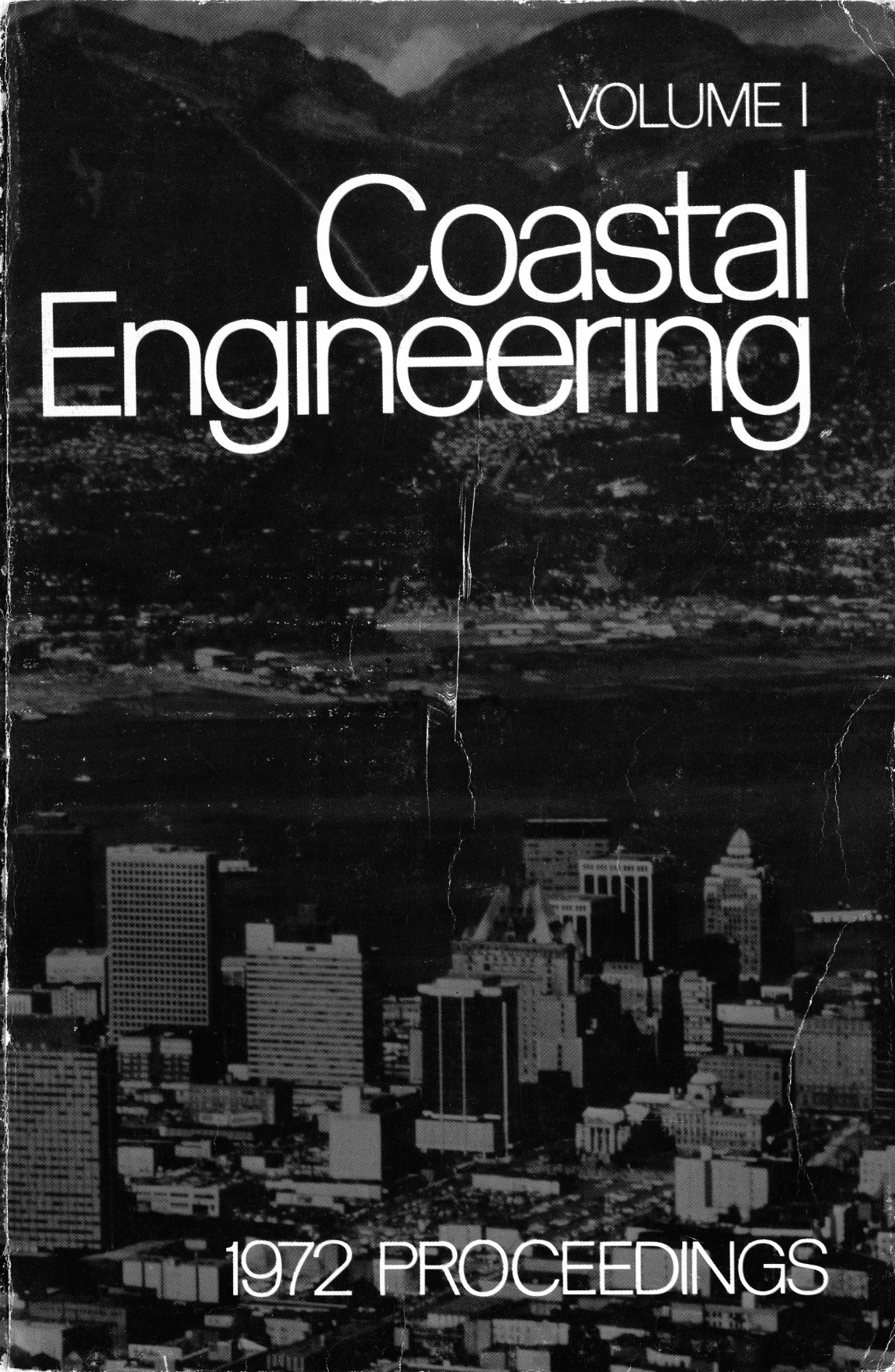
VOLUME I
Coastal Engineering
1972 PROCEEDINGS

PROCEEDINGS OF THE

Thirteenth Coastal Engineering Conference

July 10-14, 1972 • Vancouver, B.C., Canada

Volume 1

Sponsored by

Coastal Engineering Research Council
and
Waterways, Harbors and Coastal Engineering Division
ASCE

National Research Council of Canada
Department of Public Works of Canada
Queen's University
The Engineering Institute of Canada
International Association for Hydraulic Research

Published by the American Society of Civil Engineers
345 East 47th Street, New York, N.Y. 10017
Price $16.00

ACKNOWLEDGMENTS

The following engineers from Canada served as the Organizing Committee for the Thirteenth International Conference on Coastal Engineering:

M. W. Paul (Chairman)	Department of Public Works
J. Ploeg (Vice-Chairman)	National Research Council of Canada
Geroge W. T. Ashe	National Research Council of Canada
Arthur Brebner	Queen's University
Duncan Hay	Western Canada Hydraulic Laboratories Ltd.
M. K. Ward (Executive Secretary)	National Research Council of Canada

Cover and title page photographs were provided through the courtesy of the British Columbia Government Department of Travel Industry, Victoria, B.C.

CONTENTS

CONTENTS

CONTENTS

CONTENTS

CONTENTS

CONTENTS

CONTENTS

CONTENTS

CONTENTS

CONTENTS

CONTENTS

CONTENTS

CONTENTS

CONTENTS

CONTENTS

Horseshoe Bay, B. C.

PART I

WAVE THEORY, MEASUREMENTS, AND ANALYSIS

Vancouver Harbor, B.C.

SOME COMMENTS ON COASTAL ENGINEERING

M. P. O'BRIEN

Dean Emeritus, College of Engineering
University of California
Berkeley

The Canadian Organizing Committee, the Vancouver Executive Committee and the National Research Council of Canada have done a superb job in planning this conference and in carrying out the enormous amount of detail necessary for its realization. On behalf of the Coastal Engineering Research Council, the other participating organizations, and all of the attendees I thank most heartily all who participated in this work.

I am personally most grateful to those representatives of the Canadian Committee who made the final selection of papers. I should explain at this point that a small papers Committee is appointed for each of these conferences to review the summaries submitted by the authors - but this screening is intended only to appraise their appropriateness for a coastal engineering audience - and to eliminate those few papers which are promotional "blurbs". It has not been a technical review such as is made for "refereed" technical and scientific journals. The number of papers submitted for this Conference passing this simple review far exceeded the reasonable limits of the program - and for a brief period the Papers Committee faced the new and distasteful task of selection among papers acceptable under past standards.

However, the problem was handled by the Canadian Committee - applying a formula which seemed equitable and reasonable. I trust that those affected concur in this judgment.

There is a solid core of attendees who know about the origin of these conferences and about the Council which sponsors them - but there are also newcomers for whom a brief review is appropriate. About twenty-five years ago the late Professor Boris A. Bakhmeteff, while a visiting professor at Berkeley, learned about the research in coastal engineering in progress there and at a few other institutions in the United States and abroad. He became much interested in this new, small field of research and he suggested that a Research Council be proposed to the Engineering Foundation, of which he was a member of the Board. A proposal was presented and approved and the Council on Wave Research came into existence for the purpose of promoting research - but without a well-defined modus operandi. Other councils of the Foundation conducted research directly - in relatively narrow fields and with financial support from the Foundation. This pattern of operation did not fit the inter-disciplinary and international character

of coastal engineering - and the new Council floundered about for a time - seeking an effective means of promoting research. To this end, a conference was held at Long Beach, California, to bring together both researchers and practitioners for a review of the status of the field - and thus to provide a stimulus and guide for future research. The success of this conference, as evidenced by the demand for the published proceedings, indicated that the Council should sponsor at least a few similar conferences at other locations in the United States. This first conference had been heavily weighted with Pacific Coast experience - and the papers were not representative of the conditions and problems met on the Atlantic, Gulf and Great Lakes shorelines. Accordingly, conferences were held at Houston, Cambridge, and Chicago. Professor Pierre Danel of the University of Grenoble, who had attended a number of these conferences, suggested that the Council sponsor a conference at Grenoble, France; the successful meeting there led to the international sequence of biennial meetings - alternately in the United States and abroad - and so here we are.

These conferences have, I believe, stimulated research and have contributed substantially to the advancement of coastal engineering and of the related applied sciences. An indication of this result is the high percentage of references to these proceedings to be found in the bibliography of almost any published papers in the field.

However, over the years there were comments - and some criticism - of the functioning of the Council; it was a maverick among the councils sponsored by the Engineering Foundation; it should collect funds and sponsor research directly; it should evolve into an international technical society, with elected officers, committees, and a periodical publication; it should operate more democratically; and so forth. These suggestions were considered many times and at length - but each round of discussion led to the same conclusion, namely, that the international conferences served a useful purpose, with a high return in benefits for the effort expended, and that the additional activities suggested would duplicate to some degree the work of other organizations and would require much additional personal effort with doubtful incremental benefits.

There was, however, a major defect in being attached to the Engineering Foundation - namely, the lack of an established mechanism for editing, publishing, distributing and publicizing the proceedings. A logical association - and one which solved the publication problems - was to transfer the Council from the Engineering Foundation to the American Society of Civil Engineers. This was done, and in the process, the title was changed, appropriately, to the "Coastal Engineering Research Council". Under this sponsorship, the Council retains the flexibility of membership and operation which it had under the Engineering Foundation.

So much for the antecedents of this Conference.

Turning now to coastal engineering itself, anyone active in the field has viewed with consternation - and possibly some jealousy - the heavy emphasis given for a time to the exploration of the deep-sea. Recently, however, there has been evidence of a growing recognition of the fact that the greatest needs and opportunities are to be found in the coastal zone rather than the deep-sea. On this point, a recent statement of Dr. William A. Nierenberg, Director of the Scripps Institution of Oceanography of the University of California, is particularly interesting and I quote him with some relish.

> "Want to make big money on oceanography? Then forget about mining nickel from the ocean floor or refining gold from seawater. Instead, build a harbor that won't silt up or beaches that won't wash away. Learn to clean up pollution."

After the Stratton Commission of 1965 made an unrealistic but glamorous forecast of the future of deep-sea exploration, a number of major companies plunged deeply into the field only to wind-up in "the most depressed business in the United States" - to quote one of the managers involved.

The volume of research and development in coastal engineering and in the applied sciences related to it has shown a steady increase for many years; the rate of increase seems to have turned sharply upward in the last few years - stimulated by petroleum exploration and production, by the Sea Grant and other programs of the U.S. government, and by the newly-aroused interest and support of many of the coastal states. Public and private universities have created departments, institutes or laboratories devoted partially or wholly to work in coastal engineering and related fields. With this level of activity in being and in prospect the practicing coastal engineer should benefit materially in basic data, analytical methods, and design techniques available to his practice.

There is a corresponding opportunity for engineers practicing in this field to influence the character and scope of research and development by pointing out important gaps in data or methods which practice has brought to light.

It was with this point in mind that I accepted the invitation to speak on this program.

There are many topics related to research which I should like to discuss with you, but I will limit myself to a few which I have mulled over for some time and which, I believe, are partinent to plans for future work in this field.

We have been unduly optimistic, I believe, about the degree to which the results of field studies made at <u>one</u> coastal location, and under one set of environmental conditions, could be generally applied. Differences

in the wave climate, range of tide, bottom and shore materials, local winds, tidal and wind currents, shore configuration, and bottom slope tend to make each physiographic unit unique. No two such units are exactly alike in exposure to waves, wind, and tide, and in the resultant sequence of changes in the shoreline - but these differences may be so subtle as to produce evident effects only over long periods of time. These circumstances have led me to the conviction that comprehensive and continued field observations, backed by analysis and laboratory experiments, should be made along selected shorelines - and, to the extent feasible, at points of economic importance. Such studies may - and hopefully will - yield facts and principles applicable at other locations - but this objective should be secondary to the primary effort to measure and understand the complete regimen of an important segment of the coastline. The Pacific coast differs from the Atlantic and Gulf Coasts in many respects, and within these broad categories there are significant differences in the exposure and response of the shore. Clearly, one could identify so many different areas for study as to require an impossibly great effort - and for this reason it is suggested that major efforts of this type be devoted to areas of major economic importance - where the problems are usually urgent.

Regional studies continued over relatively long periods, will provide the factual basis needed for engineering design locally - and should, in the long run, provide data for appraising the validity of broad generalizations about coastal phenomena.

A comment related to the preceding discussion is that many field and laboratory investigations are what I term "half-experiments" - experiments in which only a portion of phenomena involved are observed or measured. A few examples of this are:

- observations of sediment motion without measuring the related waves and currents and, vice versa, extensive hydraulic measurements without observation of sediment movement.
- recording wave length and period without obtaining the deep water direction.
- verification of movable bed models without adequate information regarding the wave climate.
- and so on.

The circumstances which have caused this situation are understandable - inadequate budgets, personal interests, lack of effective instruments and techniques, limited time - but it is nevertheless true that these "half-experiments" are inconclusive - as much so as playing half a hole at golf. Furthermore, the results may be grossly misleading. Many coastal problems are such as to require the attention of an inter-disciplinary team - all working on the same problem with different approaches - and many of the gaps to which I have alluded would not have occurred had a broader view

been applied in planning the programs.

A major deficiency in the data essential to the planning and design of coastal structures and systems - and one which accounts for many of the half-experiments mentioned - is the relatively primitive state of our knowledge of the wave climate.

Recording shore-based wave gage data, hindcasts from meteorologists' records, and observations from ships at sea are available, but these sources have not been compared extensively to test their reliability and they have not been presented in form for application to coastal problems. The ship reports include off-shore moving waves and probably do not include much of the swell; the shore-based wave records do not include direction; the hindcasts are in question at least by the degree of the differences between forecasting methods. To be useful for engineering purposes, these data should be evaluated and combined into a "best guess" of the climate at selected deep-water stations. Such an effort would highlight gaps and discrepancies and would provide guidance for future wave observation programs.

Data on the wave climate are needed for a wide range of applications and it will be feasible to publish only the most frequently used summaries. Special requirements can be met if the basic data are readily available for scanning by computer programs designed for the purpose.

Perhaps I exaggerate the importance of the wave climate, but from my own experience I rate it as the most frustrating gap in the kit of tools available to the coastal engineers.

There are few coastal problems which do not require a judgement regarding the direction and magnitude of the littoral transport. Laboratory and field data on the relationship between wave action and rate of transport show a scatter by a factor of about 10; most of the published field data pertain to a few locations and the laboratory data suffer in credibility for a number of reasons. Reliable measurements of littoral transport are difficult - and in fact may be possible only under very special circumstances - and the scarcity of good data is understandable - but the need is urgent for data on the gross and the net annual transport at important points on the coastline - and for an ad hoc relationship of these quantities to the local wave climate. Whether or not a general correlation, such as is now applied for lack of anything better, is generally valid will not be established firmly until there are comprehensive and extended measurements of the transport and the concurrent wave "weather" at a number of localities at which the range of material characteristics, offshore bottom slope, and other parameters span the range of field conditions.

A final comment deals with the need for more case histories of failures of coastal works. There are many types of failure - physical destruction due to inadequate design or construction, limited life because of corrosion,

abrasion or fatigue, failure to perform the intended function and failure to achieve the predicted economic benefits. In addition to the human dislike of recording mistakes, there is the practical consideration that the engineers who design and build such works move on to other projects and are not in a position to observe such failures and to assess the causes. Studies of this type require a firm plan and sustained through low-key attention. They would be feasible for organizations engaged in studies of a particular coastal segment over a long period.

In brief, these few comments add up to the suggestion that plans for coastal investigations include regional studies having as their primary objective the measurement and analysis of the dynamical regimen of selected coastal segments. Such work will strongly support engineering practice in the areas studied - and will also provide a sound basis for appraising generalizations regarding coastal phenomena.

The initial program of the Beach Erosion Board included such field stations at two points on the coast of New Jersey - where measurements were made of waves, winds and currents and of the resultant response of the shore. A particular objective was to observe the effectiveness of the many groins, seawalls, and bulkheads then defacing this shore. These stations were manned for about two years. Looking back over the progress since that time, I feel that it was a mistake not to continue these observations - with improved instrumentation, backed-up by laboratory studies and analysis - and a mistake not to add stations on other coasts.

My comments may possibly be construed as advocating regression to an empirical approach but they are not so intended. What I have in mind is an addition to - and not a replacement of - the analytical, laboratory, and field work which has been so highly productive as the program of this Conference amply demonstrates.

ENVIRONMENTAL PROBLEMS AND MONITORING IN COASTAL WATERS

Arthur T. Ippen

Massachusetts Institute of Technology, Cambridge

INTRODUCTION - MAN'S CONCERN WITH THE COASTAL ENVIRONMENT

Man has been challenged by the sea from his early beginnings; he crossed the seas on rafts and boats driven by manpower and sails and adventurous cruises for booty and commerce developed into regular trade routes. With them in turn came the growth of anchorages and ports in the estuaries and inlets along the shorelines which offered the necessary protection against the storms with adequate channel depth for the constantly rising draft for larger vessels.

Probably older even than the exploits of seafaring are the manifold uses of coastal areas in man's quest for food. Fishing from the shore with nets and spears was followed with short, daily excursions into the coastal waters in small boats. As agriculture found the coastal shallows and wetlands suitable for raising crops and animals, these fertile areas were drained and diked in against the tides and storms. Today the delta regions team with life as in the Netherlands and in East Pakistan although still subject off and on to the ravages of waves and storm-tide flooding.

Exploitation of the coastal waters for commerce, fishing and agriculture is now joined in modern times of population growth by their use as sinks for all types of wastes and at the same time by the conflicting needs for food, sports, and recreation. In addition, the submerged sea bottoms have become accessible by modern technology for the extraction of minerals and oil. The apparent needs of society armed with the great potential of technology press for rapid development of the various coastal resources but also tend to endanger simultaneously these resources by conflicting goals.

Thus we stand today at the threshold of greatly accelerated growth in man's exploitation of the coastal domains, appalled by some of the apparent results of human interference. We are prone to extrapolate further unhindered activities to their surmised and fearful consequences but the basis of such predictions is often more emotionally founded than established by adequate knowledge.

Yet these serious concerns must be accepted as real and indeed helpful. We know that coastal developments of all types will be needed in man's survival. But survival has many facets, and proper balances between man's aspirations and nature's capacities for their attainment are still to be defined.

Man's happiness seems to him still best assured by interaction with nature as it is. Historically he has often good reason to distrust technological incroachments on the environment even though many of these were essential to his own well-being. Man can transform nature and even fundamentally change it over large areas, but adaptation processes in the past extended over many centuries for man and nature alike. These changes will undoubtedly go on. It is the rate of change which now gives such concern and at times causes violent reactions. These public reactions prescribe often a halt to further economic development without regard to environmental factors. Environment has acquired new values in the sense that a "high living standard" is no longer synonymous with a "high quality of life". Although the latter is not readily definable in economic terms, it

nevertheless imposes restrictions on activities which in the past were conducted without hindrance. A reconciliation of economic aims with environmental conservation is now mandatory by public demand and by its legal responses.

This poses great new tasks and challenges to scientists and engineers alike in their roles as intermediaries between the public concern with the environment and the forward thrust of purely economic needs of the same public as represented by private and public enterprises and agencies. It is to be hoped that these roles can be adequately supported as they must be and that they can thus be carried to the point where rational judgement can be rendered to resolve the questions and doubts which the public may raise. It is towards these ends that meetings such as ours must be aimed. Let us examine in the following some of the problems involved in the coastal spheres and then look at what can be done towards rational definitions by scientists and engineers armed with past experience and modern instrumentation systems presently in sight to clarify what ought to be known.

PROBLEM AREAS IN THE COASTAL ZONE

THE PHYSICAL SYSTEMS

Past coastal engineering history has taught us through many bitter experiences a most important lesson: we cannot look towards convenient remedies for local problems in coastal areas without understanding the larger systems of which these local areas form a part and with which they interact in often very complex forms. We may build dams for flood control and power but we also shut off the supply of nutrients and of sediment to estuaries and beaches. We can create new communities by filling in the wetlands near the shore but we may deplete at the same time the catch of the fish which spawned there and which attracted many new inhabitants in the first place. We have in the past discharged our wastes into the shoreline waters and found beautiful beaches closed to the public served by these outfalls. There have been numerous examples of such unexpected short circuits but have we learned the lesson?

With these experiences of detrimental effects of human interference on shorelines public as well as professional awareness has grown of the chain reactions inherently engendered by many engineering measures in coastal and ecological processes. Reluctance of conservationists to condone the continuance of present practices or the institution of new measures cannot be waved off lightly but must be countered by rapid expansion of our knowledge on coastal processes and of the various factors governing life along the shorelines. Fortunately, governmental agencies on all levels have been given wide authority to assist and to sponsor such exploration in recent years. Our capacity to measure, to record and analyze data and to display the results in meaningful ways has been vastly expanded by modern computer facilities. We have on hand now most of the tools and we stand at the beginning of implementing the organization of useful information systems on the dynamics of coastal waters. This will surely be a multi-dimensional task and its ultimate scope can as yet hardly be estimated in view of the many feedback loops linking the physical environment to biological, economic and social systems. It seems however that the physical

factors must form the building blocks for the others and that eventually their true understanding will lead to meaningful perspectives and judgements in these other spheres of human concern.

Offshore Circulation and Waves

The water masses of the oceans are in constant motion with few exceptions. We are all familiar with current systems such as the Gulf Stream or the Humboldt Current. Oceanographers have charted them and modelled them. But other forces are at work also, providing mixing and mass exchange through various mechanisms. Waves are breaking on the surface. Temperature and salinity variations produce layered systems and internal flows disturbed often by internal waves. Biological exchange takes place over the vertical and modifies water quality. Superimposed are the to and fro movements powered by tidal action. Over the long term therefore water masses are exchanged effectively at different rates depending on the topography of the shorelines. However, this rate of exchange is often over estimated in wishful thinking for convenient pollutant disposal.

Of great importance to the shoreline are the wave systems generated over the open ocean. These can be predicted now to a tolerable degree since wind conditions can be related to wave generation. But little success has been had so far in measuring waves at sea except by shipboard observation. Only as offshore structures are moved to larger depths of hundreds of feet have direct measurements of waves at these depths become possible. The waves reaching the shores are, however, transformed in many ways, by interference with other systems, by bottom friction and refraction, by partial reflection and predominant current systems. Waves provide another mechanism for internal exchange of water masses as onshore and offshore movements take place between surface and bottom.

Nearshore Interfaces

Waves arriving at the shoreline generate very powerful forces on shoreline structures erected by man and deform continuously the shoreline itself. Waves and breaker heights may be measurable here but reliable relationships between sediment transport rates and wave action still seem to escape more than very approximate estimates. Refraction and diffraction procedures have been developed for the varying bottom topography and the various boundary conditions at the shore. An important element in all calculations is wave direction, but very few attempts have been made to measure this crucial quantity and where such measurements have been attempted the complexity of the instrument systems involved defeats more general use. "Significant wave heights", no matter how expeditiously defined for engineering purposes from statistical wave records still leave us often to question the significance for specific applications to engineering structures.

The shorelines are vulnerable also to changes in water level caused by hurricanes and severe storms combined with severe wave action. Planning for such attacks is usually initiated after the damage has been done and is then confined to prevent a recurrence in areas of high investment. But such investments for structures near the shore are seldom deterred by dire

warnings, the advantages derived seem to justify the risks even if these can be quantified to some extent by environmental predictions.

The tsunamis generated by earthquakes sometimes thousands of miles away add to environmental hazards near the shore in many regions of the Pacific. Warning systems have been set up to aid vulnerable shorelines in Japan, Chile, Hawaii, and California and numerous tsunami protection structures have been built to reduce the uprush of more than 20 feet and sometimes up to 100 feet in converging inlets and bays.

Under all these wave attacks the shorelines through the ages have been eroded, whether they consist of vulnerable bluffs or gentle beaches. Man has often heedlessly accelerated these processes, through ill-considered interference and only gradually have we come to appreciate the chain reactions we may set off by local exploitation. As an example we may mention here the destruction of natural or carefully nurtured dune vegetation by dune buggies.

Inlets, Estuaries and Harbors

Human activities are perhaps most intimately intertwined with the sea through the bodies of usually shallow water contained within the bays and estuaries of the land mass. These provide with the connected wetlands the spawning grounds for fish and also the shelter required for pleasure craft and commercial shipping. These waters are confined and communicate with the open sea through the tides entering and receding through often narrow passages. Human exploitation has polluted many of these bays and estuaries to the extreme limits based on the mistaken notion of tidal flushing. We know now that such flushing action is usually very slow and involves complex dispersion processes as yet subject only to very approximate analysis. Meeting public demand many of the barrier beaches have been pierced with new inlet channels to provide convenient access to the sea from interior waters. Beaches up drift and down drift of such inlets often "protected" by extensive jetties have suffered unforeseen damage and water quality in the interior waters has been affected usually to the detriment of the ecology. But advantages to the ecology have also accrued in some instances. Our experiences have made us generally more cautious in assessing cause and effect before launching on extensive engineering works which change the existing environment. But pressures for economic use of inlet and estuary shorelines remain very high, and therefore coastal engineers and marine scientists are concentrating more and more on research in embayments and estuaries to enhance our understanding of the dynamics of the circulations and the dispersive processes related to them. One of these studies on an interdisciplinary front is presently under way on Massachusetts Bay and has brought to the forth the wide range of interrelated factors governing even a purely physical description of the flow processes. Winds and tides, temperature and salinity variations, sediment transport, varying topography, water mass exchange along the boundaries, all assume a part in the seasonally varying patterns of the flow and dispersion dynamics of the Bay waters. They, in turn, relate intimately to chemical interactions and biological processes taking place in the various parts of the Bay. Understanding the integrated behavior of the combined systems is indeed an intellectual challenge and yet one that must be met if we are to fulfill society's needs in the future in harmony with the conservation of a viable coastal environment.

The Interactions: Sea - Shore - Estuaries

The coastal environment is the meeting ground for many natural forces acting seldom in readily described patterns. Each coastal area is subject to a broad spectrum of these forces in different combinations and the land responds to the attack in different ways depending on topography and geological materials in various stages of evolution. The sea provides for wave and current attack varying with the seasons; from the interior the rivers bring mineral and organic materials, which mix with those produced on the shores by erosion and biological activity; the fresh water meeting the saline waters in estuaries reaches the sea after complex mixing processes which have their reflection in varying biological life and sedimentation patterns; finally man has added his structures and pollutants which have disturbed the natural processes in embayments, estuaries and shore areas. While natural cyclic periods, both long-term and short-term, may be discerned and certain equilibrium conditions may exist these may be upset for long periods by catastrophic events such as hurricanes and earthquakes. Hence, it is clear that purely local observations may serve only a limited purpose in predicting the shoreline changes when local structures are planned since these may affect the environment of the coastline at considerable distances from the area of the local disturbance. To sort out all the resulting consequences becomes a very complex task of environmental monitoring as coastal waters are increasingly drawn into the service of man.

HUMAN USE OF COASTAL WATERS

The coastal environment is affected by man to an ever increasing extent. There are many conflicting interests as the limits to human use are recognized and systematic planning in harmony with nature has come to be accepted as an ideal to resolve these conflicts and to extract optimal benefits for the community rather than for private gain. It is difficult to enumerate the individual facets of human use of coastal waters without getting enmeshed immediately in their relationships to other human activities as will become apparent in the following.

Fishing and Aquaculture

Traditionally, fishing for food and pleasure is one of the most obvious associations with coastal waters in the public's mind. This is expressed best by the amount of fish caught by salt water sports fishermen which may be estimated in recent years, for the U.S. alone, as close to 800,000 tons for which equipment and services sold at retail exceeded 700 million dollars. Commercial fishing went beyond these numbers, producing over 2 million tons of fish with a retail value of one and one half billion dollars. The public therefore has a considerable stake in the preservation of appropriate environmental conditions for this important resource. However, other uses of coastal waters increasingly menace such environmental conditions particularly

through various pollutants from human and industrial sources. While much of the public fervor raised on this point may be exaggerated, too little is still known on the biological processes of the food chain by which both shell fish and fin fish are sustained. Such knowledge must be developed if management of fishery resources is to be improved and if the supply of fish through aquaculture is to be enhanced. Great success has already been achieved in this area with certain variety such as salmon in the Pacific Northwest and with oysters and clams. Oyster production can be raised by a factor of over 30 when raft cultivation is employed as compared to bottom cultivation where the yield is only 600 pounds per acre per year. But successful aquaculture depends not only on better knowledge of the biological processes but also on relatively detailed information on the currents and on water quality for the waters in which the aminals are to be raised. Fish poisoning with its threat to public health is of increasing concern as pollutant levels have grown to dangerous degrees in local areas. It is not sufficient apparently to specify certain levels of pollution since fish and shellfish have the ability to concentrate certain pollutants such as mercury, DDT, or radioactive substances in their systems.

Navigation for Commerce and Pleasure

Modern shipping has produced many new problems for coastal areas and estuaries. Commercial ships have increased in size and hence draft and pleasure craft have reached tremendous numbers in our prosperous society. Much deeper channels are required and have been dredged to traditional harbor sites. Natural depths of 10-20 ft. are deepened up to 42 ft. in most of our estuaries and new harbors are in the design stage for 60 ft. depths with up to 100 ft. anticipated in the next two decades. These can only be obtained in a few coastal areas or with offshore harbor islands. Major shoreline changes must be anticipated, assessments of possible accidents with major spillage of cargo must be made, increased pollution from industrial and municipal wastes may result despite more stringent safeguards.

With the growth of pleasure craft we have already been faced with the need for suitable anchorages for home bases and for harbors of refuge at regular intervals along the shorelines. In many cases natural harbors for these purposes are not available and must be provided by new breakwaters and other structures. Inevitably natural shore processes are interrupted and dredge spoil disposal areas must be located. Detailed studies of waves and currents, of water quality and flushing characteristics, of marine biota from plankton to fish, of sediment transport and shoreline stability, seem incumbent in each case of such major interference in the marine environment.

Disposal of Wastes

Pollutants due to human activity reach the coastal waters in many ways and forms. Fertilizer components and insect sprays such as DDT come from natural run off on agricultural lands, find their way into lakes and streams where they are joined by human and industrial wastes and eventually reach the estuaries and the sea. Large population centers have evolved near the sea or interior shorelines with major industry and their liquid and solid wastes are dumped in near-shore waters with little or no treatment through pipe lines or barging. We have been alerted to the long-term consequences of such practices only in recent years and it is not apparent at this stage whether the public will be persuaded to shoulder the economic burden which a major clean up and reversal of these practices will impose.

Clear evidence also exists that many pollutants reach the sea by direct transport through atmospheric circulation and are absorbed into the water at the interface of water and air.

The ever increasing demand of society for electric power has created a new problem as the need for cooling water can no longer be met by interior sources. Considering overall use of electric power in relation to efficiency of production it is safe to assume that twice as much energy is consumed by heating the "cooling" water as finds its way to useful purposes in homes and industry. How to dispose these vast amounts of waste heat into the coastal waters without upsetting and permanently damaging ecological systems near the discharge points presents many engineering challenges. Various systems of effluent dispersal are applied but their relative merits can again be assessed only by major measuring programs extending over time and the coastal areas affected.

The proper assessment of a pollutant state for a given area is one of the most difficult tasks confronting scientists and engineers particularly when ambient environmental conditions are not known. Even with best intentions measuring programs pertaining only to major pollutants develop very quickly into projects with vast data production for which rational analysis faces considerable difficulties. What are the pollutants? Where did they come from? What are the dispersal processes? What are the chemical transfer processes? How do they affect the biological activity and interaction? Where are they finally deposited? All such questions should eventually be answerable before decisions can be made in good conscience. But it is almost evident by just asking such questions that many environmental decisions will have to be made in the near future without complete answers.

Recreation

Emotionally, recreation activities in coastal waters are most closely related to public concern. Beaches closed to swimming because of pollution, beaches eroded by structures misplaced or by natural processes, structures marring the esthetic enjoyment of a long sweep of a beach, dead fish washed up on the shores as well as other debris of human activity, clams and oysters made inedible by toxic pollutants, water fowl and other animals dying from oil pollution, all these examples have had a major impact on public thinking

and have lead to steady pressure on government agencies to adopt means of redress.

Use of beaches for recreation has assumed tremendous proportions, as illustrated by an attendance of over 70 million at the major beaches on Long Island alone. Shore property values range from 15,000 to 50,000 dollars per acre on Long Island and annual land losses over the 120 miles of shoreline exceed one million dollars. Similar figures can surely be cited even in excess of these for shorelines in other parts of the U. S. and abroad.

Table 1 Shoreline Ownership and Use in the Continental U.S.

Ownership	Length in miles	Percent of total length
Federal Government	3,900	11%
State & Local Government	4,600	12%
Private	25,800	70%
Uncertain	2,600	7%

Use	Length in miles	Percent of total length
Public Recreation	3,400	9%
Private Recreation	5,800	16%
Non-Recreational Development	5,900	16%
Underdeveloped	21,800	59%

The National Shore Line Study of the U.S. Corps of Engineers directed by Congress in the River and Harbor Act of 1968 and recently completed in August 1971 provides one of the most comprehensive summaries of the problems of our national shorelines. Along the 37,000 miles of the ocean and Great Lakes shores in the continental U.S. approximately one half were found to be subject to significant erosion with 2,700 miles of these being classified as deserving economically remedial action by protective structures. First priority is to be given to a total of 190 miles where danger to life and public safety is expected within the next five years. This will cost 240 million dollars. The study further finds that 17,800 miles of these shores could be partly protected simply by improved management practices. The economic stakes in coming to grips with shore erosion and its environmental factors are thus clearly demonstrated for all shoreline uses of which recreational use is of the greatest value for residents in the 30 coastal states as well as for those from the interior of the country. Again expanded research to improve our understanding of the near shore environment with regard to prediction of governing physical and biological factors must form the basis for rational protective measures.

Effects of Land-based Engineering

Modifications in the shorelines and in the coastal waters have been brought about in many areas as the result of land use practices and related engineering structures in the interior of the country as well as in estuaries. Much of the sediment supplied to the streams terminating in the sea has been stopped in some areas such as California through flood control measures, mainly dams impounding the flood waters but with them also the sediment. In other areas, in the center of the country, agricultural practices of the past and still to some extent in the present have vastly increased the supply of sediment as the cultivated land eroded. Other engineering works such as road construction and mining added to this sediment supply. Eventually these effects are felt in the coastal areas. Beaches erode when the supply of sediment is stopped as in some cases in Southern California, while estuaries shoal and must be dredged when excessive supplies of sediment reach them.

In addition to natural sediments the use of waterways for liquid and solid waste disposal has also changed the natural conditions in coastal waters. Increased channel depths for navigation require extensive dredging in estuaries with consequent disposal of dredge spoil on adjacent lands or in the sea. Industrial chemicals, and minerals as well as human wastes make the silt and sludge deposits often a questionable addition to offshore waters with poorly understood environmental hazards.

Offshore Mining for Minerals and Oil

Finally, this brief summary of factors involved in changing the coastal environment through human use of the coastal waters may be concluded with the most modern encroachments by man through resource developments. The most explosive issue is probably concerned with the drilling for oil, which until recently was conducted with little regard for environmental damage until the blowouts in the Santa Barbara Channel aroused a public fury. There can be little question that oil wells will continue to be drilled but also that in the future every precaution available through advanced technological safe guards will be applied. With all safety devices however, the risks will be tremendously reduced but can never by reduced to zero. Assessment of possible mishaps must therefore precede new ventures of supertanker harbors or anchorages and future drilling of new oil fields in the offshore areas. This requires again a detailed description of the dynamics and of the biota of coastal waters and points to novel and comprehensive data systems for the decision making and regulating of activities.

What pertains to exploitation of the oceanic shelves for oil applies equally to the mining of minerals and the dredging for sand and gravel in coastal waters.

As landbased sources for sand and gravel for construction and sand for beach replenishment decreases, increasing dependence must be placed on offshore sources. Naturally, dredging in these areas should be conducted with proper regard to the existing ecology so that biologically productive grounds are avoided and operations in adjacent areas do not affect animal and plant life to the extent that restoration of the biota is permanently

prevented. In contrast to sand and gravel resources the mining for other minerals will probably, with few exceptions, be concentrated in the deep portions of the oceans where Manganese nodules also rich in iron, copper, nickel, and cobalt are known to exist in large quantities. A new technology for such deep sea operations is yet to be developed as economic exploitation so far has not been feasible and has indeed been disappointing to venture-some enterprise barring a few notable exceptions.

THE NEED FOR REGULATION AND MANAGEMENT

As the actual and potential uses of coastal waters and their economic value to the many nations increased, concern for legal and regulatory authority has intensified. Numerous and frequently overlapping jurisdictions exist and are rapidly being extended. The old internationally-recognized 3 mile limit or "territorial sea", under the sovereignty of nations with shorelines, has been expanded by national edicts in many cases to 12 miles and a few nations claim jurisdiction over fishing activities up to 200 miles from shore. Peru and Ecuadore have been in conflict on this point with foreign nationals for some time and Iceland is presently fighting it out with Great Britain, as it tries to extend its sovereign rights over what have been regarded as traditional fishing grounds by the latter nation. New international agreements are obviously urgently needed to prevent such conflicts and to bring a unified approach to other pollution and resource management problems such as the dumping of hazardous and waste materials into the coastal waters. Pollution of the ocean waters has come to the fore as a threat to all nations with sources from ships as well as from natural and man-made outfalls. Offshore islands to be constructed for atomic power stations or as deep-draft harbors or transfer facilities for superships present further jurisdictional problems.

This is not the place to enumerate in detail the numerous laws and regulations enacted in recent years by federal and state legislative bodies and agencies. But a few of the principles may be recounted here in view of many misconceptions and much confusion which still exists with regard to the original meaning of the various acts. For example, the preamble of the National Environmental Policy Act of 1969 states as the Congressional purpose:

> "To declare a national policy which will encourage "productive and enjoyable harmony" between man and his environment; to promote efforts which will prevent or eliminate damage to the environment and biosphere and stimulate the health and welfare of man; to enrich the understanding of the ecological systems and natural resources important to the Nation; ....."

This is not a call for conservation only, but for responsible management of natural resources for the benefit of man in harmony with the environment. The Act emphasizes new environmentally-oriented decision-making practice and stimulates the elimination of those activities which threaten human health and ecology. In the subsequent years the Environmental Protection Agency (EPA) was established. EPA has incorporated the Water Pollution Control Program, formerly in the Department of the Interior, into its new Water Quality Office. EPA and State Officials work in concert with the U.S. Army Corps of Engineers, which has authority over numerous activities in the more broadly interpreted "navigable waters" to administer

and enforce the standards for water quality in such waters. EPA and the Corps also jointly issue permits for industrial waste discharges, a function which has been derived from a little used provision in the Refuse Act of 1899 (33 U.S.C. 407), an Act revitalized for pollution control purposes by the judiciary courts. However, the implementation of the permit system for industrial waste discharge is still faced with the difficulty of the mass of permits to be investigated and to be passed. Since the recent Kalur case, new permits must be preceded by environmental impact statements, and include consideration of fish and wildlife effects, aesthetics, water quality and other factors.

EPA reviews and approves state water quality standards and criteria, and provides guidelines for specific problems such as the disposal of dredge spoil in ocean waters. In some cases, standards, criteria and guidelines have proven impossible to apply, since natural ambient conditions alone exceed the limits set for metal and organic contents, for example.

The administration of water pollution control programs raises a number of problems on which environmental science still lacks adequate knowledge and where further research is needed on dispersal patterns, on degrees of chemical analysis for metals and organic compounds, on maximum retention methods in certain areas in preference to dispersal and on the flow dynamics especially as related to internal velocities due to waves, storms and density variations.

However, the repeated refrain, "we don't know enough and the problem requires further study" should not be accepted as a call to stop all action on needed programs. In many cases, a reasoned judgment must be rendered on the basis of rational concern by private and public agencies, and of the evidence on hand. Risks will have to be taken but their number can be reduced in the future if we agree on needed research focused on specific local problems yet also of adequate scope to build an integrated framework of information for future decisions.

The time limits and pollution control measures for water quality consistent with the "protection and propagation of fish, shellfish, and wildlife and for recreation in and on the water" may become rather specific. If Congress passes one of several bills now before it, interim goals for water quality are to be achieved by 1981, and all discharges of pollutants into navigable waters are to be stopped by 1985. The primary responsibility for proper planning and management for these goals for coastal waters is placed on the many coastal states adjacent to the shores. Much stress is now laid on public involvement in developing the necessary enforcement of effluent limitations to be applied at the source. Such measures are spelled out in great detail in the "Act to amend the Federal Water Pollution Control Act" passed by the Senate in November, 1971 (S. 2770), and now awaiting further legislative action. Of foremost interest to our professionals in water quality control is the extensive mandate to the Administrator of this Act for the development of monitoring systems and for the support of research and training "relating to the causes, effects, extent, prevention, control and elimination of water pollution".

It is clear that the enactments of such goals for unpolluted waters are setting aside many privileges of private, industrial and municipal users, which had been assumed as rights rather than privileges through many years. This may cause hardships in some cases, and impose considerable financial burdens on many. These, the public, in it's own long-term interests, must assume. Reconciliation of private claims to exploitation of coastal waters now declared to be in the public domain will be subject to many difficult decisions spanning a wide and complex array of technical, ecological, economic and social interests, often seemingly contradictory and as yet often based on vague judgments rather than objective knowledge.

A new bill recently (April 25, 1972) passed unanimously by the U.S. Senate and named the "Magnuson Coastal Zone Management Act of 1972" can contribute further to clarification of rights in the coastal zone if finally passed by the House of Representatives. This bill will provide federal aid up to 2/3 of the cost to coastal states to develop planning for coastal zones, to define permissible land and water uses ("so as to prevent such uses which have a direct significant or adverse impact upon the coastal waters"), to establish use priorities and a plan to administer the development guide lines. A further provision allows acquisition of valuable estuarine lands as sanctuaries and for baseline measurements. The bureaucracy, of course, will also be expanded through a National Coastal Resources Board under the Vice-President and with a Coastal Zone Management Advisory Committee to the Secretary of Commerce with 15 members. Most of the projected federal annual costs of 70 million dollars would go for planning and administrative grants to the states. Nevertheless, this bill would seem, if adopted, to lead to an orderly and systematic sorting out of the various private and public claims for the coastal zones and to their systematic conservation or development.

The aims of the various legislative measures either enacted already or still in an advanced state of final review in the U.S. are matched by similar efforts in other countries. International efforts are being promoted effectively by the United Nations through the Conference held in Stockholm, Sweden after detailed preparations extending over several years. The results of these deliberations unfortunately were not as yet available at the time this summary was written. However, it can safely be assumed that important principles for the preservation of the ocean environments will be agreed upon by most nations and that general guidelines for prevention of pollution, for international cooperation in monitoring and for national responsibilities in enforcement will be recommended.

MONITORING SYSTEMS

In view of the urgency bestowed on environmental quality in recent years by public pressure and it's political expression through the creation of new laws and standards the scientific and engineering community is confronted with monumental tasks. It must provide the extensive base for rational decision making through the development of reliable instrumentation systems to describe the physical, chemical and ecological interactions in the coastal waters. The necessary evaluation processes for the data collected with such instrumentation arrays must be built into effective systems for integrated analysis. Hopefully then, various mathematical

models can be constructed to not only describe on a dynamic basis the integrated behavior but to provide predictive capabilities on the response of coastal water bodies to their possible use by man in harmony with a desirable but not necessarily an unchanged environment. This is the vision before us; the modern scientific and technological means to achieve it seem to be within our grasp with the electronic and computational tools of our age. But many intellectual challenges remain to merge these tools into effective monitoring and predictive systems. We will examine in the following some of the fundamental components which must be incorporated and which must be developed further for these purposes.

THE PHYSICAL SYSTEMS

In order to understand the physical dynamics of the coastal waters conventional as well as new observation techniques must be adapted for such systems studies, the goal being a computer compatible data acquisition array for all instruments.

Tides and Currents

Tidal observation stations exist all around the coastline of the U.S. and stage predictions for average tides varying with lunar and seasonal cycles have been practiced for a long time. However, tidal currents are known in detail to a much lesser extent and current charts have been updated only after long intervals of time. For environmental studies, it is usually necessary to know more detail in local embayments concerning tidal stages and phase lags as well as about currents. Stage recorders present little difficulty and are relatively cheap to install in adequate numbers for the shorter periods of such studies, although they seem quite essential to a complete investigation especially when wind stress may modify tidal stages.

Current measurements are desirable not only for the surface but must be made in considerable number over the depth with regard to current intensity and direction. Directional changes of velocities are especially important. Unfortunately current meters with computer compatible outputs are as yet not too reliable unless frequently serviced. For propeller and cup meters fouling is a frequent occurance and they are expensive when a number are to be installed in one location to test for variations over the depth. The old standby system consists in drogues drifting at several depths which require constant observations and are therefore, providing only temporary current information. Magnetic current meters have been used with some success and are subject to fewer limitations with regard to fouling as conventional current meters since no rotating parts are involved. Further and better ideas are still needed in this field.

In many studies, particularly of pollutant transport and dispersion, very weak time-averaged currents govern the transport processes. These are particularly marked in estuaries where salinity is a variable both longitudinally and over the depth. Velocities are highly variable also over lateral sections, and an accurate assessment of net currents averaged

over time presents an almost insuperable expense in measurements. Bottom drifters may be employed to obtain long-period average trends in open coastal waters but are little suited to navigation channels in estuarine waters. Here accurate current meter surveys have proved quite successful when their expense was warranted for specific studies. In summary, new or at least improved techniques are highly desirable for current surveys in conjunction with other environmental studies to define the internal dynamics of coastal water masses. The slow exchange processes induced by wave or density generated currents here are important to our understanding of pollutant and sediment transport. Of further interest in this connection would be a suitable measuring system for turbulent fluctuations especially where salinity or temperature variations over the vertical exist.

Wave Climate and Prediction

Waves form another essential component of the processes governing the coastal environment. Generated by storms over the oceans or coastal areas they vary in amplitude and frequency over a wide range. Of importance in pollution and sedimentation studies are the mean currents produced by waves, such as the littoral currents along the shorelines, the onshore and offshore currents with variable mass transport over the depth, the turbulent mixing generated by breaking either offshore or on the beach. Wave forecasting and hindcasting have been practiced for a long time and improved as more reliable records became available from an increasing number of measuring stations around the U.S. coasts. Many of these measurements are taken however in relatively shallow water and deep water observations have only become available in very recent times as offshore structures are pushed out into deeper shelf-waters for oil exploration and production. Ship-board observations are numerous but less reliable because they depend essentially on visual observations.

When wave gauges can be mounted on fixed piers usually the capacitance wire type or a step resistance arrangement is employed. Where piers are not available, buoys have been anchored offshore but their expense is justified only in connection with other instrumentation packets for a variety of current and water quality measurements. Bottom wave sensors will record major wave action some distance from the shore and consist of electronic pressure transducers combined with local recorders or onshore recording terminals. Direct transmission of signals to a central data processing center would seem indicated however for modern requirements and for direct correlation with other environmental data.

Most systems have the shortcoming of determining wave height only and not direction. The latter property is subject to special difficulties of measuring and where this has been tried with multiple arrays of wave gauges, the data have only rarely yielded satisfactory outputs commensurate with the expense and the complexity of data analysis. Aerial photography has given some good results for directional properties under favorable weather conditions. Other systems are under development but so far it must be conceded that a routine measuring system for wave direction is still some distance off in time.

Nevertheless, for the prediction of littoral currents and of the littoral transport of beach sediments directional wave spectra will be needed in addition to prevailing wind data which are more readily available but furnish at best only an indirect approximation of the wave

attack on our shores.

Sedimentation Problems

Sedimentation processes in the marine environment are intimately associated with the current and wave systems in a coastal area. Sediment reaches the sea from land sources through our estuaries as well as from wave attack on erodible shorelines. The most abundant and for recreation the most desirable constituent of sediment on beaches is sand. Aside from small proportions of other minerals it consisty of quartz particles ($Si\ O_2$) surprisingly uniform in size (0.10 to 0.50 mm dia). Sand has moved through rivers to the seas at a slow pace estimated to take a million years per 100 miles. Its supply on beaches is therefore something to be conserved as a precious natural resource which can be readily wasted by ill-advised structures and lost to deeper portions of offshore waters.

Silt and clay form other portions of the marine sediments augmented by abraded shells and organic material. For the most part our estuaries shoal with such material in flocculated form and must be dredged to maintain artificially large depths for navigation. The interaction of turbulence and shear flow through tidal currents with the resulting periodic suspension of this material produces transport processes of considerable complexity. Man in many places has contributed large amounts of sedimentary material from his own wastes in the form of all kinds of organic and inorganic matter. The sludge of sewage plants, as in our Boston Harbor, forms extensive deposits over the years and the garbage and refuse of most larger coastal cities finds its way via barging to offshore dumping grounds. No easy solutions are at hand, considering the overall aspects of environmental quality. Burning will cause air pollution, deposition on land is often impossible for reasons of suitable sites or associated ground water pollution, dumping in the coastal sea is fraught with danger to the local biological activities and with the uncertainties of where much of the finer material will drift with the turbid currents. Man-made refuse may carry many of the unwanted pollutants to the sea often to be found afterwards in concentrated doses in shell fish and round fish making them unfit for human consumption.

Surveillance of turbidity and of suspended sediments in coastal waters is an essential facet of environmental monitoring. It is especially important in connection with dredging activities for sand and gravel offshore and in the exploration of suitable dumping grounds for sludge and dredge spoil. These should be confined to biologically inactive bottom areas.

Rapid procedures of suspended sediment assessment in quantity and quality are not at hand for these purposes. Collection by pumpout processes has been proposed as one way to replace the ancient system of bottle sampling. It may be possible to determine sediment concentration over the depth by rapid filtering at sea and storing the residues in much smaller containers for later analysis on land. Measuring sediment concentrations by light absorption is subject to many objections even under optimum conditions in view of the large variation of particle sizes and of the presence of plankton and may be used only for approximate evaluation of particle

concentrations. Again we are still in need of new ideas and devices if such may be to bring our measuring capabilities to a more economical and convenient state in sediment collection and analysis.

By contrast surveys of changes in bottom topography by sediment deposition or erosion in shoaling areas can be carried out rapidly and efficiently by means of fathometers, i.e., acoustic depth measurements combined with automatic navigation systems, of which several are on the market. Work is under way to utilize acoustic measurements not only to describe the surface of bottom deposits but to indicate by multiple reflections the layers of different composition and density. Navigation systems for effective and accurate location determinations at any instant of an environmental survey cruise are available but require as yet very skilled attendants and are quite costly in use.

Water Quality

Water quality in coastal waters is governed by natural conditions as well as by the direct and indirect input from human activities. Fine sediments reach the major streams from uplands to the extent of 1-2 billion tons annually of which one half comes from croplands. In addition to water-borne sediments, another 30 million tons are transported in the form of dusts through the atmosphere. Not all of this is detrimental to the environment. Dust in the atmosphere is needed to generate rain and water-borne sediments are needed in the coastal environment in many ways. The large streams discharging into the estuarine waters bring valuable nutrients as well as detrimental pollutants to embayments and wetlands. Their distinctive roles with the many chemical processes involved in their travel to the sea cannot always be clearly attributed to one or the other category. We simply do not know all the answers as yet.

With regard to dilution, retention and chemical transformation taking place in estuarine and coastal waters temperature and salinity distributions play an important part particularly by governing internal transport phenomena in these water bodies. The measurement of temperature and salinity distributions in coastal areas form therefore a fundamental part of all environmental monitoring and the methodology for it seems well in hand. Three instrument systems are in current use for this purpose: the bathythermograph (BT) for use in small boats and local observations, the towed thermistor array for temperature distributions over the depth and the conductivity-temperature-depth instrument (CTD). The outputs of all these instruments have been arranged to be computer compatible by tape recording and immediate or subsequent conversion to digital formats. Thus, extensive sections and areas of coastal waters can be quickly surveyed. Maps of temperature contours and, after conversion, of salinity and density distributions can be obtained. These developments have pushed extensive buoy systems for these measurements into a lesser role in environmental work. Buoy stations for continuous monitoring of water quality parameters in certain locations will be mainly used as important reference stations to which periodic overall surveys from cruises will be related.

In the newest version of the towed probe system a "hydroglider" has been designed which is buoyant and controlled from the boat. The tail surface deflections are manipulated to have the hydroglider dive up and down at approximately 45^0 at forward speeds up to 10 knots. The sensors on the glider will measure conductivity, temperature and depth and a water intake will allow water samples to be pumped on-board through a connecting hose which are identified by air bubbles released on the glider at different depths. Thus a complete water quality survey may be taken over a long section and repeated over a tidal cycle with simultaneous tape recording in FM signals of location, depth, time, temperature, salinity and of certain chemical constituents while the vessel is moving. Later, more detailed analyses may be made for additional chemical constituents in the water samples as well as for sediment concentrations.

A "Technicon" automatic chemical analyzer (auto analyzer) is used for laboratory determinations at present. It is planned to have this auto analyzer on-board for direct determination of at least phosphate concentration from the pumped samples and to store up to 160 samples for later use in a 20 meter long coil of tygon tubing separated by identifying air bubble codes.

The instrumentation and techniques reviewed here briefly have been developed and are still under development in connection with a major "Sea Grant" project at M.I.T. concerned with the "Sea Environment in Massachusetts Bay and Adjacent Waters". These systems, when fully operational, will furnish comprehensive surveys of all the basic parameters for water quality as well as for the characteristics responsible for internal currents and pollutant dispersal. These capabilities are urgently needed for assessment of input, dilution and transport of pollutants whether these originate from outfalls of sewage treatment plants processing human and industrial wastes, from dredging operations or from the condenser water discharges of atomic and fossil power stations. Many state standards must be met with regard to heat and chemical dispersal. To check conformance to these standards is a major task confronting at present environmental monitoring. To make the measuring systems reliable and comprehensive as well as fast in response and in evaluation of results is still a challenging field for engineers and scientists working in coastal waters. Many benefits will obviously accrue to our general basic knowledge of coastal dynamics and of coastal water ecology from the push received from public concern with pollution. New insights have already resulted from such studies on many aspects of water mass movement and of dispersal of properties when density variations are present.

In connection with these relatively new capabilities for massive data acquisition, another effective means of surveying coastal waters must be mentioned, the ability to distinguish surface temperature variations in coastal waters by infrared photography from the air. The entire pattern of a warm water plume originating from the condenser water of a power station may be made visible in one instant of time. Baseline data are needed in the area however for reference to evaluate the photographs quantitatively. Of course, such overflights have been used also in another facet of coastal surveys; by regular photography of the coastline to follow seasonal and long-term changes in the coastal alignments and in some cases of submarine features in shallow water as well.

THE DATA PROBLEM

With the large capacity for data acquisition through the various instrumentation systems discussed in the preceding sections and through similar systems developed elsewhere, the data processing must be automated and interfaced with available computer facilities. Large data records must be processed for extensive areas of the coastal waters covered by numerous sections for storage on magnetic tapes and possible graphic display rather than as tabulated data points for isolated measurements. The first requirement is therefore that all data acquisition be immediately designed with computer processing in mind as it has been done for the instruments discussed in the preceding sections. These give output in FM signals and record it on magnetic tape but also allow visual recording to observe proper functioning of the instruments and to plan for adjustment in cruise time and direction to cover particularly interesting features of the phenomena under investigation.

For example, in the case of the towed hydroglider the temperature sensing device furnishes output in FM format to the magnetic tape and to a pen recorder. The pen will record a dot for each desired isotherm as a function of depth and hence, as the chart moves with time and also with distance as the boat proceeds, a plot of isotherms with distance is available at once aboard for scrutiny. Other properties desired will be similarly recorded and stored for further processing.

Confronted with multi-faceted data for many current and water quality characteristics special attention must be given to systematic data filing. A multilevel hierarchy of storage is indicated. This hierarchy must be so designed that it will be useful to even untrained investigators interested in entering or recalling specific data in a conversational program. It is further desirable that the same system be used for possibly all environmental data collected by other investigators as well so as to bring together the environmental information of a large coastal area in one data storage system.

For the Massachusetts Bay study the first level of the hierarchy was chosen to contain only identification with regard to time, location and type of variables determined. On the second level more complete information is given; cruise number, purpose of stations occupied, other variables entered and related to the measurements, etc. Finally, the third level of the hierarchy will contain the actual data recorded on specific cruises for the various water quality items and other relevant oceanographic parameters.

The system has been adapted to the MIT MULTICS system which is connected to the ARPA computer network. The data files are therefore made accessible from remote computer consoles by telephone connection. Further development is needed on the software level to produce graphical or cathoderay displays of original data and of processed components such as total pollutant content in the water mass, change of water mass, or observations corrected for tidal components. It is believed that the amounts of information needed to adequately cover an environmental

description for a large body of coastal waters such as Massachusetts Bay require the fullest application of modern computer facilities. It is also believed that any environmental assessment of the effects of a local interference in these waters by dredging, power stations, sewage treatment effluents, etc., can only be rendered in the context of fairly detailed knowledge of the larger system of waters with which these local projects must interact. We have no choice therefore but to make fullest use of instrumentation and computer capabilities to define such environmental systems in their physical dynamics, their chemical constituents and their biological activities for future planning. Environmental impact statements must be based on solid ground datawise to avoid the conflicts between utilization and conservation of coastal resources which presently are producing so much emotional stress.

PREDICTIVE MODELLING

The purpose of all data collection for environmental reasons as for all others is to serve as a foundation from which rational analysis can take off. Experience with large physical systems has taught us that the inherent governing laws may be combined into either a similar physical system of more manageable size or into a mathematical model in which the different variables appear in clearly defined relations superimposed to form the system comparable to the original. Neither the physical nor the mathematical model reproduces the complex original in all essential aspects and both are subject to assumptions and boundary conditions governed by empirical factors. Both are dependent on prototype data from which these factors must be determined and both must be refined to the point where some original processes will simulate the true state but do not reproduce it. The more complex the interactions of the governing physical factors are, the more these simulations become subject to critical questions with regard to extrapolations for predictive purposes. This applies, for example, especially to predictions of dispersal processes. Furthermore, simulation for chemical and biological processes in concert with physical processes seems as yet very far off. However, it is felt that with our modern capacity for data acquisition and analysis our understanding of the physical environment can be enhanced to the point where ultimately models of the physical and of the mathematical kind with different capabilities can be made more reliable.

It is further assumed that such models of the physical environment will form a sound basis for prediction of the effects of disturbances to the system and that valid conclusions may then be drawn with regard to consequent chemical and biological phenomena.

It is clear that the need for the physical and mathematical models discussed here must have as its goal the description and performance of the essential dynamic systems and subsystems for an environmental area. So far, only long-term time-averaged systems models for pollution are available based on spotty observations in time and space and incapable of predicting unusual phenomena due to local topographic features, wind conditions, water mass exchanges at the boundaries, etc.

As an example may be cited the floating off over large distances of extensive lenses of pollutant releases from the Deer Island sewage outfall at the Boston Harbor entrance, observed in Massachusetts Bay under our Sea Grant Project. These buoyant masses of lighter water are often not mixed readily with the ambient sea water because of insufficient shear and may retain their identity for very large distances in the prevailing transporting currents. They could be spotted only accidentally by buoy observations. This mode of inadequate dispersion is obviously applicable also to heated condenser water discharges from power stations along the shores or on artificial islands. These phenomena may govern, therefore, decisions concerning location, time of release in the tidal cycle, and type of discharge system to be employed for such power stations and pollutant outfalls.

It can be stated generally for both physical models and mathematical models that in order to provide meaningful predictive capabilities for environmental decisions more comprehensive field surveys are needed covering the governing parameters simultaneously in time and space. The development of instrumentation, software and computer adaptation for systematic and immediate processing, storage, recall and display in various forms is the most important task for engineers and scientists for the near future.

THE OUTLOOK

The preceding general review of the prevalent environmental problems in coastal waters was pointed essentially at the physical phenomena as the basis for connected chemical and biological processes. In view of these important connections man's activities cannot be assessed properly unless their implications to the larger natural systems in which they interfere become definable. Recognition of coastal water regions as systems subject to many natural inputs demands an integrated approach from all those interested and active in coastal monitoring of the various components. Hence, a new degree of cooperation and coordination by many professional disciplines must be established. Surveying and monitoring by many specialists provide ample research opportunities as well as useful and necessary data bases for the solution of practical problems in resource development. Scientists and engineers may proceed from different motivations but both groups now face comprehensive tasks in which their interests are merged towards a simple end: to make known what is needed for the conservation of the coastal environment in harmony with man's aspirations for its rational use.

Where do we stand at present? We do have a large reservoir of all kinds of sensor and measuring equipment to identify the environmental characteristics from moving platforms on the sea and in the air and from anchored stations, for remote and direct recording. We have capabilities for data transfer to computer based analysis, reduction, storage, retrieval, display and future manipulation. We have a variety of suitable dissemination procedures by which information can be made available to all potential users. We do not have adequate data bases at present for most environmental processes.

Where should we go? While much of the measuring equipment is developed there are considerable shortcomings with regard to precision, reliability, convenient calibration, ease of handling, speed of operation, computer compatibility, etc. In addition, to improving and possibly standardising monitoring devices, a great deal of work must be done to resolve difficulties at the various interfaces between instrumentation and computer, the computer and useful output and dissemination. Monitoring must be planned carefully and, in view of possible overfeed, data acquisition must be confined to that essential for system definition. This necessary management phase of data collection is probably the most important aspect as well as the most difficult one in environmental monitoring. Data collection must be justified by ultimate use. A proper balance must be developed between baseline information and system simulation by mathematical models. To all these ends more cooperation is needed in the scientific and engineering community to develop generally applicable systems for integrated environmental definition. For example, what is desired in a baseline study for environmental impact assessment of engineering projects is not only knowledge on tides and tidal currents, but also on salinity, temperature distributions, sediment transport, bottom conditions, wind stress and wave state, etc., not only for one period but also at least for various seasonal states.

Will we get there in time? An appropriate development of equipment capabilities and of data management procedures will take probably an order of magnitude more manpower, money and time than we have allocated at present for such purposes. The question as to whether we will be able to provide the answers to environmental questions in time to be useful for many urgent decisions depends very much on how long we are willing to face detrimental risks. There is every expectation that major resource developments will take place in coastal waters within the next decade. Disposal for all types of refuse, oil drilling, offshore islands and harbors, recreational facilities and boating, fishing and aquaculture, etc. will all expand. The national and international economic stake therein is so vast that it is hard to conceive that we will not extend our best efforts in environmental monitoring systems. To conserve as well as to use the coastal waters in a viable ecological state we must first comprehend them. This message has been accepted and is being heeded by the scientific community as evidenced by the explosion of reports and publications by their councils, new societies, workshops and committees. The public has applied pressure through its representative agencies and their regulations, standards, hearings and permit systems. Will concern with the problem however be matched by willingness to pay? A big push is still needed to assure the allocation of adequate funds for the desirable major systems developments. A good start has been made with computer compatible instrumentation in various coastal regions of the U.S., in the Pacific Northwest, the Gulf area and in Massachusetts Bay. The full potential of modern technology however has not as yet been tapped to the necessary degree because of inadequate funds. Hopefully, this situation can be changed in time to provide us with the means to accomplish the tasks necessary for environmental protection and proper resource development in our valuable coastal water areas.

REFERENCES AND INFORMATION SOURCES

"Marine Environmental Quality"
Ocean Science Committee of the NAS-NRC Ocean Affairs Board, National Academy of Sciences, Washington, D.C. 20418, August, 1971

"Toward Fulfillment of a National Ocean Commitment"
Marine Board, National Academy of Engineering, NAS, 2101 Constitution Ave., Washington, D.C. 20418, March, 1972

"Report on the National Shoreline Study" (National Shoreline Study)
Department of the Army, Corps of Engineers, Washington, D.C. 20314 August, 1971

"Shore Management Guide Lines" (National Shoreline Study)
Department of the Army, Corps of Engineers, Washington, D.C. 20314 August, 1971

"Shore Protection Guide Lines" (National Shoreline Study)
Department of the Army, Corps of Engineers, Washington, D.C. 20314 August, 1971

"Preliminary Analysis of the Ecological Aspects of Deep Port Creation and Supership Operation"
Institute for Water Resources, Corps of Engineers, IWR Report 71-10, October, 1971, National Technical Information Service, U.S. Department of Commerce, Springfield, Va. 22151

"International Decade of Ocean Exploration"
National Science Foundation, Washington, D.C. 20050, October, 1971

"Water Spectrum - Issues, Choices, Actions"
Department of the Army Corps of Engineers, Washington, D.C. 20314, Vol. 4, No. 1, Spring 1972 (Several relevant articles)

"Abstracts - Second Coastal and Shallow Water Research Conference"
Geography Program, Office of Naval Research, University Press, University of Southern California, Los Angeles, California, September, 1971

"General Guidelines" (Technical Bulletin No. 1)
"Users Guide for NODC's Data Processing Center"
"Highlights 1961 - 1970"
National Oceanographic Data Center, NOAA, U.S. Department of Commerce Rockville, Md. 20852

"Design Characteristics for a National System to Store, Retrieve, and Disseminate Water Data"
Federal Advisory Committee on Water Data, U.S. Department of the Interior, Geological Survey, Washington, D.C., October, 1971

"Implications of a Systems Approach to Oceanography"
by John J. Walsh, "Science", Vol. 176, No. 4038, June 2, 1972

"Systems for Automatic Computation and Plotting of Position Fixing Patterns"
by H. PH. Van Der Schaaf, Rijkswaterstaat Comminications, No. 13, The Hague, Netherlands, 1972

"A Buoy System for Air-Sea Interaction Studies, Buoy Design and Operation"
by E. L. Mollo-Christensen and C. E. Dorman, M.I.T. Sea Grant Project Office, Report No. 72-1, July, 1971, Cambridge, Mass. 02139

"Current Capabilities for Data Handling to Support Ocean Exploration and Survey"
by Thomas S. Austin, Director, published in: "Environmental Data Service", NOAA, U.S. Department of Commerce, April, 1972

"Perspectives for Ocean Exploration and Survey Systems 1975-1985"
Proceedings of Workshop at Airlie House, Airlie, Va., February, 1972, Marine Board, National Academy of Engineering, Washington, D.C.

"Effects of Engineering Activities on Coastal Ecology"
by L. E. Cronin, G. Gunter and S. H. Hopkins, Research Report OCE, Department of the Army, Washington, D.C. 20314, September, 1969

"Techniques for the Use of Organic and Amorphous Materials in Source Investigations of Estuary Sediments"
by James Neiheisel, U.S. Corps of Engineers, Geological Society of America, Memoir 133,1970

"Report on Gross Physical and Biological Effects of Overboard Spoil Disposal"
Chesapeake Biological Laboratory, Ref. No. 67-34, May, 1967, University of Maryland

"Marine Sand and Gravel Mining Industry of the United Kingdom"
by Harold D. Hess, NOAA Technical Report ERL 213-MMTCI, September, 1971, U.S. Department of Commerce, Environmental Research Laboratories, Boulder, Colorado

"Environmental Effects of Oil Pollution"
by Thomas A. Murphy, Edison Water Quality Laboratory, EPA, U.S. Department of the Interior, Edison, New York, Session on Oil Pollution Control, A.S.C.E., Boston, Mass., July, 1970

"Oil at Sea"
Marine Pollution Bulletin, Vol. 1, No. 2, February, 1970, Published by Macmillan (Journals) Ltd.

"Evaluation of Water Quality Monitoring Programs in California"
prepared by California State Water Control Board in response to House Resolution 183, 1970 Regular Session, February, 1971

"Aquatic Ecosystems and Thermal Power Plants"
by Loren D. Jensen and Derek K. Brady, Journal of the Power Division, A.S.C.E., January, 1971

"Quantification of Short Term Environmental Impact of Electric Generation" I. "Aquatic Systems"
Term Project, M.I.T. Course 6.686, Seminar on Energy Problems - Policy and Planning Methods, under Prof. D. C. White

"Some Environmental Factors to be Considered in the Design of Thermal Power Plants in the Northwest"
by E. O. Salo, Fisheries Research Institute, published in: "The Trend", Journal of the University of Washington, College of Engineering, October, 1969

"Methods of Observation and Analysis of Harbor and Coastal Pollution"
Lecture Notes of Special Summer Program 19.81s, June 19-23, 1972, by Dr. A. T. Ippen, Dr. E. L. Mollo-Christensen and Associates, Massachusetts Institute of Technology, Cambridge Massachusetts

"Engineering Aspects of Heat Disposal from Power Generation"
Lecture Notes of Special Summer Program 1.76s, June 26-30, 1972, by Dr. D. R. F. Harleman and Associates, Massachusetts Institute of Technology, Cambridge, Massachusetts

THE HISTORY AND PHILOSOPHY OF COASTAL PROTECTION

by

Per Bruun

Chairman, Dept. of Port and Ocean Engineering
Technical University of Norway, Trondheim

Dedicated by the author to:
Andries Vierlingh
Dikemaster, Netherlands,
for his "Tractaet van Dijckagie" ("Treatise on Dikebuilding") 1576-1579.

"Water shall not be compelled by any 'fortse', or it will return that fortse onto you".

Abstract - This paper gives a brief review of the history of coastal defence as it has developed since the year 1,000. It makes an attempt to outline what may be termed "the philosophy" and its relation to development.

The "State of the Art" is described by figures of characteristic designs including new developments. The paper establishes some general rules for future coastal protection and gives an outlook for the future.

HOW OLD IS THE ART OF COASTAL PROTECTION

We do not know; probably very old. Adam and Eve escaped from the gardens of Paradise located on the island of Ceylon following their blunder in an apple orchard. They crossed the waters on "Adams Bridge" which was not only a "bridge" (reef) but a coastal protection for a major part of the most southern SE coast of India.

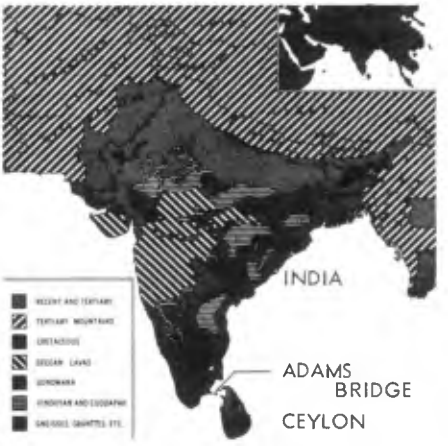

Coastal protective works of major order probably first came into existence when man was forced to protect the land which he lived on to avoid the waters digging away the ground under his feet.

COASTAL PROTECTION IN THE LOW COUNTRIES IN EUROPE AND IN ENGLAND

NETHERLANDS

Although a great many training and irrigation walls, dams or dykes were built in the Far and Middle East coastal protection per se probably first developed in the low

countries in Europe where rivers poured soft materials, mainly clay and silt, out in the ocean for settling. Consolidation was a slow process which made the land settle. In addition sea level was rising. To avoid loss of land by flooding and to protect themselves from drowning the Frisians and the Dutch first built earth mounds. Dyking started about the year 1,000. In the 13th century the Dutch had accomplished major coastal protection and reclamation works, particularly in the Dordrecht area.

Dr. van Veen in his book "The Art of a Nation" (1) writes: "The earliest written records about the Frisians (or Coastal Dutch) describe them as water-men and mud-workers. The Romans found in the North of the country the artificial hillocks upon which the inhabitants, already called 'Frisii', made a living. We shall follow their history, because written records are available about the early reclamation works they made. One and the same race, now called the Dutch, took, held and made the low country.

Pliny, who saw these mound-dwelling tribes in the year 47 A.D. described them as a poor people. He apparently exaggerated when he wrote that they had no cattle at all. Or did he see some much-exposed mounds near the outer shores where the sea had swallowed every bit of marshland? At stormtide, Pliny said, the Frisians resembled groups of miserable shipwrecked sailors, marooned on the top of their self-made mounds in the midst of a waste of water. It was impossible to say whether the country belonged to the land or to the sea. 'They try to warm their frozen bowels by burning mud, dug with their hands out of the earth and dried to some extent in the wind more than in the sun, which one hardly ever sees'.

No doubt the mud Pliny refers to was the peat which was found in the 'wolds', or swamps, some distance south of the clay marshes, where the artificial mounds had been made."

"In all they built 1260 of these mounds in the northeastern part of the Netherlands, an area of a mere 60 x 12 miles. Further East there are more of them in East Friesland. The areas of the mounds themselves vary from 5 to 40 acres; they rise sometimes to a height of 30 feet above normal sea level. The contents of a single mound may be up to a million cubic yards."

"They built their mounds on the shores of the creeks in which the tide ebbed and flowed. In their scows they went (in their language in which the roots of so many English words can be found): 'uth mitha ebbe, up mitha flood' - out with the ebb, up with the flood. The tide bore them towards the peat regions, or perhaps to the woods still farther inland and then brought them back. Or they went out with the ebb in the morning towards the sea, where they gathered their food, and returned in the evening with the incoming tide."

"The Coastal Dutch have now lived 24 centuries in their marshes and of these the first 20 or 21 were spent in peril. It was not until 1600 or 1700 that some reasonable security from flooding was achieved. During these long treacherous centuries the artificial mounds made their survival possible."

"It was a work which might be compared with the building of the pyramids. The pyramid of Cheops has a content of 3,500,000 cubic yards, that of Chephren 3,000,000 and that of Mycenium 400,000 cubic yards. The amount of clay carried into the mounds of the northeastern part of the Netherlands can be estimated at 100,000,000 cubic yards.

In Egypt it was a great and very powerful nation which built the pyramids throughout a series of dynasties. The aim was to glorify the Pharaohs. With us it was a struggling people, very small in number and often decimated, patiently lifting their race above the dangers of the sea, creating large monuments, not in stone, but in native clay."

"In this Lex Frisionum of 802 there is not yet any mention of seawalls, but the first attempts at dike building must have been made shortly afterwards. Frisian manuscripts still extant, dating from the early Middle Ages, deal chiefly with the following three points: First, the right of the people to freedom, all of them, 'the bern and the unbern'. Secondly, the 'wild Norsemen' whose invasions took place roughly from 800 to 1000, and thirdly: the Zeeburgh or Seawall.

This novel means of defence against the sea by means of a continuous clay wall was called a Burgh, or stronghold. The people were apparently very proud of this seaburgh, because they described it in poetical language as 'the Colden Hop', the Colden Hoop.

-'This is also the Right of the Land to make and maintain a Golden Hoop that lies all around our country where the salt sea swells both by day and by night'." (Plate 1, Fig. 1).

The spade, the hand barrow and the fork were the instruments used for diking, the fork presumably for the grass turfs which were used to heighten the dykes and make them stronger. Despite the tremendous efforts the sea was the strongest. "This was due partly to our insufficient technical skill and partly to lack of co-operation. For a single night, Dec. 14th 1287, the officials and priests estimated that 50,000 people had been drowned in the coastal district between Stavoren and the Ems. This is a large number considering that this was the area where so many dwelling mounds could be used as places of refuge."

The advances and successes have been tied to a few names. Says van Veen: "We often wondered who was the master engineer who created the marvellous Great Holland Polder, south of Dordrecht, the work which had included the damming off of the tidal mouth of the river Maas, and the leading of that river into the Rhine. This proved to be William I. He had already finished that gigantic undertaking by 1213. The polder was destroyed in 1421 by the St. Elisabeth's flood, described in a former chapter. William was a man of great conceptions. He surrounded the entire area of Holland-Proper with strong dikes and made several canals intended to drain the vast moors. They also served as a splendid network of shipping canals. It is likely that he made the dikes around the Zeeland islands Walcheren and Schouwen too, and that he established the still-existing administrations for the upkeep of these islands. The other part of his clever and amazing reclamation and construction programme cannot be described here, but it is very clear that he knew the geography of his county by heart. No maps as yet existed!"

The earliest reference to the art of accelerating the natural rate of accretion is the manuscript "Tractaet van Dijckagie" (Treatise on Dikebuilding), written by the Dutch dykemaster ANDRIES VIERLINGH, between 1576 and 1579. VIERLINGH discusses the construction of "cross-dams" on mud-flats which are not yet dry at low water. In this connection he also advises that old ships should be sunk and earth dumped on the top of them so as to make artificial islands or flats which should hold back the silt and sand suspended in the water. These islands should subsequently be connected with low dams. Although this method has not been used commonly it is known that shipwrecks have been used at numerous places to close dyke breaches. These wrecks formed the basis for the fill material which was secured with mats or brushwood. VIERLINGH, however, was much against closing of dyke breaches with shipwrecks due to the non-homogenity they created in the dyke structure. Nevertheless, this method was widely used over a long period of time, not only in Holland but in the (at that time Danish) Schleswig-Holstein.

"Vierlingh was found to be a real master of the dikes and waters, a man of great ability and spirit - one of the greatest of his kind. Luckily the greater part of his manuscript has survived. Its ancient picturesque style is a joy to every hydraulic engineer. This remarkable book already shows the special vocabulary of the Dutch diking people in all its present-day richness. In some ways it is even richer.

His advice is simple and sound. The leading thought is:
Water will not be compelled by any 'fortse' (force), or it will return that fortse onto you.

This is the principle of streamlines. Sudden changes in curves or cross-sections must be avoided. It is the law of action and reaction. And truly, this fundamental law of hydraulics must be thoroughly absorbed by any one who wants to be a master of tidal rivers."

The work by the dykemasters and farmers to protect and to gain land has been remarkable. Plate 1, Figs. 2 and 3 (10) give an impression of how dykes were built up gradually by adding one layer of silt, or silt and sand, shell, willow mattresses etc. on the top of each other. Remains of old ships, brick walls and pile walls were used too. No less than two-thirds of the lower part of the Netherlands is manmade, while the other third is just "natural" sea marsh or moorish swamp. Since about the year 1200 the following areas have been gained according to van Veen:

On the sea shores	940,000 acres	
By pumping lakes dry	345,000 "	
By pumping the Zuiderzee dry	550,000 "	(partly future)
	In all 1.835,000 acres	

With respect to the distribution of fill the 100,000,000 cubic yards of earth fill which the Dutch in the early centuries carried to their artificial hills were made only in a small area, covering roughly 8% of the country. Van Veen writes: "The sea walls or dikes were our second work. In 1860, that is just before the advent of steam dredging, we had about 1750 miles of them, containing about 200,000,000 cubic yards of material. Moreover, there were many old deserted dikes, whose contents may be estimated at 50,000,000 cubic yards. Those 250,000,000 cubic yards were practically all transported by handbarrows, wheel-barrows and horse-drawn carts.

The third great work was the digging of the ditches and canals. In the lower half of the country about 800,000,000 cubic yards of earth have been removed, in order to drain the land and separate the fields. Of shipping canals there are about 4800 miles in Holland, for which a figure of 200,000,000 cubic yards would be a fair estimate.

The fourth and greatest task was the digging of peat. This digging served a double purpose: the provision of fuel and the creation of lakes which, when drained, gave more fertile land than the original moors themselves.

In total we have dug according to this rough estimate the enormous volume of some 10,000,000,000 cubic yards. This includes the making of lakes as well as the digging of moors in the higher eastern regions of the Netherlands.

Compare this figure with the dredging of the Suez Canal. We constructed about 100 Suez Canals of the size made by De Lesseps. All this was done by hand, whereas De Lesseps used 60 steam dredges."

But the work would never have been completed without the dykemasters, their foremen and "polderboys", who often were the farmers themselves. Figs. 4 and 5 (Plate 1) show them repairing dykes and building willow mattresses for bottom protection, an old but still active art.

A special kind of dykebuilding was the weed-dykes. Construction was limited to West-Friesland and the Zuiderzee-area, where sea-weed or sea-grass was found in ample quantities along the coast. The West-Frisian sea dyke were for a long time reinforced with seaweed, and so were some of the Wieringen dykes. It is not known with certainty how old the weed-dykes are, but weed dykes were constructed from the 8th century. A 16th-17th-century weed dyke was built at the northernmost point of the Island of Schokland, and another one in 1734 in the Northern part of Noord-Holland. Sea-grass for dyke building was collected offshore in the Zuiderzee and the Wadden area. Following drying, a broad, tough layer was placed on the sea side of the dike.

As ambition grew, dykes also grew. Moving them still closer to the dangers it became necessary to reinforce the dykes by hard surfaces like basalt blocks and/or other structures parallel as well as perpendicular to shore. These reinforcing or supporting structures developed as experience and exposure increased. The gradual reinforcement by structures like seawalls and groynes may have made a contribution to a not fully justified sense of security. It has been claimed that dykes were not raised rapidly enough in step with the sinking of the land and the rise of sea level, and that dykes were not subjected to thorough investigation of their structural soundness.

On February 3-4th, 1953, a spring tide whipped up by a raging gale overwhelmed the sea defences, and made tremendous breaches in the dykes (Plate 2, Fig. 6) and most of the islands in the south-west were inundated. 1850 people lost their lives. All the available material and manpower was mobilized and within a year all the gaps in the dykes had been closed and the flooded areas once more reclaimed, (Plate 2, Fig. 7). On November 5th, 1957, the "Delta Bill" was passed, containing plans for closing the tidal entrances in the south-west (Plate 2, Fig. 8). When this project has been completed the Dutch coast will have been shortened by 700 kilometers. The Delta project provides for the closure by means of massive dams of four broad, deep sea inlets, viz. the Haringvliet (1968), Veerse Gat (1961), the Brouwershavense Gat (1972) and the Eastern Scheldt (1978) and for the building of secondary dams in the Zandkreek, the

Grevelingen and the Volkerak. The Rotterdam Waterway and the Western Scheldt will be left open, since they provide access to the ports of Rotterdam and Antwerp respectively. This sequence was chosen after due consideration, since the transition from small to large sea arms enables experience gained to be profitably used in the larger projects. Another reason is the desire to achieve a higher degree of safety for the largest possible area in the shortest possible time. This - the world's largest coastal protection project - is thoroughly described in a number of publications and in the Dutch periodical "Deltawerken" published by the "Delta dienst". The status of this project at this time (July 1972) is that the Veerse Gat and the Haringvliet have been closed according to schedule: Two sections of the Brouwershavense Gat were closed in the spring of 1971, and the work will be completed by 1972. The southern gap was closed by telpher, (concrete blocks dumped from cable cars), the northern one by means of 14 caissons. The closing of the last gap meant that tidal currents involving the movement of 360 million cubic metres of water into and out of the inlet (each movement taking about 6 hours) ceased to flow. There remains the dam which will close off the Eastern Scheldt. This will be about 9 kilometres long and will stop tidal currents involving the movement of 1,100 million cubic metres of water into and out of the inlet every twelve hours. The construction of 3 artificial islands was needed to build the dam: the first was completed in 1969, the second in 1970 and the third in 1971. This dam, the last and largest to be constructed (it fills up channels as deep as 35 metres), is expected to be completed by 1978.

The construction of the large sluices presented enormous problem, which were solved. Protection of the bottom was obtained by placement of large "Zinkstükken", upholding a 1,000 year old tradition. Although many tool and construction practices have changed, willow mattresses (Plate 2, Fig. 9) are still in use but they may in some cases have been replaced by mattresses of asphalt or synthetic sheets (Plate 2, Fig. 10). The cost of the Deltaproject by 1978 is estimated to be approximately 3,500 million guilders ($ 1,1 billion). It is an expensive project but it ensures greater safety for the entire South-west of the Netherlands, reduces the cost of dyke maintenance due to the coastline's shortening by nearly 700 km, opens up a whole series of islands, reduces silting, offers fast traffic links across the dams, and improves control of the supply of fresh water in almost the whole of Holland. In addition it provides new recreational possibilities for the vast population in the southwest urban areas and the provision of unique aquatic sports areas.

The development of Dutch groins. - A few remarks should be made specifically on the Dutch groins. The first groins were probably built at the beginning of the 16th century, but groin-like structures may have been built much earlier. We do not know exactly how they looked but the history of development during the latest 100 to 150 years is known (Plate 3, Fig. 11) and represents a continuous line of development of a streamlined structure exposing itself as little as possible to "the fortse" of currents and waves. Although groins have grown in size the principles are the same: Stone pitching on gravel on mattress in the middle and stones on mattresses on the sides with two or more pile walls as supports (12).

Today's length is usually approximately 200 meters and space between them is of the same order as described in more detail in a later section. Offshore elevations are about M.S.L. Occasionally groins are provided with piggy backs (Plate 3, Fig. 12) to break the longshore currents. Analyses by Bakker and Joustra (2) have demonstrated the ability of the Dutch groin protection which has not only decreased or stopped erosion in certain areas but has even caused accretion. The reason may be sought in the fact that (tidal) currents combined with swell action provided the shore with material from offshore so that the groins did not suffer starvation as often as is normally the case. While the situation at many other places where groins have been built is that erosion continues outside the extreme ends of the groins this, generally speaking, does not seem to be the case along the Dutch ocean shores. It may be said that nature itself made a demonstration of "artificial nourishment" in Holland. The groins, however, are not corner stone in the protection of Holland. This has always been the dykes. But foreigners who came and saw the results of the Dutch groins sometimes misinterpreted the situation very seriously. The massive Danish North Sea groins, Fig.43, which gradually increased in length to several hundred meters at the Thyborøn Barriers due to continued shore recession, is just one of these misinterpretations by

which enormous quantities of materials were sacrified because of earlier insufficient understanding of the mechanism involved. One may ask: Could they have done anything else? The answer apparently is that it would have been difficult in the past but it is much easier today - for which reason it should be done. Misinterpretations also found their way to the New World, with the groins at Miami Beach (Plate 8, Fig. 45) being one of the most startling examples of how groins alone are inadequate as coastal protection. On the other hand it may be fair to say that the Long Island Atlantic shore groins are examples of efforts by groins to live up to the Dutch example. And there are several other examples where conditions were favorable (Plate 8, Figs.42,47).

"The Art of a Nation" became an export article. The Dutch also carried out many dyke and drainage projects in France. According to van Veen (1) the "Hollandries" were most abundant in Germany, Poland and Russia. Along the Molotschna there were 46 Dutch villages in 1836; the district Chortitza had at that time 20 such villages. In Poland there were about 2,000 villages inhabited by the descendants of the Dutch immigrants; in Posen there were 830 villages. The first great canal in the United States, the Erie Canal, was financed in 1772 by the Dutch and its locks were devised by Dutch engineers. Until 1798 the United States of America had no other creditor than Holland.

ENGLAND

In England coastal protection also has a long history because of the continuous erosion of strategic areas on the South Coast, in Lincolnshire, South Yorkshire and in many estuaries. There is already clear evidence of reclamation works by construction of "walls" (dykes) in the Dungeness area during the Roman occupation, the Rhee wall being the best known example. Historical evidence gives a consistent picture of the incursion of the sea along the Lincolnshire coast, by references to loss of land and damage to "sea banks", which had been a necessary defence since the 13th century. In 1335, according to records, the waves breached the sea banks at Mablethorpe and the land was flooded. By 1430 the sea-wall again needed repair. Erosion continued and the history of this area is one tough fight against the sea.

As in Holland, the first measures against erosion were "sea banks", the design being modified to serve as sea walls according to the local situation. Some were just earth dams, others were fascine or pilewalls (7). Later, vertical bulkheads were developed (Plate 3, Fig. 13). On the English shingle beaches abrasion presented a severe problem and called for the application of flint, basalt, or other suitable materials (backed by concrete) to resist abrasion (Plate 3, Figs. 14 a and b). The block walls at Pett Level (Dungeness) (Plate 6, Fig. 25) and Walland (Plate 6, Fig. 26), are mentioned later as examples of modern sloping walls providing flexibility rather than rigidity and low reflection of wave energy thereby being more considerate to the beach in front than vertical or slightly curved structures (11).

Groins were used as an additional protective measure. They were put into use in early times, probably as a result of observations of the effect of hard points protruding from the shore. This was likely to have been the case at Hornsea, South Yorkshire (9) where during an inquisition held in 1609 concerning heavy losses by erosion it was stated that "there was a peere at Hornsea Beach, during the continuance whereof the decay was very little". In 1864 six groins were built on the heavily eroding Spurn Head, South Yorkshire, at the entrance to the River Humber, where nature's forces were assisted by man's removal of shingle from the beach. The groins were of the King Pile type with horizontal boards which could be adjusted similar to the Withernsea Groynes erected in the 1870's (Plate 3, Fig. 15). They were strutted at the down-drift side to resist the pressure of the accumulating beach on the updrift side. Sheet pile groins were also tested, but the result was less satisfactory than the results with King Pile groins. The former were too rigid and lacked any means of adjustment.

Some enthusiasm seems to have resulted from the result of groin construction works of limited length along the shore but observations about ill effects in the form of down-drift erosion were also made. In a discussion of an article by Mr. J. Murray on "Sunderland Docks" printed in the Proc. of Inst.Civ.Engrs. 1849, Mr. Rennie and Mr. Walker refering to a report of 1832 admit "that groins were, under certain circumstances the best defence for a coast, for wherever the waves brought the sand and shingle in quantities, the seaward side filled up while on the lee side it was generally scooped out, but by a judicious distribution of these groins, such an accumulation of material might

be produced, as would effectually protect a shore, or any sea works".

Inexpensive types were devised. Mr. Murray in Proc. of the Inst. of Civ.Engrs., 1847, discusses the design of groins and says "Groins might be formed with stones, timber, or fascines, either of the two first-named materials lasted well, but in cases where the deposit was rapid, and of such nature as to entirely fill up interstices, and prevent decay, the latter material would be sufficiently durable for all ordinary purposes".

The entire situation with respect to Sea Protection works was reviewed by a "Royal Commission on Coast Erosion etc." whose report was printed in 1911 by H.M. Stationary Office. One of the most significant references in this report is the statements that sea walls, unless properly constructed are "agents of their own destruction". In particular it refers to scour at the toe and the necessity of constructing a special toe, apron or groin protection in front of the sea wall to prevent undercutting.

With respect to groins advantages and disadvantages were fully realized. "The evidence laid before us goes to show that in many cases on the coast of the United Kingdom groins have been constructed of a greater height than was necessary to fulfil the required conditions, with the result that they have so unduly interfered with the travel of the shingle as to lead to impoverishment of the beach to leeward, causing in many districts serious injury to the coast".

The length of groins and the distance between them is discussed and 1 to 1 ratios are common but "satisfactory results were also obtained by 1 to 2 ratios". Alignment at right angles to the shore was best and provision for adjustment by adding or removing planks was preferable as low groins often proved to be more efficient than high ones being less adverse to downdrift beaches at the same time.

Reading this British document more than 60 years old, one regrets that the wisdom it contained was realized so late elsewhere and that designs as contradictory as possible to the century old British experience were advocated for a long period of time and to some extent still are being promoted. The difference between British and Dutch practice in groin design is related to the grain size of the material which the groins are composed expected to accumulate. In England a good many beaches are of shingle, and some of them experience a high rate of beach drift and significant fluctuations in beach profiles. A high (but adjustable) groin may therefore be practical. Energy loss along the stem is of less importance due to the coarseness of the material. Conversely in Holland all beaches consist of fine to medium sand which moves easily and fluctuations of beach profiles are of relatively small magnitude. Smooth streamlined cross sectional geometry causing little turbulence is therefore best for such conditions and groins should be low to conform with relatively gentle sand slopes. Groins having high vertical walls would result in scour and lowering of the beach on the either side of the groin.

DENMARK

In Denmark coastal protection started on the North Sea Coast in 1840 with a government project to increase the height of dunes on the Lime Fiord Barriers (3). In the 1870's experimental groins were built on the West Coast using a Dutch design which soon proved to be too weak to withstand the violent wave action on that shore. The design was reinforced and over the next 50-60 years almost 100 massive groins ranging in length from ab. 100 m to ab. 400 m were built in this general area of approximately 50 km length generally using a concrete block design (Plate 8, Fig. 43) of blocks ranging from 4 to 8 ts. now often provided with side slopes of 2 to 8ts granite. Blocks are placed with specially designed cranes. Erosion continued outside the extreme end of the groins and the outer parts were not kept up. The land ends were extended gradually as the dunes and dikes were withdrawn (3). Artificial nourishment from bay or offshore sources has - surprisingly enough - not been applied yet but is urgently needed particularly on the Lime Fiord Barriers.

COASTAL PROTECTION IN NORTH AMERICA

In the New World the professional history on how local problems were solved is becoming old too, but "public history" is new. It may be described briefly with a few notes (4,5).

Before 1930, Federal interest in shore problems was limited to the protection of Federal property and improvements for navigation. At that time, an advisory "Board on Sand Movement and Beach Erosion" appointed by the Chief of Engineers was the principal instrumentality of the Federal Government in this field. In 1930, the Congress assumed a broader role in shore protection by authorizing creation of the Beach Erosion Board. Four of the seven members of the Board were Corps of Engineers officers and the other three were from State agencies. It was empowered to make studies of beach erosion problems at the request of, and in co-operation with, cities, counties, or States. The Federal Government bore up to half of the cost of each study but did not bear any of the construction costs unless federally owned property was involved.

This important first step was followed by a series of improvements, in 1945, 1955, 1962, 1965 and 1968 demonstrating a still increasing interest and involvment in the matter by federal authorities (4, 5). Several states created their own beach erosion and shore development agencies which established co-operation with the local U.S. Army Corps of Engineers District and Division offices and with the Office of the Chief of Engineers. A great number of studies of actual beach erosion problems followed by reports to Congress by the Secretary of the Army authorizations and finally by federal contributions to actual improvements. These efforts were supported by research projects by the Beach Erosion Board and from 1963 by the Coastal Engineering Research Center (CERC). A number of special projects were handled by model tests at the Waterways Experiment Station of the USCE and CERC.

Structurally speaking the art of coastal protection suffered shortcomings compared to the low contries in Europe. Patented more or less useless coastal protection devices as e.g. permable groins, have had a bigger chance in U.S. business than elsewhere but the newest and most effective measure, artificial nourishment, although not born in the States, was raised there and has so far been most successful in the United States.

Being "philosophical" one may say that the difference between the European low country and the American coastal protection practice lies in "the scale" and in "the degree of involvement". The European is "high", but "short" and often "complex". The American is "long", relatively "low" (excluding hurricane protections) but "relatively simple".

The European practice is tough and silent, the American is flexible and it makes some noise because it is not only a measure but also a "nourishing machine".

WHAT WAS PAST EXPERIENCE? HOW SHALL IT BE UTILIZED?

The combined experience, gained through years of struggling, may be expressed briefly as

1) Whatever you do, avoid waves and currents turning their full fortse onto you (Vierlingh, 1570's).
2) Don't be nearsighted, think large if you possibly can. It is better to solve problems of some kilometers or miles than only of some meters or feet.
3) Look oceanward, landward and up and down the shore and evaluate carefully how your plans may be influenced by or influence the surrounding areas of land and water.
4) Coastal Protection does not necessarily need to be just coastal defence. Old Dutch experience and military tradition seems to favour defence by attack. In a war it is always best to keep the initiative and not leave it to the enemy.

An American version of this experience may be expressed as "the best protection for real estate is plenty of real estate in front of the real estate you want to protect", an approach which suits miles and kilometers and also matches economy as the general experience is that you (almost) always get a bargain when you order large quantities.

REASONS FOR BEACH EROSION

In order to define and discuss the problem it is necessary to go back to its roots. Erosion is caused by the forces of nature, sometimes assisted by man-made structures or by man's active erosion by removal of material from the shore.

Table 1 is a review of reasons for natural and man-made erosion. If no erosion is to take place from a particular shore there must be a balance between the quantity of material which arrives and the quantity of material which departs. Let us consider a shore which is not in balance but is losing material partly offshore by transversal

drift and partly to the sides by imbalance in longshore drift or

$$\left|dE_{rosion}\right| = dT_{ransversal\ drift} + dL_{ongshore\ drift}$$

$dT_{ransversal}$ - With reference to long range development transversal drift is caused by sea level rise (disregarding sand drift by wind which in some cases may be of considerable importance).

Sea level rise (refs. 19 and 20) may sound innocent, but, realizing how narrow the beach is compared to the offshore area which is to be nourished by erosion of the beach in order to balance the rise of sea level with an equal amount of deposits of material on the bottom (Plate 4, Fig. 16 and ref. 15), it can be understood how an average rise of just 1/8 in per year may cause shoreline recessions ranging from 2 to 5 ft along the Eastern Seaboard of the United States. A general "rule of thumb" is that the shoreline recedes 1 ft for every millimeter which the sea level rises. There is, needless to say, a phase lag between rise and recession (15). An impression of the most recent sea level rises along the U.S. eastern seaboard may be obtained from the following figures by the U.S. Dept. of Commerce, National Oceanic and Atmospheric Administration:

Ave. rise 1940-1970:

Eastport, Maine	1930-69	.338 cm/yr
Portsmouth, New Hampshire	1927-70	.165 "
Woods Hole, Massachusetts	1933-70	.268 "
Newport, Rhode Island	1931-70	.210 "
New London, Connecticut	1939-70	.229 "
New York, New York	1893-70	.287 "
Sandy Hook, New Jersey	1933-70	.457 "
Baltimore, Maryland	1903-70	.259 "
Washington, D.C.	1932-70	.244 "
Portsmouth, Virginia	1936-70	.341 "
Charleston, South Carolina	1922-70	.180 "
Fort Pulaski, Georgia	1936-70	.198 "
Mayport, Florida	1929-70	.155 "
Miami Beach, Florida	1932-70	.192 "
Pensacola, Florida	1924-70	.040 "
Eugene I., Lousiana	1940-70	.905 "
Galveton, Texas	1909-70	.430 "

It is obvious that the only way in which this erosion can be counteracted is by artificial nourishment replacing the material eroded by other material whether from land or from offshore sources, the latter becoming more and more popular due to shortage of land borrow areas. The integrated transversal transport of material including seasonal and long range movements is usually much larger than the longshore. Earlier planning tended to put the main emphasis on longshore transport and measures like groins, breakwaters and sea walls largely concentrated on a "different distribution" or "redistribution" of the material available - but on average there was always a net loss. Partly due to lack of recognition of that fact and partly due to lack of proper equipment to handle the "transcersal problem" effectively it was not until the last two decades that it was realized that ultimately the only way in which erosion may be fought is by artificial nourishment replacing the material eroded by other material. The only place where this general rule may be disregarded is where nature itself provides the nourishment. It was the "New World" which on purely coastal protective basis carried the initiative and it was there that efforts concentrated on the main and large problem of bringing material back to shore to replace the quantity which was lost by "submerging of the profile".

$dL_{ongshore}$ - It is generally accepted and justified by a great number of laboratory and field observations that the longshore transport of material (Q) has an almost linear relationship to the longshore input of wave energy (E) or:

$$\frac{dQ}{ds} = k \frac{dE}{ds}$$

when k is a factor which depends upon material and profile characteristics. Only wave induced currents are assumed to be present. This in turn means that the longshore transport depends upon the curvature of the shoreline. In nature this curvature is a

function of natural geological and coastal morphological conditions like the existence of headlands, bedrock and river outlets (Table 1). This may upset the balance equation so that

$$\frac{dQ}{ds} \gtrless k \frac{dE}{ds}$$

in case of $>$ accumulation will result
in case of $<$ erosion will result

Nature demonstrates both cases e.g. by updrift accumulation and downdrift erosion at headland.

Table 1. Causes of Erosion by Nature and by Man

Nature	Man
Rise of Sea Level	Dams, dykes and other coastal structures causing rise and concentrations of tides
Protruding headlands, reefs and rocks causing downdrift erosion	Groins, breakwaters, jetties etc. causing downdrift erosion
Tidal entrances and rivers causing interruption of littoral drift	Man-made entrances causing interruption of littoral drift
Shoreline geometry causing rapid increase of drift quantity	Fills protruding in the ocean to such an extent that they change local shoreline geometry radically
Blocking of river outlets carrying sediments to the shore by flood stage barriers, change of location of outlets due to floods, erosion, tectonic movements etc.	Damming up of rivers without providing material sluices Irrigation projects decreasing flow of water and sediments to the shore Removal of material from beaches for construction and other purposes

What destruction effect nature in its abundance has demonstrated man unfortunately has imitated. Man-made erosion is a black spot on man's association with shores. It is a deplorable fact that all coastal protective measures apart from artificial nourishment (may) have an adverse affect on adjoining shores. An example is provided by a group of groins built in the 30'ies on the Danish North Sea Coast which caused severe lee-side erosion, up to 30 ft recession per year (situation corrected at a later date). Dams in California cut off river supply of sediments. Long harbor breakwaters and navigation channels often became almost complete littoral barriers causing severe erosion.

To evaluate the erosion quantitatively, records of erosion of profiles are needed. Such information may be available for areas of limited size but only a few countries have kept continuous records of areas of larger size through a long period of time. This includes the low countries in Europe e.g. parts of Denmark, England, France, Germany and Holland. Mostly only shoreline movements have been followed. A very illustrative example is given by Bakker and Joustra (2) whose paper does not only include data on shoreline movements on the open shore and at tidal entrances but also compares shoreline movements of groined and non-groined shores appraising the effectiveness of groin protection. Similar records are available in a few other places, e.g. in Denmark, Germany and some places in the U.S.A.

Several publications and books give considerable information on the development of erosion and on coastal morphological features (2, 3, 7, 9, 17, 21, 22, 24, 69). A great number deal with seasonal changes (13, 14, 18).

Space photography is now providing a tool for large scale checking of coastal movements (23 and re-references).

A very special type of erosion occurs in Norwegian fjords, demonstrating that disasters of tremendous dimensions can occur in subaqueous slopes in fine sand and coarse silt.

The explanation of why these slides frequently reach very large dimensions can be found

in the two characteristic properties of these materials: The first property is the complete loss in strength after a shear failure which is characteristic for loose fine sand and coarse silt. As the result of this property the slide masses assume the character of a viscous liquid and, in the first place, flow downwards from the slide scar and possibly initiate new slides by erosion. In the second place, the disappearance of the slide debris means that the faces of the slide scar are left unsupported, involving the risk of an extension of the slide in an uphill direction by a retrogressive, slice by slice, development.

The second property of submarine deposits of fine sand and coarse silt responsible for the disasterous character of the slides is their exceptionally high erodability. The reason why these deposits are easily attacked by erosion is partly the lack of cohesion of fine sand and coarse silt particles and partly the lack of a protective cover of top soil and vegetation in submarine deposits. The consequence of the high erodability is that if a flow slide descends over this type of deposit, it will cut deep canyons into the slopes and undermine any obstruction which deflects it from its original path. The scars of such an erosion can lead to the development of a new series of retrogressive slides which can contribute both by extending the slide and by adding further liquid sand to the flowing masses. In the postglacial deltas and estuaries occupying the head of the fjords in middle Norway, the fine sand and silt slopes frequently stand steeply. In most cases the deposits are continuously growing as a result of accumulation of sandy and silty material being carried out into the fjords by the rivers. Under these conditions even small man-made fillings may initiate a slide of considerable size. A factor which may contribute to the instability of the submarine slopes in these fjords is artesian pore pressure conditions originating from high water pressures in the fissures of the bedrock beneath the deposits.

For further information on this "soil mechanics" erosion the reader is referred to a paper by Dr. L. Bjerrum, Proceedings of "The First International Conference on Port and Ocean Engineering", the Technical University of Norway, August 1971, pp. 24-38.

NATURE'S COASTAL PROTECTION. MAN'S COUNTERPARTS

By good luck nature has not only demonstrated how to erode but also how to protect. It may safely be said that there is no protection initiated by man which has not beforehand been invented by nature, and nature obtained all the good results as well as all the bad results before man did. Consequently we can learn from nature if we will only make the effort of opening our eyes and looking. It must be admitted that nature has been more imaginative and has had more success than man. Perhaps one reason for this may be sought in the fact that what we see is mainly the result of the successes. In the case of failures little or nothing was left! Coastal geographers and geologist, often unintentionally, describe natures coastal protection (e.g. 24 and 69).

Table 2. Nature's Coastal Protection. Man's Counterparts

Nature	Man
Shore rock	Sea wall
Rock reef	Submerged bulkhead or mound
Rock Island	Offshore breakwaters
Headland	Large breakwater perp. to or at an angle with the shoreline
Rock perp. to shore	Groins
Sea floor vegetation	Bottom Mattresses
Sea surface vegetation	Floating Breakwater
Dune	Dyke
Material transfer to shore by:	
Wind drift	Artificial nourishment from land sources
Rivers	
Shore erosion	
Longshore Littoral Drift	
Sea bottom transfer	
Natural by-passing of drift at tidal inlets	Artificial nourishment from offshore sources Mechanical by-passing of drift at tidal inlets

Table 2 gives examples of nature's protective measures and imitations of them by man. It is obvious that nature has immense resources and is able to play a "full orchestra" where man's instrumentation is somewhat limited by the lack of proper tools and adequate funding, one depending upon the other.

Plate 4 Fig. 17 shows updrift accumulation at a large rock headland, "Portland", on the Icelandic South coast. Plate 4 Fig. 19 demonstrates natural offshore breakwater protection causing tombolo formation in Dorset, England; Plate 4 Fig. 18 pocket beaches formed by outcroppings of coral rock and natural rock sea walls on the east coast of Puerto Rico (Palmas Del Mar) and Plate 4 Fig. 20 huge outpours of material by a glacial river in the Arctic. All glaciers have outbreaks of water reservoirs during the summer season. In Iceland subglacial vulcanoes, when erupting, occasionally cause discharges of the order of 1 billion cubic yards of material including bed load "particles" of 20 ts.

COASTAL PROTECTION A B C

The main cases of need for coastal protection are listed in Table 3, distinguishing between measures to be taken on large and on small scales.

Table 3. Main Cases of Needs for Coastal Protection

	Large Scale	Local (small) Scale
Reclamation of land and protection of the reclaimed land	x	
Protection of property and structures on the coast	x	x
Construction and protection of beaches	x	Pocket beaches

Table 4 is an attempt to establish a detailed classification of the types of coastal protection which are available today. Distinction is made between functional, operational and hydraulic or wave mechanics characteristics.

Table 5. Various Coastal Protection Measures Classified in Accordance with their Ability to Provide Protection of Extensive and Local Areas and their Influence on Adjoining Shores.

	Large Scale	Small Scale	Effect	Influence on neighbouring shores
Groins	(x)	x	May stop or decrease shoreline recession but not if offshore erosion continues	Adverse, often very severely
Sea Walls	x	x	Stop erosion where they are built but do not stop offshore erosion	May to some extent become adverse
Shore parallel breakwater	(x)	x	Will probably stop erosion and build up beach where they are erected	Adverse, often very severely
Artificial nourishment	x		Widens beaches Provides full protection if well maintained	Beneficial

(x) less attractive solution

TABLE 4. DETAILED CLASSIFICATION OF TYPES OF COASTAL PROTECTION

Groins		Training walls, Shore parallel structures, Seawalls, Revetments.	
a) Classification:		a) Classification:	
i Beach groin	A coastal structure usually built perpendicular to shoreline to trap littoral drift and thereby retard erosion of shore. Narrow in width with its length varying from less than 100 ft. to several hundred feet. Stabilizes or restores or widens beach.	i Training wall	A structure placed parallel or nearly parallel to shoreline affording protection against waves and/or currents and retaining and preventing sliding of upland areas.
ii Current breaker groin	A groin with primary purpose to intercept currents which cause movement of material along beach. Light to heavy design with lengths up to 1,000 to 2,000 ft.	ii Sea Wall Bulkhead	A vertical or nearly vertical structure primarily designed to retain fill and stop erosion at a certain point or line
b) Type:		iii Revetment	A sloping facing with primary purpose of providing protection against erosion of a dune scarp and beach in front. Sand accumulation in front is a secondary result from reduced wave energy.
i Nonadjustable	A fixed groin high enough to block most of normal littoral drift but low enough to allow over-topping by storm waves carrying sand over groin.	b) Type:	
ii Adjustable	Groin with length and height adjustable.	i Vertical	A massive structure with variations in shape such as stepped and re-entrant curved face, vertical face, non re-entrant curved face, stepped face, inclined face, cellular sheet pile and rubble mound.
iii Impermeable	A solid or nearly solid structure preventing littoral drift passing through structure.	ii Sloping (revetment)	A concrete or stone facing placed on seaward slope.
iv Permeable	A groin with openings through structure of sufficient size to permit passage of littoral drift through openings will obstruct currents to some (variable) extent.	iii Impermeable	A solid or nearly solid structure. Seapage through structure through properly located drains only.
		iv Permeable	A stone crib vertical wall or sloping rubble mound or rough stone revetment allowing movement of water inward and outward thereby dissipating energy.

Offshore Breakwaters		Artificial Nourishment	
a) Classification:		a) Classification:	
i Shore-parallel breakwater	A structure built parallel to and at a distance from the shore to absorb and/or dissipate wave energy and thus prevent or reduce wave action on the lee side.	i Direct nourishment of beaches	Operation of replenishing and nourishing an eroded beach directly by artificial means, that is, supply of dredged or other sediment material to eroded areas as a whole.
ii Shore-perpendicular breakwater	A structure connected to the shore in a perpendicular or nearly perpendicular direction mainly used to provide a protected area or harbor.	ii Bypassing at inlets and entrances	Operation by which normal littoral drift interrupted by inlets or entrances (littoral barriers) is restored on downdrift side by artificial means of sediment transfer across barrier.
iii Wave breakwater	An offshore structure built perpendicular or parallel to the shore to dissipate wave energy and thus prevent or reduce wave action on the lee side.		
iv Current breakwater	A structure supposed to break current.		
v Floating breakwater	A structure of hydraulic or pneumatic or barge fabricated type to serve as wave breakwater.		
b) Type:		b) Type:	
i Vertical	A vertical or nearly vertical structure of masonry concrete, concrete or steel caisson, sheet piling cells or timber crib. May be solid impermeable, permeable or of rock crib. Main purpose to protect against wave action.	i Offshore dumping method	Dredged material dumped in offshore zones of eroded areas.
		ii Stockpile method	A stockpile established on eroded area and nourished intermittently.
ii Sloping	Most common-rubble mound of natural rock or built-up precast concrete blocks. Used extensively as wave energy absorbers in the open sea as well as on shores.	iii Direct placement method	A method similar to stockpile method except entire fill spread out over entire area to be protected.
		iv Bypassing or continuous nourishment method	A mechanical method of intermittent sand bypassing from updrift (accretion) side of inlet or jetty entrance to downdrift (erosion) side without interference to navigation channel. Also continuous nourishment of eroded areas.

Table 5 lists different coastal protection measures and their relative ability in providing the protection, their influence on adjoining shores (beneficial or adverse).

Before we can evaluate which protection is preferable the situation with regard to erosion has to be appraised. This may by done by the introduction of the terminologies "undernourished", "sufficiently nourished" and "overnourished profiles" and by the terminologies "source" and "drain" of materials (38).

Beach Profiles Classified in Accordance with Nourishment - Considerations on the basis of the development of beach profiles built up of sand with grain size 0.2 to 0.3 mm seem to show that we can distinguish between profiles in another way: that is, between the "overnourished", the "sufficiently nourished", and the "undernourished profiles. These terminologies are especially valuable for an understanding of the problem of what kind of coastal protection should be preferred and how satisfactory such construction will be. The overnourished beach profiles are fed with more material than the waves can shape into real beach profiles. These, therefore, are irregular and often perform as irregular shoals. There are two different types of sufficiently-nourished profiles. At one of them the profiles are not fed with more material than the wave can shape into a profile having the same "equilibrium form". At the other, the loss of material equals the supply of material and the profile still has the same equilibrium form. The undernourished beach profiles are eroded: that is, the coastline retrogrades. The undernourished beach profiles will always keep an equilibrium form but the form may change from one locality to another, depending on the conditions in general. It seems, therefore, that progradation of a coast may take place with or without equilibrium profiles while retrogradation of a shoreline can take place only with equilibrium profiles having a maximum steepness corresponding to the quantity of littoral drift, the waves and the material. An actual equilibrium profile therefore should be defined as a stable profile with maximum steepness. Needless to say, we cannot expect that all undernourished profiles will always have the same shape, but we can expect that all undernourished and sufficiently-nourished profiles will have certain standard forms, which in turn means that where one of the standard erosion forms occurs, we know that the erosion is probably not temporary. This information is very important. If on the other hand no erosion takes place we can expect that only a slight change in the littoral drift balance may start erosion.

A source of materials is a coastal area which delivers materials to other beaches. A source might be an area where erosion takes place, a shoal in the sea, for instance; the shallow area in front of an inlet which has been closed; a river which transports sand material to the nearshore sea territory, or sand drift from dunes to the beach. Artificial nourishment of any kind is also a source.

A drain of materials is a coastal area where materials are deposited. A drain might be a marine foreland of any kind, a spit, recurved spit, a tombolo, angular foreland, etc. It might also be a bay, an inlet, or a shoal. Man-made constructions such as jetties, groins, or dredged sand traps, are also drains.

Both terminologies are used in the section dealing with coastal morphology in relation to problems of beach erosion and coastal protection. In practical coastal protection technology the following general rules are valid:

1) A coastal protection should be built in such a way that it functions as a drain. It should therefore have a source but not a drain on the updrift side. If there is a drain the coastal protection will not be very successful unless material is supplied artificially.

2) A harbor or an improved inlet on a littoral drift coast should not act as a drain. It should therefore have no source but if possible a drain on the updrift side. Meanwhile it is very difficult to find a place where ideal conditions exist, and many other factors play an important role. Most harbors are built in a sheltered area, an inlet, a bay or in a river mouth. In such areas depositions will almost always take place either from the littoral drift or as silting, which means that the harbor actually functions as a drain. This is the case with numerous harbors all over the world, notably on the East Coast of the United States. Protection against the littoral drift can be effected by the construction of jetties, making the "improved inlet". An improved inlet acts as a drain and protects the inlet, but at the same time it cuts off the supply of material to the beaches on the lee side which again means that these

TABLE 6. COASTAL PROTECTION IN RELATION TO SOURCE OF MATERIALS AND CONDITION OF BEACH PROFILES
(Regarding beneficial versus adverse effects, see Table 5).

Coastal Situation: Actual Conditions of Source of Material, and Beach Profiles			Groins (Adjustable, Impermeable & Nonadjustable)	Seawalls and Revetments	Offshore Breakwaters	Artificial Nourishment: Offshore dumping	Artificial Nourishment: Direct Stockpile Placement	Artificial Nourishment: Bypassing Nourishment
A. Plenty of source material. Overnourished profiles.			Not Necessary	Might be necessary to avoid attack under extreme high-water and storm conditions. Should be built in such a way that they contribute to erosion of beach as little as possible. Vertical walls built too close to shoreline increase erosion. Energy absorbing walls, revetments or rubble mounds, are usually preferable.	Not necessary	Not Necessary		
B. Source material available. Sufficiently nourished profiles. Balance between material eroded and deposited.			Necessary if beach-widening is wanted in a particular location. Could be low or adjustable thereby permitting material to pass from updrift side to downdrift side as soon as they are filled with material.	Same as above. (A)	Able to build up a wider beach at a particular location.	If a beach is wanted in a particular location in short time, groins may be necessary to maintain the beach especially if the beach protrudes in proportion to the adjacent shoreline. Sand selected must have the same gradation as the beach sand if original beach slope is to be maintained. Sand may have to be obtained by offshore dredging.		Necessary if erosion is to be prevented on the downdrift side of an inlet. Groins may help retain material.
C. Only limited source of material or none at all. Undernourished beach profiles.	C.a Erosion only up to limited depth in the sea.	C.a.1 Source of material.	If extended beyond the depth up to which erosion takes place, they should be able to maintain beach. May be low or adjustable.	Can stop erosion provided they are stable at the depth at which erosion takes place. Even if groins are built, a seawall might also be necessary to avoid attack at foot of dune or cliff under extreme high water and storm conditions. It is very important that they be built in such a way that they contribute to erosion as little as possible. Sloping walls, revetments and rubble mounds work better than other types in avoiding frontal (beach) erosion.	Able to build up and maintain a local beach.	If a beach is wanted in a particular location in a short time, groins may be necessary for maintenance of beach. Selection of suitable sand for nourishment is important Sand may have to be obtained by offshore dredging.		Necessary if erosion is to be prevented on the downdrift side of the inlet or entrance. Extra supply of material probably necessary. Groins help retain material.
		C.a.2 No source of material.	Will not work even if extended beyond the depth up to which erosion takes place unless material is supplied artificially. May be low or adjustable.	Same as above. (C.a.1.)	Will provide local protection of shore but are unable to build up and maintain a beach.	Only continuous nourishment to balance erosion totally can maintain the beach or restore eroded areas. Groins may help retain fill. Selection of suitable sand for nourishment is important. Sand may have to be obtained from offshore areas.		
	C.b Erosion up to deep water in the sea.	C.b.1 Source of material.	Will retard retrogradation of shoreline temporarily after construction. Erosion will continue and continuous prolongation of land ends will be necessary if artificial nourishment is not made to balance erosion. Extension to deep water not important. May be low or adjustable.	Unless material is supplied artificially to balance erosion and groins are built, they will work only for a limited time before collapsing. It is very important that they be built in such a way that they contribute to erosion as little as possible. Sloping walls, revetments and rubble mounds contribute by themselves little frontal (beach) erosion compared to other types.	Able to build up and maintain a local beach but have to be reinforced as deep water erosion proceeds.	Periodic nourishment in quantities which balance total erosion can maintain beach. Groins may help maintain beach. Selection of suitable sand is important. Sand may have to be obtained from offshore areas.		Necessary to decrease downdrift erosion. Extra supply of material necessary. Groins help retain material.
		C.b.2 No source of material.	Will not work well unless continuously nourished to balance total erosion. Extension to deep water not important. May be low or adjustable.	Unless material is supplied artificially for total balance of erosion and groins are built, they will work only for a limited time before collapsing. It is very important that they be built in such a way that they contribute to erosion of beach as little as possible. Sloping walls, revetments and rubble mounds contribute to themselves little frontal (beach) erosion compared to other types.	Will provide local protection of shore but are unable to build up and maintain beach and have to be reinforced as deep water erosion proceeds.	Only continuous supply in the same quantity as total erosion can maintain beach or restore eroded areas. Groins may help retain fill. Selection of suitable sand is important. Sand may have to be obtained from offshore areas.		

TABLE 7. DETAILS OF THE PERFORMANCE OF SEA WALLS.

			Comments:
1.	What is wanted:	Storm tide and/or extreme storm protection of shore and beach. Protection of specific valuable areas (industry, buildings, highways etc.)	Energy-absorbing wall or revetment on dyke or dune. Any type of substantial wall with as little adverse affects as possible.
2.	Layout and geometry:	As streamlined as possible. It is best to leave and maintain a beach in front of the wall.	Erosion may be stopped at the wall but artificial nourishment may be needed to maintain beach in front of the wall.
		Influence on adjoining shores.	Leeside erosion may result if erosion continues leaving wall as protruding headland or if wall is built too far seaward and is not streamlined in horizontal geometry. Transfer of sand or other nourishment of downdrift shore may be needed.
3.	Combination with other coastal protective measures:	Groins.	To break longshore current and possibly build up beach in front of wall.
		Artificial nourishment.	To maintain beach in front of wall and/or to check downdrift erosion.
4.	Design:	Energy-absorbing (sloping and/or mound type).	Considerate to beach stability due to friction and low reflection.
		Non-energy-absorbing (vertical sheet pile or slab).	May create local erosion due to less friction against currents and more reflection.

TABLE 8. DETAILS OF THE PERFORMANCE OF GROINS.

				Comments:
1.	Degree of efficiency wanted:	Just beach stabilization.		Short groins mainly covering the beach.
		Also widening of beach.		Longer groins, possibly extending beyond bar or breaker zone.
2.	Layout and geometry:	Streamlined in horizontal geometry. No sharp turns or corners.		Reaction of shore protected: Stable or widening and then stable. Influence on adjoining shores: Usually beneficial or neutral updrift but adverse downdrift.
3.	Combinations with other coastal protective measures:	Sea Walls.		To cope with extreme conditions incl. storm surges.
		Artificial Nourishment.		To fill groins and widen beach initially and maintain width.
				To eliminate adverse effects on downdrift beaches.
4.	Design:			
	Length in agreement with point 1. Height to match beach profile wanted to the practical extent possible.	Impermeable:	Energy absorbing.	Less reflection, less loss of sand.
			Non energy absorbing.	More reflection, more loss of sand.
			Adjustable elevation.	May be operated to match fluctuations of beach
			Fixed elevation.	Can not be operated to match fluctuations of beach.
	Length/space ratio from 1:1 to 1:4 depending upon quantity of drift and beach material. Most common ratio is 1:2.	Permeable:	May be adjustable or fixed.	"To blow and have flour in your mouth at the same time". May provide beneficial results where currents are the main agents in the transport of materials, that means in rivers and estuaries.

TABLE 9. DETAILS OF THE PERFORMANCE OF OFFSHORE BREAKWATERS.

			Comments:
1.	What is wanted:	Protection, or protection and beach.	If breakwater is built on littoral drift shore both are usually obtained.
2.	Layout and geometry:	Parallel to shore or largely following depth contours.	Tombolo formation will result on shore to be protected. Severe downdrift erosion may result due to littoral barrier effect.
3.	Combination with other coastal protective measures:	Groins.	This combination is unlikely unless groins are used to check downdrift erosion, thereby transferring problem further downdrift.
		Sea Walls.	May be built to protect against extreme storms and tides or to check downdrift erosion.
		Artificial Nourishment.	May be used to create beach more rapidly if natural supply of material is limited or to check downdrift erosion.
4.	Design:	Energy absorbing structures preferable. See Table 7. Combination with natural reefs often advantageous.	

TABLE 10. DETAILS OF THE PERFORMANCE OF ARTIFICIAL NOURISHMENT.

1.	What is wanted:	Protection and beach.
2.	Layout and geometry:	Follow natural shoreline closely on straight or streamlined shores. Fill in pockets on headland shores and artificial pockets.
3.	Combinations with other coastal protective measures:	Groins: to create or maintain beach to eliminate leeside erosion Sea Walls: to protect wall and/or create or maintain beach in front of wall to eliminate leeside erosion Offshore Breakwaters: to create and maintain beach
4.	Design:	Nourishment from land or offshore sources. Offshore equipment under development. Various methods tested in actual operation. Sand shall be suitable for nourishment. Main requirement is that sand should be as coarse or coarser than the natural beach material and of no less specific gravity. By-passing - arrangements by fixed or movable plants incl. weirs and floating plants. Movable arrangements preferable.

beaches starve - having no source on the updrift side. It will be seen, therefore, that coastal protection problems are the reverse of harbor problems.

Table 6 is a general outline of the function of the type of coastal protection in relation to the actual situation of the beach and bottom profiles and to source and drain. When these factors are known, it is possible to evaluate the effects of various kinds of coastal protection and in that way determine the type which is most suitable.

Tables 7 to 10 give basic information on various types of coastal protection: putting the protection including sea walls, groins, offshore breakwaters and artificial nourishment in relation to "what is wanted" and giving some specific information on layout and geometry, combinations with other coastal protective measures and on designs. Plate 5 Figures 21-24, with accompanying note sheets following the plate sheets illustrates dyke protection and dune building. Plates 6-9 Figures 25-55 and the accompanying note sheets describe each particular measure: sea walls, groins, offshore breakwaters and artificial nourishment incl. by-passing of sand. Due to lack of space the number of figures had to be limited to characteristic examples of "the State of the Art". Adequate information function is available in the list of references and bibliography which has been separated in sections referring to each particular measure. Space limitations had to be considered also on this matter. By-passing of material is mentioned specifically in the next section on future coastal protection.

HOW WILL COASTAL PROTECTION DEVELOP IN THE FUTURE

In future coastal protection one must think large. It will therefore develop as a function of the combined political, administrative and technical structure. There will be little or no use for "one-man shows". Large groups and large areas will have to be accomodated - by large scale measures. Needs will be concentrated on protective and recreational projects and all combinations thereof. Pressure will increase by the need for recreational beaches. Protection will be achieved simultaneously. The question of which protective measure will be most practical under such circumstances may be answered by just looking at Tables 5-10 which clearly demonstrate that artificial nourishment with suitable material offers the best large-scale protection. This, however, does not mean that it always suffices. It may need support from dikes and/or sea walls because of the possibility of storm surges or it may need groins to break scouring currents running close to shore. One main technical advantage associated with artificial nourishment is that it is "smooth" and "streamlined" and therefore not only has no adverse leeside effects, but, on the contrary, benefits adjoining shores by a gradual release of material. Other measures, particularly groins and offshore breakwaters, have definite adverse effects on neighbouring shores. The importance of streamlining is obvious from the following elementary reasoning: Most littoral drift formulas relate the quantity of longshore drift, Q, to the longshore component of wave energy as:

$$Q = (K\,we)\sin 2\alpha_b$$

If the breaker angle α_b increases, Q increases too, assuming that $_b$ changes only one degree up or down. The resulting relative increase (decrease) of material transport within various ranges of α_b is indicated in Table 11.

Table 11. Relative Increase or Decrease of Longshore Material Transport when α_b various ± 1 (one) degree

Range of α_b	Increase or decrease, approx. Percentage
10^o 5^o	20%
20^o 5^o	10%
30^o 5^o	5%

From these figures it is obvious that any (natural or) man-made discontinuity in shoreline geometry may have a considerable effect on adjoining shores. The beneficial effect is welcome but the adverse is not and it is often severe.

The "face" of the coastal protection will vary from place to place, depending upon

local conditions. In Holland protection will have the main saying but recreation will become more and more important. In the United States more and more people are moving to the coastal zone. It is estimated (68, Herbich) that approximately 50% of the entire population will live in the coastal zone by the year 2000. In Florida and in most places along the Eastern Seaboard of the United States coastal protection and recreational beaches will be combined. In California needs are mostly recreational. In Japan the need for recreational beaches is tremendous. In England sea walls and groins are needed for their steep shores but the demands for sandy beaches in lieu of shingle beaches will increase. In Denmark the massive expensive groin protection on the West Coast will be supported and partly replaced or in some cases abandoned by artificial nourishment from offshore and from bay shoals whenever possible. Accepting this inevitable trend of development it will be an increasing demand for just sand. In addition at some places measures will be needed and justified to hold on to the sand to decrease maintenance. In many areas all over the world reclamation will continue and this requires dykes and reinforcement of dykes by seawalls or recetments. From a technical as well as a coastal ethics point of view there can therefore hardly be any doubt that future coastal protection will comprise of the single or combined measures listed in Table 12.

Table 12. Future Coastal Protective Measures
AN = Artificial Beaches and Nourishment
GR = Groins
SW = Sea Walls and Offshore Breakwaters

Large Scale	Small Scale
AN possibly combined with artificial dunes or dykes providing storm tide protection	SW to protect a particular area sloping structures preferable
AN + SW SW to reinforce dyke or dune against extreme conditions of waves and tides	GR may be justified in local areas if well planned and kept filled by nature and/ or by man
AN + GR when GR are justified economically to decrease maintenance costs	SW + GR to protect a particular area where groins are needed as current breakers
AN + SW + GR in unusual difficult cases	

The question which now arises is: how do we provide the optimal solution, technically, economically - and aesthetically? This question may be converted to: how do we get fill suitable for beach nourishment in ample quantities most economically? If it is necessary to build supporting structures as sea walls and/or groins, which design is then the most suitable? The problem which we are faced with concerns an optimalization of coastal protection considering all factors, the initial design as well as future maintenance.

As the need for sand increases the possibilities of securing the fill from land, bay or lagoon sources decreases which means that suitable fill to a still increasing extent must be secured from offshore sources. Such material must fulfill the following demands (54, 57, 61):

a) Grain size shall be as coarse or coarser than natural beach sand
b) Material shall be relatively well sorted with a distribution of particle size to cover all grain sizes present in the original environment

It shall include as little fine material (< 0.15 mm) as possible and also little coarse material e.g. particles $>$ 2 mm to avoid separation and a steep and unstable - ever changing - beach.

c) It must be resistant against abrasion (quartz, feldspar and similar minerals)
d) Needless to say, it must also be clean without content of clay, silt and organic matters

e) But - very important - not all material needed to fill a beach has to be "first class". It is enough that all the exposed material is suitable. Below the lower level of fluctuation less adequate material may be placed - just to provide volume and support for the upper floor of "beach material".

Where do we find suitable material? - Every artificial nourishment project includes a hunt to locate proper material which can be secured in an economic bay. Such material may be found in borrow areas in nearby lagoons and bays where it is usually fairly easy to dredge it and dump it where it is wanted. Most artificial nourishment projects so far have been based on bay, lagoon and land sources. But it may also be secured from offshore sources. The "sand inventory program" carried out by the U.S. Army Corps of Engineers on the U.S. East Coast revealed the existence of such deposits - of varying origin almost everywhere - but not always within an economic pumping distance (61).

Is sand in ample quantities available offshore? - This depends upon the geological structure and the recent - that means the quarternary-geological development. All shores and shore areas have been subjected to changes in sea level. During submerges shores and beaches were drowned. We find old shores including shore material everywhere. Coastal geomorphologist have dealt extensively with ancient shores (69). During emerges materials returned to shore. Land areas which were subjected to glaciations - and deglaciations - and therefore to high fluctuations in pressure moved up and down with the ice load. At the same time oceans subjected to glaciations received tremendeous quantities of icecarried material incl. gravel, sand and clays and this was dropped in the ocean when the ice melted away. The North Sea and Baltic Sea offshore moraines and meltwater deposits are typical examples of that. The consequence is that many sea territories are able to deliver materials suitable for beach nourishment in ample quantities - but, this is not enough. The material also has to be available within a reasonable distance from shore and at depths which makes recovery practical and economical. To investigate the availability of material, core samples should be taken up to the depth of the planned borrow. It is selfexplanatory that the borrow pit must not be located so close to shore that it present a danger to beach stability. This question is dealt with in ref. 59. The 20 ft contour may be the boundary for milder conditions but 30 ft should probably be the minimum depth for conditions on the eastern seaboard of the United States.

How will we then bring this material back to shore? - As it cannot creep itself the only practical way of moving it is by hydraulic power, pumps and pipes. For this we need machinery and a device to carry the machinery. For the latter, three different possibilities seem to exist:

a) offshore mining from a surface vehicle (ship)
b) offshore mining from a vehicle operating on the bottom
c) offshore mining from a fixed or movable platform

re. a - Offshore mining from a surface vehicle - A test on mining of sand offshore was run by the U.S. Army Corps of Engineers in 1966 (67). The U.S. Hopper-Dredge "Goethals" was selected for the operation (Plate 9, Fig. 50). The mooring barge used for discharging from the hopper dredge was anchored in approximately 30 ft of water and its discharge pipe was connected to a 28-inch diameter, 2.000 ft long submerged pipeline running ashore. The line between the discharge piping on the barge and the submerged line, to form a connection from the plant to the ocean floor, needed both flexibility and ruggedness to withstand the lateral and vertical movement and the forces anticipated in this severe service. Much experience of operation and equipment was gained by this test by which fifty-two hopper loads, comprising more than 250,000 cubic yards of sand, were pumped ashore along a 7/10th-mile stretch of beach. The sand fill was piled on the beach to elevations about 5 feet higher than existed previously and the beach was extended seaward some 50 feet.

The Corps of Engineers beach nourishment experiment at Sea Girt, New Jersey, demonstrated that a suitably equipped seagoing hopper dredge could pump sand onto an ocean beach from an offshore mooring, thereby further enhancing the versatility and usefulness of this type of hydraulic dredging plant.

In 1971 a comprehensive nourishment from offshore sources was run at Pompano Beach,Fla.

by C.E.Bean, Inc., La. This work was performed between late April and October of 1970 by a cutterhead-suction dredge. During this period approximately 1,100,000 cubic yards of material was pumped on the beach. The material was located approximately 3-4,000 feet offshore in depths of 30-50 feet of water. The depth of sand available seldom exceeded 15 feet and never exceeded 20 feet. The dredge was 215 ft long, 45 ft wide, and 10 ft deep with a displacement of approximately 2,000 short tons. The pump engine was 3700 h.p. The pipeline used was 25" I.D. The floating line was conventional. The Pompano Beach project was described by the contractor as being "routine in every respect, with the exeption of sea conditions". The operation was limited by the inability of the floating pipeline to remain intact when the seas exceeded 4-5 ft in height. It is felt by the operators that the dredge could have operated in seas up to 5-6 ft provided the wave period was relatively short. Long-period waves tended to affect the dredge's capability while short-period waves had more effect on the floating pipeline. Subsurface pipes have now been developed for use in cases where a pipeline must be able to remain in position in bad weather.

The largest beach restoration or creation project is probably the 14 million cubic meters beach fill which was carried out in 1971 at Hook van Holland to create a 100-hectare (250 acres) beach north of the north breakwater of the Rotterdam Waterway. The material was dredged in the deep water channel serving Europort, Rotterdam's new gigantic seaport (62).

re. b - Offshore mining from a vehicle operating on the bottom - The underwater dredge is an old dream which appeared at intervals during the latest two decades. Underwater dredging for minerals has been known for long. Submergence of pipelines in the ocean bottom by jet pumps is of recent date. Similar large scale projects for placement of tunnel pipes across the Straits of Dover and elsewhere have been advocated during recent years. The underwater dredge (Plate 10 Fig. 52) which was put in operation on a test basis in 1970 at Ft. Pierce, Fla., was a result of many years of trial and error (66). A total of 63,000 cubic yards was discharged on the beach from the borrow area 1,200 ft offshore. Many improvements still seem to be needed to make such an operation successful technically and economically. 700,000 thousand cubic yards were pumped ashore by a convential dredge in continuation of this work.

re. c - Pumping from a platform - Another type of offshore dredge is a result of research undertaken by IHC, Holland, over a long period of years, which resulted in the development of the "platform-dredge" (56). Using this dredge a high rate of production can be achieved at considerable depth in currents and swells. Plan and side views of the platform are given in Plate 9, Fig. 51, which shows the dredge with the ladder lowered for dredging at the maximum depth of 25 meters. Supported on three legs, the platform can be moved by means of three twin-spud rotors, in any direction. Length of the L-sides is 30 m. The cutter ladder projects about 22 m when in the raised position. The legs are approximately 38 m in length. At a dredging depth of 25 m and a cutter penetration depth of 2 m, the platform can be jacked up to a height of 4 m above water. Table 13 is a list of data predicted by the IHC (56) comparing output capacities of conventional dredges to the cutter platform dredge.

Table 13. Output Capacity by Conventional and by Platform Dredge (56)

	Conventional cutter dredger with spuds	Conventional cutter dredger with swing wires	Cutter platform
Basic output in m^3/hr	1,000	1,000	1,000
Less factor for overrunning	-	0,5 m	-
Number of pump-hours attainable per year in calm water	3,100	3,100	3,100
Maximum wave height in even swell	0,30 m	0,75 m	2,0 m
Percentage of workable hours	15%	37%	80%
Actual pump-hours per year	465	1,145	2,480
Annual production in m^3	465,000	573,000	2,480,000

Maintenance - Any artificial nourished beach will suffer loss of material. This raises the question of how to decrease loss of artificially nourished material. This may be accomplished by structures. It is generally accepted that groins are able to

slow down longshore drift but loss by transversal drift is probably far more severe, particularly on shores with steep offshore profiles. Addition of shoreparallel breakwaters at the extreme end making a "T-groin" or "mini pocket beach" is an improvement which has been used with success e.g. at Deerfield Beach, Fla. (Plate 8 Figs. 46 and 49) on Lido Key, Fla., on Hilton Head Island, S.C. etc. Another solution is the construction of an "offshore sill". Such sills have been used e.g. on some of the Chicago beaches and on Singer Island, Fla. It is in fact some kind of an offshore breakwater. The difference is that while offshore breakwaters are built in single sections sills are continous training walls providing an offset or step in the bottom profile.

Looking at the experience available in Florida, it may be said that many shores in Florida are already protected by some kind of offshore breakwater in the form of the limestone, coquina, and beach rock reefs, which are found along a good part of the S. E. coast as well as part of the lower Gulf coast. It is a known fact that deterioration of some of the offshore reefs had caused increased erosion (e.g. at Jupiter Island, Fla., Atlantic Coast and on Casey Key, Fla., lower Gulf Coast). Model experiments carried out at the University of Florida in 1965 demonstrated the ability of the sill (reef) to make a step in the bottom but also revealed the scour problem, particularely inside the wall. It is, however, quite evident that the offshore bulkhead or training wall has had a beneficial effect on the profile. The result, needless to say, is quantitative,but compared to field experience it indicates the trend correctly.

A very special type of "offshore training wall" has been built at Durban, South Africa. It consists (1972) of an almost 3 km (2 miles) long offshore deposit of 5 million m^3 of sand placed in 1966-1972 on 17-18 m depth, crown elevation at approximately 7,5 m below M.S.L., maximum waves ab. 6 meters (ref. 55 brought up to date by private comm. with Mr. J.A. Zwamborn). This "wall" or breakwater has so far been remarkably stable although it fluctuates slightly, the upper developing gentler slope during storms and steeper slopes during fair weather (swell) conditions. Losses have been small and the breakwater has caused considerable decrease of wave action during storms, benefiting the beaches.

Considering the coastal geomorphological side of the problem,nature has established large pocket beaches (Plate 4, Fig. 18). Improvments of natural conditions may be undertaken taking advantage of natural headlands and extending then by breakwater - additions. Such pocket beaches have been established at several places, e.g. on the Venezuelan shores at Los Caracos and at the Sheraton-Macuto Hotel. Pockets may also be established by stockpiling of sand on the beach at intervals. This will undoubtedly cause some (temporary) slow down of longshore drift creating a (temporary) leeside erosion problem. More material will probably be lost offshore however.

STRUCTURES

With respect to structures - whether groins, offshore breakwaters or seawalls including revetments - it may be expected that prefab. elements will take over to a still increasing extent. The shore-parallel structures will be in the lead because they fulfill requirements of consideration to adjoining property, recreational needs and aesthetics better than shore-perpendicular structures. Where the latter are built they are most likely needed for special "interlocking purposes" as "pocket" or "perched" beaches. Most structures will probably either be mass-produced in elements as large as practical or needed - or mass-produced in sheets of various materials easy to handle and place. This trend is already evident. A sloping sea wall e.g. may be split up in the following units: prefab. toe protection, prefab. mattress, prefab. armor, prefab. wave screen and prefab. overslash protection, totalling five "units". Groins may be made up of prefab. stem elements + possibly a T-head which could also be of prefab. elements.

Bypassing of material - Bypassing of littoral drift at tidal and other entrances cannot be considered "artificial nourishment". It is a re-establishment of natural processes which were disturbed due to man's adverse interference. This may be accomplished by "bypassing plants" or by "bypassing arrangements" (59, 60, 63, 65, 68).

Table 14. Sand By-passing Status in the United States

Location	By-passing arrangement	Status, 1970-1971
Bakers Haulover, Fla.	Bay shoal dredging	Permanent transfer from bay shoal trap suggested
Boca Raton, Fla.	Trap in entrance	Transfer from trap behind updrift jetty connected breakwater suggested
Canaveral Harbor, Fla.	Dredging of channel	Fixed plant to be constructed(?)
Channel Islands Harbor, Calif.	Trap behind breakwater	Operational
East Pass, Fla.	Depressed weir and trap	Weir jetty completed
Fire Island, L.I., N.Y.	Transfer from bay shoal	Has been studied/model study on trap arrangement
Ft. Pierce, Fla.	Transfer from bay shoals	Has been studied/suggested
Hillsboro, Fla.	Depressed weir and trap	In operation since 1952
Houston, Corpus Christi, Tex.	Bay and ocean shoal dredging	Sidecasting in operation
Jupiter, Fla.	Transfer from bay shoal	Depressed weir and trap/proposed
Masonboro, N.C.	Depressed weir and trap	Operation 3 years
Moriches Inlet, L.I.,N.Y.	Fixed plant proposed	By-pass of jetties to be extended authorized
New Pass, Fla.	Ocean shoal dredging	Occasional transfer from ocean shoals
Newport, Calif.	Undetermined or being studied	Recirculation by trap at lower end of ½-mile reach being studied
Ocean Beach, Calif.	Trap inside updrift jetty	By-pass from trap inside
Palm Beach, Fla.	Fixed plant	Revision planned
Perdido Pass, Ala.	Dredging of channel	Weir jetty completed
Ponce DeLeon, Fla.	Depressed weir and trap	Almost completed
Port Everglades, Fla.	Ocean shoal dredging	Transfer from shoals in ocean and entrance suggested (model)
Port Hueneme, Calif.	Trap behind updrift jetty	Transfer from trap behind updrift breakwater
St. Lucie, Fla.	Depressed weir and trap	Construction recommended
Santa Barbara, Calif.	Transfer from shoal inside updrift breakwater	Extension of west jetty, construction of east jetty and detached breakwater authorized
Sebastian, Fla.	Bay shoal dredging	Permanent transfer from bay shoal trap suggested
Shinnecock, L.I., N.Y.	Undetermined or being studied	By-pass of jetties to be extended authorized
S. Lake Worth, Fla.	Fixed plant	New jetties and pump in 1968
Twin Lakes Harbor, Santa Cruz, Calif.	Fixed plant	Operational 1972
Virginia Beach, Va. (Rudee Inlet)	Fixed plant	Revision planned; being studied

Table 14 shows the status of by-passing procedures in the United States 1970-1971. It may be observed that the flexible arrangements: dredging from traps behind depressed weirs or detached breakwaters or other traps now are in the lead compared to fixed or movable plants on jetties or trestles. Major movable plant installations are found in Durban, South Africa (stopped in 1953) and at Paradip, State of Orissa, Bay of Benegal, India. A small movable plant mounted on a trestle which may be closed or opened for passage of drift by "shutters" or "needles" is found at Nagapatam, State of Madras, India. The jetty is left open during the monsoon period.

Plate 10, Fig. 55, shows schematically various by-passing plants and arrangements. Hydraulic "lift procedures" (63) are being considered in a few places (U.S.A., India, Denmark).

DATA NEEDED FOR DESIGN

The data needed for design, needless to say, depends upon what one intends to design. If you are "scientific" you may make up a menu-card with 57 courses or so and start eating the appetizers without accomplishing any work of actual improvements. If you are "over-practical" and "over-experienced" you may wind up with a quick judgement with accompanying 50% change of failure. Table 15 summarizes what, in the opinion of the author, is necessary to secure information needed for a sound evaluation and design. With respect to artificial nourishment reference is made to the preceeding section.

Table 15. Basic Data Needed for Design of Coastal Protection

Structures	Beaches
Adequate tide data incl. data on storm tides (statistically and hindcasted).	
Adequate wave data incl. data on extreme storms (statistically and hindcasted).	
Current data to the extent needed for the particular location. Longshore and transversal currents are related to tides, winds, bottom topography, discharges from rivers, tidal inlets etc.	
Profile data incl. long range and short range (seasonal) movements of profiles and shorelines normally up to at least 30 ft depth. Knowledge about undulations of shoreline and changes in bar geometry.	Profile data incl. long range and short range (seasonal) movements of profiles and shorelines normally up to at least 30 ft depth. Knowledge about undulations of shoreline and changes in bar geometry.
Grain size analyses of sand from beach and nearshore offshore bottom.	Grain size analyses of beach and offshore bottom extending to min. depth of seasonal and/or long range fluctuations. Seasonal fluctuations of grain characteristics. Detailed investigations of borrow pit materials based on core sampling. Tracing preferably by fluorescent tracers advantageous for evaluation of stability and future maintenance.

Some may claim that the experienced designer needs less data than the in-experienced. Practice, however, often tends to demonstrate the opposite because the experienced person is more aware of the difficulties and he is therefore more careful with his planning. It is also experience that advocators of patented "super marked" devices, e.g. within the branch of permeable groins, usually need little or no data at all. The designer's "experience" is based on "faith" or on "just business". Consequently they can also be proud of having the absolute record of absolute failures.

PLANNING. ADMINISTRATIVE ASPECTS

With respect to planning of coastal protective measures even the best "philosophy" and professional (technical) approach will not work unless the administrative and political aspects are planned as well. In the United States national (federal), state, county or other public body if requested may grant specific favours in accordance with rules and laws but support by local groups is very essential and may be gained through confidence and detailed exposure of the program. The responsibility of developing plans that reconcile conflicting demands is the responsibility of all levels of government. Although planning criteria must be orientated towards the multiple-use concept based on local desires, it must also consider State and National needs. The State (province or county) should have - and some actually have - a single agency with the administrative and technical ability, financial resources, and enforcement authority to regulate coastal protective measures and provide cooperative support to help blend local interests with the State interests. It can also supply some expertise and files of basic data. And not least it should support with funds.

With respect to public administrative control with coastal protective structures it should always be an absolute requirement that what you do and ensure a positive result

for yourself should not be allowed to have any adverse effect upon property belonging to others. It is generally accepted that one should not deprive anyone of the water which flows to his property by which he upholds his living e.g. by farming or by industry. Neither should anyone cut roads or accesses over somebody else's property. Why should it then ever be permitted to rob your neighbour of his shore property by increasing nature's forces on his shore or by decreasing the flow of beach materials to his property? These are essential for maintaining it - just as important as water is for farming the land. Neither should anybody be permitted to expand the public access road constituted by the public ocean on the cost of any neighbour or shore property owner. It is peculiar that for a long period of time the most simple analogies in public administration were not recognized. The reason was probably twofold: first the mechanics of the matter were not understood and, next, public agencies were often responsible for the errors made either by direct sponsorship of the ill-advised structure or by permits granted to erect the structures. The consequence was that "face savings" and other "bureaucratic reasons" often became more important than recognition of facts. The peculiar situation therefore developed that it was the courts who were forced to look into such problems because a few individuals were hardheaded and wealthy enough not to bend their neck for certain shortcomings of public administration.
One of the major problems for progress in coastal protection, however, is that funds for planning have been difficult to obtain - or very late in coming. Most coastal states in the U.S.A. still have not provided adequate agencies and funding and the lack of coordination and planning of coastal protective measures has gradually become a national problem. The Federal Government has taken an active - but still incufficiently funded - interest. The most difficult task, however, seems to lie on the local government and group level because the democratic system does not advocate the kind of discipline which is a necessity in all warfare including the tough fight against the sea. Practices in Europe and in the United States differ to some extent due to differences in the political and administrative pattern. In Europe, particularly in the low countries and in the countries rimming the North Sea, problems are often fully national. Contributions by local governments or groups are minor or non existing but they may handle the problems partly or wholy on less exposed shores.

Ten demands in Coastal Protection are listed in Table 16. They are as strict and demanding as those listed in Deuteronomy. But if we do not obey them we may soon need a number of "Adams Bridges" for escape - because nothing can stop the forces by tides, waves and currents. King Canute of Denmark and England placed his royal throne on the beach but the waves washed over his feet. He withdrew. Flexible defence costs less and mostly it is the most successful and it does not prohibit stand-by positions when needed.

Table 16. The Ten Demands for Coastal Protection

1)	Thou shalt love thy shore and beach
2)	Thou shalt protect it gainst the evils of erosion
3)	Thou shalt protect it wisely yea, verily and work with nature
4)	Thou shalt avoid that nature turns its full fortse gainst ye
5)	Thou shalt plan carefully in thy own interest and in the interest of thine neighbour
6)	Thou shalt love thy neighbour's beach as thou lovest thy own beach
7)	Thou shalt not steal thy neighbour's property, neither shalt thou cause damage to his property by thy own protection
8)	Thou shalt do thy planning in cooperation with thy neighbour and he shalt do it in cooperation with his neighbour and thus forth and thus forth. So be it
9)	Thou shalt maintain what thou has built up
10)	Thou shalt show forgiveness for the sins of the past and cover them up in sand

Acknowledgement - The author wants to express his appreciation for the assistance offered him in preparation of the historic sections of this paper by colleagues in the Netherlands, Mr. J.F. Agema, Chief Engineer, Rijkswaterstaat, Mr. T. Edelman, Chief, Coastal Research Department, Rijkswaterstaat and Mr. J. Battjes, Research Engineer, Delft University of Technology and in England by Mr. D.L. Newman, Research Engineer, the Hydraulic Experiment Station in Wallingford.

PLATE 1

Fig. 1. "Golden Hoop" in the Netherlands.
Currentbreaker of later date in front (van Veen, 1962)

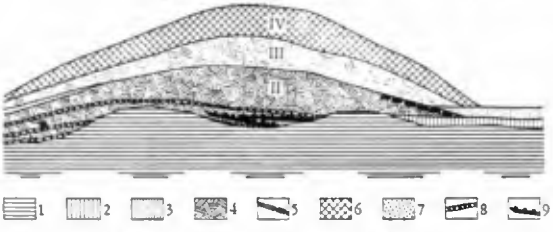

1. PEAT PRESENT IN SUB SOIL
2. COVER OF CLAY ON PEAT
3. YOUNGER CLAY COVER
4. CLAY WITH CLODS
5. CLODS OF PEAT
6. CLAY (WHICH WAS "BROUGHT IN")
7. MARINE SHELLS
8. MAT OF BRUSHWOOD
9. PARTS OF SHIPS HULL

Fig. 2. Cross section of ancient dike, Netherlands.
("Antiquity and Survival", 1959)

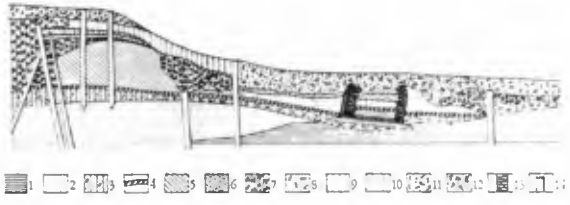

1. PEAT PRESENT IN SUB SOIL
2. CLAY
3. CLAY WITH SAND AND SHELLS
4. REED
5. SEA - GRASS (WEED)
6. PEAT
7. CLAY WITH RUBBLE
8. SAND WITH SHELLS
9. CLAY
10. CLAY WIYH SAND
11. CLAY WITH SHELLS
12. RUBBLE WITH SHELLS
13. MASONRY
14. PILE

Fig. 3. Cross section of ancient dike with pile support.
("Antiquity and Survival", 1959)

Fig. 4. Polder boys repairing dike with willow,
Netherlands (van Veen, 1962)

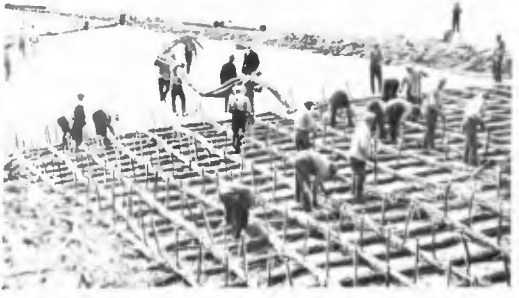

Fig. 5. Willow mattress, Netherlands (van Veen, 1962)

PLATE 2

Fig. 6. Breakthrough at Vosmer, Netherlands, Febr., 1953 (van Veen, 1962)

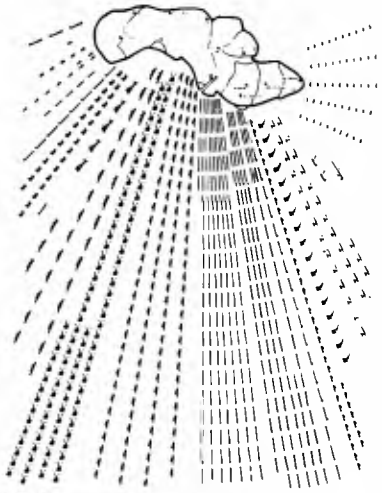

Fig. 7. Equipment parade at closing of breaches in the dikes of Schouwen - Duiveland (van Veen, 1962)

Fig. 8. The Delta Plan. (Rijkswaterstaat, 1971)

Fig. 10. Placement of zinkstuk of synthetic materials. (Deltawerken No. 58, 1971)

Fig. 9. Towing of willow mattress for bottom protection (van Veen, 1962)

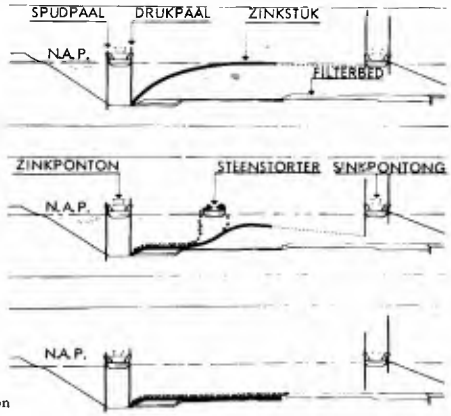

PLATE 3

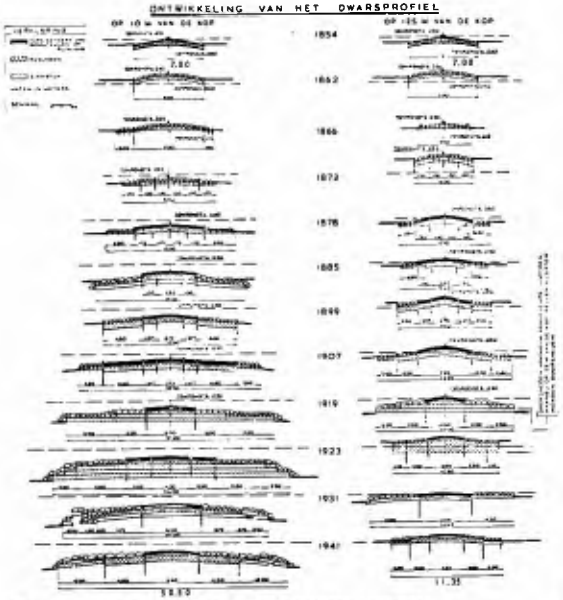

Fig. 11. Development of groins in Holland 1854-1941. (Visser, 1953)

Fig. 12. Dutch groin with piggy back

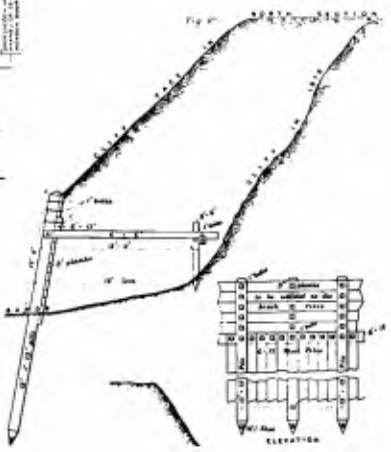

Fig. 13. Hornsea sea wall. (Journ. Inst. Civ. Engrs., 1877-78)

Fig. 14 b. Beaconsfield Sea Wall, Bridlington, under wave action

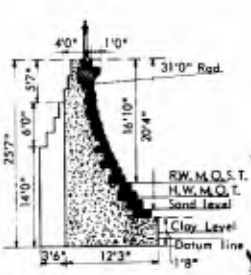

Fig. 14 a. Beaconsfield Sea Wall, Bridlington (Mattews, 1934)

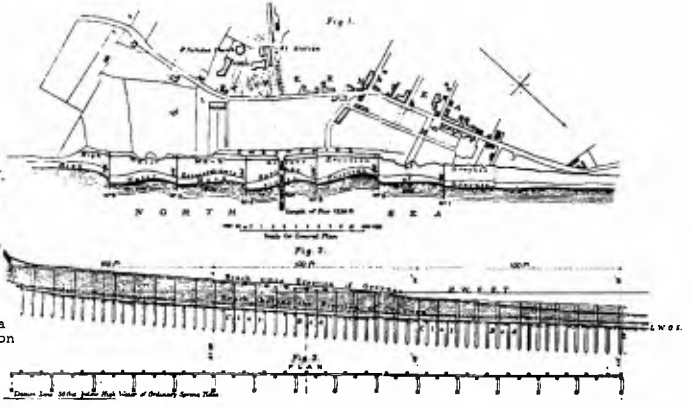

Fig. 15. Whithernsea Groins (Journ. Inst. Civ. Engrs. 1877-78)

PLATE 4

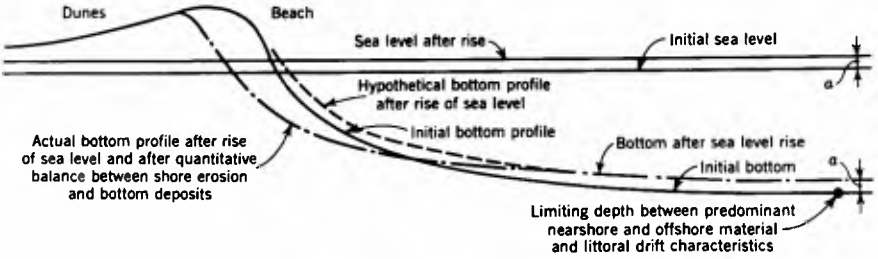

Fig. 16. The influence of sea level rise on erosion (Bruun, 1962)

Fig. 17. Dyrholaey, headland and natural breakwater on the Icelandic South Coast

Fig. 18. Rock outcroppings make natural sea walls and form pocket beach in Puerto Rico

Fig. 19. Man o'War Rocks, Oorset, makes offshore breakwater (Steers, 1947)

Fig. 20. River pouring material into the sea nourishing beach and offshore profiles on the Icelandic south coast

PLATE 5

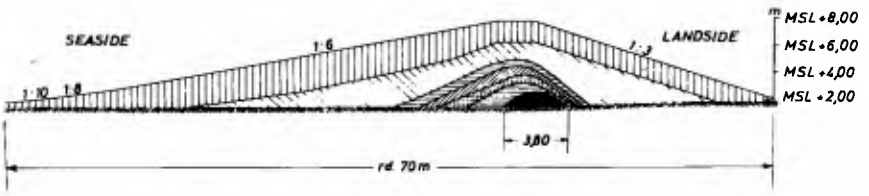

Fig. 21. Comparison of elder with modern dike profiles (Kramer, 1971)

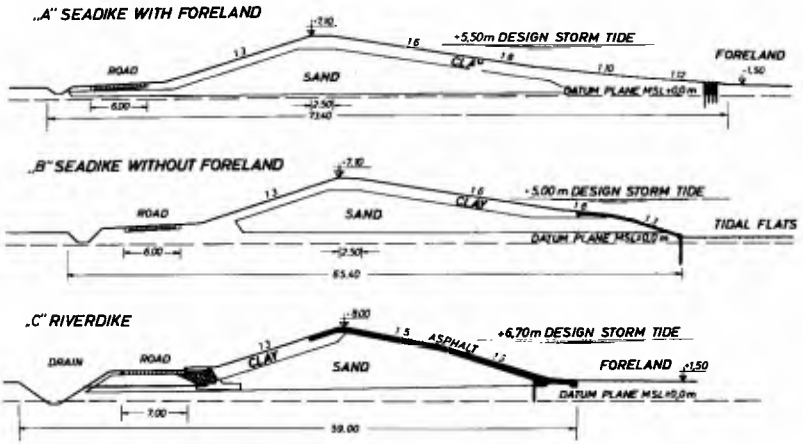

Fig. 22. Cross sections of dikes with sand core and clay or asphalt cover (Kramer, 1971)

Fig. 24. Dune building by sand fences (NPS, USA)

PLATE 6

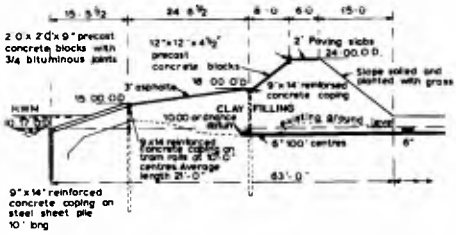

Fig. 25. Pett Level Sea wall (Thorn, 1960)

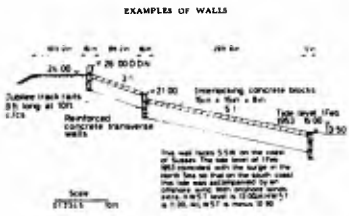

Fig. 26. Walland Sea wall (Thorn, 1960)

Fig. 27. Stone pitching revetment and stone pitching piggy back groin (Rijkswaterstaat)

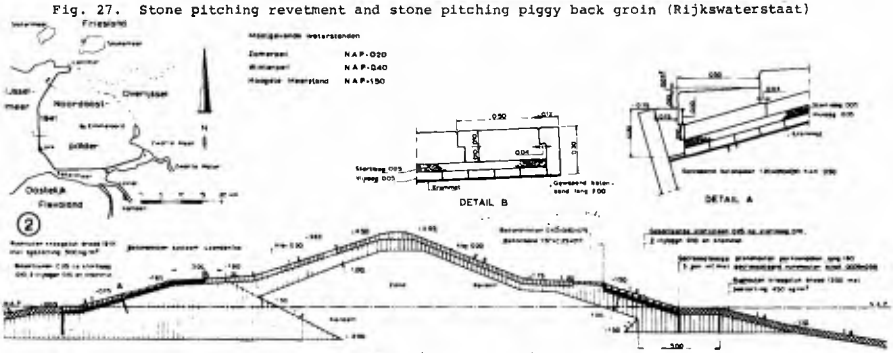

Fig. 28. Noordostpolder revetment on dike (Rijkswaterstaat)
Legend: Basaltzuilen (basalt prisms), stortlaag (gravel layer), vlijlagen (láver of brick), krammat (straw mat), kraagstuk (willow mattress), bestorting (rock), beton (concrete), klei (clay dug from canals and marshes)

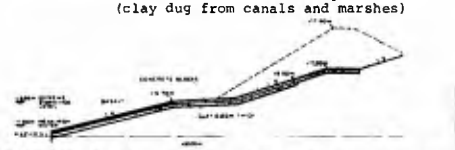

Fig. 29. Revetment at Zoutelande (Rijkswaterstaat)

Fig. 30. Sea Carpet at Europeport, Netherlands (Hydrospace, Oct. 71)

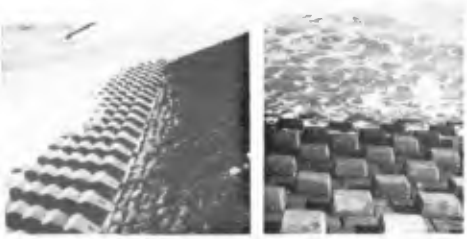

Fig. 31 a and b. Concrete blocks with friction arrangements (Rijkswaterstaat)

PLATE 7

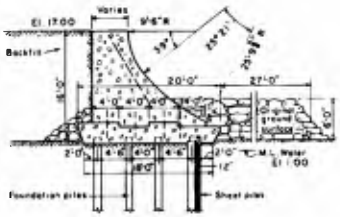

Fig. 32. The Galveston Wall, Texas (USCE = U.S. Army Corps of Engineers)

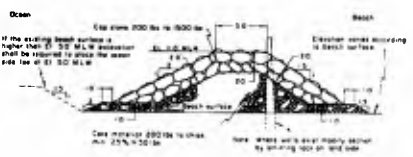

Fig. 33. The Fernandina Wall, Florida (USCE)

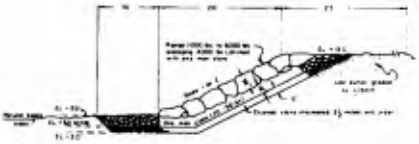

Fig. 34. The Ft. Story Wall, Va. (USCE)

Fig. 35. Indian Sea Wall (Kerala State)

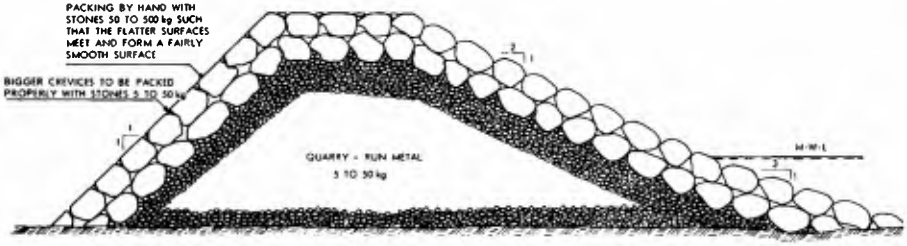

Fig. 36. Vertical wall on Jupiter Island under heavy wave attack, 1962 (Bruun and Manohar, 1963)

Fig. 37. Interlocking block revetment on Jupiter Island under heavy wave attack (Bruun and Manohar, 1963)

PLATE 8

Fig. 38.
Dutch basalt pitching groin at Petten

Fig. 39. Dutch group of groins, Walcheren (Rijkswaterstaat)

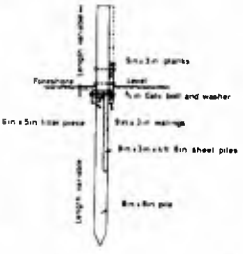

Fig. 40 a and b. British adjustable king pile groin (Thorn)

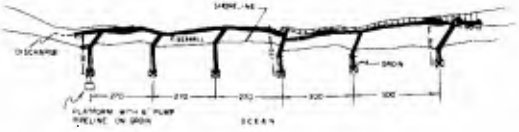

Fig. 42. Group of groins with slanting land ends at the Old Skaw, Denmark (Bruun and Manohar, 1963)

Fig. 43. Groin built of 4-8 ts concrete blocks in the crown and 2-8 ts granite in the slopes. The Lime fiord barriers, Danish North Sea Coast (Hofdahl)

Fig. 41. Adjustable groin at South Palm Beach (Greiser)

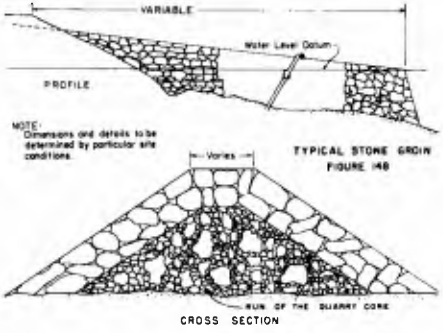

Fig. 44. American rock groin (USCE)

Fig. 45. Groins, mostly steel sheet piling, at Miami Beach, Florida

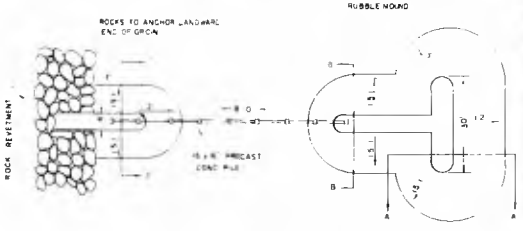

Fig. 46. T-groin design for Deerfield Beach, Fla. Adjustable king pile stem, rock T-head (Bruun and Manohar, 1963)

Fig. 47. T-groins at Deerfield Beach, Fla. (Bruun and Manohar, 1963)

PLATE 9

Fig. 48. Offshore breakwaters form pocket beaches, at Monte Carlo (Terra, Holland, No. 1, 1972)

Fig. 49 a and b. Artificial nourishment from land sources, 1,6 mill cuyds on 16,000 ft of shore, Hilton Head Island, S.C.

a b

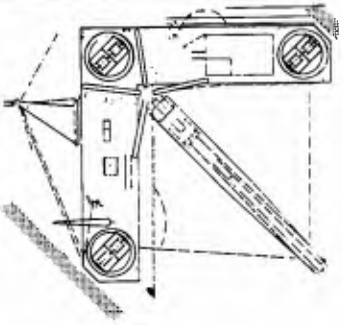

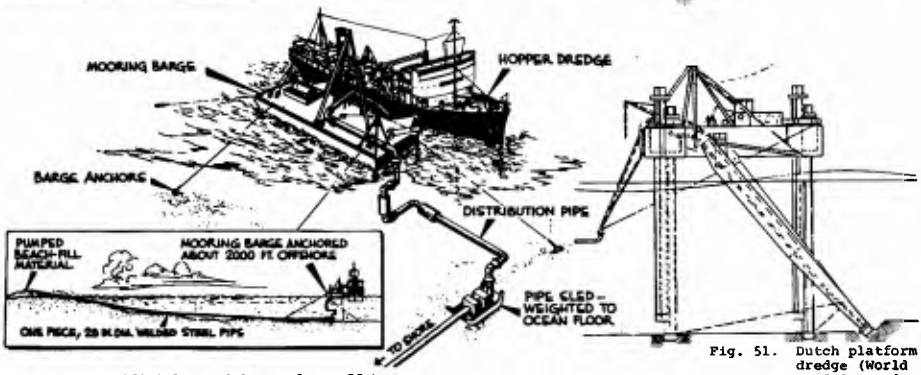

Fig. 50. Artificial nourishment from offshore by hopper dredge. See Girt, N.J. (Mauriello, 1966)

Fig. 51. Dutch platform dredge (World Dredging and Construction, Jan. 1972)

PLATE 10

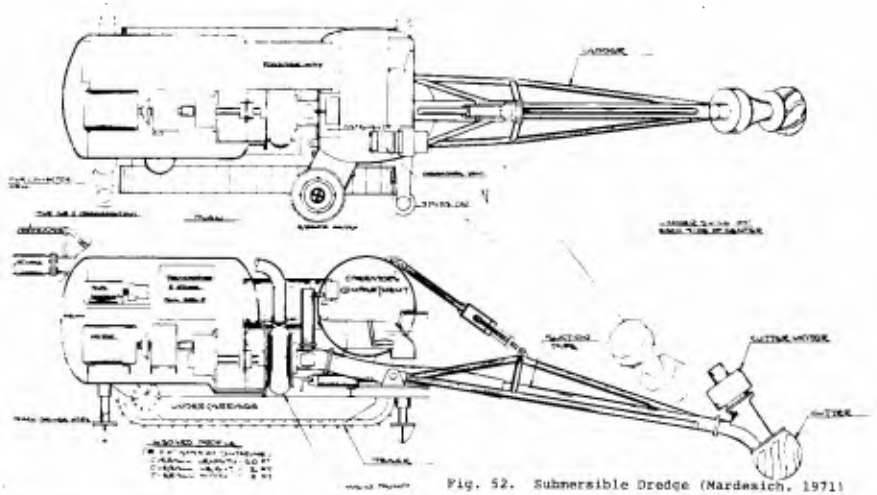

Fig. 52. Submersible Dredge (Nardesich, 1971)

Fig. 53. Artificial nourishment by dragscraper on Jupiter Island, Fla. (Bruun, 1967)

Fig. 54. Bulldozer operation at Deerfield Beach, Fla., following the March 1962 storm (Bruun and Purpura, 1963)

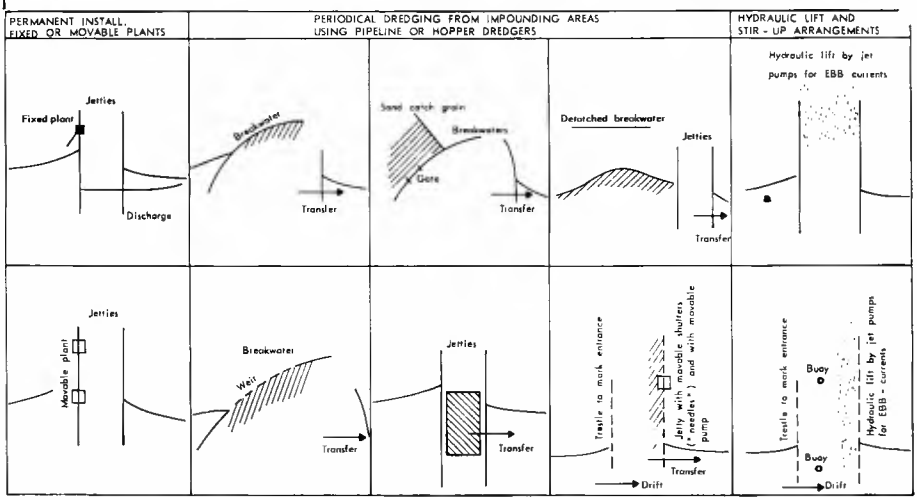

Fig. 55. Various bypassing arrangements (schematics)

NOTES ON DUNES AND DIKES

1 The dune is a natural dike which was created by wind-blown sand and was possibly vegetated by nature. Man's counterpart to the natural dune is the artificial dune or dike. The difference between dune and dike lies solely in the fact that the dune usually has land higher than sea level behind it, while the dike may protect low lying land which would otherwise be flooded.

Dunes are always built of sand, using mechanical equipment like draglines, scrapers, hydraulic pumps etc. The experience on the North Sea Coast is that an outer slope of 1 in 7 and an inner slope of 1 in 3 is practical (25). The width and elevation of the crown depends upon the actual exposure and upon the expected combined tide and wave elevations. Dunes, however, may also be erected with the assistance of wind and sand fences (28, 30). See Plate 5, Fig. 24.

They may be protected by dune vegetaion of various kinds (26, 27, 31, 32, 33). Most common are species of Ammophila - (arenaria or brevigulata, the latter called American Beach Grass in the U.S.A.). Planting machines have been developed. See Plate 5, Fig. 23 (29) and considerable research has been undertaken on fertilization etc. (32).

2 The dike is by its nature a more solid design because its tasks and obligations are more severe. The modern dike is a result of almost 1.000 years development. Plate 5, Fig. 21 (42) is a comparison of older and modern dike profiles on the German part of Nord Friesland. The oldest dike built about 1.000 A.D. had a width of 3.80 m and steep slopes. The 1962 dike was higher, had gentler slopes and a width of about 70 m. In some vulnerable areas "sea dykes" and "withdrawn dykes" have been built parallel to each other to provide satety against breakthroughs of the sea dike (25).

Dike design and construction has developed in various directions in accordance with actual needs. Plate 5, Fig. 22 shows various cross sections all fulfilling specific requirements. Plate 6 shows examples of hard pavements described in a great number of publications (11, 34, 38, 40, 42).

3 A new type of dike protection consists of various kinds of synthetic materials incl. polypropylene and nylon fabrics used as replacement for willow and other types of mattresses which are much heavier and difficult to handle. One of the best known is the Dutch-German "Sea Carpet". Plate 6, Fig. 30 demonstrates an application in reclamation work at Europeport, Netherlands. This carpet is a combination of natural reed and woven polypropylene fabric which has a tensile strength of 2 to 10 metric tons per meter. It is claimed that it is unaffected by wet conditions and is very durable, remaining stable against chemical and bacteriological influences. An additive incorporated into the polypropylene gives it high resistance to ultra-violet rays. Its specific gravity of 0.9 enables it to float, while its lasting filtering properties permit the water, but not the sand, to pass through. The reeds assist in the filtering action of the fabric and increase bouyancy enabling it to be towed to the site and protect the fabric against damage from stone used to sink the carpet and keep it in position when it is used as a mattress. Not all synthetic fabrics or impermeable sheets offer adequate protection against ultra-violet light and generally speaking experiences are best when the sheets are not subjected to light but covered with other materials.

For further information on various commercially available brands in the United States and in Europe the reader is referred to articles in Proc. of the recent Coastal Engineering Conferences (Japan, 1966, London, 1968, Washington, 1970) and to commercially available catalogues.

NOTES ON SEA WALLS

1 Wave run-up - An important design parameter for sea walls and revetment is the wave run-up which depends upon spectral characteristics. According to Battjes(35) explicit expressions for the run-up on a smooth slope are obtained for waves of which the heights and periods squared have a bivariate Raleigh distribution. For further information the reader is referred to refs. (11, 35 and 44) and to several papers on this topic in the Proc. from the 11th Conf. on Coastal Engineering, London, 1968, part 2. Furthermore the Proc. from the 10th, 11th and the 12th Conf. on Coastal Engineering include a great number of papers on wave forces on all kinds of coastal structures, fixed as well as floating.

2 The scour problem in front of sea walls is important and has to be considered. Wave height is the most significant variable to the depth of scour (39 and 41). Other important parameters are the position of the wall in the profile, the beach slope, the wave length, characteristics of beach material (41) and longshore current velocities. As the beach slope flattens, scour decreases. Scour decreases as the angle of inclination of the wall decreases, which indicates that scour decreases with decrease of reflection. Each case has to be considered separately. Model studies will be able to give qualitative information on the relative magnitude of scour. A 10 to 20 ft scour (toe) protection is usually necessary.

3 Plate 6 and 7 - Ordinary design criteria for a revetment call for sufficient weight of blocks including interlocking effect to withstand the combined effect of hydrodynamic uplift pressures due to wave breaking, down-rush and hydrostatic pressure which both cause uplift. Normally a filter layer is placed partly to make an even slope and partly to drain water, which will inevitably penetrate through the joints between the blocks. This needless to say, requires a proper "filter ratio" between block layer and filter material. If the filter material is too small it may disappear out through the joints of the blocks and if it is too large this may increase hydrodynamic and hydrostatic pressures with adverse affects on stability. Drain holes may then replace the space between blocks.

Slope should not be steeper than the core material has a stable slope in fully saturated condition apart perhaps from the uppermost less exposed section of the revetment when - as proved by experiments - the weight of blocks is useful for squeezing blocks in the lower part of the slope together. Fill material must be well compacted to minimize settlings. Examples of failures e.g. in Holland and Florida can often be traced back to inadequate compaction e.g. caused by negligence during construction. Revetments of blocks are not used in Holland where wave action exceeds 10 ft. In Florida the limit may be set a little lower due to the predominance of sand fill and less experience in building such walls, which require good workmanship and in addition on exposed shores a protective apron and/or beach in front (38, 40).

Research on revetments for reservoirs carried out in the U.S.S.R. (43), has proven that the stability of a revetment may be improved by reducing thickness of or eliminating the filter layer entirely. The flexibility of the armor layer and the porosity of the underlying soil are important parameters.

Regarding design principles for rubble mound revetments, reference is made to a paper by Johannesson and Bruun (51).

4 Plate 7, Fig. 35 - The "developing countries" have sometimes been wiser than the "developed countries". As an example the Indian standard stone-pitched rock mound used extensively for sea walls particularly at many places along the SW coast (State of Kerala) is an excellent example of long time experience adopted to "what we have and what we can do with available tools". It is startling to see the similarity in several respects between old Dutch and old Indian experience.

5 Plate 5 and 6: Asphalt and bitumous products have been used considerably for breakwaters and revetments under small to moderate wave action (34). In several cases maintenance has presented some problems and in some respects the application of asphalt is still in an experimental stage.

NOTES ON GROINS

1 Layout and geometry - The general experience is that groins should be built perpendicular to shore although some laboratory experiments may have revealed that efficiency increases a little by turning them downdrift e.g. to 70 degrees in case waves approach the beach under 70 degrees. Length/spece ratio may vary according to littoral drift capacity and exposure from 1:1 to 1:4. Streamlining downdrift is often advantageous (6 to 10 degrees tapering off).

2 The design of a groin protection also depends upon the beach material as well as the material available for construction. Unless beach material is coarse (pebble up to shingle) a streamlined design is preferable and the optimal design undoubtedly is the one which is streamlined and energy-absorbing at the same time. The Dutch groins (Plate 3 and 8) with their wide stone pitching fulfil such requirements. The vertical face sheet pile or king pile groins do not, but their function may be greatly improved

by adding roughness on their sides, e.g. in the form of rubble mounds.

One rule should always be obeyed: If groins are nonadjustable they should be low or the beach will be nourished continuously. If groins are high they should be of the adjustable type and be kept adjusted to the actual beach profile, that means they largely should follow its movement. Their function is to decrease beach fluctuations, not to hinder them.

3 The efficiency of and distance between groins may be increased by adding a shore-parallel breakwater at the extreme making a T or L-shaped geometry (Plate 8, Figs. 46 and 47). This appears to be a definite advantage on steep shores but costs increase. Scour may develop at the breakwater ends if groins extend to depth when wave action is more violent.

4 Sand filled tubes of synthetic materials have been tested in Denmark, Holland and Germany. Diameter may be from 2' to 6'. Generally speaking, experience has been rather satisfactory but the tubes are exposed to sabotage and have to be protected against ultra-violet light by special treatment.

5 Please do not use groins unless they are naturally or artificially supplied with adequate quantities of sand fill.

NOTES ON OFFSHORE BREAKWATERS

1 Some offshore breakwaters are shore-connected and some are not. Plate 9, Fig. 48 from Monaco is an example of the former. Many Southern European (Italian and Spanish) offshore breakwaters are not shore-connected. Refs. 49, 50, 53 and 54 advise on design principles and practical design and construction. Ref. 51 is a review of the ressons for failures of rubble mound breakwaters.

2 Submerged breakwaters - submerged sills and training walls are mentioned in the main paper. Ref. 52 is a comprehensive paper on wave mechanic aspects of the function of submerged breakwaters. Some patented devices are also on hand. They all have in common the fact that they suffer from scour problems, and they should never be placed in the breaking zone or where longshore currents are strong.

3 The submerged sand breakwater built at Durban, South Africa, mentioned in the main paper, is an interesting invention which so far has been successful. One of its main advantages is that should it fail as a breakwater its material will function as artificial nourishment. This experiment therefore advocates offshore dumping of sand material in certain cases.

4 Various laboratory and field tests have been run with a special type of shoreparallel protection, namely, artificial seaweed; but the results are inconclusive, although it appears that it may have an application mainly in uni-directional flow (C.F. Wicker, Shore and Beach, Oct. 1966).

NOTES ON ARTIFICIAL NOURISHMENT

1 Suitable sand - It should always be remembered that not all material for artificial nourishment needs to be suitable as beach material. In cases when heavy erosion has taken place, requiring large quantities for replacement, the lower layers may be "fill which may be separated from the upper layer by a sheet of synthetic material.

2 Heavy sand - Tests have been run with heavy sand. Laboratory tests confirm the suitability but the quantities needed makes practical application highly questionable apar from enclosed areas of limited size.

REFERENCES AND BIBLIOCRAPHY

History, Erosion and Coastal Protection Measures of various kind have been listed in separate sections and should be interpreted as characteristic examples of literature.

HISTORY AND LARCE SCALE PLANNINC

1 Van Veen. J., "Dredge, Drain, Reclaim, The Art of a Nation", Martinus Nijhoff, The Hague, 1962.

2 Bakker. W.T. and Joustra, D.Sj., "The History of the Dutch Coast in the last Centuty", Chapter 43 in Proc. of the 12th Coastal Engineering Conference, Washington, 1970. Publisher ASCE, New York.

3 Bruun, P., "Coast Stability", Danish Society of Civ.Engrs.Press, 1954.

4 Department of the Army, Chief of Engineers, "Shore Protection Program", July 1970.

5 Department of the Army, Chief of Engineers, "Shore Protection Cuidelines", Aug.1971.

6 Massachusetts Institute of Technology, "Economic Factors in the Development of a Coastal Zone", 1970.

7 Matthews, E.R., "Coast Erosion and Protection", Charles Criffin and Co., London 1934.

8 Merselis, Wm.B., "The Necessity of local Support in Coastal Zone Planning", Preprints, 7th Annual Conference by the Marine Technology Society, pp. 447-451, 1972.

9 Pickwell, Robert, "The Encroachment of the Sea from Spurn Point to Flamboro Head, and the Works executed to prevent the Loss of Land", Proc.Inst.Civ.Engrs., Paper No. 1.515, 1877/78.

10 Rijksdienst voor het oudheidkundige Bodemonderzoch, "Antiquity and Survival", Vol.II, No. 5-6, The Hague, 1959.

11 Thorn, R.B., "The Design of Sea Defence Walls", Butterworks Scientific Publication, London, 1960.

12 Visser, J.C., "De Noordzeekust van Vlieland", Waterbounkundig Tijdschrift, OTAR, 1953, (Dutch text).

EROSION, SEA LEVEL RISE, NATURES COASTAL PROTECTION

13 Berg, Dennis W., "Systematic Collection of Beach Data", Proc. 11th Conference on Coastal Engineering, London, 1968. Publisher: Am.Soc. of Civ.Engrs.(ASCE), New York.

14 Bruun, P., "Coast Stability", Danish Technical Press, 1954.

15 ___ "Sea Level Rise as a Cause of Shore Erosion", Proc. ASCE, Journal Waterways and Harbors Division, 1962, No. WW1, pp. 117-130.

16 ___ "Coastal Protection Procedures", Engineering Progress at the University of Florida, Vol. XVIII, No. 12, 1964.

17 Coldsmith, V. and Colonell, J.M., "Effects on Nonuniform Wave Energy in the Littoral Zone", Chapter 47 in Proc. of the 12th Conference on Coastal Engineering, Washington, D.C., 1970.

18 Harrison, W. and Krumbein, W.C., "Interaction of the Beach-Ocean-Atmosphere System at Virginia Beach, Va.", U.S. Army CERC,, Tech. Memo No. 7, 1964.

19 Hicks, S.D. and Shofnos, Wm., "Yearly Sea Level Variations for the United States", Proc. ASCE, Journal of the Hydraulics Division, 1965, No. HY5, pp. 23-32.

20 ___ "Sea Level - A changing Reference in Surveying and Mapping", Surveying and Mapping, Vol. XXVIII, 1968, No. 2, pp. 285-289.

21 King, C.A.M., "Beaches and Coast", Edward Arnold, Ltd., London, 1959.

22 McAleer, John B., "The State of the Shorelines", Shore and Beach, April, 1971.

23 Nichols, M.M., "Coastal Processes from Space Photography", Chapter 39 in Proc. of the 12th Conference on Coastal Engineering, Washington, D.C., 1970, Publisher ASCE, New York.

24 Steers, J.A., "A Picture Book of the whole Coast of England and Wales", Cambridge University Press, London, 1947.

DUNES AND DIKES

25 Bruun, P., "Withdrawn Dykes and Preservation Lines", Shore and Beach, Oct. 1964 and "Coastal Protection Procedures", Engineering Progress at the University of Florida, Vol. XVIII No. 12, 1964.

26 Davis, John H., "Dune Formation and Stabilization by Vegetation and Plantings", Tech. Memo No. 101, Beach Erosion Board, Office of the Chief of Engineers, USCE, 1957.

27 Kidson, C. and Carr, A.P., "Dune Reclamation at Braunton Burrows, Devon", The Chartered Surveyer, Dec. 1960, London.

28 Manohar, M. and Bruun, P., "Mechanics of Dune Growth by Sand Fences", The Dock and Harbour Authority, Vol. L1, No. 600, 1970.

29 Myers, James B., "The Cape Hatteras Mechanical Transplanter", Newsletter of the American Shore and Beach Preservation Association, May, 1964.

30 Nash, E., "Beach and Sand Dune Erosion Control at Cape Hatteras National Seashore", Paper presented for the National Park Service, Dept. of the Interior at the 36th Meeting of the American Shore and Beach Preservation Association, Nags Head, N.C.

31 Wiersma, A.G., "Turfing on Sea Walls", Inst. of Civ.Engrs., Vol.15, 1960, pp.273-277

32 Woodhouse, W.W. and Hanes, R.E., "Dune Stabilization with Vegetaion on the Outer Banks of North Carolina", Tech. Memo No. 22, CERC, U.S. Army Corps of Engineers, 1967.

33 Work Croup on Dike Vegetation, "Grasmart op Dijken", Kononklijk Instituut van Ingenieurs afdeling voor Bouw - en Waterbouwkunde and Koninklijk Cenootschap voor Landbouwvetenschappen, 1958 (Dutch text).

SEA WALLS, REVETMENTS

34 d'Angremond, K. et al., "Use of Asphalt in Breakwater Construction", Chapter 98 in Proc. 12th Conference on Coastal Engineering, 1970. Publisher ASCE, New York.

35 Battjes, J.A., "Run-up Distributions of Waves breaking on Slopes", Proc. ASCE, Journal of the Waterways, Harbors and Coastal Engineering Division, Vol. 97, 1971, No. WW1, pp. 91-114.

36 Deltadienst, Den Haag, Holland, "Driemaandelijks Bericht", No. 58, 1971, Section: De boden bescherming van een sluitgat, pp. 413-418 (Dutch text).

37 Bruun, P., "Breakwaters for Coastal Protection", Proc. of the XVIII International Navigation Congress, 1953, S11-Q1.

38 ___and Manohar, M., "Coastal Protection for Florida", Bulletin, Progress at the University of Florida, Vol. XVII, No. 8, 1963.

39 Chesnutt, C.B. and Schiller, R.E., "Scour of Simulated Gulf Coast Sand Beaches due to Wave Action in Front of Sea Walls and Dune Barriers", Texas A and M, C.O.E. Report No. 139, 1971.

40 Cerritsen, F. and Bruun, P., "Dutch and Florida Practices on Revetment Design", Proc. IXth Conference on Coastal Engineering, Lisbon, 1964, Publisher ASCE, New York.

41 Herbich, John B. and Ko, Stephen C., "Scour of Sand Beaches in Front of Sea Walls", Chapter 40 of Proc. of the 11th Conf. on Coastal Engineering, 1968, Publisher ASCE, New York.

42 Kramer, Johann, "Design Criteria for North Sea Dikes", Proc. ASCE, Journal Waterways, Harbors and Coastal Engineering Division, Vol. 97, 1971, No. WW4, pp. 703-719.

43 Molero, F., "Protection against Wave Action based on Hydrodynamic Effect", Chapter 53 in Proc. of the 12th Internat Conference on Coastal Engineering, 1970, Publisher ASCE, New York.

44 Technische Adviescommissie voor de Waterkeringen, "Colfoploop en Colfoverslag", Deel II, Oploop van Regelonatige Colven, 1970, Holland (Dutch text).

45 Abstracts of Papers, Vancouver Conference, Papers A-36 to A-44.

CROINS

46 Reference is made to "An Annotated Bibliography" by J.H. Balsillie and R.O. Bruno, Miscellaneous Paper No. 1-72, April 1972, by the U.S. Army Corps of Engineers, Coastal Engineering Research Center with comprehensive review of all aspects pertaining to groins, their function design and the experience gained up to date. This publication was distributed at the Vancouver Conference. References are therefore left out in this paper due to space limitations.

47 "Croynes-Documentation" has been published by Rijkswaterstaat-Directie Waterhuishouding en Waterbeweging, Afdeling Kustonderzoek, Netherlands, 1968.

48 Abstracts of Papers, Vancouver Conference, Papers T-26 to T-28.

BREAKWATERS FOR COASTAL PROTECTION

49 Calvin, Cyril, "Breaker Travel and Choice of Design Wave Height", ASCE, Journal of the Waterways and Harbors Division, Vol. 95, WW2, 1969, pp. 175-200.

50 Hudson, R.Y., "Laboratory Investigations of Rubble Mound Breakwaters", Trans. ASCE, 1961, Vol. 126, Part IV.

51 Johannesson, Palmi and Bruun, P., "Hydraulic Performance of Rubble Mound Breakwaters. Reasons for Failure", Proc. of the First International Conference on Port and Ocean Engineering under Arctic Conditions, Trondheim, Aug. 1971, pp. 326-359.

52 Nakamura, M., Shiraishi, H. and Sasaki, Y., "Wave Damping Effect of Submerged Dike", Chapter 17 of Proc. of the 10th Conference on Coastal Engineering, Tokyo, 1966. Publisher ASCE, New York.

53 Permanent International Association of Navigation Congresses, Brussels, SII-Q1, see also: "New Designs of Breakwaters with vertical Sides and of Structures with sloping Faces", SII-S1, 1965.

54 U.S. Army Corps of Engineers, CERC, "Coastal Protection, Planning and Design", Tech. Report No. 4, 1961 and 1966.

55 Zwamborn, J.A., Fromme, C.A.W. and Fitz Patrick, J.B., "Underwater Mound for the Protection of Durban Beaches", Chapter 62, Proc. 12th Conference on Coastal Engineering, Washington, D.C., 1970, Publisher ASCE, New York.

ARTIFICIAL NOURISHMENT, BYPASSINC, BACKPASSING

56 Anonymous, "New Dutch Dredging Systems", World Dredging and Marine Construction, Jan. 1972, pp. 20-26.

57 Berg, Dennis W. and Duane, David B., "Effect on Particle Size and Distribution on Stability of artificially filled Beach, Presque Isle Peninsula, Pa", Proc. 11th Conference Great Lakes Res., 1968, pp. 161-178, International Assoc. Great Lakes Research.

58 Bruun, P. and Purpura, J.A., "Emergency Measures to combat Beach Erosion", Engineering Progress at the University of Florida, Vol. XVII, No. 6, 1963.

59 ___ "Bypassing and Backpassing with Reference to Florida", Proc. ASCE, Journal of the Waterways and Harbor Division, Vol. 93, WW2, 1967, pp. 101-128. See also: "Offshore Dredging, Influence on Beach and Bottom Stability", The Dock and Harbour Authority, Vol. XLV, No. 530, 1964.

60 ___ "Tidal Inlets and Littoral Drift", University Book Company, Oslo, Norway, 1966, 220 pp.

61 Duane, D.B., "Sand Inventory Program", Shore and Beach, Oct. 1969.

62 IHC, Holland, "14 million cubic metres of Sand for a new Beach", Ports and Dredging, No. 74, 1972.

63 Inman, D.L. and Harris, R.W., "Crater-sink Sand Transfer System", Chapter 58, Proc. 12th Conference on Coastal Engineering, Washington, D.C., 1970, Publisher ASCE, New York.

64 Krumbein, W.C., "A Method for Specification of Sand for Beach Fills", Techn. Memo No. 102, Beach Erosion Board, Office of the Chief of Engineers, USCE, 1957.

65 Magnuson, Nils C., "Planning and Design of a Low-weir Section Jetty", Proc. ASCE,

Journal Waterways and Harbors Division, WW2, 1967, pp. 27-40.

66 Mardesich, John A., "The Design and Construction of an Underwater Dredge", Society of Automotive Engineers, Earthmoving Industry Conference, Central Illinois Section, Peoria, Ill, 1971.

67 Mauriello, Louis J., "Rehabilitation of Beaches with Hopper Dredges", Shore and Beach, Oct. 1966, and Proc. ASCE, Journal Waterways and Harbors Division No.WW2, 1968.

68 Texas, A. and M., "Dredging Seminar", Part 1, Ocean Industry Digest, Oct. 1971.

69 Natures constructive work dealt with by many authors, e.g. by Zenkovich, V.P., "Coastal Morphology", USSR Academy of Sciences, 1962.

70 Abstracts of Papers, Vancouver Conference, Papers T-30 to T-35.

CHAPTER 1

COASTAL ENGINEERING MEASUREMENTS

by
J.A. Zwamborn* K.S. Russell** J. Nicholson**

ABSTRACT

Research during the past ten years into coastal problems around the coasts of South Africa has resulted in the development of measuring instruments and techniques which, although specifically designed for conditions around these coasts, could possibly be used equally well in other areas.

This paper deals specifically with measuring instruments and techniques used for collecting data on offshore and nearshore currents, wave conditions and beach profiles extending through the surf zone. Also included are examples of the data collected and some discussion on the accuracy of these data.

INTRODUCTION

Proper design of coastal structures, commercial harbours, marinas, single buoy mooring systems, offshore ore loading facilities, coastal development works, reclamation schemes, coastal protection works, submarine outfalls for effluent disposal and anti-shark protection works should be based on reliable coastal engineering data. These data should be collected over a period of time of sufficient length to include all the significant changes taking place in the coastal environment concerned. For example (see Figure 1) an intensive programme of field measurements

Fig. 1 Richards Bay field measurements

*Head, Hydraulics Research Unit, South African Council for Scientific and Industrial Research, Stellenbosch.
**Chief Research Officer, Hydraulics Research Unit.

lasting more than three years was carried out prior to the development of Richards Bay, which is situated 160 km north of Durban on South Africa's east coast, as a major port for bulk export of coking coal.

This programme included the following measurements

(a) On a continuous or regular basis

- Recording of wave heights, periods and directions
- Deep sea and nearshore current measurements
- Wind recordings
- Tidal recordings in the sea and in the estuary
- Sand tracer tests in the littoral zone and in deeper water (up to 18 m)
- Water temperature and salinity measurements in the sea and in the Bay
- Flood and suspended solid records in the Umhlatuzi river which discharges into the Bay

(b) Every three months (at the end of each season)

- Beach survey extending through the breaker zone
- Offshore depth soundings
- Depth soundings of the estuary area
- Aerial photographs of the estuary mouth
- Beach sediment survey

(c) Once per year

- Sedimentological survey of the sea bottom
- Sub-bottom survey of the nearshore area
- Depth survey of the Bay

Similar field programmes were executed or are still in progress for several other harbour and beach improvement schemes on the coast of Southern Africa.

Measurements of sea and sea-bottom conditions, particularly in the breaker zone, are extremely difficult and in several instances new techniques had to be developed in order to complete the planned data collection programmes.

A brief description is given of the measuring techniques used for the collection of coastal engineering data with particular reference to the techniques developed in South Africa. Typical results of the collected data and discussions on the reliability of the data are also included.

MEASUREMENT OF CURRENT VELOCITIES AND DIRECTIONS

Reliable data on currents are required for various applications such as sediment transport calculations, effluent dispersion studies, determination of current effects on ship movements and model investigations into the effect of structures on current patterns. Various techniques for the determination of nearshore and offshore surface and bottom currents have been used with varying degrees of success. Some of these techniques were developed in the Hydraulics Research Unit of the South African Council for Scientific and Industrial Research to meet particular circumstances.

Dye techniques for current measurements

Breaker zone current directions and velocities can be determined by timing the longshore movement of small fluorescent dye floats (such as a tennis ball filled with dye). The tests, when undertaken daily over an extended period, give a good indication of the predominant current direction and the range of velocities.

Fluorescent dye is also very effective for *nearshore circulation* studies including rip currents. The movement of a dye patch resulting from ½ kg fluorescent dye is plainly visible and can be recorded photographically from aircraft or from a high vantage point on the shore. The nearshore circulation patterns can also be observed by aerial photography of estuarine silt discharges.

To improve the accuracy of dye tracking especially in the *offshore zone*, a so-called dye bomb technique was developed[1]. A dye 'bomb' consists of a weighted canister preferably with fins to ensure vertical entry into the water. A bag containing a float and fluorescene dye is packed into the bottom of the canister and attached to the canister by a thin nylon cord while the upper section of the canister contains a bag of Rhodamine dye also attached to a small float to which a collapsible (cloth) drogue is connected by a thin cable (see Figure 2).

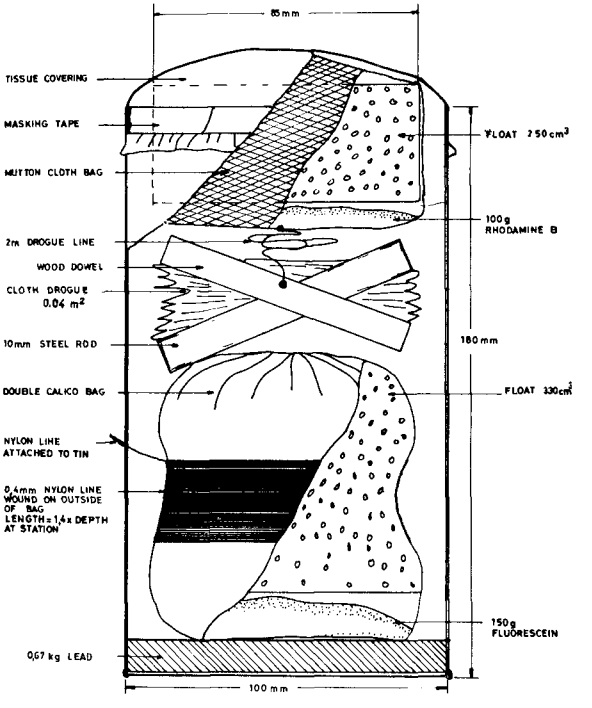

Fig. 2. Dye 'bomb'

The length of this cable depends on the depth at which the current is to be measured. On entering the water, the canister sinks to the bottom, but the bag of Rhodamine dye comes to the surface immediately and with the attached drogue begins to drift under the influence of the current. The deposition point is marked by the fluorescene dye leaking from the bag attached to the canister. In practice a series of 'bombs' and their movement are photographically recorded from an aircraft. Current direction and speed can be estimated from the relative positions of the two dye patches, provided the aircraft course and altitude are recorded (see Figure 3).

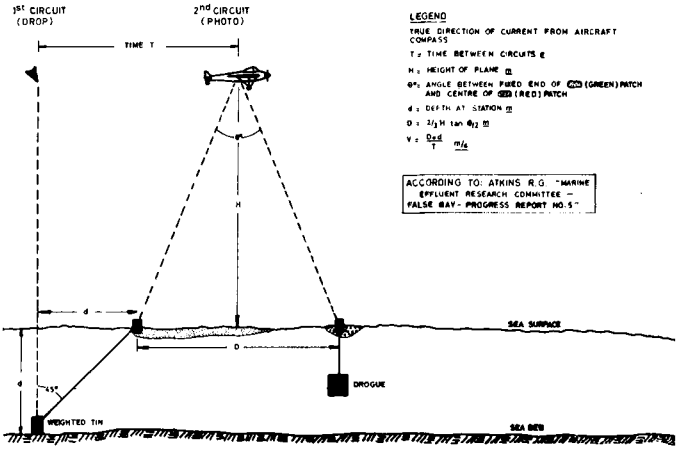

Fig. 3. Dye 'bomb' drop principle

Floats and current meters

To obtain information on the general pattern of *sea currents*, drogue floats consisting of a brightly coloured float to which a cloth drogue is attached at the required depth are used (see Figure 4)[2].

Again a series of drogue floats are released at various points from a boat or from the air and their movements are tracked either photographically from the air or by shore instruments.

In most cases sea current data are required on a regular basis. For measuring current directions and velocities near the sea bottom (e.g. 2 m above the sea bottom) extensive use is made of self-contained Kiel Hassee propeller current meters which are anchored in a fixed position. These current meters, which are not described in detail in this paper, photographically record current directions and velocities.

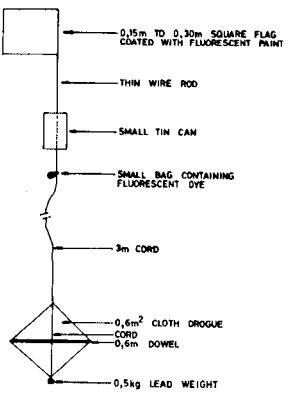

Fig. 4. Drogue float

Current measurements using a system of moored buoys

A simple method was developed to obtain near surface current directions and velocities from observations of the movements of a system of three moored buoys using binoculars specially adapted for the purpose. As can be seen from Figure 5 the system consists of an anchored buoy A connected by means of a nylon rope to a second buoy B, the so-called directional buoy. Buoy B is in turn connected to a third buoy C, the so-called velocity buoy, by means of a chain to which a weight is attached halfway along its length. A drogue is suspended below buoy C at the depth where the current is to be measured.

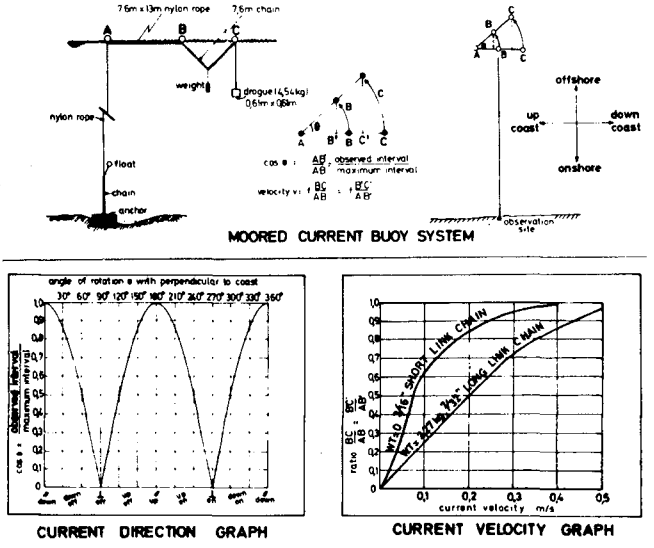

Fig. 5. Moored current buoy system and current direction and velocity graphs.

The *direction* of the current at the buoy system is determined from the distance between the anchored buoy A and the "directional" buoy B. The binoculars used in the readings are fitted with a graticule on which are inscribed a series of equally spaced vertical lines and the distance between buoys A and B is expressed in terms of the number of graticule divisions observed between the buoys. When the line of the buoys is at right angles to the sighting line the greatest number of graticule divisions will obviously be observed between buoys A and B. This maximum reading depends on the distance between the observer and the buoys and the magnification of the binoculars. When the buoys swing through an angle θ, say, as shown in Figure 5 and line themselves up parallel to the direction of the current, the apparent distance between the buoys becomes AB' and θ is given by

$$\text{Cos } \theta = \frac{AB'}{AB}$$

Curves are plotted of cos θ versus θ as shown in Figure 5. As the observer must also indicate whether the current direction is upcoast or downcoast and onshore or offshore the current direction can easily be determined if the bearing of the line of sight is known.

The current *velocity* at the buoy system is determined from the ratio of the distances between adjacent buoys. As the drag force on the drogue attached to the "velocity" buoy C depends on the velocity of the current, the greater the current velocity, the greater the distance between buoys B and C. The current velocity, V, is therefore given by the relationship:

$$V = f\left(\frac{\text{distance BC}}{\text{distance AB}}\right) = f\left(\frac{\text{observed distance B'C'}}{\text{observed distance AB'}}\right) \quad \text{(see Figure 5)}$$

where f indicates "function of".

Various systems were calibrated, both in the field and in the laboratory, from which curves giving the relationship between the ratio B'C'/AB' and current velocity are obtained. Typical calibration curves are included in Figure 5 from which actual sea current velocities can be determined from the binocular readings.

Since moored current buoy systems are inexpensive, easy to place in the sea (by ski-boat) and to maintain, extensive use is made of this system for measuring near surface (usually at 3 m from the surface) sea currents along the coast of South Africa. Once an observer is available, who can make measurements at regular intervals (usually three times daily) it is often worthwhile to place a number of current buoy systems at different distances offshore.

The *readings* of the moored current buoys are summarised both on a seasonal and a yearly basis and are presented in the form of current roses. A typical example for Richards Bay is given in Figure 6.

To illustrate the resolution and *accuracy* which can be achieved when using a moored buoy system, the layout at Richards Bay is again taken as an example. At this location three buoy systems were placed 600 m, 1200 m and 2400 m offshore, the corresponding maximum distances between buoys A and B, i.e. AB, as measured by the graticule of the binoculars, being 2,0, 1,0 and 0,5 divisions respectively. The accuracy of reading is 0,1 graticule divisions.

For the purpose of investigating the accuracy of the *current direction* measurements derived from the buoy systems consider the system moored a distance 600 m offshore. Assume that

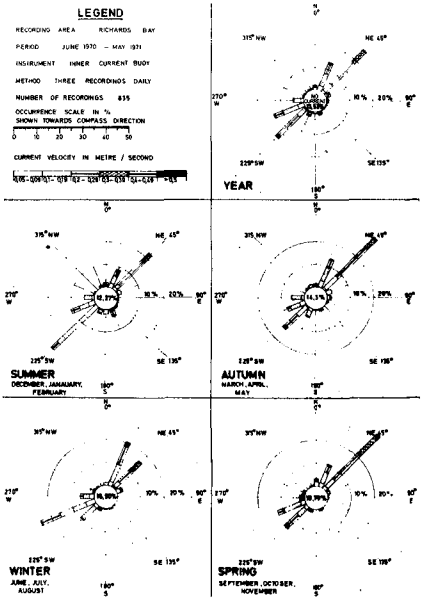

Fig. 6. Example of current roses

the current is such that the buoys are aligned in a downcoast, offshore, direction (see Figure 5) and AB' is say 0,35 thus AB'/AB = 0,175. The value of θ can then be read off from the current direction graph in Figure 5 as about 80°. As can be discerned from this graph an error of $\pm 1{,}5^{\circ}$ would have been made if the reading had been taken as 0,3 (AB'/AB = 0,15, $\theta = 81{,}5^{\circ}$) or 0,4 (AB'/AB = 0,20, $\theta = 78{,}5^{\circ}$) instead of 0,35 (AB'/AB = 0,175, $\theta = 80^{\circ}$). However, if readings of 1,9 (AB'/AB = 0,95, $\theta = 18^{\circ}$) or 2,0 (AB'/AB = 1,0, $\theta = 0^{\circ}$) had been observed instead of 1,95 (AB'/AB = 0,975, $\theta = 13^{\circ}$), when the buoy system is virtually perpendicular to the line of sight, larger errors would have been incurred, viz. $+5^{\circ}$ or -13° respectively.

For the buoy systems 1 200 m and 2400 m offshore, the possible errors are much greater. This is because the graticule readings can still only be made to the nearest 0,1 division and hence the possible errors for the 1200 m offshore system are twice and those for the 2400 m offshore system four times the above values.

From the above it is clear that the greatest accuracy as regards current direction measurements is achieved when (i) the distance between the mooring point and observation sight is not excessive and (ii) when cos θ is less than approximately 0,9 or, in other words, when θ is greater than about 25°.

As regards the *current velocity* measurements derived from the moored buoy systems the readings are most accurate when the buoy intervals AB' and B'C' (see Figure 5) are both large. Thus the buoy system generally becomes more accurate when moored comparatively close to the shore and cos θ exceeds 0,10, say, which corresponds to a value of θ less than 85°. Under these conditions the accuracy of the current velocity readings is estimated to be about 25%.

It can, therefore, be stated that the moored current buoy system provides an inexpensive, simple and effective method of determining current directions and velocities provided the above limitations of the system are taken into account. The accuracy of reading generally reduces proportionally to the distance offshore, and direction errors are minimal when the angle between the line of buoys and the perpendicular to the line of sight, θ, is greater than 25° and the velocity errors are minimal when θ is less than 85°.

Other factors which influence the accuracy and reliability of this method of measuring current directions and velocities are:

(a) the difficulty of distinguishing whether the current is onshore or offshore - particularly with increasing distance between the buoys and the observation point;

(b) the possibility of the anchor dragging makes it necessary to make constant checks on the bearing of the buoy system;

(c) the effect of wind was investigated and although its influence was found to be complex the resulting errors were found to be within the limits of accuracy accredited to the system;

(d) tangling of the chain connecting the "direction" and "velocity" buoys can occur, but experienced observers soon become aware of such an eventuality having arisen.

The accuracy of the current buoy systems as used at present could be further improved by increasing the distance between the buoys and by using binoculars with a higher magnification. These improvements should be considered if the distance between the buoys and the observer considerably exceeds 1 km.

RECORDING OF WAVE CONDITIONS

In most cases, reliable data on wave conditions are even more important than those on currents. Wave conditions have been recorded along the coastline of Southern Africa for many years, in particular since 1967, when the Ocean Wave Research Programme was launched and recording stations were established along the entire coast[3]. Various instruments are used for the wave recording programme including:

(i) Wave clinometers (visual measurement),
(ii) INES (Inverted Echo Sounder) wave recorders,
(iii) Ospos wave recorders (pressure type),
(iv) Wave riders (accelerometer) and
(v) NIO shipborne recorders.

The Wave clinometer and the INES wave recorder were developed in the Hydraulics Research Unit and are discussed in some detail in the following paragraphs.

Wave Clinometer

The wave clinometer was developed as a simple instrument which could be operated by non-technical personnel in remote and undeveloped coastal areas for recording wave conditions. Basically it is an instrument for measuring wave directions although it can also be used to give approximate wave height and period values. It is being used extensively in the wave climate studies along the South African coastline.

The instrument consists of a specially adapted hunting telescope mounted on a stand in such a way that its axis can be depressed relative to the horizontal at one of three fixed angles, namely 3^{o}, 5^{o} or $7\frac{1}{2}^{o}$ (see Figure 7). It is installed on an elevated position onshore at a

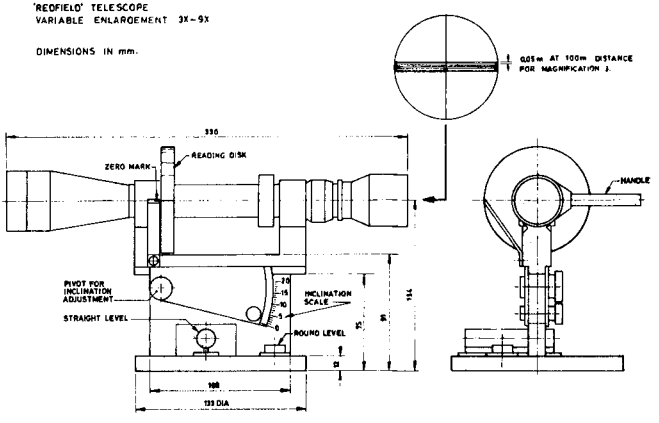

Fig. 7. Wave clinometer assembly

fixed compass direction and the angle of depression of the telescope fixed at one of these angles so that it can be focussed on the observation point at sea where a buoy (0,5 m dia. polyform buoy) is anchored. The general arrangement is shown in Figure 8.

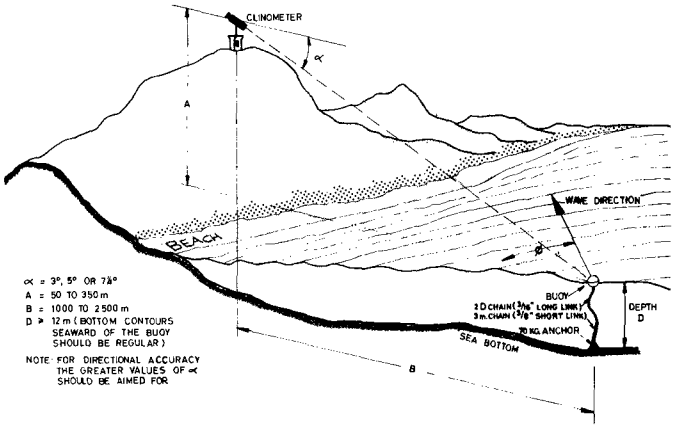

Fig. 8. Typical clinometer and clinometer buoy layout

For *wave direction* measurements the clinometer telescope is equipped with a graticule consisting of a metal ring which supports a series of equally spaced lateral cross hairs. The wave direction is measured by rotating the telescope about its optical axis until the cross hairs are aligned with the wave crests, the angle of rotation from the horizontal position, Θ, being read off on a graduated disc mounted on the telescope. The angle ϕ between the direction of wave approach and the fixed bearing of the instrument is related to the angle of rotation Θ by the following formula:

$$\tan \Theta = \sin \alpha . \tan \phi$$

where α is the angle of depression of the clinometer. The graduated disc fitted to the barrel of the telescope can thus be scribed to indicate directly the angle of wave approach for any angle of depression.

The *wave height* is measured by observing the movements of the buoy relative to the graduations on the clinometer telescope graticule, the buoy movements being observed over a period of about five minutes in order to obtain an average reading. The graticule graduations in the instruments at present in use are so spaced that one division is equivalent to 0,05 m of wave height for every 100 m of distance between the instrument and the buoy, the telescope having a magnification of x3. The standard graticule contains seven graduations. It is not possible to increase the number of graduations without obscuring the field of view and thereby adversely affecting the wave direction observations. If no direct correlation with instrument recorded wave heights is available, the wave heights recorded with the wave clinometer may be assumed to be equal to the significant wave height, H_s.

The *wave periods* are also determined with the aid of the graticule graduations by noting the time taken for twenty wave crests to pass the buoy, the dominant wave period being the value recorded.

Wave clinometer *recordings* are normally made three times daily - early morning, mid-day and early evening. The records are combined to give seasonal and yearly distributions and typical examples of direction/height and direction/period roses for Richards Bay are illustrated in Figures 9 and 10. Wave clinometer records are usually made in relatively shallow water. Using well-known refraction theory these records can, however, be converted to deep sea wave conditions which are applicable to a much larger area of the coast.

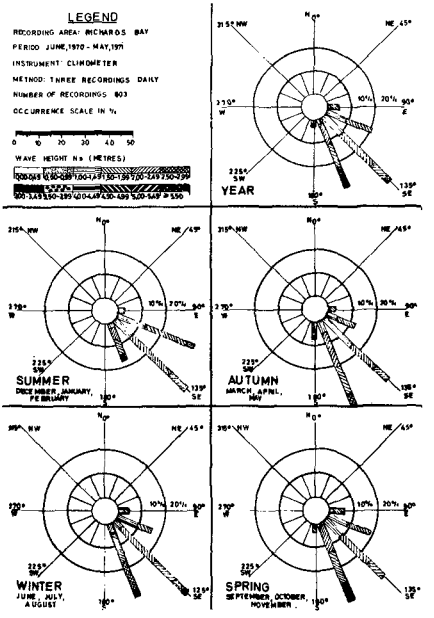

Fig. 9. Typical clinometer wave height roses

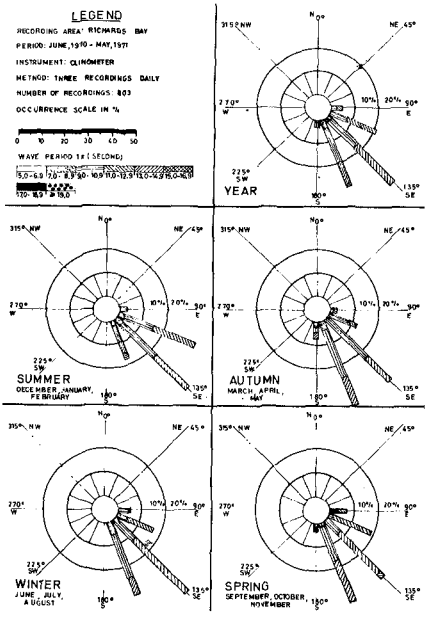

Fig. 10. Typical clinometer wave period roses

The *directional accuracy* of the wave clinometer is primarily dependent on the angle of depression of the instrument. As the angle of depression, α, increases the corresponding values for the angle of rotation of the telescope, θ, for given directions of wave approach, $\emptyset$, become more evenly distributed around the perimeter of the measuring disc. This can be seen from Table I below which is based on the relationship $\tan \theta = \sin \alpha . \tan \emptyset$.

Table I : Angular rotation of the clinometer telescope as a function of direction of wave approach

ø	Values of θ		
	α = 3°	α = 5°	α = 7½°
10°	00° 32'	00° 53'	01° 19'
20°	01 06	01 49	02 43
30°	01 44	02 53	04 19
40°	02 30	04 11	06 15
50°	03 34	05 56	08 50
60°	05 11	08 35	12 44
70°	08 11	13 29	19 43
80°	16 32	26 19	36 30
90°	90 00	90 00	90 00

The instrument is normally positioned so that its line of sight makes an angle of about 45° to the dominant wave direction in order to ensure that the majority of the readings occur in that area of the measuring disc where the graduations are spaced relatively far apart. However, it is usually desirable to record the wave direction in comparatively deep water, a requirement that leads to an instrument bearing which is often nearly parallel to the dominant wave direction. In addition the angle of depression of the telescope tends to be small under these circumstances. The values ultimately chosen for these two variables are therefore a compromise between accuracy and the need to obtain wave data in comparatively deep water.

The *accuracy of wave height* measurements depends mainly on the distance between the instrument and the reference buoy, the magnification of the telescope and the size of the graticule divisions. For a telescope with a magnification of x3, a graticule division calibration factor of 0,05 m per 100 m and with the distance from the reference buoy being 1500 m, each graticule division represents a wave height of 0,75 m. Thus by estimating to the nearest half division the wave height can be read off to the nearest 0,4 m approximately. The ability to estimate to the nearest half division is influenced by the size of the buoy which, if large relative to the size of the graticule divisions, makes observations more difficult. In general it has been found that the most satisfactory arrangement is for the buoy and graticule divisions to be of the same size.

Due to the fact that the instrument is clamped in a fixed position, under certain tidal conditions the buoy may not be in the centre of the field of view. Thus for very large waves the image of the buoy may move beyond the extreme graticule divisions and the wave height reading has to be estimated. The accuracy of the instrument is therefore reduced under these conditions.

It is not possible to arrive at quantitative conclusions regarding the *accuracy of the wave periods* measured with the clinometer. Under regular swell conditions there is no reason to doubt the reliability of

the results. Under choppy local "sea" conditions, however, the measured periods may tend to be too high because the shortest waves in the spectrum create small movements of the buoy which may not be noticed by the observer.

It can therefore be *concluded* that individual wave height and period data derived from a clinometer have a limited degree of accuracy. For this reason it is of little use when isolated wave measurements are required but its value has already been proved in the field when information is required on a regular basis extending over a recording period of a year or more.

Suggested *improvements* to the wave clinometer envisage the addition of a second and separate telescope which would be used to measure the wave heights and periods while the existing instrument would be used to measure the wave directions. The advantage of this arrangement is that the latter could then be fitted with a graticule containing one horizontal cross hair only thus leaving a large unobstructed field of view for the observations. A further possible improvement is to increase the diameter of the circular measuring disc mounted on the barrel of the telescope. This modification would increase the space between the graduations and enable the wave direction to be estimated more precisely. The second telescope, on the other hand, would have a magnification of x6 or x9. One graticule division would then correspond to wave heights of 0,025 m and 0,017 m per 100 m respectively. Thus if the distance between the instrument and the buoy is 1500 m and the observer can gauge the wave heights to the nearest half division wave heights could be estimated to the nearest 0,2 m and 0,1 m respectively as against 0,4 for the present instrument. In addition the number of graticule divisions could be increased from seven to about twenty making it unlikely that the image of the buoy would move off the scale under extreme tide and wave conditions.

INES wave recorder

The INverted Echo Sounder or INES* wave recorder is an acoustic type recorder developed by the Hydraulics Research Unit. A photograph of an INES wave recorder is given in Figure 11. It is a self-contained instrument consisting of a conventional echo sounder which is converted to carry a large supply of recording paper. It has a rechargeable battery with an operational life of four weeks and a control mechanism with a clock which can be set to operate the instrument at

Fig. 11. INES wave recorder

*INES recorders are now commercially available

any pre-set time interval. The instrument is enclosed in a fibre-glass canister which is light, strong and resistant to corrosion. The canister is placed on the sea bed in a metal tripod to which a marker buoy is attached. A transducer is fitted on the lid of the canister and the acoustic waves are reflected from the air-water interface giving a continuous record of the sea surface. For wave recording, the instrument is generally set to operate for 15 minuts every 6 hours. The INES recorder can be used in water up to 30 m deep.

The INES wave recorder including its tripod can be lowered onto and raised from the seabed if a sufficiently large boat with lifting tackle is available (e.g. a fishing boat). Alternatively the recorder can be removed from the tripod and a replacement fitted by skindivers operating from a small ski-boat. In theory the instrument need only be serviced every twenty eight days, but in practice it has been found to give a much higher percentage coverage if serviced at fourteen day intervals. To ensure recovery the master buoy must be anchored in such a way that the chance of losing this buoy is minimal. The anchoring system shown in Figure 12 has proved to be the best for prevailing South African sea conditions.

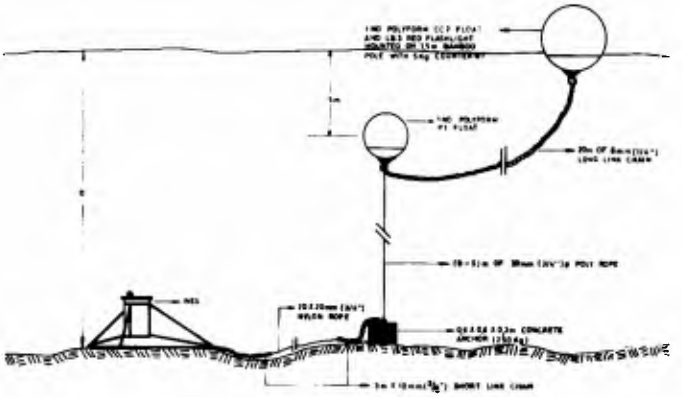

Fig. 12. INES anchoring system

A short length of a typical *wave record* obtained with an INES recorder is given in Figure 13.

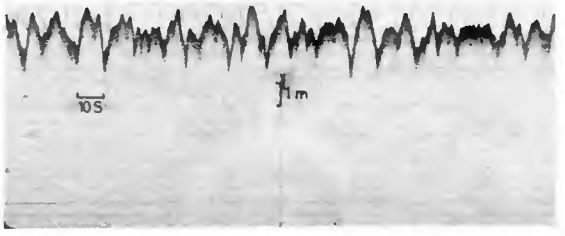

INSTRUMENT NO. W.2.
LOCATION RICHARDS BAY
PERIOD 18 00 hrs. 15th APRIL 1970

Fig. 13. Typical INES wave record

The records are analysed by the standard Draper method[4] and the results are plotted in the form of wave height and period occurrence tables and combined into exceedance curves for significant wave heights and zero crossing periods. An example of a wave height exceedance curve is given in Figure 14.

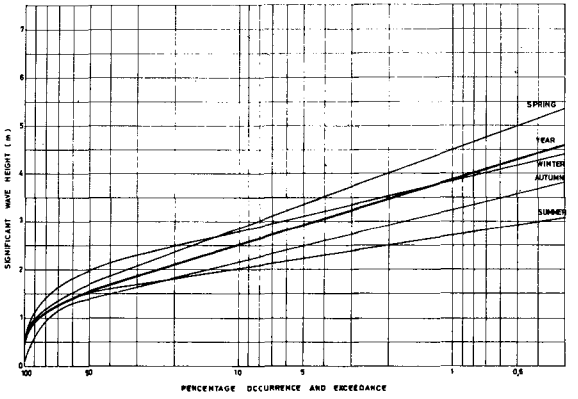

Fig. 14. Typical INES wave height exceedance curve

The *accuracy* of the INES recorder is affected by changes in the temperature and salinity of the sea water, the precision of the timing clock and the divergence of the acoustic beam.

The extreme water temperature and salinity conditions experienced at one fixed recording station may produce inaccuracies exceeding 5 per cent. It is therefore advisable to check the calibration of the instrument every three months if it is used at one fixed location, or every time it is moved to a new position where the salinity or temperature conditions are considerably different.

Inaccuracies in the timing clock are extremely unlikely to be so large as to affect an individual 15 minute wave record. However, during a monitoring period of fourteen or twenty eight days the accumulated error of a slow or fast running clock may result in the waves being recorded at the wrong time of the day.

The accuracy of the INES is also affected by the divergence of the acoustic beam, the beam divergence of a standard instrument being 20^{o}. The fact that a circular area of the sea surface is surveyed instead of a point causes distortion of the ascending and descending slopes of the waves as well as a flattening effect on their crests. The resulting error has yet to be quantified but it is most pronounced when the waves are steep. Fortunately the majority of the wave records are unlikely to be seriously affected because the ratio of the beam width at the water surface to the wave length is small. For example the beam width is only 7 per cent of the wave length for an INES placed in 20 m of water recording waves with a period of 8 s.

Bearing in mind the above limitations it is *concluded* that the INES recorder can be used effectively for measuring coastal wave conditions. A further improvement to this instrument would be to record the output

on magnetic tape instead of in the form of a graph. Consideration is at present being given to this possibility.

Correlation of wave recordings of various instruments

In an attempt to check on the overall accuracy of the various wave recording instruments a comparison has been made of their outputs. Comparisons of wave height and period values as well as energy spectra obtained from simultaneous records of five different instruments were included in an earlier paper[3]. The results were found to be in general agreement although significant differences in individual values of certain parameters were found to occur.

In a further comparison between different recording instruments, an INES *recorder* and a *waverider buoy* operated simultaneously for three months in virtually the same position (100 m apart), 1,6 km offshore in a water depth of 17,5 m at Richards Bay (see Figure 15).

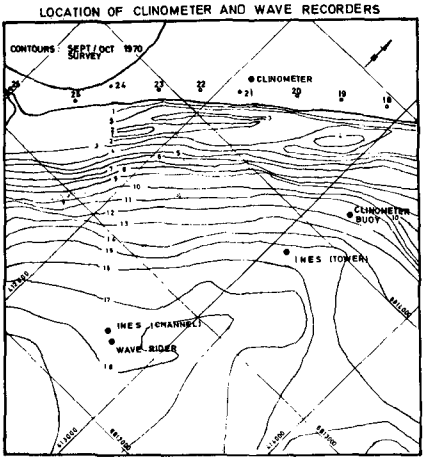

Fig. 15. Instrument positions

In Figure 16 the results of the two instruments are compared by correlating their respective significant wave heights and zero crossing periods, as given by the standard Draper method of analysis[4]. Although a good correlation is evident there are values which exhibit a poor measure of agreement. For small wave heights (up to 1 m) the waverider gives slightly smaller values than the INES, whereas for wave heights in excess of 1 m the waverider values are somewhat greater than those of the INES. The wave period correlation shows much greater differences for the two instruments. Again the waverider periods are shorter in the lower ranges (below 7s) and larger in the higher ranges (above 7s). However, it is clear from these correlations that the INES and waverider outputs on average compare well although in individual cases they can differ by more than 50 per cent.

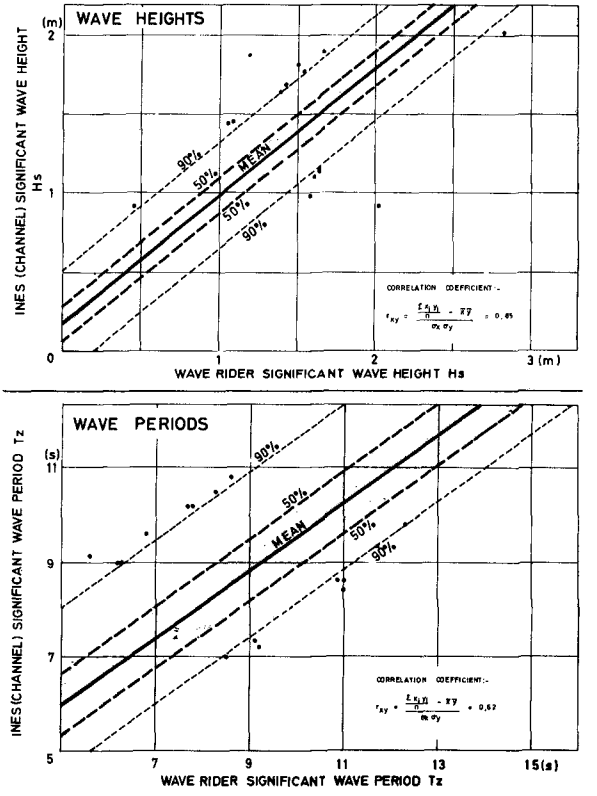

Fig. 16. Correlation of INES and waverider wave heights and periods

A detailed comparison was also made between data obtained at Richards Bay using a *wave clinometer* and those from an INES *recorder* installed approximately 350 m from the clinometer buoy. The disposition of the instruments is shown in Figure 15, the INES recorder referred to being marked INES (Tower) in the figure.

The results given in Figure 17 clearly show, that, although the distance between the two recording points is much greater than in the above case and the recordings were not simultaneous (1 to 2 hours difference between INES and clinometer recordings), there was a reasonably good correlation between the respective wave height values. For wave heights above 1 m the wave clinometer generally gives higher values than the INES recorder.

Since the same applied to the wave rider heights, in the case of Richards Bay the wave clinometer heights should compare even better with the waverider data. It must, however, be realised that wave clinometer readings depend on the particular installation (i.e. distance of buoy to instrument) and to some extent on the observer. The correlation found

for the Richards Bay case, therefore, does not necessarily hold for other measuring stations. As regards the periods, the wave clinometer values at Richards Bay are on average 2 to 4 s greater than the INES values. This has been found in all other cases and can be explained by the tendency of the observer to record the period of the main swell, neglecting the small, short period waves, whereas for the determination of the zero crossing period of the INES records all the waves are taken in to account.

Although the wave clinometer was primarily developed as a wave direction measuring instrument, reasonably reliable wave height and wave period data can still be obtained with this instrument which is extremely cheap, easy to operate and very reliable. Correlation of the wave clinometer data for each particular installation with a wave recording instrument over a short period will further improve the reliability of its output.

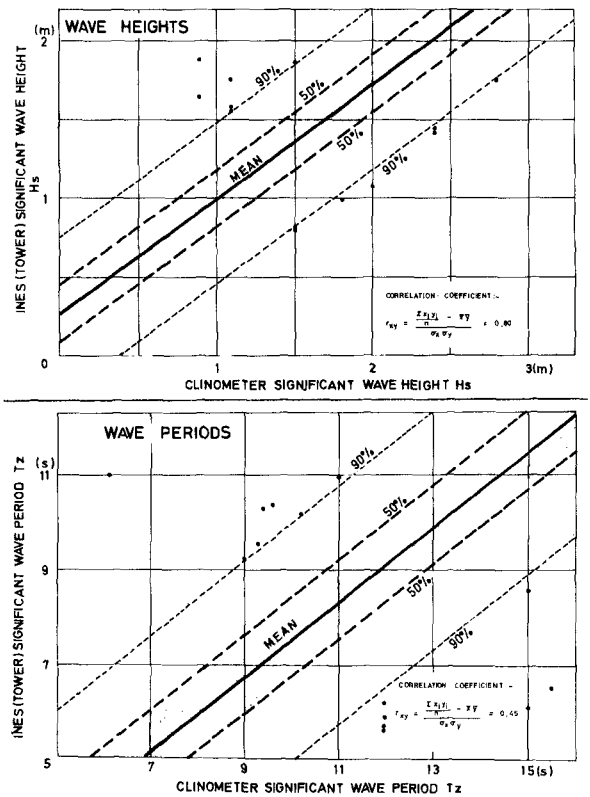

Fig. 17. Correlation of INES and Clinometer wave heights and periods

BEACH PROFILES EXTENDING THROUGH THE SURF ZONE

Until fairly recently it was not possible, on the unprotected coasts of Southern Africa, and presumably on other coasts with similar heavy swell and surf conditions, to measure beach profiles extending through the breaker zone on a regular basis. Various methods were tried with little success including the use of a pressure gauge which was attached to a line, fired across the breaker zone by rocket and then pulled back to shore while recording the water depth. The main disadvantage of this method was the large friction force caused by the line "cutting into" the offshore sand bar through which it had to be dragged.

About three years ago, a technique for measuring profiles through the breaker zone was developed by the Hydraulics Research Unit using light and highly manoeuvrable ski-boats (see Figure 18) equipped with echo-sounding equipment and operated by skilled personnel. This technique has been used successfully since its adoption.

Fig. 18. Ski-boat in the surf returning to sea

The ski-boat is kept *on course* using two theodolites and radio communication. One theodolite sights along the profile line and keeps the boat heading in the right direction while the second theodolite intersects the boat position from a point further along the beach. At each intersecting fix the echo-sounding trace is simultaneously "marked". Ski-boat surveys are normally undertaken during high spring tide conditions and extended into a water depth of as little as 0,5 m. The "dry" beach profiles are surveyed during low tide and extended as far as possible into the water. In this way it is possible to obtain an overlap of "dry" and "wet" profiles, thus providing an excellent check on the profiles measured by ski-boat. For obvious safety reasons and to keep the reference level of the echo-sounder as constant as possible the ski-boat travels at the same speed as the waves, remaining during the entire run in the same wave trough.

A complete profile through the surf zone can be measured in a few minutes and the operation must, of necessity, be extremely well organised and requires considerable skill from the ski-boat operator. Under favourable conditions a 5 km length of coast, with sections at 200 to 300 m intervals, can be profiled in less than a day using this technique.

Originally Inshore Ferrograph echo-sounders, which are very simple instruments, were used for this work, but they were later replaced by high resolution Atlas Deso 10 and Elac echo-sounders which give much more accurate results. A typical echo-sounding profile using an Atlas Deso 10 echo-sounder is given in Figure 19.

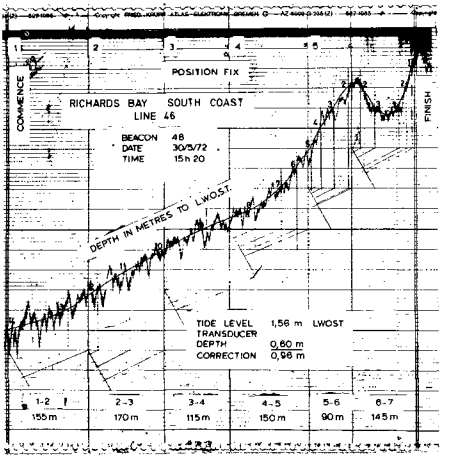

Fig. 19. Beach profile as recorded by an Atlas Deso 10 echo-sounder.

The *accuracy* of profiling by ski-boat has been checked by repetitive runs along a particular section combined with depth measurements taken by lead line at regular intervals. From the results of these checks, it was established that water depths which include tidal reductions, elimination of wave action and temperature effects, could be determined to within 0,5 m. When comparing successive hydrographic surveys differences of less than 1 m should therefore be considered as insignificant.

A valuable *application* of this technique is the study in detail of the formation and movement of sand bars along the coastline by comparison of successive surveys. When the measurements are made at regular intervals, the changes in the profiles and the general bottom topography can be related to the sea conditions which occurred in the period between the two surveys.

A very good example of nearshore bottom changes at Richards Bay in the spring of 1969 established by the above type of survey is shown in Figure 20.

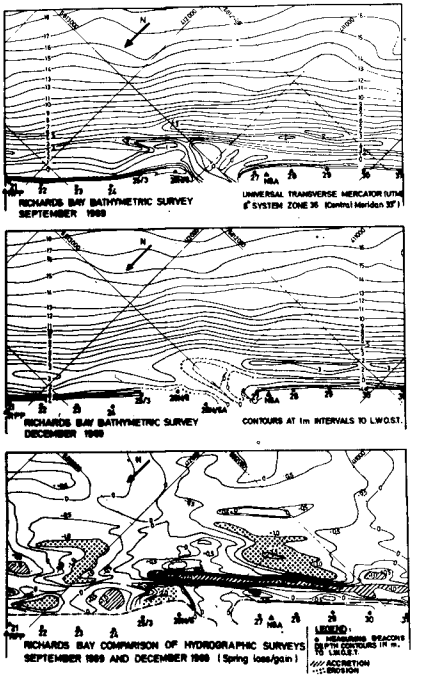

Fig. 20. Comparison of hydrographic surveys

CONCLUSIONS

Accurate data on sea conditions and the related coastal morphology are essential for the proper design of all coastal works. Coastal measurements, however, are inherently difficult and normally expensive which often results in a curtailing of the data collection programme. It is believed that a number of simple and economic measuring techniques developed in South Africa over the past ten years may be of use in the systematic collection of coastal data on a limited budget.

ACKNOWLEDGEMENTS

The assistance given in the preparation of this paper by Messrs. J.W. Kluger, C. van Schaik, A. Harper and A. Duncan is gratefully acknowledged. The photograph used in Figure 1 was supplied by Mr. D. Greaves, A.I.P.

REFERENCES

1. ATKINS, R.G. "Marine effluent research committee - False Bay - Progress Report No. 5"

2. NATIONAL INSTITUTE FOR WATER RESEARCH. "Some techniques in Coastal Oceanography". CSIR Report 222, Pretoria, South Africa, 1964.

3. ZWAMBORN, J.A., VAN SCHAIK, C. and HARPER, A. "Ocean Wave Research in South Africa". Proc. XIIth Conference on Coastal Engineering Vol. I, Washington, D.C., September, 1970.

4. DRAPER, L. "The analysis and presentation of wave data - a plea for uniformity". Proc. Xth Conference on Coastal Engineering, Tokyo, 1966.

CHAPTER 2

SIMULTANEOUS DATA SYSTEM FOR INSTRUMENTING THE SHELF

by

Robert L. Lowe, Douglas L. Inman and Birchard M. Brush

Scripps Institution of Oceanography, University of California

La Jolla, California 92037

ABSTRACT

A system, designed to give maximum flexibility and portability, has been developed to collect wave, current and other physical data within the dynamic environment from the surf zone to the edge of the shelf. The system consists of a radio-linked shore station, housed in a mobile van and as many as six shelf stations mounted in bottom referencing spars.

A shelf station can be deployed from a small boat with minimum diver time. The ease of deployment of the shelf stations coupled with the mobile self-contained shore station, allows the use of a modern data acquisition system, and rapid deployment of sensors, for the field study of remote coastal areas.

Each of the shelf stations is designed to accomodate as many as fifteen sensors. All simultaneous sensor outputs are digitized and transmitted by radio to the mobile shore station, where the received signals are processed and selected for recording on strip charts or digital magnetic tapes for computer analyses. Very high sampling rates and a real time system are used to insure precise time correlation between all data channels including those from separate shelf stations.

A single shelf station would transmit data from an array of wave sensors, thus providing continuous wave climate including the two dimensional wave spectra. Some different combinations of shelf station ensembles are shown.

INTRODUCTION

In order to observe more comprehensively the broad tapestry of energy translation which occurs as a result of the action of waves and currents incident to the coastlines, a multipurpose data acquisition system for instrumentation of the surf zone was developed several years ago (Koontz and Inman, 1967). This early system enabled the evaluation of the longshore transport of sand as a function of wave power (Inman, et al, 1969; Komar and Inman, 1970). Subsequently it became an important factor in the study of the mechanics of rip currents and mixing in the surf zone (Bowen and Inman, 1969; Inman, et al, 1971). Because the early system was limited in scale and resolution, it became attractive to consider a second generation data acquisition system which would increase resolution and greatly expand the capacity to achieve accurate data over much larger areas.

A project in 1971 for assimilating larger amounts of data than formerly available in the nearshore zone and on the continental shelf led to a new system; the Shore and Shore System (SAS System), which included an

economical vertical spar which could be placed in varying depths of water for the purpose of relaying data to a shore station and make it available for further processing and analysis. The SAS System was designed so that it would be possible to rapidly exchange transmitting and battery modules, while using a small boat as an operational base.

Original evaluation of a design concept suitable for use as the shelf station ran the gamut from a single tethered subsurface sphere (an oscillator at certain wave periods and subject to periodic torsional rotation); consideration of a redundantly anchored subsurface sphere (again, complex because of intensive anchor placement, and the requirements necessary for accurate anchor spotting); and, surface buoyant devices (sometimes wavelength-coupled and fraught with seakeeping problems). The final choice for the shelf station was a vertical spar shape which is securely anchored to the bottom through a universal joint. This arrangement prevents vertical motion, but allows motion in the horizontal plane. Vertical sections of filament wound pipe may be added for varying depths using sexless couplings. Tests performed in the hydraulics laboratory have verified that the heave-free spar tends to rectify the prevailing current direction, and implies integration of the water column, though its surge response is still being studied.

As of August 1972, a prototype has been successfully exposed to all wave regimes and storms in 20 meters of water off Scripps Pier. The survival of the shelf station in inclement periods of weather leads to speculation that storms for the first time may be instrumented; these are occasions of compelling interest in the study of nearshore processes.

The SAS System, shown schematically in Figure 1, has the following major subassemblies: 1) a shelf station, which has a benthic power supply and a vertical spar which may accomodate various ensembles of sensors; and, 2) a shore station, which receives coded data and records it virtually simultaneously for further processing and visual assay. The most frequently used sensors, on the shelf station, have been digital wave staffs, absolute pressure sensors, and passive electronic current meters. In addition, depending upon the type of operation being used for special studies, a suspended sediment meter, thermal measuring devices, and bottom roughness profiler will utilize other data channels on the shelf station. Portions of the capability for synchronous binary counting will enhance the ability to relate underwater photography to time series, and allow individual frames of motion pictures to be correlated with data taken at the same instant.

The SAS System contains a data acquisition system using a multiple radio link, pulse code modulated (PCM) telemetry link. Up to six shelf stations each having the capacity to transmit up to 15 data channels (i.e., 15 sensor inputs) can be processed simultaneously. All sensor outputs are converted to digital (10 bit binary) before transmission to the shore station. Each shelf station operates on a different RF frequency to provide isolation between shelf station transmissions.

The van mounted shore station receives the transmitted information from the shelf stations simultaneously, processes the data to provide outputs in the form of hard copy, strip chart records, and digital tape. The digital tape provides the means for inputing the data into a computer system for detail spectral and cross spectral analysis.

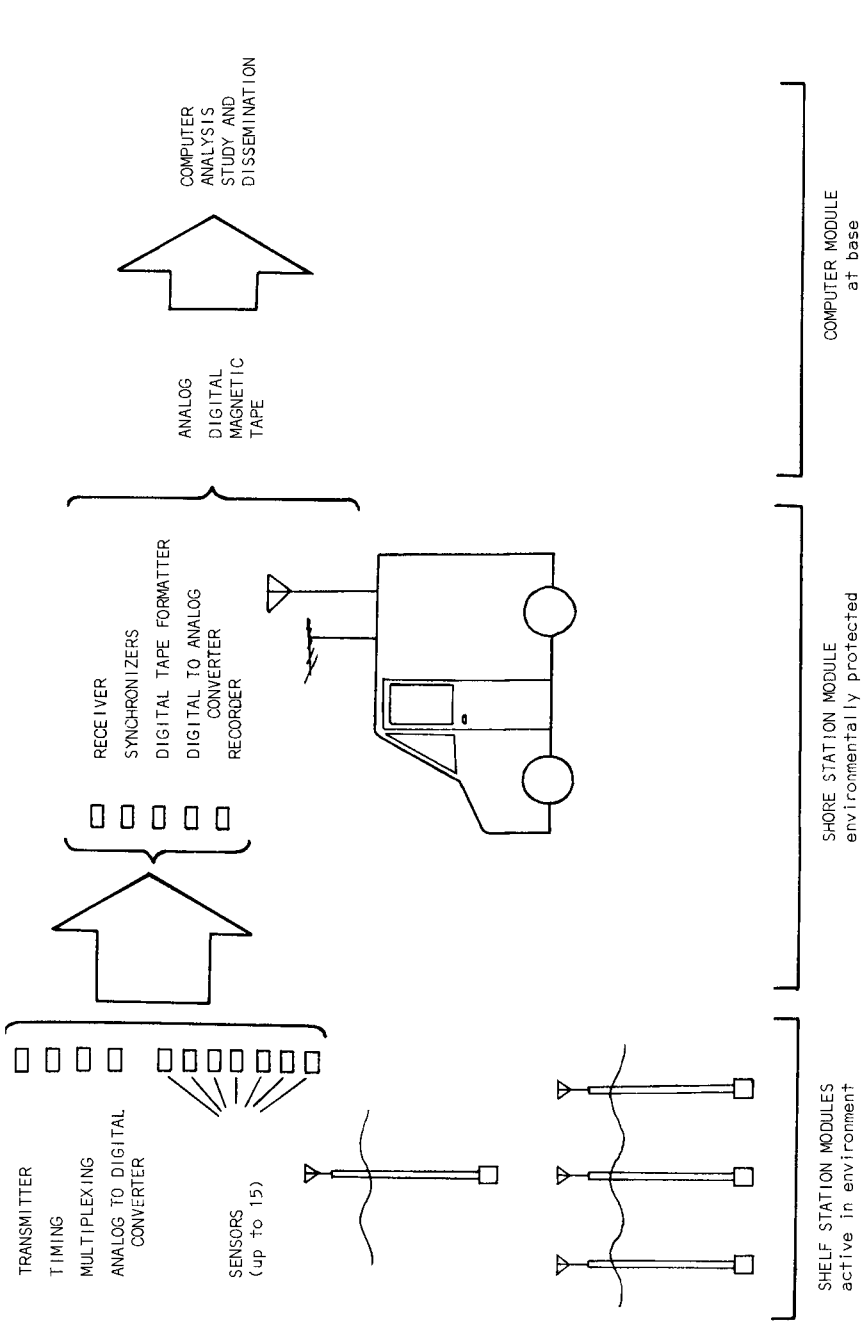

Figure 1. Schematic diagram of the shelf and shore system (SAS System). The system accepts data from six spar shelf stations, and each station will accomodate up to 15 sensors. Data is telemetered to a shore van recording station, thence to computer analysis.

In order to provide the maximum close range support, an especially modified van is capable of positioning the shore station, in the field, on coastal terrain. The component racks of the shore station are designed to be enclosed by the van and will operate from within. Major components of the SAS System are now available, and may be transported to a field location by road or on shipboard so that field conditions need not be primative as far as data acquisition is concerned. The SAS System appears to offer a versatile shelf study tool and continues to suggest itself for other applications as a basic field tool.

SHELF STATION

The shelf station consists of a vertical spar with airtight ends (Figure 2), utilizing a standard pipe size of 3.5 inches OD with a wall thickness of 0.144 inches. Standard lengths are used for modular assembly, and can be assembled to provide the desired total length. The pipe is filament wound with 75% glass and 25% epoxy resin (Table 1). In depths of water over 20 meters, the bottom sections are free-flooded.

The couplings are sexless, forged, anodized aluminum with two cadmium steel plated bolts each (Roylyn Div., Rucker Corp). These couplings are modified with a larger than standard seal to prevent loss of integrity when experiencing bending moments imposed by wave action. The sealing unit or "oreo" seal (Figure 3) consists of layers of elastomeric compound (usually neoprene with a 40 to 50 shore durometer hardness) interleaved with circular metal plates. A single axial bolt compresses the elastomer between the circular plates and exerts a bearing stress against the inside of the pipe. The pipe is bias wound (45^{o}) to tolerate the induced loop strain. When properly installed, a 3 inch oreo seal will withstand an axial load in excess of 1000 lbs by friction alone.

Two sizes are used; a 3 inch diameter seal for the top and the bottom of the shelf station, and a 2 inch diameter seal for the internal cartridges. Redundant sealing is used so that in case of damage to the shelf station spar the individual packages and circuits might be more likely to survive immersion. Where possible, transmitters, logic packages, and support modules are intentionally packaged as long slender units which will correspond to the configuration of the shelf station spar. As an alternative, the cylindrical package may be strapped alongside on the outside of the spar. A section of filament wound pipe may be cut to any desired length and sealed at each end with an oreo seal to provide additional volume with watertight integrity, including provision for watertight passage of wires and cables. The anchor assembly is shown in Figure 4: above the captive pivot pin, the positioning and trim weight platform can accept 40 lb weight modules as an aid in positioning the spar while attaching the pin. The anchor platform will accept up to six weight modules depending on the length and buoyancy of the spar. Normally, access to the lower oreo seal is only required on land, and is performed with a socket wrench and extension, through the lower clevis slot.

The univeral joint allows the spar to maintain a preferential direction without resisting. It is a standard automotive part, encased in a silicone oil filled bellows to prevent corrosion.

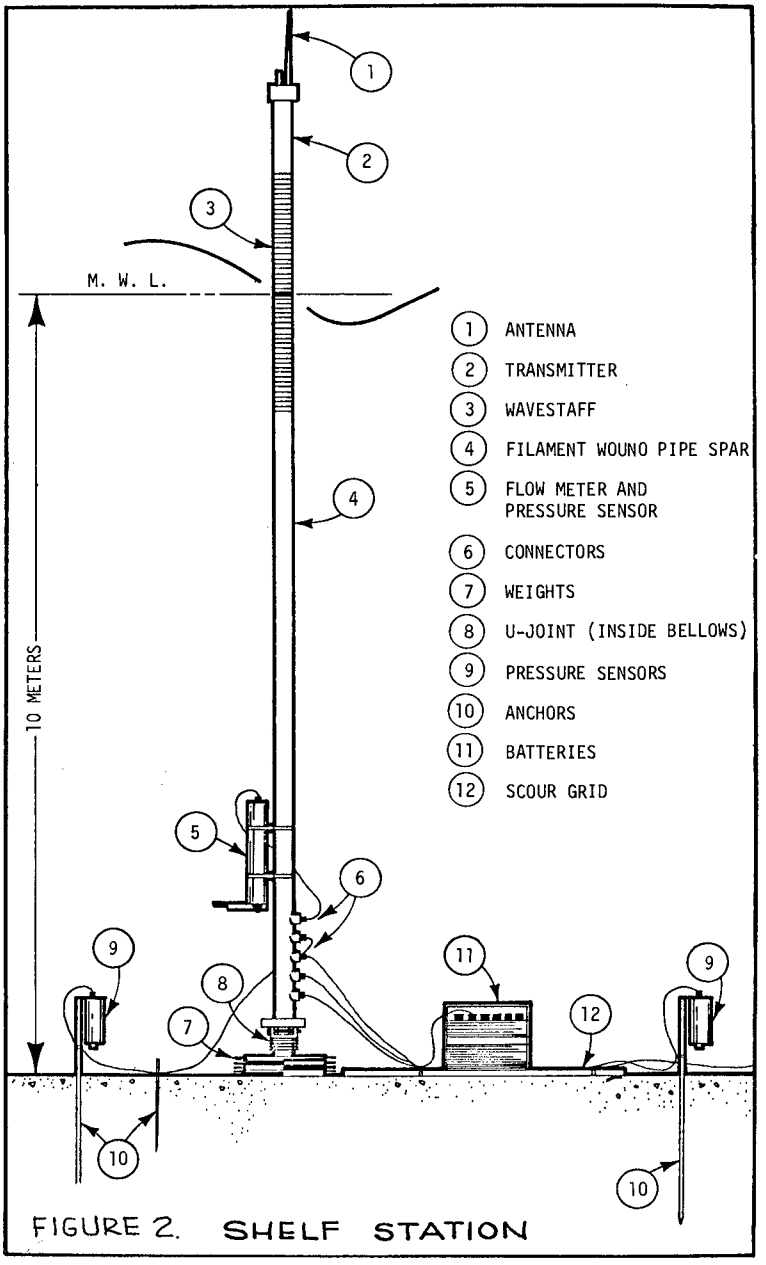

FIGURE 2. SHELF STATION

Table 1. Properties of filament wound pipe as used for the vertical buoyant section of the SAS shelf station. *

Outside Diameter	3.5 inches
Thickness of Wall	0.144 inches
Mean Radius	1.68 inches
Cross Sectional Area	1.48 in^2
Buoyancy (air filled)	3.07 lbs/foot
Weight per foot	1.2 lbs.
Section Modulus	1.195 in^3
Polar moment of Inertia	4.179 in^4
Moment of Inertia	2.098 in^4
Density	.076 lbs/in^3
Glass/Resin Ratio (weight)	3/1
Ultimate Tensile Stress	80,000 psi
Yield Stress	12-14,000 psi
Young's Modulus of Elasticity	5×10^6 psi
Poissons ratio	0.29
Expansion Coefficient	8.8×10^{-6} $in/in/^oF$
Conductivity	1.7 $BTU/ft^2/^oF$ @ 50^oF
Internal (working) Pressure	120.5 psi
External (working) Pressure	69.6 psi

* Bondstrand #2000 series, Ameron Div., Brea, California

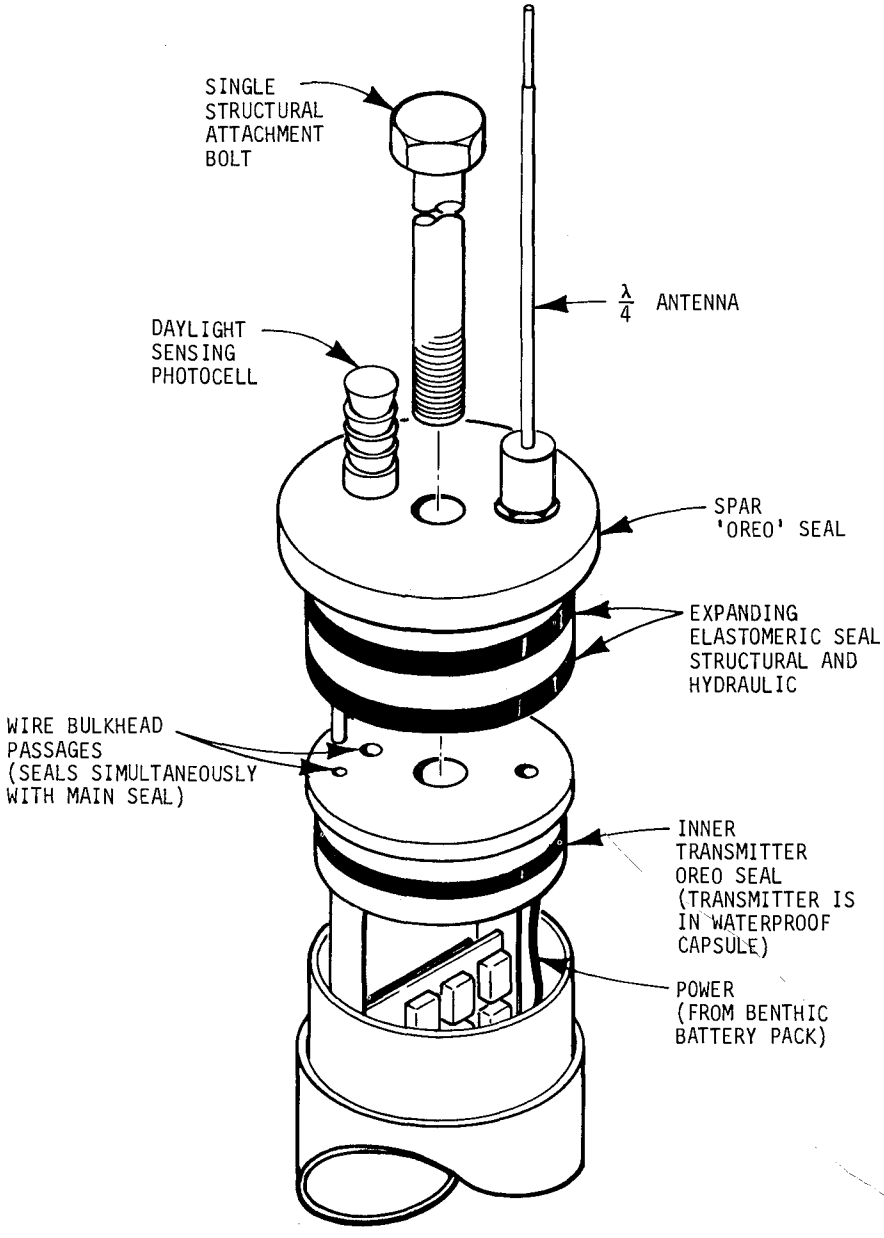

Figure 3. To facilitate rapid exchange while on station, the transmitter capsule may be removed and replaced with a centrally bolted 'oreo' seal which combines structural integrity with watertightness.

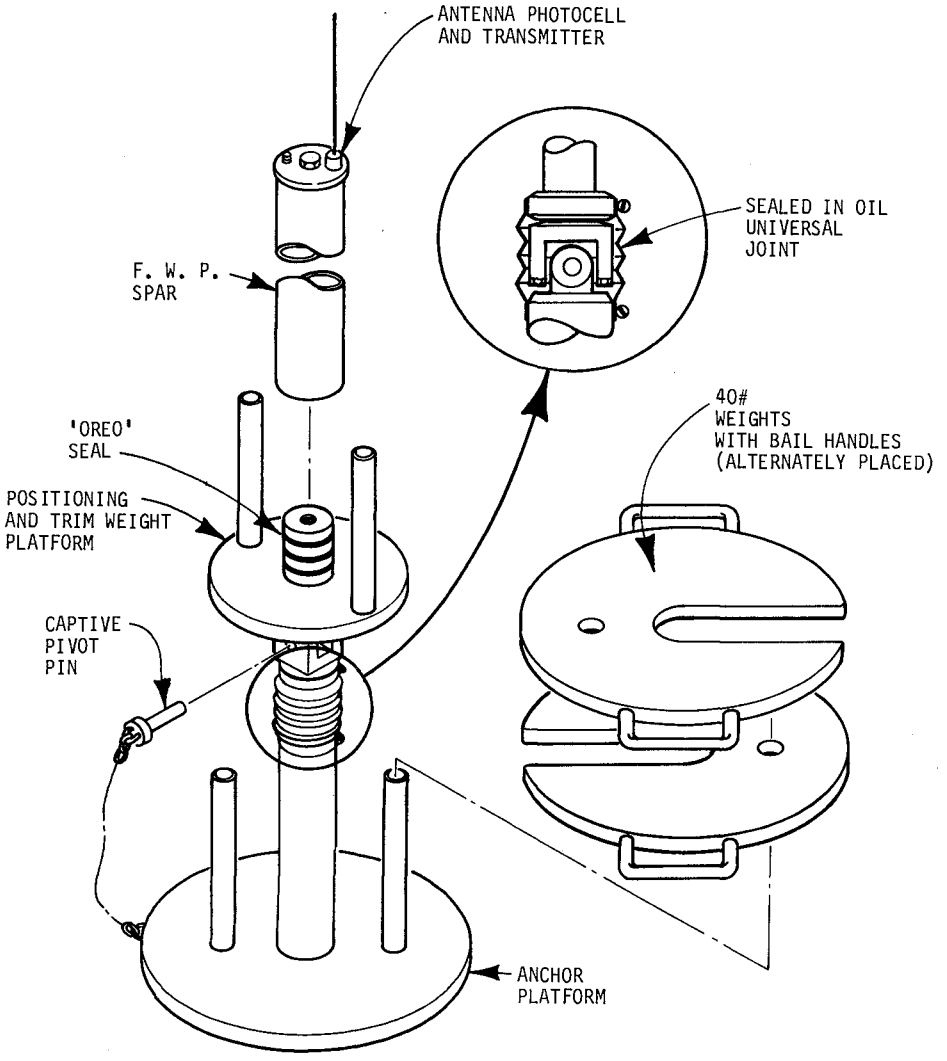

Figure 4. The lower portion of the station separates to facilitate installation and removal of components. Weights added to the trim weight platform enable the buoyant spar to be engaged to the anchor assembly.

DATA ACQUISITION AND PROCESSING

The SAS System has been designed to acquire data from a large array of sensors simultaneously. In order to accomplish this task, state-of-the-art telemetry techniques must be utilized. A completely digital data transmission scheme known as Pulse Code Modulation (PCM) is employed on six assigned UHF (ultra high frequency) frequencies within the band between 216 and 219.6 mega Hertz. Six shelf stations can therefore be operated simultaneously; each on its own UHF frequency band.

Shelf Station Electronics

Sensors can be located either within, clamped to the outside or on the bottom near the base of the shelf station. As many as 15 sensors can be accomodated by a single station. Among the most frequently used sensors are digital wave staffs, absolute pressure sensors, passive electronic current meters and accelerometers (accomodation for other sensors which might be developed in the future, whose output is in volts is assured).

A functional block diagram of the shelf station electronics is shown in Figure 5. The system is designed to accept 8 analog type sensors (e.g., pressure sensors) and 7 digital type sensors (e.g., digital wave staffs). Signals emanating from sensors having an analog format are amplified, attenuated, or offset in the signal conditioning section. Signal conditioning is necessary in order to take advantage of the entire dynamic range of the analog to digital converter. Sensors having an inherent digital format are interrogated by the digital multiplexer and their data is serially shifted into the PCM encoder.

The PCM encoder functions as a master controller establishing the sampling rates for the sensor, converting all analog signals to digital, converting parallel data into serial,and generating a unique 10 bit pattern called a frame sync word. Timing is established by dividing down a high frequency oscillator to establish bit-time or clock, word time, and frame time. From these divider outputs, the necessary timing control signals can be derived.

There are two interlocked multiplexers; one for analog data channels and one for digital data channels. The PCM format is designed to handle 16 channels; 8 analog and 7 digital and 1 frame sync word. The frame sync word is assigned the first word in the frame; and is used by the receiving equipment to identify the start of the frame. During the second word time, the first analog channel is sampled, followed by the first digital channel. Alternating between analog and digital channels continues until all input channels have been sampled. This process constitutes a total frame of data. Frame after frame of data is formatted in this fashion giving a continuous serial stream of binary data.

This serial bit stream of data consisting of a binary "1's" and "0's" is known as non-return to zero level code (NRZ-L). The NRZ-L signal turn is converted into a phase encoded signal called biphase level code (biϕ-L). In a Biϕ-L code the information (data) is contained in the clock phase (i.e., a binary "1" is represented by 0^{o} clock and a binary "0" by 180^{o} clock). It is this Biϕ-L code, after it has been filtered at approximately twice the bit rate, that is transmitted over a UHF radio channel. The selection of Biϕ-L code for transmission was motivated by one important characteristic; its

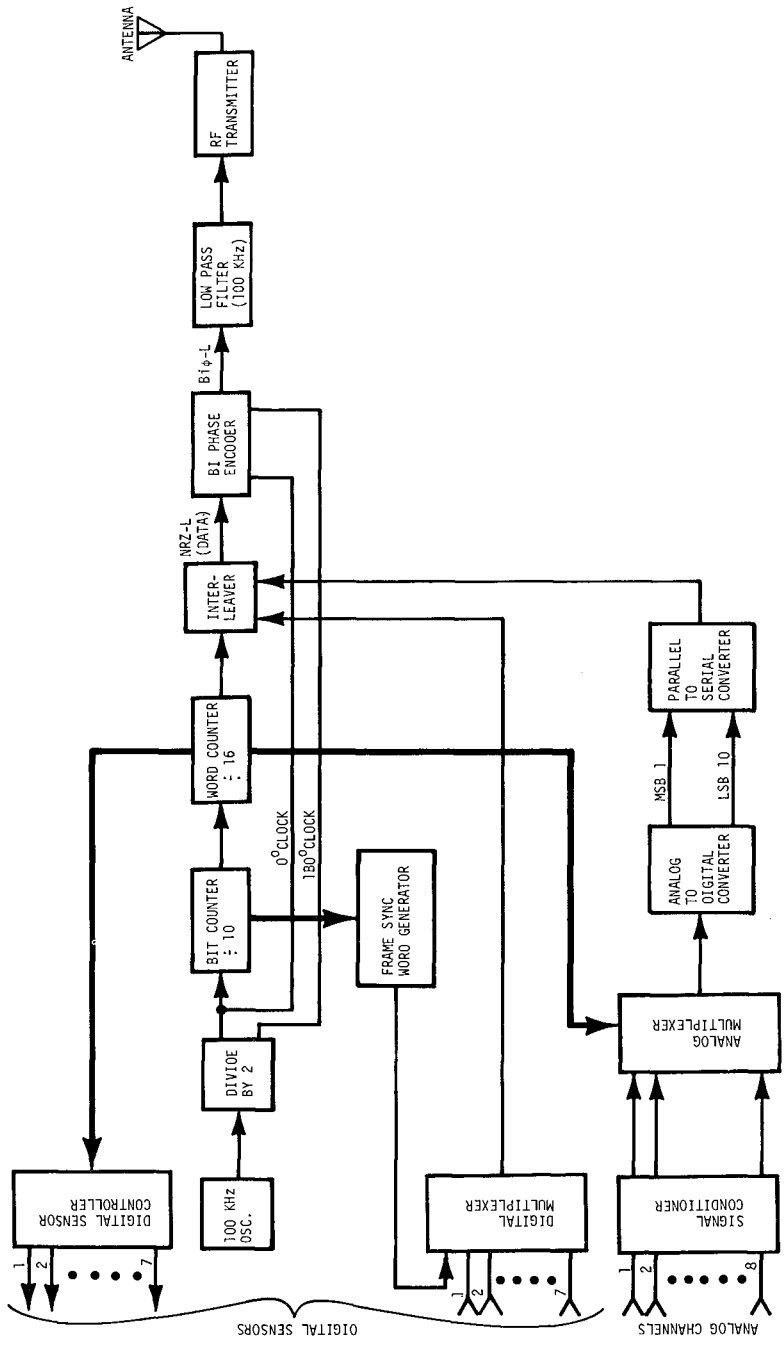

Figure 5. Up to fifteen different sensors or combinations of sensors may be accomodated by the SAS System. It is designed to accept 8 analog output sensors, and seven digital type sensors.

power spectrum density is zero at zero frequency, which is not true of other binary code types. This characteristic is important in this system for two reasons: (1) the design of the RF transmitter and receiver is much simpler because the RF system does not need dc response; and, (2) direct recording on a wide band analog tape record of the receiver output is more readily accomplished. A price must be paid for this desirable trait however; Biϕ-L code requires approximately twice the bandwidth for the same information rate than does NRZ-L. In the present system this increased bandwidth did not pose a problem.

Presently the PCM encoder is set-up to operate at 50,000 bits per second which provides a single sensor sampling rate of approximately 300 samples per second. Although the sampling process used is sequential, this high rate insures virtually simultaneous data from all 15 sensors.

Power Supply

The shelf station and its complement of sensors are powered by especially packaged lead-acid batteries. A sketch of the power pack is shown in Figure 6. Two 12 volt batteries are connected in series to provide 24 volts for operating the system. For a typical installation, 80 amp-hr rated batteries will operate a shelf station continuously for 120 hours; or slightly longer if intermittently operated.

In order to protect the battery's plates from the intrusion of sea water, a special oil mixture is used. The density of the oil is adjusted between that of the electrolyte and that of sea water. The oil allows the gas formed during battery discharge to escape, yet prevents sea water from mixing with the electrolyte.

Most installations are in water shallow enough to have intensive wave action at the bottom and thus bottom scour is a potential problem. To prevent the power pack from tumbling a grid of aluminum tubing is used to support the batteries and extend support beyond the scour pit in the immediate vicinity of the battery. The power pack is diver recoverable and reuseable. Approximately four recharge cycles can be expected.

Shore Station Electronics

The shore station of the SAS System is a complete self-contained PCM ground station. It is housed in a mobile van to allow field work to be conducted at remote sites. Four 6 foot high racks of equipment comprise the electronics of the shore station. Data outputs from the system are in two forms: 1) hard copy in the form of 8 channel strip chart records; and, 2) 9 level IBM compatible digital magnetic tapes.

A functional block diagram of the shore station electronics is shown in Figure 7. A 6 channel receiver system was custom designed to receive the RF signal transmitted by as many as six shelf stations simultaneously. The six outputs of the receiver system are in the serial encoded Biϕ-L format. All six Biϕ-L signals are directly recorded on the 7 track, wide band analog tape recorder. This process is known as predetection recording.

Along with the data, on the 7th track of the record, a precision time reference, IRIG standard time code format "B" (IRIG, 1960) is recorded. This time code uses amplitude modulation of a 1 KHz carrier to record the time of day in hours, minutes, and seconds.

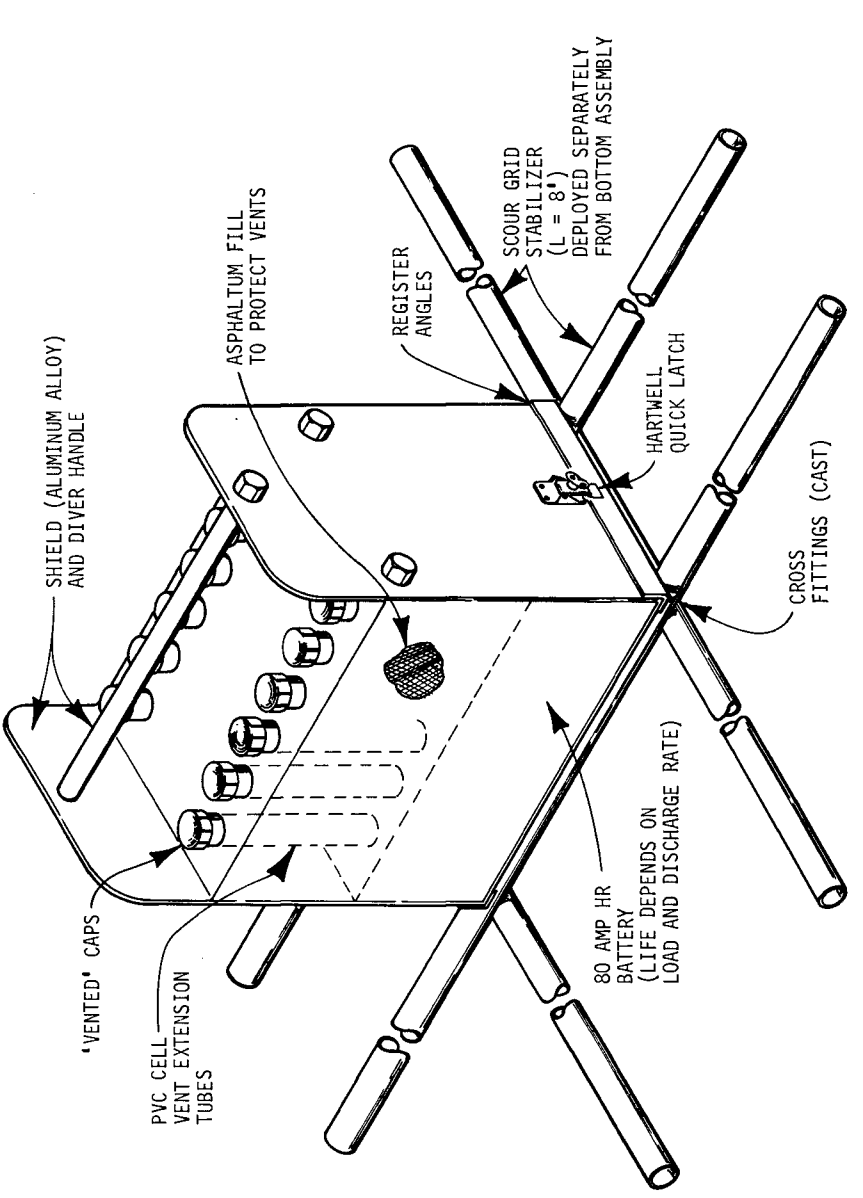

Figure 6. The benthic power pack. The necks of the cells are extended to allow the intermediate specific gravity fluid to be placed between the electrolyte and the ambient sea water. No hydrostatic pressure modifications are required with standard batteries.

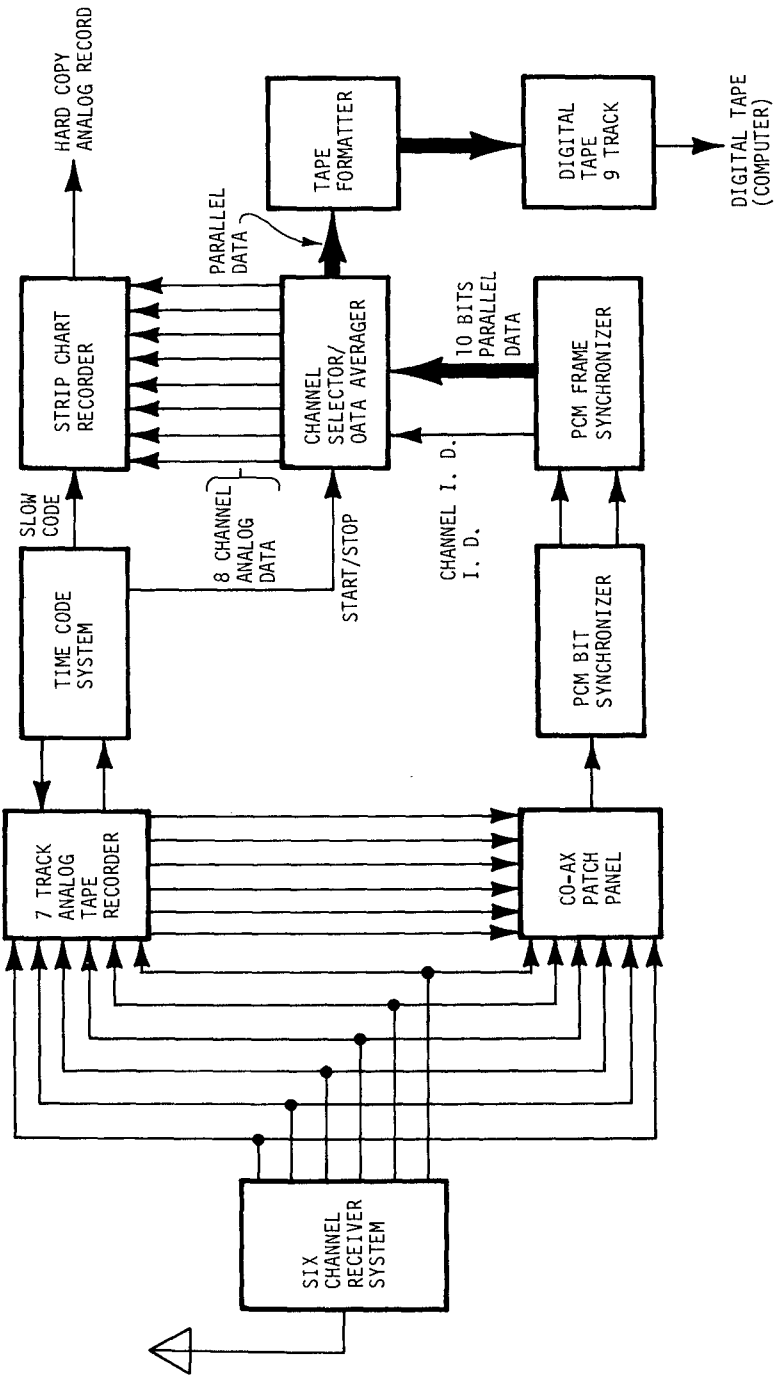

Figure 7. Functional block diagram of the shore station. The equipment is housed in a mobile van to allow data acquisition in remote areas.

Any one of the shelf stations can be selected for data reduction by the PCM system via the co-ax patch panel. The selection stations signal is applied to the PCM synchronization equipment. Synchronization must first be established with the serial Biφ-L encoded data. A PCM bit synchronizer, using a special type of phase lock loop, produces a coherent bit rate clock. The bit synchronizer also detects and converts the serial Biφ-L data back to NRZ-L.

Recovered NRZ-L data and clock is used by the frame synchronizer which is programmed to recognize and synchronize to the frame sync word generated by the PCM encoder in the shelf station. The frame synchronizer is equipped with bit and word counter identical to those in the PCM encoder, therefore when the frame sync word is detected, these counters are forced into step with the counter generating the data. Once synchronization is established all data channels can be identified by their location in the PCM frame. The frame synchronizer groups the data into 10 bit words and presents these words in parallel to the channel selector/data filter along with frame location identification.

The channel selector/data filter allows the system operator to select any eight of the possible 15 data channels to be displayed on the strip chart recorder. Each selected channel can be filtered using a running-mean digital filter which averages the data over 2^n samples where n can range between 0 and 7. The selected data channels are formatted for digital magnetic tape for later computer analyses. Most analysis involves computation of power spectrum using fast fourier techniques. This technique requires a record length 2^n where n is any positive integer. In our computer programs n is usually 12 (i.e., 4096 data points). The system allows flexibility in selecting the sampling rate which produces the 4096 data points. The operator can select a rate from as low as one sample every two seconds to as high as 16 samples per second. In order to insure simultaneous data from all 8 channels, a memory is provided in the channel selector/data filter to store the data until requested by the tape formatter.

Simultaneous samples from all six shelf stations are made possible by the serial time code recorded along with the data on the analog tape recorder. Precise control of the start time in the playback mode insures simultaneous sampling of the data. Playing the analog tape through the system while holding the start time constant, enables all shelf stations to be sampled at the same time.

Applications

The SAS System has many possible modes of operation, some of which are depicted in Figure 8. The general configuration shown in A might be used to study surface waves coupled through a thermocline, or to study the interaction of internal and surface waves. This configuration distributes sensors along the water column. 'Wave climate' can be obtained using a single shelf station as shown in B and C. Configuration B uses an array of pressure sensors placed along the bottom from which wave energy and directional spectra can be inferred by computation. Configuration C uses a passive electronic current meter to resolve direction and a pressure sensor for measuring wave energy. Finally, an array of shelf stations can be used to study larger scale phenomena such as edge waves, and the study of circulation and mixing over the shelf.

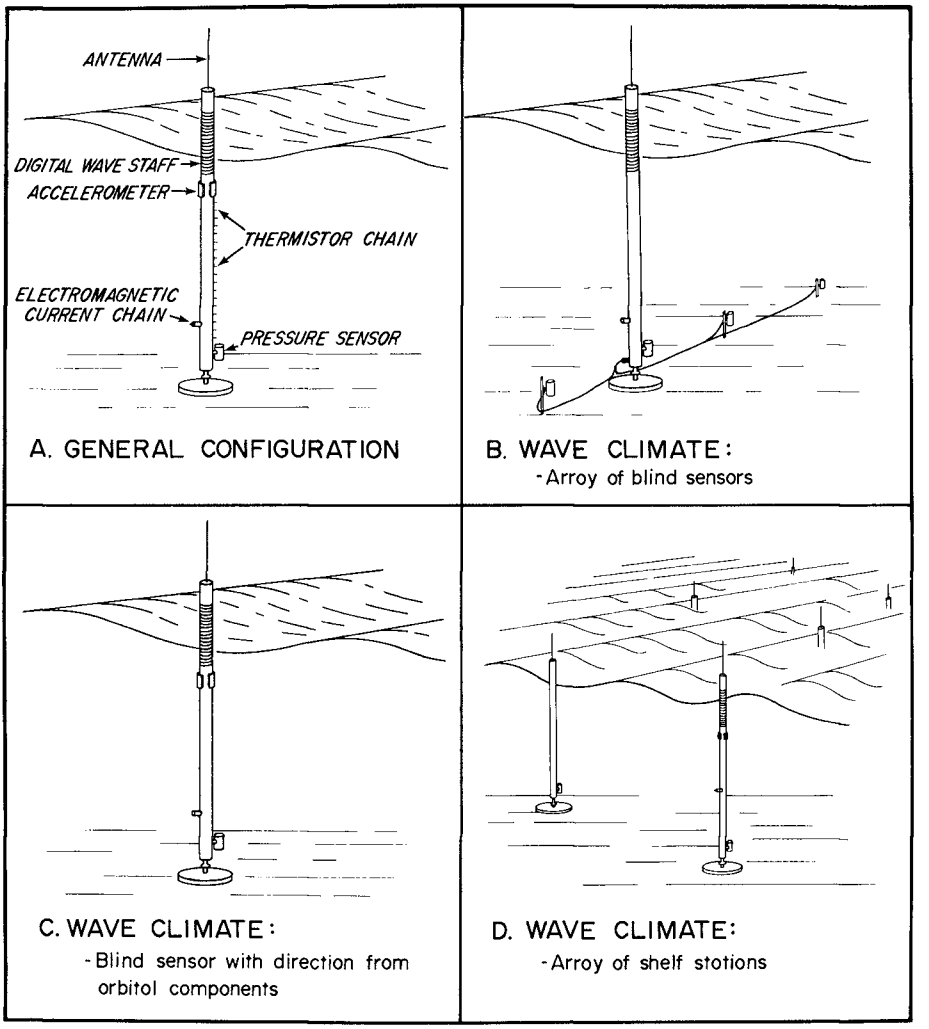

Figure 8. The shelf station is shown in four arrangements, each one of which uses common modules. Survival of prototype units have encouraged speculation that storm data may be taken continuously.

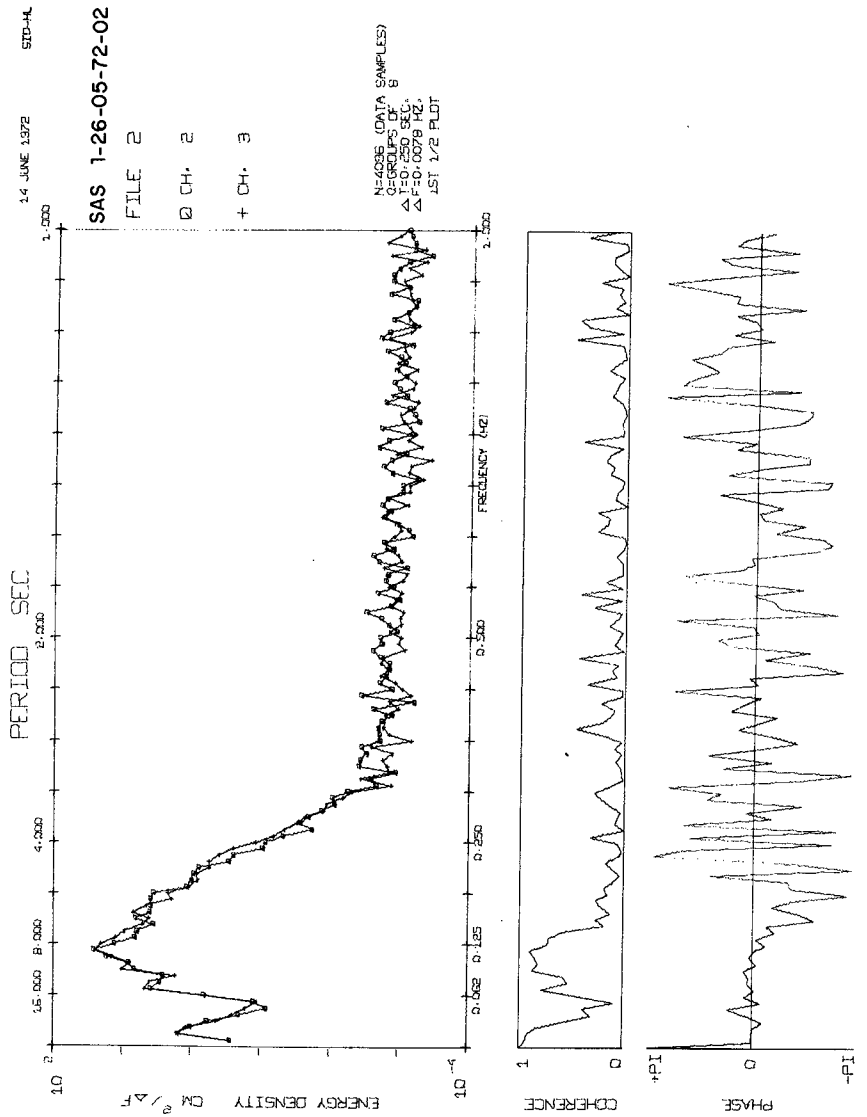

Figure 9. A typical energy density spectra presented by computer analysis. Perfection of this technique has led to new insights into the driving processes of the nearshore zone.

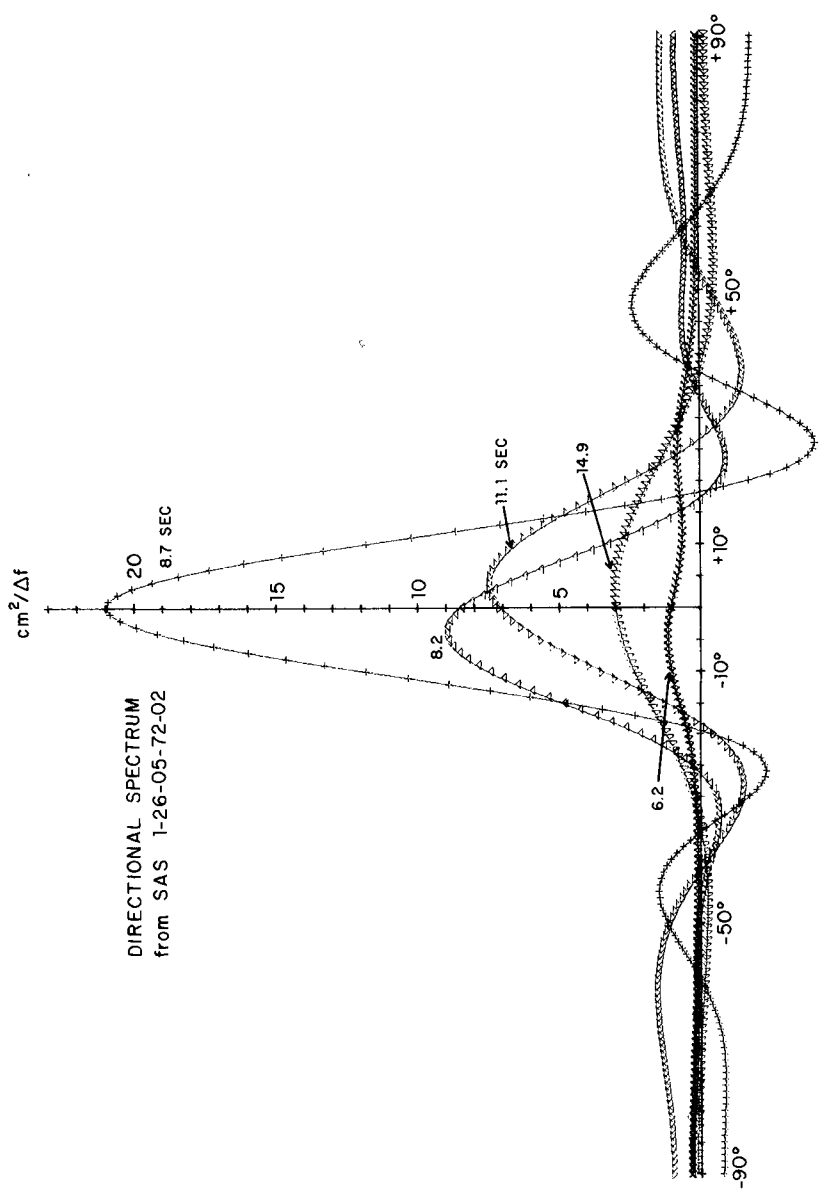

Figure 10. A directional spectrum plotted from the analytical results of SAS 1-26-05-72-02. In such plots as this the synoptic collection of data contributes to unifying theories.

The use of the SAS System is exemplified in a wave climate study. For this study a shelf station was deployed in 10 meters of water along with a four element pressure sensor array. The array was placed parallel with the beach and with a spacing of 30 meters, 60 meters, 30 meters (1-2-1). Figure 9 shows the energy spectra computed from 4096 data samples. Sampling rates for all sensors was 4 samples per second. The maximum energy occurs at a wave period of 8.7 seconds. The directions of various wave periods were computed, and are shown in Figure 10. Note that the direction of the waves is frequency dependent varying from -5 degrees for the wave of 8.2 seconds and less through 0 degrees for the 8.7 second wave to +5 degrees for the longer period wave of 11.1 seconds and greater.

Work is continuing on software for computing the directional spectra from the array data. The example given here represents preliminary results from this effort.

SUMMARY

The SAS System provides a nontraditional approach to simultaneity of measurement from large sensor arrays. Each record provides background for other measurements, and for cross-spectral analysis between various measurements. Synoptic collection of data is essential for a comprehensive and unifying study of the dynamic environment of the nearshore area.

ACKNOWLEDGMENTS

Development of the SAS System has been under sponsorship of the U. S. Department of Commerce, NOAA, Sea Grant Program.

REFERENCES

Bowen, A. J. and D. L. Inman, 1969, "Rip currents; Part 2: laboratory and field observations", Jour. Geophys. Res., vol 74, p 5479-90.

Inman, D. L., P. D. Komar and A. J. Bowen, 1969, "Longshore transport of sand", Proc. Eleventh Conf on Coastal Engin., London, Amer. Soc. Civil Engin., vol 1, p 298-306.

Inman, D. L., R. J. Tait and C. E. Nordstrom, 1971, "Mixing in the surf zone", Jour. Geophys. Res., vol 76, no 15, p 3493-3514.

Komar, P. D. and D. L. Inman, 1970, "Longshore sand transport on beaches", Jour. Geophys. Res., vol 75, no 30, p 5914-5927.

Koontz, W. A. and D. L. Inman, 1967, "A multipurpose data acquisition system for field and laboratory instrumentation of the nearshore environment", Coastal Engineering Research Center, U. S. Army Corps of Engineers, Tech Memo 21, 38 pp.

CHAPTER 3

A Discussion of Some Measured Wave Data

by

J.R. Wilson[1] and W.F. Baird[2]

ABSTRACT

The significant wave height and peak period as derived from the spectral analysis of 171 measured wave records taken in the ocean off Western Head, Nova Scotia are compared to the more classical parameters derived from individual wave heights and by the Tucker method. The highest surface elevation and the maximum wave height occurring in the records are compared to values predicted by Cartwright and Longuet-Higgins (1956), Goda (1970), and Longuet-Higgins (1952).

1. Introduction

The Canadian Wave Climate Study has been in operation since 1968, as a joint venture between the Department of Public Works and the Department of the Environment. The present study was patterned after the pioneer one conducted earlier by the National Research Council of Canada in Lake Superior and the Gulf of St. Lawrence. The purpose of the effort was to obtain data in direct support of specific engineering projects, and to provide general coverage of large areas of the coastline. This has led to the maintenance by the study during the past two years of in excess of twenty-five wave recording stations, each recording for 20 minutes every 3 hours.

Because of the large quantity of wave records being collected, it became necessary to employ digital computing techniques if the analysis was to keep pace with the field program. Accordingly, a suitable recording and digitizing system, similar in general philosophy to the one employed earlier by the National Research Council, was developed. The main difference in the new system was its orientation towards the production of a permanent file of wave profiles on digital magnetic tape in addition to an analysis for wave parameters.

At that point it became necessary to make a decision as to the analysis technique to be employed. It soon became obvious that the most economical and practical method was to compute the spectrum of each 20 minute wave record using the fast fourier transform algorithm developed by Cooley and Tukey. The reasons for this were, firstly, that the signals recorded often contained some low and high frequency noise outside the wave frequencies. This made it necessary to digitally low pass and, in some cases, even band pass filter the data before reliable results could be obtained from a

---

1. Wave Climate Study, Federal Department of the Environment, Ottawa
2. Design & Construction, Federal Department of Public Works, Ottawa

computer algorithm for picking off crests, troughs, zero crossings, etc., for a traditional analysis. Secondly, the computer algorithm developed to pick off the crests, etc., and perform the traditional analysis, proved to be slightly more expensive than the fourier transform. Adding to this the cost of filtering, the traditional analysis became prohibitively expensive. The spectral analysis of a 20 minute wave record presently costs the study about 32 cents.

A drawback of adopting this technique as our standard analysis procedure was that it has not been that commonly used. Consequently, many applications and design techniques are based on parameters that are not directly derived from the spectrum. The zero crossing period, for example, has no spectral equivalent. Design may require the most probable maximum crest to trough wave height or the significant wave height defined as the mean of the highest one-third of the waves. Present theory permits derivation of these quantities directly from the specturm only when the spectrum consists of a single narrow band of frequencies.

The work reported here was undertaken to gain some insight, for ourselves and users of our data unfamiliar with the spectrum approach, into the empirical relations between the spectral parameters and the more classical ones. In particular, we are interested in this comparison for routinely gathered wave data featuring a range of spectral widths. Also because design techniques often require information on extreme wave heights or maximum water elevations, we required to compare observed values with those predicted by theory.

2. Wave Data

The wave data presented here was collected off Western Head, Nova Scotia, between May 1970 and July 1971. The wave measuring device employed was the Dutch waverider accelerometer buoy. It was moored at a point where the water depth was approximately 20 fathoms, as shown in Figure 1. The water surface height was telemetered to the navigation light station at Western Head and recorded as an F.M. signal on a commercial quality stereo tape recorder.

In selecting the records to be used in the analysis, care was taken to obtain a reasonably uniform distribution of spectral widths. The lowest value measured in the 15 months was 0.41, the highest 0.91. The distribution was fairly uniform from 0.5 to 0.8 with a few values between 0.41 and 0.5 and between 0.8 and 0.9. In all, 171 records were used in the exercise.

The data was first passed through our standard system of programs to obtain the spectral parameters. In computing the spectrum the records were broken into 8 sections, each section consisting of 1,024 samples of water surface height. The time step between samples was chosen to give about 60 estimates of spectral density in the frequency band corresponding to 2 to 20 second period waves. The spectral density was then computed as the mean of the 8 values at each frequency.

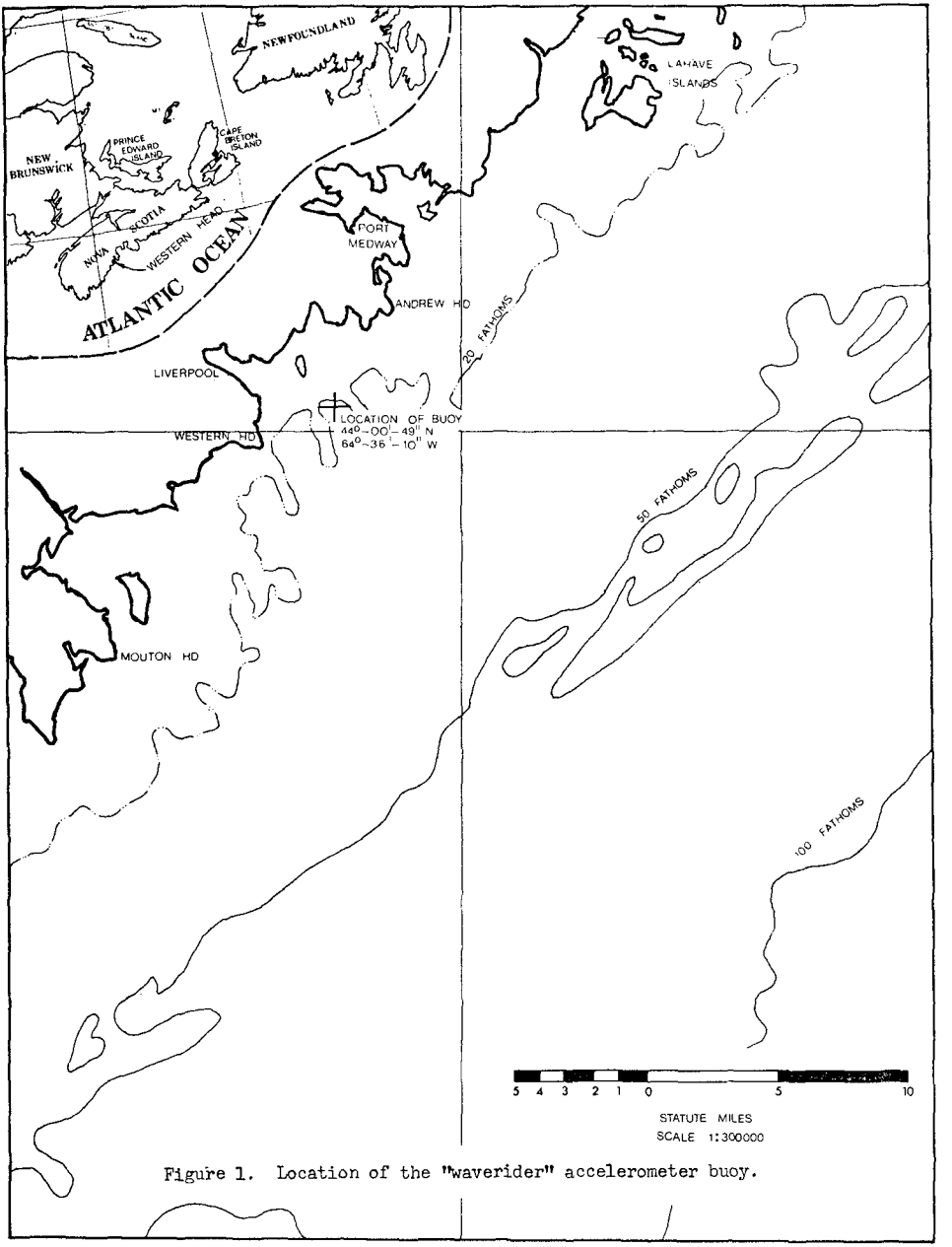

Figure 1. Location of the "waverider" accelerometer buoy.

Secondly, the data was filtered with a sharp cut-off phase shiftless digital band-pass filter which effectively removed frequencies above 0.7 and below 0.025 Hz. Algorithms were then developed to pick off crests, troughs, zero crossings, etc., and compute from these the non-spectral parameters discussed in the following section.

3. Experimental Results

3.1 Significant Wave Height

Figure 2 shows the comparison between the significant wave height defined as $4m_o^{\frac{1}{2}}$ and $H_{\frac{1}{3}}$, the mean of the highest 1/3 of the crest to trough waves. Here m_o is defined as the zeroth moment of the spectrum integrated between frequencies corresponding to periods of 2 and 20 seconds. The crest to trough wave is defined as the difference in height between a crest and the preceeding trough.

The slope of the least squares line is 0.8. The spectrum has generally yielded a significant wave height of the order of 25 percent greater than $H_{\frac{1}{3}}$. The cluster of points in the lower left corner of the plot is contributed by the records with the smaller values of spectral width. As would be expected the scatter is considerably less and this data would be better fitted by a line of steeper slope.

Figure 3 shows the comparison of the significant wave heights as derived by the Tucker and spectrum methods. The second highest crest and lowest trough were used for the Tucker analysis in this case. The scatter has slightly increased but general agreement is improved as the slope of the least squares line is 0.87.

Figure 4 shows the comparison of the mean of the highest 1/3 of the zero upcrossing waves and the significant wave height from the spectrum. The zero upcrossing wave was calculated as the difference in height between the highest surface elevation between a zero upcrossing and the following downcrossing and the the lowest surface depression between the previous zero downcrossing and upcrossing. The slope of the least squares line is 0.94 and the correlation coefficient is 1.00.

The rather good agreement should not be surprising. The slope of the spectrum for most of the records considered would be a steep rise at the low frequency end to a peak followed by a fall at a rate something like f^{-5}. The integral under the spectrum would be relatively insensitive to the presence of higher frequencies because of the f^{-5}. By calculating the zero upcrossing waves as defined, the effect of small waves carried on large waves has essentially been ignored. It would seem, therefore, that both analyses have been determined by waves with frequencies in the neighbourhood of

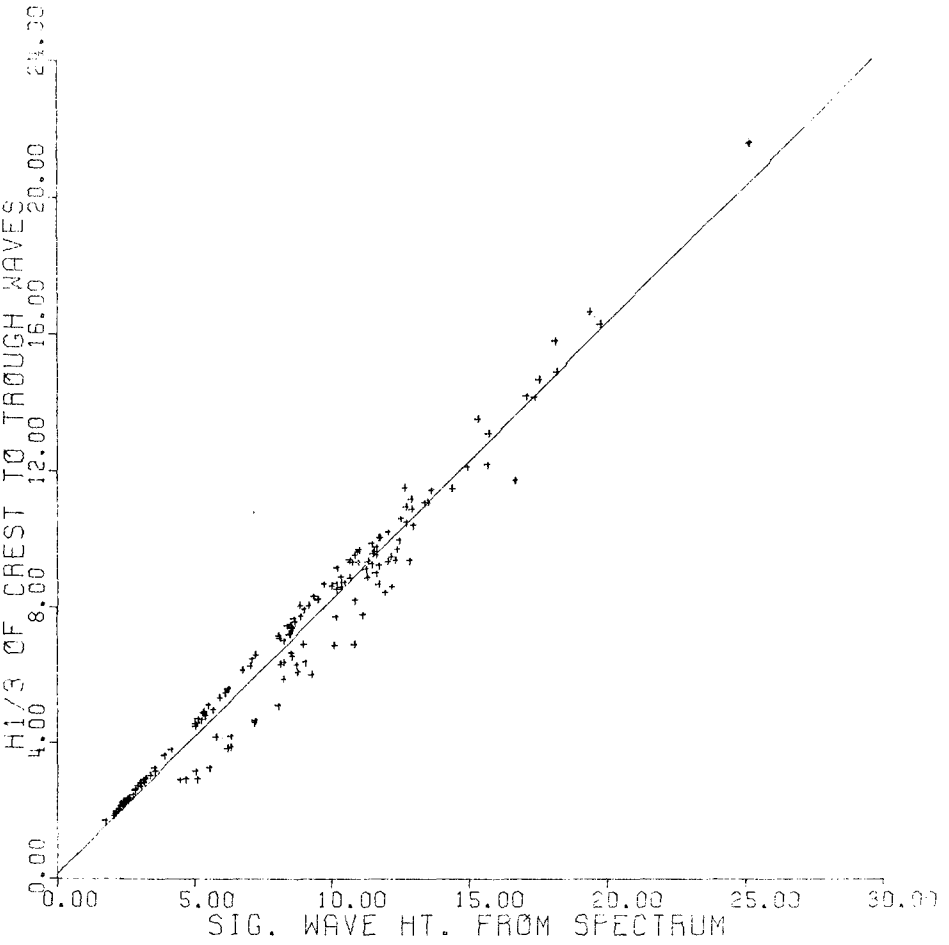

Figure 2. H 1/3, in feet, of crest to trough waves plotted against the significant wave height, in feet, as obtained from integration under the spectrum. The correlation coefficient is 0.99 and the slope of the least squares line is 0.80.

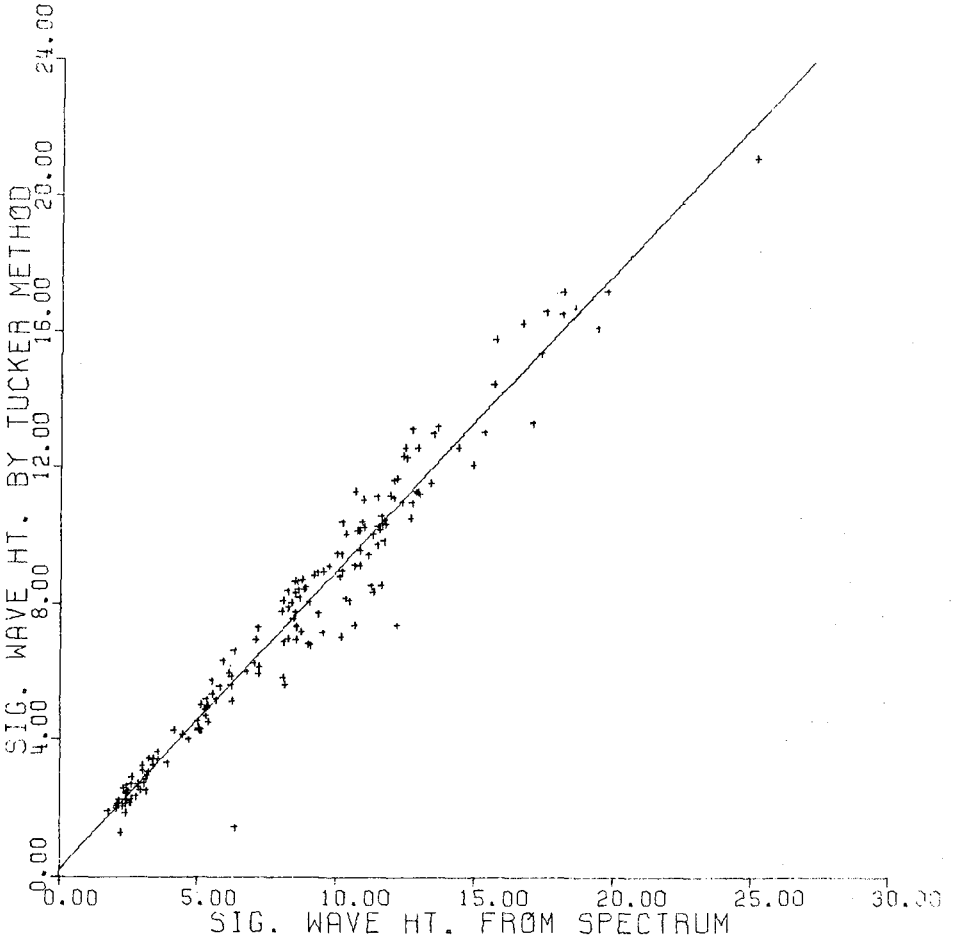

Figure 3. Significant wave height in feet as obtained by the Tucker method plotted against significant wave height as obtained from integration under the spectrum. The correlation coefficient is 0.98 and the slope of the least squares line is 0.87.

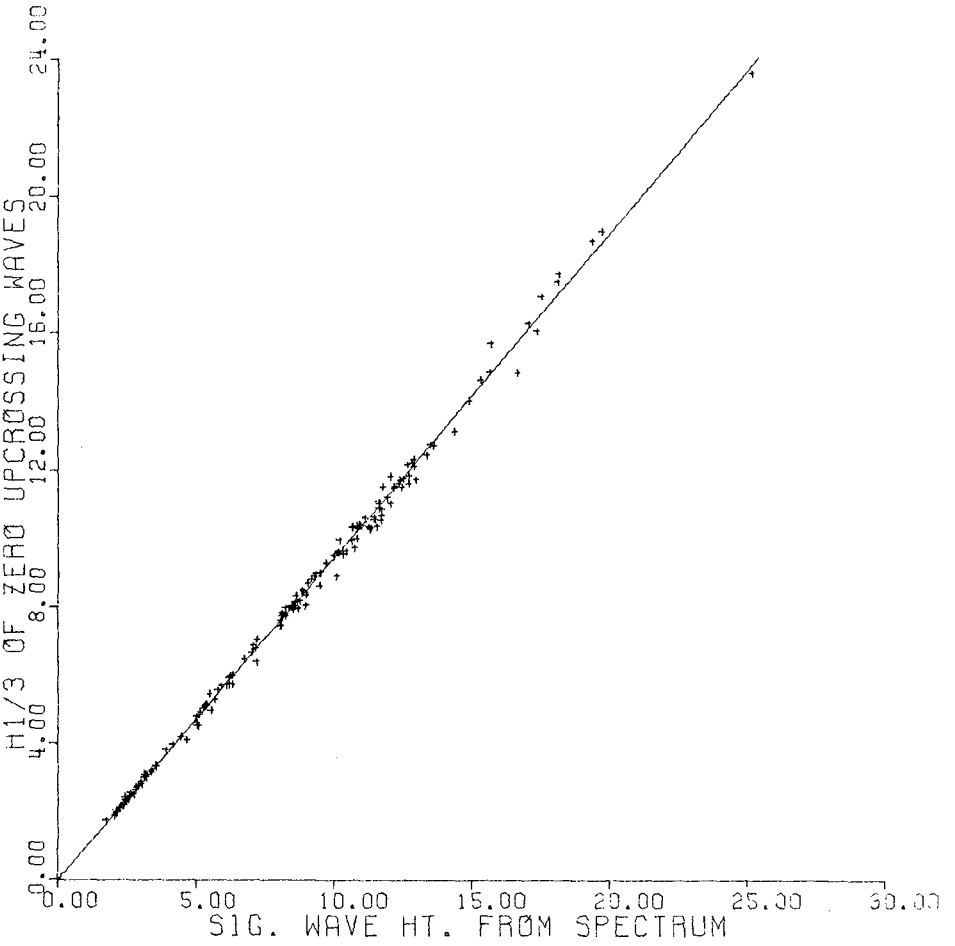

Figure 4. H 1/3 in feet of zero upcrossing waves plotted against the significant wave height as obtained from integration under the spectrum. The correlation coefficient is 1.00 and the slope of the least squares line is 0.94.

the peak of the spectrum. Consequently, the statistics of the zero upcrossing waves should be rather similar to those of the crest to trough waves in the case of a wave record featuring a single narrow band of frequencies. This is in part borne out by the observations that zero upcrossing waves are Rayleigh distributed irregardless of spectral width. These comments, of course, do not necessarily apply to a double peaked spectrum.

3.2 Wave Period

Figures 5, 6 and 7 are the comparisons between the peak period of the spectrum, and the zero crossing, significant crest to trough and significant zero upcrossing periods respectively. The peak period of the spectrum is defined as the inverse of the frequency at which the maximum spectral density occurred. The zero crossing period was computed in the usual manner. The significant crest to trough period is the mean of the periods of the highest one-third of the crest to trough waves. The significant zero upcrossing period is the same parameter for the zero upcrossing waves.

The correlation coefficients of 0.89 to 0.98 came as a surprise as various people had commented to us that these correlations did not exist. In retrospect it is clear that for the type of wave records analysed they must exist. If the type of waves encountered are those associated with more or less fully developed wind generated seas, then the spectrum will usually be of the single peaked f^{-5} type discussed earlier. If this is the case, the waves in the neighbourhood of the peak of the spectrum will essentially determine when the surface crosses zero. Lacking strong phase coherence, the other waves simply do not possess enough amplitude to overcome the large waves very often.

Since most of the wave records analysed here had significant wave heights in excess of 5 feet, the fully developed condition usually existed and, therefore, the high correlation. If lower significant wave heights had been considered, more double peaked spectra might have been encountered with a resulting decrease in the correlation.

3.3 Height of the Maxima of Surface Elevation

A comprehensive theory has been developed for the statistical behaviour of the maxima of surface elevation by Cartwright and Lonquet-Higgins (1956). The maxima are defined as the heights of the crests above the zero line. The theory shows that the statistical distribution of these maxima when normalized by $m_o^{1/2}$ is a function

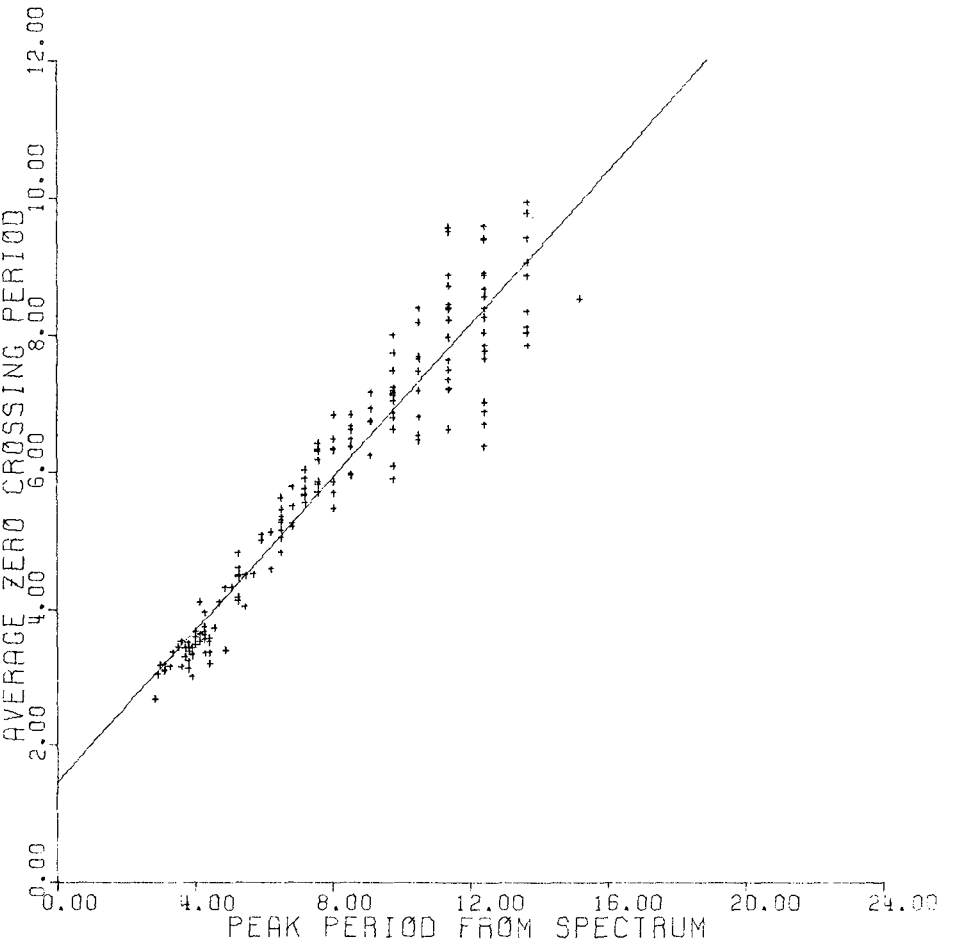

Figure 5. Average zero upcrossing period in seconds plotted against the peak period of the spectrum. The correlation coefficient is 0.96 and the slope of the least squares line is 0.56.

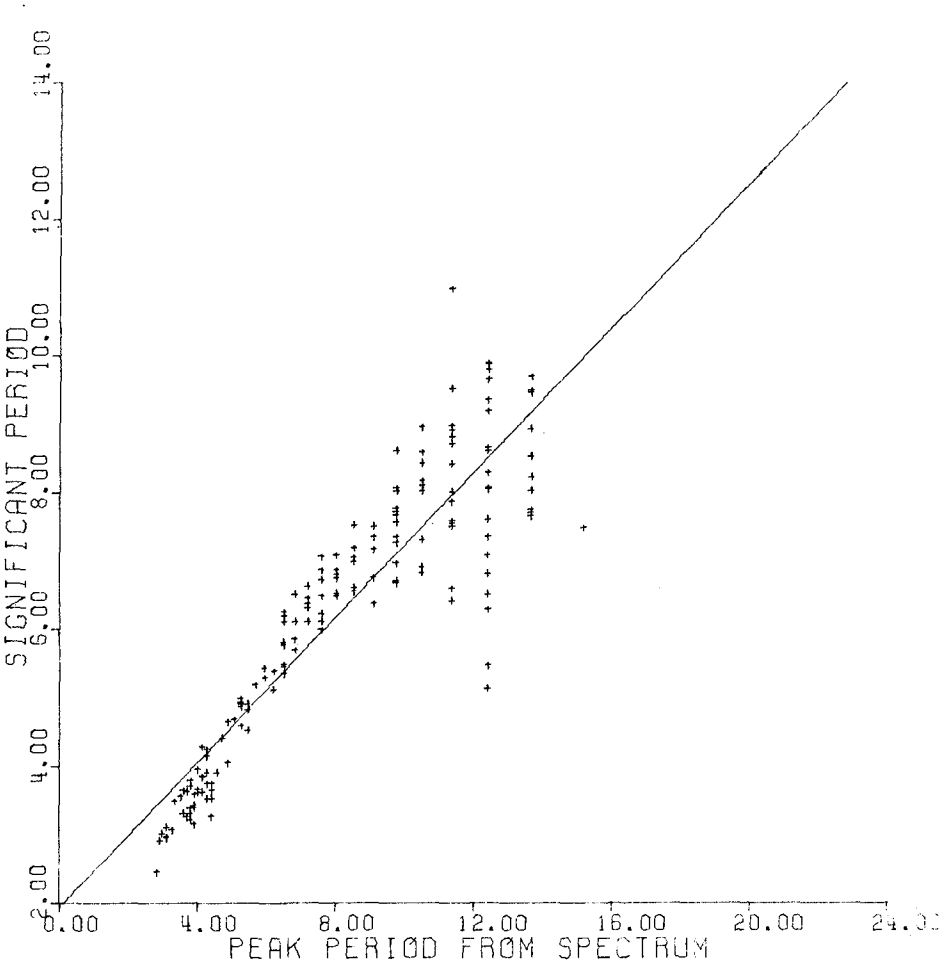

Figure 6. Significant period in seconds of the crest to trough waves plotted against the peak period of the spectrum. The correlation coefficient is 0.90 and the slope of the least squares line is 0.53.

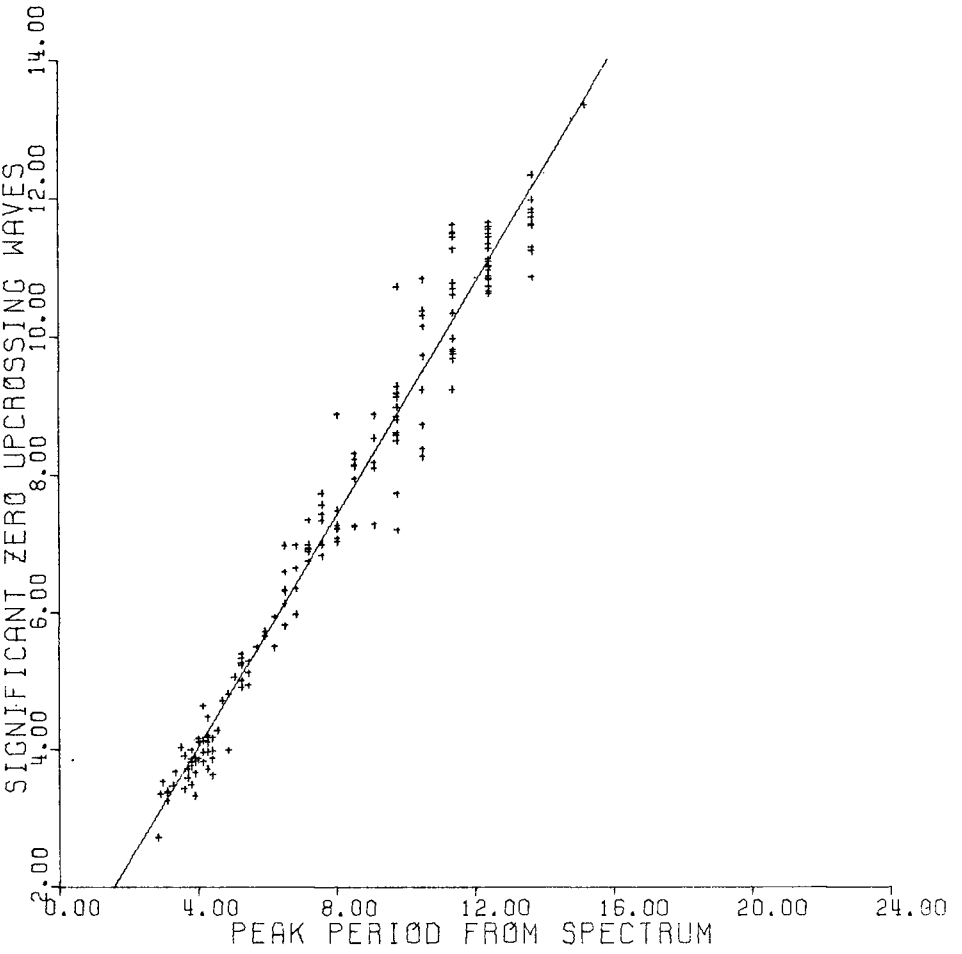

Figure 7. Significant period in seconds of the zero upcrossing waves plotted against the peak period of the spectrum. The correlation coefficient is 0.98 and the slope of the least squares line is 0.84.

only of the spectral width. $m_o^{1/2}$ is the square root of the integral under the spectrum and the spectral width is defined as:

$$\varepsilon^2 = \frac{m_o m_4 - m_2^2}{m_o m_4}$$

where m_n is the n^{th} moment of the spectrum taken about zero.

From the distribution the following relations are developed:

$$\mu_2' = 2 - \varepsilon^2$$

$$\overline{\eta_{max}} = \sqrt{2}\left\{ \left(\ln\left((1-\varepsilon^2)^{1/2} N\right)\right)^{1/2} + \frac{\gamma}{2}\left(\ln\left((1-\varepsilon^2)^{1/2} N\right)\right)^{-1/2} \right\}$$

where μ_2' is the second moment of the normalized maxima, η taken about zero, $\overline{\eta}_{max}$ is the expected mean of the highest maximum in the sample, and N is the No. of waves in the sample.

This leads to:

$$\frac{\overline{\eta_{max}}}{(\mu_2')^{1/2}} = \frac{\left[\ln\left((1-\varepsilon^2)^{1/2} N\right)\right]^{\frac{1}{2}} + \frac{\gamma}{2}\left[\ln\left((1-\varepsilon^2)^{\frac{1}{2}} N\right)\right]^{-1/2}}{\left(1-\frac{1}{2}\varepsilon^2\right)^{\frac{1}{2}}}$$

which describes the ratio of the maximum in a sample to the root-mean-square as a function of spectral width.

Figure 8 shows a comparison of the above theoretical relations with the observed values for the first 100 maxima in each of the 171 wave records. The records were grouped according to spectral width and then the means and standard deviations in the means were plotted as the error bars. The smooth curve in each case is the expected theoretical value.

In the upper plot only the first point shows significant departure of $(\mu_2')^{\frac{1}{2}}$ from the theoretical value. Both the first and last points were determined by only a few records. These records were characterized by significant wave heights small enough so that the signal to noise ratio of the recording system might have been important. Little weight can therefore be given to the departure.

The middle plot describing the normalized expected maximum in 100 waves as a function of spectral width shows good agreement with the theory with no significant departures.

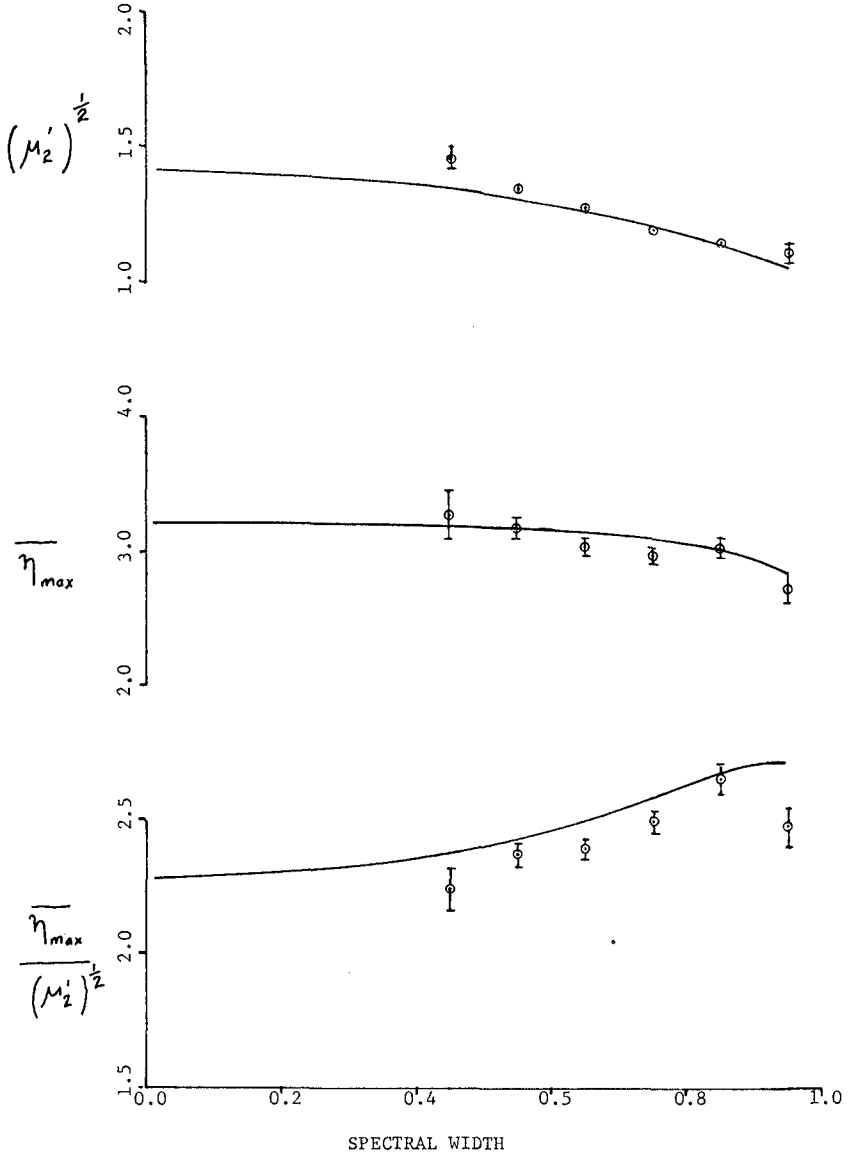

FIGURE 8. Parameters of Cartwright and Longuet-Higgins (1956) plotted against spectral width. The error bars represent the mean and the standard deviation in the mean of the observed values. The continuous lines are the values predicted by the theory.

The lower plot shows the mean of the ratio of the largest in the sample to the root-mean-square as a function of spectral width. The points corresponding to the smallest and largest values of the absissa are in doubt as mentioned earlier. Although it would appear that the other observed points tend to take a slightly lower value than the theoretical, the agreement must be considered good as the largest deviation is approximately 4%.

Figure 9 is a comparison of the experimentally observed distribution of the highest maximum in a train of 100 zero upcrossing waves compared to the theoretical distribution as developed by Goda (1970) from the theories of Cartwright and Longuet-Higgins (1956) and Davenport (1964). It is expected that the records for which the signal to noise ratio was poor would in this case also tend to yield too small values of the highest maximum. This might account for the excess of low values. However, the conclusion reached by Goda in his simulation study that the observed concentration was narrower than the theoretical would not seem to be justified here. The number of observed values in excess of 4 is greater than the theory predicts.

The theoretical curve is given by $P(\eta_{max}) = \eta_{max} \xi e^{-\xi}$

where, $\xi = N_o e^{-\frac{\eta_{max}^2}{2}}$ $\quad N_o = 100$

3.4 Maximum Wave Amplitude

Figure 10 shows plots of the ratio of the maximum wave amplitude to the root-mean-square wave amplitude as a function of spectral width for the first 100 waves of each record. The upper plot is for zero upcrossing waves and the lower for crest to trough waves. The horizontal line corresponds to the expected value of 2.28 proposed by Longuet-Higgins (1952) for 100 waves. In the case of the crest to trough waves the observed values increase with spectral width as expected. The value for the small spectral widths is less than the expected theoretical value by about 3 to 5%. In the case of the zero upcrossing waves the observed value appears to be nearly independent of spectral width as would be expected under the assumption that the statistics of the zero upcrossing waves are similar to crest to trough waves with a small value of spectral width. The value is also slightly lower than the predicted 2.28 however.

3.5 Runs of Waves greater than $H_{1/3}$.

A run of waves of length j is said to have occurred when j waves in a row have exceeded some predetermined value. Goda (1970) gives the probability of a run of waves greater than $H_{1/3}$ and of length j occurring as:

$$P_1(j) = p^{j-1}q$$

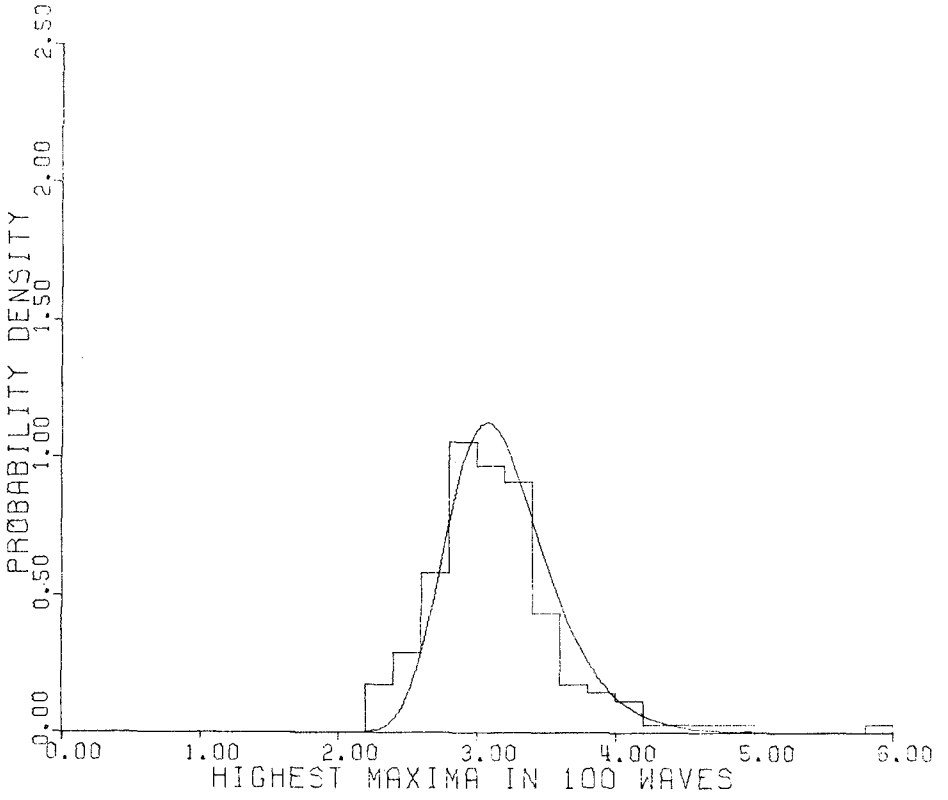

Figure 9. Observed and theoretical values of the highest maxima (normalized) in 100 zero upcrossings plotted gainst the probability density. The bar graph is the observed data and the smooth curve the predicted probability density function.

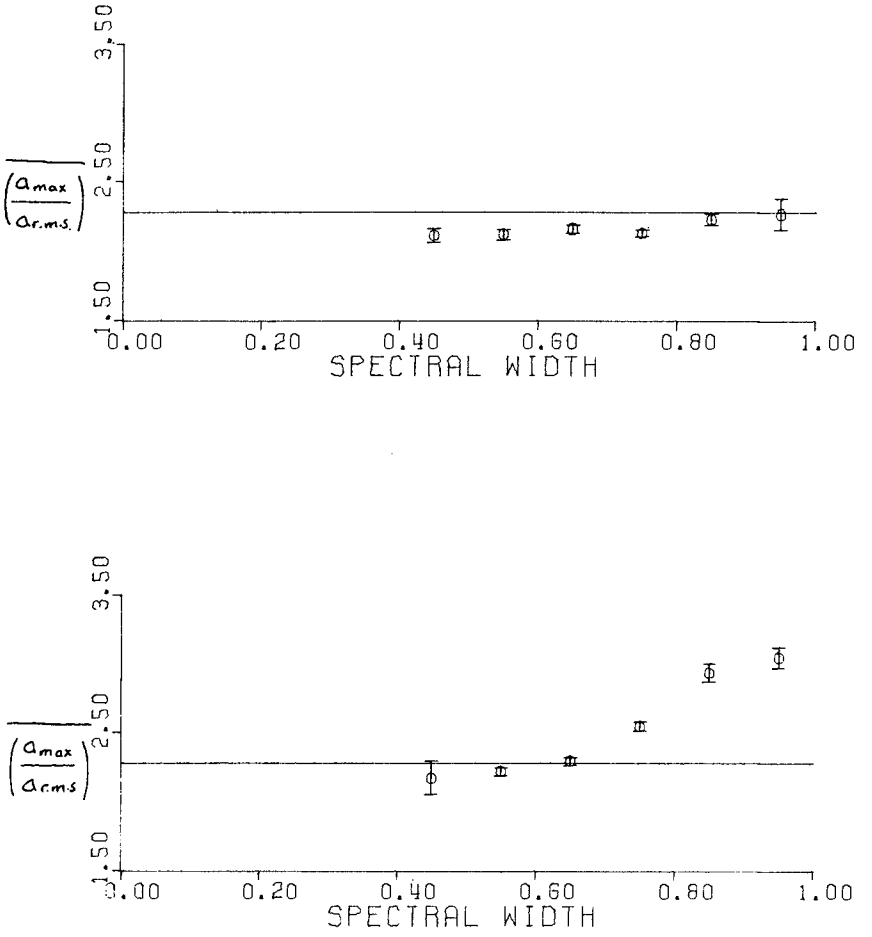

Figure 10. The observed ratio of the highest wave amplitude in a train of 100 waves to the root-mean-square wave amplitude plotted against spectral width. The top plot is for zero upcrossing waves and the bottom plot is for crest to trough waves. The horizontal line represents the value of 2.28 predicted by Longuet-Higgins (1952) for a narrow band spectrum.

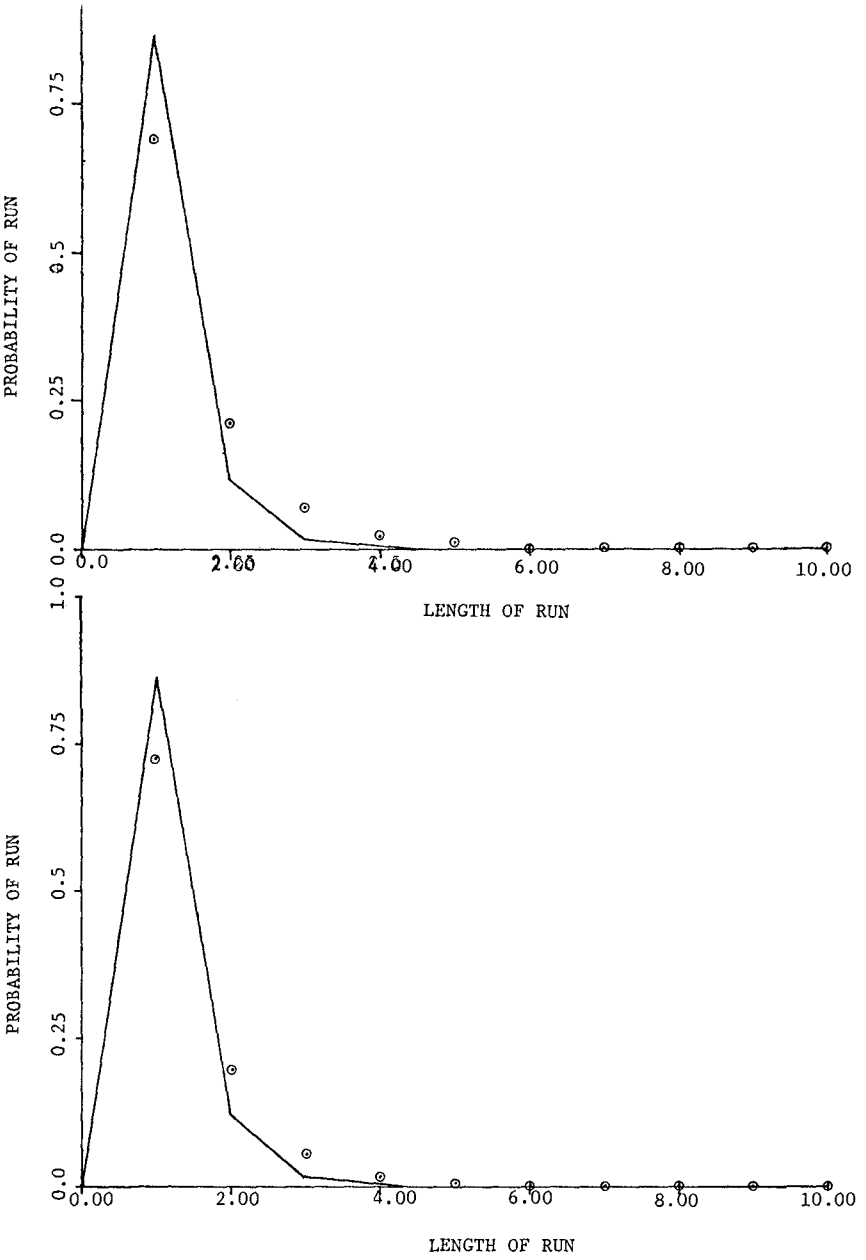

FIGURE 11. The observed and theoretical values of the probability of a run of waves greater than H 1/3 versus the length of the run. The top plot is for zero crossing waves and the bottom plot is for crest to trough waves.

where P is the probability of a wave exceeding $H_{1/3}$ (=0.134) and Q = 1-P.

Figure 11 shows a comparison of the observed results for zero upcrossing waves (top plot) and crest-to-trough waves (bottom plot). The line is the theoretical value and the points the observed probabilities. The results are very similar. Both tend to show runs of waves tend to occur much more frequently than the simple theory suggests.

4. Conclusions

The significant wave height computed from the integral under the spectrum most nearly represents the mean of the highest one-third of the zero upcrossing waves and is independent of spectral width for the type of records analyzed here.

There are strong correlations between the zero crossing period, significant period and significant zero upcrossing period respectively and the peak period at least in the case of fully developed seas featuring a singly peaked spectrum with an f^{-5} behaviour.

The theories of Cartwright and Longuet-Higgins predict very well the values of the ratio of the largest in a sample of maxima to the root-mean-square as a function of spectral width for values of spectral width between 0.5 and 0.9, the largest observed deviation being about 4%. The theoretical distribution presented by Goda (1970) for the maximum water surface height in 100 zero upcrossings fits the observed distribution reasonably well. However, the deficiency of high values found by Goda in his simulation experiment has not occurred here.

Runs of waves greater than $H_{1/3}$ and of lengths greater than 1 seem to occur in some cases several times more frequently than indicated by simple theory based on the probability that the event will occur at one trial.

References

Cartwright, D.E. and Longuet-Higgins, M.S. 1956, Proceedings of the Royal Society, A, 237, 212.

Davenport, A.G. 1964, Proc. Inst. Civil Engineering, 28, 187.

Goda, Y. 1970, Report of the Port and Harbour Research Institute, 9, No. 3.

Longuet-Higgins, M.S. 1952, Journal of Marine Research, XI, No. 3, 245.

CHAPTER 4

SOME RESULTS OF A DIRECTIONAL WAVE RECORDING STATION

by

J. Ploeg*

ABSTRACT

An experimental deep water wave recording station has been operated in Lake Ontario, Canada, from 1969 to 1971. The station included a triangular array with four wave sensors and a stable platform. The aim of the study was to obtain a better understanding of the usually rather vaguely defined wavelength parameter of a wind-generated sea and to record the direction of wave propagation directly in the wave generation field.

The station has also been used to test newly developed wave sensors, or to check and calibrate some of the existing wave recording systems, including staff gauges, pressure cells and accelerometers.

The paper describes briefly the mooring system of the floating stable platform and the triangular array. A comparison is made between various wave recorders, mainly by using spectral analysis, and some results of the wavelength and wave direction study are discussed.

INTRODUCTION

A general wave climate study of the Great Lakes and the Gulf of St. Lawrence for the Canadian Ministry of Transport in the late sixties resulted in some 20,000 wave frequency spectra. These wave data were presented in a report, which listed the significant wave heights and frequencies of the peak of the spectra as the two basic parameters defining the recorded sea state. ("Wave Climate Study - Great Lakes and Gulf of St. Lawrence", J. Ploeg, May 1971, NRC Report MH-107A or T- and R-Bulletin 2-17, Society of Naval Architects and Marine Engineers.) A number of other parameters was derived from the two basic parameters, such as the wavelength, which was calculated from the frequency of the peak of the spectrum, using the first order, small amplitude wave theory, $L = \frac{g \times 2\pi}{\omega^2}$.

However, it was felt that no information was available on the physical meaning of this computed wavelength parameter. In the past, the mean wave period has often been used to calculate the wavelength, mainly because spectral

*Head, Hydraulics Laboratory, National Research Council, Ottawa, Canada, K1A 0R6.

analysis was not readily available.

Just as the original significant wave height definition was chosen to correspond to the wave height estimated visually by an experienced observer, the wavelength should perhaps also be defined as a physically more meaningful parameter, possibly corresponding to the obvious periodicity of the sea, which can be observed on so many aerial photographs.

More directional information of wind generated seas in areas of limited fetch lengths, such as the Great Lakes, was also desirable.

Lake Ontario was chosen to install an experimental wave recording station, from which the above mentioned studies could be conducted. The development of new wave recorders and the calibration of some of the existing instruments was a natural extension of the main study.

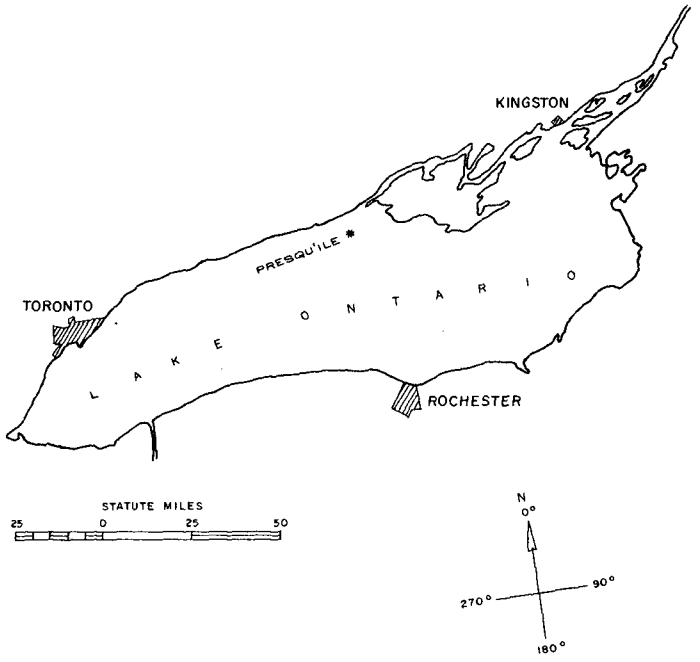

Fig. 1. Location of Wave Direction Study Station

MOORING SYSTEM OF THE STATION

The station was installed near Presqu'ile Point, Ont., about 7 miles offshore in 155 ft of water, guaranteeing the recording of true deep water wave conditions. The maximum fetch was approximately 110 miles from the S.W. (Fig. 1). The station consisted of a stable floating platform, built up from 8 inch diameter tubular steel, with an 8 ft triangular cross-section and an overall length of 100 ft. The 10,000 lbs positive buoyancy was supplied by two steel tanks, housed within the triangular framework; the vertical stability of the platform was excellent. Two buffered guy wires prevented rotational movements of the platform. On top of the platform, which protruded 12 ft above the mean water level, a 60 ft high fibreglass mast was mounted to install the meteorological sensors (Fig. 2). All power supply and recording equipment was mounted in waterproof cabinets on top of the platform.

The array of wave sensors was moored to a 60 ft triangular anchor, built up from tubular steel and guy wires. It was placed about 100 ft away from the platform. Four, 60 ft long slender spar buoys, made up of steel and plastic pipes, with 600 lbs buoyancy each, were suspended from the three apexes of the triangle and from the centroid. Pressure type wave sensors were installed on top of the buoys, 15 ft below the mean water level. A small triangular framework was attached to the buoys just below the pressure cells, to guarantee the exact geometry of the array. The 60 ft dimension of the array was chosen as half the most frequently occurring wavelength on Lake Ontario.

INSTRUMENTATION AND ANALYSIS

The platform was instrumented with a step resistance type wave staff gauge, a transmission line type wave staff gauge and an absolute and differential pressure cell type wave sensor. The array was equipped with four absolute pressure cells. All these instruments were developed and built at the National Research Council. Two commercial accelerometer type wave recorders were moored a short distance away from the platform, namely a B.I. wave recorder made in Canada and a Waverider, made in the Netherlands.

The step resistance type staff gauge and the pressure cells were of fairly standard design and no details are given here. The transmission line gauge used a relatively new approach and is briefly described next.

The gauge consisted of two concentric metal tubes, the outside one 2 inches in diameter, the inside one 1 inch in diameter. The outside tube was perforated to allow the

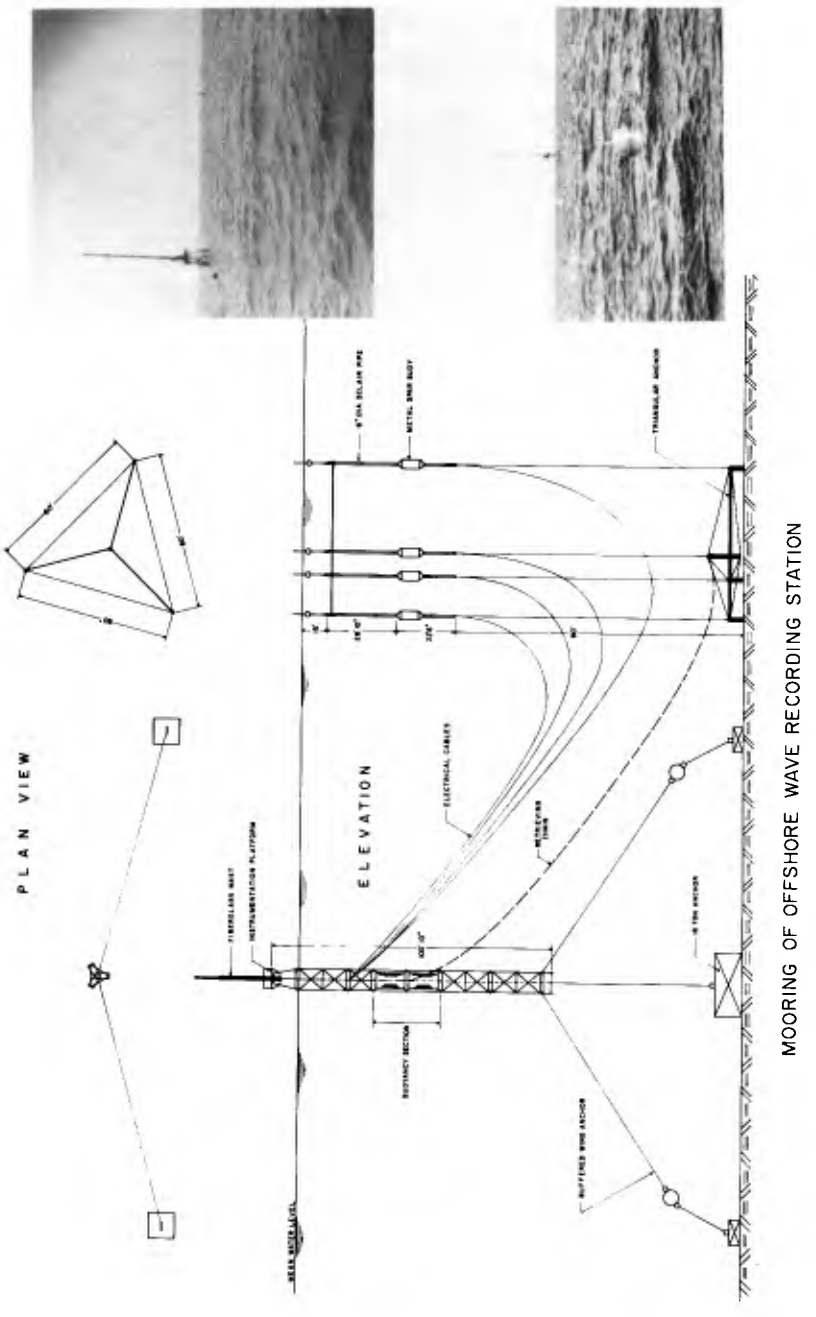

Fig. 2. Mooring Diagram of Offshore Wave Recording Station

water level inside the tube to follow the wave profile. The two tubes formed a coaxial transmission line. An electromagnetic wave generated at the top of the gauge and guided by this transmission line, reflected upon the water surface, where the permittivity changed by a ratio of 1:81 (air/water). The reflected wave travelled back to the top of the gauge, where it was used to generate a new wave, but of opposite polarity. The result, of course, was a square wave oscillation with the period linearly proportional to the wave height. The frequency of the oscillation was typically several megahertz and had to be scaled down to be recorded on tape.

Output signals of all wave recording instruments were transmitted by cables to the recorders on the platform to eliminate noise problems. The pulse frequency or period modulated signals were simultaneously recorded on a multichannel tape recorder. Only the Waverider system was transmitted to a shore station and recorded separately as an analog signal on an F.M. tape recorder.

The analysis of the recorded data was done on a small digital computer, which had an extensive analog to digital interface. A special programme was written, which allowed the analysis to be carried out as a one-pass computation, with a minimum of manual intervention from the operator. The programme allowed a simultaneous input of up to four channels. Demodulation of the signal into an analog voltage preceded the power spectral density analysis, which used the Fast Fourier Transform technique. The spectra were displayed to enable the operator to select frequency limits, if so desired, to compensate the "pressure spectra" using the Airy theory to obtain wave height spectra. Filtering of the data to specific bands of frequency could be done next. The computation of the RMS values of the four records was used to normalize the data, before the cross-correlation functions were computed.

The various calculations were done for the spectra as a whole as well as for different filtered portions of the spectra, with the filter limits selecting the frequency bandwidth defined by the location of peaks in the spectra. The bandwidths of the filtered spectra were typically 0.1 to 0.2 rad/sec. The time delays, resulting from the 6 cross-correlation functions were then used to compute the direction of wave progagation and the wave celerity. The wavelength was obtained by multiplying this wave celerity with the period corresponding to the frequency of the peak of the unfiltered or filtered spectrum. A flow chart of the programme is shown in Fig. 3.

COMPARISON OF WAVE RECORDERS

Although a comparison of wave recorders was originally not the reason for this study, it certainly turned out to be

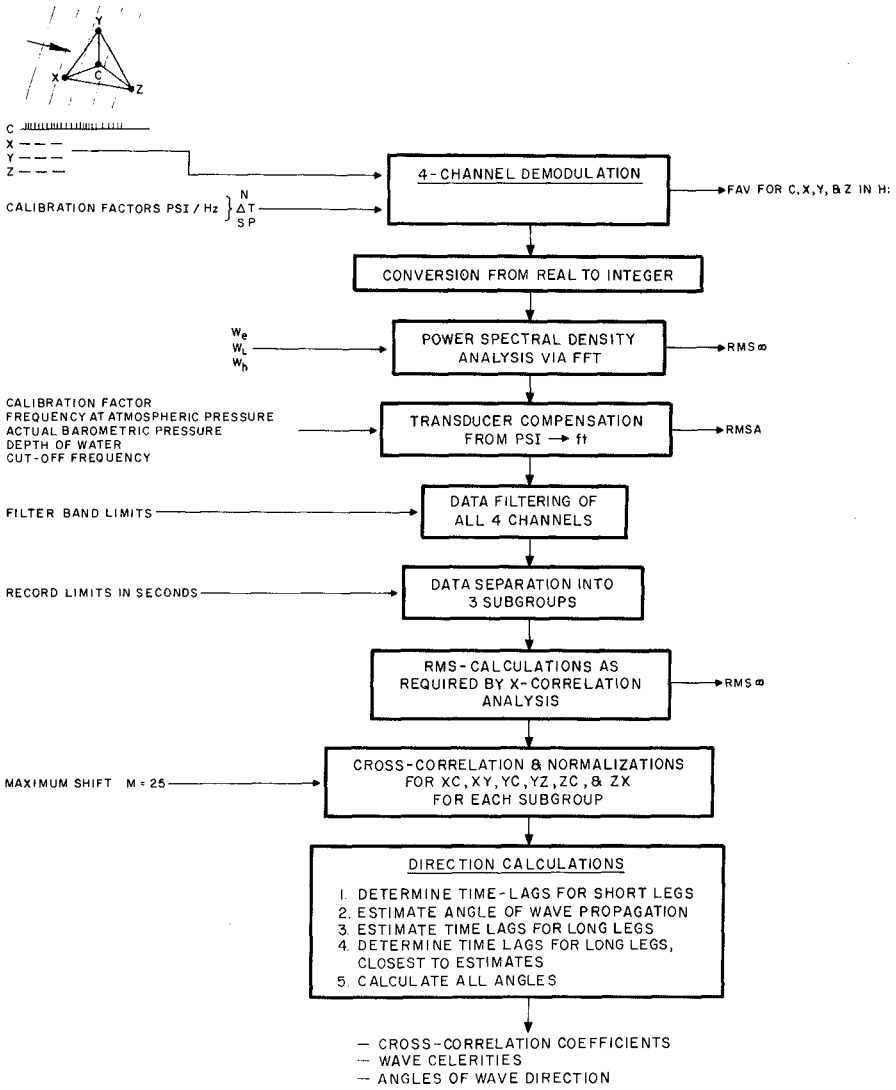

Fig. 3. Flow Chart of Directional Wave Analysis

an integral part of the programme. The entire facility lent itself pre-eminently for this purpose and the results were rather interesting.

The two different types of staff gauges yielded nearly always identical results in the power spectral densities, as well as the demodulated analog signal of the wave heights. Figure 4 is a typical example of the excellent comparisons obtained between the two instruments. The distance between the two gauges on the platform was approximately 4 ft. The transmission line wave staff gauge will be developed further by the National Research Council within the next year, because the cost and maintenance requirements turned out to be much less than any of the known staff gauge type wave recorders.

The differential pressure cell showed generally also good agreement with the wave staffs, except for frequencies higher than 0.3 Hz. The time history of wave heights from a pressure cell record was obtained by doing a Fourier transform on the recorded pressures, a compensation and conversion from pressures to amplitudes and a subsequent inverse Fourier transform to give wave height (Fig. 5).

The absolute pressure cell was slightly less accurate than the differential cell, probably because of the depth of submergence term, which had to be supplied from estimates of the mean water level. The differential cells, were of course not sensitive to the long term changes of the mean water level. Figure 6 shows an example of the typical results of a comparison between an absolute pressure cell and a wave staff gauge.

The B.I. wave recorder is not available anymore, but since it had been used extensively in the earlier quoted Wave Climate Study, this evaluation was extremely useful and a number of corrections were indeed applied to the original data as a result of this study.

The Waverider system could not be recorded on the same tape recorder with the other instruments and a direct comparison was therefore not possible. However, spectra recorded over the same time intervals compared reasonably well, both in spectral shape and in RMS values, the latter mostly within 10% of those of the wave staffs. It should be remembered that Lake Ontario does not have any high currents, which may in other locations affect some of these floating and moored wave recording systems severely.

RESULTS OF THE DIRECTIONAL ANALYSIS

The principal aim of the study was to determine a realistic wavelength parameter in a wind generated sea. The flow chart in Fig. 3 showed briefly how the outputs of the four sensors of the triangular array were used to

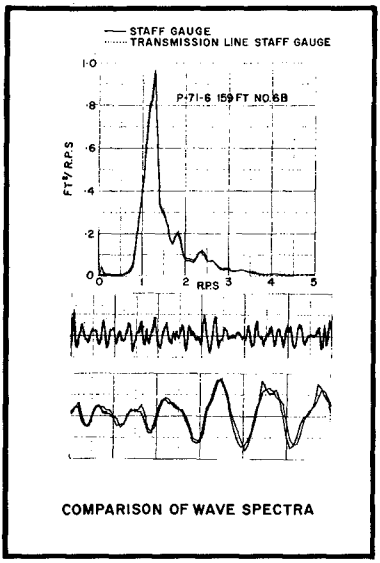

Fig. 4. Comparison of Step Resistance and Transmission Line Gauges

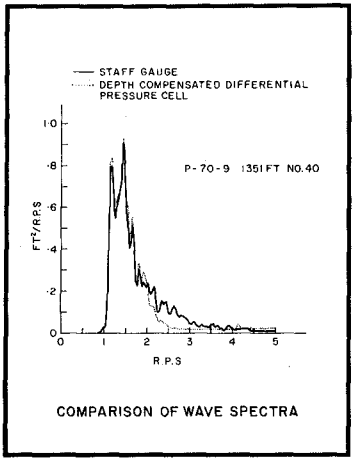

Fig. 6. Comparison of Staff Gauge and Pressure Cell

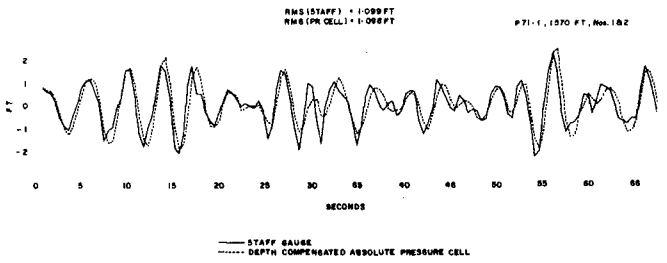

Fig. 5. Wave Record from Pressure Cell Through Inverse Fourier Transform

calculate the wave celerity and the direction of wave propagation.

In all cases the wavelengths resulting from this calculation turned out to be very close to the wavelength parameters obtained from the frequency of the peak of the unfiltered or filtered spectra and the small amplitude wave formula $L = \frac{2\pi \cdot g}{\omega^2}$. An interesting observation was that the deviations which occurred always indicated the wavelengths observed with the array to be longer than those calculated from the standard linear formula. The maximum difference was of the order of 10%. This discrepancy might be real, or might have been caused by a slight movement of the mooring system of the array. A further survey will be done in the near future to examine this in detail.

It appears reasonable to use the frequency of the peak of the spectrum to calculate a wavelength parameter, using the linear formula. This wavelength will indeed have a very real physical meaning, since it almost certainly corresponds to the length dimension between the crests of successive waves, which is so obvious when flying over a wind generated sea. It might be useful to refer to this wavelength parameter in the future as the "dominant wavelength".

As far as directional information is concerned, the results of the analysis indicated that the propagation of waves with frequencies close to the peak of the spectrum was parallel to the average wind direction, after the wind had been blowing sufficiently long from the same direction. There was some doubt about the accuracy of the observed wind direction by the meteorological mast on the platform, due to a possible rotational movement of the platform over $\pm 10^{\circ}$.

The triangular array in Lake Ontario was not very sensitive for the higher frequency components of the spectra. Directional and wavelength resolution beyond 0.3 Hz was not very good, although improvements in the results can be obtained by a more sophisticated analysis technique, which is presently being programmed.

From the results so far it appears that no definite trend in the spread of the wave direction occurred over the various bands of frequency of the spectra. It is expected that next year's study will resolve this question.

However, it should be noted that Lake Ontario has limited fetch lengths and swell does not develop. Only locally wind generated waves are observed at a recording station. In the oceans, swell will often start reaching a wave recording station long before the actual storm arrives which causes the locally generated waves. The low frequency

components of an ocean wave spectrum (the swell) will usually have a directional component different from the direction of the wind driven sea. Therefore, less spread should be expected in the Lake Ontario spectra than in the ocean spectra reported in the literature.

SOME OTHER ANALYSIS RESULTS

A number of other analyses were performed on the wave data from the Lake Ontario station and some of the preliminary results are briefly reported here because of their general interest.

Wave and meteorological data were observed and recorded continuously during an average storm on October 24 and 25, 1971. The record of a wave staff gauge was used to carry out some 200 spectral analyses over 16 minute intervals, with the starting points only 4 minutes apart, covering a total of about 13 hours of the storm. Figure 7 illustrates the spectral history of the storm, showing the familiar pattern of the build-up to a fully developed sea state with the peak of the spectrum continuously shifting to the lower frequencies and increasing its power spectral density value.

One of the conclusions to be drawn from this presentation pertains to the degree of stationarity of the input signal in the various frequency bands. Figure 8 is a plot of the power spectral density values at 13 different frequencies versus time. Typically the analysis had 20 degrees of freedom, giving a spread in the estimates of the spectral density values of about ±50%, using the 90% confidence limits of the Chi-square distribution. Figure 8 reveals that at most frequencies the spectral density values are within the ±50% band and therefore the process can be considered to be stationary. Only at the lower frequencies does the non-stationarity of the record become obvious and conclusions from spectral analysis techniques should thus be drawn with the necessary care.

The final figure, Fig. 9, is a plot of the RMS values, the peak frequencies and the meteorological data versus time for the length of this particular analysis. The RMS values over the 16 minute periods at 4 minute intervals show excellent continuity and give added confidence in the use of the RMS value for the estimation of wave heights even if the process is somewhat non-stationary as demonstrated earlier. Evidently, spectral analysis techniques are often employed to obtain RMS values because of compensation requirements.

The peak frequency curve seems to show a tendency to jump between discrete frequencies. No satisfactory physical interpretation has been found so far.

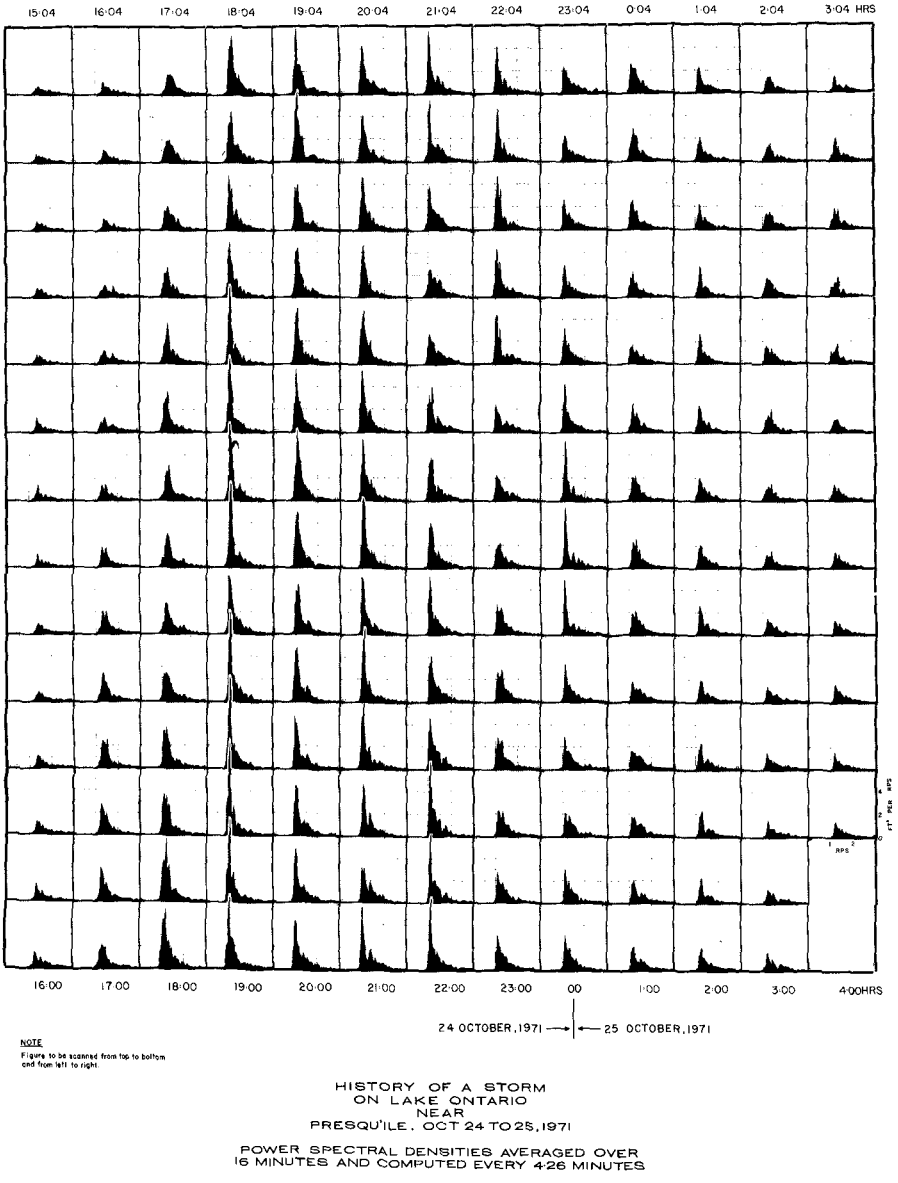

Fig. 7. History of a Storm as Power Spectral Density Curves

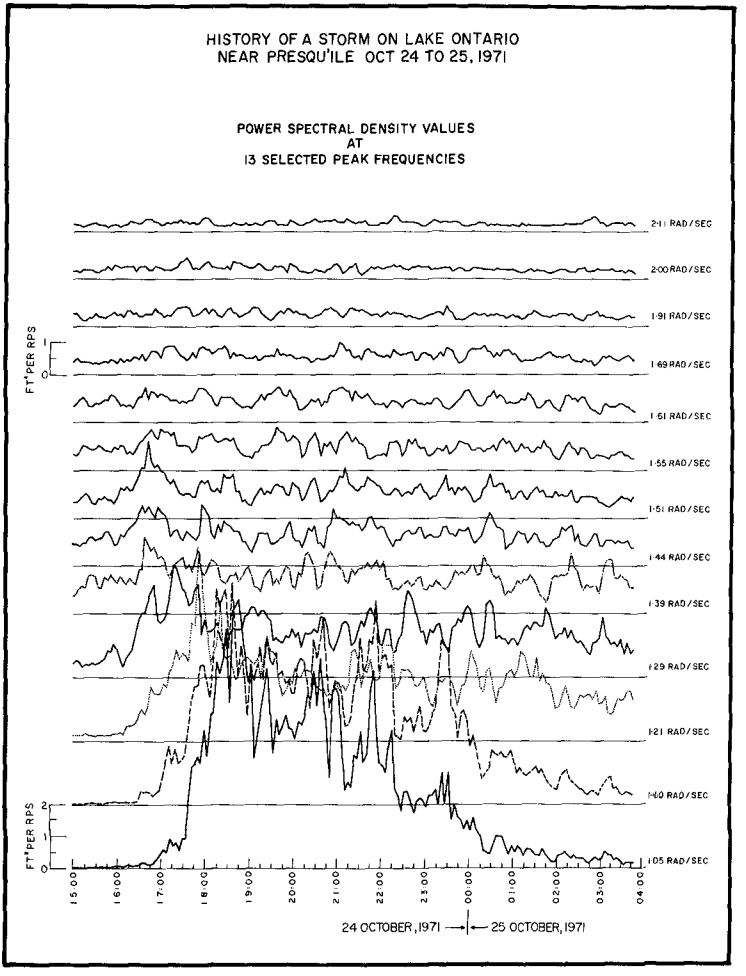

Fig. 8. Power Spectral Density Values at Different Frequencies During a Storm

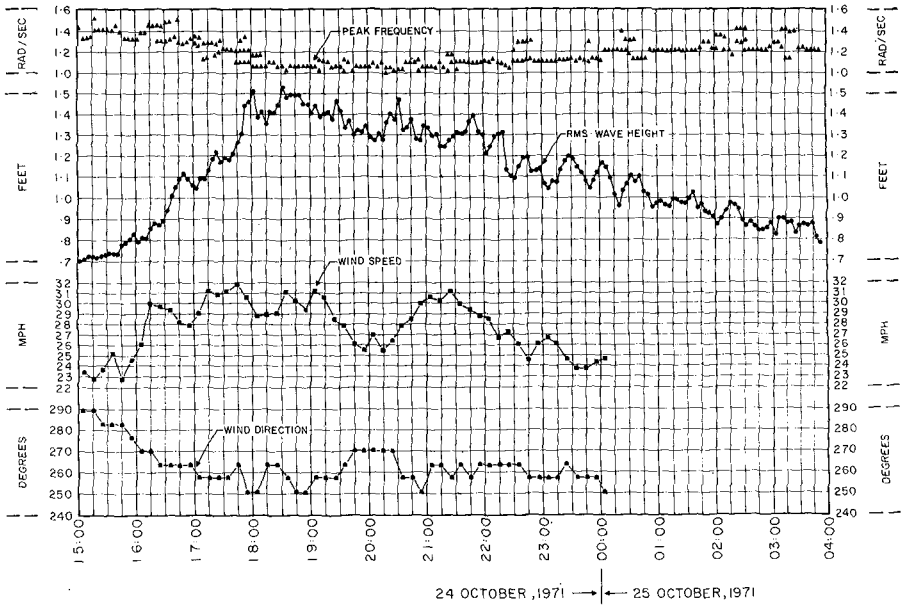

Fig. 9. Wave and Wind Parameters of a Lake Ontario Storm

The wind data were recorded 10 m above the mean water level; no attempt has been made yet to correlate the wave and wind records.

CONCLUSIONS

The study has probably up to now presented more problems than it has solved, although the question of a definition of the wavelength appears resolved. It is intended to improve on the mooring and recording aspects of the station in the coming years so that the many other questions which have arisen may also be answered, such as the up to 10% difference between measured and calculated wavelengths, the spread in the direction of wave propagation in a wind generated sea, the possibility of the occurrence of discrete frequencies in a wave spectrum and also, a further correlation between the wind and wave records.

CHAPTER 5

AN APPROACH TO AN OFF-SHORE WAVE CLIMATOLOGY

by

J.A.W. McCulloch

Atmospheric Environment Service
Canada Department of the Environment

ABSTRACT

A project to derive a wave climatology for that portion of the Atlantic Ocean between 30° and 60° N. and west of 30° W, recently begun by the Atmospheric Environment Service of Environment Canada, is described. The data base is produced from isolines of significant wave height and from plotted ship data. Details of the preparation of the basic analysis as well as the design of the remainder of the project are presented. Intermediate results will provide guidance to potential users of the wave climatology until sufficient data have been accumulated to lend statistical reliability to the analysis.

INTRODUCTION

In his opening address to the Thirteenth International Conference on Coastal Engineering, Mr. M.P. O'Brien, Chairman of the Coastal Engineering Research Council of American Society of Civil Engineers stated, inter alia, that knowledge of wave climate is primitive, and that this fact has created a " . . . most frustrating gap in the kit of tools available to the coastal engineer." A major cause of this unfortunate situation is the lack of a suitable data base for many areas of interest. This paper describes a project designed to reveal the wave climate of the portion of the Atlantic Ocean between 30° and 60° north latitude, and west of 30° west longitude, but the approach is potentially applicable to any ocean area.

Measurements are ordinarily the raw material for any statistical study. Unfortunately, in the area under consideration, few deep-water wave measurements exist, and those are strongly biased in position and time. Visual estimates of wave conditions are made by ships crossing the area, but like any visual estimate, accuracy depends strongly on the individual, the conditions to which he is exposed at the moment, and other unquantifiable variables. Furthermore, most such estimates are also biased in space and time. Hindcasts based on the surface wind field are possible, but the derivation of the latter from surface pressure gradients and isobar curvature is tedious and can produce misleading results. Perhaps within the decade, satellite-borne instruments will relieve the problem.

Faced with the immediate problem of wave statistics for the continental shelf areas of Canada's Atlantic Coast, H.J.A. Neu, an engineer on the staff of the Bedford Institute, Marine Sciences Directorate of the Canada Department of the Environment, recognized the potential of routine analyses of significant wave height (H_S) at 0001 and 1200 GMT over the northwest Atlantic made by the Atmospheric Environment Service (AES) of the Canada Department of Environment. He undertook a feasibility study (Neu, 1971), and demonstrated to the AES the desirability of undertaking a similar program on an operational basis.

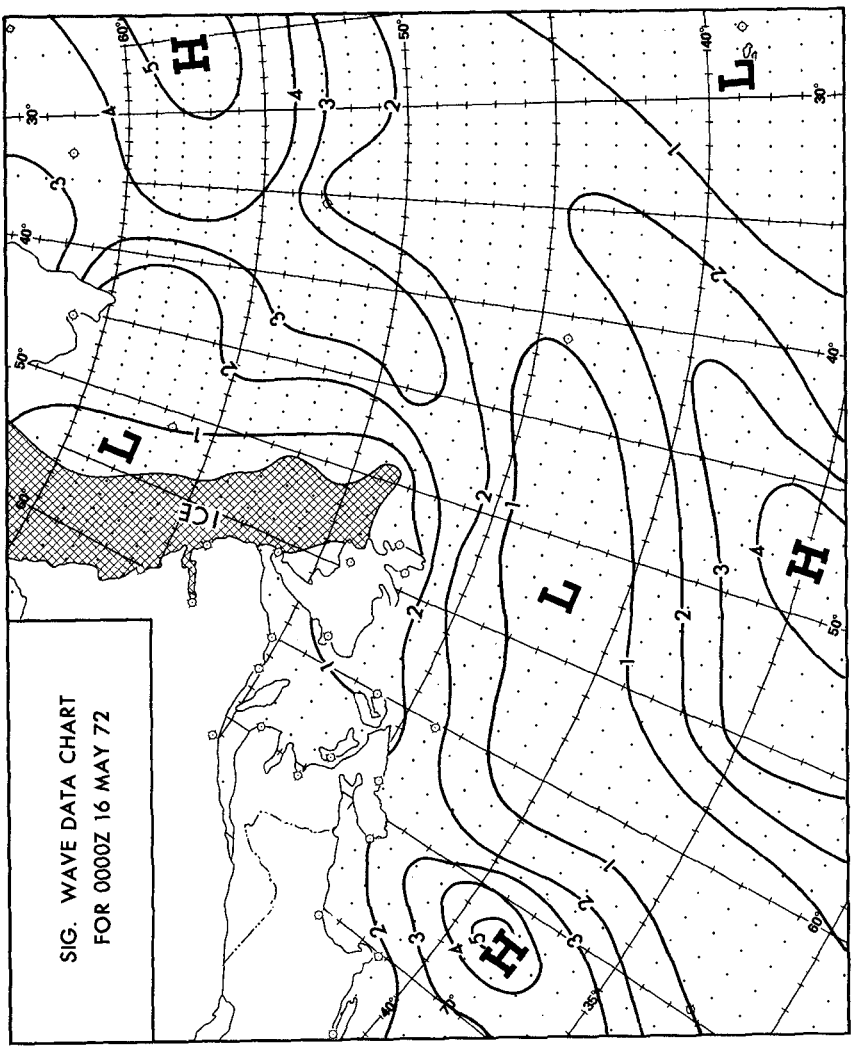

Figure 1: A sample analysis of significant wave height. The chart actually used in this project also contain plotted ship observations.

In the following sections of this paper, the procedures used in the preparation of the basic wave-height analysis are presented, Neu's pilot project is briefly described, and the AES project which has evolved is discussed in detail. While many years of data will be required to determine the wave climate, intermediate results will be of interest to those for whom alternative guidance does not exist. However, in such cases, the user of the intermediate results must recognize the limitations of the program and the hazards of using samples of insufficient size for statistical reliability.

THE BASIC ANALYSIS

To meet a portion of the requirements of maritime units of the Canadian Armed Forces, the Meteorology and Oceanography (METOC) Centre in Halifax has undertaken a program of the analysis and prognosis of significant wave height. Isolines of significant wave height at one-metre intervals are analysed twice daily (fig. 1), and are used as the base charts for 12-, 24- and 36-hour prognostics. The method of analysis combines observations from ships and offshore drilling platforms with hindcasting, while imposing spatial and temporal continuity for the control of quality.

The 12-hour prognostic of the 0001 GMT analysis becomes the first-guess field for the 1200 GMT analysis. This prognostic is prepared using extrapolation, including simple trends, as well as compatability with the forecast surface weather map.

When the observational data arrive, they are plotted on a blank chart. With the earlier prognostic chart as an underlay, discrepancies between the expected pattern and the observational data become obvious. Resolution of these may require several approaches. Prime suspect must be the first guess field, for errors in judgement about the intensification of a weather system (and thus, a wave system), or about the speed or direction of movement of such systems must be expected. However, observing, transmission or plotting crrors must not be overlooked. For example, a ten-degree error in latitude or longitude of the ship can be caused by the mistaking of a dot for a dash during communication; ordinarily, this can be detected on the weather chart since wind, pressure, previous position and water temperature could singly or collectively provide evidence. The forcing of temporal and spatial continuity and compatability with the weather map on the resulting analysis provide the best quality controls possible in these circumstances.

Once the large discrepancies are resolved, the first-guess field is adjusted to account for the observed data and unexpected developments in the wind field. In general, adjustments are mainly in the location, strength or shape of troughs, ridges or centres of low or high significant wave height.

While only one set of isolines is produced, many observations show sea and swell separately. Such observations are used to calculate a combined wave whose H_S is the square-root of the sum of the squares of the significant wave height of each train.

Large portions of the area analyzed lie off regualar sea lanes; observed data in these sections are scarce. To make the "analyses" more meaningful in such regions, hindcasts based on the current weather map and its recent history are made. The nomograms used in this task are those due to Suthons (1945) as modified by Morgan (1971).

The resulting isolines of combined significant wave height (in metres) are transmitted by radio-facsimile to Canadian naval vessels and merchant ships of all nations with appropriate receiving equipment. Figure 1 demonstrates an analysis with the plotted data (which are usually transmitted as well) missing. At the same time, the prognostic patterns of significant wave height for 12-, 24- and 36-hours are also transmitted. As a measure of the quality of the analyses, the prognostics which are based upon them are routinely verified against subsequent observations and analyses. During 1971, the AES products at 24- and 36-hours had a lower monthly root-mean-square error (over a ten-point grid which includes the ocean weather ships) than the other forecast available for the area, the U.S. N.W.S. computer-derived prognostics. This applied to all twelve months at 24 hours and to eleven of the twelve at 36 hours. It is reasoned that this fact is evidence that the analysis is a useful representation of the actual conditions.

THE PILOT PROJECT

Neu recognized the potential of the routine analysis described above to serve as a data base for a wave climatology of the shelf areas off Canada's Atlantic coast. He undertook a pilot project (Neu, 1971) to establish the feasibility of the approach. A grid system 2.5 degrees latitude by 2.5 degrees longitude (termed Neu-Squares by this writer and his colleagues) was established. From each analysis, and from a linear interpolation between them providing a time scale of six hours, Neu abstracted the average significant wave height in each grid square along with an appropriate direction and period. The latter two quantities were inferred from the plotted data.

In the report on this pilot project, (Neu, 1971), the data are presented in several ways:

(a) for each month of 1970, and for each Neu-square, the total energy per metre of wave crest is presented graphically;

(b) for each month of 1970, for each Neu-square, and for each of eight directions, graphs of total energy per metre of wave crest as functions of wave period are given;

(c) for each month of 1970, for each Neu-square and for each of eight directions, the number of occurrences by height and period class is shown in tables.

The graphs and tables contained in this report are the only readily available wave statistics for the whole area in print at the present time. Because the AES required time to adapt and take over the program on an operational basis, Neu continued the project through 1971 and it is hoped that he will publish those data as well.

As an interesting sidelight, Neu's 1971 analysis brought to light an unexpected flaw in the operational wave information service of the AES. Unknown to the forecasters at the METOC Centre, the various drill rigs had been reporting maximum waves over differing time intervals. It had been assumed that the heights being reported were significant wave heights. In the higher wave situations where the difference between the maximum and the significant waves was large, the quality control procedures outlined in the section above detected the discrepancy and the data were modified. However, a bias toward higher values remained, especially since one reaches the stage where present

techniques cannot determine with certainty that a particular value of significant wave height is inconsistent with history and weather. This bias resulted in an anomalous bulge of high energy in all months into the Neu-squares occupied by the rigs, signalling very clearly the existence of an observational problem. Once identified the problem was resolved through consultations with the operators.

PROGRAM MODIFICATIONS

Neu reasoned, quite justifiably, that the concept had been proven valid and should be carried on by an operational agency. The AES concurred and began a modified program on May 1, 1972 after the completion of a further, but relatively small, feasibility study. The modifications were necessary to permit the program to be undertaken within existing resources.

The relationships between the space and time scales chosen by Neu was deemed suitable. However, Neu was interested mainly in the shelf areas, while the AES had to consider a much large portion of the northwest Atlantic Ocean. To keep the activity to a size such that it could be undertaken within existing resources, it was decided to consider areas five degrees latitude by five degrees longitude with a time base of 12 hours. No time resolution was being sacrificed because the 6-hour "data" used by Neu were simply linear interpolations between the basic analyses. Considerable spatial resolution is sacrificed, but intelligent interpretation of the results will offset this to some extent. Doubling both the space and time scales reduces the effort involved by about one order of magnitude.

The other major change from Neu's design is the quantity being abstracted. When one considers a point, at any time there is a single significant wave height. However, when one is dealing with an area, unless circumstances are exceptional there is a variation of H_S across this area at any one time. The problem resolves itself into determining what quantity one should abstract. Neu chose an average H_S over his areas. The AES felt that the following types of questions are the ones that would be asked:

(a) What is the probability that the significant wave height at a point will equal or exceed a particular value in a particular month; or

(b) What is the significant wave height that will be exceeded, say, five percent of the time in a given month at a particular place? Using standard statistical results, the above questions could treat the average wave, or the maximum wave instead of the significant wave.

On the reasoning outlined above, the AES has chosen to abstract the highest significant wave height occurring at analysis time within each of the grid squares. This quantity will permit the derivation of a climatology of extremes (such as those for temperatures, humidities and winds used by heating and cooling engineers) so that questions similar to those posed above may be answered. Furthermore, the highest significant wave in an area at map time is easier to determine and is less affected on a percentage basis by irregularities in the analysis than is the average over the area.

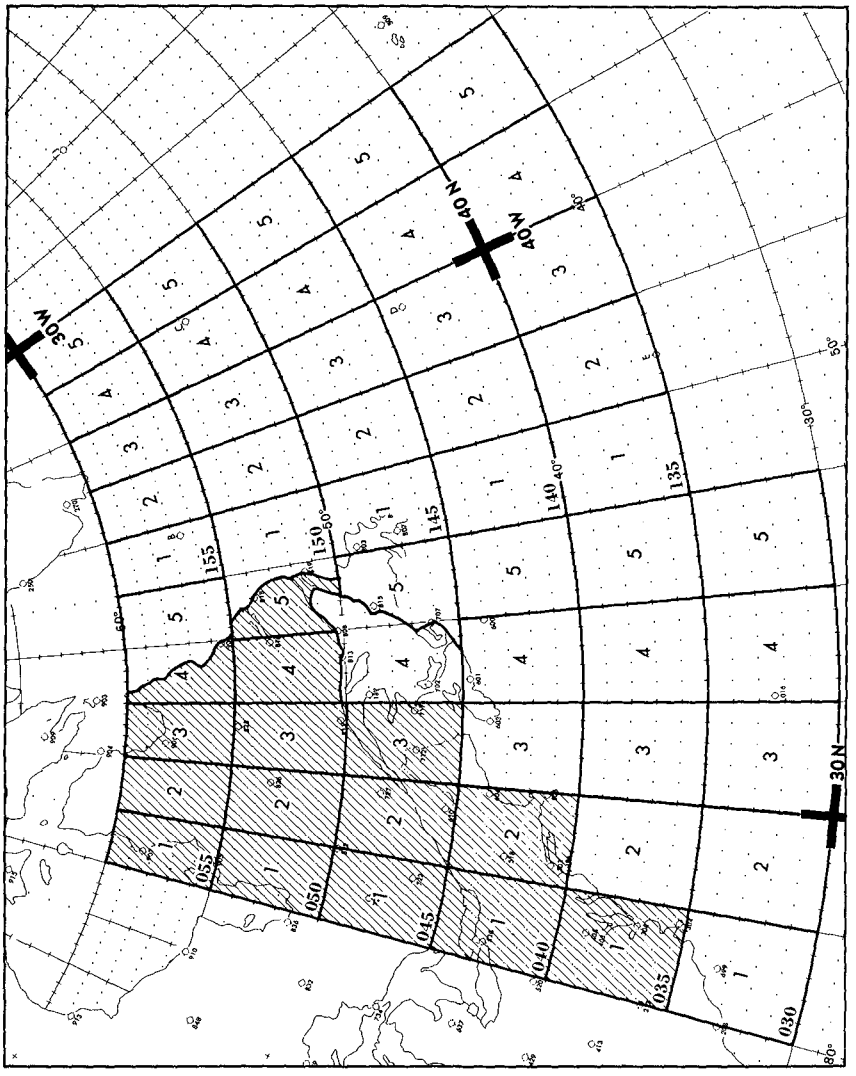

Figure 2: Area of interest and grid square identification. The hatched areas are invalid.

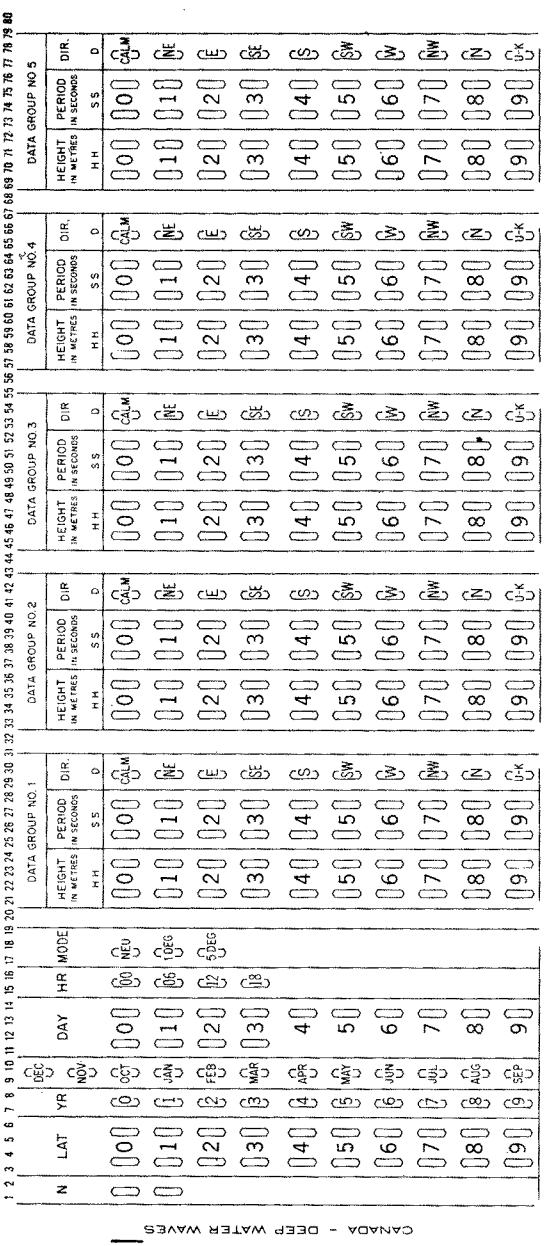

Figure 3: The optical mark recognition (OMR) card used for communicating the data to the computer.

THE AES PROJECT

Figure 2 shows the area covered by this project along with the system of identification of each grid square. The squares are grouped in fives, with the group identification consisting of the latitude of the southern boundary prefixed by a "O" or "1". For those groups whose western boundary is 80° W. longitude, the prefix is "O". If the western boundary of the group is 55° W longitude, the prefix is "1". Within each group, the squares are numbered one through five.

It should be noted that some squares are invalid because they are largely or completely land. Furthermore, some boundaries have been distorted to conform to the coastline. For example, the western boundary of square number five in group 055 has been extended to the coastline of Labrador, and all other squares in that group are invalid. Similarily, square one of group 150 has been extended westward to the coastline, and group 050 is completely invalid. Square four of group 045 constitutes the Gulf of St. Lawrence.

Data are recorded by the analyst on optical mark recognition (OMR) cards such as the one illustrated in figure 3. The first several columns are for the identifying information of the group (identifier, date/time, and mode – in this case, 5-degrees), and the remainder for the data for each square in the group. Ten such cards are produced from each chart. At the end of each month, the accumulated cards and copies of the analyses from which they were produced are forwarded to the AES headquarters for processing.

The first pass through the computer is to detect and note reading or coding errors. These are corrected on the original cards by headquarters staff, referring where necessary to the copies of the base charts. Second pass is for sorting and punching cards (as a permanent archive because the contents of two OMR cards can be recorded on one standard 80-column punched card).

Sorting is by month, area, wave direction, and classes of height and period. Initially, the height and period classes described in table 1 will be used because of the number of data available. After several years have passed, it may prove necessary to increase the resolution in height and period, but this may be easily accomplished at that time because the original data are still available on the punched cards.

TABLE 1:

Limits of Height and Period Classes

Height Classes – Metres		Period Classes – Seconds	
H1	0.5 – 1.4*	S1	<4
H2	1.5 – 3.4	S2	5 to 7
H3	3.5 – 5.4	S3	8 to 9
H4	5.5 – 7.4	S4	10 to 12
H5	7.5 – 10.4	S5	>12
H6	$\geqslant 10.5$		

*Waves with height less than 0.5m are classed as "calm", and the total of such cases listed in the area summary.

TAB 251 DEEP WATER WAVE CLIMATOLOGY PROJECT NO. 41671 PAGE 5

PERIOD OF RECORD 1972 - 1972 MONTH 5 SQNO= 9 SW-CORNER= 55N, 40W MODE= 5 DEG.

NW

	H1	H2	H3	H4	H5	H6	SH
S1	0	0	0	0	0	0	0
S2	0	6	4	0	0	0	10
S3	0	0	3	0	0	0	3
S4	0	0	1	0	0	0	1
S5	0	0	0	0	0	0	0
SI	0	0	0	0	0	0	0
SV	0	6	8	0	0	0	14

EXTR. HH(SS)=05(09),SS(HH)=10(04)
YR/DA/HR 72/29/00 , 72/28/12

N

	H1	H2	H3	H4	H5	H6	SH
S1	0	0	0	0	0	0	0
S2	0	6	0	0	0	0	6
S3	0	0	1	0	0	0	1
S4	0	0	0	0	0	0	0
S5	0	0	0	1	0	0	1
SI	0	0	0	0	0	0	0
SV	0	6	1	1	0	0	8

EXTR. HH(SS)=06(12),SS(HH)=12(06)
YR/DA/HR 72/26/00 , 72/26/00

NE

	H1	H2	H3	H4	H5	H6	SH
S1	0	0	1	0	0	0	1
S2	0	1	0	0	0	0	1
S3	0	1	1	0	0	0	2
S4	0	0	1	0	0	0	1
S5	0	0	0	0	0	0	0
SI	0	0	0	0	0	0	0
SV	0	2	3	0	0	0	5

EXTR. HH(SS)=05(08),SS(HH)=11(04)
YR/DA/HR 72/25/12 , 72/25/00

T O T A L S

W

	H1	H2	H3	H4	H5	H6	SH
S1	0	0	0	0	0	0	0
S2	1	2	1	0	0	0	4
S3	0	1	3	0	0	0	4
S4	0	0	1	1	0	0	2
S5	0	0	0	0	0	0	0
SI	0	0	0	0	0	0	0
SV	1	3	5	1	0	0	10

EXTR. HH(SS)=06(10),SS(HH)=11(04)
YR/DA/HR 72/28/00 , 72/19/12

	ICE	CLM	H1	H2	H3	H4	H5	H6	H1	SH
		0								0
S1		0	0	1	1	0	0	0	0	2
S2		0	2	22	12	2	0	0	0	38
S3		0	0	3	13	0	0	0	0	16
S4		0	0	1	3	1	0	0	0	5
S5		0	0	0	0	1	0	0	0	1
SI		0	0	0	0	0	0	0	0	0
SV	0	0	2	27	29	4	0	0	0	62

EXTR. HH(SS,D)=06(12, N1,SS(HH,D)=12(06, N1
YR/DA/HR 72/26/00 , 72/26/00

E

	H1	H2	H3	H4	H5	H6	SH
S1	0	0	0	0	0	0	0
S2	0	1	2	0	0	0	3
S3	0	0	0	0	0	0	0
S4	0	0	0	0	0	0	0
S5	0	0	0	0	0	0	0
SI	0	0	0	0	0	0	0
SV	0	1	2	0	0	0	3

EXTR. HH(SS)=05(05),SS(HH)=06(02)
YR/DA/HR 72/07/12 , 72/23/12

SW

	H1	H2	H3	H4	H5	H6	SH
S1	0	0	0	0	0	0	0
S2	1	3	3	1	0	0	8
S3	0	0	2	0	0	0	2
S4	0	0	0	0	0	0	0
S5	0	0	0	0	0	0	0
SI	0	0	0	0	0	0	0
SV	1	3	5	1	0	0	10

EXTR. HH(SS)=06(06),SS(HH)=09(05)
YR/DA/HR 72/03/00 , 72/13/12

S

	H1	H2	H3	H4	H5	H6	SH
S1	0	0	0	0	0	0	0
S2	0	1	1	1	0	0	3
S3	0	1	2	0	0	0	3
S4	0	0	0	0	0	0	0
S5	0	0	0	0	0	0	0
SI	0	0	0	0	0	0	0
SV	0	2	3	1	0	0	6

EXTR. HH(SS)=06(06),SS(HH)=08(03)
YR/DA/HR 72/02/00 , 72/01/12

SE

	H1	H2	H3	H4	H5	H6	SH
S1	0	1	0	0	0	0	1
S2	0	2	1	0	0	0	3
S3	0	0	1	0	0	0	1
S4	0	1	0	0	0	0	1
S5	0	0	0	0	0	0	0
SI	0	0	0	0	0	0	0
SV	0	4	2	0	0	0	6

EXTR. HH(SS)=05(08),SS(HH)=10(02)
YR/DA/HR 72/15/00 , 72/19/12

WAVE HEIGHT IN METERS
CLM 0 - 0.4
H1 0.5- 1.4
H2 1.5- 3.4
H3 3.5- 5.4
H4 5.5- 7.4
H5 7.5-10.4
H6 GE 10.5
HI INDETER.

PERIOD IN SEC.
S1 0- 4
S2 5- 7
S3 8- 9
S4 10-12
S5 GE 12
SI INDETER.

SH=HOR. SUM
SV=VERT.SUM

ICE MORE THAN 75% COVERED

Figure 4: A sample print-out.

During the sorting program, the extreme significant wave height for the area for the month for each direction is flagged along with its associated period and date of occurrence. Similarily, the longest period is noted along with the accompanying height and date.

Printer output will be in the form of tabulations of actual occurrences of height and period classes for each of the eight directions, and for the whole area regardless of direction. This will exist for actual and for collective month (all Januarys grouped together, for example). A model of the printer output is presented in fig. 4.

The project will be continued until the frequency of occurrence of the various classes for the collective month becomes stable, and thus can be used as a predictor of the probability of occurrence of the classes in the future. It is not possible to estimate at this time how long it will require to reach that stage.

If an area is more than 75 % ice covered, no attempt is made to abstract the wave information. Instead, a code "88" is used in the position reserved for wave height. The number of such occurrences will provide a very rough guide to the temporal extent of ice cover.

SUMMARY

In response to a long-standing need, the Atmospheric Environment Service of Environment Canada has embarked on a project that ultimately should provide a definitive wave climatology for the northwest Atlantic Ocean. In place of "measurements" the data base will be drawn from analyses of significant wave height based on a combination of observations and hindcasting within the constraints of continuity both in space and time.

Both the data base and the study design contain flaws, but the best compromises possible under the circumstances have been made. With suitable care by the user, the intermediate results may be used as interim guidance in the absence of other sources. Even inshore interests may find these results useful provided they take bottom and other boundary processes into account.

It must be emphasized that:

(a) the wave height parameter being abstracted is the highest significant wave height at map time anywhere within the grid square, in order that an extremes climatology could be produced. Since these are significant wave heights, they may be interpreted in terms of maximum wave heights using standard techniques.

(b) the period and direction are the values which, in the judgement of the analyst, are representative of the height chosen. These quantities are not analyzed separately but are deduced from the surrounding plotted data and the analyst's knowledge of how the present wave situation has evolved.

ACKNOWLEDGEMENTS

The writer is spokesman for persons too numerous to mention who have participated in the development of the program. Special mention is due Mr. B.S.V. Cudbird, Chief of the Data Processing Division of AES, Mr. M.R. Morgan, OIC of the METOC Centre at Halifax, and the staffs of both organizations. Mr. M.S. Webb also played a major role in the development of the project.

REFERENCES

Morgan, M.R., 1971, "The Analysis and Forecasting of Sea and Swell Conditions in Deep Water", TEC 763, Atmospheric Environment Service, Downsview, Ontario, 32 p.

Neu, H.J.A., 1971, "Wave Climate of the Canadian Atlantic Coast and Continental Shelf – 1970", AOL Report 1971 – 10, Bedford Institute, Dartmouth, N.S. 28 p + 24 appendix figures.

Suthons, C.T., 1945, "The Forecasting of Sea and Swell Waves", Memo No 135/45, Naval Weather Service, British Admiralty, London, 84 p.

CHAPTER 6

EXTREME WAVE CONDITIONS IN BRITISH AND ADJACENT WATERS

LAURENCE DRAPER
NATIONAL INSTITUTE OF OCEANOGRAPHY
Wormley, Godalming, Surrey, Great Britain.

ABSTRACT

Information on extreme wave conditions is needed in the design of offshore structures. This paper present the results of calculations of the parameters in the 50-year storm; the work has been based on extreme wind data and on instrumental wave measurements. The results are complementary, and are combined in two maps, one of extreme wave height and the other of the corresponding wave period.

INTRODUCTION

Systematic measurements of waves in British and adjacent waters have been made during the last quarter of a century. Estimates of extreme wave parameters for specific sites have been required for a number of purposes, but until recently no attempt had been made to produce a coherent picture of conditions in all these waters. The need for such an overall picture has existed for some time, but the study has been precipitated by the imminent government regulations required by the Mineral Workings (Offshore Installations) Act 1971. This Institute was requested by the Department of Trade and Industry to provide guidance on the oceanographic parameters which the installations must be designed to withstand. Of these, probably the most critical single phenomenon is that of wave activity.

Before such a task could begin, certain basic criteria had to be laid down. The first concerns the return period for the parameters being forecast. A typical estimated life-span for many of these structures was in the region of 20 years. The probability of occurrence of, for example, a 50-year return-period wave is 0.332 during a 20-year life-span, whilst there is an even probability of its occurrence in a 35-year life-span (Borgman 1963). This does not mean that the structure can be expected to fail during, say, a 40-year life-span, as safety factors used in the design are likely to reduce the failure probability.

Because of these and other considerations, it was decided, for the governmental 'Guidance Notes' on offshore environmental parameters, to quote the characteristics of the 50-year storm as the minimum acceptable parameters.

The second basic criterion to be decided is that of storm duration. The 50-year storm hourly-mean wind speed is predicted by Shellard (1965), but its duration is not known. The average relationships between that speed and the mean speed over other durations, such as 6, 12, 18 and 24 hours, have been calculated. The average wind speed for a given storm decreases as duration increases, but the ratio of the height of the highest wave in the storm to the significant wave height increases. Because of this, the postulated storm duration is not critical over the range of storm durations likely to occur. A short storm will yield a high significant wave height but the ratio of the likely height of the highest wave to significant height will not be very high; a longer storm (but of lower mean speed over the longer duration) will in practice yield a lower significant wave height but, because of the longer duration, the ratio of likely height of the highest wave to the significant height will be higher. These two effects tend to cancel out. In addition, the number of waves will be slightly different in the two cases. Experience has shown that a 12-hour duration yields marginally higher waves than any other duration when the Darbyshire and Draper (1963) curves are used. Because of this, a duration of 12-hours has been postulated for the 50-year storm.

Methods used in this Study

The primary sources of wave information are forecasts based on

estimates of the 50-year extreme wind calculated by Shellard (1965), and extrapolations of data obtained from instrumental measurements made by Ocean Weather Ships and Light Vessels.

Estimates based on Wind Data

The wind information is applied to established forecasting techniques such as Darbyshire and Draper (1963) which was derived entirely from instrumental measurements in the waters presently considered, or Bretschneider (1970 revision). Because of the large amount of wind data available over the whole country, the wave field can be forecast for most sea areas.

The 50-year hourly-mean wind speed is converted to mean speeds over longer durations using relationships (unpublished) provided by the Meteorological Office. This is applied to the appropriate wave forecasting graphs, from which the required parameters are obtained.

The wave heights derived from the Darbyshire system are of the most probable value of the height of the highest wave in a ten-minute record. These values can be used to derive the significant wave height, and the most probable value of the height of the highest wave in some longer time, very often 3-hours (Draper 1966), but in this case 12-hours as previously stated. The Bretschneider method yields the significant height directly, from which other parameters are speedily derived in the same way. The period forecast by both methods is the significant period, T_s.

Estimates based on Instrumentally-measured Wave Data

The records, which must normally be a sample representative of one or more complete years, are analyzed following the standard N. I. O. routine (Draper 1966). One parameter which is derived is the most probable value of the height of the highest wave likely to have occurred in a 3-hour interval, H max (3 hours). These values are then plotted as cumulative exceedances on log-normal probability paper, and extrapolated to yield an estimate of the 50-year wave height appropriate to a 3-hour interval. Wave period data, in this case zero-crossing period T_z, is usually a best fit on linear probability paper, but it is not always as well behaved as is the height data. This yields an estimate of T_z in the 50-year storm. The value of H max (storm)

for the 50-year storm assuming it lasts for 12 hours is then derived using the number of waves (T_z) expected to occur in the storm, using Longuet-Higgins statistics (Draper 1963). In addition, the methods used by Battjes (1970) are also employed to make a further estimate of H max (storm).

There are two essential checks which must be made on data derived from instrumental measurements. The first is that all the records showing the highest waves of the series must be examined individually and the significant height determined from either the spectrum or by the traditional method of taking the average height of the highest one third of all the waves. The most probable value of the height of the highest wave in a typical record must be determined from this reliably-determined significant height and must be used instead of the value determined by the standard method. This must be done to eliminate the fairly high probability, for such records, of employing an unusually high wave height as a base from which to calculate extremes. Secondly, the wind data for the year in which the wave measurements were made must be compared with some longer-term average to ensure that the deviations from normal can be taken into account. The two simplest comparisons which can be made are of the relationship between the annual mean speed during the year in which wave measurements were made, and that over many years, and also between the number of hours of gale in the year and that in the longer-term average.

Use of this Information

This information has been compiled to give an indication of the likely extreme wave parameters in these waters. Very little account has been taken in this study of the details of the sea-bed topography, except at measurement locations where this information is, obviously, already incorporated in the data. Before any structure can be erected it will be necessary for a detailed study to be undertaken covering a large area around the site to ensure that no focussing of waves, even from large distances, or severe confused seas are likely to occur at the site. Although in principle it might be technically feasible to produce a detailed picture covering all these areas, the cost would be enormous, and in only a few areas would the information be used

before the planned increase in measurement activity yields further data which could modify the picture significantly.

Presentation of Results

Agreement between the two main approaches of derivation has been comfortingly good, more especially so in height. The results are expressed in two maps. Figure 1 gives the height data and Figure 2 the period data. The height map, presenting the most probable value of the height of the highest wave in the 50-year storm, is based largely on wave forecasts, supplemented wherever possible by data derived from instrumental measurements. Heights are now expressed in metres, in accordance with the change to the metric system. Periods are expressed in seconds; the parameter presented is the zero-crossing period T_z derived from instrumental measurements, supplemented where necessary by estimates of T_z derived from forecasts of T_s. The relationship found by Darbyshire between T_s and T_z has been summarized (Draper 1965) and, in general, T_s is slightly larger than T_z. However, in this study no systematic relationship was found between wind-forecast and extrapolated instrumentally-measured period data, although the differences were small.

The basic pattern of wave height is similar to that on the map produced in the spring of 1971. Since that time there has been a significant increase in the amount of data available, the most noticeable change being in the eastern English Channel where more data has resulted in a decrease in predicted extreme wave height of 2 metres. There are minor variations in the positions of some of the contours elsewhere, but the extent of the changes is difficult to discern when comparing this height map with the previous one, because in the previous map the heights are expressed in feet. There was no previous publication of wave period information, except in tabular form.

Location of Reference Points

The locations are indicated by dots, together with a code letter based on the name of the station. With the exception of Dowsing and Royal Sovereign these locations are stations at which instrumental measurements have been made and analyzed. Data from Dowsing are being analyzed at present. To

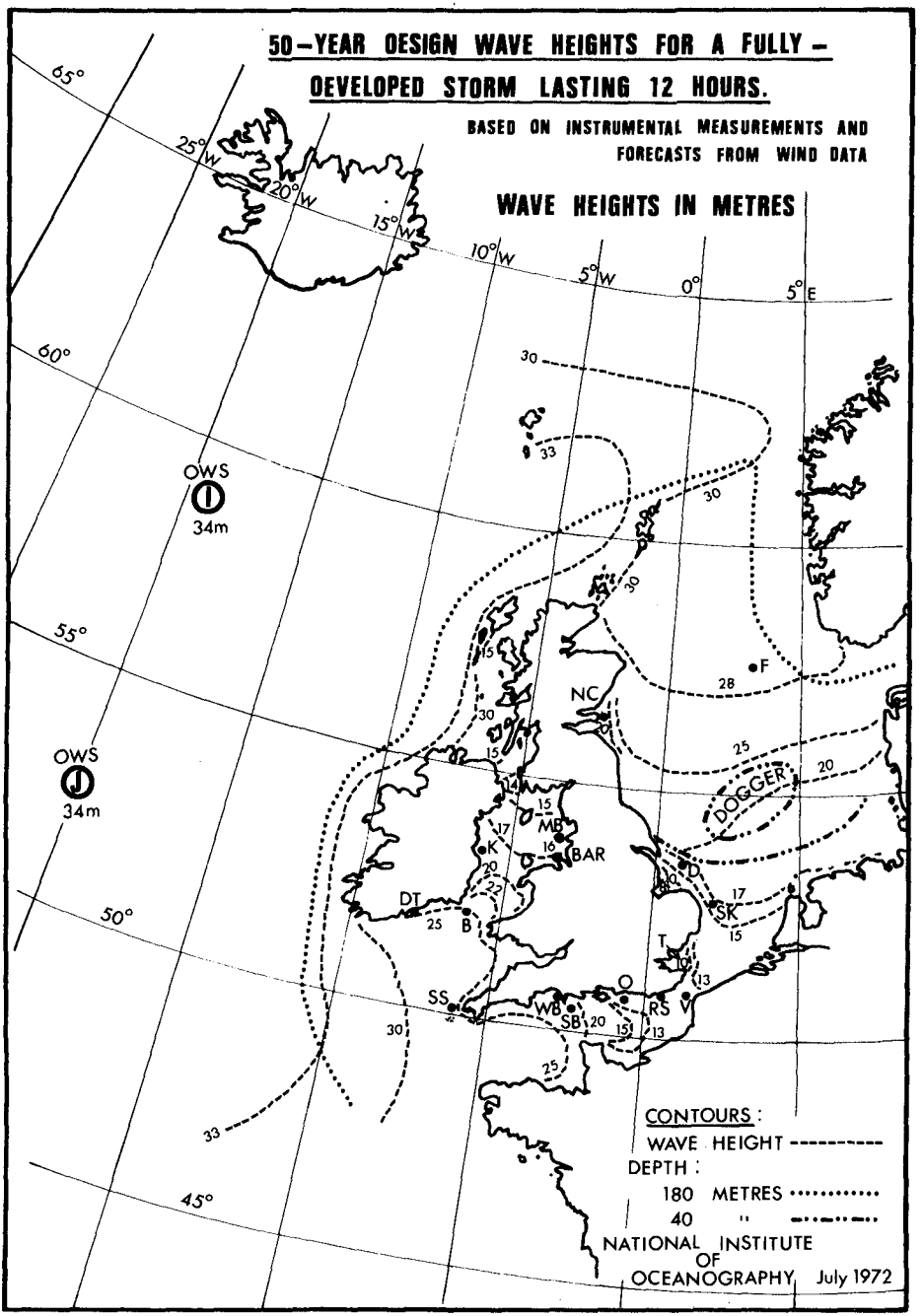

Figure 1: The most probable value of the height of the highest wave likely to occur in the 50-year storm.

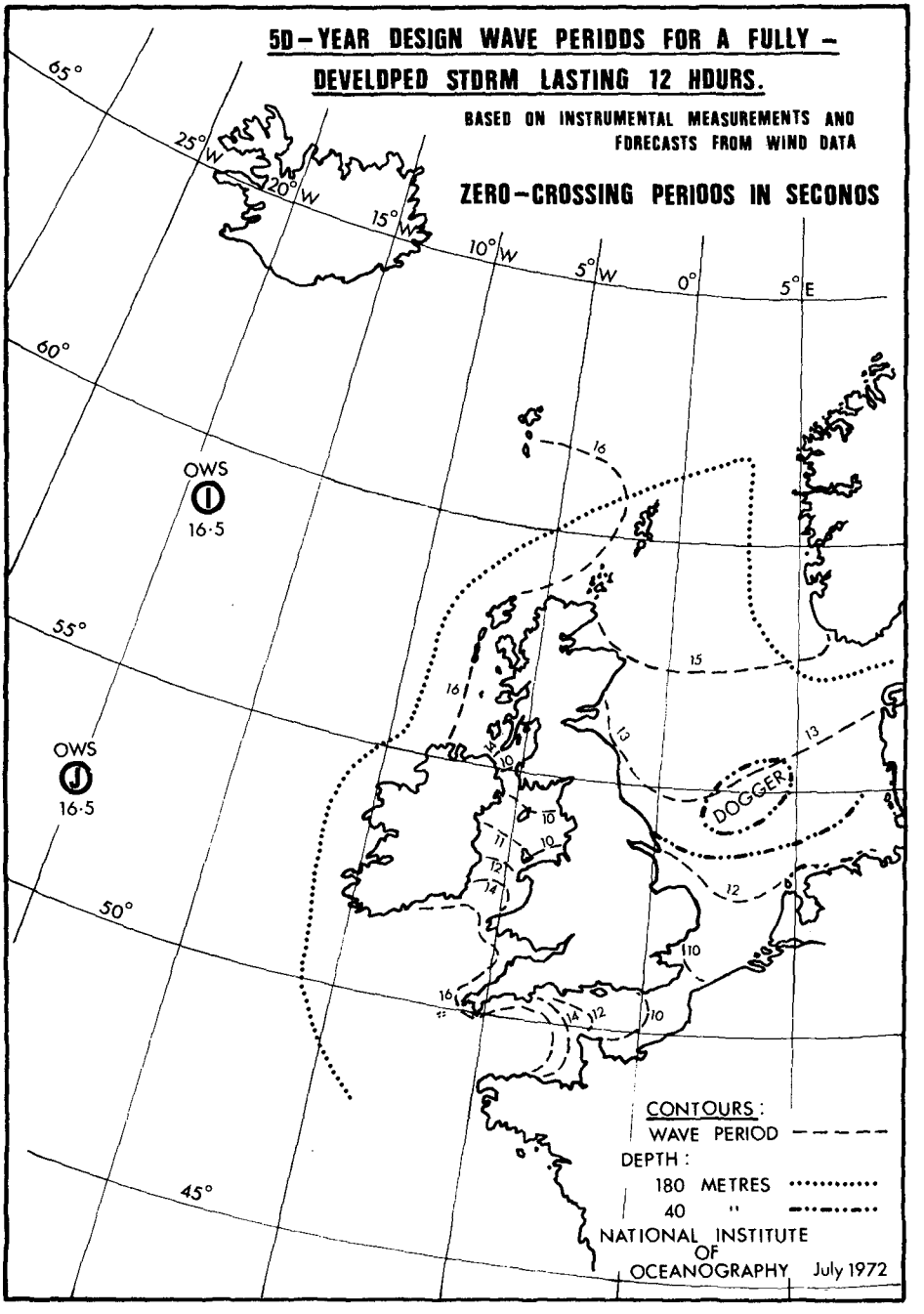

Figure 2: The most probable value of zero-crossing period likely to occur in the 50-year storm.

reduce the length of this paper, details of N. I. O. data publications for these locations are omitted from the Reference, but can be obtained from the author.

B	Barrels L. V.	OWS	Ocean Weather Ship Stations, I and J
BAR	Bar L. V.	RS	Royal Sovereign
D	Dowsing L. V.	SB	Shambles
DT	Daunt L. V.	SK	Smith's Knoll L. V.
F	FAMITA	SS	Sevenstones L. V.
K	Kish Bank	T	Tongue L. V.
MB	Morecambe Bay	V	Varne L. V.
NC	North Carr L. V.	WB	West Bexington
O	Owers L. V.		

Acknowledgements

The author wishes to express his gratitude to all those people and organisations, far too numerous to list, who have contributed to this work. The wave measurements and forecasts have been the responsibility of N. I. O. staff, with the exception of the data from Barrels, Daunt and Kish, for which the author is grateful to Mr. A. D. H. Martin, (Martin 1971) Chief Engineer of the commissioners of Irish Lights, and the data from West Bexington which were obtained by Mr. P. Hardcastle (Hardcastle and King, 1972) of the Unit of Coastal Sedimentation, Taunton.

References

BATTJES, J. A. 1970 Long-term Wave Height Distribution at Seven Stations around the British Isles. N. I. O. Internal Report A44.

BORGMAN, L. E. 1963 Risk Criteria. Journal of Waterways and Harbours Division Proc. ASCE 3607, WW3, August.

BRETSCHNEIDER, C. L. 1970 Forecasting Relations for Wave Generation. Look Lab/HAWWAll 1, 3, 31-34.

DARBYSHIRE, M. and DRAPER, L. 1963 Forecasting Wind-generated Sea Waves. Engineering (Lond) 195, 482-484.

DRAPER, L. 1963 Derivation of a 'design wave' from instrumental Measurements of Sea Waves. Proc. Instn. civ. Engrs. 26 291-304.

DRAPER, L. 1965 Wave spectra provide best basis for Offshore Rig Design. Oil and Gas Internat. 5, 6, 58-60.

DRAPER, L. 1966 The analysis and Presentation of wave data - a plea for Uniformity. Proc. 10th Conf. Coastal Engr. Tokyo, Vol, 1, Chapt. 1.

HARDCASTLE, P. J. and KING, A. C. 1972 Chesil Beach Sea Wave Records. Civil Engineering and Public Works Review, March, 1972.

MARTIN, A. D. H. 1971 Wave Data for Kish Bank L. V., Barrels L. V. and Daunt Rock L. V.
Institution of Engineers of Ireland.

SHELLARD, H. C. 1965 Extreme wind speeds over the United Kingdom for Periods Ending 1963. Met. Off. Climat. Memo. London, No. 50.
This work has recently been substantially extended at the request of the Department of Trade and Industry, but has not been formally published.

CHAPTER 7

REVISIONS TO HURRICANE DESIGN WAVE PRACTICES

BY

CHARLES L. BRETSCHNEIDER

Professor of Ocean Engineering
University of Hawaii
Honolulu, Hawaii

1. ABSTRACT

The 1959 paper "Hurricane Design Wave Practices" (ref. 1) has been widely used in the past for obtaining design wave criteria. Additional wave data and revisions in wave forecasting procedures, including computing techniques, ideas and experience, make it possible to bring these techniques up to date.

This paper should be considered also as an extension of the paper "A Non-Dimensional Hurricane Wave Model" (ref. 2) as well as revisions to the 1959 paper (ref. 1).

Graphs, formulae and procedures are presented making it possible to calculate the entire deep water wave fields from model hurricane wind fields.

The revisions have been applied to the U.S. East and Gulf coasts past historical hurricanes and also to the U.S. Weather Service standard project and probable maximum hurricanes for deep water conditions. The results of these calculations are presented in figures and tables and can serve as inputs for particular locations to calculate design storm surge and design wave criteria over the continental shelf to the coast line, making use of the material in the references listed at the end of this paper.

2. SUMMARY BASIC RELATIONSHIPS FOR STATIONARY MODEL HURRICANE WIND FIELDS

Detailed equations are given in reference 2. Specifically,

$$1) \quad \frac{U_r}{U_R} = -\tfrac{1}{2}\,\frac{fR}{U_R}\,\frac{r}{R} + \sqrt{\left(1+\frac{fR}{U_R}\right)\frac{R}{r}\,e^{(1-R/r)} + \left(\tfrac{1}{2}\,\frac{fR}{U_R}\right)^2}$$

where U_r and U_R are the wind speeds at radial distance r and R (radius of maximum wind) from the hurricane center, ϕ is latitude, ω is angular velocity of the earth, and $f = 2\,\omega \sin \phi$. (See list of symbols)

For wave generation we consider only U_r for $r \geq R$, and avoid entering into the eye of the hurricane. Fig. 1 shows relationships for eq. 1 for $r/R \geq 1.0$. The wind speed U_R is given (ref. 5) by

$$2) \quad U_R = K \sqrt{\Delta P} - 0.5\, fR$$

where ΔP is the central pressure reduction in inches of mercury from normal pressure, and the constant K varies from 67 at 20 to 25 degrees latitude to about 63 at 45 degrees latitude for U.S. coasts.

The sustained wind speed at the 10-meter reference plane above mean sea level is given (ref. 5) by

$$3) \quad U_{Rs} = K^* U_R \text{, where } K^* = 0.865 \text{ for all U.S. East Coast and Gulf Coast zones, except } K^* = 0.886 \text{ for Gulf Coast Zone B.}$$

The components U_x/U_R and U_y/U_R of the wind speeds depend upon the angular position of r/R and the incurvature angle β that the wind makes with the tangent to the isobars.

3. SUMMARY BASIC RELATIONSHIPS FOR STATIONARY MODEL HURRICANE DEEP WATER WAVE FIELDS

Detailed expressions are given in reference 2. Specifically, the component wind fields are used together with wave forecasting relationships to calculate component wave fields H_x/H_R and H_y/H_R, and the final resultant wave field becomes

$$4) \quad H_r = \sqrt{H_x^2 + H_y^2} \quad \text{and} \quad 5) \quad H_R = K' \sqrt{R\Delta P}$$

Fig. 2 in analogy to Fig. 1 gives relationships for H_r/H_R, based on calculations for 51 model stationary hurricanes. Fig. 3 can be used to determine K' for use in eq. 5. K' in Fig. 3 must be increased by $0.886/0.865 = 1.024$ for Zone B of the Gulf of Mexico.

4. MOVING HURRICANE

The stationary model hurricane wave field is directly coupled with the corresponding model hurricane wave field. Any change in the wind field will result in a directly related change in the wave field. For a moving hurricane the changes in wind speed components are

6) $\Delta U_y = \frac{1}{2} V \cos \Theta$ and 7) $\Delta U_x = 0$, where V is the forward speed of the hurricane, whose path is parallel to the y- axis and Θ is the angle of radius r measured counterclockwise from the x- axis. There will also be a change in effective fetch length as a result in movement of the hurricane.

There is a critical forward speed of the hurricane, when the hurricane moves in phase with the group velocity of the waves, afterwhich a faster forward speed will result in the hurricane moving ahead of the maximum waves.

Eqs. for critical forward speed are as follows:

8) $V_c = 1.515\ T_c$ knots

9) $$T_c = T_R \left[1 - \frac{.7575\ T_R}{U_{Rs}} \right]^{-1} = T_R \left[1 + \frac{1}{2} \frac{V_c}{U_{Rs}} \right]$$

10) $$H_c = H_R \left[1 + \frac{1}{2} \frac{V_c}{U_{Rs}} \right]^2$$

and the wave period can be obtained from

11) $$\frac{T}{U} = 0.4 \tanh \left\{ 1.07 \left[\operatorname{arc\,tanh} \frac{40H}{U^2} \right]^{0.6} \right\}$$

In eq. 11 $T = T_c$ and T_R in sec, $H = H_c$ and H_R in feet and $U = U_{Rs} + \frac{1}{2} V_c$ in knots. Eqs. 10 and 11 can be used also for actual forward speed of the hurricane when $V_a \leq V_c$, by replacing V_c with V_a, H and H_c with H_a, and $U = U_{Rs} + \frac{1}{2} V_a$.

For complete development of the above equation, see reference 2. Figs. 1, 2, 3 and 4 are selected from reference 2.

5. APPLICATION TO HISTORICAL, STANDARD PROJECT AND PROBABLE MAXIMUM HURRICANES

The parameters of the hurricanes for various zones and latitudes are R, ΔP , and V_a (see refs. 5 and 6). The summary of relationships given in this paper were used to calculate the deep water wave characteristics. The range in critical forward speed seems to be between about 18 and 28 knots. Only a few of the Gulf of Mexico hurricanes exceed the critical forward speed. However, there are quite a few Atlantic hurricanes, particularly for higher latitudes that exceed the critical forward speed. Calculations are made for H_R , H_c and H_a and T_R , T_c and T_a . However, when $V_a > V_c$ we use the values of H_c and T_c in place of H_a and T_a respectively.

The results of these calculations are given in appendix A for the historical hurricanes and in appendix B for the standard project and probable maximum hurricanes, all for the U.S. Gulf of Mexico Coast and the U.S. East Coast. Fig. 5 shows the various zones for the Gulf of Mexico and the U.S. Eastern seaboard.

6. PRESENTATION OF RESULTS

6.1 Historical Hurricanes (See Figs. 6, 7, 8 and 9 and appendix A)

The above are for the historical hurricanes. Generally, the maximum significant wave heights occur for the East Coast. Most of the hurricanes for about latitude 30°N enter the U.S. mainland from the Gulf of Mexico. The extreme range in critical forward speed of the hurricanes for maximum significant wave heights fall between 18 and 28 knots. For latitudes lower than about 30°N latitude, the actual forward speeds are less than the critical forward speed. For latitudes greater than about 30°N latitude, many of the hurricanes exceed the critical forward speed. The maximum intensity of the hurricanes seem to be reached at about 30°N latitude. At higher latitudes the actual forward speeds of many of the hurricanes greatly exceed the critical forward speed.

Generally speaking R increases and ΔP decreases with increase in latitude, and $R\Delta P$ increases with latitude to about 30 or 35°N latitude. According to Fig. 3 K' decreases with increase in latitude. Thus the product $K' \sqrt{R\Delta P}$ increases to a maximum at about 30°N latitude and then decreases northward. This, of course, is for deep water conditions. The effect of the depth and width of the continental shelf will result in other possible modifications. The total water depth, including storm surge will have an effect on the maximum waves over the continental shelf.

6.2 Standard Project and Probable Maximum Hurricanes (See Figs. 10 through 14 and appendix B)

The above are for the standard project and probable maximum hurricanes for the East Coast U.S.A. These figures show that the worst hurricane deep

water wave conditions occur around 30°N latitude. Fig. 10 adds emphasis to the fact that there is a sudden increase in actual forward speed between 30°N and 35°N latitude, and these speeds exceed the critical forward speed. Figs. 13 and 14 show the limiting wave height conditions as governed by the critical forward speed.

The standard project hurricane is estimated as that extreme hurricane that can be reasonably expected to occur within a particular zone on the average of once every 100 years. Similarly the probable maximum hurricane has the 1000-year recurrence interval.

It is interesting to compare the historical with the standard and probable maximum hurricane. The maximum significant wave height calculated for the historical hurricane moving at actual speed and that for the maximum standard project hurricane are about H_R = 60 feet. The maximum significant wave height calculated for the historical hurricane assuming critical forward speed and that for the maximum probable maximum hurricane are about H_R = 70 feet. Thus the wave energy spectrum of the 1000-year hurricane as compared to the 100-year hurricane will be in the ratio of $(70/60)^2$ = 1.36.

7. WAVES OVER THE CONTINENTAL SHELF

The standard project and probable maximum hurricanes given in appendix B can be moved over the continental shelf. The data in the tables can be used as input data, together with previous expressions for calculating the storm surge (see ref. 1, 2, & 4). Each location will have to be treated as a separate problem. The two-dimensional hydrodynamical equations for storm surge should be used to determine the total water depths. The generation of waves over the continental shelf will have to take into account the modifications of wave height due to bottom friction, percolation, refraction and diffraction, and a regeneration due to the wind, and finally the breaking wave criteria.

8. REFERENCES

1. Bretschneider, C.L. (1959) "Hurricane Design Wave Practices", Trans. ASCE, Vol. 124, pp. 39-62.

2. Bretschneider, C.L. (1972) "A Non-Dimensional Stationary Hurricane Wave Model", Proc. 1972 Offshore Tech. Conf., Houston, Texas, May 1972, Paper No. 1517.

3. Bretschneider, C.L. (1970) "Revisions in Wave Forecasting", Look Lab/Hawaii (a quarterly of the U. of Hawaii) Vol. 1, No. 3, pp. 31-34.

4. Bretschneider, C.L. (1967) "Storm Surge" Advances in Hydroscience, pp. 341-418, ed. Ven Te Chow, Academic Press, N.Y. & London.

5. Graham, H.E. and D.E. Nunn (1959) "Meteorological Considerations Pertinent to Standard Project Hurricane, Atlantic and East Coasts of the U.S.", National Hurricane Research Proj. Report No. 33, U.S. Weather Service.

6. U.S. Dept. of Commerce (May 7, 1968) "Meteorological Characteristics of the Probable Maximum Hurricane, Atlantic and Gulf Coasts of the U.S.", Int. Rept., Memo to Corps of Engrs., HUR 7-97.

9. LIST OF SYMBOLS

e	base of natural logarithms
f	Coriolis parameter
H	significant wave height (in general)
H_a	significant wave height due to actual increase in forward speed of hurricane
H_c	maximum significant wave height for hurricane moving at critical forward speed
H_R	significant wave height at R, stationary hurricane
H_x	component of H along x-axis
H_y	component of H along y-axis
K	constant varying from 67 at 20 to 25 degrees latitude to about 63 at 45 degrees latitude for U.S. coasts
K^*	0.865 for all U.S. East Coast and Gulf Coast Zones and 0.886 for Gulf Coast Zone B
K'	coefficient (see Figure 3)
ΔP	central pressure reduction from normal in inches of mercury
R	radius of maximum wind, nautical miles
r	radial distance
T	significant wave period
T_a	significant wave period at R for actual forward speed of hurricane
T_c	significant wave period at R for critical forward speed
T_R	significant wave period at R for stationary hurricane
U	wind speed (general)
U_R	geostrophic wind speed at distance R from hurricane center
U_r	geostrophic wind speed at distance r from hurricane center
U_{Rs}	surface wind speed at distance R from hurricane center

U_x	component of wind speed along x-axis
U_y	component of wind speed along y-axis
ΔU_x	change in x component of wind speed for a moving hurricane
ΔU_y	change in y component of wind speed for a moving hurricane
V	forward speed of the hurricane
V_a	actual forward speed of a hurricane
V_c	critical forward speed of a hurricane
β	incurvature angle of the wind vector
θ	angle position of the radius measured counterclockwise from the x-y axis
ϕ	latitude
ω	angular velocity of the earth

FIGURES

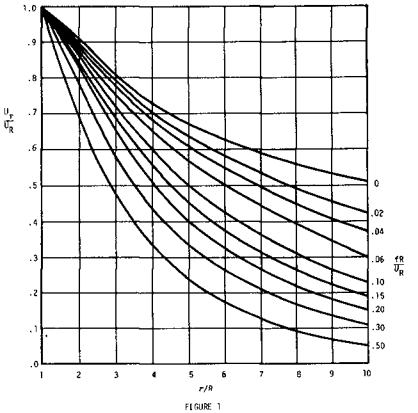

FIGURE 1

U_r/U_R VS r/R FOR VALUES OF fR/U_R (SEE EQ. 1)

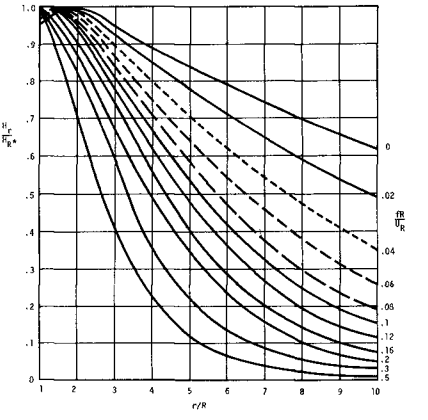

FIGURE 2

H_r/H_R* VS r/R FOR VALUES OF fR/U_R

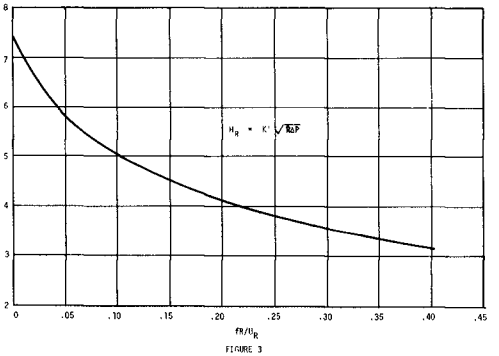

FIGURE 3

K' VS fR/U_R FOR $\beta = 25^\circ$

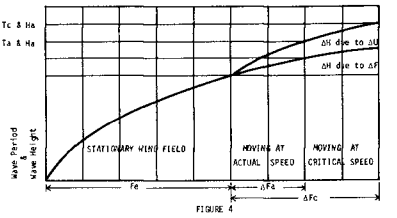

FIGURE 4

SCHEMATIC DIAGRAM FOR MOVING HURRICANE WHEN $V_a < V_c$

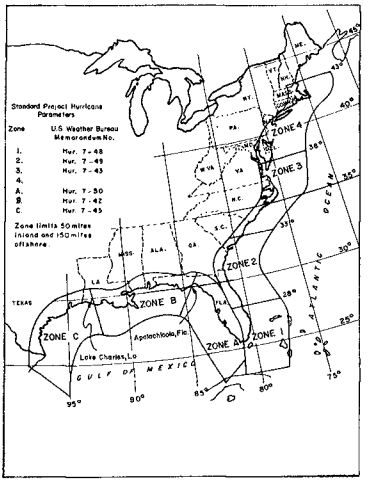

FIGURE 5
HURRICANE ZONES, ATLANTIC AND GULF COAST, U.S.A., FOR U.S. WEATHER SERVICE

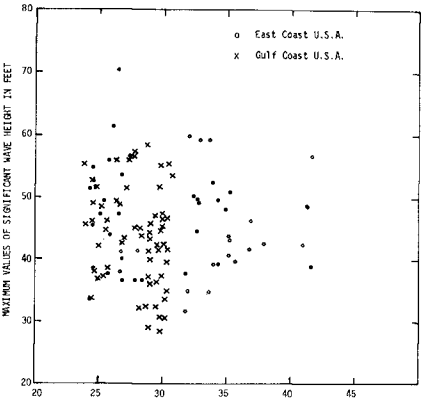

FIGURE 6
HISTORICAL HURRICANE HINDCAST SIGNIFICANT WAVE HEIGHTS (ACCORDING TO CRITICAL FORWARD SPEED) VS LATITUDE

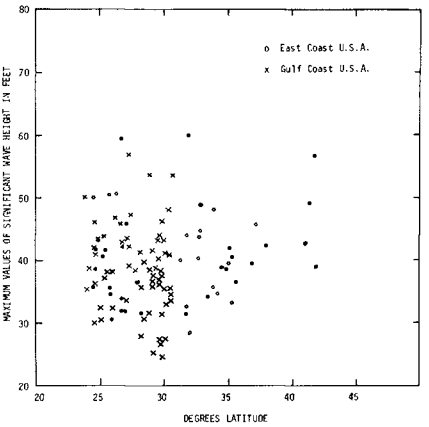

FIGURE 7
HISTORICAL HURRICANE HINDCAST SIGNIFICANT WAVE HEIGHTS (ACCORDING TO ACTUAL FORWARD SPEED) VS LATITUDE

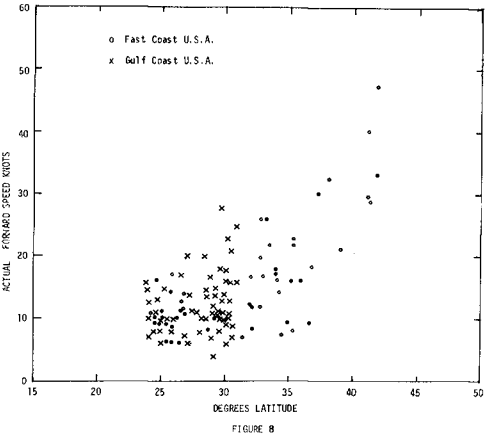

FIGURE 8
ACTUAL FORWARD SPEED IN KNOTS VS LATITUDE

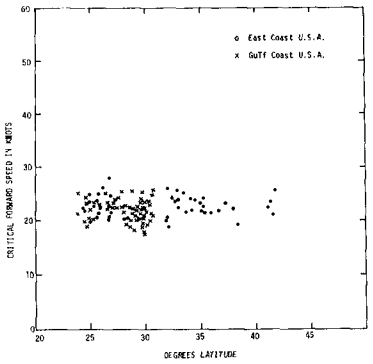

FIGURE 9

CRITICAL FORWARD SPEED IN KNOTS VS LATITUDE

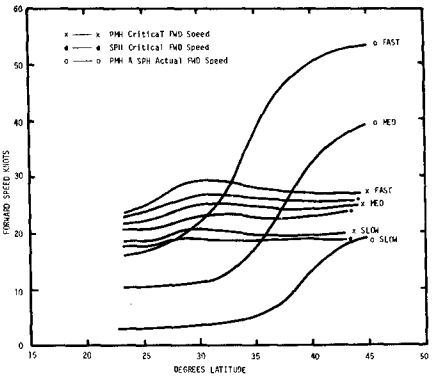

FIGURE 10

STANDARD PROJECT AND MAXIMUM PROBABLE HURRICANE FORWARD SPEED AND CRITICAL FORWARD SPEEDS, VS LATITUDE, EAST COAST U.S.A.

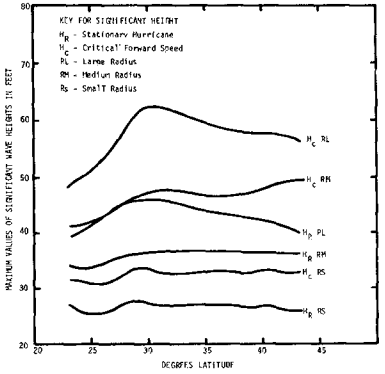

FIGURE 11

STANDARD PROJECT HURRICANE MAXIMUM VALUES OF SIGNIFICANT WAVE HEIGHT FOR STATIONARY HURRICANE AND CRITICAL FORWARD SPEED, EAST COAST, U.S.A.

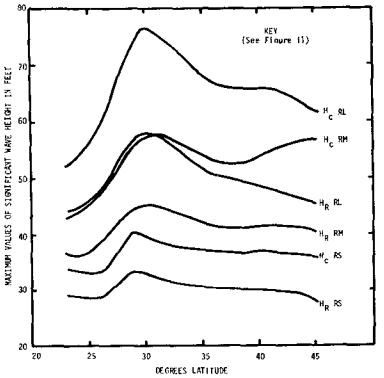

FIGURE 12

PROBABLE MAXIMUM HURRICANE MAXIMUM VALUES OF SIGNIFICANT WAVE HEIGHT FOR STATIONARY HURRICANE AND CRITICAL FORWARD SPEED, EAST COAST U.S.A.

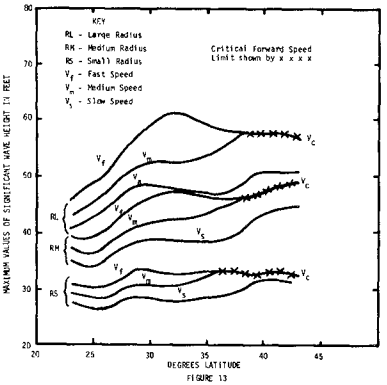

FIGURE 13

STANDARD PROJECT HURRICANE MAXIMUM VALUES OF SIGNIFICANT WAVE HEIGHT FOR SLOW, MEDIUM AND FAST SPEEDS OF FORWARD MOTION, EAST COAST U.S.A.

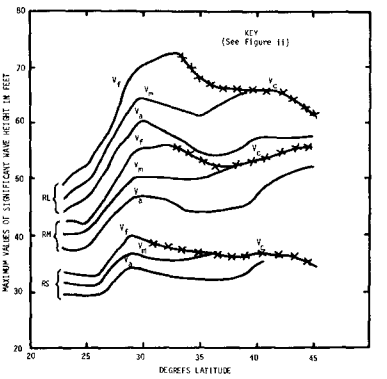

FIGURE 14

PROBABLE MAXIMUM HURRICANE MAXIMUM VALUES OF SIGNIFICANT WAVE HEIGHT FOR SLOW, MEDIUM AND FAST SPEEDS

APPENDIX A

TABLES I AND II

Deep Water Hurricane Wind and Wave Calculations for Historical Hurricanes, Hindcasts for U.S. Gulf Coast and U.S. East Coast.

TABLE I

Atlantic Ocean U.S. East Coast Historical Hurricanes Zones One to Four

TABLE II

Gulf of Mexico U.S. Coast Historical Hurricanes Zones A, B, and C.

Notations in the Above Tables:

ϕ	latitude degrees
R	radius of maximum wind nautical miles
ΔP	central pressure reduction from normal in inches of H_g
U_R	maximum sustained 10-minute average wind velocity above friction layer for stationary hurricane in knots
U_{Rs}	0.865 U_R - 10-minute average at the 10-meter level for stationary hurricane (except Zone B)
U_{Rs}	0.886 U_R for Zone B only
V_c	critical forward speed in knots
U_{Rc}	$U_{Rs} + \frac{1}{2} V_c$
V_a	actual forward speed in knots
U_{Ra}	$U_{Rs} + \frac{1}{2} V_a$
H	(1) H_R, (2) H_c, (3) H_a significant wave height feet at R for (1) stationary, (2) critical speed and, (3) actual speed respectively T_R, T_c, T_a significant wave period seconds at R for (1) stationary, (2) critical speed and (3) actual speed respectively.

TABLE I - 1

ATLANTIC OCEAN U.S. EAST COAST HISTORICAL HURRICANE ZONE ONE

No	Date	Lat ϕ	R	ΔP	STATIONARY				CRITICAL SPEED				ACTUAL SPEED			
					U_R	U_{RS}	H_R	T_R	V_c	U_{Rc}	H_c	T_c	V_a	U_{Ra}	H_a	T_a
		Degrees	N.M.	In Hg	Knots	Knots	Feet	Sec	Knots	Knots	Feet	Sec	Knots	Knots	Feet	Sec
1	Sept. 2, 1935	24.8	6	3.57	125	108	32.5	12.1	20.0	118	38.8	13.2	9	113	35.3	12.6
2	Sept. 9, 1919	24.8	15	2.48	103	89	38.4	13.6	23.3	101	49.0	15.4	8	93	41.9	14.2
3	Oct. 20, 1926	24.6	21	2.40	101	87	41.9	14.3	24.8	99	54.6	16.3	16	95	50.0	15.6
4	Sept. 10, 1960	24.5	(25.8)**	2.37									9			
5	Sept. 18, 1926	25.8	24	2.33	99	86	42.5	14.5	25.1	99	55.9	16.6	17	94	51.4	15.9
6	Sept. 16, 1928	26.7	53	2.30	95	82	51.2	16.0	28.5	96	70.6	18.8	13	89	59.6	17.3
7	Sept. 17, 1947	26.2	34	2.16	94	81	44.8	15.0	26.3	94	60.5	17.4	10	86	50.5	15.9
8	Sept. 4, 1933	26.9	29	1.94	89	77	39.9	14.1	24.8	89	53.7	16.3	11	83	45.8	15.1
9	Sept. 15, 1945	25.5	24	1.83	88	76	36.9	13.5	23.7	88	49.3	15.6	10	81	41.9	14.4
10	Sept. 8, 1965	25.2	22	1.78	87	75	35.4	13.2	23.2	87	47.2	15.3	11	80	40.8	14.2
11	Sept. 28, 1929	24.9	28	1.77	86	74	38.0	13.7	24.3	86	51.4	16.0	10	79	43.3	14.7
12	Aug. 26, 1949	26.7	23	1.76	85	74	35.2	13.2	23.1	86	47.1	15.3	14	81	42.2	14.5
13	Oct. 17, 1950	25.8	(25.8)**	1.72									6			
14	Oct. 11, 1909	24.5	22	1.62	83	72	33.6	13.0	22.7	83	45.2	15.0	10	77	38.5	13.8
15	July 28, 1926	28.0	14	1.58	82	71	28.2	11.7	20.4	81	36.8	13.4	(11)***	76		
16	Sept. 22, 1948	26.8	16	1.51	80	69	29.0	12.0	21.0	80	38.1	14.0	11	75	34.0	13.0
17	Sept. 27, 1964	25.5	(25.8)**	1.35									9			
18	Nov. 4, 1935	(25.8)*	(25.8)**	1.19									(11)***			
19	Oct. 20, 1924	25.8	25	1.09	67	58	27.2	11.7	21.0	69	37.9	13.8	6	61	30.1	12.3
20	Sept. 11, 1903	25.8	43	1.08	64	55	30.3	12.4	22.7	67	43.9	14.9	8	59	34.8	13.3
21	Oct. 18, 1906	26.9	35	1.08	65	56	28.8	12.1	21.9	67	41.0	14.4	6	59	31.9	12.7
22	Oct. 5, 1948	25.8	31	1.07	65	56	28.2	11.9	21.5	67	39.9	14.2	13	63	35.0	13.3
23	June 17, 1906	26.9	26	1.01	64	55	25.8	11.4	20.5	65	36.3	13.5	12	61	31.7	12.7

* Average of all latitudes Zone One
** Average of all R Zone One
*** Average of all V_a Zone One

TABLE I - 2

ATLANTIC OCEAN U.S. EAST COAST HISTORICAL HURRICANES ZONE TWO

No	Date				STATIONARY				CRITICAL SPEED				ACTUAL SPEED			
					U_R	U_{RS}	H_R	T_R	V_c	U_{Rc}	H_c	T_c	V_a	U_{Ra}	H_a	T_a
		Degrees	N.M.	In Hg	Knots	Knots	Feet	Sec	Knots	Knots	Feet	Sec	Knots	Knots	Feet	Sec
1	Sept. 26, 1958	32.7	19	2.40	100	87	38.6	13.7	23.6	99	49.8	15.6	12	93	44.1	14.6
2	Oct. 15, 1954	32.0	36	2.26	95	82	44.4	14.9	26.1	95	59.7	17.2	(26)	95	59.7	17.2
3	Sept. 29, 1959	32.0	(29.3)**	1.87									12			
4	July 28, 1926	28.4	14	1.58	82	71	28.1	11.7	20.3	82	36.7	13.4	8	75	31.3	12.4
5	Aug. 30, 1954	(31.4)*	(29.3)**	1.57									(12.6)***			
6	Aug. 12, 1955	32.5	45	1.52	75	65	35.7	13.4	24.1	77	50.2	15.9	7	69	39.7	14.2
7	Sept. 10, 1960	32.9	33	1.45	75	65	32.5	12.8	22.8	76	44.9	15.0	(26)[1]	78	44.9	15.0
8	Sept. 19, 1955	32.8	50	1.41	71	61	34.5	13.2	23.9	73	49.1	15.8	10	66	40.3	14.3
9	Sept. 9, 1964	33.1	(29.3)**	1.39									17			
10	Oct. 15, 1947	32.1	13	1.33	75	65	24.2	10.9	19.0	74	31.9	12.5	17	73	31.0	12.4
11	Sept. 16, 1928	29.5	(29.3)**	1.77									(12.6)***			
12	Aug. 11, 1940	32.0	27	1.14	67	58	26.9	11.6	20.8	68	37.4	13.7	12	64	32.7	12.8
13	Oct. 25, 1921	29.0	(29.3)**	1.01									10			
14	Sept. 15, 1945	29.0	(29.3)**	1.01									(12.6)***			
15	Aug. 28, 1911	32.1	27	1.00	62	54	24.7	11.2	20.1	64	34.7	13.2	8	58	28.5	12.0

* Average all latitude Zone Two
** Average all R Zone Two
*** Average all V_a Zone Two
( )[1] $V_a > V_c$

TABLE I - 3

ATLANTIC OCEAN U.S. EAST COAST HISTORICAL HURRICANES ZONE THREE

					STATIONARY				CRITICAL SPEED				ACTUAL SPEED			
		Lat ϕ	R	ΔP	U_R	U_{Rs}	H_R	T_R	V_c	U_{Rc}	H_c	T_c	V_a	U_{Ra}	H_a	T_a
No	Date	Degrees	N.M.	In Hg	Knots	Knots	Feet	Sec	Knots	Knots	Feet	Sec	Knots	Knots	Feet	Sec
1	Sept. 27, 1958	34.0	25	2.26	96	83	40.0	14.0	24.4	95	52.7	16.1	18	92	49.2	15.6
2	Oct. 15, 1954	33.0	36	2.26	94	81	44.0	14.8	26.0	94	59.2	17.2	26	94	59.2	17.2
3	Sept. 21, 1938	33.7	50	2.06	88	76	44.0	14.9	26.5	89	59.2	17.2	(17)*	85	54.4	16.6
4	Sept. 14, 1944	35.2	(39)*	2.04	90	78	33.4	12.8	22.0	89	43.3	14.5	(23)[1]	90	43.3	14.5
5	Sept. 10, 1954	(34.8)*	17	1.95												
6	Sept. 16, 1933	35.2	42	1.67	78	68	36.6	13.6	24.3	80	50.9	16.0	9	72	41.6	14.5
7	Aug. 28, 1958	34.0	(39)*	1.66									17			
8	Aug. 30, 1954	33.4	(39)*	1.57									(17)			
9	Sept. 11, 1960	37.4	36	1.57	76	66	33.5	13.0	23.2	78	46.4	15.3	(30)[1]	81	46.4	15.3
10	Aug. 12, 1955	34.5	45	1.52	75	66	35.1	13.3	24.0	77	49.3	15.8	7	68	39.0	14.0
11	Sept. 19, 1955	35.0	50	1.41	71	61	33.7	13.1	23.7	73	48.1	15.6	9	65	38.9	14.0
12	Sept. 18, 1936	35.2	34	1.39	72	62	31.2	12.5	22.4	74	43.4	14.8	16	71	39.7	14.1
13	Aug. 23, 1933	36.9	36	1.29	68	59	29.6	12.2	22.0	70	41.6	14.5	18	68	39.3	14.1
14	Aug. 25, 1924	35.2	34	1.22	67	58	28.6	12.0	21.6	69	40.3	14.3	(22)[1]	69	40.3	14.3
15	Sept. 3, 1913	35.8	41	1.11	63	55	27.6	11.8	21.5	66	39.7	14.2	16	63	36.4	13.6
16	Aug. 24, 1949	33.5	24	1.06	65	56	24.7	11.2	19.9	66	34.3	13.1	22	67	34.3	13.1
17	Dec. 2, 1925	34.2	54	.97	47	41	26.4	11.6	21.4	51	39.2	14.2	14	56	34.5	13.3
18	Sept. 16, 1967	36.6	(39)*	.95									9			
19	Sept. 17, 1906	34.0	61	.94	55	48	26.1	11.6	21.5	59	39.2	14.2	16	56	35.6	13.5

* Average for Zone 3 ( )[1] $V_a > V_c$

TABLE I - 4

ATLANTIC OCEAN U.S. COAST HISTORICAL HURRICANES ZONE FOUR

					STATIONARY				CRITICAL SPEED				ACTUAL SPEED			
		Lat ϕ	R	ΔP	U_R	U_{Rs}	H_R	T_R	V_c	U_{Rc}	H_c	T_c	V_a	U_{Ra}	H_a	T_a
No	Date	Degrees	N.M.	In Hg	Knots	Knots	Feet	Sec	Knots	Knots	Feet	Sec	Knots	Knots	Feet	Sec
1	Sept. 21, 1938	41.8	50	2.06	82	71	40.8	14.3	25.7	84	56.8	16.9	(47)[1]	95	56.8	16.9
2	Sept. 11, 1954	41.3	(44)	1.95									(40)[1]			
3	Sept. 16, 1933	(40.3)*	(44)	1.67									(33)[1]			
4	Sept. 14, 1944	41.4	48	1.61	72	62	34.4	13.2	23.8	74	48.8	15.7	(30)[1]	77	48.8	15.7
5	Sept. 11, 1960	38.0	(44)	1.57									(32)[1]			
6	Aug. 31, 1954	41.8	22	1.54	75	65	28.8	12.0	21.2	76	39.1	14.0	(33)[1]	82	39.1	14.0
7	Sept. 18, 1936	38.0	34	1.39	71	61	30.4	12.4	22.2	73	42.4	14.6	(33)[1]	78	42.4	14.6
8	Aug. 26, 1924	41.3	66	1.22	59	51	28.7	12.1	22.4	62	42.7	14.8	(29)[1]	66	42.7	14.8
9	Aug. 29, 1958	39.0	(44)	1.19									21			

*Average Zone 4 ( )[1] $V_a > V_c$

TABLE II - A

GULF OF MEXICO U.S. COAST HISTORICAL HURRICANES ZONE A

No	Date	Lat φ	R	ΔP	STATIONARY				CRITICAL SPEED				ACTUAL SPEED			
					U_R	U_{Rs}	H_R	T_R	V_c	U_{Rc}	H_c	T_c	V_a	U_{Ra}	H_a	T_a
		Degrees	N.M.	In Hg	Knots	Knots	Feet	Sec	Knots	Knots	Feet	Sec	Knots	Knots	Feet	Sec
1	Sept. 2, 1935	24.8	6	4.00	125	108	32.5	12.1	20.0	118	39.0	13.2	9	113	35.3	12.6
2	Sept. 9, 1919	24.6	15	2.50	103	89	38.4	13.6	23.3	101	49.1	15.4	8	93	42.0	14.2
3	Oct. 20, 1926	23.8	21	2.40	101	88	42.2	14.4	24.9	100	55.0	16.4	16	95	50.2	15.7
4	Sept. 10, 1960	26.0	(18.6)*	2.37	-	-	-	-	-	-	-	-	9	-	-	-
5	Sept. 21, 1948	24.5	7	2.30	100	87	27.4	11.3	19.0	106	33.7	12.5	8	91	30.0	11.8
6	Oct. 17, 1910	24.5	16	2.12	95	83	35.8	13.2	22.8	94	46.3	15.0	11	88	40.7	14.1
7	Sept. 8, 1965	25.2	21	2.00	90	78	36.6	13.4	23.4	90	48.4	15.5	15	86	44.0	14.7
8	Oct. 18, 1944	24.6	27	1.90	89	77	39.3	14.0	24.6	90	52.8	16.2	13	83	46.2	15.2
9	Sept. 17, 1947	26.4	34	1.90	88	76	41.1	14.3	25.3	87	55.9	16.7	(10.7)**	75	47.1	15.3
10	Sept. 18, 1926	26.5	24	1.90	88	76	37.1	13.5	23.7	88	49.4	15.7	17	85	45.8	15.1
11	Sept. 28, 1929	24.8	28	2.00	86	74	38.0	13.8	24.3	86	51.4	16.0	10	79	43.3	14.7
12	Oct. 25, 1921	28.1	18	2.00	83	72	31.0	12.4	22.0	83	41.0	14.2	10	77	35.4	13.2
13	Oct. 11, 1909	24.3	22	2.00	83	71	33.7	13.0	22.7	83	45.3	15.0	10	76	38.6	13.8
14	Sept. 16, 1928	27.7	53	2.00	78	68	40.3	14.3	25.8	81	57.0	17.0	(10.7)**	67	57.0	17.0
15	Sept. 4, 1950	29.1	(18.6)*	2.00	-	-	-	-	-	-	-	-	(10.7)**	-	-	-
16	Aug. 26, 1949	27.2	23	2.00	80	69	32.5	12.7	22.4	80	43.8	14.8	14	76	39.4	14.0
17	Sept. 15, 1945	25.5	24	2.00	80	69	33.1	12.8	22.7	81	44.8	15.0	10	74	38.0	13.8
18	Oct. 6, 1964	24.0	(18.6)*	1.45	-	-	-	-	-	-	-	-	15	-	-	-
19	Sept. 4, 1933	27.8	29	1.44	76	66	32.9	12.8	22.8	78	46.2	15.1	11	72	38.6	14.0
20	June 9, 1966	30.0	(18.6)*	1.28	-	-	-	-	-	-	-	-	9	-	-	-
21	Oct. 19, 1924	25.0	19	1.22	72	62	27.0	11.6	20.5	72	36.8	13.5	8	66	30.6	12.4
22	Nov. 4, 1935	25.0	(18.6)*	1.20	-	-	-	-	-	-	-	-	(10.7)**	-	-	-
23	Sept. 11, 1903	27.0	43	1.10	64	56	30.0	12.3	22.5	66	43.3	14.8	7	59	33.8	13.1
24	Oct. 18, 1906	25.0	35	1.10	65	57	29.3	12.2	22.1	68	42.0	14.6	6	60	32.5	12.9
25	Oct. 5, 1948	24.0	31	1.10	66	57	28.7	12.1	21.8	68	40.8	14.4	13	63	35.6	13.4
26	Oct. 18, 1950	28.0	(18.6)*	1.04	-	-	-	-	-	-	-	-	(10.7)**	-	-	-
27	June 17, 1906	25.1	26	1.01	64	56	26.3	11.5	20.7	66	37.0	13.7	(10.7)**	55	37.0	13.7
28	Oct. 4, 1966	24.2	(18.6)*	1.00	-	-	-	-	-	-	-	-	7	-	-	-
29	Oct. 7, 1941	29.8	18	1.00	62	54	22.0	10.5	18.7	63	30.3	12.3	11	59	26.7	11.6

NOTE:
*Average all R Zone A **Average all V_a Zone A

TABLE II - B

GULF OF MEXICO U.S. COAST HISTORICAL HURRICANES ZONE B

No	Date	Lat φ	R	ΔP	STATIONARY				CRITICAL SPEED				ACTUAL SPEED			
					U_R	U_{Rs}	H_R	T_R	V_c	U_{Rc}	H_c	T_c	V_a	U_{Ra}	H_a	T_a
		Degrees	N.M.	In Hg	Knots	Knots	Feet	Sec	Knots	Knots	Feet	Sec	Knots	Knots	Feet	Sec
1	Sept. 8, 1900	27.0	(14)[2]	2.28	98	87	37.3	14.0	23.2	98	49.0	15.3	(13.8)**	94	43.5	15.0
2	Sept. 10, 1965	28.9	32	2.13	93	83	43.8	14.7	25.8	95	58.6	17.0	17	91	53.3	16.3
3	Sept. 29, 1915	29.9	29	2.05	91	81	41.3	14.3	25.0	94	55.1	16.5	10	86	46.6	15.2
4	Sept. 14, 1919	27.0	(31)*	2.00	-	-	-	-	-	-	-	-	20	-	-	-
5	Sept. 20, 1926	30.5	17	1.72	85	75	31.7	12.5	21.6	86	41.4	14.2	7	79	34.7	13.0
6	July 21, 1909	25.8	19	1.61	82	73	32.3	12.6	22.0	84	42.7	14.5	(13.8)**	72	42.7	14.5
7	Aug. 25, 1926	29.6	27	1.61	81	72	35.0	13.2	23.3	83	47.3	15.4	10	77	40.1	14.1
8	Oct. 3, 1964	29.0	21	1.59	81	72	32.5	12.7	22.2	83	43.3	14.0	7	75	35.7	13.3
9	July 5, 1916	30.7	50	1.54	76	67	38.2	14.0	25.0	80	53.8	16.5	25	80	53.8	16.5
10	July 31, 1936	30.5	19	1.46	78	69	29.7	12.1	21.2	79	39.5	14.0	9	73	33.7	13.0
11	Sept. 28, 1917	30.4	33	1.44	75	67	33.8	13.0	23.2	78	46.6	15.3	13	73	40.8	14.3
12	Sept. 27, 1906	30.6	73	1.42	69	62	38.0	14.0	25.4	74	55.3	16.8	16	69	48.5	15.7
13	June 16, 1934	30.0	37	1.40	74	66	34.2	13.1	23.5	77	47.6	15.5	16	73	43.1	14.7
14	Sept. 19, 1947	30.0	33	1.35	73	65	32.6	12.8	22.8	76	45.2	15.1	16	73	41.2	14.4
15	Aug. 14, 1901	30.0	33	1.20	69	61	30.2	12.4	22.1	72	42.3	14.6	14	68	37.6	13.8
16	Oct. 18, 1916	30.4	19	1.16	69	61	25.8	11.4	20.0	71	35.0	13.2	21	72	35.0	13.2
17	Aug. 7, 1940	29.0	11	1.16	70	62	22.1	10.4	18.1	71	29.0	12.0	8	66	25.0	11.1
18	Sept. 23, 1956	30.0	22	1.16	69	61	27.0	11.6	20.6	71	37.0	13.6	10	66	31.6	12.6
19	July 27, 1943	28.2	16	1.14	69	61	24.7	11.1	19.4	71	32.1	12.8	8	65	28.0	11.8
20	Sept. 30, 1929	30.1	65	1.12	62	55	32.0	13.8	23.5	66	47.2	15.5	6	58	35.6	13.5
21	Aug. 30, 1950	30.2	21	1.00	64	57	24.3	11.1	19.7	66	33.5	13.0	23	68	33.0	13.0
22	Sept. 21, 1920	29.6	28	.99	63	55	25.8	11.4	20.5	65	36.3	13.6	(28)[1]	69	36.3	13.6
23	Sept. 20, 1909	29.9	88	.98	54	48	29.3	12.3	23.0	60	45.0	15.2	11	54	36.4	13.7
24	Oct. 7, 1941	29.9	18	.94	62	55	22.5	10.6	18.8	65	30.8	12.4	11	62	27.2	11.7
25	Sept. 15, 1960	28.1	19	1.04	91	81	35.0	13.0	23.0	92	45.0	15.0	10	87	41.2	14.2

NOTE: ( )[1] $V_a > V_c$ ( )[2] Estimated *Average of all R **Average of all V

TABLE II - C

GULF OF MEXICO U.S. COAST HISTORICAL HURRICANES ZONE C

No	Date	Lat φ	R	ΔP	STATIONARY				CRITICAL SPEED				ACTUAL SPEED			
					U_R	U_{Rs}	H_R	T_R	V_c	U_{Rc}	H_c	T_c	V_a	U_{Ra}	H_a	T_a
		Degrees	N.M.	In Hg	Knots	Knots	Feet	Sec	Knots	Knots	Feet	Sec	Knots	Knots	Feet	Sec
1	Sept. 20, 1967	26.0	(19.9)*	2.66	-	-	-	-	-	-	-	-	(11.2)**	-	-	-
2	Sept. 11, 1961	27.2	20	2.28	98	85	39.3	13.9	24.0	97	51.2	15.8	6	88	42.1	14.3
3	Sept. 8, 1900	29.2	14	2.28	99	85	34.7	12.9	22.2	96	44.3	14.6	10	90	38.9	13.7
4	Aug. 13, 1932	29.1	12	2.09	95	82	31.4	12.3	21.0	92	40.0	13.9	15	89	37.4	13.4
5	June 27, 1957	29.2	19	1.97	91	79	35.0	13.1	22.7	90	45.8	15.0	14	86	41.5	14.3
6	Aug. 18, 1916	27.5	35	1.92	88	76	41.3	14.4	25.4	89	56.3	16.8	11	82	47.5	15.4
7	Sept. 14, 1919	27.7	(19.9)*	1.92	-	-	-	-	-	-	-	-	20	-	-	-
8	Sept. 5, 1933	25.9	20	1.90	90	78	35.6	13.2	23.0	89	46.9	15.2	8	82	39.3	13.9
9	Aug. 30, 1942	28.5	18	1.85	88	76	33.3	12.8	22.2	88	43.7	14.6	14	83	39.7	14.0
10	Aug. 16, 1915	29.8	32	1.78	85	73	37.8	13.7	24.3	86	51.4	16.0	11	79	43.7	14.8
11	June 22, 1921	29.7	17	1.75	86	74	31.4	12.4	21.6	85	41.2	14.2	11	80	36.3	13.3
12	July 21, 1909	29.0	19	1.61	82	71	31.1	12.4	21.6	82	41.2	14.3	12	77	36.5	13.4
13	Sept. 23, 1941	29.7	21	1.61	82	71	31.8	12.6	22.0	82	42.5	14.5	13	77	38.0	13.7
14	Aug. 27, 1945	29.0	18	1.35	75	65	27.5	11.7	20.5	75	36.8	13.5	4	67	29.2	12.0
15	June 28, 1929	28.5	13	1.30	74	64	24.4	11.0	19.1	74	32.2	12.6	15	72	30.5	12.2
16	Aug. 7, 1940	29.9	11	1.16	70	61	21.5	10.3	17.9	70	28.3	11.8	8	65	24.4	11.0
17	July 27, 1943	29.5	16	1.14	69	60	23.9	10.9	19.2	68	32.2	12.6	8	64	27.2	11.6
18	Aug. 4, 1933	25.9	25	1.12	68	59	27.6	11.8	21.1	69	38.4	13.9	10	64	32.5	12.8
19	Oct. 4, 1949	28.9	28	1.04	64	56	26.3	11.5	20.7	66	37.0	13.7	11	61	31.7	12.7

*Average of all R Zone C **Average of all V_a Zone C

APPENDIX B

TABLES III TO VI

Deep Water Hurricane Wind and Wave Calculations for Standard Project Hurricanes, Probable Maximum Hurricanes. Predictions for U.S. Gulf of Mexico: Zones A, B, and C; U.S. East Coast: Zones 1, 2, 3 and 4.

TABLE III

Standard Project Hurricanes for Gulf Coast U.S. Zones A, B and C.

TABLE IV

Probable Maximum Hurricanes for Gulf Coast U.S. Zones A, B and C.

TABLE V

Standard Project Hurricanes for East Coast Zones 1, 2, 3 and 4.

TABLE VI

Probable Maximum Hurricanes for East Coast Zones 1, 2, 3 and 4.

Notations in the Above Tables:

ϕ	latitude degrees
ΔP	central pressure reduction from normal inches of H_g
R	radius of maximum wind nautical miles
U_R	maximum sustained 10-minute average wind velocity above friction layer for stationary hurricane, knots
V	forward speed of hurricane in knots (V = 0 stationary, V = V_c critical speed, V = slow, medium or fast speed of translation as indicated)
U_{Rs}	maximum 10-minute average sustained wind speed at 10 meter water level, knots
U_{Rs}	$0.865\ U_R + \frac{1}{2}\ V$, knots (except Zone B)
U_{Rs}	$0.886\ U_R + \frac{1}{2}\ V$, knots for Zone B only
H_R	significant wave height in feet at R
T_R	significant wave periods in seconds at R

TABLE III- A
DEEP WATER WAVES
STANDARD PROJECT HURRICANES FOR GULF COAST U.S. ZONE A

		Stat	Crit	Slow	Med	Fast	Stat	Crit	Slow	Med	Fast	Stat	Crit	Slow	Med	Fast
1				Small R = 4					Medium R = 7					Large R = 11		
Lat ϕ = 24°	U_R	121.5					121.1					120.7				
Δ P = 3.34 in Hg	V	0	17.7	3.0	10.0	17.0	0	20.6	3.0	10.0	17.0	0	23.2	3.0	10.0	17.0
	U_{RS}	105.1	114.0	106.6	115.1	113.6	104.8	115.1	106.3	114.8	113.3	104.4	116.0	105.9	105.4	112.9
	H_R	26.5	31.1	27.2	29.0	30.9	33.5	40.5	34.5	36.8	39.2	40.6	50.1	41.7	44.6	47.4
	T_R	10.8	11.7	10.9	11.3	11.7	12.4	13.6	12.5	13.0	13.4	13.8	15.3	14.0	14.4	14.9
2				Small R = 4					Medium R = 7					Large R = 12		
Lat ϕ = 25°	U_R	119.6					119.3					118.7				
Δ P = 3.24 in Hg	V	0	17.6	3.0	10.0	17.0	0	20.4	3.0	10.0	17.0	0	23.5	3.0	10.0	17.0
	U_{RS}	103.5	112.3	105.0	108.5	112.0	103.2	113.4	104.7	108.2	111.7	102.7	114.5	104.2	107.7	111.2
	H_R	26.0	30.6	26.7	28.5	30.4	32.9	39.7	33.9	36.2	38.5	41.3	51.3	42.5	45.4	48.4
	T_R	10.7	11.6	10.8	11.2	11.6	12.3	13.5	12.4	12.9	13.3	13.9	15.5	14.1	14.6	15.1
3				Small R = 4					Medium R = 8					Large R = 14		
Lat ϕ = 26°	U_R	116.8					116.3					115.6				
Δ P = 3.09 in Hg	V	0	17.4	4.0	11.0	17.0	0	20.9	4.0	11.0	17.0	0	24.1	4.0	11.0	17.0
	U_{RS}	101.0	109.7	103.0	106.5	109.5	100.6	111.1	102.6	106.1	109.1	100.0	112.1	102.0	105.5	108.5
Marco, Florida	H_R	25.2	29.8	26.2	28.1	29.7	33.8	41.2	35.2	37.6	39.8	42.4	53.2	44.1	47.1	49.9
	T_R	10.6	11.5	10.8	11.1	11.4	12.5	13.8	12.7	13.2	13.6	14.2	15.9	14.5	15.0	15.4
4				Small R = 5					Medium R = 10					Large R = 18		
Lat ϕ = 27°	U_R	112.1					111.5					110.6				
Δ P = 2.86 in Hg	V	0	18.1	4.0	11.0	18.0	0	21.8	4.0	11.0	18.0	0	24.8	4.0	11.0	18.0
	U_{RS}	97.0	106.1	99.0	102.5	106.0	96.5	107.4	98.5	102.0	105.5	95.6	108.0	97.6	101.1	104.6
Lemon Bay, Florida	H_R	26.5	31.7	27.6	29.6	31.7	35.5	44.0	37.0	39.7	42.5	43.6	55.6	45.4	48.8	52.2
	T_R	10.9	12.0	11.2	11.6	12.0	12.9	14.4	13.2	13.7	14.1	14.5	16.4	14.8	15.3	15.9
5				Small R = 6					Medium R = 12					Large R = 21		
Lat ϕ = 28°	U_R	106.7					105.9					104.8				
Δ P = 2.60 in Hg	V	0	18.6	4.0	11.0	19.0	0	22.2	4.0	11.0	19.0	0	24.9	4.0	11.0	19.0
	U_{RS}	92.3	101.6	94.3	97.8	101.8	91.6	102.7	93.6	97.1	101.1	90.7	103.2	92.7	96.2	100.2
Ounedin, Florida	H_R	27.2	32.9	28.3	30.5	* *	36.0	45.2	37.5	40.4	43.8	42.9	55.5	44.9	48.3	52.4
	T_R	11.2	12.3	11.4	11.8	* *	13.1	14.7	13.4	13.9	14.4	14.5	16.4	14.8	15.3	16.0
6				Small R = 6					Medium R = 13					Large R = 24		
Lat ϕ = 29°	U_R	104.1					103.2					101.8				
Δ P = 2.48 in Hg	V	0	18.4	4.0	11.0	20.0	0	22.3	4.0	11.0	20.0	0	25.2	4.0	11.0	20.0
	U_{RS}	90.0	99.2	92.0	95.5	100.0	89.2	100.4	91.2	94.7	99.2	88.0	100.6	92.0	93.5	98.0
	H_R	26.4	32.1	27.6	29.7	* *	35.7	45.2	37.3	40.2	44.1	43.2	56.4	45.2	48.7	53.5
	T_R	11.0	12.1	11.3	11.7	* *	13.1	14.7	13.4	13.9	14.5	14.5	16.6	14.9	15.4	16.2
7				Small R = 7					Medium R = 14					Large R = 26		
Lat ϕ = 30°	U_R	102.4					101.4					99.9				
Δ P = 2.41 in Hg	V	0	19.0	4.0	11.0	21.0	0	22.4	4.0	11.0	21.0	0	25.3	4.0	11.0	21.0
	U_{RS}	88.5	98.0	90.5	104.0	99.0	87.7	98.9	89.7	93.2	98.2	86.4	99.1	88.4	91.9	96.9
Carbur, Florida	H_R	27.7	33.9	28.9	31.2	* *	35.7	45.4	37.4	40.4	44.8	43.2	56.7	45.2	48.8	54.3
	T_R	11.3	12.6	11.6	12.0	* *	13.1	14.8	13.4	13.9	14.7	14.6	16.7	14.9	15.5	16.3

* * FORWARD SPEED GREATER THAN CRITICAL FORWARD SPEED

TABLE III- 8
DEEP WATER WAVES
STANDARD PROJECT HURRICANES FOR GULF COAST U.S. ZONE 8

		Stat	Crit	Slow	Med	Fast	Stat	Crit	Slow	Med	Fast	Stat	Crit	Slow	Med	Fast
1		Small R = 7					Medium R = 14					Large R = 27				
Lat ϕ = 30°	U_R	101.5					100.6					98.9				
ΔP = 2.37 in Hg	V	0	19.1	4.0	11.0	28.0	0	22.5	4.0	11.0	28.0	0	25.6	4.0	11.0	28.0
	U_{RS}	89.8	99.4	91.8	95.3	103.8	89.0	100.3	91.0	94.5	103.0	87.5	100.3	89.5	93.0	101.5
Apalachicola, Florida	H_R	28.1	34.3	29.3	31.6	* *	36.2	45.9	37.8	40.8	* *	44.2	58.1	46.2	49.9	* *
	T_R	11.4	12.6	11.7	12.1	* *	13.2	14.8	13.5	14.0	* *	14.7	16.9	15.1	15.7	* *
2		Small R = 7					Medium R = 14					Large R = 28				
Lat ϕ = 30°	U_R	100.8					99.9					98.1				
ΔP = 2.34 in Hg	V	0	19.1	4.0	11.0	28.0	0	22.4	4.0	11.0	28.0	0	25.7	4.0	11.0	28.0
	U_{RS}	89.2	98.8	91.2	94.7	103.2	88.4	99.6	92.4	93.9	102.4	86.8	99.6	88.8	92.3	100.8
Grayton Beach, Florida	H_R	27.9	34.1	29.1	31.4	* *	35.9	45.6	37.6	40.5	* *	44.3	58.4	46.4	50.1	* *
	T_R	11.4	12.6	11.6	12.1	* *	13.1	14.8	13.4	13.9	* *	14.8	17.0	15.1	15.7	* *
3		Small R = 7					Medium R = 14					Large R = 29				
Lat ϕ = 30.5°	U_R	100.5					99.6					97.6				
ΔP = 2.33 in Hg	V	0	19.0	4.0	11.0	28.0	0	22.4	4.0	11.0	28.0	0	25.8	4.0	11.0	28.0
	U_{RS}	88.9	98.4	90.9	94.4	102.9	88.1	99.3	90.1	103.6	102.1	86.4	99.3	88.4	91.9	100.4
Pensacola, Florida	H_R	27.8	34.0	29.0	31.3	* *	35.7	45.4	37.4	40.3	* *	44.5	58.8	46.6	50.3	* *
	T_R	11.4	12.6	11.6	12.1	* *	13.1	14.8	13.4	13.9	* *	14.8	17.0	15.2	15.8	* *
4		Small R = 7					Medium R = 14					Large R = 30				
Lat ϕ = 30.5°	U_R	100.3					99.4					97.2				
ΔP = 2.32 in Hg	V	0	19.0	4.0	11.0	28.0	0	22.3	4.0	11.0	28.0	0	25.9	4.0	11.0	28.0
	U_{RS}	88.8	98.3	90.8	94.3	102.8	87.9	99.1	89.9	93.4	101.9	86.0	99.0	88.0	91.5	100.0
	H_R	27.7	34.0	29.0	31.2	* *	35.6	45.3	37.3	40.2	* *	44.8	59.3	46.9	50.7	* *
	T_R	11.3	12.6	11.6	12.0	* *	13.1	14.7	13.4	13.9	* *	14.9	17.1	15.2	15.8	* *

* * FORWARD SPEED GREATER THAN CRITICAL FORWARD SPEED

TABLE III- 8
DEEP WATER WAVES
STANDARD PROJECT HURRICANES FOR GULF COAST U.S. ZONE 8
(CONTINUED)

		Stat	Crit	Slow	Med	Fast	Stat	Crit	Slow	Med	Fast	Stat	Crit	Slow	Med	Fast
5		Small R = 7					Medium R = 14					Large R = 30				
Lat ϕ = 30°	U_R	100.4					99.5					97.4				
ΔP = 2.32	V	0	19.0	4.0	11.0	28.0	0	22.4	4.0	11.0	28.0	0	26.0	4.0	11.0	28.0
	U_{RS}	88.9	98.4	90.9	94.4	102.9	88.0	99.2	92.0	93.5	102.0	86.2	99.2	88.2	91.7	100.2
New Orleans, Louisiana	H_R	27.7	34.0	29.0	31.3	* *	35.7	45.4	37.4	40.3	* *	45.0	59.5	47.1	50.9	* *
	T_R	11.4	12.6	11.6	12.1	* *	13.1	14.8	13.4	13.9	* *	14.9	17.1	15.2	15.8	* *
6		Small R = 7					Medium R = 14					Large R = 29				
Lat ϕ = 29.5°	U_R	100.7					99.8					97.8				
ΔP = 2.33 in Hg	V	0	19.1	4.0	11.0	28.0	0	22.4	4.0	11.0	28.0	0	25.9	4.0	11.0	28.0
	U_{RS}	89.1	98.7	91.1	94.6	103.1	88.3	99.0	90.3	93.8	102.3	86.6	99.6	88.6	92.1	100.6
Lake Barre, Louisiana	H_R	27.8	34.1	29.1	31.4	* *	35.9	45.6	37.6	40.6	* *	44.8	59.2	46.9	50.7	* *
	T_R	11.4	12.6	11.6	12.1	* *	13.1	14.8	13.4	14.0	* *	14.9	17.1	15.2	15.8	* *
7		Small R = 7					Medium R = 14					Large R = 29				
Lat ϕ = 29.5°	U_R	100.9					100.0					98.0				
ΔP = 2.34 in Hg	V	0	19.1	4.0	11.0	28.0	0	22.5	4.0	11.0	28.0	0	25.9	4.0	11.0	28.0
	U_{RS}	89.3	98.9	91.3	94.8	103.3	88.5	99.8	90.5	94.0	102.5	86.8	99.8	88.6	92.3	100.8
March Island, Louiana	H_R	27.9	34.2	29.2	31.4	* *	36.0	45.8	37.7	40.6	* *	44.9	59.3	47.0	50.8	* *
	T_R	11.4	12.6	11.6	12.1	* *	13.2	14.8	13.4	14.0	* *	14.9	17.1	15.2	15.8	* *
8		Small R = 7					Medium R = 14					Large R = 29				
Lat ϕ = 30°	U_R	101.3					100.4					98.5				
ΔP = 2.36 in Hg	V	0	19.1	4.0	11.0	28.0	0	22.5	4.0	11.0	28.0	0	25.7	4.0	11.0	28.0
	U_{RS}	89.6	99.2	91.6	95.1	103.6	88.8	100.1	90.8	94.3	102.8	87.2	100.2	89.2	92.7	101.2
Grand Chenier, Louisiana	H_R	28.0	34.3	29.3	31.5	* *	36.1	45.8	37.8	40.7	* *	44.5	58.7	46.6	50.3	* *
	T_R	11.4	12.6	11.7	12.1	* *	13.2	14.8	13.5	14.0	* *	14.8	17.0	15.1	15.7	* *

* * FORWARD SPEED GREATER THAN CRITICAL FORWARD SPEED

TABLE III- C
DEEP WATER WAVES
STANDARD PROJECT HURRICANES FOR GULF COAST U.S. ZONE C

		Stat	Crit	Slow	Med	Fast	Stat	Crit	Slow	Med	Fast	Stat	Crit	Slow	Med	Fast
1				Slow R = 7					Medium R = 14					Large R = 27		
Lat ϕ = 30°	U_R	101.7					100.8					99.1				
	V	0	19.0	4.0	11.0	28.0	0	22.3	4.0	11.0	28.0	0	25.4	4.0	11.0	28.0
Δ P = 2.38 in Hg	U_{Rs}	88.0	97.5	90.0	93.5	102.0	87.2	98.4	89.2	92.7	101.2	85.7	98.4	87.7	91.2	99.7
Port Arthur, Texas	H_R	27.5	33.7	28.7	31.0	* *	35.5	45.1	37.1	40.1	* *	43.3	57.1	45.4	49.0	* *
	T_R	11.3	12.5	11.6	12.0	* *	13.1	14.7	13.4	13.9	* *	14.6	16.8	14.9	15.5	* *
2				Slow R = 7					Medium R = 14					Large R = 26		
Lat ϕ = 29°	U_R	102.2					101.3					99.8				
	V	0	19.0	4.0	11.0	28.0	0	22.4	4.0	11.0	28.0	0	25.4	4.0	11.0	28.0
Δ P = 2.4 in Hg	U_{Rs}	88.4	97.9	90.4	93.9	102.4	87.7	98.9	89.7	93.2	101.7	86.3	99.0	88.3	91.8	100.3
Galveston, Texas	H_R	27.7	34.0	28.9	31.2	* *	35.8	45.6	37.5	40.5	* *	43.3	57.0	45.4	49.0	* *
	T_R	11.3	13.0	11.6	12.1	* *	13.1	14.8	13.4	14.0	* *	14.6	16.7	14.9	15.5	* *
3				Slow R = 6					Medium R = 13					Large R = 25		
Lat ϕ = 29°	U_R	103.0					102.1					100.6				
	V	0	18.3	4.0	11.0	28.0	0	22.2	4.0	11.0	28.0	0	25.3	4.0	11.0	28.0
Δ P = 2.43 in Hg	U_{Rs}	89.1	98.3	91.1	94.6	103.1	88.3	99.4	90.3	93.8	102.3	87.0	99.7	89.0	92.5	101.0
Bay City, Texas	H_R	26.1	31.8	27.3	29.4	* *	35.3	44.7	36.9	39.8	* *	43.2	56.6	45.2	48.8	* *
	T_R	11.0	12.1	11.2	11.6	* *	13.0	14.6	13.3	13.8	* *	14.6	16.7	14.9	15.5	* *
4				Slow R = 6					Medium R = 13					Large R = 24		
Lat ϕ = 28°	U_R	103.9					103.1					101.7				
	V	0	18.4	4.0	11.0	28.0	0	22.3	4.0	11.0	28.0	0	25.2	4.0	11.0	28.0
Δ P = 2.47 in Hg	U_{Rs}	89.9	99.1	91.9	95.4	103.9	89.2	100.4	91.2	94.7	103.2	88.0	100.6	90.0	93.5	102.0
San Antonio Bay, Texas	H_R	26.4	32.1	27.6	29.7	* *	35.8	45.3	37.4	40.4	* *	43.4	56.7	45.3	48.9	* *
	T_R	11.0	12.2	11.3	11.7	* *	13.1	14.7	13.4	13.9	* *	14.6	16.7	14.9	15.5	* *
5				Slow R = 6					Medium R = 12					Large R = 23		
Lat ϕ = 27°	U_R	105.5					104.8					103.5				
	V	0	18.5	4.0	11.0	28.0	0	22.2	4.0	11.0	28.0	0	25.3	4.0	11.0	28.0
Δ P = 2.54 in Hg	U_{Rs}	91.3	99.1	91.9	95.4	103.9	90.6	100.4	91.2	94.7	103.2	89.5	100.6	90.0	93.5	102.0
Sarita, Texas	H_R	26.9	32.6	28.1	30.2	* *	35.7	45.0	37.3	40.1	* *	43.8	57.1	45.8	49.4	* *
	T_R	11.1	12.2	11.4	11.8	* *	13.0	14.6	13.3	13.8	* *	14.6	16.7	15.0	15.5	* *
6				Slow R = 6					Medium R = 11					Large R = 20		
Lat ϕ = 26°	U_R	107.7					107.1					106.1				
	V	0	18.7	4.0	11.0	28.0	0	22.0	4.0	11.0	28.0	0	24.9	4.0	11.0	28.0
Δ P = 2.64 in Hg	U_{Rs}	93.1	102.5	95.1	98.6	107.1	92.6	103.6	94.6	98.1	106.6	91.7	104.2	93.7	97.2	105.7
Brownsville, Texas	H_R	27.5	33.3	28.7	30.9	* *	35.5	44.4	37.1	39.9	* *	43.3	55.8	45.2	48.6	* *
	T_R	11.2	12.4	11.5	11.9	* *	13.0	14.5	13.3	13.7	* *	14.5	16.5	14.8	15.4	* *

* * FORWARD SPEED GREATER THAN CRITICAL FORWARD SPEED

TABLE IV - A
DEEP WATER WAVES
PROBABLE MAXIMUM HURRICANES FOR GULF COAST U.S. ZONE A

		Stat	Crit	Slow	Med	Fast	Stat	Crit	Slow	Med	Fast	Stat	Crit	Slow	Med	Fast
1				Small R = 4					Medium R = 7					Large R = 11		
Lat ϕ = 24°	U_R	132.5					132.1					131.7				
	V	0	18.4	3.0	10.0	17.0	0	21.3	3.0	10.0	17.0	0	24.1	3.0	10.0	17.0
Δ P = 3.97 in Hg	U_{Rs}	114.6	123.8	116.1	119.6	123.1	114.3	125.0	115.8	119.3	122.8	113.9	126.0	115.4	118.9	122.4
	H_R	29.0	33.9	29.8	31.6	33.5	36.8	44.0	37.8	40.1	42.5	44.5	54.5	45.7	48.5	51.4
	T_R	11.2	12.1	11.4	11.7	12.1	12.9	14.1	13.0	13.4	13.8	14.4	15.9	14.6	15.0	15.4
2				Small R = 4					Medium R = 7					Large R = 12		
Lat ϕ = 25°	U_R	130.4					130.1					129.5				
	V	0	18.2	3.0	10.0	17.0	0	21.2	3.0	10.0	17.0	0	24.4	3.0	10.0	17.0
Δ P = 3.85 in Hg	U_{Rs}	112.8	121.9	114.3	117.8	121.3	112.5	123.1	114.0	117.5	121.0	112.0	124.2	113.5	117.0	120.5
	H_R	28.5	33.3	29.2	31.1	32.9	36.1	43.2	37.1	39.4	41.8	45.3	55.7	46.5	49.4	52.4
	T_R	11.1	12.0	11.3	11.6	12.0	12.8	14.0	12.9	13.3	13.7	14.5	16.1	14.7	15.2	15.6
3				Small R = 4					Medium R = 8					Large R = 14		
Lat ϕ = 26°	U_R	127.5					127.0					126.3				
	V	0	18.0	4.0	11.0	17.0	0	21.7	4.0	11.0	17.0	0	25.1	4.0	11.0	17.0
Δ P = 3.68 in Hg	U_{Rs}	110.3	119.3	112.3	115.8	118.8	109.9	120.8	111.9	115.4	118.4	109.3	121.9	111.3	114.8	117.8
	H_R	27.7	32.4	28.7	30.6	32.2	37.2	44.9	38.5	41.0	43.1	46.9	58.3	48.7	51.2	54.5
Marco, Florida	T_R	11.0	11.9	11.2	11.5	11.8	13.0	14.3	13.3	13.7	14.0	14.9	16.6	15.1	15.6	16.0
4				Small R = 5					Medium R = 10					Large R = 18		
Lat ϕ = 27°	U_R	124.1					123.5					122.5				
	V	0	18.9	4.0	11.0	18.0	0	22.7	4.0	11.0	18.0	0	26.1	4.0	11.0	18.0
Δ P = 3.50 in Hg	U_{Rs}	107.3	116.8	109.3	112.8	116.3	106.8	118.2	108.8	112.3	115.8	106.0	119.1	108.0	111.5	115.0
	H_R	29.6	35.0	30.7	32.7	34.8	39.6	48.5	41.1	43.8	46.6	49.1	61.9	51.0	54.4	57.8
Lemon Bay, Florida	T_R	11.5	12.5	11.7	12.1	12.4	13.6	15.0	13.8	14.3	14.7	15.3	17.2	15.6	16.1	16.6
5				Small R = 6					Medium R = 12					Large R = 21		
Lat ϕ = 28°	U_R	121.0					120.3					119.1				
	V	0	19.6	4.0	11.0	19.0	0	23.6	4.0	11.0	19.0	0	26.5	4.0	11.0	19.0
Δ P = 3.34 in Hg	U_{Rs}	104.7	114.5	108.7	110.2	114.2	104.0	115.8	106.0	109.5	113.5	103.1	116.4	105.1	108.6	112.6
	H_R	31.1	37.2	32.3	34.4	37.0	41.6	51.5	43.2	46.1	49.5	49.8	63.5	51.8	55.3	59.5
Ounedin, Florida	T_R	11.8	12.9	12.1	12.5	12.9	14.0	16.6	14.2	14.7	15.3	15.5	17.5	15.8	16.3	16.9
6				Small R = 6					Medium R = 13					Large R = 24		
Lat ϕ = 29°	U_R	118.7					117.8					116.4				
	V	0	19.4	4.0	11.0	20.0	0	23.7	4.0	11.0	20.0	0	26.8	4.0	11.0	20.0
Δ P = 3.22 in Hg	U_{Rs}	102.7	112.4	104.7	108.2	112.7	101.9	113.8	103.9	107.4	111.9	100.7	114.1	102.7	106.2	110.7
	H_R	30.4	36.4	31.6	33.7	* *	41.6	51.9	43.3	46.2	50.2	50.5	64.9	52.5	56.2	61.0
Yankeetown, Florida	T_R	11.7	12.8	12.0	12.4	* *	14.0	15.7	14.3	14.8	15.4	15.6	17.7	15.9	16.5	17.2
7				Small R = 7					Medium R = 14					Large R = 26		
Lat ϕ = 30°	U_R	116.8					115.9					114.3				
	V	0	20.1	4.0	11.0	21.0	0	23.8	4.0	11.0	21.0	0	27.0	4.0	11.0	21.0
Δ P = 3.13 in Hg	U_{Rs}	101.0	111.1	103.0	105.5	111.5	100.2	112.1	102.2	105.7	110.7	98.8	113.3	100.8	104.3	109.3
	H_R	31.9	38.5	33.1	35.4		41.7	52.2	43.4	46.4	50.9	50.5	65.3	52.6	56.3	62.0
	T_R	12.1	13.3	12.3	12.7		14.1	15.7	14.3	14.8	15.5	15.7	17.8	16.0	16.5	17.3
Carbur, Florida																

* * FORWARD SPEED GREATER THAN CRITICAL FORWARD SPEED

TABLE IV - B
DEEP WATER WAVES
PROBABLE MAXIMUM HURRICANES FOR GULF COAST U.S. ZONE B

		Stat	Crit	Slow	Med	Fast	Stat	Crit	Slow	Med	Fast	Stat	Crit	Slow	Med	Fast
1		Small R = 7					Medium R = 14					Large R = 27				
Lat ϕ = 30°	U_R	115.8					114.9					113.2				
	V	0	20.2	4.0	11.0	28.0	0	24.0	4.0	11.0	28.0	0	27.3	4.0	11.0	28.0
Δ P = 3.08 in Hg	U_{Rs}	102.5	112.6	104.5	108.0	116.5	101.7	113.7	103.7	107.2	115.7	100.2	113.9	102.2	105.7	114.2
Apalachicola, Florida	H_R	32.3	39.0	33.6	35.9	* *	42.3	52.8	43.9	46.9	* *	51.8	66.9	53.9	57.6	* *
	T_R	12.1	13.3	12.4	12.8	* *	14.1	15.8	14.4	14.9	* *	15.9	18.0	16.2	16.7	* *
2		Small R = 7					Medium R = 14					Large R = 28				
Lat ϕ = 30°	U_R	115.3					114.3					112.5				
	V	0	20.2	4.0	11.0	28.0	0	23.9	4.0	11.0	28.0	0	27.4	4.0	11.0	28.0
Δ P = 3.05 in Hg	U_{Rs}	102.0	112.1	104.0	107.5	116.0	101.2	113.2	103.2	106.7	115.2	99.6	113.3	101.6	105.1	113.6
Grayton Beach, Florida	H_R	32.1	38.8	33.4	35.7	* *	42.0	52.5	43.7	46.7	* *	52.0	67.3	54.1	57.9	* *
	T_R	12.1	13.3	12.4	12.8	* *	14.1	15.8	14.4	14.9	* *	15.9	18.1	16.2	16.8	* *
3		Small R = 7					Medium R = 14					Large R = 29				
Lat ϕ = 30°	U_R	114.7					113.8					111.8				
	V	0	20.1	4.0	11.0	28.0	0	23.8	4.0	11.0	28.0	0	27.6	4.0	11.0	28.0
Δ P = 3.02 in Hg	U_{Rs}	101.5	111.6	103.5	107.0	115.5	100.7	112.6	102.7	106.2	114.7	98.9	113.7	100.9	104.4	112.9
Pensacola, Florida	H_R	32.0	38.6	33.3	35.5	* *	41.8	52.2	43.4	46.5	* *	52.2	67.8	54.4	58.2	* *
	T_R	12.1	13.3	12.3	12.7	* *	14.1	15.7	14.3	14.8	* *	15.9	18.2	16.3	16.8	* *
4		Small R = 7					Medium R = 14					Large R = 30				
Lat ϕ = 30°	U_R	114.7					113.8					111.7				
	V	0	20.1	4.0	11.0	28.0	0	23.8	4.0	11.0	28.0	0	27.7	4.0	11.0	28.0
Δ P = 3.02 in Hg	U_{Rs}	101.5	111.6	103.5	107.0	115.5	100.7	112.6	102.7	106.2	114.7	98.8	113.7	100.8	103.3	112.8
Mobile, Alabama	H_R	32.0	38.6	32.3	35.5	* *	41.8	52.2	43.4	46.5	* *	52.8	68.6	54.9	58.8	* *
	T_R	12.1	13.3	12.3	12.7	* *	14.1	15.7	14.3	14.8	* *	16.1	18.3	16.4	16.9	* *

* * FORWARD SPEED GREATER THAN CRITICAL FORWARD SPEED

TABLE IV - B
DEEP WATER WAVES
PROBABLE MAXIMUM HURRICANES FOR GULF COAST U.S. ZONE B

(CONTINUED)

		Stat	Crit	Slow	Med	Fast	Stat	Crit	Slow	Med	Fast	Stat	Crit	Slow	Med	Fast
5		Small R = 7					Medium R = 14					Large R = 30				
Lat ϕ = 30°	U_R	114.7					113.8					111.7				
	V	0	20.1	4.0	11.0	28.0	0	23.8	4.0	11.0	28.0	0	27.7	4.0	11.0	28.0
Δ P = 3.02 in Hg	U_{Rs}	101.5	112.6	103.5	107.0	115.5	100.7	112.6	102.7	106.2	114.7	98.8	112.7	100.8	104.3	112.8
New Orleans, Florida	H_R	32.0	38.6	33.3	35.5	* *	41.8	52.2	43.4	46.5	* *	52.8	68.6	54.9	58.8	* *
	T_R	12.1	13.3	12.3	12.7	* *	14.1	15.7	14.3	14.8	* *	16.1	18.3	16.4	16.9	* *
6		Small R = 7					Medium R = 14					Large R = 29				
Lat ϕ = 30°	U_R	115.1					114.1	23.9	4.0	11.0		112.2				
	V	0	20.2	4.0	11.0	28.0	0				28.0		27.6	4.0	11.0	28.0
Δ P = 3.04 in Hg	U_{Rs}	101.8	111.9	103.8	107.3	115.8	101.0	113.0	103.0	106.5	115.0	99.3	113.2	101.4	104.9	113.4
Lake Barre, Louisiana	H_R	32.1	38.8	33.4	35.7	* *	41.9	52.4	43.6	46.6	* *	52.5	68.1	54.6	58.4	* *
	T_R	12.1	13.3	12.3	12.8	* *	14.1	15.8	14.4	14.9	* *	16.0	18.2	16.3	16.9	* *
7		Small R = 7					Medium R = 14					Large R = 29				
Lat ϕ = 30°	U_R	115.4					114.5					112.6				
	V	0	20.2	4.0	11.0	28.0	0	23.9	4.0	11.0	28.0	0	27.6	4.0	11.0	28.0
Δ P = 3.06 in Hg	U_{Rs}	102.2	112.3	104.2	107.7	116.2	101.4	113.4	103.4	106.9	115.4	99.6	113.4	101.6	105.1	113.6
March Island, Louisiana	H_R	32.2	38.9	33.5	35.8	* *	42.1	52.6	43.8	46.8	* *	52.7	68.3	54.8	58.6	* *
	T_R	12.1	13.3	12.4	12.8	* *	14.1	15.8	14.4	14.9	* *	16.0	18.2	16.3	16.9	* *
8		Small R = 7					Medium R = 14					Large R = 28				
Lat ϕ = 30°	U_R	116.2					115.3					113.4				
	V	0	20.2	4.0	11.0	28.0	0	24.0	4.0	11.0	28.0	0	27.5	4.0	11.0	28.0
Δ P = 3.10 in Hg	U_{Rs}	102.8	112.3	104.2	107.7	116.2	102.0	113.4	103.4	106.9	115.4	100.4	113.4	101.6	105.1	113.6
Grand Chenier, Louisiana	H_R	32.4	39.1	33.7	36.0	* *	42.4	53.0	44.1	47.1	* *	52.5	67.9	54.7	58.5	* *
	T_R	12.2	13.4	12.4	12.8	* *	14.2	15.8	14.4	14.9	* *	16.0	18.2	16.3	16.9	* *

* * FORWARD SPEED GREATER THAN CRITICAL FORWARD SPEED

TABLE IV - C
DEEP WATER WAVES
PROBABLE MAXIMUM HURRICANES FOR GULF COAST U.S. ZONE C

		Stat	Crit	Slow	Med	Fast	Stat	Crit	Slow	Med	Fast	Stat	Crit	Slow	Med	Fast
1				Small R = 7					Medium R = 14					Large R = 27		
Lat ϕ = 30°	U_R	117.0					116.0					114.3				
Δ P = 3.14 in Hg	V	0	20.1	4.0	11.0	28.0	0	23.9	4.0	11.0	28.0	0	27.2	4.0	11.0	28.0
	U_{RS}	101.2	111.3	103.2	106.7	115.2	100.4	112.4	102.4	105.9	114.4	98.9	112.5	100.9	104.4	112.9
Port Arthur, Texas	H_R	31.9	38.6	33.2	35.5	* *	42.0	52.3	43.4	46.5	* *	51.2	66.2	53.3	57.0	* *
	T_R	12.1	13.3	12.3	12.7	* *	14.1	15.7	14.4	14.8	* *	15.8	18.0	16.1	16.7	* *
2				Small R = 7					Medium R = 14					Large R = 26		
Lat ϕ = 29°	U_R	118.2					117.3					115.8				
Δ P = 3.20 in Hg	V	0	20.2	4.0	11.0	28.0	0	24.0	4.0	11.0	28.0	0	27.2	4.0	11.0	28.0
	U_{RS}	102.2	112.3	104.2	107.7	116.2	101.5	113.5	103.5	107.0	115.5	100.1	113.7	102.1	105.6	114.1
Galveston, Texas	H_R	32.3	39.0	33.6	35.9	* *	42.5	53.1	44.2	47.2	* *	51.5	66.5	53.6	57.3	* *
	T_R	12.1	13.4	12.4	12.8	* *	14.2	15.9	14.5	15.0	* *	15.8	18.0	16.1	16.7	* *
3				Small R = 6					Medium R = 14					Large R = 25		
Lat ϕ = 29°	U_R	119.4					118.4					117.0				
Δ P = 3.26 in Hg	V	0	19.5	4.0	11.0	28.0	0	24.2	4.0	11.0	28.0	0	27.1	4.0	11.0	28.0
	U_{RS}	103.3	113.1	105.1	108.8	117.3	102.4	114.5	104.4	107.9	116.4	101.2	114.8	103.2	106.7	115.2
Bay City, Texas	H_R	30.6	36.6	31.8	33.9	* *	42.9	53.7	44.6	47.7	* *	51.5	66.2	53.6	57.2	* *
	T_R	11.8	12.9	12.0	12.4	* *	14.3	15.9	14.5	15.0	* *	15.8	17.9	16.1	16.7	* *
4				Small R = 6					Medium R = 14					Large R = 24		
Lat ϕ = 28°	U_R	120.8					119.8					118.6				
Δ P = 3.33 in Hg	V	0	19.6	4.0	11.0	28.0	0	24.4	4.0	11.0	28.0	0	27.2	4.0	11.0	28.0
	U_{RS}	104.5	114.3	106.5	110.0	118.5	103.6	115.8	105.6	109.1	117.6	102.6	116.2	104.6	108.1	116.6
San Antonio Bay, Texas	H_R	31.0	37.1	32.2	34.4	* *	43.7	54.6	45.4	48.5	* *	51.8	66.5	53.9	57.6	* *
	T_R	11.8	12.9	12.1	12.5	* *	14.4	16.1	14.7	15.1	* *	15.8	17.9	16.1	16.7	* *
5				Small R = 6					Medium R = 14					Large R = 23		
Lat ϕ = 27°	U_R	122.4					121.4					120.3				
Δ P = 3.41 in Hg	V	0	19.7	4.0	11.0	28.0	0	24.6	4.0	11.0	28.0	0	27.2	4.0	11.0	28.0
	U_{RS}	105.8	114.3	106.5	110.0	118.5	105.0	115.8	105.6	109.1	117.6	104.1	116.2	104.6	108.1	116.6
Sarita, Texas	H_R	31.5	37.7	32.7	34.9	* *	44.6	55.7	46.3	49.4	* *	52.2	66.8	54.3	57.9	* *
	T_R	11.9	13.0	12.1	12.5	* *	14.5	16.2	14.8	15.3	* *	18.9	18.0	16.2	16.7	* *
6				Small R = 6					Medium R = 14					Large R = 20		
Lat ϕ = 26°	U_R	124.1					123.2					122.5				
Δ P = 3.50 in Hg	V	0	19.9	4.0	11.0	28.0	0	24.8	4.0	11.0	28.0	0	26.7	4.0	11.0	28.0
	U_{RS}	107.3	117.3	109.3	112.8	121.3	106.5	119.3	108.5	112.0	120.5	105.9	119.3	107.9	111.4	119.9
Brownsville, Texas	H_R	32.0	38.3	33.3	35.4	* *	45.6	56.8	47.3	50.4	* *	51.1	64.8	53.1	56.6	* *
	T_R	12.0	13.1	12.2	12.6	* *	14.7	16.4	14.9	15.4	* *	15.7	17.6	15.9	16.5	* *

* * FORWARD SPEED GREATER THAN CRITICAL FORWARD SPEED

TABLE V - 1
DEEP WATER WAVES
STANDARD PROJECT HURRICANES FOR EAST COAST U.S. ZONE 1

		Stat	Crit	Slow	Med	Fast	Stat	Crit	Slow	Med	Fast	Stat	Crit	Slow	Med	Fast
1		Small R = 4					Medium R = 7					Large R = 10				
Lat ϕ = 23°	U_R	122.9					122.6					122.3				
	V	0	17.8	3.0	10.0	16.0	0	20.7	3.0	10.0	16.0	0	22.8	3.0	10.0	16.0
Δ P = 3.42 in Hg	U_{Rs}	106.3	115.2	107.8	111.3	114.3	106.1	116.5	107.6	111.1	114.1	105.8	117.2	107.3	110.8	113.8
	H_R	26.9	31.6	27.6	29.5	31.1	34.1	41.1	35.1	37.4	39.4	39.6	48.6	40.7	43.4	45.8
	T_R	10.9	11.8	11.0	11.4	11.7	12.5	13.7	12.6	13.0	13.4	13.6	15.0	13.8	14.2	14.6
2		Small R = 4					Medium R = 7					Large R = 11				
Lat ϕ = 24°	U_R	121.5					121.1					120.7				
	V	0	17.7	3.0	10.0	17.0	0	20.6	3.0	10.0	17.0	0	23.2	3.0	10.0	17.0
Δ P = 3.34 in Hg	U_{Rs}	105.1	113.9	106.6	110.1	113.6	104.8	115.1	106.3	109.8	113.3	104.4	116.0	105.9	109.4	112.9
	H_R	26.5	31.1	27.2	29.0	30.9	33.5	40.5	34.5	36.8	39.2	40.6	50.1	41.7	44.6	47.4
	T_R	10.8	11.7	10.9	11.3	11.7	12.4	13.6	12.5	13.0	13.4	13.8	15.3	14.0	14.4	14.9
3		Small R = 4					Medium R = 7					Large R = 12				
Lat ϕ = 25°	U_R	119.6					119.3					118.7				
	V	0	17.6	3.0	10.0	17.0	0	20.4	3.0	10.0	17.0	0	23.5	3.0	10.0	17.0
Δ P = 3.24 in Hg	U_{Rs}	103.5	112.3	105.0	108.5	112.0	103.2	113.6	104.7	108.2	111.7	102.7	114.5	104.5	107.7	110.2
	H_R	26.0	30.6	26.7	28.5	30.4	32.9	39.7	33.9	36.2	38.5	41.3	51.3	42.5	45.4	48.4
	T_R	10.7	11.6	10.8	11.2	11.6	12.3	13.5	12.4	12.9	13.3	13.9	15.5	14.1	14.6	15.1
4		Small R = 4					Medium R = 8					Large R = 13				
Lat ϕ = 25.5°	U_R	118.5					118.0					117.5				
	V	0	17.5	3.0	10.0	17.0	0	21.0	3.0	10.0	17.0	0	23.9	3.0	10.0	17.0
Δ P = 3.18 in Hg	U_{Rs}	102.5	111.3	104.0	107.5	111.0	102.1	112.6	103.6	107.1	110.6	101.6	113.6	102.1	106.6	110.1
	H_R	25.7	30.2	26.4	28.2	30.1	34.4	41.9	35.4	37.9	40.4	42.2	52.7	43.4	46.4	49.5
	T_R	10.6	11.5	10.8	11.2	11.5	12.6	13.9	12.8	13.2	13.6	14.1	15.8	14.3	14.8	15.3
5		Small R = 4					Medium R = 8					Large R = 14				
Lat ϕ = 26°	U_R	116.8					116.3					115.6				
	V	0	17.4	4.0	11.0	17.0	0	20.9	4.0	11.0	17.0	0	24.1	4.0	11.0	17.0
Δ P = 3.09 in Hg	U_{Rs}	101.0	109.7	103.0	106.5	109.5	100.6	111.1	102.6	106.1	109.5	100.0	112.1	102.0	105.5	108.5
	H_R	25.2	29.8	26.2	28.1	30.7	33.8	41.2	35.2	37.6	39.8	42.4	53.2	44.1	47.1	49.9
	T_R	10.6	11.5	10.8	11.1	11.5	12.5	13.8	12.7	13.2	13.6	14.2	15.9	14.5	15.0	15.4
6		Small R = 5					Medium R = 10					Large R = 18				
Lat ϕ = 27°	U_R	112.1					111.5					110.6				
	V	0	18.1	4.0	11.0	18.0	0	21.8	4.0	11.0	18.0	0	24.8	4.0	11.0	18.0
Δ P = 2.86 in Hg	U_{Rs}	97.0	106.1	99.0	102.5	106.0	96.5	107.5	98.5	102.0	107.5	95.6	108.0	97.6	101.1	104.6
	H_R	26.5	31.7	27.6	29.6	31.7	35.5	44.0	37.0	39.7	42.5	43.6	55.6	45.4	48.4	52.2
	T_R	10.9	12.0	11.2	11.6	12.0	12.9	14.4	13.2	13.7	14.1	14.5	16.4	14.8	15.3	15.9

TABLE V - 2
DEEP WATER WAVES
STANDARD PROJECT HURRICANES FOR EAST COAST U.S. ZONE 2

		Stat	Crit	Slow	Med	Fast	Stat	Crit	Slow	Med	Fast	Stat	Crit	Slow	Med	Fast
1		Small R = 6					Medium R = 12					Large R = 25				
Lat ϕ = 28°	U_R	106.5					105.7					104.1				
	V		18.6	4.0	11.0	19.0	0	22.2	4.0	11.0	19.0	0	25.7	4.0	11.0	19.0
Δ P = 2.59 in Hg	U_{Rs}	92.1	101.4	94.1	77.6	101.6	91.4	102.5	93.4	96.9	90.9	90.1	103.0	92.1	95.6	99.0
	H_R	27.1	32.8	28.3	30.4	* *	35.9	45.1	37.5	40.3	43.7	45.2	59.0	47.2	50.8	55.2
	T_R	11.1	12.3	11.4	11.8	* *	13.1	14.7	13.4	13.9	14.4	14.9	17.0	15.2	15.8	16.4
2		Small R = 7					Medium R = 15					Large R = 32				
Lat ϕ = 29°	U_R	102.7					101.6					99.5				
	V	0	19.1	4.0	11.0	20.0	0	22.8	4.0	11.0	20.0	0	26.0	4.0	11.0	20.0
Δ P = 2.42 in Hg	U_{Rs}	88.8	98.4	90.8	95.5	98.8	87.9	99.2	89.9	92.4	97.9	86.0	99.0	88.0	91.5	96.0
	H_R	27.8	34.1	29.1	31.4	* *	36.8	47.0	38.5	41.6	45.7	46.2	61.5	48.4	52.3	57.6
	T_R	11.4	12.6	11.6	12.1	* *	13.3	15.0	13.6	14.2	14.8	15.1	17.4	15.5	16.1	16.9
3		Small R = 7					Medium R = 17					Large R = 38				
Lat ϕ = 30.5°	U_R	100.0					98.7					95.9				
	V	0	18.8	4.0	11.0	21.0	0	23.0	4.0	11.0	21.0	0	26.7	4.0	11.0	21.0
Δ P = 2.42 in Hg	U_{Rs}	86.5	95.9	88.5	92.0	97.0	85.3	96.8	87.3	90.8	95.8	83.0	96.4	85.0	88.5	93.5
	H_R	27.0	33.2	28.2	30.5	* *	36.9	47.6	38.7	41.9	46.6	46.2	62.3	48.5	52.5	58.7
	T_R	11.2	12.4	11.5	11.9	* *	13.4	15.2	13.7	14.2	15.0	15.2	17.6	15.5	16.2	17.1
4		Small R = 7					Medium R = 17					Large R = 38				
Lat ϕ = 30°	U_R	99.2					97.9					95.1				
	V	0	18.8	4.0	11.0	22.0	0	22.9	4.0	11.0	22.0	0	26.5	4.0	11.0	22.0
Δ P = 2.3 in Hg	U_{Rs}	85.8	95.2	87.8	90.3	96.9	84.7	96.2	86.7	90.2	95.7	82.2	95.5	84.2	87.7	93.2
	H_R	26.8	32.9	28.0	30.3	* *	36.5	47.1	38.3	41.4	46.7	45.6	61.5	47.9	51.9	58.7
	T_R	11.2	12.4	11.4	11.9	* *	13.3	15.1	13.6	14.2	15.0	15.1	17.5	15.4	16.1	17.1
5		Small R = 7					Medium R = 18					Large R = 40				
Lat ϕ = 31°	U_R	98.9					97.4					94.4				
	V	0	18.8	4.0	11.0	23.0	0	23.1	4.0	11.0	23.0	0	26.6	4.0	11.0	23.0
Δ P = 2.26 in Hg	U_{Rs}	85.5	94.9	87.5	91.0	79.0	84.2	95.8	86.2	89.7	95.7	81.7	95.0	83.7	87.2	93.2
	H_R	26.7	32.8	27.9	30.2	* *	37.0	47.8	38.8	42.0	47.8	45.8	62.0	48.1	52.2	59.6
	T_R	11.2	12.4	11.4	11.9	* *	13.4	15.3	13.7	14.3	15.2	15.1	17.6	15.5	16.1	17.2
6		Small R = 7					Medium R = 18					Large R = 40				
Lat ϕ = 32°	U_R	98.6					97.1					94.0				
	V	0	18.7	4.0	12.0	26.0		23.0	4.0	12.0	26.0	0	26.5	4.0	12.0	26.0
Δ P = 2.26 in Hg	U_{Rs}	85.3	94.7	87.2	91.3	98.3	84.0	95.5	86.0	90.0	97.0	81.4	94.7	83.4	87.4	94.4
	H_R	26.6	32.8	27.9	30.5	* *	36.8	47.5	38.5	42.2	* *	45.4	61.4	47.7	52.4	61.1
	T_R	11.1	12.4	11.4	11.9	* *	13.4	15.2	13.7	14.3	* *	15.0	17.5	15.4	16.2	17.5

* * FORWARD SPEED GREATER THAN CRITICAL FORWARD SPEED

TABLE V - 3
DEEP WATER WAVES
STANDARD PROJECT HURRICANES FOR EAST COAST U.S. ZONE 3

		Stat	Crit	Slow	Med	Fast	Stat	Crit	Slow	Med	Fast	Stat	Crit	Slow	Med	Fast
1		Small R = 7					Medium R = 18					Large R = 14				
Lat ϕ = 33°	U_R	98.6					97.1					93.9				
ΔP = 2.27 in Hg	V	0	18.7	4.0	13.0	30.0	0	23.0	4.0	13.0	30.0	0	26.4	4.0	13.0	30.0
	U_{Rs}	85.3	94.7	87.3	91.8	95.3	84.0	95.5	86.0	90.5	99.0	81.2	94.6	83.2	87.7	91.7
	H_R	26.6	32.8	27.9	30.8	* *	36.6	47.4	38.4	42.5	* *	45.2	61.1	47.4	52.7	* *
	T_R	11.1	12.4	11.4	12.0	* *	13.3	15.2	13.7	14.4	* *	15.0	17.4	15.4	16.2	* *
2		Small R = 7					Medium R = 17					Large R = 37				
Lat ϕ = 34°	U_R	99.5					98.0					95.1				
ΔP = 2.32 in Hg	V	0	18.8	5.0	15.0	34.0	0	22.8	5.0	15.0	34.0	0	26.2	5.0	15.0	34.0
	U_{Rs}	86.1	95.5	88.6	93.6	103.1	84.8	96.2	87.3	92.3	101.8	82.3	95.4	84.8	89.8	99.3
	H_R	26.8	33.0	28.4	31.7	* *	36.3	46.7	38.5	43.0	* *	44.7	60.0	47.4	53.2	* *
	T_R	11.2	12.4	11.5	12.2	* *	13.3	15.0	13.7	14.4	* *	14.9	17.3	15.4	16.3	* *
3		Small R = 7					Medium R = 17					Large R = 35				
Lat ϕ = 35°	U_R	99.9					98.4					96.7				
ΔP = 2.36 in Hg	V	0	18.9	5.0	17.0	38.0	0	22.8	5.0	17.0	38.0	0	26.0	5.0	17.0	38.0
	U_{Rs}	86.4	95.4	88.9	94.9	105.4	85.1	96.5	87.6	93.6	104.1	82.8	95.8	85.3	91.3	101.8
	H_R	27.0	33.3	28.6	32.6	* *	36.4	46.9	38.6	44.1	* *	44.3	59.2	47.0	53.8	* *
	T_R	11.2	12.5	11.6	12.3	* *	13.3	15.1	13.7	14.6	* *	14.8	17.1	15.3	16.3	* *
4		Small R = 7					Medium R = 17					Large R = 34				
Lat ϕ = 35.5°	U_R	99.9					98.3					95.8				
ΔP = 2.37 in Hg	V	0	18.9	5.0	18.0	40.0	0	22.8	5.0	18.0	40.0	0	25.8	5.0	18.0	40.0
	U_{Rs}	86.4	95.9	88.9	95.4	106.4	85.1	96.5	87.6	94.1	105.1	82.8	105.7	85.3	91.8	102.8
	H_R	27.1	33.3	28.7	33.0	* *	36.4	46.9	38.6	44.5	* *	43.9	58.7	46.6	54.0	* *
	T_R	11.2	12.5	11.6	12.4	* *	13.3	15.1	13.7	14.7	* *	14.8	17.1	15.2	16.4	* *
5		Small R = 7					Medium R = 17					Large R = 34				
Lat ϕ = 36°	U_R	99.6					98.1					95.5				
ΔP = 2.37 in Hg	V	0	18.9	6.0	20.0	42.0	0	22.8	6.0	20.0	42.0	0	25.8	6.0	20.0	42.0
	U_{Rs}	86.2	95.7	89.3	96.2	107.2	84.8	96.2	87.8	94.8	104.8	82.6	95.5	85.6	92.6	103.8
	H_R	27.0	33.3	28.9	* *	* *	36.3	46.7	38.9	45.4	* *	43.7	58.5	47.0	55.0	* *
	T_R	11.2	12.5	11.6	* *	* *	13.3	15.1	13.7	14.8	* *	14.7	17.0	15.3	16.5	* *
6		Small R = 7					Medium R = 17					Large R = 35				
Lat ϕ = 37°	U_R	98.7					97.2					94.3				
ΔP = 2.35 in Hg	V	0	18.8	7.0	22.0	45.0	0	22.7	7.0	22.0	45.0	0	25.8	7.0	22.0	45.0
	U_{Rs}	85.4	94.8	88.9	96.4	107.9	84.0	95.4	87.5	95.0	105.9	81.6	104.5	85.1	92.6	104.1
	H_R	26.8	33.1	29.1	* *	* *	35.9	46.3	39.0	46.0	* *	43.4	58.2	47.2	55.9	* *
	T_R	11.2	12.4	11.7	* *	* *	13.2	15.0	13.8	14.9	* *	14.7	17.0	15.3	16.7	* *

* *FORWARD SPEED GREATER THAN CRITICAL FORWARD SPEED

TABLE V - 4
DEEP WATER WAVES
STANDARD PROJECT HURRICANES FOR EAST COAST U.S. ZONE 4

		Stat	Crit	Slow	Med	Fast	Stat	Crit	Slow	Med	Fast	Stat	Crit	Slow	Med	Fast
1		Small R = 7					Medium R = 18					Large R = 37				
Lat ϕ = 38°	U_R	97.6					95.8					92.7				
ΔP = 2.32 in Hg	V	0	18.8	9.0	25.0	47.0	0	22.8	9.0	25.0	47.0	0	25.8	9.0	25.0	47.0
	U_{Rs}	84.4	93.8	88.9	96.9	107.9	82.9	94.3	97.4	95.3	106.4	80.2	93.1	84.7	92.7	103.5
	H_R	26.6	32.8	29.5	* *	* *	36.1	46.7	40.1	* *	* *	43.2	58.3	48.2	* *	* *
	T_R	11.2	12.4	11.8	* *	* *	13.3	15.1	14.0	* *	* *	14.7	17.0	15.5	* *	* *
2		Small R = 7					Medium R = 19					Large R = 39				
Lat ϕ = 39°	U_R	95.9					93.9					90.6				
ΔP = 2.27 in Hg	V	0	18.7	11.0	27.0	49.0	0	22.9	11.0	27.0	49.0	0	25.8	11.0	27.0	49.0
	U_{Rs}	82.9	92.3	98.4	96.4	107.4	81.2	92.7	86.7	94.7	106.7	78.4	101.3	83.9	91.9	102.9
	H_R	26.2	32.5	29.8	* *	* *	36.0	46.8	41.0	* *	* *	42.7	57.9	48.9	* *	* *
	T_R	11.1	12.3	11.8	* *	* *	13.3	15.1	14.2	* *	* *	14.6	17.0	15.6	* *	* *
3		Small R = 8					Medium R = 21					Large R = 43				
Lat ϕ = 40°	U_R	93.8					91.6					87.9				
ΔP = 2.21 in Hg	V	0	19.1	14.0	32.0	50.0	0	23.2	14.0	32.0	50.0	0	25.8	14.0	32.0	50.0
	U_{Rs}	81.2	90.8	88.2	79.2	106.2	79.3	90.9	86.3	95.3	104.3	76.0	88.9	83.0	92.0	101.0
	H_R	26.9	33.7	31.8	* *	* *	36.2	47.6	42.9	* *	* *	42.4	58.0	50.5	* *	* *
	T_R	11.3	12.6	12.3	* *	* *	13.3	15.3	14.5	* *	* *	14.6	17.0	15.9	* *	* *
4		Small R = 8					Medium R = 22					Large R = 45				
Lat ϕ = 40.5°	U_R	92.9					90.5					86.6				
ΔP = 2.18 in Hg	V	0	19.1	14.0	33.0	51.0	0	23.3	14.0	33.0	51.0	0	25.8	14.0	33.0	51.0
	U_{Rs}	80.3	89.9	87.3	96.8	105.8	78.3	90.0	85.3	94.8	103.8	74.9	87.8	81.9	91.4	100.4
	H_R	26.7	33.4	31.5	* *	* *	36.3	47.9	43.1	* *	* *	42.2	57.9	50.4	* *	* *
	T_R	11.2	12.6	12.2	* *	* *	13.4	15.4	14.6	* *	* *	14.5	17.1	15.9	* *	* *
5		Small R = 8					Medium R = 24					Large R = 48				
Lat ϕ = 41°	U_R	91.7					88.9					84.8				
ΔP = 2.14 in Hg	V	0	19.0	15.0	34.0	51.0	0	23.4	15.0	34.0	51.0	0	25.9	15.0	34.0	51.0
	U_{Rs}	79.3	88.8	86.8	96.3	104.8	76.9	88.6	84.4	93.9	102.0	73.4	86.4	78.9	90.4	98.9
	H_R	26.3	33.0	31.5	* *	* *	36.5	48.4	43.9	* *	* *	41.9	58.0	50.9	* *	* *
	T_R	11.2	12.5	12.2	* *	* *	13.4	15.5	14.7	* *	* *	14.5	17.1	16.0	* *	* *
6		Small R = 8					Medium R = 27					Large R = 52				
Lat ϕ = 42°	U_R	89.6					86.2					81.9				
ΔP = 2.07 in Hg	V	0	18.8	16.0	36.0	52.0	0	23.6	16.0	36.0	52.0	0	25.8	16.0	36.0	52.0
	U_{Rs}	77.5	86.9	85.5	95.5	103.5	74.6	86.4	82.6	92.6	100.6	70.8	81.7	76.8	86.8	96.8
	H_R	25.7	32.3	31.3	* *	* *	36.4	48.9	44.6	* *	* *	41.1	57.4	50.9	* *	* *
	T_R	11.1	12.4	12.2	* *	* *	13.4	15.6	14.9	* *	* *	14.4	17.0	16.0	* *	* *
7		Small R = 9					Medium R = 31					Large R = 57				
Lat ϕ = 43°	U_R	87.0					83.1					78.5				
ΔP = 1.99 in Hg	V	0	19.0	17.0	37.0	52.0	0	23.8	17.0	37.0	52.0	0	25.6	17.0	37.0	52.0
	U_{Rs}	75.3	84.8	83.8	93.8	101.3	71.9	83.8	80.4	90.4	97.9	67.9	80.7	76.4	86.4	93.9
	H_R	25.9	32.9	32.1	* *	* *	36.3	49.3	45.4	* *	* *	40.0	56.4	50.6	* *	* *
	T_R	11.2	12.6	12.4	* *	* *	13.5	15.7	15.1	* *	* *	14.2	16.9	16.0	* *	* *

* *FORWARD SPEED GREATER THAN CRITICAL FORWARD SPEED

TABLE VI - 1
DEEP WATER WAVES
PROBABLE MAXIMUM HURRICANES FOR EAST COAST U.S. ZONE 1

		Stat	Crit	Slow	Med	Fast	Stat	Crit	Slow	Med	Fast	Stat	Crit	Slow	Med	Fast
1		Small R = 4					Medium R = 7					Large R = 10				
Lat ϕ = 23°	U_R	132.6					132.3					132.0				
ΔP = 3.98 in Hg	V	0	18.4	3.0	10.0	16.0	0	21.4	3.0	10.0	16.0	0	23.5	3.0	10.0	16.0
	U_{RS}	114.7	123.9	116.2	119.7	122.7	114.5	125.2	116.0	119.5	122.5	114.2	126.0	115.7	119.2	122.2
	H_R	29.2	34.0	29.9	31.8	33.4	37.0	44.2	38.0	40.3	42.3	43.0	52.3	44.1	46.8	49.2
	T_R	11.3	12.2	11.4	11.7	12.0	12.9	14.1	13.1	13.5	13.8	14.1	15.5	14.3	14.7	15.1
2		Small R = 4					Medium R = 7					Large R = 11				
Lat ϕ = 24°	U_R	132.5					132.1					131.7				
ΔP = 3.97 in Hg	V	0	18.4	3.0	10.0	17.0	0	21.3	3.0	10.0	17.0	0	24.1	3.0	10.0	17.0
	U_{RS}	114.6	123.8	116.1	119.6	123.1	114.3	125.0	115.8	119.3	122.8	113.9	126.0	115.4	118.9	122.4
	H_R	29.0	33.9	29.8	31.6	33.5	36.8	44.0	37.8	40.1	42.5	44.5	54.4	45.7	48.5	51.4
	T_R	11.2	12.1	11.4	11.7	12.1	12.9	14.1	13.0	13.4	13.8	14.4	15.9	14.6	15.0	15.4
3		Small R = 4					Medium R = 7					Large R = 12				
Lat ϕ = 25°	U_R	130.9					130.6					130.0				
ΔP = 3.88 in Hg	V	0	18.3	3.0	10.0	17.0	0	21.2	3.0	10.0	17.0	0	24.5	3.0	10.0	17.0
	U_{RS}	113.3	123.8	114.8	118.3	121.8	113.0	223.6	114.6	118.0	121.5	112.5	124.8	114.0	117.5	121.0
	H_R	28.6	33.4	29.4	31.2	33.0	36.3	43.4	37.2	39.5	41.9	45.5	55.9	46.7	49.6	52.6
	T_R	11.2	12.1	11.3	11.6	12.0	12.8	14.0	13.0	13.4	13.8	14.6	16.1	14.8	15.2	15.7
4		Small R = 4					Medium R = 8					Large R = 12				
Lat ϕ = 25.5°	U_R	130.4					130.0					129.4				
ΔP = 3.85 in Hg	V	0	18.2	3.0	10.0	17.0	0	21.9	3.0	10.0	17.0	0	24.9	3.0	10.0	17.0
	U_{RS}	112.8	121.9	114.3	117.8	121.3	112.4	123.4	113.9	117.4	120.9	111.9	124.4	113.4	116.9	120.4
	H_R	28.4	33.2	29.2	31.0	32.9	38.1	45.9	39.2	41.6	44.1	46.8	57.8	48.0	51.0	54.1
	T_R	11.1	12.0	11.3	11.6	12.0	13.2	14.5	13.4	13.8	14.2	14.8	16.4	15.0	15.5	15.9
5		Small R = 4					Medium R = 8					Large R = 14				
Lat ϕ = 26°	U_R	129.7					129.3					128.5				
ΔP = 3.81 in Hg	V	0	18.2	4.0	11.0	17.0	0	21.8	4.0	11.0	17.0	0	25.3	4.0	11.0	17.0
	U_{RS}	112.2	121.3	114.2	117.7	120.7	111.8	122.7	113.8	117.3	120.3	111.2	123.9	113.2	116.7	119.7
	H_R	28.2	33.0	29.3	31.1	32.7	37.9	45.6	39.2	41.7	43.9	47.9	59.4	49.6	52.7	55.5
	T_R	11.1	12.0	11.3	11.6	11.9	13.1	14.4	13.4	13.8	14.1	15.0	16.7	15.3	15.8	16.2
6		Small R = 5					Medium R = 10					Large R = 18				
Lat ϕ = 27°	U_R	127.6					127.0					126.1				
ΔP = 3.7 in Hg	V	0	19.1	4.0	11.0	16.0	0	23.0	4.0	11.0	16.0	0	26.4	4.0	11.0	16.0
	U_{RS}	110.4	120.0	112.4	115.9	118.4	109.9	121.4	111.9	115.4	117.9	109.0	122.2	111.0	114.5	117.0
	H_R	30.5	36.0	31.6	33.6	35.1	40.8	50.0	42.3	45.0	47.0	50.8	63.8	52.6	56.0	58.5
	T_R	11.6	12.6	11.8	12.2	12.5	13.7	15.2	14.0	14.4	14.7	15.5	17.4	15.8	16.3	16.7

TABLE VI - 2
DEEP WATER WAVES
PROBABLE MAXIMUM HURRICANES FOR EAST COAST U.S. ZONE 2

		Stat	Crit	Slow	Med	Fast	Stat	Crit	Slow	Med	Fast	Stat	Crit	Slow	Med	Fast
1		Small R = 6					Medium R = 12					Large R = 25				
Lat ϕ = 28°	U_R	124.6					123.8					122.2				
ΔP = 3.54 in Hg	V	0	19.9	4.0	11.0	19.0	0	23.9	4.0	11.0	19.0	0	27.8	4.0	11.0	19.0
	U_{RS}	107.8	117.8	109.8	113.3	117.3	107.1	119.1	109.1	112.6	115.6	105.7	119.6	109.7	111.2	115.2
	H_R	32.1	38.3	33.3	35.4	38.0	42.9	53.0	44.5	47.4	50.9	54.5	69.7	56.5	60.3	64.7
	T_R	12.0	13.1	12.2	12.6	13.1	14.2	15.8	14.4	14.9	15.4	15.2	18.4	16.5	17.1	17.7
2		Small R = 7					Medium R = 15					Large R = 32				
Lat ϕ = 29°	U_R	122.0					121.0					118.8				
ΔP = 3.41 in Hg	V	0	20.5	4.0	11.0	20.0	0	24.8	4.0	11.0	20.0	0	28.8	4.0	11.0	20.0
	U_{RS}	106.0	116.3	108.0	111.5	116.0	104.7	117.1	104.7	110.2	114.7	102.8	117.2	106.8	108.3	112.8
	H_R	33.5	40.3	34.7	37.0	40.1	45.1	56.4	46.8	50.0	54.1	56.9	74.0	59.2	63.2	68.5
	T_R	12.3	13.5	12.6	13.0	13.5	14.6	16.4	14.9	15.4	16.0	16.7	19.0	17.0	17.6	18.3
3		Small R = 7					Medium R = 17					Large R = 38				
Lat ϕ = 30°	U_R	119.6					118.2					115.5				
ΔP = 3.28 in Hg	V	0	20.3	4.0	11.0	21.0	0	25.1	4.0	11.0	21.0	0	29.3	4.0	11.0	21.0
	U_{RS}	103.4	113.6	105.4	108.9	119.4	102.3	124.9	104.3	107.8	112.8	99.9	114.6	101.9	105.4	110.4
	H_R	32.7	39.4	34.0	36.2	* *	45.6	57.5	47.4	50.6	55.4	58.0	76.3	60.3	64.6	70.8
	T_R	12.2	13.4	12.4	12.9	* *	14.8	16.6	15.0	15.5	16.3	16.9	19.4	17.2	17.8	18.7
4		Small R = 7					Medium R = 17					Large R = 38				
Lat ϕ = 30.5°	U_R	118.7					117.4					114.6				
ΔP = 3.24 in Hg	V	0	20.2	4.0	11.0	22.0	0	25.0	4.0	11.0	22.0	0	29.2	4.0	11.0	22.0
	U_{RS}	102.7	110.8	104.7	108.2	113.7	101.5	114.0	103.5	107.0	112.5	99.1	113.7	101.1	104.6	110.1
	H_R	32.4	39.1	33.7	36.0	* *	45.1	56.9	46.9	50.2	55.4	57.4	75.5	59.7	63.9	70.8
	T_R	12.2	13.4	12.4	12.8	* *	14.7	16.5	15.0	15.5	16.3	16.8	19.3	17.1	17.7	18.7
5		Small R = 7					Medium R = 18					Large R = 40				
Lat ϕ = 31°	U_R	117.8					116.3					113.4				
ΔP = 3.2 in Hg	V	0	20.2	4.0	11.0	23.0	0	25.2	4.0	11.0	23.0	0	29.2	4.0	11.0	23.0
	U_{RS}	101.9	112.0	103.9	107.4	113.4	100.6	113.2	102.6	106.1	112.1	98.1	112.7	100.1	103.6	109.6
	H_R	32.2	38.9	33.4	35.7	* *	45.5	57.6	47.3	50.6	56.5	57.2	75.5	59.5	63.8	71.4
	T_R	12.1	13.3	12.4	12.8	* *	14.8	16.6	15.1	15.6	16.4	16.8	19.3	17.1	17.7	18.8
6		Small R = 7					Medium R = 18					Large R = 40				
Lat ϕ = 32°	U_R	116.4					114.9					111.9				
ΔP = 3.14 in Hg	V	0	20.1	4.0	12.0	26.0	0	25.0	4.0	12.0	26.0	0	29.0	4.0	12.0	26.0
	U_{RS}	100.7	110.8	102.7	106.7	113.7	99.4	111.9	103.4	105.4	112.4	96.8	111.3	98.8	102.8	109.8
	H_R	31.8	38.4	33.0	35.7	* *	44.7	56.7	46.5	50.3	* *	56.0	74.1	58.4	63.2	72.1
	T_R	12.1	13.3	12.3	12.8	* *	14.6	16.5	14.9	15.5	* *	16.6	19.1	17.0	17.7	18.9

* * FORWARD SPEED GREATER THAN CRITICAL FORWARD SPEED

TABLE VI - 3
DEEP WATER WAVES
PROBABLE MAXIMUM HURRICANES FOR EAST COAST U.S. ZONE 3

		Stat	Crit	Slow	Med	Fast	Stat	Crit	Slow	Med	Fast	Stat	Crit	Slow	Med	Fast
1				*Small* R = 7					*Medium* R = 18					Large R = 40		
Lat ϕ = 33°	U_R	115.4					113.9					110.7				
	V	0	20.0	4.0	13.0	30.0	0	24.8	4.0	13.0	30.0	0	28.7	4.0	13.0	30.0
Δ P = 3.1 in Hg	U_{Rs}	99.9	109.9	101.9	106.4	114.9	98.5	110.9	100.5	115.0	113.5	95.8	110.2	97.8	102.3	110.8
	H_R	31.5	38.1	32.7	35.7	* *	44.1	56.0	45.9	50.1	* *	55.1	72.9	57.5	62.9	* *
	T_R	12.0	13.2	12.2	12.8	* *	14.5	16.4	14.8	15.5	* *	16.5	19.0	16.8	17.6	* *
2				Small R = 7					Medium R = 17					Large R = 37		
Lat ϕ = 34°	U_R	114.4					113.0					110.0				
	V	0	19.9	5.0	15.0	34.0	0	24.4	5.0	15.0	34.0	0	28.2	5.0	15.0	34.0
Δ P = 3.1 in Hg	U_{Rs}	99.0	109.0	101.5	106.5	116.0	97.7	109.9	100.2	105.2	114.7	95.2	109.1	97.7	102.7	112.2
	H_R	31.2	37.8	32.8	36.1	* *	42.8	54.1	45.0	49.6	* *	53.3	70.3	56.2	62.1	* *
	T_R	12.0	13.2	12.3	12.9	* *	14.3	16.1	14.7	15.4	* *	16.2	18.6	16.6	17.5	* *
3				Small R = 7					Medium R = 17					Large R = 35		
Lat ϕ = 35°	U_R	113.3					111.8					109.1				
	V	0	19.9	5.0	17.0	38.0	0	24.3	5.0	17.0	38.0	0	27.8	5.0	17.0	38.0
Δ P = 3.03 in Hg	U_{Rs}	98.0	108.0	100.5	106.5	117.0	96.7	108.9	109.2	105.2	115.7	94.4	107.7	96.4	102.9	113.9
	H_R	30.9	37.5	32.5	36.5	* *	42.3	53.6	44.5	50.1	* *	51.9	68.3	54.7	61.7	* *
	T_R	11.9	13.1	12.2	13.0	* *	14.2	16.0	14.6	15.5	* *	16.0	18.3	16.4	17.4	* *
4				Small R = 7					Medium R = 17					Large R = 34		
Lat ϕ = 35.5°	U_R	112.7					111.2					108.6				
	V	0	19.9	5.0	18.0	40.0	0	24.2	5.0	18.0	40.0	0	27.5	5.0	18.0	40.0
Δ P = 3.01 in Hg	U_{Rs}	97.5	107.5	100.0	106.5	117.5	96.2	108.3	98.7	104.2	116.2	93.9	107.7	96.4	102.9	113.9
	H_R	30.8	37.4	32.4	36.7	* *	42.0	53.6	44.2	50.3	* *	51.1	67.2	53.9	61.4	* *
	T_R	11.9	13.1	12.2	13.0	* *	14.2	16.0	14.6	15.5	* *	15.9	18.2	16.3	17.4	* *
5				Small R = 7					Medium R = 17					Large R = 34		
Lat ϕ = 36°	U_R	112.0					110.5					107.9				
	V	0	19.8	6.0	20.0	42.0	0	24.1	6.0	20.0	42.0	0	27.4	6.0	20.0	42.0
Δ P = 2.99 in Hg	U_{Rs}	96.9	106.8	99.9	106.8	117.9	95.6	107.7	98.6	105.6	116.6	93.3	107.0	96.3	103.3	114.3
	H_R	30.6	37.2	32.6	* *	* *	41.7	52.9	44.4	50.9	* *	50.7	66.7	54.0	62.2	* *
	T_R	11.9	13.1	12.2	* *	* *	14.1	15.9	14.6	15.6	* *	15.8	18.1	16.3	17.5	* *
6				*Small* R = 7					*Medium* R = 17					*Large* R = 35		
Lat ϕ = 37°	U_R	110.8					109.2					106.3				
	V	0	19.8	7.0	22.0	45.0	0	24.0	7.0	22.0	45.0	0	27.4	7.0	22.0	45.0
Δ P = 2.95 in Hg	U_{Rs}	95.8	105.7	99.3	10.8	119.3	94.4	106.4	97.9	104.4	116.9	92.0	105.7	95.5	103.0	114.5
	H_R	30.4	36.9	32.6	* *	* *	41.2	52.3	44.3	51.3	* *	50.2	66.3	54.1	63.0	* *
	T_R	11.8	13.0	12.3	* *	* *	14.1	15.9	14.6	15.7	* *	15.7	18.1	16.3	17.6	* *

* * FORWARD SPEED GREATER THAN CRITICAL FORWARD SPEED

TABLE VI - 4
DEEP WATER WAVES
PROBABLE MAXIMUM HURRICANES FOR EAST COAST U.S. ZONE 4

		Stat	Crit	Slow	Med	Fast	Stat	Crit	Slow	Med	Fast	Stat	Crit	Slow	Med	Fast
1		Small R = 7					Medium R = 18					Large R = 37				
Lat ϕ = 38°	U_R	109.0					107.3					104.2				
Δ P = 2.89 in Hg	V	0	19.7	9.0	25.0	47.0	0	24.1	9.0	25.0	47.0	0	27.4	9.0	25.0	47.0
	U_{RS}	94.3	104.1	98.8	106.8	117.8	92.8	104.9	97.3	105.3	116.3	90.1	103.8	94.6	102.6	113.6
	H_R	30.0	36.5	32.9	* *	* *	41.2	52.6	45.3	* *	* *	49.8	66.1	54.9	* *	* *
	T_R	11.8	13.0	12.3	* *	* *	14.1	15.9	14.8	* *	* *	15.7	18.1	16.5	* *	* *
2		Small R = 7					Medium R = 19					Large R = 39				
Lat ϕ = 39°	U_R	107.2					105.2					101.9				
Δ P = 2.83 in Hg	V	0	19.6	11.0	27.0	49.0	0	24.2	11.0	27.0	49.0	0	27.3	11.0	27.0	49.0
	U_{RS}	92.7	102.5	98.2	106.2	117.2	91.0	103.1	96.5	104.5	115.5	88.2	101.9	93.7	101.7	112.7
	H_R	29.5	36.1	33.2	* *	* *	41.1	52.7	46.2	* *	* *	49.3	65.8	55.6	65.5	* *
	T_R	11.7	12.9	12.4	* *	* *	14.1	16.0	15.0	* *	* *	15.6	18.0	16.6	18.0	* *
3		Small R = 8					Medium R = 21					Large R = 43				
Lat ϕ = 40°	U_R	104.8					102.6					98.9				
Δ P = 2.75 in Hg	V	0	20.2	14.0	32.0	50.0	0	24.5	14.0	32.0	50.0	0	27.4	14.0	32.0	50.0
	U_{RS}	90.7	100.8	97.7	106.7	115.7	88.8	101.1	95.8	104.8	113.8	85.6	99.3	92.6	101.6	110.6
	H_R	30.6	37.8	35.5	* *	* *	41.4	53.5	48.1	* *	* *	48.9	65.9	57.3	* *	* *
	T_R	12.0	13.3	12.9	* *	* *	14.2	16.1	15.3	* *	* *	15.6	18.1	16.9	* *	* *
4		Small R = 8					Medium R = 22					Large R = 45				
Lat ϕ = 40.5°	U_R	103.7					101.3					97.4				
Δ P = 2.71 in Hg	V	0	20.1	14.0	33.0	51.0	0	24.6	14.0	33.0	51.0	0	27.4	14.0	33.0	51.0
	U_{RS}	89.7	99.8	96.7	106.2	115.3	87.6	99.9	94.6	104.1	113.1	84.2	97.9	91.1	100.7	109.7
	H_R	30.3	37.4	35.2	* *	* *	41.4	53.8	48.3	* *	* *	48.7	65.8	57.1	* *	* *
	T_R	11.9	13.2	12.8	* *	* *	14.2	16.2	15.4	* *	* *	15.6	18.1	16.9	* *	* *
5		Small R = 8					Medium R = 24					Large R = 48				
Lat ϕ = 41°	U_R	102.4					99.6					95.5				
Δ P = 2.66 in Hg	V	0	20.0	15.0	34.0	51.0	0	24.8	15.0	34.0	51.0	0	27.5	15.0	34.0	51.0
	U_{RS}	88.6	98.5	96.0	105.5	114.4	86.2	98.6	93.7	103.2	112.0	82.6	96.4	90.1	99.5	108.4
	H_R	29.9	37.0	35.2	* *	* *	41.9	54.8	49.5	* *	* *	48.4	65.9	57.6	* *	* *
	T_R	11.8	13.2	12.8	* *	* *	14.3	16.4	15.6	* *	* *	15.6	18.1	17.0	* *	* *

* * FORWARD SPEED GREATER THAN CRITICAL FORWARD SPEED

TABLE VI - 4
DEEP WATER WAVES
PROBABLE MAXIMUM HURRICANES FOR EAST COAST U.S. ZONE 4

CONTINUED

		Stat	Crit	Slow	Med	Fast	Stat	Crit	Slow	Med	Fast	Stat	Crit	Slow	Med	Fast
6		Small R = 8					Medium R = 27					Large R = 52				
Lat ϕ = 42°	U_R	100.0					96.6					92.2				
Δ P = 2.57 in Hg	V	0	19.8	16.0	36.0	52.0	0	25.0	16.0	36.0	52.0	0	27.4	16.0	36.0	52.0
	U_{RS}	86.5	96.9	94.5	104.5	112.5	83.6	96.0	91.5	101.5	109.6	79.8	93.5	87.8	97.8	105.8
	H_R	29.2	36.2	34.8	* *	* *	41.8	55.2	50.2	* *	* *	47.5	65.3	57.6	* *	* *
	T_R	11.7	13.1	12.8	* *	* *	14.4	16.5	15.7	* *	* *	15.4	18.1	17.0	* *	* *
7		Small R = 9					Medium R = 31					Large R = 57				
Lat ϕ = 43°	U_R	97.4					93.4					88.8				
Δ P = 2.48 in Hg	V	0	20.1	17.0	37.0	52.0	0	25.2	17.0	37.0	52.0	0	27.3	17.0	37.0	52.0
	U_{RS}	84.2	94.3	92.7	102.7	110.2	80.8	93.4	89.3	99.3	106.8	76.8	90.5	85.3	95.3	102.8
	H_R	29.5	37.0	39.8	* *	* *	41.8	55.9	51.1	* *	* *	46.6	64.7	57.5	* *	* *
	T_R	11.8	13.3	13.0	* *	* *	14.4	16.7	15.9	* *	* *	15.3	18.0	17.0	* *	* *
8		Small R = 9					Medium R = 36					Large R = 61				
Lat ϕ = 44°	U_R	94.7					89.8					85.2				
Δ P = 2.38 in Hg	V	0	19.9	18.0	38.0	53.0	0	25.4	18.0	38.0	53.0	0	27.1	18.0	38.0	53.0
	U_{RS}	81.9	91.9	90.9	100.9	108.4	77.7	90.4	86.7	96.7	104.2	73.7	87.3	82.7	92.7	100.2
	H_R	28.7	36.1	35.3	* *	* *	41.7	56.5	51.9	* *	* *	45.1	63.2	50.6	* *	* *
	T_R	11.7	13.1	13.0	* *	* *	14.4	16.8	16.1	* *	* *	15.1	17.9	16.9	* *	* *
9		Small R = 9					Medium R = 41					Large R = 66				
Lat ϕ = 45°	U_R	91.6					85.7					81.1				
Δ P = 2.26 in Hg	V	0	19.6	19.0	39.0	53.0	0	25.4	19.0	39.0	53.0	0	26.7	19.0	39.0	53.0
	U_{RS}	79.3	89.1	88.8	98.8	105.9	74.1	86.8	83.6	93.6	100.6	70.1	83.5	79.6	89.6	96.6
	H_R	27.7	35.0	34.8	* *	* *	40.9	56.2	52.1	* *	* *	43.3	61.4	55.8	* *	* *
	T_R	11.5	12.9	12.9	* *	* *	14.3	16.8	16.2	* *	* *	14.8	17.6	16.8	* *	* *

* * FORWARD SPEED GREATER THAN CRITICAL FORWARD SPEED

CHAPTER 8

PERIOD BY THE WAVE-GROUP METHOD

Warren C. Thompson, Professor of Oceanography
Naval Postgraduate School, Monterey, California

ABSTRACT

The wave-group period, T_g, is obtained by a simple manual procedure from the periodic wave groups and sequences that appear in strip-chart records. A dozen or more values are commonly derived from a 20-minute record. When plotted as a time-series, T_g values form patterns that represent individual wave trains, each generated by a synoptic weather event. Swell trains and wind-wave trains can be distinguished by their characteristic period distributions.

For swell trains, the mean wave-group frequency, $\overline{f}_g$, obtained from the best-fit line to the time-series plot of f_g values (reciprocal T_g values), is equivalent to the frequency of maximum energy density, f_m, obtained from spectral analysis. The distance and time of origin for a swell train can be determined from the time rate of change of $\overline{f}_g$, and with the use of weather maps the generating area can be identified and the deep-water arrival direction of the swell train at the wave gage determined.

The zero-line crossing period, T_z, represents an integration of the waves from all wave trains present and has no synoptic significance.

INTRODUCTION

Period is ordinarily obtained from a wave record by computer analysis of the wave information in digitized form to produce an energy density spectrum, or by manual analysis of an analog trace written on a strip chart to produce one or more of a half dozen kinds of period measures. Computer algorithms have also been developed for picking off crests, troughs, and zero-line crossings from analog data for use in obtaining several of the latter period measures.

Spectral analysis has an important advantage over other methods in that it yields the energy-density distribution over the full range of frequencies considered, although from this writer's observations it is only the period associated with the dominant frequency peak present that is used in most practical applications. In addition, there is adequate demonstration of the fact that prominent maxima in the spectrum represent wave trains from individual generating areas. The latter frequently can be followed in the wave records for several days.

Among the non-spectral procedures for processing analog records, the wave-group method has received little attention in the literature (Harris, 1970; Thompson, 1970). Nevertheless, as will be demonstrated, the

wave-group period is equivalent to the spectral peak period for swell, and in addition it is similarly identified with individual wave trains and is therefore a synoptically significant period parameter. The zero-line crossing method, which may be regarded as the standard non-spectral method of analysis by reason of its common use and frequent reference in the literature, is also examined in relation to the wave-group and spectral methods.

The results presented in this paper are principally drawn from the analysis of swell generated in moving cyclonic storms and propagated over distances of several hundred miles or more to wave gages on the California coast located in the general direction of storm advance. The data were recorded using pressure-type sensors mounted in 25 to 40 feet of water.

Period and frequency are referred to interchangeably throughout the paper in accord with conventional useage and ease of visualization.

WAVE-GROUP METHOD

Those who work with analog strip-chart records are familiar with the sequences of more or less periodic waves that appear at intervals in the record. Examples are illustrated in Figure 1. All wave sequences that can be identified in a record are here termed wave groups, whether they appear as discrete groups, as in Figure 1(a), or combined with other waves to form an irregular profile.

The wave-group period, T_g, can be obtained by identifying the first and last waves in a periodic sequence, and dividing the time interval between by the number of waves in the sequence. The measurement is made between those equivalent parts of the wave form that the analyst judges to give the best measure in each case, e.g., between selected crests, troughs, centers of wave mass, or zero-line crossings. Measurement between centers of mass are most useful when the wave shape is irregular and crest or trough measures are unsatisfactory (Figure 1(b)). Zero-line crossings should in general be avoided because most wave sequences are not symmetrical with respect to the zero line of the record due to superimposition on other waves that are ordinarily present. Occasionally, more than one wave sequence can be identified from the same time interval (Figure 1(d)). A quick check of the period of each wave in the sequence is recommended to avoid sequences containing phase changes.

The identification of periodic sequences requires judgment and seems at times to be quite subjective; nevertheless, even T_g values derived from waves of highly irregular form ordinarily prove to be associated with a recognized wave train. Rapid improvement in the identification and evaluation of wave sequences comes with a little practice, and the measurement of T_g for a selected sequence is a very quick operation. Best results in both quantity and quality of the data obtained requires the judgment of an analyst having a basic understanding of the fundamentals of wave interference, such as are given by Manley (1945).

A 20-minute record will frequently contain a dozen or more sequences of 3 or more waves. The T_g values obtained should be identified whenever

possible with individual wave trains present, as described in the next section. Averaging of the values from a given wave record without segregating them will yield an integrated period measure of uncertain significance, and a primary advantage of the wave-group method will have been discarded. The wave-group method is meant here to include both the mechanics of obtaining the wave-group period from a wave sequence and the association of the T_g values with wave trains present so as to yield synoptically significant period information.

SYNOPTIC WAVE TRAINS

Values of T_g plotted as a time series usually form well-defined patterns, each representing an individual wave train generated by a synoptic weather event, such as a cyclonic storm, occurring locally or at a distance from the recording station. These synoptic wave trains can ordinarily be recognized, from their distinctive period distributions, either as swell generated at a distance from the wave gage or as wind waves and associated young swell of local origin. Wave trains may appear singly in the T_g data, but two or more frequently are present at once. Most of the time individual trains can be distinguished from one another, but at times their period distributions merge and cannot be separated, and at other times during periods of very low waves the T_g values fall in a random pattern across the spectrum and no wave trains can be recognized. The identification of wave trains and their recognition as sea or swell from the period data are usually correctly confirmed by the associated wave-height data and weather maps.

Figure 2 presents values of T_g derived from 5-minute records made hourly for 7 days at Monterey, California, and reveals three successive wave trains arriving during otherwise quiet sea conditions. The continuous decrease of period with time from the initial appearance of each train clearly marks them as swell. The T_g distribution in a typical swell train also displays a relatively small scatter about the mean, which is consistent with the narrow spectral bandwidth character of swell. About the time of appearance of the first T_g values in a newly arriving swell train, the wave height normally rises above the energy level of the existing waves; however, on uncommon occasions during intervals of very low wave height (half a foot or less) the period distribution has unmistakably revealed the presence of a swell train when its height did not rise above the energy level of the background. When one swell train replaces another in time, the T_g values associated with each train during the interval of overlap (when the energy levels are of the same order of magnitude) may appear either as independent distributions, as in the case of Trains 1 and 2 of Figure 2, or they may form a continuous transition zone, as occurs from Train 2 to Train 3. Whether the period distribution is continuous or discontinuous appears to be determined by the magnitude of the period separation between the trains. The swell properties described here are typical of swell generated in approaching cyclonic storms.

Wind waves and associated local swell are revealed in the T_g data by the initial appearance of short periods, which increase with time as the sea grows until the wave height peak is reached. The T_g values display wide scatter, consistent with the broadband spectral nature of a sea, but tend to be concentrated near the upper envelope of the distribution. Following

passage of the wave peak, the T_g values for the young swell trailing in after the wind has fallen off diminish with time, and the period distribution takes on more the appearance of a distant swell train. No clearcut example of a wind-wave train is available for illustration.

T_g values obtained from the analysis of a series of wave records can be put to practical use best by fitting a curve to the time-series data associated with each wave train identified. In the case of a swell train, a curve fitted to the T_g values will represent the mean wave-group period for the train, $\overline{T}_g$. If reciprocal f_g values are plotted instead, as shown in Figure 3 for the swell trains of Figure 2, the best-fit curve will be, similarly, the mean wave-group frequency for the train, $\overline{f}_g$; this curve should properly be linear for distant swell trains, as discussed in a later section. The $\overline{f}_g$ curve, as will be shown in the next section, agrees closely with the frequency of maximum energy density, f_m, for the swell train as determined by spectral analysis. In the case of wind-wave trains, no comparative analyses of the same wave records have been made by the wave-group and spectral methods; however, inductive evidence indicates that a curve drawn near the upper envelope of the T_g distribution and through the densest concentration of values will give a reasonable approximation of T_m for the wave train.

In this manner, a time series of T_m curves (or f_m curves) can be produced from which the user can pick off the value or values prevailing for any selected time. When more than one wave train is recognized to be present at a given time, the dominant train can be identified by the fact that its period will be associated with the wave sequences of largest amplitude. The dominant train can often be identified also from examination of the wave-height distribution in relation to the period data. For most practical applications, when more than one wave train is present the ocean surface can be characterized by using the observed wave height along with the period of the dominant train.

EQUIVALENCE OF $\overline{f}_g$ AND f_m FOR SWELL

In the case of swell trains generated in wind areas located several hundred miles or more from the recording station, the mean wave-group frequency, $\overline{f}_g$, and the spectral peak frequency, f_m, derived from the same wave records by the respective methods of analysis have been found to agree closely in all comparisons made.

By way of demonstration, a swell train recorded at Monterey during otherwise quiet wave conditions was selected, and 20-minute strip-chart records made every 6 hours for its 2-day life were analysed by the two methods. The analog traces, written at a chart speed of 2 inches per minute, were converted for spectrum computation to digital data using a digitizer, and analysis was performed using the Blackman-Tukey (1958) method. The energy densities were computed to an upper limit of 0.24 Hertz using a frequency increment of 4.16 milliHertz, with 90 per cent confidence limits estimated at 0.60 and 2.10. The results are presented in the form of spectral density topography in Figure 4.

The prominent ridge in the topography extending across the lower part of the figure represents the swell train of interest. The frequency along

the ridge line, or spectral peak, is f_m, and is seen to increase with time in the characteristic manner of swell. The swell train reached its maximum height of two feet at 0200Z on 29 November. Several hours later, a new swell train with considerably more energy and of lower frequency began to arrive and caused the frequency peak to shift (just off the graph) in the same manner as shown in Figure 3 between Trains 2 and 3.

Values of f_g obtained from periodic sequences in the wave records are shown as dots in Figure 4, and are seen to be concentrated about the ridge line of the swell train in the lower part of the graph and to be scattered about a dying wave train in the upper left corner. This association of the f_g values with the spectral masses of the two trains is also illustrated in Figure 6, which shows the 14 f_g values obtained from Wave Record No. 2.

The f_g values shown in Figure 4 for the swell train of interest were averaged to obtain $\overline{f}_g$, and these values are plotted in Figure 5. Also plotted are the values of maximum energy density frequency, f_m, obtained from the spectral computation for each wave record. The two sets of values are also tabulated in Table 1. f_m exceeded $\overline{f}_g$ in six of the seven records by an average amount, expressed as period, of 0.3 seconds. Agreement within one second is typical of all comparisons we have made on swell trains.

$\overline{f}_g$ for a given wave record can be obtained, as just illustrated, by averaging the f_g or T_g values associated with the swell train of interest. It can also be obtained in the form of the mean or the median of the distribution of frequency or period of the individual waves composing the appropriate wave sequences. These procedures each give results that agree closely. The simplest and most practical means of obtaining $\overline{f}_g$ for an entire swell train, however, is to fit a straight line visually to the time plot of the f_g values for the train, as illustrated in Figure 3.

It is pertinent here to note that Harris (1970) compared six kinds of period measures and found the highest correlation to occur between the most prominent period in a 7-minute wave record and the spectral peak period. He stated that the period correlation might be improved if the data were stratified in some way so as to make the data samples more homogeneous. The present study indicates that stratification of a basic sort can usefully be performed on Pacific Coast wave data by differentiating between swell and wind waves where possible before manipulating the data, and that correlation can be further improved by use of a larger sample of periods such as is derived from the wave sequences appearing in wave records.

ZERO-LINE CROSSING METHOD

The zero-line crossing method (also called zero-upcrossing and zero-crossing method) involves determining the mean water level or zero line, usually visually, then counting the number of intervals between upcrossings (or downcrossings) of the zero line and dividing this number into the duration of the wave record to obtain T_z. The zero-line crossing method and the wave-group method are similar in that both basically involve the measurement of wave intervals relative to a datum surface, but differ in

that the datum used in the first method is of constant elevation and represents the still water level for the entire wave record (after the tides are filtered out) and the datum in the second method is the ordinarily irregular water surface on which a wave sequence is superimposed. Because of the difference in datums, T_z can be obtained by use of a computer algorithm that picks off zero crossings (Wilson, Wu, and Baird, 1972), but the task of discriminating individual wave sequences and measuring T_g remains beyond the accomplishment of computer programming.

The relationship of the zero-line crossing period, in the form of its reciprocal, f_z, to $\overline{f}_g$ and f_m is illustrated for the swell train of interest in Figures 5 through 7. In Figure 5, and in Table 1, f_z is seen to differ considerably from the other two values and to display large variability from record to record. In the first four wave records f_z migrates from near the spectral peak of the dying wave train in Record No. 1 toward the spectral peak of the growing swell train. Subsequently, f_z roughly approximates $\overline{f}_g$ and f_m for the dominant swell train. The relationship of f_z to the spectra of the first four records is best shown in Figure 7.

This example serves to illustrate the fact that T_z is not equivalent to $\overline{T}_g$ or T_m in the case of a swell train (wind waves have not been examined sufficiently), and that it has no synoptic significance, i.e., it gives no information about the number of wave trains present, their dominant periods, or their identification as sea or swell, and unlike $\overline{T}_g$ and T_m it yields no information about the wind field that produced the swell (discussed in next section). Since a single period value is derived from a given record, T_z is clearly an integration of the waves associated with all wave trains present. It is evident that the zero-line crossing period should be used with these characteristics and limitations in mind.

In other evaluations, Harris (1970) found a poor correlation between the zero-line crossing period (T_{ZUC}) and the period corresponding to the frequency of maximum energy density per unit frequency (T_{FM}) from wave records recorded at Atlantic City, and presented a short series of comparative data showing T_z to be smaller than T_m in every record analysed. Wilson, Wu, and Baird (1972) compared T_z and T_m from recordings made at Western Head, Nova Scotia and Ocean Station Papa and stated they found no strong correlations.

SOME APPLICATIONS

Swell Source and Direction Determination

Using spectrally analysed wave data, Munk, et al., (1963), showed that swell trains arriving from generating areas located at distances greater than a few hundred miles from the wave gage are revealed on a frequency-time graph by ridges in the spectral energy density topography, and noted that the ridge axes are linear or very nearly so. A straight ridge line implies a point source for the swell train in space and time. In view of the fact that a storm system produces swell for the duration of its passage over the ocean, the point source computed from wave records appears to represent that location and moment in the storm history at which the maximum energy density in the sea directed toward the wave gage was generated.

The distance from the wave gage to the effective swell source, D_o, can be computed from the slope of the ridge line, df_m/dt, using the relationship

$$D_o = \frac{g}{4\pi\, df_m/dt}$$

or

$$D_o = \frac{1.515}{df_m/dt}$$

where D_o is in nautical miles, f_m is in Hertz, and t is in hours. The effective origin time, t_o, is given by the intercept of the ridge line with zero frequency.

In view of the equivalence of wave-group frequency and spectral peak frequency in swell, it is evident that the effective origin of a swell train can also be computed using frequencies obtained manually through application of the wave-group method. In regard to the swell train presented in Figure 4, for example, a straight line fitted to the f_g data has a slope of 0.4220 milliHertz per hour, giving a source distance of 3590 nautical miles from the wave gage at Monterey and an origin time of 0918Z/23 November, or about 5-1/2 days before the swells were first detected. A straight-line fit to the spectral peak frequencies derived from the same wave records (Figure 5) gives df_m/dt = 0.4175 milliHertz per hour, D_o = 3622 nautical miles, and t_o = 0654Z/23 November. The swell source in space and time computed from the two data sets is seen in this example to agree within approximately $1/2^o$ latitude and 2-1/2 hours.

With regard to application of this procedure, it should be pointed out that the peak frequency theoretically can shift as a wave train passes through shoal water to the wave gage due principally to differential amplification of the spectral components by refraction. A significant shift could produce an erroneous computed swell source; however, it can be demonstrated that because of the narrow-banded character of swell spectra no shift effectively occurs, even when the rate of change of the refraction factor with frequency for a given shoal-water site is large. It may be concluded that nearly everywhere in shoal water the peak frequency of swell is conserved for purposes of swell origin computation.

Records from a single wave gage provide no directional information that can be used to locate the wind area in which the swell was generated. The storm responsible can be identified, however, using the computed origin distance and time derived from the wave records combined with weather charts. An arc of great-circle radius D_o drawn on a weather chart of or near time t_o will be found to intersect the storm system. The effective swell source point within the storm can be taken as the point of intersection of the arc of radius D_o and the axis of the maximum winds directed toward the recording station, as illustrated in the example in Figure 8.

When the location of the source point is established, a great-circle trajectory drawn from the point to the wave gage may be considered for practical engineering purposes to give the deep-water swell direction Ψ_o, for the wave-gage site (and for any other location on the adjacent coast).

Because the wave-group method yields information equivalent to that from spectral analysis for determining swell origin and deep-water swell direction, this method has particular attraction as a practical tool in economic situations and geographic regions where computer facilities are unavailable or technical expertise is limited. In this regard, it may be noted that a wave gage is not a necessity, since the mean wave-group period of the dominant swell train present can be obtained from the larger wave sequences by an observer with a stopwatch.

Additional discussion of the applications described here is given by Thompson (1970) and Austin (1972).

Surf Forecasting

Height and period measured during the early stages of arrival of a swell train can be used to make a forecast for the remainder of the train. Measurement of the dominant period, $\overline{T}_g$ or T_m, from wave records or visually over an interval of 6 to 12 hours when converted to frequency will give the rate of change of frequency with time, from which can be obtained an accurate forecast of frequency until the train has passed. The swell height can be predicted to increase continuously until the peak is observed to pass, then to decrease continuously until the train is gone or masked by a new train. Swell trains generated in distant wind-areas are generally observed to last 2 to 5 days. This procedure has proven useful to the Marine Corps, Camp Pendleton, California for forecasting surf.

AREAS FOR FURTHER INVESTIGATION

The distinctive period signature of oceanic swell trains described herein is typical of swell recorded on the west coast of North America. These waves originate in generally approaching cyclonic storms which cross the Pacific in the latitudes of the prevailing westerlies in both hemispheres. Similar swell properties can be expected on any coast where an approaching storm situation occurs, i.e., on most coasts of the oceans. This investigator has not examined wave records from coasts which receive swell trains generated in retreating storms, as occurs on the east coasts of the continents in middle and higher latitudes. There is reason to believe that the period signature of such swell trains may be different, and this question merits investigation.

It is evident from the limited attention given in this paper to wind-wave trains that the relationship between T_g values and wind-wave spectra obtained from analysis of the same wave records needs to be probed further.

The height of the larger waves composing a wave sequence is observed to be related to the height of the wave train with which they are associated in the case of swell. When more than one swell train is present, the dominant train is readily identified by its larger wave groups. This relationship should be examined quantitatively. Possible relationship between the height of a wave sequence and the energy density in the frequency band represented by the wave sequence also appears to merit investigation, and may prove of particular significance in regard to boardband spectra.

There is an important area of engineering application in which the wave-group method may provide information that cannot be provided by computation of the spectrum. Wilson, Wu, and Baird (1972) pointed out that "some marine structures react to individual or groups of waves rather than spectra and there is a real requirement for parameters other than r.m.s. water surface deviation, the moments of the spectrum and some sort of characteristic period". It would appear that such parameters should be developed from knowledge of the wave sequences appearing in wave records. The properties of wave groups and their relationship to the wave train have not been examined to the writer's knowledge beyond what is presented in this paper.

ACKNOWLEDGMENTS

This work was supported by the Fleet Numerical Weather Central, Monterey. Spectral analysis of wave records studied was performed by Lieutenant Marshall H. Austin, Jr., USN, the manuscript was typed by Joann Madler, and the figures were drafted by DM3 Peter Belcher, USN of the Naval Postgraduate School, Monterey.

REFERENCES

Austin, M. H., Jr., 1972. Determination of the Deep Water Arrival Direction of Ocean Swell at a Coastal Station. M.S. Thesis, Naval Postgrad. Sch., Monterey, 47 pp.

Barber, B. F., and F. Ursell, 1948. The Generation and Propagation of Ocean Waves and Swell. Phil. Trans. Roy. Soc., A, 240, 527-560.

Blackman, R. B., and J. W. Tukey, 1958. The Measurement of Power Spectra. Amer. Tel. and Tel. Co., reprinted by Dover Publ., N.Y.

Harris, D. L., 1970. The Analysis of Wave Records. Amer. Soc. Civil Engrs., Proc. of Twelfth Coastal Engr. Conf., Chap. 6, 85-100.

Manley, R. G., 1945. Waveform Analysis. Wiley & Sons, N.Y., 275 pp.

Munk, W. H., G. R. Miller, F. E. Snodgrass, and N. F. Barber, 1963. Directional Recording of Swell from Distant Storms. Phil. Trans. Roy. Soc., A, 255, 505-584.

Thompson, W. C., 1970. Swell and Storm Characteristics from Coastal Wave Records. Amer. Soc. Civil Engrs., Proc. of Twelfth Coastal Engr. Conf., Chap. 3, 33-52.

Wilson, J. R., H. J. Wu, and W. F. Baird, 1972. A Discussion of Some Measured Wave Data. Thirteenth Internat. Conf. on Coastal Engr., Abstracts, 359-360.

Table 1: SWELL TRAIN PERIOD (FREQUENCY) BY DIFFERENT METHODS

Wave Record No.	Arrival Time/Date (GMT/1971)	Period in seconds (Frequency in 10^{-5} Hertz) Spectral T_m (f_m)	Wave-Group $\overline{T}_g$ ($\overline{f}_g$)	Zero-Line T_z (f_z)
1	1204/27 Nov	21.83 (4580)	22.55 (4434)	12.24 (8167)
2	1808/27 Nov	20.70 (4830)	20.95 (4773)	12.85 (7784)
3	2355/27 Nov	19.69 (5080)	19.98 (5005)	13.82 (7236)
4	0600/28 Nov	19.05 (5250)	18.90 (5290)	17.40 (5749)
5	1207/28 Nov	17.79 (5620)	18.11 (5522)	15.28 (6546)
6	1810/28 Nov	17.54 (5700)	17.56 (5695)	16.45 (6079)
7	2356/28 Nov	16.21 (6170)	16.54 (6046)	14.30 (6991)

Note: The zero-line method integrates all wave trains present.

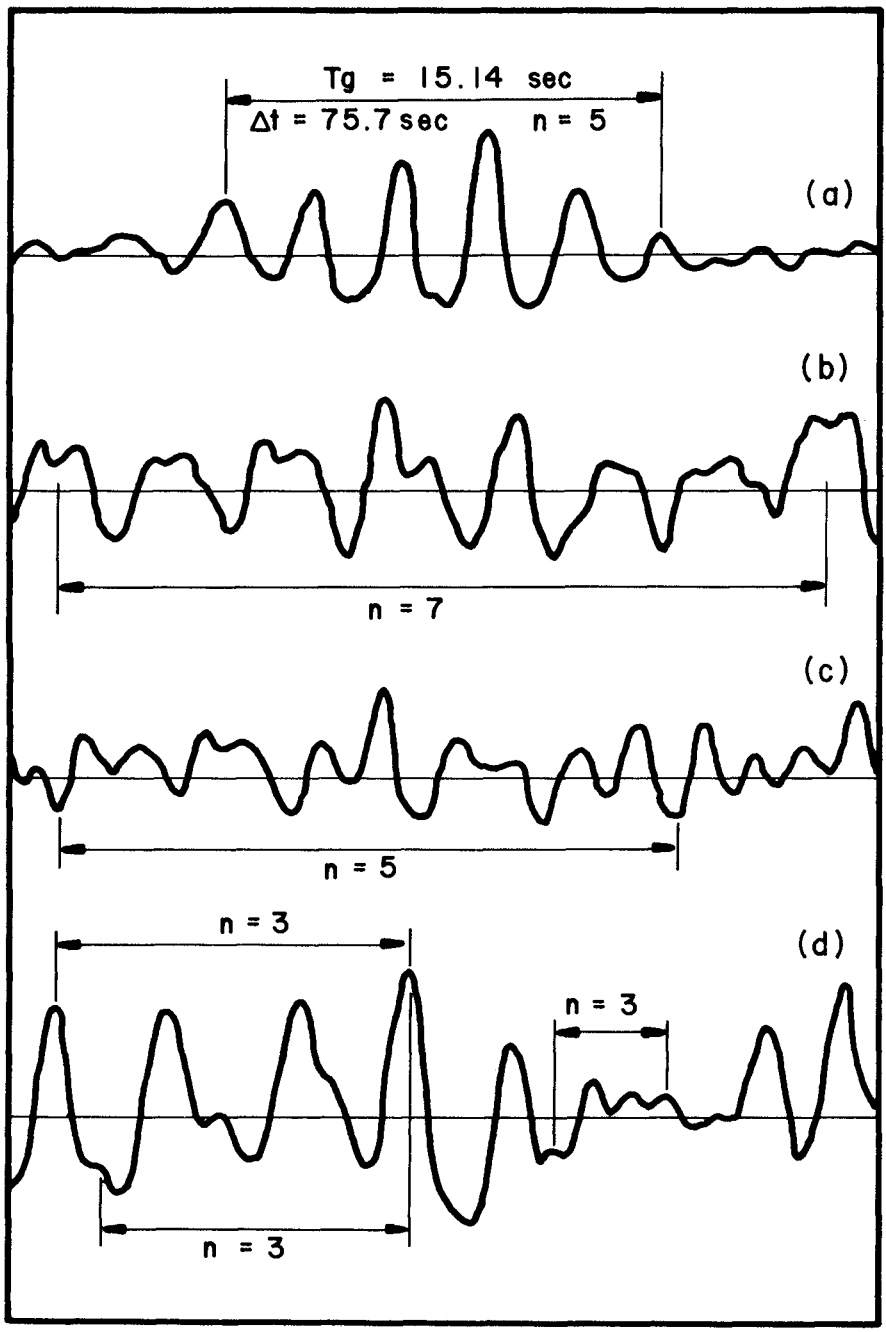

Figure 1: PERIODIC WAVE SEQUENCES

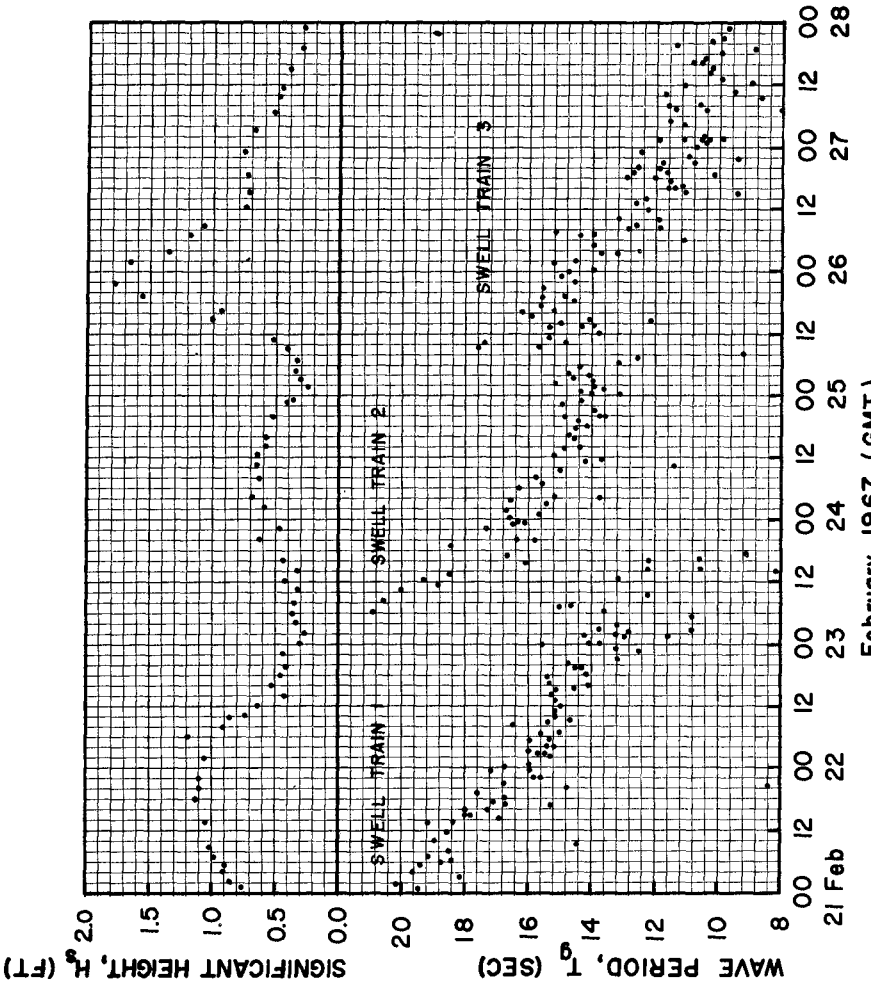

Figure 2: WAVE DATA FOR THREE SWELL TRAINS

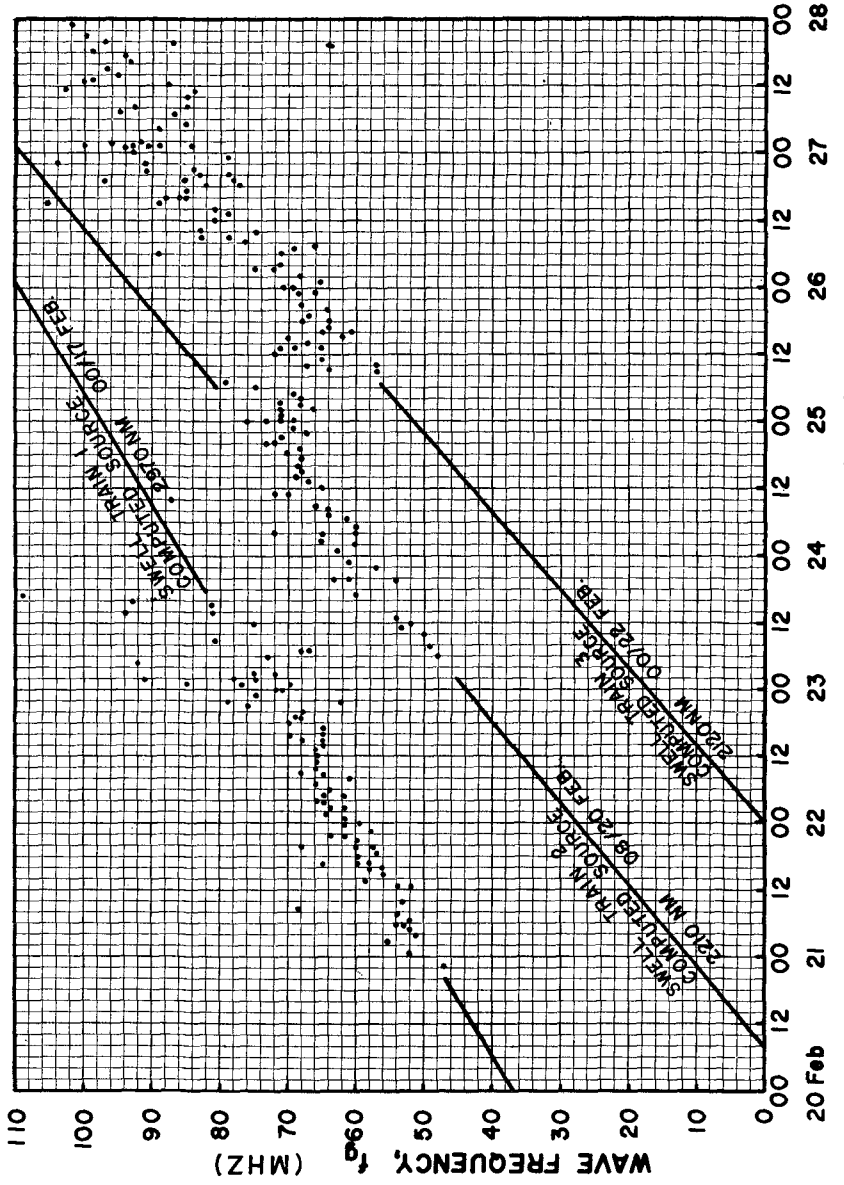

FIGURE 3: FREQUENCY–TIME DISTRIBUTION FOR THREE SWELL TRAINS

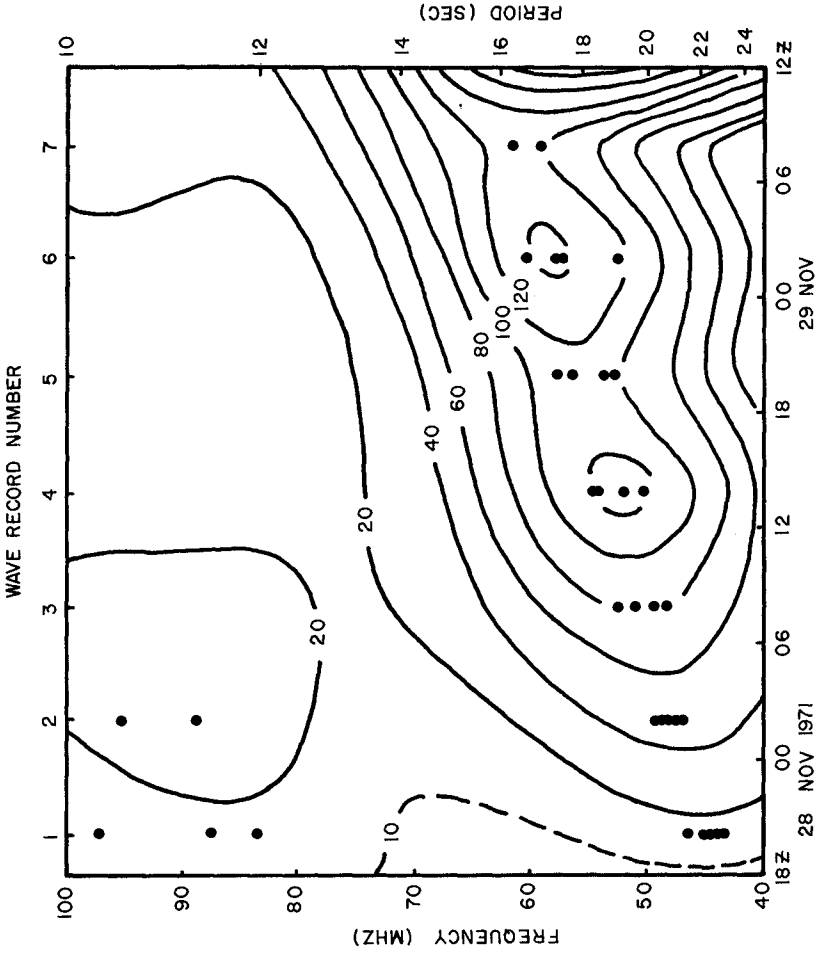

Figure 4: VALUES OF fg SUPERIMPOSED ON SPECTRAL DENSITY TOPOGRAPHY

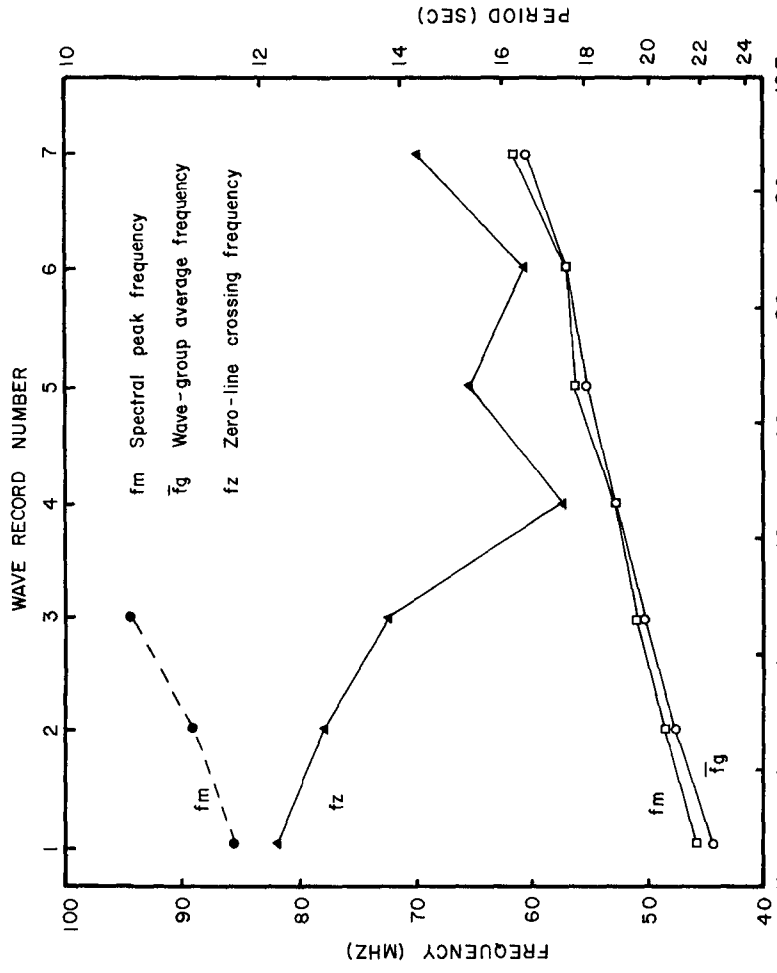

Figure 5: COMPARISON OF FREQUENCIES OBTAINED FROM MANUAL AND SPECTRAL ANALYSES

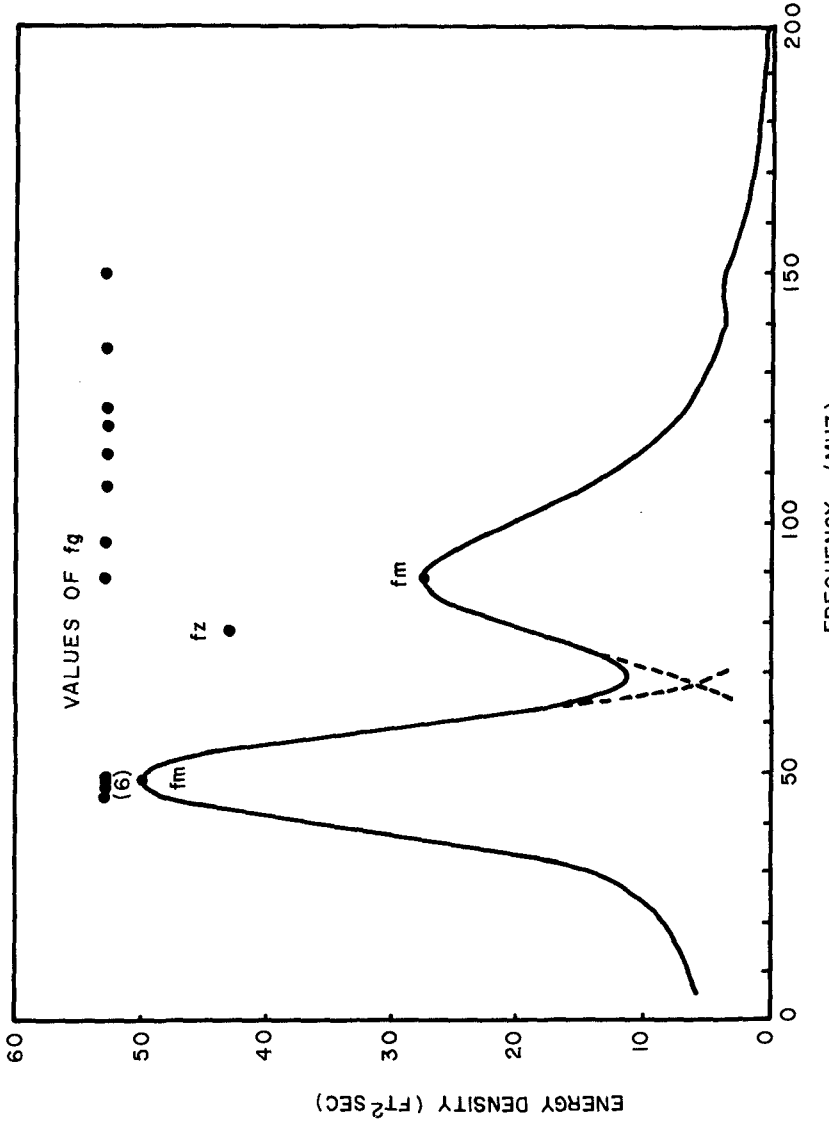

Figure 6: FREQUENCY SPECTRUM OF WAVE RECORD NO. 2

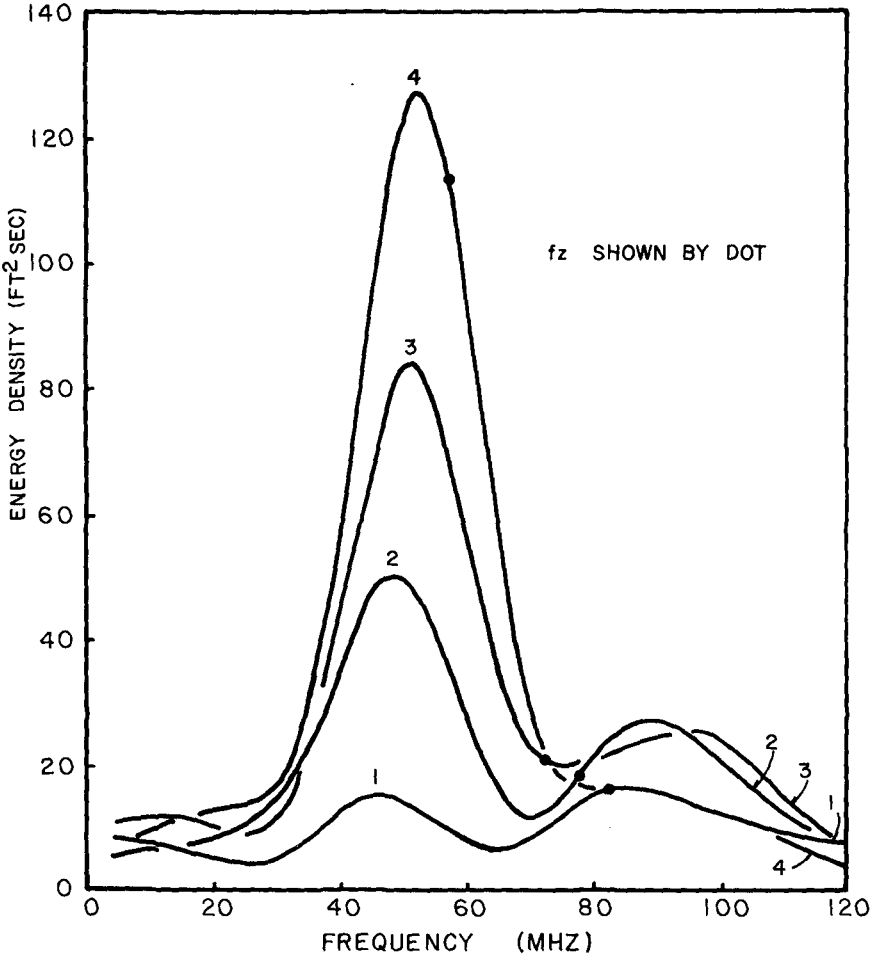

Figure 7: FREQUENCY fz IN RELATION TO SPECTRA FOR WAVE RECORDS I THROUGH 4

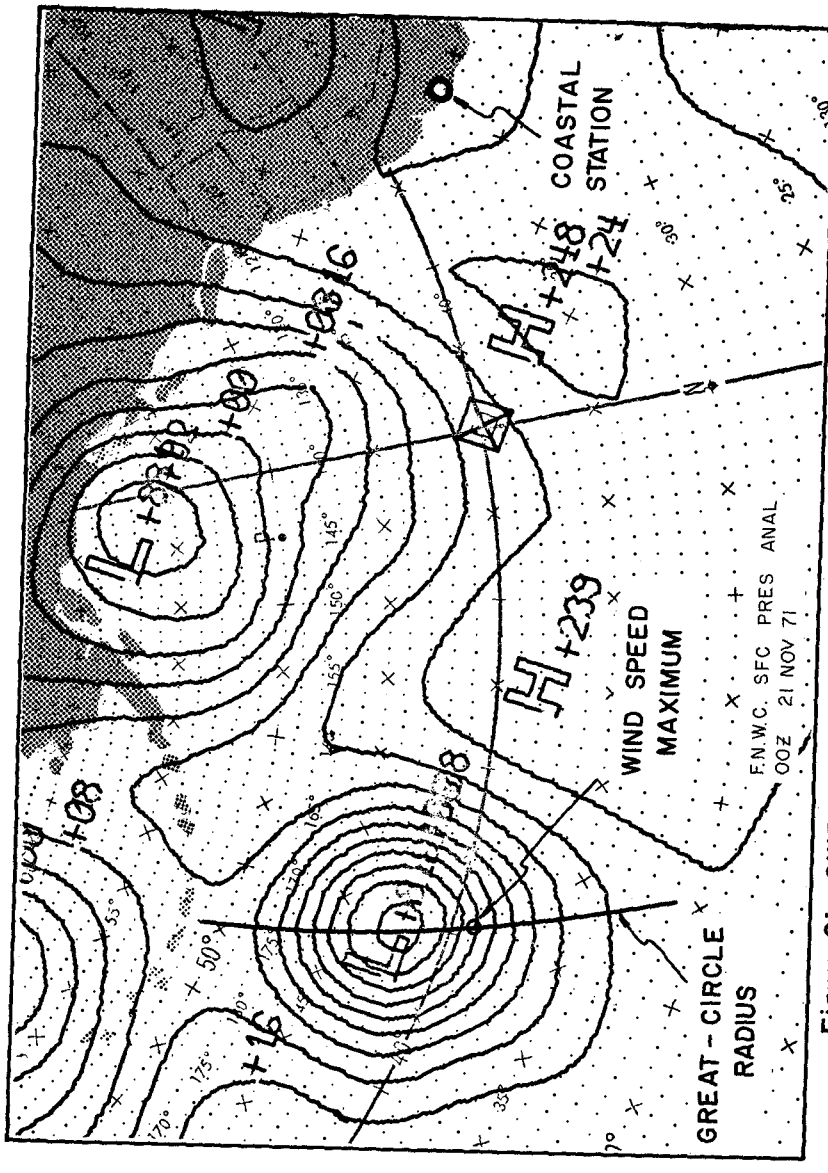

Figure 8: SWELL GENERATION POINT WITH RESPECT TO A COASTAL STATION

CHAPTER 9

A PRELIMINARY STUDY OF STORM SURGES IN HUDSON BAY

by
K.B. Yuen and T.S. Murty
Oceanography Branch, Marine Sciences Directorate,
Department of the Environment,
Ottawa, Ontario.

Abstract

In view of resource exploration, hydro-electric power development and other activities, there is a clear need for a better understanding of the hydrodynamics of Hudson Bay. One particular area that has received little attention in the past is storm surges. It is likely that a storm surge prediction will be very useful in the future and towards this goal a two-dimensional homogenous model has been constructed. A hindcast of the storm of October 15, 1969 is presented here. The calculated surge for Churchill, Manitoba compares favourably with observed residues. The overall response of the basin and the types of oscillations that are produced are also described here. In addition, the differences in behavior between James Bay and Hudson Bay proper are demonstrated. Finally the results also indicate the steady circulation which the storm has produced.

INTRODUCTION

Hudson Bay is one of the most complex and least known large water bodies in Canada. For its vast size it is extremely shallow and the topography is complicated by islands. Storm surges in most Canadian waters are not nearly as large or as devastating as those found in more tropical areas, nevertheless the prediction of storm surges is of great importance in the planning of human activity and resource management. As an initial step, a numerical model of Hudson Bay. was constructed for the purpose of studying the behaviour of storm surges in the Bay.

THE MODEL

In Figure 1 is shown the grid that was used to approximate Hudson Bay. It is 74 x 80 in dimension and is in polar coordinates. The actual configuration is a staggered grid and the black dots represent the Z or water level points, which are spaced two grid lengths apart. The components of the velocity are calculated at points midway between the Z points. This particular configuration facilitates the application of central difference operators.

Figure 2 shows the depth configuration of Hudson Bay with a contour interval of 100 metres.

Figure 2 shows the depth configuration of Hudson Bay with a contour intervals at 100 metres. The Bay is quite shallow, except for several deep areas which reach 300 metres. James Bay is much shallower, with maximum depths of about 60 metres. The average depth in the model of Hudson Bay is about 111 metres and James Bay about 38 metres.

The linearized equations used by Heaps (1969) in his work on storm surges in the North Sea are given by:

$$\frac{\partial M}{\partial t} = 2\Omega N \sin\phi - \frac{gh}{a\cos\phi}\frac{\partial \eta}{\partial \chi} - \frac{h}{\rho a \cos\phi}\frac{\partial P_a}{\partial \chi} + \frac{1}{\rho}\left[\tau_{S_\chi} - \tau_{B_\chi}\right]$$

$$\frac{\partial N}{\partial t} = -2\Omega M \sin\phi - \frac{gh}{a}\frac{\partial \eta}{\partial \phi} - \frac{h}{\rho a}\frac{\partial P_a}{\partial \phi} + \frac{1}{\rho}\left[\tau_{S_\phi} - \tau_{B_\phi}\right]$$

$$\frac{\partial \eta}{\partial t} = -\frac{1}{a\cos\phi}\left[\frac{\partial M}{\partial \chi} + \frac{\partial}{\partial \phi}(N\cos\phi)\right]$$

where χ is East longitude, ϕ is North Latitude, M and N are the χ and ϕ components of the flow, τ_S is the surface wind stress, τ_B is the bottom stress, and P_a is the atmospheric pressure. For the calculations, a quadratic wind stress law and a linear bottom stress law were used. The grid spacing was 10 min. of latitude and 15 min. of longitude. For the solution of the equations all the derivatives are approximated by central finite differences both in time and space; the calculations leapfrog in time, with water levels calculated at even time steps and flow components at odd time steps. The stability criterion was calculated to be 157 seconds, but a value of 60 seconds was used.

THE METEOROLOGICAL DATA

In Figure 3 is displayed four typical storm tracks. The present study concerns the storm of October 15, 1969 which is depicted by the dotted line. The centre of this storm was located to the north of Hudson Bay and sat there

for about the first three days of our calculations, but then moved south over the Bay during the next two days. The calculations commenced at 1800 hrs, Greenwich Mean Time, October 15, 1969 and covered approximately five days.

In earlier studies of the circulation in Hudson Bay (Murty and Yuen, 1972) the method of introducing the pressure data was to extract such information from six-hourly weather charts onto a coarse grid and then polynomials were fitted to interpolate the data onto the finer grid of the hydraulic model. However, this procedure is time comsuming and such fine interpolation of the pressure may not be justified by the accurracy of the data. Instead we divided the Hudson Bay area into a number of regions, (See Figure 4) for each of which we approximated the pressure gradient from the weather maps. Surface winds were then calculated from the geostrophic approximation, with a modification of .6 in amplitude and a 20 degree rotation. Time wise, values of the pressure gradient and wind stresses were interpolated linearly between the six hourly intervals. The points shown in Figure 5 are sample points at which time series plots are shown below and these are numbered for easy reference.

CALCULATIONS AND RESULTS

As a gross measure of the storm itself, the vector mean pressure gradients are shown in Figure 6 as a function of time. The direction of the mean pressure gradient lies in a narrow range from about 25 to 55 degrees but after about 90 hours or so it drops rapidly down towards zero. This is when the centre of the storm started to move southward along the east shore of Hudson Bay. At the bottom of Figure 6 are plotted the water levels at two sample points along the shore that are approximately diametrically opposite to each other at an angle of about 30 degrees. Superimposed upon these two curves is the amplitude of the pressure gradient. In the first case, the pressure curve is reversed because the point represents the point for the west shore. If the higher frequency oscillations are ignored, one can see some sort of correlation between the mean atmospheric pressure gradient and the low frequency variations in the two water levels, the so-called inverse barometric effect.

In Figure 7 is a comparison of the observed surge at Churchill, which is the only permanent station for the area, and the calculated surge at the closest Z point to it. The two curves are very similar but differ somewhat in exact detail. One major difference is the existence of a large spike at about time 104 hrs. which is not found in the observed. It is about this time that the centre of the storm started to move south over the Bay. The wind direction has shifted around from a northwesterly wind to one coming from the northeast thus causing this surge at the southwest corner of the model.

The calculated surge also shows a number of higher frequency oscillations which are found throughout most of Hudson Bay. These can be seen more clearly in Figure 8 where the water levels at a number of sample points around the shore of the main part of Hudson Bay have been plotted. The order of points begins along the north shore and progresses anti-clockwise around the Bay. One can easily detect two predominant periodicities in the high frequency oscillations, one of period 6.1 hrs. and the other of period 9.2 hrs. In some earlier preliminary calculations we had applied wind impulses and then the basin was permitted to oscillate on its own. In those calculations, one predominant period was found to be 9.2 hrs. Our suspicion therefore was that these two periodicities were related to the two lowest modes. The topography and shape of Hudson Bay are somewhat irregular but the Bay is very roughly a square. The average depth

of the basin, excluding James Bay, was found to be 111 metres. Very roughly, by using Merian's formula, it was estimated that the period of the lowest non-rotating mode would be somewhere between 14 to 15 hrs. From these estimates we referred to Rao's (1966) paper on the free gravitational oscillations in rotating retangular basins. Assuming an average inertial period of 17 hrs. for Hudson Bay, we then interpolated from Tables 1 and 2 of Rao's work to find the periods with rotation. For the 14 to 15 hour periods, the first rotating period would correspond to between 8.7 to 9.5 hrs. and the second period 5.8 to 6.3 hrs. The two figures of 9.2 and 6.1 from the calculations are very consistent, corresponding to a non-rotating period of 14.6 hrs.

In Figure 8 one can follow some of the disturbances around the edge of the basin, since it is basically a rotating system. For example, at the top of the Figure there are several large surges early in the calculations and these progress down anti-clockwise along the western shore. In the vicinity of the south shore, it becomes more difficult to identify them. Another feature is that the higher frequency oscillations are much smaller along the east half of the basin and this is partly due to the fact that that particular side of the Bay is sprinkled with a number of islands so that although the water is shallow there, surges never have a chance to propagate too far. In contrast, the western shore is virtually clear from the north end all the way down to the mouth of James Bay. Indeed, for this storm we found that most of the surges seemed to be generated along the north shore. For point number 10, spikes at 10 hrs., 20 hrs., 68 hrs., 86 hrs., and 96 hrs. correspond to surges at point 27 along the north shore. Generally, not only is the west shore the area of the largest oscillations but the southwest corner seems to be a very sensitive area.

The identity of the disturbances tend to become lost as they progress towards James Bay. Taking a closer look, one actually finds that these high frequency oscillations are damped out in James Bay. In Figure 9, the curves for points 15, 16, 17, 18, 4 and 5 represent a progression from the western side of the mouth of James Bay down to the head, while 6 and 7 progress along the eastern shore. Quite clearly the lower frequency response is propagated into the Bay and this response is found to correspond to the barometric pressure. The higher frequency oscillations are damped out and for point 5 there is barely an indication of their existence. The sequence at the bottom of the Figure, 20, 21, 22 are along a line down

the centre of James Bay, and here again is displayed the propogation of the low frequency response and the damping of the higher frequency oscillations.

In Figure 10 is shown another aspect of the behaviour of the surge in James Bay. For the low frequency response to the barometric pressure, James Bay behaves in a very predictable fashion in that it rotates anti-clockwise. The contours here are shown at times which correspond to the zero levels and highs and lows for Point 5 which is at the head of the basin. The surface is more or less flat at 22 hrs., the down hill slope of the surface is southward at 28 hrs., eastward at 33 hrs., northward at 40 hrs, approximately westward at 55, south at 68, slightly southeast at 76 and approximately northerly at 86 hrs. Very roughly then, the major part of the disturbance in James Bay is the response to the barometric pressure and in addition the system rotates so that one could probably develop a very simple model by which the water levels throughout James Bay could be estimated quite quickly. Some caution must be taken here of course because it is quite likely that in certain circumstances some of the surges in the main part of the Bay could very well be propagated into James Bay and be amplified quite greatly there because of the shallow depths.

In Figure 11 is displayed the surface over the whole Bay which is shown at a contour interval of 20 cm. at times 5, 10, 15, and 20 hours. One can immediately see some of the disturbances travelling along the western shoreline southward. At 5 hrs. there is a -40 cm. depression along the west shore. Its progression down into James Bay is easily followed. The contours in Figure 12 are at a later time and here we find a positive surge at the southwest corner which is propogated around the basin. The speed of this disturbance is generally in the 15 to 30 metre/second range in the main part of the Bay and down to the order of 10 to 15 metre/second or less in James Bay. In relation to the depths, these speeds are well within the correct order of magnitude.

In Figure 13 are seen some surface contours towards the end of the calculation and once again, the same general features are found to persist. There is one significant difference between these contours and the earlier contours however; by this time the atmospheric disturbance has persisted for quite some time and what results is the development of a depression of about 20 cm. in the western half of the basin. Around this depression, the disturbances are generally positive.

In order to see this quasi-steady development more clearly, we then attempted to find the mean surface by simple arithmetic averages. The result at time 81 hrs., and at 102 hrs. is shown in Figure 14. The basic pattern of a negative depression of 20 cm. shows up quite clearly. In association with this depression, there is a net circulation which was also obtained by some very rough averages over time. The currents at approximately the same times are shown in the bottom of Figure 14. A very steady coastal jet was found, hugging the shoreline in the anti-clockwise direction. Along the main part of the Bay, particularly along the south shore, there is a large, steady jet of up to 40 cm/second which is also quite wide. Some similar occurrences are found along the eastern shore, but these jets are not found in the northwest corner of the basin. Some of these jets, particularly the ones along the southwest shore, were found to persist throughout the entire calculation, the result of the steady interaction between the wind stress and the shallow depth; but because Hudson Bay is rather flat, this gives rise to a very wide jet.

Summary

A relatively simple two-dimensional model of Hudson Bay has been constructed, which does not include any non-linear terms. Nevertheless, by this simplicity we have managed to gain insight into some of the hydrodynamical characteristics of Hudson Bay. Clearly the inverse barometric pressure effect is very predictable, but much more study is yet required in understanding the excitation of some of the lower free modes. Another aspect that was demostrated was the existence of very wide coastal jets. There is a danger of over generalizing some of these results since they represent but one storm. Nevertheless, they provide the groundwork for a series of calculations of much more complex storms. It is hoped that this programme of study will establish more clearly the necessity and feasibility for storm surge prediction services in Hudson Bay and perhaps indicate the types of empirical methods that may be employed for such prediction services.

References

Heaps, N.S. 1969. A two-dimensional sea model. Phil. Trans. A 265, 93-137.

Rao, D.B. 1966. Free gravitational oscillation in rotating rectanglular basins. J. Fluid Mech. 25, 523-555.

Murty, T.S. and K.B. Yuen. 1972. Geostrophic versus balanced wind stress on Hudson Bay. Submitted to J. Fish. Res. Bd.

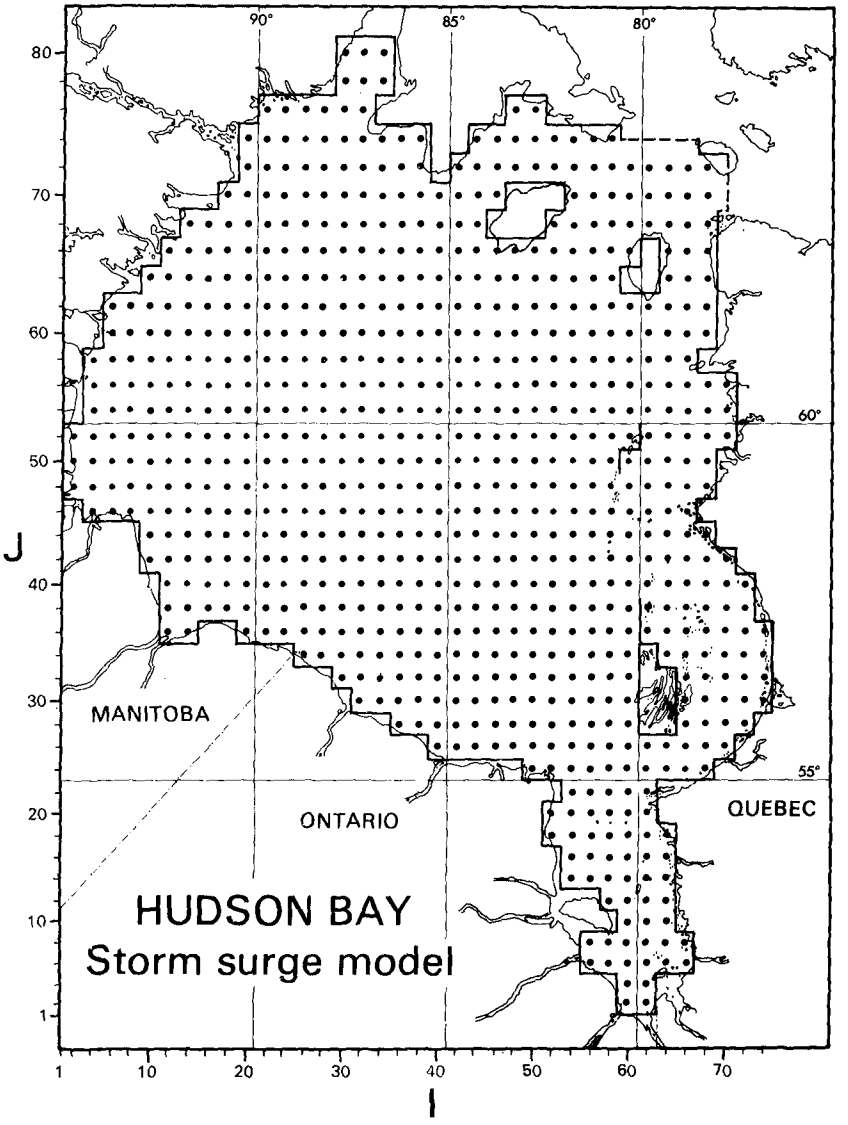

Figure 1. The grid system for the model, with the dots representing water level points.

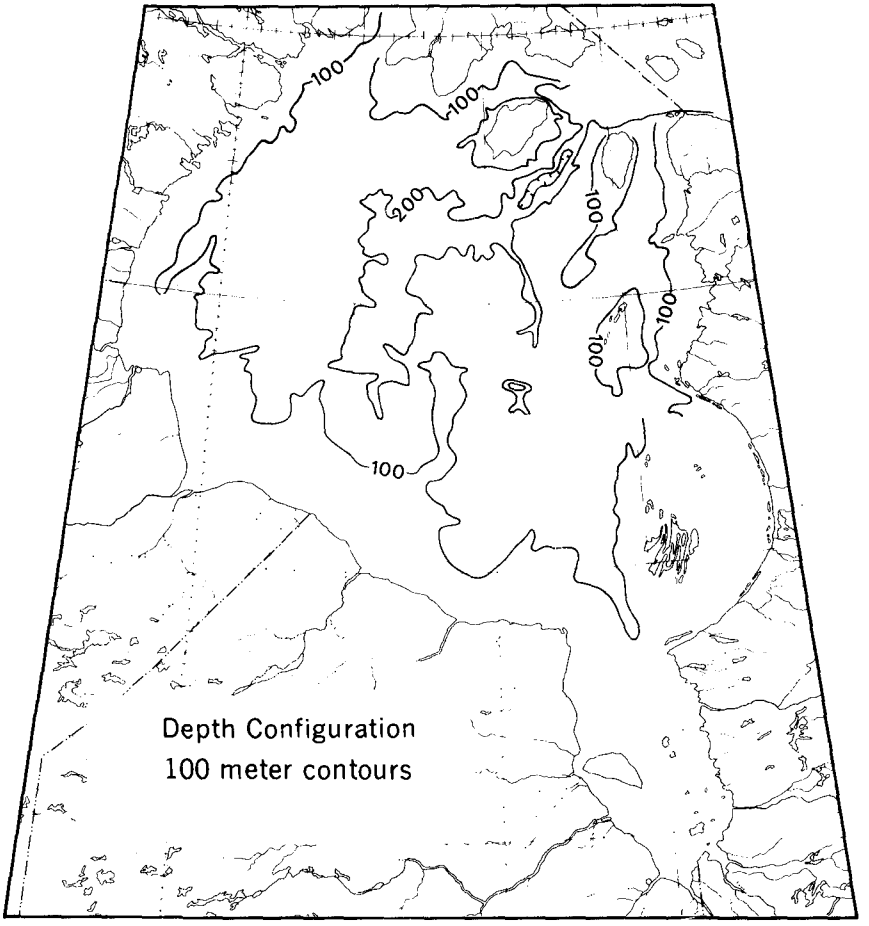

Figure 2. The depth configuration for Hudson Bay, with a contouring interval at 100 metres.

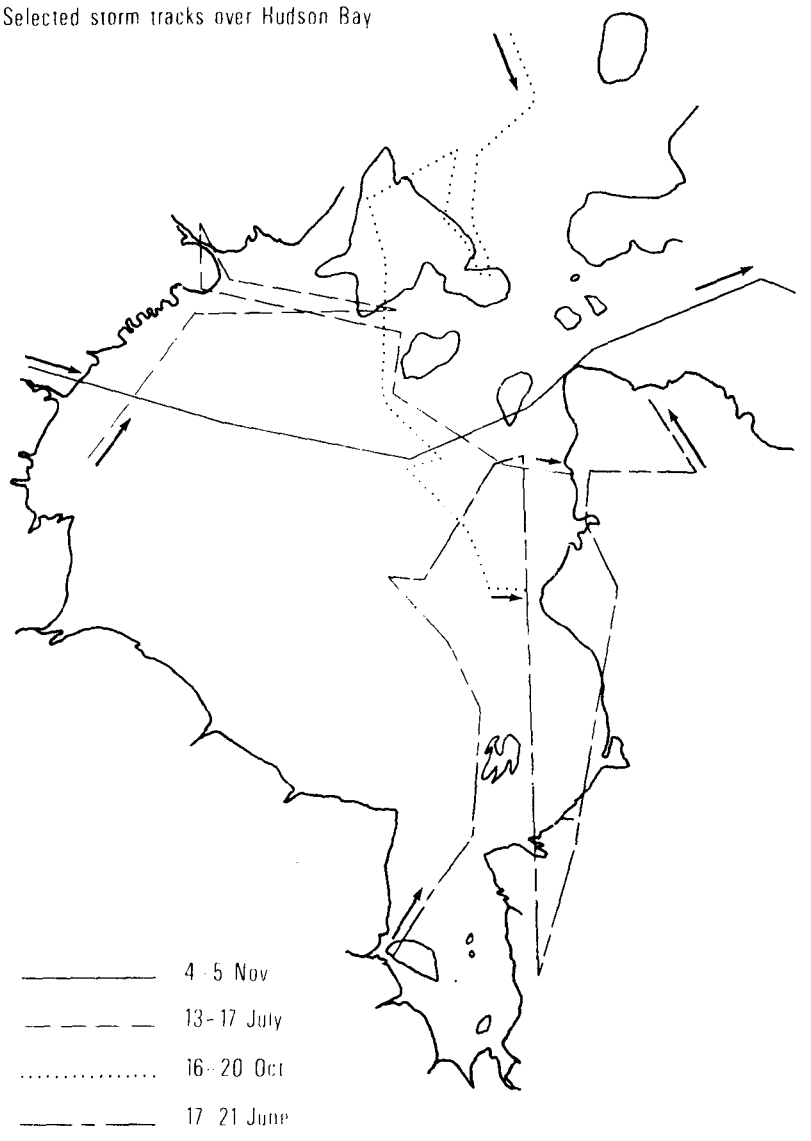

Figure 3. Some typical storm tracks over Hudson Bay. The calculation presented here is for the storm of October 16 to 20, 1969.

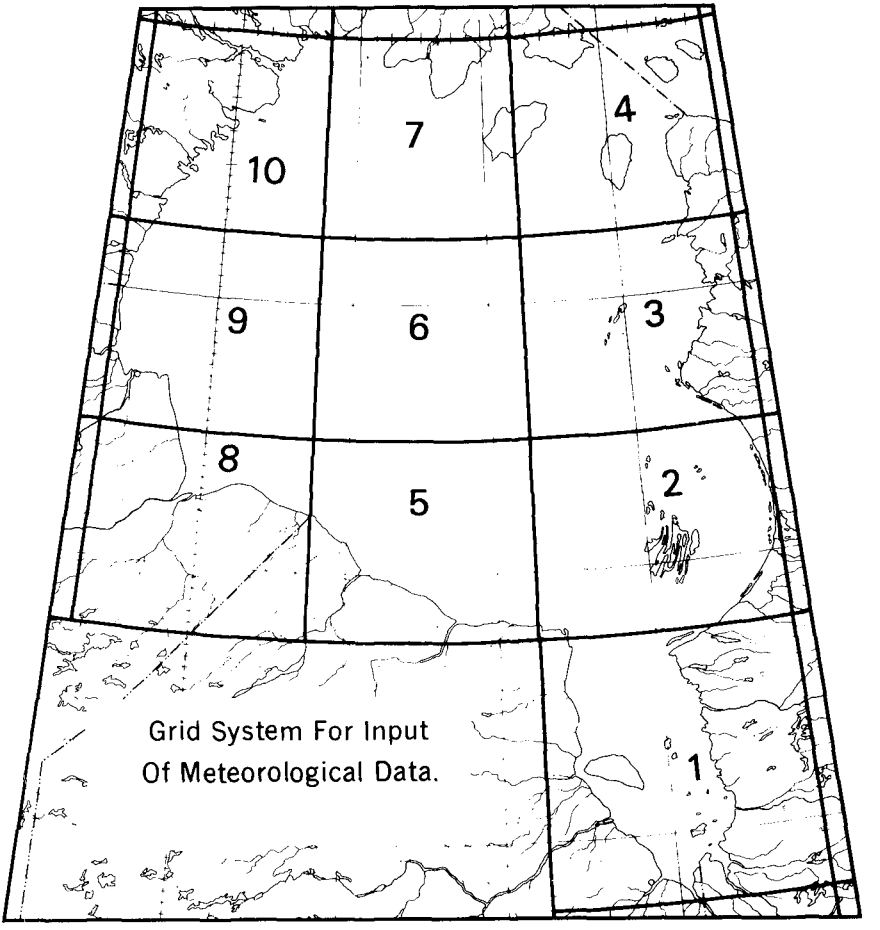

Figure 4. The grid system for the imput of meteorological data. Pressure gradients and wind stresses are calculated for each grid section.

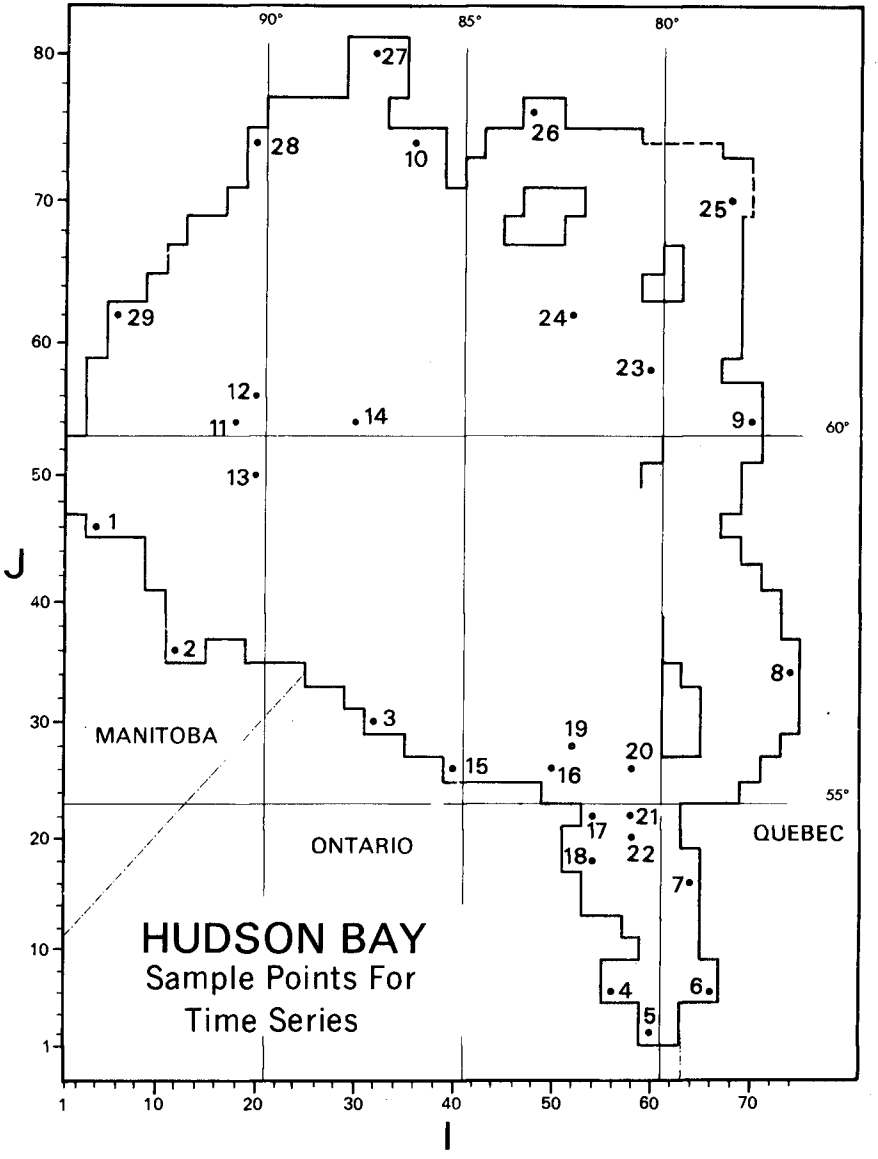

Figure 5. The numbering system for sample water level points, with reference to the time series shown in the following figures.

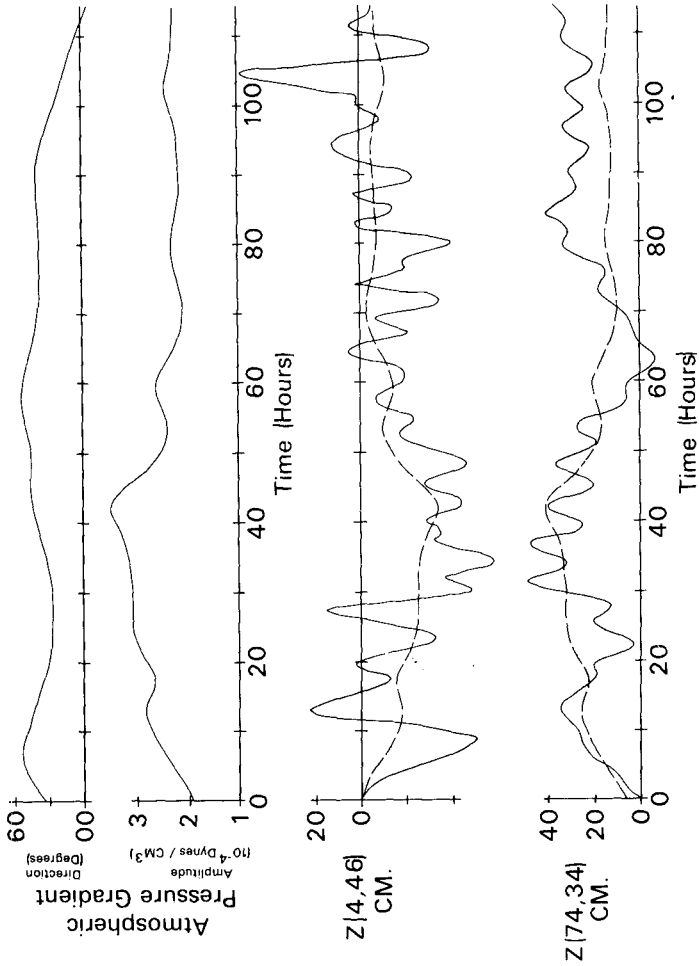

Figure 6. The curves at the top of the figure represent the mean pressure gradient (amplitude and direction) averaged over Hudson Bay. The amplitude curve is superimposed upon the two time series at the bottom of the figure to demonstrate the so-called inverse barometric effect.

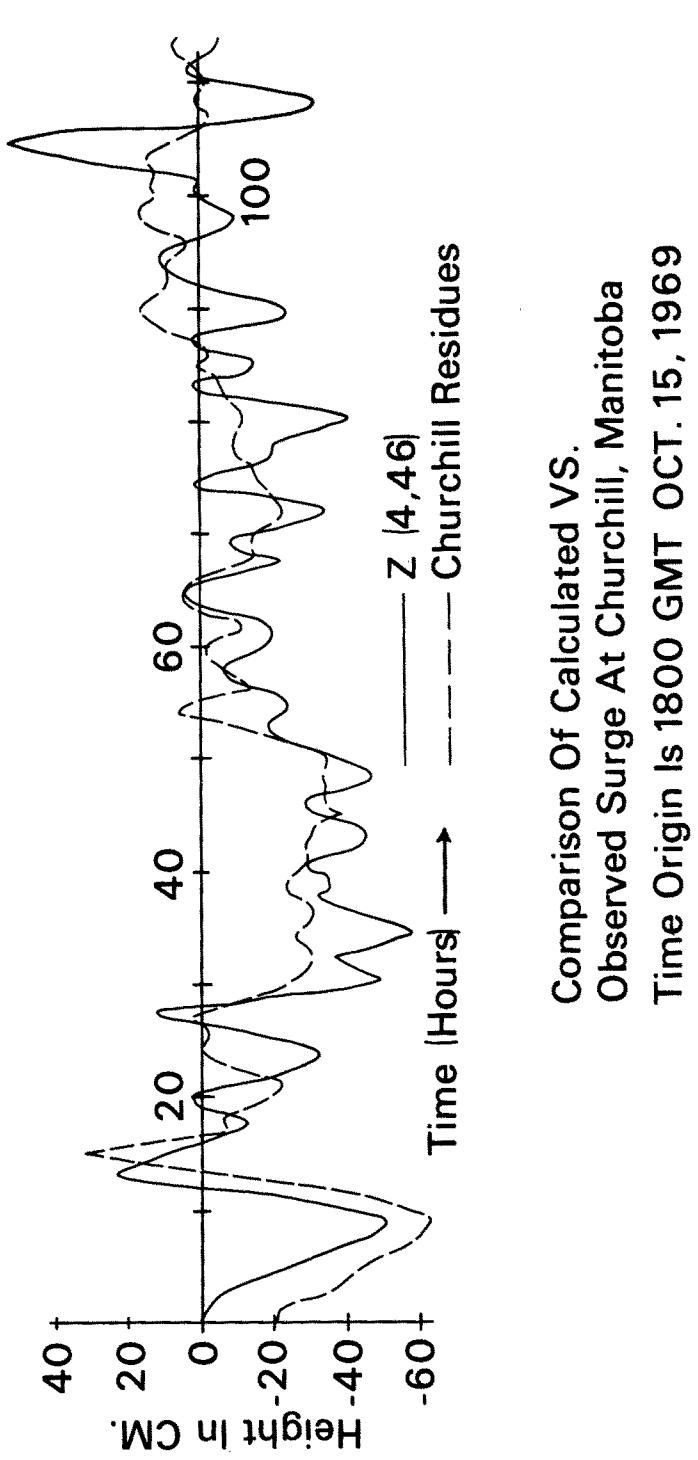

Figure 7. A comparison of the calculated versus observed surge at Churchill, Manitoba.

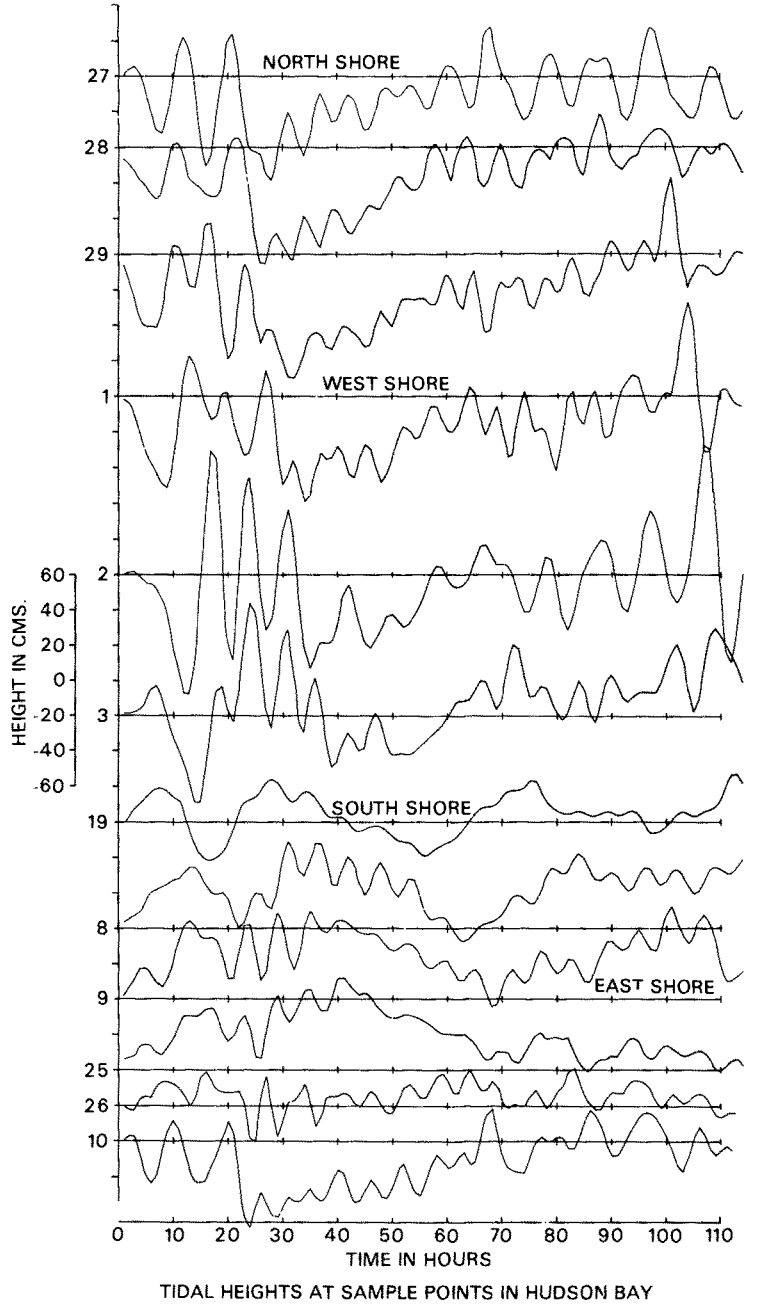

Figure 8. Time series for a sequence of water level points around the perimeter of Hudson Bay. The anti-clockwise progression of disturbances around the perimeter can be clearly seen.

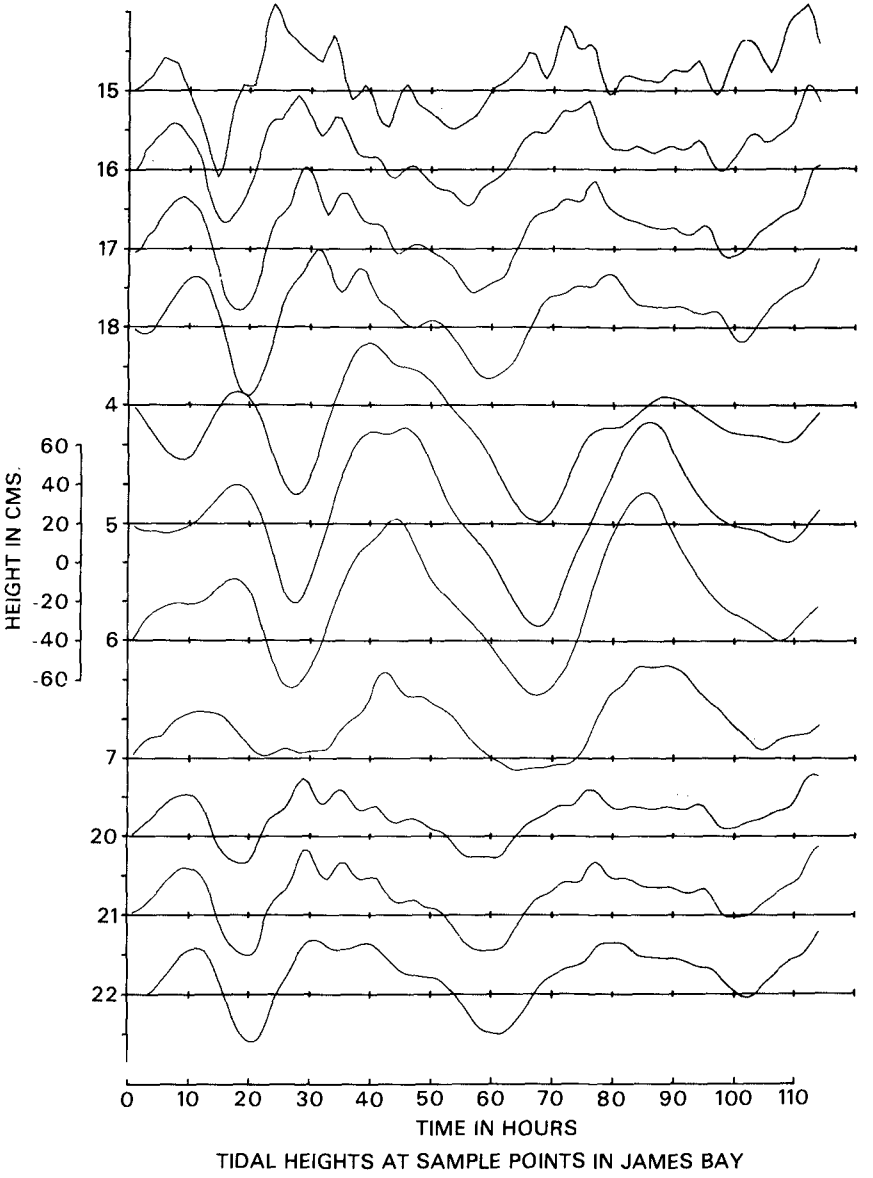

Figure 9. Time series for a number of water level points in James Bay. These curves demostrate the damping of the higher frequency oscillations from the mouth towards the head of James Bay.

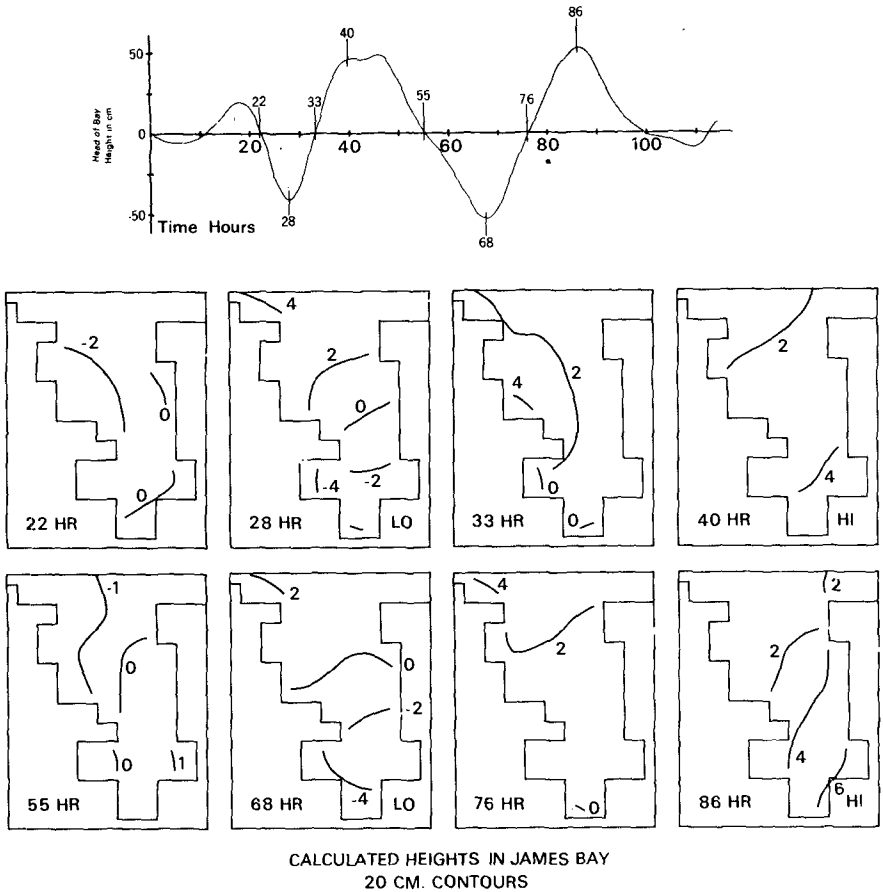

Figure 10. Surface contours in James Bay at 22, 28, 33, 40, 55, 68, 76, and 86 hours. This series demonstrates the rotation of the water surface in James Bay.

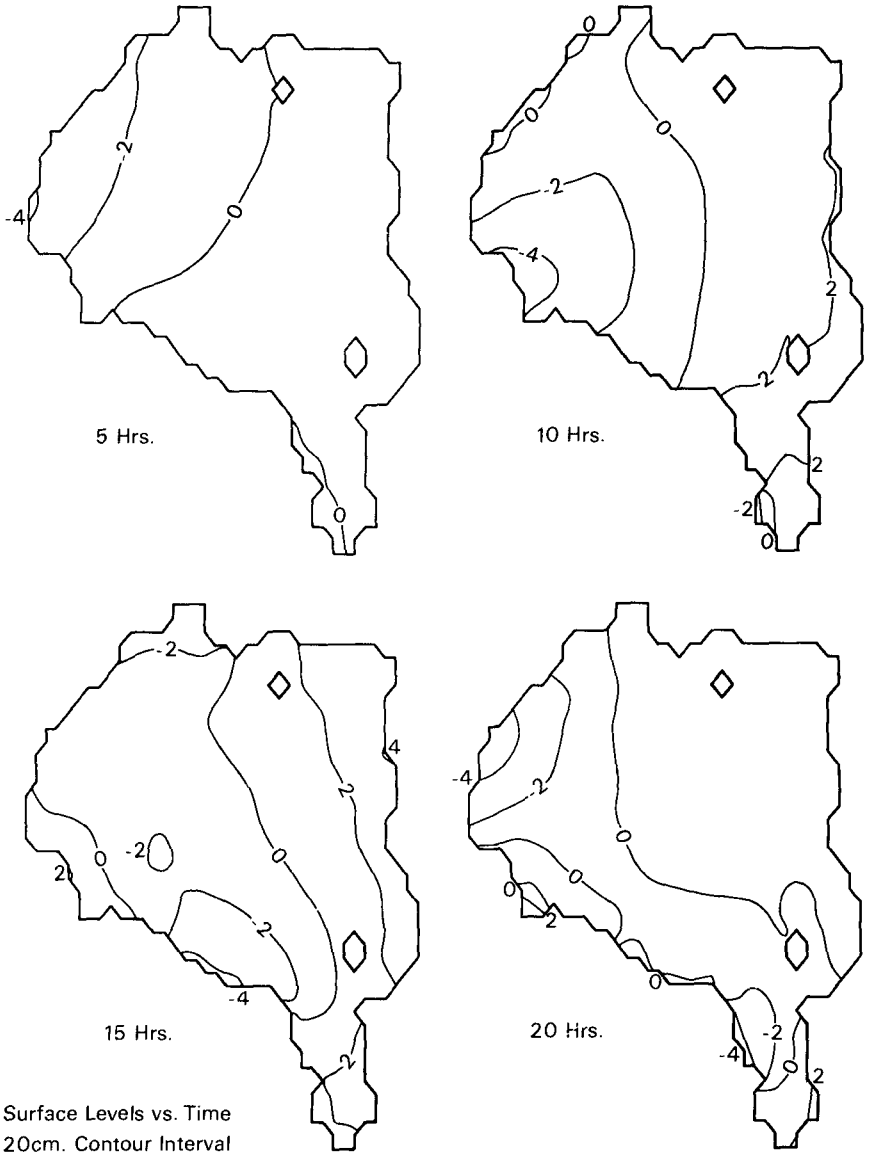

Figure 11. Surface contours in Hudson Bay at 5, 10, 15 and 20 hours. This sequence shows the progression of disturbances in the anti-clockwise direction around the perimeter of the Bay.

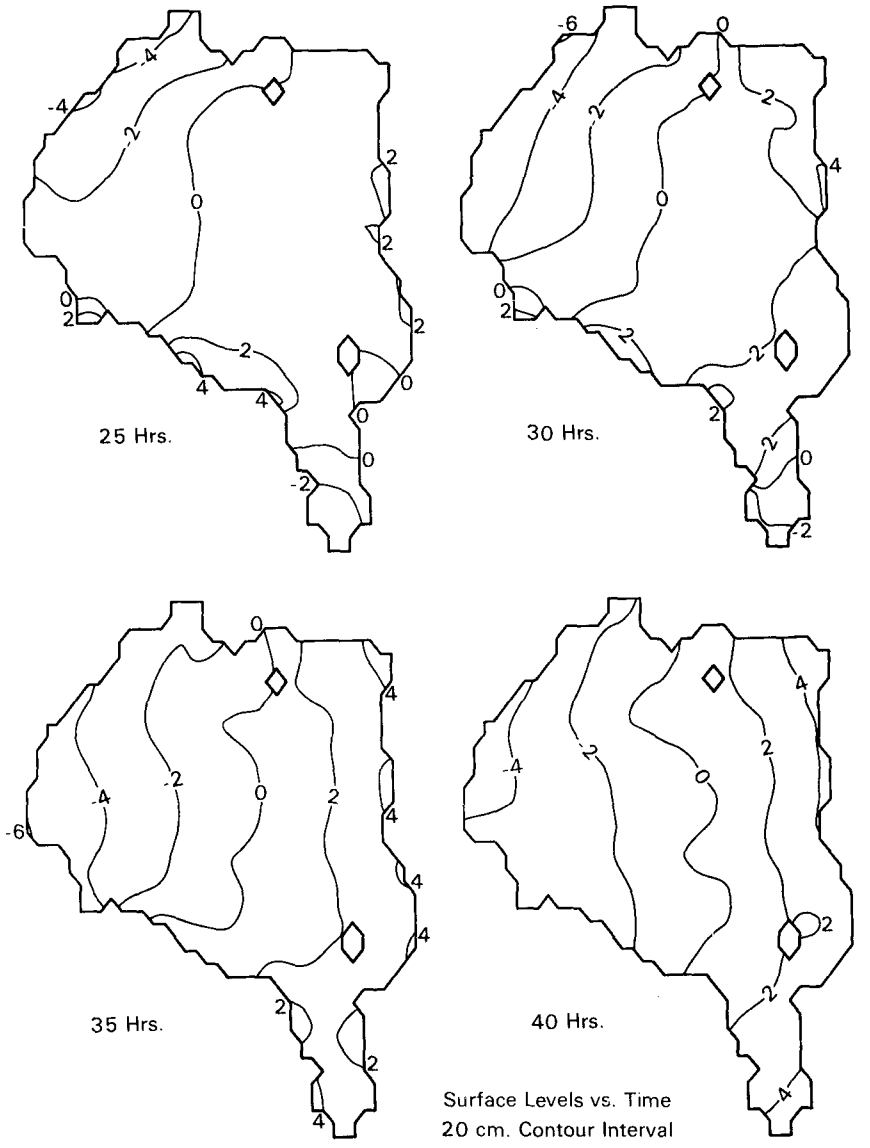

Figure 12. Surface contours in Hudson Bay at 25, 30, 35 and 40 hours. The progression of disturbances around the perimeter is again demostrated.

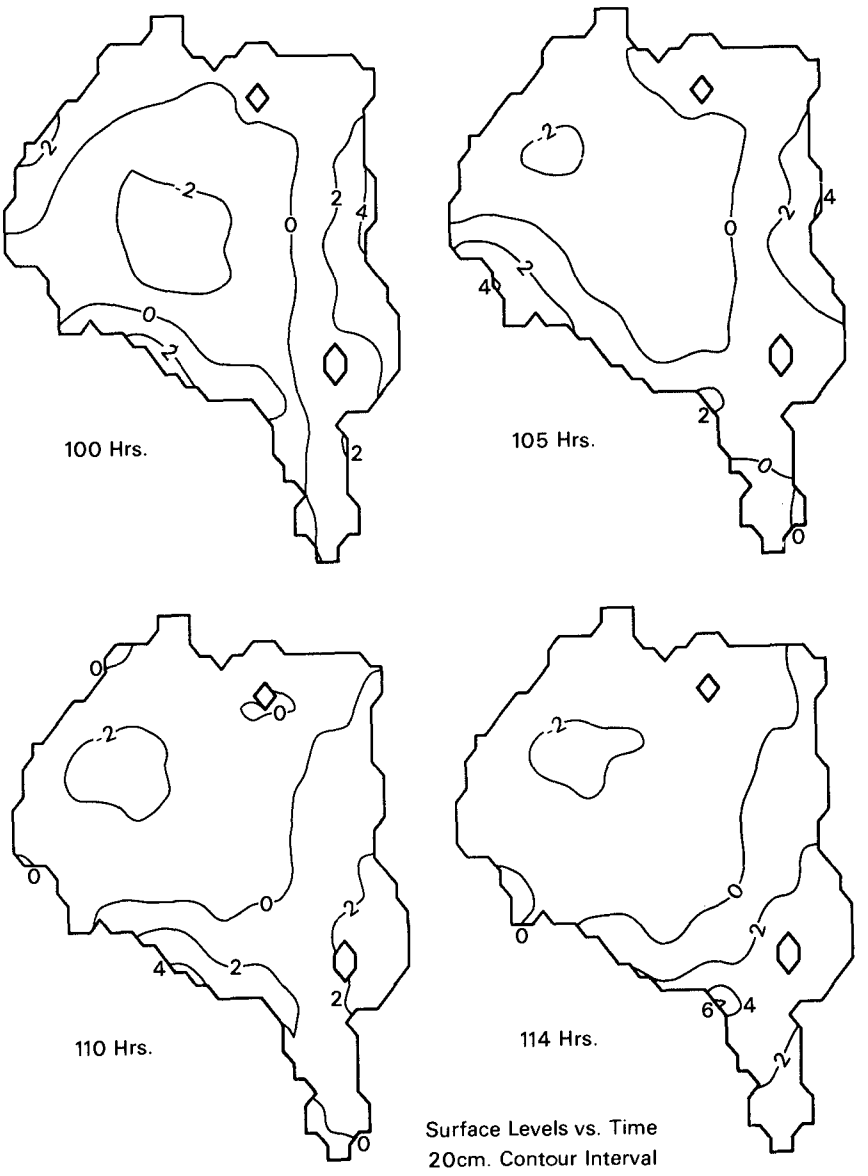

Figure 13. Surface contours in Hudson Bay at 100, 105, 110 and 114 hours. The steady depression in the western half of Hudson Bay has resulted from the persistence of the storm.

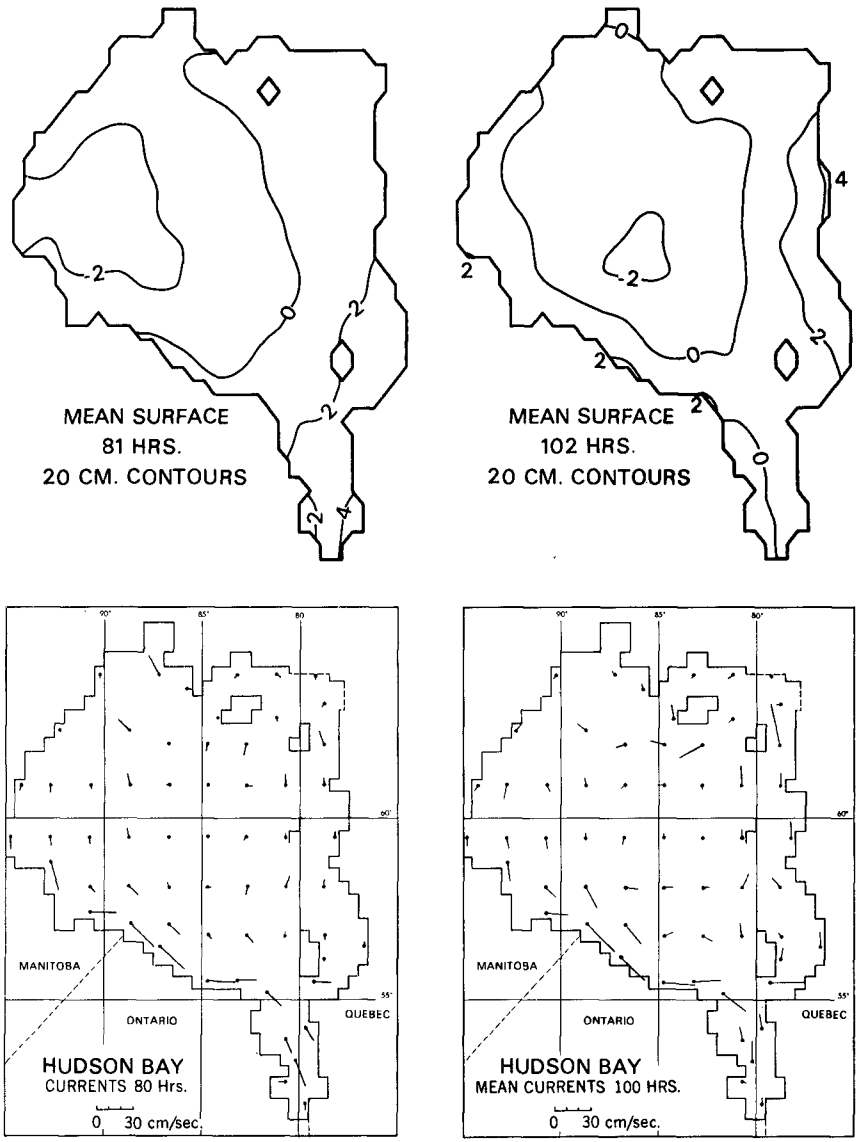

Figure 14. Surface contours for the mean water surface at 81 and 102 hours. The vectors in the bottom of the figure show the mean circulation at 80 and 100 hours.

CHAPTER 10

CONFIDENCE INTERVALS FOR OCEAN WAVE SPECTRA

Leon E. Borgman

University of Wyoming
Laramie, Wyoming

ABSTRACT

The random nature of ocean wave records introduces statistical variability into the wave spectrum estimates based on these records. This may cause inaccuracy in subsequent calculations such as the prediction of the primary wave direction or the estimation of structural response. Confidence intervals on such estimates are needed to evaluate whether adequate estimate accuracy has been obtained.

The chi-squared confidence interval commonly used for wave spectra is based on the assumption of a Gaussian sea surface. Its applicability for hurrican size waves has been open for question. Therefore, after a brief outline of the relevant statistical relations basic to the chi-squared procedure, wave data from Hurrican Carla is empirically analyzed and compared with the theoretical conclusions. A simulation procedure is used to proceed from the data to probability interval statements. A comparison of these with the correponding chi-squared statements shows the chi-squared relations to be fairly reasonable approximations for spectral estimates averaged over bands of at least eight values. The empirical simulation procedure can be extended to subsequent calculations based on the spectral estimates while the chi-square method encounters difficulty for such problems.

INTRODUCTION

The use of the wave height spectrum to characterize ocean wave conditions is widely used and generally accepted as a very significant mode of analysis for confused sea conditions. If the wave system is unidirectional and produces Gaussian (i.e., multivariate normal) water level elevations, the wave spectrum provides the information for a complete characterization of the statistical properties of the sea surface fluctuations. For a multidirectional wave system, the directional wave spectrum (if it can somehow be estimated accurately) also completely characterizes the statistical properties of the random sea surface provided the sea surface is Gaussian.

The Gaussian assumption is not true for wave systems involving wave heights of appreciable magnitude. It is well known that wave crests typically extend higher above mean water level than the troughs fall below the same level. This would not occur if the sea surface were Gaussian. It has been shown [Pierson, 1955, Brown, 1967, p. 32-37] that the water level elevation in confused sea conditions will be Gaussian if there are no spectral lines present and if linear wave theory holds.

The wave situation of interest to engineers is usually the high sea condition such as occurs in a hurricane. It is very difficult to justify linear wave theory and the Gaussian sea assumption for these circumstances. Nevertheless, the wave spectrum still provides a useful, although not complete, characterization of the statistical properties of the sea surface. Other spectrum-type functions, such as the bispectrum, yield additional information.

Typical wave spectra for hurricanes have been computed and presented by Robinson, Brannon, and Kattawar (1967) and others. These are particularly useful in the study of resonant response and fatigue in engineering structures. They also help give a climatological perspective to the wave conditions which might be encountered. It is expected that as time goes on, more and more engineering design criteria will be tied computationally to the design wave spectrum.

This raises the statistical question of confidence for the spectral estimates. It is desirable to know the approximate accuracy of the estimate. As long as the sea surface was Gaussian and a relatively long record was available for analysis, asymptotic confidence intervals (Blackman and Tukey, 1958, p. 21), based on the chi-squared distribution could be used. This procedure is no longer strictly applicable for the nonlinear wave conditions in a hurricane. What should be used then? For that matter, what are the statistical properties of the wave spectrum values for hurricane conditions? These questions will be examined in detail.

WAVE SPECTRUM ESTIMATION

Two basic procedures have been used for estimating the wave spectrum. The first of these (Blackman and Tukey, 1958) is based on using the data to estimate the covariance function and then numerically making the cosine Fourier transform of the covariance function to get the raw wave spectrum. The second method (Bingham, Godfrey, and Tukey, 1967) uses the "fast Fourier transform" computer algorithm to get the raw wave spectrum directly from the data.

The word "raw" in the above paragraph refer to the spectrum before it is smoothed or modified in various ways to improve the statistical properties of the spectrum estimate. Both basic procedures give the same general results, if the modifications could be deleted. This is difficult for the covariance method since the estimation of the covariance intrinsically causes an equivalent spectral smoothing.

From the viewpoint of simplicity, computational speed, and the preservation of information, the fast Fourier transform procedure is preferrable. Therefore it will be the method used in the following analysis. The fast Fourier transform (here after designated FFT) is a computer algorithm for rapidly computing

$$A_m = \Delta t \sum_{n=o}^{N-1} \eta_n \exp(-i2\pi mn/N) \qquad (1)$$

or its inverse

$$\eta_n = \Delta f \sum_{m=o}^{N-1} A_m \exp(i2\pi mn/N) \qquad (2)$$

Here Δt represents a time increment and Δf is a frequency increment. This notation is used since with it the FFT is directly and obviously the finite difference approximation to the integral Fourier transform. In order for equations (1) and (2) to be exact inverses of each other, Δt and Δf must satisfy

$$(\Delta t)\ (\Delta f) = 1/N \tag{3}$$

The significance of relations (1) and (2) for wave analysis can be seen if η_n (n=0, 1, 2, ..., N-1) is taken to be water level elevations above mean water level from a wave recorder digitzed at Δt increment apart. Then is real-valued and (2) reduces to

$$\eta_n = \Delta f \sum_{m=o}^{N-1} [U_m \cos(2\pi mn/N) + V_m \sin(2\pi mn/N)] \tag{4}$$

$$= \Delta f \sum_{m=0}^{N-1} \sqrt{U_m^2 + V_m^2}\ \cos\left(2\pi \frac{mn}{N} - \phi_m\right) \tag{5}$$

where

$$A_m = U_m - iV_m$$

and

$$\phi_m = \arctan(V_m/U_m)$$

Thus, computation of A_m provides the coefficients for a trigonometric series representation of the wave record. The mean-square fluctuation (variance) attributable to the m-th senusoid is (with $n/N = n\Delta t/N\Delta t = t/T$)

$$\text{mean-square} = \frac{1}{T}\int_0^T [\Delta f \sqrt{U_m^2 + V_m^2}\ \cos(2\pi mt/T - \phi_m)]^2\, dt$$

$$= \frac{(\Delta f)^2}{T}\int_0^T (U_m^2 + V_m^2)\ [1/2 + 1/2 \cos 2\ (2\pi mt/T - \phi_m)]\, dt$$

$$= (\Delta f)\ (U_m^2 + V_m^2)/\ (2T) \tag{6}$$

Here, the relation (3) together with $T = N\Delta t$ has been used to obtain $\Delta f = 1/T$ The variance per unit frequency or spectral density is, thus,

$$\frac{\text{mean-square}}{\Delta f} = \frac{U_m^2 + V_m^2}{2T} = \frac{|A_m|^2}{2T} \tag{7}$$

It follows from (1) that $|A_{N-m}|^2 = |A_m|^2$. Hence it is only necessary to list the expression in (7) for m = 0, 1, 2, ..., N/2 since from there on the values are mirror images of the preceding ones. The frequency, $N\Delta f/2$, corresponding to m = N/2 is called the Nyquist freqency. It is a useful convention to tabulate double the expression in (7) versus m = 0, 1, 2, ..., N/2 so that $|A_m|^2/T$ gives the variance for the m-th and the (N-m)-th terms combined. Hence raw spectral density estimates are defined as

$$S_m^* = |A_m|^2/T \tag{8}$$

THEORETICAL STATISTICAL PROPERTIES

Because the chi-squared confidence interval for the wave spectrum is so often used blindly without an appreciation of the applicability of the method to that particular wave data, the theoretical basis for the chi-squared confidence interval will be outlined in some detail.

If the sequence of sea surface elevations $\{\eta_n, n= 0, 1, 2, ..., N-1\}$ are regarded as a random vector with intercorrelated components, a number of results can be derived for the real and imaginary parts of A_m. It will be assumed that the stochastic sequence is second-order stationary and η_n has zero expectation. The theoretical covariance sequence and spectral density will be defined as

$$C_k = E[\eta_n \eta_{n+k}] \tag{9}$$

$$S_m = \Delta t \sum_{k=0}^{N-1} C_k \exp(-i2\pi mk/N) \tag{10}$$

The expression $E[\cdot]$ denotes the expectation operator (Freund, 1962, Chapter 4, p. 90).

From the above frame work, it is possible to derive a number of statistical properties for

$$U_m = \Delta t \sum_{n=o}^{N-1} \eta_n \cos(2\pi mn/N) \tag{11}$$

$$V_m = \Delta t \sum_{n=o}^{N-1} \eta_n \sin(2\pi mn/N) \tag{12}$$

It can be shown that (1) U_m and V_m have zero expectations, (2) U_m and V_m are asymptotically independent, (3) the components of the vectors (U_m, V_m) and $(U_{m'}, V_{m'})$ are asymptotically independent of each other, and (4) the variances of U_m and V_m, for $0<m<\frac{N}{2}$ are the same and equal to $TS_m/2$. The word "asymptotic in the above results refers to N approaching infinity while the covariance sequence is zero for k larger than some fixed integer.

Asmptotically, then,

$$E[S_m^*] = E\left[\frac{U_m^2 + V_m^2}{T}\right] = \frac{Var(U_m) + Var(V_m)}{T}$$

$$= \frac{1}{T}\left(\frac{TS_m}{2} + \frac{TS_m}{2}\right) = S_m \qquad (13)$$

and S_m^* is asymptotically unbiased as an estimate of S_m.

If, in addition to the above assumptions, $\{\eta_n,\ n = 0, 1, 2, \ldots, N-1\}$ is a multivariate normal vector it follows that $(U_m, V_m, U_{m'}, V_{m'})$ is also a multivariate normal random vector. This is true since any linear transformation of a normal vector is again normal (Lindgren, 1960, p. 129) and equations (11) and (12) show that U_m and V_m are linear combinations of the η_n. Hence $U_m/\sqrt{TS_m/2}$ and $V_m/\sqrt{TS_m/2}$ are standard normal random variables and, as mentioned above, asymptotically independent. The sum of the squares of two independent standard normal random variables is a chi-square random variable with 2 degrees of freedom (Freund, 1962, p. 194). Thus

$$\frac{S_m^*}{S_m} = \frac{U_m^2 + V_m^2}{TS_m} = \tfrac{1}{2}\left[\left(\frac{U_m}{\sqrt{TS_m/2}}\right)^2 + \left(\frac{V_m}{\sqrt{TS_m/2}}\right)^2\right] = \frac{\chi_2^2}{2} \qquad (14)$$

(asymptotically)

Now suppose $\hat{S}_{m_o}$ is the average of b values of S_m^* and that S_m is constant over the b values. Then asymptotically

$$\hat{S}_{m_o} / S_{m_o} = \frac{1}{b}\sum_{j=r}^{b+r}(S_m^* / S_m) = \frac{\chi_{2b}^2}{2b} \qquad (15)$$

where r is the first in value in the band and m_o is the mid frequency of the band. Equation (15) holds since the sum of independent chi-squares is again a chi-squared random variable with degrees of freedom equal to the sum of the degrees of freedom of the individual summands (Freund, 1962, p. 194).

The relation (15) is the basis for the chi-squared confidence interval used so often for wave spectra.

$$P\left[\frac{2b\hat{S}_m}{\chi^2_{2b,\,1-\frac{\alpha}{2}}} < S_m < \frac{2b\,\hat{S}_m}{\chi^2_{2b,\,\frac{\alpha}{2}}}\right] = 1-\alpha \qquad (16)$$

In the above expression, $\chi^2_{2b,c}$ refers to the c-th percentile of a chi-squared variate with 2b degrees of freedom.

What then should the user beware of relative to the chi-square confidence interval for wave spectra? Some of the points to consider are as follows. (a) the Length of record analyzed (i.e., the value of N) should be as large as possible consistent with avoiding non-stationary conditions. For most wave situations, a commonly used choice is 20 mintes of record. (b) the covariance function should be essentially zero for lags substantially less than the wave record length. One published suggestion is that the maximum covar-

iance lag with appreciable non-zero covariance values should be on the order of one-tenth of the record length (Blackman and Tukey, 1958, p. 11). (c) The closer the wave conditions come to satisfying linear wave theory, the better will be the confidence interval approximation provided by (16), and vice-versa.

EMPIRICAL DATA ANALYSIS

Wave data from hurricane Carla was selected to test the accuracy of the chi-squared confidence interval under extreme conditions. Water level elevations (4096 values) digitized at an inverval of 0.2 seconds apart and starting at noon, September 8, 1961 were used. The wave records were made in 100-ft. water depth by the Chevron Research Company on a Chevron platform in South Timbaker Block 63, Gulf of Mexico, as a part of their Wave Project II (Thrasher and Aagaard, 1970) and have been released to the National Oceanographic Data Center. The FFT coefficient, A_m, were computed by the NLØGN subroutine (Robinson, 1967, p. 63) and S_m^* was tabulated for $m = 0, 1, 2, \ldots, 4095$. The values of S_m^* for $6 < m < 305$ were selected by inspection as being significantly different from zero. These values, graphed in Fig. 1 versus $f = m\Delta f$, are the basic initial information from which the wave spectrum is estimated.

The scattered points must be averaged in some manner to produce a mean curve. Fig. 2 shows the results of two different averaging methods. The dashed line gives the results of straight arithmetic averaging in blocks of 8 lines. The solid line gives the spectrum as determined from the following weighted average

$$S_m^* = \left[\sum_j W_{m-j} S_j^* \right] / \left[\sum_j W_{m-j} \right] \tag{17}$$

where

$$W_{m-j} = e^{-[(m-j)\Delta f]^2 / (2\sigma^2)} \tag{18}$$

$$\sigma = 3\Delta f$$

This averaging will be referred to as Gaussian smoothing because of the analogy to the normal or Gaussian density. The two spectral estimates are almost identical. The Gaussian smoothing was selected as preferrable for the present study because it gives the greatest emphasis in averaging to nearby points and the least emphasis to points further away. This is different from the block averaging which equally weights points within the block.

The scatter of the raw spectrum points about the Gaussian-smoothed spectrum estimate was examined next. The residuals, or deviations of S_m^* from the spectrum estimate

$$R_m = \hat{S}_m - S_m^*$$

are plotted at the bottom of Fig. 3. As would be expected the residuals are the biggest for frequencies where the spectrum is large. The magnitude of the residuals at different frequencies was characterized by three different root-mean-square values. These were

$$\begin{aligned} \sigma_m &= \text{r.m.s. } R_m \\ \sigma_{m+} &= \text{r.m.s. positive } R_m \\ \sigma_{m-} &= \text{r.m.s. negative } R_n \end{aligned} \tag{19}$$

The first formula uses (17) and (18) as written except R_j^2 is substituted for S_j^*. The second formula applies (17) and (18) only to the R_j^2 where R_j is greater than zero. The third formula does the same for the negative R_j. All three Gaussian averages are then square-rooted to get the root-mean-square values. The quantities σ_{m+}, and σ_{m-} are graphed versus frequency in Fig. 4. Although computed, σ_m is not shown since it did not prove to be useful in later parts of the study.

As Fig. 4 shows, σ_+ has a much larger maximum than σ_-. Also both maxima more or less coincide with the peak of the spectral density.

The residuals were first normed by dividing them by σ_m. These values are graphed as the normed residuals shown in Fig. 3. Originally it was intended to use these normed residuals as the stationary noise characterization of the spectrum deviations. However a careful examination of the normed residuals shows that their minimum values are larger around 0.10-0.15 Hertz than elsewhere. Thus the noise in this form does not appear to be stationary.

The residuals were then normed by dividing positive R_m by σ_{m+} and dividing negative R_m by σ_{m-}. These symmetrically normed residuals are plotted at the top of Fig. 3. A Smirnov k-sample test applied to six groups of 50 each of these (Conover, 1971, p. 322) leads to an acceptance that the noise represented by the symmetrically normed residuals is essentially stationary (See Fig. 6). Thos noise was therefore used to characterize the fluctuations about $\hat{S}_m$.

The empirical distribution function of the symmetrically normed residuals is shown as the solid line in Fig. 7. The corresponding probability density function was estimated from the slope of the straight line fitted by least squares to the empirical distribution function using the values in a band of width $\pm$ 0.5 about the abscissa value for which the density is being estimated. A graph of the density is given in Fig. 8.

A COMPARISON WITH THEORY

How do the above empirical results compare with the theory outlined previously? Theoretically, the S_m^* are supposed to be asymptotically independent. This would imply that the symmetrically normed residuals would also be independent. This would imply that the symmetrically normed residuals would also be independent. As a partial test of this property, the m-th symmetrically normed residual was graphed versus the (m+1)-th corresponding value as

shown in Fig. 5. The scatter shows no clear cut trend except for a tendency to produce a square cloud of points. The squareness is explained by the abrupt start and termination of the density function in Fig. 8. If the density were uniform, for example, and the residuals independent a perfectly square cloud would be expected. Thus, Fig. 5 does not appear to contradict the asymptotic independence.

The chi-square distribution with two degrees of freedom which theoretically should approximately hold for S_m^* was checked next. Symmetrically norming a χ_2^2 random variable produces a variable with a distribution function shown by the dash-dot curve in Fig. 7. The corresponding theoretical density function is graphed in Fig. 8. The discontinuity results from the abrupt change in norming constant at zero.

A Kolmogarov test for goodness-of-fit at the .05 level can be performed by inspection of Fig. 7. The distribution function for the symmetrically normed χ_2^2 variate passes outside the 90% Kolmogorov confidence band (Conover, 1971, p. 299) and therefore causes a rejection of the hypothesis that the data follow that theoretical distribution.

Despite this rejection, it is interesting to compare the chi-squared probability predictions with what would follow from the symmetrically normed noise. By Monte-Carlo procedures, independent noise having the empirical distribution function given in Fig. 7 was assigned at random to the different m values. Then σ_+, σ_-, and $\hat{S}_m$ were used to reconstruct the S_m^* values consistent with this noise. Finally a new set of $\hat{S}_m$ values were computed by Gaussian smoothing. These $\hat{S}_m$ values would be an equivalent possibility to that which actually occurred if the noise had just been shifted around to an equally likely realization. Three hundred such sets of $\hat{S}_m$ values were developed and 90% probability intervals were established from the 5th and 95th percentiles of simulated values. These are shown in Fig. 9.

The Gaussian smoother used in deriving the original $\hat{S}_m$, had a width roughly equivalent to band of 8 spectral lines.(Its standard deviation was 3 lines and the width is somewhat larger than $\pm\sigma$.) Hence it seems reasonable to compare the probability intervals with that for a chi-squared with b = 8, or 2b = 16. This is shown in Fig. 10. The two probability interval sets are slightly but not terribly different. One would have to conclude that the chi-squared approximation is reasonably adequate, even for hurricane waves. This seems true despite the disagreement relative to the S_m^* values. Something like a central limit theorem seems to be pulling the distributions into agreement for averages of bands including as many as 8 raw spectral values.

ADDITIONAL DOCUMENTATION PLANNED

Empirical Analysis has continued on the Hurrican Carla data. About half of the available data sets have been analyzed. The empirical distribution functions and probability densities for these (seven more records) are all remarkably identical with Figs. 7 and 8. The Smirnov k-sample test overwhelmingly accepts that they all have the same distribution function. It is planned that the detailed empirical analysis of the Hurricane Carla spectra and of a variety of spectra for other wave conditions will be issued as a project report as soon as the analysis is complete.

CONCLUSIONS

The available data supports the use of the chi-squared approximation for a confidence interval on spectrum estimates. It is difficult however to extend the chi-squared approximation to yield confidence intervals on subsequent quantities computed from wave spectra. For such situations, simulation procedures based on the empirical properties of the spectral noise would seem to provide a reasonable approach to developing confidence intervals.

ACKNOWLEDGEMENTS

This investigation was supported by Contract DACW72-72-C-0001 with the Coastal Engineering Research Center, Corps of Engineers, U.S. Army. Appreciation is expressed to Mr. Richard Whitaker and Mr. Jack Wolff, graduate students at the University of Wyoming, for their assistance in computer calculations.

REFERENCES

Bingham, C., Godfrey, M. D., and Tukey, J. W. (1967), "Modern Techniques of Power Spectrum Estimation" IEEE Trans. Audio and Electroacoustics, vol. AU-15, no. 2, pp. 56-66.

Blackman, R. B., and Tukey, J. W. (1959), "The Measurement of Power Spectra," Dover, New York.

Brown, L. J. (1967), "Methods for the Analysis of Non-stationary Time Series with Applications to Oceanography," Hydraul. Eng. Lab. Rep. HEL 16-3, College of Eng., University of California, Berkeley.

Conover, W. J., (1971), "Practical Nonparametric Statistics," John Wiley and Sons, Inc., New York.

Freund, J. E., (1962), "Mathematical Statistics," Prentice-Hall, Inc., Englewood Cliffs, New Jersey.

Lindgren, B. W., (1960), "Statistical Theory," Macmillan Co., New York.

Pierson, W. J., Jr., (1955) "Wind-Generated Gravity Waves," Advances in Geophysics, vol. 2, pp. 93-178.

Robinson, E. A., (1967), "Multichannel Time Series Analysis with Digital Computer Programs," Holden-Day, San Francisco.

Robinson, R. J., Brannon, H. R., and Kattawar, G. W., (1967), "Storm Wave Characteristics," Trans. Soc. of Petroleum Eng. of AIME, vol. 240, pp. 87-98.

Thrasher, L. W., and Aagaard, P. M., (1970), "Measured Wave Force Data on Offshore Platforms," Jour. Petroleum Technology, vol. 22, pp. 339-346.

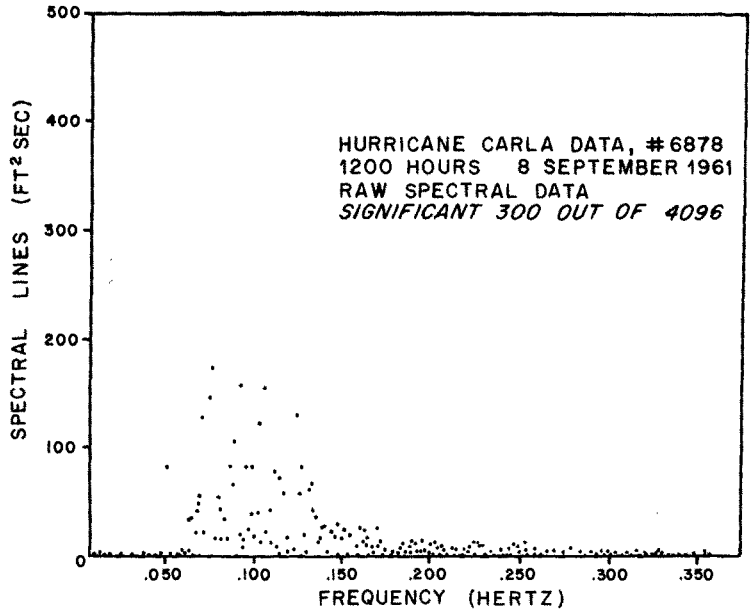

Fig. 1. Values of S_m^* versus $m\Delta f$

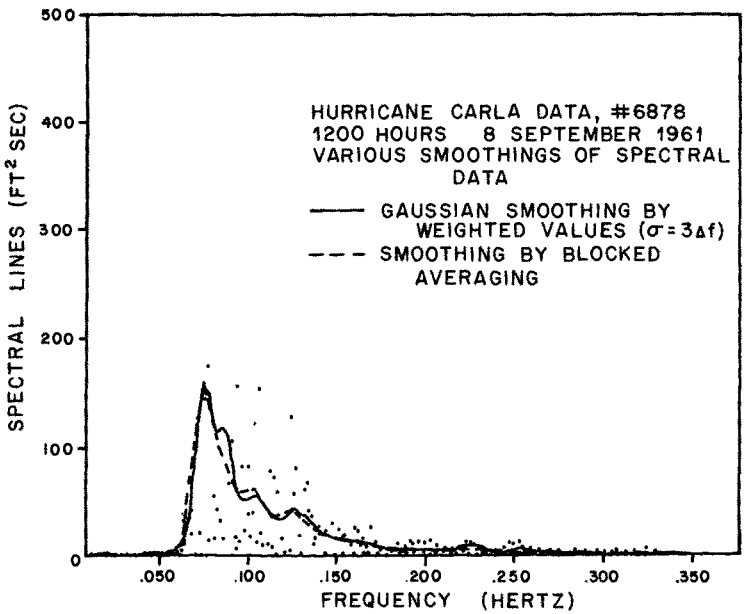

Fig. 2. The spectrum estimate $\hat{S}_m$ determined by two different methods.

Fig. 3. Various versions of residuals plotted versus frequency.

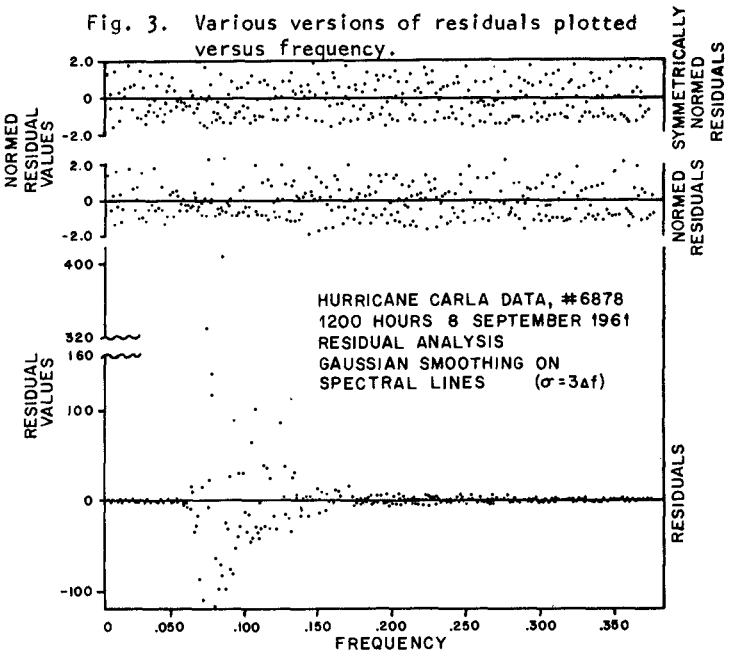

Fig. 4. Local estimates of standard deviation.

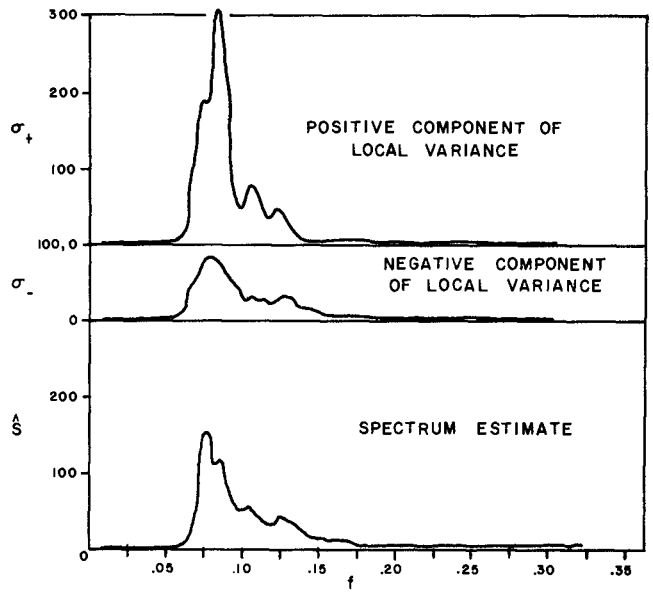

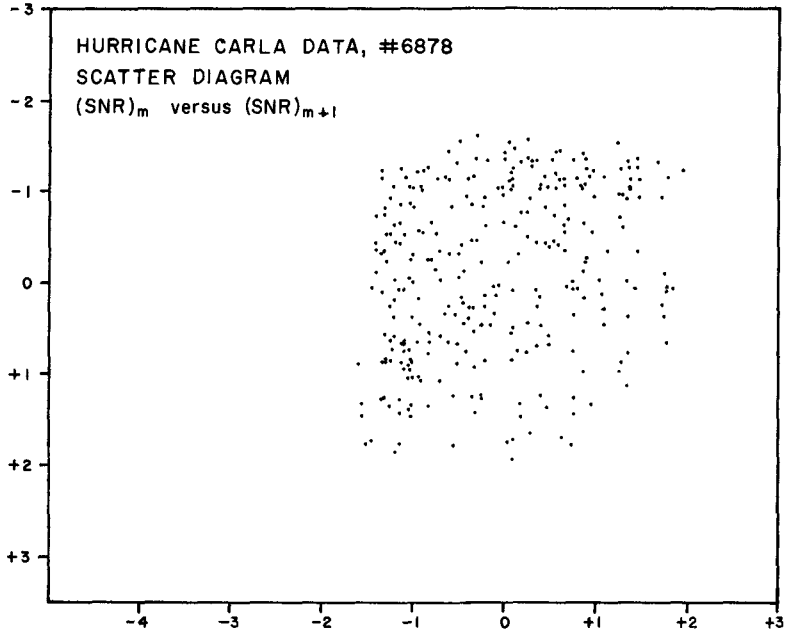

Fig. 5. Scatter diagram of the m-th symmetrically normed residual plotted versus the (m+1)-th value.

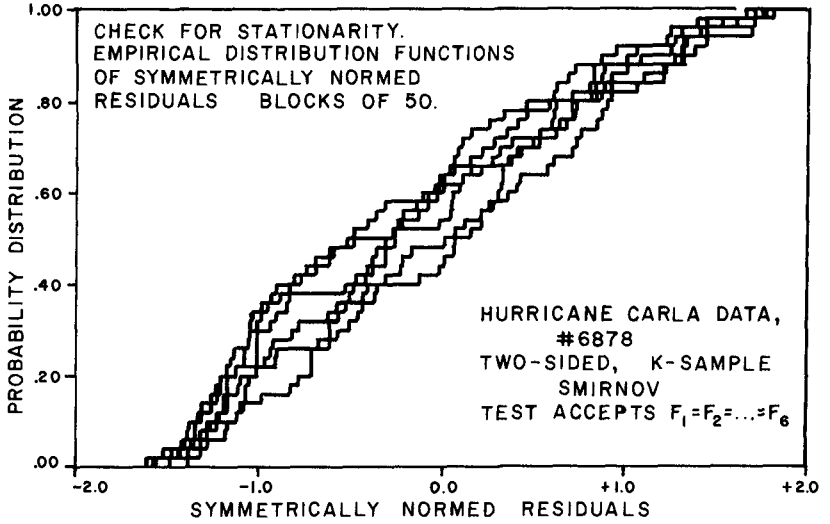

Fig. 6. Smirnov test of noise stationarity.

Fig. 7. The empirical distribution function of the noise as compared with a symmetrically normed chi-square distribution function.

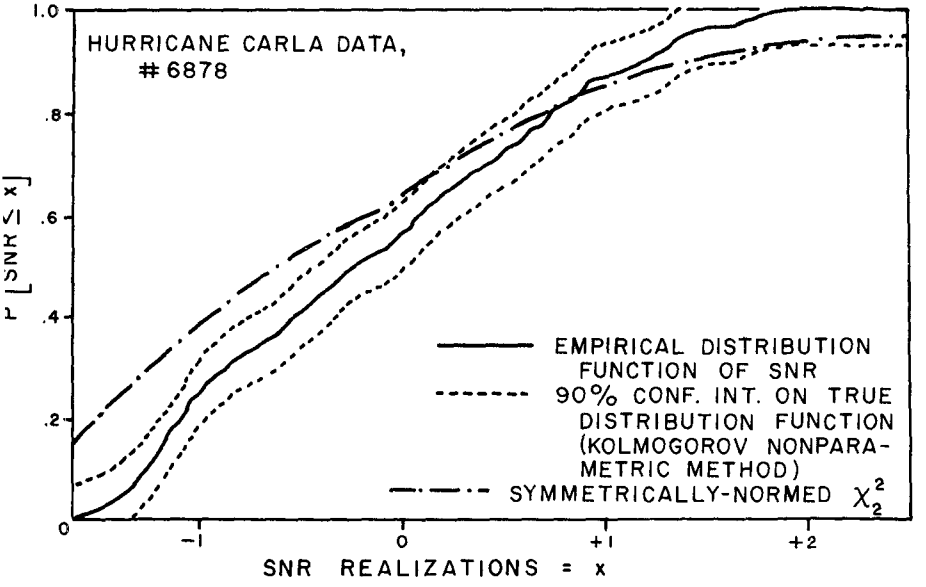

Fig. 8. Probability densities for the noise and a symmetrically normed chi-squared random variable.

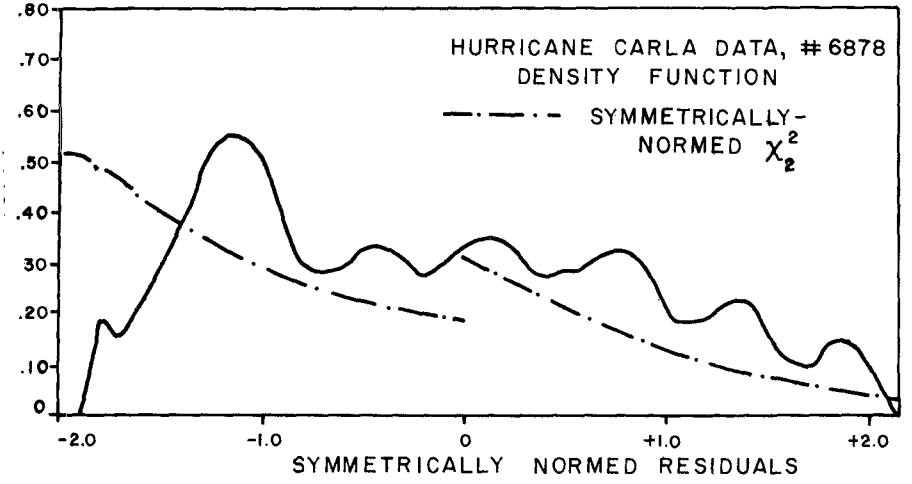

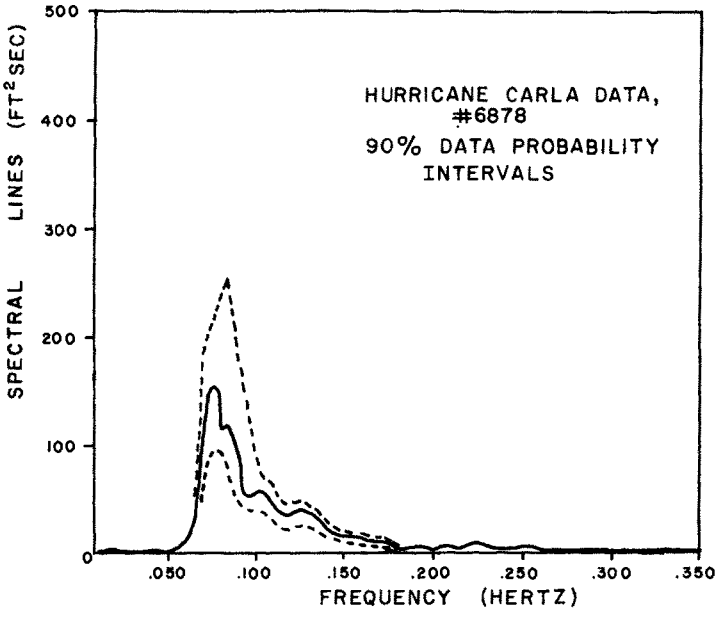

Fig. 9. Empirical probability intervals as determined from simulation.

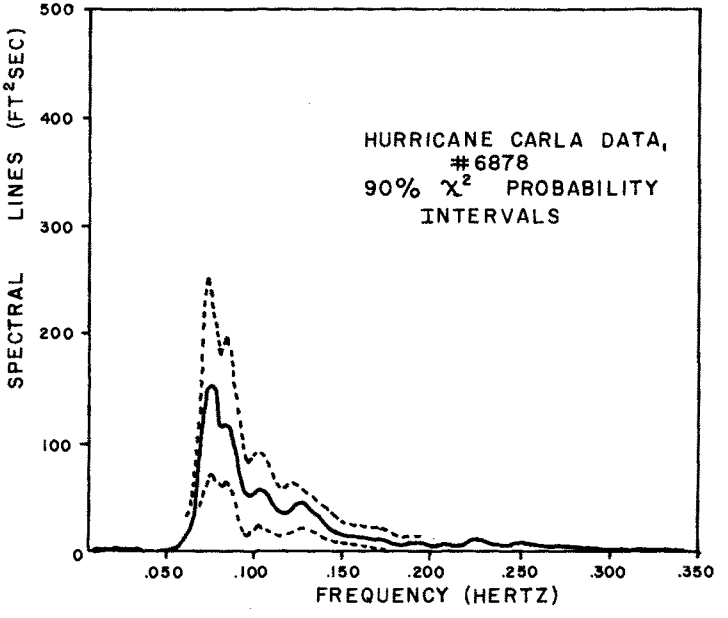

Fig. 10. Chi-square probability intervals (16 degrees of freedom).

CHAPTER 11

NON-STATIONARY SPECTRUM ANALYSIS OF OCEAN WAVES

by

Mehmet Aziz Tayfun, Cheng Yi Yang, and George Chia-Chu Hsiao*

ABSTRACT

Priestley's method [1, 2, 3]** of non-stationary spectral analysis is extended to the case of digitally sampled records. A computation procedure previously proposed in an earlier work [4] is further investigated. This procedure compensates for the inherent difficulties in the theory and computes time-dependent spectra from a sample in an iterative manner. Validities of the theory and the iterative procedure are tested with a simulated non-stationary process. Results establish a general agreement with theory, especially when spectra vary smoothly with time and frequency. Consequently, the procedure is applied to estimate non-stationary spectra for two wave records. A comparison is made between the non-stationary estimates and the stationary results derived from the same set of wave records.

1. INTRODUCTION

Since the pioneering work of Pierson and Marks [5], stochastic spectral analysis of wave records is well accepted. Among many available published works on the subject, references [6, 7, 8, 9, 10, 11, 12] are excellent sources of information on the analysis, significance and the current state of the wave spectrum approach.

The most important constraint of the conventional spectral analysis is the assumption of stationarity, i.e., the fundamental character of the wave field does not change with time. Unfortunately, in many realistic situations, this

* Research Fellow of Civil Engineering, Professor of Civil Engineering and Assistant Professor of Mathematics, respectively; University of Delaware, Newark, Delaware, 19711.

** Brackets refer to references in the Appendix.

is an unsatisfactory restriction imposed by the lack of a physically meaningful and mathematically rigorous non-stationary spectrum concept. A few analysts tried an intuitive approach to compensate for time-dependency. For example, Wilson [13] computes time-variant spectra from overlapping segments of a wave record. Such attempts are useful but are still unsatisfactory because they do not have a formal basis for guidance and a clear design rationale for practical application.

Recently, Priestley has made a major effort to define a non-stationary spectrum as a smooth extension of the classical concepts and discussed a method of estimating time-dependent spectra from a single realization. This method is a generalization of the conventional analog approach. Therefore, it involves all the difficulties of the stationary analysis as well as new ones imposed by time-dependency. Specifically, the optimal design of a spectral computation requires a prior knowledge of frequency- and time-domain characteristics of the spectrum of the underlying process. These are normally unavailable in a realistic situation. Tayfun, et al [4], suggested a practical procedure to compute these parameters and time-dependent spectra in an iterative manner. The procedure was successfully tested on an artificially generated process in which spectral components have the same time-history, which is called a uniformly modulated process.

Processes that arise in applications such as ocean waves are realistically non-uniformly modulated. The purpose of this study is, therefore, to investigate the validities of the estimation method and the iterative procedure in the more general case of a non-uniformly modulated process, and, consequently, to be able to apply the iterative procedure to estimate time-dependent spectra for ocean wave records.

The discussion will mostly be limited to the basic ideas and the operational results in the case digitally sampled records. The concepts are simple extensions of those of the continuous case given in references [1, 2, 3]. The reader is referred to these references for details and elegant mathematical analysis of the underlying theory.

2. DEFINITIONS AND ASSUMPTIONS

A zero-mean non-stationary process $x(t)$ is represented in the frequency-domain as [1].

$$x(t) = \int_{-\infty}^{\infty} A(t,\omega)\, e^{i\omega t}\, dZ(\omega) \qquad (2.1)$$

where $Z(\omega)$ is a process with uncorrelated increments, and $A(t,\omega)$ is a deterministic modulating function. We see that, if $A(t,\omega)$ equals one, the natural representation of a stationary process is recovered in terms of its generalized Fourier transform process, $Z(\omega)$.

The above representation (2.1) provides a spectral decomposition of the process $x(t)$ in terms of harmonic components with different frequencies and time-variant random amplitudes $A(t,\omega)dZ(\omega)$. The mean-square function of $x(t)$ is

$$E|x(t)|^2 = \int_{-\infty}^{\infty} |A(t,\omega)|^2 \, E|dZ(\omega)|^2 \tag{2.2}$$

where $E\{\cdot\}$ denotes an ensemble-average. Note that $E|x(t)|^2$ depends on time t, as expected, by virtue of the modulating function $A(t,\omega)$. From the definition that the spectral density is the frequency distribution of the mean-square, it follows that the spectral density at time t is

$$f(t,\omega) = |A(t,\omega)|^2 \, f(\omega) \tag{2.3}$$

where

$$f(\omega)\, d\omega = E|dZ(\omega)|^2,$$

with $f(\omega)$ regarded as the spectral density, say, at time t_o if we assume that $A(t_o,\omega) = 1$. Hence, the function $|A(t,\omega)|^2$ describes the change or evolution of that density at subsequent times.

Assume that a sea-surface record collected at a fixed spacial reference as a continuous function of time is a sample of a zero-mean process which admits a representation of the form (2.1). If the record is digitally sampled at a periodic sampling interval of Δt sec., then we form the sequence $x_1, x_2, \ldots, x_N$, where $x_t = x(t\Delta t)$, and $N = T/\Delta t$ with T the total record length in seconds. Furthermore, assume that the interval Δt is so chosen that

$$f(t\Delta t,\omega) = 0 \ , \ |\omega| \geq \pi/\Delta t, \text{ all } t \tag{2.4}$$

so as to make sure that no error will be introduced due to the well-known aliasing effects.

At this point it is convenient to regard the sequence x_t as if it consisted of prints at unit time intervals. This is equivalent to transforming the original frequency scale into a standardized dimensionless frequency, say ω', which is defined in $(-\pi, \pi)$ and such that $\omega' = \omega\Delta t$. Consequently, the spectral density, say $f_d(t,\omega')$, of the sequence x_t and that of the actual wave record $x(t\Delta t)$ relate to each other in the form

$$f(t\Delta t,\omega'/\Delta t) = \Delta t \cdot f_d(t,\omega') \ , \ |\omega'| < \pi \tag{2.5}$$

Associated with the discrete process from which the sequence x_t is assumed to be sampled, three dimensionless parameters, B_x, B_o and B_f are respectively defined as the "characteristic width," the time and frequency domain bandwidths of the spectral density f_d as a function of t and ω'. The characteristic width, B_x, is a measure of the maximum interval over which the statistical properties of the process are approximately stationary. B_o and B_f are of the order of magnitudes of the physical bandwidths based on the "half-power points" of the major

peaks of $f_d(t,\omega')$ as a function of only t, and then ω', respectively. Both B_x and B_o are imposed by time dependency introduced through the modulating function $A(t,\omega')$. They relate to the inverse time-rate of change of $A(t, \omega)$, and therefore, to one another in the sense that if one is large, so is the other, and conversely. The explicit definitions of these parameters are given in [1, 2, 3].

3. ESTIMATION OF NON-STATIONARY SPECTRAL DENSITY

The "raw" and "smooth" spectral estimates of $f_d(t,\omega')$ in the neighborhood of t and ω' are given respectively by

$$|U_t(\omega')|^2 = \left| \sum_{u=t-N}^{t} g_u X_{t-u} e^{-i\omega'(t-u)} \right|^2 \tag{3.1}$$

and

$$\hat{f}_d(t,\omega') = \sum_{t-N}^{t} W_{T',u} |U_{t-u}(\omega')|^2 \tag{3.2}$$

where g_u is a digital "filter," and $W_{T',u}$ is a weight-sequence which depends on a parameter T'. Associated with the filter g_u and its Fourier transform $\Gamma(\omega')$, two parameters, B_g and B_Γ are respectively defined as measures of bandwidths in time and frequency. These parameters indicate the concentration of the functions g_u and $|\Gamma(\omega')|^2$ near their origins. We likewise define a parameter B_w as a measure of bandwidth for the weight-sequence $W_{T',u}$. Explicit definitions of the parameters B_g, B_Γ and B_w as well as certain suitability conditions which g_u and $W_{T',u}$ must satisfy are given in [1, 2, 3].

The raw estimate, $|U|^2$, is essentially a digital filtering of the sequence x_t through a filter g_u with a frequency response, $\Gamma(\omega')$, centered on frequency ω'. Under the conditions, $B_g << B_x$ and $B_\Gamma << B_f$, Priestley [1] shows that

$$E|U_t(\omega')|^2 \simeq f_d(t,\omega') \tag{3.3}$$

Hence, $|U|^2$ is an approximately unbiased estimate of $f_d(t,\omega')$. The condition $B_g << B_x$ implies that this filtering is to be done through a filter with a narrow bandwidth so that over the effective range of the filter the statistical properties are approximately constant. The condition $B_\Gamma << B_f$ requires that the spectral window, $|\Gamma(\omega')|^2$, be narrow enough just like a slit through which the value $f_d(t,\omega')$ can be observed without any contamination from neighboring values. As is well-known, a small bandwidth, B_g, in the time-domain corresponds to a large bandwidth, B_Γ, in the frequency-domain. Consequently, the estimation would be accurate for processes with spectra changing slowly over time and frequency (i.e., large B_x, B_o and B_f), so that a fulfillment of one of the conditions, $B_g << B_x$ and $B_\Gamma << B_f$, would not delete the other.

Note that the raw estimate is derived through a linear transformation of the random sequence x_t. Hence, it also is random in character, and not a useful estimate for practical purposes. It may be recalled that, in the conventional analog approach when x_t is in fact stationary, a stationary spectral estimate is obtained simply by averaging the raw estimates of the form (3.1) over the total length of the record. This enables one to approximate an ensemble-average as well as to obtain more stable estimates. Such an approach is not valid in the non-stationary case, since one cannot replace an ensemble-average with a time-average. Therefore, in order to account for the unstable nature of the raw estimate, $|U_t|^2$, it is smoothed over neighboring values of t, as implied by (3.2), resulting in a more stable "smooth" estimate, $\hat{f}_t$. This smoothing is done through a weight-sequence $W_{T',u}$ depending on the parameter T' which satisfies the condition $B_g << T' << N$. The last condition implies that smoothing with $W_{T',u}$ should be over a range that is substantially larger than the effective width of g_u to achieve satisfactory stability. On the other hand, T' should be small enough so as to prevent excessive "smudging" of the temporal characteristics of the raw estimates.

Finally, note that, once $\hat{f}_d(t,\omega')$ is computed, we can obtain the smooth estimate, say $\hat{f}(t\Delta t,\omega)$, corresponding to the actual wave process through the transformation (2.5), i.e.,

$$\hat{f}(t\Delta t,\omega'/\Delta t) = \Delta t \cdot \hat{f}_d(t,\omega') \ , \ |\omega'| < \pi \tag{3.4}$$

is a smooth estimate of $f(t\Delta t,\omega)$ at time $t \cdot \Delta t$ (sec) and frequency $\omega = \omega'/\Delta t$ (rad $\cdot$ sec^{-1}).

4. SAMPLING PROPERTIES AND DESIGN RELATIONS

The overall sampling quality of the estimate $\hat{f}_d(t,\omega')$ is measured by its relative mean-square error at time t and frequency ω', i.e.,

$$M(h,T') = \frac{E|\hat{f}_d(t,\omega') - f_d(t,\omega')|^2}{f_d^2(t,\omega')} \sim \frac{1}{4}\left\{\frac{B_w^2}{B_o^2} + \frac{B_\Gamma^2}{B_f^2}\right\}^2 + \frac{C}{T'}\int_{-\pi}^{\pi} |\Gamma(\omega')|^4 d\omega' \tag{4.1a}$$

where h is a parameter related to the functional form of g_u, and C is a constant determined from the weight-sequence $W_{T',u}$.

Design of a spectral estimate involves determining the functions g_u and $W_{T',u}$. Functional form of these may be chosen from a standard collection of filter windows that already exists in the classical analysis. For example, in terms of the parameters h and T', we may choose a rectangular filter g_u and a discrete Daniell window $W_{T',u}$ of the forms

$$g_u = \begin{cases} \dfrac{1}{\sqrt{2\pi(2h+1)}} \ , & u = 0, \pm 1, \ \ldots, \pm h \\ 0 \ , & |u| > h \end{cases} \tag{4.2}$$

and

$$W_{T',u} = \begin{cases} \frac{1}{T'+1} , & u = 0, \pm 1, \ldots, \frac{1}{2}T' \\ 0 , & |u| > \frac{1}{2}T' \end{cases} \tag{4.3}$$

The above functional forms will be adopted in the subsequent discussion and applications for illustrative purposes. On the basis of (4.2), (4.3) and from (4.1a), we may show that, for large values of h and T'

$$M(h,T') \simeq \frac{1}{4}\left\{\frac{B_w^2}{B_o^2} + \frac{B_\Gamma^2}{B_f^2}\right\}^2 + \frac{4h}{3T'^2} \tag{4.1b}$$

where $B_w \simeq T'/\sqrt{12}$ and $B_\Gamma \sim \pi/h$, an approximation based on half-power points of the major peak of $|\Gamma(\omega')|^2$.

The parameters h and T' may now be determined as follows:

(a) Fixed Frequency-Domain Resolution: For each t, $\hat{f}_d(t,\omega')$ is required to have a prescribed degree of resolution in frequency-domain, i.e., we require $B_\Gamma/B_f = \lambda$, where λ is a small prescribed constant. Here, $B_\Gamma \sim \pi/h$. Hence, given B_f, h is the largest integer smaller than

$$\frac{\pi}{\lambda B_f} \tag{4.4}$$

Now, T' is chosen so as to minimize the relative mean-square error, M, now a function of only T'. Subject to the condition $B_g < T' < N$, the optimum value of T' is easily obtained from (4.1b) as the largest even integer smaller than

$$[192\ h\ B_o^4]^{1/5} \tag{4.5}$$

(b) Fixed Resolution in Time and Frequency-Domains: In this case, we set $B_\Gamma/B_f = \lambda$ and $B_w/B_o = \mu$, where μ is likewise a small prescribed constant. Assuming B_o and B_f are available, h and T' are determined from

$$h \sim \frac{\pi}{\lambda B_f} , \text{ and } T' \sim \sqrt{12}\, B_o \mu \tag{4.6}$$

The sampling quality of the estimates is now determined by the above conditions and from (4.1b), the relative mean-square error.

5. FEATURES AND INHERENT DIFFICULTIES

The estimation method described above is a smooth generalization of the conventional analog approach to non-stationary cases. Especially with the particular choice of $W_{T',u}$ here, the technique is roughly equivalent to estimating spectra from overlapping segments of a record. This is achieved through a formal consideration of the temporal characteristics (i.e., B_x and B_o) of the underlying process. In the limit case of stationarity, B_x and B_o both become infinite and smoothly disappear from the formulations as the analysis reduces to the conventional results. In that case, a stationary spectral estimate, say $\hat{f}(\omega)$, is obtained by

$$\hat{f}(\omega'/\Delta t) = \frac{\Delta t}{N-2h} \sum_{t=h+1}^{N-h} |U_t(\omega')|^2, \tag{5.1}$$

where $|U_t|^2$ is given by (3.1) and limits are chosen over the range of t in (1, N) for which $|U_t|^2$ can be evaluated from (3.1) by using a filter g_u of the form (4.2). This simply corresponds to an averaging of the squared filter output, $|U_t|^2$, over the complete record length, just as in the conventional analog approach.

The method involves all the difficulties associated with the classical analysis as well as new ones imposed by time-dependency. A rational application requires a knowledge or a rough estimate of the parameters B_x, B_o and B_f as a background information for design. These are unavailable a priori on the basis of a given sample record in a realistic situation such as ocean waves, and therefore, form the major source of difficulty in application.

6. A PRACTICAL PROCEDURE

Consider a practical situation where it is required to estimate the non-stationary spectral density, $f(t\Delta t,\omega)$, of a wave process on the basis of a digitally sampled record $x(t\Delta t)$, where $t = 1, \ldots, N$.

The first objective is to determine the process parameters B_x, B_o, and B_f in a rational way. At present, there seems to be no way of estimating a lower bound for the characteristic width B_x on the basis of a sample record. However, we recall that the parameters B_x and B_o are related to each other in the sense that if one is large, so is the other, and conversely. Hence, if we could estimate B_o, then it could be used as a measure of the temporal characteristics of the wave process. Furthermore, design relations are dependent on B_o and B_f. A rational design for the parameters h and T' requires, therefore, a background information about B_o and B_f. An iteration scheme may be suggested to compute the parameters B_o and B_f, and consequently, h and T' in the following manner.

We perform a pilot-estimation by using "trial values" for h and T´ such that $h < T' < N$. Accordingly, a value h can be chosen arbitrarily. Then, we may choose $T' \sim rh$, where r is a constant larger than unity, and $f_d(t,\omega')$ is "pilot-estimated" for several values of t. Recall, from (4.1b), that the dimensionless variance of the estimates is given by

$$\frac{\text{var } \hat{f}_d(t,\omega')}{f_d^2(t,\omega')} \sim \frac{4h}{3T'} \sim O(\frac{1}{r}) \tag{6.1}$$

Therefore, the larger r is, the more stable the pilot-estimates will be. It now becomes possible to estimate B_o and B_f on the basis of the pilot-estimates of $f_d(t,\omega')$ and according to the definitions of these parameters conceptually illustrated in Figure 1. After B_o and B_f are computed, using one of the design criteria discussed in Section 4, we determine "refined values" h and T´. The same procedure is iterated for enough number of times until the parameters B_o and B_f (therefore h and T´) simultaneously attain a convergent behavior. The spectral estimate $\hat{f}(t\Delta t,\omega)$ corresponding to the wave process is derived from the values $\hat{f}_d(t,\omega')$ in the convergent cycle through the transformation (3.4).

Intuitively, the success of the procedure would be affected by the degree of "smoothness" of the true spectral density $f(t\Delta t,\omega)$ as a function of t and ω. This is due to "blurring" and "smudging" effects of filtering and smoothing operations as discussed previously. The more detailed features of true $f(t\Delta t,\omega)$ as a function of t and ω are likely to be obscured by the estimation procedure.

7. APPLICATIONS

An Artificial Non-Uniformly Modulated Process

This example is a non-stationary process in discrete time with a frequency-domain representation of the following general form, i.e.,

$$x_t = \int_{-\pi}^{\pi} A(t,\omega)\, e^{it\omega}\, dZ(\omega) \tag{7.1}$$

In general, a process x_t of the form (7.1) has an equivalent interpretation in the time-domain in terms of a linear time-variant filter and a suitable stationary process (see Priestley [1]). For example, we may write

$$x_t = \sum_{u=-\infty}^{\infty} h_{t,u}\, V_{t-u}\ , \tag{7.2}$$

if we formally define

$$h_{t,u} = \frac{1}{2\pi} \int_{-\pi}^{\pi} A(t,\omega)\ e^{iu\omega}\ d\omega \tag{7.3}$$

as a time-variant filter, and specify V_t as a second-order stationary process of the form

$$V_t = \int_{-\pi}^{\pi} e^{it\omega}\ dZ(\omega) \tag{7.5}$$

in the frequency-domain. Note that $E|dZ(\omega)|^2 = f_v(\omega)d\omega$, with $f_v(\omega)$ defined as the spectral density corresponding to the stationary process V_t.

The theoretical spectral density, say $f_x(t,\omega)$, of the non-stationary process x_t is, by definition

$$f_x(t,\omega) = |A(t,\omega)|^2\ f_v(\omega) \tag{7.6}$$

In order to illustrate and test the estimation method and the iterative scheme on a non-uniformly modulated process of the form (7.1), we may now choose some explicit functional forms for the processes V_t and X_t such that

$$V_{t+2} + 0.5\ V_t = N_t \tag{7.7}$$

in which N_t are independent random variables, identically distributed as $N(0,3^2)$, and

$$A_{t,\omega} = 5\left(\frac{t}{500}\right)^2 \left\{\frac{e^{-0.2|\omega|}}{4}\left(\frac{t}{600}\right)^2 - e^{-0.1|\omega|}\ \frac{t}{600} + 1\right\} \tag{7.8}$$

where $|\omega| < \pi$, and $t = 0, 1, \ldots, 1400$. It can easily be shown that the process V_t given by (7.5) has a frequency-domain representation of the form (7.5) with

$$f_v(\omega) = \frac{3^2}{2\pi} \frac{1}{(0.25 + 2\cos^2\omega)}\ ,\ |\omega| < \pi \tag{7.9}$$

The above form of $A(t,\omega)$ is, for any frequency ω, basically a fourth-order polynomial of the form $at^4 + bt^3 + ct^2$. The coefficients as functions of the parameter ω are deliberately so chosen that the function $A(t,\omega)$ smoothly changes

with respect to t, and its transform with respect to ω, i.e., $h_{t,u}$ given by

$$h_{t,u} = \frac{5}{2\pi} \left(\frac{t}{600}\right)^2 \left\{\left(\frac{t}{600}\right)^2 \frac{0.1}{0.04+u^2} \left[(-1)^{u+1} e^{-.2\pi} + 1\right] - \left(\frac{t}{600}\right) \frac{0.2}{0.01+u^2} \left[(-1)^{u+1} e^{-.1\pi} + 1\right] + 2\pi \delta_{0,u}\right\} \tag{7.10}$$

falls off rapidly to zero as u becomes large. Therefore, these functional forms are of convenience in the simulation of a sample of x_t. This is done as follows: we first generate a sufficient number of independent normal variables with zero means and standard deviation 3 corresponding to N_t. A sample of V_t is obtained through (7.7) iteratively. In so doing, a sufficient number of initial V_t's are neglected to account for the transient. Finally, the sample x_t is obtained through (7.10) and (7.2), using only a finite number of terms in the summation. The sample simulated in the described manner is shown in Figure 2 for values t = 0, 10, ..., 1400, to give a general idea on the temporal behavior of the process studied.

The process parameters B_o (~210) and B_f (~0.70) are approximately estimated from the theoretical spectral density $f_x(t,\omega)$. For this example, a fixed frequency-time-domain resolution criterion with $\lambda = 1/2$, $\mu = 1/3$ is adopted. Therefore, from (4.6), we have h (~9) and T′(~240). The corresponding relative mean-square error is approximately 8%. Some of the theoretical spectra, $f_x(t,\omega)$, and the estimates $\hat{f}_x(t,\omega)$ at various times based on the simulated sample with the above values of h and T′ are illustrated in Figure 3 with solid and dashed lines (simulation 1), respectively. The estimates compare favorably with the theoretical ones, and indicate to the validity of the concepts and the estimation method.

Table 1 illustrates convergence of process and design parameters in the iterative procedure based on the same design criterion and two pairs of trial values h and T′. The convergent parameters h (~12), T′ (~210 and 220), B_o (~180) and B_f (~.5) compare fairly with those (i.e., h = 9, T′ = 240, B_o = 210, B_f = 0.70) obtained on the basis of a prior knowledge about the underlying process x_t. The estimates based on the iterated parameters h = 12 and T′ = 220 are also presented in Figure 3 by dotted solid lines (simulation 2) for comparison with the first estimates as well as the theoretical ones. In this case, again, the comparison is fairly satisfactory and indicates the validity of the iterative scheme.

Atlantic City Record

The example we consider here is a twenty-minute sample from the wave data collected at Atlantic City, New Jersey, on May 23, 1969 (14:00 ~ 14:20). The data was available in the form of punched cards, and sampled at intervals Δt = 0.25 sec. Table 2 shows the convergence of design and process parameters in interation based on the trial values h (~10 sec.) and T′ (~100 sec.), and a fixed frequency-domain resolution criterion with $\lambda = 1/2$. Some of the non-stationary estimates corresponding to the convergent parameter h (~24 sec.) and T′ (~270 sec.) are presented in Figure 4 at various times. The relative mean-square of an estimate at any time and frequency is approximately 13%.

For comparison, a stationary analysis was also performed on the same wave record. This is done using results of the non-stationary analysis for the special limit case of stationarity as described briefly in section 5. The stationary estimate, also shown in Figure 4, is similarly based on a frequency resolution of $\lambda = 1/2$, and a relative mean-square error of 6% with 60 equivalent degrees of freedom.

A comparison of the non-stationary spectral estimates at various times with the stationary estimate indicates that they generally differ in both magnitude and shape. The location of the major spectral peak and the magnitudes of the non-stationary estimates differ from the conventional in an unconservative manner, indicating that the wave field is in a general time-dependent state. We believe that the stationary analysis in this case, by smearing and smoothing out the temporal changes, may not provide all the critical spectral characteristics of waves.

	TRIAL VALUES	ITERATIONS				
		1	2	3	4	5
ATLANTIC CITY	h (sec) 10	16	21	22	24	24
	T' (sec) 100	172	216	260	270	270
	B_o (sec)	90	100	132	134	134
	B_f (sec^{-1})	.4	.3	.28	.26	.26
HURRICANE DORA	h (sec) 8	11	11	13	13	
	T' (sec) 120	176	220	280	284	
	B_o (sec)	90	120	160	165	
	B_f (sec^{-1})	.6	.56	.52	.5	

Table 2. Convergence of Parameters in Iteration For Atlantic City and Hurricane Dora Records.

Hurricane Dora

This is an approximately twenty-five minute sample from the wave data collected offshore Panama City, Florida, during Hurricane Dora while it crossed the northern part of Florida on September 9-10, 1965. The data was collected at a multi-legged tower (Stage I) in about 100 ft. of water at 11 nautical miles offshore. The record time of the waves examined here is 17:00 - 17:25 on September 10, the same data analyzed by J. I. Collins [14] through the conventional autocorrelation method of Blackman and Tukey.

On the basis of the trial values h (~8 sec.) and T´ (~120 sec.), and a fixed-frequency-domain criterion with $\lambda = 1/2$, the iterative scheme is carried out. The convergence of the parameters in iteration is presented in Table 2. Some of the non-stationary estimates corresponding to the convergent parameters h (~13 sec.) and T´ (~284 sec.) are presented in Figure 5 together with the stationary estimate obtained on the same record with respect to the same design criterion with $\lambda = 1/2$. The non-stationary estimates and the stationary one have 12% and 4% relative mean-square errors, respectively. The equivalent degrees of freedom corresponding to the stationary estimate is 150.

The non-stationary estimates generally differ from the stationary results. However, these differences in magnitude and shape are not very significant, indicating the waves are in a more or less steady state. In this case, we believe that the conventional analysis seems to provide the essential spectral characteristics of the wave field. This also confirms the fact that the results reduce to the conventional when stationarity dominates.

8. SUMMARY AND CONCLUSIONS

Priestley's estimation method and an approximate iterative procedure applicable to the realistic spectral analysis of ocean wave records with intrinsic non-stationarity have been examined. The validities of the concepts and the suggested iterative procedure have been tested with a simulated non-stationary process, and consequently applied to estimate time-dependent spectra for two wave records. Some characteristics results have been presented.

We may summarize the results of this study as follows: the results of the estimation method from a simulated non-stationary process compare favorably with the theoretical ones. This is especially true when the underlying spectrum changes smoothly with time and frequency. We believe that ocean wave records intrinsically satisfy these conditions. The subsequent application of the concepts to two actual wave records indicates that the time-dependent estimates generally differ in magnitude and form from the conventional stationary results. Differences in terms of magnitudes, shape and location of a major spectral peak are significant in one instance, but not so in the other. This may suggest that the stationary spectral analysis may not provide all the spectral characteristics of a wave process due to a smearing effect of the temporal changes. However, the method is generalized in the sense that the results reduce to the conventional if stationarity is dominant.

Note that the estimation method does not depend on an explicit knowledge of the modulating function $A(t,\omega)$. However, accuracy of the estimates directly relates to how "slowly" time-variant $A(t,\omega)$ is implicitly. During the conference presentation of the paper, J. I. Collins and L. E. Borgman raised the question whether one can determine the squared modulating function, $|A(t,\omega)|^2$. It seems that an approximate estimation of this function is possible via fitting a non-stationary time-series model with time-dependent parameters to the given sample record. For the details of such an approach, the reader is referred to the work of T. S. Rao [15].

It is hoped that this study, although limited in particular applications here, will provide some insight to the problem in general, as well as be a practical tool for application.

ACKNOWLEDGEMENTS

Support of this work is provided to the first author through a research fellowship by the Department of Civil Engineering; to the second author in part by the Office of Naval Research under contract 2-970-815 (N00014-69-A0407); and to the third author in part through a University Research Foundation Grant (2-970-414) from the University of Delaware. Data for Atlantic City was obtained through the courtesy of D. L. Harris of CERC, and that for Hurricane Dora through the courtesy of J. I. Collins of Tetra Tech. and C. Bennet of Naval Ship and Research Laboratory.

APPENDIX - REFERENCES

1. Priestley, M. B., "Evolutionary Spectra and Non-Stationary Processes," J. R. Stat. Soc., B, 27, 204-236 (1965).

2. Priestley, M. B., "Power Spectral Analysis of Non-Stationary Random Processes," J. Sound Vibr., 6, 86-97 (1967).

3. Priestley, M. B., "Design Relations for Non-Stationary Processes," J. R. Stat. Soc., B, 28, 228-240 (1966).

4. Tayfun, M. A., Yang, C. Y., and Hsiao, G. C., "On Non-Stationary Random Wave Spectra," Proc. First Inter. Symp. on Stochastic Hydraulics, Pittsburgh (1971).

5. Pierson, W. J., and Marks, W., "The Power Spectrum Analysis of Ocean Wave Records," Trans. Amer. Geophysical Union, Vol. 33, No. 6, 835-844 (1952).

6. Jenkins, G. M., and Watts, D. G., Spectral Analysis and Its Applications, Holden Day (1969).

7. Anderson, T. W., The Statistical Analysis of Time Series, John Wiley (1971).

8. Proc. of the Twelfth Coastal Engineering Conference, Vol. I, ASCE, Washington (1970).

9. Shinozuka, M., and Wen, Y. K., "Non-Linear Dynamic Analysis of Offshore Structures: A Monte Carlo Approach," Proc. First Inter. Symp. on Stochastic Hydraulics, Pittsburgh (1971).

10. Shinozuka, M., "Simulation of Multivariate and Multidimensional Random Processes," J. Acoustical Soc. America, Vol. 49, No. 1, 357-368 (1971).

11. Goda, Y., "Analysis of Irregular Wave Action for Engineering Design," Proc. First Inter. Symp. on Stochastic Hydraulics, Pittsburgh (1971).

12. Edge, G. L., and Mayer, P. G., "Dynamic Structure-Soil-Wave Model for Deep Water," J. of Waterways, Harbors and Coastal Engg. Div., Proc. ASCE, 97, WW1, 167-184 (1971).

13. Wilson, D. G., "A Procedure for Computing and Displaying Time-Varying Power Spectra Illustrated by Application to a Geophysical Process," Tech. Dep. 67, Chesapeake Bay Institute, The Johns Hopkins University (1970).

14. Collins, J. I., "Wave Statistics from Hurricane Dora," J. of Waterways and Harbors Div., Proc. ASCE, Vol. 93, WW2 (May 1967).

15. Rao, T. S., "The Fitting of Non-Stationary Time Series Models with Time-Dependent Parameters," J. R. Statist. Soc., B, 32, 312-322 (1970).

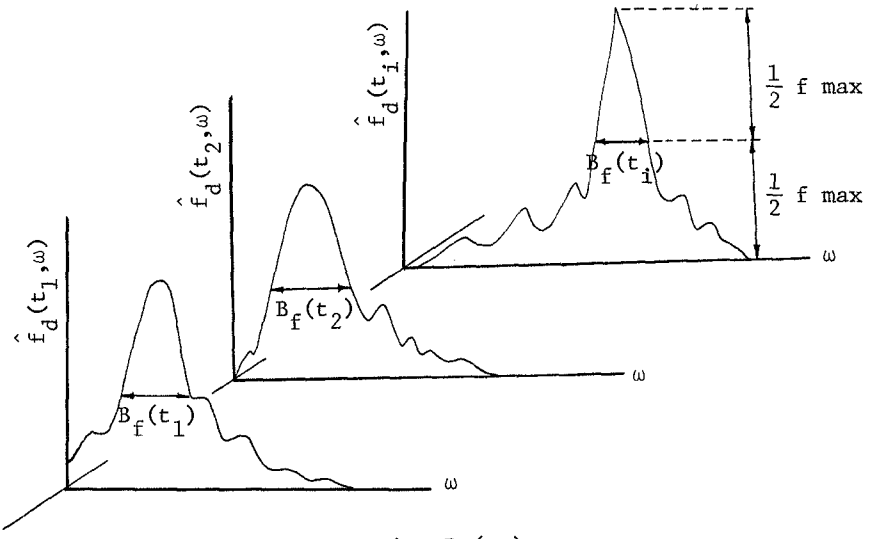

$$B_f = \min_{t_i} B_f(t_i)$$

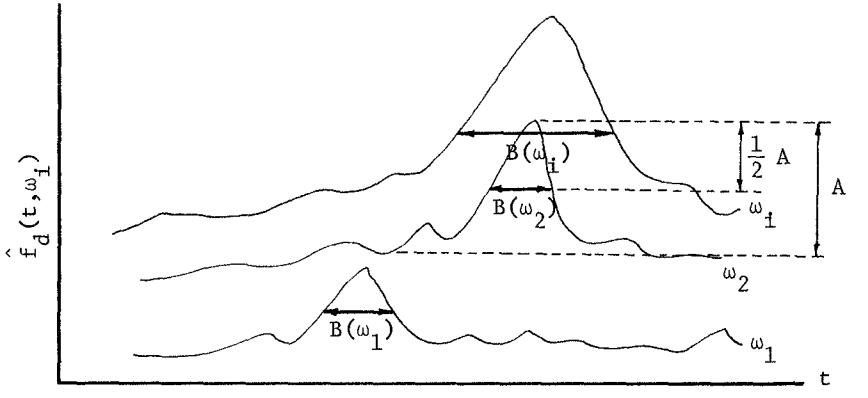

$$B_o = \frac{1}{2} \min_{\omega_i} B(\omega_i)$$

Figure 1. Estimation of B_o and B_f.

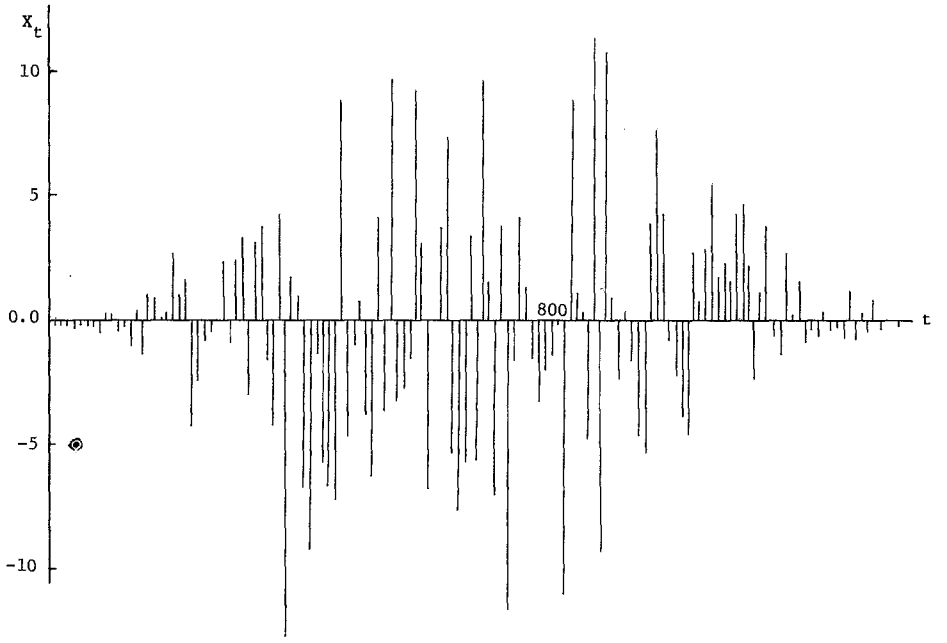

Figure 2. Simulated Non-Stationary Sample (t = 0, 10, ..., 1400).

TRIAL VALUES		ITERATIONS 1	2	3
h	5	9	12	12
T´	120	200	230	220
B_o		200	190	180
B_f		0.7	0.5	0.5
h	20	16	12	12
T´	350	230	210	210
B_o		200	180	180
B_f		0.4	0.5	0.5

Table 1. Convergence of Parameters in Iteration For the Simulated Example.

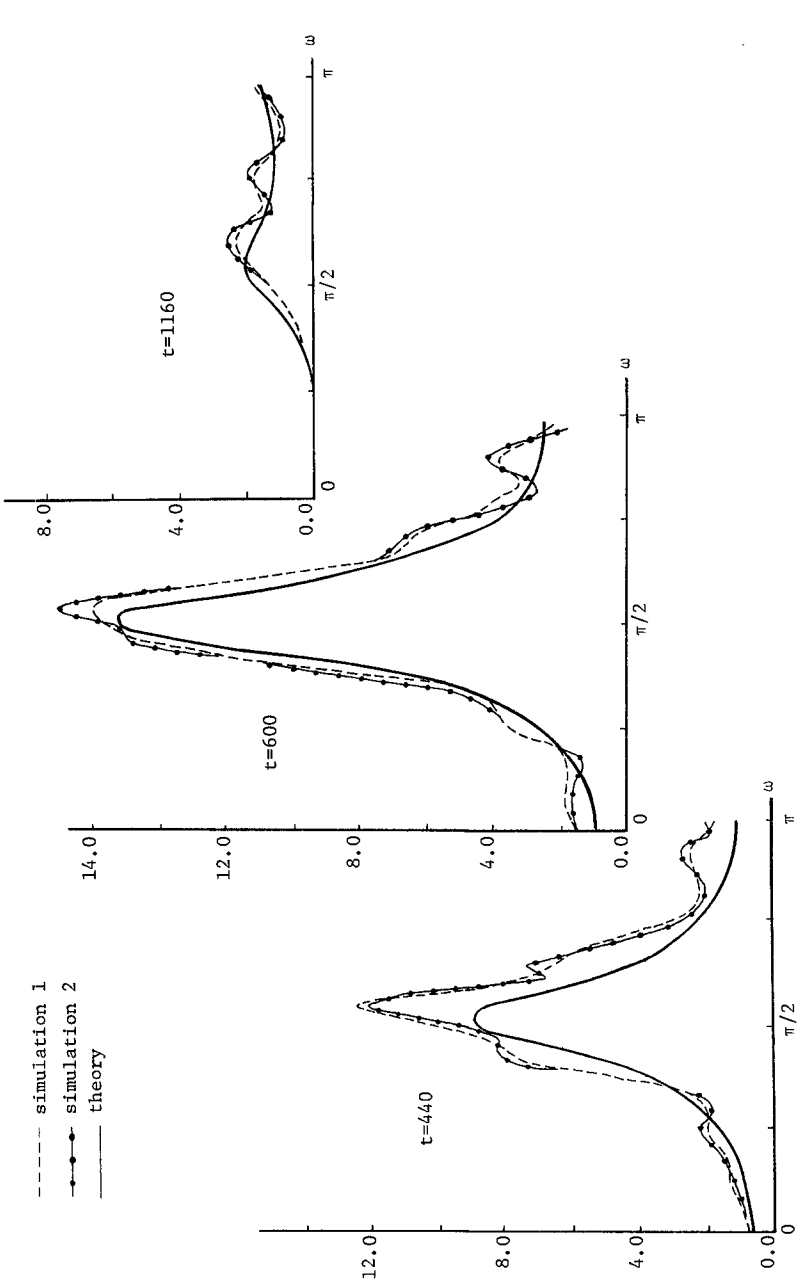

Figure 3. Non-Stationary Spectra for the Simulated Example.

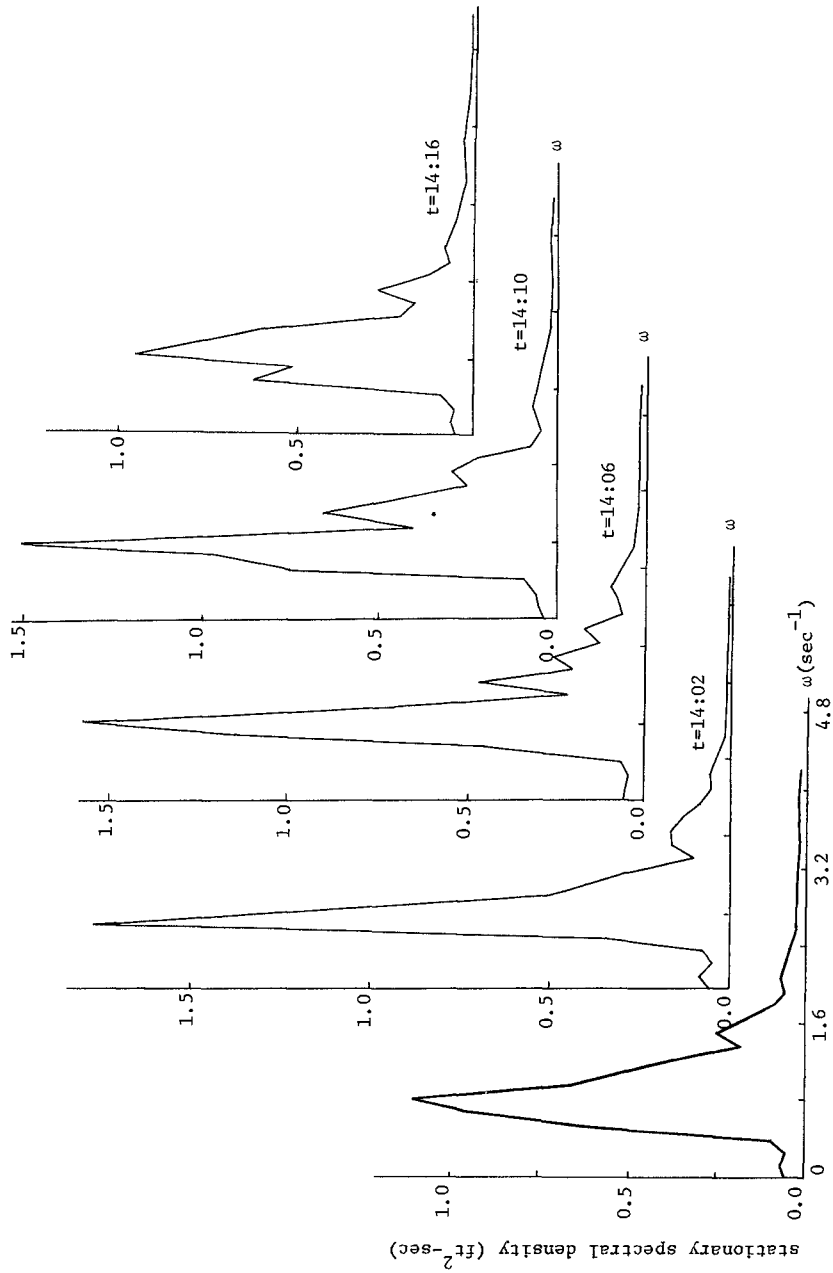

Figure 4. Stationary and Non-Stationary Estimates for Atlantic City.

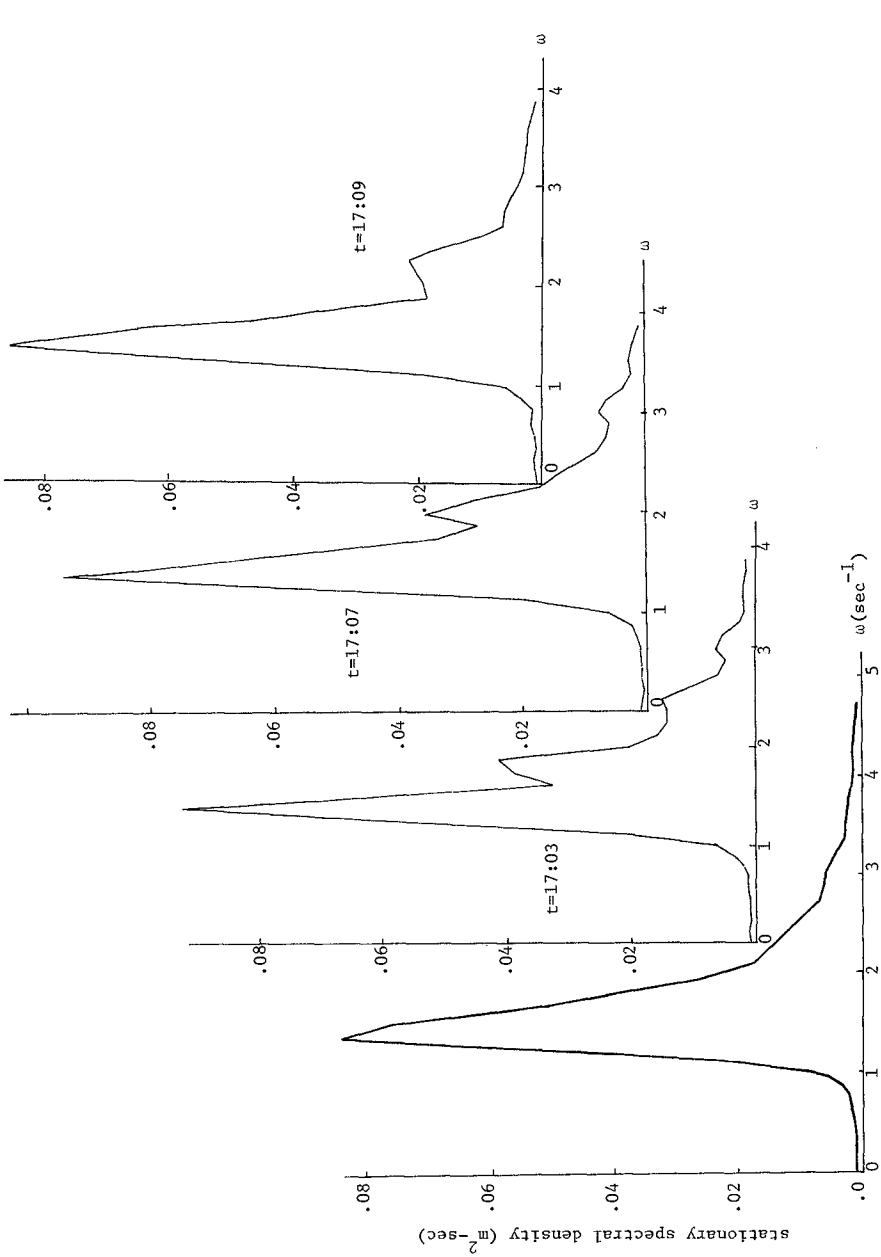

Figure 5. Stationary and Non-Stationary Estimates for Hurricane Dora.

CHAPTER 12

RESEARCHES ON THE DEFORMATION OF WAVE SPECTRA IN INTERMEDIATE WATER AREA BY CALCULATION

by

Frederick L. W. Tang, Dr. Eng.
Professor and Chairman
Hydraulic Engineering Department
National Cheng Kung University
Tainan, Taiwan, Republic of China

and

Shan-Hwei Ou
Graduate Student,
Ditto

ABSTRACT

In order to devise more rational approach to predicat the wave features in intermediate water area, energy spectra in deep water area are to be changed to histograms, and every stripe of the histogram is to represent an elementary small amplitude wave. The deformation of such elementary waves over intermediate water area can be calculated theoretically by energy flux equation. Spectra in intermediate area can be worked out by summing up the wave energies deformed by shoaling, bottom friction and refraction.

Calculation are carried out by computer. The peak of spectra will never change when it propagates from deep water to intermediate water area if the bottom contours are parallel to the shore line. Tangible process for using this approach to practical engineering problems is pending investigation.

1. INTRODUCTION

From a practical point of view, the semi-empirical relations for wave forecasting can be classified by two methods: the S-M-B method and the P-N-J method. Both methods utilize the wave height

distribution function derived theoretically by Longuet-Higgins, that is, the distribution of wave height is a Gamma distribution in a state of narrow band-width spectrum. The are related to the deep water. However, the transformation of irregular ocean waves over the water area where they feel the bottom is a complicated process which is not yet fully understood. One method of treating the problems is to represent the actual wave system by the superposition of elementary sinusodial wave series of different height, period, phase and direction. Such a system would have a two-dimensional energy spectrum. When the waves propagate over the intermediate water area, they are deformed by bottom friction, shoaling, refraction and percolation, etc. As an overall effects, the deformation of wave spectrum results that the wave height can no longer defined by the special type of Gamma distribution such as the Rayleigh distribution.

Traditional forecasting methods in shallow water were roughly due to Thijsse-Schijf (1949) and Bretschneider (1954) in two entirely different approaches. Nevertheless, they were done by making use the deep water forecasting relationships originally developed by S-M-B, and establishing an numerical procedure for computing the wave in shallow water (Tang, 1970), without regarding the complicated component waves.

A new approach of calculating the shallow water waves was first introduced by Bretschneider (1963) according to the shallow water spectrum. Also Karlsson (1969) calculated the shallow water waves from shallow water spectra on the effect of refraction only. In this paper a reasonable way has been made to investigate the deformation of wave spectra in intermediate water area by assuming the deep water spectra being already known. A special type of topographical configuration with constant bottom slope and parallel contour lines was adopted. Comparison of traditional forecasting method and the following method was made.

2. FUNDAMENTAL ASSUMPTIONS

The basic assumptions needed in this development are:

(1) The waves in deep water are assumed to be fully arisen, and have been existing for quite a long time. Consequently, the velocity dispersion is not necessary to be considered during calculation.

(2) Pierson-Moskowitz's one-dimensional spectrum (P-M spectrum) is to be adopted for calculation, i.e.

$$S(\sigma) = \alpha g^2 \sigma^{-5} \exp\left[\beta\left(\frac{g}{U\sigma}\right)^4\right] \qquad (1)$$

where $\alpha = 0.0081$

$\beta = -0.74$

g = gravity acceleration constant

U = Wind velocity

σ = angular frequency ($\sigma = \frac{2}{T}$), T = wave period

(3) The coordinate system to be used in this development is that shown in Fig. 1. The bottom slope is denoted by"s", water depth by "d" and wave direction by "θ". Whereas, the shallow water spectrum is a function of (x,y,z,σ,θ,d).

(4) Assumes that the shore line is straight and that the slope of sea bottom is uniform. So the contour lines are parallel to the shore line.

(5) The width of the fetch area of deep water waves is supposed to be considerably large, and the points of interest are located in the middle of the fetch width. Accordingly, the effect of angular spreading is not essential in this case.

(6) Each component wave which represents a stripe of histogram is small amplitude wave and its deformation in shallow water area is able to be calculated by following equation of energy flux.

$$(EGb)_1 - (EGb)_2 = -\frac{\partial (EGb)}{\partial x} = P_d\, b \qquad (2)$$

where G = group velocity
b = width between orthogonals
P_d = rate of energy dissipation between section 1 and 2
E = total wave energy per unit area
x = wave propagates direction

Neglecting the effect of infiltration, P_d is mainly due to internal and bottom friction.

3. SOME CONSIDERATIONS OF ONE-DIMENSIONAL SPECTRA IN INTERMEDIATE WATER AREA

The amount of friction losses was first given by Hough (1896) basing on the small amplitude wave theory. He found that

$$P_d = \frac{K}{2\pi}\int_{-d}^{0}\int_{0}^{L}\mu\left[\left(\frac{\partial w}{\partial x}-\frac{\partial u}{\partial z}\right)^2 - 4\left(\frac{\partial u}{\partial x}\frac{\partial w}{\partial z}-\frac{\partial u}{\partial z}\frac{\partial w}{\partial x}\right)\right]dx\,dz$$

$$= \frac{\pi^2\mu\beta H^2}{2T^2(\sinh kd)^2}\left[1+\frac{2K}{\beta}\sinh 2Kd+\cdots\right] \qquad (3)$$

where u and w are components of fluid velocity in x and z direction respectively; $k = \frac{2\pi}{L}$, L : wave length, μ : viscosity of fluid, $\beta = \left(\frac{\sigma}{2\nu}\right)^{\frac{1}{2}}$, $\sigma = \frac{2\pi}{T}$, $\nu = \frac{\mu}{\rho}$, T : period, ρ : unit mass of fluid, H : wave height.

3.1 Situation of predominant wave direction perpendicular to shore line

If the wave direction is perpendicular to shore line, every component wave front remains parallel to the contour lines when it propagates into shallow water. Then the width between any two orthogonals are constant. According to Eq. (2), we have

$$\frac{\partial (EG)}{\partial x} = G\frac{\partial E}{\partial x} + E\frac{\partial G}{\partial x} = -P_d \qquad (4)$$

The total wave energy E per unit surface area is given by

$$E = \frac{1}{8} \rho g H^2 \tag{5}$$

which is transmitted across the unit area with group velocity G. The group velocity changes from deep water into shallow water according to

$$G = n c = \frac{1}{2} \left(1 + \frac{2 kd}{\sinh 2 kd}\right) \frac{gT}{2\pi} \tanh kd \tag{6}$$

where c is the wave celerity and n is the transmission coefficient. From Fig. 1, we see

$$d = \frac{Lo}{2} - sx \tag{7}$$

where Lo is wave length in deep water, s is bottom slope, both d and s are positive values. We obtain following formulas from Eq. (7)

$$dx = -\frac{1}{s} d(d) = -\frac{1}{s} L \; 2n \, d\xi = -\frac{gT^2}{2\pi s} \frac{1}{k_s^2} d\xi \tag{8}$$

where $\xi = \frac{d}{L}$, $k_s^2 = \frac{2 (\cosh 2\pi\xi)^2}{\sinh 4\pi\xi + 4\pi\xi}$, which is the so-called shoaling coefficient.

By using Eq.(3), (5), (6), (8) together with changing variables, Eq. (4) can be expanded to yield

$$\frac{dH}{H} = J \, d\xi \tag{9}$$

where

$$J = -\frac{\pi (\sinh 4\pi\xi - 2\pi\xi \cosh 4\pi\xi + 2\pi\xi)}{(\cosh 2\pi\xi)^2 \left[(\sinh 2\pi\xi)^2 + 2\pi\xi \tanh 2\pi\xi\right]}$$

$$+ \frac{\sqrt{2}\, \pi \nu^{\frac{1}{2}} \sigma^{\frac{3}{2}}}{g s (\sinh 2\pi\xi)^2} + \frac{8 \pi \nu \sigma^3}{g^2 s} (\coth 2\pi\xi)^2 \tag{10}$$

By integrating Eq.(10) and seting the lower limit of integration

in deep water where $\xi_o = d/L_o = \frac{1}{2}$ and the upper limit in shallow water of any depth, we obtain

$$H/H_o = \exp\left(\int_{\xi_o}^{\xi} J \, d\xi \right) \tag{11}$$

where H_o is the wave height in deep water.

Since the power spectrum density for a particular frequency is proportional to the square of wave height, i.e., $S(\sigma)\, d\sigma \sim H^2$. The ratio of shallow water spectrum density, $S(\sigma)$, to the deep water spectrum density, $S_o(\sigma)$, results in

$$\frac{S(\sigma)}{S_o(\sigma)} = \exp\left[2 \int_{\xi_o}^{\xi} J \, d\xi \right] \tag{12}$$

Using P-M spectrum, the shallow water one-dimensional frequency spectrum in this case is written as follows:

$$S(\sigma) = 0.0081 g^2 \sigma^{-5} \exp\left[-0.74 \left(\frac{g}{U\sigma} \right)^4 \right] \cdot \exp\left[2 \int_{\xi_o}^{\xi} J \, d\xi \right] \tag{13}$$

Each stripe of histogram of shallow water spectrum based on Eq.(13) at the place where $d/L_{op} = 0.2$ (L_{op} is the deep water wave length of optimum frequecy wave) were plotted smoothly in Fig. 2. The dash line was given by Tsuchiya and Inoue (1961), which was based on the wave decay due to bottom friction in the uniform slope sea bottom. It gave

$$\ln\left(\frac{H}{H_o} \right) = -4\pi^2 \sqrt{\pi} \left(\frac{\nu}{g^2 T^3} \right)^{\frac{1}{2}} \cdot \int_{\xi}^{\xi_o} \frac{\tanh 2\pi\xi + 2\pi\xi \left(\operatorname{sech} 2\pi\xi \right)^2}{\left(1 + 4\pi\xi \operatorname{csch} 4\pi\xi \right) \tanh 2\pi\xi \left(\sinh 2\pi\xi \right)^2} \, d\xi$$

$$- \frac{\ln\left[\left(1 + 4\pi\xi \operatorname{csch} 4\pi\xi \right) \tanh 2\pi\xi \right]}{2 \left(1 + 4\pi\xi_o \operatorname{csch} 4\pi\xi_o \right) \tanh 2\pi\xi_o} \tag{14}$$

Eq. (13) can be computed by numerical procedure to yield significant wave height. Fig. 3 shows the corresponding variation of the ratio of the shallow water significant height, H_s, to the deep water

significant wave height, H_{os}, for various values of d/L_{op}.

3.2 Situation of predominant wave direction inclined to shore line

In the case of wave direction inclined to the shore line, the waves are affected by refraction that tend to align the their fronts to the depth contours.

Eq. (2) to be written as

$$b \frac{\partial (EG)}{\partial x} + (EG) \frac{\partial b}{\partial x} = -P_d \, b \tag{15}$$

By utilizing Snell's law directly, following equation is obtained

$$b = \frac{b_o}{\cos \theta_o} \sqrt{1 - (\tanh 2\pi\xi \sin \theta_o)^2} \tag{16}$$

where b_o is the width between two orthogonals in deep water, and θ_o is the angle between the deep water wave and the contour line.

Substituting Eq. (3), (5), (6) and (16) in Eq.(15), we obtain

$$\frac{\partial (EG)}{\partial \xi} + (EG) f(\xi, \theta_o, \sigma) = 0 \tag{17}$$

where

$$f(\xi, \theta_o, \sigma) = \frac{2\pi \tanh 2\pi\xi (\sin \theta_o \operatorname{sech} 2\pi\xi)^2}{(\sin \theta_o \tanh 2\pi\xi)^2 - 1} - \frac{4\sqrt{2}\,\pi \nu^{\frac{1}{2}} \sigma^{\frac{3}{2}}}{g s} \left[1 + \frac{4\sqrt{2}\,\nu^{\frac{1}{2}} \sigma^{\frac{3}{2}}}{g} (\cosh 2\pi\xi)^2 \right] \tag{18}$$

Integrating Eq. (17) to give

$$\frac{EG}{(EG)_o} = \exp\left[- \int_{\xi_o}^{\xi} f(\xi, \theta_o, \sigma) \, d\xi \right] \tag{19}$$

The symbol "O" refers to the case of deep water. Hence

$$\frac{H^2}{H_o^2} = \frac{S(\sigma)}{S_o(\sigma)} = K_s^2 \exp\left[- \int_{\xi_o}^{\xi} f(\xi, \theta_o, \sigma) \, d\xi \right] \tag{20}$$

where $K_s^2 = \frac{G_o}{G} = C_o/2nc$

Using P-M spectrum, the shallow water spectrum in this case is to be the following form

$$S(\sigma) = 0.0081\, g^2 \sigma^{-5} \exp\left[-0.74\left(\frac{g}{U\sigma}\right)^4\right]$$

$$\cdot K_s^2 \exp\left[-\int_{\xi_0}^{\xi} f(\xi, \theta_0, \sigma)\, d\xi\right] \qquad (21)$$

For S = 0.05, U = 30 Knots, $\theta_0 = \pi/12$, the relationship between H_s/H_{os} and d/L_{op} is shown in Fig. 4

4. DEFORMATION OF DIRECTIONAL SPECTRUM IN INTERMEDIATE WATER AREA AND ITS COMBINATION

In the foregoing sections we use the one-dimensional frequency spectrum in deep water to compute the frequency spectrum in shallow water. And assume that every component wave serves is a simple sinusodial wave. In this section, we will take a more reasonable approach, namely the directional spectrum is to be used to calculate the deformation in shallow water, and then combine the shallow water directional as well as frequency spectrum to give the wave characteristics.

For practical use, the directional spectrum may be obtained from the Pierson-Moskowitz's spectrum for a fully developed sea and the directional function such as that obtained in the Stereo Wave Observation Project (SWOP), or that used by Pierson, Neumann and James (1955).

The directional function used by P-N-J and later adopted in the so-called DSA forecasting method has the form

$$\theta(\theta) = \begin{cases} \frac{2}{\pi}\cos^2\Omega & |\Omega| < \frac{\pi}{2} \\ 0 & |\Omega| > \frac{\pi}{2} \end{cases} \qquad (22)$$

where $\Omega = \theta - \psi_0$, θ is the travel direction of any component wave, ψ_0 is the predominant direction of the combined waves.

We designate the incident angle in deep water of predominant direction by ψ_0, as shown in Fig. 5. For any component wave of angular frequency σ_i and travel direction θ_j, the directional spectrum in deep water is then given by

$$S_0(\sigma_i, \theta_j) = 0.0081 g^2 \sigma_i^{-5} \exp\left[-0.74\left(\frac{g}{U\sigma_i}\right)^4\right] \cdot \frac{2}{\pi} \cos^2(\theta_j - \psi_0) \quad (23)$$

whereas the corresponding shallow water directional spectrum is obtained according to Eq. (20) as follows

$$S(\sigma_i, \theta_j') = S_0(\sigma_i, \theta_j) K_s^2 \exp\left[-\int_{\xi_0}^{\xi} f(\xi, \theta_j, \sigma_i) d\xi\right] \quad (24)$$

Shallow water frequency spectrum is written as

$$S(\sigma_i) = \int_0^{2\pi} S(\sigma_i, \theta_j') d\theta_j' \quad (25)$$

where θ_j' is the refracted direction angle in shallow water which was originally denoted by θ_j in deep water.

From Snell's law

$$d\theta_j' = \frac{\tanh 2\pi\xi \cos\theta_j}{\sqrt{1 - (\tanh 2\pi\xi \sin\theta_j)^2}} d\theta_j \quad (26)$$

Consequently, we finally obtain the frequency spectrum of shallow water as follows

$$S(\sigma_i) = \int_\alpha^\beta 0.0081 g^2 \sigma_i^{-5} \exp\left[-0.74\left(\frac{g}{U\sigma_i}\right)^4\right] \frac{2}{\pi} \cos^2(\theta_j - \psi_0)$$
$$\cdot K_s^2 \exp\left[-\int_{\xi_0}^{\xi} f(\xi, \theta_j, \sigma_i) d\xi\right] \frac{\tanh 2\pi\xi \cos\theta_j}{\sqrt{1 - (\tanh 2\pi\xi \sin\theta_j)^2}} d\theta_j \quad (27)$$

where $\alpha = -\frac{\pi}{2} + \psi_0$, $\beta = \frac{\pi}{2}$ because the component waves which direct toward offshore should be excluded here.

The double integrals were evaluated by using finite difference method for a single angular frequency. Fig. 6 and Fig. 7 show the deformation of frequency spectra at various values of d/L_{op} for

$\psi_o = 0^\circ$ and $\psi_o = \frac{\pi}{6}$ respectively. Fig. 8 shows the comparison of frequency spectrum deformation obtained from considering directional spectrum to that of neglecting direction function, with the value of d/L_{op}=0.2 and $\psi_o = 0$. Fig. 9 shows the relationship between the relation of significant wave height and the values of d/L_{op}.

5. COMPARISON IN RESULT OF FOREGOING METHOD AND THE TRADITIONAL METHOD

5.1 Traditional method

In order to compare the two method at the same basic conditions, Preison-Moskowitz's spectrum was adopted to calculate the deep wave height and period in the case of the fully arising spectrum in U = 30 knots, we have

$$H_o = 4\sqrt{E} = 5.31 \text{ m}$$
$$T_{op} = 11 \text{ sec} \qquad (28)$$

For bottom slope s = 0.002, the shore line locates far from the origin of coordinate system (Fig. 1) at the distance of x = 47,000 m.

The traditional method for calculating shallow water waves based on the equation shown by

$$H = K_s K_{ra} K_d H_o \qquad (29)$$

where K_s is the shoaling coefficient; K_{ra} is the refraction coefficient and can be obtained by drowing the refraction diagram with straight shore and parallel contours; K_d is the decay coefficient, here we consider friction loss only.

A numerical procedure is utilized by subdividing the whole distance x into small segments; in each increment Δx, the depth is considered constant; and numerical calculations are performed

step by step. The significant wave height at the depth d=10 m is computed to be H = 2.42 m, here we assumed the bottom friction coefficient f = 0.01.

5.2 The abovementioned method

As discussed in previous sections, the parameter d/L is a variable according to the wave period. Since wave length L is the function of period, the same value of d/L does not denote the same point in the shallow water. Hence, in practical computation, one must change the Eq.(27) into the parameter of depth d instead of relative depth d/L. Through long term of derivations, we obtain

$$S(\sigma) = \int_{-\frac{\pi}{2}+\Psi_0}^{\frac{\pi}{2}} 0.0081\, g^2 \sigma^{-5} \exp\left[-0.74\left(\frac{g}{U\sigma}\right)^4\right] \frac{2}{\pi} \cos^2(\theta_j - \Psi_0)$$

$$\cdot \exp\left[\int_{0 \le L_0}^{d} \left\{ \frac{2\pi \left(\sin\theta_j \sinh\frac{2\pi d}{L}\right)^2}{\left[1-\left(\tanh\frac{2\pi d}{L}\sin\theta_j\right)^2\right]\left[L_0\left(\sinh\frac{2\pi d}{L}\right)^2 + 2\pi d\right]} \right.\right.$$

$$- \frac{8\pi\left(\frac{1}{2}\sinh\frac{4\pi d}{L} - \frac{\pi d}{L}\cosh\frac{4\pi d}{L} + \frac{\pi d}{L}\right)}{\left(\sinh\frac{4\pi d}{L} + \frac{4\pi d}{L}\right)\left[L_0\left(\sinh\frac{2\pi d}{L}\right)^2 + 2\pi d\right]} + \frac{4\sigma^3\nu\beta}{g^2 S}\left(\coth 2\frac{\pi d}{L}\right)^2$$

$$\left.\left. \cdot \frac{\left(1+\frac{4\pi d}{L\beta}\sinh\frac{4\pi d}{L}\right)}{\sinh\frac{4\pi d}{L} + \frac{4\pi d}{L}} \right\} d(d) \right] \frac{\tanh\frac{2\pi d}{L}\cos\theta_j}{\sqrt{1-\left(\tanh\frac{2\pi d}{L}\sin\theta_j\right)^2}}\, d\theta_j \qquad (30)$$

At the depth d = 10 m, the spectral density is shown in Fig. 10. We find that $H_{1/3} = 4\sqrt{E} = 1.51$ m.

6. SUMMARY AND CONCLUSION

(1) From the computation as shown in Fig. 6 and Fig. 7, the peak of spectrum will never change when wave propagates over the intermediate water area where the contour lines are parallel to the shore line. However, if the configuration of sea bottom is complex, the results will be different.

(2) The wave theory adopted herein was the linear wave theory. The foregoing method is adequate for the range of $d/L \geq 0.2$.

(3) The foregoing approaches did not take the effect of wind in transformation area into consideration, it can only be adequate to swell in the present state.

(4) In actual engineering problems, numerical method calculating spectra deformation on irregular sea bottom can be devised basing on abovementioned principles. However, it would not be accuracy until the caustic effect of wave rays has satisfactory explanation.

REFERENCES

(1) Bretschneider, C.L. (Technical Editor): Ocean wave Spectra, Proc., Conference sponsored by the U. S. Navy Oceangraphic Office and the Div. of Earth Sci., National Academy of Sci., National Res. Council Easton, Maryland, May 1-4, 1961. Prentice-Hall, Inc. Englewood Cliffs, N. J., 1963.

(2) Bretschneider, C. L. (1963): Modification of wave spectra on the continental shelf and in the surf zone, Proc. of 8th conference on coastal engineering, PP. 17-33.

(3) Bunting, D. C. (1970): Evaluating forecasts of ocean wave spectra, J. of Geophys. Res., 21, pp. 4131.

(4) Hasselmann, K., and Collins, J. I. (1967): Spectral dissipation of finite-depth gravity wave due to turbulent bottom friction, J. of Marine Res., vol. 26, No. 1.

(5) Harrison, W., and Wilson, W. S. (1964): Development of a method for numerical calculation of wave refraction, U. S. Coastal Eng. Res. Center, Tech. Memo., No. 6.

(6) Kinsman, B.: Wind wave, Prentice-Hall, Inc., Englewood Cliffs, N. J., 1965, Chap. 3, 4, 6, 7, 8, 9, 11.

(7) Kitaigorodskii, S. A. (1962): Application of the theory of similarity to the analysis of wind generated wave motion as a stochastic process, Izv. Akad. Nauk SSSR, Ser. Geofiz., 9, pp. 1221-1228; English Transl., 9, pp. 765-769, 1962.

(8) Karlsson, T. (1969): Refraction of continuous ocean wave spectra, Proc. of the Amer. Society of Civil Eng. pp. 437-448, WW4, Nov., 1969.

(9) Pierson, W. J., Jr., and Moskowitz, L. (1964): A proposed spectral form for fully developed wind sea based on the similarity theory of S. A. Kitaigorodskii, J. of Geophys, Pes., vol. 69, No. 24, 1964.

(10) Silvester, R. and Vongvisessomjai, S. : Energy distribution curves of developing and fully arisen seas, J. of Hyd. Res., IAHR, vol. 8, No. 4, pp. 493-521, 1970.

(11) Tang, Frederick L. W. (1970): Researches on the calculation of waves on long shoaling beacher, J. of Civil & Hydraulic Eng., National Cheng Kung Univ., Republic of China, vol. 1, pp. 105-164.

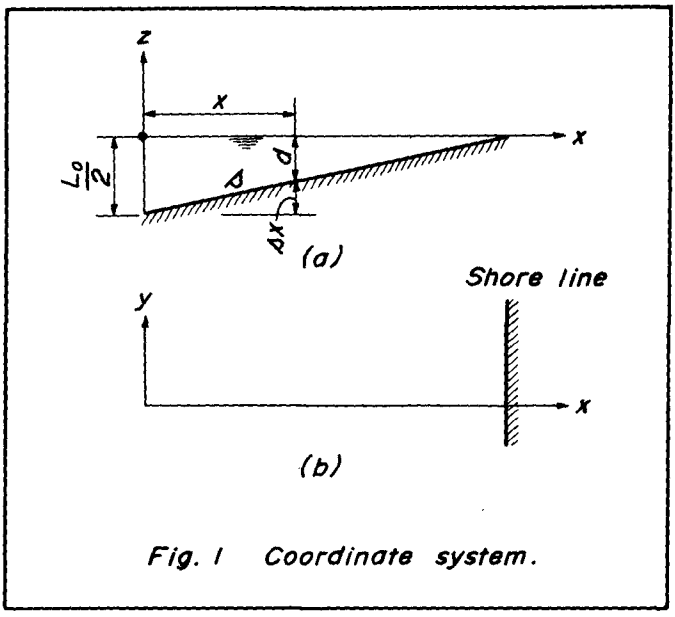

Fig. 1 Coordinate system.

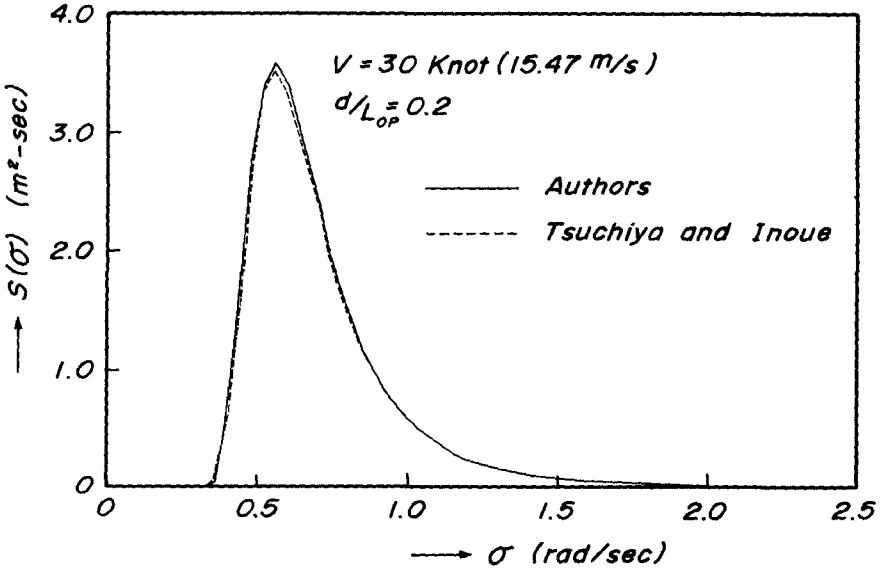

Fig. 2 Shallow water frequency spectrum.

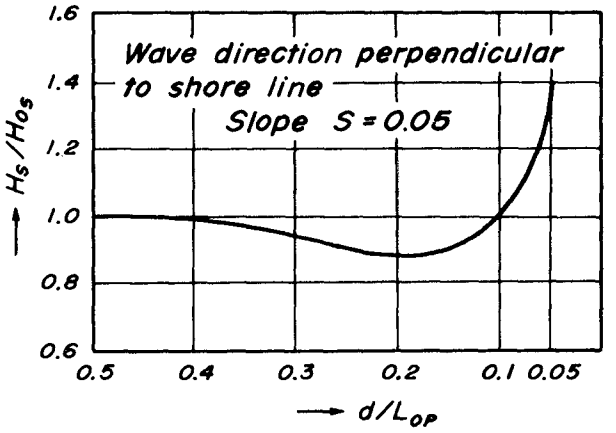

Fig. 3 Ratio of significant wave heights.

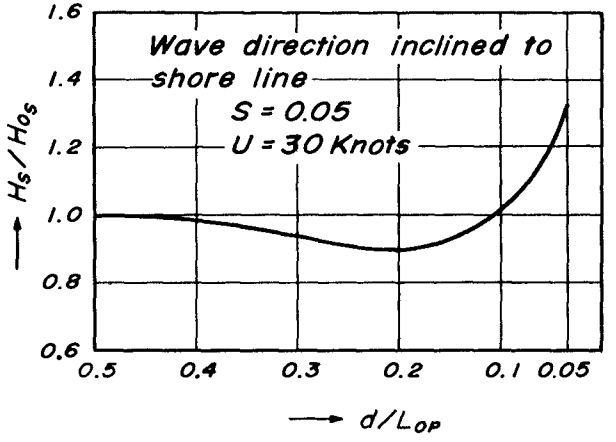

Fig. 4 Ratio of significant wave heights

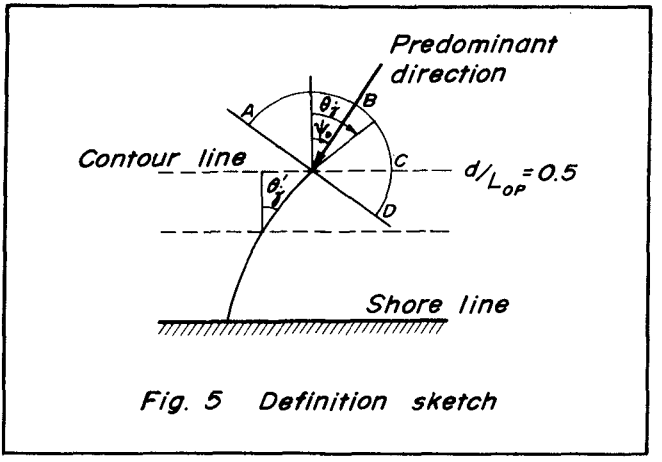

Fig. 5 Definition sketch

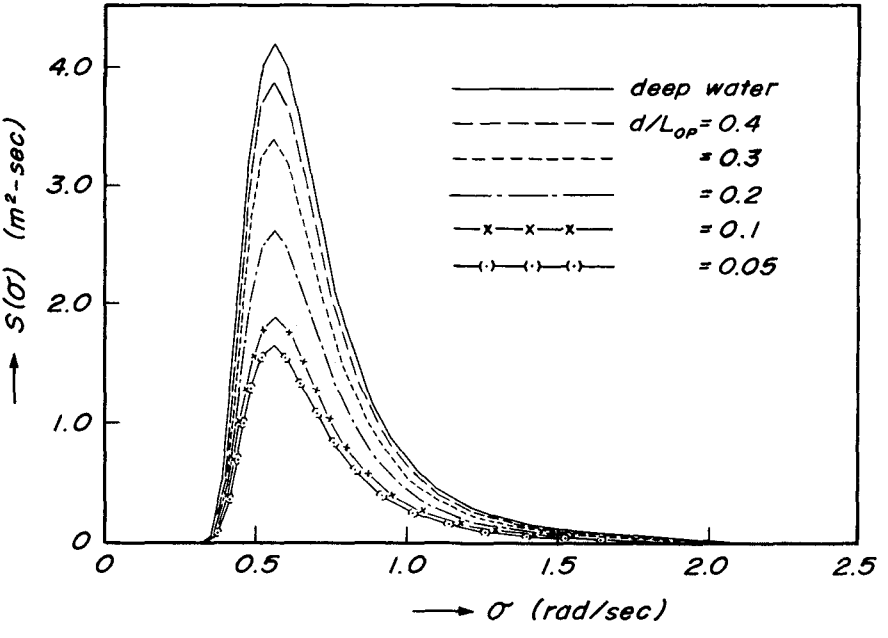

Fig. 6 Deformation of frequency spectra for $\psi_0 = 0°$

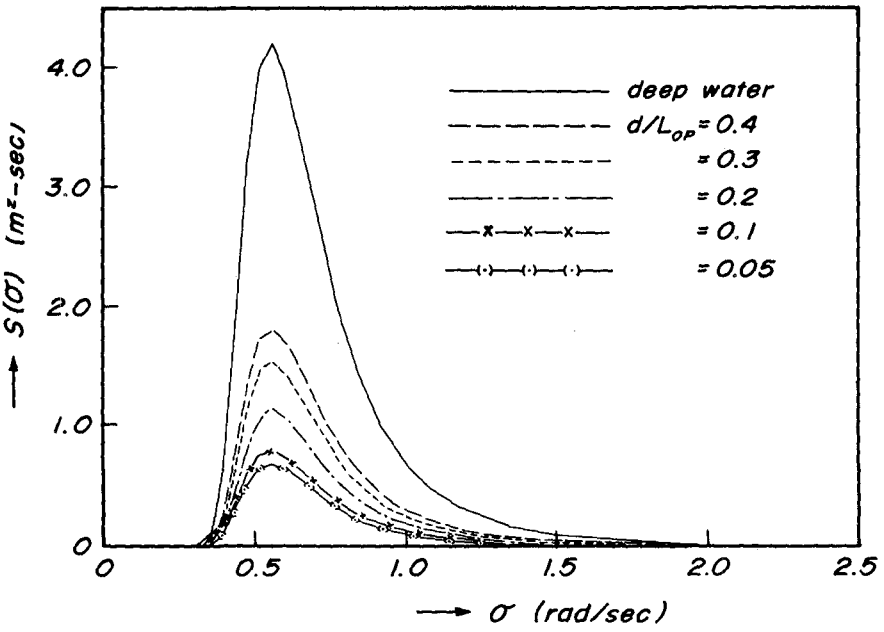

Fig. 7 Deformation of frequency spectra for $\Psi_0 = \frac{\pi}{6}$

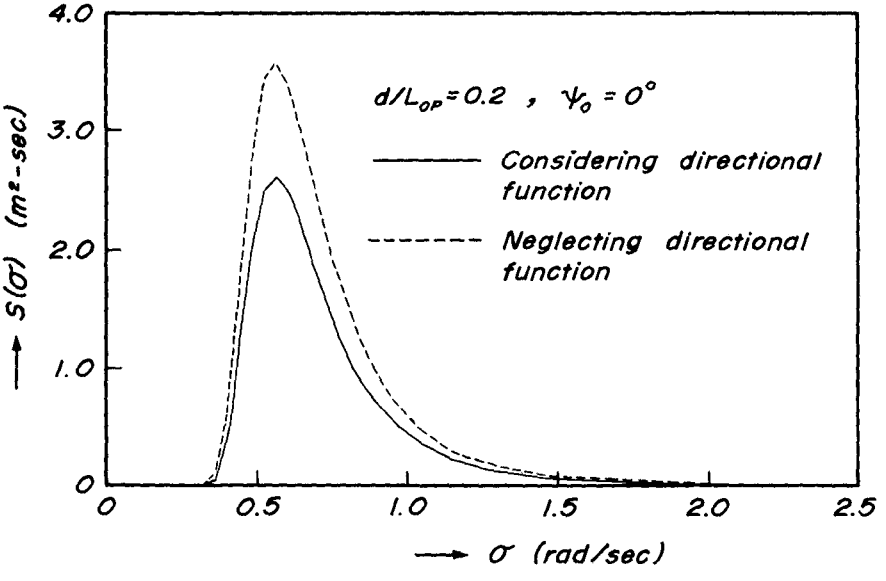

Fig. 8 Comparison of deformation of frequency obtained by different approaches.

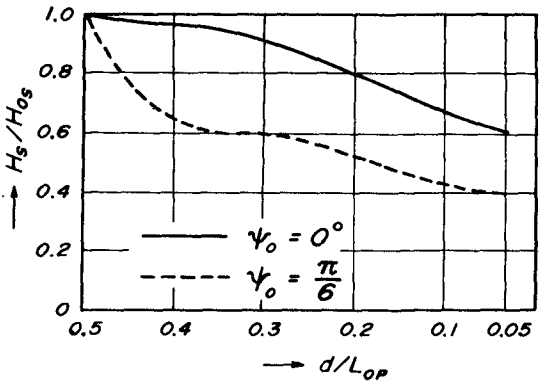

Fig. 9 Ratio of significant heights obtained from directional spectrum.

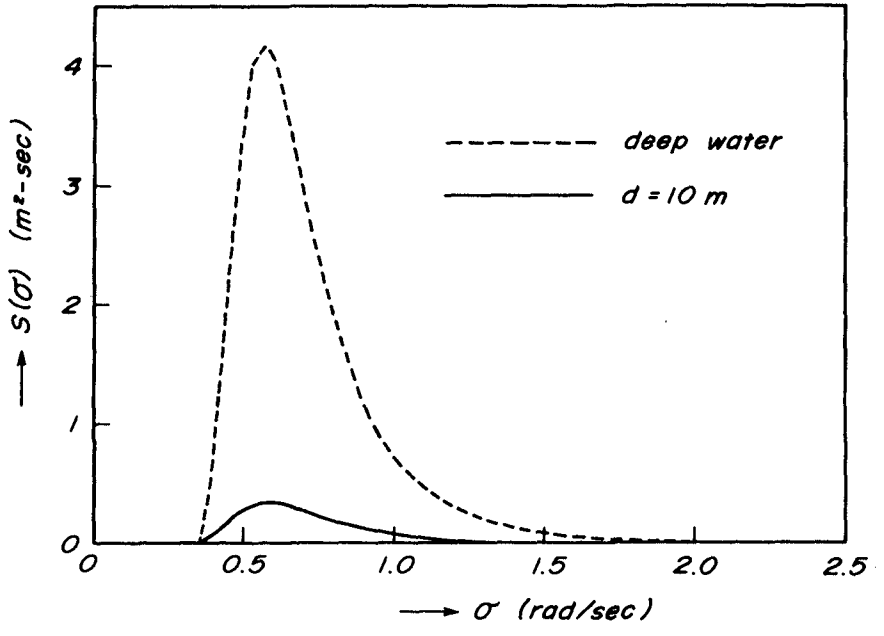

Fig. 10 Computed frequency spectral density.

CHAPTER 13

THE ONE-DIMENSIONAL WAVE SPECTRA AT LIMITED FETCH

Hisashi Mitsuyasu

Professor of Kyushu University,
Research Institute for Applied Mechanics,
Fukuoka, Japan.

ABSTRACT

The data for the spectra of wind-generated waves measured in a laboratory tank and in a bay are analyzed using the similarity theory of Kitaigorodski, and the one-dimensional spectra of fetch-limited wind waves are determined from the data. The combined field and laboratory data cover such a wide range of dimensionless fetch $\hat{F}$ (= gF/u_*^2) as $\hat{F}$: $10^2 \sim 10^6$. The fetch relations for the growthes of spectral peak frequency ω_m and of total energy E of the spectrum are derived from the proposed spectra, which are consistent with those derived directly from the measured spectra.

INTRODUCTION

In a series of recent papers (Mitsuyasu 1968, 1969 and 1970, hereinafter denoted by I, II and III) the author attempted to uncover the growth characteristics of the spectrum of wind-generated waves at short fetch. In I the low frequency part of the wave spectrum was mainly studied by using the wind and wave data measured in a laboratory tank and in a bay. The low frequency parts of the measured spectra were analyzed using the similarity theory of Kitaigorodski (1961), and the dependence on dimensionless fetch $\hat{F}$ of the constants " a " and " b " in the expression

$$\log_{10}\hat{\phi} = a + b\,\hat{\omega} \quad , \qquad (1)$$

where $\hat{\phi} = \phi(\omega)\,\omega^5/g^2$,

was determined from the data, where g is the acceleration of gravity, F the fetch, u_* the friction velocity of the wind, $\phi(\omega)$ the frequency spectrum of the wind waves, ω the angular frequency and $\hat{\omega}$ the dimensionless frequency defined by $\hat{\omega} = u_*\omega/g$. Patching together the spectral form for low frequency part and the equilibrium spectrum proposed by Phillips (1958), the author proposed the form of the wave spectrum at limited fetches. The fetch relation for the growth of the dimensionless spectral peak frequency $\hat{\omega}_m$ was determined from the proposed spectrum but the fetch relation for the growth of the dimensionless wave height $\sqrt{\hat{E}}$ (= $g\sqrt{E}/u_*^2$) was not determined due mainly to the difficulties of the mathematical integration of the proposed spectrum, where E

is total energy of the wave spectrum defined by

$$E = \int_0^\infty \Phi(\omega)\, d\omega \left(= \overline{\eta^2},\ \eta : \text{surface elevation}\right) . \quad (2)$$

In II a high frequency part of the measured wave spectrum was carefully analyzed by using the recent theory of Longuet-Higgins (1969) . It was shown that, as had been predicted by Longuet-Higgins, the equilibrium range constant β was not a universal constant but that β decreased with increasing the dimensionless fetch $\hat{F}$. A tentative empirical relation between β and $\hat{F}$ was determined from the various data of measured wave spectra. Detailed discussions were also made in II on the " overshooting and undershooting effects " of the spectra of wind-generated waves. The excess energy concentration of the wave spectrum near the spectral peak frequency was related to the overshooting effect of the spectral component in the stage of its growth with fetches.

In III the results of the earlier two studies I and II were summed up for obtainning the dimensionless spectral form $\hat{\Phi}$ $(= \Phi(\omega)\omega^5/g^2)$ of fetch-limited wind waves. That is, the following spectral form determined in I was used as the spectrum for low frequency part ;

$$\hat{\Phi} = 1.66 \times 10^{-9} \exp\left[3.94 \left(\hat{F} \right)^{0.283} \hat{\omega} \right], \quad \text{for } \omega < \omega_m , \quad (3)$$

The spectral form for high frequency part was determined from the results of study II as

$$\hat{\Phi} = \left[21.0 \log_{10} \hat{F} - 34.5 \right]^{-1} \quad \text{for } \omega > \omega_m . \quad (4)$$

The fetch relation for the growth of the dimensionless spectral peak frequency $\hat{\omega}_m$ could be obtained from the proposed spectrum (3) and (4), though the fetch relation for the dimensionless wave height $\sqrt{\hat{E}}$ could not be obtained from the proposed spectrum.

Recently, however, closed comparisons of the proposed spectrum (3) and (4) with the measured spectra have shown that the agreement between them is not so good in some cases. Furthermore, the agreement between the fetch relation for the growth of the dimensionless wave heicht $\sqrt{\hat{E}}$ directly measured and that obtained from the proposed spectrum by numerical integration of the spectrum has been shown to be not so good . Therefore, the author attempt in this paper to revise the spectral forms proposed in III in order to obtain the spectral forms which fit to the measured spectra more closely than the previous one. In the courses of the present study, reanalysis is done on the previous data, some new data have been added, and only the data carefully checked are used for determinning the spectral forms. Patching together the new results for high and low frequencies, the author proposes the revised form of the wave spectrum which can be useful for practical forcasting. The fetch relation for the growth of the dimensionless spectral peak frequency is determined from the revised form of the wave spectrum. The fetch relation for the dimensionless wave hight $\sqrt{\hat{E}}$ is also determined from the revised form of the wave spectrum by the numerical integration of the present spectrum. The both fetch relations agree quite well to those determined directly from the measured spectra.

WIND AND WAVE DATA

The wind and wave data used in the present study are almost the same to those used in our previous study I and II except that two new data measured in Hakata Bay are added. That is, the data obtained in a laboratory tank (Fig. 1) and in Hakata Bay (Fig. 2) are used. As shown in Fig. 1, the wave tank has been divided tentatively by the dividing wall and the ceiling connecting to the wind blower so as to form the ordinary wind-wave channel. In both measurements waves have been measured by capacitance-type wave gages and the vertical wind profiles over the water surface have been measured respectively by traversing a pitot-tube in the laboratory tank and by cup-anemometers at different heights of the observation tower (Fig. 3) in Hakata Bay. The friction velocity u_* of the wind has been determined by the application of the logarithmic law to the measured wind profiles. Many of the wind and wave data in Hakata Bay have been measured when the wind is blowing from the north, and corresponding fetch length is approximately 4.5 km. The spectral analysis of the wave data has been done in the ordinary Blackman-Tukey's method. The degrees of freedom of the measured spectra are approximately 90. The ranges of the dimensionless fetch $\hat{F}$ covered by the present data are $10^2 \sim 10^3$ for the laboratory data and $10^5 \sim 10^6$ for the field data.

SIMILARITY CONSIDEREATION OF THE WAVE SPECTRUM

Kitaigorodski (1961) extensively applied the similarity theory to the description of wave spectra. By a close analogy to the spectrum of turbulence, he has shown that the wave spectrum can be devided into various frequency ranges which respectively have different main controlling factors as schematically shown in Fig. 4. Furthermore, from considerations of similarity theory, he obtained the following general forms of the wave spectrum for each frequency range :

(1) linear [I] and intermediate [II] intervals, $\omega < \omega_0$,

$$\hat{\Phi} = F_1 (\hat{\omega}, \hat{F}), \qquad (5a)$$

$$F_1 = 10^{a + b\hat{\omega}} , \qquad (5b)$$

where " a " and " b " are the dimensionless constants which, in a general case, are the functions of $\hat{F}$.

(2) interval of small scale turbulence [III], $\omega_0 < \omega < \omega_1$,

$$\hat{\Phi} = \overline{\Psi}_1 (\varepsilon_m \omega / g^2) , \qquad (6)$$

where ε_m is the rate of energy dissipation from the frequency range with the maximum value of $\Phi(\omega)$ to the range of high frequencies corresponding to small-scale turbulence. By introducing the relation

$$\varepsilon_m = \alpha \, u_* g \qquad (7)$$

(6) becomes

$$\hat{\Phi} = \bar{\psi}_1 (\alpha \hat{\omega}) \quad , \qquad (8)$$

where α is a dimensionless constant which, in a general case, is a function of dimensionless fetch $\hat{F}$.

(3) equilibrium interval (Phillips 1958) [IV], $\omega_1 < \omega < \omega_2$ and $\omega \ll \omega_\gamma = (4g^3/\gamma)^{1/4}$,

$$\hat{\Phi} = \beta \quad , \qquad (9)$$

where γ is the ratio of surface tension σ to water density ρ_w , and β is a dimensionless constant (equilibrium range constant).

(4) interval of small-scale isotropic turbulence [V], $\omega_2 < \omega < \omega_4$,

$$\Phi(\omega) \sim \varepsilon_m \omega^{-4} = \alpha u_* g \omega^{-4} \quad , \qquad (10a)$$

or

$$\hat{\Phi} \sim \alpha \hat{\omega} \qquad (10b)$$

(5) capillary-turbulence interval [VI], $\omega_4 < \omega < \omega_5$,

$$\Phi(\omega) \sim \varepsilon_m \omega^{-4} \bar{\psi}_2 (\gamma^{2/3} \omega^{5/3} / \varepsilon_m)$$
$$\sim \alpha u_* g \omega^{-4} \bar{\psi}_2 (\gamma^{2/3} \omega^{5/3} / \alpha u_* g) \quad , \qquad (11a)$$

or

$$\hat{\Phi} \sim \alpha \hat{\omega} \bar{\psi}_2 (\gamma^{2/3} \omega^{5/3} / \alpha u_* g) \quad . \qquad (11b)$$

In addition to these spectra, he also proposed the following spectra ; gravity-capillary interval

$$\hat{\Phi}(\omega) \sim \psi (\gamma \omega^4 / g^3), \qquad (12)$$

and pure capillary interval

$$\Phi(\omega) \sim \gamma^{2/3} \omega^{-7/3} \quad . \qquad (13)$$

(12) can be considered as a more general formula of the equilibrium spectrum (9), where the frequency range is extended to higher frequency side and the capillary effect is included. (13) can be obtained when the effect of molecular viscosity is neglected in a pure capillary interval where the condition $\omega \gg \omega_\gamma$ is satisfied and $\Phi(\omega)$ does not explicitly depend on g.

In our present study, the discussions of the wave spectrum will be confined only to the gravity wave range in which the influences of the surface tension and molecular viscosity are neglisible, because the highest frequency of our measured spectra is at most 7 Hz which is smaller than f_γ ($= 1/2\pi \cdot [4g^3/\gamma]^{1/4}$) $\doteqdot$ 14 Hz. The interval of small scale

isotropic turbulence is tentatively neglected because, as will be shown later, the frequency dependence " ω^{-4} " of the measured spectra can not be found in our measured spectrum. Therefore, the frequency ranges of our measured spectra extend from the linear interval [I] to the equilibrium interval [IV] in the classification by Kitaigorodski. According to the above discussions the spectral form (8) can be modified into

$$\hat{\Phi} = \Psi_3 (\hat{\omega}, \hat{F}) . \qquad (14)$$

because α in (8) is assumed to be a function of $\hat{F}$. On the other hand, according to our previous study II equilibrium spectrum (9) can be shown, in a more general form, as

$$\hat{\Phi} = \beta (\hat{F}) , \qquad (15)$$

because β has been shown to be a function of $\hat{F}$. Comparing (5a), (14) and (15), it will be natural to assume that the general form of our measured spectrum which is in a frequency range $0 < \omega < \omega_2$ can be shown, in a general expression, as

$$\hat{\Phi} = \Phi (\hat{\omega} , \hat{F}) . \qquad (16)$$

LOW FREQUENCY PART OF THE WAVE SPECTRUM

Fig. 5 shows our measured spectra which are normalized according to (16). It will be seen from Fig. 5 that the functional form of (16) for the low frequency part $\omega < \omega_m$ can well be approximated by (1). In our previous study I, the dependence on the dimensionless fetch $\hat{F}$ of the constants " a " and " b " in (1) have been determined from three groups of data, i.e., the data obtained in our laboratory tank, the data obtained in Hakata Bay and Burling's data analyzed by Kitaigorodski (1961). In the present determinations of the constants, however, we will not use Burling's data, because the spectral form (1) is very sensitive to the value of " b " and Burling's data on " b " seem to deviate slightly but systematically from our data as shown in Fig. 6. Furthermore, some of our previous data are reanalyzed in order to obtain more reliable results.

Fig. 6 shows the revised relations between the dimensionless fetch $\hat{F}$ and the constants " a " and " b ", which have been obtained by using the reanalyzed data. Other data obtained by Burling (1959), Moskowitz (1964) and Stevens (1965) are shown for the comparison. The following simple relations can be obtained by the method of least squares :

$$a = -9.04 , \qquad (17)$$

$$b = 1.53 \hat{F}^{0.312} . \qquad (18)$$

On substituting (17) and (18) into (1) we can determine the functional form of the wave spectrum as

$$\hat{\Phi} = 9.12 \times 10^{-10} \exp 3.55 \hat{F}^{0.312} \hat{\omega} . \qquad (19)$$

(19) can be considered as the spectral form in a frequency range lower than the spectral peak frequency ω_m . It should be mentioned here that the spectrum $\Phi(\omega)$ derived from (19) has the minimum value at some frequency near $\omega_c = 0.3\ \omega_m$, the values of which depend weakly on the dimensionless fetch $\hat{F}$, and for $\omega < \omega_c$ $\Phi(\omega)$ increases with decreasing ω approaching finally to ∞ for $\omega \to 0$. Therefore, strictly speaking, (19) should be used for the frequency range greater than a cut-off frequency ω_c ($\fallingdotseq 0.3\ \omega_m$). This restriction for the spectral form introduces no problems for the practical applications of the spectrum, because the spectral energy at near the cut-off frequency ω_c is neglisibly small.

HIGH FREQUENCY PART OF THE WAVE SPECTRUM

The following equilibrium form proposed first by Phillips (1958) is used tentatively as the functional form of (16) for the high frequency part

$$\hat{\Phi} = \beta(\hat{F}) \qquad \text{for} \quad \omega > \omega_m \ , \qquad (20)$$

Although Phillips (1958) had conjectured β being universal constant, it was shown in our previous study II that β depend on the dimensionless fetch $\hat{F}$ as had been predicted by Longuet-Higgins (1969). It was also shown in II that high frequency part of the measured wave spectrum showed, in some cases, the oscillatory deviation from the spectral form given by (20)*). In other words, the " overshooting " and " undershooting " were seen in some of the measured spectra. These facts mean that β depend not only on dimensionless fetch $\hat{F}$ but also on dimensionless frequency $\hat{\omega}$. These results may be partly attributed to the facts that the equilibrium form (20) has been originally proposed only for the spectrum in some narrow frequency range

$$\omega_m \ll \omega \ll \omega_\beta \ , \qquad (21)$$

but we have applied it to the spectrum in such a wide frequency range as $\omega > \omega_m$. Therefore, the interval of small-scale turbulence, which is a function of $\hat{\omega}$ and $\hat{F}$ as shown in (8), is included in (20). However, if we take some kind of average of $\hat{\Phi}$ ($\hat{\omega}$, $\hat{F}$) with respect to $\hat{\omega}$ we can derive a functional form which is only a function of $\hat{F}$. The assumption of (20) for the spectral form for high frequency part corresponds to such procedure.

In II, β has been determined in three different ways, i.e., (i) β which is the mean value of $\hat{\Phi}$ with respect to $\hat{\omega}$ in a frequency range $\hat{\omega} > \hat{\omega}_m$, (ii) β_1 which is determined by

$$\beta_1 = \int_{\omega_m}^{\infty} \Phi(\omega)\, d\omega \Big/ \int_{\omega_m}^{\infty} g^2 \omega^{-5}\, d\omega \ , \qquad (22)$$

(iii) β_2 which is determined by the method of least squares, under the assumption that the spectral form is $\Phi(\omega) = \beta_2\, g^2\, \omega^{-5}$. The dependence of β defined by (i) on $\hat{F}$ has been mainly studied in II.

*) Such a characteristic can be seen in the laboratory spectra shown in Fig. 5.

However, we will use β_1 for the present study, because it is more reasonable to use β_1 for the discussion of the total energy of the wave spectrum. In the previous study II, the following relation has been determined by using the theory of Longuet-Higgins (1969) ;

$$\beta = [D \log_{10} \hat{F} - G]^{-1} \qquad (23)$$

D and G are dimensionless constants, and they have been determined from the measured values of β and $\hat{F}$. In the present study, however, the measured values of β_1 and $\hat{F}$, which has been also shown in II (Table 1)*), are used for determining, by the method of least squares, the constant D and G in (23). The relation finally obtained in the present analysis is given by

$$\beta_1 = [\, 24.3 \log_{10} \hat{F} - 47.1 \,]^{-1} . \qquad (24)$$

In addition to this relation, the following empirical relation is obtained from the same data ;

$$\beta_1 = 0.589\, \hat{F}^{-0.308} . \qquad (25)$$

As can be seen from Fig. 7 the relation (25) fits quite well to the observed results and it is better than the relation (24) within a range of $\hat{F}$: $10^2 \sim 10^6$. Therefore, the relation (25) will be used for the present study. Now, substituting (25) into (20), the high frequency part of the wave spectrum can be determined as

$$\hat{\Phi} = 0.589\, \hat{F}^{-0.308} . \qquad (26)$$

(26) can be considered as a kind of equilibrium spectrum of fetch-limited wind waves.

A. PROPOSED SPECTRUM OF WIND WAVES AT LIMITED FETCH

In the preceding sections, on the basis of the accurately measured wave spectra, we have experimentally determined the forms of the spectrum of wind waves at short fetches. Applying (19) to the spectrum in the low frequency range $\omega_c < \omega \lesssim \omega_m$, and (26) to that in the high frequency range $\omega \gtrsim \omega_m$, and defining conventionally the spectral peak frequency ω_m as the intersection of the both spectral forms one can get the spectral form of wind waves at limited fetch, which is schematically shown in Fig. 8. When the frequency is measured in cycles instead of radian, the proposed spectral form can be writen as

$$\hat{\Phi} = 5.86 \times 10^{-13} \exp [\, 22.1\, \hat{F}^{0.312}\, \hat{f} \,], \quad \hat{f}_c < \hat{f} \lesssim \hat{f}_m , \qquad (27)$$

$$\hat{\Phi} = 3.79 \times 10^{-4}\, \hat{F}^{-0.308}, \quad \hat{f} \gtrsim \hat{f}_m , \qquad (28)$$

where $\hat{f}$ is the dimensionless frequency defined by

$$\hat{f} = \hat{\omega} / 2\pi \quad (= u_* f / g) . \qquad (29)$$

*) In Table 1 β_1' is shown instead of β_1, but β_1 can be obtained from β_1' by using the relation $\beta_1 = (2\pi)^4 \beta_1'$.

Figs. 9a, 9b and 9c show some examples of the comparison of the measured spectra with the proposed spectrum. As can be seen from these figures, the proposed spectra fit quite well to the measured spectra.

At the intersection of the spectral forms (19) and (26) or (27) and (28), which corresponds to the spectral peak, the following relations are satisfied :

$$\hat{\omega}_m = (5.76 - 0.201 \log_{10} \hat{F}) \hat{F}^{-0.312}, \qquad (30)$$

$$\hat{f}_m = (9.17 - 0.320 \log_{10} \hat{F}) \times 10^{-1} \hat{F}^{-0.312}. \qquad (31)$$

(30) or (31) represents the fetch relation by which the dimensionless frequency of spectral peak can be determined as a function of the dimensionless fetch $\hat{F}$. (31) can be simplified, with sufficient accuracy, to the following equation*) ;

$$\hat{f}_m = 0.917 \hat{F}^{-0.327} \quad . \qquad (32)$$

(32) is very close to the following fetch relation which is determined directly from the measured spectra ;

$$\hat{f}_m = 1.00 \hat{F}^{-0.330} \quad . \qquad (33)$$

On the other hand, it is difficult to determine the fetch relation for the total energy of our proposed spectrum, because the integration of (19) or (27) is analytically difficult. That is, in order to obtain the fetch relation for the total energy of the proposed spectrum it is necessary to perform the following integrations ;

$$\begin{aligned} E = E_1 + E_2 &= \int_{\hat{f}_c}^{\hat{f}_m} \Phi \, d\hat{f} + \int_{\hat{f}_m}^{\hat{f}_N} \Phi \, d\hat{f} \\ &= 5.86 \times 10^{-13} \int_{\hat{f}_c}^{\hat{f}_m} (\hat{f})^{-5} \exp [22.1 \hat{F}^{0.312} \hat{f}] \, d\hat{f} \\ &\quad + 3.79 \times 10^{-4} \int_{\hat{f}_m}^{\hat{f}_N} (\hat{f})^{-5} \hat{F}^{-0.308} \, d\hat{f} \quad , \end{aligned} \qquad (34)$$

where $\hat{f}_c$ is the dimensionless cut-off frequency and $\hat{f}_N$ the dimensionless Nyquist frequency. The second integration can be easily done reducing to

$$E_2 = 9.48 \times 10^{-5} \hat{F}^{-0.308} [(\hat{f}_m)^{-4} - (\hat{f}_N)^{-4}], \qquad (35)$$

but the first integration is difficult. Therefore, the first integration has been done numerically for some typical values of $\hat{F}$ which are within the range $\hat{F} : 10^2 \sim 10^7$. The results have been then added to E_2 obtaining finally the total energy E . By using the values of the total energy E thus obtained corresponding to the dimensionless fetch $\hat{F}$, the following fetch relation has been determined by the method of least squares

$$\hat{E} \; (= g\sqrt{E} / u_*^2) = 1.22 \times 10^{-2} \hat{F}^{0.514} \quad . \qquad (36)$$

*) This is performed by taking the logarithm of the both sides of (31) and taking the first term in the expansion of the type of $\ln (1 - x) = -x - x^2/2 - \cdots\cdots$

(36) is very close to the following fetch relation obtained directly from the measured spectra ;

$$\hat{\sqrt{E}} = 1.13 \times 10^{-2} \hat{F}^{0.504} \quad . \qquad (37)$$

Fig. 10 shows the fetch relations for the growth of dimensionless spectral peak frequency $\hat{f}_m$ and for the growth of dimensionless wave height $\hat{\sqrt{E}}$, which have been determined directly from the measured spectra. Fig. 10 also includes the following fetch relations ;

$$\hat{f}_m = 9.46 \times 10^{-1} \hat{F}^{-1/3} \quad , \qquad (38)$$

$$\hat{\sqrt{E}} = 1.5 \times 10^{-2} \hat{F}^{1/2} \quad , \qquad (39)$$

which are determined from Wilson's formulas IV (Wilson 1965) under the present assumptions ;

$$U_{10} = 25\, u_* \quad , \qquad H_{1/3} = 4\sqrt{E} \quad , \qquad T_{1/3} = 1/1.05\, f_m \qquad (40)$$

Although the fetch relation (32) and (36) which have been determined from our proposed spectra are not shown in Fig. 10 to avoid the congestion of the figure, they are very close to our directly measured one and Wilson's one. Therefore, it can be said that the proposed spectrum not only fits quite well to the measured spectra but also gives quite accurate fetch relations both for f_m and for E . For convenience, the present spectral form will be called as Formula I (revised).

DISCUSSIONS AND CONCLUSION

In a previous paper (Mitsuyasu 1971), starting from a simple assumption that the general form of the wave spectrum can be given by

$$\phi(f) = k_1 f^{-5} \exp [- k_2 f^{-4}] \quad . \qquad (41)$$

where k_1 and k_2 are undetermined constants, and using the empirical fetch relations (33) and (37) for determining the constants k_1 and k_2, the author has derived the following spectral form of fetch-limited wind waves (Formula II).

$$\hat{\Phi} = 8.58 \times 10^{-4} \hat{F}^{-0.312} \exp [- 1.25 \hat{F}^{-1.32} \hat{f}^{-4}] \quad . \qquad (42)$$

It was also shown that (42) is almost the same to the simplified spectral form of Bretschneider (1968) and (42) approaches to the spectral form of Pierson-Moskowitz (1964) at near $\hat{F} = 10^7$.

Obviously, Formula II gives quite consistent results for the growthes of the spectral peak frequency f_m and of the total energy E of the wave spectrum, because the empirical fetch relations for f_m and E have been used in its derivation. However, slight differences exist between its spectral form and measured spectra particularly at a low frequency part and at near the spectral peak. In this respect, present spectral form [Formula I (revised)] gives much better agreement to the measured spectra, though its spectral form is not so simple as Formula II. Therefore, the selection of either spectra will depend on the application

purpose of the wave spectrum.

REFERENCES

Bretschneider, C. L. (1968) : Significant wave and wave spectrum, Fundamental in Ocean Engineering Part 7, Ocean Industry, Feb. 40 - 46.

Burling, R. W. (1959) : The spectrum of wave at short fetches, Dtsch. Hydrogr. Z. 12, 45 - 64, 96 - 117.

Kitaigorodski, S. A. (1961) : Applications of the theory of similarity to the analysis of wind-generated wave motion as a stochastic process. Izv., Geophys. Ser. Acad. Sci., U.S.S.R. I, 105 - 117.

Longuet-Higgins, M. S. (1969) : On wave breaking and the equilibrium spectrum of wind-generated waves. Proc. Roy. Soc. A, 310, 151 - 159.

Mitsuyasu, H. (1968) : On the growth of the spectrum of wind-generated waves (I). Rep. Res. Inst. for Appl. Mech., Kyushu Univ., Vol. XVI, No. 55, 459 - 482.

Mitsuyasu, H. (1969) : On the growth of the spectrum of wind-generated waves (II). Rep. Res. Inst. for Appl. Mech., Kyushu Univ., Vol. XVII, No. 59, 235-248.

Mitsuyasu, H. (1970) : On the growth of the spectrum of wind-generated waves, Coastal Engineering in Japan, Vol. 13, 1 - 14.

Mitsuyasu, H. (1971) : On the form of fetch-limited wave spectrum, Coastal Engineering in Japan, Vol. 14, 7 - 14.

Moskowitz, L. (1964) : Estimate of power spectrum for fully developed seas for wind speed of 20 to 40 knots, J. Geophys. Res., Vol. 69, No. 24, 5161 - 5179.

Phillips, O. M. (1958) : The equilibrium range in the spectrum of wind-generated waves, J. Fluid Mech., 4, 426 - 434.

Pierson, W. J. and Moskowitz, L. (1964) : A proposed spectral form for fully developed wind seas based on the similarity theory of S. A. Kitaigorodski, J. Geophys. Res., Vol. 69, No. 24, 5181 - 5190.

Stevens, R. G. (1965) : On the measurement of the directional spectra of wind generated waves using a linear array of surface elevation detectors, Reference No. 65 - 20, Woods Hole Oceanographic Institution. 118Pp.

Wilson, B. W. (1965) : Numerical prediction of ocean waves in the North Atlantic for December 1959, Dtsch. Hydrogr. Z. 18, 3 , 114 - 130.

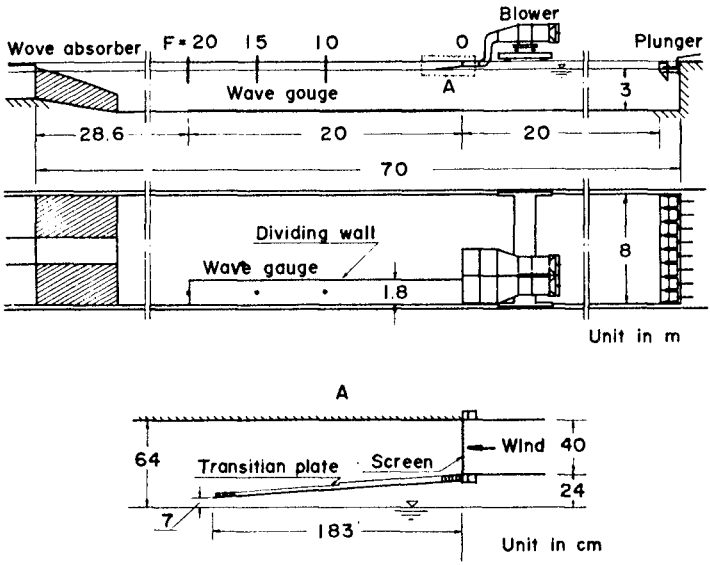

Fig. 1. WIND-WAVE FACILITY

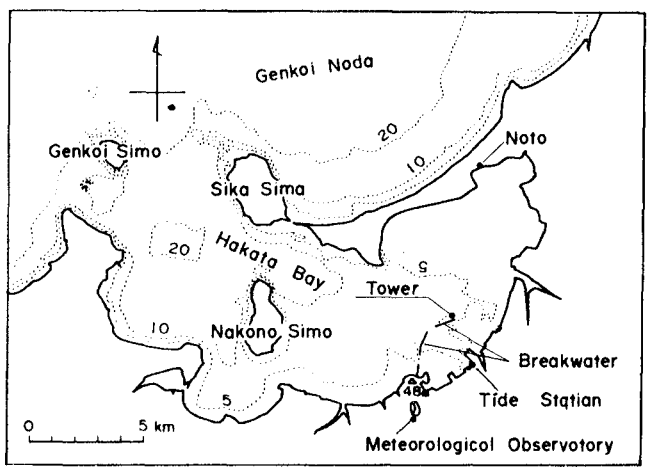

Fig. 2 SITE OF THE FIELD OBSERVATION
(HAKATA BAY)

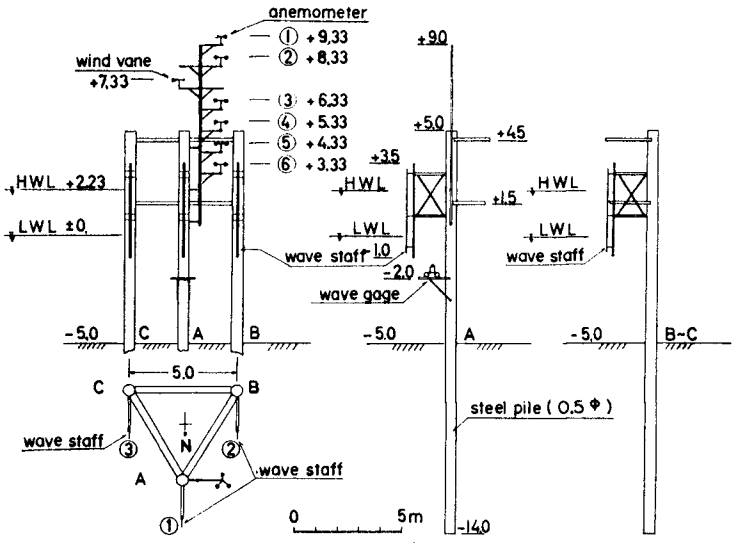

Fig. 3 OBSERVATION TOWER, UNIT IN M

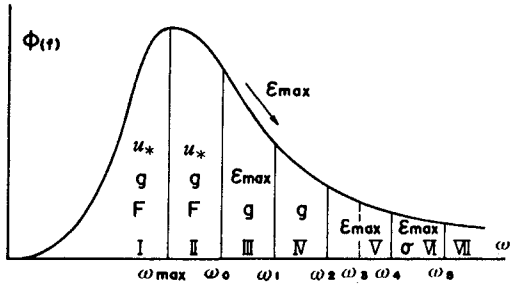

I linear interval
II intermediate interval
III interval of small scale turbulence
IV equilibrium interval (breaking)
V interval of small scale isotropic turbulence
VI capillary turbulence interval
VII dissipation interval

Fig. 4 SCHEMATIC REPRESENTATION OF WIND-WAVE SPECTRUM (KITAIGORODSKI, 1961)

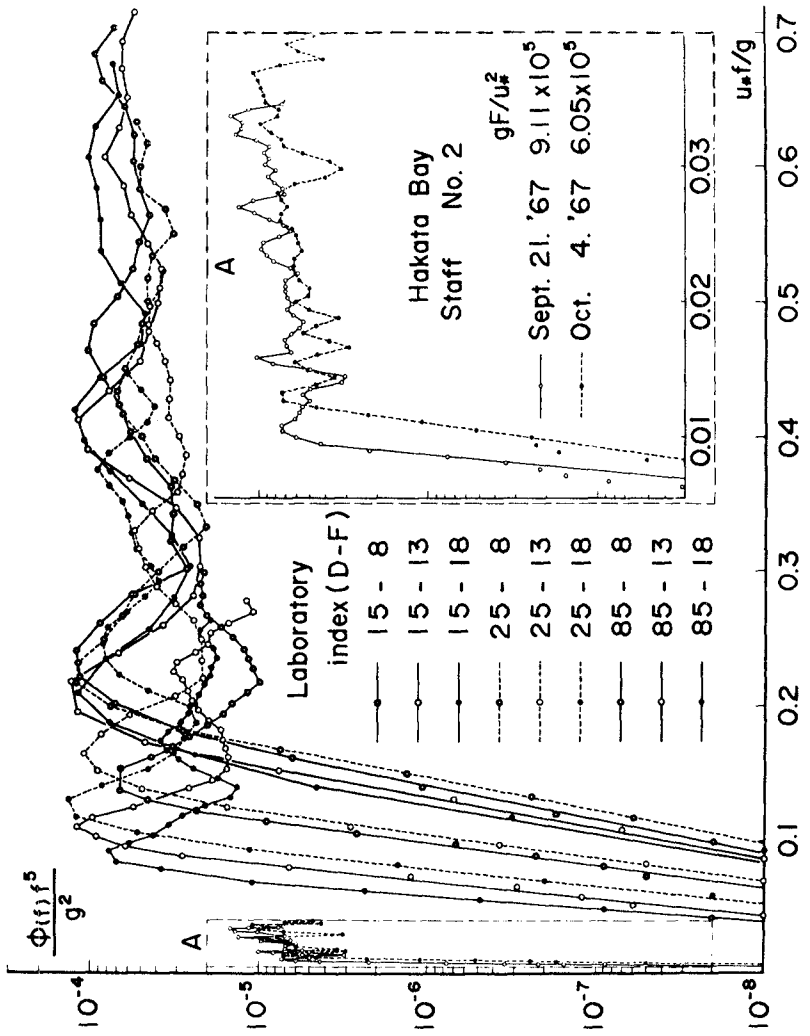

Fig. 5 NORMALIZED WAVE SPECTRUM

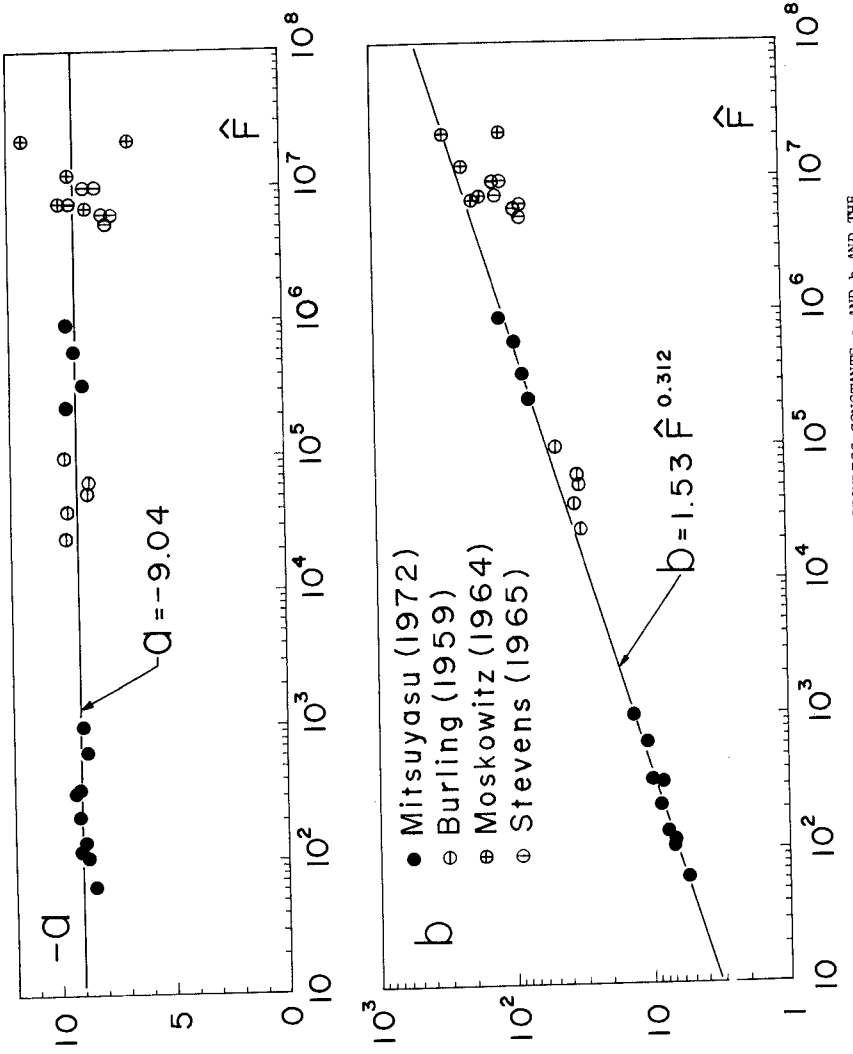

Fig. 6 THE RELATION BETWEEN DIMENSIONLESS CONSTANTS a AND b AND THE DIMENSIONLESS FETCH $\hat{F}$

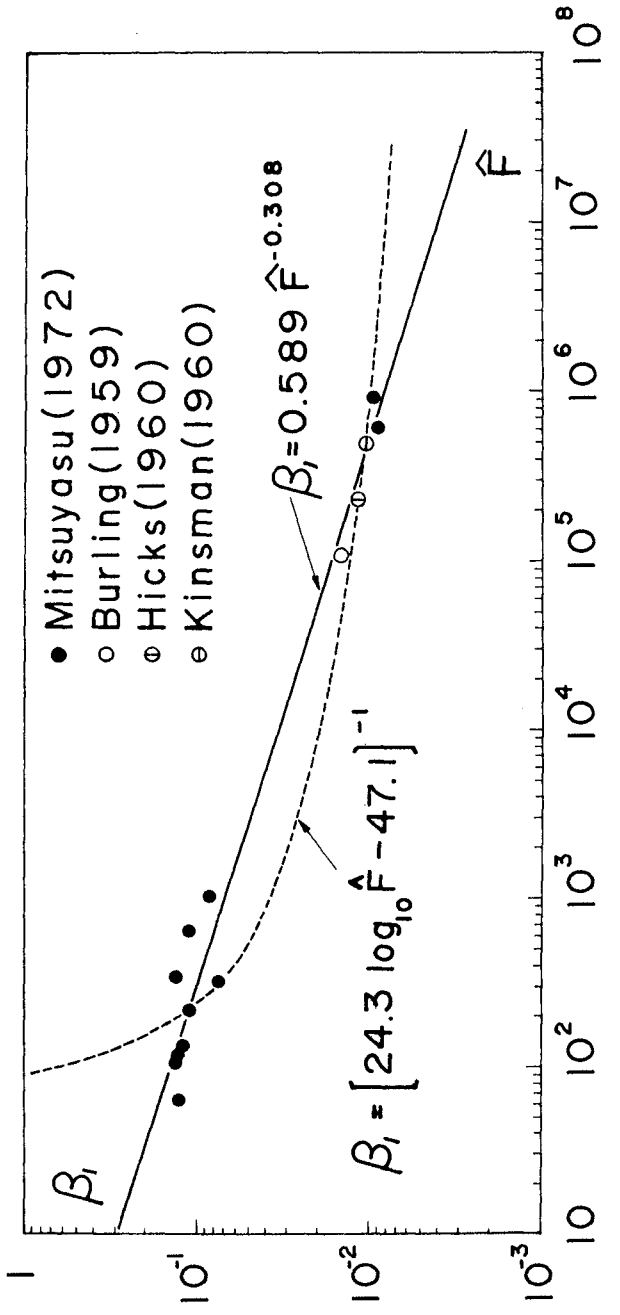

Fig. 7 THE RELATION BETWEEN EQUILIBRIUM RANGE CONSTANT β_1 AND THE DIMENSIONLESS FETCH $\hat{F}$.

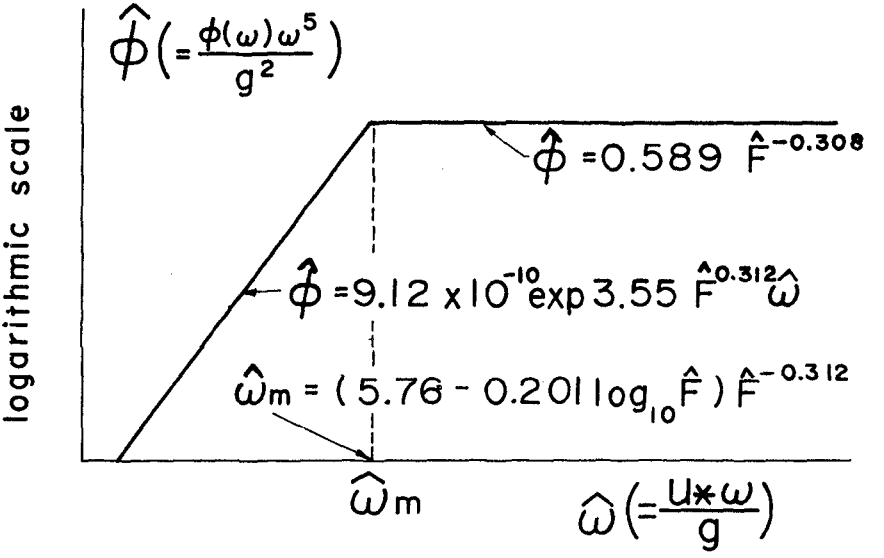

Fig. 8 PROPOSED FORM OF WIND-WAVE SPECTRUM

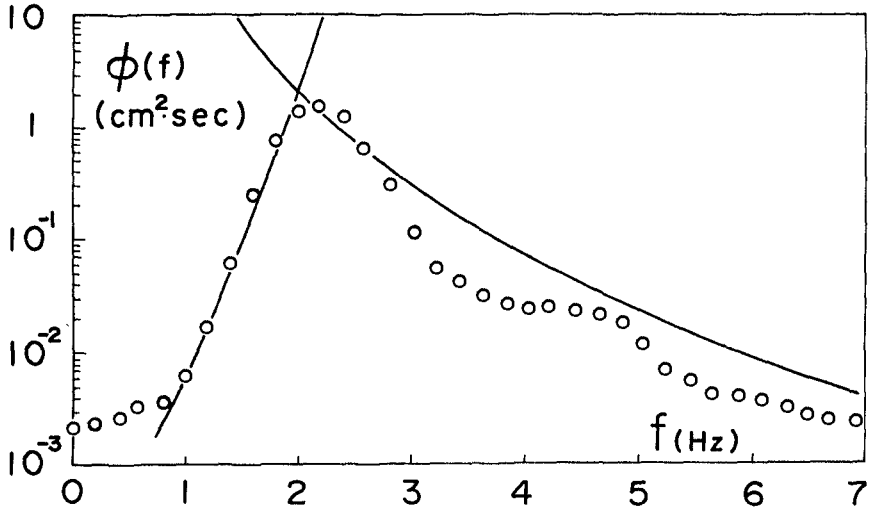

Fig. 9a COMPARISON OF THE PROPOSED SPECTRUM WITH THE MEASURED ONE.
(LABORATORY, $\hat{F} = 2.15 \times 10^2$)

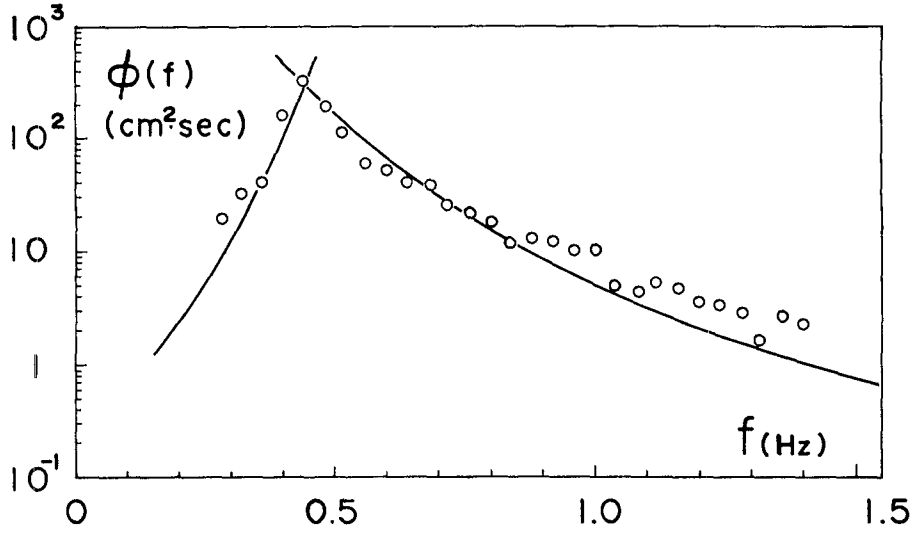

Fig. 9b COMPARISON OF THE PROPOSED SPECTRUM WITH THE MEASURED ONE.
(HAKATA BAY, $\hat{F} = 9.11 \times 10^5$)

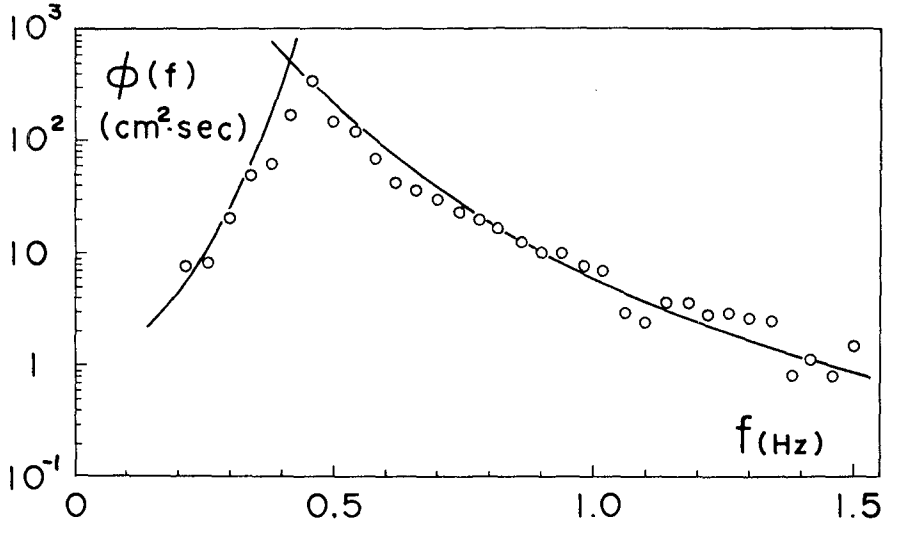

Fig. 9c COMPARISON OF THE PROPOSED SPECTRUM WITH THE MEASURED ONE.
(HAKATA BAY, $\hat{F} = 6.05 \times 10^5$)

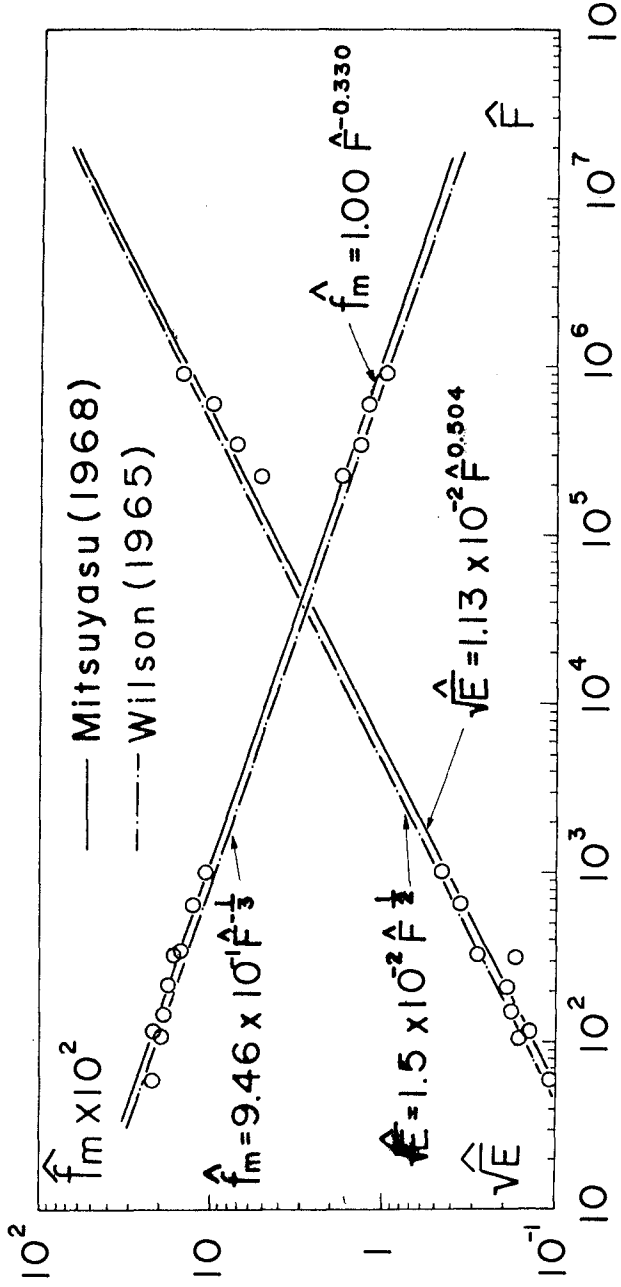

Fig. 10 FETCH GRAPH : DIMENSIONLESS SPECTRAL PEACK FREQUENCY $\hat{f}_m$ AND DIMENSIONLESS WAVE HEICHT $\sqrt{\hat{E}}$ VERSAS DIMENSIONLESS FETCH $\hat{F}$

CHAPTER 14

STRUCTURE OF SEA WAVE FREQUENCY SPECTRUM

By S.S. Strekalov [1], V.Ph. Tsyploukhin [2], S.T. Massel [3]

INTRODUCTION

A knowledge of the frequency spectrum is necessary for working a number of applied problems concerning wave parameter calculations, ship rolling, effects of wave loads upon sea structures and so on.

According to the data of work /1/ the frequency spectrum in deep sea may be represented as the following equation:

$$S(\mu) = A\mu^{-l}\exp(-B\mu^{-k}) \qquad (1)$$

The spectra obtained from the experiments on parameter values of l and k may be divided into three groups (Table 1).

Table 1

The parameter values of l and k on the data of various authors

Groups	Authors	l	k
I	W. Pierson and L. Moskowitz /3/	5	4
II	G. Neumann /2/, S. Strekalov /4/, B. Glukhovskii /5/	6	2
III	Yu. Krylov /5/	7	4

1) Scientific worker, M.Sc.Tech., USSR, Moscow, Sojuzmorniiproject.

2) Scientific worker, M.Sc.Tech., USSR, Moscow, Sojuzmorniiproject.

3) Scientific worker, M.Sc.Tech., Poland, Gdansk, The Institute for Water Economy of the Polish Academy of Sciencies.

At present, it is well-known that there is the Phillips' equilibrium range /6/ in the high-frequencies part of spectrum.

In this range the spectral density adheres to the equation

$$S(\mu) = \alpha g^2 \mu^{-5} \qquad (2)$$

In accordance with the Phillips' data $\alpha = 0,74 \cdot 10^{-2}$. In cosecquence of this the spectra of groups II-III (l= 6, 7) describe inaccurately the behavior of a spectral density in the high-frequency range in distinction of Pirson's and Moskowitz's (l = 5), which is in agreement with the experimental data for this range. In the range of maximum the spectral density of power falls out of the equilibrium range. In this case a high degree of approximation to full-scale data from spectra groups I-III is given by the Krylov's spectrum /5/. And hence, considering the equation (1) it is impossible to describe the spectrum correctly in the whole range of frequencies.

BASIC ANALYSIS DATA

The authors have made an attempt to refine the structure of spectrum for deep sea conditions on the basis of measurements taken on various seas of the USSR. For this purpose the wave recordings were used with the wind generated waves in the range of 7-12 m/sec. wind velocities and 50-200 km fetches. The wind flow velocity along the fetch was a practically constant.

The electrocontact wave recorders of "ГМ-16"-type were also used. Wave recording data were handled by the computer "Razdan-3". Each calculated spectrum was normalized by the equation:

$$S(\mu)/\bar{\tau}\, D = S(\mu/\bar{\mu}) \qquad (3)$$

ANALYSIS DATA

In fig. 1 the generalized empirical spectrum is shown by a solid curve line (1), and the confidence limit of 90% probability is presented by dushed lines (2). The spectrum (curve 1) has two peaks: low-frequency ($\mu_1/\bar{\mu}$ = 0,8) and high-frequency ($\mu_2/\bar{\mu}$ = 1,1). Another important character of the spectrum is in keeping of conditinn (2) in the range of high-frequencies (fig. 1-b). Here the generalized spectrum (curve 1) is described by function of $0,22(\mu/\bar{\mu})^{-5}$ (curve 3). The spectral density deviates gradually from the equilibrium range when frequencies are $\mu/\bar{\mu}$ = 1,5 and lower. Availability of two peaks in the generalized empirical spectrum is typical for calculated individual spectra.

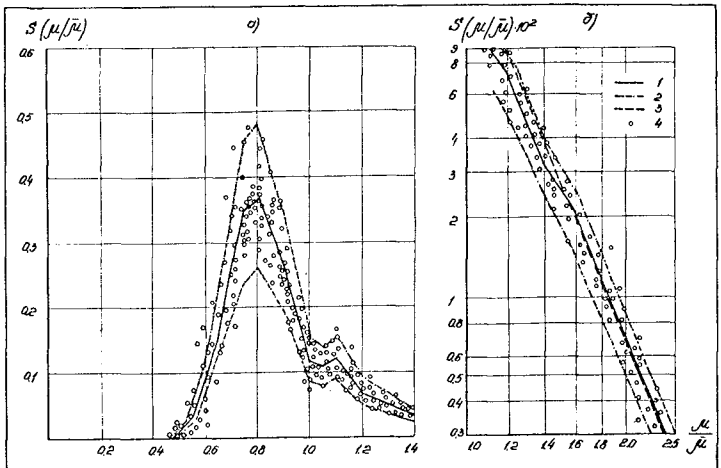

Fig.1. - Generalized empirical spectrum (curve 1) in the range of low (a) and high (б) frequencies. Confidence limit of 90% probability are showed by a dotted line (2), function (3) $0{,}22(\mu/\bar{\mu})^{-5/3}$ by a dushed one and individual spectra by spots (4)

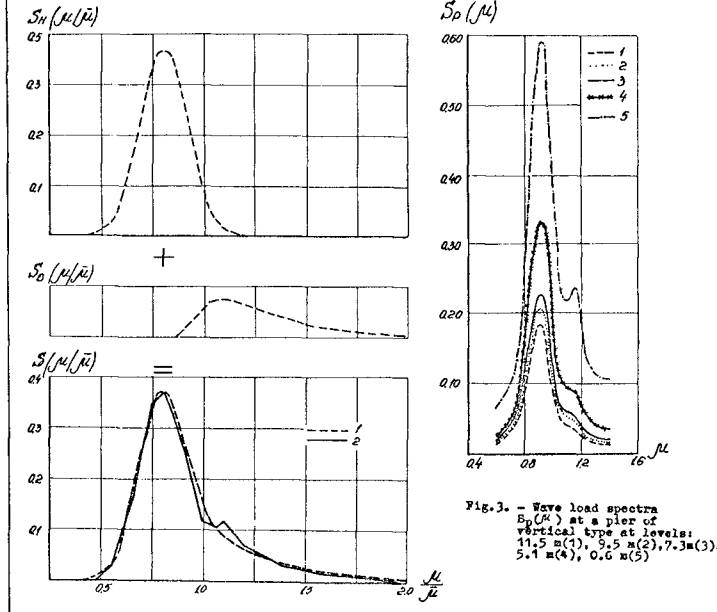

Fig.2. - Dimensionless spectrum $S(\mu/\bar{\mu})$ in form of sum $S_H(\mu/\bar{\mu})$ and $S_D(\mu/\mu)$. Curve 2 is a generalized empirical spectrum

Fig.3. - Wave load spectra $S_D(\mu)$ at a pier of vertical type at levels: 11.5 m(1), 9.5 m(2), 7.3 m(3), 5.1 m(4), 0.6 m(5)

SPECTRUM FORM

The form of frequency spectrum is determined as a sum of a low-frequency $S_H(\mu/\bar{\mu})$ and a high-frequency $S_B(\mu/\bar{\mu})$ parts /7/

$$S(\mu/\bar{\mu}) = S_H(\mu/\bar{\mu}) + S_B(\mu/\bar{\mu}) \qquad (4)$$

The spectral density may be expressed by such a function:

$$S_B(\mu/\bar{\mu}) = a(\mu/\bar{\mu})^{-n} \exp\left[-b(\mu/\bar{\mu})^{-m}\right] \qquad (5)$$

where n=5, a=0,22; b, m - parameters which to be determined. By means of expression (5) the single-peak unsymmetric curve is described. Maximum of this curve conforms the frequency of $\mu_2/\bar{\mu} = 1,1$. From this condition for the derivative

$$dS_B(\mu/\bar{\mu})/d(\mu/\bar{\mu}) = 0, \qquad (6)$$

"b" is determined

$$b = \frac{n}{m}(\mu_2/\bar{\mu})^m = \frac{5}{m}(1,1)^m$$

Assuming that $S_P(\mu/\bar{\mu})$ on the frequency μ_2/μ is a negligible quantity, and $\mu_1/\bar{\mu} = 0,8$; $S(\mu/\bar{\mu}) = 0,37$ from fig.1, m=8, b = 1,34 are obtained from expressions (5-6). In the final analysis the high-frequency part of spectrum may be written as

$$S_B(\mu/\bar{\mu}) = 0,22(\mu/\bar{\mu})^{-5}\exp\left[-1,34(\mu/\bar{\mu})^{-8}\right] \qquad (7)$$

In the frequency range of $\mu/\bar{\mu} \geq 1,5$ the relation (7) with regard to the normalized expression (3) will be calculated as:

$$S_B(\mu) = 0,22(2\pi)^2(\bar{\delta}^*)^2 g^2 \mu^{-5}, \qquad (8)$$

where

$$\bar{h} = \sqrt{2\pi D'}, \qquad (9)$$

$$\bar{\delta}^* = \bar{h}\Big/\frac{g\bar{\tau}^2}{2\pi} \qquad (10)$$

and $\bar{\delta}^*$ - parameter characterizing a steepness of waves. When $\alpha = 0,22(2\pi^2).(\bar{\delta}^*)^2$ the equation (8) is equivalent to the Phillips' formula (2). Considering that the parameter $\bar{\delta}^*$ is the dimensionless fetch function gx/v^2 the following equation is obtained

$$\alpha = \alpha(gX/v^2) \qquad (11)$$

TABLE 2.-VARYING OF PARAMETER α ACCORDING TO THE DATA OF FULL-SCALE OBSERVATIONS /9/

Nos. of wave recordings	99	95	135	150	148	144	147	235	68	124	49	198	6	203	43
Wind velocity, v, in m/sec.	18,4	14,4	17,0	10,4	11,8	10,6	12,5	9,8	17,2	15,2	14,7	7,1	13,6	6,7	12,6
Fetch, X, in km	3,7	2,3	8,9	5,2	11,1	11,1	20,0	41,0	180	280	330	116	625	157	550
Average height, h, in m	0,65	0,47	0,74	0,40	0,56	0,49	0,74	0,64	2,25	2,00	2,09	0,60	2,52	0,59	2,05
Average period, $\bar{\tau}$, in sec.	3,2	2,8	3,8	2,7	3,2	3,1	3,9	3,9	7,0	6,6	7,2	3,8	7,7	3,9	7,0
$\frac{gX}{v^2} \cdot 10^{-3}$	0,11	0,11	0,30	0,47	0,78	0,97	1,25	4,19	5,93	11,9	15,0	22,6	33,1	34,3	37,5
$\alpha \cdot 10^{-2}$	1,46	1,25	0,94	1,06	1,06	0,94	0,83	0,63	0,73	0,73	0,59	0,63	0,63	0,54	0,63

It is pointed by S.Kitaigorodsky and O.Phillips that the parameter α is a variable. The authors estimated variable range of α from the formula (11) using actual measurement data. The values of α proved to be enclosed within $0{,}54 \cdot 10^{-2} \leq \alpha \leq 1{,}46 \cdot 10^{-2}$.

As the parameter of gX/v^2 increases the values of decreases. It is characteristic that the value of constant $\alpha = 0{,}74 \cdot 10^{-2}$ determined before by O.Phillips (6) is an approximately average value for the conditions of rough sea when $\bar{\delta}^* = 0{,}025 - 0{,}030$.

The low-frequency part of spectrum $S_H(\mu/\bar{\mu})$ to be found in the form of difference /7/:

$$S_H(\mu/\bar{\mu}) = S_э(\mu/\bar{\mu}) - S_B(\mu/\bar{\mu}), \qquad (12)$$

where $S_э(\mu/\bar{\mu})$ - values of the generalized empirical spectrum, and
$S_B(\mu/\bar{\mu})$ - already known function (7).

The low-frequency part of spectrum (12) with sufficient accuracy may be presented as a symmetric Hauss-type curve with a maximum displaced on frequency scale from the origin by $\mu_1/\bar{\mu} = 0{,}8$;

$$S_H(\mu/\bar{\mu}) = \frac{p_1}{\sqrt{2\pi}\sigma} \exp\left\{-\frac{[1/\bar{\mu}(\mu-\mu_1)]^2}{2\sigma^2}\right\} \qquad (13)$$

According to the calculations when $p_1 = 0{,}11$ and $S(\mu_1/\bar{\mu}) = 0{,}37$

$$\sigma = \frac{p_1}{\sqrt{2\pi}\, S(\mu_1/\bar{\mu})} \simeq 0{,}12 \qquad (14)$$

The total spectrum $S(\mu/\bar{\mu})$ consisting of members (3) and (4) is given in fig.2. In the dimension form the spectrum $S(\mu)$ is written as

$$S(\mu) = D\bar{\tau}\left([p_1/\sqrt{2\pi}\sigma]\exp\left\{-\frac{[1/\bar{\mu}(\mu-\mu_1)]^2}{2\sigma^2}\right\} + a(\mu/\bar{\mu})^{-5}\exp\left[-b(\mu/\bar{\mu})^{-8}\right]\right. \qquad (15)$$

SPECTRUM UNIVERSAL PROPERTIES

The authors realized that the spectrum form (15) is not universal for all the stages of wave development. However, the spectrum describes specific wave properties at the particular stages. In fig.3 the full-scale wave load spectra $S_R(\mu)$, $(T/M^2)^2$ sec. at a pier of vertical type at various levels are shown /10/. Two maxima with the relation of frequencies close to the relation in spectrum (15) are followed at all the levels. The low-frequency part of spectrum may be described by a symmetric function of (13)-type, and the high-frequency part by an unsymmetric one of (7) - type.

CONCLUSIONS

1. Two maxima in frequency spectrum are followed.
2. The low-frequency part of spectrum may be approximately described by a Hauss symmetric type curve.
3. The high-frequency part is an unsymmetric owing to the presence of the equilibrium range.

APPENDIX I.-REFERENCES

1. Burling A. The spectrum of waves at a short fetches. "Dtsch.hydrogr.Z.", 1959, 12, 1, 3.
2. Neumann G., Pierson W. A detailed comparison of theoretical wave spectra and wave forecasting methods. "Dtsch.hydrogr.Z.", 1957, 10, 3.
3. Pierson W., Moskowitz L. A proposed spectral form for fully developed seas, based on the similarity theory of S.A. Kitaigorodskii. "J.Geophys. Res.", 1964, 69, №24.
4. Стрекалов С.С. К определению аналитического вида энергетического спектра развитого волнения. "Океанология", 1961, I, вып. 3
5. Крылов Ю.М. Спектральные методы исследования и расчёта ветровых волн. Л., Гидрометеоиздат, 1966
6. Phillips O. The equilibrium range in spectrum of wind generated waves. "J. Fluid. Mech.", 1958
7. Strekalov S.S., Massel S. Niektore zagdneenia widmowej analizy falowania wiatrowego. Apch. Hydrotechniki. T. XVII, Z 4, Poland, 1971.
8. Китайгородский С.А. Физика взаимодействия атмосферы и океана. Л., Гидрометеоиздат, 1970
9. Ржеплинский Г.В., Крылов Ю.М., Матушевский Г.В., Стрекалов С.С., Назаретский Л.Н. Новый метод анализа и расчёта элементов ветровых волн. Труды Гос. Океанографического института, вып. 93, 1968
10. Крылов Ю.М. и др. Волноизмерительная станция в порту Шесхарис на Черном море. Информационные материалы по гидрологическим приборам и методам наблюдений. Сб., 1971, вып. 46

APPENDIX II.-NOTATION

A, B = dimensional parameters
a, b, n, m = dimensionless parameters of spectrum (5)
D = dispersion
g = acceleration of gravity
h = average height
l, k = dimensionless parameters
p = normalizing factor
$S(\mu)$ = spectral density of power $[L^2T]$
$S_p(\mu)$ = spectral density of wave pressure in $(T/M^2)^2$sec.
$S_3(\mu/\bar{\mu})$ = experimental value of spectral density
v = wind velocity in m/sec.
X = fetch
α = dimensionless Phillips' constant
μ = frequency in rad./sec.
$\bar{\mu} = 2\pi/\bar{\tau}$ - average frequenoy in rad./sec.
μ_1 = frequency of low-frequency maximum (rad./sec.)
μ_2 = frequency of high-frequency maximum (rad./sec.)
$\bar{\tau}$ = average period
σ = parameter characterizing spectrum form (13)

CHAPTER 15

METHODES DE MESURE ET TRAITEMENT DE LA HOULE

par René BONNEFILLE
Laboratoire National d'Hydraulique - 78 - CHATOU (France)

Résumé :

Un sondeur à ultra-son inversé, un manographe immergé au fond et une bouée accélérométrique ont été utilisés pour mesurer la houle, au même point. Les enregistrements, dont certains sont simultanés, ont été soumis à divers traitements en vue de comparaisons et de critiques orientées vers la connaissance de la précision des appareils et le choix économique de la méthode de dépouillement.

LES APPAREILS DE MESURE

D'octobre 1970 à mars 1971 fut installé au large de Cap Couronne, par fonds de 18 m, près de Marseille (France) un ensemble de trois houlographes en vue de comparer les appareils et les méthodes de traitement de leurs enregistrements :

a) Un écho-sondeur inversé type Electricité de France [1] était posé sur le fond et relié à terre par un câble. Le transducteur donne un pinceau conique d'ultra-son à la fréquence 200 kHz, d'ouverture utile 8° ; il permet d'enregistrer sans déformation les houles de périodes supérieures à 4 s, mais il est inutilisable pour enregistrer les agitations de la surface libre de période inférieure à 2 s. Etant donné sa précision, ce houlographe est considéré pour cette étude comme l'appareil de référence. Les informations de l'appareil sont digitalisées (1 mesure toutes les 0,2 s) et enregistrées sur bande de papier perforé, en code binaire-décimal.

b) Un manographe autonome(2) type Laboratoire National d'Hydraulique était immergé à proximité. Les enregistrements de la pression au fond sont obtenus sur film, ce qui présente deux inconvénients majeurs : La lecture automatique du film en vue du traitement des données est délicate ; il convient de calculer l'agitation en surface à partir des fluctuations de pression au fond.

c) Une bouée accélérométrique "Datawell" appartenant au Service des Phares et Balises flottait en surface. Les informations sont transmises à terre par radio. A la réception le signal analogique est numérisé et enregistré sur bande magnétique. Ce dispositif présente deux inconvénients majeurs : L'ensemble bouée-ligne de mouillage a une période d'oscillation propre qui perturbe la mesure (le degré de nuisance de cet effet est un des buts de l'étude) ; la transmission radioélectrique des signaux analogiques est entachée d'erreurs dues aux perturbations hertziennes qui ne sont malheureusement pas décelables par les méthodes de traitement simples.

Les aléas de fonctionnement du houlographe à pression et les difficultés de traitement des données de la bouée, n'ont permis d'obtenir que quelques enregistrements de 20 mn vraiment simultanés de deux des appareils (8 avec la bouée et 4 avec le manographe) ; néanmoins, ces comparaisons sont très instructives au niveau de l'étude de la précision des appareils et de l'intérêt économique des méthodes de traitement automatique.

LES METHODES DE TRAITEMENT

Deux grandes classes de méthodes de traitement furent utilisées :

a) Les méthodes statistiques s'appuient sur l'analyse de l'enregistrement au niveau des vagues, c'est-à-dire des distances des crêtes à creux successifs. L'étude de l'ensemble des vagues permet de construire les histogrammes (creux, période, croisés creux-périodes) et de déterminer les grandeurs classiques (creux maximal, creux significatif, périodes moyennes). A côté de cette méthode d'analyse globale, est utilisé un procédé proposé par DRAPER (3) , consistant à déduire les grandeurs caractéristiques d'une séquence d'enregistrement de la mesure des deux plus grandes oscillations en s'appuyant sur des hypothèses assez plausibles sur la répartition statistique de l'agitation.

b) Les méthodes d'analyse spectrale, conduisent à la connaissance de la répartition de l'énergie de l'enregistrement suivant les fréquences. Moyennant des hypothèses sur la répartition statistique de l'agitation, elles permettent d'estimer les caractéristiques de la houle._

COMPARAISON ECHO-SONDEUR INVERSE - BOUEE ACCELEROMETRIQUE

La comparaison des résultats du traitement par l'analyse spectrale des enregistrements par écho-sondeur inversé et bouée accélérométrique conduit aux résultats suivants, lorsque les parasites ne perturbent pas la transmission radio-électrique :

- Les moments d'ordre zéro (m_o) de la répartition d'énergie coïncident (Fig. 1) ; l'énergie totale contenue dans le processus est la même.

- Le moment d'ordre deux (m_2) donné par la bouée est de l'ordre du double de celui du houlographe à ultra-son (Fig. 2) ; la bouée amplifie les mouvements de faible période, alors que le sondeur les atténue.

En admettant que le processus soit gaussien, les caractéristiques classiques s'en déduisent, en particulier si le spectre est étroit :

- creux moyen : $\overline{H} = \sqrt{2\pi m_o}$

- creux significatif : $H_{1/3} = 4\sqrt{m_o}$

- période moyenne : $T = \sqrt{m_o/m_2}$

Les creux moyens et significatifs coïncident, mais la différence sur m_2 fait que les creux maximaux donnés par la bouée sont environ 10 % supérieurs et que les périodes moyennes sont d'environ 20 % inférieures à celles obtenues par le houlographe à ultra-son. En revanche, la période d'énergie maximale coïncide bien.

COMPARAISON ECHO-SONDEUR INVERSE - MANOGRAPHE

La comparaison des enregistrements par les houlographes à ultra-son et à pression a d'abord permis de préciser la valeur du coefficient de restitution K utilisé dans la relation :

$$z(t) = K\, p(t)\, \mathrm{ch}\, 2\pi \frac{d}{L}$$

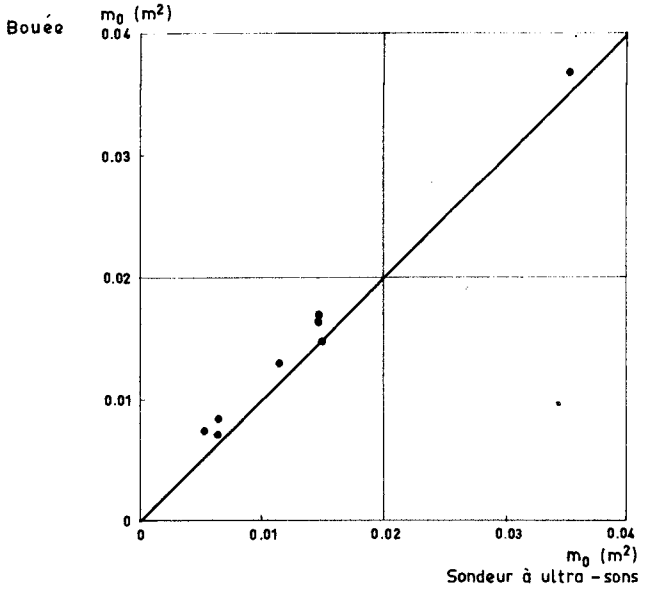

Fig.1–COMPARAISON DES PREMIERS MOMENTS DU SPECTRE, m_0

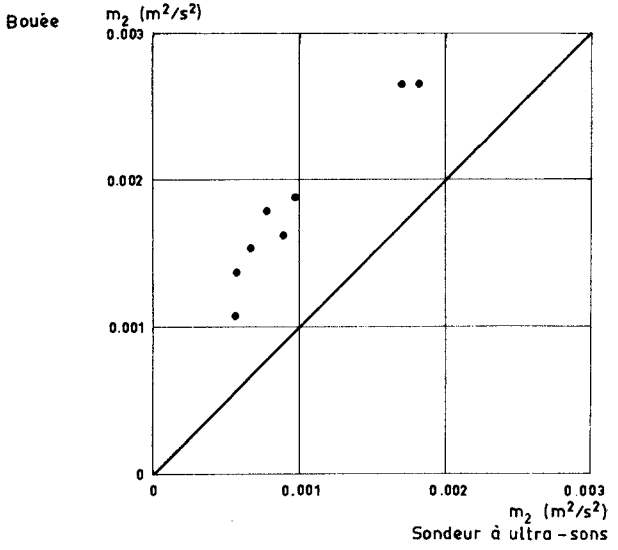

Fig.2-COMPARAISON DES SECONDS MOMENTS DU SPECTRE, m_2

pour passer des fluctuations de pression p(t) à la profondeur d, à celle de la surface libre z(t) de longueur d'onde L. En fait, pour les vagues de faible période le terme en cosinus hyperbolique est grand et peut donc introduire des erreurs appréciables ; dans cette étude ce terme est arbitrairement conservé constant (égal à 12,35) pour les périodes inférieures à 5,33 s, ce qui revient à éviter de donner trop de poids aux courtes périodes.

La comparaison des m_o déduits des analyses spectrales des enregistrements des deux houlographes conduit alors à choisir :

$$K = 1,11$$

En revanche, les moments d'ordre deux sont encore différents ; celui donné par le houlographe à pression ne vaut que 86% de celui du houlographe à ultra-son, ce qui conduit à penser que la réduction des faibles périodes est trop atténuée. Cependant, cet écart est trop faible pour empêcher que les creux moyens, significatifs et maximaux ne soient pas bien restitués avec K = 1,11 (Fig.3). La période moyenne est évidemment trop faible (10%); les périodes d'énergie maximale coïncident.

En résumé, avec le coefficient de restitution proposé et une troncature du spectre du côté des petites périodes, les enregistrements de deux appareils traités par l'analyse spectrale conduiraient à des résultats concordants.

COMPARAISON DES METHODES DE TRAITEMENT

La comparaison des résultats obtenus par les différentes méthodes de traitement donne les résultats suivants :

Les méthodes d'analyse statistique, par histogramme ou DRAPER , et d'analyse spectrale donnent des résultats concordants à partir des enregistrements du sondeur à ultra-son inversé (Fig.4).Elles ne diffèrent que par leur prix de revient variant dans le rapport de 2 à 5. La méthode des histogrammes coûte deux fois plus cher que la méthode DRAPER ; l'analyse spectrale coûte 5 fois plus cher ; il est vrai que dans ces prix sont inclus le tracé des histogrammes ou du spectre.

Appliquées aux résultats du houlographe à pression, les méthodes d'analyse statistiques conduisent à des creux significatifs environ 13% inférieurs à ceux obtenus par l'analyse spectrale. La différence peut provenir de la restitution de l'agitation à partir de la pression ; dans

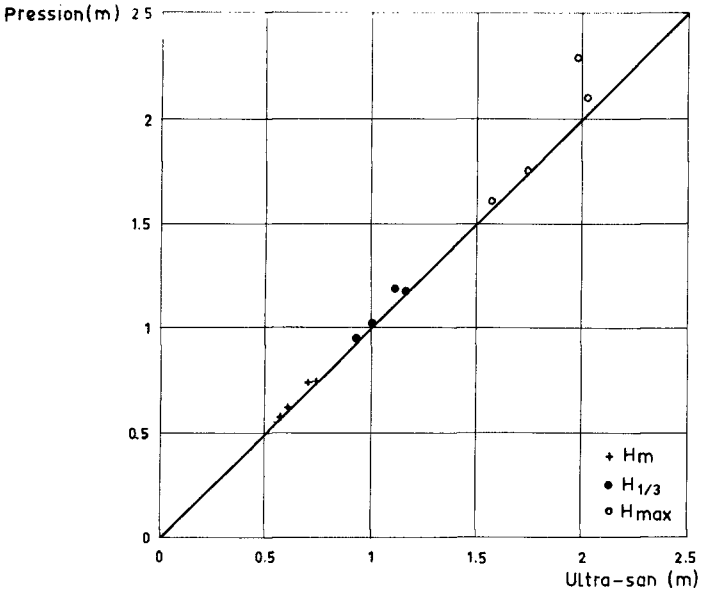

Fig:3- COMPARAISON DES DONNEES DES HOULOGRAPHES A ULTRA-SON ET A PRESSION (K=1.11)

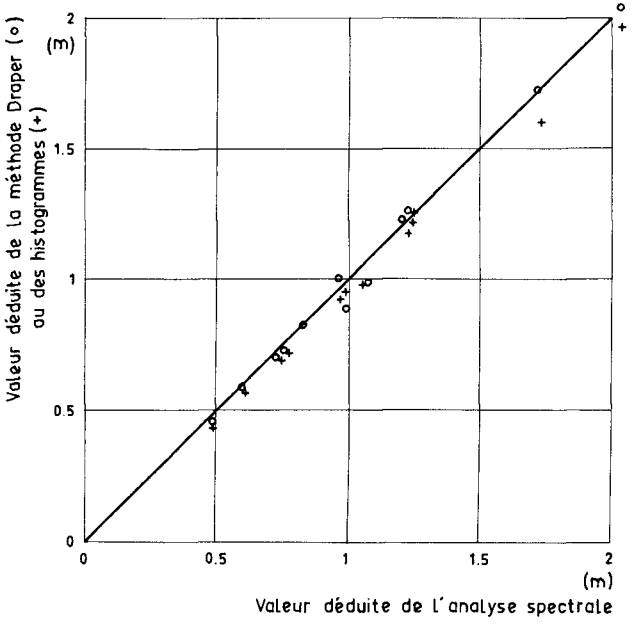

Fig:4- COMPARAISON DES DONNEES DU HOULOGRAPHE A ULTRA-SON TRAITES PAR DIFFERENTES METHODES

le facteur de restitution K ch $2\pi\frac{d}{L}$, la longueur d'onde L est fonction de la période dans l'analyse spectrale ; elle est celle de la vague effectivement mesurée dans l'analyse statistique. Il semble donc que le coefficient de restitution global K déduit de l'analyse spectrale, soit trop faible, et qu'il conviendrait de le majorer d'environ 13 %, c'est-à-dire prendre :

$$K = 1{,}25$$

pour les restitutions vague par vague ou par la méthode DRAPER.

COMPARAISON DES RESULTATS AVEC LES MODELES THEORIQUES

La disponibilité des enregistrements de houle sous forme facile à soumettre aux traitements automatiques permet d'estimer la validité des modèles théoriques.

L'étude a porté sur les points suivants :

- vérification de la loi de probabilité gaussienne des passages des niveaux par une cote donnée z :

$$P(z) = \frac{1}{\sqrt{2m_o}} e^{-z^2/2m_o}$$

- étude statistique :
  - . des cotes des maximums η_{max} et des minimums η_{min}
  - . des hauteurs H^* de toutes les vagues, c'est-à-dire la distance verticale entre une crête et le creux suivant (T^* désigne la période associée calculée entre 2 crêtes successives)
  - . des hauteurs H entre les crêtes et les creux successifs situées de part et d'autre du niveau moyen, T est leur période associée définie par le temps qui sépare 2 passages successifs au niveau moyen.

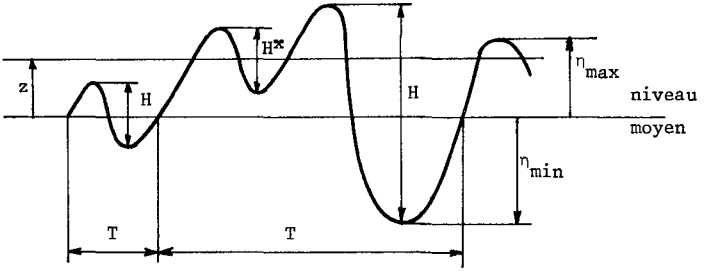

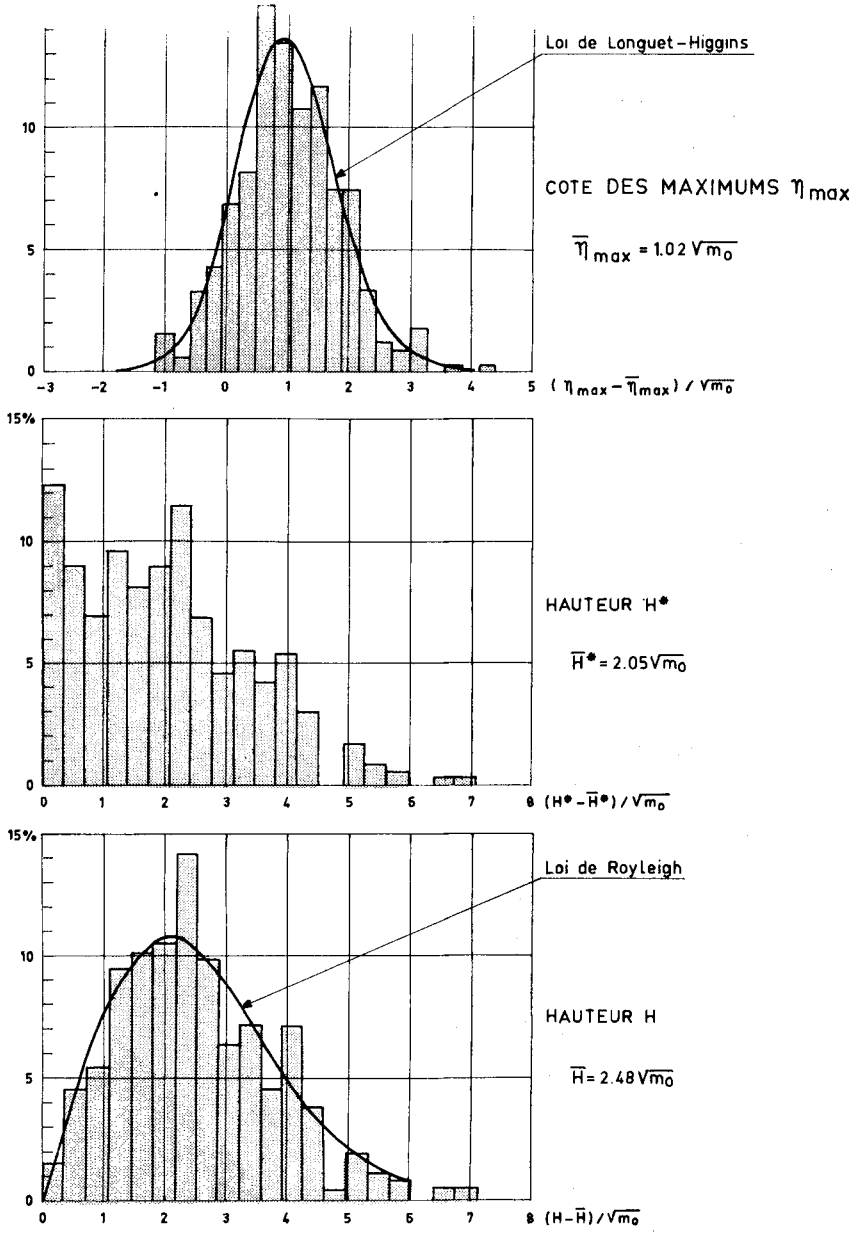

Fig.5 - EXEMPLES DE REPARTITIONS STATISTIQUES
(le 7 Octobre 1970 à 7h) $\sqrt{m_o} = 0.367m$

La loi de probabilité gaussienne étant vérifiée, les résultats théoriques, qui en découlent, moyennant les hypothèses de stationnarité et d'ergocité, doivent être aussi bien vérifiées. Les figures 5 et 6 illustrent les faits suivants :

- Les cotes η_{max} (et de même η_{min}) se répartissent suivant la loi de Longuet-Higgins (4) ; leurs valeurs moyennes suivent bien la loi théorique en fonction de la largeur ε du spectre par :

$$\overline{\eta}_{max} = \frac{1}{2}\sqrt{2\pi m_o(1 - \varepsilon^2)}$$

avec

$$\varepsilon^2 = 1 - (N_o/N_1)^2 = 1 - m_2^2/m_o m_4$$

ε étant donc estimé à partir du rapport entre le nombre N_o de passage par le niveau moyen et le nombre N_1 de creux et crêtes, ou à partir des moments m_o, m_2 et m_4 des spectres d'énergie.

- Les valeurs significatives $(\eta_{max})_{1/3}$, $(\eta_{min})_{1/3}$ dérivent par rapport aux lois théoriques quand η augmente ; $(\eta_{max})_{1/3}$ est supérieur, $(\eta_{min})_{1/3}$ est inférieur, de sorte que :

$$\eta = \frac{1}{2}\left[(\eta_{max})_{1/3} + (\eta_{min})_{1/3}\right]$$

suit assez bien la loi théorique.

La loi de Rayleigh ne peut pas être retenue pour représenter la distribution des hauteurs H^* entre toutes les crêtes et creux ; en conséquence, on ne dispose pas de loi théorique pour représenter $H^*_{1/3}$ et $\overline{H}$. Cependant la figure 6 montre que la valeur moyenne $\overline{H}^*$ varie comme η_{max} en fonction de ε.

- Les hauteurs H entre crêtes et creux de part et d'autre des niveaux moyens se répartissent suivant la loi de Rayleigh ($\varepsilon = 0$) :

$$P(H) = \frac{H}{4m_o} e^{-H2/2m_o}$$

les grandeurs caractéristiques correspondantes doivent donc être indépendantes de ε, ce que montre la figure 6 ; cependant les valeurs moyennes et significatives $\overline{H}$ et $H_{1/3}$ prennent des valeurs un peu inférieures (2,5 et 4 %) aux valeurs théoriques $\sqrt{2\pi m_o}$ et $4\sqrt{m_o}$ déduites de la distribution de Rayleigh ; de même $H_{1/10}$ est 7 % inférieur à la valeur théorique $5{,}09\sqrt{m_o}$.

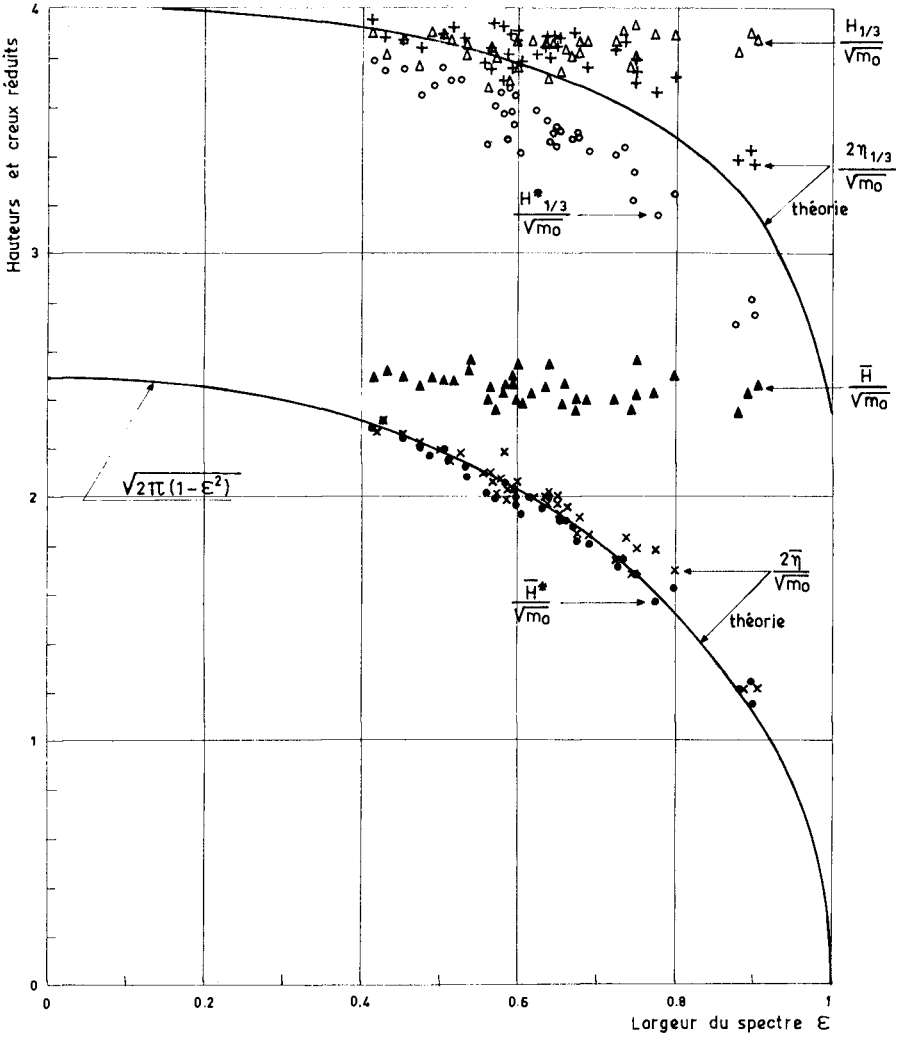

Fig.6 - PROPRIETES DES VALEURS SIGNIFICATIVES ET MOYENNES DE η, H^* ET H

RECOMMANDATIONS SUR LES METHODES DE TRAITEMENT

En conclusion de l'analyse des enregistrements de pression au fond, le coefficient K du facteur de restitution doit être pris égal à :

1,11 dans le cas de l'analyse spectrale

1,25 dans le cas de l'analyse statistique

L'imprécision du calcul de m_2 (et à fortiori de m_4) provient de la part importante que jouent les ondes de petites périodes de hauteur mal connue : il en résulte une mauvaise connaissance de la largeur du spectre ε et par suite des valeurs caractéristiques des hauteurs η_{max}, η_{min}, $\overline{H}^{x}$. L'étude de ε et m_o en fonction de la fréquence de coupure f_c au-dessus de laquelle il n'est pas tenu compte des mesures, ne fait pas apparaître de singularités dans la courbe $\varepsilon(f_c)$; en revanche, la fonction $m_o(\varepsilon)$ varie assez vite au-dessous d'un certain seuil de fréquence (figure 7). Ceci suggère de définir la fréquence de coupure à l'aide de l'erreur qu'entraînerait le calcul de m_o en ne considérant que les fréquences inférieures à f_c. Une valeur intéressante est celle pour laquelle cette erreur est 2 % : elle est définie par

$$\int_0^{f_c} S(f)\, df = 0{,}98 \int_0^{\infty} S(f)\, df = 0{,}98\, m_o$$

S(f) étant la distribution spectrale d'énergie en fonction de la fréquence f. Dans le cas de la figure 7, ε vaudrait alors 0,56 et devrait être désigné par ε_{98} ainsi que toutes les grandeurs qui en découlent $(m_2)_{98}$, $(\eta_{max\,1/3})_{98}$, etc ....

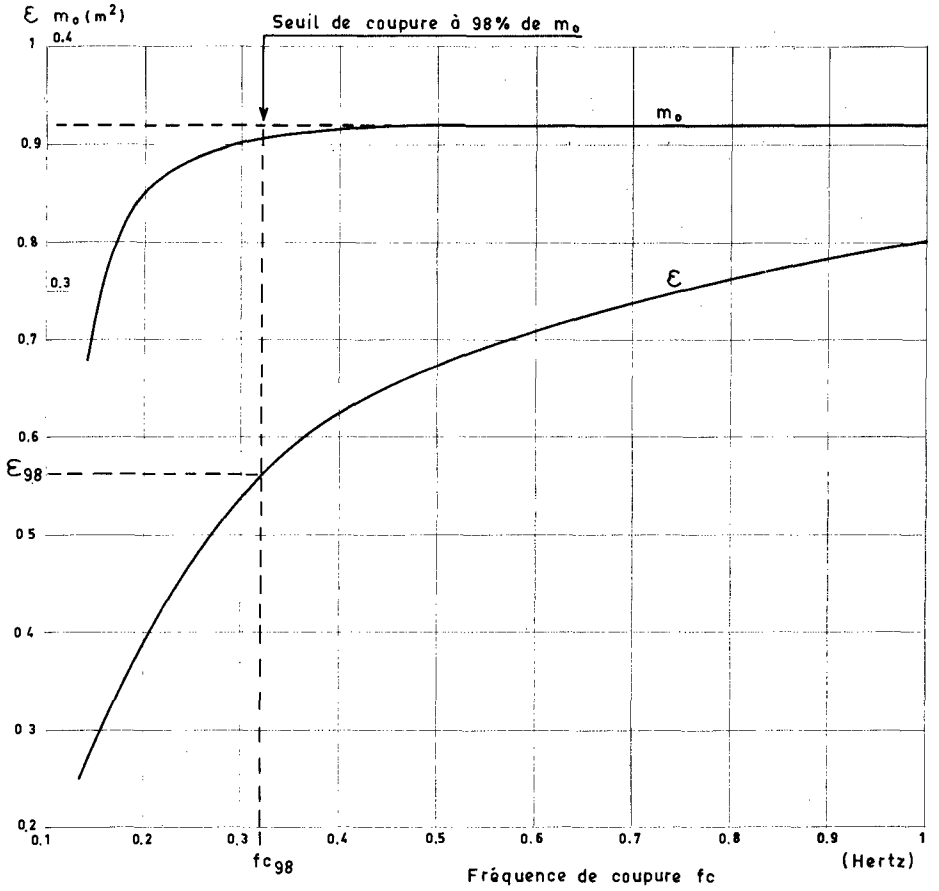

Fig.7-EXEMPLE DE VARIATION DE ε et m_0 EN FONCTION DE LA FREQUENCE DE COUPURE

(1) R. BONNEFILLE - P. CORMAULT - J. VALEMBOIS - "Progrès des méthodes de mesure de la houle naturelle au Laboratoire National d'Hydraulique". - Proceedings Xth Conference on Coastal Engineering - Tokyo 1966.

(2) J. VALEMBOIS - "Les appareils réalisés à Chatou pour la mesure de la houle naturelle". - Proceedings VIth Conference on Coastal Engineering - Grenoble 1954.

(3) L. DRAPER - "Wave recording instruments for civil engineering use". - National Institute of Oceanography - Wormley 1968.

(4) M.S. LONGUET-HIGGINS - "On the Statistical Distribution of the Height of Sea Waves".-Journal of Marine Research, Vol. XI, n° 3, 1952.

CHAPTER 16

SHALLOW WATER WAVE CHARACTERISTICS

by

Winfried Siefert*)

Abstract

Prototype data from 24 wave stations on and around the tidal flats south of the Elbe estuary enable us to elaborate special shallow water wave characteristics, concerning the variations and correlations of heights, periods, lengths and velocities. This paper deals with some interesting aspects from the engineer's point of view. It turns out that the steepness factor $\frac{\overline{H}}{\overline{L}}$ or $\frac{\overline{H}}{g \cdot \overline{T}^2}$ of breaking waves is much smaller than of non-breaking waves and that steepness is no suitable parameter to describe a natural wave spectrum in shallow waters.

On the tidal flats the maximum wave heights only depend on the depth of water, not on the steepness. Moreover the possible wave height proves to become much higher than theoretically predicted, especially in depths of water less than 2 m.

Introduction

In 1962 the Coastal Engineering Research Group in Cuxhaven, a branch of the City of Hamburg Harbour Authority, was established to carry out a general programme of hy-

*) Dr.-Ing., Strom- und Hafenbau Hamburg, Coastal Engineering Research Group "Neuwerk", 219 Cuxhaven, West Germany

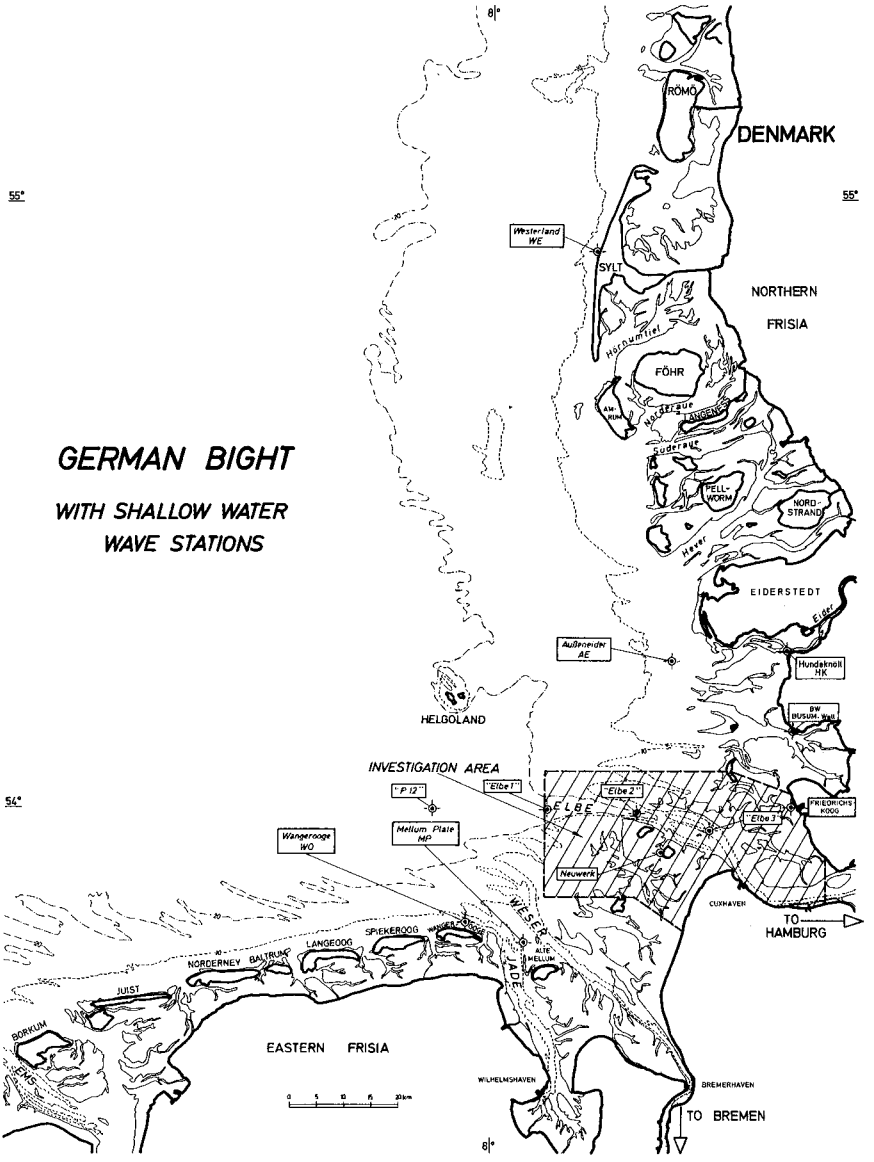

Fig. 1
Coast of the German Bight

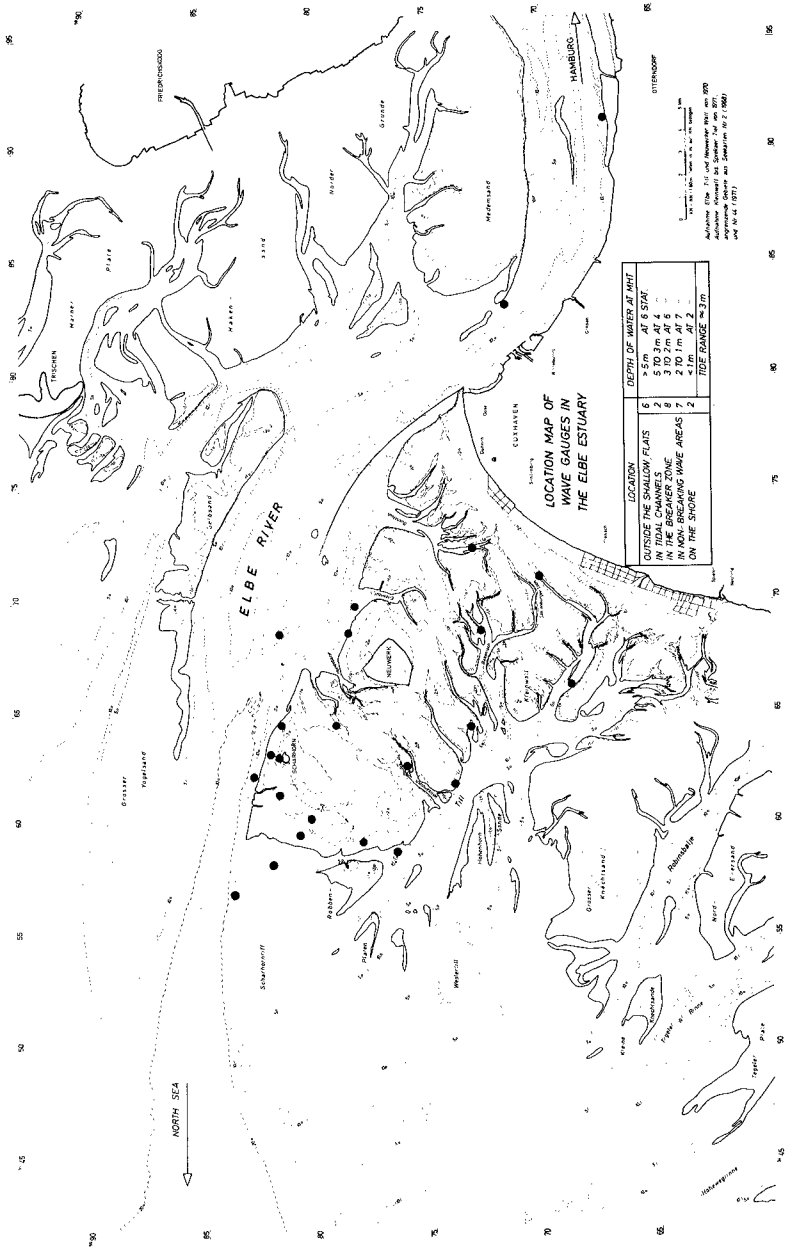

Fig. 2
Wave Investigations in the Elbe Estuary

drologic, hydrodynamic and morphologic investigations in the Elbe estuary. One part of these are wave measurements in an area that is morphologically very complicated. The location map (fig. 1) shows the structure of extended tidal flats, interrupted by tidal channels of variing width and depth with 2 small islands on the higher part of the flats.

To get a sufficient survey of the wave conditions in an area with strongly changing depths and under the influence of mean tide ranges of about 3 m, detailed research is necessary. Till 1972 the number of measuring stations amounts to 24 in water depths from 30 cm to 10 m (fig. 2). To give an impression of one special investigation programme, fig. 3 shows two of these stations on the beach of the dune island of Scharhörn with a distance of 20 m between them.

Fig. 3

Previous evaluations gave strong connections between mean wave height and wave height distribution, morphologic structure and wave period distribution, $\overline{H}$ and $\overline{T}$ and wind conditions, and others (Siefert, 1971). The following examples shall indicate the variation of some simple para-

meters, as $\overline{H}$, $H_{1/3}$, $\overline{T}$, $\overline{L}$ and $\overline{c}$, due to changing water depths and wave character, especially in depths below 1 m, whereof prototype data have not yet been available.

Waves in Very Shallow Water ($d < 1$ m)

Fig. 4 contains data from the two above mentioned beach stations in water depths not over 1 m on a beach slope of about 1:70. Waves are breaking here for the second time, as most of them already broke in the flat area in front of the beach. In a few words the results can be resumed as follows:

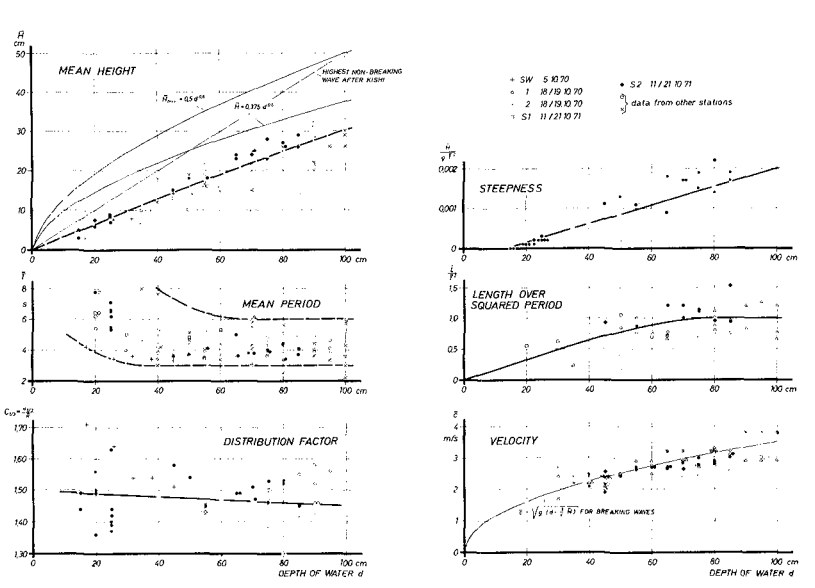

Fig. 4

1. $\overline{H}$ increases nearly proportional to depth, and the highest mean values are lower than in the first breaker zone (see last chapter) and even than the highest non-breaking waves after Kishi (1959).

2. $\overline{T}$ decreases with increasing depth, until for $d > 0.5$ m $\overline{T}$ reaches the range from 3 to 6 s that is typical for

waves on tidal flats in the southern part of the North Sea.

3. The weak decrease of the wave height distribution factor $C_{1/3}$ with increasing depth indicates that the width of the wave height distribution becomes smaller with deeper water and consequently higher waves. Besides this the distribution is obviously narrower than theoretically expected with $C_{1/3} = 1.60$.

4. Concerning the wave steepness factor $\frac{\overline{H}}{g \cdot \overline{T}^2}$, it may be remembered that it is generally used only in connection with sinusoidal waves and waves of constant profile in a wave tank. As a ratio of mean prototype data it receives a different valuation. This fact will be discussed later.

   Fig. 4 indicates that the steepness factor increases with increasing depth and increasing wave height, though it remains very small with $\frac{\overline{H}}{g \cdot \overline{T}^2} = 0.002$ for d = 1 m.

5. The relation $\frac{\overline{L}}{\overline{T}^2}$ in very shallow water increases with decreasing period and becomes constant about 1 at depths over 0.7 m. So usually $\overline{L}$ equals $\overline{T}^2$, as was determined in deeper water areas by earlier investigations. Consequently the steepness factor $\frac{\overline{H}}{g \cdot \overline{T}^2}$ really equals $\frac{\overline{H}}{\overline{L}}$ except the constant acceleration due to gravity.

6. The theoretical relation between mean wave velocity $\overline{c}$ and depth of water in very shallow water

$$c = \sqrt{g \cdot d}$$

   is valid only for non-breaking waves. Concerning breaking waves, it must be regarded that the crests of these waves lie $\frac{3}{4}$ H above still-water-level (Wiegel, 1964) and that the velocity-distribution in the wave is different, thus

getting

$$c = g(d + \frac{3}{4} H).$$

Prototype data on fig. 4 state that they represent breaking waves and - what is likely more important - that the theoretical formula for single waves can be used to describe the mean velocity of waves of a natural spectrum by using the mean wave height under the root.

Waves on Tidal Flats

At the southern and eastern coast of the North Sea, beaches with those wave characteristics are usually surrounded by shallow flats, where also special, but of course different wave characteristics are dominating. Fig. 5 gives a comprehensive impression of these. It is relatively easy to divide

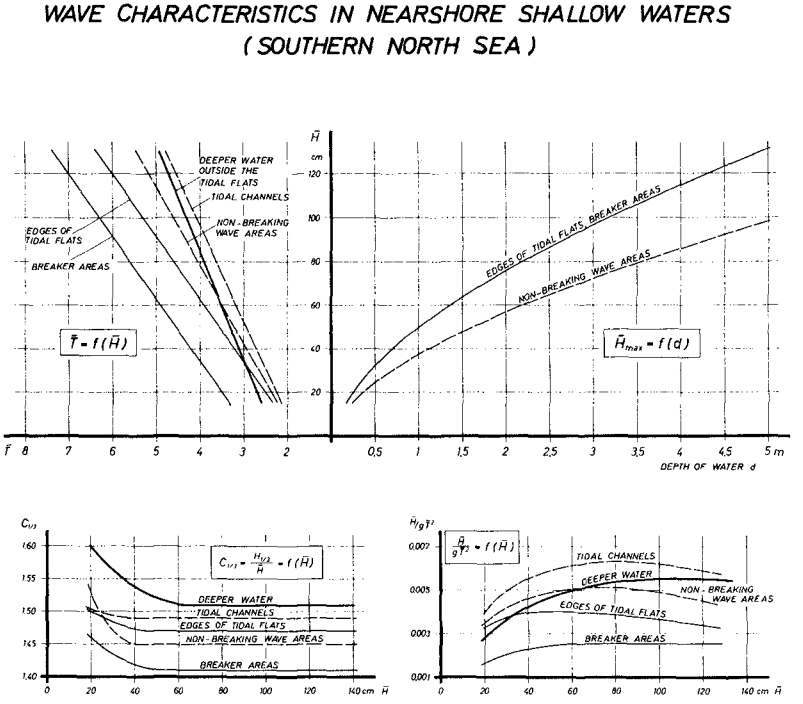

Fig. 5

such an area into some parts with constant characteristics. The first criterion is the depth of water, that separates the tidal flats from the deeper water area in front of them and from the tidal channels. The exposure to deeper water areas determines, whether mainly breaking or non-breaking waves are to be expected. This is of greatest importance for the determination of the highest possible mean wave heights, $\overline{H}_{max}$, as a function of the depth of water (Siefert, 1973).

The connections of $\overline{H}$ and d are given on the upper right side of fig. 5. Later on we will look at them again. The round about linear connections between $\overline{H}$ and $\overline{T}$ are plotted on the upper left side. For each area of special wave characteristics there is a different line, the result being somewhat surprising but reasonable:

Waves of a certain height obviously proceed with different periods. Mean waves of 60 cm height for example have a period of 3.5 s in deeper water outside the flats. In tidal channels waves of the same height proceed with a 10% shorter period, due to strong wave deformation by refraction, the period being even shorter than in the neighbouring non-breaking wave areas on the tidal flats. Waves of this height within the breaker areas have much longer periods, up to 5 s (fig. 5). The consequence for engineering projection is that the type of coastal area and its special wave characteristics are of high interest for the determination of design waves.

The variation of wave characteristics during the transition of two wave height groups from the deep Elbe fairway on to the shallow flats is generalized on fig. 6 for waves with (left) and without breaking, resuming the results as before mentioned:

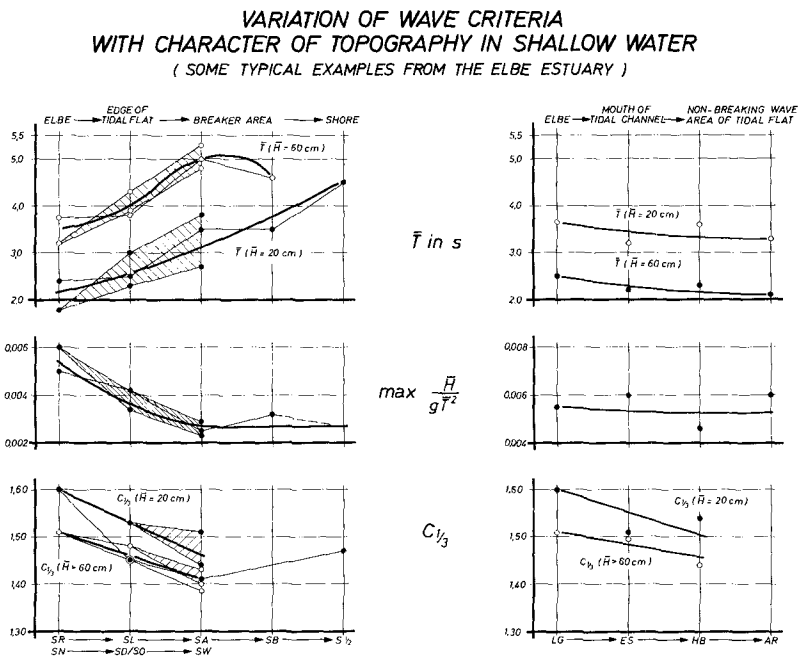

Fig. 6

1. Increase of period for breaking waves of constant height, slow decrease of period for non-breaking waves,

2. Decrease of maximum steepness factor for breaking waves (from 0.0055 to 0.0027), nearly constant steepness for non-breaking waves at about 0.0055,

3. Narrowing of the wave height distribution factor for all waves.

The increase of period with decreasing depth at MHW for waves of the same height can clearly be indicated on fig. 7. In water depths deeper than 4 m the period range is about

INFLUENCE OF TOPOGRAPHY ON SHALLOW WATER WAVE CHARACTERISTICS

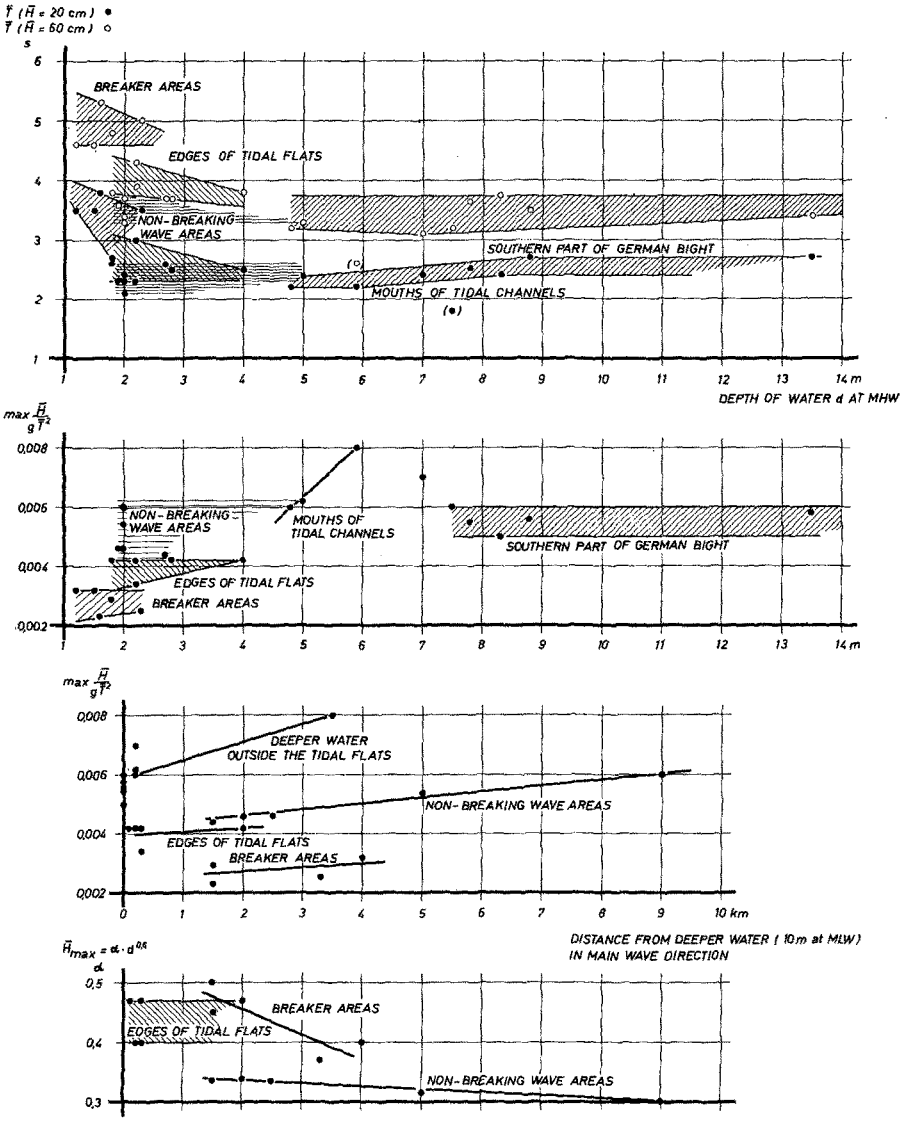

Fig. 7

constant. With the following transition into the tidal flats, going from right to left on the 2 upper graphs of fig. 7, the period range changes concerning to the wave character, as shown on fig. 6.

Wave Height Distributions

Prototype data on the tidal flats in the Elbe estuary proved wave heights and periods to follow Rayleigh-distributions (Siefert, 1971). The distribution functions of the heights are represented by the distribution factor $C_{1/3}$, i.e. significant over mean wave height (fig. 8). Now the data indicate, that combined with the increase of wave height up to $\overline{H}$ = 60 cm there is a clear narrowing of the wave height distribution, as represented by the factor $C_{1/3}$ on fig. 5 and 6. In the breaker zone on tidal flats this value becomes 1.41 instead of 1.60 in deep water. It can be seen than the determination of a realistic distribution is of remarkable importance for the choise of a design wave height. For example, the distribution of Longuet-Higgins with $C_{1/3}$ = 1.60 on fig. 8 delivers a value for the 10% highest waves of 2.03 $\overline{H}$ instead of 1.72 $\overline{H}$, as can be expected in the breaker zone on the tidal flats.

Steepness of Waves in Shallow Water

The periods of waves of constant height growing longer on the way into the breaker zone consequently reduce the steepness factor (fig. 5 and 6). Though these graphs do not represent simultanous waves in different areas, the tendency can be generalized: Waves running from deeper water into the tidal flats loose up to 50% of their height, while the period remains constant or gradually increases, the result always being a distinct decrease of the so-called steepness factor.

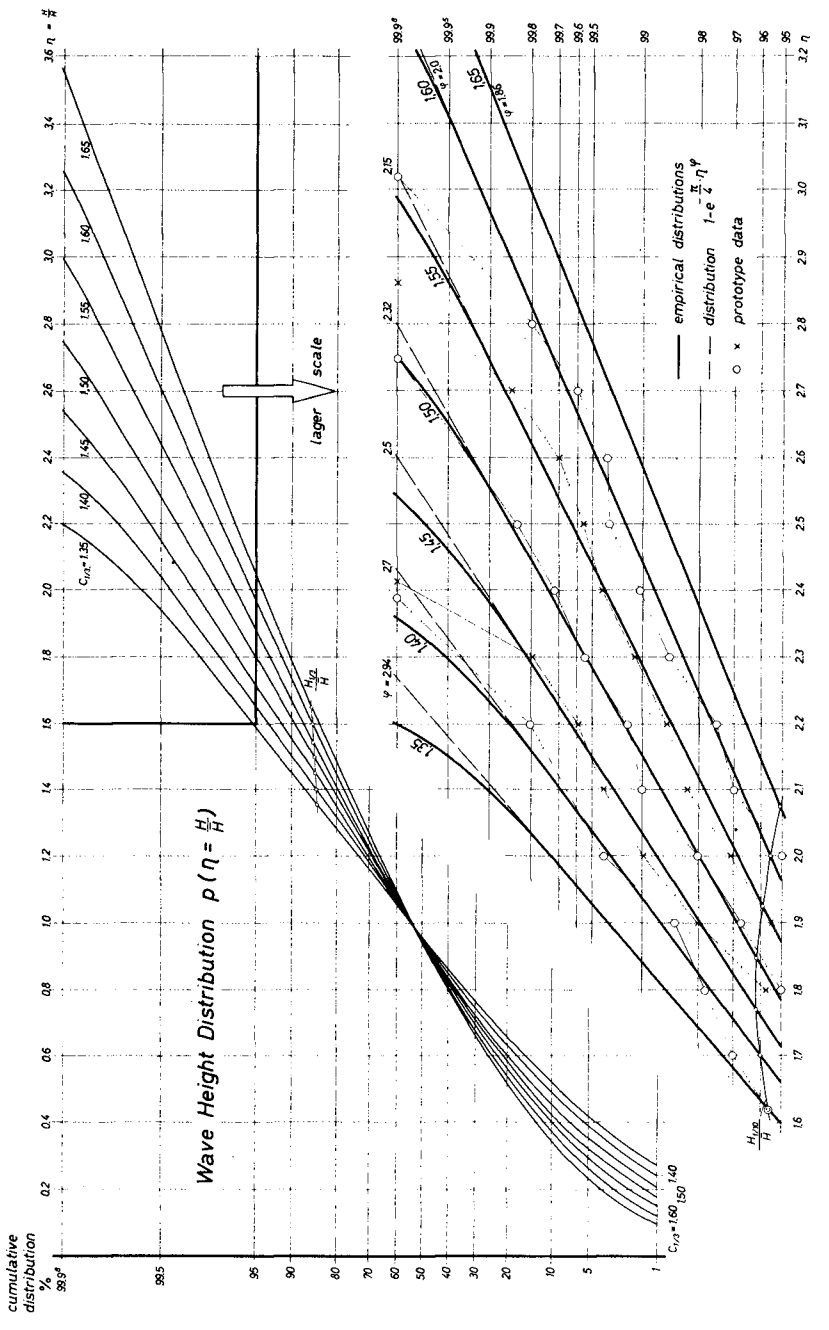
Wave Height Distribution $p(\eta = \frac{H}{\bar{H}})$
cumulative distribution %
larger scale
empirical distributions
distribution $1-e^{-\frac{\pi}{4}\eta^2}$
prototype data
$\frac{H_{1/3}}{\bar{H}}$
$\frac{H_{1/10}}{\bar{H}}$
$\eta = \frac{H}{\bar{H}}$
$C_{1/3}$=1.35
$C_{1/3}$=1.60
φ=2.34
φ=2.20
φ=1.86

Fig. 8

Comparing maximum steepness of breaking and non-breaking waves, fig. 5 to 7 show, that the steepness-factor of breaking waves on tidal flats is clearly smaller than of non-breaking waves. This is also indicated by the upper limits of the scattering areas for two stations with non-breaking and breaking waves respectively (fig. 9).

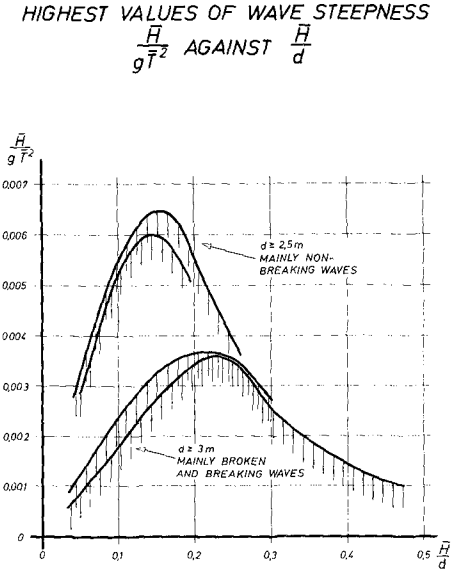

Fig. 9

Apparently the steepness factor is very small for small relative wave heights, i.e. small wind waves on the flats, and again becomes small for great relative heights, i.e. breaking waves in shallow water. The steepness factor does not increase continuously with relative wave height, indicating that not steepness but water depth is the criterion for the highest wave heights in shallow water. Neither does $\frac{\bar{H}}{\bar{L}}$ sufficiently represent the steepness of breakers with long troughs, and steep slopes only near

the crests. So the ratio $\frac{\overline{H}}{g \cdot \overline{T}^2}$ seems to be unsuitable as an item to describe wave characteristics in shallow water. A factor would be much more valuable that represents the asymmetric profile of a wave in shallow water. But as there is no correlation between heights and periods of single waves in a natural spectrum, the asymmetry must become smaller the higher the mean waves are. This again leads to a somewhat peculiar conclusion.

Highest Waves in Shallow Water

The height of the highest possible waves in shallow water has to be discussed with special respect to the conclusions for design waves. Data from 8 stations in breaking areas on shallow flats delivered a very simple empirical formula for the highest possible mean wave heights (Siefert, 1973)

$$\overline{H}_{max} = 0.5 \cdot d^{0.6}$$

indicating higher waves than usually are thought to be possible. In areas with mainly non-breaking waves the highest mean waves reach three quarters of these values, i.e.

$$\overline{H}_{max} = 0.375\ d^{0.6}$$

(fig. 4 and 5).

The values for the extreme waves in the wave spectrum with a probability of occurence 1:5000, i.e. once during a tide, are much higher than usually recognized, especially in water depths below 2 m. They can be evaluated as functions of d and $C_{1/3}$ as shown in fig. 5:

$$C_{1/3} = f(\overline{H}) \text{ with } \overline{H} = f(d)$$

Fig. 8 then delivers

$$H(1:5000) = H_{max}(\overline{H}_{max}) = f(C_{1/3})$$

as the highest possible single wave in a spectrum. It is

$$H_{max}(\overline{H}_{max}) = 1.2\ d^{0.6}$$

in breaker areas and

$$H_{max}(\overline{H}_{max}) = 0.95\ d^{0.6}$$

in areas with mainly non-breaking waves (fig. 10). Ratios H over d higher than 1.0 and even 1.5 are realistic. In 1 m deep water the extreme wave measures 1.2 m, and in half a meter deep water the highest possible wave is double as high as the often used 0.78 d (fig. 10).

With respect to a recent publication concerning breaker travel and breaking processes (Galvin, 1969), the maximum breaker heights on slopes were determined for three height groups and different depths of water (fig. 11).

Galvin's breaker travel distance X_b reads

$$X_b = 2 \cdot (4.0 - 9.25\ m) \cdot H_b$$

with m = slope $\tan\alpha$

H_b = breaker height

Galvin recommends to calculate the design wave height as the height at a distance of $\frac{1}{2} X_b$ before the structure. The safest way is of course to regard X_b completely, as is done on fig. 11. Further investigation has to be done on the problem of the definition of H_b. Unter the supposition that H_b can be replaced by any mean height of a breaking wave group of the natural spectrum, the curves on fig. 11 can

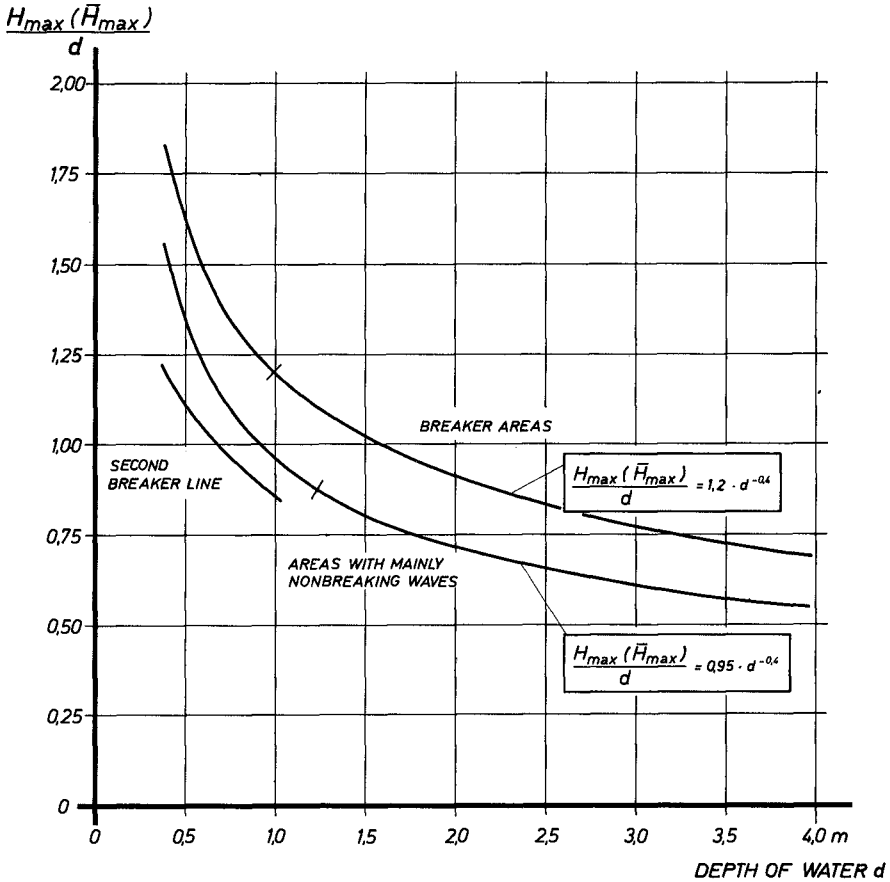

Fig. 10
Highest Possible Single Waves in Shallow Water
(Prototype Data from Elbe Estuary)

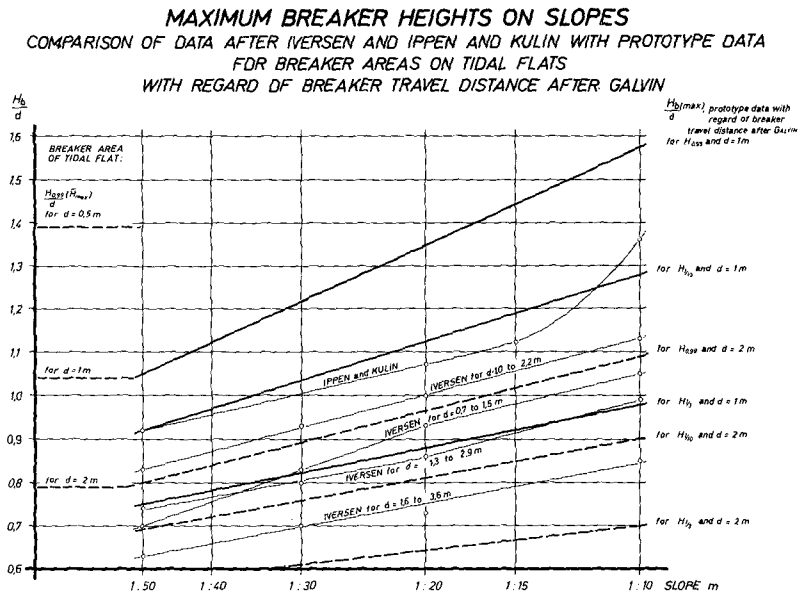

Fig. 11

be constructed, i.e.

$$X_b\ (H_{1/3}) = 2 \cdot (4.0 - 9.25\ \text{m}) \cdot H_{1/3}$$

If treated in this way, it turns out that even the highest heights of Ippen and Kulin do not represent the highest possible values. They seem to be sufficient for waves in water depths no less than 2 m.

References

GALVIN, C.J. jr.: Braker Travel and Choice of Design Wave Height. Journal of the Waterways and Harbors Div., ASCE, Vol. 95, No. WW 2, 1969

KISHI, T.: The Possible Highest Gravity Waves in Shallow Water. Coastal Eng. in Japan, Jap. Soc. of Civil Eng., Tokyo 1959

SIEFERT, W.: Wave Investigations in Shallow Water. Proc. 12th Coastal Eng. Conf., 1970. ASCE, New York, 1971

SIEFERT, W.: Über den Seegang in Flachwassergebieten. (In preparation for publication in 1973)

WIEGEL, R.L.: Oceanographical Engineering. Prentice-Hall Inc., Englewood Cliffs, N.J., 1964

CHAPTER 17

SHOALING OF FINITE AMPLITUDE LONG WAVES ON A BEACH OF CONSTANT SLOPE

Yuichi Iwagaki
Professor
and
Tetsuo Sakai
Assistant Professor

Department of Civil Engineering
Kyoto University
Kyoto, Japan

ABSTRACT

A solution of finite amplitude long waves on constant sloping beaches is obtained by solving the equations of the shallow water theory of the lowest order. Non-linearity of this theory is taken into account, using the perturbation method. Bessel functions involved in the solution are approximated with trigonometric functions. The applicable range of this theory is determined from the two limit conditions caused by the hydrostatic pressure assumption and the trigonometric function approximation of Bessel functions.

The shoaling of this finite amplitude long waves on constant sloping beaches is discussed. Especially, the effects of the beach slope on the wave height change and the asymmetric wave profile near the breaking point are examined, which can not be explained by the concept of constancy of wave energy flux based on the theory of progressive waves in uniform depth. These theoretical results are presented graphically, and compared with curves of wave shoaling based on finite amplitude wave theories.

On the other hand, the experiments are conducted with respect to the transformation of waves progressing on beaches of three kinds of slopes (1/30, 1/20 and 1/10). The experimental results are compared with the theoretical curves to confirm the validity of the theory.

INTRODUCTION

As waves progress in shallow water, wave transformations occur due to the presence of the sea bottom. Especially, the changes of wave height, celerity and length in shoaling water are generally explained by using the assumption that the wave energy flux based on the theory of progressive waves in uniform depth is kept constant in shoaling water[1),2)]. On the other hand, some investigator[3),4)] have attempted to obtain a solution of wave transformation on the sloping beach considering the change of water depth as the bottom condition. The existing results of observations and experiments show that the

change of wave height, celerity and length are well explained by the concept of constancy of energy flux based on theories of finite amplitude wave in uniform depth[2].

However, on sloping beaches, not only the wave height increases but also the wave profile becomes asymmetric[5]. Further, as Goda[6] pointed out recently, it is obvious that the beach slope affects the breaking wave height. Similarly, the beach slope will affect the wave transformations before breaking. These two problems, i.e. the asymmetry of wave profile and the effect of beach slope, can not be explained by using the approximate method of energy flux of waves in uniform depth. They will be explained by the solution of progressive waves on the beach mentioned above. However, none of existing theoretical investigations has given any solution to clarify these problems, except Biesel's investigation[7] which proposed a quantity representing the asymmetry of wave profile.

This paper treats analytically the two-dimensional wave transformation on constant sloping beaches in order to explain the asymmetry of wave profile and the beach slope effect on wave transformation. As the method to obtain the solution of progressive waves on the beach, two approximate methods exist, which are the small amplitude approximation and the shallow water approximation. In this paper, the shallow water theory of the lowest order[8] is used as the basic equations. These equations are non-linear, and the linear solution was already obtained[9]. It is seems that two problems mentioned above can be explained by taking this non-linearity into account. Carrier and Greenspan[10] and Ichiye[11] solved this non-linear shallow water theory already, but did not make clear these problems.

The non-linearity of this shallow water theory is taken into account herein by using the perturbation method as Ichiye did. Further, by using the asymptotic expansion of Bessel functions with trigonometric functions, the general solution of finite amplitude long waves progressing on the beach of a uniform slope is obtained. Based on this solution, the graphs showing the effects of beach slope on the wave height change and the asymmetry of wave profile are presented. On the other hand, the experiments with respect to wave shoaling on beaches of three kinds of slopes (1/30, 1/20 and 1/10) are conducted. The experimental results are compared with the theoretical ones in order to confirm the validity of this theory.

DERIVATION OF SOLUTION

BASIC EQUATIONS

The equations of two-dimensional shallow water theory of lowest order are as follows (see Fig.1) :

$$\left.\begin{aligned} u_t + u \cdot u_x + g \cdot \eta_x = 0 \,, \\ \eta_t + \{ u \cdot (\eta + h) \}_x = 0 \,, \end{aligned}\right\} \quad (1)$$

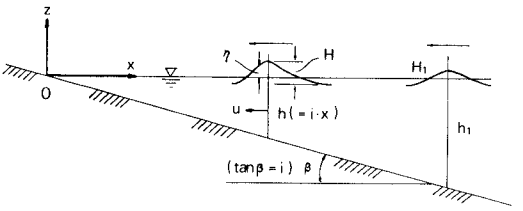

Fig.1 Sketch of waves on sloping beach

where h = h(x) is the water depth, $\eta = \eta(x,t)$ the height of water surface above still water level and u = u(x,t) the water particle velocity in the x-direction which is not dependent on the vertical coordinate. This implies that the pressure distribution is approximated with the hydrostatic distribution. Suffixes t and x denote the differentiations with t and x respectively. Eq.(1) is non-linear and frequently solved numerically with the method of characteristics. In this paper, the perturbation method is used in order to represent the non-linear effect analytically. That is, η and u are assumed to be expressed as the power series of a small quantity α as follows :

$$\eta = \alpha \cdot \eta^{(1)} + \alpha^2 \cdot \eta^{(2)} + \cdots\cdots , \quad u = \alpha \cdot u^{(1)} + \alpha^2 \cdot u^{(2)} + \cdots\cdots . \qquad (2)$$

Substituting Eq.(2) into Eq.(1) and rearranging with respect to α and α^2, the coefficients of α and α^2 lead respectively

$$u^{(1)}{}_t + g \cdot \eta^{(1)}{}_x = 0 , \quad \eta^{(1)}{}_t + \{ u^{(1)} \cdot h \}_x = 0 , \qquad (3)$$

and

$$u^{(2)}{}_t + u^{(1)} \cdot u^{(1)}{}_x + g \cdot \eta^{(2)}{}_x = 0 , \quad \eta^{(2)}{}_t + \{ u^{(1)} \cdot \eta^{(1)} + u^{(2)} \cdot h \}_x = 0 . \qquad (4)$$

SOLUTION OF $\eta^{(1)}$ AND $u^{(1)}$

Eliminating $u^{(1)}$ in Eq.(3), the following equation is derived :

$$\eta^{(1)}{}_{tt} - g \cdot \{ \eta^{(1)}{}_x \cdot h \}_x = 0 . \qquad (5)$$

If the beach slope i is constant and the water depth h is ix (see Fig.1), Eq.(5) is further reduced as follows :

$$\eta^{(1)}{}_{tt} - g \cdot \{ \eta^{(1)}{}_{xx} \cdot i \cdot x + \eta^{(1)}{}_x \cdot i \} = 0 . \qquad (6)$$

$\eta^{(1)}$ is assumed to be expressed as

$$\eta^{(1)}(x, t) = \eta(x) \cdot \cos \sigma t . \qquad (7)$$

Therefore, from Eqs.(6) and (7), the equation of $\eta^{(1)}$ is obtained as follows :

$$x \cdot \eta_{xx} + \eta_x + (\sigma^2 / g i) \cdot \eta = 0 . \qquad (8)$$

When the variable x is replaced with w through the relationship[12],

$$x = (g i / 4 \sigma^2) \cdot w^2 , \qquad (9)$$

Eq.(8) is modified as

$$\eta_{ww} + (1 / w) \cdot \eta_w + \eta = 0 . \qquad (10)$$

It is evident that Eq.(10) posesses a solution consisting of Bessel function $J_0(w)$ and Neumann function $N_0(w)$. A similar result is obtained when $\eta^{(1)}$ is assumed as

$$\eta^{(1)}(x,\ t) = \eta(x)\cdot\sin\sigma t\ . \qquad \cdots\cdots (11)$$

When x (therefore w) approaches infinite, Bessel and Neumann functions are expanded asymptotically as follows :

$$\left.\begin{aligned} J_\nu(w) &\sim \sqrt{2/\pi w}\cdot\cos(w-\nu\pi/2-\pi/4)\ , \\ N_\nu(w) &\sim \sqrt{2/\pi w}\cdot\sin(w-\nu\pi/2-\pi/4)\ . \end{aligned}\right\} \qquad \cdots\cdots (12)$$

Accordingly the solution $\eta^{(1)}$ corresponding to the waves progressing in the negative x-direction (see Fig.1) is given as[9]

$$\eta^{(1)}(x,\ t) = a\cdot\{\cos\sigma t\cdot J_0(2\sigma\sqrt{\frac{x}{gi}}) - \sin\sigma t\cdot N_0(2\sigma\sqrt{\frac{x}{gi}})\}, \qquad \cdots\cdots (13)$$

where a is a constant related to the wave height. Using the relationships,

$$Z_0'(w) = -Z_1(w)\ ,\quad Z_1'(w) = Z_0(w) - w^{-1}\cdot Z_1(w)\ , \qquad \cdots\cdots (14)$$

and Eq.(3), $u^{(1)}$ is obtained as

$$u^{(1)}(x,\ t) = a\sqrt{\frac{g}{i}}\cdot x^{-1/2}\cdot\{\sin\sigma t\cdot J_1(2\sigma\sqrt{\frac{x}{gi}}) + \cos\sigma t\cdot N_1(2\sigma\sqrt{\frac{x}{gi}})\}\ . \qquad \cdots\cdots (15)$$

Eqs.(13) and (15) are the solutions of Eq. (1) when the non-linearity is neglected. Due to the natures of J_0 and N_0, the amplitude of $\eta^{(1)}$ increases with decrease in x. Therefore the solution $\eta^{(1)}$ can explain the fact of wave height increase in shoaling water. However, the wave profile of $\eta^{(1)}$ with time has the form of sine function, and can not explain the experimental fact of asymmetric and forward inclined wave profile on the sloping beach (see Fig.2[5]).

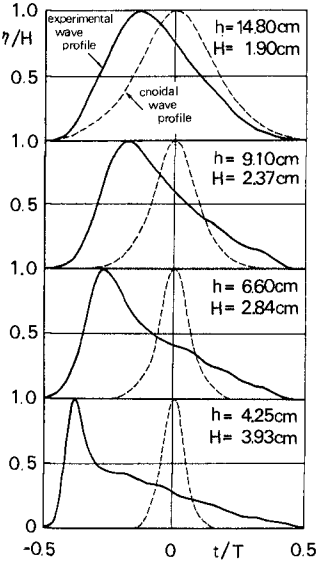

Fig.2 Asymmetric wave profile on sloping beach[5]

SOLUTION OF $\eta^{(2)}$ AND $u^{(2)}$

When $u^{(2)}$ is eliminated and the relation h = i×x is used in Eq.(4), the following equation is obtained.

$$\eta^{(2)}{}_{tt} - g\cdot\{\eta^{(2)}{}_{xx}\cdot i\cdot x + \eta^{(2)}{}_{x}\cdot i\} = -\{u^{(1)}\cdot\eta^{(1)}\}_{xt} + \{u^{(1)}\cdot u^{(1)}{}_{x}\}_{x}\cdot i\cdot x + \{u^{(1)}\cdot u^{(1)}{}_{x}\}\cdot i\ . \qquad \cdots\cdots (16)$$

After substituting Eqs.(13) and (15) into Eq.(16), rearranging by using the relation of Eq. (14), the right side of Eq.(16) becomes as follows :

$$\cos 2\sigma t\cdot\{-\frac{3}{2}a^2\frac{\sigma^2}{i}x^{-1}\cdot(J_0^2 - J_1^2 - N_0^2 + N_1^2)$$

$$+\frac{5}{2}a^2\sqrt{\frac{g}{i}}\cdot\sigma\cdot x^{-3/2}\cdot(J_0J_1-N_0N_1)$$

$$-a^2\cdot g\cdot x^{-2}\cdot(J_1^2-N_1^2)\}$$

$$+\sin 2\sigma t\cdot\{3a^2\frac{\sigma^2}{i}x^{-1}\cdot(J_0N_0-J_1N_1)$$

$$-\frac{5}{2}a^2\sqrt{\frac{g}{i}}\cdot\sigma\cdot x^{-3/2}\cdot(J_1N_0+J_0N_1)$$

$$+2a^2\cdot g\cdot x^{-2}\cdot J_1N_1\}$$

$$+\{\frac{1}{2}a^2\frac{\sigma^2}{i}x^{-1}\cdot(J_0^2-J_1^2-N_0^2+N_1^2)$$

$$-\frac{3}{2}a^2\sqrt{\frac{g}{i}}\cdot\sigma\cdot x^{-3/2}\cdot(J_0J_1-N_0N_1)+a^2\cdot g\cdot x^{-2}\cdot(J_1^2-N_1^2)\}. \quad \cdots\cdots(17)$$

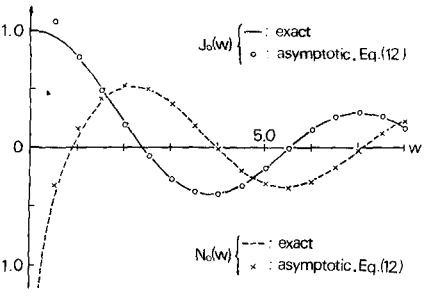

Fig.3 Approximate values by asymptotic expansion of Bessel and Neumann functions

In Fig.3, the approximate values of J_0 and N_0 based on Eq.(12) are compared with the exact ones. It is seen that the approximate values are accurate enough for the large value of w. When Bessel and Neumann functions in Eq.(17) are approximated with the trigonometric functions of Eq.(12), Eq.(17) becomes

$$\cos 2\sigma t\cdot\Big[-3a^2\frac{\sigma}{\pi}\sqrt{\frac{g}{i}}\cdot x^{-3/2}\cdot\cos\{2(2\sigma\sqrt{\frac{x}{gi}}-\frac{\pi}{4})\}$$

$$+\frac{5}{2}a^2\frac{g}{\pi}x^{-2}\cdot\sin\{2(2\sigma\sqrt{\frac{x}{gi}}-\frac{\pi}{4})\}+a^2\frac{g}{\pi\sigma}\sqrt{gi}\cdot x^{-5/2}\cdot\cos\{2(2\sigma\sqrt{\frac{x}{gi}}-\frac{\pi}{4})\}\Big]$$

$$+\sin 2\sigma t\cdot\Big[3a^2\frac{\sigma}{\pi}\sqrt{\frac{g}{i}}\cdot x^{-3/2}\cdot\sin\{2(2\sigma\sqrt{\frac{x}{gi}}-\frac{\pi}{4})\}$$

$$+\frac{5}{2}a^2\frac{g}{\pi}x^{-2}\cdot\cos\{2(2\sigma\sqrt{\frac{x}{gi}}-\frac{\pi}{4})\}-a^2\frac{g}{\pi\sigma}\sqrt{gi}\cdot x^{-5/2}\cdot\sin\{2(2\sigma\sqrt{\frac{x}{gi}}-\frac{\pi}{4})\}\Big]$$

$$+\Big[a^2\frac{\sigma}{\pi}\sqrt{\frac{g}{i}}\cdot x^{-3/2}\cdot\cos\{2(2\sigma\sqrt{\frac{x}{gi}}-\frac{\pi}{4})\}$$

$$-\frac{3}{2}a^2\frac{g}{\pi}\cdot x^{-2}\cdot\sin\{2(2\sigma\sqrt{\frac{x}{gi}}-\frac{\pi}{4})\}-a^2\frac{g}{\pi\sigma}\sqrt{gi}\cdot x^{-5/2}\cdot\cos\{2(2\sigma\sqrt{\frac{x}{gi}}-\frac{\pi}{4})\}\Big]. \quad \cdots\cdots(18)$$

The solution of $\eta^{(2)}$ is assumed to be expressed as

$$\eta^{(2)}(x,t)=\cos 2\sigma t\cdot A(x)+\sin 2\sigma t\cdot B(x)+C(x). \quad \cdots\cdots(19)$$

Substituting Eq.(19) into the left side of Eq.(16), it becomes

$$\cos 2\sigma t\cdot\{-4\sigma^2\cdot A(x)-g\cdot i\cdot x\cdot A''(x)-g\cdot i\cdot A'(x)\}$$

$$+\sin 2\sigma t\cdot\{-4\sigma^2\cdot B(x)-g\cdot i\cdot x\cdot B''(x)-g\cdot i\cdot B'(x)\}$$

$$+\{-g\cdot i\cdot C''(x)-g\cdot i\cdot C'(x)\}. \qquad \cdots\cdots (20)$$

Comparing Eqs.(18) and (20), A(x), B(x) and C(x) are determined as follows :

$$A(x)=-a^2\frac{1}{\pi i}\cdot x^{-1}\cdot\sin\{2(2\sigma\sqrt{\frac{x}{gi}}-\frac{\pi}{4})\}-\frac{3}{10}a^2\frac{1}{\pi\sigma}\sqrt{\frac{g}{i}}\cdot x^{-3/2}\cdot\cos\{2(2\sigma\sqrt{\frac{x}{gi}}-\frac{\pi}{4})\}, \qquad \cdots\cdots (21)$$

$$B(x)=-a^2\frac{1}{\pi i}\cdot x^{-1}\cdot\cos\{2(2\sigma\sqrt{\frac{x}{gi}}-\frac{\pi}{4})\}+\frac{3}{10}a^2\frac{1}{\pi\sigma}\sqrt{\frac{g}{i}}\cdot x^{-3/2}\cdot\sin\{2(2\sigma\sqrt{\frac{x}{gi}}-\frac{\pi}{4})\}, \qquad \cdots\cdots (22)$$

$$C(x)=\frac{1}{4}a^2\frac{1}{\pi\sigma}\sqrt{\frac{g}{i}}\cdot x^{-3/2}\cdot\cos\{2(2\sigma\sqrt{\frac{x}{gi}}-\frac{\pi}{4})\}-\frac{1}{16}a^2\frac{g}{\pi\sigma^2}\cdot x^{-2}\cdot\sin\{2(2\sigma\sqrt{\frac{x}{gi}}-\frac{\pi}{4})\}. \qquad \cdots\cdots (23)$$

Substituting Eqs.(21), (22) and (23) into Eq.(20), the left side of Eq. (16) becomes

$$\begin{aligned}
&\cos 2\sigma t\cdot\Big[-3a^2\frac{\sigma}{\pi}\sqrt{\frac{g}{i}}\cdot x^{-3/2}\cdot\cos\{2(2\sigma\sqrt{\frac{x}{gi}}-\frac{\pi}{4})\}\\
&\quad+\frac{5}{2}a^2\frac{g}{\pi}x^{-2}\cdot\sin\{2(2\sigma\sqrt{\frac{x}{gi}}-\frac{\pi}{4})\}+\frac{27}{40}a^2\frac{g}{\pi\sigma}\sqrt{gi}\cdot x^{-5/2}\cdot\cos\{2(2\sigma\sqrt{\frac{x}{gi}}-\frac{\pi}{4})\}\Big]\\
&+\sin 2\sigma t\cdot\Big[3a^2\frac{\sigma}{\pi}\sqrt{\frac{g}{i}}\cdot x^{-3/2}\cdot\sin\{2(2\sigma\sqrt{\frac{x}{gi}}-\frac{\pi}{4})\}\\
&\quad+\frac{5}{2}a^2\frac{g}{\pi}x^{-2}\cdot\cos\{2(2\sigma\sqrt{\frac{x}{gi}}-\frac{\pi}{4})\}-\frac{27}{40}a^2\frac{g}{\pi\sigma}\sqrt{gi}\cdot x^{-5/2}\cdot\sin\{2(2\sigma\sqrt{\frac{x}{gi}}-\frac{\pi}{4})\}\Big]\\
&+\Big[a^2\frac{\sigma}{\pi}\sqrt{\frac{g}{i}}\cdot x^{-3/2}\cdot\cos\{2(2\sigma\sqrt{\frac{x}{gi}}-\frac{\pi}{4})\}-\frac{3}{2}a^2\frac{g}{\pi}\cdot x^{-2}\cdot\sin\{2(2\sigma\sqrt{\frac{x}{gi}}-\frac{\pi}{4})\}\\
&\quad-a^2\frac{g}{\pi\sigma}\sqrt{gi}\cdot x^{-5/2}\cdot\cos\{2(2\sigma\sqrt{\frac{x}{gi}}-\frac{\pi}{4})\}+\frac{1}{4}a^2\frac{g^2}{\pi\sigma^2}\cdot i\cdot x^{-3}\cdot\sin\{2(2\sigma\sqrt{\frac{x}{gi}}-\frac{\pi}{4})\}\Big].
\end{aligned} \qquad \cdots\cdots (24)$$

From the comparison between Eqs.(18) and (24), it is found that the difference exists between the constants in the third terms of coefficients of cos2σt and sin2σt. Further, the forth term in the last part (independent on t) exists only in Eq.(24). Three terms in the coefficients of cos2σt and sin2σt involve $x^{-3/2}$, x^{-2} and $x^{-5/2}$ in turn, and the forth term in the last part of Eq.(24) involves x^{-3}. Using the relationships of $T = 2\pi/\sigma$ and $h = i\cdot x$, the ratios of the second, third and forth terms to the first term become :

2nd/1st term $\sim \{(gT/2\pi)/\sqrt{gh}\}\cdot i$, 3rd/1st term $\sim [\{(gT/2\pi)/\sqrt{gh}\}\cdot i]^2$,

and 4th/1st term $\sim [\{(gT/2\pi)/\sqrt{gh}\}\cdot i]^3$.

Therefore the higher term becomes smaller in proportion to i.

The third terms in the coefficients of cos2σt and sin2σt have $\cos\{2(2\sigma\sqrt{x/gi}-\pi/4)\}$ and $\sin\{2(2\sigma\sqrt{x/gi}-\pi/4)\}$ respectively, and are in the same phase as that of the first term. If i = 1/10, h = 20cm and T = 3sec, the ratio of third to first term $[\{(gT/2\pi)/\sqrt{gh}\}i]^2$ becomes smaller than 1/10, and the difference

between constants of the third terms is negligible. Similarly, the forth term in the last part of Eq.(24), which has $\sin\{2(2\sigma\sqrt{x/gi}-\pi/4)\}$ is in the same phase as that of the second term, and also negligible.

Therefore, Eq.(19) with Eqs.(21), (22) and (23) is the solution of Eq. (16), and expressed as follows :

$$\eta^{(2)}(x,\ t)=\cos 2\sigma t\Big[-a^2\frac{1}{\pi i}\cdot x^{-1}\cdot\sin\Big\{2\Big(2\sigma\sqrt{\frac{x}{gi}}-\frac{\pi}{4}\Big)\Big\}$$

$$-\frac{3}{10}a^2\frac{1}{\pi\sigma}\sqrt{\frac{g}{i}}\cdot x^{-3/2}\cdot\cos\Big\{2\Big(2\sigma\sqrt{\frac{x}{gi}}-\frac{\pi}{4}\Big)\Big\}\Big]$$

$$+\sin 2\sigma t\cdot\Big[-a^2\frac{1}{\pi i}x^{-1}\cdot\cos\Big\{2\Big(2\sigma\sqrt{\frac{x}{gi}}-\frac{\pi}{4}\Big)\Big\}$$

$$+\frac{3}{10}a^2\frac{1}{\pi\sigma}\sqrt{\frac{g}{i}}\cdot x^{-3/2}\cdot\sin\Big\{2\Big(2\sigma\sqrt{\frac{x}{gi}}-\frac{\pi}{4}\Big)\Big\}\Big]$$

$$+\Big[\frac{1}{4}a^2\frac{1}{\pi\sigma}\sqrt{\frac{g}{i}}\cdot x^{-3/2}\cdot\cos\Big\{2\Big(2\sigma\sqrt{\frac{x}{gi}}-\frac{\pi}{4}\Big)\Big\}$$

$$-\frac{1}{16}a^2\frac{g}{\pi\sigma^2}\cdot x^{-2}\cdot\sin\Big\{2\Big(2\sigma\sqrt{\frac{x}{gi}}-\frac{\pi}{4}\Big)\Big\}\Big]\ . \qquad \cdots\cdots(25)$$

Using the relationship of Eq.(12), $\eta^{(1)}$ of Eq.(13) becomes

$$\eta^{(1)}(x,\ t)=a\cdot\Big(\frac{\sqrt{gi}}{\pi\sigma}\Big)^{1/2}\cdot x^{-1/4}\cdot\cos\Big(\sigma t+2\sigma\sqrt{\frac{x}{gi}}-\frac{\pi}{4}\Big)\ . \qquad \cdots\cdots(26)$$

For the sake of comparison with Eq.(26), Eq.(25) is finally reduced as follows :

$$\eta^{(2)}(x,\ t)=a^2\frac{1}{\pi i}\cdot x^{-1}\cdot\cos\Big\{2\Big(\sigma t+2\sigma\sqrt{\frac{x}{gi}}-\frac{\pi}{4}\Big)+\frac{\pi}{2}+\tan^{-1}\Big(\frac{3}{10}\frac{\sqrt{gi}}{\sigma}\cdot x^{-1/2}\Big)\Big\}$$

$$+\Big[\frac{1}{4}a^2\frac{1}{\pi\sigma}\sqrt{\frac{g}{i}}\cdot x^{-3/2}\cdot\cos\Big\{2\Big(2\sigma\sqrt{\frac{x}{gi}}-\frac{\pi}{4}\Big)\Big\}-\frac{1}{16}a^2\frac{g}{\pi\sigma^2}\cdot x^{-2}\cdot\sin\Big\{2\Big(2\sigma\sqrt{\frac{x}{gi}}-\frac{\pi}{4}\Big)\Big\}\Big]. \qquad \cdots\cdots(27)$$

APPLICABLE RANGE OF SOLUTION

The basic equation (1) is the shallow water theory of the lowest order[8], and the pressure distribution is assumed to be hydrostatic. Therefore these solutions are applicable only when the water depth is considerably smaller than the wave length. If the wave celerity is equal to that of long waves $\sqrt{gh}$,

$$h\ /\ L=1\ /\ (T\sqrt{g\ /\ h})\ . \qquad \cdots\cdots(28)$$

The upper limit of h/L implies that the lower limit of $T\sqrt{g/h}$ exists and that the upper limit of the water depth h exists if the wave period is given. On the other hand, the lower limit of h also exists. As the solution of $\eta^{(1)}$, Eq.(26) is used in which Bessel and Neumann functions are approximated with

trigonometric functions by Eq.(12), which is the asymptotic expansion when $|w| \to \infty$. Comparing between the exact and approximate values of J_0, N_0, J_1 and N_1, it is found that the approximate values are accurate enough when $|w| \geqq 1.0$. Using Eq.(9), this condition is rewritten as follows :

$$T\sqrt{g/h} \leq 4\pi/i \quad \cdots\cdots(29)$$

This means that the lower limit of h determined by the beach slope exists when the wave period is given. Two conditions mentioned above are shown in Fig.4. Two lines showing the lower limit of $T\sqrt{g/h}$ are given for the two limiting values of h/L.

DETERMINATION OF α

The second part of the right side of Eq.(27) consists of two terms involving $x^{-3/2}$ and x^{-2} respectively. The ratios of these to the first term in the first part of the right side are $\{(gT/2\pi)/\sqrt{gh}\}i$ and $\{(gT/2\pi)/\sqrt{gh}\}i\}^2$ respectively. Therefore the second part is smaller than the first part by the order of $\{(gT/2\pi)/\sqrt{gh}\}i$. Further, because of independence of t, the second part affects only the still water level and does not affect the wave height and wave profile. Becuase this paper deals with the beach slope effect on the wave height change and wave profile asymmetry, the second part of the right side of Eq.(27) is neglected.

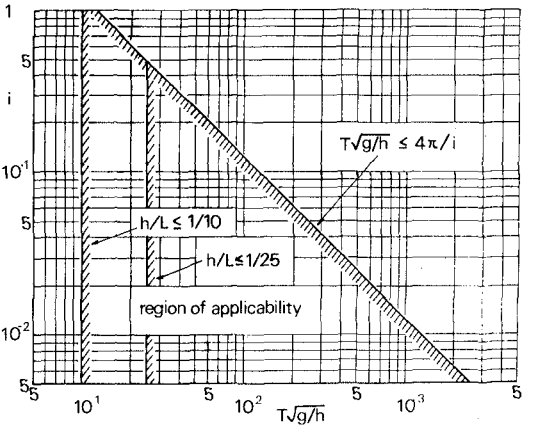

Fig.4 Applicable range

Substituting $\eta^{(1)}$ of Eq.(26) and $\eta^{(2)}$ of Eq.(27) into Eq.(2), the wave profile is given by

$$\eta(x,t) = \alpha \cdot a \cdot \left(\frac{\sqrt{gi}}{\pi\sigma}\right)^{1/2} \cdot x^{-1/4} \cdot \cos\left(\sigma t + 2\sigma\sqrt{\frac{x}{gi}} - \frac{\pi}{4}\right)$$

$$+ \alpha^2 \cdot \frac{a^2}{\pi i} \cdot x^{-1} \cdot \cos\left\{2\left(\sigma t + 2\sigma\sqrt{\frac{x}{gi}} - \frac{\pi}{4}\right) + \frac{\pi}{2} + \tan^{-1}\left(\frac{3}{10}\frac{\sqrt{gi}}{\sigma} \cdot x^{-1/2}\right)\right\} . \quad (30)$$

Now, h_1/L_0 is applied as the small quantity α, where h_1 is the largest water depth in the applicable range of this solution (see Fig.4) and L_0 is the deep-water wave length of the small amplitude wave theory, $gT^2/2\pi$.

DETERMINATION OF a

Substituting $\alpha = h_1/L_0$ into Eq.(30) and rearranging, Eq.(30) is simply rewritten as follows :

$$\eta / h_1 = A^{(1)} \cdot \cos\theta + A^{(2)} \cdot \cos(2\theta + \delta), \quad \cdots\cdots(31)$$

where $A^{(1)}$, $A^{(2)}$, θ and δ are are given by

$$\left.\begin{aligned} A^{(1)} &= 2^{-1/4} \cdot \pi^{-3/4} \cdot i^{1/2} \cdot (h_1 / L_0)^{3/4} \cdot (h_1 / h)^{1/4} \cdot (a / h_1), \\ A^{(2)} &= \pi^{-1} \cdot (h_1 / L_0)^2 \cdot (h_1 / h) \cdot (a / h_1)^2, \\ \theta &= 2\pi / T \cdot t + 2\pi\{\sqrt{2/\pi} \cdot (h / L_0)^{-1/2}\} \cdot x / L_0 - \pi / 4, \\ \delta &= \pi / 2 + \tan^{-1}\{3 / 10 \cdot \sqrt{2\pi}^{-1} \cdot i \cdot (h / L_0)^{-1/2}\}. \end{aligned}\right\} \quad \cdots\cdots(32)$$

If $A^{(1)}{}_1$ and $A^{(2)}{}_1$ denote $A^{(1)}$ and $A^{(2)}$ at $h = h_1$ respectively, these are

$$\left.\begin{aligned} A^{(1)}{}_1 &= 2^{-1/4} \cdot \pi^{-3/4} \cdot i^{1/2} \cdot (h_1 / L_0)^{3/4} \cdot (a / h_1), \\ A^{(2)}{}_1 &= \pi^{-1} \cdot (h_1 / L_0)^2 \cdot (a / h_1)^2. \end{aligned}\right\} \quad \cdots\cdots(33)$$

Because $\tan^{-1}\{\ \}$ in δ of Eq.(32) is smaller than $\pi/2$ at h_1, it is neglected. Therefore the wave profile η_1 at h_1 is given as follows :

$$\eta_1 / h_1 = A^{(1)}{}_1 \cdot f(\theta), \quad (34)$$

where

$$f(\theta) = \cos\theta - b \cdot \sin 2\theta,$$

$$b = A^{(2)}{}_1 / A^{(1)}{}_1. \quad (35)$$

Fig.5 shows the profile of $f(\theta)$ in the range of $-\pi \leqq \theta \leqq \pi$. It is evident that the relative wave height H_1/h_1 at h_1 is given

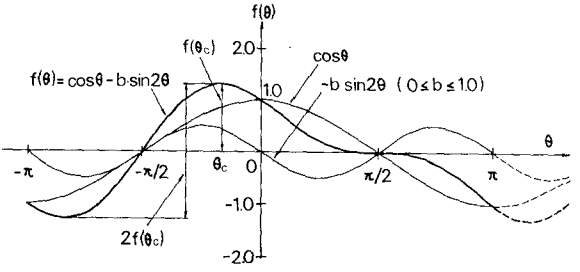

Fig.5 Profile of $f(\theta)$

$$H_1 / h_1 = 2 \times A^{(1)}{}_1 \cdot f(\theta_c). \quad \cdots\cdots(36)$$

θ_c is determined from $df/d\theta = 0$. After all, considering $-\pi/2 \leqq \theta_c \leqq 0$,

$$\sin\theta_c = (1 / 4b - \sqrt{1/16b^2 + 2}) / 2. \quad \cdots\cdots(37)$$

In Eq.(36), $A^{(1)}{}_1$ is the function of a/h_1, and $f(\theta_c)$ is also the function of a/h_1 because b ($= A^{(2)}{}_1/A^{(1)}{}_1$) is dependent on a/h_1. Therefore a is determined from H_1 by using Eq.(36).

DISCUSSION OF SOLUTION

For simplicity, the second term of right side of Eq.(31) is assumed to be smaller than the first term at h_1 and negligible. Therefore the wave height H_1 is equal to twice of the amplitude of the first term. Using this relationship, Eq.(31) is reduced as follows :

$$\eta / h_1 = 1/2 \cdot (H_1 / h_1) \cdot (h_1 / h)^{1/4} \cdot \cos\theta + \sqrt{2\pi} \cdot (h_1 / L_0)^{1/2} \cdot i^{-1} \cdot (H_1 / 2h_1)^2 \cdot (h_1 / h) \cdot \cos(2\theta + \delta) . \quad (38)$$

As seen in Eq.(38), the amplitude of the first term (the linear solution) is inversely proportional to the 1/4th power of the water depth h, and independen on the beach slope i. This agrees with Green[13]'s law with respect to the long wave transformation on very gentle sloping beaches without wave reflection and energy loss. On the other hand, the amplitude of the second term representing the nonlinear effect is inversely proportional to h, and the rate of wave height increase with decrease in the water depth is much larger than that of the first term. Further it depends on h_1/L_0 and the beach slope i. Especially, the amplitude of the second term increases inversely proportionally to the beach slope i, the effect of which has not been made clear previously.

The authors[2),5)] presented previously the theoretical curves of wave shoaling based on the wave energy flux of the hyperbolic wave theory which is the approximate representation of Laitone's cnoidal waves of the second approximation[14)]. Before these investigations, as the preliminary step, Iwagaki[15)] obtained the theoretical equation of wave height change based on the first approximation. The characteristics of this equation agree with the relationship between the amplitude of the second term and the water depth that the amplitude is inversely proportional to the water depth h. Furthermore, the period of the second term is a half of that of the first term, and the phase of the second term is in advance of that of the first term by δ. As seen from Eq.(32), δ consists of $\pi/2$ and $\tan^{-1}\{(3/10)\cdot(2\pi)^{-1/2}\cdot i\cdot(h/L_0)^{-1/2}\}$, which increases with decrease in the water depth. As descrebed later, the difference of phase explains the asymmetry of wave profile.

NUMERICAL COMPUTATION

RESTRICTION ON NUMERICAL COMPUTATION

As shown in Fig.4, the applicable range of the water depth h exists when the wave period T and the beach slope i are given, which is determined by two limit conditions of the hydrostatic pressure assumption and the trigonometric function approximation of Bessel and Neumann functions. However, some arbitrarity exists in determination of the limiting value of h/L, which corresponds to the largest water depth h_1 in the range. In this paper, the following value is adapted :

$$h / L \leq 1/20 . \quad (39)$$

From Eqs.(28) and (39), the following equation is obtained :

$$T\sqrt{g/h} \geq 20 . \quad (40)$$

Using the deep-water wave length $L_0 = gT^2/2\pi$, h_1 is given by

$$h_1 / L_0 = 0.0157 . \quad (41)$$

Before the changes in the wave height and profile with decrease in the water depth on the beach of constant slope i are discussed numerically, the wave height H_1 at h_1 is calculated by using the theoretical curves of wave height change, which the authors[2),5)] obtained based on the wave energy flux of the hyperbolic wave theory. If the value of deep-water wave steepness H_0/L_0 (H_0 : deep-water wave height) is given, the value of H_1/H_0 is obtained from the theoretical curve when $h_1/L_0 = 0.0157$ and the value of $H_1/h_1 = (H_1/H_0)\times(H_0/L_0)/(h_1/L_0)$ is calculated. According to the theoretical curves of hyperbolic waves, when $H_0/L_0 \geq 0.006$, waves already break at the water depth where $h_1/L_0 = 0.0157$. Therefore, the deep-water wave steepness to which this theory is applicable is restricted to considerably small values.

When the beach slope i is given, the value of a/h_1 can be calculated as described previously. However, the value of $A^{(2)}_1/A^{(1)}_1$ increases with decrease in i for a constant value of H_0/L_0 and with increase in H_0/L_0 for a constant value of i. The numerical computation is restricted in the range of $A^{(2)}/A^{(1)} \leq 1$. Therefore, for the larger value of H_0/L_0, the value of i for which the computation can be made becomes larger.

RESULTS OF NUMERICAL COMPUTATION

The numerical computations were conducted for the cases that the deep-water wave steepness $H_0/L_0 = 0.004$, 0.002, 0.001, 0.0004, 0.0002 and 0.0001. As mentioned above, for each value of H_0/L_0, the value of H_1/H_0 was calculated using the theoretical curves by the energy flux method[2),5)], for the largest water depth $h_1/L_0 = 0.0157$, where the computation was started. Further, the values of a/h_1 were calculated for given values of i. The values of i in computations were 1/10, 1/20, 1/30, 1/50, 1/100 and 1/200. However, due to the restriction on the beach slope mentioned above, the computations were conducted for the larger values of i than 1/100 when $H_0/L_0 = 0.001$, 1/50 when $H_0/L_0 = 0.002$, and 1/20 when $H_0/L_0 = 0.004$.

For each value of H_0/L_0 and i, using Eqs.(31) and (32), η/h_1 was computed for many values of h/L_0 which are smaller than h_1/L_0. The numerical computations were performed with FACOM 230-60 at the DATA PROCESSING CENTER, KYOTO

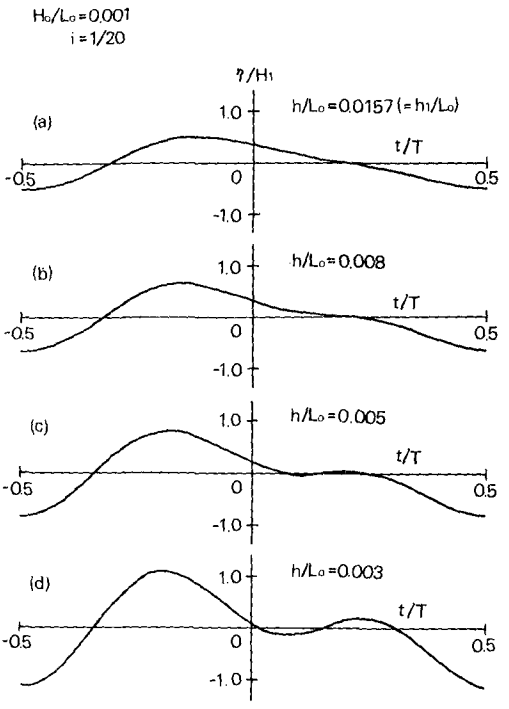

Fig.6 Wave profile change with decrease in water depth

UNIV.. One example is shown in Fig.6, for the case that $H_0/L_0 = 0.001$ and $i = 1/20$. The wave profile η is divided by the wave height H_1 at the water depth h_1. Therefore $(\eta/H_1)_{max} - (\eta/H_1)_{min} = 1.0$ in (a). This value increases with decrease in the water depth h (in order of (b), (c) and (d)), and it becomes larger than 2.0 in (d). Further, it is found that the slope of front face of the wave becomes steeper and that of back face becomes more gentle, so that the wave profile becomes more asymmetric and forward inclined. Thus, the asymmetric deformation of the wave profile in shoaling water can be explained by this solution.

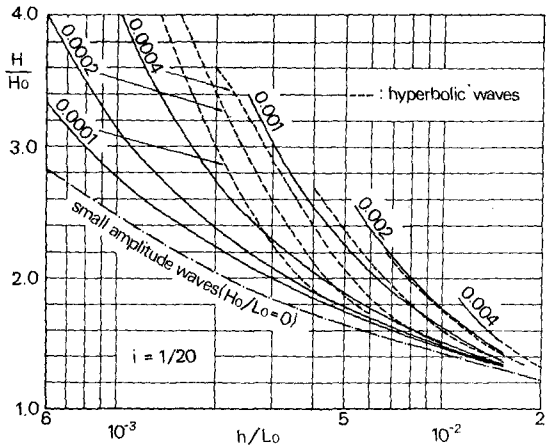

Fig.7 Effect of deep-water wave steepness on wave height change

Several examples of wave height change are shown in Figs.7 and 8. The beach slope i is constant (1/20) in Fig.7 and the deep-water wave steepness H_0/L_0 is constant (0.001) in Fig.8, which shows the effect of the beach slope on wave height change. The theoretical curves obtained under the assumption of constancy of energy flux of hyperbolic waves[2),5)] are also shown with broken lines. Similarly the curve of small amplitude waves is shown with chain line. At the upper end of each curve of this theory (full line) the value of $A^{(2)}/A^{(1)}$ approaches 1.0.

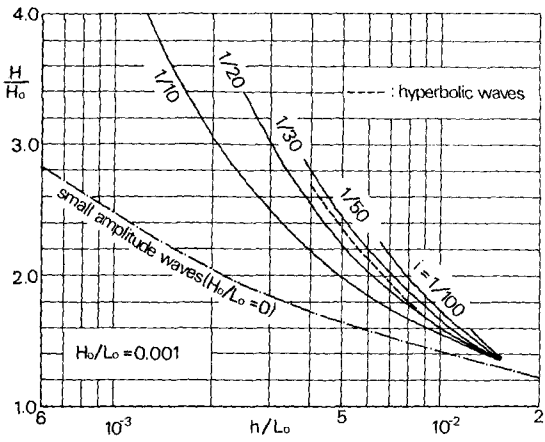

Fig.8 Effect of beach slope on wave height change

In general, the wave heights by this theory are always larger than those of small amplitude waves, and the rate of wave height increase with decrease in the water depth is larger than that of small amplitude waves. Further, as well as the curves of hyperbolic waves, the rate of wave height increase is larger for the larger value of the deep-water wave steepness. However, as the deep-water wave steepness becomes smaller, the value itself of this theory becomes smaller than that of hyperbolic waves. On

the other hand, for a constant deep-water wave steepness as in Fig.8, when the beach slope i is small, tha rate of wave height increase becomes large. This effect of the beach slope is expected from the fact that i^{-1} is involved in the coefficient of the second term of Eq.(38). Thus, this theory clarifies the effect of beach slope on the wave height change, which has not been made clear theoretically before.

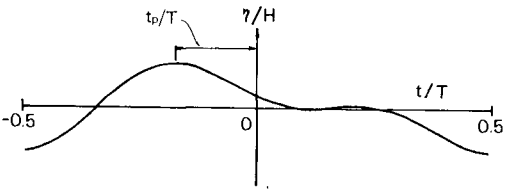

Fig.9 Parameter of asymmetry of wave profile

As a parameter representing the degree of asymmetry of the wave profile, t_p/T shown in Fig.9 is taken. Several examples of the change of t_p/T in shoaling water are shown in Fig.10 and 11. Fig.10 shows the case that the beach slope is constant (1/20) and Fig.11 is for the constant deep-water wave steepness (0.001). It is obvious that the value of t_p/T increases with decrease in the water depth and the wave profile becomes more asymmetric and forward inclined. It is found from the figures that the wave profile becomes more asymmetric for the larger deep-water wave steepness and for the smaller beach slope.

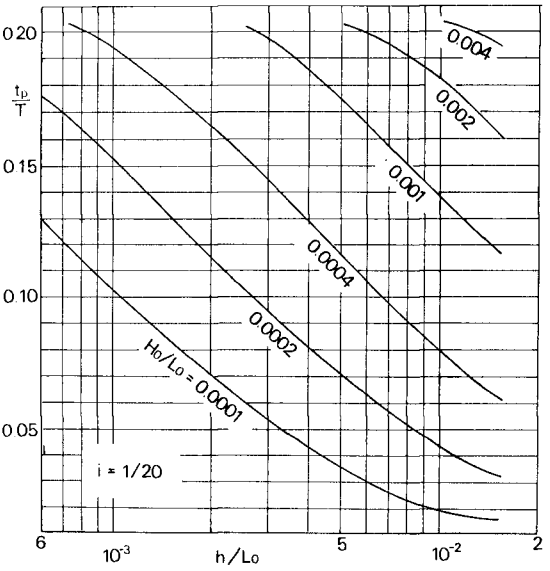

Fig.10 Effect of deep-water wave steepness on wave profile asymmetry

As mentioned above, Biesel[7] derived theoretically the average value of the slopes of front and back faces of the wave profile, while the parameter t_p/T is same as the " wave horizontal asymmetry " discussed experimentally by Adeyemo[16]. The wave profile asymmetry corresponds to the asymmetry of time variation of water particle velocity, and affects the time variations of wave forces on coastal structures and motions of bed materials. Therefore, the parameter t_p/T may has more important engineering significance than Biesel's parameter.

COMPARISON WITH EXPERIMENTAL RESULTS

The equipment and procedure of the experiments with respect to wave shoaling on beaches were same as that described by Iwagaki[2], in which the experiments for the beach slope of only 1/20 were conducted.

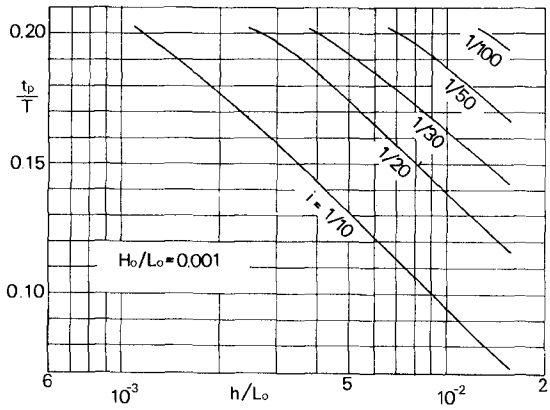

Fig.11 Effect of beach slope on wave profile asymmetry

WAVE HEIGHT CHANGE

In Fig.12 (1) ∿ (3), the experimental results of wave height change for the beach slopes of 1/30, 1/20 and 1/10 are shown. In Fig. 12 (1) (i = 1/30), although the experimental values can not be directly compared with the theoretical values by this theory because of the lack of data for corresponding values of H_0/L_0, it seems that the trend of the experimental values agrees roughly with that by this theory and the values are larger than those by the hyperbolic wave theory[2),5)]. In Fig. 12 (2) (i = 1/20), the experimental values when H_0/L_0 = 0.0026 agree with those by this theory and all of the experimental values agree well with those by the hyperbolic wave theory. In Fig.12 (3) (i = 1/10), the experimental values are much smaller than those by this theory. Therefore, the experimental results confirm the prediction by this theory that the wave height becomes larger on the gentle slope beach than on the steep slope beach.

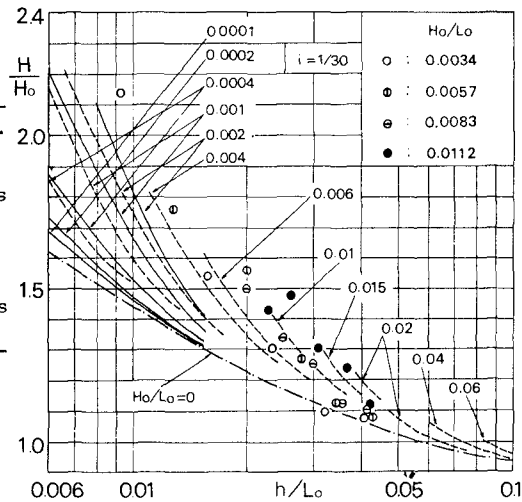

Fig.12 (1) Comparison with experimental results of wave height change (i = 1/30)

WAVE PROFILE ASYMMETRY

In Fig.13 (1) ∿ (3), the experimental results of wave profile asymmetry for the beach slopes of 1/30, 1/20 and 1/10 are shown. The experimental values of a parameter t_p/T increase with decrease in the water depth. This agrees with the behaviour of the curves by this theory. However, the experimental values

themselves are considerably different from those of theoretical curves. Although the common range of values of h/L_0 and H_0/L_0 between the experimental results and the theoretical curves is limited, it is found that the experimental values begin to increase at the larger value of h/L_0 than the theoretical curves and the rates of increase are also larger than those of theoretical ones. It seems that the experimental values of t_p/T are larger for larger values of the deep-water wave steepness. This trend of the experimental values agrees with that of this theory. However, because of scatter of experimental values, the effect of the beach slope on the wave profile asymmetry can not be confirmed by the experimental results.

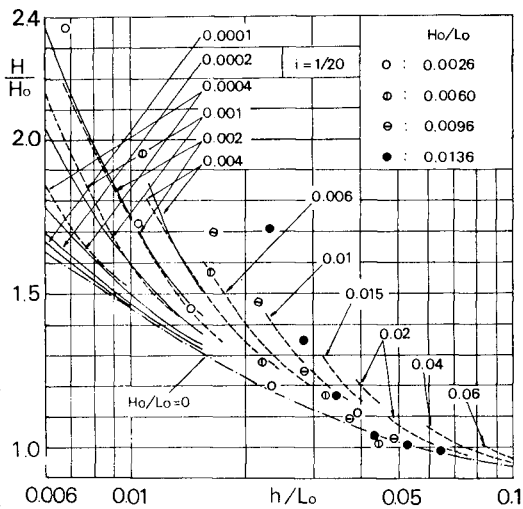

Fig.12 (2) Comparison with experimental results of wave height change (i = 1/20)

CONCLUSION

A solution of finite amplitude long waves on beaches of constant slope was obtained by solving the shallow water theory of the lowest order with the perturbation method. This solution was used to explain the beach slope effect on the wave height change and the wave profile asymmetry in shoaling water, which have not been made clear theoretically. The theoretical results were shown graphically. On the other hand, the experiments on wave shoaling were conducted in order to confirm the validity of this theory.

It was found theoretically that the rate of wave height increase is larger on

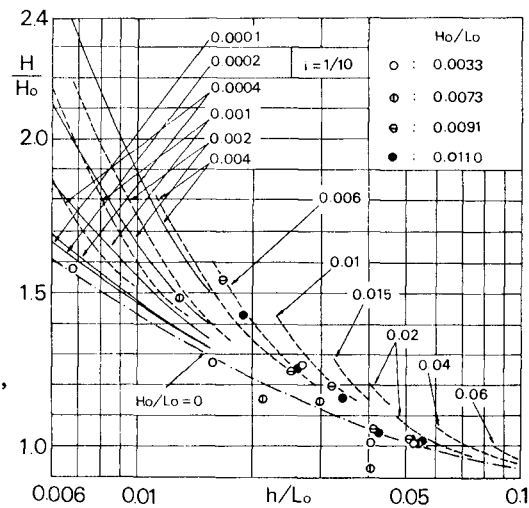

Fig.12 (3) Comparison with experimental results of wave height change (i = 1/10)

the gentle slope beach than on the steep slope beach. The experimental results agreed qualitatively with this theoretical prediction.

It was found theoretically that the wave profile becomes asymmetric with decrease in the water depth and more asymmetric for the larger deep-water wave steepness and smaller beach slope. The experimental results confirmed the theoretical prediction on the effects of the water depth and the deep-water wave steepness.

This study is the part of the authors' investigations on the finite amplitude waves and their shoaling during recent several years. The authors wish that the results of this study contribute to advance of investigations on these problems and practical applications.

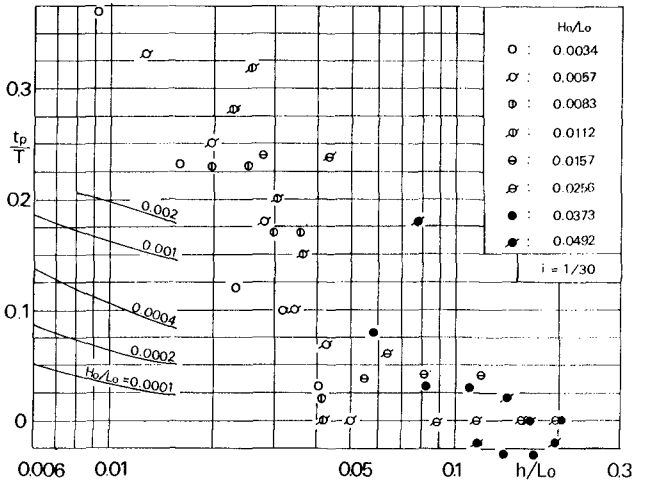

Fig.13 (1) Comparison with experimental results of wave profile asymmetry t_p/T (i = 1/30)

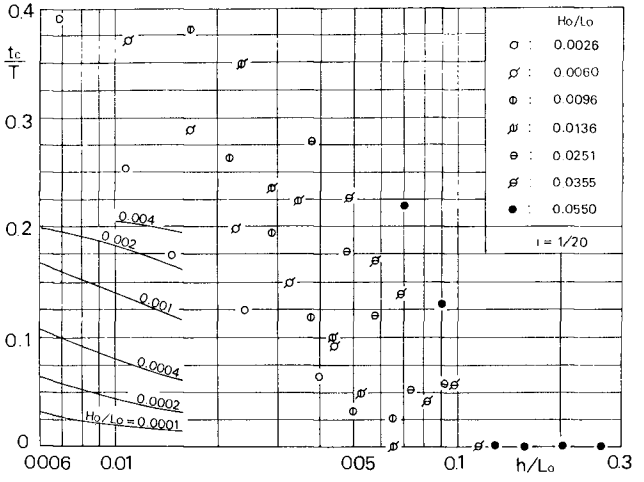

Fig.13 (2) Comparison with experimental results of wave profile asymmetry t_p/T (i = 1/20)

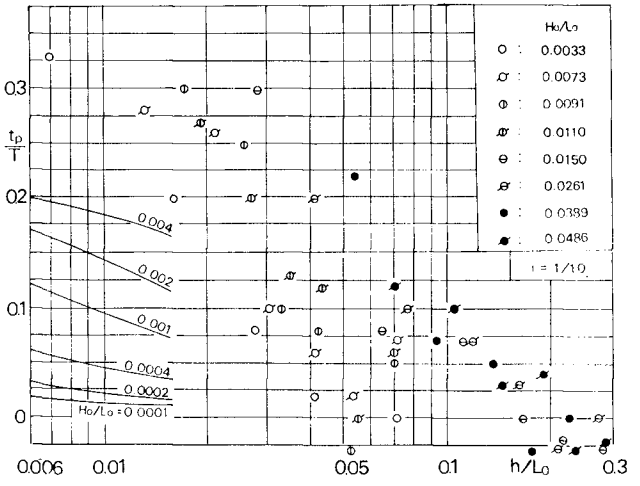

Fig.13 (3) Comparison with experimental results of wave profile asymmetry t_p/T (i = 1/10)

REFERENCES

1) Le Méhauté, B. and L.M. Webb : Periodic gravity waves over a gentle slope at a third order of approximation, Proc. 9th Conf. Coastal Eng., pp.23-40, 1964.
2) Iwagaki, Y. : Hyperbolic waves and their shoaling, Proc. 11th Conf. Coastal Eng., pp.124-144, 1968.
3) Friedrichs, K.O. : Water waves on a shallow sloping beach, Comm. Pure and Applied Math., Vol.1, pp.109-134, 1948.
4) Tlapa, G.A., C.C. Mei and P.S. Eagleson : An asymptotic theory for water waves on beaches of mild slope, M.I.T. Hydrodynamics Laboratory Report No. 90, 1966.
5) Iwagaki, Y. and T. Sakai : On the shoaling of finite amplitude waves (2), Proc. 15th Conf. Coastal Eng. in Japan, pp.10-15, 1968 (in Japanese).
6) Goda, Y. : A synthesis of breaker indices, Trans. JSCE, Vol.2, Part 2, pp. 227-230, 1970.
7) Biesel, F. : Study of wave propagation in water of gradually varying depth, Gravity Waves, Circular No.521, Nat. Bureau of Standard, Washington D.C., 1951.
8) Stoker, J.J. : Water Waves, Interscience Pub. Inc., New York, pp.22-32, 1957.
9) Homma, M. : Deformation of long waves, Jour. JSCE, Vol.19, No.9, 1933 (in Japanese).
10) Carrier, G.H. and H.P. Greenspan : Water waves of finite amplitude on a sloping beach, Jour. Fluid Mech., Vol.4, pp.97-109, 1958.
11) Ichiye, T. : Some remarks on the non-linear theory of shallow water waves on a sloping beach, The Oceanographical Magazine, Vol.4, No.4, pp.159-166, 1953.
12) Bourodimos, E.L. and A.T. Ippen : Wave transformation in an open channel transition, Proc. ASCE, Vol.94, HY.5, pp.1317-1329, 1968.
13) Green, G. : On the motion of waves in a variable canal of small depth and width, Camb. Trans. Vol.VI, 1837.
14) Laitone, E.V. : The second approximation to cnoidal and solitary waves, Jour. Fluid Mech., Vol.9, pp.430-444, 1961.
15) Iwagaki, Y : Wave transformation, Lecture note of the 1967 summer seminor on hydraulic engineering B, JSCE, 1967 (in Japanese).
16) Adeyemo, M.D. : Effect of beach slope and shoaling on wave asymmetry, Proc. 11th Conf. Coastal Eng., pp.145-172, 1968.

CHAPTER 18

SHOALING OF CNOIDAL WAVES

I. A. Svendsen

O. Brink-Kjær

Institute of Hydrodynamics and Hydraulic Engineering
Technical University of Denmark

ABSTRACT

An equation is derived which governs the propagation of a cnoidal wave train over a gently sloping bottom. The equation is solved numerically, the solution being tabulated in terms of f_H (Eq. 47) as a function of $E_1 = (E_{tr}/\rho g)^{1/3}/gT^2$ and $h_1 = h/gT^2$. Results are compared with sinusoidal wave theory. Two numerical examples are included.

0. INTRODUCTION

Although discovered almost 80 years ago and having received increasing attention during the last 10 years cnoidal waves have still not achieved the position of a tool for engineers, which one would expect from the demand for a consistent and reasonably accurate long wave theory.

One of the reasons is of course their complexity. Unlike the sinusoidal wave theory the velocity of propagation and thus the wave length depends on the wave height already in the lowest order of approximation and further the shape of the surface profile is characterised by the much more complicated elliptic function cn.

Another reason may be related to the fact that it has not hitherto been possible to determine how the main parameters such as wave height and wave length change if the wave propagates over a slowly varying bottom.

The main object of this paper is to analyse this transformation process which for sinusoidal waves is usually termed "shoaling". It is throughout assumed that the propagation is without refraction.

It is well known, see e.g. [3], that on a horizontal bottom the first approximation of the cnoidal wave theory predicts the speed of wave propagation c as

$$c = (gh)^{1/2}\left\{1 + H/mh\ \left(2 - m - 3\ E(m)/K(m)\right)\right\}^{1/2} \qquad (1)$$

where h is water depth, H wave height, E and K are complete elliptic

integrals with m as parameter. m satisfies the equation

$$H\,L^2/h^3 = 16/3\;m\;K(m)^2 \qquad (2)$$

where L is the wave length.

Let us consider two-dimensional wave trains. The concept of shoaling is based on the assumption that for sufficiently gentle variations of the bottom, the reflexion is negligible and the local value of c is given by Eq. 1 with h the local depth.

To define the local cnoidal wave uniquely under such conditions two magnitudes have to be specified in addition to the depth. Therefore, to follow a wave as it propagates over the gently sloping bottom we must know the variation - or constancy - of two magnitudes. These are the wave period T and the energy transport E_{tr}, which together do define the wave. Both these magnitudes stay constant during the propagation. Thus

$$L = c\,T \qquad (3)$$

defines a wave length L locally in the same sense as c, and Eq. 2 yields a local value of m.

1. ENERGY TRANSPORT

To carry on the development the energy transport in a cnoidal wave must be expressed in terms of the main parameters H and L (or T). We first determine the energy flux through a control section A, i.e. a section fixed in the x-direction (Fig. 1).

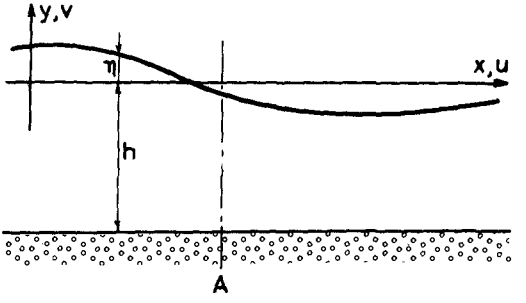

Fig. 1 Definition sketch

Using the definitions in the figure, the energy flux through A is

$$E_f = \int_{-h}^{\eta} \rho\,u\,\{g\,y + p/\rho + \tfrac{1}{2}(u^2 + v^2)\}\,dy \qquad (4)$$

where p is the pressure.

By introduction of the excess pressure p^+ defined as

$$p^+ \equiv p + \rho\,g\,y \qquad (5)$$

Eq. 4 can be rewritten

$$E_f = \int_{-h}^{\eta} \rho u \{ p^+/\rho + \tfrac{1}{2}(u^2 + v^2) \} \, dy \tag{6}$$

In cnoidal waves the first approximation to the horizontal velocity u is

$$u = c \, \eta/h \tag{7}$$

The corresponding expression for p^+ is

$$p^+ = \rho g \eta \tag{8}$$

(see e.g. [5]) and η is given by

$$\eta = H \left(\frac{1}{m} \left(1 - E(m)/K(m) \right) - 1 + cn^2 \left(2 K(m) \left(\frac{t}{T} - \frac{x}{L} \right) | m \right) \right) \tag{9}$$

where cn is a Jacobian elliptic function, m its parameter.

Since we are only interested in the leading term in the expression for E_f, the relative magnitude of the terms in Eq. 9 must be considered.

The theory of cnoidal waves is based on the assumption that the dimensionless Ursell-parameter UR founded on a characteristic horizontal length λ is

$$UR \equiv H \lambda^2/h^3 = O(1) \tag{10}$$

From this we obtain, by introducing the small parameter $\varepsilon \equiv h/\lambda$ that

$$\eta/h = O(H/h) = O(h^2/\lambda^2) = O(\varepsilon^2) \tag{11}$$

so that Eq. 7 yields

$$\frac{u}{c} = O(\varepsilon^2) \tag{12}$$

Since in long waves $v << u$ we need only consider the first two terms in Eq. 6. By Eqs. 7 and 8 we have

$$\frac{\rho u^2}{2p^+} = \frac{c^2 \eta}{2gh^2} \tag{13}$$

and as $c^2 = O(gh)$ we get

$$\frac{\rho u^2}{p^+} = O\left(\frac{\eta}{h}\right) = O(\varepsilon^2) \tag{14}$$

In other words, we may write

$$E_f = \int_{-h}^{0} u \, p^+ \, dy + O(\varepsilon^2 E_f) = \rho g \eta^2 c \tag{15}$$

since also $\int_0^{\eta}$ represents a small term.

The energy transport E_{tr} is defined in the same way as for Stokes waves, viz. as the transport per wave period

$$E_{tr} = \int_0^T E_f \, dt = \rho g c \int_0^T \eta^2 \, dt \tag{16}$$

Introducing for η Eq. 9 and noting that

$$\int_0^{2K} cn^2 \, \theta \, d\theta = (2/m) \, (E - (1 - m)K) \tag{17}$$

$$\int_0^{2K} cn^4 \, \theta \, d\theta = (2K/3m^2) \left(3m^2 - 5m + 2 + (4m - 2)E/K \right) \tag{18}$$

the expression for E_{tr} finally becomes

$$E_{tr} = \rho g H^2 L/m^2 \left(\frac{1}{3} \left(3m^2 - 5m + 2 + (4m - 2) \frac{E}{K} \right) - \left(1 - m - \frac{E}{K} \right)^2 \right) \tag{19}$$

(Eq. 17 may be obtained from e.g. [1] and Eq. 18 can be determined by suitable substitutions but is actually given in [4] directly.)

2. THE "SHOALING EQUATION"

Since the main parameters of the wave at each depth must satisfy Eqs. 1, 2 and 3 with h as local depth and since the wave period T and energy transport E_{tr} stay constant during the propagation, the four equations governing the shoaling process can be written

$$\frac{c^2}{gh} = 1 + \frac{H}{h} A \tag{20}$$

$$U = 16/3\, m K^2 \tag{21}$$

$$L = c\, T \tag{22}$$

$$E_{tr}/\rho g = H_r^2 L_r B_r = H^2 L B \tag{23}$$

where we for convenience have introduced the following definitions

$$A = A(m) \equiv 2/m - 1 - 3E/(mK) \tag{24}$$

$$U = U(m) \equiv H L^2/h^3 \tag{25}$$

$$B = B(m) \approx \frac{1}{m^2} \left(\frac{1}{3} \left(3m^2 - 5m + 2 + (4m - 2) \frac{E}{K} \right) - \left(1 - m - \frac{E}{K} \right)^2 \right) \tag{26}$$

The variation of A is shown in Fig. 2. The variation of B is shown in Fig. 3. Numerical results for both A and B are given in Table 1. We see that B is a dimensionless measure for the energy transport. In the formulas index $_r$ means "reference", indicating values corresponding to the water depth h_r where the wave is initially specified.

This is a system of four simultaneous transcendent equations. The four unknowns are H, L, c, and m, all values corresponding to the water depth h, and to solve these equations means finding these wave data at the water depth h provided T and E_{tr} are specified in some way by data at h_r (say H_r and L_r or H_r and T).

However, it is obvious that only one parameter, i.e. m, appears in transcendental form in the equations, namely as the independent variable in the elliptic functions E and K.

Thus in principle it is possible to reduce the four equations to one transcendental equation in m by eliminating the other three unknowns. As the manipulations are fairly trivial the result is presented directly as the following equation

$$M f_1(m) + N f_2(m) = 1 \tag{27}$$

where

$$M \equiv (H_r^2 L_r B_r)^{2/3}$$

$$N \equiv M^{-1} h/gT^2$$

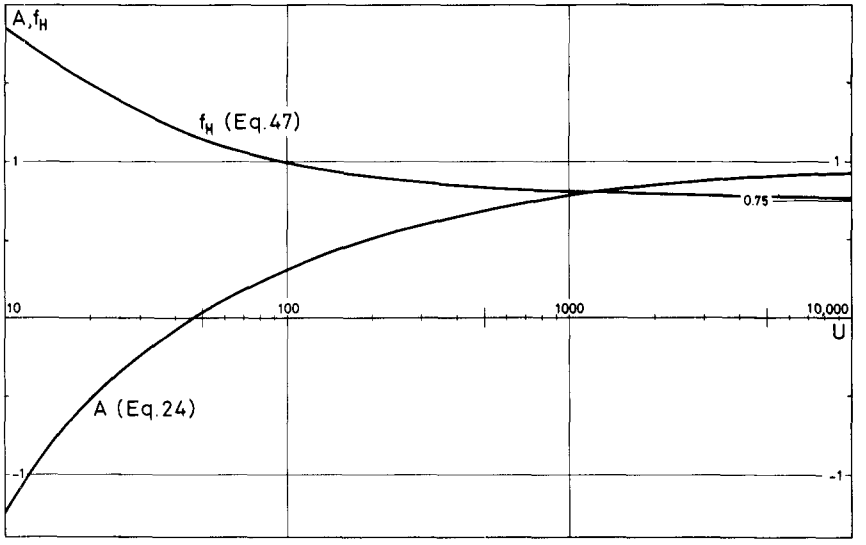

Fig. 2 A and f_H versus U

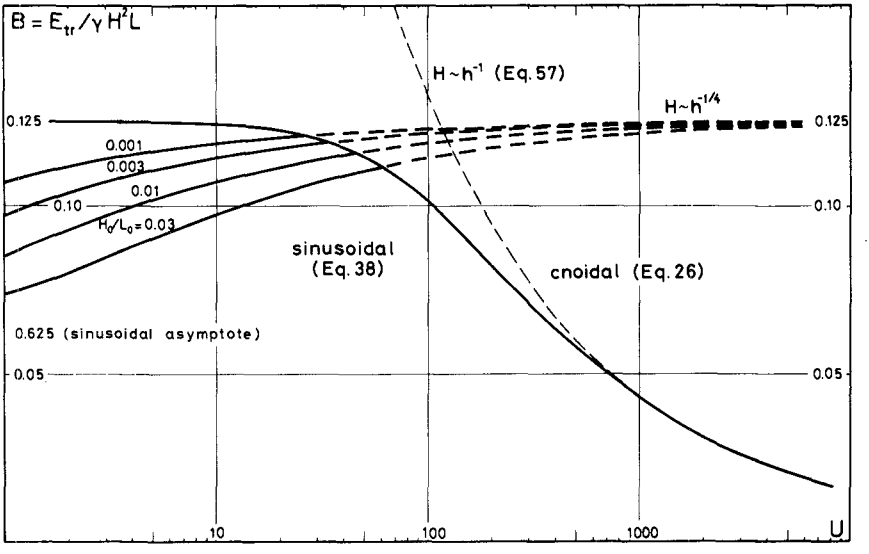

Fig. 3 B versus U

$$f_1 \equiv - U^{-1/3} B^{-2/3} A \tag{30}$$

$$f_2 \equiv U^{4/3} B^{2/3} \tag{31}$$

A closer investigation of Eq. 21 would reveal the (well-known) fact that U is a monotonous function of m. In the following we will choose to consider the problem in terms of U as independent variable. By this change we bring in the main parameters H, L and h for the wave directly and at the same time avoid the inconveniencies caused by the singularity in the K(m)-function for m = 1. Hence we may write

$$\boxed{M f_1(U) + N f_2(U) = 1} \tag{32}$$

where in Eqs. 30 and 31 A and B are to be regarded as functions of U.

Eq. 32 may be called the "Shoaling Equation". From the solution U of this equation H, c and L can be determined by the original equations 20 - 23.

3. SOLUTION OF THE SHOALING EQUATION

As mentioned above the wave may be specified at water depth h by, say, H and L. Thus three lengths are necessary to define the problem. From this we conclude that the problem has two (independent) dimensionless parameters, a result verified by Eq. 32 which requires the two parameters M and N to be defined.

The solution of Eq. 32 could of course be presented as a function of M and N. However, it proves more useful to note that M and N can be expressed as

$$M = E_1^2 h_1^{-2} \tag{33}$$

$$N = E_1^{-2} h_1^3 \tag{34}$$

where

$$E_1 = \frac{(H_r^2 L_r B_r)^{1/3}}{g T^2} = \frac{(E_{tr}/\rho g)^{1/3}}{g T^2} \tag{35}$$

$$h_1 = \frac{h}{g T^2} \tag{36}$$

In the following E_1 and h_1 will be used as parameters. This has the advantage - among others - that for a wave of a given period and height at a certain depth E_1 is independent of h, i.e. the shoaling process is represented by a variation of h_1 only. Variations in E_1 represent changes in the initial wave data.

The shoaling equation has been solved numerically on a digital computer. It appears that the equation has two roots. One of them, however, is readily shown to be false as it does not assume the value U_r when h is h_r. Hence if this argument of "continuity" is included there is one root U for each set of parameters E_1 and h_1 in the cnoidal region. For sufficiently large values of h_1 and small values of E_1 (corresponding to the sinusoidal region) the negative values of A dominates and the shoaling equation has no roots. The variation of U is shown in Fig. 4.

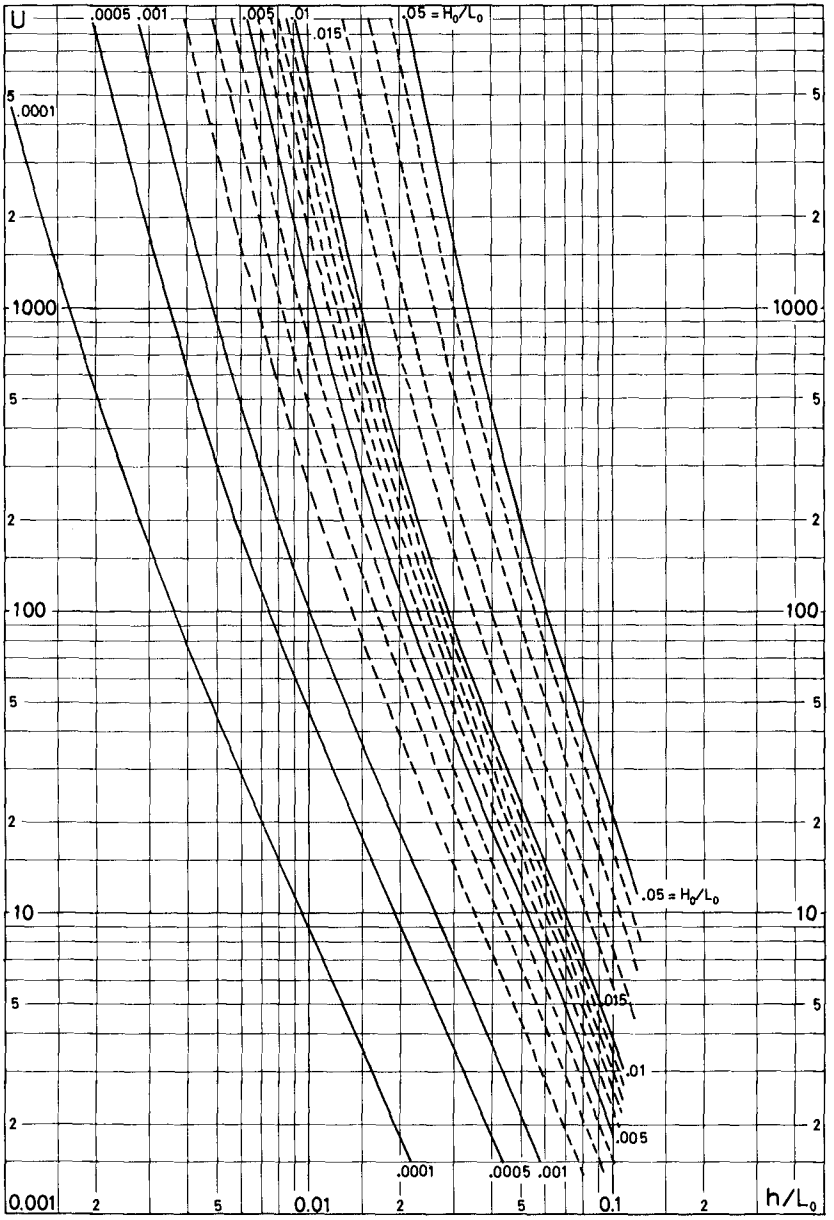

Fig. 4 Solution of shoaling equation

4. RELATION TO SINUSOIDAL WAVE THEORY

The basic equations 20 - 23 show that the only way in which the initial wave enters the data is through the wave period in Eq. 22 and the specification of the energy transport in Eq. 23.

This means that in the case, where the initial wave is specified at a depth so great that sinusoidal wave theory must be applied instead of cnoidal, we instead of Eqs. 23 and 26 have to determine the energy transport from

$$E_{tr}/\rho g = H_r^2 L_r B_r \tag{37}$$

where we for B_r use the well-known expression

$$B_r = \frac{1}{16}\left(1 + \frac{2k_r h_r}{\sinh 2k_r h_r}\right) \tag{38}$$

$k_r = 2\pi/L_r$ being the wave number.

This result is of particular interest because it makes it possible at any water depth to compare the results of the two theories for a wave which is characterised by data at any other water depth including deep water. For a closer discussion on this point the reader is referred to section 7.

Fig. 3 shows the variation of B according to Eq. 38. Since the abscissa U does not specify the kh parameter uniquely the value of B in this plot depends on another parameter too, which is for convenience chosen as the deep water steepness H_o/L_o. Comparison between the curves representing Eqs. 26 (cnoidal theory) and 38 (sinusoidal theory) shows that the amount of energy which according to the two theories is transported by a wave of a certain height and length varies in a very different way. Thus we can expect considerable differences in the wave heights and wave lengths predicted for the same period and energy transport.

Another important aspect appears by noting that the deep water wave length is

$$L_o = gT^2/2\pi \tag{39}$$

Hence the parameter h_1 may be rewritten

$$h_1 = \frac{1}{2\pi}\frac{h}{L_o} \tag{40}$$

and E_1 as

$$E_1 = (H_r^2 L_r B_r)^{1/3}/2\pi L_o \tag{41}$$

which by virtue of Eqs. 23 and 38 becomes

$$E_1 = (H_o^2 L_o B_o)^{1/3}/2\pi L_o = (2\pi \sqrt[3]{16})^{-1} (H_o/L_o)^{2/3} \quad \left(= 0.0632\,(H_o/L_o)^{2/3}\right) \tag{42}$$

In other words, the parameters E_1 and h_1 are proportional to h/L_o and $(H_o/L_o)^{2/3}$, index $_o$ referring to deep water values.

TABLE 1

U	A	B	f_H	U	A	B	f_H	U	A	B	f_H
2	-6.565	0.124	3.175	50	0.028	0.114	1.148	425	0.663	0.062	0.847
4	-3.261	0.124	2.521					450	0.673	0.060	0.844
6	-2.150	0.124	2.203	55	0.072	0.113	1.122	475	0.682	0.059	0.841
8	-1.588	0.124	2.003	60	0.110	0.111	1.099				
				65	0.144	0.110	1.080	500	0.690	0.058	0.839
10	-1.245	0.124	1.862	70	0.175	0.108	1.063				
								550	0.704	0.055	0.834
12	-1.012	0.124	1.754	75	0.202	0.107	1.048	600	0.717	0.053	0.830
14	-0.842	0.123	1.669					650	0.728	0.052	0.826
16	-0.711	0.123	1.599	80	0.227	0.106	1.035	700	0.738	0.050	0.823
18	-0.607	0.123	1.540	85	0.250	0.104	1.023				
				90	0.271	0.103	1.012	750	0.747	0.049	0.820
20	-0.521	0.122	1.490	95	0.290	0.102	1.003				
								800	0.755	0.047	0.818
22	-0.449	0.122	1.447	100	0.308	0.100	0.994	850	0.762	0.046	0.815
24	-0.387	0.122	1.408					900	0.769	0.045	0.813
26	-0.333	0.121	1.375	125	0.380	0.095	0.959	950	0.775	0.044	0.812
28	-0.285	0.121	1.345	150	0.434	0.090	0.935				
				175	0.476	0.085	0.918	1000	0.780	0.043	0.810
30	-0.242	0.120	1.318								
				200	0.510	0.082	0.904	2000	0.845	0.031	0.791
32	-0.204	0.120	1.294					3000	0.873	0.026	0.783
34	-0.169	0.119	1.272	225	0.538	0.078	0.893	4000	0.890	0.023	0.778
36	-0.137	0.118	1.251	250	0.561	0.076	0.884				
38	-0.108	0.118	1.233	275	0.582	0.073	0.876	5000	0.902	0.020	0.775
				300	0.600	0.071	0.870	6000	0.910	0.018	0.773
40	-0.081	0.117	1.216					7000	0.917	0.017	0.771
				325	0.615	0.068	0.864	8000	0.922	0.016	0.770
42	-0.056	0.117	1.200	350	0.629	0.067	0.859	9000	0.926	0.015	0.768
44	-0.033	0.116	1.186	375	0.642	0.065	0.855				
46	-0.011	0.116	1.172					10000	0.930	0.014	0.767
48	0.009	0.115	1.160	400	0.653	0.063	0.851				

5. DETERMINATION OF WAVE HEIGHT H

When the Shoaling Equation has been solved H can be found in several ways.

The most natural way is to consider the expression Eq. 23 for the energy transport and eliminate L by means of Eq. 25. We have

$$(L/h)^2 = U\ (H/h)^{-1} \tag{43}$$

Eq. 23 can be rewritten

$$\frac{H}{h} = \frac{H_r}{h}\left(\frac{L_r}{h}\right)^{1/2}\left(\frac{L}{h}\right)^{-1/2}\left(\frac{B}{B_r}\right)^{-1/2} \tag{44}$$

which after introduction of Eq. 43 becomes

$$\frac{H}{h} = \left(\frac{H_r}{h}\right)^{4/3}\left(\frac{L_r}{h}\right)^{2/3}\left(\frac{B}{B_r}\right)^{-2/3} U^{-1/3} \tag{45}$$

or

$$\frac{H}{H_r} = \frac{h_r}{h}\,\frac{f_H\,(U)}{f_H\,(U_r)} \tag{46}$$

where we have defined

$$f_H\,(U) \equiv U^{-1/3}\,B^{-2/3} \tag{47}$$

and

$$U_r \equiv H_r L_r^2 / h_r^3 \tag{48}$$

The relation between f_H and U is given in Table 1 and Fig. 2. However, since f_H is a monotonous function of U, f_H has been tabulated directly as a function of E_1 and h_1 in Table 2, which will facilitate the practical applications. Thus we can either determine U from Fig. 4 and f_H from Table 1 or f_H directly from Table 2.

If the reference depth h_r where we initially have data for the wave train is infinite we must consider $h_o/f_H(U_o)$ instead of $f_H(U_o)$. We see that

$$h_o/f_H(U_o) = H_o^{1/3} L_o^{2/3} B_o^{2/3} \tag{49}$$

so that Eq. 46 becomes (B_o being 1/16 according to Eq. 38)

$$\frac{H}{H_o} = 0.157 \left(\frac{H_o}{L_o}\right)^{1/3} \left(\frac{h}{L_o}\right)^{-1} f_H \tag{50}$$

Eqs. 46 and 50 are of course only valid for a wave height H in the cnoidal region.

H can also be determined by eliminating L and c from Eqs. 20, 22 and 25.

Rewriting Eq. 20 as

$$\frac{c^2}{g\,h} = \frac{L^2}{g\,T^2 h} = \frac{h^2}{g\,T^2}\,\frac{U}{H} = 1 + \frac{H}{h}\,A \tag{51}$$

we see that when U and T are known and hence A, Eq. 51 represents an equation for H/h which can be rearranged into the following

$$A\left(\frac{H}{h}\right)^2 + \frac{H}{h} - \frac{h\,U}{g\,T^2} = 0 \tag{52}$$

From this we obtain

$$\frac{H}{h} = \left((1 + 4\,A\,h\,U/gT^2)^{1/2} - 1\right)/2\,A \tag{53}$$

However, for the true cnoidal wave $H/h \ll 1$ the first term in Eq. 52 will be small, so that the exact calculation of H/h from Eq. 53 will be represented numerically by a small difference between two almost equal numbers. Thus it can only be recommended using Eq. 53 if $4\,A\,h\,U/g\,T^2$ is larger than, say, unity.

For $4\,A\,h\,U/g\,T^2 \leq 1$ Eq. 52 can be solved by iteration. We write

$$\frac{H}{h} = \frac{h\,U}{g\,T^2} - A\left(\frac{H}{h}\right)^2 \tag{54}$$

and start with the approximation $H/h \sim h\,U/g\,T^2$ which is used in the last term on the right hand side etc.

The asymptotic behaviour of H for vanishing h can be derived from Eq. 46. If H/h is assumed small enough to avoid breaking, decreasing h means rapidly increasing U, whereby the elliptic parameter m approaches unity. Hence Eq. 26 yields

$$B \to \frac{2}{3\,K} \qquad \text{for} \quad U \to \infty \tag{55}$$

which substituted into Eq. 47 together with U from Eq. 21 yields

$$f_H(U) \to \left(\frac{16\,K^2}{3}\right)^{-1/3} \left(\frac{2}{3\,K}\right)^{-2/3} = \frac{3}{4} \qquad \text{for } U \to \infty \tag{56}$$

Thus for large values of U, f_H approaches the fixed value 3/4. Substituting into Eq. 46 we get

$$\frac{H}{H_o} = \text{const}\ h^{-1} \qquad \text{for} \quad U \to \infty \tag{57}$$

This variation is illlustrated by the dotted curve in Fig. 3. It shows that the wave height in very shallow water increases considerably faster with decreasing h than the variation as $h^{-1/4}$ predicted by the classical linear long wave theory (see e.g. [6] § 185). For large values of U each of the crests in the cnoidal wave train more and more resembles a solitary wave in profile. Thus for large U the wave will show all the features of the solitary wave. It is therefore relevant to recall that the same result was obtained directly for a solitary wave by Grimshaw [2].

Another of the solitary wave characteristics can be demonstrated if we consider the energy transport. Substitute Eq. 55 for B and $\frac{3}{16} H L^2/h^3$ for K (from Eqs. 21 and 25) into Eq. 23. We then get

$$E_{tr}/\rho g = \tfrac{2}{3} H^{3/2} h^{3/2} \tag{58}$$

which shows that the energy transport does not depend on the wave length L.

Although in most practical cases this limit corresponds to H/h values which are far in excess of any breaking point the tendency that the wave height grows faster than $h^{-1/4}$ is felt even at moderate values of U (section 7).

6. DETERMINATION OF WAVE LENGTH L

The wave length is determined from Eqs. 20 and 22. Once f_H or U are known the value of A can be obtained from Table 1 so that Eq. 20 gives c when H has been calculated, and then L is readily determined from Eq. 22.

Another method which is less accurate consists in using Eq. 25. When U and H/h are known this equation gives a value for L/h. However, as in many cases U does not have to be determined very accurately for the purpose of getting accurate results for H by means of f_H, this method cannot be recommended except as a guidance.

If T is known the following method can also be used.

Initial Wave Data Supplied as H_r and T

A problem related to the determination of L arises if the initial wave data are in terms of wave height and wave period. This will for example usually be the case when they originate from a wave recorder. In the cnoidal wave theory L_r cannot be determined explicitly from H_r and T, and neither can U_r, A_r or B_r.

For this case Table 3 gives values of L/h as a function of H/h and $T\sqrt{g/h}$. The values in the table represent the solution of Eq. 52 with respect to U and determination of L/h by Eqs. 20 and 22.

TABLE 2(a)

E_1 \ h_1	0.001	0.002	0.003	0.004	0.005	0.006	0.007	0.008	0.009	0.010	0.011	0.012	0.013	0.014	0.015
.0002	1.168	1.908	2.591	3.226	3.826										
4	0.929	1.363	1.835	2.283	2.708	3.118	3.514	3.901							
6	0.856	1.140	1.505	1.866	2.212	2.546	2.871	3.188	3.499	3.806					
8	0.822	1.023	1.313	1.619	1.917	2.206	2.487	2.761	3.031	3.298	3.562	3.825			
.0010	0.802	0.954	1.188	1.452	1.716	1.973	2.224	2.470	2.711	2.950	3.187	3.423	3.660	3.899	
12	0.789	0.909	1.101	1.331	1.569	1.802	2.031	2.255	2.475	2.693	2.910	3.126	3.342	3.561	3.790
14	0.780	0.879	1.038	1.240	1.455	1.670	1.881	2.088	2.292	2.493	2.694	2.894	3.095	3.297	3.504
16	0.774	0.856	0.990	1.168	1.364	1.563	1.759	1.953	2.144	2.332	2.520	2.707	2.895	3.085	3.278
18	0.770	0.839	0.954	1.111	1.290	1.475	1.659	1.841	2.021	2.199	2.375	2.552	2.729	2.908	3.090
.0020		0.826	0.926	1.065	1.229	1.401	1.575	1.747	1.917	2.086	2.253	2.421	2.589	2.759	2.932
22		0.815	0.903	1.027	1.177	1.338	1.502	1.666	1.828	1.988	2.148	2.308	2.468	2.630	2.795
24		0.807	0.885	0.995	1.133	1.284	1.439	1.595	1.750	1.903	2.056	2.209	2.363	2.518	2.676
26		0.800	0.870	0.969	1.095	1.236	1.384	1.533	1.681	1.829	1.975	2.122	2.270	2.419	2.570
28		0.794	0.857	0.946	1.062	1.195	1.335	1.477	1.620	1.762	1.903	2.045	2.187	2.330	2.477
.0030		0.789	0.846	0.927	1.033	1.158	1.291	1.428	1.565	1.702	1.838	1.975	2.112	2.251	2.392
32		0.785	0.836	0.911	1.008	1.125	1.252	1.383	1.515	1.647	1.779	1.912	2.044	2.179	2.315
34		0.781	0.828	0.897	0.987	1.096	1.216	1.342	1.470	1.598	1.726	1.854	1.983	2.113	2.246
36		0.778	0.821	0.884	0.967	1.069	1.184	1.305	1.428	1.552	1.676	1.801	1.926	2.053	2.182
38		0.776	0.815	0.873	0.950	1.046	1.155	1.271	1.390	1.510	1.631	1.752	1.874	1.997	2.123
.0040		0.773	0.810	0.863	0.935	1.025	1.128	1.240	1.355	1.472	1.589	1.707	1.826	1.946	2.068
45		0.769	0.799	0.843	0.904	0.980	1.071	1.172	1.278	1.387	1.497	1.607	1.719	1.832	1.948
50			0.790	0.828	0.880	0.945	1.025	1.115	1.213	1.315	1.418	1.523	1.629	1.736	1.845
55			0.784	0.816	0.861	0.918	0.987	1.069	1.158	1.253	1.350	1.450	1.550	1.652	1.756
60			0.779	0.807	0.846	0.895	0.957	1.030	1.111	1.199	1.291	1.385	1.481	1.579	1.678
65			0.775	0.799	0.833	0.877	0.931	0.997	1.071	1.153	1.239	1.329	1.420	1.513	1.609
.0070			0.772	0.793	0.823	0.862	0.910	0.969	1.037	1.112	1.193	1.278	1.366	1.455	1.546
75			0.769	0.788	0.815	0.849	0.893	0.945	1.007	1.077	1.153	1.233	1.316	1.402	1.490
80				0.784	0.808	0.839	0.877	0.925	0.981	1.045	1.116	1.192	1.272	1.354	1.439
85				0.780	0.802	0.830	0.865	0.907	0.959	1.018	1.084	1.155	1.231	1.310	1.391
90				0.777	0.796	0.822	0.854	0.893	0.939	0.993	1.055	1.122	1.194	1.270	1.348
95				0.775	0.792	0.815	0.844	0.880	0.922	0.972	1.029	1.092	1.161	1.233	1.308
.0100				0.772	0.788	0.809	0.836	0.868	0.907	0.953	1.006	1.065	1.130	1.199	1.271
120					0.777	0.792	0.811	0.835	0.863	0.897	0.936	0.981	1.031	1.088	1.148
140					0.770	0.781	0.796	0.814	0.835	0.860	0.890	0.924	0.964	1.008	1.058
160						0.774	0.786	0.799	0.816	0.836	0.859	0.886	0.916	0.951	0.991
180						0.769	0.778	0.789	0.803	0.818	0.837	0.858	0.883	0.911	0.943
.0200							0.773	0.782	0.793	0.806	0.821	0.838	0.858	0.881	0.907
220							0.769	0.777	0.786	0.796	0.809	0.823	0.840	0.859	0.880
240								0.772	0.780	0.789	0.800	0.812	0.826	0.842	0.860
260								0.769	0.776	0.784	0.793	0.803	0.815	0.828	0.844
280									0.772	0.779	0.787	0.796	0.806	0.818	0.831
.0300									0.769	0.775	0.782	0.790	0.799	0.809	0.820
320										0.772	0.778	0.785	0.793	0.802	0.812
340										0.770	0.775	0.781	0.788	0.796	0.805
360											0.772	0.778	0.784	0.791	0.799
380											0.770	0.775	0.781	0.787	0.794
.0400											0.768	0.773	0.778	0.783	0.790
450												0.768	0.772	0.776	0.781
500														0.771	0.775
550															0.771
600															
650															
700															
750															
800															
850															
900															
950															
.1000							f_H = 0.750								
.1200															

f_H as a function of E_1 and h_1

TABLE 2(b)

E_1 \ h_1	0.016	0.017	0.018	0.019	0.020	0.021	0.022	0.023	0.024	0.025	0.026	0.027	0.028	0.029	0.030
.0002															
4															
6															
8															
.0010															
12															
14	3.716	3.940								sinusoidal region					
16	3.477	3.687	3.919							(no roots)					
18	3.278	3.476	3.696												
.0020	3.112	3.298	3.507	3.820											
22	2.965	3.145	3.343	3.640											
24	2.839	3.011	3.201	3.486											
26	2.727	2.893	3.075	3.342											
28	2.627	2.787	2.962	3.220											
.0030	2.538	2.691	2.861	3.105											
32	2.457	2.605	2.770	3.003											
34	2.383	2.527	2.686	2.909											
36	2.315	2.455	2.610	2.823											
38	2.252	2.389	2.539	2.745											
.0040	2.194	2.327	2.473	2.672											
45	2.066	2.191	2.329	2.510											
50	1.958	2.076	2.205	2.372											
55	1.863	1.976	2.099	2.253											
60	1.781	1.888	2.005	2.148											
65	1.707	1.810	1.921	2.055											
.0070	1.641	1.739	1.845	1.971											
75	1.581	1.675	1.777	1.895											
80	1.526	1.617	1.715	1.826											
85	1.476	1.564	1.657	1.763											
90	1.429	1.514	1.604	1.705	1.863										
95	1.387	1.468	1.555	1.651	1.779										
.0100	1.347	1.426	1.509	1.601	1.716										
120	1.213	1.281	1.354	1.432	1.519										
140	1.112	1.170	1.232	1.299	1.372	1.456									
160	1.035	1.084	1.137	1.195	1.257	1.325	1.405								
180	0.979	1.019	1.063	1.112	1.165	1.222	1.287	1.363							
.0200	0.936	0.969	1.006	1.047	1.092	1.141	1.195	1.255	1.327						
220	0.904	0.932	0.962	0.996	1.034	1.076	1.121	1.172	1.229	1.297					
240	0.880	0.903	0.928	0.957	0.988	1.024	1.062	1.105	1.153	1.207	1.271				
260	0.861	0.880	0.902	0.926	0.952	0.982	1.015	1.052	1.092	1.137	1.188	1.249			
280	0.846	0.862	0.880	0.901	0.924	0.949	0.977	1.009	1.043	1.081	1.124	1.172	1.231		
.0300	0.833	0.847	0.863	0.881	0.901	0.922	0.947	0.973	1.003	1.036	1.072	1.113	1.159	1.214	
320	0.823	0.836	0.849	0.865	0.882	0.901	0.922	0.945	0.970	0.999	1.030	1.064	1.103	1.147	1.200
340	0.815	0.826	0.838	0.852	0.866	0.883	0.901	0.921	0.943	0.968	0.995	1.025	1.058	1.095	1.137
360	0.808	0.818	0.828	0.840	0.854	0.868	0.884	0.902	0.921	0.943	0.966	0.992	1.021	1.052	1.088
380	0.802	0.811	0.820	0.831	0.843	0.856	0.870	0.885	0.902	0.921	0.942	0.965	0.990	1.017	1.048
.0400	0.797	0.805	0.813	0.823	0.833	0.845	0.858	0.872	0.887	0.903	0.922	0.942	0.964	0.988	1.015
450	0.787	0.793	0.800	0.807	0.816	0.825	0.834	0.845	0.857	0.869	0.883	0.898	0.915	0.932	0.952
500	0.780	0.785	0.790	0.796	0.803	0.810	0.818	0.826	0.836	0.846	0.856	0.868	0.881	0.895	0.910
550	0.775	0.779	0.783	0.788	0.794	0.800	0.806	0.813	0.820	0.828	0.837	0.846	0.857	0.868	0.879
600	0.771	0.774	0.778	0.782	0.787	0.792	0.797	0.803	0.809	0.815	0.823	0.830	0.839	0.848	0.857
650		0.771	0.774	0.777	0.781	0.785	0.790	0.795	0.800	0.806	0.812	0.818	0.825	0.832	0.840
700		0.768	0.771	0.774	0.777	0.780	0.784	0.788	0.793	0.798	0.803	0.808	0.814	0.821	0.827
750			0.768	0.771	0.773	0.776	0.780	0.783	0.787	0.791	0.796	0.801	0.806	0.811	0.817
800				0.768	0.771	0.773	0.776	0.779	0.783	0.786	0.790	0.794	0.799	0.803	0.808
850					0.768	0.771	0.773	0.776	0.779	0.782	0.786	0.789	0.793	0.797	0.802
900						0.768	0.771	0.773	0.776	0.779	0.782	0.785	0.788	0.792	0.796
950							0.769	0.771	0.773	0.776	0.778	0.781	0.784	0.788	0.791
.1000		$f_H \to 0.750$						0.769	0.771	0.773	0.776	0.778	0.781	0.784	0.787
.1200												0.769	0.771	0.773	0.775

f_H as a function of E_1 and h_1

TABLE 3

$T\sqrt{g/h}$ \ H/h	0.01	0.02	0.03	0.04	0.05	0.10	0.15	0.20	0.25	0.30	0.35	0.40	0.45	0.50	0.60	0.70	0.80
6.0	-	-	-	-	-	-	-	-	-	-	-	-	-	-	-	-	-
7.0	-	-	-	-	-	-	-	-	-	-	-	-	-	-	5.8	6.1	6.4
8.0	-	-	-	-	-	-	-	-	6.9	6.9	7.0	7.1	7.2	7.3	7.6	7.8	8.1
9.0	-	-	-	-	-	-	-	8.1	8.2	8.3	8.4	8.5	8.6	8.7	9.0	9.3	9.7
10.0	-	-	-	-	-	-	9.2	9.3	9.4	9.5	9.6	9.7	9.9	10.0	10.4	10.7	11.1
11.0	-	-	-	-	-	10.3	10.4	10.4	10.6	10.7	10.8	11.0	11.2	11.3	11.7	12.1	12.5
12.0	-	-	-	-	-	11.4	11.5	11.6	11.7	11.9	12.0	12.2	12.4	12.6	13.0	13.5	13.9
13.0	-	-	-	-	-	12.5	12.6	12.7	12.9	13.0	13.2	13.4	13.7	13.9	14.4	14.8	15.3
14.0	-	-	-	-	-	13.5	13.7	13.8	14.0	14.2	14.4	14.7	14.9	15.1	15.7	16.2	16.7
15.0	-	-	-	-	14.5	14.6	14.7	14.9	15.1	15.4	15.6	15.9	16.1	16.4	16.9	17.5	18.1
16.0	-	-	-	-	15.5	15.7	15.8	16.0	16.3	16.5	16.8	17.1	17.4	17.6	18.2	18.8	19.4
17.0	-	-	-	16.6	16.6	16.7	16.9	17.1	17.4	17.7	18.0	18.3	18.6	18.9	19.5	20.2	20.8
18.0	-	-	-	17.6	17.6	17.8	18.0	18.2	18.5	18.8	19.1	19.5	19.8	20.1	20.8	21.5	22.1
19.0	-	-	18.6	18.6	18.6	18.8	19.0	19.3	19.6	20.0	20.3	20.7	21.0	21.4	22.1	22.8	23.5
20.0	-	-	19.6	19.7	19.7	19.9	20.1	20.4	20.8	21.1	21.5	21.9	22.2	22.6	23.4	24.1	24.9
21.0	-	-	20.7	20.7	20.7	20.9	21.2	21.5	21.9	22.3	22.7	23.1	23.4	23.8	24.6	25.4	26.2
22.0	-	-	21.7	21.7	21.7	22.0	22.3	22.6	23.0	23.4	23.8	24.2	24.7	25.1	25.9	26.7	27.6
23.0	-	22.7	22.7	22.7	22.8	23.0	23.4	23.7	24.1	24.6	25.0	25.4	25.9	26.3	27.2	28.1	28.9
24.0	-	23.7	23.7	23.7	23.8	24.1	24.4	24.8	25.3	25.7	26.2	26.6	27.1	27.5	28.5	29.4	30.3
25.0	-	24.7	24.7	24.8	24.8	25.1	25.5	25.9	26.4	26.9	27.3	27.8	28.3	28.8	29.7	30.7	31.6
26.0	-	25.7	25.7	25.8	25.8	26.2	26.6	27.0	27.5	28.0	28.5	29.0	29.5	30.0	31.0	32.0	33.0
27.0	-	26.7	26.8	26.8	26.9	27.2	27.7	28.1	28.6	29.2	29.7	30.2	30.7	31.2	32.3	33.3	34.3
28.0	-	27.7	27.8	27.8	27.9	28.3	28.7	29.2	29.8	30.3	30.8	31.4	31.9	32.5	33.6	34.6	35.7
29.0	-	28.8	28.8	28.8	28.9	29.3	29.8	30.3	30.9	31.4	32.0	32.6	33.1	33.7	34.8	35.9	37.0
30.0	-	29.8	29.8	29.9	29.9	30.4	30.9	31.4	32.0	32.6	33.2	33.8	34.4	34.9	36.1	37.2	38.4
31.0	-	30.8	30.8	30.9	31.0	31.4	32.0	32.5	33.1	33.7	34.3	35.0	35.6	36.2	37.4	38.5	39.7
32.0	31.8	31.8	31.8	31.9	32.0	32.5	33.0	33.6	34.3	34.9	35.5	36.1	36.8	37.4	38.6	39.9	41.0
33.0	32.8	32.8	32.9	32.9	33.0	33.5	34.1	34.7	35.4	36.0	36.7	37.3	38.0	38.6	39.9	41.2	42.4
34.0	33.8	33.8	33.9	33.9	34.0	34.6	35.2	35.8	36.5	37.2	37.8	38.5	39.2	39.9	41.2	42.5	43.7
35.0	34.8	34.8	34.9	35.0	35.1	35.6	36.3	36.9	37.6	38.3	39.0	39.7	40.4	41.1	42.4	43.8	45.1
36.0	35.8	35.8	35.9	36.0	36.1	36.7	37.3	38.0	38.7	39.5	40.2	40.9	41.6	42.3	43.7	45.1	46.4
37.0	36.8	36.8	36.9	37.0	37.1	37.7	38.4	39.1	39.9	40.6	41.3	42.1	42.8	43.5	45.0	46.4	47.8
38.0	37.8	37.8	37.9	38.0	38.1	38.8	39.5	40.2	41.0	41.7	42.5	43.3	44.0	44.8	46.2	47.7	49.1
39.0	38.8	38.9	38.9	39.0	39.2	39.9	40.6	41.3	42.1	42.9	43.6	44.4	45.2	46.0	47.5	49.0	50.5
40.0	39.8	39.9	40.0	40.1	40.2	40.9	41.6	42.4	43.2	44.0	44.8	45.6	46.4	47.2	48.8	50.3	51.8

L/h as a function of H/h and $T\sqrt{g/h}$

7. NUMERICAL COMPARISON BETWEEN SINUSOIDAL AND CNOIDAL WAVE THEORY

As mentioned in section 4 it is possible to trace a wave train as it propagates from deep water into shallower water and determine the wave heights, lengths etc. according to both the sinusoidal as well as the cnoidal theory.

Fig. 5 shows the variation of the wave height. The abscissa is h/L_o so the values for the cnoidal theory split up into curves, one for each value of H_o/L_o. The significant feature is that the cnoidal wave height grows faster with decreasing depth although at intermediate water depths its value is up to 10% less than that predicted by sinusoidal wave theory. Waves with considerable deep water steepness (2-3%) will break at a depth where the cnoidal wave height is only slightly larger than that of sinusoidal waves. Waves with small deep water steepness, however, such as swells pass to much smaller depth before they break and consequently a major part of their shoaling process is governed by the cnoidal theory. For these waves the two theories will yield results for the wave height differing by factors of up to 2

For the wave length L the opposite applies, as can be seen from Fig. 6. In sufficiently shallow water in particular, the length of swell type waves is almost independent of the water depth. This is caused by the increase in H influencing c through the second term on the right hand side in Eq. 20.

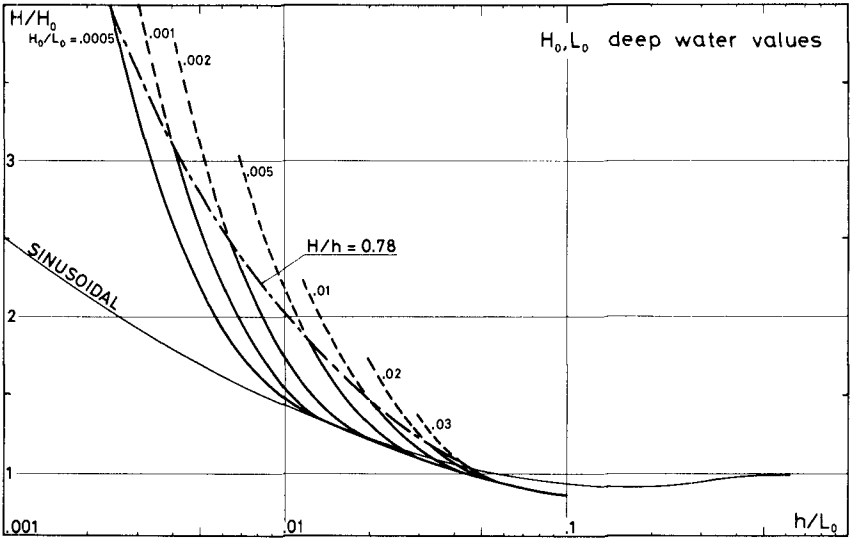

Fig. 5 H/H_o versus h/L_o for various H_o/L_o

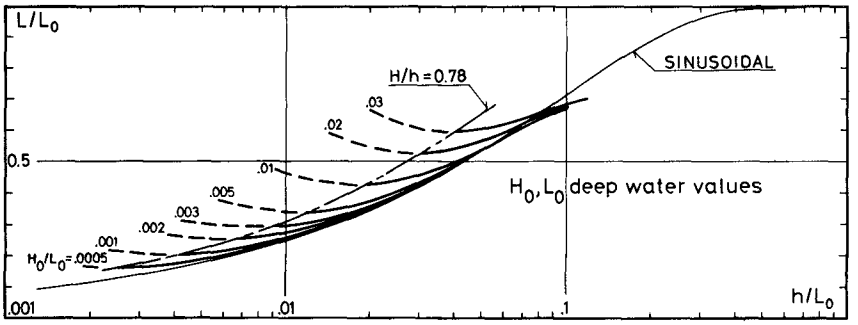

Fig. 6 L/L_o versus h/L_o for various H_o/L_o

8. NUMERICAL EXAMPLES

1. Consider wave forecast predicting a deep water wave height H_o = 3 m and a corresponding wave period T = 10 s.

We want to determine the wave height and wave length at h = 5 m.

We have directly

$$L_o = g/2\pi \cdot T^2 = 156 \text{ m}$$

$$h/L_o = 5/156 = 0.032$$

$$H_o/L_o = 3/156 = 0.0192$$

and by virtue of Eqs. 40 and 42

$$E_1 = 0.0632 \quad 0.0192^{2/3} = 0.00454$$

$$h_1 = 0.032/2\pi = 0.0051$$

Table 2 then yields

$$f_H = 0.910$$

so that by virtue of Eq. 50

$$\frac{H}{H_o} = 0.157 \cdot 0.0192^{1/3} \cdot 0.032^{-1} \cdot 0.910 = 1.20$$

or

$$H = 3.60 \text{ m}$$

We observe that since U = 190 (Table 1) we are within the cnoidal region.

If the sinusoidal wave theory is used we get

$$\frac{H}{H_o} = 1.11 \quad \text{or} \quad H = 3.33 \text{ m}$$

i.e. 7.5% less.

From H/H_o we get H/h as

$$\frac{H}{h} = \frac{H}{H_o}\frac{H_o}{L_o}\frac{L_o}{h} = 1.20 \cdot 0.0192/0.032 = 0.72$$

and since the other parameter of Table 3 is $T\sqrt{g/h} = 14$ we get from that table L/h = 16.3.

As was mentioned in section 6 L/h can also be determined by virtue of Eqs. 20 and 22. Table 1 yields

$$A = 0.50$$

and Eqs. 20 and 22

$$\frac{L}{h} = T\sqrt{\frac{g}{h}}\sqrt{1+\frac{H}{h}A}$$

or

$$\frac{L}{h} = 14\sqrt{1+0.72 \cdot 0.50} = 16.3$$

2. Data from a wave recorder at $h_r = 10$ m show $H_r = 1.20$ m, T = 18 s.

Looking for the wave height at h = 3.5 m we have

$$H_r/h_r = 1.20/10 = 0.12$$

$$T\sqrt{g/h_r} = 18\sqrt{9.81/10} = 17.8$$

Table 3 yields directly $L_r/h_r = 17.7$ so that $U_r = H_r L_r^2/h_r^3 = 0.12 \cdot 17.7^2 = 37.6$ which is within the cnoidal region. Table 1 supplies the values $B_r = 0.118$ and $f_H(U_r) = 1.237$.

Hence (Eqs. 35 and 36)

$$h_1 = h/gT^2 = 3.5/9.81 \cdot 18^2 = \underline{0.00110}$$

$$E_1 = (H_r^2 L_r B_r)^{1/3}/gT^2 = (H_r/h_r)^{2/3}(L_r/h_r)^{1/3} B_r^{1/3} (T\sqrt{g/h_r})^{-2}$$

$$= 0.12^{2/3} \cdot 17.7^{1/3} \cdot 0.118^{1/3} \cdot 17.8^{-2} = \underline{0.00099}$$

We then get from table 2

$$f_H = 0.818$$

so that Eq. 46 yields

$$\frac{H}{H_r} = \frac{10}{3.5} \cdot \frac{0.818}{1.237} = 1.89$$

or

$$\underline{H = 2.27 \text{ m}}$$

If sinusoidal theory is used we get, using wave tables [7]

$$\frac{H}{H_r} = \frac{H}{H_o}\frac{H_o}{H_r} = 1.565/1.229 = 1.27$$

or

$$\underline{H = 1.53 \text{ m}}$$

i.e. 33% smaller wave height.

9. CONCLUSION

A method has been developed by which the cnoidal wave theory can be used to calculate changes in wave height and wave length due to shoaling of waves.

The basis is a calculation of the energy transport in cnoidal waves presented in section 1.

It is shown that the problem has two independent parameters which are chosen as $E_1 = (E_{tr}/\rho g)^{1/3}/gT^2$ and $h_1 = h/gT^2$ which define the parameters in the shoaling equation (32). The solution U of this equation is shown in Fig. 4. Numerical results for the function $f_H(U)$ (Eq. 47) which is used for determination of the wave height H (Eq. 46) are given in Table 2.

The relation to sinusoidal wave theory is established. Thus E_1 and h_1 can be related to deep water wave data (Eqs. 40 and 42). Hence it can be shown (sections 5 and 6) how wave height and wave length can be determined if sufficient data is specified for the wave either at a point in the region where the cnoidal theory is valid or at a point where sinusoidal theory applies, including deep water.

Results for wave height and wave length predicted by the two theories are compared in Figs. 5 and 6. They show that in particular swell type wave motions will undergo a much more rapid increase in wave height according to the cnoidal wave theory.

The limits of validity of theory have not been investigated.

10. NOMENCLATURE

c	propagation velocity
$f_1(U)$	function of U (Eq. 30)
$f_2(U)$	function of U (Eq. 31)
f_H	dimensionless wave height factor (Eq. 47)
g	acceleration of gravity
h	water depth
h_1	parameter (Eq. 36)
k	$= 2\pi/L$ wave number
m	elliptic parameter
p	pressure
p^+	excess pressure (Eq. 5)
t	time
u,v	particel velocities (Fig. 1)
x,y	rectangular coordinates (Fig. 1)
A	function of m (Eq. 24)

B function of m (Eq. 26)

E complete elliptic integral of second kind

E_1 parameter (Eq. 35)

E_f energy flux

E_{tr} energy transport per wave period

H wave height

K complete elliptic integral of first kind

L wave length

M,N parameters (Eqs. 28 and 29)

T wave period

U parameter (Eq. 25)

UR Ursell-parameter (Eq. 10)

η surface elevation (Fig. 1)

ρ specific density

index $_r$: reference i.e. initial wave data

index $_o$: deep water data

11. REFERENCES

The following references have been used in the paper.

[1] Abramowitz, M. and Segun, I.A. (Ed.)
Handbook of Mathematical Functions.
Dover Publications, New York 1965.

[2] Grimshaw, R.
The solitary wave in water of variable depth.
J. Fl. Mech. (1970), 42, part 3, pp. 639-656.

[3] Keulegan, G.H. and Patterson, G.W.
Mathematical theory of irrotational translation waves.
J. Res. Nat. Bur. Stand. (1940), 24, pp. 48-101.

[4] Laitone, E.V.
Limiting conditions for cnoidal and Stokes' waves.
J. Geophys. Res. (1962), 67, No. 4.

[5] Laitone, E.V.
Higher approximation to non-linear water waves and the limiting heights of cnoidal, solitary, and Stokes' waves.
Tech. Mem. 133, (1963), Beach Erosion Board, Corps of Engineers.

[6] Lamb, H.
Hydrodynamics
Cambridge Univ. Press, 1932.

[7] Wiegel, R.L.
Gravity waves, tables of functions.
Council on Wave Res., The Engrg. Foundation, 1954.

CHAPTER 19

TRANSFORMATION OF WAVES PASSING A SUBMERGED BAR

By

Pierce L. Chandler, Jr.[1] and Robert M. Sorensen[2]

ABSTRACT

This study investigates the transformation of nonbreaking waves that pass over a submerged longshore bar. An envelope for the occurrence of transformation of nonbreaking waves is established and compared with existing information. Power spectral analyses are made of both the incident and transformed waves to determine quantitatively the change in wave characteristics. The conclusion is made that the transformation process is a nonlinear phenomenon occurring over the bar, but, in the deeper water in the lee of the bar, a combination of linear wave forms results.

INTRODUCTION

Winter and hurricane weather conditions in the Gulf of Mexico produce waves of considerable height and steepness. As they reach the shore, these waves remove material from the beaches and deposit it some distance from the shoreline. Deposition of this eroded material soon creates longshore bars. The typical bar will have a cross section with the following properties: a gently sloping face toward the sea, a rounded crest, and a steep slope downward into a trough in the lee of the crest. These bar formations are usually transient both in shape and in location.

Water depths over these bar formations are often reduced to the point that waves passing over the bar begin to shoal and their steepness increases. Leeward of the bar, in the deeper water of the trough, the waves decrease in steepness and transmit shoreward the energy that was not reflected or expended in passage over the bar. Often the waves appearing in the lee of the bar have noticeably shorter period components superposed on the fundamental wave form.

---

1. Research Hydraulic Engineer, USAE Waterways Experiment Station, Vicksburg, Mississippi.

2. Associate Professor, Division of Coastal and Ocean Engineering, Department of Civil Engineering, Texas A&M University, College Station, Texas.

The characteristics of these modified wave forms in the lee of the bar are of interest both in the area of structural design and in the study of beach processes. The object of the research described herein was to establish limits for the occurrence of modified wave forms and to quantitatively define some of the characteristics of these transformed waves in the lee of the bar.

A REVIEW OF THE LITERATURE

It was noted in studies of the passage of waves over submerged bars, breakwaters, and docks that transformation of waves occurs in the lee of the obstruction in certain instances.

Mason and Keulegan (10) in 1944 investigated the profiles of waves passing over three different configurations of rectangular reefs. Their study developed a criterion for the "regular" passage of waves over the reef—regular meaning without forming multiple crests. Their criterion for regular transmission is given as

$$\left(H_i L_i\right)^{1/2} \leq 2C_b$$

where H_i and L_i are the incident wave height and length, respectively, and C_b is the water depth over the reef.

Horikawa and Wiegel (4) verified the criterion of Mason and Keulegan (10) for regular transmission in similar experiments conducted in 1959. In addition to these verifying tests, investigations were made in a channel containing no bottom discontinuities. A wave filter was used in the generator end of the channel, and a wave absorber was utilized in the other end. Various wave characteristics and channel depths were investigated for possible multiple wave crest formation. Some multiple crests did appear and their appearance agreed closely with a theoretically derived criterion for the limit applicability of the second order profile of the free surface developed by Miche (11).

Jolas (6) also studied the characteristics of wave encountering a submerged rectangular bar. These studies were primarily for the determination of reflection and transmission coefficients and their comparison with theoretical results. However, his analysis of wave profiles indicated the increasing formation of harmonics of the incident wave frequency as the depth over the bar to the incident wave length decreased.

Williams (13) investigated wave transformation occurring over a submerged dock. The waves on either side of the dock were "deepwater" waves

(water-depth-to-wavelength ratio greater than 0.5) and the top of the dock was submerged less than twenty percent of the water depth. He showed that the nonlinear wave forms appearing over the dock reduce to a system of linear harmonic waves, the fundamental frequency of which is identical to that of the incident waves, in the deep water past the bar. Of note is his conclusion that the amplitudes of the harmonics are affected more by the dock length than the end conditions.

At Texas A&M, McNair (8) in investigating the characteristics of monochromatic waves breaking over a representative submerged bar noted that the broken waves reformed into a complex wave form. Applying power spectral analysis methods to his wave records, he found that the reformed wave had a fundamental period equal to the period of the incident waves. In addition, energy was present at frequencies harmonic to the fundamental wave. He also noted that these complex waves resulted from steep waves that passed over the bar without breaking.

In 1969, Byrne (2) studied the field occurrences of multiple wave formed in passage over a naturally occuring submerged bar. He found that the number of waves appearing past the bar was double the number of waves encountering the bar. The wave conditions for these occurrences were bar-depth-to-wavelength ratio (C_b/L_b) of 0.045 and wave-height-to-depth ratios (H_b/C_b) of 0.4 to 0.5. The ratio of bar depth to trough depth was approximately 0.6.

Madsen and Mei (9) turned their attention to the transformation of a solitary wave over an uneven bottom both numerically and experimentally for height-to-depth ratios (H_i/d) of 0.1 to 0.2 and depth-to-wavelength (d/L_i) ratios of 0.03 to 0.05. Of particular interest is their description of the nature of the transformation: when the wave, distorted by climbing a mild (1:20) slope, passes onto a following shelf, a hump of smaller height appears at the rear and gradually trails behind the main wave. Profiles are illustrated and a comparison with Byrne's (2) field observations is made. Madsen and Mei (9) further note that some of the transformed waves may more closely resemble cnoidal or even possibly sinusoidal waves rather than solitary waves.

Galvin (3) found that finite amplitude, periodic, sinusoidal waves generated in constant depth shallow water breakdown into two or more waves traveling at speeds dependent on their height. Galvin (3) calls these waves "solitons" after an analogous phenomenon in plasma physics. One of the more interesting characteristics of solitons occur when a larger wave temporarily decreases during the resulting interaction. This decrease in amplitude is explained by the acceleration and subsequent spreading of the larger soliton when its leading edge reaches the deeper water of the smaller soliton. After passing through the smaller wave, the larger wave regains its initial amplitude. In Galvin's (3) study, the interaction of solitons periodically reproduced the initial wave form if followed far enough down the wave tank.

He ran tests over a very wide range of depth-to-wave length (d/L_i) and height-to-depth (H_i/d) ratios to define areas of soliton appearance. The results of his definition of soliton production are shown in Fig. 5. As can be seen, varying numbers of solitons will be produced for a given $d/L_i < 0.09$ and $H_i/d > 0.05$.

The attention of Galvin (3) is also applied to the previously cited works of Mason and Keulegan (10), Byrne (2), and Horikawa and Wiegel (4) and it is shown that much of their work was in the area of soliton genration.

THE LABORATORY STUDY

A laboratory experiment was designed to investigate the characteristics of gravity water waves that had passed over a submerged longshore bar. A model simulating a longshore bar formation was installed in a two-dimensional wave channel of the Hydromechanics Laboratories of Texas A&M University. Monochromatic waves were generated toward the submerged bar. Time histories of the water surface were recorded both windward and leeward of the bar. Analysis of these recordings allowed comparison of the characteristics of the modified waves with the characteristics of the incident waves.

The Model.--The model simulating the bar formation is the same as used by McNair (8). The profile of the model is shown in Fig. 1.

The Flume.--The wave channel used in this study was a 2-ft wide by 3-ft deep by 120-ft long flume equipped with a mechanical wave generator (see Fig. 2). The flume walls were of glass so that tests might be observed visually and photographically. A pendulum type wave generator was used to generate the incident waves. A wire mesh wave filter was utilized near the generator to attenuate the higher frequency wave (noise) present in the generated wave. At the opposite end of the flume, a semipermeable wave absorber was used to minimize reflection of the transformed waves back into the area of the bar. Prior to installation of the bar, a variety of waves with periods and heights representing the range of this study were generated at the wave absorber. Reflection measurements showed negligible reflection for the wave conditions investigated in this study.

Measuring Equipment.--Water surface time histories were obtained through the use of an ultrasonic profiler. The choice of an ultrasonic profiler was dictated by its excellent linearity characteristics. In operation, the sonar transceiver "reads" the surface thirty times a second. The resulting signal was amplified and supplied to a strip chart recorder. A second transceiver was used to monitor the relative position of the bar. The profiler was securely mounted to a movable carriage fitted to rails on either side of the channel. The movable carriage allowed records to be taken at any point in the channel.

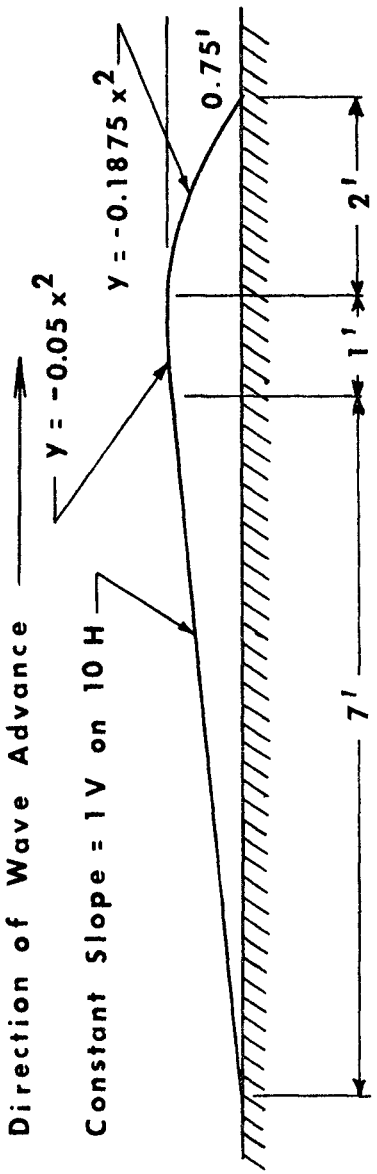

FIG. 1. - MODEL OF THE LONGSHORE BAR FORMATION

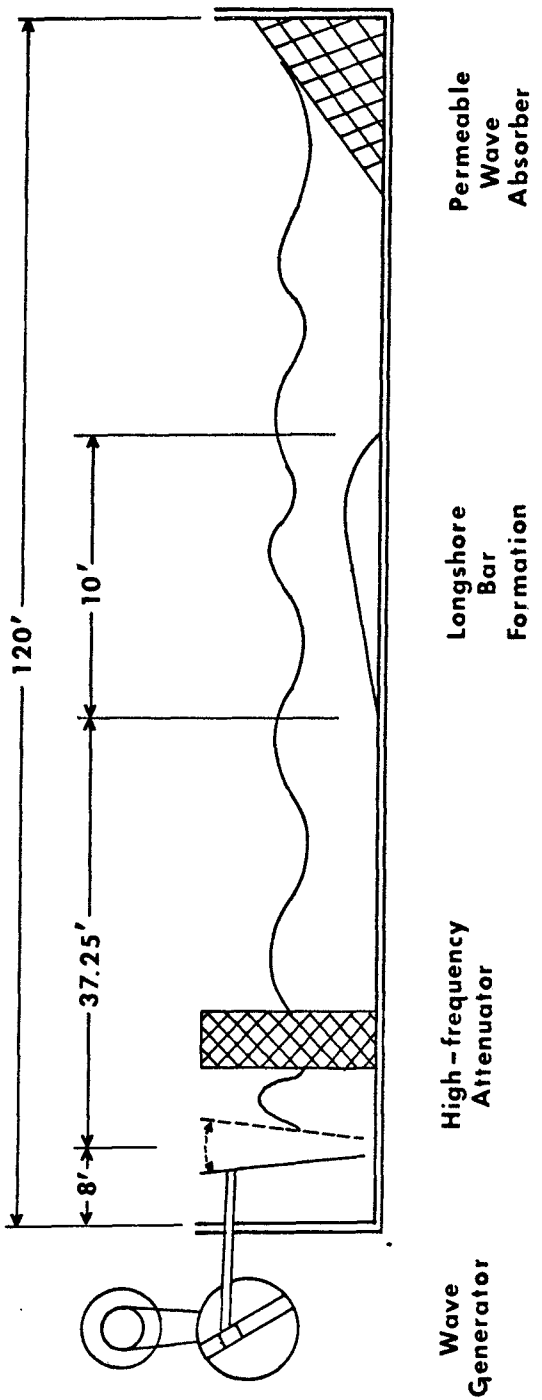

FIG. 2. - THE WAVE FLUME

Measurement of depth and dynamic calibration of the recording system were accomplished through the use of point gages.

Scope of the Study.--Waves of a range of periods (0.7 to 2.0 seconds) and heights (0.5 to 6.0 inches) were generated at the bar for several water depth (3.0 to 15.0 inches) over the bar. To reduce the limits of this investigation, primarily those waves which are transformed without breaking in passage over the bar were considered. However, several breaking conditions as well as the condition of waves passing the bar relatively unaffected were utilized in the envelope study.

It should be noted that a naturally occurring longshore bar is a steeper discontinuity in an already sloping beach. However, the effects of this beach slope are not accounted for in this study as the flume floor or representative ocean bottom was at a constant elevation. In addition, the axis of the bar was perpendicular to the direction of wave advance, so refractive effects would not be present in the wave forms.

EXPERIMENTAL PROCEDURE

With the water in the flume completely stilled, the recorder was switched on long enough to record a still-water level. Next, the wave generator was started and the excitation within the tank was allowed to come to a steady state. The recorder was switched on, and the profiler was slowly moved down the flume before the bar using a movable carriage. This procedure yielded a record for determining reflection coefficients and the height of the incident wave. These characteristics were determined using the envelope method of the linear wave theory. The period of the wave was determined by by using a stopwatch and a revolution counter on the generator flywheel. Any transformation was observed either visually or by utilizing the profiler/recorder system.

For the data necessary for power spectral density calculations, the above procedure was repeated. Once the incident wave height had been determined the profiler was located at a point in the flume having that wave height. Varying lengths of record were then made. Leeward of the bar, the profiler was stopped in several places, and records were again run at these locations. No specific locations were used as in the case of the records before the bar, as preliminary runs without the bar had indicated negligible reflection from the permeable wave absorber for the range of wave periods considered. These leeward records were also used to check for any wave "setup" that might be present.

EXPERIMENTAL RESULTS

The data obtained were in the form of strip chart records of the water-surface time-histories for locations before and after the bar. Samples of the wave profiles are shown in Fig. 3.

The Transformation Envelope.--For a given period, depth of water, and incident wave height derived from the analysis of the incident wave record, various relations were calculated. To eliminate problems of scale, only nondimensional relations were computed. Evidence of transformation was confirmed visually or by analysis of the leeward wave record.

The nondimensional relations and information on transformation were plotted in various ways to determine any functional relationships and to develop an envelope for the occurrence of transformation. The various plots showed that a wave-height-to-depth (H_I/C_b) ratio versus a depth-to-wavelength (C_b/L_i) ratio best defined a transformation envelope (see Fig. 4). This fact is in good agreement with Galvin (3).

Incident wave characteristics were used rather than wave conditions over the bar for two reasons: Incident wave characteristics can be more easily measured in the prototype; and there is difficulty in determining wave characteristics over the crest of the bar if the transformation process has already begun.

In Fig. 4, the demarcation between transformation and regular transmission for (C_b/L_i) approximately equal to 0.13 is not very distinct. The magnitude of the secondary waves in this region becomes so small as to be barely distinguishable. Thus, this boundary should probably be labeled the limit of measurable transformation. The same description should be applied to the boundary occurring for (H_i/C_b) of approximately 0.10.

Power Spectral Analysis.--The digital program used to evaluate power spectra in this study is based on procedures detailed in Blackman and Tukey (1). Additional description of their method applied to ocean waves is contained in Kinsman (7) and Robinson et al. (12).

In this study, a frequency bandwidth capable of evaluating third harmonics was used for maximum accuracy. For a given test, a frequency increment for energy computation was chosen such that the frequency interval was about a tenth of the fundamental frequency. This condtion allows very sharp definition of the energy peaks and their corresponding frequencies. Selection of the above values determined the sampling rate and the length of the record required. With this information, wave records from before and after the bar for nine different tests were digitized and supplied to the IBM 360/65 for analysis.

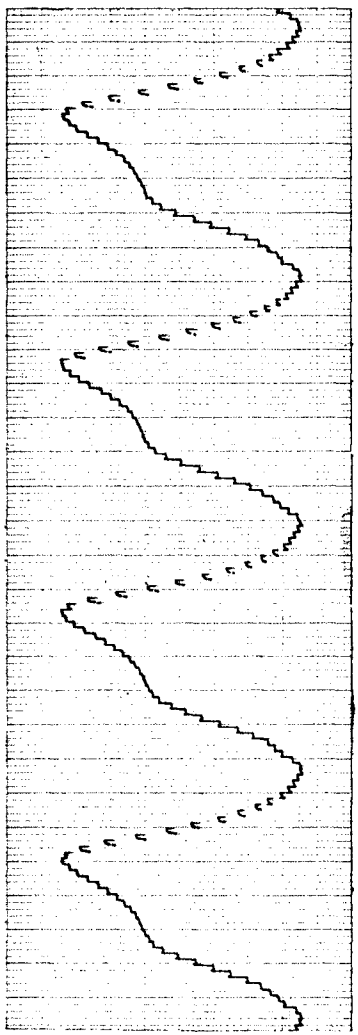

Reformed Wave Record

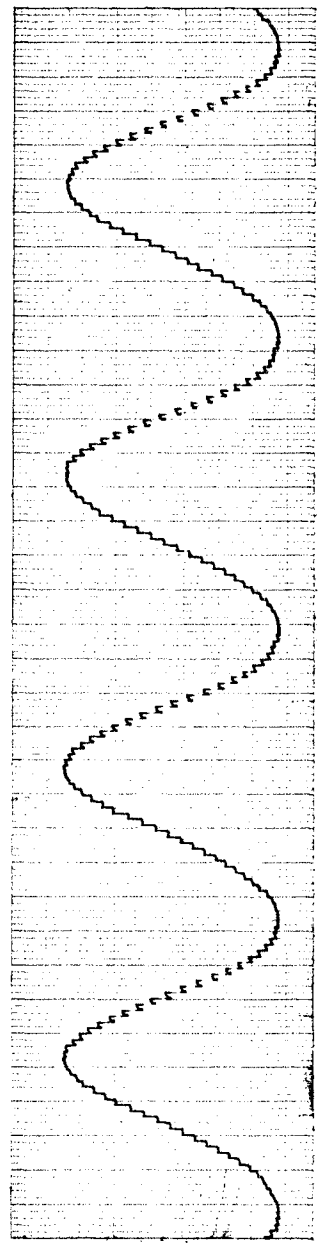

Incident Wave Record

FIG. 3. - TYPICAL WAVE RECORDS

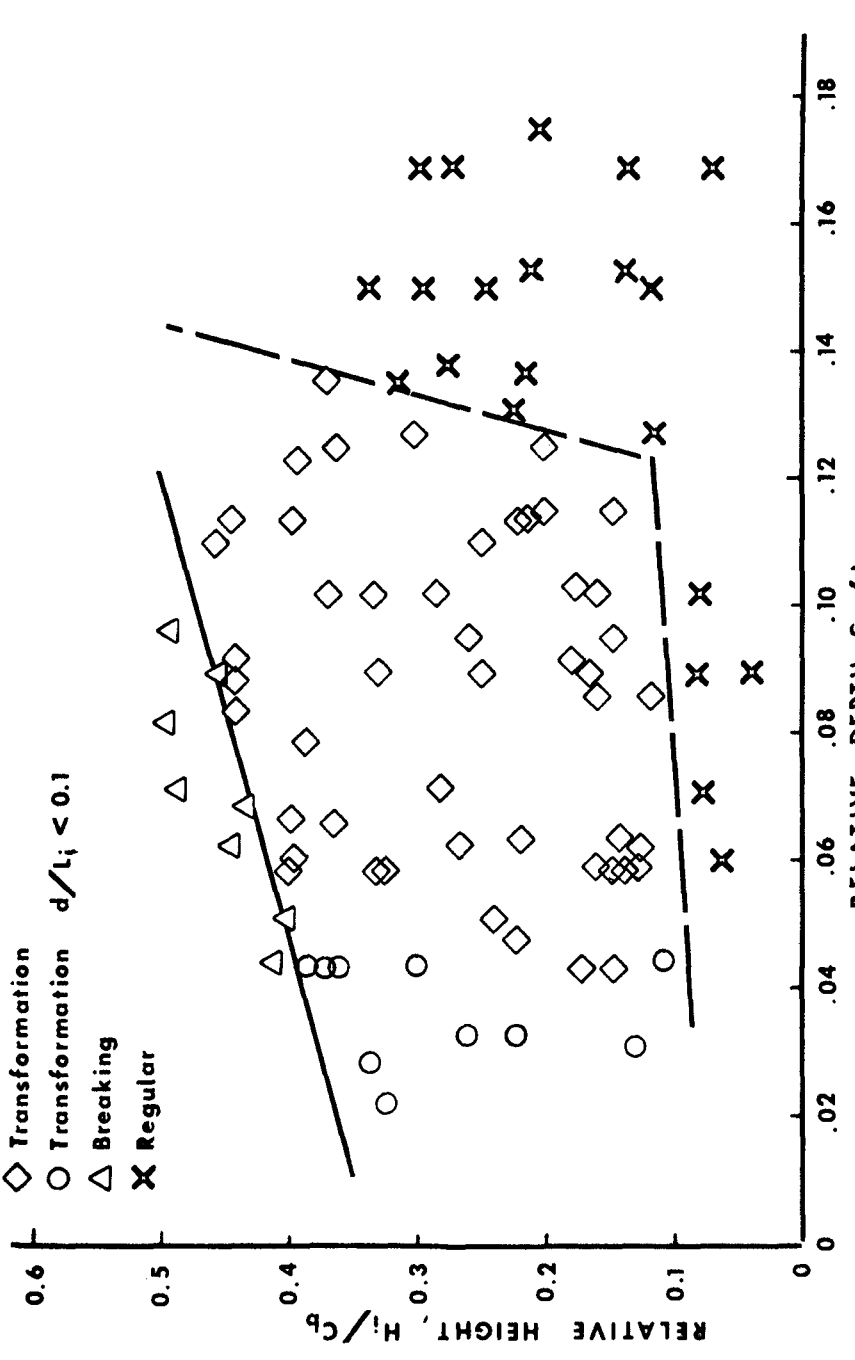

FIG. 4. - THE ENVELOPE OF TRANSFORMATION

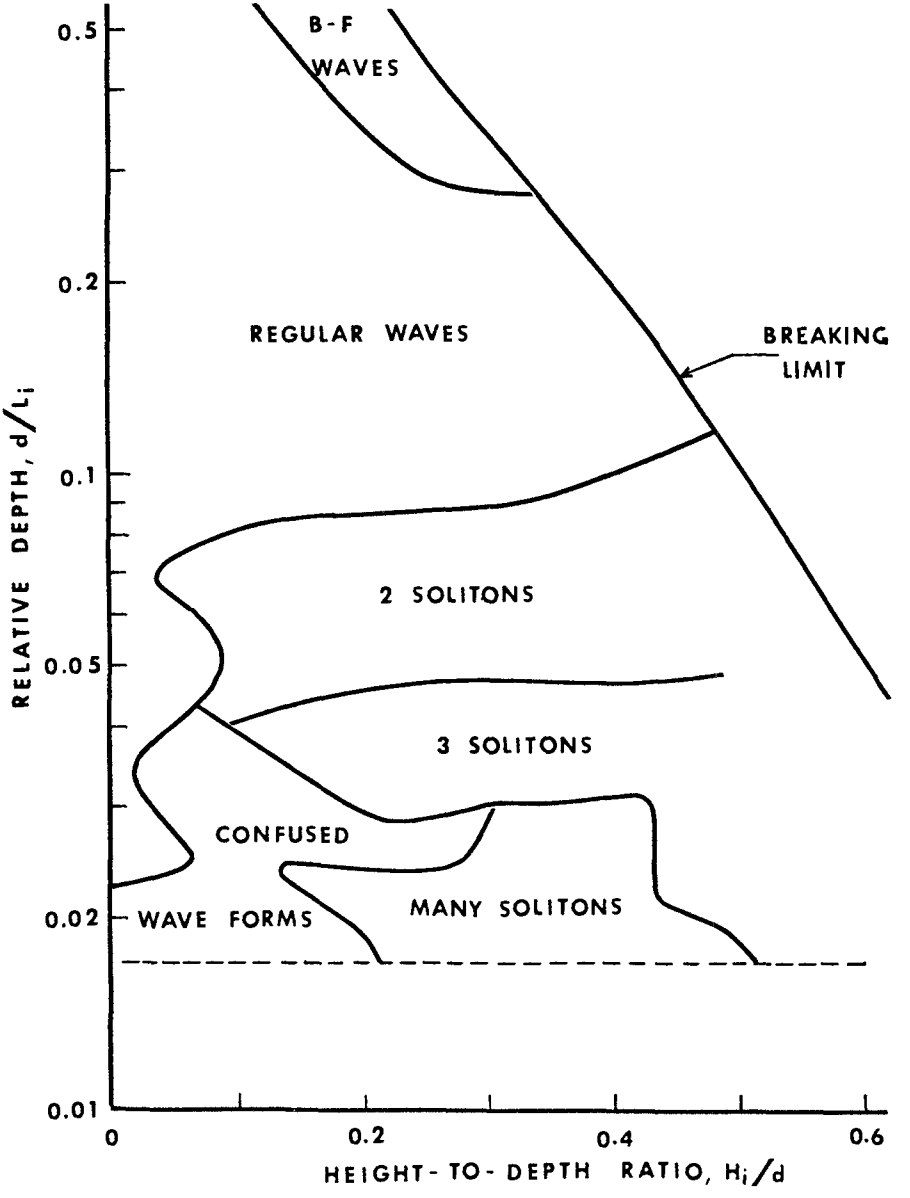

FIG. 5. - WAVE FORMS PRODUCED IN CONSTANT DEPTH BY A PERIODIC WAVE GENERATOR - AFTER GALVIN (3)

The digital program was verified using several combinations of sine waves. In each case, the output matched the input exactly. As a further check, the obtained power spectra of the incident wave was checked against the input conditions, again with excellent agreement for the nine tests used.

The power spectra show the reformed waves are definitely harmonic in composition. The amount of energy present in the various harmonics are tabulated in Table 1. The ratio of the harmonic energy to that of the fundamental wave $\left(E_h/E_{f_1}\right)$ is plotted in Fig. 6. Analysis of this energy transfer shows that the relative energy of the second harmonic increases with increasing $\left(H_i/C_b\right)$ for a given $\left(C_b/L_i\right)$, and the relative energy decreases with increasing $\left(C_b/L_i\right)$ for a given $\left(H_i/C_b\right)$.

The Transformed Wave.—The components of the transformed wave in the lee of the bar exhibit small-amplitude-theory characteristics of linear superposition and propagation velocities proportional to their respective periods. This lack of coupling between the various components was visually observed and was confirmed by the wave records. A typical series of wave profiles measured at foot increments leeward of the bar (Fig. 7) shows the phasing and superposition of the transformed wave elements very graphically. Sighting horizontally along the crests or troughs indicates the effects of these properties.

Fig. 8 shows the alteration of the incident wave as it passes over the bar. This alteration agrees closely with experiments by Madsen and Mei (9) on the transformation of solitary waves encountering a sloping bottom.

CONCLUSIONS

The experimental results clearly defined an envelope for transformation (Fig. 4). This envelope was determined using parameters involving incident wave characteristics and the depth over the bar.

The envelope for transformation seems to be somewhat similar to that of soliton wave appearance in a flat channel defined by Galvin (3) and reproduced in Fig. 5. The one significant difference in the depth-to-wavelength limit for regular transmission of waves which seems to be significantly higher. This difference is probably accounted for by the presence of the bar formation.

Although short period waves very close to the breaking limit were not analyzed spectrally because of difficulties previously explained in obtaining good profiles, the spectral analyses performed indicated that the secondary waves possed as much as six-tenths of the energy of the total

TABLE I

POWER SPECTRA CHARACTERISTICS

PARAMETER	Power Spectral Density Run								
	1	2	3	4	5	6	7	8	9
T in seconds	1.0	1.8	2.0	1.2	2.0	2.0	1.2	1.4	1.4
L_i in feet	4.9	10.5	12.8	6.6	12.8	12.8	6.6	8.2	8.2
H_i in feet	0.203	0.112	0.112	0.163	0.246	0.329	0.335	0.342	0.136
H_i/L_i	0.0379	0.0106	0.00872	0.0169	0.0192	0.0238	0.0508	0.0417	0.0166
C_b in feet	0.50	0.50	0.75	0.75	0.75	0.75	0.75	0.75	0.75
d in feet	1.25	1.25	1.50	1.50	1.50	1.50	1.50	1.50	1.50
H_i/C_b	0.372	0.223	0.149	0.218	0.328	0.405	0.447	0.456	0.181
C_b/L_i	0.104	0.0476	0.0586	0.1136	0.0586	0.0586	0.1136	0.0915	0.0915
E_h/E_{f_1}	0.092	0.281	0.065	0.040	0.633	0.603	0.121	0.085	0.045
E_{f_1} in inches^2	0.468	0.140	0.185	0.403	0.67	0.998	1.63	2.12	0.311
E_{f_2} in inches^2	0.403	0.0327	0.012	0.016	0.413	0.552	0.197	0.14	0.014
E_{f_3} in inches^2	------	0.0066	------	------	0.011	------	------	0.04	------
E_T in inches^2	0.511	0.179	0.197	0.419	1.094	1.60	1.84	2.30	0.325
E_I in inches^2	0.591	0.230	0.2185	0.524	1.17	1.74	2.31	2.31	0.351
$C_{TRANS} = E_T/E_i$	0.865	0.780	0.90	0.80	0.935	0.920	0.797	0.995	0.926
E_i in inches^2	0.620	0.225	0.225	0.500	1.15	1.67	2.02	2.10	0.333
C_{REFL}	0.077	0.313	0.231	0.074	0.186	0.096	0.040	0.050	0.060

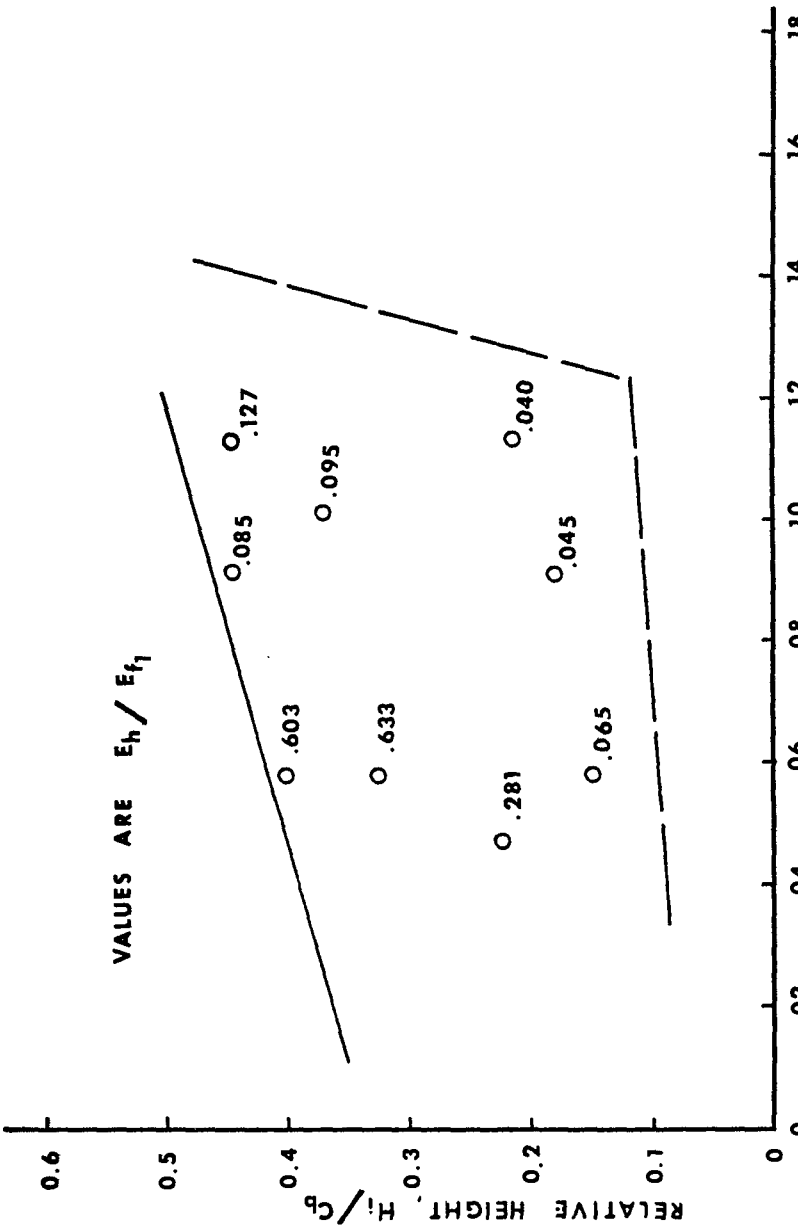

FIG. 6. - RELATIVE ENERGY TRANSFORMED TO HIGHER FREQUENCIES

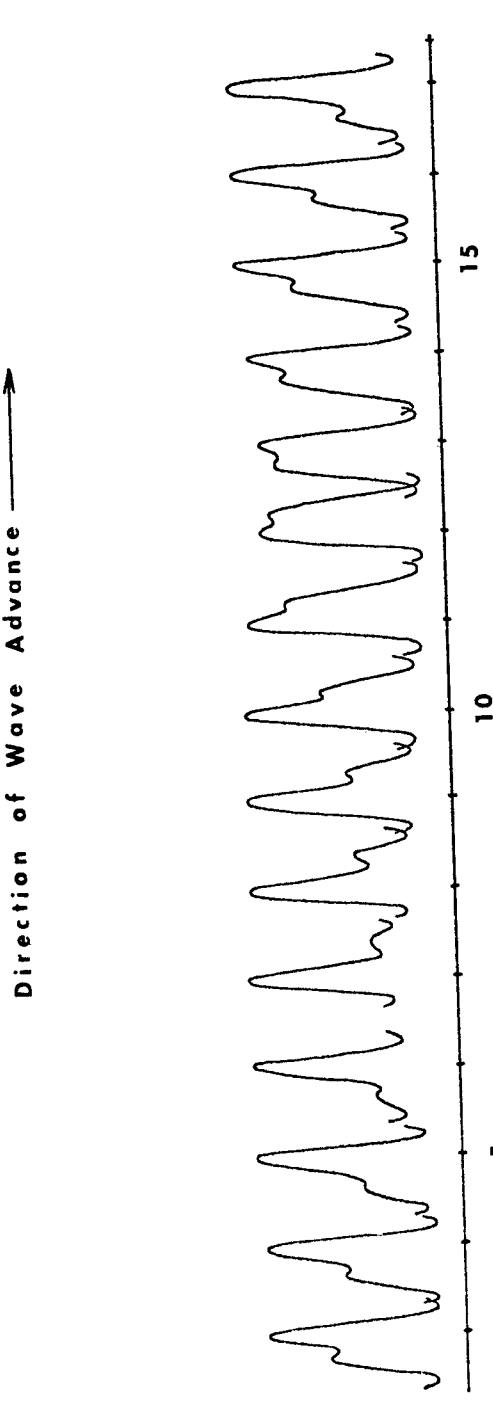

FIG. 7. - TYPICAL WAVE PROFILES LEEWARD OF THE BAR

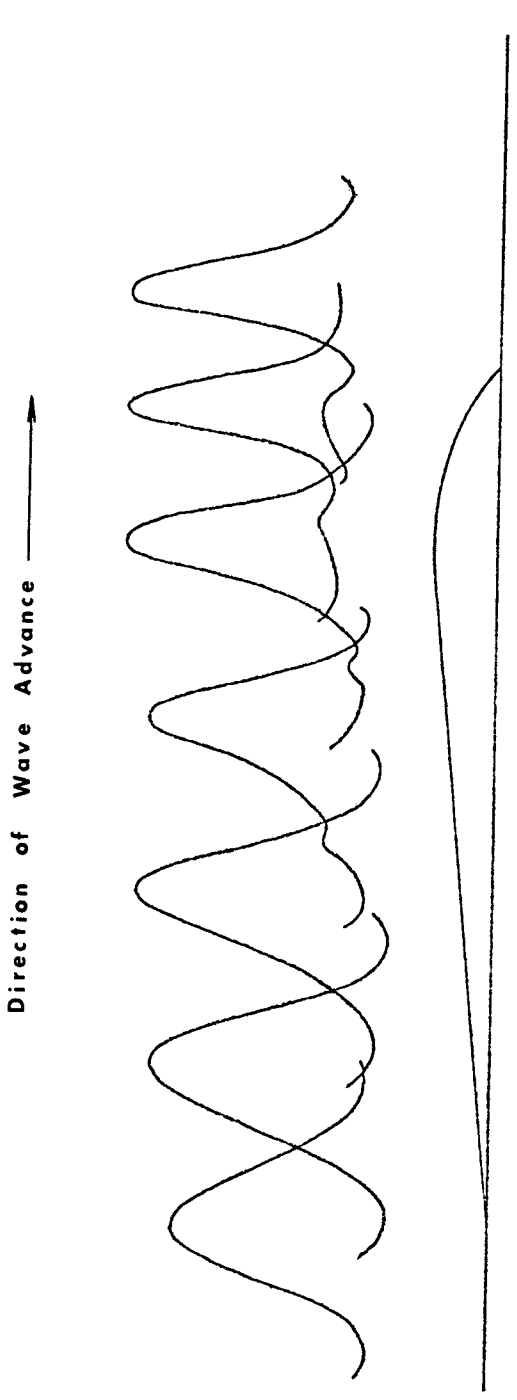

FIG. 8. - TRANSFORMATION OF A WAVE OVER THE BAR

energy of the transformed wave. The power spectra also show that this secondary crest has a frequency twice that of the primary wave.

Assuming that the depth-to-wavelength ratio in the channel before the bar precludes the formation of solitons, it is felt that the phenomenon of wave transformation is due to the generation of nonlinear wave forms in passage of the incident wave over the bar. In the deeper water in the lee of the bar, the nonlinear wave is altered into a sinusoidal form secondary to the main wave propagating with a speed proportional to its period as shown in Fig. 6. The actual alteration of the wave profile over the bar as shown in Fig. 7 agrees closely with experiments by Madsen and Mei (9) on the transformation of solitary waves moving up a sloping bottom.

This study has left many questions unanswered due to the limited scope of the experiments. In addition, this effort has probably generated further questions. Williams' (13) conclusion that the length of the submerged object has the greatest effect on transformation would suggest that several different bar formations, including a vertical plate, should be investigated. Further, power spectral analysis should be performed for a wide variety of conditions to determine functional relationships for the energies of the secondary waves.

NOTATIONS

The following symbols are used in this paper:

C_b = Water depth over the bar crest measured from still-water level.

C_{REFL} = Coefficient of reflection using small amplitude theory.

C_{TRANS} = Coefficient of transmission.

d = Water depth in the flume measured from still-water level.

E_{f_1} = Energy of fundamental harmonic of reformed wave.

E_{f_2} = Energy of second harmonic of reformed wave.

E_{f_3} = Energy of third harmonic of reformed wave.

E_h = Total energy of harmonics.

E_I = Energy of incident wave.

E_i = Energy of incident wave using small amplitude theory $= H_i^2/8$.

E_T = Total energy of reformed wave.

H_b = Wave height measured over the bar.

H_i = Incident wave height.

L_b = Wavelength over the bar.

L_i = Incident wavelength.

REFERENCES

1. Blackman, R. B., and J. W. Tukey, The Measurement of Power Spectra, Dover Publications, Inc., New York, 1958.

2. Byrne, R. J., "Field Occurrences of Induced Multiple Gravity Waves," Journal of Geophysical Research, Vol. 74, No. 10, May 15, 1969.

3. Galvin, C. J., "Finite-Amplitude, Shallow Water-Waves of Periodically Recurring Form," Paper presented at Longwave Symposium, University of Delaware, September 1970.

4. Horikawa, K., and R. L. Wiegel, "Secondary Wave Crests," University of California, Berkeley, Institute of Engineering Research Report, Series 89, Issue 4, February 1959.

5. Ippen, A. T., Ed., Estuary and Coastline Hydrodynamics, McGraw-Hill Book Company, Inc., New York, 1966.

6. Jolas, P., "Passage de la Houle sur un Seuil," La Houille Blanche, No. 2, Mars-Avril, 1960, pp. 148-152.

7. Kinsman, Blair, Wind Waves, Their Generation and Propagation on the Ocean Surface, Prentice-Hall, Inc., Englewood Cliffs, New Jersey, 1965, Chapter 9.

8. McNair, E. C., Jr., and R. M. Sorensen, "Characteristics of Waves Broken by a Longshore Bar," Proceedings of the Twelfth Coastal Engineering Conference, Vol. 1, Chapter 26, ASCE, New York, 1970.

9. Madsen, O. S., and C. C. Mei, "The Transformation of a Solitary Wave Over an Uneven Bottom," Journal of Fluid Mechanics, Vol. 39, Part 4, 1969, pp. 781-791.

10. Mason, M. A., and G. H. Keulegan, "A Wave Method for Determining Depths Over Bottom Discontinuities," Technical Memorandum No. 5, Beach Erosion Board, Corps of Engineers, Military Intelligence Division Office, Chief of Engineers, U. S. Army, May 1944.

11. Miche, M., "Mouvements ondulatories de la mer en profondeur constante ou decroissant," Annual des Ponts et Chausees, Tome 114, 1944.

12. Robinson, R. J., H. R. Brannon, and G. W. Kattawar, "Storm Wave Characteristics," Society of Petroleum Engineers Journal, March 1967, pp. 87-98.

13. Williams, John A., "A Nonlinear Problem in Surface Water Waves," Dissertation presented to University of California, Berkeley, in partial fulfillment of the requirements for the degree of Doctor of Philosophy, 1964.

CHAPTER 20

AIRY WAVE THEORY AND BREAKER HEIGHT PREDICTION

Paul D. Komar and Michael K. Gaughan

School of Oceanography
Oregon State University
Corvallis, Oregon 97331

ABSTRACT

Using a critical value for $\gamma_b = H_b / h_b$ as a wave breaking criterion, where H_b and h_b are respectively the wave breaker height and depth, applying Airy wave theory, and assuming conservation of the wave energy flux, one obtains

$$H_b = k\, g^{1/5} \left(T^2 H_\infty \right)^{2/5}$$

relating H_b to the wave period T and to the deep-water wave height H_∞. Three sets of laboratory data and one set of field data yield $k = 0.39$ for the dimensionless coefficient.

The relationship, based on Airy wave theory and empirically fitted to the data, is much more successful in predicting wave breaker heights than is the commonly used equation of Munk, based on solitary wave theory. In addition, the relationship is applicable over the entire practical range of wave steepness values.

INTRODUCTION

Engineers and scientists interested in the nearshore region often find it necessary to calculate the expected breaker heights of a wave train from its deep-water characteristics. Wave forecast procedures, for example, yield estimates of the deep-water wave height, H_∞, and period T. From these values it is desirable to estimate the heights of these waves when they arrive and break on a particular beach.

The procedure that is commonly followed (CERC Tech. Report No. 4, 1966) is to utilize the theoretical equation

$$H_b = \frac{H_\infty}{3.3 \left(H_\infty / L_\infty \right)^{1/3}} \qquad (1)$$

or its graphical equivalent, where H_b is the breaker height. This relationship, introduced by Munk (1949), is based on an evaluation of the breaker wave energy and celerity with the theoretical solitary wave equations of Boussinesq (1877). The application of the solitary wave was suggested by the obvious resemblance between the theoretically derived solitary wave profile and the observed profiles of oscillatory waves nearing the breaker zone.

Several studies, such as those of Ippen and Kulin (1954) and Kishi and Saeki (1966), have demonstrated that when a solitary wave travels up an inclined slope, as it would in approaching a beach, the observed changes in amplitude, celerity, wave profile, etc., deviate markedly from the theoretical values determined from solitary wave theory. Such results, plus the usual doubt in applying solitary wave theory to periodic oscillatory waves, casts doubts on the foundations and applicability of equation (1).

The purpose of this paper is to examine the applicability of linear Airy wave theory to evaluate wave breaker heights. Such an application is encouraged by the recent successes of Airy theory in examining longshore current generation (Bowen, 1969; Longuet-Higgins, 1970). In addition, based on the fit of the wave theories to the free surface boundary conditions, Dean (1970) determined that Airy wave theory may be applicable to a wide range of near breaking conditions.

Using Airy wave theory, a new relationship is deduced from which the breaker height H_b can be predicted from the deep-water wave parameters H_∞ and T. As will be seen, the resulting relationship can predict with excellent success breaker heights that agree with those observed.

THEORETICAL DEVELOPMENT

In his derivation of equation (1), Munk (1949) made use of the conservation of energy flux

$$\left(E\, Cn \right)_b = \left(E\, Cn \right)_\infty \qquad (2)$$

where E is the wave energy and Cn is the wave group velocity, the rate at which the energy travels. This links the deep-water wave conditions (denoted by the subscript ∞) to the wave breaking parameters (denoted by the subscript b). As written, equation (2) does not include the effects of refraction. Munk evaluated the deep-water

parameters with Airy wave theory and applied solitary theory to the breaking wave. In this paper, Airy wave theory will be used for both the deep-water and breaking wave conditions. The energy of the breaking wave then becomes

$$E_b = \frac{1}{8} \rho g H_b^2 \tag{3}$$

where ρ is the density of water, and the celerity in shallow water is given by

$$C_b = \sqrt{g h_b} \tag{4}$$

where h_b is the water depth at breaking.
Munk (1949) made use of the substitution

$$\gamma_b = H_b / h_b = 0.78 \tag{5}$$

for a breaking criterion. This value was determined theoretically by McCowan (1894) for solitary waves. Field measurements reported in Scripps Institution of Oceanography Wave Report 24 (1944) and again in Sverdrup and Munk (1946) confirm this value of γ_b for beaches with very low gradients. Several laboratory studies have demonstrated that γ_b actually varies with the beach slope, increasing as the slope increases. γ_b also varies somewhat with the deep-water wave steepness, H_∞ / L_∞. In light of the poor showing of the solitary wave theory in studies such as those of Ippen and Kulin (1954) and Kishi and Saeki (1966) the success of γ_b as a breaking criterion must be fortuitous and cannot be taken as an indication of the success of the solitary wave theory as implied by Munk (1949).

Following Longuet-Higgins and Stewart (1964), Bowen et. al. (1968), Bowen (1969) and Longuet-Higgins (1970), we shall apply $\gamma = H/h$ as a similarity criterion without reference to the solitary wave theory. $\gamma_b = H_b / h_b$ will be accepted as a breaking criterion and used in conjunction with the Airy wave theory. This is commonly done in practice in computer programs for wave refraction.

Using γ_b as a breaking criterion, applying Airy theory, and assuming conservation of the energy flux (equation 2), one obtains the relationship

$$H_b = \left| \frac{\sqrt{g \gamma_b}}{4 \pi} T H_\infty^2 \right|^{2/5} \tag{6}$$

relating the breaker height H_b to the wave period T (assumed constant) and the deep-water wave height H_∞. According to equation (6), if we plot H_b against $g^{1/5} (T H_\infty^2)^{2/5}$ we should obtain a straight line whose slope is dependent upon the value of γ_b. Since γ_b is known to vary with the beach slope, we might expect a separate straight line for each beach slope. However, the one-fifth power of γ_b is involved so that the expected variations in γ_b should not produce a very marked change in the line slope. A comparison with the data bears this out.

DATA TESTS

Three sets of extensive laboratory data and the one existent set of field data have been utilized to test the proposed relationship of equation (6).

The wave flume measurements of Komar and Simmons, collected in 1968, give a considerable range to the required wave parameters needed to test equation (6). This data, which has not been previously published, will be discussed fully in Gaughan (in prep). The technique of the study was very similar to that of the well-known study of Iverson (1951) and provided measurements of H_b and T and values of H_∞ computed from the wave height measurements in the constant depth portion of the wave channel. The corresponding measured values of H_b and the computed values of the parameter $g^{1/5} (T H_\infty^2)^{2/5}$ are plotted in Figure 1. It is seen that there is a good linear relationship as predicted by equation (6), which yields

$$H_b = 0.39\, g^{1/5} \ (T H_\infty^2)^{2/5} \qquad (7)$$

There is no apparent systematic dependence on the beach slope although the data extends over a range of slopes from 2 to 6 degrees.

The line slope value 0.39 corresponds to a $\gamma_b = 1.42$ in equation (6). This γ_b value is higher than those actually measured by Komar and Simmons (which ranged from 0.7 to 1.1). Apparently the line fitted to the data must empirically correct for the fact that Airy wave theory, when applied to the amplitude changes of a shoaling oscillatory wave near breaking, tends to give a predicted height lower than observed.

In Figure 2 are plotted the laboratory measurements of Iverson (1951), generally considered to be the best available laboratory data. The straight line shown is the same as that of Figure 1 and given by equation (7), established by the data of Komar and Simmons. It is apparent that there is good agreement between the two sets of data in establishing equation (7). The trend of the Iverson data does demonstrate a systematic dependence on the beach face slope, the higher gradient giving a somewhat higher line slope. Such a dependence is expected from the observed changes in γ_b with variations in the beach slope. Iverson found a much greater variation in γ_b with beach

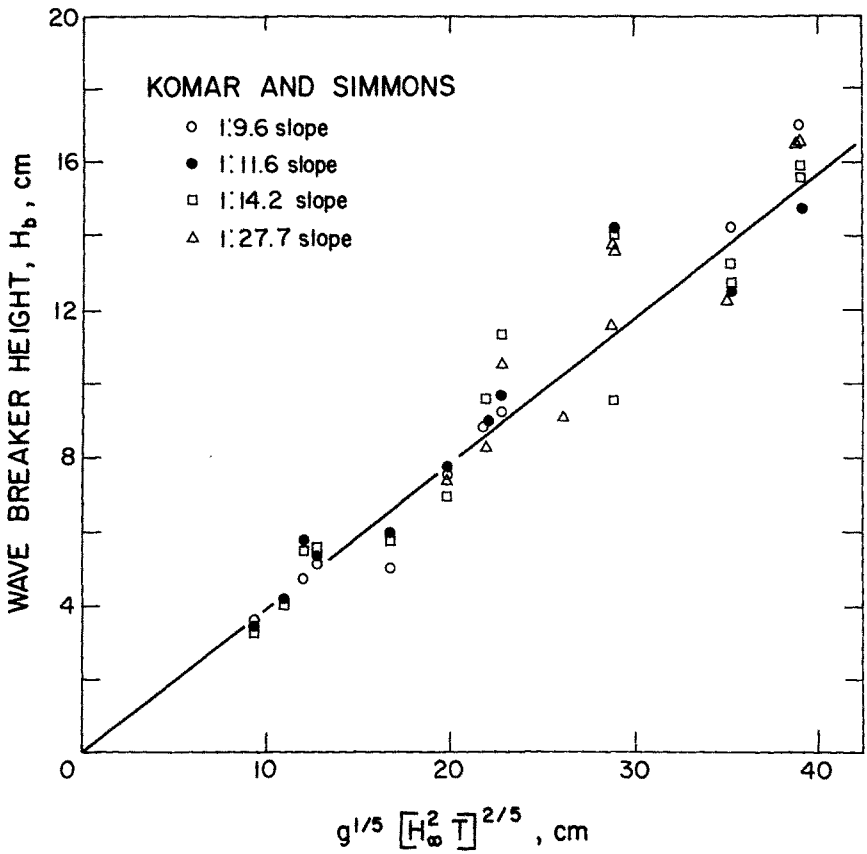

Figure 1: Laboratory breaking wave data of Komar and Simmons. The straight line, fitted by eye, has a slope of 0.39 and yields equation (7).

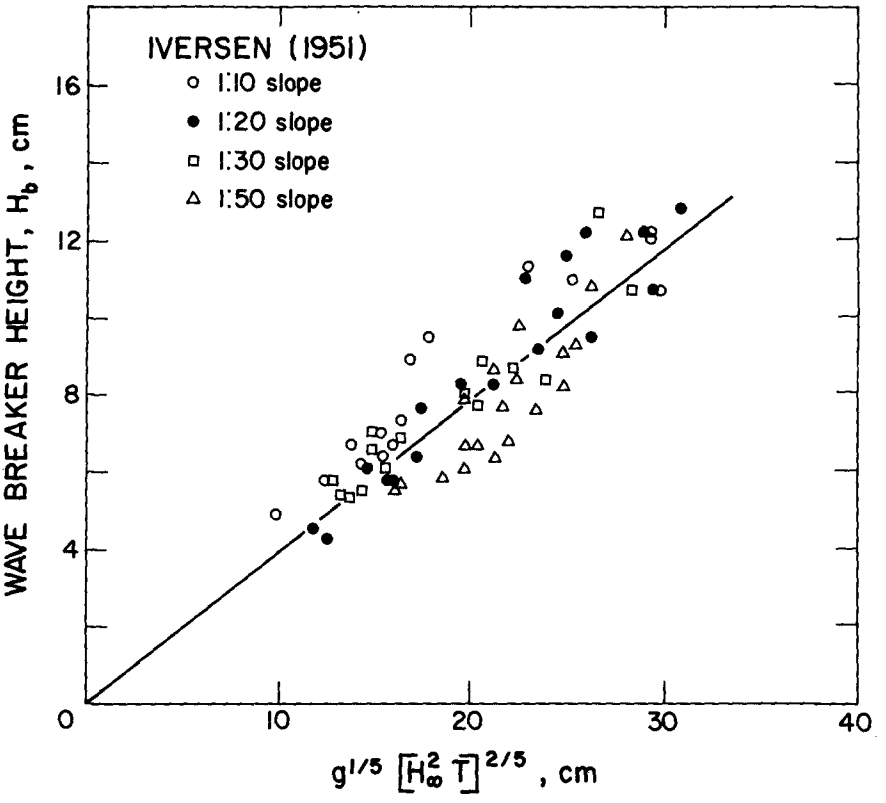

Figure 2: The straight line of equation (7) in comparison to the laboratory breaking wave data of Iverson (1951).

slope than did Komar and Simmons (see Gaughan, in prep) and this greater dependence is reflected in the plots of Figure 1 and 2.

The laboratory data of Galvin (1969) are also utilized to test equation (6); the results are shown in Figure 3. The data does not follow quite as well the straight line based on the data of Komar and Simmons. The main difficulty here is that Galvin defined his breaker heights differently than did Iverson or myself, and so should systematically plot above the line. In addition, he calculated the deep-water wave heights directly from the paddle stroke rather than from wave measurements in the constant depth portion of the channel; this may account for the increased scatter in the data plot. No systematic dependence on the beach slope appears.

The real test for the relationship of equation (6) comes in examining the available field data. The only field data of breaking waves suitable for such a test is that reported by Munk (1949). The data is referred to as Leica, Types 1 and 2. The Type 2 data represents waves which break behind a bar in water of increasing depth while the more normal breaking conditions are included in the Type 1 data. Both sets of field data are plotted in Figure 4 along with the highly extrapolated straight line of equation (7) obtained from Figure 1. The degree of agreement between the trend of the data and the straight line is remarkable in view of the degree of extrapolation involved. To illustrate the extent of the extrapolation, the data of Komar and Simmons and the field data of Munk are plotted together on a log-log graph in Figure 5.

Linear regression analysis of the above laboratory and field data yields the equation

$$H_b = 0.383\ g^{1/5}\ (\ T\ H_\infty^2\ )^{2/5} \quad + \quad 0.73\ cm \qquad (8)$$

with a sampling correlation coefficient of $r = 0.98$. This remarkably high value of the correlation coefficient confirms our visual approval of the correlation.

COMPARISON WITH SOLITARY WAVE THEORY

By using the relationship $L_\infty = g\ T^2 / 2\pi$ between the deep-water wave length L_∞ and the period T, equation (7) can be modified to the dimensionless form

$$H_b / H_\infty = \frac{0.56}{(\ H_\infty / L_\infty\ )^{1/5}} \qquad (9)$$

which indicates that H_b is a function of the deep-water wave steepness

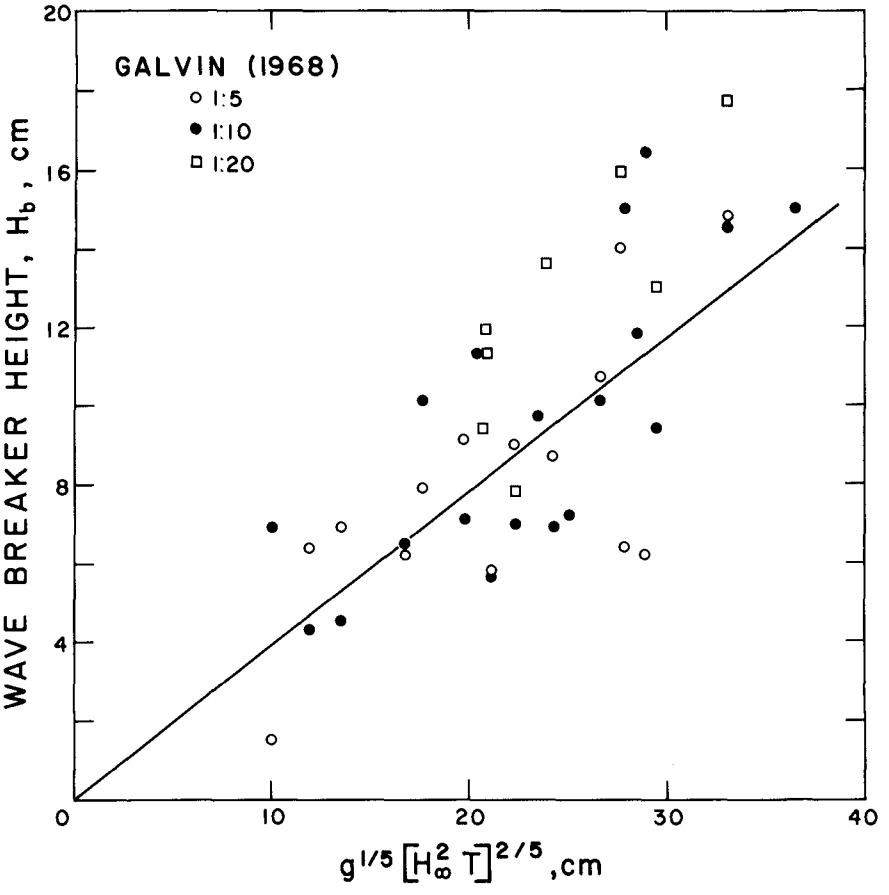

Figure 3: The straight line of equation (7) in comparison to the laboratory breaking wave data of Galvin (1968).

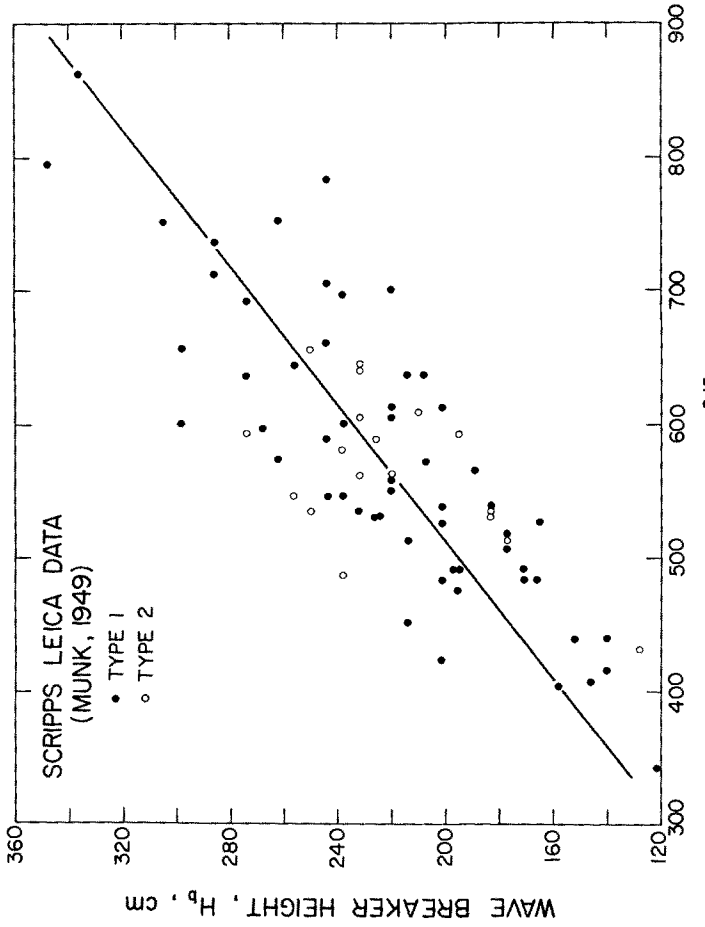

Figure 4: The straight line of equation (7) in comparison to the field breaking wave data reported in Munk (1949). The sampling correlation coefficient is 0.81.

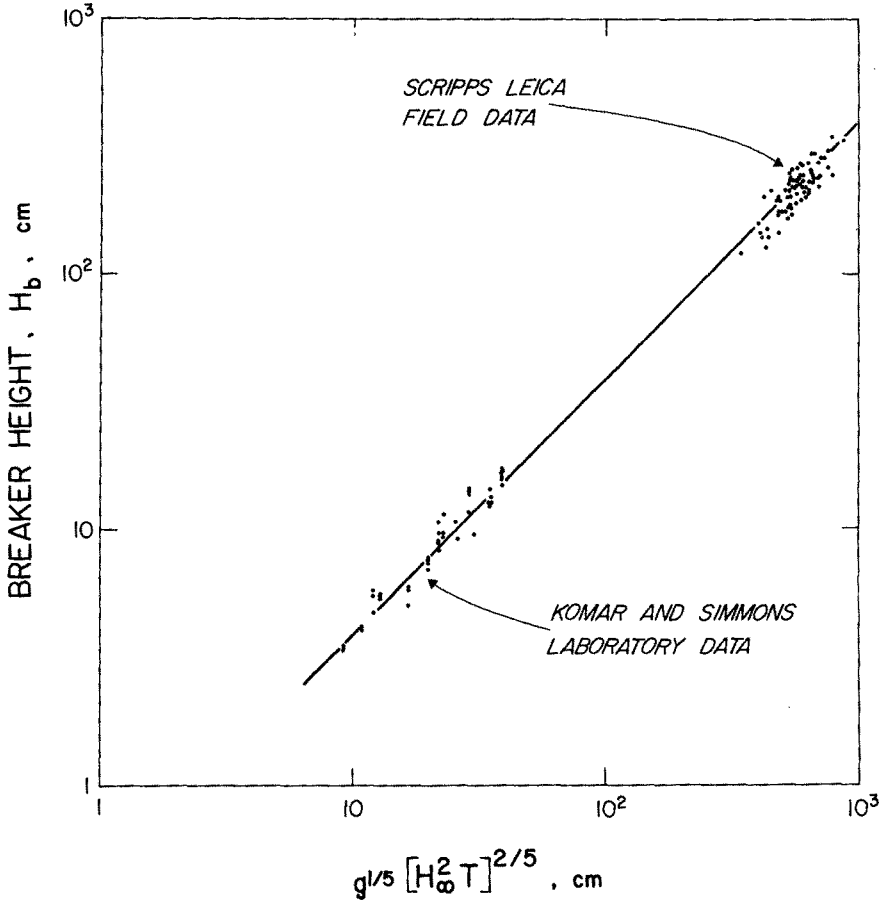

Figure 5: A log-log plot of the laboratory data of Komar and Simmons and the field data of Munk (1949). The straight line is that of equation (7).

H_∞ / L_∞. This relationship is similar to equation (1) obtained by Munk (1949) using solitary wave theory, the principal difference being that H_∞ / L_∞ is to the - 1/5 power rather than to the - 1/3 power. It is also very close to the empirical equation of Le Mehaute and Koh (1967) which gives H_∞ / L_∞ to the - 1/4 power.

Figure 6 is the well-known graph of H_b / H_∞ versus H_∞ / L_∞ from Munk (1949) showing the line from solitary wave theory, equation (1), fitting the data best for low H_∞ / L_∞ values and a line at high wave slopes from regular Airy wave theory. Connecting the two, at intermediate values is an empirical line through the data. Superimposed on this graph is the line (solid) corresponding to equations (7) and (9). It is seen that this curve fits the data very well over the entire range of H_∞ / L_∞ values, nearly lying atop the empirical curve of Munk. Because of this success over the entire range of wave slope values, equation (9) should be very useful for engineering design and field application.

CONCLUSIONS

Both the available laboratory and field data support the relationship in equation (7), derived from Airy wave theory and the use of $\gamma_b = H_b / h_b$ as a breaking wave criterion. The relationship is successful over the entire practical range of wave steepness values and therefore is much more useful than the standard relationship derived from solitary wave theory by Munk (1949) which is limited only to small H_∞ / L_∞ values. The proposed relationship can also replace the empirical curve given by Munk for the intermediate range of wave slope values.

ACKNOWLEDGMENTS

We wish to thank J. H. Nath and L. S. Slotta for critically reading the manuscript, and N. Pisias for the statistical analysis of the data. This study was supported in part by the National Oceanographic and Atmospheric Administration (maintained by the U. S. Department of Commerce). Institutional Sea Grant 2-35187.

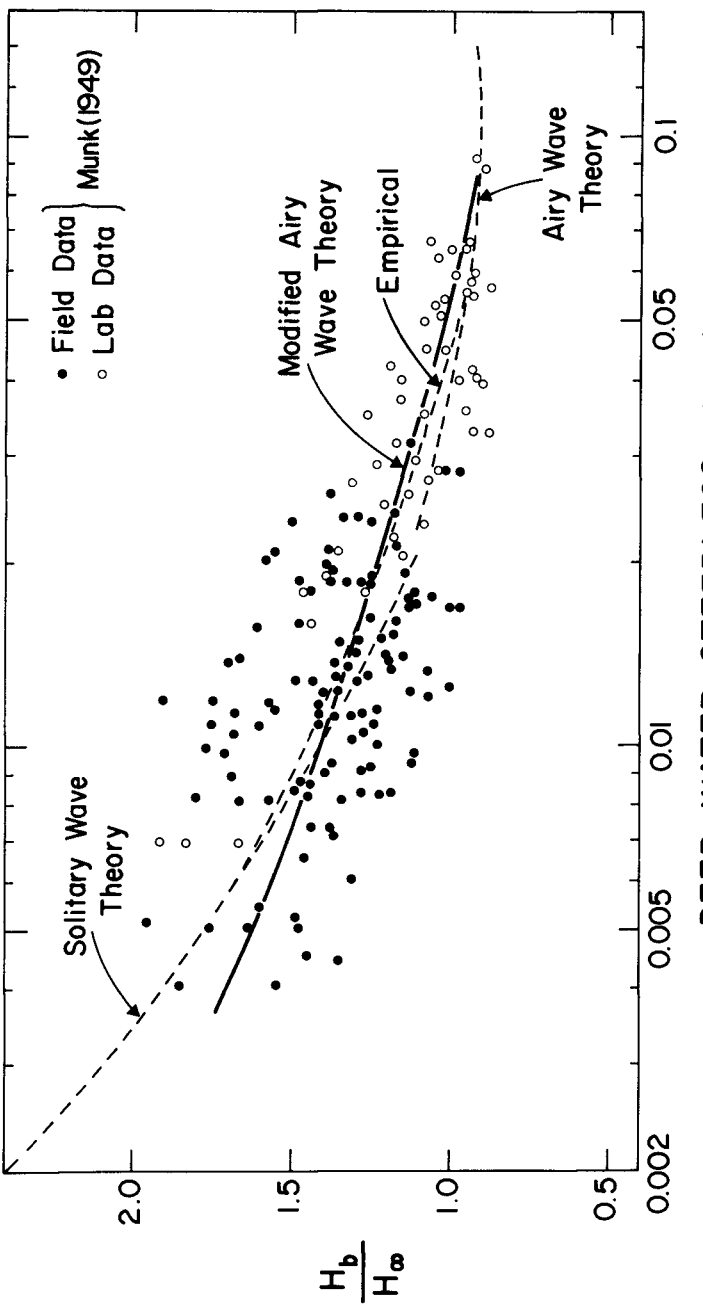

Figure 6: Wave breaker height related to the deep-water wave steepness (after Munk, 1949). The dashed curves are the theoretical and empirical curves given by Munk (1949). The solid curve corresponds to equation (9), the dimensionless form of equation (7).

REFERENCES

Boussinesq, J., Essai sur la theorie des eaux courantes, Memoires par divers savants, 23, 24, 1877.

Bowen, A. J., The generation of longshore currents on a plane beach, Jour. Marine Res., 37, 206, 1969.

Bowen, A. J., D. L. Inman, and V. P. Simmons, Wave 'set-down' and set-up, Jour. Geophys. Res., 73(8), 2569, 1968.

Coastal Engineering Research Center, Shore protection, planning and design, Technical Report No. 4, U. S. Army, Corps of Engineers, 1966.

Dean, R. G., Relative validities of water wave theories, Proc. Amer. Soc. Civil Engr., 96 (WW1), 105, 1970.

Galvin, C. J., Jr., Breaker travel and choice of design wave height, Proc. Amer. Soc. Civil Engr., 95 (WW2), 175, 1969.

Gaughan, M. K., Gravity water wave breaking criteria: A review of theory and data (in preparation).

Ippen, A. T. and G. Kulin, The shoaling and breaking of the solitary wave, 5th Conf. on Coastal Engr., Chapt. 4, 27, 1954.

Iverson, H. W., Studies of wave transformation in shoaling water, including breaking, Gravity Waves, Nat. Bureau of Standards, Circular 521, 1951.

Kishi, T. and H. Saeki, The shoaling, breaking and runup of the solitary wave on impermeable rough slopes, Proc. 10th Conf. on Coastal Engr., Chapt. 21, 322, 1966.

Le Mehaute, B. and R. C. Y. Koh, On the breaking of waves arriving at an angle to the shore, Jour. of Hydraulic Res., 5 (1), 67, 1967.

Longuet-Higgins, M. S., Longshore currents generated by obliquely incident sea waves, parts 1 and 2, Jour. Geophys. Res., 75 (33), part 1: 6778, part 2: 6790, 1970.

Longuet-Higgins, M. S. and R. W. Stewart, radiation stresses in water waves; a physical discussion, with applications, Deep-Sea Res., 11, 529, 1964.

McCowan, J., On the highest wave of permanent type, Phil. Mag. XXXVII (5), 351, 1894.

Munk, W. H., The solitary wave theory and its applications to surf problems, New York Acad. Science Annals, 51, 376, 1949.

Scripps Institution of Oceanography, Effect of bottom slope on breaker characteristics as observed along the Scripps Institution pier, Wave Report No. 24 (unpublished), 1944.

Sverdrup, H. V. and W. H. Munk, Theoretical and empirical relations in forecasting breakers and surf, Trans. Amer. Geophys. Union, 27, 828, 1946.

CHAPTER 21

MAXIMUM BREAKER HEIGHT FOR DESIGN

J. Richard Weggel
Coastal Engineering Research Center
Washington, D. C. 20016

ABSTRACT

A re-evaluation of previously published breaking wave data is used to develop a relationship for the maximum breaker height in terms of the depth in which the wave breaks, breaker steepness and the local beach slope. This relationship is used with the breaker travel distance equation of Galvin (3)* to estimate the maximum breaker height to which a coastal structure might be subjected. In addition, the range of depths in which a wave of given height will break is found by examination of the upper bound of observed values of d_b/H_b . An example problem is presented to illustrate the use of the general maximum breaker height design curves.

INTRODUCTION

Coastal structures such as groins, jetties and breakwaters are usually subjected to waves breaking directly against them. The range of breaker heights to which such a structure is subjected depends critically on the range of depths at the structure site with the largest breaker occurring for the greatest depth at the site. It is necessary to determine this breaker height since it usually establishes the critical design condition for the structure. This maximum design breaker height, H_b, is a function of depth at the structure, d_s, wave period, T, and the post-construction beach slope, m, on which the structure is situated. The relationship between the above variables and breaker height must be based on empirical data since it is not at present possible to adequately describe breaking waves in mathematical terms. This paper presents a re-evaluation of some previously published breaker data in order to establish this maximum breaker height and to present the results in a form easily applied to engineering design calculations.

BREAKING WAVES IN SHALLOW WATER

In relatively deep water $(d/L > 0.5)$ wave breaking is initiated when the wave steepness becomes greater than some limiting value. Michell (11) found that theoretically this limiting steepness is given by,

$$\left\{\frac{H}{L}\right\}_{limiting} = \frac{H_b}{L_b} = 0.142 \approx \frac{1}{7} \qquad (1)$$

For a finite amplitude wave in deep water having the above limiting

*Numbers in parentheses correspond with references listed in Appendix I.

steepness, the wave length, as a function of wave period, is given approximately by,

$$L_b = 1.2 \frac{gT^2}{2\pi} \tag{2}$$

and consequently breaking occurs when

$$\frac{H_b}{T^2} = 0.875 \tag{3}$$

As a wave moves into shoaling water the local water depth also influences the initiation of breaking. Miche (10) found theoretically that this dependence on depth could be approximated quite well by,

$$\frac{H_b}{L_b} = 0.142 \tanh\left(\frac{2\pi d_b}{L_b}\right) \tag{4}$$

For small values of d_b/L_b , $\tanh(\frac{2\pi d_b}{L_b})$ approaches $\frac{2\pi d_b}{L_b}$ and equation 4 reduces to

$$H_b = 0.89 d_b \tag{5}$$

McCowan (9), using a solitary wave theory analysis, found that the breaker height in shallow water is given by

$$H_b = 0.78 d_b \tag{6}$$

Experimental studies by Collins and Wier (1), Galvin (2, 3) and Iversen (5, 6) have shown that the ratio H_b/d_b also depends on the beach slope in shallow water. For plunging breakers, Galvin (2) found

$$\frac{H_b}{d_b} = \frac{1}{\beta_b} \tag{7}$$

with $\beta_b=0.92$ for $m \geq 0.07$ and $\beta_b=1.40-6.85m$ for $m \leq 0.07$ where m is the beach slope (tangent of the angle the beach makes with the horizontal). Collins and Weir (1) give

$$\frac{H_b}{d_b} = 0.72 + 5.6\, m \tag{8}$$

for the relationship between H_b/d_b and beach slope.

The present analysis takes into consideration the dependence of H_b/d_b on wave steepness in addition to its dependence on beach slope.

DATA ANALYSIS

In order to arrive at an expression for H_b/d_b in terms of beach slope, m, and the wave steepness parameter, H_b/T^2 , the data presented by Iversen (6), Galvin (2), Jen and Lin (8), Weggel and Maxwell (13) and Reid and Bretschneider (12) have been used. These

data are shown on Figure 1 along with McCowan's equation based on solitary wave theory (equation 6), Michell's limiting steepness in deep water (equation 1) and Miche's transition equation (equation 4). In spite of the considerable amount of scatter in the data shown on the figure, a general trend of decreasing H_b/d_b with increasing H_b/T^2 for each beach slope is apparent. An increase in H_b/d_b with increasing beach slope for a given steepness is also in evidence. Thus a given deepwater wave will have a higher H_b/d_b on a steep beach than it will have on a flat beach.

A series of straight line envelope curves were constructed to the data so that they would be tangent to Miche's transition curve at the higher values of H_b/T^2. Consequently, the form of the relationship between H_b/d_b and H_b/T^2 is taken to be

$$\frac{H_b}{d_b} = b[m] - a[m]\frac{H_b}{T^2} \tag{9}$$

where b[m] and a[m] are functions of beach slope. The function, b[m] is the value of H_b/d_b when H_b/T^2 equals zero and -a[m] is the slope of the envelope curve. Values of 1/b[m] and a[m] found from the empirical envelope curves are shown on Figure 2. Two sets of data for 1/b[m] and -a[m] are shown for each function; one set (solid circles and squares) is based on an envelope curve over all the data for the given slope while the second set (open circles and squares) is based on an envelope curve to the data with the highest data point omitted. Approximating equations for 1/b[m] and a[m] are also given on Figure 2. The forms of the approximating functions were chosen because of their asymptotic behavior for flat and steep slopes. As the beach slope approaches zero, b[m] approaches 0.78 (1/b[m] $\rightarrow$1/0.78 = 1.28) and a[m] approaches zero so that H_b/d_b is independent of H_b/T^2 and equals McCowan's value of 0.78. As the slope approaches infinity (a vertical wall), the assumed upper limit on H_b/d_b was taken as twice the theoretical value of 0.78 or 1.56; consequently, the limiting value of 1/b[m] is 1/1.56 or 0.64. The equations for a[m] and b[m] are shown on Figure 2 and are given by,

$$a[m] = 1.36\left(1.0 - e^{-19m}\right) \qquad (\text{sec}^2/\text{ft}) \tag{10}$$

and

$$b[m] = \frac{1.0}{0.64\left(1.0 + e^{-19.5m}\right)} \tag{11}$$

Straight line envelope curves based on equations 9, 10 and 11 are shown on Figure 1 for beach slopes of 1:∞, 1:50, 1:20, 1:10, and 1:0. The relationship in terms of d_b/H_b as a function of m and H_b/T^2 is shown on Figure 3 along with an upper envelope to d_b/H_b defined by the data (corresponding to the lower H_b/d_b envelope on Figure 1).

For flat slopes, a transition may be defined by the intersections of the sheath of curves defined by equations 9, 10 and 11. This is obtained by solving for the intersections of equation 9 and the equation,

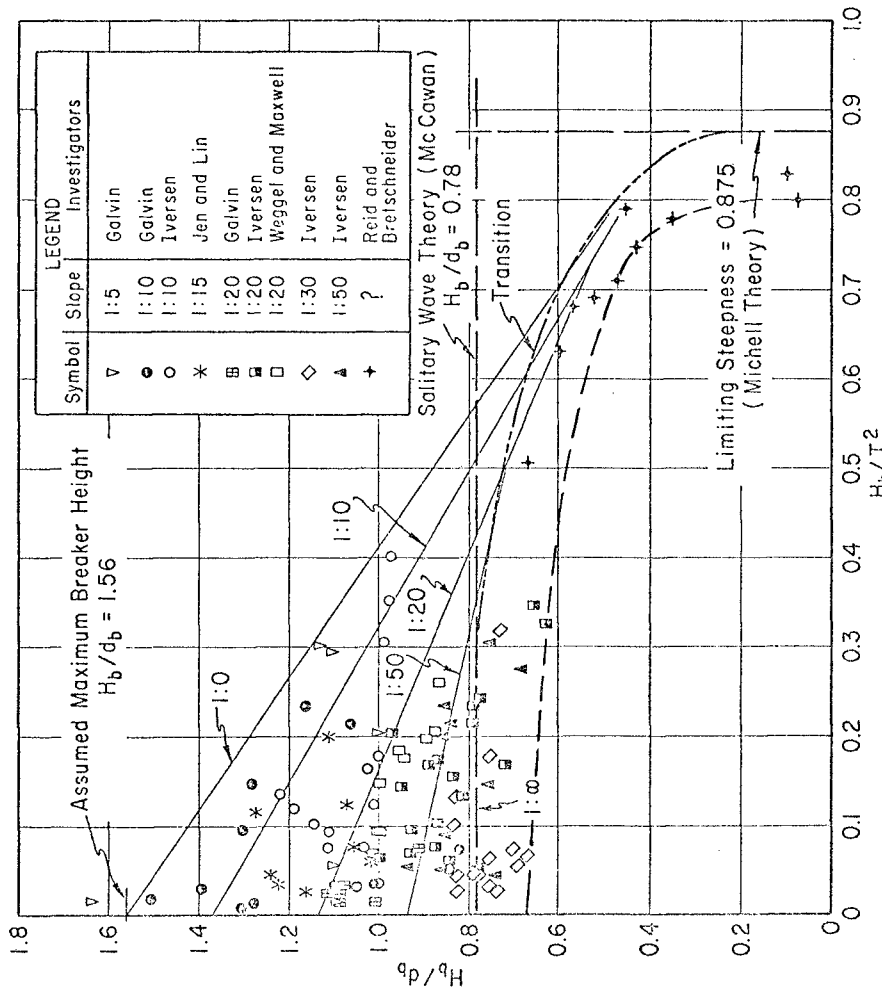

Figure 1. Experimental Observations of d_b/H_b vs. Breaker Steepness, H_b/T^2.

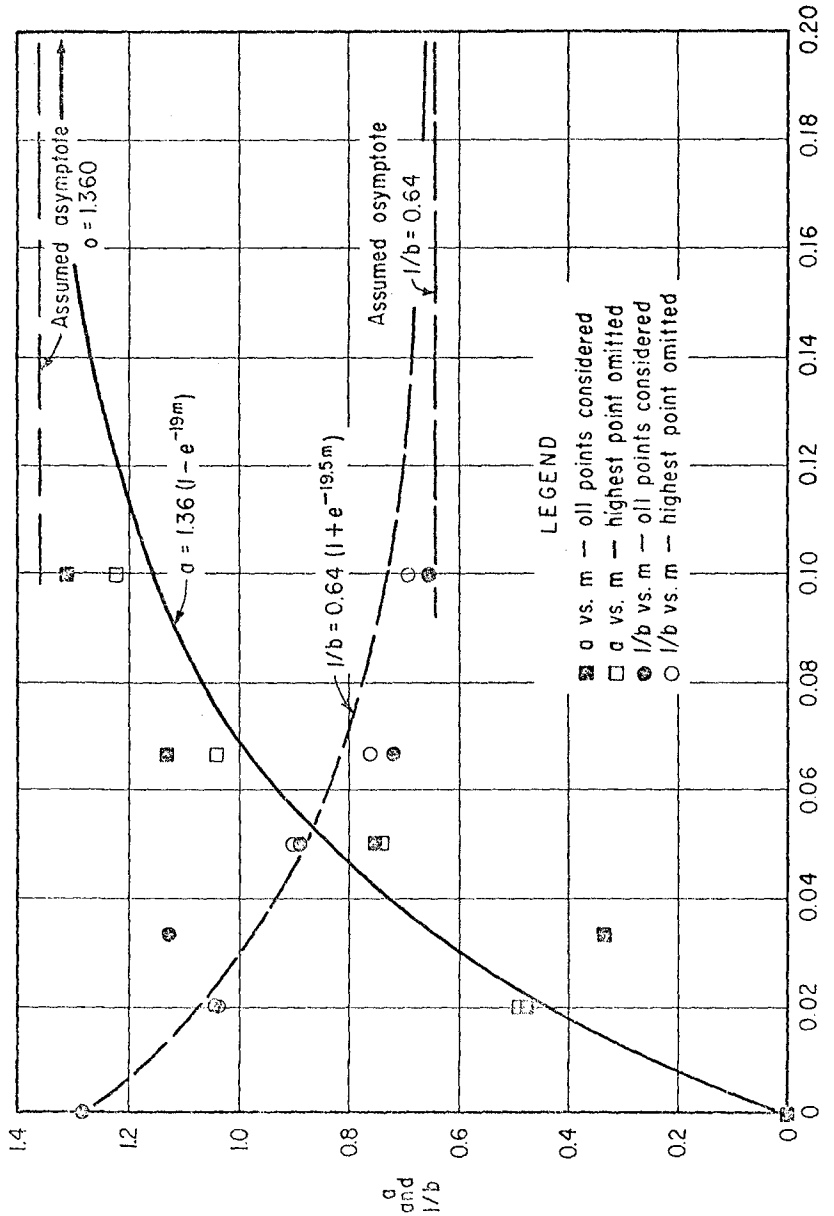

Figure 2. Variations of the Functions a and 1/b with Beach Slope.

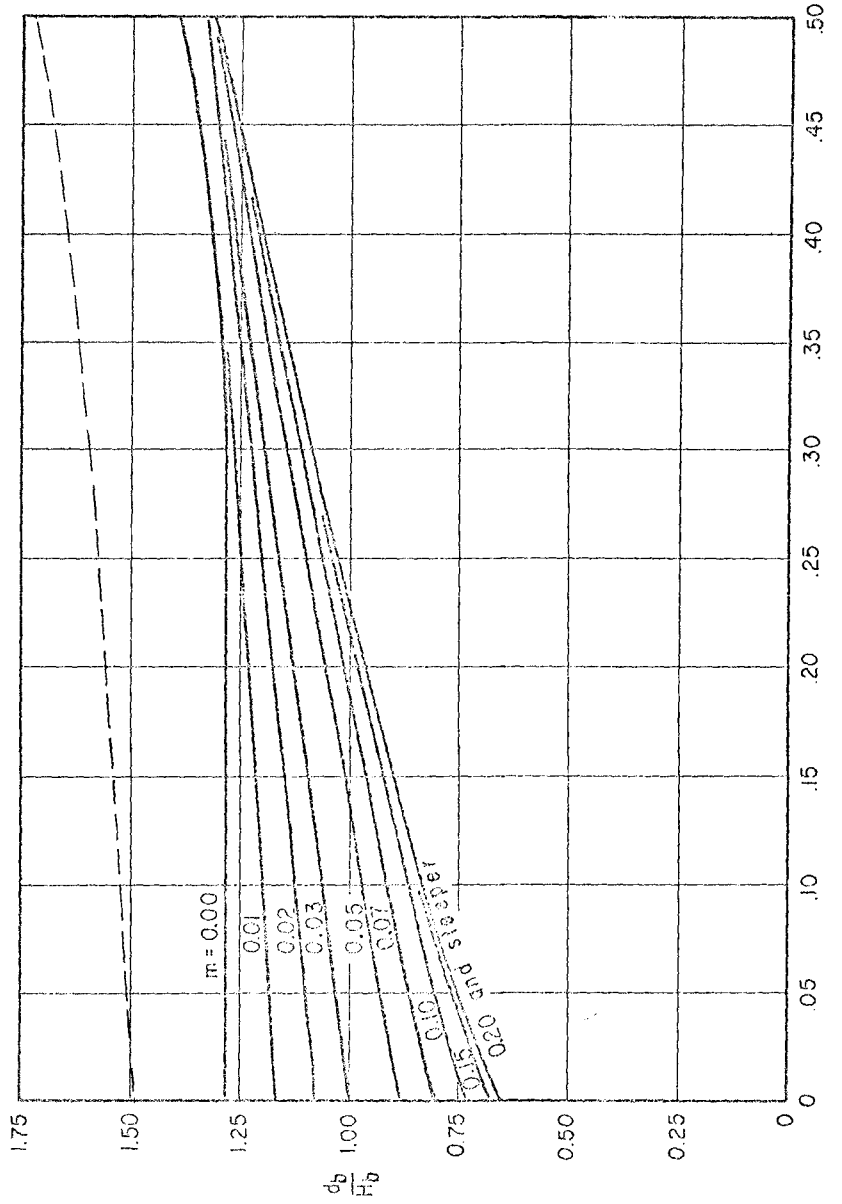

Figure 3. Empirical Equation of d_b/H_b vs. Breaker Steepness for Various Values of Beach Slope

$$\frac{H_b}{d_b} = b[m+dm] - a[m+dm]\,\frac{H_b}{T^2} \tag{12}$$

This empirical transition is given in parametric form by,

$$\frac{H_b}{d_b} = b[m] - a[m]\left\{\frac{d\,b[m]}{dm}\right\}\left\{\frac{dm}{da[m]}\right\} \tag{13a}$$

and

$$\frac{H_b}{T^2} = \left\{\frac{d\,b[m]}{dm}\right\}\left\{\frac{dm}{da[m]}\right\} \tag{13b}$$

for $0 \le m \le 0.105$. The transition given by equation 13 is defined for $0.30 < H_b/T^2 < 0.875$. Evaluating the derivatives in equation 13 gives,

$$\frac{H_b}{d_b} = \frac{1.56 - 1.6\,e^{-0.5m} + 4.72\,e^{-19.5m} - 1.6\,e^{-20m} + 3.16\,e^{-39m}}{(1.0 + e^{-19.5m})^3} \tag{14a}$$

and

$$\frac{H_b}{T^2} = \frac{1.18\,e^{-0.5m}}{(1.0 + e^{-19.5m})^2} \tag{14b}$$

for the transition. Equation 14b also gives the largest value of H_b/T^2 for which equation 9 should be used. For values of H_b/T^2 greater than this maximum value, the value of m which satisfies equation 14b for the given H_b/T^2 should be used in equation 14a to determine H_b/d_b. Alternatively, equation 4 could be used.

MAXIMUM DESIGN BREAKER HEIGHT

The maximum breaker height that actually strikes a coastal structure can be somewhat higher than the value obtained by simply substituting the depth at the structure toe into equation 9. The breaker height data analyzed pertain to the point where breaking is initiated; consequently if breaking is initiated some distance seaward of the structure and the wave travels to the structure during the breaking process a larger breaker than that predicted by equation 9 will strike the structure. If the depth at the toe of the structure is denoted by d_s, geometrical considerations give a relationship between d_s and the critical breaking depth, d_b, which results in the maximum breaker height. This relationship is given by,

$$d_s = d_b - m X_b \tag{15}$$

where m is the beach slope and X_b is the distance traveled by the wave during breaking. If H_b is used to make equation 15 dimensionless, equation 16 results;

$$\frac{d_s}{H_b} = \frac{d_b}{H_b} - m\,\frac{X_b}{H_b} \tag{16}$$

Galvin (2, 3) investigated the distance traveled by plunging breakers and found,

$$\frac{X_b}{H_b} = 4.0 - 9.25m \tag{17}$$

Strictly, equation 17 should be applied only to plunging breakers; however, in the absence of breaker travel data for other breaker types, it will be assumed generally applicable. Combining equations 9, 10, 11, 15 and 16 results in a quadratic equation for H_b/d_s in terms of m and d_s/T^2. The dimensionless variables H_b/d_s and d_s/T^2 are selected here because m, d_s and T are usually known at the outset of a design problem; hence, the unknown H_b can be found from known variables. The expression for H_b/d_s is given by,

$$\frac{H_b}{d_s} = \left\{\frac{1.0}{ma(18.5m-8.0)}\right\}\left\{a + \frac{1}{d_s/T^2}\left[1.0 + 9.25m^2b - 4.0mb\right] - \sqrt{\left[a + \frac{1}{d_s/T^2}(1.0 + 9.25m^2b - 4mb)\right]^2 - \frac{4mba}{d_s/T^2}(9.25m - 4.0)}\right\} \tag{18}$$

where a and b are given by equations 10 and 11. For ease of application equation 18 is presented in graphical form on Figure 4 for several specific beach slopes.

ILLUSTRATIVE EXAMPLE

Figure 4 may be used to obtain an estimate of the maximum breaker height a coastal structure could experience. For example, given a structure sited in water having a maximum design depth, d_s = 20 ft, and fronted by a beach having a slope of 1:20 (m = 0.050), determine the maximum breaker height for a 10 second design wave period. Calculate $d_s/T^2 = 20/(10)^2 = 0.20$ and enter Figure 4 to the curve for m = 0.050 and read $H_b/d_s = 0.83$. Therefore $H_b = 0.83\ d_s$ or H_b = 16.6 ft. Breakers larger than 16.6 feet will break farther offshore from the structure and will have dissipated a sizable amount of their energy before reaching the structure. While smaller breakers may strike the structure, they will not establish a critical design condition. Thus the bathymetry in front of a structure can be thought of as a filter for the wave spectrum causing larger waves to break farther offshore and permitting only breakers with heights less than or equal to the maximum breaker height to reach the structure. Figure 3 (or equations 9, 10, and 11) may now be used to establish the critical depth in which breaking is initiated. Calculate $H_b/T^2 = 16.6/(10)^2 = 0.166$ and enter the figure using the curve for m = 0.050. Read $d_b/H_b = 0.64$; hence, $d_b = 0.64\ H_b = 0.64\ (16.6) = 10.6$ ft. The breaking depth for the given breaker height can be bracketed by using the upper envelope (dashed) curve to all the breaker data shown on Figure 3. For the given wave steepness $H_b/T^2 = 0.166$, the upper limit for d_b/H_b is 1.55 and therefore $\{d_b\}_{max} = 25.7$ ft with the critical breaking depth being d_b = 10.6 ft.

In order to establish the deepwater wave height that results in the maximum breaker height, refraction data for the site and the

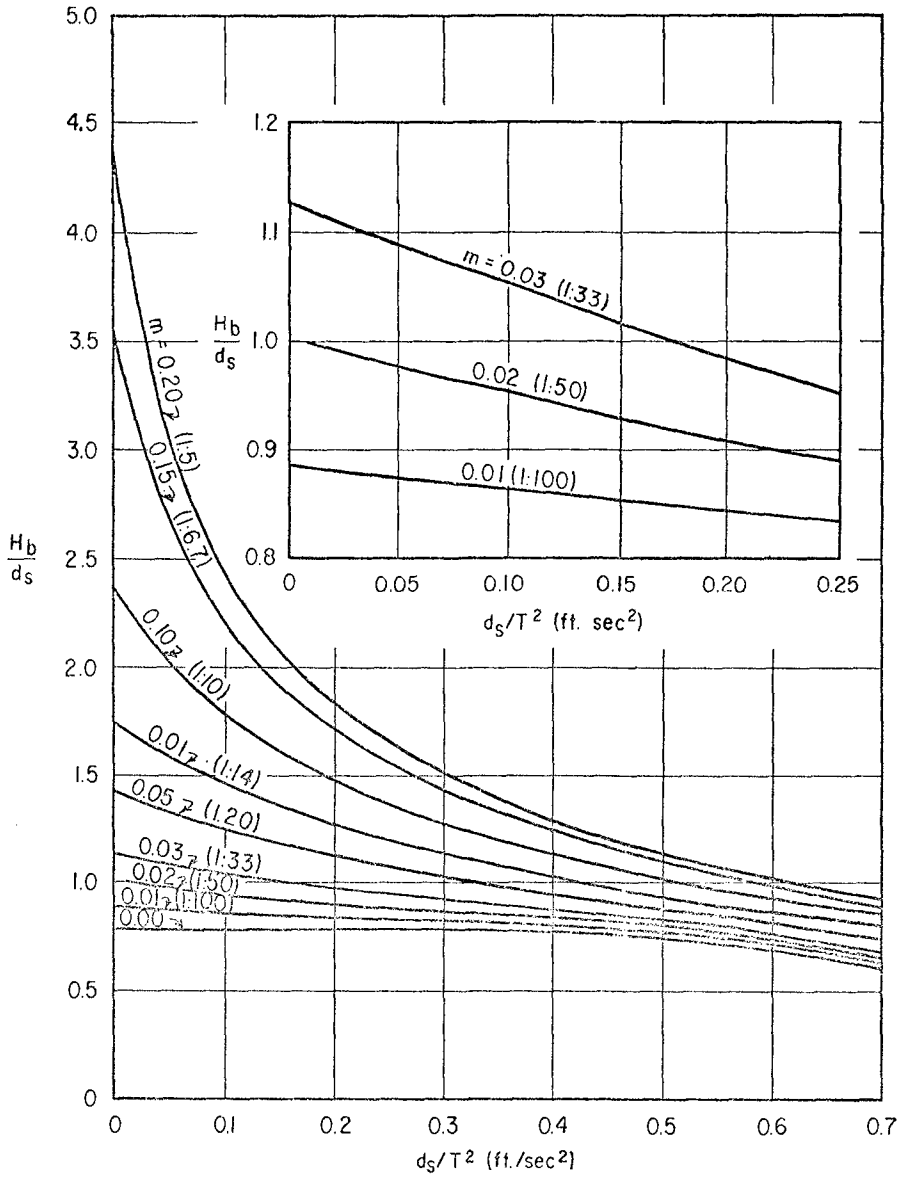

Figure 4. Dimensionless Maximum Breaker Height, H_b/d_s, vs. Depth at Structure, d_s/T^2.

breaker height index, H_b/H_o', is required. Figure 5, which presents the breaker height indices of Goda (4) in a modified form, can be used to find the desired deepwater wave height. If, for example, the refraction coefficient for waves having a period of 10 seconds approaching from a given direction is $K_r = H_o'/H_o = 0.95$, where H_o' is the unrefracted deep water height and H_o is the actual deep water height, enter Figure 5 with the calculated $H_b/T^2 = 0.166$ and from the curve for $m = 0.020$ read $H_b/H_o' = 1.12$. Then, $H_o' = H_b/1.12 = 16.6/1.12 = 14.8$ ft and $H_o = H_o'/K_r = 14.8/0.95 = 15.6$. Consequently a 15.6 ft deepwater wave with T = 10 sec. approaching from the given direction will result in the maximum breaker height on the structure.

If the slope fronting the structure is irregular an average slope between the depth at the toe of the structure and the depth at breaking should be used in equations 16 and 17 and the slope seaward of db used in equations 9, 10 and 11. Equation 18 and Figure 4 were derived by assuming that a constant beach slope extends some distance seaward of the structure; that is, the slope on which the wave breaks is identical to the slope used in equation 16. This assumption is not valid for the case of a varying beach slope, hence the appropriate slopes should be used with the equations to establish the upper limit on breaker height.

DISCUSSION AND CONCLUSIONS

The applicability and validity of the methods presented here are limited by the experimental conditions under which the data were obtained. With the exception of a few of the data points shown on Figure 1, the data were obtained in laboratory wave tanks and are subject to the scale effects and reflections often inherent in such facilities. In addition, the studies were conducted on impermeable, smooth, uniform, unobstructed slopes with monochromatic waves. The effects of interaction between waves of different heights and periods were not present. Also the effects of reflections from structures on the slope were not considered. Jackson (7) presents some data on a rubble structure's influence on breaking conditions on a 1 on 10 beach slope. Figure 6 gives a comparison of Jackson's data with the data of Iversen (6) and Galvin (2) for the 1:10 slope. The equations of Galvin (2) and Miche(10) are also shown on Figure 6 along with an equation based on the present analysis and Airy wave theory (solid line).

The method proposed here for estimating maximum breaker height is believed reasonably conservative. For beach slopes steeper than 1:10, additional verification is recommended and additional research on the effects of reflecting structures on breaker conditions is indicated.

ACKNOWLEDGEMENT

Some of the data on breaker heights and depths were made available to the author through the courtesy of Dr. Cyril J. Galvin. The work described herein was conducted under the Civil Works Program of the United States Army Corps of Engineers by the Coastal Engineering Research Center. Permission to publish this information is appreciated. The finding of this paper are not to be construed as official Department of the Army position unless so designated by other authorized documents.

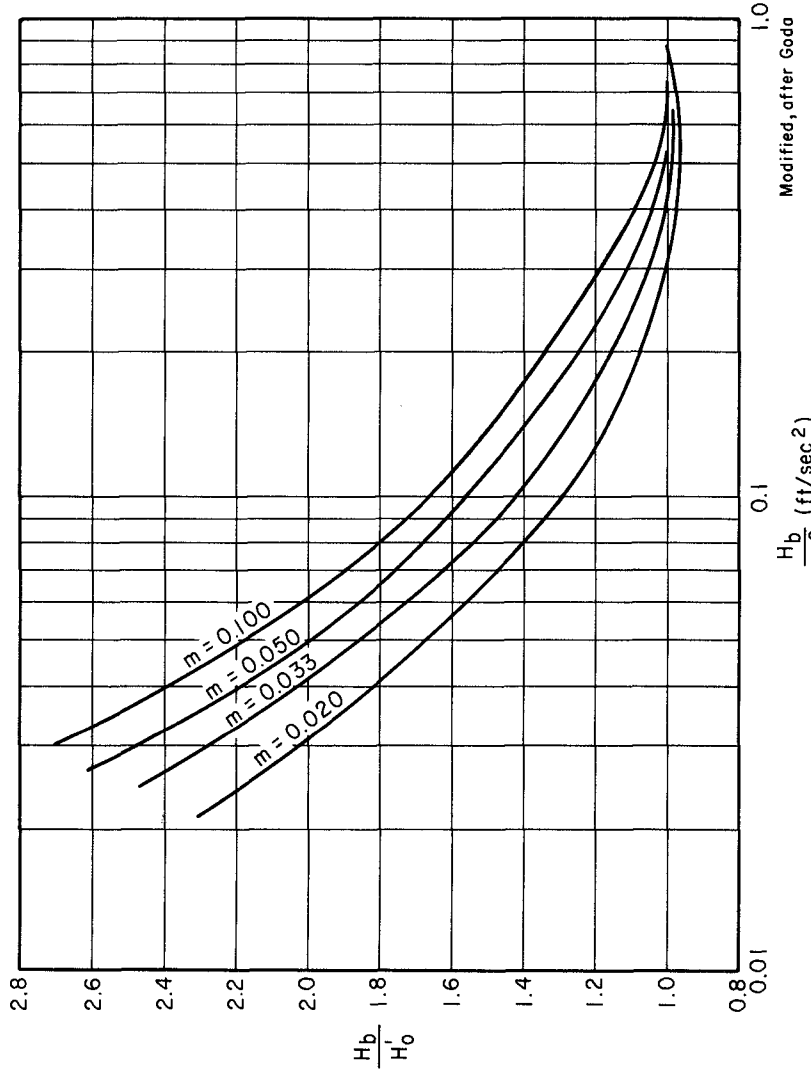

Figure 5. Breaker Height Index vs. Breaker Steepness, H_b/T^2

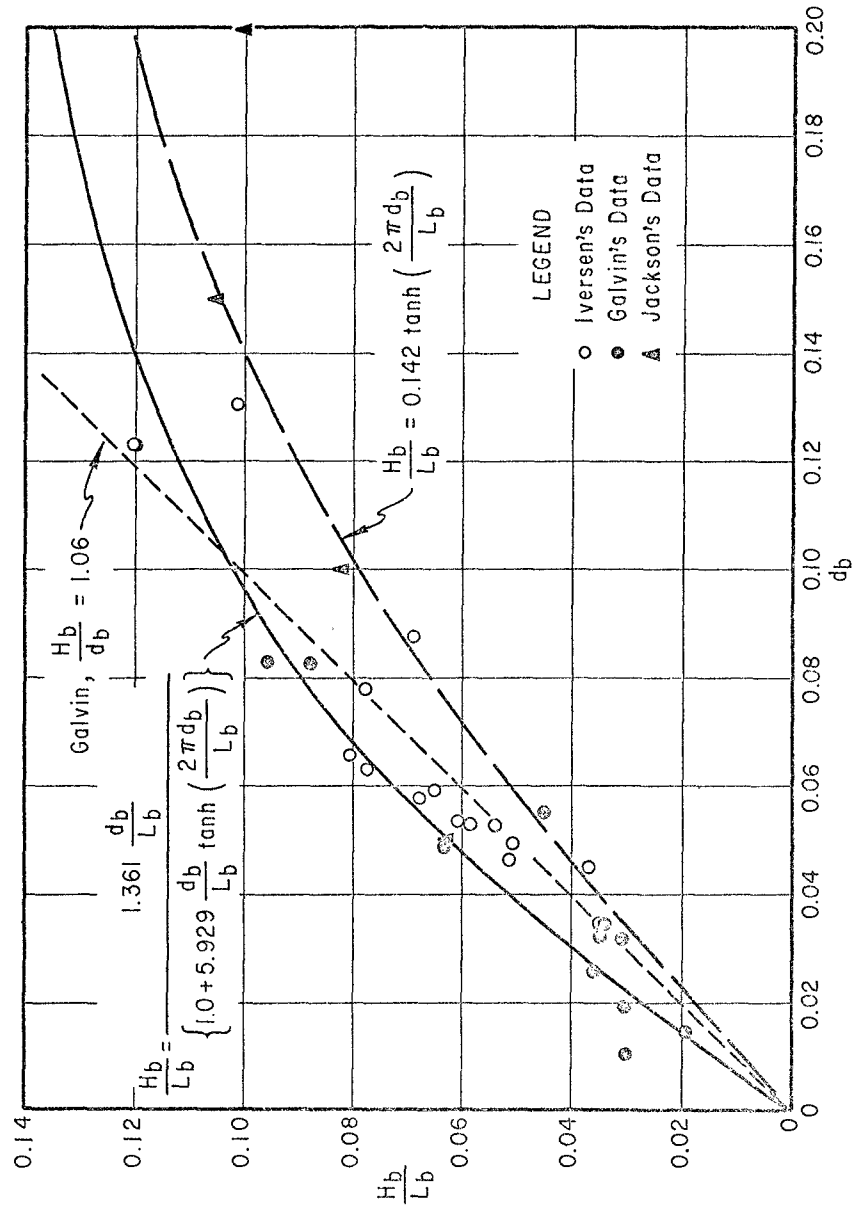

Figure 6. Breaker Steepness, H_b/L_b, vs. Breaker Depth, d_b/L_b, for a Beach Slope of 1:10.

APPENDIX I REFERENCES

1. Collins, J. I. and W. Wier, "Probabilities of Wave Characteristics in the Surf Zone", Tetra Tech Rpt #TC-149, September 1969.

2. Galvin, C. J. Jr., "Breaker Travel and Choice of Design Wave Height" Journal of the Waterways and Harbors Division, ASCE, May 1969, #6569.

3. Galvin, C. J. Jr., "Horizontal Distance Travelled by a Plunging Wave", ASCE, National Meeting on Transportation Engineering, San Diego, California, February 19-23, 1968, Preprint #630.

4. Goda, Y., "A Synthesis of Breaker Indices," Transactions, Japanese Society of Civil Engineers, Vol. 2, Part 2, 1970.

5. Iversen, H. W., "Waves and Breakers in Shoaling Water", Proceedings Third Converence on Coastal Engineering, Berkeley, California, October 1952.

6. Iversen, H. W., "Laboratory Study of Breakers," Gravity Waves, U. S. Bureau of Standards, Circular 52, 1952.

7. Jackson, R. A., "Limiting Heights of Breaking and Non-Breaking Waves on Rubble Mound Structures", Tech. Rpt. H-68-3, U. S. Army Waterways Experiment Station, Vicksburg, Mississippi, June 1968.

8. Jen, Y. and P. M. Lin, "Plunging Wave Pressures on a Semi-Cylindrical Tube", Proceedings, Twelfth Conference on Coastal Engineering, Washington, D. C., September 1970.

9. McCowan, J., "On the Solitary Wave", London, Edinburgh, Dublin Philosophical Magazine, Journal of Science, Vol. 32, 5(1891).

10. Miche, Robert, "Mouvements ondulatoirs des mers en profondeur constante on décroissant", Annals des Points et Chaussées (1944) (translation by Lincoln and Chevron, University of California at Berkeley, Wave Research Laboratory, Series 3, Issue 362, June 1954).

11. Michell, J. H., "On the Highest Waves in Water", Philosophical Magazine, Vol, 36, 5th Series, 1893, pp. 430-437.

12. Reid, R. O. and C. L. Bretschneider, "Surface Waves and Offshore Structures", The Texas A&M University, Technical Report #53-10, October 1953.

13. Weggel, J. R. and W. H. C. Maxwell, "Experimental Study of Breaking Wave Pressures", Second Annual Offshore Technology Conference, Houston, Texas, April 1970, OTC-1244.

APPENDIX II - NOTATION

The following symbols are used in this paper;

$a[m]$ = slope of H_b/d_b vs H_b/T^2 line, a function of beach slope.

$b[m]$ = value of H_b/d_b for $H_b/T^2 = 0$, a function of beach slope.

d = depth.

d_b = depth at which breaking is initiated.

d_s = depth at the toe of a structure.

g = gravitational acceleration.

H = wave height

H_b = wave height at breaking (breaker height)

H_o' = unrefracted deepwater wave height

m = beach slope.

L = wave length.

L_b = wave length at breaking.

L_o = wave length in deep water

T = wave period.

x_b = distance traveled by a plunging wave during breaking

β_b = ratio of d_b to H_b, a function of beach slope.

CHAPTER 22

THE ROLE OF SURFACE TENSION IN BREAKING WAVES

Robert L. Miller

Professor, Department of Geophysics
University of Chicago

Abstract.

Breaking criteria in the vicinity of the crest, such as limit crest angle and limit form, and larger dimensions such as limit height (H/L) and breaker height (H_b/d_b), are found experimentally to be significantly affected by change in surface tension. A number of wave types were examined, including periodic waves, solitary waves, and standing waves, over both constant depth and uniform slopes. Variations in natural waters in some cases were found to be of equivalent magnitude to those induced for the experiments. The conclusion is drawn that surface tension should be taken into account in development of a satisfactory theory of breakers. It is also an important factor in experimental studies, particularly engineering model studies involving breaking waves.

Introduction.

Experimental studies made several years ago, of run-up and transitions in bores brought out an interesting sequence of events during the breaking process. The first definite breaking at the crest was preceeded by a surface pattern of ridges or streaks normal to the crest, on the back side of the wave. These later coalesced, to form a pattern of cell-like indentations. Following this, the surface ruptured just at the crest and the wave broke. Miller 1968a and also Witting 1964.

It thus appeared that the breaking process in its earliest stages, may be a surface phenomenon, at the least in part. Accordingly, a preliminary series of experiments, Miller 1968b, were made with undular bores first at normal surface tension; and then repeated with the surface tension reduced by adding a detergent. Figure 1 gives a summary of the results. The ordinate represents the distance down-channel at which initial breaking of the lead undulation occurs, as it progresses over a flat bottom. D is the distance down-channel from the generating piston and d is the undisturbed water depth. The abscissa is in units of crest velocity converted in a second scale to Froude numbers. For a given Froude number, comparison is made of D/d for surface tension at a "normal" 73 dynes/cm vs surface tension reduced to 39 dynes/cm;

Froude no. at initial breaking	D/d T_{73}	T_{39}
1.256	(not breaking)	11.0
1.261	(not breaking)	14.75
1.267	9.75	9.50
1.271	5.0	4.5
1.278	12.3	10.4

Several conclusions were drawn. 1) For a given Froude number, the normal surface tension wave remains stable for a greater distance down-channel. 2) Breaking is observed for lower Froude numbers at surface tension T_{39} than at normal surface tension T_{73}. These results indicated that a more general study should be made.

Accordingly, a survey of the published literature was made, with respect to limit form, and breaking criteria in the vicinity of the crest. In addition, a search was made for papers on the role of surface tension at the crest particularly with respect to breaking waves. Table 1 gives a summary of the limit form and breaking criteria at the crest. The summary is not intended to be a complete reference list, but hopefully

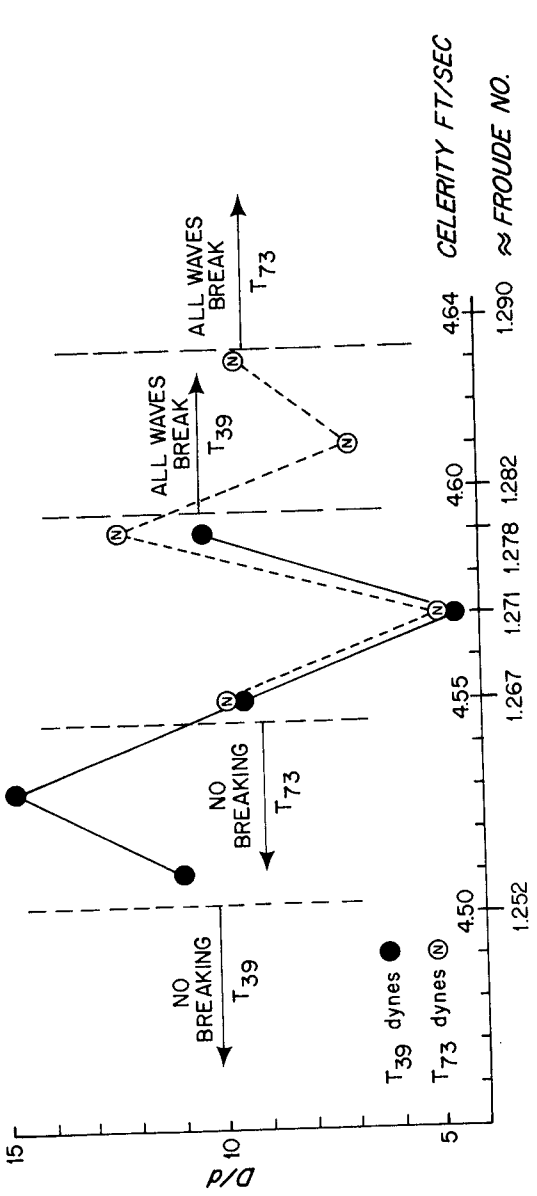

Figure 1 Undular Bore: Average Distance From Piston To Initial Breaking, vs. Celerity

Table 1 Summary of limit form and breaking criteria, at the crest.

Wave type	Limit Crest Angle	Symmetry[1]	Vertical Acceleration of fluid particle[2]	Initial Breaking Process[3]
Periodic Progressive (Deepwater)	120° Stokes 1880	Symmetrical almost a vertical plane.	½g in vicinity of crest, directed away from crest. Directly beneath crest = ½g, directed downward. Just at crest, acceleration is indeterminate. Longuet-Higgens 1963	? May be related to the parasitic capillary waves which form on the forward face. Longuet-Higgens 1963
Periodic Progressive (Constant depth)	120° ?	Wave front vertical Stoker 1948		Vertical front collapses and wave "curls over". Stoker 1948
Periodic Progressive (Uniform slope)	? May be less than 90°	Steep slope Vertical front face → plunging.	Mason 1951 Stoker 1948 Galvin 1968	Formation of downward curving jet at vertical face which strikes water surface in front of wave. Rapid collapse of wave.
		Gentle slope Vertical front face at crest? → Spilling.		A turbulent zone with air entertainment confined to vicinity of crest. Slow subsidence of wave.

[1] Analagous to "limiting shape" criterion which suggests that for plunging breaker for example, "breaking occurs when some part of shoreward face of wave becomes vertical" Ippen and Kulin 1954.

[2] In appropriate cases, such as progressive waves, the fluid particle may be subject to the "limiting velocity" criterion which states that "breaking occurs when the velocity of particles at some point along the wave usually at the crest, equals the celerity of the wave" Ippen and Kulin, 1954.

[3] The specific effect of wind in the keaking process is not known. For smaller waves, Cox 1958 has shown that capillaries will form in the absence of wind.

Wave type	Limit Crest Angle	Symmetry	Vertical Acceleration of fluid particle	Initial Breaking Process
Standing Wave	90° Penney-Price 1952 G. I. Taylor 1953	Symmetrical about vertical plane. Truly Periodic waves not established theoretically: thus perfect symmetry may not exist.	g directed downwards Penney-Price 1952 G. I. Taylor 1953	Surface at crest bursts followed by a plume, then violent instability G. I. Taylor 1953 and present paper
Clapotis	Assumed same as standing wave			
Solitary: (const. depth)	120° McCowan 1891	Symmetrical about vertical plane.		?
Solitary: shoaling (uniform shape)	? May be less than 90° Front face vertical Back face subparallel to bottom.	For steep slopes: vertical forward face → "plunging breaker" For gentle slopes small vertical face at the crest? → spilling breaker.[1]		formation of a jet from the vertical face which strikes the water surface in front of the wave

[1] Note: under certain conditions, a shoaling wave may not "break" at all but simply subside into the run up phase. Caldwell 1949 Galvin 1969

Wave type	Limit Crest Angle	Symmetry	Vertical Acceleration of Fluid Particle	Initial Breaking Process
Undular bore First undulation (constant depth)	120° McCowan (assumed similar to solitary wave)	Symmetrical about vertical plane.		Turbulent zone with air entrainment, at vicinity of crest followed by collapse of lead undulation, and transformation to fully developed bore form; turbulence rapidly engulfs trailing undulations. Miller 1968
Undular bore First undulation shoaling over uniformly sloping bottom.	(assumed similar to solitary wave)	vertical face at crest on front side.		Analogous to plunging breaker for steep slope and to spilling breaker for gentle slope. Miller 1968
Reforming Solitary wave				
Very short crested waves superposition of to oppositly progressing wave trains.	90° (Analogous to standing wave?) (present paper) Observation, 98°	varies	g directed downward? analogous to standing wave?	bursting upward at crest or overturning crest (present paper)

does include a reasonably complete list of breaking criteria and limit form, in the vicinity of the crest. Thus, breaker classifications such as that of Miller and Zeigler, 1964 and Galvin 1968, are not considered, in this study.

Experimental procedure.

Several wave types exhibit a cusped profile, prior to breaking. In the vicinity of the crest, however, the profile limbs are approximately straight as shown in Figure 2, except at the apex, where the radius of curvature R, becomes an important consideration. Pressure difference across the air-water interface may be expressed as $\Delta P = 2T/R$ where T is the surface tension and R is the radius of curvature. The highest pressure is on the concave side of the interface.

For progressive waves, α is defined as the angle the front face makes with the vertical line to the apex. β is the angle formed by the trailing face of the wave. As in Figure 2, $\alpha + \beta$ = the crest angle, and symmetry is expressed by comparison of α with β.

A primary aim of the study is to assess the effect of surface tension on crest angle, on symmetry, and where appropriate, on larger scale breaker characteristics as secondary effects. The experimental plan is to measure the above properties for surface tension normal, and reduced to several lower values.

A number of additives intended to reduce surface tension were tried. The most satisfactory of these were Triton X-45 and Triton CF32. It was determined that a solution of 0.01% reduces surface tension of pure water from normal 72 dynes/cm at 20°C to about half at 36 dynes/cm. An anti-foaming agent, G. E. AF-60, was also added at a strength of about 25 parts/million.

Test for change in viscosity indicated a drop of about 2% when the surface tension was reduced to 35 dynes/cm using the above solution. The surface tension gradient, surface to bottom, was checked by withdrawing fluid at various levels, taking care to withdraw slowly thru glass pipette to insure a local sample. The results showed a slow decrease at the surface, indicating a concentration of the Triton at the surface with time. However, when the fluid was thoroughly mixed by agitation, the surface tension remained essentially constant throughout the tank for a period of several hours. It is well known that surface films which tend to increase surface tension will form on open water with time, even in the cleanest of laboratories. It was necessary in this study to insure the absence of surface films, and the absence of surface concentration of the detergent. Thus, a procedure was established whereby the tank was drained and refilled with fresh water, before each set of experiments. The Triton plus AF-60 was then immediately added in the desired proportion and thoroughly mixed with the tank water, followed by a check of the resulting surface tension on the ring tensiometer. The tank was again agitated by running the wave generator. Elapsed time for the above procedure after the tank is refilled, is about 20 minutes. Experiments were then run immediately. I feel that the surface film and surface concentration of detergent were eliminated satisfactorily.

Several methods were tried for measuring surface tension. It was found that the ring tensiometer method was most satisfactory in terms of repeatability, ease of operation, and time required to obtain a measurement. It was, however, necessary to establish a careful procedure including cleaning the ring by flaming and rinsing after each measurement. Calibration of the ring tensiometer was checked repeatedly against standards during the course of this study.

Most of the experiments were conducted in a wave tank approximately 90 feet long. The waves were of the order of $L \simeq 2.25$ ft. and $H \simeq 0.20$ ft. for the progressive waves and $H \simeq 0.30$ ft. for the solitary wave and undular bore. The standing wave experiments were conducted in a small aquarium sized tank with waves of the order of $L = 35$ cm. in an undisturbed depth of $\simeq 18$ cm.

Attempts to measure crest angles from oscillograph records proved arduous and inaccurate. The following method proved satisfactory. 16 mm motion picture films were taken through a reference grid on the glass wall of the tank, at 64 frames/sec.

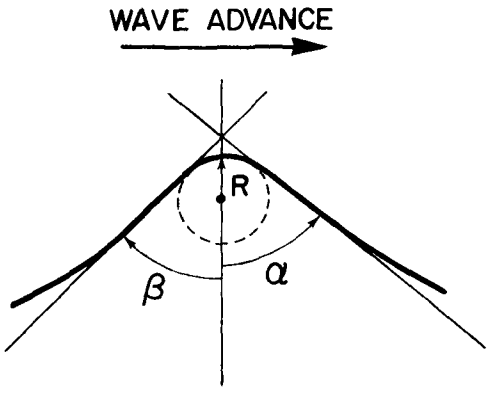

Figure 2 Detail of Crest Angle and Symmetry.

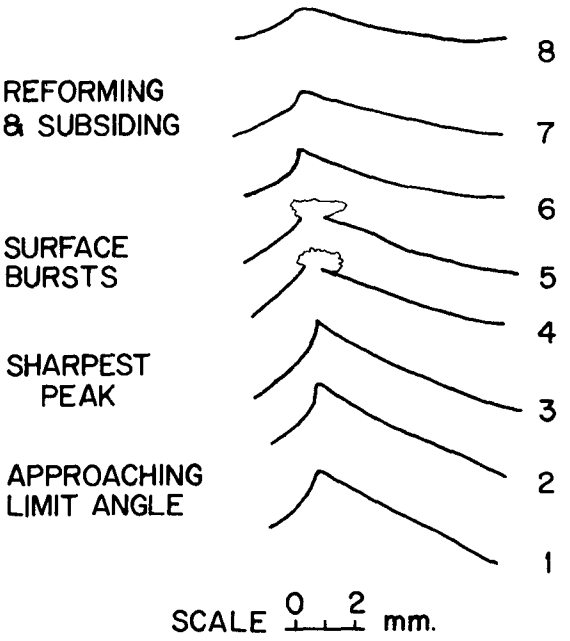

Figure 3 Breaking and Reforming Sequence. Standing Wave, at 64 Frames/Sec., Motion Picture Sequence. The Possibility of Calculating Bursting Pressure is Suggested.

A "stop-action" projector was utilized against a white background wall to locate a satisfactory breaking sequence and then the film was advanced one frame at a time to obtain the maximum unbroken profile. By projecting upon a smooth white surface at a suitable distance, sufficient image enlargement was acquired to aid in accurate measurements. Sharp contrast in the color film was gained by using rhodamine dye in the water. Tests indicated that the slight addition of rhodamine dye did not affect either the surface tension or viscosity. Larger scale dimensions of the waves were measured in the same way.

Experimental results.

A summary of experimental results is given in table 2. Several of the notable results are indicated in the following discussion.

1) Limit crest angle

It seems clear that the limit crest angle of 120° is significantly exceeded when surface tension is reduced, for progressive periodic waves in deep water or over constant depth bottom. This latter case also includes solitary waves and the lead undulation in the undular bore. A similar conclusion is drawn for the 90° limit crest angle for standing waves, including clapotis.

The limit crest angle concept, does not appear to apply at all to waves shoaling on a plane beach, dispite statements to the contrary, i.e. Kinsman 1965 p. 273. Rather than 120°, the limit angle by implication is approximately 90° with a vertical front face, and a back face sub-parallel to the bottom slope. (Figure 5). It seems reasonable that the subsequent stage is effected by surface tension whether collapse of the vertical face (waves shoaling over low angle slopes) or jet-like overturn (waves shoaling over steep slope). This merits careful experimental study.

2) Symmetry

Periodic progressive waves in deep water do not preserve symmetry up to the point of breaking, but rather the front face is notably steeper than the trailing face. However, the solitary wave over constant depth, and the standing wave, do preserve symmetry to initial breaking i.e. α approximately equal to β. The observations of clapotis indicate that α (the wave face toward the reflecting plate) is considerably smaller than β for the wave face away from the reflecting plate. However, the waves recorded in these observations may not have reached the stable standing wave configuration. This could account for the asymmetry. It is also interesting to note that symmetry is reversed in the reforming solitary wave, with the rear face being the steepest.

3) Limit steepness (H/L)

If the breaking mechanism at the crest is affected by changes in surface tension, it is reasonable to expect secondary effects on larger scale breaker properties. The next three properties are of this nature, and as can be seen, several of these do show the effect of change in surface tension. Periodic progressive waves showed a progressive increase in limit steepness for decreasing surface tension, although the steepest waves observed were less steep than the theoretical prediction of Michell, 1893.

In the case of standing waves the limit steepness for surface tension normal was very close to that observed by G. I. Taylor, and slightly higher for surface tension reduced.

4) Breaker height (H_b/d_b) over sloping bottom.

For periodic progressive waves and solitary waves over a low slope, breaker height is slightly higher for surface tension reduced. For solitary waves over steep slope breaker height is significantly lower! The magnitude of H_b/d_b, however, is much greater for solitary than for periodic waves. It is possible that the backwash of the previous wave with its "tripping" effect may be involved in some manner, since it is present in the periodic case and absent in the solitary wave case.

5) Limit height (H/d) constant-depth bottom.

Table 2 Summary of experimental results.

Wave	Limit Crest Angle	Symmetry	Limit Steepness H/L	Breaker Height (H_b/d_b) or Limit Ht(H/d)	Breaker Distance (x_b) from shoreline. (actual scale)
Periodic Progressive d/L = 0.311 ("Intermediate depth" wave)	Theory: 120° Observed: T_{74} = 129° T_{53} = 123° T_{40} = 116°	Theory: $\alpha = \beta = 60°$ Observed: T_{74}: α = 57°, β = 72° T_{53}: α = 35°, β = 88° T_{40}: α = 44°, β = 72°	Theory: 0.142 (Michell 1893) Observed: T_{74}: 0.088 T_{53}: 0.093 T_{40}: 0.120		
Periodic Progressive (Shealing over uniform slope) 9°	Theory $\leq$ 90° Observed: T_{73} : 81° T_{40} : 85°	Theory: vertical front Observed: T_{73} : α = 0, β = 81 T_{40} : α = 5, β = 80		(H_b/d_b) Theory: ? Observed: T_{73} : 0.74 T_{40} : 0.80	T_{73} = 0.73 ft. T_{40} = 0.60 ft.
Solitary (constant depth)	Theory: 120° Observed: T_{73} = 129° T_{74} = 113°	Theory: $\alpha = \beta = 60°$ Observed: T_{73} : α = 63°, β 66° T_{40} : α = 54°, β = 59°		(H/d) Theory: $\simeq$ .78 McCowan 1894 Observed: T_{73} = 0.73 T_{40} = 0.80	

Wave	Limit Crest Angle	Symmetry	Limit Steepness H/L	Breaker Height H_b/d_b (slope) or Limit Height H/d (flat)	Breaker Distance (x_b) from shoreline (actual scale)
Solitary (uniform slope)	6° Theory ? Observed: T_{73} = 90° T_{40} = 90° front verticle back horizontal	Theory ? Observed: T_{73} α = 90° β = 0 T_{40} α = 90° β = 0		(H_b/d_b) Theory ? Observed: T_{73} = 4.28 T_{40} = 3.78	T_{73} = 0.16 ft. T_{40} = 0.30 ft. averages over 18 runs each.
	2°30' Observed: T_{74} = 90° T_{39} = 90°	Observed: T_{74} α = 90° β = 0 T_{40} α = 90° β = 0		(H_b/d_b) Observed: T_{74} = 1.55 T_{39} = 1.67	T_{74} = 1.55 ft. T_{39} = 1.67 ft. averages over 18 runs each.
Solitary Reforming Wave (constant depth)	Theory ? Observed: T_{73} = 149° T_{40} = 140°	Theory ? Observed: T_{73} : α = 77° β = 74° T_{40} : α = 72° β = 68°		(H/d) Theory ? Observed: T_{73} = 0.65 T_{40} = 0.65	
Standing Wave	Theory: 90° Observed: T_{74} = 93° T_{35} = 80°	Theory: $\alpha = \beta$ = 45° Observed: T_{74}: α = 46° β = 47° T_{35}: α = 41° β = 39°	Theory 0.141 (Penney and Price 1952) Observed: T_{74} = 0.122 (0.125, Taylor 1953) T_{35} = 0.131		

Wave	Limit Crest Angle	Symmetry	Limit Steepness H/L	Breaker Height H_b/d_b (slope) or Limit Height H/d (flat)	Breaker Distance (x_b) from shoreline. (actual size)
"clapotis"	Theory: 90° Observed: T_{74} = 101° T_{55} = 99° T_{40} = 80°	Theory: ? Observed: T_{74} α = 47° β = 54° T_{55} α = 57° β 42° T_{40} α = 37° β 43°			
Very short Crested Superposition of solitary progressing opp. direction to wave train	Theory ? Observed: T_{73} = 99° T_{40} = 66°				
Undular Bore; lead undulation "constant depth"	Theory ? Observed: T_{73} = 130° T_{35} = 111°	Theory ? Observed: T_{73} α = 62° β = 68° T_{35} α = 43° β = 68°		(H/d) T_{73} = 0.78 T_{35} = 0.85	

All "Observed" values are averages of three lowest measurements, except where noted otherwise.

Figure 5. Solitary wave breaking sequence on 6° slope. Images at 1/64 sec. from motion picture camera study.

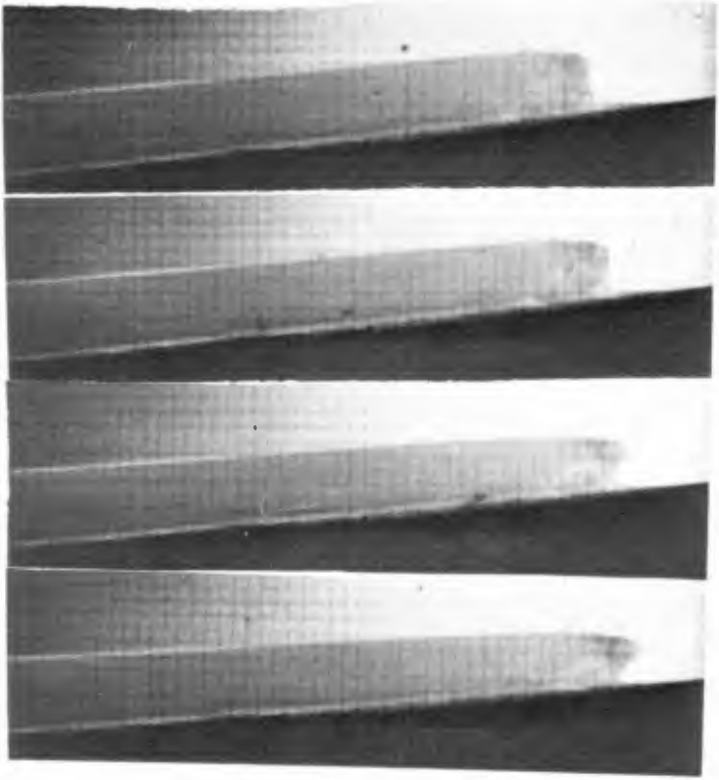

When surface tension is reduced, the limit height is significantly greater for both solitary wave and lead undulation of undular bore. The "reforming" solitary wave, as should be expected, has lower height that the limit height noted just before breaking.

6) Breaker distance from shoreline

In the case of the periodic progressive wave, the initial breaking occured consistently closer to the shore when surface tension was reduced. On the other hand, the solitary wave initial breaking was consistently further from the shore for surface tension reduced, the magnitude being greater for lower slope, as would be expected. As in the case of breaker height, it is possible that the presence of backwash in the case of the periodic waves accounts for the differences noted.

Ippen and Kulin 1954 show a series of graphs of breaking amplitude to breaking depth ratio. Figure 4 shows a similar graph for data acquired during the present study. Although the bottom slope is steeper than the steepest given by Ippen and Kulin, the same general trend is noted in the data points. However, for a second quite distinct curve results, for data points obtained when surface tension is reduced! It would appear that for a given initial amplitude, the breaking amplitude to breaking depth ratio is significantly greater.

Variation in surface tension in natural waters.

In view of the results described previously for surface tension adjusted under experimental conditions, it is of interest to consider the variation which may be observed in natural waters. A series of samples were taken over a period of several years. The procedure involved taking the water sample in carefully cleaned containers at a standard depth of 30 cm. below the surface. In this manner, surface films which can yield considerable variation in surface tension (i.e. Jarvis 1967, Lumby and Folkard 1956), were excluded from the sample. Measurements were made on a ring tensiometer in the same manner as for the laboratory experiments. The results, intended only to give some indication of natural variation, are given in table 3. A rather surprising range of variation was noted, particularly in the vicinity of organic concentrations.

Conclusions

The most useful conclusion that can be drawn from this study is that surface tension should not be neglected as a significant factor in the breaking process. It seems reasonable to suggest that it should be included in any realistic theoretical study.

In view of the relatively small size of the experimental waves, some consideration of scaling is needed, perhaps similar to the studies by Diephuis, 1957, and Maxwell, Hall, and Weggel, 1969 on related topics. It is evident that surface tension is a significant factor when breaking waves are included in engineering design scale models. Some extension of the present study should be made, including consideration of Froude and Weber numbers.

Another interesting possibility is an extension by varying surface tension, of the experiments of Cox 1958 with attention focused on the parasitic capillary waves of Longuet-Higgens 1963. A study of bursting pressures (Figure 3) would also be of interest.

Acknowledgements.

Robert V. White, Associate Engineer, contributed importantly to all phases of the experimental program. Michael Penney and A. Hanson carried out the surface tension measurements. The study was supported by the Office of Naval Research, Geography Programs, N000 14-67-A-0285-0013, N. R. 388-074.

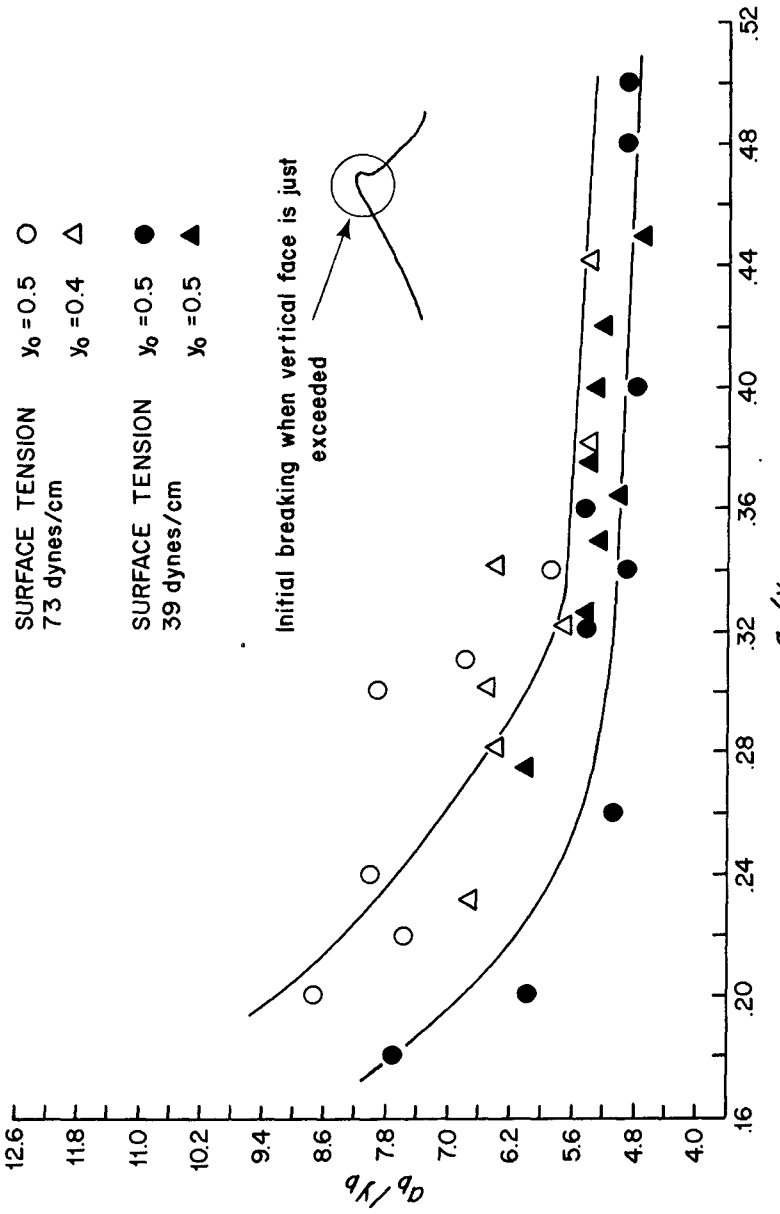

Figure 4 Solitary Wave 6° Slope: Initial Amplitude/S.W.L. vs. Breaking/Depth

Table 3 Variation in surface tension in natural waters.

Location	Description	Deviation from standard at given temperature.[1]
Atlantic Ocean		
Cape Cod, Mass.		
Great Harbor	Max. tide at 2.6 knots	+ 0.95 dynes/cm
Woods Hole Channel	rapid choppy flow	+ 0.25
Vineyard Sound	open ocean	-13.15
Great Harbor	WHOI dock	-15.15
	MBL club beach	-14.25
	Marsh creek mouth	- 9.05
	Sewage outfall	-14.65
Buzzards Bay	slick off Quisset	+ 0.35
	dumping grounds	-14.05
	mouth, Wild Harbor	- 3.65
Pacific Ocean		
Tomales Bay, Calif.		
open ocean	well mixed surf	+ 1.0
Great Rock	rapid channel flow	-16.1
Lawson's Pier	" " "	-15.9
Walker Creek		-12.9
Nicks Cove	Sewer outfall	-11.4
Millerton Creek	Brackish water	+ 0.1
Chicago		
Garfield Park	Fresh water	- 0.1
Lake Michigan	Near-shore	- 0.2

[1]Standard surface tension for seawater at S ‰ = 30 and for fresh water at S ‰ = 0, from Riley and Skirrow 1965, Deviation from standard value at temperature at which measurement was made.

References

Caldwell, J. M. 1949, Reflection of solitary waves. U.S. Army Corps. of Engineers, Beach Erosion Board Tech. Memo. No. 11.

Cox, D. S., 1958, Measurements of slopes of high-frequency waves. Jour. of Mar. Research. V 16, pp. 199-225.

Diephuis, J.G.H.R., 1957, Scale effects involving the breaking of waves. Proceedings 6th Conf. Coastal Engineering Florida Publ. by Council for Wave Res. Berkeley, California.

Galvin, C. J. 1968, Breaker type classification. Jour. Geophys. Res. V. 73:12, pp. 3651 ff.

Ippen, A. T. and G. Kulin, 1954, The shoaling and breaking of the solitary wave. Proceedings 5th Conf. Coastal Eng. Grenoble, France. Publ. by Council for Wave Res. Univ. Calif., Berkeley, California.

Jarvis, N. L. 1967, Adsorption of the surface active material at the sea-air interface. Limnology and Oceanography V12:2, pp. 213-221.

Kinsman, B., 1965, Wind Waves, Prentice-Hall, Inc. Englewood Cliffs, New Jersey, p. 273.

Longuet-Higgens, M. S., 1963, The generation of capillary waves by steep gravity waves. J. Fluid. Mech. 16, pp. 138-159.

Lumby and Folkard 1956 (quoted in Riley and Skirrow 1965 ibid, p. 117.)

Mason, M. A. 1951, Some observations of breaking waves. Paper 24, Gravity Waves, Circ. 521 Nat Bur. Standards, Washington, D. C.

McCowan, J., 1891, On the solitary wave. London, Edinburgh, Dublin, Phil. Mag. J. Sci. 32:5, pp. 45-58.

Michell, J. H., 1893, On the highest waves in water, Phil. Mag. Ser. 5, V 36, pp. 430-437.

Miller, R. L. and J. M. Ziegler, 1964. Internal velocity field in breaking waves. Proceed. 9th Conf. on Coastal Engineering, Lisbon, Portugal. Publ. by Council for Wave Res. Univ. of Calif. Berkeley, California.

Miller, R. L., 1968a, Experimental determination of run-up of Undular and fully developed bores. Jour. Geophys. Res. V73:14, pp. 4497-4510.

Miller, R. L. 1968b, The effect of surface tension on the limit form of waves. Trans. Am. Geophys. Union, V 49, pp. 209.

Penney, W. G. and A. T. Price, 1952. Finite periodic stationary gravity waves in a perfect liquid. Phil. Soc. Roy, Soc. London, Ser. V. 244, pp. 254-284.

Riley, J. Paul and G. Skirrow, 1965 (Editors) Chemical Oceanography (Table XIV p. 117). V. 1, Academic Press, New York.

Stokes, G. G., 1880, On the theory of oscillatory waves,(1847) Reprinted in Math. and Physical Papers V. 1, Cambridge, University Press.

Taylor, G. I., 1953, An experimental study of standing waves. Proc. Roy. Soc. London,

Ser. A:218, pp. 44-59.

Witting, J. M. 1964, Dissipation Mechanisms in weak shock waves in collisionless plasmas. Ph.D. Dissertation Dept. Physics, Mass. Inst. of Technology.

Stoker, J. J. 1948, The formation of breakers and bores. Communications, Pure and Applied Math. Vol. 1, pp. 1-87.

CHAPTER 23

Wave Refraction Theory in a Convergence Zone

Robert W. Whalin

U. S. ARMY ENGINEER WATERWAYS EXPERIMENT STATION, VICKSBURG, MISSISSIPPI

ABSTRACT

An experimental investigation utilizing nonbreaking waves and one bottom topography with parallel circular contours symmetric about the center of the basin was performed to assess the limits of applicability of linear wave refraction theory in a convergence zone. Analytical computations of reflections from underwater topographic variations and of viscous dissipation of energy at the bottom agreed with experimental measurements. It was vividly illustrated that a significant amount of energy was involved in diffraction along the wave crest, thus the necessity of developing a theory to include the stepwise computation of diffraction processes simultaneously with the computation of wave refraction is now evident. Nonlinear transfer of energy from lower to higher frequency components was investigated by performing a harmonic analysis over one wave period. As expected, nonlinear effects increased with both wave period and wave height (for a given wave period). Only 20 percent of the energy remained in the fundamental component for the longest period largest amplitude wave tested. Higher frequency components ranged from being completely coupled to the fundamental frequency to almost completely uncoupled. It was clearly demonstrated that in some circumstances the consideration of nonlinear effects becomes extremely important.

INTRODUCTION

The objective of this investigation is to ascertain, as a function of the incident wave characteristics for a given bottom topography, the error incurred by utilizing the usual linear wave refraction theory in a convergence zone with energy conservation between orthogonals and without reflection or nonlinear effects. This study is limited to nonbreaking waves and one bottom topography; however, the variation of wave period and height allows for a wide range of refraction coefficients and relative steepness. The deviation of the experimental data from the usual theory is attributed to the effects reflection, diffraction, and nonlinearities according to their respective magnitudes.

One of the practical problems confronting the (coastal) physical oceanographer and design engineer is to determine the expected wave environment in an area of proposed coastal construction. Occasionally one must cope with the problem of determining a design wave for a structure in an area where a strong convergence of wave orthogonals can occur. The present method utilized is to compute a linear wave refraction coefficient assuming no reflection from underwater topographic variations, no diffraction of energy along the wave crest, and certainly no consideration of nonlinear effects. This investigation was initiated in order to obtain an experimental indication of the relative importance of these phenomena in more realistic theories of wave refraction.

The economic impact of the topics under investigation cannot be overemphasized. Each phenomenon affecting the refraction coefficient (diffraction, reflection, and nonlinear effects) tends to decrease the design wave for a particular structure (with some slight reservation relative to the nonlinear effects). Nonlinearities tend to peak the wave crest and redistribute the energy through the mechanism of energy transfer to higher frequency components. The data and analyses which follow indicate conclusively that a much better understanding of the dynamics of wave propagation in a strong convergence zone of wave orthogonals is necessary before analytical computations of the wave environment can be made with confidence.

MODEL DESIGN

The bottom topography utilized in the model consisted of circular bottom contours of the same radius, the center of the circles lying along the centerline of the test basin as illustrated in Figure 1. A crushed rock wave absorber with slope of 1:14 and a layer of rubberized horsehair were installed at the end of the model to eliminate reflections back into the measurement area.

Computations of the wave reflection coefficient from the sloping topography in the model were made from three different theories. The long wave theory of Cochran and Arthur (for which the Lamb theory is a special case for normal incidence) utilizing a vertical step with depths of 0.1524 m (0.5 ft) and 0.4572 m (1.5 ft) resulted in a reflection coefficient of 0.268 which is certainly too large. The Ogawa and Yoshida theory which also employs the long wave assumption was solved for the case of a weak reflection with a constant sloping bottom. The first order reflection coefficient, R_{r_1}, is 0.0045 (T = 1 sec), 0.0197 (T = 2 sec), and 0.0089 (T = 3 sec). Figure 2 illustrates the reflection coefficient as a function of wave period. The oscillatory behavior of the Ogawa and Yoshida theory appears to be a result of attempting to apply the theory where the basic assumption of a long wave is not satisfied. The primary point illustrated by the Ogawa and Yoshida theory is that reflections from the underwater topographic variations are indeed small (less than 0.02).

The most sophisticated linear reflection theory available for underwater topographic variations is due to Rosseau (1952). This theory provides an analytical solution which makes no assumption on the wave form other than linear small amplitude progressive waves emanating from $+\infty$ and the bottom profile must be described by a specified function which approaches a depth h_2 as $y \to -\infty$ and h_1 as $y \to +\infty$. This theory is quite complicated requiring the fitting of a bottom contour to model topography. Details of the application of this theory can be found in Rosseau (1952), Webb (1965), and Whalin (1971).

The reflection coefficient from the Rosseau theory is given by

$$R_r = \frac{\tanh \pi\lambda_1 - \tanh \pi\lambda_2}{\tanh \pi\lambda_1 + \tanh \pi\lambda_2}, \qquad (1)$$

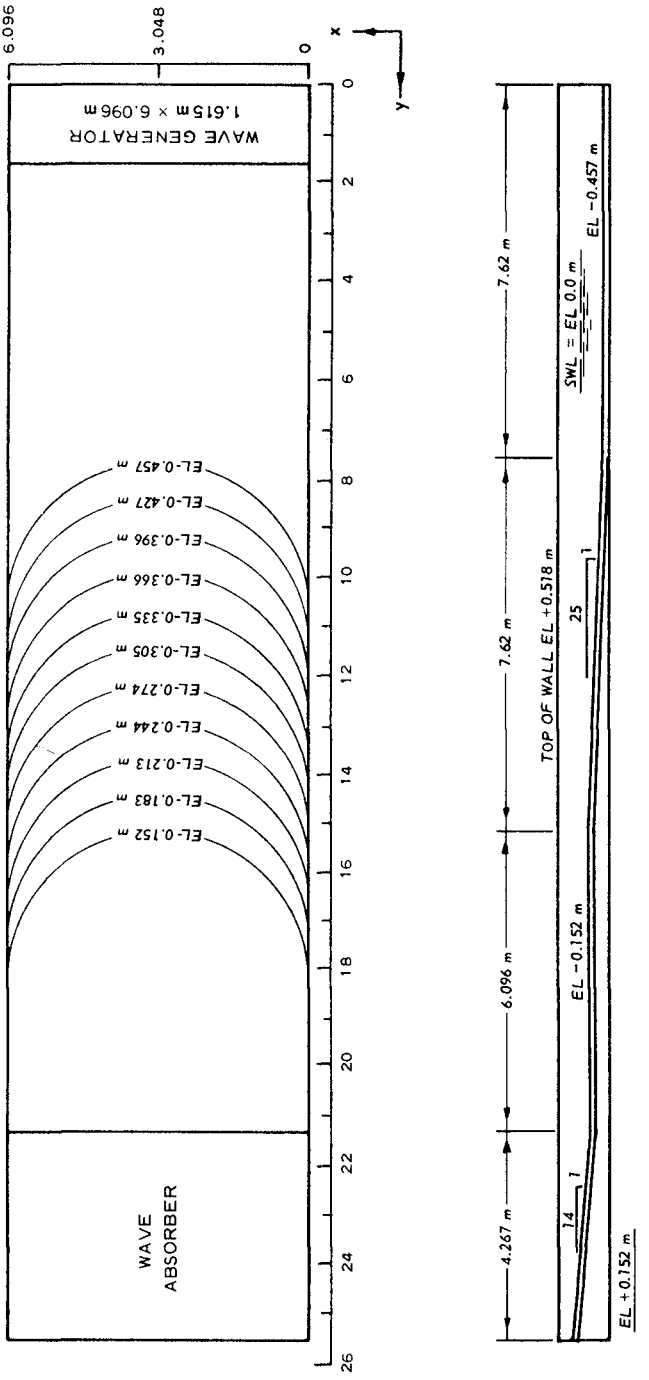

Figure 1. Model Topography

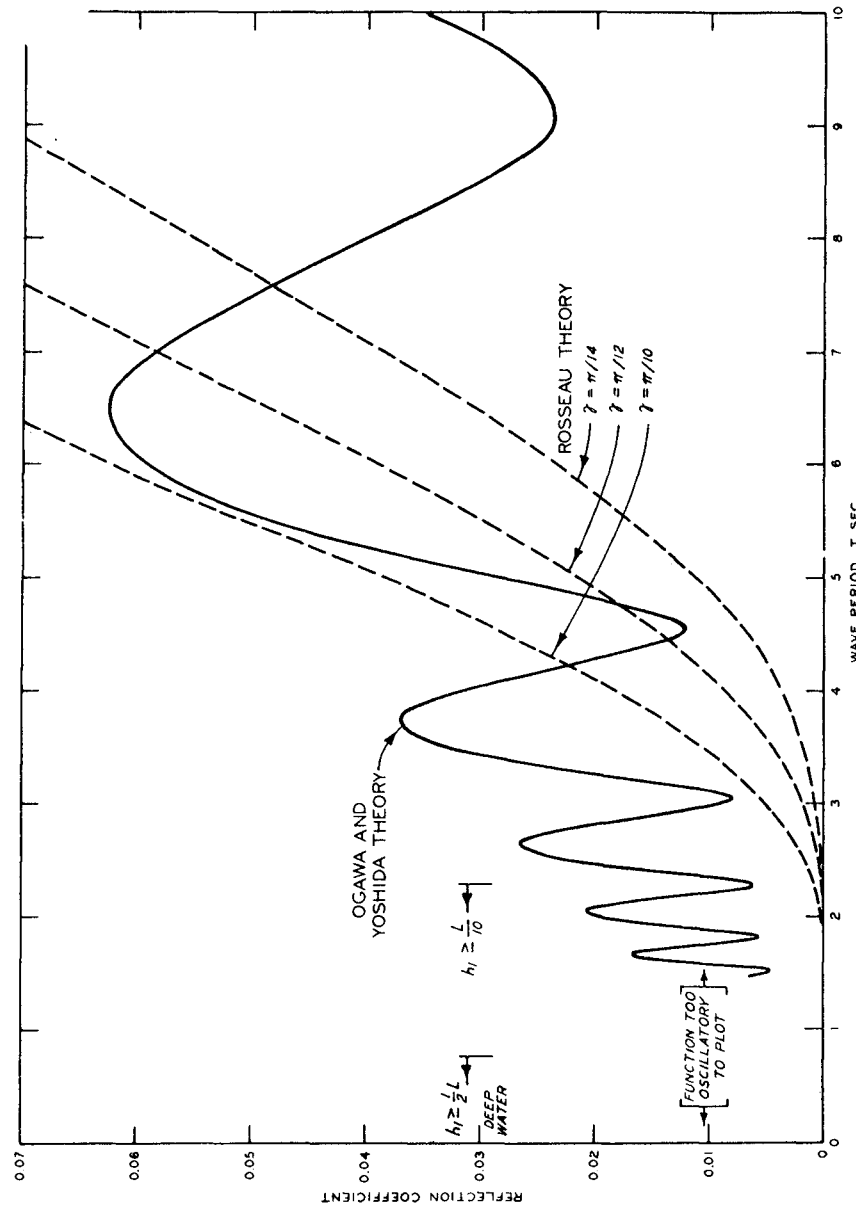

Figure 2. A Comparison of Rosseau and Ogawa and Yoshida Reflection Coefficients, T<10 sec

where λ_1 and λ_2 are solutions of

$$\lambda_i \tanh \gamma\lambda_i - \frac{\omega^2 h_i}{g\gamma} = 0;\ i = 1,2;\ \gamma = \pi/N \qquad (2)$$

In order to compare the Ogawa and Yoshida (1959) reflection theory with the Rosseau (1952) theory, a Rosseau bottom contour was selected to obtain the best fit to the centerline of the wave basin. Figure 3 illustrates the best fit which was obtained for $\gamma = \pi/14$ (N = 14); however, the curve for $\gamma = \pi/12$ also is shown. The reflection coefficient from the Rosseau (1952) theory is obtained from (1) as a function wave period upon solution of (2) for λ_1 and λ_2. Figure 2 shows a comparison of the reflection coefficient from the Rosseau (1952) theory and the Ogawa and Yoshida (1959) theory for three values of γ. The oscillatory behavior of R_{r_1} exhibited by the Ogawa and Yoshida (1959) theory is absent from the Rosseau (1952) theory. This is interpreted as being a consequence of attempting to apply the theory of Ogawa and Yoshida (1959) to a situation where the basic assumption (a long wave) is not valid. The reflection coefficients computed from the Rosseau (1952) theory (Figure 2) were 2.5×10^{-11}, 1.3×10^{-5}, and 6.1×10^{-4} for wave periods of 1, 2, and 3 sec, respectively, and $\gamma = \pi/14$. Figure 2 illustrates the sensitivity of the reflection coefficient to the parameter γ. Both reflection theories approach the Lamb (1932) value for normal incidence as $T \to \infty$.

A theory has been developed by Keulegan (1950) to compute the wave damping due to viscous dissipation of energy. This theory applies to slowly damped periodic progressive water waves in the absence of refraction, diffraction, or shoaling. Computations indicated that the wave height attenuation over the entire measurement area was between 0.01 and 0.03 which was considered sufficiently small to be neglected.

A 20-channel wave-height measuring system was used to secure data at 60 points in the wave basin for the basic test series and at 40 other points for an alternate test series. Actual gage locations are shown in Figure 4. The wave generator spanned the width of the test basin with approximately a 1 cm clearance at each of the sidewalls. The generator moves in simple harmonic motion in the vertical. Data were acquired at the 60 basic wave gage locations shown in Figure 4 for wave periods of 1, 2, and 3 sec and for three wave amplitudes for each period. These data formed the basic set of measurements from which the refraction coefficients were computed and compared with linear theory. In order to ascertain if there were any measurable reflections from either the bottom topography or the end of the test basin, 40 wave gages were installed at the alternate positions shown in Figure 4. Since only 20 wave gages were available, the locations delineated by A, B, and C (for the basic test series) and A and B (for the alternate test series) represent positions to which the gages were moved and the same series of tests repeated. Two permanent monitor gages were set in the positions denoted on Figure 4 (M-1 and M-2) and were not moved during the entire test series in order to eliminate any errors in resetting the wave generator stroke for the alternate gage locations.

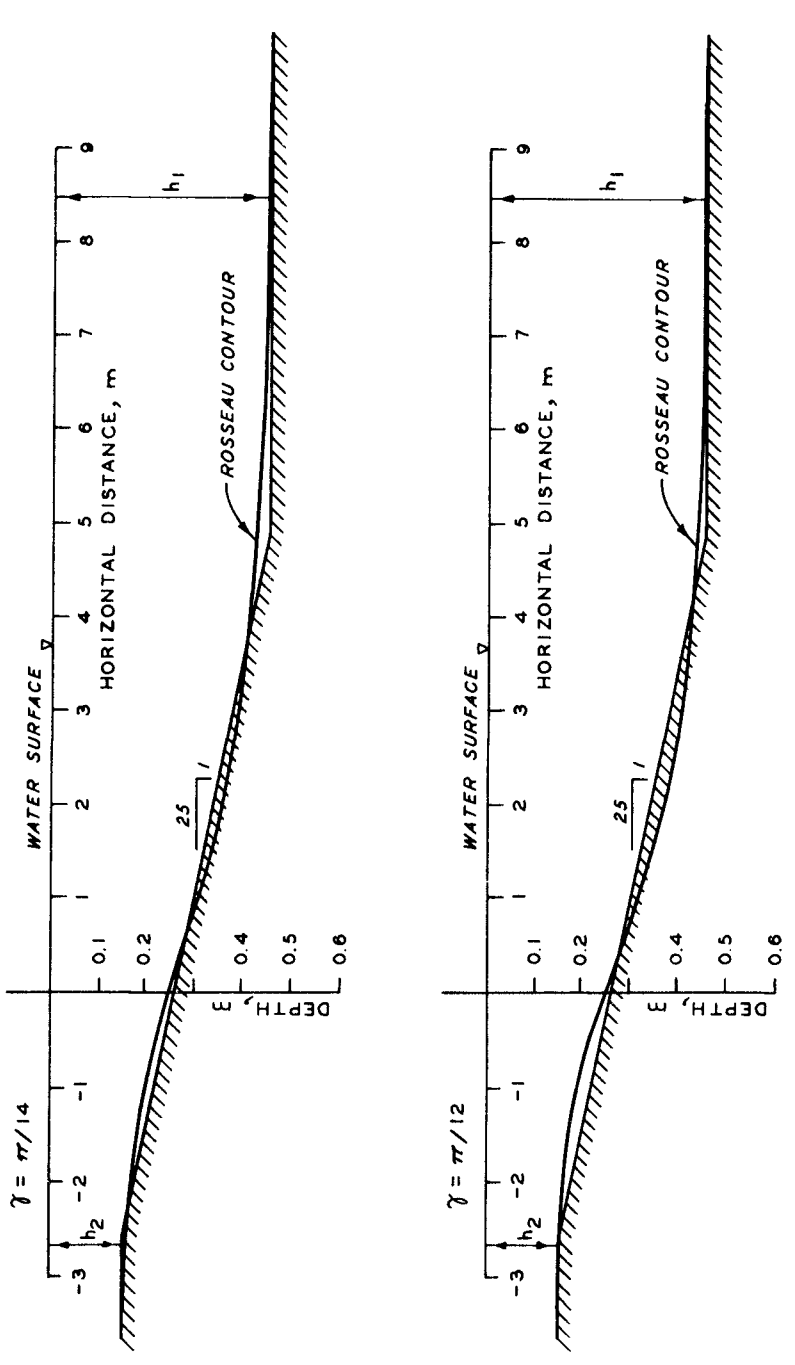

Figure 3. Rosseau Contours for Topography Along the Centerline of the Wave Basin

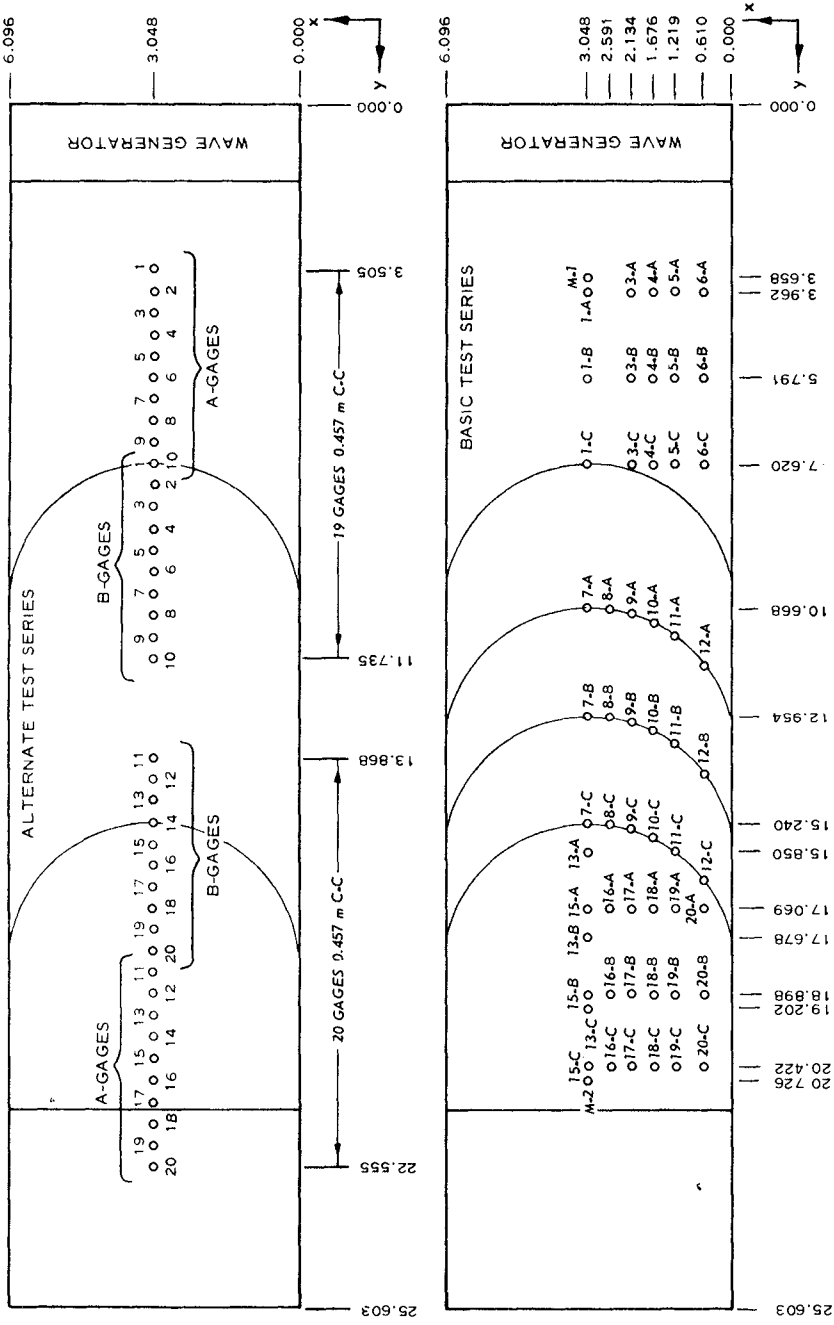

Figure 4. Wave Gage Locations

DATA ANALYSIS

The analysis of these data is predicated on the assumption that the total energy or wave power is equally divided between potential and kinetic energy as is the case for the Airy wave theory. The departure from an equal partitioning of kinetic and potential energy is small and the effect of this departure on the analysis will be even smaller. The important point relative to the data analysis is that the same ratio between potential and kinetic energy be preserved over the measurement area.

One of the primary assumptions of the linear wave refraction theory being investigated is that no energy is diffracted laterally along the wave crest; that is, for steady conditions of wave generation the same wave power exists at all positions between any two orthogonals. Moreover, since the property of interest is the energy transmitted per unit time one must deal with the group velocity rather than the phase velocity. The actual quantity to be computed from the data is the energy transmitted per unit crest width over one wave period; the units of this quantity being energy per unit width (joule m^{-1}). The potential energy per unit crest width over one wave length is given by

$$\frac{PE}{W} = \frac{\rho g}{2} \int_0^L \eta_1^2 \, (y,t) \, dy \tag{3}$$

where W is the width along the wave crest, ρ the water density, g the acceleration due to gravity, η_1 the water level anomaly above equilibrium level, and L the wave length. After appropriate transformation of equation (3) to correspond to a wave record obtained at a fixed point, a computer program was written to perform the integration given a number of values η at equally spaced intervals over one wave period.

In addition the program also performed a harmonic analysis of the wave form to determine the amplitude and phase of the fundamental (that corresponding to the period set on the wave generator) and the higher order harmonics. These data were then utilized to interpret the magnitude of the nonlinear effects during propagation of the waves over the topography in terms of the amount of deviation of the generated wave form from purely sinusoidal. The output of the harmonic analysis routine (the mean adjusted to zero) was expressed in the form

$$\eta_1(t) = \sum_{k=1}^{n} (a_k \cos k\omega t + b_k \sin k\omega t) \tag{4}$$

or

$$\eta_1(t) = \sum_{k=1}^{n} c_k \cos (k\omega t - \theta_k) \tag{5}$$

where

$$c_k = \left[a_k^2 + b_k^2\right]^{\frac{1}{2}} \text{ and } \theta_k = \tan^{-1}\frac{b_k}{a_k} \tag{6}$$

For k = 1, the wave crest occurs at $\omega t_o = \theta_1$. Letting $t' = t - t_o$

$$k\omega t - \theta_k = k\omega t' + \theta_k' \tag{7}$$

wbere $\theta_k' = k\theta_1 - \theta_k$ represents the phase lead of the higher order harmonics relative to the phase of fundamental (k = 1) frequency. If θ_k' is positive, the higher order harmonics are leading the fundamental; if negative, they are lagging the fundamental. If θ_k' increases as a function of propagation distance, the higher order harmonics are catching up with or are propagating faster than the fundamental (a situation for which there is no easy explanation) and if θ_k' decreases as a function of propagation distance, the higher order harmonics are continually lagging the fundamental.

If θ_k' remains constant, this can be interpreted as a verification that the higher order frequencies are completely coupled to the fundamental frequency and hence the wave acts as a Stokes type of nonlinear wave.

In performing the analytical computation of the refraction coefficient from linear theory, expressions are needed for the phase velocity, its first and second order derivatives with respect to x and y, the bottom topography, and its first and second derivatives with respect to x and y. The equation of the sloping portion of the bottom topography is given by

$$h(x,y) = h_1 + \frac{1}{25}\left\{y_o + \frac{1}{2}w - y - \left[x(w - x)\right]^{\frac{1}{2}}\right\} \tag{8}$$

where y is measured along the wave basin, x across the wave basin, y_o is the coordinate of the first circular bottom contour along the centerline of the wave basin, h_1 is depth in the deep portion of the basin (0.4572 m) and w is the width of the basin (6.096 m). Note that any line parallel to the y axis has a slope of 1:25 over the variable portion of the bottom. This expression for the bottom topography makes it possible analytically to compute the phase velocity and its derivatives at any location (x,y) in the basin.

Figure 5 illustrates the computed and measured refraction coefficient for a wave period of 3 sec. Similar comparisons for periods of 1 and 2 sec are given in Whalin (1971). The dotted lines represent a caustic. The computed refraction coefficient is merely the square root of the ratio of the potential energy transmitted per unit crest width over one wave period at any particular wave gage to the average of the potential energy transmitted per unit crest width over one wave period at either gages 1A to 6A, 1B to 6B, or 1C to 6C depending upon whether A, B, or C gage is being analyzed (remembering that A, B, and C locations represent locations to which the gages were moved and the same test repeated).

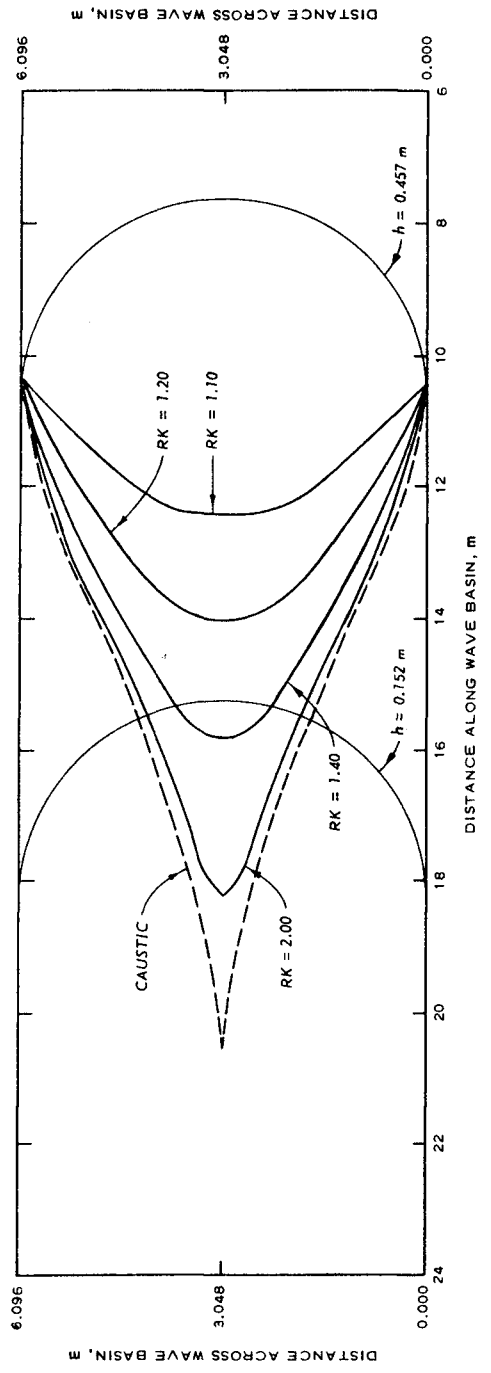

Figure 5. Theoretical Refraction Pattern, T = 3 sec

A word of caution should be interjected at this point relevant to the interpretation of the computed refraction coefficients. The theoretical refraction coefficient implies energy conservation between orthogonals, a condition which is in the process of being investigated. On the other hand, what we are computing from the data is merely the square root of the ratio of the energy transmitted since, as will be illustrated shortly, a significant amount of energy has been diffracted. In short, a refraction coefficient alone is insufficient in this case except in areas on the sloping portion of the topography where little diffraction has occurred. More properly one should have a refraction coefficient, a diffraction coefficient, a friction coefficient, a shoaling coefficient, and a reflection coefficient.

Caution must be exercised in analyzing the amount of transmitted energy involved in diffraction processes. However, one very meaningful estimate of this quantity can be obtained from the three gage alignments in the shallow portion of the wave basin. Gages 15-20A, 15-20B, and 15-20C can be analyzed to ascertain the amount of diffraction of transmitted potential energy (or total energy transmitted through the assumption that transmitted energy is equally partitioned between kinetic and potential energy). Since the caustic boundary intersects each of these gage alignments, all potential energy transmitted outside the caustic line must be diffracted with the exception of the energy refracted from the opposite side of the centerline of the wave basin. Therefore, a computation of the percent energy measured outside the caustic line minus the theoretical amount refracted into this region from the opposite side of the wave basin was made for each condition tested and for each gage alignment. Figure 6 illustrates the distribution of measured potential energy transmitted per unit width relative to the distribution obtained by linear wave refraction theory. The percent energy diffracted represents 100 times the ratio of the intergrated potential energy (from the caustic to the edge of the basin) transmitted per unit width minus the amount refracted to the left of the caustic from the opposite side of the wave basin to the total potential energy transmitted (integrated from the centerline to the edge of the basin). Table 1 summarizes the data for all test conditions.

Table 1

Percent of Transmitted Energy Diffracted Over One Wave Period

Period sec	S cm	15-20A %	15-20B %	15-20C %
3	15.24	59.58	84.73	48.20
	10.16	59.98	85.38	48.22
	7.62	63.16	83.98	48.21
2	10.16	44.84	80.57	70.87
	7.62	44.51	79.06	69.57
	5.08	46.83	75.24	68.68
1	5.08	26.20	36.04	54.24
	2.54	24.84	37.48	54.87
	1.27	22.49	26.95	32.88

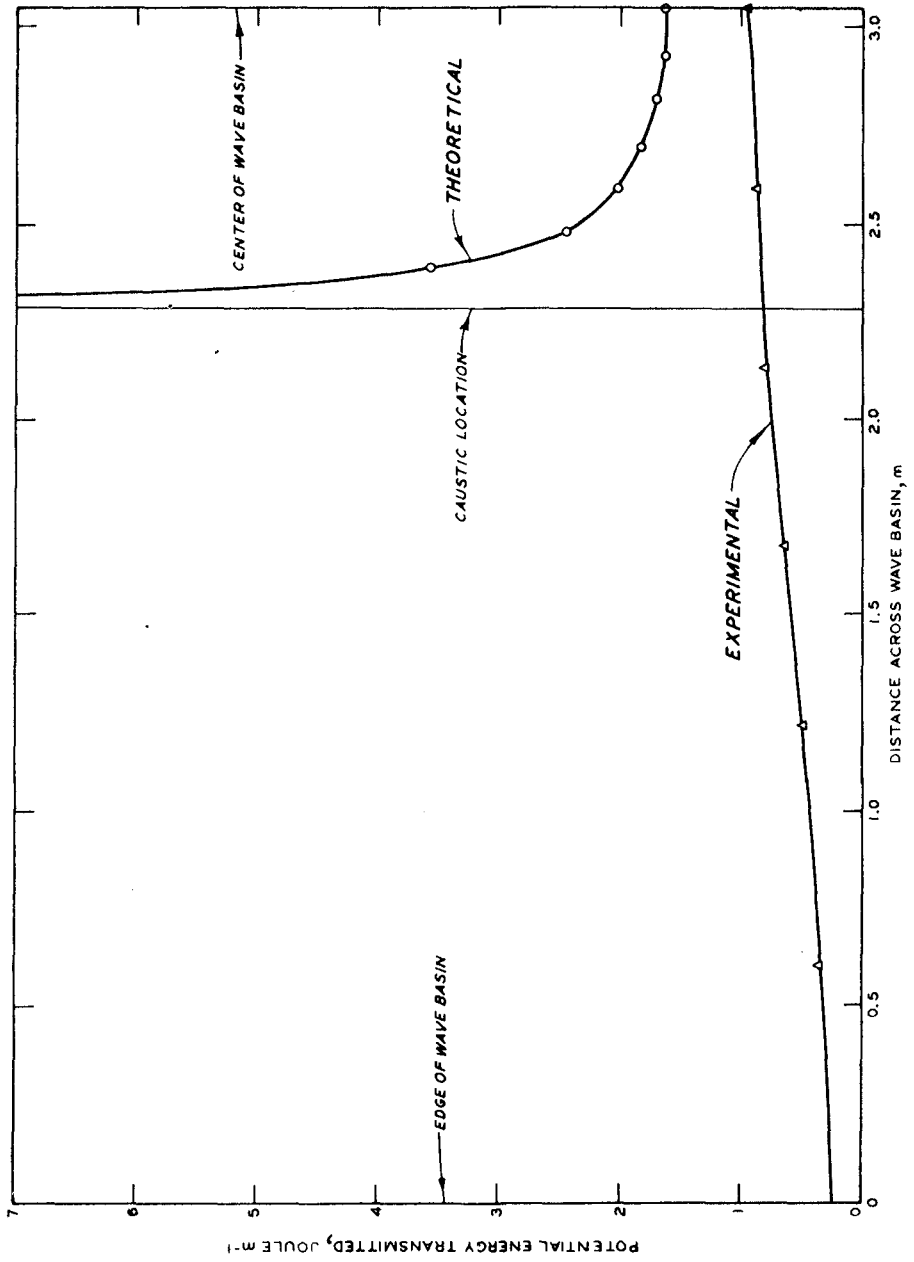

Figure 6. Diffraction of Transmitted Potential Energy, T = 3 sec, S = 7.62 cm, Gages 15-20A

The lower values in the right hand column of Table 1 (gage alignment 15-20C) for the 2- and 3-sec waves arise because there is a significant amount of energy refracted across the caustic from the opposite side of the centerline of the wave basin. Gage alignment 15-20C for wave periods of 2 and 3 sec was the only situation where a significant (greater than 2 percent) amount of energy was refracted (according to the linear theory) across the centerline into the shadow zone. It is obvious that diffraction of energy must be considered in order to obtain an accurate estimate of the wave height; the assumption of energy conservation between orthogonals is certainly not valid at any location in the shallow end of the wave basin.

Nonlinear effects were analyzed by performing a harmonic analysis over one period of all data acquired during the test series. It was observed during the course of data acquisition that the wave form changed quite rapidly along the centerline of the wave basin at the top of the sloping portion of the topography. Over a propagation distance of less than 2 m, the wave form became very steep at the crest with a long trough. Therefore, an alternate series of tests were designed with two purposes in mind, one to verify the computation of a negligible wave reflection coefficient and more importantly, to investigate (through a harmonic analysis) the nonlinear effects occurring, especially along the centerline of the wave basin. Gage locations for this test series are illustrated in Figure 4 (alternate test series).

Figure 7 shows the amplitude of the first three components from the harmonic analysis. Data for the other test conditions can be found in Whalin (1971). The amplitudes are represented by c_1, c_2, and c_3 and correspond to frequencies of ω, 2ω, and 3ω where ω is the frequency of the fundamental component. The limits of the sloping topography are shown in each figure and it is easily seen that a considerable amount of energy is transferred to the higher frequency components. Figure 8 shows the percent of potential energy transmitted by the fundamental frequency component, c_1 as a function of distance along the centerline of the wave basin for the 3-sec waves. The total energy per unit width available to be transmitted (along the centerline) is of course increasing with distance due to refraction. Relative to the 3-sec data (Figure 8) the ratio of energy transfer to the higher frequency components always seems to be greater than the rate of increase due to refraction. The rate of energy loss by diffraction in the fundamental frequency component must also be considered, hence the interpretation is not so simple. In order for the percent energy in the fundamental frequency component to increase, the rate of transmitted energy increase (per unit width) by refraction must be greater than the rate of transmitted energy loss (per unit width) by diffraction and nonlinear transfer to higher frequency components.

A further insight into the nonlinear processes occurring is gained from Figure 9 which shows the relative phase ($\theta_{\frac{1}{2}}$ and $\theta_{\frac{1}{3}}$) of the 2ω and 3ω frequency components for the 3-sec wave. These relative phases are defined by (7).

The trend was essentially identical for all conditions tested, the phase of the 2ω and 3ω frequency components relative to the ω component

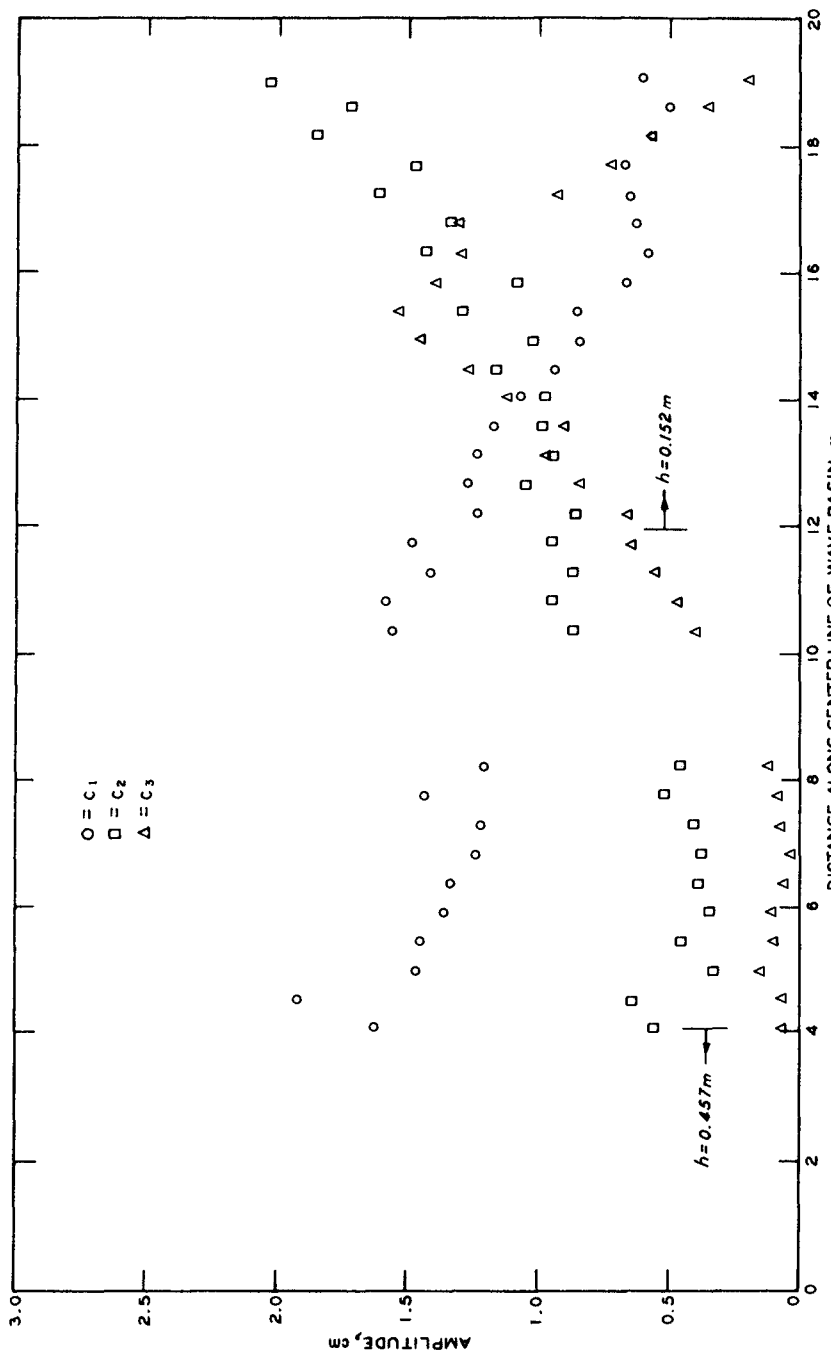

Figure 7. Values of c_1, c_2, and c_3 as Functions of Distance, T = 3 sec, S = 15.24 cm

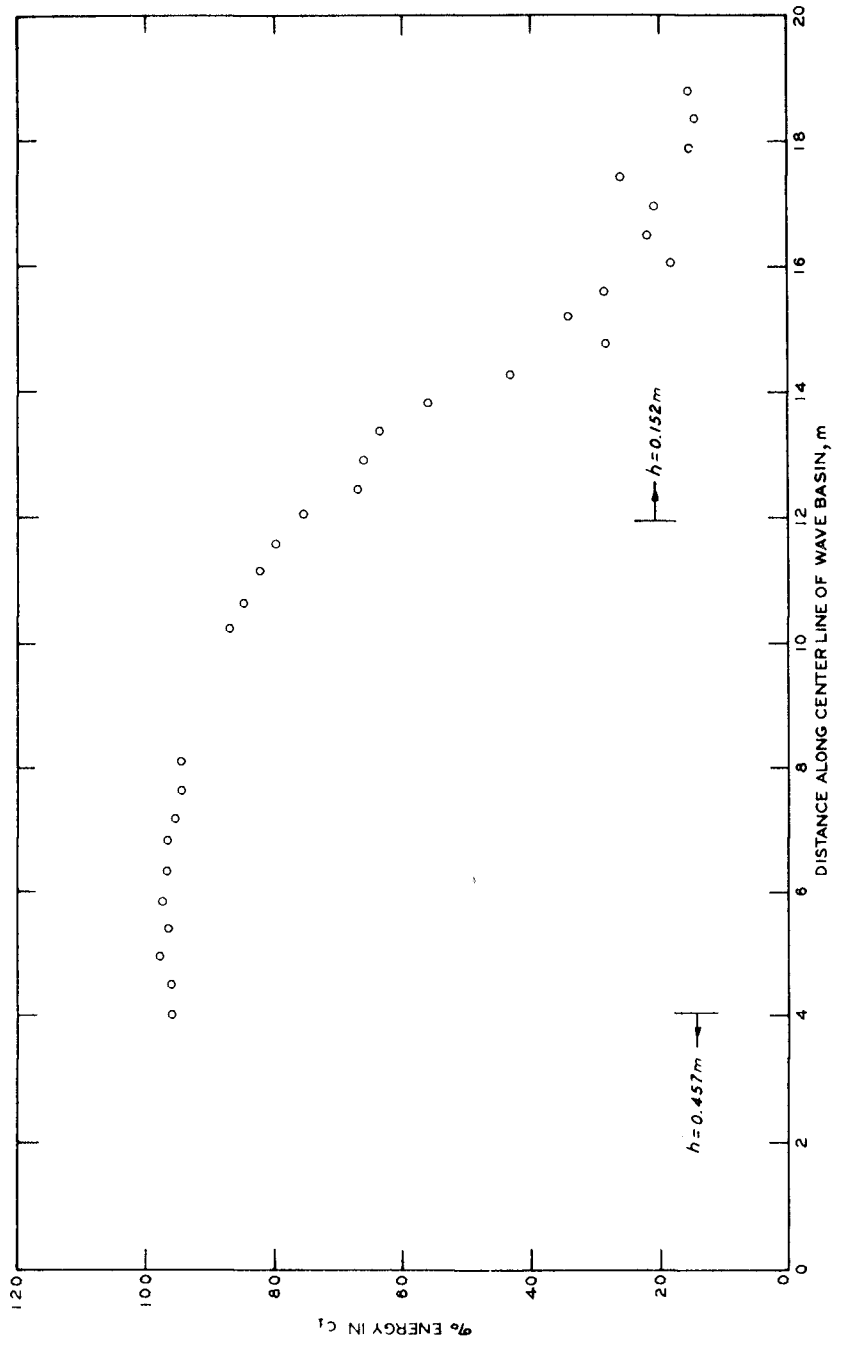

Figure 8. Percent Energy in Fundamental Frequency Component, T = 3 sec, S = 15.24 cm

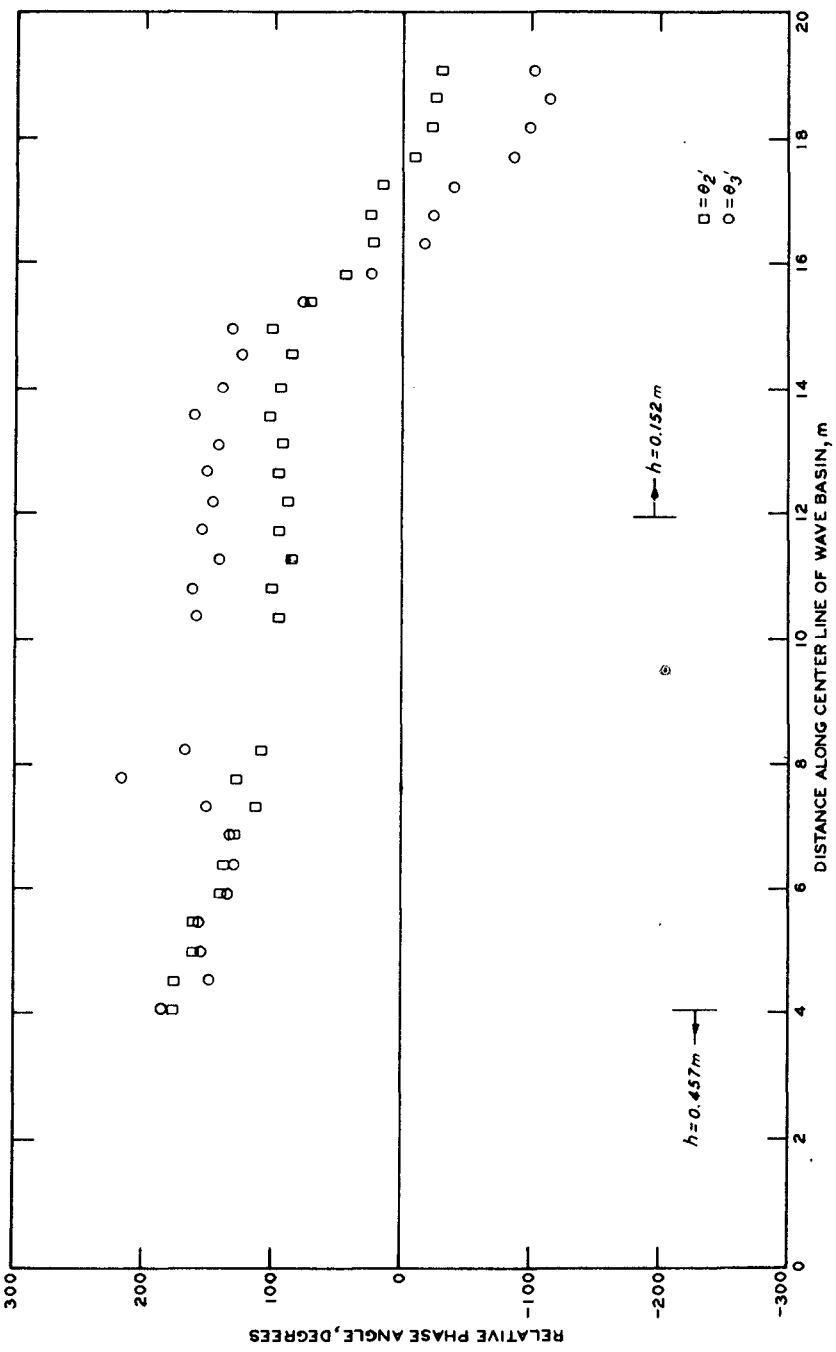

Figure 9. Phase of 2ω and 3ω Relative to the ω Component, T = 3 sec, S = 15.24 cm

decreases with distance propagated down the flume. The interpretation of this is very clear; if the relative phase does not change with distance then the higher order harmonics are completely coupled to the fundamental frequency and they propagate at its velocity. Since the relative phase of the higher order harmonics is decreasing, it means that they are continually lagging the fundamental frequency or are propagating slower. In order to investigate the possibility that the harmonics are completely uncoupled, one can compute the change in the relative phase over a given propagation distance. This computation revealed that the higher order harmonics were (1) completely coupled for the 1-sec waves, (2) quasi-coupled for the 2-sec waves, and (3) completely uncoupled for the 3-sec waves.

The data indicate that the magnitude of nonlinear effects increases with the wave period for a given topographic variation. Further, the energy transfer to higher frequency components becomes quite significant (as much as 80 percent for the largest amplitude and longest period wave) and these higher frequency components may or may not be coupled to the fundamental component.

One phenomenon not analyzed but observed during the course of this investigation was the effect of wave height on the phase velocity. At the top of the sloping portion of the topography, the wave crest in the middle of the basin was lagging slightly behind that toward the basin edges; however, by the time the wave reached the absorber material, the middle portion of the wave crest was leading. The effect of wave height on propagation speed is always neglected in refraction computations. The change in propagation speed across the wave front may alter the refraction coefficient by a significant amount in instances of a strong convergence of orthogonals. Furthermore, if the relative position of the wave front is important in any particular design problem, then this effect should be included in the refraction computation. It is an effect which can be relatively easily accounted for, although it certainly will necessitate a slightly longer running time on the computer.

CONCLUSIONS

A number of conclusions have arisen as a result of the rather extensive data acquisition and analysis phases of this investigation. Any conclusions drawn from the investigation must be interpreted with a view toward the effects of a more general type of bottom topography since the experimental data were acquired for only one topography. The conclusions of this investigation are enumerated below.

In the tests conducted, linear refraction theory was completely inadequate for predicting the refraction coefficient. Even for values of the refraction coefficient as low as 1.1 to 1.2, diffraction of energy along the wave crest completely altered the form of the isolines of equal refraction coefficient. Actually one cannot speak of a refraction coefficient alone whenever diffraction is significant since by definition refraction means conservation of energy between orthogonals thus implying no diffraction. In situations where a convergence zone exists it is imperative to include diffraction effects and speak of a design wave height of a design wave profile which includes the effects of diffraction,

convergence of energy by the bottom topography (rather than refraction), reflection, frictional energy dissipation and nonlinear effects. No analyses are available at the present time which combine the computation of refraction and diffraction simultaneously. Such a combination of linear theories must be developed into a working numerical scheme in the form of a computer program which can routinely handle this type of problem. In the absence of a refraction theory which includes diffraction effects, the best approach to determining a design wave is to conduct a model study.

The magnitude of nonlinear effects, in particular the transfer of energy to higher frequency components, was found to be quite significant for the longest wave period (3 sec) and the largest wave height tested. In this case, less than 20 percent of the energy remained in the fundamental frequency component. Once the energy transfer to higher frequency components was initiated, it continued over the extent of the measurement area. In the case of the 1-sec wave period, practically all energy remained in the fundamental frequency component over the entire measurement area. The percent energy remaining in the fundamental frequency component for the 2-sec period exhibited an unusual behavior. It decreased and reached a minimum of approximately 80 percent and then increased again to the end of the measurement area. This is interpreted as meaning that the rate of energy being transferred to the higher frequency components is initially greater than the rate at which energy is being supplied by refraction but later becomes less.

The higher frequency components produced by the nonlinear transfer of energy from the fundamental component were not completely coupled to the primary wave except for the 1-sec period. The phase of the higher frequency components relative to the phase of the fundamental component indicated that a moderate coupling existed for the 2-sec period tested and a very weak coupling existed for the 3-sec waves tested. The amount of coupling decreased as the wave period increased and also as the wave height increased (for a given period) as one would expect. The significance of these findings is that it is clearly exhibited that an extremely complicated process is occurring; therefore to accurately predict the wave form (which may be important for the design of certain coastal structures) at a given location within a strong convergence zone of orthogonals, it is necessary to develop a nonlinear theory capable of describing not only the development of a nonlinear wave profile, but also the transition from coupled to uncoupled higher order frequency components. It seems apparent that the small amplitude assumption should be abandoned when there is a marked increase (for the 3-sec waves) in the nonlinear energy transfer to higher frequency components as the initial wave height increases. Values of the relative wave height vary from approximately 0.15 to 0.4 at the top of the sloping topography for the 3-sec waves. The maximum wave steepness was approximately 0.03, 0.022, and 0.015 for periods of 1, 2, and 3 sec, respectively, indicating that wave steepness is relatively unimportant with regard to the nonlinear effects analyzed.

An interesting point which was vividly illustrated in the present investigation was the effect of wave height on the phase velocity of the wave profile. Along with the inclusion of wave diffraction, one should also include effect of a finite wave height on the phase velocity of wave since this can alter the refraction coefficient obtained (especially in a zone of large convergence of wave orthogonals).

The computation of a wave reflection coefficient from underwater topographic variations requires some careful consideration of both the Ogawa and Yoshida (1959) long wave theory and the more general (in terms of assumptions relative to the wave form) theory of Rosseau (1952). The oscillatory behavior of the Ogawa and Yoshida (1959) theory seems to be unwarranted and evidently is a consequence of the error introduced by using the long wave theory in deep to intermediate water depths. Furthermore, the Ogawa and Yoshida (1959) theory usually overestimates the reflection coefficient. On the other hand, the difficulty of the Rosseau (1952) theory is that it probably underestimates the reflection coefficient due to the nature of the bottom profile (asymptotically approaching constant water depths on both sides of the topographic variation). A computation by both methods is recommended in order to bracket the actual value of the reflection coefficient with the preference toward one theory or the other depending on the characteristics of the actual bottom contour (how well this can be matched by a Rosseau bottom contour) and the relative water depth involved (the validity of the long wave assumption).

Viscous dissipation of energy at the bottom and sides of the wave basin was shown to result in a wave height attenuation of approximately 3 percent over the entire measurement area. The theory of Keulegan (1950) seems to be very satisfactory as long as the basic assumptions of small amplitude waves and small damping are satisfied as was the case in the present investigation.

The economic impact of the phenomena studied in this investigation cannot be overemphasized. The point is that diffraction acts to decrease the wave height computed by linear refraction theory, thus decreasing the design wave for any coastal structure located in such an environment. The nonlinear effects observed may act to either increase or decrease the design wave height and more importantly they need to be predictable where significant in order to evaluate such practical design considerations as wave forces, breaking wave heights, and longshore components of velocity. Therefore, future analytical investigations should be aimed first at including the effects of a linear diffraction theory and secondly toward describing the nonlinear effects adequately. The fact that the phenomena studied tend to decrease the design wave height can produce a very significant savings in the cost of breakwaters and jetties alone if they are situated shoreward of a convergence zone.

ACKNOWLEDGEMENTS

The author wishes to acknowledge Professor Robert O. Reid for many stimulating classroom lectures and helpful suggestions relative to this paper which is extracted from a dissertation submitted to Texas A&M University in partial fulfillment of the requirements for the degree of Doctor of Philosophy, Mr. Fred R. Brown, COL Levi A. Brown, and COL Ernest D. Piexotto who were primarily responsible for funding this project under the In-House Laboratory Initiated Research Program at the Waterways Experiment Station, Mr. Charles W. Brasfeild and SP4 Tom Anderson for their invaluable assistance in data acquisition and analysis, Mr. R. Y. Hudson for suggesting the topic of investigation, and the Office, Chief of Engineers for granting permission to publish this paper.

REFERENCES

COCHRAN, J. D. and R. S. ARTHUR, 1948, Reflection of Tsunamis. J. Mar. Res., 7(3): 239-251.

KEULEGAN, G. H., 1950, The Gradual Damping of a Progressive Oscillatory Wave with Distance in a Prismatic Rectangular Channel. Ntl Bur. Stds. Rept. 75 pp.

LAMB, H., 1932, Hydrodynamics. Cambridge Univ. Press, Sixth ed.; 738 pp.

OGAWA, K. and K. YOSHIDA, 1959, A Practical Method for a Determination of Reflection of Long Gravitational Waves. Records of Ocn. Works in Japan, 5(1): 38-50.

ROSSEAU, M., 1952, Contribution a la theorie des ondes liquides de gravite en profondeur variable. Publ. Sci, et Tech. du Ministere de l'Air, No. 275; 73 pp.

WEBB, L. M., 1965, Contributions to the Mono Lake Experiments, Vol. IlI, Linear Theory of the Propagation of Periodic Waves over a Continental Slope. Natl Engr. Sci. Co., Rept No. S-256-2; 36 pp.

WHALIN, R. W., 1971, The Limit of Applicability of Linear Wave Refraction Theory in a Convergence Zone. WES Res Rept H-71-3; 156 pp.

CHAPTER 24

Computation of Combined Refraction - Diffractian

by

J.C.W. Berkhoff,

Delft Hydraulics Laboratory,
Mathematical Branch,
The Netherlands

Abstract

This paper treats the derivatian af a two-dimensional differential equation, which describes the phenomenon of cambined refraction - diffraction for simple harmonic waves, ond a method of solving this equation. The equation is derived with the aid of a small parameter development, and the method of solution is based on the finite element technique, together with a source distribution method.

Introduction

It would greatly help designers of harbaurs ond offshore structures if it were passible to get same quantitative infomation about the wave penetration ond wave height which can be expected in the harbour and around the structures. For simple harmonic linear water waves mathematical models exist in the case of diffraction [3, 4] or refraction [5, 7] separately. The combined effect in the cose of long waves is described by the linear two-dimensional shallow water equatian [10], but for short waves the describing equation has not yet been derived. Battjes [1] proposed a set of equations fram which the equation derived in this paper differs in one term.

Independently of the writer of this paper Schönfeld [8] derived the same equation written in another form and obtained in a different way. Solving the equation and treating the boundary conditions in the horizontal plane is possible in various ways. This paper gives a method which solves the equation in an area in which the combined effect of refraction and diffraction is impartant, with a finite element technique [12] and treats the Sommerfeld radiatian condition [9] with a source distribution method [4]. Numerical results in the case of Tsunami response of a circular island with parabolic water depth [11], propagation of plane waves over a parabolic shoal, and response of o rectangular harbour with o constant slope of the bottom ore given and compared with analytical or numerical results from other methods. The accuracy of the numerical treatment is not yet known in detail and will be the subject of further study, so the interpretation of the results must be done with care. An attempt was made to compare the results for short waves over a parabolic shoal with measurements by Holthuysen [6]

Derivation of the equation

The theory will be restricted to irrotational linear harmonic waves, and loss of energy due to friction or breaking is not token into account. A two-dimensional equation which is applicable to waves in the range from shallow water to deep water has been derived by means of o small parameter development and on integration over the water depth.

Basic equatians

The equatians with which the derivotion starts ore:

(i) The three-dimensional patentiol equatian

$$\frac{\partial^2 \phi}{\partial x^2} + \frac{\partial^2 \phi}{\partial y^2} + \frac{\partial^2 \phi}{\partial z^2} = 0 \qquad (1)$$

(ii) The linearised free-surface conditian far harmonic waves

$$\frac{\partial \phi}{\partial z} + \frac{\omega^2}{g} \phi = 0 \qquad \text{ot } z = 0 \qquad (2)$$

(iii) The battom condition

$$\frac{\partial \phi}{\partial z} + \frac{\partial \phi}{\partial x} \frac{\partial h}{\partial x} + \frac{\partial \phi}{\partial y} \frac{\partial h}{\partial y} = 0 \qquad \text{ot } z = -h\,(x, y) \qquad (3)$$

with x, y : harizantal caardinates.
z : vertical coardinates.
ϕ : three-dimensianal velacity patential.
ω : angular frequency.
g : accelerotian due ta gravity.
h : woter depth.

Dimensianless caordinates

Intraduce dimensianless quantities with the aid af a vertical length H (mean water depth) and a harizantal length λ (wove length carrespanding ta H)

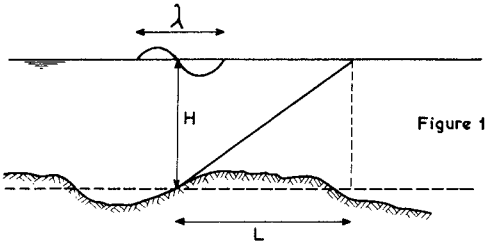

Figure 1

$$x' = x/\lambda \; ; \quad y' = y/\lambda \; ; \quad z' = z/\lambda \; ; \quad d = h/H$$

The equatians written in these dimensianless quantities are:

$$\Delta' \phi + \frac{\partial^2 \phi}{\partial z'^2} = 0 \tag{4}$$

$$\frac{\partial \phi}{\partial z'} - \delta \phi = 0 \qquad \text{at } z' = 0 \tag{5}$$

$$\frac{\partial \phi}{\partial z'} + \mu \, (\nabla' \phi \, . \, \nabla' d) = 0 \qquad \text{at } z' = - \mu d \tag{6}$$

with $\Delta' = \nabla'^2 = (\frac{\partial^2}{\partial x'^2} + \frac{\partial^2}{\partial y'^2})$; $\nabla' = (\frac{\partial}{\partial x'} , \frac{\partial}{\partial y'})$

$$\delta = \frac{\omega^2 \lambda}{g} \qquad \text{and} \qquad \mu = \frac{H}{\lambda}$$

Gradient of the bottom

Instead of the horizontal length λ it is more correct to use the horizontol length L (see figure 1 for the definition) as a characteristic length corresponding to the slope af the bottom.
If $\bar{x} = x/L$ ond $\bar{y} = y/L$ then $\nabla h = \gamma \bar{\nabla} d$ with $\gamma = \frac{H}{L}$ and $\bar{\nabla} = (\frac{\partial}{\partial \bar{x}} , \frac{\partial}{\partial \bar{y}})$.

Assume ($\bar{\nabla} d$. $\bar{\nabla} d$) and $\bar{\nabla}^2 d$ are of order one.
Now

$$\nabla' d = \frac{\lambda}{H} \nabla h = \epsilon \, \bar{\nabla} d$$

and ($\epsilon = \frac{\lambda}{L}$)

$$\nabla'^2 d = \epsilon^2 \bar{\nabla}^2 d$$

(From now on the primes will be omitted for simplicity in notation.)

Power - series

Assume the potential function ϕ has the farm

$$\phi (x, y, z) = Z (d, z ; \mu) \; \varphi (x, y, \sqrt{\epsilon} z)$$

or

$$\phi = Z (d, \zeta ; \mu) \; \varphi (x, y, \nu \zeta) \tag{7}$$

with $\zeta = z/\mu$ and $\nu = \mu\epsilon^{\frac{1}{2}}$ ($= H/\sqrt{\lambda}\, L$), φ will be developed into a power - series with respect to $\nu\zeta$

$$\varphi = \varphi_o(x, y) + \nu\,\zeta\varphi_1(x, y) + \nu^2\zeta^2\varphi_2(x, y) + \ldots\ldots\ldots \tag{8}$$

The porometer μ can vary independently from the parometer ν between zero (shollow water) and infinity (deep water). Assuming that the function Z is such that for small values of μ the derivatives with respect to d are of order μ^2, then $\frac{1}{\mu^2}\frac{\partial Z}{\partial d}$ and $\frac{1}{\mu^2}\frac{\partial^2 Z}{\partial d^2}$ are finite for every value of the parometer μ $(0 \leqslant \mu < \infty)$.

Substitution into the boundary conditions

Substitution of (7) and (8) into the condition (6) using the relation

$$\nabla Z = \epsilon \frac{\partial Z}{\partial d}\,\bar{\nabla}\, d \tag{9}$$

gives in the limit $\nu \longrightarrow 0$ the results:

(i) $\frac{\partial Z}{\partial \zeta} = 0$ at $\zeta = -d$ (10)

(ii) The odd numbered functions φ_k are identically zero.

(iii) The even numbered functions φ_k can be expressed in the function φ_o with the aid of recurrence relations.

Substitution of (7) and (8) into the condition (5) gives

$$\frac{\partial Z}{\partial \zeta} = \delta\,\mu\, Z = 0 \qquad \text{at } \zeta = 0 \tag{11}$$

As the unknown functions the two-dimensionol potential function φ_o and the function Z remain.

Substitution into the differential equation

Remembering the previous assumption obout the function Z, substitution of (7) and (8) into the differentiol equotion (4) gives in first opproximotion for small values of ν the equation:

$$\mu^2 Z\,\Delta\varphi_o + \frac{\partial^2 Z}{\partial \zeta^2}\,\varphi_o = 0$$

or

$$\frac{\Delta\varphi_o}{\varphi_o} = -\frac{1}{\mu^2 Z}\frac{\partial^2 Z}{\partial \zeta^2} \tag{12}$$

The left-hand side of equation (12) is a function of x and y only, so the right-hond side also must be a function of x and y only.

Now put

$$\frac{1}{\mu^2 Z}\,\frac{\partial^2 Z}{\partial \zeta^2} = \chi^2(x, y) \tag{13}$$

with χ an arbitrary function of x and y only.

The function Z

Equation (13) together with condition (10) and the imposed condition Z = 1 at $\zeta = 0$ gives the solution:

$$Z = \frac{\cos h \{\chi\mu (\zeta + d)\}}{\cos h \{\chi \mu d\}} \tag{14}$$

Dispersion relation

The function χ (dimensionless wave number) is fixed by equation (11) which results in the dispersion relation

$$\delta = \chi \tan h \{\chi \mu d\} \tag{15}$$

The dispersion relation is the same as is given in the theory with a constant water depth. The wave number χ is the real root of equation (15) and will now be a function of x and y corresponding to the local water depth d.

The function φ_o

To get an equation for the two-dimensional function φ_o in a higher degree of approximation than is given by equation (12), equation (4) is integrated with respect to ζ from -d to zero after multiplicotian with the function Z. With the aid of the relations

$$\int_{-d}^{0} Z^2 \frac{\partial^2 \varphi}{\partial \zeta^2}\, d\zeta = Z^2 \frac{\partial \varphi}{\partial \zeta}\Bigg|_{\zeta = -d}^{\zeta = 0} - \int_{-d}^{0} \frac{\partial \varphi}{\partial \zeta}\,\frac{\partial Z^2}{\partial \zeta}\, d\zeta$$

and

$$\int_{-d}^{0} Z\,\varphi\,\frac{\partial^2 Z}{\partial \zeta^2}\, d\zeta = \mu^2 \chi^2 \int_{-d}^{0} Z^2 \varphi\, d\zeta ,$$

the power - series development of the function φ and the recurrence relations between the even numbered

functions φ_k , the integrated equotion becomes

$$\left(\int_{-d}^{0} Z^2 \, d\zeta \right) \Delta \varphi_o + \chi^2 \left(\int_{-d}^{0} Z^2 \, d\zeta \right) \varphi_o + \frac{\nu^2}{\mu^2} \frac{\partial}{\partial d} \left(\int_{-d}^{0} Z^2 \, d\zeta \right)$$

$$(\nabla \varphi_o \cdot \bar{\nabla} d) + O(\nu^2) + \frac{1}{\mu^2} O(\nu^4) = 0 \qquad (16)$$

The function φ_o must be o solution of this equation. Now

$$\int_{-d}^{0} Z^2 \, d\zeta = \frac{n\delta}{\chi^2 \mu} \quad \text{with} \quad n = \tfrac{1}{2} \left(1 + \frac{2\chi\mu d}{\sin h\{2\chi\mu d\}}\right) ,$$

ond the following relotion exists between the porameters δ and μ according to the definition of λ ond H (see figure 1):

$$\delta = 2\pi \tan h (2\pi\mu) \qquad (17)$$

So for smoll volues of μ the integral $\int_{-d}^{0} Z^2 \, d\zeta$ is of order one. A distinction is now mode between three cases:

Case A: Assume $\mu \gtrsim 1$. In practice this is the case of "deep" woter, giving no voriotion in the wave number. Neglecting the terms of the order $O(\nu^2)$ gives the equotion in dimensional quontities:

$$\Delta \varphi_o + \frac{\omega^2}{g} \varphi_o = 0 \qquad (18) ,$$

which is the diffraction equotion for deep water.

Case B: Assume $\mu = \nu \ll 1$, which means the woter is shollow, ond neglect ogain terms of the order $O(\nu^2)$. It is eosy to see thot in this cose $Z = 1 + O(\nu^2)$ and the dimensionless wave number $\chi = \frac{2\pi}{\sqrt{d}} + O(\nu^2)$.

In dimensional coordinates and variables the equation (16) becomes

$$\nabla \cdot (c^2 \nabla \varphi_o) + \omega^2 \varphi_o = 0 \qquad (19)$$

with $c = \sqrt{gh}$ (phase velocity).

This is the linearised shallow water equation.

Case C: Assume $\nu < \mu < 1$ and neglect in equation (16) terms of order $O(\nu^2)$. The resulting equation in dimensional quantities is:

$$\Delta \varphi_o + k^2 \varphi_o + \frac{k^2}{n} \frac{\partial}{\partial h} \left(\frac{n}{k^2} \right) (\nabla \varphi_o \cdot \nabla h) = 0$$

or, written in onother form,

$$\nabla \cdot (c\, c_g \nabla \varphi_o) + \frac{\omega^2 c_g}{c} \varphi_o = 0 \qquad (20)$$

with $c = \frac{\omega}{k}$; $c_g = n\, c$ (group velocity)

$$\omega^2 = g\, k \tanh (k\, h) \quad ; \quad n = \tfrac{1}{2} \left(1 + \frac{2\, k\, h}{\sinh \{2\, k\, h\}} \right)$$

Properties of equation (20)

Equation (20) changes into the well-known diffraction equation in the case of constant water depth and is also usable in the limiting cases of deep and shallow waters. Substitution of the expression $\varphi_o = a\, e^{i\, S}$, where a is the amplitude and S the phase of the wave, gives the equations:

$$\frac{1}{a} \left\{ \Delta\, a + \frac{1}{c\, c_g} \nabla\, a \cdot \nabla (c\, c_g) \right\} + k^2 - (\nabla S \cdot \nabla S) = 0 \qquad (21)$$

and

$$\nabla \cdot (a^2\, c\, c_g \nabla S) = 0 \qquad (22)$$

If the term between curly brackets in equation (21) is neglected, the refraction equations remain [5]. Equation (20) therefore contains all limiting situations as special cases and is generally applicable.

Battjes [1] gives the equations:

$$\frac{1}{a} \Delta\, a + k^2 - (\nabla S \cdot \nabla S) = 0 \text{ and } \nabla \cdot (a^2\, c\, c_g \nabla S) = 0$$

as the describing equations for the refraction - diffraction phenomenon. The combination of these equations, however, does not pass into the linear shallow water equation when the water depth is small.

Method of Solution

General description:

The solution of the differential equation (20) in an arbitrary area can be found by minimizing the corresponding functional over the area, taking into account the conditions at the boundaries, i.e., full reflection at rigid walls and the Sommerfeld condition at sea. The solution at sea, where the water depth is assumed to be constant, will be a superposition of the incident and an outgoing wave which is caused by the presence of the harbour or an obstacle. This outgoing wave will represented by a superpasition of waves from point sources at the boundary between the sea and the area of interest. The solution at this baundary must be continuaus with respect to wave height and phase.

The functional

The functionol which must be minimised to get the solution in area I in which the water depth is variable (see figure 2) reads [2] :

$$J = \tfrac{1}{2} \iint_I \left[c\, c_g\, (\nabla \varphi_1 \cdot \overline{\nabla \varphi_1}) - \omega^2 \frac{c_g}{c} \varphi_1 \overline{\varphi}_1 \right] dx\, dy \qquad (23)$$

The overbar denotes the conjugote complex value. Minimizing (23) gives a solution with the natural boundary conditions:

$$\frac{\partial \varphi_1}{\partial n} = 0 \qquad \text{at } \Gamma_1 \text{ and } \Gamma_2$$

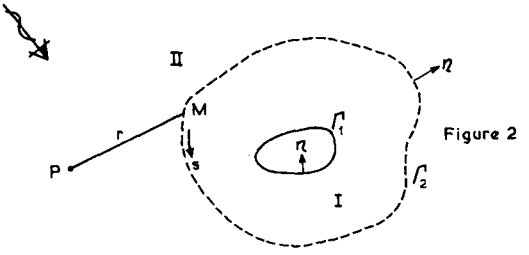

Figure 2

If the boundary condition at Γ_2 is $\frac{\partial \varphi_1}{\partial n} = f$, the following term must be added to the functional J [2] :

$$-\tfrac{1}{2} \int_{\Gamma_2} (f\, \overline{\varphi}_1 + \overline{f}\, \varphi_1)\, c\, c_g\, ds \qquad (24)$$

Saurce distribution

In area II, where the water depth h_a is constant, the solution con be written in the form [3] :

$$\varphi_{II}(P) = \tilde{\varphi}(P) + \int_{\Gamma_2} \mu(s) \frac{1}{2i} H_o^2 (k_o r)\, ds \qquad (25)$$

with $\tilde{\varphi}$: The potential function af the known incident wave.
$\mu(s)$: The strength of a source distribution an the baundary Γ_2 .

H_o^2 : Hankel function of the second kind.
k_o : Constant wave number.
r : Distance from point P to the point M at the boundary Γ_2 (see figure 2).
i : $\sqrt{-1}$.

Formulation (25) gives a solution in area II that satisfies the Sommerfeld radiation condition. From this expression it can be derived that

$$\frac{\partial \varphi_{II}}{\partial n} = \frac{\partial \tilde{\varphi}}{\partial n} - \mu(P) + \int_{\Gamma_2} \mu(s) \frac{\partial}{\partial n} \left[\frac{1}{2i} H_o^2 (k_o r) \right] ds \qquad (26)$$

if the point is situated on the boundary Γ_2 [3].

Continuity conditions

Taking together the two continuity conditions between the solutions φ_I and φ_{II} at the boundary Γ_2

$$\varphi_I = \varphi_{II} \quad \text{and} \quad \frac{\partial \varphi_{II}}{\partial n} = \frac{\partial \varphi_I}{\partial n} \quad (= f) \qquad (27)$$

the problem is well-defined and the unknown functions $\mu(s)$ and $\varphi_I(x, y)$ can be found.

Numerical method

The functional written in real terms ($\varphi = \varphi_1 + i\varphi_2$) reads:

$$J = \tfrac{1}{2} \iint_{II} \left[c\, c_g \left\{ \left(\frac{\partial \varphi_1}{\partial x}\right)^2 + \left(\frac{\partial \varphi_1}{\partial y}\right)^2 + \left(\frac{\partial \varphi_2}{\partial x}\right)^2 + \left(\frac{\partial \varphi_2}{\partial y}\right)^2 \right\} \right.$$

$$\left. - \omega^2 \frac{c_g}{c} (\varphi_1^2 + \varphi_2^2) \right] dx\, dy - \int_{\Gamma_2} c\, c_g (f_1 \varphi_1 + f_2 \varphi_2)\, ds \qquad (28)$$

The numerical treatment is based on the finite element method to find the minimum of the functional [12]. Now area I is split up into elements of triangular form and the functions φ_1, and φ_2 are approximated in each element by a linear expression. As the treatment of both functions φ_1 and φ_2 is the same, in the following the subscript will be omitted. After the linear approximation of φ, the functional will be a function of the M nodal values $\varphi_1, \varphi_2, \ldots\ldots\ldots, \varphi_M$. The functional must be minimal with respect to variation in these values, so

$$\frac{\partial J}{\partial \varphi_m} = 0 \qquad m = 1, 2, 3, \ldots\ldots\ldots, M \qquad (29)$$

This gives a set of linear equations in the unknown nodal values. The function f is also unknown, and therefore the integral will be approximated by a summation over N segments in which c$_g$f is assumed to be a constant and equal to the value in the centre point P (see figure 4).

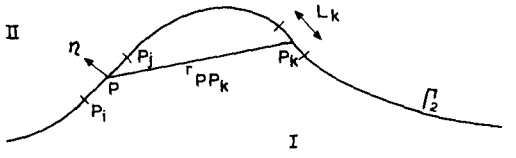

Figure 4

With the aid of equations (26) and (27) the unknown values f in the N points P on the boundary Γ_2 can be expressed in terms of the strength μ of the source distribution:

$$(f)_P = \left(\frac{\partial \overset{\sim}{\varphi}}{\partial n}\right)_P - \mu(P) + \sum_{k=1}^{N} \mu(P_k) \frac{\partial}{\partial n}\left[\frac{1}{2i} H_o^2 (k_a r_{PP_k})\right] L_k \qquad (30)$$

The cantinuity condition for the wave height gives the additional set of equatians ta provide M + N equations in the M + N unknown values $\varphi_1, \varphi_2, \ldots\ldots \varphi_M$ and $\mu_1, \mu_2, \ldots\ldots\ldots, \mu_N$:

$$\tfrac{1}{2}(\varphi_{P_i} + \varphi_{P_j}) = \overset{\sim}{\varphi}(P) + \sum_{k=1}^{N} \mu(P_k) \frac{1}{2i} H_o^2 (k_o r_{PP_k}) L_k \qquad (31)$$

The value of φ in the source point P is approximated by the average of the values in the twa neighbouring nodal points P_i and P_j on the boundary Γ_2 (see figure 4). The full set of equatians, which must be solved ta get the complex values φ and μ in the nodal and source points respectively, becames in matrix natatian:

$$\begin{aligned} A\,\underline{\varphi} + B\,\underline{\mu} &= \underline{r} \\ D\,\underline{\varphi} + T\,\underline{\mu} &= \underline{s} \end{aligned} \qquad (32)$$

$\underline{\varphi}$ is the vectar of the unknawn complex values $\varphi_1, \varphi_2, \ldots\ldots, \varphi_M$ and $\underline{\mu}$ the vectar of the strength of the source distribution in the N source points on the baundary Γ_2.

A is a real symmetric M x M matrix with a band structure generated by the finite element methad.

B is a camplex M x N matrix which has non-zera values in the raws carresponding with the nadal points on the boundary Γ_2.

D is a real N x M matrix generated by the averaging procedure in equatian (31).

T is a complex N x N matrix with coefficients consisting of Hankel functions according to equation (31). The known vectors $\underline{r}$ and $\underline{s}$ are provided by the indicent wave $\tilde{\varphi}$ This system of equations is solved by a direct solution method. First the vector $\underline{\mu}$ is computed according to

$$\underline{\mu} = (T - DA^{-1}B)^{-1} (\underline{s} - DA^{-1}\underline{r}) \tag{33}$$

and then the vector $\underline{\varphi}$ follows from

$$\underline{\varphi} = A^{-1}\underline{r} - A^{-1} B \underline{\mu} \tag{34}$$

In computing the decomposition of the matrix A, the symmetrical band structure of the matrix has been taken into account.

Results

It is not the intention of this paper to give accurate solutions of some of the problems but more to show the possibilities of the method of solution which has been described.

The quantitative aspects of the accuracy of the method will be the subject of further study.

(i) Tsunami response for a circular island

A good comparison with other computations without large computing time can be obtained in the problem of tsunami response for a circular island with a parabolic bottom profile. Vastano and Reid [11] have solved this problem with a finite difference technique and compared their results with analytic solutions. The results of the method given in this paper are shown in figures 5 - 9.

Figure 5 gives the configuration of the finite elements in the area of variable depth. First the problem with a constant water depth has been computed to check the method of solution (figure 6) and then the problem with a parabolic bottom profile has been solved and compared with the results of Vastano and Reid (figure 7). It has still to be seen whether the accuracy of the method is better when the wave length becomes greater with respect to the size of the elements.

(ii) Propagation of tsunami waves over a parabolic shoal

The influence of a shoal with parabolic bottom profile on the propagation of tsunami waves has been computed and the results are given in figures 8 - 10. Figure 8 indicates how the area of variable depth has been split up into triongular elements. Figures 9 - 10 show lines of equal phase and amplitude. The phase of the wave is expressed in degrees, so a difference of 360 degrees corresponds to one wave length.

(iii) Propagation of short waves over a shoal

An interesting problem with respect to the combined effect of refraction and diffraction of waves is the propagation of short waves (short with respect to the size of the disturbance of the bottom) over a shool with a parabolic bottom profile, because the presence of a caustic curve (see figure 11) following from the refraction theory is an indication that diffraction effects cannot be neglected. An attempt was made to compare the results in this case with the measurements of

Halthuysen [6] . To save memory and computing time the area, which has been split up into finite elements, was reduced to a circle segment with an angle at the top of 60 degrees (figure 12). It was assumed that the solution at the boundary AO (see figure 11) does not deviate from the solution following from the refraction theory (ray-method) according to the measurements. The solution of the ray-method has been imposed as a boundary condition on the boundary AO, and the results of the computation are given as lines of equal phase (fiure 13), lines of equal amplitude (figure 14) and lines of equal water elevation at some time (figure 15). A good comparison with the measurements over a large area was not possible because of the lack of information about the phase and because of the unreliability of the quantitative results of the measurements in an area above the shoal. Qualitatively the computer results seem reasonable.

(iv) Response of a rectangular harbour

The last problem of which the results will be given is the response of a rectangular harbour with a constant slope of the bottom. The amplitude of the standing wave in the centre line of the harbour is given for different slopes of the bottom in figure 16. In the first instance the wave height in the harbour decreases as a result of the increasing slope of the bottom, but with a slope of 1/3 the phenomenon of resonance of the harbour becomes important.

References

1. Battjes, J.A. — Refraction of water waves; Proc. Am. Soc. Civ. Eng., 94, WW 4, Nov., 1968, pp. 437-451.
2. Courant, R. and Hilbert, R. — Methods of mathematical physics, Volume I; Interscience Publishers Inc., New York, 1962.
3. Daubert, A. and Lebreton, J.C. — Diffraction de la houle sur des obstacles a parois verticales; La Houille Blanche, 20, numero 4, 1965, pp. 337-344.
4. Delft Hydraulics Laboratory — Computation of the phenomenon of diffraction (in Dutch); Research report S5-I, 1969.
5. Delft Hydraulics Laboratory — Wave refraction; derivation and numerical solution of the refraction equations; Research report S5-II, 1970.
6. Holthuysen, L.H. — An investigation of two-dimensional wave propagation problems; Report R 1971/10/H, 1971, Delft University of Technology.
7. Keller, J.B. — Surface waves on water of nonuniform depth; Journal of Fluid Mech., 4, no. 6, 1958, pp. 607-614.
8. Schönfeld, J.Ch. — Propagation of two-dimensional short waves; Delft University of Technology, manuscript (in Dutch).
9. Sommerfeld, A. — Partielle Differentialgleichungen der Physik, Akademische Verslagsgesellschaft, Leipzig, 1958.
10. Stoker, J.J. — Water waves; Interscience Publishers Inc., New York, 1957.
11. Vastano, A.C. and Reid, R.O. — Tsunami response for islands, Verification of a numerical procedure; Journal of Marine Research, 25, No. 2, 1967, pp. 129-139.
12. Zienkiewicz, O.C., Taylor, C. and Patil, B.S. — Harbour oscillation; a numerical treatment for undamped natural modes; Proc. Inst. Civ. Engrs, 43, 1969, pp. 141-155.

Notation

A	matrix
a	amplitude
B	matrix
c	phase velocity
c_g	group velocity
D	matrix
d	dimensionless depth
f	function
g	gravity constant
H	mean water depth
H_o^2	Hankel function
h	water depth
i	$\sqrt{-1}$
J	functional
k	wave number
k_o	constant wave number
L	horizontal length
L_k	length of k-th segment
M	number of nodal points
N	number of source points
n	shoaling factor
$\underline{n}$	normal vector
$\underline{r}$	known vector
S	phase
s	distance along the boundary
$\underline{s}$	known vector
T	matrix
x, y	horizontal coordinates
z	vertical coordinate
Z	function
Γ_1, Γ_2	boundaries
γ	parameter (H/L)
Δ	Laplace operator
δ	parameter $(\omega^2 \lambda/g)$
ϵ	parameter (λ/H)
$\varkappa$	dimensionless wave number
λ	mean wave length
μ	parameter (H/λ)
$\mu(s)$	strength of the source distribution
$\underline{\mu}$	vector of strength of the sources
ν	parameter $(H/\sqrt{\lambda L})$
Φ	three-dimensional potential function
φ	two-dimensional potential function
$\hat{\varphi}$	potential of incident wave
φ_I, φ_{II}	potential functions in areas I and II respectively
$\underline{\varphi}$	vector of values of φ in the nodal points
ω	angular frequency
ζ	stretched vertical coordinate z/μ
∇	nabla operator.

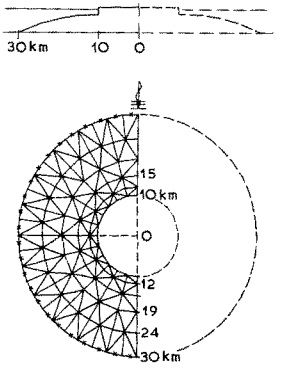

Figure 5

Tsunami response for a circular island
Configuration of elements and horizontal dimensions

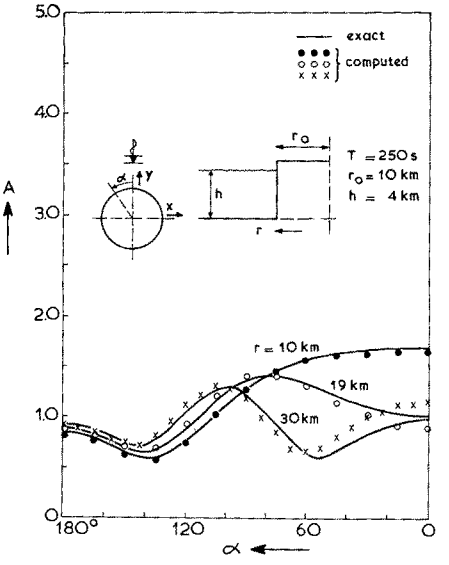

Figure 6

Tsunami response for a circular island
Wave amplitude by constant depth

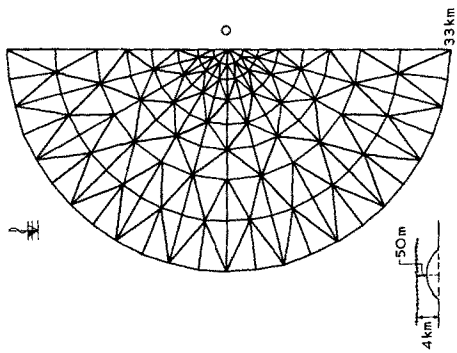

Figure 8

Long wave propagation over a shoal
Configuration of elements and dimensions

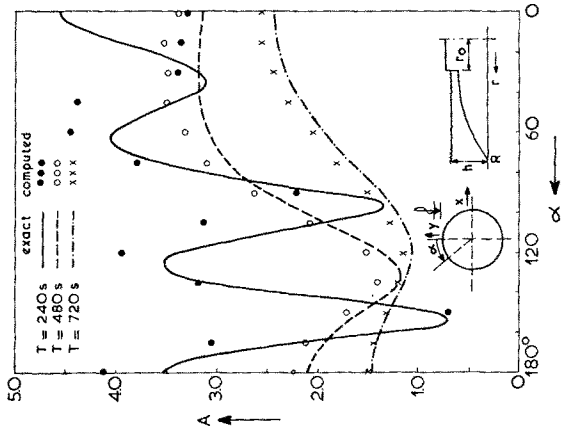

Figure 7

Tsunami response for a circular island
Wave amplitude along the shore
Variable depth. $h(r_o) = 400$ m; $h(R) = 4$ km

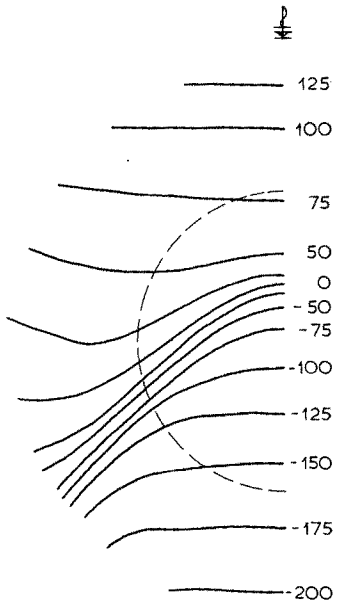

Figure 9

Long wave propogation over o shoal
Lines af equal phase
Variable depth (50 ≤ h ≤ 4000 m); T = 720 s

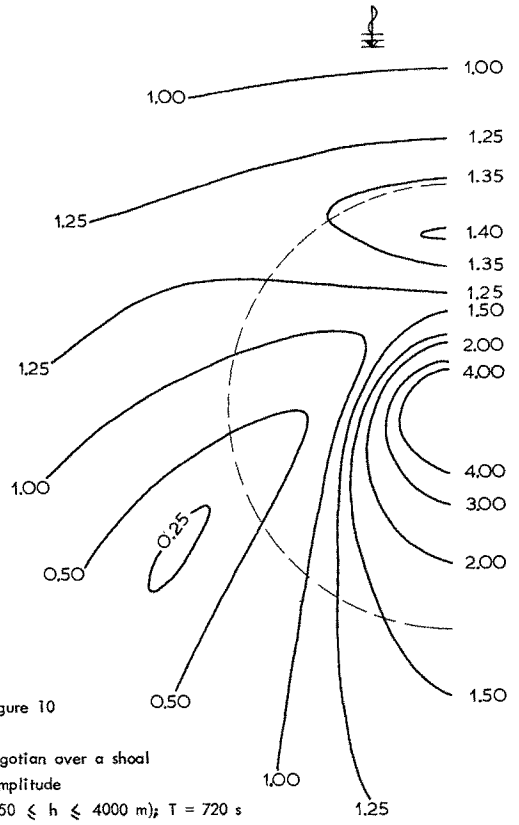

Figure 10

Lang wave propagotian over a shoal
Lines of equal amplitude
Variable depth (50 ≤ h ≤ 4000 m); T = 720 s

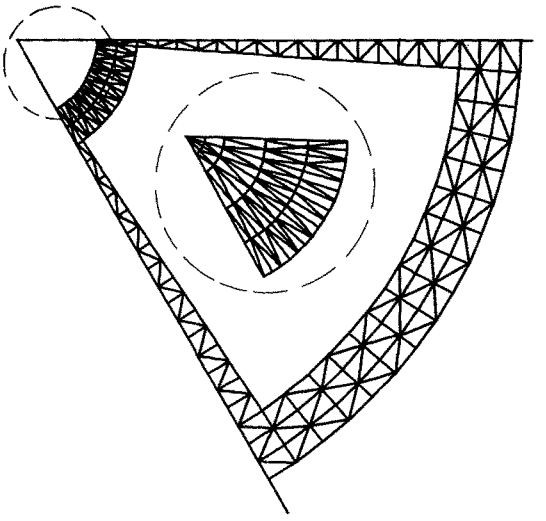

Figure 12

Short wave propagation over a shoal
Configuration of elements

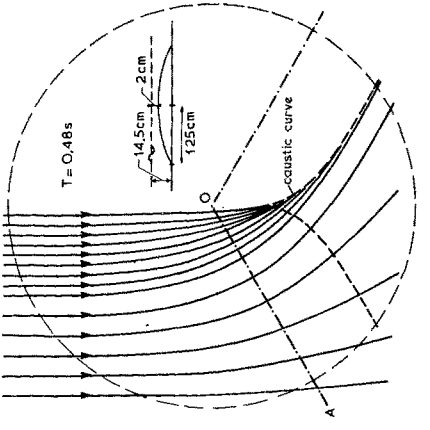

Figure 11

Short wave propagation over a shoal
Dimensions and wave rays according to the refraction theory

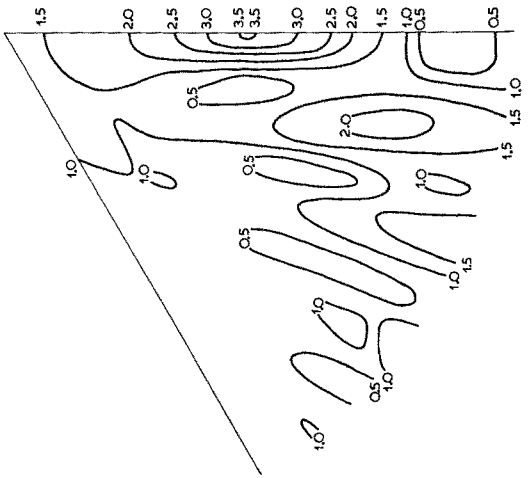

Figure 14

Short wave propagation over a shoal
Lines of equal amplitude

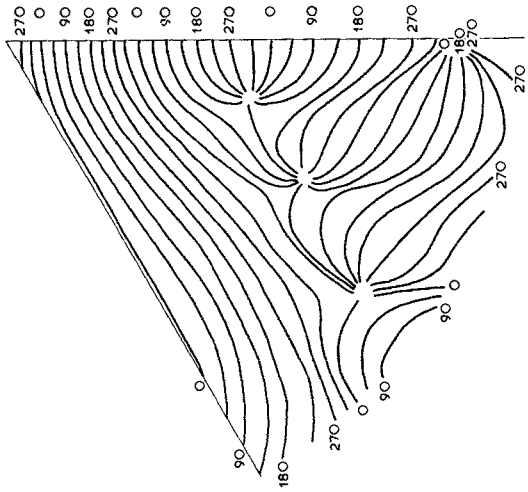

Figure 13

Short wave propagation over a shoal
Lines of equal phase

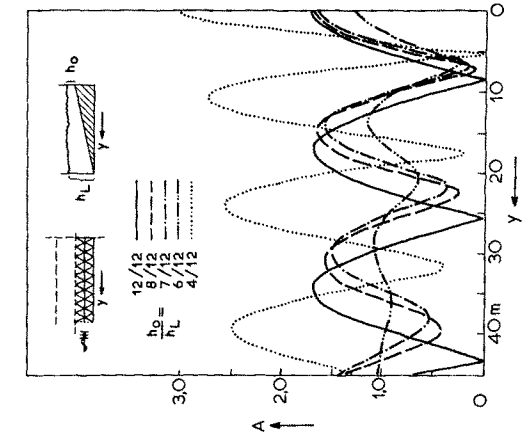

Figure 16

Response of a rectangular harbour
Wave amplitude for different bottom slopes

Figure 15

Short wave propagation over a shoal
Lines of equal water elevation $\eta = a \cos S$
Contour lines every 0.5 units

CHAPTER 25

REFRACTION DE LA HOULE AVEC DIFFRACTION MODEREE

FRANCIS BIESEL
DIRECTEUR, OMNIUM TECHNIQUE OTH
DIVISION HYDRAULIQUE
FRANCE

RESUME

La méthode "géométrique" de construction des épures de houle n'est qu'une approximation qui cesse d'être applicable, par exemple, lorsque deux orthogonales se croisent. En effet, la règle de calcul de l'amplitude donnerait alors une valeur infinie au point de croisement, ce qui n'a évidemment pas de sens physique.

Pour traiter de tels cas, d'ailleurs fréquents, il est indispensable d'utiliser une approximation meilleure, et pour cela de revenir aux équations fondamentales. Ceci est typique des problèmes où les effets de diffraction cessent d'être négligeables, cependant ceux-ci n'ont pas l'importance qu'ils prennent en présence de discontinuités brutales (contournement de l'extrémité d'une jetée, par exemple). Nous disons donc qu'il y a diffraction modérée.

Ce que nous présentons ici est une méthode de construction d'épures de propagation de la houle qui peut tenir compte de ce type de diffraction. Cette méthode a l'avantage d'être une construction front d'onde par front d'onde, comme pour l'approximation géométrique, mais les orthogonales ne peuvent plus être calculées indépendamment les unes des autres. Au total, le calcul est plus long, mais il reste cependant beaucoup moins lourd que les calculs de diffraction tenant compte également des variations de profondeur.

Pour le calcul de la propagation de la houle par profondeurs variables, les épures de réfraction classiques sont un outil pratique et relativement peu coûteux. Elles reposent essentiellement sur les hypothèses suivantes :

A. La longueur d'onde de la houle est donnée en chaque point, en fonction de la profondeur, par les formules valables en profondeur constante.

B. L'énergie transmise par la houle ne traverse pas les orthogonales aux fronts d'onde.

C. L'énergie transmise est donnée en chaque point, en fonction de la profondeur et de l'amplitude, par les formules valables en profondeur constante.

On sait que ces hypothèses sont grossièrement fausses lorsque les phénomènes de diffraction jouent un rôle important. L'exemple le plus simple, illustré par la figure 1 est celui d'une houle cylindrique, en profondeur constante abordant une jetée verticale semi indéfinie. Seules les orthogonales sont représentées sur cette figure, on voit que l'application brutale des hypothèses ci-dessus amènerait à conclure que l'orthogonale figurée en pointillé est une ligne de discontinuité séparant une zone, à gauche, où la houle serait celle du large, d'une zone, à droite, où l'agitation serait nulle.

Dans ce cas l'échec provient évidemment de la discontinuité brutale introduite par l'extrémité A de la jetée, la diffraction est alors un phénomène essentiel et nous dirons que c'est un cas type de diffraction forte. Dans un tel cas il est nécessaire de recourir à des méthodes de calcul complètement différentes, également schématisées sur la figure 1, et consistant essentiellement à reconstituer l'agitation en un point P par la somme d'ondes élémentaires émises par des sources S réparties sur la "passe" prolongeant la jetée.

Le calcul résultant est sensiblement plus lourd, et se complique considérablement, si la profondeur est variable, car l'influence de chaque source sur chaque point P pose alors de multiples problèmes de calcul de réfraction.

Chacun de ces problèmes, et d'une façon générale n'importe quelle épure de réfraction, peut se heurter à une autre difficulté très commune. Il s'agit du croisement éventuel d'orthogonales voisines construites suivant les règles de "l'optique géométrique". La figure 2 illustre ce cas dans un exemple très simple où la réfraction est causée par un haut fond, ou dôme sous-marin, dont le contour est figuré en traits interrompus. Là encore seules les orthogonales sont représentées et trois d'entre elles se croisent au point A. D'après les hypothèses B et C ci-dessus l'amplitude devrait être infinie en ce point. On sait que cette conclusion est fausse et que le champ de houle reste partout fini et continu. En fait le comportement

de la houle au voisinage du point A pourrait être calculé par les méthodes de sommation décrites plus haut pour la diffraction. Cependant il semble raisonnable d'espérer que ces méthodes coûteuses ne soient pas indispensables dans un problème dont les conditions aux limites sont elles mêmes très régulières et ne contiennent aucune discontinuité. En fait les phénomènes de diffraction (que l'on peut définir comme tout ce qui s'écarte de l'"optique géométrique") n'ont plus le caractère dominant qu'ils avaient dans l'exemple précédent, on peut donc penser qu'il suffit de n'en introduire que l'essentiel à titre de correction de l'épure classique.

Ce qui est essentiel peut d'ailleurs se juger à deux points de vue :

- tout d'abord, ce qui permet de lever l'impasse où se trouvent les épures classiques, c'est-à-dire éviter ou résoudre le problème des croisements d'orthogonales, tout en conservant, au moins en partie, l'avantage de rapidité de ces épures et la possibilité de construire tout un champ de houle à l'avancement crête après crête (la construction par orthogonales isolées n'étant plus possible).

- ensuite, bien sûr, ce qui permet de faire une correction aussi parfaite que possible. Nous allons discuter de ce point en détail.

Il importe de souligner tout d'abord qu'une correction parfaite est théoriquement impossible car on ne peut pas construire numériquement la solution d'un problème d'onde (équation elliptique) en partant d'une seule condition aux limites (front de départ). Ce genre de construction ne réussit dans les épures classiques que parce qu'elles simplifient excessivement le problème. La question sera donc de savoir si l'on peut concilier l'introduction des corrections essentielles, au moins jusqu'à un certain ordre d'approximation, avec la stabilité des calculs "à l'avancement".

Il n'a pas été fait d'analyse théorique complète de cette question fondamentale, mais des résultats obtenus antérieurement ont permis d'orienter le choix des termes à conserver.

Dans une communication antérieure (F. BIESEL - Coastal Engineering 1964) des corrections du type défini ici ont été calculées à partir d' équations hydrodynamiques approchées de la houle en profondeur variable. Ces équations ont montré que les hypothèses B et C des épures classiques pouvaient être conservées, à l'approximation atteinte, à condition de perfectionner l'hypothèse A, c'est-à-dire d'introduire une correction uniquement sur le calcul de la longueur d'onde locale.

Parmi les différents termes correctifs ceux liés aux variations d'amplitude le long des crêtes étaient de beaucoup les plus prépondérants. Au contraire les corrections liées à la pente du fond semblaient toujours devoir être d'un ordre de grandeur négligeable.

Nous reviendrons sur la première remarque; en ce qui concerne la seconde elle permet intuitivement de penser que l'on fera des erreurs négligeables en admettant que la houle en profondeur variable satisfait à une équation du type :

$$\Delta \varphi + m_o^2 \varphi = 0 \qquad (1)$$

où m_o, fonction de x et y, a la valeur classique pour une profondeur constante ayant la valeur de la profondeur locale h.

En d'autres termes, on a :

$$k^2 = m_o \; g \; \text{th} \; m \; h \qquad (2)$$

où $k = 2\pi / T$

T étant la période de la houle.

φ, dans l'équation (1), est une quantité complexe liée à la dénivellation a (par exemple) par une relation du type :

$$a = R \left[A(h) \; \varphi \; e^{-ikt} \right] \qquad (3)$$

Le symbole R signifiant "partie réelle de"

A (h) étant une fonction appropriée de la profondeur que nous définirons plus loin.

Il est toujours possible d'écrire :

$$\varphi = r \, e^{if} \qquad (4)$$

r étant le module de φ (réel positif) et
f étant son argument à $2K\pi$ près (réel).

En séparant les parties réelles et imaginaires facteur de e^{if}, l'équation (1) se transforme en deux relations équivalentes :

$$(\text{grad } f)^2 = m^2 = m_o^2 + \frac{\Delta r}{r} \qquad (5)$$

$$\text{div } (r^2 \; \text{grad } f) = 0 \qquad (6)$$

Si l'on donne à A (h) la valeur :

$$A(h) = 2 \, m_o / \left[\varrho g \, k \left(1 + \frac{2m.h}{\text{sh}2m.h} \right) \right]^{1/2} \qquad (7)$$

r^2 grad f se ramène à la valeur classique (m = mo) du veoteur flux d'énergie.

(6) exprime donc simplement la conservation de l'énergie transportée par la houle. Cette équation permet également d'écrire :

$$r^2 \frac{\partial f}{\partial x} = \frac{\partial w}{\partial y} \; , \quad r^2 \frac{\partial f}{\partial y} = \frac{\partial w}{\partial x} \qquad (8)$$

w étant un scalaire défini a une constante près.

Il est clair d'après ces relations que f et w définissent un système de coordonnées orthogonales. Les lignes f = constante sont des lignes d'égale phase de la houle, c'est-à-dire des fronts d'onde successifs. Leur écartement est régi par la formule (5) qui introduit une correction du nombre d'onde m ($2\pi/L$) par rapport à la valeur classique m_0. Les lignes w = cte sont des orthogonales aux fronts d'onde et sont les trajectoires de l'énergie, le flux de celle-ci entre les lignes w_1 et w_2 étant $|w_1 - w_2|$. Ce système de fronts d'onde et d'orthogonales satisfait donc bien aux hypothèses B et C la condition (5) remplaçant l'hypothèse A.

L'équation (5) peut s'exprimer dans le nouveau système de coordonnées par des transformations classiques, elle devient :

$$m^2 = m_0^2 + m^2 r \left[\frac{\partial^2}{\partial w^2} \left(\frac{r^3}{3}\right) - \frac{\partial^2}{\partial f^2} \left(\frac{1}{r}\right) \right] \quad (9)$$

On peut réaliser plusieurs algorithmes de calculs en différences finies qui construisent successivement des fronts d'onde f = n Δ f par la méthode géométrique classique mais en utilisant m au lieu de m_0, c'est à dire :

$$L = \frac{2\pi}{m} \text{ au lieu de } Lo = \frac{2\pi}{m_0}$$

Des itérations successives pourront être nécessaires, en particulier pour la dérivée seconde en f qui nécessite la connaissance de r en avant du front d'onde pour calculer une dérivée seconde centrée.

Notons également que la valeur de r sera donnée par (8) sous la forme :

$$r^4 \, (\text{grad } f)^2 = (\text{grad } w)^2$$

soit

$$r = \sqrt{\frac{|\text{grad } w|}{m}}$$

|grad w| se déduit immédiatement de la construction géométrique des fronts d'onde (l'écartement de deux orthogonales voisines est $\Delta w / |\text{grad } w|$).

Ainsi que nous l'avons souligné plus haut, l'intégration rigoureuse, front d'onde par front d'onde, ne pourrait que diverger. Nous n'avons pas pu établir une règle théorique précise permettant de savoir exactement quels étaient les sacrifices indispensables à l'obtention de la stabilité.

Nous n'avons cependant pas procédé entièrement au hasard dans la recherche des simplifications indispensables. Finalement, nous avons été amenés à supprimer le terme $\partial^2/\partial f^2(1/r)$ de l'équation (8) pour les raisons suivantes :

- Une analyse de cas simples montre que ce terme est responsable d'une instabilité pour les intégrations le long de la variable f. C'est d'ailleurs souvent le cas des termes d'ordre le plus élevé dans les équations différentielles de ce type.

- Notre première ambition est de traiter des cas de diffraction "modérée", c'est-à-dire des cas ne s'écartant pas trop des conditions de validité des épures classiques. On pourrait donc accepter d'être moins bons pour les cas de convergence très brutale que pour les cas (fréquents en pratique) où les orthogonales voisines se coupent sous un angle très aigu. Or dans de tel cas, les dérivées en f sont petites même au voisinage du point de croisement, car si r tend à croître rapidement avec f, par contre les valeurs de 1/r et leurs dérivées restent faibles. Au contraire, même dans ces conditions quasi classiques, les dérivées en w peuvent prendre des valeurs élevées.

- Notre étude antérieure, déjà citée, plus rigoureuse sous l'angle hydrodynamique, avait montré que les dérivées le long de la crête semblaient donner la seule correction d'importance pratique pour la longueur d'onde.

Le programme de calcul que nous avons finalement établi n'a encore qu'un caractère provisoire et expérimental, il n'utilise que les schémas de différences finies les plus élémentaires et, outre la simplification majeure que nous venons de décrire, il néglige des termes du second ordre par rapport à $|m - mo|$.

L'intérêt de ce calcul est qu'il montre qu'il y a presque sûrement une voie ouverte entre les calculs de réfractions classiques, parfois trop simplistes, et les calculs rigoureux, impossibles à mener front d'onde par front d'onde. En particulier, le problème des croisements d'orthogonales semble disparaître. Lorsque la topographie du fond provoque le rapprochement de deux d'entre elles, elles paraissent se repousser et s'écarter à nouveau. Ces changements de direction se font avec une courbure notable et il a été nécessaire de resserrer le pas, c'est-à-dire de diminuer Δ f, lorsque le calcul passait par ces cas. Ces variations de Δ f, sont réalisées automatiquement par le programme.

Les diagrammes résultants sont très différents des épures classiques, en particulier les orthogonales peuvent être très sinueuses même en profondeur constante. Il a donc semblé utile, ne serait-ce que pour augmenter la crédibilité des résultats, de montrer un exemple de calcul rigoureux de ces trajectoires de l'énergie pour un cas simple. C'est celui de la figure 3, où seules les orthogonales sont représentées, et qui montre la superposition de deux houles de même fréquence, en profondeur constante, l'une se propageant dans le sens des x et l'autre, d'amplitude $\sqrt{2}$ fois plus faible, se propageant dans le sens des y.

La pente générale des orthogonales est 1/2, ce qui correspond bien à la direction résultante du transfert d'énergie, mais elles s'éloignent et se rapprochent constamment les unes des autres, les zones de rapprochement, telles que V, étant des ventres d'agitation verticale et les zones d'écartement, telles que N, étant des noeuds.

La figure 4 montre un résultat de calcul tracé directement sur table Benson-Lehner, pour un cas analogue à celui figuré schématiquement par la figure 2. On voit qu'à la zone B de cette figure, où des ondes d'origine différentes se croisent, correspond sur la figure 4 une zone d'interférence analogue à celle de la figure 3. C'est un des avantages notables de ce type de calcul, de pouvoir suivre en un seul passage des propagations qui nécessiteraient plusieurs épures classiques superposées.

La figure 5 représente le calcul du contournement d'un ouvrage à talus. Il est vraisemblable que les résultats ainsi obtenus seront plus proches de la réalité que des calculs de diffraction négligeant l'influence du talus.

En conclusion, nous tenons surtout à préciser que le travail présenté ici n'a qu'un caractère exploratoire. De grandes améliorations restent possibles au niveau des algorithmes à mettre en oeuvre, d'autre part, des comparaisons avec l'expérience, ou avec des théories plus complètes, devront être faites pour justifier les approximations et définir les limites d'applicabilité de ce genre de calcul.

Il faut souligner également que l'intérêt de ces épures ne se limite pas au cas de la diffraction modérée mais est aussi de permettre le calcul du champ créé, en profondeur variable, par des sources élémentaires du type utilisé pour les calculs de diffraction-réfraction. Ainsi les coefficients d'influence de ces sources pourront être calculés sans ambiguité, comme dans le cas de la profondeur constante, et la validité des modèles mathématiques portuaires en profondeur variable, et compte tenu du talus des ouvrages, pourra reposer sur des bases plus solides.

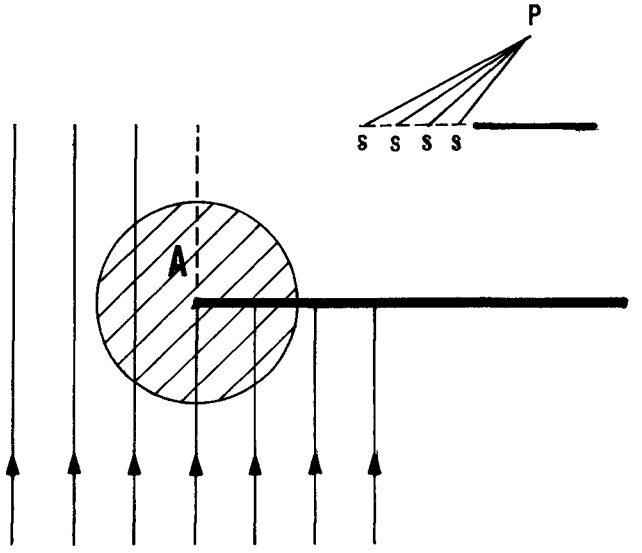

Figure 1

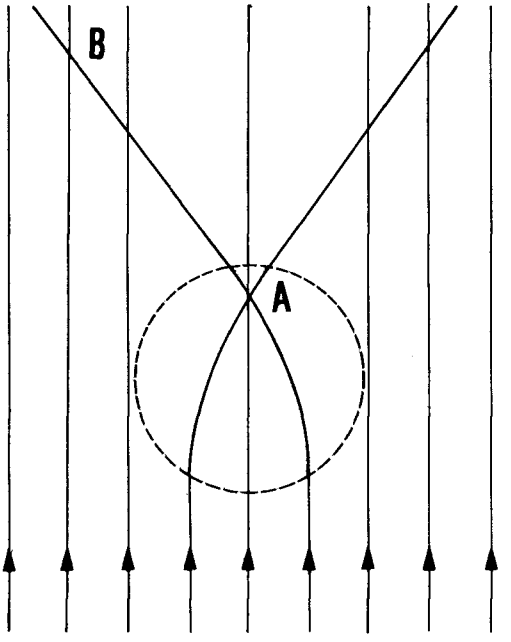

Figure 2

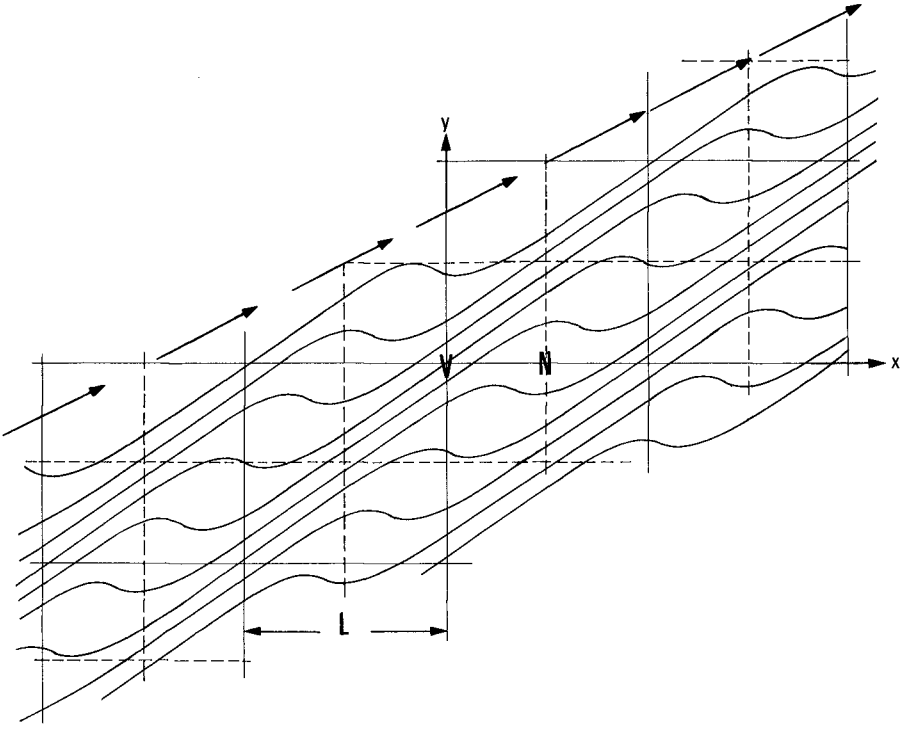

Figure 3

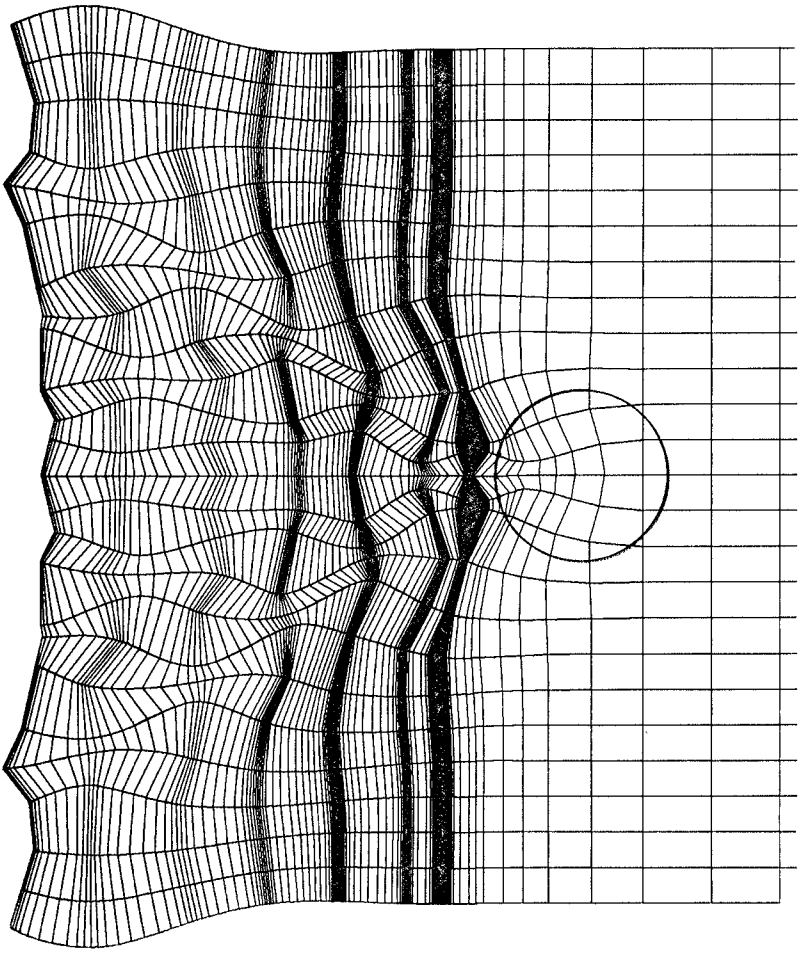

Figure 4

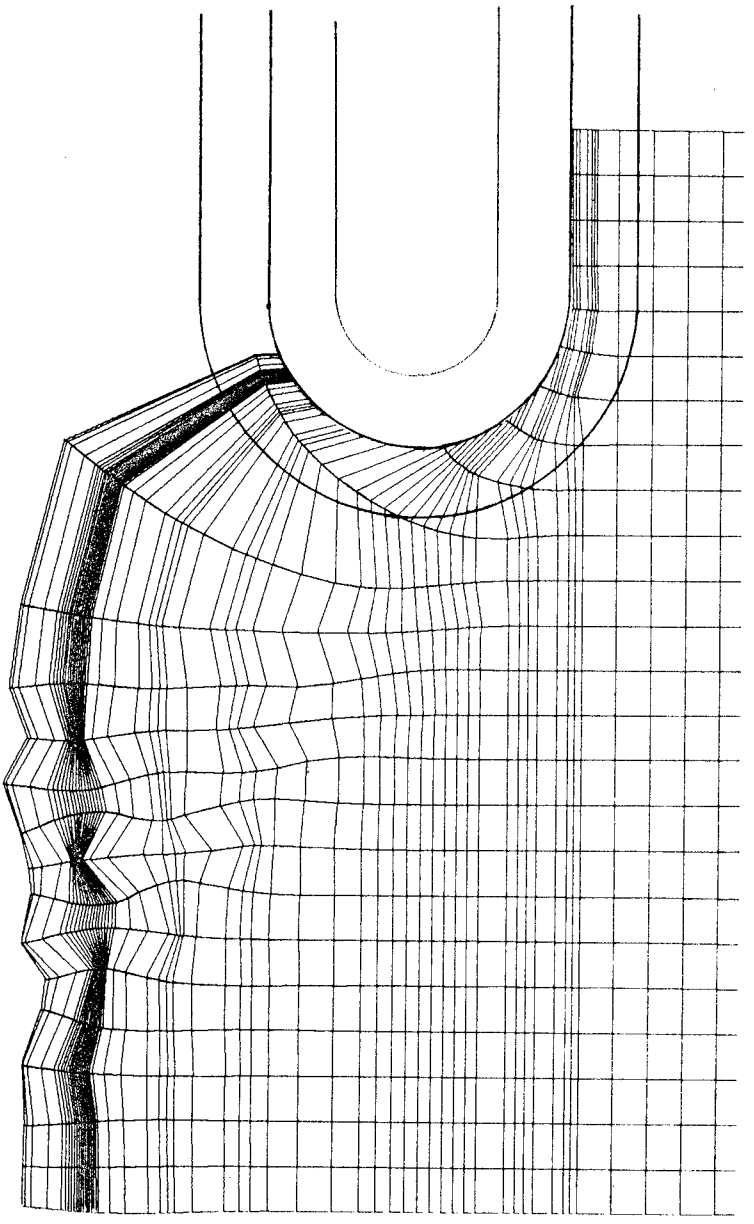

Figure 5

CHAPTER 26

A METHOD OF NUMERICAL ANALYSIS OF WAVE PROPAGATION
--- APPLICATION TO WAVE DIFFRACTION AND REFRACTION ---

by

Yoshiyuki ITO* and Katsutoshi TANIMOTO*

ABSTRACT

A method is presented to obtain numerically wave patterns in the region of arbitrary shape. The principle is to solve the linearized wave equations under given boundary conditions from a certain initial state.

In this paper, two principal applications of our method of numerical analysis are presented in the fundamental fashion.

The first application of our method is related to wave diffraction. The distribution of wave height along a semi-infinite breakwater and a detached breakwater is calculated and compared with that obtained from the conventional analytic solutions to confirm the validity of our numerical method. Three examples of application are presented to the wave height distribution along breakwaters of arbitrary shape and of arbitrary reflecting power and to wave force upon a large isolated vertical structure.

The second application is to wave refraction. In particular, this method of numerical analysis is applicable to the analysis of wave propagation in the region of ray intersections which are indicated by the conventional geo-optic wave refraction theory. An example of application to a submerged shoal with concentric circular contours where a cusped caustics is formed is presented and the calculated wave height distribution around the shoal is compared with that obtained from hydraulic model experiments.

Our method of numerical analysis might be applied to the calculation of wave height distribution in the region of more realistic bottom topography and it is possible to include vertical boundaries of arbitrary shape.

1. INTRODUCTION

When we examine the calmness in a harbour with respect to the sheltering effect of breakwaters, only the consideration of wave diffraction is not sufficient, but the effect of reflected waves from other boundaries and water depth variation in the harbour should be taken into account.

* Hydraulic Engineering Division, Port and Harbour Research Institute, Ministry of Transport, 3-1-1, Nagase, Yokosuka, Japan.

In most cases, a realistic wave height distribution in a harbour is obtained by the performance of hydraulic model tests. If we could treat theoretically together with all factors of disturbance in a harbour as diffraction, reflection, and refraction of waves, it will be of great help for the examination of an appropriate arrangement of breakwaters.

From such a standpoint, recent studies in France are noticeable by Biesel and Ranson(1), Gaillard(2), and Barailler and Gaillard(3). In these papers, examples of calculation of wave height distribution in an arbitrary shape harbour of constant or variable water depth are presented. Most recently, Berkhoff(4) has discussed the computation of combined refraction-diffraction. All of these methods of calculation are to solve basic wave equations as a boundary value problem.

On the other hand, the authors have studied to obtain the height and flow distribution of long waves in an arbitrary shape harbour from the standpoint of the effect of breakwaters against tsunamis, since the Chilian Earthquake Tsunami in 1960(5-8). In this method, a train of tsunamis is supposed to propagate into a calm region and the solution both in transient state and in stationary state can be obtained by calculating step by step the basic hydrodynamic equations for long waves under the given boundary conditions from a certain initial state.

In this paper, this method of numerical analysis have developed so as to be applicable to waves in any region from deep water to shallow water. For short waves, since it is an aim, in general, to obtain the solution in stationary state, the calculation in transient state can be regarded as a process to reach the end, whereas in case of tsunamis the transient state is significant as an actual phenomenon.

The basic equations in our numerical analysis method are the linearized wave equations including unknown functions at the water surface only such as the water surface elevation and the components of particle velocity, which are derived on the basis of a small amplitude assumption in a constant water depth from the Eulerian equations of motion and of continuity.

The wave height distribution around an arbitrary alignment of breakwaters can be obtained by the application of our method of numerical analysis and it is not difficult to include other vertical walls behind the breakwaters. For a simple alignment of breakwater, the effect of reflecting power can be included in the diffraction diagram by our modified calculation method which is named the "Wave generator method". This modified method is based on the principle that the effect of breakwater is equivalent to a hypothetical wave generator which makes the corresponding reflecting waves at the front face and waves cancelling the incident waves at the rear face of the breakwater.

Since it is not irrational to loose the condition of constant water depth to variable water depth, as far as the variation of water depth is gentle. In particular, an interesting application of our method is the analysis of wave propagation in the vicinity of caustics where ray intersections occure. It has been pointed out that the conventional geo-optic wave refraction theory fails to predict the wave height at and near caustics. Pierson(9) has discussed the existence of caustics and suggested some theoretical approaches for the solution of the caustic problem. Our basic wave equations are equivalent to what Pierson has suggested as the general basic equation of wave refraction.

For a smooth caustic, Chao(10) has developed the uniform asymptotic solution, and Chao and Pierson(11) have compared the calculated wave heights with those obtained by hydraulic model tests for a straight caustic. Most recently, Whalin(12) has pointed out that the effect of diffraction in wave refraction is vividly significant in the vicinity of a cusped caustics from his results of model experiments, and Biesel(13) has discussed the general calculation method of wave refraction including the effect of diffraction as a boundary value problem.

In this paper, several examples of application of our numerical analysis method are presented in the fandamental fashion to demonstrate its applicability to various problems of wave propagation. Being associated to wave diffraction, calculations of wave height distribution along a breakwater and of wave force upon a large isolated vertical structure are shown. As to wave refraction, an example of application to the wave height distribution around a submerged shoal with consentric circular contours where the conventional geo-optic refraction theory indicates the formation of a cusped caustics and the calculated wave heights are compared with those obtained by hydraulic model experiments.

2. BASIC EQUATIONS

2.1 Equations of motion and of continuity and boundary conditions

Propagation of small amplitude waves in the region of constant water depth of ideal fluid is treated in this analysis and irrotational motion is assumed.

The Eulerian equations of motion and of continuity and boundary conditions at the water surface and the bottom for a linearized wave are as follows;

$$\left.\begin{aligned} \frac{\partial u}{\partial t} &= -\frac{1}{\rho}\frac{\partial p}{\partial x} \\ \frac{\partial v}{\partial t} &= -\frac{1}{\rho}\frac{\partial p}{\partial y} \\ \frac{\partial w}{\partial t} &= -\frac{1}{\rho}\frac{\partial p}{\partial z} - g \end{aligned}\right\} \qquad (2.1)$$

$$\frac{\partial u}{\partial x} + \frac{\partial v}{\partial y} + \frac{\partial w}{\partial z} = 0 \qquad (2.2)$$

$$p = 0, \quad \text{at } z = \eta \qquad (2.3)$$

$$w = \frac{\partial \eta}{\partial t}, \quad \text{at } z = \eta \qquad (2.4)$$

$$w = 0, \quad \text{at } z = -h \qquad (2.5)$$

where u,v,w are components of water particle velocity, p is pressure, η is water surface elevation, and h is water depth.

2.2 Derivation of basic wave equations at water surface

Equations (2.1) ∿ (2.5) are transformed into the wave equations including only unknown functions at the water surface, which can be solved by a numerical method. For convenience sake of transformation, the motion is considered in the field of a velocity potential.

The velocity potential in a constant water depth can be expressed in the following form, after considering the bottom boundary condition of Eq.(2.5),

$$\phi = \psi(x,y,t) \cosh k(h+z) \tag{2.6}$$

where k is a constant. Equation (2.6) is different a little from the ordinary one, since a term on time t is not separated off.

Using this velocity potential, the components of water particle velocity can be written as follows;

$$\left.\begin{aligned} u &= \frac{\cosh k(h+z)}{\cosh kh} u_o(x,y,t) \\ v &= \frac{\cosh k(h+z)}{\cosh kh} v_o(x,y,t) \\ w &= \frac{\sinh k(h+z)}{\sinh kh} w_o(x,y,t) \end{aligned}\right\} \tag{2.7}$$

where u_o, v_o, w_o are the components of unknown water particle velocity at the water surface.

Now, consider the pressure p.

By integrating equations of motion into which the velocity potential of Eq.(2.6) is substituted, we get

$$-\cosh k(h+z) \frac{\partial \psi}{\partial t} + \frac{p}{\rho} + gz = 0$$

Considering the free surface condition of Eq.(2.3), following well known relation of the pressure p is obtained,

$$p = \rho g \frac{\cosh k(h+z)}{\cosh kh} \eta(x,y,t) - \rho g z \tag{2.8}$$

Since w_o in the Eq.(2.7) is given by the kinematic boundary condition at the water surface of Eq.(2.4), the unknown functions u,v,w and p in the original basic equations have been represented by a constant k and the unknown functions u_o, v_o, and η at the water surface. By substituting these relations into the first and the second equation of Eq.(2.1) and into Eq.(2.2), following modified equations of motion and of continuity are derived,

$$\left.\begin{aligned} \frac{\partial u_o}{\partial t} &= -g \frac{\partial \eta}{\partial x} \\ \frac{\partial v_o}{\partial t} &= -g \frac{\partial \eta}{\partial y} \\ \frac{\partial \eta}{\partial t} &= -\frac{1}{k} \tanh kh \left(\frac{\partial u_o}{\partial x} + \frac{\partial v_o}{\partial y} \right) \end{aligned}\right\} \tag{2.9}$$

Thses are the basic wave equations at the water surface in our analysis.

From the third equation of Eq.(2.1), the following relation is obtained for a constant value k,

$$\frac{\partial \eta^2}{\partial t^2} = - kg \tanh kh \cdot \eta$$

When η has a period T ($= 2\pi / \sigma$), this relation is equivalent to

$$\sigma^2 = kg \tanh kh \qquad (2.10)$$

This is the well-known relationship between the wave period and the wave length in the conventional small amplitude wave theory, if the k is interpreted as the wave number $2\pi/L$.

An arbitrary profile wave can be considered as a composite wave of such components of which each satishfies the relation of Eq.(2.10) respectively.

2.3 Non-dimensional basic wave equations

It is advantageous to perform calculation in a non-dimensional system, because of the generality of results. To obtain the non-dimensional wave equations, we introduce the non-dimensional variables defined by,

$$\left.\begin{aligned} x_* &\equiv \frac{x}{L} = \frac{x}{cT} \\ y_* &\equiv \frac{y}{L} = \frac{y}{cT} \\ t_* &\equiv \frac{t}{T} \end{aligned}\right\} \qquad (2.11)$$

$$\left.\begin{aligned} u_* &\equiv \frac{u_o}{ag/c} \\ v_* &\equiv \frac{v_o}{ag/c} \\ \eta_* &\equiv \frac{\eta}{a} \end{aligned}\right\} \qquad (2.12)$$

where a is the amplitude of incident waves.

Substituting these relations into Eq.(2.10), the following non-dimensional wave equations are obtained,

$$\left.\begin{aligned} \frac{\partial u_*}{\partial t_*} &= - \frac{\partial \eta_*}{\partial x_*} \\ \frac{\partial v_*}{\partial t_*} &= - \frac{\partial \eta_*}{\partial y_*} \\ \frac{\partial \eta_*}{\partial t_*} &= - \frac{\partial u_*}{\partial x_*} - \frac{\partial v_*}{\partial y_*} \end{aligned}\right\} \qquad (2.13)$$

3. METHOD OF NUMERICAL CALCULATION

3.1 Computing region

Let us consider a simple example where incident waves are progressing normally to a semi-infinite breakwater and suppose we intend to obtain only the distribution of wave height along the breakwater.

We may consider the propagation of waves around the breakwater,in the sense of geometrics, to resolve into incident waves, reflected waves, and diffracted waves as shown in Fig.-3.1.

Since we are going to calculate only the wave height along the breakwater, it is sufficient if computing points of water elevation are included in an effective computing region. To continue calculations for the pur incident waves, however, wider region than the effective region must be considered as a computing region. In our calculation, a rectangular computing region is adopted as shown in Fig.-3.2, of which the circumference boundary is a wall reflecting the incoming waves perfectly. This boundary is an imaginary boundary, because it is only for the performance of calculation.

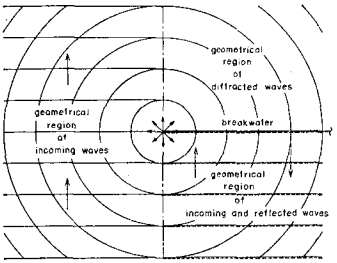

Fig.-3.1 Propagation pattern of geometrical waves

The required region for computing depends on the alignment of breakwater, the direction of incident waves, and the length of breakwater for which effective calculation should be made. In this example, since there exists no obstruction up to the front of breakwater, initial conditions can be given as a state when the front of incident wave trains have reached the breakwater.

Suppose we are going to calculate effectively over two wave length from the tip of the breakwater. Then, it is sufficient if the calculation is continued over four periods from the initial state, and the rectangular imaginary boundary can be put as shown in Fig.-3.2. In this figure, the propagation pattern of diffracted waves from the tip of breakwater (real line) and its reflection pattern from the imaginary boundary (dotted line) are shown. Patterns of incident waves and reflected waves from the breakwater can be drawn in a similar way and these reflected waves by the imaginary boundary reach around the breakwater after four periods calcu-

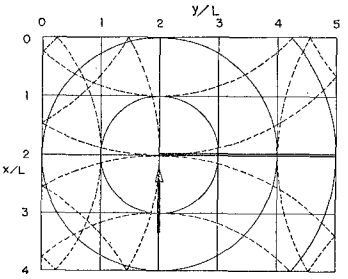

Fig.-3.2 Region of computation and propagation pattern of of geometrical diffracted waves (after four periods)

lations. At the offshore imaginary boundary, the particle velocity of incident waves must be given at least two periods long to supply incident waves of four periods long to the breakwater.

This technique of calculation is equivalent to the practical method in hydraulic model experiments on waves as the measurements are finished before the time when re-reflected waves at the wave generator reach the model site of structures to keep the same condition of incident waves during the tests.

3.2 Difference equations

The non-dimensional basic differential equations are converted into following difference equations for the arrangement of computing points as shown in Fig.-3.3.

$$\left.\begin{aligned}
\eta(i,j)^{t+\Delta t/2} &= \eta(i,j)^{t-\Delta t/2} \\
&\quad - \frac{\Delta t}{\Delta x}\{u(i+1,j)^t - u(i,j)^t\} \\
&\quad - \frac{\Delta t}{\Delta y}\{v(i,j+1)^t - v(i,j)^t\} \\
u(i,j)^{t+\Delta t} &= u(i,j)^t \\
&\quad - \frac{\Delta t}{\Delta x}\{\eta(i,j)^{t+\Delta t/2} - \eta(i-1,j)^{t+\Delta t/2}\} \\
v(i,j)^{t+\Delta t} &= v(i,j)^t \\
&\quad - \frac{\Delta t}{\Delta y}\{\eta(i,j)^{t+\Delta t/2} - \eta(i,j-1)^{t+\Delta t/2}\}
\end{aligned}\right\} \qquad (3.1)$$

where the substript $_*$ which means the non-dimensional quantity is droped to avoid unwieldly notation.

3.3 Initial and Boundary conditions

(1) Initial conditions

In this calculation, a sinusoidal wave train propagating in the negative direction of x axis is considered as the incident waves. The time when the front of the incident wave train reaches the front of breakwater ($i = i_o$) is counted zero, then the following initial conditions are given from the conventional small amplitude wave theory.

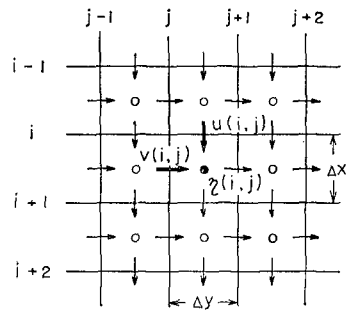

Fig.-3.3 Arrangement of computing points

Initial calm region ($i < i_o$)

$$\left.\begin{aligned}
\eta(i,j)^{-\Delta t/2} &= 0 \\
u(i,j)^0 &= 0 \\
v(i,j)^0 &= 0
\end{aligned}\right\} \qquad (3.2)$$

Initial wave region ($i \geq i_o$)

$$\left.\begin{aligned} \eta(i,j)^{-\Delta t/2} &= \sin\left[2\pi\left\{(i-i_o)\Delta x + \frac{\Delta x}{2} - \frac{\Delta t}{2}\right\}\right] \\ u(i,j)^{0} &= -\sin\left\{2\pi(i-i_o)\Delta x\right\} \\ v(i,j)^{0} &= 0 \end{aligned}\right\} \qquad (3.3)$$

(2) Boundary conditions

There are two types of boundaries in the computing plane; the one is the imaginary boundary and the other is the internal boundary corresponding to the breakwater. At the offshore imaginary boundary, the velocity of incident waves is given and at the other three sides the velocity component is given zero.

Offshore boundary condition*

$$u(i_e,j)^{n\Delta t} = -\sin n\theta \qquad (3.4)$$

where,

$$\left.\begin{aligned} \cos\theta &= 1 - \left(\frac{\Delta t}{\Delta x}\right)^2 (1-\cos\phi) \\ \phi &= 2\pi\Delta x \end{aligned}\right\} \qquad (3.5)$$

Internal boundary condition

$$V_n\big|_s = 0 \qquad (3.6)$$

where s is the circumference of the internal boundary and V_n is the normal velocity component to it.

Equation (3.6) is the condition for the boundary of perfect reflection. The condition of boundary with arbitrary reflecting power will be trated in 4.3.

3.4 Stability condition of numerical calculation

A following relation between the space interval x, y and the time interval t must be satishfied to perform stable calculations.

$$\Delta t \leq \frac{1}{\left(\frac{1}{\Delta x} + \frac{1}{\Delta y}\right)^{1/2}} \qquad (3.7)$$

All the calculation in present paper are conducted by using following intervals,

$$\Delta x = \Delta y = \Delta s = \frac{1}{15}$$

$$\Delta t = \frac{1}{24}$$

* This is the velocity obtained as a solution of difference equations of which the initial conditions are given by Eq.(3.3) in the initial wave region. Details can be reffered to the reference paper (5).

4. WAVE HEIGHT DISTRIBUTION ALONG A BREAKWATER

4.1 Comparison with analytical solutions

The diffraction pattern around a semi-infinite breakwater has been solved as the Sommerfeld solution and also around a deatached breakwater has been obtained by solving the Mathieu equation. It has been already confirmed that these analytical solutions agree well with hydraulic model experimental results. The applicability of our numerical method to wave diffraction, therefore, can be verified by comparing the computed wave heights with those obtained from the conventional analytic solutions for a semi-infinite breakwater or a detached breakwater.

For this purpose, the following three calculations are conducted,
1) a semi-infinite breakwater, normal incident wave direction (θ = 90°)
2) a detached breakwater, normal incident wave direction (θ = 90°)
3) a semi-infinite breakwater, oblique incident wave direction (θ = 45°)

(1) Wave height distribution along a semi-infinite breakwater (θ = 90°)

The distribution of wave height calculated by our numerical analysis method is compared with that obtained from the conventional analytic solution in Fig.-4.1. The wave heights in the numerical analysis are calculated at the computing points apart from the faces of the breakwater by $\Delta s/2$ (= L/30, in this case), because of the finite difference. Analytical solutions both at the face of the breakwater and at the computing points of water elevation are shown.

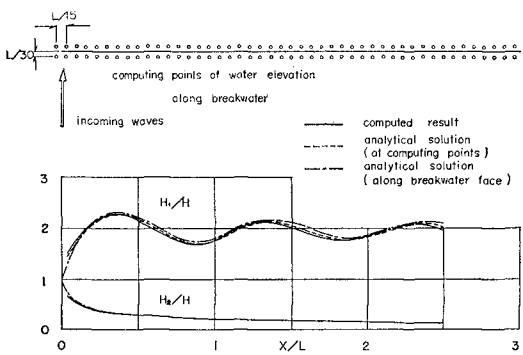

Fig.-4.1 Wave height distribution along a semi-infinite breakwater

The undular distribution of wave height along the front face is well realized in the calculated result as predicted by the analytical solution. The wave height distribution along the rear face of breakwater by both methods extremely agree with each other.

(2) Wave height distribution along a detached breakwater (θ = 90°)

The wave height distribution along a detached breakwater of which the

length is 2L is calculated for the incident waves approaching normally to it.

Fig.-4.2 shows the comparison of results obtained by the numerical analysis and by the conventional solution. A little difference around the tip of breakwater may be due to the difference of calculating points.

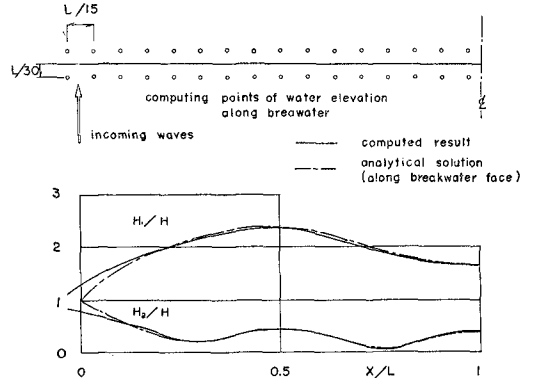

Fig.-4.2 Wave height distribution along a breakwater with the length of 2L

(3) Wave height distribution along a semi-infinite breakwater (θ = 45°)

We take the direction of incident waves on one axis of the grid system and make the oblique breakwater bear a close resemblance to a staircase shape. The results are shown in Fig.-4.3 where the staircase breakwater

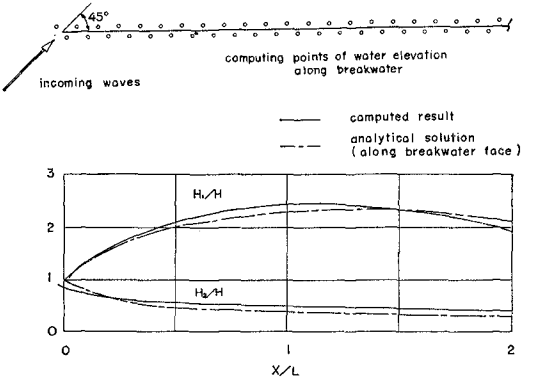

Fig.-4.3 Wave height distribution along a semi-infinite breakwater due to obliquely incoming waves

is drawn as a straight line. Some difference is noticed between the calculated result and the analytical solution. This degree of difference, however, could be reduced by using finer space intervals.

4.2 Wave height distribution along a breakwater of arbitrary shape

As an example of application to a breakwater of arbitrary shape, the distribution of wave height along a semi-infinite breakwater with a short wing is calculated.

Fig.-4.4 shows the calculated result for the case the length of the short wing is 0.4L and the direction of incident waves is normal to the main part of the breakwater. It is noticed apparently that the non-uniformity of wave height is increased due to the existence of the short wing.

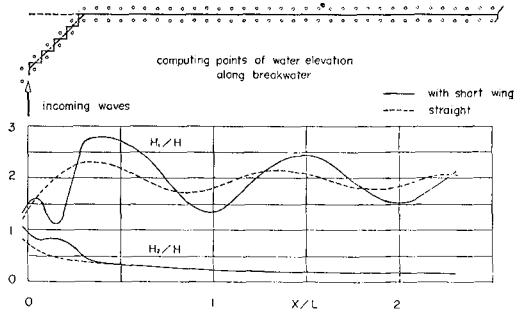

Fig.-4.4 Wave height distribution along a semi-infinite breakwater with a short wing

4.3 Wave height distribution along a breakwater of arbitrary reflecting power

There exists a number of breakwaters which are not of perfect reflection, for examples, rubble mound breakwaters and vertical walls protected by artificial blocks. For these breakwaters, the authors have devised a special calculation way named the Wave generator method.

Let us explain the principle of the wave generator method for a straight breakwater of perfect reflection. In this case, the velocity potential can be expressed as a sum of the velocity potential of incident waves (ϕ_i) and that of scattered waves by the breakwater (ϕ_d),

$$\phi = \phi_i + \phi_d \tag{4.1}$$

Furthermore, since the scattered waves can be considered as a sum of waves generated at the front face (ϕ_f) and at the rear face of the breakwater (ϕ_r), ϕ_d is expressed as,

$$\phi_d = \phi_f + \phi_r \tag{4.2}$$

We can interprete obviously that waves generated at the front face are waves corresponding to reflected waves by the breakwater and waves generated at the rear face are waves cancelling the incident waves. Such waves must be generated at the both faces of the breakwater so as to satishfy the following conditions;

$$\frac{\partial \phi_f}{\partial n}\Big|_s = -\frac{\partial \phi_i}{\partial n}\Big|_s \tag{4.3}$$

$$\frac{\partial \phi_r}{\partial n}\Big|_s = -\frac{\partial \phi_i}{\partial n}\Big|_s \tag{4.4}$$

where s designates the circumference of the breakwater and n designates the normal direction to it.

Since the breakwater is replaced by a special wave generator, the authors have named this calculation way the Wave generator method. In this method, the calculation is performed by following procedure;

1) Calculation of incident waves in the absence of breakwater
2) Calculation of waves generated by the hypothetical wave generator at the boundary of the breakwater, by using the calculated velocity component of incident waves in 1)
3) Summation of simultaneous results of incident waves and generated waves

The wave height distribution along a semi-infinite breakwater which was calculated by this wave generator method has been confirmed to agree perfectly with that obtained by the ordinary calculation method of our numerical analysis.

In case that the arbitrary reflection coefficient r(s) distributes along the face of a breakwater, the following equation is used for Eq. (4.3),

$$\frac{\partial \phi_f}{\partial n}\Big|_s = -\, r(s)\, \frac{\partial \phi_i}{\partial n}\Big|_s \tag{4.5}$$

It should be noted that this wave generator method is directly applied only to the case in which velocities of all the incoming waves with normal component to the boundary can be obtained. As to the case of the semi-infinite breakwater, both waves generated at the front face and waves generated at the rear face are propagating along the breakwater when they reach the other face and they have no normal velocity component to it. Therefore, it is enough that only incident waves are considered as incoming waves to the breakwater.

However, if there are two separate breakwaters, and waves generated at one of the breakwaters reach the other with normal velocity component to it, it is necessary to repeat the calculation procedure at any computing time step.

Fig.-4.5 shows the wave height distribution along a semi-infinite breakwater of perfect reflection, of no reflection along the breakwater, and of no reflection only at the heading part. Two remarks are pointed out from these results: 1) The wave height in the vicinity of no reflection part is approximately equal to that of the incident wave at the front face. 2) Little effect of the reflecting power is brought on the wave height along the rear face.

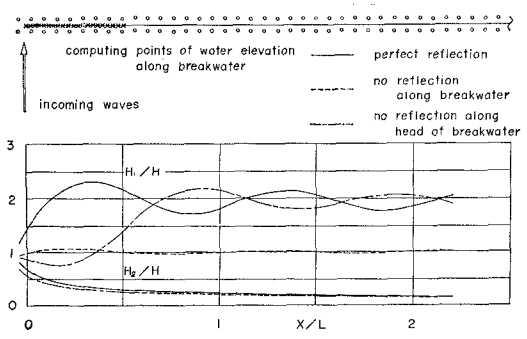

Fig.-4.5 Effect of reflecting power on wave height distribution

4.4 Application to wave force upon a large isolated vertical structure

An interesting application of our method of numerical analysis is the calculation of wave force upon a large isolated vertical structure of arbitrary shape.

Components of wave force upon a structure can be obtained from the following relation, when the water surface elevation along the structure is calculated by the numerical analysis,

$$F_x = \oint\int_{-h}^{0} p\,dz \cdot l(s)\,ds = \frac{\rho g}{k} \tanh kh \oint \eta_s\, l(s)\,ds$$
$$F_y = \oint\int_{-h}^{0} p\,dz \cdot m(s)\,ds = \frac{\rho g}{k} \tanh kh \oint \eta_s\, m(s)\,ds \qquad (4.6)$$

where s is the circumference of the structure and (l,m) is the directional cosine of the inward normal line.

As an example of application, wave force upon a rectangular body which

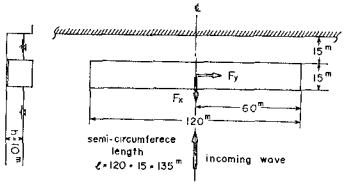

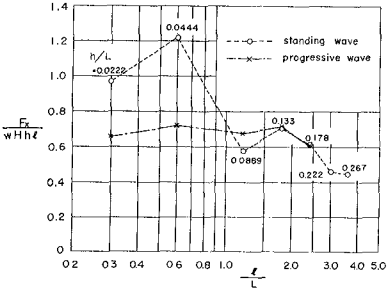

Fig.-4.6 Arrangement of a rectanglar vertical body and calculated wave force

is a simplified treatment for a moored ship is calculated. Fig.-4.6 shows the arrangement of the moored ship and calculated wave forces with and without a vertical quay wall of infinite length.

5. APPLICATION TO THE REGION OF VARIABLE WATER DEPTH

5.1 Correction factor of shoaling

For the propagation of waves in the region of variable water depth $h(x,y)$, we assume that the wave frequency σ is constant and the local wave number k is given by Eq.(2.10). Then, our wave equations include the variation of wave height due to shoaling caused by the variation of water depth as well as due to refraction caused by the variation of wave phase velocity.

The variation of wave height due to shoaling, however, is not the function of the group velocity but of the phase velocity in our wave equations.

As a simple example of water depth variation, let us consider the region where the water depth changes in step-shape at $x = 0$ from h_1 to h_2 as shown in Fig.-5.1.

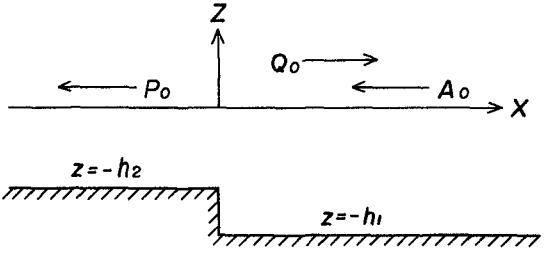

Fig.-5.1 Change of water depth in step-shape

The velocity potential for this situation is expressed in the following form,

$$\left.\begin{aligned}
\phi_1 &= (A_0 e^{ikx} + Q_0 e^{-ikx})\, e^{i\sigma t}\, \frac{\cosh k(z+h_1)}{\cosh kh_1} \\
&\quad + \sum_{m=1}^{\infty} A_m e^{-k_m x} e^{i\sigma t}\, \frac{\cosh k_m(z+h_1)}{\cosh k_m h_1} \quad , \qquad x \geq 0 \\
\phi_2 &= P_0 e^{ik'x} e^{i\sigma t}\, \frac{\cosh k'(z+h_2)}{\cosh k'h_2} \\
&\quad + \sum_{n=1}^{\infty} P_n e^{k'_n x} e^{i\sigma t}\, \frac{\cosh k'_n(z+h_2)}{\cosh k'h_2} \quad , \qquad x \leq 0
\end{aligned}\right\} \qquad (5.1)$$

And,

$$\sigma^2 = kg \tanh kh = -k_m g \tanh k_m h \tag{5.2}$$

Unknown coefficients in Eq.(5.1) can be determined from the following boundary conditions at x = 0,

$$\phi_1 = \phi_2 \quad \text{,(continuity of pressure)}$$
$$\frac{\partial \phi_1}{\partial x} = \frac{\partial \phi_2}{\partial x} \quad \text{,(continuity of horizontal particle velocity)} \tag{5.3}$$

As obvious from Eq.(5.1), the strict solution includes an infinite series and the term of group velocity c_g appears through mathematical development for the determination of unknown coefficients. Waves corresponding to the infinite series, however, are not progressive waves and does not contribute the energy transport over one period. Consequently, the following relation of energy conservation can be obtained,

$$p^2 c_{g*} + q^2 = 1 \tag{5.4}$$

where,

$$p = \left| \frac{P_0}{A_0} \right| \quad \text{, (transmission coefficient)}$$

$$q = \left| \frac{Q_0}{A_0} \right| \quad \text{, (reflection coefficient)}$$

$$c_{g*} = c_{g_2} / c_{g_1}$$

The c_{g_1} and c_{g_2} are the group velocities respectively in the region of water depth h_1 and h_2, and the group velocity is given by,

$$c_g = nc = \frac{1}{2} \left(1 + \frac{2kh}{\sinh 2kh}\right) c \tag{5.5}$$

The basic wave equations of our method of numerical analysis include only waves corresponding to the first term of the strict solution Eq.(5.1) and does not include waves corresponding to the infinite series.

Now we consider the analytic solution of our wave equations for the situation as shown in Fig.-5.1. Starting from the finite difference equations, the following coefficients of transmission and reflection are obtained,

$$p = \frac{2}{1 + c_*}$$
$$q = \left| \frac{1 - c_*}{1 + c_*} \right| = | p - 1 | \tag{5.6}$$

where,

$$c_* = c_2 / c_1$$

From these relations, we get

$$p^2 c_* + q^2 = 1 \tag{5.7}$$

Comaring Eq.(5.7) with the strict solution of Eq.(5.4), it is noticed that the group velocity in Eq.(5.4) is replaced by the phase velocity in Eq.(5.7).

If reflection can be neglected, the transmission coefficient is written as,

$$p = c_{g*}^{-1/2} \quad \text{, from Eq.(5.4)} \tag{5.8}$$

$$p = c_{*}^{-1/2} \quad \text{, from Eq.(5.7)} \tag{5.9}$$

This relation is kept for a sloping bottom, if reflection is neglected, and the coefficient of Eq.(5.8) is equivalent to the conventional shoaling factor. To keep this conventional relation of shoaling factor, therefore, the shoaling factor in our analysis should be multiplied with the following correction factor of shoaling,

$$f_s = n_*^{-1/2} = \{(1 + \frac{2k_1h_1}{\sinh 2k_1h_1})/(1 + \frac{2kh}{\sinh 2kh})\}^{1/2} \tag{5.10}$$

When the deep water is taken as a reference region, this value of correction factor varies from 1 in deep water to 0.707 in the region of long waves.

In the application of our method of numerical analysis to a submerged shoal with concentric circular contours which is treated in the next section, final results of wave height are multiplied with this correction factor of shoaling.

5.2 Wave height distribution in the vicinity of ray intersections

Since the conventional wave refraction theory is based on the geometrical optic approximation, it fails to predict wave height at and near caustics where ray intersections occur. It has been already pointed out that the effect of diffraction in wave refraction should be included in the analysis of waves in the vicinity of ray convergence. Our method of numerical analysis is applicable to the region where caustics are formed.

As an example , our method is applied to wave propagation on a submerged shoal with concentric circular contours where the conventional refraction theory indicates the formation of a cusped caustics as shown in Fig.-5.2.

Figure 5.3 shows the arrangement of the shoal in the numerical calcultion.

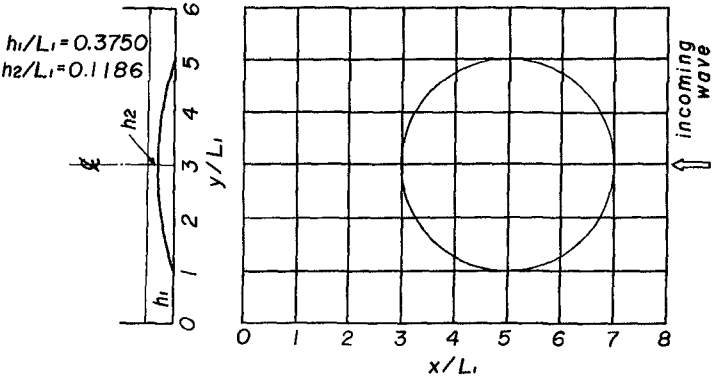

Fig.-5.3 Arrangement of a shoal

Hydraulic model experiments for same situation are conducted to confirm the validity of our method. The water depth and the wave length in the model are as follows,

$$h_1 = 15 \text{ cm}, \quad h_2 = 5 \text{ cm}, \quad L_1 = 40 \text{ cm}.$$

All tests are conducted for non-breaking waves.

Both results of the numerical calculation and the hydraulic model tests are presented in Fig.-5.4,5.5, and 5.6. In Fig.-5.4, the wave height which is not corrected for the shoaling factor is also shown. It is noticed that experimental results agree better with the corrected value than that of non-correction. Maximum wave height in the calculated results is 2.1 H_i near the rear end of the shoal.

6. SUMMARY AND CONCLUSIONS

A method has been presented to obtain numerically wave patterns in any region of arbitrary shape from deep water to shallow water. The principle is to solve the linearized wave equations under the given boundary conditions from a certain initial state, which are derived from the Eulerian equations of motion and of continuity and include only unknown functions at the water surface.

By applying our method of numerical analysis, it is possible to investigate various problems of wave propagation in the region of arbitrary shape and of variable water depth. In this paper, we have presented several examples of application of our method to wave diffraction and to wave refraction in the fundamental fashion.

The applicability of our method to wave diffraction has been confirmed by the comparison of the distribution of wave height along a semi-infinite breakwater and a detached breakwater by our numerical method with that obtained from the conventional analytic solutions. As an example of application to a breakwater of arbitrary shape, the distribution of wave height along a semi-infinite breakwater with a short wing is calculated. The result shows that the non-uniformity of wave height along the breakwater is apparently increased due to the existence of the short wing.

For a breakwater of arbitrary reflecting power, a modified method which is named the "Wave generator method" is devised. Two examples of application of this modified method to semi-infinite breakwaters of no reflection and of no reflection only at the heading part are shown. The effect of reflecting power on the wave height distribution along the rear side of the breakwater is a little.

In addition, an interesting application of our method with respect to wave diffraction is the calculation of wave force upon a large isolated vertical structure of arbitrary shape. As an example of application, wave forces upon a rectangular body which is regared as a moored ship are calculated with and without a vertical quay wall behind the body.

As to the application to the region of variable water depth, the correction factor of shoaling has been introduced, since the shoaling factor for our basic wave equations is a function of the phase velocity instead of the group velocity in the conventional relation. This value of correction factor varies from 1 in deep water to 0.707 in the region of long waves, when the deep water is taken as a reference region.

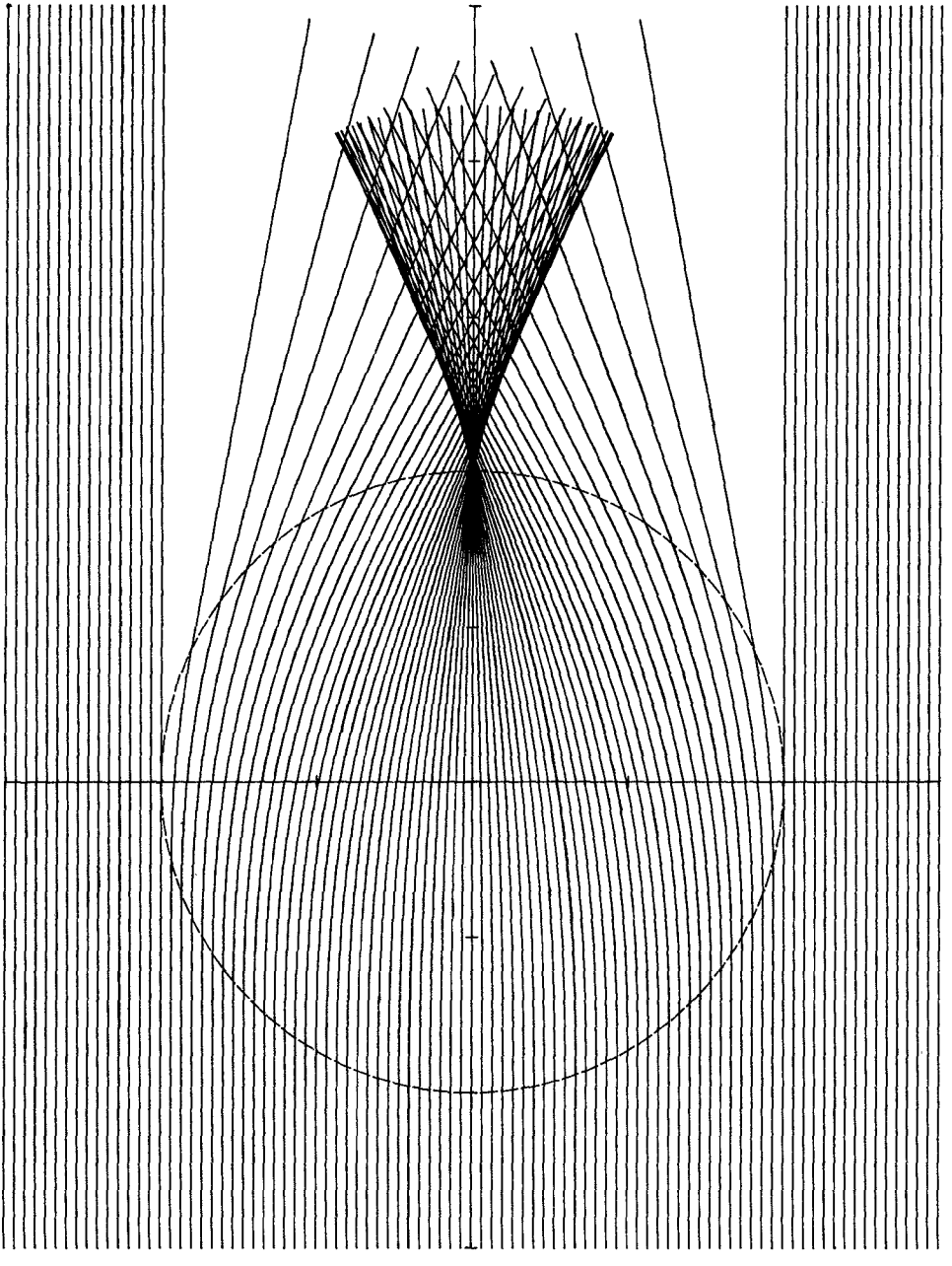

Fig.-5.2 Formation of a cusped caustics

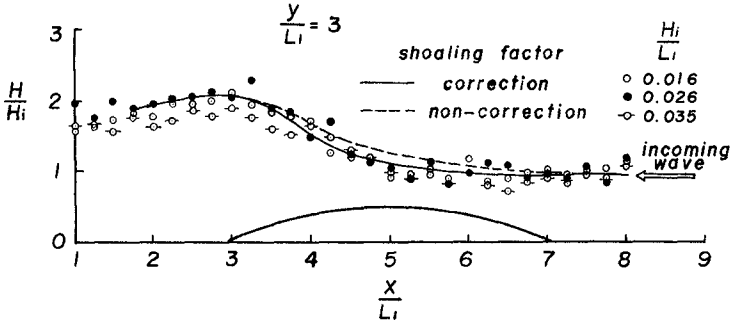

Fig.-5.4 Comparison of calculated wave height and experimental results (1)

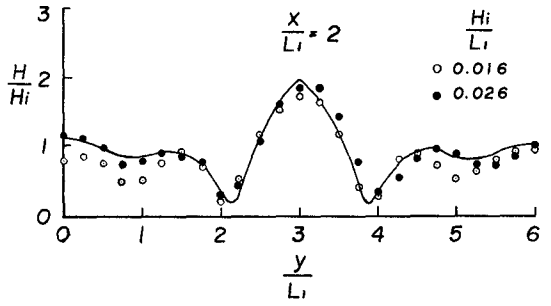

Fig.-5.5 Comparison of calculated wave height and experimental results (2)

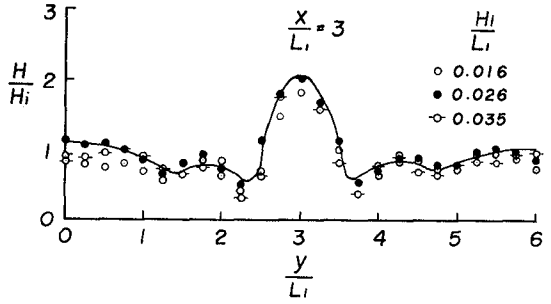

Fig.-5.6 Comparison of calculated wave height and experimental results (3)

Our method of numerical analysis is applicable to the analysis of wave propagation in the region of ray convergence. An example of application is shown to a submerged shoal with concentric circular contours where the conventional geo-optic wave refraction theory indicates the formation of a cusped caustics. Hydraulic model experiments are conducted to verify the validity of our method for a cuastic problem. Calculated wave heights agree very well with those obtained from the model tests. The maximum wave height is 2.1 H_1 at the rear end of the shoal where the geo-optic refraction theory gives the infinite wave height.

Our method of numerical analysis might be applied to the calculation of wave patterns in the region of more realistic bottom topography and it is possible to include vertical boundaries of arbitrary shape.

REFERENCES

1) Biesel,F.,R.Ranson : Calculs de diffraction de la houle, Congrès de l'A.I.R.H., 1961
2) Gaillard,P. : Sur l'amplitude de la houl émise par une sourse ponctuelle isotrope dans un domaine de profondeur variable, La Houille Blanche, No.5,1964
3) Barailler,L.,P.Gaillard : Évolution récente des modèles mathématiques d'agitation due á la houl. Calcul de la diffraction en profondeur non uniforme, La Houille Blanche. No.8,1968
4) Berkhoff,J.C.W. : Computation of combined refraction-diffraction, 13th International Conference on Coastal Engineering,1972,Conference Abstracts
5) Fuku-uchi,H.,Y.Ito : On the effect ob breakwaters against tsunami, Proc. 10th Conference on Coastal Engineering, 1966
6) Ito,Y. : On the effect of Ofunato tsunami-breakwater against 1968 Tsunami, Proc. 13th Congress of IAHR, 1969
7) Ito,Y. : Head loss at tsunami-breakwater opening, Proc. 12th Conference on Coastal Engineering,1970
8) Ito,Y. : On the effect of tsunami-breakwater, Coastal Engineering in Japan,Vol.13,1970
9) Pierson,W.J.Jr. : The interpretation of crossed orthogonals in wave refraction phenomena, Technical Memorandum No.21,Beach Erosion Board, Corps of Engineers,1951
10) Chao,Y.Y. : The theory of wave refraction, including the effects of caustics and spherical earth, Tech. Rept.,TR-70-7, New York University, Geophysical Research Labs.,1970
11) Chao,Y.Y.,W.J.Pierson,Jr. : An experimental study of gravity wave behavior near a straight caustic, Tech. Rept.,TR-70-17, New York University, Geophysical Research Labs.,1970
12) Whalin,R.W. : Wave refraction theory in a convergence zone, 13 th International Conference on Coastal Engineering,1972,Conference Abstracts
13) Biesel,F. : Réfraction de la houle avec diffraction modérée, 13th International Conference on Coastal Engineering,1972,Conference Abstracts

CHAPTER 27

ENERGY TRANSFER MECHANISM FOR FINITE AMPLITUDE WAVES

by Konstantin Zagustin Ph.D.
Asoc. Prof. and Head Hydraulic Laboratory
Universidad Central de Venezuela
Caracas, Venezuela.

ABSTRACT.-

A basic mechanism is proposed to explain the growth of finite amplitude water waves due to the effect of normal stresses. The proposed mechanism can probably be applied to the whole range of wave's growth, starting from a small amplitude wave up to the case of a limiting and breaking wave condition. The transfer of energy from air flow to the water wave is explained by the existance of a circulation flow pattern above the water surface, which is responsable for a phase-lag of the normal stress distribution in relation to the wave's profile. Such a circulation flow pattern extends throughout the whole wave length and it is quite different from the classical concept of flow separation, as postulated by Jeffrey's. The difference becomes as a result of considering a different boundary condition at the interface. Experiments performed on wavy models with moving boundary conditions, for small amlitude waves and finite amplitude waves showed that the normal stress distribution is similar in both cases, and displays a noticible phase-lag with respect to the wave's profile. It was observed that for both cases a circulating flow pattern was present above the water surface, which indicated some relation between the flow vorticity above the wave and the normal stress distribution.

To prove the role of circulation in the energy transfer mechanism, a model was built with water and mercury as working fluids. In this model the interface was initially non disturbed, when both fluids move in opposite directions. However, when a forced circulation was applied by means of a variable speed rotor located above the interface, a wave would form. The wave would be inicially of small amplitude, but with an increase of circulation would become of finite amplitude, then reach the angular crest condition and finally would reproduce the breaking condition at the crest.

The obtained experimental results proved the importance of the circulation flow pattern present above the wave surface, and suggest that a mathematical model could be formulated based on vorticity analysis, which would be able to provide an explanation for the energy transfer mechanism due to normal stresses at all stages of wave's growth.

INTRODUCTION.-

It has been proven both theoreticly (ref. 1,2) and experimentally (ref. 3,4), that in the case of already formed small amplitude waves , the normal stress distribution displays a phase-lag with respect to the wave's profile, which accounts for the energy transfer due to this stresses from wind to the water waves. However, these linear theories fail when the wave reaches a finete amplitude, being the only available mechanism that of Jeffrey's (ref.5) based on flow separation. The experimental data used to estimate Jeffrey's

sheltering coefficient where obtained from fixed boundary wavy models tested in wind tunnels or water channels. Such an empirical approach had not been succesufull to provide a good agreement between the predicted values and real observations, and hence the problem remain unsolved. Since most of the water waves observed in nature are of finite amplitude, it is important to understand the basic mechanism of their growth, and this paper intend to provide new basic ideas to develop a better understanding on the subject.

To properly analyse the air motion over a wave profile which is fixed in space, a coordinate system which moves with the wave has to be introduced. In this moving coordinate system the air flow (far away from the interface) will move at a speed U-C, while water will flow in opposite direction with a speed equal to the wave celerity C. At the interface the water particle velocity will vary with location along the wave, being larger than C at the trought and smaller than C at the crest. A graphical representation of the coordinate transformation is shown in fig. 1 .

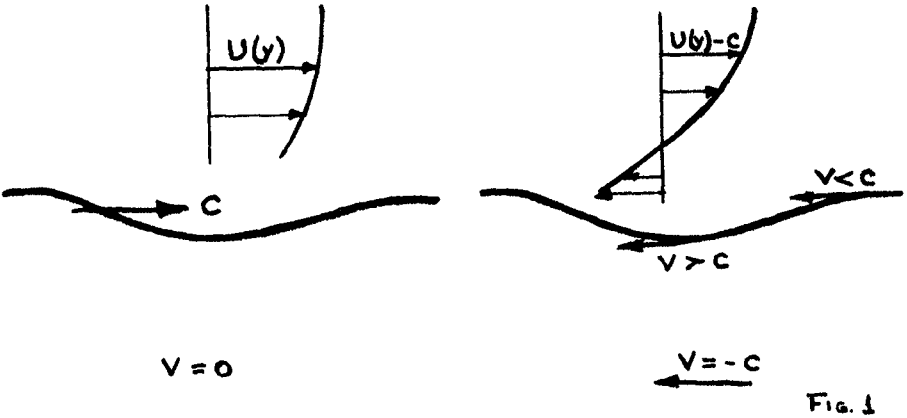

Fig. 1

Unsteady Flow Picture Steady Flow Picture

When the wave's amplitude is small as compared with the wave's length the difference of particle velocities at the interface is small and can be neglected. Experimental results obtained in wavy models with constant velocity boundary conditions (ref.3,4) showed that the effect of the moving boundary is to produce a phase-lag in the normal stress distribution. In fig. 2 a comparison is presented between the obtained experimental results for normal stress distribution with fixed and movin boundary conditions. This phase-lag in the pressure distribution has been also obtained in laboratory measurements over wind generated waves (ref. 6), and in the field (ref. 7).

Experimental results for finite amplitude waves with the appropiate moving boundary conditions were reported by the author at the XIIth Conference on Coastal Engineering held in Washington in 1970 (Unfortunately was not published in the proceedings). The obtained results, which will be briefly described in this paper, showed that for finite amplitude waves the pressure distribution looks almost the same as in the case of small amplitude waves, and is quite different from the normal stress distribution

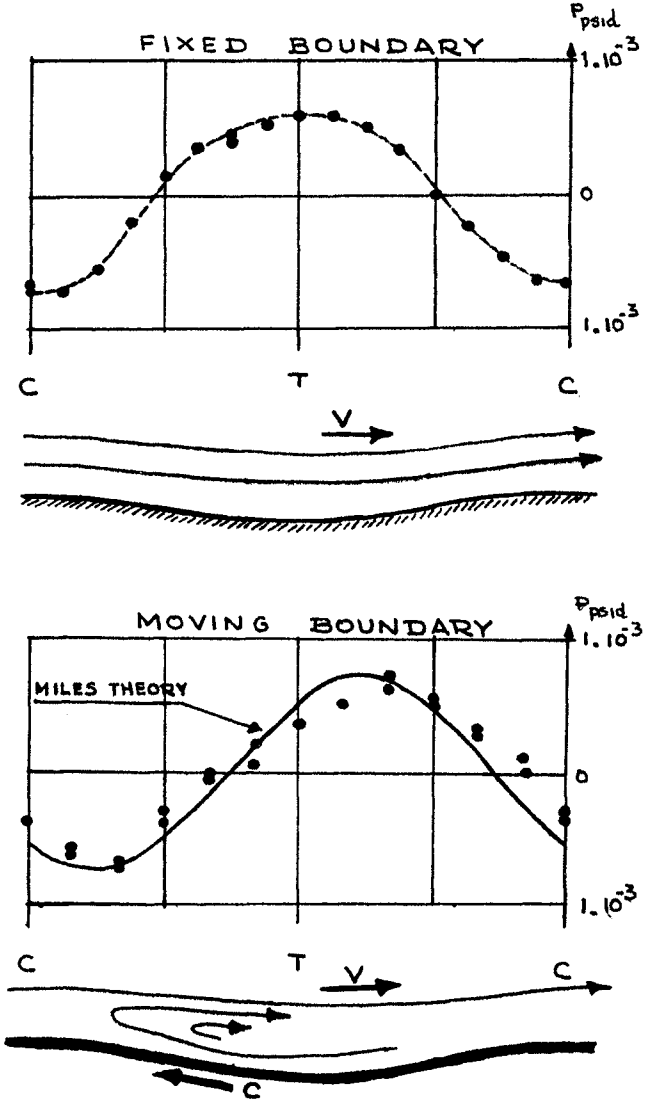

PRESSURE DISTRIBUTION OVER SMALL AMPLITUDE WAVES

Fig. 2

obtained from fixed boundary experiments as reported by Motzfeld (ref. 8) and others. A comparison between both results can be seen in fig. 5. Flow visualization showed that instead of a classical separated region as obtained in fixed models (fig. 6), the flow over the wave displaied a large circulation region which extend throughout the wave's length (fig. 7), as if the flow would separate from one crest to the another one. This flow picture coincided with that proposed by the author in 1966 (ref. 3) for a limiting wave profile.

The obtained experimental results for pressure distribution and flow visualization suggested that the circulation flow pattern above the wave surface is responsable for the phase-lag observed in the normal stress distribution, and hence, for the growth of the wave. If that is true, a theory could be developed based on vorticity which will cover the whole range of wave's growth. However, the role of circulation in the process of energy transfer is not obvious, and it is the purpose of this paper to provide a definite foundation for a future mathematical model based on vorticity, which would provide the answer to such important problem.

MOVING BOUNDARY EXPERIMENTS FOR FINITE AMPLITUDE WAVES.-

The result of this experimental work were presented at the XIIth. Conference on Coastal Engineering held in Washington in 1970, and therefore only a summary of the used procedure and the main results will be included in this paper.

Since in the case of a finite amplitude wave the boundary can not be considered as moving with a constant speed, an approximation to the real particle velocity distribution along the wave surface had to be introduced. Such an approximation was made by dividing the wave profile in several regions, each of them, moving at different constant velocities.

Such a moving boundary model was built in a water tunnel at the Hydraulic Laboratory of the Central University of Venezuela, where three waves with 50 cm. wave length and 5,5 cm heigth were represented. The total test section had the dimenssions of 1,8 x 0,5 x 0,1 mt. and the water flow velocity could be varied from 0 to 3 mt./sec. The moving boundary was set to move at a speed corresponding to the celerity of a gravity water wave of the same wave length, and the velocity distribution along the boundary was adopted in the form shown in fig. 3 . The motion of each section of the wave surface was achieved through a combination of wheels with different diameters connected by chains. A view of the installation can be seen in fig. 4.

A series of test were performed with several water flow velocities, for both cases, of fixed and moving boundary conditions. For each case pressure distribution was obtained by means of a series of static pitot tubes located just above the wave's profile, measuring the pressure difference with a highly sensitive pressure transducer. Also, flow visualization was obtained for each run by adding bouyant plastic particles to the water flow and taking pictures of the flow field above the wave's profile.

In fig. 5 a typical set of data is shown for the normal stress distribution for both cases os fixed and moving boundary conditions, being in the later case the ratio between the water velocity and the mean boundary speed equal to unity. In fig. 6 and 7 the corresponding flow visualization is presented. From these results it can be concluded that in the case of a fixed boundary model, the normal stress distribution and the flow visualization coincides with the known experimental data. However, when the boundary is moving , the normal stress distribution curve presents an astonishing re-

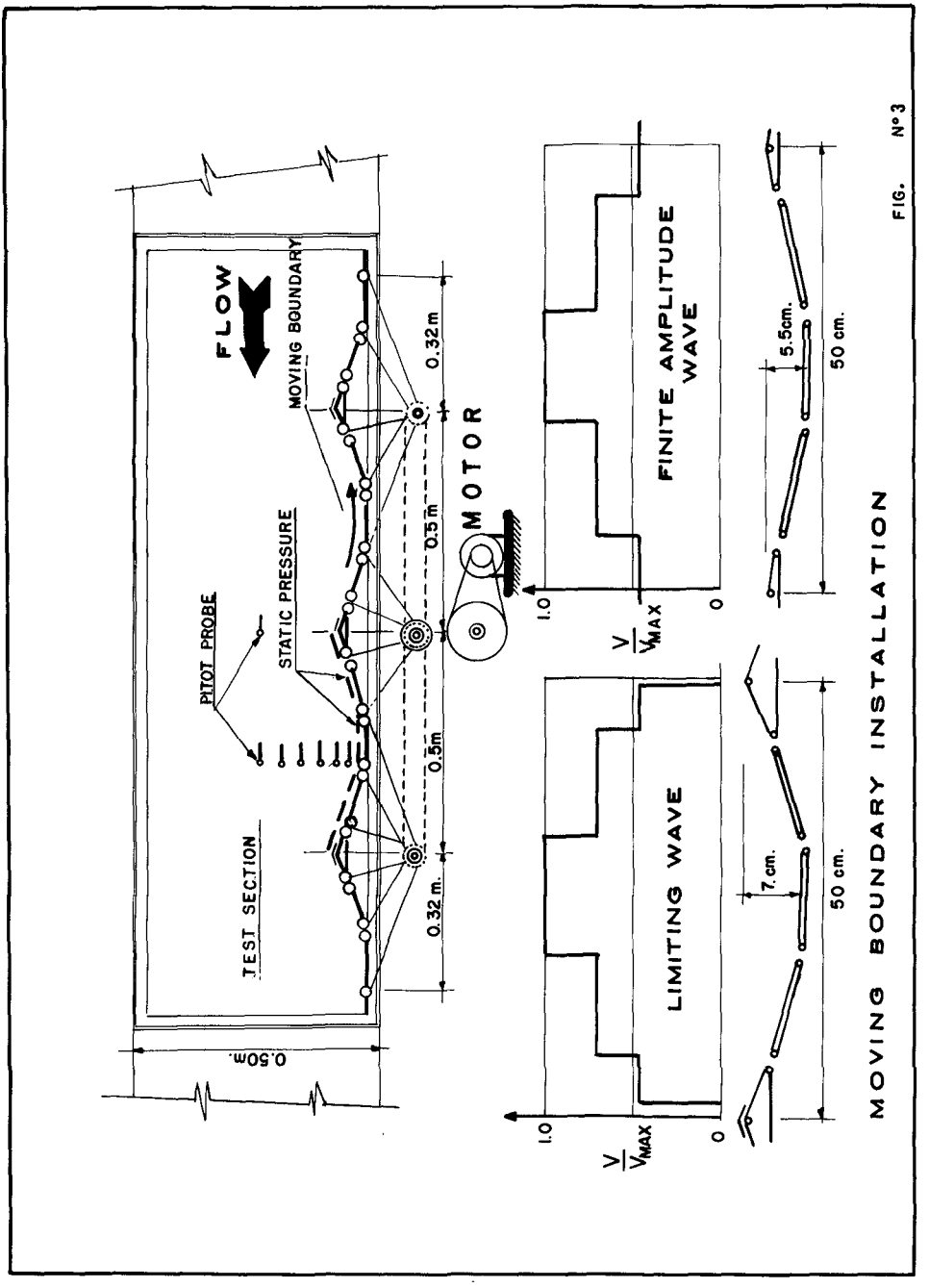
FLOW
MOVING BOUNDARY
0.32m
0.5m
0.5m
0.32m
MOTOR
PITOT PROBE
STATIC PRESSURE
TEST SECTION
0.50m
FINITE AMPLITUDE WAVE
LIMITING WAVE
1.0
0
V/VMAX
5.5cm.
50 cm.
7.cm.
50 cm.
MOVING BOUNDARY INSTALLATION
FIG. N°3

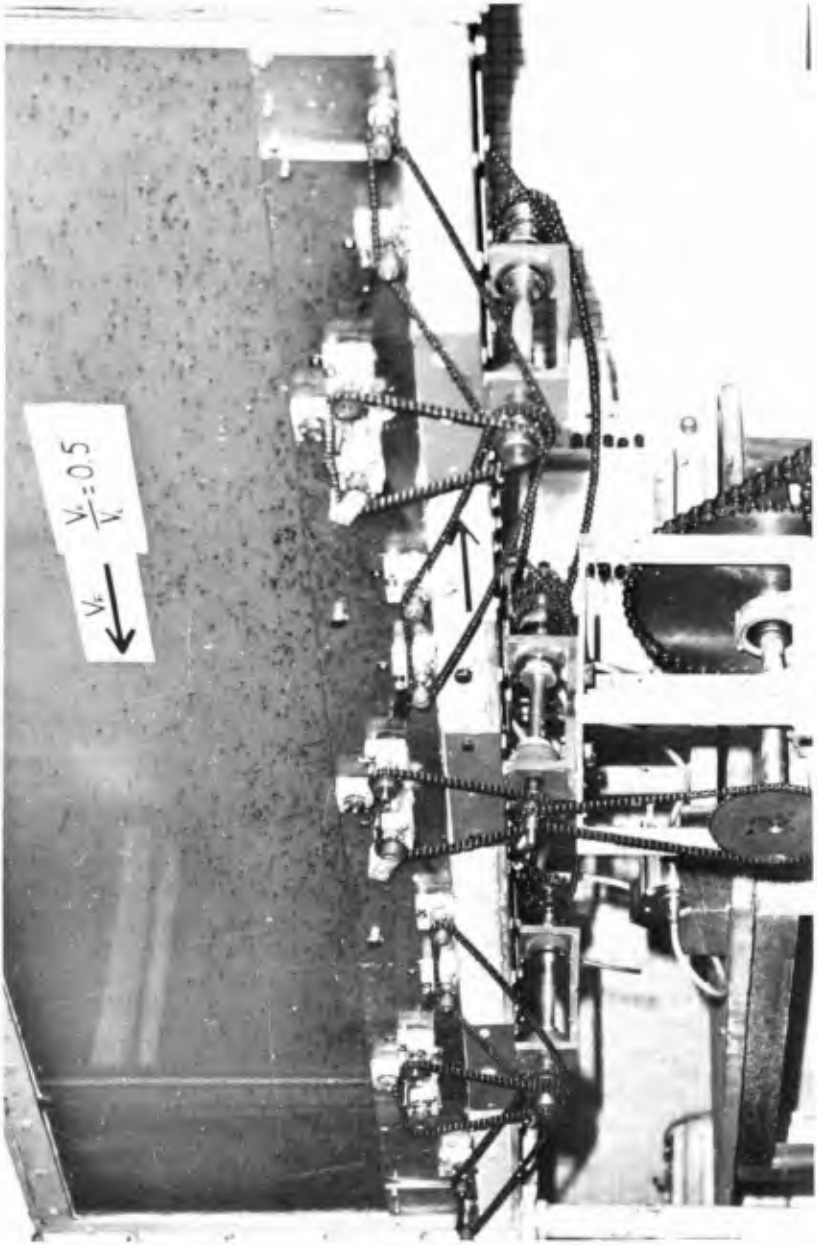

Fig. 4.- General View of the Moving Boundary Installation for Finite Amplitude Waves

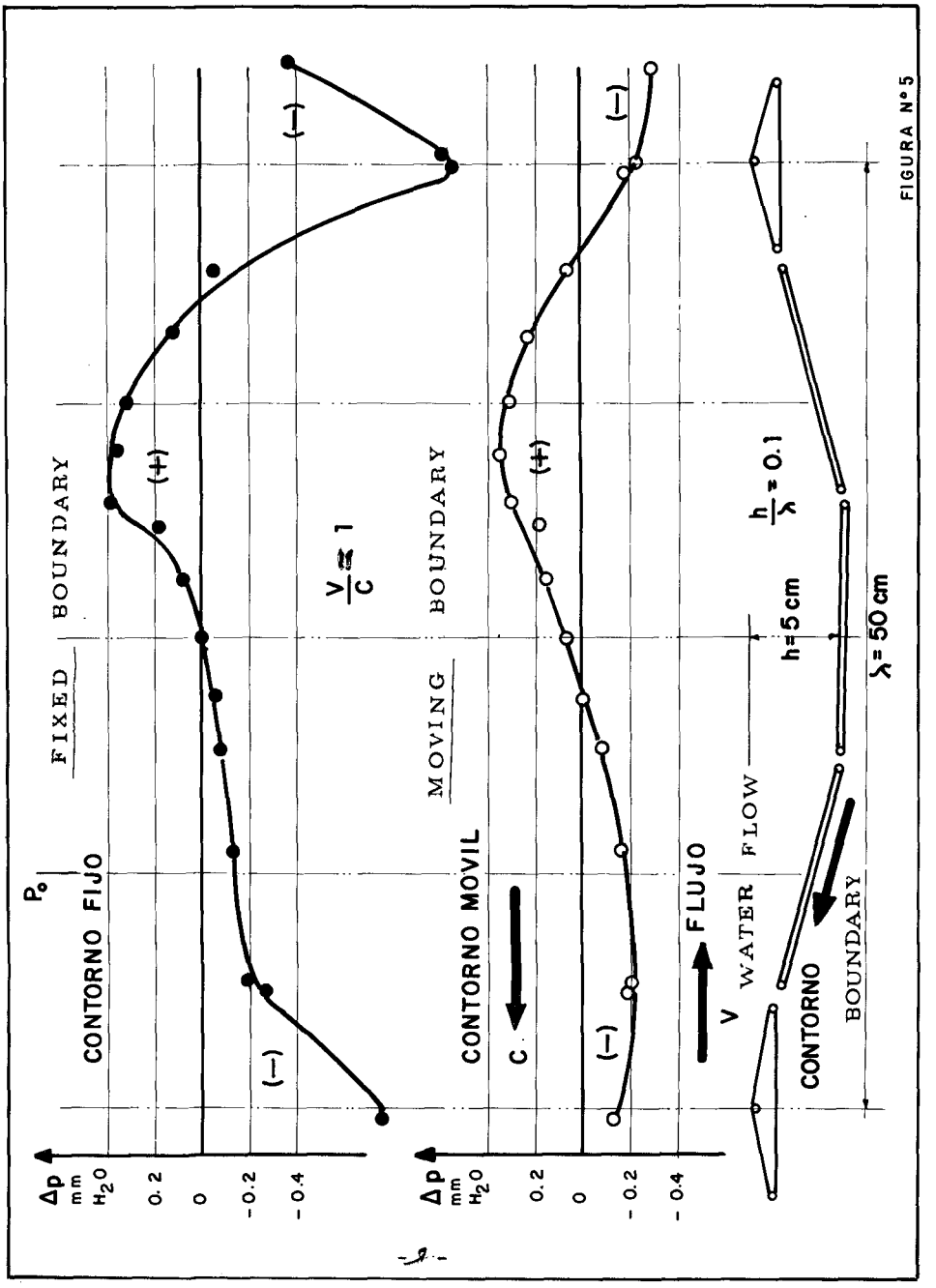
Δp mm H2O
0.2
0
-0.2
-0.4
Po
FIXED BOUNDARY
CONTORNO FIJO
(+)
(-)
V/C ≅ 1
MOVING BOUNDARY
CONTORNO MOVIL
C
FLUJO
V
WATER FLOW
h=5 cm
h/λ = 0.1
λ= 50 cm
CONTORNO BOUNDARY

FIGURA N°5

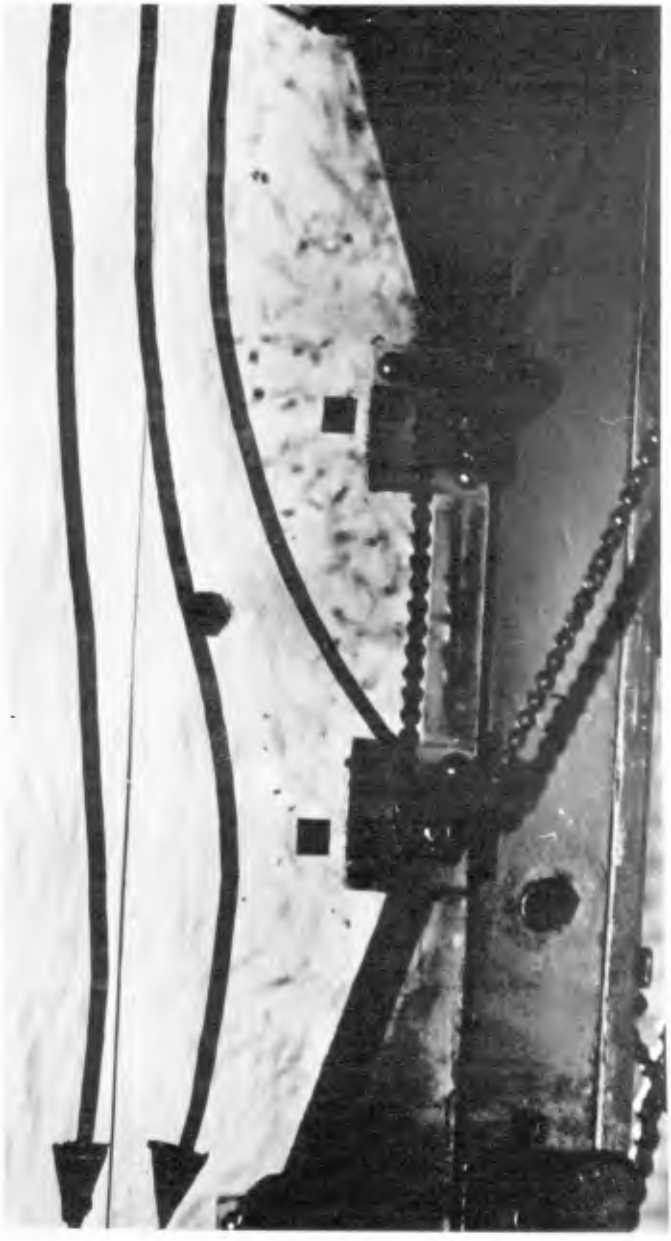

Fig. 6. Flow Characteristics Over a Fixed Wavy Boundary.

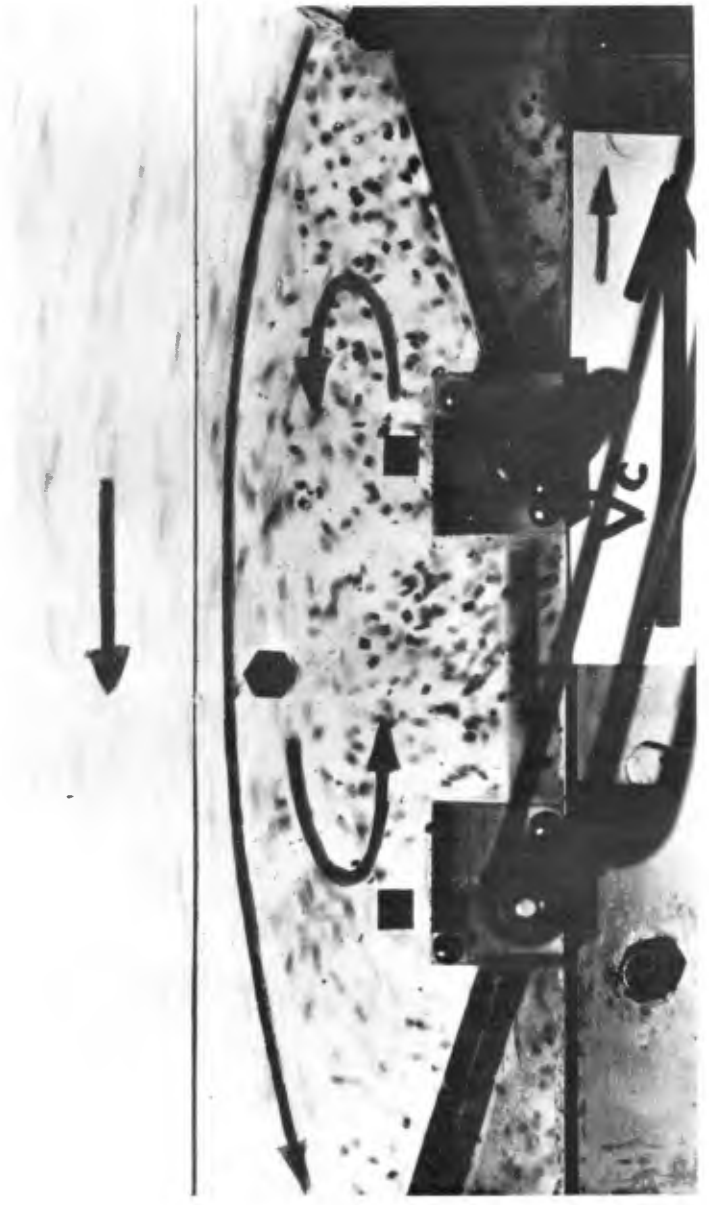

Fig. 7.- Flow Characteristics Over a Finite Amplitude Wave With Moving Bondaries

Fig. 8.- Flow Characteristics Over a Limiting Wave With Moving Boundaries.

gular form, and it is almost similar to the one shown in fig. 2 for the case of small amplitude waves. The variation of the pressure magnitude between both crests is due to the fact that the pressure difference was recorded in relation to a fixed point in the water tunnel. From fig. 7 it can be seen that the flow pattern above the wavy surface presents a large circulation which extends from one crest to the other one. This result coincides with the flow picture obtained by the author in 1966 for the case of a limiting wave profile (ref. 3), which is shown in the picture of fig. 8.

The fact that the pressure distribution curve is similar in shape and in phase-lag (for the same ratio of flow velocity to wave celerity), for small and finite amplitude waves, suggest that the mechanism that produces such effect must be similar in both cases. Since in small amplitude wave experiments a circulation flow pattern over the wave was also observed, it is almost certain that such phenomena has something to do with the phase-lag of the pressure distribution curve. To prove this statement, a different experimental installation was built, and its description follows.

STRATIFIED FLOW EXPERIMENTS WITH FORCED CIRCULATION.-

To prove the role of vorticity on the process of wave's growth, a model was built with two stratified flows moving in opposite directions with a forced circulation produced above the interface. If vorticity has something to do with the process of wave's growth, a wavy disturbance on the interface should occur when a forced circulation is applied above the interface.

The working fluids for such a model were mercury and water, which were moved in opposite directions in a closed test sections with dimenssions 1,2 x 0,7 x 0,01 mt. The motion of both fluids was achieved by means of pumps and the mean velocity could be controlled by valves . Circulation was produced by mechanical means, using a cross made out of stainless steel which rotated in a clockwise direction with a speed that could be varied by an electrical motor.

When both fluids moved without any applied circulation the interface remained undirsturbed. However, as soon as circulation was applied a small amplitude wave would form at the interface. The wave location in relation to the vortex coincided with the expected position, if the pressure distribution would be similar to that obtained from the moving boundary experiments. With the increase of circulation the wave profile would grow, until it reaches the angular shape at the crest, any further increase in the magnitude of circulation produced a breaking effect at the wave's crest. In fig. 9 and 10 a general view of the apparatus is shown, along with a set of pictures of the water-mercury interface for different degrees of the applied circulation. It can be seen that the position of the vortex in relation to the formed wave remains the same regardless of the amplitude of the wave , and coincides with the expected location based on the pressure distribution along the wave's profile obtained from the moving boundary experiments. Also, this experiments showed that the wave length was a function of the mercury mean velocity, as it should be expected from the steady state analysis of a deep water gravity water wave.Therefore, for a given mercury mean velocity a set of waves could be generated by installing a series of rotors located at intervals equal to the wave's length.

General View of the Stratified Flow Installation.

Interface Disturbance when a Small Circulation is Applied

Fig.9

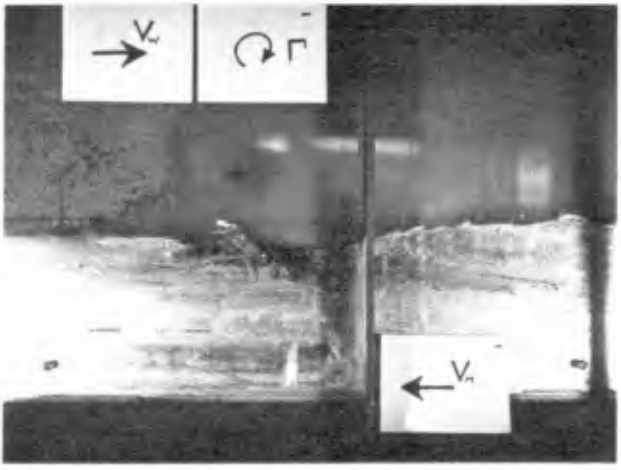

Wave at the Interface Reaching Almost the Limiting Condition

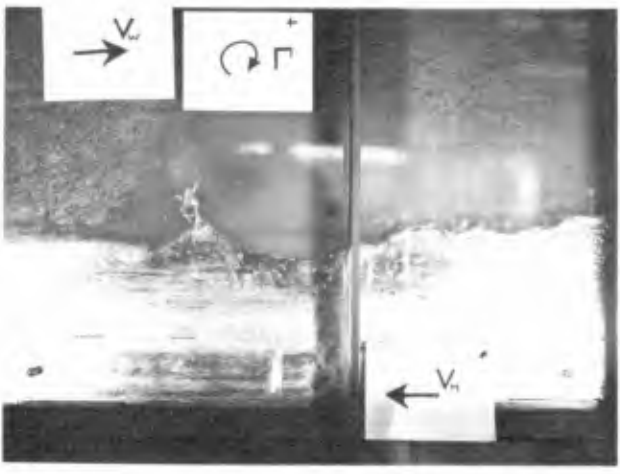

Breaking of the Crest Produced by too Much Applied Circulation

Fig. 10

CONCLUSIONS.-

The obtained experimental results proved that the circulating flow pattern prevailing over the wave surface of small or finite amplitude waves, plays an important role in the energy transfer process from air flow to the water waves, due to the effect of normal stresses. The role of this circulation is to produce a phase-lag in the pressure distribution curve, in relation to the wave's profile. The magnitud of the phase-lag is the same for small or finite amplitude waves, provided that the ratio of flow velocity to wave celerity remains constant.

The fact that the wave's growth can be reproduced by a variable strength vortex located above the interface of two stratified flows, suggest the possibility of developing a mathematical model based on vorticity considerations, which could be applied for the whole history of wave's growth.

AKNOWLEDMENT.-

Finantial support for this project was supplied by " Consejo de Desarrollo Cientifico y Humanistico de la Universidad Central de Venezuela". The author would like to aknowledge the help provided by Mr. R. Lozano during the design and construction of all experimental installations.

REFERENCES.-

1- Miles, J.W. " On the Generation of Surface Waves by Shear Flows". Jour. of Fluid Mech. Vol 3, Part 3,1957, pp 185-204.
2- Benjamin,T.B. " Shearing Flow Over a Wavy Boundary", Jour. of Fluid Mech. Vol 6, Part 2, 1959,pp 161-205
3-Zagustin, K. " Flow Over a Moving Boundary in Relation to Wind-Generated Waves" Ph.D. Thesis, Stanford Univ. 1966
3a- Zagustin, K. Hsu,E.Y. , Street, R.L., Perry,B. " Flow Over Moving Boundary in Relation to Wind-Generated Waves", Tech. Report No. 60 C.E. Dept, Gov't No. AD488373, Stanford Univ., Stanford, Calif. 1966
3b- Zagustin K., Hsu E.Y., Street R.L., " Turbulent Flow Over Moving Boundary" , Jour. Waterways and Harbor Div. A"S.C.E. WW4, Nov 1968 pp.397-414
4- Zagustin K. " Pressure Distribution Over a Moving Wavy Boundary" Proc. XIth Conf. on Coastal Eng., London Sept. 1968.
5- Jeffrey H. " On the Formation of Water Waves by Wind", Proc. Roy. Soc. Ser. A, 110, pp 241-247, 1926.
6- Shemdin O.H., Hsu E.Y. " The dynamic of Wind in Vecinity of Progressive Water Waves", Tech. Rep. No. 66, C.E. Dept. Stanford Univ. 1966.
7 -Chang P.C. " Measurements of air-flow Over Wind Waves", Ph.D. Thesis Colorado State Univ. 1968.
8- Motzfeld H. " Die Turbulente Stromung an Welligen Wanden" Z. angew Math. Mech. Vol 17, 1937, pp 193-212.

CHAPTER 28

WIND-GENERATED CURRENT AND PHASE SPEED OF WIND WAVES[1]

Omar H. Shemdin
Coastal and Oceanographic Engineering Laboratory
University of Florida, Gainesville, Florida 32601

ABSTRACT

Measurements of drift were made in a wind and wave facility at different elevations below the mean water level. The drift profiles were obtained for reference wind speeds, U_r = 3.1, 5.7 and 9.6 m/sec. The measurement technique involved tracing the movement of small paper discs which were soaked in water to become neutrally buoyant at the elevation of release. A logarithmic drift profile is proposed. The water shear velocity, U_{*w}, predicts a surface stress, $\tau_s = \rho_w U_{*w}^2$, in agreement with that obtained from the wind shear velocity, $\tau_s = \rho_a U_{*a}^2$, where ρ_a and ρ_w refer to air and water densities, respectively.

The influence of wind on phase speeds of waves was investigated by solving the first order perturbation problem of the coupled shear flows in air and water. The air velocity profile was described by a logarithmic distribution and the drift profile was described by the proposed drift profile. Adequate agreement is found between the calculated and measured phase speed using Doppler radar in the wave number range 1.9 - 10 cm^{-1}. In the wave number range 0.05 - 0.5 cm^{-1}, measurements of phase speeds were obtained by using two wave gages. The waves were mechanically generated without wind and the wave gages were spaced to obtain coherent signals. The wind was then allowed to blow over the waves and the distance between wave gages was increased to maintain coherence. The wave length and frequency were obtained from the distance between the gages and from the generator frequency, respectively. The measured phase speeds were found to increase with wind speed consistent with theoretical computations.

I. INTRODUCTION

Wind action over water generates both waves and surface drift. Waves contribute to the surface drift through Stokes mass transport. A portion of the total rate of momentum transfer to the water is through the normal stress acting on the disturbed surface and the other portion is due to the tangential stress which contributes, at least in part, to the surface drift. The details of the transfer of momentum and energy from air to water by the normal and tangential stresses are not completely understood yet.

The purpose of this investigation is to shed light on the interaction between the wind generated waves and the wind-induced current. That such an interaction exists can be observed in a wind and wave facility in which waves can be generated mechanically. In the absence of wind, mechanical waves with a preselected length can be generated and detected by two wave gages spaced an integral number of wave lengths apart. The simultaneous wave records under these conditions are coherent. When wind is allowed to blow over the mechanically generated waves the wave records exhibit a phase shift which increases with

[1] Also submitted to the Journal of Physical Oceanography

wind speed. The experimental and anlaytical results of this study suggest that surface drift induced by wind alters significantly the dispersion relationship for small amplitude waves.

Previous investigations of surface drift were obtained by Van Dorn (1953) in a pond and by Keulegan (1951), Wu (1968), Plate and Trawle (1970) and Wright and Keller (1971) in the laboratory. The first two observers found the surface drift to be about 3 percent of the wind speed under turbulent conditions. The surface drift was found to be independent of surface waves which they were able to show by suppressing the waves by spreading detergent over the water surface. The other investigators recorded surface drifts in the range 2.5 - 4.0 percent of the wind speed.

Observations by Francis (1951), Cox (1958), Hide and Plate (1966) and Plate and Trawle (1970) all indicated phase speeds of wind generated waves greater than the calculated values based on the linear wave theory. The difference was found to be greater than that due to the finite amplitude of the waves and was accordingly attributed to the surface drift. An analytical solution by Plate and Trawle (1970) based on a linear drift profile below the surface was found to produce unsatisfactory agreement with observations. They concluded that the need existed for a careful computation of phase speeds based on a reasonable drift profile below the interface.

An interesting computation of surface drift based on Stokes mass transport was carried out by Kenyon (1969) for a fully developed sea. The computation suggests that the entire wind stress is supported by waves in a fully developed sea. However, fetch limited laboratory and field observations do not verify this result.

II. LABORATORY EXPERIMENTS

a. The Wind Wave Facility

The wind and wave facility at the University of Florida was used to conduct experiments on wind generated drift and phase speed of waves under the influence of wind generated drift. The facility is described by Lai and Shemdin (1971). Briefly, the wave channel is 1.83 meters wide and 45.7 meters long, and is divided into two bays of equal width. The height of the facility is 1.93 meters and the water depth is maintained at 91.5 cm by a small water pump. One bay is provided with a roof and is used as a wind channel. The wind intake is modified to produce a turbulent flow regime throughout in the wind channel. Waves can be generated mechanically by an electrohydraulic system. The wave energy is absorbed at the down-wind end of the tank by baskets mounted on a steel ramp and filled with stainless steel turnings.

The wind velcoity profile over the water surface was measured by a standard pitot-static tube manufactured by United Sensors, Inc. and a sensitive differential pressure transducer. The velocity profiles near the air-water interface were found to follow a logarithmic distribution as shown by Lai and Shemdin (1971). From the slopes of the logarithmic distributions the shear velocity, U_{*a}, was obtained and used to evaluate the boundary shear stress at different wind speeds.

b. Wind Generated Drift Profile

The drift of neutrally buoyant particles below the surface was measured by

using small paper discs 6 mm in diameter. The discs were obtained by a standard paper hole puncher. When soaked in water for a few seconds the paper discs became neutrally buoyant and followed the wind-induced drift. It was found desirable to soak the discs at the elevation of the release since a vertical temperature gradient existed in the water which affects the buoyancy of the discs. Normally a few discs were released, some ascended and other descended in the flow but invariably a few remained at the elevation of the release and drifted horizontally. Particle speeds of ten discs were averaged at each elevation to obtain a mean value for that elevation.

The drift profiles for three reference wind speeds, U_r = 3.1, 5.4 and 9.1 m/sec. are shown in Fig. 1. The reference probe is located at 183 cm downstream of the air intake and 16.5 cm below the roof plate and is used to insure repeatability of experiments. The drift profiles exhibit a sharp gradient immediately below the surface and follow a logarithmic distribution when graphed downward with respect to the surface as shown in Fig. 2. A logarithmic profile of the form

$$U_w(o) - U_w(z) = \frac{U_{*w}}{\kappa} \ln \frac{z}{z_{ow}}, \tag{1}$$

is proposed where $U_w(o)$ is the surface drift, $U_w(z)$ is the drift at elevation z below the surface, κ is the universal von Karman constant and z_{ow} is a roughness height. Such a profile was observed by Bye (1967) to describe the ocean drift measurements reasonably well. This profile has a number of desirable features: (i) it has an analogous form to the profile associated with a rough turbulent boundary layer past a rigid boundary and suggests that the drift current is turbulent in nature; (ii) it yields a shear velocity, U_{*w}, which provides an independent method to estimate the surface stress, τ_s, defined by

$$\tau_s = \rho_w U_{*w}^2, \tag{2}$$

where ρ_w is the water density; and (iii) it provides a shear profile to investigate analytically the properties of the wind generated waves superimposed on the wind generated drift.

The surface stress, τ_s, can also be estimated from the wind velocity profiles by the relationship

$$\tau_s = \rho_a U_{*a}^2 , \tag{3}$$

where ρ_a is the air density and U_{*a} is obtained by fitting the log relation (17) to the wind profile. The surface stress values obtained using both wind and drift profiles are compared in Fig. 3 for different free stream (maximum at station in the wind tunnel) wind speeds, U_∞. The three dirft profiles shown in Fig. 2 were used to obtain the surface stresses according to (2). Four other wind profiles corresponding to reference wind speeds, U_r = 1.95, 2.96, 4.57 and 10.66 m/sec were available and were used to obtain the surface stress according to (3). The best fit curve through all the data is given by

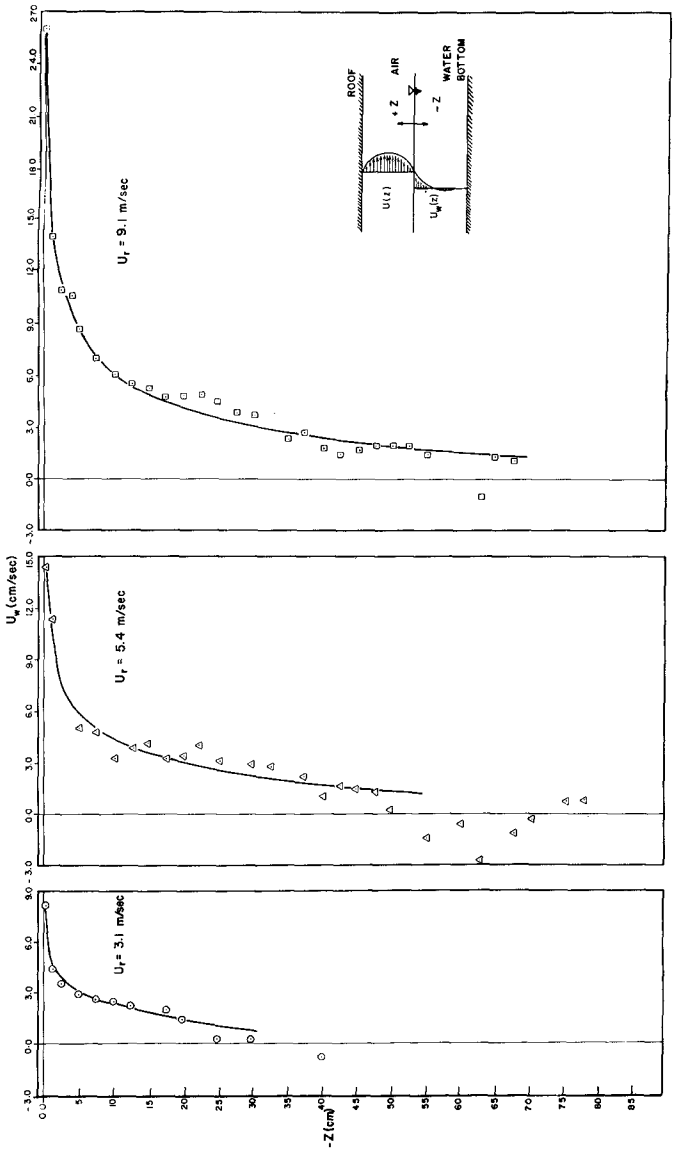

Figure 1 Wind generated drift profiles associated with the three reference air speeds.

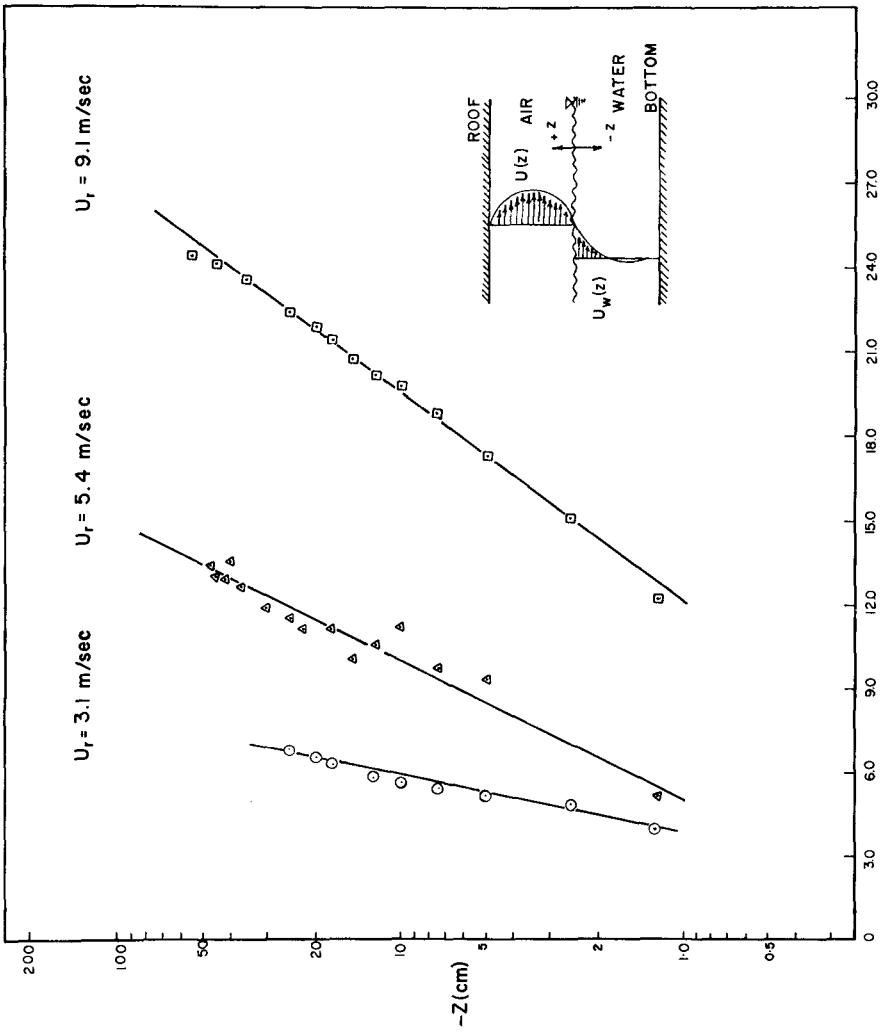

Figure 2 Logarithmic fit of the wind generated drift profiles.

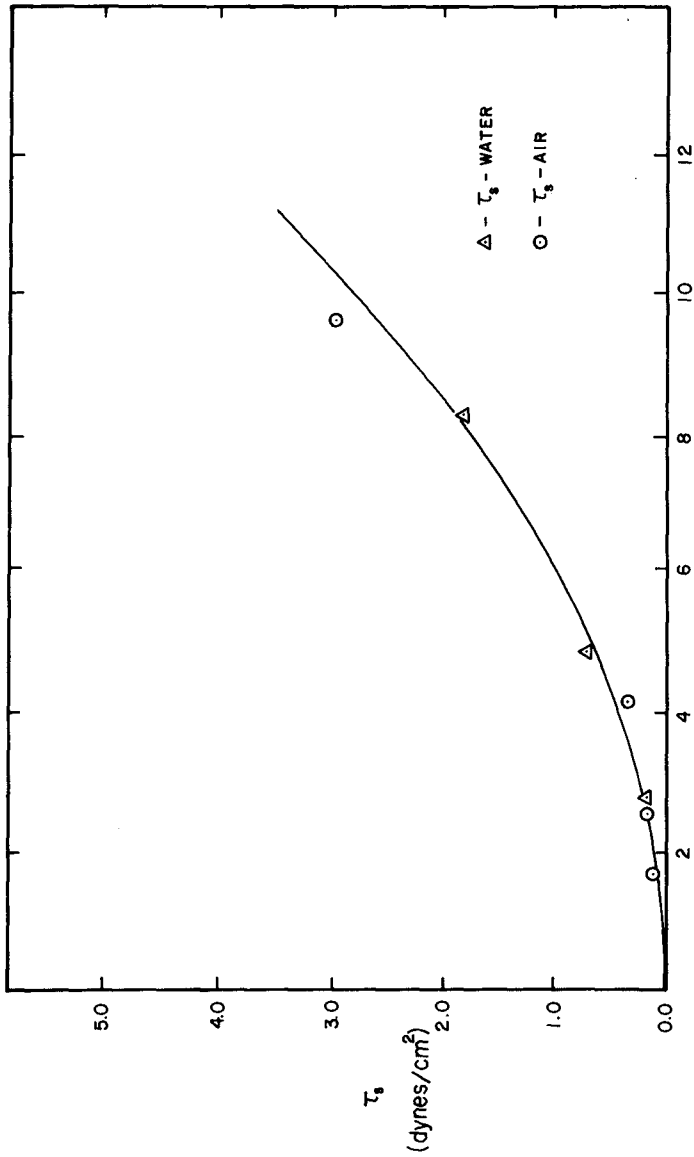

Figure 3 Surface stress obtained from both the air and the drift profiles.

(4)

where the drag coefficient 2.45×10^{-3} is consistent with other laboratory measurements.

In a fully developed sea, it was suggested by Bye (1967) and Kenyon (1969) that the wind induced drift is due primarily to Stokes mass transport, S, given by

$$S = a_o^2 \sigma k e^{-2kz} , \tag{5}$$

where a_o, σ and k are the wave amplitude, frequency and wave number, respectively. Integrating over the frequency range in a wave spectrum from σ_U (angular frequency corresponding to minimum wave speed under gravity and surface tension) to σ_L (angular frequency corresponding to spectrum peak) Bye obtained the following relationship for surface drift, $U_w(o)$

$$U_w(o) = \frac{30}{\sigma_L} \text{ cm/sec.} \tag{6}$$

The measured wind wave spectrum peak for U_r = 9.1 m/sec was found to correspond to σ_L = 12.56 rad/sec. Using (6) the surface drift is computed to be 2.4 cm/sec which is one order of magnitude smaller than the measured value of 26.2 cm/sec. Some doubts remain regarding the mechanism of surface drift in the absence of wind. Longuet-Higgins (1960) estimated the surface drift to be twice the Stokes mass transport because of viscosity. This was disputed by Hwang (1970), however. Regardless of the dominating mechanism the above computation suggests that in a fetch limited case the wind generated drift is primarily due to the direct shear stress action of wind. This conclusion is consistent with the observations of both Keulegan (1951) and Van Dorn (1953) who found the surface drift to remain unchanged when wind generated waves were suppressed by spreading detergent over the water surface. The surface drift, $U_w(o)$, for all the three cases shown in Fig. 1 was found to be 3% of the free stream velocity, U_∞, and in agreement with the results of Keulegan and Van Dorn. More recently drift measurements were obtained by Wu (1968) who reported a linear drift profile near the surface from which he found the surface drift to vary from 3.0 - 5.0% of U_∞. These drift profiles were measured in a layer 3.8 mm below the surface. Estimates of the surface stress based on such a linear gradient can be subject to errors due to the steep gradient near the surface which is perturbed by wind generated ripples.

c. Phase Speed of Wind Waves

As indicated in Section I the phase speeds of wind generated waves were found by other investigators to be greater than calculated values based on the linear wave theory. In order to verify these results and to provide complete data for comparison with an analytical prediction (to be discussed in Section III), measurements of phase speeds were obtained in the wind wave facility by using mechanically generated waves and two capacitance wave gages. Initially no wind was allowed and the two wave gages were spaced an integral number of wave lengths apart to obtain a coherent signal. Then wind was allowed to blow over the water surface and one wave gage was moved away from the other until the signals became coherent again. The new distance between the wave gages was taken to

represent an integral multiple of the mechanically generated wave length in a current-wave field. From the wave length and frequency the phase speed, C, was computed. This procedure was followed for waves with wave numbers in the range 0.05 - 0.5 cm^{-1} and free stream velocity, U_∞, from 0 to 8.0 m/sec. Both C and U_∞ were normalized with respect to C_0 defined by

$$C_0^2 = g/k + T\, k/\rho_w, \tag{7}$$

where g is the gravitational constant and T is the surface tension. The results are shown in Fig. 4 for different mechanically generated waves. It is noted that at high wind speeds the wind generated waves drowned the mechanical wave signal and a phase averaging device was used to enhance the periodic wave signal and to suppress the random wind generated ripples. Use was made of a signal averager Model 281 manufactured by Fabri-Tek Instruments, Inc.

The results of Fig. 4 suggest a linear relationship between c and U_∞. Other experimental results by Wright and Keller (1971) obtained for higher wave numbers from doppler spectra of radar backscattering from wind generated waves indicate that the relationship between C and U_∞ need not be a linear one.

III. LINEAR COUPLING BETWEEN WIND AND WAVES

The influence of the wind on the dispersion relation for simple harmonic waves is investigated here via a linear model similar to that of Miles (1957), which was concerned primarily with wave generation. The present formulation is not intended to improve the Miles' model for the air flow, by including the effects of viscosity and non-linear terms (cf., Shemdin, 1969, Saeger and Reynolds, 1971), but rather to include the shear flow on the water side which has heretofor been neglected. It will be demonstrated that the inclusion of the water shear flow can significantly change the dispersion relationship for the waves in the presence of wind, particularly for capillary waves.

Attention is confined to the displacement, η, of the interface being of simple harmonic progressive form:

$$\eta = \mathrm{Re}\,[a e^{ik(x-ct)}]\,. \tag{8}$$

a. Equations of Motion for Flow Below the Interface

Considering a coordinate system defined in Fig. 5 where waves propagate in the positive x-direction with crests parallel to the y-direction and z positive in the vertical direction the equations of motion governing small perturbation of a two dimensional shear flow $U_w(z)$ in an incompressible inviscid fluid with density ρ_w are

$$\frac{\partial U_w}{\partial t} + U_w \frac{\partial U_w}{\partial x} + W_w \frac{\partial U_w}{\partial z} = -\frac{1}{\rho_w} \frac{\partial p_w}{\partial x}\,, \tag{9a}$$

$$\frac{\partial W_w}{\partial t} + U_w \frac{\partial W_w}{\partial x} = -\frac{1}{\rho_w} \frac{\partial p_w}{\partial z} - g\,, \tag{9b}$$

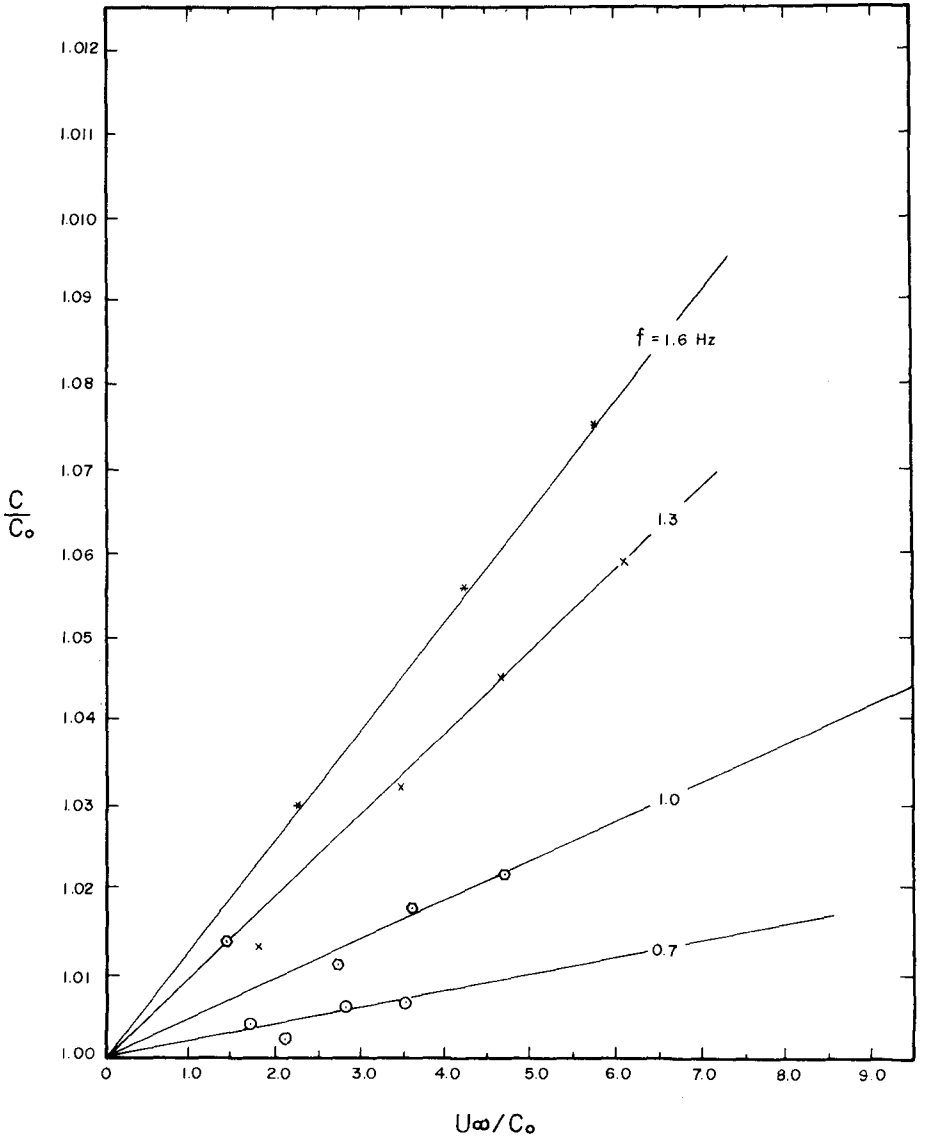

Figure 4 Dependence of phase speed on wind speed, U_∞.

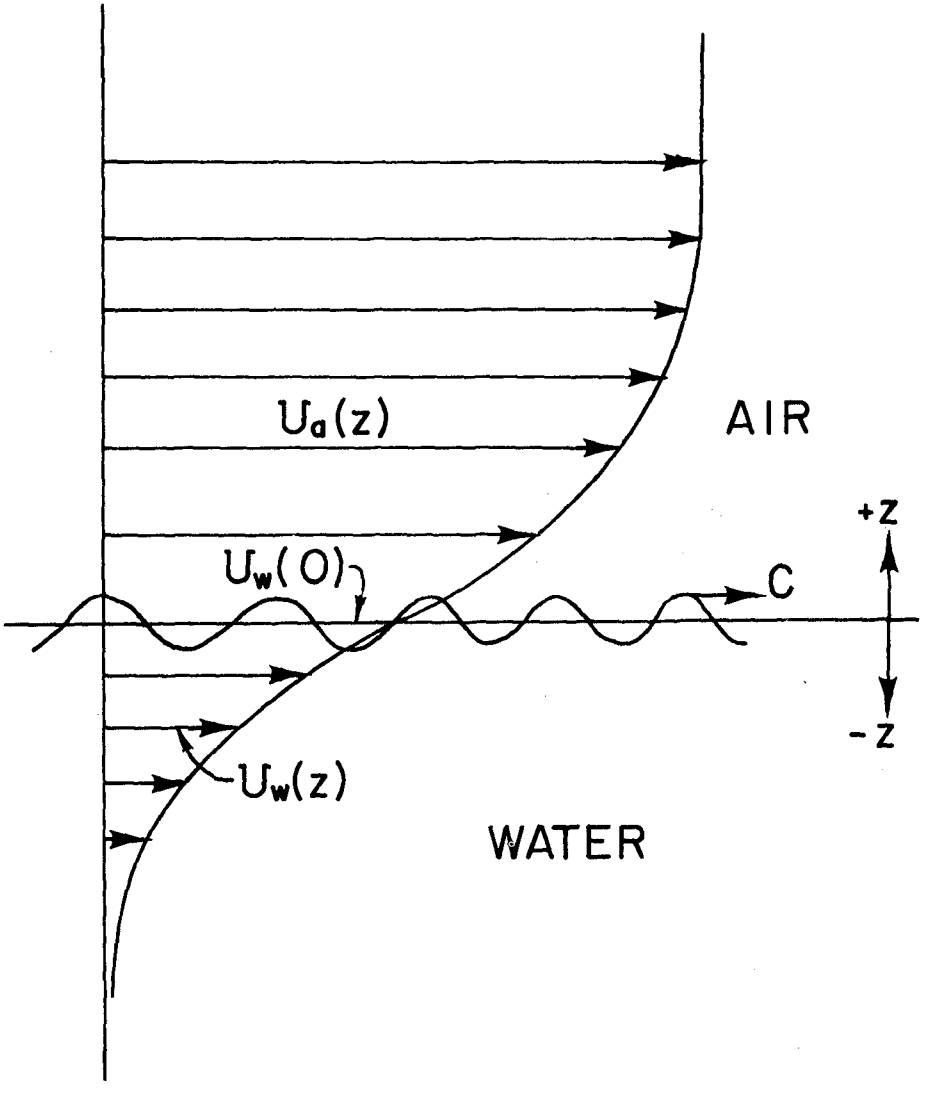

Figure 5 Definition sketch.

$$\frac{\partial U_w}{\partial x} + \frac{\partial W}{\partial z} = 0 \ , \tag{9c}$$

where U_w and W_w are the x- and z- components of the perturbation velocity and p_w is the perturbation pressure. Introducing a stream function defined as

$$U_w = \frac{\partial \psi_w}{\partial z} \ , \ W_w = - \frac{\partial \psi_w}{\partial x} \ ,$$

and assuming ψ_w and p_w to have the same dependence on x and t as η in (8)

$$\psi_w = \hat{\psi}_w \, e^{ik(x-ct)} \ , \quad p_w = \hat{p}_w \, e^{ik(x-ct)} \ ,$$

the following equations are obtained

$$(U_w - C) \frac{\partial \hat{\psi}_w}{\partial z} - \hat{\psi}_w \frac{\partial U_w}{\partial z} = - \frac{\hat{p}}{\rho_w} \ , \tag{10a}$$

$$(U_w - C) \frac{\partial \hat{\psi}_w}{\partial x} = - \frac{1}{\rho_w} \frac{\partial \hat{p}}{\partial z} \ . \tag{10b}$$

Elimination of p_w yields the Rayleigh equation

$$(U_w - C) \frac{\partial^2 \hat{\psi}_w}{\partial z^2} - [k^2 (U_w - C) + \frac{\partial^2 U_w}{\partial z^2}] \hat{\psi}_w = 0 \ . \tag{11}$$

The flow field below the interface may be obtained by solving (11) subject to the boundary conditions

$$\frac{\partial \hat{\psi}_w}{\partial z} = (U_w - C) \frac{\partial \eta}{\partial x} \quad \text{at } z = \eta \simeq 0 \ , \tag{12}$$

$$\hat{\psi}_w \to 0 \text{ as } z \to - \infty \ . \tag{13}$$

A convenient form for $U_w(z)$ is that given by (1).

b. Equations of Motion for Flow Above the Interface

For the lack of a superior model the inviscid model proposed by Miles (1957) will be adopted. The x- and z- components of the perturbation velocity are U_a and W_a, respectively, the perturbation pressure is p_a and the stream function is ψ_a. The following Rayleigh equation and boundary conditions can be derived in a manner similar to that for ψ_w

$$(U_a - C)\frac{\partial^2\hat{\psi}_a}{\partial z^2} - \left[k^2(U_a - C) + \frac{\partial^2 U_a}{\partial z^2}\right]\hat{\psi}_a = 0 \ , \tag{14}$$

$$\frac{\partial \psi_a}{\partial x} = (U_a - C)\frac{\partial \eta}{\partial x} \text{ at } z = \eta \simeq 0 \ , \tag{15}$$

$$\hat{\psi}_a \to 0 \text{ as } z \to +\infty \ . \tag{16}$$

The mean shear flow in air was assumed to have the form

$$U_a(z) = \frac{U_{*a}}{\kappa} \ln \frac{z}{z_{oa}} \ , \tag{17}$$

where z_{oa} is the roughness height.

c. Matching Conditions at the Interface

From the experimental results discussed previously it was found that the shear velocities in the air and in the water could be matched through the surface stress according to

$$\tau_s = \rho_a U_{*a}^2 = \rho_w U_{*w}^2 \ . \tag{18}$$

The normal pressures above and below the interface are matched according to

$$p_w - p_a + T\frac{\partial^2 \eta}{\partial x^2} = 0 \quad \text{at } z = \eta \simeq 0 \ , \tag{19}$$

where T is the surface tension. The pressures are obtained from the equations of motion for the water and the air, respectively

$$\frac{\hat{p}_w}{\rho_w} = \hat{\psi}_w \frac{\partial U_w}{\partial z} - (U_w - C)\frac{\partial \hat{\psi}_w}{\partial z} - g \ a \text{ at } z \simeq 0, \tag{20}$$

$$\frac{\hat{p}_a}{\rho_a} = \hat{\psi}_a \frac{\partial U_a}{\partial z} - (U_a - C)\frac{\partial \hat{\psi}_a}{\partial z} - g \ a \text{ at } z \simeq 0 \ . \tag{21}$$

Eliminating the pressures in (19) yields

$$\frac{1}{ka}\left[\hat{\psi}_w \frac{\partial U_w}{\partial z} - (U_w - C)\frac{\partial \hat{\psi}_w}{\partial z}\right] = \frac{g}{k}\left(1 - \frac{\rho_a}{\rho_w}\right) + \frac{Tk}{\rho_w}$$
$$+ \frac{1}{ka}\left[\hat{\psi}_a \frac{\partial U_a}{\partial z} - (U_a - C)\frac{\partial \hat{\psi}_a}{\partial z}\right] \text{ at } z \simeq 0 \ . \tag{22}$$

d. Method of Solution

Solution of the boundary value problem for the air was obtained numerically by Conte and Miles (1959). The surface pressure was defined

$$\hat{p}_a = (\alpha_m + i\,\beta_m)\,\rho_a\,\left(\frac{U_{*a}}{\kappa}\right)^2 ka, \tag{23}$$

where α_m and β_m were evaluated from (21)

$$(\alpha_m + i\beta_m)\left(\frac{U_*}{\kappa}\right)^2 = \frac{1}{ka}\left[\hat{\psi}_a \frac{\partial U_a}{\partial z} - (U_a - C)\frac{\partial \hat{\psi}_a}{\partial z}\right] - \frac{g}{k} \text{ at } z = 0\,. \tag{24}$$

Eq. (22) becomes for given α_m and β_m

$$\frac{1}{ka}\left[\hat{\psi}_w \frac{\partial U_w}{\partial z} - (U_w - C)\frac{\partial \hat{\psi}_w}{\partial z}\right] = \frac{g}{k} + \frac{Tk}{\rho_w}$$

$$+ (\alpha_m + i\beta_m)\frac{\rho_a}{\rho_w}\left(\frac{U_{*a}}{\kappa}\right)^2\,. \tag{25}$$

It is noted that in the water, the phase speed is mostly greater than U_w so that a critical layer is normally not present. Under these conditions $\hat{\psi}_w$ is real. For waves that grow or decay the phase speed is complex

$$C = C_r + i\,C_i\,.$$

Equating real and imaginary parts of (25) yields

$$\frac{1}{ka}\left[\hat{\psi}_w \frac{\partial U_w}{\partial z} - (U_w - C_r)\frac{\partial \hat{\psi}_w}{\partial z}\right] = \frac{g}{k} + \frac{Tk}{\rho_w} + \alpha_m \frac{\rho_a}{\rho_w}\left(\frac{U_{*a}}{\kappa}\right)^2 \text{at } z = 0, \tag{26a}$$

$$C_i \frac{\partial \hat{\psi}_w}{\partial z} = \beta_m \frac{\rho_a}{\rho_w}\left(\frac{U_{*a}}{\kappa}\right)^2 ka \quad \text{at } z = 0\,. \tag{26b}$$

The propagation speed is given by C_r and was computed from (26a).

The proceudre followed in computing C_r was an iterative one where an initial C_r value was assumed. The boundary value in the air was then solved to yield α_m, the boundary value problem in water was solved to yield $\hat{\psi}_w$ and its first derivative, and using (26a) a new value for C_r was computed. The computation was then repeated for the new C_r value. Solutions to the boundary value problems were obtained by numerical methods similar to the procedure followed by Conte and Miles (1959). The independent variables needed for a solution were U_{*a}, z_{oa} and z_{ow}. The experimental results exhibit considerable scatter in z_{oa} and z_{ow} depending on the velocity profile fit. In most cases it was found that both z_{oa} and z_{ow} were of the same order of magnitude. In the computations it was assumed that $z_{oa} = z_{ow}$ so that a complete computation could be obtained by

simply specifying a logarithmic velocity profile for the air, i.e. specifying U_{*a} and z_{oa}. The surface drift velocity was experimentally found to be 3% of the free stream velocity or 0.6 U_{*a}. Convergence for C_r was normally obtained after 3-6 iterations depending on the input values of U_* and z_{oa}. Convergence was assumed where $\Delta C_r \leq 0.05\ C_r$ was achieved.

IV. RESULTS AND DISCUSSION

Numerical computations were carried out for cases corresponding to the available experimental results. In the wave number range 1.9 - 15.8 cm^{-1} a comparison between the numerical predictions of the phase speed and the measured values by Wright and Keller (1971) are shown in Table 1. The difference in most cases is below 10%. It is noted that a free stream wind velocity of 7.9 m/sec can increase the minimum phase speed ($k = 3.7\ cm^{-1}$) by 100%. Convergence in this range of k was achieved readily. However, for the smaller wave numbers which corresponded to the experimental results discussed in Section 2 convergence could not be obtained. Either overflow or underflow invariably occurred in the computations. Modification of the numerical procedures appear to be necessary to extend the computations to the lower wave numbers.

By way of summarizing the experimental and numerical results it was found convenient to parameterize the phase speed of waves in a shear flow according to

$$c = c_0 + \alpha U_\infty , \tag{27}$$

where α is a shear flow parameter which can be dependent on U and wave frequency, σ. Figure 6 shows the dependence of α on σ for the experimental results described in this paper (denoted by UF) and the experimental results of Wright and Keller (1971) (denoted by NRL). Numerical computations for $U_\infty = 2.25$ and 7.9 m/sec are also shown. The following observations are drawn under laboratory conditions:

i) When the surface drift is small or equal to the orbital wave velocity the motion in water is dominated by the orbital motion and a negligible increase in phase speed is produced by the wind induced drift.

ii) When the surface drift is large compared to the orbital wave velocity the surface wave is simply advected by the drift.

iii) When the surface drift is of the same order of magnitude or slightly larger than the orbital velocity a noticeable increase in phase speed can be expected.

The factor α represents the relative influence of the wind induced drift on the phase speed of waves. It is observed that in the laboratory the wind induced drift is large enough to produce a significant increase in phase speeds of capillary waves. In the field where wind speeds greater than 100 mph are found under hurricane conditions a significant increase in phase speeds of gravity waves are to be expected.

TABLE I

COMPARISON BETWEEN COMPUTED AND MEASURED

PHASE SPEED

k (cm^{-1})	U_∞ (m/sec)	Computed C_c (cm/sec)	Measured C_m (cm/sec)	% Difference
1.90	7.9	51.4	51.6	-0.4
3.86	7.9	49.1	48.0	2.2
5.80	7.9	50.5	49.2	2.6
9.07	7.9	53.7	47.0	12.5
15.80	7.9	61.7	50.0	19.0
1.86	2.25	32.15	30.0	6.7
3.98	2.25	30.3	29.5	2.6
5.90	2.25	30.6	30.0	2.0
9.00	2.25	33.5	32.0	4.5
15.70	2.25	38.4	32.0	16.5

V. CONCLUSIONS

The following conclusions are derived from this investigation:

1. The dispersion relationship governing small amplitude waves is significantly altered by the wind induced surface drift when the surface drift is large compared to the orbital wave velocity.

2. Strong interaction can exist between waves and the surface drift when the latter is not small. This can play a significant role in energy transfer among waves with different wave numbers in a spectrum.

3. The wind induced drift profile can be conveniently approximated by a logarithmic distribution.

4. When extending the above results to the open sea conditions care must be exercised to allow for the absence of lateral constraints.

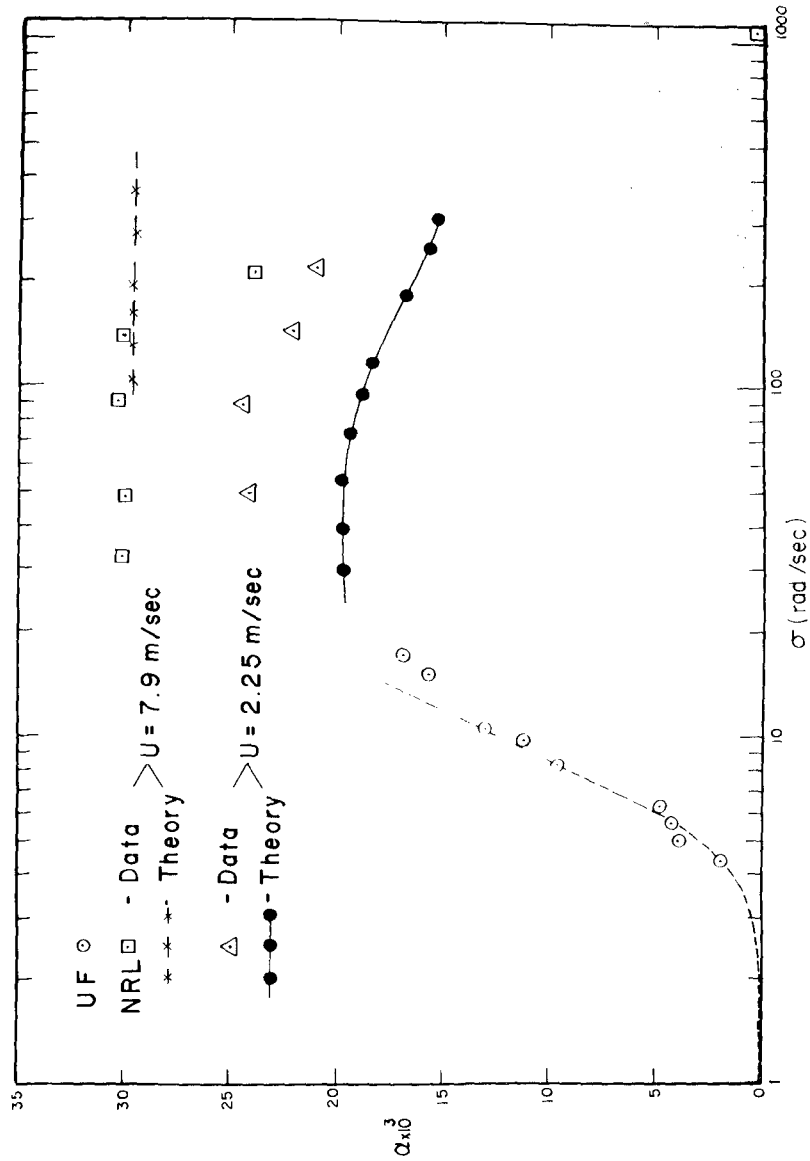

Figure 6 Dependence of α on σ and U_∞ from numerical and experimental results.

ACKNOWLEDGEMENT

The author acknowledges the contribution of Dr. A. Verma in the early phase of the numerical study and the efforts of Messrs. P. M. Lin and C. Horstmann in the experimental phase of the study. The research was supported by the National Science Foundation under Grant GK-3986 and the Coastal Engineering Rdsearch Center under Contract No. DACW 72-71-C-0020. Significant interaction with Dr. J. W. Wright at the Naval Research Laboratory facilitated parts of this study. His results were presented as a companion paper at the Symposium on Sea-Air Interaction.

REFERENCES

Bye, J.A.T., (1967) "The Wave-Drift Current," J. Marine Res., 25, 95-102.

Conte, S.D. and Miles, J.W., (1959), "On the Numerical Integration of the Orr-Sommerfeld Equation," J. Soc. indust. Appl. Math., 1, 361-366.

Cox, C.S., (1958), "Measurements of Slopes of High-Frequency Wind Waves," J. Marine Res., 16, 199-225.

Francis, J.R.D., (1961), "The Aerodynamic Drag of a Free Water Surface," Proc. Roy. Soc., Ser. A, 2D6, 387-4D8.

Hide, G.M. and E. J. Plate, (1966), "Wind Action on Water Standing in a Laboratory Wave Channel," J. Fluid Mech., 26, 651-687.

Huang, N.E., (1970), "Mass Transport Induced by Wave Motion, J. Marine Res., 20, 35-50.

Kenyon, K.E., (1969), "Stokes Drift for Random Gravity Waves," J. Geophys. Res., 74, 6991-6994.

Keulegan, G.H., (1951), "Wind Tides in Small Closed Channels," J. Res. Nat'l Bureau of Standards, 46, 358-391.

Lai, R.J. and Shemdin, O.H., (1971), "Laboratory Investigation of Air Turbulence Above Simple Water Waves," J. Geophys. Res., 76, 7334-7350.

Longuet-Higgins, M.S. (196D) "Mass Transport in the Boundary Layer at a Free Oscillating Surface", J. Fluid Mech., 8, 293-306.

Miles, J.W., (1957), "On the Generation of Waves by Turbulent Wind", J. Fluid Mech., 2, 417-445.

Plate E. and Trawle, M., (197D), "A Note on the Celerity of Wind Waves on a Water Current", J. Geophys. Res., 75, 3537-3544.

Saeger, J.C. and Reynolds, W.C., (1971), "Perturbation Pressures over Traveling Sinusoidal Waves with Fully Developed Turbulent Shear Flow," Dept. of Mechanical Engineering, Tech. Report No. FM-9, Stanford University, Stanford, California.

Shemdin, O.H., (1969), "Instantaneous Velocity and Pressure Measurements above Propagating Waves," Dept. of Coastal and Oceanographic Engineering, Technical Report No. 4, University of Florida, Gainesville, Florida.

Van Dorn, W.G., (1953), "Wind Stress on an Artificial Pond," J. Marine Res., 12, 249-276.

Wright, J.W. and Keller W.C., (1971), "Doppler Spectra in Microwave Scattering from Wind Waves," The Physics of Fluids, 14, 466-474.

Wu, J., (1968), "Laboratory Studies of Wind Wave Interactions," J. Fluid Mech., 34, 91-122.

CHAPTER 29

HORIZONTAL AND VERTICAL WATER PARTICLE VELOCITIES INDUCED BY WAVES

Yoshito Tsuchiya
Professor of Coastal Engineering

and

Masataka Yamaguchi
Research Assistant of Coastal Hydraulics

Disaster Prevention Research Institute
Kyoto University, Kyoto, Japan

ABSTRACT

Measurements of horizontal and vertical water particle velocities induced by regular waves, wind waves generated by a wind wave tank and ocean waves in shallow water were made using a Doppler-type sonic current meter. For regular waves, the validity of wave theories such as Stokes and cnoidal waves is investigated by comparison between theoretical curves and the experimental results. For wind waves and ocean waves, power spectra of water particle velocities and cross-correlations between surface displacement and water particle velocity are considered, especially in the latter case, directional spectra calculated from both the records are compared each other.

INTRODUCTION

To obtain the water particle velocities induced by waves is of very importance for the investigation of various phenomena on coastal engineering such as wave force, littoral drift and so on. Although the horizontal water particle velocity by regular waves was measured by Goda (1964), Le Méhauté, Divoky and Lin (1968) and Iwagaki and Sakai (1969) using a propeller-type current meter, tracers of neutrally buoyant particles, tracers of hydrogen bubbles and a hot-film anemometer respectively and compared the results of experiment with finite amplitude wave theories, their conclusions are different each other because of difficulty of the measurement. Moreover, there have little been the previous works on the vertical water particle velocity by regular waves, the water particle velocities by wind waves in a laboratory and ocean waves in shallow water except for the some observational results.

This paper deals with the experimental and observational investigations on the horizontal and vertical water particle velocities by regular waves, wind waves and ocean waves measured using a Doppler-type sonic current meter.

EXPERIMENT ON WATER PARTICLE VELOCITIES BY REGULAR WAVES

(1) Experimental Equipment and Procedure

The wave tank used in the experiment is 78 m long, 1.0 m wide and 1.5 m deep which has the sloping model beach of 1/100, 45 m long, as shown in Fig. 1.

The measurements of horizontal and vertical water particle velocities were

made using the Doppler-type sonic current meter of three components, which was set the output of one component to be zero. The principle of this current meter is to make use of the frequency shifts of sonic beam due to the Doppler effect by the motion of buoyant particles in water. Static calibration of this current meter was made moving the carrier equipped with the one, with a various constant speed, and in view of the characteristics of low pass filter which transforms the frequency shifts into the variation of voltage, the response frequency is deduced to be approximately 2 cps, although the dynamic calibration was not carried out. In the experiments, time variations of water particle velocities at a point and the vertical distributions of them including the wave height at the same time were respectively measured for the wide range of wave characteristics.

The wave characteristics used in the experiment are tabulated in Table 1, in which T, h, H and g indicate the wave period, the depth of water, the wave height and the acceleration of gravity respectively.

(2) Experimental Results and Considerations

Fig. 2 shows the comparison between the theoretical curves of finite amplitude waves and the experimental results for horizontal particle velocities at phase of wave crest and wave trough u_c and u_t respectively, in which the notations 1, 2, 3, 4 and c indicate the theoretical curves by Stokes wave theories of each order approximate solution derived by Skjelbreia and Hendrickson (1961) and the cnoidal wave theory of the second approximation by Laitone (1965). These figures show that the degree of increase of water particle velocity at phase of wave crest with wave height is not so large enough to be obtained by the finite amplitude wave theories and that the experimental results at phase of wave trough agree relatively well with the theoretical curves of Stokes waves of the 4th orders and cnoidal waves.

The variation of maximum value of vertical water particle velocity with wave height is given in Fig. 3, which shows that the experimental values are to be good agreement with the cnoidal wave theory, as the value of $T\sqrt{g/h}$ increases.

Fig. 4 shows the vertical distribution of horizontal water particle velocity at phase of wave crest. The experimental results agree with the theoretical curves of the 4th order solution in the case of relatively small value of $T\sqrt{g/h}$ and disagree to be plotted between the theoretical curves of small amplitude and finite amplitude wave theories in the case of large value of $T\sqrt{g/h}$, especially the cnoidal wave theory gives considerably excessive values for large wave height.

Some examples of the time variations of horizontal and vertical water particle velocities which are designated by white and black circles respectively and wave profile are shown in Fig. 5. It is found that the theories are coincided with the experimental results in the figures.

In the experiment of this time, it was verified from above consideration that although the finite amplitude wave theories are applicable for estimation of water particle velocities in the case of relatively small wave height, the deviation of both the results becomes considerably larger with the increase of wave height.

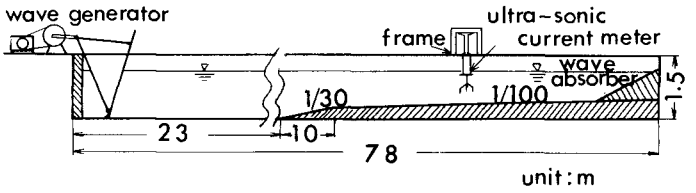

Fig. 1 Schematic sketch of wave tank used

Table 1 Wave characteristics used in experiment by regular waves

T_{sec}	h_{cm}	$T\sqrt{g/h}$	H_{cm}
1.50	55.6	6.30	9.4 ~ 25.3
2.00	55.6	8.40	9.0 ~ 39.6
2.50	55.6	10.50	6.2 ~ 39.1
3.00	55.6	12.60	6.6 ~ 42.2
2.50	27.8	14.85	5.7 ~ 19.5
3.00	27.8	17.82	4.7 ~ 24.8

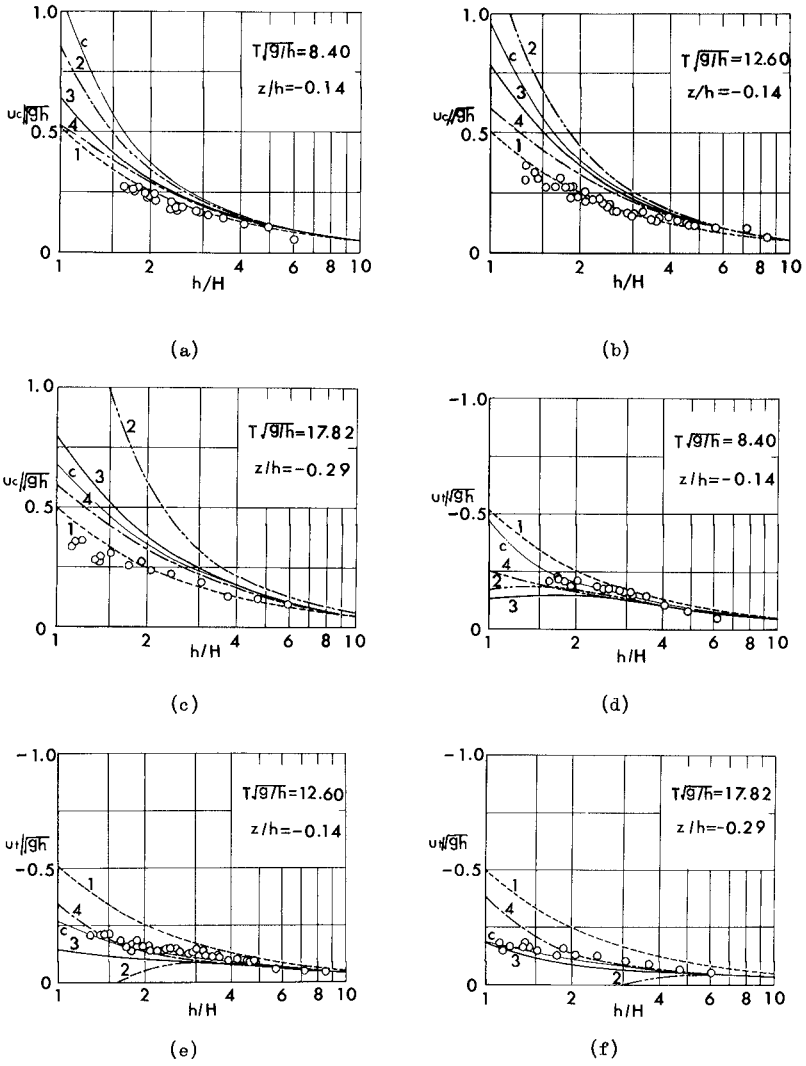

Fig. 2 Variations of horizontal water particle velocity at phase of wave crest and wave trough with wave height

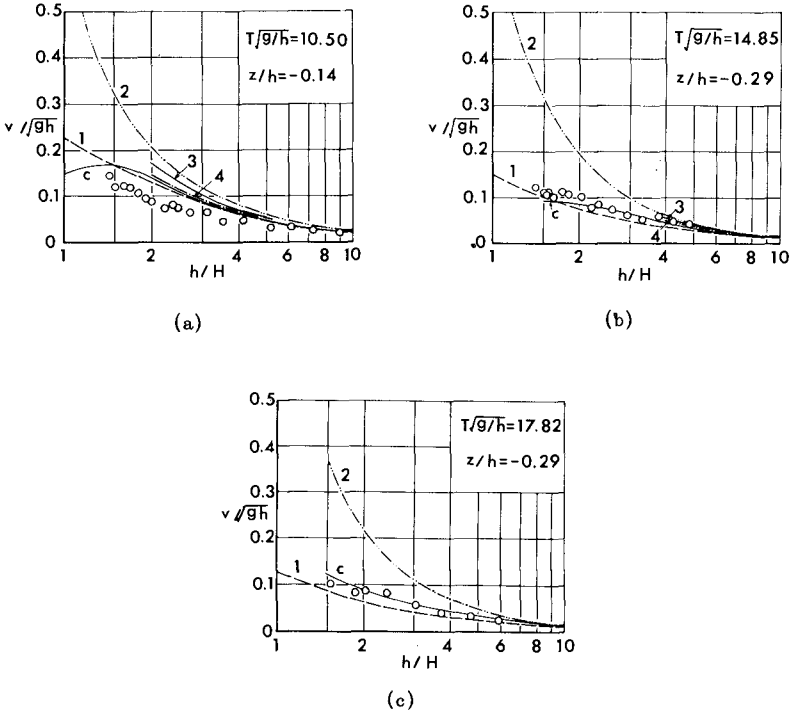

Fig. 3 Variation of maximum value of vertical water particle velocity with wave height

Some factors for this cause are picked up, such as the poor responsibility of this current meter for higher frequency, sheltering and blocking effects for wave motion by the submerged portion of the current meter and so on, in addition to the question for the validity of applying the theories of comparatively lower approximation on a uniform depth to large amplitude waves near wave breaking on a gently sloping beach. Moreover, the more important one may be the wave celerity in most of Stokes wave theories to be calculated on the basis of Stokes' first definition. It has been made clear in the authors' experiment on the vertical distribution of mass transport velocity by waves that the experimental results agree with the theoretical curves derived by Stokes' second definition better than the first definition. This means that the generated waves in a laboratory satisfy approximately the condition of the second definition, which is the average mass transport velocity over a wave length to be zero by addition of a uniform motion. In fact, the 4th order approximate solution calculated using the second definition accounts for the experimental results for wave celerity and water particle velocities better than the first definition. The theo-

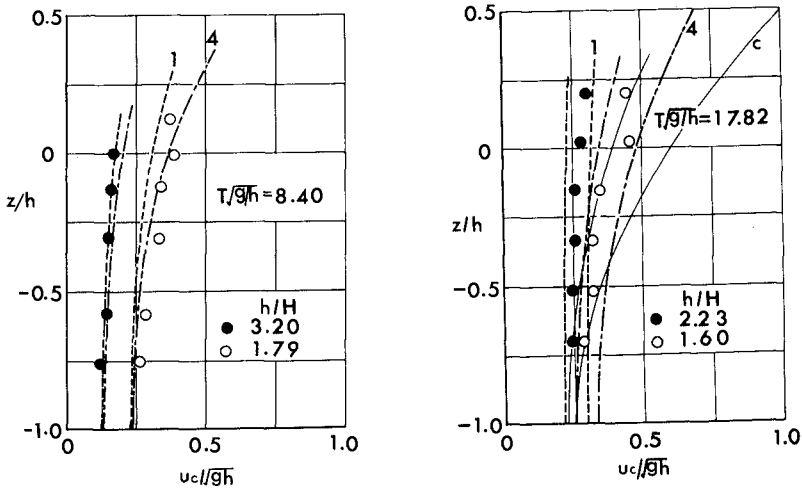

Fig. 4 Vertical distribution of horizontal water particle velocity at phase of wave crest

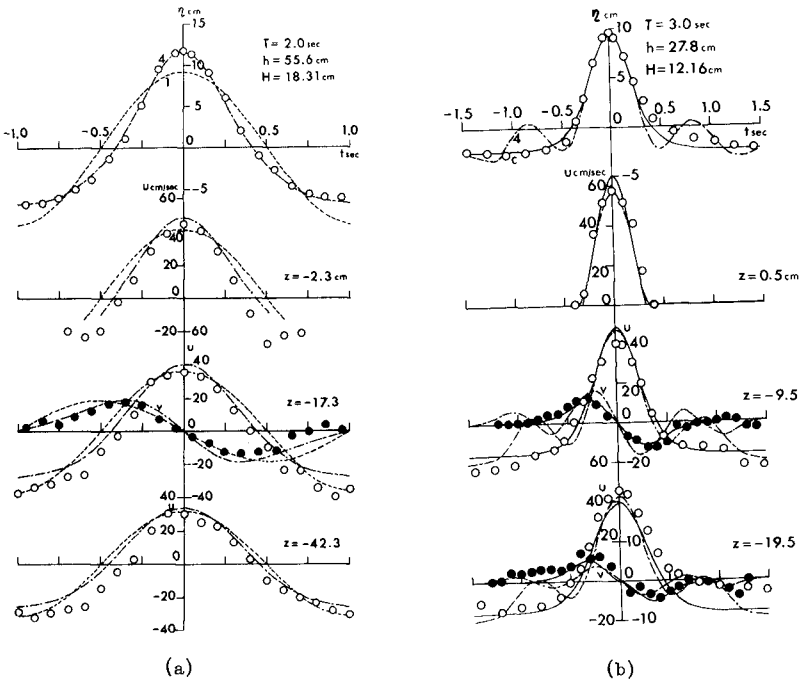

Fig. 5 Time variations of water particle velocities and wave profiles

retical curves of horizontal water particle velocity by the second definition become considerably smaller at phase of wave crest and a little larger at phase of wave trough than those by the first definition and approach the experimental results.

EXPERIMENT BY WIND WAVES IN A LABORATORY

(1) Experimental Equipment and Procedure

A random wave generator used in the experiment is a recirculating wind wave tank which consists of a doughnut-shaped wind wave tank, a blower, a wave direction controller and an experimental straight tank as shown in Fig. 6.

The experiment was carried out by changing wind speed U at constant water depth in the unsteady state that the generated waves are recirculating in the wave tank (called especially recirculating in this paper) and in the steady state such as a usual straight wind wave tank (called non-recirculating). The surface displacement and water particle velocities in quasi-steady and steady states were measured at a portion of recirculating wind wave tank and an experimental straight tank in both the cases. The records were sampled at intervals of 0.1 sec for 1 or 2 minutes and power and cross spectra were computed by the Blackman-Tukey method.

(2) Experimental Results and Considerations

Fig. 7 shows the power spectra of surface displacement and water particle velocities and their coherences ($C_{\eta u}$ and $C_{\eta v}$), in which f is the frequency. It

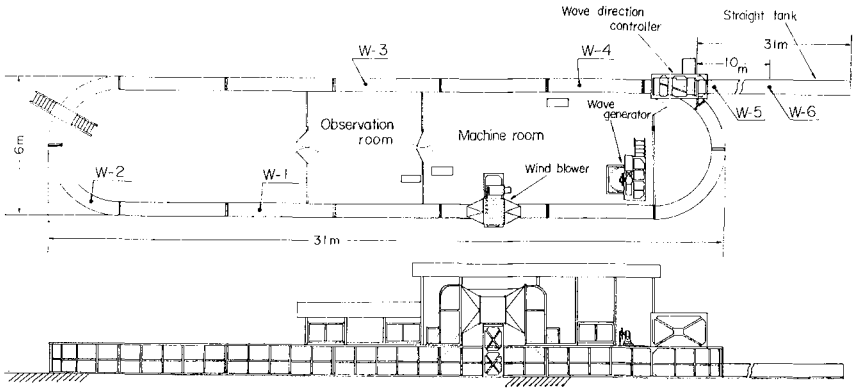

Fig. 6 General view of recirculating wind wave tank

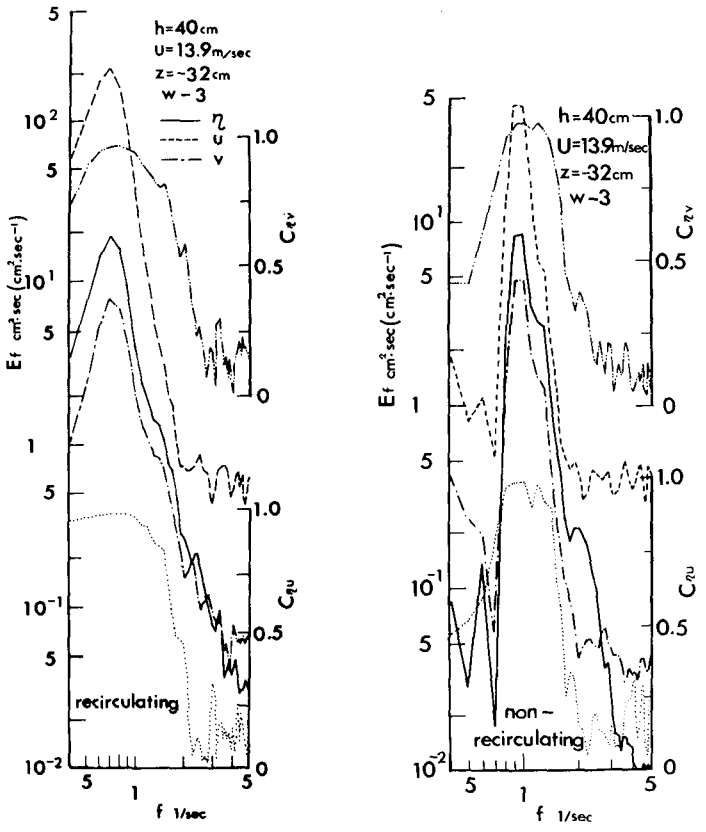

Fig. 7 Power spectra of water particle velocities and surface displacement of wind waves

is found that the correspondence between them is good in the neighbour of peak frequency, but that poor in the region of higher frequency because of the noise, and less responsibility of this current meter and the effect of hydraulic filter. This is also obvious from the characteristics of their coherence.

Fig. 8 is an example of the comparison between the experimental results and the curves of Gaussian distribution, in which N, σ, $\sqrt{\beta_1}$, β_2, and $H_{1/3}$ are the number of samples, standard deviation, skewness, kurtosis and significant wave height respectively. It shows that the frequency distributions of them are ap-

proximately described by Gaussian distribution in spite of a little distortion on the left side.

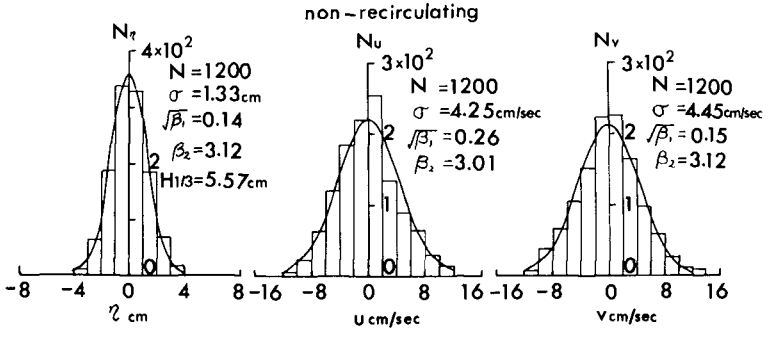

(a) (b) (c)

Fig. 8 Frequency distribution of surface displacement and water particle velocities

In the next, the cross-correlation between them is considered introducing the correction coefficients, because in general the frequency response function calculated from measured records by the spectral analysis G(f) disagrees with the one from small amplitude wave theory due to the effects of non-linearity, irregularity of waves and so on. The correction coefficients for horizontal and vertical water particle velocities n_u' and n_v' are given respectively as

$$n_u' = \{2\pi f \cosh k(h+z)/\sinh kh\}/G(f), \quad n_v' = \{2\pi f \sinh k(h+z)/\sinh kh\}/G(f)$$

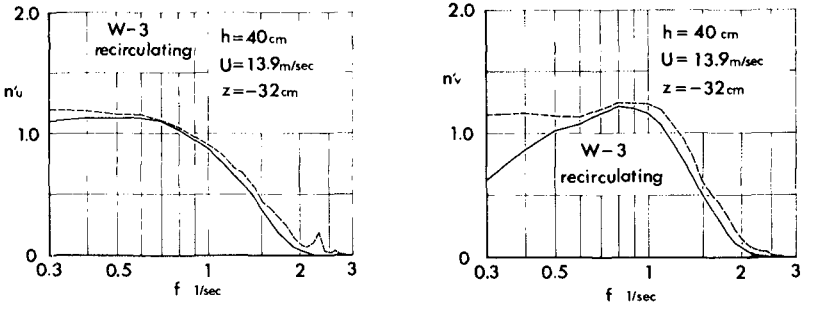

(a) (b)

Fig. 9 Correction coefficient for water particle velocities of wind waves

Some examples are shown in Fig. 9, in which full and dotted lines are correction coefficients determined by power spectra and cross-spectra respectively. It can be seen that the values of them are a little larger than 1 in the neighbour of peak frequency and that rapid decrease appears in the higher frequency region. In this way, the power spectra for horizontal and vertical water particle velocities can be inferred from the surface displacement when the characteristics of these correction coefficients are given.

OBSERVATION BY OCEAN WAVES IN SHALLOW WATER

(1) Observational Method

The simultaneous obserbations of ocean waves and water particle velocities in shallow water were made at the pier on the Ogata Coast facing the Japan Sea in October 1971. Waves were measured by capacitance wire gages arranged the Delta prove array at three stations (St-1, St-2 and St-3) of which distances are 15.4 m (St-1 ~ St-2), 18.8 m (St-1 ~ St-3) and 18.8 m (St-2 ~ St-3) respectively and water particle velocities of three components by the sonic current meter mentioned above which was set on the almost same place as the wave gage (St-2) at the location of 1.65 m below the still water level. The direction of sensors of this current meter was decided by photographs taken directly downwards from the pier. The average depth of water is about 5.7 m.

These records for 5 or 10 minutes were digitalized at intervals of 0.4 sec and power and cross spectra were computed as well as in the previous section.

(2) Observational Results and Considerations

Fig. 10 is one of examples for power spectra of surface displacement at three stations. Spectral form of each other is closely similar and the law of f^{-5} proved by Phillips (1958) holds good in the equilibrium range of higher frequency.

Fig. 11 is the power spectra of water particle velocities of three components and corresponding surface displacement, in which u_x and u_y are two horizontal velocity components in the orthogonal directions and it shows good correspondence each other. An example of correction coefficients for vertical water particle velocity is shown in Fig. 12.

Various methods to measure directional spectra have been proposed. For example, Barber (1961) gave a method of calculating the directional resolving power for array of wave gages and directional spectrum and Nagata (1964) described the directional spectrum to be calculated using a current meter of three components on the basis of the same method as Longuet-Higgins et al (1961).

The directional spectra for peak frequency obtained from simultaneous records of three wave gages and sonic current meter of three components are compared in Fig. 13. In most cases, mutual correspondence is poor owing to the lack of directional resolving power, as shown in Fig. 14 which indicates the one of this array for each direction of incident waves α in the case of frequency of 0.2 cps. Fig. 14 is one of examples for the directional spectra obtained during the observations.

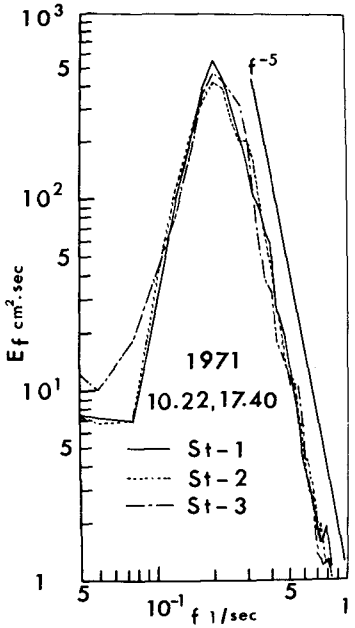

Fig. 10 Power spectra of surface displacement of ocean waves at three stations

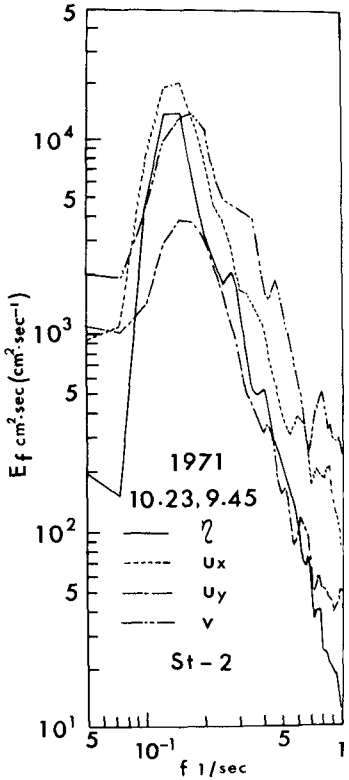

Fig. 11 Power spectra of water particle velocities and surface displacement of ocean waves

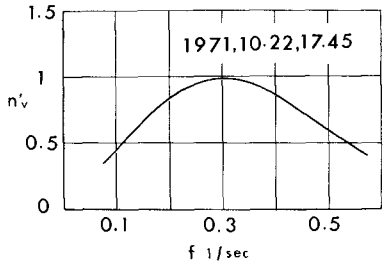

Fig. 12 Correction coefficient for vertical water particle velocity of ocean waves

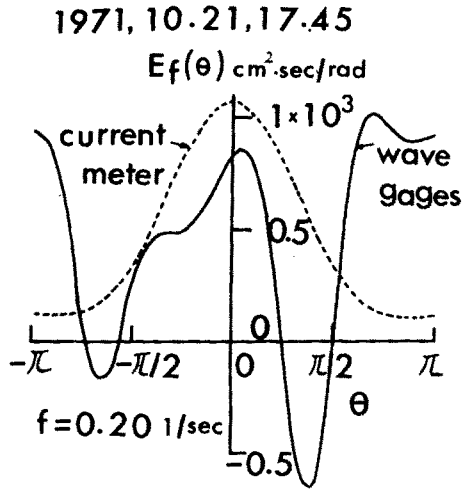

Fig. 13 Comparison between directional spectra obtained from records of waves and water particle velocities

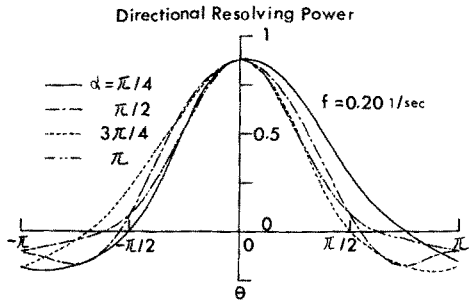

Fig. 14 Directional resolving power for Delta array used in observation

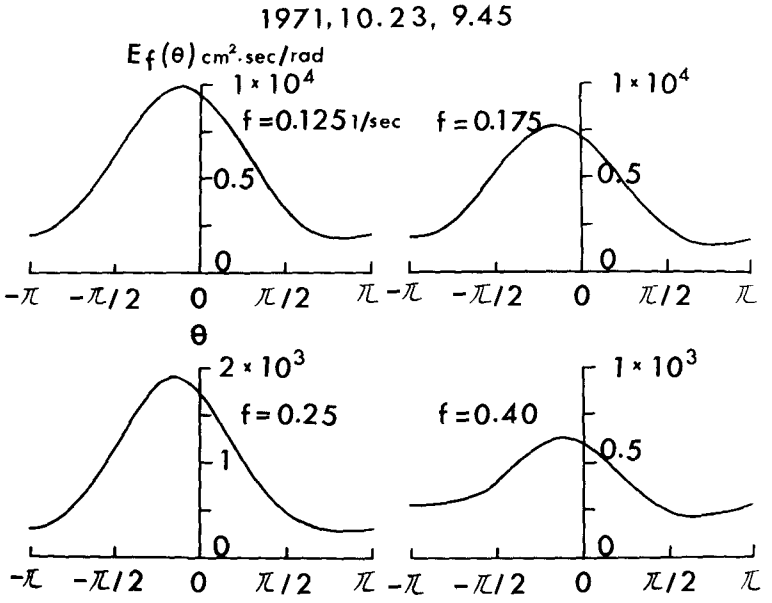

Fig. 15 An example of directional spectra of ocean waves obtained by sonic current meter

CONCLUSIONS

The experimental and observational investigations on the validity of theoretical expressions for horizontal and vertical water particle velocities induced by regular waves, wind waves and ocean waves in shallow water were made using the Doppler-type sonic current meter. For regular waves, it was verified from comparison between the theoretical curves of finite amplitude wave theories and the experimental results that the theories are applicable in the case of relatively small wave height. For wind waves, a method of estimation of power spectra for water particle velocities was proposed. In addition, the directional spectra obtained from the records of waves and water particle velocities at the Ogata Coast were compared each other.

ACKNOWLEDGEMENT

Part of this investigation was accomplished with the support of the Science Research Fund of the Ministry of Education, for which the authors express their appreciation. Thanks are due to Mr. T. Shibano, Research Assistant, for his cooperation during this investigation.

REFERENCES

Goda, Y. (1964). Wave Forces on a Vertical Circular Cylinder, Experiments and a Proposed Method of Wave Force Computation, Report of Port and Harbour Tech. Res. Inst., No. 8, pp. 1-74.

Le Méhauté, B., Divoky, D. and Lin, A. (1968). A Comparison of Theories and Experiments, Proc. 11th Conf. Coastal Eng., Vol. 1, pp. 87-101.

Iwagaki, Y. and Sakai, T. (1969). Experiment on Horizontal Water Particle Velocity of Finite Amplitude Waves, Proc. 16th Conf. Coastal Eng. in Japan, pp. 15-21(in Japanese).

Skjelbreia, L. and Hendrickson, J. A. (1961). Fifth Order Gravity Wave Theory, Proc. 7th Conf. Coastal Eng., Vol. 2, pp. 184-196.

Laitone, E. V. (1965). Series Solutions for Shallow Water Waves, Jour. Geophys. Res., Vol. 70, No. 4, pp. 995-998.

Phillips, O. M. (1958). The Equilibrium Range in the Spectrum of Wind-Generated Waves, Jour. Fluid Mech., Vol. 4, pp. 426-434.

Nagata, Y. (1964). The Statistical Properties of Orbital Wave Motions and Their Applications for the Measurement of Directional Wave Spectra, Jour. Oceanogr. Soc. Japan, Vol. 19, No. 4, pp. 169-181.

Barber, N. F. (1961). The Directional Resolving Power of an Array of Detectors, Proc. Conf. Ocean Wave Spectra, pp. 137-150.

Longuet-Higgins, M. S., Carwright, D. E. and Smith, N. D. (1961). Observations of the Directional Spectrum of Sea Waves Using the Motion of a Floating Buoy, Proc. Conf. Ocean Wave Spectra, pp. 111-132.

CHAPTER 30

VELOCITY AND SHEAR STRESS IN WAVE BOUNDARY LAYERS

P. G. Teleki
Coastal Engineering Research Center
Washington, D. C. 20016

SYNOPSIS

The critical force for the entrainment of sediment on the ocean floor is the maximum, instantaneous shear force. A numerical estimate for the stress is made from the third approximation of a second order boundary layer theory for oscillating laminar flow. The analytical derivation satisfies both the case of flow in an oscillating water tunnel and the case of a progressive (Airy) wave, where the shear distribution depends on the form of the velocity distribution in the boundary layer. Solution for the velocity is on the basis of iteration in an infinite series, where the convective terms are numerically evaluated from lower order solutions. For the boundary shear, the phase lead is found to be less than predicted by linear theory, and although the correction at the third approximation is small compared to lower approximations, the modified vertical distribution provides a basis for the correction of shear measurements, obtained by indirect means, to the boundary value.

INTRODUCTION

In coastal engineering, one of the critical problems is the prediction of the motion of sediment or solid pollutants in the marine environment. Although it is realized that the critical parameter for the entrainment of sedimentary particles is the instantaneous shear force, an accurate assessment of its numerical value for various wave and boundary conditions has been difficult to obtain. In part this stems from the difficulty in analytical modeling of the velocity and shear stress distributions near a solid boundary, but it is also the result of the scarcity of experimental data on these parameters in the zone of shoaling waves. The importance of understanding boundary layer behavior under ocean waves can be well illustrated with the findings of Stone and Summers (1972) who have determined that 95% of the total load moves within 15 cm of the bottom in the nearshore zone and 80% of which is carried as bedload. These figures agree with Saville's (1950) results, where 40-100% of the sediment was found to be transported as bedload in a model basin.

In this paper we are concerned with the modeling of the velocity distribution in laminar flow of oscillating boundary layers of the form found in oscillating water tunnels and of a progressive (Airy) wave. Consequently, we evaluate the shear stress distribution analytically and appraise the contribution the third approximation makes on the phase and amplitude of the instantaneous friction in order to understand the force distribution at the boundary.

The boundary layer theory of Schlichting (1932) is the basis of developments reported herein, with higher approximations of Kestin and others (1961, 1967) and Shah (1970). Similar approaches can be found in the studies of Hill and Stenning (1960), Hori (1962), Hunt and Johns (1963), Dore (1968), Noda (1971) and others.

THE BOUNDARY LAYER

1. The velocity distribution

The distribution of velocity in the potential flow region of harmonically varying flows without displacement is of the form:

$$U(x,t) = U_o(x)\cos\omega t = Re\,(U_o(x)e^{i\omega t}) \tag{1}$$

where U_o is the velocity amplitude at the edge of the boundary layer, $\omega = 2\pi/T$ is the characteristics frequency of oscillation of period T, and Re denotes the real part of the complex variable.

The periodic flow in the free stream region produces oscillations in the fluid near the solid boundary. If the amplitudes of fluctuation are small, such as $(ka, a/d) \ll 1$, the boundary layer behavior can be calculated by using Fourier series for arbitrary fluctuations of the free stream with time (Hill and Stenning, 1960). This method involves linearization of the stream function $\psi(x,y,t)$, which is expanded in an infinite series

$$\psi(x,y,t;\varepsilon) = \varepsilon(\psi_1(z) + \varepsilon\psi_2(z) + \varepsilon^2\psi_3(z) + \ldots)e^{i\omega t} \tag{2}$$

following Schlichting's (1932) technique. According to Kestin and others (1967)

$$\psi = \delta^{-1}U_o(x)\sum_{n=1}^{\infty}\chi_n(\eta,t) \tag{3}$$

given

$$\eta = y/\delta \tag{4}$$

and

$$\delta = (\omega/2\nu)^{1/2} \tag{5}$$

where δ is the thickness of the boundary layer. The parameter χ_n represents the dimensionless stream function.

For incompressible, irrotational flow the stream function and the velocity potential can be equated through the velocity terms, so that

$$-\frac{\partial \psi}{\partial y} = \frac{\partial \phi}{\partial x} = u$$
$$\frac{\partial \psi}{\partial x} = \frac{\partial \phi}{\partial y} = v \tag{6}$$

where $\psi(x,y,t)$ and $\phi(x,y,t)$ meet the requirement

$$\nabla^2 \phi = \nabla^2 \psi = 0 \tag{7}$$

Considering now, that motion is only periodic in the potential flow region, i.e. steady flow is externally not superimposed on the boundary layer, we can write the velocity distribution in the two-dimensional case in two Fourier series

$$u(x,y,t) = u_0(x,y) + \sum_{n=1}^{\infty} u_n(x,y) e^{in\pi t} + \sum_{n=1}^{\infty} u_n^*(x,y) e^{-in\pi t}$$
$$v(x,y,t) = v_0(x,y) + \sum_{n=1}^{\infty} v_n(x,y) e^{in\pi t} + \sum_{n=1}^{\infty} v_n^*(x,y) e^{-in\pi t} \tag{8}$$

where u_0, v_0 are components of the steady "streaming" arising from the second approximation and u^*, v^* represent the complex conjugates of u, v. Complex variable theory is used to minimize computations in this expansion procedure.

We shall now establish the motion in the boundary layer by writing the appropriate momentum equation to $O(\epsilon^2)$

$$\frac{\partial u_1}{\partial t} + u_1\frac{\partial u_1}{\partial x} + v_1\frac{\partial u_1}{\partial y} +$$

$$\frac{\partial u_2}{\partial t} + u_1\frac{\partial u_2}{\partial x} + u_2\frac{\partial u_1}{\partial x} + u_2\frac{\partial u_2}{\partial x} + v_1\frac{\partial u_2}{\partial y} + v_2\frac{\partial u_1}{\partial y} + v_2\frac{\partial u_2}{\partial y} +$$

$$\frac{\partial u_3}{\partial t} + u_1\frac{\partial u_3}{\partial x} + u_3\frac{\partial u_1}{\partial x} + v_1\frac{\partial u_3}{\partial y} + v_3\frac{\partial u_1}{\partial y} = \tag{9}$$

$$\frac{\partial U_o}{\partial t} + U_o\frac{\partial U_o}{\partial x} + V_o\frac{\partial U_o}{\partial y} + \ldots +$$

$$\nu\left(\frac{\partial^2 u_1}{\partial y^2} + \frac{\partial^2 u_2}{\partial y^2} + \frac{\partial^2 u_3}{\partial y^2}\right)$$

If initially we assume $u = O(1)$ and $v = O(\epsilon)$ where $\epsilon = U_o/\omega\delta$ is the perturbation parameter, we can neglect all convective acceleration terms involving $v_{1,2,3}$ and V_o. We also assume the pressure gradient across the layer to be small compared to its magnitude just outside the layer, and use this term to match the flows across the upper boundary. We now make use of the reduced equation:

$$\frac{\partial}{\partial t}(u_1 + u_2 + u_3) + \frac{\partial u_1}{\partial x}(u_1 + u_2 + u_3) +$$

$$\frac{\partial u_2}{\partial x}(u_1 + u_2) + u_1\frac{\partial u_3}{\partial x} =$$

$$\frac{\partial U_o}{\partial t} + U_o\frac{\partial U_o}{\partial x} + \ldots + \nu\frac{\partial^2}{\partial y^2}(u_1 + u_2 + u_3) \tag{10}$$

to the third approximation. Each of the velocity terms in Eq.10 must sepa-

rately satisfy continuity, therefore

$$\begin{aligned} \frac{\partial u_1}{\partial x} + \frac{\partial v_1}{\partial y} &= 0 \\ \frac{\partial u_2}{\partial x} + \frac{\partial v_2}{\partial y} &= 0 \\ \frac{\partial u_3}{\partial x} + \frac{\partial v_3}{\partial y} &= 0 \end{aligned} \tag{11}$$

As $u_2 = u_{21} + u_{22}$, where u_{21} is the periodic and u_{22} is the steady component, the boundary conditions appropriate to Equations 10, 11 are

$$u_1 = \begin{cases} 0 \text{ at } & y = 0 \\ U_0 \text{ at } & y = \delta \end{cases}$$

$$u_{21} = u_3 = \begin{cases} 0 \text{ at } & y = 0 \\ 0 \text{ at } & y = \infty \end{cases}$$

$$u_{22} = \begin{cases} 0 \text{ at } & y = 0 \\ O(\varepsilon) \text{ at } & y = \delta \end{cases}$$

$$v_1 = v_2 = v_3 = \begin{cases} 0 \text{ at } & y = 0 \\ < \varepsilon \text{ at } & y = \delta \end{cases}$$

According to Stuart (1963), the steady velocity at the outer edge of the boundary layer is of the order εU_0, which defines a Reynolds number $R_s = U_0^2/\omega\nu = a^2/\delta^2$. This second perturbation parameter is of $O(1)$ when $\varepsilon \ll 1$, which condition is required for maintaining a non-decaying man transport velocity in the "outer boundary layer", defined by Stuart (1966), and also to validate linearizing the equations of motion. When R_s is large, u_{22} progressively diminishes in the outer layer, the interaction between flow within and outside the boundary layer can be shown to remain negligible, and the steady streaming will not be influenced significantly by the presence of potential flow.

Following Kestin et al (1967), the general expression for the stream function to the nth approximation is of the form:

$$\psi = \frac{1}{\delta}\left[\frac{U_o^{n-1}}{\omega^{n-1}}\frac{d^{n-1}U_e}{dx^{n-1}}\left\{\zeta_{na1}(\eta)e^{ni\omega t} + \zeta_{nb1}(\eta)e^{(n-2)i\omega t} + \ldots\right\} + \frac{U_o^{n-2}}{\omega^{n-1}}\frac{dU_e}{dx}\frac{d^{n-2}U_e}{dx^{n-2}}\left\{\zeta_{na2}(\eta)e^{ni\omega t} + \zeta_{nb2}(\eta)e^{(n-2)i\omega t} + \ldots\right\} + \ldots\right] \tag{12}$$

Differentiating and retaining the real part, three approximations of the horizontal velocity components are obtained.

$$u_1 = Re\left[U_o \zeta'_{1a0}(\eta)e^{i\omega t}\right] \tag{13}$$

$$u_2 = Re\left[\frac{U_o}{\omega}\frac{dU_o}{dx}\left(\zeta'_{2a1}(\eta)e^{i2\omega t} + \zeta'_{2b1}(\eta)\right)\right] \tag{14}$$

$$u_3 = Re\left[\left(\frac{U_o}{\omega}\right)^2\frac{d^2U_o}{dx^2}\left(\zeta'_{3a1}(\eta)e^{i3\omega t} + \zeta'_{3b1}(\eta)e^{i\omega t}\right) + \frac{U_o}{\omega^2}\left(\frac{dU_o}{dx}\right)^2\left(\zeta'_{3a2}(\eta)e^{i3\omega t} + \zeta_{3b2}(\eta)e^{i\omega t}\right)\right] \tag{15}$$

As $y \to \delta$ the steady component becomes

$$u_{22} = -3/4\left(U_o/\omega\ dU_o/dx\right) \tag{16}$$

The third approximation for the velocity component normal to the boundary, and the differential equations for ζ with their pertinent boundary conditions are omitted for the sake of brevity. These can be found in the article by Shah (1970). The first two terms have been determined by Schlichting (1932).

$$\zeta_1(\eta) = \zeta_{1a0}(\eta) = \frac{1-i}{2} + \eta + \frac{1-i}{2}e^{-(1+i)\eta} \tag{17}$$

$$\zeta_{2a}(\eta) = \zeta_{2a1}(\eta) = \frac{1+i}{4\sqrt{2}}e^{-\sqrt{2}(1+i)\eta} + \frac{i}{2}\eta e^{-(1+i)\eta} - \frac{1-i}{4\sqrt{2}} \tag{18}$$

$$\zeta_{2b}(\eta) = \zeta_{2b1}(\eta) = \frac{13}{8} - \frac{1}{8}e^{-2\eta} - \frac{3}{2}e^{-\eta}\cos\eta - e^{-\eta}\sin\eta - \frac{\eta}{2}e^{-\eta}\sin\eta - \frac{3}{4}\eta \tag{19}$$

For the third approximation Shah (1970) obtained

$$\zeta_{3a}(\eta) = \zeta_{3a1}(\eta) = (1-i)\left\{\left(\frac{5}{16\sqrt{3}} + \frac{1+2\sqrt{2}}{16(\sqrt{2}+1)} - \frac{1}{4}\right) - \frac{5}{16\sqrt{3}}\, e^{-\sqrt{3}(1+i)\eta} - \frac{1}{4\sqrt{2}}\, e^{-\sqrt{2}(1+i)\eta} - \frac{1}{8}\left[(1+i)\eta - \left(1+\frac{1}{\sqrt{2}}\right)\right] e^{-(1+i)\eta} + \frac{1-\sqrt{2}}{16(\sqrt{2}+1)}\, e^{-(\sqrt{2}-1)(1+i)\eta} + \frac{1}{8}\, e^{-2(1+i)\eta}\right\} \tag{20}$$

$$\zeta_{3b}(\eta) = \zeta_{3b1}(\eta) = \left[\frac{1}{8}(2-i)\eta^2 - \frac{1}{8}(1+2i)\eta + \frac{1}{1200}(608-521i)\right] e^{-(1+i)\eta} - \left[\frac{1}{8}\eta + \frac{1}{16}(5+7i)\right] e^{-(1-i)\eta} - \frac{i}{80}\, e^{-(3+i)\eta} - \frac{1}{48}(1-i)\, e^{-2(1+i)\eta} - \left[\frac{1}{20}(2+i)\eta + \frac{1}{200}(47+96i)\right] e^{-2\eta} - \frac{3}{4}i\eta + \frac{1}{600}(37+806i) \tag{21}$$

$$\zeta_{3c}(\eta) = \zeta_{3a2}(\eta) = -\frac{3}{16\sqrt{3}}(\sqrt{2}+1)(1-i)\, e^{-\sqrt{3}(1+i)\eta} - \left[\frac{1}{2}\eta - \frac{1+\sqrt{2}}{4\sqrt{2}}(1-i)\right] e^{-\sqrt{2}(1+i)\eta} + \left[-\frac{1}{4}(1+i)\eta^2 + \frac{1}{4}\eta + \frac{1-3\sqrt{2}}{8\sqrt{2}}(1-i)\right] e^{-(1+i)\eta} + \frac{3-2\sqrt{2}}{16(\sqrt{2}+1)}(1-i)\, e^{-(\sqrt{2}+1)(1+i)\eta} + \frac{1-i}{16\sqrt{6}(\sqrt{2}+1)}(12+9\sqrt{2}-7\sqrt{6}+2\sqrt{3}) \tag{22}$$

$$\zeta_{3d}(\eta) = \zeta_{3b2}(\eta) = \left[\frac{i}{12}\eta^3 + \frac{1}{16}(11+3i)\eta^2 + \frac{1}{16}(16-13i)\eta + \frac{1}{800}(903-951i)\right] e^{-(1+i)\eta} + \left[-\frac{1}{20}(3+4i)\eta + \frac{1}{200}(12-159i)\right] e^{-2\eta} - \left[\frac{1}{8}(1-i)\eta^2 + \frac{1}{8}(9+2i)\eta + \frac{1}{16}(13-31i)\right] e^{-(1-i)\eta} + \frac{1}{80}\, e^{-(3+i)\eta} - \frac{3}{2}i\eta + \frac{1}{800}(-311+3137i) \tag{23}$$

Distribution of the horizontal velocity for phase angles $\omega t = 0, \pi/3, \pi/2, 2\pi/3, \pi$ is shown in Figure 1 for $4/\omega(dU_\infty/dx) = 16/\omega^2(U_\infty d^2U_\infty/dx^2) = 1$. Comparison of the velocity profiles indicate that the third approximation is effective near

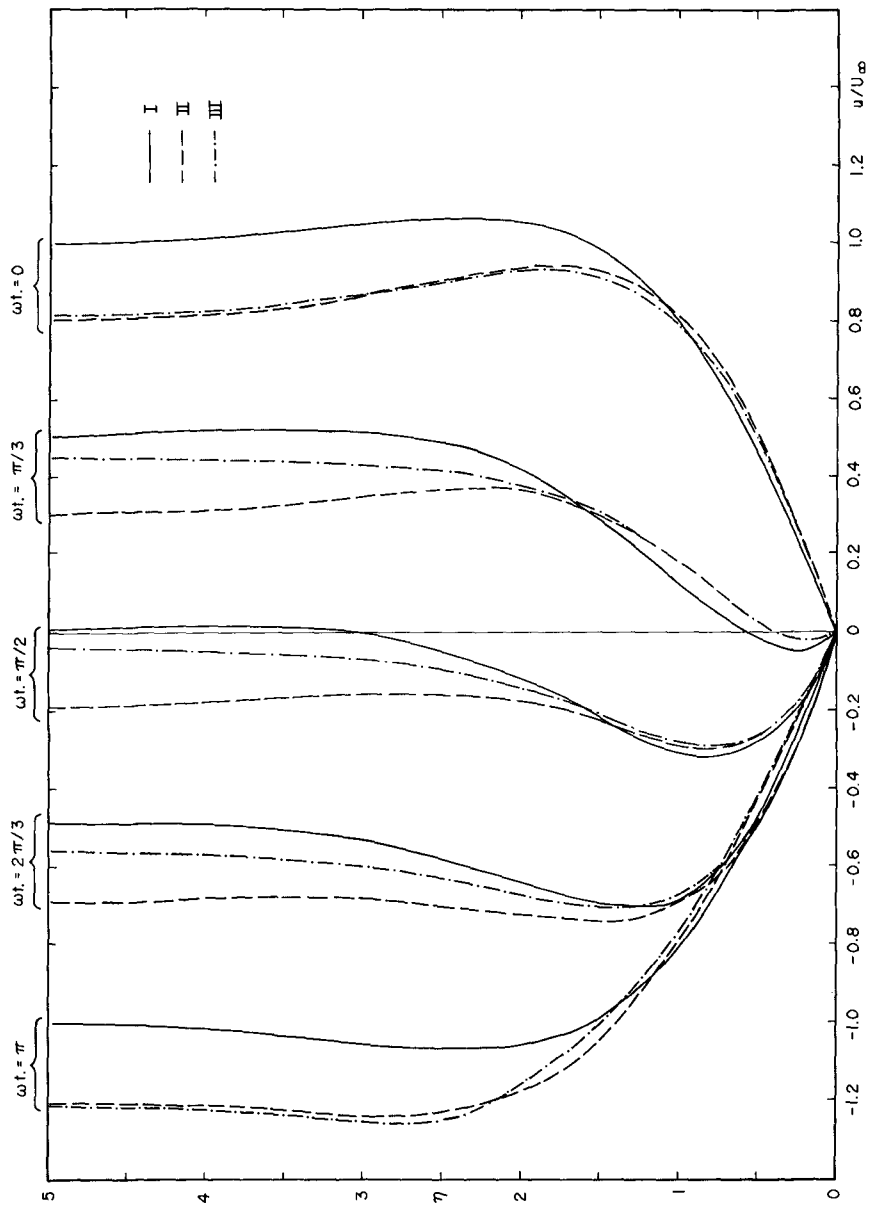
I
II
III
ωt. = 0
ωt. = π/3
ωt. = π/2
ωt. = 2π/3
ωt. = π
u/U∞
1.2
1.0
0.8
0.6
0.4
0.2
0
-0.2
-0.4
-0.6
-0.8
-1.0
-1.2
η
5
4
3
2
1
0

Figure 1

the outer edge of the boundary layer, and especially near flow reversal. It does not, however, contribute to the mass transport velocity owing to the fact that all velocity functions in the third approximation are periodic.

2. Case of a progressive wave

When the external flow is represented by a progressive gravity wave, the appropriate form of the stream function, according to Dore (1968) and Johns (1968), is

$$\psi(x,y,t;\varepsilon) = \frac{a\omega d}{\sinh k_0 d}\left[\psi_0(z)+\varepsilon\psi_1(z)+\ldots\right]e^{i(k_0x-\omega t)} \tag{23}$$

where

$$z = y+d \tag{24}$$

and the wave number can be expanded as

$$k = k_0 + \varepsilon k_1 + \ldots \tag{25}$$

The second term was given by Biesel (1949) as

$$k_1 = \frac{k_0^2 d\,(1+i)}{2k_0 d + \sinh 2k_0 d} \tag{26}$$

The boundary conditions are

$$\psi_0 = \psi_1 = 0 \qquad \text{at} \quad z = d$$

$$\psi_0 = \psi_1 = \text{constant} \quad \text{at} \quad z = 2d+\xi$$

where the free surface is specified by

$$\xi = ae^{i(k_0x-\omega t)}$$

and the depth d, has its origin at the still water surface.

With a change of variables for the zero order stream function we can write

$$\Psi_o(y)e^{i(k_o x-\omega t)} = A \sin ik_o z \sin(k_o x-\omega t) \tag{27}$$

where

$$A = -\frac{a\omega}{k_o \sinh k_o d} \tag{28}$$

Retaining the real part and displacing the coordinate system by $\pi/4$, we obtain the horizontal velocity by differentiation of Eq. 27

$$-\frac{\partial \Psi_o}{\partial y} = U_o = -Ak_o \cosh k_o z \cos(k_o x-\omega t) \tag{29}$$

at the outer edge of the boundary layer. Similarly,

$$\frac{\partial U_o}{\partial x} = Ak_o^2 \cosh k_o z \sin(k_o x-\omega t) \tag{30}$$

$$\frac{\partial^2 U_o}{\partial x^2} = -Ak_o^3 \cosh k_o z \cos(k_o x-\omega t) \tag{31}$$

We assume now, that as $\eta \to 1$, terms of $O(\varepsilon, \varepsilon^2)$ in $k_o d$ remain small for the fixed viscosity in order that the condition of viscous effects outside the boundary layer be avoided. Therefore it follows, that the zero order velocity is considered to adequately describe the free stream oscillation. This is justifiable, since the point of interest is not in the flow far from the boundary, where mass transport and interaction terms are significant; rather in establishing the magnitude of shear stress near $\eta = 0$; which is discussed in the following section. The argument is based on R_s being large, whereby interaction between the mass transport velocity and the inviscid flow in the potential region are neglected, following Stuart's (1966) arguments. When R_s is of $O(1)$, however, the periodic component of the horizontal velocity, obtained in the second approximation, must be matched asymptotically with the

first order velocity εU_1 at the interface, so that the boundary condition reflected in Equation 9 is satisfied. That is,

$$u_{21}(x,y) = Re\left[\frac{U_0}{\omega}\frac{dU_0}{dx}\zeta'_{2b}(\eta)\right]e^{i2\omega t} - \varepsilon U_1(x,y,t) \qquad (32)$$

as shown by Longuet-Higgins (1953) and Noda (1971). Evaluation of interaction terms resulting from the simultaneous perturbation of inner and outer flows remains a continuing research interest of the author.

THE SHEAR STRESS DISTRIBUTION

To assess the potential force available, say for the entrainment of sediment, it is important to know the maximum value of the instantaneous shear at the bottom, its distribution normal to the boundary and its phase advance in respect to the horizontal velocity.

In laminar flow, the shear stress distribution is derived from the velocity gradient

$$\tau = \nu\rho\left(\frac{\partial u}{\partial y}\right) \qquad (33)$$

which expanded to the third approximation becomes, in general

$$\sum_{n=1}^{3}\tau_n = \nu\rho\left[\frac{\partial u_1}{\partial \eta} + \frac{\partial u_2}{\partial \eta} + \frac{\partial u_3}{\partial \eta}\right] \qquad (34)$$

where u_1, u_2 and u_3 are given in Equations 13, 14, and 15 respectively.

The boundary conditions for the auxiliary functions are

$$\left.\begin{matrix}\zeta_1''(\eta), \zeta_{2a}''(\eta), \zeta_{2b}''(\eta) \\ \zeta_{3a}''(\eta), \zeta_{3b}''(\eta), \zeta_{3c}''(\eta), \zeta_{3d}''(\eta)\end{matrix}\right\} = \begin{cases}\text{finite at } \eta = 0 \\ 0 \text{ at } \eta = \infty\end{cases}$$

Solutions for all ζ'' are:

$$\zeta_1''(\eta) = (1+i)\,e^{-(1+i)\eta} \tag{35}$$

$$\zeta_{2a}''(\eta) = -\frac{\sqrt{2}\,(1-i)}{2}\,e^{-\sqrt{2}(1+i)\eta} - e^{-(1+i)\eta}\,(\eta - (1-i)) \tag{36}$$

$$\zeta_{2b}''(\eta) = e^{-\eta}\left[\cos\eta - 2\sin\eta + \eta\cos\eta\right] - \frac{1}{2}e^{-2\eta} \tag{37}$$

$$\zeta_{3a}''(\eta) = -\frac{1}{2}i\eta e^{-(1+i)\eta} + \frac{1+i}{4}\left[\left(3+\frac{1}{\sqrt{2}}\right)e^{-(1+i)\eta} - \frac{5\sqrt{3}}{2}e^{-\sqrt{3}(1+i)\eta} - 2\sqrt{2}\,e^{-\sqrt{2}(1+i)\eta} - \frac{1}{2}e^{-(\sqrt{2}+1)(1+i)\eta} + 4e^{-2(1+i)\eta}\right] \tag{38}$$

$$\zeta_{3b}''(\eta) = \frac{1}{8}\left[\left\{(2+4i)\eta^2 - (6+2i)\eta + \frac{521+608i}{75}\right\}e^{-(1+i)\eta} + \left(2i\eta - (5-3i)\right)e^{-(1-i)\eta} + \frac{3-4i}{5}\,e^{-(3+i)\eta} - \frac{4}{3}(1+i)\,e^{-2(1+i)\eta}\right] - \frac{1}{10}\left(2\eta(2+i) + \frac{27+86i}{5}\right)e^{-2\eta} \tag{39}$$

$$\zeta_{3c}''(\eta) = \frac{3\sqrt{3}\,(\sqrt{2}+1)(1+i)}{8}\,e^{-\sqrt{3}(1+i)\eta} + \frac{1}{4}\left[2(1-i)\eta^2 + 10i\eta - \left(4+\frac{1}{\sqrt{2}}\right)(1+i)\right]e^{-(1+i)\eta} + \left[-2i\eta + \left(\frac{1}{\sqrt{2}} + \sqrt{2} + 1\right)\cdot(1+i)\right]e^{-\sqrt{2}(1+i)\eta} - \frac{2\sqrt{2}-3}{8}(\sqrt{2}+1)(1+i)\,e^{-(\sqrt{2}+1)(1+i)\eta} \tag{40}$$

$$\zeta_{3d}''(\eta) = \frac{1}{4}\left[-\frac{2}{3}\eta^3 + (1-i)\eta^2 + \frac{1}{2}(4+5i)\left\{(1+i)\eta^2 - 2\eta\right\} + \frac{7-3i}{4}\left\{(1+i)\eta - 1\right\} + \frac{113+414i}{50}\right]e^{-(1+i)\eta} + \frac{3+4i}{10}\left[-2\eta+1\right]e^{-2\eta} + \frac{27+139i}{50}\,e^{-2\eta} + \frac{4+3i}{40}\,e^{-(3+i)\eta} + \frac{1}{4}\left[(1+i)\eta^2 - 2i\eta - 2(6-5i)\right]e^{-(1-i)\eta} \tag{41}$$

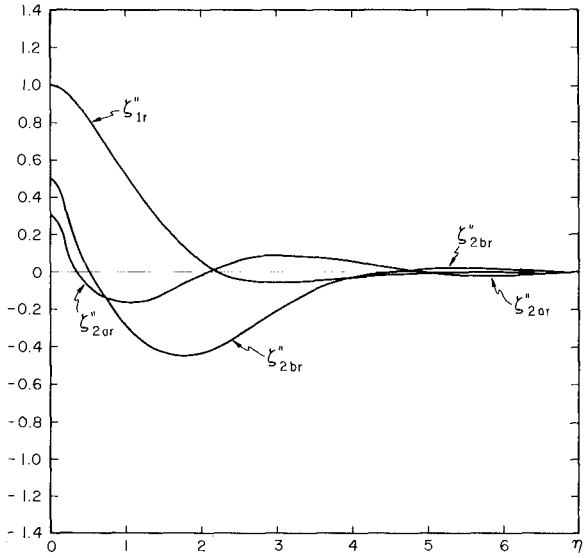

Figure 2

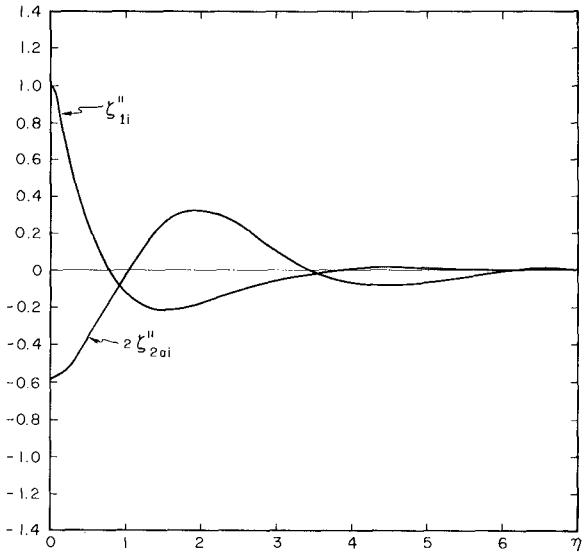

Figure 3

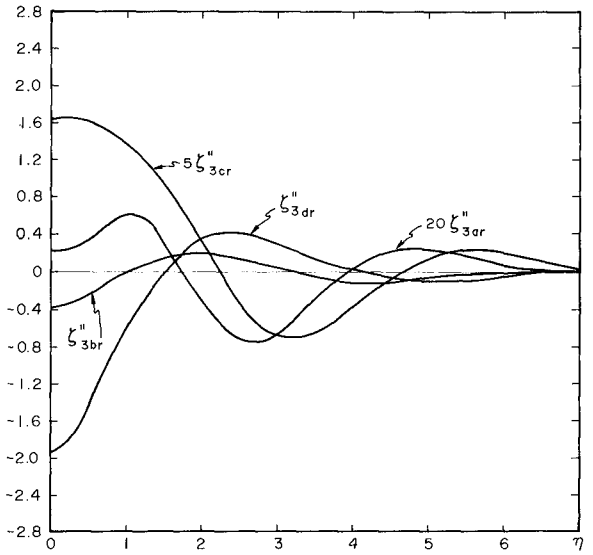

Figure 4

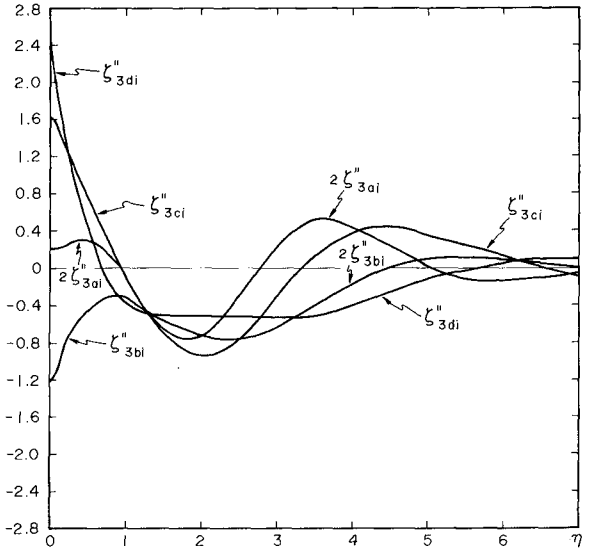

Figure 5

Equations 35-37 are the auxiliary functions of the first and second approximations; these are depicted in Figures 2 and 3 separated into real and imaginary components. Similarly, Figures 4 and 5 show components of the third approximation (Equations 38-41). It is evident, that $\zeta_1''(\eta)$ considerably outweighs the numerical contribution of all other components, except that of $\zeta_{3d}''(\eta)$. However, this function is only effective in correcting the first approximation.

We can now write the complete expression for the shear stress distribution correct to

$$\left(\frac{\tau}{\rho U_o^2}\right)\frac{U_o}{\delta} = \frac{dU_o}{dx}\zeta_{2b}''(\eta) + \left\{\omega\zeta_1''(\eta) + \frac{U_o}{\omega}\frac{d^2U_o}{dx^2}\zeta_{3b}''(\eta) + \frac{1}{\omega}\left(\frac{dU_o}{dx}\right)^2\zeta_{3d}''(\eta)\right\}e^{i(\omega t-\theta)} + \frac{dU_o}{dx}\cdot \zeta_{2a}''(\eta)\,e^{i2(\omega t-\theta)} + \left\{\frac{U_o}{\omega}\frac{d^2U_o}{dx^2}\zeta_{3a}''(\eta) + \left(\frac{dU_o}{dx}\right)^2\zeta_{3c}''(\eta)\right\}e^{i3(\omega t-\theta)} \tag{42}$$

The first term on the right side is the steady contribution equivalent to $\partial u_{zz}/\partial\eta$. The phase advance is represented by θ. It is seen from this equation, grouped to equivalence in the harmonic terms, that the contribution made by the third approximation is two-fold, one of which is correct terms of $O(\varepsilon^0)$. In fact, this is numerically more significant, than all terms of $O(\varepsilon^2)$. In other words, the contribution of the third approximation to the distribution of $\tau(y)$ is small.

An example of the shear stress distribution of Equation 42 is given for an Airy wave of H = 2.0 ft, T = 10 sec and d = 30 ft in Figure 6, where the normalized shear is shown as a function of η. Phase advance of the maximum shear over the forcing velocity is found to be near $\theta = \pi/6$ in absolute units, instead of $\pi/4$ predicted by linear theory. This is equivalent to 30°, and compares well with the experimental phase lead obtained by Jonsson (1966) in an oscillating water tunnel, although the flow in his boundary layer was turbulent. It appears, therefore, that the additional nonlinearity due to the Reynolds stresses, or the diffusion of vorticity into the inviscid region reduces the phase lead of the stress; this is supported in part by the analytical work of Srivastava (1966) who

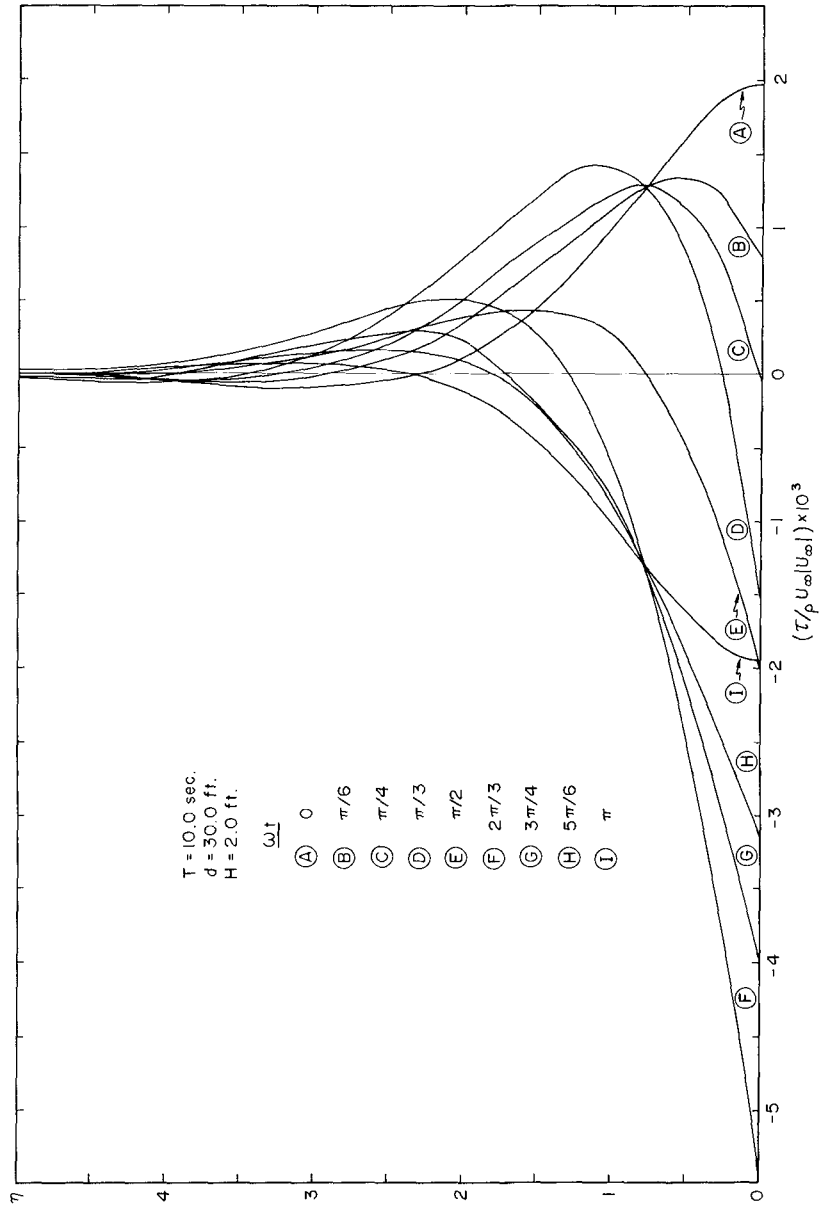

Figure 6

obtained progressive reductions in the phase by increasing the order of the solution for the shear stress.

CONCLUSIONS

An analytical solution for the shear stress distribution to the third approximation in the boundary layer of laminar flow established the following:

(1) The maximum, instantaneous shear stress has a phase difference $\theta = \pi/6$ over u, agreeing with Jonssons's (1966) experimental data;

(2) The third approximation modifies the numerical estimate of the second approximation boundary shear by no more than 6 percent, which is below the experimental error associated with shear measurements;

(3) When the shear stress is measured indirectly at some elevation above the solid boundary, the perturbation procedure described herein enables one to correct the experimental data for the true value of the bottom skin friction. This is particularly applicable to experiments where current meters or Preston probes are used to survey the velocity distribution near the boundary.

ACKNOWLEDGEMENTS

For continuous encouragement in regard to the theoretical aspects of this study, the author expresses his gratitude to his colleague Dr. J. R. Weggel and for computer programming help to Mr. P. A. Turner. Portion of this work was conducted under the civil works program of the U. S. Army Corps of Engineers at the Coastal Engineering Research Center. Permission of the Chief of Engineers to publish this information is appreciated. The findings of this paper are not to be construed as official Department of the Army position unless so designated by other authorized documents.

REFERENCES

Biesel, F., 1949, Calcul de l'amortissement d'une houle dans un liquide visqueux de profondeur finie; La Houille Blanche, V. 4, No. 5 pp. 630-634.

Dore, B. D., 1968, Oscillations in a non-homogeneous viscous fluid; Tellus, V. 20, No. 3, pp. 514-523.

Hill, P. G. and Stenning, A. H., 1960, Laminar boundary layers in oscillatory flow; Trans. ASME, Jour. Basic Eng., V. 82, pp. 593-608.

Hori, Ei-ichi, 1962, Unsteady boundary layers, Fourth report; Bull. Jap. Soc. Mech. Eng., V. 5, No. 19, pp. 461-470.

Hunt, J. N. and Hones, B., 1963, Currents induced by tides and gravity waves; Tellus, V. 15, No. 4, pp. 343-351.

Johns, B., 1968, The damping of gravity waves in shallow water by energy dissipation in a turbulent boundary layer; Tellus, V. 20, No. 2, pp. 330-337.

Jonsson, I. G., 1966, On the existence of universal velocity distribution in an oscillatory, turbulent boundary layer; Coastal Eng., Tech. Univ. Denmark, Prog. Report No. 12, pp. 2-10.

Kestin, J., Maeder, P. F. and Wang, H. E., 1961, On boundary layers associated with oscillating streams; Appl. Sci. Res., Sec. A. V. 10, No. 1, pp. 1-22.

Kestin, J., Persen, L. N. and Shah, V. L., 1967, The transfer of heat across a two-dimensional, oscillating boundary layer; Zeitschrift für Flugwissenschaften, V. 15, No. 8/9, pp. 227-285.

Noda, H., 1971, On the oscillatory flow in turbulent boundary layers induced by water waves; Bull. Disas. Prev. Inst., Kyoto Univ., V. 20, pt. 3, No. 176, pp. 127-144.

Saville, T. Jr., 1950, Model study of sand transport along an infinitely long, straight beach; Trans. Am. Geophys Union, V. 31, No. 4, pp. 555-565.

Schlichting, H., 1932, Berechnung ebener periodischer Grenzschichtstromungen; Phys. Zeitung, V. 33, pp. 327-335.

Shah, V. L., 1970, Contribution to the calculation of oscillatory boundary layers; Trans. ASME, Jour. Heat Transfer, V. 92, pp. 661-664.

Srivastava, A. C., 1966, Unsteady flow of a second order fluid near a stagnation point; Jour. Fluid Mech., V. 24, pt. 1, pp. 33-39.

Stone, R. O. and Summers, H. J., 1972, Study of subaqueous and subaerial sand ripples; Univ. S. Cal., Dept. Geol. Sci., Report 72-1, 293 p.

Stuart, J. T., 1963, Unsteady boundary layers; Ch. 7 in Rosenhead, L., ed., Laminar boundary layers; Clarendon Press, Oxford, England pp. 349-408.

Stuart, J. T., 1966, Double boundary layers in oscillatory viscous flow; Jour. Fluid Mech., V. 24, pt. 4, pp. 673-687.

NOTATION

a	Wave amplitude	$z=y+d$	Normalized distance or coordinate
d	Local water depth	δ	Boundary layer thickness
e	Exponential	ε	Perturbation parameter
g	Gravitational acceleration	ζ	Function of η
H	Wave height	$\eta=y/\delta$	Dimensionless coordinate, normal to boundary
i	$\sqrt{-1}$	θ	Phase advance of the shear str
$k=2\pi/L$	Wave number	ν	Kinematic viscosity
L	Wavelength	ξ	Vertical displacement of water surface from still water level
Re	Real part of complex number	ρ	Density of fluid
$R_s=U_0/\omega\nu$	Reynolds number	τ	Horizontal shear stress
T	Wave period	$\omega=2\pi/T$	Wave number
t	Time	ϕ	Velocity potential
U_Q	Free stream velocity	χ	Dimensionless stream function
$u_{1,2,3}$	Velocity in the boundary layer horizontal component	ψ	Stream function
$v_{1,2,3}$	Velocity in the boundary layer vertical component	∇	Laplacian operator
x	Horizontal distance or coordinate		
y	Vertical distance or coordinate		

CHAPTER 31

MEASUREMENT OF BED SHEAR STRESS UNDER WAVES

H.P. Riedel[1], J.W. Kamphuis[2] and A. Brebner[3]

ABSTRACT

Shear stress measurements on both smooth and sand roughened beds were carried out in an oscillating water tunnel using a flexurally supported shear plate. The range of simulated wave boundary layers covered practically any situation possible in the field or laboratory.

In the laminar range good agreement is obtained with the theoretical shear stress calculated from first order wave theory. However, in the turbulent flow regimes the experimental data indicates that theory results in an overestimate of the shear force by 20-50%. Limits of laminar, smooth turbulent and rough turbulent flow regimes are determined and it appears that the rough turbulent flow regime may itself be subdivided into two sections, each having different turbulence characteristics.

INTRODUCTION

Many researchers have devoted their time in recent years to the study of waves in flumes, model basins and in the field, but the state of knowledge on the interaction of waves and the bed is still limited. A better understanding of the oscillatory boundary layer at the bed is necessary because most shallow water wave phenomena are largely influenced by bottom friction.

For any study of the oscillatory boundary layer a means of generating the wave boundary layer must be found and appropriate tools are needed to measure the relevant boundary layer parameters. An oscillating water tunnel was built to satisfy the first requirement and both prototype and model scale wave boundary layers could be simulated. With respect to measurement, the most useful boundary layer parameter is

---

1. Research Associate,

2. Associate Professor of Civil Engineering,

3. Professor and Head of Civil Engineering,

Coastal Engineering Research Laboratory, Queen's University at Kingston Canada.

velocity, however, velocity meters which do not disturb the flow and which are capable of measuring the unsteady flow within thin boundary layers are only now being developed. Consequently, an alternative parameter, bed shear stress, was measured by a shear stress transducer which did not interfere with the boundary layer flow.

To date experimental methods of determining shear stress have only yielded a limited amount of data e.g. Bagnold (1), Iwagaki et al (2), Inman & Bowen (3), Jonsson (4), Yalin & Russel (5), and Teleki & Anderson (6). As a result, theoretical expressions for shear stress at the bed outside the laminar range, as given by Jonsson (4) and Kajiura (7), have not been adequately verified experimentally.

EXPERIMENTAL EQUIPMENT

Wave boundary layers were simulated in an oscillating water tunnel illustrated in figure 1. The construction is all concrete and glass which gives minimum leakage and a maximum viewing area in the working section. The working section is 12 m long, 1 m high and 0.5 m wide. Nine 13 mm thick plate glass windows (.9 m x 1 m) on each side allow a clear view throughout the working section. Access to the working section is provided by hatches located above each window.

A 2 m square piston moves the water with periods ranging from 2.5 to 15 seconds and strokes up to 1 m. With an 8:1 reduction in cross-sectional area between the piston "bore" and the working section, orbital diameters of 8 m in length are possible in the working section. The honeycombs at the entrance to the working section straighten the flow and prevent large scale eddies, which may be generated in the bends, from entering the working section. The sediment trap prevents granular material from reaching the piston and fouling it.

A 18.7 KW Reeves Varispeed motor drives the piston through a 31.4:1 Philadelphia reducer giving a continuously variable output speed range of 4.3 - 56.5 R.P.M. The output shaft of the gearbox drives a crank arm with an eccentricity that may be adjusted from 0-0.5 m. Then a connecting rod and shaft transfer this motion to the piston.

Superimposed unidirectional currents may be added by means of a

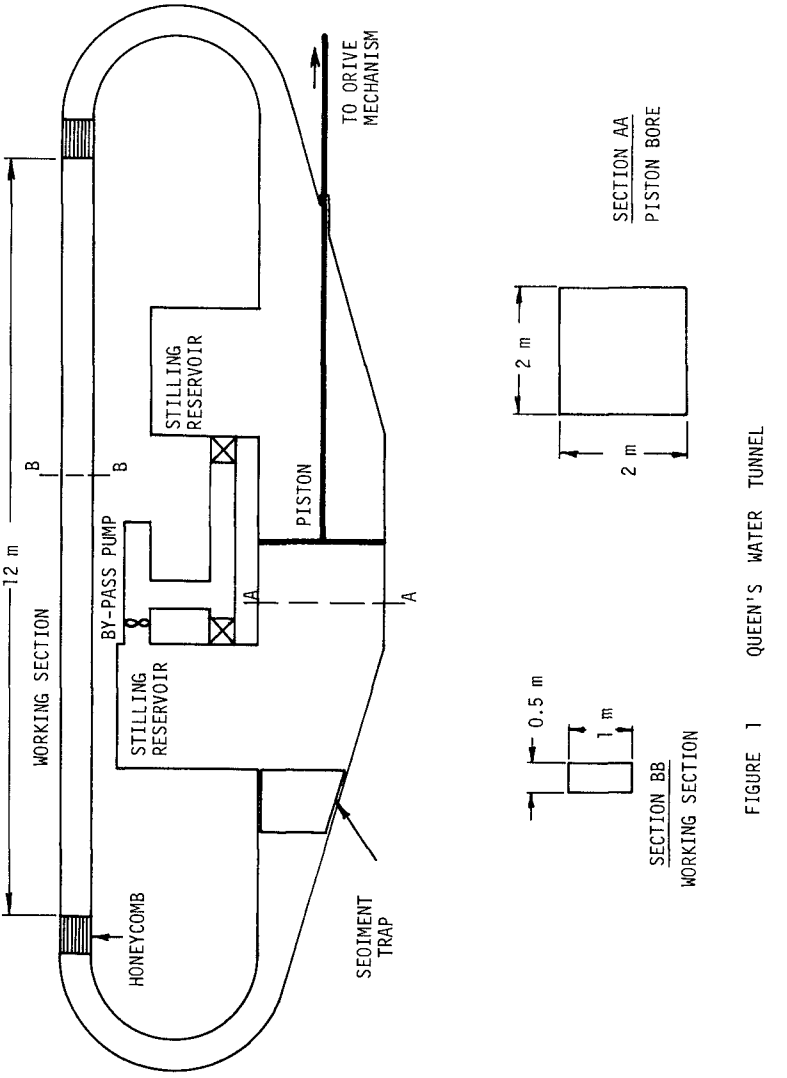

FIGURE 1 QUEEN'S WATER TUNNEL

by-pass pump. The stilling reservoirs are included to dampen the turbulence resulting from the pump discharge.

Shear stress was measured using the shear plate shown as a centre-line section in figure 2. The rectangular shear sensitive plate (6), 0.048 square metres in surface area, is mounted inside an outer plate (1) so that in its equilibrium position there is a gap of 1 mm at each end through which the plate can deflect. Clearance gaps of 0.5 mm are provided at the sides of the plate. The position of the shear plate can be adjusted by the fastening blocks (2, 11). Similar blocks not seen in the view of figure 2 locate the shear plate laterally. In this way the level of the shear sensitive surface can be adjusted to match the outer plate within 0.1 mm.

The shear plate is supported at its corners by 4 thin stainless steel legs (4) which are clamped to the base plate (12, 13) and bonded to the shear sensitive plate. A buffer plate (8) and flow interruptor (7), impede the flow of secondary currents under the shear plate. Pressure tappings P_1, P_2, P_3 and P_4 monitor the pressure in the freestream as well as under the shear plate. With this system both end pressure forces, which act on the leading and trailing edges of the plate, and vertical pressure forces can be determined. The apparent measured shear is then corrected for these forces. The 1.65 mm thick stainless steel plate is stiffened longitudinally by two 6.5 mm square bars fitted onto the bottom edges (9). This arrangement gives a relatively small frontal area but is still stiff enough to prevent bowing of the shear plate under vertical loading.

Strain gauges mounted in pairs on the upstream support legs sense any deflection of the shear plate and a temperature compensated full bridge circuit is used which gives a linear output over the full-scale range of shear ($\pm 100 N/m^2$). The shear plate output is stable for sensitivities as low as $0.015 N/m^2$.

A complete flushing system was installed to cope with loose sand grains and any other dirt in the tunnel. The outer plate assembly provides a four walled enclosure within which the shear plate is located. Water under mains pressure can be fed into this enclosure via flushing pipes (10, 15) and a third one not seen in figure 2. The only way the water can escape is through the gaps around the shear

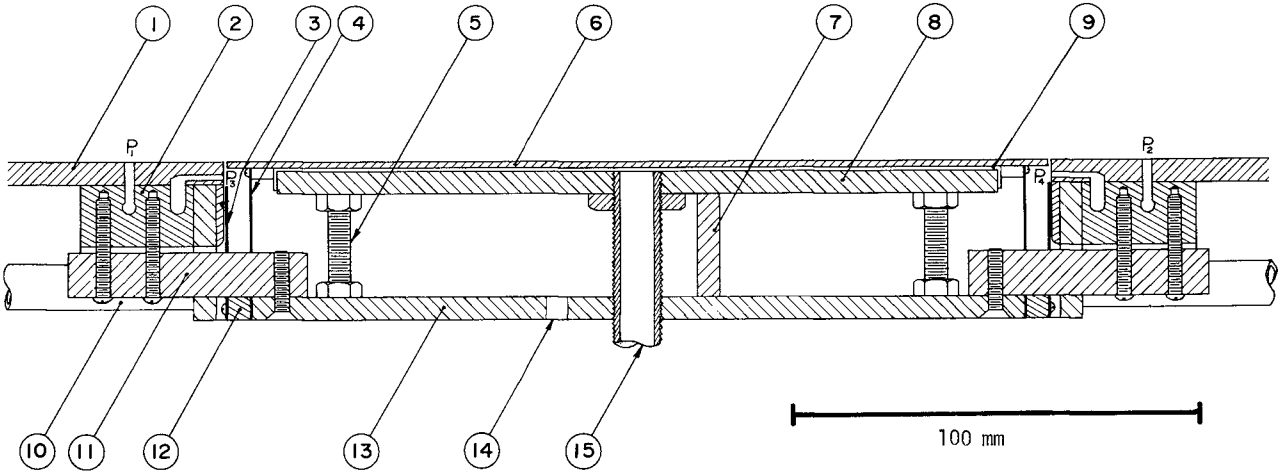

1 OUTER PLATE
2 SHEAR ASSEMBLY OUTER FASTENING BLOCK
3 DEFLECTOR
4 STAINLESS STEEL FLEXURE LEGS
5 BUFFER PLATE ADJUSTING SCREWS
6 SHEAR PLATE
7 FLOW INTERRUPTOR
8 BUFFER PLATE
9 SHEAR PLATE STIFFENER
10 END FLUSHING PIPE
11 SHEAR ASSEMBLY INNER FASTENING BLOCK
12 CLAMPING BAR
13 BASE PLATE
14 STRAIN GAUGE WIRING OUTLET
15 BUFFER FLUSHING PIPE

FIGURE 2 SHEAR PLATE ASSEMBLY

plate and so a jet-like flushing system is established.

Sand roughened beds as illustrated in figure 3, were used. Table 1 lists the equivalent sand roughness k_s for each of the surfaces.

TABLE 1. Equivalent sand roughness data

Material No.	D_{50}(mm)	D_{90}(mm)	k_s(mm)
1	0.37	0.50	1.41
2	1.65	2.20	8.43
3	3.13	4.22	15.8
4	9.8	12.3	51.5
5	50	50	139

EXISTING SHEAR STRESS THEORIES

Over the laminar range use of first order wave theory and solution of the resultant boundary layer equation, (e.g. Jonsson (4)) yields

$$\hat{\tau} = \rho \hat{U}_\delta^2 / \sqrt{RE} \qquad (1)$$

where $\hat{\tau}$ is the maximum shear stress at the bed, ρ the density of water, $\hat{U}_\delta$ the maximum orbital velocity just outside the boundary layer and RE the maximum amplitude Reynolds number for sinusoidal motion which is equal to $\hat{U}_\delta a_\delta / \nu$ where a_δ is the orbital amplitude just outside the boundary layer and ν the kinematic viscosity of water.
Eq. 1 may be rewritten as

$$f_w = \frac{2}{\sqrt{RE}} \qquad (2)$$

where $f_w = 2\hat{\tau}/\rho \hat{U}_\delta^2$, a wave friction factor as defined earlier by Jonsson (4).

Expressions for wave friction factor, or shear stress have been theoretically derived in the smooth turbulent and rough turbulent flow regimes by Kajiura (7). The derivation followed along the lines of

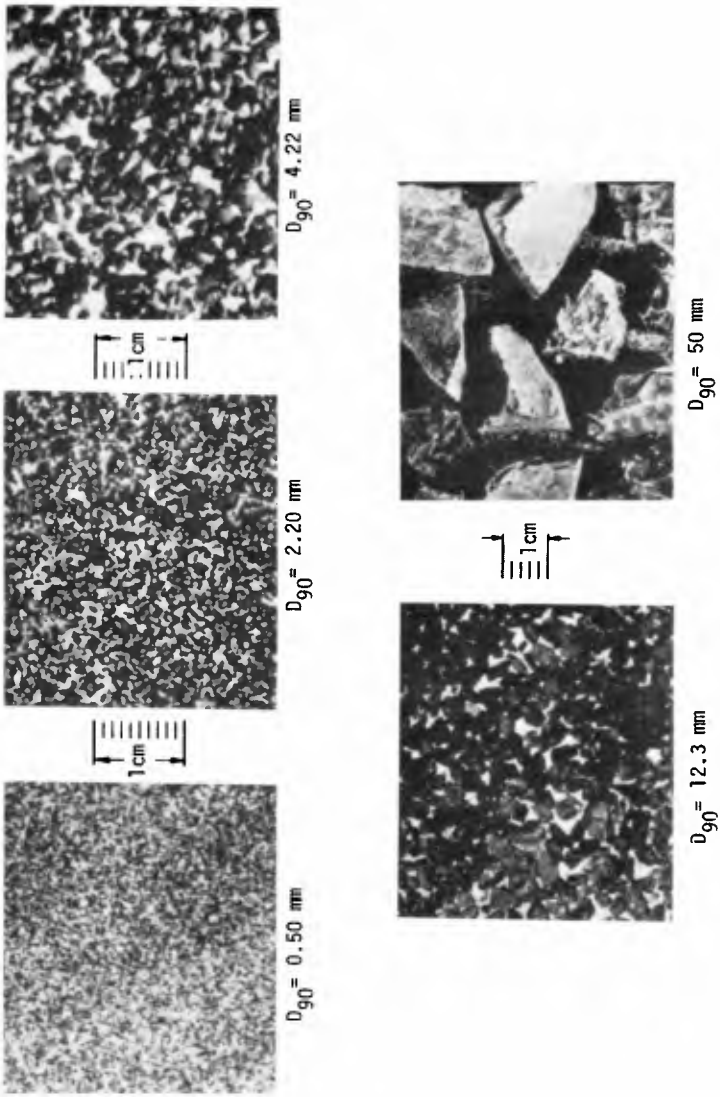

FIGURE 3 ROUGH BEDS

unidirectional turbulent boundary layer theory as presented by Mellor & Gibson (8). In this approach the boundary layer was sub-divided into inner, overlap and outer layers and for each of these a different form of eddy viscosity was assumed. The boundary layer equations were then solved. However, the theory has its limitations because it assumes an average state of turbulence over the wave period. Also constants evaluated from unidirectional flow measurements are used. On the other hand a better theoretical formulation cannot be developed until detailed velocity studies within the boundary layer have been completed.

For the smooth turbulent flow regime Kajiura obtained

$$\frac{1}{8.1\sqrt{f_w}} + \log \frac{1}{\sqrt{f_w}} = -0.135 + \log \sqrt{RE} \qquad (3)$$

Over rough beds Kajiura gives

$$\frac{1}{4.05\sqrt{f_w}} + \log \frac{1}{4\sqrt{f_w}} = -0.254 + \log \frac{a_\delta}{k_s} \qquad (4)$$

Jonsson (4) deduced a similar expression based on the measurement of velocity profiles of one wave simulated in a water tunnel.

$$\frac{1}{4\sqrt{f_w}} + \log \frac{1}{4\sqrt{f_w}} = -0.08 + \log \frac{a_\delta}{k_s} \qquad (5)$$

RESULTS

For the smooth bed and for each of the sand roughened beds, from 37 to 63 shear measurements were made over the Reynolds number range $300 < RE < 5.5 \times 10^6$. The measured shear stress and pressure differences between the various tapping points were recorded on chart paper and from there the data was transferred to punched cards. In this way corrections were made to the recorded shear(i) for end pressure forces resulting from the pressure difference across the shear plate and the roughness elements glued to it, (ii) for vertical pressure loading which resulted because the freestream pressure was not being transmitted under-

neath the plate and (iii) for vertical dead-weight loading of the roughness elements. (i) Depends only on the frontal area of the plate, roughness size and packing,and the pressure gradient. The effects of (ii) and (iii) also depend on the magnitude of the shear stress which deflects the plate in the direction of the flow. i.e. the deflection of the plate from its mean position will influence its response to a vertical load.

Using this method of analysis, the maximum shear stress was obtained for each record and the wave friction factor calculated. The results are presented in the form of a wave friction factor diagram where f_w is plotted against RE. This diagram has a similar format to the Stanton diagram for pipe flow. Jonsson (4) first presented a diagram of this form but it was based on very little data. The data obtained in the present experiments is sufficient to define the wave friction factor diagram over the range of practical use.

Figure 4 shows the experimentally determined wave friction factor diagram. For ease of interpretation this figure 4 has been reproduced in figure 5 with the data points omitted. Inspection of these figures shows:

(a) Within the laminar range the agreement between theory and experiment is very good. This agreement indicates that the shear plate operation was satisfactory and that the corrections for secondary forces were adequate.

(b) The upper limit of the laminar range occurs for RE $\simeq 10^4$ which corresponds approximately to the middle of the observed range of values of transition for wave flume and oscillating plate tests. However, the transition in wave flumes and on oscillating plates was determined by observation of dye streaks. The conclusions drawn for these depend largely on the observer's interpretation.

(c) In the smooth turbulent range the data points define a curve which lies 25-30% below that predicted by Kajiura (7). This difference is remarkably small considering the assumptions that were made in the derivation of the theoretical expression. The lower limit of the smooth turbulent regime was found to be RE = 6×10^5. This corresponds quite well with that derived by Kajiura.

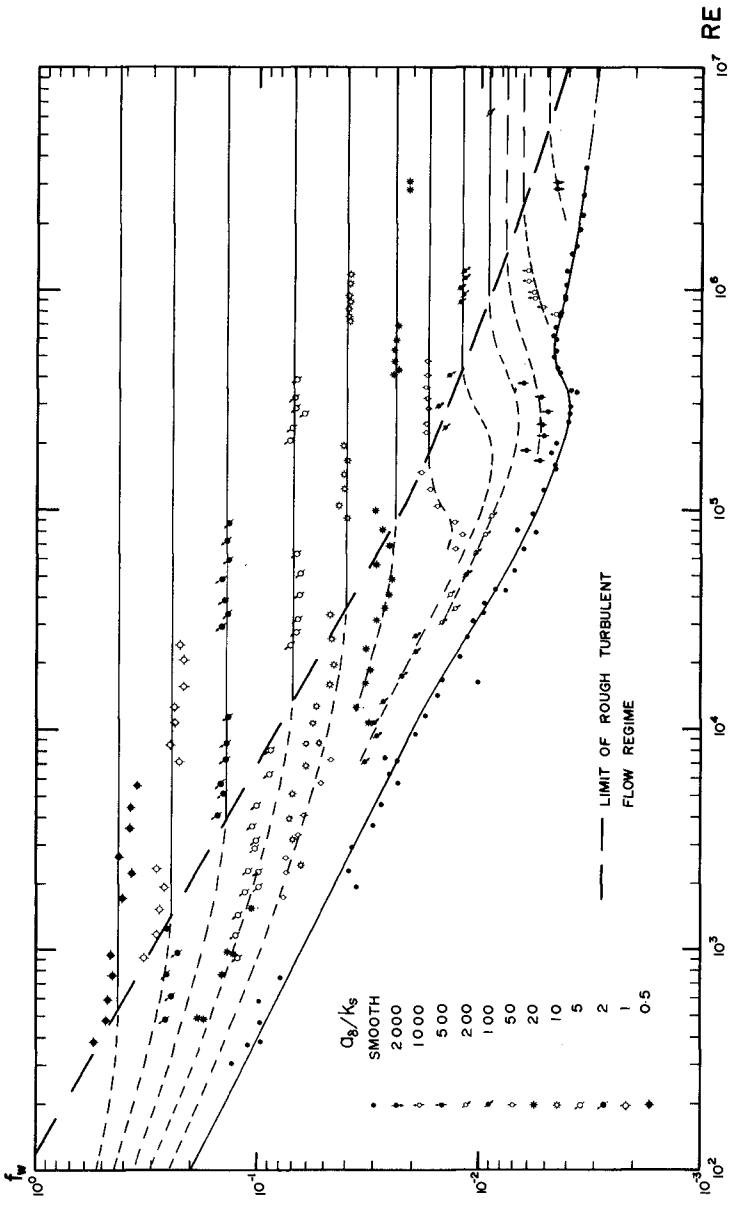

FIGURE 4 EXPERIMENTAL WAVE FRICTION FACTOR DIAGRAM

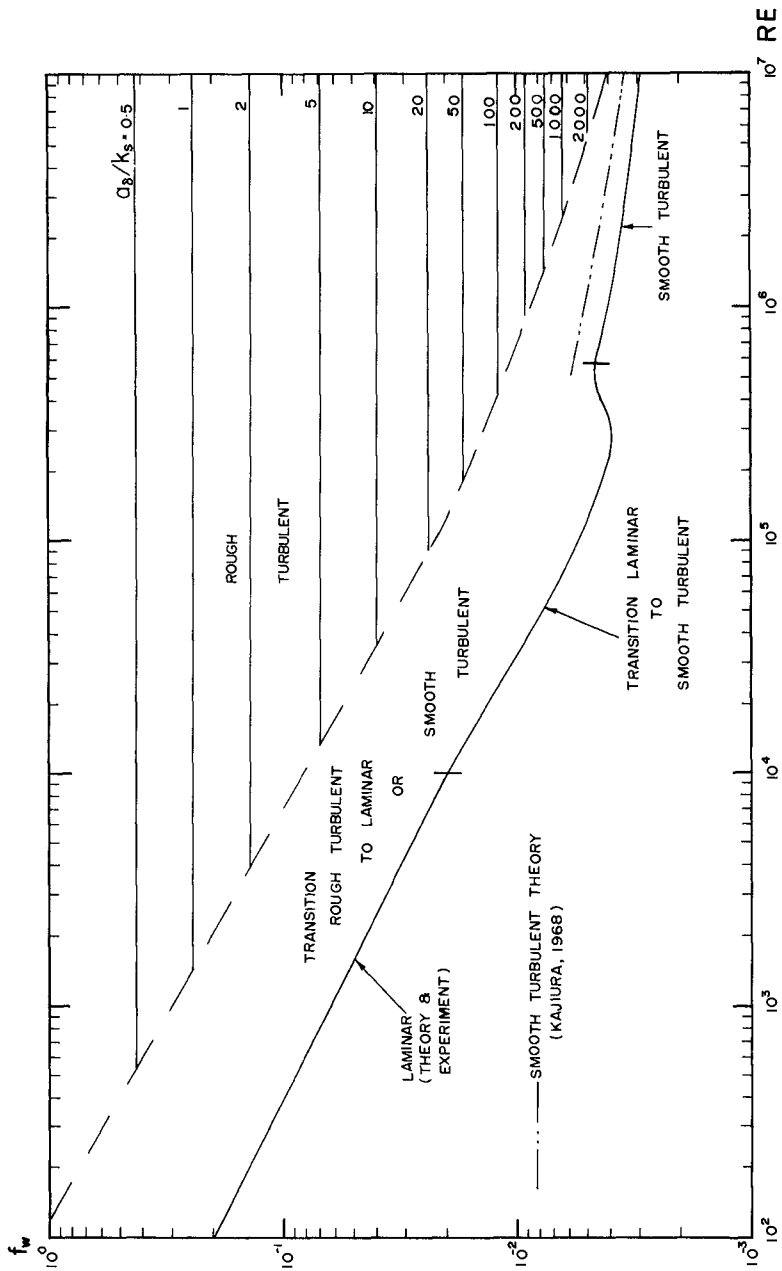

FIGURE 5 WAVE FRICTION FACTOR DIAGRAM SHOWING FLOW REGIMES AND THEORETICAL CURVES.

(d) The lower limit of the rough turbulent regime is defined by the dashed line which was drawn through the points where the family of a_δ/k_s lines curves away from the horizontal (in the rough turbulent regime the friction factor is independent of RE). This lower limit may be expressed in terms of the roughness Reynolds number $k_s v_*/\nu$ (Table 2). It may be seen that for $a_\delta/k_s < 25$, $k_s v_*/\nu$ has a constant value of approximately 500. As a_δ/k_s becomes larger $k_s v_*/\nu$ becomes smaller and it would be expected that as $a_\delta/k_s \to \infty$, $k_s v_*/\nu \to 70$ as for unidirectional flow. Values of other commonly used transition parameters $k_s \hat{U}_\delta/\nu$ and k_s/δ_L have been included in Table 2 for completeness.

(e) In the transition region between rough turbulent flow and laminar or smooth turbulent flow the data points tend to be less ordered. The parameter k_s has because of its definition been measured in the rough turbulent flow regime, and consequently its physical significance is restricted to that regime. In the transition region the flow is a function of the shape of the individual roughness elements and their packing density and not a known function of k_s. Hence these curves must be used with caution within the transition flow regime.

The data for the rough turbulent frow regime has been replotted as f_w against a_δ/k_s since RE is no longer important. (Figure 6). Using a least squares fitting technique, the following equation results

$$\frac{1}{4.95\sqrt{f_w}} + \log \frac{1}{4\sqrt{f_w}} = 0.122 + \log \frac{a_\delta}{k_s} \qquad (6)$$

This equation is consistent with the assumption that a logarithmic velocity law exists near the bed. For $a_\delta/k_s > 25$ the actual data points are in good agreement with this curve. Here the orbital amplitudes are relatively large and as $a_\delta/k_s \to \infty$ unidirectional flow is approached. Also the phase difference between the freestream velocity and the shear stress at the bed approaches zero as $a_\delta/k_s \to \infty$. So it may be concluded

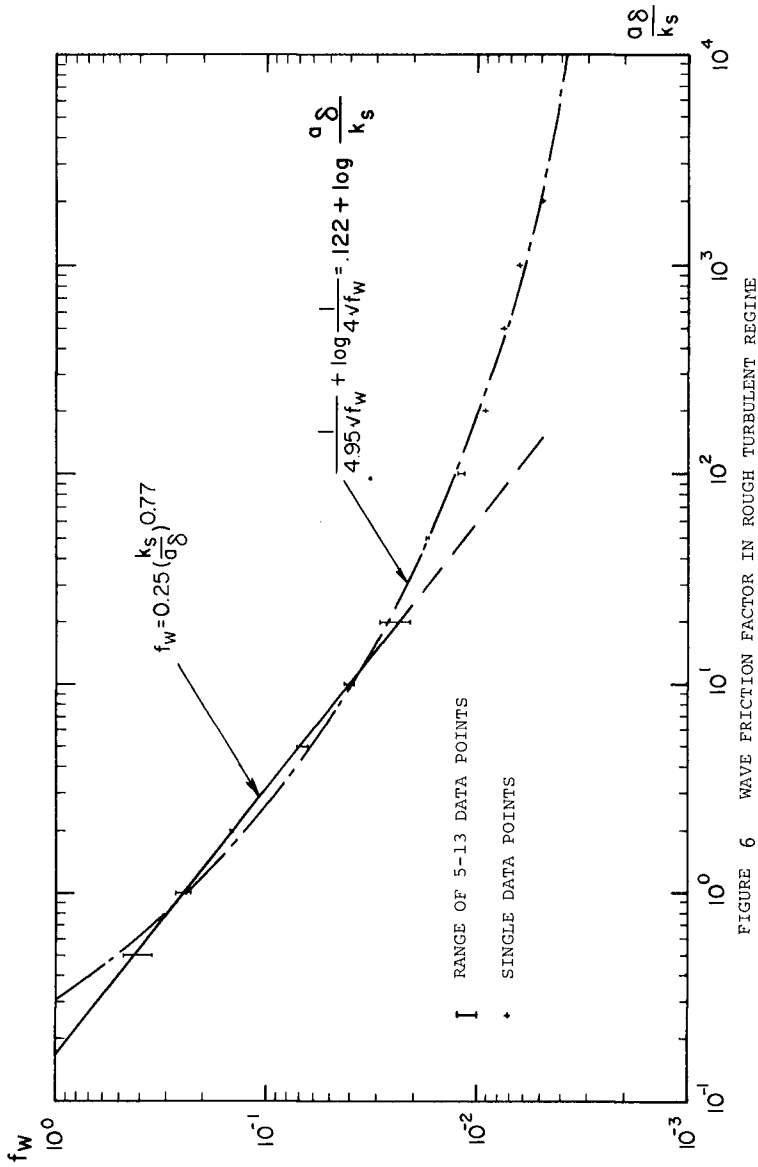

FIGURE 6 WAVE FRICTION FACTOR IN ROUGH TURBULENT REGIME

that the assumption of a logarithmic velocity profile at the instant of maximum freestream velocity is reasonable.

TABLE 2. Lower limits of rough turbulent flow regimes.

$\frac{a_\delta}{k_s}$	$\frac{k_s v_*}{\nu}$	$\frac{k_s \hat{U}_\delta}{\nu}$	$\frac{k_s}{\delta_L}$
0.5	490	1060	32.5
1	490	1400	26.4
2	512	1925	21.9
5	487	2600	16.1
10	495	3500	13.1
20	487	4450	10.6
50	325	3500	5.92
100	340	4400	4.70
200	290	4300	3.30
500	170	2700	1.65
1000	135	2350	1.08
2000	135	2700	0.82

For $a_\delta/k_s < 25$ the data points deviate systematically from the curve defined by equation 6. This results from a large phase difference between the shear stress at the bed and the freestream velocity ($\simeq 45^o$) and this phase difference has a controlling influence on the boundary layer velocity profile. i.e. the velocity profile is not logarithmic near the bed. For $a_\delta/k_s < 25$ the data points fit very closely on a straight line given by

$$f_w = 0.25 \left(\frac{k_s}{a_\delta} \right)^{0.77} \qquad (7)$$

It is then recommended that equation 7 be used to calculate friction factor or bed shear in the rough turbulent regime for $a_\delta/k_s < 25$ and

equation (6) be used for $a_\delta/k_s > 25$. Jonsson's (4) and Kajiura's (7) curves are included in figure 7 for comparison. It may be seen that Kajiura's predicted friction factor is 30-50% higher than the experimentally determined line, while Jonsson's curve falls 20-40% above the line. Experimentally determined wave friction factors in the rough turbulent regime by Bagnold (1) and Inmann and Bowen (3) fall between the experimental curve and Jonsson's curve.

CONCLUSIONS

Direct measurement of bed shear stress was attempted for a wide range of oscillatory flows produced in a water tunnel. The following conclusions were reached.

1. A wave friction factor diagram similar to the Moody diagram for unidirectional flow was obtained experimentally. The parameters a_δ and T for a wave motion over a bed of roughness, k_s, define the flow regime within the boundary layer and allow the maximum shear stress at the bed to be computed.

2. Transition between flow regimes may be expressed in terms of numerical values of the Reynolds numbers RE and $k_s v_*/\nu$. For a smooth bed the upper limit of the laminar flow regime occurs at $RE = 9\times10^3$ while the lower limit of the smooth turbulent regime occurs at $RE = 6\times10^5$. For rough beds with $0.1 < a_\delta/k_s < 25$ the lower limit of the rough turbulent flow regime is given by $k_s v_*/\nu = 500$. As a_δ/k_s becomes larger the value of $k_s v_*/\nu$ at transition reduces so that as $a_\delta/k_s \to \infty$, $k_s v_*/\nu \to 70$.

3. In the rough turbulent flow regime the wave friction factor may be expressed as

$$f_w = 0.25 \left(\frac{k_s}{a_\delta} \right)^{0.77} \quad ; \quad 0.1 < a_\delta/k_s \leq 25$$

$$\frac{1}{4.95\sqrt{f_w}} + \log \frac{1}{4\sqrt{f_w}} = 0.122 + \log \frac{a_\delta}{k_s} \quad ; \quad a_\delta/k_s > 25$$

4. The assumption of a logarithmic velocity profile for the oscillatory boundary layer is reasonable for $a_\delta/k_s > 25$. For $a_\delta/k_s < 25$ the experimental data indicates that this assumption needs to be modified.

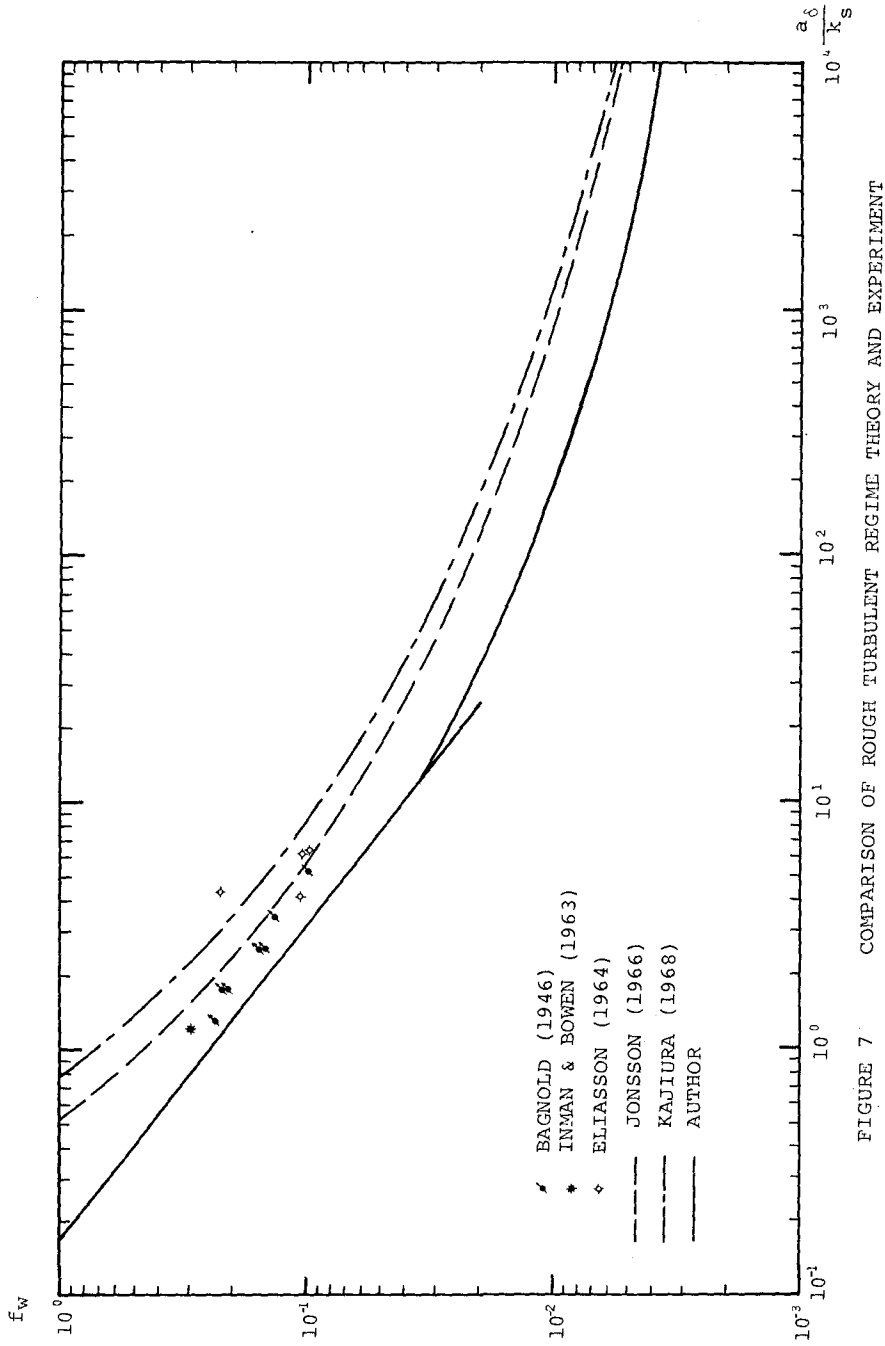

FIGURE 7 COMPARISON OF ROUGH TURBULENT REGIME THEORY AND EXPERIMENT

ACKNOWLEDGMENTS

Financial support for this program of study came from the National Research Council of Canada while the senior author was sponsored under the Canadian Commonwealth Scholarship Scheme.

REFERENCES

Bagnold, R.A. (1946) "Motion of Waves in Shallow Water. Interactions between Waves and Sand Bottoms", Proc. Roy. Soc. Lond., Series A, Vol. 187, pp 1-18.

Inman, D.L. & Bowen, A.J. (1963) "Flume Experiments on Sand Transport by Waves and Currents", Proc. of 8th Conference on Coastal Engineering, Mexico City, pp. 137.

Iwagaki, Y., Tsuchiya, Y. & Sakai, M. (1965) "Basic Studies on the Wave Damping due to Bottom Friction", Coastal Eng. in Japan, Vol. 8, pp. 37.

Jonsson, I.G. (1963) "Measurements in the Turbulent Wave Boundary Layer", 10th Congress IAHR, Lond., pp. 85.

Kajiura, K. (1968) "A Model of the Bottom Boundary Layer in Water Waves", Bull. Earthquake Res. Inst., Vol. 46, pp. 75.

Mellor, G.L. & Gibson, D.M. (1966) "Equilibrium Turbulent Boundary Layers", J. Fluid Mech., 24, pp 235.

Teleki, P.G. & Anderson, M.W. (1970) "Bottom Boundary Shear Stresses on a Model Beach ", Proc. of 12th Coastal Engineering Conference, Washington D.C., Vol. 1, pp. 269-288.

Yalin, M.S. & Russell, R.C.H. (1966) "Shear Stresses due to Long Waves", J. Hyd. Res. 4, No. 2, pp. 55.

CHAPTER 32

DISSIPATION OF WAVE ENERGY DUE TO OPPOSING CURRENT

by

Toshio Iwasaki
Professor of Tohoku University,
Sendai, Japan

and

Michio Sato
Assistant of Tohoku University,
Sendai, Japan

ABSTRACT

Energy dissipation and wave height attenuation were analysed theoretically for surface waves propagating against uniform flow. Energy dissipation was estimated from evaluation of work by internal and boundary shear stresses. Experiments were conducted in a test flume of 20m long, 0.8m wide and 0.5m high. Results showed that tested values of rate of wave height attenuation were comparable with theoretical values.

INTRODUCTION

When waves travel against current, wave energy is transfered from current by so called radiation stress at the one hand, but is dissipated by internal and boundary shear stress at the other hand. Thus the wave height variation in the course of travelling against the current is effected by these two controversing action and as the result, wave height may be increased in some time or may be decreased in othertime owing to their relative magnitude. In deep water, the shear stress can be neglected, for which several investigators such as Unna[1,2,3], Yu[4], Longuet-Higgins & Stewart[5], and Witham[6] have contributed. In shallow water and especially in estuary, the shear stress cannot be neglected. The friction factor for a current superimposed by waves was, due to the auther's knowledge, firstly treated by Ivar G. Jonsson[7] theoretically as,

$$f_{w+c} = \frac{U_b}{U + U_b} f_{wo} + \frac{U}{U + U_b} f_c \qquad (1)$$

where U, U_b mean current velocity and maximum amplitude of velocity of waves respectively, f_{wo} means a friction coefficient of waves in case of no current and f_c means that of current in case of no waves. In this

paper, energy dissipation was estimated from evaluation of work by internal and boundary shear stresses.

Experiments were conducted in a test flume of 20m long, 0.8m wide and 0.5m high.

Analytical results showed that the attenuation rate due to boundary shear was nearly constant over full range of current velocity, but effect by internal friction become remarkable as the opposing current velocity increased. The latter dominated tendency of total dissipation.

THE ENERGY EQUATION FOR WAVES RIDING OVER CURRENT

The motion to be discussed will be assumed to occur in two dimensions on incompressible fluid.

Space co-ordinates x and y are chosen along and perpendicular to the bottom respectively (Fig. 1).

Basic equations for unsteady disturbance riding over uniform flow are,

$$\frac{\partial u}{\partial t} + (U+u)\frac{\partial u}{\partial x} + v\frac{\partial (U+u)}{\partial y} = g\sin\theta - \frac{1}{\rho}\frac{\partial p}{\partial x} + \frac{1}{\rho}\frac{\partial \tau}{\partial y} \qquad (2)$$

$$\frac{\partial v}{\partial t} + (U+u)\frac{\partial v}{\partial x} + v\frac{\partial v}{\partial y} = -g\cos\theta - \frac{1}{\rho}\frac{\partial p}{\partial y} \qquad (3)$$

$$\frac{\partial u}{\partial x} + \frac{\partial v}{\partial y} = 0 \qquad (4)$$

where u and v are the components of disturbance velocity in x and y directions respectively, U is the current velocity and is assumed as a function of y such as $U_1 f(y)$ in which U_1 means the velocity at $y=h$, ρ, g, θ, p and τ denote density, accerelation of gravity, angle of bottom to the horizontal, pressure intensity and shear stress.

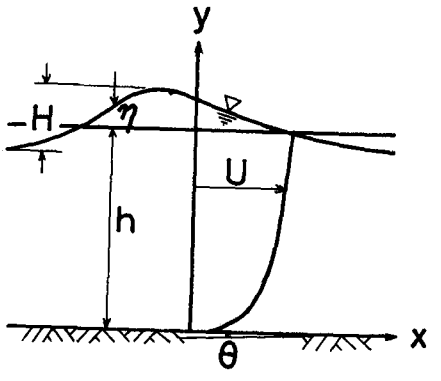

Fig.1

If τ is considered

to be the sum of shear stress due to current τ_c and that due to disturbance τ_w, then gradient of τ_c in y direction is compensated with $\rho g \sin\theta$ when flow is uniform without waves, because then remaining terms beside $g\sin\theta$ and $\frac{1}{\rho}\frac{\partial \tau_c}{\partial y}$ are all vanished in eq.(2).

Eq.(2), then, becomes

$$\frac{\partial u}{\partial t} + (U+u)\frac{\partial u}{\partial x} + v\frac{\partial (U+u)}{\partial y} = -\frac{1}{\rho}\frac{\partial p}{\partial x} + \frac{1}{\rho}\frac{\partial \tau_w}{\partial y} \qquad (2)'$$

Combination of eqs.(2)', (3) and (4) and integration from zero to $h+\eta$ with respect to y leads to the following equation for average values over a period,

$$\frac{\partial}{\partial t}\{\overline{\int_0^{h+\eta}\frac{\rho}{2}(u^2+v^2)dy+\frac{1}{2}\rho g\eta^2}\} + \frac{\partial}{\partial x}\overline{\int_0^{h+\eta}\{\frac{\rho}{2}(u^2+v^2)+p+\rho g(y-h)\}udy}$$
$$+\frac{\partial}{\partial x}\overline{\int_0^{h+\eta}\frac{\rho}{2}(u^2+v^2)Udy} + \overline{U_{h+\eta}\frac{\partial}{\partial x}(\frac{1}{2}\rho g\eta^2)} + \overline{\int_0^{h+\eta}\rho uv\frac{\partial U}{\partial y}dy} = \overline{\int_0^{h+\eta}u\frac{\partial \tau_w}{\partial y}dy} \qquad (5)$$

where bar means average over a period, h is the undisturbed depth and η is the surface elevation, and in the derivation of eq.(5), the surface condition (6) and the bottom condtion (7) are used with taking cos θ as unity.

$$v = \frac{\partial \eta}{\partial t} + (U+u)\frac{\partial \eta}{\partial x} \qquad \text{at } y=h+\eta \qquad (6)$$

$$v = 0 \qquad \text{at } y=0 \qquad (7)$$

As $U_{h+\eta}$ is approximately equal to $U_h + \eta\frac{dU}{dy}\Big|_{y=h}$, the fourth term in the left side of eq.(5) is written as $\frac{\partial}{\partial x}(\frac{1}{2}\rho g\overline{\eta^2}U_h)$ to the second order in the amplitude.

The last term is written as follow,

$$\overline{\int_0^{h+\eta}\rho uv\frac{\partial U}{\partial y}dy} = \overline{\int_0^{h}\rho uv\frac{\partial U}{\partial y}dy} + \overline{\eta(\rho uv\frac{\partial U}{\partial y})_{y=h}}$$

and is zero to the second order in the amplitude because $\overline{uv}$ is zero. Consequently eq.(5) is written as follows

$$\frac{\partial}{\partial t}\{\overline{\int_0^{h+\eta}\frac{\rho}{2}(u^2+v^2)dy+\frac{1}{2}\rho g\eta^2}\} + \frac{\partial}{\partial x}\{\overline{\int_0^{h+\eta}\{\frac{\rho}{2}(u^2+v^2)+p+\rho g(y-h)\}udy}$$
$$+\overline{\int_0^{h+\eta}\frac{\rho}{2}(u^2+v^2)Udy+\frac{1}{2}\rho g\eta^2 U_h}\} = \overline{\int_0^{h+\eta}u\frac{\partial \tau_w}{\partial y}dy} \qquad (8)$$

In eq.(8), the term in the first bracket is the energy density $\bar{E}$. That in the second bracket is the energy flux and is expressed by $\overline{E}\cdot\overline{C_G}'$ physically, where C_G' is the energy transfer velocity. Then the physical expression of eq.(8) is simply as,

$$\frac{\partial \bar{E}}{\partial t} + \frac{\partial}{\partial x}(\overline{E \cdot C_G'}) = \overline{\int_0^{h+\eta} u \frac{\partial \tau}{\partial y} W dy} \tag{9}$$

The term in the right side is the dissipated energy $\bar{E}_d$. Evaluation of $\bar{E}$ or $E \cdot C_G'$ must be given by disturbance velocity (u,v), pressure p, surface elevation η with current velocity assumption U. Strictly to say the energy transfer velocity is not necessarily equal to the group velocity in general,[8] which is defined by

$$\bar{C}_G = \frac{d(Cm)}{dm} \tag{10}$$

where m is the circular wave number $2\pi/L$ and L is the wave length. As this caluculation is very troublesome, C_G' is approximated by $\bar{C}_G$ in the following. Then,

$$\frac{\partial \bar{E}}{\partial t} + \frac{\partial}{\partial x}(\overline{E \cdot C_G}) = \overline{\int_0^{h+\eta} u \frac{\partial \tau}{\partial y} W dy} \tag{9}'$$

Furthermore, $\bar{E}$ is approximated as that of regular sinusoidal waves,

$$\bar{E} = \frac{1}{8}\rho g H^2 \tag{11}$$

where H denotes wave height.

The term in the right side is dissipated energy $\bar{E}_d$ and contribution to this term is partly due to those in main part, $\bar{E}_{dI}$ and partly due to in the boundary layer, $\bar{E}_{dB}$.

For steady flow with regular waves, the first term in (9)' vanishes and putting $-2\bar{E} \cdot G$ for the right side of eq.(9)', eq.(12) is obtained.

$$\frac{d\bar{E}}{dx} = -2\bar{E} \cdot \frac{G}{C_G} \tag{12}$$

as C_G is constant.

Then,

$$\bar{E} = E_o e^{-\frac{2G}{C_G}x} \tag{13}$$

$$H = H_o e^{-\frac{G}{C_G}x} \tag{14}$$

Eq.(13) gives the rate of energy dissipation. Eq.(14) gives the wave height attenuation. G/C_G gives the physical meaning of Inman's a.[9]

Then,

$$G = -\frac{1}{2\bar{E}} \overline{\int_0^{h+\eta} u \frac{\partial \tau}{\partial y} W dy} = -\frac{1}{\frac{1}{4}\rho g H^2}(\bar{E}_{dI} + \bar{E}_{dB}) \tag{15}$$

in which

$$\bar{E}_{dI} = -\overline{\int_\delta^{h+\eta} u \frac{\partial \tau}{\partial y} W dy} \quad \text{and} \quad \bar{E}_{dB} = -\overline{\int_0^{\delta} u \frac{\partial \tau}{\partial y} W dy} \tag{16}$$

where δ is the depth of the boundary layer. Evaluation is now to be divided into the main part of flow and the boundary layer.

DERIVATION OF WAVE DISTURBANCE ON CURRENT IN THE MAIN PART

As shown in Fig.2 local disturbance (u,v) is assumed to be the sum of disturbance velocities (u_1,v_1) neglecting effects of boundary layer due to the wave motion and that (u_2,v_2) to be corrected for effects of boundary layer. Then,

$$u = u_1+u_2 , \qquad v = v_1+v_2 \tag{17}$$

To evaluate $\bar{E}_{dI}$ in the main part of flow, u can be replaced by u_1 because u_2 may be neglected. The shear stress in the main part is estimated to be,

$$\tau_w = \rho\varepsilon\frac{\partial u_1}{\partial y} \tag{18}$$

where ε is the eddy viscosity and is assumed as

$$\varepsilon=\kappa h U_*(1-\frac{y}{h})\frac{y}{h} \tag{19}$$

in which U_* is the shear velocity and κ is the Karman's universal constant.

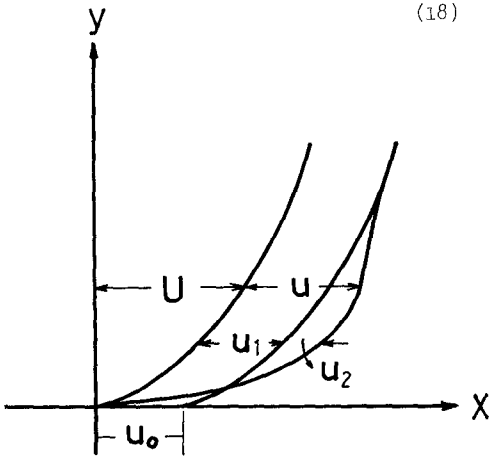

Fig.2

Then $\bar{E}_{dI}$ is approximated as,

$$\begin{aligned}\bar{E}_{dI}&=-\int_\delta^h \overline{u_1\frac{\partial}{\partial y}(\rho\varepsilon\frac{\partial u_1}{\partial y})}dy\\&=\int_\delta^h \rho\varepsilon\overline{(\frac{\partial u_1}{\partial y})^2}dy+[\frac{\rho\varepsilon}{2}\cdot\overline{\frac{\partial u_1^2}{\partial y}}]_{y=\delta}\\&=\frac{1}{4}\rho g H^2\cdot G_1\end{aligned} \tag{20}$$

Derivation of (u_1,v_1) neglecting effects of boundary layer due to the wave motion is the next problem. For this purpose linearized equations of (2)' and (3) are used. Then,

$$\frac{\partial u_1}{\partial t} + U\frac{\partial u_1}{\partial x} + v_1\frac{\partial U}{\partial y} = -\frac{1}{\rho}\frac{\partial p}{\partial x} \tag{21}$$

$$\frac{\partial v_1}{\partial t} + U\frac{\partial v_1}{\partial x} = -g - \frac{1}{\rho}\frac{\partial p}{\partial y} \tag{22}$$

and linearized surface conditions are

$$\left.\begin{aligned} \frac{\partial \eta}{\partial t} + U_1\frac{\partial \eta}{\partial x} &= v_1 \\ \frac{\partial p}{\partial t} + U_1\frac{\partial p}{\partial x} &= v_1\rho g \end{aligned}\right\} \quad \text{at } y=h \tag{23}$$

(24)

where U_1 is the current velocity at $y=h$ as already mentioned.

The stream function ψ is introduced as

$$u_1 = -\frac{\partial \psi}{\partial y} \qquad v_1 = \frac{\partial \psi}{\partial x} \tag{25}$$

Elimination of p between (21) and (22) leads to the equation

$$(\frac{\partial}{\partial t} + U\frac{\partial}{\partial x})\nabla^2\psi - U_1 f''(y)\frac{\partial \psi}{\partial x} = 0 \tag{26}$$

in which $\nabla^2=\partial^2/\partial x^2+\partial^2/\partial y^2$ and the primes denote differential with respect to y.

Putting

$$\psi = \phi(y)e^{im(x-ct)} \tag{27}$$

and substituting (27) in (26)

$$\frac{\partial^2 \phi}{\partial y^2} - (m^2 + \frac{U_1 f''(y)}{U_1 f(y)-c})\phi = 0 \tag{28}$$

As $\phi(0)=0$ from the bed condition (7), the solution of eq.(28) is

$$\phi(y) = A \sinh my + \frac{U_1}{m}\int_0^y \frac{f''(y)\sinh m(y-t)}{U_1 f(t)-C}\phi(t)\,dt \tag{29}$$

where A is constant to be determined.

Substituting $\phi(y)=\sum_0^\infty (U_1/\sqrt{gh})^n \phi_n(y)$ in eq.(29), and equating coefficients, the solution becomes as follows to the first order of $U_1/\sqrt{gh}$.

$$\phi(y) = A\{\sinh my + \frac{U_1}{m}\int_0^y \frac{f''(y)\sinh m(y-t)\sinh mt}{U_1 f(t)-C}dt\} \tag{30}$$

By putting $\eta=\frac{H}{2}\cdot e^{im(x-ct)}$, A is obtained from (23) as,

$$A = \frac{H}{2}\cdot\frac{U_1-C}{\sinh mh\{1+\frac{U_1}{m}\int_0^h \frac{f''(t)\sinh m(h-t)\sinh mt}{(U_1 f(t)-C)\sinh mh}\,dt\}} \tag{31}$$

Now the current field is assumed to be logarithmic in the main part and to be linear in the viscous sublayer. Thus,

$$U = \begin{cases} (5.5+\frac{1}{\kappa}\ln\frac{U_* y}{\nu})U_* = U_1 + \frac{U_*}{\kappa}\ln\frac{y}{h} & (y_s \leqq y \leqq h) \qquad (32) \\ \frac{U_*^2}{\nu}\, y & (0 \leqq y \leqq y_s) \qquad (33) \end{cases}$$

where κ is the Kármán's constant (=0.4), U_* is the shear velocity, ν is

the kinematic viscosity coefficient and y_s is the depth of viscous sublayer.

$$y_s = 11.6\,\frac{\nu}{U_*} \tag{34}$$

Then, from (30), (31) and (32),

$$\phi(y) = \frac{H}{2}\cdot(U_1-C)\cdot\frac{\sinh my}{\sinh mh}\cdot F_2(y) \tag{35}$$

$$F_2(y) = \frac{1+\dfrac{U_*}{\kappa m}\displaystyle\int_{y_s}^{y}\frac{\sinh m(y-t)\,\sinh mt}{\{C-U_1-(U_*/\kappa)\ln(t/h)\}t^2\sinh my}\,dt}{1+\dfrac{U_*}{\kappa m}\displaystyle\int_{y_s}^{h}\frac{\sinh m(h-t)\,\sinh mt}{\{C-U_1-(U_*/\kappa)\ln(t/h)\}t^2\sinh mh}\,dt} \tag{36}$$

From (25), (27) and (35), u_1 and v_1 are obtained as follows,

$$u_1 = \frac{H}{2}\cdot\frac{m(C-U_1)\cosh my}{\sinh mh}\cdot F_1(y)\cos m(x-Ct) \tag{37}$$

$$v_1 = \frac{H}{2}\cdot\frac{m(C-U_1)\sinh my}{\sinh mh}\cdot F_2(y)\sin m(x-Ct) \tag{38}$$

where

$$F_1(y) = \frac{1+\dfrac{U_*}{\kappa m}\displaystyle\int_{y_s}^{y}\frac{\cosh m(y-t)\,\sinh mt}{\{C-U_1-(U_*/\kappa)\ln(t/h)\}t^2\cosh my}\,dt}{1+\dfrac{U_*}{\kappa m}\displaystyle\int_{y_s}^{h}\frac{\sinh m(h-t)\,\sinh mt}{\{C-U_1-(U_*/\kappa)\ln(t/h)\}t^2\sinh mh}\,dt} \tag{39}$$

Elimination of p between (21) and (24) leads to the following equation.

$$(C-U_1)\frac{\partial\phi}{\partial y}\Big|_{y=h} + \{(C-U_1)\frac{\partial U}{\partial y}\Big|_{y=h} - g\}\phi_{y=h} = 0 \tag{40}$$

Substituting (35) in (40), C is obtained as

$$C = U_1 - \frac{U_*\tanh mh}{2\kappa mhF_1(h)} \pm \sqrt{\left(\frac{U_*\tanh mh}{2\kappa mhF_1(h)}\right)^2 + \frac{g\tanh mh}{m\,F_1(h)}} \tag{41}$$

Using eq.(10), the group velocity C_G is derived as

$$C_G = U_1 + \frac{(C-U_1)}{g+\{1+D_1(C-U_1)\}\{g-(C-U_1)(U_*/\kappa h)\}}\Big[\{\{2mh\,\mathrm{cosech}\,2mh + D_1(C-U_1)-D_2\}\{g-(C-U_1)\frac{U_*}{\kappa h}\}+g\Big] \tag{42}$$

where

$$D_1 = \frac{\dfrac{U_*}{\kappa m}\displaystyle\int_{y_s}^{h}\frac{\sinh m(h-t)\,\sinh mt}{\{C-U_1-(U_*/\kappa)\ln(t/h)\}^2t^2}\,dt}{\sinh mh+\dfrac{U_*}{\kappa m}\displaystyle\int_{y_s}^{h}\frac{\sinh m(h-t)\,\sinh mt}{\{C-U_1-(U_*/\kappa)\ln(t/h)\}t^2}\,dt}$$

$$-\frac{\frac{U_*}{\kappa m}\int_{y_s}^{h}\frac{\cosh m(h-t)\,\sinh mt}{\{C-U_1-(U_*/\kappa)\ln(t/h)\}^2t^2}\,dt}{\cosh mh+\frac{U_*}{\kappa m}\int_{y_s}^{h}\frac{\cosh m(h-t)\,\sinh mt}{\{C-U_1-(U_*/\kappa)\ln(t/h)\}t^2}dt} \tag{43}$$

$$D_2=\frac{\cosh^2mh+\frac{U_*}{2\kappa}\int_{y_s}^{h}\frac{t\cosh 2m(h-t)-(h-t)\cosh 2mt+h}{\{C-U_1-(U_*/\kappa)\ln(t/h)\}t^2}\,dt}{\cosh^2mh+\frac{U_*}{\kappa m}\cosh mh\int_{y_s}^{h}\frac{\cosh m(h-t)\,\sinh mt}{\{C-U_1-(U_*/\kappa)\ln(t/h)\}t^2}\,dt}$$

$$-\frac{\sinh^2mh+\frac{U_*}{2\kappa}\int_{y_s}^{h}\frac{t\cosh 2m(h-t)+(h-t)\cosh 2mt-h}{\{C-U_1-(U_*/\kappa)\ln(t/h)\}t^2}\,dt}{\sinh^2mh+\frac{U_*}{\kappa m}\sinh mh\int_{y_s}^{h}\frac{\sinh m(h-t)\,\sinh mt}{\{C-U_1-(U_*/\kappa)\ln(t/h)\}t^2}\,dt} \tag{44}$$

Evaluation of $\bar{E}_{dI}$ is now capable by putting (19) and (37) into (20) and approximating δ as y_s. Thus,

$$G_1=\frac{U_*^3}{2\kappa gh}\left\{\frac{m(C-U_1)}{\sinh mh+\frac{U_*}{\kappa m}\int_{y_s}^{h}\frac{\sinh m(h-t)\,\sinh mt}{\{C-U_1-(U_*/\kappa)\ln(t/h)\}t^2}\,dt}\right\}^2$$

$$\times\left[\int_{y_s}^{h}(h-y)y\{(\frac{\kappa m}{U_*}+\frac{1}{m\{C-U_1-(U_*/\kappa)\ln(y/h)\}y^2})\sinh my+\right.$$

$$\left.+\int_{y_s}^{y}\frac{\sinh m(y-t)\,\sinh mt}{\{C-U_1-(U_*/\kappa)\ln(y/h)\}t^2}\,dt\}^2dy\right.$$

$$\left.+\frac{1}{2}\frac{\kappa}{U_*}(h-y_s)y_s(\frac{\kappa m}{U_*}+\frac{1}{m\{C-U_1-(U_*/\kappa)\ln(y_s/h)\}y_s^2})\sinh 2my_s\right] \tag{45}$$

DERIVATION OF WAVE DISTURBANCE IN THE BOUNDARY LAYER

In the boundary layer, eq.(2)' can be linearized as,

$$\frac{\partial u}{\partial t}+U\frac{\partial u}{\partial x}+v\frac{\partial U}{\partial y}=-\frac{1}{\rho}\frac{\partial p}{\partial x}+\frac{1}{\rho}\frac{\partial \tau_w}{\partial y} \tag{46}$$

Putting eq.(17) into (46) and using eq.(21), the following equation is derived.

$$\frac{\partial u_2}{\partial t}+U\frac{\partial u_2}{\partial x}=\frac{1}{\rho}\frac{\partial}{\partial y}(\rho\varepsilon\frac{\partial u_2}{\partial y}) \tag{47}$$

in which v_2 and $\partial u_1/\partial y$ are neglected.

Substituting $u_2=\hat{u}_2e^{i(mx-\omega t)}$ in (47)

$$\frac{d}{dy}(\varepsilon\frac{\partial\hat{u}_2}{\partial y})+i\omega(1-\frac{U}{C})\hat{u}_2=0 \tag{48}$$

Expanding $\hat{u}_2$ as a power series of U_1/C and substituting in (48), the following equations are obtained.

$$\begin{cases} \dfrac{d}{dy}\left(\varepsilon\dfrac{d\hat{u}_{20}}{dy}\right) + i\omega\hat{u}_{20} = 0 & (49) \\ \dfrac{d}{dy}\left(\varepsilon\dfrac{d\hat{u}_{21}}{dy}\right) + i\omega\hat{u}_{21} = i\omega\left(\dfrac{U}{U_1}\right)\hat{u}_{20} & (50) \end{cases}$$

From eq.(18), ε is assumed as

$$\varepsilon = \begin{cases} \nu & \text{for } 0 \leqq y \leqq y_s \quad (51) \\ \kappa U_* y & \text{for } y_s \leqq y \quad (52) \end{cases}$$

because $y/h \ll 1$.

Substituting in (49) and (50), the equations to be solved are

$$\begin{cases} \dfrac{d^2\hat{u}_{20}}{dy^2} + \dfrac{i\omega}{\nu}\hat{u}_{20} = 0 & \text{for } 0 \leqq y \leqq y_s \quad (53) \\ \dfrac{d^2\hat{u}_{20}}{dy^2} + \dfrac{1}{y}\dfrac{d\hat{u}_{20}}{dy} + \dfrac{i\omega}{\kappa U_*}\dfrac{1}{y}\hat{u}_{20} = 0 & \text{for } y_s \leqq y \quad (54) \end{cases}$$

$$\begin{cases} \dfrac{d^2\hat{u}_{21}}{dy^2} + \dfrac{i\omega}{\nu}\hat{u}_{21} = \dfrac{i\omega}{\nu}\dfrac{U}{U_1}\hat{u}_{20} & \text{for } 0 \leqq y \leqq y_s \quad (55) \\ \dfrac{d^2\hat{u}_{21}}{dy^2} + \dfrac{1}{y}\dfrac{d\hat{u}_{21}}{dy} + \dfrac{i\omega}{\kappa U_*}\dfrac{1}{y}\hat{u}_{21} = \dfrac{i\omega}{\kappa U_*}\dfrac{1}{y}\dfrac{U}{U_1}\hat{u}_{20} & \text{for } y_s \leqq y \quad (56) \end{cases}$$

The boundary conditions are

$$\hat{u}_{20} = -\hat{u}_1(0) = -\hat{u}_0 \qquad \text{at } y=0 \quad (57)$$

$$\hat{u}_{21} = 0 \qquad \text{at } y=0 \quad (58)$$

where

$\hat{u}_{20}$, $d\hat{u}_{20}/dy$, $\hat{u}_{21}$, $d\hat{u}_{21}/dy$ are to be continuous at $y=y_s$ respectively (59)

In addition to them, $\hat{u}_{20}$ and $\hat{u}_{21}$ must be bounded at large y.

The solutions become finally as,

$$u = u_1 + u_2 = u_1 + R_e\{(\hat{u}_{20}+(U_1/C)\hat{u}_{21})e^{i(mx-\omega t)}\}$$

$$= \Bigg\{ u_1 - \hat{u}_0 R_e\Bigg\{\Bigg[\frac{H_0^{(1)}(2\beta_2\sqrt{y_s})\cos\beta_1(y_s-y)+\frac{\beta_2}{\beta_1\sqrt{y_s}}H_1^{(1)}(2\beta_2\sqrt{y_s})\sin\beta_1(y_s-y)}{H_0^{(1)}(2\beta_2\sqrt{y_s})\cos\beta_1 y_s+\frac{\beta_2}{\beta_1\sqrt{y_s}}H_1^{(1)}(2\beta_2\sqrt{y_s})\sin\beta_1 y_s}$$

$$-\frac{\beta_1}{\{H_0^{(1)}(2\beta_2\sqrt{y_s})\cos\beta_1 y_s+\frac{\beta_1}{\beta_1\sqrt{y_s}}H_1^{(1)}(2\beta_2\sqrt{y_s})\sin\beta_1 y_s\}^2}\{(H_0^{(1)}(2\beta_2\sqrt{y_s})\cos\beta_1(y_s-y)$$

$$+\frac{\beta_2}{\beta_1\sqrt{y_s}}H_1^{(1)}(2\beta_2\sqrt{y_s})\sin\beta_1(y_s-y))\Big\}\int_0^{y_s}\left(\frac{U}{C}\right)(H_0^{(1)}(2\beta_2\sqrt{y_s})\cos\beta_1(y_s-\xi)$$

$$+\frac{\beta_2}{\beta_1\sqrt{y_s}}H_1^{(1)}(2\beta_2\sqrt{y_s})\sin\beta_1(y_s-\xi))\sin\beta_1\xi d\xi$$

$$+\left(H_0^{(1)}(2\beta_2\sqrt{y_s})\cos\beta_1 y_s\right.$$

$$+\frac{\beta_2}{\beta_1\sqrt{y_s}}H_1^{(1)}(2\beta_2\sqrt{y_s})\sin\beta_1 y_s)\int_y^{y_s}(\frac{U}{C})(H_0^{(1)}(2\beta_2\sqrt{y_s})\cos\beta_1(y_s-\xi)$$

$$\left.+\frac{\beta_2}{\beta_1\sqrt{y_s}}H_1^{(1)}(2\beta_2\sqrt{y_s})\sin\beta_1(y_s-\xi))\sin\beta_1(y-\xi)d\xi\right\}e^{i(mx-\omega t)}\Bigg\}$$

for $0\leq y\leq y_s$ (60)

$$u_1 - \hat{u}_0 R_e\Bigg\{\Bigg[\frac{H_0^{(1)}(2\beta_2\sqrt{y})}{H_0^{(1)}(2\beta_2\sqrt{y})\cos\beta_1 y_s+\frac{\beta_2}{\beta_1\sqrt{y_s}}H_1^{(1)}(2\beta_2\sqrt{y_s})\sin\beta_1 y_s}$$

$$-\beta_1\frac{H_0^{(1)}(2\beta_2\sqrt{y})\int_0^{y_s}(\frac{U}{C})(H_0^{(1)}(2\beta_2\sqrt{y_s})\cos\beta_1(y_s-\xi)}{\{H_0^{(1)}(2\beta_2\sqrt{y_s})\cos\beta_1 y_s+\frac{\beta_2}{\beta_1\sqrt{y_s}}H_1^{(1)}(2\beta_2\sqrt{y_s})\sin\beta_1 y_s\}^2}$$

$$\underline{\left.+\frac{\beta_2}{\beta_1\sqrt{y_s}}H_1(2\beta_2\sqrt{y_s})\sin\beta_1(y_s-\xi))\sin\beta_1\xi d\xi\right]}$$

$$-\frac{i\pi\beta_2^2}{2}\frac{\int_{y_s}^{y}(\frac{U}{C})H_0^{(1)}(2\beta_2\sqrt{\xi})(H_0^{(1)}(2\beta_2\sqrt{y})H_0^{(2)}(2\beta_2\sqrt{\xi})}{H_0^{(1)}(2\beta_2\sqrt{y})\cos\beta_1 y_s+\frac{\beta_2}{\beta_1\sqrt{y_s}}H_1^{(1)}(2\beta_2\sqrt{y_s})\sin\beta_1 y_s}$$

$$\underline{\left.-H_0^{(2)}(2\beta_2\sqrt{y})H_0^{(1)}(2\beta_2\sqrt{\xi}))d\xi\right]e^{i(mx-\omega t)}}\Bigg\}$$

for $y_s\leq y$ (61)

where

$$\beta_1=\sqrt{\frac{\omega}{\nu}}e^{i\frac{\pi}{4}}\qquad \beta_2=\sqrt{\frac{\omega}{\kappa U_*}}\,e^{i\frac{\pi}{4}} \tag{62}$$

in which $H_\nu^{(1)}(z)$ and $H_\nu^{(2)}(z)$ are the first and the second kind of Hankel function respectively.

From eq.(16), (17) and (18),

$$\bar{\bar{E}}_{dB}=-\overline{\int_0^\delta u_1\frac{\partial}{\partial y}(\rho\varepsilon\frac{\partial u_2}{\partial y})dy}-\overline{\int_0^\delta u_2(\frac{\partial}{\partial t}+U\frac{\partial}{\partial x})u_2 dy} \tag{63}$$

in which the second term is derived from eq.(47) and vanishes due to the wave periodicity. Assuming that $\partial u_1/\partial y$ is approximately equal to zero in the layer and $\partial u_2/\partial y$ is approximately zero at the outer edge of the layer, $\bar{\bar{E}}_{dB}$ becomes from eq.(63) as,

$$\bar{\bar{E}}_{dB}=\mu u_1\frac{\partial u_2}{\partial y}\Big|_{y=0}=\frac{1}{4}\rho g H_1^2 G_2 \tag{64}$$

$$G_2=\frac{\nu}{2g}\{\frac{m(C-U_1)F_1(0)}{\sinh mh}\}^2 R_e\{\beta_1\frac{H_0^{(1)}(2\beta_2\sqrt{y_s})\sin\beta_1 y_s-\frac{\beta_2}{\beta_1\sqrt{y_s}}H_1^{(1)}(2\beta_2\sqrt{y_s})\cos\beta_1 y_s}{H_0^{(1)}(2\beta_2\sqrt{y_s})\cos\beta_1 y_s+\frac{\beta_2}{\beta_1\sqrt{y_s}}H_1^{(1)}(2\beta_2\sqrt{y_s})\sin\beta_1 y_s}$$

$$-\beta_1^2\frac{\int_0^{y_s}(\frac{U}{C})(H_0^{(1)}(2\beta_2\sqrt{y_s})\cos\beta_1(y_s-\xi)+\frac{\beta_2}{\beta_1\sqrt{y_s}}H_1^{(1)}(2\beta_2\sqrt{y_s})\sin\beta_1(y_s-\xi))^2 d\xi}{(H_0^{(1)}(2\beta_2\sqrt{y_s})\cos\beta_1 y_s+\frac{\beta_2}{\beta_1\sqrt{y_s}}H_1^{(1)}(2\beta_2\sqrt{y_s})\sin\beta_1 y_s)^2}\} \tag{65}$$

Thus, the rate of the wave height variation can be calculated from eq.(14) by using eq.(42) for C_G, eq.(45) for G_1 and (65) for G_2 , in which

$$G = G_1 + G_2 \tag{66}$$

is used.

EXPERIMENT

A glass walled flume, 20m long, 0.8m wide and 0.5m high shown in Fig.3 was used for experiments. Flow was circulated and regular waves were generated by a plunger type generator from the most downstream end. Velocities were measured by a propeller type current-meter in which electric pulses were transduced by a photo-electric cell for each rotation of the propeller. An electric resistance type wave gauge and an electromagnetic oscillograph were used to record water surface. To avoid errors due to difference of characteristics between different gauges, only one wave gauge was used to measure waves at different points, for which a gauge carrier on wheels was used. Wave heights at each points were determined by averaging those of eight waves which become steady just after the beginning of movement of the generator.

As shown in Table-1, surface velocities were between 6 cm/sec and 33 cm/sec and undisturbed depth was in the range between 10 and 15 cm. Wave periods were 0.85~1.25 sec and wave heights were 1~4 cm. Water temperature was adjusted between 13°C and 16°C.

Fig.4 shows the wave height variation with travel distance, which is exponential as shown eq.(14).

Fig.5 shows the relationship between the rate of wave height attenuation $\alpha L_0=\frac{G}{C_G}L_0$ and U_1/C_0 in which C_0 and L_0 are the wave celerity

and the wave length without current. Full lines represent theoretical results for the water temperature of 15°C. White circles are experimental values.

It is shown that the rate of wave height attenuation becomes larger as the opposing current velocity increases. The attenuation rate due to boundary shear α_2 is nearly constant over full range of current velocity. Although as shown by $\alpha_1 L_0$ effect by internal friction can be neglected in compare with that by boundary shear when the current velocity is small, the former becomes remarkable as the opposing current velocity increases, which dominates tendency of total dissipation.

However evaluation of energy dissipation in the boundary layer is too low which suggests turbulence due to wave motion must be analysed.

Fig.5 shows velocity distributions calculated in the boundary layer.

As given in eq.(31) and (32), discontinuity is shown at $y=y_s$. However y_s is too small to give serious effects by this continuity.

CONCLUSION

Mechanics of energy dissipation of waves traveling against currents are analysed theoretically in this paper. The rate of energy dissipation or wave height attenuation is given physical meaning by eq.(14). This is the ratio of the dissipated energy and the energy transfer velocity.

Energy dissipation in the boundary layer is nearly constant over full range of current velocity. Effect of internal eddy viscosity is negligible when current velocity is small, but become remarkable as the opposing current velocity increases. In this case, this internal eddy viscosity dominates thendency of total dissipation.

The effect of the wave motion on turbulence in the boundary layer is not treated in this paper. However experimental results showed they should be taken into consideration.

REFERENCE

(1) Unna, P.J., (1941): White horses., Nature, London, 148

(2) Unna, P.J., (1942): Waves and tidal streams., Nature, London, 149

(3) Unna, P.J., (1947): Sea waves., Nature, London, 159

(4) Yu, Yi-Yuan., (1952): Breaking of waves by an opposing currents., Trans. A.G.U, Vol.33 No.1

(5) Longuet-Higgins & Stewart., (1960): The changes in amplitude of short gravity waves on steady non-uniform currents., Jour. of Fluid Mech., Vol.10

(6) Whitham, G.B.,(1962): Mass, momentum and energy flux in water waves., Jour. of Fluid Mech., Vol.12

(7) Jonnson, I.G., (1966): The friction factor for a current superimposed by waves., Basic Reserch-Progress Report, No.11, Coastal Engineering Laboratory, Techn. Un. of Denmark.

(8) Hamada, T., (1971): On the properties of surface waves in a shear flow., Proc. 18th Conf. on Coastal Engineering in Japan, Japan Soc. Civil Engineers. (in Japanese)

(9) Imnam, D.L. & Bowen, A.J., (1962): Flume experiments on sand transport by waves and currents., Proc. 8th Conf. Coastal Engineering., Mexico

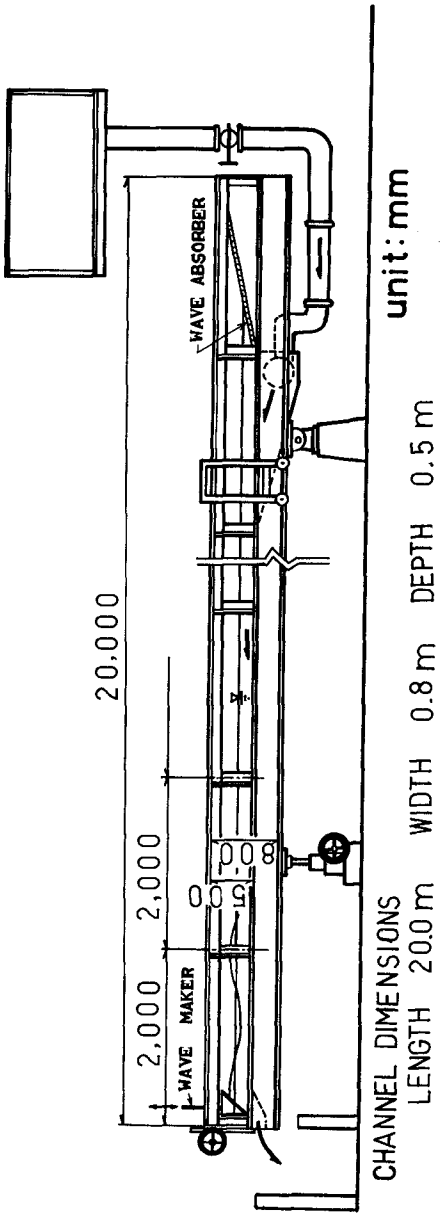

Fig.3 Experimental apparatus

Table-1

h (cm)	T (sec)	U_1 (cm/sec)	H_0 (cm)	α (cm^{-1})	Temp. (°C)
10.0	0.85	6.3	2.02	0.79×10^{-4}	14.2
10.0	0.94	6.4	1.45	2.13	15.3
10.0	0.94	6.4	2.16	1.85	15.3
10.0	0.94	12.0	1.53	1.91	14.4
10.0	0.96	33.2	1.63	4.51	14.3
11.4	1.02	16.1	1.91	1.37	16.0
10.0	1.05	12.0	1.63	3.29	14.4
11.4	1.05	23.1	3.15	4.26	16.0
10.0	1.07	6.3	2.42	2.27	14.2
10.0	1.08	33.2	1.66	4.53	14.3
10.0	1.10	10.4	1.48	2.11	13.2
10.0	1.10	10.4	2.04	1.68	13.2
12.0	1.15	23.1	2.71	3.15	16.0
12.0	1.15	23.1	3.33	3.77	16.0
11.5	1.15	27.1	2.92	4.89	10.8
10.0	1.25	10.4	1.70	2.54	13.2
10.0	1.25	10.4	2.13	1.81	13.2
10.0	1.24	33.2	1.38	6.42	14.3
15.0	0.85	6.3	2.34	0.52	14.1
15.0	0.85	13.1	1.37	2.09	14.9
15.0	0.86	14.6	2.36	2.14	14.3
15.0	0.84	19.5	1.33	2.68	15.1
15.0	0.84	19.5	2.12	3.48	15.1
15.0	0.83	20.3	1.49	2.97	15.0
15.0	0.85	29.4	1.36	2.76	15.0
15.0	0.95	6.3	1.91	1.74	14.1
14.8	0.94	13.1	1.21	1.54	13.1
15.0	0.95	14.6	1.95	2.67	14.3
15.0	0.94	16.9	2.07	3.88	12.4
15.0	0.94	19.5	1.37	2.42	15.1
15.0	0.93	20.3	1.72	2.11	15.0
15.0	0.94	29.4	1.50	2.64	15.0
15.0	1.05	6.3	2.16	1.91	14.1
15.0	1.06	13.1	1.20	1.61	15.0
15.0	1.05	19.5	1.44	2.75	15.1
15.0	1.06	20.3	1.86	2.71	15.0
15.0	1.08	14.6	1.47	3.00	14.3
15.0	1.08	16.9	3.46	2.72	12.4
15.0	1.23	6.3	2.00	0.91	14.1
15.0	1.24	13.1	1.11	1.33	15.0
15.0	1.26	16.9	2.15	2.93	12.4
15.0	1.24	19.5	1.24	1.08	15.1
15.0	1.23	20.3	2.51	2.11	15.0

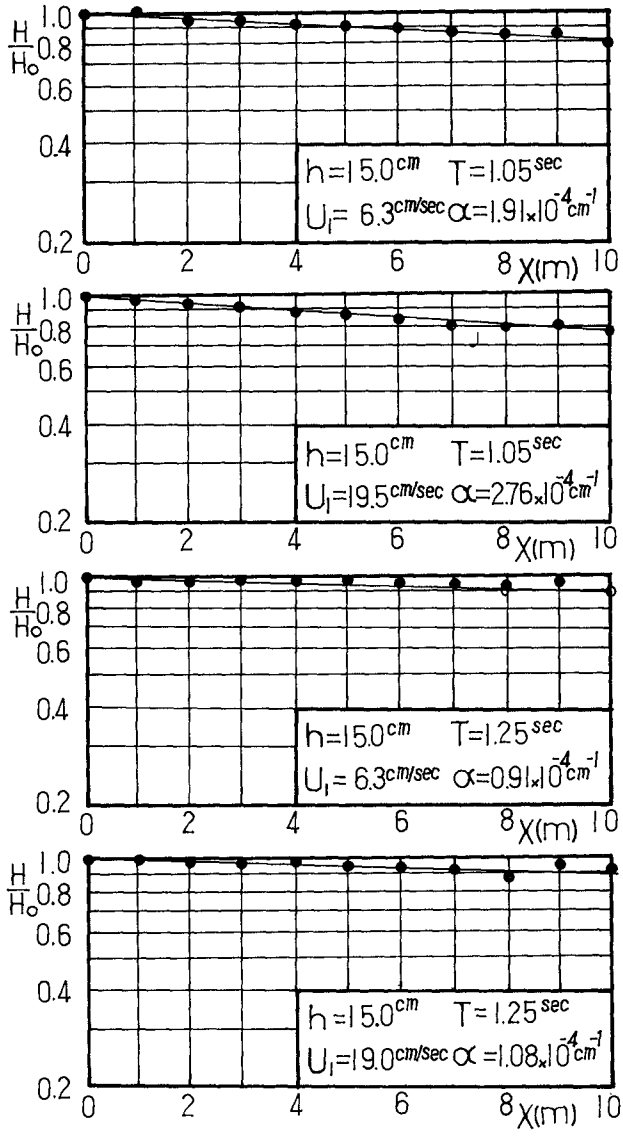

Fig.4

Wave height variation with distance

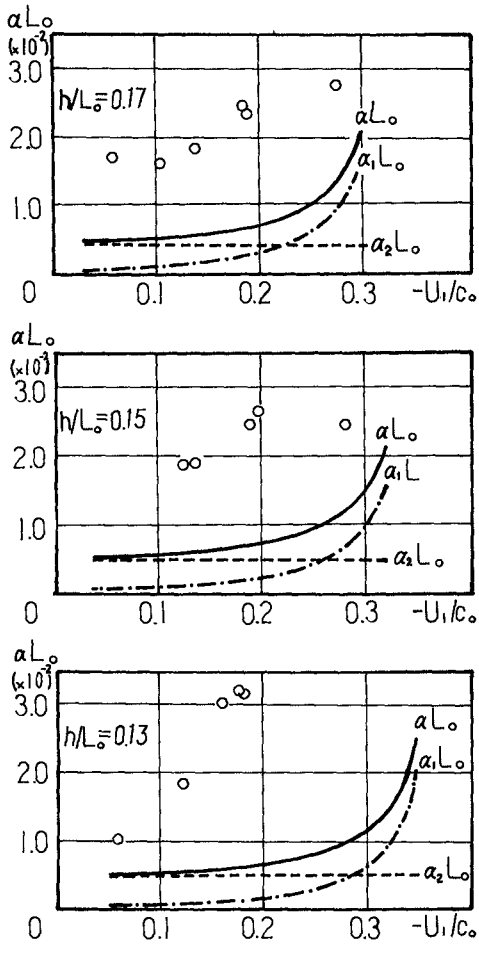
αL₀
(×10³)
3.0
2.0
1.0
0
h/L₀=0.17
αL₀
α₁L₀
α₂L₀
0.1
0.2
0.3
-U₁/c₀
αL₀
(×10³)
3.0
2.0
1.0
0
h/L₀=0.15
αL₀
α₁L
α₂L₀
0.1
0.2
0.3
-U₁/c₀
αL₀
(×10³)
3.0
2.0
1.0
0
h/L₀=0.13
αL₀
α₁L₀
α₂L₀
0.1
0.2
0.3
-U₁/c₀

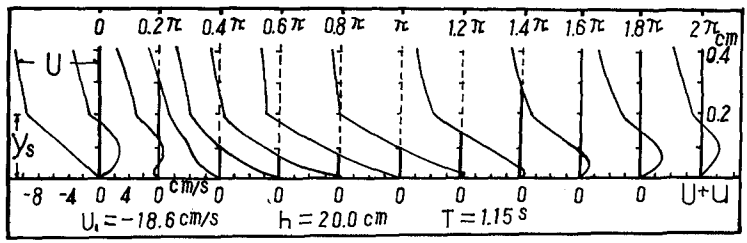

Fig.6

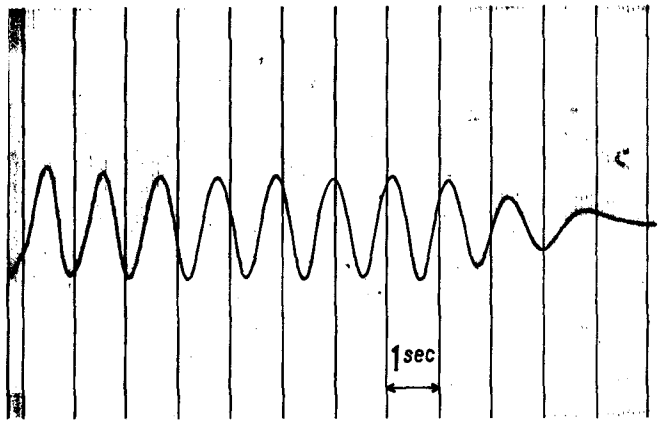

Fig.7

Example of wave record

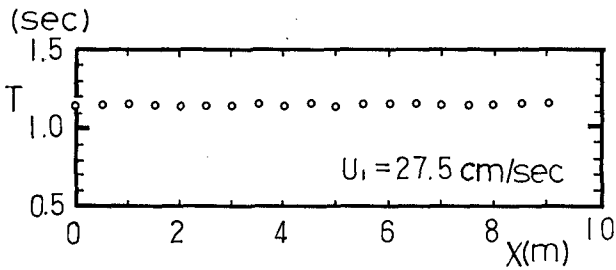

Fig.8

Wave period variation with travel distance

CHAPTER 33

TURBULENT CURRENTS IN THE PRESENCE OF WAVES

Helge Lundgren

Professor, Technical University of Denmark
Scientific Director, Danish Hydraulic Institute

1. ABSTRACT

This paper presents an approximate theory for the reduction of the velocity of a current due to the presence of sinusoidal waves.

For a given slope, S, in water of constant depth, d, the current velocity profile is

$$U(z) = U_f \left(2.5 \ln \frac{z}{z_o} - A\right) \qquad (1)$$

as a function of the height, z, above the bed. Eq. 1 is valid only above the thin wave boundary layer near the bed, the roughness of which is $k = 30\, z_o$. U_f is the current friction velocity defined by

$$\rho\, U_f^2 = \gamma\, d\, S = \tau_{cw} \qquad (2)$$

where τ_{cw} is the current shear stress in the presence of waves.

Values of A can be found from:

Fig. 2 where A_1 applies when the direction of wave propagation is parallel to the current direction, and

Fig. 3 where A_2 applies when the direction of wave propagation is perpendicular to the current direction,

cf. Notation in Sec. 2.

The theory is based upon a number of assumptions (see Sec. 4).

2. NOTATION

A_1 Constant of velocity defect for a current parallel to the direction of propagation of the waves.

A_2 Constant of velocity defect for a current perpendicular to the direction of propagation of the waves.

a_b Amplitude of particle orbit at bed for sinusoidal wave according to potential theory.

d Depth of water.

f_w Characteristic friction coefficient in wave boundary layer.

k Roughness of bed (Nikuradse).

n_c Turbulent (kinematic) viscosity in a pure current.

n_{cw} Turbulent viscosity in combination of current and waves.

n_w Average turbulent viscosity in pure wave motion.

r Wave friction velocity ratio u_f/u_b.

S_1 Slope of still water level for a current in the direction of wave propagation (for constant depth).

S_2 Slope of still water level for a current perpendicular to the direction of wave propagation (for constant depth).

U_1 Current velocity in the direction of wave propagation.

U_2 Current velocity perpendicular to the direction of wave propagation.

U_f Current friction velocity.

u Velocity in wave boundary layer.

u_b Maximum orbital velocity at bed for sinusoidal wave according to potential theory.

u_f Maximum wave friction velocity.

v Velocity.

z Height above bed.

z_o Roughness parameter = $k/30$.

γ Specific gravity.

δ Characteristic thickness for wave viscosity decreasing exponentially with height above bed.

ρ Specific density.

τ_c Shear stress in a current.

τ_{cw} Current shear stress at the bed in the presence of waves.

τ_w Shear stress in the wave boundary layer.

3. INTRODUCTION

In recent years there has been much progress with respect to the theory of interaction of currents and waves. Most of this progress, however, has taken place within the realm of potential flow, i.e. without consideration of bed friction and turbulence.

Much less has been done with a view to the influence of the bed friction on the combination of currents and waves, for the simple reason that the turbulence problems of the wave boundary layer and of the

combined flow are very complicated. In some cases it has been attempted to approach the turbulence problem of the combination by simple assumptions taken from the turbulence theory of steady flow, for example that the Prandtl mixing length be known. Indeed, to-day no theory of the combined bed friction would be possible without a number of simplifying and, perhaps, quite hypothetical assumptions.

In the potential theory of the interaction of waves and currents, the main problem is the influence of varying depths and current velocities, and most interesting results have been obtained. However, the very solution of the problems in nature cannot be obtained without knowledge of the bed friction since a natural problem will normally be posed in the following manner: "For a region exposed to a given wave motion the mean water levels are known along the boundary, for example as a result of tides or storm surges; it is then desired to determine the current and wave fields within the region, with due consideration of the interaction effects and the bed friction hampering the current."

In general, no methods are available for the rational solution of such problem because of the influence of wave breaking. For problems outside the breaker zone, however, the approximate theory in this paper, which assumes sinusoidal waves, might be of some value.

Since no experiments, against which the theory could be tested, are available, the present results may be taken only as an indication of the order of magnitude of the reduction of the current velocities due to the influence of waves.

In addition, it must be stressed that the theory is valid for fixed beds only. If the sediments of the bed are brought into motion by the waves, they are expected to act as a "lubricating" agent, with the result that the current is less hampered or, perhaps, for heavy suspension of sediments, even enhanced by the waves.

For the turbulent interaction of currents with sinusoidal waves over a fixed bed, one may distinguish between 4 zones from the surface to the bed:

Z_1 Zone of Low Current Frequencies: In this zone the dominant frequencies of the turbulent stresses are much lower than the wave frequency, so that turbulent production, diffusion and dissipation take place independently of the waves.

Z_2 Zone of Intermediate Current Frequencies: In this zone the nonlinear terms may give some interaction between the turbulent stresses and the wave frequency. The wave-produced bed turbulence has no influence.

Z_3 Transition Zone: In this zone the turbulent viscosity produced by the wave boundary layer near the bed is of the same order of magnitude as the viscosity pertaining to the current turbulence. The dominant frequencies of the turbulence become much larger than the wave frequency towards the lower boundary of this zone.

Z_4 Zone of Dominant Wave Viscosity: In this zone the wave-produced viscosity is much larger than the current-produced viscosity. If the waves are low and the current strong, zone Z_4 may vanish, with Z_3 extending all way to the bed.

In order to give a picture of the extent of these zones, the following situation may be considered: Water depth $d = 10$ m, bed roughness $k = 0.1$ m, current velocity $U = 0.5$ m/s, wave period $T = 10$ s, wave height $H = 3$ m. Then the transition between the zones takes place approximately at the following elevations above the bed: $z_{1-2} \sim 5$ m, $z_{2-3} \sim 0.5$ m, $z_{3-4} \sim 0.1$ m.

The reason for the reduction of the current velocity by the presence of the waves lies in the zones Z_3 and Z_4 where the resulting viscosity is larger, respectively, much larger than the normal current-produced viscosity. When the viscosity is increased the current velocity gradient pertaining to a given current bed shear stress is reduced. This reduction of gradient is largest near the bed where the velocity gradients are particularly large for a pure current.

4. ASSUMPTIONS

The main assumptions of the theory presented below are:

(a) The bed is fixed. It has the equivalent sand roughness $k = 30\, z_o$, where z_o is the roughness parameter used in the following.

(b) The water depth, d, is constant, the still water level and the bed having the same slope, S.

(c) The wave motion at the bed is sinusoidal.

(d) The current velocity, U, is so small compared with the wave celerity, c, that the relative wave motion - as seen by an observer moving with the current - can be calculated from Stokes' first-order theory, cf. Sec. 5.

(e) The interaction between the turbulent stresses of the current and the wave frequency in the zone Z_2 (see Sec. 3) can be neglected.

(f) In the zones Z_3 and Z_4 the pulsations of the current with the wave frequency are not considered, but only the average of the current velocity over the wave period.

(g) The turbulence is everywhere fully developed with negligible molecular viscosity.

(h) The gradient, dU/dz, in the vertical direction, z, of the average current velocity, U(z), can be derived from the current shear stress, τ_{cw}, in the presence of waves and from the combined turbulent viscosity, n_{cw}, by the same formula as for a pure current, cf. Sec. 10.

(i) In the zone Z_3 the combined viscosity, n_{cw}, may be calculated from the current-produced viscosity, n_c, and the wave produced viscosity, n_w, by means of the formula

$$n_{cw} = n_c + n_w \tag{3}$$

for a current in the direction of propagation of the waves, and the formula

$$n_{cw}^2 = n_c^2 + n_w^2 \tag{4}$$

for a current perpendicular to the wave direction, cf. Sec. 9.

(j) At any level above the bed, the current viscosity, n_c, is related to the current velocity gradient, dU/dz, by the same formula as for a pure current, cf. Sec. 6.

(k) Whereas the viscosity in the boundary layer of a pure wave motion actually varies with a frequency twice the wave frequency, it suffices to use an average value, n_w, over the wave period, cf. assumption (f).

(l) The average wave viscosity, n_w, may be calculated from average (numerical) values of the shear stresses and the velocity gradients, as found from measurements in the wave boundary layer, cf. Sec. 7.

5. POTENTIAL WAVE MOTION

For a sinusoidal wave of height H, wave length L, and period T relative to the current, the amplitude of the orbital motion at the bed according to potential theory is

$$a_b = \frac{H}{2} \frac{1}{\sinh (2\pi\, d/L)} \tag{5}$$

The maximum orbital velocity at the bed is

$$u_b = \frac{2\pi}{T} a_b \tag{6}$$

With good approximation the wave boundary layer at the bed is uniquely determined by a_b and u_b together with the roughness parameter z_o, independent of L and d.

6. CURRENT VISCOSITY

For steady flow the general relation between a shear stress τ and the velocity gradient dv/dz is

$$\tau = \rho\, n\, dv/dz \tag{7}$$

where n is the turbulent (kinematic) viscosity. If this formula is applied to the usual velocity profile of a steady current

$$U(z) = 2.5\, U_f \ln (z/z_o) \tag{8}$$

where U_f is the current friction velocity, the viscosity is found to be

$$n_c = 0.4\, U_f\, z\, (1 - \frac{z}{d}) \tag{9}$$

the coefficient 0.4 being von Kármán's constant.

Since the velocity gradient is

$$dU/dz = 2.5\ U_f/z \tag{10}$$

U_f can be eliminated from Eq. 9 giving

$$n_c = 0.16\ z^2\ (1 - \frac{z}{d})\ \frac{dU}{dz} \tag{11}$$

where the coefficient 0.16 is the square of von Kármán's constant.

Because of assumption (e) in Sec. 4, these formulae apply directly above the wave boundary layer, i.e. above the layer where the wave viscosity has any influence.

In the wave boundary layer z is so small compared with d that Eq. 11 may be written

$$n_c = 0.16\ z^2\ \frac{dU}{dz} \tag{12}$$

Thus the wave boundary layer is within the constant stress layer of the current.

The constant stress layer of a pure current is characterized by the equilibrium between local production and local dissipation of turbulence, i.e. the current viscosity is locally produced, with no essential contribution from diffusion of turbulence. The physical basis of Eq. 12 is the similarity within the constant stress layer, with the vertical mixing length, 0.4 z, as length scale and the velocity gradient, dU/dz, as frequency scale.

When a wave motion is superimposed upon the current, the viscosity is increased within the wave boundary layer because of the wave turbulence, resulting in a reduction of the current velocity gradient, dU/dz, for a given current shear stress, τ_{cw}. It will be assumed, however, that the viscosity, n_c, originating from the current, is still locally produced according to Eq. 12, whereby the mixing length is supposed to play the same role as in a pure current.

Within the wave boundary layer Eq. 9 could not be used, because this formula involves a velocity scale U_f of the current-produced turbulence, and the current-produced vertical velocity fluctuations will be strongly influenced by the wave-produced turbulence. There is much better hope that the mixing-length of the current-produced turbulence is largely independent of the wave-produced turbulence.

7. WAVE VISCOSITY

In the present context the wave viscosity is of interest inasmuch as it influences the current velocity gradient, but not as a factor governing the development of the wave boundary layer, because the latter must anyway be studied by means of experiments.

It would be of little or no use to define the instantaneous value of the wave viscosity by means of Eq. 7, because τ and dv/dz do not vanish at the same time. Hence, the values of n thus calculated would now be zero, now infinite, whereas the wave viscosity that participates

in controlling the current velocity gradient must always be a positive, finite quantity.

Since it is not intended to study the pulsations of the current with the pulsating wave viscosity, cf. assumption (f), it is natural to average the wave viscosity over the period. In analogy to Eq. 7, the average wave viscosity, n_w, can most simply be introduced as a function of z by the following formula

$$n_w(z) = \frac{\int |\tau_w(z)/\rho| \, dt}{\int |\partial u(z)/\partial z| \, dt} \tag{13}$$

where the integrals are taken over the wave period. It is necessary to use the numerical values of the shear stresses and the velocity gradients because both change sign every half period.

In the oscillating water tunnel of the Technical University of Denmark two tests have been run with measurements in the wave boundary layer, and the main results published in Refs. 1 and 2, respectively. The characteristic data of these tests are:

	TEST 1	TEST 2
a_b	2.85 m	1.79 m
u_b	2.11 m/s	1.53 m/s
k	23 mm	63 mm
u_f	0.208 m/s	0.210 m/s
r	0.0984	0.1371
f_w	0.0194	0.0376
δ	42 mm	52 mm

The quantities u_f, r, f_w and δ will be explained in Sec. 8.

The basic data from the tests have been introduced in Eq. 13, and the resulting empirical wave viscosities plotted in Fig. 1 with dimensionless coordinates.

8. WAVE VISCOSITY FORMULA

In order to generalize the test results to other values of the parameters a_b, u_b and k, the following formula has been constructed

$$n_w = \frac{0.4 \, u_f \, z}{1 + 1.34 \sqrt{r} \, \frac{z}{\delta} \exp \frac{z}{\delta}} \tag{14}$$

The determination of u_f, r and δ will be explained below. This formula satisfies two basic requirements: (a) Near the bed n_w is proportional to z. (b) In the upper part of the wave boundary layer n_w decreases exponentially with z.

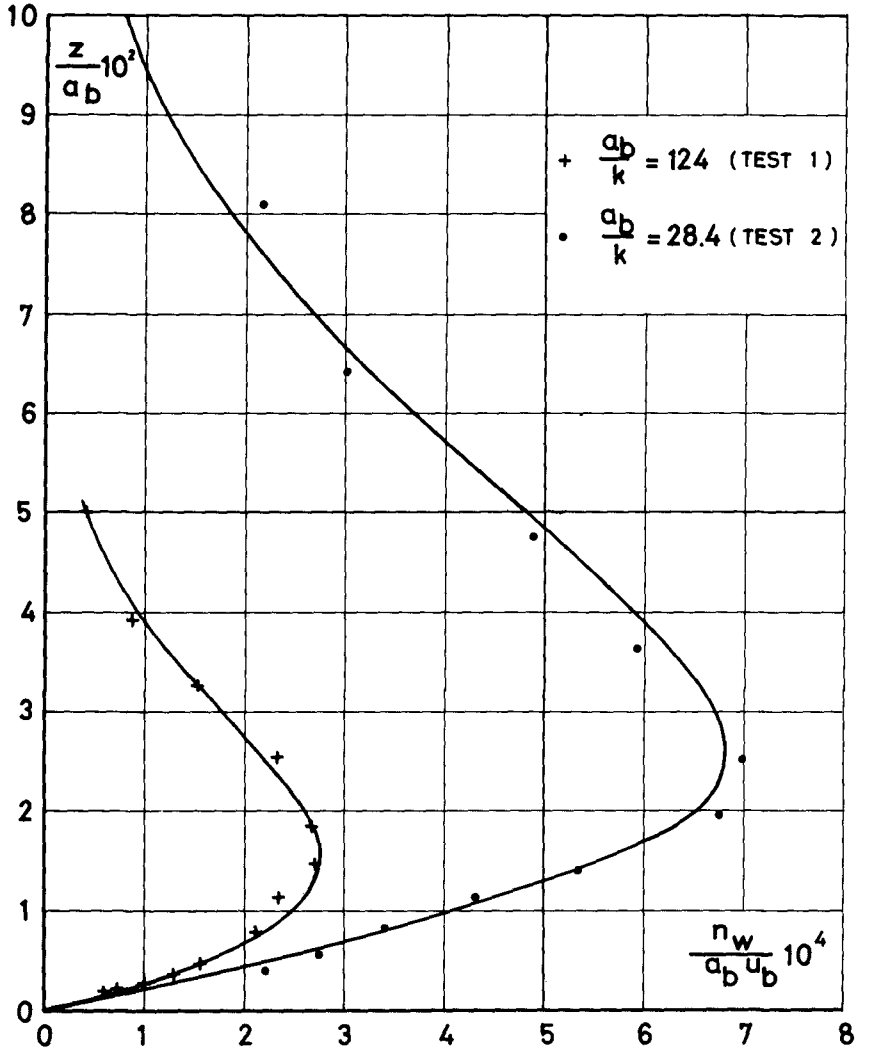

Fig. 1 Wave viscosity, n_w, as a function of z

For Tests 1 and 2 the full curves in Fig. 1 show the variation of the wave viscosity according to Eq. 14.

In a wave boundary layer the maximum bed shear stress, $\tau_{w,max}$, occurs before the maximum velocity, u_b, in the potential flow, the phase shift being about 30^o. The maximum wave friction velocity, u_f, and the characteristic wave friction coefficient, f_w, are defined by

$$\tau_{w,max} = \rho u_f^2 = \tfrac{1}{2} f_w \rho u_b^2 \qquad (15)$$

The wave friction velocity ratio, r, is defined as

$$r = u_f/u_b = \sqrt{\tfrac{1}{2} f_w} \tag{16}$$

and can be determined from the following equation

$$\frac{0.174}{r} + \log \frac{0.174}{r} = - 0.077 + \log \frac{a_b}{k} \tag{17}$$

According to Eq. 14, δ is a characteristic thickness for the upper part of the wave boundary layer, where the viscosity decreases exponentially with z. δ can be calculated from

$$\frac{2.74\ \delta}{k} \log \frac{2.74\ \delta}{k} = 0.0282\ \frac{a_b}{k} \tag{18}$$

The compositions of Eqs. 17-18 have been derived by very simplified considerations of the growth of the wave boundary layer in accelerated potential flow (Ref. 3).

The procedure for calculating the wave viscosities is then:

(a) Solve Eq. 17 for 0.174/r and find r.

(b) Solve Eq. 18 for 2.74 δ/k and find δ.

(c) Calculate $u_f = r\ u_b$, cf. Eq. 16.

(d) Calculate n_w from Eq. 14.

The validity of Eq. 14 has been tested partly by Fig. 1, partly by the following method: For Tests 1 and 2, a semilogarithmic diagram was plotted of two dimensionless quantities: $n_w/z \cdot u_b$ (logarithmic scale) versus $z/f_w \cdot a_b$ (linear scale), whereby the curves for the two tests came very close to each other over a large range. This diagram was used for an independent extrapolation of the viscosities to the ratio $a_b/k = 540$. The extrapolated curve fitted Eq. 14 very well.

9. COMBINED VISCOSITY

For the combination of a current with waves the total viscosity is n_{cw}.

Above the wave boundary layer n_w is negligible, and $n_{cw} = n_c$ can be determined from Eq. 9. Here the current friction velocity U_f is defined by

$$\tau_{cw} = \rho\ U_f^2 = \gamma\ d\ S \tag{19}$$

where τ_{cw} is the current shear stress at the bed.

Within the wave boundary layer the situation is very complicated because both n_c and n_w contribute to n_{cw}. It was decided to find n_{cw} by adding a vector n_c in the current direction to a vector n_w in the wave direction, because such vectorial combination would be correct in the case of two currents U' and U" in arbitrary directions, cf. Eqs. 8-9.

The vectorial combination of n_c and n_w is probably the most questionable of the assumptions of the present theory, because the structures of the current-produced turbulence and the wave-produced turbulence are

widely different. There are two zones, however, where the error of n_{cw} is believed to be small: The zone where n_w varies linearly with z, and the zone where n_c is essentially larger than n_w. Between these zones the error may be larger but will probably have a rather limited influence on the resulting velocity profile.

The vectorial combination has been applied only when the angle between the current and wave directions is 0° or 90°, resulting in the Eqs. 3 and 4.

10. CURRENT VELOCITY PROFILES

Throughout the wave boundary layer, where the current shear stress is constant, the velocity profile U(z) has been found by numerical integration of

$$\tau_{cw} = \rho\, n_{cw} \frac{dU}{dz} \tag{20}$$

Near the bed the velocity gradient dU/dz is essentially reduced because of the influence of the wave viscosity.

The numerical integration has been carried out by Mr. Roger B. Wallace of the Danish Hydraulic Institute, for all combinations of the values

$$\frac{a_b}{k} = 28.4 - 124 - 540 \tag{21}$$

and

$$\frac{\tau_{cw}}{\rho\, u_b^2} = 10^{-5} - 10^{-4} - 10^{-3} - 10^{-2} \tag{22}$$

both for parallel and perpendicular directions of the current and the waves.

Above the wave boundary layer the velocity profile becomes

$$U(z) = U_f \left(2.5 \ln \frac{z}{z_o} - A\right) \tag{23}$$

It has the normal logarithmic shape but is reduced by the constant velocity $A\, U_f$. The constant, A, of velocity defect can be found from Figs. 2 and 3, for parallel and perpendicular directions, respectively. The values of A_1 and A_2 must be seen in relation to the value of $2.5 \ln (d/z_o)$, which is normally of the order of magnitude of 20.

For waves propagating at an arbitrary angle with the current, the friction velocity U_f is determined from the total slope S by means of Eq. 19 as usual. It is suggested to calculate the current velocity profile without waves and then deduct A_1 or A_2, respectively, from the velocity components parallel and perpendicular to the wave direction.

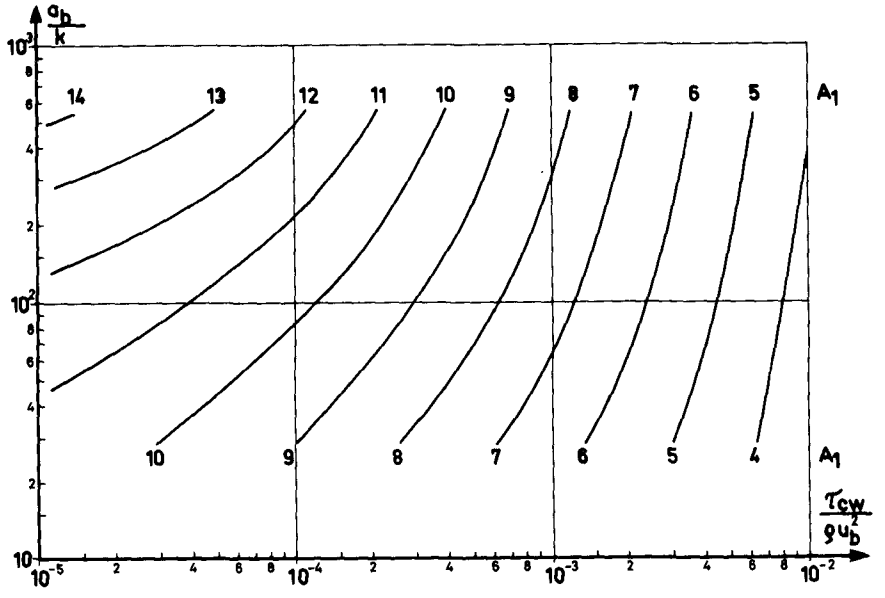

Fig. 2 Constant, A_1, of velocity defect for current || wave direction

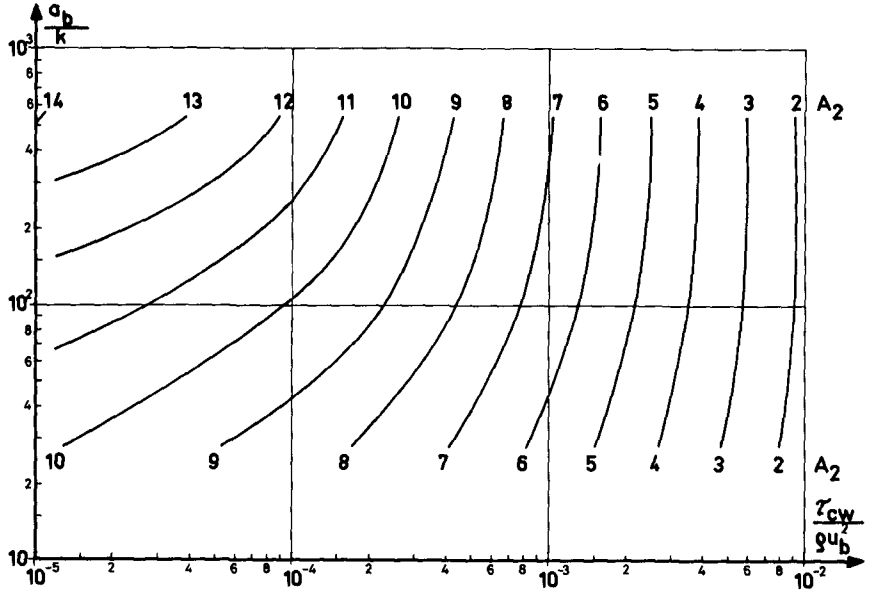

Fig. 3 Constant, A_2, of velocity defect for current $\perp$ wave direction

11. REFERENCES

1. Jonsson, I. G.: Measurements in the turbulent wave boundary layer. Int. Ass. Hydr. Res., 10th Congr., London 1963, vol. 1, 85-92.

2. Carlsen, N. A.: Measurements in the turbulent wave boundary layer. Coastal Engng. Lab. & Hydr. Lab., Techn. Univ. Denmark, Progress Report 14, 2-3, July 1967.

3. Jonsson, I. G. & H. Lundgren: Derivation of formulae for phenomena in the turbulent wave boundary layer. Coastal Engng. Lab. & Hydr. Lab., Techn. Univ. Denmark, Progress Report 9, 8-14, Aug. 1965.

CHAPTER 34

FIELD OBSERVATIONS OF NEARSHORE CURRENT SYSTEM

Kiyoshi Horikawa
Professor
and
Tamio Sasaki
Postgraduate

Department of Civil Engineering
University of Tokyo
Tokyo, Japan

ABSTRACT

The two systems based on the principle of photogrammetric surveying have been developed in order to accomplish the field observations of nearshore current system induced by waves, and were applied to the field investigations on the Shonan Coast, Kanagawa Prefecture, Japan (Horikawa, Sasaki et al, 1970). The first is called as the Balloon Camera System and the other is the Synchronized Helicopter System. The main efforts were concentrated to the simultaneous observations of waves and current fields in and out the surf zone. Even there still exist some difficulties to be overcome in applying the present systems, the validity and usefulness of these systems were demonstrated by the obtained data. In this paper are presented the details of the developed systems and a part of the analyzed results by using the data obtained in field.

INTRODUCTION

The nearshore current system is of very importance in connection with the coastal processes, and the characteristics of the nearshore current have strong influences on the recreational activities and water pollution problems in the coastal area.

Several mathematical models of longshore current and/or of nearshore current system have been proposed very recently by Bowen (1969), and Bowen & Inman (1969, 1971) based on the concept of radiation stress. On the other hand the field measurements of nearshore current have been conducted very actively by Sonu (1972). From the engineering point of views it is of

essentially importance that all of the factors taken into the mathematical models of nearshore current system should be determined by the physical parameters such as the height, period, and incident direction of waves, and bottom configuration especially inside the surf zone. The proposed models are at present qualitative ones, and their applicability should be investigated by using the reliable data obtained in field under the numerous conditions.

The principal difficulties in the field observations of nearshore current result from the fact that the phenomena of current system extend to the broad area in and near the surf zone. Therefore the main efforts so far have been devoted to the velocity measurements of longshore current which is a part of the nearshore current system except the pioneering works by Shepard & Inman (1950) and leading works by Sonu (1969, 1972).

Figure 1 is a well-known schematic diagram of nearshore current system drawn originally by Shepard & Inman (1950), and revised by Inman and Bagnold (1962). In order to investigate the whole pattern of this current system, it is desirable to measure the wave characteristics such as height, period, and direction, the current field and the bottom topography in and out of the surf zone simultaneously. From that point of view, the aerial photographic surveying seems to be the most suitable way to accomplish the systematic observations in the nearshore area. Therefore the following two systems were developed and applied to the field observations in order to take successive pictures at certain interval from air. At any rate this is the initial stage of the research project on the nearshore current at the Coastal Engineering Laboratory, University of Tokyo.

FIELD OBSERVATION SYSTEMS

Balloon Camera System

Figure 2 is the schematic diagram of the Balloon Camera System which is shortly named as BACS. The Balloon of this system is to hang the capsule in which a motor-drive camera (Hasselbrad 500EL) is contained as shown in Figure 3. The balloon has its inner volume of 33 m^3 filled with hydrogen gas. The reasons why hydrogen gas is prefered are as follows:

(1) The cost of hydrogen gas is fairly cheaper in Japan, and its specific gravity is relatively small, therefore the gained buoyancy is relatively large, in comparison with helium gas.

(2) Although hydrogen gas is easy to detonate in case of mixing with air, it is practically easy to operate with safety under the desired care.

The detailed descriptions of the Balloon Camera System are given in Table 1.

As shown in the table 70 mm film is used instead of 35 mm with the purpose of getting better resolution of pictures. The stability of the photo coverage was practically well in the air. The camera was set for shotting at 6 sec interval and for taking successive 20 frames or more.

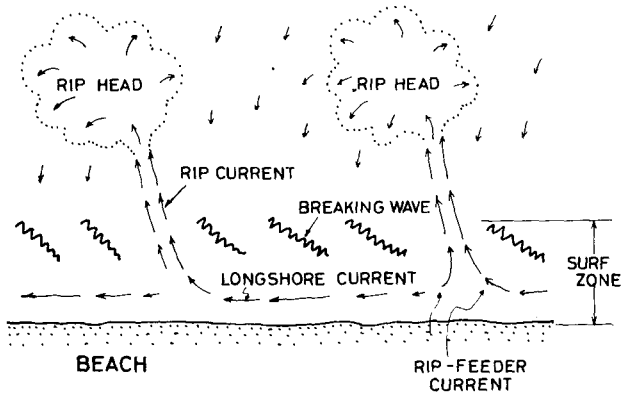

Fig. 1 Schematic diagram of nearshore current system. (After Inman & Bagnold)

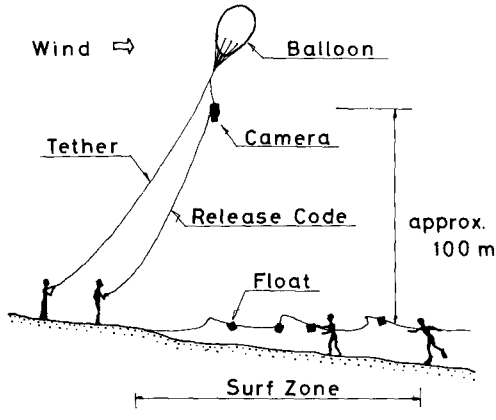

Fig. 2 Schematic diagram of BACS.

Fig. 11 A part of Fig. 10 enlarged. Two rip channels are seen on left and center of the photograph. (SIHEL-515,,swell)

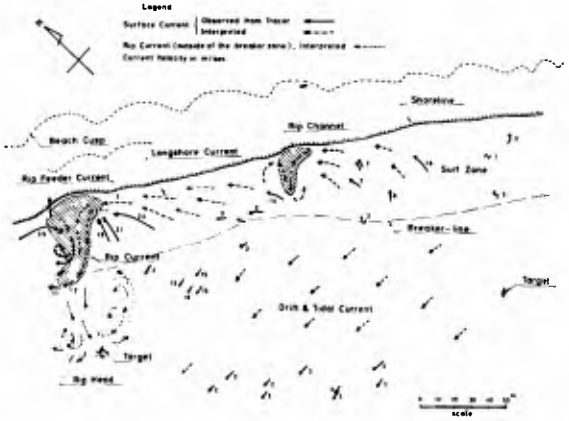

Fig. 12 An example of velocity field obtained by SIHELS. (cf. Fig. 11, SIHEL-515, swell)

The defects of the present system are as follows:

(1) The wind speed should be less than 7 - 8 m/sec.

(2) The actual distribution of wave height can not be read from successive pictures due to non stereophotogrammetry.

(3) The area covered by each photograph is relatively small as 100 m x 100 m in horizontal scale.

Synchronized Helicopter System

Figure 4 is the schematic diagram of the Synchronized Helicopter System which is shortly named as SIHELS. The descriptive outline of this system is given in Table 2, from which it is recognized that the area covered by single photograph is pretty large in comparison with the Balloon Camera System. The following facts were the reasons why the helicopter was used. The airplane except helicopter needs at least 5 min. to return to the questioned site, but the helicopter is able to stay for certain period at a defined location with constant altitude owing to its hovering capacity.

The accuracy of the results is very high and satisfactory in the quantitative sense for the present purpose, but the largest defect is the operation cost being extremely high.

The helicopters used are too small to stay for longer time at the specified locations accurately (Figure 5). The accuracy is requested to get stereophotographic pictures. Owing to the above limitation, 40 sec period was selected for the operation of taking pictures.

The method for synchronization of taking pictures was as follows. The trigger signal was transmitted from "MASTER" camera mounted on the commanding helicopter to "REMOTE" camera mounted on the other helicopter at the initiation of operation, ever since then the timing mechanism installed in each camera was operated to take the following successive 5 - 7 frames at interval of 6 - 8 sec.

Floats

The principle of both systems stated above is basically the same as follows: numerous floats throwing by hand along the specified lines from shore to breaker line were traced by the successive pictures taken at a certain interval. Various kinds of floats were tested in order to find out the adequate type of floats for tracing the velocity field of nearshore current as accurately as possible. The float of cube made from polyurethane foam with 25 cm or 33 cm in edge length was finally selected. The outer surface was coated by membrane of vinyl with yellow and/or orange colour. This kind of device was successful to distinguish the location of float on colour film under the white foamed surf zone condition.

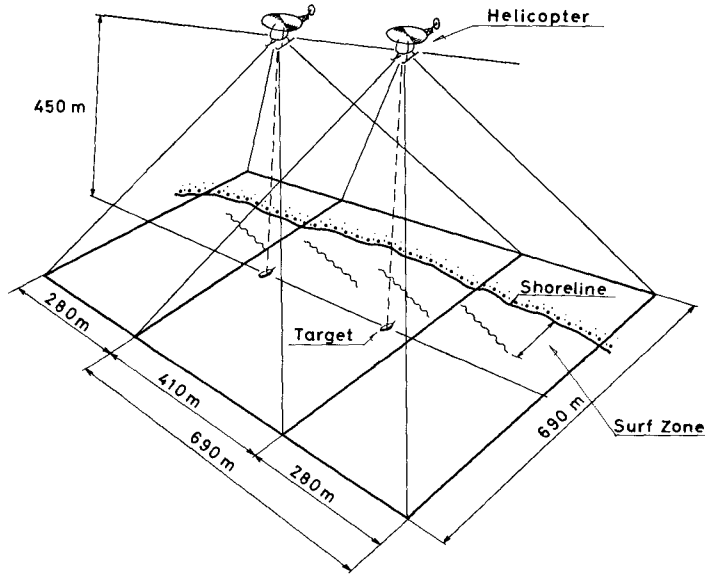

Fig. 4 Schematic diagram of SIHELS.

Table 2 Outline of SIHELS.

HELICOPTER	Bell KH-4
CAMERA	Zeiss RMK 15/23
FILM	Kodak Aerocolour-N
PHOTO SCALE	1/3000
ALTITUDE	450 m
COVERAGE	690m X 410m (stereo)
	690 m X 970m (mono)

Fig. 5 Helicopters used for SIHELS.

Fig. 6 Polyurethane floats for nearshore current observations.

FIELD INVESTIGATIONS AND ANALYZED RESULTS

Test Sites and Wave Climates

The two systems stated above were practically applied to the field observations on the Shonan Coast near Enoshima Island in Kanagawa Prefecture, Japan. This is one of the busiest summer health resorts in Japan owing to the relatively short distance from the Tokyo Metropolitan Area, namely the distance from Tokyo to Enoshima Island is about 50 km. The survey area is divided into two, one is named as Area A, and the other Area B as shown in Figure 7.

Table 3 gives the available information about the date and time of observations, the wind conditions, the wave characteristics of breakers, and the width of surf zone. The classification of wave climate was also indicated as wind wave or swell condition. The hydrographic surveying could not be conducted at the time when the stated field observations were done, but the hydrographic chart made by the Kanagawa Prefecture in 1969 was available to be used. According to this chart the foreshore slope was in the range of 1/20 through 1/40. Here the authors wish to mention that has been observed the flow field under the rather rough sea condition such as the maximum breaker height being over 2.5 m in comparison with most of the previous data which were obtained under the relatively small wave condition.

Some Results of Field Observations

Figure 8 gives one example of photographs taken by the Balloon Camera System. Analysis of these successive photographs gives the velocity field in the surf zone as demonstrated in Figure 9. In this diagram the solid line arrows indicated the actual trace of floats, while the dotted line arrows indicate the interpreted flow pattern. The wave climate, when the field investigation was conducted, was swell condition with its breaker height of about 0.6 m, and the spacing between two neighbouring rip channels was about 100 m.

Figure 10 is one example of photographs taken by the Synchronized Helicopter System. It is needless to say that the original one was colour picture. The existence of many rip channels was clearly taken in this photograph. In order to make much more clear picture of rip channels and rip heads, the right hand half of the original photograph was enlarged as shown in Figure 11, where the rip channels, the targets ship and numerous floats were indicated. The wave climate at that time was swell with breaker height of 0.5 - 0.8 m. The wave steepness was relatively small, hence the breaker was classified into plunging breaker type with rather long wave crest. The analyzed diagram is given in Figure 12, where the flow pattern and the rip head were interpreted. The shape of the rip head is quite similar to a cauliflower. At any rate the flow pattern is surprisingly similar to the illustration given in Figure 1. The synchronization was unsuccessful at this operation, hence the stereoscopic analysis could not be applied.

On the other hand, under the wind wave condition the situation of flow

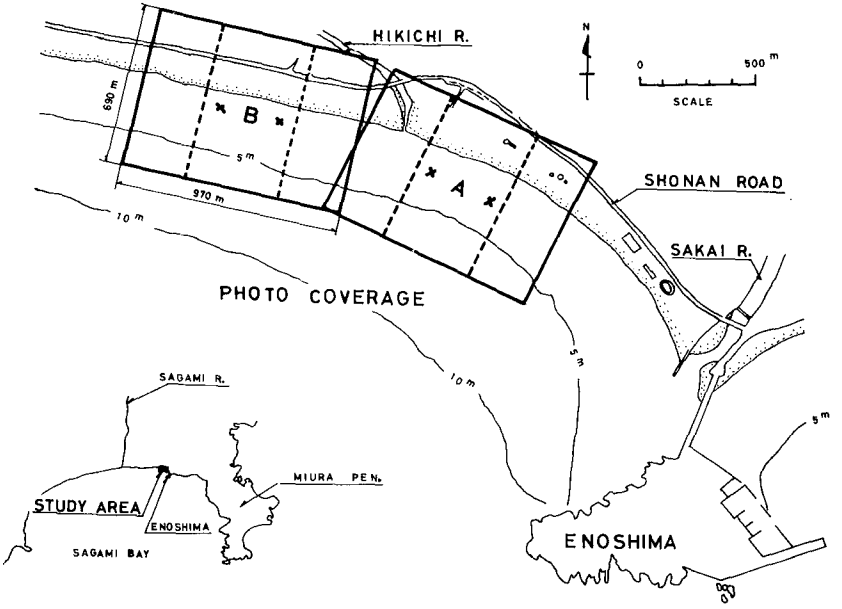

Fig. 7 Location map of field boservation site.

Table 3 Wave and climate condition associated with field observations executed.

SIGN		SIHELS-515		SIHELS-611		BACS-624	SIHELS-705	
DATE		1971. 5. 15.		1971. 6. 11.		1971. 6. 24.	1971. 7. 05.	
AREA		A	B	A	B	A	A	B
TIME		12:35	14:23	13:47	15:26	11:40	14:10	15:40
WIND	VELOCITY(m/sec)	(8)	(8)	6.6	4.3	2.5	5.3	6.7
	DIRECTION	(NNE)	(NE)	SW	SSW	NNW	SSW	SSW
WAVE (breaker)	HEIGT (m)	0.8	0.8	1.4 ~ 1.7	1.3 ~ 2.5	0.6	1.4 ~ 1.7	1.2 ~ 1.5
	ANGLE (deg.)	7	7	9	0	10	4	2
	LENGTH (m)	15~30	20	15~25	20~30	20 ~ 30	6 ~ 12	10~25
	PERIOD(sec.)	—	—	—	—	7.0	(4 ~ 5)	
	CONDITION	SWELL		WIND WAVE		SWELL	WIND WAVE	
SURF ZONE WIDTH (m)		50	50	100	90	60	40	50

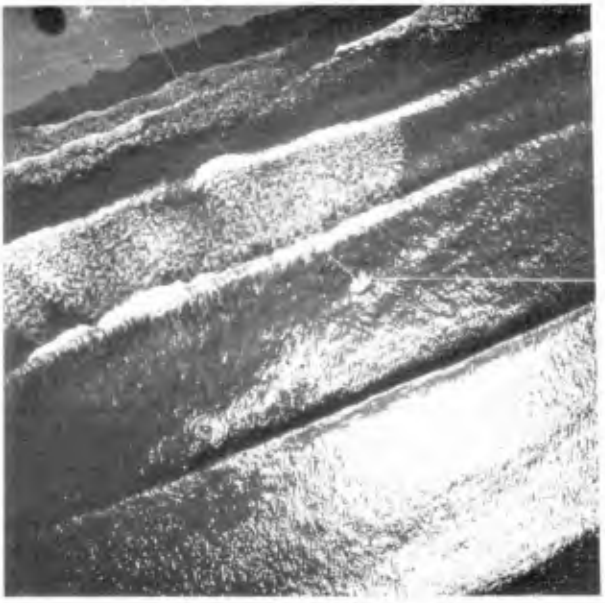

Fig. 8 An example of photograph taken by BACS.

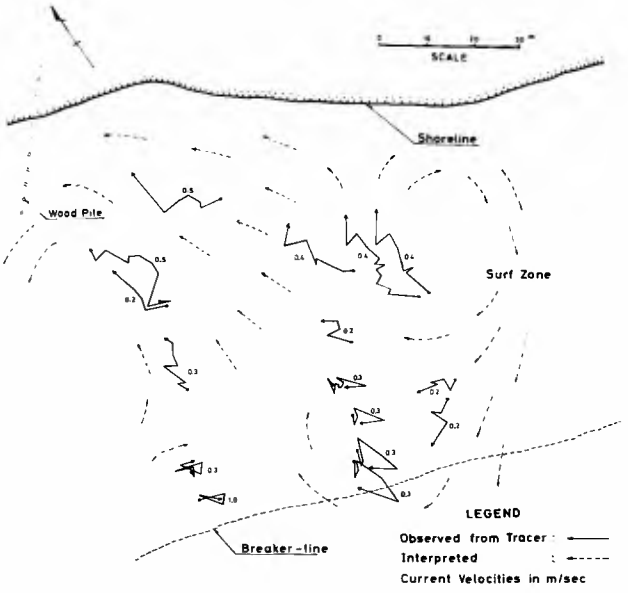

Fig. 9 An example of velocity field by BACS. (BACS-624, swell)

Fig. 10 An example of photographs taken by SIHELS. (SIHELS-515, swe11)

Fig. 3 Balloon and camera capsule of BACS.

Table 1 Outline of BACS.

BALLOON	Ovoid type gas balloon volume : 33 m^3
CAMERA	Hasselbrad 500EL 70 mm moter drive
LENS	Distagon 50 mm
TETHER	ø5 mm polyester
ALTITUDE	100 ~ 150 m
FLOAT	Polyurethane foam

Fig. 13 An example of photographs taken by SIHELS. (SIHELS-611, wind wave)

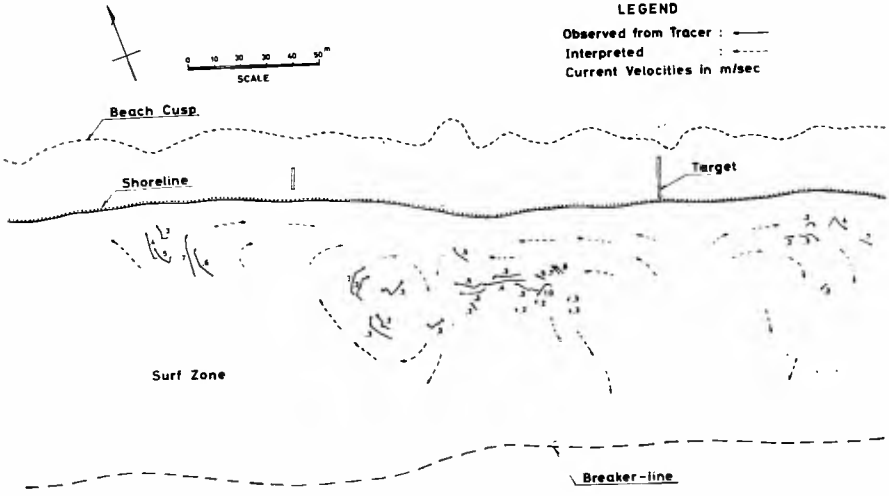

Fig. 14 An example of velocity field by SIHELS. (SIHEL-611, wind wave)

pattern seems to be really complicated. Figure 13 is one example of photographs taken during the wind waves, the breaker height of which was approximately 2.5 m.

The distributed pattern of floats was unfortunately not adequate to catch the whole flow pattern of nearshore circulation system as shown in the analyzed diagram of Figure 14. The main reason of this situation was that the handling of floats was extremely limited in the technical sense due to the rough sea. In spite of this limitation stated above, it was successful to figure the successive configuration of water surface as shown in Figure 15. By using these successive diagrams the contour map for the maximum elevation of water surface above the estimated mean water level is shown in the following fugures. Figure 16 is for the wind waves corresponding to Figures 13, 14, and 15. That is to say the breaker height for Figure 16 was as large as 2.5 m, while the breaker height for Figure 17 was about 1.0 m. From these diagrams it is easily recognized the existence of the periodical distribution of highs and lows along the shoreline. Following the hypothesis presented by Bowen (1969), that is the rip current appeares at the site of the lowest breaker height, the location of rip current was assumed as indicated in Figures 16 and 17. The generation theory of rip current proposed by Bowen & Inman (1969) is as well-known based on the interaction of edge waves with incoming waves.

On the other hand Sonu (1972) stresses that the bottom undulation existed in the surf zone is also to be the cause of nearshore circulation even in the case of uniform breaker height of the waves coming normaly to the shoreline. He stresses also the existence of meandering current in the case of oblique incident waves. In the case of Sonu's hypothesis it must be essentially needed to solve the problem by what reason such an undulation of bottom contour was caused.

In order to clarify the actual phenomena occurred in nature, further field observation data is highly requested.

CONCLUSIONS

The conclusions of the present investigations are as follows:

(1) The two systems developed at the Coastal Engineering Laboratory, University of Tokyo, were verified in field to be successful measures to observe the nearshore current system.

(2) The pattern of the current system described by the previous researchers is characterized only in the case of swell condition, while the pattern generated by wind waves seems to be more complex due to the existence of numerous circulations with vertical axis.

(3) The Synchronized Helicopter System is the most suitable one at present, but the Balloon Camera System must be also very effective due to its simplicity and mobility in the operation provided with an additional camera

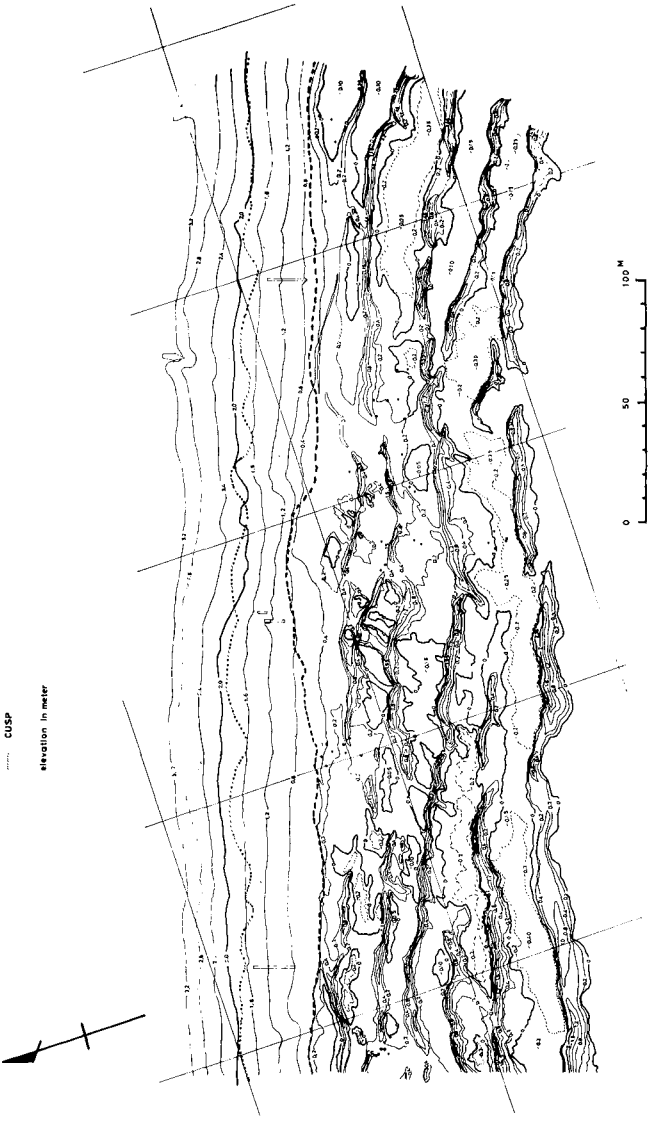

Fig. 15 Water surface configuration obtained from successive photographs. (SIHEL-611, wind wave)

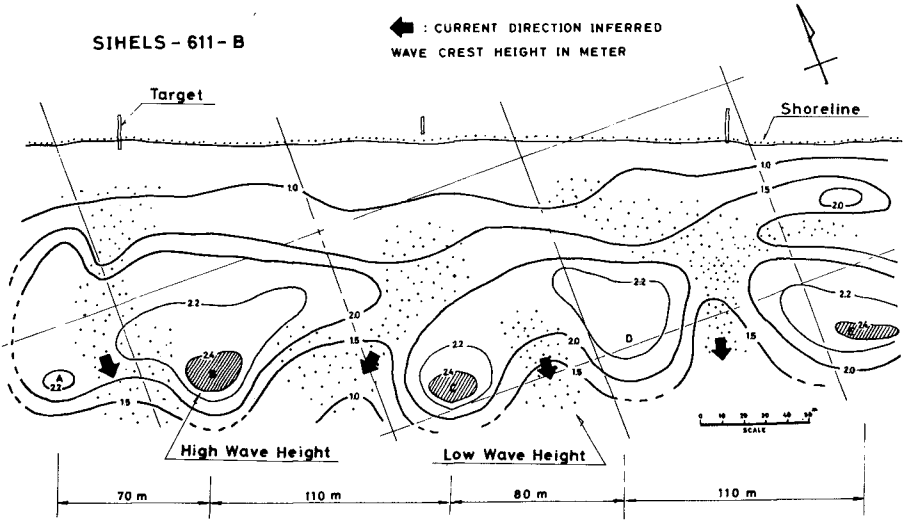

Fig. 16 Maximum water surface distribution above the estimated mean water level. (SIHEL-611-B, wind wave)

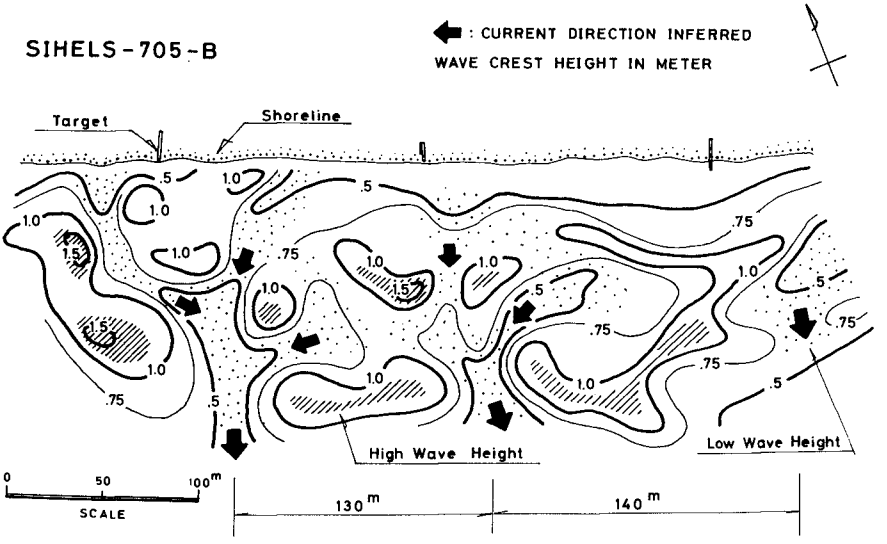

Fig. 17 Maximum water surface distribution above the estimated mean water level. (SIHEL-705-B, wind wave)

to make the pictures stereographic.

(4) The floats presently used are useful to trace the flow pattern in the case of plunging breaker and also in the case of spilling breaker with its height less than 1 m.

(5) The following two problems should be solved in the near future in order to obtain the valuable data under the stormy wave conditions; the first is to find a new type of float which is effective to the spilling breaker, and the second is to apply one more helicopter for throwing a number of floats in a short tim e in an interested broad area.

ACKNOWLEDGEMENTS

The field investigations conducted on the Shonan Coast were supported by the Ministry of Construction and the Kanagawa Prefectural Government. The authors are deeply indebted to Dr. Choule J. Sonu, Louisiana State University, for valuable informations and suggestions given to the authors in connection with the development of the Balloon Camera System, and to H. Igarashi, H. Kito and Y. Uchida at the Coastal Engineering Laboratory, University of Tokyo, for providing essential contributions to the execution of field operations.

REFERENCES

Bowen, A. J.: Rip currents, 1, Theoretical investigations, J. Geophys. Res., Vol. 74 (23), 1969.

Bowen, A. J. and D. L. Inman: Rip currents, 2, Laboratory and field observations, J. Geophys. Res., Vol. 74 (23), 1969.

Bowen, A. J. and D. L. Inman: Edge waves and crescentic bars, J. Geophys. Res., Vol. 76 (36), 1971.

Horikawa, K., T. Sasaki, H. Igarashi, and H. Kito: Development of "Balloon Camera System" for nearshore current observation, Annual Conv. of Japan Soc. of Civil Eng., 1971. (in Japanese)

Horikawa, K., T. Sasaki, N. Fukui, H. Igarashi and H. Kito: A study on nearshore current, Rept. 1, Field observation techniques and some results of field observations conducted on the Shonan Coast, Proc. 18th Conf. on Coastal Eng. in Japan, 1971. (in Japanese)

Inman, D. L. and R. A. Bagnold: Beach and nearshore processes, in the Sea, Vol. 2, Chap. 2, John Wiley & Sons, N. Y., 1962.

Shepard, F. P. and D. L. Inman: Nearshore water circulation related to bottom topography and wave refraction, Trans. Amer. Geophys. Union, Vol. 31 (4), 1950.

Sonu, C. J.: Tethered balloon for study of coastal dynamics, Proc. Symposium on Earth Observations from Balloons, Amer. Soc. of Photogrammetry, 1969.

Sonu, C. J.: Field observation of nearshore circulation and meandering currents, J. Geophys. Res., Vol. 77 (18), 1972.

CHAPTER 35

RIP - CURRENTS

by

Edward K. Noda
Tetra Tech, Inc.
Pasadena, California

ABSTRACT

The generation and stabilization of rip - current circulation patterns is considered herein. An analytic model is developed to simulate the wave hydrodynamic processes in the nearshore zone, strongly influenced by the local bottom topography. The wave induced nearshore circulation pattern is computed and the results compared to prototype field data.

INTRODUCTION

One of the most common hydrodynamic features of the nearshore zone is the generation and stabilization of rip - current circulation patterns. While the rip - current phenomenon is well known visually, its generating mechanism is not well understood. This understanding of the characteristics of rip - current processes and nearshore circulation is an important link in analyzing the complicated interaction between hydrodynamics and sedimentation in the coastal zone.

Presently there are two theories concerning the generation of nearshore rip - current patterns. Bowen (1) proposed a driving mechanism consisting of a longshore variation of average wave height across a rip - current cell with waves impinging normally onto a plane beach. Bowen suggested that this longshore variation of wave height might be due to edge waves. While the circulation patterns appear qualitatively realistic, the quantitative results are not so optimistic.

Sonu (6) suggests that rip - current circulation patterns are strongly influenced by the local bottom topography. The coupling of the wave characteristics and bottom topography produced the necessary driving

mechanism. A schematic description of the types of stream line patterns occurring in the nearshore zone is described in Figure 1 from Sonu. Detailed quantitative field data is shown in Figures 5 and 8 to correlate with Figure 1.

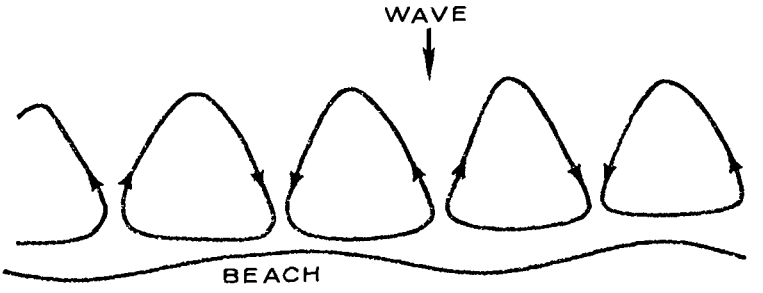

1. Circulation under normal wave incidence

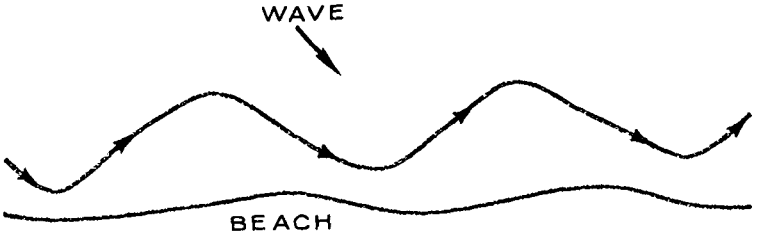

2. Meander under oblique wave incidence

Figure 1: Schematic Display of Current Patterns due to Normal and Oblique Wave Incidence [Sonu (6)].

In the following analysis an analytic model is developed to correlate rip - current patterns with wave characteristics affected by the local non-uniform bottom topography.

THEORY

Figure 2 describes the coordinate system. To obtain the wave height and direction field the "geometrics optics" approximation is utilized where the ray equations describing the x, y and θ values along the ray are

$$\frac{dx}{ds} = \cos\theta \tag{1}$$

$$\frac{dy}{ds} = \sin\theta \tag{2}$$

and

$$\frac{d\theta}{ds} = \frac{1}{c}\left[\sin\theta\frac{\partial c}{\partial x} - \cos\theta\frac{\partial c}{\partial y}\right] \tag{3}$$

where s is displacement along the ray and c is the wave celerity defined by

$$c = \frac{gT}{2\pi}\tanh\left(\frac{2\pi d}{cT}\right) \tag{4}$$

Eqs. (1) to (3) are kinematic equations describing the ray location. To find the wave height, the intensity equation as given by Munk and Arthur (5) is used

$$\frac{d^2\beta}{ds^2} + p(s)\frac{d\beta}{ds} + q(s)\beta = 0 \tag{5}$$

where

$$p(s) = -\cos\theta\left[\frac{1}{c}\frac{\partial c}{\partial x}\right] - \sin\theta\left[\frac{1}{c}\frac{\partial c}{\partial y}\right] \tag{6}$$

and

$$q(s) = \sin^2\theta\left[\frac{1}{c}\frac{\partial^2 c}{\partial x^2}\right] - 2\sin\theta\cos\theta\left[\frac{1}{c}\frac{\partial^2 c}{\partial x\partial y}\right] + \cos^2\theta\left[\frac{1}{c}\frac{\partial^2 c}{\partial y^2}\right] \tag{7}$$

The wave height due to refraction alone is then given by

$$H = \frac{Ho}{\sqrt{\beta}} \tag{8}$$

where Ho is the deep water wave height.

To solve Eqs. (1) to (4) a 4th order Runga-Kutta technique is utilized where

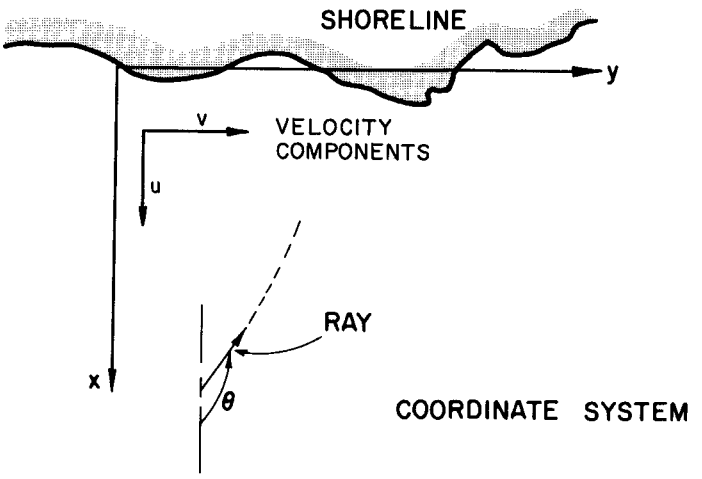

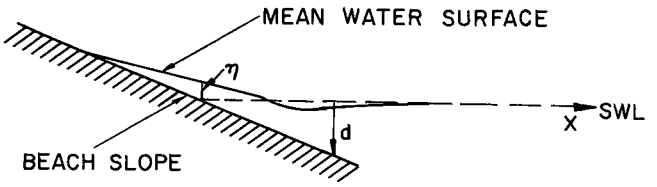

Figure 2: Coordinate System

Eq. (4) is divided into two (2) first order equations. Thus, the simultaneous solution of five (5) first order equations yields the wave height and direction field.

As the wave propagates into shore, the effects of refraction and shoaling can produce a breaking wave. Consequently, an empirical breaking criterion is imposed. From Miche (4) the limiting wave steepness is

$$\frac{H_b}{L_b} = 0.142 \tanh \left(\frac{2\pi d_b}{L_b}\right) \tag{9}$$

although an examination of experimental data of waves breaking over a horizontal bottom by LeMéhauté and Koh (2) indicates a better criterion is

$$\frac{H_b}{L_b} = 0.12 \tanh \left(\frac{2\pi d_b}{L_b}\right) \tag{10}$$

For the following analysis Eq. (10) has been utilized. Note that breaking characteristics may be influenced by "local" bottom slope which is not considered herein.

Once the wave height and direction fields are known, the nearshore circulation pattern can then be computed. To facilitate the analysis, the momentum and continuity equations have been vertically integrated and the time dependent and nonlinear terms neglected to yield

$$g\frac{\partial \eta}{\partial x} = M_x - F_x \tag{11}$$

$$g\frac{\partial \eta}{\partial y} = M_y - F_y \tag{12}$$

and the continuity equation

$$\frac{\partial [u(\eta+d)]}{\partial x} + \frac{\partial [v(\eta+d)]}{\partial y} = 0 \tag{13}$$

where the radiation stress terms are [Longuet-Higgins and Stewart (3)]

$$M_x = -\frac{1}{\rho(d+\eta)}\left[\frac{\partial \sigma_{xx}}{\partial x} + \frac{\partial \tau_{xy}}{\partial y}\right] \tag{14}$$

$$M_y = -\frac{1}{\rho(d+\eta)}\left[\frac{\partial \sigma_{yy}}{\partial y} + \frac{\partial \tau_{xy}}{\partial y}\right]$$

and the friction terms are

$$F_x = \frac{2c_f u H}{(\eta+d)T \sinh kd} \tag{15}$$

$$F_y = \frac{2cvH}{(\eta+d)T \sinh kd} \tag{16}$$

where

$$\sigma_{xx} = \frac{3}{16}\rho g H^2 \cos^2\theta + \frac{1}{16}\rho g H^2 \sin^2\theta \tag{17}$$

$$\sigma_{yy} = \frac{3}{16}\rho g H^2 \sin^2\theta + \frac{1}{16}\rho g H^2 \cos^2\theta \tag{18}$$

$$\tau_{xy} = \tau_{yx} = \frac{1}{16}\rho g H^2 \sin 2\theta \tag{19}$$

and c is the friction coefficient and $k = 2\pi/L$ is the wave number.

Assuming that

$$\eta + d \cong d \tag{20}$$

and defining a stream friction Ψ such that

$$\frac{\partial \Psi}{\partial y} = -ud \tag{21}$$

$$\frac{\partial \Psi}{\partial x} = +vd, \tag{22}$$

automatically satisfies the continuity requirement. Cross-differentiating Eqs. (11) and (12) and utilizing (21) and (22) produces the governing circulation equation

$$\frac{\partial^2 \Psi}{\partial x^2} + \frac{\partial^2 \Psi}{\partial y^2} + \frac{\frac{\partial F}{\partial y}}{F}\frac{\partial \Psi}{\partial y} + \frac{\frac{\partial F}{\partial x}}{F}\frac{\partial \Psi}{\partial x} =$$

$$\frac{g}{F}\left\{\frac{\partial}{\partial y}\left[\frac{1}{d}\left(\frac{\partial \bar{\sigma}_{xx}}{\partial x} + \frac{\partial \bar{\tau}_{xy}}{\partial y}\right)\right] - \frac{\partial}{\partial x}\left[\frac{1}{d}\left(\frac{\partial \bar{\sigma}_{yy}}{\partial y} + \frac{\partial \bar{\tau}_{xy}}{\partial x}\right)\right]\right\} \tag{23}$$

where

$$F = \frac{2cH}{d^2 T \sinh kd} \tag{24}$$

$$\bar{\sigma}_{xx} = H^2\left(\frac{3}{16}\cos^2\theta + \frac{1}{16}\sin^2\theta\right) \tag{25}$$

$$\bar{\sigma}_{yy} = H^2 \left(\frac{3}{16}\sin^2\theta + \frac{1}{16}\cos^2\theta\right) \tag{26}$$

$$\bar{\tau}_{xy} = \bar{\tau}_{yx} = \frac{1}{16} H^2 \sin 2\theta \tag{27}$$

NUMERICAL COMPUTATION

To initiate the computation, the bottom topography must be everywhere defined. An examination of the field data from Sonu (6), Figure 5 indicates that an approximate analytic representation can be obtained by the relationship

$$d(x,y) = 0.025x\left[1 + 20e^{-3\left(\frac{x}{20}\right)^{1/3}} \sin^{10}\left(\frac{\pi y}{80}\right)\right] \tag{28}$$

This produces a straight beach line (y-axis) and a periodic rip - current channel decaying exponentially offshore into a plane beach.

The first case to be analyzed is that of normal wave incidence. The computation proceeds by tracking the rays or orthogonals from deeper water where Shell's law is valid into the area defined by Eq. (28). Figure 3 indicates the rays on one-half of the periodic beach since the solution is symmetrical about the line y=0. The dotted line indicates the position of wave breaking and notice that a caustic occurs as the wave rays merge. While the "geometric optics" approximation breaks down near a caustic, the wave has already broken so that the wave height computation is determined from Eq. 10. The kinematical equations (1) to (3) still produce results independent of the caustic and these are assumed sufficient to provide wave direction data.

Following the ray solution, a algorithm is utilized to transform the essentially "random" locations of wave height and direction into a uniform grid by a two-dimensional interpolation scheme. The grid data is then used to solve Eq. 23 by application of a Gauss-Seidel relaxation algorithm with the boundary conditions.

$$\Psi = 0 \text{ at } y = 0 \text{ and } y = 40 \text{ meters}$$

$$\Psi = 0 \text{ at } x = 0 \text{ and } x = 385 \text{ meters}$$

The final stream line solution for normal incidence is shown in Figure 4. As a test case, a full period of 80 meters was used and the results were identical with Figure 4 with similar stream line patterns mirror imaged about y = 0 and 40 meters except that these streamlines are negative in value. While qualitatively the results are reasonable, quantitatively the maximum rip - current velocity is about 4 meters/second. This seems to be much larger than existing prototype measurements from Sonu (6), Figure 5.

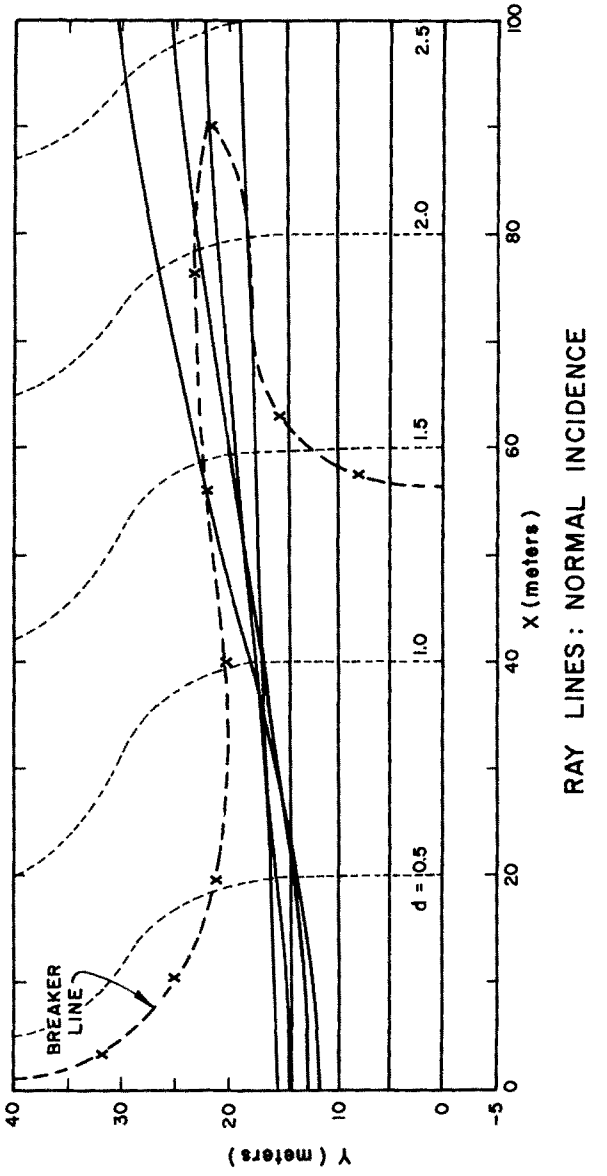

Figure 3: Schematic View of Wave Orthagonals with Normal Incidence

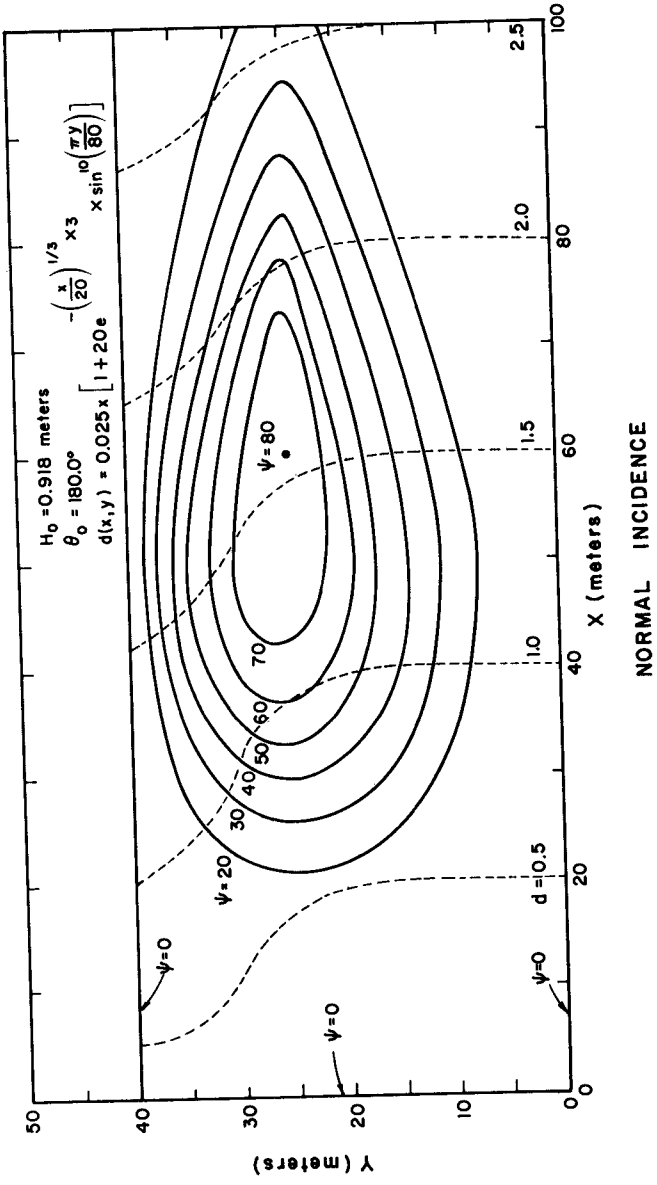

Figure 4: Numerical Stream Function Solution with Normal Wave Incidence

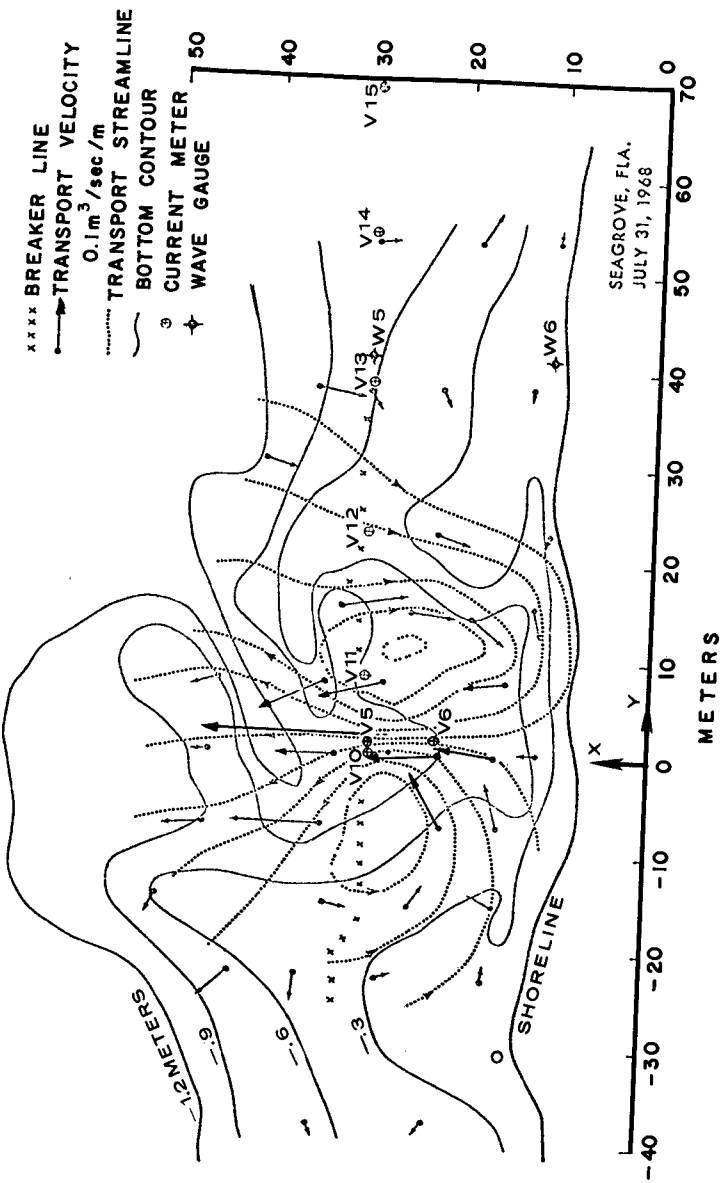

Figure 5: Distribution of Transport Velocities and Streamlines in a Circulation Cell. Streamline Separation is 0.4m^3/sec, H_b = 0.395 meters, T_b = 5 sec [From Sonu (6)]

The next case examined was that of wave attack at an oblique angle to the shore line. For this case, a deep water angle and wave height of

$$\theta_o = 153^o, \; H_o = 1.0 \text{ meters}$$

was used. Typical rays are described in Figure 6 with the associated breaker line. In this problem while the shore line and off-shore boundary conditions are well defined as

$$\Psi = 0 \text{ at } x = 0 \text{ and } x = 385 \text{ meters}$$

the longshore boundary conditions are as yet unknown. Since this is a boundary value problem, the longshore Ψ conditions must be apriori constrained before a solution can be found. To solve this problem, the numerical relaxation algorithm was allowed to update Ψ along the line $y = 0$ and the periodic condition was imposed that

$$\Psi(x, y=80) = \Psi(x, y=0)$$

Convergence for this case required about 700 iterations since the imposed accuracy was very high. The solution for the stream function field is shown in Figure 7. Notice the existance of a small negative area of Ψ which is a degeneration of the previously described negative cell produced by normal wave incidence.

An examination of the prototype field data from Sonu (6) Figure 8 indicates a optimistic qualitative agreement. Quantitatively the numerically computed maximum rip - current velocities are about 4 meters/second which is much larger than observed values. Also, notice that the incoming rip - current velocity is of the same magnitude as the outgoing velocity which is not observed in the field and also the maximum rip velocity direction is oblique to the imposed bottom topography.

RESULTS AND CONCLUSIONS

As previously indicated, while the analysis for normal wave incidence Figure 4 yields qualitatively reasonable results, quantitative estimates of the rip - current velocity are much larger than field measurements. An examination of Figure 3 shows that in the channel area the breaker line extends almost to the shoreline at $y = 40$ meters and out to $x = 90$ meters at $y = 20$ meters. Examining Figure 5, the field data does not indicate this large variation in the breaker line and consequently this suggests that there may be a strong wave-current interaction which would produce a more uniform breaker line. Since this effect would yield a more uniform longitudional wave height distribution, it is expected that the rip - current velocity would be greatly reduced. The analysis for wave-current interaction has been completed and the numerical algorithm generated although presently no results are available.

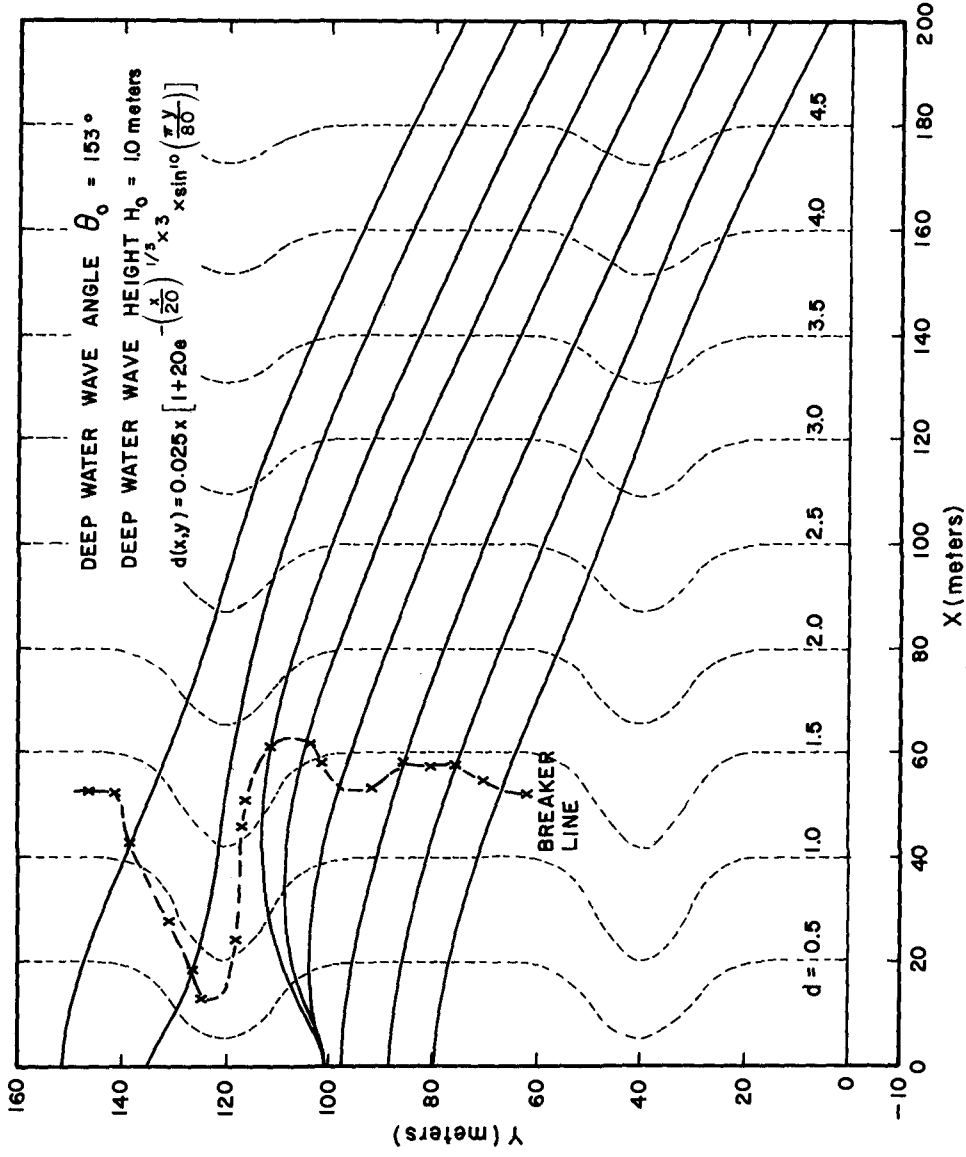

Figure 6: Wave Orthagonals for Oblique Incidence

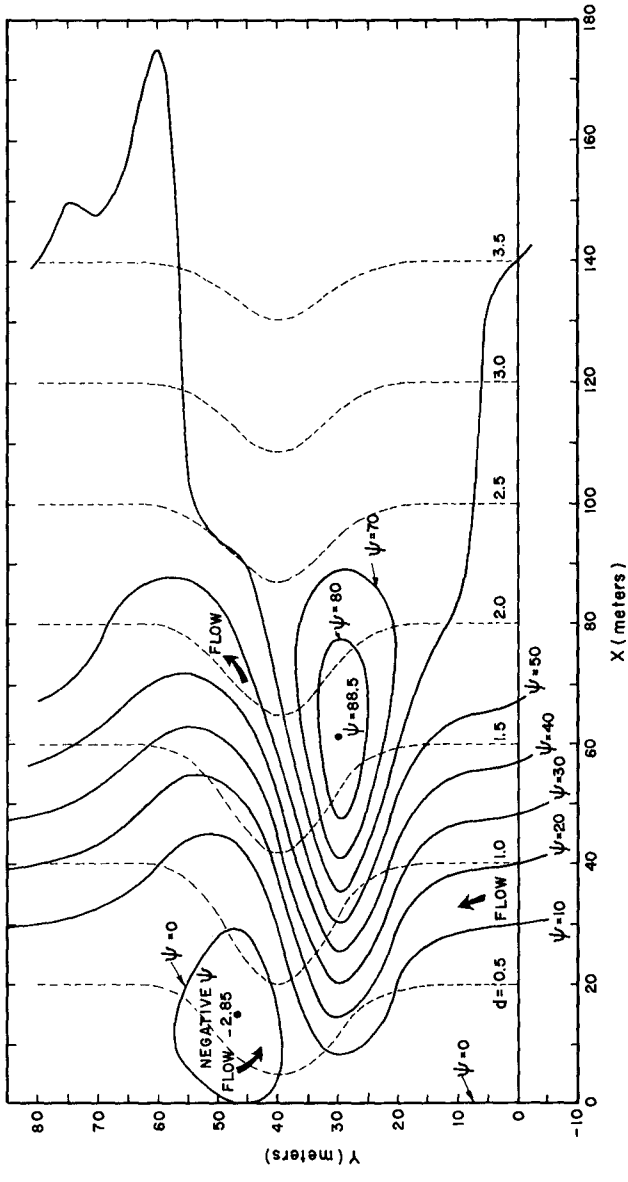

Figure 7: Numerical Stream Function Solution for Oblique Incidence

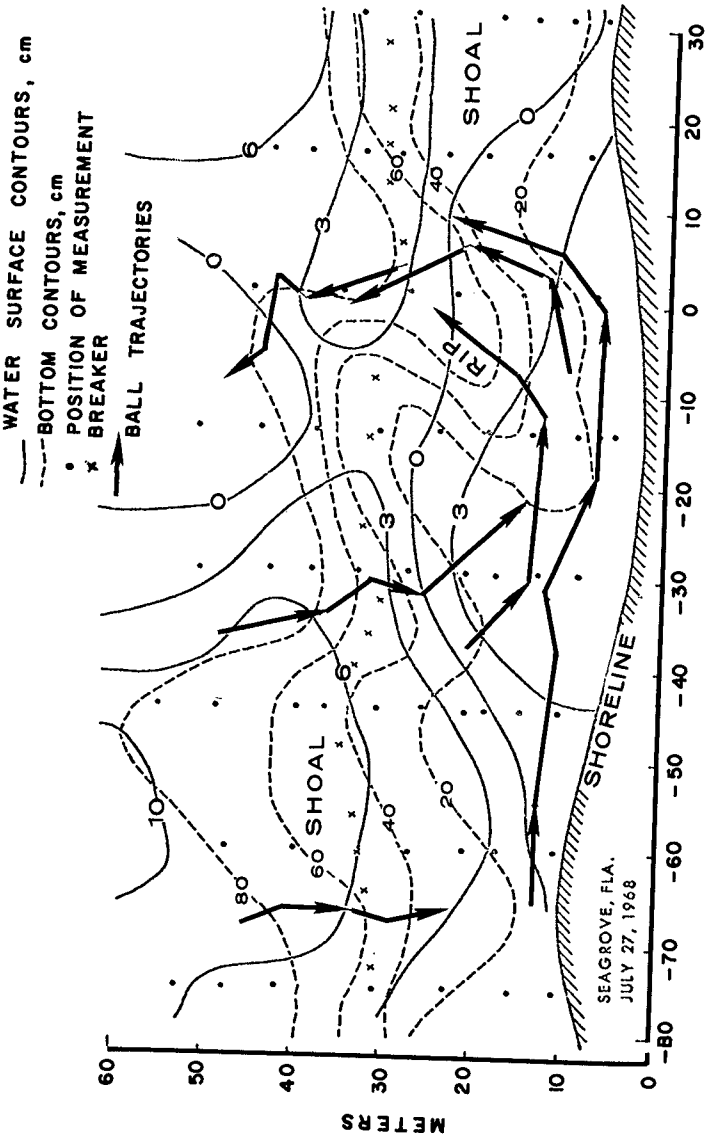

Figure 8: Nearshore Circulation due to Oblique Incidence [From Sonu (6)]

The case of oblique wave attack again yields much larger velocities than field data. Since the field data Figure 8 shows a definite skewing of the rip - channel in line with the current vector, the following depth configuration was recently imposed

$$d(k,y) = 0.025x\,[1 + 20e^{-3(\frac{x}{20})^{1/3}} \sin^{10} \frac{\pi}{80}(y - x\tan\alpha)] \qquad (29)$$

where $\alpha = 30^{o}$. This depth function effectively skewed the rip - channel 30^{o} to the x-axis and performing the ray computations through the relaxation procedure produced a solution very similar to Figure 8 except that now the maximum rip - current velocity was about 1.8 meters/second and the incoming rip - current velocity was much smaller than the outgoing velocity. This then indicates the importance of the bottom topography and also shows that such a profile as given by Eq. (28) would probably be scowed by oblique waves and possibly produce a bottom profile similar to Eq. (29). Unfortunately at press time a graphical display of the stream function solution to Eq. (29) is not available.

The previously described results is part of a continuing research effort to describe the hydrodynamic and littoral nearshore environment. The preliminary results herein are very optimistic and indicate that the local bottom configuration may be very important in the determination of the nearshore wave-induced circulation pattern.

ACKNOWLEDGMENT

This study was sponsored by the Office of Naval Research, Geography Programs under Contract No. N00014-69-C-0107. The author would like to express appreciation to Dr. J. Ian Collins for stimulating discussions and to Mr. Wayne Wier for valuable computer programing services.

REFERENCES

1. Bowen, A.J. (1969), "Rip Currents, 1, Theoretical Investigation", Journal of Geoghys. Res., No. 74, Vol. 23, pp. 5467-5478.

2. LeMéhauté, B. and Koh, R. C.Y. (1967), "On the Breaking of Waves Arriving at an Angle to the Shore", Journel of Hyd. Res., No. 1, Vol. 5, pp. 67-88.

3. Longuet-Higgins, M.S. and Stewart, R.W. (1964), "Radiation Stress in Water Waves, a Physical Discussion with Application", Deep Sea Research, No. 11, Vol. 4, pp. 529-563.

4. Miche, R. (1944), "Mouvements Ondulatoires de la Mer en Profondeur Constante ou Décroissante", Ann. des Ponts et.

5. Munk, W.H. and Arthur, R.S. (1951), "Wave Intensity along a Refracted Wave", Circular 521, U.S. Dept. of Commerce, National Bureau of Standards, pp. 95-108.

6. Sonu, C.J. (1972), "Field Observations of Nearshore Circulation and Meandering Currents", J. of Geophys. Res., Oceans and Atms., No. 18, Vol. 77, pp. 3232-3247.

CHAPTER 36

TIDAL INLET CURRENT--OCEAN WAVE INTERACTION

by

Lyndell Z. Hales[1] and John B. Herbich[2]

Abstract

An experimental study was conducted in a three-dimensional wave basin to investigate the manner in which surface gravity waves propagating toward a tidal inlet are altered. Dimensional analysis of the pertinent variables indicates that a functional relationship exists between as many as five dimensionless terms, and the functional relationship is displayed in graphical non-dimensional form to apply to all scales. Results indicate the ebb current increases the steepness in the ocean region to such an extent that the wave begins to lose energy by the crest spilling down the front of the wave, and the wave characteristics in the inlet proper may never reach the breaking limit unless factors other than a current alone are involved.

Introduction

The non-uniform current created by tidal flow through the relatively narrow inlets connecting many bays and estuaries to the open ocean can have a significant influence on the characteristics of surface gravity waves propagating toward the inlets. For a flood flow, the waves will be lengthened and will experience a decrease in height. The ebb current is seen to compress the wave length and concentrate the energy of the wave form which is reflected in a dramatic increase in height. This has a direct bearing on the energy propagation through the inlet and into the bay or estuary, as well as implications regarding the flushing of littoral drift and sediment from the inlet.

The pattern of the build-up of the non-uniform tidal current on the flood stage from the region of essentially zero velocity offshore to its maximum value at the inlet throat is distinctly different from the decay of the ebb current as it is discharged into the ocean. The ebb flow emanates from the inlet as a jet and can be detected much further offshore

[1]Hales, Lyndell Z., Research Hydraulic Engineer, Coastal Section, U. S. Army Engineer, Waterways Experiment Station, Vicksburg, Mississippi, U. S. A.
[2]Herbich, John B., United Nations Expert, Poona-4, India, Presently on leave-of-absence from position of Head, Division of Coastal and Ocean Engineering, Texas A&M University, College Station, Texas, U. S. A.

than can the flood currents. This jet action creates a channel effect through the offshore bar and shoal region, and it is often this natural channel which will be improved and maintained for navigation. On the other hand, the flood currents form smaller flood channels to the sides of this main ebb flow channel.

Coastal inlets in a natural state are subjected to opposing forces which alternately try to close or enlarge the passage. During the flood stages, the littoral transport of sand in the surf zone tends to be swept into the tidal inlet by the wave action and strong currents created by the rising tide. On the ebb flow, the estuary experiences a flushing condition and sediment, both suspended and bed load, may be swept through the tidal inlet and passed down coast or lost to deep water. A river may also drain into the bay, augmenting the ebb flow. When a balance of these forces exists the inlets tend to be stable and remain open. Otherwise the inlets may try to migrate or close completely.

It is desirable that the inlet location and geometry remain fixed, so decisions are frequently made that corrective engineering works be undertaken to insure the stability of a tidal inlet on an erodible coast. To prevent the lateral movement of the coastal inlet, jetties are often constructed which extend seaward from the shore and become essential to the operation of a dependable inlet for navigation purposes. When both a jetty system and maintenance dredging of a navigation channel through the offshore bar are required, the characteristics of the surface gravity waves being propagated toward the inlet can be significantly altered.

An understanding of the phenomena connected with the interaction of tidal inlet currents and ocean waves is important for several reasons. The current will alternately oppose or flow with the waves as they are propagated upstream. During the ebb flow, waves which are entering the estuary will have their steepness increased and hazards to navigation are accordingly produced. In the alternate case, waves traveling with the tidal current will have their lengths increased and the energy propagation into the estuary occurs at a rate proportional to the vector sum of the group celerity and the current velocity plus an additional interaction term. The energy propagation and dispersion into the estuary will frequently affect harbor facilities and marinas and knowledge of the amount of energy amplification or reflection at a tidal entrance is desirable

Previous Studies

Considerable analytical effort has been expended in an attempt to explain the mechanism by which a current can alter a wave's characteristics, but the subject has had only a limited amount of experimental input. A two-dimensional study of the point where waves become unstable and break as they are propagated against a current was performed for deep water conditions by Yu (1). Experimental studies of hydraulic breakwaters were performed by Herbich, Ziegler, and Bowers (2) to determine the effect of wave characteristics and breakwater requirements on wave attenuation. Another two-dimensional study was made by Sarpkaya (3) to determine the conditions of stability of progressive, oscillatory waves in flowing water.

Collins (4) performed a two-dimensional study of the effects of currents on the mass transport of progressive water waves, and Hughes (5) created a Couette-type flow between two concentric cylinders in which he studied waves with lengths of the order of 2.5 cm and periods of the order of 0.1 sec. No experimental work is known to exist for a three-dimensional situation where the current can vary in the direction of wave propagation.

Historically, the classic analysis was given by Unna (6) in which he showed that when the current opposes the wave propagation and has a velocity of one-fourth the wave celerity in deep water, the waves must break however small their initial steepness. But Unna assumed without justification that the wave energy is propagated with a velocity equal to the sum of the group velocity and the local stream velocity, and that no coupling takes place between the waves and the current. On the contrary, it was shown later by Longuet-Higgins and Stewart (7) that gravity surface waves riding on non-uniform currents are modified to a much greater extent than would be predicted if there were no interchange of energy between the wave system and the current.

Johnson (8) made a theoretical development for deep-water conditions of a wave train crossing a current at an angle, in terms of the initial wave length and direction, and the magnitude of the current. He showed that refraction of the waves by the current effects a change in the wave length and stretches or compresses the wave crest. Classical shallow-water theory for the propagation of long waves in running water was modified by Burns (9) to include the effects of the vorticity present in the main stream as the result of the action of viscosity. Hunt (10) analytically considered some particular cases of the effects of a non-uniform current. For linear waves on a current varying as the one-seventh power of the depth, the velocity of propagation was found as a power series in the square root of the Froude number. For the non-linear solitary and cnoidal waves, both the profile and the velocity were found to depend on the value at the free surface of the current and its first derivative. Longuet-Higgins and Stewart (7) theoretically studied the changes in wave length and wave amplitude of surface gravity waves riding on steady non-uniform currents. They recognized an interaction term for which they coined the phrase "radiation stress". It appears this same phenomenon had been deduced previously and quite independently by Lundgren (11).

The limited experimental work has all been performed under certain specific conditions to obtain particular information about one facet of the overall subject. It appears that no experimental work of a three-dimensional nature has been performed in an effort to either verify or refute the analytical conclusions.

Experimental Apparatus

An experimental study was conducted at the U. S. Army Corps of Engineers, Waterways Experiment Station to determine quantitatively the manner in which surface gravity waves are altered by non-uniform tidal inlet currents. A wave basin of dimensions 150 ft long, 50 ft wide, and 3 ft deep, shown in Fig. 1, was used in which a relatively narrow opening was constructed to connect the ocean with a bay region. All flow was required to pass through

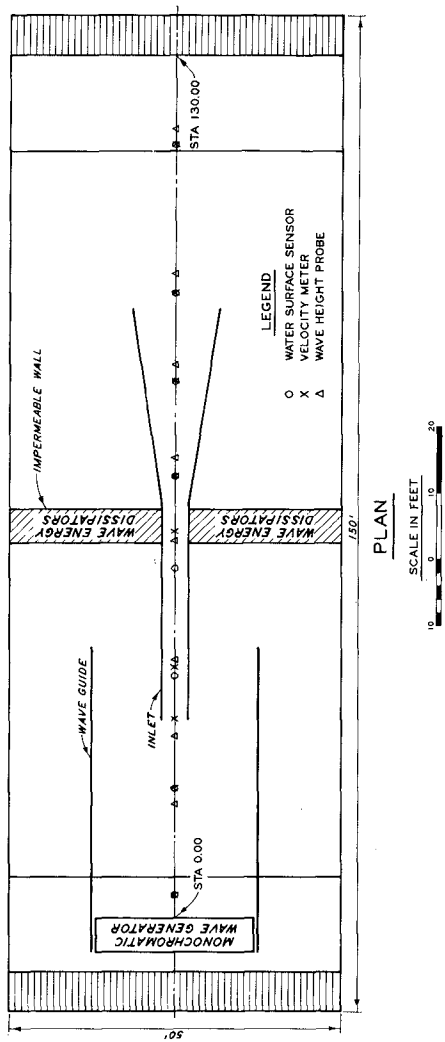

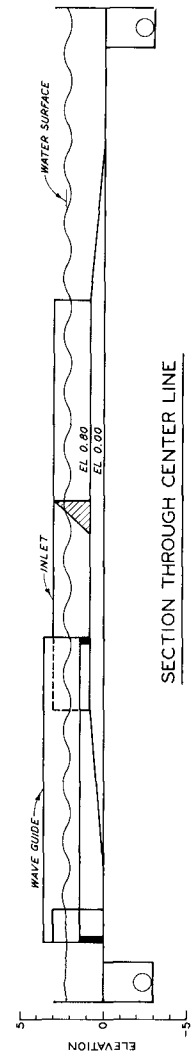

FIG. 1-THREE-DIMENSIONAL WAVE BASIN AND EXPERIMENTAL APPARATUS

this simulated tidal inlet which had dimensions 4 ft wide and 32 ft long and was situated in the center section of the basin. The bottom of the inlet was horizontal and elevated 0.8 ft above the basin floor with a slope of 0.033 ft/ft approaching the inlet from the ocean side, and the same slope at the rear of the inlet into the bay region. This caused the approaching waves to experience a shoaling effect as well as refraction due to the tidal inlet current, typical of prototype inlets.

The wave generator was placed perpendicular to the inlet throat and data measurements were taken at 8 selected points along the inlet axis from the ocean into the bay. In the absence of a current, the wave characteristics were recorded by direct print oscillograph at these selected locations. A steady non-uniform flood current was then created by circulating flow from the bay region and discharging into the ocean with a reversible variable-speed pump. The intake and discharge manifolds were carefully adjusted so that negligible disturbance occurred in the still water region. For this steady-state flow condition, velocity measurements were taken at the predetermined locations and the wave characteristics were again recorded. Then the flow would be changed, steady-state conditions achieved and measurements once more recorded. Ultimately the data obtained consisted of current and wave measurements recorded at 8 locations for no flow condition, 4 flood conditions, and 4 ebb conditions for each wave generator setting.

Results and Conclusions

Some authors, for example Barber (12) and Barber and Ursell (13), have argued that waves crossing a tidal stream on the open ocean experience a change in the apparent wave period. Wilson (14) has expressed the belief that when waves are being propagated onto a non-uniform current, they suffer a Doppler shift in frequency, causing a decrease in period in a following current and vice versa.

The water surface time histories of the fluctuating wave motion recorded by wave gage no. 2, located in the ocean region near the entrance to the inlet, were analysed by spectral means to determine if, under steady-state flow and monochromatic waves, a shift in the generated frequency would occur. This gage was chosen because it experienced the effect of both ebb and flood currents. The results of the spectral analysis are shown in Fig. 2, and it appears the peak of the energy spectrum occurs at the same period under all flow conditions. Further study reveals the period remains constant with space as well as time for steady-state flow conditions. There does appear to be a flow of energy to other frequencies, as reflected by the shift of the curves for the accumulated percent of the total energy in the wave form occurring at periods greater than a specified period. The ebb flow shift is particularly dramatic, indicating for a given percentage of the total energy, the ebb condition occurs at a slightly higher period. This appears to be in line with the hypothesis of Wilson (14), although in the absence of local accelerations the flow of energy to other periods was not enough to cause a shift in the peak of the energy spectrum.

Changes in the Inlet:

Dimensional analysis of the pertinent variables indicates that for the

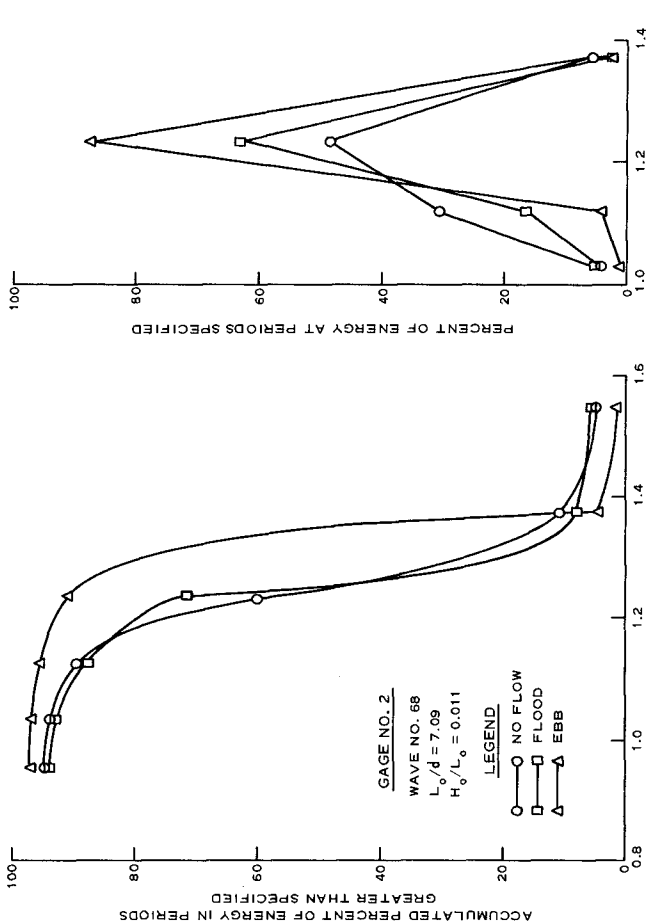

FIG. 2-ENERGY SPECTRUM RECORDED AT GAGE NO. 2. (Curves are for percentages of total energy, and do not reflect the actual magnitude of the energy of the wave form.)

inlet proper, a functional relationship exists of the form

$$\phi(L_o, L, H_o, H, d, U, C_o) = 0 \quad \ldots\ldots (1)$$

which can be rearranged to produce

$$\frac{L}{L_o} = f'\left(\frac{L_o}{d}, \frac{H_o}{L_o}, \frac{U}{C_o}\right) \quad \ldots\ldots (2)$$

and

$$\frac{H}{H_o} = f''\left(\frac{L_o}{d}, \frac{H_o}{L_o}, \frac{U}{C_o}\right) \quad \ldots\ldots (3)$$

The determination of such functional relationships is frequently very difficult if not completely impossible by analytical means, so recourse is often taken to hydraulic model studies. The strength of dimensional analysis lies in its ability to provide insight into the manner in which certain variables are related, and thus initiates the planning of the research program.

The functional relationships of Eqs. 2 and 3 were substantiated by random plots of the change in wave length and wave height as a function of the current parameter. The relationship can be displayed as a series of charts for different values of H_o/L_o, each chart containing a family of curves for different values of L_o/d, where the subscript zero always refers to still water conditions in the inlet where the water depth is d.

Because the data obtained from the model was for random values of L_o/d and H_o/L_o, the technique of fairing the experimental data was applied so that the results could be displayed in a more systematic form. Figs. 3 and 4 show the manner in which the wave height and wave length changed as the flow in the inlet increased, at a constant value of H_o/L_o. For the range of data obtained, the change in wave length appeared as a straight line; however, the analytical studies indicate that the curves will eventually approach an asymptotic value similar to the change in wave height. For ebb currents flowing through the inlet, the change in wave height and wave length are shown in Figs. 5 and 6. It was noted in the experimentation that in the inlet, the waves increased in height and decreased in length for the ebb flow until a certain condition was reached, at which time the wave records showed a decrease in height with increased ebb current. The steepness of the waves at this condition was determined, and it was found that most of the waves were not even approaching the limiting steepness for breaking waves in still water. It was observed that the ebb flow emanating as a turbulent free jet into the ocean region was causing the waves to increase in steepness and lose energy by the crest spilling down the front of the wave as it continued to propagate onto the current. Consequently, when the wave reached the inlet, it had decreased in height because of energy losses in the ocean region, and not because of breaking in the inlet. Hence, the approximate limits for stable waves shown in Figs. 5 and 6 do not really reflect a cause-and-effect relationship in the inlet, but are a reflection of events which occurred in the ocean.

Changes in the Ocean:

Photographic documentation of the ebb and flood conditions occurring

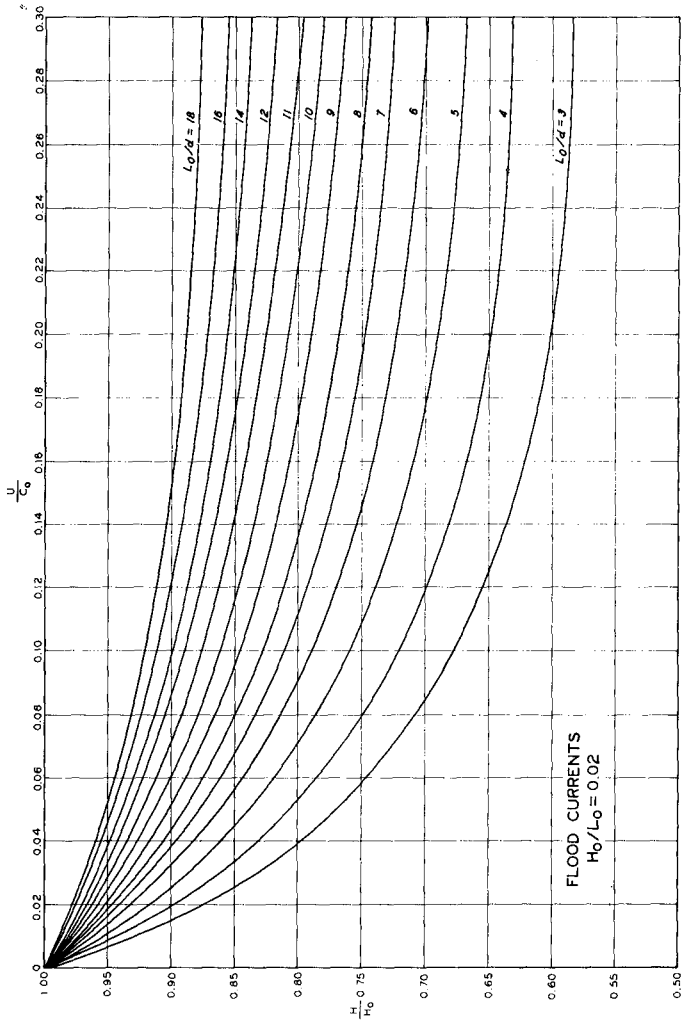

FIG. 3-CHANGE IN WAVE HEIGHT IN THE INLET PROPER UNDER CHANGING FLOOD CURRENT CONDITIONS FOR A CONSTANT VALUE OF H_o/L_o

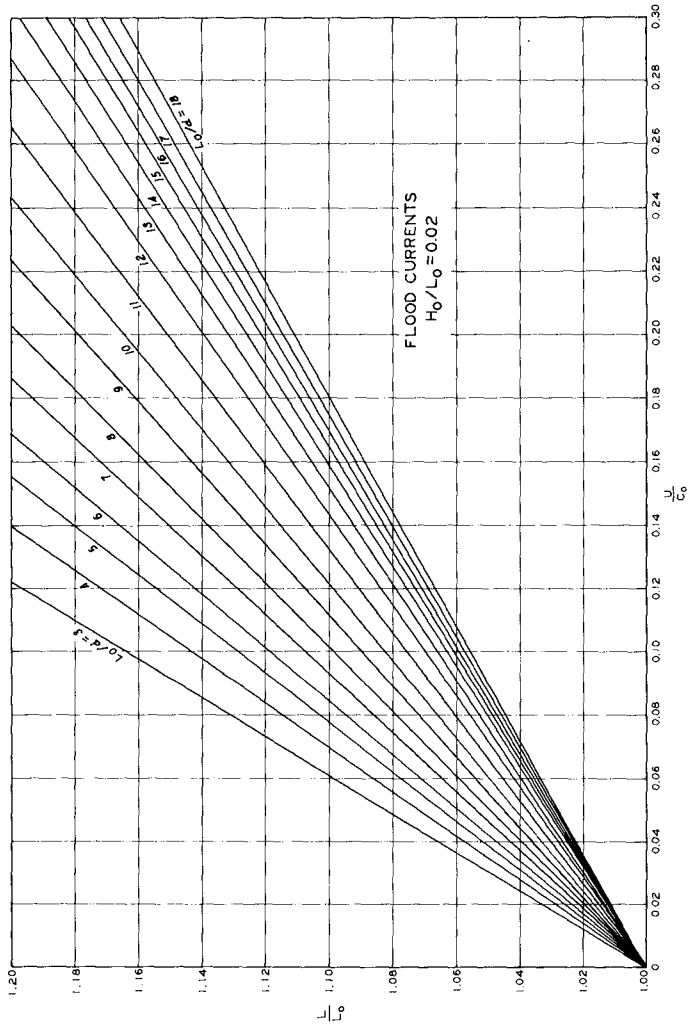

FIG. 4-CHANGE IN WAVE LENGTH IN THE INLET PROPER UNDER CHANGING FLOOD CURRENT CONDITIONS FOR A CONSTANT VALUE OF H_o/L_o

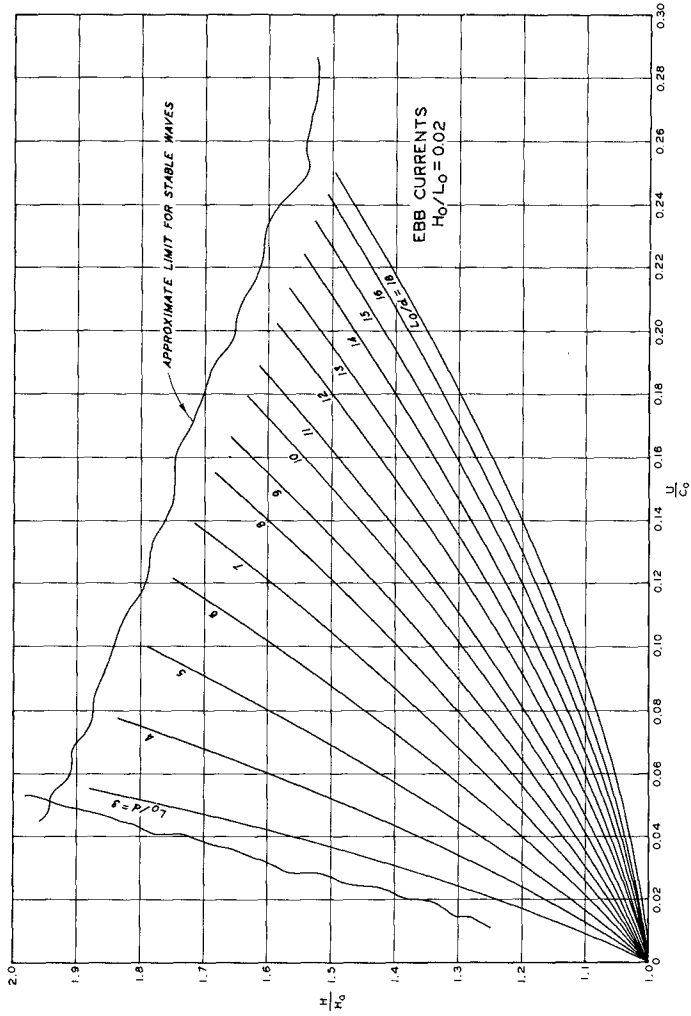

FIG. 5-CHANGE IN WAVE HEIGHT IN THE INLET PROPER UNDER CHANGING EBB CURRENT CONDITIONS FOR A CONSTANT VALUE OF H_o/L_o

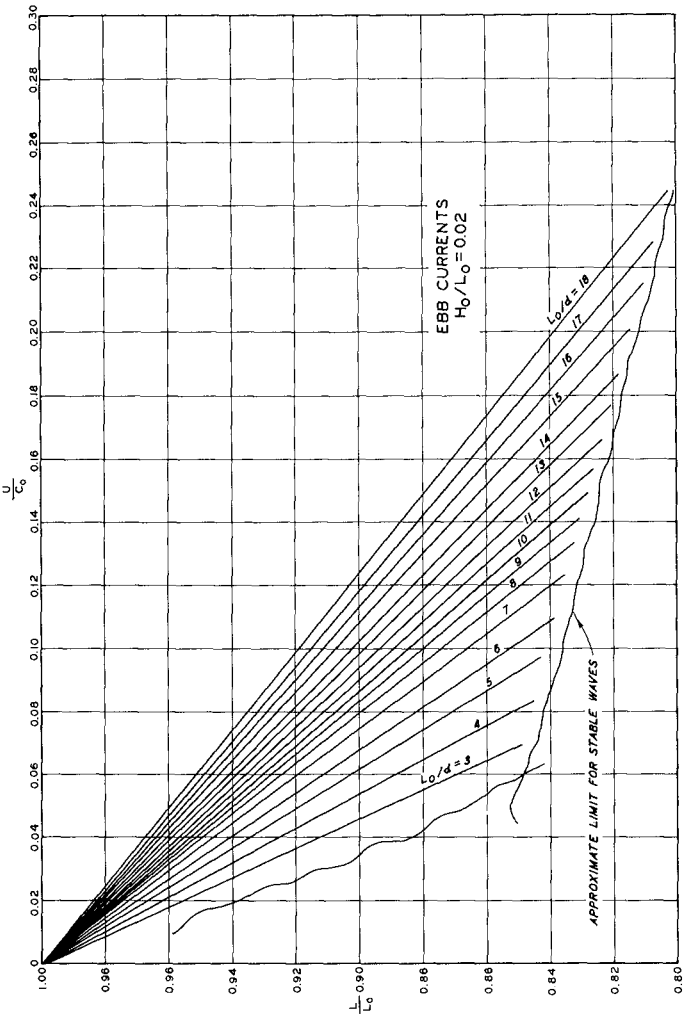

FIG. 6-CHANGE IN WAVE LENGTH IN THE INLET PROPER UNDER CHANGING EBB CURRENT CONDITIONS FOR A CONSTANT VALUE OF H_o/L_o

in the ocean near the entrance to the inlet indicated the flood pattern to be relatively insignificant when compared with the flow pattern of the ebb current. Fig. 7 is a typical dye and confetti pattern photograph of the ebb flow emanating from the inlet and dispersing as essentially a turbulent free jet. For the simplified two-dimensional free jet turbulent flow, French (15) has shown that the ratio (distance from exit)/(inlet width) is a pertinent dimensionless quantity for completely describing the manner in which the flow field changes. Accordingly, it is deduced that in addition to the four previously defined dimensionless parameters necessary for displaying the experimental data obtained in the inlet, to adequately describe the functional relationship existing between variables in the ocean region, Eqs. 2 and 3 must be re-written as

$$\frac{L}{L_o} = f'''\left(\frac{L_o}{d}, \frac{H_o}{L_o}, \frac{U}{C_o}, \frac{x}{W}\right) \quad \text{..... (4)}$$

and

$$\frac{H}{H_o} = f''''\left(\frac{L_o}{d}, \frac{H_o}{L_o}, \frac{U}{C_o}, \frac{x}{W}\right) \quad \text{..... (5)}$$

where x is the distance from the entrance of the inlet to the point of interest and W is the width of the inlet. The conclusions by French (15) from momentum considerations include the face that the depth of flow in the inlet is apparently mot pertiment for describing the flow patterns coming from the inlet.

When the experimental data obtained from sensors located in the ocean region of the facility are displayed in dimensionless form, the relationships implied by Eqs. 4 and 5 are apparent. It was observed during the data collection phase of the study that a given current would alter some waves in a particular manner but would have little or no effect on other waves. To project a feel of advancing with distance from the inlet into the ocean, the data were displayed with the ratio x/W as the abscissa with the wave length and wave height alterations as the ordinate. The faired experimental data then generated curves of constant values of L_o/d for constant values of H_o/L_o and constant values of the current parameter U/C_o. The effect of a given current on selected waves noted in the experimentation can be seen reflected in the data curves of Figs. 8, 9, and 10, which show the manner in which the wave height is altered in the ocean for given incipient conditions.

The physical picture of the waves losing energy by spilling at the wave crest can be seen in Figs. 11, 12, and 13. These are photographs of three different waves being propagated onto the same magnitude of ebb current. The refraction of the wave train by the strong velocity gradients and vorticity in the horizontal plane is an area for further investigation.

Acknowledgements

Appreciation is extended to Mr. R. A. Sager, Chief, Coastal Section, Waterways Experiment Station, for use of the experimental facilities. The assistance of Mrs. E. K. Lever, Mr. O. H. Rhodes, and Mr. J. A. Boyd in data reduction is acknowledged. Permission of U. S. Army Engineers to publish this paper is greatly appreciated. The work was performed in

FIG. 7-EBB CURRENT EMANATING FROM THE INLET AND DIFFUSING AS A TURBULENT FREE JET IN THE OCEAN

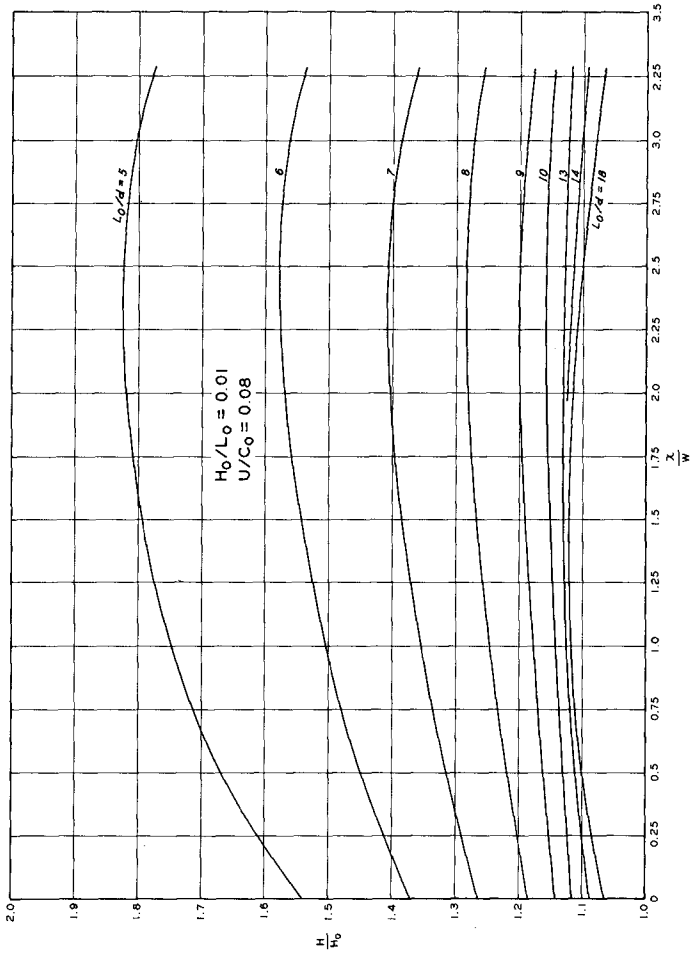

FIG. 8-CHANGES IN WAVE HEIGHT IN THE OCEAN UNDER CHANGING EBB CURRENT CONDITIONS FOR CONSTANT VALUES OF H_o/L_o and U/C_o

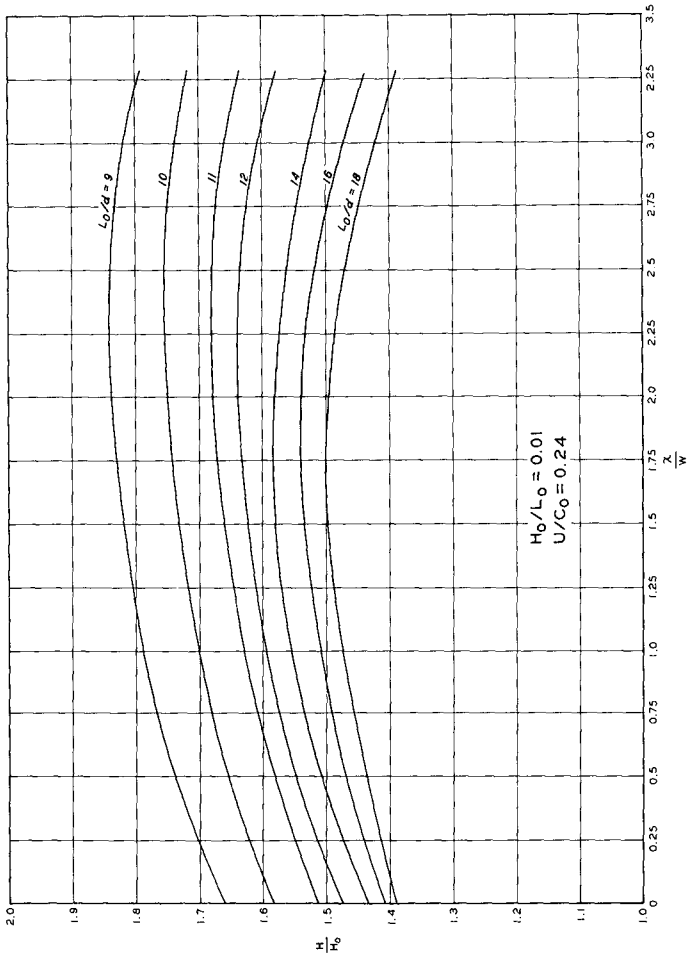

FIG. 9-CHANGES IN WAVE HEIGHT IN THE OCEAN UNDER CHANGING EBB CURRENT CONDITIONS FOR CONSTANT VALUES OF H_o/L_o and U/C_o

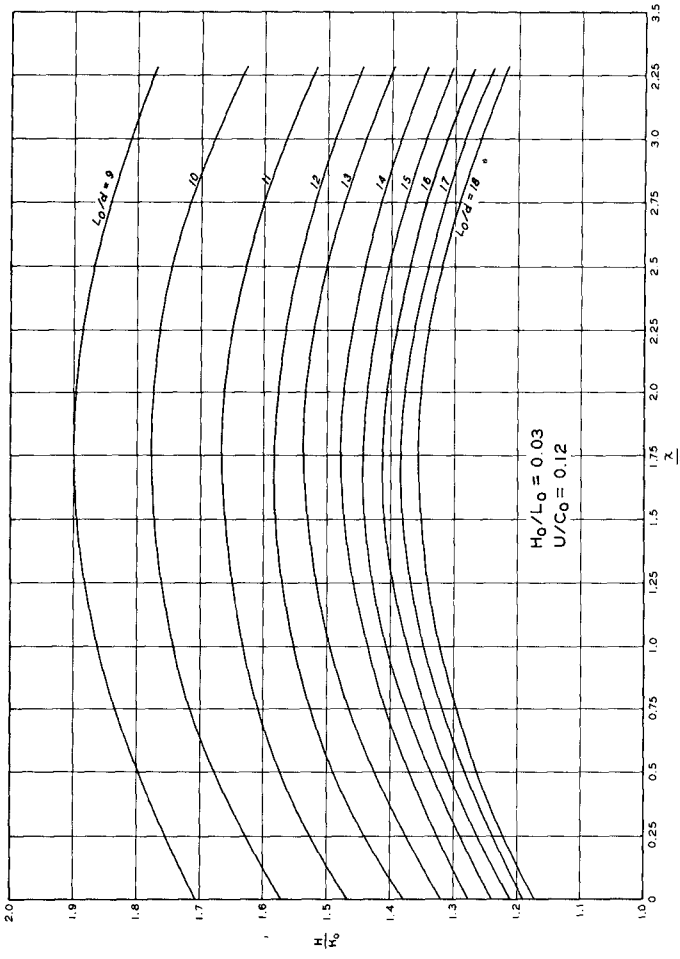

FIG. 10-CHANGES IN WAVE HEIGHT IN THE OCEAN UNDER CHANGING EBB CURRENT CONDITIONS FOR CONSTANT VALUES OF H_o/L_o and U/C_o

FIG. 11-WAVE TRAIN PROPAGATING ONTO AN EBB CURRENT. $U/c_o = 0.097$, $L_o/d = 5.37$, $H_o/L_o = 0.021$

FIG. 12-WAVE TRAIN PROPAGATING ONTO AN EBB CURRENT. $U/C_o = 0.101$, $L_o/d = 4.58$, $H_o/L_o = 0.028$

FIG. 13-WAVE TRAIN PROPAGATING ONTO AN EBB CURRENT. $U/C_o = 0.115$, $L_o/d = 3.24$, $H_o/L_o = 0.057$

partial fulfillment of graduate degree requirements and may subsequently be used as part of the Ph. D. dissertation material at Texas A&M University.

References

1. Yu, Y-Y., Transactions, American Geophysical Union, Vol. 33, 1952, pp. 39-

2. Herbich, J. B., Ziegler, J. and Bowers, C. E., Project Report No. 51, St. Anthony Falls Hydraulic Laboratory, Univ. of Minnesota, June 1956.

3. Sarpkaya, T., Transactions, American Society of Civil Engineers, Vol. 122, 1957, pp. 564-586.

4. Collins, J. I., Journal of Geophysical Research, Vol. 69, pp. 1051-1056.

5. Hughes, B. A., Masters Degree thesis, University of British Columbia, Vancouver, British Columbia, Canada, 1960.

6. Unna, P. J. H., Nature, Vol. 149, 1942, pp. 219-220.

7. Longuet-Higgins, M. S. and Stewart, R. W., Journal of Fluid Mechanics, Vol. 10, 1961, pp. 529-549.

8. Johnson, J. W., Transactions, American Geophysical Union, Vol. 28, 1947, pp. 867-872.

9. Burns, J. C., Proceedings, Cambridge Philosophical Society, Vol. 49, 1953, pp. 695-703.

10. Hunt, J. N., Proceedings, Royal Society of London, Vol. 231, 1955, pp. 496-504.

11. Lundgren, H., Basic Research--Progress Report No. 3, Coastal Engineering Laboratory, Technical University of Denmark.

12. Barber, N. F., Proceedings, Royal Society of London, Vol. 198, 1949, pp. 81-93.

13. Barber, N. F. and Ursell, F., Philosophical Transactions, Royal Society of London, Vol. 240, 1948, pp. 527-560.

14. Wilson, B. W., Deficiencies in Research on Gravity Surface Waves, Council on Wave Research, compiled by J. W. Johnson, Berkeley, California, 1961.

15. French, J. L., Tidal Flow in Entrances, Technical Bulletin No. 3, Committee on Tidal Hydraulics, Corps of Engineers, U. S. Army.

CHAPTER 37

THE SPIRAL WAVEMAKER FOR LITTORAL DRIFT STUDIES

Robert A. Dalrymple[1] and Robert G. Dean[2]

Abstract

A technique for simulating an infinitely long beach in the laboratory is introduced, with the objective of eliminating end effects usually present with short straight beach sections. The technique involves the spiral wavemaker generating waves in the center of a circular basin.

The wavemaker, consisting of a vertical right-circular cylinder oscillating in a small circle about its axis, is described in detail. Theoretical developments, using small-amplitude wave assumptions, show that the surface wave crests generated by the wavemaker may be described, at a particular time, as an Archimedian-type of spiral, with the wavemaker at its origin. Also, the crests impinge on the circular beach everywhere at the same angle of incidence.

Experiments with a prototype spiral wavemaker verify the theory, with close results for shallow water waves. Littoral drift applications of the wavemaker are given.

Introduction

There have been numerous laboratory studies of littoral drift rates since the first experiments of Krumbein (7) and Saville (8) over 20 years ago. In addition many other model studies have been conducted to determine the effects of groins, jetties and inlets on the adjacent beach. For all of these studies, a short straight beach section has been used, usually with provisions to add sand at the updrift end to simulate infinitely long beaches in nature.

The spiral wavemaker eliminates the end effects present in a straight beach laboratory study by operating in the center of a circular wave basin with a circumferential beach. The waves, which propagate away from the wavemaker in a spiral pattern, impinge on the beach everywhere at the same angle.

In this paper, the linear theory of the spiral wavemaker is presented, along with experimental verification of its validity, and some general results from its use for littoral drift studies.

The Linear Spiral Wavemaker Theory

The theory of wave generation by the spiral wavemaker belongs to a class of water wave problems, which has been extensively investigated, both theoretically and experimentally, particularly for the two-dimensional cases, such as piston and flap wavemaker motions (see, for example, Havelock (6), Ursell, Dean and Yu (9), Biesel and Suquet (1), Galvin (4), and recently Gilbert, Thompson and

---

[1] Graduate Research Associate
[2] Professor, Department of Civil and Coastal Engineering, University of Florida, Gainesville, Florida

Brewer (5)). The case of a vertically-oscillating horizontal cylinder at the water surface has been investigated by Yu and Ursell (10).

The three-dimensional problem of vertical cylinder wavemakers has been examined previously by Havelock (6), who studied the vertical oscillation of an upright cylinder and by Dean (3), for sway (piston) and roll (flap) motion of the cylinder; both of these studies resulted in circular or semi-circular wave crests propagating away from the wavemaker. Recently Black and Mei (2) examined semi-immersed and fully submerged oscillating cylinders in heave, sway and roll. The theory for a pulsating cylindrical wavemaker could also be easily derived. The spiral wavemaker differs from these previous studies by producing waves with an angular dependence that varies with time and distance from the wavemaker.

Assuming an incompressible fluid and irrotational motion, the velocity potential ϕ exists and is governed by the Laplace equation,

$$\nabla^2\phi = \phi_{rr} + \frac{1}{r}\phi_r + \frac{1}{r^2}\phi_{\theta\theta} + \phi_{zz} = 0 \qquad (1)$$

in polar coordinates. The subscripts denote partial differentiation. See Figure 1 for the notation. The boundary condition imposed at the bottom is that of no flow through the bottom.

$$-\phi_z = 0 \text{ at } z = -h \qquad (2)$$

At the surface, the Cauchy-Poisson condition, which is composed of the linearized dynamic free surface boundary condition ($\eta = \phi_t/g$ at $z = 0$) and the kinematic free surface boundary condition ($-\phi_z = \eta_t$ at $z = 0$), is applied.

$$\phi_z - (\sigma^2/g)\,\phi = 0 \text{ at } z = 0\ , \qquad (3)$$

where it has been assumed that the wave motion is periodic in time and of the form $e^{-i\sigma t}$, here σ($= 2\pi/T$) is the angular frequency. The boundary condition on the cylinder wall ($r = a'$) is determined by assuming that a small perturbation propagates with time around the circumference of the cylinder of radius a, i.e.

$$a' = a + \epsilon(z)\sin(\theta - \sigma t) \qquad (4)$$

where the amplitude of the perturbation $\epsilon(z)$ may be a function of the elevation, z. The instantaneous radius a' may be rewritten in complex form as

$$a' = a - \epsilon(z)\, i\, e^{i(\theta - \sigma t)} \qquad (5)$$

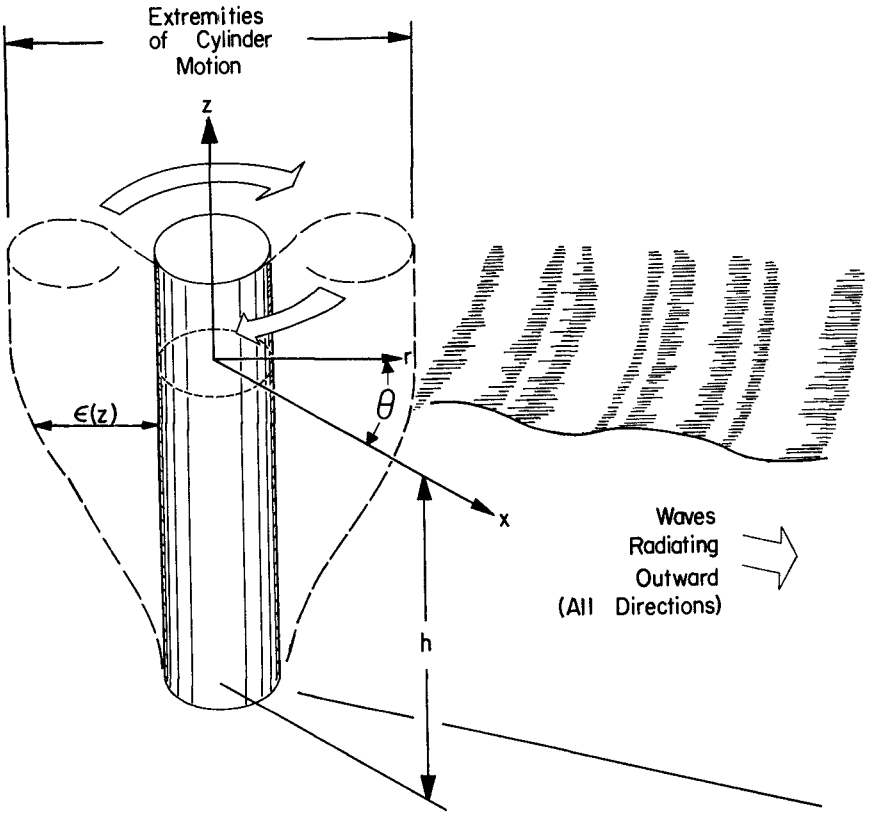

FIGURE 1 SPIRAL WAVEMAKER

The radial velocity, u_r, is

$$u_r = \frac{da'}{dt} = \mathrm{Re}\ \{-\sigma\ \varepsilon\ (z)\ e^{\ i(\theta\ -\ \sigma t)}\} \tag{6}$$

and, under the assumption that $\varepsilon(z)/a << 1$, it is prescribed at the mean position of the cylinder wall, $r = a$.

The final boundary condition to be imposed is that, at $r = \infty$, all waves propagate away from the wavemaker; this is the so-called radiation boundary condition.

The solution of this boundary value problem follows readily from separation of variables. In the z direction, the resulting ordinary differential equation with the two homogeneous boundary conditions is a proper Sturm-Liouville problem and it can be shown that the complete set of eigenfunctions in this coordinate direction is $\{\cosh\ k_o(h + z),\ \cos\ k_m(h+z), m=1, 2...\infty\}$, with the relationships

$$\sigma^2 = gk_o\ \tanh\ k_o h \tag{7}$$

$$\sigma^2 = -gk_m\ \tan\ k_m h \tag{8}$$

Here k is a wave number. The subscript zero is used to denote the wave mode associated with the relationship in Eq. 7, and is not to be confused with the customary notation for deep water conditions. The total solution for the velocity potential which gives outward propagating waves is, therefore,

$$\phi(r,\theta,z,t) = A_o\ H_1^{(1)}\ (k_o r)\ \cosh\ \ k_o(h + z)\ e^{i(\theta-\sigma t)}$$

$$+ \sum_{m=1}^{\infty} B_m\ K_1(k_m r)\ \cos\ k_m(h+z)\ e^{i(\theta-\sigma t)} \tag{9}$$

where $H_1^{(1)}(k_o r) = J_1(k_o r) + i\ Y\ (k_o r)$, is the Hankel function of the first kind and $K_1(k_m r)$ is the modified Bessel function of the second kind. The remaining cylinder wall boundary condition (Eq. 6) is used to determine the unknown A_o and the B_m coefficients. Equating the radial velocity of the wall with that determined from the velocity potential, $-\phi_r$, at $r = a$, and using the orthogonality properties of the eigenfunctions in z, A_o and B_m are found to be

$$A_o = \frac{4\sigma \int_{-h}^{0} \varepsilon(z)\ \cosh\ k_o(h+z)dz}{H_1^{(1)'}(k_o a)(\sinh\ 2k_o h + 2k_o h)} \tag{10}$$

$$B_m = \frac{4\sigma \int_{-h}^{0} \epsilon(z) \cos k_m(h+z)dz}{K_1'(k_m a)(\sin 2k_m h + 2k_m h)} \tag{11}$$

where the primes denote differentiation with respect to the arguments. The wave profile, η, is found from the dynamic free surface boundary condition,

$$\eta = \frac{1}{g}\phi_t\Big|_{z=0} = R_e \{ \frac{-i\sigma A_o}{g} H_1^{(1)}(k_o r) \cosh k_o h \, e^{i(\theta-\sigma t)} - \sum_{m=1}^{\infty} \frac{i\sigma B_m}{g} K_1(k_m r) \cos k_m h \, e^{i(\theta-\sigma t)} \} \tag{12}$$

The waves represented by the summation terms decay rapidly with distance, r, as $K_1(k_m r)/K_1'(k_m a)$ becomes much less than unity with distances of order (h). Thus the waves in the sum in Eq. 12 do not propagate from the cylinder, and only exist near it to provide water motion necessary to match the motion of the cylinder wall.

For two simple types of wavemaker motion, the A_o terms have been evaluated.[1] These are: Case 1, sway, a uniform displacement over depth, analogous to a piston wavemaker motion, and Case 2, a rolling motion with no movement at the bottom, analogous to a flap wavemaker motion.

$$\text{Case 1:} \quad A_o = \frac{4\sigma (\frac{S}{2}) \sinh k_o h \, e^{-i\nu}}{k_o \sqrt{J_1'(k_o a)^2 + Y_1'(k_o a)^2}\,(\sinh 2k_o h + 2k_o h)} \tag{13}$$

$$\text{Case 2:} \quad A_o = \frac{4\sigma (\frac{S}{2}) (k_o h \sinh k_o h - \cosh k_o h + 1) \, e^{-i\nu}}{k_o^2 h \sqrt{J_1'(k_o a)^2 + Y_1'(k_o a)^2}\,(\sinh 2k_o h + 2k_o h)} \tag{14}$$

---

[1] These A_o terms are exactly the same as those derived by Dean (3) for sway and roll motion of the cylinder wavemaker, which generates semicircular waves. His velocity potential was

$$\phi(r,\theta,z,t) = A_o H_1^{(1)}(k_o r)\cosh k_o(h+z) \cos\theta \, e^{-i\sigma t} + \sum_{m=1}^{\infty} B_m K_1(k_m r) \cos k_m(h+z) \cos\theta \, e^{-i\sigma t}$$

The B_m term may be found from Eq.11.

Here (S/2) is the amplitude of the wavemaker displacement ($\varepsilon(0)$) at the surface and the phase, $\nu=\tan^{-1}\left(Y_1'(k_o a)/J_1'(k_o a)\right)$.

The dimensionless theoretical wave amplitudes, $|\eta|/(S/2)$, have been shown in Figures 2 and 3 for these two cases as a function of $k_o h$ and evaluated at the wavemaker (r=a).

Far from the wavemaker, the wave profile, η, becomes asymptotically

$$\eta = \mathrm{Re}\left\{\frac{-i\sigma A_o}{g}\sqrt{\frac{2}{\pi k_o r}}\cosh k_o h\, e^{\,i(k_o r+\theta-\sigma t-3\pi/4)}\right\} \qquad (15)$$

The asymptotic wave direction, α, that is, the angle between the normal to the wave crest and the radial direction, r, is determined by the gradient of the phase function, $\psi(=k_o r+\theta-\sigma t-3\pi/4-\nu)$ and is expressed as

$$\alpha = \tan^{-1}\left(\frac{1}{k_o r}\right) = \tan^{-1}(L_o/2\pi r) \qquad (16)$$

This relationship is shown in Figure 4. It should be noted that, in the limit as $r \to \infty$, the wave direction is not a function of the size of the wavemaker, being solely a function of the period of and distance from the wave maker and the water depth. Also the direction of the wave tends to be more radial with increasing distance. The pattern of the wave crest is found by setting the phase function equal to a constant, say $\pi/2$. Rearranging, the following equation of the form of an Archimedian spiral results.

$$r = \frac{1}{k_o}(5\pi/4 - \theta + \sigma t + \nu) \qquad (17)$$

The power necessary to produce the propagating waves is easily found by two means. (Note that theoretically the standing waves require no energy after they have been initially established). The first is to integrate the dynamic pressure dotted with u_r, the radial velocity, over the wetted surface of the cylinder, and then taking the time average,

$$P = \overline{\int_0^{2\pi}\int_{-h}^{0} -\rho g\, \phi_t\, \phi_r\, dz\, a\, d\theta} \qquad (18)$$

where Bernoulli's equation has been used, or by equating the power to the averaged energy flux of the propagating wave far from the cylinder, say, at r = b,

$$P = \int_0^{2\pi} \frac{\rho g|\eta|^2}{2} C_g\, b\, d\theta \qquad (19)$$

where C_g is the group velocity of the waves.

$$C_g = \frac{\sigma}{2k_o}\left(1 + \frac{2k_o h}{\sinh 2k_o h}\right) \qquad (20)$$

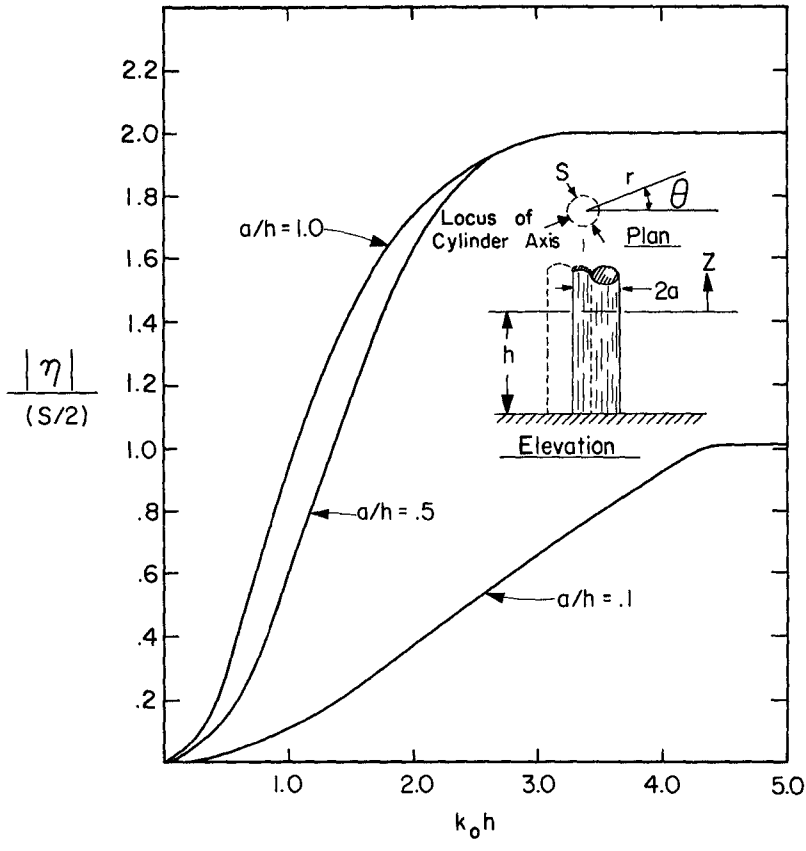

FIGURE 2 DIMENSIONLESS PROGRESSIVE WAVE AMPLITUDE EVALUATED AT CYLINDER, CASE I

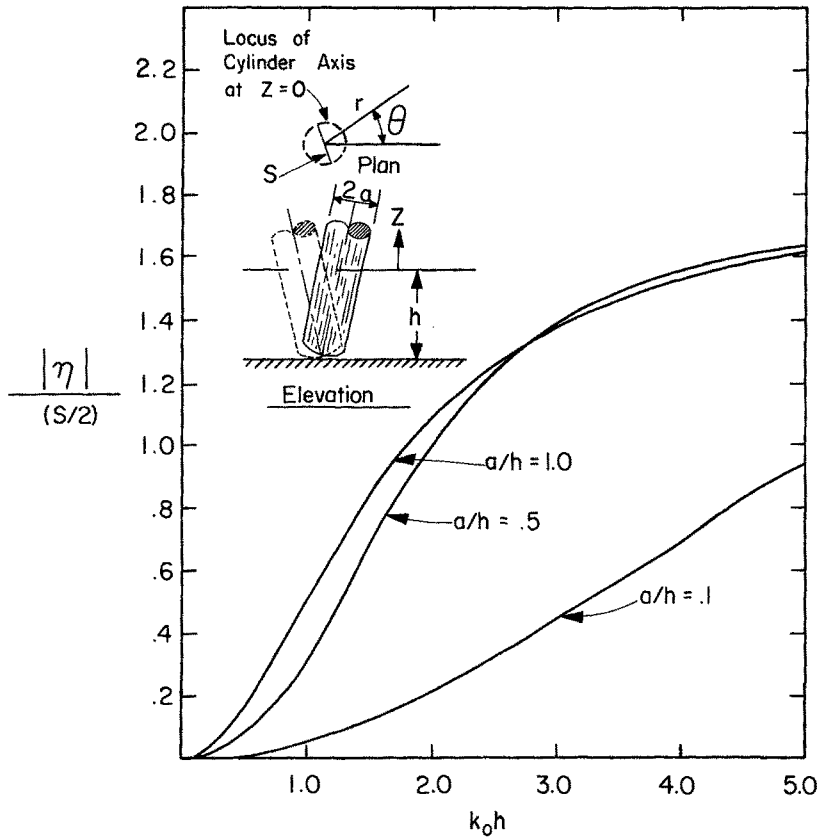

FIGURE 3 DIMENSIONLESS PROGRESSIVE WAVE AMPLITUDE EVALUATED AT CYLINDER, CASE 2

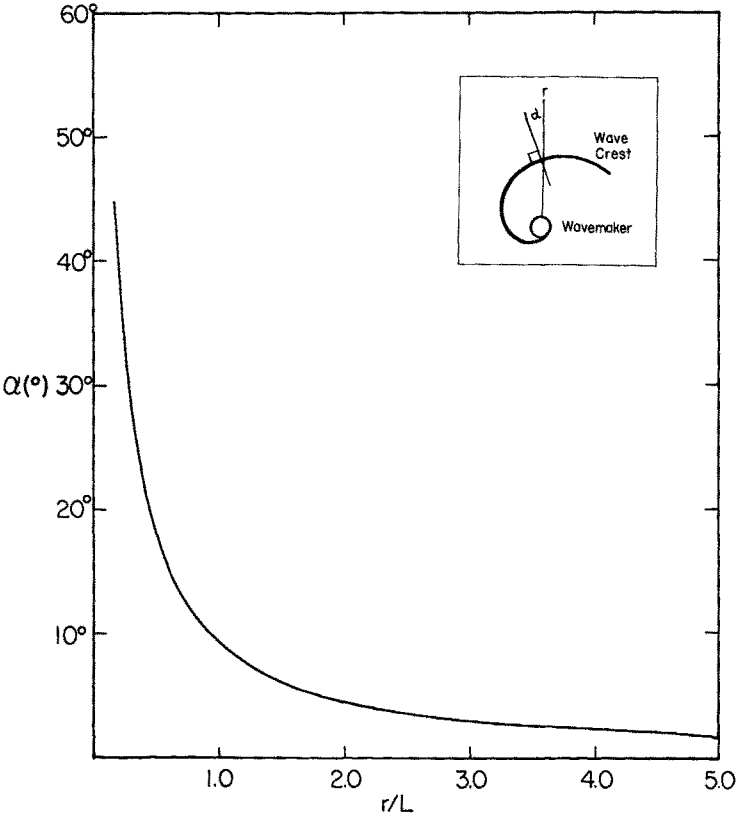

FIGURE 4 ASYMPTOTIC WAVE DIRECTION AS A FUNCTION OF DISTANCE FROM WAVEMAKER

In either case, the power is expressed as

$$P = \rho \frac{|A_o|^2}{2k_o} \sigma (\sinh 2k_o h + 2k_o h) \qquad (21)$$

The dimensionless power for the two cases of wavemaker motion is shown in Figure 5. As expected, the rolling spiral wavemaker (Case 2) is the more efficient wave generator in deep water while in shallow water the converse is true.

Experimental Results

A prototype spiral wavemaker has been constructed and tested against the theory. The wavemaker is composed of a 2' tall, 12.5" diameter steel drum, mounted on an offset shaft which was pulley-driven. The offset of the rotating shaft could be located at either 1" or 2" from the axis of the cylinder. The shaft fit into a floor-mounted bearing and at the top into a cantilevered arm from the electric motor platform. The steel drum was rotated, rather than moved irrotationally, about the axial shaft.

Experimental runs to determine wave heights were conducted in a large 75' x 40' basin filled with 10" of water. The wavemaker was run at different periods to provide a range of relative depths, $k_o h$. Measurements of the spiral wave heights were made at 3' and 9' from the wavemaker and were obtained using a resistance wire gage and recorded by a Hewlett-Packard recorder. The tests were each run twice in succession and independently analyzed by the authors. As an example of the data, see Figures 6 and 7. The tabulated results represent the averaged data for each test. The measured data were then extrapolated to the wavemaker (r = a) via the theory, by multiplying by the ratio,

$$\left[\frac{J_1(k_o a)^2 + Y_1(k_o a)^2}{J_1(k_o r_m)^2 + Y_1(k_o r_m)^2} \right]^{\frac{1}{2}}$$

where r_m represents the distance of the wave gage from the wavemaker. The results are also plotted versus the theory in Figure 8. The results are remarkably good for small $k_o h$, particularly in view of the rotational motion of the wavemaker and because of a 3/4" gap between the wavemaker bottom and the floor of the basin. The poor agreement at $k_o h$ greater than 2.0 is attributable to the violations of the conditions of potential flow. For instance, for the $k_o h$ value of 4.55, the wavemaker was rotating at 125 revolutions per minute, and separation occurred behind the cylinder perturbation as it rotated.

Littoral Drift Test

A 16' diameter circular basin was placed around the wavemaker and a fine sand beach was constructed in 9" of water. The wavemaker was operated at a 1 second period and produced waves of approximately 1" in height at the beach.

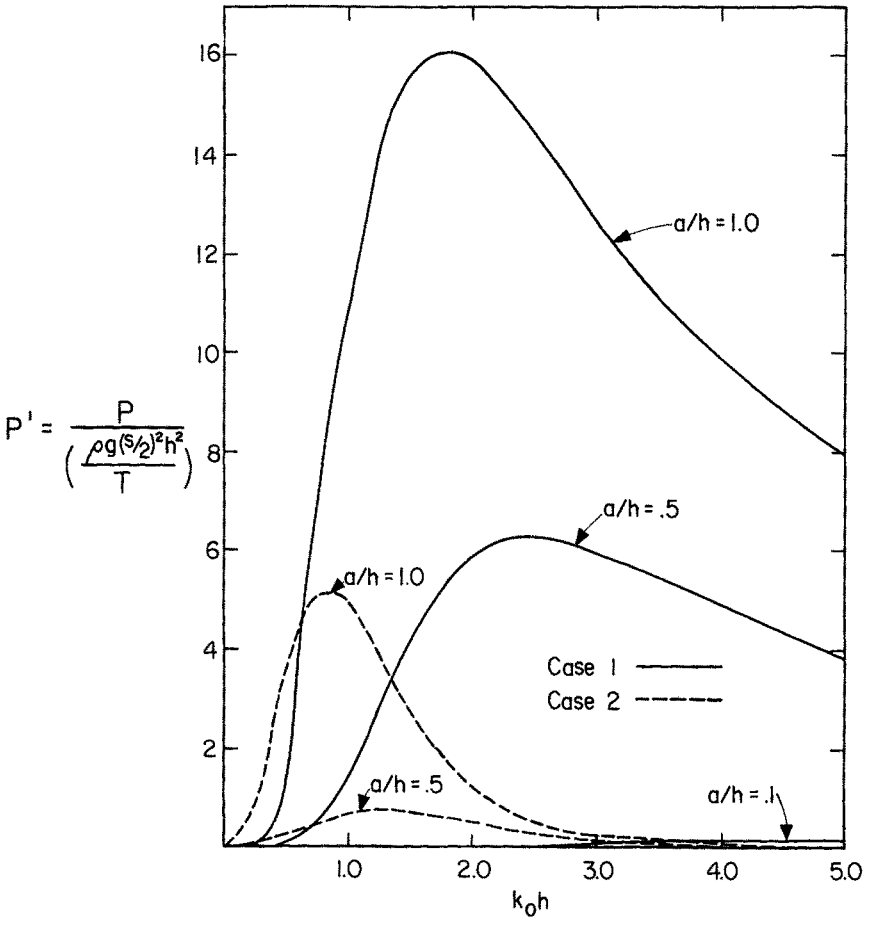

FIGURE 5 DIMENSIONLESS POWER, P', FOR CASES 1 AND 2

EXAMPLES OF TEST DATA

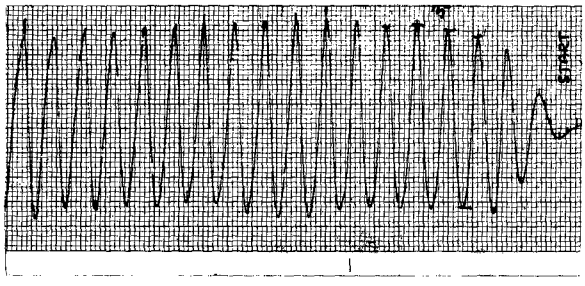

FIGURE 6. Recorded data (3' from wavemaker)
Test Condition: h = .833', T = .615 sec, $|\eta|/(S/2)$ = .667
a = .52', (S/2) = 1"

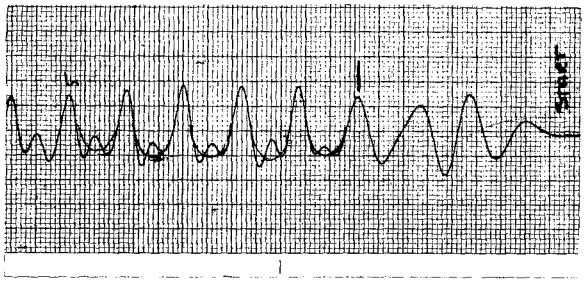

FIGURE 7. Recorded data (9' from wavemaker)
Note presence of first harmonic.
Test Condition: h = .833', T = 1.18 sec., $|\eta|/(S/2)$ = .109
(not to same scale as above) a = .52', (S/2) = 1".

Table 1. Measured and Predicted Spiral Wave Amplitudes for Water Depth of 10" and 12.5" Wavemaker Diameter

Wave Period (sec)	Measured Dimensionless Wave Amplitude $\lvert\eta\rvert/(S/2)$ at Gage	Distance from Wavemaker (feet)	Dimensionless Wave Amplitude Calculated at Wavemaker from Measured Wave	Predicted Dimensionless Wave Amplitude at Wavemaker	% Error
(S/2)=1"					
1.135	.236	3.0	.690	.748	7.83
1.13	.150	9.0	.766	.760	-7.36
1.61	.055	9.0	.318	.327	2.63
1.55	.108	3.0	.348	.358	2.76
3.11	.0367	3.0	.148	.073	-101.4
2.98	.0087	9.0	.0644	.0805	20.09
3.74	.0068	9.0	.0553	.0494	-12.03
3.82	.0094	3.0	.0402	.0472	14.85
1.19	.213	3.0	.631	.670	5.81
1.18	.109	9.0	.565	.681	16.97
1.99	.0297	9.0	.186	.199	6.35
2.33	.0401	3.0	.147	.140	-6.16
.62	.667	3.0	1.683	1.955	13.90
.48	.479	3.0	1.173	2.041	42.53
.80	.386	3.0	1.025	1.504	31.85
(S/2)=2"					
1.04	.224	3.0	.695	.907	23.36
2.70	.0165	3.0	.0636	.100	36.40
1.405	.130	3.0	.406	.452	10.25

* $$\%\ \text{Error} \equiv \frac{\eta_{\text{Predicted}} - \eta_{\text{Measured}}}{\eta_{\text{Predicted}}} \times 100$$

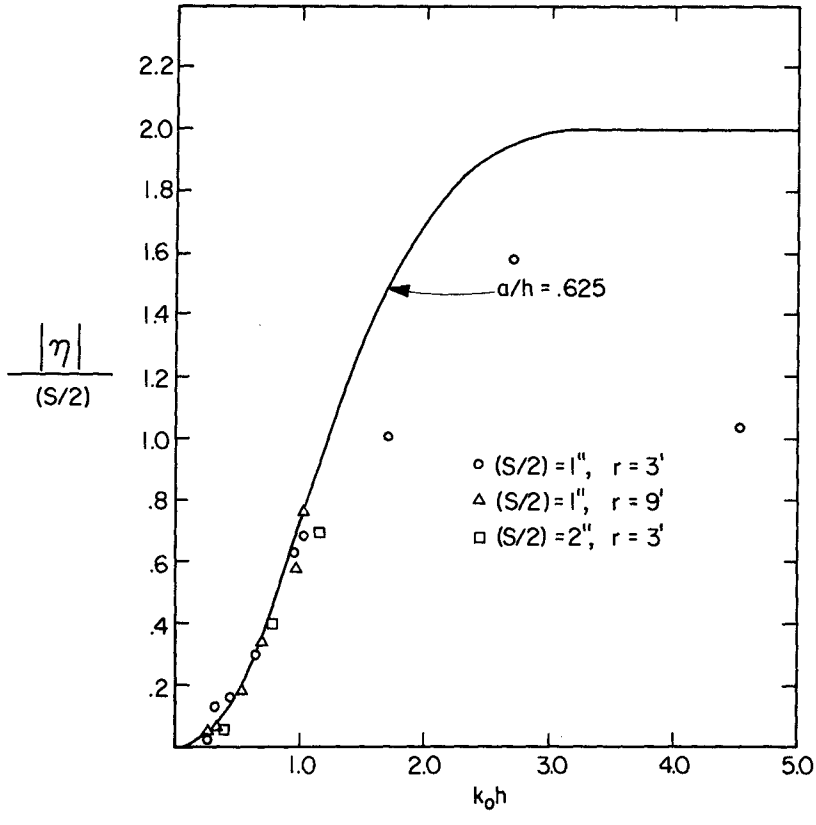

FIGURE 8 THEORETICAL AND EXPERIMENTAL DIMENSIONLESS PROGRESSIVE WAVE AMPLITUDE EVALUATED AT CYLINDER (a=.52') FOR CASE I

Photograph of Spiral Wavemaker With 16' Diameter Circumferential Beach for Littoral Drift Tests. (Cement blocks and sand were removed for wave height measurements).

A steep beach was immediately formed with a shallow foreshore, dropping off at the plunge point of the waves to about 8" in depth. Around the basin, despite obvious reflections due to the beach steepness, a noticeable time lag in wave breaking around the basin was apparent. Fluorescent sand tracer placed in a strip across the foreshore moved readily in the direction of the wavemaker rotation. A rock groin placed across the beach and offshore, showed after two hours of testing, the usual downdrift scour and updrift deposition pattern, despite noticeable leakage of tracer through the groin. After testing, the current attributable to the stirring action of the wavemaker was measured as .05 ft./sec. approximately 2' from the beach, a velocity much lower than the incipient motion velocity of the sand. No qualitative tests were made to determine drift rates.

Conclusions and Recommendations

From this study it is apparent that the spiral wavemaker can be both a practical and a useful research tool for time-dependent littoral drift studies. A much larger spiral wavemaker should be built, in part, to produce large waves and also to keep $\varepsilon(z)/a \ll 1$; see below. If possible, the wavemaker motion should be irrotational and the clearance between the wavemaker and the basin floor should be a minimum.

The linear spiral wavemaker theory adequately describes the spiral wave for $k_o h < 2.0$. For larger $k_o h$ values separation effects were encountered in these experiments.

The ratio, $\varepsilon(z)/a$, is of importance in the generation of higher wave harmonics. Due to the small but finite displacement of the cylinder from origin, the cylinder wall boundary condition at $r = a$ is in actuality,

nonlinear, giving rise to higher harmonics. From geometrical considerations, it can be shown for Case 1 motion that the ratio of the first harmonic amplitude to the fundamental mode is proportional to $\varepsilon(o)/2a$; however, the wave height response to the first harmonic is usually greater due to the increased relative water depth as a result of doubling the angular frequency. In other words, the higher harmonics may be amplified greatly, and therefore the requirement of $\varepsilon(z)/a << 1$ is a strict one. For example, for the data shown in Figure 7, $\varepsilon(z)/2a = .08$; however, the response for the first harmonic is double that of the fundamental, and therefore at the wavemaker, the amplitude of the first harmonic is 16% that of the fundamental wave.

Finally, one possible disadvantage should be emphasized. The angle of the wave to the radial direction of the beach is fixed by the wave period, the water depth, and the distance from the wavemaker. Thus the experimenter does not have a wide range of wave attack angles for littoral drift studies. Should this range be necessary, one possible solution is to change the diameter of the wave basin, or possibly, increase the number of lobes the wavemaker.

Acknowledgement

This work was sponsored, in part, by the NOAA Office of Sea Grant, Department of Commerce, under Grant No. SGP 2-38.

References

1. Biesel, F. and F. Suquet,"Laboratory Wave Generation Apparatus," Proj. Rept. 39, St. Anthony Falls Hydraulic Laboratory, University of Minnesota, Minneapolis, English Translation, 1953.

2. Black, J. L. and C. C. Mei,"Scattering and Radiation of Water Waves," M.I.T., Water Resources and Hydrodynamics Laboratory, Rept. No. 121, April, 1970.

3. Dean, R. G.,"Water Waves Generated by Oscillating Plane and Cylindrical Wavemaker," Unpublished Lecture Notes, University of Hawaii, May 7, 1968.

4. Galvin, C. J., Jr.,"Wave Height Predictions for Wave Generation in Shallow Water," U.S. Army Coastal Engineering Research Center, T.M. 4, 1964.

5. Gilbert, G., D. M. Thompson and A. J. Brewer, "Design Curves for Regular and Random Wave Generations,"J. Hyd. Res., IAHR, Vol. 9, No. 2, 1971.

6. Havelock, T. H., "Forced Surface-Waves on Water," Philosophical Magazine, Vol. VIII, Oct. 1929.

7. Krumbein, W. C.,"Shore Currents and Sand Movements on a Model Beach", U. S. Army Beach Erosion Board T.M. 7, Sept., 1944.

8. Saville, T., Jr.,"Model Study of Sand Transport along an Infinitely Straight Beach," Trans. A.G.U., Vol. 31, No. 4, 1950.

9. Ursell, F., R. G. Dean and Y. S. Yu, "Forced Small-Amplitude Water Waves: A Comparison of Theory and Experiment", J. Fluid Mechanics, Vol. 7, Pt. 1, 1960.

10. Yu, Y. S. and F. Ursell, "Surface Waves Generated by an Oscillating Cylinder on Water of Finite Depth: Theory and Experiment, J. Fluid Mech. Vol. 11, 1961.

CHAPTER 38

WAVES INDUCED BY NON-PERMANENT PADDLE MOVEMENTS

by C.Campos MORAES*
F.Silveira RAMOS**
M.Mendes de CARVALHO**

ABSTRACT

In a flume equipped with an irregular wave maker the motion of the paddle and the resulting waves may be thought of respectively as input and output of a system which, if linear, is for some purposes described by the so-called gain function.
A theoretical and experimental study of this function is carried out making use of paddle movements that produce transient surface motion.

1. INTRODUCTION

At the Laboratório Nacional de Engenharia Civil, a new flume was recently built for reproducing irregular (random) waves (fig.1). Length, width and depth of the flume are respectively 50, 1.60 and 1.20 m and the maximum water depth is 0.8 m. Waves are generated by the motion of a paddle actuated by a hydraulic jack, which is controlled, through a servo-valve, by an electrical signal of programmable characteristics, such as a given spectrum, if the signal is stationary, a given amplitude, if it is a sinusoid, etc. The structure linking paddle and actuator, a four-bar system, is such that the paddle may either be kept normal to the shaft of the actuator during motion (translation) or it may undergo a rotation as shown in fig. 1.
For the simulation of sea waves it is necessary to know the relationship between paddle motion and generated surface motion. For our purposes it is convenient to consider the flume a system for which input and output are respectively x(t), the (horizontal) displacement of the actuator shaft, and y(t), the water surface at a point, as functions of time. Of course, the system will be different for different water depths and for different positions of the points A and B in the four-bar structure that supports the paddle. In this paper, only the translation case is

* - Research Officer, Laboratório Nacional de Engenharia Civil, Lisbon, Portugal.
** - Trainee Research Officer, Laboratório Nacional de Engenharia Civil, Lisbon, Portugal.

considered and the water depth is 0.50 m, unless otherwise stated.
We assume that the system $\{x(t), y(t)\}$ is time-invariant. If it is also linear, we have

$$y(t) = h(t) * x(t) \tag{1}$$

where * denotes convolution and h(t) is a function which characterises the system. If we put

$$G(f) = \left|TF\left[h(t)\right]\right| \tag{2}$$

where TF indicates Fourier transform, it is well known that
(i) if x(t) and y(t) are realisations of stationary stochastic processes with variance spectra $P_x(f)$ and $P_y(f)$, respectively, then

$$P_y(f) = G^2(f)P_x(f) \tag{3}$$

(ii) if x(t) and y(t) are transient functions, then

$$\left|TF\left[y(t)\right]\right| = G(f)\left|TF\left[x(t)\right]\right| \tag{4}$$

(iii) if x(t) and y(t) are sinusoids of frequency f_o and amplitudes A_x and A_y respectively, then

$$A_y = G(f_o)A_x \tag{5}$$

G(f) is the gain function of the system and $G^2(f)$ is sometimes called its transfer function.
Thus, if the system is reasonably linear and if we are able, as is the case, to control the characteristics of the input, a knowledge of G(f) will suffice to generate, for instance, waves with a given spectrum, $P_y(f)$.
A relationship of the form (5) for sinusoids has been obtained theoretically by Biésel & Suquet (1951), not for each frequency f but for each wave number, k. After adaptation for frequency, their formula is plotted in fig. 2. This relationship was derived using the linearised Hydrodynamics equations, a simplification we will also adopt.
Thus, apart from energy losses due to leakage around the paddle edges and the like, the problem of determining G(f) may be considered solved if for this purpose one may assume that the system $\{x(t), y(t)\}$ is linear, which allows the use of the formula not only for sinusoids but for any movements. This assumption may be studied theoretically making use of the solution by Kennard (1949) for the linearised equations of Hy

drodynamics, precisely in the case of waves generated by paddle movements. One procedure is the following: a transient motion of the paddle and the corresponding surface profile at a point, computed by Kennard's formula, are considered; these are Fourier transformed and (4) is applied. The obtained G(f) is then compared with the one by Biésel & Suquet. If results are similar one may infer that in what concerns the determination of G(f) the linearity assumption for the system $\{x(t), y(t)\}$ is justified, at least as long as the linearised equations are applicable to water waves. Another procedure, this one with approximate results only, is based on the fact that, for a time-invariant linear system, if

$$x(t) = U(t) \tag{6}$$

where U(t) is the unit step function, that is, $U(t) = 1$ for $t > 0$ and $U(t) = 0$, for $t \leqslant 0$, then

$$h(t) = \frac{dy}{dt} \tag{7}$$

and so

$$G(f) = \left| TF\left[\frac{dy}{dt}\right] \right| \tag{8}$$

Kennard's solution does not allow the use of such an input. However, if instead of U(t) we use

$$\tilde{U}(t) = \begin{cases} 0 & , \quad t \leq 0 \\ \frac{t}{T} & , \quad t \in (0,T) \\ 1 & , \quad t \geq T \end{cases}$$

with T sufficiently small, then $\tilde{y}(t)$ being the resulting surface by Kennard's formula, we will have

$$G(f) \approx \left| TF\left[\frac{d\tilde{y}}{dt}\right] \right| \tag{10}$$

Similar and other procedures may be used for an experimental study in the flume using actual records of inputs and outputs instead of theoretical inputs and Kennard's outputs. This will permit to see not only whether the linearisation of the Hydrodynamics equations is too gross an approximation for our purposes, but also whether the linear assumption for the system is supported by experimental evidence. Experimental tests will also help in judging the accuracy of numerical integration necessary for Kennard's formula.

2. USE OF NON - PERMANENT PADDLE MOVEMENTS

We call non-permanent those paddle movements which produce transient surface motion. The importance of such movements in the determination of G(f) and the testing of the system linearity, as described above, results from several facts:

(i) with sinusoidal movements the system behaviour as regards linearity cannot be tested. Even assuming linearity, many flume experiments must be made to test the appropriateness of the B & S formula.

(ii) realisations of stationary stochastic processes have the drawback that spectra must be estimated from limited lengths of record.

(iii) non-permanent motions of the paddle are simpler to use with Kennard's formula especially those with constant absolute values of the velocity such as are shown in fig. 3, and which for lack of better names will be called "impulses" and "steps".

(iv) these impulses have simple Fourier transforms to apply in (4); the steps are such that it is simple to determine $\frac{dy}{dt}$ for use in (10).

(v) tests in the flume, with such inputs are quite simple to perform and take little time.

3. THEORETICAL TESTS

3.1 - Theory

The two-dimensional surface profile for waves produced by the movements of a paddle is, as obtained by Kennard (1949) from the linearised Hydrodynamics equations and quoted by Madsen (1970),

$$\eta(x,t) = -\frac{2}{\pi}\int_0^{+\infty} dk \int_0^t d\tau \int_0^d dz \, \frac{\cos\sigma(t-\tau).\cos kx.\cosh k(z+d)}{\cosh kd}\, u(z,\tau) \qquad (11)$$

where $\eta(x,t)$ is the surface elevation on time t and at distance x from the paddle, $\sigma = (gk \tanh kd)^{1/2}$, k being the wave number, d is the water depth and $u(z,\tau)$ is the horizontal velocity of the paddle on instant τ and on ordinate z. Of course, if there is no rotation, u is independent of z.

We will have then for a step

$$u(\tau) = \begin{cases} v\,, & \tau \in (0,T) \\ 0\,, & \tau \notin (0,T) \end{cases} \qquad (12)$$

and for an impulse

$$u(\tau) = \begin{cases} v/2 \ , & \tau \in (0,T/2) \\ -v/2 \ , & \tau \in (T/2,T) \\ 0 \ , & \tau \notin (0,T) \end{cases} \qquad (13)$$

where $v = H/T$.

After some manipulation, we obtain for the surface time profiles at distance x from the paddle

$$\eta_s(x,t) = \frac{4v}{\pi} \int_0^{+\infty} W(k,x) \cos \sigma(t - \frac{T}{2}) dk \qquad (14)$$

$$\eta_i(x,t) = -\frac{8v}{\pi} \int_0^{+\infty} Q(k,x) \sin \sigma(t - \frac{T}{2}) dk \qquad (15)$$

where subscripts s and i indicate step and impulse respectively, and

$$W(k,x) = \frac{1}{k\sigma} \tanh kd . \cos kx . \sin \frac{\sigma T}{2} \qquad (16)$$

$$G(k,x) = \frac{1}{k\sigma} \tanh kd . \cos kx . \sin^2 \frac{\sigma T}{4} \qquad (17)$$

The derivative of η_s is simple to obtain

$$\frac{d\eta_s}{dt} = -\frac{4v}{\pi} \int_0^{+\infty} W(k,x) . \sigma . \sin \sigma(t - \frac{T}{2}) dk \qquad (18)$$

The Fourier transform of the theoretical input impulse is in absolute value

$$A(f) = \frac{HT}{2} \left(\frac{\sin \pi f \frac{T}{2}}{\pi f \frac{T}{2}} \right)^2 \qquad (19)$$

3.2 - Use of Kennard's solution

To have an experimental equivalent to the theoretical impulse to be used, a test was performed in the irregular wave flume with the experimental impulse shown in fig. 5. The width was the smallest that could be achieved by the actuator. In the manner of fig. 3, the values of $H = 3.16$ cm and $T = 0.54$ s were obtained for the "equivalent" theoretical impulse. As there were actual records from the flume at distances $x = 5$ m and $x = 29$ m from the paddle, Kennard's theoretical outputs were then computed by formula (15), for these distances, using Simpson's rule

for the numerical integration. After some trials, the upper limit of integration and the step size were chosen to be 0.8 and 0.0005 respectively, the length unit being the centimetre.

Comparison of the theoretical (fig. 4) and the experimental (fig. 5) outputs for x = 5 m shows good agreement in periods and heights, except perhaps in the shorter periods towards the end. For x = 29 m agreement was still good in the longer periods but worse in the end as there was earlier dampening in the experimental record. This was ascribed to the numerical error in the integration and studies were confined to the x = 5 m case.

No comparison was made of surfaces produced by steps, as in the theoretical case there was no intermediate surface computation. The derivative of the surface was obtained instead by formula (18).

3.3 - The theoretical gain function

The function G(f) was computed by (4) for x = 5 m from the theoretical impulse mentioned in 3.2, that is, with H = 3.16 cm and T = 0.54 s. The Fourier transform of the corresponding Kennard surface profile was computed by the FFT algorithm. $\left|TF\left[x(t)\right]\right|$ is given by (19). G(f) values are plotted in fig. 6 (squares). G(f) was also computed by (10) for x = 5 m from a theoretical step with H = 1 cm and T = 0.05 s. $\frac{dy}{dt}$ was obtained by (18) with a numerical integration similar to the impulse case. The Fourier transform was also computed numerically by the FFT algorithm and and the resulting G(f) values are plotted in fig. 6 (circles). It is seen that the G(f) values obtained by two procedures through Kennard's formula agree quite well with the Biésel-Suquet curve for translation which is also shown in fig. 6. The points resulting from the step (circles) show some dispersion, perhaps due to the fact that (10) is merely an approximative formula.

This good agreement seems to indicate that if the linearised Hydrodynamics equations are a sufficiently good approximation, then the system $\{x(t), y(t)\}$ may be taken as linear.

In the following section some experimental results are now presented.

4. EXPERIMENTAL TESTS

4.1 - Preliminary tests

For the determination of the gain function there had been some preliminary tests with sinusoids and white noise, that is, with permanent

paddle movements. In what concerns spectral width, this corresponds to the use of two extremes: inputs with extremely wide and extremely narrow spectra.

Thus, for frequencies in the range of interest, that is, up to 2.0 cps, sinusoidal inputs of several amplitudes were used. The corresponding G(f) values, computed by (5), for x = 29 m are plotted in fig. 7. The scatter reveals that in practice there is some non-linearity in the system $\{x(t), y(t)\}$ in what concerns multiplication by a constant. However the overall agreement is good at least for $f \leq 1.5$ cps.

The white noise was provided by a white noise generator with an upper frequency limit of 1.5 cps[1], which is still within the range of interest. Nevertheless the test was made, input and output spectra were estimated and G(f) was computed by (3), also for x = 29 m, and plotted in fig. 7. What small energy there was in the input above 1.5 cps still provided some points for f>1.5 cps, which however should be viewed with some reserve, as according to Tick (1963), when computing the transfer function one should "use inputs that were rich in all frequencies of interest to obtain proper estimates".

The agreement between the two sets of points is good until $f \approx 1.3$ cps. Above this frequency the G(f) values obtained through white noise fall rapidly below the theoretical value of 2 cps. This may be due to two facts: (i)G(f) estimates are poor because of the 1.5 cps limitation of the available white noise; or (ii) there is in practice a lack of linearity which is specially felt above 1.3 cps. This seems to be related to the already mentioned differences between experimental and Kennard surfaces in the shorter periods and is probably caused by energy losses due to the variations of velocity and acceleration that occur in irregular waves.

4.2 - Experimental tests with non-permanent paddle movements for comparison with theory

In the experimental test referred to in 3.2, with an impulse (test nº.101) records were made at distances x = 5 m, x = 19 m and x = 29 m. G(f) was computed by (4) for the three distances. All Fourier transforms including that of the input were calculated numerically.

Results are shown in fig. 9.

---

(1) -In fact there were greater upper limits, but the next one available was 5 cps, already too high to use as input for the actuator.

Let us consider for the moment only the 29 m G(f) values. It is seen that the experimental values while showing reasonable agreement until f ≈ 1.6 cps then fall well below the theoretically obtained ones. It should be noted that theoretically and in practice the input energy will not reach zero values before about 4 cps and that at 2 cps the input energy is still about 40 percent of its maximum. Thus it seems that the fall in G(f) values is real, above 1.6 cps, that is, it must be explained at least in part by a lack of linearity in the higher frequencies. Results from the experimental step shown also in fig. 5 were not good enough. The derivative of the function represented by the record was computed and then Fourier transformed to obtain an approximation of G(f) according to (10). Results, shown in fig. 8, were not good, probably because the width T = 0.27 s of the step was too large, although it was the smallest the equipment could produce. The theoretical step, which gave reasonable results, had one fifth of the width.

4.3 - Tests with non-permanent movements for studying the influence of certain parameters on the experimental gain function

4.3.1 - Variation along the flume

Fig. 9 shows the variation along the flume of the gain function G(f) as computed from records made at 5 m, 19 m and 29 m from the paddle in test no. 101 (fig. 5). There is a distinct dampening of G(f) as x increases which may be ascribed to energy losses in the wave propagation. The absolute values of the Fourier transform F(f) of the surface profile at each one of the three distances is shown in fig. 10. Another feature is the overshooting of experimental G(f) values at 5 m above the theoretical ones in the range 1.1-1.9 cps. This may possibly have one or both of the following explanations: (i) there is still turbulence in the surface at 5 m from the paddle in this case; (ii) on the one hand the B & S formula is not so well verified in practice, but on the other hand the energy loss along the flume is such that at 19 m and 29 m it brings down the G(f) values in a way which makes them approximate the theoretical curve. This needs further investigation.

4.3.2 - Variation with impulse parameters

Besides the experimental impulse of test no. 101, other experimental tests were made with impulses with different values of H and T. In table 1, these tests are summarised.

This table shows that the impulses of tests 102, 103 and 104 are proportional to that of test 101 and so if the system $\{x(t), y(t)\}$ is linear then the resulting surface profile should be the same, only with a different scale of elevation. That this was indeed approximately so is reflected in the fact that variations in the corresponding G(f) values are but small, fig. 11.

Table 1 - Experimental impulse inputs used

Test no.	H (cm)	T (s)
101	3.16	0.536
102	2.46	0.536
103	2.05	0.536
104	1.62	0.536
105	3.54	0.760
106	3.98	1.04
107	4.00	1.36
108	3.91	1.76

The result of using impulses with successively larger T, as in tests 101, 105, 106, 107 and 108 is shown in fig. 12. The larger the T, the sooner the fall in the G(f) values. This is explained by the fact that wide impulses are poorer in the higher frequencies. In fact it can be shown that the impulse input energy falls down to zero when f reaches the value $\frac{1}{2T}$. This value is about 4, 2.6, 2.0, 1.5, 1.1 cps, respectively, for the five tests, and it is seen that the last three are still within the frequency range of interest. On the other hand, while the zero value for the impulse of test no. 101, which had the smallest width possible, is not reached before 4 cps, the G(f) curve is still below the theoretical curve for $f > 1.6$ cps and so, lack of linearity seems to play a part in this fall; it would be interesting to see curves for narrower experimental impulses if it were possible to obtain them, which it is not, owing to mechanical and hydraulic limitations.

4.3.3 - Variation with water depth

As mentioned in the introduction, the water depth used for all the tests described was 0.50 m. However, tests with impulses similar to that of test no. 101 have also been made for other depths. Fig. 13 shows G(f) computed by (4) for x = 29 m and for depths d = 0.20, 0.30, 0.40, 0.50 and 0.80 m. The B & S curves for 0.20, 0.50 and 0.80 m are also indicated for comparison.

Non-linearity is apparent at all depths especially at the shallower ones, where deviation of experimental G(f) values from B & S curves is evident at all frequencies. Thus for each surface spectrum to be used in tests, the corresponding input will probably have to be determined by successive approximations, possibly starting with the experimental G(f) obtained through the use of a narrow impulse input.

In the higher depths there is however a reasonable agreement between experimental G(f) points and the B & S curves in the lower frequencies, that is, the system may be considered for these frequencies as approximatively linear. In fact, d'Angrémond & Van Oorschot (1969) report good results using the B & S curves for a depth of 0.40 m. The spectra they used had only a small percentage of their energy out of the range where for that depth non-linearity is more strongly felt. It is interesting to note, however, that they also report somewhat lower values than expected in the output spectra for the higher frequencies, which is in accordance with the fall observed in all experimental G(f) values after 1.5, 1.6 cps.

5. CONCLUSIONS

A summary of the more important conclusions drawn in preceding sections is:

- The linearised equations of Hydrodynamics from which the B & S curves were derived for sinusoidal movements imply that the system $\{x(t), y(t)\}$ is linear and so those theoretical curves should apply even for non-sinusoidal movements whenever the linearised equations are a good model for water waves. In practice it was found that non-linearity of the system was present at all depths especially at the shallower depths and higher frequencies. However, in many cases where higher depths and lower frequencies, only, are of interest it is to be expected that the mentioned non-linearity will not prevent the validity of the use of an approximate gain function possibly coincident with the ascending branch of the B & S curves.

- In what concerns variation along the flume a slight decrease in the wave energy was detected as distance from the paddle increased.
- Non-permanent paddle movements of the impulse type were found to be quite convenient for these gain function studies both for use with Kennard's formula and for experimental tests. As expected narrower impulses produce better results and so the narrowest impulses compatible with mechanical and hydraulic limitations should be used.

6. BIBLIOGRAPHY

1. BIESEL, F.and F.SUQUET - Les appareils générateurs de houle en laboratoire, La Houille Blanche, nos. 2, 4, 5 - 1951, 6 - 1952.

2. D'ANGREMOND, K.and J.H. VAN OORSCHOT - Generation of irregular waves on model scales, Proceedings of the Symposium Research on Wave Action, Delft Hydraulics Laboratory, Delft, the Netherlands, 1969.

3. KENNARD, E.H. - Generation of surface waves by a moving partition, Quarterly of Applied Mathematics, vol. 7, No. 3, 1949.

4. MADSEN, O.S. - Waves generated by a piston type wavemaker, Proceedings of the Twelfth Coastal Engineering Conference, Washington, 1970.

5. TICK, L.J. - Conditional Spectra, Linear Systems and Coherency, Proceedings of a Symposium on Time Series Analysis, edited by M.Rosenblatt, John Wiley and Sons, Inc, New York, 1963.

6. DAS, M.M. and R.L.WIEGEL - Water waves generated by horizontal motion of a vertical wall, Tech. Rep. HEL 16-7, University of California, Hydraulic Engineering Laboratory, Berkeley, 1971.

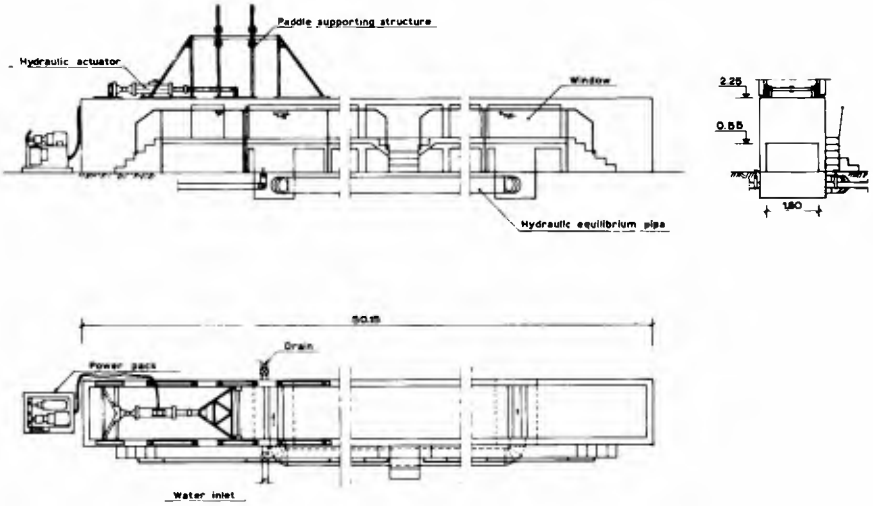

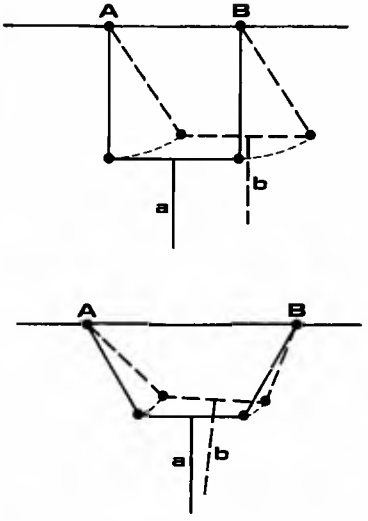

Fig. 1 - Irregular wave flume

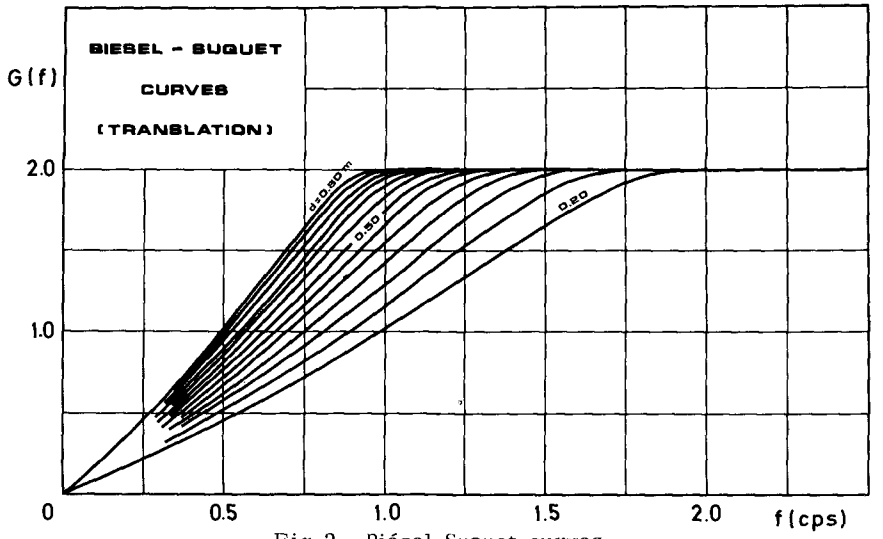

Fig. 2 - Biésel-Suquet curves

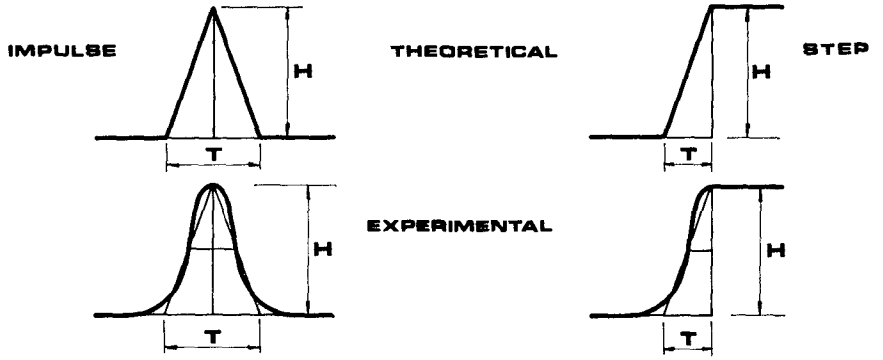

Fig. 3 - Definition sketch for impulses and steps

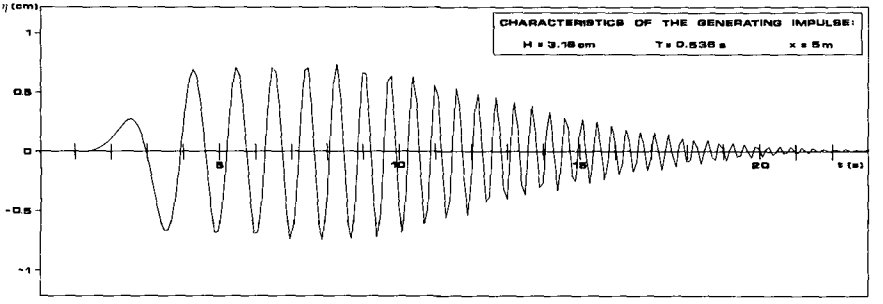

Fig. 4 - Kennard surface profile generated by an impulse

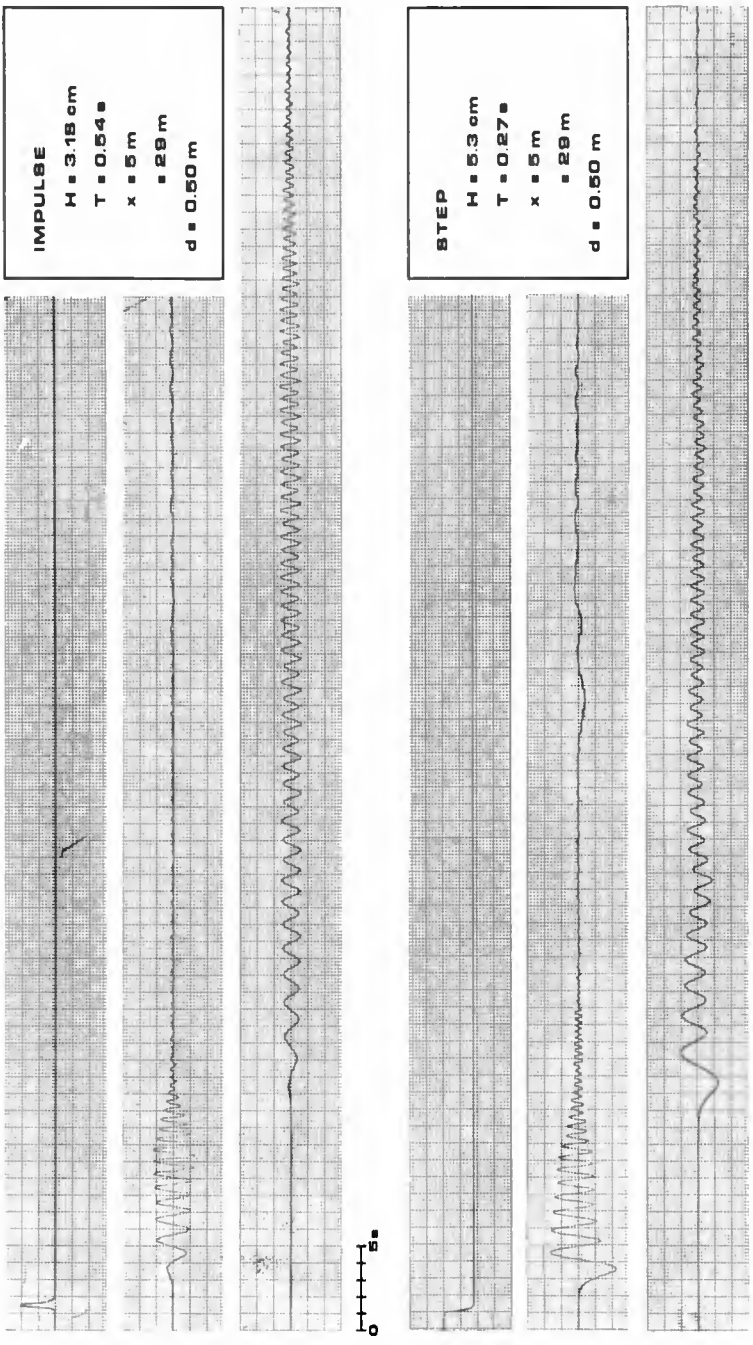

Fig. 5 - Experimental impulse and step and corresponding records

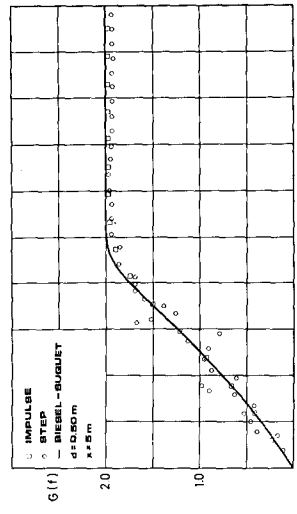

Fig. 6 - Theoretical gain functions from impulse and step compared with Biésel-Suquet curve

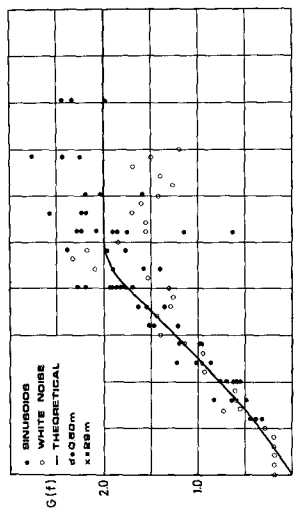

Fig. 7 - Experimental gain functions from sinusoids and white noise

Fig. 8 - Experimental gain function from step

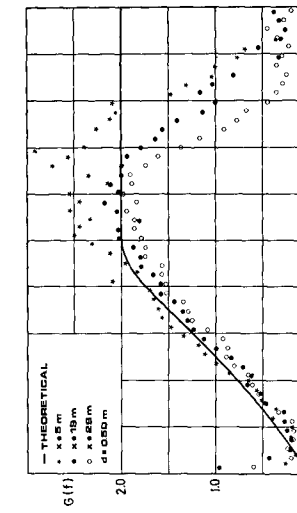

Fig. 9 - Variation of experimental gain function along the flume

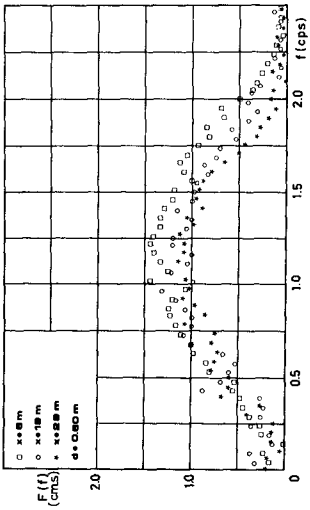

Fig. 10 - Variation of experimental surface Fourier transform along the flume

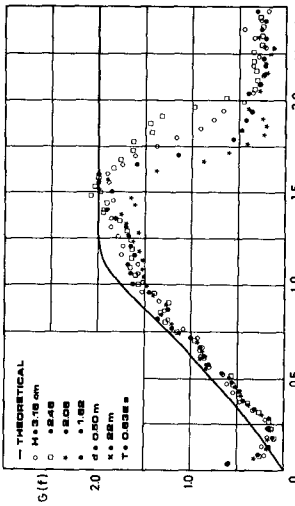

Fig. 11 - Variation of experimental gain function with impulse height

Fig. 12 - Variation of experimental gain function with impulse width

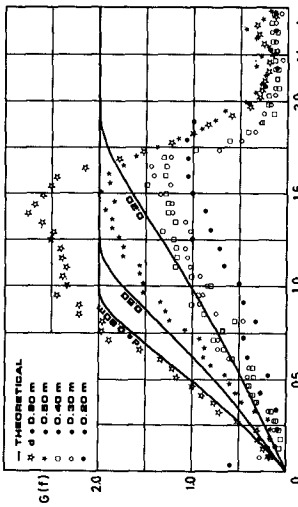

Fig. 13 - Variation of experimental gain function with water depth

Long Beach, Vancouver Island, B.C.

PART II

COASTAL SEDIMENT PROBLEMS

Breaker Beach, Vancouver Island, B.C.

CHAPTER 39

TIME-INTERVAL PHOTOGRAPHY OF LITTORAL PHENOMENA

by

Dennis W. Berg[1], M, ASCE

and

Eugene F. Hawley[2]

ABSTRACT

The collection of most data on littoral phenomena usually is based on the requirement of personnel and equipment actually being on-site for specific periods of time.

An approach to minimize this requirement involves the use of a photographic technique, using time-interval cinematography. Two such systems have been used at sites in California; Point Mugu and Newport Beach. This method incorporates commercially available 16 mm motion picture cameras with automatic lenses, remotely programmed to shoot selected lengths of film at predetermined periods during a day, everyday. At Point Mugu the camera, housed in a weatherproof enclosure mounted atop an existing 100-foot tower, records shoreline conditions, wave characteristics and existing weather twice a day for a period of 20 seconds per exposure.

The cameras are normally serviced on a weekly basis but are capable of longer unattended operation. To date this method has provided data which on preliminary anaylsis has revealed it to be of significant value for the purposes intended.

INTRODUCTION

In the last few years, increased use has been made of ground and aerial photography to provide a permanent record of the dynamic and interrelated forces that converge at the shoreline. The requirement for trained individuals to operate the wide variety of cameras and accessory equipment, and that the recorded image represents but a minute instant of time are the most serious drawbacks to such methods of documentation.

[1]Chief, Evaluation Branch, Engineering Development Division, U. S. Army Coastal Engineering Research Center, Washington, D. C.

[2]Hydraulic Engineer, Evaluation Branch, Engineering Development Division, U. S. Army Coastal Engineering Research Center, Washington, D. C.

In an attempt to provide continued documentation of the littoral zone, cinematography has been employed to record shoreline conditions over long periods of time. This method, called time-lapse photography (Beck, 1971), provides a number of still pictures taken at precise time periods but does not reveal in real time the rapidly changing forces that are present in the littoral zone. Time-interval photography similar to time-lapse photography but significantly different in its mode of operation, does reveal this dynamic interplay of forces.

Time-interval photography consists of taking motion pictures for a time period separated by another relatively longer time period. It thus differs from time-lapse photography in the number of actual frames exposed. Figure 1 illustrates this comparison. Its advantage is that for areas of interest where motions of the subject occur over very short periods of time, such as wave action, the motion is documented. Because of the time period between exposures, excess film is not used indiscriminately and economy is achieved as in time-lapse photography. Also, it enables the time history of a subject to be compressed and easily reviewed in a matter of minutes versus normal cinematography which could require hours for similar periods of observation.

The U. S. Army Corps of Engineers has employed this system of photography to document shoreline conditions and littoral forces at two locations in southern California. The Coastal Engineering Research Center (CERC), in a comprehensive study of the functional effects of groins, has used a time-interval photographic system to supplement those methods usually used to document shoreline and sea surface conditions. This field study, entitled Prototype Experimental Groin (PEG), located near Point Mugu, California, has been in operation since the spring of 1969 and film has been collected for nearly the entire period of time. The U. S. Army Engineer District, Los Angeles, has used a similar system to collect data on a beach erosion control project at Newport Beach, California, for approximately two years.

EQUIPMENT

Basically, the system of time-interval photography depends on the use of a relatively precise 16 mm motion picture camera with an automatic lens, a self contained power source, a timing device to actuate the camera, and a suitable housing to protect this equipment from the corrosive atmosphere of the coastal environment and vandalism. Other than these considerations, the system merely requires coordination of commercially available equipment to attain the desired objectives. The two systems employed by the U. S. Army Corps of Engineers are similar, though each uses different components. Detailed descriptions of each are presented.

A. Prototype Experimental Groin (PEG), Point Mugu, California

1. Location of Installation. The Prototype Experimental Groin (PEG), Point Mugu, is located on property of the U. S. Pacific Missile Range,

Point Mugu, California. This site, approximately 60 miles northwest of Los Angeles and 10 miles downcoast of Port Hueneme. A description of the PEG project has been made by Riese (1971) and the U. S. Army Engineer District, Los Angeles (1968). This area is one of active longshore material movement and is near the site of a major U. S. Army Corps of Engineers project where sand bypassing operations across a submarine canyon have been in progress since 1953 (Savage, 1957, Herron and Harris, 1966).

An oblique aerial photograph of the PEG field site is shown on Figure 2. The location of the remotely operated time-interval camera is on top of a 100-foot tower situated on the back beach area. The camera is oriented seaward and diagonally downward to include a view of the experimental structure, approximately 600-feet of shoreline and the nearshore water surface. A typical view as seen by the camera is shown in Figure 3.

2. Basic Components. The time-interval photography system employed at this site utilizes the following equipment:

(a) Bolex, model H-16, Rex 4, 16 mm motion picture camera.

(b) Vario Switar 86 EE, automatic zoom lens. Zoom range 18 to 86 mm, angle of view 34° to 5.2°, maximum aperture f/2.5, minimum aperture f/16.

(c) Bolex Perfectone Motor. This motor runs the camera at a synchronous 24 frames per second.

(d) Power supply; two systems are available: a portable 12 VDC battery pack and a 110-120 VAC to 12-13 VDC converter.

(e) CERC designed intervalometer.

(f) CERC designed weatherproof aluminum shelter.

Detailed information on this photographic equipment is published in Paillard Incorporated Catalogue (1966) and the Professional Photographic Catalogue (Fuller and d'Albert, Inc. 1971).

Figure 4 shows the combined camera, lens and motor. Components of the power supply have been combined with the intervalometer, and a schematic of this portion of the system is shown as Figure 5. (A list of parts used in this installation is attached as part a. of Appendix I.) A photograph of the completed unit is shown as Figure 6.

As mentioned in the list of equipment, an all weather enclosure made of aluminum was designed to provide protection of the basic equipment. It is a 2-foot cube, all welded unit with a flanged hatch for access, and a 6-inch viewing port for the camera. This port, protected by plexiglass and a movable door, provides the window for the camera. The interior of the enclosure has been lined with a 2-inch thick layer of polyurethane foam to provide insulation and vapor barrier for any possible passage of humid air. Figure 7a shows initial stages of construction of the enclosure; Figure 7b presents the completed product, ready for field installation.

2. Mode of Operation. As designed the intervalometer allows the selection of up to and as many as 24 different periods of operation per day. Since the film selected for use and the automatic lens of the camera require sufficient ambient light for operation, the actual number of exposure periods are restricted to daylight hours, normally from 2 hours after sunrise to 2 hours before sunset.

Once the time(s) of exposure(s) has been selected the entire operation then becomes automatic. At the selected hour(s) the timer energizes a motor which opens the door of the camera view port; furnishes electrical power to the camera; allows the automatic iris of the lens to adjust to ambient light; starts the camera motor, which in this case runs for 20 seconds, exposing 480 frames of film; then turns off the electrical power to the camera; closes the view port door and recycles the timing mechanism to its start position. It is then ready for the next programmed exposure whether it is 1 or 24 hours later. The entire sequence of operation actually takes approximately 3.5 minutes of which 20 seconds are used for film documentation.

The period of programmed exposure may be varied from 10 to 30 seconds. Because the camera has only the capacity for 100-feet of film the 20 second exposure period was selected, enabling approximately 8 days of unattended operation with one exposure period taking place each day.

B. Beach Erosion Control Project, Newport Beach, California

1. Location of Installation. The Beach Erosion Control Project; Newport Beach, California, is located some 50 miles southeast of Los Angeles. It is an area of intensive shoreline development and the beach is used extensively for recreational purposes. Deterioration of the shoreline has required the reconstruction and periodic sand nourishment of the beach. Subsequent installation of a groin system to stabilize the beach has provided protection for the developed residential area and necessary room for beach recreation. A detailed description of this project and adjoining area has been published by the U. S. Army Engineer District, Los Angeles (1972).

An oblique aerial photograph of the study area for the time-interval camera installation is shown as Figure 8. The camera is located on the top of a 40-foot telephone pole and is oriented to view the beach, nearshore water surface and groin system in a northerly direction. A typical view as seen by the camera is shown in Figure 9.

2. Basic Components. The time-interval photography system employed at this site utilizes the following equipment:

(a) Beaulieu, Model R16, automatic 16 mm motion picture camera.

(b) Angenieux 4 x 17 automatic zoom lens. Zoom range 17 to 68 mm, angle of view 41° to 11° maximum aperature f/2.2, minimum aperature f/22.

(c) Power supply; Beaulieu Model R16 electric handgrip with rechargeable battery and 110-120 VAC.

(d) U. S. Army Engineer District, Los Angeles, designed intervalometer.

(e) U. S. Army Engineer District, Los Angeles, designed camera enclosure.

Detailed information on this photographic equipment is published in Beaulieu R16 Instruction Manual and Professional Photographic catalogue (Fuller and d'Albert, Inc. 1971).

A schematic of electrical circuitry of the camera, intervalometer and power supply is shown on Figure 10. A photograph of the assembled unit is shown as Figure 11.

The enclosure used in this installation is a modified electronic equipment cabinet that, although not completely weatherproof, has provided sufficient protection over extended periods of time. It is insulated with styrofoam and screen type filters for temperature control and exclusion of humid air. A list of parts used in this installation is attached as part b. of Appendix 1.

3. Mode of Operation. Similar to the mode described for the preceding site, this installation differs only in the length of exposure. Because of the selection of time delay relays, the exposure time is limited to 8 seconds.

EXAMPLES OF DATA

Installations of equipment of this type are overly comprehensive of the data recorded. Usually there will be more information available than planned for; much of which could possibly be used in other analyses. Each investigator will, by design, be interested in a selected number of parameters and ignore a number of others visible in the film. The fact that with proper care the film will last indefinitely allows other investigators to review the film innumerable times, each to his own satisfaction. The two installations described are intended to record littoral forces and responses of the shoreline; however, there is additional data recorded for purposes other than those intended, such as recreational use of a beach, the number of people present on the beach, and recording construction progress of shore protection structures.

A. Prototype Experimental Groin (PEG), Point Mugu, California

The original intention of the camera installation was to qualitatively document wave climatology of the area, shoreline responses, and the functional effects of a littoral barrier in retaining materials. These data are to supplement that obtained by conventional means which normally are obtained at much longer time intervals than those prescribed for the camera.

Detailed analysis of the photographic data is in progress. However, for the purpose of this paper an example of the type of analysis being made is presented. Table 1 shows data extracted from the film for the month of March 1972. From this table it can be seen that positive wave period (for a minimum

of two wave crests) can be determined; estimates of direction of wave approach, wave height and tide condition can be made. Additionally, should the area be used for recreational purpose, the number of persons and their activity can be counted and delineated. Less specific conditions of the beach and the nearshore environment are also recorded. Construction activity, weather conditions and visibility, outstanding beach features such as scarps and debris, types of waves which are breaking on the beach are a few examples noted.

Correlation of the data shown in Table 1, especially that of wave conditions was made from independent sources and shows strong agreement. If no other source of data were available it would prove invaluable; in this example it allowed data normally obtained by observers and/or electronic instruments which were either not present or missing because of equipment failures to be determined. Correlation and comparison of the data from two such sources reinforces the reliability of each.

At the present time, the functional response of a groin as it reacts to littoral forces has not been determined from the photographic data. Steps are being taken to apply mathematical solutions to this problem by rectification of the oblique view to that equal to a vertical view. This will enable direct measurements to be made. As presently envisioned this will not require true photographic rectification but simply measurements made on the viewed image which are then mathematically corrected to those which would appear in a vertical view.

B. Beach Erosion Control Project, Newport Beach, California

Data for the installation at Newport Beach, California, could be shown but the analysis would be similar for that shown in Table 1; therefore for brevity, detailed analysis will not be pursued in this paper.

OPERATIONAL PROBLEMS

For the most part minor operational problems have been encountered; those which have occurred are worthy of mention.

One problem has been that concerned with salt air corrosion of the various electro-mechanical parts. If care is not taken to prevent the free exchange of the atmosphere from the camera enclosure, such parts will readily corrode to a point where the equipment will not function properly. The addition of a low heat source within the enclosure (a 15-25 watt light bulb) or sufficient vapor barrier protection was found to be a solution to this problem.

The location of the camera installation and proper planning of the exposure interval and repetitive exposure sequence will reduce the problem of servicing the camera. Primarily such servicing is concerned with changing the film. A solution to this problem is, of course, the use of cameras with

larger film magazines than those used so far. Cameras having 400 and 800-foot capacity are available and will essentially extend the period of operation by a factor of 4 and 8 compared to those used to date.

Positioning of the camera equipment with the requirements for easy access and supplementary power, although not always easy, can be made easier if existing facilities can be utilized. In the case of the installation at Point Mugu, a 100-foot tower was available for the camera installation. At Newport Beach, a 40-foot telephone pole had to be installed. At first glance each seemed satisfactory, and in general each is, but climbing the tower in strong winds can be hazardous to personnel. If sufficient height can be attained in nearby buildings, access and enclosure problems can be reduced by using a window in the upper floors of the building.

To date, detailed mathematical analysis of film has proved extremely difficult because of the lack of a visible horizon in the field of view. If sufficient visual coverage can be attained while still maintaining the object of interest, and include a horizon, the analysis will be greatly simplified.

FUTURE IMPROVEMENTS

The rapid advances being made in optical surveillance and measurement systems can only enhance the methods described so far. Remotely controlled, closed-circuit television systems are presently in use for numerous purposes. Examples are monitoring passage of ships through locks, fish counting dams, monitoring instruments located at distant locations and recording man's endeavors on the moon. Application of such a closed-circuit television can allow many locations to be monitored and recorded at a single central location. The ability of panning, tilting and zooming in are all remotely controlled and should allow important occurrences to be recorded for later analysis. Should sequences recorded be of little or no value, rendered useless with time, or analysis completed, present systems allow reuse of the magnetic recording tape a distinctive financial saving over that using photographic films.

Until recently nightfall has restricted the use of cameras and television. Recent advances in light amplification systems (GTE Sylvania, 1972) are becoming available which now allow available light, moonlight, starlight, earthshine and infra-red radiations to be used as the sole source of illumination. These devices, although costly, do allow night observation of the parameters previously described, where at present few comprehensive instruments recording during this period of the day can be compared to the visual image.

Applications of remotely controlled closed-circuit television and camera systems using light amplification devices can add information to that which is presently being collected.

CLOSURE

Use of a camera as a scientific tool for recording pertinent data have been established (Janke, 1972). The applications described have shown it to be a useful complement to the usual and accepted methods of recording littoral phenomena and in some instances a supplement to those methods or sole source of data. Increased use will allow expanded coverage, with a greater time base, of the littoral environment and the forces which converge at the shoreline.

"Data presented in this paper, unless otherwise noted, were obtained from research conducted by the United States Army Coastal Engineering Research Center under the Civil Works research and development program of the United States Army Corps of Engineers. Permission of the Chief of Engineers to publish this information is appreciated. The findings of this paper are not to be construed as official Department of the Army position unless so designated by other authorized documents."

"The contents of this paper are not to be used for advertising or promotional purposes. Citation of trade names does not constitute an official endorsement or approval of the use of such commercial products."

Table 1. Data obtained from time-interval camera, P.E.G. Pt. Mugu, Ca.

March 1972

Day	Time	Breaker Period	Wave Direction	Surf Condition	Tide Condition	No. of Surfers in Area	Comments
1	0900	-	-	-	-	-	-
	1500	-	-	-	-	-	-
2	0900	-	-	-	-	-	-
	1500	-	-	-	-	-	-
3	0900	-	-	-	-	-	-
	1500	11.0	WSW	2	L-	0	Clear, Sunny; Large beach scarp.
4	0900	8.5	WSW	3	H+	0	" "
	1500	9.5	SW	2	H-	0	Clear, Sunny; Beach scarp.
5	0900	0	0	0	0	0	Fog, zero visibility.
	1500	13.8 (?)	0	0	0	0	Fog, limited visibility.
6	0900	16.8	SW	2	0	0	Fog, Visibility 700-800feet.
	1500	16.6	SW	1	H-	0	Overcast, good visibility; Beach scarp.
7	0900	13.1	SSW	1	H+	0	Haze, visibility 2500 feet; Beach scarp.
	1500	17.2	SSW	1	H+	0	Overcast skies; Beach scarp; Observers on beach.
8	0900	18.5	SW	1	H-	0	Overcast skies; Beach scarp flattening.
	1500	19.3	SW	1	H-	0	Clear, Sunny; Beach scarp flattening.
9	0900	13.2	SSW	1	H-	0	" "
	1500	14.2	WSW	2	L-	0	Clear, Sunny, Strong offshore wind.
10	0900	15.6	SW	2	L-	0	Clear, Sunny; Slight beach scarp.
	1500	13.6	SW	3	L+	0	Clear, Sunny; Observers on beach.
11	0900	0	0	0	0	0	Fog, Visibility 600-700 feet.
	1500	13.7	SW	1	L+	0	Fog, Visibility 1500 feet.
12	0900	17.3	SW	3	H+	0	Overcast skies, Rain (?); Beach scarp.
	1500	14.0	SW	4	L-	8	Overcast skies, Waves have overtopped berm.
13	0900	12.1	SW	2	H+	0	Overcast skies, Slight haze, Beach scarp.
	1500	17.3	SW	2	L+	0	Overcast skies; Survey party on beach.
14	0900	13.3	WSW	1	H-	1	Overcast skies; Survey in progress.
	1500	12.3	SW	2	L+	0	Overcast skies; Survey in progress.
15	0900	6.6	SW	2	H-	0	Overcast skies, rain; Beach scarp.
	1500	19.3	SSW	1	L+	0	Overcast skies; Survey in progress; No scarp.
16	0900	15.7	WSW	1	H-	3	Overcast skies; Survey in progress; Wave overtopped berm.
	1500	-	SW	2	L-	0	Overcast skies.
17	0900	15.8	SW	1	H-	0	Overcast skies; Survey in progress.
	1500	6.2	SW	2	H-	0	Overcast skies; Survey in progress.
18	0900	12.0	SW	2	H-	2	Overcast skies; Slight haze.
	1500	9.8	SW	2	H-	0	Clear, Sunny.
19	0900	9.4	SW	1	L+	5	Overcast skies; Waves have overtopped berm.
	1500	15.6	SSW	2	H-	0	Clear, Sunny; Beach scarp.
20	0900	12.6	SW	1	L-	0	Overcast skies; Two people on beach.
	1500	15.8	SW	2	H-	2	Clear, Sunny.
21	0900	14.4	SW	2	L+	3	Overcast skies.
	1500	12.7	SW	2	H+	0	Clear, Sunny; Beach scarp.
22	0900	12.0	SW	1	H-	0	Overcast skies; Survey in progress.
	1500	6.5	WSW	1	L-	0	Clear, Sunny; Local wind wave; Kelp on beach.
23	0900	12.4	WSW	2	H-	0	Clear, Sunny; Large beach scarp.
	1500	14.3	SW	2	L-	0	Clear, Sunny; Large beach scarp.
24	0900	10.5	WSW	3	H+	0	Clear, Sunny; Observers on pier; Beach scarp.
	1500	6.8	WSW	2	L-	0	Clear, Sunny; Navy beach patrol; Beach scarp.
25	0900	11.8	SW	2	H+	0	Clear, Sunny; Navy beach patrol; Beach scarp.
	1500	7.9	SW	2	L-	0	Clear, Sunny; Large beach scarp.
26	0900	6.0	SW	3	H-	0	Overcast skies; Beach scarp.
	1500	5.5	WSW	3	L+	0	Clear, Sunny; Navy beach patrol; Beach scarp.
27	0900	7.0	WSW	3	H-	0	Clear, Sunny; Observers on pier; Large beach scarp.
	1500	14.4	WSW	3	H-	0	Clear, Sunny; Construction second groin begins.
28	0900	13.5	WSW	1	H-	3	Clear, Sunny; Scarp smoothing.
	1500	11.9	SW	1	L-	0	Clear, Sunny; Excavation for new groin.
29	0900	6.0	WSW	2	H-	2	Clear, Sunny; Plunging breakers.
	1500	6.7	WSW	2	L-	0	Clear, Sunny; Continued construction.
30	0900	13.8	SW	1	H-	2	Clear, Sunny; No scarp.
	1500	14.8	SSW	1	L-	3	Clear, Sunny; Welding taking place.
31	0900	10.0	SW	1	H+	0	Clear, Sunny; Driving sheet pile.
	1500	15.6	SW	1	L+	2	Clear, Sunny; Driving sheet pile.

NOTES
1. All times shown Pacific Standard Time.
2. Breaker period in seconds.
3. Wave direction from which waves are coming; Groin oriented in SW - NE direction
4. Surf condition qualitative using Beaufort Scale for Sea State.
5. Tide condition H+ Rising to high tide (flood)
H- Falling from high tide (ebb)
L- Falling to low tide (ebb)
L+ Rising from low tide (flood)

REFERENCES

Beaulieu Co., Operational Manual for R16 Automatic Camera, undated.

Beck, J. R., Use of Time-Lapse Photography Equipment for Hydrologic Studies: USGS Open File Report, September 1971.

Fuller and d'Albert Incorporated, Professional Photographic Catalog, 1971.

GTE Sylvania, Sociosystems Products Organization, Advertisement for Night Viewing Device: PMI Magazine, April 1972, pg. 75.

Herron, W. J. and Harris, R. L., Littoral Bypassing and Beach Restoration in the Vicinity of Port Hueneme, California: Proceedings of Tenth Conference on Coastal Engineering, September 1966, pp. 651-675.

Janke, N. C., Field Measurements with Common Equipment: Photogrammetric Engineering, Vol. XXXVIII, No. 1, January 1972, pp. 37-47.

Paillard Incorporated, Bolex H 8-H16, Camera Catalogue, April 1966.

Riese, R. C., Experiment in Shore Protection: The Military Engineer, Vol. 63, No. 413, May-June 1971, pp. 181-182.

Savage, R. P., Sand Bypassing at Port Hueneme, California: BEB Technical Memorandum No. 2, March 1957.

U. S. Army Engineer District, Los Angeles, Design Memorandum, General Design, Experimental Prototype Groin, U. S. Naval Air Station, Point Mugu, California, January 1968, Revised May 1968.

Design Memorandum for Stages 4B and 5 Construction, Beach Stabilization with Groins and Beach Fill at Newport Beach, Orange County, California, March 1972.

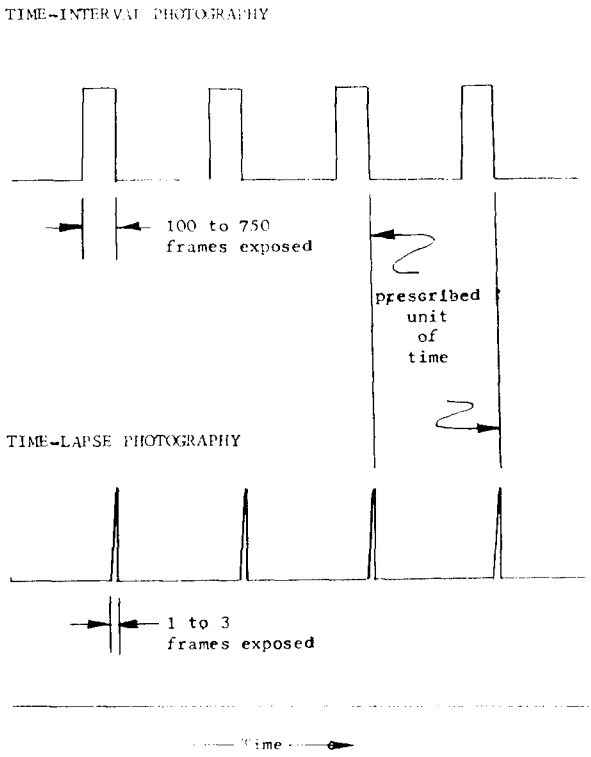

Figure 1. Comparison of time-interval and time-lapse cinematography, showing relation of time of exposure to time between exposures.

Fig. 2. Oblique aerial of CERC's Prototype Experimental Groin, Point Mugu, California

Fig. 3. Typical view of shoreline as seen by the remote time-interval camera, Point Mugu, California

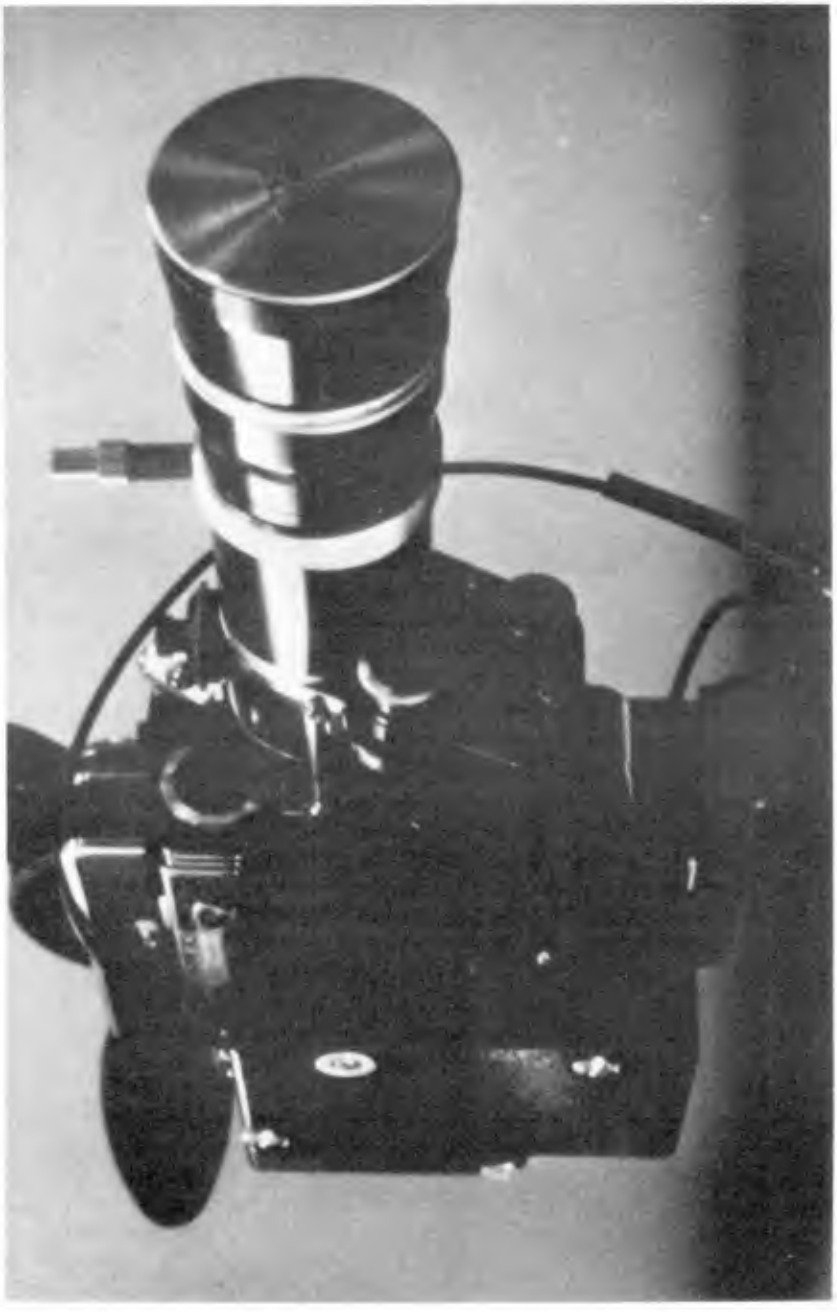

Fig. 4. View of CERC Bolex 16 mm movie camera used for time-interval photography

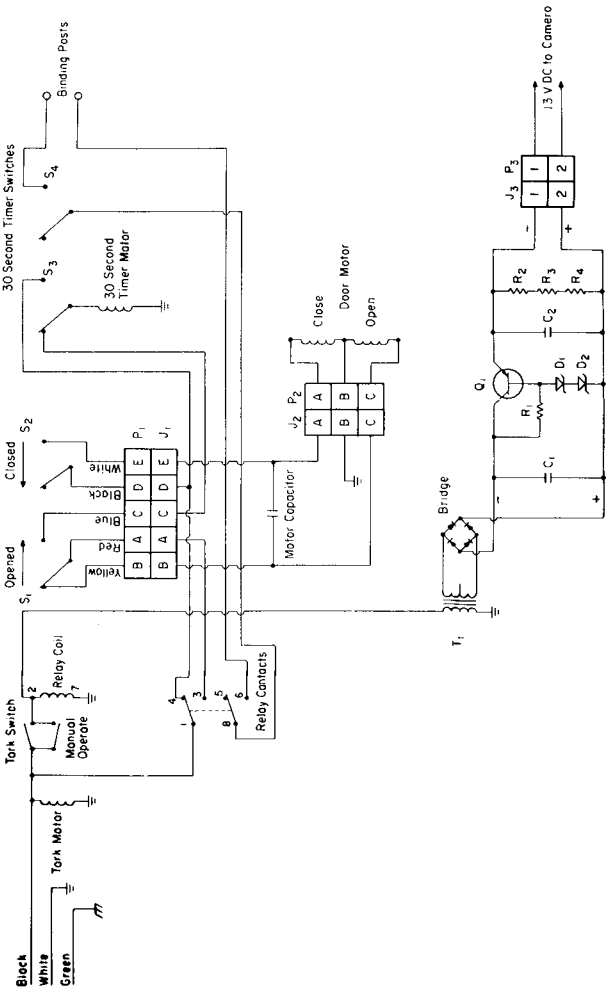

Fig. 5. Schematic of CERC time-interval photography camera, power supply and intervalometer

Fig. 6. Photograph of completed CERC time-interval photography, power supply and intervalometer

Fig. 7a. View of CERC time-interval photography weatherproof shelter in its initial stages of construction

Fig. 7b. View of CERC time-interval photography weather-proof shelter as installed in the field

Fig. 8. Oblique aerial of Newport Beach, California

Fig. 9. Typical view of shoreline as seen by the remote time-interval camera, Newport Beach, California

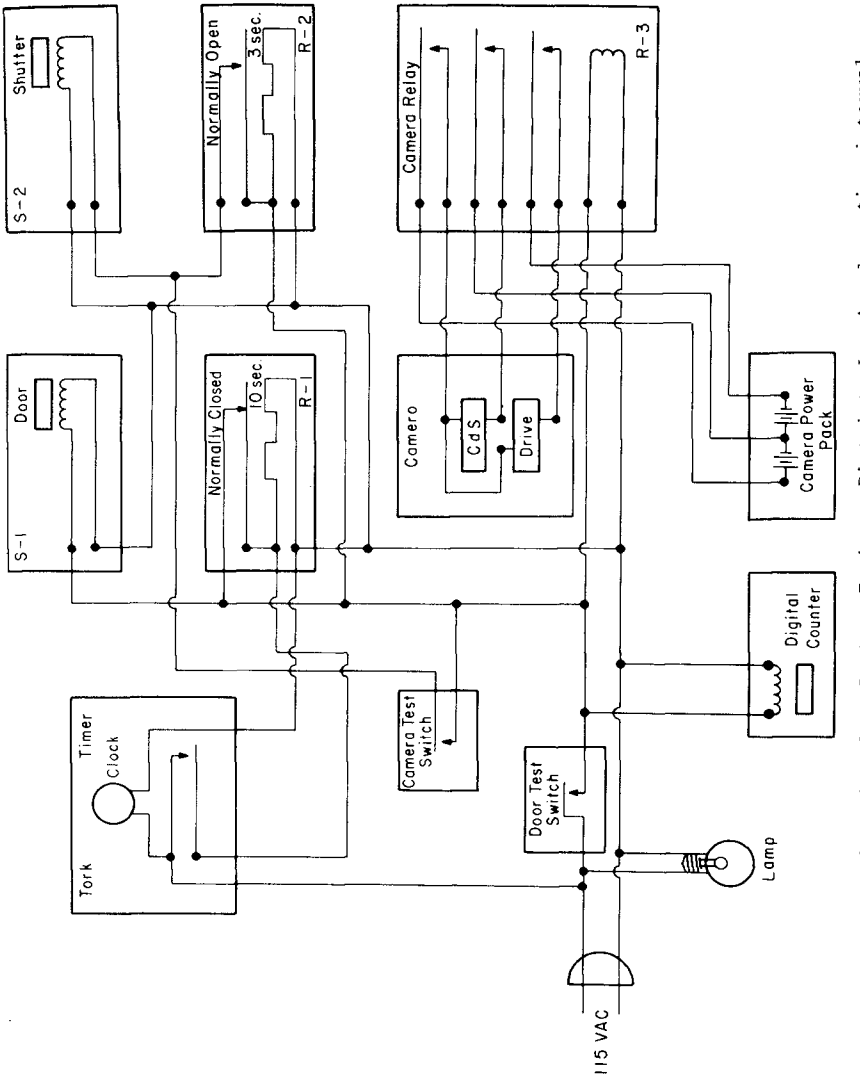

Fig. 10. Schematic of U. S. Army Engineer District, Los Angeles, time-interval photography camera, power supply and intervalometer

Fig. 11. Photograph of assembled U. S. Army Engineer District, Los Angeles, time-interval camera and accessories in enclosure

APPENDIX

A. List of electronic parts, time-interval camera, Prototype Experimental Groin, Point Mugu, California (refer to schematic, figure 5).

relay	Potter & Brumfield; No. KRP11AG
S_1, S_2 (door switches)	Robertshaw; No. BRD 2-2M
30 second timer	Industrial Timer Corp.; Mode 1MC-2
Door motor	Bodine 115 VAC, 60 cycle, single phase, 7.5 watts imput, 2 rpm, continuous duty, 95 oz. in, capacity 0.85 mfd, type KYC-22RC.
Motor capacitor	0.8-0.9 mfd; 220 VAC
J_1	Amphenol No. 145-55
J_2	Amphenol No. 165-16
J_3	Amphenol No. 80-PC2F
P_1	Cannon No. CA 3106 B145-5P-A105
P_2	Amphenol No. 165-13
P_3	Amphenol No. 80-MC2M
T_1	Triad No. F-25X, fillament 12.6 VCT
Bridge	Motorola No. MDA 952-2
C_1, C_2	Mallory No. HC-2060KK, 6000 mfd, 2 VSP
R_1	150-2
R_2, R_3, R_4	11-2, 5W
D_1	Motorola No. IN3016
D_2	Motorola No. IN3829
Q_1	Motorola No. 2N1544
Manual switch	Arrow Hart No. 81015AW

B. List of electronic parts, time-interval camera, Newport Beach, California (refer to schematic, figure 10).

S-1	Guardian switch 18 contact, 115 amp, 115 VAC
S-2	Control Corp. push solenoid No. 831-401, 115 VDC, 1"
R-1	Amperite time delay relay, No. 24F2329, 115 C 10
R-2	Amperite time delay relay No. 24F2329 115 No. 3
R-3	Potter & Brumfield, general purpose relay, 3PDT, No. 24F2893

CHAPTER 40

SEQUENTIAL PHOTOGRAPHY OF COASTAL WATER[1]

Maynard M. Nichols, Associate Professor
Virginia Institute of Marine Science
Gloucester Point, Virginia 23062

ABSTRACT

Sequential photographs from aircraft and satellites provide a source of data for studying dynamic features of coastal waters. Procedures for detecting features in sequential photos follow two approaches; (1) application of sequential signatures, (2) simple comparative analysis. For quantitative analyses images of two or more frames must have proper registration and comparable tones, i.e. tones free of photographic variance from film processing, varying exposure and solar illumination. After a normalization correction for variance is determined through use of density control points, density of successive frames is measured with a microdensitometer, the correction is applied and tonal differences determined. Such differences relate to the time character of a feature and to causal processes. Application of correction values and numerical differencing is best accomplished in a digital or computerized densitometer. However, corrections and differencing can also be accomplished graphically from line traces or plots of an objective densitometer. Application of the procedures is demonstrated by analyses of tonal patterns of suspended sediment concentration in an estuary.

INTRODUCTION

Coastal features are so dynamic, constantly changing in content and position in response to waves, tides and man-made stress, they are difficult to characterize and monitor over large areas. The scientist or coastal engineer is often faced with a number of questions, for example: How stable are the sedimentary materials of tidal inlets and estuaries? How can sediment pollution be detected? What is the circulation pattern and direction of sediment transport? What are the effects of storms and floods? - the environmental impacts of man in his effort to fill land and dredge channels? Many such questions can be answered by remote sensing techniques. Already satellites and repetitive aerial flights are capable of generating volumes of sequential photography but procedures for its analysis are not fully known.

---

[1] Contribution 493 of the Virginia Institute of Marine Science

For example, how can the tonal appearance of coastal water in aerial photographs be used to analyze their movement. This paper aims to show how temporal data can be extracted from sequential photography and reduced to useful information about the dynamic distribution of sediment suspended in coastal waters.

BACKGROUND

As defined by Colwell (1968), the term "sequential photography" pertains to photography taken of any given area at two or more different times. By comparing images in a sequence of photographs, certain time-dependent features may be detected or discriminated, changes evaluated and time-history determined. There are two principal aspects to utilizing the time element: (1) a "sensing" aspect in which the characteristic temporal variations of a feature's reflectance or emittance are used for detection and identification, (2) a change detection aspect in which differences in a feature's shape, position or tone from time to time are utilized to determine water movement or variations in load. Thus, sequential photographs may be used to sense changes in the amount of reflectance from the water as well as to determine varying position and shape of tonal anomalies.

Already a great deal has been accomplished with sequential photographs and related time-coverage. They are widely used for measuring shoreline changes (e.g. Stafford, 1971 and Moffitt, 1969), for visualizing flow in models, and for direct flow measurements by recording successive positions of moving targets (e.g. Waugh, 1963 and Waldichuk, 1966) or by application of a stereo time-lapse Cameron (1962). By utilizing satellite observations they provide information on movement of weather patterns (e.g. Sikdar and Suomi, 1971) and changes of terrestrial features (Sissala, 1972). At the present state of progress satellites and aerial flights are capable of generating volumes of sequential imagery but procedures for its analyses are not well known.

Rationale for sensing

The temporal character of coastal features emerges mainly from the periodic nature of coastal processes that affect a feature's size, shape and position, or its content and composition. Such time-dependent processes include wave action, rise and fall of the tide, ebb and flood currents, heating and cooling, melting and freezing, changes in marine aquatic or plankton populations. They present a wide spectrum of time scales panning minutes, hours, months and years, as illustrated in Figure 1. Variations with short-time scales and large geometric scales are most pronounced, e.g. those due to waves and tides, but any time variation that is characteristic and distinct should have diagnostic value.

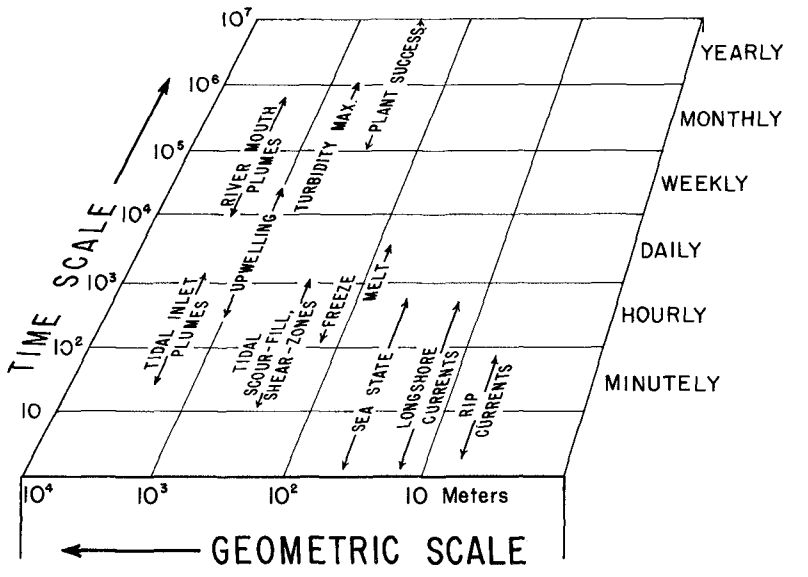

Figure 1. Time scales of some time-dependent coastal features at different geometric scales. Full range of geometric scale for each feature not shown.

Sequential Signatures

Time sensing is based on the fact that a feature reflects or emits electromagnetic energy with a specific and distinctive frequency or period. Just as spectral signatures are characteristic of a feature in multiband images so too "sequential signatures" are diagnostic of time-dependent features in repetitive imagery. At infrared wavelengths, time variations are mainly due to cyclic heating and cooling. Because contrasting coastal materials like mud, sand and water, differ widely in their heat capacities and radiative behavior diurnal changes are especially strong at wavelengths longer than 4μ. At visible wavelengths time variations are mainly due to changing reflectance. Figure 2 shows some examples of prospective sequential signatures developed from surface observations. But continuous measurements of reflectance or

emission with time in coastal waters are scarce; successive photographs yield incomplete signatures, and discrimination becomes difficult because signatures are susceptible to contamination by meterological events, by varying water "penetration" or sun glint, and by the dissipation of energy through different party of the temporal spectrum.

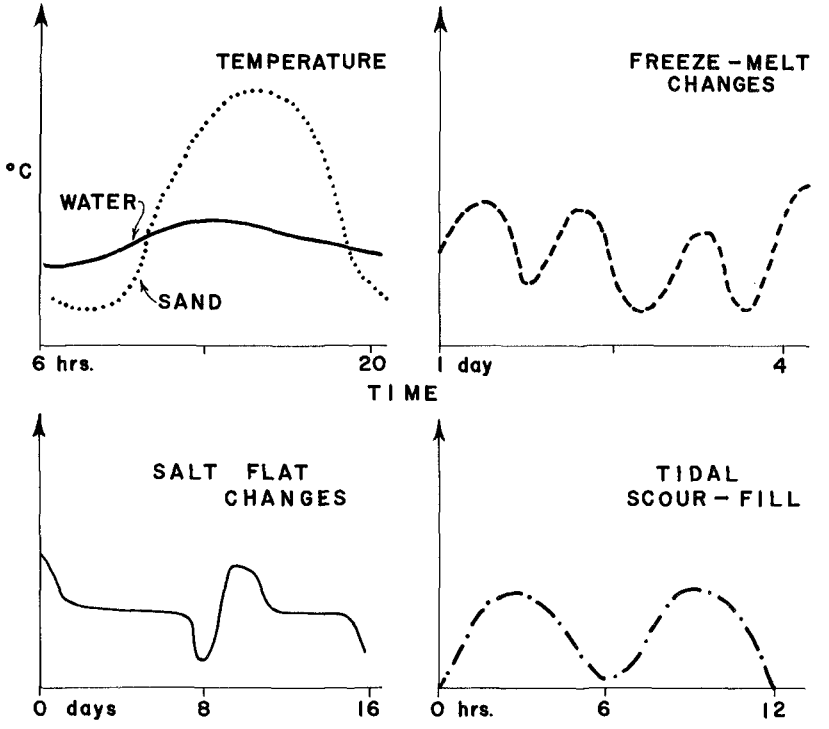

Figure 2. Examples of prospective sequential signatures developed from surface observations. Relative magnitude of reflectance (or emission) is directed along ordinate, time on abscissa.

MULTIPLE "LOOK" TECHNIQUE

A more fruitful approach for detecting time-dependent features is to compare successive photographs visually and identify features by simple photo interpretation. For example, the sequence presented in Figure 3 illustrates some dynamic features of a tidal inlet that are best identified through comparative analysis supplemented by surface observations. In the second photograph (0 hour) a large light-toned patch representing a plume of discolored water (p) extends seaward (to the right) off a tidal inlet through barrier islands. Breakers, recorded in very light tones (b), mark an area of shoals. But between the breakers and the plume proper light tones represent either reflectance from submerged shoals or from sediment suspended in the plume overlying the shoals. The two features cannot be differentiated, nor can growth or decay of the plume associated with tidal suspension or settling out be determined from a single photograph. But by comparing the photograph with others taken two hours before and two to four hours after, it should be evident that the plume was mainly dissipating along its seaward edge, except for a lateral extension (downward) at 0-hour (e). Light tone areas in the inlet mouth (m) persist throughout the series indicating relatively stable shoals, in contrast to the more transient tidal plumes. Various small scale patterns are also displayed, e.g. turbid rip plumes and whirlpool patterns, but a much shorter time scale is required for detection. Thus, a single time interval or "net" does not "catch" all features at all time scales. And the minimum time scale depends on the smallest time scale involved plus the diversity of other time-dependent features in the scene or "background".

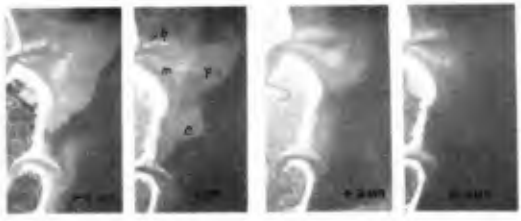

Figure 3. Sequential photographs of Ship Shoal Inlet, Virginia, U. S. East Coast, showing 2-hour variations in a sediment plume. For explanation of symbols see text. Black and white reproductions of 70mm color infrared aerial photos taken from 25,000 foot altitude, Oct. 12, 1971. Reproduction of tones necessarily varies from original. Tidal current is flooding at 0, +2 & +4 hours.

The multiple "look" method yields a maximal amount of information from large volumes of aerial photography. It is useful for qualitative evaluations of storm changes, for assessing ecological deterioration or growth and effects of dredging and filling operations. In practice, comparative analysis is facilitated by compiling composites of tonal information on an acetate overlay. Multiple image correlators such as the I²S Addcol used without color filters, enable viewing four or more sequential frames at a time in register. Features which cannot be identified from study of single photographs often are positively identified through comparative analysis of sequential photography.

TONE ANALYSIS

Image tone consists of variations of gray of "blackening" manifest in the film density. Film density depends mainly on the exposure received and the development time given the film. This relationship is illustrated in Figure 4, which describes the "characteristic curve" of the film for a given development time. Along the straight line portion of the curve (BC), densities increase proportionately to the log exposure whereas densities on the "toe" and "shoulder" do not. Thus, the level and range of density are partly controlled by exposure and developing time.

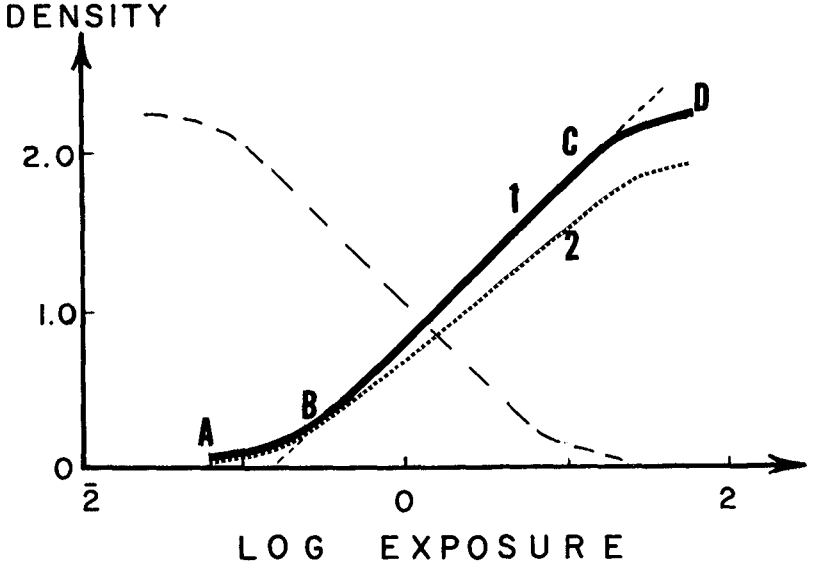

Figure 4. Characteristic curves of a photographic film; A-B is "toe", C-D "shoulder". Dotted curve (2) shows typical variance from ideal curve (1) due to developing time. Dashed line is typical curve of negative in contrast to positive solid line.

The tone or brightness of a feature in a photograph mainly represents the amount of reflectance recorded on the film. Such changes however, are influenced by many factors other than changes in reflectance of water itself with its variable load of particle backscatters. A part of the reflectance is due to changes of solar intensity and direction of incidence. Another part may be due to changes in atmospheric scattering or absorption, or to changes in surface roughness which affect reflection at the surface. Additionally, spectral reflectance of the water may change temporally with changes in depth or light penetration. In clear or shallow water, reflectance often varies with the amount of light backscattered from the bottom. Therefore, when a time-sequence of photographs is obtained, the reflectance recorded on the film is affected by variations in energy from the water surface, the water column as well as the bottom. Additionally, variations associated with optics and film characteristics or photographic processing must be taken into account. While all these factors appear to limit analysis, in practice they may be controlled or corrected within limits.

Analyses of sequential photography requires (1) proper image registration and (2) comparable image tones in successive frames. The chief procedural problem is to remove unwanted photographic and environmental variance and bring tones to a common datum.

Normalizing

To bring the density of two or more scenes to a common reference or datum for comparing transient tonal anomalies, it is necessary to normalize the density distributions. For accurate measurements a calibrated step wedge is exposed with each scene at the time of photography and processed to a 1:1 density-log exposure relation. However, wedge-film exposures are not commonly obtained in aircraft photography. As an alternate, panels of known reflectance are installed on the ground, or where not available, the reflectance of objects such as runways, or road surfaces is measured and their density values are used to construct a characteristic curve. Subsequently, densities in successive frames are adjusted by ratioing to what they would have been had each frame been processed to a 1:1 density-log exposure relation.

As an expedient a series of relatively stable objects are selected to serve as density control points. The densities of these points, which consist of common geographic points or identical objects in successive frames, are read in a microdensitometer and the average density difference of three or more points is applied, added or subtracted, to the densities of transient features in frames that require normalization. In practice, selection of suitable control points is critical to normalization. The following criteria are suggested:

1. Locate control points close to the transient feature that requires normalization. Avoid tonal fall-off in corners and

outer edges; locate points in central two-thirds of frame. In scenes with many prospective locations, a grid of points can be established and normalizing values applied throughout a series of reference quadrants.

2. Density of the points should cover a range that lies within the density range of the feature to be normalized.

3. Density of both the points and the feature to be normalized must fall within the straight-line portion of the characteristic curve.

4. Points must have "stable" reflectance characteristics, e.g. objects free of shadows, wind stirring, and relief. Paved runways, parking lots, or roadways are good; ponds and grass lawns are often stable.

5. Density within large "points" must be uniform.

Success of selecting control points can be checked by examining the range of differences between sets of points in successive frames. If optical characteristics of the normalized features are known from surface observations, differences from time to time should be proportional to corresponding density differences.

Positive-Negative Composites

A simple means of detecting tonal changes is to prepare a composite of oppositely matched positive and negative transparencies; i.e. a positive taken at time "1" and a negative taken at time "2". When tones are "matched", like images cancel out by contrasting bright-dark film density whereas unlike tones are displayed. Thus, differences are simply and effectively highlighted; and conventional enhancing techniques (Colwell, 1969; Ross, 1969) can be used to reveal subtle differences. Registration is accomplished by superposition on a light table but scale variations and geometric distortions often require correction. Matching tones of frames processed under different conditions is difficult and requires a great deal of patience in the dark room. However, frames exposed and processed under the same conditions, i.e. one roll at one time, can be matched by processing duplicate positive-negative frames to a 1:1 density-log exposure relation. This is accomplished by using a film, developer and developing time of known specifications that yields a 1:1 density-log exposure.

Comparative Densitometry

A microdensitometer is employed for quantitative analyses of tonal changes. Density control points are established, scenes singly read or scanned and the pre-determined normalizing correction applied. After the output is registered, differences are determined graphically or by computation, areas of change delineated and further related to causal processes as dictated by the problem. Figure 5

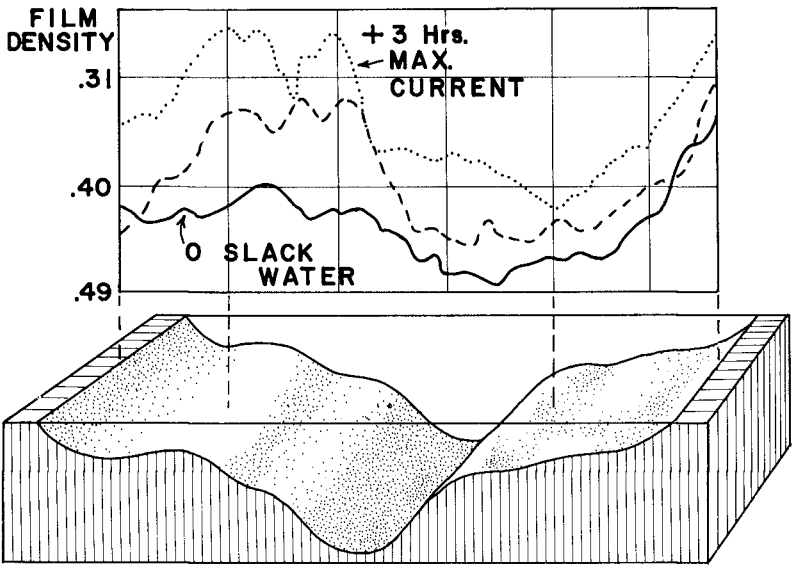

Figure 5. Graph of film density in a transect across the James Estuary, Virginia. Derived from Joyce Loebl microdensitometer tracing across frames 1, 2 and 3 reproduced in Figure 6A.

shows the distribution of film density at approximately 2-hour intervals across an estuary reach as illustrated in Figure 6A. It is in the form of normalized line traces derived from a Joyce Loebl microdensitometer. Differences between solid and dotted lines indicate the magnitude of density change, in this case a change due to differences in suspended load that varies with current strength. Outputs in the form of X-Y plots are treated similarly. Changes are revealed by comparing changes in the magnitude of density, by recording varying locii of maximum and minimum densities, or by examining the changing position of isodensity lines, their symmetry, character or axial position. Figure 6B shows the distribution of density change in surface water of the same reach shown in Figure 5. Changes from slack water to maximum current are greatest over the shoals.

Once a sequence of normalized density plots have been prepared many different sorts of analyses can be performed. Figure 7 gives the concept of a film density "stack" from which densities may be averaged or integrated over a given time span. A time "thread" through the stack at one point (small arrow) yields a time-distribution of film density representative of a sequential signature for suspended sediment concentrations that varies with tidal current velocity.

Figure 6A. Sequential photographs of a portion of the James River estuary taken at approximately 2-hour intervals, Oct. 12 1971. Reproduced from black and white red band photographs. Tones necessarily differ from originals due to reproduction and printing.

6B Distribution of density change between frames 1 and 3 above derived by computing density differences after normalization.

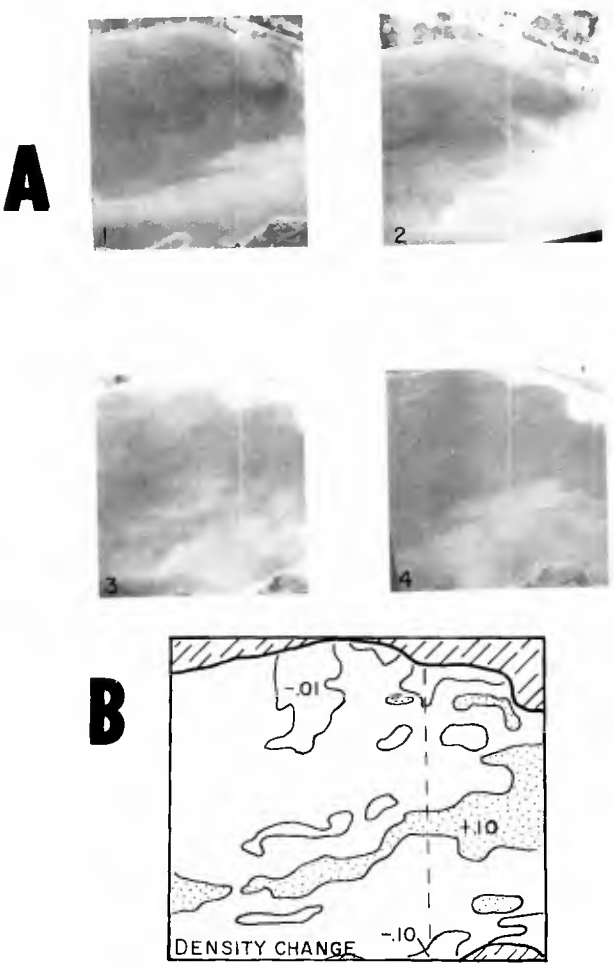

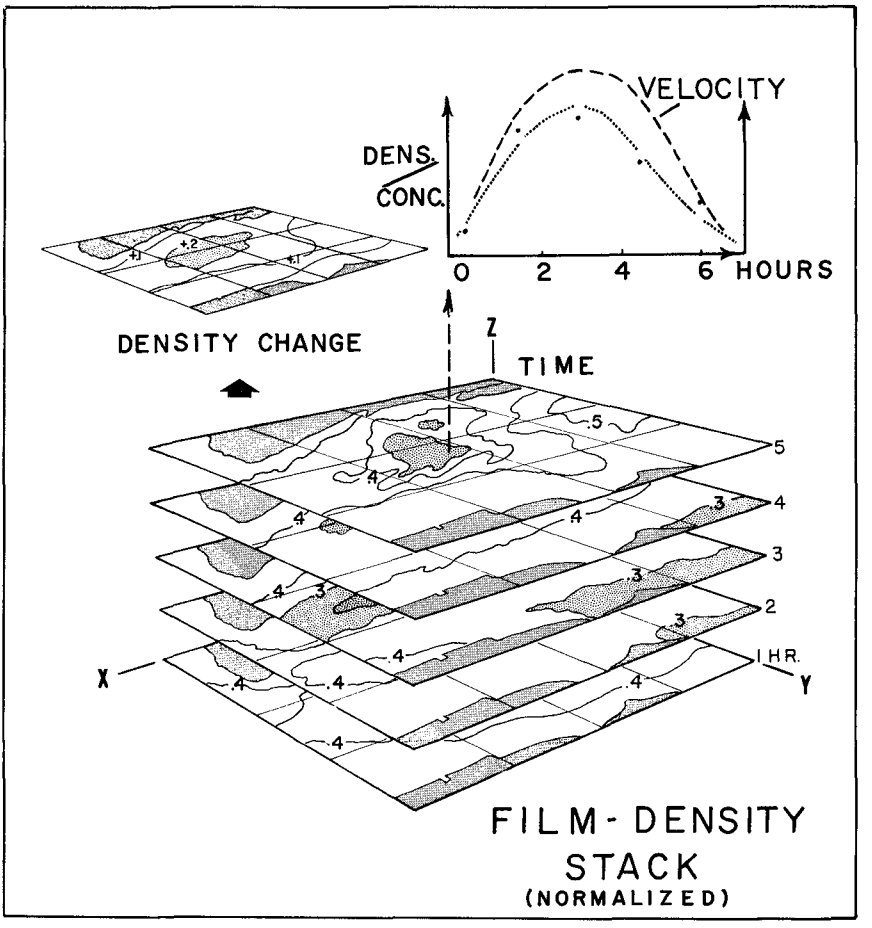

Figure 7. Concept of the film density "stack"; schematic. For explanation see text.

A great deal of comparative densitometry can be rapidly accomplished by employing an image scanning vidicon camera system such as the Spatial Deta Systems, "Data Color", or I^2S "Digicol". The equipment is most useful when extensive normalization or high resolution are not required. Two or more frames can be examined on a display screen at one time. The systems allow great flexibility in selection of density range and distributions that relate to surface observations.

Digital Densitometry

Normalizing film densities and computing differences, averages etc. of sequential photographs is best accomplished with a computerized system or a densitometer having a digital output. Densities, including both those of control points and transient features, are scanned, digitized and identified in a geographic matrix system prior to storage on magnetic tape in register. The computer is programmed to make density corrections and "change" computations as well as to electronically process photo-like displays of "change" distributions.

PROCEDURAL SUMMARY

Steps for analyzing sequential photos are summarized schematically in Figure 8.They are as follows:

1. Obtain photographs repetitively on the same flight line or track with the photos centered on the same image points to facilitate registration. Constant flying altitude and minimal aircraft and camera tilt are required, in addition to uniform time intervals and constant exposure-shutter speeds.
2. Process film in a single "batch" under controlled conditions and close to a 1:1 density-log exposure relation. A step wedge exposed on the head and tail of each roll provides a record to compare processing results from roll to roll.
3. Scrutinize film to determine if quality allows registration, density normalization and differencing.Geometric distortions may require rectification. If density level and range appear to preclude further analyses,some improvements may be accomplished by reprocessing duplicate transparencies.
4. Select density control points using criteria previously presented. Read film density in a microdensitometer and compute average correction values. Program corrections as necessary for normalizing subsequent outputs.
5. Scan film in a microdensitometer utilizing reference marks for subsequent registration of the output. Use the same instrument settings throughout each sequence taking into account the full density range of the sequence.

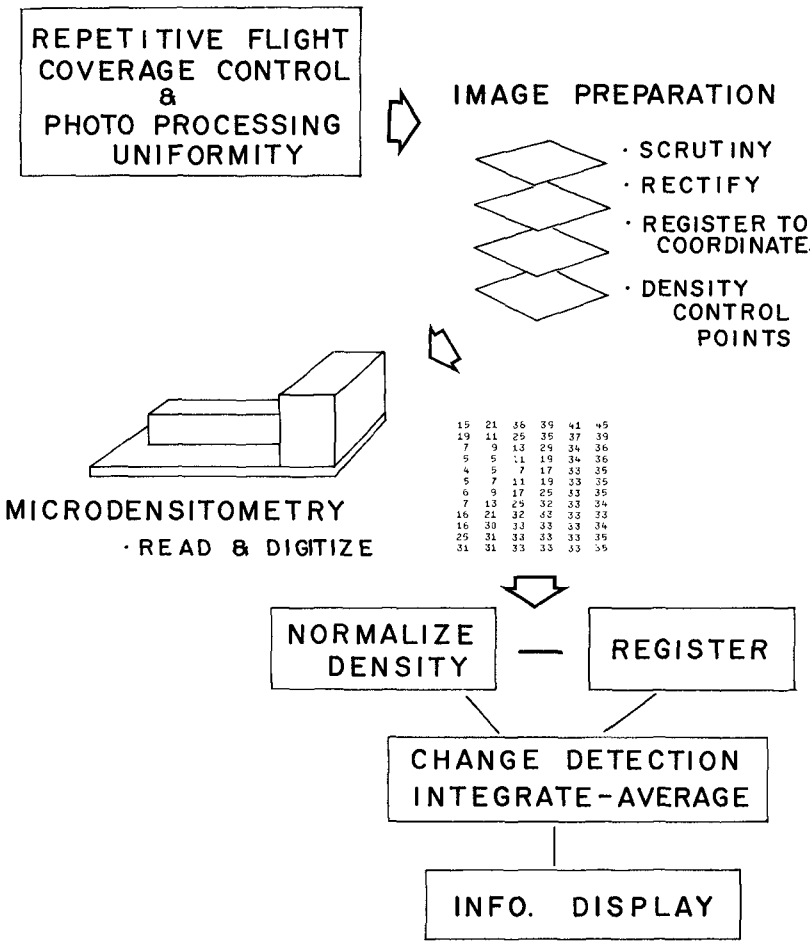

Figure 8. Schematic summary of procedural steps for densitometric analyses of sequential photographs. For details see text.

6.Apply normalization value to density distributions under examination.
7.Register frames to be compared utilizing predetermined reference marks.
8.Compute changes or averages as required.
9.Contour change distributions and relate to environmental processes or impacts as problem dictates.

ACKNOWLEDGEMENTS

This study is sponsored by the NOAA Space Craft Ocenography Project through the Geography Programs Office of Naval Research, contract N00014-72C-0268. Analyses were accomplished on equipment of the NASA Langley Research Center, the University of Virginia and the EROS program of the U. S. Geological Survey.

REFERENCES CITED

Cameron, H. L., 1962. Water current and movement measurement by time-lapse air photography. Photogrammetric Engr. v. 28, p. 150-163.

Colwell, R. N., 1968. Photographic studies and applications of the NASA Earth Resources Survey Program: NASA Earth Resources Aircraft Program Status R view. v. 2, p. 28-1 to 28-35.

Moffitt, F. H., 1969. History of Shore Growth from Aerial Photographs: Shore and Beach, v. 37, No. 1, P. 23-27.

Sikdar, D. N., Suomi, V. E., 1971. Time Variation of Tropical Energetics as Viewed from a Geostationary Altitude: Journal of the Atmospheric Sceinces, v. 28., p 170-180.

Sissala, J. E., 1972. The Utilization of the Various Time Scales of Meteorological Satellite Observations to Monitor Terrestrial Changes: Allied Research Associates, Inc., 18 p.

Waldichuk, M., 1966. Currents from aerial photography in coastal pollution studies: 3rd Intern. Conf. Water Pollution Res., Sec. III, Paper No. 13, 22 pp.

Waugh, J. E., 1963. Photogrammetric measurement of tidal currents: Jour. Sur. and Mapping, v. 3857, p. 17-29.

CHAPTER 41

HYDRAULICS AND SEDIMENTARY STABILITY OF COASTAL INLETS

by

M. P. O'Brien* and R. G. Dean*

ABSTRACT

A method is presented for investigating the stability of coastal inlets against closure due to transport and deposition of sand in the inlet cross-section. The method utilizes earlier contributions by: (1) Keulegan representing the hydraulics of inlets, (2) O'Brien which describes an equilibrium relationship between the cross-sectional area of an inlet and the bay tidal prism, and (3) Escoffier which relates to the stability of an inlet under changes in conditions which tend to close or enlarge an inlet. A "stability index" is defined which incorporates the buffer storage area available in the inlet cross-section, prior to the onset of closure and also includes the capability of the inlet to transport excess sand from its cross-section. In order to apply the method, geometric and hydraulic data representing the inlet are necessary; the minimum data required include a survey of the inlet throat cross-section and the lag between high (or low) water in the ocean and the following slack water in the inlet. In addition, it is necessary to conduct measurements or make assumptions concerning the minor and gradual hydraulic loss coefficients. Based on assumed depositional patterns in the inlet, the method is applied to five real inlets and the stability indices are presented.

INTRODUCTION

Some inlet-bay systems are inherently more stable than others against closure due to sand deposition in the inlet cross-section. It is clear that the larger and jettied inlets are generally more resistant to closure than the smaller and unjettied inlets. A review of the histories of various inlets show that some inlet-bay systems appear to be marginally stable, with closure generally occurring within a period of several years to a decade or more often after opening by severe storm activity. Other water systems separated by a barrier island from a tidal sea are closed soon after breaching. A better understanding of the hydraulics and sedimentary responses of inlets is necessary in order to improve capabilities in the design and maintenance planning of these coastal features.

The subject of the hydraulic and sedimentary characteristics of inlets has been one of a great deal of previous investigation. The classic paper of E. I. Brown[1] provides a lucid description of the processes of importance in

* Coastal and Oceanographic Engineering Laboratory, University of Florida, Gainesville, Florida 32601.

the vicinity of an inlet on a sandy coast and also presents an approach for calculating the hydraulics of tidal inlets. Brown's method considers the bay and ocean water level variations to be sinusoidal and the channel cross-sectional area to be constant with time. More recently, Keulegan[2] has extended the approach of Brown to include the effect of a non-sinusoidal bay tide; however, the other restrictions are the same. The methods of both Brown and Keulegan strictly apply for the case of a bay connected to the ocean by a single inlet and for a bay water level which rises and falls uniformly over the entire bay area, see Figure 1. Moreover, their considerations are limited to inlets forming a definite flow constriction, the discharge into and from the inlet being governed by a head loss which is quadratic in the velocity. For some large inlet features, such as the Chesapeake Bay Entrance,the flow is probably describable as due to a partial standing wave system. Keulegan's results include the phase lag between bay and ocean tides, and dimensionless values of maximum inlet velocity and bay amplitude; these results are presented as functions of the so-called "repletion coefficient," K, defined as

$$K = \frac{T}{2\pi a_o} \frac{A_c}{A_B} \frac{\sqrt{2ga_o}}{\sqrt{K_{en} + K_{ex} + \frac{f\ell}{4R}}} \qquad (1)$$

See Figures 2, 3 and 4 for the phase lag, ε, dimensionless velocity and bay amplitude. Other hydraulic studies of inlets include those of Baines[3], Van de Kreeke[4], Moto Oliveira[5], and Shemdin and Forney[6].

O'Brien[7,8] has presented data summarizing the relationship between the inlet throat cross-sectional area, and the tidal prism passing through that inlet during spring tide conditions. Very briefly, these results indicate that equilibrium conditions of an inlet are represented by a balance of the tidal prism tending to enlarge the cross-section and the supply of sand transported to the inlet by waves and currents tending to reduce the cross-section.

The relationship, shown in Figure 5 can also be interpreted as a unique relationship of maximum spring tidal velocity, V_{max}, versus inlet equilibrium cross-sectional area, A_{CE}.

Escoffier[9] has presented a concept of the stability of an inlet under the influences of depositional conditions which tend to enlarge or reduce the size of the inlet cross-section. The concept considers the maximum velocity in an inlet connected to a bay; this velocity varies with the inlet cross-sectional shape and area. A representative case is shown in Figure 6, in which it is seen that the V_{max} curve has a peak at some cross-sectional area, A_c^*. This curve applies only for one tidal range, whereas in nature, the ratio of spring to neap tidal ranges can vary from a reasonably small factor (1.2 at Miami Beach, Florida) to a much larger factor (18 at Pensacola Bay Entrance, Florida). Referring to Figure 6, the following will be shown:

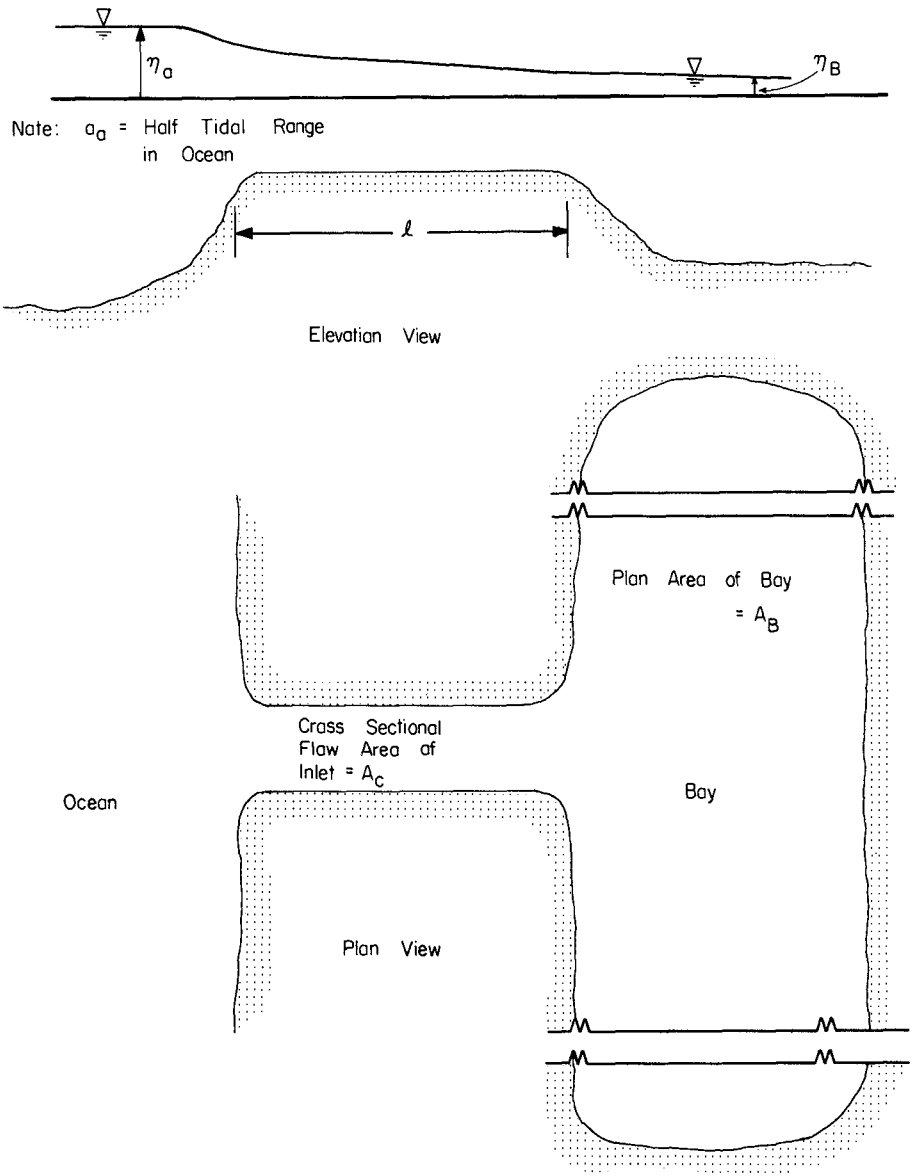

FIGURE 1. DEFINITION SKETCH OF INLET/BAY SYSTEM

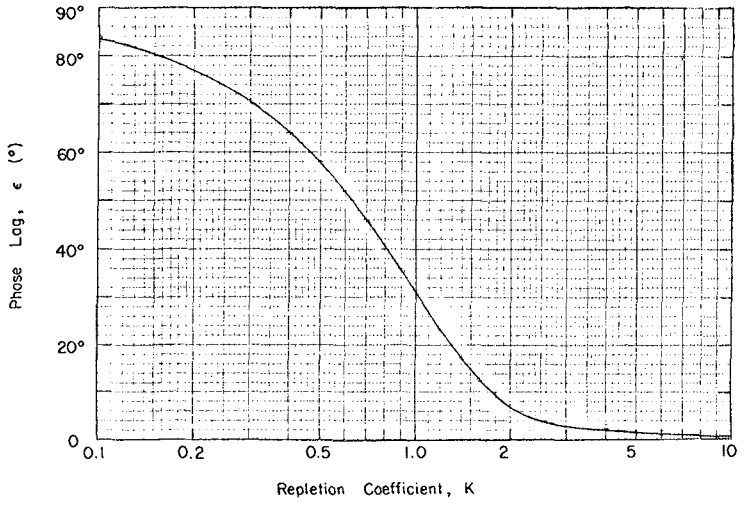

FIGURE 2. VARIATION OF PHASE LAG, ϵ, WITH REPLETION COEFFICIENT, K. KEULEGAN'S METHOD

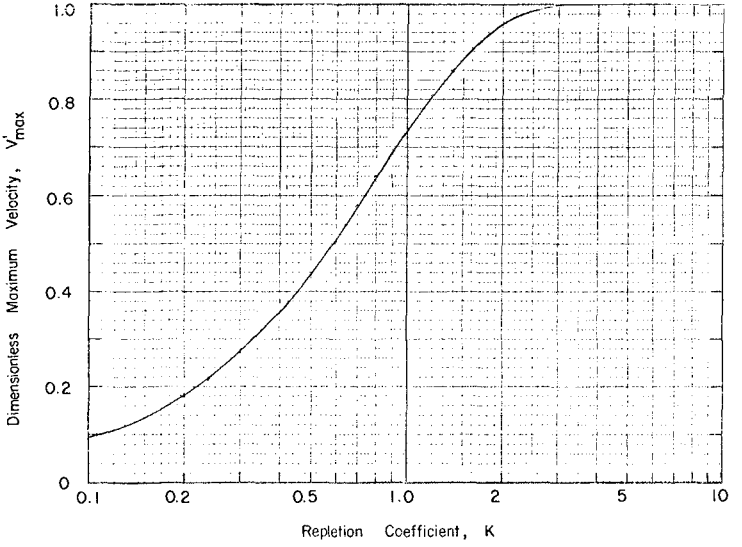

FIGURE 3. VARIATION OF DIMENSIONLESS MAXIMUM VELOCITY WITH REPLETION COEFFICIENT, K. KEULEGAN'S METHOD

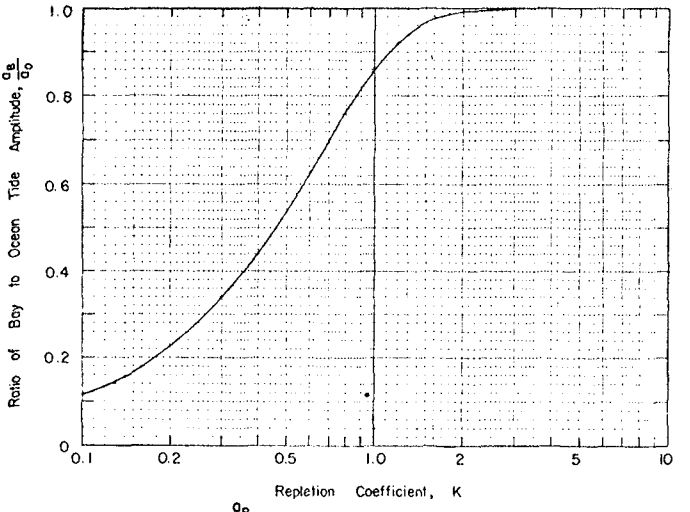

FIGURE 4. VARIATION OF $\frac{a_B}{a_o}$ WITH REPLETION COEFFICIENT, K. KEULEGAN'S METHOD

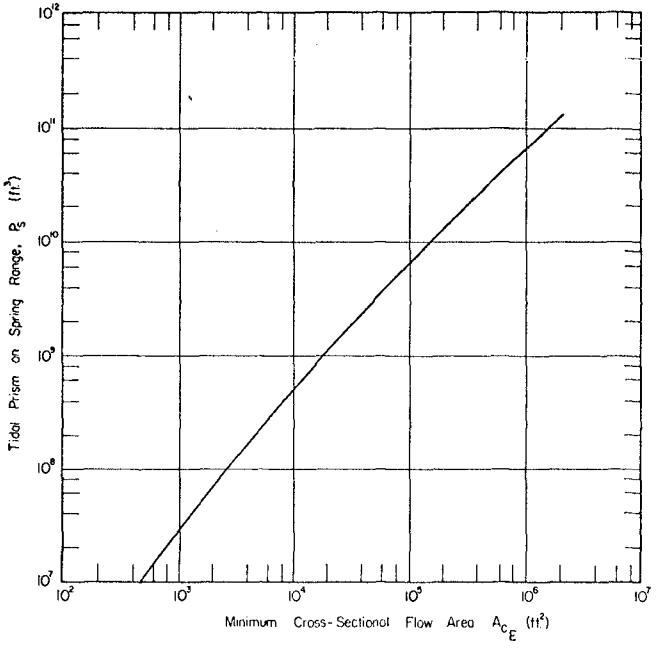

FIGURE 5. EQUILIBRIUM CROSS-SECTIONAL AREA AND TIDAL PRISM RELATIONSHIP (FROM O'BRIEN)

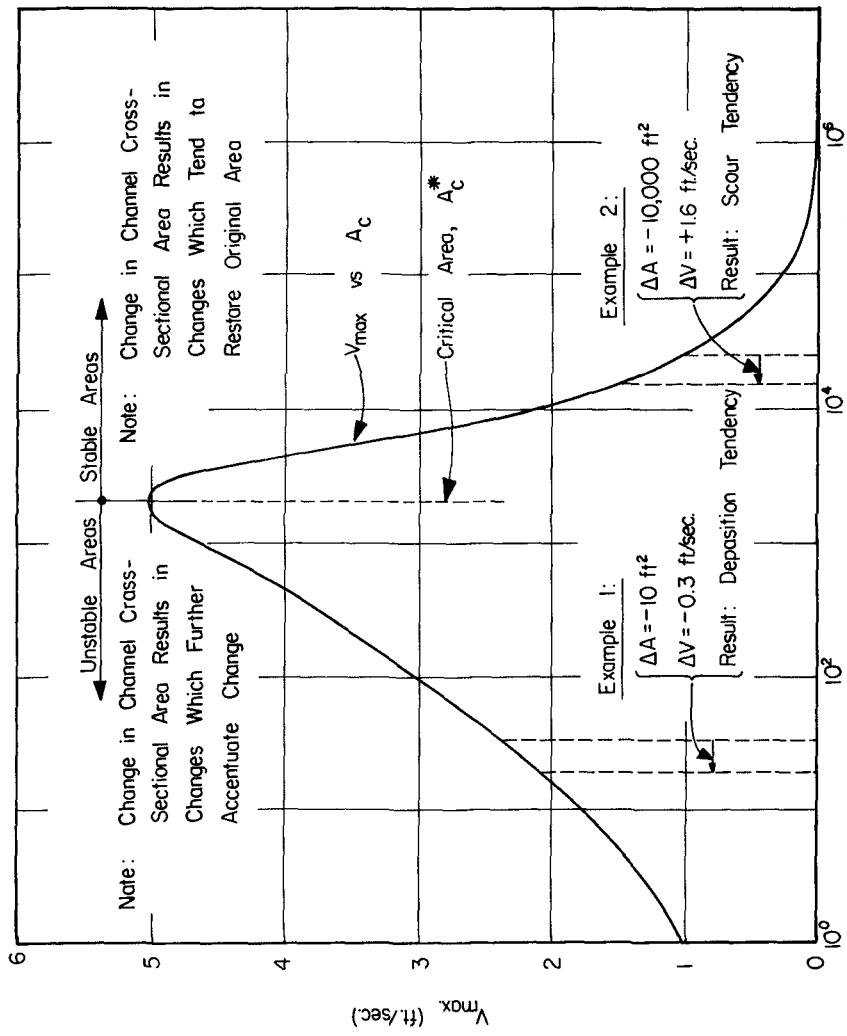

FIGURE 6. ILLUSTRATION OF ESCOFFIER'S STABILITY CONCEPT

$A_c > A_c^*$ → This inlet is stable against changes in closure tendencies

$A_c < A_c^*$ → This inlet is unstable against changes in closure tendencies

Consider first the right hand side of the curve. If an unusual amount of littoral drift is carried into the inlet, the cross-sectional area will decrease, thereby resulting in an increase in inlet velocity and an increase in scouring capacity; therefore, the inlet tends to be stable by countering against any area change by a velocity change that will tend to reduce the area change. It is also noted that any enlargement in area will result in a decrease in velocity and an associated increase in deposition tendency, thereby causing the inlet to tend to stabilize about the equilibrium area. Consider next the left hand side of the curve. Any decrease in cross-sectional area will result in a decrease in velocity and a tendency for the area to decrease further. Also any increase in area will perpetuate this increase by an increase in inlet velocity. The cross-sectional area, A_c, characterized by

$$\frac{\partial V_{max}}{\partial A_c} = 0$$

is denoted A_c^* and represents a division between stable and unstable conditions. The stable region is primarily governed by the changes in velocity resulting from a change in cross-sectional area, whereas the characteristics of the unstable region are due to the increasing friction with decreasing cross-sectional area, (and hydraulic radius, R). Finally, in concluding the discussion on stability, it is clear that in nature, the tidal ranges change with time and an equilibrium cross-sectional area as well as critical area would only be meaningful in terms of some average tidal range conditions. Furthermore, if the maximum velocity V_{max} associated with A_c^* is less than the "threshold velocity" required to move sand, it is clear that the inlet would tend to close under the depositional action of waves and currents. The presence of a net fresh water outflow would also be an important factor in favorably affecting the stability of an inlet.

METHOD OF CALCULATING INLET STABILITY

The method involved in calculating inlet stability requires some available information describing existing inlet conditions; these existing conditions are assumed to represent equilibrium conditions. Based on the equilibrium conditions and assumptions regarding minor and gradual head loss terms, it is possible to calculate the inlet stability characteristics for an assumed form of deposition in the inlet cross-section.

Inlet Hydraulics

It is assumed that the inlet hydraulic characteristics are adequately represented by the Keulegan method, even though the bay system may be interconnected to other bays or may be served by more than one inlet. Although

this is not strictly valid, it does allow calculation of the inlet stability and it can be shown that the effect is an overestimate of the stability.

Estimate of the Repletion Coefficient, K

There are several types of field observations which can be used to yield an estimate of the repletion coefficient, K. Referring to Figures 2, and 4, it is seen that estimates could be obtained as shown in Table 1.

TABLE I

ALTERNATE METHODS FOR ESTIMATING K

Field Measurements	Figure
Lag between ocean high (or low) tide and following slack water in the inlet, ε	2
Ratio of bay to ocean amplitudes, a_B/a_o	4

After comparing various methods, it appears that the most convenient and reliable field measurement is the lag between the ocean tide extreme and the following slack water in the inlet. Tide and current tables contain adequate information for some inlets. For example, Figure 7 represents the lag, ε, from tide[10] and current[11] tables for Government Cut, Florida for the month of January, 1972. The different lags following high and low ocean tides represent a departure from the Keulegan predictions, and it is recommended that an average value be taken. The values of K as determined from Figure 2 are also presented in Figure 7 for two values of ε. The representative value of ε and K for Government Cut were taken as 56^o and 0.53 respectively.

Estimate of Inlet and Bay Characteristics

Considering the inlet throat cross-sectional area to be known from surveys, and to be in equilibrium with the tidal prism, P, in accordance with O'Brien's relationship, it is possible to determine the head loss coefficient $K_{en} + K_{ex} + \frac{f\ell}{4R}$. Expressing the repletion coefficient, K

$$K = \frac{T}{2\pi a_o} \frac{\sqrt{2ga_o}}{\left[K_{en} + K_{ex} + \frac{f\ell}{4R}\right]^{\frac{1}{2}}} \frac{A_c}{A_B} = \frac{T}{\pi} \frac{\sqrt{2ga_o}\cos\varepsilon}{\left[K_{en} + K_{ex} + \frac{f\ell}{4R}\right]^{\frac{1}{2}}} \frac{A_c}{P} \quad (2)$$

in which the tidal prism P has been equated to $2a_B A_B$ and $\cos\varepsilon = a_B/a_o$. It should be recognized that the bay area as defined is not the actual bay area but an area consistent with the tidal prism and the bay tidal amplitude, a_B,

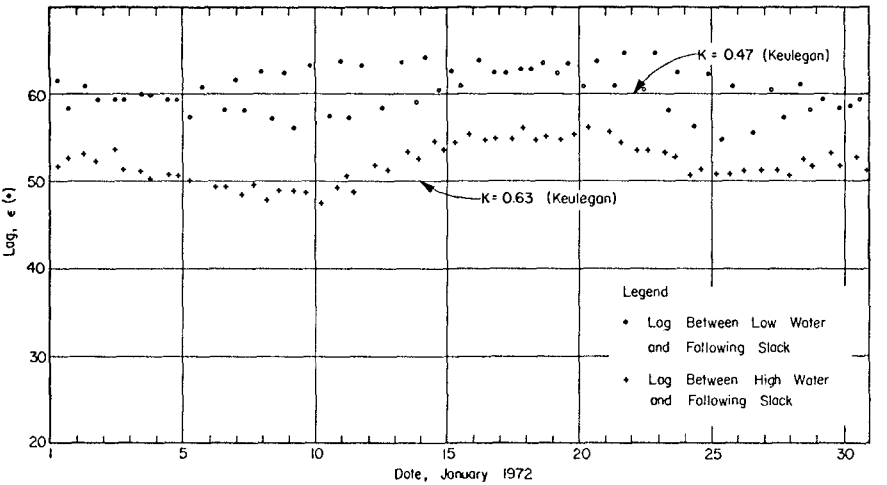

FIGURE 7. LAG BETWEEN HIGH AND LOW WATERS AND FOLLOWING SLACKS FOR GOVERNMENT CUT, FLORIDA DETERMINED FROM TIDE AND CURRENT TABLES

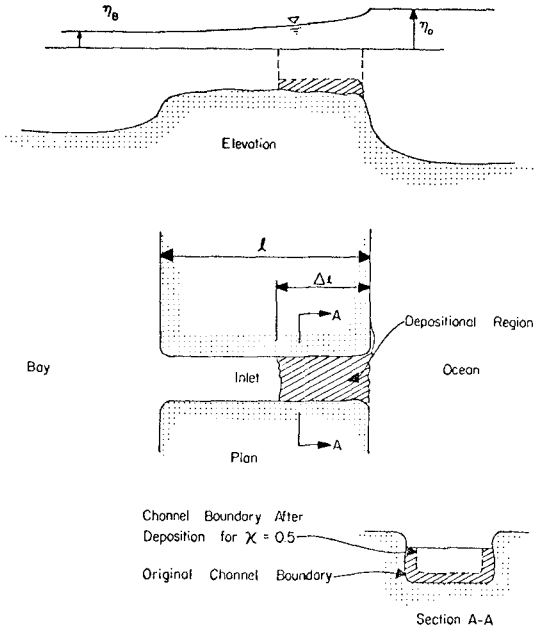

FIGURE 8. DEPOSITIONAL PATTERN IN INLET

just inside of the inlet. Because the tidal amplitude within the bay is generally less than this value, it follows that the effective bay area will be less than the actual bay area.

Considering the inlet cross-section to be in equilibrium with the tidal prism, Equation (2) may be solved for the head loss terms, i.e.

$$K_{en} + K_{ex} + \frac{f\ell}{4R} = \left[\frac{T}{\pi} \frac{\sqrt{2ga_{om}} \cos \varepsilon}{K} \frac{A_c}{P_m} \right]^2 \qquad (3)$$

One slight refinement is introduced in the calculation indicated by Equation (3). The equilibrium area-tidal prism relationship applies for spring or diurnal tides, whereas the head loss terms are solved for the mean tidal range. The values of a_o and the tidal prism, P, in Equation (3) should therefore refer to mean tide conditions. Denoting P_s and P_m as the tidal prisms associated with spring and mean tides, respectively, it can be shown that

$$P_m = P_s \left[\frac{(a_o)_m}{(a_o)_s} \right]^n$$

in which $0.5 < n < 1.0$ depending on the repletion coefficient, K, and the subscripts m and s refer to mean and spring tidal ranges respectively. The tidal prism value employed in Equation (3) is P_m with n taken to be 0.5.

The hydraulic radius is known from the inlet cross-sectional surveys and if $K_{en} + K_{ex}$ and f can be estimated, than an equivalent inlet length, ℓ, based on an inlet cross-section of uniform area with length, is estimated as

$$\ell = \left\{ \left[K_{en} + K_{ex} + \frac{f\ell}{4R} \right] - (K_{en} + K_{ex}) \right\} \frac{4R}{f} \qquad (4)$$

where the terms in the square brackets are estimated from Equation (3) and $K_{en} + K_{ex}$ and f were estimated to be 1.3 and 0.03, respectively.

In summary of the calculated inlet-bay properties, it is possible to estimate: K, A_B, ℓ in which A_B and ℓ are "effective" or "equivalent" properties

Stability Calculations

With the calculated values of the existing inlet characteristics and the assumption that the inlet is in equilibrium, the response of an inlet to deposition of sand will be investigated.

Consider a quantity of sand driven into an inlet by waves and currents and deposited, thereby reducing the inlet cross-section. The constriction of the cross-section will tend to increase the inlet currents whereas the

increase in friction due to the lesser depths will tend to decrease the currents. It therefore is apparent that the manner in which the inlet is loaded with sand is of importance. Obviously, in carrying out stability calculations, it would be preferable to assume deposition in each inlet in a manner that is consistent with the particular hydrography and wave climate of the vicinity. This type of information, however, is generally not available and, for purposes of consistency, it was decided to "load" all inlets in the same manner which is reasonably realistic; the results would therefore represent the response of a group of inlets to the same depositional pattern.

As noted previously, the pattern of deposition affects the response of the inlet to a decrease in area. For example, if the sand is deposited primarily along the sides of a channel, the hydraulic radius will be affected only slightly and the resulting maximum velocity will be larger relative to the case where the deposition resulted in a depth decrease but no decrease in width. Similarly, deposition along the entire inlet length will influence the response differently than the same reduction in cross-sectional area, but the decrease limited to a portion of the inlet length. In the calculations, it was assumed that the reduced cross-sectional area was geometrically similar to the equilibrium (measured) cross-sectional area. Denoting the equilibrium values by the subscript, E,

$$A_c = \kappa A_{c_E} \tag{5}$$

where κ is to be specified as the parameter of area reduction. It can be shown that the hydraulic radius is related to the equilibrium hydraulic radius R_E by

$$R = \sqrt{\kappa}\, R_E \tag{6}$$

Governing Equations

Referring to Figure 8, it can be shown that for a given area reduction and depositional length, denoted by κ and $\Delta\ell$, respectively, the repletion coefficient is given by

$$K = \frac{T}{2\pi a_o} \frac{A_{c_E}}{A_B} \frac{\sqrt{2ga_o}}{\left[\frac{K_{en} + K_{ex}}{\kappa^2} + \frac{f\Delta\ell}{4\sqrt{\kappa}R_E\kappa^2} + \frac{f(\ell - \Delta\ell)}{4R_E}\right]^{1/2}} \tag{7}$$

in which it is assumed that no change in the effective bay area, A_B, occurs due to the deposition and the same hydraulic minor loss coefficients apply at the transition from A_{c_E} to A_c, except the coefficients are multiplied by the difference in velocity heads. With the repletion coefficient known for the considered deposition, V'_{max} is determined from Figure 3 and V_{max} is determined

from

$$V_{max} = V'_{max} \frac{2\pi}{T} a_o \frac{A_B}{A_c} \tag{8}$$

This is the maximum velocity that would pertain in the deposition region and would be the velocity of importance in tending to restore the area to equilibrium conditions. In employing Equations (7) and (8), the spring tidal range was used as the condition considered most effective in governing stability.

Stability Index, β

A measure of stability, β, was defined to represent the capacity of an inlet to remain stable under conditions of deposition. The best definition of the stability index is not apparent; however, it is clear that the definition should recognize that inlets with equilibrium areas much larger than the critical area A_c^* have more storage area and therefore, will be more resistant to closure. Also the definition should reflect the capacity of large velocities to transport sand out of an inlet.

The relationship between sediment transport, q_s, and water velocity is not precisely known, however it is generally agreed that the sediment discharge is proportional to some power, j, of the velocity

$$q_s = C(V - V_T)^j \tag{9}$$

where C is some constant (or function) and V_T represents a "threshold velocity" for sand transport.

In consideration of the sediment discharge relationship, and the factors noted, the stability index, β was defined as

$$\beta \equiv \int_{A_c^*}^{A_{c_E}} (V_{max} - V_T)^3 \, dA_c \tag{10}$$

The index β has units of $(\text{length})^5/(\text{time})^3$.

Example Calculation

To illustrate the effects of various deposition lengths, $\Delta\ell$, consider a hypothetical inlet and the following parameters:

$$R_E = 8 \text{ ft.}$$

$$A_{c_E} = 10{,}000 \text{ ft.}^2$$

$$a_o = 2 \text{ ft.}$$

$$\varepsilon_E = 60^o$$

$$K_{en} + K_{ex} = 1.3$$

$$f = 0.03$$

The equilibrium repletion coefficient, K_E, determined from Figure 2 is 0.465 and the equilibrium tidal prism from Figure 5 is 4.86×10^8 ft.^{3}. The effective bay area A_B is determined as

$$A_B = \frac{P_E}{2a_{B_E}} = \frac{P}{2\, a_o \cos \varepsilon} = \frac{4.86 \times 10^8}{2(2)(0.5)} = 2.43 \times 10^8 \text{ ft.}^2$$

The head loss coefficients are determined from Equation (3) as

$$\left[K_{en} + K_{ex} + \frac{f\ell}{4R}\right] = 12.74$$

from which the effective length is (Equation 4)

$$\ell = 12{,}200 \text{ ft.}$$

This completes the determination of existing conditions, The stability calculations for V_{max} as a function of A_c for various $\Delta\ell$ values are carried out in accordance with Equations (7) and (8) and are plotted in Figure 9.

From Figure 9 it is seen that the stability results depend markedly on the deposition length, $\Delta\ell$. For small deposition lengths, the inlet is more stable because the total friction is less; hence the velocities are higher than for the larger deposition lengths. Based, in part, on inspection of photographs of deposition along inlets, a standard deposition length was taken as 1000 ft. in all calculations related to natural bay-inlet systems.

The stability indices for the five values of $\Delta\ell$ presented in Figure 9 and determined from Equation (10) are summarized in Table II.

TABLE II

EXAMPLE INLET
EFFECT OF DEPOSITION LENGTH

Relative Deposition Length ($\Delta\ell/\ell$)	A_{c_E}/A^*_c	Stability Index, β (ft.^{5}/sec.^{3})
0.0	∞	16.4×10^5
0.2	3.7	1.38×10^5
0.4	2.1	0.58×10^5
0.6	1.8	0.34×10^5
0.8	1.4	0.16×10^5
1.0	0.0	0.0

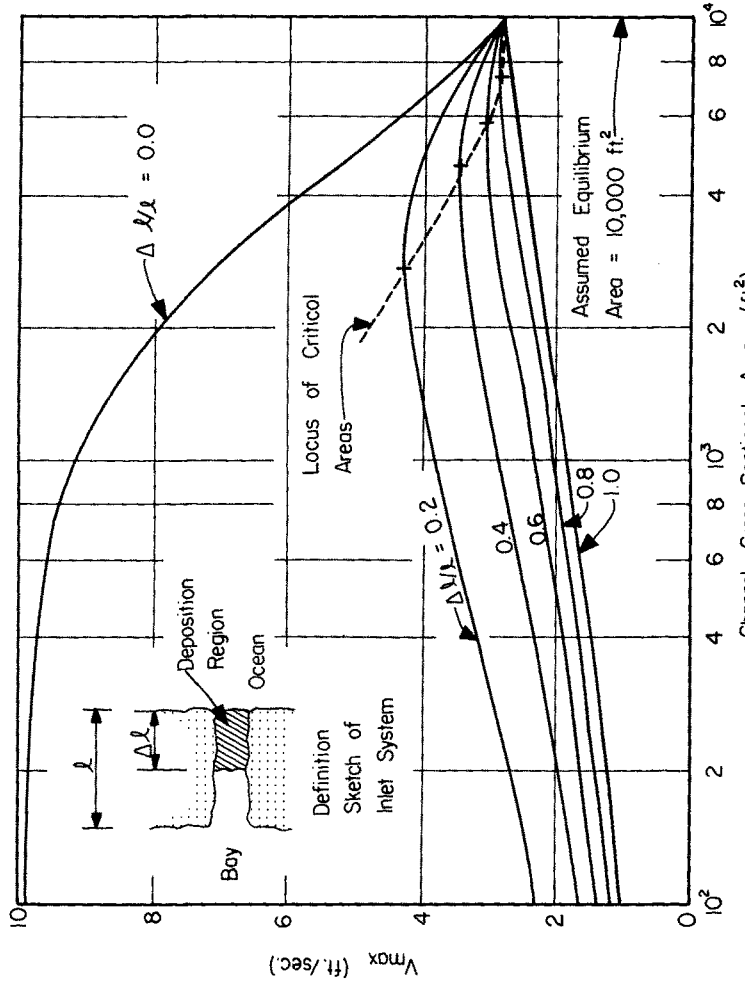

FIGURE 9. STABILITY CONSIDERATIONS FOR EXAMPLE INLET, EFFECT OF DEPOSITION LENGTH

RESULTS OF CALCULATIONS FOR NATURAL INLET-BAY SYSTEMS

Calculations were carried out for four Florida inlets and one inlet along the New York shoreline.

1. Government Cut, Florida

Government Cut, Florida, is a jettied and dredged inlet at the south end of the barrier island on which Miami Beach is located. The existing (1970) cross-sectional area, A_{cE}, was determined by survey to be 19,600 ft.^{2} Other characteristics are summarized in Table III. The results of the stability calculations are presented in Figure 10 where it is seen that the critical cross-sectional area is 3000 ft.^{2}. The calculated stability index, β is 11.5 x 10^5ft.^{5}/sec.^{3}.

2. Broad Creek, Florida

Broad Creek comprises a natural system of inlet channels through a limestone reef, although sedimentary material is present along much of the bottom of these channels. The inlet characteristics and results of the stability calculations are summarized in Table III, and Figure 11. The equilibrium and critical areas are 9200 and 1800 ft.^{2} respectively. The calculated stability index is 1.7 x 10^5 ft.^{5}/sec.^{3}.

3. Boca Raton Inlet, Florida

Boca Raton Inlet is a natural inlet with very short jetties. The inlet has a history of closure in an approximate period of 1-3 years if maintenance dredging is not carried out. The information of interest and results of the stability calculations are presented in Table III and Figure 12. The stability index for Boca Raton Inlet is 0.12 x 10^5 ft.^{5}/sec^3.

4. Stump Pass, Florida

Stump Pass is a small inlet located on the west coast of Florida. The inlet cross-sectional area determined by a 1972 survey[12] was 4940 ft.^{2} and the stability index, β, determined as described is 0.75 x 10^5 ft.^{5} /sec.^{3}, see Figure 13.

5. Shinnecock Inlet, New York

Considerable data are available describing the hydraulic characteristics and history of Shinnecock Inlet. The 1955 inlet cross-sectional area[13] is assumed to represent equilibrium conditions; see Table III and Figure 14 for the summarized results. The stability index for Shinnecock Inlet is 0.96 x 10^5 ft.^{5}/sec.^{3}.

TABLE III

SUMMARY OF NATURAL INLET COMPUTATIONS

Inlet	A_{c_E} ($ft.^2$)	A^*_c ($ft.^2$)	Stability Index, β (ft^5/sec^3)
Government Cut, Florida	19,600	3,000	11.5×10^5
Broad Creek, Florida	9,200	1,800	1.7×10^5
Boca Raton Inlet, Florida	1,410	230	0.12×10^5
Stump Pass, Florida	4,940	900	0.75×10^5
Shinnecock Inlet, New York	5,500	1,400	0.96×10^5

SUMMARY

Based on earlier concepts and techniques relating to inlet hydraulics, equilibrium inlet conditions, and inlet stability, as developed by Keulegan, O'Brien and Escoffier respectively, and assuming idealized depositional patterns within the inlet, a method has been developed to calculate the stability of an inlet as affected by deposition. A stability index, β, has been defined, based on considerations of idealized depositional patterns, allowing the comparison of stabilities of various inlet systems. The stability indices are calculated and compared for five natural inlet systems.

ACKNOWLEDGEMENT

This work was sponsored, in part, by the NOAA Office of Sea Grant, Department of Commerce, under Grant No. SGP 2-38.

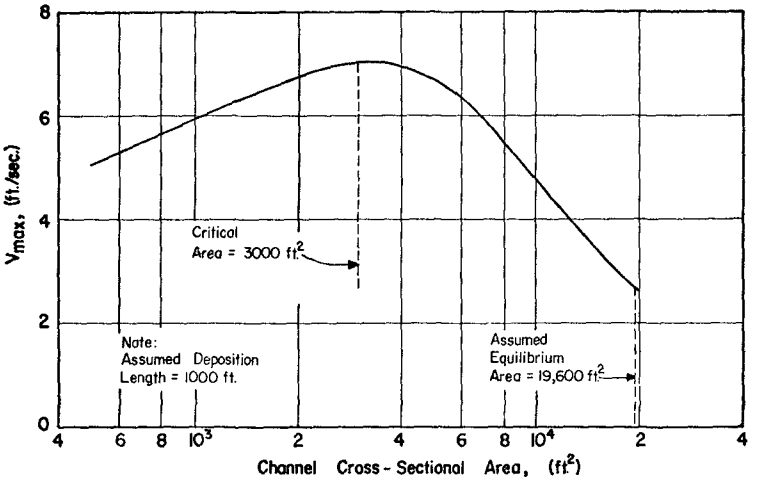

FIGURE 10 STABILITY CONSIDERATIONS FOR GOVERNMENT CUT, FLORIDA

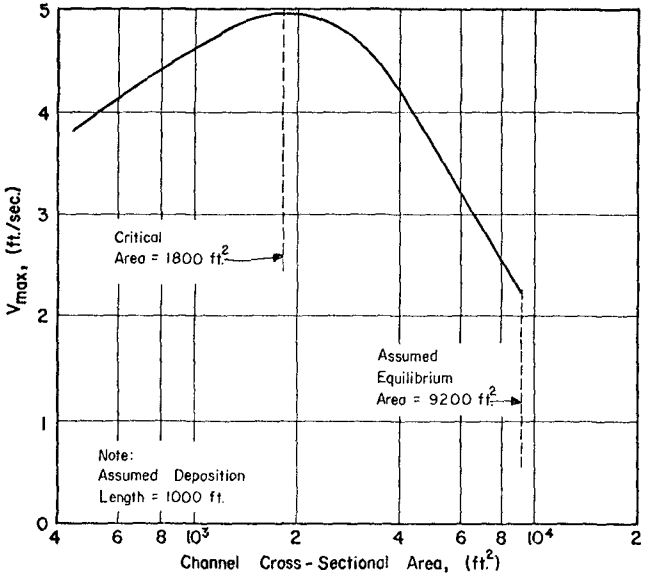

FIGURE 11. STABILITY CONSIDERATIONS FOR BROAD CREEK, FLORIDA

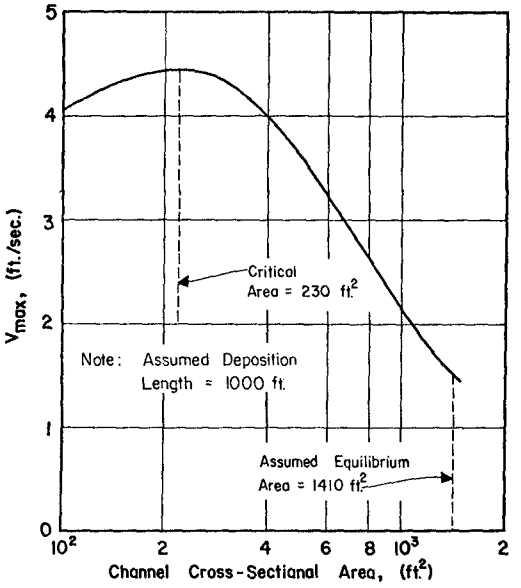

FIGURE 12. STABILITY CONSIDERATIONS FOR BOCA RATON INLET, FLORIDA

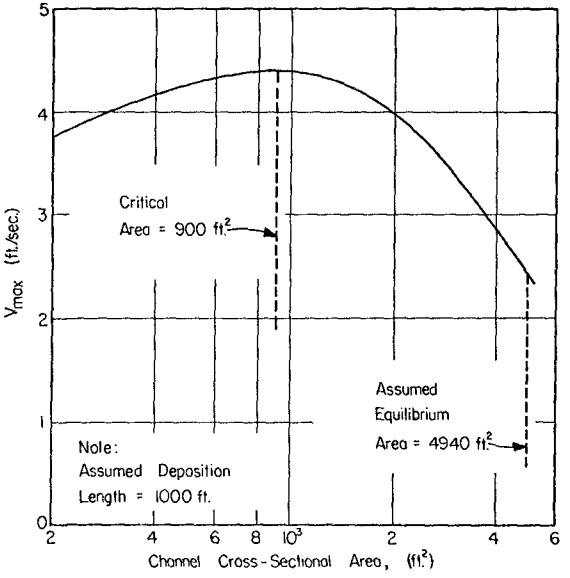

FIGURE 13. STABILITY CONSIDERATIONS FOR STUMP PASS, FLORIDA

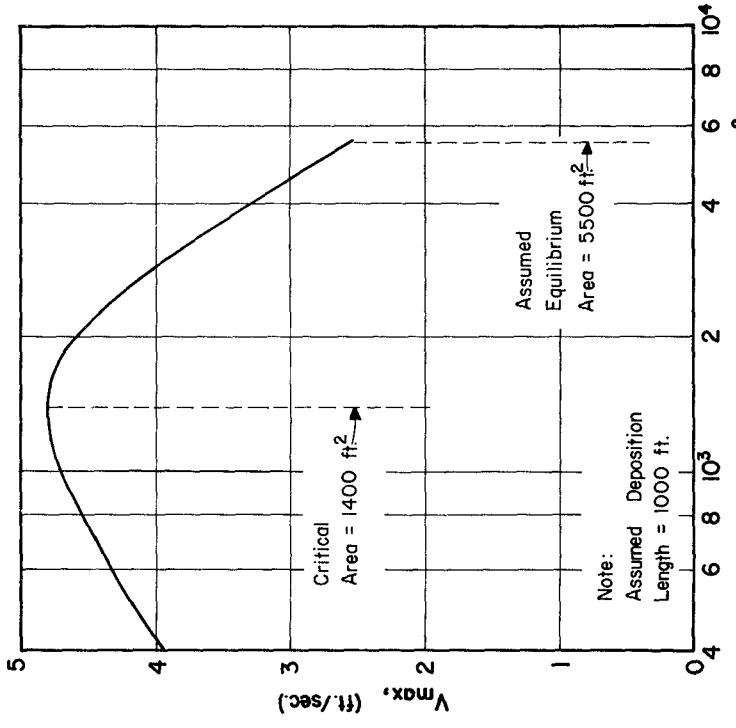

FIGURE 14. STABILITY CONSIDERATIONS FOR SHINNECOCK INLET, NEW YORK

REFERENCES

1. Brown, E. I., "Inlets on Sandy Coasts," Proceedings, ASCE, Vol. LIV, pp. 5D5-553, 1928.

2. Keulegan, G. H., "Tidal Flows in Entrances. Water Level Fluctuations of Basins in Communication with Seas," Third Progress Report, National Bureau of Standards Report, No. 1146, 1951.

3. Baines, W. D., "Tidal Currents in Constricted Inlets," Proceedings, Sixth Conference on Coastal Engineering, pp. 545-561, 1957.

4. Van de Kreeke, J., "Water-Level Fluctuations and Flow in Tidal Inlets," Journal, Waterways and Harbors Division, ASCE, Vol. 93, No. WW4, pp. 97-1D6.

5. Mota, Dliviera, I.B., "Natural Flushing Ability in Tidal Inlets," Proceedings, Twelfth Conference in Coastal Engineering, pp. 1827-1B45, 197D.

6. Shemdin, D.H., and R. Forney, "Tidal Motion in Bays," Proceedings, Twelfth Conference on Coastal Engineering, pp. 2225-2242, 197D.

7. O'Brien, M.P., "Estuary Tidal Prisms Related to Entrance Areas," Civil Engineering, Vol. 1, No. B, pp. 738-739, 1931.

8. D'Brien, M. P., "Equilibrium Flow Areas of Inlets on Sandy Coasts," Journal, Waterways and Harbors Division, ASCE, Vol. 95, No. WW1, pp. 43-52, Feb. 1969.

9. Escoffier, F. F., "The Stability of Tidal Inlets," Shore and Beach, Vol. 8, No. 4, pp. 114-115, 1940.

10. "Tide Tables, East Coast of North and South America," National Ocean Survey, U.S. Department of Commerce, 1972.

11. "Tidal Current Tables, Atlantic Coast of North America," National Ocean Survey, U.S. Department of Commerce, 1972.

12. Tackney, D., "Survey Notes for Stump Pass, Florida," Unpublished, 1972.

13. U.S. Army Corps of Engineers, "Survey Report on Moriches and Shinnecock Inlets, Long Island, New York. Appendix A - Characteristics of the Inlets and Adjacent Shorelines," No Date Given on Publication Available.

CHAPTER 42

CHARACTER AND STABILITY OF A NATURAL TIDAL INLET

By

Curtis Mason[1] and Robert M. Sorensen[2]

ABSTRACT - An environmental study was conducted at Brown Cedar Cut, a natural unstable barrier beach inlet connecting East Matagorda Bay, Texas, with the Gulf of Mexico. The objectives of this study were to determine the physical and hydraulic properties of the inlet, and to investigate the inlet's historical stability, as well as its short-term response to a number of physical processes. Results of the study indicate that hurricanes and continuing erosion of adjacent beaches enhance the long-term stability of the inlet. During winter months, the rapid passage of strong frontal systems and associated winds, as well as substantial amounts of rainfall, are primarily responsible for the day-to-day viability of the channel boundaries. In the absence of such forces, the predominance of littoral drift over the limited flushing ability of astronomical tidal currents leads to degradation of the inlet channel and westward migration of the entire inlet system.

INTRODUCTION - The coastline of Texas is characterized by a barrier island and lagoon regime which extends over 80% of the coastline. Separating these islands are over a dozen tidal inlets of various sizes, ranging in width from a few hundred feet to over one mile. Although these inlets have been studied to some extent in the past by Price (6,7,8,9,10) and Carothers and Innis (1), little attempt has been made to correlate the various environmental factors with observed changes in the inlet's geometric properties. Therefore, a field investigation of a small tidal inlet was undertaken to identify and establish the relative importance of those natural processes influencing the behavior of the inlet, and to determine its long and short-term stability.

The inlet selected for study was Brown Cedar Cut, located about twenty-five miles south of Freeport, Texas, as shown in Figure 1. This inlet is the sole direct connection between the Gulf of Mexico and East Matagorda Bay, a shallow estuary some fifty-four square miles in area. This site was selected for its small size and because maintenance of the channel is due entirely to natural processes.

HISTORICAL BACKGROUND - Brown Cedar Cut was formed during a hurricane in 1929 (4), and since that time has exhibited considerable variation in size and location, actually closing for three years between 1964 and 1967. An analysis of historical charts and photographs revealed that the inlet's behavior is characterized by a periodic sequence of events. The initial break through the barrier island results from the action of large waves, high tides, and torrential rainfall associated with hurricanes, which establish a wide, relatively deep channel. Subsequently, the northeast side of the inlet elongates toward the southwest in response to dominant wave conditions and related depositional processes. As the inlet migrates westward, the channel lengthens, tidal velocities decrease, and deposition occurs throughout the channel. If undisturbed by severe weather conditions, migration continues until the inlet closes. Usually, however, the channel is re-enlarged at the original position before closure occurs.

---

1. Oceanographer, USACE Coastal Engineering Research Center, Washington, D.C.
2. Assoc. Prof. Dept. of Civil Engineering, Texas A&M University, College Station, Texas.

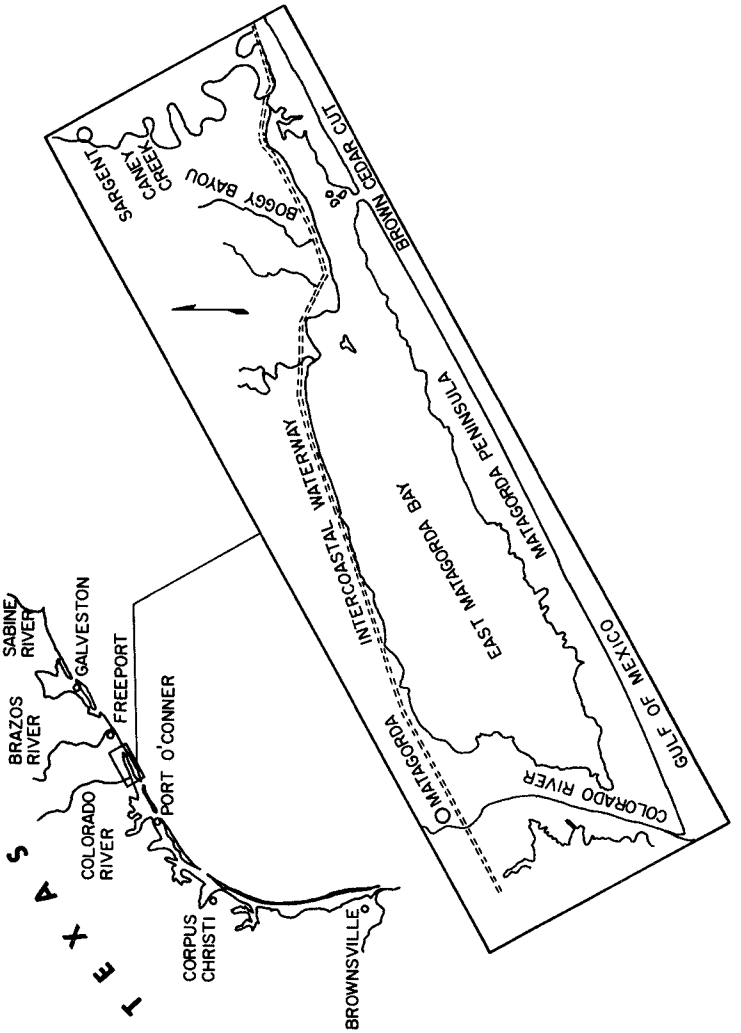

FIGURE I. EAST MATAGORDA BAY AND ENVIRONS

In addition to the generally erosive forces of hurricanes and other storms another factor appears to have played a major role in the stability of Brown Cedar Cut. Analysis of coastal charts indicates that since 1929, the adjacent shoreline has receded over 1500 feet. Thus, the effective length of the channel has been reduced, and the resulting decrease in frictional resistance has allowed velocities to remain relatively high, precluding closure.

INLET PROCESSES - Comprehensive surveys of the inlet were initiated in October, 1970, to determine those factors influencing changes in shape, size, and stability. Beach and shallow water elevations were determined using standard surveying equipment and a fathometer. Data obtained were employed in the analysis of the inlet's response to natural processes as follows.

Local contours of the mean water level were drawn for each pair of consecutive surveys, thus delineating the nature of gross changes. Determination of environmental conditions prevailing during the interim was important, but considerably more difficult. Current velocities between surveys were computed from measured tidal differential time histories obtained from tide gages. However, observations of wave conditions were available only for brief periods, so an indirect method for determining the nature of the wave activity was employed.

Although wave characteristics are not always proportional to wind direction and magnitude at the site, it was felt that a reasonable correlation could be made. Wind observations taken at a nearby location at six hour intervals and occurring between survey dates were first sorted according to direction - those having a strong north component, i.e. north, north-northwest, and north-northeast, were grouped together as north. Similar groups were established for east, south, and west. Winds from the northeast, southeast, southwest, and northwest formed four other groups of wind velocity observations. The velocities in each group were then summed, and these sums were divided by the number of days in the observation period. The resulting values are daily averages of the relative forces of prevailing winds. Computations were performed for each survey interval and plotted in the form of a wind force rose on the corresponding shoreline comparison figure.

A detailed discussion of the nature and probable causes of changes in inlet geometry is presented below in chronological order.

October 24: The general configuration of the inlet and prominent reference points are indicated in Figure 2. The distance between shorelines at the mouth was about 1450 feet, but wide shoal areas extended outward from the banks, and the portion of the channel greater than six feet deep was only about four hundred feet wide. The inlet exhibited the typical north-south orientation of other Texas inlets (10), and the main channel followed a winding path through interior islands to the bay. The east side of the inlet was a sand spit that exhibited a well defined "hook" configuration. The origin of hooked or recurved spits was reported by Evans (2), who concluded that they form as a result of wave refraction around the spit end. However, Evans' findings require that for growth of such structures, waves must approach the spit obliquely from the mainland or upcoast side, in this case from the east or southeast. Waves approaching normal to the beach or from a southerly direction will not transport sand to the spit end, and may in fact actively erode the spit area. The converse is true for the west spit; growth due to wave refraction will occur only when waves strike the beach with a predominately south or west component. In both cases, however, refraction of offshore waves by the adjacent gulf shoals may cause local directional variability.

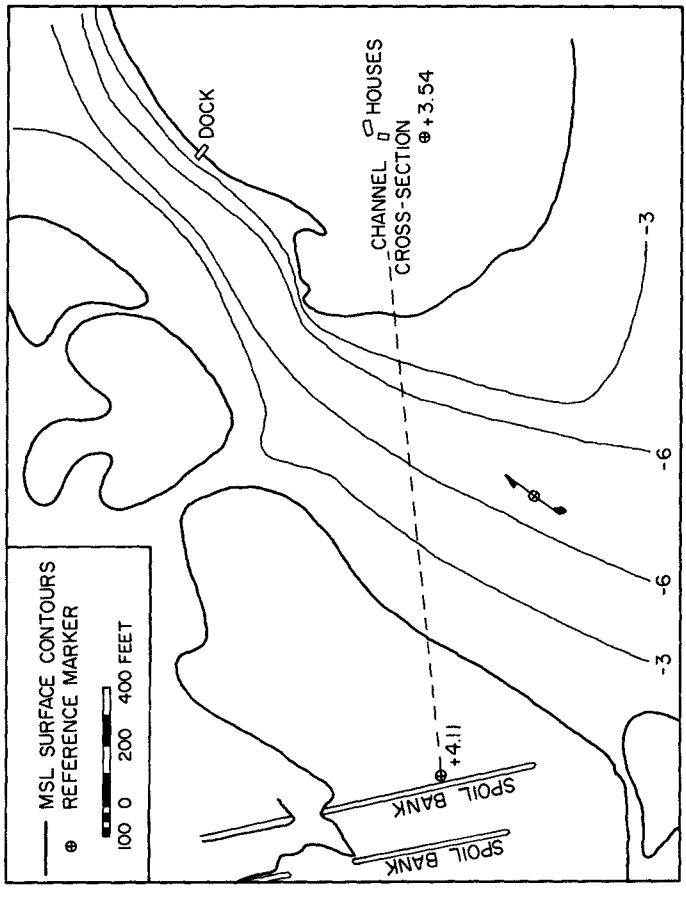

FIGURE 2. BROWN CEDAR CUT LOCATION CHART, 24 OCTOBER, 1970

October 24 to February 20, Figure 3: The first presentation of shoreline comparisons indicates significant spit growth on both sides of the inlet during the four month interval. Wind activity during this period was moderate, and exhibited a north and east predominance. Rainfall throughout the period was below normal. Casual observations of spit contours in December indicated that growth was minor until January. By February, the eastern recurved spit had extended about three hundred thirty feet towards the southwest, and a total of 21,600 cubic yards of sand had accumulated shoreward of the February 20 mean water contour. The growth of the west spit a distance of 535 feet northward is attributed primarily to refraction of waves from both the south and east. However, the action of tidal currents may have contributed to the total deposition of 14,400 cubic yards landward of the February 20 mean water contour.

February 20 to 27, Figure 4: During this period the second hook on the east spit was modified considerably. Predominant wind direction was from the east, and deposition occurred along the entire southwest edge. Wave activity on the 27th was of great magnitude and almost directly from the east, and a southwestward flowing longshore current of over three feet per second was measured near the inlet. Current velocities during this period showed a strong predominance for ebb flow resulting from the passage of a frontal system on the 21st, which depressed the bay waters for over three days. Therefore, wave refraction patterns were modified by the outward flowing water during that time. Although not exhibiting a hook configuration, a considerable area at the end of the spit did experience growth, as indicated by the cross-hatching in Figure 4. Much of this growth occurred in the form of a beach ridge, as shown in the profiles of Figure 4. Numerous investigators (3,11,12) have commented upon conditions required for growth of such a feature, and the primary factors appear to be significant wave activity and relatively constant water level. Tidal records from an inlet tide gage indicated that semi-diurnal neap tides prevailed between February 25 and 27, and averaged less than one-half foot in range. In addition, the mean water level during this time was considerably above the long term mean water level, which would enhance growth of the ridge. Wind data indicated that winds from the east and southeast blew continuously from the 24th to the 27th, meaning that the observed wave activity had probably been in effect for some time. Thus, all evidence points to rapid building of the ridge by wave run-up. A series of similar ridges was formed between March 4 and 20, and these also corresponded to periods of small tidal fluctuations and high wave activity. As will be shown later, an entire series of these recurved beach ridges subsequently formed across the northeast spit.

February 27 to March 4, Figure 5: Wind and current activity during this period were dominated by the effects of a strong frontal system which passed through the area on March 2. The maximum recorded value of tidal differential occurred on March 3, when the Bay level was 1.8 feet higher than that of the Gulf, producing ebb velocities in excess of 3.5 feet per second. The west spit was effectively unchanged over the period, and the mean water contours at the southeast corner of the east spit also maintained position. However, the first hook was eroded about twenty feet and the tip of the spit migrated seaward about two hundred feet. Observations of the banks at both locations revealed the existence of small vertical bluffs extending about one foot above the water's edge. Although the exact cause of this erosion is unknown, degradation of the spit end during the morning of March 4 was observed to result from refracted waves from the Gulf. However, it is highly doubtful that the extensive erosion experienced at interior locations was due to similar processes. More likely is the possibility that strong ebb currents flowed along the shore and eroded large sections of the banks into the vertical configurations exhibited.

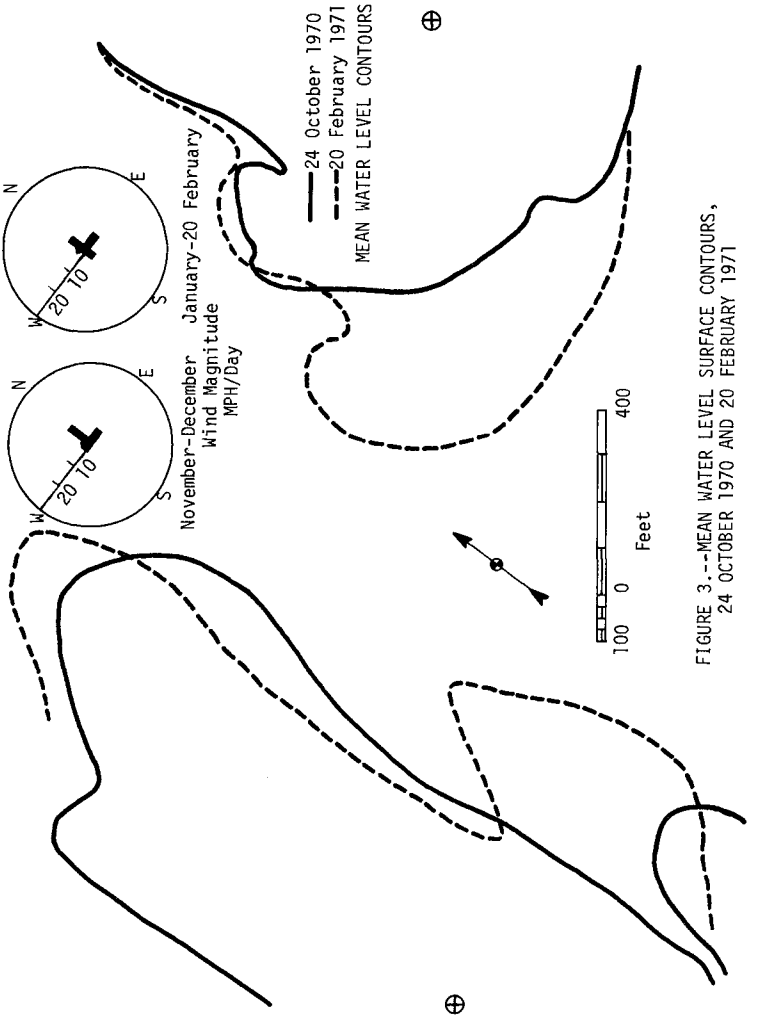

FIGURE 3.--MEAN WATER LEVEL SURFACE CONTOURS, 24 OCTOBER 1970 AND 20 FEBRUARY 1971

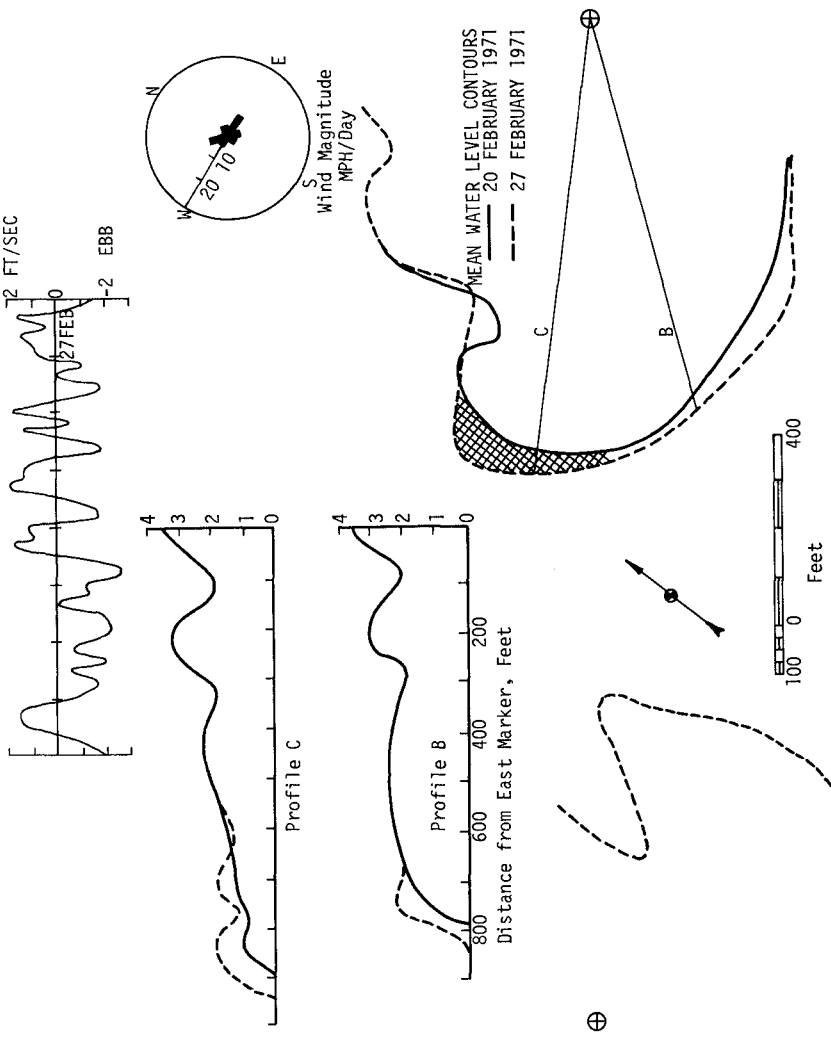

FIGURE 4.--MEAN WATER LEVEL SURFACE CONTOURS, 20 AND 27 FEBRUARY, 1971

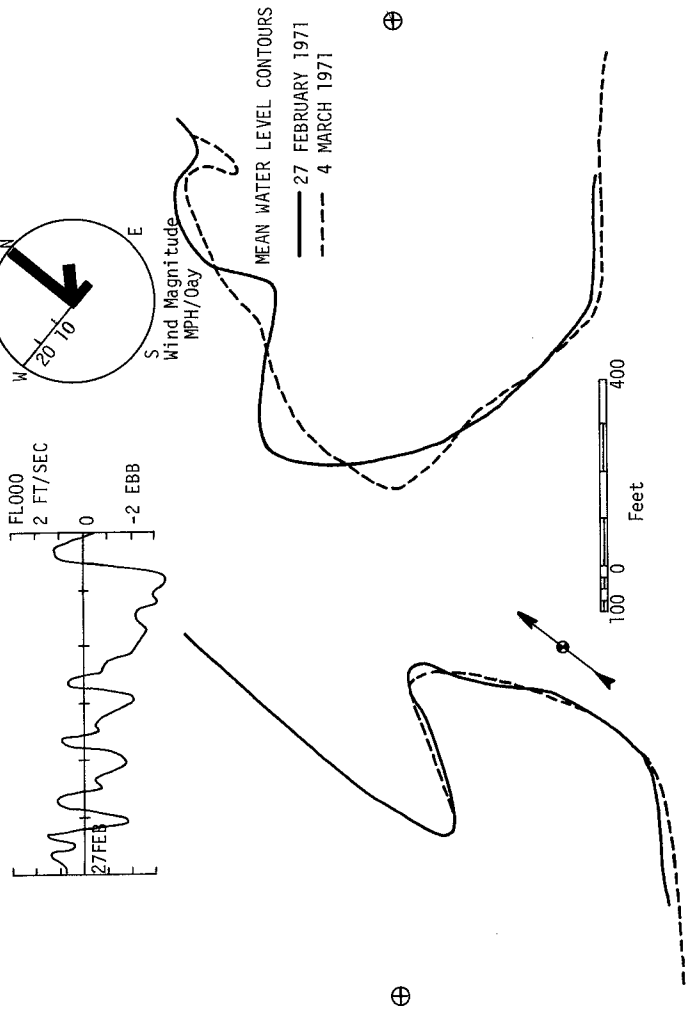

FIGURE 5.--MEAN WATER LEVEL SURFACE CONTOURS, 27 FEBRUARY AND 4 MARCH, 1971

March 4 to 20, Figure 6: Strong winds from the south and moderate flood currents predominated during this period, although the passage of two frontal systems did produce short-term ebb currents of significant magnitude. The inlet apparently responded primarily to wave activity from the south. The west spit acquired a slight bulge at the southeast corner, and built northward, exhibiting a pronounced recurved configuration. Waves and currents moving inward through the channel caused significant degradation of the east bank, but some deposition of this material occurred on the north side.

March 20 to April 3, Figure 7: Diurnal tidal ranges during this period were far above normal, averaging about 1.4 feet. Therefore, current velocities in the order of 1.6 feet per second prevailed, and were about evenly balanced between flood and ebb. Wave conditions were observed at three different occasions during this period and above-average breaker heights of about four feet were evidenced each time. Steep waves from the south and east, in combination with some of the highest recorded water levels, are assumed to be responsible for the recession of the west spit shoreline. Wave action from the east would usually cause cross-channel growth of the east spit. However, during this period the only growth experienced was in a northerly direction up the channel. It is theorized that the strong tidal currents, acting in concert with southerly waves, precluded any permanent effects of easterly waves, and in fact actively eroded the east bank. However, the material eroded was apparently transported northward, and subsequent deposition occurred in a pattern characteristic of wave refraction processes, i.e. a well-defined recurved spit.

Although waves and currents are responsible for most changes in the inlet, the influence of two additional natural forces must be considered. First, movement of beach sand by strong winds will contribute to changes in the exposed regions of the spit. Examination of the survey data revealed moderate spit modification above the high water mark, which probably resulted from wind action. Large-scale wind erosion is tempered by the existence of vast quantities of shells, which enhance the surface stability. In addition to wind effects, the influence of surface runoff and rainfall is very important. Significant amounts of fresh water contributed to the Bay can produce substantial differences in elevation between Bay and Gulf waters. The resulting ebb currents possess a potential for eroding the inlet banks and enlarging the channels.

HYDRAULIC PROPERTIES - The characteristics and stability of a tidal inlet are governed primarily by the exchange of water through its channels between the ocean and enclosed bay. The quantity of water exchanged and the velocities developed through the inlet are dependent upon the magnitude of the astronomical and meteorological tidal differentials. In order to determine the hydraulic properties at Brown Cedar Cut, it was necessary to obtain a continuous record of either the velocity or the tidal differential. Since instrumentation of the inlet for velocity information was prohibitively expensive and subject to interference by natural human forces, a plan for installation of two recording tide gages was implemented. Velocity time histories were then computed from the tidal differential histories using Manning's equation. Discharge measurements were taken over a complete tidal cycle to calibrate the inlet.

TIDAL DATA - Collection of tide records was performed using Leupold and Stevens Water Level Records Type F, Model 68, which were installed at the positions indicated in Figure 8. They were operated from February 1 to April 9, 1971, and sufficient data were collected to allow meaningful calculations of tidal differentials over most of the recording period.

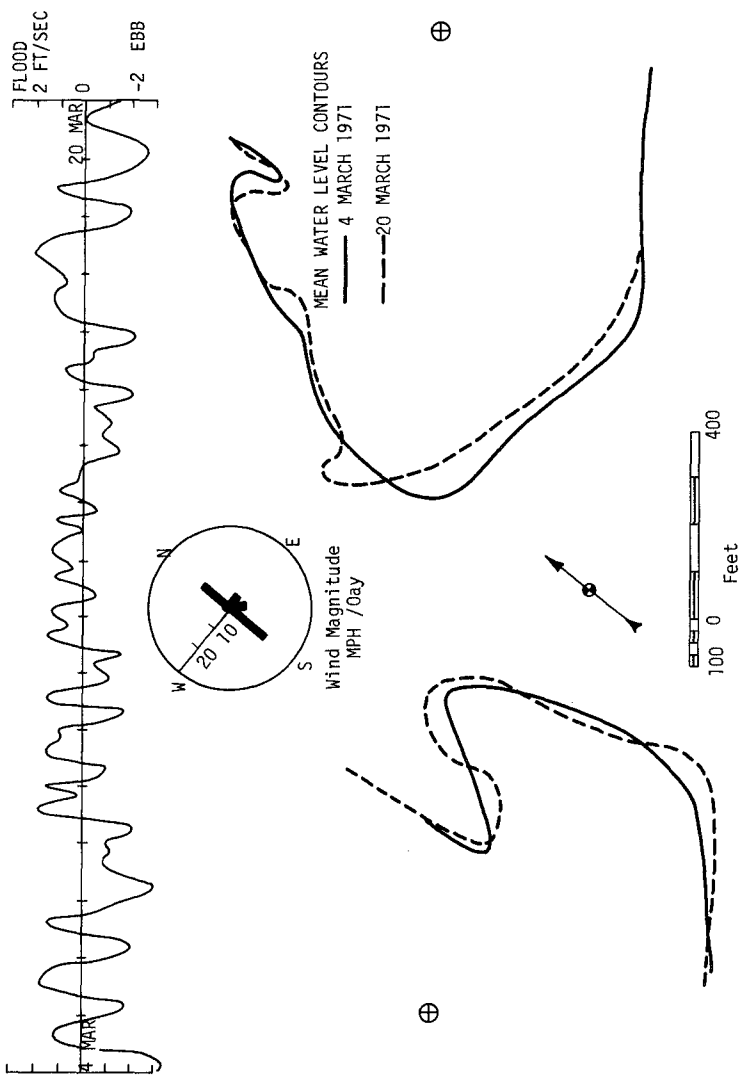

FIGURE 6.--MEAN WATER LEVEL SURFACE CONTOURS, 4 AND 20 MARCH, 1971

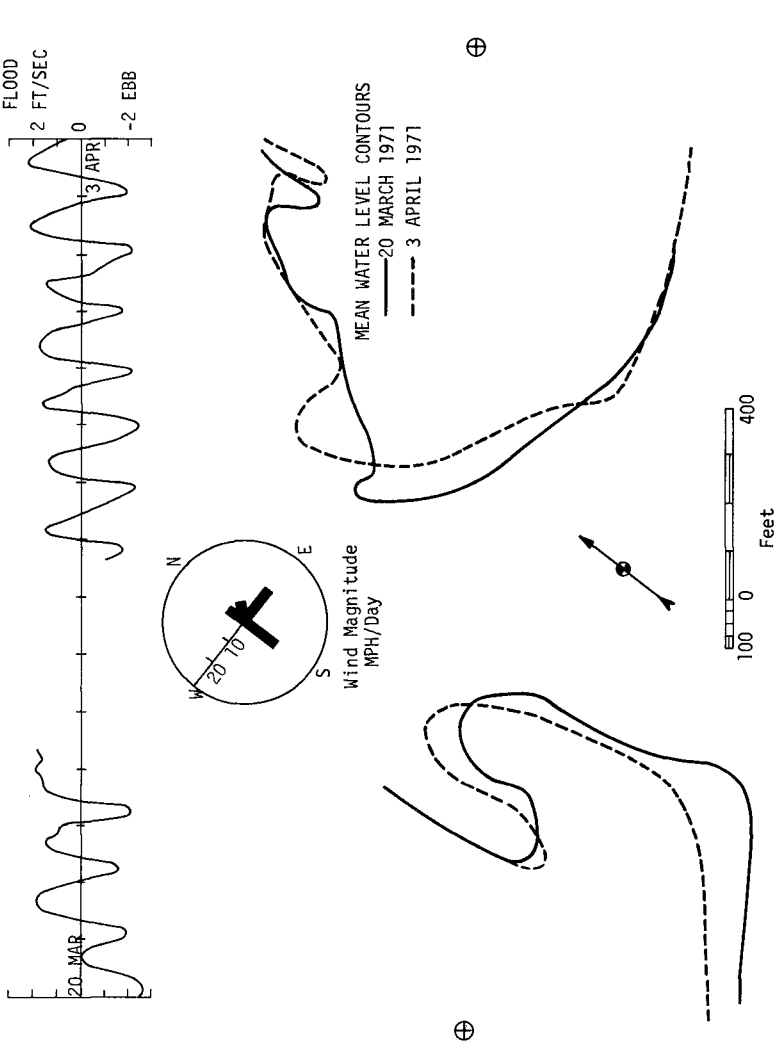

FIGURE 7.--MEAN WATER LEVEL SURFACE CONTOURS, 20 MARCH AND 3 APRIL, 1971

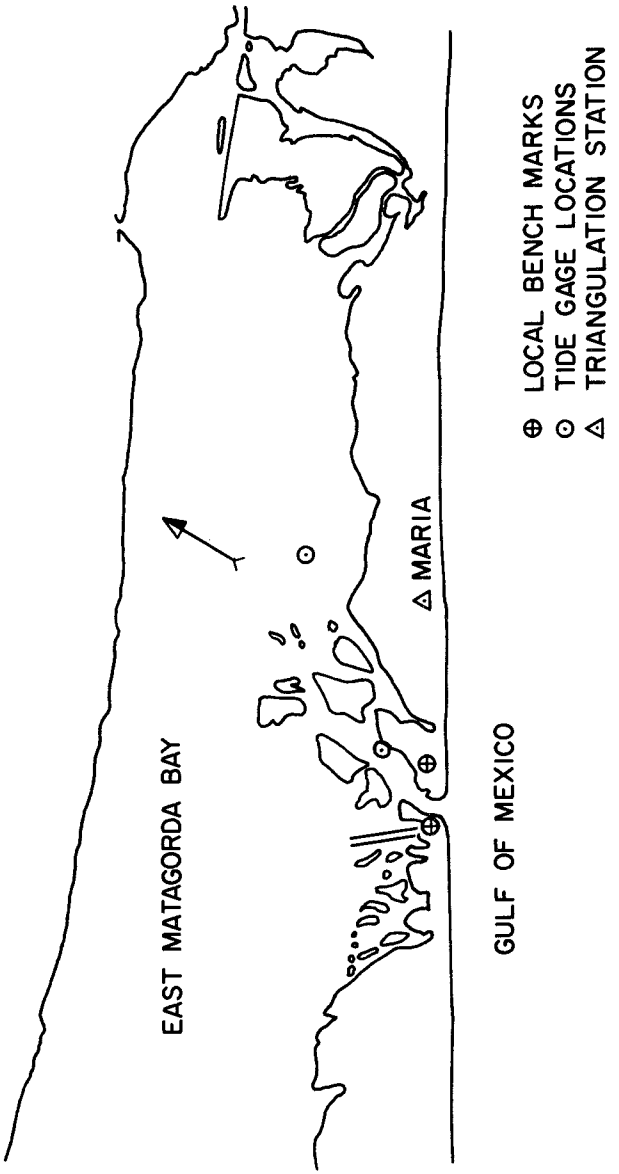

FIGURE 8. POSITIONS OF SEMI-PERMANENT MARKERS, BROWN CEDAR CUT

Analysis of the records was performed to determine the mean water level (MWL) over the reporting period. This value was ob ained by determining the average elevation of the water surface, using data points on the inlet tide record spaced at two hour intervals. The averaged values were then assumed to represent mean water level in both the Bay and Gulf. In addition to determining the MWL value, other tidal data required for related calculations were obtained and are presented in Table 1.

Tide Gage	Mean Low Water	Mean High Water	Mean Range	Maximum Low Water	Maximum High Water	Maximum Range
#1 (Inlet)	-.44	+.37	.81	-2.40	+1.40	3.80
#2 (Bay)	-.10	+.14	.24	-0.92	+1.20	2.12

TABLE 1 TIDAL CHARACTERISTICS AT BROWN CEDAR CUT, FEET FROM MWL DATUM, FEBRUARY 1 TO APRIL 9, 1971.

VELOCITY DATA - Knowledge of the current velocities through Brown Cedar Cut was important for the determination of the Bay tidal prism, as well as for correlations with the observed patterns of erosion and deposition discussed previously. For the purposes of this study, Manning's equation was considered sufficiently accurate for calculations of the velocity time history:

$$V = \frac{1.486\ R^{2/3} S^{1/2}}{n} \qquad (1)$$

where n = Manning coefficient (0.02), R = hydraulic radius (4.43 ft), S = slope of water surface ($\Delta H/L$), L = inlet length (6000 ft), and ΔH = ocean-bay tidal differential. Thus,

$$V = 2.60\ |\Delta H|^{1/2} \text{ (sign } \Delta H).$$

Applying this relationship to the previously determined tidal differential data, the current velocity time histories were computed. Additional statistics obtained during the analysis are presented in Table 2.

Tidal Current	Velocity, fps			Per Cent of Time		
	V_{max}	V_{avg}	Current Direction	V>1.8fps	V>2.2fps	V>2.6fps
Flood	2.2	1.1	44	1.6	0	0
Ebb	3.5	1.5	56	14.0	7.3	3.0

TABLE II VELOCITY CHARACTERISTICS AT BROWN CEDAR CUT, FEBRUARY 1 TO APRIL 9, 1971.

Considering the large number of assumptions required for the use of Manning's equation, it was considered desirable to compare the theoretical velocities with experimentally determined values. Therefore, a twenty-five hour velocity measurement study was performed on March 4 and 5, 1971.

A Gurley-Price current meter suspended on a rod from a small boat was used to determine velocity vs. depth profiles. These measurements were taken at approximately two hour intervals at the stations indicated in Figure 9. The channel cross-section was obtained using both a graduated rod and an ultrasonic fathometer. The following geometric parameters were established: cross-

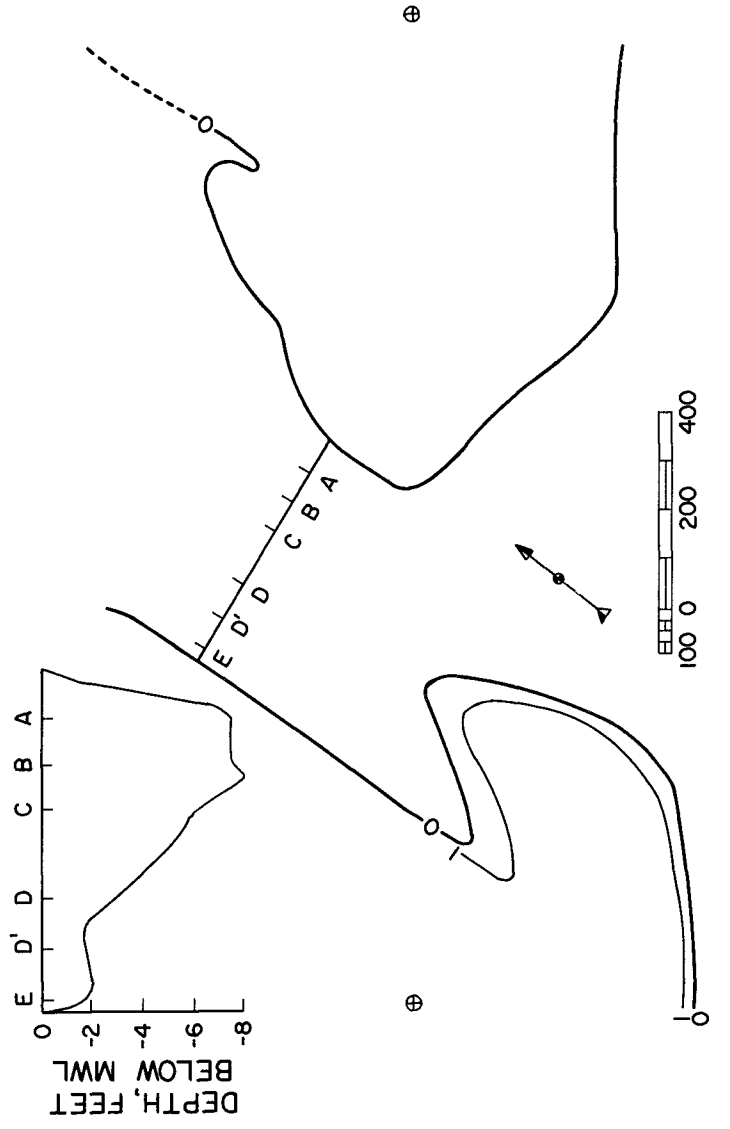

FIGURE 9. LOCATION OF VELOCITY MEASUREMENT STATIONS

sectional area, 2480 square feet; wetted perimeter, 560 feet; hydraulic radius, 4.43 feet.

The measured velocities are plotted against $\sqrt{\Delta H}$ in Figure 10 with a straight line best-fitted to the points. The slope of the line shows almost perfect agreement with Manning's equation. However, for a ΔH of zero, the experimentally determined velocities indicate a value of 0.5 feet per second. The origin of this excessive flood component is unknown. It may result from the transport of water into the inlet by littoral currents or wave action. Breakers on the offshore bar were about four feet in height, and the longshore current velocities were approximately 2 feet per second.

TIDAL PRISM COMPUTATIONS - To evaluate the flushing capability of the inlet, and for comparison with theoretical stability criteria, a determination of the tidal prism of Matagorda Bay was made using two methods. From an analysis of tide gage data, a prism, P_I is obtained from:

$$P_I = A_B h$$

where P = tidal prism, A_B = area of bay (1.5×10^9 ft^2), and h = range of bay tide (0.24 ft). Thus,

$$P_I = 3.6 \times 10^8 \text{ ft}^3.$$

A second method equates the prism to the velocity of water flowing through the inlet:

$$P_{II} = VA_C T$$

where V = average velocity through inlet (1.26 ft/sec), A_C = cross-sectional area of inlet (2480 ft^2), and T = tidal period (89280 seconds). This gives

$$P_{II} = 2.8 \times 10^8 \text{ ft}^3.$$

The first method yields a value 25% higher than that from the velocity method. This is understandable, since the tidal fluctuation is not uniform throughout the bay, decreasing with distance from the inlet. Also, error is introduced by the influx of an unknown amount of water from the Intracoastal Waterway through numerous connecting channels. However, errors in the velocity values may also influence the comparison. Therefore, for purposes of future computation, a representative tidal prism of 3.0×10^8 cubic feet will be assumed.

A comparison with O'Brien's theoretical stability criteria can now be made. In an analysis of the tidal prism, cross-sectional area ratio for a large number of inlets, O'Brien (5) reported the following linear relationsbip was approximated for most non-jettied stable inlets:

$$A_c = 2 \times 10^{-5} P.$$

Based on the representative tidal prism of 3×10^8 cubic feet, and a March 4 cross-sectional area of 2480 square feet:

$$A_c = .83 \times 10^{-5} P.$$

Thus, relatively good agreement is indicated, as Brown Cedar Cut exhibits a tendency for closure.

RECENT STABILITY - Since the final complete topographic survey of April, 1971, the inlet has been monitored on an infrequent basis. However, through the use of aerial photographs and occasional cross-channel profiles, several interesting features have been observed.

Figure 11 indicates that in July, 1971, the west spit continued to elongate toward the north. The gorge closely skirted this spit, but the channel appears to turn sharply southwestward a short distance seaward of the beach face, paralleling the shore for a few hundred feet before turning sea-

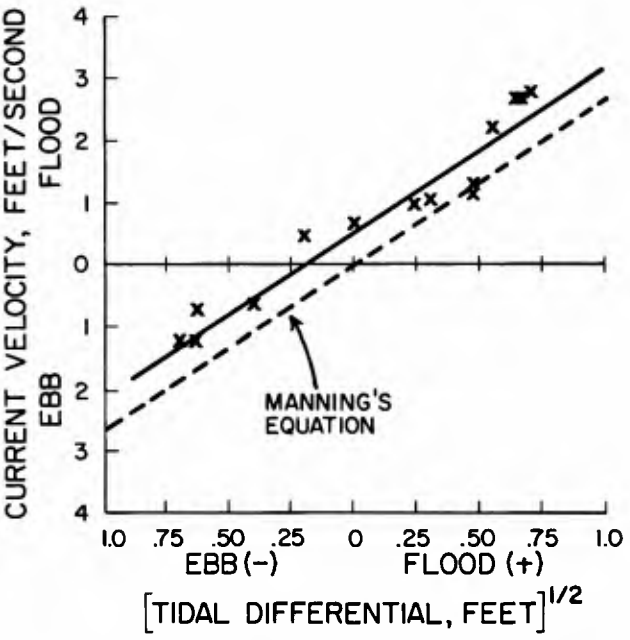

FIGURE 10. OBSERVED CURRENT VELOCITY VS. TIDAL DIFFERENTIAL

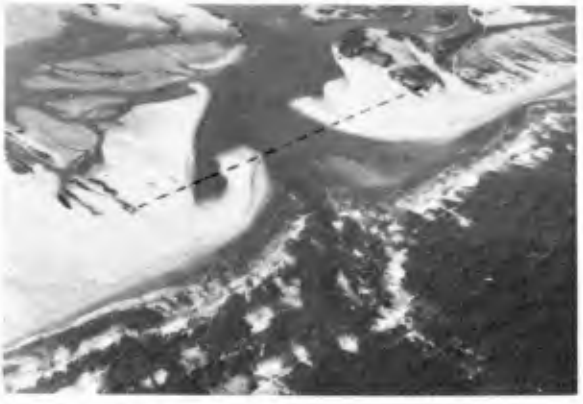

FIGURE 11 --BROWN CEDAR CUT, JULY, 1971

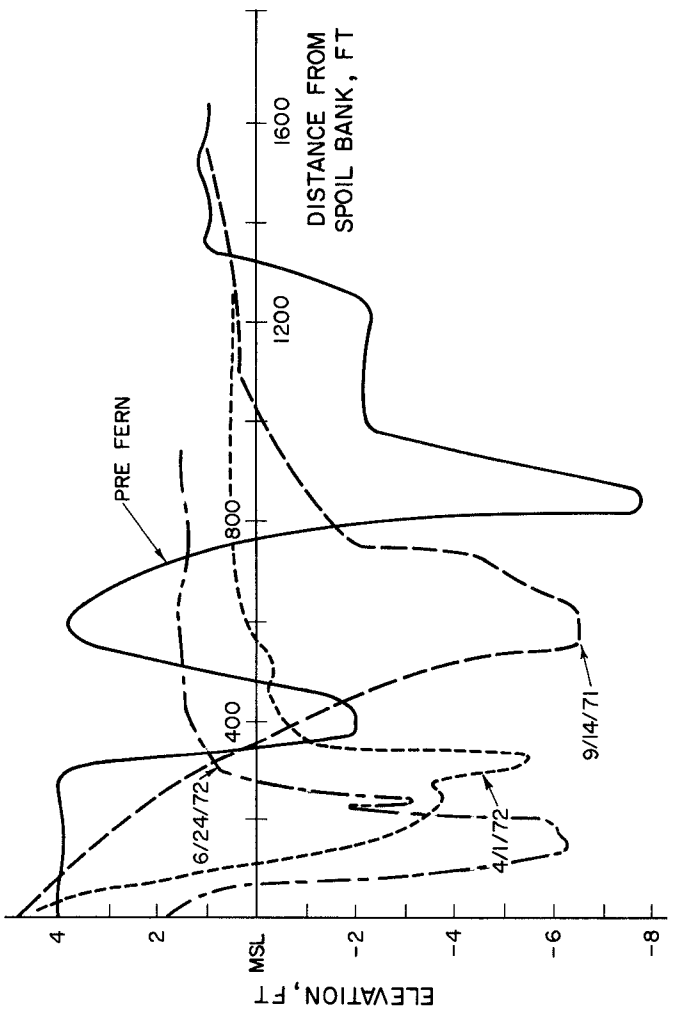

FIGURE 12. PROFILES ACROSS BROWN CEDAR CUT

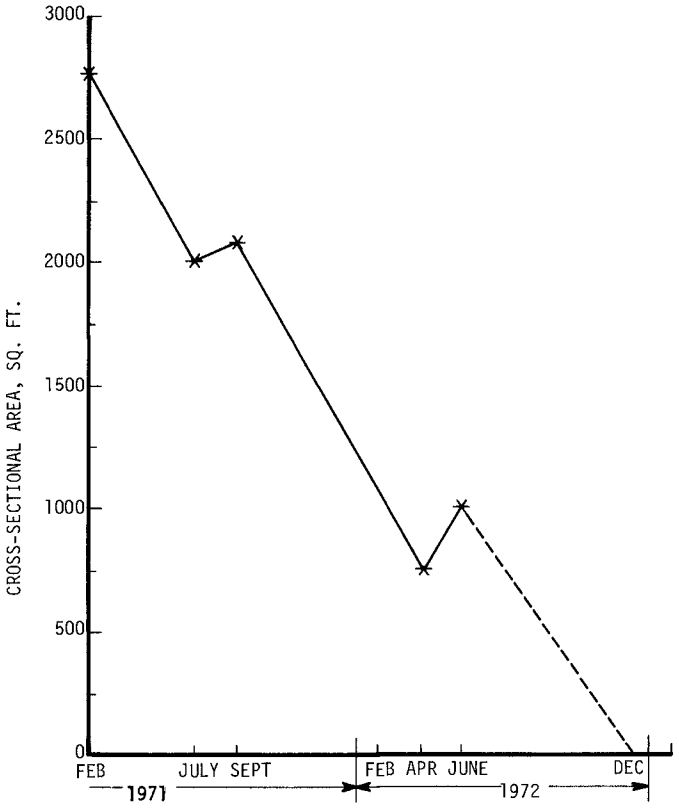

FIGURE 13.--VARIATION OF CROSS-SECTIONAL AREA, 1971-1972

ward. Growth of a major shoal area above the mean low water line is indicated adjacent to the east spit.

In September, 1971, Hurricane Fern crossed the coast within a few miles of the inlet, and provided an unusual opportunity to evaluate the effects of a storm on the inlet. Pre and post hurricane cross-sectional profiles along the line indicated in Figure 11 were compared in Figure 12. Complete eradication of the west spit occurred, and the gorge migrated 250 feet westward, occupying virtually the same position as the former spit. However, the east spit experienced some growth, although the storm increased water levels at the site to about five feet above MWL. Therefore, only a minor increase of 200 square feet in the cross-sectional area of this profile was experienced.

A profile taken in April, 1972, also shown in Figure 12, indicates that the gorge migrated approximately 300 feet westward since September, and the area was reduced from 2100 square feet to 760 square feet.

On June 24, 1972, a final cross-channel profile was obtained. The continuing migration of the gorge, a distance of about 200 feet since April 1, is illustrated in Figure 12. However, since April the cross-sectional area had increased to about 1000 square feet, apparently the result of locally heavy spring rains in the Matagorda Bay watershed.

Using the cross-sectional variation with time as documented from the profiles, it is felt that a rough prediction concerning the possibility of closure of Brown Cedar Cut can be made. Figure 13 illustrates the rather rapid decrease in area since February 1971. With the exception of slight increases resulting from Hurricane Fern and spring rains, the inlet appears to be closing at an average rate of 200 square feet per month. Barring the occurrence of hurricanes or above-average rainfall, and assuming the above rate of closure, the dashed line in Figure 13 indicates that Brown Cedar Cut will close naturally in December, 1972. Periodic surveys of the inlet are to be taken to evaluate the accuracy of this prediction.

ACKNOWLEDGEMENT - This work was supported by a grant from the NOAA Sea Grant Program at Texas A&M University. Funding for the senior author's travel and time in connection with the presentation of the paper was furnished by the U.S. Army Corps of Engineers.

REFERENCES

1. Carothers, H.P., and Innis, H.C., "Design of Inlets for Texas Coastal Fisheries," Journal of the Waterways and Harbor Division, ASCE, Vol. 86, No. WW3, Sept., 1960, pp. 103-128.

2. Evans, O.F., "The Origin of Bars, Spits, and Related Structures," Journal of Geology, Vol. 50, 1942, pp. 846.

3. King, C.A.M., Beaches and Coasts, Edward Arnold Ltd., London, 1959, pp. 186-191.

4. Mason, C., and Sorensen, R.M., Properties and Stability of a Texas Barrier Beach Inlet, Texas A&M Sea Grant Report TAMU-SG-71-217, August, 1971.

5. O'Brien, M.P., "Equilibrium Flow Areas of Tidal Inlets on Sandy Coasts," Journal of the Waterways and Harbors Division, ASCE, Vol. 95, No. WW1, Feb., 1969, pp. 43-52.

6. Price, W.A., "Equilibrium of Form and Forces in Tidal Basins of Coasts of Texas and Louisiana," Bulletin of the American Association of Petroleum Geologists, Vol. 31, No. 9, Sept., 1947, pp. 1619-1663.

7. _____, "Reduction of Maintenance by Proper Orientation of Ship Channels Through Tidal Inlets," Proceedings, Second Conference on Coastal Engineering, Council on Wave Research, Houston, Texas, Nov., 1951, pp. 243-255.

8. _____, "Shorelines and Coasts of the Gulf of Mexico," U.S. Fisheries Bulletin, Vol. 55, No. 89, 1954, pp. 39-65.

9. _____, "Hurricanes Affecting the Coast of Texas from Galveston to the Rio Grande," Beach Erosion Board Technical Memorandum No. 78, U.S. Army Corps of Engineers, Washington, D.C., 1956.

10. _____, "Patterns of Flow and Channeling in Tidal Inlets," Journal of Sedimentary Petrology, Vol. 33, No. 2, June, 1963, pp. 279-290.

11. Wiegel, R.L., Oceanographical Engineering, Prentice-Hall, Inc., Englewood Cliffs, N.J., 1964, pp. 361-372.

12. Yasso, W.E., "Geometry and Development of Spit-Bar Shorelines at Horseshoe Cove, Sandy Hook, New Jersey," Technical Report No. 4 of Project NR 388-057, Department of Geology, Columbia University, New York, N.Y., 1964.

CHAPTER 43

CASE HISTORY OF MISSION BAY INLET SAN DIEGO, CALIFORNIA

by
William J. Herron, Jr.
Moffatt & Nichol, Engineers
Long Beach, California

ABSTRACT

The Mission Bay Inlet was designed as a "Non-Scouring" entrance channel by the Los Angeles District, Corps of Engineers, in 1946. Construction of the inlet was completed in 1959 and the entire project was completed in 1963. A channel with over twice the cross-sectional area required by the "O'Brien" equation was developed to reduce the average cross-sectional tidal currents to less than two feet per second. The design depth of -20 feet MLLW eliminated bottom movement induced by wave action- except during the most severe storms. The jetties are sealed to the +4 foot elevation and extend to the -25 foot depth almost entirely eliminating the intrusion of littoral drift. The channel has shoaled at a rate of less than 20,000 cubic yards per year since final dredging in 1959, indicating the soundness of this concept. This case history was prepared under contract to the Coastal Engineering Research Center, U. S. Army, Corps of Engineers, and project data and aerial photographs were obtained from the Los Angeles District, U. S. Army, Corps of Engineers, and the City of San Diego.

HISTORY

Mission Bay, prior to 1946, was a natural estuary of over 4,000 acres (Photo 1). The major drainage feature into the estuary was the San Diego River with a drainage area of 435 square miles. San Diego is a semi-arid area and the river is normally dry, but during severe floods it may flow in excess of 100,000 cubic feet per second and carry large quantities of silts, sands, cobbles and floating debris. There has not been a flood of this magnitude since 1927. The San Diego River originally discharge into either San Diego Bay or into the southeast corner of Mission Bay. The latter entrance to the ocean was a natural inlet through a sandy beach. While the thread of the inlet meandered constantly, it generally had a controlling depth of 6 feet mean lower low water. The tidal currents in the natural inlet could exceed 4 knots and were sufficient to counteract the force of waves and infringement of littoral drift and maintain a permanently open tidal inlet.

It was realized that if the San Diego River were allowed to continue to discharge into San Diego Bay, serious shoaling would result and would interfere with commercial shipping. In 1876 a permanent levee was constructed, protecting San Diego Harbor. From 1876 to 1946 the river was permitted to discharge its debris into the "useless" Mission Bay.

DESCRIPTION OF AREA

Geomorphology

Indian legend has it that Pt. Loma was originally an island. This is undoubtedly true. There is also little doubt that a few hundred years ago there was much more rainfall than at present and the San Diego River supplied a great deal more sediment to the coastal plain. However, the history of the river up to 1876 was alternate discharge into either San Diego Bay or Mission Bay, or False Bay as it was originally called.

Littoral Drift

Studies by the Beach Erosion Board of the Corps of Engineers in 1942(2) and 1949-50(3) indicate that the Mission Bay area is essentially a beach compartment extending from La Jolla on the north to Point Loma on the south. The San Diego River, originally discharging through Mission Bay, is the principal source of beach sand. It was observed that while there was some upcoast sand movement in the summer and downcoast in the winter the area was essentially in littoral balance. They also found in their 1950 studies that there was a very positive onshore-offshore movement from summer to winter.

Tides

At the entrance to Mission Bay the mean range of tide is 3.8 feet and the diurnal range is 5.4 feet. The extreme range varies from 2.5 feet below to 7.0 feet above mean lower low water. Mean sea level is 2.8 feet above MLLW. The tides are characterized by a diurnal inequality and, as the maximum run is from higher high tide to lower low tide, inlets in southern California generally have higher ebb-tide than flood-tide velocities. This infers an ability to move more sediments during periods of ebb tide than during flood tides.

Waves

Wave action is generally mild in this area having periods of 6 to 16 seconds and heights of less than 3 feet. However, waves 18 feet in height can occur at the entrance to Mission Bay and a significant wave height(H) of 16 feet was used for design of the jetty structures.

Also, based upon experience and consideration of the larger storm waves it was decided to use a navigation project depth of -20 feet MLLW to insure the occurrence of non-breaking waves in the entrance channel at all times except during the most severe storms.

Winds

Winds rarely exceed 30 knots, and their main import is how they affect the maneuverability of boats under sail.

Rainfall

Average annual rainfall in this semi-arid region ranges from 10 inches along the coast to 38 inches in the mountains. 80% falls from December to March inclusive and, in the lower reaches, the San Diego River is dry most of the time. The last major runoff was in 1927. During peak floods it may run as high as 100,000 cubic feet per second. Thus, while the river has almost no influence on the tidal characteristics of the bay and its ocean inlet, the sediments carried during periods of major runoff can be of large quantity and materially affect the bay and/or the adjacent shoreline.

ANALYSIS OF DESIGN

Project Authorization (Fig.1)

The first mention of plans for development of Mission Bay as a navigation area was in 1941 in studies by the City of San Diego and the Corps of Engineers to improve the lower San Diego River for purposes of flood control. As this study progressed it became evident that maximum benefits could be obtained by a combined flood control-navigation project.

The combined project was adopted by Congress in July 1946, as presented in House Document No. 760, 79th Congress, 2nd Session. Detailed design and cost estimates were presented by the Corps of Engineers in "Definate Project Report on San Diego River and Mission Bay", dated January 1949. The Federal Government was responsible for the main channel and its sideslopes, the dredging of the east and west basins, the dredging of the navigation entrance channel and construction and maintenance of the three jetties defining the navigation and flood control channels. Navigation depths of -20 feet MLLW were authorized. The Ventura Boulevard Bridge and everything inland of it was the responsibility of the City, and navigation areas were to be dredged to a depth of -8 MLLW. The Federal portion of this project was essentially completed in 1959 at a cost of about $10,000,000. Local public interests have expended about $19,000,000 to date and private interests over $18,000,000. Ultimate public recreational development is expected to exceed $50,000,000 (4).

Design Objectives

A well conceived harbor, among other considerations, represents a balanced sedimentation system. It is hopefully a large quiet body of water with a relatively narrow protected channel to the sea


SAN DIEGO
SAN DIEGO RIVER
MISSION BAY
PACIFIC BEACH
MISSION BEACH
OCEAN

Figure 1.

requiring minimal maintenance. Due to waves, tides or river discharge, currents of varying rates may be created. If these currents have sufficient velocity, they will either initiate movement and transport sediments or if sediments are already moving, continue them in motion. These currents and resultant sediment movement may cause internal changes in bottom depths or may cause a net gain or loss of sediments to the total harbor complex with resultant shoaling or scouring, either of which may be detrimental.

Engineers in Southern California learned as early as 1876 that if the rivers of this semi-arid country were diverted out of the harbor area and preferably discharged into the sea on the down-drift (littoral) side of the entrance a major source of harbor shoaling could be eliminated. This was demonstrated (successfully accomplished) in 1876 when the San Diego River was diverted out of San Diego Bay and in 1916 when the Los Angeles River was diverted out of Los Angeles-Long Beach Harbor.

The other major exterior source of shoaling is sand from the adjacent beach being carried into the entrance by tide and/or wave induced littoral current, creating shoals either in the entrance or in the quiet water area of the harbor. If the entrance jetties are sand tight, of sufficient elevation, and are extended seaward of the area of littoral drift, most of this type shoaling is eliminated. However, in areas of predominantly uni-directional littoral drift, a sand-bypass system will ultimately have to be established to prevent the impounded sand from being carried over or around the seaward end of the intercepting jetty and thus shoaling the entrance. Jetties extended to the 25 to 40 foot depth contour at Newport Beach in 1936 and Pt. Hueneme in 1941 had demonstrated this concept.

Even though there are no external sources of sediments to cause shoaling of a harbor or its entrance channel and the discharge from the uplands has been diverted, tidal or other currents still are a liability. They may either cause internal movement of sediments (with adverse shoaling or scouring effects) or interfere with the safe and efficient operation of boats using the harbor.

These experiences resulted in a concept known as a "non-scouring" tidal channel, i.e., enlarge the inlet cross section to a point where tidal current velocities are reduced below their capability to move bottom material. A secondary benefit in such reduced velocities is the elimination of hazards to boats. Such a maximized cross-sectional area requires a balanced design between width and depth. Increased depth permits deeper draft boats to use the harbor, prevents a breaking wave, or reduces the steepness of waves during the storms, making for a safer entrance. Wave induced bottom movement can also be eliminated, or greatly reduced. The principal effects from increased width of channel is less boat traffic congestion and greater maneuver area for sail boats. On the minus side are increased dredging costs, sometimes more costly jetties, increased land acquisition costs and the introduction of more wave energy into the inner harbor to the possible detriment of berthed boats and interior land perimeters.

BASIS OF INLET DESIGN 1946 to 1949

1. The design relationship between the dimensions of a harbor or bay and its channel connection to the ocean at this time was largely an emperical one. The most acceptable work in this field had been done by Lt. Col. T.M. Robins of the Corps of Engineers(6), and Morrough P. O'Brien of the University of California at Berkeley (5). They had developed the following relationships based strictly on observations of existing harbors, bays and estuaries.

In 1931 O'Brien developed the equation $A = 1{,}000\ T^{0.85}$ where A = area of the entrance section below mid-tide in square feet. T = volume of the tidal prism in square-mile feet between MLLW and MHHW, and has a value ranging between 7.0 and 3000. In 1933 Robins published the relationship developed by C.I. Grimm of his staff as $A = T$ where A = Area of channel cross-section at mid-tide in square feet and T = The Tidal prism in acre-feet between MLLW and MHHW.

2. Mission Bay in its natural state reportedly had a tidal prism of about 10,400 acre feet (Photo 1). The minimal cross-sectional area of the entrance channel as surveyed in 1947 was 6000 square feet (Fig.2a). Compared to this field data, the Robins' equation shows a computed equilibrium entrance area of 10,400 sq.ft. while the O'Brien equation shows an area of 9,100 sq. ft. The reported 10,400 acre-feet of tidal prism may be in error or, if correct, the very flat slopes of the marshlands and the constructions of tidal flow at the two Ingraham Boulevard bridges may have reduced the resultant required channel cross-section from the O'Brien derivation of 9100 sq. ft. to the actual 6000 sq. ft.

3. The designers of Mission Bay increased the cross-sectional area of the planned entrance channel to 19,800 square feet below mean tide level and even though creation of the Aquatic Park resulted in some 30,000,000 cubic yards of dredging, the net result was a tidal prism of about 9,200 acre feet. However, the flat slopes of the marshland areas were eliminated and there is very little frictional or time loss in disposing of the tidal prism. Thus, using the O'Brien equation, the jettied entrance channel computes at an equilibrium flow area of 8900 square feet as compared to the design area of 19,800 sq. ft. Treating the tidal current produced from a spring tidal drop of 5.4 feet in 6 hours, average channel velocity would be 0.97 ft. per second. It was felt that maximum velocity would not exceed 2 ft. per second except during spring tides, and scouring velocity along the bottom of the channel should be even less.

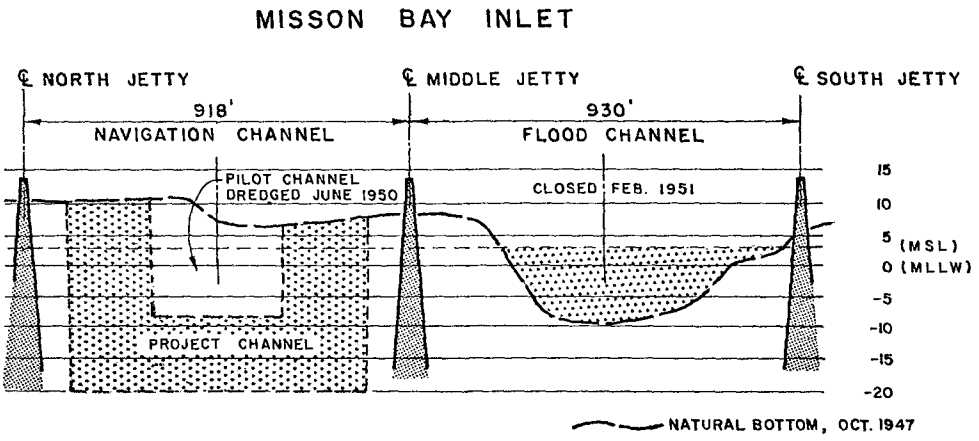

Station 40+00
FIGURE 2a

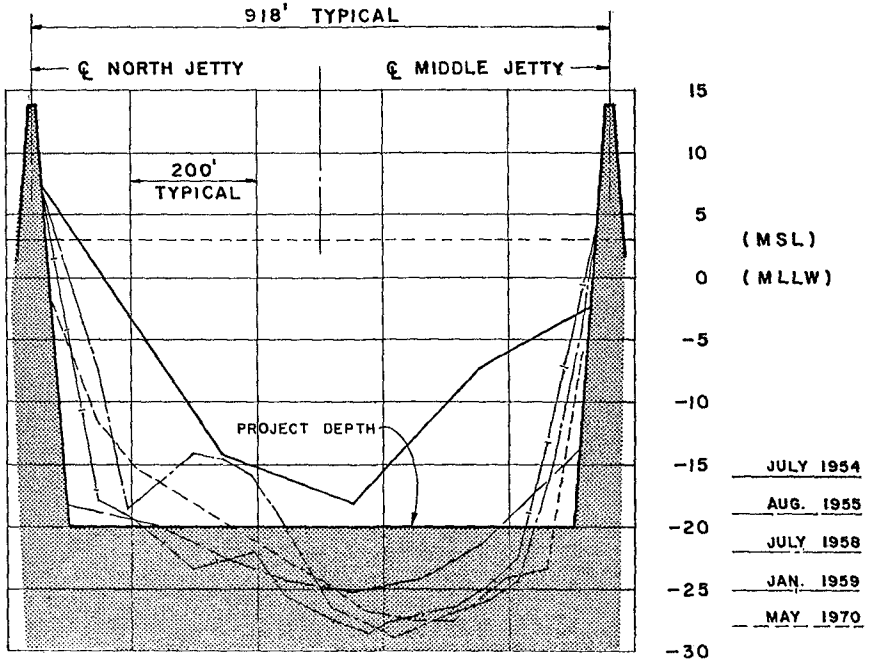

Station 48+00
FIGURE 2b

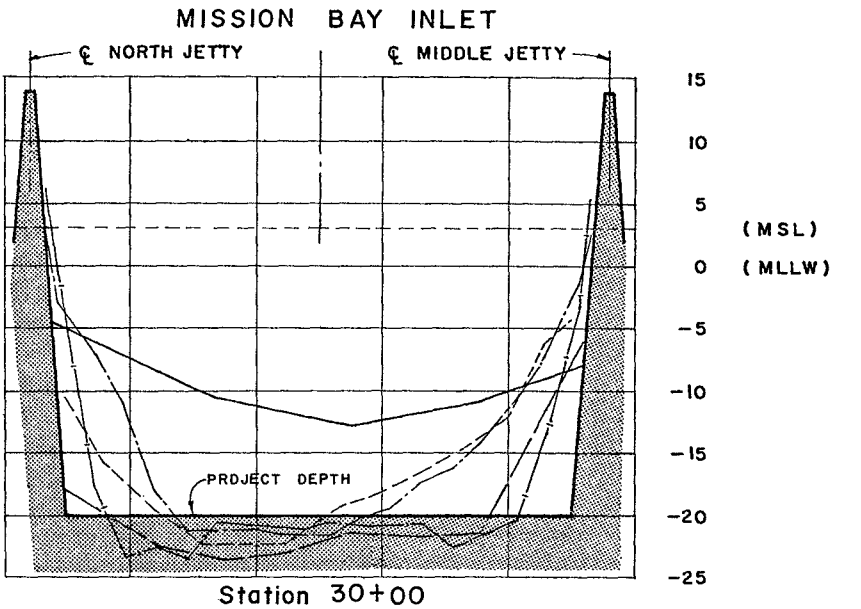

Station 30+00
FIGURE 2c

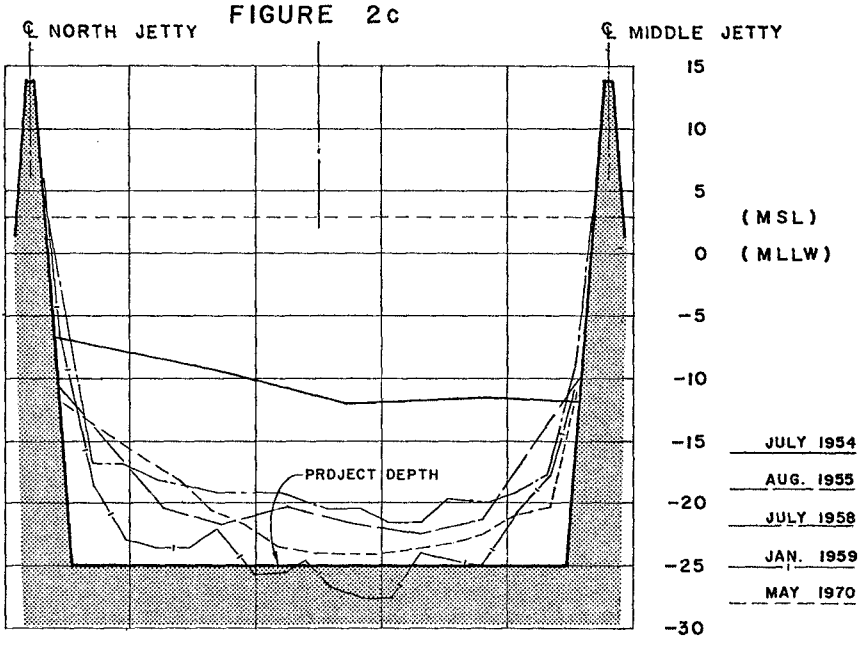

Station 13+00
FIGURE 2d

BEFORE CONSTRUCTION
GENERAL CONFIGURATION OF BAY AT HIGH TIDE
1947 **NO. 1**

START INTERIOR CONSTRUCTION
NOTE CONFIGURATION OF NATURAL INLET
FEB. 1948 **NO. 2**

START ENTRANCE CONSTRUCTION
MIDDLE AND SOUTH JETTIES
JULY, 1948 NO. 3

COMPLETION OF FLOOD CONTROL CHANNEL OUTLET
MIDDLE AND SOUTH JETTIES
FEB. 1949 NO. 4

NAVIGATION AND FLOOD CONTROL CHANNEL JETTIES
COMPLETION OF NORTH JETTY
NOV. 1950 NO. 5

NAVIGATION AND FLOOD CONTROL CHANNELS
MIDDLE JETTY CLOSED, CREATING TWO CHANNELS
SEPT. 1951 NO. 6

DEVELOPMENT OF WEST MISSION BAY
NOTE CLOSURE OF FLOOD CHANNEL
JAN. 1953 **NO. 7**

START OF DEVELOPMENT OF EAST MISSION BAY
NOTE COMPLETED DREDGING OF ENTRANCE CHANNEL
JAN. 1958 **NO. 8**

COMPLETION OF MISSION BAY - SAN DIEGO RIVER PROJECT
1963 NO. 9

HYDRAULIC MODEL STUDY - MISSION BAY ENTRANCE
1969 NO. 10

CONSTRUCTION PROCEDURE

In any project of this magnitude, construction problems during an extended construction period (1946 to 1963) can create problems and misunderstandings. The time s quence for creation of the bay and the jettied entrance channel was as follows:

1946: Dredging and filling of interior portions of the bay were initiated by the City. (Photo 2, 1948).
May 1948: The Corps of Engineers initiated construction of the south (flood control) jetty and the middle (combined flood control and navigation) jetty. (Photo 3, 1948); Photo 4, 1949).
June 1949: The Corps of Engineers initiated construction of the north (navigation) jetty.
November 1949: The south and middle jetties were completed.
September 1950: The north jetty was completed (Photo 5, 1950).
June 1950: A pilot channel (300 feet wide) was dredged to the -8 foot MLLW depth to divert tidal flow of the bay to between the navigation jetties. (Photo 5, 1950).
February 1951: The flood control channel was completed and the final section of the middle jetty was closed, separating the Flood Control Channel from Mission Bay. (Photo 6, 1951).
March 1951 to Nov. 1954: The Corps of Engineers project was shut down because of the Korean War. During this time period, the City essentially completed their dredge and fill program for the bay westerly of Ingraham Street (Photo 7, 1953).
December 1954: Dredging of the outer entrance channel by the Corps of Engineers was resumed.
May 1955: An experimental attempt was made to seal the jetties to prevent littoral sand from entering the navigation channel through voids in the jetty cap rock.
July 1955: The outer entrance channel was completed to full width and depth.
January 1957 to December 1957: The Corps of Engineers dredged a portion of the main channel and Quivera Basin to a depth of -20 feet MLLW. This relatively coarse sand was pumped to the eastern perimeter of the bay to stabilize the mud deposits along U. S. 101 Highway. This dredging essentially permitted full and unimpeded tidal flow through the West Bay, the main channel and the entrance channel. (Photo 8, 1958).
July 1958: The Corps of Engineers dredged the main channel and the west anchorage basin (Mariner's Basin) to a depth of -15 feet, MLLW. At the same time, the City initiated a 12 million cubic yard dredging contract to complete the development of the east bay. This project, completed in 1963, essentially completed the City's dredge and fill program, and while the natural tidal prism was reduced by about 10%, flow characteristics were greatly improved by elimination of the large marshy areas with flat slopes between high and low tide. (Photo 9, 1963).
August 1959: The middle and north jetties were sealed with concrete grout from mean lower low water to the +4 foot elevation through the littoral zone to prevent future shoaling of the navigation channel by intrusion of littoral sand through the large voids in the cap rock.

October 1966 to June 1969: Field studies, resulting in a hydraulic model study were made by the Corps of Engineers to develop a solution for occasional undesirable wave action in the two deepwater anchorage basins (Photo 10, Hydraulic Model Study).
1972: Maintenance dredging is planned to remove about 300,000 cubic yards of sand from the entrance channel.

DISCUSSION OF PROBLEMS ENCOUNTERED DURING CONSTRUCTION

The shutdown of this project as a result of the Korean War had a most adverse effect. While the flood channel was completed, only a minimum effort was made to open the bay to the sea by dredging a pilot channel through the barrier beach. The pilot channel was to be 300 feet wide to the -8 foot depth (Fig. 2a). In other words, looking at O'Brien's equilibrium equation the cross-sectional area of less than 4000 feet was completely inadequate and the channel shoaled and spread the full width between jetties to form a very dangerous bar. (Figs. 2c and 2d). From an engineering point of view this was a very successful maneuver because in accord with the equilibrium relationship and because of the west coast tidal character of getting maximum tidal run from MHHW to MLLW, the minimal cross-sectional area of the entrance channel increased to about 11,000 $ft.^2$ by July 1954, and over 250,000 cubic yards of sand were scoured from the channel and apparently carried out to sea. However, the boatmen were not adequately informed as to the hazards of this partial channel, and before its closure by City Ordinance in 1953, several boats were capsized and 11 lives lost.

Another major problem was the intrustion of littoral sand into the entrance channel. However, until 1954, in Southern California, it was the practice to only bring core rock, or "C" rock up to MLLW for jetties and then to continue construction through the wave zone with large cap rock. Thus both navigation jetties at Mission Bay consisted of 2 to 8 ton cap stone from MLLW to the +14.0 foot elevation. It was realized during the initial dredging of the entrance channel in early 1955 that a very appreciable amount of littoral sand was being carried through the voids of the cap rock and shoaling the navigation channel. In May 1955 a plan was conceived to introduce a concrete grout diaphram into the center of the cap rock section (7). After considerable testing, this was accomplished by drilling holes along the centerline of the structure and forcing a mixture of concrete and bentonite (driller's mud) through the holes and into the central voids of the cap rock. The intent was to create a diaphram with a minimum elevation of +4 feet. Some 2200 feet of the middle jetty and 600 feet of the north jetty were sealed in this manner.

During this same period of developing the entrance channel, it was observed that, all too frequently, waves were either breaking in the entrance channel or were so steep as to constitute a serious hazard to small boats. As a final move, in June 1960 the outer 1000 feet were dredged to the -25 foot depth. This appears to have greatly improved the navigability of this outer portion.

The remaining inlet problem at Mission Bay is excessive wave action inside the bay. It has been learned at Mission Bay, Alamitos Bay, Newport Harbor and Marina del Rey that while they are excellent harbors, so far as navigability and low maintenance are concerned, these excessively wide entrances do admit a great deal of wave energy which must be disposed of. Alamitos Bay is partially sheltered by the outer harbor breakwater and much of the interior perimeter is still in sand beaches which can absorb considerable wave energy. Much the same is true at Newport; the jetties are skewed some 20° to the south,and the north jetty acts, in part, as a breakwater. Newport Bay also consists mostly of sand beaches around its perimeter, and has had no interior wave problems. A very bitter lesson was learned at Marina del Rey, where subsequent to construction of jettied entrance, the interior walls were changed from rock revetment to vertical concrete bulkheads which almost totally reflected wave energy. An offshore breakwater had to be constructed across the entrance to keep this wave energy out of the boat basins. At Mission Bay, a wave problem exists in the two deepwater anchorages: Quivera Basin and Mariner's Basin. Very soon after installation of boat slips in 1959 and 1960 in Quivera Basin, there were complaints of waves as high as 2.5 feet at the berths with damage to both boats and floats. Studies were made in the field (8) and by hydraulic model at the Corps of Engineers' Waterways Experiment Station (9) and it was concluded that the main problem was excessive wave energy reaching the inshore end of the entrance channel. The inshore end of the entrance channel makes a 90° left into the main channel, and the shore is protected by a semi-circular rock revetted slope. This revetment not only tends to reflect too much wave energy, it also tends to focus this reflected energy towards the entrance to Mariner's Basin. Several corrective measures were tested and the most promising was to convert the revetted semi-circular end of the channel to a series of straight revetted sections in echelon that would tend to reflect this energy back out the entrance channel to sea (Photo 10). Estimated cost of this modification is about $1,000,000, and until there is further development of the two basins and the need is strongly demonstrated, no action is planned.

REVIEW OF DESIGN 1972

The design of the inlet for Mission Bay, as developed in 1946-1949, has since proved to be fundamentally correct. Dean O'Brien reviewed his work in 1969 (10) and arrived at the basic equation: $A = 4.69 \times 10^{-4} P^{0.85}$, expressing P in cubic feet rather than his original expression of square-mile feet. Thus the minimal cross-sectional area of the entrance channel for equilibrium flow would still be in the order of 9000 square feet. Since completion of the entrance channel dredging in 1959, the cross-sectional area has varied from 16,400 sq. ft. to the design area of 19,800 sq.ft. which is well above the minimal. The first maintenance dredging of the entrance is scheduled for the latter part of 1972. Making due allowance for sand entering the channel before completion of jetty sealing, the average maintenance dredging of the entrance between 1954 and 1972 amounts to less than 20,000 cubic yards per year.

In Feb. ,1972, Professor J. W. Johnson published a paper comparing the various tidal inlets of California, Oregon and Washington (11). His work confirmed the equilibrium curve developed by O'Brien. He realized, as did O'Brien, that factors other than tidal prism should have an influence on the equilibrium cross-sectional area of the inlet. In an attempt to prove this point, he compared the characteristics which he believed should have certain modifying effects on the equilibrium ratio. He gave identifying symbols to the plotting points for inlets with two,one or no jetties and with various degrees of exposure to wave action. He also made separate plots of his data adding such parameters as tide range and tide-cycle duration. Surprisingly, these factors and parameters showed no sifnigicant modifying trends. All inlets plotted within reasonable proximity of the equilibrium curve with the exception of Morro Bay, Marina del Rey, Alamitos Bay and Newport Bay, all of which showed entrance sections far larger than their tidal prisms should have allowed. Prof. Johnson stated that these radical departures from the norm appeared to be "primarily a function of wave climate and the limited movement of littoral drift as affected by long jetties and the possible initial over-dredging of the entrance channels". He concluded that since these inlets and a few others, including the Mission Bay Entrance,showed no evidence of shoaling, they were not in equilibrium in the usual sense for unimproved inlets because of the effects of limited wave action, low littoral drift or long jetties. It is apparent from Figure 3 of this study that, at least in the case of San Diego Bay, Mission Bay, Newport Bay, Marina del Rey and Alamitos Bay, the inlet has not been over-dredged by mistake, but the cross-section has been deliberately increased beyond "equilibrium" limits. This was done to reduce the tidal currents and to prevent appreciable sand transport in the entrance channel.

The various relationships between the tidal prism and the area of the inlet since start of construction in 1946 are shown in Figure 3 and Table 1. It is apparent that there has been a very major change in the relationship of tidal prism to inlet area with a resultant reduction in tidal velocities, yet no significant entrance shoaling has occurred as the equilibrium formula would have predicted.

During the original design of Mission Bay and its inlet, it was only possible to make a rough approximation of tidal current velocities through the critical sections. Since 1948, a great deal of study has been done on this subject and one of the most widely accepted methods for computing velocity of inlet currents was developed by Dr. G.H. Keulegan, as described in the U.S. Army Corps of Engineers' Committee on Tidal Hydraulics, Technical Bulletin No.14. His procedure takes into account the tidal oscillation in the ocean, the physical properties of the inlet channel, the physical properties of the basin and inflow from streams or rainfall, and it develops a mathematical relationship between the tidal range in the basin and the maximum velocity in the connecting channel.

TABLE 1
MISSION BAY INLET STUDY
RELATION TIDAL PRISM TO INLET

Date	Min. Cross Section-Area of Inlet A(Sq.Ft)		Tidal Prism Spring Tide Range P (Cu.Ft).		Ratio $P/Ax10^4$	
1947	$7.2x10^3$	(1)	4.5×10^8		6.3	
July 1954	$1.11x10^4$	(2)	4.4×10^8		4.0	
Aug. 1955	$1.95x10^4$	(3)	4.4×10^8		2.1	
July 1958	$1.55x10^4$		4.3×10^8		2.8	
Jan. 1959	$1.86x10^4$		4.3×10^8		2.3	
June 1963	$1.78x10^4$		4.0×10^8	(4)	2.3	
May 1970	$1.64x10^4$		4.0×10^8		2.4	
June 1971	$1.72x10^4$		4.0×10^8		2.0	(6)
Fall 1972	$1.98x10^4$	(5)	4.0×10^8		2.0	(6)

1. Natural Channel, including San Diego River
2. Adjusted pilot channel, dredged in June 1950
3. Entrance channel dredged to full dimensions
4. Tidal Prism completed to full dimension
5. Proposed Maintenance dredging of entrance channel
6. The O'Brien equilibrium equation for the relationship between the entrance channel with two jetties and the tidal prism for a tidal prism(P) of $4.0x10^8$ cu.ft. gives an equilibrium cross-sectional area(A) of $1.0x10^4$sq.ft. and P/A is $4.0x10^4$. This is twice the value of P/A for a "Non-Scouring" channel.

Mr. John M. Nichol, Moffatt & Nichol, Engineers, had occasion to use Dr. Keulegan's method in a study of currents at Channel Islands Harbor (13) in 1970. He developed the following maximum entrance current velocities for the "non-scouring" entrance channels of Southern California:

San Diego	2.1 ft/sec.
Mission Bay	1.9
Newport Bay	1.5
Alamitos Bay	1.1
Marina del Rey	0.4

Thus it is seen that "tidal scour" is a very minor or non-existant factor in design and maintenance of these particular harbors.

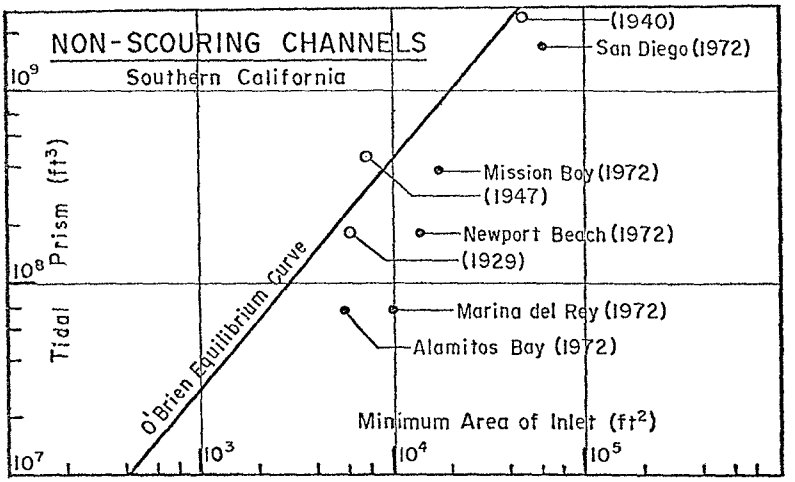

FIGURE 3

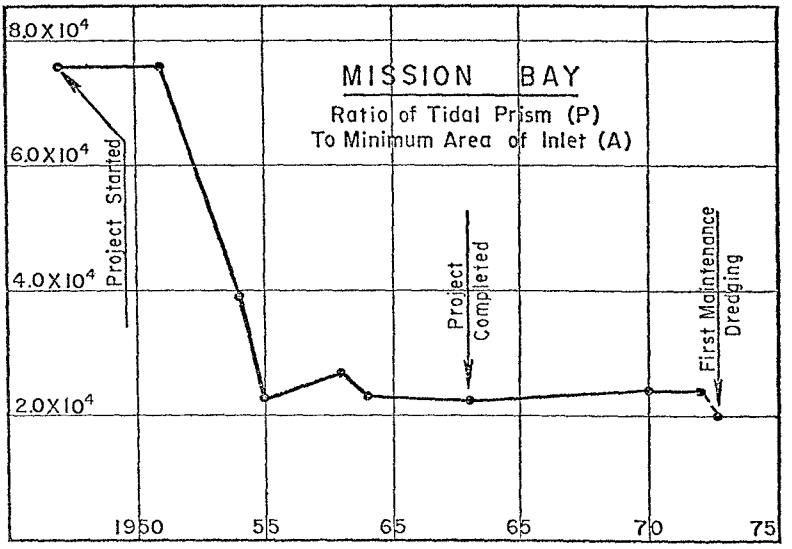

FIGURE 4

CONCLUSIONS

The principle of a "non-scouring-non-shoaling" channel, such as was developed for Mission Bay in 1946-49, is sound so long as the following criteria are satisfied: 1) there must be no exterior supply of shoaling material either from upland drainage or from littoral drift; 2) tidal velocities must be reduced to where there is no movement of bottom sediments within the bay or the entrance channel; 3) the entrance channel must be of sufficient depth to prevent appreciable movement of bottom sediments by wave induced currents.

Problems created by this type channel are: 1) possibility of such low tidal velocities as to fail to create adequate flushing action and cause pollution problems; 2) a wide entrance channel may permit excessive wave energy to be delivered to the inner basins. Measures must be taken to properly dispose of this energy by either absorption or reflection.

The most serious problem at Mission Bay resulted from the suspension of work on the project from 1951 to 1955 because of the Korean War, and the failure of the boating public to appreciate the hazards of using a partially dredged entrance channel. Completion of the entrance channel to full dimension eliminated this hazard.

A jetty-design deficiency had to be corrected because of the use of cap rock only in the tide and wave zone above mean lower low water level. The large voids (35 to 40%) inherent in caprock placement permitted an excessive amount of littoral sand to pass through the jetty into the channel. Sealing of portions of the jetties to the +4 foot elevation effectively reduced this shoaling factor.

Since completion of the entrance channel to full design dimension in 1959, there has been no serious shoaling or navigation problems. The first maintenance dredging scheduled for the latter part of 1972 indicates an average annual rate of shoaling of less than 20,000 cubic yards.

* * * *

REFERENCES

1. Westway Magazine(Oct. 1967). Southern California Auto Club.

2. Beach Erosion Board, U.S.Army, Corps of Engineers (Nov. 1942). Beach Erosion Study of Mission Beach, California.

3. Beach Erosion Board, U.S.Army, Corps of Engineers (1951). Unpublished Report by D. L. Forrest.

4. Patterson, John K. (Oct. 1965). Mission Bay, 1939-1965. City Engineering Dept., City of San Diego.

5. O'Brien, Morrough P. (May 1931). Estuary Tidal Prisms Related to Entrance Areas. Civil Engineering Vol. 1, No. 8, pp 738.

6. Robins, Thomas M. (Jan. 1933). Maintenance and Improvement of Entrance Channels to the Pacific Coast Ports. World Ports, Jan. 1933.

7. Los Angeles District, U.S. Army Engineers (March 1958). Addendum No. 1 to Definate Project Report, dated Jan. 1949, on San Diego River and Mission Bay.

8. Marine Advisers (Sept. 1961). A Study of Sea Swell and Seiches in Mission Bay. Wave Study at Mission Bay, Calif. (Sept. 1963).

9. U.S. Army Engineer Waterways Experiment Station, Vicksburg, Miss. (1970). Wave Action in Mission Bay, Technical Report No._____.

10. O'Brien, Morrough P. (Feb. 1969). Equilibrium Flow Areas of Inlets on Sandy Coasts. Journal of the Waterways and Harbor Division. Proceedings of the American Society of Civil Engineers Vol. 95, No. WW 1, Feb. 1969.

11. Johnson, J. W. (Feb. 1972). Tidal Inlets on the California, Oregon and Washington Coasts. University of California Hydraulic Engineering Laboratory. HEL-24-12, Berkeley,Calif.

12. Keulegan, G.H. (1967). Tidal Flow in Entrances. Technical Bulletin No. 14, Committee on Tidal Hydraulics, Corps of Engineers, U. S. Army.

13. Nichol, John M. (April 1970). A Study of the Effects of Waterway Expansion, Channel Island Harbor.

CHAPTER 44

SEDIMENT TRANSPORT IN A TIDAL

John R. Ritter
Hydrologist
U.S. Geological Survey
Water Resources Division
Menlo Park, California

ABSTRACT

Tidal flow and suspended-sediment discharge were measured in or near the inlet to Bolinas Lagoon through seven ebbtides and six floodtides. The highest flows and suspended-sediment discharges occurred during the major daily ebbtide. Most transported sediment was sand and most sediment deposited in the lagoon was sand. Computations from a relation of suspended-sediment discharge and tidal range indicated that the annual suspended-sediment discharge of ebbtides exceeded that of floodtides by 9,000 tons. The highest concentration of suspended sediment occurred near the east shore of the inlet, which is at the end of a sand spit.

The measured volume of water moved by a tide ranged from 180 to 2,740 acre-feet and the maximum flow measured was 7,900 cubic feet per second. The highest average velocity for a measurement was 4.9 feet per second. The maximum average velocity in the inlet occurred within an hour after midtide during a floodtide and usually at about one-third tide during an ebbtide. The relation of average tidal velocity ($\bar{u}_t$) to tidal range (R), was $\bar{u}_t = 1.21R^{.508}$; the average flow for a tide can be estimated by multiplying this calculated average velocity by the average cross section of the inlet.

INTRODUCTION

Five series of measurements of the quantity of sediment being transported by tides into and out of Bolinas Lagoon, Calif., were made as part of a study to determine the rate of sediment deposition in the lagoon and to define the sources and movement of the sediment (Ritter, 1970). Three series of measurements were made at the inlet, and two series of measurements were made in two channels inside the lagoon not far from the inlet (fig. 1). In all, the suspended-sediment discharge for seven ebbtides and six floodtides was determined. The measurements were made during periods when inflow to the lagoon from upland sources was negligible; therefore, the values of sediment discharge represent those caused chiefly by tidal action.

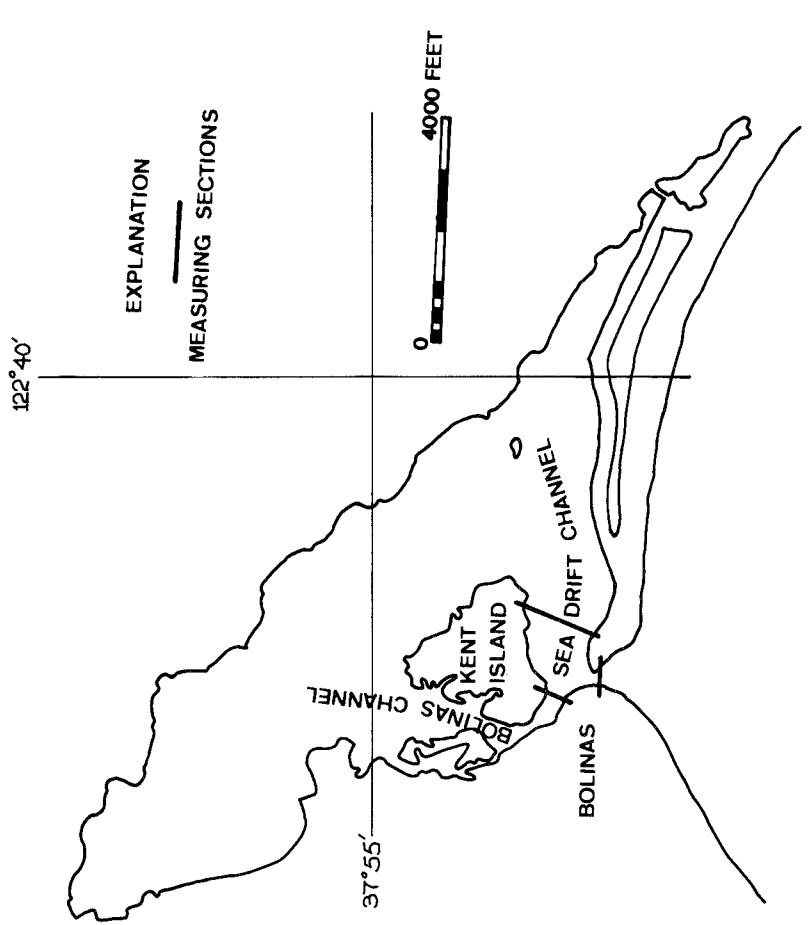

FIGURE 1.--Map of Bolinas Lagoon showing sections used to measure suspended-sediment discharge.

Bolinas Lagoon, the seaward end of a rift valley created by the San Andreas fault, is about 15 miles northwest of San Francisco. The lagoon has a triangular shape with maximum dimensions of 1 by 3 miles and an area of about 1,100 acres. Most of the lagoon is under water at high water, whereas over 50 percent of the lagoon is usually exposed at low water. The lagoon has been filling with sediment in historic time.

The mineral content of the bottom sediment in the lagoon, studies of the littoral drift, and observations of the littoral current, suggest that a major source of the bottom sediment is the cliff west of the inlet. This cliff is eroding at a rate of 2.5 feet per year (A. J. Galloway, oral commun., 1967).

The inlet to Bolinas Lagoon cuts between the end of a spit and the cliffs of a headland (fig. 2). The eastern or spit side of the inlet is composed of sand; the bottom of the middle of the inlet is bedrock or sediment larger than sand; the west side is bedrock but usually is covered by a narrow sandy beach abutting a high cliff. Tidal deltas have formed on both the lagoon and ocean sides of the inlet.

The inlet is 250 to 350 feet wide at mean sea level; the thalweg of the inlet is about 11 feet below mean sea level. The sides of the inlet have a slope as much as 16 percent. The thalweg remained about the same during the study; however, the width of the inlet changed greatly, especially between elevations of 2 and 8 feet above mean sea level (fig. 3).

During the first year of the study no large-scale changes in the width of the inlet were observed, but in the summer of 1968 the inlet was observed to widen considerably. Between August 1967 and December 1968, the inlet was eroded as much as 300 feet laterally and often more than 4 feet vertically. Most of the erosion occurred along the spit side of the inlet during the summer of 1968. By July 1969 deposition had replaced much of the sediment that had been removed by erosion, and the cross section of the inlet was becoming similar to that of August 1967 (fig. 3). Erosion of the end of the spit similar to that observed in 1968 probably recurs at intervals of several years but has not occurred recently (probably not within the last decade) judging from the quantity of vegetation on the dunes prior to erosion. The cause of the widening of the inlet in 1968 is not known; no correlation with wave conditions or littoral drift was observed.

Time-lapse photography by Beck (1971) from a cliff overlooking the inlet pictorially recorded changes in the configuration of the inlet during daylight hours for the period January 1968 to July 1969. That photography shows that erosion first began on the ocean side of the spit and that erosion moved progressively northward into the lagoon. Thus, forces responsible for the erosion must have originated in the ocean or from nearshore processes.

FIGURE 2.--Inlet to Bolinas Lagoon at low water. Pacific Ocean in background, Kent Island in right foreground, and spit midleft. Town of Bolinas at base of headland cliff and atop headland.

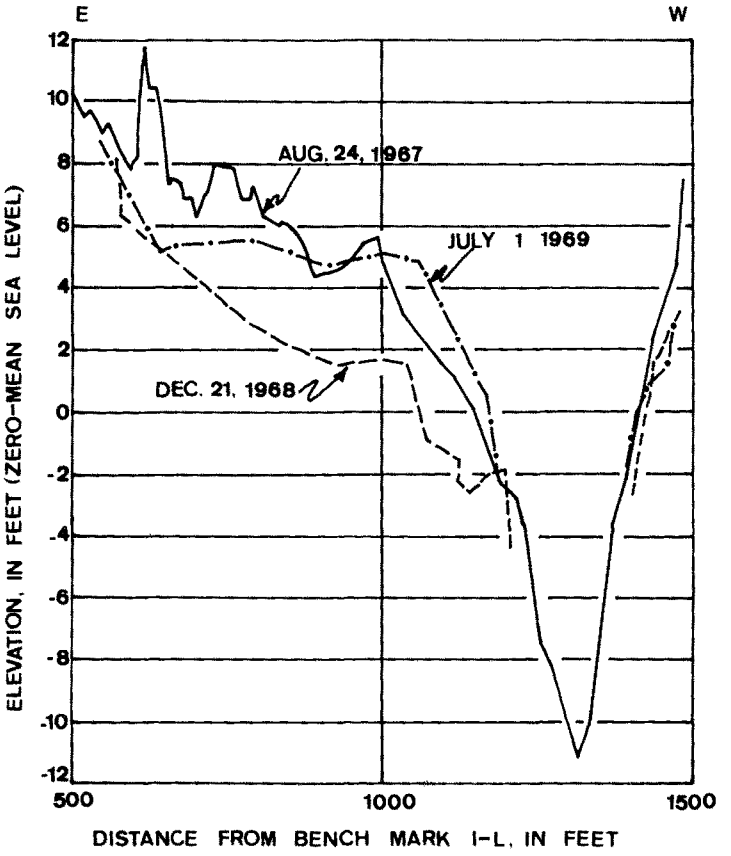

FIGURE 3.--Cross sections of the Bolinas Lagoon inlet, August 24, 1967, December 21, 1968, and July 1, 1969.

DESCRIPTION OF SEDIMENT-TRANSPORT MEASUREMENTS

Suspended-sediment transport in the inlet was measured on June 22, 1967, October 24-25, 1967, and May 16-17, 1968. Measurements spanning a 25-hour period were attempted during each series of measurements so that data for an entire tidal day would be obtained; however, only on October 24-25, 1967, was that successfully accomplished.

A moving-boat technique, in which the boat moved at a rate of about 10 fpm (feet per minute) along a cable stretched across the inlet, was used to measure the flow of water at the inlet. Two current meters, which were suspended from the boat and adjusted for changes in depth, measured the velocity of the current continuously at 0.2 and 0.8 of the depth. The direction of flow, sensed by a current-orienting compass, depth of water, station, meter revolutions, and time were continuously registered on a panel of counters aboard the boat. The panel was photographed about every 30 seconds by an automatically triggered 35-mm camera. The difference in the total count of meter revolutions per 30 seconds was used to determine the average velocity for the increment of width traversed. Then by multiplying the average depth of the increment by its width, the area of the increment was obtained. The area multiplied by the velocity corrected for the angle of the current to the measuring section was the flow for the increment. The total flow was the sum of the flows of the increments. The above calculations were made by computer from data tabulated from the film. Measurements of flow took from 9 to 25 minutes. The measured flow was assumed to equal the flow at the midpoint of the time interval of the measurement.

Suspended-sediment samples were collected from the same boat while flow was being measured. Depth-integrated samples were collected at five to seven stations during each measurement. On another boat, also in the inlet, point samples of suspended sediment were collected from various depths, and samples of sediment moving along the bottom of the inlet were collected with an Arnhem sampler so that bedload could be calculated.

An example of the temporal variations of tidal stage, average velocity, water flow, suspended-sediment discharge, and average concentration of suspended sediment for the three series of measurements is shown in figure 4. Tidal ranges during the three measuring periods varied from 0.2 to 5.7 feet (table 1); both extreme ranges were during ebbtides.

The maximum average velocity of a flow measurement, 4.9 fps (feet per second), occurred during the ebbtide having the maximum tidal range; the maximum instantaneous velocity at a vertical, 6.7 fps, also occurred then. The flow velocity in the inlet was consistently higher near the middle of the channel except sometimes when the tide was beginning to reverse. The inlet would be considered a neutral channel as there was no difference in the zones of maximum velocity for floodtide and ebbtide. Therefore, presence of flood and ebb channels could not be detected. The average velocity of the flow of each tide measured ranged from 0.4 to 2.8 fps (table 1).

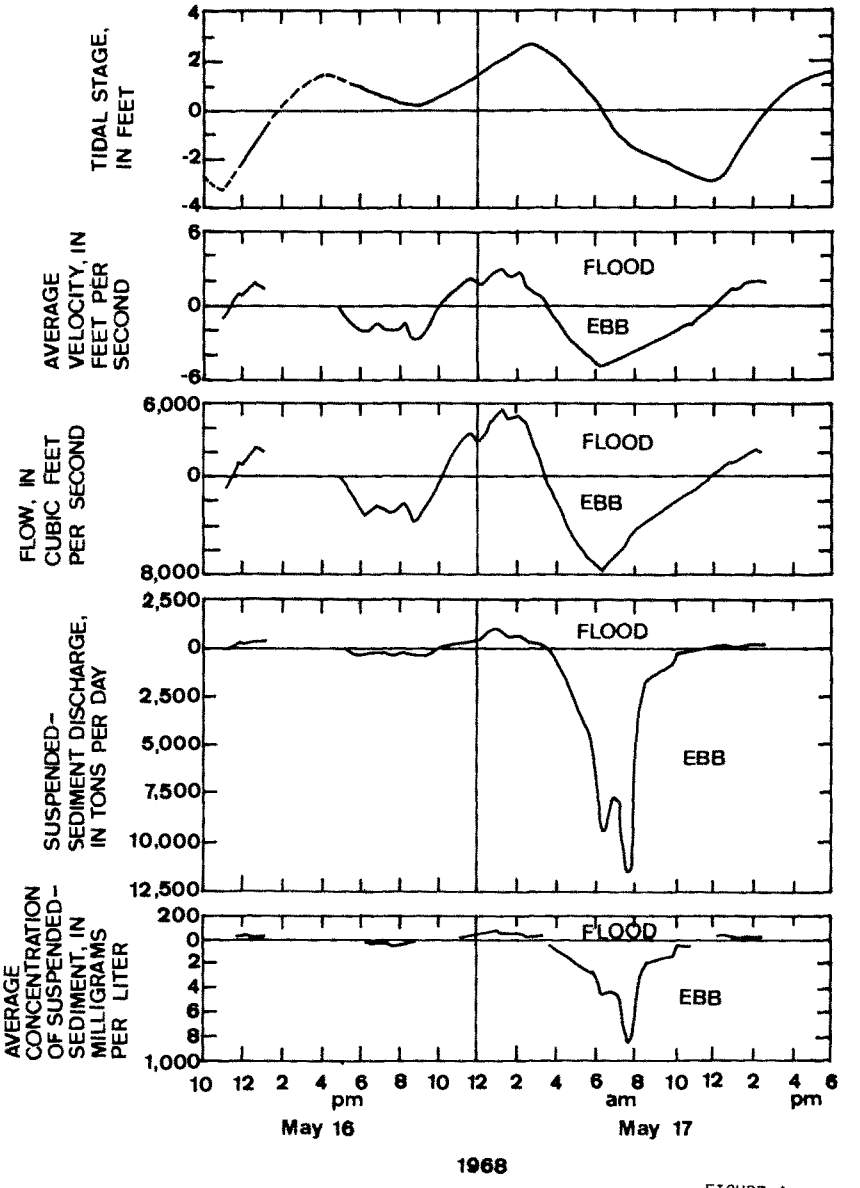
TIDAL STAGE, IN FEET
4
2
0
-2
-4
AVERAGE VELOCITY, IN FEET PER SECOND
6
0
-6
FLOOD
EBB
FLOW, IN CUBIC FEET PER SECOND
6,000
0
8,000
FLOOD
EBB
SUSPENDED-SEDIMENT DISCHARGE, IN TONS PER DAY
2,500
0
2,500
5,000
7,500
10,000
12,500
FLOOD
EBB
AVERAGE CONCENTRATION OF SUSPENDED-SEDIMENT, IN MILLIGRAMS PER LITER
200
0
2
4
6
8
1,000
FLOOD
EBB
10 12 2 4 6 8 10 12 2 4 6 8 10 12 2 4 6
pm
am
pm
May 16
May 17
1968

FIGURE 4.

TABLE 1.--*Summary of tidal range, average velocity, volume of water moved, and suspended-sediment discharge for each tide measured in the inlet*

Date	Tide	Tidal range (ft)	Duration (hours)	Number of flow measurements	Average velocity (fps)	Volume of water (acre-feet)	Suspended-sediment discharge (tons)
June 22, 1967	Flood	[1]4.3	6	10	2.3	2,000	152
	Ebb	1.2	4	6	1.5	770	36
Oct. 24-25, 1967	Flood	1.3	6	11	1.6	1,340	85
	Ebb	4.5	9	17	2.8	2,330	495
Flood	Flood	3.2	7	13	1.8	1,330	85
	Ebb	.2	3	5	.4	180	3
May 16-17, 1968	Ebb	1.1	5	6	1.6	950	44
	Flood	2.4	5.5	9	1.8	1,410	96
	Ebb	5.7	8.5	14	2.8	2,740	1,150

[1]Elevation of lower low water was estimated.

The maximum flow measured during an ebbtide was 7,900 cfs; that during a floodtide was 5,810 cfs. Maximum flow usually coincided with the occurrence of maximum average velocity; however, maximum flow during the floodtide of June 22, 1967, followed the occurrence of maximum velocity when the increase in area of the channel offset the decrease in velocity. Conversely during some ebbtides maximum flow in an inlet may precede maximum velocity when the decrease in channel area offsets the increase in velocity. The total volume of water transported during an ebbtide ranged from 180 to 2,740 acre-feet during the measurement period (table 1). The volume of water for the measured floodtides ranged from 1,330 to 2,000 acre-feet.

Average concentration of suspended sediment for a flow measurement ranged from 5 to 862 mg/l (milligrams per liter). The lowest average concentration occurred during the ebbtide having the minimum tidal range (0.2 foot) and the minimum average velocity (0.4 fps) of the tides studied; the highest concentration occurred during the ebbtide having the maximum range (5.7 feet) and the maximum average tidal velocity (2.8 fps). Average concentrations during floodtides ranged from 9 to 125 mg/l. Thus, the maximum average concentration measured during an ebbtide was about 7 times greater than the maximum measured during a floodtide.

The highest concentrations of suspended sediment usually occurred near the end of the spit and probably were caused by the local erosion of sand from the spit. Concentrations also increased with depth. Most of the temporal, lateral, and depth fluctuations of suspended-sediment concentration were caused by changes in the concentration of suspended sand. The concentration of suspended sediment finer than sand remained relatively constant.

The measured instantaneous suspended-sediment discharge was as much as 11,600 tons per day, 98 percent of which was suspended sand. The total discharge of suspended sediment for the floodtides ranged from 85 to 152 tons, and the total discharge for ebbtides ranged from 3 to 1,150 tons (table 1).

Nineteen bedload measurements were made in the inlet during the series of suspended-sediment measurements. The maximum instantaneous bedload measured was 370 tons per day, but the high velocity in the inlet prevented sampling at the higher flows when probably much more bedload was transported. If the total load is assumed to be the sum of bedload and suspended-sediment discharge, then as much as 48 percent of the total load was bedload and the average was 16 percent. Most of the sediment transported as bedload moved along the bottom of the eastern or spit side of the inlet, the area of the highest suspended-sediment concentration. The size of the sediment moved as bedload generally increased from the end of the spit toward the center of the inlet, and the median size of the bedload material ranged from 0.2 to 8.9 mm. Dune movement of at least part of the bedload is suggested as dunes with amplitudes of as much as 2 feet were observed along the end of the spit at low water.

Between May 17 and November 14, 1968, the inlet to Bolinas Lagoon widened to such an extent that the wave action in the inlet precluded measuring sediment discharge in the inlet for the last two series of measurements. Instead, the measurements were made simultaneously at two cross sections inside the lagoon, one in Seadrift channel and the other in Bolinas channel (fig. 1). Discharges were measured only during one ebbtide and one floodtide each time.

The measurements of flow and suspended-sediment discharge in the Bolinas and Seadrift channels were made by a combination of wading measurements and boat measurements, using standard Geological Survey techniques (Buchanan and Somers, 1969). The tidal range during the measurements was as much as 4.7 feet and as small as 2.0 feet (table 2). Both extreme ranges occurred during ebbtides.

The maximum average velocities for flow measurements in Seadrift channel and in Bolinas channel (2.2 and 1.4 fps), were much lower than those measured in the inlet. The highest velocity for each flow measurement in Seadrift channel occurred in the south part of the channel during ebbtide and the north part of the channel during floodtide. Thus, ebb and flood channels seem to have developed with the main current of the ebbtide flowing close to the spit and that of the floodtide near Kent Island. No consistent difference in the zones of maximum velocity for ebbtide and floodtide were observed in the Bolinas channel, which seemed to be a neutral channel.

The instantaneous suspended-sediment discharge measured in Seadrift channel was as much as 1,830 tons per day for an ebbtide and as much as 1,080 tons per day for a floodtide; and in Bolinas channel it was as much as 78 tons per day for an ebbtide and as much as 57 tons per day for a floodtide. The total suspended-sediment discharge measured in Bolinas channel averaged about 5 percent of the total suspended sediment measured in both channels.

Bedload was measured intermittently in the Seadrift and Bolinas channels on November 14, 1968. Bedload was collected only in three of the seven attempts and the maximum bedload was only 10 tons per day which represents about 1 percent of the total load. In contrast, two bedload measurements, 136 and 28 tons per day were made at the inlet during the measurements of suspended-sediment discharge in the Seadrift and Bolinas channels in May 1969. These bedloads represent about 24 and 29 percent of the total load. These observations suggest that most of the bedload transported in the inlet probably moved only in the area in and near the inlet. It is interesting, however, that some fluorescent sand placed in the inlet on November 14, 1968, at slack tide was collected as bedload at the measuring cross section in Seadrift channel 2 hours later.

TABLE 2.--*Summary of tidal range, average velocity, volume of water moved and suspended-sediment discharge for each tide measured in Seadrift channel and Bolinas channel*

Date	Tide	Tidal range (ft)	Duration (hours)	Channel	Number of flow measurements	Average velocity (fps)	Volume of water (acre-ft)	Suspended-sediment load (tons)
Nov. 14, 1968	Ebb	2.0	6.5	Seadrift	7	0.8	1,490	68
				Bolinas	6	.5	150	11
						Total	1,640	79
	Flood	2.3	6.0	Seadrift	4	.9	1,680	137
				Bolinas	4	.6	200	8
						Total	1,880	145
May 20, 1968	Ebb	4.6	9.5	Seadrift	16	1.4	2,680	248
				Bolinas	10	.6	220	7
						Total	2,900	255
	Flood	3.4	6.5	Seadrift	14	.8	1,040	48
				Bolinas	4	.3	60	1
						Total	1,100	49

DISCUSSION

Although data collected through only seven ebbtides and six floodtides are hardly adequate for a thorough analysis of tidal parameters, certain trends are discernible by studying the interrelations between the various parameters and comparing the data with data and observations by others.

The figures given previously show that the maximum velocity, flow, suspended-sediment concentration, and suspended-sediment discharge of the measured tides all occurred during ebbtide. This was expected because, generally, lower low water follows higher high water, and the major daily ebbtide at Bolinas Lagoon occurs then; therefore, under normal conditions a larger volume of water and sediment would be moved during that ebbtide than during a floodtide. However, no measurements were made during a storm, which may cause floodtides to transport more sediment into the lagoon than they normally would.

Velocity of Flow

The equation that relates the average velocity of a tide to tidal range at Bolinas inlet is:

$$\bar{u}_t = 1.21R^{.508} \tag{1}$$

where $\bar{u}_t$ = the average tidal velocity and
R = the tidal range.

This indicates that average tidal velocity is approximately proportional to the square root of the range. The average difference between the nine measured velocities and velocities calculated from corresponding tidal ranges using equation 1 is about 12 percent; the maximum difference is 19 percent.

The equation for the curve of relation of the average velocity for each flow measurement made at the inlet to the maximum velocity observed during that measurement is:

$$u_{max} = 1.64\bar{u}^{.825} \tag{2}$$

where u_{max} = the maximum velocity and
$\bar{u}$ = the average velocity for a flow measurement.

It is interesting to note that, in the inlet, the maximum velocity measured in a vertical for each floodtide ranged only from 3.9 to 4.3 fps, but the tidal ranges for these floodtides ranged from 1.3 to 4.3 feet. In contrast, the maximum velocity in a vertical for each ebbtide that had similar tidal ranges (1.3 to 4.5 feet) ranged from 3.0 to 5.5 fps.

The two highest mean inlet velocities for a measurement were 4.90 and 4.71 fps. The Froude numbers for those two velocities were 0.31 and 0.33, about 50 percent greater than 0.2, which was given by Bruun (1967, p. 173) as the Froude number for tidal inlets at the maximum current velocity. However, Bruun (1966, 1967) also reported that the maximum mean velocity in tidal inlets should be about 1 meter per second (3.28 fps), a velocity well below the maximum mean instantaneous velocity observed in the Bolinas inlet. The Froude number computed for the Bolinas inlet for velocities nearest 3.28 fps for each of the three periods of measurement ranged from 0.19 to 0.24, which are comparable to the Froude number of 0.2 given by Bruun.

The maximum velocity of floodtide at the Bolinas inlet generally occurred within an hour after midtide, but the maximum velocity of three of the five ebbtides that were measured occurred near one-third tide and preceded half tide by as much as 90 minutes. The maximum velocity of the May 16 ebbtide (table 1) occurred at about three-quarters tide, but some erratic velocities measured during that tide probably were related to the tsunami that struck the coast that day. The maximum velocity of the ebbtide of October 25 (table 1), occurred about half tide, but the tidal range was only 0.2 foot and the flow was very small. Therefore, at Bolinas inlet the maximum velocity of floodtide probably occurs slightly after half tide and the maximum velocity of ebbtide probably occurs at about one-third tide.

Because the maximum velocity often is reached early in an ebbtide, the ebbtide velocity often increases more rapidly to its maximum than it decreases to its minimum as slack water approaches. In other words, a plot of velocity and time during an ebbtide is skewed toward the later part of the tide. The temporal relation for the floodtide velocity is more symmetrical with perhaps a slightly more rapid decrease than increase.

Flow

The average flow through the inlet for a tide can be estimated by multiplying the average velocity, as computed from equation 1, by the average area of the cross section for that tide as determined from a hydrographic survey. The average difference between the calculated flow and the measured flow was 13 percent, and the differences ranged from 0 to 50 percent (table 3).

The ebbtide flow in the inlet and in Seadrift and Bolinas channels generally increased more rapidly than it decreased. A combination of higher velocities and a larger channel cross section before the middle of ebbtide produced the more rapid increase. Conversely during floodtide, because the cross section increased throughout the tide and higher velocities occurred at or after half tide, maximum flow occurred after midtide and thus the rate of flow decreased more rapidly than it increased.

TABLE 3.--*A comparison of average tidal flow calculated from computations of average velocity and average channel area with average flow determined by tidal measurement*

Date	Tide	Tidal range (ft)	Average velocity[1] (fps)	Average channel area[2] (sq ft)	Average flow[3] (cfs)	Measured average flow (cfs)	Difference in flow (cfs)	Percent difference
June 22, 1967	Flood	4.3	2.5	1,440	3,600	4,000	-400	10
	Ebb	1.2	1.3	1,790	2,300	2,300	0	0
Oct. 24-25, 1967	Flood	1.3	1.4	1,840	2,600	2,700	100	4
	Ebb	4.5	2.6	1,460	3,800	3,100	+700	23
	Flood	3.2	2.2	1,250	2,800	2,300	+500	22
	Ebb	.2	.5	1,600	800	700	+100	14
May 16-17, 1968	Ebb	1.1	1.3	1,620	2,100	2,300	-200	9
	Flood	2.4	1.9	1,860	3,500	3,100	+400	13
	Ebb	5.7	2.9	1,500	4,400	3,900	+500	13
Nvo. 14, 1968	Ebb	2.0	1.7	1,680	2,900	3,100	-200	6
	Flood	2.3	1.8	1,740	3,100	3,800	-700	18
May 20, 1969	Ebb	4.7	2.6	1,520	4,000	3,700	+300	8
	Flood	3.5	2.3	1,300	3,000	2,000	+1,000	50

[1]Calculated from equation 1.
[2]Calculated from average channel area determined from survey of August 1967.
[3]Product of average velocity and average channel area.

The volume of water that flowed into and out of the lagoon by tides as determined from the tidal measurements was from 0.47 to 0.98 of the volume of water computed from the tidal prism of the lagoon. The average rate of change in tidal stage during an ebbtide or floodtide may be related to these ratios. If the stage for an entire tide rose or fell at an average rate of more than 0.3 foot per hour, the average ratio was about 0.65; if the average rate was less, the average ratio was about 0.95. These ratios were particularly consistent for the measurements made at the inlet. The measurements did not equal the volume of the prism because the water level in the lagoon is not horizontal. Tide records showed that the elevations of the tidal stage at various points in the lagoon differed as much as 2 feet at a given time.

Sediment Discharge

The maximum concentration of suspended sediment during a tide usually was observed within about a half hour of the time of the highest measured velocity for that tide. Postma (1967, p. 163), observed that usually there was a lag between the time of slack tide, when the average velocity is zero, and the time of the lowest concentration of suspended sediment. The lag was explained by the fact that, during a period of decreasing velocity, time is needed for sediment to settle and that during the succeeding period of increasing velocity, it takes time to reach a velocity that will resuspend sediment. At Bolinas Lagoon the concentration of suspended sediment sometimes decreased slightly during the first two measurements made after slack tide, an indication of the lag noted by Postma. The lowest overall concentrations for a tide occurred during an ebbtide with a tidal range of about 0.2 foot and a maximum average velocity of only about 1 fps. The ebbtide lasted only 3 hours, and the concentration of suspended sediment decreased progressively from 26 to 5 mg/l during that time.

Maximum average concentration of suspended sediment and tidal range for the five ebbtides measured at the inlet seemed to be directly correlated. No such correlation was perceived for the floodtides.

Suspended-sediment discharge is related to availability of erodible sediment, velocity, tidal range, and water flow. Colby (1964) showed that in sand-bed streams a relation existed between stream velocity and the discharge of sand. Data from measurements made at the inlet and at Seadrift and Bolinas channels were used to relate the discharge of suspended sediment in the inlet to average velocity (fig. 5). Discharge of suspended sand was similarly related and a comparison of the two curves is shown in figure 5. The sand discharge became almost the total suspended discharge when an average velocity of about 3 fps was reached.

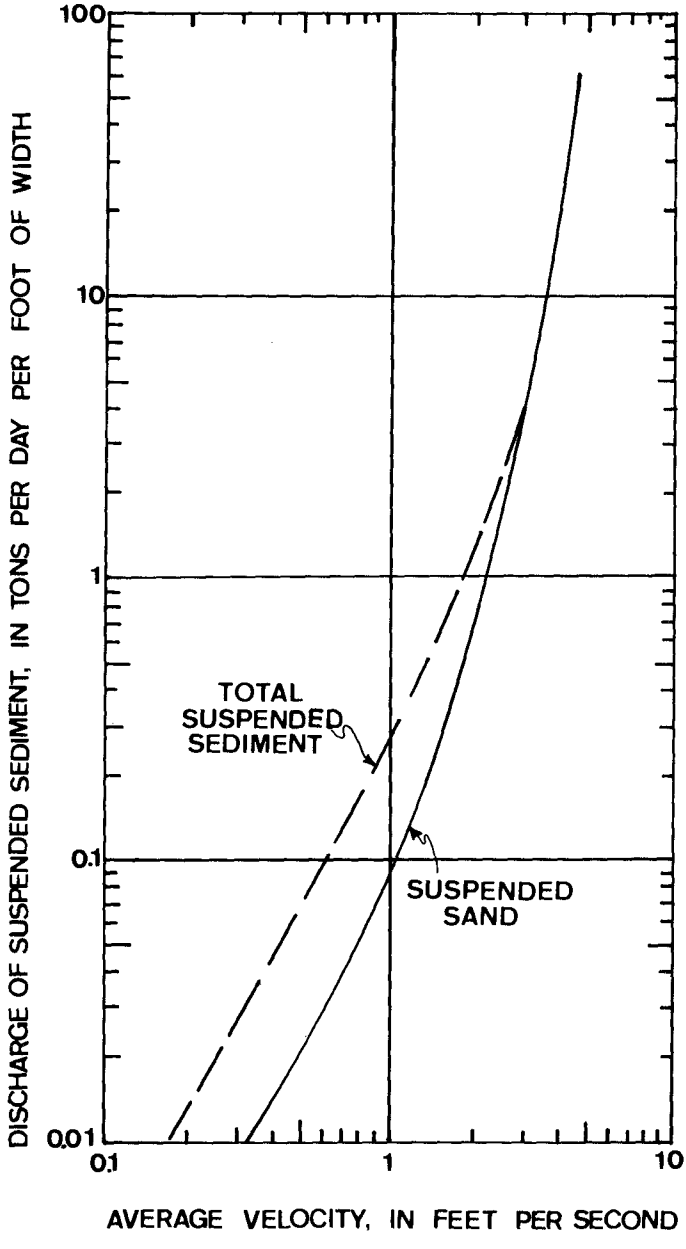

FIGURE 5.--Comparison of the relations of average velocity to the discharge of total suspended sediment and to the discharge of suspended sand per foot of width.

The relation of flow to suspended-sediment discharge for each of the periods of measurement was fairly consistent. This relation, however, changed during the tide. The suspended-sediment discharge for a given flow and the suspended-sediment concentration for a given velocity were larger in the later part of the ebbtide than they were in the earlier part. Except for the maximum flow, a given flow occurs twice during a tide; therefore, a plot of flow and suspended-sediment discharge and that for velocity and suspended-sediment concentration form loops which are counterclockwise with respect to time (fig. 6). The variation in suspended-sediment discharge at a given flow at the inlet was less than the variation at Seadrift channel. Part of the reason for this loop relation is the fact that an eroding velocity greater than a transporting velocity must be reached before sediment will move. In other words, once sediment is suspended by a moving current, less velocity is required to keep it moving.

The curve representing the floodtide relation of flow velocity to suspended-sediment discharge tends to loop in a clockwise direction (fig. 7). In this case, the rate of sediment transport was greater when a given flow first occurred than when it occurred again. The difference in the direction of the loop at floodtide and at ebbtide can be explained by differences in the relation of velocity and area of the channel during floodtide and ebbtide. The area of the channel is greater and the tidal velocity is less when the given flow first occurs than when it occurs later. During a floodtide, the process is reversed; the area increases and velocity decreases between the first and second time that a given flow occurs. Because suspended-sediment concentration is related to velocity, the concentration at a given flow is less early in an ebbtide than it is later in the ebbtide, and the concentration is higher early in a floodtide than it is later when the given flow again occurs.

Maximum suspended-sediment discharge and maximum flow seldom occurred at the same time. Usually maximum flow occurred before maximum suspended-sediment discharge although maximum flow occurred later during three of the tides measured.

Several methods of computing the suspended-sediment discharge were tried. The method that provided the best estimate was the simple relation of the suspended-sediment discharge per tide (Q_S) to the tidal range (R). The equation of the line of relation is:

$$Q_S = 31.3R^{1.433}. \qquad (3)$$

However, the difference between the suspended-sediment discharge calculated from the above equation and that determined from tidal measurements was as much as 201 percent; and averaged 49 percent.

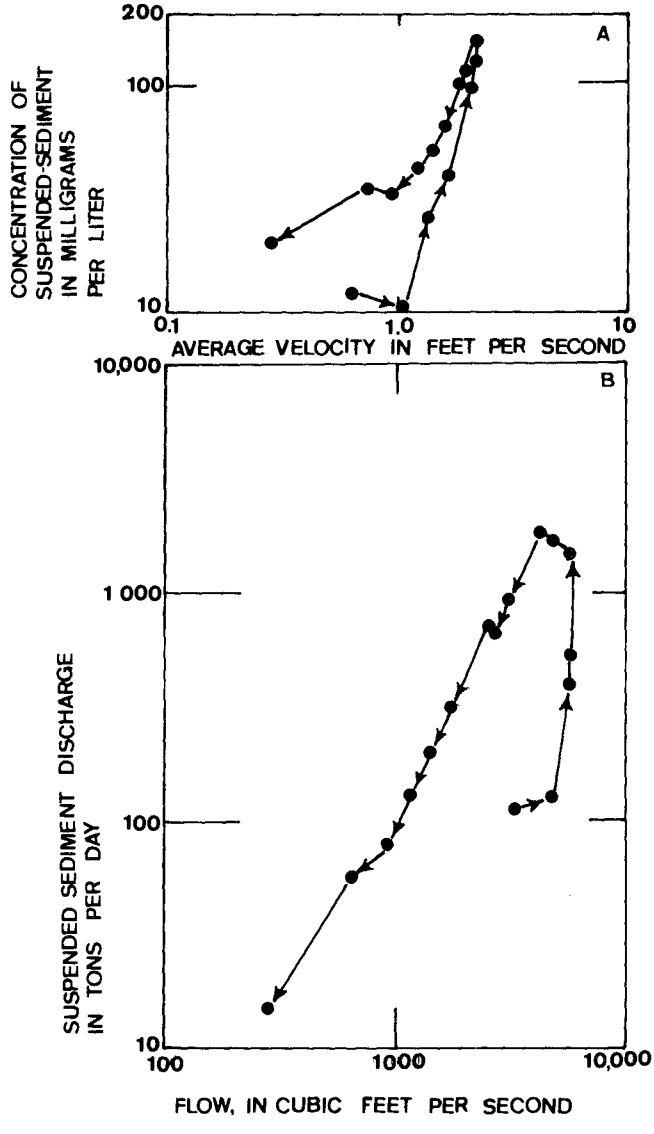

FIGURE 6.--Temporal variation during ebbtide of the relation of: A. average velocity to suspended-sediment concentration and B. flow to suspended-sediment discharge, Seadrift channel, May 20, 1969. Arrows indicate measurements.

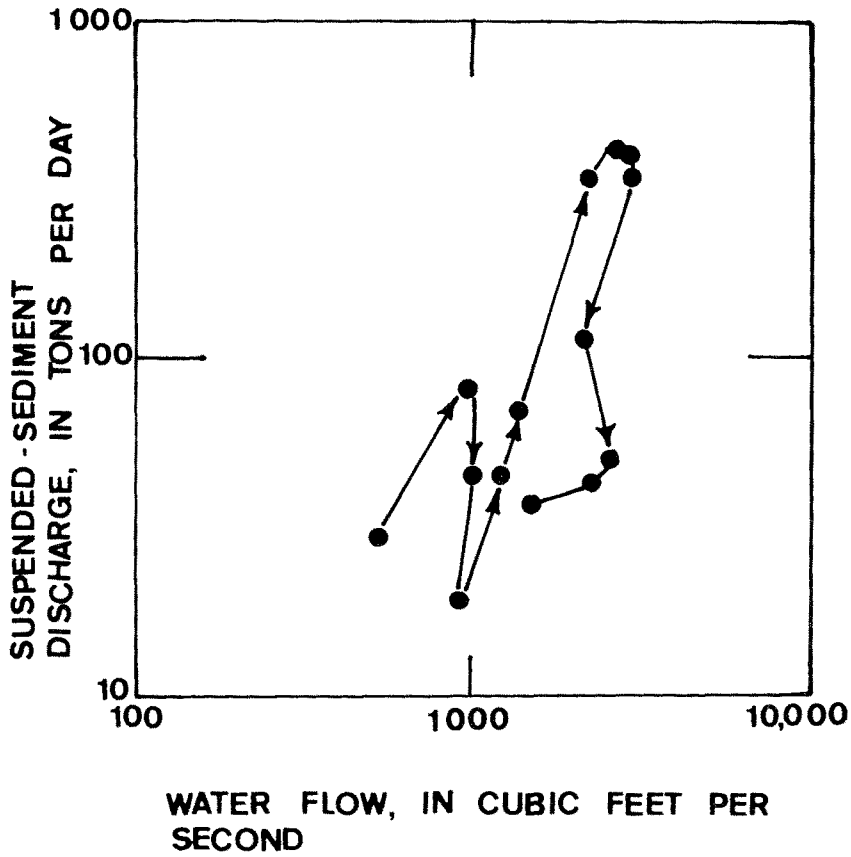

FIGURE 7.--Temporal variation during floodtide of the relation of flow to suspended-sediment discharge, Seadrift channel. Arrows indicate measurements.

Although the accuracy of suspended-sediment discharges calculated from equation 3 may seem questionable, annual suspended-sediment discharges for 2 years were computed using the equation. Floodtides carried an average of 115,000 tons per year of suspended sediment into the lagoon and ebbtides carried an average of 124,000 tons per year of material out of the lagoon. Thus, suspended sediment transported out of the lagoon exceeded that transported into the lagoon by about 9,000 tons per year. Bedload transported by ebbtides was 2,000 tons more than bedload transported by floodtides. Other calculations of sediment transport showed that about 46,000 tons per year were added to the lagoon by streams, wind, and bank erosion. The average net quantity of sediment added to the lagoon each year, therefore, is 35,000 tons. That weight of sediment, assuming 79 lbs/cu ft, represents a depositional rate of 21 acre-feet per year which is comparable to the rate of 16 acre-feet per year determined from surveys of the lagoon made in 1939 and 1968. Thus, calculations made from equation 3 seem to be adequate.

REFERENCES

Beck, J. R., 1971, Use of time-lapse photography equipment for hydrologic studies: U.S. Geol. Survey open-file rept., 10 p.

Bruun, Per, 1966, Tidal inlets and littoral drift: Oslo, Univ. Book Co., 193 p.

_____1967, Tidal inlets housekeeping: Jour. Hydraulics Div., Am. Soc. Civil Engineers, v. 93, no. HY5, p. 167-184.

Buchanan, T. J., and Somers, W. P., 1969, Discharge measurements at gaging stations: U.S. Geol. Survey Techniques Water Resources Inv., book 3, chap. A8, 65 p.

Colby, B. R., 1964, Discharge of sands and mean-velocity relationships in sand-bed streams: U.S. Geol. Survey Prof. Paper 462-A, 47 p.

Postma, Henrik, 1967, Sediment transportation and sedimentation in the estuarine environment in Lauff, G. H., Estuaries: Washington, Am. Assoc., Av. Science, p. 158-179.

Ritter, J. R., 1970, A summary of preliminary studies of sedimentation and hydrology in Bolinas Lagoon, Marin County, California: U.S. Geol. Survey Circ. 627, 22 p.

CHAPTER 45

COASTLINE CHANGES NEAR A TIDAL INLET

By

Emmanuel Partheniades, Professor
Department of Civil and Coastal Engineering
University of Florida, Gainesville, Florida, U.S.A.

and

James A. Purpura, Associate Professor
Department of Civil and Coastal Engineering
University of Florida, Gainesville, Florida, U.S.A.

ABSTRACT

Extensive coastline changes around the Ponce de Leon Tidal Inlet, Florida, are described, discussed and explained. These changes started developing immediately after the beginning of the construction of two jetties on both sides of the inlet forming part of a plan to stabilize the inlet, improve navigation conditions and bypass sand effectively. The mean annual littoral transport of sand was considered to be from north to south.

Rapid sand accretion south of the south jetty started immediately after the beginning of its construction in 1969, reaching by November, 1971, a volume of approximately 1,400,000 cu. yds. Aerial photographs suggest that the sand was transported there from the south during the summer periods of northerly drift and from the offshore bar by refracted waves from the north. The accumulated sand is well protected by the south jetty during the winter storms from the northeast. Coastline and duneline recession occurred north of the inlet due, at least partially, to the described sand retention.

It is concluded that for inlets where the littoral drift reverses its direction, the net annual rate of littoral transport is not a unique design criterion. Instead the total sand volumes transported annually in either direction should be considered.

INTRODUCTION

The importance of estuaries and bays as centers of population growth and industrial development is well-known, and man's historical development has been closely linked with these two geomorphological features. It is sufficient to only mention that about one-third of

the population of the United States lives and works near estuaries and that most of the world's large metropolitan areas, such as London, New York, Tokyo, Shanghai, Buenos Aires, San Francisco, Osaka, Montreal and New Orleans, border estuarine and bay areas.

Estuaries and bays are semienclosed water bodies with one or more free connections with the open sea through which the tidal energy and the sea salts are transmitted. When the discharge of fresh water derived from upland sources is sufficient to measurably dilute the sea water within the semienclosed body then the latter is called an estuary, (1),* otherwise it is referred to as a bay.

Geomorphologically bays and estuaries can be classified into the following four subdivisions (1): (a) drowned river valleys; (b) fjords; (c) bar-built and (d) generated by tectonic processes. The first, and most common, type has been formed by the inundation of an alluvial plain by sea water during the postglacial period. It is normally characterized by an abundance of fresh water supply and river born sediment, flat slopes and relatively low depths. The second, encountered predominantly in zones subjected to heavy glaciation, are inundated U-shaped valleys gouged out by glaciers. They have narrow long shapes, high depths, a shallow entrance sill in certain cases and steep ground slopes. Fresh water supply may or may not be significant. The third type is formed where offshore barriers, sand islands and spits build above sea level forming a chain between headlands broken by one or more inlets. The enclosed water body has generally an elongated shape parallel to the main coastline. Similar sand barriers can be formed across the mouth of drowned river valleys in the presence of intense littoral sand transport. The fourth subdivision is very general and it encompasses all these coastal indentures formed by faulting and local ground subsidence.

Navigation is particularly critical through tidal inlets between sand barriers due to: (a) gradual shifting of the inlet in the dominant direction of sand transport; (b) shoaling and shifting of the natural channels; (c) existence of an offshore bar, completely or partially submerged with relatively shallow depths and intense wave breaking and (d) intense currents due to tides and to wave action.

Stabilization of such tidal inlets and improvement of navigation conditions has been one of the major problems confronting coastal engineers. The normal method of inlet improvement has been to provide jetties flanking the inlet channels. Such jetties, however, obstruct the littoral transport of sand, so that sand accretion at the updrift side of the inlet and erosion at the

---

*Numbers in parenthesis indicate references at the end of the paper.

downdrift side may develop. Eventually at the updrift side the accumulated sand may reach the offshore tip of the jetty and enter into the channel, whereas at the downdrift side the erosion may reach objectionable proportions. The reestablishment of the sand balance can be accomplished by bypassing the sand artificially from the updrift accretion zone to the downdrift depleted beaches (2,3).

An optimum inlet stabilization system should provide maximum safety to navigation at the lowest possible construction and maintenance cost. A relatively new design consists of two jetties, a submerged weir, forming the near-coast portion of the updrift jetty, and an impoundment basin close to the weir, between the updrift jetty and the entrance channel. The main objectives of the design are: (a) to control the sand accretion at the updrift side of the inlet, by allowing sand to pass over the submerged weir portion of the jetty and (b) to collect any sand passing over the weir into the protected impoundment basin from where it can be conveniently dredged and placed on the downdrift side.

Such a system has recently been completed at the Ponce de Leon Inlet in Florida, U.S.A. A project supported by the Coastal Engineering Research Center of the U.S. Army Corps of Engineers was initiated in the summer of 1970 at the University of Florida in order to determine the effect of the jetties on the adjacent coastline and to estimate the percentage of littoral transport passing over the weir and entrapped into the impoundment basin. The coastline changes to February, 1972, north and south of the inlet are herein presented and discussed. These changes already provide valuable information regarding the function of a jetty-weir-impoundment basin system at inlets where the littoral transport periodically reverses its direction although the net drift is always unidirectionally the same on an annual basis.

BACKGROUND INFORMATION

Location and Physical Characteristics

The Ponce de Leon Inlet is located in Volusia County on the east coast of Florida, about 65 miles south of St. Augustine Harbor and about 57 miles north of Canaveral Harbor. Figure 1 shows an aerial photograph of the inlet and of the immediately adjacent area. The inlet connects the Atlantic Ocean with the Halifax River and the Indian River North. The former extends from the inlet northward about 24 miles whereas the latter extends southward from the inlet to the Mosquito Lagoon (4). Both rivers, however, are essentially bar-built tidal estuaries.

Fig. 1. Ponce de Leon Inlet on April 4, 1967.

The mean tidal range is 4.1 ft. in the ocean and 2.3 ft. just inside the inlet. Spring ranges are 4.9 ft. and 2.7 ft., respectively. The estimated mean and spring tidal prisms are 8000 acre-feet and 9000 acre-feet, respectively. The beach is low and flat and, prior to the construction of the jetties, it was 400 to 500 ft. wide just south of the Ponce de Leon Inlet (4).

The beach sand is, like for the most part of the Volusia County, clean, fine, relatively uniform with a mean grain size around 0.2 mm and hard packed. The shell content is very small but it begins to increase about 8 miles south of the inlet resulting in a steeper profile and a softer beach. Past records (4) indicate an average annual recession in the 2-mile reach immediately north of the inlet of about 7 ft. per year. For the 4-mile reach immediately below the inlet shoreline recession is accompanied by accretion of

the offshore part of the profile. This phenomenon could be caused by displacement of material from the upper part of the profile offshore into the lower or seaward part of the profile and by similar displacement of drifting material by the "jet effect" of the ebb tide. Moreover, there are indications that the shores in the neighborhood of the inlet underwent periodic revulsions whereby material accumulated on the north beach over a period of some years disassociated itself from the mainland and was transported across the inlet to the south beach, thereby creating an apparent eroding condition north and an accreting condition south of the inlet.

The movement of sand along the ocean shoreline of the South Atlantic coast of the United States varies seasonally. During the summer months gentle winds from the south create waves and swells which move the sand in a south to north direction. However, the more violent northeast waves and storms generate a higher littoral transport rate from north to south so that the predominant annual drift is to the south. The estimated average annual littoral transport rates (4) for the zone between Oregon Inlet, North Carolina, to Key West, Florida vary widely from negligible to a maximum of 500,000 cu. yds.; however, the volume of material being transported past a fixed point onshore in one direction can amount to well over 1,000,000 cu. yds. annually. According to the same estimates the net annual littoral transport in the neighborhood of the Ponce de Leon Inlet is 500,000 cu. yds., i.e., one of the highest. Gross annual drift rates are estimated to be about 600,000 cu. yds. southerly and 100,000 cu. yds. northerly.

Navigation

Navigation through the original natural inlet had always been difficult and hazardous; nevertheless, according to historical accounts, the inlet has been used for navigation for more than two hundred years. A typical fan shaped sandbar lies across the ocean entrance over which intense wave breaking takes place. Inadequate depths across the bar and continuous shifting of the channel crossing that bar cause the principal difficulties and hazards to navigation. In fact prior to the jetty construction the bar-channel shifted so rapidly and so often that it was difficult for the Coast Guard to maintain channel markers in proper positions (5). Substantial shifts have been reported by boatmen occurring between their outbound and inbound passages on the same day. The situation becomes particularly hazardous during periods of low tides and high seas or swells. At least six lives have been reported lost between 1957 and 1963 as a result of boat capsizing in the inlet.

Prior to the present improvement plan, engineering operations to improve navigation conditions in the Ponce de Leon Inlet have

been minimal. The earliest engineering structure is a lighthouse provided by Congress in 1882 and constructed shortly after on the north shore of the inlet. From 1936 to 1949 occasional dredging operations were attempted; however, any newly dredged channel filled very rapidly. In September, 1962, the inlet channel extended in an easterly direction with depths ranging from less than 6 ft. across the bar to 35 ft. in the gorge (5).

The Present Inlet Stabilization Plan

In general the project plan, outlined in Fig. 2, consists of an entrance channel, a pair of jetties and an impoundment basin south of the north jetty. The north jetty contains a submerged weir section to allow the southward moving sand to pass over it and deposit in the impoundment basin. This basin would then be dredged periodically with the material being placed on the beach south of the inlet. This design was based on the previously mentioned mean annual rate of littoral southerly drift, an expected rapid accretion north of the north jetty, negligible accretion immediately south of the south jetty and beach erosion further south of the inlet. The design details are given in (6).

The north jetty is composed of 500 ft. of prestressed concrete sheet piling, 1800 ft. of weir and 1750 ft. of rubble mound section. The first 250 ft. section of sheet piling has a crest elvation of +10.00 ft. with the crest of the remaining 250 ft. sloping linearly to an elevation of +4.00 ft. The weir section is composed of a series of prestressed concrete king piles 3 ft. deep and 2 ft. wide with slots for the fitting of the beams. The latter, also of prestressed concrete, are properly keyed to each other. It was intended initially to have an adjustable crest weir; however, because of construction difficulties, the design was changed into a fixed crest weir. The first 300 ft. of the weir crest are at an elevation of +4.00 ft. whereas the crest elevation of the remaining 1500 ft. of the weir is 0.00, which is taken at mean low water level. The crest elevation of the 1750 ft. of the rubble mound offshore section of the jetty is +7.00 ft.

The south jetty has a total length of about 3800 ft. It is entirely rubble mound construction of variable composition (6).

The impoundment basin, shown in Fig. 2, is located between the weir and the channel. Its horizontal area is about 600,000 ft.^{2} and it is to be dredged to an elevation of -20.00 ft. The average natural bottom elevation at the location of the impoundment basin was about -2.00 ft. Thus an 18 ft. initial dredging depth is anticipated corresponding to about 400,000 cu. yds. of dredged material. The outlined design was based on an amount of littoral drift of 310,000 cu. yds. expected to pass over the weir annually.

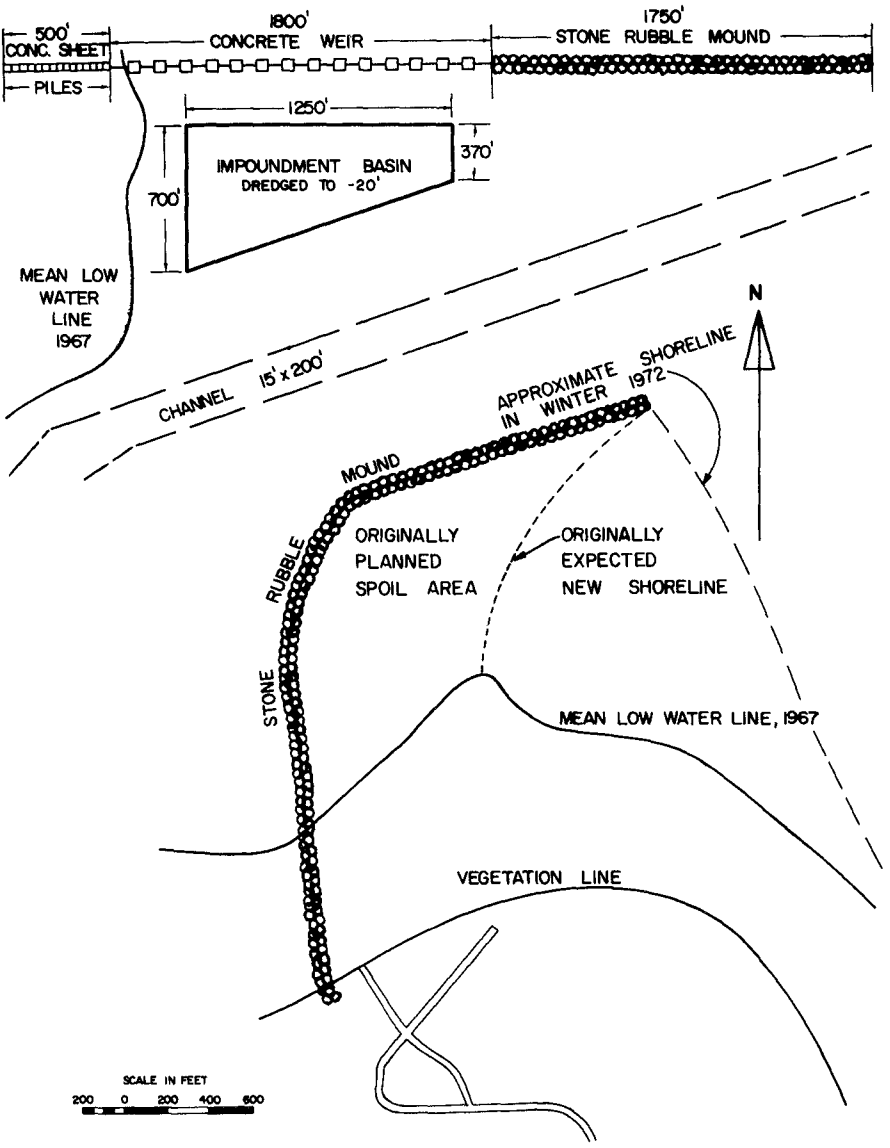

Fig. 2 Outline of the Ponce de Leon Stabilization System

A 7,200 ft. long entrance channel leads from the ocean to the Halifax and Indian River north, where it divides into two inner channels following these two rivers. The entrance channel has been designed with a width of 200 ft., a depth 12 and 15 ft., an overdepth of 2 ft. and a side slope (vertical on horizontal) 1 on 5. Its excavation quantity including the overdepth is 178,000 cu. yds. The inner channels have been designed with a width of 100 ft., depths of 7 and 12 ft., overdepth of 1 ft. and side slopes of 1 to 3. The excavation quantity including the overdepth is 74,000 cu. yds. The initial cost estimate for the entire project was approximately $3,000,000 (6).

The original plans provided distinct dredge disposal sites. Of interest to the present work is that material excavated from the entrance channel and the impoundment basin was to be disposed immediately south of the south jetty in order to assure a strong land connection between the west end of the south jetty and the existing barrier beach. Figure 2 shows an outline of the present shoreline at M.L.W. and of the expected new shoreline after the dredge disposal.

The following have been the various stages of construction in chronological order:

1. The construction of the south jetty started in July, 1968, and was completed in October, 1969.

2. The driving of the sheet piling section of the north jetty started in September, 1968, and was completed in October, 1968.

3. The driving of the king piles of the weir section started in October, 1968, and was completed in March, 1969.

4. The 1800 ft. rubble mound section of the north jetty began in January, 1970, and was completed in July, 1971.

5. The horizontal weir beams were placed between March and July, 1971.

6. The dredging of the impoundment basin began in August, 1971, and was continued to February, 1972, at which time it was interrupted due to bad weather conditions. It was resumed in May, 1972, and it was completed in August, 1972.

7. The dredging of the interior channel on the Indian River began in September, 1971, and was completed in February, 1972.

8. The dredging of the entrance channel started in July, 1971, but it was interrupted in February, 1972, also because of bad weather conditions. That dredging has not been resumed as of July 1, 1972.

THE COASTLINE CHANGES

Dramatic changes in the coastline south of the inlet started occurring immediately after construction of the south jetty. These changes can most readily be observed in a sequence of aerial photographs taken apart at low tides between April, 1967, and February, 1972, at an original scale of 1:9600. Some of these aerials are reproduced in this paper at a scale of approximately 1:21600.

Figure 1 shows the inlet on April 4, 1967, more than a year before the beginning of any engineering operations. The interior and exterior shoals and the main channel can be observed. The large number of breakers is, moreover, indicative of the low offshore bottom slope. The angle of the wave crests with the north coastline suggests a southerly wind direction; however, there is an obvious refraction pattern around the inlet modifying the direction of the wave crests and causing them to converge towards the inlet from both directions.

Figure 3 shows the beach developments at the inlet in August 1969, about a year after the beginning of the construction of the south jetty. The north jetty did not provide until that date any obstruction to littoral transport since only the king piles were driven and the construction platform placed, as shown. Thus, insignificant coastline changes occurred in the north coastline; however, the changes in the coastline south of the south jetty were enormous and spectacular. The coastline at low water level advanced by about 1500 ft. right next to the jetty, about 600 ft. at a distance of 1500 ft. south of the tip of the jetty and about 200 ft. south of the point where the original coastline bends to its north-south direction. The entrapment of water indicates that sand advanced from the south to the jetty bent over the originally shallow offshore zone with part of it passing through the jetty into the inlet. The refraction pattern with wave crests converging to the inlet from both directions is again obvious; so are the offshore shoals as demonstrated by the breakers. A patch of shoal just offshore of the new M.L.W. line and the refraction pattern suggests that sediment is being transported from the offshore shoals towards the beach. Likewise the near coast shoaling patterns immediately south of the north jetty and the direction of the wave crests suggest sand transport inside the inlet.

Fig. 3 Ponce de Leon Inlet - August, 1969

Fig. 4 Ponce de Leon Inlet - December 12, 1969

Figure 4 shows the situation around the inlet on December 12, 1969, i.e., shortly after the completion of the south jetty. The M.L.W. line at the jetty has advanced since August, 1969, by approximately 600 ft. The refraction pattern and the related direction of sand movement to the south coast are about the same as in Fig. 3.

Figure 5 shows the inlet on the 7th of April, 1970. The coastline at the jetty, during these last 4 months advanced only 150 feet seaward in contrast to the 600 ft. advancement during the previous 4 month interval. It appears, therefore, that the sand entrapped south of the south jetty is well protected against the storms from the north, which are dominant from late fall to late spring; in fact the refraction pattern indicates that these storms may even contribute to the building of the south beach by transporting sediment from the offshore bar, which, in turn, is supplied by sediment transported to the inlet from the north. In the same figure, a shoal can be observed creeping to the north, as suggested by its shape and by the pattern of the refracted wave crests. Other significant observations are the increased volume of sand deposited at the inlet west of the north-south section of the south jetty, the beginning of a sand build-up north of the sheet piling section of the north jetty and an initiation of beach erosion south of that sheet piling. Between August, 1969, and April, 1970, the beach immediately north of the sheet piling has advanced by 200 ft. whereas the average recession south of the sheet piling is about 100 ft.

The aerial survey of June 8, 1970, shown in Fig. 6, disclosed little change in the entire situation except some recession north and south of the sheet piling section of the north jetty, which is believed to be a short term phenomenon. However, as Fig. 7 indicates, during the summer of 1970 the beach at the south jetty advanced eastward by approximately another 500 ft. This was the result of a northward advancement of the previously mentioned shoal 2000 ft. south of the jetty first observed in April of 1970. When this shoal reached the jetty it entrapped water thus creating an internal lagoon. Waves and tidal currents initiated subsequently an erosion process with the eroded sand being washed through the breakwater into the inlet. The first 800 feet right south of the jetty from the bend point, which in July, 1970, were covered with dense sand, were submerged by December of the same year even at low tides. The only sand supply to the internal lagoon is wind blown. No significant changes are observed in Fig. 7 in the neighborhood of the sheet piling of the north jetty. The crest of the apparently light waves seem to push sand towards the beach right next to the north jetty platform, whereas the refracted waves further onshore seem to erode the beach south of the sheet piling transporting sand towards the entrance channel.

Fig. 5 Ponce de Leon Inlet - April 7, 1970

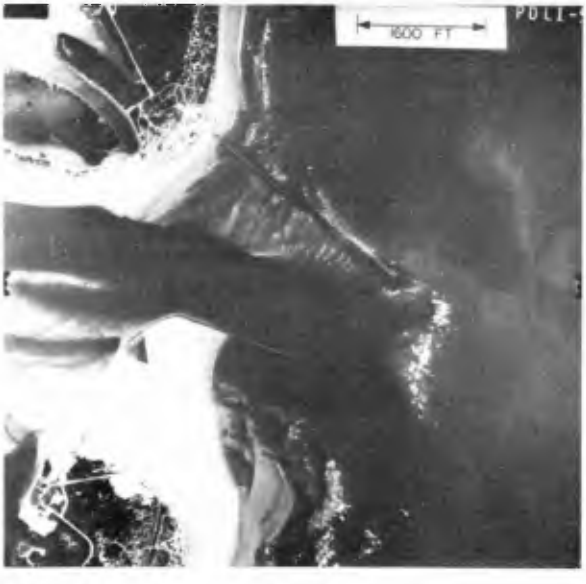

Fig. 6 Ponce de Leon Inlet - June 8, 1970

Fig. 7 Ponce de Leon Inlet - December 22, 1970

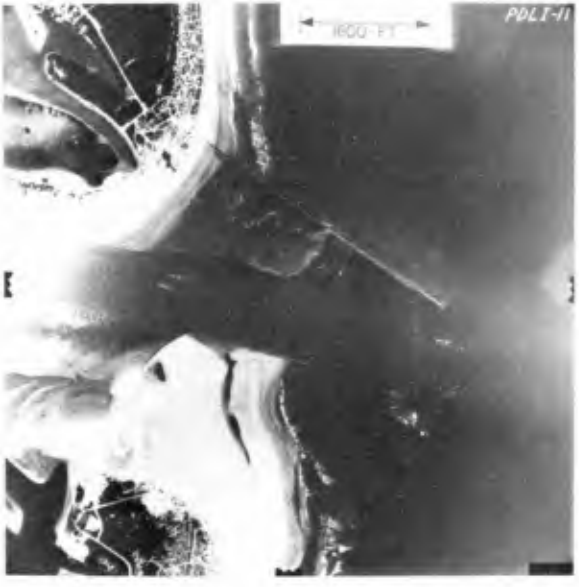

Fig. 8 Ponce de Leon Inlet - April 9, 1971

By April 9, 1971, the south coastline advanced by only 100 ft. (Fig. 8). This is just about equal to that which occurred between December, 1969, and April, 1970 (Figures 4 and 5). However, right north of the sheet piling the shoreline advanced by about 200 ft. whereas the beach south of the sheet piling remained practically unchanged. The area of the internal lagoon had been somewhat reduced apparently due to wind blown sand.

By July 18, 1971, the south beach advanced by another 50 ft. towards the tip of the jetty (Fig. 9) with negligible change in the internal lagoon. By the same date the beach north of the sheet piling advanced by another 100 ft. However, the erosion immediately south of the sheet piling started becoming obvious with an average recession of about 200 ft. in 3 months. Again the advancement of sand from the offshore bar to the inlet becomes obvious.

By November, 1971, the coastline reached the eastern tip of the south jetty. By that time the dredging of the entrance channel had begun by a pipeline dredge disposing the dredged material south of the south jetty and filling the internal lagoon.

The aerial of December 13, 1971, shows a similar situation to that of November, 1971 (Fig. 10) with an advancement of the coastline to the tip of the south breakwater. Little future advancement of the coastline may be expected at this location and the south beach appears to be near its new quasi equilibrium profile with seasonal localized erosions and accretions. This conclusion is confirmed by Figures 11 and 12 showing aerials taken on January 28, 1972, and February 22, 1972, respectively.

The approximate final coastline is outlined in Fig. 2 together with the original one and the coastline which was initially expected by the designers to develop after the disposal of sand from the dredged entrance channel and the impoundment basin (6). The comparison of these three coastlines is indicative of the difference between the expected and the actual behavior of nature in certain cases.

Figures 13 and 14 show the approximate location of the M.L.W. lines at the indicated dates north and south of the inlet as obtained by field surveys. Some data on dune recession north of the inlet are included in Fig. 13. Thus a net coastline recession, ranging approximately from 100 to 200 feet, has occurred up to January, 1972, between stations 28N and 50N. The accretion right north of the sheet piling section of the north jetty and the erosion southwest of the same section can also be observed.

The total volume of sand accumulated south of the south jetty between September, 1967, and November, 1971, has been estimated to about 1,400,000 cu. yds., of which only about 100,000 cu. yds. of

Fig. 9 Ponce de Leon Inlet - July 18, 1971

Fig. 10 Ponce de Leon Inlet - December 13, 197

Fig. 11 Ponce de Leon Inlet - January 28, 1972

Fig. 12 Ponce de Leon Inlet - February 22, 1972

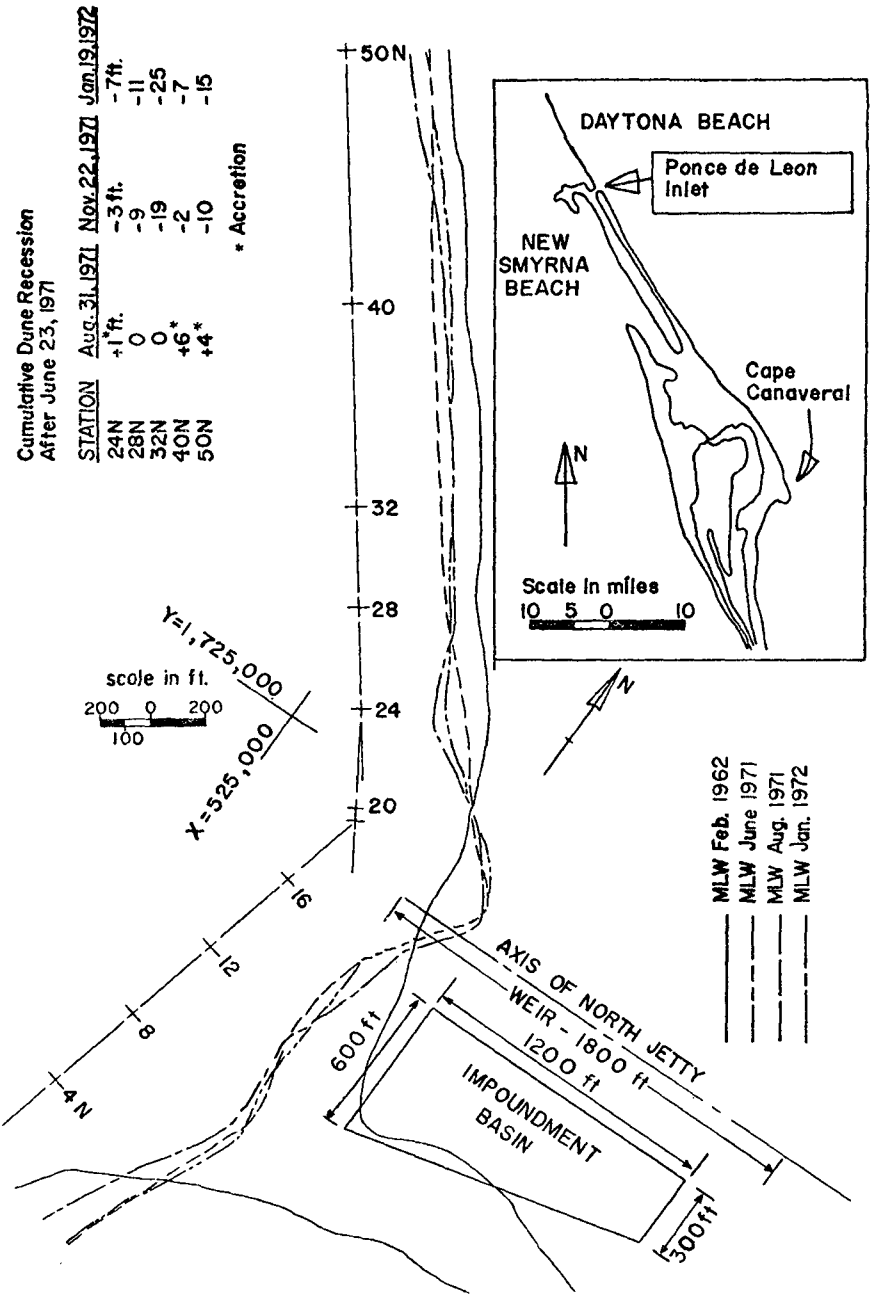

Fig. 13 Coastline Changes North of the Ponce de Leon Inlet

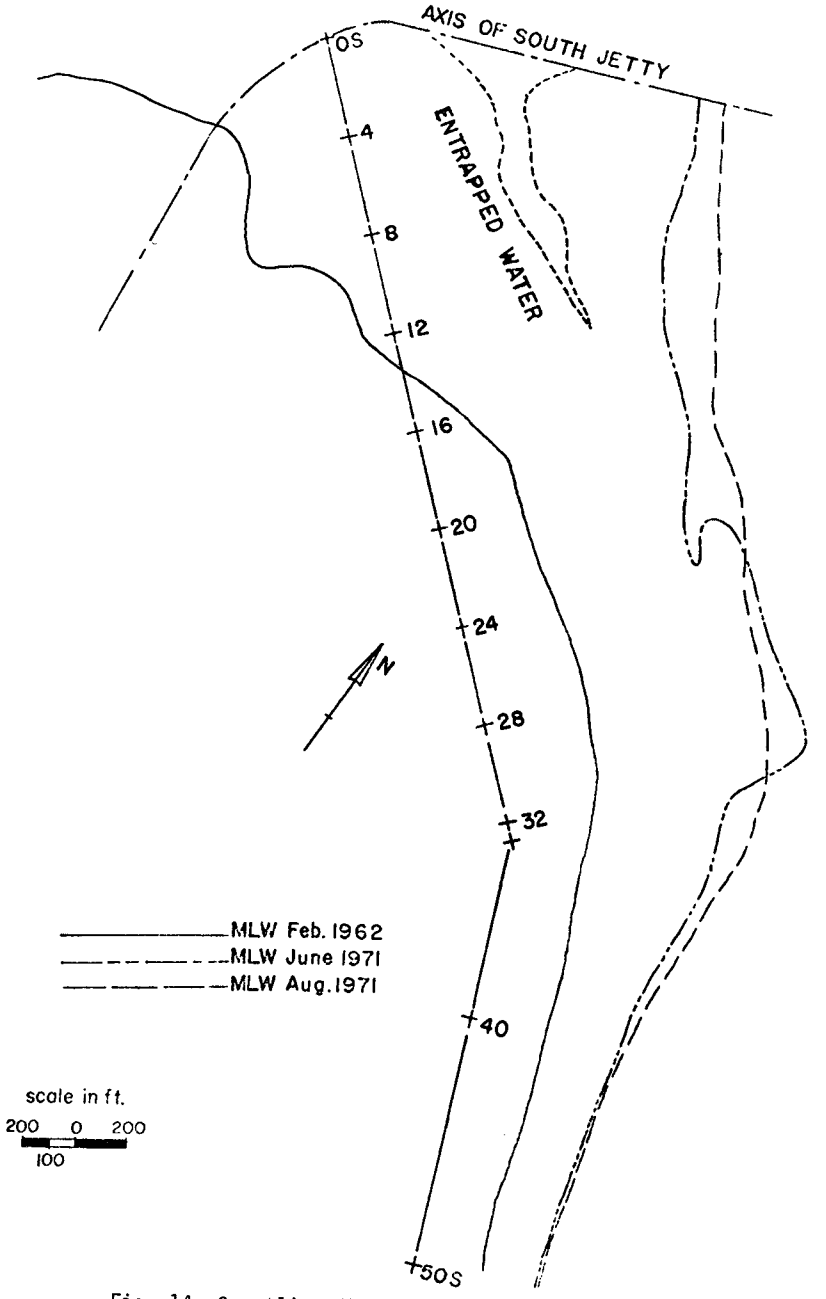

Fig. 14 Coastline Changes South of the Ponce de Leon Inlet

sand have been accumulated between June, 1971, and November, 1971. A minor portion of these volumes comes from the dredged material since little dredging had been done to that date. It should be pointed out, however, that these figures have been based on limited ground-elevation data before the jetty construction and limited field surveys and should be considered only as approximate estimates representative of the order of magnitude of the total accretion and indicative of the littoral process in the neighborhood of the inlet.

It is of interest that recent estimates of the littoral transport rates along the coast of Florida by Walton (7) based on ship wave observations have indicated a net northerly annual drift rate of 309.000 cu. yds. and a net southerly drift rate of 386,000 cu. yds. in the neighborhood of Ponce de Leon Inlet. These volumes are drastically different from those assumed in the design of the stabilization system. According to them if all the northerly moving sand is assumed to be entrapped south of the south jetty then the total accretion volumes from the beginning of construction to date (occurred predominantly during 4 summers) would have been close to 1,2000,000 cu. yds., a figure much closer to the one obtained from the field surveys.

Much additional work is needed for a reasonably accurate and dependable prediction of littoral transport rates. Our stage of knowledge on littoral processes is still incomplete and direct estimates of sand drift by field measurements and tracings are very time consuming and expensive. All that can be said at this point is that the unexpected high sand accretion south of the south jetty is most likely due to both underestimates of the northerly sand drift and to a change of the refraction pattern, which causes southerly moving sand to be deflected in a westerly direction towards the area protected by the south jetty.

SUMMARY AND CONCLUSIONS

Rapid and unexpected changes of the coastline near the Ponce de Leon Inlet during and after the construction of two jetties have been presented and discussed. The most important and spectacular change has been the rapid sand accretion south of the south jetty in spite of the estimate of a net annual littoral transport of 500,000 cu. yds. of sand from north to south. The total accretion volume from the summer of 1968 to the late fall of 1971 amounts to approximately 1,400,000 cu. yds. Evidence from a series of aerial photographs suggests that the sand was transported predominantly in a northerly direction during the summer months and from the offshore bar by the action of refracted waves.

It appears that the sand entrapment south of the inlet reduced the sediment supply to the beach north of the inlet during the periods of northerly drift thus upsetting the preexisting balance between sediment supply and erosion. As a result the recession of the coastline and duneline north of the jetty after its construction have been considerably higher than the mean annual recession before the jetty construction. Sand accretion, however, immediately north of the weir has already started.

The described changes lead to a number of fundamental conclusions regarding the design of inlet stabilization systems, the most important of which are the following:

1. The net annual rate of littoral transport cannot be used as a unique criterion in designing stabilization and sand bypassing systems in inlets where the littoral drift reverses its direction. Instead the total sand volumes transported annually in either direction should be considered.

2. The refraction pattern of waves in the immediate neighborhood of the inlet as well as the effect of jetties on that pattern should carefully be studied. Refracted waves may transport sand locally in a direction opposite to that of littoral transport along a nearby straight beach. This may be particularly important in bar-built estuaries and bays with extensive offshore bars.

3. There is a need for more precise techniques for the estimate of littoral transport of sand and for the correlation of the latter with the wave climate.

4. In cases where development of new beaches and/or extension of existing ones is anticipated as a byproduct of an inlet stabilization by jetties, appropriate filters should be designed to prevent washing of sand through the jetties and avoid erosion of the beach internally by waves and tidal currents.

ACKNOWLEDGEMENTS

This study is being supported by the Coastal Engineering Research Center through the Department of the Army, Jacksonville District, Corps of Engineers under contract No. DACW17-70-0079. Messrs. David Tackney, B. G. Beechley and E. Olsen, research assistants in the Department of Civil and Coastal Engineering of the University of Florida, participated in various phases of the field surveys and in the analysis of field data.

REFERENCES

1. Prichard, D. W., "What is an Estuary: Physical Viewpoint," Estuaries, Edited by Lauft, G. H., Publication No. 83, American Association for the Advancement of Science, Washington, D.C., 1967.

2. U.S. Army, Coastal Engineering Research Center, "Shore Protection Planning and Design," Technical Report No. 4, Third Edition, 1966.

3. Ippen, A. T. (Editor), "Estuary and Coastline Hydrodynamics," Chapter 10, McGraw-Hill, 1966.

4. U.S. Army Engineer Division, South Atlantic Corps of Engineers, Atlanta, Georgia, "National Shoreline Study and Regional Inventory Report, South Atlantic - Gulf Region, Puerto Rico and the Virgin Islands," August, 1971.

5. U.S. Army Engineer District, Jacksonville, Corps of Engineers, Jacksonville, Florida, "Survey Review Report on Ponce de Leon Inlet, Florida," Serial No. 61, September 30, 1963.

6. Department of the Army, Jacksonville District, Corps of Engineers, Jacksonville, Florida, "General and Detail Design Memorandum, Ponce de Leon Inlet, Florida," Serial No. 17, November 29, 1967.

7. Walton, T. L., Jr., "Littoral Drift Computations Along the Coast of Florida by Use of Ship Wave Observations," Thesis presented to the University of Florida at Gainesville in Partial Fulfillment of the Requirements for the Degree of Master of Science in Coastal and Oceanographic Engineering, June, 1972.

CHAPTER 46

SAND TRANSPORT DURING CLOSURE OF TIDAL CHANNELS

J.N. Svasek[1], J.H.J. Terwindt[2]
and A.W. Walther[2]

Abstract

A method is presented for estimating the dredger capacity required for closing tidal gaps with sand as the only building material.

The method is based essentially on a relation between parameters describing the flow of the water and the resulting sand transport.

Empirically determined coefficients are used to approximate the effects of the non-stationary flow in the gap and the supply of suspended material at the dumping site.

The experiences gained at a number of closure operations are discussed and compared with the computations.

Introduction

The choice of the construction to be applied during the last phase of a closure operation of dams in tidal waters depends largely on the current velocities occurring in the remaining gap.

Tbe material to be used should have either sufficient weight to resist erosion or be supplied in such large quantities so that the main portion is not carried away by the currents. In the latter case sand or gravel are possible materials.

If currents velocities in the closing gap reach high values (order 3 m/sec or more) large scale methods are necessary (caissons, concrete blocks, etc.). Due to the high velocities costly bottom protection works are required.

If the currents are of moderate magnitude (order 2.5 m/sec or less) local sand may be used. A part of this material will be

1. Consulting Engineer, Rotterdam Airport, The Netherlands.
2. Coastal Research Section, Delta Service, The Hague, The Netherlands.

lost in the closing operation. However, the costs of the expensive bottom protection are saved. Therefore, the losses of sand may well be accepted in the overall economics of the works.

Recently a number of tidal channels both in The Netherlands and in Germany were closed successfully by pumping sand into the gap. This was mainly possible because of the increased capacity of the modern suction dredgers.

This paper describes a method with which the required capacity of the dredgers can be estimated for a given closure operation. The method can be used to determine the most economical scheme of an operation. The effect of a temporary decrease or interruption of the sand supply can also be evaluated.

Method of calculation

The method is essentially based on the computation of the suspended sediment load. The suspension transport is considered only because relatively fine sands (diameter 0.120 to 0.250 mm) were used in the closure operations realised until now. Then the bed load may be neglected compared with the suspension load. When coarser sands are used, however, the bed load should also be considered.

The suspended sediment load can be calculated using the relations presented by LANE AND KALINSKE, further elaborated by MORRA and summarized by DRONKERS (1970).

The equations describing the suspended sediment load apply to steady flow in a condition of equilibrium between erosion and sedimentation.

The first condition is not satisfied in a tidal area. MORRA, however, proved that acceptable results can be obtained if the current velocity curve during the tide is schematized by a number of time intervals with constant current velocities.

The second condition, equilibrium of erosion and sedimentation is also not satisfied, because of the acceleration and deceleration of the water flow in the area of the closure gap.

The closure gap may be divided into two areas: the sloping

head of the sandfill where the sand is supplied and the area outside this head which is only affected by the accelerated water flow. In both areas there is an increase in sand transport capacity (q_{cap}) which is the quantity of transported sand under equilibrium conditions, calculated with the above mentioned formulae.

The increase in sand transport capacity (q_{cap}) along the streamlines of the gap will result in a certain amount of erosion. However, a certain distance is necessary for the erosion of an additional amount of sand from the bed to distribute it over the vertical and so create a new equilibrium. Usually this distance is larger than the zone of accelerated flow.

Therefore the transport of eroded sediment (q_{LE}) in the closure gap outside the head of the fill is smaller than the sand transport capacity q_{cap}.

The proportionality factor (A) between q_{LE} and q_{cap} may be estimated afterwards from the comparison of the observed quantities of erosion and calculated q_{cap} in closure gaps. This factor cannot be determined precisely enough. The amount of erosion which cannot be computed very accurately from soundings is related to the period between the soundings. In practice, however, the current measurements are limited to one tidal cycle only within such a period. It is doubtful whether the results of these measurements are representative for the whole period, because the closure operations proceed further.

It was found that the factor A varies between 0.05 and 0.6 while its mean value is about 0.1. In the computations realised until now the factor A was estimated to be 0.25.

At the head of the fill in front of the discharge pipes all sand is supplied in suspension flowing down along the submerged slope of the head. The quantity of sand in the water far exceeds the sand transport capacity (q_{cap}) in this area. Some time is required for the settling of this sand. As a result a certain part of it is transported by the currents and settles outside the base of the closure dam.

The loss of sand in this part of the gap (q_{LD}) was assumed

to be $q_{LD} = B.q_{cap}$, with B = 2 for sand with a mean diameter of 0.120 to 0.250 mm. The total loss of sand per unit of time is $q_{LD} + q_{LE}$, both being computed from q_{cap} using above mentioned factors A and B.

The variables necessary for the calculation of q_{cap} (see Dronkers, op.cit.) are the average current velocity over the vertical, the waterdepth, the Chézy coefficient, the mean diameter of both the sand that will be supplied and that of the bed material in the gap.

The current velocities during the successive phases of the closure operation can be derived from model tests or from tidal computations.

The Chézy coefficient is determined from prototype measurements; q_{cap} is expressed by $m^3/m'/$unit of time.

In order to calculate q_{cap} over the entire longitudinal section of the gap during one tide the following procedure may be applied.

The longitudinal section of the gap should be schematized into parts. In each of these parts, both the depth and the current conditions are supposed to be constant within a time interval Δt (figure 1).

When a_i is the length of part i in meters, then the sand transport capacity per unit of time in part i is: $a_i.q_{cap\ i}$, varying during the tidal cycle.

The time intervals are usually chosen either $\frac{1}{2}$ or 1 hour. (There is a diurnal tide along the Dutch coast).

The total sand transport capacity q_i for part i over the total tidal cycle is computed by summation.

The sand loss per tide over the longitudinal section (q_{LT}) can now be evaluated taking into account that the sand loss over the dumping site is 2 q_i and in the rest of the section 0,25 q_i.

The same procedure should be repeated for the successive stages of narrowing the closure gap.

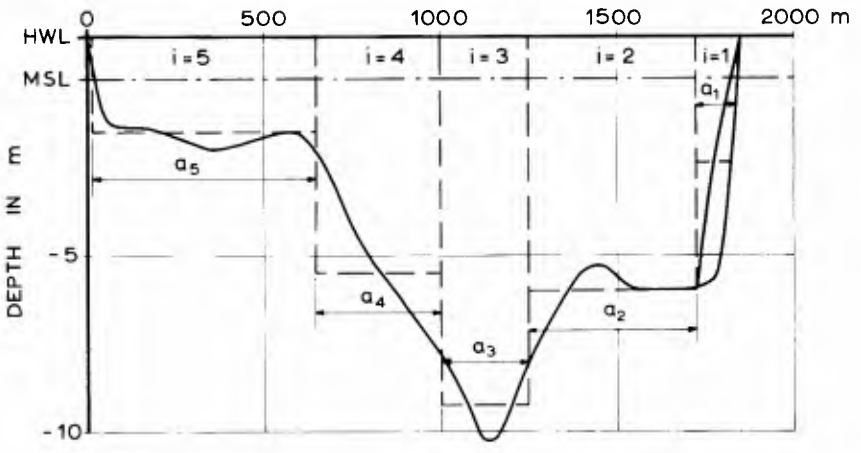

LONGITUDINAL SECTION OF A CLOSURE GAP
Fig. 1

Fig. 2

Experiences

With the procedure outlined above an optimalization of the closure operations can be set up. If the time of the entire closure operation has been fixed the necessary dredger capacity can be estimated.

On the other hand if the dredger capacity has been fixed the time of the closure operation can be determined.

The method was applied to the closure of the following tidal channels in The Netherlands (figure 2), Brielse Gat (1966), Zuidwal, Lauwerszee (1968), Noord Pampus, Haringvliet (1968), Springersdiep, Brouwershavense Gat (1969) and Geul, Oosterschelde (1972, in execution), figure 3. Some data of these channels are presented in table 1.

The following experiences were obtained. Obviously the actual closure of the channels was realised with a minimum width of the primary dam in order to finish the enclosure in a short time and to reduce the loss of sand. In practice a crest width is determined by the number of discharge pipelines and was chosen at 50 to 100 m. The height of these dams is determined by accepted risks for destruction of the pipelines and was chosen between 2 and 3 m above M.S.L.

The final dam of larger dimensions was realised after the closure operation of the primary dam. It appears that a large part of the quantity of sand transported from the closure gap settles within the cross-section of the final dam. The computed loss of sand during the closure operation should consequently not be considered to be the loss in the overall work. It determines the duration of the operation and is the base for the choice of the total capacity of the dredgers.

The total economy of a project, however, is determined by the losses of sand outside the base of the final dam.

In order to evaluate the accuracy of the computations, observed losses were compared with both the predicted and the calculated losses.

The observed sand loss is the difference between the dredger production and the sedimentation within the designed cross-

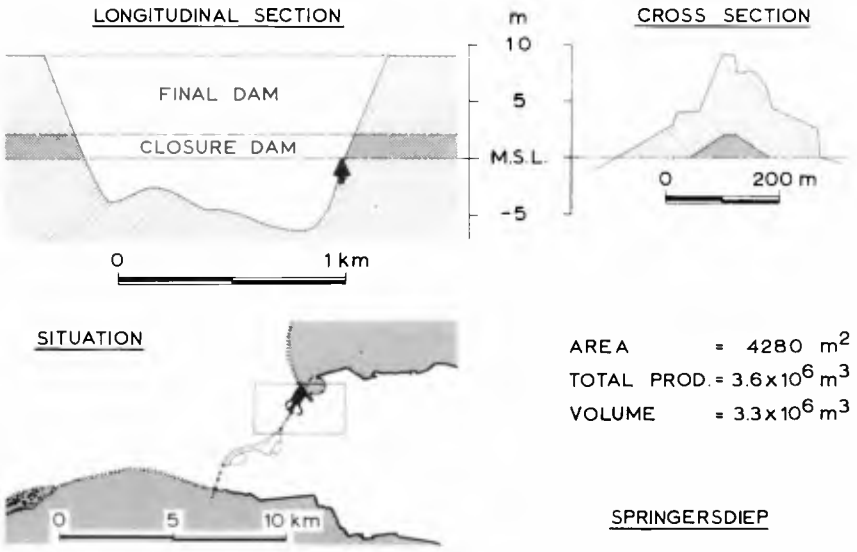

Fig. 3[a] EXAMPLE OF MODERATE DEEP CLOSURE GAP

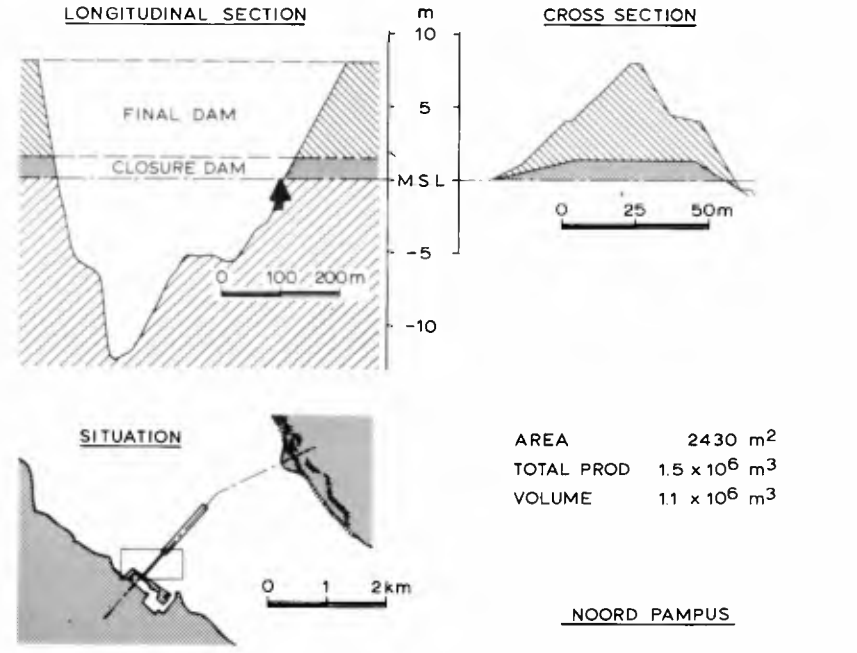

Fig. 3[b] EXAMPLE OF DEEP CLOSURE GAP

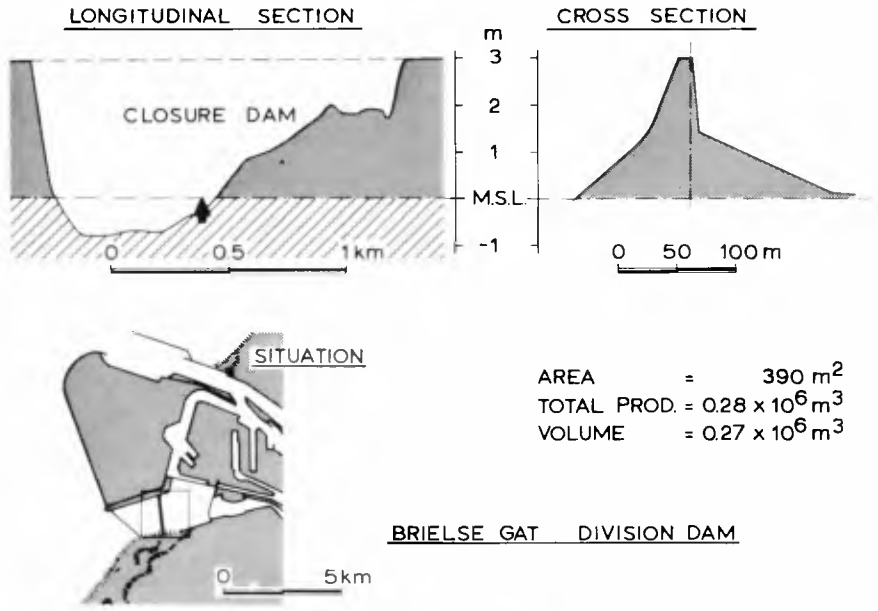

Fig. 3c EXAMPLE OF SHALLOW CLOSURE GAP

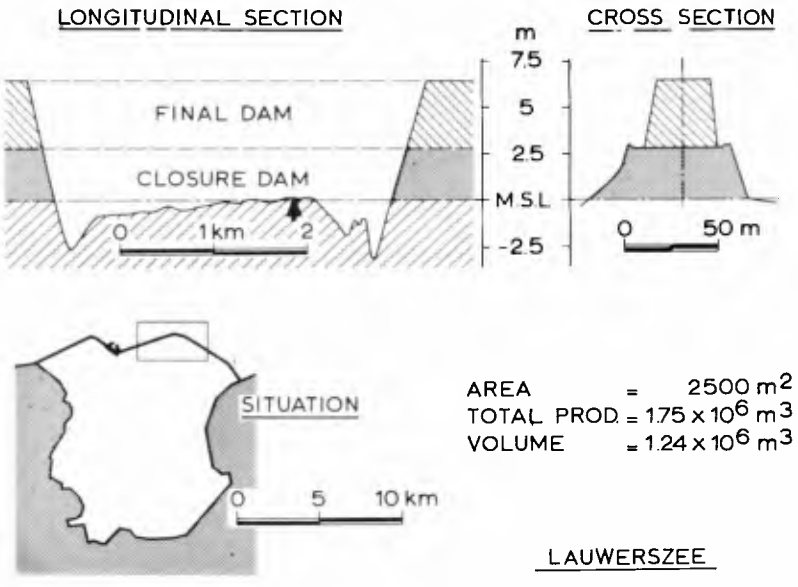

Fig. 3d EXAMPLE OF SHALLOW CLOSURE GAP

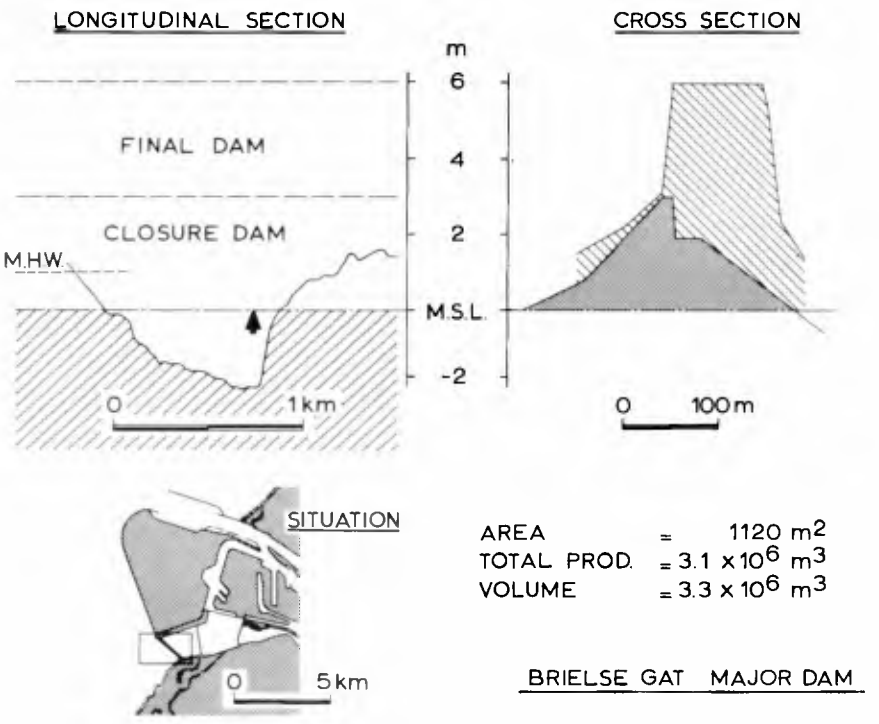

Fig. 3e EXAMPLE OF SHALLOW CLOSURE GAP

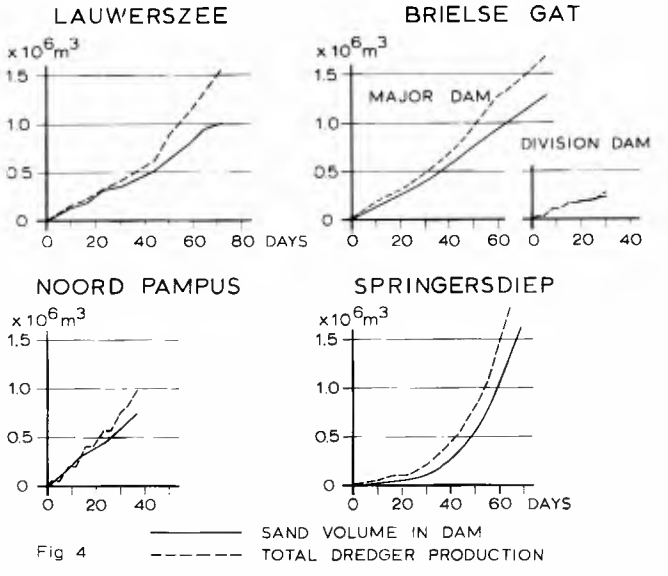

Fig. 4

		Lauwerszee Zuidwal	Brielse Gat Division Dam	Brielse Gat Major Dam	Noord Pampus	Springers-diep
Mean tidal range	m	2.6	2.2	2.2	1.85	2.60
Length of closure gap	m	3351	1720	1820	400	1000
Area of closure gap	m^2	4280	390	1120	2430	4280
Volume of closure dam	10^6 m^3	1.04	0.22	1.19	0.75	1.62
Volume of final dam	10^6 m^3	1.24	0.23	3.28	1.10	3.34
Total production of dredgers during closure	10^6 m^3	1.56	0.27	1.72	0.97	1.87
Total production of dredgers in overall work	10^6 m^3	1.75	0.28	3.10	1.50	3.60
Total observed loss of sand during closure	10^6 m^3	0.52	0.06	0.53	0.22	0.25
Total observed loss of sand in overall work	10^6 m^3	0.51	0.05	+ 0.18	0.40	0.26
Time of closure operations	days	70	36	63	37	66
Maximum number of dredgers		3	1	2	2	3
Maximum production per tide	10^3 m^3	16	10,5	20	25	25
Maximum predicted loss of sand per tide	10^3 m^3	1.48	6	12	6	7.8
Number of sides of sand fill		2	1	2	1	1
Mean grain size of supplied sand	microns	130	-	-	135	200

Table 1. Data of closure gaps and dredging operations

section of the final dam. It may be noted that the actual side slopes of the sand dam may deviate from the designed ones. If there is any wave action, almost an equilibrium beach profile is developing during the operation. The material eventually deposited outside the design cross-section contributes to this equilibrium profile and therefore should not be considered as lost to the volume of the dam. Moreover, the dredger production is measured as volume of spoil, consisting of sand and mud. The mud, however, is hardly found in the sand dam. So a part of the observed sand loss consists of the mud suspended in the spoil.

The predicted sand loss is that which has been calculated before the works started. The data are estimates, derived from tidal computations or model experiments. These data may deviate from the actual ones, operating during the closure procedure. Furthermore the outline of the closure procedure may deviate from the planning and the data introduced in the calculation of the predicted sand loss are no longer reliable. Moreover, variations in weather conditions cannot be included in the computation.

Therefore, the calculated sand loss was introduced. This is the sand loss computed from data derived from actual measurements made during the closure operation (hindcast).

The discrepancies between calculated and observed sand losses are then mainly due to the inaccuracy of the method or that of the current measurements.

From some closure operations there were enough acceptable data to compare the predicted, the calculated and the observed sand losses. Table 2 gives the results. In figure 4 the dredger production and losses are illustrated.

It may be concluded that in most cases the calculated and observed sand losses are of the same order of magnitude. The predicted sand losses deviate in most cases considerably from the observed losses. This indicates that much care should be given to the data on which the prediction is based.

From table 1 it can be learned that successful operations were executed when the maximum dredger production per tide was at least four times the predicted maximum losses of sand per tide.

			Lauwerszee	Brielse Gat Division Dam	Brielse Gat Major Dam	Noord Pampus	Springers-diep
Total dredger productions	(D)	(10^6 m^3)	1.56	0.27	1.72	0.97	1.87
Observed losses of sand	(O)	(10^6 m^3)	0.52	0.06	0.53	0.22	0.25
Predicted losses of sand	(P)	(10^6 m^3)	0.90	*	*	0.20	0.70
Calculated losses of sand during closure operation	(C)	(10^6 m^3)	0.45	0.10		0.06	0.35
Percentage O ÷ D			33	22	31	25	15
Percentage P ÷ D			60			20	42
Percentage C ÷ D			29	37		6	21
$\frac{P - O}{P}$			0.43			- 0.20	0.64

* Execution of closure operation deviated very much from planning; predicted losses of sand unreliable

Table 2. Dredger productions and losses of sand

Some illustrations of the optimalization of the closure operations can be presented here.

lt appeared that in most cases an increase in dredger capacity results in a reduction of the sand losses during closing. This is indicated in table 3.

Assumed dredger productions m^3/week	Time of closure operation weeks	Calculated loss of sand 10^6 m^3
230,000	5	0.50
300,000	$3\frac{1}{2}$	0.35
350,000	$2\frac{1}{2}$	0.25

Table 3. Calculated loss of sand. Dam through Springersdiep for several dredger productions.

Furthermore the computations may show at which stages of the closing the largest sand losses are to be expected (figure 5). It may be wise to reach this stage during neap tide conditions.

This determines the beginning time of the operation. The difference in sand loss during spring and neap tide is illustrated in figure 6 for the closure of a gap from one side. It can be seen that during the ten weeks closure operation the actual losses vary with the tidal range.

Also the computations may indicate the most feasible way of operations viz. closing from one side to the other, or tbe reverse or from both sides together. There can be a great difference in current pattern and velocities in the closing gap for different ways of operations.

Table 4 shows for example that in the North Pampus channel the calculated sand losses are much higher when proceeding the dam from N to S than from S to N.

	Loss of sand in 10^6 m^3
Operation from S to N	0.10
Operation from N to S	0.19

Table 4. Calculated loss of sand, Dam through Noord Pampus.

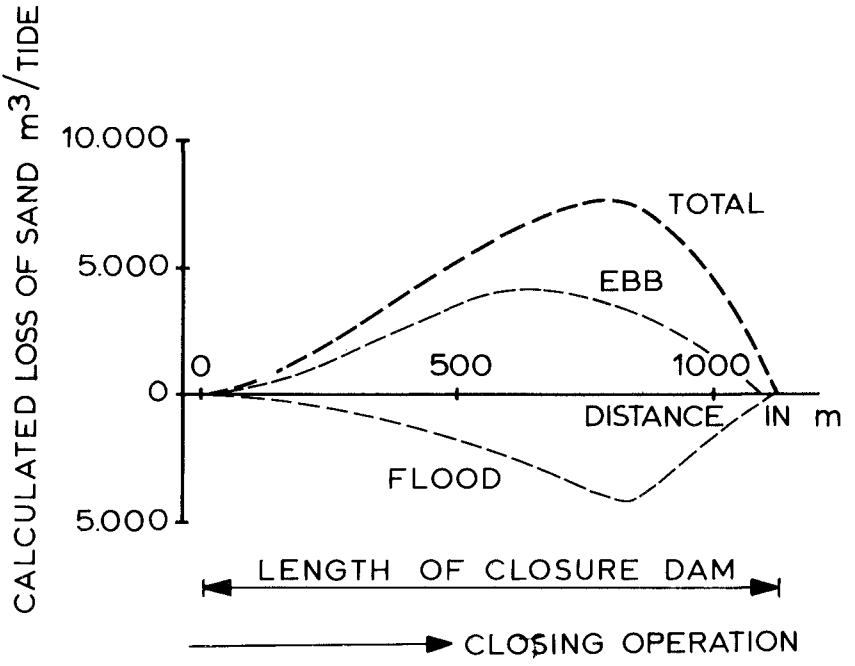

Fig. 5

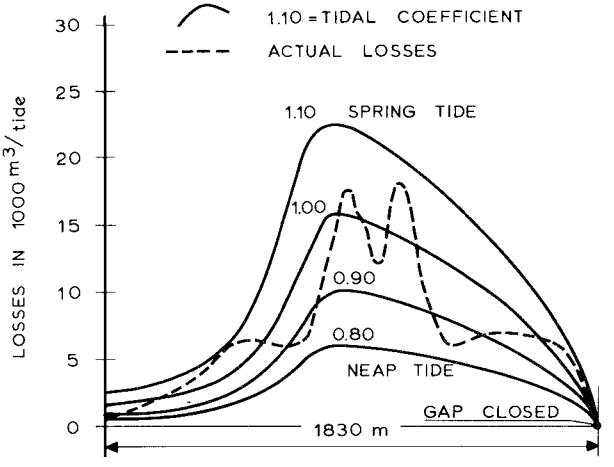

Fig. 6 CALCULATED LOSSES DURING THE CLOSURE OF A GAP

The representative grain size, which may be introduced into the computations may be established as follows. From samples of borings of the winning pit the variation of grain size with depth can be found (figure 7) and schematized. The schematized data of several borings can be put together in order to obtain an overall indication of the variation of the grain sizes with depth. Then an overall grain size distribution of all the material can be determined.

For each grain size fraction the sand transport capacity per unit of time can be calculated taking into account the percentage material present in that particular fraction. The cumulative distribution of the transport capacities of all fractions gives the total sand transport for that grain size distribution ($q_{cap\ f}$) (figure 8).

Furthermore the sand transport capacity can also be calculated for each fraction assuming a uniform grain diameter $q_{cap\ u}$. (So in every fraction there is 100% of material). The representative diameter is that one for which $q_{cap\ u} = q_{cap\ f}$ (figure 8).

Finally it was observed that the submerged slopes of the dumping site were 1 : 15 to 1 : 20 for grain sizes of .15 to .20 mm, whereas the emerged slopes were about 1 : 30.

From experience and calculations it appeared that usually the most favourable location of the final gap of the sand dam is a shallow part of the cross-section. This is due to the fact that the current velocities in the final gap situated in a shallow area are lower compared with those in a deep final gap. Moreover, the length of the sloping fill head is less and consequently also the losses of saud.

Furthermore the sand volume needed for the final stage of the closure operation is lower. Altogether, shorter time is needed with the final stage in a shallow area. Then both the amount of erosion in the gap and the losses out of the base of the dam are reduced while the current velocities reach their maximum values.

Success of the operation also depends on the working method, the layout of the pipelines, the sand-water ratio of the spoil

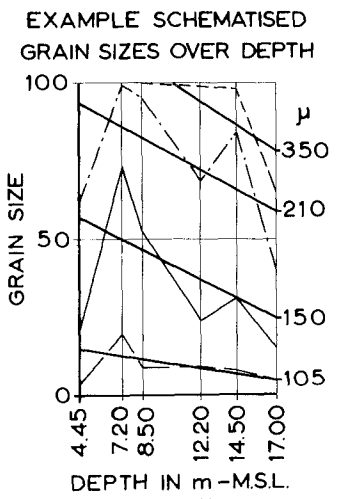
EXAMPLE SCHEMATISED
GRAIN SIZES OVER DEPTH
100
50
0
GRAIN SIZE
μ
350
210
150
105
4.45
7.20
8.50
12.20
14.50
17.00
DEPTH IN m -M.S.L.

Fig. 7

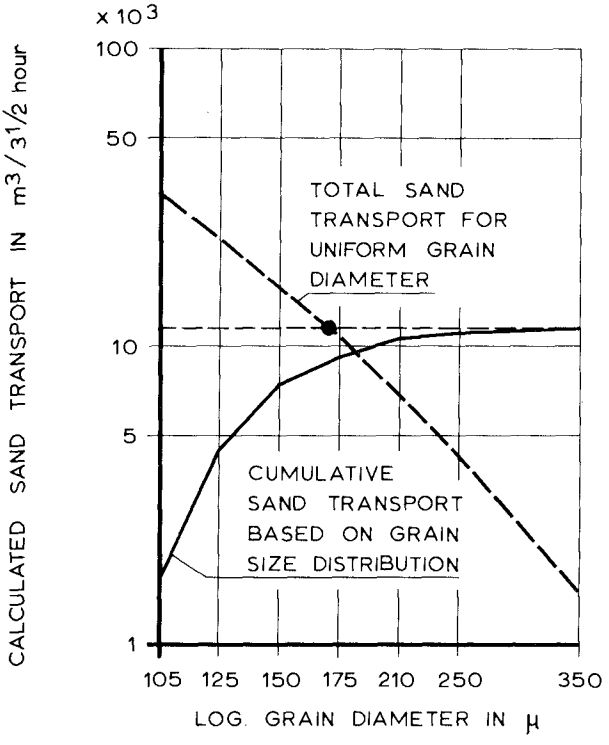
x 10³
100
50
10
5
1
CALCULATED SAND TRANSPORT IN m³/3½ hour
TOTAL SAND
TRANSPORT FOR
UNIFORM GRAIN
DIAMETER
CUMULATIVE
SAND TRANSPORT
BASED ON GRAIN
SIZE DISTRIBUTION
105 125 150 175 210 250 350
LOG. GRAIN DIAMETER IN μ

Fig. 8

and the working time of the dredgers.

In the final gap, bulldozers and draglines should operate on the fill to control the sand deposition above the water level, (see photo 1).

A special problem is to control the supplied water eroding channels while running down the fill, especially when dredgers with large discharge capacities are used. Normally these channels are rapidly filled when the tide is rising.

The method of computation presented above can be of great help to determine the feasibility of the closing of a tidal channel by means of a sand dam. Further it gives reliable data on the optimum dredger capacity and the time involved in the closure operation. Finally it fcan contribute to the choice of the best operational scheme.

Reference:

Dronkers, J.J., 1970. Research for the coastal area of the Delta region of the Netherlands.
XIIth Conf. on Coastal Engineering, Washington D.C.

Photo 1. Final gap. Bulldozers and draglines operating on the fill

CHAPTER 47

MODELING SEDIMENTATION AT INLET AND COASTAL REGION

Pang-Mou Lin,[1] A.M., ASCE
Civil Engineer Assistant
Dept. of County Engineer, County of Los Angeles
California, U.S.A.

ABSTRACT

Sediment transport in the vicinity of inlets and coastal regions depends on the combined bottom shear stresses due to both currents and waves. The modeling of the movement of bedload is controlled by the Froude law, bottom shear stress, wave steepness, and friction factor. Assuming Einstein's theory of bedload function can be applied to this study, an analysis was performed after conducting experiments in the flume and model basin. A series of results obtained from the flume tests is to insure the relationship between the fluid characteristic and the movement of bedload. The final results concerning the longshore sediment transport appeared satisfactory with the estimated curves. The bottom configurations in the inlet after each test were also shown satisfactorily similar. The sedimentological time scale for the three bed materials were not in satisfactory agreement, however, more discussion of the results was presented in this paper.

INTRODUCTION

Problems dealing with sediment transport in the vicinity of inlet and coastal region are very comlex and difficult. Very often, analytical solution fall short because of insufficient knowledge of phenomena, or because of complex geometry. In such cases, a model study with a movable bed is desirable and is a valuable quide to the engineer in the design of coastal structures and navigational channels.

---

1) Former graduate assistant, Dept. of Coastal and Oceanographic Engineering, University of Florida. Gainesville, Florida, U.S.A.

It is desirable to use lighter movable bed material to reduce the operation time of the model. In this research, the similarity of movable beds was studied by using sand, walnut shell, and coal. The characteristics of bed materials is shown below

Material	Spec. Gravity	D_{80}	D_{50}	D_{20} (mm)
Sand	2.67	0.23	0.16	0.14
Walnut shell	1.35	1.60	1.60	1.25
Coal	1.25	0.84	0.76	0.53

The movement of sand along the coast and in the inlet is induced by both currents and waves action. Many investigators have arrived at a relationship between currents and sediment transport (1), and to a lesser extent, between waves and sediment transport (2). The combined action of waves and currents in sediment transport is not completely understood yet. In order to have a better understanding of this problem, a series of tests was conducted in which different materials were used to verify the similarity laws. The test program consisted of (I) a basic investigation of grain movement of different materials in a one-dimensional flume, and (II) a model study of waves and currents in a inlet and a coastal region under consideration similar to the ones found in nature. Separate tests were conducted for inlet currents, waves approaching the coastal line at an angle, and a combination of waves and currents. The acquired measurements consisted of currents in the inlet, wave heights, and longshore sediment transports. After each run, the bottom configuration was contoured and recorded photographically.

THEORETICAL REVIEW

The consideration of modeling velocity parameters in the model basin is shown in Figure 1_a and the respective flow equations are expressed below

EBB FLOW

$$V_x = \frac{V_m}{2C_2} \cdot \frac{B_1}{x} \exp\left(-\frac{1}{2C_2^2} \cdot \frac{y^2}{x^2}\right) \qquad (1)$$

$$V_y = \frac{V_m}{2C_2} \cdot \frac{B_1 \cdot y}{x^2} \exp\left[-\frac{y^2}{2C_2^2 x^2}\right] \tag{2}$$

FLOOD FLOW

$$\cosh^2 \log \frac{V}{q} = \tfrac{1}{2}\left\{(e^{\frac{2\pi\phi}{Q}} + 1) + \left[(e^{\frac{2\pi\phi}{Q}} + 1)^2 - 4e^{\frac{2\pi\phi}{Q}} \sin^2\left(\frac{\pi\psi}{Q}\right)\right]^{\frac{1}{2}}\right\} \tag{3}$$

where $V = \frac{2+\pi}{\pi} V_m$

LONGSHORE CURRENT

$$V_L^2 = \frac{3}{8} \frac{gH_b^2 \cdot n_b}{d_b} \cdot \frac{\sin\alpha \cdot \sin\theta_b \cdot \sin 2\theta_b}{f} \tag{4}$$

where $f = \left[2 \log_{10}\left(\frac{d_b}{k_e}\right) + 1.74\right]^{-2}$

HORIZONTAL ORBITAL VELOCITY

$$u = \frac{H}{2} \frac{\cosh ky}{\sinh kd} \sin(kx - \sigma t) \tag{5}$$

The basic analytical treatment of channel expansion of ebb flow is assumed to be the same as that for a half circular jet expansion. The theory of circular jet expansion was first described in detail by Tollmien (3) and later investigators, for example, Albertson, Dai, Jensen and Rouse (4) and Baines (5). It is resonable to apply this theory in the course of the analysis of ebb flow pattern. Concerning the flood flow pattern,

the basic analytical treatment was presented by French (6) in his research. It is resonable to apply potential flow phenomenon to the flood flow condition. The longshore current is based on Eagleson's experimental result (7). No direct measurement of longshore current velocity was conducted in this study, however, the friction coefficient f was obtained by using the Karman-Prandtl resistance equation for steady uniform flow. The values of absolute roughness height k_e in thepresent study were assumed according to both Eagleson's report and the velocity profiles measured in the flume tests. The average values of roughness height k_e are shown below

Material	k_e (ft.)
Sand	0.0058
Walnut shell	0.00092
Coal	0.00054

It is assumed that the bedload transport, due to the combined action of waves and currents, is a function of bottom shear stress. Apply Prandtl's turbulent shear stress equation

$$\tau = \rho \ell^2 \left(\frac{\partial V(y)}{\partial y} \right)^2 \tag{6}$$

and make the assumption that the velocity profile

$$V(y) = \frac{V_*}{\kappa} \log \frac{y}{k_e} \tag{7}$$

from the edge of the vicous sublayer to the granular surface, is linear. The combined shear stresses are expressed as follows.

Ebb flow inside channel

$$\tau(t) = \rho V_{m_*}^2 \left| 1 - \xi \frac{p_1 u_o}{V_m} \cos\theta \sin\sigma t \right| \left(1 - \xi \frac{p_1 u_o}{V_m} \cos\theta \sin\sigma t\right) \tag{8}$$

Ebb flow parallel to the shoreline

$$\tau(t) = \rho V_{L_*}^2 \left| \frac{V_L - V_y}{V_L} + \xi \frac{p_1 u_o}{V_L} \sin\theta \sin\sigma t \right| \left(\frac{V_L - V_y}{V_L}\right.$$

$$+\xi\frac{p_1 u_o}{V_L}\sin\theta\ \sin\sigma t) \tag{9}$$

Flood flow inside channel

$$\tau(t) = \rho q_*^2 \left| \frac{q_x}{q} + \xi\frac{p_1 u_o}{q}\cos\theta\ \sin\sigma t \right| \left(\frac{q_x}{q} + \xi\frac{p_1 u_o}{q}\cos\theta\ \sin\sigma t\right) \tag{10}$$

Flood flow parallel to the shoreline

$$\tau(t) = \rho V_{L*}^2 \left| \frac{V_L - q_y}{V_L} + \xi\frac{p_1 u_o}{V_L}\sin\theta\ \sin\sigma t \right| \left(\frac{V_L - q_y}{V_L} + \xi\frac{p_1 u_o}{V_L}\sin\theta\ \sin\sigma t\right) \tag{11}$$

where $\xi = \dfrac{C_z \cdot K}{g^{\frac{1}{2}}}$

p_1 is the coefficient of horizontal orbital velocity above the viscous sublayer and was determined experimentally in this study. After integration for a wave period (see appendix I) the shear stress can be expressed in terms of the shear velocity and a dimensionless coefficient η_x as expressed below

$$\tau = \rho V_*^2 \cdot \eta_x \tag{12}$$

where $\eta_x = \dfrac{1}{T}\displaystyle\int_o^T \frac{\tau(t)}{\rho V_*^2}\,dt$

Bagnold (8) found that the bed shear stress τ_c required to

maintain the motion of bedload is shown in the equation

$$\tau = (\rho_s - \rho_f)\, g.d_e.\theta' \qquad (13)$$

where $\theta' = C_o \tan\alpha_1$ a dimensionless shear stress parameter

where C_o is static volume concentration of bed material, α_1 is the internal friction angle of bed material. The magnitude of θ' does affect the intensity of the movement of bed material. Considering the similarity law, θ' is one of the essential parameters to simulate the bed shear stresses between two different bed materials. The dimensionless critical shear stress parameter θ_c for each bed material was obtained from the results of flume tests.

Applying an empirical relationship between shear stress and sediment transport rate by the Einstein's result as shown below

$$\frac{q_s}{F_o.\left[g(S_s - 1)d_e^3\right]^{\frac{1}{2}}} = 40\left(\frac{\tau}{\rho g(S_s - 1)\, d_e}\right)^3 \qquad (14)$$

$$\text{where } F_o = \left[\frac{2}{3} + \frac{36\nu^2}{gd_e^3(S_s - 1)}\right]^{\frac{1}{2}} - \left[\frac{36\nu^2}{gd_e^3(S_s - 1)}\right]^{\frac{1}{2}}$$

and the equation of conservation of sediment mass transport

$$\frac{dy}{dt} + \frac{1}{\rho_w g(S_s - 1)(1 - p)} \frac{dq_w}{dx} = 0 \qquad (15)$$

The time scale of sediment transport is obtained and shown as

$$\lambda_t = \frac{\lambda_{C_z}}{\lambda_V^6} \cdot \lambda_{d_e}^{3/2} \cdot \frac{\lambda_{(S_s - 1)}^{5/2} \cdot \lambda_L^2}{\lambda_{\eta_x}^3 \cdot \lambda_{F_o}} \tag{16}$$

From the above analysis, it is possible to summarize the movable bed parameters by a functional relationship of the form

$$f_1 \left[d_e(S_s - 1)\theta_c, d, V, g, V_*, H, L \right] = 0 \tag{17}$$

The choice of parameters implies that the particle shape and its size distribution, fluid characteristics, wave characteristics, and movement of bedload are significant. Using the Buckingham π - theorm, a functional relationship among four dimensionless parameters is expressed below

$$f_2 \left[\frac{V}{\sqrt{gd}}, \frac{V_*^2}{g(S_s - 1)d_e \cdot \theta_c}, \frac{V}{V_*}, \frac{H}{L} \right] = 0 \tag{18}$$

It is to be noted that velocity scale is determined first from the experimental result of the value of θ_c and C_z, then the depth scale and time scale of wave period are calculated from the undistorted model law.

TEST PROCEDURE AND RESULTS

A schematic diagram of the flume is shown in Figure 1b. The flume is 60 feet long, 3 feet deep, and 2 feet wide and has maxium slope of 2 per cent and a maximum discharge of 5.8 cfs. The tests in the flume were conducted for three types of granular beds. These were made of sand, ground walnut shell, and bituminous coal. Water was allowed to flow until the flow was statistically steady and uniform in the test section. For each bed material, a series of tests was carried out with various combinations of mean depth and flow velocity. Velocity measurements were obtained at different elevations in the test section. A propeller-type velocity meter, manufactured by A. Ott Kempten (Germany), was used for this purpose.

The bed materials were arranged in the middle portion of the flume at a thickness of 2 inches along a 30 foot test section. In order to obtain the velocity profile which produces the critical shear stress, the water discharge was increased slowly in small increments spaced by ten-minute intervals. When the bed material underwent intermittent motion, the velocity profiles were measured at that stage. The values of θ_c obtained from velocity profiles at critical stage are shown below

Material	θ_c
Sand	0.0914
Walnut shell	0.0378
Coal	0.0436

The relationship between the mean velocity $\bar{V}$ and the shear velocity V_* for the three bed materials are shown in Figure 2. The bedload transport rate in the flume tests were measured by taking samples from a pan trap. The quantity by weight of the sediment was determined after drying. On the average, three samples per run were taken. The mean sediment transport rates were considered to be the average of the three samples. The latter was assumed to represent the long-time average bedload transport prevailing in the flume. The results of sediment transport tested in the flume are shown in Figure 3.

A schematic plan view of the model basin is shown in Figure 4. The maximum still water depth in the constant depth portion was approximately 11 inches. The channel connecting the two basin was 10.75 feet long and 2.75 feet wide. The beach was arranged to have a 1:20 slope (i.e., $\tan\alpha = 0.05$). The velocity profile in the channel was measured by the propeller-type velocity meter at different depths. The mean velocity was then taken by averaging the velocities over the full water depth. The three types of sediment materials used in the flume were also used in the model basin study. The water depth for each material was selected to satisfy the similarity laws. Waves were generated by a flap-type wave generator with variable periods and wave heights. The waves were made to approach the shore at an angle of ten degrees with respect to the normal of the shoreline. The flood and ebb flows were controlled by weir boxes and gates. The bedload transport rates in the model on the ocean side were measured by taking samples from a pan trap located under the sand weir.

TABLE 1

Test conditions in the model basin

Conditions	Sand	Walnut Shell	Coal
Depth in the channel (in.)	5.25	5.62	4.06
Depth in the ocean (in.)	8.125	8.57	7.72
Velocity in the channel (ft/sec.)			
Flood	0.646	0.665	0.568
Ebb	0.675	0.724	0.598
Wave period (sec.)	0.859	0.875	0.729
Wave height (ft.)	0.093	0.102	0.073
Test duration* (min.)	180	29	85

*The test duration was determined experimentally as the duration for accumulating equal volumes of bed material in the weir trap.

The results of longshore bedload transport is shown in Figure 5. After the completion of each test, the bottom configurations were contoured and recorded photographically. Three bottom section profiles, based on photographic records, are shown in Figure 6 through Figure 8 for the analysis.

DISCUSSION

The results of the velocity profiles measured in the flume tests were used to determine the dimensionless shear stress coefficients θ_c. The value of θ_c for sand in this study is approximate the same as that shown by Bagnold in his study (9). The grain size used in his study was 0.31 mm, and the θ_c was found at the range of values from 0.05 to 0.14. According to Bagnold, θ_c is a function of static volume concentration and the internal friction angle of bed material. The magnitude of θ_c does affect the intensity of the movement of bed material.

The linear relationship between the mean velocities and shear velocities are shown for the purpose of selecting the constant friction coefficients. The results of the velocity measurements were taken both in plane and dune beds. The reason for selecting the friction coefficient as constant is that the test velocity was scaled to a little higher than the velocity for bedload movement in the critical condition. The error introduced cannot be very significant as a linear velocity distribution in the boundary layer was assumed.

Figure 3 is a graphical comparison of the results by using Einstein's bedload function theory. The data for coarse bed materials fit Einstein's bedload function very well. The experimental results by Bishop, Simons and Richardson (10) showed that A_* and B_* are not universal constants but are related to the median diameter of the bed material. The results of the present study showed that the values of A_* increase with increasing grain size, and the values of B_* decrease with increasing grain size and that A_* and B_* are independent of the types of bed material. These characteristics of A_* and B_* are similar to the results shown by Bishop *et al*.

For the tests in the model basin, it is assumed that the bedload transport due to combined action of waves and currents is a function of bottom shear stress. Since the movement of

bedload due to wave action is related to the probability characteristics, the theory of Einstein's bedload function can be assumed to be valid in this study provided the dependence of the bottom shear stress on the oscillatory mean flows is taken into account. The equations of combined shear stresses were derived for this purpose. However, these derivations were based on the assumption that the velocity profile, from the edge of the viscous sublayer to the granular surface, is linear. Some discrepancy may occur for low water velocity. The error introduced by this can be reduced due to the effect of oscillating bottom water particle velocity, and the error is usually insignificant (11).

The velocity of longshore current was introduced according to Eagleson's formula. The derivation of Eagleson's formula was based on the conservation of momentum transported parallel to the shoreline. In the vicinity of an inlet, a similar analysis of momentum normal to the shoreline may be made and is seen to give a net flux of momentum into the inlet. The latter may be interpreted in terms of net velocity into the inlet in analogy to the longshore current in Eagleson's analysis. Consequently, the value of bottom shear stress should be higher than the one calculated by equation of flood flow inside inlet channel.

The coefficient p_1 of horizontal orbital velocity above the viscous sublayer was determined experimently in this study. The value of p_1 was determined from the duration of a test to accumulate a predetermined volume of sediment. From Figure 5, the shear stress was estimated, and using the combined shear stress equation, p_1 was evaluated. Using the three different bedload materials, three values of p_1 were obtained for three test durations which corresponded to the same volume transport rate. The final value of p_1 was evaluated according to results that have the best fit both in sediment transport rate and sedimentological time as compared with the estimated curves and the test durations. The value of p_1, in this atudy, was found to be 0.24. Bijker (11) derived the value of p_1 on the basis of Prandtl's shear stress equation and p_1 was found to be a constant value of 0.39. His experimental result of p_1, however, was 0.48. The reason his experimental result of p_1 was higher than the one found in this study may be due to many sand traps introduced during the test. Too many sand traps introduced during

the test may chang the bottom roughness and increase the value of p_1.

The bedload transport rate in the inlet was not directly. However, the bottom configurations were recorded photographically. It is possible to analyze the variation of bottom configurations by using those photographs. Three bottom section profiles in tne vicinity of inlet are shown in Figure 6 through Figure 8 for the analysis. Generally speaking, the results of hydrographical variation at the same location are similar to each other for flood and ebb flow with waves but exibit a difference for coal under the action of waves only. Although a complete justification for this difference is not know, the existence of a small current may interact the waves to produce a significant difference in shear stress.

Based on Newton's second law, Eagleson, Glenne and Dracup derived the equilibrium conditions for a stable beach (12). It is important to consider this equilibrium condition if one tries to obtain reasonable results. According to this equilibrium condition, there is no bedload movement in the direction normal to the beach under the action of a certain value of wave height. If the wave height is higher than this value, the beach slope changes. In this study, all the tests with coal, walnut shell,and sand had this consideration. The final results concerning the longshore sediment transport appeared satisfactory with the estimated curves.

CONCLUSIONS

From the basic study of bedload movement and the test results, the parameters involved in the modeling of sediment transport oan be expressed as the function of Froude number, bottom shear stress, friction factor, and wave steepness. The parameters, so selected, give better corelation for various movement of bedload in the ooastal environment. The dimensionless bedlaod intensity ϕ' was obtained aocording to the theory of Einstein's bedload function $\phi' = f(\psi')$. The dimensionless shear intensity ψ', however, was determined from the combined shear stresses due to the waves and currents. The results of longshore sediment transport rate were favorable compared with the estimated values for each bed material. However, they were not in close agreement for the tests of walnut shell and sand under the combined action due to waves and ebb flow.

In this study, the values of friction coefficient C_Z for each bed material were obtained with reasonable accuracy in the flume test. However, if the friction coefficient C_Z in the prototype cannot be well estimated, the results obtained in the model test will be influenced. Since it is always difficult to predict these values with sufficient accuracy, computation of the scale factor will have to be performed with different values of C_Z. From these computations, the possible variation in the scale factors, resulting from a wrong evaluation of the friction, can then be predicted.

For sediment transport research, most people are interested in knowing how accurate the sediment time scales are by introducing a weir trap in the model basin. The results show that the predicted sedimentological time ran 31 per cent less than the test durations for walnut shell and 36 per cent for coal. The scaled sedimentological time for each bed material will affect the changes in bottom configuration. If the considered parameters were perfect in scale, the bottom configuration should result in the same scaled topography during the test of the scaled sedimentological time. The results of the bottom configuration in this study are similar to each other except for the wave test on coal.

Although certain difficulties remain for predicting the sedimentological time scale, owing to the inadequate knowledge of flow near rough boundaries, the equation shown in this study is still useful in estimating test duration in model studies.

ACKNOWLEDGMENTS

This is a condensed report from a master thesis originally presented to the Graduate Council of the University of Florida, in August 1969.

The author is indebted to Dr. O. H. Shemdin and Dr. R. G. Dean for valuable guidance, suggestions and critical reading of the master thesis. The author also wishes to express his gratitude to Dr. B. A. Christensen for his review of the analytical results and for his constructive suggestions.

APPENDIX I

INTEGRATION OF BED SHEAR STRESSES DUE TO THE COMBINED ACTION OF WAVES AND CURRENTS

Equation (8) through Equation (11) can be integrated for one wave period by the following considerations.

Ebb flow inside channel

$$\text{If } \left(1 - \xi \frac{p_1 u_o}{V_m}\cos\theta\right) \geq 0,$$

$$\tau = \frac{1}{T}\int_0^T \tau(t)\,dt = \frac{1}{T}\rho V_{m_*}^2 \left[1 + \frac{1}{2}\left(\xi \frac{p_1 u_o}{V_m}\cos\theta\right)^2\right] \qquad \text{(I-1}$$

$$\text{If } \left(1 - \xi \frac{p_1 u_o}{V_m}\cos\theta\right) < 0,$$

$$\tau = \frac{1}{T}\int_0^T \tau(t)\,dt = \frac{1}{T}\rho V_{m_*}^2 \left[1 + \frac{1}{2}\left(\xi \frac{p_1 u_o}{V_m}\cos\theta\right)^2 - 2\int_{t_1}^{t_2} \left(1 - \xi \frac{p_1 u_o}{V_m}\cos\theta \sin\sigma t\right)^2 dt\right] \qquad \text{(I-2}$$

where $t_1 = \frac{1}{\sigma}\sin^{-1}\left(\frac{V_m}{\xi p_1 u_o \cos\theta}\right)$ $\qquad t_2 = \pi - t_1$

Simplifying Equation (I-2), it follows that

$$\tau = \frac{1}{T}\int_0^T \tau(t)\,dt = \frac{1}{T}\rho V_{m_*}^2 \left\{\left[1 + \frac{1}{2}\left(\xi \frac{p_1 u_o}{V_m}\cos\theta\right)^2\right]\left[1 - (2\pi - 4t_1)\right] + \frac{8}{\sigma}\left(\xi \frac{p_1 u_o}{V_m}\cos\theta\right)\cos\sigma t_1\right\} \qquad \text{(I-3)}$$

Ebb flow parallel to the shoreline

$$\tau = \frac{1}{T}\int_0^T \tau(t)\,dt = \pm \frac{1}{T}\rho V_{L_*}^2 \left[\left(\frac{V_L - V_y}{V_L}\right)^2 + \frac{1}{2}\left(\xi \frac{p_1 u_o}{V_L}\sin\theta\right)^2\right] \qquad \text{(I-4)}$$

where

"+" sign for $\frac{V_L - V_y}{\xi p_1 u_o \sin\theta} \geq 1$

"-" sign for $\frac{V_L - V_y}{\xi p_1 u_o \sin\theta} \leq -1$

If $0 < \left(\frac{V_L - V_y}{\xi p_1 u_o \sin\theta}\right) < 1$ or $-1 < \left(\frac{V_L - V_y}{\xi p_1 u_o \sin\theta}\right) < 0$

$$\tau = \frac{1}{T}\int_0^T \tau(t)\, dt = \pm \frac{1}{T}\rho V_{L*}^2\left\{\left[\left(\frac{V_L - V_y}{V_L}\right)^2 + \frac{1}{2}\left(\xi \frac{p_1 u_o}{V_L}\sin\theta\right)^2\right]\right.$$
$$\left.\left[1 - (2\pi - 4t_1)\right] + \frac{8}{\sigma}\left(\xi \frac{p_1 u_o}{V_L}\sin\theta \cos\sigma t_1\right)\right\} \quad \text{(I-5)}$$

where

$$t_1 = \frac{1}{\sigma}\sin^{-1}\left(\frac{V_L}{\xi p_1 u_o \sin\theta}\right)$$

and

"+" sign for $0 < \frac{V_L - V_y}{\xi p_1 u_o \sin\theta} < 1$

"-" sign for $-1 < \frac{V_L - V_y}{\xi p_1 u_o \sin\theta} < 0$

If $\frac{V_L - V_y}{\xi p_1 u_o \sin\theta} = 0$

$$\tau = \frac{1}{T}\int_0^T \tau(t)\, dt = 0 \quad \text{(I-6)}$$

Flood flow inside channel

If $\frac{\frac{q_x}{q}}{\xi \frac{p_1 u_o}{q}\cos\theta} \geq 1$

$$\tau = \frac{1}{T}\int_0^T \tau(t)\, dt = \frac{1}{T}\rho q_*^2\left[\left(\frac{q_x}{q}\right)^2 + \frac{1}{2}\left(\xi \frac{p_1 u_o}{q}\cos\theta\right)^2\right] \quad \text{(I-7)}$$

If $0 < \dfrac{\frac{q_x}{q}}{\xi \frac{p_1 u_o}{q}\cos\theta} < 1$

$$\tau = \frac{1}{T}\int_0^T \tau(t)\,dt = \frac{1}{T}\rho q_*^2 \left\{ \left[\left(\frac{q_x}{q}\right)^2 + \frac{1}{2}\left(\xi \frac{p_1 u_o}{q}\cos\theta\right)^2 \right] \left[1 - (2\pi - 4t_1)\right] + \frac{8}{\sigma}\left(\xi \frac{p_1 u_o}{q}\cos\theta\right)\cos\sigma t_1 \right. \quad \text{(I-8)}$$

where

$$t_1 = \frac{1}{\sigma}\sin^{-1}\left(\frac{q}{\xi p_1 u_o \cos\theta}\right)$$

Flood flow parallel to the shoreline

$$\tau = \frac{1}{T}\int_0^T \tau(t)\,dt = \pm \frac{1}{T}\rho V_{L_*}^2 \left[\left(\frac{V_L - q_y}{V_L}\right)^2 + \frac{1}{2}\left(\xi \frac{p_1 u_o}{V_L}\sin\theta\right)^2 \right] \quad \text{(I-9)}$$

where

"+" sign for $\dfrac{V_L - q_y}{\xi p_1 u_o \sin\theta} \geq 1$

"-" sign for $\dfrac{V_L - q_y}{\xi p_1 u_o \sin\theta} \leq -1$

If $0 < \dfrac{V_L - q_y}{\xi p_1 u_o \sin\theta} < 1$ or $-1 < \dfrac{V_L - q_y}{\xi p_1 u_o \sin\theta} < 0$

$$\tau = \frac{1}{T}\int_0^T \tau(t)\,dt = \pm \frac{1}{T}\rho V_{L_*}^2 \left\{ \left[\left(\frac{V_L - q_y}{V_L}\right)^2 + \frac{1}{2}\left(\xi \frac{p_1 u_o}{V_L}\sin\theta\right)^2 \right] \left[1 - (2\pi - 4t_1)\right] + \frac{8}{\sigma}\left(\xi \frac{p_1 u_o}{V_L}\sin\theta\right)\cos\sigma t_1 \right\} \quad \text{(I-10)}$$

where

$$t_1 = \frac{1}{\sigma}\sin^{-1}\left(\frac{V_L}{\xi p_1 u_o \sin\theta}\right)$$

and

$$\text{"+" sign for } 0 < \frac{V_L - q_y}{\xi p_1 u_o \sin\theta} < 1$$

$$\text{"-" sign for } -1 < \frac{V_L - q_y}{\xi p_1 u_o \sin\theta} < 0$$

If $\frac{V_L - q_y}{V_L} = 0$

$$\tau = \frac{1}{T}\int_0^T \tau(t)\, dt = 0 \qquad \text{(I-11)}$$

NOTATIONS

A_*, B_*	Constants determined experimentally
B_1	Channel width
C_z	Chēzy's coefficient
C_o	Static volume concentration of bed material
C_2	Empirical constant
d	Water depth in the channel
d_b	Water depth at breaker
d_e	Grain size of bedload which is 50 per cent finer by weight
F_o	Dimensionless parameter
f	Darcy-Weisbach's coefficient
g	Gravity acceleration
H	Wave height
H_b	Wave height at breaker
k	Wave number
k_e	Roughness height
L	Wave length
n_b	Ratio of group velocity with respect to wave celerity at breaker
p	Porosity of bed material
p_1	Coefficient of horizontal orbital velocity above the laminar sublayer
Q	Rate of water discharge

q	Velocity in potential flow field
q_s	Volume discharge of sediment transport per unit time per unit width
q_w	Weight discharge of sediment transport per unit width
q_x	Velocity component of q in x-direction
q_y	Velocity component of q in y-direction
q_*	Shear velocity in potential flow
S_f	Specific gravity of water
S_s	Specific gravity of bedload
u	Orbital velocity in x-dircetion
u_b	Orbital velocity at bottom
V_L	Longshore velocity
V_m	Velocity in the approach flow
V_x	Velocity in the region of channel expansion
V_*	Shear velocity
V_{m_*}	Shear velocity in the approach flow
V_{x_*}	Shear velocity in the region of channel expansion
α	Beach slope angle
α_i	Internal friction angle
κ	Von Karman's universal constant
θ	Angle that the velocity vector in potential flow makes with the positive x-axis
ϕ	Velocity potential
ψ	Stream function

REFERENCES

1. Einstein, H. A. The Bed Load Function for Sediment Transportation in Open Channel Flow, U.S. Dept. of Agr., Tech. Bull. No. 1026, 1950.

2. Kalkanis, G. Transportation of Bed Material Due to Wave Action. U.S. Army Corps of Engr., Tech. Memo. No. 2, 1964.

3. Tollmien, W. Momentum Transfer Theory for a Jet, Translation, Tech. Memo. 1085, NACA (currently, NASA), Washington, D.C., 1945; originally in Z.A.A.M., Vol. 6, pp. 468-475, 1926.

4. Albertson, M. L., Dai, Y. B., Jensen, R. A., and Rouse, Hunter, Diffusion of Submerged Jets, Proceedings, ASCE, Vol. 74, No. 10, pp. 1157-1196, 1948.

5. Baines, W. Douglas, Discussion of "Diffusion of Submerged Jets" by M. L. Albertson, Y. B. Dai, R. A. Jensen, and Hunter Rouse, Transactions, ASCE, Vol. 115, pp. 677-684, 1950.

6. French, J. L. Tidal Flow in Entrances, U.S. Army Corps of Engrs. Tech. Bull. No. 3, 1960.

7. Eagleson, P. S. Theoretical Study of Longshore Currents on a Plane Beach, M.I.T. Hydrodynamics Lab., Rep. No. 82, 1965.

8. Bagnold, R. A. An Approach to the Sediment Transport Problem from General Physics, Geological Survey, Prof. Paper 422-I, 1966.

9. Bagnold, R. A. Flow of Cohesionless Grains in Fluids, Philo. Trans. of Royal Soc., Vol. 249, pp. 235-197, 1956.

10. Bishop, A. A., Simons, D. B., and Richardson, E. V. Total Bed Material Transport, Journal of Hydr. Div., ASCE, Vol. 91, No. HY2, March, 1965.

11. Bijker, E. W. Some Considerations about Scales for Coastal Model with Movable Bed, Delft Hydr. Lab. Report, Publ. No. 50, 1967

12. Eagleson, P. S., Glenne, B., and Dracup, J. A. Equilibrium Characteristics of Sand Beaches, Journal of Hydr. Div., ASCE, Paper No. 3387, pp. 35-37, January, 1963.

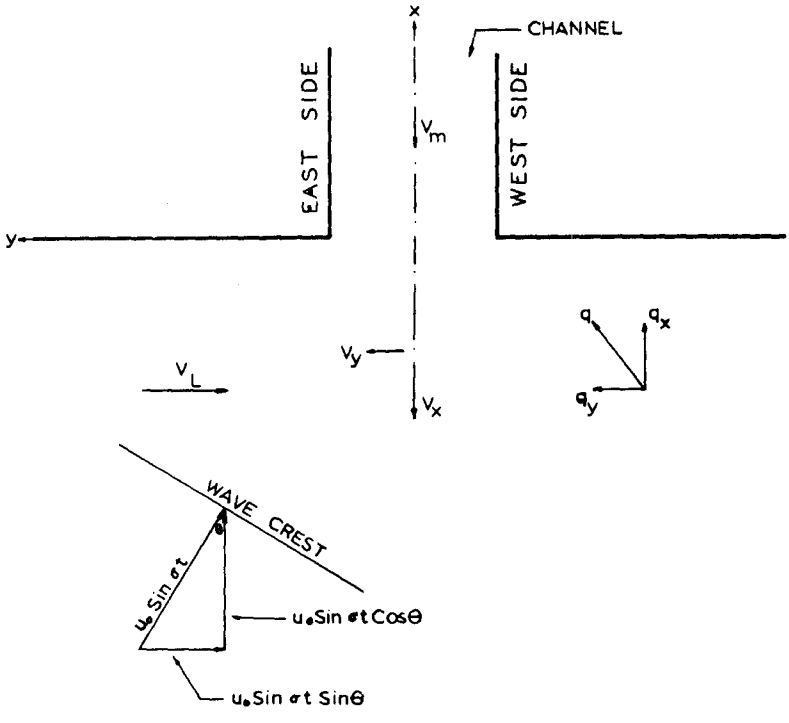

Fig. I_a General representation of currents and waves

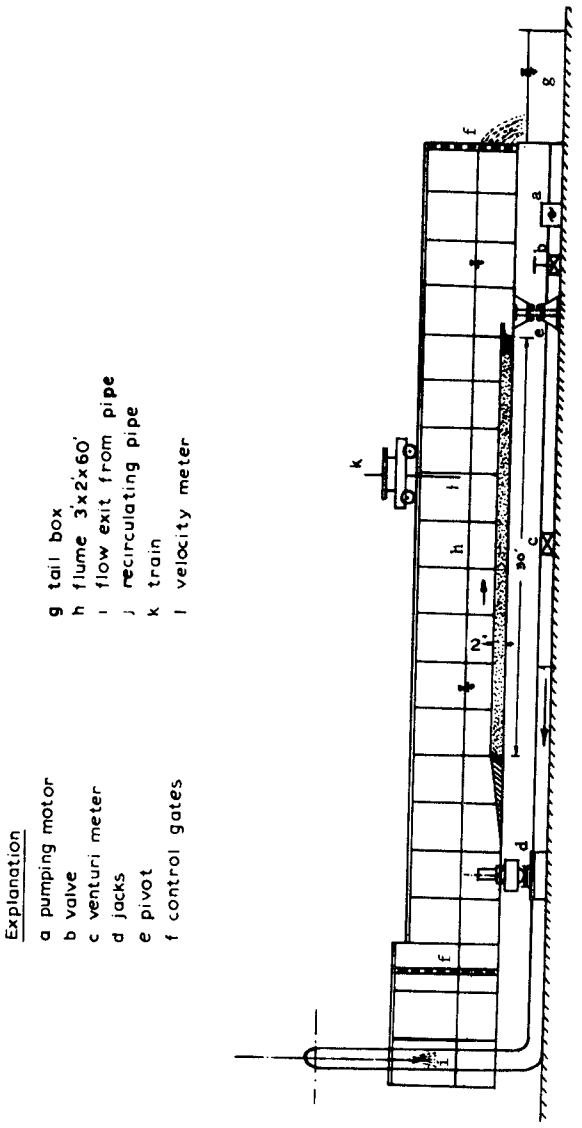

Fig. 1b Schematic diagram of the flume

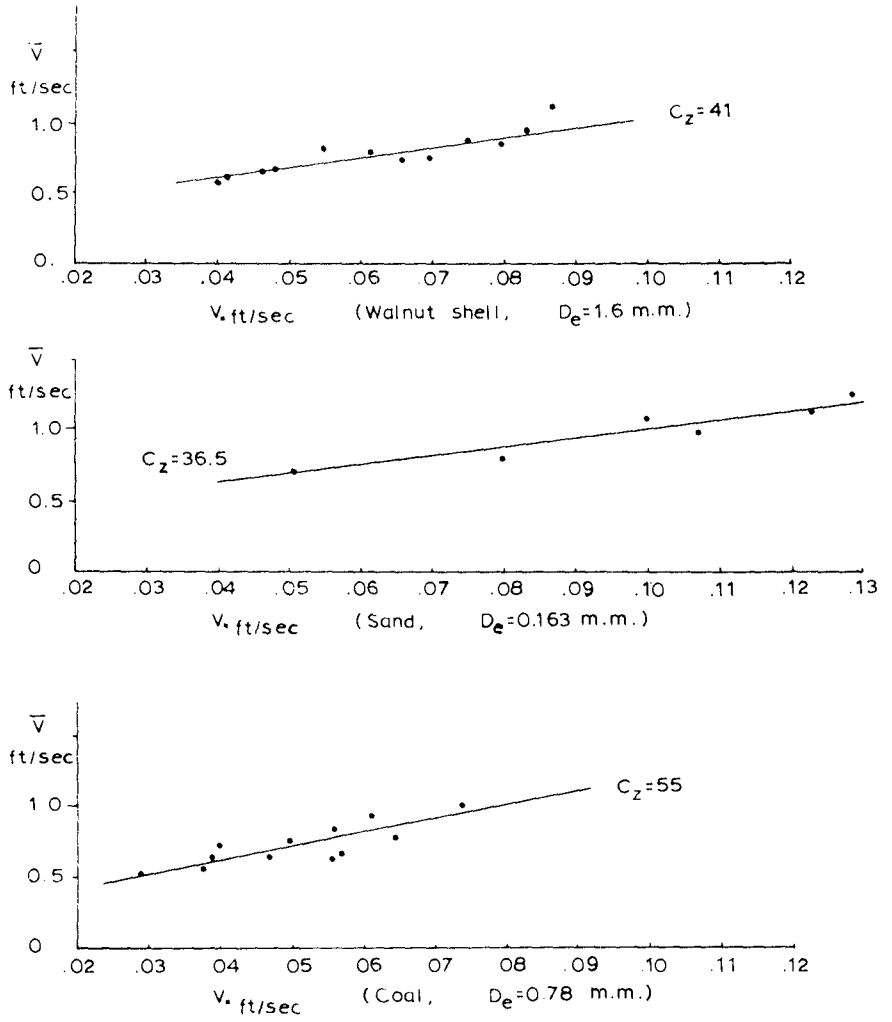

Fig 2 $\bar{V}$ vs. V_* for plane and dune beds

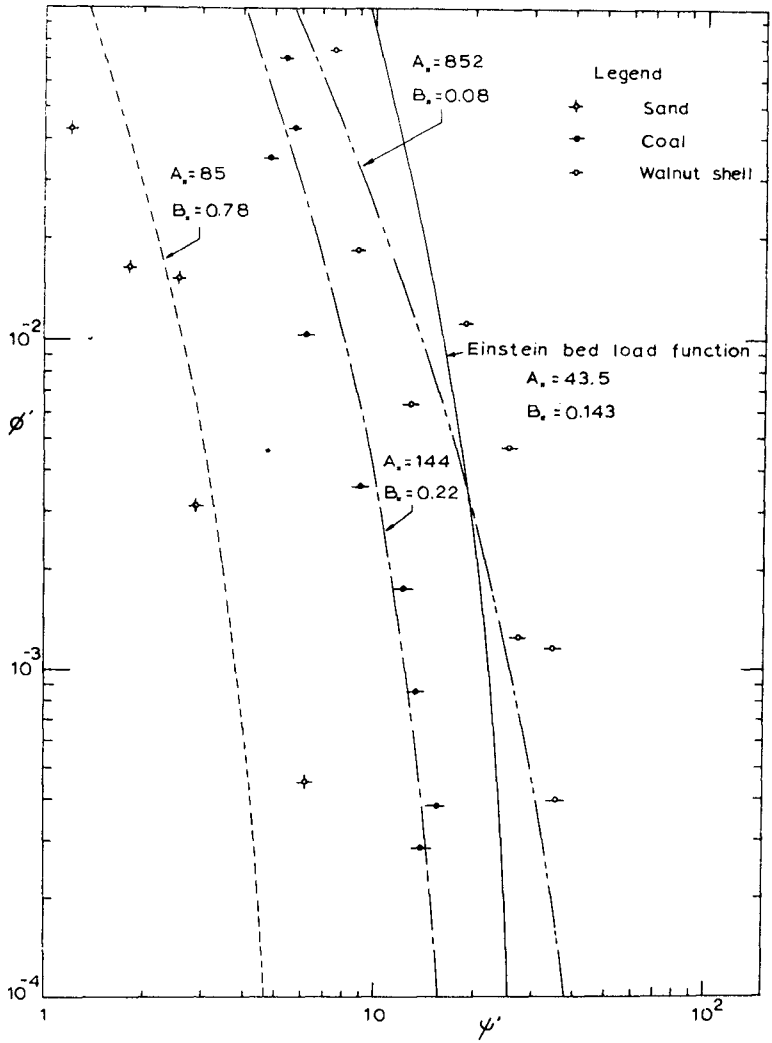

Fig. 3 ϕ'-ψ' curves for the three different bed materials tested in the flume

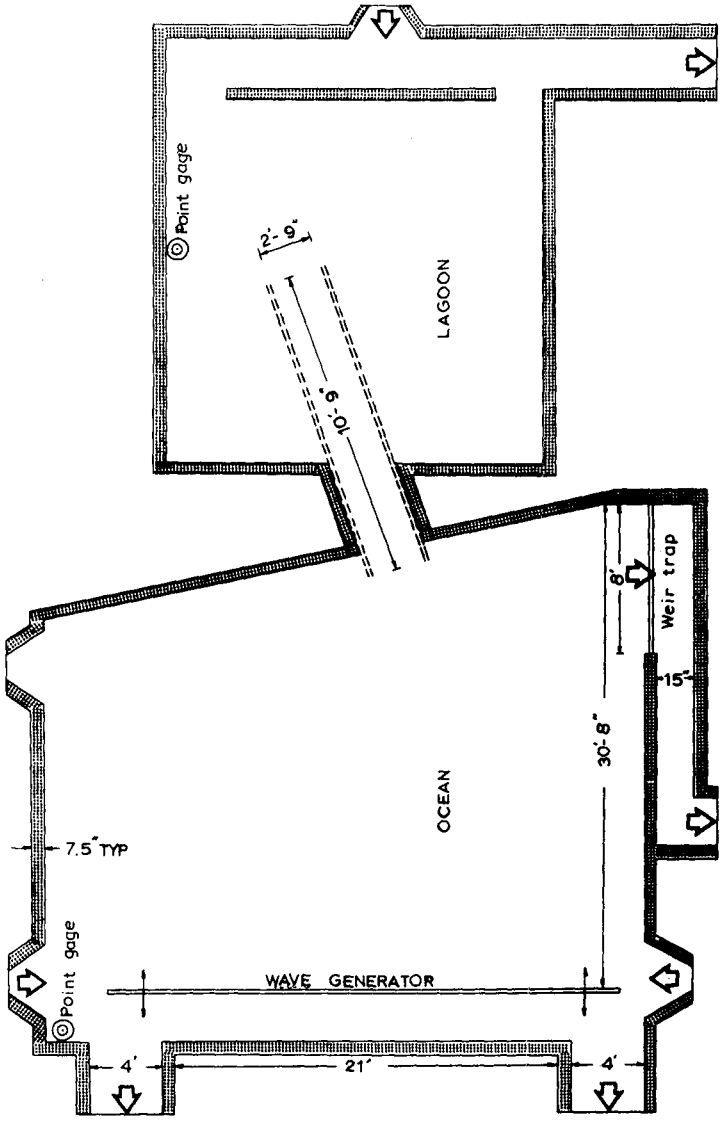

Fig. 4 Schematic diagram of model basin

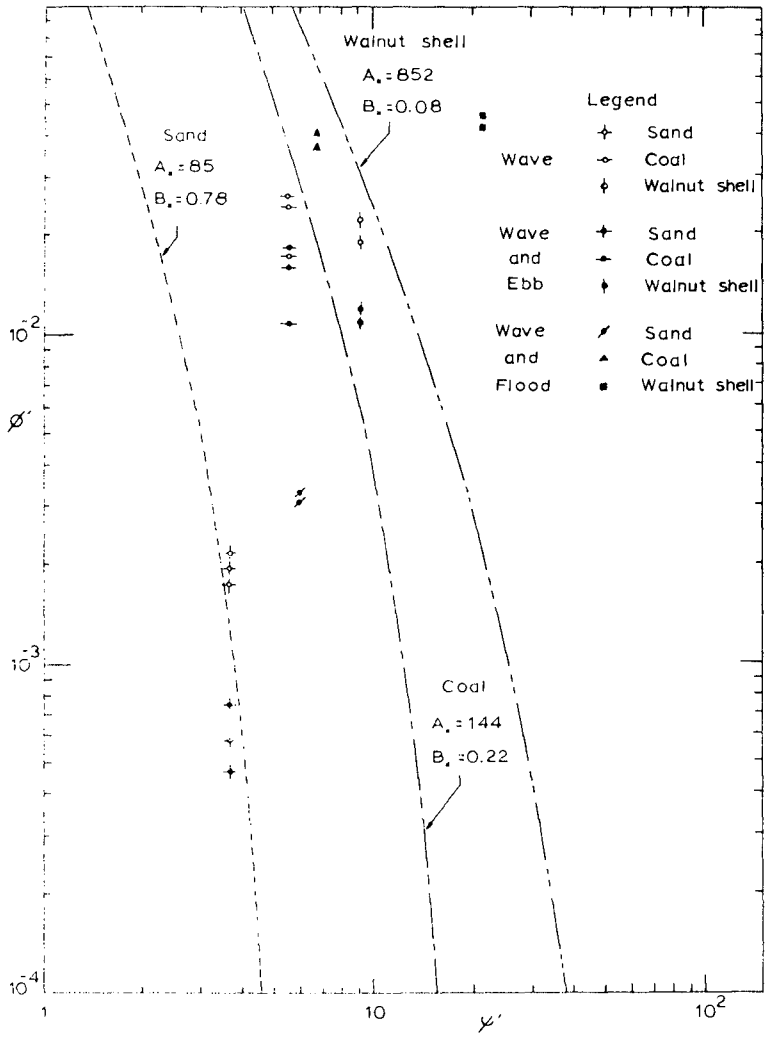

Fig. 5 The tested results in the model basin as compared with the estimated ϕ'- ψ' curves

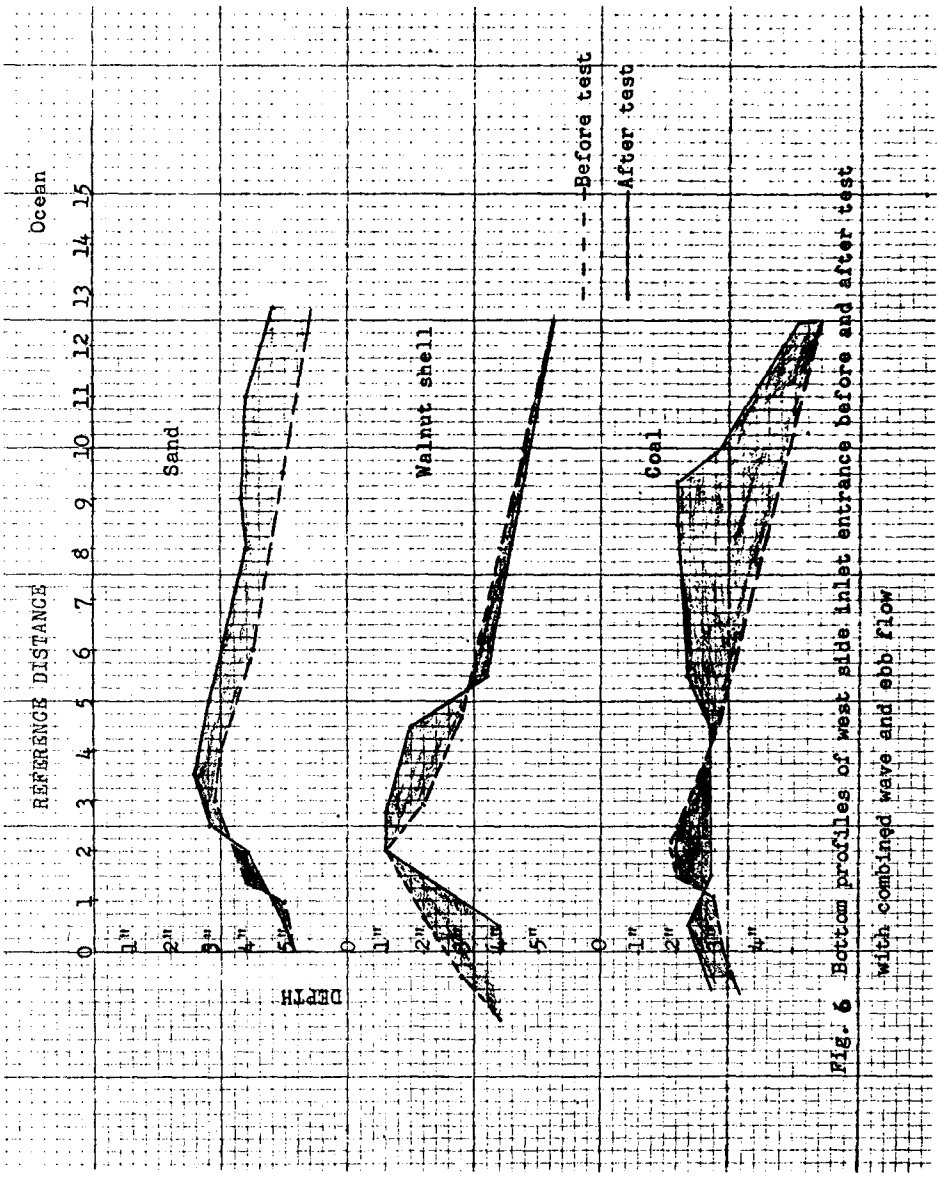

Fig. 6 Bottom profiles of west side inlet entrance before and after test with combined wave and ebb flow

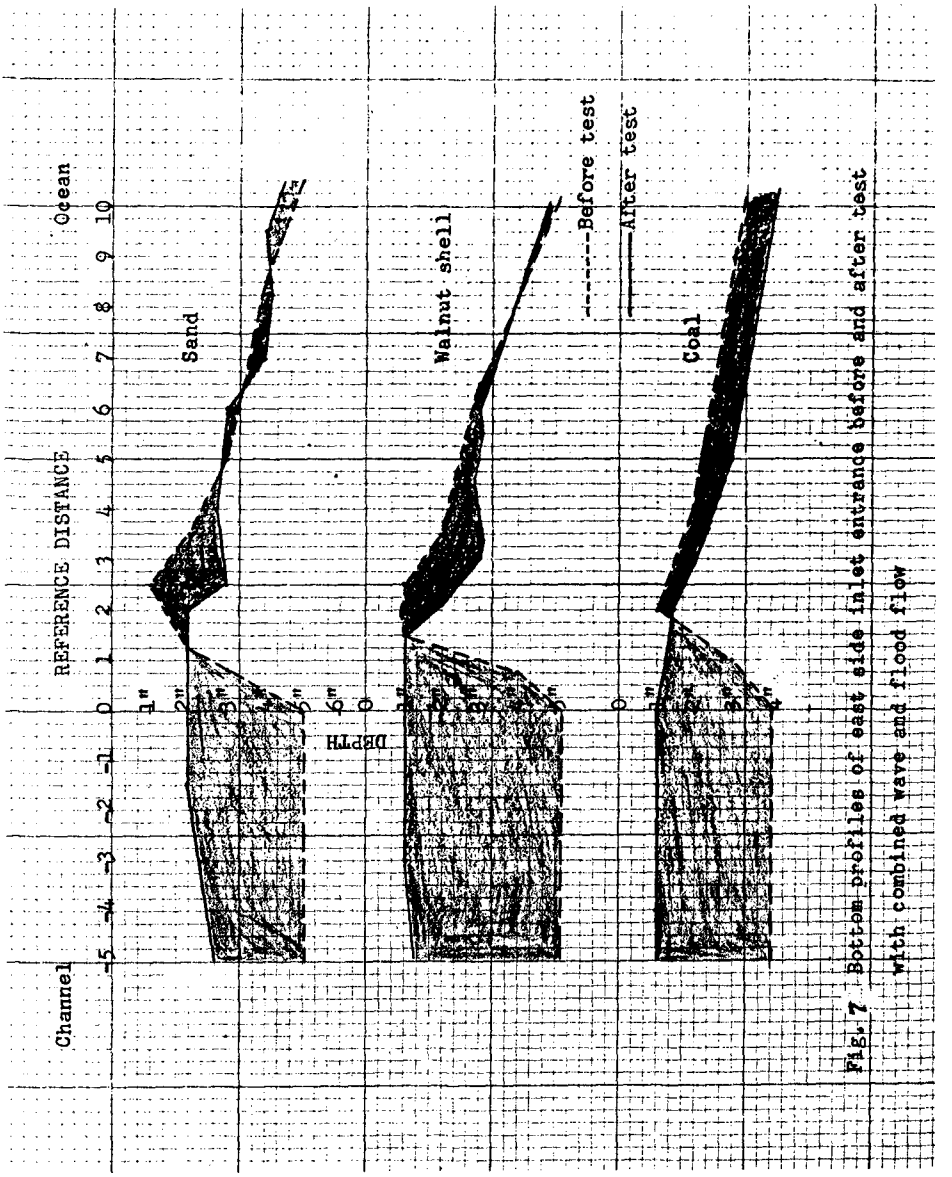

Fig. 7 Bottom profiles of east side inlet entrance before and after test with combined wave and flood flow

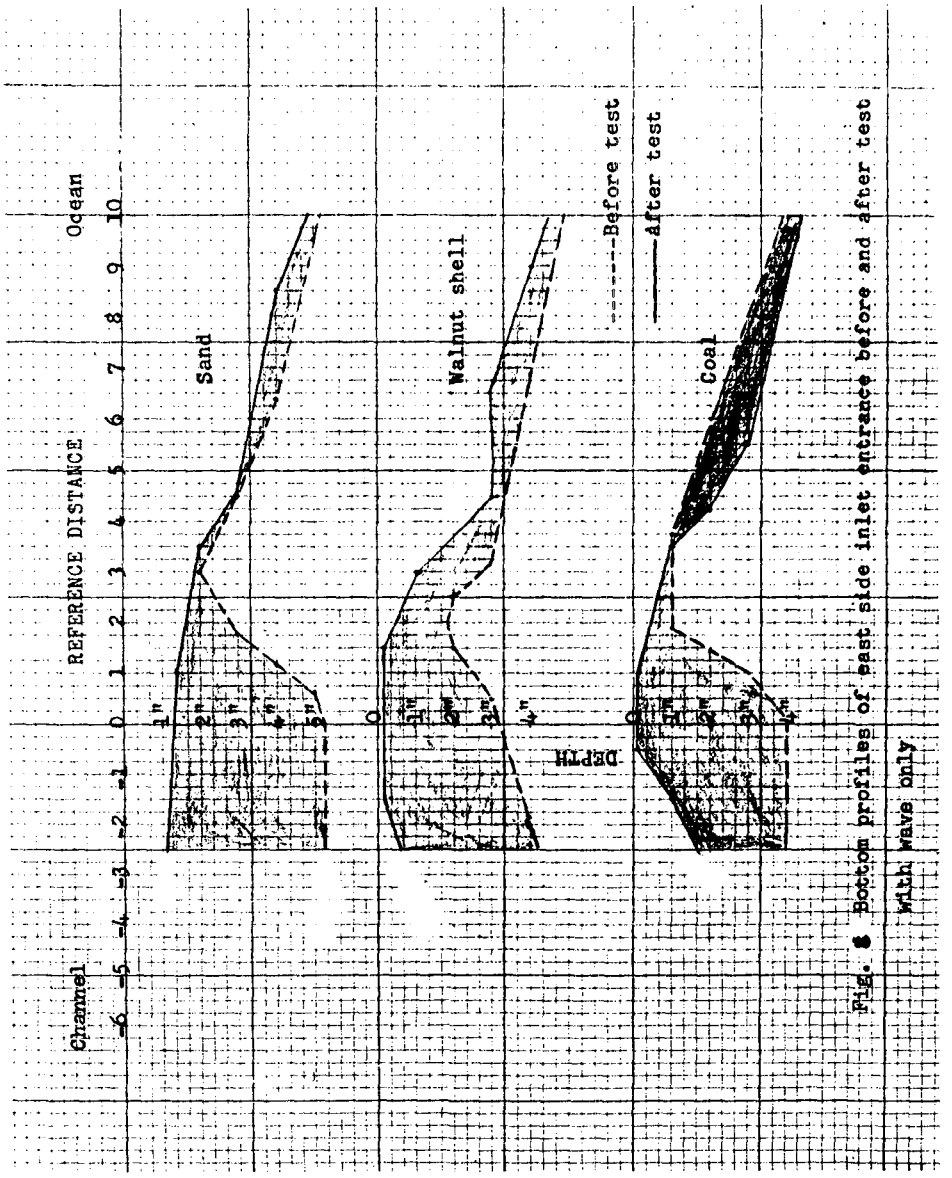

Fig. 8 Bottom profiles of east side inlet entrance before and after test with wave only

CHAPTER 48

SAN FRANCISCO BAR DREDGE MATERIAL DISPOSAL

Richard M. Ecker [1] and John F. Sustar [2]

ABSTRACT

Studies were conducted on San Francisco Bar in June 1971 and February 1972 to monitor dredge material disposal. The purpose of the study was to determine the effects of dredging and material disposal on the physical and biological environment and to develop dredging procedures and disposal sites to mitigate possible adverse effects. This paper presents the results of the material dispersion portion of the study including bottom deposition, current measurements and aerial photography. The biological studies and water quality monitoring are not presented.

INTRODUCTION

Since its organization, the United States Army Corps of Engineers' primary function has been maintenance of navigable waterways. In our awakening toward the total environment, waste products in many cases have become natural resources. Maintenance dredging of the San Francisco Bar is such a case. The "waste" is a nonpolluted fine sand along a coast which has both severe erosion problems and a heavy demand for beach recreation. Hopper dredge operations on the Bar began in June 1971 to increase the depth of the Main Ship Channel to a new authorized depth of fifty-five feet, mean lower low water (MLLW).[3]

Past procedure for dredge material disposal has been to waste the material in deep water outside the Bar. Disposal in deep water prevents the material, a native sand of the Bar, from reentering the littoral regime, resulting in the loss of the sand as a natural resource. Dr. Hans Einstein of the University of California, Berkeley, serving as a consultant for the San Francisco District, Corps of Engineers, suggested that dispersion of the material on the Bar south of the channel would retain the material in the littoral regime with the possible effect of nourishing the coastline to the south. Acting upon the recommendation of Dr. Einstein, the San Francisco District now disperses dredged material from the Main Ship Channel on the San Francisco Bar south of the channel.

While dispersing dredge material on the Bar keeps the material in its natural environment, it remains that the material is still being displaced and that the displacement does have an effect on the existing physical and biological environment of the Bar. As mentioned previously, the material is a nonpolluted fine sand. It is not a sediment containing pollutants,

1/ Geological Oceanographer, Navigation and Shoreline Planning Branch, U.S. Army Engineer District, San Francisco, California

2/ Civil Engineer, Navigation and Shoreline Planning Branch, U.S. Army Engineer District, San Francisco, California

such as heavy metals and pesticides, or large amounts of clays and silts. Disposal of Bar material does not involve in anyway the contamination of the ocean or the Bay. Disposal of Bar material does involve the possible accumulation and suffocating effects of the material on marine organisms. To determine these effects knowledge of the dispersal pattern from the hopper dredge operations, of the subsequent movement of the material on the Bar and of the marine organisms which exist on the Bar is necessary.

DESCRIPTION OF SAN FRANCISCO BAR

The San Francisco sand bar, a crescent shaped bar, extends in an arc about 5 miles west of the Golden Gate as shown on Figure 1. The Bar is separated from the mainland by Bonita Channel on the north and by South Channel on the south. Depths across the Bar are 24 feet MLLW or less on the northern portion known as Four-fathom Bank or Potatopatch and about 36 feet MLLW on the remainder of the Bar. The width of the Bar varies from about one to two miles. The Main Ship Channel which cuts through the Bar has been maintained since 1935 at an authorized depth and width of 50 and 2,000 feet, respectively. The channel is subject to maintenance dredging on the order of 1 million cubic yards per year.

The formation and continuance of the Bar result from a complex of phenomena difficult to precisely evaluate. Previous studies of San Francisco Bar have been by Gilbert,[4] early in the century, and by Grimm in 1930.[5] The Bar is in approximate dynamic equilibrium due to the prevailing wave action which tends to move sediment eastward, tidal currents occurring during ebb flows from San Francisco Bay which move sediment westward and coastal currents. Very little information is available to further define this equilibrium.

Median grain size studies have been made by Professor Byron Schatz of the University of California, Berkeley.[6] Median grain size of bottom surface material range from 0.6mm at a depth of 90 feet outside the Golden Gate to 0.2mm on the top of the Bar. Median grain size of samples obtained in the channel from previous maintenance dredging operations has been decreasing with 0.22mm in 1956, 0.16mm in 1962 and 0.14mm in 1970.

Historical movement of the Bar from 1855 to 1957 has been generally landward. However, as noted in the Technical Report on Barriers,[7] significant shifts have occurred seaward during major flood on the Bay tributaries, indicating a sensitive equilibrium. The tidal prism for an average tidal range of 4-1/4 feet at the Golden Gate is about 1.2 million acre-feet (390 billion gallons). The prism for extreme ranges is estimated to be about 2.7 million acre-feet. Tides at San Francisco are semi-dirunal. During the summer, prevailing winds and swells are from the northwest with some distant storms from the southwest. In addition to this, the California coast exhibits three distinct oceanographic seasons. They are the Upwelling occurring in spring with an overturning of the upper layers from moderate depths, Oceanic in fall with southward movement of both surface and deep currents, and Davidson in winter northward surface currents near shore.[8]

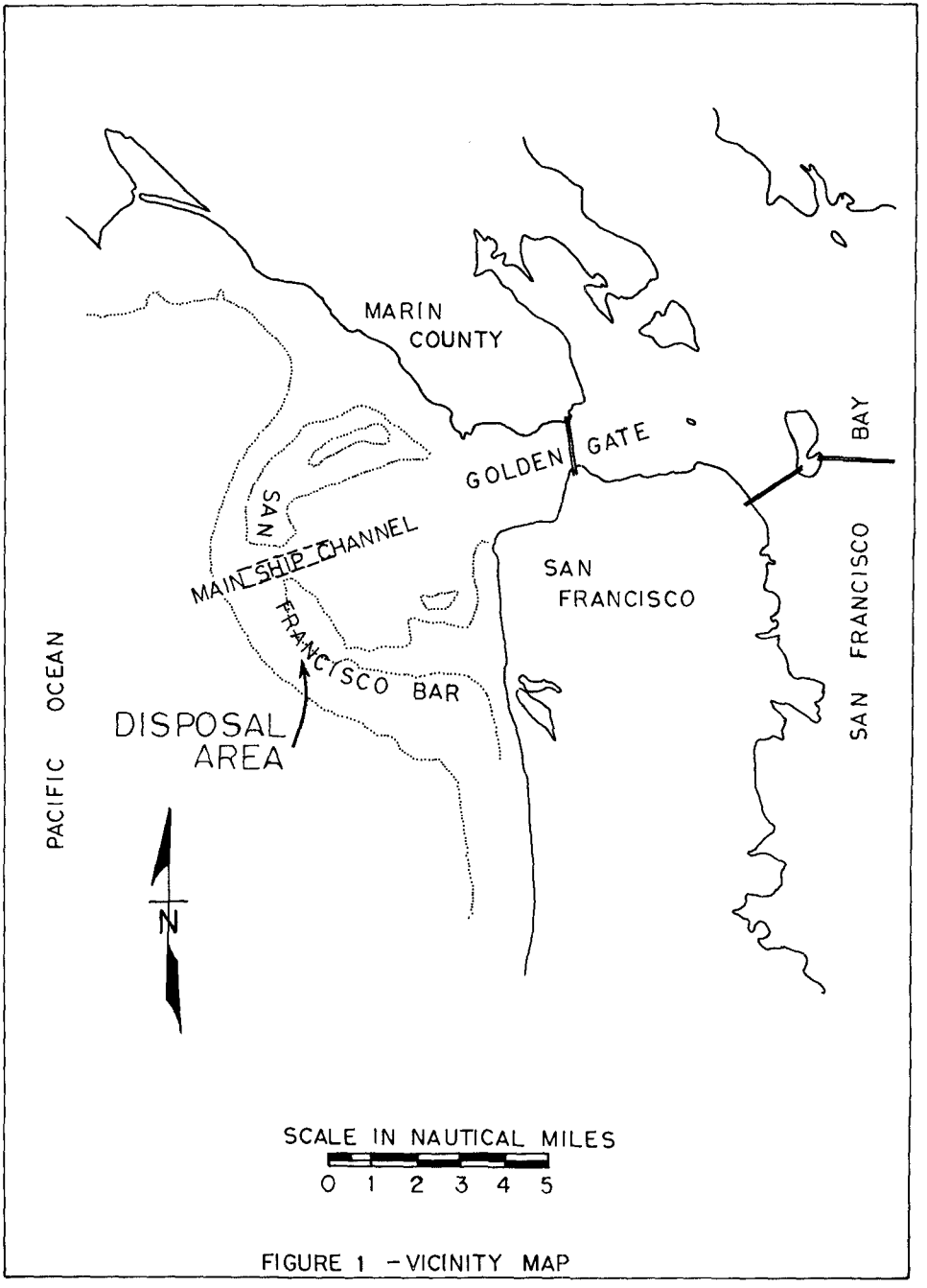

FIGURE 1 – VICINITY MAP

Littoral transport of sand along the coast of norhtern California is generally directed southward. Street, Mogel and Perry[9] in their littoral transport studies along the shores of San Francisco, using automatic data processing methods, found a sizeable breaker zone along the crest of the San Francisco Bar that supports the hypothesis that transportation phenomena exist along the crest of the Bar. Further, tracer studies by A.M. Kamel (1962)[10] found local maximum concentrations of radioactive thorium and heavy minerals on the crest of Bar and at San Francisco Beach, thereafter, decreasing to the south, indicating the transportation phenomena on the crest of the Bar.

MATERIAL DISPERSION

Three programs were set up to determine the material dispersion and deposition. They were (1) bottom deposition evaluation using measurements and sampling at specified underwater stations, underwater photography and observations, (2) current measurements including both current velocity-direction and current paths, and (3) aerial and surface observations. The programs were conducted during June 1971 and February 1972 except for the current paths which were conducted on three occassions. Location of the test sites is shown on Figure 2.

Objectives

The objectives of the material dispersion study were to observe directly and indirectly the immediate and long-term dispersion of dredge material after release on San Francisco Bar. The bottom deposition and current-velocity and direction programs were designed primarily to observe and predict the immediate dispersion and deposition of dredge material while the aerial photography and current path programs were designed to observe the long-term dispersion.

Program

The initial program in June 1971 was conducted by the consulting firm of Towill, Inc. A test site was established by the San Francisco District about 3,000 feet south of the Main Ship Channel in 35 to 40 feet MLLW. Delay in dredge arrival, high sea state and adverse weather conditions prevented the programs from being carried out simultaneously. The actual study was extended over 19 days. The studies were as follows:

8 June	Current velocity-direction
10 June	Test releases and diving operation
14 June	Aerial photography
18 June	Test releases and diving operation
25-26 June	Current Path

The second program was conducted by the San Francisco District on 8-9 February 1972. Four underwater stations with 200-foot spacing established a test section. Test releases, diving operations and aerial

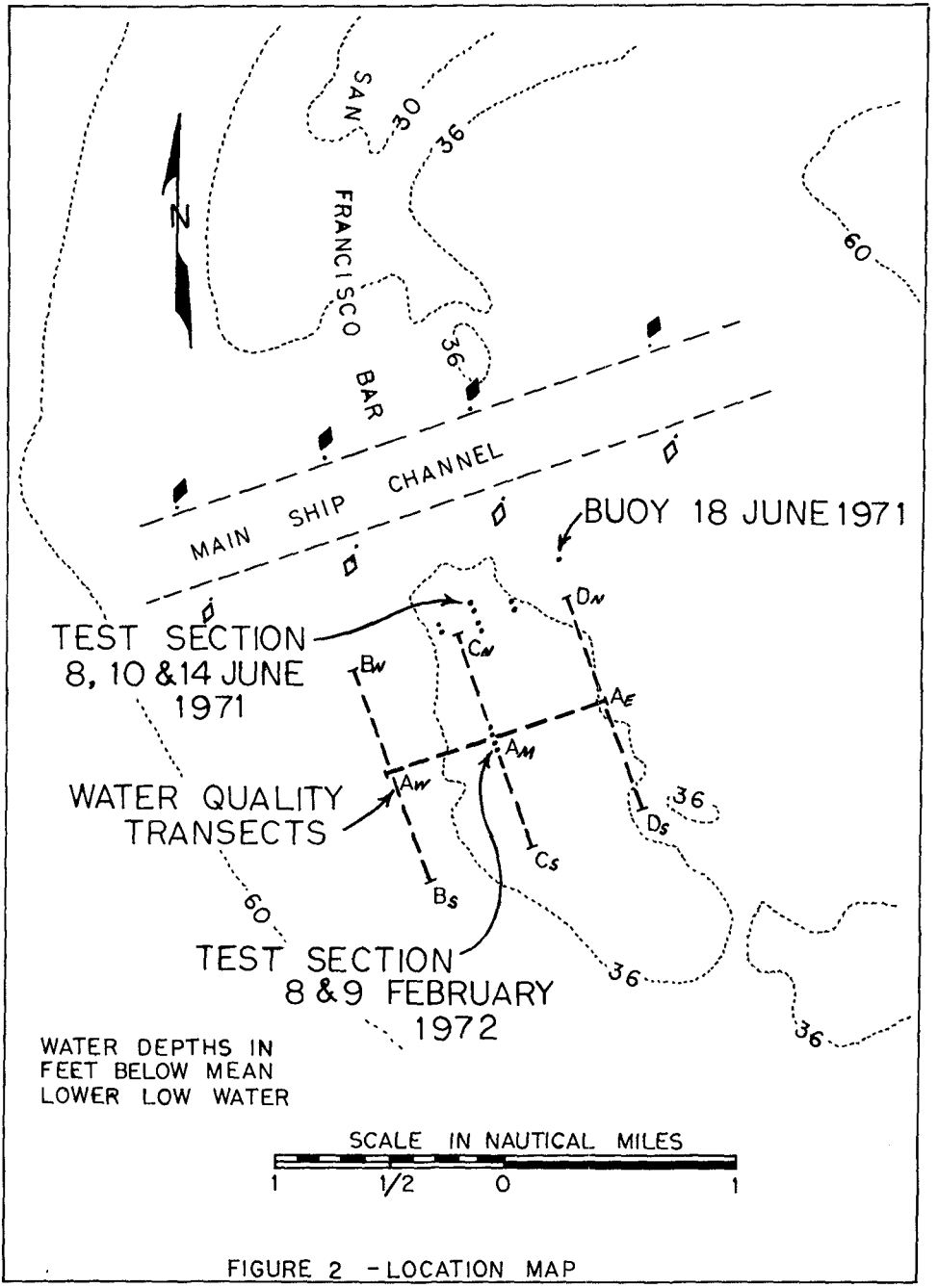

FIGURE 2 - LOCATION MAP

photography were accomplished on 8 February with current velocity-direction measurements made on both days.

The current path studies in addition to 25-26 June 1971 were conducted on 5-7 November 1971 and 1-2 February 1972.

TEST RESULTS

Bottom Deposition

Bottom deposition measurements and observations for 10 June, 18 June 1971 and 8 February 1972 are tabulated on Table 1, 2, and 3 respectively. Measurements made on 10 and 14 June utilized graduated stakes and flat plates. On 8 February divers measured accumulation by taking core samples instead of using stakes as used previously. Accumulation measurements were made using the distinct difference in grain size between the material on the top of the Bar and new construction material from within the Bar.

Current Measurements

Current velocity-direction measurements were taken over a 24-hour period on 7-8 June 1971 at depths of 1, 6 and 12 meters below the surface. Wind velocity during the test ranged from 10 to 25 miles per hour with sea state varying from 2 to 6 feet. The current velocity-direction for the three depths is shown on Figure 3. The center point denotes the location of the current meter during the study. The length of the lines radiating from the center point equals the velocity of the current in knots and the direction of the radials indicate the current direction in reference to the north arrow at that particular time. The curved line with the arrows is the continuity of time curve and represents the progression of the direction-time relationship for the duration of the study. The small circle in sequence represent one hour increments.

Similar measurements were made on 8 and 9 February 1972 over periods of six and eight hours, respectively. The lower depth was 10 meters as compared to 12 meters in June. The current velocities for the three days together with the predicted current at the Golden Gate are shown on Figure 4. The directions used to divide ebb and flood flows are 172° to 351° to 171°, respectively, for the 7-8 June plot. All measurements for 8 and 9 February are plotted as ebb flow since the directions are not defined for that area of the Bar and the flows for the Bay were ebbing. However, although the upper water column was in ebb direction, measurements at 6 and 10 meters showed a reversal of flow. Maximum recorded current on 8 and 9 February was 2.3 knots on the surface.

Current path studies using free floating drogues at a fixed depth of 15 feet were made on three occasions. For determining long-term movement of the dredged material, the path studies were scheduled to represent the three oceanographic seasons. The current path studies were conducted as shown in Table 4. The paths are plotted on Figure 5.

TABLE 1

DIVING OPERATION DATA
10 JUNE 1971

TEST RELEASE/ DIVE LOCATION	TIME OF DIVE	TIDAL CURRENT/ TIME	PHYSICAL DATA					BIOLOGICAL DATA	
			STAKE READING*	ACCUMULATION OR SCOUR	VISIBILITY TURBIDITY, CURRENT	SEDIMENT CHARACT. TOPO, TYPE, COMPACT	TASKS PERFORMED	MARINE LIFE	ORGANIC MATERIAL
BEFORE RELEASE		Slack 0936			Very dark below 15 ft. Suspended sed. in water. Visibility 6 in. Current.	6" unconsolidated sand, compacted below.	Set plate sampler and stake.	Many Sand Dollars, some buried.	None
Buoy 4A	0953		1.0						
Buoy 4	1030		2.4		Very dark. Suspended sand in water. Strong current. Divers must hang on to cable.	6" unconsolidated sand. Very loose sand ripples, 4 1/2" x 1 1/2"	Set plate and stake. Attempted core sample. Took grab sample.	Sand Dollars on edge. 12 per sq. ft. 3" Crab.	None
Buoy 3	1128		3.5		Visibility of about 2 ft. Very turbid layer to 10 ft. above bottom.	2" loose sand. Hard underneath.	Set stake only; current too strong to set plate.	Sand Dollars.	None
Buoy 3A	1204	Flood 1217	2.0		1 ft. visibility.	Fine sand, 4" ripples, 1" depth	Obtained grab sample. Set stake but not plate.	Sand Dollar density: 12/sq. ft.	None
FIRST TEST RELEASE	1227		STATION 3A LOST						
AFTER FIRST AND BEFORE SECOND RELEASE				Scour is taking place. 6" deep around anchor.	Visibility 3 ft., current is slacking, no suspended material.			Sand Dollars on edge and flat.	None
Buoy 4A	1310		1.5	No sand on plate.					
Buoy 4	1344		1.9	Some accumulation on plate x 1/2" scouring continuing.	Fine sand in suspension.			Sand Dollars.	None
Buoy 3	1355		1.9		Visibility 2 ft.		Set plate sampler.	Many Sand Dollars on surface and buried.	None
Buoy 3	1436						Attempted to obtain 2" core sample. Drove to 18". Sed. too fluid.		
SECOND TEST RELEASE	1535								
AFTER 2ND RELEASE									
Buoy 4A	1600	Slack 1612	1.9	Some accumulation	Same	Same		Same	None
Buoy 4	1609		2.2	Plate was clear.	Same	Same		Same	None
Buoy 3	1613		could not find	Sed. accumulation on plate sampler 15", could not find to recover	1 ft. visibility, turbid water. Divers could feel suspended sand.	Sed. seemed more compacted.	Attempted core sample. Drove pipe 24" Could not recover.		

*One unit of stake reading equals three inches.

TABLE 2

DIVING OPERATION DATA
18 JUNE 1971

TEST RELEASE 1 STATION ONLY	TIME OF DIVE	TIDAL CURRENT TIME	PHYSICAL DATA					BIOLOGICAL DATA	
			STAKE READING*	ACCUMULATION OR SCOUR	VISIBILITY TURBIDITY, CURRENT	SEDIMENT CHARACT. TOPO, TYPE, COMPACT	TASKS PERFORMED	MARINE LIFE	ORGANIC MATERIAL
BEFORE FIRST RELEASE	0703	Flood 0717	3.0		Visibility 1-1/2 ft. with light bottom turbid layer extending 15 ft. above bottom. Bottom current slight although there were surges.	Compacted sand. Smooth topography.	Set graduated stake; set sampler plate; photograph of devices in place.	None	None
FIRST TEST RELEASE	0736								
AFTER FIRST RELEASE	0801		2.5	Very little accumulation on plates.	Same.	Same.	Grab sample. Water sample Photographs.	None	None
BEFORE SECOND RELEASE	1015	Slack 1048	2.5 and 3.7	Scour at stake forming 6" diameter depression around stake.	Visibility 1-2 1/2 ft. at 2 ft. above bottom. Bottom layer turbid. No current on bottom.	Divers could dig 14" into sediment with hands	Pipe core sample 18" deep obtained. Water sample. Underwater photographs	None	None
SECOND TEST RELEASE	1047								
AFTER SECOND AND BEFORE THIRD RELEASE	1129		2.5 and 4.2	1/2" sed. accumulated on plate Anchor shows scour. Est. 3-4"	Visibility 1-2 ft. at 3 ft. above bottom and 10 feet above that.	Sand ripples, 3"x 1/2"	Grab sample Water sample Photographs	Sand Dollar density 3-4 ft^2 Small jellyfish 20 ft. above bottom.	None
THIRD TEST RELEASE	1230	Ebb 1241							
AFTER THIRD RELEASE	1250		2.5 and 4.3	No accumulation on plate. Depression around stake 2 ft. in diameter.	Visibility 1 ft. Turbid layer increasing from bottom to surface.	Same	Photographs		None

*One unit of stake reading equals three inches. The second readings are those of the surrounding areas.

TABLE 3

DIVING OPERATION DATA
8 FEBRUARY 1972

TEST RELEASE/ DIVE LOCATION	TIME OF DIVE	TIDAL CURRENT/ TIME	PHYSICAL DATA						
			CORE NUMBER	ACCUMULATION OR SCOUR	VISIBILITY TURBIDITY, CURRENT	SEDIMENT CHARACT. TOPO, TYPE, COMPACT	TASKS PERFORMED	MARINE LIFE	ORGANIC MATERIAL
BEFORE RELEASE		Slack 0724			2 feet visibility; no material in suspension observed; moderate bottom surge; no prevailing current.	Fine compacted sand; Can penetrate finger only about 1/4 to 1/2 inch; Ripple marks 7mm ht. and 60mm wave length.	Set substations, yellow rock and rod. Obtained a 3 liter grab sample.	One juvenile Sanddab; dense aggregations of Sand Dollars; 8-14/ft^2	Shell fragments only
STATION 1	0920								
					2 feet visibility; some material put into suspension by divers. Light surge on bottom, strong surface ebb current.	Fine sand; highly compacted. Penetration only 1/4 inch. Ripple marks, ht. 6-7mm.	Set substations, yellow rock, rod, and pan.	Sand Dollars	None
STATION 2	0955								
STATION 3	1021				Same	Same	Set substations, yellow rock and rod.	Sand Dollars	None
STATION 4		EBB	FIRST DIVE AT THIS STATION WAS ABORTED						
FIRST TEST RELEASE	1108	1042							
			1	+0.2 inches	Visibility somewhat reduced.	Sediment less compacted; penetration 1/2 inch. Ripple marks are present.	Set white rock; marked rod; obtained two core samples.	Same	None
			2	+0.5 inches					
STATION 1	1227								
STATION 2			SECOND DIVE AT THIS STATION WAS ABORTED						
			1	+1.8 inches		Sediment somewhat less compacted	Set white rock; marked rod; obtained two core samples	A colony of Siphonphores were passing through area. No samples taken.	None
			2	+2.2 inches	Same				
STATION 3	1342								
STATION 4	1304					Same	Set substations, white rock & rod.	Same	None
SECOND TEST RELEASE	1427								
			1	+1.1 inches	The visibility was somewhat reduced and is partially attributable to weather and time of day.	Same	Obtained two core samples and a 3 liter grab sample.	Sand Dollars, some scattered but majority grouped 7/ft^2	None
			2	+1.4 inches					
STATION 1	1511	SLACK 1514							
			1	+2.5 inches	Light surge near bottom; strong surface current.	Same	Obtained two core samples; marked rod; and recovered rod and pan.	Sand Dollars	None
			2	+3.2 inches					
STATION 2	1457								
			1	+2.7 inches	Slight surge near bottom, negligible bottom current.	Same	Obtained one core sample	Free floating siphonphores (unidentified) density 3-4/ft^3	None
STATION 3	1544								
			1	+0.5 inches	Same	Same	Obtained one core sample.	Sand Dollars	None
STATION 4	1558	FLOOD 1825							

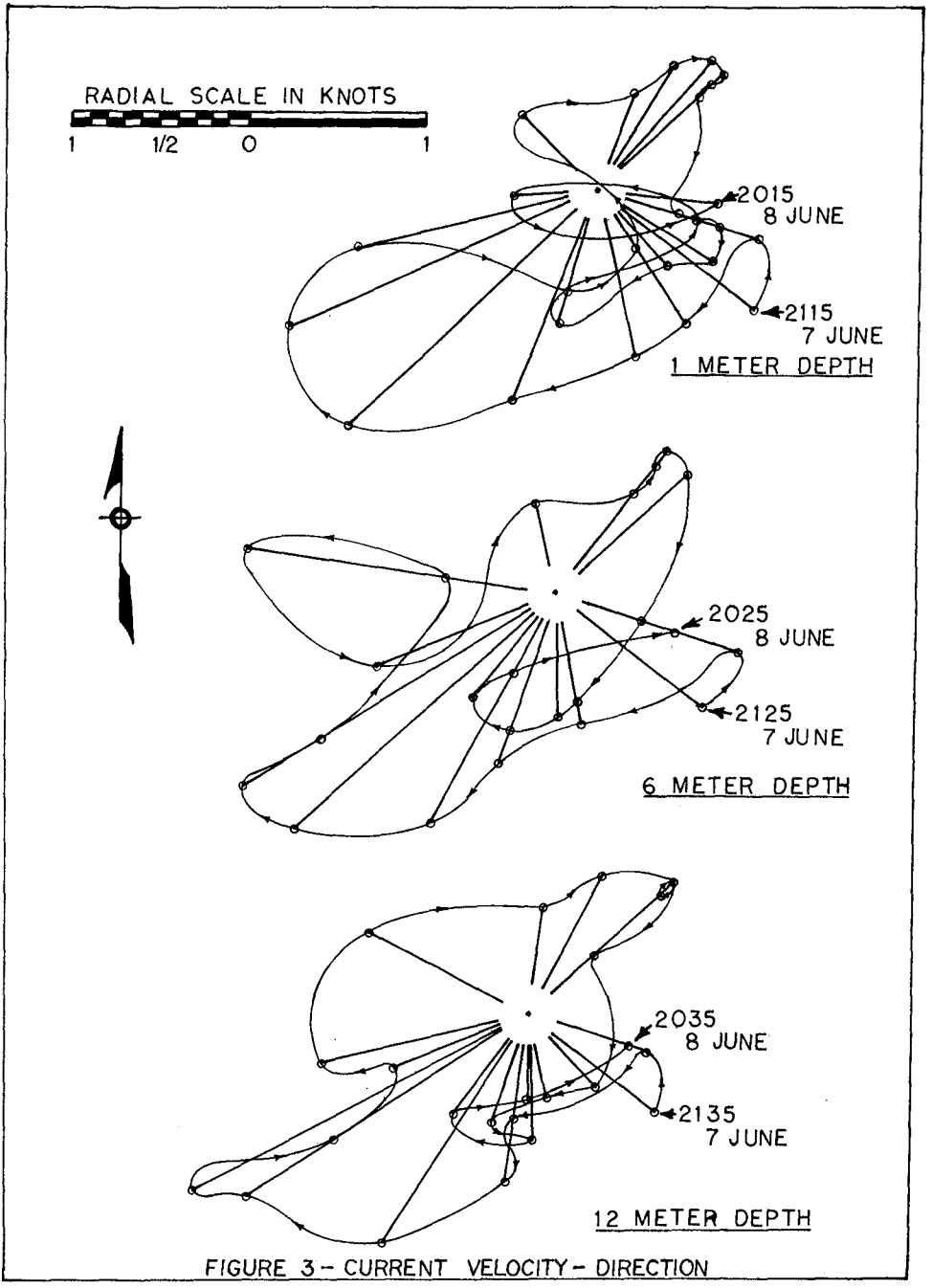

FIGURE 3 – CURRENT VELOCITY – DIRECTION

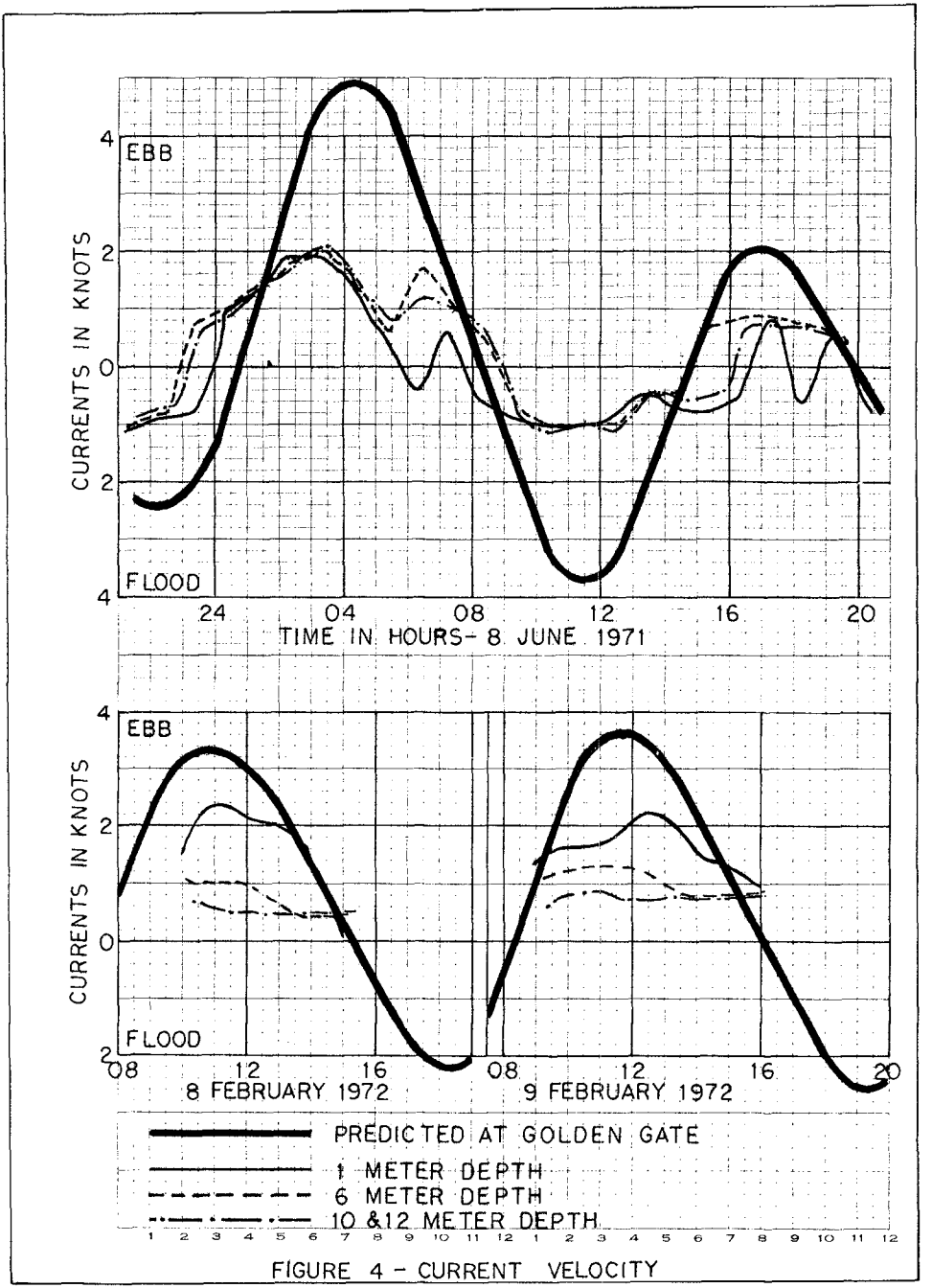

FIGURE 4 - CURRENT VELOCITY

TABLE 4

CURRENT PATH STUDIES

Conditions	25-26 June 71	5-7 November 71	1-2 February 72
Season	Upwelling	Oceanic	Davidson
Length	24 hours	47 hours	30 hours
Wind	0-10 mph W-SW	0-20 mph N-NW	0-20 mph
Sea State	1-2 feet W-SW	1-6 feet W-NW	0-6 feet W-NW

Aerial Photography

The aerial photography of dredging operations on 14 June 1971 using Kodak Aerocolor Negative Film 2445 and GAF 1000 Blue Insensitive Color Film Type 2575, was flown at scales of 1:6,000 and 1:9,000 during slack and flood currents. The photographs using the non-blue emulsion film were overexposed and interpretation of the imagery was not possible. Color photographs showed some discoloration during all phases of the dredging-release operation with the discoloration greastest during the dredging in the channel. This corresponds with the observations made from the dredge and at the test site during operations.

The discoloration is a result of fine material being introduced into the water column from the overflow of the hoppers. The photographs showed that dispersion of the fine material in suspension occurs rapidly. The concentration of the suspended material is then diluted and the discoloration vanishes within a few minutes after the dredge passes. Photographs of the dredge in transit and other vessels in the area indicated small setting rates for the fine material. In both cases, the wash from the vessels propellers re-agitated the fine material and again discolored the surface water.

Low altitude aerial photography on 8 February 1972, used Kodak EF 8442 color positive film with a yellow filter. The combination of film, filter and exposure has been found to provide the greatest resolution of suspended sediments. However, the photographs showed no discoloration at the test site following the release of material. The lack of discoloration is due to the decrease of fines and increase in median grain size of the material being dredged with the new construction.

High altitude remote sensing, including earth satelite simulation photography experiments, were utilized to interpret the larger scale suspended sediment patterns off the Golden Gate and along the California coast.

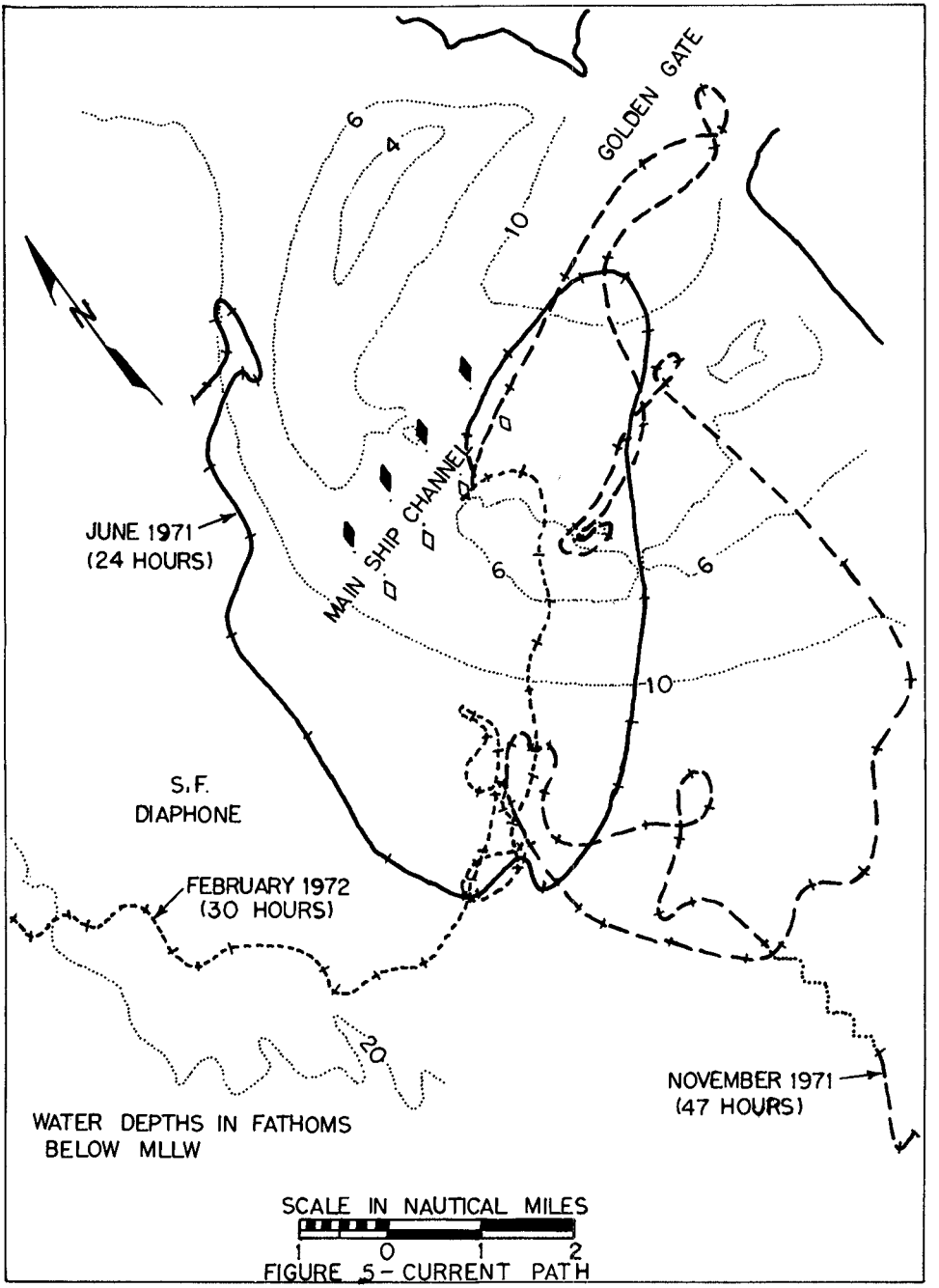

FIGURE 5 – CURRENT PATH

DISCUSSION AND EVALUATION

The aerial and surface observation, bottom deposition and current measurement programs were developed to provide an understanding of the immediate and long-term dispersion of dredge material after release on the Bar. The bottom deposition and current velocity-direction programs were conducted to define the immediate dispersion while the current path and aerial programs dealt with the long-term dispersion of dredge material.

Immediate Dispersion

Results of the bottom deposition program have shown that at no time during diving operations on the Bar did the accumulation of released material exceed two inches in depth during any one release. The maximum recorded accumulation during an entire operation was four inches. Prestudy predictions concerning accumulation estimated the maximum and minimum to occur after one release would be 2.5 inches and 0.25 inches, respectively. The horizontal displacement for the maximum and minimum accumulation conditions would be 100 feet and 1,700 feet, respectively. The maximum accumulation would occur when the line of release was parallel to the current direction and the minimum accumulation would occur when the line of release was perpendicular to the current direction. The above values were estimated using the following parameters: speed of the vessel during release was 4 knots; the time required for discharge of the load was 5 minutes; the total load discharged was 3,000 cubic yards; the current velocity was 1 knot over the entire water column; sediment size ranged from 0.22 millimeters to 0.84 millimeters using the 84th and 16th percentiles of the cumulative distribution curve; and the sediment accumulated was distributed evenly over the area. The maximum accumulation of 2 inches did fall within the predicted ranges of accumulation.

Figure 6 is a normal distribution curve developed using the core sample measurements from 8 February 1972. The curve was calculated using an accumulation of 2 inches under the centerline of the dredge release and 0.8 inches at a location two hundred feet on either side of the centerline. Observed values for the three sets of data are compared with a normal distribution value based on position of the release to the particular station. The normal distribution readings are 96 percent and 93 percent of the observed accumulation values for 8 February 1972 and 18 June 1971, respectively. These percentages exceed any expected accuracy of predicted accumulation values for the Bar under prevailing conditions. Other measurements made on 18 June 1971 (not included in the above percentages) indicated the occurrence of about 1.5 inches of scour around the stake during the entire testing period.

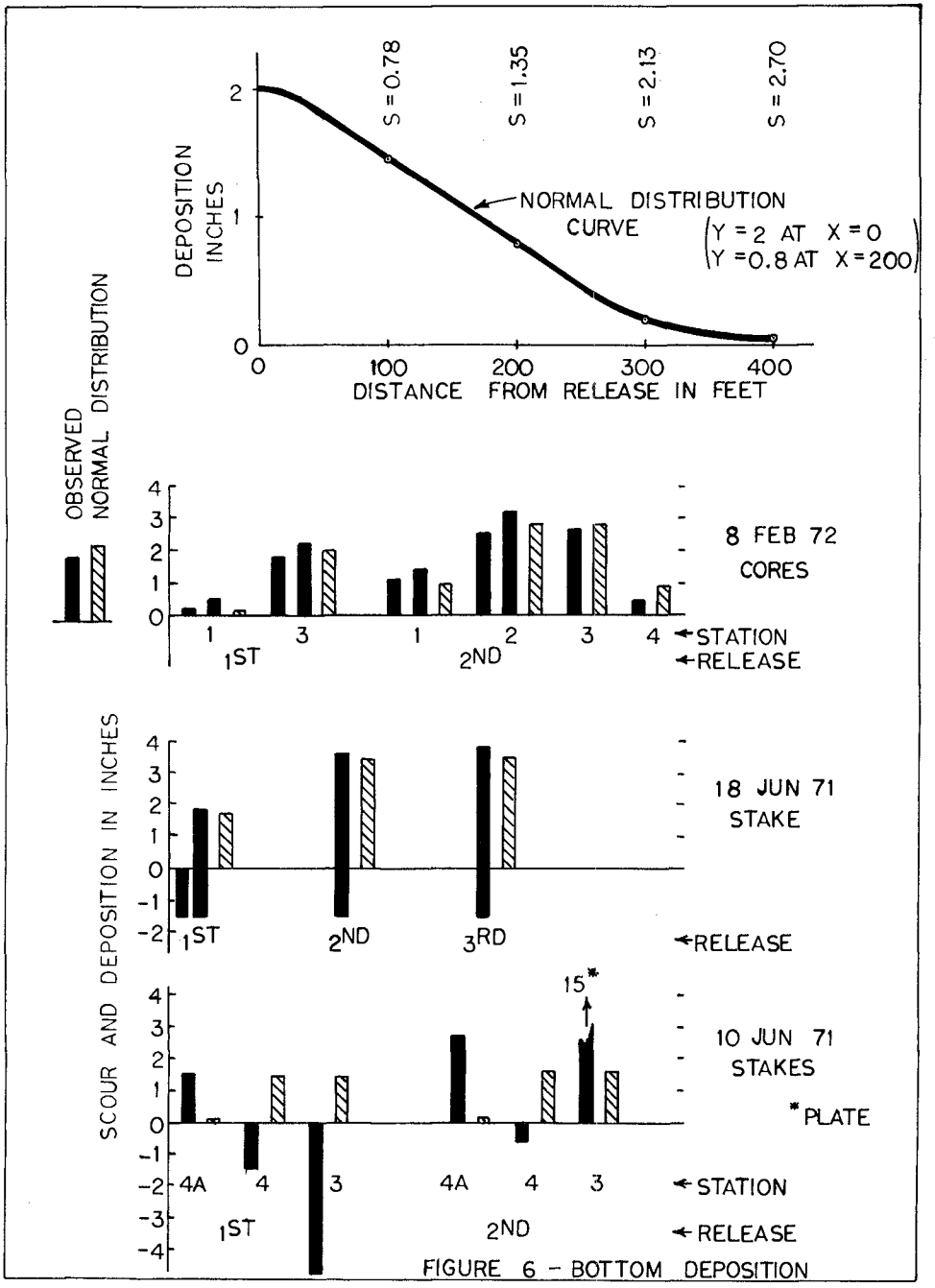

FIGURE 6 – BOTTOM DEPOSITION

No correlation has been found between the observations on 10 June 1971 and the above analysis. Of six observations on 10 June 1971, three indicated only scour ranging from 0.6 inches to 4.7 inches whereas observations on 18 June indicated a consistent scour of 1.5 inches. The three remaining observations indicated only accumulation whereas all observations on 18 June indicated accumulation and scour. The stations indicating accumulation on 10 June were all up current from the release whereas the stations indicating only scour were either near the line of release or were down current. For these reasons the deposition and scour data for 10 June 1971 have been disregarded. Some factors contributing to the decision are; (1) local scour around stakes was not accounted for in measuring accumulation; (2) divers were unfamiliar with stake gradation marks; and, (3) sea state and visibility hindered diver operations. Furthermore, one observation on 10 June indicated an accumulation of 15 inches. This was the last observation of the day and the diver reported excessive turbidity due to sea state. The diver made the 15 inch accumulation observation from the plate rod and not the stake as was done with all other observations since the stake could not be located. When the diver returned to recover the stake and plate neither could be located.

Current velocity-direction studies on 8 June 1971 indicate that bottom currents at times reach maximum ebb velocities exceeding two knots. Figure 3, the current rose plots for the depths of 1, 6 and 12 meters, show that on this particular day the currents at the three depths were fairly homogenous and showed a definite southwest predominance. One can infer that the net movement of suspended dredge material would be to the southwest. The subsequent dispersion of material after deposition can be described as the vector sum of the bottom tidal currents, wind induced currents, the coastal currents and the wave induced turbulence (surge). The observed velocity-direction measurements are the sum of the tidal, coastal, and wind induced currents. The wave induced motion near the bottom-water interface is primarily oscillatory in nature and, thus, is mainly a suspending force. One can then assume that the dispersion of the deposited dredge material will be in the direction of the bottom currents as observed during the current velocity-direction measurements.

The current velocity-direction measurements observed on 8 June 1971 are not indicative of the annual currents on the Bar. During high freshwater outflows from the Bay, current reversals with depth may be encountered on the Bar. During the freshets, a net water discharge from the Bay will occur in the upper water column whereas in the lower column a net influx into the Bay of more saline water will occur. The currents will also differ during different phases of the lunar tide. Therefore, the currrent velocity-direction measurements on the Bar in June 1971 may not be used as an indicator of current magnitudes and directions for other than the period of observation. For a complete understanding of immediate dispersion of dredge material,

continuous recording current stations would have to be placed on the Bar during all dredge disposal operations. However, the bottom deposition program and current velocity-direction program indicated that accumulation of dredge material does not exceed two inches during any one release and that the material deposited on the bottom is dispersed quickly as a result of the suspending wave induced turbulence and the transporting bottom currents.

The divers observed four distinguishable sediment layers in the water-sediment column (Fig. 7). They were the upper water column extending from 25 to 35 feet below the sea surface, the turbid layer extending from 3 to 15 feet above the bottom, the fluid sediment layer 3 to 6 inches deep on the bottom, and the underlying compacted sediment.

The turbid and fluid sediment layers were found to be the transport strata for material on the Bar. The turbid layer was composed of suspended sediment, moving horizontally along the water-bottom interface. It was observed before, during and after all test releases throughout the entire study. The depth and sediment concentration of the turbid layer were found to be a function of current velocities and sea state. As the currents and sea state increased, the depth of the layer and concentration of sediment in the layer increased. The maximum and minimum depth encountered during the study were 15 feet and 3 feet, respectively. The minimum conditions existed during calm seas with only slight bottom currents. Water samples in the turbid layer showed the presence of considerable suspended sand in the 200-275 micron range, the same range as that found in the fluid and compacted sediment layers. The fluid sediment layer was composed of uncompacted sand moving as bed load. It was observed to be absent during calm conditions and a more compacted layer of sediment in its place. As the sea state became more active the fluid layer again appeared.

The minimum condition of sediment transport that existed on the Bar during the study was in the more advanced stage of sediment motion as described by Shepard[11] from observations in a simple flume. Shepard's advanced stage of sediment transport consists of both bed load and suspended load transport of sediment. The sediment that is transported by bed load is moved by saltation and is associated with the formation of ripple marks. The sediment transported by suspended load is put into suspension by turbulence over the bed and is associated with a high Reynolds' Number which is a function of height above the bed, the flow over the bed and the viscosity of the water. However, in an environment such as San Francisco Bar, large Reynolds' Numbers are always present and are mainly associated with stresses due to sea state and internal waves (surge). Although the Reynolds' Number due to current flow was sufficient to maintain the suspended load in the turbid layer, the major component of turbulence was due to the activity of the surface waves and the existing surge. The major suspending force on the Bar is the wave induced turbulence. Tidal flows are responsible for net horizontal movement. At all times during the study the wave induced turbulence was great enough to keep material in suspension. The existing conditions precluded the actual observations of bed load transport of sediment; however, ripple marks with a wave height of 1-1/2 inches and wave length of 4 inches indicated that such a transport was occurring.

The maximum condition of sediment transport that existed on the Bar during the study was observed during increased sea state and surge action. The presence of a thick turbid layer and a fluid sediment layer indicates the existence of Shepard's maximum condition of both a large suspended load and sheet flow. Due to the turbulence on the Bar, there is no threshold velocity associated with the sediment transport.

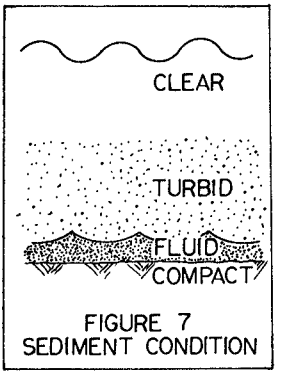

FIGURE 7
SEDIMENT CONDITION

Long-Term Dispersion

The net long-term dispersion of dredge material is a function of the forces acting on the medium in which the material has been introduced. The forces in this case are the various currents induced by tidal, wave, wind, and other generating phenomenon causing the movement of the water mass. The net movement of the water mass, as measured with the current path program then is an approximation of the sum of the forces acting on the water. Assuming the water column is uniform, the direction of net movement of dredge material can be approximated by the direction of the net movement of the water mass.

A depth of 15 feet was chosen for the drogue studies based on the average flow over the water column of the fixed current studies in June 1971. However, fixed current studies in February 1972 indicated the presence of stratified flows on the Bar. The stratified flow consisted of ebb currents in the upper water column and flood currents on the bottom. Therefore, the uniform flow assumption is incorrect and the 15 feet depth can not be considered representative of the entire water column. For this reason, the current path method has proven inadequate for measuring long-term sediment movement on the bar.

CONCLUSIONS

Studies conducted on dredge material disposal on San Francisco Bar during June 1971, February 1972 dredging operations indicate that immediate accumulation of material on the Bar does not exceed two inches for each release. Although no observations were made of the impact on material and potential smothering of marine organisms, time lags for the deposition and the types of marine organisms found in the Bar environment indicated that smothering does not take place. Movement of material on the Bar takes place in two transport strata, the fluid sediment layer and the turbid suspension layer. The thickness of the turbid layer is a function of the surge and wave generated currents. The long-term accumulation of dredged material does not occur due to the high energy environment and dynamic equilibrium characteristics of the Bar.

ACKNOWLEDGEMENT

The material in this paper is based on data and studies made during the Corps of Engineers investigation of dredge material disposal on San Francisco Bay. Publication of this paper has been approved by the Corps of Engineers but any views, interpretations or conclusions developed are those of the writers only.

REFERENCES

3. "San Francisco Bay to Stockton, California," 26 April 1965, H.D. 208, 89th Cong., 1st Ses.

4. Gilbert, C. K., Hydraulic-Mining Debris in the Sierra Nevada, U. S. Ceological Survey Professional Paper 105, 1917.

5. "Sacramento, San Joaquin and Kern Rivers, California," 27 June 1933, H.D. 191, 73rd Cong., 2nd Ses.

6. Schatz, Byron, "A Restudy of Bottom Sediments Near the Entrance of the Colden Cate," Univ. of California, Hydraulic Engineering Lab., Berkeley, Calif., Nov. 1963.

7. "Technical Report on Barriers," U. S. Army Engr. Dist, San Francisco, Calif., July 1963.

8. Sverdrup, H. V.; Johnson, Martin W.; and Fleming, Richard H.; The Oceans, Their Physics, Chemistry, and General Biology; Pretice-Hall, Inc., Englewood Cliffs, New Jersey, 1964.

   Wiegel, Robert L., Oceanographical Engineering, Prentice-Hall, Inc., Englewood Cliff, New Jersey, 1964.

9. Street, Mogel and Perry, Computation of the Littoral Regime of the Shores of San Francisco County, California, Automatic Data Processing Methods. Contract No. DACW07-68-C-0054, U. S. Army Engineer District, San Francisco, 1 January 1969.

10. Kamel, A. M. Littoral Studies Near San Francisco Using Tracer Techniques, Beach Erosion Board, TM No. 131, November 1962.

11. Shepard, Francis, Submarine Ceology, 2nd Ed., Harper and Row, New York, Evanston and London, 1963.

CHAPTER 49

SEDIMENT TRANSPORT BY WAVE ACTION

by

H. A. Einstein
Emeritus, Professor of Hydraulic Engineering
University of California
Berkeley, California

This paper summarizes the results of a continuing study at the hydraulic laboratory at the University of California at Berkeley on this subject, which is supported by the Coastal Engineering Research Center (CERC) and which has resulted over the years in the Theses of Huon Li (1954), M. Manohar (1955), G. Kalkanis (1957, 1963), M. M. Abou-Seida (1965), M. M. Das (1968) and is at this time being continued by T. C. Mac Donald. All these researchers have greatly contributed to the success of this work while the author was mostly responsible for the continuity of the study.

The aim of the study was to see if it is possible to establish for the description and prediction of sediment transport by waves a general system of approach similar to that which the author published in 1950 under the title "The Bed-Load Function for Sediment Transport in Open Channel Flows".[3] It was hoped at the time that many of the basic steps of such a description may at least be similar to those used for uni-directional flow. It became apparent that such similarities of approach were quite feasible; but another difficulty became apparent from the beginning. While in the uni-directional flow many details of the flow, such as velocity distributions, boundary layers and turbulence had been studied and described previously, such knowledge was almost entirely lacking for wave motion. The first part of the study consisted entirely of hydraulic measurements and of their analysis. In order to determine the necessary scope of such hydraulic studies, the analogy with sediment transport in uni-directional flow was used. Some of the principles governing uni-directional flow transport are:

1. Sediment motion can be divided into bed-load motion or surface creep and suspension.

2. While moving as bed load, the particle weight is to a large part transmitted directly to the nonmoving bed, not to the flow.

3. The rate of bed-load motion is defined by the equilibrium exchange of sediment between the bed-load and the nonmoving bed.

4. This equilibrium gives a direct relationship between the sediment rate and the flow conditions near the bed, including the turbulence.

5. The flow condition near the bed can be predicted for a uni-directional boundary layer as a function of the bed shear and the bed roughness, only.

6. The bed particles moving as bed load in the rather thin bed layer define in this layer a sediment concentration.

7. Above the bed layer, bed particles move in suspension, i.e., continuously transmitting their weight to the surrounding water.

8. The distribution of the concentration in a suspension is defined by the equation of equilibrium exchange of particles through the various horizontal planes, with the bed-load concentration in the bed layer as boundary condition.

All these eight principles are assumed (and seem) to apply equally to the problem of sediment transport by wave action except No. 5. All unidirectional equilibrium flows moving sediment on a bed of the same kind of particles are friction controlled; they represent in their totality a boundary layer. The basic variable describing such a flow is, therefore, the rate of friction or of shear stress at the boundary. A wave motion, on the other hand, is mainly an exchange between potential and kinetic energy and may in the first approximation be described as a frictionless motion--it does not by itself define a shear stress at the boundary. Such a shear stress can be derived only if the additional condition of zero-velocity at the boundary is introduced. That shear stress and the resulting boundary layer are caused by the wave motion and take their energy from the wave energy, but are in deep water of negligible magnitude compared with the total wave energy. For our purpose of predicting the sediment motion near the bed the description of this boundary layer is of prime importance, because it defines the shear forces on the bed and the velocity distribution in its vicinity from which the bed-load motion may be derived. It is also the only source of turbulence from which the suspension may be derived, except where the waves become very steep and begin to break, which case is excluded from this present treatment. In case of wave breaking this additional source of turbulence must be introduced separately and its effect on the sediment transport must be combined with that of the bottom friction.

Like any other boundary layer, also this reversing layer may be either laminar or turbulent. The laminar boundary layer between an oscillating fluid and a still boundary, or between a still fluid and an oscillating boundary has been known for a long time (see for instance (8)). Kalkanis (6) showed that from the viewpoint of the boundary layer the two cases are exactly equivalent, even if there is a minor difference with respect to the ability of the two to move sediment.

If an extended plain boundary moves parallel to itself at constant speed with respect to a large mass of still fluid, the resulting boundary layer motion always becomes turbulent eventually. In contrast, if this same boundary undergoes an oscillatory motion parallel to itself, the resulting boundary layer may remain permanently laminar. If the amplitude or period of this motion is properly changed, the motion in the boundary layer becomes turbulent and the entire flow condition changes drastically. Lamb in the above-quoted reference gives the solution of the laminar boundary layer, but no source could be found which defines the limiting conditions

at which the flow becomes turbulent. It was thus decided to define this limiting flow condition experimentally as the first step of the entire study.

THE CRITICAL REYNOLDS NUMBER OF THE BOUNDARY LAYER

The turbulence in a frictional flow is caused by an instability of the laminar flow. Its stability may be tested by comparing the magnitude of the inertia forces with that of the frictional forces; instability will occur when the inertia forces become large compared with the friction forces, or when the Reynolds Number which expresses the ratio of the two types of forces becomes larger than a certain limiting value. The Reynolds Number is obtained by multiplication of a characteristic length with a characeristic velocity and by division of the product by the kinematic viscosity of the fluid. Which characteristic values must be chosen can often be decided by logical arguments, but if too many variables of the same dimension are involved it may become necessary to determine the proper variables empirically. The critical value of the Reynolds Number must always be found by experiment.

If the wave theory predicts near the bed at a given location the flow velocity u

$$u = u_o \sin(\omega t) \qquad -1-$$

with ω the angular velocity of the motion $\omega = 2\pi/T$ and T the wave period. The constant $u_o = a\omega$ where a is the amplitude or half excursion of the motion. For thin boundary layers one may neglect all gradients in the x-direction parallel to the horizontal bottom as compared with the corresponding gradients in the vertical direction z. In that case Eq. 1 may be interpreted as the oscillatory motion of a long horizontal bottom under an infinite body of still water, and one obtained in both cases a velocity distribution of

$$u = u_o e^{-\beta z} \sin(\omega t - \beta z) \qquad -2-$$

with respect to the fluid outside the boundary layer (at infinity) where β has the value $\sqrt{\omega/2\nu}$. $1/\beta$ is the scale of the distance z above the bottom. Equation 2 is the description of the boundary layer for the laminar case (8) and may be written in the more general form

$$u = u_o f_1(z) \sin(\omega t - f_2(z)) \qquad -2a-$$

which will be used for the turbulent boundary layer, too. In the laminar case β = constant in Eq. 2. The motion may be interpreted as a shear wave moving away from the bottom with the constant speed $(\omega/\beta) = (\omega\nu)^{\frac{1}{2}}$, simultaneously reducing its amplitude exponentially.

In order to describe the effect of a wave motion over a still bottom, the time history of the velocity in a given cross section is found by a simple transformation of the coordinates in the form

$$u = u_o \{\sin(\omega t) - e^{-\beta z} \sin(\omega t - \beta z)\} \qquad -3-$$

or again in more general terms

$$u = u_o \{\sin(\omega t) - f_1(z) \sin[\omega t - f_2(z)]\} \qquad -3a-$$

Here u is a function of z and t, but the two f-functions depend only on z. Since both motions of Eqs.3 and 3a are sine-functions of the same frequency, it is possible to describe the composite motion in the form of an Eq. 2 or 2a. The two motions have different phases and, therefore, must be combined vectorially. This is done for Eq. 3a in Eq. 4

$$\left.\begin{aligned} u &= u_o f_1^*(z) \sin\{\omega t - f_2^*(z)\} \\ f_1^* &= \{1 + f_1^2(z) - 2 f_1(z) \cos f_2(z)\}^{\frac{1}{2}} \\ f_2^* &= \tan^{-1}\left\{\frac{f_1(z) \sin[f_2(z)]}{1 - f_1(z) \cos[f_2(z)]}\right\} \end{aligned}\right\} \qquad -4-$$

The thickness of the layer affected by friction may be estimated as the distance z from the smooth bed at which the friction-induced motion is reduced to 10% of its original value, i.e., where $e^{-\beta z}$ becomes 0.1. For a kinematic viscosity of $\nu = 10^{-5}$ ft^2/sec and a period T = 15 sec the thickness of the layer becomes 1/4 inch. This shows that the boundary layer is actually thin, as previously assumed.

The limiting flow condition at which the laminar boundary layer becomes unstable, as well as the turbulent velocity distribution, was determined empirically; the latter showed different solutions for smooth, two- and three-dimensional roughness investigated.

THE EXPERIMENTAL EQUIPMENT

After the decision was made to restrict the study to conditions of long wave periods it became possible to simplify the equipment by moving the bottom harmonically under still water. The velocity in the laminar boundary layer is then described by Eq. 2, and Eq. 4 may be used to derive from it the solution of the wave problem. In setting up the differential equations for both cases it is easily seen that the same considerations also apply to turbulent boundary layer. However, there is one acceleration term different in the two cases when the motion of particles with a density different from that of the fluid is described. This term contains the acceleration of the wave motion which is believed small compared to local accelerations of the flow near particles and due to turbulence. It was thus decided to incur this small mistake for the sake of a much smaller, simpler, and more flexible instrumentation.

The tank in which the measurements and observations were taken, contains a horizontal platform about half the length of the tank located 4" above the tank bottom, moving first on fixed rollers, later sliding on two rails, pulled by an endless steel tape. The tape followed the bottom and aorund wheels along the two end plates at the inside. This design avoided seals for the drive. A sled moving on rails above the tank was rigidly connected to

tape loop and directly driven by a crank mechanism with variable speed and amplitude. The tank was 12 ft long, 3 ft deep and 1 ft wide. A pair of displacement cylinders were arranged, one at each end, and connected by a cable such that they would make opposite vertical movements. They were driven by the same drive at such adjustable amplitude and phase as to compensate for the standing wave excited by the motion of the platform. The higher harmonics of the standing wave were negligible without compensation.

The amplitude of the platform was directly measured as the eccentricity of the crank. The period was measured by stop watch or by recording electric pulses from a switch at the crank. Turbulence was detected by introduction of dye from the free surface. Velocities were measured with a sensitive pitot device directly connected to a diaphragm, the motion of which was recorded by means of a capacitance gage.

THE CRITICAL FLOW CONDITION

The smooth case may be idealized by a half-space filled with the fluid at rest which has the kinematic viscosity ν, bounded by an infinite plane oscillating in its own plane with the angular velocity ω and the amplitude a. The total displacement of the plane $d_1 = 2a$ at the onset of turbulence was plotted in Fig. 1 against ω/ν in a log-log graph and gave a straight line of slope -1/2 except at the highest values of ω where vibrations of the system may have caused somewhat more unstable conditions. This means that $d_1^2\ \omega/\nu = \text{const.} = 6.8 \cdot 10^5$. This combination has the character of a Reynolds Number and is composed of the only parameters of the problem. In terms of amplitude one may write for the critical case

$$N_R = a^2\ \omega/\nu = 1.7 \cdot 10^5 \qquad -5-$$

That the value of the critical Reynolds Number is much higher than that for pipe flow has no significance since it describes the stability of an entirely different flow geometry. It is of the same order as that of the steady flow boundary layer.

Next rough surfaces were investigated, both with two- and three-dimensional roughness. For the two-dimensional roughness cylindrical rods of a given diameter were arranged side by side on the platform with their axes cross-wise. To reduce the displacement of the moving platform half-cylinders were used for the large diameters.

For each roughness a graph of the type of Fig. 4 was plotted indicating that the combination $d_1\ \omega/\nu = \text{const.}$ held. This value changed from roughness, to roughness, however, One would not expect such a parameter with the dimension of L^{-1} to be constant. From dimensional considerations one would expect the Reynolds Number $\varepsilon d_1\ \omega/\nu$ to become constant if ε is the size of the roughness. ε was plotted against a ω/ν and it was found that both for two- and three-dimensional roughness lines resulted with the slope -1. in a log-log graph. They define the critical Reynolds Numbers for rough surface as

$$\varepsilon\ a\ \omega/\nu = 640 \text{ for two-dimensional roughness} \qquad -5a-$$

$$\varepsilon\ a\ \omega\ \nu = 104 \text{ for three-dimensional roughness} \qquad -5b-$$

These values apply for

$$\frac{a}{\varepsilon} < \begin{cases} 266 \text{ for two-dimensional roughness} \\ 1630 \text{ for three-dimensional roughness} \end{cases}$$

All other cases behave hydraulically smooth.

TURBULENT VELOCITY DISTRIBUTION NEAR AN OSCILLATING SMOOTH WALL

It was first unsuccessfully attempted to describe the velocity distribution using the known methods of vorticity and momentum exchange which are both successful in unidirectional flow, but it was soon found that momentum exchange was not applicable in any case, and that vorticity exchange could describe the velocity distribution along a smooth wall, but was not applicable along rough walls. It was thus decided to use Eqs. 2a, 3a and 4 and to describe f_1 and f_2 empirically as well as could be done by power and exponential functions. A double-sided symmetric Pitot tube was used exclusively and proved to be very reliable.

The results are given in Fig. 2 in which the velocity amplitude is given as a function of the distance from the wall. In order to obtain a unique relationship for all different flow conditions, the two variables were plotted in dimensionless form. The distance z from the wall was measured in units of $(\nu/\omega)^{\frac{1}{2}}$ and the velocity u was measured in units of u_o, the velocity amplitude of the movable bottom (or of the wave motion near the bottom in the wave case). The dashed curve gives the predicted velocity distribution of the laminar boundary layer for comparison. The velocity u here is the velocity amplitude at various distances from the wall of the sinusoidal velocity component with the same frequency as that of the bed motion (or of the wave). From this one may derive the function f_1 for the smooth boundary

$$f_1(z) \approx 0.3\, e^{-75\, z/a} \qquad -6-$$

with a the amplitude (half excursion) of the moving bed (or of the particle motion as predicted by wave theory).

Figure 3 gives the corresponding values for the phase shift ωt in terms of the dimensionless distance $z/(\nu/\omega)^{\frac{1}{2}}$. Again the deviation from the laminar prediction is significant. The function f_2 for the smooth boundary may be derived from this

$$f_2(z) \approx 1.55\, (z/\sqrt{2\nu/\omega})^{\frac{1}{3}} \qquad -7-$$

The two functions $f_1(z)$ and $f_2(z)$ are purely empirical. They may be used in connection with Eqs. 2a, 3a, and 4.

TURBULENT VELOCITY DISTRIBUTION NEAR AN OSCILLATING ROUGH WALL

For the two-dimensional roughness half-cylinders of diameter D were used and arranged with their axes at right angle to the motion. The three-dimensional roughness were sand and gravel of sieve diameter D glued to the movable bottom. Only uniform roughnesses fully covering the bottom were considered. The following descriptions were found:

For two-dimensional roughness

$$f_1(z) = e^{-1000 \frac{z/\sqrt{2\nu/\omega}}{a\ D}} \qquad -8-$$

$$f_2(z) = 0.5\ (z/\sqrt{2\nu/\omega})^{\frac{2}{3}} \qquad -9-$$

For three-dimensional roughness

$$f_1(z) = e^{-\frac{133\ z/\sqrt{2\nu/\omega}}{a\ D}} \qquad -10-$$

$$f_2(z) = 0.5\ (z/\sqrt{2\nu/\omega})^{\frac{2}{3}} \qquad -11-$$

These expressions which are strictly empirical have been obtained by experiments covering the following ranges:

$0.0039\ \text{ft} \leq D \leq 0.104\ \text{ft}$ $0.104\ \text{ft} \leq a \leq 2.00\ \text{ft}$ $0.174\ \text{rad/sec} \leq \omega \leq 10.4\ \text{rad/sec}$	Two-dimensional roughness
$0.0009\ \text{ft} \leq D \leq 0.0453\ \text{ft}$ $0.104\ \text{ft} \leq a \leq 2.00\ \text{ft}$ $0.169\ \text{rad/sec} \leq \omega \leq 6.82\ \text{rad/sec}$	Three-dimensional roughness

All experiments used water between 66° and 75° F. The scatter of the measured points is about the same as in Figs. 2 and 3. All the above expressions may be applied in connection with Eq. 2a for moving bottom and to Eqs. 3a and 4 for wave motion over a still bottom. The system of reference coordinates is standing still in both cases.

It is interesting to observe how much faster two-dimensional roughness elements permit the velocity amplitude $f_1(z)$ to reduce than the three-dimensional roughness while the phase shift for both is the same.

THE TRANSPORT OF BED PARTICLES BY WAVE MOTION

A strictly symmetric oscillation, as the wave motion near the bed has been assumed to be, can only result in an equally symmetric motion of the sediment particles. It cannot cause any net motion of sediment. Its most important function is that of keeping continuously a greater or smaller

number of particles per unit bed area in motion. These particles move with the water near the bed and will follow the water in any direction in which it flows. If the water has, in addition to the wave motion, a small additional one-directional velocity, such as littoral current caused by the angular incidence of the waves or a secondary circulation caused by the geometry of the beach, then one must expect a systematic transport of the moving particles parallel or normal to the shoreline, respectively.

In an attempt of predicting such a transport one may thus first find the number of particles which a given wave motion keeps in motion. This mass is then subjected to the systematic motion. In this study no attempt was made to study the small systematic motion since that should best be done in the prototype. However, the particles available for transport by being in motion at a given time by wave action is easily studied in the laboratory, using the same installation as for the velocity measurements. The platform was for this purpose covered with loose sand. At half-length a tray was built into the platform covering the full width of the sand bed. Its sides were level with the bed as to not hinder any motion of sand into it. When the platform was moving towards the left sand from the left would move into the tray, during motion towards the right sand would enter from the right. The total sand Q_s collected in the tray after T seconds of wave motion over the width B permitted the determination of a specific sediment rate q_s.

$$q_s = \frac{Q_s}{BT} \qquad -12-$$

which is a measure for the rate of transport independent of direction. If the velocity of the particles composing q_s is v_q, then the amount of sediment in motion per unit of bed area S_o is

$$S_o = \frac{q_s}{v_q} \qquad -13-$$

which is the value that was to be found. The two values q_s and v_q must be determined separately: q_s by measurement and by available sediment theory, v_q by calculation from the boundary layer description.

CALCULATION OF THE SEDIMENT LOAD

Before one can begin to describe successfully the transport of sediment by water, it is necessary to observe the motion of the particles. This can be done easily in a laboratory flume, but observation at the beach or in a river shows exactly the same picture. Some particles seem to slide and roll along the nonmoving bottom. At higher rates of motion an entire sheet of moving particles appears to cover the bed. Even within this layer the particles roll, giving the layer an aspect of being continuously mixed. In this layer the particles' weights are still supported by the bed even if the flow exerts a lifting force on the top particles of the bed and thus initiates their motion from time to time. This type of motion is usually called bed-load motion and has been described in the past (1) as an equilibrium between the rate at which bed-load particles are deposited on the bed and that at which bed particles are picked up by the flow and made part of the bed load.

One factor simplified the description of the motion. Observation shows that most beach sands are well sorted, i.e., contain only a narrow range of grain sizes. The derivation will thus be made for uniform material. The experimental sands were also well sorted. The following derivation will essentially follow the procedure of reference (3) at least up to the point where the effective velocity near the particles is introduced to find the force on a nonmoving particle in the top layer of the bed. Reference (7) gives more detail; only the main steps are given here except for the new points which are particular to the application of the transport description in wave motion.

In order to describe the rate at which particles are settled out on the bed, an empirical piece of information is used which was obtained about 35 years ago by the author: every particle moving as bed load will--as an average--travel a distance of 100 diameters until it finds another suitable location for deposit. If at that spot the local instantaneous lift force due to flow conditions prevents deposition, another 100 diameter step is added and so on. In the following all constants of proportionality are omitted as they are in the end determined empirically.

The rate at which particles are deposited per unit bed area and per unit of time is proportional to

$$\sim \frac{q_s}{L\, D^3\, \gamma_s} \qquad -14-$$

if q_s is the sediment rate in weight per unit of width, L the length of the average step, D the diameter and γ_s the specific weight of the particles. The value of the average step L can be expressed as

$$L = 100\, D/(1 - p) \approx D/(1 - p) \qquad -15-$$

if p is the fraction of the bed at which at a given time, or the fraction of time at which at a given point, the lift force on a particle of size D and of specific weight γ_s is larger than its weight. With this the rate of deposition per unit area of bed becomes proportional to

$$\frac{q_s\,(1 - p)}{D^4\, \gamma_s} \qquad -16-$$

The rate at which particles are eroded from the bed and which is equal to the rate of deposition in Eq. 16 may be expressed by dividing the number of particles per unit area, which is proportional to D^{-2} through the time t_1 necessary for one exchange of a particle and by multiplication with p as defined above, t_1 may be estimated as

$$t_1 \approx \frac{D}{v_s} \qquad -17-$$

Being a characteristic of the grain, t_1 should be a function of other grain characteristics such as the diameter and the settling velocity in still water. If the turbulent settling velocity is used, one obtains

$$v_s \approx \sqrt{\frac{g\,(\gamma_s - \gamma_f)\,D}{\gamma_f}} \qquad -18-$$

and the rate of scour becomes

$$\approx \sqrt{\frac{g\,(\gamma_s - \gamma_f)\,D}{\gamma_f}}\;\frac{p}{D^2\,D} \qquad -19-$$

By combining expressions Eqs. 16 and 19 and by introduction of the constant A_* of proportionality, the following expression is obtained

$$\frac{p}{1-p} = A_* \left[\frac{q_s}{\gamma_s}\sqrt{\frac{\gamma_s}{g(\gamma_s - \gamma_f)}}\,D^{-\frac{3}{2}}\right] = A_*\,\Phi \qquad -20-$$

which may be solved for p

$$p = \frac{A_*\,\Phi}{1 + A_*\,\Phi} \qquad -21-$$

Now we must express that p is the probability for an exchange to take place at a given place of the bed. This probability, however, expresses basically only the fraction of time during which the lift on a particle of the bed surface is larger than its weight. The weight is constant and is submerged proportional to

$$W \approx (\gamma_s - \gamma_f)\,D^3 \qquad -22-$$

while the lift force is porportional to

$$L \approx \gamma_f\,\frac{u^2}{g}\,D^2 \qquad -23-$$

The ratio $\frac{W}{L}$ may thus be written

$$\frac{W}{L} = B_*\left[\frac{\gamma_s - \gamma_f}{\gamma_f}\,\frac{Dg}{u^2}\right] \qquad -24-$$

Reference (4) shows that in a boundary layer the instantaneous lift force may be derived from the instantaneous velocity at a distance 0.35 D above the theoretical boundary, that the turbulent component of the force follows statistically the normal error law and that its root-mean-square value is proportional to the corresponding lift derived from the average velocity. In the case of the wave-induced transport the problem is complicated by the fact that the lift due to the main motion also varies with time, but in contrast to the turbulent part periodically. The problem of finding the resulting probability may best be explained by Fig. 4. This isometric sketch shows three axes: towards the right that of the turbulent lift,

towards the rear that of the phase ωt, and vertically that of the probability for a given L' to occur. If we focus our interest on a quarter period, the time which is covered in Fig. 4 by Gauss-curves, the total time is given by the volume under these probability-curves. The time of motion is given by the condition $W - \bar{L} < L'$ which is demonstrated in the figure as follows: the weight W is plotted as a line parallel to the ωt-axis. From this value of L' the sinusoidal $\bar{L}$ was subtracted. All values $L' > W - \bar{L}$ are to the right of this line $W - \bar{L}$ and the cross-hatched part of the time volume under the probability curves represents the "favorable" part of the time. The ratio of the favorable time to the total time is equal to p.

This may be written mathematically as

$$p = \frac{2}{\pi \sqrt{2\pi}} \int_0^{\pi/2} \int_{B_* \psi - 1/\eta_o}^{\infty} e^{-\frac{m^2}{2}} \, dm \, d(\omega t) \qquad -25-$$

if

$$\psi = \frac{\gamma_s - \gamma_f}{\gamma_f} \frac{Dg}{u_a^2} \qquad -26-$$

where u_a is the velocity amplitude at 0.35 D from the boundary, η_o is the scale ratio between $\bar{L}$ and L' and m is a variable of integration. Elimination of p between Eq. 21 and Eq. 25 produces the bed-load equation.

$$\frac{A_* \Phi}{1 + A_* \Phi} = \frac{2}{\pi \sqrt{2\pi}} \int_0^{\pi/2} \int_{B_* \psi \xi - 1/\eta_o}^{\infty} e^{-\frac{m^2}{2}} \, dm \, d(\omega t) \qquad -27-$$

For this equation A_*, B_*, and η_o must be determined empirically. This was done in Fig. 5. First the four theoretical curves according to Eq. 27 and $A_* = B_* = 1$ and for $\frac{1}{\eta_o} = 1.0, 1.5, 2.0$, and 2.5 were calculated and plotted. Then, for all transportation experiments the values Φ and ψ were calculated and also plotted in Fig. 5. As the plotting is done on a log-log graph, the constants A_* and B_* represent only a parallel shift in the Φ and ψ direction, respectively. A reasonable fit was achieved with the values

$$\left.\begin{aligned} A_* &= 13.3 \\ B_* &= 6.0 \\ 1/\eta_o &= 2.0 \end{aligned}\right\} \qquad -28-$$

which define the bed-load equation for the bed-load movement of uniform sediment by wave motion in deep water.

The correction factor ξ for the parameter ψ is the analogous correction which had been introduced as "hiding factor" in unidirectional flow (3). There, it indicates the ability of small sizes of a sediment mixture to hide between the larger grains and also the ability of small grains to hide

in the viscous sublayer. The first case is not applicable here because of the assumption of uniform sands. The second application, on the other hand, is very important and has been studied by Abou-Seida (1), who ran special sets of experiments in the flume with the movable botton with especially fine sands (D_{50} = 0.000475 ft and D_{50} = 0.000984 ft diameter) to study this effect. The results are given in Fig. 6 as a graph of ξ against $\frac{D}{1.39\ \delta^*}$. Herein D is the grain size and δ^* the displacement thickness of the sublayer. Both, the curve of Fig. 6 and the definition of δ^* are different from those for unidirectional flow. In unidirectional flow the velocity distribution and the sublayer thickness are expressed in terms of boundary shear or u_*. In the boundary layer due to wave action the shear stress could not be expressed. The sublayer thickness is thus determined according to Einstein and Li (5) using for the sublayer a critical Reynolds Number $N_R = 4\ \delta^*\ U/\nu = 1100$, where U is the amplitude of the velocity near the bottom. This represents the minimum thickness of the sublayer over the wave period, not a constant value as in unidirectional flow, giving rise to an entirely different curve (Fig. 6). Figure 5 includes all points which were obtained by Abou-Seida (1) in addition to the measurements of Kalkanis (7).

Already Kalkanis had proposed to apply this theory to sediment transport by surface waves in wave channels. The main wave motion sets the bed particles in motion while the superimposed "mass transport current" of the same wave pattern provided the systematic velocity causing a unidirectional transport. Abou-Seida performed a set of such experiments and attempted the analysis of their results, as well as those of similar experiments performed by Vincent (12). Herein he expressed the mass transport velocity according to Longuet-Higgins (10) multiplied it with the average concentration of bed particles per unit of bed area in motion due to the oscillating wave motion. This concentration was obtained by division of the oscillating transport rate q_s of Eq. 26 by the layer thickness 2D and the average flow velocity in that layer.

Comparison of the measured with the predicted sediment rates showed very significant deviations with the measured transport. The measured values were consistently high. He explained the deviation by the fact that the theory was derived for waves of long period and low height while the experimental waves were all of short length and period and steep. In order to test this explanation he argued that in steep and short waves acceleration effects could not be neglected compared with the velocity effects on the grain. He introduced, therefore, the parameter $u^2/(\partial u/\partial t)\ D$ as an indicator for the acceleration effects. He plotted a correction factor M by which the measured transport is higher than the predicted against this acceleration parameter and found systematically decreasing deviations M for increasing acceleration parameters or, with other words, for decreasing acceleration effects.

One may conclude that for the prototype conditions of long-period waves in deep water the theory must apply satisfactorily without this acceleration correction.

SUSPENSION IN THE OSCILLATING BOUNDARY LAYER

The study of suspension due to wave action which is being pursued actively at this time is restricted to the particle motion caused by turbulence created in the boundary layer. Any turbulence created by breaking of the waves is for the time being excluded. Like in the description of the bed load it is attempted to follow the same thoughts which led to a solution in unidirectional flow, but, unfortunately, some of the most basic assumptions in the derivation of the unidirectional suspension do not apply here. In unidirectional flow the turbulence, which is responsible for the suspension is described by the shear stress at the boundary. In wave action it was not possible to find a usable expression for the shear stress; boundary layer has been shown to be very thin. The suspension, on the other hand, was found to be covering a much larger range of elevations. It appears to be impossible to derive the particle exchange in wave action from the momentum or vorticity exchange of the velocity distribution.

It was decided to attack the suspension problem in a strictly empirical way, i.e., to try to establish an approximate description of the suspended concentration distribution empirically with sufficient accuracy to complement the bed-load motion, which cannot be expected to include any suspension. Unfortunately, this work has not been advanced sufficiently to permit any results to be presented here.

The work on the suspension by the boundary layer under wave action was mostly hampered by the utter lack of any observation of the turbulence of this flow, as well as the nonexistence of the proper instrumentation to obtain such information. A method of measuring turbulent velocity components in turbulence without the presence of an average velocity was developed for this purpose by Das (2), who also developed an optical method of measuring the sediment concentrations which makes the measurement without any interference with the flow. It is hoped that soon results will be available that will permit to estimate this effect with sufficient accuracy to complement the bed-load predictions.

SUMMARY AND CONCLUSIONS

In order to describe the sediment transport due to wave action near the bed, the velocities were divided into

1. A symmetric wave motion assumed to be a horizontal sine motion with the frequency of the waves,
2. A boundary layer motion caused by the friction along the bed, including turbulence, and
3. A systematic motion, which may or may not be connected with the wave motion, but has a time-average velocity different from zero.

Of these velocities 1. and 2. are assumed to be sufficiently large to cause the motion of the bed particles; 3. may or may not be of that strength. From the velocity components 1. and 2. an average amount of sediment is derived which is at any time in motion without being permanently displaced by these

motions. While they are in motion these particles are assumed to be also under the influence of 3. which displaces them permanently and causes the sediment transport. The motion as bed load along the bed seems to be satisfactorily developed; the resulting suspension is still under investigation.

REFERENCES

1. Abou-Seida, M. M., "Bed Load Function due to Wave Action," Univ. of California, Berkeley, Calif., Hydraulic Engineering Lab. Tech. Rept. HEL 2-11, January 1965.

2. Das, M. M., "Extended Application of a Single Hot-Film Probe for the Measurement of Turbulence in a Flow Without Mean Velocity," Univ. of California, Berkeley, Calif., Hydraulic Engineering Lab. Tech. Rept. HEL 2-20, December 1968.

3. Einstein, H. A., "The Bed-Load Function for Sediment Transport in Open Channel Flows," U. S. Dept. of Agriculture, SCS, Tech. Bulletin No. 1026, September 1950.

4. Einstein, H. A., and El S. A. El Samni, "Hydrodynamic Forces on a Rough Wall," Rev. Mod. Phys., Vol. 21, 1949, pp. 520-524.

5. Einstein, H. A., and Huon Li, "The Viscous Sublayer Along a Smooth Boundary," Jour. of Engrg. Mechanics Div., Proc. ASCE, Vol. 28, Paper 945, 1956, pp. 1-27.

6. Kalkanis, George, "Observations of Turbulent Flow near an Oscillating Wall," M.S. Thesis, also Beach Erosion Board, Technical Memo No. 97, 1957.

7. Kalkanis, George, "Transportation of Bed Material due to Wave Action," Univ. of California, Berkeley, Calif., Hydraulic Engineering Lab. Tech. Rept. HEL 2-4, February 1963; also Tech. Memo No. 2, U. S. Army Coastal Engineering Research Center, February 1964.

8. Lamb, Sir Horace, Hydrodynamics, 6th edition, 1932, pp. 619-621.

9. Li, Huon, "Stability of Oscillatory Laminar Flow along a Wall,: Ph.D. Thesis; also Beach Erosion Board, Tech. Memo. No. 47, 1954.

10. Longuet-Higgins, M. S., "Mass Transport in Water Waves," Philos. Trans. Royal Society of London, Series A, Mathematical and Physical Sciences, No. 903, Vol. 245, 31 March 1953, pp. 535-581.

11. Manohar, Madhav, "Sand Movement Mechanics in Deep Water," Univ. of California I.E.R. Report Series 72, Issue 2, October 1953.

12. Vincent, G. E., "Contribution to the Study of Sediment Transport on a Horizontal Bed due to Wave Action," Proc. of Sixth Conf. on Coastal Engineering, Council on Wave Research, The Engineering Foundation, 1958, pp. 326-354.

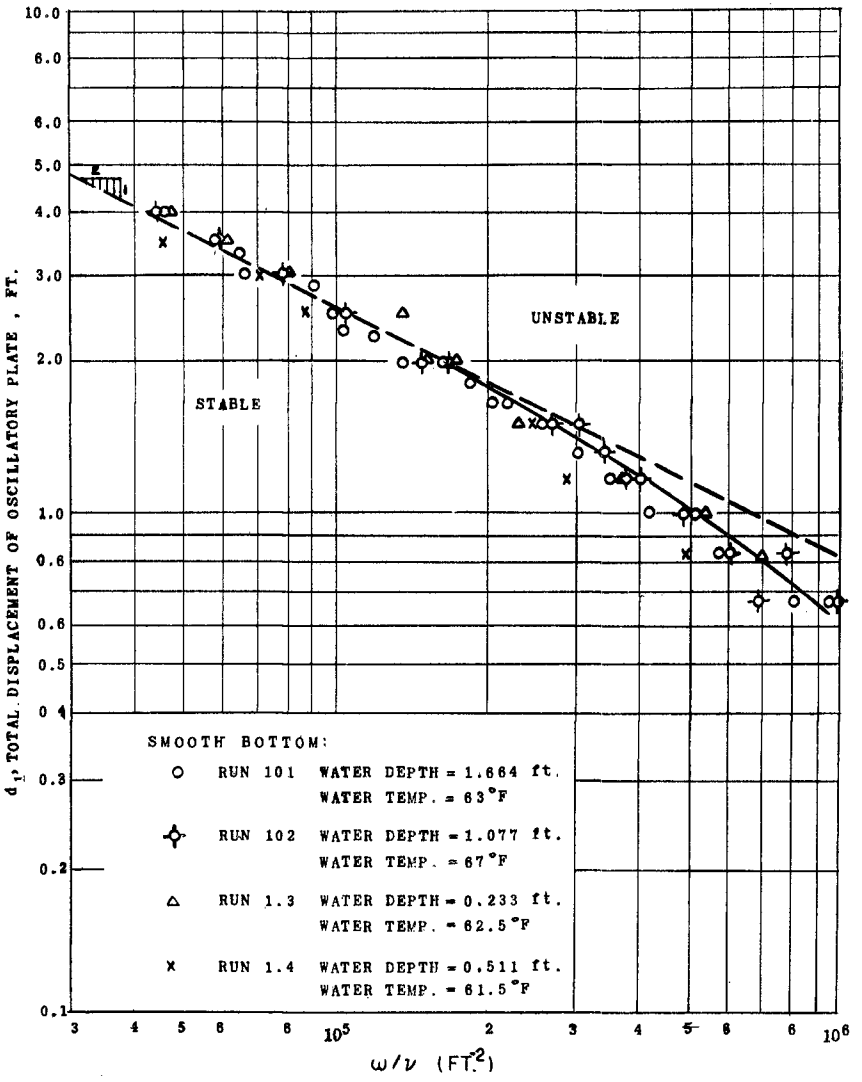

EXPERIMENTAL RESULTS OF TRANSITION INVESTIGATION OF OSCILLATORY MOTION
SMOOTH BOTTOM
FIGURE I

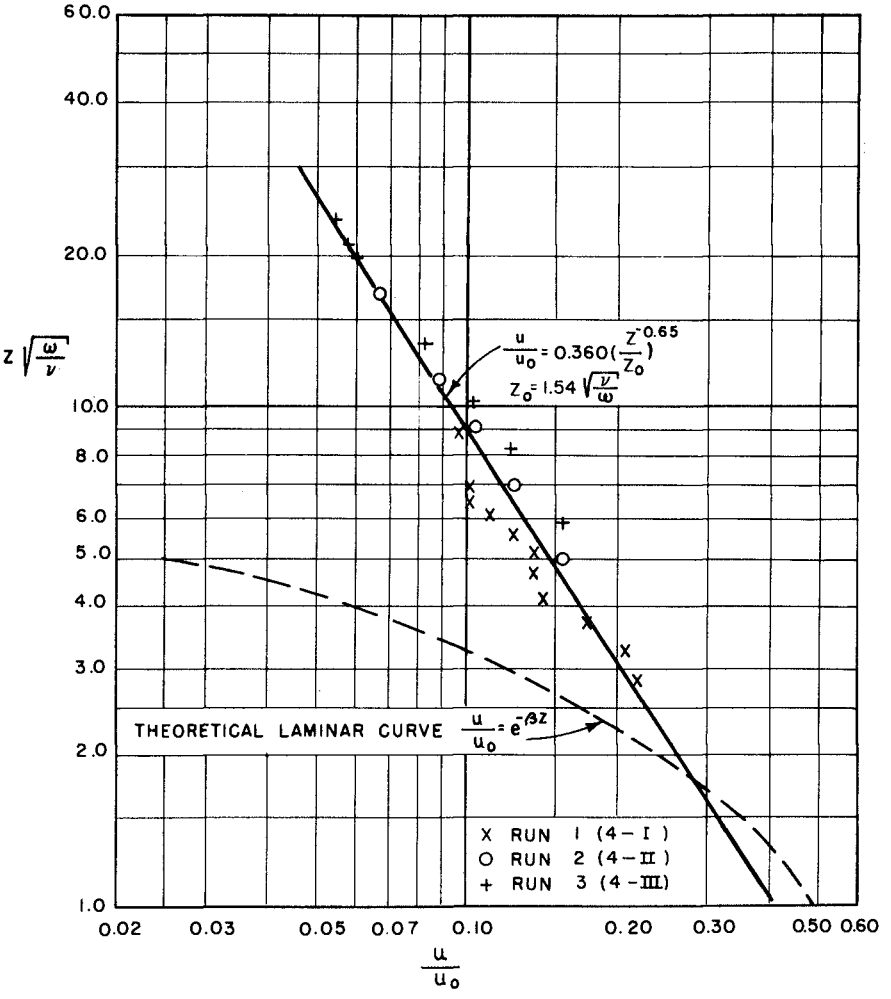

FIG. 2. PLOTTING OF EXPERIMENTAL DATA OF VELOCITY MEASUREMENT (SMOOTH BOTTOM)

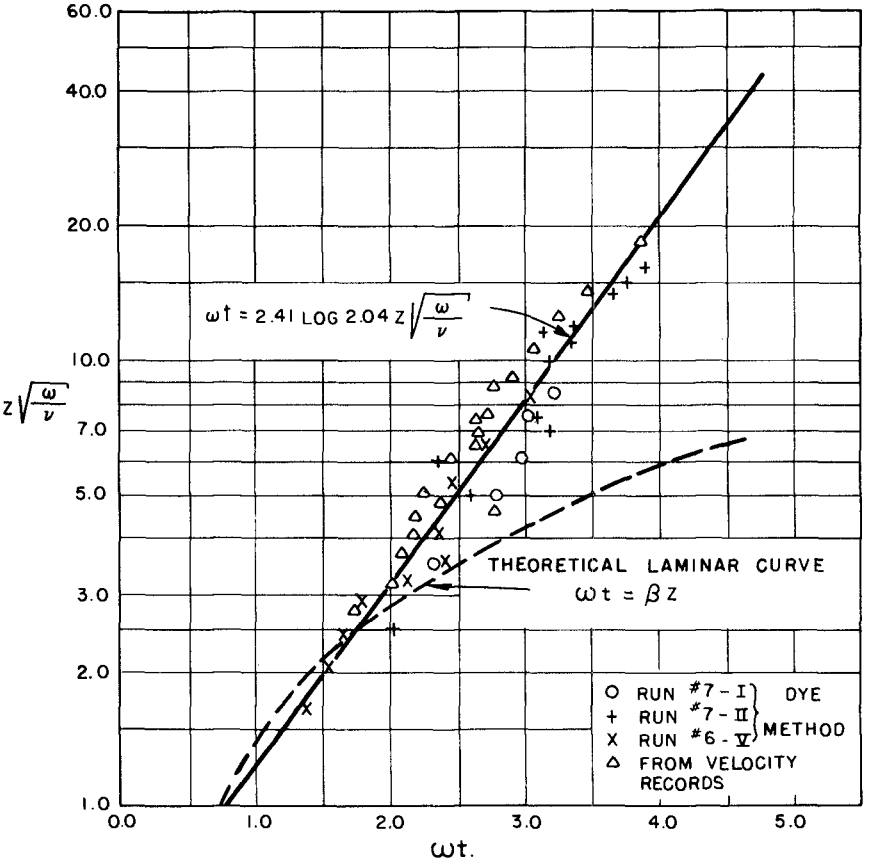

FIG. 3. PLOTTING OF EXPERIMENTAL DATA OF PHASE SHIFT MEASUREMENT (SMOOTH BOTTOM)

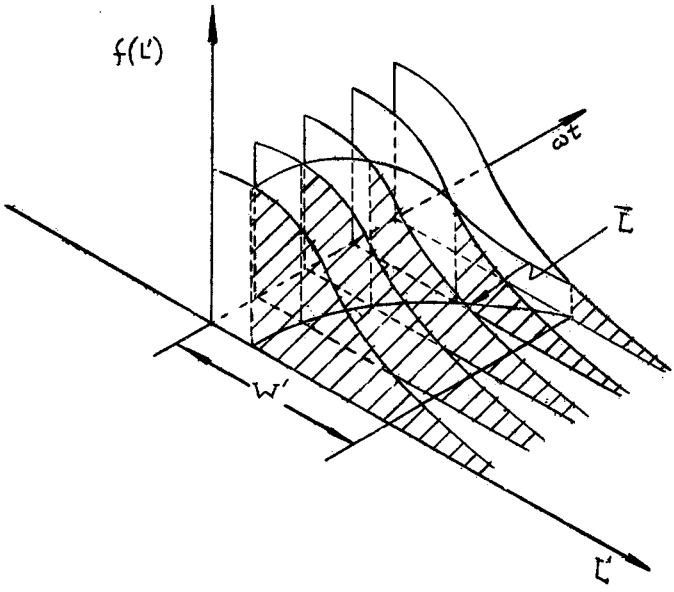

FIG. 4.

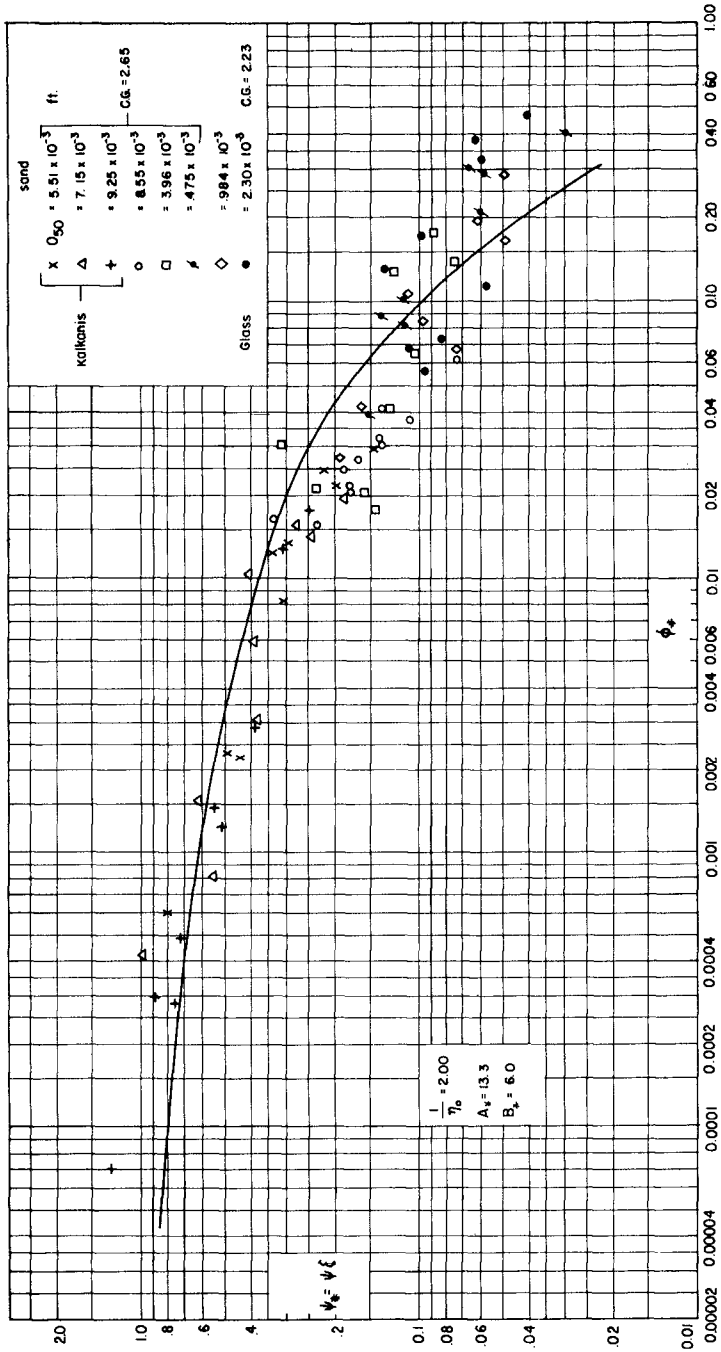

FIG. 5. GRAPHICAL REPRESENTATION OF THE BED LOAD EQUATION, $\phi_* - \psi_*$ CURVE

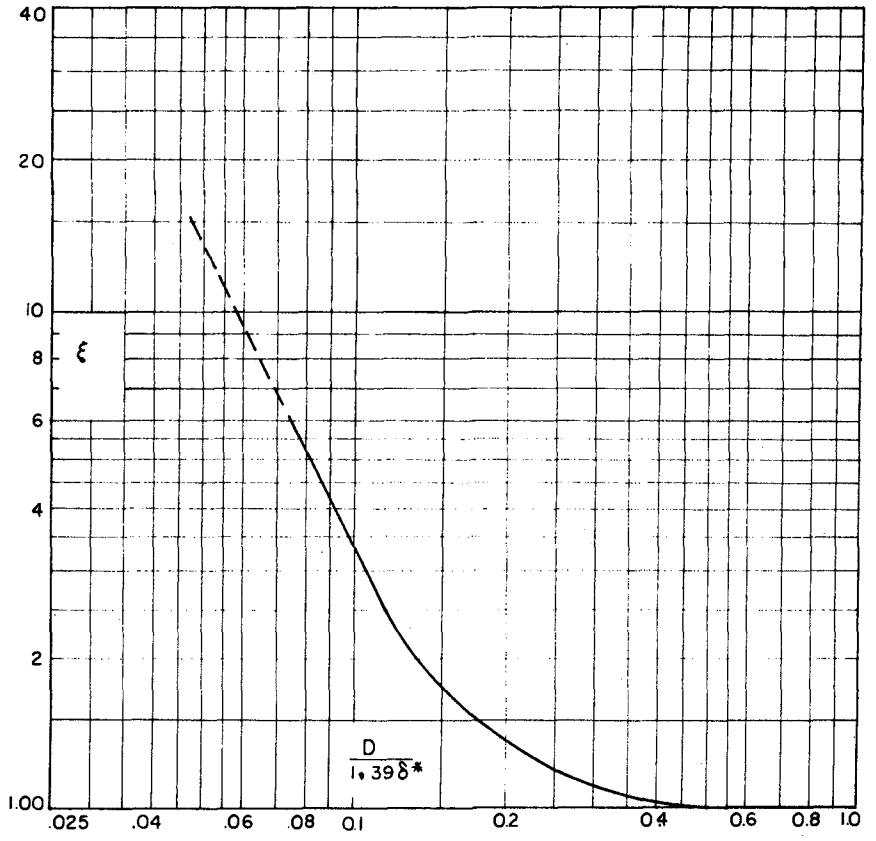

FIG. 6. PRESSURE REDUCTION IN THE SUBLAYER

CHAPTER 50

A GROSS LONGSHORE TRANSPORT RATE FORMULA

by

Cyril J. Galvin, Jr.,[1] A.M. ASCE

ABSTRACT

Gross longshore transport rates for 11 long-term field measurements are predicted reasonably well by the empirical relation, $Q=2H^2$, where Q is longshore transport rate in 100,000 yd^3/yr, and H is a mean breaker height in feet. A physical explanation of this empirical relation assumes: (1) most littoral drift is transported in suspension; (2) longshore current velocity is predicted by $V=gmT\sin 2\theta_b$; (3) the empirical relation is an equation for conservation of suspended sediment in the longshore current.

INTRODUCTION

Definitions. Littoral drift is the material moved in the littoral zone by waves and currents. For this paper, the littoral zone is a strip which follows the shoreline, bounded by the runup limit on the landward side and by a depth on the seaward side at which large waves begin to move bottom sediment in significant quantities.

The rate at which littoral drift is moved parallel to the shoreline is the longshore transport rate. Since this rate is directed parallel to the shoreline, there are two possible directions of motion, which may be called the right and left directions, if defined for an observer standing on the shore looking out to sea. Anything moving from the observer's right to his left is moving in the left direction, indicated by the subscript $_\ell$. A similar definition holds for the right direction, indicated by the subscript $_r$.

A gross longshore transport rate is defined for a given point on a shoreline as the sum of the amounts of littoral drift transported to the right and to the left, past that point on the shoreline, in a given time period.

Similarly, a net longshore transport rate is defined as the difference between the amounts of littoral drift transported to the right and to the left, past that point on the shoreline, in a given time period.

Longshore transport rates are usually given in units of volume per time (cubic yards per year in the U.S.). Typical rates for oceanfront beaches range from 10^5 to 10^6 yd^3/yr. These volumes include about 40% voids and

[1]Chief, Coastal Processes Branch, Coastal Engineering Research Center, Washington, D. C. 20016. This paper delivered at 12th Coastal Engineering Conference, Washington, D. C., on 15 September 1970, but completed too late to be published in the proceedings of that conference. Text thru page 15 completed on 4 December 1970.

about 60% solids. The solids commonly are fine to medium sand-sized material, either quartz with a specific gravity of 2.65, or carbonates or silicates with slightly higher specific gravities.

It is convenient to indicate the longshore transport rate by the symbol Q. Then, the gross longshore transport rate, Q_g, is, by definition,

$$Q_g = Q_r + Q_\ell \tag{1}$$

where Q_r is the transport to the right and Q_ℓ is the transport to the left. Similarly, the net longshore transport rate, Q_n, is

$$Q_n = Q_r - Q_\ell \tag{2}$$

The quantities Q_r, Q_ℓ, Q_n and Q_g all have specific engineering uses: Q_g is needed to predict shoaling rates in uncontrolled inlets; Q_n is needed for design of protected inlets and for predicting beach erosion on the open coast; Q_r and Q_ℓ are needed for design of jetties and impoundment basins behind weir jetties. In addition, Q_g provides an upper bound on the other quantities since, by (1) and (2), $Q_g \geq Q_n$. Note that $Q_g = |Q_n|$ if either Q_r or Q_ℓ is zero, as may happen on partially sheltered coasts.

Purpose. This paper presents an empirical relation between gross longshore transport rate, Q_g, and the local mean breaker height, H, as a first approximation for engineering predictions. An hypothesis is also presented to explain the empirical relation.

Present (1970) Practice. Longshore transport rates are predicted by the following methods:

1. The best way to predict longshore transport rate at a given site is to adopt the best known rate from a nearby site, with modifications based on local conditions.

2. If rates from nearby applicable sites are not known, then the next best way to predict transport rates at a given site is to compute them from data showing historical changes in the topography of the littoral zone (charts, surveys, and dredging records are primary sources).

3. If neither Method 1 nor Method 2 is practical, then it is accepted practice to use either measured or calculated wave conditions along with the curve relating "Longshore component of wave energy and Littoral transport rate" which appears in CERC Technical Report Number 4 (Coastal Engineering Research Center, 1966, Figure 2-22, p. 175).

Method 1, if applicable, depends largely on engineering judgement. Method 2, if applicable, is a straight-forward, but tedious, application of historical data, which gives useable answers, provided the basic data are reliable, the calculations are correct, and the interpretation is based on a thorough knowledge of the locality. By choosing only a few representative wave conditions, Method 3 can usually supply an answer with less work than Method 2, but with correspondingly less certainty. Because calculation of needed wave statistics in Method 3 follows an established routine, it is often easier than researching the records and computing the changes necessary for Method 2. Thus, there is a tendency to apply Method 3 where possible.

Transport Rate - Energy Flux Correlation. The curve on which Method 3 is based (CERC, 1966, p. 175), taken from Savage (dashed line of Figure 7 in Savage, 1962), shows a correlation between longshore transport rate and energy flux. Savage's dashed line is his modification, based on laboratory data, of an earlier curve given by Caldwell (1956) that is based on two sets of field data (Caldwell, 1956; Watts, 1953) which are generally accepted as the best prototype longshore transport data now (1970) available. The curves of both Savage and Caldwell, as adapted from Savage (1962), are shown on Figure 1 of this paper.

The variables plotted on Figure 1 are Caldwell's adaption of a somewhat cryptic suggestion in the fifth appendix of an unpublished report prepared by the Los Angeles District, Corps of Engineers (dated October 1, 1948; see also Eaton, 1951). It appears probable that the suggestion in the 1948 report was, in turn, based on work done at the Scripps Institution of Oceanography shortly before that date (S.I.O., 1947).

The relation shown on Figure 1 has been criticized (Galvin, 1963; Longuet-Higgins, private communication, 1969; Komar and Inman, 1970) for, among other things, confusing scalar energy with vector energy flux. See, for example, the legend on the horizontal axis of Figure 2-22 in TR4 (CERC, 1966, p. 175). However, for the practicing engineer looking for an answer to his problem, this objection is a mere quibble, provided that the straight line gives a reasonably accurate answer. Although the present state of the art is such that a reasonably accurate answer is one good within a factor of 2, it is doubtful that the relation on Figure 1 is that good. Thus, further work on the subject is justified.

GROSS TRANSPORT RATE FORMULA

Empirical Relation. It appears intuitively obvious that the longshore transport rate, Q, must be closely related to wave height at breaking, H. On a naive level, the bigger the waves, the more energy they have to move sand around. Or the bigger the waves, the greater the cross-sectional area of the surf zone through which the sediment might move. Thus, a relation between drift rate and breaker height is expected, and, indeed, such a relation already exists in the longshore transport curves of Caldwell and Savage, since the horizontal axis of Figure 1 is a term including H^2.

At the Coastal Engineering Research Center (CERC), visual observations of waves along U.S. coasts are routinely collected as a first step towards

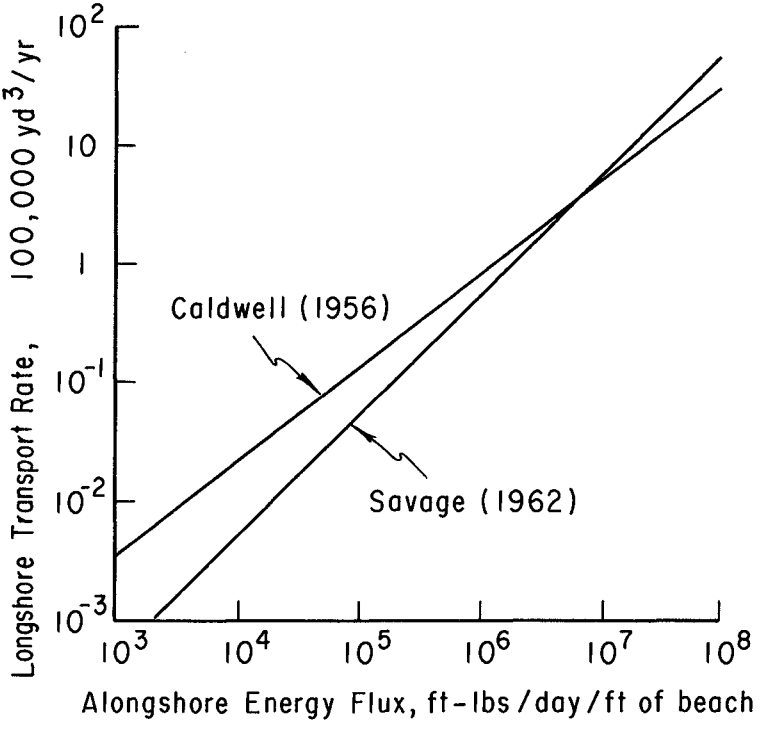

TRANSPORT RATE - ENERGY FLUX CORRELATION

Figure 1

defining the wave climate of these coasts. Much of these data are collected by Coast Guard personnel or other volunteers in the Cooperative Surf Observation Program (COSOP), the Beach Evaluation Program (BEP), and the Littoral Environmental Observation Program (LEO). (See Darling, 1968; Galvin, et al., 1969, 1970; Szuwalski, 1970). There is also an extensive program of wave gaging on U. S. coasts (Darling and Dumm, 1967).

Also at CERC, there is frequent occasion to discuss coastal engineering problems requiring information on longshore transport rates for U. S. coasts, many of which are tabulated by Johnson (1957). Familiarity with these wave and transport data impressed on the writer that measured transport rates and observed mean breaker heights are highly correlated on U. S. coasts. This led to the following empirical relation. If longshore transport rate, Q, is plotted against mean breaker height, H, a curve given by

$$Q = 2H^2 \tag{3}$$

forms an envelope (Figure 2) over all but two known (Q,H) pairs, when Q is in units of 100,000 yd^3/yr and H is in feet.

The Data. The 17 longshore transport rates plotted on Figure 2 and tabulated in Table 1 include rates obtained from 13 Corps of Engineer field studies (points 1 through 10, and 15 and 16). All but one of these 13 rates (point 9b) are based on changes measured by Method 2 for periods of at least one year. Three other shorter field studies are plotted, including two tracer studies (points 11 and 12) and one special study (point 14), all having durations measured in hours or days. One laboratory point (14) is plotted, which is the maximum transport rate obtained by Fairchild (1970).

The plotted transport rates are all supposed to be gross transport rates. In some cases, the sources report the data as gross rates, or as nearly gross rates. In the three short-term field studies (points 11, 12, and 14) and in the single laboratory case (point 13), the source description leads to the assumption that gross rates are involved. For point 16, the source (Committee on Tidal Hydraulics, 1964) give Q_ℓ and Q_r, so equation (1) was used. Point 6 (southwest Lake Michigan) is the maximum of 6 values of Q_n given by Johnson (1957), assuming from equations (1) and (2) that $Q_g \geq Q_n$.

For points 9a, 9b, and 10, only the net rates were given, but gross rates were computed from the net rates by equation (4),

$$Q_g = Q_n(1+\alpha)/(1-\alpha) \tag{4}$$

which is obtained by dividing equation (1) by (2) and defining $\alpha = Q_\ell/Q_r$. In these cases, the gross rates were calculated by assuming that the ratios of waves from the south to waves from the north (points 9a and 9b from Watts, 1953b) and the corresponding ratio of longshore energy fluxes (point 10 from Caldwell, 1956) were identical to α in (4). Note that equation (4) is not useful when α approaches 1, i.e., when the net transport rate is a small fraction of the gross transport rate.

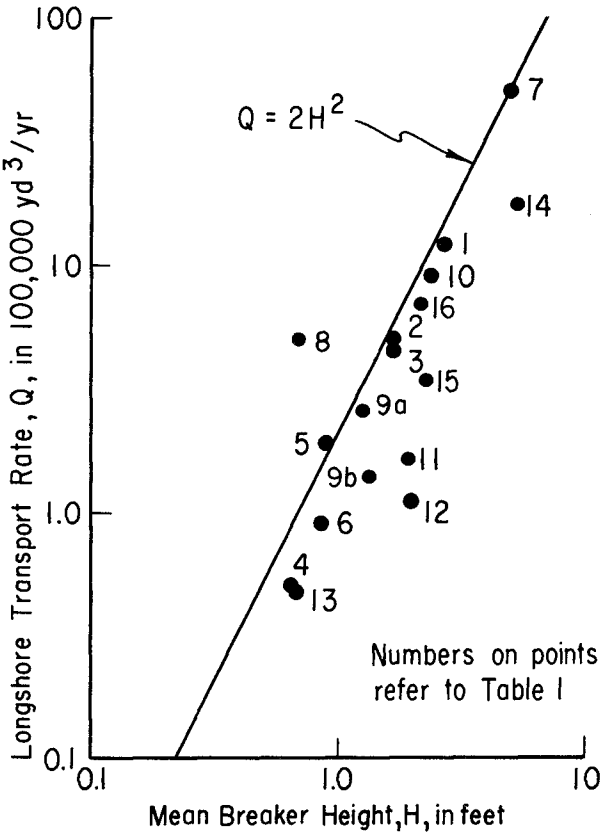

EMPIRICAL PREDICTION OF
GROSS LONGSHORE TRANSPORT RATE

Figure 2

GROSS LONGSHORE TRANSPORT RATES

No.	Locality	Measured ($10^5 yd^3/yr$)	Predicted($2H^2$) ($10^5 yd^3/yr$)	H (ft)	Sources for Data* Transport Rate	Height
1	Port Hueneme	12	15.1	2.75	Herron & Harris, 1966.	LEO & Gage 715,1962
2	Sandy Hook	4.93	5.7	1.69	Caldwell, 1966	COSOP (Monmouth Beach)
3	Fire Island Inlet	4.50	5.8	1.70	Taney, BEB TM 128	COSOP (Short Beach)
4	Tampa Bay Entrance	0.50	0.87	0.66 0.66	Jacksonville Dist. and Caldwell	COSOP (Cape San Blas) Naples Wave Gage (59-60)
5	Presque Isle	1.91	1.6	0.9	Berg	Saville, BEB TM 37
6	SW L. Michigan	0.90	1.5	0.87	Johnson, 1957	Saville, BEB TM 36
7	Columbia R. Estuary	50	50.0	5.01	Caldwell	COSOP (Yaquina Bay)
8	Galveston	3.30	1.0	0.70		Gage (Apr, May, 47)
9a	Lake Worth	2.5	3.2	1.26	Watts, BEB TM 42	COSOP(Hillsboro,all year)
9b	S. Lake Worth	1.37	3.6	1.34	Watts, BEB TM 42	COSOP(Hillsboro in Mar, Apr, May)
10	Anaheim	8.85	11.5	2.40	Caldwell, BEB TM 68	Huntington Beach Gage
11	Virginia Beach	1.60	6.5	1.80	Boon, 1969	Harrison, 1968
12	El Moreno	1.10	8.0	2	Komar, 1969	Komar, 1969
13	CERC Lab	0.48	0.92	0.68	Fairchild, 1970	Fairchild, 1970
14	Cape Thompson	17.1	60.5	5.5	Moore and Cole, 1960	Moore and Cole, 1960
15	Carolina Beach	3.4	10.1	2.25	Wilmington District	COSOP (Atlantic & Oak Island averaged)
16	Ponce de Leon	7.0	9.2	2.15	Com. on Tidal Hyd.	COSOP (Ponce de Leon)

*COSOP: CERC-US Coast Guard Cooperative Surf Observation Program. Nearest open coast station given in ( ).

*LEO: CERC Littoral Environment Observation Program, from Berg and Szuwalski.

The wave data plotted on Figure 2 and tabulated in Table 1 are mean values of the height of waves breaking or shoaling on beaches. Of the 17 plotted points, 12 are based at least in part on visual estimates of breaker height. These include 8 COSOP heights, one LEO height, and 3 heights from published sources (see Table 1). The COSOP heights are simple averages of all observations available from the locality listed. The minimum length of record for any of the 8 COSOP localities is 4 years. Each observation is a visual estimate of the height of the highest one third of the waves breaking on the beach. Other work (Galvin, et al., 1969; Galvin, et al., 1970) has shown that mean annual heights obtained in this way are internally consistent and that the distribution of these heights around the U. S. coasts agrees with known climatic conditions.

Five sets of wave gage records are used, including one set from laboratory wave gages for point 13. Two gage records have not been shoaled to the breaking point, although all were obtained in fairly shallow water. The two data points from the Great Lakes (points 5 and 6) use wave heights from hindcasts by Saville (1953a; 1953b), taken from the percent of total time curves, including the effect of ice cover, but not shoaling to the breaking point. The wave height for point 12 from Komar's (1969) tracer study is listed as 2 feet, but the author gives only the range of wave heights observed (1 to 3 feet).

In all cases, the best available wave height data were chosen, with measured or visually observed values given preference over hindcast values. Where it is possible to compare data from different sources, the data usually agree. For example, the visual and unshoaled gage data for point 4, Table 1, are precisely, although accidentally, equal.

In the case of point 15, the height listed is the average of the nearest COSOP stations from either side of Carolina Beach, North Carolina - Oak Island to the south where the H is 1.18 feet, and Atlantic to the north where the H is 3.32 feet. Despite this disparity, which is caused by differing exposure of the localities, the mean of the two COSOP stations agrees well with four months of visual and gage records obtained at Wrightsville Beach, only a few miles from Carolina Beach.

Long-term Rates. The 17 points on Figure 2 are not all on the same basis, particularly in terms of length of record. For this reason, only the (Q,H) pairs for which both the Q and the H data are based on more than one year of record have been plotted in Figure 3. It then becomes obvious that, in eliminating data based on shorter lengths of record, a significant amount of the scatter in Figure 2 is also eliminated. This reduction of scatter by elimination of shorter term data increases confidence in equation (3) as an empirical prediction of gross longshore transport rates.

Of the 6 shorter term points that have been eliminated in going from Figure 2 to Figure 3, the two that fall furthest below the curve are the only two tracer tests in Table 1 (points 11 and 12). If there is validity to the empirical relation (3), then the fact that points 11 and 12 have significantly lower rates of drift than is predicted by (3) is consistent with the hypothesis that the burial and delayed erosion of tracers produce indicated transport rates lower than actual rates (Galvin, 1965).

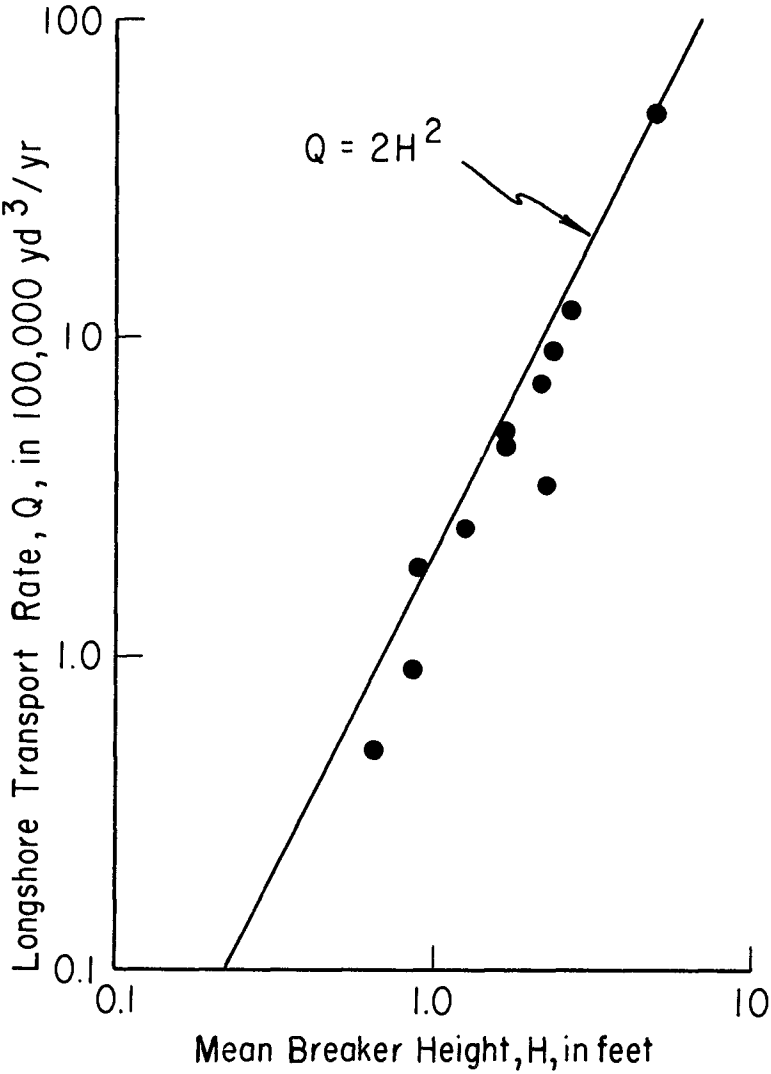

EMPIRICAL PREDICTION FOR LONG TERM RATES

Figure 3

It is emphasized that the field data plotted on Figure 2 and tabulated in Table 1 include all known (Q,H) pairs for which Q equals, or nearly equals, Q_g. That is, the plotted and tabulated transport rates are intended to be gross rates only. There are many more (Q,H) pairs where Q equals Q_n when $Q_n < Q_g$. In all of these Q_n cases, the (Q,H) pairs plot below the curve given by equation (3), so that the equation, $Q=2H^2$, is really an envelope above the measured longshore transport rates.

Instead of this envelope, a better fit of the curve to the gross transport data on Figure 3 could be had by changing the constant 2 in equation (3) to 1.5. However, historical estimates of longshore transport rates, somewhat like estimates of the age of the earth, are nearly always revised upward and only rarely revised downward. Therefore, it is safer, as well as more convenient, to keep 2 as the constant in equation (3).

PHYSICAL HYPOTHESES

Energy Flux. The simplicity of equation (3) and the unexpected, but empirically good, fit of the data to it prompt an attempt at a physical explanation. The fact that H enters equation (3) as a squared term suggests that energy flux may be involved. However, since H is defined as the breaker height, the energy flux ought to depend on $H^{5/2}$, assuming that the energy density is proportional to H^2 and that the group velocity depends on $H^{1/2}$ near breaking. But the slope of the H^2 curve seems to fit the data better than the slope of an $H^{5/2}$curve (compare Figures 3 and 4).

Continuity. However, another likely explanation is that equation (3) is a version of the conservation of mass, or continuity equation,

$$Q = D\ c\ V\ A \qquad (5)$$

where c is a mean sediment concentration in the surf zone, V is a mean longshore current velocity, and A is the cross sectional area of the surf zone. D is a factor added to keep the units correct. If Q is 10^5 yd^3/yr and V and A are ft/sec and ft^2, then D = 11.68 ($sec\text{-}yd^3/yr - ft^3$).

In the following paragraphs, it is shown by plausibility arguments how equation (5) can be worked into a form like that of equation (3). In order to do this, it is necessary to have relations for c, V, and A. Since there does not appear to be any way of predicting concentration in the surf zone, c will be obtained from measurements (Watts, 1953a; Fairchild, unpublished). It is then necessary to obtain relations for the longshore current velocity, V, and the cross sectional area, A.

There are many equations available which purport to predict the mean longshore current velocity, V, but it has been shown that only two of them agree with both the best field and the best laboratory data (Galvin, 1967). One of these two equations, developed from elementary continuity considerations (Galvin and Eagleson, 1965), is

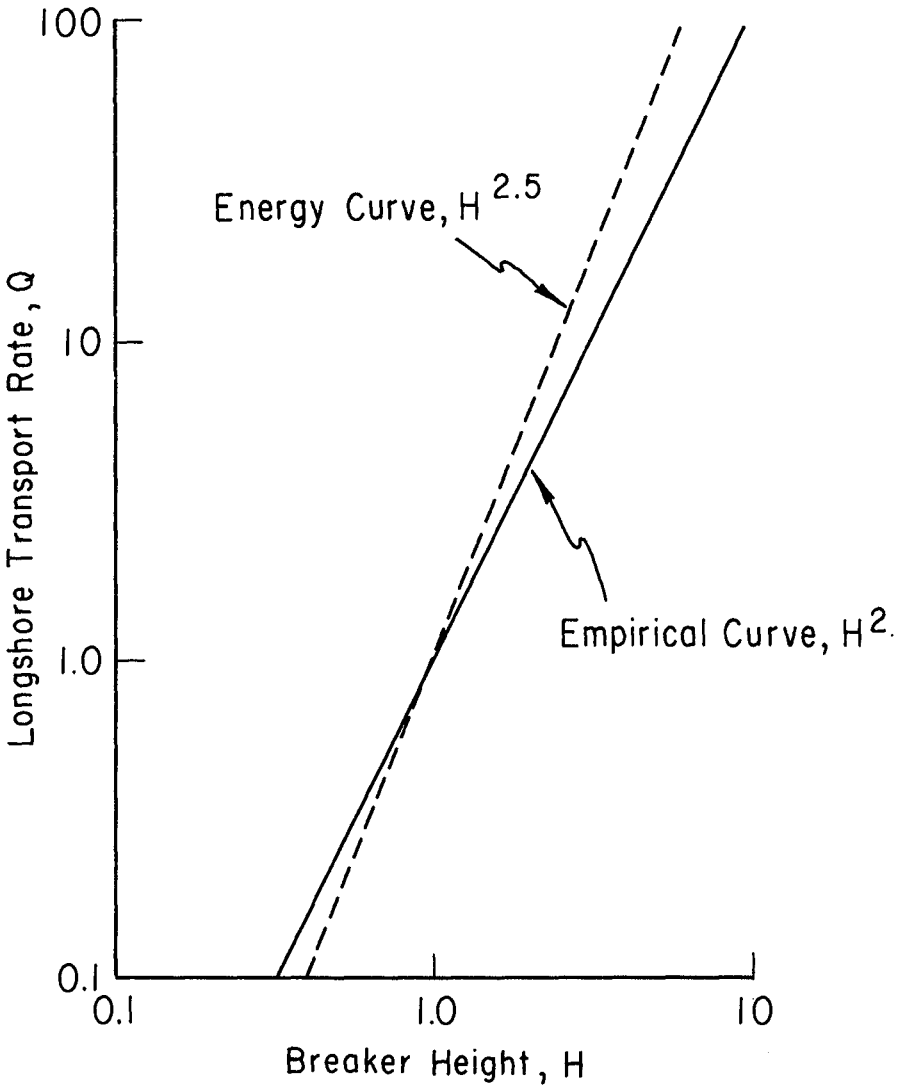

HEIGHT DEPENDENCE OF ENERGY AND EMPIRICAL CURVES

Figure 4

$$V = g\, m\, T \sin 2\theta_b \tag{6}$$

where g = acceleration of gravity; m = beach slope as defined in Figure 5; T = wave period; and θ_b = the angle between the wave crest at breaking and the shoreline. Since equation (3) attempts to predict gross transport rates, direction does not matter, and the sign of angle θ_b in (6) can be ignored.

For mean cross-sectional area, A, the surf zone will be approximated by a triangle bounded on the seaward side by a depth equal to βH, where β is the breaker depth-to-height ratio for the given slope, as shown in Figure 5. The area, A', of the triangle for a given wave height is thus

$$A' = (\beta H)^2/(2m) \tag{7}$$

which is how H^2 gets into equation (5). The area A' is somewhat less than the true area of the surf zone (Figure 5). Since (7) refers to A' for a specific wave condition, it is necessary to convert this to the annual mean area (A) for use in equation (5), by a factor K, where

$$K = \frac{\text{annual mean of individual } H^2}{\text{square of annual mean}} \tag{8}$$

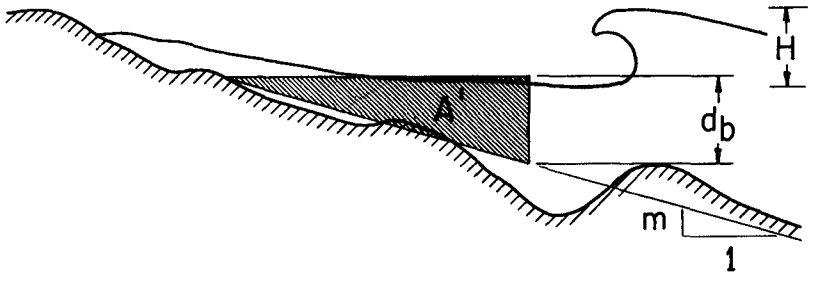

AREA OF SURF ZONE

Figure 5

Thus, the average annual area is

$$A = K\ (\beta H)^2/(2m) \tag{9}$$

Putting equations (6) and (9) into (5) results in (10)

$$Q = D\ K\ g\ \beta^2 c\ T\ H^2\ \sin\ \theta_b \tag{10}$$

assuming that $\sin 2\theta_b = 2 \sin \theta_b$ for the small angles involved. Note that the slope, m, present in both velocity (6) and area (9), has cancelled out of the equation for transport rate (10).

Check on Continuity Hypothesis. If equation (10) is an explanation of the empirically derived equation (3), then the factors on the right side of (10), exclusive of H^2, should be equivalent to or less than the factor 2 on the right hand side of equation (3). That is,

$$D\ K\ g\ \beta^2\ c\ T \sin\ \theta_b \leq 2 \tag{11}$$

where the $\leq$ enters because the curve on Figure 3 is an envelope above almost all known values, and because A was derived as a minimum value. It is now of interest to see whether reasonable values of K, β, c, T, and θ_b will satisfy (11).

Data for concentration are adopted from Watts (1953a) and Fairchild (unpublished) according to the following calculation:

$$c = c_w \gamma_{sw}/(\gamma_q(1-\varepsilon)) \tag{12}$$

where c is the concentration given in (5), c_w is the concentration by weight given by Watts (1953a); $\gamma_{sw} = 64$ lbs/ft^3; $\gamma_q = 62.4 \times 2.65 = 165.4$ lbs/ft^3; and ε is the ratio (voids in beach sand)/(voids + solids in sand) assumed to equal 0.4. With these substitutions, equation (12) becomes

$$c = 0.65\ c_w \tag{13}$$

From Watts' paper, an average value of c_w is about 0.5×10^{-3}, so that $c = 0.32 \times 10^{-3}$, a concentration which includes allowance for void space. Fairchild's data average around 0.46×10^{-3}.

The value of β is taken to be 1.3, a value traditionally used by engineers and one which has some experimental and theoretical basis (Iversen, 1952). Values of K have been obtained from calculation of equation (8) using visually estimated breaker heights from the COSOP data. Wave period T is also taken from the COSOP data. The value of θ_b is assumed to be 8°, which is a mean of three field studies tabulated by Galvin and Nelson (1967) and which also is a representative mean value for data obtained in the CERC Beach Evaluation Program.

Tests of equation (11) for five coastal localities are shown in Table 2, where ( ) is used as a symbol for the left side of equation (11). The data in Table 2 show that ( ) is indeed less than 2, averaging about 0.50. While this is not compelling evidence in favor of the continuity hypothesis, these data do suggest that the hypothesis is worth further examination.

Table 2. CHECK ON CONTINUITY HYPOTHESIS

Locality	K -	T sec	c vol/vol	( )* -	( )/2 -
Short Beach, N.Y.	1.5	6.8	0.00046	0.42	0.21
Monmouth Beach, N.J.	1.4	6.4	0.00046	0.36	0.18
Hillsboro Inlet, Fla.	2.2	5.8	0.00046	0.52	0.26
Cape San Blas, Fla.	3.4	5.5	0.00046	0.76	0.38
Yaquina Bay, Ore.	1.3	13.0	0.00032	0.48	0.24

*( ) = $Dg\beta^2KcT \sin\theta_b$ as in equation (11)

where D = 11.68 sec-yd^3/yr-ft^3

g = 32.2 ft/sec^2

β = 1.3

θ_b = 8^o

Assumptions of Continuity Hypothesis. The following paragraphs discuss the principal assumptions underlying the continuity hypothesis. Ad hoc reasons for favoring a continuity approach to surf zone motion have been previously advanced (Galvin, 1967, p. 299-300).

Assumption 1. The passage of waves through the littoral zone initiates sediment motion, so that this sediment may be moved alongshore even by weak longshore currents. Explicit statements of this assumption are given by the Beach Erosion Board (1933, paragraph 5/7), Kalkanis (1964, p.2), and Caldwell (1966, p. 146), and it seems well verified by observation.

Assumption 2. Longshore transport of littoral drift is accomplished principally as suspended load transport. There are some field and laboratory data which support this assumption. On the basis of his field measurements, Watts (1953a, p. 41) concludes that "the total suspended material movement can be an important factor in a littoral drift analysis". The data of Thornton (1969, Appendix B), based on measurement of transport rates with bedload traps, yield transport rates between a tenth and a hundredth of the value that would be expected from the longshore transport rate-energy flux correlation on

Figure 1 (M. M. Das, personal communication, 1970). If the traps were functioning properly, and if order-of-magnitude faith in Figure 1 is justified, then Thornton's data indicate that bedload is less important than suspended load in longshore transport. Saville (1950, p. 564) concludes, on the basis of his laboratory experiments, that "On equilibrium storm beaches, the sediment transportation was produced mainly by the movement of material in suspension by the littoral current." On the other hand, Komar (1969, p. 54) suggests that "suspended load transport of sand in the surf zone is less important than bedload transport" since his measurements appear to be explained by a bedload theory (Komar and Inman, 1970, p. 5921).

Assumption 3. Suspended sediment concentration in the surf zone can be approximated by a single average value. Watts (1953a, p. 40) states that there is some evidence for a uniform concentration across much of the surf zone, but there is little data available on this point.

Assumption 4. The mean longshore current velocity is given by equation (5). Comparison with data shows that this equation is one of two that fit the best data, it resembles the equation of Longuet-Higgins (1970, p. 6784), and it is consistent with the continuity hypothesis in that it was derived from continuity assumptions also (Galvin, 1967).

CONCLUSIONS

1. Gross longshore transport rates obtained from long-term field measurements are correlated with mean breaker height (Figure 3) by the empirical relation, $Q = 2H^2$, where Q is in 10^5 yd^3/yr and H is in feet (if measured in 10^5 m^3/yr and meters, the empirical relation becomes $Q = 16.5H^2$).

2. The empirical relation is conservative in predicting gross longshore transport rates now known (1970). Seven of 11 gross longshore transport rates from long-term field measurements are between 75 and 100% of their respective $2H^2$ values, and only one of the 11 rates is numerically greater than $2H^2$ (Figure 3).

3. All known net longshore transport rates which differ significantly from the gross rates have measured Q values that are numerically less than $2H^2$. In other words, the empirical relation approximately predicts the gross longshore transport rates and forms an envelope above the net longshore transport rates.

4. A physical explanation of $Q= 2H^2$, supported by some data from published studies, suggests that littoral drift is moved primarily as suspended load during longshore transport.

5. The physical explanation assumes conservation of suspended sediment in a longshore current whose mean velocity is given by equation (6) and whose cross-sectional area is a triangle having the breaker depth as its seaward side (Figure 5). The resulting expression (10) for Q is independent of beach slope and consistent with the limited field data available (Table 2).

ACKNOWLEDGEMENTS

This work was done at the U. S. Army Coastal Engineering Research Center. It evolved from a study of Coast Guard wave observations and J. W. Johnson's compilation of longshore transport rates, and from discussions with J. M. Caldwell and others of the CERC staff. T. Saville, Jr., and R. P. Savage reviewed an earlier version of this paper, and numerous others have contributed ideas and data, among whom are D. W. Berg, M. M. Das, J. C. Fairchild, J. J. Fisher, J. T. Jarrett, P. C. Pritchett, W. N. Seelig, A. Z. Szuwalski, L. W. Tenney, and L. Vallianos.

Data presented in this paper, unless otherwise noted, were obtained from research conducted by the United States Army Coastal Engineering Research Center under the Civil Works research and development program of the United States Army Corps of Engineers. Permission of the Chief of Engineers to publish this information is appreciated. The findings of this paper are not to be construed as official Department of the Army position unless so designated by other authorized documents.

REFERENCES

Beach Erosion Board, Interim Report, Office of Chief of Engineers, 1933.

Berg, D. W., and D. B. Duane, Effects of particle size and distribution on stability of artificially filled beach, Presque Isle Peninsula, Pennsylvania, Proc. 11th Conf. Great Lakes Res., 161-178, 1968.

Boon, J. D., Quantitative analysis of beach sand movement, Virginia Beach, Virginia, Sedimentology, 13, 85-103, 1969.

Caldwell, J. M., Wave action and sand movement near Anaheim Bay, California, U. S. Army Beach Erosion Board Tech. Mem. 68, 1-21, 1956.

Caldwell, J. M., Coastal processes and beach erosion, J. Soc. Civil Engrs, 53, 142-157, 1966.

Coastal Engineering Research Center, Shore protection, planning and design, Tech. Report 4, 1-401, 1966.

Committee on Tidal Hydraulics, Shoaling and beach stability problem, Ponce de Leon Inlet, Florida, Corps of Engineers, 1-7, 1964.

Darling, J. M., Surf observations along the United States' coasts, J. Waterways Harbors Div. Am. Soc. Civil Engrs., 94, 11-21, 1968.

Darling, J. M., and D. G. Dumm, the wave record program at CERC, U. S. Army Coastal Engr. Res. Center Misc. Paper 1-67, 1-30, 1967.

Eaton, R. O., Littoral processes on sandy coasts, Proc. 1st Conf. Coastal Engineering , 140-154, Council on Wave Research, 1951.

Fairchild, J. C., Longshore transport of suspended sediment, Proc. 13th Conf. Coastal Engr., ASCE, 1972.

Fairchild, J. C., Laboratory tests of longshore transport, Proc. Twelfth Conf. Coastal Engr., ASCE, 1970.

Galvin, C. J., Discussion of "Laboratory determination of littoral transport rates" by R. P. Savage, J. Waterways Harbors Div. Am. Soc. Civil Engrs, 89, 57-59, 1963.

Galvin, C. J., Longshore current velocity: a review of theory and data, Reviews of Geophysics, 5, 287-304, 1967.

Galvin, C. J., A theoretical distribution of waiting times for tracer particles on a sand bed, U. S. Army Coastal Eng. Res. Center Bull., 1, 13-22, 1964.

Galvin, C. J., D. G. Dumm, B. R. Sims, and L. W. Tenney, Nearshore visual wave observations for United States coastlines (abstract) Transactions American Geophysical Union, 50, 192, 1969.

Galvin, C. J. and P. S. Eagleson, Experimental study of longshore currents on a plane beach, U. S. Army Coastal Engr. Res. Center Tech. Mem. 10, 1-80, 1965.

Galvin, C. J. and R. A. Nelson, Compilation of longshore current data, U. S. Army Coastal Engr. Res. Center Misc. Paper 2-67, 1-19, 1967.

Galvin, C. J. and W. N. Seelig, Surf on U. S. coastline, Unpublished Laboratory Report, CERC, 1-12, 1969.

Galvin, C. J., L. W. Tenney, and W. N. Seelig, Differences between coastal and offshore wave climates (abstract), Trans. Am. Geophys. Union, 51, 322, 1970.

Harrison, W., A time series from the beach environment, ESSA Research Laboratories Tech. Mem. - AOL 1, 1-28, 1968.

Herron, W. J., and R. L. Harris, Littoral Bypassing and beach restoration in the vicinity of Port Hueneme, California, Proc. Tenth Conf. Coastal Engr., 651-675, ASCE, 1966.

Iverson, H. W., Waves and breakers in shoaling water, Proc. Third Conf. Coastal Engr., 1-12, Council on Wave Research, Richmond, Calif., 1953.

Johnson, J. W., the littoral drift problem at shoreline harbors, J. Waterways Harbors Div., 83 , Am. Soc. Civil Engrs., 1211-37, 1957.

Kalkanis, G., Transportation of bed material due to wave action, U. S. Army Coastal Engr. Res. Center Tech. Mem. 2, 1-38, 1964.

Komar, P. D., The longshore transport of sand on beaches, doctoral thesis, Univ. of Cal. at San Diego, 1969.

Komar, P. D., and D. L. Inman, Longshore transport on beaches, J. Geophys Res., 75, 5914-5927, 1970.

Longuet-Higgins, M. S., Longshore currents generated by obliquely incident sea waves, 1, J. Geophys. Res., 75, 6778-6789, 1970.

Moore, G. W., and A. Y. Cole, Coastal processes vicinity of Cape Thompson, Alaska, in geologic investigations of Cape Thompson, NW Alaska - Preliminary Report USCS Trace Element Investigation, Report 753, 1960.

Savage, R. P., Laboratory determination of littoral transport-rates, J. Waterways Harbors Div., Am. Soc. Civil Engrs., 88, 69-92, 1962.

Saville, T., Model study of sand transport along an infinitely long straight beach, Trans. Am. Geophys. Union, 31,555-565, 1950.

Saville, T., Wave and lake level statistics for Lake Erie, U. S. Army Beach Erosion Board Tech. Mem. 37, 1-14, 1953a.

Saville, T., Wave and lake level statistics for Lake Michigan, U. S. Army Beach Erosion Board Tech. Mem. 36, 1-23, 1953b.

Scripps Institution of Oceanography, A statistical study of wave conditions at five open sea localities along the California coast, S. I. O. Wave Report 68, 1-34, 1947.

Szuwalski, A., Littoral environment observation program in California preliminary report February-December 1968, U. S. Army Coastal Engr. Res. Center Misc. Paper 2-70, 1-14, 1970.

Taney, N. E., Geomorphology of the south shore of Long Island, New York, U. S. Army Beach Erosion Board Tech. Mem. 128, 1-50, 1961.

Thornton, E. B., Longshore current and sediment transport, Dept. of Coastal and Ocean Engr. Tech. Report 5, Col. of Engr., U. of Fla., 1-171, 1969.

U. S. Army Corps of Engineers, Jacksonville District, Cooperative study of the Gulf of Mexico shoreline of Pinellas County, Florida, Corps of Engineers, 1-67, 1957.

U. S. Army Corps of Engineers, Los Angeles District, Harbor and shore protection in the vicinity of Port Hueneme, California, Corps of Engieners, 1-71, 1948.

U. S. Army Corps of Engineers, Wilmington District, Investigation of erosion Carolina Beach, N. C., Corps of Engineers, 1-69, 1970.

Watts, C. M., Development and field tests of a sampler for suspended sediment in wave action, U. S. Army Beach Erosion Board Tech. Mem. 34, 1-41, 1953a.

Watts, C. M., A study of sand movement at South Lake Worth Inlet, Florida, U. S. Army Beach Erosion Board Tech. Mem. 42, 1-24, 1953b.

CHAPTER 51

TRANSPORT LITTORAL : ESSAIS ET CALCULS

par J.P. LEPETIT[1]

Résumé :

Des essais de transport littoral en cuve à houle ont été effectués avec de la bakélite. L'étude de l'influence d'un épi isolé a permis de montrer une corrélation entre la position du musoir de l'épi par rapport à la distribution du débit solide le long du profil et le débit solide arrêté par l'épi.

Un programme de calcul sur ordinateur permet de déterminer l'évolution de la ligne de rivage d'une côte sableuse sous l'action de diverses houles incidentes. Le calcul, de forme itérative, est basé sur une loi de débit solide déduite des essais en cuve à houle. Il fait intervenir les caractéristiques au rivage des houles de diverses provenances dont la propagation est calculée et diverses hypothèses relatives à l'évolution des profils de la plage en cours de sédimentation ou d'érosion. Le calcul a été appliqué à des cas concrets (ports de Dunkerque et Deauville) et les résultats obtenus dans le cas d'action d'un épi isolé ont été comparés à ceux des essais en cuve à houle.

1 - GENERALITES

L'étude du transport littoral, en cours au Laboratoire National d'Hydraulique de Chatou, a deux buts :

- analyser le mécanisme de transport des sédiments le long d'une plage en houle oblique, et déterminer une loi de débit charrié en fonction des paramètres : angle d'incidence, période de la houle, densité et diamètre du sédiment ;

(1) Docteur-Ingénieur Chercheur au Laboratoire National d'Hydraulique - Chatou (France).

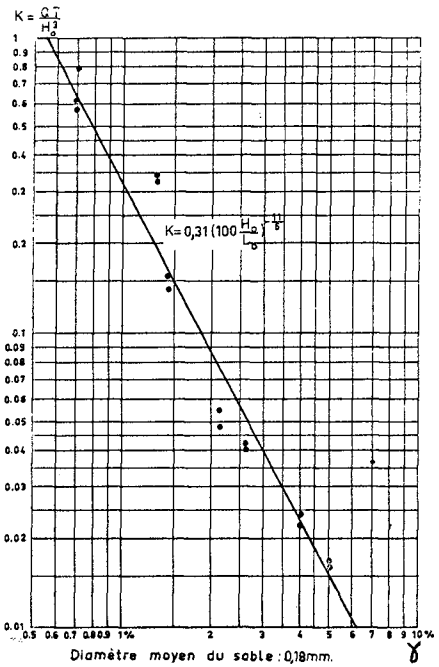

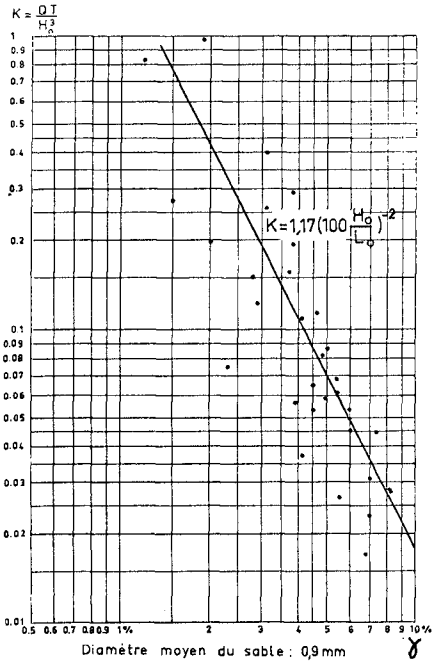

VARIATION DU COEFFICIENT K EN FONCTION DE γ

$$Q = K(\gamma, D)\frac{H^3}{T} f(\alpha)$$

Fig.1 - SABLE -

LOI DE DEBIT SOLIDE

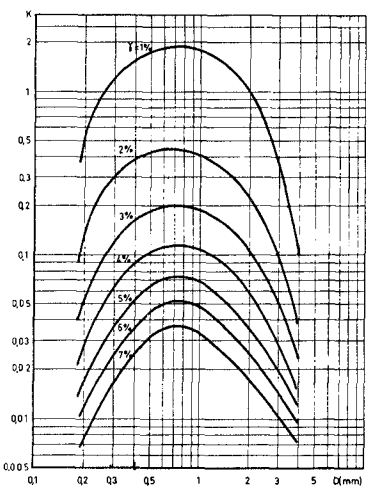

VARIATION DE K EN FONCTION DE γ ET D

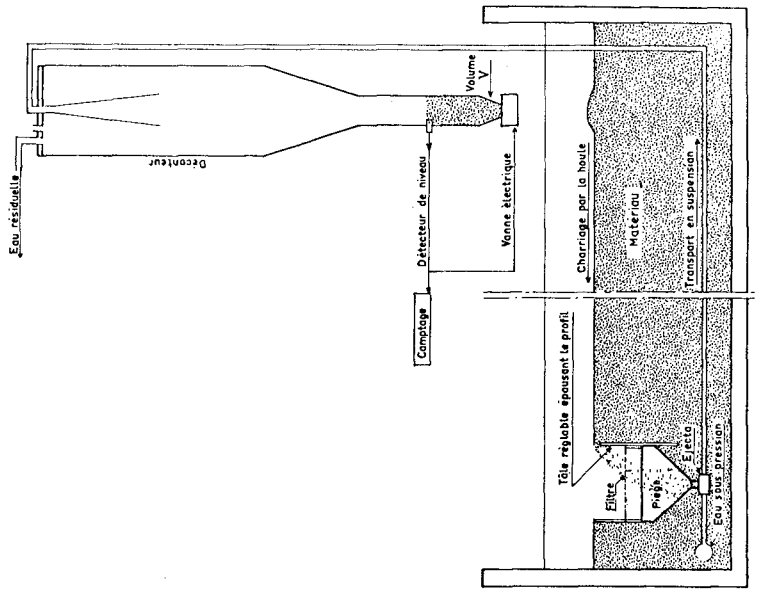

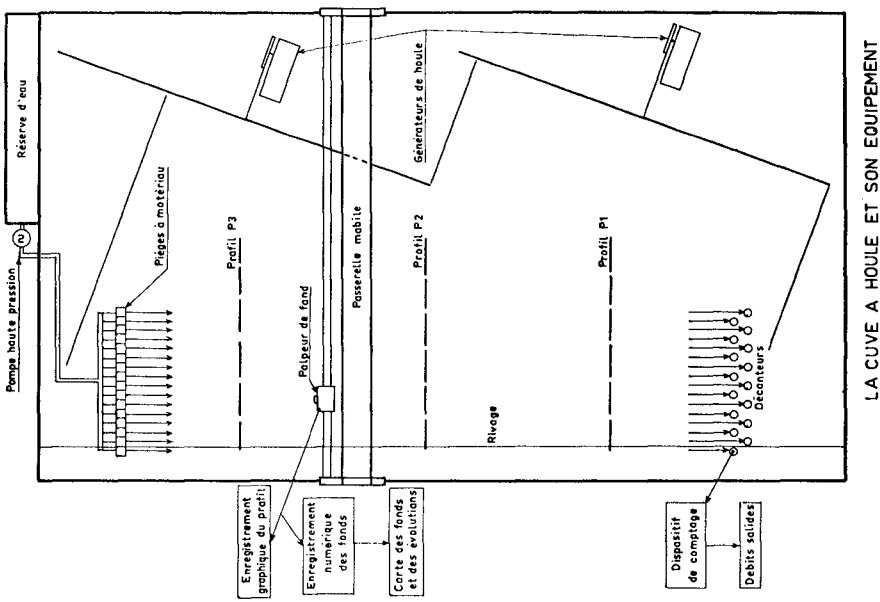

Fig.2 - DISPOSITIF EXPERIMENTAL

- élaborer ou améliorer des méthodes d'étude de problèmes posés par le transport littoral, soit sur modèle réduit physique, soit par calcul sur ordinateur.

Une précédente série d'essais avec du sable a permis d'établir une loi de débit charrié de la forme :

$$Q = \frac{H^3}{T}\, k(\gamma,D)\, f(\alpha) \qquad \text{avec} \qquad \begin{cases} T,L,H & \text{période, longueur d'onde et creux de la houle} \\ \gamma = \frac{H}{L}, D & \text{cambrure de la houle et diamètre du sable} \\ f(\alpha) & \text{fonction de l'angle d'incidence de la houle (par ex. } \sin\alpha\sqrt{\cos\alpha}) \end{cases}$$

$\frac{H^3}{T}$ représente l'énergie de la houle considérée comme une succession d'ondes solitaires. La fonction $k(\gamma,D)$ décroît lorsque γ croît, et passe par un maximum vers $D \approx 0{,}8$ mm (fig. 1).

Cette formule, extrapolée à la nature, donne des résultats d'un ordre de grandeur comparable à certaines mesures in situ.

2 - ESSAIS EN CUVE A HOULE

2.1. La cuve à houle :

Les études expérimentales sont faites dans une cuve à houle de 30 x 15 m dotée des équipements suivants (fig. 2) :

- deux générateurs de houle synchronisés, orientables et réglables en période et creux ;
- une rangée de 16 pièges (de 25 cm chacun, disposés à l'aval de la cuve perpendiculairement au rivage) captant le débit solide charrié près du fond en différents points du profil de la plage ;
- des circuits de reprise et de transport hydraulique vers l'amont des sédiments piégés ;
- une rangée de 16 décanteurs disposés à l'amont de la cuve (chacun étant à une distance du rivage égale à celle du piège qui lui correspond) réinjectant le matériau capté à l'aval ;

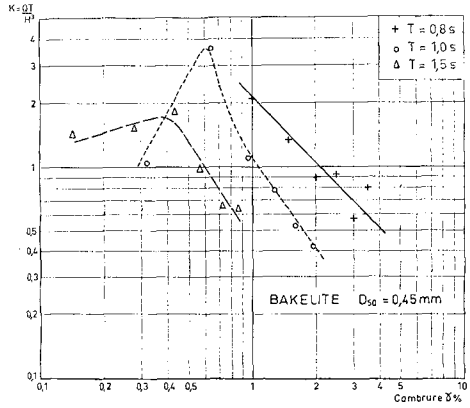

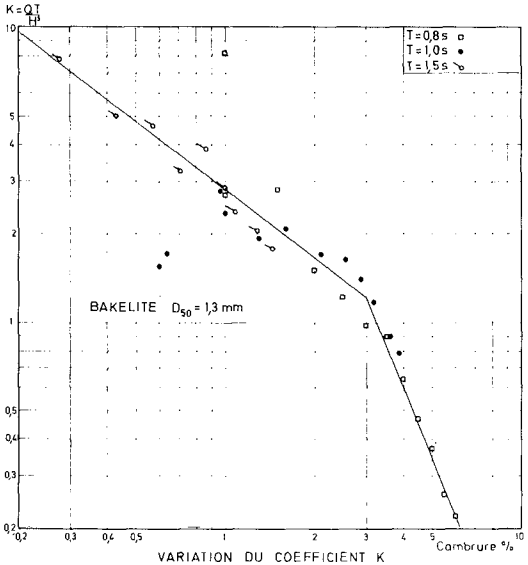

VARIATION DU COEFFICIENT K
EN FONCTION DE LA CAMBRURE

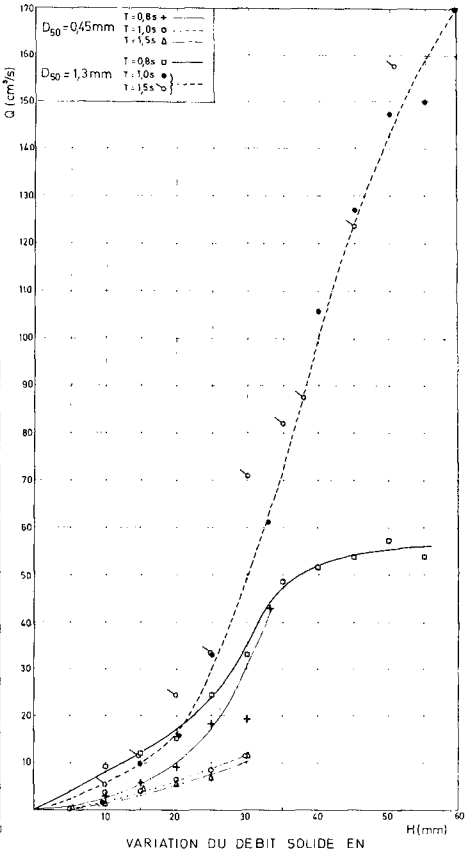

VARIATION DU DEBIT SOLIDE EN
FONCTION DU CREUX DE LA HOULE

Fig 3 - BAKELITE - RESULTATS EXPERIMENTAUX

- un système de mesure du débit solide transitant dans chaque décanteur (compage de volumes élémentaires avec ouverture automatique de vannes fermant le décanteur) ;
- une passerelle de mesure portant un "palpeur de fond", appareil mesurant la profondeur à l'aide d'une sonde mécanique asservie électroniquement à partir de la différence de conductivité du matériau par rapport à l'eau.

Le système de pièges, décanteurs et de comptage de volumes élémentaires permet d'assurer le recyclage du débit solide entre l'aval et l'amont de la cuve (simulant ainsi une plage infinie) et la mesure de sa valeur et de sa répartition le long du profil de la plage.

Le palpeur de fond fournit le tracé automatique du profil de la plage ou, par enregistrement numérique d'un ensemble de profils et traitement sur ordinateur, le tracé automatique d'une carte bathymétrique de la plage (ex. fig. 5) et le calcul de volumes déposés et érodés.

2.2. Plage libre :

Les essais concernent actuellement l'étude de matériaux légers en vue de leur utilisation en modèle réduit et d'une généralisation de la loi de débit solide.

Les mesures portent sur les profils d'équilibre, le débit charrié et sa répartition le long du profil de la plage. Chaque essai est poursuivi (pendant 15 à 40 heures) jusqu'à obtention d'une stabilité satisfaisante du profil et du débit solide.

Les premiers essais ont concerné la bakélite (densité 1,4) de diamètre D = 0,45 et 1,3 mm (fig. 3). Les débits solides mesurés se groupent bien suivant une loi semblable à celle du sable pour D = 1,3 mm. Par contre pour D = 0,45 mm, les points se dispersent en fonction de la période, ce qui laisse supposer un mode d'action différent de la houle sur les grains fins et légers. Les essais se poursuivent avec un diamètre de 0,8 mm qui permettra de préciser cette influence.

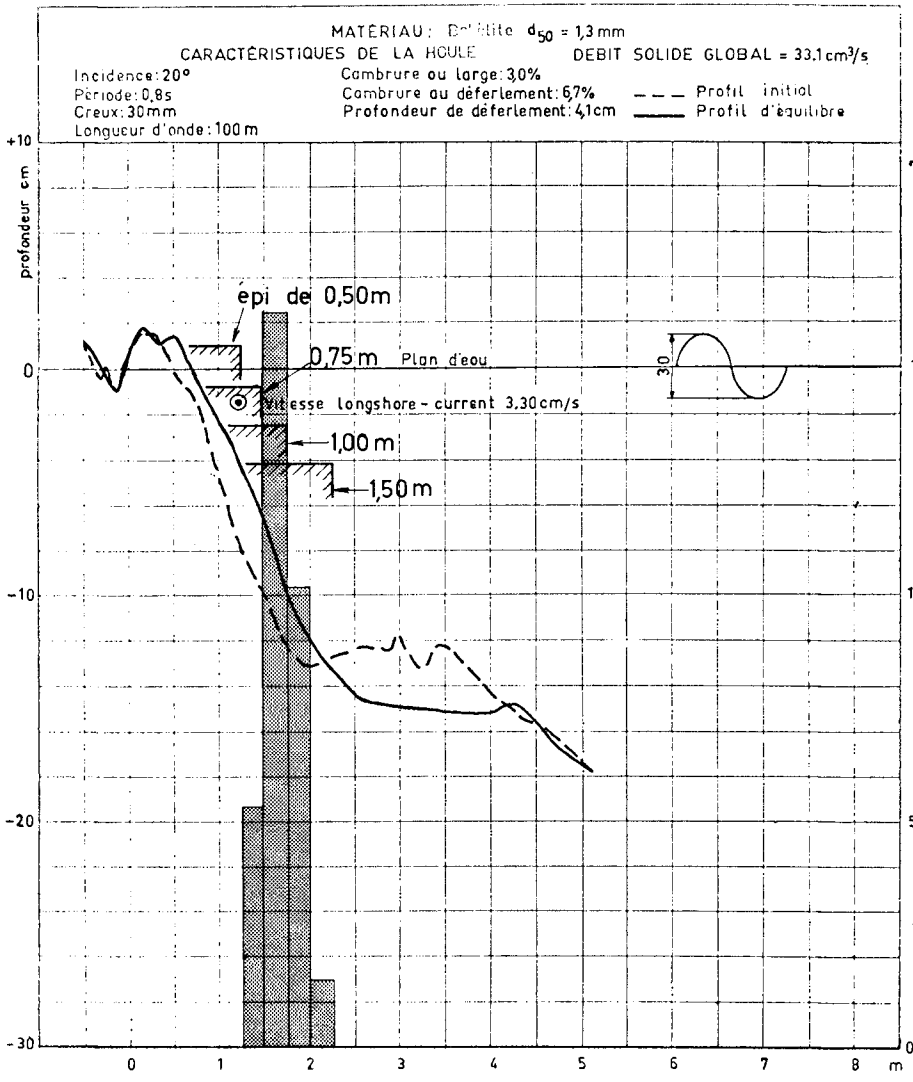

Fig. 4 _ ETUDE D'UN EPI ISOLE

PROFIL DE LA PLAGE ET HISTOGRAMME DE DEBIT SOLIDE

Les résultats obtenus ont permis d'effectuer avec succès deux études de plage (Dunkerque et Capbreton) en modèle réduit. La distorsion des échelles a été choisie en fonction des profils d'équilibre relevés en cuve à houle, et les débits solides mesurés ont constitué une bonne base de détermination de l'échelle des temps sédimentologique.

2.3. Plage avec épi :

L'étude d'un épi isolé a pour but de déterminer son influence sur la plage, de mesurer le débit solide arrêté par l'épi en fonction de sa longueur et de le relier à la distribution de débit le long du profil de la plage, mesurée en plage libre. Les essais ont été réalisés sur une plage en bakélite de 1,3 mm de diamètre, sur un profil sans barre et sur un profil avec barre.

Sur le profil sans barre (la figure 4 montre le profil de la plage, l'histogramme de débit solide et les positions du musoir de l'épi par rapport à celui-ci), le débit solide arrêté par l'épi (mesuré par cubature des dépôts et érosions de part et d'autre) est sensiblement égal à celui transitant normalement entre le musoir de l'épi et le rivage, débit qui peut être déterminé à partir de la répartition de débit le long du profil : le tableau 1 compare le coefficient de perméabilité de l'épi (rapport du débit solide qui laisse passer l'épi au débit solide total existant sur la plage libre) mesuré, à celui déduit de l'histogramme de débit solide en sommant la fraction de débit transitant normalement au-delà du musoir de l'épi.

Le profil de plage au voisinage de l'épi est différent de celui en plage libre : il est plus accore à l'amont dans la zone de dépôt et moins accore à l'aval dans la zone d'érosion (fig. 5).

Sur le profil avec barre il n'a pas été possible de chiffrer le débit arrêté, l'épi provoquant d'importants déplacements de matériau perpendiculaires au rivage. L'effet de l'épi est lié à la position de son musoir par rapport à la barre ; il est très faible si l'épi n'atteint pas la barre et s'il la dépasse nettement, la barre disparaît à l'aval et augmente à l'amont (fig. 5).

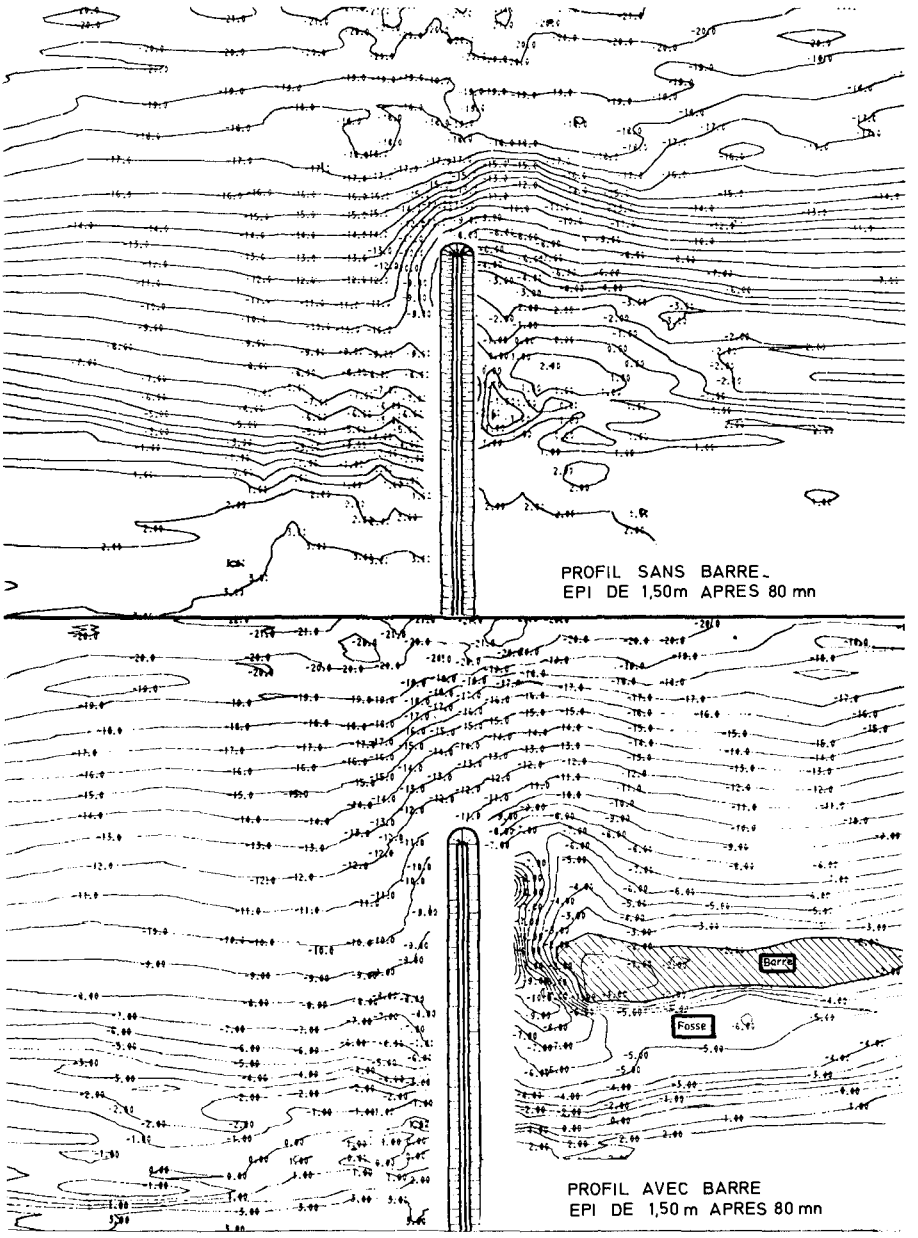

Fig. 5 - ETUDE D'UN EPI ISOLE - EXEMPLES DE LEVES

Longueur de l'épi (m)	Temps (m)	Débit solide aux limites (cm^3/s)	Volumes (dm^3)		Coefficient de perméabilité	
			Sédimentation amont	Erosion aval	mesuré	déduit de l'histogramme de débit solide
0,50	0 - 40 40 - 80	42 40	néant	néant	1	1
0,75	0 - 40 40 - 80 80 -120	39 37 38	12 ε ε	18 ε ε	0,8 # 1 # 1	0,84
1,00	0 - 40 40 - 80 80 -120	37 32 38	60 48 ×	65 44 ×	0,23 0,42 ×	0,37
1,50	0 - 40 40 - 80 80 -120	38 40 39	65 80 ×	90 60 ×	ε 0,1 ×	0

ε quantité faible non mesurable

× mesure inexistante (levé entâché d'erreur)

Tableau 1 : Coefficient de perméabilité d'un épi sur un profil sans barre.

3 - CALCULS SUR ORDINATEUR

3.1. Méthode (fig. 6)

La formule de débit charrié est utilisée dans un calcul sur ordinateur donnant l'évolution du rivage à partir d'un état initial donné et connaissant les diverses houles incidentes. Les principales hypothèses faites sont les suivantes :

- la loi de débit solide, établie en régime uniforme, est valable en chaque point du rivage en régime non uniforme ;

- les profils en travers de la plage gardent la même forme et subissent une translation horizontale en cas de sédimentation ou d'érosion ;

- aux limites de l'emprise du calcul le rivage garde une position ou une orientation fixe.

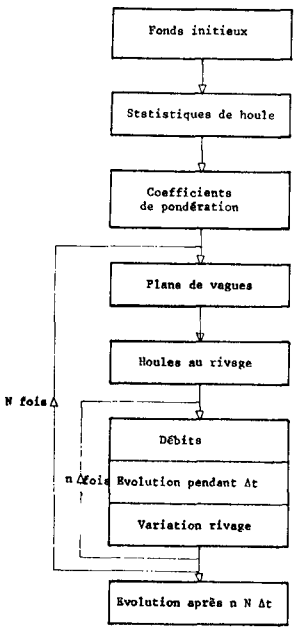

ORGANIGRAMME DE PRINCIPE

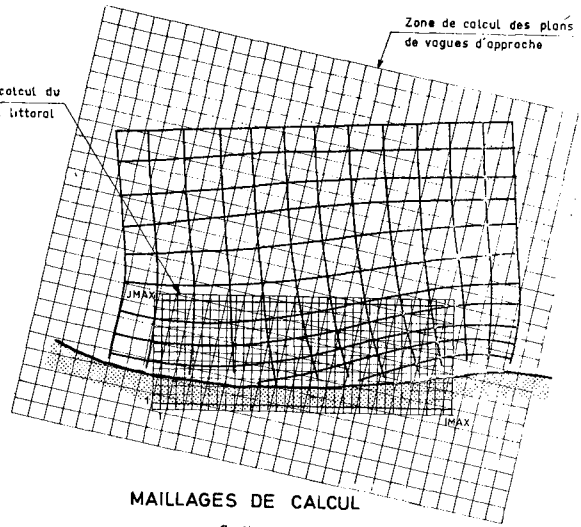

MAILLAGES DE CALCUL

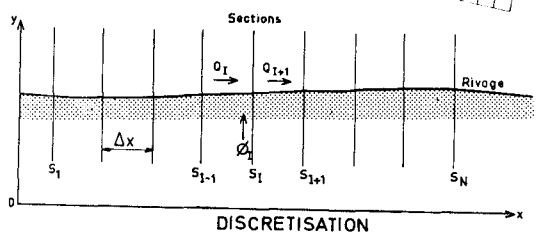

DISCRETISATION

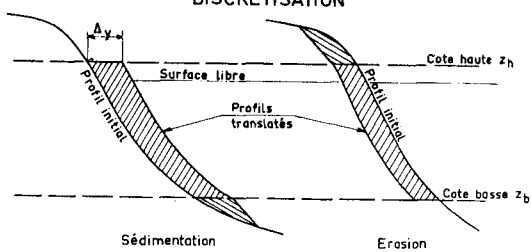

EVOLUTION DES PROFILS

$$\frac{\partial s}{\partial t} = \emptyset - \frac{\partial Q}{\partial x}$$

$$Q = \frac{H^3}{T} K(\gamma, D) f(\alpha)$$

EQUATIONS

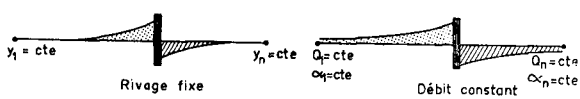

CONDITIONS AUX LIMITES

Fig. 6 - PRINCIPE DU MODELE MATHEMATIQUE

Les caractéristiques de houle au rivage (creux, cambrure, angle d'incidence) sont déterminées (par le calcul de plans de réfraction) pour diverses provenances et périodes de houle représentatives du site considéré, ce qui permet de calculer, en chaque point du rivage, le débit solide dû à chacune des houles, et par sommation algébrique pondérée par leurs fréquences respectives, le débit solide résultant.

L'équation de continuité, qui s'écrit :

$$\frac{\partial Q}{\partial x} + \frac{\partial S}{\partial t} - \emptyset = 0 \quad \text{avec} \quad \begin{cases} \frac{\partial Q}{\partial x} & \text{gradient de débit solide} \\ S & \text{aire solide de la section en travers du rivage} \\ \emptyset & \text{apport extérieur par unité de longueur du rivage,} \end{cases}$$

permet d'en déduire la variation des aires S en fonction du temps et donc, par translation des profils, les modifications de la ligne de rivage.

Pratiquement, le calcul est discrétisé dans l'espace et dans le temps avec une itération à deux niveaux permettant de faire varier progressivement le débit solide en fonction des modifications du rivage et, avec une fréquence moindre, les conditions d'approche de la houle.

L'action d'obstacles naturels ou artificiels (épis par exemple) est schématisée par l'introduction d'un coefficient de perméabilité égal au rapport du débit solide qui laisse passer l'ouvrage à celui qui existerait sur la plage libre.

Le calcul a été appliqué à deux cas concrets : études de la stabilité d'une plage artificielle à Dunkerque et de l'influence d'un port de plaisance à Deauville.

3.2. Application au cas d'un épi isolé (fig. 7) :

L'épi isolé sur une plage sans barre étudié en cuve à houle, a été introduit dans le calcul avec un coefficient de perméabilité déduit de la distribution de débit solide mesurée. Le calcul donne des résultats

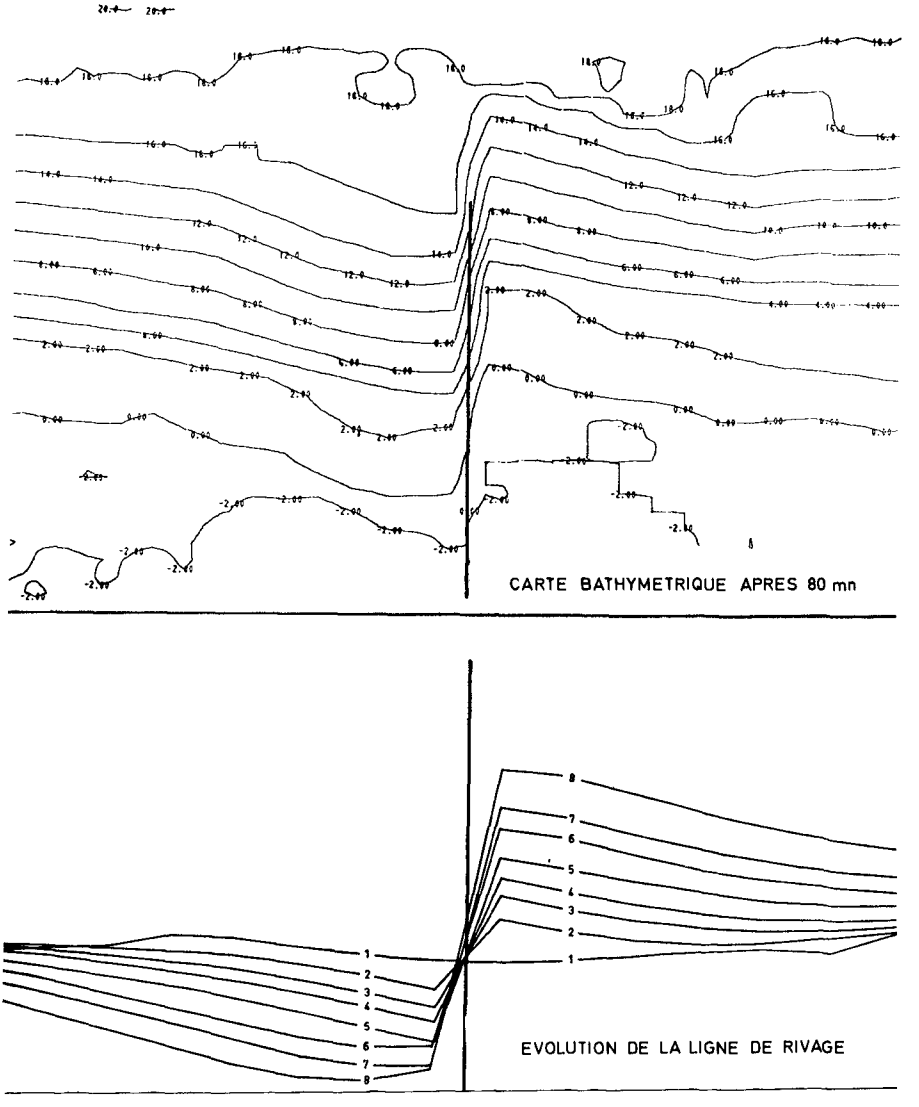

Fig.7_ EXEMPLES DE RESULTATS DU CALCUL_
CAS D'UN EPI DE 1,50m

(volumes de dépôt, d'érosion et recul du rivage près de l'épi) d'un ordre de grandeur comparable à celui de l'expérience (tableau 2) avec cependant deux différences importantes :

- le recul du haut de plage à l'aval de l'épi est moins important que dans la cuve, l'adoucissement du profil n'étant pas introduit dans le calcul (et inversement à l'amont) ;

- le contournement de l'épi après un certain temps n'est pas pris en compte dans le calcul (si l'on garde le même coefficient de perméabilité).

Longueur de l'épi (m)	Temps (m)	Coef. de perméabilité	Volumes (dm^3)				Décrochement des lignes bathymétriques (cm)		
			Sédimentation amont		Erosion aval		Calcul	Expérience	
			Calcul	Expérience	Calcul	Expérience		ligne -4cm	ligne -10cm
1,00	0 - 40	0,20	51	60	41	65	55	55	25
	40- 80	0,40	44	48	29	44	75	60	40
	80-120	0,57	43	-	23	-	90	70	50
1,50	0 - 40	0	53	65	43	90	57	90	60
	40- 80	0	46	80	32	60	80	120	80
	80-120	0	49	-	28	-	95	130	95

Tableau 2 : Epi sur un profil sans barre - Comparaison Calcul-Expérience

4 - CONCLUSION

Les études en cours ont apporté :

- une meilleure connaissance du comportement de la bakélite et de ses possibilités d'utilisation en modèle réduit ;

- un modèle mathématique schématique permettant d'étudier rapidement des cas simples d'évolution du rivage.

Les essais seront poursuivis par l'étude d'autres matériaux légers (par exemple plexiglas) et le modèle mathématique sera perfectionné en introduisant progressivement des variations de profil de plage avec débits solides perpendiculaires au rivage et une prise en compte plus précise des ouvrages.

CHAPTER 52

RATE OF SEDIMENT MOTION USING FLUORESCENT TRACER

Abdel-Latif A.Kadib

Head of the Coastal Engineering Section
Suez Canal Research Centre,Egypt

ABSTRACT

A rational design of coast protection works requires a knowledge of the behaviour of beach under natural conditions. The estimation of the littoral drift rate is thus a necessary preliminary to the analysis of the cause of beach erosion and the evaluation of the effect of projected remedial measures.

This study presents a method for estimating the rate of littoral drift along sandy beaches. The derived method is based on the use of fluorescent tracer, and observing the tracer concentration reaching the different profiles along the study zone, as function of location and time of sampling. Steps followed in estimating the rate of littoral drift, using the derived formula, are included in this paper.

INTRODUCTION

It is a known fact that sand movement along beaches is caused primarily by the action of littoral current systems generated in the swash zone and shoreward of the breaking point by wave breaking at an angle to the beach. Attempts to study beach drifting quantitavely have been relatively few because of the complexity and expense of such study. Studies of this kind required not only the observation of sand movement but also simultaneous recording of the waves, currents and various parameters contributing to the sediment motion. Research and study into problems of sand drifting followed three principle lines :

1. Studies of erosion or accretion in the vicinity of littoral barriers.
2. Model studies of the behaviour of artificial beaches in laboratory wave tanks.
3. Tracer studies of the movement of marked particles on natural beaches.

The first method of using erosion-accretion studies have been the most successful in producing quantitative data in the past. The method necessitates periodical surveying of the area and continuous recording of the different wave and current parameters.

Model studies have determined many useful details about the mechanism of sediment transport, but because of the difficulties of assessing the influence of scale effect and of reproducing the complex pattern of waves, currents and sediment particles, this technique can reveal little about the rate of sediment movement at a given area. Studies of sediment transport using fluorescent tracer have been conducted by many investigators (1,2,3,4)(*). Most of these studies are concerned with the attempt to advice a simple, unexpensive technique for marking sand and gravel with fluoresoent dye while very few studies (2) have used tracers in estimating rates of littoral drift.

The present study is an attempt to develop a simple method for estimating the rate of littoral drift along eroding beaches using fluorescent tracer technique. The method was tried for Ras-El-Bar eroding beach along the Northern Coast of Egypt. Both the rate and direction of sediment motion at different points along the beach were estimated.

THEORETICAL CONSIDERATIONS

Consider a mobile bed over which the average intensity of sediment discharge Q, varies from one section to the other along the bed. The value of Q can be determined by injecting a known quantity of tracer sediment, at a reasonable rate, and then observing the surface tracer concentration along different lines normal to the flow direction. Tracer sampling should continue from the time the tracer starts to reach a given sampling line till its complete disappearance from the study reach.

Before dealing with the mathematical derivations of the sediment equation, it may be useful to illustrate the different variables and elements relevant to these derivations, as given in Figure (1), where :

Q = average rate of littoral drift per unit width at any distance X from the injection point.

q = average rate of tracer per unit width reaching any sampling section at any distance X from the injection point.

C = concentration by weight of tracer in the sediment at any sampling point.

dy = length of a typical element of any sampling line.

L = length of any sampling line along which tracer is found.

(*) For referenoes see page 19 please.

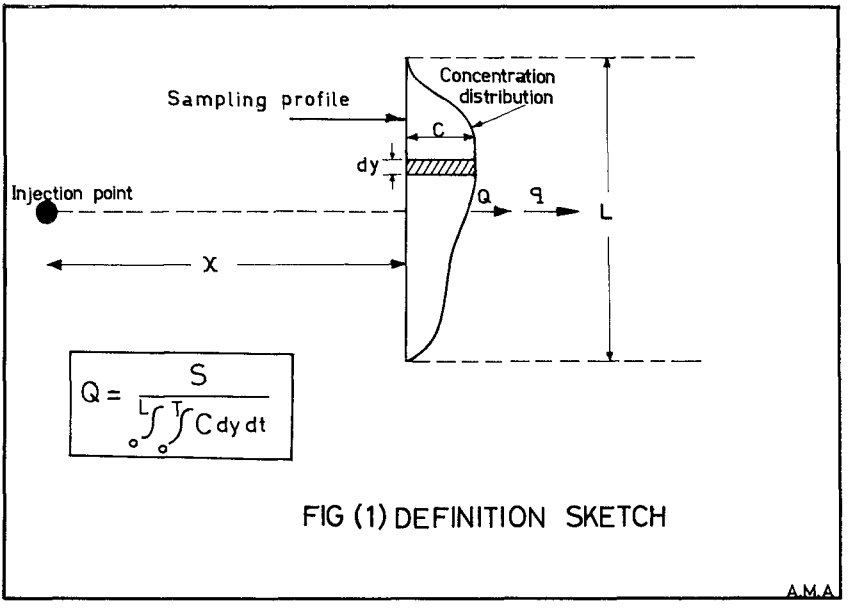

FIG (1) DEFINITION SKETCH

A.M.A

Now, by definition :

$$C = \frac{q}{Q} \quad \ldots\ldots\ldots\ldots\ldots\ldots\ldots\ldots\ldots\ldots\ldots\ldots\ldots\ldots \quad (1)$$

$$\text{or} \quad q = C\,Q \quad \ldots\ldots\ldots\ldots\ldots\ldots\ldots\ldots\ldots\ldots\ldots\ldots\ldots\ldots \quad (2)$$

At any time, t , the amount of tracer, ds , contained in any sampling section may be calculated as follows :

$$ds = \int_0^L q \; dy \quad \ldots\ldots\ldots\ldots\ldots\ldots\ldots\ldots\ldots\ldots\ldots\ldots\ldots\ldots \quad (3)$$

$$\text{or} \quad ds = \int_0^L C\,Q \; dy \quad \ldots\ldots\ldots\ldots\ldots\ldots\ldots\ldots\ldots\ldots\ldots\ldots\ldots\ldots \quad (4)$$

Now, the total amount of tracer S_x , which passes any sampling section during any period, T , may be written as :

$$S_x = \int_0^L \int_0^T C \; Q \; dy \; dt \quad \ldots\ldots\ldots\ldots\ldots\ldots\ldots\ldots\ldots\ldots\ldots\ldots\ldots\ldots \quad (5)$$

where, T is the time between the first arrival of tracer to any sampling section and its complete disappearance.

Equation (5) may be written as :

$$S_x = Q \int_0^L \int_0^T C \; dy \; dt \quad \ldots\ldots\ldots\ldots\ldots\ldots\ldots\ldots \quad (6)$$

and hence the average rate of littoral drift Q may be calculated as :

$$Q = \frac{S_x}{\int_0^L \int_0^T C \; dy \; dt} \quad \ldots\ldots\ldots\ldots\ldots\ldots\ldots\ldots \quad (7)$$

The use of equation 7 should be governed by the following conditions :

1. If the littoral drift has a unique direction all over the study period, then S_x should equal to the total amount of tracer sand, S, used for injection.

2. If the littoral drift has a minor direction for a small percentage of time, then one gets :

   (a) the value of S_x will be less than S by the amount moved to the opposite direction. Therefore, if one uses $S_x = S$, over estimation of the littoral drift rate will be obtained if one uses equation 7.

   (b) due to the double passage of the tracer sand over any sampling section, the value of $\int_0^L \int_0^T C \; dy \; dt$ in Equation 7 will be increased by the same order of magnitude mentioned before. Therefore, as one uses the measured values of $\int_0^L \int_0^T C \; dy \; dt$ there will be a possibility of underestimating the littoral drift rate by almost the same order of magnitude of the overestimation due to the use of $S = S_x$.

   (c) from (a) and (b) it may be concluded that for beaches where the littoral drift has a major direction, not less than 80% of the time, using $S = S_x$ in Equation 7 will give a reasonable estimate of the littoral drift rate along that beach.

   The use of Equation 7 requires the following conditions :

   1. Littoral drift should have a major direction.

   2. Sampling lines should not be far from injection.

   3. Sampling should cover the entire distance from the shore line to any depth seawards where tracer could be found.

   4. Sampling should continue till all tracer disappears from the study area.

APPLICATION OF THE DERIVED METHOD FOR THE STUDY OF LITTORAL DRIFT ALONG RAS-EL-BAR, EGYPT.

The field work reported in this paper was carried out[6] at Ras-El-Bar beach, Egypt, and as shown in Figures (2) and (3). This study was made during the period October-February 1969. The beach consists of fine sand, 0.12 mm average grain size, and 1.2 sorting coefficient. Fig.(4) shows the grain size distribution of the beach sand. Wave attacks the study area from the west, NW and NNW directions[5]. The fluoreecent tracer sand used in this etudy is Rhodamine B which gives fluoresce red under ultra-violet light. Fig. (4) shows the mechanical analyeis of the tracer sand used which have almost the same characteristics as the natural sand at Ras-El-Bar.

1. Location of the study area and injection point.

The general location of the study area is usually choeen by some epecific local sediment problems. In Ras-El-Bar case, and from Fig.(3) it can be noticed that erosion predominatee to the western side of the jetty for a distance of 4.00 kilometers, and shoaling inside the Damietta estuary is in progress. Fig.(5) shows the reach of Ras-El-Bar shore line chosen for this study. This reach extends for a distance of 8 kilometers west of the jetty and for more than one kilometer east of Damietta estuary. Injection was made at a point 3.25 kilometers west of the jetty where the shore line is straight and wave disturbance is the least compared with the other parte of the shore line.

2. Injection and Sampling.

Fig.(5) shows the general plan for the injection and sampling locations where the following steps were considered :

(1) injection point was chosen at a distance of 20 meters from the shore line. It was decided to use injection at a point instead of injection along a line in order to eliminate possible losses of tracer to deeper water.

(2) a total amount of 1050 kilogrammes of tracer were injected at a rate of 50 kilogrammes/2 days.

(3) sampling period of 2 daye was chosen and eampling start from the first arrival of tracer to the sampling and continued till all fluorescent particles disappeared from the study area.

(4) sand samples were taken for analyeis from the uppermost two centimeters of the bed with a straight sided can ehape.

(5) each eample was kept inside a nylon eac and was identified by its location and eampling date and was eent to the laboratory for ooncentration analysis.

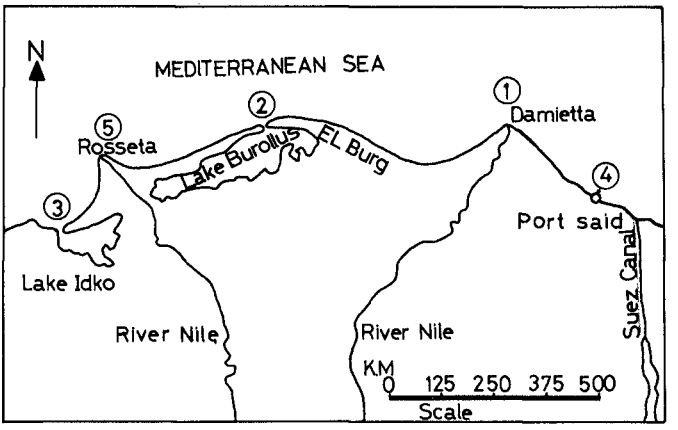

FIG(2) GENERAL MAP OF PROBLEM REGIONS ALONG THE EGYPTION COAST

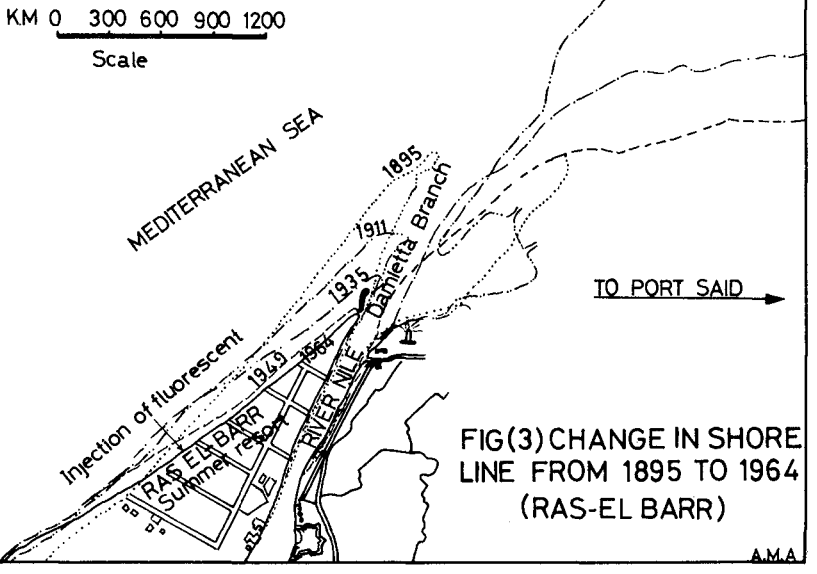

FIG(3) CHANGE IN SHORE LINE FROM 1895 TO 1964 (RAS-EL BARR)

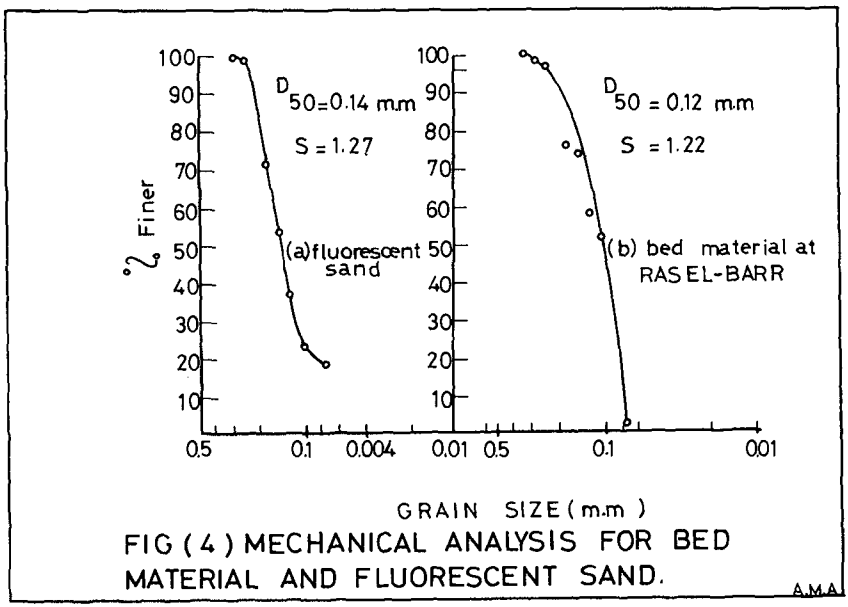

FIG (4) MECHANICAL ANALYSIS FOR BED MATERIAL AND FLUORESCENT SAND.

A.M.A

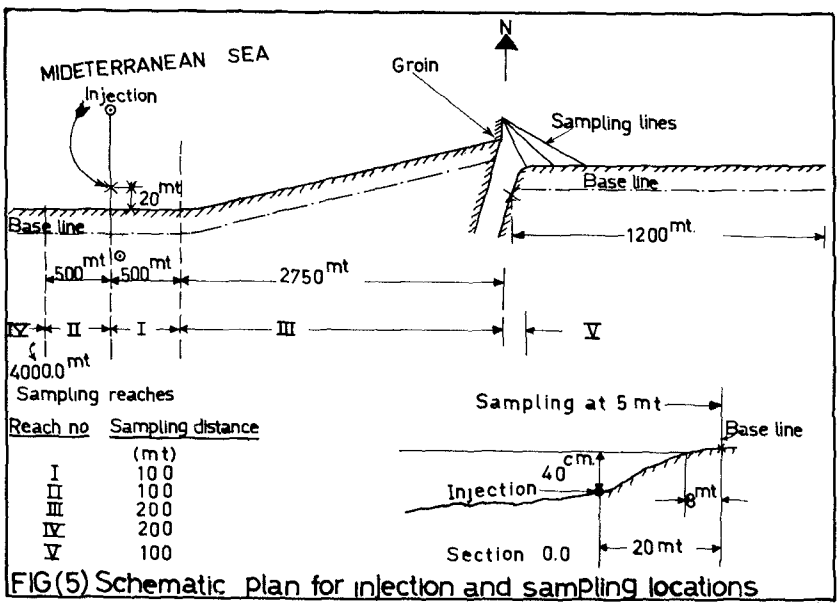

FIG(5) Schematic plan for injection and sampling locations

A.M.A

3. Methods of fluorescent particles counting and concentration.

A specially designed dark box with two ultra violet lamps was used to measure the tracer concentration in each sample, as follows :

(1) Each sample was spread out in a layer of at least one centimeter thick over a plate 100 cm^2 surface area.

(2) The number of visible tracer particles on the surface of each sample was counted and converted into concentration.

In order to convert figures expressed as number of visible particles per 100 cm^2 into concentration, a calibration experiment was carried out as follows :

(1) Tracer and beach sand were mixed in different known concentrations.

(2) For each concentration, the number of visible particles/100 cm^2 were counted using ultra violet lamp.

(3) Each mixing and counting was carried out fifty times for each concentration, and the counts averaged.

(4) The best straight line through the average points was drawn and represented by the equation :

$$C = n \times 10^{-5} \quad \ldots\ldots\ldots\ldots\ldots\ldots\ldots\ldots\ldots\ldots \quad (8)$$

where, C = tracer concentration by weight and n = number of visible particles/100 cm^2 surface area.

4. Littoral current observation.

Both the direction and intensity of the littoral current were observed at ten different locations along the study area. Figure 6 shows the average results obtained from the littoral current measurements. From Fig. 6 it can be seen that there is a decided majority of currents towards the NE direction with 80% probability of motion towards that direction.

EXPERIMENTAL RESULTS AND ANALYSIS OF DATA

1. Direction of littoral drift.

Before each injection, sampling for tracer concentration was carried out. During the early stages of the study, sampling did not cover the whole area shown in Fig. 5, but starts at small distances from both sides of the injection point and then were increased latter on to cover the whole area, shown in Fig. 5 as the tracer advanced in these areas. Fig. 7 shows the average tracer concentration along the different sampling line and during the injection period. It is clear from Fig. 7 that the majority of tracer moved to the NE direction during the injection period. It should be noticed that, after the last injection was made, sampling continued till all the tracer partioles disappeared from the study area. Fig. 8 shows the distribution of tracer along the

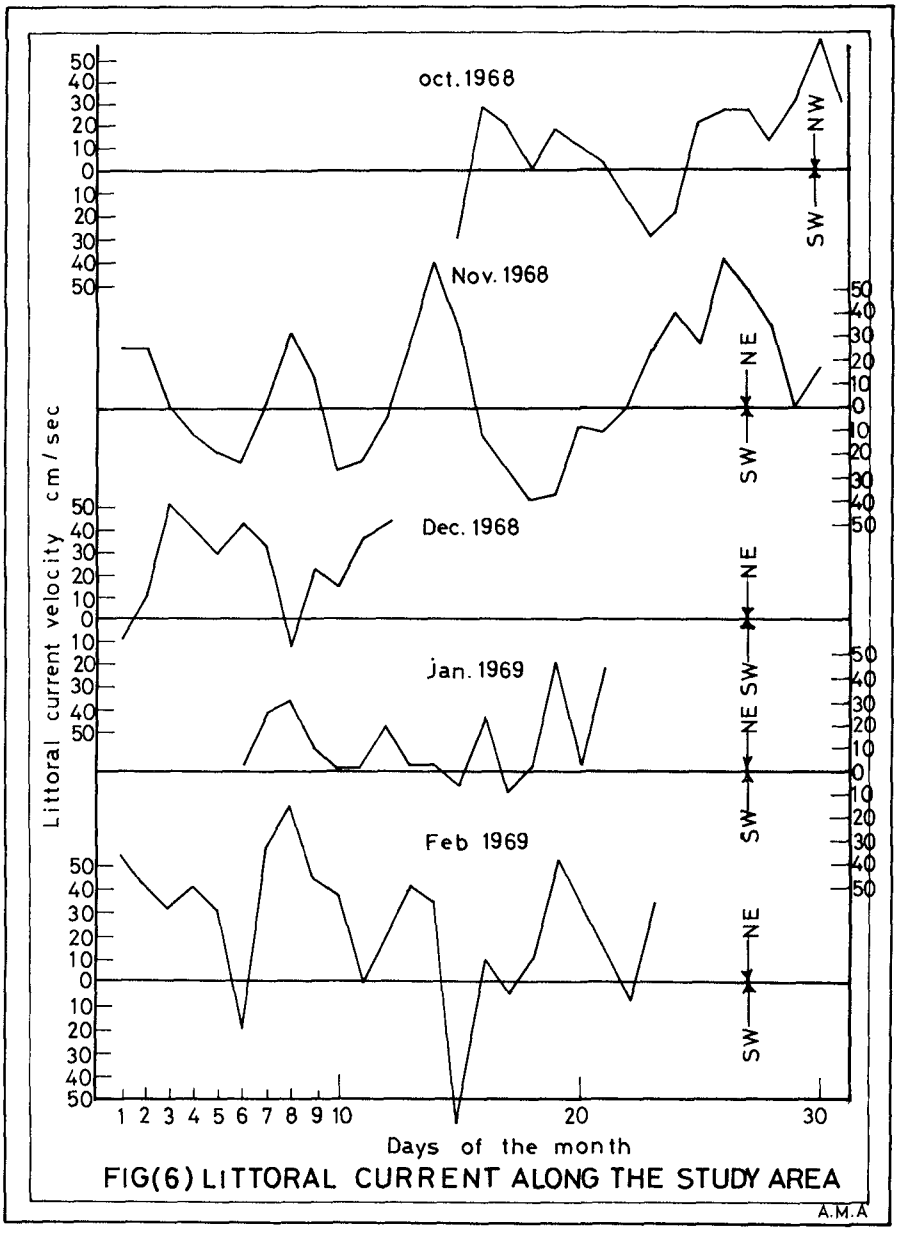

FIG(6) LITTORAL CURRENT ALONG THE STUDY AREA

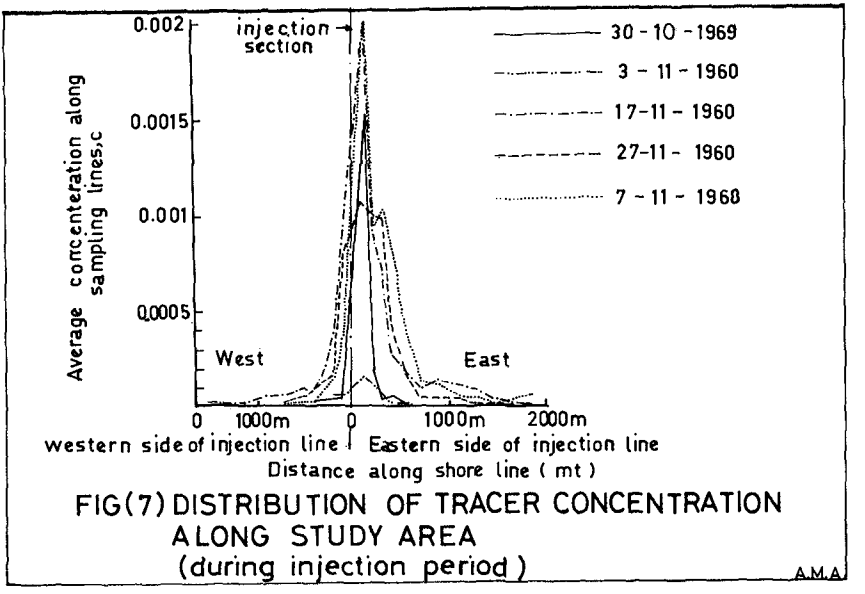

FIG(7) DISTRIBUTION OF TRACER CONCENTRATION ALONG STUDY AREA (during injection period)

A.M.A

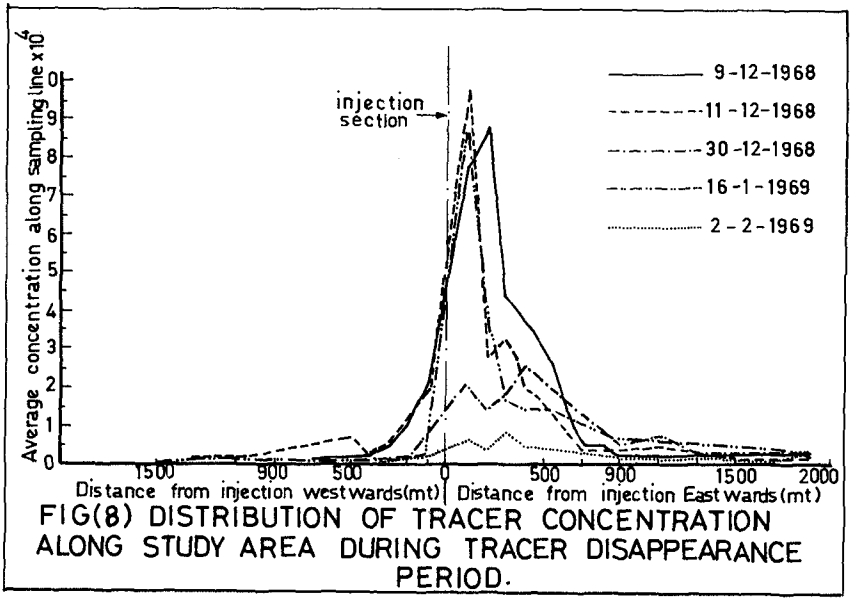

FIG(8) DISTRIBUTION OF TRACER CONCENTRATION ALONG STUDY AREA DURING TRACER DISAPPEARANCE PERIOD.

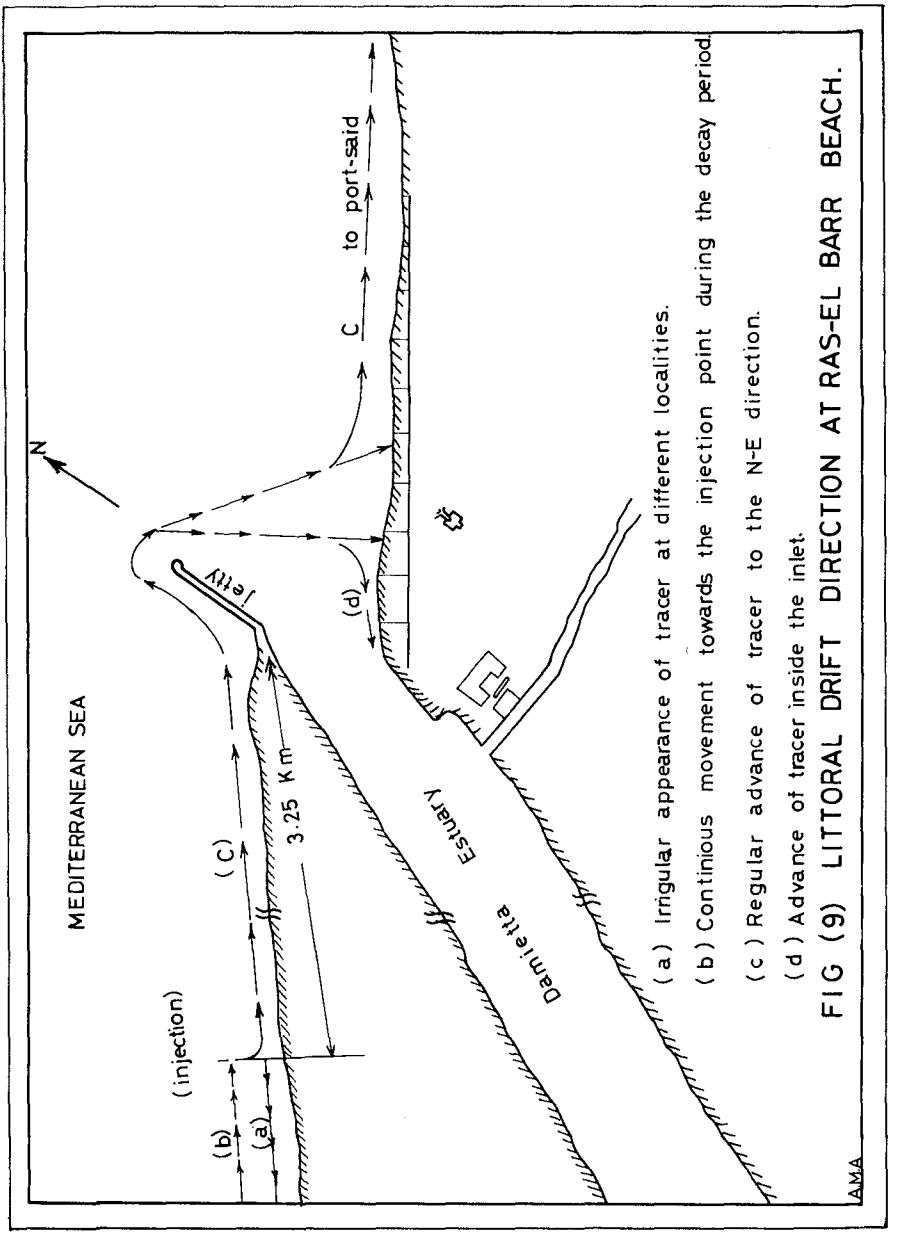

FIG (9) LITTORAL DRIFT DIRECTION AT RAS-EL BARR BEACH.

study reach after the last injection was made and during the period which may be called "tracer disappearance period". It is clear from Fig. 8 that the tracer continued to advance to the NE direction with continuous disappearance from the western side of the injection point. Due to the remarked advance of the tracer to the NE direction, sampling was carried out to the eastern side of the Nile exit and inside the inlet, as shown in Fig. 5. Fig. 9 summarizes the main results obtained on the direction of littoral drift motion at the study area, as follows :

(1) The main direction of littoral drift at Ras-El-Bar is from SW to NE direction.

(2) The littoral drift which moves along Ras-El-Bar beach, turns around the jetty by wave diffraction and proceeds to the eastern side of the exit where it partially deposits inside the inlet and partially moves to the NE direction towards Port Said.

2. Speed of littoral drift advance(Pioneer particles).

Pioneer tracer particles advance was followed along the study area. Both the location and the time from the first injection, for the appearance of those particles were recorded at the different points along the beach. Fig.10 shows the plotting of these data where the following may be concluded :

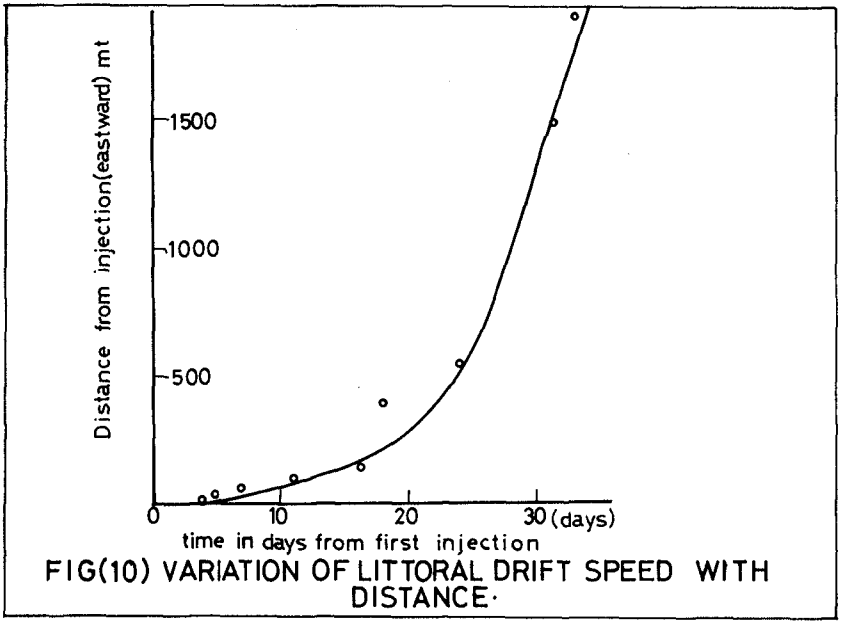

FIG(10) VARIATION OF LITTORAL DRIFT SPEED WITH DISTANCE.

(1) Speed of littoral drift along Ras-El-Bar increases as one moves from the injection point towards the jetty.

(2) For the two kilometers, west of the jetty and where heavy erosion takes place, the littoral drift moves at a speed of about 145 meter/day.

3. Effective zone of littoral movement.

There is no doubt that the movement of beach material takes place largely within the breaker zone, motived by the wave action and littoral current. It is, therefore, believed that once the tracer is injected at a certain point in the breaker zone (as in this study it was), tracer particles will find themselves among the original bed particles and behave in the same manner. It is also known that sediment motion within the breaker zone follows a zig-zag path under the action of the swash and back wash of the waves. Due to this action, tracer particles will behave in that manner and should give an idea about the effective zone of littoral drift motion. Fig. 11 shows the distribution of tracer partcles inside the breaker zone for different sampling sections along the beach. It is clear from Fig. 11 that the effective zone of tracer dispersion took place within fifty meters width of the breaker zone. The same result was obtained for all samples taken all over the study period and specially for the reach 500 meters to both sides of the injection point. One may conclude that at least for the mentioned reach, there is no loss of tracer to the off-shore area.

4. Calculation of the littoral drift rate, using Equation 7.

As a result of the present field study, one may observe the following :

a. Littoral drift is directed to the NE direction with probability more than 80%.

b. For the 500 meter reach to the east side of the injection point, tracer losses to the offshore area could be neglected.

From the above and the fact that sampling continued from the moment tracer reaches the given sampling line till its complete disappearance from that section, the main requirements for the application of Equation 7 are fullfilled, and it was used for Ras-El-Bar beach as follows :

(1) Five sampling sections to the eastern side of the injection point where considered for the calculations, namely at 100, 200, 300, 400 and 500 meters from the injection point.

(2) Sampling along these lines continued according to the method given in this paper.

(3) For each sampling section and period, the data were plotted, as shown in Fig. 11. The value of $\int_0^L c\,dy$ was calculated, where c is the tracer

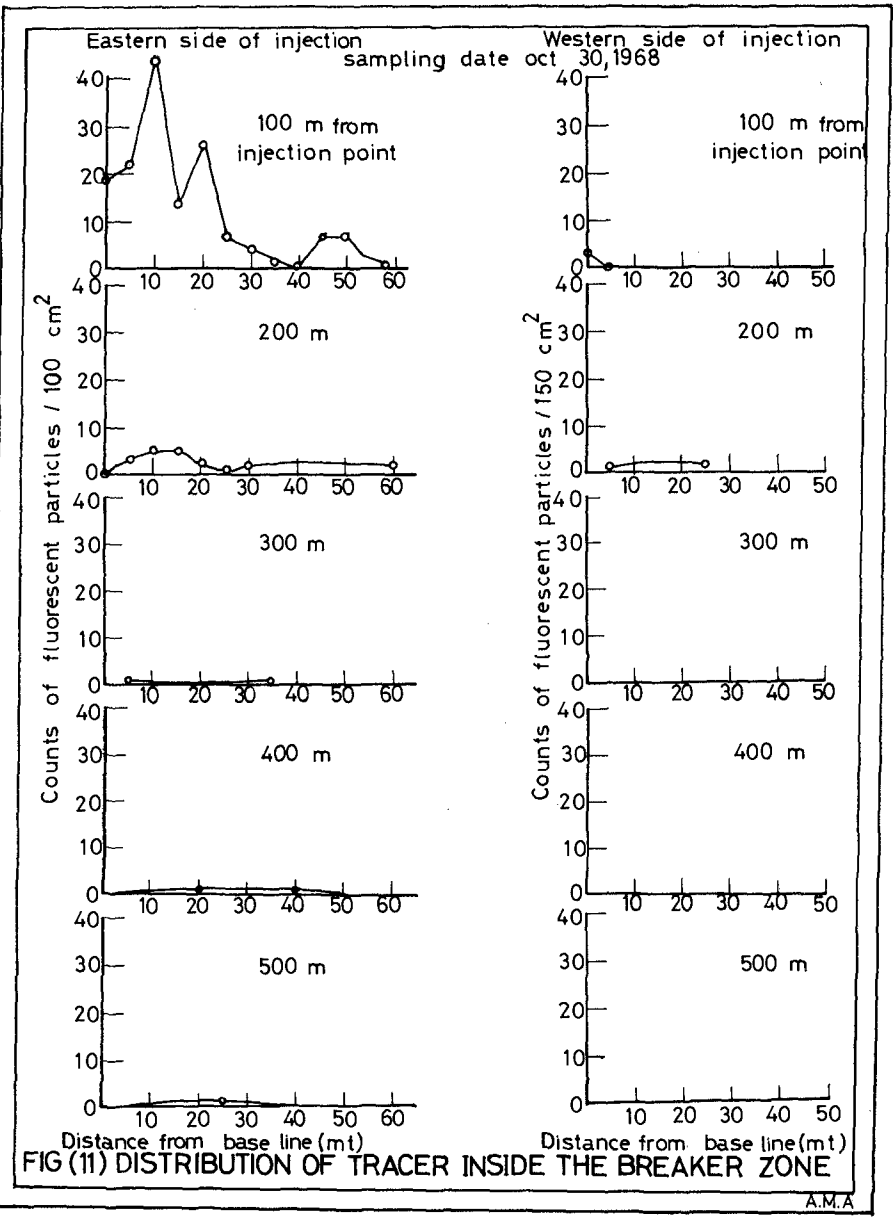

FIG (11) DISTRIBUTION OF TRACER INSIDE THE BREAKER ZONE

A.M.A

concentration at any point at distance y from the shore line and L is the effective length of sampling line along which tracer is dispersed.

(4) The values of $\int_0^L C\,dy$ and their corresponding sampling period, t , from the first injection were plotted as shown in Fig. 12.

(5) From Fig. 12 the value $\int_0^L \int_0^T C\,dy\,dt$ was calculated for each sampling section by integrating the area under each $\int_0^L C\,dy$ vs. time curve of Fig. 12.

(6) The estimated rate of littoral drift Q may be calculated using

$$Q = \frac{S_x}{\int_0^L \int_0^T C\,dy\,dt} \quad \text{where ,}$$

S_x = Total amount of tracer injected = 1.05 tons

T = Time, in days, between the first arrival of tracer to any sampling section and its complete disappearance = about 105 days in this study.

(7) The estimated rate of littoral drift is shown in Table (1).

Table (1) - Rate of littoral drift using Equation 7.

Distance from injection (mt)	$\int_0^L \int_0^T C\,dy\,dt$ (mt.day)	Q ton/mt. day	Q m^3/day (*)
100	0.342038	3.08	54.00
200	0.137770	7.60	142.00
300	0.075588	13.90	260.00
400	0.054925	19.00	360.00
500	0.046137	22.00	430.00

(*) Effective width of movement was taken as 50 meters.

Table (1) shows a remarkable eastern increase of the littoral drift rate. This increase is expected due the followings :

a. Increased erosion as one moves from the injection point towards the old Nile exit. This is clear from Fig. 3 where erosion history along that area is shown.

b. Continuous supply of sand to the breaker zone under the action of western and northern waves. This effect was studied[6] using a developed continuity equation for the sediment movement at Ras-El-Bar and introducing all possible factors involved in the supply and loss of sand to a coast as given by J.W. Johnson[7]. This study gave an estimated supply of 0.75 m^3/mt of coast to the breaker zone due to the waves attacking the area.

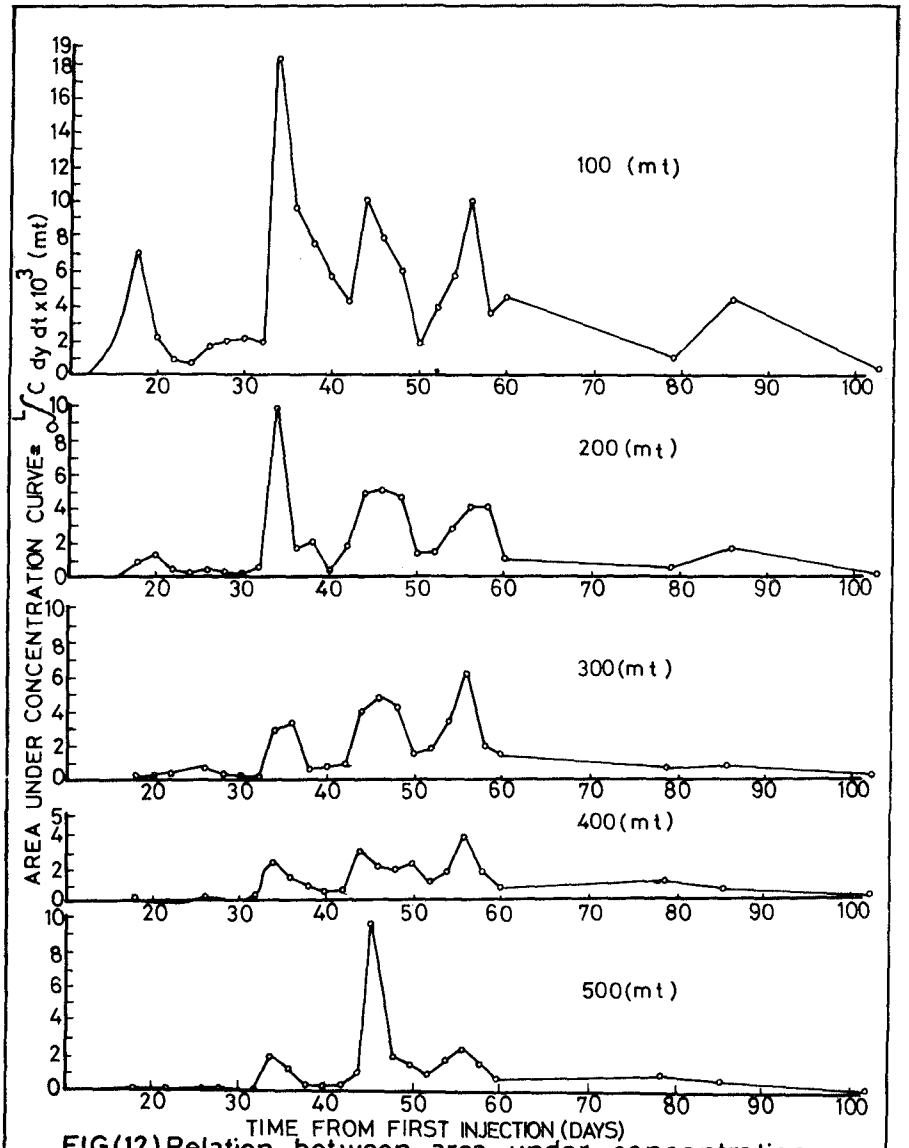

FIG(12) Relation between area under concentration curve and time, along different sampling lines.

5. Thickness of the moving layer.

From Fig. 10, one can estimate the average speed of littoral drift, V_s, at different points along the study area. Table (1) shows the calculations for the littoral drift rate Q at five different locations along the coast. The thickness, δ, of the moving layer of sediment at any locality, may be calculated from the following equation :

$$\delta = \frac{Q}{V_s} \quad \ldots\ldots\ldots\ldots\ldots\ldots\ldots\ldots\ldots\ldots\ldots\ldots\ldots\ldots\ldots\ldots\ldots\ldots\ldots\ldots\ldots\ldots(9)$$

The thickness of the moving layer at 100, 200, 300, 400 and 500 meters from the injection point is shown in Table (2).

Table (2) - Calculations for the moving layer thickness.

Distance from injection (mt)	Q m^3/mt.day	V_s mt./day	δ (mt.)	δ (cm.)
100	1.08	12.6	0.085	8.5
200	2.85	31.50	0.091	9.1
300	5.20	42.00	0.122	12.2
400	7.20	65.00	0.11	11.0
500	8.60	145.00	0.06	6.0
				Σ 46.8

average moving layer thickness δ = 9 cm.

From Table (2), the average thickness of the moving sediment layer, at the breaker zone of Ras-El-Bar, is estimated as 9 centimeters. A formula for relationship between wave height and depth of sand disturbance is given by King[8] ; that for each foot of deep water wave height there is a disturbance to one centimeter. Application of King's formula to Ras-El-Bar coast gives disturbance thickness ranging from 3 to 12 centimeters which is comparable with the thickness of the moving layer calculated. Accordingly, for any future study, collection of sand for either marking or analysis should be taken within this layer.

SUMMARY AND CONCLUSIONS

The present investigation is concerned with the study of sediment movement at Ras-El-Bar coast, using fluorescent tracer technique. A method for calculating the rate of littoral drift was developed. This method is based on the use of tracer and observing the concentration reaching different profiles along the shore line as a function of space and time. The method was used for estimating the rate of drift movement along the eroding beach of Ras-El-Bar. The main findings of this study can be summarized as follows :

(1) The main direction of littoral drift at Ras-El-Bar is from the SW to the NE direction.

(2) Accretion inside the old River Nile exit is partially contributed by erosion from Ras-El-Bar beach.

(3) The average speed of littoral drift along the eroding zone of the beach reaches 145 meters per day.

(4) Reasonable estimate of the littoral drift rate, at a certain point along shore lines, could be obtained using fluorescent tracer and Equation 7, under the following conditions :

a. Littoral drift movement should have a major direction for most of the period.

b. Sampling of tracer along the profile concerned should continue from the moment tracer starts to reach that section till its complete disappearance from it.

c. Sampling periods of two days interval seems to be reasonable.

d. Sampling should cover any seawards distance wherever tracer may be found.

(5) Littoral drift along Ras-El-Bar is originated from the continuous erosion along the area.

(6) Most of the littoral drift along the breaker zone is supplied by wave action which is originated from erosion in the off shore area.

(7) For the three kilometers coast length, west of the Nile exit, erosion increases as one moves to the N E direction.

(8) For the same reach above littoral drift rate also increases in the same direction. This finding was obtained by Saville[9] who found that greater long shore transport of sand occurred when the beach is eroding than when they were prograting.

(9) The average thickness of the moving sediment layer along the breaker zone, is estimated to be about 9 centimeters.

ACKNOWLEDGEMENTS

The author wishes to express his gratitude to Prof.H.Ismail and Dr.A.A.Ammar for their help and advice and to various members of staff and personnel of the Suez Canal Authority Research Centre for their cooperation.

Thanks are also due to Mr. El Zogby, Mr. El Saay, Mr. Abbas for their assistance in collection and analysis of data. Mrs. Thetis Calambichis typed the manuscript.

REFERENCES

1. Zencovitch,V.P., "Emploi des Luminophores pour l'étude du mouvement des alluvios sablonneuses", Bulletin d'Information du Comité Central d'Oceanographie et d'Etude des Côtes, V.19, No.5, 1958.

2. Russell,R.C.H., "The use of fluorescent tracer for the measurement of littoral drift", Proceedings of Seventh Conference on Coastal Engineering, The Hague, Netherlands, Vol. 1, 1958.

3. Jolliffe, Ivan P., "A study of sand movements on the Lowestuft sand-bank using fluorescent tracers", Geographical Journal, V. 129, 1963.

4. Wright, F.F., "The development and application of a fluorescent marking technique for tracing sand movement on beaches", Columbia University, Dept. of Geology, ONR Technical Report No. 2, 1962.

5. Mobarek, I., Kadib A.A. and El-Ghamry, M., "New Harbour at Damietta - Field Investigations", Suez Canal Research Centre Technical Report No.34, 1966.

6. Kadib, A.A., "Study of the Littoral Drift at Ras-El-Bar Using Fluorescent Tracer", Suez Canal Research Centre Technical Report No. 42, April 1969.

7. Johnson, J.W., "The supply and loss of sand to the coast", Journal of the Waterways and Harbour Division, ASCE, Vol.85, Sept.1959, pp 227-251.

8. King, C.A.M., "Depth of Disturbance of sand on sea beaches by waves" , Jour. Sed. Pet., V. 21, 1951.

9. Saville, Thorndike, Jr., "Model study of sand transport along an infinitely long straight beach", Trans. Amer. Geophys. Union, 31, 4 August, 1950.

CHAPTER 53

THE MEASUREMENT OF OFFSHORE SHINGLE MOVEMENT

Crickmore, M J, Waters, C B and Price, W A
The Hydraulics Research Station, Wallingford,
Berkshire, England

Abstract

The objective was to obtain quantitative data on the movement of shingle under wave action in water depths of about 10 to 20 m by tracking pebbles tagged with radioactive material.

The paper describes the method of tagging, the method of position fixing, and the development of an underwater detection vehicle with a wide field of view. The field tracer tests demonstrated both increased mobility with decreasing depth and the existence of a small landward movement of shingle inshore of a depth of 12 m. Existing predictive data on the threshold of movement under waves, based on the results of previous work in the laboratory, was confirmed.

INTRODUCTION

The Hydraulics Research Station is often approached to assess the likely physical consequences on nearby coastlines, that could arise from the commercial dredging of offshore banks of gravel and shingle. In these cases attention is given to two major effects that may occasion damage to the shore-line. First, the locally increased depths of the dredged area can alter the angle of incidence of waves on to the beaches. Erosion and accretion as the coast re-adjusts to the new wave situation may have adverse consequences on amenity. Secondly, removal of offshore shingle may deprive the shore-line of its natural source of beach material. It is necessary, therefore, to assess whether the shingle that is to be dredged is moving towards the land under the present circumstances of waves and tides. Clearly, if it is not, there is no danger as far as source considerations are concerned.

The object of the study was to obtain, for the first time, quantitative data on the mobility of shingle under wave action in water depths of about 10 to 20 m.

The area offshore of Worthing was chosen as being suitable for an exploratory study of shingle movement. This part of the south coast of England is already the subject of a number of applications for commercial dredging licences. Thus research here is directly relevant to helping the licensing authorities to deal with these applications. Also, from the point of view of general study the area is attractive: the bottom topography being simple and wave conditions fairly typical of British coastal waters.

PREDICTION OF SHINGLE MOVEMENT

Existing predictive data on shingle movement under waves are based on a limited number of laboratory tests. Many of these attempted to model prototype shingle motion by means of scaled-down waves and granular bed material in laboratory wave tanks. Possible scale distortions make difficult the interpretation of the results of such tests. More reliable guidance is given by experiments in a pulsating water tunnel (Ref 1) in which full-scale oscillatory motions under waves can be represented. The conditions necessary to initiate movement of a variety of materials have been explored thoroughly with this facility and, given knowledge of the typical wave conditions, go a long way towards answering the question whether bed shingle is stationary or not.

It is found that, for the particular case of 25 mm diameter shingle, maximum oscillatory velocities of 1.4 to 1.6 m/s at the bed are required, to initiate movement for typical wave

periods of 6 to 10 s. At water depths of 20 m, 10 s waves of about 6 m height are necessary to give oscillatory velocities of this magnitude. For 8 s waves, wave heights of nearly 8 m are needed. As the wave advances into shallower water, orbital velocities increase rapidly and bed shingle is progressively more vulnerable to movement. For the simple case of waves approaching a straight coast with parallel submarine contours, it is seen (Fig 1) that at 6 m water depth, threshold velocities for 25 mm diameter shingle are exceeded by waves with deep water heights of only 3 m and with periods as short as 6 s.

The quoted threshold velocities apply to shingle on a shingle bed. If shingle is present as a thin veneer on a hard rock basement, higher mobility can be expected. On the other hand, for the case of shingle coexisting with sand, the threshold velocities are probably underestimated because the sand occupies the interstices between the shingle, thus reducing the area on which drag and lift forces can be exerted.

Motion under non-breaking waves is primarily of an oscillatory nature, and as such may be expected to cause shingle to disperse normal to the wave front. This oscillation can cause a landward drift of shingle because on the forward-moving stroke the water velocity is higher and, therefore, more likely to move shingle, than the longer duration motion in the opposite direction. When pebbles have been lifted off the bed they can be entrained by tidal currents or by a second order wave-induced translatory flow known as the mass transport current. The latter arises because the orbits described by water particles under waves are not closed so that there exists a slow transference of water that is in the direction of wave propagation near the bed. Following Longuet-Higgins (Ref 2), the mass transport current at the bed increases with increasing wave height and with decreasing depth. Thus a 10 s wave, 6 m high, gives a mass transport bed current of less than 0.3 m/s in 20 m depth, but of 0.8 m/s in 10 m depth. A 10 s wave, 3 m high, gives values of less than 0.1 m/s and of 0.2 m/s for 20 and 10 m depths, respectively.

It is seen, therefore, that smaller depths are associated not only with increased bed mobility due to exposure to stronger oscillatory flows, but also, under large waves, with a net transfer of bed material in the direction of wave propagation on account of the mass transport current. In normal circumstances and neglecting tidal currents, this drift will be towards the shore. The question arises as to the likely magnitude of the bed material drift. Unfortunately, no data are available to predict the drift of solids beyond the threshold conditions. Consequently, if reliable estimates of drift quantities are to be made, recourse has to be made to field measurements of shingle movements.

EXPERIMENTAL AREA

Reserves of shingle exist offshore of Worthing in the vicinity of the 20 m mean water depth contour. Fears are expressed by the local coastal authorities that these offshore areas are sources for the shingle beaches of the nearby coastal resorts, and that the exploitation of the reserves will deprive the beaches of their natural supply.

It was decided to explore bottom shingle movement at a number of depths (9 to 18 m mean water depth), extending inshore from the shoreward boundary of the possible licence areas, by introducing marked pebbles and subsequently mapping their movement.

For the tests to be representative of areas of high dredging potential it was desired to introduce the marked pebbles on to a natural shingle floor. This condition was not easily satisfied in the case of the more inshore sites of the Worthing area. A bed reconnaissance by divers from H.M.S. Vernon, Portsmouth, extending offshore from Worthing, failed to find extensive shingle areas inshore of about 15 m water depth. The sea-floor between the reserve area and the shore at this point is very variable; sometimes bare chalk, sometimes patches of shingle, large stones and silt, and widespread weed cover. Clearly this was not a satisfactory experimental site and the search area was moved about 7 km east to offshore of Shoreham. Further diver reconnaissance eventually found locations (Fig 2) displaying suitable bottom conditions over the required depth range.

This stretch of coast is open to waves throughout the sector from ESE to WSW. The longest fetch coincides with the prevailing southwesterlies and consequently in a normal year the dominant wave attack would be expected from the southwest quarter. For the greater part of the duration of the experimental study, wave records were taken with a National Institute of Oceanography shipborne wave recorder installed on the Owers Light Vessel. These records were analysed for wave height and period after Tucker (Ref 3).

Tidal currents run generally parallel to the shore and are relatively weak: peak surface velocities being 0.8 m/s at Spring tides, and 0.5 m/s at Neap tides. These currents are insufficient to move shingle, but in conjunction with the mass transport current, they could be important in determining the direction of movement of shingle that has been already lifted from the bed by oscillatory flow under heavy wave action.

EXPERIMENTAL METHOD

In the past, qualitative studies of shingle movement have been undertaken using fluorescent or radioactive tracer pebbles (Refs 4 and 5). Although fluorescent tracers offer a convenient means of tracking movement on beaches above the low water mark where visual identification of the marked pebbles is possible;

the inability to detect them remotely from a boat is a severe handicap for deeper water operations. In this respect, the radioactive tracer method has a distinct advantage, with its capability of identifying tracer units using a radiation detector dragged over the sea-floor behind a boat.

Tracer pebbles

Previous radioactive tracer work on coastal shingle movement has been short-term using short half-life radioisotopes. In the present case, the objective was to follow movements for at least one year and the radioisotope Silver 110 m was selected as being sufficiently long-lived (half-life, 253 days) for the purpose. Again, on account of the duration of the tracking period, a tag sealed into the centre of a pebble was preferred to the alternative of a surface coating: the latter being susceptible to abrasion losses. The technique consisted of placing a short length (3 mm) of activated silver wire (20 μCi Silver 110 m) in a hole in each pebble and then filling the hole with a clear epoxy resin. Abrasion tests lasting over a week, tumbling tagged pebbles in a mixer with other beach pebbles and sand, showed no sign of damage, apart from a scratching of the epoxy resin surface which masked the presence of the underlying wire tag.

The pebbles of this part of the coast are flint and considerable difficulty was experienced in drilling holes in them. 4000 tagged pebbles were required and the failure rate of diamond drills was so high that only about 300 pebbles were prepared by drilling. It was found more economical to collect natural pebbles already having suitable holes in them (Plate 1). Only pebbles passing through a 38 mm sieve and retained on a 19 mm sieve (corresponding roughly to coarse aggregate grading) were accepted for tagging.

Pebble seeding

The four selected sites with mean water depths of 9, 12, 15 and 18 m, were each seeded with 1000 tracer pebbles in mid-September 1969. To provide a reasonably well-ordered initial distribution, the pebbles were laid by divers on the surface of the bed over a rectangular area 30 m by 60 m. The discovery of an almost completely buried mine within the seeded area at 15 m depth and subsequent failure to re-locate the mine for disposal, led to the abandonment of this site. It was considered that the risks involved in repeatedly traversing the area with a large underwater wheeled vehicle were too great to permit tracking in this area.

Pebble detection

An inherent difficulty of shingle tracer experiments is that of detecting a sufficiently high proportion of the injected tracer units to permit quantitative interpretation of the

measured spatial distributions. Tracer preparation is inevitably tedious, and the number of pebbles introduced is consequently low. There is clearly the need to optimise the areal coverage of the detector. Underwater detectors for normal applications are unable "to see" a pebble over a band much greater than one metre wide, when moving over the bed at a speed of 1 m/s. Thus, if the tracking boat runs parallel courses about 20 m apart, only 50 pebbles of a total of 1000 are likely to be detected.

In order to overcome the narrow sweep handicap, a detector with a wide field of view was developed (Plate 2). Five scintillation counters are distributed over the width of a 3-wheeled vehicle drawn behind a boat, so that they view the sea-bed over a band-width of 6 m. The vehicle weighs about 350 kg and is towed at speeds of about 1 m/s, using 90 m stainless steel tow rope (12 mm dia.) incorporating the electrical cable as its core. Detector output is provided on three twin-channel pen recorders on-board the tracking vessel. The presence of a tagged pebble is readily distinguished on the chart record as a well-defined pulse above the natural background radiation. The spare recorder channel indicates the vehicle's speed over the sea-floor, using the output from a rev. counter on the leading wheel of the vehicle.

In addition to the main tracking detector for measuring the horizontal distribution of the pebbles, a subsidiary diver-held, portable detector was employed for assessing the depth of burial of individual pebbles. Divers intensively explored the bed in the seeded area and obtained a series of maximum bed surface radiation readings, directly above tagged pebbles. With the radioactivity in each pebble being closely similar, the reading indicated the extent to which the emitted radiation was absorbed, and the depth of overburden was given from laboratory calibration of the detector.

Position-fixing

Shingle tracking imposes rather stringent requirements with respect to position-fixing. To achieve effective combing of the search area there is the need to run courses at slow speeds on parallel lines not greater than 20 m apart. At this spacing 30 per cent registration of the seeded pebbles could be obtained with the wide-view detector.

Hydrodist MRB2 was hired to provide the necessary precision. Operating at 3000 mc/s the system gives a nominal position-fixing accuracy of $\pm$ 2 m. In this specific case, the siting of slave transponder stations at Shoreham and Rottingdean yielded satisfactory intersection angles of the lattice lines throughout the working area. Apart from occasional spurious distance shifts at the most offshore site, the system proved reasonably reliable throughout the study, but it made extravagant demands on manpower.

Although the boat's position was accurately given by Hydrodist fixes, the position of the detector behind the boat was more indeterminate. Normally the detector was taken as being on the line of the boat's course, but displaced some distance behind the boat according to the length of tow. Errors would be introduced in the presence of a strong cross-wind or when tracking across the tide, and it is estimated that tolerances of 5 to 10 m on detector position are realistic.

Surveys

A preliminary bed background radiation survey was made in early September 1969 before the seeding operation. No background radiation anomalies were recorded.

Following the seeding in mid-September, subsequent surveys were made in October, November/December 1969, March and August 1970, April/May 1971. Normal practice was to run parallel courses roughly E-W along the tidal direction, maintaining a constant distance off the Shoreham slave station. Tracking was not possible with a beam sea, so when sea conditions were bad, the alternative procedure of running courses to and from the coast was adopted, holding a constant distance off the Rottingdean slave station. The running of parallel courses was greatly facilitated by the adoption of courses with a fixed Hydrodist reading on one or other of the two slaves.

Measurements of the depth of shingle burial were made on the last three surveys only.

RESULTS

The results of the various surveys are illustrated in Figs 3 to 5. The following points should be borne in mind when examining these figures:-

1. The delimitation of maximum tracer extent is subject to considerable random error, being based on the detection of a single pebble. Consequently the boundary can shift markedly in areas of low tracer density, dependent on whether or not, a particular pebble is coincident with the detector track width. The profiles of tracer pebble density with distance from the centre of the seedee zone are more valid guides to the degree of movement between surveys.

2. Profiles are not given for surveys based on tracking courses running to or from the shore, because these would not be comparable with profiles based on the more customary tracking direction.

3. The shaded rectangular area is a somewhat idealistic representation of the initial tracer distribution. The actual seeding only approximated to this form.

4. To economise on space the full extent of tracking coverage is not shown. The courses were much longer than indicated, and

normally, further parallel courses were run to the north and to the south. However, no tracer pebbles were detected at these more remote positions.

The most striking feature of the mapped distributions is the small degree of movement at all sites: even single tracer pebbles are very rarely encountered as far as 100 m from the centre of the original seeded area.

The inshore sites, at 9 and 12 m mean water depth, exhibit typical tracer distributions, with a low density scatter of tracer pebbles extending in an approximately NNE direction from a high density cluster coincident with the originally seeded area. The net drift of pebbles is small but is clearly discernible above possible experimental errors referred to earlier. Average landward pebble movement over the total observation period of 20 months is assessed at 40 and 15 m for 9 and 12 m depths, respectively.

Although Fig 5 shows a small westerly shift in the mapped tracer distribution at 18 m depth compared with the seeded position, there is no sign of the characteristic scatter of pebbles at low density. All the distributions at this site display an abrupt boundary: there are either tracer pebbles at high density, or there are none. Past experience suggests that tracer units do not shift as a group without a concomitant dispersal similar to that given at sites 1 and 2. It is concluded that the small positional shifts at site 4 are spurious and represent fixing errors between surveys. Thus no net pebble drift was recorded at 18 m depth.

After one winter, measurement of the vertical distribution of 120 tracer pebbles by divers using the portable radiation monitor at the two inshore sites showed that they were still confined to the surface 50 mm. After two winters, the vertical position of 50 tracer pebbles at each site was determined in the same manner. The mixing depth was found to be 125 mm, 50 mm and 60 mm at sites 1, 2 and 4 respectively. Further evidence of low mobility was demonstrated by the recovery of tracer pebbles by divers in May 1971. These pebbles still showed a clear resin plug through which the silver wire was visible and obviously had suffered negligible abrasion in the experimental period.

DISCUSSION

From the plots of tracer pebble distributions the most obvious movement took place early in the experiment in November 1969 when strong westerly winds gave 8 s waves with significant heights in excess of 5 m. The wave climate prevailing between each survey is shown in Fig 6 and it can be seen that the severe conditions of November 1969 were repeated in a storm during the 1970-71 winter. However, on this second occasion the horizontal displacement of the tracer pebbles was not so apparent because the pebbles were dispersed over a thicker bed layer by that time. During the summer period the tracer pebbles at all sites showed very little

horizontal movement in spite of significant wave heights in excess of 3 m at Owers Light Vessel.

The extent to which the tracer results can be regarded as typical is best judged by comparison of the wave conditions prevailing during the study with the long-term average. Unfortunately wave data outside the experimental period are limited. Additional records at Owers Light Vessel are available (Ref 6) for one year (October 1968 to September 1969) only and show that wave conditions then were less severe than during the present study.

Recourse has to be made to wind frequency comparison for a longer-term standard. Analysis of 5 years of wind records for Calshot suggests that sea conditions were less disturbed during the winters 1968 to 1971 than the long-term average. It is seen (Fig 7) that strong winds from the southwest quarter i.e. those capable of generating higher and longer period waves, were less frequent during the experimental period than normal.

Wave records at Owers Light Vessel with suitable adjustments to take account of shoaling have been used to calculate bottom current conditions at each of the tracer sites. For this purpose the significant wave height i.e. the mean of the third highest waves, and the mean zero crossing period are used to compute the peak oscillatory velocity at the bed. The frequency of occurrence of bottom-water oscillations having instantaneous peak values that exceed a number of specific velocities is shown for each site, alongside the final tracer distributions, in Fig 8. The results are qualitatively consistent with data obtained from the pulsating water tunnel (Ref 1). The laboratory tests showed that maximum bed oscillatory velocities of 1.4 to 1.6 m/s were required to move 25 mm shingle. In the field the peak recorded at 18 m depth was about 1.2 m/s; so it is not surprising that the tracer distribution suggested a non-mobile bed at that depth. On the other hand, significant movement occurred at 12 m depth where peak values reached 1.7 m/s.

It appears that mass transport currents associated with heavy wave action are more important than tidal currents in determining the direction of net pebble movement at the nearshore sites. These bring about a landward drift across the tidal stream direction. The volume of shingle drift may be obtained from the product of the shift in centroid position of the horizontal tracer distributions and of the thickness of the layer in movement. The drift after two winters and one summer is estimated at 2.5 and 0.5 m^3 per metre width for the 9 and 12 m water depth, respectively.

It is evident from the absence of movement at 18 m water depth that the drift occurring at the more inshore sites is not supported by an offshore feed. Thus the nearshore shingle drift is either replenished by alongshore movements of shingle or is slowly drawing from geological reserves.

CONCLUSIONS

The field tracer test demonstrated both increase in bed mobility with decreasing depth and the existence of landward movement of shingle inshore of 12 m water depth. However, even at the two inshore sites the quantities of shingle transported towards the shore were found to be small, amounting to 1000 to 1500 m^3 and less than 500 m^3 per kilometre length of coast per annum from 9 and 12 m water depth, respectively. Dredging at these depths could interrupt the slow landward creep but the manifestation of this on the beaches would be long-delayed. For instance, the centroid shifts at the two sites indicate that the average pebble will take about 200 years to advance the 3 km from the 12 to 9 m contour. It is debatable whether changes on such a long time scale are significant when there is a strong probability that beach levels are controlled primarily by spatial and temporal variations in the littoral movement of shingle close inshore. However, at these depths, beach changes arising from alterations of wave refraction might be the primary consideration.

It is considered that shingle movements offshore of the 18 m contour along this piece of coastline will be negligible at all times. Furthermore, at these depths the mass transport current at the bed is too small to promote preferential landward drift.

ACKNOWLEDGEMENTS

This report is published with the permission of the Director of the Hydraulics Research Station, Wallingford, England. The work was financed by the Crown Estate Commissioners.

The services of Navy divers from H.M.S. Vernon proved valuable at various stages in the tests. The permission of the Ministry of Defence for the diver participation and the willingness of the individuals concerned are gratefully acknowledged.

The authors are also indebted to the National Institute of Oceanography of the Natural Environment Research Council for making available the processed wave data for Owers Light Vessel.

REFERENCES

1. RANCE, P J and WARREN, N F The threshold of movement of coarse materials in oscillating flow. Paper 127. Coastal Eng. Conf. 1968.

2. LONGUET-HIGGINS, M S Mass transport in water waves. Phil. Trans. Roy. Soc. Series A. No 903, Vol 245, 1953.

3. TUCKER, M J Analysis of records of sea waves. Proc. Instn. Civ. Engrs. Vol 26, 1963.

4. REID, W J and JOLLIFFE, I P Coastal experiments with fluorescent tracers. Dock and Harbour Authority, Vol XLI, No 484, 1961.

5. KIDSON, C and CARR, A P The movement of shingle over the sea bed close inshore. The Geographical Journal, Vol CXXV, Parts 3-4, 1959.

6. DRAPER, L and SHELLARD, H C Waves at Owers Light Vessel Central English Channel, National Institute of Oceanography; Internal Report No A.46, 1971.

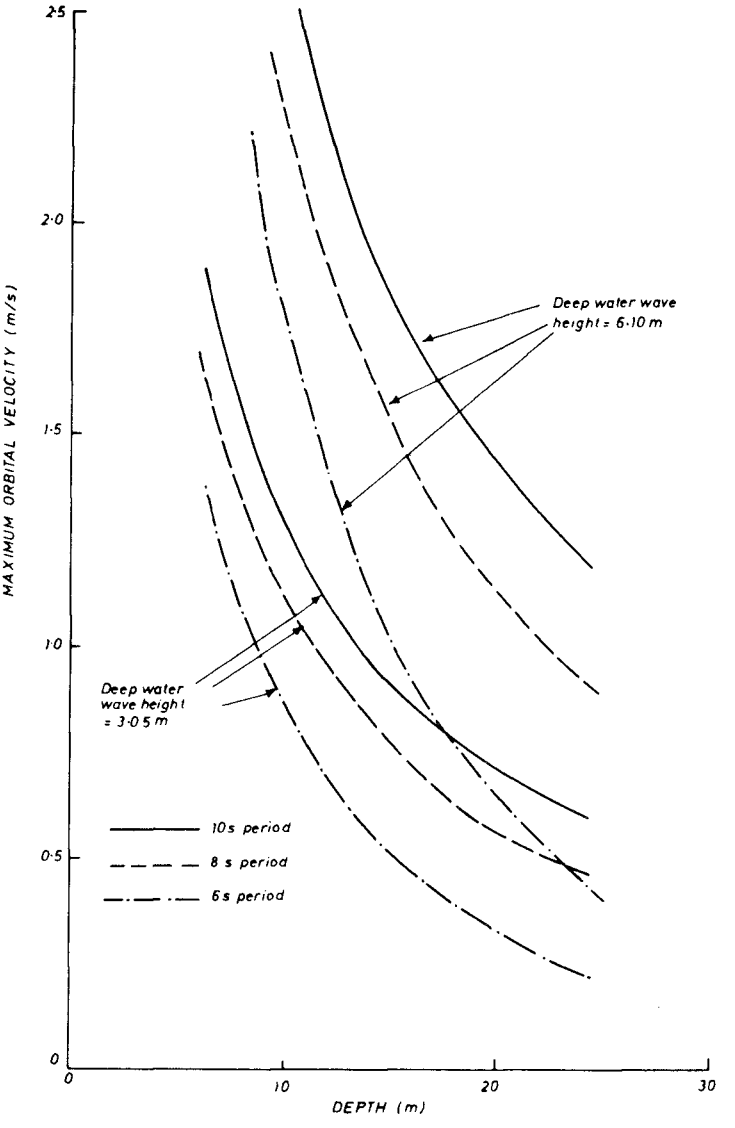

EFFECT OF DEPTH ON MAXIMUM ORBITAL VELOCITY AT BED

FIG 1

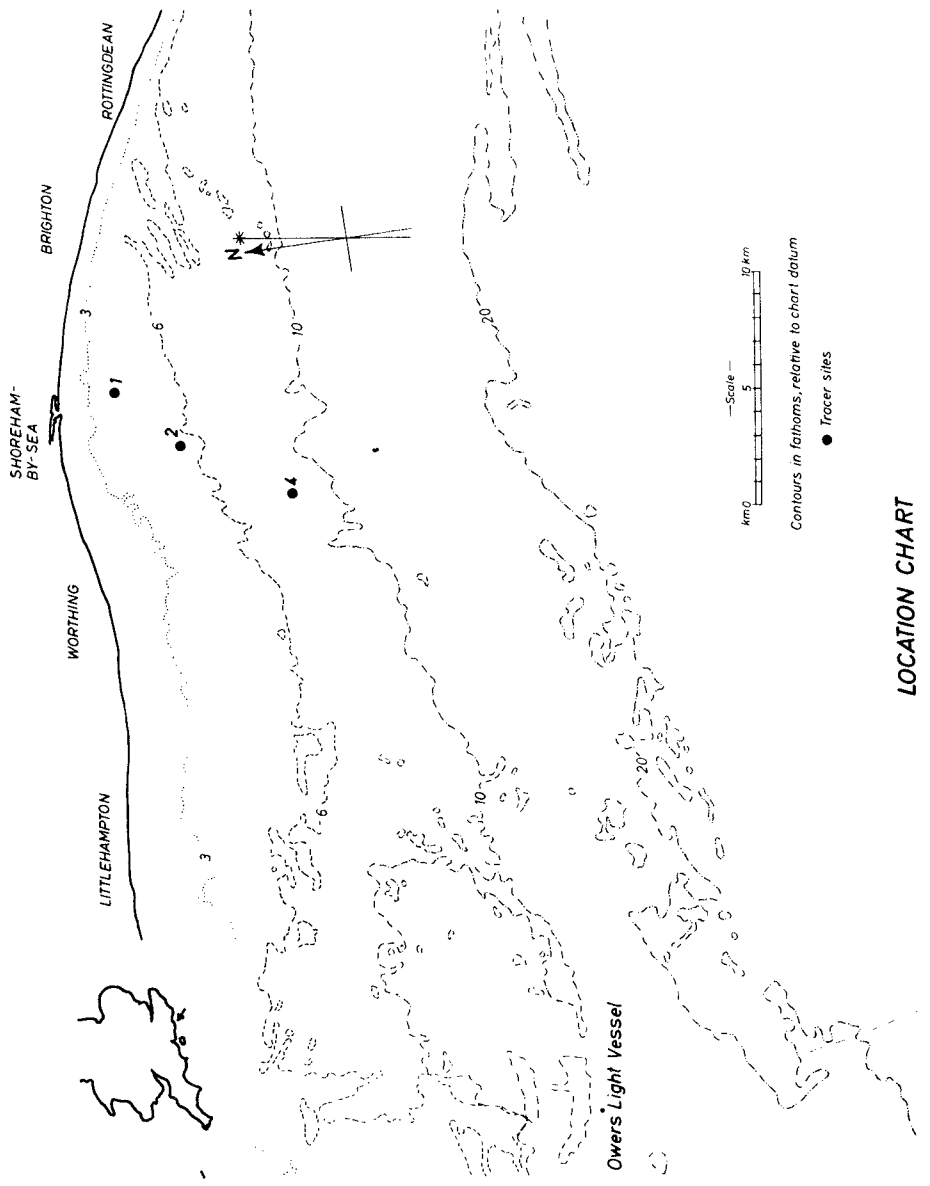
SHOREHAM-BY-SEA
BRIGHTON
ROTTINGDEAN
WORTHING
LITTLEHAMPTON
Owers Light Vessel
N
—Scale—
5
km 0
10 km
Contours in fathoms, relative to chart datum
Tracer sites
LOCATION CHART

FIG 2

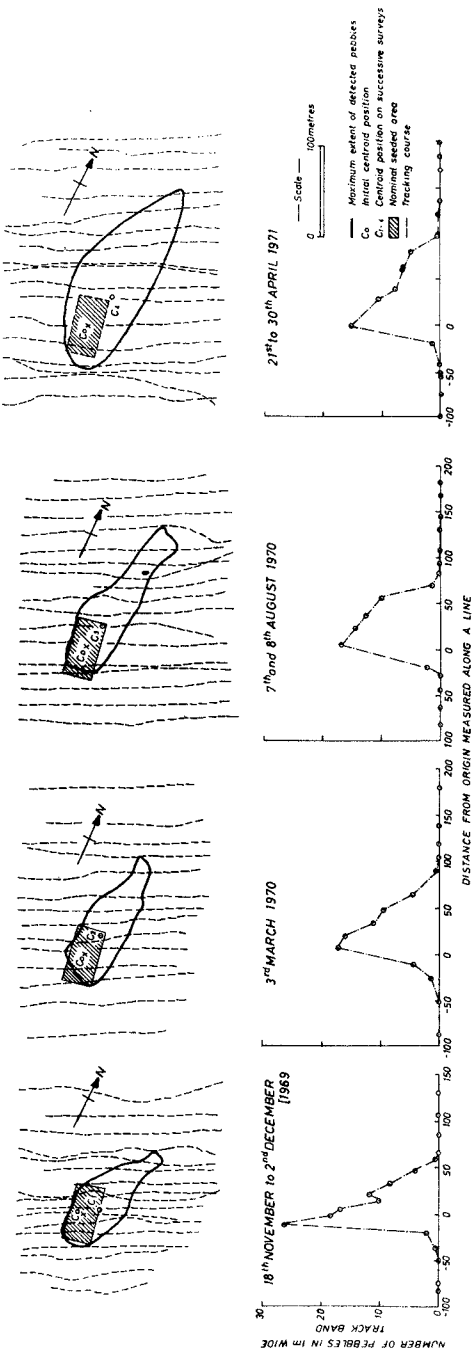

TRACER PEBBLE DISTRIBUTIONS - SITE 1

FIG 3

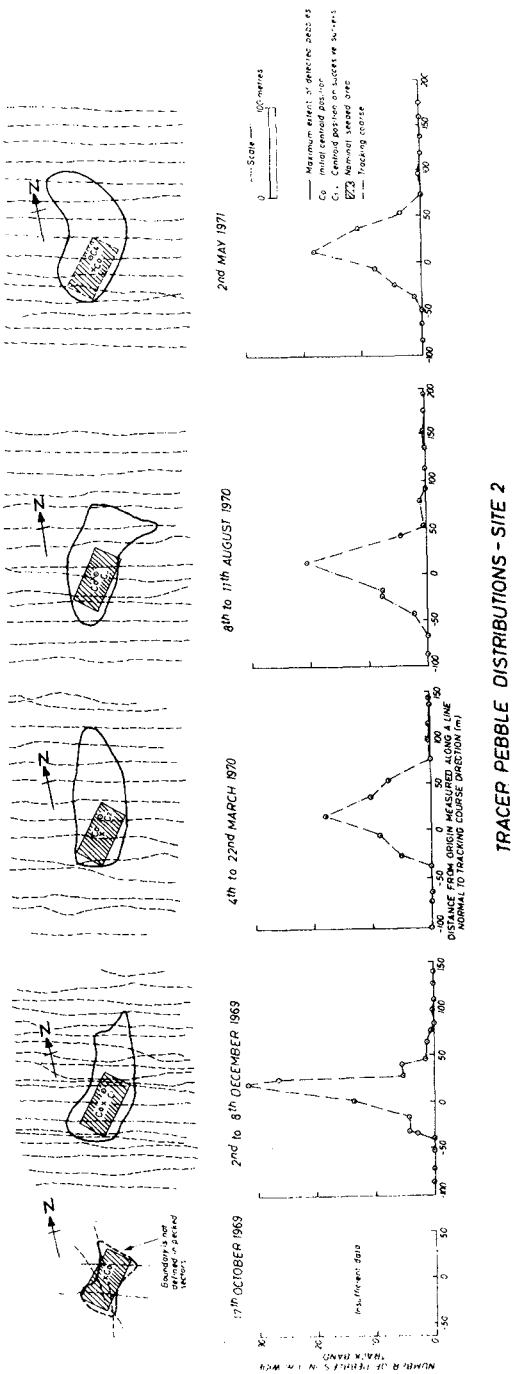

FIG 4

TRACER PEBBLE DISTRIBUTIONS - SITE 2

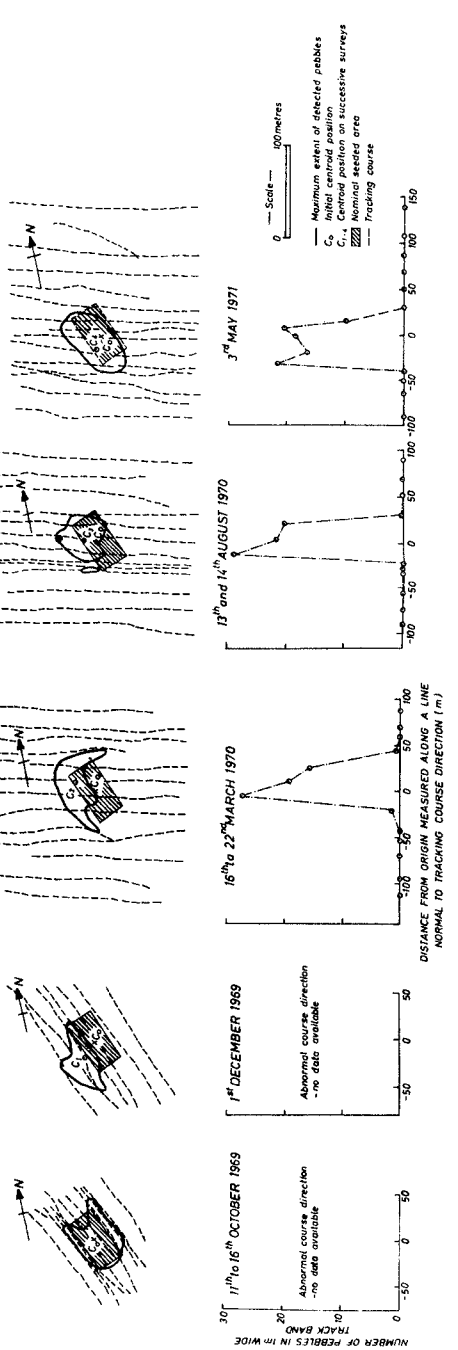

TRACER PEBBLE DISTRIBUTIONS - SITE 4

FIG 5

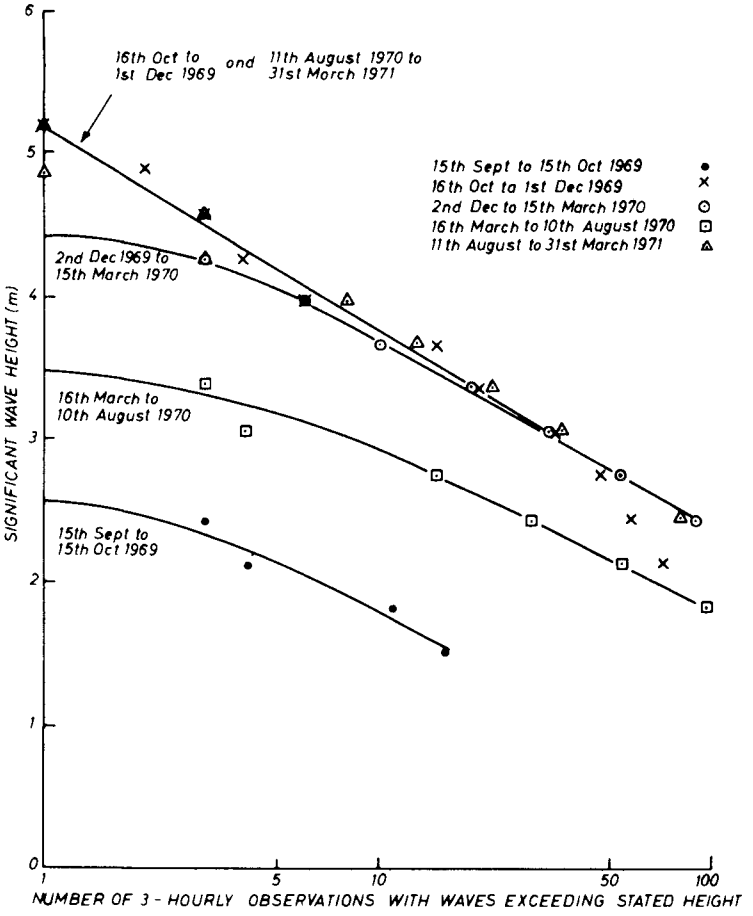

SIGNIFICANT WAVE HEIGHT EXCEEDANCES -OWERS LIGHT VESSEL

FIG 6

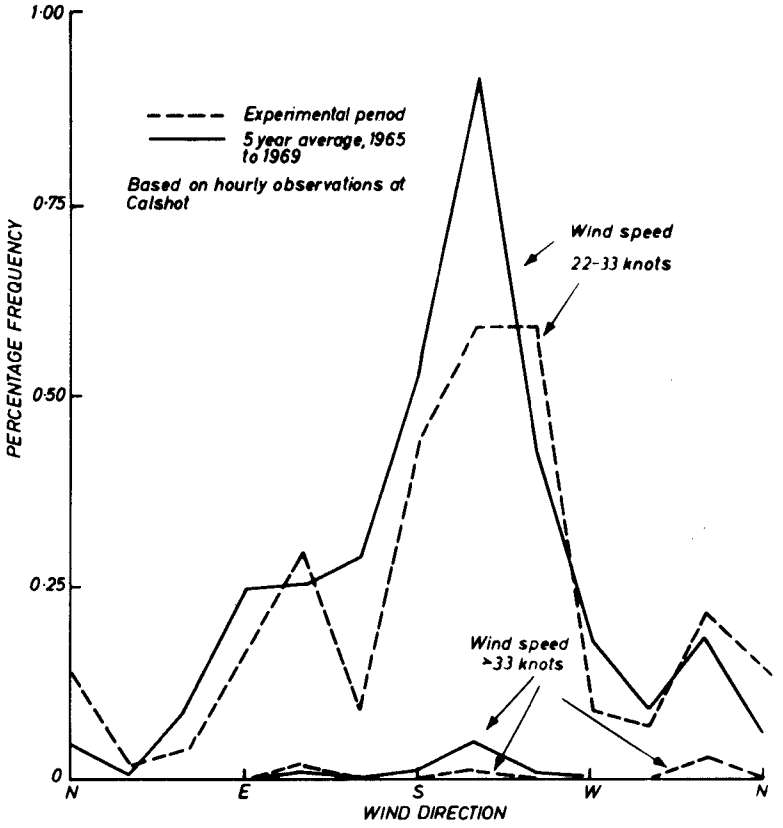

WIND FREQUENCY COMPARISON

FIG 7

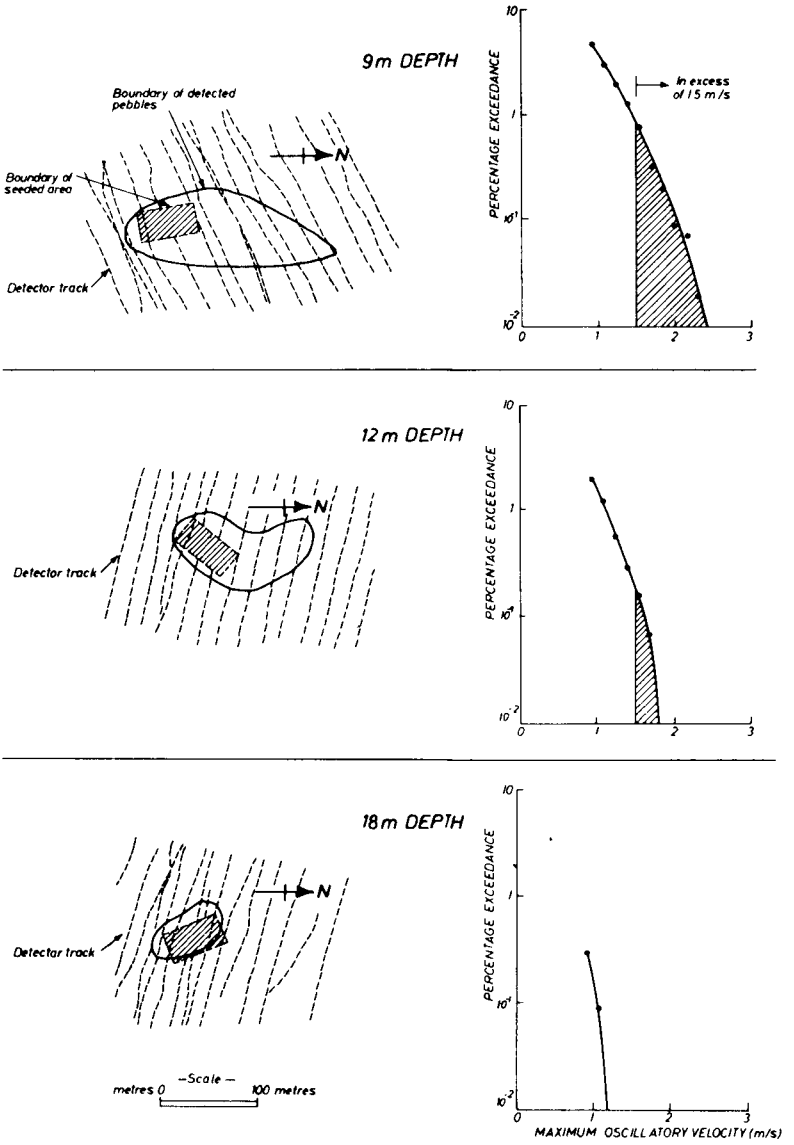

MAXIMUM EXTENT OF TRACER PEBBLES AND FREQUENCY DISTRIBUTION OF MAXIMUM OSCILLATORY VELOCITIES AFTER 20 MONTHS

FIG 8

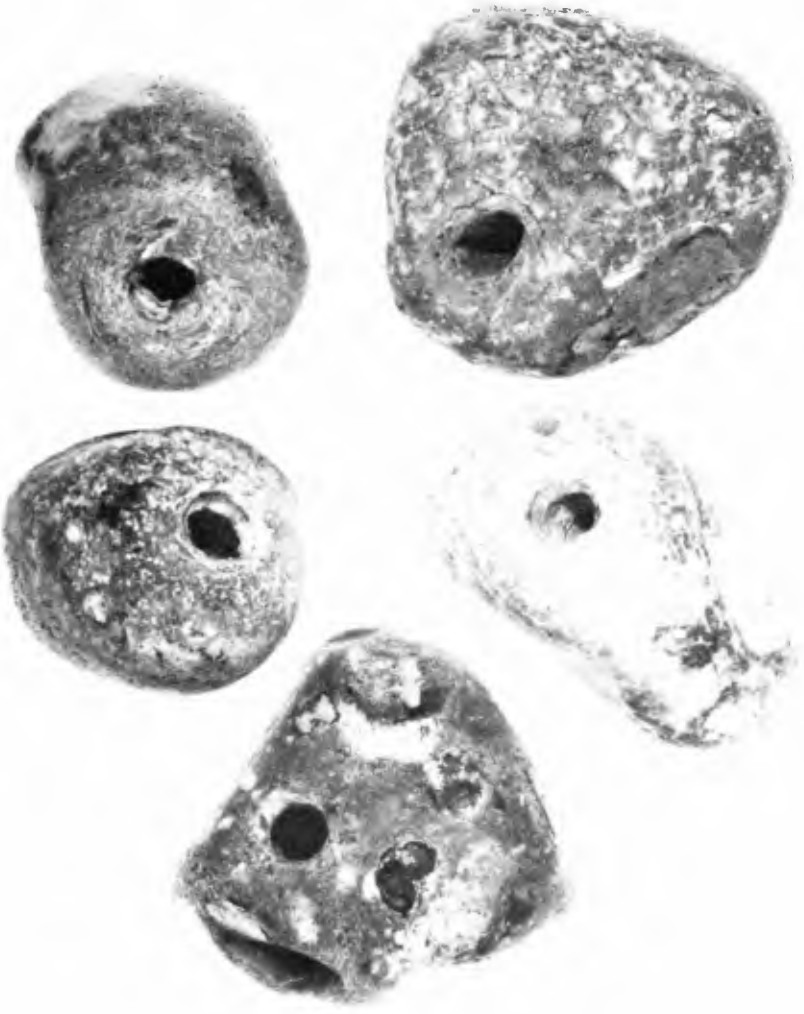

Plate 1 Natural holes in flint beach pebbles

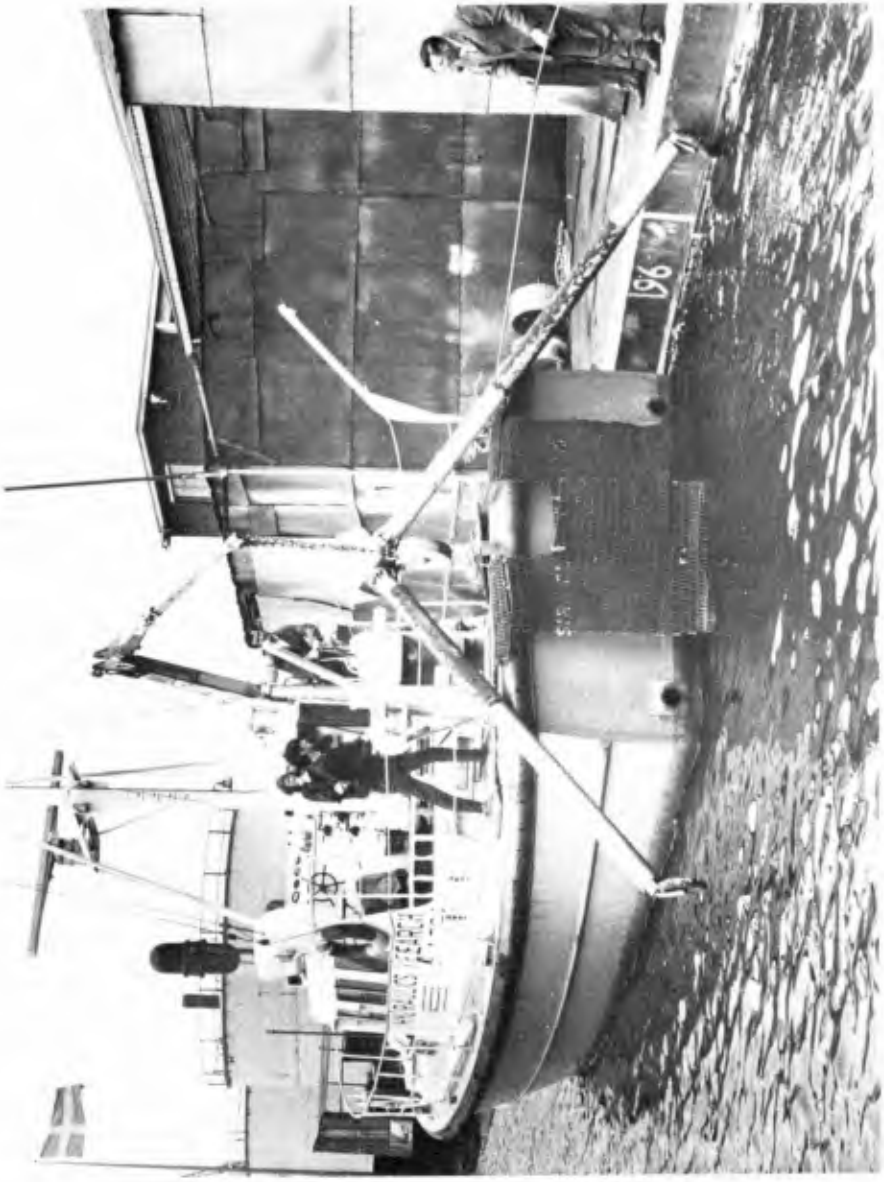

Plate 2 Wide-sweep radiation detector

CHAPTER 54

SUSPENDED SEDIMENT AND LONGSHORE SEDIMENT TRANSPORT DATA REVIEW

BY

M. M. Das*, M. ASCE

ABSTRACT

A review of laboratory and field studies on suspended sediment under waves shows that although about five analytical or semi-empirical approaches have been attempted to predict the vertical distribution of suspended sediment, none of the approaches has had its general validity proven. This is mainly due to the lack of knowledge about the characteristics of turbulence of the wave boundary layer and to the lack of a suitable suspended sediment measuring technique for use in waves. Six different suspended sediment measuring techniques have been used in the studies reviewed. Although none of them gives completely reliable laboratory or field measurements, an optical system appears to show promise in obtaining information on the mechanics of suspension under waves.

The reanalysis of longshore sediment transport data and tests of the relationships $Q = A_1 E_a$, $Q = A_2 E_a^B$, and $I_\ell = A_3 E_a$, where Q is volume transport rate in cubic yards per day, E_a is longshore component of wave energy flux in lbs per day per foot of beach and I_ℓ is immersed weight transport rate in lbs per day, for different subsets of data and using the method of least squares, showed that a single set of A_1, A_2 and B does not fit all subsets of data with minimum average percentage deviation of observed values from those predictable by the relationships. The subset of data consisting of all but the observations with light weight sediments can be described by the line of fit, $Q = 1.93 \times 10^{-4} E_a$, with the observed data differing from the predicted ones by 74 percent on the average.

INTRODUCTION

There is no proven prediction method of general validity for quantitative estimates of onshore-offshore and longshore sediment transport rates. The reasons are (a) inadequate knowledge of the turbulent flow field in water waves, due partly to lack of velocity measurement technique and (b) nonavailability of reliable techniques to measure sediment transport rates in the near-shore zone. It is agreed in principle that the oscillatory flow due to wave motion stirs up the sediment and makes it available for net movement by the mass transport current associated with the wave motion, or by any other net current. It has also been concluded from laboratory (Saville, 1950;Shinohara et al, 1958) and

*Research Hydraulic Engineer, U. S. Army Coastal Engineering Research Center, Washington, D. C.

field studies (Watts, 1953; Thornton, 1969; Cook and Gorsline, 1972) that sediment transport both onshore and offshore of the surf zone occurs in two modes - suspension and bed load. Equations (1) and (2) below are an expression of this. But their relative contribution to total transport still remains unspecified in both zones.

The total sediment transport rate per unit width in the zone outside the breakers can be written as,

$$q_T = q_b + q_s = \int_o^a C_0 \bar{u}(y)dy + \int_a^y \bar{C}(y)\bar{u}(y)dy \qquad (1)$$

where, q_b and q_s are the bed load and suspended load rates per unit width, C_0 is the average bed layer concentration, a is a measure of the thickness of bed layer, $\bar{u}(y)$ is the net current profile within the bed layer and in the interior of the fluid.

The total longshore sediment transport in the surf zone may be written as

$$Q_T = \int_o^{z_s}\int_o^a C_0(z)\bar{u}_l(y,z)dydz + \int_o^{z_s}\int_a^{h(z)} \bar{C}(y,z)\bar{u}_l(y,z)dydz \qquad (2)$$

where, $\bar{u}_l$ is the net current alongshore, the z co-ordinate is the distance across the surf zone, z_s is the width of the surf zone and h(z) is the local water depth.

For better design of future studies on nearshore sediment transport, two reviews have been made, one on the existing analytical approaches to predict suspended sediment distribution, $\bar{C}(y)$, with a summary of the techniques used or under development to measure suspended sediment concentration under waves, and the other on the readily available longshore transport data (Das, 1971). The reviews are, however, not exhaustive.

SUSPENDED SEDIMENT REVIEW

The equilibrium exchange equation is given by,

$$v_s \bar{C}(y) = -\overline{v'c'} = -\overline{v'\ell e}\ \frac{d\bar{C}(y)}{dy} = -\varepsilon_s \frac{d\bar{C}(y)}{dy} \qquad (3)$$

Integrating, $$\ell n \frac{\bar{C}(y)}{\bar{C}(a)} = -v_s \int_a^y \frac{dy}{\varepsilon_s} \qquad (4)$$

The determination of the exchange coefficient ε_s and its relation to known or easily accessible flow parameters is the central issue of the problem of sediment suspension.

In the case of open channel flows where the entire flow is a turbulent boundary layer or shear flow, the solution of the equilibrium exchange equation (3) under the conditions of linear shear stress distribution, Kármán's log-velocity distribution, and the Reynolds analogy between the momentum and mass diffusion coefficients defines the vertical distribution of suspended sediment concentration in terms of a reference concentration (Rouse, 1937) as,

$$\frac{\bar{C}(y)}{\bar{C}(a)} = \left(\frac{h-y}{y} \cdot \frac{a}{h-a}\right)^z \qquad (5)$$

where, $z = (v_s/\kappa U_*)$.

It is widely used in unidirectional flows. Bijker (1971) used it for computation of suspended sediment transport in the combination of waves and current and reported good agreement between measured and computed values of longshore transport.

In the case of waves, the boundary layer, usually very thin compared to the entire depth of flow, is the only source of turbulence to cause suspension of bed material, except near the breakers. Therefore, knowledge of the boundary layer turbulence is necessary to predict the distribution of suspended sediment concentration.

ANALYTICAL APPROACHES

If the exchange coefficient ε_s, is independent of the space variable y, then one obtains the exponential distribution of mean concentration from equation (4).

$$\frac{\bar{C}(y)}{\bar{C}(a)} = \exp\left[-\frac{v_s}{\varepsilon_s}(y-a)\right] \qquad (6)$$

The experimental results of Shinohara et al (1958) from a sloping beach with 0.2 mm sand and 0.3 mm pulverized coal showed the mean concentration to be exponentially distributed with depth. Figure (1) is a typical result from Shinohara et al with coal as sediment. Unlike the profiles with sand the concentration profile with coal shows a break point and this break point was considered as the lower limit of suspension. Using equation (6) and the known value of the settling velocity v_s, the exchange coefficient ε_s was calculated at various sections along the beach. The coefficient was found to increase slowly with decrease of depth, increasing faster before breaking and attaining maximum value near the breaker point and then decreasing shorewards, the decrease being faster in case of pulverized coal.

Hom-ma and Horikawa (1962) obtained a solution of the equilibrium exchange equation with the following assumptions. Prandtl's type mixing length hypothesis was used to characterize the eddy diffusion coefficient,

$$\varepsilon_y = \beta b^2 \left| \frac{du}{dy} \right| \tag{7}$$

where β is a constant, b is the vertical dimension of the water particle orbit, and u is the horizontal velocity of the water particle due to wave motion. Airy's wave theory was used to obtain b and u. The temporal variation of mean concentration during a wave period was expressed in the form,

$$C = \bar{C}(y) \left[1 + \xi \sin 2 \left(kx - \frac{2\pi t}{T}\right)\right] \tag{8}$$

where C is the instantaneous concentration, k is the wave number, and ξ is a constant. Under the above assumptions the solution of the steady state diffusion equation was obtained as,

$$\frac{\bar{C}(y)}{\bar{C}(a)} = \exp\left[-\alpha \frac{v_s}{c} \left(\frac{H}{L}\right)^3 \left(\frac{h}{L}\right) \mathrm{Sinh}^3 kh \, (F(n,kh))\right] \tag{9}$$

where, $n = \frac{y}{h}$, $n_a = \frac{h-a}{h}$, $\alpha = \frac{3}{\beta}$, $c = \frac{L}{T}$.

$$F(n,kh) = \frac{1}{2kh} \left[\frac{\mathrm{Coshkn}_a h}{\mathrm{Sinh}^2 kn_a h} - \frac{\mathrm{Coshknh}}{\mathrm{Sinh}^2 knh} \right] + \log \left| \frac{\tanh \frac{kn_a h}{2}}{\tanh \frac{knh}{2}} \right|$$

in which $\bar{C}$ (a) is the mean concentration at a reference depth above the bed, h is the undisturbed water depth, L is the wave length, H is the wave height, v_s is the settling velocity, and T is the wave period. The agreement between the theory and the experimental results was reported to be satisfactory.

Hom-ma, Horikawa, and Kajima (1965) modified the distribution function (9), by using Kármán's mixing length hypothesis,

$$\varepsilon_y = \kappa \ell^2 \left| \frac{du}{dy} \right| \tag{10}$$

and considering empirically the effects of ripple geometry on suspension. Velocity u, and the mixing length ℓ were determined from potential wave theory, and ε_y was given as,

$$\varepsilon_y = \frac{1}{K} \frac{Hc}{\mathrm{Sinhkh}} \frac{\mathrm{Sinh}^3 k(y+h)}{\mathrm{Cosh}^2 k(y+h)} \tag{11}$$

The concentration distribution was given by

$$\frac{\bar{C}(y)}{\bar{C}(a)} = \exp\left\{-K\frac{v_s}{cH}\ \frac{\text{Sinh}kh}{2k}\ [F(n_a, kh) - F(n, kh)]\right\} \qquad (12)$$

where,

$$F(n, kh) = \frac{\text{Cosh } nkh}{\text{Sinh}^2 nkh} - \log\left|\tanh\frac{nkh}{2}\right|$$

and,

$$n = \frac{y+h}{h},\ n_a = \frac{h-a}{h}\ ,\ c = \frac{L}{T}$$

The value of n_a was chosen arbitrarily as 0.05 and 0.1 in the analysis of laboratory and field data respectively.

The values of K were determined using the equation (12) from the measurements of mean concentration in the field and laboratory and were found to be a function of the relative depth n and a function of $\frac{H}{L}\cdot\frac{h}{\eta}$ or $\frac{H}{L}\cdot\frac{h}{\lambda}$ where η and λ are the height and length of the ripples respectively. The equation for K was obtained graphically as,

$$K = 0.161\ \left(\frac{y+h}{h}\right)^{0.833}\left(\frac{H}{L}\cdot\frac{H}{\lambda}\right)^{0.142}\left(\frac{H}{\lambda\text{sinh}kh}\right)^{0.270} \qquad (13)$$

from best fits of available data. While the effect of ripple geometry on sediment suspension is considered, the inconsistency of using potential velocity to derive turbulent diffusion coefficient existed and also the arbitrariness in the choice of the reference depth and concentration persisted. Fig. 1 shows a typical experimental result of Hom-ma et al (1965) using a horizontal bed of 0.178mm sand.The distributions of mean concentration both above a ripple crest and trough appear to be exponential as suggested by equation (12).

Noda (1967, 1971) derived the one-dimensional mass balance equation from the complete two-dimensional unsteady mass conservation equation under some simplifying assumptions. His measurements of suspended sediment concentration under standing waves using poly vinyl chloride grains of 0.13 mm diameter and of 1.13 specific gravity yielded profiles similar to those of Shinohara et al (1958) with pulverized coal.

From a comparison of the distributions of ε_s derived from his experimental results, from those of Hom-ma, Horikawa and Kajima (1965) and from the available field measurements and using the eddy diffusivity models of Hom-ma and Horikawa (1962), Hom-ma, Horikawa and Kajima (1965), Kishi (1964) and Kajiura (1964) he concluded that the distribution of ε_s was strongly dependent on the flow conditions near the bed and the bed roughness.

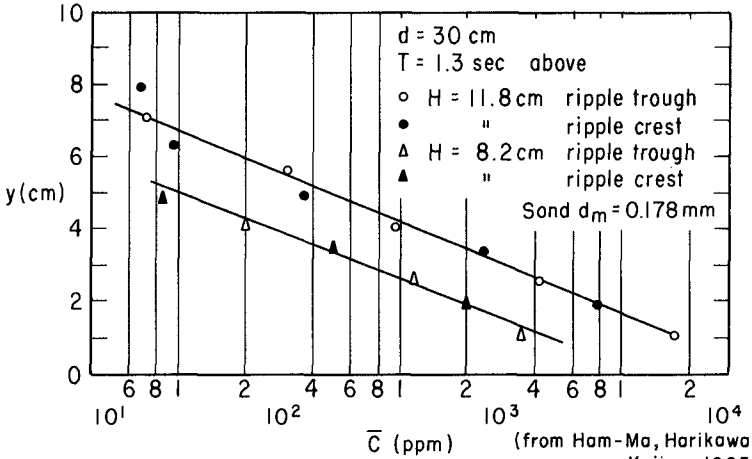

DISTRIBUTION OF $\overline{C}$

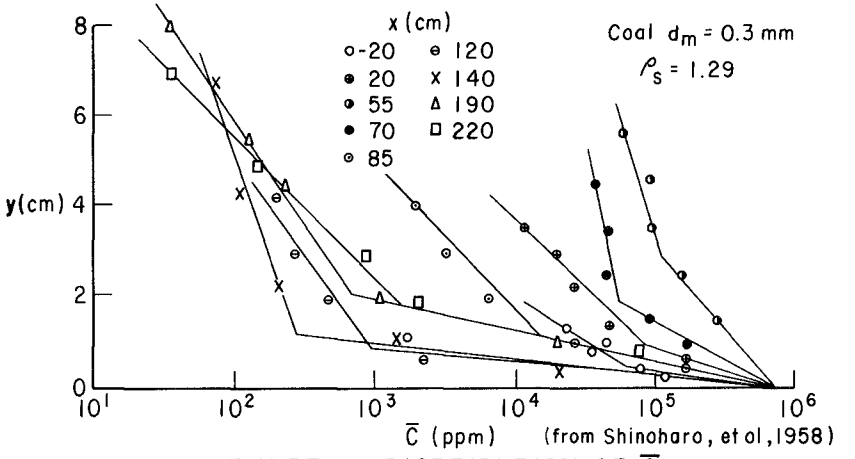

FIGURE 1. DISTRIBUTION OF $\overline{C}$

Noda (1971) assumed a constant ε_s and expressed the vertical distribution of concentration as,

$$\frac{\bar{C}(y)}{\bar{C}(a)} = \exp\left[-\left(\frac{v_s h}{\nu}\right)\left(\frac{\nu}{\varepsilon_s}\right)\left(\frac{y-a}{h}\right)\right] \tag{14}$$

He tried to investigate the relationship between the agitation parameter $\frac{\varepsilon_s}{\nu}$ and Reynolds number $\frac{U_o \delta}{\nu}$ ($\delta = \sqrt{\nu T/2\pi}$, U_o = amplitude of bottom velocity) using the mean concentration data above the break point in the profile where ε_y is constant. He also attempted to relate nondimensionalized height of the break point in the mean concentration profile, $\frac{a}{\delta}$ to $\frac{U_o \delta}{\nu}$. Since the range of Reynolds number in the data was narrow (60-200) he could not arrive at definite conclusions. But he felt that the height of break point was closely connected with the size of sand ripples and the diameter of the eddies they generate. He also felt that detailed study of the velocity field near the ripples was necessary for further clarification of the mean concentration profiles.

Hattori (1969) presented an analytical approach for two-dimensional distribution of suspended sediment concentration under standing waves. In this approach he introduced a delay distance caused by the relative motion between the sediment and fluid particles. He assumed the coefficient of diffusion and delay distance to be independent of space variables. He also assumed the instantaneous concentration to be made up of a mean and a fluctuation from the mean given as:

$$C(x,y,t) = \bar{C}(x,y) + C_j'(x,y) \sin 2j\omega t \tag{15}$$

where $\omega = \frac{2\pi}{T}$ and C_j' is the concentration fluctuation.

Under the above assumptions the distribution of mean concentration of suspended sediment under a standing wave was obtained as,

$$\bar{C}(x,y) = \bar{C}(o, a) \exp\left[\alpha(1-\text{Cos}kx) - \frac{\beta}{h}(y-a)\right] \tag{16}$$

where $\alpha = 2HL\left|\delta_x\right| / \pi \varepsilon_{sx} Th$

$\beta = v_s h / \varepsilon_{sy}$

δ_x is the delay distance and ε_{sx} and ε_{sy} are diffusion coefficients in the x and y directions respectively. He found close agreement between his theoretical and

experimental results (1969, 1971) on horizontal and vertical distribution of mean concentration under standing waves. Fig. 2 shows typical experimental results of Hattori (1969) and of Noda (1967). The agreement between theory and experiment is, however, dependent on the suitable choice of the parameters α and β, which in turn depend on the unknown quantities δ_x, ε_{sx} and ε_{sy}. Hattori (1971) obtained relationship between the delay distance δ_x and the characteristics of standing waves, on the assumption that the diffusion coefficient in the horizontal direction is almost equal to that in the vertical direction. The relationship obtained is,

$$\frac{|\delta_x|}{\xi} = 1.35\ (v_s/u)^{3/2} . \tag{17}$$

where $\xi = \frac{H}{h/L}$, a quantity proportional to the amplitude of the mean horizontal displacement, and u is the amplitude of the mean horizontal velocity of fluid particles under standing waves. Further his experimental results showed that the delay distance in the horizontal direction has a tendency to decrease with the increase in the mean horizontal velocity of fluid particles.

If the exchange coefficient is linearly dependent on the space variable y, the resulting concentration distribution would be linear on a log-log plot. The results of Kishi (1964), Bhattacharya (1971) and Das (1971) show such a tendency (Fig. 3). The results of Das (1971) were obtained in a swing flume where the oscillary boundary layer flow is reproduced on a prototype scale.

In data shown in Fig. 4, Horikawa and Watanabe (1968) attempted to demonstrate the agreement between the calculated eddy diffusivity using the constant eddy diffusivity model proposed by Kajiura (1964) for the inner layer and the estimated ε_y from measured distribution of mean concentration. Although acceptable agreement is apparent from the figure, the applicability of the Kajiura's eddy diffusivity model deserves further consideration. In bottom Fig. 4 Horikawa and Watanabe (1970) compared the eddy diffusivity ε_y obtained from point measurements of turbulent velocity fluctuations with the exchange coefficient determined from measured distribution of mean concentration. The authors have felt it necessary to improve their instrumentation techniques to attain greater accuracy in such measurements, needed for explication of the suspension mechanism under waves.

Using Bagnold's energy principle approach, Thornton (1969) proposed the following relationships for the mean suspended sediment transport rate per unit width of the profile outside the surf zone,

$$\overline{q_s} = \frac{S}{g(1 - \frac{\rho}{\rho_s})} \frac{V}{v_s} \left| \overline{u_{wh}\, \tau_h} \right| \tag{18}$$

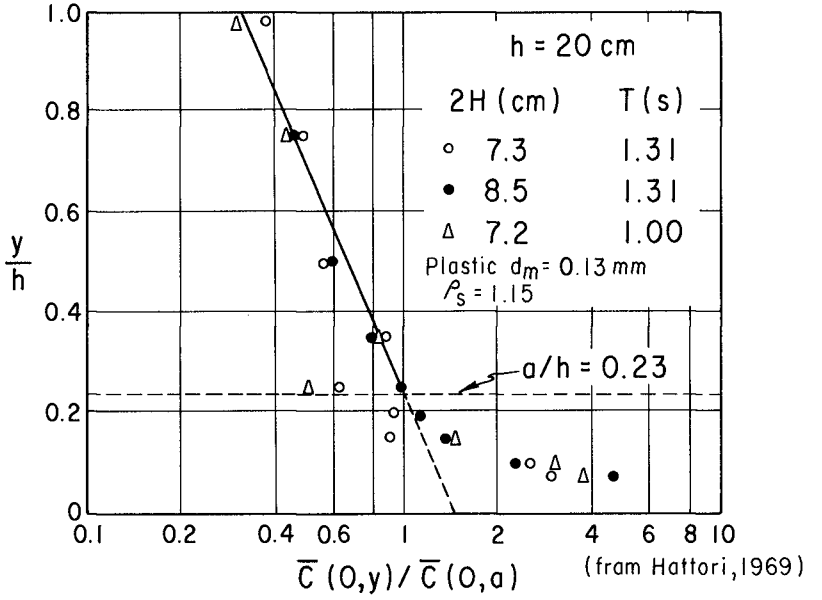

EXPERIMENTAL VALUES FROM NODA, 1967

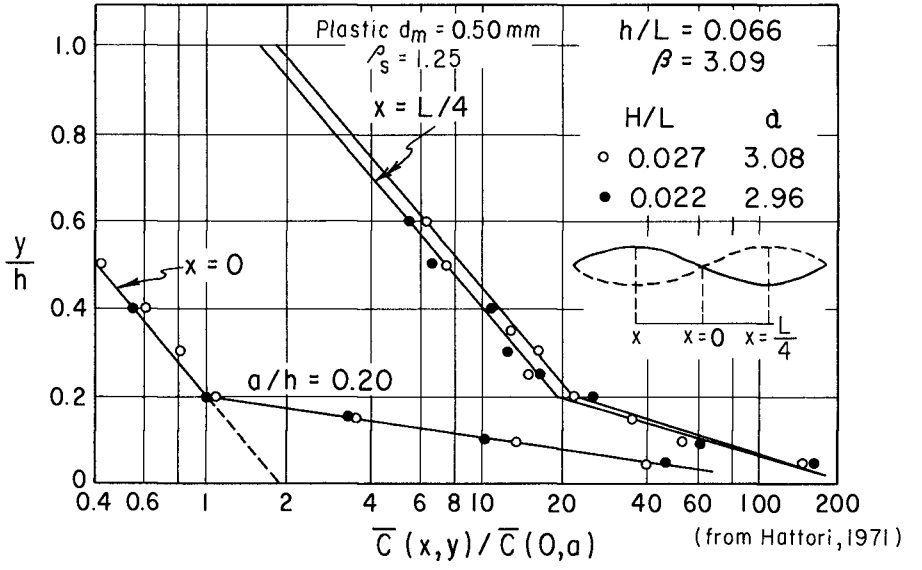

FIGURE 2. VERTICAL DISTRIBUTION OF SUSPENDED SEDIMENT CONCENTRATION (STANDING WAVES)

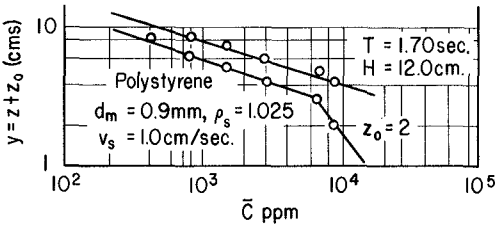

(Fram Kishi, 1964)

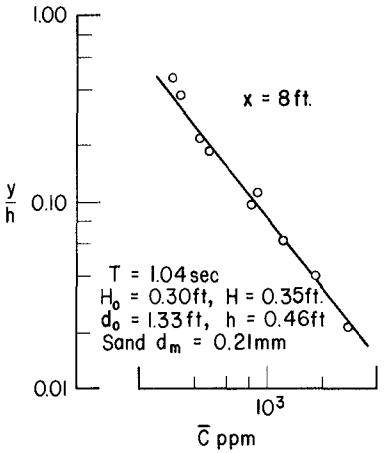

(From Bhattacharya & Kennedy, 1971)

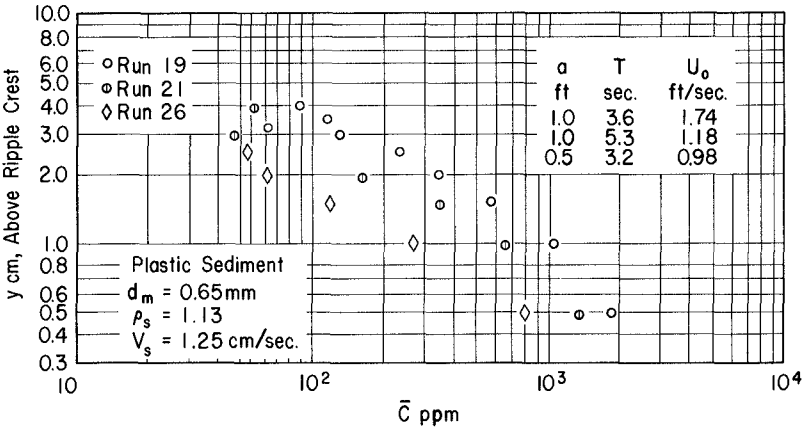

(From Das, 1971)

FIGURE 3. DISTRIBUTION OF $\bar{C}$

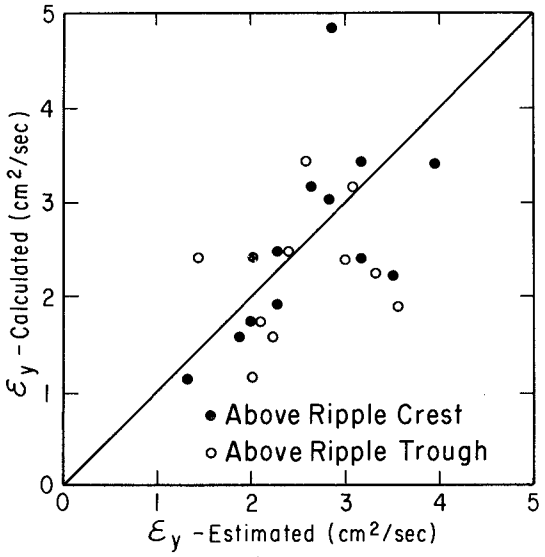

(from Horikawa and Watanabe, 1968)

COMPARISON BETWEEN ESTIMATED AND CALCULATED $\mathcal{E}_y$

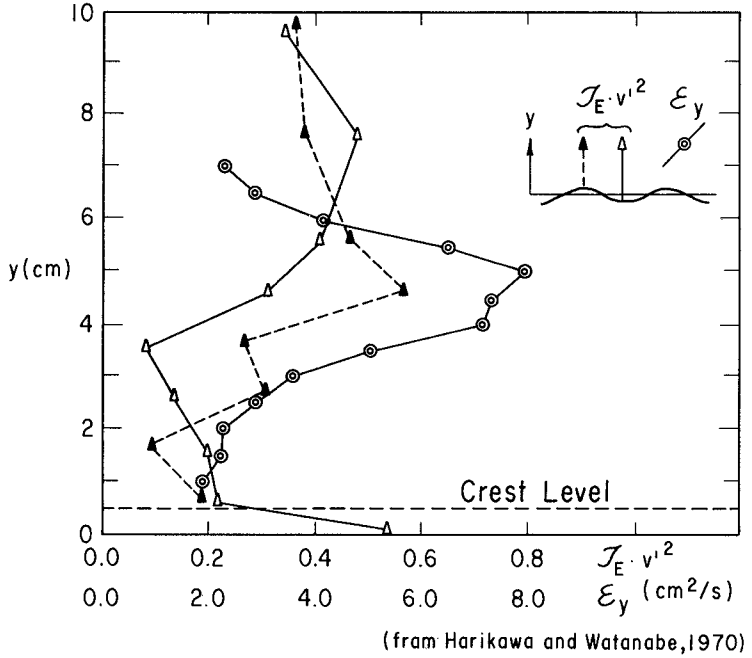

(from Harikawa and Watanabe, 1970)

FIGURE 4. COMPARISON BETWEEN $\mathcal{T}_E \cdot v'^2$ AND $\mathcal{E}_y$

and inside the surf zone,

$$\overline{q_s} = \frac{-S_s}{g(1 - \frac{\rho}{\rho_s})} \frac{V}{v_s} \frac{\partial ECg}{\partial x} \qquad (19)$$

where S and S_s are proportionality factors associated with suspended sediment transport, V is mean velocity component parallel to the beach, u_{wh} is water particle velocity due to wave motion at the bed, τ_h is shear stress at the bed, E is wave energy density, Cg is group velocity, and ρ and ρ_s are densities of fluid and sediment respectively. No measurements of suspended sediment transport rates are reported in the study for verification of the proposed relationships.

Bhattacharya (1970) and Kennedy and Locher (1971), time-integrating the complete two-dimensional mass conservation equation under the assumption of $\frac{\partial}{\partial x} << \frac{\partial}{\partial y}$ and using the concept of a delay time between motions of sediment and fluid particles similar to the delay distance concept of Hattori (1969), obtained the one-dimensional mass conservation equation given as,

$$\overline{C_p \left[v_p - \tau \frac{\partial v_p}{\partial t}\right]} - v_s \overline{C} = \varepsilon_y \frac{d\overline{C}}{dy} \qquad (20)$$

where, C_p is the periodic component of concentration and v_p is the vertical component of fluid velocity due to orbital motion and τ is the delay time. However, motion picture photography of sediment suspension process led Kennedy and Locher (1971) to postulate that the periodic part of velocity near the bed is composed of wave orbital motion, velocity due to the eddies and the velocity perturbation due to the waviness of the bed. Therefore C_p also includes all the three above effects and the convective term $\overline{C_p[v_p - \tau \frac{\partial v_p}{\partial t}]}$ reflects suspension due to all the three effects. But considering ε_y and τ as constant and only the effect due to vertical orbital motion v_p Bhattacharya (1970) and Kennedy and Locher (1971) obtained the solution to (20) as,

$$\frac{d\overline{C}}{dy}\left[\frac{\tau k_1 \eta^2 \sigma^2}{2h^2} y^2 + \varepsilon_y\right] = - v_s \overline{C} \qquad (21)$$

and upon integration,

$$\ln \frac{\bar{C}_o}{\bar{C}(y)} = \frac{hv_s}{\eta\sigma\sqrt{\frac{\tau k_1 \varepsilon_y}{2}}} \tan^{-1}\left\{\frac{\eta\sigma}{h}\sqrt{\frac{\tau k_1}{2\varepsilon_y}}\ \frac{y - y_o}{1 + \frac{\eta\sigma}{h}\sqrt{\frac{\tau k_1}{2\varepsilon_y}}\ yy_o}\right\} \quad (22)$$

where h is the undisturbed water-depth, η is wave amplitude and $\sigma = \frac{2\pi}{T}$.

Arguing that turbulent diffusion under wave motion is limited to regions near the boundary and wave induced convection dominates in the interior of the fluid, ε_y can be approximated to zero. With this argument Kennedy and Locher (1971) obtained the following distribution function from (20).

$$\ln \frac{\bar{C}(y)}{\bar{C}o} = \frac{2v_s h^2}{\tau k_1 \eta^2 \sigma^2}\ [\frac{1}{y} - \frac{1}{y_o}\ ] \quad (23)$$

Arguing the other way that close to the bed turbulence is predominant and wave induced convection is small and therefore considering $k_1 = 0$ the classical Schmidt equation was obtained,

$$v_s \bar{C} + \varepsilon_y \frac{d\bar{C}}{dy} = 0, \quad (24)$$

considering the functional dependence of ε_y as,

$$(\frac{\varepsilon_y}{\varepsilon_o}) = (\ \frac{y}{y_o}\ )^{\alpha} \quad (25)$$

where $\varepsilon_o = \varepsilon_y\ (y_o)$. Kennedy and Locher (1971) obtained the following distribution functions after integration of (24),

$$\alpha = 1 \qquad \frac{\bar{C}(y)}{\bar{C}_o} = (\frac{y}{y_o})^{\frac{-v_s y_o}{\varepsilon_o}} \quad (26)$$

$$\alpha \neq 1 \qquad \ln \frac{\bar{C}(y)}{\bar{C}_o} = \frac{v_s y_o}{(1 - \alpha)\ \varepsilon_o}\ [1 - (\frac{y_o}{y})^{\alpha - 1}\ ] \quad (27)$$

$$\alpha = 0 \qquad \frac{\bar{C}(y)}{\bar{C}_o} = \exp\ [-\frac{v_s}{\varepsilon_o}\ (y - y_o)] \quad (28$$

Bhattacharya's (1970) experimental results from a laboratory study under equilibrium sloping beach conditions using .21 mm quartz sand did not support the distribution functions (22), (23) and (28). His results of mean concentration $\bar{C}$ varied linearly with depth on a logarithmic graph (middle Fig. 3) suggesting a power type distribution given as,

$$\frac{\bar{C}(y)}{\bar{C}_o} = \left(\frac{y}{h}\right)^{-z} \tag{29}$$

which corresponds to the distribution given by (26).

Bhattacharya (1970) then used a simple dimensional analysis to determine the exponent z, and found to be equal to $\frac{v_s T}{\varepsilon_o h}$ where

$$\varepsilon_o = \frac{\varepsilon_y T}{hy} = f\left(\frac{\eta}{h}, \frac{\eta}{gT^2}\right) \tag{30}$$

Using his experimental results he obtained the variation of ε_o against h/η with η/gT^2 as a parameter.

Kennedy and Locher (1971) from further tests using horizontal bed with fixed ripples and using small quantity of 0.14 mm diameter sand, tried to verify the validity of the mean concentration distribution functions given by (22), (23), (26) and (28). The fixed bed ripples were used with the purpose of removing the arbitrariness in defining the depth of concentration measurements due to ripple migration and change of ripple height. The electro-optical meter utilized in Bhattacharya's study (1970) was further developed for higher sensitivity and better performance and smaller sediment size was used to increase measurement accuracy at lower concentrations at higher distances from the bed. The verification yielded positive results for all the four functions in their expected regions of validity. Fig. 5 displays a typical example of data verifying the distribution given by equation (26).

SUMMARY

Analytical approaches:

The four or five analytical approaches which exist to predict the suspended sediment distributions simply illustrate the complex nature of the problem of sediment suspension under waves. A satisfactory solution to the problem still does not exist. It must be recognized that turbulence is the major cause of suspension of sediment in a turbulent flow. The only source of turbulence under waves is the boundary layer, except near breakers. In the equilibrium exchange equation the effect of turbulence is considered through the exchange coefficient. Future research must, therefore, concentrate on the detailed study of the boundary layer turbulence and hence the exchange coefficient. Precise measurements of suspended sediment concentration under suitable flow conditions and with properly developed instrumentation will supplement the effort on the determination of the exchange coefficient from measurements of boundary layer turbulence and its relation to flow parameters and bed roughness. This will provide a relative distribution of concentration in terms of a reference concentration C_o, which may be determined

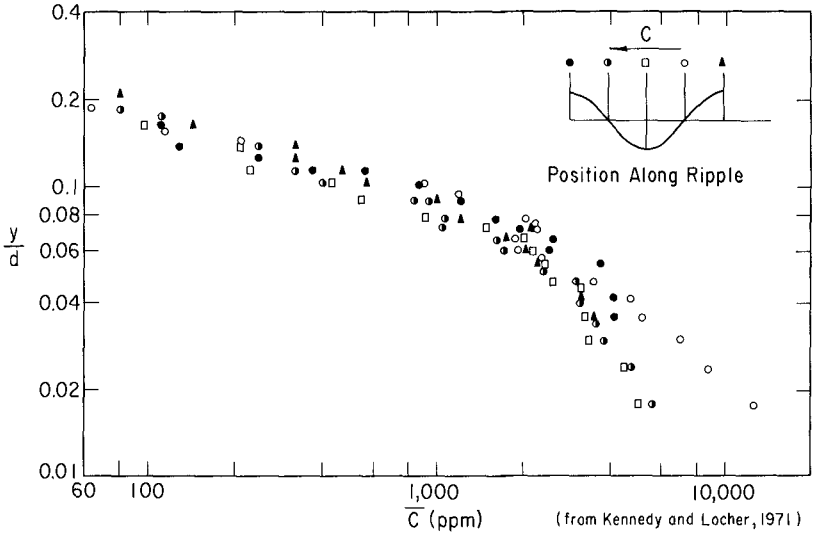

FIGURE 5. VARIATION OF $\bar{C}$ WITH y/d

from the basic approach presented by Einstein (1971). However, in order to be able to compute the net transport rate in any direction the next problem would be to obtain the distribution of net current in that direction in the suspension layer as indicated by equation (1). This problem will continue to be a field of active research for several years to come.

Suspended sediment measuring techniques:

Three types of time-integrated samplers, namely pump samplers (Watts, 1953; Fairchild, 1956; 1959; Noda, 1967, 1971), syphon samplers (Shinohara et al, 1958; Hom-ma and Horikawa, 1962) and bamboo samplers (Fukushima and Mizoguchi, 1958; Fukushima and Kashiwamura, 1959; Noda, 1967) and three types of in situ measuring techniques, namely photography (Bijker, 1971), various configurations of electro-optical meters (Hom-ma, Horikawa and Kajima, 1965; Horikawa and Wantanabe, 1970; Noda, 1971; Bhattacharya, 1970; Bhattacharya and Kennedy, 1971; Kennedy and Locher, 1971; Das, 1971) and electronic particle counter (Hattori, 1969, 1971) have been used in the studies reviewed. In laboratory applications negligible disturbance to flow and precision in measurements are the most important requirements. Quantities to be measured are the long time mean and unsteady mean concentrations at a point. Although a random concentration fluctuation does exist conceptually, its measurement using sediment particles is apparently difficult to interpret. It appears that the electro-optical meters offer the best possibility in most laboratory applications. With suitable design this can be used in the field. A particle counter appears to be good at low concentrations, where the probability of two or more particles occupying the probe volume simultaneously is very small. However, the particle velocity must be determined in order to compute concentration from particle counts. Pump samplers with their sampling efficiency properly evaluated are simple and easily operable tools for field applications.

LONGSHORE SEDIMENT TRANSPORT DATA REVIEW

The longshore transport data compiled by Das (1971) form the basis of this review and analysis. The data are taken from six laboratory studies with 177 observations and from four field studies with 25 observations. An observation has been defined here as a data point, for which the transport rate and the associated wave and sediment characteristics are known. The purposes of the review were to see if the empirical relationships between longshore transport rate and the alongshore component of wave energy flux could fit the available data with reasonable scatter and specifically to up-date the visual line of fit in CERC TR-4.

The relationships tested were $Q = A_1 E_a$, $Q = A_2 E_a^B$ and $I_\ell = A_3 E_a$ where, Q is volume transport rate in cubic yards per day, E_a is alongshore component of wave energy flux in lbs per day per foot of beach and I_ℓ is immersed weight transport rate in lbs per day. The volume transport rate Q is related to the immersed weight transport rate I_ℓ (Bagnold, 1963) by,

$$I_\ell = (\rho_s - \rho) g a' Q \qquad (31).$$

where, a' is a correction factor for pore space and it has been assumed as 0.6 in the analysis. The alongshore wave energy flux E_a has been computed in the 177 laboratory observations by using the relationship suggested in CERC TR-4.

$$E_a = \frac{E_o}{2} N K_R^2 \text{ Sin } \alpha_b \text{ Cos } \alpha_b \qquad (32)$$

where $E_o = \frac{\gamma H_o^2 L_o}{8}$, γ is unit weight of sea water H_o and L_o are deep water wave height and wave length, N is number of waves per day, K_R is refraction coefficient and α_b is the breaker angle.

In case of the field studies of Watts (1953), Caldwell (1956) and Komar (1969), the energy flux computed by the investigators have been used, except that the energy flux values of Watts and Caldwell were reduced by a factor 2 to correspond to energy based on root-mean-square wave height, rather than the significant wave height used by them (Inman and Frautschy, 1966). This is consistent with the theoretical prediction of Longuet-Higgins (1952) for narrow band wave spectrum with waves of random phases.

Fig. 6 is the plot of Q vrs E_a for the data reviewed. The data of Johnson (1952) and of Thornton (1969) are also plotted. But these two sets of data are not included in the least square procedure to examine the empirical relationships. The reasons are that Johnson's data do not include the observation of wave angles and Thornton's data do not provide transport measurement across the whole width of the surf zone and, moreover, he apparently measured only the bed load transport. The figure shows only two lines of best fit using $Q = A_1 E_a$ for all data and for all but light weight material data and the line proposed in CERC TR-4. Figure 7 shows only the scatter-areas of plots of I_ℓ against E_a. The reduction of scatter in laboratory data due to inclusion of density of material in I_ℓ can be noticed. In this figure are shown the line of best fit now obtained for all available data, the line proposed by Komar (1969) for field data and the line proposed by Inman and Frautschy (1966) on the basis of data available at that time and using significant wave energy flux for the data of Watts and Caldwell.

SUMMARY

As a rule-of-thumb the volume rate relationship $Q = 1.93 \times 10^{-4} E_a$ where Q is in cubic yards per day and E_a is in ft-lbs per day per foot of beach, or the immersed weight rate relationship $I_\ell = .35\ E_a$ may be used as a guide. It is suggested and also indicated by equation (2) that the near-future studies, both in the laboratory and in the field should include, (1) simultaneous measurements of bed load and suspended load; (2) simultaneous measurement of velocity field in and shoreward of the breaker zone and the imposed wave conditions, and that systematic laboratory studies be made to evaluate scale model relationships by simulating known prototype conditions for better interpretation and the extrapolation of laboratory data to field conditions.

ACKNOWLEDGEMENT: Data presented in this paper, unless otherwise noted, were obtained from research conducted by the United States Army Coastal Engineering Research Center under the Civil Works research and development program of the United States Army Corps of Engineers. Permission of the Chief of Engineers to publish this information is appreciated. The findings of this paper are not to be construed as official Department of the Army position unless so designated by other authorized documents.

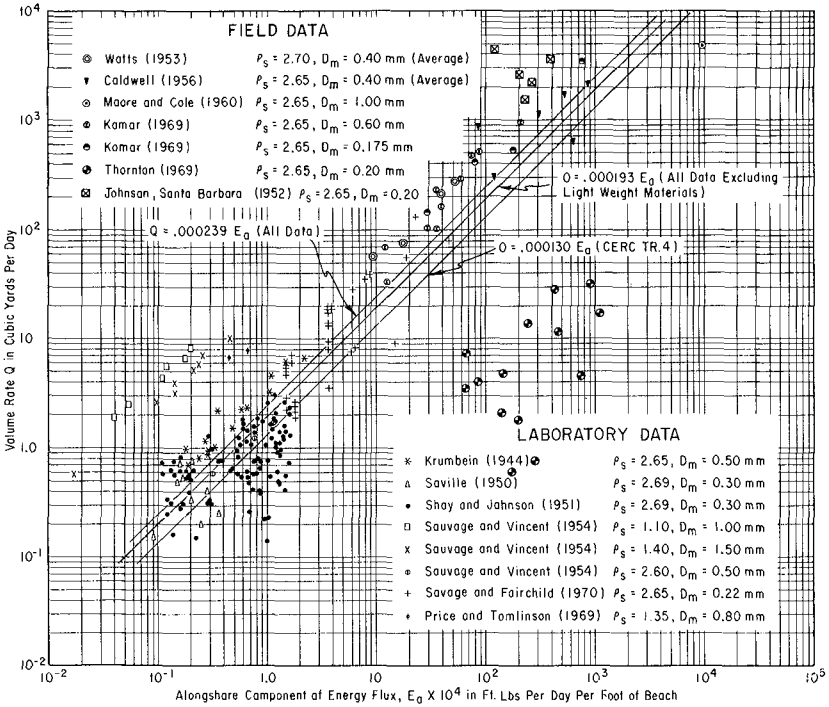

FIGURE 6. RELATION BETWEEN Q AND E_a

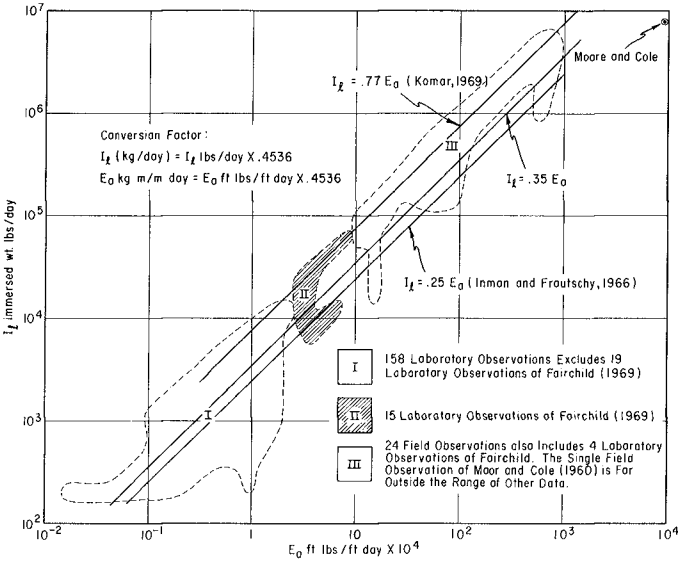

FIGURE 7. RELATION BETWEEN IMMERSED WEIGHT LITTORAL TRANSPORT RATE I_l AND LONGSHORE COMPONENT OF WAVE ENERGY FLUX PER UNIT LENGTH OF BEACH E_o

REFERENCES

Suspended Sediment

Bhattacharya, P. K., 1971, "Sediment Suspension in Shoaling Waves," Ph. D. Thesis, The University of Iowa.

Bhattacharya, P. K. and John F. Kennedy, 1971, "Sediment Suspension in Shoaling Waves," 14th Congress of IAHR, Paris, vol. 4.

Bijker, E. W., "Longshore Transport Computations," Journal of WH&C Div. ASCE, Nov. 1971.

Cook, D. O. and D. S. Gorsline, 1972, "Field Observations of Sand Transport by Shoaling Waves," Marine Geology, vol. 13, no. 1.

Das, M., 1971, "Mechanics of Sediment Suspension Due to Oscillatory Water Waves," Proc. of Sedimentation Symposium, Univ. of California, Berkeley, 1971, (Publication, Colorodo State Univ., Fort Collins)

Einstein, H. A., 1971, "A Basic Description of Sediment Transport on Beaches," U. C., Berkeley, HEL 2-34.

Fairchild, J. C., "Development of Suspended Sediment Samplers for Laboratory Use under Wave Action," Beach Erosion Board, Bulletin, Vol. 10, No. 1, July. 1956.

Fairchild, J. C., "Suspended Sediment Sampling in Laboratory Wave Action," Beach Erosion Board, Tech. Memo. No. 115, June, 1959.

Fukushima, H. and Y. Mizoguchi, Field Investigation of Suspended Littoral Drift, Coastal Engineering in Japan, vol. 1, 1958.

Fukushima, H. and M. Kashiwamura, Some Experiments on Bamboo Samplers, Coastal Engineering in Japan, Vol. 4, 1961.

Glover, J. R., P. K. Bhattacharya, and J. F. Kennedy, 1969, "An Electro-Optical System for Measurement of Mean and Statistical Properties of Sediment Suspensions," Iowa Institute of Hydraulic Research, The Univ. of Iowa, IIHR Rep. No. 120.

Hattori, M., 1969, "The Mechanics of Suspended Sediment Due to Standing Waves," Coastal Engineering in Japan, 12.

Hattori, M., 1971, "A Further Investigation of the Distribution of Suspended Sediment Concentration due to Standing Waves," Coastal Engineering in Japan, Vol. 14.

Hom-ma, M. and K. Horikawa, 1962, "Suspended Sedimnt Due to Wave Action," Proc. Eighth Conf. on Coastal Engineering, Mexico City.

Hom-ma, M. and K. Horikawa, 1963, "A Laboratory Study on Suspended Sediment Due to Wave Action," Proc. Xth Congress of the IAHR, London.

Hom-ma, M., K. Horikawa, and R. Kajima, 1965, "A Study of Suspended Sediment Due to Wave Action," Coastal Engineering in Japan, 8,

Horikawa, K, and A. Wantanabe, 1970, "Turbulence and Sediment Concentration Due to Waves," 12th International Conference Coastal Engineering.

Kajiura, K., "On the bottom Friction in an Oscillatory Current," Bull. Earthq. Res. Inst., Vol. 42, pp 147-174.

Karaki, S., "Modern Measuring Techniques," Chapter 15, River Mechanics, Vol. 1, Colorado State Univ., 1971.

Kennedy, J. F. and F. A. Locher, 1971, "Sediment Suspension by Water Waves", Univ. of Iowa, Institute of Hydraulic Research, Iowa City, Iowa.

Kishi, C., "Research Notes on the Flotation of Sediment Due to Waves," Research News on Coastal Disaster, No. 2, 1964.

Noda, H., "Suspension of Sediment Due to Wave Action," Proc. of 14th Conf. on Coastal Engineering in Japan, Dec. 1967, pp 306-314. (Translation by Coastal Eng. Research Center)

Noda, H., T. Iwasa, "Mechanism of Bottom Sediment Suspension by Waves," 18th Coastal Engineering Conference, 1971, Japan, pp 349-352.

Rouse, H., 1937, "Modern Conceptions of the Mechanics of Turbulence," Trans. Am. Soc. Civil Engrs., Vol. 102.

Saville, T., Jr., "Model Study of Sand Transport Along an Infinitely Long, Straight Beach," Transactions, AGU, Vol. 31, No. 4, August, 1950, pp. 555-565.

Shinhara, K., et al, 1958, "Sand Transport Along a Model Sandy Beach by Wave Action," Coast. Eng. in Japan, Vol. 1.

Thornton, E. B., 1969, "Longshore Current and Sediment Transport," Dept. of Coastal and Oceanogr Eng, Univ. of Florida, Gainesville, Tech REport No. 5.

Longshore Sediment Transport Data

Caldwell, Joseph M., "Wave Action and Sand Movement Near Anaheim Bay, California," BEB Tech Memo No. 68, Corps of Engineers, U. S. Department of the Army, Washington, D. C., February, 1956.

Coastal Engineering Research Board, Subcommittee Report, "Analysis of Data on Littoral Transport," February, 1970 (unpublished).

Das, M. M., "Longshore Sediment Transport Rates," CERC Miscellaneous Paper No. 1-71, Sept. 1971.

Fairchild, John C., "Laboratory Tests of Longshore Transport," Proceedings 12th Conference in Coastal Engineering, Washington, D. C., 1970.

Inman, D. L. and J. D. Frautschy, "Littoral Processes and the Development of Shorelines," Coastal Engineering, 1966, ASCE, p. 511-536.

Johnson, J. W., 1952, "Sand Transport by Littoral Cu-rents," IER, Wave Research Lab., U. C., Berkeley Tech. Report Series 3, Issue 338.

Komar, P. D., "The Longshore Transport of Sand on Beaches," Ph. D. Thesis, University of California, San Diego, 1969.

Komar, P. D., "The Mechanics of Sand Transport on Beaches," JGR, Vol. 76, No. 3, Jan 20, 1971, p. 713-721.

Krumbein, W. C., "Shore Currents and Sand Movement on a Model Beach," BEP Tech. Memo. No. 7, Office of the Chief of Engineers, Washington, D. C., September, 1944.

Longuet-Higgins, M. S., "On the statistical distribution of the height of sea waves," Journal of Marine Research, Vol. 11, 1952, p. 245-266.

Manohar, M., "Discussion of Laboratory Determination of Littoral Transport Rates," Journal of the Waterways and Harbors Division, Proc. ASCE, Vol. 38, No. WW4, November 1962, p. 144-147.

Moore, G. W., and J. Y. Cole, "Coastal Processes in the Vicinity of Cape Thompson, Alaska," Geologic Investigations in Support of Project Chariot in the Vicinity of Cape Thompson Northwestern Alaska - Preliminary Report Final report U. S. Geol. Sruvey Trace Elements Investigations Report 753, 1960.

Price, W. A. and K. W. Tomlinson, "The Effect of Groynes on Stable Beaches," Proceedingsof 11th Conference on Coastal Engineering, Vol. 1, September, 1968, and Personal Communication with Mr. Tomlinson, December 8, 1970.

Sauvage, M. G. and M. G. Vincent, 1954, "Transport Littoral Formation de Leches et de Tombolos," Fifth Conference on Coastal Engineering, Grenoble, France.

Savage, R. P., "Laboratory Determination of Littoral Transport Rates," Journal of the Waterways and Harbors Division, ASCE, No. WW2, May, 1962, p. 69-92.

Saville, Thorndike, Jr., "Model Study of Sand Transport Along an Infinitely Long, Straight Beach," Transactions, AGU, Vol. 31, No. 4, August, 1950, p. 555-565.

Saville, Thorndike, Jr., "Discussion of Laboratory Determination of Littoral Transport Rates," Journal of Waterways and Harbors Division, ASCE, Vol. 38, No. WW4, Nov. 1962, p. 141-143.

Shay, E. A., and J. W. Johnson, "Model Studies on the Movement on Sand Transported by Wave Action Along a Straight Beach," Issue 7, Series 14, Inst of Eng'g Research, University of California, Berkeley, California, 1951.

Thornton, E. B., 1969, "Longshore Current and Sediment Transport," Dept. of Coastal and Oceanog. Engineering, Univ. of Florida, Gainesville, Tech. Report No. 5.

Watts, George M., "A Study of Sand Movement at South Lake Worth Inlet, Florida," BEB Tech. Memo. No. 42, Corps of Engineers, U. S. Army Washington, D. C., October, 1953.

CHAPTER 55

DISTRIBUTION OF SEDIMENT TRANSPORT ACROSS THE SURF ZONE

Edward B. Thornton
Assistant Professor of Oceanography

Naval Postgraduate School
Monterey, California

ABSTRACT

The wave-induced sand transport alongshore is investigated by an energy principle approach. Although the energy approach has been used before, this is the first application to comparing theory and measurements of the distribution of littoral transport along a line perpendicular to the beach. Bed load transport equations are formulated for outside and inside the surf zone. Sand transport data were collected in the field using bed load traps. Wave, tide, wind, and current information was collected simultaneously in order to verify the derived predictive equations for longshore current and sediment transport. Quite reasonable predictions are obtained for the relative distribution of bed load transport, both inside and outside the surf zone.

INTRODUCTION

The wave induced sand transport alongshore is investigated using an energy principle approach. This method relates the work expended in transporting a quantity of sand to the energy available for transporting purposes. The development follows basically that of Bagnold [1] with some modifications to better suit the assumed conditions. The analysis is similar to Komar's [2] which was also based on Bagnold's approach. The inherent advantage of an energy approach is the simplicity and ease of physical interpretation. This type of approach also has had the most success for engineering applications in the oceans.

Bed load transport due to combined wave and current action is considered. The areas inside and outside the surf zone are discussed separately. Bagnold applied his analysis only to waves in deeper water, but the principle would be expected to be equally valid inside the surf zone.

The quantity of sand transported is a function of the energy available for transporting the sediments. This

energy is related to the energy utilized in bottom friction, viscous dissipation, and turbulence. For the case of waves and currents superposed, wave energy is utilized to put the sediment in motion, and, once in motion, the sediments can be acted upon by weak secondary currents. Hence, littoral drift can be considered as a stirring by the waves, which induces little net motion, and transport by the longshore current, which has net motion in the direction parallel to shore.

Energy dissipation outside the surf zone is primarily due to bottom friction, that is, most of the work is done on the bottom. Hence, the primary mode of transport outside the surf zone is by bed load. Energy is dissipated inside the surf zone both by the turbulence in the breaking waves and by friction acting on the bottom so that bed and suspended load transport are important.

BED LOAD TRANSPORT

It is assumed, in the problem being considered, that the bottom contours are straight and parallel so that the bed slope in the direction of net sand transport (parallel to the beach in the y-direction) is zero. It is further assumed that the slope of the beach is very small and that it is in dynamic equilibrium such that there is no net transversal (perpendicular to the beach in the x-direction) movement of sand. Hence, the slope of the beach will not affect the net sand transport and can be neglected. This is to say that the sand grains will maintain, on the average, the same relative position with respect to the bottom profile (distance offshore).

The average rate of work per unit bed area, P_h, required to overcome the resisting stress and maintain the bed load movement is proportional to the immersed weight of moving sand times the velocity of the sand grains moving along the bed, u_{sh}

$$P_h \propto \left(1 - \frac{\rho}{\rho_s}\right) g m_h \overline{|\vec{u}_{sh}|} \qquad (1)$$

where ρ is the density of the fluid, ρ_s the density of the sediments and m_h the mass of the bed load transport. The absolute value sign is necessary since the sand grains can oscillate back and forth in response to the wave motion. The fluid motion responsible for the sediment transport is that of the waves and currents. The waves are assumed simple harmonic with zero mean motion, so that the net transport is due to the mean current in the longshore direction only. The net mass transport of the sediment per unit time per unit width perpendicular to the beach is defined

$$\bar{q}_h(x) = \bar{m}_h V_{sh} \tag{2}$$

where $\bar{m}_h = \bar{m}_h(x)$ is the average mass of moving sediment per unit area of the bed with the mean velocity, $V_{sh}(x)$ in the longshore direction.

Substituting Equation (2) into (1) leads to the expression for bed load transport.

$$\bar{q}_h \left(1 - \frac{\rho}{\rho_s}\right) g \frac{|\bar{u}_{sh}|}{V_{sh}} \propto P_h \tag{3}$$

The actual mean velocities of the sand grains are very difficult to measure. The mean sand grain velocities must be related to more measurable quantities in order to make Equation (3) workable. It is assumed, as a first approximation, that the mean velocity of the moving sand grains is proportional to the mean shear velocity in the direction of the sand particle motion. The mean shear velocity is defined

$$|\overline{u_*}| = \sqrt{\frac{|\bar{\tau}_h|}{\rho}} \tag{4}$$

where $\bar{\tau}_h$ is the total mean bed shear stress. The ratio of the mean particle velocities is then given by

$$\frac{|\bar{u}_{sh}|}{V_{sh}} = b \left|\frac{\bar{\tau}_h}{\bar{\tau}_{hy}}\right|^{\frac{1}{2}} \tag{5}$$

where b is a constant of proportionality. It was shown by Thornton [3] that the ratio of the total mean bed shear stress $\bar{\tau}_h$ to the mean bed shear stress due to the mean current in the y direction, $\bar{\tau}_{hy}$, is given by

$$\frac{\bar{\tau}_h}{\tau_{hy}} = \frac{2}{\pi} \frac{u_{mh}}{V} \tag{6}$$

where V is the mean longshore current and u_{mh} is the maximum particle velocity of the waves at the bed. Hence, the ratio of the sand velocities is proportional to the square root of the water particle velocity ratio

$$\frac{|\bar{u}_{sh}|}{V_{sh}} \propto \left(\frac{u_{mh}}{V}\right)^{\frac{1}{2}} \tag{7}$$

The mean rate of bed load transport of sand per unit width in the longshore direction can then be expressed

$$\bar{q}_h \propto \frac{1}{g(1 - \frac{\rho}{\rho_s})} \sqrt{\frac{V}{u_{mh}}} P_h \tag{8}$$

The basic idea to underline is that the mass of sand transported is proportional to the available power.

A. Bed Load Transport Outside the Surf Zone

The mean work done in transporting the bed load and the available power are assumed proportional to each other. The fluid power available to transport the bed load is measurable as the product of the bottom shear stress due to the motion of the fluid times a representative flow velocity. This available power is equal to the work done on the bottom. The bed shear stress must be considered composed of both the wave and mean current components. The action of this combined, or total bed shear stress, can be thought of as the loosening of the sand grains off the bed which are then available for transport by the mean current. The mean current is the longshore current alone as the wave motion has little or no net motion. The total power expended is due to the combined wave and current action.

Outside the surf zone, there is normally little turbulent energy dissipated. Provided percolation can be neglected, the frictional energy dissipated on the bottom represents most of the energy dissipated. The reduction in wave energy, measurable as a decrease in wave height, is then indicative of the energy spent in sediment transport. In this case, the available power for sediment transport would be proportional to the total change in energy flux.

$$P_h = \frac{-\partial E \vec{c}_g}{\partial x} = \left| \overline{u_{wh}\ \tau_h} \right| \tag{9}$$

where E is the wave energy density and c_g the group velocity of the waves. u_{wh} is the water particle velocity at the bed due to the waves. The bottom shear stress assuming small wave angles of approach is given by

$$\tau_h = \frac{\rho f_w}{2} u_{wh} \left| u_{wh} \right| \tag{10}$$

where f_w is a friction factor.

Jonsson [4] showed that the friction factor for wave motion alone for rough turbulent boundary layers could tentatively be represented by

$$\frac{1}{4\sqrt{f_w}} + \log \frac{1}{4\sqrt{f_w}} = -0.08 + \log \frac{\xi_h}{r} \tag{11}$$

where r is a measure of roughness given by the ripple height and ξ_h is the maximum water particle excursion amplitude of the fluid motion at the bottom as predicted by linear wave theory. This representation is used in this formulation.

The longshore current formulation is based on the "radiation stress" concept where the changes in excess momentum flux due to the wave motion is balanced by the bottom shear stress due to the mean current (see Thornton [3]). The formulation includes changes in the mean water level. The longshore current outside the surf zone is given by

$$V = -\frac{\pi\sigma}{pg\ kf_w H} \cosh kh \frac{\partial}{\partial x} \left(E \frac{c_g}{c} \sin 2\alpha\right) \tag{12}$$

where k is the wave number, σ is the radial frequency, H is the wave height, α is the angle between the wave crest and bottom contour, c is the wave speed, and h is the depth of water.

The mean bed load transport of sand per unit time per unit width in the longshore direction can then be expressed

$$\bar{q}_h = \frac{B}{g(1 - \frac{\rho}{\rho_s})} \sqrt{\frac{V}{u_{mh}}} \left|\overline{\tau_{wh}\ \tau_h}\right| \tag{13}$$

where all the proportionality factors have been combined into B and must be determined experimentally.

B. Bed Load Transport Inside Surf Zone

Inside the surf zone, the dissipation of energy is greatly increased and is largely due to turbulent dissipation. The transport inside the surf zone is much greater than outside, and a large proportion of the transport is suspended load for which there is more energy available for transporting purposes. The actual bed load is still a function of the energy dissipated on the bottom which decreases with decreasing depth. There is also an additional amount of work done on the bed by turbulent energy being diffused and convected downward due to the breaking waves. It is assumed that inside the surf zone the bed load as well as the suspended load is a function of the total energy dissipated including both the energy dissipated on the bottom due to friction and turbulent energy dissipation due to the breaking waves.

$$P_h = \frac{-\partial \vec{Ec}_g}{\partial x} \tag{14}$$

In the present analysis, it is assumed that the waves act as spilling breakers inside the surf zone and that they follow the breaking index, $\kappa = 0.78$, as predicted by the solitary wave theory. The wave height inside the surf zone is then given by

$$H = \kappa D \tag{15}$$

It is further assumed that the total wave energy can be described in terms of the wave height which is a function of the depth

$$E = \frac{1}{8} \rho g \kappa^2 D^2 \tag{16}$$

This is a non-conservative statement of the energy distribution within the surf zone. The wave speed is approximated using solitary wave theory and for shallow water

$$c_g = c = \sqrt{g(1 + \kappa)D} \tag{17}$$

The total mean transport inside the surf zone is then

$$\bar{q} = \frac{-1}{g(1 - \frac{\rho}{\rho_s})} \left[B_s \sqrt{\frac{V}{u_{mh}}} \right] \frac{\partial \vec{Ec}_g}{\partial x} \tag{18}$$

where B_s is the proportionality factor for inside the surf zone. For transport of sand in the surf zone, the proportionality factor will certainly be a function of the manner in which the waves break--just as are the wave-induced currents inside the surf zone.

The longshore current distribution inside the surf zone as given by Thornton [3] is used

$$V(x) = -\frac{5}{8} \frac{\pi \kappa}{f_w} \left(1 - \frac{\kappa^2}{8(1+\kappa)}\right) c_b \sin\alpha_b \cos\alpha_b \frac{D}{D_b} \frac{\partial D}{\partial x} \tag{19}$$

where b subscript refers to conditions at the breaker line.

Equations (13) and (18) are rational equations for predicting the bed load sediment transport due to combined waves and longshore current outside and inside the surf zone. Unfortunately, unknown proportionality factors, or energy coefficients, have been introduced. Experiments have been conducted in laboratory flumes by Inman and Bowen [5] to experimentally determine the functional relationship of the coefficients. These experiments were

conducted by superposing waves on a current moving in the same direction. Unfortunately, no such relationships have evolved empirically to date.

FIELD EXPERIMENTS

A meaningful investigation of the sand transport processes in the surf zone requires the synoptic measurement of a number of hydrodynamic and sediment variables. Fairly complete and extensive data are required to evaluate the validity of the proposed sand transport relationships.

Field experiments were conducted in the surf zone at Fernandina Beach, located on the northeastern coast of Florida. The emphasis of the tests was to obtain information concerning the distribution of alongshore sand transport across the surf zone and the physical processes causing such movement. Sediment transport about the surf zone has been shown to be caused by a combination of shear stresses and turbulence due to wave and current action. Hence, an attempt to correlate sediment transport with physical parameters must include adequate wave and current measurements.

Experiments were initiated in 1962 and conducted intermittently at this location. Data from experiments conducted between 1964 and 1967 are used for testing the equations. In the course of this time, the method of measuring the various parameters changed, evolving to a relatively sophisticated level. Much of the test equipment was designed and developed especially for these experiments and is unique.

The experiments were conducted at various times of the year so that a variety of wave and weather conditions prevailed during the experiments. The measurements were taken from a pier traversing the surf zone seaward to the outer bar. A plan of the pier and location of the instrumentation are shown in Figure 1. A typical bottom profile taken adjacent to the pier is also shown in this figure. The beach and nearshore bottom profile is typically a one-or-two bar system with a gentle slope of 2 to 3 percent. The experiments were limited to the study of the sand transport in the area bounded by the outer and inner bar.

The sand characteristics have been studied thoroughly including size distribution, mineral composition, and differences of characteristics across the surf zone. The results generally showed the sand to be evenly sorted in the area of the sand transport measurements. The mean grain diameter at Fernandina Beach is approximately 0.2 millimeters.

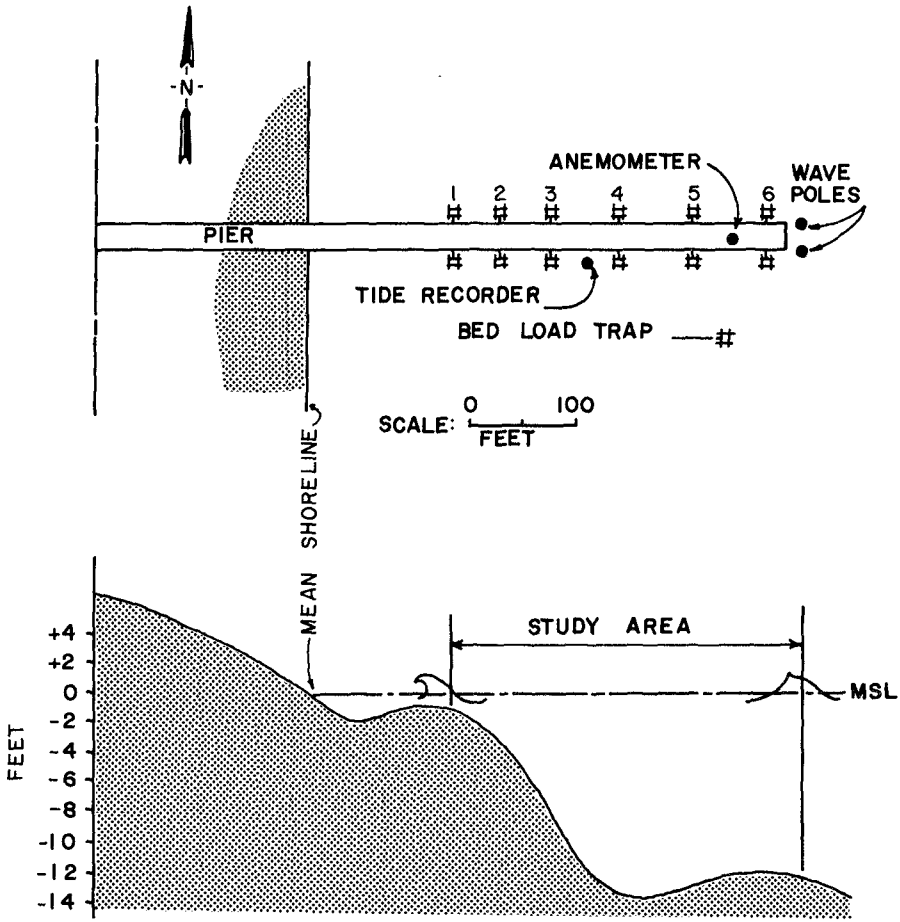

Figure 1.
Plan of Pier Showing Instrument Locations and Typical Bottom Profile at Fernandina Beach, Florida

The physical parameters measured during the experiments were the wave height, wave direction, currents, tides, wind direction and speed, quantity of sediment transport, bottom contour profiles, and sediment characteristics. The experiments were conducted typically over approximately half a tidal cycle, usually four to six hours. The mean tidal range is 5.6 feet. The tide recorder, anemometer, and sand traps operated continuously during the experiment. Current measurements were taken by means of floats and current meters. The wave heights and direction were measured simultaneously. The instrumentation and details of measurements have been previously discussed by the author (Thornton [6]).

Taking measurements in the surf zone is usually a difficult problem due, in part, to the tremendous forces exerted by the waves. It is almost essential for synoptic measurements to have a stable platform from which to work. This platform, a fishing pier in this case, exerts some local influence on the environment being measured and care must be taken to minimize this effect. Thus, all measurements were made as far from the pier and its piling as possible, and the measurements were taken on the updrift side of the pier on which the incident waves impinge first.

A. Sand Transport Measurements

The quantity of sand transport was measured by means of bed load traps. The traps are aligned in the direction of the longshore current and are designed to intercept the bed load portion of the littoral drift. These traps rest on the bottom and sample an area 20 centimeters high by 40 centimeters wide. The bed load movement here is defined by the height of the traps and, as such, includes saltation. Up to six traps were operated simultaneously from from the pier and are located as indicated in Figure 1. The unique design of these traps evolved over several years of use, and they have proven to be very rugged and dependable for the severe conditions to which they are subjected. An abbreviated description is given below. For a more complete description of the traps and attendant system, see Thornton [6] and Bruun and Purpura [7].

The body of the traps is elliptical in shape which serves two functions: to decrease current velocities due to the divergence from the entrance allowing sediment to fall from suspension during sampling, and to act as a circular tank in which a swirling motion is developed to put sediment in suspension for pumping out. The trap base is a sheet metal apron which is extended to reduce scour. Tag lines were attached to assure proper orientation. The traps were run typically on a sampling sequence of 15 minutes sampling with the doors open and 5 minutes pumping out with the doors closed. The doors operate pneumatically

from the pier. During the pumping-out cycle when the doors are closed, two jets of fresh water from inside the trap create a swirling action to put sediment in suspension. Simultaneously, the water-sand mixture is pumped out of the traps into filter baskets and drained of the water. The wet sand is put in sample bags and taken back to the laboratory where it is dried and weighed.

The accuracy of the sand traps is dependent on their efficiency in retaining the sand that passes into the trap. The trap efficiency is dependent on the wave conditions, being more efficient for light wave conditions where the turbulence and induced currents are less. The traps tend to become clogged for very heavy wave conditions, and all the sand cannot be pumped out in the sampling cycle; the traps also tend to bury themselves for extreme wave conditions. The traps were observed in the laboratory and field under light wave conditions and appeared to function very well. It was not possible to observe the traps under heavier wave conditions due to the increased turbidity of the water. A trap efficiency of between 40 and 100 percent is estimated as the representative range for most conditions.

B. Current Measurements

Simultaneous with the sand transport measurements was a complete measurement of the physical environment. The currents were measured using two means: floats in the earlier experiments and combined floats and a current meter in later tests. The float measurements consisted of filling large balloons (one foot in diameter when filled) with fresh water and releasing these from the pier and measuring their travel time over a prescribed distance. The fresh water makes the balloons slightly buoyant so that just the top of the balloon is visible. These proved to be a very effective means of measuring the longshore currents.

The direct measurement of water particle velocities in the presence of a wave field, such as the surf zone, has long been a problem. An electromagnetic flowmeter was used during these experiments and proved applicable for use in the surf zone.

C. Wave Measurements

The waves were measured by a variety of methods including mechanical, pressure, and resistance wire wave meters. The measurements were made at one or several locations along the pier.

Waves, as they occur in nature, are essentially aperiodic or random in appearance and, as such, have to be

treated as a statistical phenomenon. The studies were conducted over a relatively short duration of time, and the physical environment may be assumed quasi-stationary. Hence, spectral analysis or other statistical inference can be employed in treating this aperiodic phenomenon. Spectral analysis was used in the later experiments and provided valuable information concerning the energy distribution in and about the surf zone. The relations derived previously assume a single component wave system and are not formulated to accommodate a spectrum of waves. For this reason, and due to the variety of methods used in measuring waves, it is convenient to extract from the wave measurements a single parameter characterizing the energy content of the waves. This parameter was selected as the significant wave height which is defined statistically as the average of the highest one-third waves.

The wave direction was measured by sighting with a compass and noting the angle between the pier alignment and the wave crest. Aerial photography was also employed in a number of the experiments. The incident wave angle at particular points inside and outside of the surf zone were determined in this manner. These measurements refer to the angle of the "significant" wave. Wave measurements conducted in the later experiments, using two wave staffs stationed at the end of the pier and aligned parallel to the shore, allowed directional features of the waves to be determined. A directional spectrum is obtained by computing the Fourier transform of the cross-correlation function of the two wave records which associates one direction with each frequency component and is essentially a measure of the phase difference between the two sensor locations for each Fourier component. A more complete description of the spectral aspects of the experiments is given by Thornton [6].

The angle of wave incidence is the most importantly weighted variable in the predictive equations for the longshore current and sediment transport equations; it is also the most difficult parameter to measure accurately. Galvin and Savage [8] compared several methods for measuring waves from a pier using a compass and sighting along the wave crests. They concluded that the error in measuring wave angle may be easily ± 2 degrees, and this same variability will be assumed here. This amount of uncertainty in the measured angle can result in considerable error in the longshore current and sediment transport calculations--particularly, for small angles of approach.

The wave heights generally were determined from wave records greater than five minutes in length. Hence, the significant wave height was determined with a high degree of confidence. Visual measurements were used in the first experiments. Galvin and Savage (op. cit.) state an

accuracy of the breaking wave height of ± 25 percent for both wave meter and visual measurements. There is an uncertainty even for the wave meter measurements since there is a spatial variation due to variations in bottom topography. The wave meter measures only at one point that may not be representative of the general area.

RESULTS AND COMPARISON WITH THEORY

Thirty-one experiments were conducted in all, fourteen of which were judged appropriate for comparison with theory. The other experiments were deleted because of the presence of rip currents, lack of correlating data, equipment failure, or unfavorable weather.

The sand transport, like the waves and water particle motion causing the transport, is a stochastic process. The bed load transport was seen to vary considerably with time. All data used are mean values representing an assumed stationary system.

The data are used to test the bed load transport theory, Equation (13) for outside the surf zone and Equation (18) for inside the surf zone. It is necessary to make several assumptions in the application of the predictive equations. It is assumed that the ripple height was everywhere constant and equal to 0.05 feet. The same ripple height was used for predicting the mean longshore currents inside the surf zone and gave reasonable results. A constant ripple height is not necessarily a good assumption, but was made as a first approximation due to there not being enough information to assume otherwise.

Percolation losses have been found empirically to be very small for sand sizes less than 0.5 millimeters. Energy losses due to percolation have been neglected for application to the Fernandina Beach data because the mean grain size is much less than this value. A mean specific gravity of 2.65 was measured for Fernandina Beach sand, and this value was used in all calculations.

The theory requires wave and current information everywhere along the profile. The measured wave parameters, taken at one location, are used to obtain wave characteristics at each trap location by theoretically carrying the waves shoreward accounting for shoaling, refraction, and frictional dissipation. Predicted longshore currents were used in the littoral transport equations since there was a lack of measurements at each station. The objective is to obtain equations that can be easily utilized to predict the littoral transport from the measured physical environment, and the wave information at one point is all that is usually available.

The distribution of the measured and predicted bed load transport are compared for Test Numbers 19 and 22 in Figures 2 and 3. During Test number 19, all the traps were outside the breaker line which was the case in most of the experiments. The significant wave height was 3.8 feet, the mean wave period 6 seconds and the mean angle of wave approach 3.5 degrees.

Different values of the proportionality factor B were chosen for predicting the sediment transport distribution so that a best fit between theory and experiment for each test could be obtained. The rationale, in doing so, is that if one of the measured variables in the experiments, such as wave height or direction, was substantially in error, this error could change the absolute value of the prediction considerably, but have little effect on the relative distribution along the profile. The B values for inside the surf zone range from 0.42 to 1.0 for all tests except one. The exception was Test Number 25 for which a value of B = 0.13 was used.

There appears to be a definite correlation of sediment transport with depth of water which is graphically illustrated in Figure 2 for Test Number 19. The energy density of the waves in the process of shoaling outside the surf zone generally increases with decreasing depth (provided frictional energy dissipation is not too great) to a maximum at near breaking. Since the energy density is generally a function of depth, the correlation of sediment transport with depth is explained. Indeed, the transport is shown to be a minimum in the trough of the profile, greater over the bar, and a maximum near the breaker line where the energy density is greater.

Measurements both inside and outside the surf zone were obtained in Test Number 22. In this experiment, the significant wave height was 3.8 feet, the mean wave period 8 seconds, and mean angle of wave approach 4 degrees. Again, there is a general correspondence of transport with depth outside the surf zone; a maximum occurs at the breaker line. The energy density gradually decreases for spilling breakers inside the surf zone, and a corresponding decrease in sediment transport is expected. This is clearly shown in Figure 3. It should be noted that a different proportionality factor has been used for inside and outside the surf zone which might be expected.

All the results for outside the surf zone are summarized in Figure 4. The same constant of proportionality, B = 1.0, has been used for all the predicted values so as to provide a comparison between the various tests. There are forty values in all to form the correlation. As can be seen, the data span a very large range of values, almost three decades on a log-log graph. The heavy line

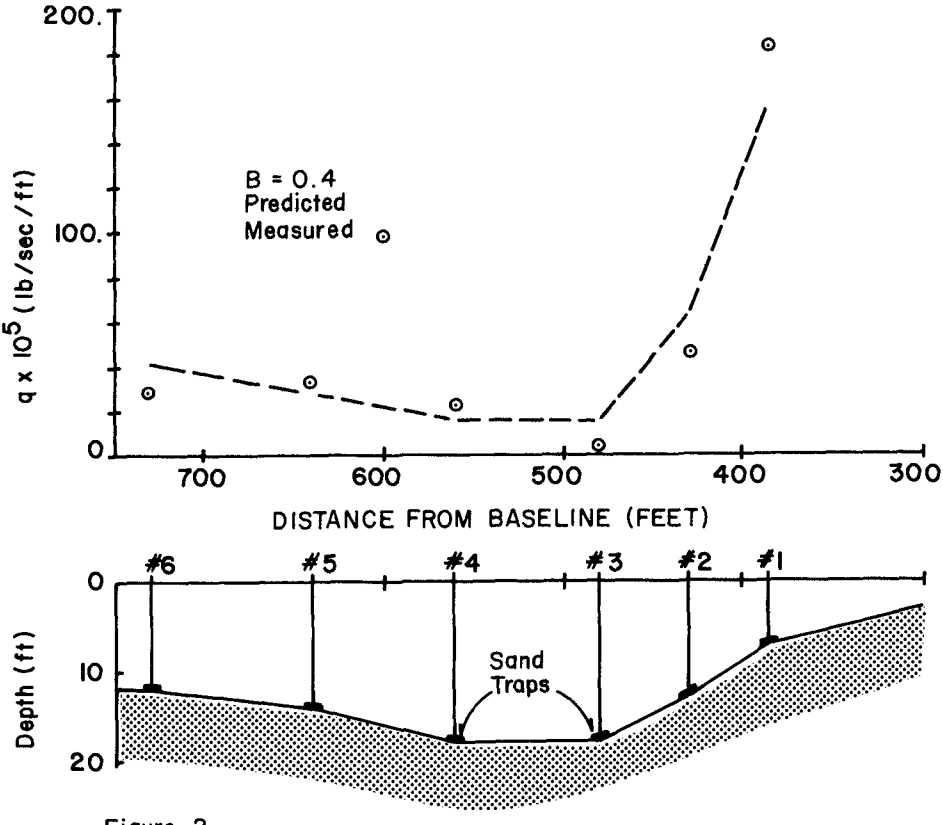

Figure 2.
Distribution of Bed Load Transport outside the surf zone, Test Number 19

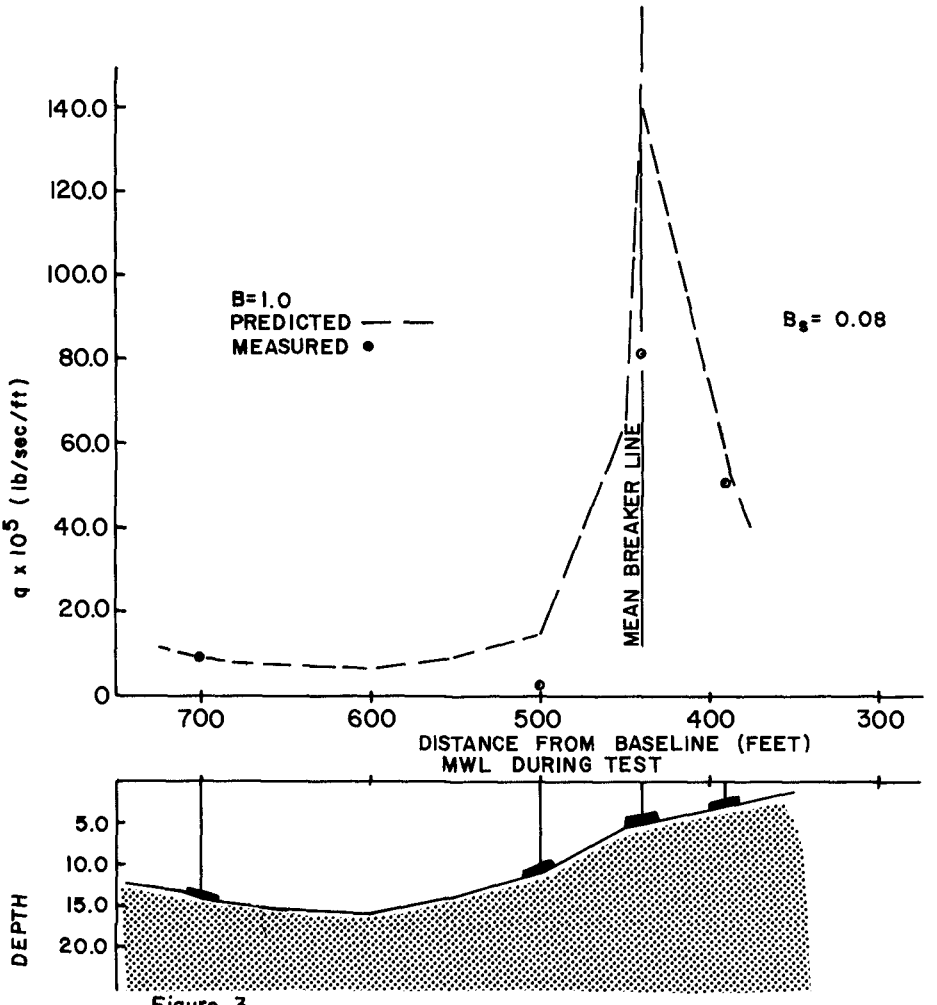

Figure 3.
Distribution of Bed Load Transport across the Surf Zone
Test Number 22

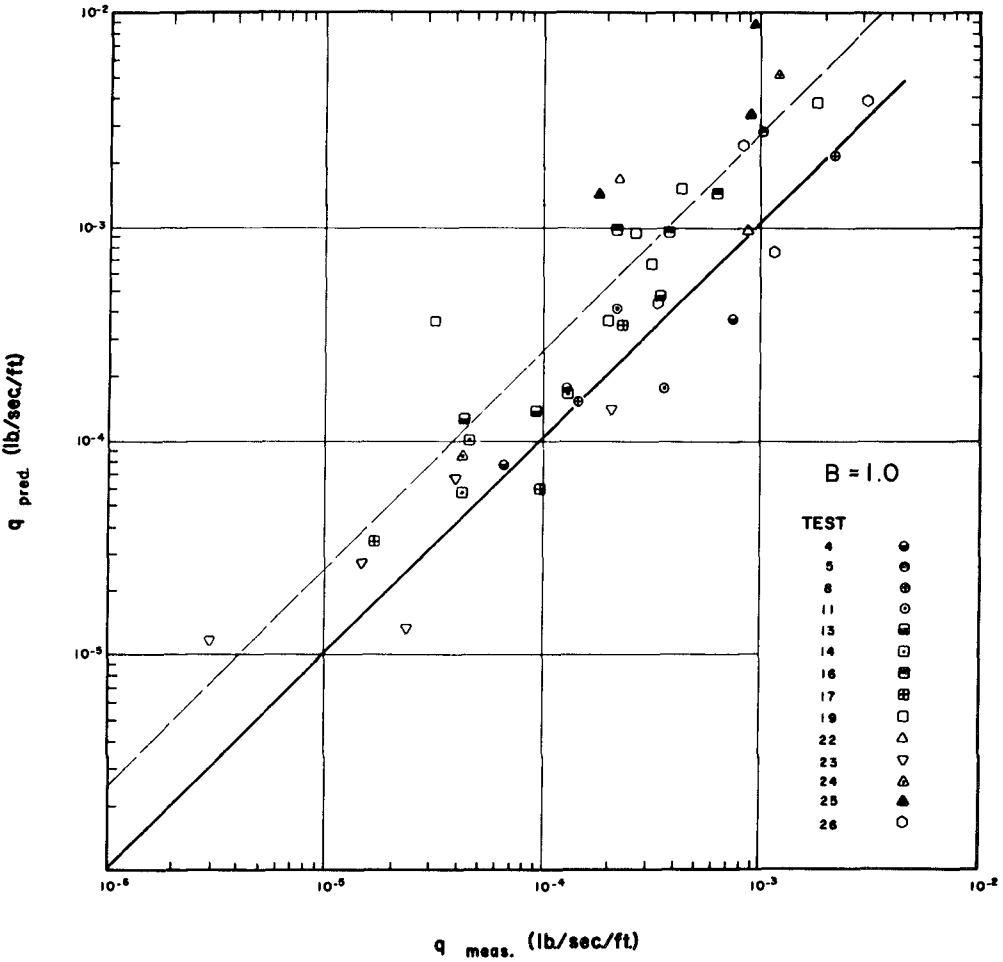

Figure 4.

Measured and Predicted Bed Load Transport outside the Surf Zone

denotes a one to one correspondence between predicted and measures values for the proportionality factor given by B. The dashed line indicates the expected range of variability of the measured values due to the efficiency of the traps in catching the bed load. The dashed line as drawn indicates that the traps are estimated to be at least 40 percent efficient in collecting the bed load. It is possible that, in some cases, the traps were more than 100 percent efficient, that is, they collected more than the actual net littoral transport. This might happen when there is no net flow in one direction alongshore, and the traps would collect sand moving in both directions, indicating a larger than actual net transport.

The predicted and measured values for inside the surf zone are shown in Figure 5. Unfortunately, there is a paucity of data for sediment transport inside the surf zone. This is primarily due to the design of the traps in that they function poorly for very high transport rates as generally occurs inside the surf zone and have a tendency to become buried. A proportionality factor of $B = 0.08$ was used for all experiments inside the surf zone. The estimated limits of variability extend the same range as before. All the values except one fall within the estimated variability of traps. This, in itself, is considered to be very good correlation for predicting conditions so complicated and varied as occurring inside the surf zone.

The values of B are necessarily limited to the particular sediment characteristic found at Fernandina Beach. The most important characteristics are the mean grain size, $d = 0.2$ millimeter and the specific gravity equal to 2.65. Although the distributions were indicative of only one grain size, the relative distributions are expected to vary little. This is due to the fact that the influence of grain size (provided percolation is not important) would be primarily to change the factor B and the friction factor f_w. Since B is assumed to be constant, and f_w varies only slowly, the relative distribution would not be expected to differ substantially for different grain sizes.

As mentioned previously, the measured currents were not used in comparing the results. The measured longshore currents outside the surf zone are generally several times greater than the predicted values. The bathymetry at Fernandina Beach is not ideal for the application of the derived theory in that there is typically a bar-trough formation. The bar may tend to trap the shoreward mass transport of the waves between the bar and the shoreline. This fluid contribution over the bar could constitute a considerable influence on the longshore velocity outside the breaker line. The discrepancies between theoretical and measured longshore currents could also be a result of neglecting the influence of internal shear stresses. The

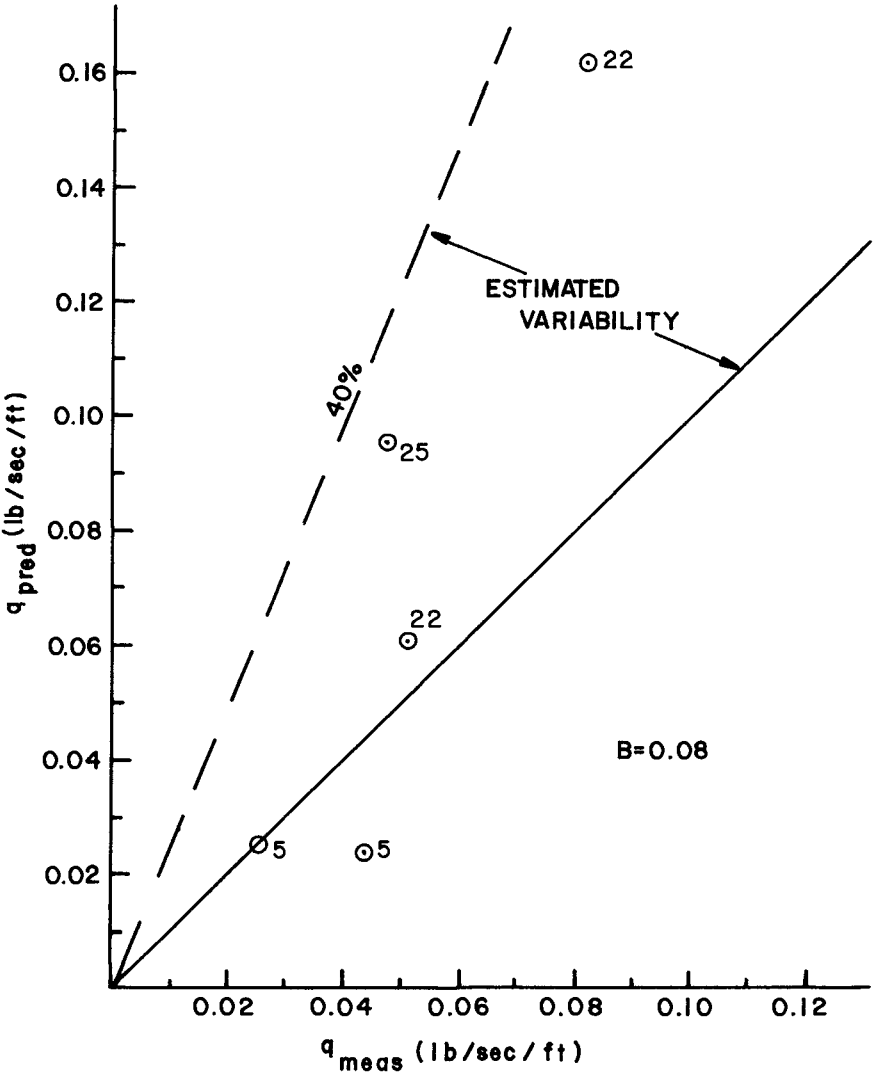

Figure 5.
Comparison of Measured and Predicted Bed Load Transport inside the Surf Zone.

coupling across the breaker line, due to lateral transport of momentum offshore, would increase the predicted longshore current values outside the surf zone.

If the actual values of the longshore current were used, instead of the predicted values, the proportionality factor B would be decreased for outside the surf zone. This would result in the proportionality factors, applicable to inside and outside the surf zone, being more nearly equal. The predicted and measured longshore current velocities inside the surf zone correspond well so that the substitution of the measured values would not substantially change the B_s value inside the surf zone.

CONCLUSIONS

The wave-induced sand transport alongshore was investigated by an energy principle approach. The aim of the investigation was to present usable predictive formulas. Bed load transport equations were formulated for outside and inside the surf zone. Although the energy approach has been used before, this is the first application to comparing theory and measurements of the distribution of littoral transport along a line perpendicular to the beach.

Sand transport data were collected in the field using bed load traps. Wave, tide, wind, and current information was collected simultaneously in order to verify the derived predictive equations for longshore current and sediment transport. The longshore current formulation including only bottom shear stress was used in the sediment transport predictive equations.

The field data were correlated with the predictive equations to determine separate proportionality factors for inside and outside the surf zone. The proportionality factors are limited to the particular parameters found at the experimental site. In particular, the sediment transport rates would certainly be dependent on the sand characteristics such as grain size and sediment density. However, the comparison of theory and experiment show that the relative distributions, which would be expected to have little dependence on sand characteristics, were fairly well predicted. Quite reasonable predictions were obtained for the relative distribution of bed load transport, both inside and outside the surf zone; although, the absolute values were not as well predicted. Hence, the equations could be used as a qualitative predictive relationship for engineering application.

BIBLIOGRAPHY

1. Bagnold, R. A. Mechanics of Marine Sedimentation, The Sea, Interscience Publishers, New York, 3:507-528, 1963.

2. Komar, P. D. The Mechanics of Sand Transport on Beaches, J. of Geophysical Research, Vol. 76, No. 3, Jan. 20, 1971.

3. Thornton, E. B. Variations of Longshore Current Across the Surf Zone, Proc. Twelfth Coastal Engineering Conf., ASCE, 1970.

4. Jonsson, I. G. Wave Boundary Layers and Friction Factors, Proc. Tenth Conf. Coastal Eng., ASCE, 127-148, 1966.

5. Inman, D. L. and Bowen, A. J. Flume Experiments on Sand Transport by Waves and Currents, Proc. Eighth Conf. Coastal Eng., Council on Wave Research, 137-150, 1963.

6. Thornton, E. B. A Field Investigation of Sand Transport in the Surf Zone, Proc. Eleventh Coastal Engr. Conf., ASCE, 1968.

7. Bruun, P. and Purpura, J. Quantitative Research on Littoral Drift in Field and Laboratory, Proc. Ninth Conf. Coastal Eng., ASCE, 267-288, 1964.

8. Galvin, C. J. and Savage, R. P. Longshore Currents at Nags Head, North Carolina, Coastal Eng. Res. Center Bull. 2, U.S. Army Corps of Engrs., Washington, D.C., 1966.

CHAPTER 56

LONGSHORE TRANSPORT OF SUSPENDED SEDIMENT

by

John C. Fairchild*

ABSTRACT

In excess of 800 suspended sediment samples were collected from stations along the City Pier, Ventnor, New Jersey and Jennettes Pier, Nags Head, North Carolina using a tractor-mounted pump sampler. Most samples were collected within the surf zone at the Ventnor site. At the Nags Head site, sample collections included the surf zone, but generally extended over a wider range of the nearshore zone. Average sampling time was 3 minutes. Nozzle elevation varied from 3 inches above the bottom up to a maximum about mid-depth, generally not greater than 2.5 feet above bottom. Maximum concentrations at Ventnor ranged up to 2.6 ppt by weight and at Nags Head were about 4.0 ppt. Median size at Ventnor ranged from 0.12 to 0.15 mm and averaged about 0.20 mm in depths of 4 feet and less at Nags Head. Results are summarized in a series of scatter plots which relate suspended sediment concentration to nozzle height, wave height, water depth and sampling distance from an observed wave-breaker-line. Results are compared to CERC laboratory data, to two excerpted concentrations from unidirectional flow tests and to the CERC TR-4 design curve of longshore wave energy versus longshore transport.

Introduction

Design criteria for problems involving sediment transport by wave action could be greatly improved by development of empirical relationships from field measurements covering a wide range of wave conditions. In the absence of adequate data or predictive techniques, the coastal engineer has relied on historical compilations of dredging and survey records to obtain longshore transport estimates. Better techniques are needed and therefore, field and laboratory studies of sediment transport are needed to gain added knowledge of natural beach processes, leading to better predictions of longshore transport rates. This paper reports on some data on suspended loads gathered in both ocean and laboratory waves.

Longshore transport of suspended sediment is one of the two basic modes of wave induced sediment transport, the other mode being bedload transport whereby the bed sediment is pushed or rolled along the nearshore bottom by wave action, and the resulting shear stress in the bottom boundary layer. The total amount of suspended material moving along a given shore over a given time depends on the complex interactions of several factors, including wave conditions, water depth, beach slope, characteristics of the beach materials and total range of the tide. Important among the several inter-

* Research Hydraulic Engineer, Coastal Engineering Research Center, Washington, D. C.

actiona is the generation of the longshore current during the wave breaking proceas. This current transporta large amounts of bottom materials forced into suspension by wave-generated currents and turbulence.

An early estimate of the longshore transport of suspended sediment was made by Watts (1), using pump samplings of suspended sediment from a pier at Pacific Beach, California. Updated estimates of the longshore transport of suspended aediment may be made from field and laboratory data, including suspended aediment concentrations and related wave parameters, now on hand at CERC (2). Thia data was obtained at two Atlantic coast sites, and in the CERC laboratory wave facilities using pump sampling techniques.

The paragraphs which follow briefly describe the field sampling, compare the field results to CERC-laboratory data and to two excerpts of data from unidirectional flow tests, and finally, compare computed longshore tranaport rates to the Coastal Engineering Research Center TR-4 design curve of longshore transport versus longshore wave energy flux.

Field Sampling

In excess of 800 suspended sediment samples were collected from stations along the City Pier, Ventnor, New Jersey and Jennettes Pier, Nags Head, North Carolina, using a tractor-mounted pump sampler (3). Figure 1 is a achematic illustration of the sampler on a fishing pier. Most samples were obtained

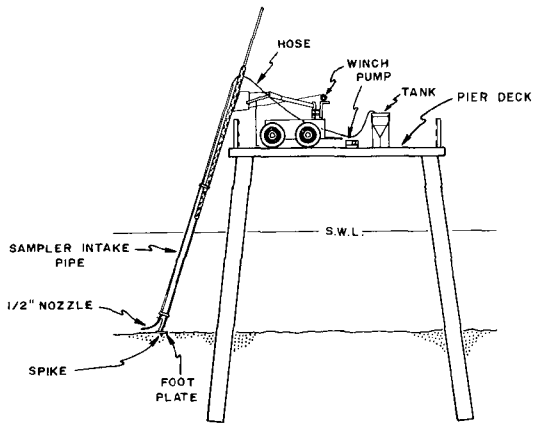

FIGURE 1: SCHEMATIC VIEW OF A TRACTOR-MOUNTED SUSPENDED SAND SAMPLER ON A PIER

within the surf zone at Ventnor, N. J. under varying intensities (types and proximities) of wave breaking. Nags Head samples were collected in the surf zone, but generally extended over a wider and deeper range of the nearshore zone. Figure 2 is a schematic illustration of the areas of interest in the sample collections which shows a surf zone, a swash zone and an offshore zone. Average samplings of 3 minutes time were made from a height of 3 inches above the bottom up to a maximum height at about the mid-depth level. Each sample, as initially pumped through a 1/2-inch intake nozzle, was a 40 gallon volume of water-sediment mixture which was decanted in the field to a sample-size quantity of wet sand. Laboratory analysis and data reduction at CERC yielded a suspended sediment concentration and a size distribution for each sample. In the Ventnor data, maximum concentrations were about 2.6 ppt by weight (equivalent to 380 grams (.84 lb) of sand in 40 gallons of seawater) and minimum concentrations were of the order of .025 ppt (less than 4 grams in 40 gallons). In the Nags Head data concentrations above 1.0 ppt by weight occurred more frequently with two measured values which were above 4 ppt. However, there was also a greater percent occurrence of concentrations below .01 ppt in the Nags Head data. Median diameter of the suspended sediment ranged from .12 to .15 mm for the Ventnor data and averaged 0.20 mm in depths of 4 feet or less at Nags Head. In depths of 8 to 12 feet at Nags Head, median diameter of suspended sediment samples averaged about 0.17 mm.

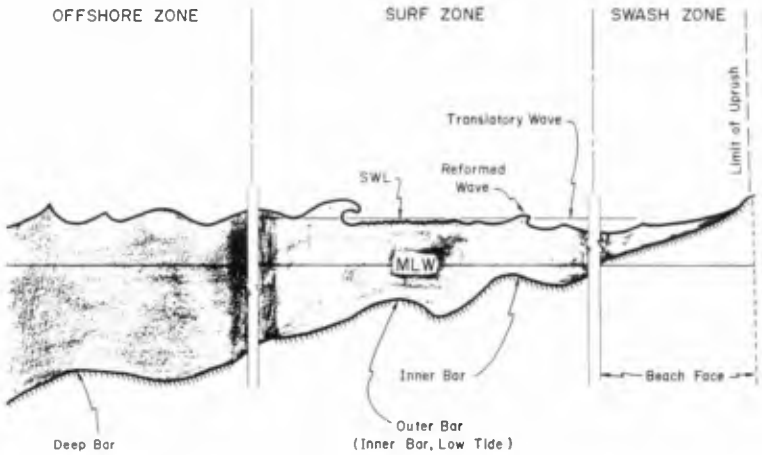

FIGURE 2: SCHEMATIC PROFILE OF A SURF ZONE

Discussion of Results from Sample Collections

Table 1 lists the principal variables considered in this study. The concentration, C_w, is considered to be a dependent variable determined by an unknown function of elevation, depth, wave height, and distance from the wave-breaker-line

$$C_w = f\ (E_B,\ d,\ H,\ S_B).$$

The variables Q and θ_b are used in the final section of this paper.

Table 1. DEFINITION OF VARIABLES

C_w - suspended sediment concentration (ppt by wgt)

E_B - elevation of suction nozzle (ft above bottom)

d - water depth at sampling station (ft)

H - significant wave height (ft)

S_B - distance from the wave-breaker-line (ft, + is landward)

Q - longshore transport rate (100,000 yd^3/yr

θ_b - angle between a wave breaking crest and the shoreline (designated α_b in Fig. 13, CERC TR-4)

The results from the sample collections at Ventnor, N. J. and Nags Head, N. C. are summarized in a series of scatter plots which relate suspended sediment concentrations, C_w, in parts per thousand (ppt) by weight to the 4 independent variables. Sediment concentration is presented in the several figures which follow by sampling stations, and by all stations plotted together on general scatter plots. The sampling station scatter plots show data collected at a specific station on the pier usually within a period of 3 hours or less. The general scatter plots are representative of all the data collected and so may have more significance than data collected at a specific station and over periods of - say 2 to 3 hours.

Figures 3 and 4 are single station scatter plots which show the vertical distribution of suspended sediment concentration for two pier stations at Ventnor, and two pier stations at Nags Head, respectively. Note that the ordinate in each figure represents concentrations of suspended sediment, C_w in ppt by weight and that the abscissa represents sampling nozzle heights, E_B, in feet above the ocean bottom. Two sets of points are plotted in the right-side graph in Figure 3, with the open circles representing samplings before 1200 hours and the filled circles representing samplings after 1300 hours. It was observed during the samplings that there was an abrupt increase in the wave activity at about 1300 hours and this graph shows how quickly the concentration level responds to the increased wave height, and how much flatter the trend is for the higher waves ($\bar{H} \approx 1.82$ ft).

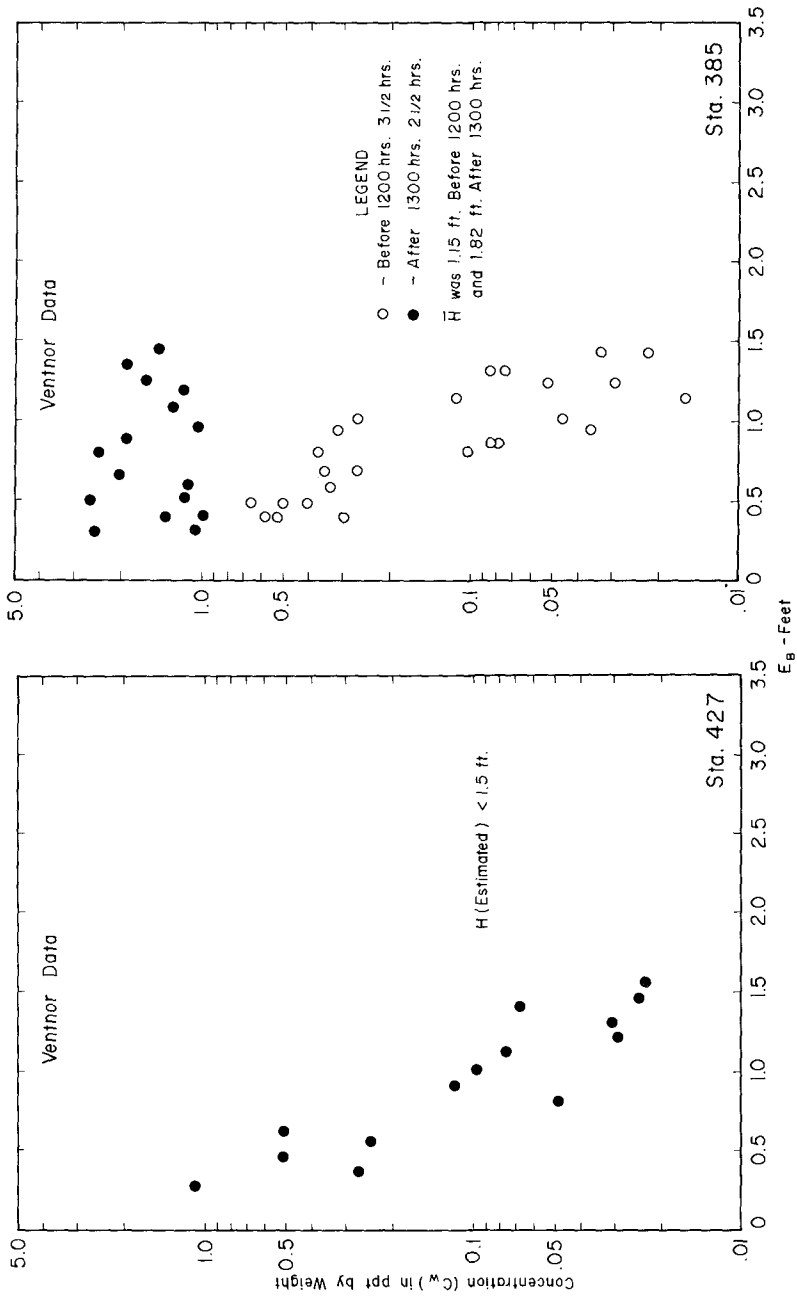

FIGURE 3: VERTICAL DISTRIBUTION OF SUSPENDED SEDIMENT CONCENTRATION

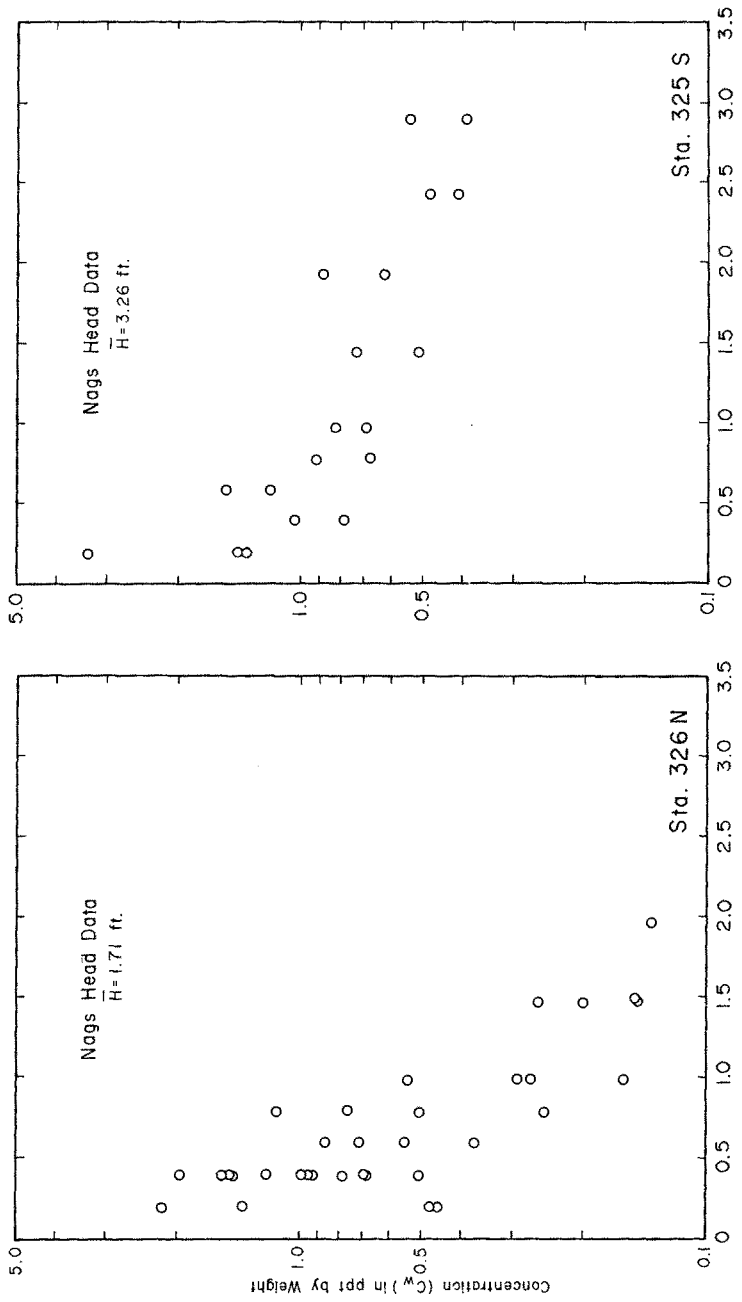

FIGURE 4: VERTICAL DISTRIBUTION OF SUSPENDED SEDIMENT CONCENTRATION

Also, note the considerable difference in the steepness of the scatter trends in Figure 4 for the Nags Head data. Based on a study of numerous plots, it was found that a higher wave or more intense wave activity was usually aassociated with the flatter distribution trends.

Figure 5 relates concentration of suspended sediment to the distance of the sampling station from an observed wave-breaker-line for the Ventnor data. The top graph relates suspended sediment concentration to distance from a moving wave-breaker-line for a single station during an eight hour period. The bottom graph shows the same type of relationship but for shorter periods of time on three separate dates. Based on the author's examination of the effect of other factors such as wave height, water depth, nozzle height, it is his judgement that the type of wave breaking (surging, plunging or spilling) is what caused the particular distribution of the three data groups shown in this scatter plot.

The next three figures, 6, 7 and 8 are more representative of all the data collected than the last three figures which gave results for data collected at a single station and generally over times of two or three hours. The first of these, Figure 6, relates suspended sediment concentration, C_w, in ppt by weight, to distance from the wave-breaker-line, S_B, for two nozzle height ranges above the ocean bottom at Ventnor, N. J. The next scatter plot, Figure 7, shows the relationship of suspended sediment concentration, C_w to the parameter, H/d, wave height over water depth. Note that the left graph in Figure 7 shows the results for the Ventnor data and the right-side graph shows results for the Nags Head data. Figure 8 concludes this phase of the results with an additional graph relating suspended sediment concentration, C_w, to the parameter, H/d, wave height over water depth, for samples collected above 0.5 feet and less than 1.0 feet above the ocean bottom. The legend of the left side graph for the Ventnor data divides the data into two classes, one class for samples collected seaward of the wave-breaker-line, another class for samples collected shoreward of the wave-breaker-line. Note that the right-side graph for the Nags Head data in Figure 8 appears to have a gap in the data scatter appearing just about where the peak occurs in the data scatter for the Ventnor data, left graph in the figure.

The results presented in Figures 5-8 may be explained as follows: As the shallow water waves approach breaking, the concentration of suspended sediment increases sharply from barely non-breaking waves to fully breaking waves with shoreward advance and with increase in H/d (wave height over water depth). Scatter configurations (Note Figures 7 and 8) indicate that the suspended sediment concentration peaks near the wave breaker index (H/d = 0.78)(4) and that concentrations decrease gradually with the shoreward advance of spilling translatory waves and with further increase in H/d.

The next two figures present all data collected in these field studies. The first of these, Figure 9, relates suspended sediment concentration to H^2 (wave height squared). These data show very much scatter. In noting the scatter in this figure, it must be recognized that the plotted concentrations were collected at a range of elevations above the ocean bottom - E_B from 0.25 to 2.50 feet. Scatter plots presented earlier have indicated that this elevation variable significantly affects the total scatter in the graphs. The scatter trend in the top graph in Figure 9 appears to change noticeably near an H^2 of 1.5 and trend toward the upper right.

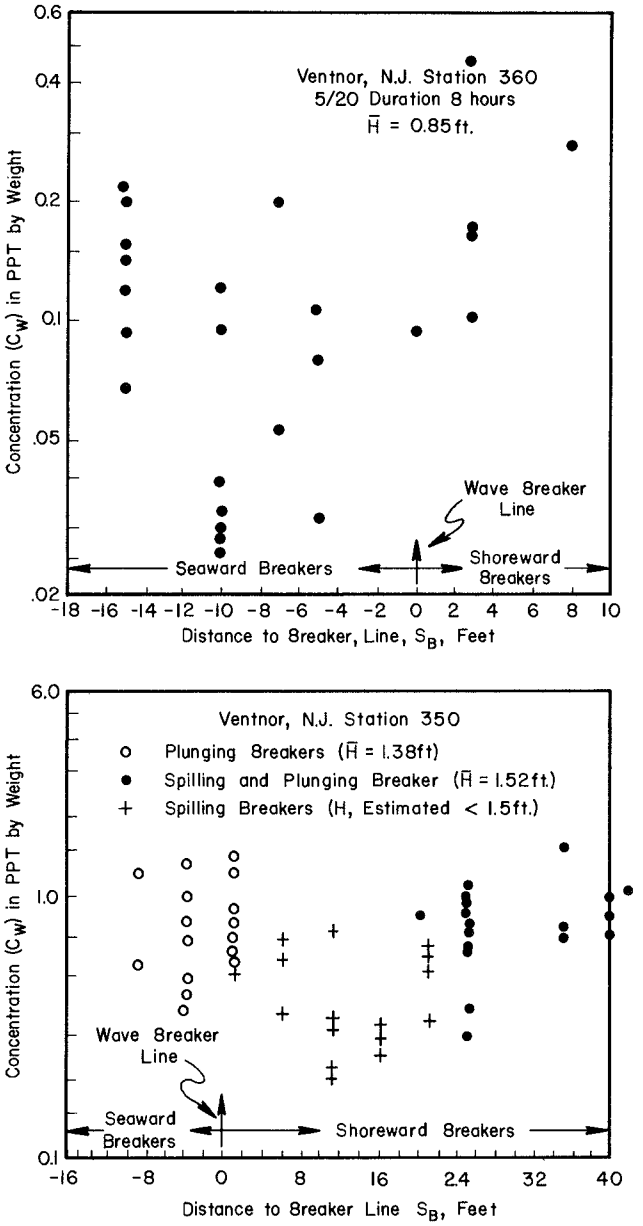

FIGURE 5: VARIATION IN SUSPENDED SEDIMENT CONCENTRATION ACROSS A MOVING BREAKER LINE

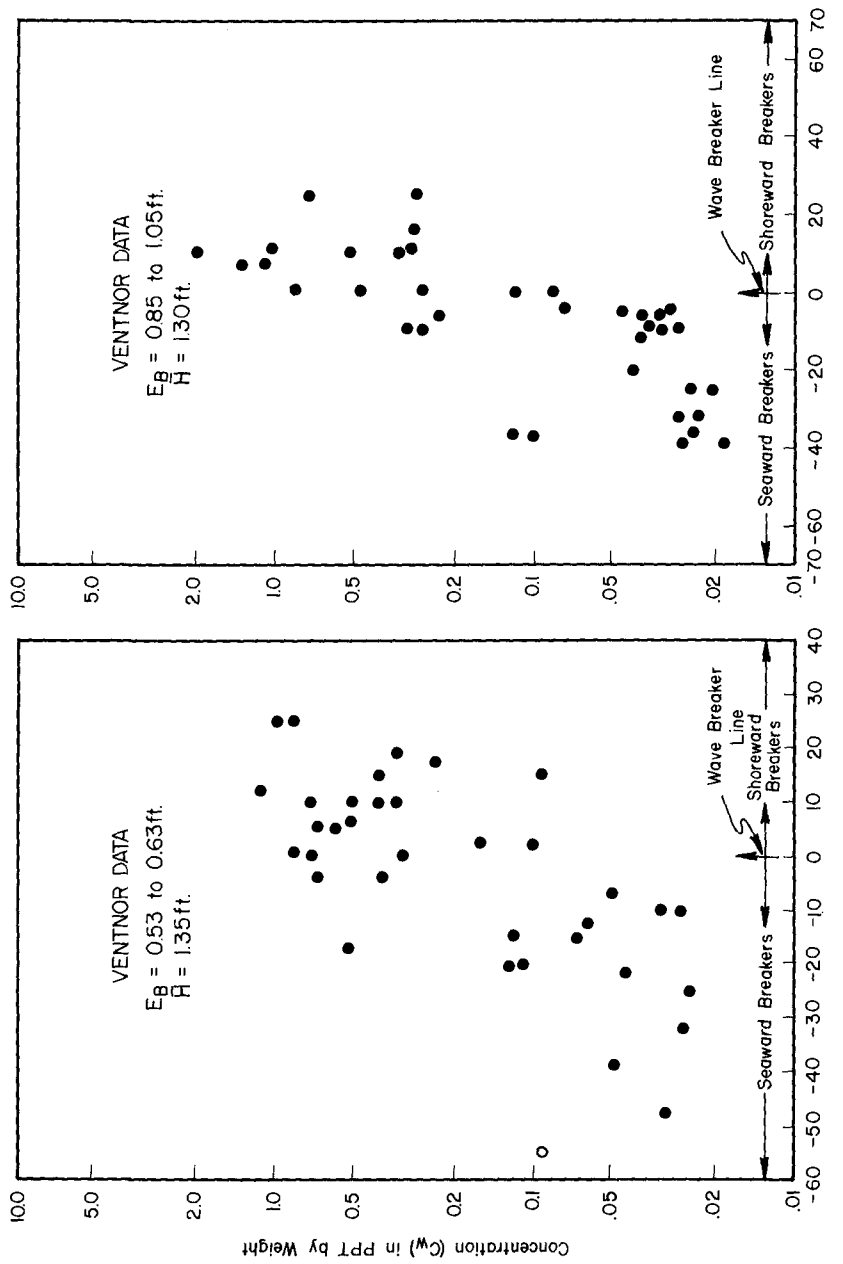

FIGURE 6: VARIATION IN SUSPENDED SEDIMENT CONCENTRATION ACROSS A MOVING BREAKER LINE

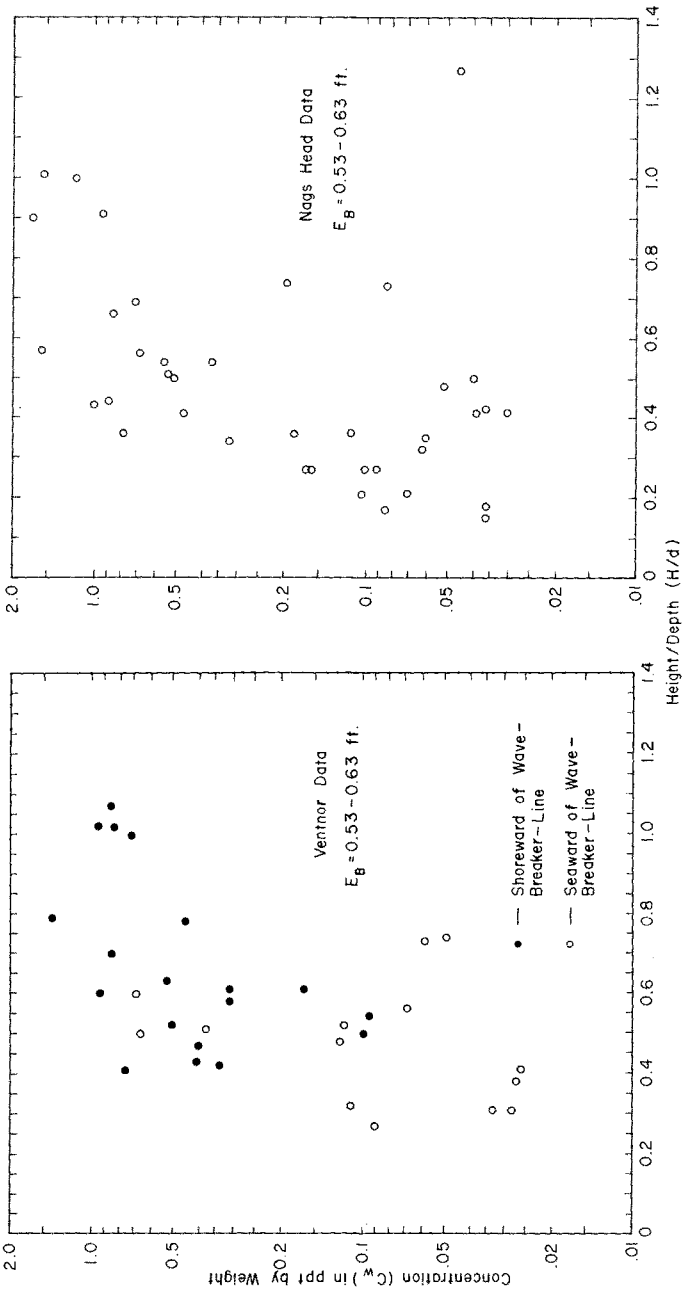

FIGURE 7: RELATIONSHIP OF SUSPENDED SEDIMENT CONCENTRATION TO (H/d) WAVE HEIGHT/WATER DEPTH

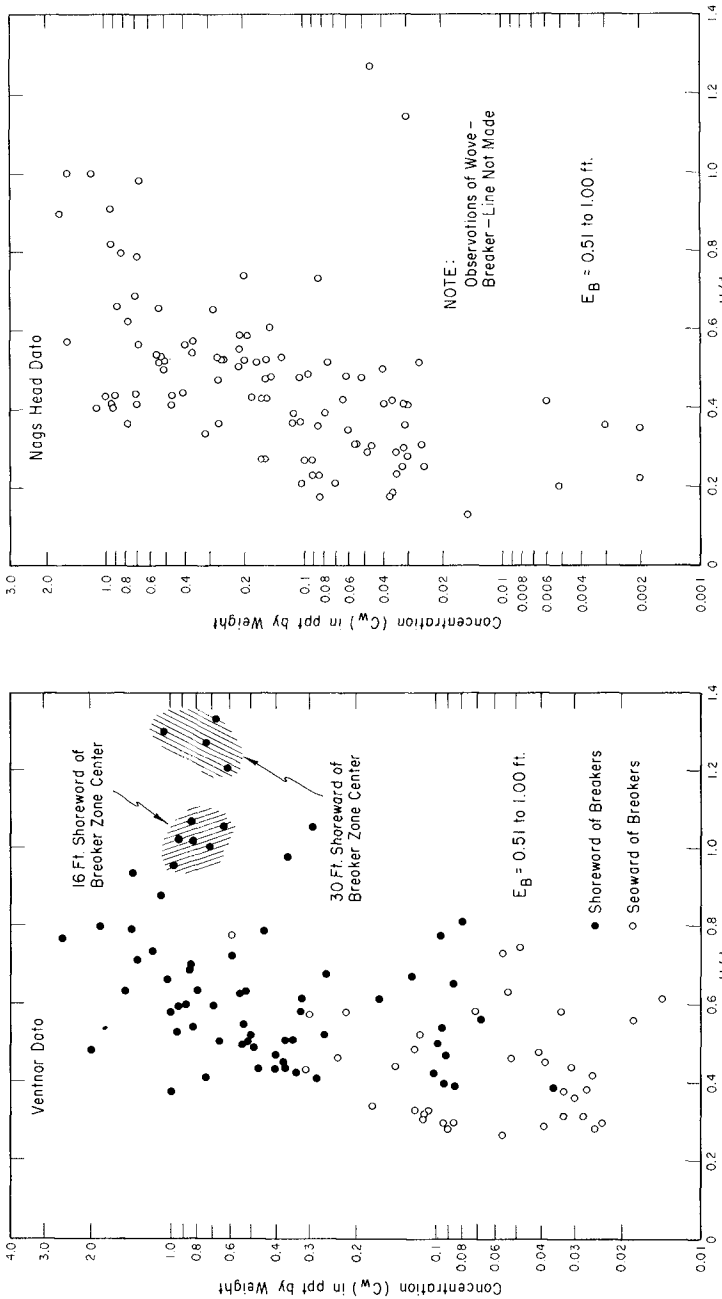

FIGURE 8. CONFIGURATION OF THE SCATTER IN A PLOT OF SUSPENDED SEDIMENT CONCENTRATION VERSUS WAVE HEIGHT OVER WATER DEPTH

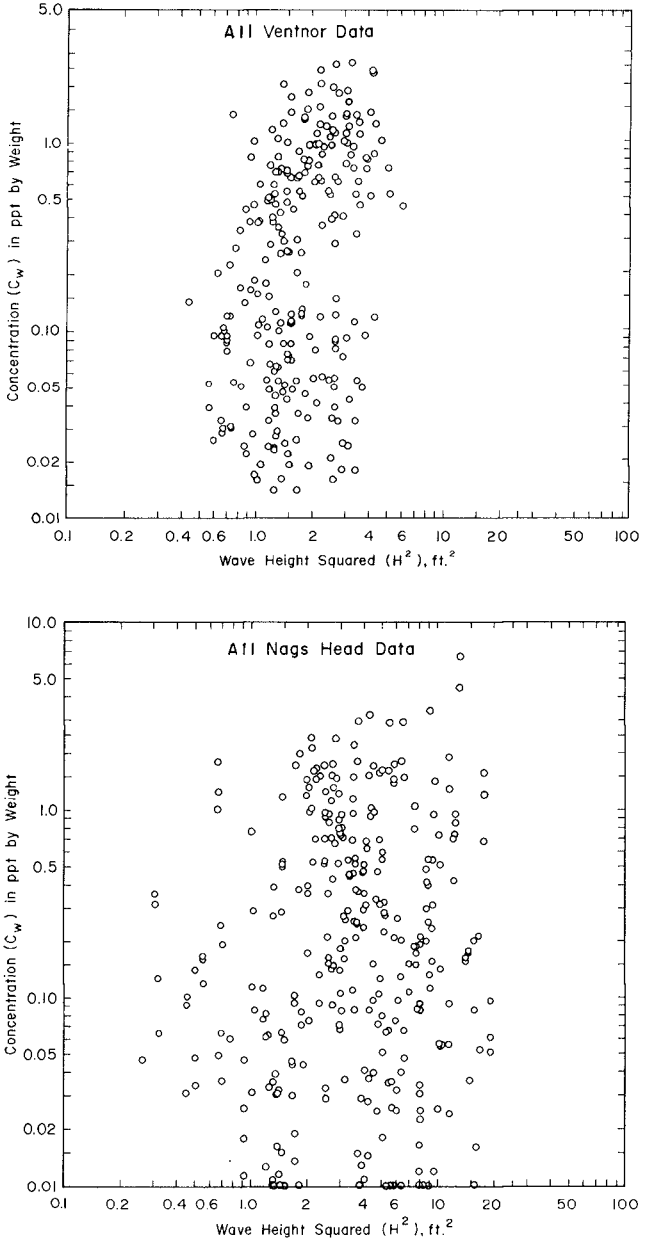

FIGURE 9: VARIATION OF SUSPENDED SEDIMENT CONCENTRATION IN RELATION TO WAVE HEIGHT SQUARED

In the next all-data scatter plot, Figure 10, C_w is plotted against the parameter, H/E_B wave height over sampling nozzle elevation above the ocean bottom. The total scatter in these plots, especially that for the Ventnor data on the left, is significantly less than in the last Figure of C_w versus H^2; the reduced acatter in Figure 10 results largely from the inclusion of E_B in the denominator of the abscissa, which accounts for the effect of variable nozzle elevation above the bottom. By overlaying the two sections of this figure, it was observed that the Ventnor data has a somewhat steeper slope than the Nags Head data. This may be explained by the fact that the median diameter of the Ventnor sand (0.12 - 0.15 mm) is significantly less than that of the Nags Head sand (about 0.20 mm), so that the Ventnor sand is more uniformly mixed, and being significantly smaller may be sustained in suspension at relatively higher elevations by a given energy or turbulence input.

Particle size effects in relation to wave-induced suspended sediment are summarized in Figure 11. The two scatter plots in this figure relate the median particle size and the coarser 5th percentile of the samples to water depth and nozzle height above bottom for the Nags Head data. These scatter trends show a very gradual decrease in median particle size with increase in water depth, and also with increase in E_B, nozzle height above bottom. Scatter trends for the Ventnor data were very similar but an actual points plot for the Ventnor data was not included due to space limitations. Instead, as the legend in Figure 11 shows, a visual best fit curve from the actual Ventnor data is displayed near the bottom of each graph.

Figure 12 is a composite plot of suspended sediment concentration versus wave height squared, as indicated for sampling elevation, $E_B \leq 1.00$ foot above the bottom, enabling comparison of the Ventnor, N. J. and Nags Head, N. C. results, with other field and laboratory results. The upper graph shows plotted points from two sets of laboratory tests (SPTB and 72 ft wave tank) and three sets of CERC large wave tank tests grouped about the plots from the two field tests at Ventnor, N. J. and Nags Head, N. C. This graph gives an overview of variations in the concentrations of wave-induced suspended sediment in laboratory and in average condition ocean waves - from small tank waves with 3 to 6 inch heights up to CERC large-wave tank waves with 7.0 feet breaker heights. The lower graph in Figure 12 is an averaged version of the upper one, where each scatter grouping has been averaged as a single point. The SPTB data actually comprised three data sets as the lower-graph legend shows. In addition, the lower graph includes three added points as follows: one point from data collected at Mission Bay, California and reported by Watts (1); and, two points from measurements of suspended sediment in the Missouri River and in a laboratory flume.(5) In plotting the unidirectional flow data, the flow depth is assumed analogous to the wave breaker height, since breaker depth equals breaker height to a first approximation.

In summary, the various data plotted in Figure 12 show an expectable relationship (C_w increasing with H^2). These results suggest the possibility of further application of suspended sediment results from unidirectional flow in studies of wave-induced suspended sediment. The unidirectional flow

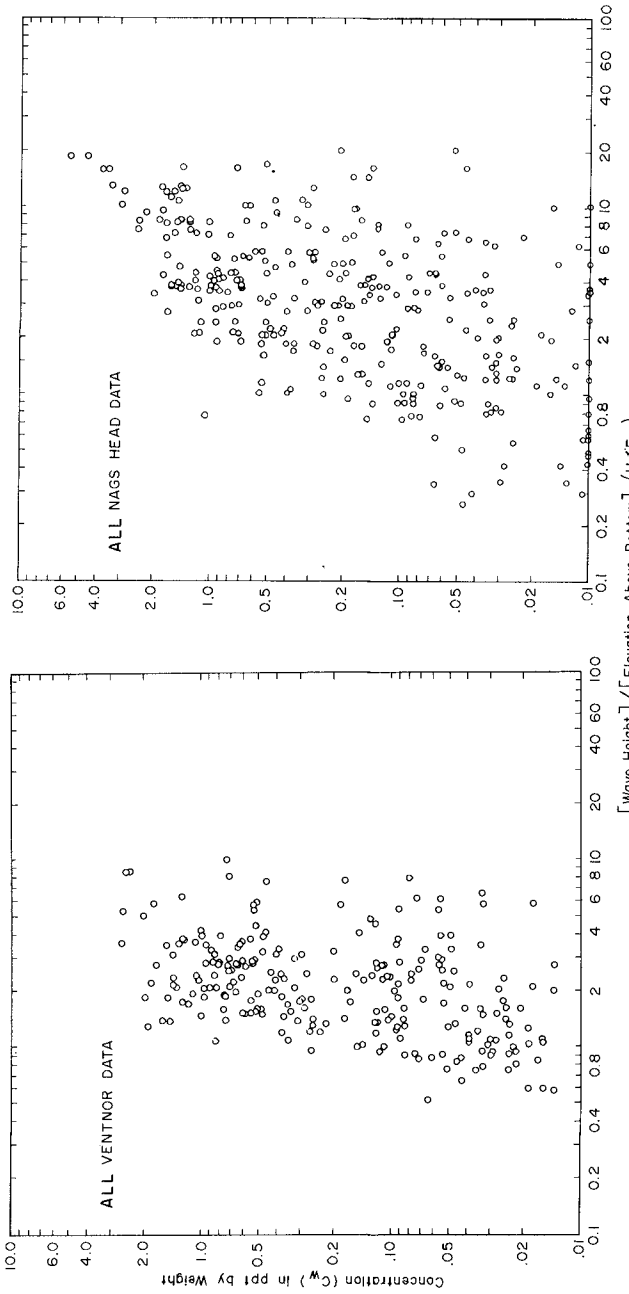

FIGURE 10: VARIATION OF SUSPENDED SEDIMENT CONCENTRATION IN RELATION TO WAVE HEIGHT OVER NOZZLE HEIGHT

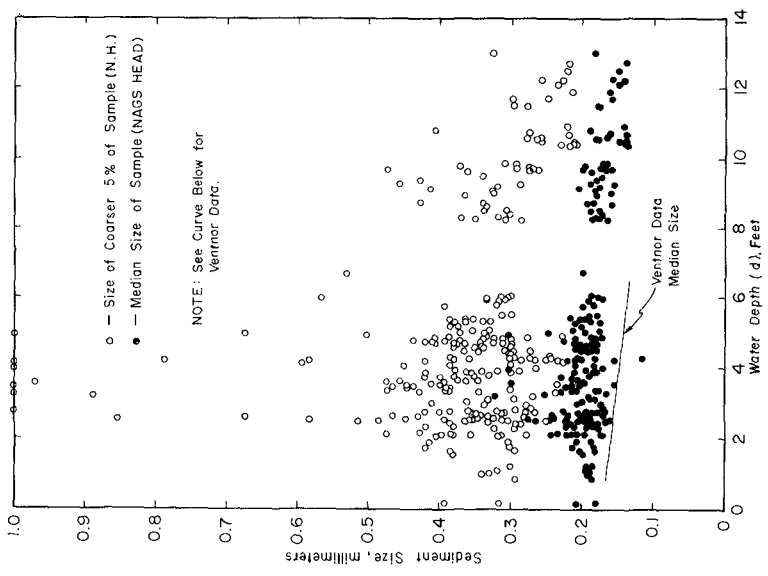

FIGURE 11A: RELATION OF SUSPENDED SEDIMENT SIZE TO WATER DEPTH

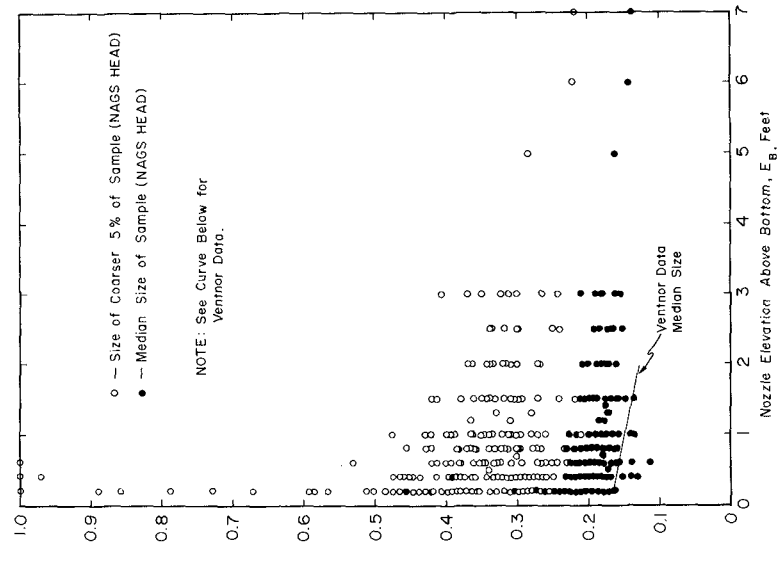

FIGURE 11B: RELATION OF SUSPENDED SEDIMENT SIZE TO NOZZLE ELEVATION

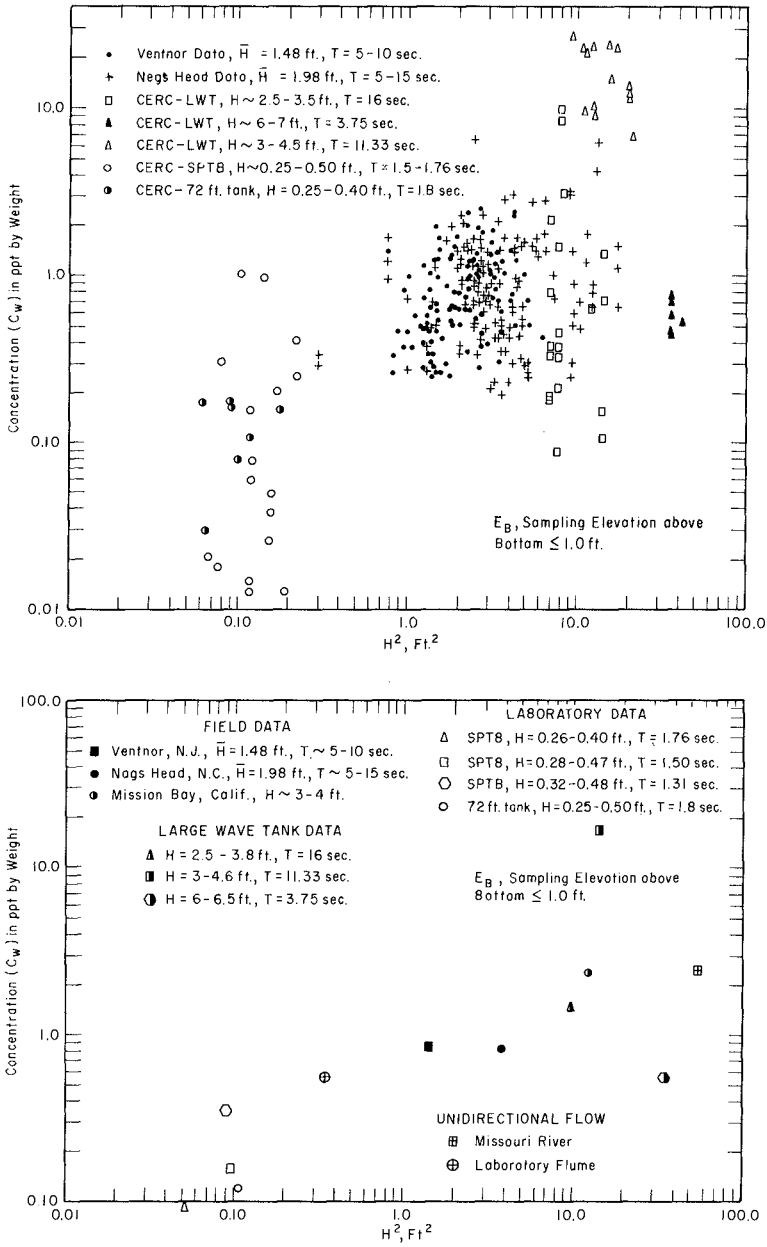

FIGURE 12. SUSPENDED SEDIMENT CONCENTRATIONS IN OCEAN AND LABORATORY WAVES

conditions are very different from those in the surf zone. However, much data, and empirical and theoretical development are available from unidirectional flow studies which will provide useful concepts, relationships and ideas to test out in surf zone studies.

Longshore Transport Rate From Suspended Sediment Data

Figure 12, discussed in the two paragraphs above indicated the relationship between representative concentrations of suspended sediment and their respective wave height squared (a wave energy parameter). A further and interesting use of the CERC field and laboratory data on suspended sediment may be made by approximating longshore transport rates for comparison with the transport rates indicated by the TR-4 design curve of longshore wave energy flux versus longshore transport rate.(6) Computations may be made by a formula developed by Galvin and included in his abstract at the 12th Conference on Coastal Engineering.(7) This formula is as follows: $Q = DgcT(\beta H_b)^2 \sin \theta_b$, where g is gravity, c is suspended sediment concentration in ppt by volume, β is a wave breaker index d_b/H_b, taken as 1.3, H_b is wave breaker height, θ_b is the angle between a wave breaking crest and the shoreline and D is a coefficient equal to 11.68 which changes ft^3/sec into units of $100{,}000\ yd^3/yr$.

Seven values of the longshore transport rate have been computed, using Galvin's formula along with their corresponding longshore components of wave energy at breaking using the formula, $Ea/wave = 1/8\ \rho g H_b^2 \left(1 - M \frac{H_b^2}{L_b^2}\right) \sin \theta_b \cos \theta_b K_R^2$. (6)

In Figure 13 these seven rates and their corresponding longshore wave energies are shown as plotted points for comparison with the TR-4 design curve of longshore wave energy flux versus longshore transport rate.

Wave breaker angles used in the computations were obtained from a nomograph of d/Lo versus θ_o under the assumption that the deep water angle between wave crest and shoreline could be approximated by an average value of 30°. Wave breaker angles (θ_b) were observed in conjunction with the collection of suspended sediment samples at Ventnor, N. J. Values observed ranged from 3 to 10 degrees for low height swell waves (1-2 ft) with wave period of 7 seconds or more. Breaker angles were not observed in the collection of suspended sediment at Nags Head, N. C. Large wave tank values of θ_b are necessarily hypothetical, since this is a test facility where wave breaker angle (θ_b) is actually zero.

The plotted points of computed longshore transport rates in Figure 13 compare reasonably well with the suggested design curve. The dotted line in the figure paralleling the TR-4 design curve extends the comparison to include recent indications by Inman (8) and Das (9) that the curve should be changed to reflect rms values of wave height. The TR-4 (6) design curve (solid line) is based on the significant wave height. The author recognizes that significant though not unreasonable assumptions have been made to obtain this plot.

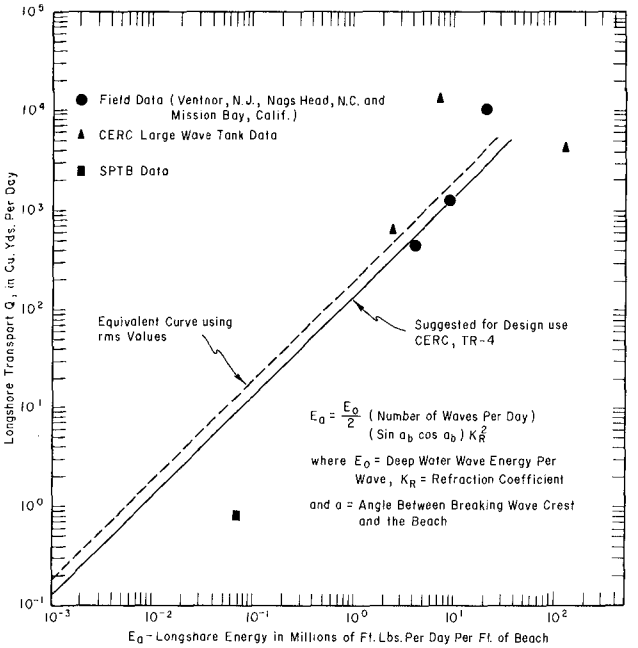

FIGURE 13. LONGSHORE TRANSPORT FROM SUSPENDED SEDIMENT DATA COMPARED TO CERC TR-4 LONGSHORE TRANSPORT CURVE

Summary and Conclusions

This paper has presented a summary of suspended sediment data from two Atlantic Coast sites with implications for its use in compiling longshore transport design criteria within the context of three main points as follows:

1. Discussion of the results from the field collections of suspended sediment at Ventnor, N. J. and Nags Head, N. C. These results show large variation in the suspended sediment concentration, but that the concentrations did depend on elevation above bottom, wave height, and position in the surf zone.

2. Comparison of these field results with earlier CERC field data (1) from Pacific Beach, California, and with CERC laboratory measurements (2) showed a trend when suspended sediment concentration was plotted against wave height squared. This comparison also included two sets of suspended sediment concentration measurements from unidirectional flow (5) - one in the Missouri River and one in a laboratory flume, under the assumption that to a first approximation the flow depth is analogous to the wave breaker height.

3. Reasonable correlation was found between longshore tranaport rates, computed from representative values of suspended sediment concentration and wave conditions, and the TR-4 design curve of wave energy flux va longshore transport rates.

The data and results presented and discussed appear to support the following conclusions:

1. Field data suggest that 3-minute averages of surf zone concentration in waves up to 4 feet high, show significant variation in concentration with elevation above the bottom. The higher the level of wave activity the less concentration varies with elevation above bottom, and hence the flatter the trend in the distribution curve.

2. Scatter configurations also suggest that for waves approaching their breaking depth, the concentration of suspended sediment rises sharply just before the wave breaks, peaking at a wave height-to-water depth ratio of about 0.78 (theoretical breaker index). Concentration then drops off more slowly shoreward of the initial wave breaking;

3. Concentrations measured in the field compare realistically with those obtained in CERC large and small wave tank tests;

4. Median size of the suspended sediment samples decreases gradually with increase in water depth and with increase in sampling elevation above the ocean bottom. There is some implication that a flatter distribution of sand size with nozzle height, as found in the smaller size Ventnor sand, may be indicative of higher concentrations for smaller more uniformly mixed sands;

5. An empirical check on longshore transport rates computed from field and laboratory data on suspended sediment compare reasonably well with the TR-4 suggested design curve.

ACKNOWLEDGEMENT

This paper was written while the author was a member of the Coastal Processes Branch, Research Division. C. J. Galvin, Jr., Chief, Coastal Processes Branch reviewed this paper.

Data presented in this paper, Longshore Transport of Suspended Sediment, unless otherwise noted, were obtained from research conducted by the United States Army Coastal Engineering Research Center under the Civil Works research and development program of the United Statea Army Corps of Engineers. Permission of the Chief of Engineers to publish this information is appreciated. The findinga of this paper are not to be construed as official Department of the Army position unless so designated by other authorized documents.

REFERENCES

1. Watts, G. M., "Development and Field of a Sampler for Suspended Sediment in Wave Action," Beach Erosion Board Technical Memorandum No. 34, March 1953.

2. Fairchild, J. C., "Suspended Sediment Sampling in Laboratory Wave Action," Beach Erosion Board Technical Memorandum No. 115, June 1959.

3. Fairchild, J. C., "A Tractor-Mounted Suspended Sand Sampler," Coastal Engineering Research Center R. 4-66, Reprinted from Shore and Beach, June 1966.

4. Fairchild, J. C., "Suspended Sediment Concentration in the Surf Zone," Transactions Abstract (EOS), American Geophysical Union, April 1971.

5. "Sediment Transportation Mechanics: Suspension of Sediment" Progress Report, Task Committee on Preparation of Sedimentation Manual, HY 5, ASCE, Sept 1963.

6. "Shore Protection, Planning and Design," Coastal Engineering Research Center, Technical Report No. 4, Third Edition, 1966.

7. Galvin, C. J. Jr., "A Gross Littoral Drift Rate Formula," Abstracts, 12th Conference on Coastal Engineering, 1970.

8. Inman, D. L. and J. D. Frautschy, "Littoral Processes and the Development of Shorelines," Coastal Engineering, 1966, ASCE, p. 511-536.

9. Das, M. M., "Longshore Sediment Transport Rates," Coastal Engineering Research Center Miscellaneous Paper No. 1-71, Sept 1971.

CHAPTER 57

INSTRUMENT FOR LONG-TERM MEASUREMENT OF SUSPENDED MATTER (SILT GAUGE)

Harald Göhren
Hans Laucht

Strom- und Hafenbau
Hamburg, W. Germany

ABSTRACT

With financial support by the German Research Association (Deutsche Forschungsgemeinschaft) an instrument for automatic long-term measurement of suspended matter has been developed by the authors. It works on a settling method. A sample of 20 l of water is pumped into a conical settling bottle every hour. The suspended sediments settling in a measuring tube at the bottom of the bottle are recorded by a camera. The device called "Silt Gauge" is intended for long-term measurements in shallow coastal water.

INTRODUCTION

In estuaries as well as in the surf zone in front of sandy coasts the transport of material in form of "suspended load" is of great importance. Various instruments and methods to determine the concentration of suspended matter in water have been developed. Most of them are based on the analysis of weight or volume of the suspended sediment in a water sample, using filters, centrifuges or special settling receptacles. The samples are taken by pumping systems or bottle traps which have been constructed in

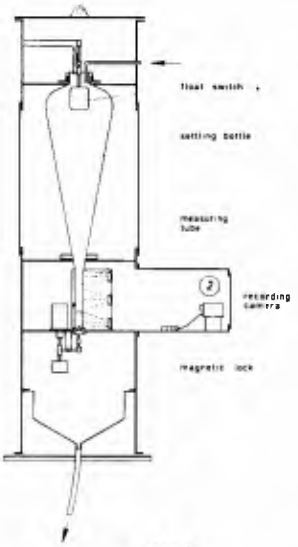

Fig. 1
SILT GAUGE

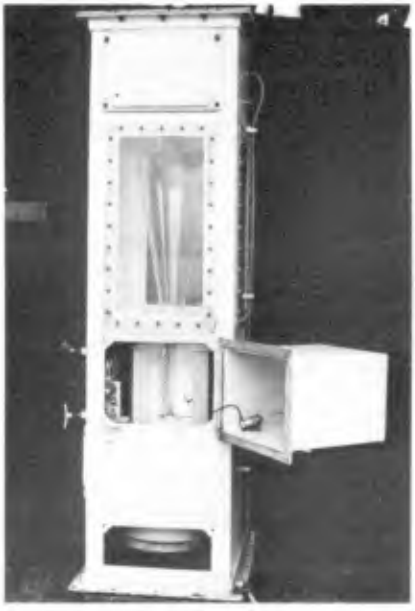

Fig. 2
SILT GAUGE

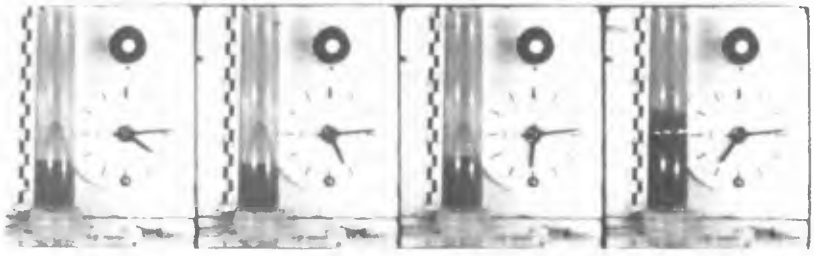

Fig. 3
SECTION OF A RECORD (orig. 8 mm film)

numerous variations. They all require manual handling and hence are not suitable for automatic long-term measurements. Another indirect method applies the effect that light is absorbed or scattered by the suspended particles. This principle provides a good basis for the construction of an automatic instrument, but unfortunately the absorbtion or scattering of light mainly depends on the grain diameter and not on the weight or volume. Another problem is the fouling of the optical windows which must be submerged into the liquid.

DESIGN AND CONSTRUCTION OF THE SILT GAUGE

The development of the Silt Gauge was started in 1967 after establishing the following principle: In regular time intervals 20 l of water are pumped into a settling bottle of 1 m height. The bottle is of conic shape, ending in a narrow measuring tube of 25 mm diameter. The slope of the bottle sides is designed that way that falling particles will slide off and settle in the tube. The settling bottle is manufactured from glass in order to have the walls as smooth as possible and to avoid any corrosion. After one hour settling time (which may be varied) the deposition is recorded by a camera. Then sediment and water are released through a magnetically operated lock (fig. 1 and 2). This cycle is reiterated hourly, controlled by an electronic unit. The recording set consists of a simple 8 mm camera and a magnetic trigger. The film capacity is sufficient for a two month's measuring time. The camera takes a picture of the measuring tube, a scale and a clockface, giving accurate time control. A special test lamp indicates whether the settling bottle is filled in the moment the foto is taken and provides a function check. Fig. 3 shows a section of a record.

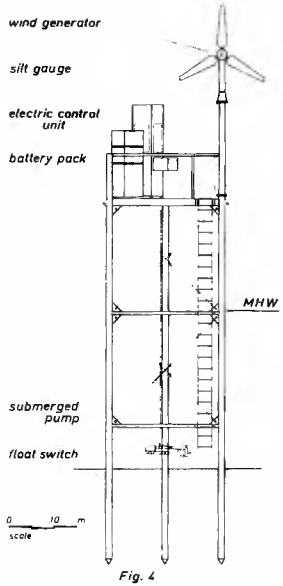

Fig. 4
SILT GAUGE PLATFORM FOR TIDAL FLAT

Fig. 5
THE PLATFORM FOR THE SILT GAUGE IS ERECTED

Fig. 6
THE WIND-MILL GENERATOR IS MOUNTED ON THE PLATFORM

Fig. 7
SUBMERGED PUMP AND FLOAT SWITCH

The Silt Gauge has been developed for investigations in the tidal flats of the southern North Sea coast. The complete instrument, installed in a steel box (dimensions 20 x 20 x 80 in.), is based on a threepod platform which easily can be set up by a vessel (fig. 4 to 6). A windmill generator in combination with a set of storage batteries provides an independent power supply. The submerged pump, fitted with an intake nozzle of 11 in. length and 0.6 in. diameter, is fastened at one of the platform legs (fig. 7). A special float switch is mounted on the pump, stopping it if the water level sinks below the switch.

CALIBRATION

Due to the "settling principle" the Silt Gauge can only measure the amount of suspended particles which sink down with a velocity $\geq$ 1 m per hour. Very fine stuff having a lower settling velocity is not recorded. The settling velocity mainly depends on grain size, specific weight and density of the liquid. This measuring principle may be a drawback in particular cases. But generally it seems to be advantageous since in all processes of coastal erosion and sedimentation only that part of suspended load is of importance that is able to sink down in calm water within a limited space of time. With regard to the dimension of the settling bottle and the "Stokes law" a theoretical deposition curve can be evaluated (fig. 8) indicating that a grain size of about 0.02 mm diameter confines the measuring range. However it is obvious that this theoretical boundary does not exist under natural conditions. Due to some complicate electrolytic, chemical and even biological effects fine suspended particles tend to generate flakes, these having a higher settling velocity in calm water than the single grains.

From a series of analyses using water samples taken in the tidal flat the deposition curve in fig. 9 has been

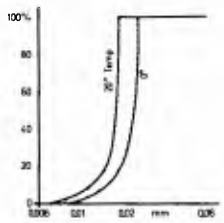

Fig. 8

RATE OF DEPOSITION IN THE BOTTLE VERSUS GRAIN SIZE (THEOR.)

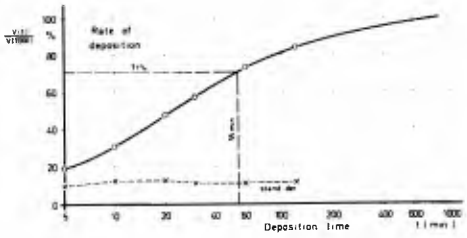

Fig 9

DEPOSITION IN THE TUBE VERSUS TIME
(EVALUATED BY TESTS UNDER NATURAL CONDITIONS)

Fig. 10

SILT GAUGE STATION IN THE TIDAL FLAT

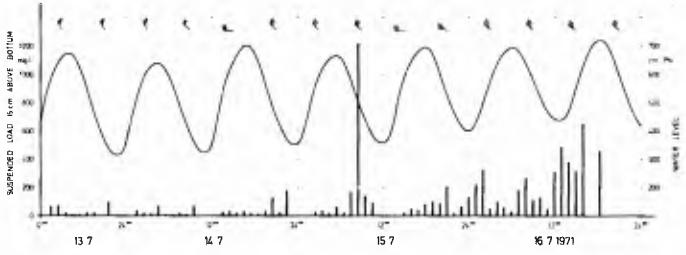

Fig 11

DATA OBTAINED FROM A "SILT GAUGE STATION" IN THE NEUWERK TIDAL FLATS, INDICATING WIND INFLUENCE ON SUSPENDED LOAD

evaluated. An average rate of 70% of the suspended load can be expected to settle in the measuring tube during one hour.

EXPERIENCE

After having completed the device in 1968, a thorough test programme was performed which lead to several technical improvements. Particular difficulties were caused by the submerged pump (Type Benthos, 24 V D.C.). The pump, announced as "deep sea pump", was found to be not waterproof. After protracted trials in connection with the manufacturer to improve this type, which was most suitable because of its voltage and capacity, it was necessary to take another type of a submerged pump, operating with 220 V A.C. and thus requiring additional electric units.

After having accomplished all improvements, the device is operating with great reliability. It has been working on several stations in the tidal flats of the Elbe Estuary. The particular aim of these measurements is an investigation of the influence of waves and drift currents on suspended load in a tidal flat. As vessels cannot operate in the shoals at stormy weather, the employment of an automatic instrument is the only method to advance in that programme.

Fig. 10 shows the Silt Gauge in the tidal flat at high water. Records of currents and waves are taken simultaneously by a wave gauge and a current meter, both instruments likewise equipped for automatic long-term measurements.

Fig. 11 shows a section of a measurement carried out with the Silt Gauge. The increase of suspended load with increasing wind velocity gives an impression of the predominant wind influence on litoral transport in the shoals. It is intended to continue investigations of this kind over several years in order to abtain sufficient data

for a statistical evaluation of relationships between suspended load, currents, waves, water temperature and other parameters and in this way to enable trusty computations of suspended transport and its dependence on tide and weather variations.

REFERENCES

Fairchild, J.C. (1965). Suspended sand sampler. Shore and Beach, Oct. 1965

Göhren, H. and Laucht, H. (1972). Entwicklung eines Gerätes zur Dauermessung suspendierter Feststoffe. Deutsche Gewässerkundliche Mitteilungen, 16. Jg., H. 3, 1972

Laucht, H. (1971). Entwicklung eines automatischen Schwebstoffmeßgerätes für den Brandungsbereich. Forschungsbericht - Sandbewegung im Küstenraum. Deutsche Forschungsgemeinschaft, 1971

Nelson, M. and Bendict, C. (1950). Measurement and analysis of sediment load on streams. Am. Soc. Civ. Eng. Vol. 76, 1950

Watts, G.M. (1953). Development and field test of a sampler for suspended sediment in wave action. Beach Erosion Board, Techn. Mem. 34

CHAPTER 58

MEASUREMENT OF SEDIMENT SUSPENSION IN COMBINATIONS OF WAVES AND CURRENTS

J. Kirkegaard Jensen[x] and Torben Sørensen[xx]

ABSTRACT

The paper describes a procedure for obtaining field data on the mean concentration of sediments in combination of waves and currents outside the breaker zone, as well as some results of such measurements. It is assumed that the current turbulence alone is responsible for the maintenance of the concentration profile above a thin layer close to the bottom, in which pick-up of sediments due to wave agitation takes place. This assumption gives a good agreement between field data and calculated concentration profiles.

1. INTRODUCTION

An extensive investigation programme was carried out in 1971 to predict the sedimentation in a proposed dredged entrance channel to the Port of Karachi. During the summer the area is exposed to monsoon waves and to tidal currents.

The programme involved both field and laboratory measurements of concentrations of suspended sediment, and the results were interpreted on the basis of simultaneous recordings of waves and currents. This paper deals with the determination of concentration profiles in the region outside the breaker zone.

x) Research Engineer, Danish Hydraulic Institute, Copenhagen, Denmark

xx) Director, Danish Hydraulic Institute, Copenhagen, Denmark

2. NOTATION

- c - Concentration
- c_r - Concentration at a reference level
- D - Water depth
- u - Maximum orbital velocity of wave movement at the bottom
- U_f - Friction velocity
- w - Settling velocity of suspended grains
- y - Vertical coordinate
- z - $w/\kappa \cdot U_f$
- ε_s - Diffusion coefficient for suspended sediment
- κ - v. Karman's constant

3. THEORETICAL CONSIDERATIONS

In a turbulent flow, the concentrations of suspended sediments are determined by an equilibrium between settling of sediments, due to gravity, and diffusion of sediment grains towards levels with lower concentrations. This mechanism may be described by the equation:

$$c \cdot w = -\varepsilon_s \frac{\partial c}{\partial y} \tag{1}$$

In a fully turbulent two-dimensional steady and uniform flow, this equation may be integrated to yield

$$c = c_r \left(\frac{D - y}{y}\right)^z \tag{2}$$

in which

$$z = \frac{w}{\kappa \cdot U_f}$$

if ε_s is assumed to be equal to the eddy viscosity of the flow. The concentration c_r at a reference level has to be determined by measurements.

In pure sinusoidal waves, sediment suspension occurs only within a thin turbulent layer near the bottom. It is known from several investigations that the thickness of the wave boundary layer is of the order of magnitude of a few

centimetres. However, suspended sediments have been found above this layer in a number of tests. The suspension mechanism under such circumstances cannot yet be described mathematically, which means that in neither of the cases, pure wave motion and wave motion combined with currents, can equation (1) be integrated in this region.

For the present purposes, it is assumed that the wave motion provides a boundary condition, from which a c_r in equation (2) may be found. This boundary condition is assumed to be related only to the wave conditions whereas the profile above the level of this c_r is calculated by equation (2), and is thus assumed not to be influenced by the presence of waves.

4. FIELD MEASUREMENTS

4.1 Hydrographic Conditions

Measurements of concentration profiles were carried out at 11 m water depth off Karachi during the southwest monsoon season of 1971. During this season the coast is constantly exposed to high waves. Wave measurements performed with a Waverider system simultaneously with the water sampling showed significant heights of 1.4-2.7 m, and zero-crossing periods of 7-9 s. The currents generated by the predominantly semidiurnal tide of maximum range 3.5 m reached a maximum velocity of 0.5 m/s at the sampling position.

The bottom sediments are silt and fine sand with a median diameter of 0.08 mm.

4.2 Measuring Technique

The main problem of these measurements was to establish a fixed location of the sampling levels relative to the bottom. This is very critical, especially when sampling from levels close to the bottom, because the concentration

gradient is very large.

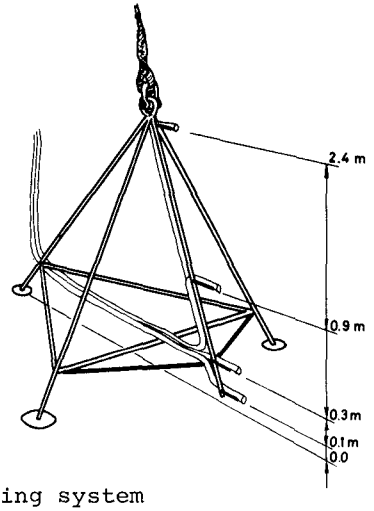

Fig. 1 - Sampling system

The sampling system was constructed as a tripod frame of steel bars, figure 1, which was lowered to the bottom from a vessel anchored at the sampling position. The frame was supported on feet shaped as part of a sphere to reduce scouring around the feet. Four suction hoses were attached to intake nozzles mounted on this frame and a fifth hose was lowered with a sinker for sampling at mid depth.

Every 45 minutes, two 1 litre samples from each of the five levels, were pumped on board the vessel, each sample representing an average over 30 s. The sediment concentrations of these routine samples were determined by filtration. In addition to this 20 l samples were taken for determination of the settling velocity distribution by the hydrometer method.

In order to investigate the relationship between wave conditions and the concentrations near the bottom, samplings were carried out during eight periods, each of them covering one half tidal cycle.

4.3 Results

Figure 2 presents the results of measurements during one flood tide. The results did not show any systematic variation of the concentrations arising from the variation of the tidal current velocity. Therefore, the measurements are correlated with the average characteristics of the tidal current over the flood tide. The calculated mean profile is based on the settling velocity distribution as determined in the boundary layer 0.05 m above the bottom, and the average concentration of the 12 samples from the 0.3 m level. The friction velocity in equation (2), could not be determined by the current measurements performed. Hence, an approximate value of 0.05 times the average velocity over depth was used.

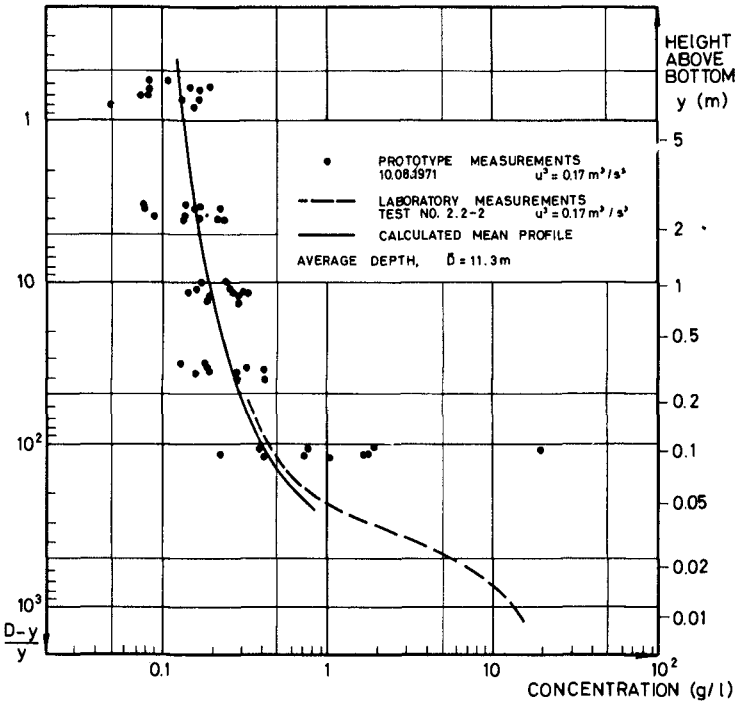

Fig. 2 - Sediment concentration profiles

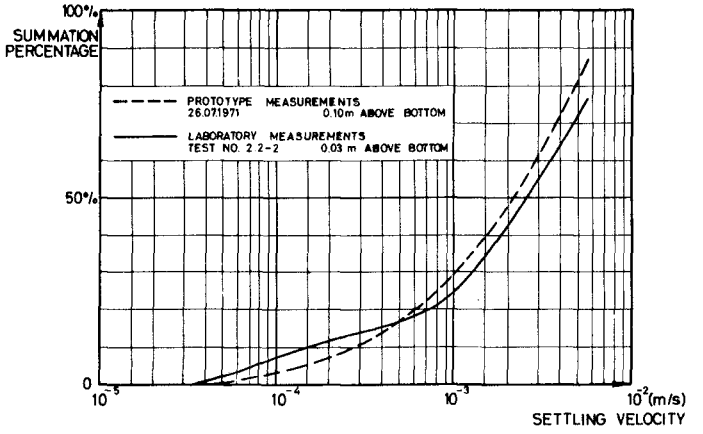

Fig. 3 - Settling velocity distributions

The agreement between the calculated profile, shown by a solid curve in figure 2, and the averages of measured sediment concentration is demonstrated by the following table:

Height above bottom	Concentrations measured	calculated
5.5 m	0.122 g/l	0.12 g/l
2.4 m	0.154 g/l	0.15 g/l
0.9 m	0.238 g/l	0.20 g/l
0.3 m	0.265 g/l	0.265g/l
0.1 m	0.282 g/l	0.40 g/l

Except for the level closest to the bottom, the agreement appears to be very good. Close to the bottom, however, the measurements show considerably higher sediment concentration than the calculated profile.

The most likely explanation of this discrepancy is that the frame does not fulfil the requirement of being a fixed reference system, but sinks a little into the bed, so that the lowermost nozzle is, in fact nearer to the

bottom than assumed. This explanation is supported by the fact that in many cases the concentration close to the bed increased with time after placing the frame on the bed. Another explanation could be the existence of bed undulations of a size comparable to the size of the frame.

Sometimes during the samplings very sudden, bursts of exceptionally high concentration were observed. This could be the effect of eddies separated from the bottom, either associated with the orbital movements or with scouring around the feet of the frame.

5. LABORATORY MEASUREMENTS

In nature it appears to be very difficult to obtain sufficiently accurate results close to the sea bed, as appears from the concentrations obtained at the 0.1 m level. Therefore, supplementary tests were carried out in the Institute's oscillating water tunnel. In this device orbital motions of the water particles near the bed, as generated by regular waves can be reproduced to the scale 1:1.

A number of tests at various periods and amplitudes were performed on bottom material recovered from the site. A concentration profile obtained in the water tunnel at conditions similar to the prototype condition is presented in figure 2.

Figure 3 shows settling velocity distributions of suspended sediment samples taken close to the bottom as determined from samples taken in the laboratory as well as the field.

For comparison of conditions in the oscillating water tunnel and in the nature it has been assumed that the height of regular waves creating the orbital motion simulated in the water tunnel corresponds to the RMS wave height of the prototype wave train.

In figure 2 the wave conditions are represented by

the parameter u^3, as the data both from the prototype and from laboratory measurements suggested a proportionality between the concentration near the bed and u^3. The validity of this relationship could, however, not be satisfactorily confirmed on the basis of the present measurements.

6. CONCLUSIONS

The following conclusions may be drawn from the work described in this paper:

1. The field measuring procedure used is satisfactory at levels not too close to the bottom (from 0.3 m and upwards). However, improvements are required in order to obtain reliable field data closer to the bottom than 0.3 m. The procedure described appears to be satisfactory in principle, when the transported sediments are predominantly silt and finer grains.

2. In a combination of waves and currents the concentration profile may be divided in an upper part where the characteristics of the current determine the profile, and a boundary layer, in which the wave motion determines the rate of pick-up of sediments from the bottom. The boundary layer in this respect is not well defined, and further investigations in this region are urgently required.

ACKNOWLEDGEMENT

This paper is presented with the kind permission of Karachi Port Trust, the United Nations Development Program, and of the International Bank of Reconstruction and Development.

CHAPTER 59

SEDIMENT BUDGET OF THE LOWER FRASER RIVER

By Nick Tywoniuk*

ABSTRACT

The Lower Fraser River, being continually developed for better navigation and larger port facilities, is an area of active sedimentation. The dynamic processes influenced by river discharge, tides and winds are probably the most important factors in the transport and deposition of sediments in the estuary. The main part of the Fraser Estuary is vertically homogeneous (non-stratified) and the sediments are transported progressively seaward and are accumulated near the limit of net landward flow. The lower estuary is stratified and coarse sediments are trapped near the toe of the salt wedge while the fine sediments are carried seaward with the outflowing river water.

The hydrometric and sediment survey of the lower Fraser River are described. Survey results are used in determining the sediment balance of the river reach. In the budget analysis, the river and estuary are divided into four consecutive reaches, the sediment discharges are subdivided to represent about 10 particle size ranges and the balance is then determined for each reach and particle size range.

Conclusions are drawn with respect to the sediment transport and depositional characteristics, annual variations, and the agreement between the sediment entering the estuary and the sediment dredged.

* Studies Engineer, Water Survey of Canada, Inland Waters Branch, Department of the Environment, Ottawa, Canada.

INTRODUCTION

A comprehensive hydrometric and sediment survey was started on the Lower Fraser River by the Water Survey of Canada in 1965. Flow and sediment data were required in the assessment of problems related to the maintenance and improvement of the navigation channel of the Lower Fraser River. Proper economic and engineering design for increased depths and widths, whether by dredging, training works or combinations of these two, required reliable and accurate data. Decisions related to extension of the deep sea channel to Mission City and of improvements to the navigation channel for barge traffic between Mission City and Hope awaited more reliable hydraulic and geomorphologic data in the Lower Fraser River reaches.

Navigation was only one of several problems associated with the Fraser River which would benefit from a comprehensive hydrometric and sediment survey. The data obtained would be essential in design of projects related to bank stabilization, protection dykes, land reclamation, harbour and mooring facilities, flood control and fisheries. The availability of these type of data for possible litigation during construction and operation of hydraulic projects should not be overlooked.

The analysis of data included the computation of a sediment budget. In this analysis, the sediment balance was determined for four consecutive parts of the lower river reach or estuary. The sediment discharges were subdivided to be representative of several particle size ranges and the balance was then determined for each part and each particle size range.

A general description of the hydrometric and sediment survey, the details of the budget analysis and some of the results are described and illustrated in this paper.

RIVER HYDRAULICS

The Fraser River with its tributaries drain 90,000 square miles of central and northern British Columbia into the Pacific Ocean near Vancouver. At the Fraser River at Hope, approximately 100 miles upstream from the mouth, the mean discharge is 94,600 cfs; the average annual runoff is in the order of 68,500,000 acre-feet. The Lower Fraser River, the reach between Hope and the Strait of Georgia, is illustrated in Figure 1.

The station, Fraser River at Hope, has been operational since March 1912, and has served as a useful base station in the prediction and calculation of flows below this point. The daily discharge at this station has varied from a low of 12,000 cfs on January 8, 1916 to a high of 536,000 cfs on May 31, 1948. The tributary inflow between Hope and Port Mann is about 30 percent of the total flow at Hope.

The suspended sediment discharge at the Fraser River at Hope is 20.6 million tons per year (average of 1966 to 1970 inclusive) and has varied from a daily low of 119 tons per day on January 16, 1967, to a daily high of 911,000 tons per day on May 11, 1966.

To further illustrate the river hydraulics, a flow duration curve obtained using daily flows for the Fraser River at Hope for the period October 1, 1946 to September 30, 1966, is shown in Figure 2. A frequency curve is shown in Figure 3 for this same station. The frequency curve was developed by the method of maximum likelihood (Chow, 1964) and is in terms of natural flows; that is, the flows have been adjusted to compensate for the effect of upstream river regulation.

Between Hope and the mouth, the natural channel has an average width of 2,000 feet, which expands to more than 3 miles in some areas. In this reach, Hope to the Strait of Georgia, the river falls approximately 125 feet of which the first 100 feet occur within the first 43 miles. In this eastern reach of the Lower Fraser River, particularly just east of the Sumas River, the spring freshets deposit coarse gravel material in the form of gravel bars. West from the mouth of the Sumas River the river slope is smaller and sands are deposited.

A large portion of the Lower Fraser River reach is affected by tides. During low flow the upstream limit of tidal effect is Chilliwack Mountain, approximately 15 miles east of Mission City. The high flow limit falls between Mission City and Whonock. This tidal effect within the survey reach has made the survey extremely complex. Deviation from standard methods of hydrometric and sediment measurement and computation were required in the determination of unsteady flows and the resulting sediment movement. A comparatively large amount of data were required to determine the pattern of sediment movement and to obtain a suitable understanding of unsteady flow in tidal portions of the study reach.

The complexity of the river hydraulics downstream from Port Mann is further increased by river branching. The approximate branching and flow distributions are illustrated by Figure 4 (Keane, 1957).

HYDROMETRIC AND SEDIMENT SURVEY

Some hydrometric data for the Lower Fraser River date back to 1876. However, it is only during the last 15 or 20 years in which a comprehensive hydrometric program in this area has been made operational. (Water Survey of Canada, 1970).

Much of the data that are collected in the lower tidal reaches are in the form of water surface elevations rather than discharge data normally required by the design engineer. Measurement and computation of tidal flow is relatively complex. Daily water level fluctuations which can exceed ten feet, variations and reversals in river flows, and the relatively large river depths, widths and velocities have produced a need for deviation from standard hydrometric techniques and have resulted in development of more sophisticated methods in the study of hydrometry of this river reach.

Discussion of the hydrometric survey of the Lower Fraser River cannot be entirely separated from the sediment survey since some of the recent developments in hydrometry have resulted from the needs of the sediment survey. The main sediment survey stations which required as a basis a complete hydrometric program were as follows: the four Fraser River stations located at Hope, Agassiz, Mission City and Port Mann; and the five tributary

stations Pitt River near Port Coquitlam, Stave River at Stave Falls, Chilliwack River at Vedder Crossing, Harrison River near Harrison Hot Springs and Silverhope Creek near Hope. This network of stations is illustrated in Figure 1. Continuous daily sediment and flow data have been obtained by the Water Survey of Canada at these stations since 1965.

The sediment data are of two types: suspended sediment and bed load. Bed load is the sediment that moves in essentially continuous contact with the bed of the stream whereas suspended sediment is the sediment supported by the flow. Bed load data were collected at only three stations of the main channel of the Fraser River; at Port Mann, Mission City and Agassiz.

Complementary to the sediment survey, records of public and private dredging have been kept by several agencies. These dredging data were used in the sediment budget analysis as these were the only quantitative data for the river downstream from Port Mann.

ANALYSIS DETAILS AND RESULTS

A number of simplifications or assumptions were made to facilitate the analysis. These were as follows: suspended sediment and bed load inflow from the tributaries could be ignored; the density of the material dredged was 90 pounds per cubic foot; the provisional data, some of which were used in these analysis were accurate; and the dissolved solids component was negligible. These assumptions could be readily justified, for example: suspended sediment inflow from four main tributaries is in the order of one percent of the suspended sediment discharge of the Fraser River at Hope; densities of deposited sands vary from 10 to 120 pounds per cubic foot (Inter-Agency Committee on Water Resources, 1963) and so on.

The budget is based on daily flow, suspended sediment and bed load data. The sediment discharge at a station is represented by:

$$QS(QB,QSB) = \sum_{i=1}^{n} QS(QB,QSB)_i \qquad (1)$$

Continuity within a reach is represented by:

$$QS(QB,QSB)_{xi} = QS(QB,QSB)_{yi} - SS_{xyi} \qquad (2)$$

Also of interest is a comparison of sediment measured at Port Mann with the material dredged downstream:

$$QSB_i - DSB_i = OSB_i \qquad (3)$$

In these equations, QS, QB and QSB are suspended sediment, bed load, and total load respectively. DSB and OSB are respectively the total load dredged and outflowing total load, that is, total load transported past the area of dredging. The particle size ranges are represented by subscript i, number of particle size ranges by n, upstream and downstream stations of a reach by x and y, and storage or deposition within a reach by SS, SB and SSB for suspended sediment, bed load and total load respectively.

The particle size distributions for both the suspended sediment and the bed load were determined for each day for the Fraser River stations from available data. The seasonal variations were found to be quite significant. These are illustrated in Tables 1 and 2, showing the particle size distributions for January 10 and June 10, 1969 for suspended sediment and bed material respectively. (The flow at Hope on January 10 was 42,000 cfs and on June 10, 274,000 cfs).

With the daily particle size distributions, and daily flow and sediment discharges, it was possible to perform the budget analyses on a daily basis using equations 1 and 2. Thus, the suspended sediment transported by the river was computed for the four Fraser River stations on a daily basis for the particle size ranges 0.000 - 0.062, 0.062 - 0.125, 0.125 - 0.500, and 0.500 - 1.000 mm. Bed load transported was also computed on a daily basis for these particle size ranges and also, where applicable, for the ranges 1.000 - 2.000, 2.000 - 4.000, 4.000 - 8.000, 8.000 - 19.10, 19.10 - 38.10, 38.10 - 76.20 and 76.20 - 152.4 mm. Bed load data were not available for the Fraser River at Hope.

The daily details are too numerous for illustrating in this paper. Furthermore, these are more meaningful on an annual basis and are thus represented for each main channel station in Tables 3, 4 and 5. These tables show, respectively, the annual suspended sediment, bed load and total load discharges for the four main channel stations for the years of available data. Partial year data are not shown.

The total load budgets, as determined by equation 2, are illustrated in Figures 5 and 6 for the Agassiz to Mission City and Mission City to Port Mann reaches respectively. Similar budgets could be prepared for suspended sediment and bed load discharges from data shown in Tables 3, 4 and 5.

Finally, annual data were used in equation 3 for comparing the total sediment discharge at Port Mann with the material dredged downstream from this location. It is convenient to illustrate these results in terms of percent of material dredged of the total sediment discharge at Port Mann. The percentages for the various particle size ranges are shown in Figure 7.

CONCLUSIONS

A number of observations with respect to the sediment balance in the Lower Fraser River can be made.

Gravels and boulders are transported by the river during very high flow only and are deposited at about the tidal limit between Agassiz and Mission City. Within the tidally influenced reach, a natural sorting of grain sizes occurs, the coarser particles being deposited in the upstream reaches. In the most active dredging reach, between Port Mann and Steveston, which is also within the reach of salt water intrusion, the sorting appears to terminate resulting in a river bed composed of relatively uniform grain sizes. The results shown in Tables 1 to 5 inclusive illustrate this phenomenon.

It is evident from Table 2 that clay and silt sizes (sizes finer than 0.062 mm) constitute only a very small fraction of the bed material at

the four Fraser River stations and in the main channel downstream from Port Mann. For this reason the silt and clay sizes were not subdivided for the budget computations but were instead treated together in the particle size range 0.000 to 0.062 mm. The absence of this fraction in the dredging region, as far downstream as Steveston indicates that the silts and clays are transported into the Strait of Georgia and must be deposited nearer to the foot of the delta.

The comparison of dredged and measured quantities is illustrated in Figure 7 and is perhaps relatively more difficult to interpret. The results perhaps indicate that more coarse material is dredged than is transported by the river to the dredging region considered. At least part of the difference must be the result of the settling out, in the dredging area, of some of those sediments which are in suspension at Port Mann. It has been observed in other tidal rivers that the upstream tip of a saline wedge is a focal point for sediment deposition. This factor and the fact that it is during the peak of the freshets that the bed of the river becomes most active in shoaling and scouring, could account for much of the heavy shoaling which occurs at Steveston. There is evidence that the salt water intrusion does not extend much further upstream than Steveston during a freshet. (Pretious, 1972). Other possible explanations for the measured and dredged differences are possible, for example, removal of large quantities of material for construction of the international airport and of bridge approaches; redistribution of the bed within the dredging area; undersampling of bed load, in the sense that suspended sediments in suspension at one point of measurement could become bed load at a downstream point; the distribution of total sediment load into the various channels of the lower estuary is not known and hence the possibility of overdredging of only one channel could not be evaluated; all dredged material was assumed to be represented by the average particle size distribution of the bed material in the main channel; and other factors. In summary, this part of the analysis is inconclusive because of insufficient data downstream from Port Mann.

Finally, one other observation should perhaps be noted: the sediment balance in the two river reaches Agassiz to Mission City and Mission City to Port Mann. Figures 5 and 6 illustrate that there is a net degradation of the upstream reach and a net aggradation of the downstream reach. In both reaches, however, there is an aggradation of coarse sediments. Hence these figures further verify the sorting process which is occurring in the Lower Fraser River.

ACKNOWLEDGEMENTS

The study was done utilizing the data, facilities and staff of the Water Survey of Canada, Department of the Environment. Data on dredging quantities were supplied by the Department of Public Works, the Fraser River Harbour Commission and the North Fraser River Commissioners. The author wishes to express his gratitude to Mr. W. Stichling and other staff of the Water Survey of Canada for their guidance and assistance throughout the study.

LITERATURE CITED

Chow, V.T., 1964. Editor-in-Chief. Handbook of Applied Hydrology, McGraw-Hill, New York.

Keane, J.C.B., 1957. "Report on the Hydrometric Surveys and Discharge Computations for the Fraser River Estuary for May, June and August, 1954". A Technical Monograph, Fraser River Board, Victoria, B.C. Open File Report.

Water Survey of Canada, 1970. "Hydrometric and Sediment Survey, Lower Fraser River, Progress Report, 1965-68". Inland Waters Branch, Department of Energy, Mines and Resources, Ottawa, Canada.

Inter-Agency Committee on Water Resources, 1963. A Study of Methods used in Measurement and Analysis of Sediment Loads in Streams. Report No. 14. Determination of Fluvial Sediment Discharge, U.S. Government Printing Office, Washington, D.C.

Pretious, E.S., 1972. "Downstream Sedimentation Effects of Dams on Fraser River, B.C." Water Resources Series No. 6, Department of Civil Engineering, The University of British Columbia.

TABLE 1

Particle Size Distributions for Suspended Sediment for January 10 and June 10, 1969.

Station	Day	Percent finer than indicated size (mm)					
		0.062	0.125	0.250	0.500	1.000	2.000
Fraser River at Port Mann	Jan. 10	100	100	100	100	100	100
	June 10	51.2	71.6	87.1	96.7	100	100
Fraser River At Mission City	Jan. 10	100	100	100	100	100	100
	June 10	42.7	58.4	82.3	96.9	100	100
Fraser River near Agassiz	Jan. 10	89.8	95.0	100	100	100	100
	June 10	59.6	72.0	88.9	97.6	100	100
Fraser River at Hope	Jan. 10	90.0	95.0	100	100	100	100
	June 10	57.1	74.0	90.4	93.3	100	100

TABLE 2

Particle Size Distributions for Bed Material
for January 10 and June 10, 1969

Station	Day	Percent finer than indicated size (mm)											
		0.062	0.125	0.250	0.500	1.000	2.000	4.000	8.000	19.10	38.10	76.20	152.4
Fraser River at Port Mann	Jan. 10	1.0	5.0	36.2	92.0	100							
	June 10	1.0	3.9	30.7	89.9	100							
Fraser River at Mission City	Jan. 10	0.0	3.0	20.0	70.1	100							
	June 10	0.0	3.0	28.8	77.9	100							
Fraser River near Agassiz*	Jan. 10	0.7	100	100	100	100	100	100	100	100	100	100	100
	June 10							0.0	0.1	24.6	64.5	89.8	100
Fraser River at Hope	Jan. 10	) No data available											
	June 10	)											
Material below Port Mann**	-	0.5	2.7	29.2	90.3	95.7	96.2	98.4	100				

* Particle Size distributions of bed load which were assumed to be equivalent to bed material sizes.

** Average of 29 samples taken at 5 locations in main channel in active dredging region (March 19, 1971).

TABLE 3

Fraser River Suspended Sediment Budget (per Station)

Location	Year	0.000-0.062 [a]	0.062-0.125	0.125-0.250	0.250-0.500	0.500-1.000	Total
Hope	1966	14,400 [b]	2,590	2,420	1,270	1,660	21,800
	1967	17,600	3,410	2,370	1,220	1,250	25,900
	1968	18,100	3,050	4,470	1,550	681	27,900
	1969	9,340	1,910	1,920	894	477	14,500
Agassiz	1967	17,700	4,170	3,530	2,020	536	28,000
	1968	16,100	3,710	2,600	944	258	23,600
	1969	9,580	1,690	1,680	897	252	14,100
Mission City	1966	14,400	1,900	3,360	1,160	1,110	21,900
	1967	19,300	4,850	3,700	2,810	1,490	32,200
	1968	16,800	3,080	2,760	2,590	613	25,800
	1969	9,360	3,030	2,880	1,560	503	17,300
Port Mann	1966	14,000	2,730	1,600	960	323	19,600
	1967	15,400	3,800	3,650	1,440	2,420	26,700
	1968	16,100	2,550	2,500	1,080	447	22,700
	1969	8,990	1,760	1,310	669	279	13,000

(a) figures indicate particle size ranges in millimeters.

(b) figures represent thousands of tons suspended sediment discharge per year.

TABLE 4

Fraser River Bed Load Budget (per Station)

Location	Year	0.000-0.062 [a]	0.062-0.125	0.125-0.250	0.250-0.500	0.500-1.000	1.000-2.000	2.000-4.000	4.000-8.000	8.000-19.10	19.10-38.10	38.10-76.20	76.20-152.4	Total
Hope			Bed load data were not available											
Agassiz [b]	1967	146 [b]	4270	4960	1620	129	25.5	4.10	383	115,000	248,000	180,000	77,100	632,000
	1968	108	3390	7150	2900	174	33.9	5.40	612	66,900	102,000	65,300	26,500	275,000
	1969	70.2	3000	5080	2850	249	48.2	7.50	710	29,400	29,500	16,500	6,370	93,800
Mission City [c]	1967	0 [c]	41.6	281	724	104	27.7	27.7	97.0	83.2	0	0	0	1,390
	1968	0	28.3	181	492	52.8	18.9	9.43	37.7	123	0	0	0	943
	1969	0	19.9	161	314	63.0	6.64	6.64	26.6	59.8	6.64	0	0	664
Port Mann [c]	1966	19.7 [c]	45.4	708	1030	132	39.4	0						1,970
	1967	17.2	90.8	507	976	108	17.2	0						1,720
	1968	8.98	47.6	270	475	79.0	18.0	0						899
	1969	10.6	42.8	315	595	36.3	63.8	0						1,060

(a) figures indicate particle size ranges in millimeters.

(b) figures represent tons bed load discharge per year.

(c) figures represent thousands of tons bed load discharge per year.

TABLE 5

Fraser River Total Load Budget (per Station)

Location	Year	0.000-0.062 (a)	0.062-0.125	0.125-0.250	0.250-0.500	0.500-1.000	1.000-2.000	2.000-4.000	4.000-8.000	8.000-19.10	19.10-38.10	38.10-76.20	76.20-152.4	Total
Hope		Total load data were not available												
Agassiz	1967	17,700 (b)	4,170	3,530	2,020	536	0.026	0.004	0.383	115	248	180	77.1	28,600
	1968	16,100	3,710	2,610	947	258	0.034	0.005	0.612	66.9	102	65.3	26.5	23,900
	1969	9,580	1,690	1,690	900	252	0.026	0.004	0.315	22.6	27.0	16.0	6.30	14,200
Mission City	1967	19,300	4,890	3,980	3,530	1,590	27.7	27.7	97.0	83.2	0	0	0	33,500
	1968	16,800	3,110	2,940	3,080	666	18.9	9.43	37.7	123	0	0	0	26,800
	1969	9,360	3,050	3,040	1,870	566	6.64	6.64	26.6	59.8	6.64	0	0	18,000
Port Mann	1966	14,000	2,780	2,310	1,990	455	39.4	0						21,600
	1967	15,400	3,890	4,160	2,420	2,530	17.2	0						28,400
	1968	16,100	2,600	2,770	1,560	526	18.0	0						23,600
	1969	9,000	1,800	1,630	1,260	315	63.8	0						14,100

(a) figures indicate particle size ranges in millimeters.

(b) figures represent thousands of tons total load discharge per year.

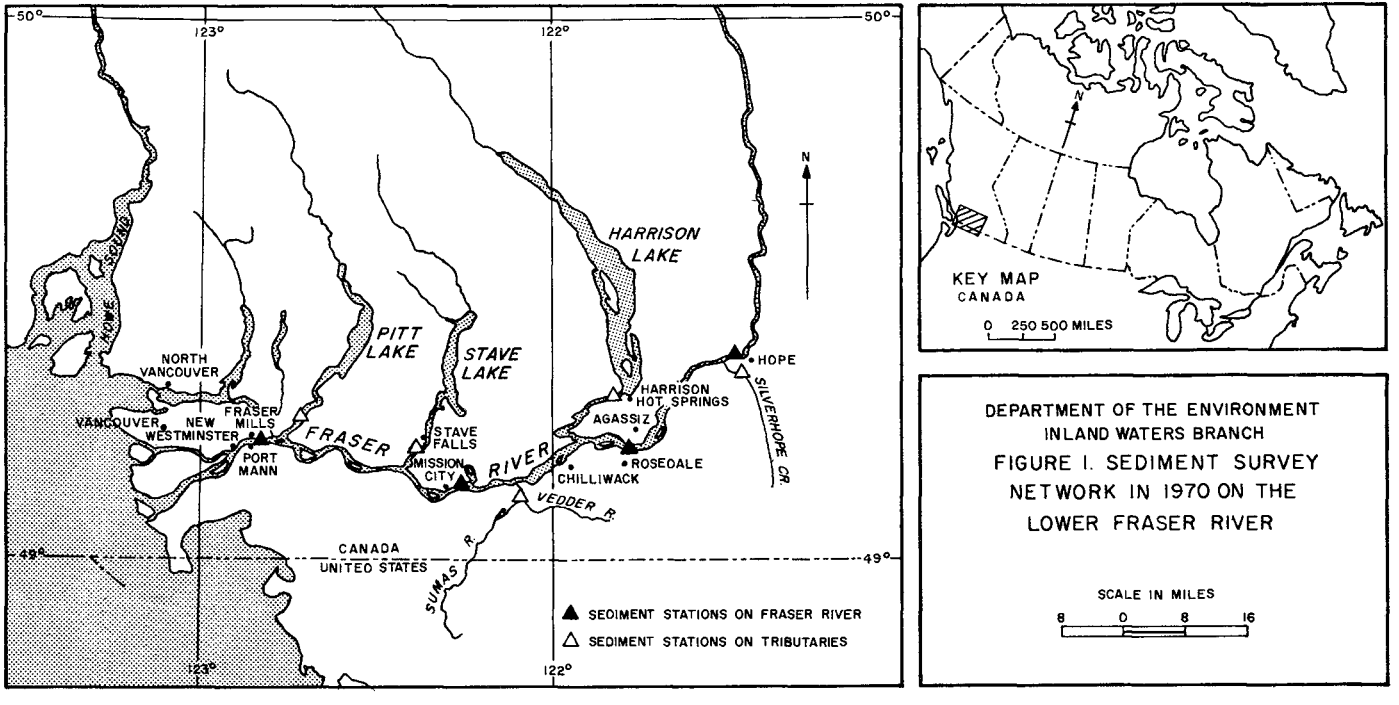
50°
123°
122°
49°
HARRISON LAKE
PITT LAKE
STAVE LAKE
FRASER RIVER
NORTH VANCOUVER
VANCOUVER
NEW WESTMINSTER
FRASER MILLS
PORT MANN
STAVE FALLS
MISSION CITY
HARRISON HOT SPRINGS
AGASSIZ
HOPE
SILVERHOPE CR.
CHILLIWACK
ROSEDALE
VEDDER R.
SUMAS R.
CANADA
UNITED STATES
SEDIMENT STATIONS ON FRASER RIVER
SEDIMENT STATIONS ON TRIBUTARIES
KEY MAP
CANADA
0 250 500 MILES
DEPARTMENT OF THE ENVIRONMENT
INLAND WATERS BRANCH
FIGURE I. SEDIMENT SURVEY NETWORK IN 1970 ON THE LOWER FRASER RIVER
SCALE IN MILES
8 0 8 16

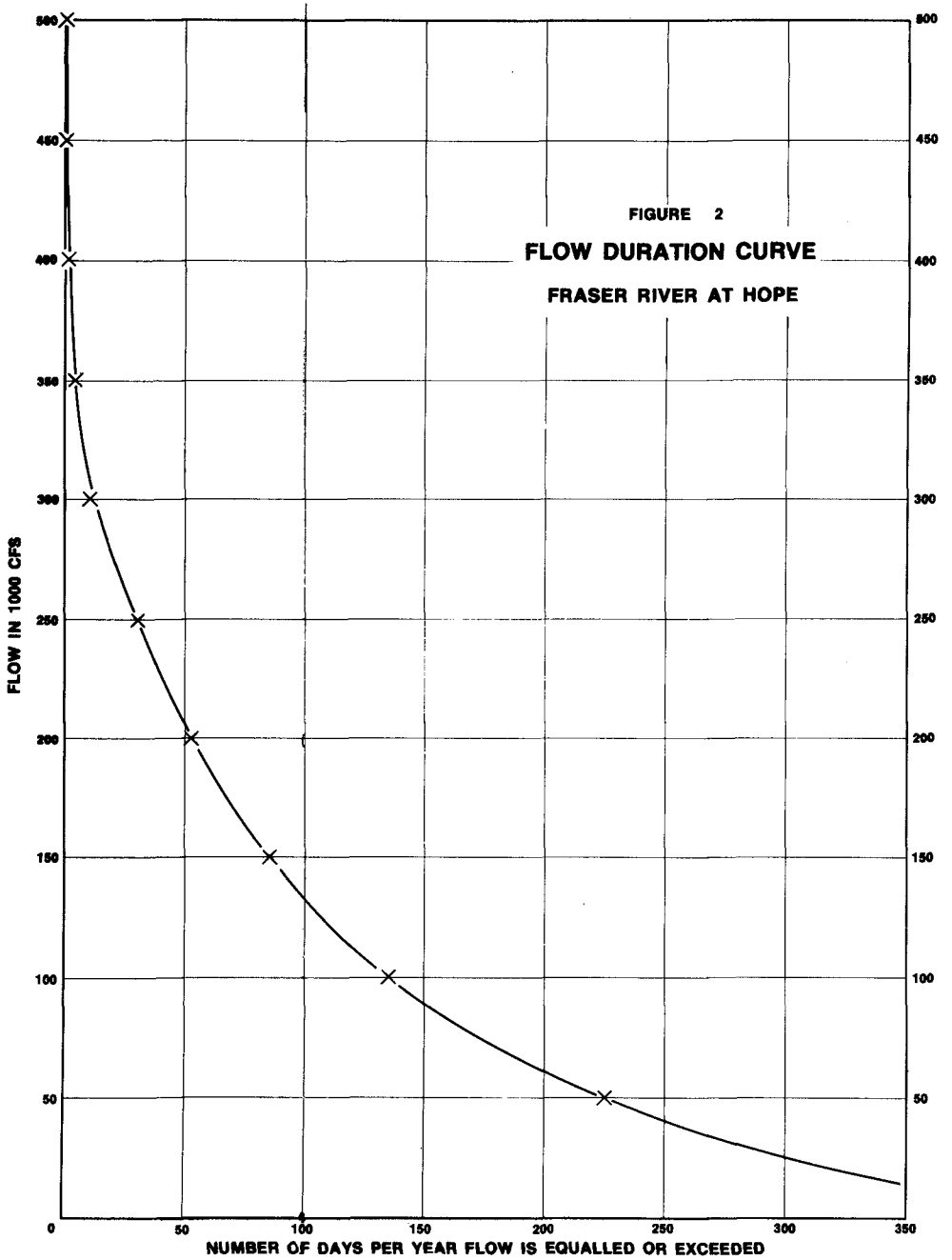
FIGURE 2
FLOW DURATION CURVE
FRASER RIVER AT HOPE
FLOW IN 1000 CFS
500
450
400
350
300
250
200
150
100
50
0
50
100
150
200
250
300
350
NUMBER OF DAYS PER YEAR FLOW IS EQUALLED OR EXCEEDED

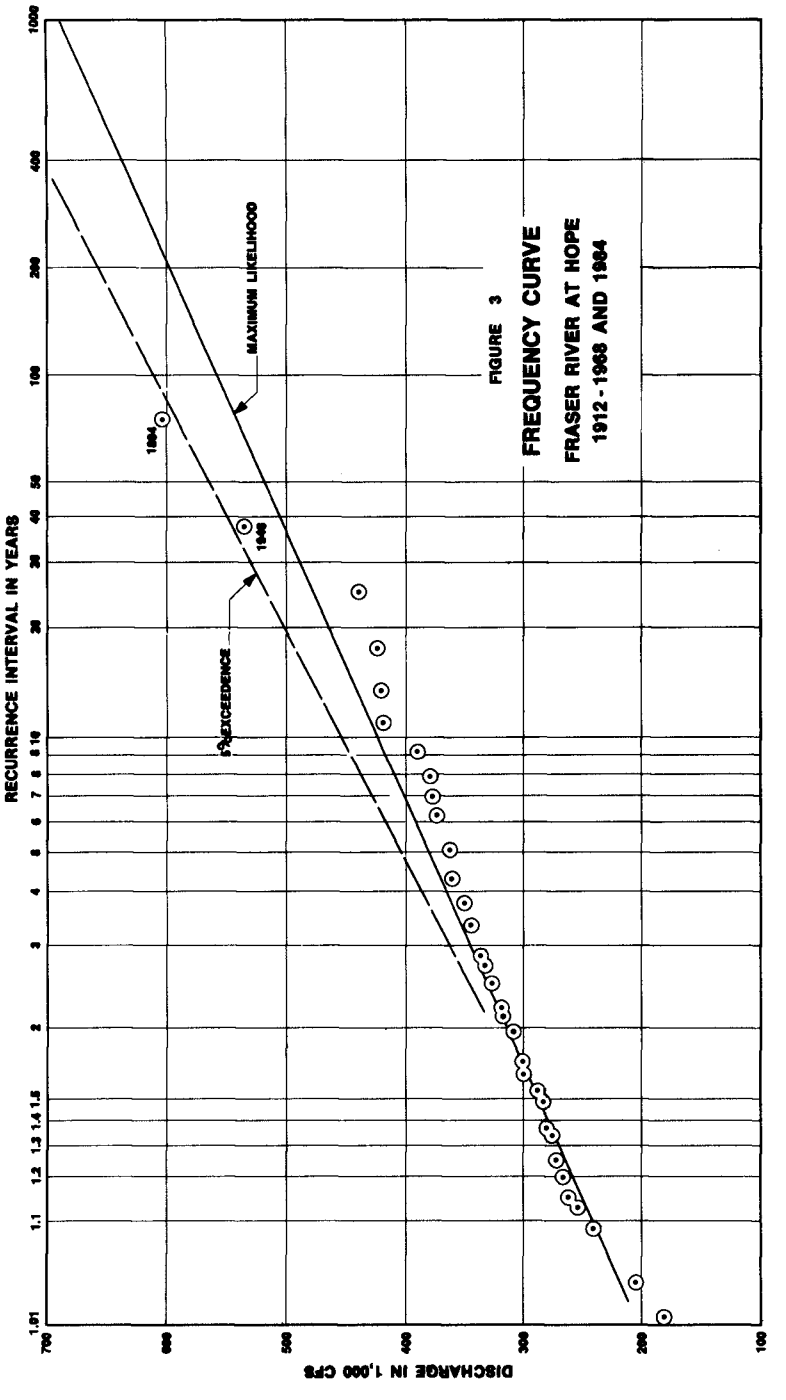
FIGURE 3
FREQUENCY CURVE
FRASER RIVER AT HOPE
1912 - 1968 AND 1984
MAXIMUM LIKELIHOOD
5% EXCEEDENCE
1894
1948
RECURRENCE INTERVAL IN YEARS
DISCHARGE IN 1,000 CFS

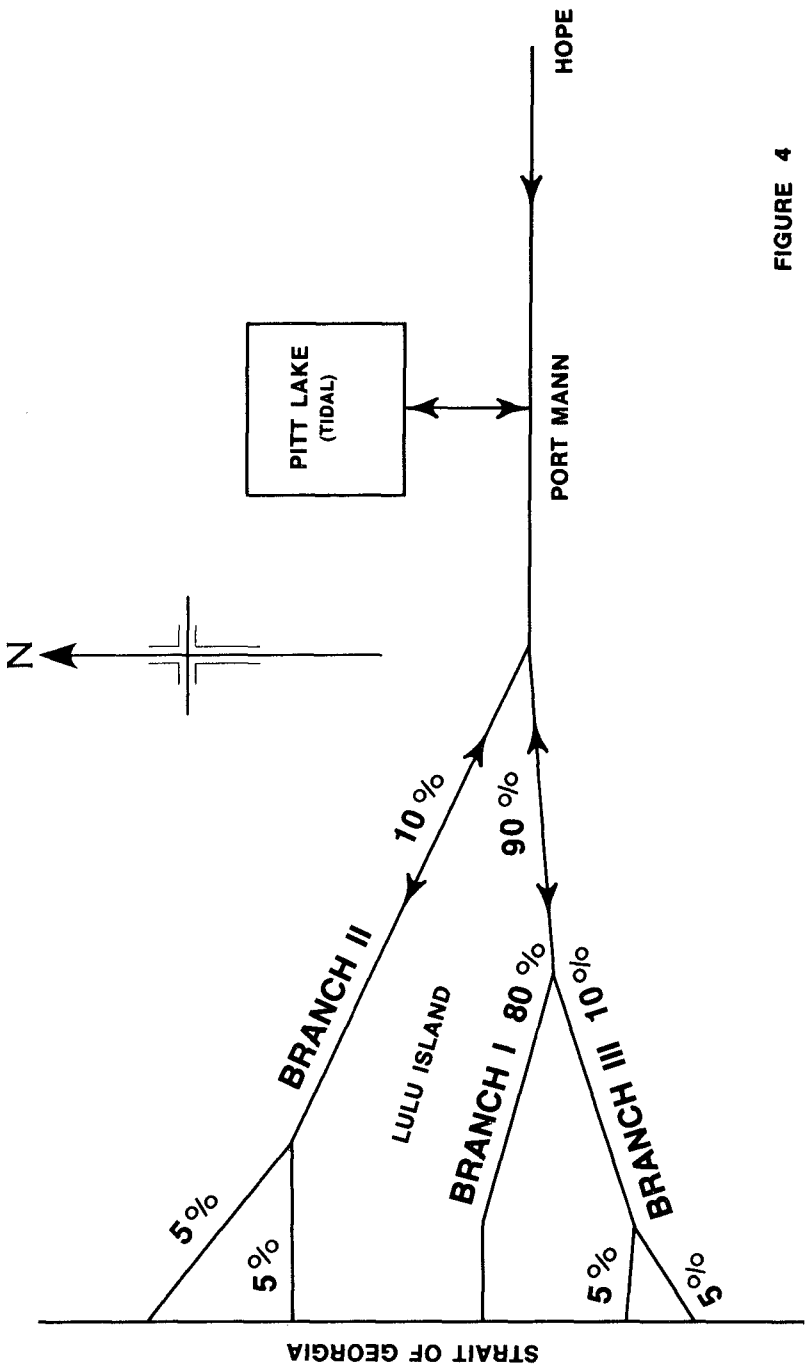

FIGURE 4

FLOW DISTRIBUTION

FRASER RIVER DELTA

(NOT TO SCALE)

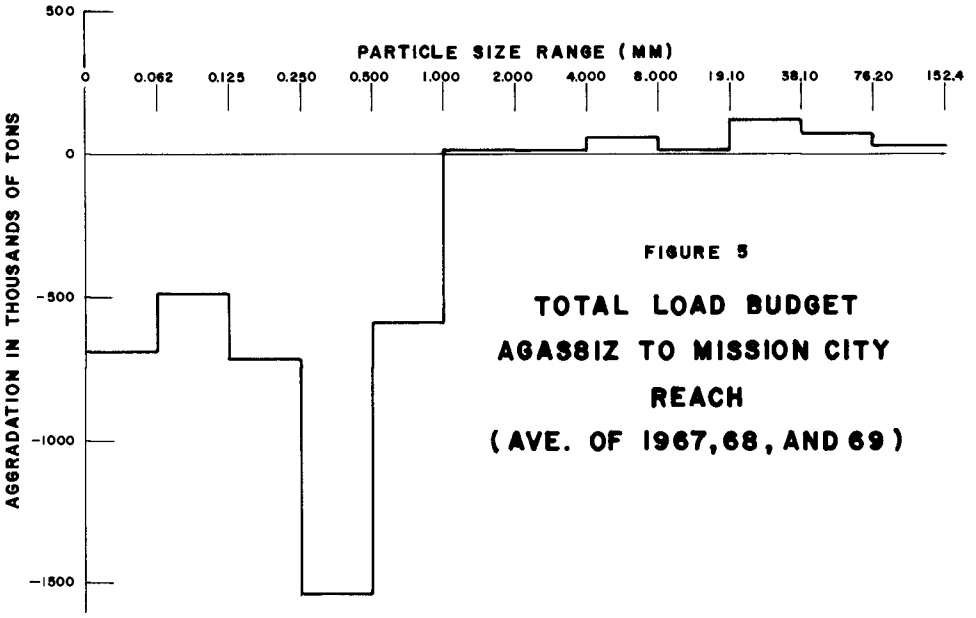

FIGURE 5

TOTAL LOAD BUDGET
AGASSIZ TO MISSION CITY
REACH
(AVE. OF 1967,68, AND 69)

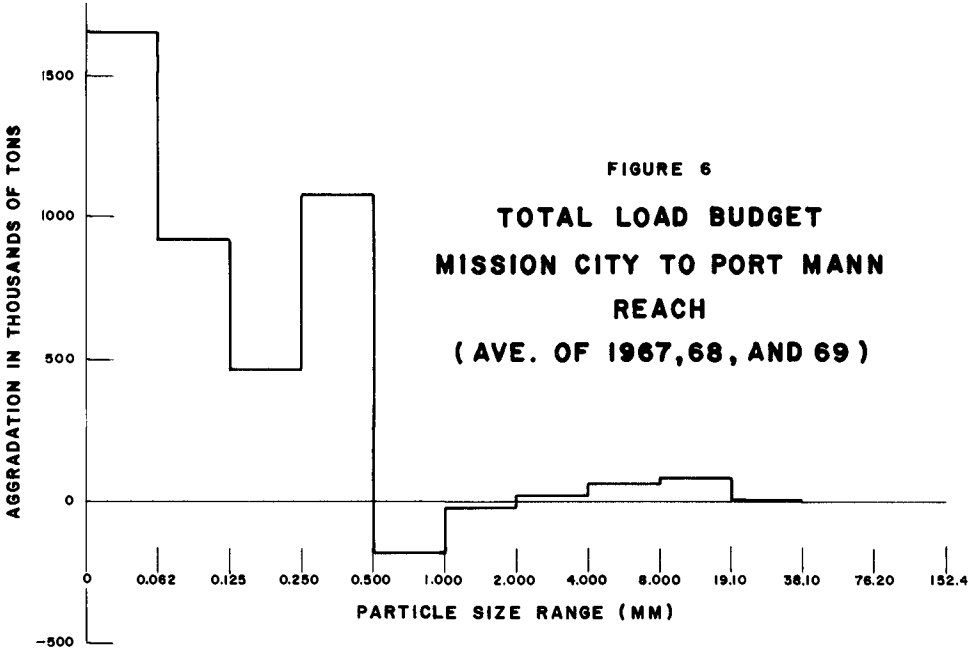

FIGURE 6

TOTAL LOAD BUDGET
MISSION CITY TO PORT MANN
REACH
(AVE. OF 1967,68, AND 69)

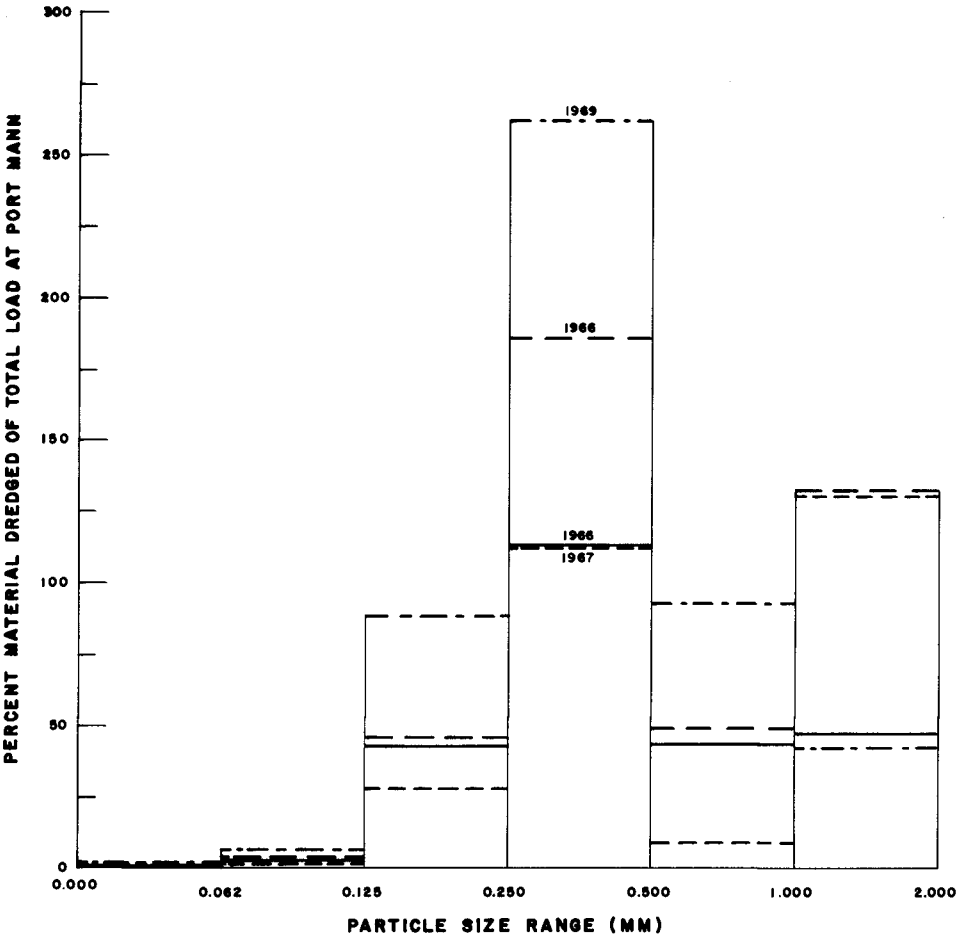

FIGURE 7

PERCENT OF MATERIAL DREDGED OF TOTAL LOAD AT PORT MANN

CHAPTER 60

EXPERIMENTS ON BED FORM GENERATION BY WAVE ACTION

by

G.R. Mogridge[1] and J.W. Kamphuis[2]

ABSTRACT

Experiments to determine the length, height and steepness of bed forms generated by wave action have been conducted in a laboratory wave flume and an oscillating water tunnel. The effects of a wide range of oscillatory flows were examined on polystyrene (specific gravity 1.05, diameter 1.54 mms), bakelite (specific gravity 1.60, diameter 0.52 mms), bakelite (specific gravity 1.51, diameter 0.67 mms) and sand (specific gravity 2.68, diameter 0.36 mms).

From the results of the experiments design curves were plotted which make it possible to predict the length and height of bed form that will develop on any specified sediment bed for given conditions of fluid oscillation.

INTRODUCTION

Knowledge about the formation of sand waves by wave action is limited when compared to what is known about sand waves caused by unidirectional flows. Yet bed forms resulting from wave action are at least as significant as those formed by unidirectional flows, since they exert an exceptionally strong influence on the sediment transport. For example, it is found in the laboratory wave flume that although sediment transport over a flat bed is in the same direction as the waves, i.e. the positive direction, when sand waves are present on the bed, the direction of net sediment transport may be either positive or negative. Therefore, as a first step to further research in sediment transport, a state of knowledge on sand waves should be reached where it is possible to predict what size sand waves form for specified sediment and wave conditions.

Different methods have been used to obtain data about the development of bed forms by the action of waves. Experiments have been conducted in laboratory wave flumes by

[1]Assistant Research Officer, Hydraulics Laboratory, National Research Council, Ottawa, K1A 0R6, Canada, formerly, Queen's University at Kingston, Canada.
[2]Associate Professor of Civil Engineering, Coastal Engineering Research Laboratory, Queen's University at Kingston, Canada.

Scott (9), Yalin and Russell (12), Kennedy and Falcon (6), Homma and Horikawa (3) and Horikawa and Watanabe (4). The range of bed form size that is obtainable beneath model waves is limited, however, and attempts have been made to extend this range by the use of prototype scale fluid motions. Thus, Bagnold (1) and Manohar (7) have studied bed forms using an oscillatory plate in still water Carstens et al (2) studied the bed forms produced by the oscillatory flow generated in an oscillating water tunnel. Inman (5) actually measured the bed forms occurring in the ocean up to depths of 52 m and produced a valuable analysis of the data.

The present study commenced with wave flume experiments and was completed by extending the range of fluid amplitude and period of oscillation in an oscillating water tunnel. A number of wave flume experiments were repeated in the water tunnel to confirm that all experiments belonged to the same population.

DIMENSIONAL ANALYSIS

If Q is a quantitative property of the phenomenon of sand wave formation then it may be described by the following characteristic parameters,

$$Q = f_Q(\rho, \mu, U_m, a_\delta, D, \rho_s, g), \tag{1}$$

where ρ is the density and μ the dynamic viscosity of the fluid; U_m is the maximum fluid velocity and a_δ is the amplitude or semi-orbital diameter of the fluid motion, immediately outside the boundary layer. D is the median diameter and ρ_s is the density of the sediment. The acceleration due to gravity, g, is only necessary to describe the submerged weight of the sediment particle, i.e. it only appears in the submerged unit weight of the sediment, i.e. $\gamma_s = (\rho_s - \rho) \cdot g$. Therefore, equation 1 may be rewritten as,

$$Q = f'_Q(\rho, \mu, U_m, a_\delta, D, \rho_s, \gamma_s) \tag{2}$$

Dimensional analysis yields,

$$\pi_Q = \Phi_Q\left(\frac{U_m D}{\upsilon}, \frac{\rho U_m^2}{\gamma_s D}, \frac{\rho_s}{\rho}, \frac{a_\delta}{D}\right), \tag{3}$$

where $\upsilon = \mu/\rho$ is the kinematic viscosity of the fluid.

If the fluid motion is sinusoidal,

$$U_m = \text{constant} \left(\frac{a_\delta}{T}\right), \tag{4}$$

where T is the wave period and equation 3 may be simplified to,

$$\pi_Q = \Phi'_Q\left(\frac{a_\delta D}{\upsilon T}, \frac{\rho a_\delta^2}{\gamma_s T^2 D}, \frac{\rho_s}{\rho}, \frac{a_\delta}{D}\right) \tag{5}$$

Because a_δ is an important parameter in determining the bed form properties such as length and height, the variables as expressed in equation 5 are not convenient for design of the experimental procedure, since a_δ occurs in three of the four variables. To simplify the experiments, equation 5 may be written as,

$$\pi_Q = \Phi''_Q\left[\left(\frac{a_\delta \cdot D}{\upsilon \cdot T}\right)^2 \cdot \left(\frac{\gamma_s T^2 D}{\rho a_\delta^2}\right), \left(\frac{\rho a_\delta^2}{\gamma_s T^2 D}\right) \cdot \left(\frac{D}{a_\delta}\right)^2, \frac{\rho_s}{\rho}, \frac{a_\delta}{D}\right],$$

or

$$\pi_Q = \Phi''_Q\left(\frac{\gamma_s D^3}{\rho \upsilon^2}, \frac{\rho D}{\gamma_s T^2}, \frac{\rho_s}{\rho}, \frac{a_\delta}{D}\right) \tag{6}$$

As a result of mass transport, the fluid motion is rarely sinusoidal. The mass transport distance, ξ, the net distance moved by the fluid in a wave period immediately outside the boundary layer, is of minor importance in sand wave formation, and is small compared to $2 \cdot a_\delta$. During preliminary tests it was found to be difficult to exercise any control over its magnitude and therefore, instead of considering ξ as a separate parameter in equation 1, it was included with the fluid amplitude in a parameter called the effective fluid orbit length A, which is defined as,

$$A = 2 \cdot a_\delta + |\xi| \tag{7}$$

Thus the relationship finally used to describe the phenomenon becomes,

$$\pi_Q = \Phi'''_Q\left(\frac{\gamma_s D^3}{\rho \upsilon^2}, \frac{\rho D}{\gamma_s T^2}, \frac{\rho_s}{\rho}, \frac{A}{D}\right), \tag{8}$$

which will be denoted as,

$$\pi_Q = \Phi_Q''' (X_1, X_2, X_3, X_4),$$

where,

$$X_1 = \frac{\gamma_s D^3}{\rho \upsilon^2} \quad ; \quad X_2 = \frac{\rho D}{\gamma_s T^2}$$

$$X_3 = \rho s/\rho \quad ; \quad X_4 = \frac{A}{D} \tag{9}$$

The effect of each of the above dimensionless variables on sand wave formation was obtained by organising the experiments so that the dimensionless bed form properties were measured for different values of X_4. The values of the remaining dimensionless variables were then altered one at a time in order to determine the effect of each individual variable on the bed form properties. X_1 was varied by changing the temperature of the water, X_2 was varied by altering the oscillation period, X_3 was varied by using different sediments and in the wave flume X_4 was varied by increasing the wave height or altering the water depth.

EXPERIMENTAL EQUIPMENT

Experiments were conducted at the Coastal Engineering Research Laboratory of Queen's University at Kingston. The wave flume experiments were performed in a 50 m long, 1 m wide and 1.2 m deep wave flume. Waves were absorbed by a porous beach. Wave reflections varied with the wave height and period, but reflection was generally less than 8%. The sediment bed was 6 m long, 1 m wide and 7.5 cm deep.

Since it is generally recognised (8), (10), that prototype bottom conditions are difficult to model accurately in a wave flume, such oscillatory motions were reproduced to prototype scale in an oscillating water tunnel. The tunnel has a working section 12 m long, 1 m deep and 0.5 m wide, Fig. 4, and is constructed of reinforced concrete. A detailed description of the design and construction of the tunnel is given by Riedel (8). The rear portion consists of a large chamber 2 m by 2 m in cross section in which a piston moves to oscillate the water. The piston is connected by means of a shaft which extends through the wall of the tunnel, to a crank arm which is driven by a 18.7 KW variable speed motor. The amplitude of the oscillation may be varied between 2.5 cm and 4 m by adjusting the eccentricity on the

crank arm, and the period of oscillation may be varied between 2.5 and 14 seconds by varying the speed of the motor.

For the present study, a false bottom was constructed in the tunnel for the purpose of placing a sediment bed which was 4 m long and 15 cm deep. Thus, the effective tunnel depth was 85 cm. Four different sediments were used; two crushed bakelite sediments, a sieved and washed natural sand and a polystyrene sediment. Their characteristics are given in Table I.

TABLE I
Sediment Characteristics

Sediment	Specific Gravity	Median Diameter D	Geometric Standard Deviation σ_g
Bakelite	1.60	0.52 mm	1.33
Bakelite	1.51	0.67 mm	1.40
Sand	2.68	0.36 mm	1.39
Polystyrene	1.05	1.54 mm	1.09

The geometric standard deviation was determined assuming a logarithmic normal distribution of sediment grain sizes. Thus, as an example, 68.2% of the grain sizes in the distribution are within the range D/σ_g to $D \cdot \sigma_g$.

The fluid orbit lengths in the vicinity of the bed forms were measured by recording the paths of almost neutrally buoyant particles in the fluid on videotape. A General Electric television camera fitted with a 15-150 mm zoom lens was used in conjunction with a television monitor and an International Video Corporation video-recorder with facility for slow motion playback. By replaying the videotape and following the tracer particles on the television monitor, accurate measurement of the fluid orbit length could be made. Bed form lengths and heights were measured on the glass windows.

EXPERIMENTAL RESULTS

(a) Variation of $X_4 = A/D$

Figures 1 and 2 show how, for some typical tests, the bed form length and height vary with X_4 while the values of X_1, X_2 and X_3 are kept constant. Figure 1 indicates for bed form length that at low values of X_4, the data falls on a straight line of slope 1:1. This means that,

$$\Lambda = \text{constant} \cdot A,$$

and thus, the bed form length is independent of the sediment grain size and is a function of the fluid orbit length only. At high values of X_4 in Fig. 1, the relationship becomes a horizontal straight line, i.e.

$$\Lambda = \text{constant} \cdot D$$

The constant of proportionality is a function of X_2.

The curves in Fig. 2 show that bed form height increases to a maximum as X_4 increases and then begins to decrease to the stage where the height is barely measurable. The slope of the rising leg of the curve is slightly greater than 1:1 indicating that for this range of X_4, the bed form height depends largely on the fluid orbit length A, but also is slightly dependent on the grain size D. Thus, the bed form is slightly dependent on the shear stress exerted by the fluid on the sediment particles.

Figure 3 shows the effect of X_4 on bed form steepness S, which is defined as bed form height divided by length. As X_4 increases, the steepness increases to a maximum and then decreases.

Previous studies on bed forms resulting from wave action have produced results showing variation of Λ/D and Δ/D with X_4, very similar to those in Figs. 1 and 2. Bagnold (1) using an oscillatory bed in still water and Carstens et al (2), using an oscillating water tunnel, both showed that the bed form length becomes dependent only on grain size diameter for high values of X_4. Bagnold (1), Carstens et al (2) and Yalin (12), all give curves for bed form height which reach a maximum and then continuously decrease for increasing fluid orbit lengths.

It may be concluded from the results that bed form properties such as length, height and steepness are in general strongly dependent on the fluid orbit length. Therefore, the experimental results to determine the effects of X_1, X_2, and X_3 are all plotted on graphs of dimensionless bed form property against X_4.

(b) Variation of $X_1 = \gamma_s D^3/\rho\upsilon^2$

Two series of tests were conducted in the wave flume using sand as the sediment. The first series was in cold water at 6°C and the second series was in relatively warm

water at 22°C. The viscosity of the cold water was one and a half times the viscosity of the warm water, thus providing a range in viscosity similar to that normally found under prototype conditions. For the first series of tests $X_1 = 346.6$ and for the second series of tests $X_1 = 801.9$.

There was virtually no difference in bed form length, height or steepness for different values of X_1. Therefore, assuming a null hypothesis for differences in X_1, a significance test was applied to the data. For bed form length and height, there was no significant difference at the 5% probability level, between the results for the two values of X_1. However, for bed form steepness the null hypothesis was rejected as the results showed a significant difference for the two values of X_1. Therefore, although X_1 may be a significant variable, the difference it causes over a practical range is so small that it may be considered unimportant.

(c) Variation of $X_3 = \rho_s/\rho$

In previous studies it has been assumed by Yalin (12) and Carstens et al (2), that the density of the sediment particle is important only when associated with the acceleration due to gravity. That is, in the dimensional analysis, only the parameter $\gamma_s = (\rho_s - \rho) \cdot g$ was used. This assumption is satisfactory for unidirectional flows where accelerations other than gravitational are negligible, but in oscillatory flows, the fluid and therefore the sediment particles are subject to almost continuous acceleration or deceleration. As the acceleration due to gravity is not the cnly acceleration involved, the density of the sediment cannot be considered to occur only in association with g, and it must remain as a separate variable X_3.

Figures 5 and 6 show that bed forms are indeed a function of X_3. The lighter material (bakelite, $X_3 = 1.60$) produces bed forms which are both longer and higher than those produced by the denser material (sand, $X_3 = 2.68$). Bed form steepness did not appear to be as sensitive to changes in X_3. These results obtained from wave flume experiments are at a constant value of $X_2 = 21.9 \times 10^{-6}$. The effect of varying X_3 is most important at the high values of X_2 occurring for laboratory waves. Low values of X_2 occurred for experiments with large periods of oscillation in both the wave flume and the oscillating water tunnel and for these conditions the effect of the variable X_3 was found to be insignificant.

To determine why the variable X_3 affects the results as it does, the flow conditions at either end of the ranges of X_2 and X_4 were considered. At low values of X_4 and high values of X_2 as occurring mainly in the wave flume, the maximum fluid accelerations are high. Because of these high accelerations there is a substantial phase lag between the sediment particle velocities and the fluid particle velocities, particularly for sediments of high density. Therefore, the distance the fluid can transport the sediment particles is smaller for the denser sediment, and it follows that bed form lengths and heights will also be smaller. Thus, X_3 has a strong effect on bed form. As X_4 increases while X_2 decreases, fluid accelerations become smaller until at values of X_4 occurring in the water tunnel, the phase lag in velocity for the light and dense particles behind the fluid velocity is small in both cases and X_3 has no effect on the properties of the bed forms.

(d) Variation of $X_2 = \rho D/\gamma_s T^2$

Figures 7 and 8 are results of experiments in the oscillating water tunnel using polystyrene sediment. For bed form length, Fig. 7, the curves all have an initial slope of 1:1 and they appear to stem from a single straight line. In the case of bed form heights in Fig. 8, the rising slopes of the curves for each value of X_2 all have approximately the same steepness and overlap so that a straight line envelope may be drawn to the data at a slope of approximately 1:1. The curve for $X_2 = 196.3 \times 10^{-6}$ is an exception since its rising slope is much steeper than for the other X_2 curves.

Tests were also conducted in the oscillating water tunnel using sand and bakelite sediments for which much lower values of X_2 were obtained than for the polystyrene. The results for these tests are given in Figs. 9, 10, 11, 12 along with results from wave flume experiments. For $X_2 = 21.9 \times 10^{-6}$ in Figs. 11 and 12 two sets of results are presented. One was taken in the oscillating water tunnel and the other in the wave flume, while all other experimental conditions were exactly similar. The agreement between the two sets of results was quite close, giving confidence in the use of the two methods for measurement of the same phenomena.

Although the data in Figs. 7, 9 and 11 falls approximately on straight lines, closer examination reveals that each group of points for a specific value of X_2 actually defines a curve or portion of a curve similar to those shown

in Figs. 1 and 2. Each curve for X_2 describing bed form length is slightly offset to the right from the one at the next higher value of X_2, so that the data as appearing in Figs. 7, 9 and 11 seems to define one straight line at a slope slightly less than 1:1.

The experimental results for the sand and bakelite could not be extended to very high values of X_4 for constant values of X_2, due to physical limitations of the experimental equipment.

The experimental results showing the effect of variation of X_2 on the bed form steepness, are shown in Figs. 13, and 14. The data obtained using polystyrene clearly shows a series of curves for different values of X_2. The maximum steepness for a particular value of X_2, decreases as the value of X_2 increases. Thus, for the high values of X_2 obtained in the wave flume, bed form steepness was approximately 0.14. For the highest value of X_2 obtained, i.e. 196.3×10^{-6}, using polystyrene in the water tunnel, the maximum steepness was 0.115. In Fig. 14 showing bed form steepness in the bakelite experiments, there is more scatter in the data, but in some cases the characteristic rising and falling curves may be distinguished.

(e) Design Curves

From the experimental data for bed form length and height presented, it may be seen that for a specified value of X_2 there are maximum possible values of length and height. These maximum values are plotted against X_2 in the Figs. 15 and 16. Included are the results of Carstens et al (2) who also used an oscillating water tunnel. They show a reasonable agreement with the results of the present experiments.

Having obtained the two curves for maximum possible bed form length and height in Figs. 15 and 16, it is possible to plot the design curves for bed form length as in Fig. 17 and for bed form height as in Fig. 18. These curves neglect the effects of X_1 and X_3. Although neglecting X_3 at the highest values of X_2 may introduce an error of approximately 15%, for $X_2 < 20 \times 10^{-6}$ the error would be negligible.

Using Figs. 17 and 18 it is now possible to determine the length and height of bed form that will develop on any specified sediment bed for given conditions cf fluid

oscillation amplitude and period.

CONCLUSIONS

Experiments have been conducted in both a laboratory wave flume and an oscillating water tunnel to determine the characteristics of bed forms produced by wave action. From the results of these experiments the following conclusions are drawn.

1. For the variation of bed form length with X_4, as X_4 increases, bed form length is initially dependent only on the fluid orbit length. At large values of X_4, the bed form becomes directly proportional to the grain size diameter. The constant of proportionality is a function of X_2. Bed form height and steepness at first increase with increasing X_4, reach maximum values and then decrease until the bed form disappears.

2. Tests conducted over the practical range of viscosity showed that the difference in bed form caused by X_1 is so small as to be unimportant.

3. X_3 was shown to be an important variable as in the present experiments, results for $X_3 = 2.68$ and $X_3 = 1.60$ showed a difference of approximately 15% in bed form length and height. However, X_3 is an important variable only at high values of X_2, i.e. for X_2 greater than approximately 20×10^{-6}.

4. Graphs have been presented to show the variation of bed form length, height and steepness with X_2. At values of X_2 greater than approximately 200×10^{-6}, bed forms do not appear on a sediment bed.

5. Design curves have been drawn by means of which it is possible to predict the length and height of bed form that will develop on any specified sediment bed for given conditions of fluid oscillation amplitude and period.

ACKNOWLEDGEMENTS

The authors are grateful to the National Research Council of Canada for the financial support for this program of study during which the senior author was a Gledden Fellow of the University of Western Australia.

REFERENCES

1. Bagnold, R.A., "Motion of Waves in Shallow Water. Interaction between Waves and Sand Bottoms". Proc. Roy. Soc. Lond., Series A, Vol. 187, 1946, pp.1-15.

2. Carstens, M.R., Neilson, F.M. and Altinbileck, H.D., "Bed Forms Generated in the Laboratory under an Oscillatory Flow: Analytical and Experimental Study". C.E.R.C., Tech. Memo No. 28, 1969.

3. Homma, M. and Horikawa, K., "Suspended Sediment Due to Wave Action". Proc. 8th Conf. on Coastal Eng., Mexico City, 1962, pp.168-193.

4. Horikawa, K. and Watanabe, A., "A Study on Sand Movement Due to Wave Action". Coastal Eng. in Japan, Vol. 10, 1967, pp.39-57.

5. Inman, D.L., "Wave Generated Ripples in Nearshore Sands". Beach Erosion Board, Tech. Memo 100, 1957.

6. Kennedy, J.F. and Falcon, M., "Wave Generated Sediment Ripples". M.I.T. Hydrodynamics Lab. Rep. No. 86, 1965.

7. Manohar, M., "Mechanics of Bottom Sediment Movement Due to Wave Action". Beach Erosion Board, Tech. Memo 75, 1955.

8. Riedel, H.P., "Direct Measurement of Bed Shear Stress Under Waves". Ph.D. Thesis, Queen's University at Kingston, 1972.

9. Scott, T. "Sand Movement by Waves". Beach Erosion Board, Tech. Memo 48, 1954.

10. Silvester, R., "Modelling of Sediment Motions Offshore". Jr. of Hyd. Res., I.A.H.R., Vol. 8, No. 2, 1970, pp.229-259.

11. Yalin, M.S., "Mechanics of Sediment Transport". Pergamon Press, 1972 (in press).

12. Yalin, M.S. and Russell, R.C.H., "Similarity in Sediment Transport Due to Waves". Proc. 8th Conf. on Coastal Eng., Mexico City, 1962, pp.151-167.

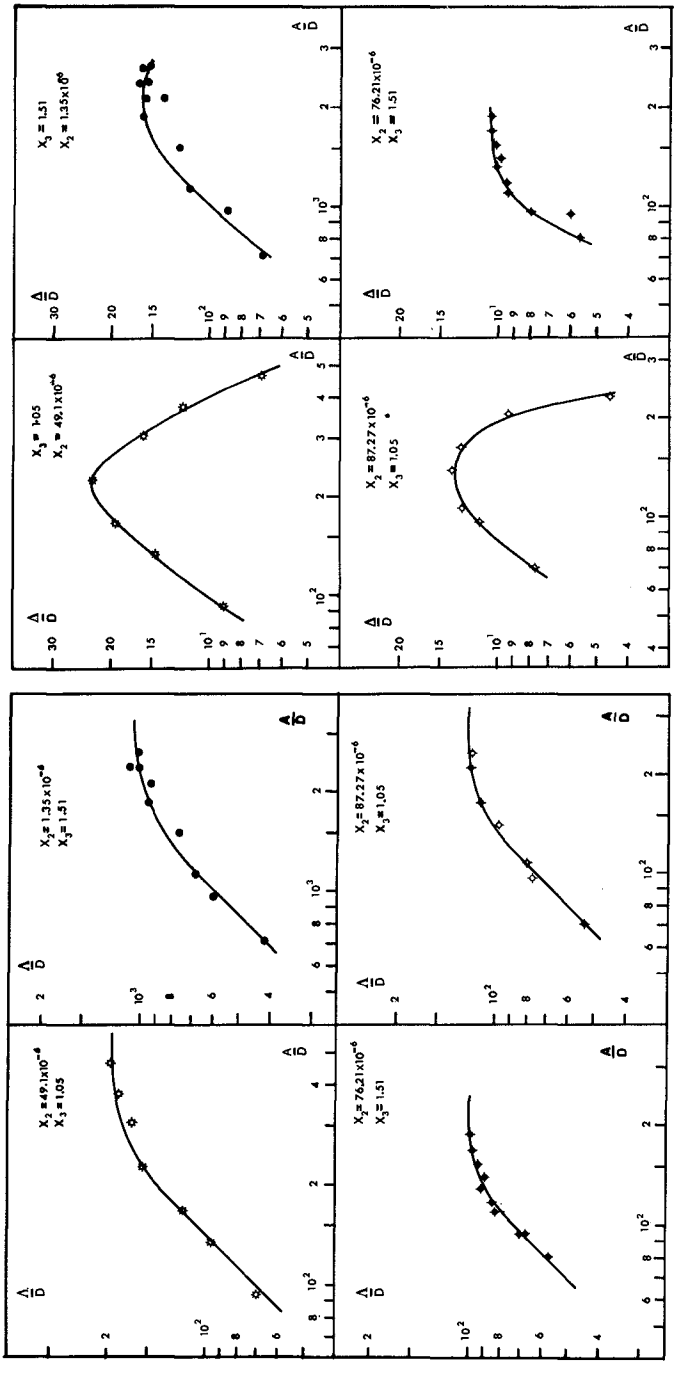

FIG.1 VARIATION OF Δ/D WITH $X_4 = A/D$

FIG.2 VARIATION OF Δ/D WITH $X_4 = A/D$

FIG. 4 THE OSCILLATING WATER TUNNEL

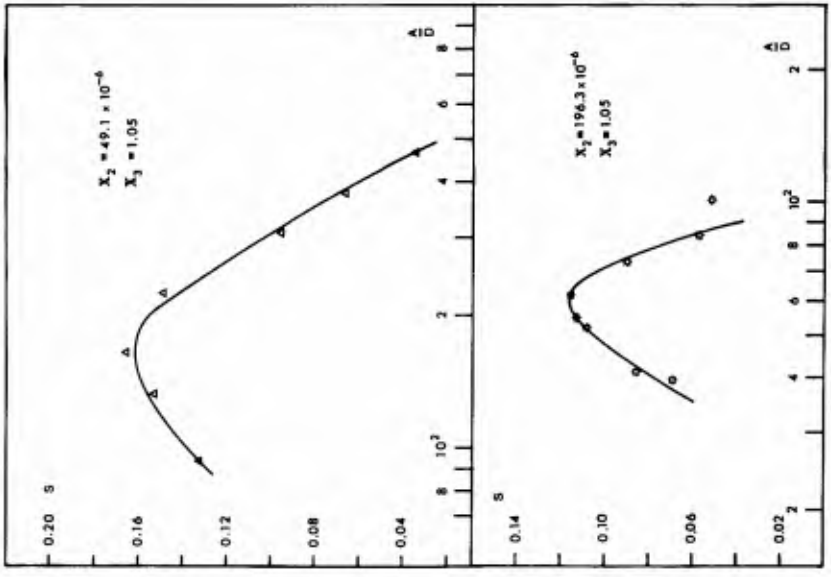

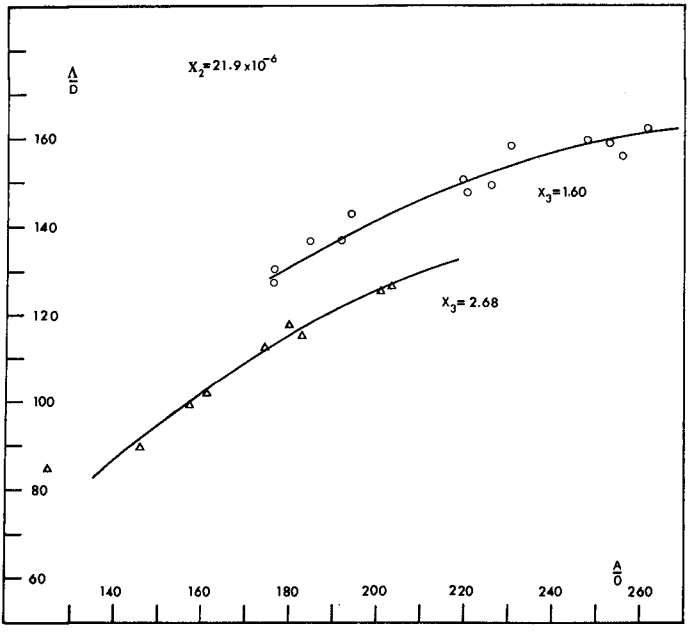

FIG. 5 VARIATION OF Λ/D WITH $X_3 = \rho_s/\rho$

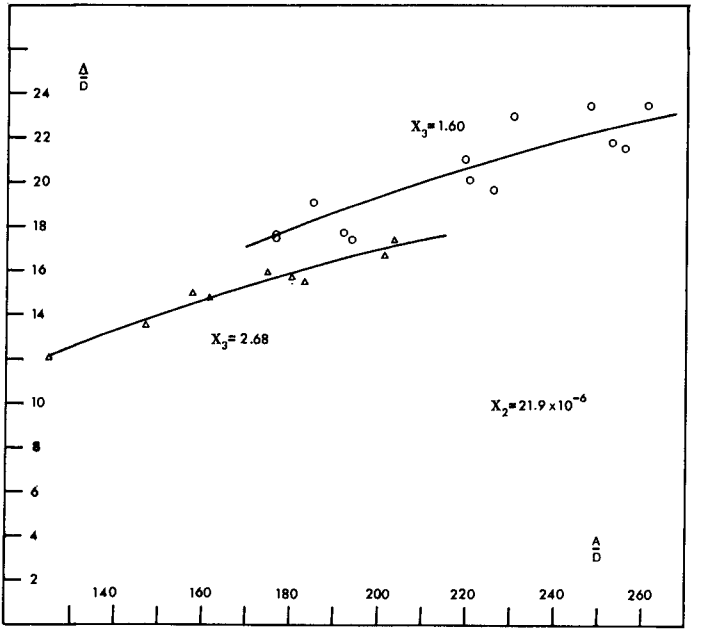

FIG. 6 VARIATION OF Δ/D WITH $X_3 = \rho_s/\rho$

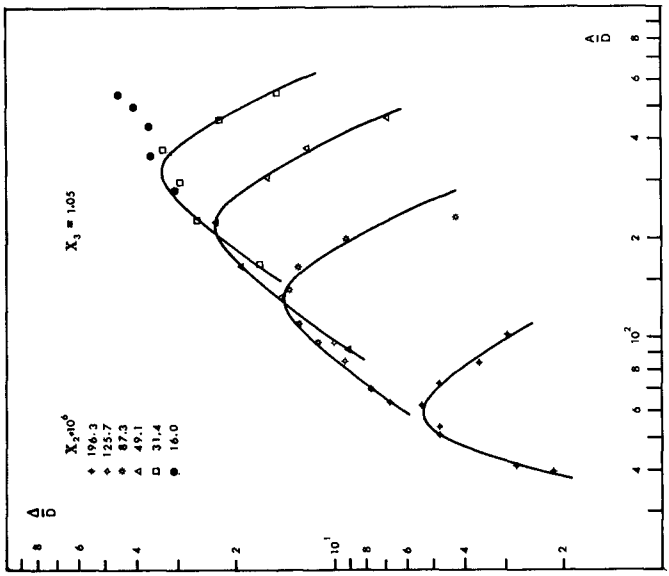

FIG. 8 VARIATION OF Δ/D WITH $X_2 = \rho D/\gamma_s T^2$ (POLYSTYRENE)

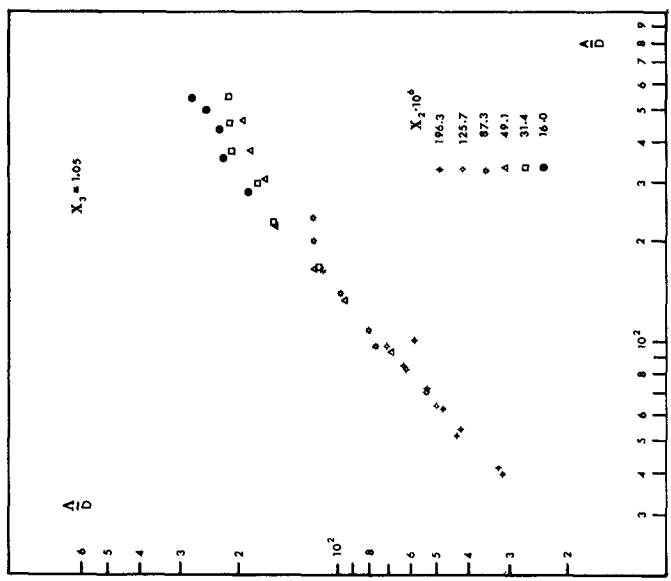

FIG. 7 VARIATION OF Δ/D WITH $X_2 = \rho D/\gamma_s T^2$ (POLYSTYRENE)

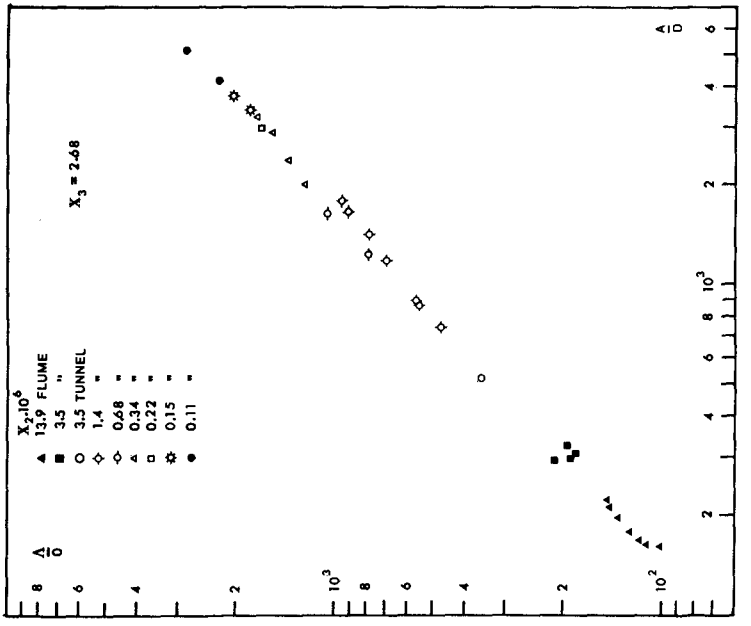

FIG. 9 VARIATION OF Δ/D WITH $X_2 = \rho D/\gamma_s T^2$ (SAND)

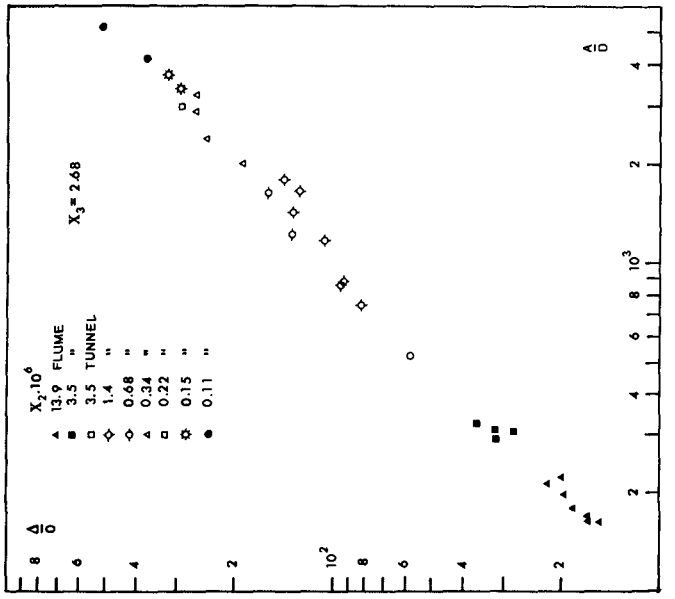

FIG.10 VARIATION OF Δ/D WITH $X_2 = \rho D/\gamma_s T^2$ (SAND)

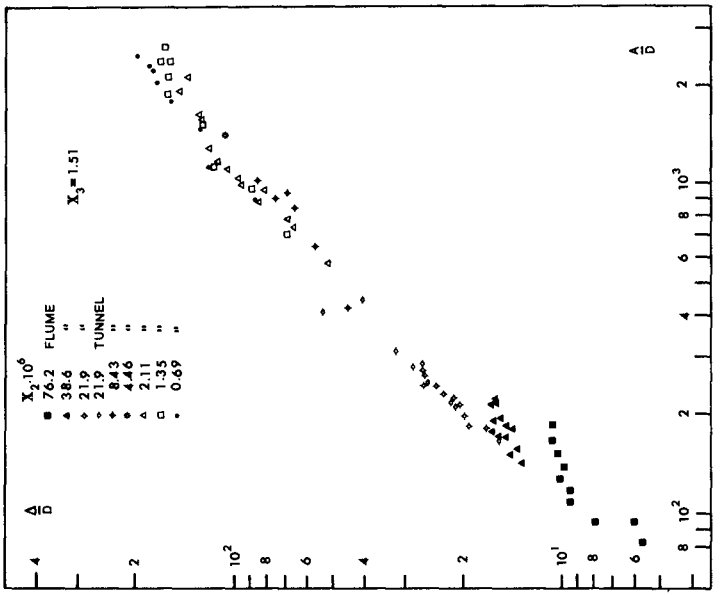

FIG.12 VARIATION OF Δ/D WITH $X_2 = \rho D/\gamma_s T^2$ (BAKELITE)

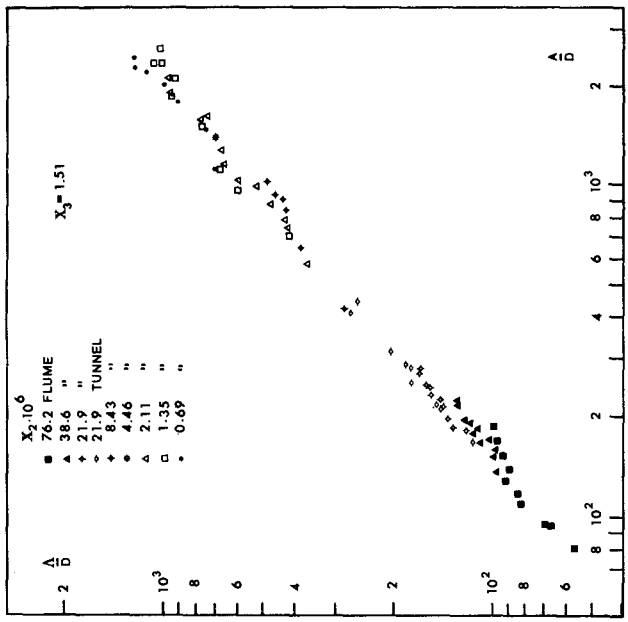

FIG.11 VARIATION OF Δ/D WITH $X_2 = \rho D/\gamma_s T^2$ (BAKELITE)

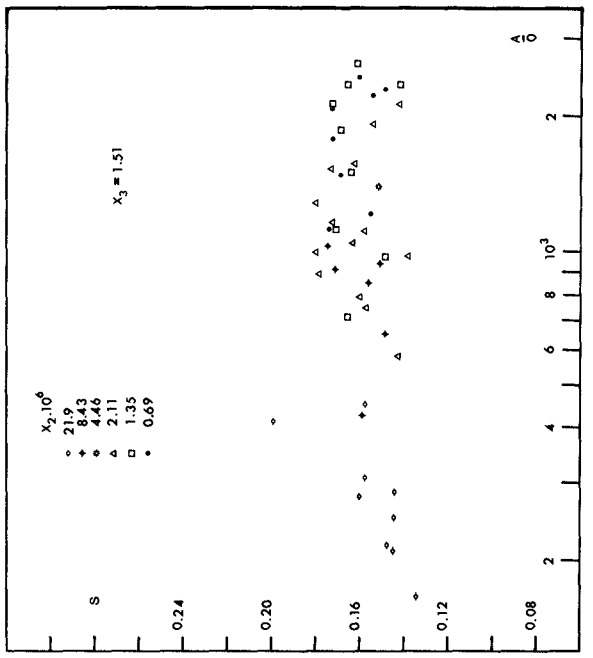

FIG.14 VARIATION OF S WITH $X_2 = \rho D/\gamma_s T^2$ (BAKELITE)

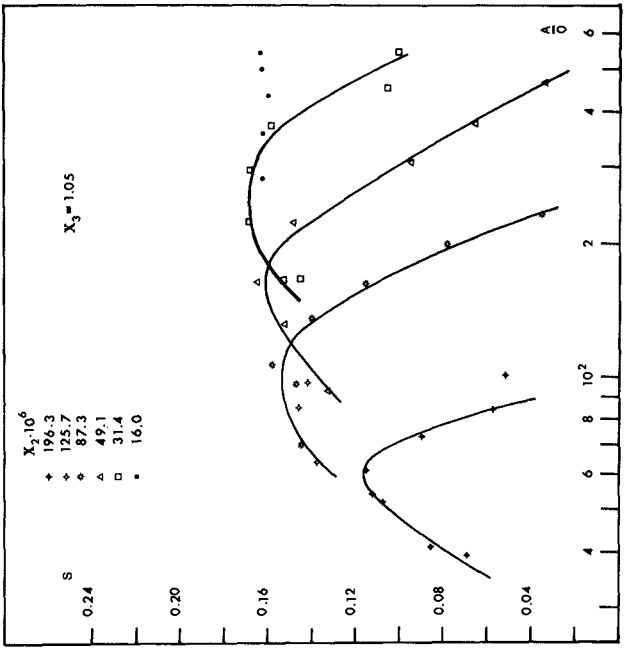

FIG.13 VARIATION OF S WITH $X_2 = \rho D/\gamma_s T^2$ (POLYSTYRENE)

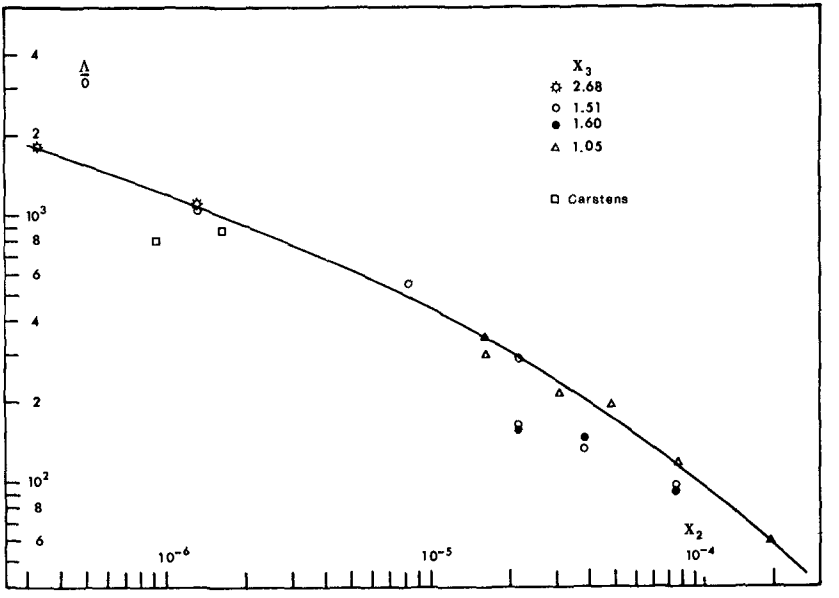

FIG. 15 MAXIMUM POSSIBLE Δ/D

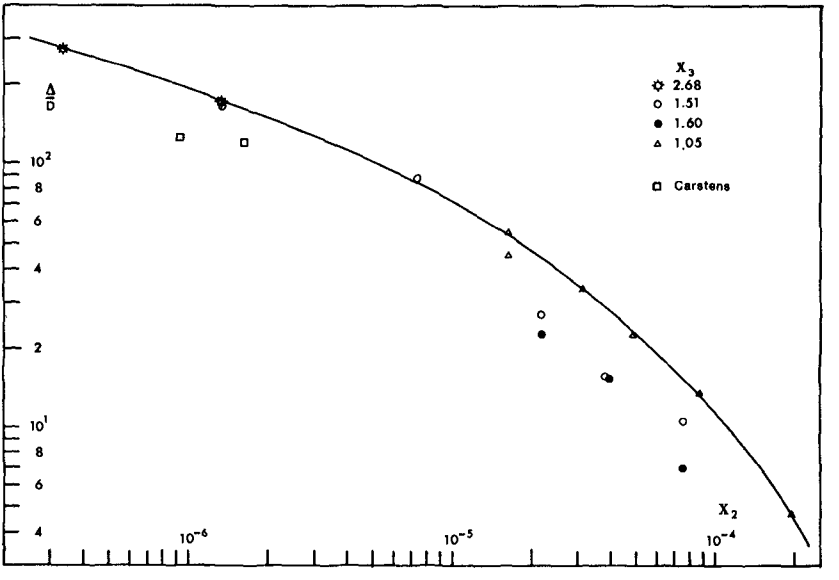

FIG. 16 MAXIMUM POSSIBLE Δ/D

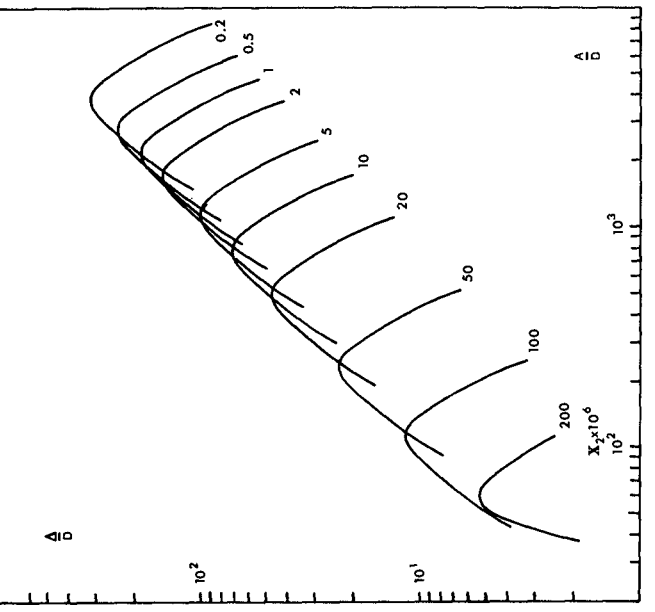

FIG.18 DESIGN CURVES FOR BED FORM HEIGHT

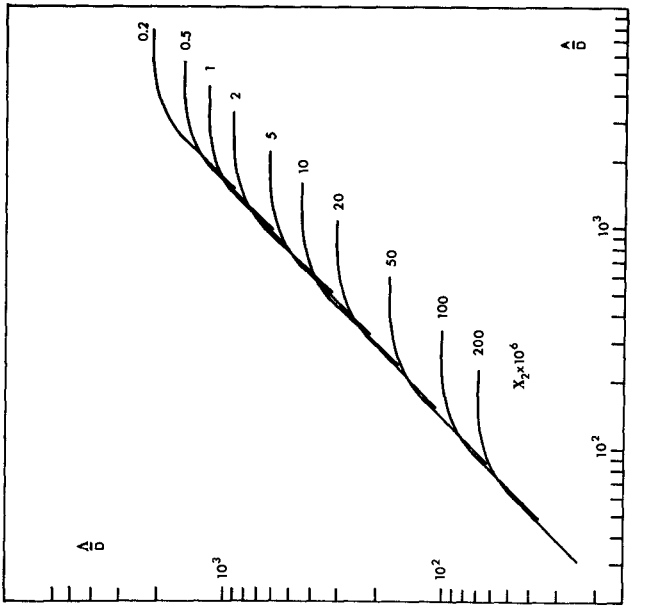

FIG.17 DESIGN CURVES FOR BED FORM LENGTH

CHAPTER 61

ON THE GEOMETRICALLY SIMILAR REPRODUCTION OF DUNES IN A TIDAL MODEL WITH MOVABLE BED

M.S. Yalin *

ABSTRACT

A model design method is suggested which is based on the principles of the theory of dimensions and which is evaluated by experimental relations for the geometric properties of dunes. The model is distorted and, in general, non Froudian. The geometrically similar model dunes are reduced in vertical model scale. The scale of the flow velocity is derived from a generalised friction equation which takes into account the influence of both skin friction and form drag. The application of the method is illustrated by a numerical example. This example indicates that a practicable set of scales is obtained if the model bed is formed by a light weight material.

INTRODUCTION

When carrying out model tests with drilling structures, buried pipelines or any other objects which are in contact with a movable bed a major consideration is that the model dunes should be geometrically similar to their counterparts in the prototype. Indeed the functioning of the structures mentioned depends to a considerable extent on how their geometry compares with the geometry of dunes around them, so that a reliable prediction of the performance of these structures can only be made if the model and prototype dunes are geometrically similar.

At present no systematic information on dunes formed by tidal flows is available. On the other hand the measurements carried out in the North Sea, Liverpool Bay, Outer Thames and Sandettie

---

* Professor of Hydraulics,
Coastal Engineering Research Laboratory, Queen's University at Kingston, Canada.

(in English Channel) indicate that the dunes produced by tidal currents should be very similar in their size and shape to the dunes produced by the equivalent unidirectional flows.* This similarity between the tidal and unidirectional dunes is, in fact, not surprising, for the formation of dunes by tidal currents takes place mainly in those parts of the periodic cycle when the whole body of the fluid moves in one direction, that is when the tidal flow becomes virtually a unidirectional flow. Considering this (fortunate) similarity between the tidal and unidirectional dunes, the present method is developed by using the existing information for unidirectional dunes.

SOME QUANTITATIVE ASPECTS OF RIPPLES AND DUNES **

It can be shown that the dimensionless combinations (variables):

$$X = \frac{v_* D}{\nu} \quad ; \quad Y = \frac{\rho v_*^2}{\gamma_s D} \quad ; \quad Z = \frac{h}{D} \quad *** \qquad (1)$$

are sufficient in order to express any dimensionless property of sand waves formed by a unidirectional tranquil ($Fr < 1$) flow (i.e. of ripples and dunes).

From the analysis of a large number of data it follows that the relative length Λ/h of dunes is a function of two variables :

$$\frac{\Lambda}{h} = f(X, Z) \qquad (2)$$

Furthermore, the same data reveals that for $X > \approx 25$ and/or $Z > \approx 5000$ the function $f(X, Z)$ reduces into a constant (2π):

$$\frac{\Lambda}{h} = 2\pi \qquad (3)$$

---

* The author is grateful to R.C.H. Russell and A.W. Price (HRS - Wallingford) for this information.

** Extensive information on all the aspects summarised in this section can be found in Chapter VII of Ref [1].

*** See "List of Symbols" at the end of the paper.

In natural estuaries, the values of X and Z are almost always large enough, as to assume that the length of dunes is given by the proportionality (3).

For the height Δ of dunes the following expression is valid

$$\frac{\Delta}{\Lambda} = \Phi \left(\frac{Y}{Y_{cr}}, X, Z \right) \qquad (4)$$

where the subscript cr signifies the "critical stage" (initiation of sediment transport), while the fundtion Φ characterises the dune steepness. Here the most important variable is Y/Y_{cr} ; the variations in Φ induced by X and Z are comparatively small. Accordingly the relation (4) can be replaced by its approximate equivalent:

$$\frac{\Delta}{\Lambda} \approx \Phi \left(\frac{Y}{Y_{cr}} \right) \qquad (5)$$

If $Z > \approx 1000$, then ripples and dunes exist in the regions shown in Fig. 1. When Z decreases from ≈ 1000 to ≈ 200 the point X_2 moves towards the fixed point $X_1 \approx 5$, as to reduce the interval $\overline{X_2X_1}$ to the point $X_2 = X_1 \approx 5$, for all Z smaller than ≈ 200. Hence, for $Z < \approx 200$ the simultaneous occurrence of ripples and dunes (in the form of ripples superposed on dunes) becomes impossible; the sand waves are either ripples or dunes. This is only natural, for ripples can be superposed on dunes only if their size $\Lambda_r = \text{const. } D$ is much smaller than the size Λ of dunes. Observe, however, that

$$\frac{\Lambda}{\Lambda_r} \text{ is proportional to } \frac{h}{D} = Z$$

and thus that Λ_r cannot be "much smaller" than Λ if Z is not sufficiently large.

It follows that the presence of ripples on model dunes will certainly be avoided if the model value of X is selected as to be larger than ≈ 25 . (Note that this requirement coincides with one of the requirements for the validity of the proportionality (3)).

SCALE RELATIONS

Let A' and A'' be the prototype and model values of a quantity A, and $\lambda_A = A''/A'$ be the scale of A.

From Eqn (5) it follows that the steepness of model and prototype dunes will be approximately the same, i.e. the approximate scale relation

$$\frac{\lambda_\Delta}{\lambda_\Lambda} \approx 1 \tag{6}$$

will be valid if the condition

$$\lambda_Y = \lambda_{Ycr} \tag{7}$$

is fulfilled.

Consider now the $X; Z$ plane shown in Fig. 2. From the text preceding Eqn (3) it follows that if the model and prototype "points" M'' (X'', Z'') and M' (X', Z') are both outside the shaded region, then

$$\lambda_\Lambda = \lambda_h \ .$$

The present method is an attempt to achieve the similarity of dunes, i.e. the scale relation:

$$\lambda_\Delta \approx \lambda_\Lambda \approx \lambda_h \tag{8}$$

by satisfying (7), and by selecting M'' outside the shaded part of the $X; Z$ plane (assuming, of course, that the prototype point M' is also outside it).

A certain prototype corresponds to a certain set of the values of the variables X, Y, Z and Y_{cr}. Knowing the prototype values X', Y', Z' and Y'_{cr}, one determines the model values X'', Y'', Z'' and Y''_{cr} from the relations:

$$X'' = \lambda_X X' \ ; \ Y'' = \lambda_Y Y' \ ; \ Z'' = \lambda_Z Z' \ ; \ Y''_{cr} = \lambda_Y Y'_{cr} \tag{9}$$

where

$$\lambda_X = \frac{\lambda_y \lambda_D}{\lambda_x^{\frac{1}{2}}} \qquad \lambda_Y = \frac{\lambda_y^2}{\lambda_x \lambda_{Y_s} \lambda_D} \qquad \lambda_Z = \frac{\lambda_y}{\lambda_D} \tag{10}$$

In the relations above, λ_x and λ_y are horizontal and vertical model scales respectively. These relations follow directly from the set (1) by substituting

$$\lambda_g = \lambda_\rho = \lambda_\nu = 1 \tag{11}$$

(model operating with water) and

$$\lambda_{v_*}^2 = \lambda_h \lambda_s \quad ; \quad \lambda_h = \lambda_y \quad ; \quad \lambda_s = \lambda_y/\lambda_x \tag{12}$$

The following procedure can be suggested for determining the model scales.

(i) Choose vertical scale and the model bed material (i.e. choose λ_y , λ_{γ_s} and λ_D);

(ii) Knowing λ_y and λ_D , determine λ_Z and thus $Z'' = \lambda_Z . Z'$;

(iii) Knowing $\gamma_s'' = \lambda_{\gamma_s} \gamma_s'$ and $D'' = \lambda_D D'$, determine Y_{cr}'' (from the Shields curve);

(iv) Knowing Y' , Y_{cr}' and Y_{cr}'', determine $\lambda_Y = Y_{cr}''/Y_{cr}'$ and $Y'' = \lambda_Y Y'$;

(v) Knowing λ_Y , determine λ_X (from second eqn of (10));

(vi) Knowing λ_y , λ_x , and λ_D , determine λ_X (first eqn of (10)) and the distortion $\lambda_y/\lambda_x = n$;

(vii) Check whether the position of the point $M''(X'' , Z'')$ on the X; Z plane and the value of n are acceptable. If not repeat the procedure for another set of values of λ_y, λ_{γ_s} and λ_D .

Nothing has been said so far on how the flow velocity scale λ_v must be determined, and it is intended now to consider this relevant aspect of the model design.

GENERALISED FRICTION FORMULA; VELOCITY SCALE

Let S_k and S_Δ be the pure friction and form drag components of the total slope (free surface slope) S

$$S = S_k + S_\Delta \tag{16}$$

Suppose the granular material is (almost) uniform. In this case, the "skin roughness" $k_s \approx D$ and the pure friction slope S_k can be expressed as

$$S_k = \frac{Fr}{[\frac{1}{\kappa} \ln(A \frac{h}{k_s})]^2} \approx \frac{Fr}{[\frac{1}{\kappa} \ln(AZ)]^2} \quad *) \tag{17}$$

while the form drag slope S_Δ can be given by

$$S_\Delta = \frac{1}{2} \cdot \frac{\Delta^2}{\Lambda h} \cdot Fr \quad **) \tag{18}$$

Hence:

$$\frac{S}{Fr} = \frac{1}{[\frac{1}{\kappa} \ln(AZ)]^2} + \frac{1}{2} \frac{\Delta^2}{\Lambda h} \tag{19}$$

Observe, that since $Fr = v^2/gh$ the eqn (19) can be written in the Chezy form

$$v = c\sqrt{gSh} \tag{20}$$

where the generalised dimensionless Chezy coefficient c reflects the influence of the skin roughness ($k_s \approx D$) as well as of the sand waves (Δ,Λ) as follows:

$$c = \left[\frac{1}{[\frac{1}{\kappa} \ln(AZ)]^2} + \frac{1}{2} \frac{\Delta^2}{\Lambda h} \right]^{-1/2} \tag{21}$$

(Note, that if the sand waves are not present (flat bed: $\Delta \equiv 0$) then the expression above reduces into the familiar form $c = (1/\kappa).\ln(AZ))$.

---

* See e.g. Ref [2] and observe that S_k/Fr implies $[v*)_k/v]^2$. The comment on the values of A is in the last footnote of the text.

** Refs [3] , [4] , [5] .

The Eqn (19) gives for the scales

$$\frac{\lambda_s}{\lambda_{Fr}} = \frac{\left[\frac{1}{\kappa}\ln(AZ'')\right]^{-2} + \frac{1}{2}\frac{\Delta''^2}{\Lambda''h''}}{\left[\frac{1}{\kappa}\ln(AZ')\right]^{-2} + \frac{1}{2}\frac{\Delta'^2}{\Lambda'h'}}$$

and thus

$$\frac{\lambda_s}{\lambda_{Fr}} = \frac{\left[1 + \frac{\ln\lambda_Z}{\ln(AZ')}\right]^{-2} + N'\left(\lambda_\Delta^2\lambda_\Lambda^{-1}\lambda_h^{-1}\right)}{1 + N'} \qquad (22)$$

where

$$N' = \frac{1}{2}\frac{\Delta'^2}{\Lambda'h'}\left[\frac{1}{\kappa}\ln(AZ')\right]^2 . \quad *) \qquad (23)$$

Since $\lambda_s = \lambda_y/\lambda_x = n$ and since the dunes are geometrically similar, i.e.

$$\lambda_\Delta^2\lambda_\Lambda^{-1}\lambda_h^{-1} \equiv 1$$

the Eqn (22) can be written as

$$\frac{n}{\lambda_{Fr}} = \frac{\left[1 + \frac{\ln\lambda_Z}{\ln(AZ')}\right]^{-2} + N'}{1 + N'} \qquad (24)$$

which gives immediately

$$\lambda_v = \xi\sqrt{\lambda_y} \quad \text{with} \quad \xi = \left[\frac{\left[1 + \frac{\ln\lambda_Z}{\ln(AZ')}\right]^{-2} + N'}{n(1 + N')}\right]^{-1/2} \qquad (25)$$

If the scales involved in the procedure explained at the end of the preceding section are determined, then λ_y and all of the terms that appear in the expression of the multiplier ξ are known, and the value of the scale λ_v can be computed from (25).

Note, that the multiplier ξ reflects the deviation from a "Froudian model". Indeed the model becomes Froudian ($\lambda_v = \sqrt{\lambda_y}$) only

---

* Note that Eqns (19) and (22) are the generalised versions of the expressions given in Ref [6].

if $\xi = 1$, i.e. only if n, λ_Z, Z' and N' are interrelated as follows:

$$n = \frac{\left[1 + \frac{\ln \lambda_Z}{\ln(AZ')}\right]^{-2} + N'}{1 + N'} \qquad (26)$$

Usually it is very difficult to select such λ_Z and n which can satisfy the condition (26) and which can, at the same time, be regarded as "reasonable" (Z' and N' being determined by the prototype). In such cases it may be wiser to relax the condition (26) and thus to allow a deviation from a Froudian model (especially if the phenomenon forming the subject of model tests is related to the vicinity of the bed rather than to that of the free surface). *

NUMERICAL EXAMPLE

Consider the prototype specified by the following characteristics: **

$$\left.\begin{array}{l} h' = 27 \text{ m } (\approx 90 \text{ ft}) \\ D' = 0.2 \text{ mm} \\ L' = 700 \text{ km} \\ H' = 7 \text{ m} \end{array}\right\} S = 10^{-5}, \quad \gamma_s'/\gamma' = 1.65 \qquad (\nu = 10^{-6} \text{ m}^2/\text{S}, \; g = 9.81 \text{ m/S}^2) \qquad (27)$$

Using Eqns (1) and the Shields' curve one determines for this prototype the following values of the dimensionless variables

$$X' = 10.3 \quad ; \quad Y' = 0.82 \quad ; \quad Z' = 1.35.10^5 \quad ; \quad Y'_{cr} = 0.052 \qquad (28)$$

If $\lambda_y = 1/45$, then $h'' = 27/45 = 0.6$ m which is reasonable. Adopting this value of λ_y and using it for various combinations of λ_{γ_s} and

---

* See more on the importance of the Froude number in Ref [7] (Introduction).

** Due to R.C.H. Russell (HRS - Wallingford).

λ_D one arrives (by applying the procedure described and the Eqn (25)) at the results shown in the table below. *

TABLE 1

Model Bed Material	λ_{γ_s}	λ_D	λ_y	λ_x	$n = \lambda_y/\lambda_x$	λ_X	λ_Y	λ_Z	ξ
polystyrene (γ_s'' = 0.05) 3.0 mm	$\frac{1}{33}$	15	$\frac{1}{45}$	$\frac{1}{532}$	11.85	7.70	$\frac{1}{1.73}$	$\frac{1}{675}$	2.50
polystyrene (γ_s'' = 0.05 2.0 mm	$\frac{1}{33}$	10	$\frac{1}{45}$	$\frac{1}{343}$	7.64	4.12	$\frac{1}{1.79}$	$\frac{1}{450}$	2.05
polystyrene (γ_s'' = 0.05) 1.35 mm	$\frac{1}{33}$	6.75	$\frac{1}{45}$	$\frac{1}{239}$	5.32	2.32	$\frac{1}{1.73}$	$\frac{1}{304}$	1.77
perspex (γ_s'' = 0.19) 1.5 mm	$\frac{1}{8.7}$	7.5	$\frac{1}{45}$	$\frac{1}{209}$	4.65	2.41	$\frac{1}{1.85}$	$\frac{1}{338}$	1.64
sand (γ_s'' = 1.65 0.12 mm	1	$\frac{1}{1.67}$	$\frac{1}{45}$	$\frac{1}{1775}$	39.5	$\frac{1}{1.78}$	1.46	$\frac{1}{27}$	5.64
sand (γ_s'' = 1.65 0.10 mm	1	$\frac{1}{2}$	$\frac{1}{45}$	$\frac{1}{1745}$	38.80	$\frac{1}{2.15}$	1.70	$\frac{1}{22.5}$	5.53

* The values of N' were computed by adopting A = 15.00. The quantity A is related to B of Ref [2] (Chapter XX) by $A = e^{\kappa B}$. Using Fig. 20.18 of Ref [3] one can show that the value of $A = f(v_* k_s/\nu)$ varies within a relatively narrow interval $16.50 > A > 11.00$ (for all $v_* k_s/\nu > 10$). Hence the reason for a constant (average) value $A = 15.00$.

Note, that sand models can hardly be regarded as acceptable (at least not for the prototype under consideration), as they require very large distortions (n) while their velocities deviate too much from the Froudian velocities (large ξ). Conversely, light weight materials yield acceptable values for n and ξ, and among them 1.35 mm - polystyrene and 1.5 mm - perspex appear to be as most favorable.

REFERENCES

1. Yalin, M.S "Mechanics of Sediment Transport". Pergamon Press, Oxford, 1972.

2. Schlichting, H. "Boundary Layer Theory". McGraw-Hill, 6th Edition, 1968.

3. Engelund, F. & Hansen, E. "The Hydraulic Resistance of Alluvial Streams". Techn. Univ. of Denmark, Coastal Eng. Lab. Prog. Rep. No. 8, 1965.

4. Yalin, M.S. "On the Average Velocity of Flow over a Movable Bed". La Houille Blanche, No. 1, 1964.

5. Yalin, M.S. "Theory of Hydraulic Models". Macmillan, London, 1971.

6. Russell, R.C.H. "Methods of Selecting Scales for Models in Use at the Hydraulics Research Station, Wallingford". Rep. No. INT 40, 1964.

7. Yalin, M.S. "River Models with Movable Bed". Proceedings of the International Symposium on River Mechanics (IAHR), Bangkok, Jan. 1973.

LIST OF SYMBOLS

h	flow depth	representative values
S	free surface slope	
v	average velocity	
v_*	shear velocity	
ρ	fluid density	
ρ_s	grain density	
γ_s	specific weight of grains in fluid	

ν	kinematic viscosity
D	typical grain size (usually D_{50})
$Fr = v^2/gh$	Froude number
X,Y,Z,W	dimensionless variables of the two phase motion as defined by Eqn (1)
a' and a"	prototype and model values respectively of a quantity a
$\lambda_a = a''/a'$	scale of a
x,y	horizontal and vertical coordinates
$n = \lambda_x/\lambda_y$	distortion
ξ	ratio of the non Froudian model velocity to the Froudian model velocity

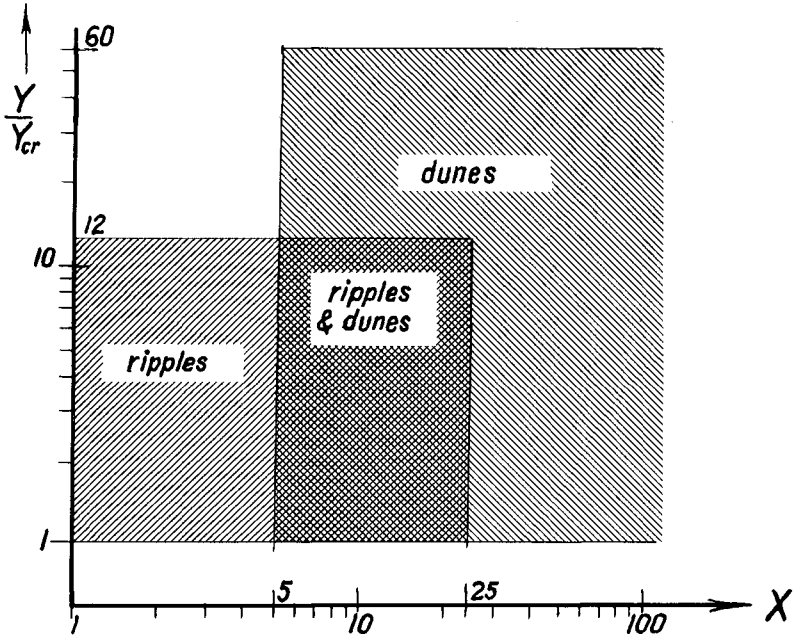
Y/Ycr
60
12
10
1
dunes
ripples & dunes
ripples
5
25
1
10
100
X

Fig. 1

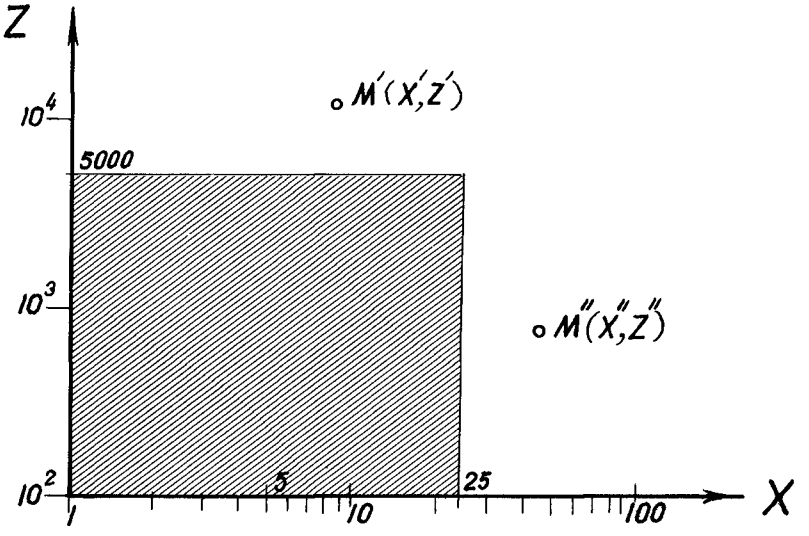
Z
10^4
5000
10^3
10^2
M'(X',Z')
M''(X'',Z'')
5
25
1
10
100
X

Fig. 2

CHAPTER 62

PHASE DEPENDENT ROUGHNESS CONTROL OF SAND MOVEMENT

by

Douglas L. Inman and Edward B. Tunstall

Scripps Institution of Oceanography, University of California

La Jolla, California 92037

ABSTRACT

Experiments with wave motion over asymmetrical "ripple-like" forms show that the difference between a net sand transport in a down-wave versus an up-wave direction is related to a subtle phase dependent mechanism associated with the intensity of vortex formation in the lee of the form. Artificial roughness modules have been developed, consisting of arrays of asymmetrical forms resembling natural ripples. The asymmetry of the forms causes an intense vortex to form in the lee of the steep face. This vortex traps and suspends sediment, which when the orbital motion reverses its phase, is lifted above the roughness element and carried in the new direction. Thus, the direction of the net sand transport is dependent upon the relation between the steep face of the roughness element and the phase of the orbital velocity; the net transport being in the direction of the orbital velocity that is out-of-phase with the maximum vortex formation.

INTRODUCTION

Progressive waves traveling over a sand bed usually produce sand ripples that are almost symmetrical in profile. This wave action over horizontal beds, in the presence of the Longuet-Higgins bed drift current, produces a net sand transport in the down-wave direction. However, experiments with waves and currents showed that asymmetrical sand ripples could cause a change in the direction of sand transport so that the net transport is opposite to the drift current and the direction of wave propagation.

Investigation of this phenomena indicates that the difference between a net sand transport in a down-wave direction versus an up-wave direction is related to a subtle phase dependent mechanism associated with the intensity of vortex formation in the lee of the ripple crest. Artificial roughness modules have been developed, consisting of arrays of asymmetrical forms resembling natural ripples. The asymmetry of the forms coupled with the oscillatory flow causes large vortices to be generated on the steep side of the crest and smaller vortices to be generated on the gentle side of the crest. These different sized vortices suspend differing amounts of sand or sediment, which when the orbital motion reverses its phase, is lifted above the roughness element and carried in the new direction. Since the larger vortex suspends a greater amount of sediment, the direction of the net sand transport is dependent upon the relation between the steep face of the roughness element and the phase of the orbital velocity: the net transport being in the direction of the orbital velocity that is out-of-phase with the maximum vortex formation. This differential vortex formation and sediment suspension is depicted in Figure 1.

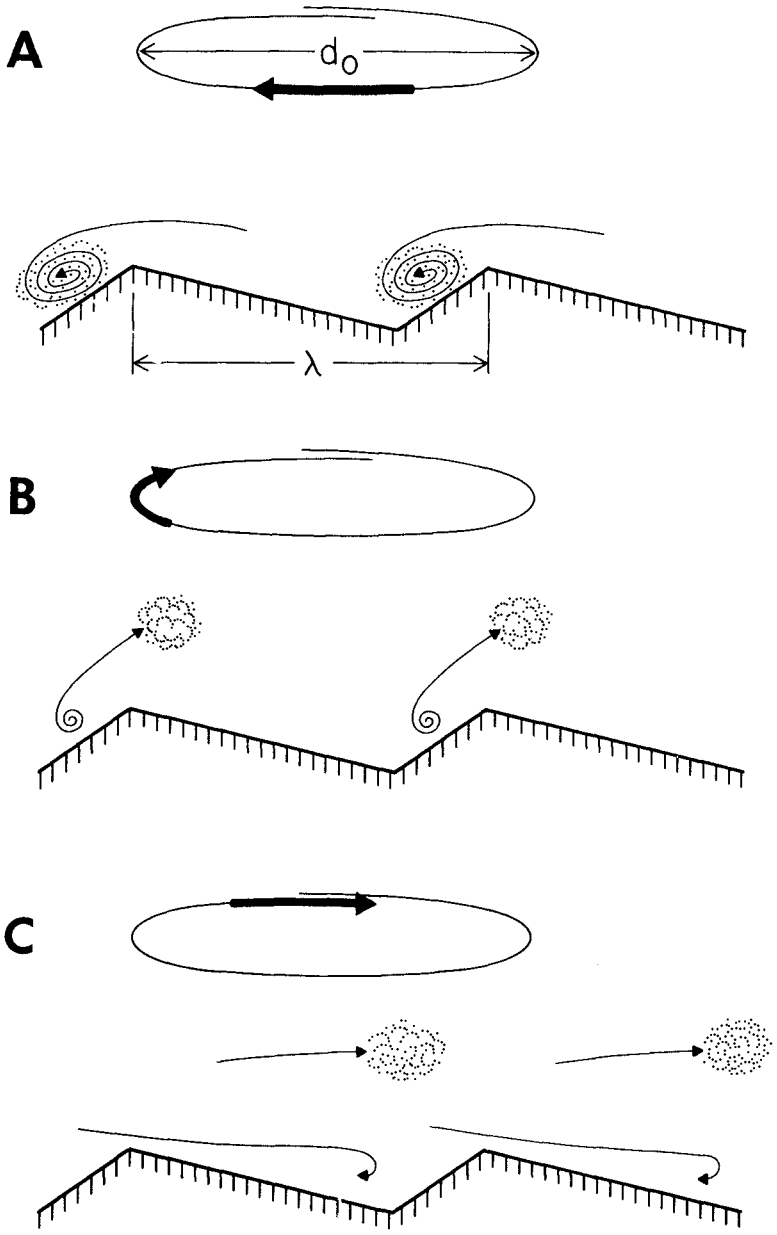

Figure 1. Asymmetrical bottom forms under oscillatory wave motion showing differential vortex formation and sediment transport. Wave travels from left to right.

It is well known that oscillatory ocean surface waves produce horizontal and vertical water particle motions in the water column which have been found to affect the bottom sediment to depths in excess of 52 meters (Inman, 1957). One of the more common effects of this motion is to form sand ripples, which in the absence of extraneous currents are generally symmetrical in profile.

The formation of vortices in the lee of the ripple crests has been described as early as 1884 (Darwin, 1884) and 1910 (Ayrton, 1910). Good photographic evidence of vortices was obtained by Bagnold (1946), and many studies have been conducted since. However, most of these studies have been conducted with standing waves or oscillating beds, which give flow conditions that differ in some respects from those of progressive waves. The oscillatory flow is seen to form the vortex over symmetrical ripples with the vortex being released into the water near the bed as the flow reverses (Figure 2). This alternate formation and release of vortices leads to the existence of a vortex sublayer near the bed under oscillating flow. This vortex sublayer is a zone of two dimensional vorticity rotating about axes that are parallel to the ripple crests. Figure 3 shows this vortex formation over symmetrical sand ripples.

Inman and Bowen, 1963, while studying the transport of sand in a wave flume with a superimposed current, found that for certain combinations of wave and current speed, the sediment could be made to move in an up-wave and up-current direction. That is, in opposition to the direction of wave propagation and flow of current. It was argued that this direction of sediment transport was caused by differing amounts of sediment suspension due to differential vortex formation. This differential vortex formation was caused by the asymmetrical form of the ripples. The asymmetry of the ripples was due to the unidirectional current superimposed upon the velocity field of the wave.

The following series of demonstrations were performed to illustrate the capability of the phase dependent roughness mechanism in controlling the net movement of sand. A roughness form in two segments with five identical asymmetrical wavelengths in each segment was used. The segments were arranged to form a test section as shown in Figure 4. For the first arrangement, particles were placed on the down-wave end of the test section. The direction of particle transport was out-of-phase with the intense vortex formation and the particles moved up-wave and off of the forms. In the second arrangement, the forms were turned around, and the particles were placed on the up-wave end of the test section and the particles moved down-wave and off of the forms. In the third arrangement, only the up-wave form was turned around and a group of particles was placed in the center of the forms. Approximately one-half of the particles moved up-wave and the other half of the particles moved down-wave, both groups of particles moving completely beyond the forms. For the fourth arrangement, both forms were turned around and particles were placed at both ends of the test section. In this case, both groups of particles moved toward the center of the test section and remained in the center.

This series of demonstrations showed that: (1) the direction of transport is not determined by currents in the wave tank; and (2) end effects are not important in determining the direction of motion of the particles. From these results, it may be stated that the direction of motion of the sediment is determined by the orientation of the asymmetrical forms.

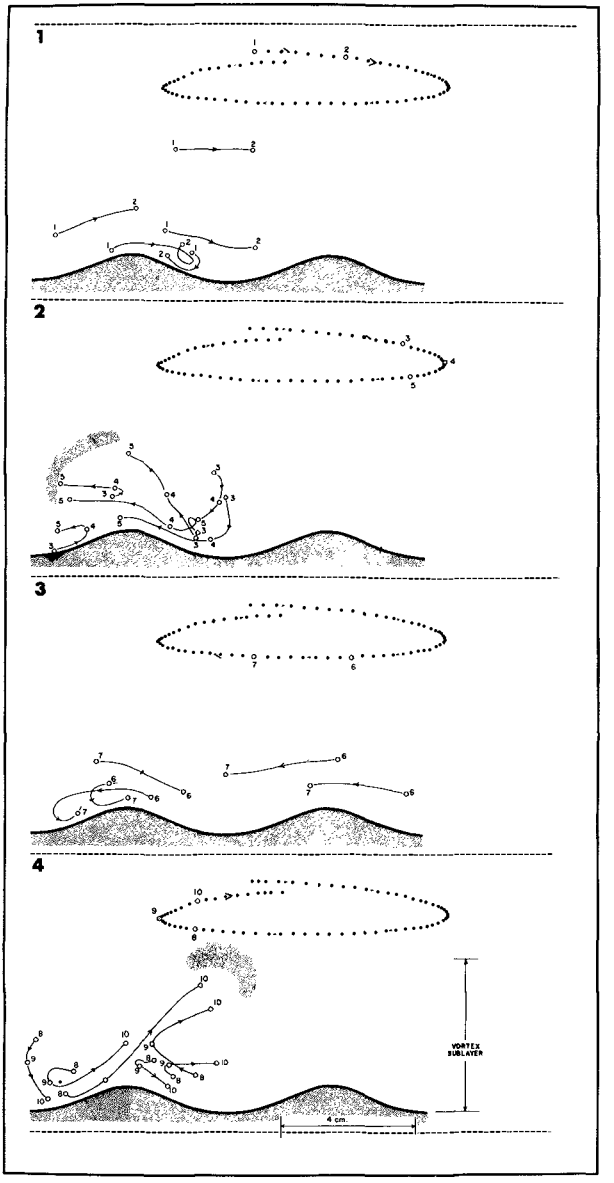

Figure 2. Particle trajectories over a rippled bed showing the height of the vortex-sublayer (after Inman and Bowen, 1963).

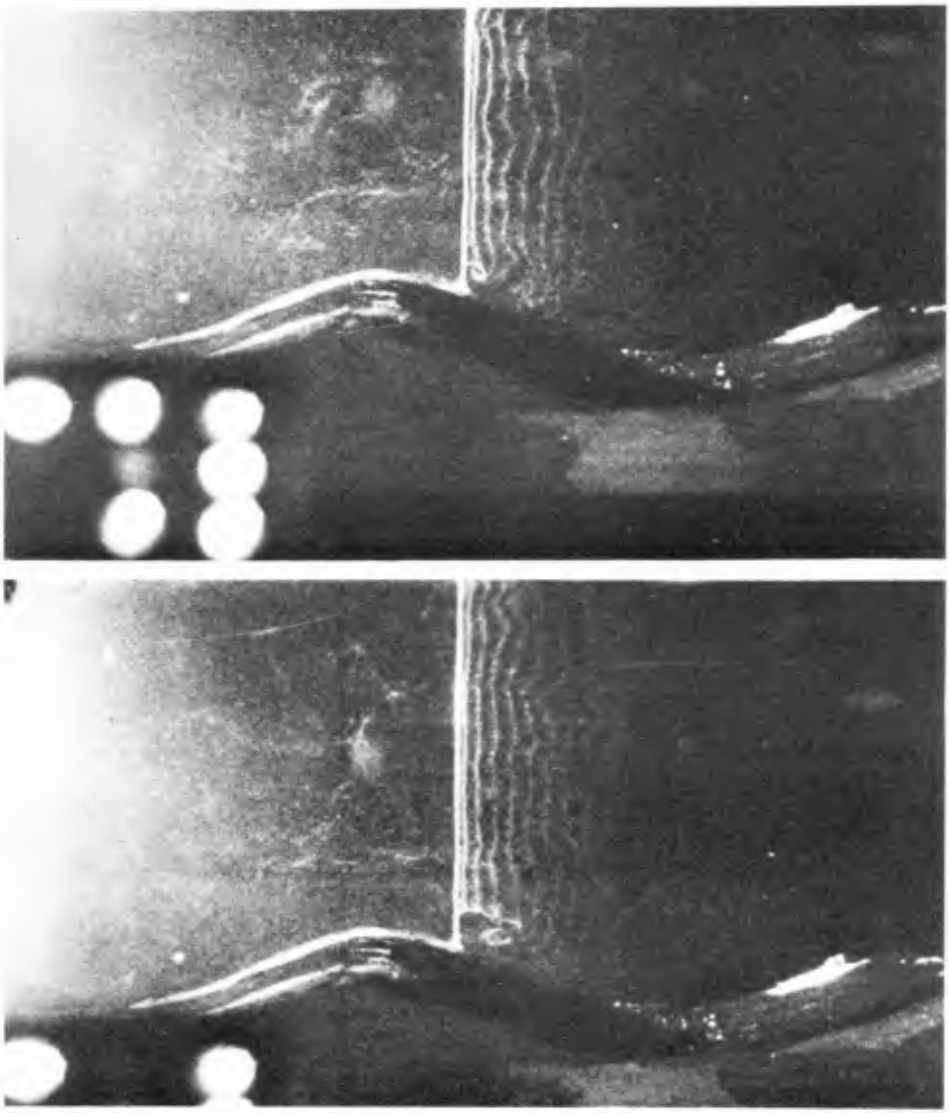

Figure 3. Vortex formation over symmetrical ripples, using the hydrogen bubble technique (note counting lights in lower left portion of figure). The wave form travels from left to right. Upper picture taken at a phase of 40 degrees, lower picture taken at a phase of 55 degrees, wave crest passage denotes zero degrees phase.

TYPICAL EXPERIMENTAL CONDITION

Water Depth	$h = 160$ cm
Wave Period	$T = 3.4$ sec
Wave Height	$H = 21$ cm
Orbital Displacement	$d_o = 24$ cm
pvc, $\rho = 1.5$ gm/cm^3 acrylic, $\rho = 1.1$ gm/cm^3	Tracers Used

ROUGHNESS DIMENSIONS

Wavelength = 10 cm Height = 1.5 cm

Asymmetry: 7.5 cm; 2.5 cm

Waves Propagate from Left to Right

Direction of Particle Transport is Shown by the Arrows

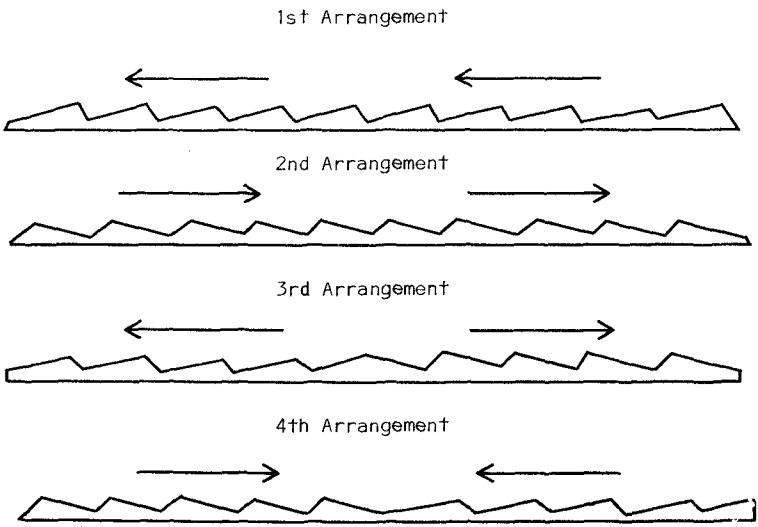

Figure 4. Laboratory demonstration of the capability of phase dependent roughness elements to control the direction of sediment transport. In each case the wave traveled from left to right.

EXPERIMENTAL PROCEDURE

In order to investigate the up-wave movement of sediment and the effect of asymmetrical ripples on this sediment transport, tests were conducted in a laboratory wave tank which is 45 m long, 2.5 m wide and 2.5 m deep. Water depths of 1.7 m were used throughout the testing program. The wave tank is equipped with a hinged paddle wave generator and a 1 in 8 slope at the far end to minimize reflection. The laboratory tests were conducted to take advantage of the benefits of good control and ease of measurements. Later tests on a full scale basis were carried out in the near-shore zone.

The tests in the wave tank were scaled to the prototype scale by using the ratio of water particle orbital diameter, d_o, to the wavelength of the asymmetrical roughness form, λ. For Airy wave theory the parameter $d_o/2\lambda$ is equal to the wave Strouhal number

$$\frac{u_m}{\sigma\lambda}$$

where $u_m = \pi d/T$ is the maximum horizontal component of the orbital velocity near the bed, $\sigma = 2\pi/T$ is the radian frequency, and T is the wave period. This scaling has been found to be a relevant parameter for naturally formed symmetrical ripples.

The first series of tests consisted of the construction of asymmetrical roughness elements and the study of the direction of particle motion caused by the wave induced flow over the forms. The testing method consisted of placing particles on the roughness forms and studying their direction of motion. Three types of particles were used: polyvinylchloride, PVC, with a density of 1.5 gm/cm^3; acrylic, with a density of 1.1 gm/cm^3; and, beach sand, with a density of 2.5 gm/cm^3. The beach sand was used in order to check that erroneous results were not being introduced by the usage of the larger and less dense synthetic particles. In all cases, the three types of particles behaved in a similar manner. The demonstration described in the introduction of this paper was first conducted during testing of the asymmetrical forms with these particles.

Once the nature of the movement of the particles was determined for various wave conditions and asymmetrical roughness elements, experiments were next conducted to study the nature of the vortex formation over the forms and the subsequent movement of these vortices. The vortices were studied using two flow visualization techniques; dye injection, and hydrogen bubble generation from a fine platinum wire. The dye injection technique proved most useful in determining the location and time of formation of the vortices and in following the path of the vortices after they were ejected from the surface of the roughness elements. The hydrogen bubble technique proved useful in studying the size and rotational characteristics of the vortices.

Motion pictures were taken of both visualization techniques. The pictures were correlated with the water surface motions by the use of timing lights in the field of view of the camera. The output of the timing lights also appearing on the strip chart of the analog record of the surface waves. The motion pictures were then analyzed frame by frame to study the motion and rotation of the vortices. Figure 5 shows a vortex generated over the steep side of one of the asymmetrical roughness elements.

Figure 5. Large vortex formed over steep side of asymmetrical roughness element. Wave form travels from left to right.

EXPERIMENTAL RESULTS

From the particle motion studies, it was found that for low values of steepness of the forms, where steepness is defined as form height/form wavelength, η/λ, the particle motion was always out-of-phase with the orbital motion causing the most intense vortex. That is, for steepnesses of about 0.15 to 0.2, the particles always moved in a direction opposite to that faced by the steep side of the roughness forms. For greater steepness values, the higher orbital velocities caused breakdown of the system and particle transport in the direction faced by the steep side of the forms.

It should be noted that the phase dependent mechanism is valid over the same range of steepnesses that are found for natural sand ripples. Figure 6 presents the results from these tests. The solid characters represent points where the direction of particle transport was as predicted by the phase dependent mechanism, while the x's represent conditions for which the particle transport was in the direction opposite to that predicted by the phase dependent mechanism.

The reversal of particle transport direction for forms with higher steepnesses was due to vortex destruction over the steep side of the ripple form. For forms with low steepness, the vortex remains well formed during the orbital motion causing it, with the consequence that the vortex is able to raise the sediment as a plume and move it up into the higher layer of reversed orbital motion (Figures 1 and 2). However, for forms with higher steepnesses the higher velocity flows caused a plaining off and destruction of the vortex on the steep side, and hence a degradation of its ability to suspend sediment. While vortices were destroyed over the steep side, the vortex over the gentle side remained well formed during the entire orbital motion. For these greater steepnesses, the vortex over the gentle side suspended more sediment than the vortex over the steep side, hence reversing the direction of preferred transport.

In unidirectional flow, vortex formation in the wake of an obstacle is due to an adverse pressure gradient caused by the presence of the obstacle. This adverse pressure gradient leads to reversed flow in the boundary layer near the obstacle, which in turn ultimately leads to the vortex roll-up observed in the lee of the obstacle. In oscillating flow there is an additional source of adverse pressure supplied by the pressure field of the oscillating fluid itself. As the velocity field passes through a maximum in one direction, it starts to be retarded by a pressure gradient in the opposite direction from that of the current velocity. This is due to the fact that under progressive waves, the pressure field has a phase lead of 90 degrees over the velocity field. Thus, under oscillating flow conditions, the phenomenon of vortex formation is optimized. The presence of asymmetrical roughness forms causes an intensification of the vortex over the steep face and minimizes the vortex over the gentle face. Thus, in oscillatory flow under progressive waves the difference in the relative intensities of the vortices determines the direction of net sediment transport.

ENGINEERING APPLICATIONS

Upon completion of the laboratory phase of the investigation, it was decided to test a 2 meter by 2 meter square array of asymmetrical roughness forms in the nearshore zone under natural wave conditions. Using Figure 6

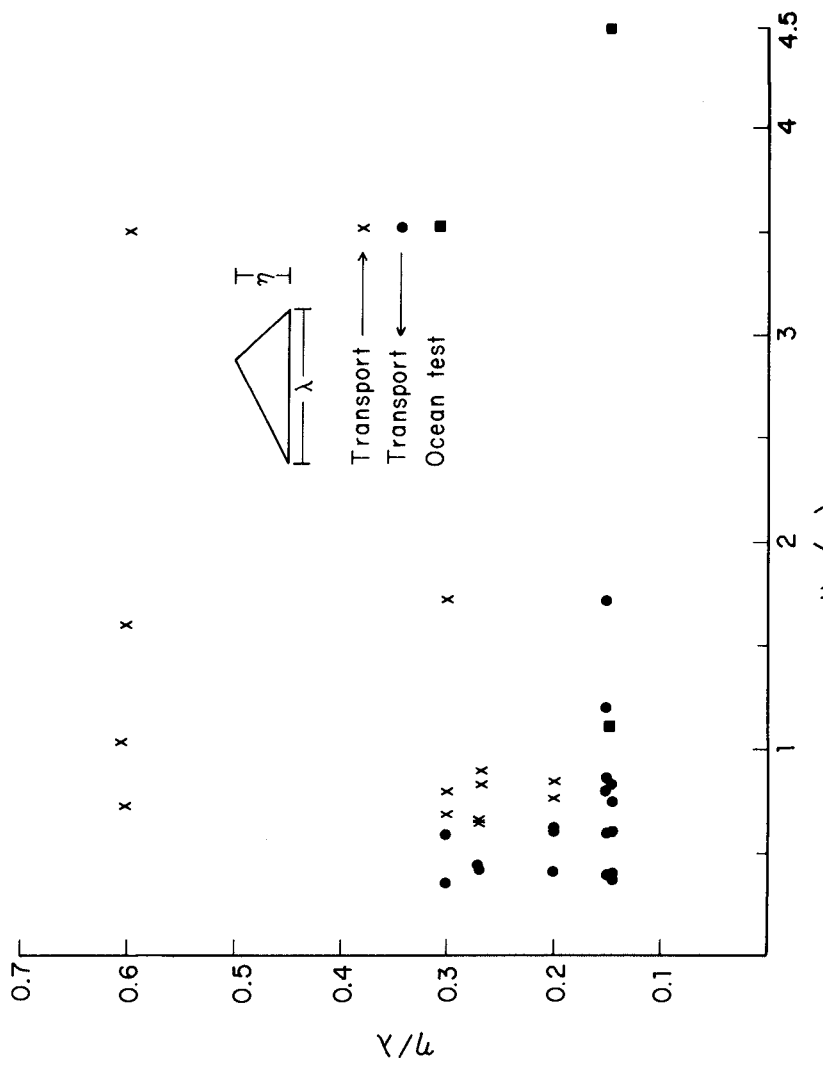

Figure 6. Transport behavior as a function of ripple steepness, η/λ, and wave Strouhal number.

as a design criterion, and a typical Southern California summer wave condition of 9 second period with wave heights of about 0.75 m, the test roughness forms were constructed with a wavelength of 40 cm and a wave height of 6 cm. This set of roughness and wave parameters corresponds to a steepness of 0.15 and a wave Strouhal number of 1.0 (Figure 6).

The roughness elements were cast with Portland cement concrete with an added 2.5 cm base for strength. Figure 7 shows the array of roughness forms just prior to installation in the nearshore environment. In addition to the asymmetrical roughness forms, two forms were cast which had the same wavelength as the asymmetrical forms, but were symmetrical in form. These forms were placed in the same locality as a control for the tests. The forms were placed in 6 meters of water, and metal rods were implanted on either side of the array in an on-offshore direction. Measurements were taken on the rods to ascertain the amount of sand loss or gain on each side of the array. The results of two weeks of observations on the array are presented in Figure 8.

The array was first arranged so as to move sediment in the offshore direction. After 24 hours in place the array had developed a pit on the inshore end of the array and had a mound on the offshore end of the array. Thus indicating that the array was having the intended effect even in this limited scale. Observations were continued for the next 6 days, with the maximum depth of the pit on the onshore side of the array attaining a depth of 13 cm below the level of the sand when the array was first installed. At the end of this one week period, the two symmetrical forms were completely buried with the crests of the ripple forms being 3 cm under the surrounding sand level. The asymmetrical array had no sand on top of it. The top portion of Figure 8 illustrates the effects of the array on the surrounding sand level.

The array was next arranged so as to move sediment in the onshore direction. After 24 hours in place, there was a 4 cm deep depression on the offshore side of the array with little noted change on the onshore side of the array. After 48 hours there were depressions on both sides of the array, with the depression on the offshore side of the array being some 2 cm deeper than the onshore side depression. It would seem that the effect of the array was not as pronounced when it was aligned in this direction. A possible explanation for the apparent lack of effectiveness in transporting sand in an onshore direction, is that at this time of year, the local beaches are accreting and sand is naturally moving toward shore (Inman and Bagnold, 1963). This sand transport rate would be sufficient to overshadow the effects of the asymmetrical array. However, when the array was arranged so as to move sediment in an offshore direction, it apparently prevented the onshore movement of sand from taking place. When the asymmetrical array was turned around, the symmetrical forms were uncovered and placed on level sand. Again within 3 days, the symmetrical forms were completely buried. The results of the second trial with the array are shown in the lower half of Figure 8.

From the preceeding discussion of the laboratory and field tests of phase dependent roughness elements, it seems likely that the phenominon is valid and should be further tested to determine the extent of its usefulness in sediment control in the nearshore zone. Along these lines, plans are underway to construct an array of roughness elements approximately 300 meters along the shore and 3 to 4 meters wide in the on-offshore direction to test their effect in preventing the loss of sand from the beach that naturally occurs during the winter storms.

Figure 7. Photograph of the phase dependent roughness forms used in the field test

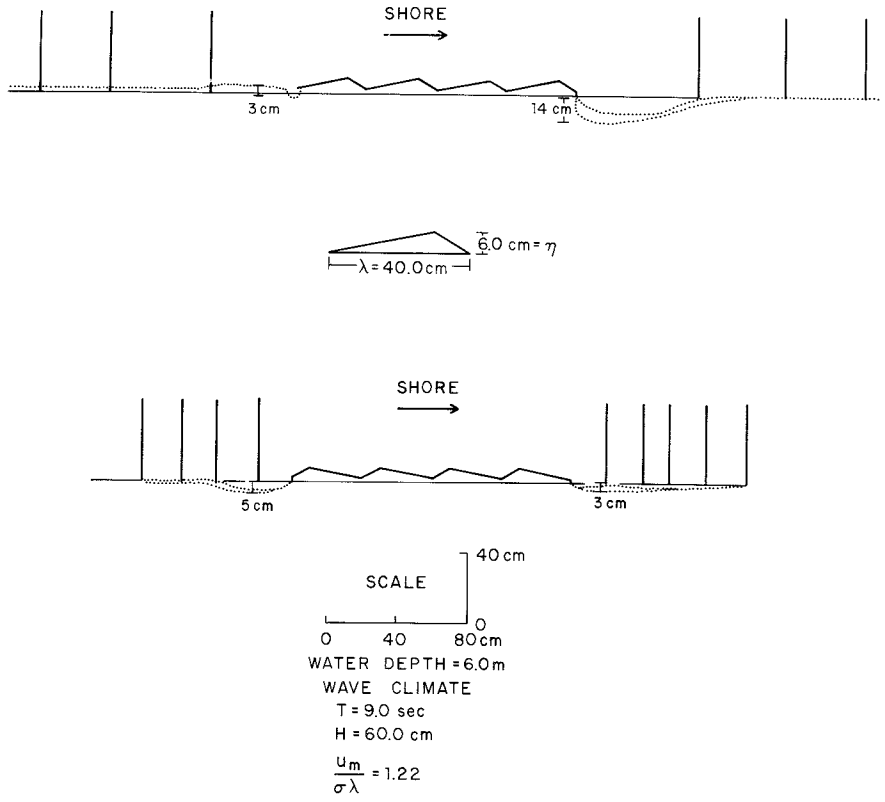

Figure 8. Results of field test in water depth of 6 meters adjacent to Scripps Institution of Oceanography Pier.

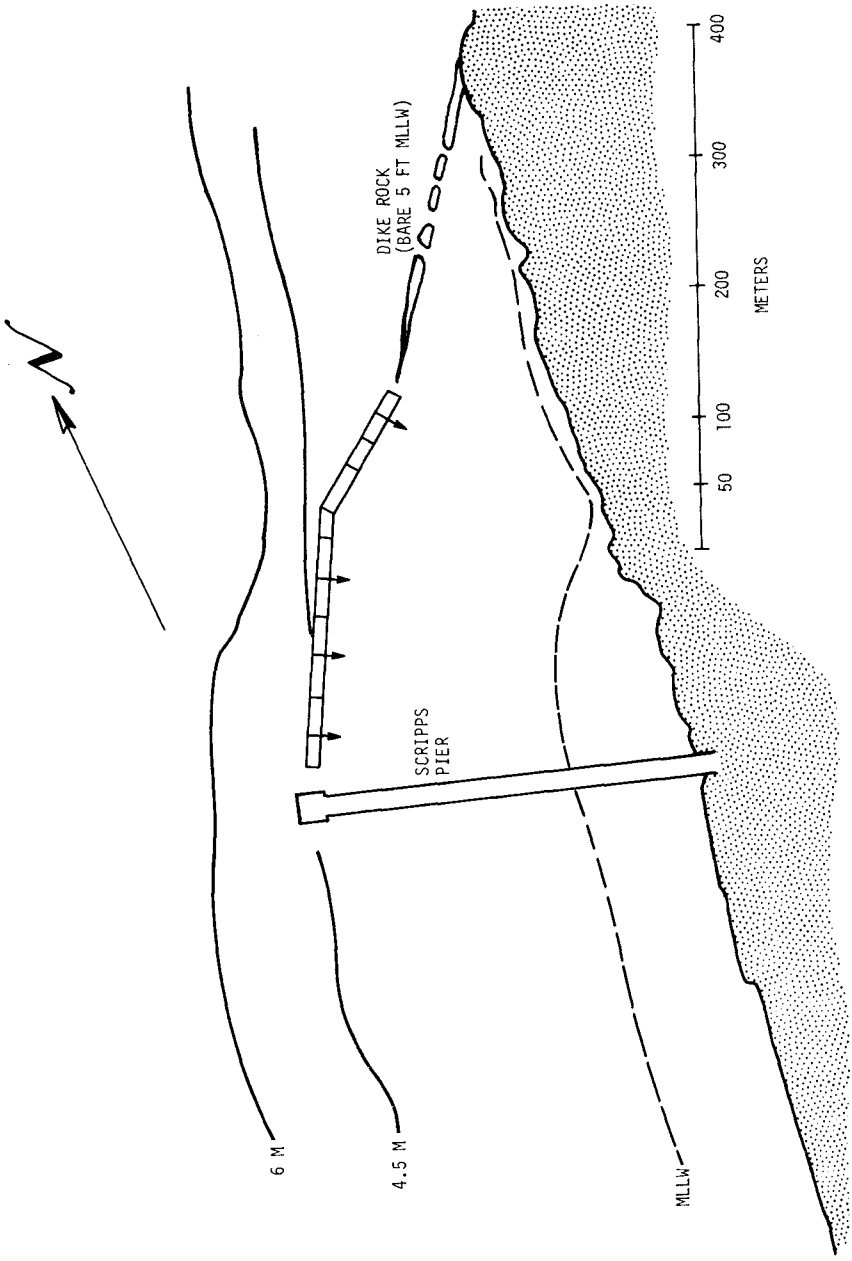

Figure 9. Proposed full scale ocean test off Scripps Beach.

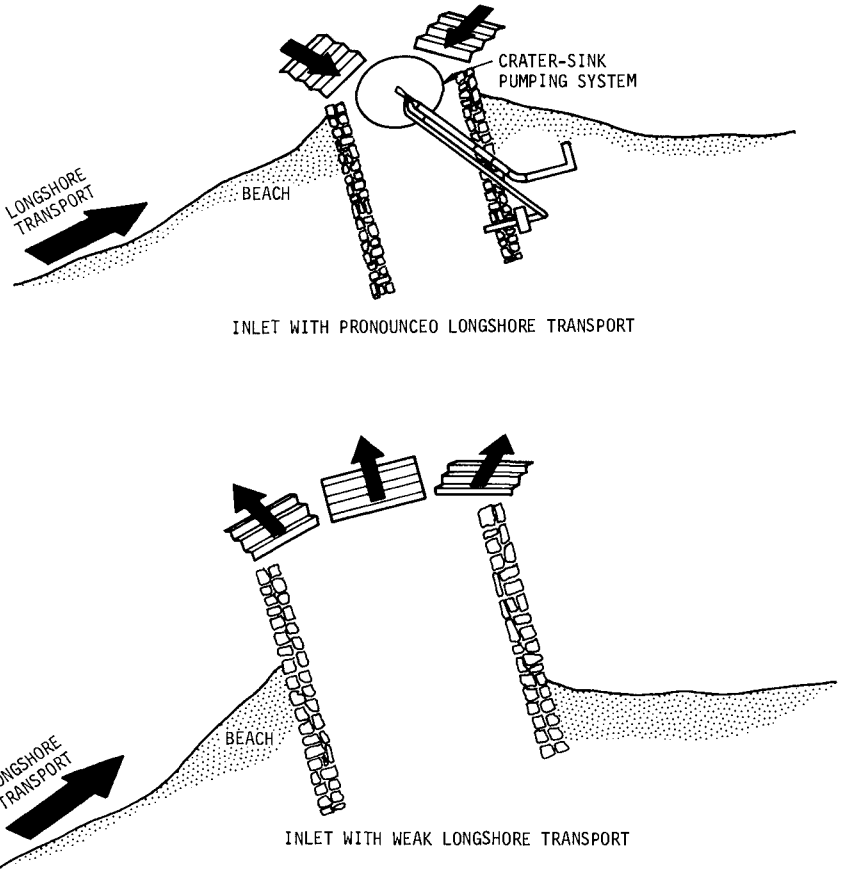

Figure 10. Possible applications for phase dependent roughness elements.

The area to be tested is a strip of beach just north of the Scripps Institution of Oceanography which is terminated by the presence of a rocky headland which will act as a barrier to "close" off one end of the experiment. The array is to be aligned with the 5 to 6 meter contour which has been found to be an area of equilibrium in terms of the seasonal on-offshore movement of sediment. In an effort to counteract the scouring effect which was present along the ends of the small test array, the 300 meter array will be placed atop a type of plastic filter cloth which will allow the passage of water, but not the passage of sand through its weave. Figure 9 is a plan view of the proposed test site showing the location and length of the test array of phase dependent roughness elements. To test the effectiveness of the system for controlling sediment movement, bottom profiles will be measured in the area of the array and also to the south of the pier to detect any differences in sand level between the "controlled" and "uncontrolled" strips of beach.

In addition to the management of beach erosion shown in Figure 9, several additional applications of phase dependent roughness elements are suggested. These are shown schematically in Figure 10. The first application is used in an area of pronounced longshore drift in which sediment continually gets around the end of a channel maintained by a jetty. The phase dependent roughness elements can be used to direct the sediment toward a dredge or crater-sink pumping system, (Inman and Harris, 1970) to increase the efficiency of the overall system in keeping the harbor entrance open.

For areas of less pronounced longshore drift, the phase dependent roughness elements could be placed at the ends of jetties to prevent the formation of a bar at the entrance to the jetty. The longshore transported sediment would be moved away from the entrance, where it would be available for longshore transport past the end of the jetty.

Present plans call for the construction of the nearshore test elements out of concrete. However, it may be possible to construct movable elements so that the roughness form could be changed as the wave conditions change, thus keeping the roughness elements operating in their most efficient range (Figure 6).

ACKNOWLEDGMENTS

This paper represents, in part, concepts developed at the Scripps Institution of Oceanography, University of California, La Jolla, under contract with the Advanced Research Project Agency. One of the authors was principally funded by a Graduate Fellowship from the Naval Undersea Research And Development Center, San Diego.

REFERENCES

Ayrton, H., 1910, "The origin and growth of ripplemark", Proc. Roy. Soc. London, Ser. A., vol 84, p 285-310.

Bagnold, R. A., 1946, "Motion of waves in shallow water--interaction between waves and sand bottoms", Proc. Roy. Soc. London, Ser. A., vol 187, p 1-18.

Darwin, G. H., 1883, "On the formation of ripple-mark in sand", Proc. Roy. Soc. London, vol 36, p 18-43.

Inman, D. L., 1957, "Wave generated ripples in nearshore sands", Beach Erosion Board, Corps of Engineers, Tech Memo 100, 42 pp.

Inman, D. L. and R. A. Bagnold, 1963, "Beach and nearshore processes: part II, Littoral processes", The Sea, M. N. Hill, ed., vol 3, p 529-553.

Inman, D. L. and A. J. Bowen, 1963, "Flume experiments on sand transport by waves and currents", Proc. Eighth Conf. Coastal Engin., p 137-150.

Inman, O. L. and R. W. Harris, 1970, "Crater-sink sand transfer system", Proc. Twelfth Conf. Coastal Engin., p 919-933.

CHAPTER 63

SCALE SELECTION FOR MOBILE BED WAVE MODELS

by

J. William Kamphuis *

ABSTRACT

A rational basis for the design of wave models with a mobile bed is presented. The discussion is of a preliminary nature and further model analysis, underway at present at Queen's University, should introduce a sounder basis for model design.

INTRODUCTION

The determination of scales for mobile bed wave models is an area of great uncertainty and a discussion at the 12th Coastal Engineering Conference in Washington in September 1970 resulted in the conclusion that in spite of a great deal of practical experimentation and model analysis relatively little is known about modelling with mobile beds.

An earlier report [1] has been written to serve as a framework for further study of modelling techniques presently under way at the Queen's University Coastal Engineering Research Laboratory. Here the derivation of scale relationships for fixed bed models as well as for mobile bed models is described in greater detail and the reader is referred to this work for further information.

FIXED BED MODEL SCALES

For wave models it is necessary to distinguish between short wave models and models of long waves and unidirectional current.

Short waves may be said to consist of two regions, the upper region, outside of the boundary layer, and the boundary layer region.

Upper region models are the normal type of fixed bed short wave

---

* Associate Professor of Civil Engineering,
Coastal Engineering Research Laboratory,
Queen's University at Kingston, Canada.

model constructed to model refraction, diffraction, reflection, etc. Often these models are distorted and the scale relationships governing these models are

$$\begin{aligned} n_H &= n_L = n_d = n_z = n_a = n \\ n_u &= n_t = n_T = n^{1/2} \\ n_x &= n_y = Nn \end{aligned} \tag{1}$$

Here n is the general model scale - prototype value divided by model value to result in integer model scales rather than fractions for the major scales. H is the wave height, L the wave length, d the depth of water, z the vertical co-ordinate, a the orbital amplitude, u the water particle velocity, t the time co-ordinate, T the wave period, x and y the space co-ordinates and N the model distortion $= n_x/n_z = n_y/n_z$.

Both N and n may be freely chosen, and each could be coined as a "degree of choice". n is usually a function of the accuracy of the field measurements of depth and wave height, model accuracies of the same quantities, minimum depths required in certain model areas and maximum slopes that can be used without causing additional effects such as separation and vortices; N is normally determined by the laboratory size and the area to be modelled. A model with two "degrees of choice" may appear to be an easier model to design, but it is based on a number of additional trade-offs, necessary in order to achieve this extra choice. These must be carefully evaluated for each model. As an example consider a refraction-diffraction model. If two "degrees of choice", i.e. a distorted model, are insisted upon, the total wave field, consisting of the model diffraction pattern and the model refraction pattern, does not correspond to the prototype wave field. Thus the effect of this discrepancy must be evaluated and, in the light of this, the number of "degrees of choice" must be determined - either one (undistorted), or two (distorted).

When the researcher is interested in the motion within the boundary layer, as he would be in the case of mobile bed models the situation

becomes considerably more complex. Only models with a rough turbulent boundary layer are considered here. Details regarding other boundary layer models may be found in Kamphuis [1].

It is not unusual that the bottom roughness k_s cannot be reproduced to model scale, because the model bottom would be too smooth. Not modelling k_s to scale represents another "degree of choice" and again constitutes certain further limitations imposed on the model. The ratio of n_{k_s} / n may be defined as the bottom roughness distortion N_{k_s}. When a larger roughness is used (usual case), $N_{k_s} < 1$.

The required model scales for fully developed rough turbulent oscillatory boundary layer flow may be derived as:

$$
\begin{aligned}
&n_H = n_L = n_d = n_z = n_Z = n_a = n \\
&n_u = n_{U_\delta} = n_t = n_T = n^{1/2} \quad ; \quad n_U = n^{1/2} N_{k_s}^{-1/42} \simeq n^{1/2} \\
&n_x = n_y = n_X = n_Y = Nn \quad ; \quad n_{k_s} = n N_{k_s} \\
&n_\delta \simeq n N_{k_s}^{1/7} \\
&n_\tau \simeq n N_{k_s}^{2/7} \quad ; \quad n_{v_*} \simeq n^{1/2} N_{k_s}^{1/7}
\end{aligned}
\tag{2}
$$

Here Z refers to the vertical co-ordinate within the boundary layer, measured from the bottom up. U is the velocity within the boundary layer, δ refers to the top of the boundary layer, τ is the shear stress and v_* is the shear velocity = $\sqrt{\tau_o/\rho}$, where τ_o is the shear stress on the bottom.

For long waves and unidirectional flow models the following scale relationships apply.

$$
\begin{aligned}
&n_d = n_Z = n \\
&n_{\bar{U}} = n_U = n^{1/2} \quad ; \quad n_t = n_T = Nn^{1/2} \\
&n_X = n_Y = n_L = Nn \\
&N_{k_s} = N^{-4} \quad ; \quad n_\tau = nN^{-1} \\
&n_C = N^{1/2} \quad ; \quad n_f = N^{-1} \quad ; \quad n_S = N^{-1}
\end{aligned}
\tag{3}
$$

Here $\bar{U}$ is the average velocity. It is capitalized because the totality of the flow constitutes a boundary layer. C, f and S are the Chezy friction coefficient, the Darcy-Weisbach friction factor and the surface slope.

Equation 3 refers to the situation where all additional roughness required as a result of model distortion is supplied on the bottom. If vertical roughness elements are used, the bottom shear may be considered to result from k_s only and

$$n_\tau = nN_{k_s}^{1/4} \tag{4}$$

while C and f refer to the combination of bottom and vertical "roughness".

When a combined model is used, i.e. short waves, long waves and unidirectional currents it becomes evident that when all the additional roughness is placed in the bottom, the short wave boundary layer thickness becomes grossly exaggerated. Thus vertical roughness elements must be used. The resulting scale relationships for such a combination model are:

$$\begin{aligned}
&n_H = n_d = n_z = n_Z = n_a = n \\
&n_u = n_{U_\delta} = {}_\ell n_{\bar{U}} \simeq {}_s n_U = n^{1/2} \\
&n_x = n_y = n_X = n_Y = Nn \quad ; \quad n_{k_s} = nN_{k_s} \\
&{}_s n_L = n \quad ; \quad {}_\ell n_L = Nn \\
&{}_s n_t = {}_s n_T = n^{1/2} \quad ; \quad {}_\ell n_t = {}_\ell n_T = Nn^{1/2} \\
&{}_s n_\tau = nN_{k_s}^{2/7} \quad ; \quad {}_\ell n_\tau = nN_{k_s}^{1/4} \\
&{}_s n_\delta = nN_{k_s}^{1/7} \\
&n_C = N^{1/2} \quad ; \quad n_f = N^{-1} \quad ; \quad n_S = N^{-1}
\end{aligned} \tag{5}$$

where $_s$ refers to short waves and $_\ell$ refers to long waves and unidirectional flow.

EQUATIONS FOR A MOBILE BED

Sediment transport along the bottom may be described by the following parameters, Yalin [2,ch 6].

$$A = f(\rho, \mu, D, \rho_s, g, \ell, v_*) \tag{6}$$

where ρ and μ are the fluid density and viscosity, D and ρ_s are the particle diameter and density, g is the acceleration due to gravity, and ℓ is a typical length.

If initiation of motion is basically considered to be a lift phenomenon it is possible to replace g by the submerged unit weight

$$\gamma_s' = (\rho_s - \rho)g \tag{7}$$

This results in the following dimensionless relationship

$$\Pi_A = \phi\left(\frac{v_* D}{\nu}, \frac{\rho v_*^2}{\gamma_s D}, \frac{\rho_s}{\rho}, \frac{\ell}{D}\right) \tag{8}$$

The first two dimensionless variables are the grain size Reynolds Number and the Shields parameter, the X and Y axes of the Shields diagram.

For a flat bed and unidirectional flow v_* is readily determined and easily varied in a definable fashion since

$$v_* = (gRS)^{1/2} \tag{9}$$

where R is the hydraulic radius of the flow. If bed forms are present

$$S = S_{k_s} + S_f \tag{10}$$

where S_{k_s} is the slope caused by the friction on the actual grains and S_f is the slope caused by the bed form. Experimentally the following two expressions have been derived, Yalin [2, ch 6].

$$S_{k_s} = \frac{\mathbf{F}}{(2.5 \ln 11 \frac{d}{k_s})^2} \quad ; \quad S_f = \frac{1}{2}\frac{\Delta^2}{\Lambda d}\mathbf{F} \tag{11}$$

where $\mathbf{F}$ is the Froude number of the flow $= \bar{U}^2/gd$, Δ is the height of the bed form and Λ its length.

Under waves v_* is not an easy variable to use and it would be convenient to rewrite Eq. 8 as

$$ {}_s\Pi_A = \phi_s \left(\frac{U_\delta D}{\nu}, \frac{\rho U_\delta^2}{\gamma_s D}, \frac{\rho_s}{\rho}, \frac{a_\delta}{D} \right) \qquad (12) $$

$$ {}_\ell\Pi_A = \phi_\ell \left(\frac{\bar{U} D}{\nu}, \frac{\rho \bar{U}^2}{\gamma_s D}, \frac{\rho_s}{\rho}, \frac{d}{D} \right) \qquad (13) $$

for short waves and long waves respectively.

This is justified when deriving model scales, if

$$ n_{U_\delta} \simeq {}_s n_{v_*} \quad \text{and} \quad n_{\bar{U}} \simeq {}_\ell n_{v_*} $$

and Eq. 5 indicates that this is not unreasonable except for the case when all roughness is bottom roughness [1,p49]. The direct determination of τ below waves is at present also under investigation at Queen's (Riedel et al [14]).

SCALE SELECTION FOR SHORT WAVE MOBILE BED MODELS

General

In order to model the boundary layer and the wave motion both simultaneously and correctly, it was seen that the boundary layer motion must be fully developed rough turbulent in case of the prototype as well as the model.

The following model scales may be derived from Eq. 8 using a_δ as the typical length for models of short waves and assuming $n_\nu = n_\rho = 1$

$$ n_{v_*} n_D = 1 \qquad (14) \qquad n_D n_{\gamma_s} = n_{v_*}^2 \qquad (15) $$

$$ n_{\rho_s} = n_\rho = 1 \qquad (16) \qquad n_D = n_{a_\delta} = n \qquad (17) $$

Equations 14 and 15 ensure that both model and prototype fall on the same point on the Shields diagram, i.e. it ascertains that when motion occurs in the prototype, motion will also occur in the model.

Valembois [3] combines these into

$$n_{\gamma_s} = n_D^{-3}$$

Equation 16 states that the density scales for the fluid and the sediment must be the same. Since n_ρ is usually equal to unity, the only proper model material is the material found in the prototype, a very restricting concept. Yalin [2,p162] states that this is only of importance when considering the motion of individual grains. When mass movement of bed form and discharge of material is of interest, this very stringent scale law may sometimes be relaxed.

Without the assumption that Eq. 16 need not be satisfied, it is impossible to construct models using larger, light-weight sediment. If the effect of ρ_s/ρ is small, the assumption introduces a scale effect, where scale effect is defined as a discrepancy in the model results caused by not adhering to all scale laws. If the effect of ρ_s/ρ is large, the model is useless. When particle ballistics are involved, e.g. in the formation of ripples or the formation of equilibrium beaches, Mogridge and Kamphuis [4], Paul, Kamphuis and Brebner [5], it may well be impossible to use light-weight material.

If the mobile bed is flat, i.e. without bed forms such as ripples, then from Eq. 2, 14 and 15

$$n_D = n^{-1/2}\, N_{k_s}^{-1/7} \quad \text{and} \quad n_{\gamma_s} = n^{3/2}\, N_{k_s}^{3/7} \tag{18}$$

For mobile beds, it is at present usual to assume that

$$n_{k_s} = n_D \tag{19}$$

and therefore Eq. 18 becomes

$$n_D = n^{-5/16} \quad \text{and} \quad n_{\gamma_s} = n^{15/16} \tag{20}$$

For beds with bedform it can either be assumed that the bottom roughness is the same as the grain roughness (Assumption I) or that it is equal to the total roughness (Assumption II). In the latter case

$$n_D = n^{-1/2}\, N_k^{-1/7} \quad \text{and} \quad n_{\gamma_s} = n^{3/2}\, N_k^{3/7} \tag{21}$$

Both assumptions are incorrect, but certain situations, e.g. long ripples may warrant Assumption I, whereas other configurations, such as short ripples may warrant Assumption II.

Bijker [6] and others follow the example of Einstein and introduce a ripple factor, α, so that $\tau' = \alpha\tau$, where τ' is the effective shear stress, i.e. the shear stress that moves the sediment. In how far this applies to ripples under waves remains to be seen and in any case, it is unlikely that the other properties such as growth of bed form, bed form dimensions, etc. are dependent on α. Furthermore, it is found that in most cases $n_\alpha \simeq 1$. Therefore the ripple factor has only a small effect on the scaling problem and this approach becomes synonymous to Assumption II.

Equation 17 has not been discussed so far and it may be seen that since $n > 1$, Eq. 17 results in $n_D > 1$ while Eqs. 18 and 21 yield $n_D < 1$. This is a conflict which must be resolved for all mobile bed models.

Large Grain Sizes

From the Shields diagram it may be inferred that when

$$\frac{v_* D}{\nu} > 100 \tag{22}$$

the grain size Reynolds number effect, i.e. Eq. 14 may be neglected and thus Eqs. 15 and 17 yield

$$n_{\gamma_s} = \frac{n_{v_*}^2}{n_D} = N_k^{2/7} \quad ; \quad n_D = n_{a_\delta} = n \tag{23}$$

where it is understood that N_k refers to total roughness or grain size roughness, depending on the assumption made. For Assumption I, since k_s varies with D, N_{k_s} is likely very close to unity and $n_{\gamma_s} \simeq 1$.

The resulting model bed consists of prototype sand material, with its grain size scaled down by the model scale. Note that in this case Eq. 16 is also satisfied automatically. For Assumption II,

N_k is a function of the grain size, as well as model wave conditions which cause the bed form. At present little is known about the variation of bed form below waves and research is underway at Queen's University [4] to determine this. It is very likely that N_k is a function of n_{γ_s}, which means that an iterative procedure may need to be followed in order to select the correct n_{γ_s} even after expressions for N_k have been determined experimentally.

Preliminary test results indicate that both ripple height Δ and ripple length Λ are primarily functions of a_δ/D. Thus if Eq. 23 is satisfied, N_k could still have a value close to one, as long as a_δ/D does not change a great deal within the model and prototype. Therefore ripple sizes scale down approximately by the model scale and again $n_{\gamma_s} \simeq 1$.

There are obvious lower limits to this type of model. Problems arise when the model boundary layer becomes smooth and laminar, or when sand size particles are modelled by clay size particles. Under those circumstances the condition in Eq. 23 must be dropped.

Smaller Grain Sizes

In most cases the flow around the individual grains is not turbulent and a conflict between Eqs. 14 and 17 exists. Since it is almost impossible to satisfy Eq. 17, especially for the smaller grain sizes, as shown above, Eq. 14 is considered, leaving the misrepresentation of Eq. 17 to scale effect. This scale effect is in addition to the scale effect resulting from not adhering to Eq. 16, which now is an impossible condition to meet.

As an example the total bed roughness k, may be considered since it influences the value of N_k which, under Assumption II, may be used eventually for scale selection. This is one problem presently under investigation at Queen's University.

$$\Pi_k = \frac{k}{D} = \phi_k \left(\frac{v_* D}{\nu}, \frac{\rho v_*^2}{\gamma_s D}, \frac{\rho_s}{\rho}, \frac{a_\delta}{D} \right) \qquad (24)$$

If the scale laws resulting from Eqs. 14 and 15 are satisfied, it may be stated in very simplified terms that

$$n_k = m_k\, n_D = \frac{m_k}{n^{1/2}\, N_{k_s}^{1/7}} = \frac{m_k}{n^{5/16}} \;;\; n_k = m_k\, n_D = \frac{m_k^{7/8}}{n^{5/16}} \qquad (25)$$

for Assumption I, and Assumption II respectively. Here m_k is the scale effect with respect to k, resulting from Eqs. 16 and 17 not being satisfied.

Yalin [2,p226] and present research at Queen's University indicate that in models, ripple height and length are indeed functions of a_δ/D and that therefore k/D must also be a function of this parameter [2,p227]. But a_δ is also a function of water depth and therefore in a single model there are many values of m_k, each corresponding to a different depth. The use of a single value of m_k is dangerous since this means that the model is designed for one distortion of roughness with respect to D. The factor m_k must therefore be thoroughly investigated.

If Assumption II is made the scale effect m_k is found back in the other scale relationships which include N_k, e.g.

$$n_\tau = n\, N_k^{2/7} = n^{5/8}\, m_k^{1/4} \;;\; n_\delta = n\, N_k^{1/7} = n^{13/16}\, m_k^{1/8}$$

$$n_D = \frac{1}{n^{5/16}\, m_k^{1/8}} \;;\; n_{\gamma_s} = n^{15/16}\, m_k^{3/8} \qquad (26)$$

The smaller powers of m_k indicate that the influence of the scale effect is not very serious for n_δ and n_D, but the actual value of m_k can conceivably be quite large since for small waves Δ and Λ are direct functions of a_δ/D, while for prototype waves this relationship may be decoupled and Δ and Λ may be independent of a_δ/D.

The sediment transport scale may be derived in a similar fashion

$$\frac{q}{v_* D} = \phi_q \left(\frac{v_* D}{\nu}, \frac{\rho v_*^2}{\gamma_s D}, \frac{\rho_s}{\rho}, \frac{a_\delta}{D} \right) \qquad (27)$$

q is the solid volume of material transported per unit width, per unit time. By analogy to the above derivation

$$n_q = m_q\, n_{v_*}\, n_D = m_q \qquad (28)$$

Thus if Eqs. 16 and 17 are not satisfied the sediment transport scale is not equal to unity. Also m_q is again a function of depth and therefore n_q is not constant throughout the model. Bijker and Svasek [7] discuss this in more detail. It is only possible to design a model for a single value of m_q. The proper choice is of extreme importance and worthy of additional study.

Model Distortion

Model distortion is a "degree of choice" for fixed bed models but must be chosen more carefully for mobile bed models. Since many models involve beaches, the model shoreline and slope must correspond to the prototype shoreline and slope so that they both represent the same conditions. If the equilibrium beach slope is denoted by Θ and the shoreline position is called x_s, then it may be stated in a simplified fashion that

$$N = F_N(\Theta, x_s) \tag{29}$$

where the function is determined by an experimental fit of model vs prototype. Equation 29 is at present under investigation at Queen's University [e.g. 5].

Summary

The scale relationships for short wave models with a mobile bed are therefore Eqs. 2 and 29, with for models with large grain size Reynolds number Eq. 23 and if N_{k_s} or N_k are near unity

$$n_{\gamma_s} \simeq 1 \quad ; \quad n_\rho \simeq n_{\rho_s} \tag{30}$$

Because of very small model grain sizes, these models quickly become physically impossible. For the more usual models with grain size Reynolds numbers below the fully turbulent range,

$$n_D = n^{-1/2}\, N_{k_s}{}^{-1/7} = n^{-5/16} \quad \text{or} \quad n_D = n^{-5/16}\, m_k{}^{-1/8} \tag{31}$$

$$n_{\gamma_s} = n^{3/2}\, N_{k_s}{}^{3/7} = n^{15/16} \quad \text{or} \quad n_{\gamma_s} = n^{15/16}\, m_k{}^{3/8}$$

$$n_k = m_k\, n^{-1/2}\, N_{k_s}^{-1/7} = m_k\, n^{-5/16} \quad \text{or} \quad n_k = m_k^{7/8}\, n^{-5/16}$$

$$n_\tau = n\, N_{k_s}^{2/7} = n^{5/8} \quad \text{or} \quad n_\tau = n^{5/8}\, m_k^{1/4} \qquad (31)$$

$$n_\delta = n\, N_{k_s}^{1/7} = n^{13/16} \quad \text{or} \quad n_\delta = n^{13/16}\, m_k^{1/8} \qquad \text{(Cont'd)}$$

$$n_q = m_q$$

for Assumption I and Assumption II respectively.

Substitutions for v_*

Although v_* has been conveniently eliminated from the scaling problem, the actual experimentation with the model still depends on the measurement of v_* as expressed in Eq. 8. It was indicated earlier that for short waves, substitution of U_δ for v_* is not unreasonable. If the wave motion is sinusoidal, Eq. 12 may be further simplified to

$$s\Pi_A = \phi_s' \left(\frac{\hat{U}_\delta D}{\nu}, \frac{\rho \hat{U}_\delta^2}{\gamma_s D}, \frac{\rho_s}{\rho}, \frac{a_\delta}{D} \right) \qquad (32)$$

where $\hat{}$ indicates the maximum value. Since for sinusoidal motion

$$\hat{U}_\delta = \text{cst} \left(\frac{a_\delta}{T} \right) \qquad (33)$$

$$s\Pi_A = \phi_s'' \left(\frac{a_\delta D}{\nu T}, \frac{\rho a_\delta^2}{\gamma_s T^2 D}, \frac{\rho_s}{\rho}, \frac{a_\delta}{D} \right) \qquad (34)$$

It must be recognized that above dimensionless quantities are not entirely constant, for instance:

$$n_{X_1} = \frac{n_{a_\delta}\, n_D}{n_\nu\, n_T} = \frac{n}{n^{1/2}} \cdot \frac{1}{n^{1/2}\, N_{k_s}^{1/7}} = N_{k_s}^{-1/7} = n^{3/16} \qquad (35)$$

or

$$n_{X_1} = \frac{n}{n^{1/2}\, n^{5/16}\, m_k^{1/8}} = n^{3/16}\, m_k^{-1/8} \qquad (36)$$

Distortion of H

At times it is suggested in the literature, e.g. Goddet and Jaffry [8] that the wave height may be distorted to force proper sediment transport conditions by waves, i.e. $n_H = N_H\, n$, since an increase in wave height has little influence on the wave refraction patterns. It must be borne in mind, however, that the position of the breaker is influenced by this distortion and therefore the effects on the model results of this "degree of choice" must be evaluated carefully. Goddet and Jaffry [8] suggest that $N_H = N^{1/4}$ is permissible.

SCALE SELECTION FOR LONG WAVE AND UNIDIRECTIONAL FLOW MOBILE BED MODELS

For long waves and unidirectional flow similar reasoning may be used. From Eq. 8, using the water depth d as a typical length, Eqs. 14, 15 and 16 are valid while Eq. 17 becomes

$$n_D = n_d = n \tag{37}$$

If the mobile bed is flat, substitution of Eq. 3 into Eqs. 14 and 15 yields

$$n_D = n^{-1/2}\, N^{1/2} \quad ; \quad n_{\gamma_s} = n^{3/2}\, N^{-3/2} \tag{38}$$

These equations are identical to those derived by Le Méhauté [9,p1091] for both short wave and long wave and unidirectional models! When multiplied together, Goddet and Jaffry's [8] expression may be derived as well as Bijker's expression [6,V3-3] assuming n_α, the ripple factor scale, to approximate one. Model distortion introduces a requirement for additional roughness and Eq. 38 presupposes that all this additional roughness is added in the form of bottom roughness. There is also again a conflict between Eqs. 37 and 38 with respect to n_D. Eq. 38a is the basis for a common expression for model distortion developed by Yalin [2,p235]. From experiment it has been found that

$$C \sim \left(\frac{d}{D}\right)^{1/5}$$

Using Eqs. 5 and 38a it is possible to derive

$$N = n^{1/2} \quad \text{or} \quad n_x = n_z^{3/2} = n^{3/2} \tag{39}$$

Yalin [2,p236] has plotted values for model studies performed at Wallingford which substantiate Eq. 39. It may be noted in passing that Eq. 39 may be derived from Lacey's regime equations. These equations are based on erodible channels in an identical soil medium where the smaller channels form "models" of the larger channels. Le Méhauté [9] calls this the natural distortion and states it is only valid when prototype material is used in the model, i.e. when n_D and n_γ in Eq. 38 are equal to unity. The above development, however, indicates that this distortion can be generally accepted for all long wave models as long as all additional roughness is added to the bottom.

Most sediment transport problems do not present a flat bed and if the model is distorted, additional roughness must be added. Thus the total model roughness may be described as the sum of grain size roughness, bed form roughness and artificial roughness, i.e. $\tau = \tau_{k_s} + \tau_f + \tau_A$. The extra roughness may be added to the bottom or consist of vertical roughness elements. The use of the latter in sediment transport models may be open to question. Roughness strips will cause substantial scour in their immediate vicinity and also, roughness strips must be present in the original bottom before erosion has taken place. It is felt, however, that the addition of roughness to the bottom causes unacceptable conditions, since the additional roughness will greatly alter the bed forming process. Also if short waves are present, it causes exaggerated bottom boundary layers. Additional vertical roughness must undoubtedly consist of a close grid of small elements in order to bring the local scour problems to a minimum.

The shear acting on the bottom particles and causing sediment movement surely excludes the artificial roughness. Therefore it is a function of the actual bottom roughness distortion N_{k_s} or N_k depending on whether Assumption I or II is used. If Eq. 37 is not satisfied, Eqs. 4, 14, 15 and 19 yield

$$n_D = n^{-1/2} N_{k_s}^{-1/8} = n^{-1/3} \quad \text{or} \quad n_D = n^{-1/2} N_k^{-1/8} \tag{40}$$

$$n_k = m_k n_D = m_k n^{-1/3} \quad \text{or} \quad n_k = m_k^{8/9} n^{-1/3} \tag{41}$$

which leads in turn to

$$n_\tau = n N_{k_s}^{1/4} = n^{2/3} \quad \text{or} \quad n_\tau = n N_k^{1/4} = n^{2/3} m_k^{2/9} \tag{43}$$

$$n_D = n^{-1/2} N_{k_s}^{-1/8} = n^{-1/3} \quad \text{or} \quad n_D = n^{-1/2} N_k^{-1/8} = n^{-1/3} m_k^{-1/9} \tag{44}$$

$$n_{\gamma_s} = n^{3/2} N_{k_s}^{3/8} = n \quad \text{or} \quad n_{\gamma_s} = n^{3/2} N_k^{3/8} = n\, m_k^{1/3} \tag{45}$$

for Assumptions I and II respectively. Here m_k is the scale effect. It is again only possible to design a model for a single value of m_k, while in fact m_k is a function of the variation in the water depth d.

Some indication as to the value of N_k or m_k may be obtained from using Eqs. 11 which may be assumed to apply to both model and prototype. These yield

$$n_{\tau_{k_s}} \simeq m_{S_{k_s}} n_d = n N_{k_s}^{1/4} \tag{46}$$

$$n_{\tau_f} \simeq \frac{n_\Delta^2}{n_\Lambda} \tag{47}$$

Yalin [10,p242] indicates that Λ is a function of d and independent of D for dunes while ripples Λ is a function of D only. Also $\frac{\Delta}{\Lambda}$ depends slightly on excess shear but may be approximated as a constant for model and prototype with considerable sediment transport.

Similar to the case of short wave models, the scale for sediment transport may be derived as $n_q = m_q$.

MOBILE BED MODELS FOR COMBINED SHORT WAVES, LONG WAVES AND UNIDIRECTIONAL FLOW

From the foregoing discussion it appears that to combine short waves with the other two, vertical additional roughness elements are necessary in distorted models. In previous studies Bijker [6], Goddet and Jaffry [8] and Le Méhauté [9] inherently assume that all the shear necessary for the long wave model portion is supplied on the bottom, hence their scale relationships are variations of

$$n_\tau = n\, N^{-1} \quad ; \quad n_D = n^{-1/2}\, N^{1/2} \quad ; \quad n_{\gamma_s} = n^{3/2}\, N^{-3/2} \tag{48}$$

This results, however, in an undue distortion of the short wave boundary layer.

Bijker [6] has performed his experiments without additional roughness. This is the method used for most wave-current models. For this case he correctly suggests that in order to achieve the correct wave-current interaction, the long wave or unidirectional current velocities must be exaggerated. The bottom shear stresses, resulting from waves and currents, must be the same. This results in

$$n_{\bar{U}} = N^{1/2}\, N_k^{1/7}\, n_{U_\delta} \tag{49}$$

Bijker's relation [7-V3-2] is slightly more simplified and compares with Goddet and Jaffry [8].

The following scale relationships for combination models may be deduced from Eqs. 5,29,31 and 41 to 45.

$$\begin{aligned}
&n_H = n_d = n_z = n_Z = n_a = n_{a_\delta} = n \\
&n_x = n_y = N_X = N_Y = Nn \quad ; \quad N = f_N(\Theta, x_s) \\
&{}_s n_u = {}_s n_{U_\delta} = {}_\ell n_{\bar{U}} = {}_\ell n_U \simeq {}_s n_U = n^{1/2} \\
&{}_s n_L = n \quad ; \quad {}_\ell n_L = Nn \\
&{}_s n_t = {}_s n_T = n^{1/2} \quad ; \quad {}_\ell n_t = {}_\ell n_T = Nn^{1/2} \\
&n_C = N^{1/2} \quad ; \quad n_f = n_S = N^{-1}
\end{aligned} \tag{50}$$

These scales are based on the assumption that additional roughness is supplied to cause $n_c = N^{1/2}$. If no additional roughness is supplied, U must be exaggerated with respect to U_δ as outlined in Eq. 49.

For Assumption I, i.e. velocity distribution is a function of grain size

$$
\begin{aligned}
{}_s n_D &= n^{-5/16} & {}_\ell n_D &= n^{-1/3} \\
{}_s n_{\gamma_s} &= n^{15/16} & {}_\ell n_{\gamma_s} &= n \\
{}_s n_k &= {}_s m_k n^{-5/16} & {}_\ell n_k &= {}_\ell m_k n^{-1/3} \\
{}_s n_\tau &= n^{5/8} & {}_\ell n_\tau &= n^{2/3} \\
{}_s n_\delta &= n^{13/16} & & \\
{}_s n_q &= {}_s m_q & {}_\ell n_q &= {}_\ell m_q
\end{aligned}
\qquad (51)
$$

For Assumption II, i.e. velocity distribution is a function of the bed form and grain size

$$
\begin{aligned}
{}_s n_D &= n^{-5/16}\ {}_s m_k^{-1/8} & {}_\ell n_D &= n^{-1/3}\ {}_\ell m_k^{-1/9} \\
{}_s n_{\gamma_s} &= n^{15/16}\ {}_s m_k^{3/8} & {}_\ell n_{\gamma_s} &= n\ {}_\ell m_k^{1/3} \\
{}_s n_k &= {}_s m_k^{7/8}\ n^{-5/16} & {}_\ell n_k &= {}_\ell m_k^{8/9}\ n^{-1/3} \\
{}_s n_\tau &= n^{5/8}\ {}_s m_k^{1/4} & {}_\ell n_\tau &= n^{2/3}\ {}_\ell m_k^{2/9} \\
{}_s n_\delta &= n^{13/16}\ {}_s m_k^{1/8} & & \\
{}_s n_q &= {}_s m_q & {}_\ell n_q &= {}_\ell m_q
\end{aligned}
\qquad (52)
$$

It may be seen that although Eqs. 51 and 52 give slightly different scales, the short wave and long wave scales are quite close and relatively similar so that if either one is chosen, the other will not be very wrong, as long as the additional roughness is supplied by vertical roughness elements.

TIME

In Eq. 50, two time scales are given and these are the time scales used for the wave motion, the forcing mechanism in a mobile bed model. For the sediment transport, the list in Eq. 6 may be extended using the general time parameter t, resulting in a time scale for individual grain motion

$$ {}_i n_t = \frac{n_D}{n_{V_*}} $$

which when using Eq. 14 becomes

$$ {}_i n_t = n_D{}^2 = \frac{1}{n_{V_*}{}^2} \tag{53} $$

where n_{V_*} is a function of Assumption I or II and whether or not vertical roughness elements are used. When dealing with erosion or deposition, it is the volume eroded or deposited which determines the time scale. Therefore, using Eq. 28, recognizing that q refers to transport of solids:

$$ {}_e n_t = \frac{n_V n_{1-p}}{n_y n_q} = \frac{N^2 n^3}{N n m_q} n_{1-p} = \frac{N n^2}{m_q} n_{1-p} \tag{54} $$

where V is the total volume of material and p is the material porosity. m_q is different for the short wave and long wave portions of the model.

Similar time scales may be derived for other model transport phenomena such as movement of sand waves, transport of tracer materials, etc.

From Eqs. 50, 53 and 54 it may be noted that

$$ {}_e n_t > {}_\ell n_t > {}_s n_t > {}_i n_t \tag{55} $$

This is very fortunate. Changes in bed formation, erosion and accretion, are very long term processes. Because ${}_e n_t$ is so large, it is possible to perform model studies on these phenomena within a reasonable time.

BREAKERS AND LONGSHORE CURRENTS

Since sediment motion in a coastal mobile bed model is brought about mainly by the agitation of sediment in the breaker zone, it is

essential that conditions in this area are modelled correctly. The breaker position will be correct if $n_H = n_d$ and the refraction pattern will be correct if ${}_s n_L = n_d$ while the beach upon which the waves act will be modelled correctly if $N = f_N(\Theta, x_s)$. All these conditions are incorporated in Eq. 50. However, if a simplified littoral transport mechanism is envisioned, in which the waves stir up the material which is subsequently transported by the wave orbital motion and the longshore current, generated by the wave action, it is essential that

$$\frac{n_w}{{}_s n_u} = 1 \quad \text{and} \quad \frac{n_w}{n_{U_L}} = 1 \tag{56}$$

where U_L is the longshore current velocity and w is the fall velocity of the sediment particles.

Yalin [10,p69] shows $\frac{wD}{\nu}$ to be a function of $\frac{\gamma_s D^3}{\rho \nu^2}$. This is also stated by Valembois [3]. Using Eqs. 51 and 52 it may be seen that $\frac{n_{\gamma_s D^3}}{n_{\rho \nu^2}} = 1$, i,e, $\frac{n_{wD}}{n_\nu} = 1$ and thus for proper reproduction of fall velocity

$$n_w = n_D^{-1} \tag{57}$$

This relation has also been derived by Bonnefille [11].

Yalin [10,p71] also demonstrates that if the X and Y parameters on the Shields diagram are the same for model and prototype, i.e. Eqs. 14 and 15 are satisfied, then $\frac{w}{v_*} = \text{cst}$ which is the same as Eq. 57.

The above argumentation is based on spherical particles but could be extended to particles of any shape, as long as the shape factors in model and prototype are similar.

The conditions expressed in Eq. 56 must now be checked. The longshore current velocity U_L is generated by the waves and many formulas are proposed for the generation of longshore currents, e.g. Fan and Le Méhauté [12,p22]. Preliminary investigations into this area, Kamphuis [13] indicate that most of these formulations

fit laboratory results adequately but do not describe field results. The single factor that appears to influence the longshore current velocity most is the wave height. Results indicate that

$$U_L = \text{cst } (H)^{\eta} \tag{58}$$

where η lies between 0.5 and 1, and from Eqs. 50, 51, 52 and 57 it may be seen that Eq. 56 is approximately satisfied. It is not very fruitful to pursue this line of thought any further until additional research has shown more clearly what drives the longshore current velocity.

FOOD FOR THOUGHT

Throughout this paper the problem of the proportion of total shear going into sediment transport has been touched upon as a basic criterion for similarity in sediment transport. It has been suggested that the prototype and model points must fall on the same location of the Shields diagram. It is obvious that if the model falls below the Shields curve for initiation of motion, while the prototype falls above, the model will be useless, but it is not entirely clear when Eqs. 14 and 15 are satisfied, that the model will represent the prototype correctly. If the bed form is identical, α , the proportion of shear going into sediment transport should be the same and the model results should represent the prototype. If the bed form is different, α must be taken into account and the following scale laws may be developed from

$$\frac{n_\alpha \rho v_*^2}{\gamma_s D} = \frac{n_\alpha^{1/2} v_* D}{\nu} = 1 \tag{59}$$

Present sediment transport relationships for unidirectional flow are usually presented in a form related to

$$\frac{q}{v_* D} = f\left(\frac{\rho v_*^2}{\gamma_s D}\right) \tag{60}$$

i.e. a simple version of Eq. 27. The relationships apply to the turbulent region of the Shields curve and it is understood that v_*

is not the total shear. Therefore, to extend this system using the present terminology, it is possible to write

$$\frac{q}{\alpha^{1/2} v_* D} = f\left(\frac{\alpha^{1/2} v_* D}{\nu}, \frac{\rho \alpha v_*^2}{\gamma_s D}, \frac{\rho_s}{\rho}, \frac{\ell}{D}\right) \qquad (61)$$

The relationship between Y and X_1 and X_2 in Eq. 61 may be represented by a modified Shields diagram with axes X_1 and X_2 projected into a third dimension thus presenting a surface as shown in Fig. 1.

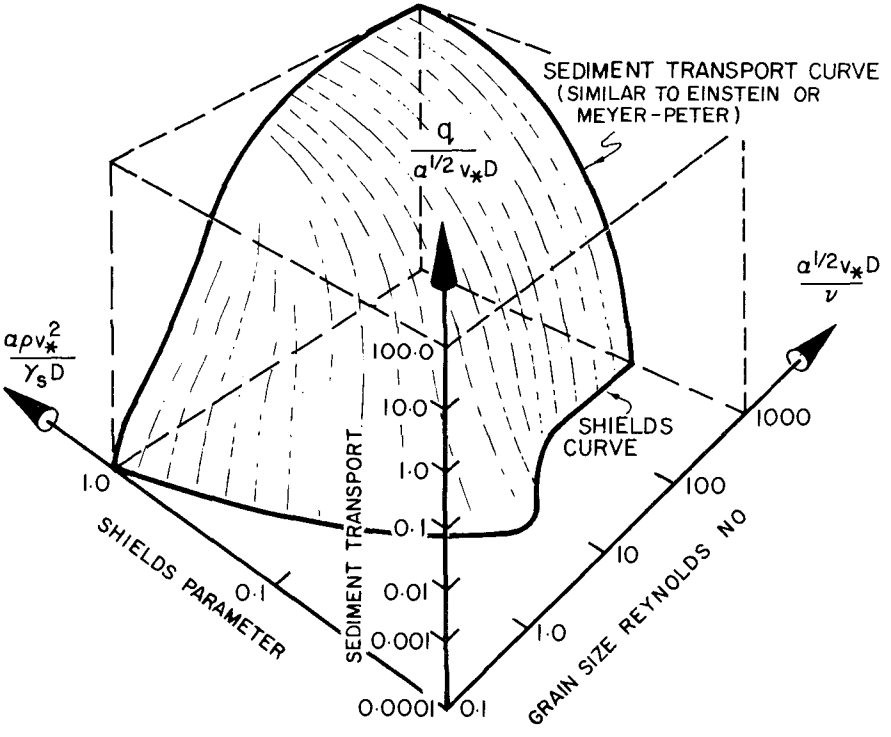

FIGURE 1 - SEDIMENT TRANSPORT SURFACE

This yields the more complete scaling laws

$$n_\alpha^{1/2}\, n_{v_*}\, n_D = 1 \quad ; \quad n_\alpha\, n_{v_*}^{2} = n_{\gamma_s}\, n_D \quad ; \quad n_q = n_\alpha^{1/2}\, n_{v_*}\, n_D$$

or

$$n_\alpha^{1/2}\, n_{v_*} = \frac{1}{n_D} \quad ; \quad n_{\gamma_s} = \frac{n_\alpha\, n_{v_*}^{2}}{n_D} = \frac{1}{n_D^{3}} \quad ; \quad n_q = 1 \qquad (62)$$

The above equations assume no scale effect in q and indicate that the derivations used in this paper are limited to $n_\alpha = 1$. The problem associated with the determination of α and n_α is of course the largest single problem in sediment transport study. It should be of prime concern, not only to the model builder, but also to the sediment transport student in general. Under oscillatory waves, the problem may be relatively simple and is very worthy of intensive investigation.

Finally it must be stated that Eqs. 27 and 61, concerned with sediment discharge are incomplete. These equations are essentially correct for unidirectional flow and long waves but for short oscillatory waves, sediment transport is highly dependent upon the asymmetry of particle accelerations, velocities and displacement. This asymmetry is a function of wave shape and relative depth d/L. The wave shape cannot be modelled in most cases; the relative depth in a propertly designed model is the same as in the prototype. Thus Eqs. 27 and 61 are adequate for scaling purposes, but the actual value of sediment transport under short waves lies considerably below the plane sketched in Fig. 1. Research underway at Queen's University indicates that under waves, sediment discharge is 1/2 - 10% of the value given by the Einstein function.

REFERENCES

1. Kamphuis, J.W., *'Scale Selection for Wave Models'* Queen's University, C.E. Report No. 7, Feb. 1972.

2. Yalin, M.S., *'Theory of Hydraulic Models'*, MacMillan, 1971.

3. Valembois, J., 'Etude sur la Modèle du Transport Littoral : Conditions de Similitude' *Coastal Engineering*, The Hague (1961), pp 277-307.

4. Mogridge, G.R., and Kamphuis, J.W., 'Experiments on Ripple Formation under Wave Action', *Coastal Engineering*, Vancouver, 1972.

5. Paul, M.J., Kamphuis, J.W., and Brebner, A., 'Similarity of Equilibrium Beach Profiles', *Coastal Engineering*, Vancouver, 1972.

6. Bijker, E.W., 'Some Considerations about Scales for Coastal Models with Movable Bed', *Delft Hydraulics Laboratory*, Publication No. 50, 1967.

7. Bijker, E.W., and Svasek, J.N., 'Two Methods for Determination of Morphological Changes Induced by Coastal Structures', Permanent International Association of Navigation Congress (PIANC), Paris, 1969, pp 181-202.

8. Goddet, J., and Jaffry, P., 'La Similitude des Transports de Sédiments sould l'Action Simultaneé de la Houle et des Courants' *La Houille Blanche*, 1960, No 2, pp 136-147.

9. Le Méhauté, B., 'Comparison of Fluvial and Coastal Similitude', *Coastal Engineering*, Washington, 1970, pp 1077-1096.

10. Yalin, M.S., *'Mechanisms of Sediment Transport'*, Pergamon Press, 1972 (in Press)

11. Bonnefille, R., 'L'utilization des Paramètres Adimensionnels dans l'Etude de l'Hydrodynamique des Sédiments' Deuxième thèse, Docteur es Sciences, Grenoble, 1968.

12. Fan, L.N., and Le Méhauté, B., 'Coastal Movable Bed Model Technology', *Tetra Tech*, Report No TC-131, 1969.

13. Kamphuis, J.W., 'Another Look at Longshore Currents', *Proceedings 15th Conference on Great Lakes Research*, Madison, Wisc., Apr. 1972.

14. Riedel, H.P., Kamphuis, J.W., and Brebner, A., "Measurement of Bed Shear Stress Under Waves', *Coastal Engineering*, Vancouver, 1972.

CHAPTER 64

MOVABLE-BED MODEL STUDIES OF PERCHED BEACH CONCEPT

by

C. E. CHATHAM, JR.

U. S. ARMY ENGINEER WATERWAYS EXPERIMENT STATION, VICKSBURG, MISSISSIPPI

ABSTRACT

Hydraulic model studies were conducted to aid in ascertaining the technical feasibility and optimum design factors of the perched beach concept. Among these were two-dimensional, movable-bed studies to determine an estimate of the amount of sand which would be lost seaward over the submerged toe structure by normal and storm wave action, the optimum elevation of the submerged toe structure, and the length of a stone blanket required to reduce seaward migration of sand to a minimum. The model beach was subjected to test waves until equilibrium was reached for a wide range of wave conditions for both the existing beach and the perched beach. Test results indicate that (a) little or no beachfill material will be lost seaward of the toe structure for normal wave conditions but the larger storm waves may cause erosion of the perched beach, (b) the installation of a stone blanket shoreward of the toe structure will reduce the amount of beach erosion, (c) if the beach fill is extended a sufficient distance seaward, the toe structure serves no useful purpose, and (d) a three-dimensional movable-bed model study is feasible and is necessary to determine the final design features of a perched beach.

INTRODUCTION

The concept of building a perched beach, that is, extending the berm of an existing beach seaward of its original position, has received favorable attention in recent years for the purpose of expanding or creating recreational areas and providing more coastal area for development. Since the beach profile in a given area is governed by the wave climate in that area, in a beach-fill project the existing profile must be reproduced for a considerable distance seaward if the fill is to be stable. The basic concept of the perched beach is to reproduce the existing beach profile to some convenient seaward point and then intersect this profile with a submerged toe structure to retain the beach in a perched position (see figure 1). Since turbulence induced by the oncoming waves as they travel over the submerged toe structure could transport quantities of beach material seaward, a stone riprap apron might be needed along the shoreward edge of the toe structure crest to reduce seaward migration of sand. In order to be effective, a perched beach must allow the natural littoral processes to continue without being supplemented by excessive beach replenishment.

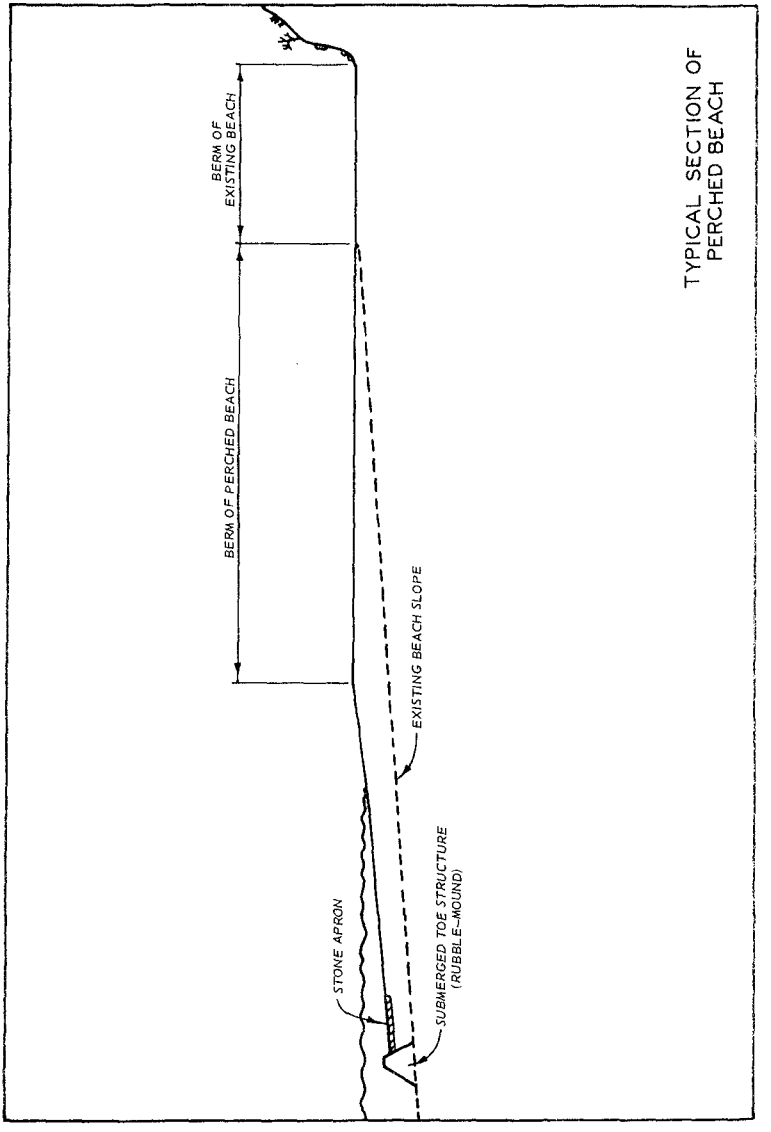
TYPICAL SECTION OF
PERCHED BEACH
BERM OF
EXISTING BEACH
BERM OF PERCHED BEACH
EXISTING BEACH SLOPE
STONE APRON
SUBMERGED TOE STRUCTURE
(RUBBLE-MOUND)

Figure 1

Hydraulic model studies were conducted to aid in ascertaining the technical feasibility and optimum design factors of the perched beach concept for a site in Santa Monica Bay, California. Among these were two-dimensional movable-bed studies to determine an estimate of the amount of sand which would be lost seaward over the toe structure by normal and storm wave action, the optimum crown elevation of the submerged structure, and the length of the stone riprap apron required to reduce seaward migration of sand to a minimum.

Scale models of hydraulic phenomena are essentially a means of replacing the analytical integration of the differential equations governing the process, including initial conditions and boundary conditions. However, before reliable information can be derived from scale models, the physical laws which cause the processes must be understood so that the relative magnitude of the forces involved remains the same.

A movable-bed model study guided by proper similitude relations and procedures can offer quantitative results which are vitally important in seeking an efficient engineering solution. In addition, by observing the display of the model, an investigator can develop a more concrete feeling of the nature of the problems which could not be achieved otherwise.

SELECTION OF SCALES

The perched beach movable-bed model was designed in accordance with the scaling relations developed by Noda (1971) which indicate a relationship or model law among the four basic scale ratios; the horizontal scale, vertical scale, sediment size ratio, and the relative specific weight ratio. These relations, which are valid mainly for the breaker zone, were determined experimentally using a wide range of wave conditions and beach materials. To determine the validity of the experimentally derived model law, Noda modeled a prototype dimension beach profile in the laboratory and comparisons of test results showed good correlation.

Using the scaling relations of Noda and the physical characteristics of the prototype sand at the perched beach site, a search was made of all readily available model beach materials, and possible model scales based on the characteristics of these materials were computed. Preliminary model tests were conducted using polystyrene (specific weight = 1.05) but this material proved to be too light and serious operational problems were encountered. Polystyrene was therefore abandoned and a quanity of crushed coal (specific weight = 1.30) was obtained. The model scales were computed as follows:

$\gamma_w = 1.00$ = specific weight of water

$\gamma_s = 2.65$ = specific weight of prototype sand

γ_c = 1.30 = specific weight of coal

$$\gamma'_s = \frac{\gamma_s - \gamma_w}{\gamma_w} = \frac{2.65 - 1}{1} = 1.65$$ = apparent specific weight of prototype sand

$$\gamma'_c = \frac{\gamma_c - \gamma_w}{\gamma_w} = \frac{1.30 - 1}{1} = 0.30$$ = apparent specific weight of coal

$$\eta_{\gamma'} = \frac{\gamma'_c}{\gamma'_s} = \frac{0.30}{1.65} = 0.182$$ = ratio of apparent specific weight

D_{proto} = 0.4 mm = median diameter of prototype sand

$$\eta_D = \frac{D_{model}}{D_{proto}}$$ = ratio of median diameters

λ = horizontal scale

μ = vertical scale

D_{model} = 0.55 mm = median diameter of available coal

$$\eta_D = \frac{0.55}{0.40} = 1.375$$

$$\mu^{0.55} = \eta_D \eta_{\gamma'}^{1.46} = 1.375\ (.182)^{1.46} \quad ;\ \mu = 0.0192 = 1/52 \text{ say } 1/50$$

$$\lambda = \mu^{1.32}\ \eta_{\gamma'}^{-0.35} = (.0192)^{1.32}\ (.182)^{-0.35} = .0098 = 1/102 \text{ say } 1/100$$

$$\Omega = \frac{1/50}{1/100} = 2$$ = model distortion using coal

To check the validity of the computed scales, equilibrium profile tests were conducted using coal as the beach material and the test results were compared with data from full scale tests run at the Coastal Engineering Research Center using natural sand as the beach material. Since these data were generally in good agreement, the computed scales were considered adequate for the movable-bed tests.

The two-dimensional movable-bed model was constructed in a 2-ft wide, 4.5 ft deep, 148-ft long wave flume. A flap-type wave generator capable

of generating waves with the required characteristics was positioned at the seaward end of the flume. Using coal as the beach material and the computed scales, average beach slopes were constructed between elevations of +20 and -60 ft.

SELECTION OF TEST CONDITIONS

Still-water levels (swl) for wave action models are selected so that the various wave-induced phenomena that are dependent upon water depths are accurately reproduced in the model. These phenomena include the refraction of waves, the overtopping of structures by the waves, the reflection of wave energy, and the transmission of wave energy through porous structures. The primary purpose of the movable-bed model was to determine the amount of beach fill material which would be lost seaward over the toe structure. Since the waves would break further seaward for lesser depths probably causing greater losses of material, a model (swl) of 0.0 mean lower low water (mllw) representing a low water stage was selected for these tests.

Measured wave data on which a comprehensive analysis of wave conditions could be based were unavailable for the Santa Monica Bay area. However, hindcast wave data were secured from deepwater stations 7 (National Marine Consultants) and A (Marine Advisers). The locations of these stations are shown in fig. 2. The data prepared by National Marine Consultants were computed in accordance with the theory of wave spectra and statistics as presented by Pierson, Neumann, and James. The data prepared by Marine Advisers were in accordance with Bretschneider's modification of the Sverdrup-Munk theory. Data for stations 7 and A were analyzed to establish the characteristics and estimated duration of deepwater sea and swell approaching the problem area from all directions clockwise from south to west. The deepwater wave data were then converted to shallow water data for use in the model by application of refraction and shoaling coefficients, and the results of this conversion are presented in table 1 for a depth of 60 ft. Since waves were to be generated from one direction (that normal to the beach) table 1 shows the estimated duration and magnitude of shallow water waves approaching the problem area from all directions combined. The following test waves were selected as being representative of those approaching the study area:

Selected Test Waves

Period, sec	Height, ft
7	5
7.9	10
10	3
10	8
10	14
11.3	12
16	4
16	8

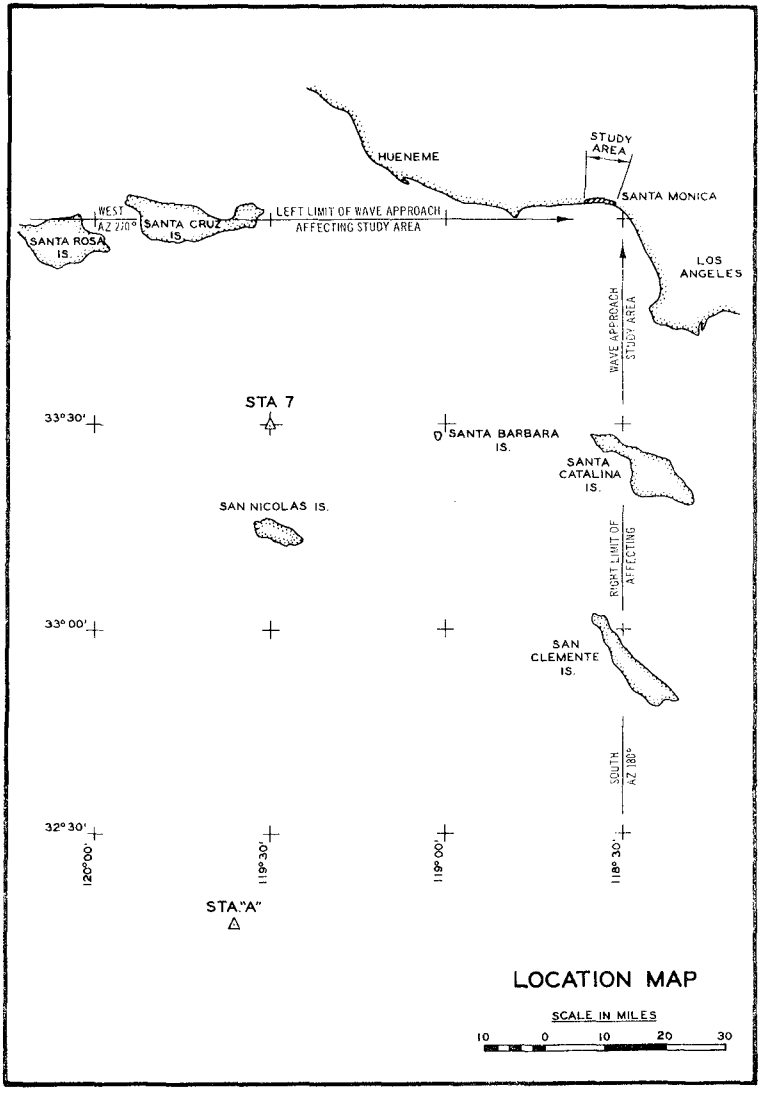
HUENEME
STUDY AREA
SANTA MONICA
LOS ANGELES
WEST
AZ 220°
SANTA CRUZ IS.
SANTA ROSA IS.
LEFT LIMIT OF WAVE APPROACH AFFECTING STUDY AREA
WAVE APPROACH STUDY AREA
STA 7
33°30'
SANTA BARBARA IS.
SANTA CATALINA IS.
SAN NICOLAS IS.
RIGHT LIMIT OF AFFECTING
33° 00'
SAN CLEMENTE IS.
SOUTH AZ 180°
32° 30'
120°00'
119°30'
119° 00'
118° 30'
STA "A"
LOCATION MAP
SCALE IN MILES
10 0 10 20 30

Figure 2

Table 1

Estimated Duration and Magnitude of Shallow-Water Waves (60-ft depth) Approaching Santa Monica Bay from all Directions (South to West)

Wave Height (ft)	Duration, hr/yr, for the Various Wave Periods (sec) at Station A										
	2-4	4-6	6-8	8-10	10-12	12-14	14-16	16-18	18-20	20-22	Total
0-0.9	395		27	47	10	612	342				1433
1-1.9	245		2	28	55	1387	982	100	29	11	2839
2-2.9		132	1	1	27	583	492	204	30	18	1488
3-3.9		159			3	91	151	118	10	2	534
4-4.9		64				13	46	99	12		234
5-5.9			22								22
6-6.9			71		9	1	3	18	1		103
7-7.9			20					9			29
8-8.9			18					1	2		21
9-9.9			1						1		2
10-10.9				3							3
11-11.9				2							2
12-12.9				1							1
TOTALS	640	355	162	82	104	2687	2016	549	85	31	6711

Wave Height (ft)	Duration, hr/yr, for the Various Wave Periods (sec) at Station 7								
	4-6	6-8	8-10	10-12	12-14	14-16	16-18	18+	Total
1-1.9	106	2	63	20	2	4			197
2-2.9	202	115	196	103	56	31	10	2	715
3-3.9	49	89	86	48	31	2	10	2	317
4-4.9		100	52	22	22	22			218
5-5.9		21	33	36	11	6	4		111
6-6.9		20	33	28					81
7-7.9			27	39	22	4			92
8-8.9			26		14	9			49
9-9.9			10	23					33
10-10.9					2	6	2		10
11-11.9				15					15
12-12.9					8				8
13-13.9				4					4
TOTALS	357	347	526	338	168	84	26	4	1850

MODEL TESTS AND RESULTS

The term "base test" as used herein denotes a test performed with existing prototype conditions installed in the model. Movable-bed tests were conducted for base test conditions and 8 variations in design elements of the proposed perched beach. Brief descriptions of the plans are given in the following subparagraphs.

a. Plan 1 consisted of a 700-ft wide perched beach (measured from the toe structure centerline to the 0.0 mllw contour) with the submerged toe structure located at the -25 ft contour and a crown elevation of -15 ft.

b. Plan 1A was the same as plan 1 with a 100-ft stone apron installed shoreward of the toe structure.

c. Plan 2 consisted of a 350-ft-wide perched beach with the submerged toe structure located at the -22-ft contour and a crown elevation of -10 ft.

d. Plan 2A was the same as plan 2 with a 100-ft stone apron installed shoreward of the toe structure.

e. Plan 3 consisted of an 1100-ft-wide perched beach with the submerged toe structure located at the -28-ft contour and a crown elevation of -20 ft.

f. Plan 3A was the same as plan 3 with a 100-ft stone apron installed shoreward of the toe structure.

g. Plan 4 consisted of a 700-ft-wide perched beach with no toe structure.

h. Plan 4A consisted of an 1100-ft-wide perched beach with no toe structure.

The movable-bed tests were conducted in the following manner. The movable-bed material (coal) was installed in the flume to correspond to one of the test plans. The wave generator was then started and allowed to run continuously until the beach profile had reached an equilibrium condition. The length of time required to reach equilibrium varied from 3 hours (model time) for the smaller waves to as much as 13 hours (model time) for some of the larger waves. Profiles were measured at regular intervals (usually hourly) to determine the bed evolution. Since initial tests indicated that

considerable wave energy was reflected from some of the steeper profiles, a wave filter was installed in front of the flap-type wave generator to dampen re-reflected waves.

The results of movable-bed tests with base test and plans 1 through 4A installed are presented in fig. 3-9. These data indicate that normal wave action on the perched beach caused no appreciable loss of beach fill, but for some of the larger storm waves, severe erosion of the perched beach occurred.

Tests to determine the effect of a 100-ft stone apron installed shoreward of the toe structure reveal that installation of such a structure in conjunction with a 700-ft perched beach (plan 1A) significantly reduced the amount of beach fill lost seaward. When installed with a 350-ft perched beach (plan 2A) however, the stone apron had little or no effect on beach erosion. When installed with an 1100-ft perched beach (plan 3A), the stone apron had a slight beneficial effect on reducing erosion, however, from a comparison of the data for base test, plan 3, and plan 3A, it appeared questionable whether the toe structure itself was beneficial in this location. Tests were therefore conducted with the toe structure removed (plan 4A) and these test results, when compared with those of plans 3 and 3A, indicated that the toe structure would have little or no beneficial effect on reducing beach erosion when located 1100-ft seaward of the 0.0 contour. Tests with the toe structure removed for the 700-ft perched beach (plan 4) revealed that beach erosion increased significantly without the toe structure.

From a comparison of all the data in fig. 3-9, it appears that plan 1A (700-ft perched beach, toe structure crown elev of -15 ft, and 100-ft stone apron) offers the greatest degree of protection to the perched beach fill of any of the plans tested.

While the overall test results using coal as a movable-bed material appear satisfactory, there are two inconsistencies which bear further discussion. The first of these is the behavior of the coal in the area above the swl. As can be seen from fig. 3-9, the amount of shoreward erosion between the 0.0 and +20 contours is inconsistent for several of the plans tested (especially for the larger waves). In addition, in some cases the profile at the shoreward limit of erosion is characterized by a vertical (or possibly undercut) bank as much as 20 ft high. This is probably due to a discrepancy in the moisture content of the coal above the water line as compared to the prototype sand (the coal appears to be more cohesive in this area). This inconsistency should be kept in mind when examining the data in fig. 3-9 and a more accurate evaluation can probably be drawn by considering only that portion of the profile which is below the swl. The second inconsistency is the formation of a series of bars seaward of the toe structure for the 16 second test waves (fig. 8 and 9). It was known, prior to the use of coal in the present study, that it had a tendency to form unrealistic ripples or waves

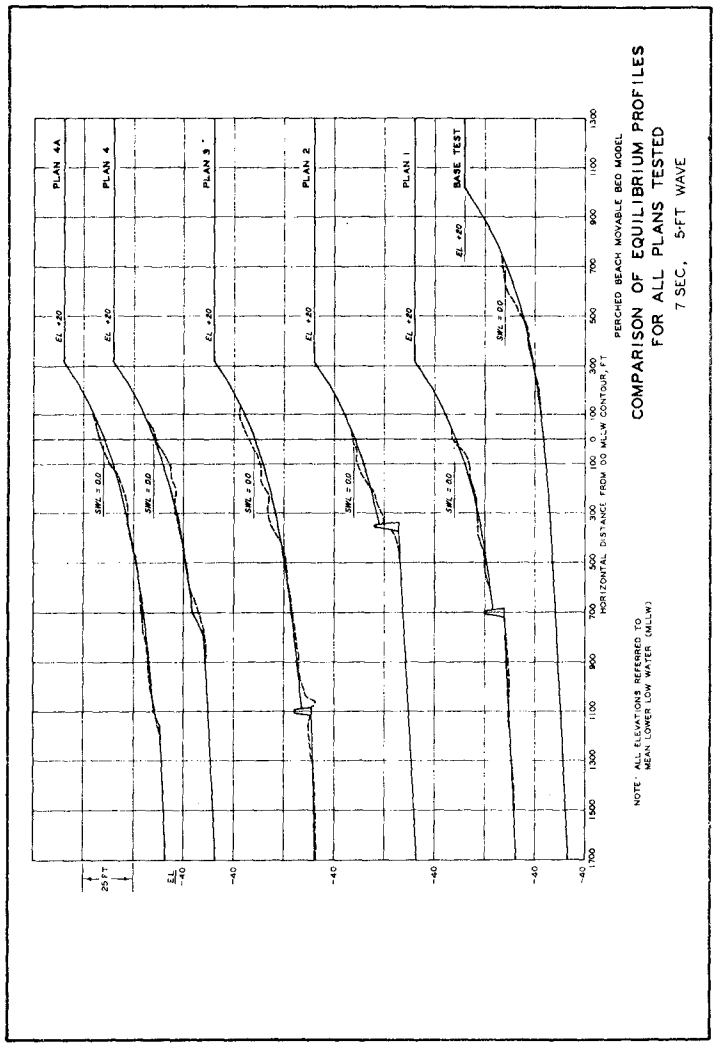
COMPARISON OF EQUILIBRIUM PROFILES
FOR ALL PLANS TESTED
7 SEC, 5-FT WAVE
PERCHED BEACH MOVABLE BED MODEL
PLAN 4A
PLAN 4
PLAN 3
PLAN 2
PLAN 1
BASE TEST
EL +20
SWL = 0.0
HORIZONTAL DISTANCE FROM 0.0 MLW CONTOUR, FT
NOTE: ALL ELEVATIONS REFERRED TO MEAN LOWER LOW WATER (MLLW)

Figure 3

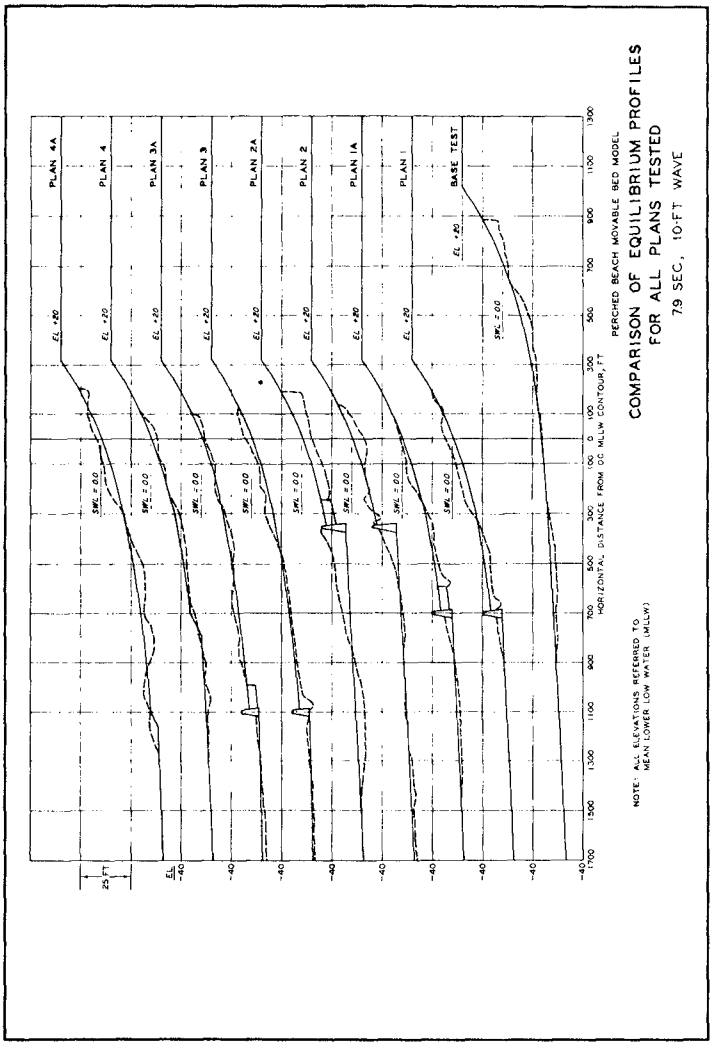
COMPARISON OF EQUILIBRIUM PROFILES
FOR ALL PLANS TESTED
7.9 SEC., 10-FT WAVE
PERCHED BEACH MOVABLE BED MODEL
HORIZONTAL DISTANCE FROM 0C MLLW CONTOUR, FT
NOTE: ALL ELEVATIONS REFERRED TO MEAN LOWER LOW WATER (MLLW)
PLAN 4A
PLAN 4
PLAN 3A
PLAN 3
PLAN 2A
PLAN 2
PLAN 1A
PLAN 1
BASE TEST
EL +20
SWL +0.0
SWL +2.0
SWL +2.00
25 FT
EL -40

Figure 4

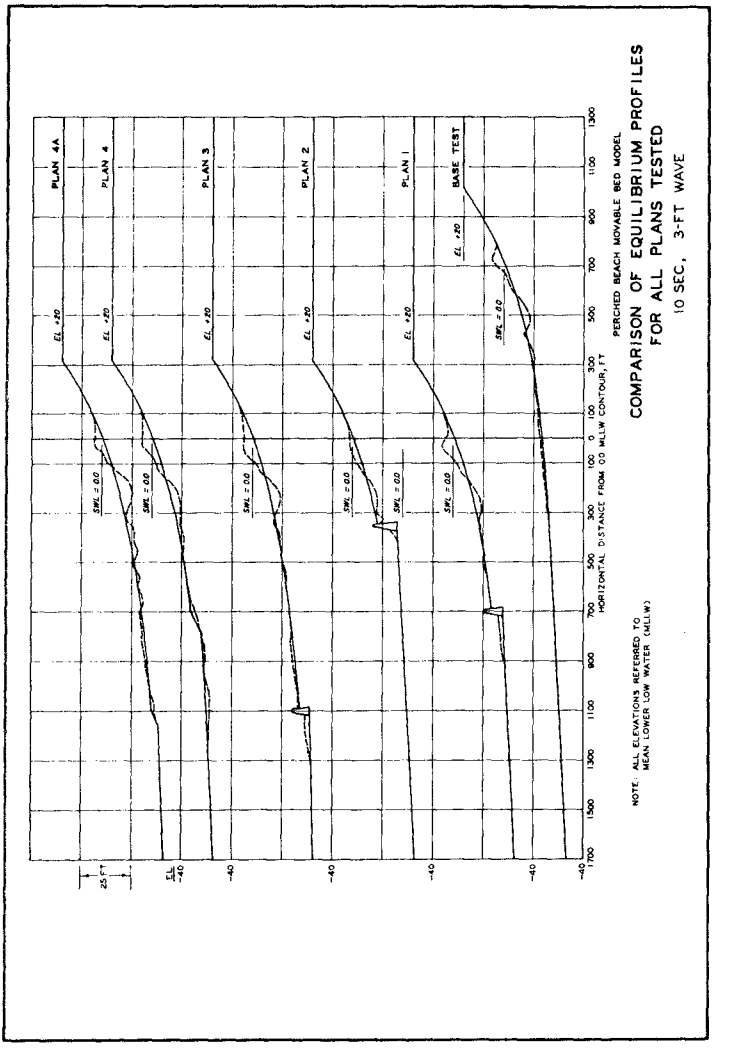
COMPARISON OF EQUILIBRIUM PROFILES
FOR ALL PLANS TESTED
10 SEC, 3-FT WAVE
PERCHED BEACH MOVABLE BED MODEL
HORIZONTAL DISTANCE FROM 0.0 MLLW CONTOUR, FT
NOTE: ALL ELEVATIONS REFERRED TO MEAN LOWER LOW WATER (MLLW)
PLAN 4A
PLAN 4
PLAN 3
PLAN 2
PLAN 1
BASE TEST
EL +20
SWL = 0.0
EL -40
25 FT

Figure 5

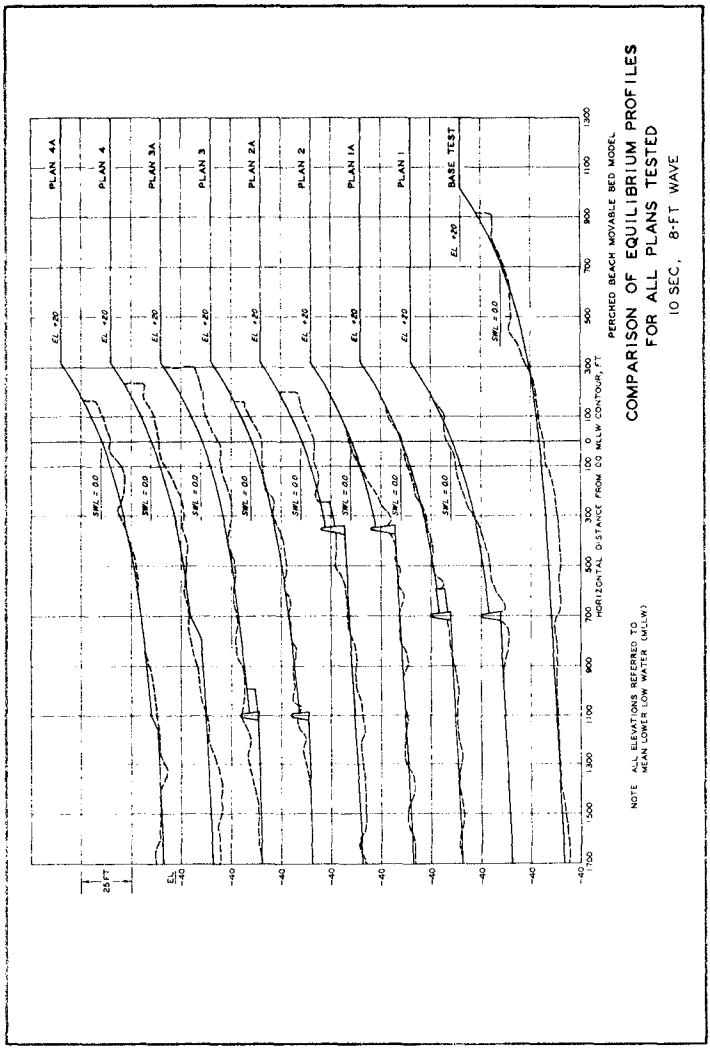
COMPARISON OF EQUILIBRIUM PROFILES
FOR ALL PLANS TESTED
10 SEC, 8-FT WAVE
PERCHED BEACH MOVABLE BED MODEL
HORIZONTAL DISTANCE FROM 0.0 MLLW CONTOUR, FT
NOTE ALL ELEVATIONS REFERRED TO MEAN LOWER LOW WATER (MLLW)
PLAN 4A
PLAN 4
PLAN 3A
PLAN 3
PLAN 2A
PLAN 2
PLAN 1A
PLAN 1
BASE TEST
EL +20
SWL = 0.0
EL -40
25 FT

Figure 6

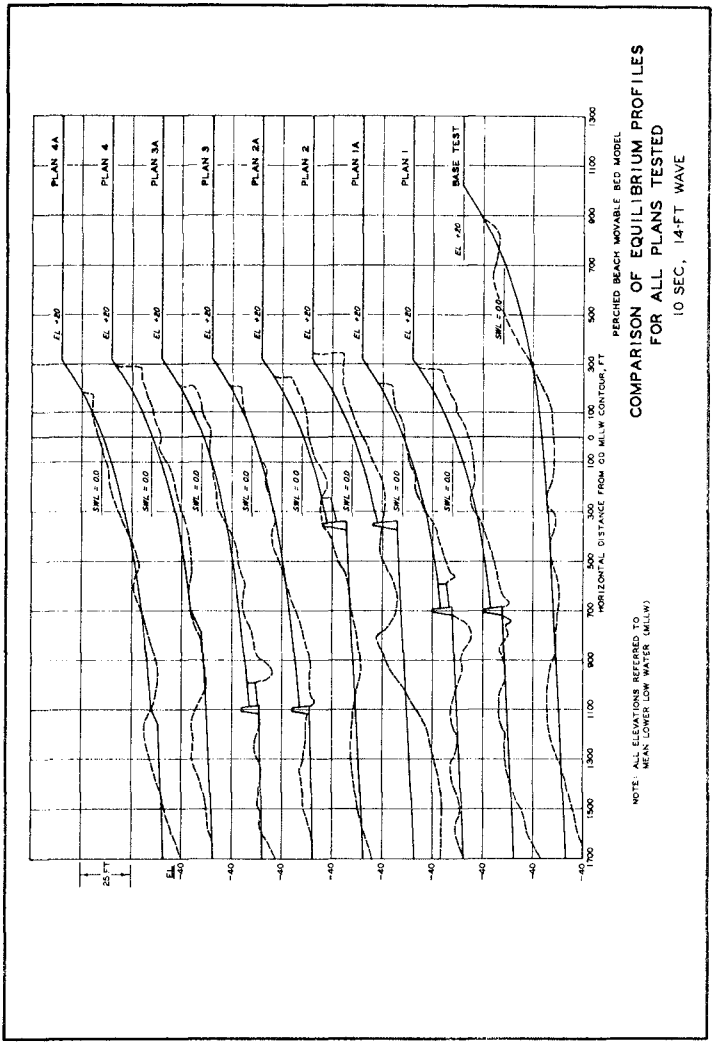
COMPARISON OF EQUILIBRIUM PROFILES
FOR ALL PLANS TESTED
10 SEC, 14-FT WAVE
PERCHED BEACH MOVABLE BED MODEL
HORIZONTAL DISTANCE FROM 0.0 MLLW CONTOUR, FT
NOTE: ALL ELEVATIONS REFERRED TO MEAN LOWER LOW WATER (MLLW)
PLAN 4A
PLAN 4
PLAN 3A
PLAN 3
PLAN 2A
PLAN 2
PLAN 1A
PLAN 1
BASE TEST
EL. +20
SWL = 0.0
SWL = 2.0
2.5 FT

Figure 7

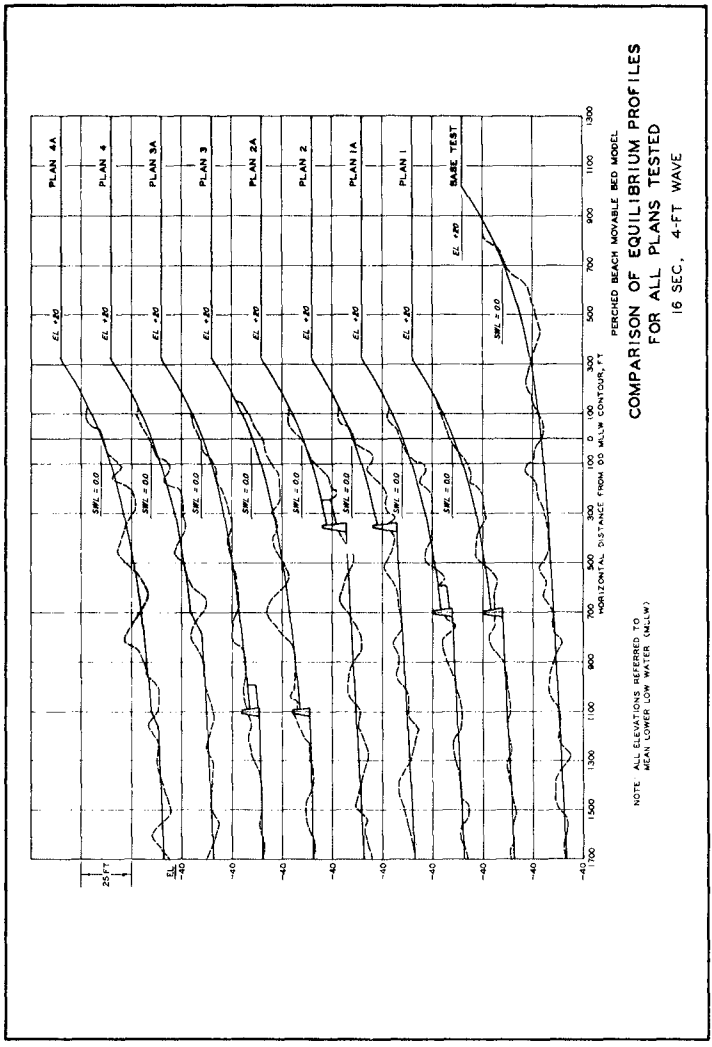
COMPARISON OF EQUILIBRIUM PROFILES
FOR ALL PLANS TESTED
16 SEC, 4-FT WAVE
PERCHED BEACH MOVABLE BED MODEL
HORIZONTAL DISTANCE FROM 0.0 MLLW CONTOUR, FT
NOTE ALL ELEVATIONS REFERRED TO
MEAN LOWER LOW WATER (MLLW)
PLAN 4A
PLAN 4
PLAN 3A
PLAN 3
PLAN 2A
PLAN 2
PLAN 1A
PLAN 1
BASE TEST
EL +20
SWL = 0.0
SWL = 2.00
25 FT
EL -40

Figure 8

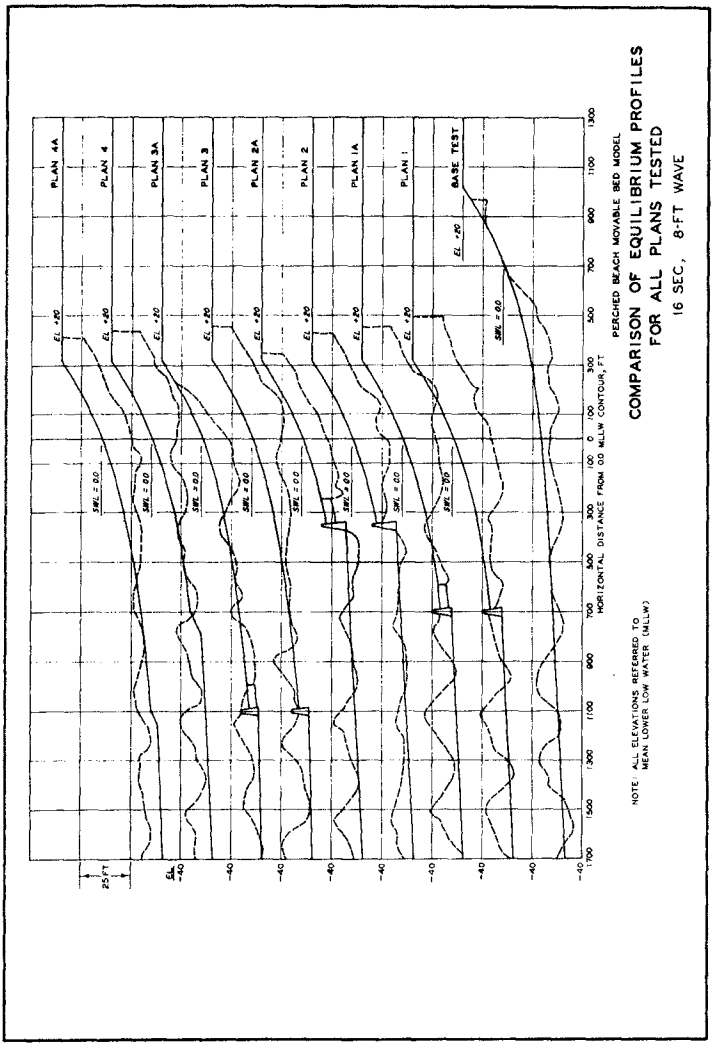
COMPARISON OF EQUILIBRIUM PROFILES
FOR ALL PLANS TESTED
16 SEC, 8-FT WAVE
PERCHED BEACH MOVABLE BED MODEL
HORIZONTAL DISTANCE FROM 0.0 MLLW CONTOUR, FT
NOTE: ALL ELEVATIONS REFERRED TO MEAN LOWER LOW WATER (MLLW)
PLAN 4A
PLAN 4
PLAN 3A
PLAN 3
PLAN 2A
PLAN 2
PLAN 1A
PLAN 1
BASE TEST
EL +20
SWL = 0.0
SWL = 0.5
25 FT

Figure 9

for higher velocity oscillatory flow (longer period, larger amplitude waves); however, the wave statistics at the Santa Monica location reveal a relatively mild wave climate, and since coal was available it was an expedient choice for the present study. It was found that coal would be satisfactory except for the longer period waves which have a low frequency of occurrence.

THREE-DIMENSIONAL MOVABLE-BED MODELS

Prior to performing a three-dimensional movable-bed model investigation, additional wave-flume tests are needed using various materials with a specific gravity range from 1.3 to 1.6 to aid in the selection of a suitable beach material. Another problem which must be analyzed during the two-dimensional tests is the size distribution of the model material. If Noda's scale relations are accepted without modification, any appreciable size distribution in the prototype will be difficult to scale correctly in the model (at certain scales) due to the sensitivity of the calculated model scales to variations in particle size. This means that one must either show that the size distribution is essentially a delta function or else the particle size distribution in the prototype has a negligible effect on the onshore-offshore transport as well as the littoral transport. It is believed that the answer to the problems lies somewhere in between these two elements. That is, the scale relations should not be quite so sensitive to particle size and, hopefully for a specific location, the size distribution will not have a large effect on the erosion and accretion characteristics of the beach.

It is well known that quantitative three-dimensional movable-bed model investigations are difficult to conduct and each area where such an investigation is contemplated must be carefully analyzed. The following computations and prototype data are considered essential for such investigations:

a. A computation of the littoral transport based on the best available wave statistics.

b. An analysis of the sand size distribution over the entire project area (offshore to a point well beyond the breaker zone).

c. Simultaneous measurement of the following items over a period of erosion and accretion of the shoreline (this measurement period should be judiciously chosen to obtain the maximum probability of both erosion and accretion during as short a time span as possible):

(1) Continuous measurements of the incident wave characteristics. This means enough sensors to obtain accurate estimates of the directional spectrum over the entire project area and a detailed analysis of these data.

(2) Bottom profiling of the entire project area using the shortest time intervals possible.

(3) Nearly continuous measurements of both littoral and onshore-offshore transport of sand. This is especially important over the erosion-accretion period. A wave forecast service is essential to this effort in order to be prepared for full operation during the erosion period.

Upon verification of the model based on the data acquired, one should then be prepared to evaluate the effectiveness of various project plans. A quantitative three-dimensional movable-bed model investigation of littoral transport is feasible and should be successful provided it is approached in the manner prescribed and provided adequate prototype data are acquired. Insofar as is known, prototype data to the extent described above have never been acquired; however, it is certainly within the state of the art to obtain such data. Admittedly the measurement of littoral and onshore-offshore transport will be most difficult, but it is felt that such measurements can be made with sufficient accuracy for model verification. It should be noted that the prototype data acquisition would include measurements of the size and intensity of rip currents in the prototype area and, if they persevere to any appreciable degree, measurements of the amount of material moved seaward in the rips would be obtained as a part of the overall data.

CONCLUSIONS

Based on the results of the two-dimensional hydraulic model studies, it is concluded that:

a. Normal wave action on the perched beach will cause no appreciable loss of beach fill.

b. For the larger storm waves, severe erosion of the perched beach may be expected.

c. The installation of a 100-ft stone apron in conjunction with a 350-ft perched beach (plan 2A) will have little or no effect on reducing beach erosion.

d. The installation of a 100-ft stone apron in conjunction with a 700-ft perched beach (plan 1A) will significantly reduce the amount of beach erosion.

e. If the beach fill is extended as far as 1100 ft seaward of the 0.0 mllw contour, the toe structure itself will have little or no beneficial effect on reducing beach erosion.

f. Of all plans tested, plan 1A (700-ft perched beach with -15-ft toe structure crown elev and 100-ft stone apron) appears to offer the greatest degree of protection against erosion of beach fill material.

g. Additional wave flume tests are needed in the specific gravity range from 1.3 to 1.6 prior to performing a three-dimensional movable-bed model investigation.

h. Provided adequate prototype data are available for use in model verification, a three-dimensional movable-bed model investigation of the perched beach is feasible and should result in a valid indication of the relative merits of various project designs.

ACKNOWLEDGEMENTS

The tests described and the resulting data presented herein were obtained from research conducted in connection with a contract between the Corps of Engineers (represented by the Los Angeles District) and the California Division of Highways (who provided the funding). We gratefully acknowledge the help and guidance provided by Messrs. C. H. Fisher and H. D. Converse of the Los Angeles District, Mr. T. Inuzuka of the Division of Highways, and Professor J. W. Johnson and Dr. D. L. Inman, Consultants for the Division of Highways. Permission was granted by the Chief of Engineers to publish this information.

REFERENCES

1. U. S. Army Engineer District, Los Angeles, CE, "Feasibility Study of Proposed Marine Locations for State Highway Route 60 and Their Shoreline Effects," August 1963.

2. Fan, L., and B. Le Méhauté, "Coastal Movable-Bed Scale Model Technology,: Tetra Tech No. TC-131, Pasadena, California, June 1969.

3. Noda, E. K., "Coastal Movable-Bed Scale Model Relationship," Tetra Tech No. TC-191, Pasadena, Calif., March 1971.

4. U. S. Army Engineer, Beach Erosion Board, CE. "The Source Transportation and Deposition of Beach Sediment in Southern California," Tech. Memo No. 22, March 1951.

5. U. S. Army Coastal Engineering Research Center, CE, "Shore Protection Planning and Design," Technical Report No. 4, 3rd ed, 1966 , Washington, D. C.

6. National Marine Consultants, Wave Statistics for Seven Deep Water Stations Along the California Coast," December 1960, Santa Barbara, Calif.

7. Marine Advisers, "A Statistical Survey of Ocean Wave Characteristics in Southern California Waters," La Jolla, Calif., Jan 1961.

8. Pierson, W. J., Jr., G. Neumann, and R. W. James, "Practical Methods for Observing and Forecasting Ocean Waves by Means of Wave Spectra and Statistics," 1953, Research Division, College of Engineering, New York University, New York.

9. Kamphuis, J. W., "Scale Selection for Wave Models," C.E. Research Report No. 71, Feb 72, Dept of Civil Engineering, Queens University, Kingston, Ontario.

10. Le Méhauté, B., "Theory, Experiments, A Philosophy of Hydraulics," Journal of Hydraulics Division, Vol. 88 Hy 1, Proc. of ASCE, pp 45-66, Jan 1962.

11. Nyak, I. V. "Equilibrium Profiles of Model Beaches" University of California, Berkeley, May 1970.

CHAPTER 65

SIMILARITY OF EQUILIBRIUM BEACH PROFILES

M.J. Paul[1], J.W. Kamphuis[2], and A. Brebner[3]

ABSTRACT

In the design of mobile bed coastal models it is inherently assumed that prototype beach processes may be modelled using lightweight sediment. At the Queen's University Coastal Engineering Research Laboratory, a long range project is currently in progress to determine scaling laws and scale effect for mobile bed coastal models. A large portion of this program is directly concerned with beach profiles and in this paper preliminary work is reported, in which a comparison is made between two dimensional laboratory beach profiles obtained from controlled "prototype", undistorted model and some distorted model tests.

INTRODUCTION

A recent publication by Nayak (1970) provides a bibliography of the work on beach profiles to date, and summarises the conclusions drawn by several investigators. Fundamental differences in definition and experimental conditions make it extremely difficult to compare the data accumulated, and in previous work very little attempt has been made to achieve model similarity for the physical processes of beach formation which is required before a valid comparison can be made with prototype data.

This paper concerns itself with the derivation and use of reasonable scale laws for modelling equilibrium beaches. In practical cases, it is seldom possible to adhere strictly to all scale laws. This causes errors between the prototype and the model, which are a direct result of non-adherance to certain scale laws. These errors

---

1. Engineer, Public Works Department of Western Australia, Formerly Research Associate, Queen's University at Kingston.
2. Associate Professor of Civil Engineering,
3. Professor and Head of Civil Engineering, Coastal Engineering Research Laboratory, Queen's University at Kingston, Canada.

are called "scale effect" in this paper and some causes and types of scale effect are discussed.

DIMENSIONAL ANALYSIS

Two phase phenomena in the vicinity of a mobile bed may be expressed as a function of

$$\rho,\ \nu,\ \gamma_s,\ D,\ \rho_s,\ \ell,\ v_*$$

where ρ is the fluid density, ν the kinematic viscosity of the fluid γ_s the submerged unit weight of the sediment, D a general length parameter which specifies the overall particle geometry, ρ_s the sediment density, ℓ a general length parameter describing the fluid motion at the bed, and v_* a typical shear velocity. For more detail see Yalin (1971) and Kamphuis (1972).

For beach profiles formed by short waves ℓ may be replaced by the wave orbital amplitude at the bed, a_b . The shear velocity v_* is time varying and is characterised here by $\hat{v}_*$, the maximum shear velocity during the wave cycle. Particle geometry cannot be adequately described by a limited number of parameters, however, in order to draw attention to the most important ones, the general length parameter D is defined as

$$D = f\,(D_{50},\ \sigma_\Phi,\ \alpha)$$

where D_{50} is the sediment median grain size, σ_Φ the standard deviation of its Φ size distribution, and α the natural angle of repose. The beach profile P , may now be expressed as

$$P = f\,(\rho,\ \nu,\ \gamma_s,\ D_{50},\ \sigma_\Phi,\ \alpha,\ \rho_s,\ a_b,\ \hat{v}_*,\ i_o,\ ) \qquad (1)$$

where i_o is the initial beach slope. Equation 1 may be rewritten in the dimensionless form

$$\Pi_p = \Phi\left(\frac{D_{50}\hat{v}_*}{\nu}\ ,\ \frac{\rho\hat{v}_*^{\,2}}{\gamma_s D_{50}}\ ,\ \sigma_\Phi,\ \alpha\ ,\ \frac{\rho_s}{\rho}\ ,\ \frac{a_b}{D_{50}}\ ,\ i_o\ \right) \qquad (2)$$

In determining practical model scale laws, it is desirable to

eliminate a_b and $\hat{v}_*$ since they vary with location and are almost impossible to measure.

Equation 2 may be rewritten - Paul (1972) - as

$$\Pi_p = \Phi \left(\frac{D_{50}\sqrt{gH_o}}{\nu}, \frac{\rho g H_o}{\gamma_s D_{50}}, \sigma_\Phi, \alpha, \frac{\rho_s}{\rho}, \frac{D_{50}}{L_o}, \frac{H_o}{L_o}, \frac{d}{L_o}, i_o \right) \qquad (3)$$

and the maximum shear velocity $\hat{v}_*$ has effectively been replaced by $\sqrt{gH_o}$.

SCALE LAWS

Since in practice it is necessary to use water in both model and prototype $n_\rho = n_\nu = n_g = 1$, where n is the scale expressed as prototype value over model value. From Equation 3 the following scale laws may be derived

$$n_{D_{50}} = n_{H_o}^{-\frac{1}{2}} \qquad (4) \qquad n_{H_o} = n_{\gamma_s} n_{D_{50}} \qquad (5)$$

$$n_{\rho_s} = n_\rho = 1 \qquad (6) \qquad n_{D_{50}} = n_{L_o} \qquad (7)$$

$$n_{H_o} = n_{L_o} = n_d = n_z \qquad (8) \qquad n_{\sigma_\Phi} = n_\alpha = n_{i_o} = 1 \qquad (9)$$

Equations 4 and 5 yield conflicting values for $n_{D_{50}}$ since 4 is essentially derived from a Reynolds number while 5 is derived from a Froude number (a type of Shields parameter). This familiar situation is discussed in detail in Kamphuis (1972). One case which has a simple solution occurs when the particle Reynolds number is large enough to ensure turbulent flow around the grains in both model and prototype. Then the influence of fluid viscosity is negligible and Equation 4 may be ignored. Equation 6 implies that lightweight sediments cannot be used, while Equation 7 indicates that particle sizes must be scaled down geometrically. The non-similarity of Equation 4 is then considered to cause scale effect. This type of model is very limited because Equation 7 quickly results in model particles in the silt and clay range, subject to suspension and electro-chemical charges.

If the particle Reynolds number is not in the turbulent range, one expedient often used is to neglect similarity of ρ_s/ρ and D_{50}/L_o, i.e.

lightweight sediment is used (Fan and Le Mehaute, 1969; Yalin, 1971; Kamphuis 1972). Thus Equations 4, 5, 8 and 9 form a basis for the design of practical scale models using lightweight sediments while the non-similarity of ρ_s/ρ and D_{50}/L_o is considered to cause "scale effect".

For a laboratory beach model, the only water depth d, over which control can be maintained is the limiting depth at the toe of the beach d_T. Thus of necessity Equation 8 has been restricted to $n_{d_T} = n_z$. This equation and $n_i = 1$, often are not satisfied when different laboratory tests are compared. Since these scale laws may be important (Paul, 1972) it is difficult to make a valid comparison between different beach profiles reported in the literature. It is generally also difficult to exercise any real control over the variable α, and thus $n_\alpha \neq 1$ contributes to "scale effect". The requirement $n_{\sigma_\phi} = 1$ is a rough indication that the shape of the grain size distribution curves for the model and prototype sediment should be similar. This can be achieved by proper mixing of materials.

EXPERIMENTAL INVESTIGATION

In order to determine the validity of the scale laws derived and the scale effects introduced by non-similarity of the various dimensionless variables, several series of two dimensional equilibrium beach profiles were tested using both lightweight and natural beach materials. Coarse sand, coarse bakelite, fine sand, fine bakelite were used and the largest beach which reasonably could be constructed in the laboratory wave flume using coarse sand, was defined as the prototype. Waves of constant period, $T_1 = 1.71$ sec, were generated in a water depth $d_T = 0.68$ m, corresponding to a fixed ratio $d_T/L_o = 0.15$. These waves impinged on an initial beach slope of 1:10, for sufficient time to form an equilibrium profile. Separate tests were undertaken at fixed values of deep water wave steepness H_o/L_o ranging from 0.016 to 0.040, the upper limit being controlled by wave stability in the flume.

The test series, using coarse bakelite and fine sand were defined as models of the coarse sand prototype. The lightweight bakelite models followed the scale laws expressed by Equations 4, 5, 8 and 9, which agree with those proposed by Fan and Le Mehaute (1969) and Yalin (1971) for a distortion, N = 1; the fine sand models were based on the

assumption that the grain size Reynolds number was in the turbulent range and thus followed Equations 5 to 9 . One additional series of tests was completed in which fine bakelite, modelled a fine sand prototype, just as the coarse bakelite modelled the coarse sand prototype. This was intended to provide an additional check on the validity of the scale laws proposed for the use of lightweight sediments. The variables involved are listed in Table 1, while the resulting values of the Reynolds numbers and Shields parameters for the various tests are listed in Table 2.

All tests were carried out in a 50 m long x 1,20 m deep x 0,60 m wide wave flume at the Queen's University Coastal Engineering Research Laboratory. A flap type wave generator was used which could be adjusted to produce waves of any desired height compatible with the practical range of wave periods, 0.6 - 2.0 secs. Wave heights were measured immediately seaward of the toe of the beach slope, using a capacitance type proximity probe. They were recorded on chart paper, at the beginning and immediately before the completion of each test. An average wave height H_1, allowing for wave reflection, was determined by moving the wave gauge, mounted on a level trolley system, along the flume centreline for a distance of at least one half a wave length at a speed of approximately 20 mm/sec. Since the waves were generated in shallow water (d_T/L_o = 0.15) allowance was made for shoaling in the determination of a deep water wave height H_o from the measured wave height H_1.

The sand beach profiles reached equilibrium within 24 hours, but were run for at least 36 hours, the bakelite beach profiles reached equilibrium within 6 hours, and were run for 12 hours. Each beach profile was measured with a blunt point gauge (10 mm dia tip) along the flume centreline. Ripples covered a portion of the beach profile following most tests. Where these were particularly prominent their heights and lengths were measured. Otherwise the profile recorded was an envelope of the ripple crests. The beach profile data were plotted in the dimensionless form x/L_o versus z/L_o, where x is the horizontal distance measured from an intersection between the initial profile and mean water level, and z is the vertical distance above mean water level.

In Figures 1, 2 and 3, the different model beach profiles are compared with their corresponding prototype beach profiles. For both coarse and fine lightweight bakelite models (Figures 1 and 2) a

TABLE 1

Comparison between variables for the different beach profile test series

Variable	Coarse Sand (Series 4)	Coarse Bakelite (Series 7)	Fine Sand (Series 5)	Fine Bakelite (Series 6)
γ_s (kg/m^3)	1710	600	1670	600
D_{50} (mm)	0.63	0.91	0.357	0.525
d_T (m)	0.68	0.34	0.38	0.19
T_1 (sec)	1.71	1.20	1.29	0.91
L_o (m)	4.54	2.26	2.57	1.28
Av. water temp. (^{o}C)	19.5	9.9	18.7	20.4
ν(cm^2/sec; stokes)	1020	1300	1040	1000
ρ_s/ρ	2.71	1.60	2.67	1.60
$(D_{50}/L_o)x10^5$	13.8	40.0	13.8	40.7
d_T/L_o	0.15	0.15	0.15	0.15
σ_Φ	0.667	0.653	0.458	0.550
α(in water)	33^{o}20'	37^{o}40'	32^{o}50'	37^{o}50'
i_o	0.10	0.10	0.10	0.10

Table 2

Variation of the dimensionless variables $X_2 = \frac{\rho g H_o}{\gamma_s D_{50}}$ and $X_1 = \frac{D_{50}\sqrt{gH_o}}{\nu}$ with wave steepness H_o/L_o

H_o/L_o	Coarse Sand (Series 4)			Coarse Bakelite (Series 7)			Fine Sand (Series 5)			Fine Bakelite (Series 6)		
	H_o(ft)	X_2	X_1	H_o(ft)	X_2	X_1	H_o(ft)	X_2	X_1	H_o(ft)	X_2	X_1
0.016	0.240	67.9	523				0.136	68.1	219	0.068	65.6	236
0.020	0.300	84.9	593	0.149	83.3	466	0.169	86.7	244	0.085	82.0	264
0.025	0.375	106.1	653	0.187	104.2	521	0.212	108.3	273	0.106	102.4	295
0.030	0.450	127.4	715	0.224	125.0	571	0.254	130.0	299	0.127	122.9	324
0.040	0.600	169.8	832	0.299	166.7	660	0.339	173.3	346	0.169	163.9	374
0.050				0.373	208.3	737						
0.060				0.448	249.9	808						

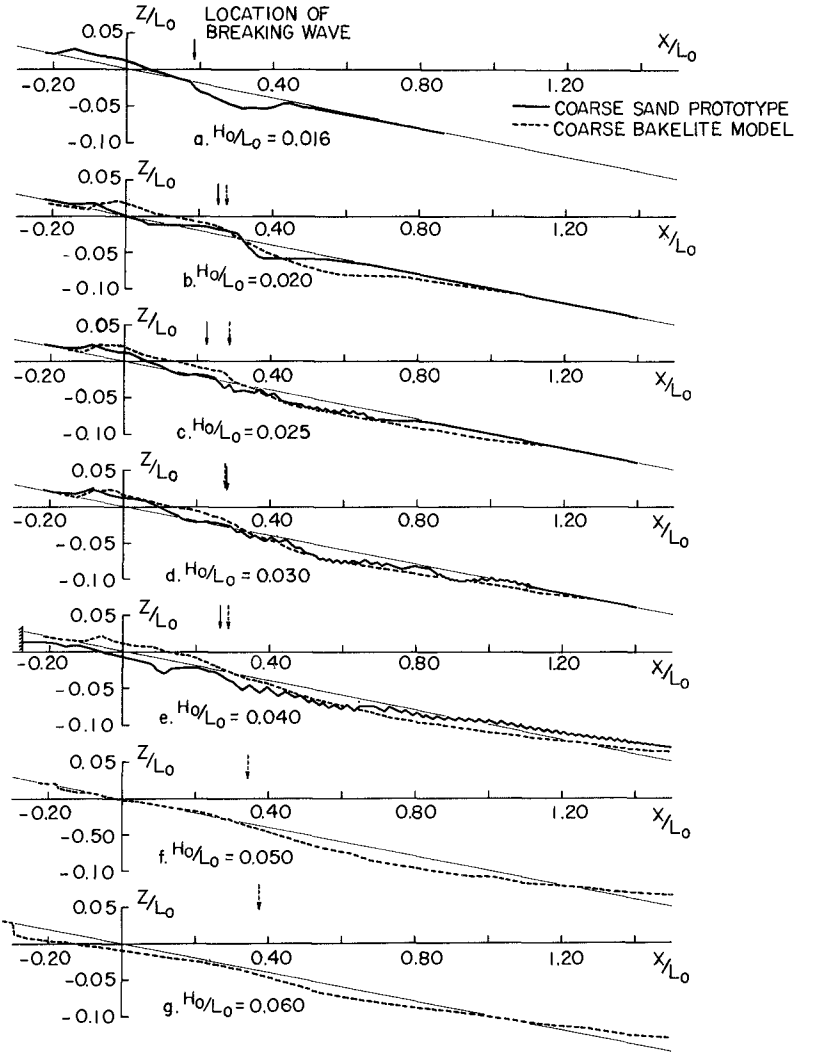

FIGURE 1 : DIMENSIONLESS COMPARISON BETWEEN PROFILES IN COARSE SAND AND COARSE BAKELITE

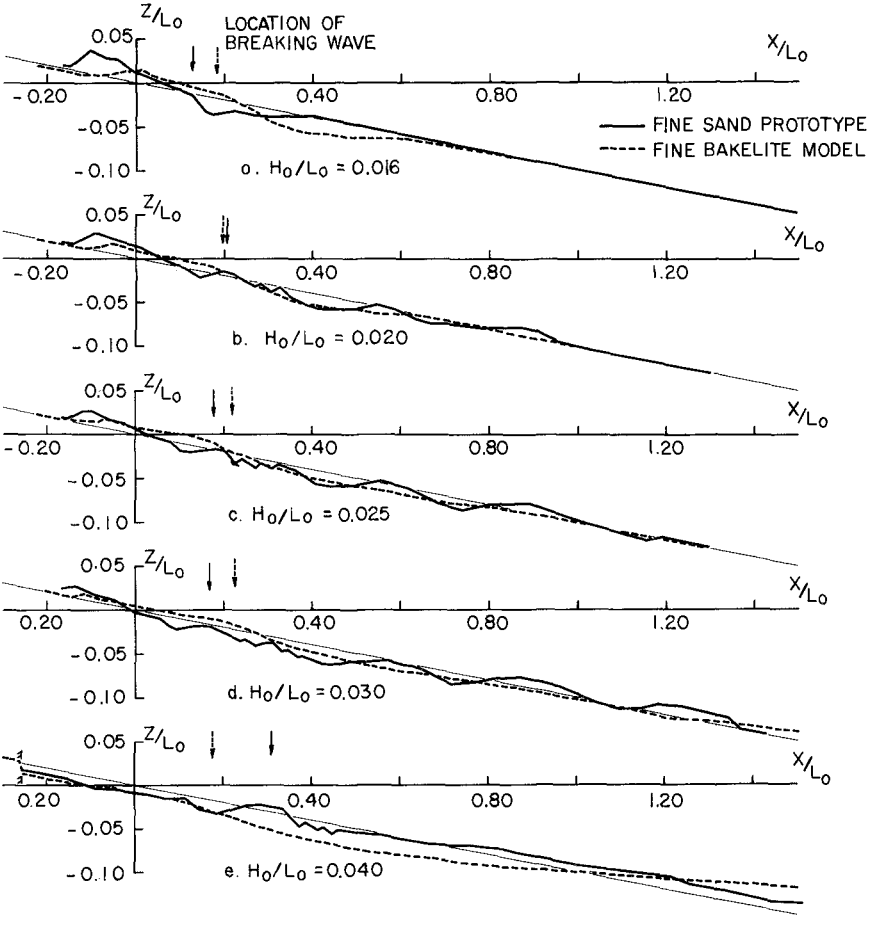

FIGURE 2 : DIMENSIONLESS COMPARISON BETWEEN BEACH PROFILES IN FINE SAND AND FINE BAKELITE.

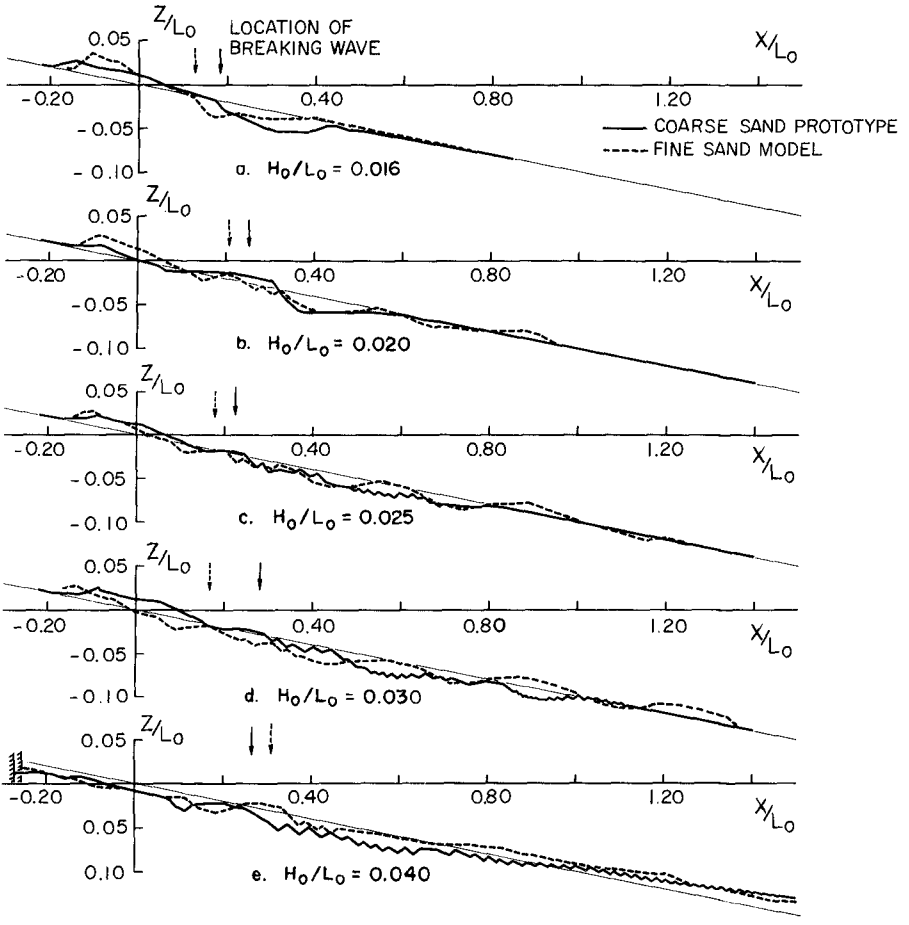

FIGURE 3 : DIMENSIONLESS COMPARISON BETWEEN BEACH PROFILES IN COARSE AND FINE SAND

considerable difference was observed between the profiles.

For all wave steepnesses (H_o/L_o) greater than 0.025 the natural sand beaches formed a "storm" profile with an offshore bar whereas the bakelite beaches showed no evidence of an offshore bar even at a wave steepness H_o/L_o = 0.060. Nayak (1970) summarised several different criteria for the generation of offshore bars (Figure 4). Superimposed on Figure 4 is the range covered by the present test data. The range is limited and therefore no general conclusions can be drawn as to the validity of the previously published criteria. However, for those tests using natural sand, transition from a "summer" to a "winter" profile occurred at wave steepnesses slightly less than those predicted by Johnson (1949) and Iwagaki and Noda (1963). On the other hand, for lightweight bakelite, no "winter" profile was evident, even for the highest values of H_o/L_o tested. This data throws considerable suspicion on the validity of any generalized criterion, such as proposed by Nayak, for the generation of an offshore bar. Instead it would appear that a separate criterion must exist for each different material. Most probably the criterion is a function of the dimensionless variable ρ_s/ρ , as well as of the reflection off the beach. It was noted that longshore bars for the sand profiles occurred at the antinodes on the reflection envelope. The bakelite beaches were much more porous in nature, and exhibited substantially smaller reflection coefficients and no appreciable offshore bars. Ripples, however, were noted for both materials at wave steepnesses exceeding 0.025.

From all profile comparisons it was evident that a greater proportion of the crushed bakelite, rather than the natural sand, had been transported shorewards. This resulted in the bakelite beach, shorewards of the wave breaking zone, being invariably higher than the corresponding natural sand beach, and the shoreline being further to sea-wards leaving the impression that the bakelite model beach was considerably steeper. Initially it was sought to explain this difference simply in terms of a "natural" distortion phenomenon. Different slope parameters similar to those postulated by Waters (1939) and Bagnold (1940) were used to characterise the beach slopes θ within the wave breaking zone. These yielded estimates of beach slope scales n_θ varying from 0.64 - 1.55, the lower values being associated with higher values of wave steepness H_o/L_o.

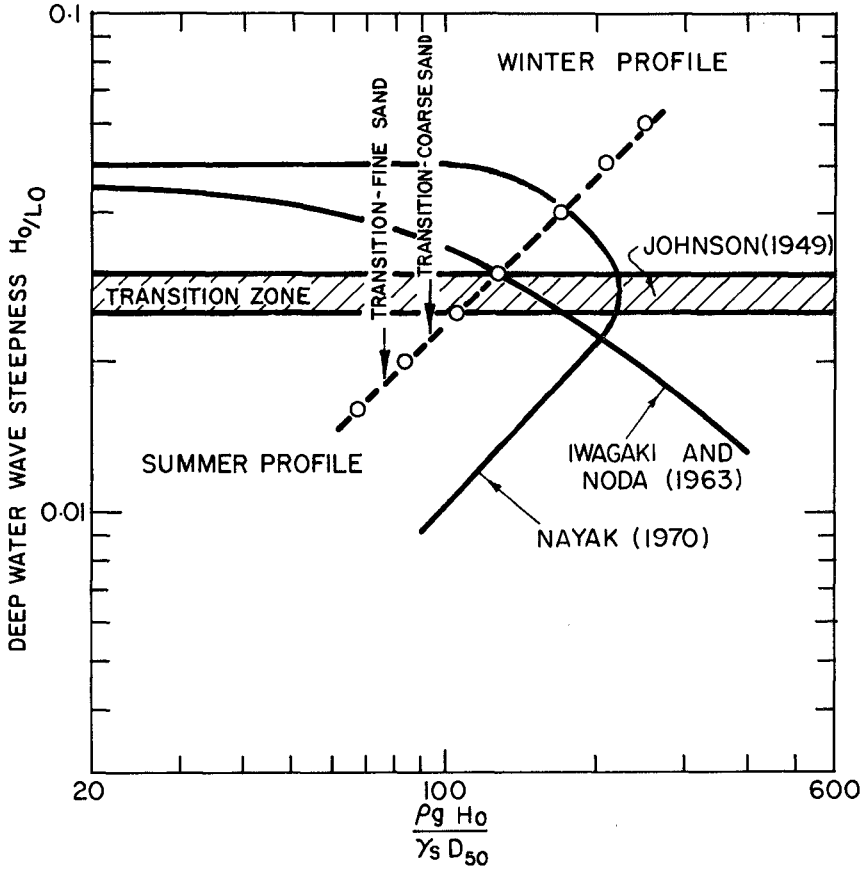

FIGURE 4 : CRITERIA FOR GENERATION OF AN OFFSHORE BAR — AFTER NAYAK (1970)

The comparison between test results for coarse and fine sand (figure 3) indicated a closer similarity between model and prototype. Offshore bars formed at corresponding values of H_o/L_o, and ripples dominated the offshore topography in both profiles, for wave steepnesses $0.025 \leq H_o/L_o \leq 0.030$. In spite of this improved similarity significant differences still existed between comparable profiles, and therefore it was concluded that fluid viscosity affected the model results, i.e. the model design was not acceptable because equation 9 (i) was not satisfied. Another possible source of difference between the sand prototype and sand model could be the replacement of v_* by $\sqrt{gH_o}$ in the scaling process. This would of course also affect the bakelite models and will be discussed later.

DISTORTED MODELS

Figure 5 indicates that for tests at wave steepnesses $H_o/L_o = 0.020$ and 0.040 a change in the initial beach slope i_o, for a lightweight sediment model, is sufficient to alter the final beach profile significantly. Although the basic shape of the beach profile in the foreshore region, from beach crest to wave breaking zone, is not greatly altered, Figure 5 shows that the position of the final shoreline, and the size of the foreshore berm are very much a function of the initial slope.

From Figures 1 and 2 it is apparent that an undistorted model beach, using lightweight bakelite invariably produced a profile in which the foreshore region was more prominent and the shoreline further to seaward than the corresponding prototype profile. Combining these two observations would indicate that distortion of the initial prototype slope in a lightweight sediment model, will reduce the beach berm, cut back the shoreline, and produce closer similarity between the model and prototype, except for the fact that offshore bars are not formed in the model at $H_o/L_o \geq 0.025$.

For a wave steepness of 0.020, a matching of the profiles and a comparison of the measured beach slope parameters indicate that if n_{i_o} were 1.2 to 1.6, the best similarity with respect to foreshore berm and shoreline would be obtained. From the earlier reference to n_θ, the beach slope scale, it may be seen that θ is very dependent upon its definition and that n_θ does not differ a great deal from 1. It is often argued that a model should be distorted so that

$$N = n_\theta \tag{10}$$

where N is the model distortion. Since n_θ has an average value of approximately 1 this would indicate all models should be undistorted. However,

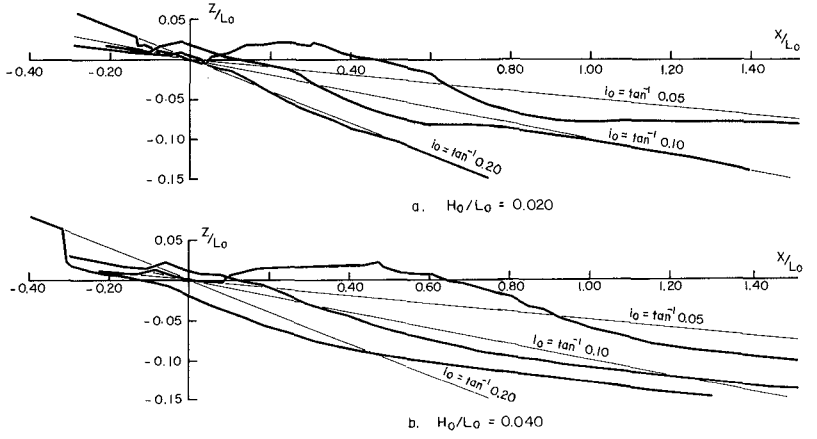

FIGURE 5 : DIMENSIONLESS COMPARISON BETWEEN PROFILES IN COARSE BAKELITE, FOR DIFFERENT INITIAL SLOPES, i_o .

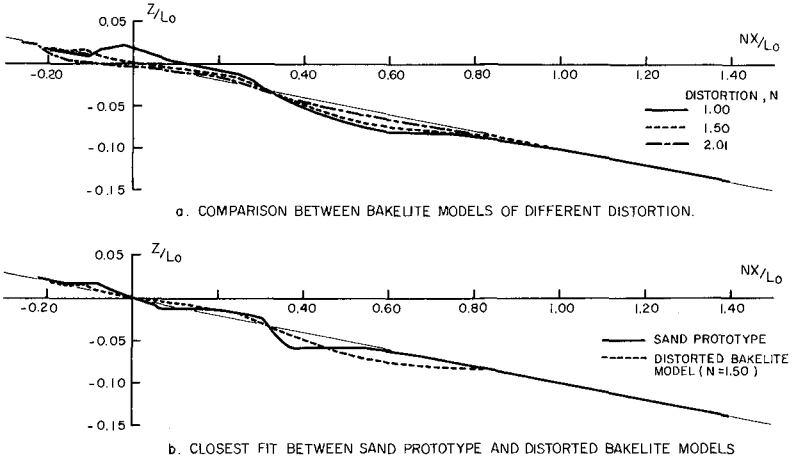

FIGURE 6: DIMENSIONLESS COMPARISON BETWEEN BEACH PROFILES USING MODEL DISTORTION, FOR TESTS AT A WAVE STEEPNESS H_o/L_o = 0.020

undistorted models do not reproduce the foreshore and shoreline correctly. This can be achieved by distorting i_o, as mentioned above. Thus the reason for model distortion is not Equation 10, but the matching of the onshore zone and shoreline.

Yalin (1971, p. 235) derives another expression for distortion

$$N = \eta_z^{\frac{1}{2}} \qquad (11)$$

which, yields a value of N = 1.42 for the lightweight bakelite model.

To determine the validity of model distortion, tests were carried out with the same coarse bakelite sediment, a constant wave steepness H_o/L_o = 0.020, and N = 1.50 and 2.01. Increasing the distortion decreases the dimensionless variable $\frac{\rho g H_o}{\gamma_s D_{50}}$, and thereby reduces the mobility of the sediment particles.

In Figure 6 a) the coarse bakelite beach profiles obtained for distortions N = 1.0, 1.50, and 2.01 are compared by plotting Nx/L_o against z/L_o. In Figure 6 b) it may be observed that the closest fit to the sand prototype data, in the foreshore region, was obtained for a distortion N = 1.50. In the offshore region beyond the wave breaking zone the fit between profiles still was not particularly good.

SCALE EFFECT IN THE ONSHORE ZONE

The equation of motion for a solid particle moving through a fluid shows that the particle trajectory is dependent on the particle specific gravity ρ_s/ρ. Only for a situation where the solid particle acceleration $du_s/dt \to 0$, does the particle motion become independent of ρ_s/ρ. For the undistorted lightweight sediment models investigated the trajectory of a model bakelite particle will be proportionally higher and longer than for a corresponding prototype sand particle. This difference in particle trajectory, caused by non-similarity of ρ_s/ρ, is a possible explanation for the observed difference between model and prototype equilibrium beach profiles, particularly in the portions of the bed where high fluid accelerations are present such as the foreshore and wave breaking zones. It seems reasonable to attribute non-similarity of the beach profile in this region primarily to non-similarity of ρ_s/ρ.

SCALE EFFECT IN THE OFFSHORE ZONE

In the comparison between beach profiles it is apparent that, beyond the breaking zone, the bakelite model sediment was moved at a proportionally greater depth than the sand prototype sediment. This is

particularly obvious for the "summer" profiles formed by low steepness waves - Figures 1 (b) and 2 (a). This "scale effect" may be explained in terms of non-similarity of a_b/D_{50} and this hypothesis was examined in some detail. Exaggerated model scour may be predicted by using the concepts developed by Riedel et al (1972). Figure 4 of their paper reproduces the experimentally determined relationship between wave friction factor, $f_w = 2(\hat{v}_*/\hat{U}_b)^2$, the maximum amplitude Reynolds Number for sinusoidal motion $RE = \hat{U}_b a_b/\nu$, and a_b/k_s the relative roughness. Here $\hat{U}_b$ is the maximum wave orbital velocity near the bed, and k_s is the equivalent sand grain roughness.

If k_s is assumed equal to D_{50} the relative roughness becomes a_b/D_{50}. Using small amplitude wave theory, it is possible to calculate values of a_b/D_{50} and $\hat{U}_b a_b/\nu$ for equivalent locations in the model and prototype, and determine corresponding values of f_w. For the test illustrated in Figure 1 b) where $H_o/L_o = 0.020$, and $d/L_o = 0.058$ at the point of scour in the prototype.

$$f_{w_{proto.}} = 2\,(\hat{v}_*/\hat{U}_b)^2_{proto.} = 0.025 \qquad (12)$$

If the model scour depth were the same, i.e. $(d/L_o)_{model} = 0.058$

$$f_{w_{model}} = 2(\hat{v}_*/\hat{U}_b)^2_{model} = 0.057 \qquad (13)$$

and $f_{w_{model}} > f_{w_{proto.}}$ for similar scour depths. More specifically

$$n_{\hat{v}_*} = \frac{n_{\hat{U}_b}}{1.5} \qquad (14)$$

for the particular depth $d/L_o = 0.058$ and the wave conditions considered. Equation 14 demonstrates that

$$n_{\hat{v}_*} < n_{\hat{U}_b} = n_{H_o}^{\frac{1}{2}} \qquad (15)$$

which is in conflict with the initial model design assumption that $v_* \propto \sqrt{gH_o}$. Since H_o/L_o and $D_{50}\sqrt{gH_o}/\nu$ are modelled correctly and d/L_o is constant in this particular example the inequality expressed in Equation 15 must be a direct result of non-similarity in D_{50}/L_o. The shear velocity and bottom shear stress for the model are exaggerated and additional scour will occur in the model. This is as observed, and the result is a deeper scour hole.

Kamphuis (1972) recognises that, for mobile bed short wave models, non-similarity of the variables ρ_s/ρ and a_b/D_{50} cause "scale effect". For a plain granular bed roughness distortion is simply equal to the particle size distortion and the following scale laws may be postulated - (Kamphuis (1972a, Eq. (31)):

$$n_{D_{50}} = n_z^{-5/16} \quad ; \quad n_{\gamma_s} = n_z^{15/16} \quad ; \quad n_\tau = n^{5/8} \qquad (16)$$

If these are used for model tests instead of Equations 4 and 5, then for the same model material ($n_{D_{50}} = 1/\sqrt{2}$), n_z would be equal to 3 instead of 2 and $n_\tau = 2$. With $n_{\hat{U}_b}$ now equal to $\sqrt{3}$, Equation 14 would become

$$n_{\hat{v}_*} = n_{\hat{U}_b} / 1.2 = n_{H_o}^{\frac{1}{2}} / 1.2 \qquad (17)$$

Thus modelling $v_* \alpha \sqrt{gH_o}$ would now give closer similarity between model and prototype in the offshore zone. In addition, the distortion is entered as a function of the fit of model and prototype profiles only, therefore the tests performed using Equations 16 may be representative of any distortion. Tests are in progress to assess the validity of Equations 16 and similar equations for rippled beds.

CONCLUSIONS

Two dimensional equilibrium beach tests, based on the scale laws developed in this paper, indicate that it is impossible to achieve exact similarity between a sand prototype beach profile and its lightweight sediment model. Closer correspondence between the profiles exists when exact geometric similarity is maintained, and sand is used in the model. For normal prototype sand beaches, however, where $D_{50} < 1.0$ mm, there is a severe limitation on the permissible scale reduction if these beaches are to be modelled using natural materials, because clay size model sediments must be avoided. This scale limitation renders these scale laws largely impractical. Practical circumstances require that water is used for the model, as well as the prototype. This invariably introduces "scale effect"

which is attributable to non-similarity of some of the dimensionless quantities since not all can be satisfied simultaneously.

For beach profile models using lightweight sediment in particular, it may be concluded that:

1. Non-similarity of the dimensionless variable ρ_s/ρ in a mobile bed short wave model causes non-similarity of the equilibrium beach profile. This scale effect is more pronounced in the foreshore and wave breaking zones where the influence of fluid accelerations is greatest.

2. For "summer" beach profiles, formed by low steepness waves ($H_0/L_0 < 0.025$), the above scale effect may be reduced by introducing a distortion N into the model design. This distortion is not equal to n_θ^{-1} since $n_\theta \simeq 1$. The distortion results from a desire to match the shoreline and foreshore in model and prototype.

3. For "winter" or "storm" beach profiles which are formed by high steepness waves ($H_0/L_0 > 0.025$) and exhibit substantial offshore bars, similarity of the beach profile cannot be achieved using lightweight sediments since the model profiles do not exhibit any bar structure. A generalised criterion for bar formation for all materials appears to be impossible to derive because of differences in specific gravity, porosity and angularity of the particles of the various materials.

4. For the offshore region, beyond the wave breaking zone, mainly non-similarity of the dimensionless variable a_δ/D_{50} causes exaggeration of the scour depths in the model.

5. For "summer" beach profiles, this "scale effect" will be reduced by revising the initial assumption that $v_* \propto \sqrt{gH_0}$, on the basis that

$$\frac{\hat{v}_*}{\sqrt{gH_0}} = f\left(\frac{a_\delta}{D_{50}}\right)$$

This leads to an increase in the vertical scale n_z, with respect to the scales n_{γ_s} and $n_{D_{50}}$, thereby decreasing both the mobility of the model sediment particles and the depth of scour. The scale laws recently proposed by Kamphuis (1972a) warrant investigation.

6. If the model beach particles have an angle of repose that is radically different from the prototype material, then this difference will significantly affect similarity of the model beach profile.

7. Natural sand beaches absorb less wave energy than those formed by lightweight bakelite. The resulting larger reflected wave may have a significant influence on the equilibrium beach profile and the formation of bars.

8. If similarity of the bottom profile is required then large distortions, permissible for rigid bed models, are not valid for mobile bed models of the coastal regime, because distortion is limited by the maximum angle of repose of the model beach material.

ACKNOWLEDGMENTS

The authors express their thanks to the National Research Council of Canada for their financial support, to Mr. J. Ploeg of the National Research Council for his interest, advice and use of some of his facilities and to the Public Work Department of Western Australia for granting leave of absence to Mr. Paul to complete this study.

REFERENCES

Bagnold, R.A. (1940) "Beach Formation by Waves, Some Model Experiments in Wave Tank", Journal of the Institution of Civil Engineers Vol. 15, pp. 27-52.

Bijker, E.W. (1967) "Some Considerations about Scales for Coastal Models with Movable Bed", Delft Hydraulics Laboratory, Publication No. 50, p. 142.

Fan, L.N. & Le Mehaute, B. (1969) "Coastal Movable Bed Scale Model Technology", Tetra Tech. Report No. TC-131, p. 122.

Iwagaki, Y. & Noda, H. (1963) "Laboratory Study of Scale Effects in Two-Dimensional Beach Processes", Proceedings of 8th Conference on Coastal Engineering, Mexico City, Chapter 14, pp. 194-210.

Johnson, J.W. (1949), "Scale Effects in Hydraulic Models Involving Wave Motion", Trans. American Geophysical Union, Vol. 30, No. 4, pp. 517-525.

Jonsson, I.G. (1966) "Wave Boundary Layers and Friction Factors", Proceedings of 10th Conference on Coastal Engineering, Tokyo, Japan, Vol. 1, Chapter 10, pp. 127-148.

Kamphuis, J.W. (1972) "Scale Selection for Wave Models", Queen's University, Civil Engineering Report No. 71.

Kamphuis, J.W. (1972a), "Scale Selection for Mobile Bed Wave Models", Proceedings of 13th Conference on Coastal Engineering", Vancouver.

Nayak, I.V. (1970) "Equilibrium Profiles of Model Beaches", University of California, Tech. Report HEL 2-25, Berkeley, p. 117.

Paul, M.J. (1972) "Similarity of Bed Evolution and Sediment Transport in Mobile Bed Coastal Models", Ph.D. Thesis, Department of Civil Engineering, Queen's University at Kingston, Canada.

Riedel, H.P., Kamphuis, J.W. and Brebner, A. (1972) "Measurement of Bed Shear Stress Under Waves", Proceedings 13th Conference on Coastal Engineering, Vancouver, Canada.

Valembois, J. (1961) "Etude sur Modele de Transport Littoral Conditions de Similitude", Proceedings of 7th Conference on Coastal Engineering, The Hague, Netherlands, Vol. 1 Chapter 18, pp. 307-317.

Waters, C.H. (1939) "Equilibrium Slopes of Sea Beaches", M.S. Thesis, Department of Engineering, University of California.

Yalin, M.S. (1971) "Theory of Hydraulic Models", MacMillan, London.

Yalin, M.S. (1972) "Mechanics of Sediment Transport", Pergamon Press, London, (in press).

CHAPTER 66

EQUILIBRIUM CONDITIONS IN BEACH WAVE INTERACTION

Dr. H. Raman and John J. Karattupuzha
Hydraulic Engineering Laboratory
Indian Institute of Technology
Madras, India

ABSTRACT

Laboratory studies were conducted in an attempt to find out a relationship between beach and wave characteristics when equilibrium conditions are reached in beach wave interaction for the simple case of regular waves acting normal to the beach. Experimental results indicate the existence of stable points on beach profiles where the coordinates of the profile do not change with time when waves of constant characteristics act on the beach. Eqperical relationship between the wave and beach properties are proposed. A new criterion for classification of beach profiles is indicated.

INTRODUCTION

In beach-wave interaction and the resultant process of mutual modification there is a tendency to attain equilibrium conditions under which beach and wave no longer cause any further change on each other. In nature however, the ever-changing meteorological factors which cause rapid changes in waves, tides and currents seldom permit this interaction to reach equilibrium conditions. Nevertheless, certain dominant tendencies in the wave pattern may persist over a season or part of a season thereby enabling us to delineate a few significant characteristics of waves to work out their influence on beach modification problems. This in turn offers us an opportunity for a meaningful determination of beach response to wave action, provided necessary numerical relationships are available for this purpose. Accurate formulae for determination of the nature and extent of changes on beach profiles for given wave conditions, though of great importance in a large number of shore problems, are not available at present. It appears that the evolution of theoretical relationships, which can be used on practical problems with a reasonable degree of accuracy, may have to wait till better tools are available to deal with problems of sediment transport in an unstable and oscillating wave velocity field. This is disoussed in detail by Silvester (1,2). Emperical relationship can however be derived for certain conditions of profile

changes. In this paper an attempt is made to derive emperical relationships for the determination of the type and quantum of beach profile changes in the simple case of regular waves acting on a beach of uniform initial slope aligned normal to wave action.

STABLE POINTS ON BEACH PROFILES

Available experimental and field data on beach profiles indicate that usually there is a stable point on beach profiles near the breaker zone which does not undergo any considerable change during the process of profile modification due to incident waves of essentially constant characteristics. In the case of storm profiles a second stable point may exist in the offshore zone depending on the steepness of the incident waves (See Fig.1). The stable point (or the second stable point in case two stable points exist) acts as a fulcrum about which the waves try to keep the material distribution in balance - erosion onshore and deposition offshore - within the active zone of the profile. For normal profiles the stable point does not exist in the strict sense, but there is one point on the modified profile which seem to serve the same function as above (See Fig.2). In this case there is erosion offshore and deposition onshore.

Neutral points on beach profiles where, material of a given size will be in oscillating equilibrium, with no net movement, have been discussed in a few previous works. Cornaglia (1898) was perhaps the first to make this observation(3). Inman's(4) observations on sediment sorting and studies of Miller and Zeigler (5) showed that there are zones of oscillating equilibrium for each sediment size for the given wave conditions. Eagleson et al (6) in their theoretical analysis of the problem of sediment transport on sloping beaches under waves equated the forces acting on a bed particle and arrived at a criterion for oscillatory equilibrium. Wells (7) defined a neutral point on the beach profile such that the skewness of the probability distribution of horizontal water velocity of second order gravity waves will be zero at the point.

The neutral positions of particle motion described by these authors indicate that particles of the same size will move in opposite directions when placed on either side of the neutral point. (A sediment particle on the seaward side will move seaward while one on the shoreward side will move shoreward of the neutral point for the same sediment size). The stable points mentioned in this paper are those which act as a fulcrum about which the profile swings while material is moved from one side of the point to the other. The net sediment motion is unidirectional, either towards shore or away from it, for appreciable distances on either side of the stable point. A directional variation is expected

only due to changes in velocity field imposed by reflection or due to changes in material size. The influence of the former is comparatively small and can be easily identified by the formation of nearly stationary humps and hollows on the bed whose spacing will be closely related to the wave length. This is easily understood from the profiles shown in Figures 3 to 8 and from the profiles given in the references cited.

Fig.3 shows the stable point on a set of natural beach profiles taken at a shore which is in equilibrium. Fig.14.22 of Ref (8) shows 12 sets of profiles on an actual beach. Each set contains 5 profiles taken during the course of two to three months at a single station. It is seen that in most cases the profiles remain stationary at a depth of 5 ft. (1.52 m).

Figures 4 to 7 show the stable points on experimental beach profiles of the storm type and Figure 8 shows the modified version of the stable point on a normal beach. In the experimental beach profile shown in Fig.14 of Ref(7) the stable point is visible at 17.5 cm depth. At this point there is no change for the original profile irrespective of the time of propagation of waves, although adjacent areas are getting altered with time of wave action.

EXPERIMENTAL SET-UP AND PROCEDURE

The experiments were conducted in a wave flume 31 m long 90 cm wide and 90 cm deep. The plunger type wave maker powered by a variable speed motor is fixed at one end for wave generation. At the other end of the flume, model beaches are laid to uniform initial slope using sand of required size. All tests in the present series were done under a constant water depth of 35 cm at the toe of the beach.

Waves of constant characteristics were generated and allowed to work on the beach till the profile showed no significant change in time. In order to locate the stable points and to find out the pattern of modifying process the beach profile was measured at 5 to 10 hour intervals. Normally it took 40 to 50 hours for the profile to reach equilibrium conditions. Wave characteristics were measured by resistance type wave gauges and a recorder unit.

EXPERIMENTAL RESULTS AND DISCUSSION

Even though experiments were done with sand of different sizes and coal powder and with different initial slopes, the results of tests on 0.3 mm sand alone is reported in this

paper. Other profiles also show the same pattern. But detailed analysis with respect to stable point is done only for 0.3 mm sand for different wave conditions and initial slopes and hence this is discussed in detail.

Typical storm type profiles for slopes 1/8, 1/10, 1/12 and 1/15 are shown in Figures 4,5,6 and 7 indicating the progressive development of profiles towards equilibrium. Similarly Fig.8 shows the development of a normal type profile on a 1/10 slope.

TYPES OF PROFILE CHANGES

It is found that mainly there are three types of profile changes:

(i) Storm type profiles with erosion on the shore and deposition in deeper waters. Erosion takes place shoreward of the second stable point when it exists or shoreward of the first stable point when the second one is absent. Long shore bar is present.

(ii) Normal profiles with deposition taking place on the shore from the material dug out by waves from offshore of the breaker by waves. Longshore bar is absent.

(iii) Storm type profile with longshore bar, but deposition takes place on the shore. Shoreward of the second stable point erosion takes place and seaward of it deposition is seen.

The last mentioned of these is an interesting phenomenon in that it is customary to think of storm profiles as indicative of shore erosion. Examination of this type of profiles show that onshore transport in storm profiles takes place when the distance between the two stable points is more than one local wave length . It appears that in such a case more than one set of mass transport circulation cells will be formed with possibility of a reversal in the direction of transport. It may be recalled that Longuet-Higgins (9) showed that mass transport circulation cells may be formed in pairs at spacings equal to half wave length for standing waves. In the present case there is reflection from the beach and hence there will be a partial standing wave. This incidentally explains why flat beaches usually show accretion on the shore while steep beaches erode for the same wave and bed material characteristics. It is interesting to note that the second stable point being the offshore limit of erosion of the original beach profile, its location is controlled by the local wave characteristics, which is primarily dependent on the depth below still water level, and bed material characteristics. The first stable

point is a product of the breaker at the longshore bar and hence is controlled by the slope of the beach also. Therefore the distance between these points is a function of the slope also. As the slope becomes flatter, the distance increases, increasing the possibility of creating more than one mass transport circulation cell. This helps in reversing the direction of transport at some point between the offshore bar and the second stable point, thereby permitting deposition on the shore.

SIGNIFICANCE OF STABLE POINTS

A stable point can exist only on a beach which is in equilibrium - ie. a beach with a shore line which may oscillate between certain shorewards and seaward positions due to seasonal changes in waves while maintaining its mean position without significant change when considered over a period of one or two decades. This means that there should not be a net loss or gain of material to the beach in its active zone either due to onshore-offshore transport or longshore transport mechanism. The presence of a stable point on a beach profile can be taken as an indication that the beach is in equilibrium.

The presence of stable points on natural beaches Fig.3 and Ref.(8) indicate that small changes in wave characteristics as may occur within a season for short periods do not annihilate the stable point or the corresponding alongshore stable zone.

EQUILIBRIUM PROFILE AND STABLE POINTS

If the local wave steepness H/L, where H is the local wave height and L the local wave length calculated from the linear theory with Rayleigh's assumptions, is plotted against the ratio of x/h for a straight uniformly sloping beach, a straight line graph will be obtained for h/Lo ratios less than nearly 0.15. Here x is the horizontal distance from a suitable origin to be chosen on the still water line (SWL) to any desired point on the bed profile and h is the depth of that point below SWL. (See Fig.1 for definition). The slope of this line is controlled by the location of the origin on the still waterline as can be seen from Fig.9. Fig.9 gives plots of H/L Vs x/h for the case of uniform beach slope of 1/10 when a wave of deep water wave height, Ho = 11.28 cm and wave period, T = 1 sec acts on the beach for different locations of origins. The straight vertical line is for origin at the intersection of the SWL with beach slope. This is the point of zero chainage also. The plot becomes flatter and flatter as the origin is shifted further and further offshore.

Available experimental results indicate that a plot of H/L Vs x/h prepared for the final equilibrium profile, even though not falling strictly into a straight line, can be approximated to one for portions of profile offshore of the longshore bar. The dashed line in Fig.9 is the line of best fit drawn in this fashion for the final profile resulting from the action of the above wave on the 1 on 10 initial beach slope. In this case the projection of the 1st stable point on SWL at ch.104 cm is taken as the origin. This line will then correspond to a straight line which represents the mean profile in the offshore part.

Fig.10 gives plots of H/L Vs x/h for the final equilibrium profiles resulting from waves of different characteristics acting on the 1 on 10 initial beach slope. In all cases the origin is chosen as the first stable point. The lines marked 1 to 4 represent storm type profiles and 5 and 6 represent normal profiles. It will be noted that the lines for the same type of profile, either storm or normal are nearly parallel to each other. Also the distances between these lines along the ordinate are nearly equal to the differences in deepwater wave steepness in the case of profiles of the same type. This perhaps, indicates the possibility of obtaining the mean profile resulting from any incident wave if H/L Vs x/h relationship for one wave condition is known for the same initial beach slope.

LOCATION OF STABLE POINTS

From the available experimental results concerning an initially uniform slope of 1/10 with material having a median dia of 0.3 mm it is found that the depth at the first stable point is a function of Ho and T for the given slope. The depth at the stable point is found to increase linearly with the nondimensional parameter $(Ho\ g\ T)/\nu$ where g is the acceleration due to gravity and ν is the kinematic viscosity of water. This is shown in Fig.11.

The second stable point, when it exists, corresponds to the point of intersection of the plots H/L Vs x/h for the initial and final profiles calculated with the origin at the first stable point for both cases. Fig.12 shows H/L Vs x/h relationships for initial and final conditions, for the four profiles shown in figures 4 to 7. These four profiles have four different initial slopes. The wave characteristics are given in the drawing. It can be easily seen that the intersection of the initial and final plots of H/L Vs x/h represents the second stable point.

CLASSIFICATION OF BEACH PROFILES

A new criterion for Johnson's(11) classification of beach profiles as 'storm and normal' is briefly examined. If the formation of a normal profile is examined it will be seen that transport of material is onshore everywhere along the profile. This would suggest that the fluid particle movement at bottom, at least predominantly if not always is towards shore. A type of wave which satisfies this condition is the solitary wave which in its ideal case has only forward movement everywhere across its depth. In shoaling water it is possible that wave condition may approximate to solitary wave. If the point of threshold movement of bed material is onshore of the point at which the wave becomes nearly solitary, only onshore movement of sediments can take place.

Taking Bagnold's (10) criterion $T = \frac{2\pi}{mh}\sqrt{\frac{h}{g}}$ to find the depth h_s at which a progressive wave may be approximated to a solitary wave for a given period T and finding the depth h_T at which threshold movement starts by equating the maximum instantaneous horizontal velocity from linear theory to the threshold velocity for material movement as given in Ref.(11), the criterion for classification of profiles can be written as:

$$\frac{h_s}{h_T} \geqslant 1 \qquad \text{normal profile}$$

$$\frac{h_s}{h_T} < 1 \qquad \text{storm profile}$$

Here, the quantity mh is given as a function of the ratio of amplitude a to depth below SWL, h by Bagnold (10) for easy extraction of the same for calculation purposes. Available experimental and field data generally confirm the validity of this test. A detailed description of the same is not attempted in this paper.

CONCLUSIONS

Available experimental and field data indicate the existence of stable points on beach profiles of equilibrium beaches. On a normal beach two stable points may be present, one near the breaker zone and one at the offshore limit of erosion of original profile seaward of the longshore bar.

The variation of the local wave steepness H/L with the ratio of coordinates x/h with the projection of stable point on SWL as the origin is nearly linear for the final equilibrium

profile. For the same initial slope and material characteristics, different wave characteristics give nearly parallel plots of H/L Vs x/h, the distance between these lines along the H/L axis being equal to the deepwater wave steepness. This indicates the possibility of getting the mean final equilibrium profile if the depth at the first stable point for the profile is known along with one plot of H/L Vs x/h for the same initial slope and bed material and any other wave characteristics.

Experiments on a 1/10 initial beach slope using 0.3 mm dia sand show that the depth at the stable point is proportional to the dimensionless parameter $(Ho\ g\ T)/\nu$

The second stable point can be fixed if the first one is determined and the plot of H/L Vs x/h plot can be drawn as already described.

ACKNOWLEDGEMENTS

The authors are greatly indebted to Professor V. Sethuraman, Professor of Hydraulic Engineering, I.I.T. Madras for his constant encouragement in this work. The authors also thank the Kerala Engineering Research Institute for permission to use the field data given in Fig.3 and Mr. Balakrishnan for his help in carrying out part of the experimental work.

REFERENCES

1. Silvester, R., "Sediment movement beyond the breaker zone", Civil Engineering Transactions, April 1970, pp 63-71

2. Silvester, R., "Beach Profiles and Littoral drift assessment", La Houille Blanche/No.6-1969, pp 615-622

3. Reference by James C. Ingle Jr., "Movement of Beach Sand" P.91, Developments in Sedimentology 5, Elsevier, New York 1966

4. Inman, D.L., "Areal and Seasonal variations in beach and near shore sediment at La Jolla, California", U.S. Army Corps of Engineers, B.E.B. Tech. Memo No.39, March 1953

5. Miller, Robert R.L. and John M. Zeigler, "A model relating dynamics and sediment pattern in equilibrium in the region of shoaling waves, breaker zone and foreshore", Journal of Geology, 66, 4 (July 1958) pp 17-41

6. Eagleson, P.S., B. Glenne and J.A. Dracup "Equilibrium characteristics of sand beaches in the offshore zone" U.S. Army Corps of Engrs., B.E.B., Tech. Memo No.126, July 1961.

7. Wells, D.R., "Beach Equilibrium and Second Order Wave Theory", Journal of Geop. Res. Vol.72, No.2, Jan 15, 1967, pp 497-504

8. Wiegel, R.L., "Oceanographical Engineering", p.365, Prentice-Hall Inc., 1964.

9. Longuet-Higgins M.S., "Mass transport in water waves", Phil. Trans. Roy. Soc. A 245 (903) 535-581.

10. Technical Report No.4, Coastal Eng. Res. Centre, U.S. Army Corps of Engrs., 1966.

11. Johnson J.W., "Scale Effects in Hydraulic Models involving wave motion" Trans. Amer. Geophys. Union, 30, 4 (1949), 517-25.

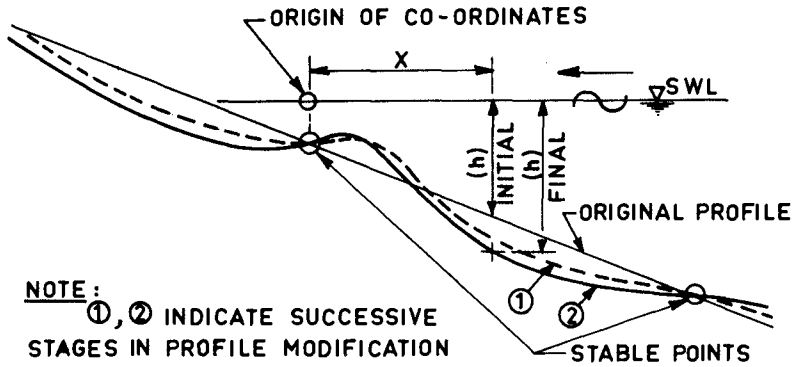

FIG.1..PROFILE MODIFICATION FOR STORM BEACH PROFILE

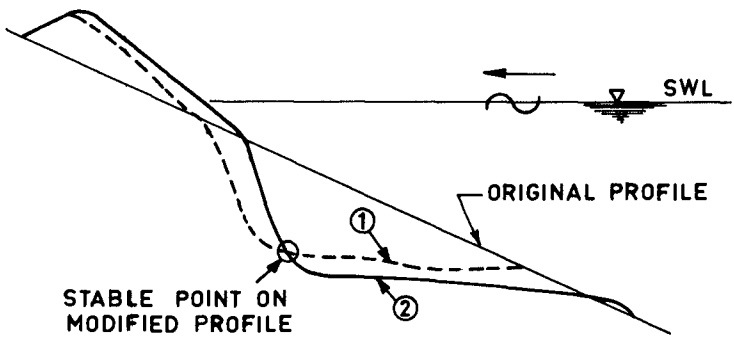

FIG.2..PROFILE MODIFICATION FOR NORMAL BEACH PROFILE

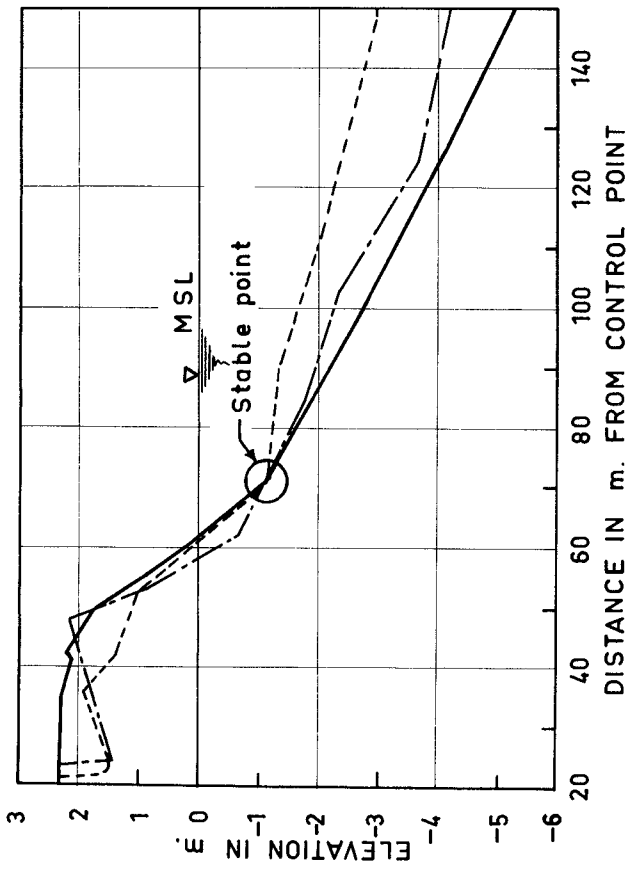

FIG.3.. STABLE POINT ON UNPROTECTED BEACH IN EQUILIBRIUM - BEACH PROFILE AT 300 m. SOUTH OF THOTTAPPALLY BAR-KERALA(INDIA)

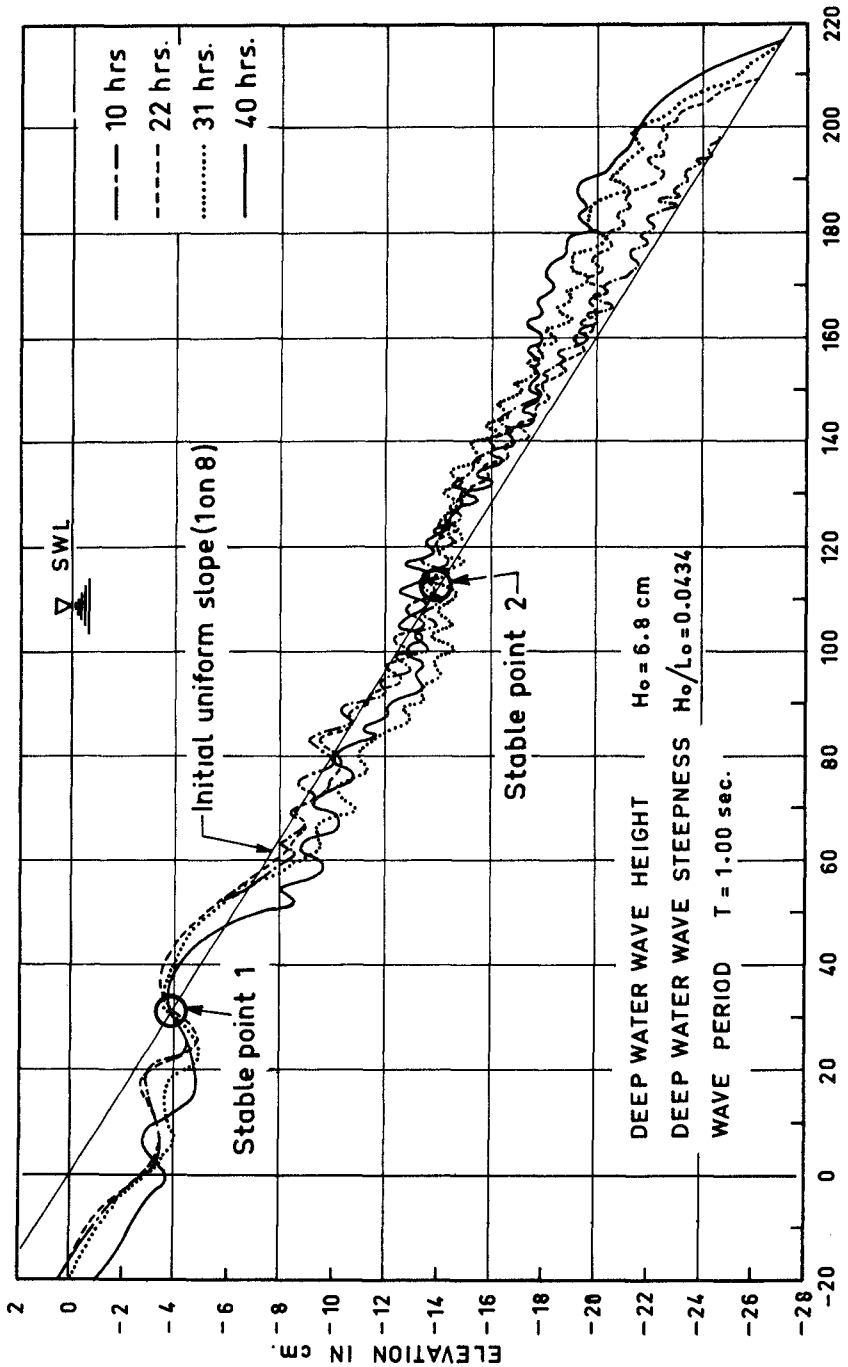

FIG. 4.. BEACH PROFILE CHANGES

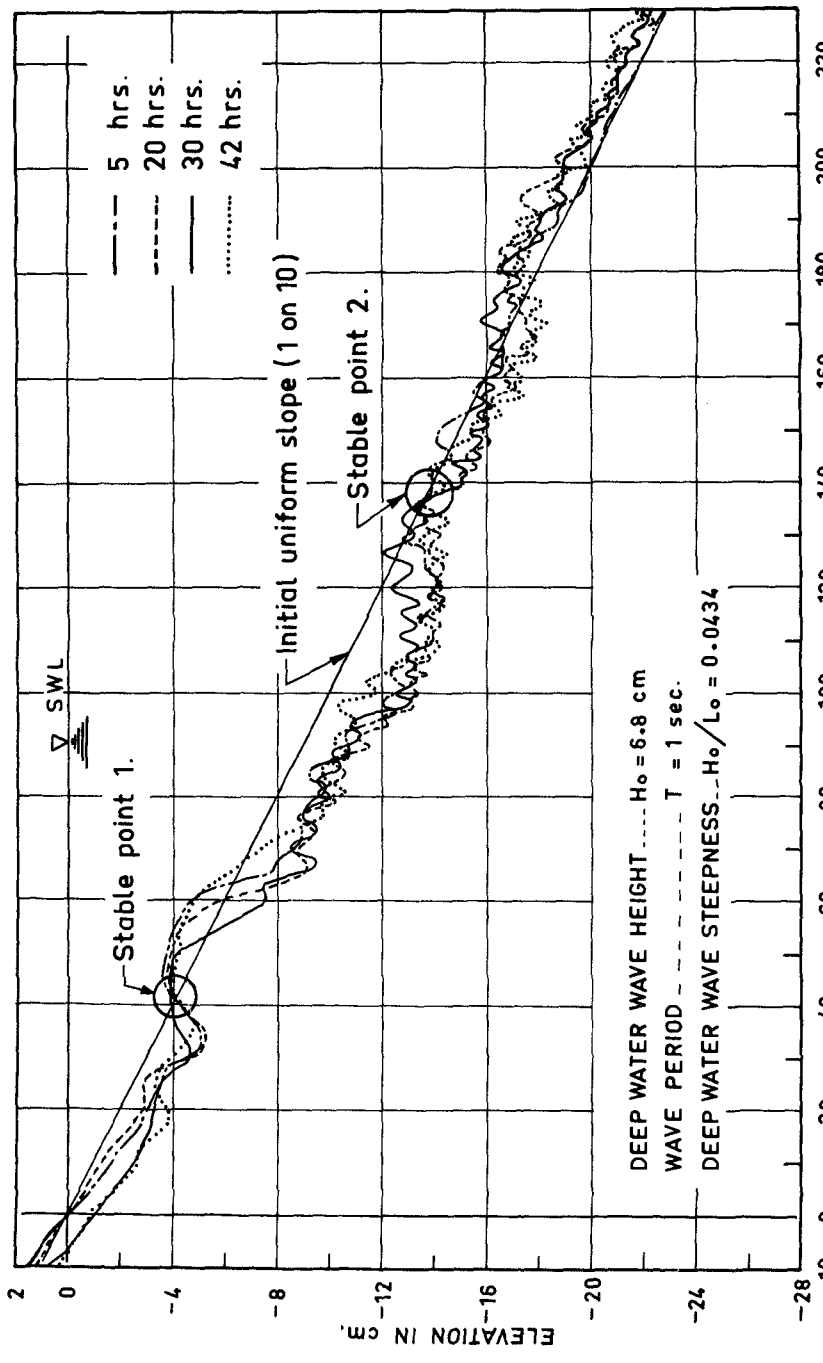

FIG. 5.. BEACH PROFILE CHANGES

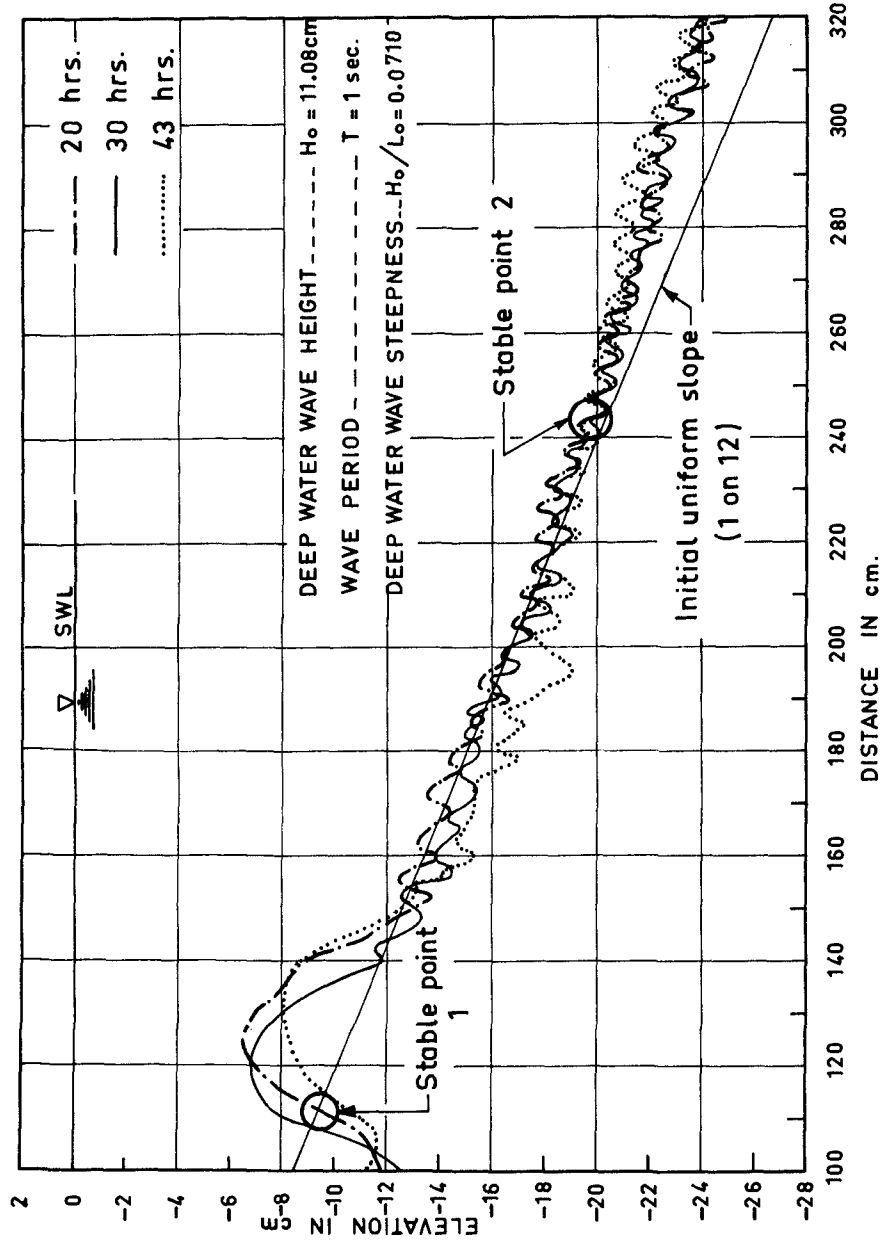

FIG. 6.. BEACH PROFILE CHANGES

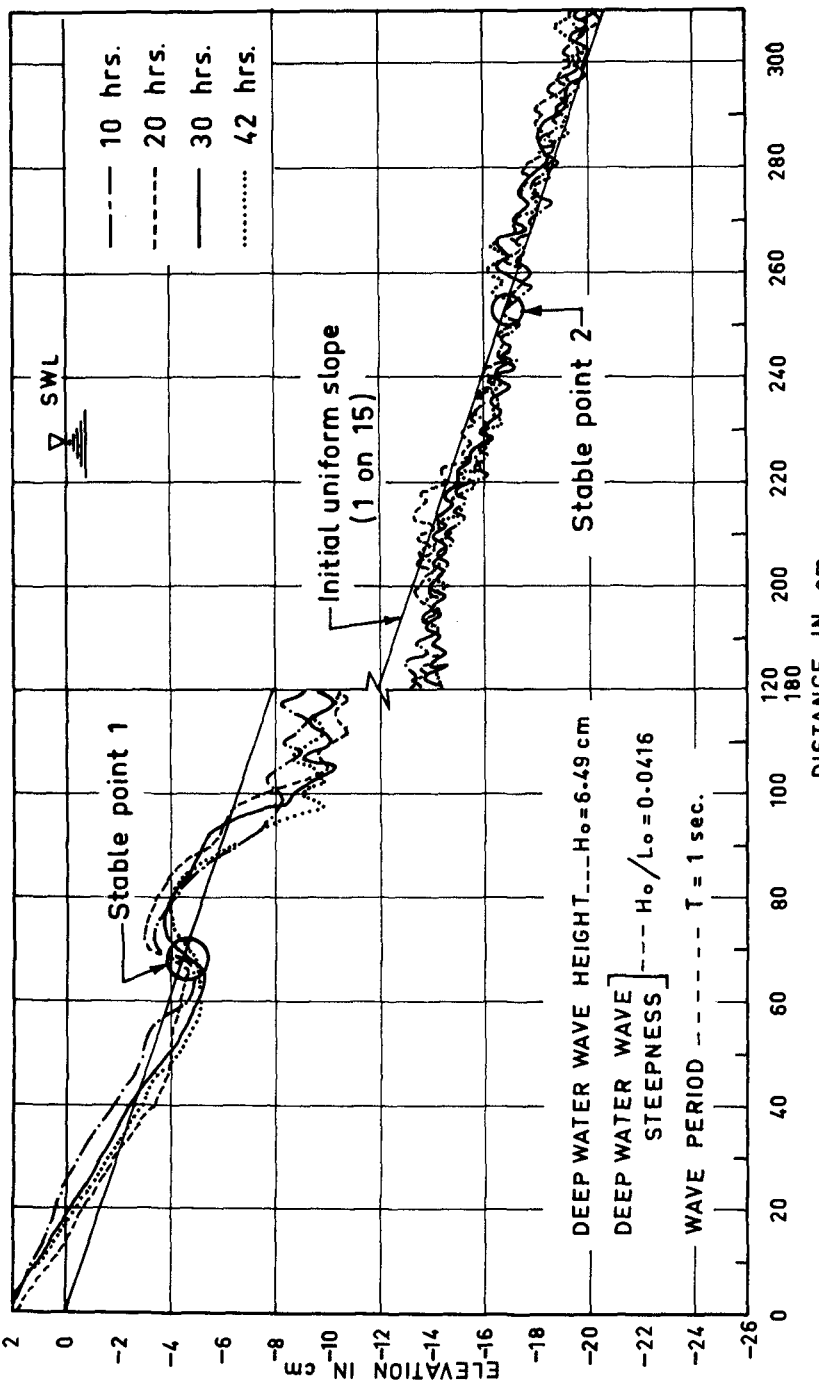

FIG. 7.. BEACH PROFILE CHANGES

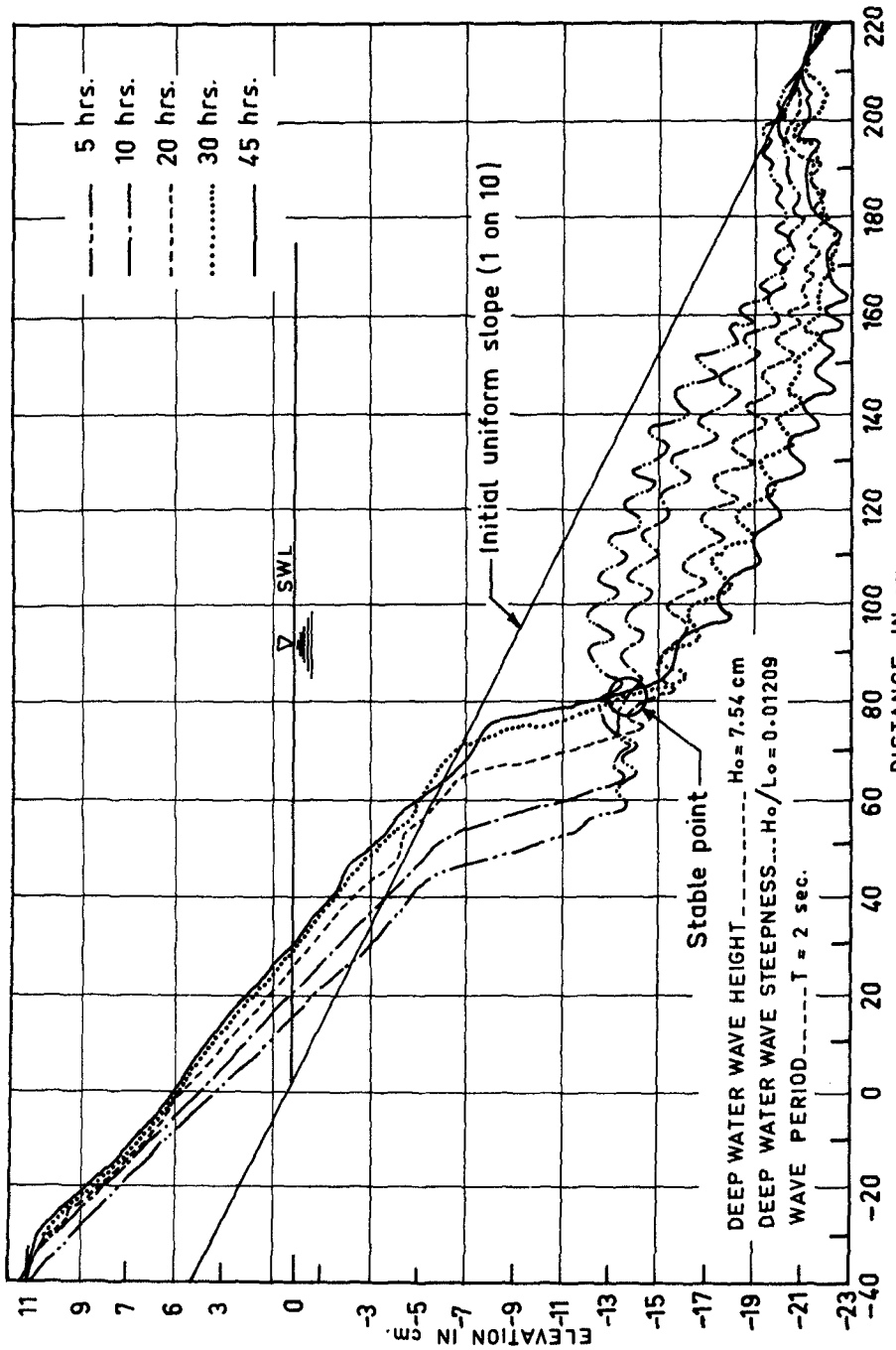

FIG. 8.. BEACH PROFILE CHANGES

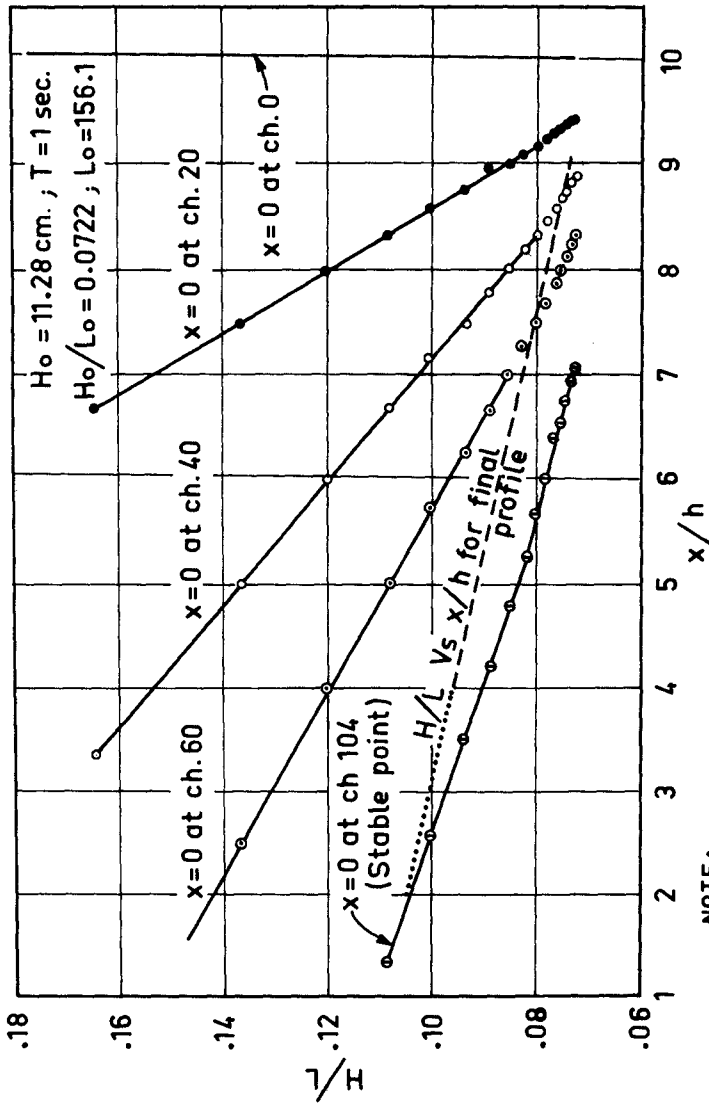

NOTE:
1. FIRM LINES ARE FOR INITIAL UNIFORM SLOPE 1 ON 10
2. DASHED LINE IS FOR THE FINAL EQUILIBRIUM PROFILE
3. CHAINAGE STARTS FROM INTERSECTION OF SWL WITH INITIAL SLOPE
4. CHAINAGE OF STABLE POINT = 104 cm.
5. THERE IS ONLY ONE STABLE POINT FOR THIS PROFILE

FIG. 9.. H/L Vs x/h FOR DIFFERENT LOCATIONS OF ORIGIN

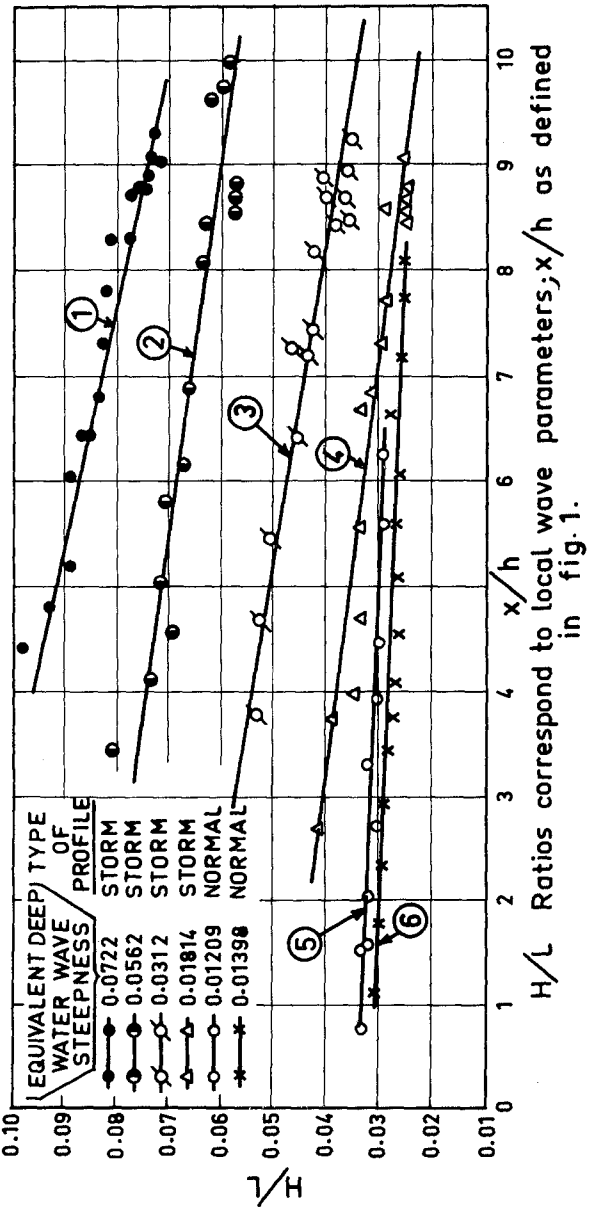

FIG.10.. H/L Vs X/h

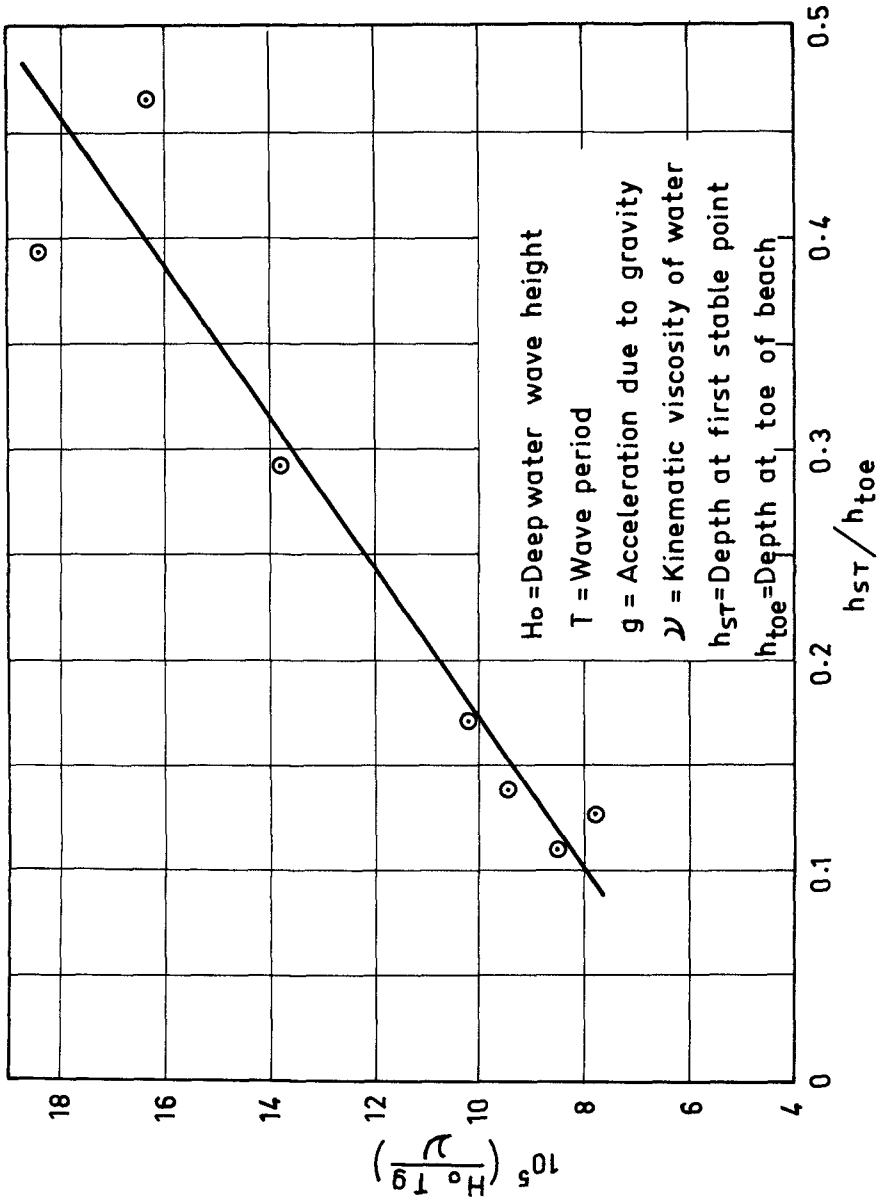

FIG.11.$(H_o g T)/\nu$ Vs h_{st}/h_{toe} FOR 1 ON 10 INITIAL SLOPE

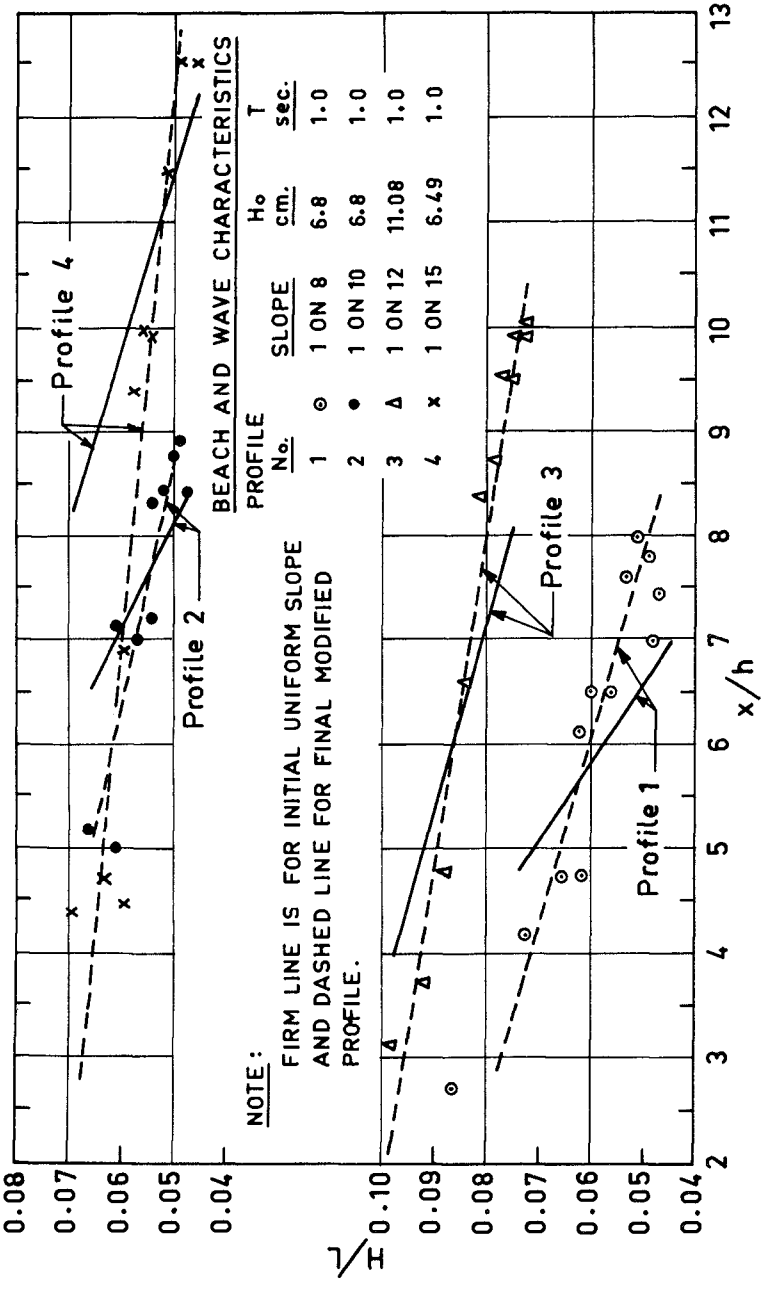

FIG.12.. H/L Vs x/h FOR INITIAL AND FINAL PROFILES

CHAPTER 67

HAWAIIAN BEACHES

BY

Frans Gerritsen
Chairman and Professor of Ocean Engineering
University of Hawaii
Honolulu, Hawaii

ABSTRACT

Hawaii's beaches are of great economical and social value; they serve a variety of purposes and are valuable both to residents and tourists alike. Like in many other parts of the world, many of Hawaii's beaches are in a state of erosion and measures of improvement must be designed to cope with this problem. Although in the past several studies have been undertaken to evaluate Hawaii's beach systems and to analyze possible measures of improvement, this study aims at an in-depth analysis of the physical factors at work in the coastal zone. A thorough understanding of these processes, it is felt, is indispensable for the application of sound and economic measures in stabilizing and maintaining Hawaii's beaches. This paper describes some preliminary results of field studies conducted in Waikiki Beach. The latter beach was chosen because of the pressing need for improvements and because of its convenient location. In order to project this study against the proper background, a short review of the general characteristics of Hawaiian beaches precedes the results of the Waikiki Beach study.

INTRODUCTION

The study of beaches in Hawaii is not new. For many years the value of these beaches has been recognized and several studies have been undertaken to define their general characteristics or to specify measures of improvement.

A prime source of information on Hawaiian beach systems is the valuable work by Moberly and Chamberlain for the State of Hawaii (ref. 1). A treatise on Hawaiian beaches can also be found in the work of Shepard and Wanless, "Our Changing Coastlines" (ref. 2).

For an evaluation of proposed measurements of improvement of several Hawaiian beaches, technical reports by the U.S. Army Engineers, Honolulu District, give background data for those projects. Previous studies of Waikiki Beach are documented in House Document No. 104, 89th Congress, 1st Session, 1965 (ref.3).

What is then the need of and use for additional studies of Hawaiian beaches? As far as improvements of Hawaiian beaches are concerned, three important factors put serious restraints on what can and what cannot be done:

-- Adverse effects to surfing should be avoided, or at least severely reduced;

-- Suitable sand for artificial nourishment is very scarce; most of it has to be trucked in or transported from the other islands;

-- Adverse effects of artificial nourishment on reef life cannot be tolerated.

The restraints mentioned above severely limit engineering solutions for the areas that need improvement. In light of recent emphasis on environmental protection, those restraints have to be considered very seriously so that more advanced and sophisticated measures have to be considered in future planning. This in turn requires a greater and more fundamental knowledge of the processes at work in the coastal zone. To provide the information that is needed for the above mentioned approach, the present beach studies at the University of Hawaii are being undertaken as part of its Sea Grant program. In order to allow a more in-depth analysis, a limited number of beach sites have been selected. These sites include Waikiki Beach, Waimanalo Beach and Haleiwa Beach on the Island of Oahu and Kaimu Beach, the black sand beach mentioned before, on the Island of Hawaii. The different beaches on Oahu are with different wave exposures; the beach at Haleiwa forms part of a hydraulic model study for Haleiwa Harbor conducted for the State of Hawaii.

CHARACTERISTICS OF HAWAIIAN BEACHES

Along most mainland beaches the littoral drift, parallel to the shoreline, plays a dominant role in the nourishment and preservation of beaches. In most Hawaiian beach systems the main transport of beach sand takes place in littoral cells, in which the transport perpendicular to the shoreline plays an essential role.

Many beaches are characterized by offshore reefs, which serve as a protection of the coastline against the attack of high waves and tsunamis. At the same time the reefs serve as an important source of (calcareous) beach sand. Chave, Smith and Roy (as reported in ref. 4) estimate that the gross production of calcium carbonate by reef communities averages between 100 and 500 tons per acre per year. This production is used for the building and maintenance of both the reef and the nearby beaches.

In many beach areas sand channels may be observed through the reef flats; these channels may serve as supply channels to nourish the beaches or they may act as rip-channels, carrying water and sand in offshore direction into deep water where extensive sand deposits may be formed. Usually these deposits of sediments consist of material finer than the beach sand (ref. 1).

Because of their important function in protecting Hawaii's shoreline, the preservation of Hawaiian reefs is a matter of great concern. Although not all damages to reefs are man-made, the interference of man with the natural environment is a major cause for this development.

The continental shelf in Hawaii is very narrow, almost non-existent. In most areas deep water is close to the shoreline. Where the protective reef does not exist, wave attack to the shoreline is very severe. An example of such heavy wave attack was experienced during the first few days of December 1969, when a severe North Pacific swell hit the north shore of Oahu causing severe damage to coastal lands and property.

Sources of Beach Sand

Sand from the Hawaiian beaches come from different sources. The most important are:

-- coastal streams and rivers
-- coastal erosion (e.g. weathering of beach rock)
-- destruction of reef by wave action
-- from organic matter by biochemical action
-- volcanic action

In Hawaii the unique situation exists that geologic activity in the form of volcanic action is still a source of both land formation and production of beach sand. This activity is concentrated on the Island of Hawaii where active volcanoes sometimes pour lava into the ocean, which is a source for the black sand beaches.

Apart from the latter, most other beaches on the islands are of composite nature; the beach sand is composed of two general types of sand mixed together in proportions that vary from place to place; the light colored calcareous grains and the darker colored silicate grains of volcanic origin (ref. 1). The calcareous sands are mostly composed of the remains of organisms that lived in the sea. Foraminifera predominate in most beaches and appear to be useful as natural tracers in the study of the beach processes. By staining the foraminifera with Rose Bengal dye it can be determined whether or not they have living protoplasm. Coral fragments usually constitute only a minor portion of the calcareous beach sands. Quartz is absent from most Hawaiian beaches; it is found in a few areas only. Most island beaches have sand of medium grain-size (0.2 - 0.6 mm). The windward beaches have usually a smaller grain-size than the leeward beaches. Courser sand is also formed on the exposed north and west coasts.

The Hawaiian Wave Climate

The natural characteristics and behavior of various Hawaiian beaches is closely associated with wave climate and exposure. The following general types of wave conditions can be recognized:

1. Northeast trade waves - generated by the northeasterly tradewinds that prevail 75-80 percent of the year.

2. Southern swell - generated by storms in the southern hemisphere. These waves have travelled over long distances, are usually of long (14-22 sec) period and low (1-4 ft) height. Time of occurrence is from April through October.

3. Kona storms - generated by local storms of extra tropical nature. They usually occur during the winter months.

4. North Pacific swell - generated by low pressure areas on the North Pacific and arriving at the Hawaiian Islands as swell. These waves create unique surfing conditions on the north and northwest coasts and are sometimes of destructive nature.

5. Hurricane waves - generated by tropical storms that travel in the vicinity of the Islands.

Whereas the wave conditions mentioned under 1-5 occur regularly in the Hawaiian waters, hurricane waves occur only with a low frequency.

Although of less serious nature than on the U.S. mainland, hurricanes do occur and their effect should be taken into consideration, in particular when the design of coastal structures is concerned. In the latter case hurricane waves may very well produce the most critical design conditions.

A special cause of change and of destruction in Hawaii are tsunamis. Examples of destruction are the heavy damages in Hilo on the Big Island during the 1946 and 1960 tsunamis. Under certain conditions the tsunami wave assumes the characteristics of a bore; the latter type is particularly destructive.

Differences in wave exposure cause beaches on opposite sides of the Islands to have different characteristics. On the windward side of the Island of Oahu, for example, a fringing reef is present along most of the shoreline. After breaking and regeneration waves arrive at the beach with reduced height and period. The beach at Waimanalo along the southeast side of the island is an example of this type of beach. It is one of the most beautiful beaches on the islands (fig. 1).

Waikiki Beach (fig. 2) is on the leeward side; waves that affect this beach are turned shoreward by refraction. Direct wave attack on this beach only occurs occasionally, e.g. during Kona storms or with a southern swell.

Wave action on the beach in Waikiki is generally mild, offering good opportunities for safe swimming. Because of the long and relatively low swell, surfing conditions in the Waikiki area are usually good, both for the experienced surfer and the beginner.

On the north shore the fringing reef is either small or non-existent. Wave attack on this coastal part is very heavy during high waves during the North Pacific swell. Surfing conditions are excellent but only for the experienced surfer.

Figure 1

Waimanalo Beach
Southeast Coast, Oahu

Figure 2

Waikiki Beach, Honolulu

Figure 3

Island of Hawaii

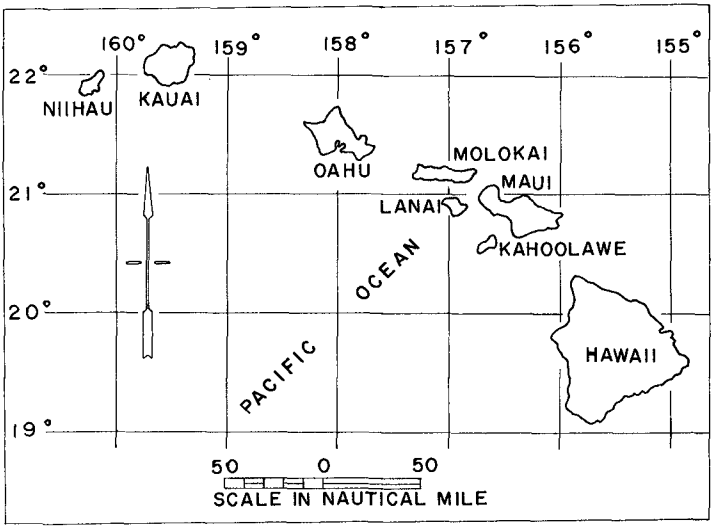

Figure 4 Hawaiian Islands

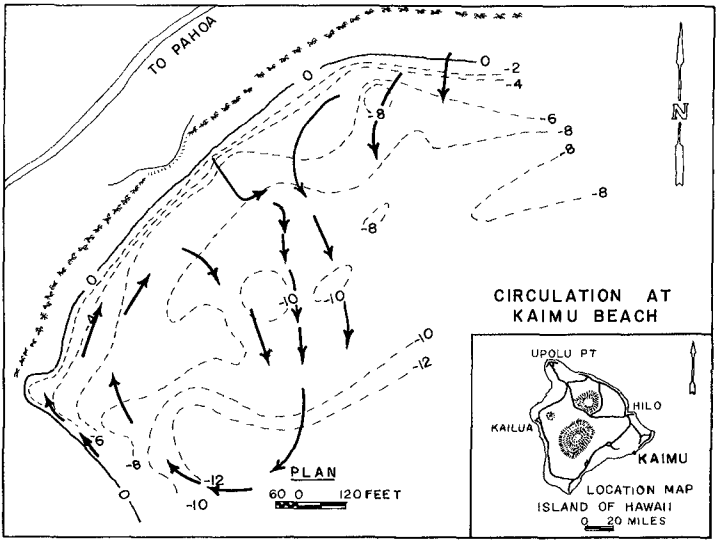

Figure 5 Current Pattern at Kaimu Beach

The scope of this paper does not allow to mention general characteristics of all neighbor island beaches. Figure 4 shows the situation of the major islands in the Hawaiian archipelago. We will mention Kaimu Beach, however, the well known black sand beach on the Island of Hawaii situated on the southeast coast of this island. Figure 3 shows a picture of this characteristic beach that is subject to serious erosion. The developing of this erosion is due, at least partly, to a lowering of the sea floor associated with a local earthquake in 1868 so that the beach became more exposed to the windward trade waves. The current circulation in the bay off Kaimu Beach, as observed on April 7, 1972 is shown in Figure 5.

The Corps of Engineers is presently studying measures to stabilize this beach. One of the solutions under consideration is the construction of a low dam across the bay, which project has met with serious resistance from various groups, because of its doubtful effectiveness and its adverse effect on the coastal environment.

DEVELOPMENT OF WAIKIKI BEACH

The site of Waikiki Beach has undergone drastic changes during the last decade, a process that is continuing today. Started as a very rural area with fishponds and insignificant beaches, its proximity to Honolulu and the ideal swimming and surfing conditions have developed it the way it did. Most of the sand in the Waikiki Beach area is brought in artificially during the various improvements that have been carried out over the years. The last improvement project, which is portion of works of larger scope presently being developed, has just been terminated; it involved artificial nourishment of a section, known as Kuhio Beach, during which about 250,000 cubic yards of sand was trucked in and deposited on the beach. The project also included some minor groin construction and a realignment of the seawall with extensive landscaping and beautification. Over the years, sand that was deposited on the beach in Waikiki has gradually moved away from the beach and deposited on the relatively shallow offshore reefs. Although the losses do not amount to great quantities, the gradual process requires a systematic nourishment of the beach areas. Whether or not the deposition of sand on the reef flats is the cause for the dying of the living reef in this area is not certain; although some reef life can be found, most of it is dead at the present time.

METHOD OF APPROACH

For each selected site a program of field observations is scheduled in which the dominant physical parameters are measured either continuously or intermittently and the behavior of the beach is analyzed by measuring of beach profiles. As many littoral variables as possible are being measured and evaluated. The success of a study, based on field observations, is highly dependent on the quality and accuracy of the data collected. For this reason suitable instrumentation is a first order of concern and much emphasis is therefore placed on obtaining and installing adequate instrumentation.

The following types of observation are being undertaken:

1. measurements of offshore wave conditions (wave height and period) with in situ wave recorders in depth of approximately 50 feet.

2. measurement of wave direction by aerial photography.

3. measurement of wave conditions on reef flat by means of self-supported capacitance wave gages.

4. measurement of currents by means of current meters, dye and drogue measurements.

5. water level recorders for measurement of vertical tide.

6. measurement of sand transport by means of sand traps and flourescent tracers.

Wave conditions and currents are basic parameters that affect the movement of sand in a beach area. It is not sufficient to characterize the wave climate offshore, but it is essential in Hawaii to evaluate energy losses over the reef and the change in wave characteristics. Often the larger waves break in deeper water, and the larger period waves break down in components of smaller period. The latter represents the effective energy available for the littoral processes in the nearshore region.

Wave Conditions and Measurements

Wave data available at present as support for the present studies include the following information:

1. a study by "Marine Advisors" regarding the wave conditions around the Islands. The results of this study of about one year came partly from hindcasting, partly from observations (ref. 1).

2. staff gage readings in the Waikiki area by the U.S. Army Corps of Engineers (about one year).

3. measurements with two bottom mounted self-recording pressure wave gages in 50 feet of water off Waikiki Beach.

4. wave measurements by pressure transducer at 36 feet depth near the entrance of Kewalo Basin, a small craft harbor west of Waikiki Beach (continuous, over about one year).

5. computations on significant wave height and period associated with a number of storms by the U.S. Army Corps of Engineers.

In order to evaluate the frequency of occurrence of waves of a given height on the leeward coast south of Honolulu, the data mentioned under 1, 4 and 5 have been used to construct a frequency diagram. Various ways of constructing such diagram have been evaluated; the form that seems most promising is presented in fig. 6. The offshore waves (representing conditions at 30-40 ft. depth) have a frequency distribution that is built up from two different categories of waves: the distribution of wave height according to daily observations, measured near the entrance to Kewalo Basin (4), and the distribution of waves obtained from hindcasting during a number of storms (5).

The data available for storm waves is of limited scope and does not allow a further breakdown as to wave period and distribution, so that a refraction and shoaling coefficient can be applied. A practical approach is to use an average value for refraction and shoaling to obtain nearshore conditions from deep water values.

The available data suggest that for Mamala Bay (fig. 6a) a combined frequency diagram, representing all conditions can best be obtained by two different lines, intersecting each other on the diagram: a steep line, representing the storm wave conditions and a more gently sloping line, representing the ordinary daily observations. The part of the frequency diagram that is to be used depends on the purpose of the analysis. When a design wave for a structure is needed, the steeper portion will have to be used; for workability and possibly littoral drift phenomena the more gentle sloping portion of the frequency diagram may be the most interesting part. A similar analysis was made for the west shore of the Island of Oahu regarding wave conditions prevailing near Pokai Bay, whereby the same distinction was made between daily wave conditions and storm waves (fig. 6b). For this area the two groups merge into one working line on the frequency diagram.

The next problem is to define the frequency distribution for shallow water (above the reef) given the conditions at 30-50 ft. depth. Under the assumption that the frequency diagrams for offshore conditions represent the significant wave height, the significant wave height for shallow water may be derived utilizing an assumed wave height distribution and a breaking criterion.

Using a Rayleigh distribution for the wave height and a simple breaking criterion: $H_b = \alpha h_b$ for the maximum wave height H_b, in which h_b represents the water depth; the significant wave heights for shallow water can be obtained by constructing diagrams of the form of fig. 6. The latter figure presents the significant shallow water wave height for various depths, given an offshore wave height of 17.5 ft. In this manner frequency distributions for shallow water can be constructed as shown in fig. 6a.

It is of interest to compare the results of this type of analysis with the North Sea investigation as reported by Paape (1969) (ref. 5). Paape reported a ratio between maximum breaking wave height and significant breaking wave of 1.5. Using an average value $\alpha = 0.78$ (from solitary wave theory) this ratio becomes about 1.34 for 30 ft., 1.04 for 20 ft. and 1.0 for 10 ft. depth.

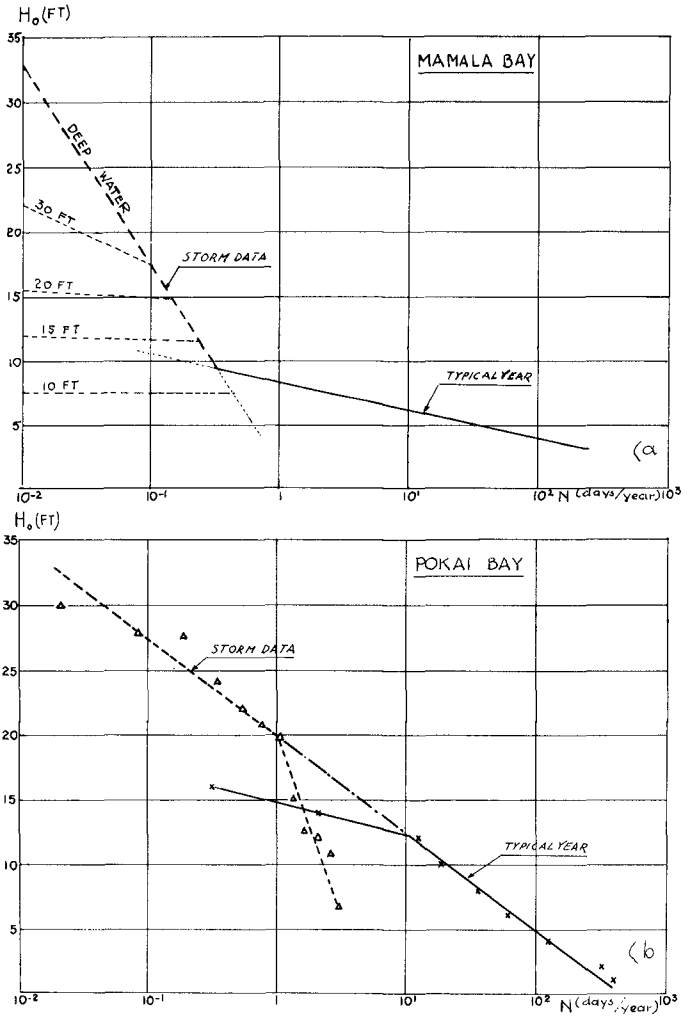

Figure 6

Frequency Diagrams for Offshore and Nearshore Waves

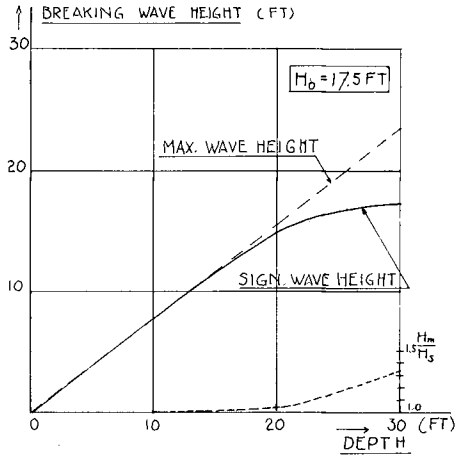

Figure 7

Significant Breaking Wave Height Versus Depth for Given Deep Water Wave Characteristics

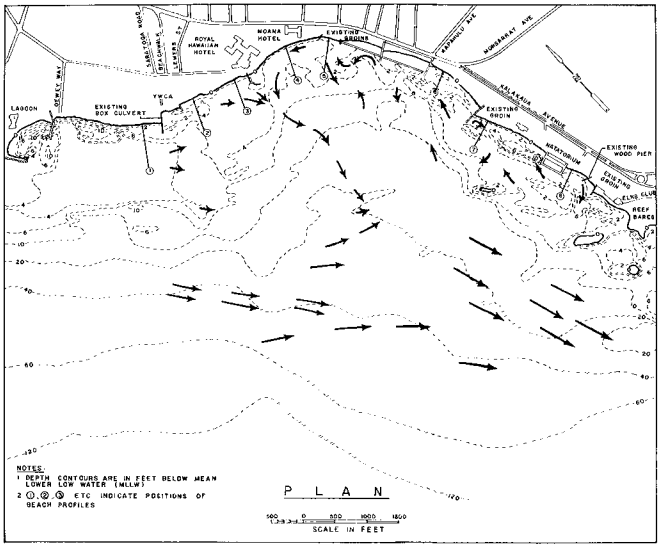

Figure 8

Waikiki Beach, Depth Contours and Circulation Pattern

Figure 9 Aerial Photograph Waikiki Beach, Showing Refraction of Waves

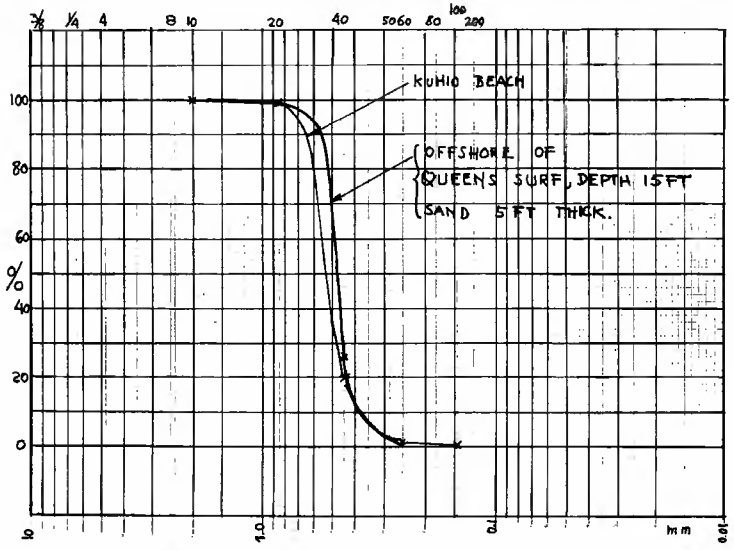

Figure 10 Sediment Characteristics for Beach and Offshore Sand at Waikiki

Realizing that for individual waves α may be larger than 0.78 and that the average depths at the measuring stations of the North Sea most likely is over 30 ft., the results suggest general agreement and therefore support the type of analysis suggested here.

Flow Measurements at Waikiki Beach

Transport of beach materials takes place under the combined action of waves and currents (Byker, ref. 6). In order to establish prevailing transport patterns, it was felt necessary to obtain a clear understanding of the prevailing current circulation. In cooperation with Dr. R. Tait of the Department of Oceanography who is involved in an analysis of environmental conditions in the Waikiki Beach area for the U.S. Army Corps of Engineers, an extensive program of current measurements was undertaken. The current measurements were taken during flood and ebb conditions both close to the shoreline and on the reef flats and in the reef channels. The methods included aerial observation of the movements of dye patches, triangulation of drogues and following of dye patches by small boats.

Without going into details, a number of preliminary conclusions came forward from the studies that have been conducted so far. Further analysis is necessary to clarify some uncertainties encountered.

Current patterns could be clearly distinguished into three groups:

1. currents associated with the tidal flow off the coast.

2. currents associated with the pattern of breaking waves (longshore currents).

3. rip currents, associated with the breaking of the (larger) waves. Where the tidal and longshore currents had principle directions parallel to the shoreline, the rip currents have directions perpendicular to the shoreline.

Regarding the nature of the above mentioned current types, the observations show the following characteristics:

Tidal Currents

Offshore currents beyond the reefs in this area are predominantly of tidal nature with reversing components parallel to the coastline. On the reefs the currents are considerably smaller than in deep water; their maximum values are of the order of 0.1-0.2 m/sec.

Flow measurements on the offshore reef areas show that in the eastern part of the study area the currents are persistently in easterly direction, both during flood and ebb periods, suggesting the existence of a large eddy during predominantly westerly flow in deep water.

In the western part of the study area currents of varying strength and direction were observed. The nature of these variations is not completely understood at this time and needs further investigation. The general circulation is shown in fig. 8.

Longshore Currents

The direction of the longshore currents inside the breaker zone and close to the beach is consistent with direction of breaking waves near the beach. They are usually small (of the order of 0.05 m/sec.) which is in agreement with the usually low wave heights near the beach. They do not reverse with the tide, but they may have a component perpendicular to the beach in the vicinity of a groin or other coastal structure. These currents are responsible for the longshore and transport, which has a predominant westerly direction eastward of the Royal Hawaiian Hotel (fig. 8). Reference is also made to fig. 9, showing the pattern of breaking waves in the Waikiki Beach offshore area.

Rip Currents

During conditions of heavy southerly swell a large rip was observed off the Royal Hawaiian Hotel, and a smaller (and shorter) rip west of the Kapahulu groin off the offshore breakwater.

Recent theoretical studies on rip currents (ref. 7, 8) indicate that the occurrence of rip currents can be associated with the phenomenon of edge waves. The latter are long period, low amplitude waves that travel in a direction parallel to the shoreline. They may be progressive waves or standing waves.

The general topography of the offshore area at Waikiki Beach (Mamala Bay) suggests that standing edge waves of a certain type could be a contributing factor to the rip current pattern. Further studies will be required to clarify this matter.

Observations of Beach Profiles

In order to study the stability of the beach in the Waikiki area, profiles have been measured at regular time intervals. Where differences between successive measurements are minimum, the beach has its highest degree of stability. Differences in stability characteristics may be observed by comparing the profiles at Stations 4, 3 and 2 of fig. 8. The maximum and minimum profiles over a period of about one-half year are presented in fig. 11. Profile No. 4 which is situated in the zone of predominantly westerly drift, is relatively stable; Profiles No. 3 and 2 are situated westward of the prevailing rip and show a higher degree of instability. The offshore reefs are relatively flat; material is moved from the beaches onto the reefs where it fills holes and channels.

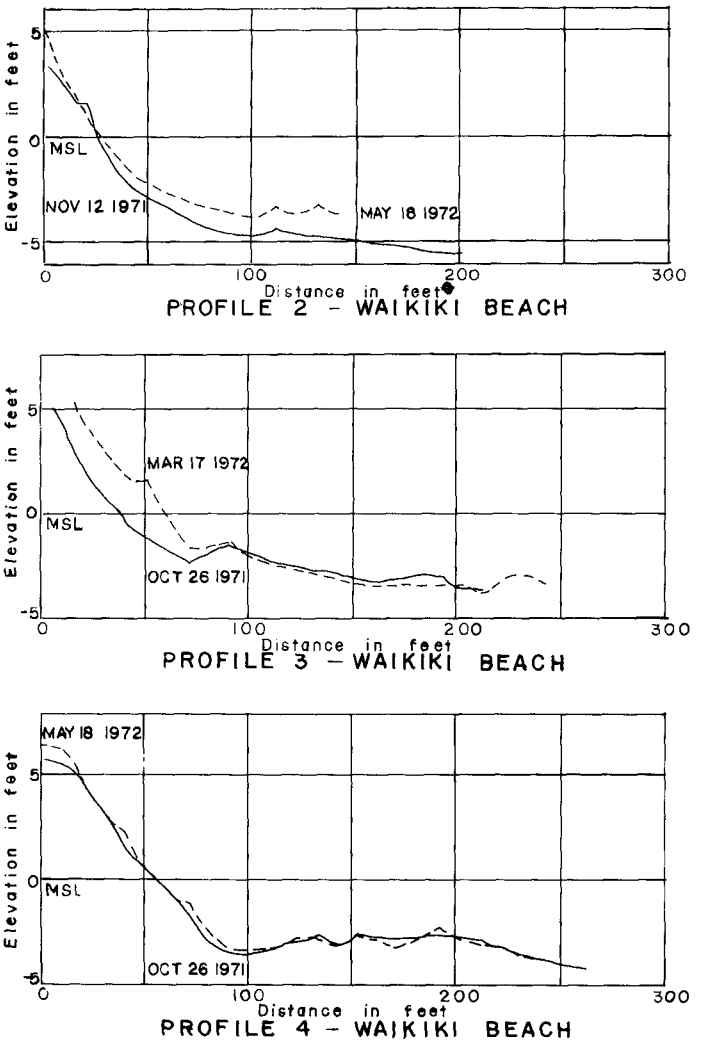

Figure 11

Characteristic Beach Profiles, Waikiki

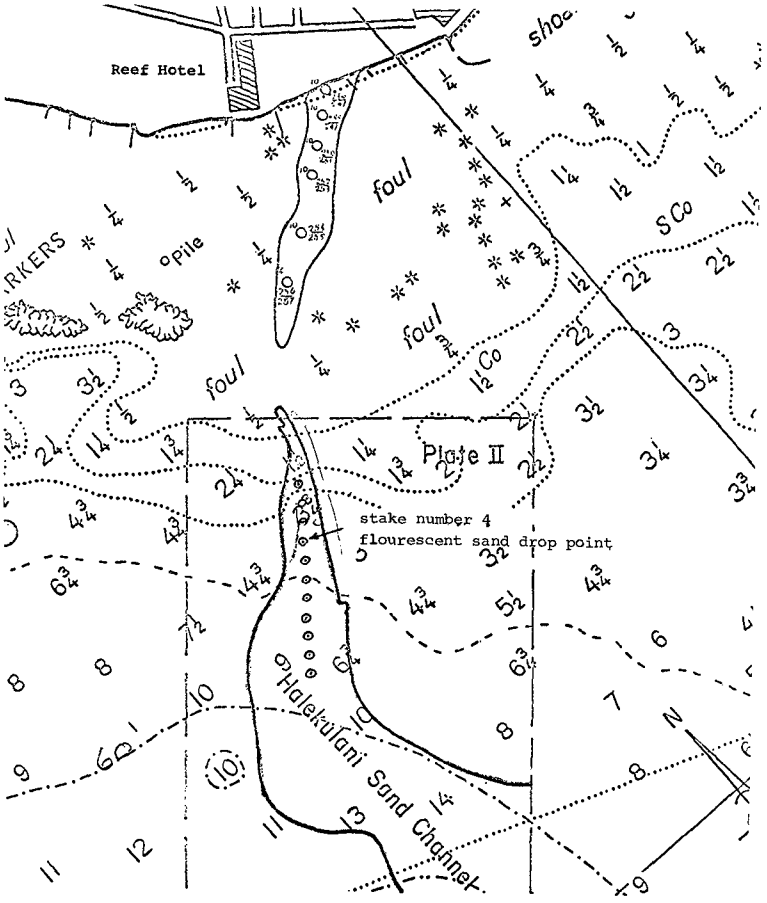

Figure 12

Stations for Measurement of Sand Transport in Halekulani Channel

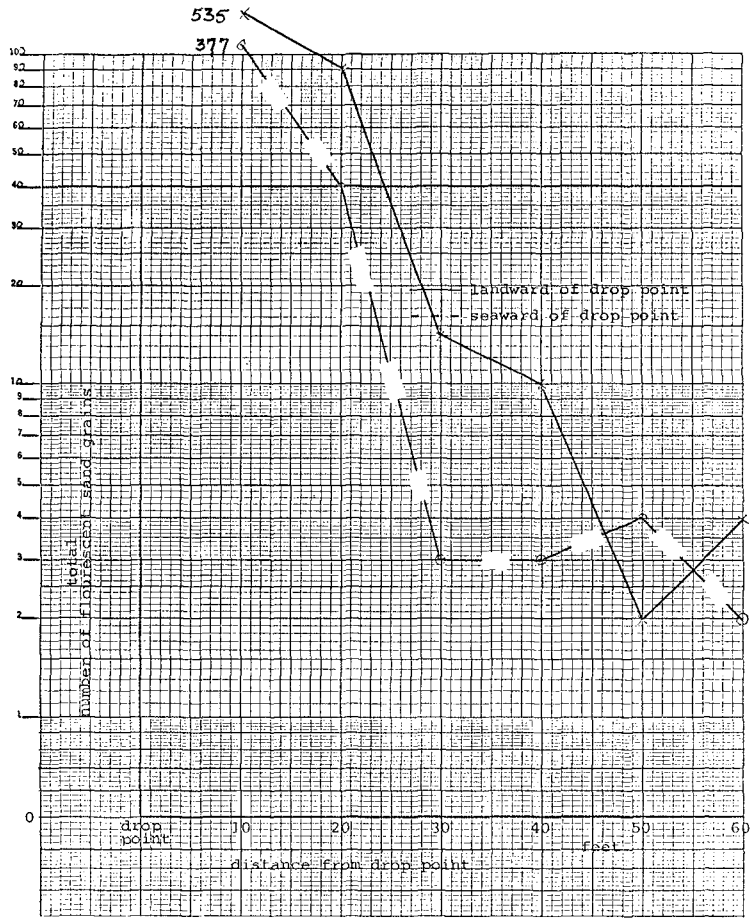

Figure 13

Tracer Counts for Transport of Sand in Halekulani Channel

It may be expected that the material found on the reefs will be of the same characteristics as the material on the beach. Analysis of beach and reef sand by Fred Casciano, as presented in fig. 10, confirms that beach and reef sand is basically of the same grain-size distribution characteristics.

Measurements of Material Transport

Both aerial photographs and bathymetric charts indicate the presence of two sand channels in the Waikiki Beach area, they appear to be the remnants of previous river mouths. The western most channel is called the Halekulani channel; it is located offshore of the Halekulani Hotel.

In earlier studies for the improvement of Waikiki Beach, it was felt that this channel could possibly function as a drain to the littoral drift, allowing sand to pass seaward from the beach.

To investigate this possibility a program of sand tracing was developed by Fred Casciano and David Kern (ref. 9). Stations in the Halekulani channel were marked by iron bars, 100 ft. apart, as indicated in fig. 12. Rhodamine B dye was used as tracer; sand from the channel was dried after which the grains were colored with the dye. An initial deposit of 362 lbs. of colored sand was made at Station 4 and observations were made to study the movement of the colored sand. On both sides of Station No. 4, a grid system of bars, 10 ft. apart was installed for detailed observations around Station No. 4. The observations consisted of the collection of surface samples by divers with the use of bottle caps, provided with a substance to let the surface grains stick to the cap. From January 23, 1970 two days after the fluorescent sand was deposited in the channel, to May 22, 1970, 13 sets of surface cap samples were taken, each on a different day. The time between successive sampling days ranged between two days in the beginning of the study and two weeks near the end. In addition to the collection of surface samples sand cores were taken at the end of the study period. At each station the number of colored grains was counted, using ultra-violet long wave light.

Assuming the number of grains counted in a surface sample to be a measure of the total sand movement the count at the stations on the seaward side and on the landward side of the deposition point indicates whether there is a resultant shoreward or landward movement of the bottom sand in the channel.

Figure 13 shows the total count at all stations in the channels. This result and the results of individual counts during each of the observations indicate a resultant sand transport in shoreward direction in the channel during the period of observation. The results of sand cores confirmed the results of the surface sampling.

An additional observation was made that gave further weight to the conclusion of resultant landward transport: at each station the height of the bar over the (average) bottom was measured during each observation. At the most landward station an increased elevation of the bottom of about 0.1 meter was observed; at the other stations, the elevation of the bottom did not change significantly.

One may ask whether the period of observation (4 months) is long enough to justify a general conclusion in the same direction. This question is partly answered by the results of the flow measurement. During the large southern swell, observed in March 1972, and also during other periods of observations no indications were found that the Halekulani channel was functioning as a rip channel; on the contrary the currents under most conditions seemed to move parallel to shoreline, possibly with a very small shoreward component. The conclusion regarding a net material transport in the Halekulani channel in a shoreward direction therefore seems to have a general significance.

CONCLUSIONS

Hawaii's beaches are of great economical and social value, and therefore worthy of careful preservation. Past actions of man have often been hap-hazardous or detrimental, because a thorough understanding of the dynamic nature of beach systems was lacking. The present study undertaken at the University of Hawaii to obtain detailed insight into the processes at work will be useful in guiding future planning and development for Hawaiian beaches. The study at Waikiki Beach has provided a better insight into the mechanics of water and sediment motion in this area:

-- It has shown that tidal currents, littoral current and rip currents contribute to the sediment motion and the formation of the littoral cell.

-- It has provided insight into the behavior and direction of the littoral drift and has given further evidence to the supposition that the Halekulani channel does not function as a drain, but rather could have a net transport in shoreward direction.

-- A main rip current was found to exist off the Royal Hawaiian Hotel at Waikiki, by which relatively large amounts of material are moved in offshore direction.

-- In the study of beach processes at Waikiki, the use of aerial photography has been of great value.

The findings of studies of this type will be valuable in further engineering of coastal protection works and will be of general use in understanding the prevalent coastal processes.

ACKNOWLEDGEMENTS

The author wishes to express his appreciation to all who have contributed to this study. He particularly wishes to thank Mr. U.B. Nayak and his group of students for all the tedious field work involved and for analyzing the data. The author thankfully acknowledges the cooperation of Dr. R. Tait and Mr. Frank Gremse for their cooperation in conducting the flow measurements. He wants to thank Mr. Fred Casciano for his help in this study, and Mr. James Walker, who helped in taking the aerial photographs. He wants to acknowledge the help of Mr. John Kelly for providing interesting historical data on various

projects. The author wishes to thank the U.S. Army Corps of Engineers and the State of Hawaii for providing available data on study sites and the Sea Grant Office for providing financial support to this study. He finally wishes to thank Mrs. Edith Katada and Mrs. Mildred Frank for administrative help and typing of the manuscript.

REFERENCES

1. R. Moberly, Jr. and Theodore Chamberlain, "Hawaiian Beach Systems", report prepared for the Harbors Division, Department of Transportation, State of Hawaii, July 1964.

2. Francis P. Shepard and Harold R. Wanless, "Our Changing Coastlines", McGraw-Hill Book Company, 1970.

3. Hawaii Beach Erosion Control Study, Waikiki Beach, Oahu, 89th Congress, 1st Session, House Document No. 104. Washington, D.C., U.S. Government Printing Office, 1965.

4. R.E. Johannes, "Coral Reefs and Pollution", paper presented at the Regional Symposium on Conservation of Nature--Reef and Lagoons, South Pacific Commission, August 1971.

5. A. Paape, "Some Aspects of the Design Procedure of Maritime Structures", XXIInd International Navigation Congress, Paris, 1969, Section II, Subject 5.

6. E.W. Byker, "Some considerations about scales for Coastal Models with Movable Bed", Delft Hydraulics Laboratory, Publication No. 50, November 1967.

7. Anthony J. Bowen and Douglas L. Inman, "Rip Currents", Laboratory and Field Observations, Journal of Geophysical Research, Vol. 74, No. 23, October 20, 1969.

8. Edward K. Noda, "Rip Currents", Proceedings 13th Int. Conference on Coastal Engineering, Vancouver, 1972.

9. David E. Kern, "A Study of Sand Movement in the Halekulani Channel off Waikiki, Hawaii", paper for presentation in Ocean Engineering seminar, University of Hawaii, as partial fulfillment of the requirements for a M.S. degree in Ocean Engineering.

CHAPTER 68

FORMS OF EROSION AND ACCRETION ON CAPE COD BEACHES

by
Victor Goldsmith[1], Joseph M. Colonell[2],
and Peter N. Turbide[3]

Abstract

Frequent measurements of beach profiles have been made at sixteen areas between Maine and Long Island since September 1965 by members of the Coastal Research Center of the University of Massachusetts. This research effort has resulted in the accumulation of approximately 2000 beach profiles along the New England coastline. The detailed analysis of profiles from Monomoy Island and Nauset Spit on Cape Cod has revealed the following erosion-accretion characteristics:

1. The most active areas of the beach profile in terms of sand transport are at the low-tide, neap high-tide, and spring high-tide zones. The center of the beach face is relatively inactive.
2. An exception to this behavior occurs during severe storms when large volumes of sand are removed from the entire beach face, producing a concave upward profile shape.
3. During periods of relatively low wave activity there is much interaction in terms of sand movement between these three zones, resulting in the formation of distinctive profile shapes.
4. These profile shapes tend to maintain themselves through sand movements which cause the berm to migrate back and forth along the profile.
5. This activity is often accomplished with little or no net sand erosion or accretion to the total profile.

These conclusions, combined with additional analyses, indicate that the traditional measurements of total beach width and high tide beach width (i.e., to the berm) are not a reliable indication of sand volume changes on beaches.

---

[1]Associate Marine Scientist, Virginia Institute of Marine Science, Gloucester Point, Virginia

[2]Associate Professor of Civil Engineering, University of Massachusetts, Amherst, Massachusetts

[3]Graduate Student, Department of Civil Engineering, University of Massachusetts, Amherst, Massachusetts

INTRODUCTION

Measurements of beach profiles have been made at sixteen areas between Maine and Long Island since September 1965 over various time intervals by members of the Coastal Research Center of the Department of Geology at the University of Massachusetts. This research effort has resulted in the accumulation of approximately 2000 detailed beach profiles along the New England coastline. Analysis of these profiles, along with other data, has provided a considerable store of information on the nature of coastal processes and the development of coastal morphology along the depositional portions of the New England coast (1,4). More specifically, these measurements have provided a means for the precise determination of sand volumes added to or removed from beaches under a wide variety of climatic conditions (2).

The characteristic response of a beach, in terms of volumetric changes and strandline migration, should be regarded as essential to the evaluation, planning, design, and operation of any coastal engineering project. It is the purpose of this paper to illustrate the type of information which is available from a detailed analysis of beach profile data and to show that the results so obtained are not always consistent with intuitive beliefs or "classical" patterns of beach behavior.

MONOMOY ISLAND AND NAUSET SPIT

Located on the "elbow" of Cape Cod, Massachusetts, Monomoy Island and Nauset Spit form a dynamic barrier island complex which originated in Holocene time (Figure 1). For a period of three years, beginning in June 1968, twelve beach profiles on Monomoy Island and four profiles on Nauset Spit were measured at intervals varying from two weeks to several months, depending upon the apparent beach activity. Very early in this study it was noted that the beach at various profile locations reacted in strikingly different manners to apparently similar beach-shaping mechanisms (5). A particular storm would cause considerable erosion at one profile location but comparatively little erosion would occur at another location as close as one mile away. This observation prompted an increased surveillance at certain locations, resulting in the collection 393 beach profiles over the twelve-mile stretch of coastline (Table I). The number of profiles measured at any single location is generally indicative of the relative activity (i.e. erosion/accretion) of the beach at that location.

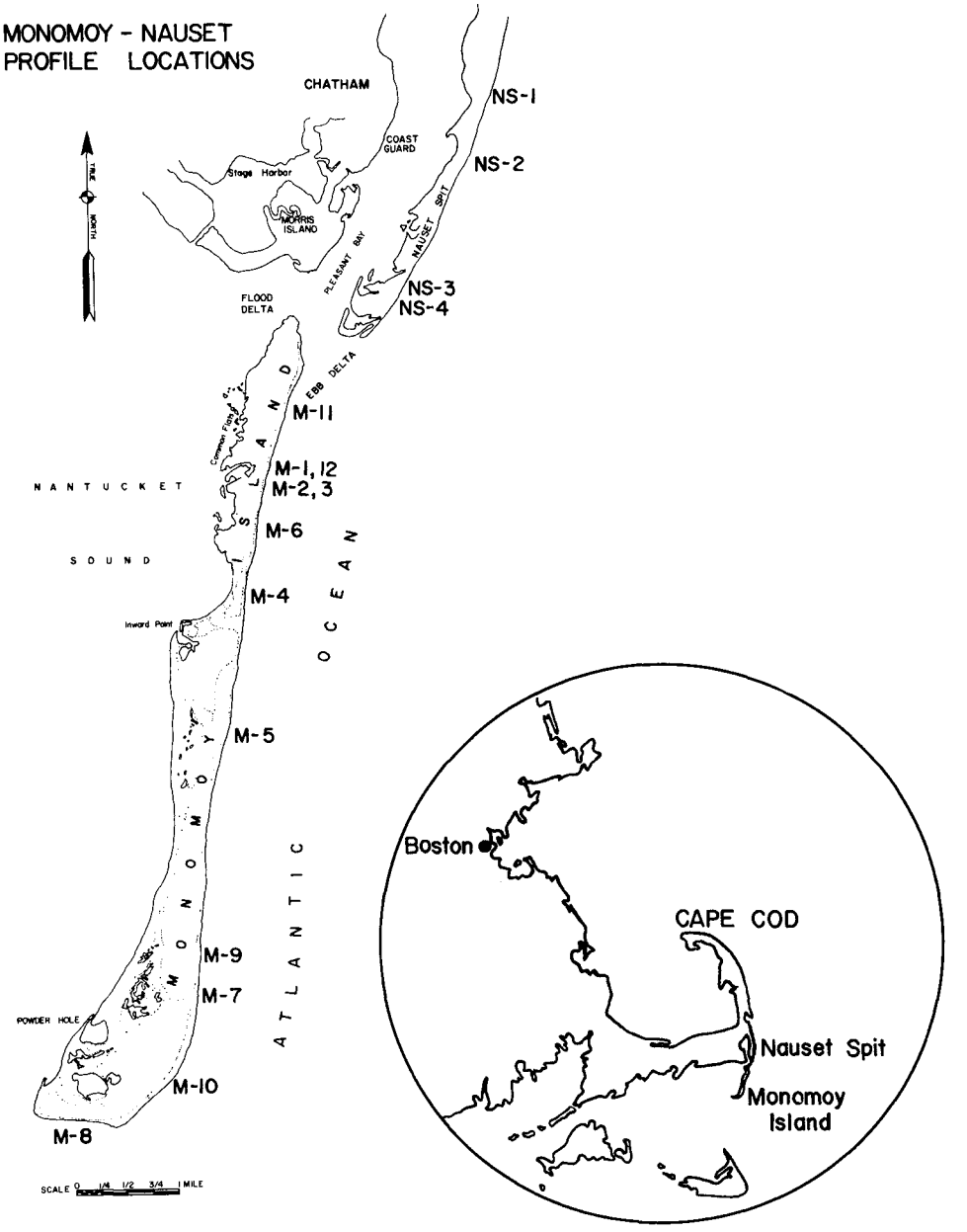

Figure 1. Location map for Monomoy-Nauset beach profile stations.

MONOMOY ISLAND

Profile Location	1	2	3	4	5	6	7	8	9	10	11	12
Number of Profiles	40	26	15	30	33	41	9	25	5	16	18	3

NAUSET SPIT

Profile Location	1	2	3	4
Number of Profiles	30	35	28	28

TABLE I. Beach profiles measured on Monomoy Island and Nauset Spit, 1968-1971. See Figure 1 for profile locations.

ANALYSIS OF BEACH PROFILE DATA

The 393 Monomoy-Nauset beach profiles were measured by means of a standard profiling technique (3). Each profile line extends seaward from a permanent stake in the foredune ridge perpendicularly across the beach to the low tide line. Vertical measurements are made at horizontal intervals of ten feet along the profile line, or at even shorter intervals when there occurs a distinctive morphological feature such as a beach ridge, an erosional scarp, or other significant break in the beach slope. The accuracy of this method is estimated to be $\pm$ 0.1 feet vertically over the total profile length.

Field data obtained by this beach profiling technique were punched on computer cards in essentially the same form as they appear on the original data sheets. These data were then converted to an x-y coordinate representation of the profile, the results being punched automatically on cards or written on magnetic tape for subsequent analysis and permanent storage. A comparative analysis of the Monomoy-Nauset profiles was made to determine detailed changes along any given profile with time.

The analysis of the beach profile data is basically a computation of changes in the total sand volume at a given profile location over the time period between measurements. By computing the areal change in a vertical cross-section of the beach at the profile location, the amount of sand that was added to or removed from the beach is estimated. These volume estimates are properly stated in the units of cubic feet of sand per lineal foot of beach (i.e. parallel to the shoreline) but, for the sake of brevity, such results are hereafter given simply in

terms of cubic feet of sand. This analysis allows not only the determination of the net change to the beach as a whole, but also provides useful information on the re-distribution of sand within the beach profile. Correlation of these results with changes in beach shape and strandline migration form the substance of this discussion.

A detailed analysis of the Monomoy Island-Nauset Spit profiles, which are typical of other New England beach profiles, has revealed several distinctive erosion-accretion characteristics. These characteristics are illustrated by Figures 2 through 7, each of which is a set of profile comparisons selected to exemplify the observations listed below.

1. The most active zones of the beach profile in terms of sand transport are at the low-tide zone, neap high-tide zone, and spring high-tide zone. The center of the beach face tends to be relatively inactive (Figures 2 and 3).

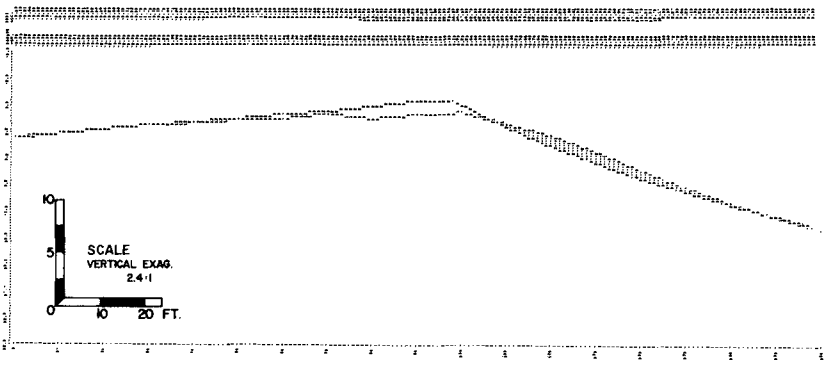

Figure 2. Comparison of the September 27, 1969, and the November 1, 1969, M-4 beach profiles, on Monomoy Island. Volumetric changes are indicated by the dark areas (erosion) and the light areas (accretion) between the two profiles. This comparison shows that 34 cubic feet of sand was removed from the beach face and 39 cubic feet of sand was added to the berm crest, resulting in a net total profile accretion of 5 cubic feet despite a neap berm retreat of 20 feet and a change in profile shape from convex to concave upward.

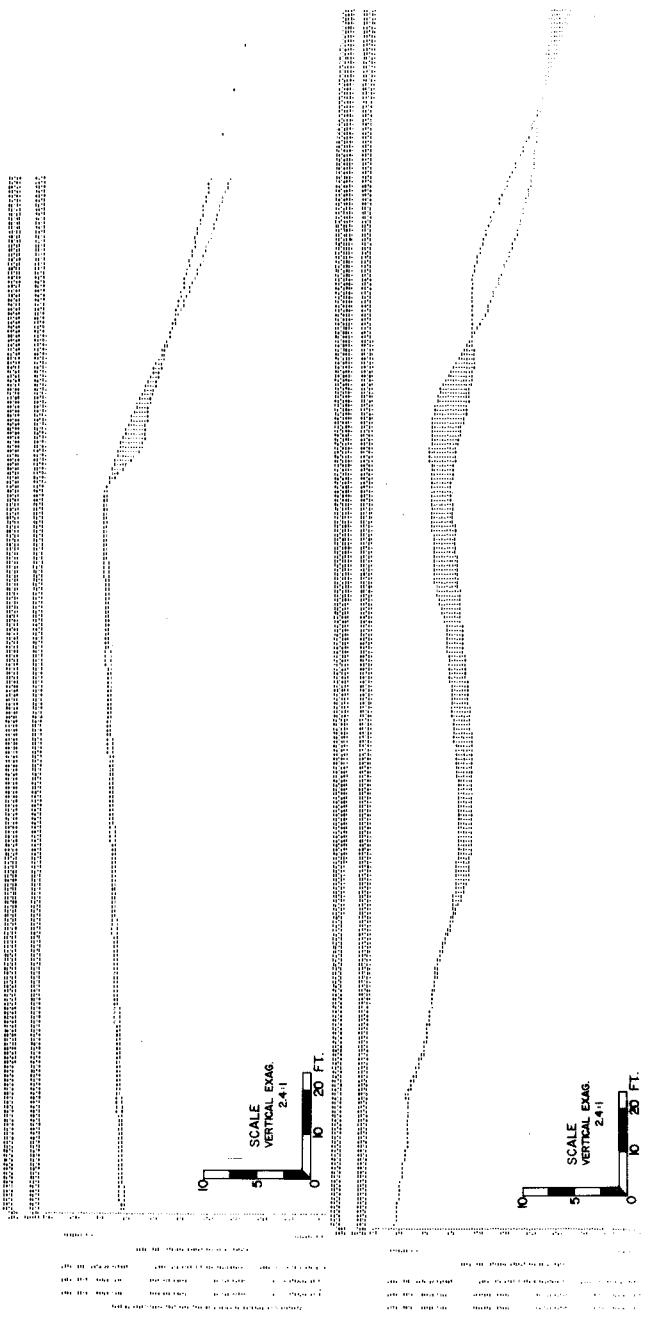

Figure 3. Comparisons between the November 1, 1969 and December 4, 1969, M-5 beach profiles (top), and July 14, 1969, and August 10, 1969, M-1 profiles (bottom), on Monomoy Island. Volumetric changes are indicated by the dark areas (erosion) and the light areas (accretion) between the two profiles. The most active areas of the profile (i.e., volumetric changes) are the low tide, neap high tide and spring high tide zones. In the upper comparison the cumulative volumetric change in these three zones was the accretion of only five cubic feet of sand. In the lower comparison, the cumulative volumetric change in these three zones was the loss of 55 cubic feet of sand. Note the changes in profile shape from convex to concave upwards.

2. An exception to the behavior noted above (#1) occurs during severe storms when large quantities of sand are removed from the entire beach face, producing a concave upward profile shape (Figure 4).
3. During periods of relatively low wave activity there is much interaction in terms of sand movement between these three zones (listed in #1), resulting in the formation of distinctive beach profile shapes (Figures 5 and 6).
4. These profile shapes tend to maintain themselves through sand movements which cause the berm to migrate back and forth along the profile (Figures 5 and 6).
5. The beach activity noted above is often accomplished with little or no net sand erosion or accretion to the total profile (Figures 2 and 7).

The observations enumerated above, supported by additional analyses, suggest that the traditional measurements of total beach width and high tide beach width (i.e., to the berm) are not necessarily a reliable indication of sand volume changes on beaches. Intuitively, one expects accretion to be accompanied by a seaward migration of the strandline and erosion to be associated with a landward migration of the strandline. Figure 8 shows that such intuitive conclusions would have been correct for about two-thirds of the 154 beach profiles represented in that illustration. It is also readily apparent from Figure 8 that the application of any general formula for estimating volumetric changes corresponding to a given strandline migration would be inappropriate for the Monomoy-Nauset beaches. For example, the U.S. Army Corps of Engineers estimation rule (6, p. 216), "... one square foot of change in beach surface area equals one cubic yard of beach material ...", fails to indicate even the trend of the beach volume change associated with strandline migration. The Monomoy-Nauset conditions, typical of other Cape Cod beaches, are obviously not amenable to such simple formulations.

Additional attempts to correlate beach volume change with strandline migration led to examination of the ratio of the former to the absolute value of the latter. Figure 9 shows the frequency of occurrence of various values of this ratio during the three-year study of the Monomoy-Nauset beaches. The significant feature of Figure 9 is the

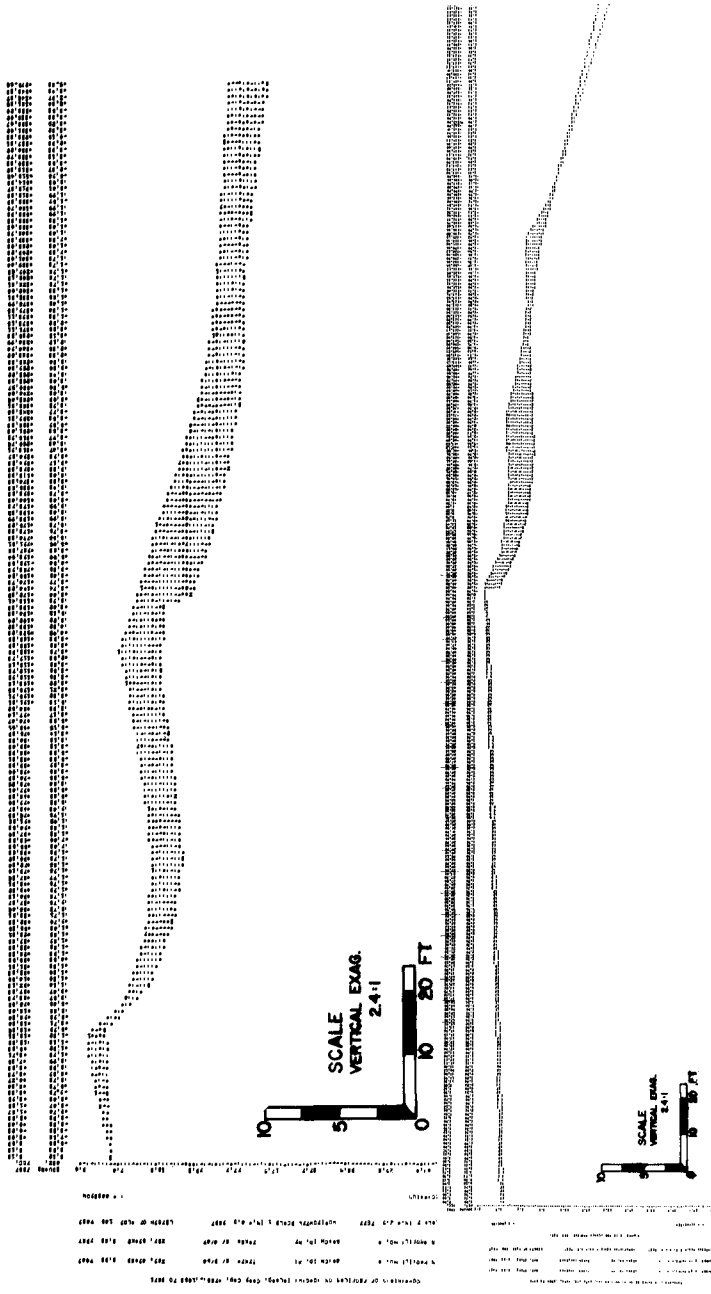

Figure 4. Comparisons between the August 3, 1969, and August 9, 1969, M-8 beach profiles (top) and the August 13, 1968, and November 14, 1969, M-5 beach profiles (bottom), on Monomoy Island. In both comparisons severe erosion had occurred through the intertidal portion of the profiles, and in both comparisons the beach was well underway towards recovery at the time the second profile was made as indicated by its convex upward shape. Nevertheless, there remained a net loss of 347 and 122 cubic feet of sand at the M-8 and M-5 profiles, respectively.

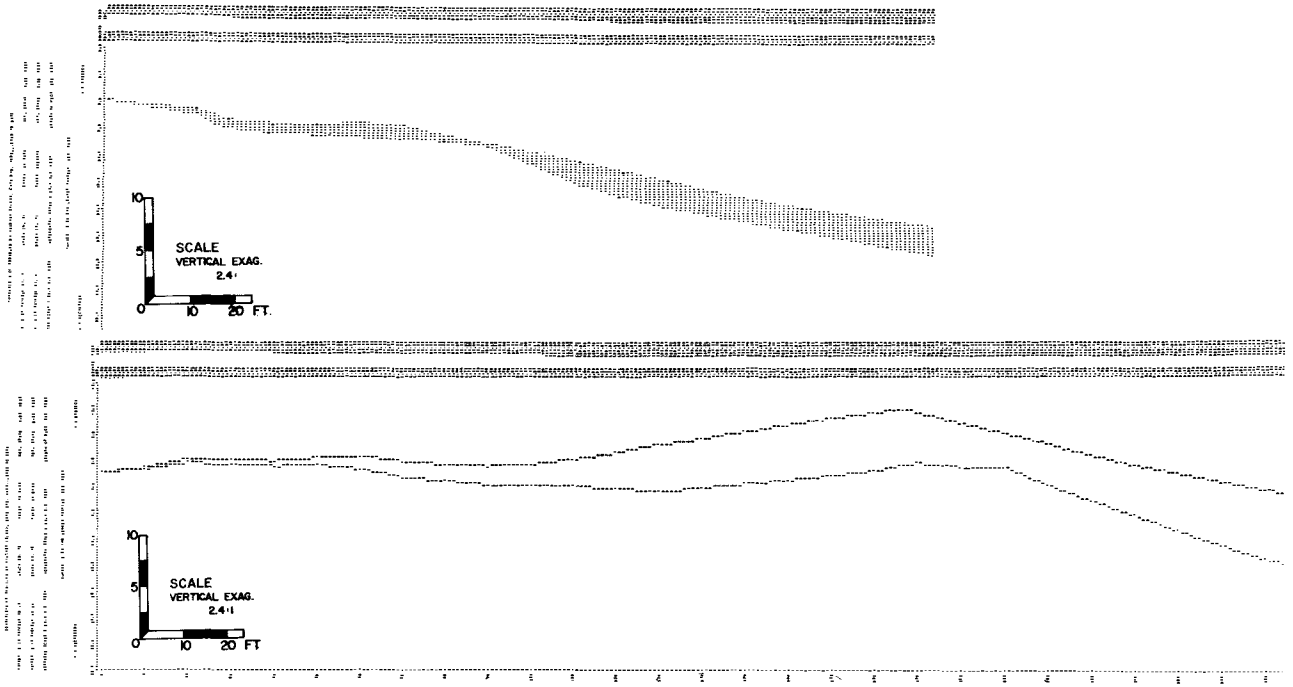

Figure 5. Comparisons between the May 9, 1970, and June 17, 1970, M-6 profiles (top) and the July 4, 1969, and August 3, 1969, M-10 beach profiles (bottom), on Monomoy Island. Volumetric changes are indicated by the dark areas (erosion) and the light areas (accretion) between the two profiles. In the upper comparison 267 cubic feet of sand was removed from the total profile, yet the berm moved 20 feet seaward. In the lower comparison 1070 cubic feet of sand per lineal foot of beach was added to the total profile, yet the berm migrated landward approximately 25 feet, resulting in an apparent narrowing of the beach. Note the similarity of the beach profiles before and after erosion (upper) and accretion (lower).

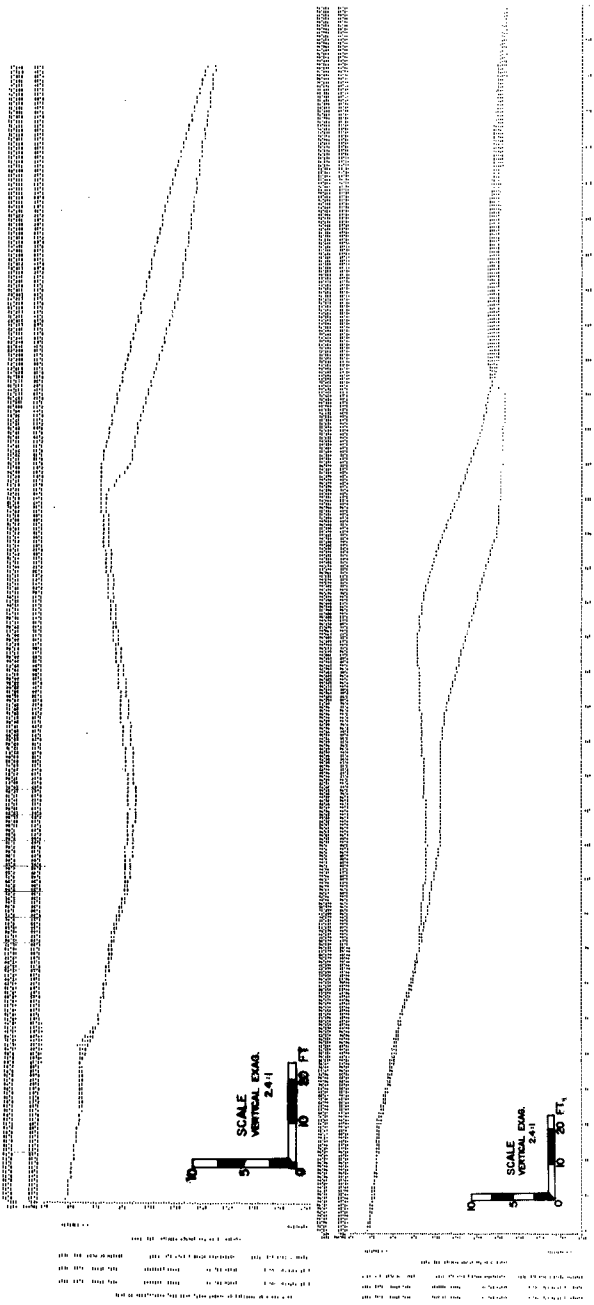

Figure 6. Comparisons between the September 26, 1969, and the October 18, 1969, NS-1 beach profiles (top) and the January 3, 1970, and April 14, 1970, NS-1 beach profiles on Nauset Spit. Volumetric changes are indicated by the dark areas (erosion) and the light areas (accretion) between the two profiles. In both comparisons, increases in beach volume (292 and 493 cubic feet, respectively) are associated with seaward berm migrations (10 and 40 feet). In the lower comparison the accretion occurred in the form of onshore ridge and runnel migration, with the ridge eventually welding onto the upper part of the beach face. Migrating intertidal ridges are typical of post-storm beach recovery on many New England beaches (1, pp. 245-265).

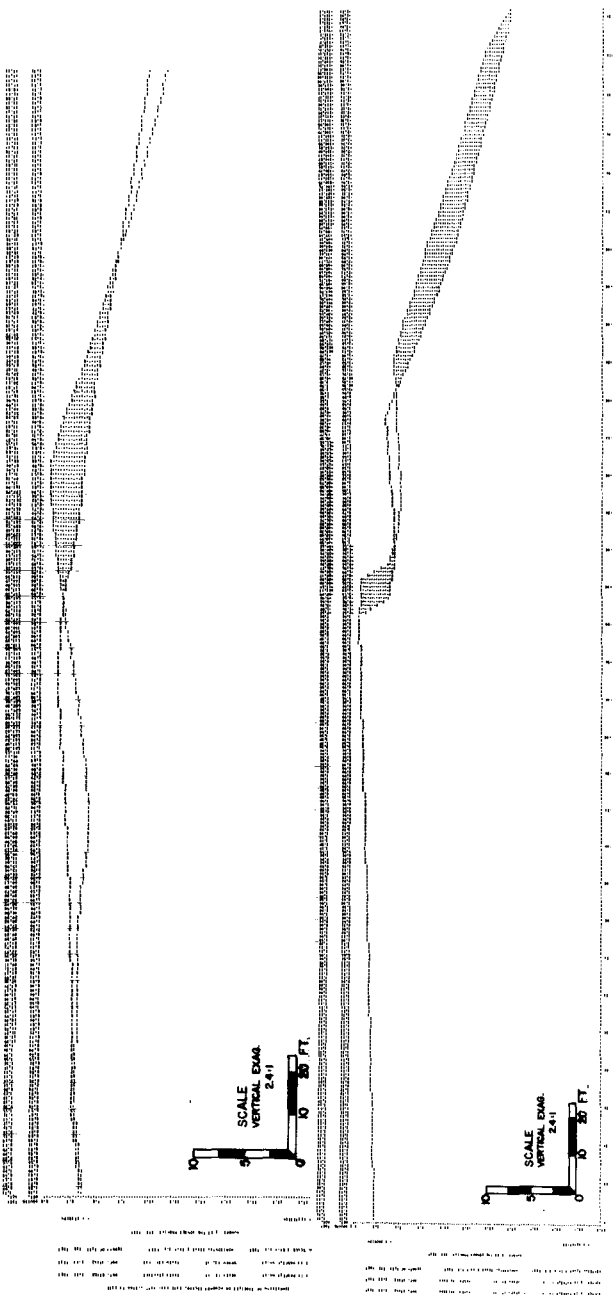

Figure 7. Comparisons between the October 19, 1969, and the December 19, 1969, M-10 beach profiles (top) and the June 19, 1969, and the July 4, 1969, M-5 beach profiles (bottom), on Monomoy Island. Volumetric changes are indicated by the dark areas (erosion) and the light areas (accretion) between the two profiles. In both locations sand was eroded from the upper beach face and berm-crest portions of the profile and was partially redeposited on the back beach portion of the profiles. This resulted in an increase of 49 cubic feet of sand in the upper comparison, and a decrease of 214 cubic feet in the lower comparison; however, at both locations the berm crest migrated landward and the profile shape changed from convex upward to concave upward.

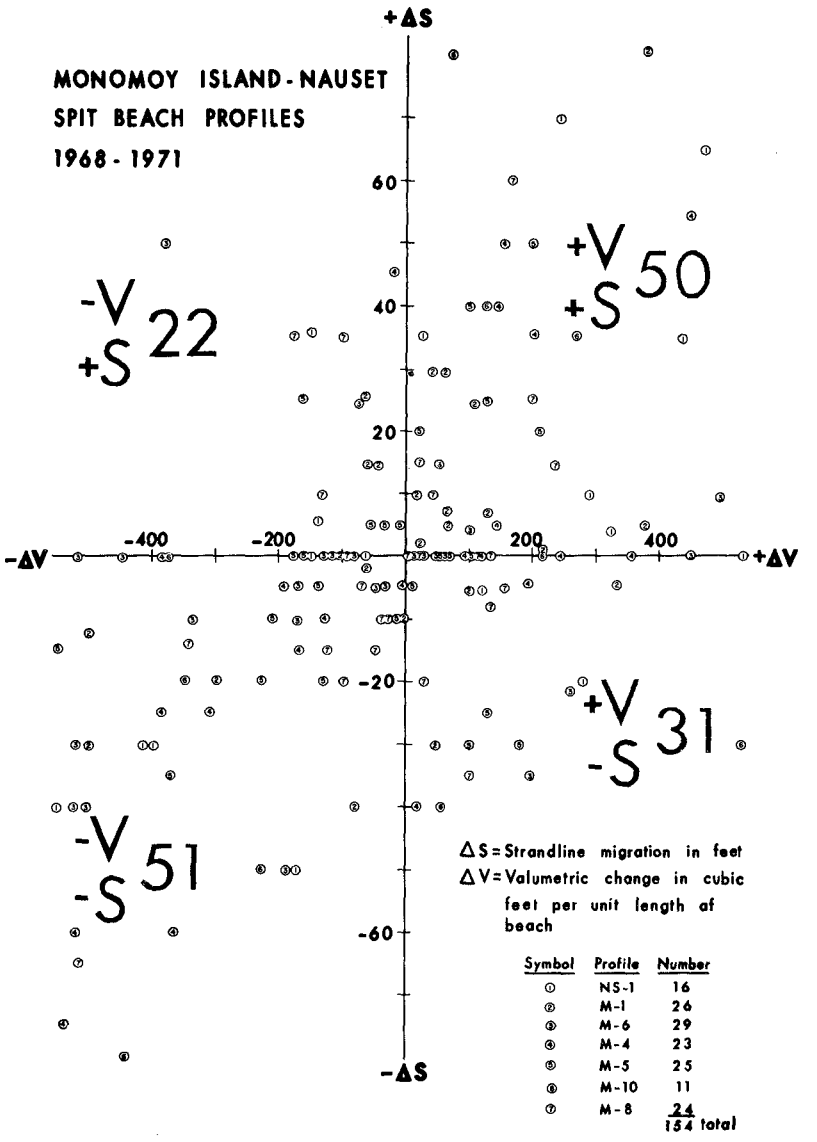

Figure 8. Graph of strandline migration versus volumetric change per unit length of beach. Large numerals indicate the number of profiles represented in each quadrant of the graph.

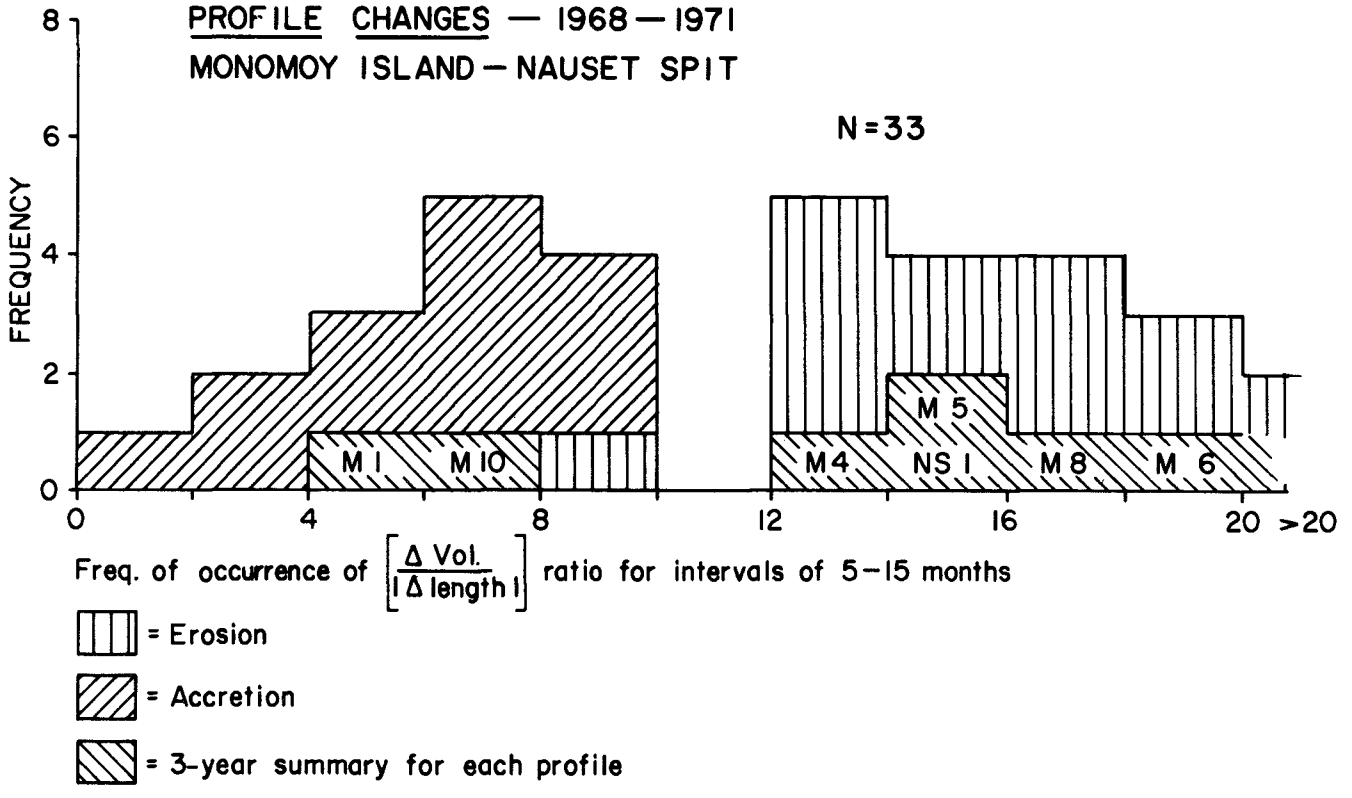

Figure 9. Ratio of change in sand volume to change in profile length at six profiles on Monomoy Island and one on Nauset Spit, for time intervals of five to fifteen months.

distinct separation of ratio values corresponding to erosional and accretional beach conditions; that is, the ratio was less than ten for accretional profiles and it was greater than twelve but less than 21 (except for one case of the 33 examined) for erosional profiles during the period of observation. The Corps of Engineers formula would predict a constant value of 27 for this ratio (i.e., 1 cu.yd./ft. = 27 cu.ft./ft.).

The three-year summary for each profile is also shown in Figure 9. The graph shows that more sand was removed per foot of beach profile (i.e., the ratio is higher) than was returned. This indicates a net dune erosion for the period, amounting from one-half to two-thirds of the sand composing the beach. Thus, it becomes even more apparent that observations of beach profile length alone can be quite misleading if the intention is to estimate beach changes in terms of sand volume.

CONCLUSIONS

An abundance of information is provided by the detailed comparative analysis of beach profiles as demonstrated by this study. Quantitative identification of erosion/accretion zones on the beach and precise determination of sand volume transport along the beach profile are facilitated by this technique. Traditional observations of beach profile length are not reliable for these purposes, as shown in the case of Monomoy Island-Nauset Spit beaches.

ACKNOWLEDGMENTS

The field work for this study was supported by the Coastal Engineering Research Center, U.S. Army Corps of Engineers, Contract DACW-72-67-C-0004, for which Dr. Miles O. Hayes was Principal Investigator. Computational analysis was supported by a grant from the University of Massachusetts Computing Center.

REFERENCES

1. Coastal Research Group, 1969, "Coastal Environments of Northeastern Massachusetts and New Hampshire: Field Trip Guidebook," Contribution CRG-1, Dept. of Geology, Univ. of Massachusetts, Amherst, 462 pp.

2. Colonell, J. M., and Goldsmith, V., 1971, "Computational Methods for Analysis of Beach and Wave Dynamics," Proc. Second Annual Geomorphology Symposium: Quantitative Geomorphology and its Applications," State University of New York, Binghamton, 38 pp.

3. Emery, K. O., 1961, "A Simple Method of Measuring Beach Profiles," Limnology and Oceanography, v. 6, pp. 90-92.

4. Goldsmith, V., 1972, "Coastal Processes of a Barrier Island Complex and Adjacent Ocean Floor: Monomoy Island-Nauset Spit, Cape Cod, Massachusetts," Doctoral Dissertation, Dept. of Geology, Univ. of Massachusetts, Amherst, 469 pp.

5. Goldsmith, V., and Colonell, J. M., 1970, "Effects of Nonuniform Wave Energy in the Littoral Zone," Proc. Twelfth Conference on Coastal Engineering, A.S.C.E., v. 2, pp. 767-785.

6. U.S. Army Coastal Engineering Research Center, 1966, "Shore Protection, Planning, and Design," Technical Report No. 4, Dept. of the Army, Corps of Engineers, Washington, D.C., 580 pp.

CHAPTER 69

BEACH CHANGES AND WAVE CONDITIONS, NEW BRUNSWICK

S. Brian McCann and Edward A. Bryant
Department of Geography,
McMaster University,
Hamilton, Ontario,
Canada.

ABSTRACT

The coast line of Kouchibouguac Bay, New Brunswick, within the southern Gulf of St. Lawrence coastal province, consists of a barrier island system of sand beaches and low dunes. It is a relatively low energy system in a protected location with the important waves entering the bay through a narrow fetch window from the northeast. The behaviour of these wave trains and their refraction patterns within the S. Gulf of St. Lawrence and Kouchibouguac Bay were simulated by the construction of a series of refraction diagrams, from which it is possible to obtain a realistic appraisal of wave conditions at the shore. Waves entering the bay from N and NE directions are concentrated on the southern part of the barrier island system, and those entering from the ENE and E are concentrated on the northern part. In greater detail, a series of wave refraction diagrams, based on former conditions of nearshore bathymetry at Richibouctо Inlet, help to explain the changes which have occurred there in the past 80 years. The simulation of wave behaviour in Kouchibouguac Bay has provided useful additional information which helps to explain the recent evolution of the barrier island system.

INTRODUCTION

Barrier island systems constitute an important part of the coastline of the southern Gulf of St. Lawrence and the Kouchibouguac Bay, New Brunswick system with its limited fetch window to the northeast provides a simplified case study with implications for other more complex systems in the southern Gulf (Fig.1). This paper concerns one aspect of a case study-- the use of wave refraction diagrams in defining the important wave regimes and the resultant areas of wave energy concentration at the shore, which have modified in the past and continue to modify today this barrier island-sandspit system. It is also concerned with a retrospective view of wave conditions over nearshore bathymetry near Richibucto Inlet since 1894 and the effect of such conditions on documented changes along the shoreline.

The Kouchibouguac barrier system consists of 29 km of sand beaches and dunes running in a gentle arc from SSE to NNW across the head of the bay. The continuity of the system is broken by three inlets of which the southerly one, Richibucto Inlet, is the largest and most stable.

Structurally the system is simple with only local developments of dune ridges. With a mean tidal range of 0.67m, the intertidal oceanside beach varies in width from 15 to 50m and is succeeded seawards by a series of offshore bars. The smooth offshore countours parallel the curve of the coastline except that in the northern and southern parts of the bay broad submarine ridges extend outwards to the shallow trough which is succeeded eastwards by the northward submarine extension of Prince Edward Island (Fig. 1).

There has been little research on the barrier islands of the Maritime provinces but it is clear that the general conditions of the barrier systems of the eastern U.S.A., with continual changes in configuration and overall shoreward retreat, are present here. For Kouchibouguac Bay long term changes have been documented from earlier air photo cover and hydrographic charts, and short term changes have been measured in the field using conventional ground survey and mapping. There has been frequent and significant breaching and infilling of the barrier in the area of the central inlet, Blacklands Gully, and similar though less frequent occurrences at the northern end and at Richiboucto Inlet over the last 150 years. Within the last thirty years at least 5 important breaches have occurred and been subsequently infilled. In the short term, beach profiles for 1970-72 show active erosion of the main dune ridge in the southern part of the bay.

METHODS

It is considered that waves generated within Kouchibouguac Bay (less than 6 seconds) are relatively insignificant in terms of changes in the gross configuration of the islands. The important waves are generated in the southern Gulf of St. Lawrence and enter the bay through the narrow window between the northern end of Prince Edward Island and Point Sapin. These wave trains, from north to east directions, and the subsequent refraction patterns within the southern Gulf and across Kouchibouguac Bay were simulated using a computer program developed by R.S. Dobson (1967).

In the absence of any suitable real wave data for the southern Gulf of St. Lawrence the selection of appropriate wave trains was based upon data contained in a comprehensive hindcast study by Quon, Keyte and Pearson (1963), which used the Pierson, Neuman and James method to compile characteristic hourly wave lengths and heights for the months March to December, 1956-60. Five wave directions were selected--north, north-northeast, northeast, east-northeast and east, and refraction diagrams constructed for each of four periods--6.25, 7.65, 8.84 and 9.88 seconds--for each direction. The procedure for the construction of the diagrams involved the use of base maps at three scales. Wave rays from the five directions, for each of four periods in turn, were first generated in deep water in the Gulf of St. Lawrence using bathymetry and a grid based on the small scale hydrographic chart. Once wave rays entered Kouchibouguac Bay they were transferred to a second larger scale grid with more detailed bathymetry and the refraction procedure continued until they reached the

shore. Those rays entering the southern part of the bay and affecting the Richibucto Inlet area were transferred again onto a still larger scale grid and the refraction procedure continued using four different bathymetries taken from detailed charts dated 1894, 1930, 1955, and 1964. For the Richibucto maps high tide depths, plus an additional value for storm surge effects were used in the construction of the wave refraction diagrams. Increased water levels due to surge conditions could reasonably be expected to occur in the Richibucto Inlet for the wave conditions, and causative weather conditions, which were modelled in the refraction diagram procedure.

RESULTS AND DISCUSSION

The series of diagrams of wave orthogonals accompanying this paper have been selected, from the more than 100 diagrams constructed for the analysis, to illustrate the refraction patterns for what appear to be the most significant waves to affect the coastline. Each stage of the analysis is represented by a separate series of diagrams--Figure 2, Gulf of St. Lawrence; Figure 3, Kouchibouguac Bay; Figure 6, Richibucto Inlet. In Figures 2 and 3, the first group of diagrams shows 7.65 second period waves from each of the 5 directions within the northeast quadrant; the second and third group of diagrams illustrate the behaviour of waves from the NNE and NE, respectively, at different periods. In Figure 6, only waves from the NNE at four different periods are illustrated for four different bottom configurations.

Wave refraction within the S. Gulf of St. Lawrence filters all large waves substantially before they enter Kouchibouguac Bay. This refraction depends on the angle of wave approach to a large submarine ridge, which is the northward extension of Prince Edward Island, and the parallel trough to the west which is directed southwards into Northumberland Strait. The ridge affects waves from ENE and E, the trough waves from the N to NE, and the tendency is to create a divergence of wave rays into Kouchibouguac Bay and a concentration on the northwest coast of Prince Edward Island for all wave directions (Fig. 2.1). The bathymetry of the S. Gulf acts most effectively on the longer period waves so that as wave period increases orthogonals diverge more into Kouchibouguac Bay and concentrate to a greater extent on the west coast of Prince Edward Island (Fig. 2.2). With NE waves (Fig. 2.3) as against NNE waves there is a somewhat greater concentration of orthogonals around Point Sapin at the northern end of Kouchibouguac Bay with the divergence within the bay increasing. Therefore, of the waves entering from the S. Gulf those of shorter period (less than 8 seconds) will be most effective at the shoreline in Kouchibouguac Bay; for longer wave periods those from the NNE and NE will be most effective.

Within Kouchibouguac Bay further wave refraction is caused by two broad submarine ridges extending northeastwards from shore. As wave period increases there is a pronounced concentration of orthogonals on the northern barrier island (Fig. 3.2, 3.3) while the southern part of the

system becomes more protected. The greatest effects of this bathymetry is observed not with a change in wave period but with change in direction of wave approach. North and northeast waves are concentrated along the southern part of the barrier island system while the northern part remains sheltered. As wave direction becomes more easterly, the southern part of the bay becomes sheltered and it is in the northern part that wave orthogonals are concentrated (Fig. 3.1). The bay is thus under the influence of two wave regimes and it is possible for long sections of the barrier islands to be unscathed during storms while other sections are being eroded. Such a situation occurred between 1970-71 when the southern dune ridges underwent marked shoreward retreat due to storms with N-NE waves while the northern end of the bay remained unchanged.

In order to obtain some idea of which part of the shoreline of Kouchibouguac Bay is receiving the most vigorous wave action, the position at shore of all the orthogonals in each of the refraction diagrams constructed for Kouchibouguac Bay was marked on a single map. An arbitrary classification of the grouping of the points into light, moderate and heavy was used to define areas of wave energy concentration (Fig.4). Those areas of heavy and moderate concentration correspond very closely with those areas which have undergone frequent change over the past 150 years, as defined from a series of accurate charts and, more recently, air photographs.

A very much more convincing demonstration of the fact that the wave refraction diagrams constructed for Kouchibouguac Bay provide a realistic simulation of sets of real world conditions is provided by the sequential retrospective construction of refraction diagrams for a series of past bathymetries at Richibucto Inlet in the southern part of the bay. The area has been accurately mapped since 1894 and there are four good hydrographic charts--1894, 1930, 1955, and 1964 (Fig.5), as well as other maps and air photography covering the last 35 years. Both the shoreline and nearshore bottom topography have undergone considerable changes in this period. The four shoal areas of 1894 have given way to a consolidated linear shoal, or bank, extending from the northern side of the inlet and defining a deep and regular river-tidal channel to the south. The 1894 shoreline position remains basically the same, though the southern side of the inlet was breached in 1930 and has undergone some erosion and the northern side shows the effect of a breakwater first noticeable on the 1894 chart.

When wave refraction diagrams are constructed using the 1894 bathymetry of Richibucto Inlet there are no marked areas of concentration or divergence of wave orthogonals. Figure 6.1 shows the situation for waves from the NNE at different periods, and the situation for all wave directions from the NE quadrant is similar. The wave refraction patterns reflect the four offshore shoal areas which have the effect of distributing wave energy evenly along the shoreline for a variety of wave periods and directions. The pattern for 1930 is substantially different. Figure 6.2, again for NNE waves, shows definite areas of wave orthogonal

concentration--at the breach on the southern beach and to either side of it. This pattern holds for all wave periods and directions out of the NE quadrant, and is a direct result of the consolidation of the offshore shoals (see Fig. 5). Whereas the nearshore bathymetry of 1894 caused wave energy to be more or less equal all along the shore, the 1930 bathymetry resulted in a concentration of wave energy at particular points onshore. By 1955 the shoals offshore from the southern side of the inlet had disappeared and the shoal extending from the northern beach had become regular in shape and depth and extended southeastwards. The 1955 wave refraction patterns are a response to these forms and there was again a fairly even distribution of wave energy along the southern beach (Fig. 6.3). The only consistent area of orthogonal concentration is to the east of the breach. Thus the extension and consolidation of the bar on the northern side, partly as a result of the construction of breakwalls, had caused wave energy to be concentrated to the east of the breach. This breach, or small inlet, was not receiving the same degree of wave attack as it did in 1930, and thus, instead of maintaining itself, was being infilled by 1955. By 1964, the offshore bar on the northern side of the inlet had grown further to the southeast and the depth of water over it had shallowed. The wave refraction pattern is very similar to that for 1955, but the waves show a response to the increased shoaling of the bar (Fig. 6.4). The old breached inlet is an area of orthogonal divergence and waves are concentrated to either side of it, particularly to the east. This is the area undergoing coastal erosion and retreat at the present time (field survey evidence 1970-72) and if the recent trends of bathymetric change continue then this erosion is likely to continue.

CONCLUSIONS

1. Wave refraction in S. Gulf of St. Lawrence affects waves from between N and E before they enter Kouchibouguac Bay, causing a divergence of wave rays within the bay and a concentration on the west coast of Prince Edward Island. Thus only the shorter waves and those from the NNE and NE for longer wave periods affect Kouchibouguac Bay to any degree.

2. Within Kouchibouguac Bay waves of less than 6.5 second periods undergo little refraction. Longer period waves from N and NE are concentrated on the southern barrier islands and waves from E and ENE are concentrated on northern barrier islands so that the bay is divided into two waves regimes.

3. Wave refraction patterns, in detail, in the area of Richibucto Inlet have changed since 1894, in response to changing bathymetry, which to some extent is due to the construction of breakwaters. The varying refraction patterns over time have produced changes in the beaches south of the inlet and will continue to erode the frontal dune ridge to the east of the 1930 breach.

REFERENCES

Dobson, R.S., 1967. Some applications of a Digital Computer to hydraulic engineering problems. Dept. Civil Engineering, Stanford University, California. Tech. Rept., No. 80.

Quon, C., F.K. Keyte, and A. Pearson, 1963. Comparison of 5 years hindcast wave statistics in the Gulf of St. Lawrence and Lake Superior. Bedford Institute of Oceanography Report 63-2, 59pp.

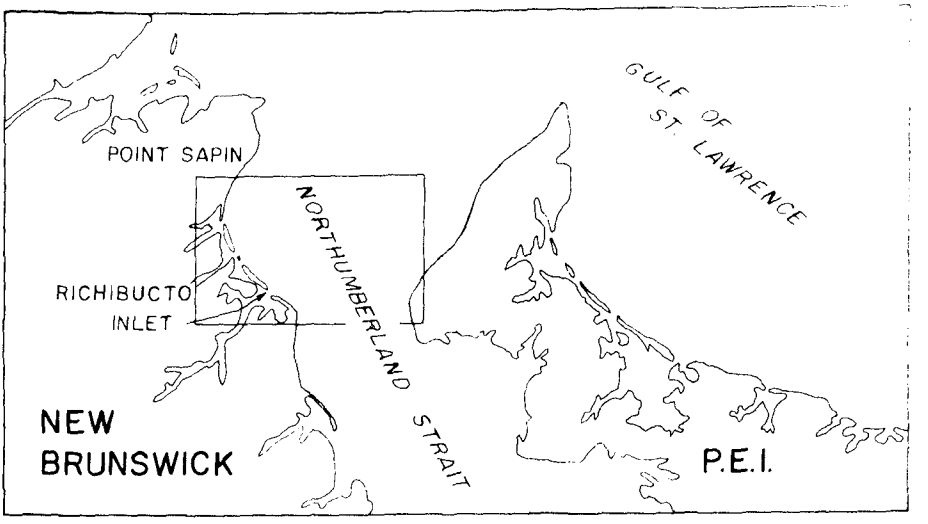
POINT SAPIN
NORTHUMBERLAND STRAIT
GULF OF ST. LAWRENCE
RICHIBUCTO INLET
NEW BRUNSWICK
P.E.I.

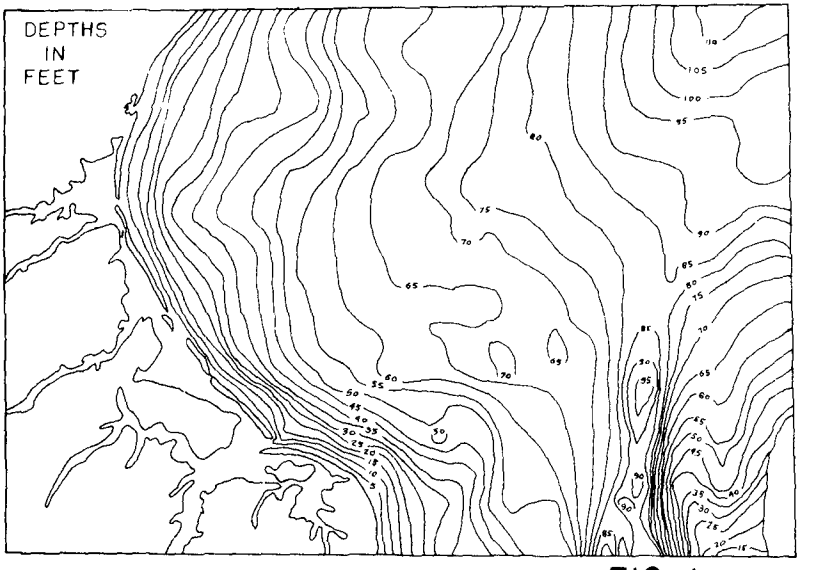
DEPTHS IN FEET

FIG. 1

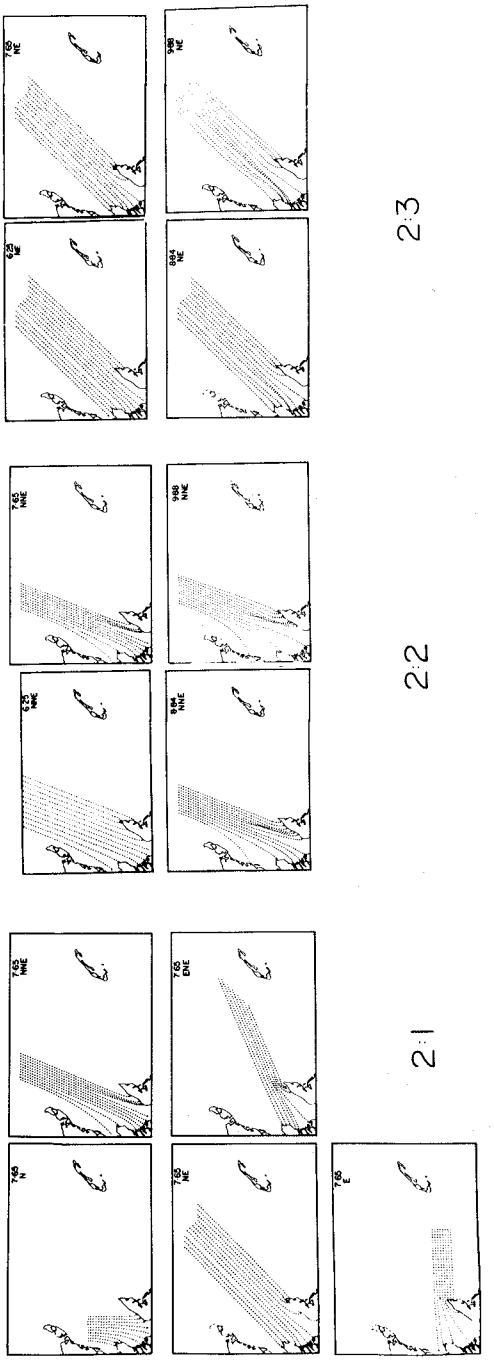
7.65 N
7.65 NNE
7.65 NE
7.65 ENE
7.65 E
6.25 NNE
6.25 NE
9.84 NNE
9.84 NE
9.88 NNE
9.88 NE
2:1
2:2
2:3

FIGURE 2

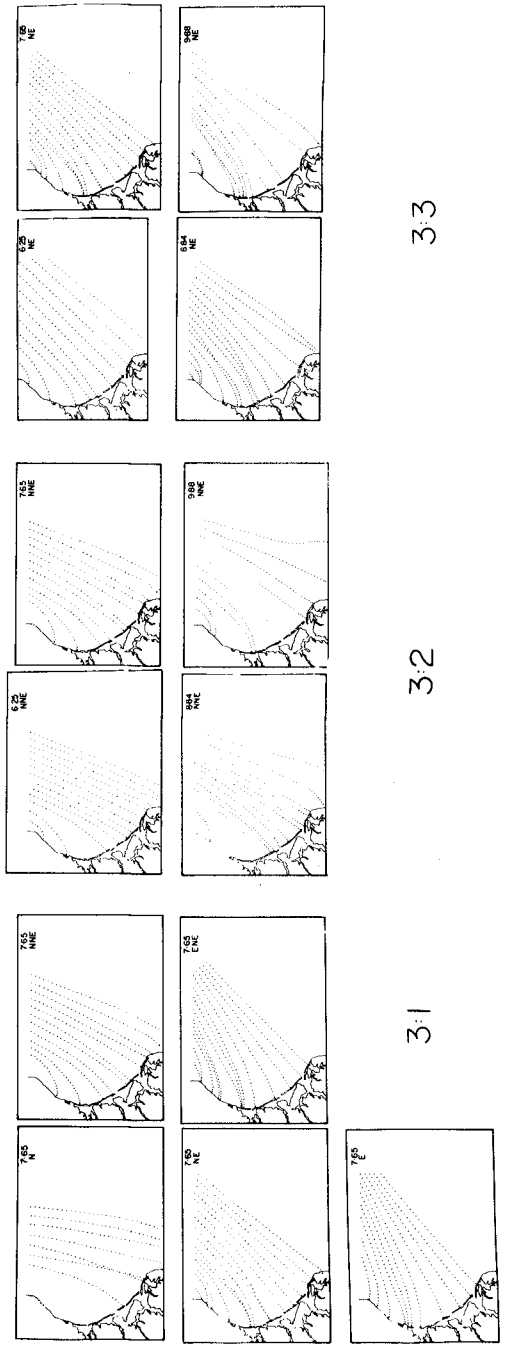
7.65 N
7.65 NNE
7.65 NE
7.65 ENE
7.65 E
6.25 NNE
7.45 NNE
8.84 NNE
9.98 NNE
6.25 NE
7.78 NE
8.84 NE
9.98 NE
3:1
3:2
3:3

PICTURE 3

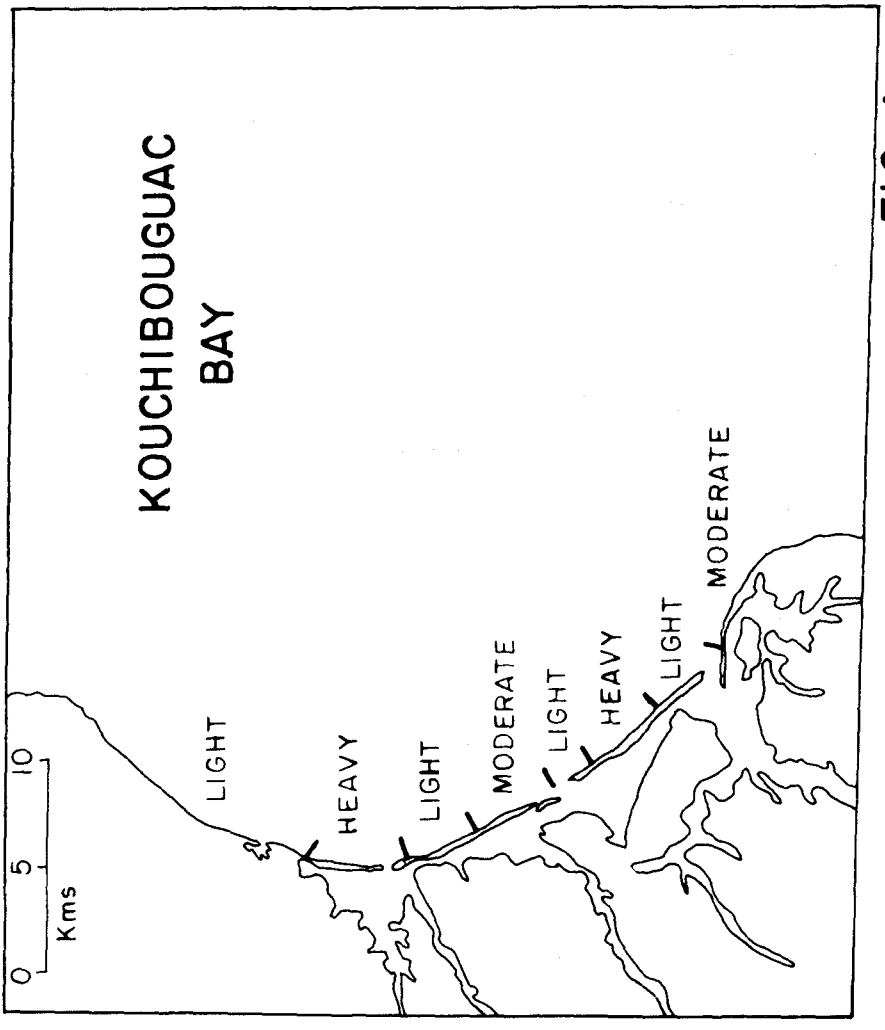
KOUCHIBOUGUAC
BAY
LIGHT
HEAVY
LIGHT
MODERATE
LIGHT
HEAVY
LIGHT
MODERATE
0
5
10
Kms

FIG. 4

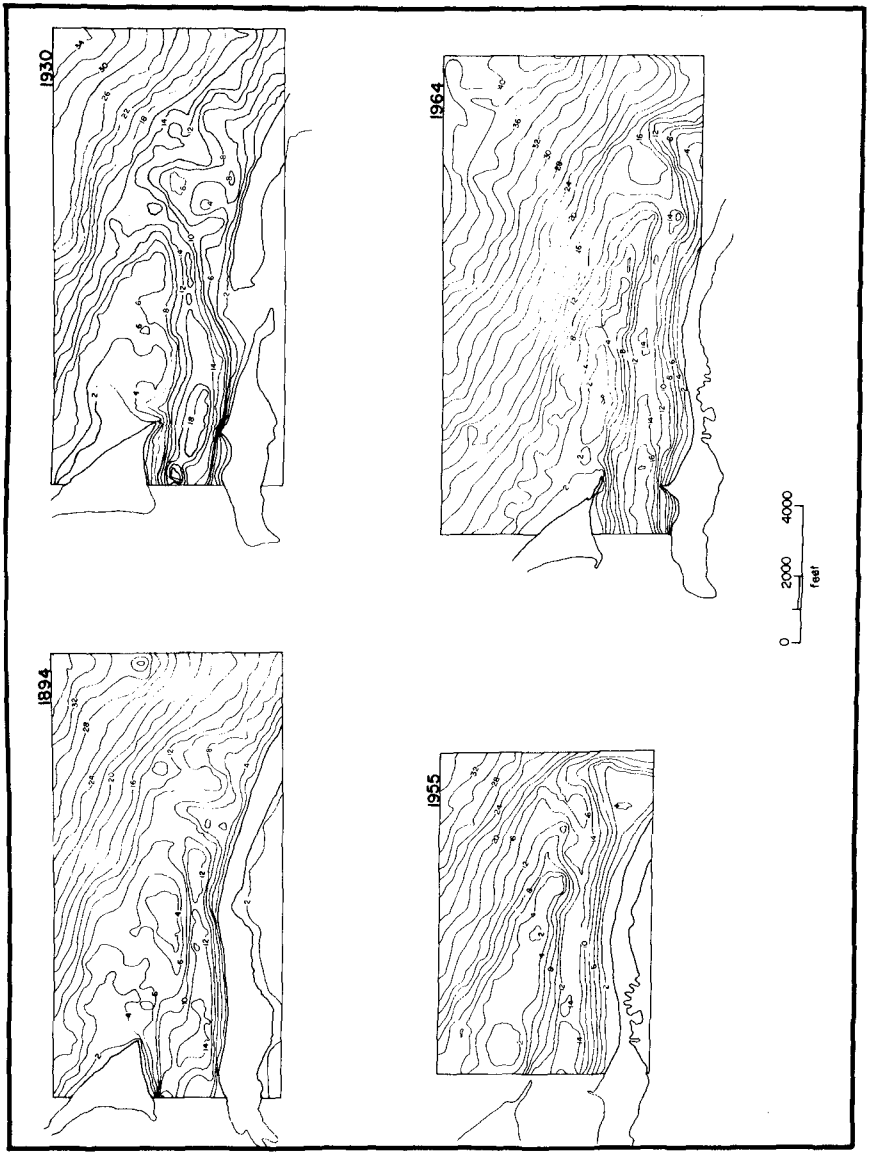

FIG. 5

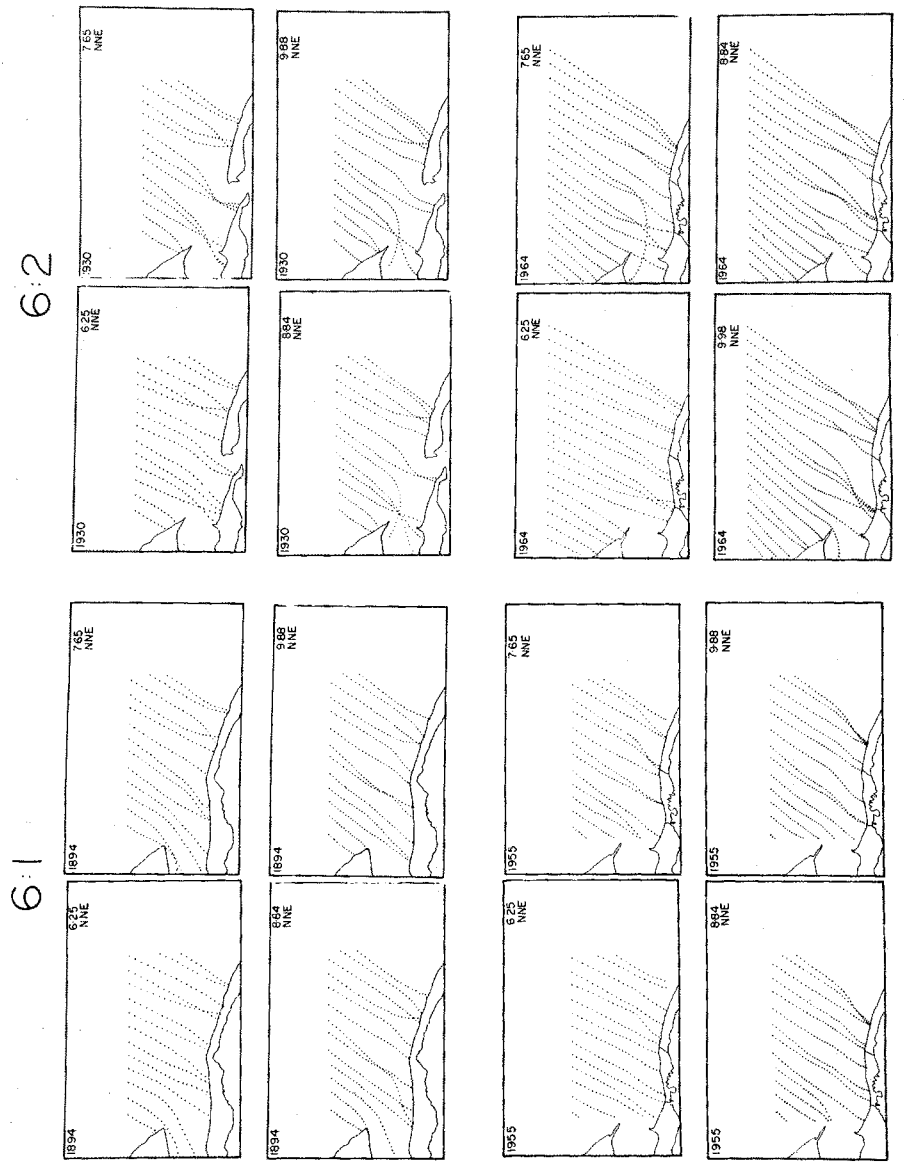

FIGURE 6

CHAPTER 70

Dune erosion during storm conditions

by T. Edelman[x)]

Abstract

Starting from a provisional hypothesis, presented by the author at the 11th Conference on Coastal Engineering, this paper deals with the further development of our knowledge about dune erosion during storm conditions. Results of measurements in the prototype are mentioned. Some speculations about the occuring processes during storms are given. However, the problem has not yet been solved. Further measurements in the prototype will be necessary.

Introduction

During the eleventh Conference on Coastal Engineering (London, September 1968) the author presented a first paper about dune erosion during storm conditions (Proceedings Volume I, chapter 46, page 719) in which he assumed, as a first approach, that after a storm the profile on the beach in cross-section was a straight line under a slope with an average value 1 in 50. This hypothesis was based on the assumption that during a storm an equilibrium slope would establish itself, comparable with the slope between highwater- and lowwater-level, as measured on the dutch beaches during normal weather conditions. It may be, that such an equilibrium slope does exist in nature, but soon it became evident, that a storm never lasts long enough to produce such a slope.

---

x) Head of the Coastal Research Department of Rijkswaterstaat Netherlands

Measurements

Since 1968 researches have been made into a large number of after-storm profiles. These investigations have revealed, that after a storm the profile of the beach is not a straight line, but a curve with a general shape as can be seen in figure 1. Only the part AC could be measured; the part lower than point C is unknown until now.

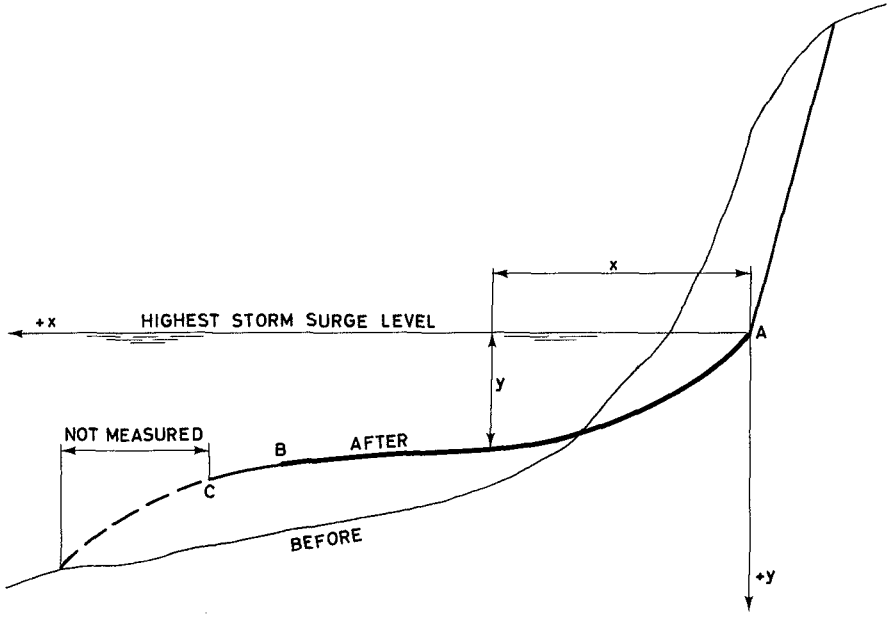

Fig. 1

The highest part of such a curve, indicated by the heavy line AB , can be represented by the formula :

$$y + 0{,}90 = 0{,}415\sqrt{x + 4{,}70} \quad \ldots\ldots\ldots\ldots \quad (1)$$

in which y = the depth below the highest storm surge level and x = the distance from the waterline A.

When $x = 0$ is $y = 0$ (point A) and when $x = 100$ meter is $y = 3,35$ meter (point B).

The remarkable fact has been observed, that, with regard to the maximum stormflood level the above parts of these curves are almost identical. Its shape appears to be almost independent of the height of this level and the formula (1) holds good for every stormflood level, that causes dune erosion. We can therefore speak of „the" after-storm profile.

Extrapolations

From figure 1 it can be seen that the slope decreases from A towards B, but that further seaward the slope increases again. It is, therefore, impossible that (1) describes the complete curve; the formula must at least be of the third degree.

We tried the simple formula:

$$y = ax^3 - bx^2 + cx \qquad (2)$$

in which a, b and c are parameters.

If we want $y = 3,35$ when $x = 100$ (thus causing the curve to go through the points A and B), we find a relation between the parameters a, b and c :

$$3,35 = 10^6 a - 10^4 b + 10^2 c \qquad (3)$$

It has been found that, if we vary the values of a, b and c within wide ranges, but stick to the relation (3), we find very small variations in the part AB of the curve. The differences with (1) remain within the range of the measurement inaccuracies. This proves that it is impossible to make a seaward extrapolation starting from part AB of the curve.

This is a pity, as we must, for the present, make use of an extrapolation, because hitherto we were not able to measure the lower part of an after-storm profile in the prototype.

Apart from the fact, that it is rather dangerous to measure this part of the profile just after a storm, we still have another difficulty. It is of little value to measure the profile only after the storm, as we must also know the profile just before the storm, in order to be able to calculate the quantity of sand sedimented upon beach and fore-shore.

Since storms never announce themselves beforehand, we have to lie in wait for a storm with our manned measuring boat during the whole winter season, measuring the excisting profiles every week and hoping for a neat, heavy storm to come within the next week. Since 1968, however, such a storm did not occur.

Moreover, even if we should have good luck during next winter, we are not satisfied. For obvious reasons, we should like to obtain data of several storms, with different levels and different time-height graphs.

It seems, therefore, that for the present we are at a dead-lock. But, perhaps, there is another way-out.

Steady shape of the profile

We have seen, that the shape of the above part of the profile is almost independent of the height of the maximum storm surge level. As a first supposition we may assume that this holds good for the complete profile.

The next assumption is, that this „storm profile" excists at any moment during the rise of the water-level. During the whole period, in which large quantities of dune sand are sliding down into the boiling sea, the under-water profile may move upward and landward, preserving its own characteristic shape. Obviously, this characteristic shape must come into existence during the preceding period and has to establish itself at the moment, that the large dune erosion begins.

Further we have to assume, that the sliding sand is spread out over the whole profile within a very short time.

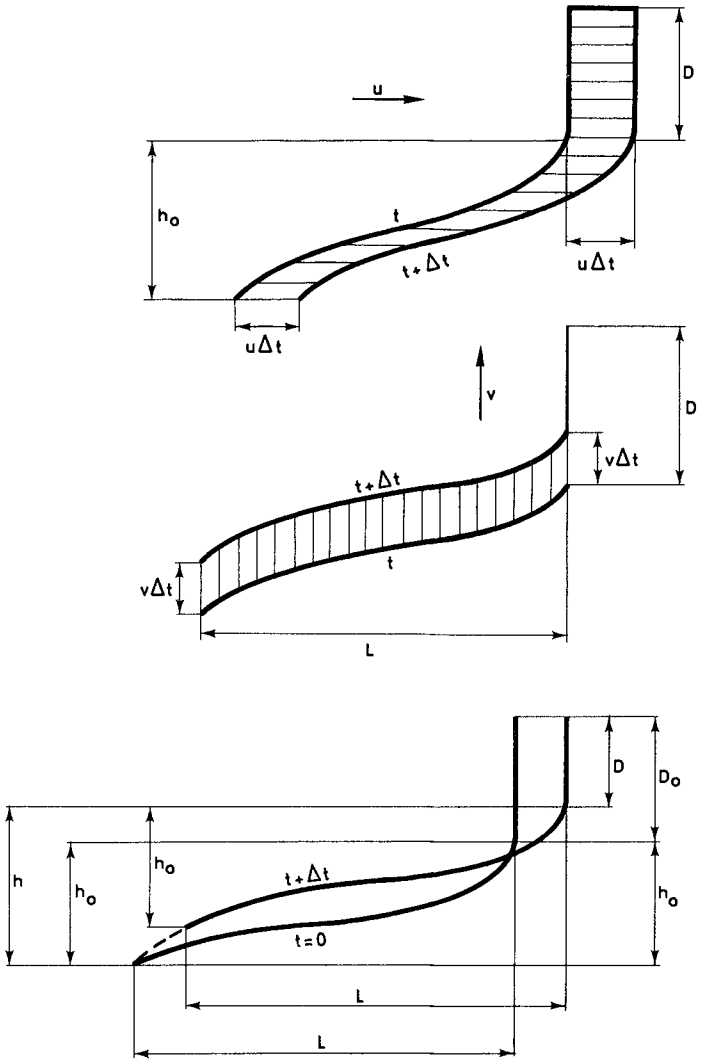

Fig. 2

If at the moment t each point of such a „storm profile" moves in horizontal direction with a velocity u and in vertical direction with a velocity v, we can derive that (see figure 2) during a time-interval $\triangle t$ the horizontal movement causes a loss of material : $(h_o + D)\ u\ \triangle t$, and the vertical movement brings a gain : $L\ v\ \triangle t$. If no sand disappears from the profile, both quantities have to be equal, from which we obtain : $(h_o + D)\ u\ \triangle t = L\ v\ \triangle t$

$$\text{or} \quad u = \frac{L}{h_o + D}\ v$$

During the storm the dune-foot moves landward over a distance

$$A = \int_{t=0}^{t=t_m} u\ d\ t$$

Since $v = \frac{dh}{dt}$ and (with a horizontal dune-surface)

$$h_o + D = D_o + 2\ h_o - h$$

we find

$$A = L\ \ln \frac{D_o + h_o}{(D_o + h_o) - (h_m - h_o)}$$

We are able to calculate A from this formula if we can establish the values of h_o and L, the height and the length of the „storm profile".

Most investigators assume, that L is the length of the breakerzone and that h_o is the breaker-depht : $h_o = \gamma H_s$ in which H_s is the significant wave height and γ is a constant, often assumed to be 1,3.

From this value of h_o the value of L can be found from the profile excisting before the storm.

However, if we put these values into our formula, we mostly find a value of A which seems to be too large and which is certainly not in accordance with the average dune-erosion we measure in the prototype. Probably the length of the storm profile is smaller than the length of the breakerzone, and $h_o < \gamma \cdot H_{sign}$.

At present, we do not understand the mechanism of the sand transport on beach and fore-shore very well. During normal weather-conditions the waves are supposed to induce a landward transport over the whole breakerzone. The much larger seaward transport of the sand from the eroding dunes during storms, however, may mainly be caused by gravity. This gravity transport could be a kind of turbidity current.

There is, however, no reason why we should assume, that this turbidity current should proceed as far as the end of the breakerzone. It is more likely, that on the landward part of the breakerzone gravity preponderates and that on the outer seaward part of the breakerzone the sand is still moving landward.

Conclusions

As pointed out before, we do not know exactly what happens in the breakerzone. Once more we see, that measurements in the prototype are necessary, with all the difficulties involved.

From the considerations and reflections pointed out here, it may be seen and understood, that it will probably take several years before a reliable answer can be given to the simple question: „How far will a dune row erode during a severe storm".

CHAPTER 71

EDGE WAVES AND THE LITTORAL ENVIRONMENT

Anthony J. Bowen

Institute of Coastal Oceanography and Tides
Bidston Observatory, Birkenhead, Cheshire,
England.

ABSTRACT

Several types of beach features seem to have a rather regular, longshore pattern. This pattern may indeed be sufficiently uniform to be described in terms of a recognisable longshore wavelength. A likely explanation for such features lies in the motion of edge waves, surface waves trapped by refraction to the shoreline. These waves, by themselves or by interaction with the normal, incoming surface waves breaking on the beach, can generate longshore features having a wavelength equal to or half the edge wave wavelength.

If a broad spectrum of edge wave modes were present any longshore variation should appear rather irregular. The existence of regular features therefore suggests that a particular edge wave mode is often dominant, the characteristics of the dominant mode depending on the geometry of the nearshore area and the width of the surf zone.

Any new, artificial structure stretching seawards provides new boundary conditions, almost certainly altering the characteristic of the edge wave spectra. This is particularly obvious in the case of a regularly spaced structure such as a set of groynes. A deeper understanding of the edge wave processes is needed so that the induced changes in the edge wave spectra are the least deleterious or, an intriguing possibility, advantageous.

INTRODUCTION

It would be very convenient if one could take measurements along a line perpendicular to a beach and assume that these were representative of any line normal to the beach. In fact, even on very long, straight beaches, this is never the case. The existence of rip currents, beach cusps, offshore bars of crescentic shape or straight bars with rip channels all provide a longshore perturbation on the system. A large number of different, and in some cases rather extraordinary, theories have been proposed to explain the existence of each of these phenomena, but in the absence of any comprehensive explanation, the engineer has been forced to regard them as annoying noise, making small scale or spot measurements of either sediment or water movement particularly difficult to interpret.

There are indeed situations where the longshore perturbations are not readily apparent, the rip currents are weak and ill defined and regular, longshore features in the sediment are rarely observed, this is the case when small waves approach a coast obliquely - a situation often studied at laboratory scale. One also has situations, perhaps common on the Californian coast where the perturbations in the flow are obvious with very well developed rip currents but the sedimentary features the bars and cusps are rarely well developed. (Shepard & Inman, 1950). Finally the sedimentary features may be so well developed that they appear to completely control the nearshore flow (Sonu, 1972).

At some stage the longshore features cease to be a minor perturbation on the system which can be eliminated by taking a bulk average. More importantly, while the existence of observable longshore features suggests the existence of the edge waves that caused them, the absence of such features does not conversely imply the absence of edge waves. Strong longshore currents will tend to destroy beach cusps, large tidal ranges will discourage the formation of crescentic bars (Bowen & Inman, 1971) but in neither case will be edge wave itself be eliminated. Even in otherwise ideal circumstances the existence of a whole spectra of edge waves could produce a very complex pattern with no obvious longshore wavelength. To examine the basic ideas associated with generation of longshore features in either the water or the sediment it is therefore very necessary to understand the properties of the edge waves which are probably responsible for their existence.

EDGE WAVES

Edge waves are surface waves trapped by refraction to the shore, having an amplitude which is a maximum at the shoreline and generally decreases in the offshore direction. Although the wave elevation decays seawards it may have several maxima and minima. An offshore modal number n gives the number of zero crossings and therefore with increasing n the edge wave becomes more complex and for a given longshore wavenumber decays seawards more slowly. (Bowen & Inman, 1969).

Ursell (1952) considered the motion on a plane beach of slope tan s and derived a dispersion relation between the angular frequency of the edge wave σ and the longshore wavenumber k where

$$\sigma^2 = gk\sin(2n+1)s \qquad (1)$$

and therefore showed that all values of n are not possible as there is a cut-off at

$$\sin(2n+1)s=1 \qquad (2)$$

Ursell found experimentally that the edge wave for this particular case, the cut-off mode, could be generated in a wave-tank and might be an important resonance. The cut-off mode may be of practical interest as it represents the longest longshore wavelength that is possible for an edge wave of a given frequency (equation 1).

Ursell's solution applies to the simplest, possible beach topography, a straight coastline with a plane beach of constant slope. Incoming wind waves would have no longshore variation and any longshore perturbations must be derived either from the motion of the edge wave itself or from its interaction with the incoming waves. The orbital motion of both waves, although very complex in the case of an edge wave with a large value of n, is purely oscillatory and leads to no net motion of the water or sediment. However, the amplitude of the edge wave at the shoreline can produce a longshore differential in the maximum run-up on the beach; in consequence, points of equal height above mean water level may be exposed to quite different hydraulic conditions, one point being totally dry for a long period while the other is in the swash zone.

Figure 1 illustrates the two possible cases

a) the edge waves are of the same period as the edge wave

b) the edge waves and the incoming waves are of different period, the edge wave usually being of lower frequency.

Two further subdivisions are useful

i) incoming wave larger amplitude than the edge wave

ii) edge wave larger than incoming wave.

If Figure 1 is regarded as a view looking down on the shoreline, given by the mean water line (MWL), the incoming wave will just move up and down the beach. The combination with a standing edge wave of the same period will produce a longshore perturbation in the water line on the beach either a(i) of the edge wave wavelength or a(ii) complex system primarily of the edge wave wavelength but with a system of smaller amplitude in between the major crests depending on the relative size of the waves.

If the edge wave is progressive the perturbation is of the same wavelength as the edge wave case a(i) independent of the relative size of the waves.

When the edge wave and the incoming wave are of different periods which have no harmonic relation, at any given time they will be of random phase. The maximum run up of the incoming waves will be within the shaded areas occasionally reaching the maximum excursion when the waves are temporarily in phase. A longshore perturbation will result only if the edge waves are standing waves and will have a wavelength half that of the edge wave.

The shaded areas are the perturbation of the run-up of the incoming wave by the edge waves. As in b(ii) the edge wave motion is dominant, the darker shading has been used to indicate the perturbation of the maximum edge wave incursion due to the incoming waves.

It is necessary to consider the relative size of the waves as at the shoreline the amplitude of the incoming wave is a minimum while that of the edge waves is a maximum, case (ii) may therefore be reasonably common.

The important interactions are those that produce steady drift velocities in the nearshore zone. The self-interaction of the incoming wave is obviously important producing drift velocities and longshore currents. However, although these may be large, they are uniform in the longshore direction.

If the edge wave is of significantly different frequency from the incoming waves, cross interactions will generate oscillations at the sum and difference frequencies rather than steady currents. However if they are of the same frequency, their interaction produces steady currents, the nearshore circulation patterns (Bowen & Inman, 1969). These, in turn, may lead to the formation of sedimentary features (Bowen & Inman, 1969; Komar, 1971). This type of interaction produces features, rip currents or beach cusps, which theoretically have exactly the same longshore wavelength as the edge waves. The interaction is independent of whether the edge wave is progressive or standing, the mechanism is the same as that shown in a(i) of Figure 1.

Steady drift velocities also arise from the second-order solution for the edge wave motion. These velocities are probably small but until accurate measurements are made of edge wave amplitudes they cannot be entirely dismissed as insignificant as the motion due to a standing edge wave provides a satisfactory explanation for the formation of crescentic bars and particularly for crescentic bars with matching cusps

(Bowen & Inman, 1971). These features have a theoretical wavelength of half that of the edge wave. The drift velocities associated with a progressive edge wave have no longshore variation although they change in magnitude and longshore direction as a function of the distance from the shore.

On an infinitely long beach a very large number of edge wave modes are possible; for each frequency there are a set of wavelengths, a different wavelength for each possible value of n. The measurement and identification of edge waves is therefore a formidable task. Fortunately one mode is often dominant giving the rather regular longshore variations which are often observed but irregular, or apparently irregular features, will be generated if more than one edge wave mode present is of significant amplitude.

In reality, the local geometry may be very important in determining the possible dominant mode. A situation of practical interest occurs when a beach is bounded by two headlands, or groynes, perpendicular to the shoreline a distance b apart. The possible wavelengths of the standing edge wave between the boundaries are given by

$$L = \frac{2b}{m} \qquad m = 1, 2, 3 \qquad (3)$$

so that m is a longshore model number. The resonant periods T of the bay are, from (1) and (3)

$$T^2 = \frac{4\pi}{g} \quad \frac{b}{m\sin(2n+1)s} \qquad (4)$$

If the width of the bay, or the groyne spacing, is about 400m, then small values of m and n give resonant periods of the order of a minute, essentially in the surf beat range. For small m the cut-off mode has a period of 10 - 20 secs. With a slope of 0.030, a reasonable value for an exposed coast, there are 26 possible values of n in addition to the cut-off mode (Table 1). All values of m are possible but the very short wavelength associated with large values of m are probably not of any practical interest.

CONCLUSIONS

It is clear that the introduction of artificial boundaries on a beach can profoundly influence the spectrum of edge wave energy. This could be particularly important if the new geometry has resonances close to the predominant frequency of incoming waves.

There is some indication that the bottom drift velocity due to the edge wave is offshore close to the shore, of order (Bowen & Inman, 1971)

$$\frac{a^2}{4g}\left[\frac{\sigma}{\tan s}\right]^3 \qquad (5)$$

where a is the amplitude of the edge wave at the shoreline.

Large edge waves of short period might therefore have a significant erosional capacity. Measurements of edge wave amplitude are required urgently so that the significance of this type of estimate can be established.

The wave periods associated with crescentic bars (Bowen & lnman, 1971) are relatively long, of the order of 30 secs, yet the drift velocities associated with these edge waves seem to explain the observed formation of large sedimentary features. This certainly suggests, as the frequency cubed enters the drift velocity relation, that edge waves of higher frequency could play a significant role in determining the equilibrium slope of the beach.

REFERENCES

Bowen, A.J. and D.L. lnman, 1969. Rip currents, 2, laboratory and field observations. J. Geophys.Res. 73. 2569-2577.

Bowen, A.J. and D.L. lnman, 1971. Edge waves and crescentic bars. J. Geophys. Res. 76. 8662-8671.

Komar, P.D., 1971. Nearshore cell circulation and distribution of giant cusps. Geol. Soc. Amer. Bull. 82. 2643-2650.

Shepard, F.P. and D.L. Inman, 1950. Nearshore circulation related to bottom topography and wave refraction.

Sonu, C.J., 1972. Field observation of nearshore circulation and meandering currents. J. Geophys. Res. 77. 3232-3247.

Ursell, F., 1952. Edge waves on a sloping beach. Proc. Roy. Soc. A214. 79-97.

TABLE I

Resonant periods for various (m, n) in seconds.

b = 400 m, = 0·030 (1°43')

n \ m	1	2	3	4	5	6	7	8	9	10	11
0	130·5	92·2	75·3	65·3	58·4	53·2	49·4	46·2	43·5	41·3	39·3
1	75·5	53·4	43·6	37·8	33·8	-	-	-	25·2	-	-
2	58·6	41·5	33·8	29·3	26·6	23·9	23·2	20·7	-	18·6	-
3	49·6	35·1	28·6	34·8	-	-	-	-	16·5	-	-
4	43·8	31·0	25·3	21·9	19·6	-	-	-	-	-	-
5	39·8	28·2	23·0	19·9	-	-	-	-	13·3	12·6	12·0
6	36·8	26·0	21·2	18·4	16·5	15·0	13·9	-	12·3	11·7	11·1
7	34·3	24·3	19·7	17·2	-	-	-	12·1	11·4	10·9	-
8	32·4	22·9	18·7	-	14·5	13·2	12·3	11·5	10·8	-	-
9	30·8	21·8	17·8	15·4	-	-	11·7	10·9	10·3	-	-
10	29·5	20·9	17·0	-	13·2	12·1	11·2	-	9·8	-	-
11	28·4	20·1	16·4	14·8	-	11·6	10·8	-	-	-	-
12	27·4	19·4	15·8	-	-	11·2	-	-	-	-	-
13	26·6	18·7	15·3	13·3	11·9	10·9	-	-	8·9	-	-
14	25·9	18·3	14·9	-	11·6	-	-	-	-	-	-
15	25·4	17·9	14·6	12·7	11·4	-	-	-	-	-	-
16	24·8	17·5	-	-	11·1	-	-	-	-	-	-
17	24·3	17·2	14·0	12·2	10·9	9·9	9·2	8·6	8·1		
18	23·9	16·9	-	12·0	-	-	-	-	-	-	-
19	23·6	16·7	13·6	11·8	10·5	-	-	-	-	-	-
22	32·9	16·2	13·2	11·5	10·2	9·4	8·7	8·1	7·6	-	-
25	22·6	16·0	13·0	11·3	10·1	-	-	-	-	-	-
Cut-off	22·6	16·0	13·0	11·3	10·1	9·3	8·6	8·0	7·5	-	-
L	500	400		200				100			

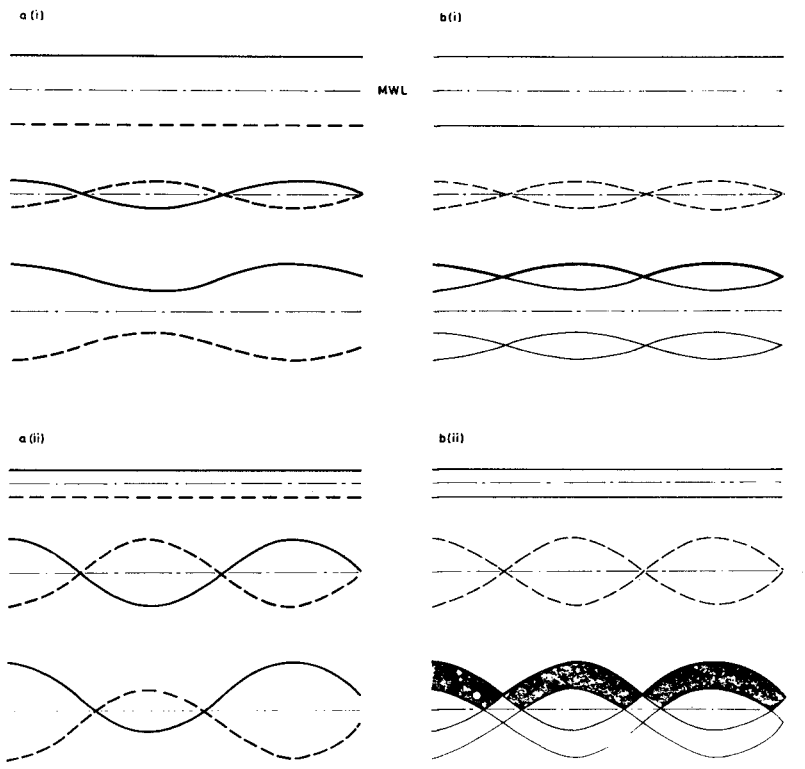

FIGURE 1.

Incoming wave/edge wave interaction a) with waves of the same frequency b) waves of different frequency. Case (i) incoming waves larger than edge waves; case (ii) edge waves dominant.

CHAPTER 72

PREDICTING CHANGES IN THE PLAN SHAPE OF BEACHES

By

W A Price
Senior Principal Scientific Officer

K W Tomlinson
Senior Scientific Officer

D H Willis
Senior Scientific Officer

The Hydraulics Research Station, Wallingford, Great Britain

ABSTRACT

A mathematical model is described that is capable of predicting changes in the plan shape of a beach following the construction of sea defences or an alteration in the wave climate. The rate of change is calculated. The technique is illustrated by comparing model predictions with results from experiments carried out in a wave basin. The importance of the method in estimating coastal changes due to offshore dredging is mentioned, and the future development of the mathematical approach is outlined.

INTRODUCTION

A frequently recurring problem in coastal engineering is the prediction of changes in the plan shape of a beach following alterations in the wave climate. Such changes can be induced by various means. The construction of groynes, breakwaters and harbour moles has a direct influence on the beach plan shape. Offshore dredging for sand and gravel may also affect the waves by changing the refraction pattern.

Changes in the plan shape of a beach and the rate of this change are of particular interest in Great Britain. Large deposits of sand and gravel exist close to the shore. The use of these offshore natural resources is becoming necessary as stocks on land are now less economically obtained.

Hence methods to forecast changes affecting general beach stability are of immediate concern to the civil engineer.

This paper describes the early development of a mathematical model to study such situations. It illustrates the application of the method to the problem of predicting beach changes following the construction of a long groyne. Results from experiments carried out in a wave basin to check predictions made by this mathematical approach are described.

MATHEMATICAL MODEL

Essentially, the mathematical model is a finite difference solution of the continuity equation in the alongshore direction:-

$$\frac{\delta Q}{\delta x} + \frac{\delta A}{\delta t} = 0$$

where Q = volume rate of alongshore sediment transport

x = distance in the alongshore direction

A = beach cross-sectional area

t = time

When the cross-sectional area is represented as the product of a beach ordinate, y, perpendicular to x, and a depth, D, as shown in Figure 1, this becomes:-

$$\frac{\delta Q}{\delta x} + D \frac{\delta y}{\delta t} = 0 \qquad (1)$$

The solution of this equation requires a means of calculating the rate of alongshore sediment transport, Q, given wave and beach properties at an instant in time. Analysis of the results of previous tests in the wave basin indicated that the Scripps Equation, as modified by Komar in Reference 1, described the submerged weight sediment transport rate reasonably well for uniform waves in the absence of tidal currents:-

$$I_L = 0.35\ E\ (nC)\ \sin 2\alpha$$

where I_L = submerged weight rate of alongshore sediment transport

E = energy density of breaking waves, $\frac{1}{8} \rho g H^2$

ρ = mass density of water

g = acceleration due to gravity

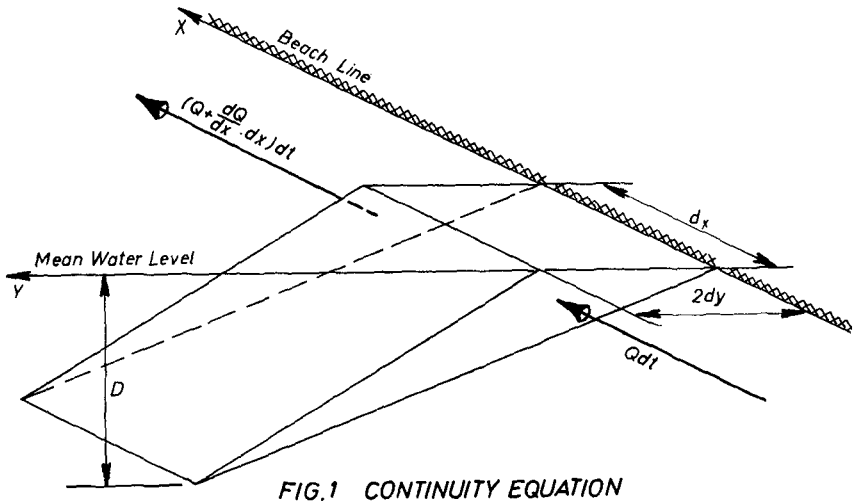

FIG.1 CONTINUITY EQUATION

H = wave height, trough to crest, at breaking

(nC) = group velocity of waves at breaking

α = angle between breaking wave front and the beach

Converted to a volume rate of transport, this becomes:-

$$Q = \frac{0.35}{\gamma_s} E(nC) \sin 2\alpha \qquad (2)$$

in which γ_s = submerged density of beach material in place

It is assumed that, for the given wave conditions, (nC) is a constant, E is a function of x only, and α is a function of x and t.

Two methods of solution have been used. In the first, Equation (2) is differentiated with respect to x and substituted in Equation (1) to obtain:-

$$\frac{0.35}{\gamma_s} (nC) \left[\sin 2\alpha \frac{dE}{dx} + 2E \cos 2\alpha \frac{\delta\alpha}{\delta x}\right] + D\frac{\delta y}{\delta t} = 0 \qquad (3)$$

In difference form, this is

$$\frac{0.35}{\gamma_s}(nC)\left\{\sin 2\alpha\,[n,t]\,\frac{E[n+1]-E[n-1]}{2\Delta x}+2E[n]\cos 2\alpha\,[n,t]\,\frac{\alpha[n+1,t]-\alpha[n-1,t]}{2\Delta x}\right\}+D\,\frac{y[n,t+1]-y[n,t]}{\Delta t}=0$$

in which $[n,t]$ refer to the number of Δx and Δt steps respectively from the origin.

Thus rewriting:-

$$y[n,t+1]=y[n,t]-\frac{0.35(nC)\Delta t}{2\gamma_s D\,\Delta x}\left\{\sin 2\alpha\,[n,t]\,(E[n+1]-E[n-1])+2E[n]\cos 2\alpha\,[n,t]\,(\alpha[n+1,t]-\alpha[n-1,t])\right\} \quad (4)$$

which can be solved, given an expression for α, see Figure 2:-

$$\alpha=\alpha_x-\tan^{-1}\frac{\delta y}{\delta x} \quad (5)$$

where α_x = the angle between the breaking wave front and the x-axis, a function of x only.

Thus, $\alpha[n,t+1]=\alpha_x[n]-\tan^{-1}\frac{y[n+1,t]-y[n-1,t]}{2\Delta x}$ (6)

The second method of solution is much simpler. In this technique, Equation (1) is converted immediately to differences:-

$$\frac{Q[n+1,t]-Q[n,t]}{\Delta x}+D\,\frac{y[n+\tfrac{1}{2},t+\tfrac{1}{2}]-y[n+\tfrac{1}{2},t-\tfrac{1}{2}]}{\Delta t}=0$$

or:-

$$y[n+\tfrac{1}{2},t+\tfrac{1}{2}]=y[n+\tfrac{1}{2},t-\tfrac{1}{2}]-\frac{\Delta t}{D\Delta x}\left\{Q[n+1,t]-Q[n,t]\right\} \quad (7$$

in which:-

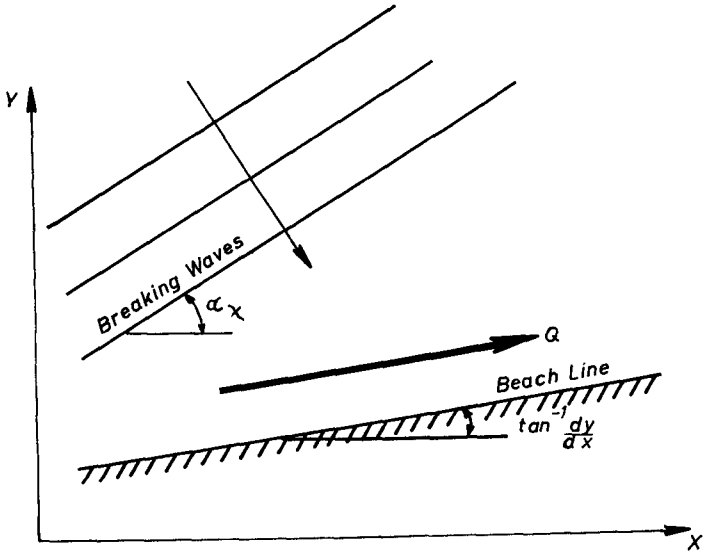

FIG.2 BREAKER ANGLE

$$Q[n,t+1] = \frac{0.35E[n](nC)}{\gamma_s}\sin 2\alpha\,[n,t+1] \qquad (8)$$

$$\alpha[n,t+1] = \alpha_x[n] - \tan^{-1}\frac{y[n+\tfrac{1}{2},t+\tfrac{1}{2}] - y[n-\tfrac{1}{2},t+\tfrac{1}{2}]}{\Delta x} \qquad (9)$$

This method has three principal advantages over the first:

1. Within the limitations of the alongshore transport calculation, it is 'exact'. That is, the budget of beach material is maintained because

$$\frac{Q[n+1,t] - Q[n,t]}{\Delta x}$$

completely describes $\frac{\delta Q}{\delta x}$ over the length Δx.

2. It can be used with alongshore transport equations that are difficult or impossible to differentiate.

3. It is more economical in computer time.

The second advantage described is probably the most important, and the second technique has already been used with a rather more complex transport equation, incorporating transport from

areas of high to areas of low wave energy when the angle of incidence is zero. This has not yet been tested but will form the subject of a future paper.

The only drawback to the second method is that, because Q and y are not known at the same points along the beach, boundary conditions are difficult to define. However, the advantages outweigh the disadvantage, and no further development of the first technique is contemplated.

Input to the mathematical model is the wave height, H, angle of incidence, α_x, and the initial beach shape, y, all as functions of x; an estimated celerity at breaking, nC, based on the observed water depth and the wave period; and an estimated depth, D, beyond which alongshore transport no longer takes place. In the present case all these were measured in the physical model, but in practice it is intended that they would be provided by an analysis of observed or forecasted wave conditions.

WAVE BASIN TESTS

A beach of crushed coal - specific gravity 1.35 and d_{50} = 0.8 mm - was subjected to waves having a period of 1.15 s and a constant height of 40 mm - the initial angle between the breakers and the beach being 4^0. Material was fed to the updrift beach at the calculated alongshore transport rate. The beach was moulded to an arbitrary profile, and waves were generated for an hour to allow the profile to adjust to the waves. A long groyne was then constructed across the foreshore as shown in Figure 3. For comparison with the mathematical predictions, beach ordinates were obtained by averaging the 0, 25, 50, 75 and 100 mm depth contours at the following times:

- before the groyne was constructed. This was the initial plan shape used in the mathematical model.
- 1 hour after construction of the groyne.
- 3 hours after construction of the groyne.
- 6 hours after construction of the groyne.

DISCUSSION

A comparison of beach plan shapes predicted by the mathematical model and those measured in the wave basin is shown in Figure 4. There is close agreement for a period of 3 hours after the introduction of the groyne. After 6 hours

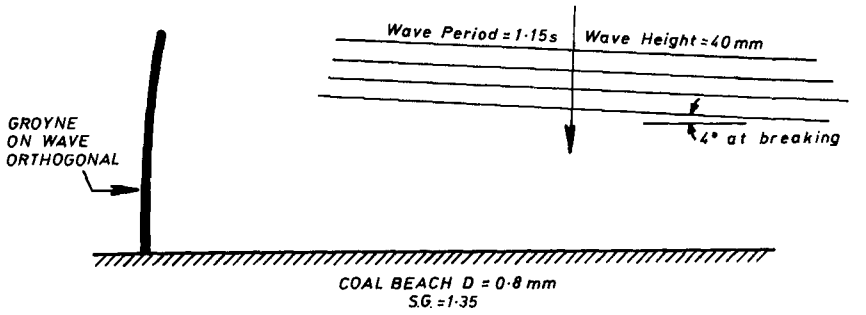

FIG. 3 TESTS IN THE WAVE BASIN

the build-up of coal near the structure sufficiently altered the wave refraction pattern to invalidate the input wave data. A complex boundary condition had also developed at the updrift end of the wave basin. No further useful comparisons could therefore be made.

The experiment to date has shown that the mathematical model, operated with the Komar equation for alongshore sediment transport, is capable of predicting the plan shape and rate of change of the plan shape of a beach with reasonable accuracy. Greater accuracy can be obtained if the relationship between alongshore sediment transport and wave height and direction can be verified for the beach in question.

The next development of the mathematical model is to link it with an existing refraction program to take account of the effect of beach changes on the waves. Further research will then be necessary to move away from the bulk flow sediment approach, as used by Komar, to a detailed description of sediment flux in terms of waves and currents; this will enable hydraulic and sediment conditions to be described for a point in space and time.

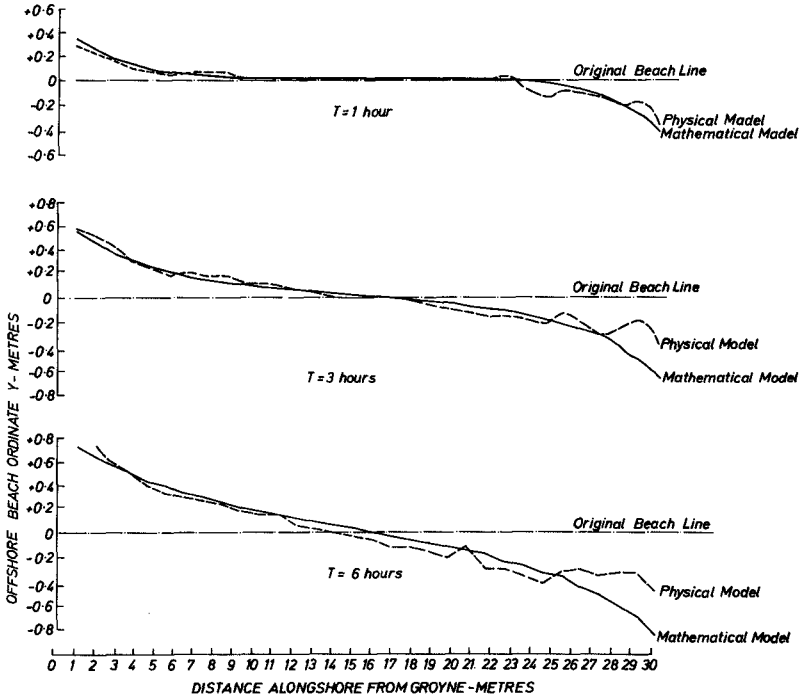

FIG. 4 CHANGES IN BEACH PLAN SHAPE

ACKNOWLEDGEMENTS

This report is published by permission of the Director of the Hydraulics Research Station, Wallingford, Great Britain. The authors gratefully acknowledge the co-operation of Ir W T Bakker, of the Rijkswaterstaat, The Netherlands. We also wish to thank Mr J M Motyka, who carried out the physical model work, wrote the computer program, and provided invaluable assistance and advice.

REFERENCES

1. KOMAR, Paul D. "The longshore transport of sand on beaches". Ph D thesis, University of California, San Diego, 1969.

2. BAKKER, W T. "The dynamics of a coast with a groyne system". Proceedings of the 11th Conference on Coastal Engineering, London, September 1968, Vol 1, pp 492-525.

3. BAKKER, W T. "The influence of diffraction near a harbour mole on the coastal shape". Studierapport W.W.K. 70-2, Rijkswaterstaat, The Netherlands.

4. PELNARD-CONSIDERE, R. "Essai de theorie de l'evolution des formes de rivage en plages de sable et de galets". Quatriemes Journees de l'Hydraulique, Paris. Juin 1956, Les Energies de la Mer, Question III, rapport 1, Vol 1, pp 289-298.

CHAPTER 73

ON THE FORMATION OF SPIRAL BEACHES

Paul H. LeBlond
Institute of Oceanography
University of British Columbia

ABSTRACT

The theory of wave-induced longshore currents is applied to problems of beach erosion. An erosion equation is derived, relating the local erosion (or deposition) rate to the form of the beach and to the characteristics of the incoming wave field. A numerical integration technique of the erosion equation is discussed and a specific example is examined: that of a linear coast line which is gradually eroded into a spiral-shaped beach in the lee of a headland.

Introduction

Hook-like beaches of the type shown in Figure 1 are quite common on exposed coasts. Such beaches have received various names: Silvester (1960) calls them "half-heart shaped bays" and Yasso (1965) "headland-bay beaches". Half-Moon Bay in California is one of the best known examples (Bascom, 1951). It was Yasso (1965) who discovered that the planimetric shape of many such beaches could be fitted very closely by a segment of a logarithmic spiral. The distance r from the beach to the center of the spiral increases with the angle ψ according to

$$r = r_o e^{\psi \cot\alpha} \qquad (1)$$

in which α is called the "spiral angle" and determines the tightness of the spiral. Bremner (1970) has also shown the logarithmic spiral to give an excellent fit for each side of a recessed beach between two headlands.

It is extremely tempting to attribute the characteristic shape of these spiral beaches (as I call them here) to wave-induced erosional processes. To confirm this suspicion, I have attempted to show, using available theories of longshore currents and beach erosion, how a spiral beach could evolve from a linear wave-swept coastline.

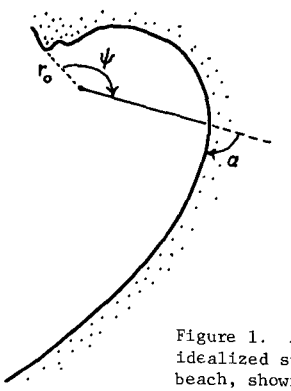

Figure 1. An idealized spiral beach, showing the coordinate system.

Longshore currents

It will be assumed that any erosion or deposition at the shoreline will be due uniquely to transport of material by wave-induced longshore currents. The theory of such currents has recently risen out of a state of semi-empiricism following a re-examination of the role of waves in producing currents (Longuet-Higgins, 1970 a, b) and of the manner in which sand is transported by these currents (Komar and Inman, 1970; Komar, 1971). Longshore currents are produced by breaking waves in the surf zone; the amplitude and direction of the incoming wave are determined by offshore conditions which are assumed to be completely uncoupled with surf zone phenomena.

To be more specific, let's consider a straight section of beach, as shown in Figure 2. Approaching waves begin to break at the mean distance x_b from the shore line, in a mean depth h_b; their amplitude upon breaking is a_b and the angle made by their propagation vector with the x-axis is ϕ_b. The wave amplitude in the surf zone ($0 \leq x \leq x_b$) is taken as proportional to the mean depth: $a = \alpha\, h$ (Longuet-Higgins, 1970a). The local wave energy density is then $E = \frac{1}{2} \rho g \alpha^2 h^2$. In beach coordinates (x,y), the radiation stress of the waves has components

$$S_{ij} = \frac{E}{2} \begin{pmatrix} 3\cos^2\phi + \sin^2\phi, & -\sin 2\phi \\ -\sin 2\phi, & 3\sin^2\phi + \cos^2\phi \end{pmatrix} \tag{2}$$

The divergence of the radiation stress S_{ij} provides the driving force for the longshore currents in the surf zone; there is no net forcing in the offshore area. Once a steady state has been reached, frictional forces will just balance the driving force and the mean longshore momentum equation will read

$$\frac{\partial}{\partial x}\left(\mu h \frac{\partial V}{\partial x}\right) - fV = \left(\frac{\partial}{\partial y} S_{yy} + \frac{\partial}{\partial x} S_{yx}\right) \qquad 0 \leq x \leq x_b$$

$$" \qquad = \qquad 0 \qquad\qquad x_b \leq x < \infty \tag{3}$$

The assumptions and simplifications leading to these equations have been discussed by O'Rourke and LeBlond (1972). The lateral eddy friction coefficient μ is taken as increasing linearly with wave velocity and with distance from the beach:

$$\mu = N \rho x \sqrt{gh} \tag{4}$$

(N is a dimensionless constant). The bottom friction parameter f is proportional to the maximum orbital velocity

$$f = \frac{2}{\pi} \rho \alpha C \sqrt{gh} \tag{5}$$

Where C is a friction coefficient for flow over rough plates. Assuming a linear depth profile which is uniform along the beach

$$h = Sx \tag{6}$$

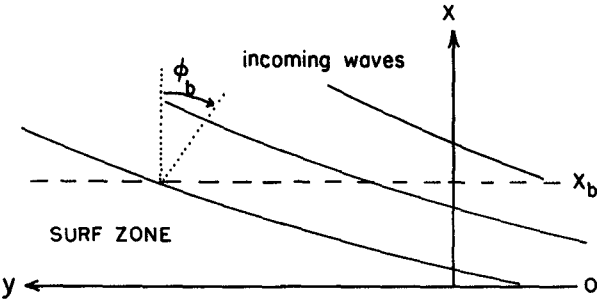

Figure 2.
Definition sketch for the linear beach.

and transforming to a scaled coordinate $\xi = x/x_b$, (3) may be rewritten

$$P \frac{\partial}{\partial \xi}\left(\xi^{5/2} \frac{\partial}{\partial \xi}\right) - \xi^{1/2} V = \sum_{i=1}^{3} V_i \xi^{1+i/2} \qquad 0 \le \xi \le 1$$
$$" \qquad = \quad 0 \qquad 1 \le \xi \le \infty \tag{7}$$

This is the same equation obtained by Longuet-Higgins (1970b), but with two more forcing terms. P is the ratio of lateral to bottom friction effects, $\left(P = \frac{\pi N S}{2\alpha C}\right)$

$$K = \frac{5\pi\alpha}{8C} g^{1/2} x_b^{1/2} S^{3/2}, \quad V_2 = \frac{2K}{5}\left(3 - 2\cos^2\phi_b\right) \frac{x_b}{a_b} \frac{\partial a_b}{\partial y}$$
$$V_1 = K \sin\phi_b \cos\phi_b \qquad V_3 = \frac{4K}{5} x_b \sin\phi_b \cos\phi_b \frac{\partial \phi_b}{\partial y} \tag{8}$$

The three forcing terms are due respectively to 1) the obliqueness of wave approach, 2) and the non-uniformity of wave amplitude and 3) of wave angle along the beach. The first term is usually the more important one.

The solution to (7) which keeps V finite and both V and $\partial V/\partial \xi$ continuous across the breaker line is

$$V = B_1 \xi^{p_1} + 2 \sum_{i=1}^{3} \frac{V_i \xi^{(1+i)/2}}{(1+4i)P-2} \qquad 0 \le \xi \le 1$$
$$= B_2 \xi^{p_2} \qquad 1 \le \xi \le \infty \tag{9}$$

in which

$$p_{1,2} = -\frac{3}{4} \pm \left(\frac{9}{16} + \frac{1}{P}\right)^{1/2}$$

$$B_1 = \frac{2}{P(p_1-p_2)} \sum_{i=1}^{3} \frac{V_i}{2p_1-(1+i)}$$

$$B_2 = \frac{2}{P(p_1-p_2)} \sum_{i=1}^{3} \frac{V_i}{2p_2-(1+i)}$$

Whenever $P = 2/(1 + 4i)$ for any one of $i = 1, 2, 3$, a singularity appears in one of the coefficients of V in (9); the solution must then be modified. For $i = 1$, $P = 2/5$, the appropriate term is $5/7\ V_1\ \xi \ln\xi$; for $i = 2$, $P = 2/9$, $V_2\ \xi^{3/2}\ \ln\xi$; and for $i = 3$, $P = 1/7$, $-14/11\ V_3\ \xi^2 \ln\xi$. We will avoid any worries by simply choosing a value of P different from 2/5, 2/9 and 1/7.

Sand transport

In relating sand transport to longshore currents I have simply assumed that the volume rate of sand transport T will be proportional to the total water transport in the surf zone, Q, times a "sand fraction" μ, so that $T = Q\mu$. Q is defined by

$$Q = Sx_b^2 \int_0^1 \xi V(\xi)\, d\xi \tag{10}$$

Sand transport is then an integral property of the surf zone, and is thus independent of ξ. It will thus not be possible with this model to examine variations in beach profile $(h\ (\xi))$ associated with differences in sand transport rates across the surf zone. Such refinements could well be brought into more advanced models, by making T an explicit function of V, as in Komar (1971).

It is useful to split Q into three parts, each one resulting from one and only one of the three forcing mechanisms mentioned earlier: thus,

$$Q = \sum_{i=1}^{3} Q_i \tag{11}$$

in which

$$Q_i = Sx_b^2 V_i \left(\frac{4}{\left((1+4i)P-2\right)(5+i)} + \frac{2}{P(p_1+2)(p_1-p_2)\left(2p_1-(1+i)\right)} \right) \tag{12}$$

We recall the source of three components of the transport: Q_1 is caused by the obliqueness of the waves, Q_2 and Q_3 by the non-uniformities of the wave amplitude and angle of approach respectively.

The Erosion Equation

The rate of erosion will be directly proportional to the divergence of sand transport $Q\mu$. As we have lost all information about the details of sand transport across the surf zone by relating the total sand transport directly to the integral of the longshore current, it will be reasonable

to simply assume that the beach profile is not modified by erosion. The slope S retains the same value, the beach being shifted laterally by sand removal or accretion, as shown in Figure 3. The parallelogram of sand (of density ρ_s) removed by erosion in a time Δt has a mass $\rho_s h_b \Delta x_o$. With $x_o(t)$ the position of the mean shore line, the rate of sand removal is then $\rho_s h_b \frac{\partial x_o}{\partial t}$. This is balanced by the divergence of sand transport in the surf zone

$$\frac{\partial}{\partial y}(Q\mu) + \rho_s h_b \frac{\partial x_o}{\partial t} = 0 \tag{13}$$

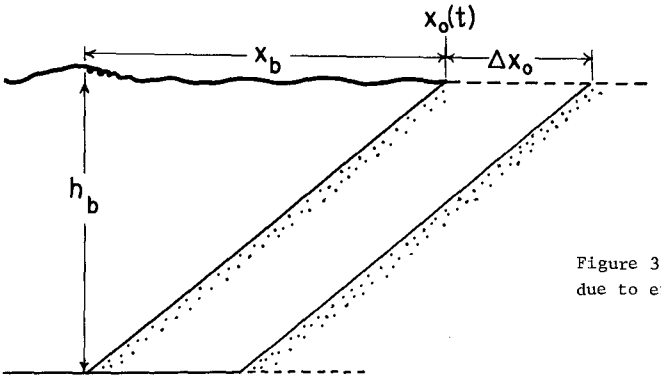

Figure 3. Beach shift due to erosion.

This derivation is strictly correct only for linear beaches. We will extend its applicability to curved beaches by appealing to the results of O'Rourke and LeBlond (1972) who found that, for semi-circular beaches, the supplementary forcing terms occuring in (3) because of beach curvature were negligible provided the radius of curvature of the beach remained much greater than the width of the surf zone. When that condition is satisfied, (13) still describes the erosional processes in a short enough section of the beach. We may now redefine local variables (x, y) as shown in Figure 4; the orientation of the beach segment to fixed axes (X, Y) will be specified by the angle θ. The rate of displacement of a point P(X, Y) which always remains on the beach may then be found from (13) as

$$\frac{\partial X}{\partial t} = -\frac{\cos\theta}{\rho_s h_b} \frac{\partial}{\partial y}(Q\mu) \tag{14a}$$

$$\frac{\partial Y}{\partial t} = \frac{\sin\theta}{\rho_s h_b} \frac{\partial}{\partial x}(Q\mu) \tag{14b}$$

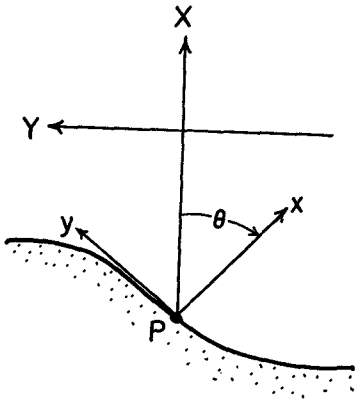

Figure 4. Definition of local coordinates for extension to curved beaches.

Computational Scheme

The initial planimetric shape of a beach may be specified by giving the coordinates (X, Y) of a sufficient number of points P_j (j = 1, ... N). Given the characteristics of the incident wave field (ϕ,a_b), the initial beach geometry (S, x_b, ρ_s) and the empirical coefficients α, N, C, μ it will be possible to calculate the sand transport $Q\mu$ and its divergence along the beach. Integrating the erosion equations (14) over a finite time interval yields values Δx_j, Δy_j by which the position of the j^{th} point is to be modified because of erosion or deposition during that time span. Repetition of this process gives a series of positions for the forms Pj and hence a series of planimetric shapes for the beach. This apparently simple-minded integration scheme is alas full of pitfalls! Having fallen victim to many of them I would like to discuss the origin and the means of avoiding the worst of them before presenting actual computational results.

First of all, there arises the problem of stability. The natural processes described by this model occur over time-scales ranging from months to centuries. The integration time-step should then be chosen large enough to make it possible to witness the evolution of the beach within a reasonable lapse of computing time. A long time step is thus desirable; it is also dangerous. Imagine for a moment a linear section of beach with a hump on it. With a uniform incident wave field ($\phi_b \neq 0$, $\partial a_b/\partial y = 0$, $\partial \phi_b/\partial y = 0$: $Q_1 \neq 0$, $Q_2 = 0 = Q_3$) there will be a tendency for this hump to be eroded away. A strong divergence of sand transport will occur on the hump, leading from (13) to a large rate of erosion ($\partial x_o/\partial t < 0$). If the time step is small enough, the hump will gradually be reduced to insignificance. Should the time step be chosen too large however the correction Δx_o to the beach shape during the time Δt may be large enough to transform the hump into a hole! This is already nonsense, but not yet instability. If the hole is less deep than the hump was high, an oscillatory approach to equilibrium will result.

Only when the hole is deeper than the original height of the hump will instability occur. It is clearly not sufficient to choose a time step small enough to avoid instability of this type; one must avoid over-correction: violent transformation of humps into holes and vice-versa within a single time step. The computer model should behave very much in the same way as a real beach does, and be endowed with a similar tendency to gradually minimize its curvature, except possibly at a few well understood and identified points, such as sand spits.

The problem of stability has to do with the mechanics of numerical computation, and is readily taken care of. A more fundamental difficulty is that of correcting the incident wave field to account for the change in planimetric shape of the beach. As indicated earlier, one of the fundamental premises of the theory of generation of longshore currents is that there is no coupling between the longshore currents in the surf zone and the wave field in the offshore zone. The longshore currents are caused by the incident wave field but do not in turn influence it. This may well be so on a time scale short compared to that during which significant modifications of the sea shore occur, but as the planimetric shape of the beach departs more and more from its initial form, the incoming wave field will suffer from refraction or diffraction to a significant extent and the forcing function for the longshore currents will be altered. There is thus a larger-time-scale coupling between longshore currents and the incident wave field, and it must be taken into account in problems of beach evolution.

Let us see how the above theory of longshore currents and the scheme of integration of the erosion equation may be applied to account for the presence of spiral beaches. We shall assume that at some initial time ($t = 0$) a completely uniform wave field is incident at an angle ϕ_o upon a linear beach (Figure 5). To simulate the presence of a rocky headland it will be assumed that half the beach ($Y \leq 0$) is a rocky strip, from which no sand can be eroded, and hence on which $\mu = 0$. The longshore water transport Q is thus initially uniform, but not the sand transport $Q\mu$, which has a discontinuity at the origin.

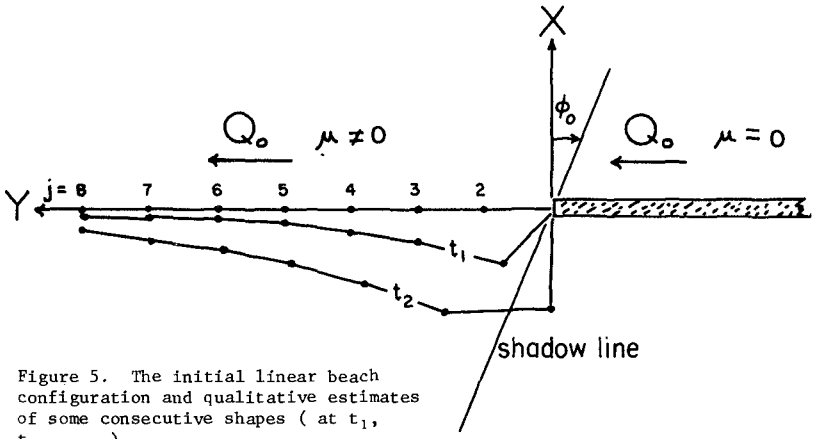

Figure 5. The initial linear beach configuration and qualitative estimates of some consecutive shapes (at t_1, t_2, . . .).

It is simple to see, at least qualitatively, how the beach will evolve. Because of the sand fraction discontinuity at the origin, the sand transport divergence will be large and positive there and, from equation (13), erosion will occur rapidly. The beach will be gradually deformed as shown in Figure 5. As the beach changes its orientation in the (X, Y) plane, so that the angle θ in (14) is no longer zero, the local angle of attack ϕ_b will change from its original value of ϕ_o to a new value $\phi_b = \phi_o - \theta$. Those parts of the transport which depend on the angle ϕ_b (Q_1) or on the longshore variation of ϕ_b (Q_3) will be changed accordingly. Further, as the nick dug in the beach gets deeper and the beach segment near the origin approaches the "shadow line", the influence of diffraction by the tip of the rocky strip (which has now become a headland) will become more noticeable, and the amplitude and direction of the waves arriving at the breaker line will have to be modified to account for the changing geometry of the shore line. The variation of Q along the beach will gradually become as important as the initial discontinuity in μ in determining the erosion rate.

The actual computations have been made following the procedure outlined earlier. A number of points, labelled $j = 1, 2 \ldots N$, are initially strung along the half line $Y \geq 0$, and are gradually displaced according to equations (14). The beach thus consists of N - 1 linear segments, the j^{th} segment being between the j^{th} and $(j + 1)^{th}$ points, and making an angle θ, with the Y-axis. Transports are calculated at intermediate points and are characteristic of a segment, not of a point (see Figure 6).

The rate of displacement of a labelled point will be proportional in magnitude to the difference in the transport in the segments on either side of it. The direction in which the point moves must be defined with more care: since the labelled points are at the intersection of beach segments, where there is usually a discontinuity in slope, as characterized by the angle θ, one cannot use equations (14) in exactly the form in which they appear. We define an angle α which is the average slope at a point:

$$\alpha_{j+1} = \frac{\theta_{j+1} + \theta_j}{2}$$

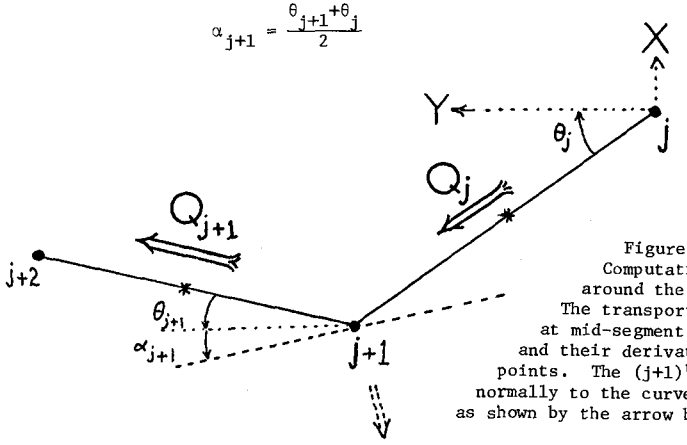

Figure 6. Computational "molecule" around the $(j+1)^{th}$ point. The transports Q are evaluated at mid-segment (starred) points and their derivative at labelled points. The $(j+1)^{th}$ point moves normally to the curve of angle α_{j+1}, as shown by the arrow beneath it.

and allow the erosion to proceed at the $(j+1)^{th}$ point as if the beach had an orientation given by the angle α_{j+1} there. In finite difference form, (14) now reads:

$$\Delta X_{j+1} = \frac{-\mu\cos\alpha_{j+1}}{\rho_s h_b} \frac{\left(Q_{j+1}-Q_j\right)}{\Delta_{j+1}} \tag{15a}$$

$$\Delta Y_{j+1} = \frac{\mu\sin\alpha_{j+1}}{\rho_s h_b} \frac{\left(Q_{j+1}-Q_j\right)}{\Delta_{j+1}} \tag{15b}$$

where $2(\Delta_{j+1})^2 = \sqrt{(X_{j+2}-X_{j+1})^2 + (Y_{j+2}-Y_{j+1})^2} + \sqrt{(X_{j+1}-X_j)^2 + (Y_{j+1}-Y_j)^2}$.

Since there can be no erosion of the rocky spit, the first point ($j = 1$) does not move: $(X_1, Y_1) = (0, 0)$ at all times.

Qualitative considerations

Even before proceeding with the integration of (15) it is possible and advisable to consider what kind of qualitative results are expected. First, as already indicated, the beach erodes at the corner, as shown in Figure 5. From the definition of α, it should be clear that erosion at point $j = 2$ should take place in a direction which will take it towards decreasing values of Y, so that erosion behind the rocky strip will ultimately result. This back-cutting is indeed seen to occur in the computed configurations (Fig. 7, 8) and is a necessary step towards attaining spiral shape (or anything which resembles a spiral).

From the nature of the erosion and deposition processes, it is also clear that humps and holes (regions of high curvature) will be rapidly smoothed away in a real beach, and should suffer the same fate in our model. Such regions of sharp curvature would appear wherever the sand transport $Q\mu$, has maxima or minima along the beach. We thus expect that once an equilibrium profile has been reached, there will be no such extrema in $Q\mu$, which will increase monotonically from zero at the headland to a maximum value at the far end of the beach. From the very beginning, the eroded beach is concave seawards near the headland, convex seawards further on. If $Q\mu$ increases monotonically from the headland, this situation will prevail at all times and there will be only one point of inflexion.

If there exists a planimetric shape which the headland beach asymptotically approaches, it must have the following properties: 1) it is first concave outwards, near the headland, and then convex outwards; 2) the sand transport increases monotonically along it; 3) erosion, by causing the beach to be displaced (inwards) normally to itself, does not change the qualitative shape of the beach. This last statement requires some explanation. If a planimetric shape is defined as a curve $f(X, Y, a_1 \ldots a_n) = 0$ where $a_1 \ldots a_n$ are parameters which define the centre, the size, the orientation, etc., of the curve, then what is stated is that a displacement of the curve normal to itself produces another curve of the same n-parameter family.

A trivial example of such a curve is a circle $(x-x_o)^2 + (y-y_o)^2 = r^2$, which is a three-parameter curve; displacing every point of the circle normally outwards by an equal amount gives another circle of greater radius. A more appropriate example would be that of a logarithmic spiral displaced normally to itself by a distance L proportional to the radius vector from the origin: $L = \beta r$. Such a shift, as could be caused by erosion, transforms a spiral into another one of the same angle but different intercept r_o. The spiral does not fulfill the first condition however. There must exist more complicated curves satisfying all of the above three conditions, and one cannot decide a priori which one will be the equilibrium one.

Because of the diffractive influence of the headland on the incident wave field, the region in the shadow of the headland, i.e. the head of the hook, is the most difficult to describe. All three terms (Q_1, Q_2, Q_3) may be important in the longshore volume flow there and it is not clear which one will dominate. The tail of the beach on the other hand should behave in a much simpler fashion since the wave field there should be nearly uniform in the longshore direction. The only contribution to longshore transport will come from Q_1, which, from (12), (8) and $\phi_b = \phi_o - \theta$, may be written

$$Q_1 = Q_o \sin\left[2(\phi_o - \theta)\right]$$

In the tail region, θ is a small angle, and $\tan\theta \simeq dX/dY$. For the same reason, $\frac{\partial}{\partial y} \simeq \frac{\partial}{\partial Y}$, so that

$$\frac{\partial Q_1}{\partial y} = -2Q_o \frac{\partial \theta}{\partial y} \simeq -2Q_o \frac{\partial^2 X}{\partial Y^2}$$

The shape of the beach may then be found from

$$\frac{\partial^2 X}{\partial Y^2} = -\frac{1}{2Q_o} \frac{\partial Q_1}{\partial Y}$$

Analytic determination of the solution curve which will satisfy the three fundamental criteria in this region and connect to an equally satisfactory curve in the head region is beyond the present effort. We may choose for the moment any Q_1 which will tend to Q_o so as to make X and all of its Y derivatives vanish as Y tends to infinity. For example, the tail region at t = 80 hours in Figure 7 is very closely fitted by $X = -X_o e^{-\beta(Y-Y_o)^2}$, with $X_o = -143$ m, $Y_o = 130$ m, and $\beta = 3.15 \times 10^{-6} m^{-2}$, so that $Q_1 = Q_o\left(1 - 4\beta X_o Y e^{-\beta(Y-Y_o)^2}\right)$ in that region.

Computed Beaches

The computed beach profiles fall into two categories according to the type of approximations made in describing the wave field in the vicinity of the headland.

It was first simply assumed that there was no diffraction whatsoever and hence no wave energy behind the "shadow line" $Y = -X \tan\phi_o$. The transport along the beach segment which intersects the shadow line (at the point P_s with coordinates (X_s, Y_s)) was reduced in proportion to the fraction of it that lies in the shadow. The reduction factor is

$$\left[(X_{j+1}-X_s)^2 + (Y_{j+1}-Y_s)^2\right]^{1/2} \Big/ \left[(X_{j+1}-X_j)^2 + (Y_{j+1}-Y_j)^2\right]^{1/2} \qquad (16)$$

Only the oblicity component Q_1 was retained in this case, to lighten the computational burden. Even under such gross approximations the results are encouraging. The successive beach shapes shown in Figure 7 were computed for $P = 0.2$, $S = 0.02$, $x_b = 62.5$ m., $C = 10^{-2}$, $\alpha = 0.4$, $\phi_o = \pi/10$, $a_b = 1$ m., $\mu = 1$ kg m^{-3}, $\rho_s = 2 \times 10^3$ kg m^{-3} and a time step Δt of 1 minute. The small time step was necessary to avoid instabilities. Except for the incredibly rapid rate of erosion of the beach, which may be attributed to the presence of an unrealistic discontinuity at the origin as well as to the absence of the Q_2 and Q_3 terms, the erosion proceeds in a reasonable fashion. Note in particular that the first two of the qualitative criteria established earlier for an equilibrium shape are satisfied: 1) the beach is concave outwards at first, convex afterwards; 2) the transport increases monotonically along the beach.

Encouraged by this moderate success I have started computations in which diffraction effects are included. As it is not in general possible to obtain closed-form solutions to the diffracted wave problem for arbitrary coast geometries, any diffraction correction to the incident wave field will necessarily be an approximation. The most obvious correction, Sommerfeld's solution to wave diffraction by a wedge (Stoker, 1957, p. 109), is too complicated for practical computations. Once the beach has been eroded back sufficiently behind the rocky coastal strip, one would expect the solution for a wedge of zero angle, i.e. a thin barrier, to be a useful approximation. The theoretical results for that case have been verified experimentally (Putnam and Arthur, 1948). In order to take into account the fact that the barrier is not infinitely thin, nor the corner angle identically zero, I have used the following correction for the wave field: if $F_o(X, Y)$ is the wave amplitude function for the thin barrier case (as given by Putnam and Arthur) then the correction factor for the amplitude used in the computations was

$$F(X, Y) = 1 - \left(1-F_o(X, Y)\right)(\theta_1/\pi)^n \qquad (17)$$

where θ_1 is the angle of the first segment ($j = 1$), as defined in Figure 4 and n is an adjustable exponent. Clearly, for $\theta_1 = \pi$, $F = F_o$ and the wave field is that behind a thin barrier; for $\theta_1 = 0$, $F = 1$, and the waves have the same amplitude everywhere. Inside the geometrical shadow (behind the shadow line: $Y < -X \tan \phi_o$) the waves are now assumed to radiate from the origin (i.e. the headland), and $\phi_b = \tan^{-1}(-Y/X) - \theta$; outside the shadow area, $\phi_b = \phi_o - \theta$, as before. An upper bound ϕ_{max} was also imposed on the angle of incidence.

Computations including all components of transport (Q_1, Q_2 and Q_3) as well as diffraction corrections have not so far been very successful.

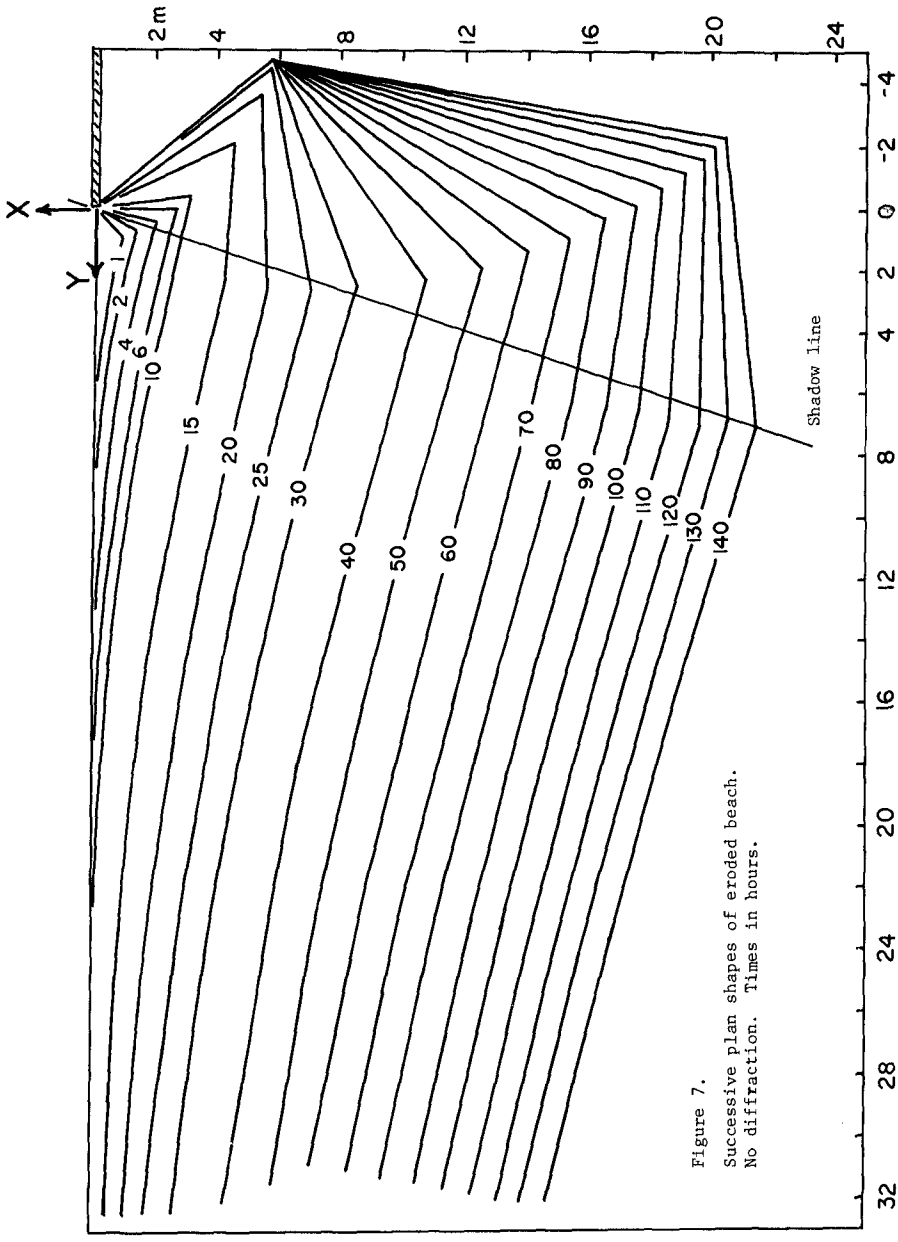

Figure 7.
Successive plan shapes of eroded beach.
No diffraction. Times in hours.

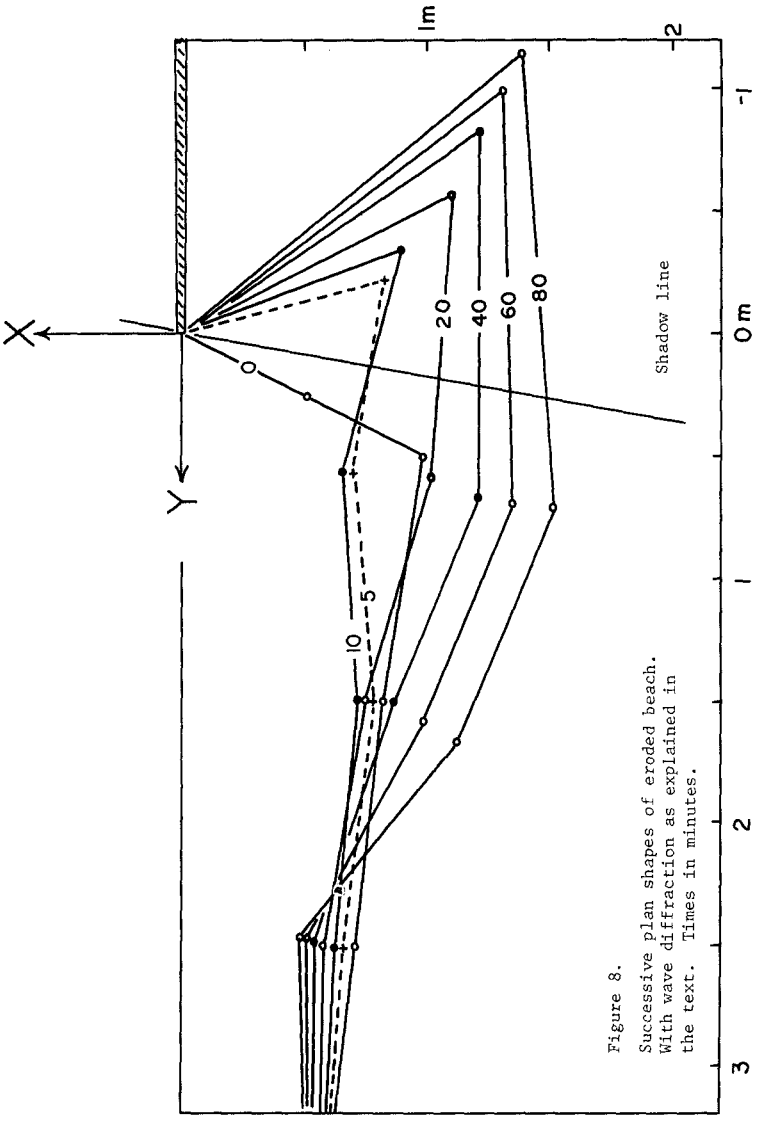

Figure 8.

Successive plan shapes of eroded beach. With wave diffraction as explained in the text. Times in minutes.

As a matter of fact, they have been plagued with instabilities to such an extent that it will be necessary to review the whole of the computational scheme. One of the more successful efforts is shown in Figure 8. In this computation, $P = 0.3$, $S = 0.083$, $x_b = 32$ m, $C = 10^{-2}$, $\alpha = 0.42$, $\phi_o = 0.17$, $a_b = 1$ m., $\mu = 1$ kg m^{-1}, $\rho_s = 2 \times 10^3$ kg m^{-3}, $\Delta t = 10$ sec and $n = 3$, $\phi_{max} = 0.35$. The computation was first run for 1 hour without diffraction corrections and with $Q_2 = Q_3 = 0$; the shape arrived at then ($t = 0$) provided the base line for the more sophisticated calculations. It is clear from Figure 8 that, after some adjustment ($t = 5$, 10), the beach digs in behind the headland, as it did in Figure 7. The transports do not become monotonic, as they did in the previous example however and a catastrophic instability occurs soon after $t = 80$ min.

Conclusions

I have shown, using the theory of wave-induced longshore currents and a simple model for beach erosion, how waves obliquely incident upon a non-uniform coast could initiate beach erosion which would eventually lead to the formation of hook-like beaches. I have however not succeeded in explaining why these beaches are such good fits to segments of logarithmic spirals, although I have presented qualitative arguments which indicate that such a shape would satisfy the requirements of an equilibrium planimetric shape.

Acknowledgement

The financial help of the National Research Council of Canada is gratefully acknowledged. Amy Carr and David Cumming performed the calculations.

REFERENCES

Bascom, W.N. 1951. The relationship between sand size and beach face slope. Trans. Am. Geoph. Un. 32, 866-874.

Bremner, J.M. 1970. The geology of Wreck Bay, B.C. M.Sc. Thesis, Univ. of British Columbia, 243 pp.

Komar, P.D. 1971. The mechanics of sand transport on beaches. J. Geophys. Res. 76, 713-721.

Komar, P.D. and D.L. Inman 1970. Longshore sand transport on beaches. J. Geophys. Res. 75, 5914-5927.

Longuet-Higgins, M.S. 1970a. Longshore currents generated by obliquely incident sea waves, I. J. Geophys. Res. 75, 6778-6789.

Longuet-Higgins, M.S. 1970b. Longshore currents generated by obliquely incident sea waves, 2. J. Geophys. Res. 75, 6790-6801.

O'Rourke, J.C. and P.H. LeBlond 1972. Longshore currents in a semicircular bay. J. Geophys. Res. 77, 444-452.

Putnam, J.A. and R.S. Arthur 1948. Diffraction of water waves by breakwaters. Trans. Am. Geoph. Un. 29, 481-490.

Silvester, R. 1960. Stabilization of sedimentary coastlines. Nature, 188, 467-469.

Stoker, J.J. 1957. Water waves. Interscience, N.Y., 567 pp.

Yasso, W.E. 1965. Plan geometry of headland-bay beaches. J. Geol. 73, 702-713.

CHAPTER 74

USE OF CRENULATE SHAPED BAYS TO STABILIZE COASTS

by

Richard Silvester[1]
Department of Civil Engineering
University of Western Australia

and

Siew-Koon Ho[2]
Housing and Development Board
Singapore

ABSTRACT

Crenulate shaped bays are the rule rather than the exception on coastal margins of oceans, inland seas or lakes where sedimentary beaches exist between headlands. They have a particular orientation to the swell or resultant wave energy vector, such that the straight tangent section is downcoast and the curved portion upcoast. The latter is a logarithmic spiral at all stages of development of the bay. When fully stable, that is no littoral drift taking place, the constant of the log-spiral equation has a specific relationship to the approach angle of the waves to the headland alignment. In this condition it is shown that diffraction and refraction are involved when waves sculpture the curved beach in the lee of the upcoast headland. A further ratio to identify stable bays appears to be the ratio of indentation length to clearance between headlands. The application of crenulate shaped bays to stabilization of a reclaimed shoreline suffering strong littoral drift on Singapore Island is described.

INTRODUCTION

The crenulate shaped bay is a pronounced feature of any coastline, be it on an oceanic margin, the coast of an inland sea, the boundary of a lake, or the beach line of a hydraulic model. As long as there is a sedimentary shoreline interspersed with headlands and waves approaching the coast obliquely there will be such bays with half-heart or half spear-head shape.

Model work[1] has shown the sculpturing of this physiographic feature to be the work of waves, particularly those which are the most persistent in their incidence and direction. Such is the case of swell which arrives almost continuously from some storm zone of the ocean. The greatest source area for this energy is the 40° to 60° latitudes in both hemispheres.[2] Successive storms are generated there which travel from west to east. This provides almost continuous swell towards the margins of these oceans, but more particularly to the eastern margins, or the western coasts of continents. Even in enclosed seas (such as the Mediterranean, Baltic etc.) or large lakes (such as those in north America) the variable wind sequences will normally have a recognisable resultant at any specific zone of the coast as far as direction is concerned.

This oblique wave approach is directly related to the crenulate bay shape, since the orthogonal will be nearly normal to the straight section which passes through the downcoast headland. Downcoast here refers to the direction towards which sediment is moved by the wave action. The remainder of the bay comprises a curved zone, which is partly in the wave shadow of the upcoast headland. The indentation of the bay, from the headland alignment, depends upon the obliquity of the waves to this alignment and the amount of sediment available for transport through the embayment. In the final equilibrium, when little or no transport is taking place, the incoming waves are being diffracted and refracted into this shadow zone in such a way that simultaneous breaking occurs around the periphery.

BAY CURVATURE

It has been shown by Yasso[3] and subsequently proved by Silvester[4] that the curved water line can be defined by a logarithmic spiral. This is given by the relationship

$$R_2/R_1 = e^{\theta \cot \alpha}$$

where, as seen in Figure 1, R_1 and R_2 are radii from an origin that are at an angle of θ (radians) apart, and angle α is the constant angle of the radii to the tangents of the curve, with e as the exponential constant. It is the factor α which dictates the curvature and an infinite series could be drawn. When available on transparencies they can be used to define the shape of any sized bay, since scale is overcome by using various sections of a single curve.

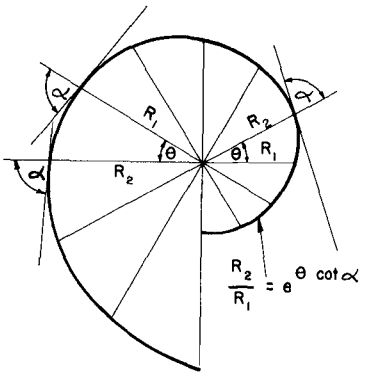

1. Definition sketch of logarithmic spiral.

Model tests(4)(5) have shown that progressive sculpturing of a bay beachline from a straight coast between headlands causes a systematic variation in the curvature or the value of α. When equilibrium is reached for the case of no renourishment from upcoast, the final α value is related in a consistent manner with the angle between the incident wave crests and the headland alignment, designated β in Figure 2. This angle is also that between the tangent shoreline and the headland alignment, since in this equilibrium state the wave crests are parallel to the beach.

STABILITY CRITERION

The connection between α and β is exhibited in Figure 2, which has been derived from two series of model tests.(5)(6) Also shown are some values from prototype bays, for which it can be rationalised that those nearest to the curve are closest to a stable condition. Points should fall above the line when there is adequate sediment still to be passed through the bay, or rivers are supplying it within the bay. Should such sand supply be decreased, or cut off altogether, the bay will become more indented as the shoreline and adjacent sea bed is eroded. Degradation will proceed until the curvature of the logarithmic spiral gives an α value which falls on the curve of Figure 2.

Evaluation of β by measuring the angle between the tangent shoreline and the headland alignment is only correct when waves are normal to this beachline. This cannot be so until all littoral drift has ceased. However, the extremity of this near-straight coastline reaches its equilibrium alignment long before the upcoast regions, so that even in early stages of bay development this angle β can be determined reasonably well.

It has been shown elsewhere(4) how the curve of Figure 2 can be utilised to test the long term stability of a bayed shoreline. The plot of α versus β falls above this line when the bay is not stable,

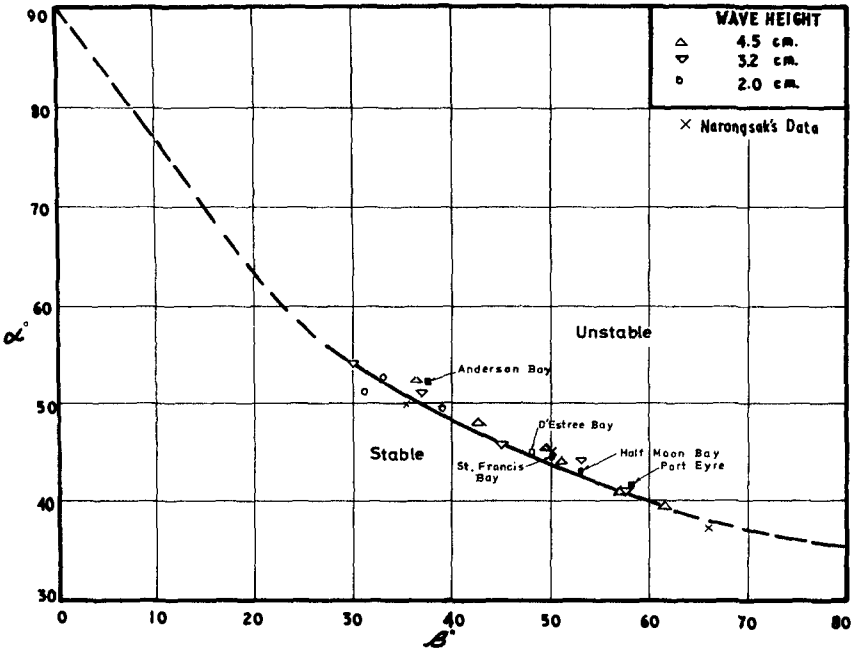

2. Relationship between log-spiral constant α and wave obliquity β.

implying that any reduction of sediment supply, from the upcoast direction or within the bay, will cause erosion of the beaches. This will be most pronounced in the curved section, particularly that part adjoining the tangent zone. This will not be prevented by groynes or sea walls in the long term, only by breaking the bay into two bays by the creation of an intermcdiate headland. The shape of the two subsequent stable bays are then predictable by using Figure 2 for the final equilibrium condition of no littoral drift.

WAVE PROPAGATION

It has been stated above that waves both diffract and refract into the shadow zone of the upcoast headland. The refraction is readily accepted due to the shoaling of the bed, but the existence of diffraction has not been proven in a prototype situation. Obviously, if the only waves present are short in period and thc water between headlands is deep, the curving crests can only be created by diffraction. Under these conditions sculpturing the shoreline entails the formation of a shallow shelf close in shore, but this would have

little effect on the overall shoreline shape in plan.

In order to test the occurrence of diffraction besides refraction, four bays were selected which appeared to be in equilibrium. Criteria used for this purpose were as follows:

(a) The downcoast tangential beach was sensibly parallel to the crests of the persistent swell.

(b) The crest alignment noted in (a) was checked against the tangential alignments of several adjacent bays when the coastline and Continental Shelf were sensibly straight.

(c) The proportionate length of the tangent section is greater when equilibrium is approached.

(d) No large rivers fed material to the bay.

(e) The wave energy level was high.

(f) Towards the downcoast end of the bay the bed contours spread, indicating a more normal approach of the waves.

(g) The approach angle β (measured between the downcoast shoreline and the headland alignment) and the logarithmic spiral factor α plotted close to the curve of Figure 2.

Details of the location and values of α and β for each bay are listed in Table I. The waterline and underwater contours are presented in Figure 3.

Table 1 - Summary of Equilibrium Bays

Name	Longitude	Latitude	β	α
Port Eyre	132°25'-133°00' E	31°57'-32°02' S	58°	41.5°
Anderson Bay	147°22'-147°38' E	40°50'-41°03' S	37.5°	52.5°
D'Estree Bay	137°35'-137°44' E	35°52'-35°59' S	48°	45°
St. Francis Bay	24°50'- 25°30' E	35°55'-34°15' S	50°	44.5°

Bed contours, or profiles normal to the beaches, of these several bays would influence refraction, but each would have also resulted from the wave climate and sediment characteristics of the area. Some average had therefore to be determined, for which purpose each bay was divided into equal distances along the coastline and the vertical profiles measured. The profiles are numbered 1 to 6 from the upcoast to the downcoast headland, and are presented on a logarithmic scale in Figure 4. The mean line through these points provided a mean profile at these locations, from which contours of an average bay in equilibrium could be derived. Such a typical bay for $\beta = 50°$ is depicted in Figure 5, with bed contours shown in fathoms.

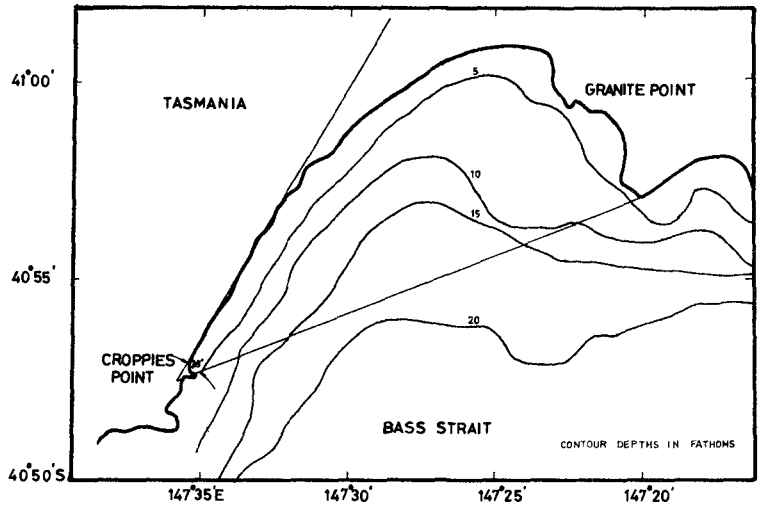

Fig 3A Plan of Anderson Bay Shoreline

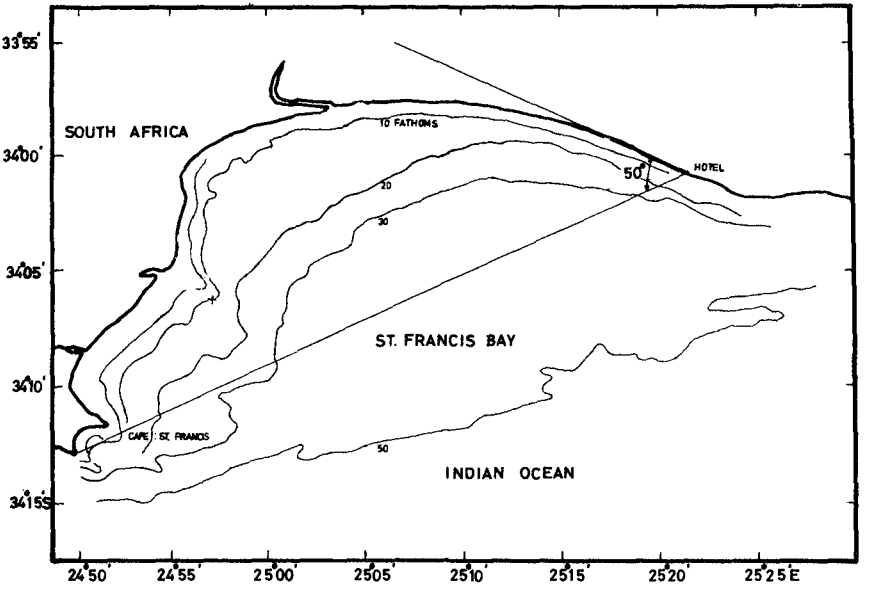

Fig.3B Plan of St.Francis Bay and fitted Logarithmic Spiral

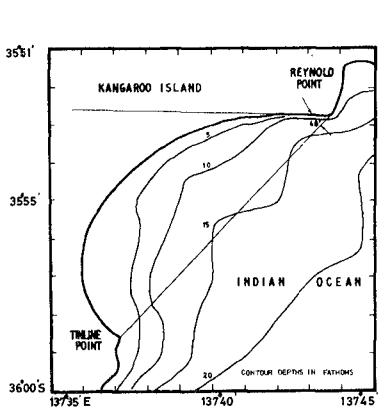

Fig.3C Plan of D'Estree Bay Shoreline

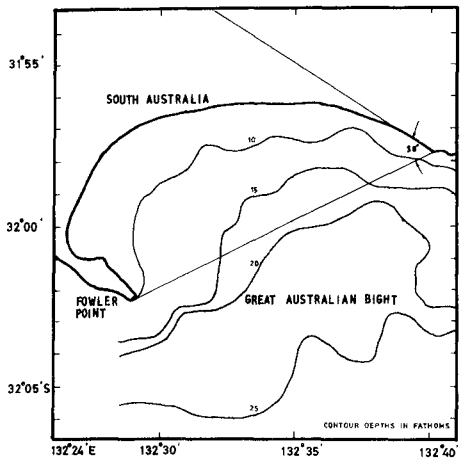

Fig.3D Plan of Port Eyre Shoreline

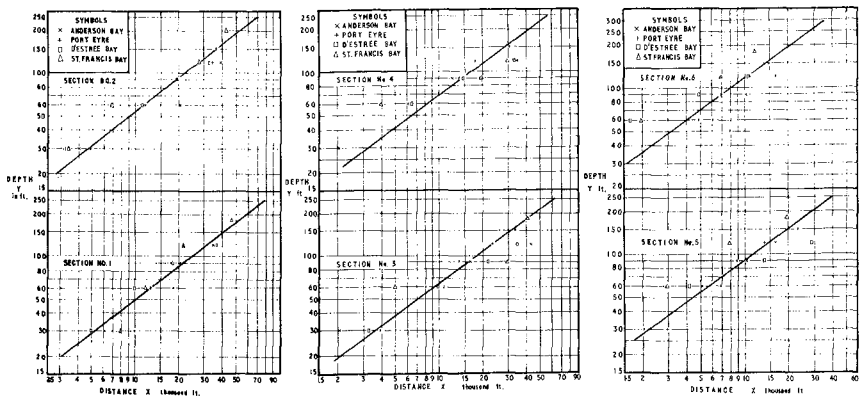

4. Bed profiles at points along the four bays detailed in Figure 3.

These bays on oceanic margins will suffer swell of various heights and periods throughout the year, but the predominant periods will be from 12 to 15 seconds, as discussed by Silvester(7)(8). These limiting bands were used in a refraction and diffraction analysis to test whether waves, whose crests in 30 fathoms are at 50° to the headland alignment, arrived at the breaker line normal to the beach. The angle $\beta = 50°$ at 30 fathoms was chosen because this depth contour essentially ran along the headland alignment and waves from there to the tangential shoreline had to traverse more or less parallel bed contours.

The wave orthogonal arriving at the tip of the upcoast headland from the 30 fathom depth is refracted across the parallel contours in front of it. The depth in the headland zone is aroung 10 fathoms so that the orthogonal direction can be obtained readily for the 12 and 15 second trains(9). These were 32.5° and 30° respectively to the normal of the breakwater or the bed contours. The waves were then diffracted and refracted over the contours within five wave lengths of the headland tip, as indicated for the 15 second wave in Figure 6(10). From there to the shoreline, refraction was determined by a computer programme, for which purpose the typical bay was divided into squares with 9840 ft sides (see Figure 5). Waves were so traced to a depth where breaking occurred, as assessed from $H_o = 4.75$ and 4.55 ft respectively for the 15 and 12 second waves respectively, with $d_b = 1.28\ H_b$, where H_b was calculated from the diffraction and refraction process. The final breaking angle of the waves was compared with the orientation of the beach at that point on the bay (see Figure 5) and an error value derived. There are two methods of finding beach alignment, (a) by direct measurement (E_m) and (b) by the orientation of the radius from the logarithmic spiral centre less the angle α of the specific bay curvature (E_c). For the 20 orthogonals treated (as detailed in Figure 5) the angular errors are listed in Table II.

Observation of Table II indicates that the errors are least for the 15 second waves, indicating that the most predominant swell is closer to this period than 12 seconds. The differences in angle are all of the same sign, such that waves are breaking at a slight angle which would cause transport of sediment downcoast. The orthogonals with the greatest error, namely 1 and 17 to 20, are those traversing bed contours at very acute angles, making for reduced accuracy in the refraction procedure. Also the strong curvature of the bed contours in this zone could be susceptible to error in position or location. Also any misjudgement of bay shape will vary the length of these orthogonals the greatest. However, the modest nature of the errors indicates that both diffraction and refraction are involved in the sculpturing process of crenulate shaped bays. Although the typical bay examined is close to equilibrium it could be rationalised that similar processes occur prior to this condition.

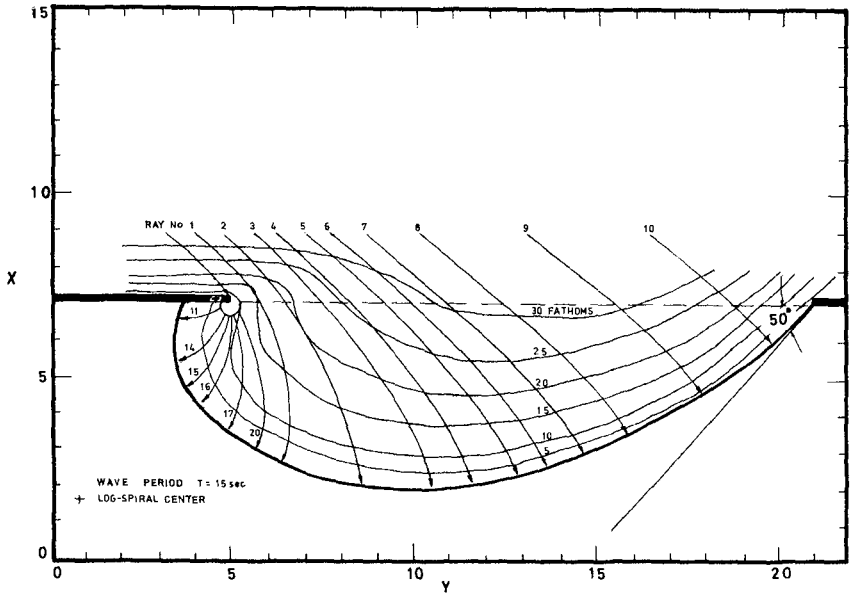

Fig.18 Typical Prototype Bay showing Refracted Orthogonals

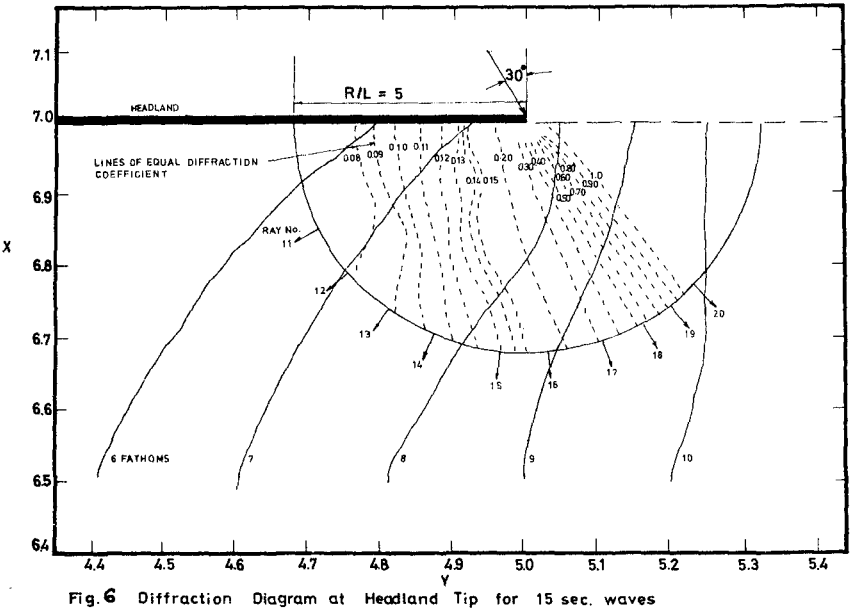

Fig. 6 Diffraction Diagram at Headland Tip for 15 sec. waves

Table II - Angular Difference in Degrees Between Orthogonal of Breaking Wave and Normal to the Beach.

Wave Period →	12 Second		15 Second	
Ray H_o	E_m	E_c	E_m	E_c
1	5.64	6.64	3.41	3.99
2	2.72	5.22	2.76	3.76
3	4.39	6.89	2.08	1.58
4	0.40	2.40	3.32	4.82
5	3.50	4.50	0.62	0.12
6	2.58	4.08	3.11	2.11
7	0.96	1.96	1.19	0.69
8	0.65	2.15	0.64	0.86
9	0.22	0.72	0.55	0.95
10	2.91	5.41	1.79	5.29
11	4.49	4.99	2.50	8.50
12	-	-	-	-
13	-	-	-	-
14	3.19	7.19	2.51	6.51
15	-	-	0.06	3.46
16	0.03	2.03	0.96	1.46
17	6.97	8.47	4.91	9.91
18	6.60	5.10	-	-
19	-	-	-	-
20	10.92	10.42	4.55	6.05

INDENTATION RATIO

Although the tangential angle β and the logarithmic spiral constant α should be sufficient to define any crenulate shaped bay, it is sometimes difficult to position the curved zone of the bay. This is because the upcoast end of the tangent section cannot be identified readily. It seems reasonable, therefore, to seek a relationship between indentation and width of bay. Such a ratio of a/b is illustrated in Figure 7

(a) for experiments conducted by Ho[6] and Vichetpan[5]

(b) the four prototype bays referred to previously, besides Half Moon Bay in California (also considered in equilibrium),

(c) the typical bay as derived before, and

(d) a bay at the upcoast end of the reclamation project in Singapore designated as Bedok (this should also be in equilibrium).

The dotted extension of the mean line through the points in Figure 7 should naturally pass through the origin (since for $\beta = 0$ $a = 0$).

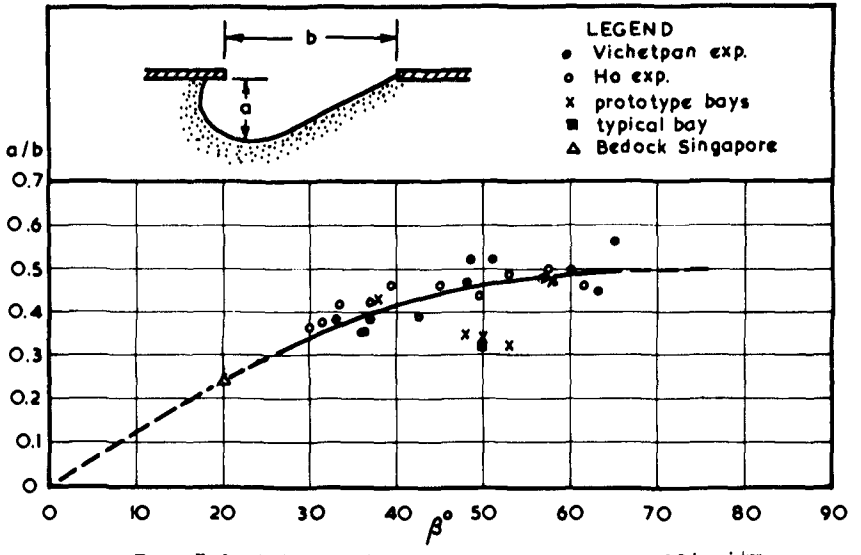

7. Indentation ratio for a range of wave obliquity.

It is seen in Figure 7 that the prototype bays of D'Estree, St. Francis, Half Moon and the typical one derived, fall below those given by experiments. This might be through slight lack of equilibrium, or the impedance to this shape by local outcrops of beach rock which cannot be identified in the scale of reproduction of the bay. The apparent lack of equilibrium in the typical prototype bay may have been the reason for the greater errors in the orthogonals numbered 1 and 17 to 20 previously noted.

SINGAPORE RECLAMATION

In order to provide suitable flat ground for large accommodation complexes the Singapore Housing Board is undertaking a large scale reclamation of shoreline to the east of the main harbour. As seen in Figure 8, this is being accomplished in four phases, the first two of which are already complete, the third due for completion in 1974 and the fourth in 1975.

Wave Incidence

Phases I and II were along a coastline facing south which is subject to wave action from the south to the east. This results in a net littoral drift from east to west, whether the waves are generated locally or are swell from the South China Sea entering Main Strait from the east (see Figure 8). The wind rose for the area indicates a predominance of winds from the NE quadrant. The largest proportion of

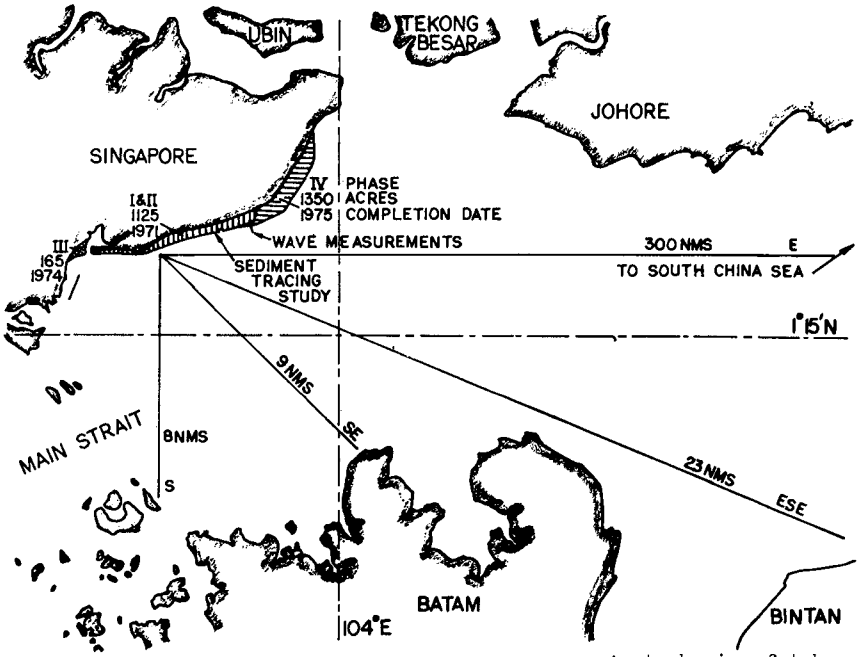

8. Location map of Singapore reclamation project showing fetch lengths for locally generated waves.

these are winds of less than 15 knots. Winds in excess of this velocity from this NE quadrant occur for less than 2% of the time, whilst from the SE quadrant none occur at all.

The major wave incidence would therefore appear to be swell arriving from the South China Sea. The predominance of this wave action is indicated by the crenulate shaped bays on the southern shoreline of Johore State (see Figure 8). These clearly indicate an east to west drift of sediment, even though locally generated waves have a reasonable fetch in the SW quadrant at this point. During March 1972 waves were recorded at the end of the jetty marked in Figure 8(11). They never exceeded 3 ft in height and were mainly around 1 ft. Their direction was essentially SE in 13 ft of water and their period around 6 seconds. Considering the general orientation of the bed contours at this point, a refraction computation indicates a deepwater approach from an easterly direction. The wave period is close to that reported in the South China Sea of 5 to 7 seconds.(11) Such swell is predominant in the months from December to March when the NE monsoons exist in the area.

Coastal Defense

The initial proposal for protecting the reclaimed land was to construct a rock revetment with seawall capstone along the straight shoreline. Such a structure was commenced at the eastern or Bedok end of the Phase I reclamation (see Figure 9). Construction was effected in the dry by overfilling the area and then trenching and dewatering the site of the seawall. However, erosion of the protecting dike was rapid and undermining of the finished wall severe, particularly at the exposed eastern corner.

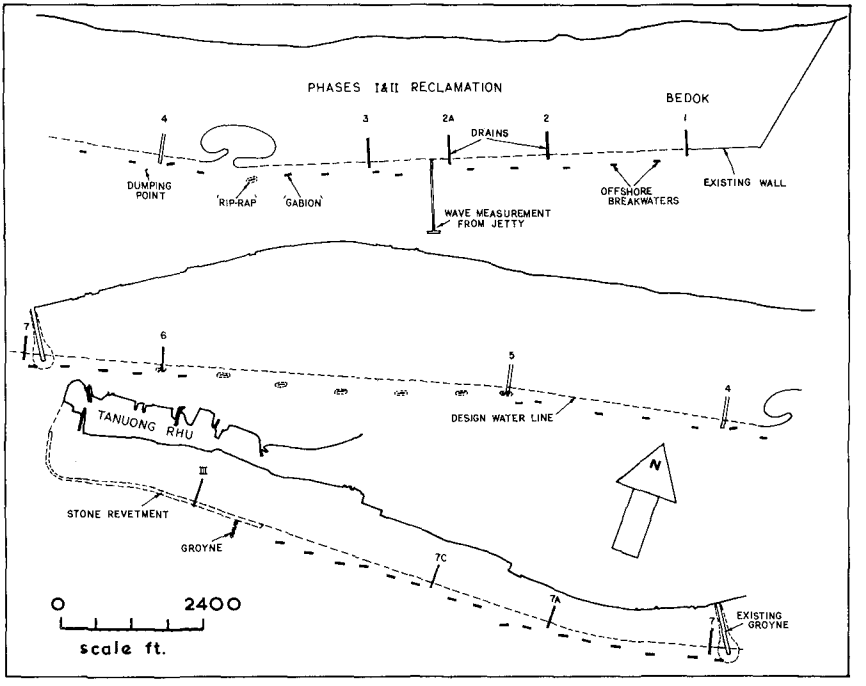

9. Location of coastal defense structures for Phase I and II reclamation.

At this time the concept of the crenulate shaped bay to stabilize coastlines was conveyed to the Board, who immediately instigated the design of offshore breakwaters or headlands to prevent erosion. These have been spaced in front of the new shoreline, as illustrated in Figure 9, and are progressively forming bays between them, as material is transported in the nearshore zone towards the west.

The tidal range in Main Strait is around 10 feet, which exposes a width of shoreline around 50 ft, for sufficient time to permit the

construction of headlands near LWL by land-based equipment. Two types of rock-fill structure have been utilised, namely, the "gabion" (with stones in steel mesh baskets) and "rip-rap" (consisting of a compacted soil mound faced with layers of rock).

The gabions consist of steel cages of 2 cubic metre capacity filled with stones of about 1 ft dimension. These rise in 4 or more layers from 2 ft below LWL to 1 ft above HWL. They extend about 100 ft along the shoreline and are located about 200 ft. from the proposed straight alignment of the reclaimed area and spaced about 800 ft apart.

The rip-rap structure is constructed in the dry by overfilling the area and compacting the soil. The mound is then shaped to give a seaward slope of 1 : 2 and landward slope of 1 on $1\frac{1}{2}$. A vinylon sheet is then spread over this, on which are placed a 6 inch layer of 2 to 6 inch stones, a second 6 inch layer of 6 to 9 inch stones, and lastly a single layer of 2 ft stones properly pitched. The structure extends from 2 ft below LWL to 3 feet above HWL, which is the same as the finished ground level. The crown of these structures is 120 ft in length and some 200ft from the design shoreline. Their spacing is similar to the gabion headlands.

As seen in Figure 9, the alignments are such as to be parallel to the incoming swell waves at high tide. Also shown in the figure are the locations of drains, which should enter the predicted bays in the lee of the upcoast headlands,(12) so as not to be silted up by the action of high waves.

Tracer Test

To check that the predominate direction of sediment transport was to the west, a tracer test was carried out at the location indicated in Figure 8 in March 1970. Fluorescent sand was dumped just westward of drain no. 4 (see Figure 9) at the low water mark, and sampled at four points across the exposed tidal beach face on normals both upcoast and downcoast. The results indicated that the predominant motion was westerly, or parallel to the shoreline. Not until the second headland was reached did the higher concentration of tracer appear at the high water mark. Downcoast of this (i.e. westwards) the tracer again moved out to the low water mark, and onwards to the next headland. Although tombolo's then existed at high tide level, the bays in question had not reached their predicted crenulate shape. They have since done this.

Overall Result

The success of the headland measure can be gauged by the aerial photos of Figures 10 to 13, which show the development of the stabilising bays at the two extremities of the Phase I and II reclamation. The advantages of this approach over the seawall originally proposed may be listed as follows:

(a) The headlands are much more economical initially. The seawall had precast capping stones on a stone revetment and required overfill for its construction. The savings have been

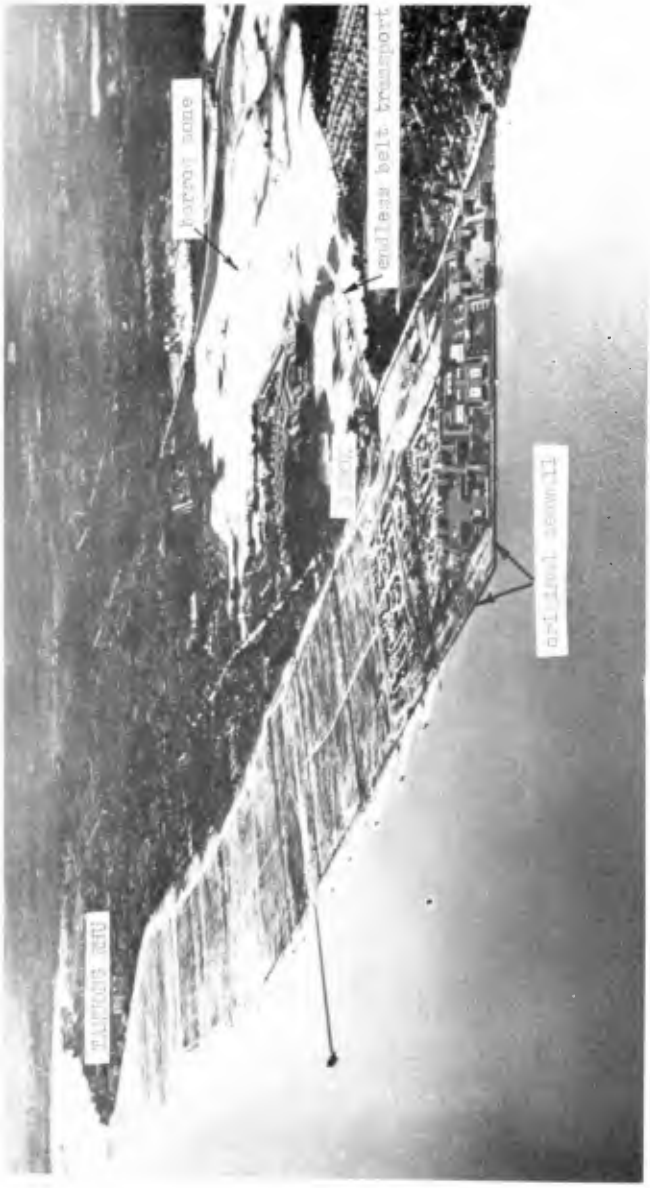

10. View of phase I and II reclamation looking west in May 1971.

11. View of bay development looking west from drain 7A (Fig. 9) in February 1972 at medium tide.

12. View of gabion headlands near Tanuong Rhu looking east in Febru 1972 at high tide.

13. Close-up view of gabion headland showing bay formation between drains 7A and 7C looking west at low tide.

estimated as around 50% for gabion headlands and 25% for the rip-rap headlands.

(b) The maintenance cost on the seawall would have been high, due to the action of the reflected waves in expediting the scouring in front of it(13). This rapid transit of material westward would have created a silting problem west of Tanuong Rhu.

(c) The residents of the new housing estate will have a sandy shoreline for their recreation. This is divided into many small embayments which are safe for children to use. The alternative revetment would have had water of some depth adjacent to it, with submerged rocks to add to the danger for infants.

(d) The reclaimed shoreline is protected by the buffer zone of the bay, with offshore bed slopes mild in character. These help break waves prior to reaching the shoreline. Less spray will be generated than if waves were smashing up against a stone revetment and coping stone. This should minimise corrosion of fittings in dwellings and the concentration of salt in the lawns of the compounds. Overtopping of the wall by standing storm waves is obviated, so reducing the cost of drainage structures to cope with such eventualities.

CONCLUSIONS

1. Crenulate shaped bays are ubiquitous features of the coastline and give a lead to man in his attempts to minimise longshore drift.

2. Such bays have a definite orientation with respect to the predominant swell on oceanic margins, and to the resultant energy vector in enclosed seas, where locally generated waves assume importance.

3. At all stages of development the sedimentary coast between two successive headlands consists of a tangential zone downcoast and a logarithmic spiral section upcoast.

4. Where full equilibrium is reached and zero longshore drift is achieved, the constant in the log-spiral equation has a specific relationship to the angle of the wave crests to the headland alignment, this latter angle equating to that between the tangent beach line and this same headland alignment.

5. The relationship noted in (4) above can serve as a measure for equilibrium of any bay on a coast, so that the limit of erosion can be determined in the event of sand supply to the bay being cut off by natural or man-made means.

6. Waves arriving at the shorelines of crenulate shaped bays both diffract and refract into the shadow zone of the upcoast headland, so producing the log-spiral shape of this zone of the bay.

7. Wave propagation as in (6) results in a normal approach to the beach at the breaker line when the bay is in complete equilibrium, so preventing a littoral current.

8. To completely predict the outline of a stable bay, when criteria (4) and (7) above are fulfilled, the ratio of indentation length to distance between headlands can be ascertained from a knowledge of the wave obliquity as designated in (4) above.

9. Application of the stable bay principle to a reclamation project in Singapore appears to have provided an economic solution to a problem involving strong littoral drift.

REFERENCES

1. Silvester, R. "Stabilisation of Sedimentary Coastlines". Nature 188, 1960, 467-469.

2. Davies, J.L. "A Morphogenic Approach to World Shorelines" Ann. of Geomorph. 8, 1964, 127-142.

3. Yasso, W.E. "Plan Geometry of Headland-bay Beaches" J. of Geology 73, 1965, 702-714.

4. Silvester, R. "Growth of Crenulate Shaped Bays to Equilibrium" Proc.ASCE. 96 (WW2), 1970, 275-287.

5. Vichetpan, N. "Development of Crenulate Shaped Bays". Thesis No. 280 submitted to the Asian Institute of Technology, Bangkok, in partial fulfilment of Master of Eng. degree, 1969.

6. Ho, S.K. "Crenulate Shaped Bays" Thesis No. 346 submitted to the Asian Institute of Technology, Bangkok, in partial fulfilment of Master of Eng. degree 1971.

7. Silvester, R. "Design Waves for Littoral Drift Models" Proc.ASCE 89, (WW3), 1963, 37-47.

8. Silvester, R. and S. Vongvisessomjai "Computation of Storm Waves and Swell" Proc. I.C.E. 48, 1971, 259-283.

9. Silvester, R. "An Aid to Constructing Wave Refraction Diagrams" Trans.I.E. Aust, CE8, 1966, 123-127.

10. Blue, F.L. Jr. and J.W. Johnson "Diffraction of Water Waves Passing Through a Breakwater Gap" Trans.Am.Geoph.Un. 30, 1949, 705-718.

11. Private correspondence from S.Y. Chew of Singapore Housing Board.

12. Bascom, W.N. "The Control of Stream Outlets by Wave Refraction" J. of Geology 62, 1954, 600-610.

13. Silvester, R. "Wave Reflection at Seawalls and Breakwaters" Proc. Inst.Civil Engrs. 51, 1972, 123-131.

ACKNOWLEDGEMENTS

The permission of the Singapore Housing and Development Board for presenting information on their reclamation scheme is deeply appreciated.

CHAPTER 75

STATE OF GROIN DESIGN AND EFFECTIVENESS

by

J. H. Balsillie[1]

and

D. W. Berg[2]

ABSTRACT

An annotated bibliography on groins, compiled by Balsillie and Bruno (1972), has provided the background for this paper. A review of functional design criteria is presented including groin length, height, spacing, permeability-adjustability, and orientation. A discussion of coastal processes and their relationship to groin design and effectiveness is also given.

INTRODUCTION

Groins have been in wide use throughout the world since before the turn of the century. They are possibly the oldest type structure whose specific purpose is to build up a sand or pebble beach where little material existed before, or to maintain an existing beach against further erosion. There are numerous examples where groins have fulfilled these purposes and as many others which have not; indeed some have actually intensified the problems they were intended to solve.

Coastal engineering is a relatively young field of science. Classically established disciplines relegated to the land, the sea, and the atmosphere all meet at the shoreline. Coastal engineers, therefore, need understanding of knowledge in all three of these areas. They must have an understanding of sedimentology, physiography, physics, mathematics, hydraulic and structural engineering, climatology, stratigraphy, to name a few. Their job is made even more difficult, for the many factors that affect the delicate stability of a beach are often impossible to measure in their entirety. As a result, the

[1]Geologist, Evaluation Branch, Engineering Development Division, U. S. Army Coastal Engineering Research Center, Washington, D. C.

[2]Chief, Evaluation Branch, Engineering Development Division, U. S. Army Coastal Engineering Research Center, Washington, D. C.

coastal engineer must rely on either his experience as gained from field or laboratory studies, or, lacking this, make judgments based upon documented reports to form the basis of remedial design criteria for a particular problem.

In pursuit of further understanding of the role that documented research plays in groin design, over 450 reports and papers, covering the period from 1900 to 1971, were reviewed during the compilation of an annotated bibliography on groins. It was determined that the majority of articles were introductory in nature, giving in many cases but a cursory glance at groin design and purpose. In other..."instances it is clear that...groins have been attributed magical properties whereby they might conjure beach material out of the sea into their outstretched arms" (Hoyle and King, 1957). Some articles, however, have contributed significant data as a result of experimental endeavors and field observation where groin geometry, spacing, degree of permeability, orientation relative to the shoreline, and materials of construction have been investigated under particular conditions of littoral drift and wave action. Such reports have formed the basis for the development of design criteria for groins. At present it is felt that the criteria as published in the Coastal Engineering Research Center's report "Shore Protection Planning and Design" (U. S. Army Corps of Engineers, 1966) represent the present state-of-the art and provides a logical design approach for groin structures.

Three basic categories form the basis for the design of groins: (1) coastal processes (wind data, wave height, period and angle, beach slopes, textural characteristics of beach sediments, etc.); (2) functional design (spacing, length, height, orientation with the shoreline, permeability, special designs); and (3) structural design (materials of construction and procedures). This paper is primarily concerned with the first two categories, since the selection of materials and construction procedures are of necessity a matter of economics and local practice. Therefore, it is the purpose of this paper to present a review of some of the more prominent criteria used in groin design as revealed by the literature, and to offer general discussion on the effectiveness of groin use.

LITTORAL PROCESSES

In undertaking the functional design of groins, a primary requisite is a comprehensive understanding of the littoral processes predominating in the locality of concern. Too often such knowledge is deficient or totally lacking and the effectiveness of the resulting structure(s) is a matter of chance.

Adequate investigation of the many faceted and interrelated oceanographic and meteorological forces and their effect on the shoreline should be made in order that understanding of the littoral processes is attained. With such understanding, the functional design of a groin(s) can proceed in a manner which best utilizes the littoral processes and yields a structure(s) attuned to the environment producing the desired objectives.

Figure 1 presents the major oceanographic and meteorological forces and their interrelationships with each other and the shoreline. It should be noted that many of these forces vary in magnitude over relatively short periods of time and that determination of specific characteristics suitable for structural design purposes is difficult. This is especially true of those elements concerned with waves and littoral currents. Elements, such as coastal and beach configurations, are relatively stable, therefore, measurable with reasonable accuracy and can easily be used in the functional design of groins. Others, particular littoral drift rates and directions and their influence on the volume of material on a beach, need additional documentation for use in the proper functional design of groins. Although conceptually understood, the means to accurately measure and thus document or predict littoral drift rates are, at present, limited.

When considering the use of groins for shoreline protection or improvement, it should be remembered that each beach is unique due to the combination of forces that are focused at that location, and that the overall configuration of the shore is constantly being reshaped. Thus any structure to be built at the shore must consider and account for these changes. Proponents of proprietary groin designs too often fail to recognize this, and attempt to use a single design as a cure-all device. "There is no such thing as a universal solution to the problem." (Schijf, 1959).

FUNCTIONAL DESIGN

Following are a series of tables, each concerned with a specific functional dimension utilized in the design of groins both singly and in a system. Six criteria are presented. They are: length, height, spacing, permeability-adjustability, orientation with respect to the shoreline, and special design innovations. The tables offer a spectrum of criteria as gained from field observation, experimental results, and personal experience. Specifics of the actual littoral zone and test conditions are not presented since space here will not allow such detailed description. All entries follow as closely as possible the original documentation. Though the list of articles represented is by no means complete, the tables do present some of the more pertinent results concerning functional design criteria for groins.

Length and Height of Groins:

In early shore protection projects, and even to a large extent today, length has remained a question of "trial-and-error". It has been defined in relative terms as short or long; the longer structures collecting larger quantities of littoral drift than shorter structures, though it is argued that shorter structures can be extended, if needed, allowing for greater economy. Many investigators have defined length to be a function of water depth, since the longshore transport rate is also a function of depth. Other investigators have utilized a concept that length is a function of the

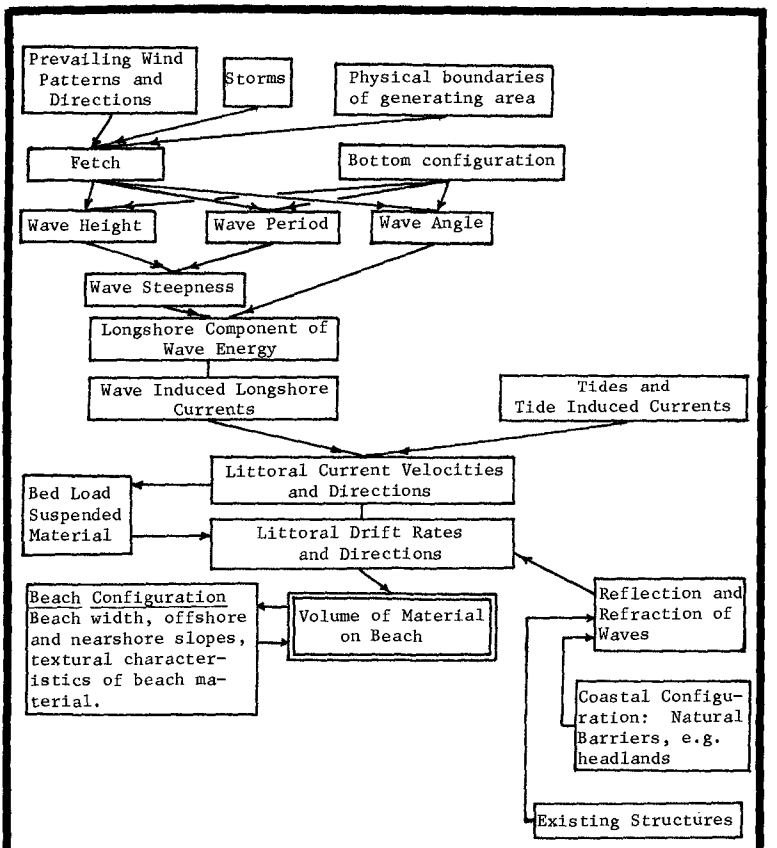

Figure 1. Environmental factors which affect shorelines.

distance from the shoreline to average breaking point of plunging waves. There are design rules that divide a groin into sections, each section of which is prescribed a certain design length. Many designs are contingent upon the amount of littoral drift they are anticipated to entrap. These and other requirements for groin length are presented in Table 1.

The evolution of requirements for the height of groins has followed the same lines as for groin length. Height, as with groin length, has been defined in relative terms, as either high or low. High groins tend to entrap and hold more material than do low groins (depending on length), thereby causing excess erosion of downdrift beaches. Scour along the immediate downdrift sides of high groins has been reported; caused by the spilling effect of water over the structure and subsequent removal of beach material which lead to failure of groins (Evans, O. F., 1943). Low groins, on the other hand, allow littoral drift to pass over the structure so that immediate downdrift scour and overall beach recession should be minimized. Many investigations also reveal that height can be more absolute; and give heights that groins should be built above the beach profile and water level for specific conditions. These results are presented by Table 2.

Height and length are utilized in various combinations to produce various effects. For instance, the use of high, impermeable groins of considerable length to permanently trap sands has been proposed, and the structures thus act as artificial headlands. They may be used at the updrift side of an inlet or submarine canyon. Wicker (1958) and Dunham (1965) have discussed such use.

Spacing of Groins in a System:

Spacing has generally been defined as a function of groin length. A spacing designation of 1:2, for instance, defines a spacing twice the length of a groin to be used in a system, assuming the groins to be of equal length.

Table 3 indicates that spacing ratios commonly fall into a range of 1:1 to 1:4. Spacing requirements are dependent upon such factors as severity of wave climate, size of beach material, steepness of the beach profile, predominant angle of wave incidence with the shoreline, and economic factors.

Permeability-Adjustability of Groins:

Permeability of groins became a design feature when it was observed that such structures could cause deposition in their immediate vicinity, yet allow significant amounts of littoral drift to pass through the structures so that abrupt offsets in shore alignment would not occur between groins, and

TABLE 1. LENGTH OF GROINS

INVESTIGATOR, YEAR	AREA OF INVESTIGATION	TYPE OF INVESTIGATION	LENGTH / REMARKS
Owen, J.S., and Case G.O., 1908	England - General	Theory - Experience	Extend at least to low water line.
Case, G.O., 1915	England, New York, New Jersey	Field - Experience	Long groins recommended - should extend from high to low water, and seaward of low water if possible.
Kressner, B., 1928	Germany	Movable bed, model study	Decreasing length downcoast: proposes principle of shortening groins downcoast at a small angle (4-6°) to insure that downcoast beaches receive littoral drift.
Coen-Cagli, M.E., 1932	General	Theory - Experience	Pebble beaches: 40-50 meters seaward from shoreline should be sufficient length. Sandy beaches: extend to 2 or 3 meter depth; will interrupt most of littoral drift.
Brown, E.I., 1939, 1940	General	Experience	Should extend at least to 6 foot depth below mean sea level. Under normal conditions, 80% of sand movement takes place at depths of less than 6 feet.
Duvivier, Jack, 1947	England	Experience	Utilize shortest length possible to stabilize the beach. Has used short groins between sets of longer groins.
Frech, F.F., 1948	New Jersey	Field	Extend to 6 feet depth of water.
Nagai, Shositiro, 1956	Japan	Movable bed, model study	Optimum distance groins extend from shore line seaward 40% of distance from shoreline to breaking point of plunging breakers where wave steepness is δ_0 = 0.01 0.02. Tests showed this gave greatest amount of deposition downdrift of groins, least updrift scour at groin sides and ends.
Horikawa, Kiyoshi, 1958; Horikawa, K., and Sonu, C., 1958	Japan	Movable bed, model study	Should extend seaward from shoreline 40-60% of distance from shoreline to breaking points of plunging waves.
Hiranandini, M.G., and Gole, C.V., 1961	Cochin, India	Field Study - prototype conditions, model study	200 foot minimum length preferred. Short groins defined as less than 150 feet.
Lee, C.E., 1961	Great Lakes	Field study	64% 100 ft. 21%: 100-150 ft. 15% 150 ft. } of 841 groins examined, these percentages reported for Great Lakes; a predominance of short groins
Rayner, A.C., and Rector, R.L., 1961	Great Lakes	Experience	Principal benefit of short groins (100' or less) on the Great Lakes is to retain a narrow protective beach from material eroded from bluffs, in order that further bluff erosion be retarded.
Kemp, P.H., 1962	England	Movable bed, model study	Groin Orientation from Normal Groin Length: 30° Updrift; Normal to Coast; 20° Downdrift Long: 43; 50; 55 Short: 67; 71; 67 } Quantities of material collected in downdrift traps as % of total material after 3 wave cycles. High, impermeable groins used.
Bruun, Per, and Manohar, Madhav, 1963	North Sea	Field Experience	Most effective when extended out to depths of 12 to 18 feet of water.
Ishihara, Tojiro, and Sawaragi, Toro 1964	Japan	Field study	Observed results showed that structures of T-groin design should be at least 60 meters in length.
Dunham, J.W., 1965	California	Field	Notes use of long groins to form artificial headlands to permanently hold sand, regardless of effects produced along adjoining segments of the shore.
Shore Protection, Planning and Design, Coastal Engineering Research Ctr., T.R. 4, 1966	General	Manual	Correct length is dependent upon prediction of ultimate stabilized beach profile. Original beach profile, conditions of littoral drift, refraction patterns, desired beach width are some of the factors utilized in methods for designing groins. Groin Type: High; High; Low; High; Low Depth to which extended below MLLW: 10' or more; 4 to 10'; 10' or more; 1 to 4'; < 10' Amount of Littoral Drift Interrupted: 100%; 75%; 75%; 50%; 50%
Barcelo, J.P., 1970	Portugal	Model study, movable bed	Inclined groins must be extended for conditions of same spacing, e.g. where α_s=20°, inclined angle =70°, inclined groins must be 30% longer than corresponding normal groins.
Kolp, Otto, 1971	Fischland, Zempin, Nevendorf	Field, Experimental	Generally recommends use of long groins, short groins fail to trap and retain sand efficiently; use of artificial fill in conjunction with long groins.

TABLE 2. HEIGHT OF GROINS

INVESTIGATOR, YEAR	AREA OF INVESTIGATION	TYPE OF INVESTIGATION	HEIGHT / REMARKS
Owen, J.S., and Case, G.O., 1908	England, General	Theory, Experience	Low, to allow some sand to pass over the structure.
Case, G.O., 1915	England, New York, New Jersey	Field	Groins should not exceed 2-3 ft. in height and should follow low profile of the beach. Low, long groins of adjustable type are recommended. High groins are too costly; stop all littoral drift and lead to erosion downdrift of groins.
Dent, E.J., 1931	East Coast United States	Field	Low groins recommended - allow sand to drift over the structure and maintain leeward beach.
Coen-Cagli, M.E., 1932	General	Theory, Experience	1 meter height above high tide sufficient for outer portion of groins on a pebble beach. Beach Section: 50-60 cm. above original beach level. Intermediate Horizontal Section: 50 cm. above low tide level. Inclined End Section: end should be 50 cm. lower than horizontal intermed. section. } Recommendations for groins maintaining a sandy beach
Brown, E.I., 1939; 1940	General	Experience	Horizontal Beach Section: berm height. Sloping Intermediate Section: berm height to below low water line; slope of groin top slightly less than natural beach slope Outer Section: gentle underwater slope seaward.
Evans, O.F., 1943	General, United States	Field	Prefers low groins as they reduce scour on downdrift side caused by wave overtopping. Recommends gradual decrease in height seaward; end should be at low water level or somewhat lower.
Duvivier, Jack, 1947; 1949	England	Experience	No higher than 3 ft. above beach level; as groin fills, it should be gradually heightened; higher groins cause scour.
Jones, J.H., 1948	United States	Movable bed, model study	Low, impermeable groins did not trap and retain as much material as high, impermeable structures.
Brater, E.F., 1953	Great Lakes	General Theory Field	1 ft. above high lake level has given good results.
"Basic Coastal Model" Hydraulic Research, London, 1957	England	Movable bed, model study	High, impermeable groins closely spaced (1:1) arrested greatest amounts of drift, but caused sand to be eroded from upper beach. Reduced drift to 1/8 of former value. Low, impermeable groins widely spaced (1:2) arrested 1/2 of littoral drift, but upper beach did not erode. Recommends use of low groins over high structures.
Wicker, D.F., 1958	General	Theory	Recommends use of high groins (see text).
Savage, R.P., 1959	United States	Movable bed, model study	Low, short groins: trapped 12% of test sand. High, short groins: " 25% of test sand. High, long groins: " 60% of test sand.
Schijf, J.B., 1959	Holland, General	Theory	Groins should remain as low as is compatible with their reducing effect on littoral drift.
Lee, C.E., 1961	Great Lakes	Field Study	Horizontal Shore Section: minimum height should be berm height of existing beach. Intermediate Section: not steeper than existing beach profile; should approximate anticipated beach slope. Seaward Section: governed by expected still water elevation at time of construction. (specific criteria given for rubble-mound structures).
Kemp, P.H., 1962	England	Movable bed, model study	Groin Type / Orientation with Shore: 30° updrift, 0°, 20° downdrift low: 51, 60, 87 high, long: 43, 50, 55 high, short: 67, 71, 67 Quantities of material collected in downdrift traps as % of total material after 3 wave cycles, for impermeable groins.
Bruun, Per, and Manohar, Madhav, 1963	General	Field, Experience	Minimum height should equal maximum water level plus height of normal wave uprush.
Shore Protection, Planning and Design, Coastal Engr. Research Ctr., TR4, 1966	General	Theory, Experience	Groin is built in 3 sections, (a.) horizontal shore section (b.) intermediate sloped section, (c.) outer section. Height dependent upon construction methods used, economics and beach profiles, wave uprush, and littoral drift (see Table 1).

TABLE 3. SPACING GROINS IN A SYSTEM

INVESTIGATOR, YEAR	AREA OF INVESTIGATION	TYPE OF INVESTIGATION	SPACING / REMARKS
Owen, J.S., and Case, G.O., 1915	England, General	Theory, Experience	1:1 - Recommended spacing.
Case, G.O., 1915	England, New York, New Jersey	Field, Experience	No greater spacing than distance from high to low water line.
Kressner, B., 1928	Germany	Movable bed, model study	1:2 - 1:3 - Tests show this to be optimum spacing requirement; smaller spacing unnecessary, wider spacing unadvisable
Coen-Cagli, M.E., 1932	General	Theory, Experience	1:1.5 to 1:2 - Initial spacing for systems on pebble beaches, then decrease until desired effect is produced. 1:1.5 - Usually spacing of groins on a sandy beach.
Steiner, C.T., 1936	Rockaway Bch, New York	Field	1:1 - Will maintain a beach about 1/2 this length.
Brown, E.I., 1939; 1940	Genaral	Experience, Wave Tank Studias	1:1 - 1:3 - 1:1 and less is never economical. 1:3 is maximum limit for spacing. Suggests that after length is decided, draw a line through the end of the groin parallel with direction of the storm approach. Projection of this line on line of connecting landward edge of groins will determine proper spacing.
Dobbie, C.H., 1946	England	Experience	1:1 to 1:1.5 - Considered as best spacing.
Frech, F.F., 1948	General		1:1.5 - Generally accepted spacing ratio.
Brater, E.F., 1953	Great Lakes	Field, General	1:1 - Where wava action is severa and beach material is fine. 1:2 - Where wave action is less severe, and beach material is coarse sand or gravel.
Nagai, Shositiro, 1956	Japan	Movable bed, model study	1:3 - Provided optimum spacing for conditions during testing.
"Basic Coastal Model" Hydraulics Research, London, 1957	England	Movable bed, model study	1:1 - High, impermeable arrested 7/8 of drift, but upper beach eroded. 1:2 - Low, impermeable arrested 1/2 of littoral drift, but upper did not erode. Use of this plan recommended.
Nagai, Shoshichiro, and Kubo, Hirokazu, 1958	Japan	Fixed bed, model study	1:3 & 1:4 - Most effective spacing found from testing.
Hiranandini, M.G., and Gole, C.V., 1961	Cochin, India	Field study-prototype conditions, model study	1:3 - Should not exceed this ratio. 1:2 - Recommended spacing at Cochin.
Lea, C.E., 1961	Great Lakes	Field study	Govarned by: 1.) Angle beach normally makes with shoreline 2.) Minimum width of beach required on the downdrift side of groins.
Bruun, Per, and Manohar, Madhav, 1963, Bruun, Per, 1955	General	Field, Experience	1:1.S - 1:4 - Generally the range of ratios used. As size of material and amount of littoral drift increases, so should spacing. As steepness of beach profile and steepness of waves increases, spacing distance should decrease. 1:1 - 1:1.5 - If ratio is less than this groins in most cases will not work well.
Ishihara, Tojiro, and Sawaragi, Toru, 1964	Japan	Field	1:1.S - 1:2 - Utilized this spacing in actual situation.
Wiegel, R.L., 1964		Lab. Tests	1:2 - 1:3 - Most desirable distance between groins; the greater the relative groin length, the smaller should be the distance between groins (After Horikawa and Sonu, 1958). 1:4 - Desirable for conditions of waves of variable direction for groins normal to shoreline (After Hoyle and King, 1955).
Shore Protaction, Planning and Design, Coastal Engr. Research ctr., TR4, 1966	General	Manual	1:2 or 1:3 - Suggested as rule of thumb method. Distance from berm crest to seaward end. Other considerations offerred in taxt. A groin system too closely spaced diverts material offshore rather than create a wide beach.
Garcelo, J.P., 1968	Portugal	Model study	1:2.S - for $\alpha_o = 20°$ Where α_o is the angle of wave inci- 1:3:S - for $\alpha_o = 10°$ dence with the shoreline. 1:4 - for $\alpha_o = 5°$
Price, W.A., and Tomlinson, K.W., 1968	England	Movable bed, model study	1:1.5 - 1:2 - These ratios caused considerable deposition during tests.
Kolp, Otto, 1971	Fischland, Zempin, Neuendorf	Field, Experimental	1:1 - A change in this ratio in terms of greater groin length will cause a reduction in rips at groin flanks.

on a broader scale that beaches downdrift from a system of groins would not suffer recession due to lack of littoral material reaching those areas. Most investigators are in agreement with the statement that "permeable groins should not be used as individual units isolated along the beach but in a group, i.e. in a system of groins" (Shay and Johnson, 1951). Other plans have used designs wherein structures are initially built low, following closely the natural beach profile, but being adjustable, they may be readily heightened as the beach builds up, or lowered as the beach loses material. Many investigators feel that groins of the low, impermeable type approach closely the capabilities that permeable groins offer, and on that basis recommend use of impermeable groins exclusively. Table 4 presents a list of articles giving views held by investigators concerning the permeability and adjustability of groins.

TABLE 4. PERMEABILITY -- ADJUSTABILITY OF GROINS

INVESTIGATOR, YEAR	AREA OF INVESTIGATION	TYPE OF INVESTIGATION	PERMEABILITY-ADJUSTABILITY	REMARKS
Case, G.O., 1915	England, New York, New Jersey	Field, Experience	Adjustable	Proposes use of adjustable groins so that they can be built up as accration progresses.
Brown, E.I., 1939, 1940	General	Experience	Impermeable	Groins should be sand-tight.
Evans, D.F., 1943	General, United States	Theory	Permeable	Appear to be sucessful where there are strong prevailing wind and shore currents, or where there is variable beach drifting and weak, variable currents.
Johnson, J.W., 1948	United States	Movable bed, model study	Impermeable	Tests showed that impermeable groins were more effective in causing accretion (single structures used in tests).
Shay, E.A., and Johnson, J.W., 1951	United States	Movable bad, model study	Permeable Impermeable	Should be used in systems only - caused deposition of from 11 to 26% sand under 2 corresponding sets of wave conditions. Much more effective than permeable groins for trapping littoral drift.
Brater, E.F., 1953	Great Lakes	Field, General	Impermeable	Permeable groins work only where wave action is mild or beach material is coarse.
Mason, M.A., 1953	Great Lakes	Field	Impermeable	Permeable structures appear to be poorly suited to Great Lakes area. The requirement of impermeability is absolute.
"Basic Coastal Model," Hydraulics Research, London, 1957	England	Movable bed, model study	Permeable	Had only a small influence on littoral drift and caused some loss of sand from upper beach. Ratio of voids to solids 1:1.
Bruun, Per, Gerritsen, F., and Morgan, W.H., 1957	Florida	Field, Experience	Permeable Impermeable	Permeable groins are usually accompanied by lee side scour. Recommend usa of low, impermeable, nonadjustable or impermeable adjustable groins on Florida shorelines.
Wicker, C.F., 1958	General	General theory	Impermeable	Recommendation for all situations.
Lee, C.E., 1961	Great Lakes	Field study	Permeable Impermeable	13% } of 841 groins examined, these % re- 87% } ported for the Great Lakes.
Hoyle, J.W., and King, C.T., 1962	England	Genaral	Impermeable	Do not recommend use of permeable groins.
Bruun, Per, and Manohar, Madhav, 1963	General	Field, Experienca	Adjustable	Recommend use of adjustable groins to regulate amount of drift supplied to downdrift beaches.
Shore Protection, Planning, and Design, Coastal Engr. Research Ctr., TR4, 1966	General	Manual	Adjustable Permeable	Useful where attempt is being made to widen beach with a minimum of damage to downdrift area. Present state of knowledge does not lend conclusions as to effectivanass.
Price, W.A., and Tomlinson, K.W., 1968	England	Movable bed, model study	Impermeable	Permeable groins had little effect on longshore drift.
Kolp, Otto, 1971	Fischland, Zempin, Neuendorf	Field, Experimental	Permeable	Found that 37% open space reduced longshore flow 50%; piling was used in groin construction.

Of groin structures utilized today, there is a greater lack of adequate understanding of permeable structures than of any other type of groin design. Generally, it has been determined that "insufficient empirical data have been compiled to establish quantitative relationships between the applied littoral forces, groin permeability, and resulting behavior of the shore" (Shore Protection Planning and Design, U. S. Army Corps of Engineers, 1966). The lack of understanding is displayed through the very term "permeable". In its present usage, the term provides but a casual explanation that permeable groins have openings through which littoral drift may pass. There is not an adequate engineering definition pertaining to the structure itself that can be used comparatively to relate a condition of "permeability" of one type of structure to another. A standard concept will need to be established in order that an organized evaluation of the structure can be made.

Model investigations have apparently used an implied definition of permeability as:

1.) ratio of void area to total area, or;

2.) a ratio of the volume of voids to total volume of the mass (porosity).

The former definition would, of course, be the easier to work with, but regardless of which is used, a standard definition is needed where, in this case, the ratios can be related to amounts of drift that pass through a structure. Few endeavors, either in the form of experiments or field studies, have been conducted which commit themselves to such a goal. Laboratory tests to date have been concerned only with voids of rectangular shape oriented in a vertical direction, although most prototype structures known to the authors have been constructed with the voids oriented in a horizontal direction. Geometric variations of both voids and their orientation other than those utilized may be more beneficial, and though the variations are almost inconceivable in number, investigations are warranted.

Orientation of Groins to the Shoreline:

Orientation of groins to the shoreline has not received as much attention as previously discussed criteria. There have, however, been several papers that have devoted considerable discussion to this topic. The potential benefits of varying the orientation from normal, as presented in the literature, and the controversial nature of the concept warrants discussion.

Generally it has been defined that orientation of groins is a function of the angle of wave approach. Various investigators have shown that groins oriented slightly updrift from the normal to the shoreline collect greater amounts of littoral material than normal groins when the angle of incidence of waves with the shoreline is relatively constant with time. Kemp (1962) suggests, from results of his experiments, that where a beach is receding due to destructive wave action (again where wave approach is relatively constant),

that groins correctly oriented to the shoreline could reorient the shore such that the erosive effect would be minimized. Where variable wave conditions exist, groins constructed normal to the coast are preferred. Table 5 presents a spectrum of opinions on groin orientation.

TABLE 5. ORIENTATION OF GROINS WITH THE SHORELINE

INVESTIGATOR, YEAR	AREA OF INVESTIGATION	TYPE OF INVESTIGATION	ORIENTATION / REMARKS
Case, G.O., 1915	England, New York, New Jersey	Field, Experience	Recommends use of normal groins only. Oblique groins are more costly, are liable to be damaged by waves because of greater surface area exposed to waves, and cause more scour than groins constructed normal to the coast.
Duvivier, Jack, 1947; 1949	England	Experience	Normal to shoreline: use where direction of drift is variable. 10° from normal, pointing away from drift: use where there is prevailing drift, and where beach material is shingle. 20° from normal, pointing away from drift: use where prevailing drift occurs, and where beach is sandy.
Nagai, Shositiro, 1956	Japan	Movable bed, model study	θ / δ / α: 30° / 100° / 110°; 40° / 110° / 100° 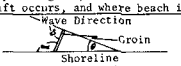 These angles satisfied test conditions; in general δ should not be less than 95° nor greater than 120°, otherwise scour is the result.
Shimano, T., Hom-ma, M., Horikawa, K., Sakou, T., 1957	Japan	Movable bed, model study	Should consider building groins upcoast (toward updrift direction).
Horikawa, Kiyoshi, and Sonu, C., 1958	Japan	Movable bed, model study	Best orientation depends upon wave steepness. Groin For steep storm waves, α=105° For relatively flat waves, α=90° (Taken from Wiegel, 1964) 
Nagai, Shoshichiro, and Kubo, Hirokazo, 1958	Japan	Fixed basin, model study	θ / α / D: 30° / 110° / 1:3; 45° / 90, 110° / 1:3; 60, 90° / 90° / 1:3-1:4  Despacing. (Deep water waves used for calculations) Above are results of fixed basin test conducted to compare with movable bed study by Nagai, 1956.
Hiranandini, M.G., and Gole, C.V., 1961	Cochin, India	Field study-prototype conditions, model study	Inclined groins did not commend themselves for adoption on this coast.
Lee, C.E., 1961	Great Lakes	Field study	Inclined groins are ineffective or too costly for the effects produced.
Kemp, P.H., 1962	England	Movable bed, model study	Orientation / Low Groin / High, Long Groin / High, Short Groin: 30° updrift: 51 / 43 / 67 Normal to Coast: 60 / 50 / 71 20° downdrift: 87 / 55 / 67 Table gives quantities of material collected in downdrift traps as % of total material after 3 wave cycles, for impermeable groins. Gives results showing that by appropriate choice of groin type and alignment, it should be possible to orient the shoreline in such a way that the effects of storm attack are minimized.
Shore Protection, Planning and Design, Coastal Engr. Research Ctr., TR4, 1966	General	Manual	Maximum economy is achieved with a straight groin normal to the shoreline. In cases where shoreline alignment may change after groin construction it may be desirable to build groins at an angle initially, so that they will be normal to expected adjustment of shore.
Barcelo, J.P., 1970	Portugal	Model study	β = 90° for α = 20° β = 70° for α = 10° β = angle of groin with shoreline. α = obliquity of waves. 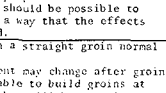 Where variable wave conditions persist, groins constructed normal to the shoreline are preferred.

Special Designs:

Variation is not only found in the design of component parts of conventional groins, but also in the overall configuration of special types of groins. Component parts of groins are constructed of rock, timber, concrete, or steel, and have assumed a variety of shapes. Groins of the Budd-Wall (E. & E. Associates, 1965) and S. M. Wood (1937, 1945) design, and structures such as the cellular and crib groins provide examples of such variations. Special features have been added to the design of conventional straight groins to produce such structures as curved-, spur-, corner-, L-, Z-, and T-groins. Each has been designed to produce special effects where they are intended to improve upon effectiveness of conventional structures.

SUMMARY COMMENTS

This paper has presented in tabular format and accompanying discussion some of the basic criteria used in the functional design of groins. From data presented here and from the review of pertinent literature in general, the following comments are offered:

1.) Prior to undertaking the design of a groin or groin system, complete understanding of littoral processes that predominate in the area of concern is required. Particular attention must be devoted to the determination of:

a.) longshore transport rates;

b.) longshore transport directions, and

c.) prediction of possible modifications of the preceding by the intended structure(s) and the effect of such structure(s) on adjoining shores.

2.) There are a number of factors concerning groin design criteria that need further investigation and refinement. Some of the factors include:

a.) standardization of a reliable formula for computing longshore transport rates, and an efficient method for obtaining or verifying longshore transport data needed. These will be utilized to produce and verify more effective designs of groins and groin systems for a particular coastal locality. Factors that modify longshore transport rates, especially storms and the onshore-offshore movement of beach material must be integrated into design formulas;

b.) a scientific definition that adequately defines the permeability of groins: experimental work has apparently implied that this

design concept can be expressed as a ratio of void area to total area, or as a ratio of void volume to total volume of mass; such concepts should be formalized into a definition for standard application where the ratios can be related to the amounts of material passing through one type of permeable structure to another; types of voids and their interstructure orientation may be a decisive factor for an increase in efficiency of such groins, especially if they are built in areas of frequent reversals of littoral drift;

c.) use of artificial nourishment: as a general rule, groins should not be built where there are inadequate supplies of longshore moving drift; where supplies are inadequate, artificial fill should be used either independently or in conjunction with groins; some investigators maintain that groin construction should always be accompanied by fill; it has been stated that where technically possible and economically feasible, artificial nourishment should be utilized exclusive to permanent structures, since the fill does not "entail a permanent commitment" (Barcelo, 1970).

3.) Of critical statements, the following is probably most pertinent in terms of the state-of-the-art in groin design. By the very nature of beaches, that no two are the same, it is erroneous to assume that one specific groin design will provide the answer to all shore erosion problems.

ACKNOWLEDGEMENTS

Data presented in this paper, unless otherwise noted, were obtained from research conducted by the United States Army Coastal Engineering Research Center under the Civil Works research and development program of the United States Army Corps of Engineers. Permission of the Chief of Engineers to publish this information is appreciated. The findings of this paper are not to be construed as official Department of the Army position unless so designated by other authorized documents.

The contents of this paper are not to be used for advertising or promotional purposes. Citation of trade names does not constitute an official endorsement or approval of the use of such commercial products.

REFERENCES

1. Balsillie, J. H. and Bruno, R. O., "Groins: an Annotated Bibliography", Coastal Engr. Research Center Misc. Paper No. 1-72, Washington, D. C., April 1972, 249 pp.

2. Barcelo, J. P., "Experimental Study of the Hydraulic Behavior of Groyne Systems", Proceedings of Eleventh Conference on Coastal Engineering, ASCE, Vol. 1, Sept. 1968, pp. 526-548.

3. Barcelo, J. P., "Experimental Study of the Hydraulic Behavior of Inclined Groyne Systems", Proceedings of the Twelfth Coastal Engineering Conference, ASCE, Vol. 2, Sept. 1970, pp. 1020-1040.

4. "Basic Coastal Model", Hydraulics Research 1957, Department of Scientific and Industrial Research, Her Majesty's Stationery Office, London, 1958, pp. 52-54.

5. Brater, E. F., "Low Cost Shore Protection Used on the Great Lakes", Proceedings of Fourth Conference on Coastal Engineering, Council on Wave Research of the Engineering Foundation, Oct. 1953, pp. 214-226.

6. Brown, E. I., "Beach Erosion Studies", Shore and Beach, American Shore and Beach Preservation Association, Vol. 7, No. 1, Jan. 1939, pp. 3-23.

7. Brown, E. I., "Beach Erosion Studies", Transactions of the American Society of Civil Engineers, Vol. 105, Paper No. 2076, 1940, pp. 869-918.

8. Bruun, P., Gerritsen, F. and Morgan, W. H., "Florida Coastal Problems", Proceedings of Sixth Conference on Coastal Engineering, Council on Wave Research of the Engineering Foundation, Dec. 1957, pp. 463-509.

9. Bruun, P. and Manohar, M., "Coastal Protection for Florida", Engineering Progress at the University of Florida, Engineering and Industrial Experiment Station, Gainesville, Bulletin Series 113, Vol. 17, No. 8, Aug. 1963, 56 pp.

10. Case, G. O., "Coast Erosion and Protection on Long Island and New Jersey", Engineering News, Engineering, Chemical and Marine Press, Ltd., London, Vol. 74, No. 10, Sept. 1915, pp. 439-442.

11. Coen-Cagli, M. E., "Protection of Coasts against the Sea, with or without Preponderating Coastal Drift of Materials", World Ports, American Shore and Beach Preservation Association, Vol. 20, No. 4, Feb. 1932, pp. 286-293.

12. Dent, E. J., "Sand Movement and Beach Erosion", Civil Engineering, ASCE, Vol. 1, No. 9, June 1931, pp. 821-826.

13. Dobbie, C. H., "Some Sea Defence Works for Reclaimed Lands", Journal of the Institution of Civil Engineers, London, Vol. 22, No. 4, Feb. 1946, pp. 267-272.

14. Dunham, J. W., "Use of Long Groins as Artificial Headlands", Coastal Engineering Santa Barbara Specialty Conference, ASCE, Oct. 1965, pp. 755-762.

15. Duvivier, J., "The Problem of Coast Erosion", Proceedings of Institution of Civil Engineers, London, 1947, 47 pp.

16. Duvivier, J., "Report to the Seventeenth International Navigation Congress", Seventeenth International Navigation Congress, Permanent International Association of Navigation Congresses, Brussels, Belgium, Section 2 - Ocean Navigation, Communication 1, 1949, pp. 75-84.

17. E. & E. Associates, 1968 Budd Groins, Brochure, Venice, Florida.

18. Evans, O. F., "The Relation of the Action of Waves and Currents on Headlands to the Control of Shore Erosion by Groins", Proceedings of the Oklahoma Academy of Science, 1943, pp. 9-13.

19. Frech, F. F., "Paper on Protective Works Adopted to Limit Erosion Along the Open Coast: How They Work", U. S. Army Corps of Engineers, Philadelphia District, June 1948, 35 pp. (Unpublished).

20. Hiranandini, M. G. and Gole, C. V., "Shoreline Advancement by Sea Wall and Groynes at Cochin", Proceedings of the Seventh Conference on Coastal Engineering, Council on Wave Research of the Engineering Foundation, Vol. 2, Aug. 1960, pp. 860-871.

21. Horikawa, K. and Sonu, C., "An Experimental Study on the Effect of Coastal Groins", Coastal Engineering in Japan, Committee of Coastal Engineering, JSCE, Vol. 1, Oct. 1968, pp. 59-74.

22. Horikawa, K., "Japanese Construction Practice on Groins", Seminar on Groin at Princeton, N. J., ASCE sponsored, Oct. 1958, (Unpublished).

23. Hoyle, J. W. and King, G. T., "The Origin and Stability of Beaches", Proceedings of Sixth Conference on Coastal Engineering, Council on Wave Research of the Engineering Foundation, Dec. 1957, pp. 281-301.

24. Hoyle, J. W. and King, G. T., "Coast Protection - Groyne Systems", Surveyor and Municipal and County Engineer, London, Vol. 121, No. 3647, April 1962, pp. 575-579.

25. Ishihara, T. and Sawarogi, T., "Stability of Beaches Using Groins", Proceedings of the Ninth Conference on Coastal Engineering, ASCE, June 1964, pp. 299-303.

26. Johnson, J. W., "The Action of Groins on Beach Stabilization", University of California, Department of Engineering, Navy Department Bureau of Ships Contract NObs 2490, Technical Report HE-116-283, April 1948.

27. Jones, J. H., "Wave Action on Beaches", University of California, M.S. Thesis, June 1948.

28. Kemp, P. H., "A Model Study of the Behavior of Beaches and Groynes", Journal of the Institution of Civil Engineers, London, Vol. 22, 1962, pp. 191-210.

29. Kolp, O., "Sea Groins Effectiveness Investigations, Dyed Sand Tests", Beitrage zur Meereskunde, Deutsche Akademie der Wissenschuften zu Berlin Institute fur Meereskunde, Berlin, Issue 17-18, 1966, pp. 6-90.

30. Kressner, B., "Tests with Scale Models to Determine the Effects of Currents and Breakers upon a Sandy Beach and the Advantageous Installation of Groins", Bautechnik, Berlin, Vol. 25, June 1928.

31. Lee, C. E., "Groins on the Shores of the Great Lakes", Journal of the Waterways and Harbors Division, ASCE, Vol. 87, No. WW2, Paper 2819, May 1961, pp. 89-111.

32. Mason, M. A., "Principles of Shore Protection for the Great Lakes", Proceedings of Fourth Conference on Coastal Engineering, Council on Wave Research of the Engineering Foundation, Oct. 1953, pp. 207-213.

33. Nagai, S., "Arrangement of Groins on a Sandy Beach", Journal of Waterways and Harbors Division, ASCE, Vol. 82, No. WW4, Paper 1063, Sept. 1956, 13 pp.

34. Nagai, S. and Kubo, H., "Motion of Sand Particles Between Groins", Journal of Waterways and Harbors Division, ASCE, Vol. 84, No. WW5, Paper 1876, Dec. 1958, 28 pp.

35. Owen, J. S. and Case, G. O., Chapter 11 Coast Erosion and Foreshore Protection, St. Brides Press, London, 1908.

36. Price, W. A. and Tomlinson, K. W., "The Effect of Groynes on Stable Beaches", Proceedings of Eleventh Conference on Coastal Engineering ASCE, Vol. 1, 1968, pp. 518-525.

37. Raynor, A. C. and Rector, R. L., "Groins on the Shores of the Great Lakes", Journal of the Waterways and Harbors Division, ASCE, Vol. 87, No. WW4, Nov. 1961, p. 137.

38. Savage, R. P., "Laboratory Study of the Effect of Groins on the Rate of Littoral Transport: Equipment Development and Initial Tests", U. S. Army, Beach Erosion Board, Technical Memorandum No. 114, June 1959, 56 pp.

39. Schijf, J. B., "Generalities on Coastal Processes and Protection", Journal of the Waterways and Harbors Division, ASCE, Vol. 85, No. WW1, Pt. 1, March 1959, pp. 1-12.

40. Shay, E. A. and Johnson, J. W., "Influence of Groins on Beach Stabilization", University of California at Berkeley, Department of Engineering, Series 14, Issue 6, Beach Erosion Board Contract W49-055-eng-2, Jan. 1951.

41. Shimano, T., Hom-ma, M., Horikawa, K. and Sakou, T., "Functions of Groins Fundamental Study on Beach Sediment Affected by Groins (1)", Proceedings of the Fourth Conference on Coastal Engineering in Japan, JSCE, 1957, pp. 111-121.

42. Steiner, C. T., "Construction and Maintenance of the Public Beach at Rockaway Beach, Borough of Queens", The Municipal Engineers Journal, Paper 181, Oct. 1936, pp. 107-122.

43. Wicker, C. F., "Summary Statement Concerning Importance of a Groin Design Criterion", Seminar on Groins at Princeton, N. F., ASCE sponsored, Oct. 1958, 2 pp. (Unpublished).

44. Wiegel, R. L., Oceanographical Engineering, Prentice-Hall International Series in Theoretical and Applied Mechanics, Fluid Mechanics Series, Prentice-Hall Incl., Englewood Cliffs, N. J., 1964, 532 pp.

45. Wood, S. M., "Jetty", U. S. Patent Office, Patent No. 2,099,249, Nov. 1937, 3 pp.

46. Wood, S. M., "Art of Beach Protection", U. S. Patent Office, Patent No. 2,387,965, Oct. 1945, 3 pp.

47. U. S. Army Corps of Engineers, "Shore Protection, Planning and Design", Coastal Engineering Research Center, Technical Report No. 4, 3rd ed., June 1966.

CHAPTER 76

CALCULATED SAND FILLS AND GROIN SYSTEMS

by

John S. Hale
Head, Ocean Engineering Group
County of Los Angeles
California

Abstract

This paper demonstrates the results of the comparison between the calculated alignment of the beach's plan view and the actual alignment that resulted from the natural wave action.

A new groin system was designed to replace an existing one. The new groin system and spacing was designed to hold the beach fill at the required width during average wave conditions as well as changing storm wave conditions. The system was designed for Las Tunas Beach, a beach near Los Angeles, California.

In other words, the energies are tabulated for all storm conditions, and the beach alignment is recalculated for changing storm conditions. As the beach plan view alignment rotates back and forth with changing storm directions, it must always meet the minimum beach width requirements. This may entail changing the groin lengths, heights and spacing several times before the design complied with all requirements.

Surveys from 1929 to 1970 showed that the beach did not have long periods, periods of several years, of constant erosion or constant accretion. If there are no major man made changes, it is safe to assume that nature will provide an adequate sand supply.

Last, but not least, the calculated beach alignments check with the empirical information gathered from years of surveying.

This paper tells of a groin system and sand fill that was calculated by the use of resultant wave energies.

The beach to be studied was widened during 1929 by damming up the littoral drift with five sheet pile groins. We plan to replace the five groins with two long rock groins and fill the groin system with sand. The new groin system and beach alignment was calculated and compared to existing alignments that have been surveyed over the years.

Plate 1 shows the beach as it was seen recently and the way it will look after widening. This beach, called Las Tunas Beach, is located along the Pacific Ocean shoreline, a few miles westerly of the City of Santa Monica in the County of Los Angeles, California. This is, of course, within the United States.

Because of the amount of survey data available over a great number of years, the natural beach has been examined much like it would be if it were a laboratory model. Surveys have been taken at various seasons of the year and during changes of wave climates.

Since the beach's five long groins dammed up the littoral drift, surveys of the natural beach would tell us how the littoral drift was impounded and indicate the plan view alignment changes with different wave climates.

Plate 2 shows the locations of our range lines along which surveys of the ocean bottom were repeated and compared.

See Plate 1 for the location of five groins and the remaining sand fillet.

Our range lines are spaced 250 feet apart along this 1500 feet of proposed shoreline development.

Plate 3 demonstrates our method of plotting and comparing the profiles.

The beach foreshore slopes remain somewhat parallel during seasonal and long term changes.

The groins have deteriorated years ago and allowed the beach to return to its present postion. Since the existing beach has remained in this position, except for seasonal changes, since surveyed during the early 1950's, it is evident that there is adequate nourishment and the beach is stable.

Plate 4 shows the comparison between the calculated alignment and present alignment. The calculated alignment was made for storms coming from south, southeast to west. The shore line on this plate goes east and west and you will note the difference in the resultant inshore wave directions.

The predominant inshore wave direction changes only slightly with different storms, while seaward of the islands the storms varied more than 120° in direction.

A more detailed discussion of what wave statistics are used will be covered later. At this time let's discuss the different alignments. Note the alignments from the westerly

PLATE 1

LAS TUNAS BEACH IMPROVEMENT PROJECT

BEFORE BEACH IMPROVEMENT

AFTER BEACH IMPROVEMENT

PLATE 2

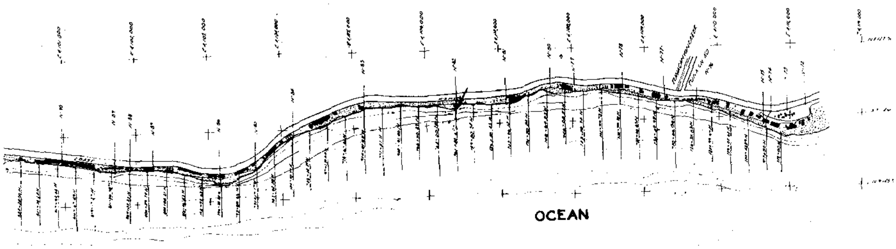

NUMBER STATION	ADJUSTED STATION	GRID COORDINATES NORTH	EAST	FROM	TO	GRID BEARING	DISTANCE
N-81	754+87.16	4,128,741.11	4,107,085.51				
				N81	N82	N86°12'02"W	684.52
N-82	761+51.68	4,128,762.63	4,106,401.51				
				N82	N83	S88°46'45"W	1264.27
N-83	774+15.95	4,126,724.69	4,105,137.62				
				N83	N84	S69°13'36"W	1,048.38
N-84	784+64.33	4,126,352.65	4,104,157.39				
				N84	N85	S50°57'58"W	676.74
N-85	791+41.07	4,125,923.61	4,103,634.20				
				N85	N86	S79°50'40"W	498.38
N-86	796+39.45	4,125,[illegible]	4,10[illegible]				
				N86	N87	N80°08'06"W	930.69
N-87	805+70.14	4,125,959.24	4,102,236.00				
				N87	N88	N87°57'58"W	312.24
N-88	808+82.38	4,125,970.35	4,101,923.00				
				N88	N89	S80°32'45"W	247.39
N-89	811+29.77	4,125,929.71	4,101,679.01				
				N89	N90	N77°19'49"W	725.24
N-90	818+55.01	4,126,088.64	4,100,971.53				

NUMBER STATION	FIELD BOOK STATION	GRID COORDINATES NORTH	EAST	FROM	TO	GRID BEARING	DISTANCE
N-72	711+66.51	4,126,661.08	4,111,172.23				
				N72	N73	S70°35'44"W	230.80'
N-73	714+00.31	4,126,584.40	4,110,946.97				
				N73	N74	S83°30'58"W	233.35'
N-74	716+38.66	4,126,555.67	4,110,715.00				
				N74	N75	S34°17'45"W	179.69'
N-75	718+18.35	4,126,407.22	4,110,613.80				
				N75	N76	N70°36'46"W	985.60'
N-76	728+03.95	4,126,734.66	4,109,684.18				
				N76	N77	N87°24'32"W	427.87'
N-77	732+31.82	4,126,754.01	4,109,256.76				
				N77	N78	N74°55'38"W	596.00'
N-78	738+27.82	4,126,908.98	4,108,681.26				
				N78	N79	S89°32'08"W	662.53'
N-79	744+90.35	4,126,903.63	4,108,018.76				
				N79	N80	N79°54'34"W	328.46'
N-80	748+18.81	4,126,961.17	4,107,695.37				
				N80	N81	S70°08'31"W	648.35'
N-81	754+87.16	4,128,741.1	4,107,085.51				

Enlarged Section

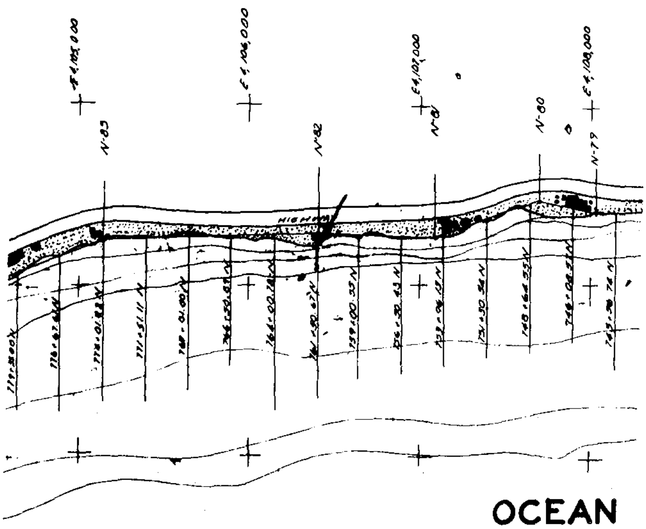

This Plate shows the onshore beach control line with "N" monuments and lines extending seaward that formed the paths for the beach profile. Direction and scale can be determined from available survey data.

PLATE 3

Beach Profile

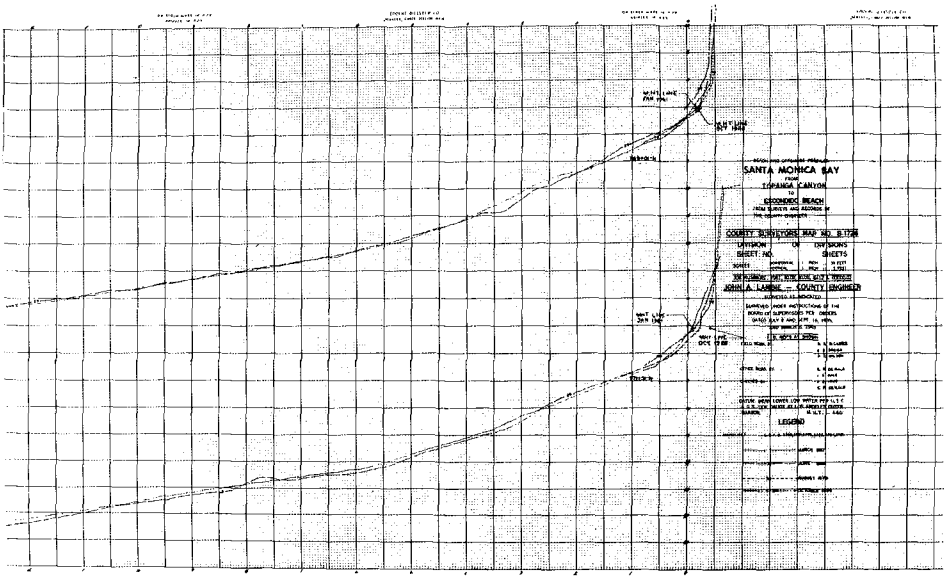

Horizontal scale: 1 inch = 365 feet
Vertical scale: 1 inch = 36.5 feet

PLATE 4A

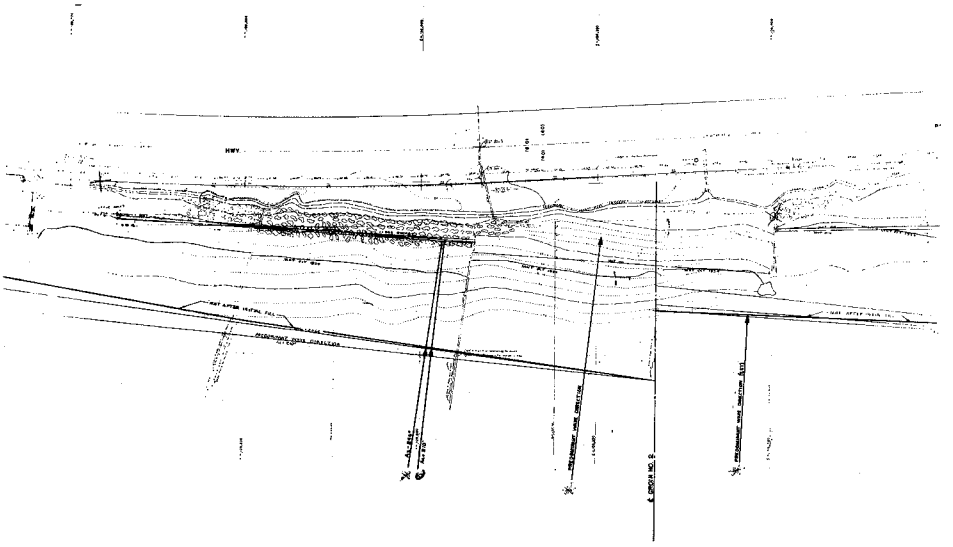

✗ Azimuth 246° is a deep water wave from the west.
● Azimuth 210° is a deep water wave from the south.
✱ Azimuth 232° is the predominant wave direction.

PLATE 48

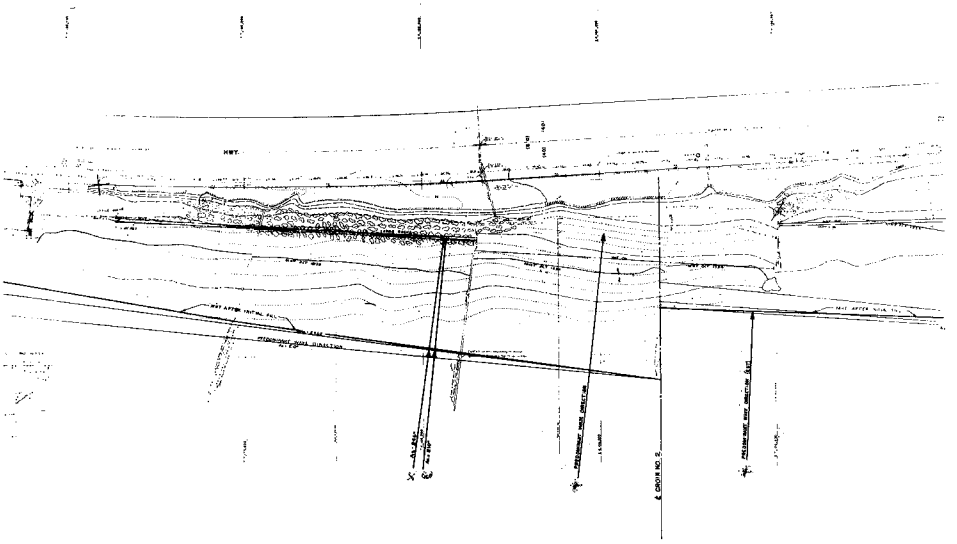

PLATE 4C

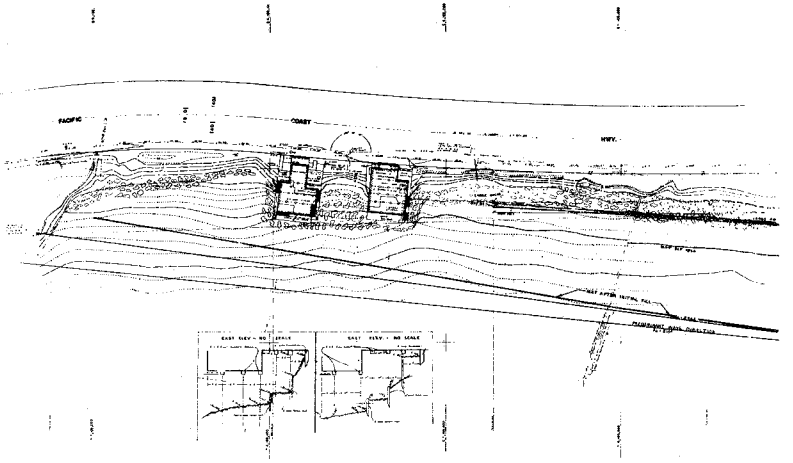

waves as they compare to those from the south and the predominant wave direction of all waves.

Since the sand fillet will attempt to align itself normal to the wave orthogonals from these predominant wave directions, we can calculate the alignment of the shoreline by knowing the inshore direction of the orthogonals.

The next question is how did we calculate these different shoreline alignments and where did we get the wave statistics to do it with.

Plate 5 shows the crux of the problem. The hindcasted wave statistics must he brought through the island maze, refraction and resultant wave directions must be calculated.

Note where the hindcasted wave statistics were compiled, Station A and Station 7, and where the wave statics were tabulated inside the island maze, lat. 33°56, long. 118° 37'.

Plate 6 shows a summary nf the work, and an explanation of the various steps that were followed.

Column No. 1 shows the wave directions at Station A, Station 7 and those used to tabulate the local winds.

The waves at Stations A and 7 were compiled within 22½ degrees arcs, of which the directions shown are the center. The local waves or those called sea, are recorded within ten degree arcs, and the directions shown are the center of these arcs.

Column No. 2 shows the resultant wave directions, based on energy calculation, of those waves shown in Column No. 1.

The first calculations were to change the wave statistics to deep water wave energy. Since relative energy was all that was needed, we calculated the <u>total</u> storm wave energy by the use of significant wave heights. You will note, I used the word "total". In other words, we calculated the wave energy for the total average annual time that given storms would occur during the year.

The next step was to calculate the resultant energy for all the storms within the 22½ degree segments represented in Column No. 1.

The resultant can be calculated by vector analysis. The length of the vector represents total annual energy for storms and the vector direction represents the direction of these storm waves. By joining these vectors end for end the resultant energy and direction can be calculated.

Column No. 3 shows a tabulation of the shift in the direction of the resultant of wave energy when the point of observation is moved from Station 7 or A to the deep water area just off Las Tunas Beach. This shift will be explained in a later plate.

Column No. 4 is a summation of Columns 2 and 3.

Column No. 5 shows the resultant relative energy that has been calculated for different storm conditions at Station A or Station 7.

Column No. 6 shows a coefficient that indicates the decimal part of this energy that gets through the island maze.

PLATE 5

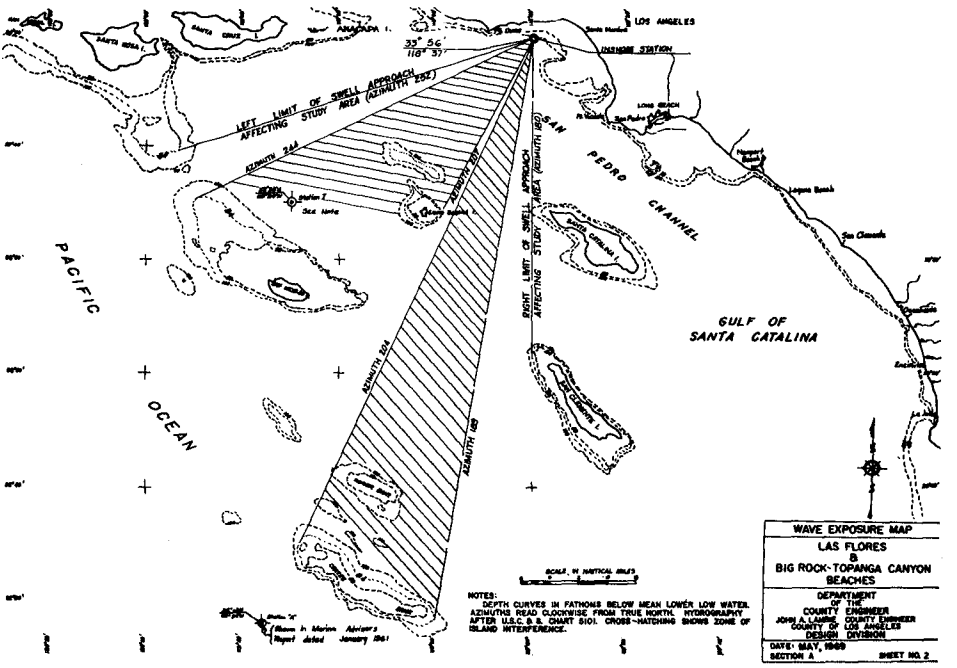

Note stations where wave statistics were compiled "⊕".

PLATE 6
WAVE STATISTICS
AT
NORTH LATITUDE 33° 55.9'
AND
WEST LONGITUDE 118° 36.7'

(ANNUAL ENERGY IN MILLIONS OF FOOT POUNDS)

(1) DIRECTION (AZIMUTH)	(2) RESULTANT DIRECTION (AZIMUTH NORTH)	(3) SHELTERING CORRECTION TO DIRECTION	(4) DIRECTION AT THE ABOVE LOCATION	(5) ENERGY AT STATION A or 7	(6) ISLAND SHELTERING COEFFICIENT (C) C	(6) C²	(7) RESULTANT ENERGY AT THE ABOVE LOCATION
			SWELL STATION A				
157.5	157.3°	+29.9	187.2°	10,400	.33	.109	1,140
180.0	174.8°	+21.9	196.7°	8,400	.47	.221	1,850
202.5	204.6°	+ 6.0	210.6°	9,500	.60	.360	3,420
225.0	226.0°	+ 3.5	229.5°	29,200	.71	.504	14,900
			STATION 7				
247.5°	247.5°	- 8.5	239.0°	5,600	.62	.384	2,130
270.0°	270.0°	-24.0	246.0°	48,500	.54	.292	14,060
			SEA				
120	145	Waves are the result of local winds blowing towards the main-land from the islands --no shel-tering correction needed.	145				22
130	148		148				7
140	157		157				53
150	167		167				84
160	175		175				46
170	182		182				78
180	187		187				50
190	194		194				137
200	204		204				217
210	213		213				190
220	217		217				65
230	219		219				180
240	226		226				120

RESULTANT - WAVE DIRECTION
(For all Waves Counted) = 231° 50'
AVERAGE WAVE PERIOD = 11.8°
NOTE: Waves from west north west have no effect on this area.

We call this the island sheltering coefficient.

Column No. 7 shows the fractional part of the energy that reaches the deep water area just off Las Tunas Beach.

Three important beach forming wave resultants exist, wave resultants from westerly waves, southwesterly waves and southerly waves.

Other waves considered in the tabulation are as follnws:

The waves from the southwest have a very high energy value but are so clnse to the predominant wave direction that no special consideration need be given them.

The local wind wave energies are tahulated at the bottom of the plate under the term sea. None of these waves have significant quantities of energy in the study area. Furthermore, the waves from 226° to 145° occur over a wide range of months and involve many small storms during the year. Thus, the energy fnr any individual storm will be quite small and will not he very effective in shaping the study area coastline.

Plate 7 shows the way the island blocking is handled. The details of this type of blocking can not be completely covered here, but in general the area under the curve shown represents total energy from the average storms and the area under the curve and not crosshatched shows the part of the energy that gets through the islands.

Because of the irregularities of wind waves within the island maze, it was expedient to divide the problem into two parts --energy resulting from deep water swells, and energy resulting from fetch, wind and local conditions.

Since little wave decay exists between Station A or 7 and Las Tunas Beach, the plate shows hnw the island sheltering affected a wave with an azimuth of 175° from Station A.

In the formula $id\theta = K(1+\cos 2\theta)d\theta$, θ is the angle on either side of the center of the waves formed and $id\theta$ is the energy for a small sector of θ. The K and $d\theta$ can be chosen to be unity without significant error. Because this wave is a deep water swell, a path nf 45° on eether side of 175° is considered and the blocking effect is shown. The energy will he reduced by 22% of the energy at Station A and the resulting wave azimuth will increase from 175° to 197°--this direction change is achieved by calculating the resultant nf the energy in the open windnws.

The unhlocked energy is reprcsented by the figure 17.13 which is the area under the total curve, and 3.81 represents the area of the open windows. Therefnre, the energy just off Las Tunas Beach equals energy calculated at Station A, times (3.81÷17.13) and equals 22% of the total energy.

During sea conditions in which the sheltering land masses are within the fetch area, a wave path of 90° on either side of the fetch directions is considered to be good. Decayed swell conditions can lead to overestimating the effects of island sheltering. The variability of wave direction for swells can be less than 45° and may be only a few degrees for very distant storms. Remember, the island windows are based on the average

PLATE 7

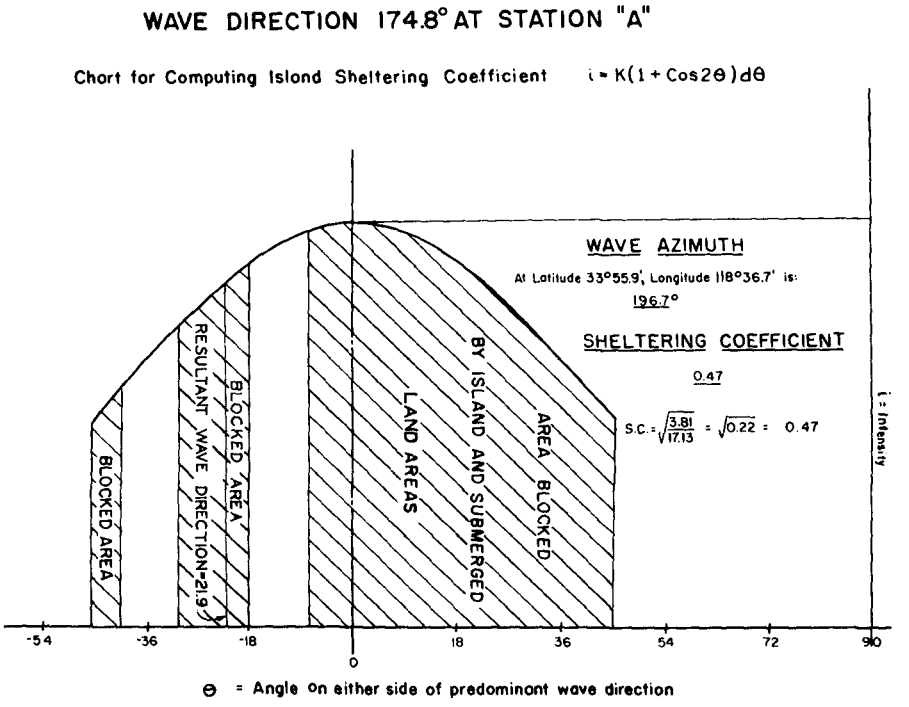

Predominant wave direction = _____

wave period for all swells, and the long period swells will not get through windows as large as those shown. Forty-five degrees prohably represents an average figure. Beaches in Los Angeles County are developed, primarily by the mid-range wave conditions and not the unusual rare occuring large wave conditions.

Investigating island sheltering necessitates considering the depth to which this island blocking will take place.

This was accomplished by determining the average wave period and taking 50 percent of the resultant deep water wave lengths as the depth to which the offshore islands will block continental hound waves.

The refraction diagrams were calculated and used to determine the resultant inshore energies.

Plate 8 shows the plotted profiles and the grouted groin area. The grout is placed on the porous cap stone to make it impermeable far enough seaward to maintain the beach at a minimum width.

The last ingredient is the question of an adequate, continuous sand supply. Surveying the heach over a great many years also gives us the answer to this question. Surveys from 1929 to 1970 showed that the beach did not have long periods--periods of several years of constant erosion and constant accretion. If there are no major man made changes, it is safe to assume that nature will provide an adequate sand supply.

Last, but not least, the calculated beach alignments check with the empirical information gathered from years of surveying.

PLATE 8

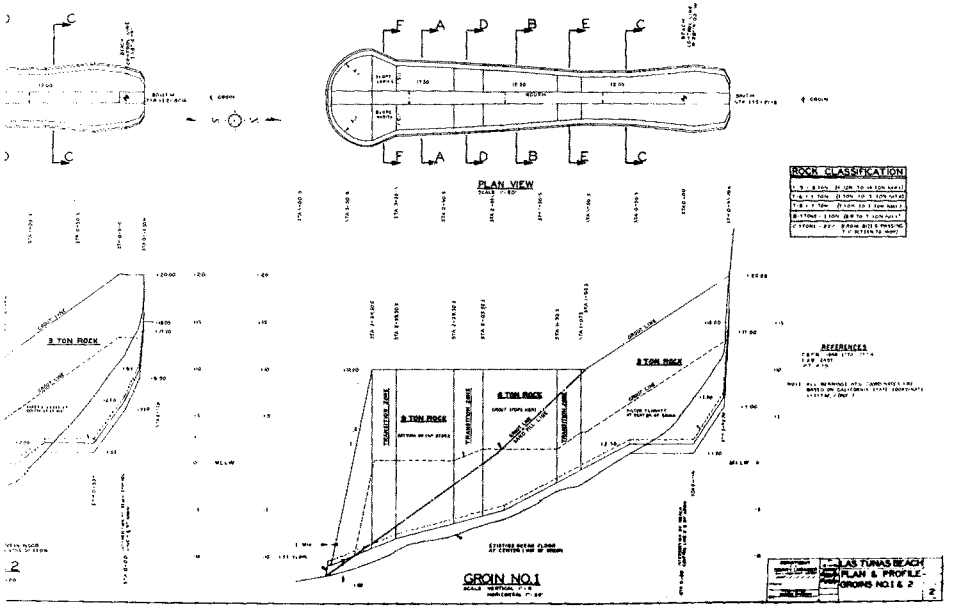
PLAN VIEW
ROCK CLASSIFICATION
3 TON ROCK
GROIN NO.1
LAS TUNAS BEACH
PLAN & PROFILE
GROINS NO.1 & 2

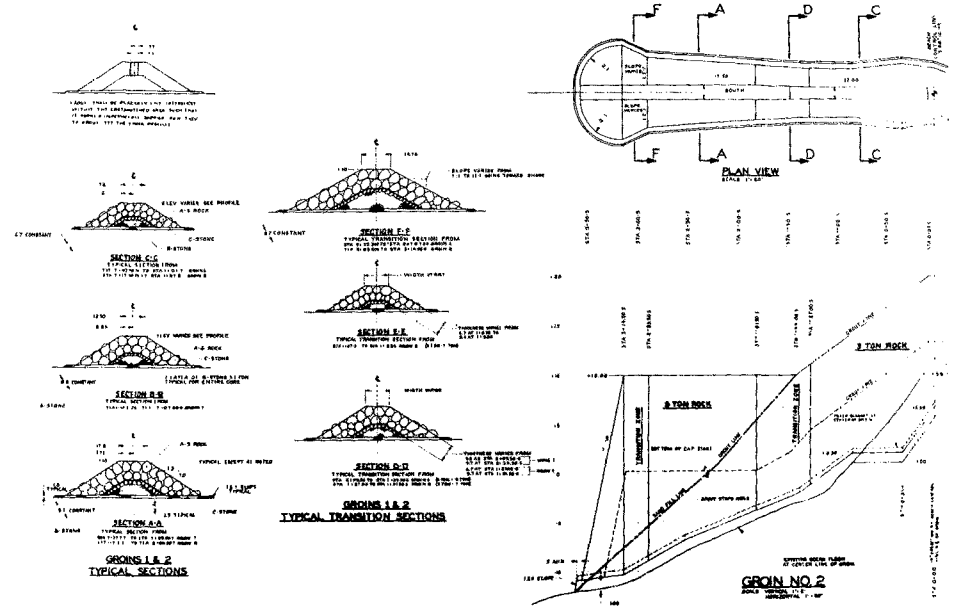
PLAN VIEW
SECTION C-C
SECTION E-E
SECTION B-B
SECTION D-D
SECTION A-A
GROINS 1 & 2
TYPICAL SECTIONS
GROINS 1 & 2
TYPICAL TRANSITION SECTIONS
3 TON ROCK
GROIN NO.2

REFERENCES

1. Shore Protection Planning and Design
(Technical Report No. 4, Third Edition)
Department of the Army, Corps of Engineers,
published 1966

2. Wave Statistics for Seven Deep Water Stations
Along the California Coast
National Marine Consultants, 1960

3. A Statistical Survey of Ocean Wave Characteristics
In Southern California Waters
Marine Advisers, January, 1961

4. A Lognormal Size Distribution Model For Estimating
Stability of Beach Fill Material
Technical Memorandum No. 16, Department of the
Army, Corps of Engineers Research Center.

5. Beach Improvement and Erosion Control Report
Design Division, Department of County Engineer,
August, 1965

6. Santa Monica Canyon to Las Flores Shoreline
Survey
County Engineer Field Books

CHAPTER 77

FIELD TESTS ON TWO PERMEABLE GROYNES

By

W A Price
Senior Principal Scientific Officer

K W Tomlinson
Senior Scientific Officer

D H Willis
Senior Scientific Officer

The Hydraulics Research Station, Wallingford, Great Britain

ABSTRACT

A section of beach on the south coast of England has been under surveillance for five years, from March 1966 until March 1971. During this period, two permeable groynes of the Makepeace Wood type were constructed. Beach cross-sectional areas and rates of accretion were compared before and after groyne construction. The groynes caused a build-up in beach levels updrift.

INTRODUCTION

Bournemouth is located on the south coast of England, see Figure 1. Because of its attractive beach it is a major tourist area. In recent years beach erosion has become a problem. To find a method of overcoming this loss of sand, the County Borough of Bournemouth have undertaken a number of sea defence schemes, advised and assisted by the Hydraulics Research Station, Wallingford.

One such scheme was the construction of two permeable groynes, in conjunction with Makepeace Wood Associates. This was in July 1968. The Hydraulics Research Station has measured beach profiles in the vicinity of the groynes at approximately 3 monthly intervals for 5 years; the first survey was in March 1966, almost 2½ years before groyne construction began, and the last was in March 1971, 2½ years after. This paper presents the results of these surveys.

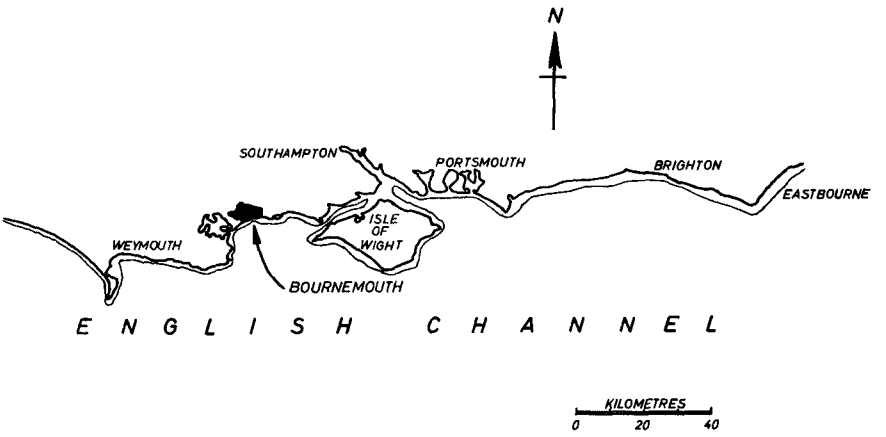

FIG 1 LOCATION

DESCRIPTION OF BEACH

The beach, mean size of sand 0.2 mm, is backed by a seawall and promenade. As shown on Figure 2, the foreshore has a slope of about 1:15 between high and low water contours, flattening to a slope of 1:200. Varying between 100 to 200 metres offshore it steepens again to approximately 1:15. Further offshore, seabed slopes are relatively small.

The tidal range at the site is about 1.7 m on spring tides, and 0.6 m on neaps. Waves approach the beach from directions between south-east and south-west, with the dominant direction being south-west. The fetch is limited in most directions by the coast of France, but some Atlantic swell does reach the site via the English Channel.

DESCRIPTION OF GROYNES

The groynes were built to a design by Sidney Makepeace Wood, see Ref 1. Each consisted of a double row of piles, interlaced with precast concrete units, and capped by a flat deck which provided a working platform during construction and added to its structural stability, see Plates 1 and 2.

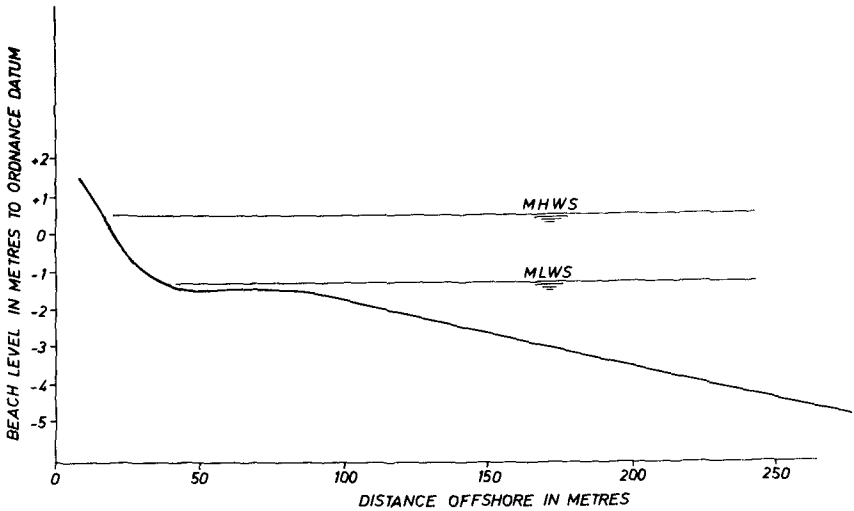

FIG 2 BEACH PROFILE

The longitudinal precast concrete units are castellated so that the groynes are permeable. The percentage of open area increases seaward as shown in Figure 4. The groynes were 190 m apart and designed to be 90 m long, although shortly after construction approximately 16 m of the seaward end of one collapsed. During the discussion of this paper at the 13th Coastal Engineering Conference a delegate reported the collapse of the seaward ends of a number of Makepeace Wood groynes in Jamaica.

DATA COLLECTION AND ANALYSIS

A general plan of the site is given in Figure 3.

On each of the 10 sections shown on this figure, beach profiles were measured at 3 monthly intervals, beginning in March 1966. In July 1968, groyne construction began. The surveys were continued until March 1971.

Beach volumes were calculated as shown in Figure 5. In order to obtain an estimate of the rate of erosion or accretion the data was subjected to regression analysis of volume on time. The slope of the regression line was then taken as the growth rate, summarised in Table 1.

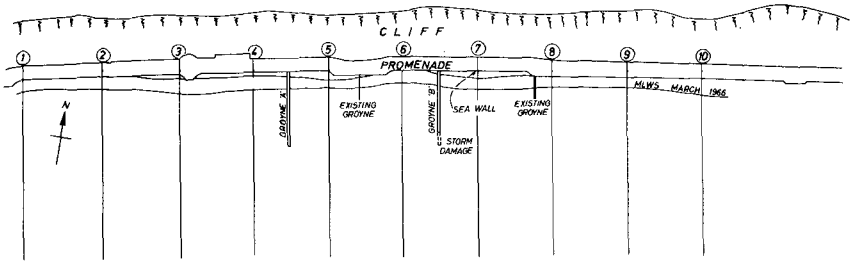

FIG 3 SITE PLAN

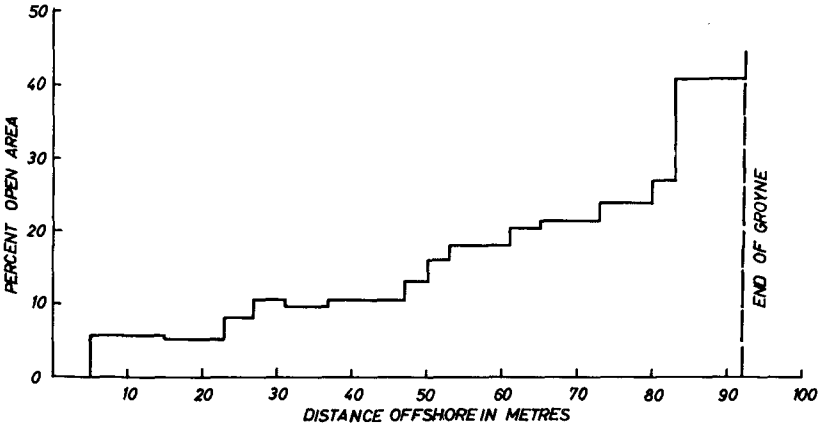

FIG 4 VARIATION OF OPEN AREA WITH DISTANCE ALONG GROYNE

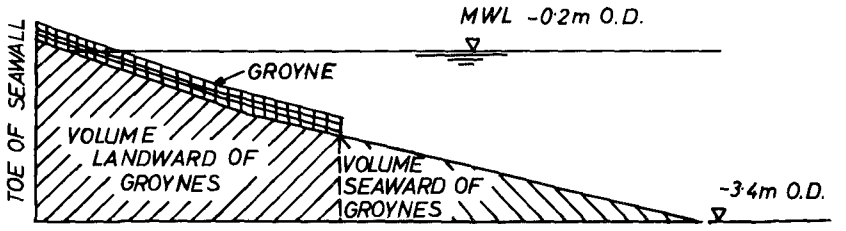

FIG 5 KEY TO CALCULATED VOLUMES

Of the 20 regression lines, it is significant that 14 showed an increase in slope following groyne construction. These increases were most marked landward of the groynes and updrift, Sections 3, 4 and 5. Although erosion downdrift was expected, Sections 6 through 10 showed some improvement as well, and it is possible that the beach as a whole would have accreted, but at a slower rate, if the groynes had not been constructed. Plate 3 shows the beach as it was before groyne construction, and Plate 4 shows it in the spring of 1971. The build-up in beach levels in the immediate vicinity of the groynes is marked; there appears to be little downdrift erosion. Figure 6 shows the changes in some typical cross-sections between March 1966 and March 1971.

CONCLUSIONS

There seems little doubt that the two Makepeace Wood groynes constructed at Bournemouth have resulted in a build-up of the beach in their immediate vicinity. Although erosion would be expected downdrift, it is not immediately obvious. Beach surveys are to be resumed.

TABLE 1
BEACH-GROWTH RATES BEFORE AND AFTER GROYNE CONSTRUCTION

Section No.	Growth Rate in Cubic Metres/Metre Per Month			
	Before Groyne Construction		After Groyne Construction	
	Landward of groynes	Seaward of groynes	Landward of groynes	Seaward of groynes
1	1.54	-0.20	0.26	0.11
2	2.97	-0.65	0.97	0.30
3	-2.45	0.71	2.63	0.69
4	-0.60	0.06	3.01	1.11
5	0.36	0.60	2.75	1.44
6	1.65	0.57	2.03	0.12
7	-0.29	0.30	1.37	0.37
8	-0.31	1.13	0.92	-0.37
9	0.48	-0.42	1.44	0.63
10	-0.19	0.30	0.66	-0.24

Plate 1. General view of groyne
Plate 2. Detail of groyne construction

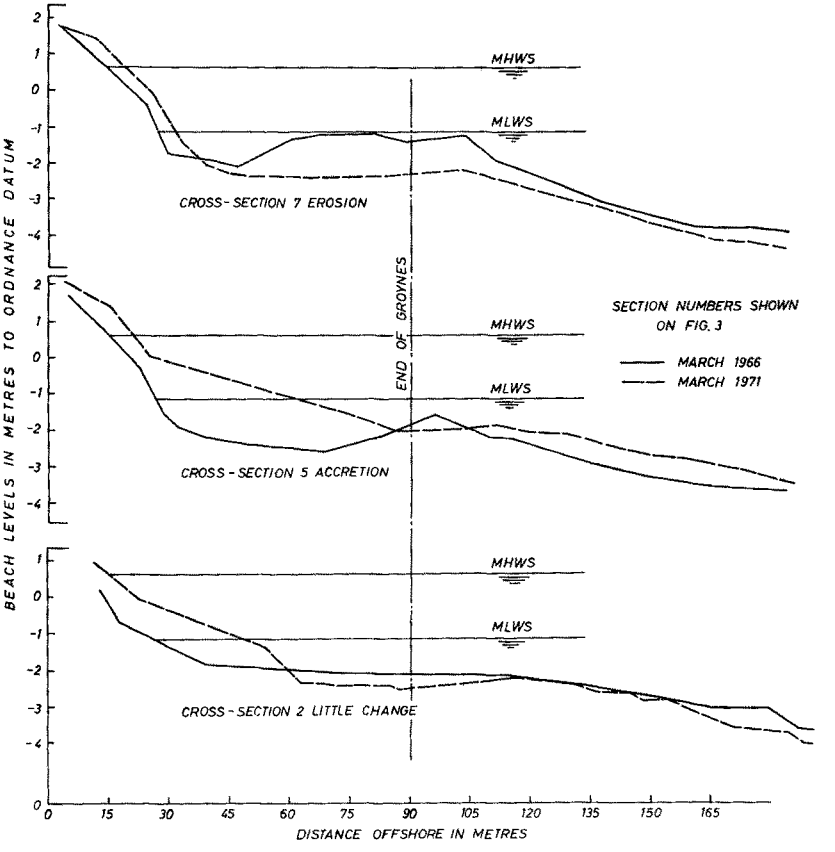

FIG 6 BEACH CROSS-SECTIONS

Plate 3. The beach before groyne construction
Plate 4. The beach in 1971

ACKNOWLEDGEMENTS

This report is published by permission of the Director of Hydraulics Research, Wallingford, Great Britain. The authors gratefully acknowledge the help and co-operation of the Office of the Borough Engineer, County Borough of Bournemouth.

REFERENCES

1. MAKEPEACE WOOD, S. "Erosion of our Coastal Frontiers", Bulletin of the Associated State Engineering Societies, April, 1938, pp 32.

CHAPTER 78

THE NILE DELTA COASTAL PROTECTION PROJECT

Ismail E.Mobarek

Deputy Co-Manager,Beach Protection Project,Egypt
Member and Executive Secretary,Beach Protection Board of Egypt

ABSTRACT

The Nile Delta Coast on the Mediterranean Sea was formed through many centuries. The two existing main branches of the River Nile, i.e. Rosetta and Damietta, succeeded over the ages in forming two peninsulas or protrusions in the sea. By the end of the 19th century erosion started at several important points of the coast, causing damages to the national economy, either directly or indirectly. This erosion has increased tremendously during the last decade.

Several field and laboratory studies were carried out during the last few years, concentrating on the severely attacked areas, such as Ras-El-Bar, Burullos, Rosetta,Maadia.

Based on the quick field and laboratory studies, remedial constructions are designed for the locations of severe erosion. Groins for Ras-El-Bar with artificial sand feeding and stone pitching and a wall for the Damietta estuary. A large groin for Burullos outlet which developed some advantageous changes even before finishing its execution,, and sea wall for Maadia. All the above projects are discussed and explained.

A long term study project was started early in 1971 to collect the data necessary for a better understanding of the problem. The aims of this project are as follows: (1) To determine the historical formation of the Delta and forecasting future changes ; (2) Study the Meteorology and the Hydrodynamics of the area ; hindcasting and starting a new forecasting technique for them; (3) Planning and design of protective constructions for the coast is to be gained.

All the above will be based on an extensive field data collection programme, mathematical models and hydraulic scale models.

Introduction

The Nile Delta Coast, on the Mediterranean Sea, was found through many centuries. The existing main branches of the River Nile, i.e. Rosetta and Damietta, succeeded over the ages in forming two peninsulas or protrusions in the sea. By the end of the 19th century, erosion was observed at several important points of the coast, causing damage to the national economy, either directly or indirectly. This erosion is increased tremendously during the last decade.

The relative stability of a shoreline within a given area is dependent on the material and energy available to the shore. Forecasting the behaviour of a certain shore area requires data on the different aspects of the phenomena. But since most of the phenomena affecting a coast-line are random, they require many years of record in order for the result to be statistically significant.

Data are scarce on the different phenomena occuring on the Coast of Egypt. However, the problem areas cannot wait for many years for collecting field data. Therefore, the beach protection plan for the Northern Coast of Egypt is divided into two parts, viz, the short term plan and the long term plan.

The purpose of this paper is to explain the different technical aspects of these two plans and what has been accomplished.

Description of the Problem

The present Delta region, as shown in Fig.(1) has been created by the continuous discharge of large quantities of sediment into the Mediterranean by the Nile during thousands of years. In the course of time the supply of sediment by the Nile exceeded the losses due to wave and current action, resulting in a continuous advance of the shoreline towards the sea. This process continued until sometime in the last century, when it seemed to be reversed. Around the year 1900, the loss of land from Damietta and Rosetta peninsulas was observed. Figs.(2),(3) show the historical changes recorded at both these two locations. Between 1998 and 1954, the Rosetta peninsula receeded about 1.7 km., whilst between 1902 and 1940 the Damietta peninsula receeded about 1.8 km.

The problem has not attracted the proper attention until it started to affect the National economy and the welfare of the people living on the coast. Erosion attacked the beach summer resorts, waves flooded villages on the coast, estuaries blocked, fisheries are deteriorating and danger existed of severe salt water intrusion. The annual loss was estimated in 1970 to be about six million Egyptian Pounds (about $\$ 15 \times 10^6$).

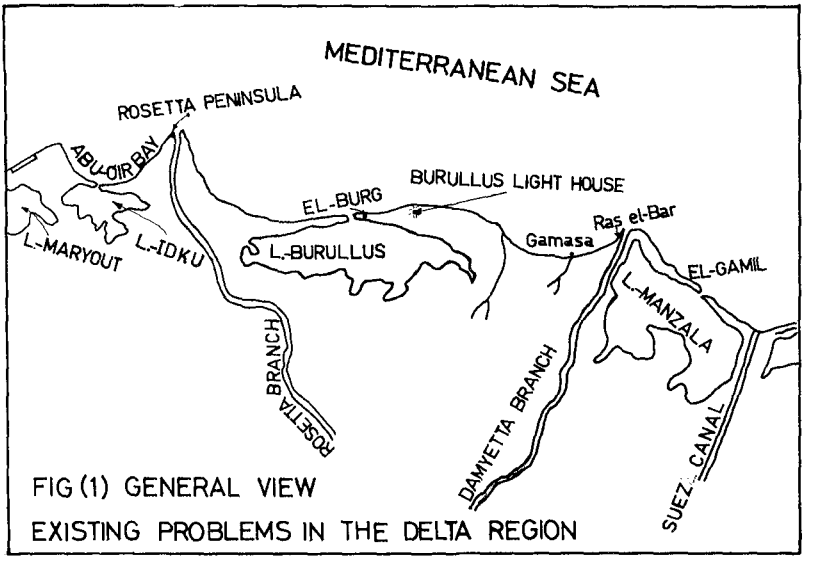

FIG (1) GENERAL VIEW
EXISTING PROBLEMS IN THE DELTA REGION

In 1964, the Suez Canal Research Centre, by a contract from the Ministry of Scientific Research, completed the first systematic study both in the field and laboratory about Lake Menzala exit.(1) The exit was migrating to the east at a fast rate, at the same time it is blocked for fishermen a sizable portion of the year. A short groin on the east side and stone pitching to the east side of the exit have been recommended. However, it was not executed due to financial difficulties.

Then the Suez Canal Research Centre carried out a thorough field and laboratory study, in 1965, 1966 by a contract with the Ports and Lighthouses Administration, for the New Damietta Harbour(2). The Ras-El-Bar area, east of the Damietta branch of the Nile, was covered in this study. The study included wave and current recordings, hindcasting of sea waves, water level variations, littoral current, beach profile changes and borings.

During the same years, the Ministry of Irrigation Experiment Station carried out a laboratory test for Lake Burullos exit(3) and a long groin on the west side was recommended to keep the exit open all over the year.

Until 1968, the interests of the beach protection were scattered around concerned Ministries and Departments, but the

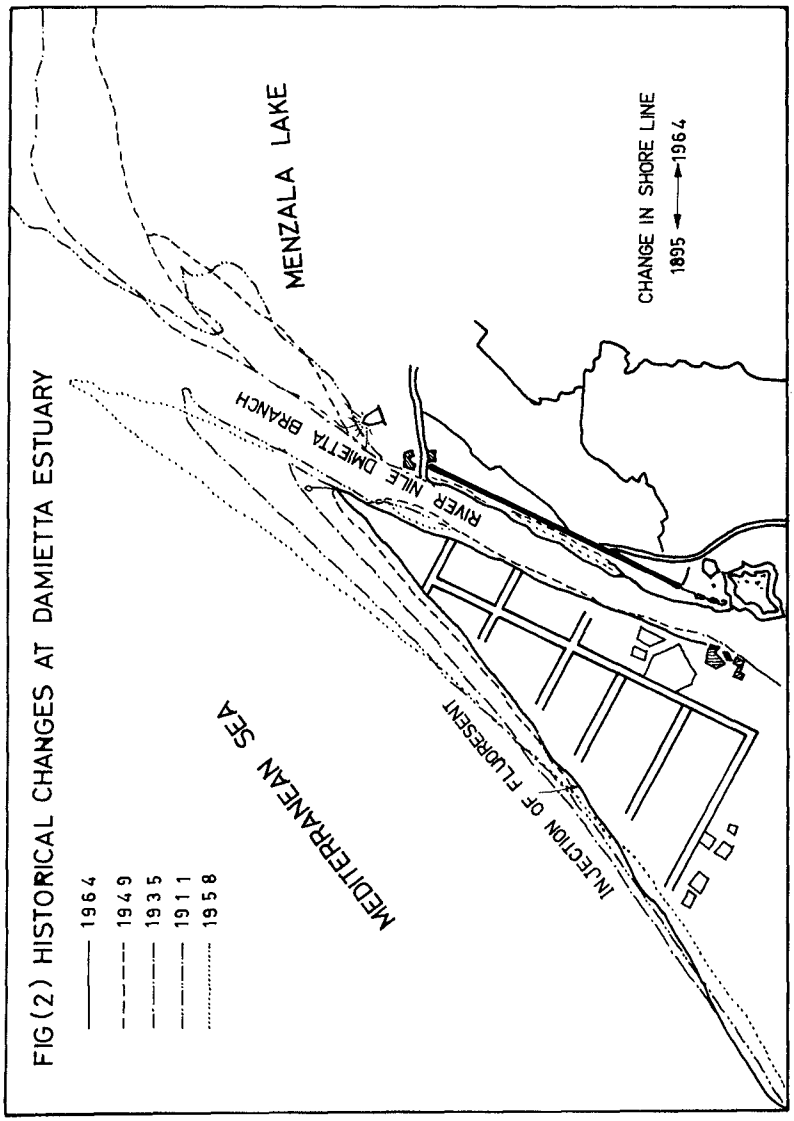
FIG(2) HISTORICAL CHANGES AT DAMIETTA ESTUARY
1964
1949
1935
1911
1958
MEDITERRANEAN SEA
MENZALA LAKE
RIVER NILE DMIETTA BRANCH
INJECTION OF FLUORESENT
CHANGE IN SHORE LINE
1895 ⟵ ⟶ 1964

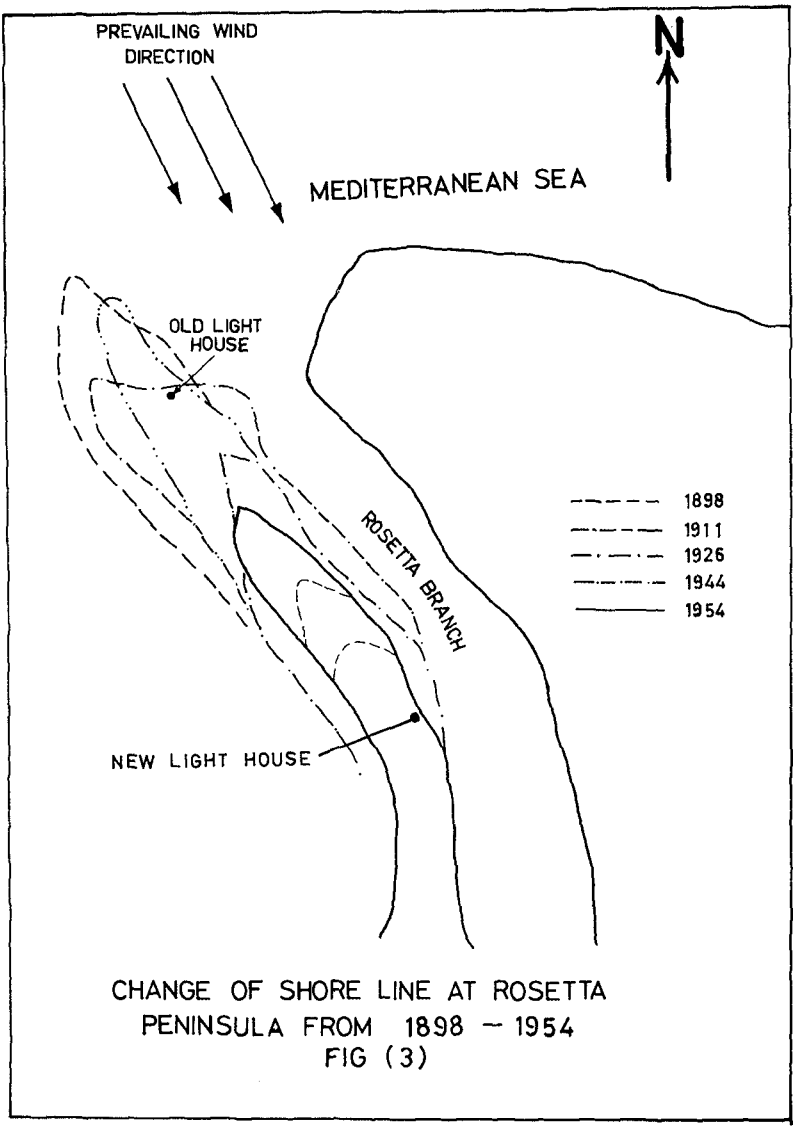

CHANGE OF SHORE LINE AT ROSETTA PENINSULA FROM 1898 – 1954
FIG (3)

whole beach protection problem did not take any serious consideration. But in 1968, the Beach Protection Board of Egypt was reformed and immediately it started the beach protection plan of the Northern coast. This plan is divided intc two parts, viz, the short term plan and the long term plan.

The Short Term Plan

For the areas that cannot wait for the extensive long term study, a one year study programme was planned and executed in certain areas, amomng which the following examples are thosem :

1. Ras-El-Bar and the Damietta Estuary.
2. Burullos Lake Exit.
3. Idku Lake Exit.

The study plan included measurements of wave heights using the O.S.P.O.S. (Van Essen, Holland) and the Ultrasonic (Sogreah) Wave Recorders. Puddle Wheel and OTT Current Meters were used to measure the currents. Tide gauges were used to record the continuous variation of the water levels. Topographic and hydrographic maps were prepared. Meteorological data were recorded and waves hindcasted from the synoptic weather charts. Fluorescent tracer experiments were carried out to determine mainly the direction of the littoral drift and its magnitude whenever possible.

Then remedial measures were suggested, designed and executed in the danger areas. A summary for each location is given in the following :

1. (a) Ras-El-Bar Summer Resort

The beach of Ras-El-Bar is shown in Fig.(4). The beach extends west of the Damietta estuary to a length of about 4.0 km. It has a direction approximately NE to SW. The following data were concluded from the fast study programmes :

a - Wind and Waves. The predominant wind direction comes somewhere between the NW and WNW directions. The wind rose at the Ras-El-Bar beach is shown in Fig.(5). Most of the storms occur in the winter season and they mostly have the same direction as the predominant wind.

The waves were recorded a good part of the years 1964 and 1965. When the wave gauges were not in operation for a reason or another, hindcasting from the weather charts were carried out. The characteristics of the recorded waves are :

Maximum recorded wave height	=	3.95 meters
Maximum recorded wave period	=	9.30 sec.
Significant wave height	=	1.56 meters
Significant wave period	=	7.5 sec.

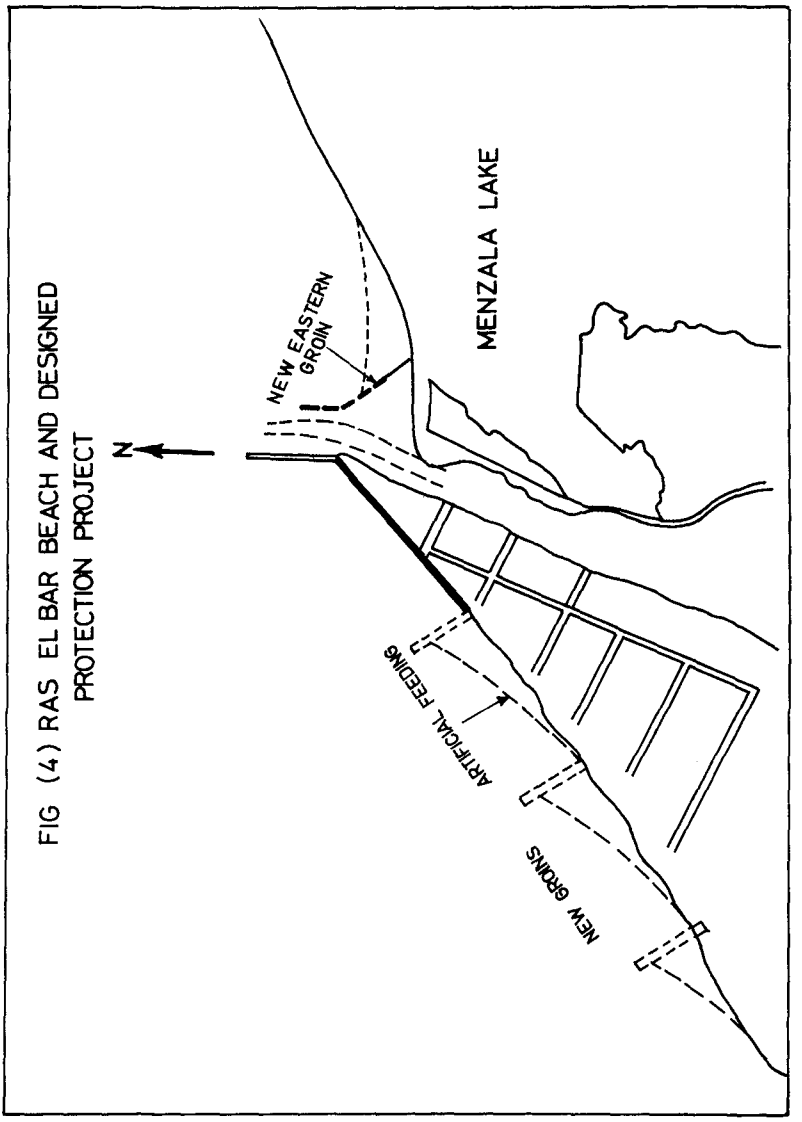

FIG (4) RAS EL BAR BEACH AND DESIGNED PROTECTION PROJECT

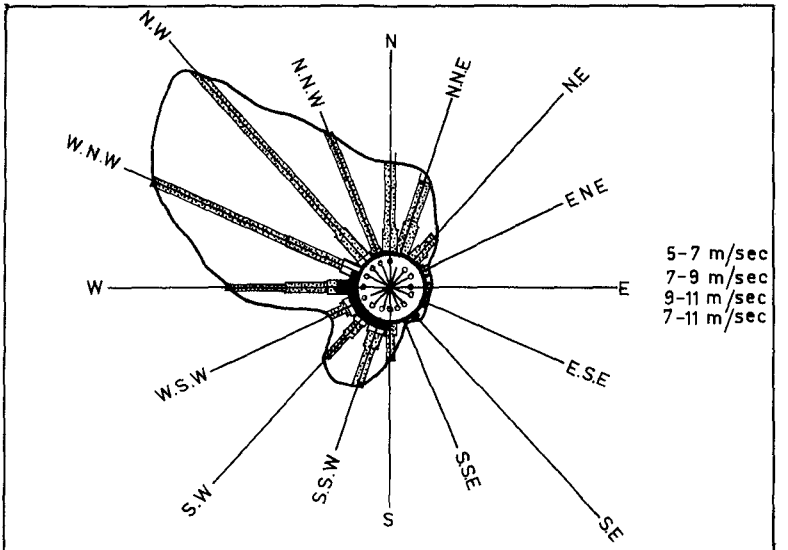

FIG (5) WIND ROSE AT RAS EL-BAR

b - Littoral Characteristics. Fig.(6) gives the wave energy rose. The littoral drift was estimated using Caldwell's formula[4]. Simultaneously some studies with fluorescent tracers[5] showed that the littoral drift to be from SW to NE.. Also, there are some indications that the sediment motion is concentrated in the breaker zone and no exchange of sediment occurs between the off-shore, on-shore areas.

c - Sediment Characteristics. The sediment constituting the beach is formed of silty sand with d_{50} = 0.12. The grain size increases as the estuary is approached from the west side.

d - Tides. Tidal variations in this part of the Mediterranean are not of a significant value. They are of the same order of magnitude as the wind set-up. The tidal range is about 30 cm. The maximum rise in the water level due to all the factors was found to be 1.00 m above datum, the datum being the lowest low water level.

e - Soundins. Several soundings were carried out to determine the characteristics of the soil layers.

Based on the above studies, groins and artificial feeding to build the eroded beach were chosen as remedial measures. Fig.(4) shows the plan of the new project. The

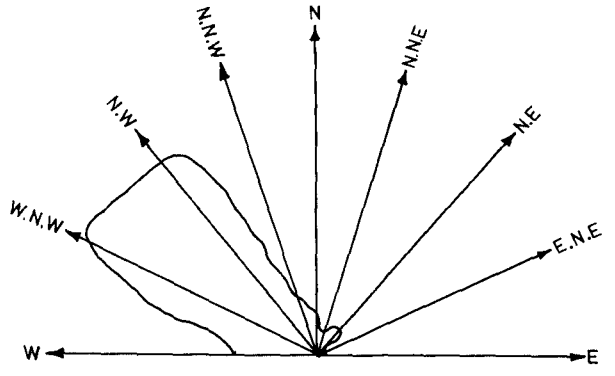

FIG (6)ENERGY ($H^2.T$) CONTAINED IN WAVES ADVANCING IN THE DIFFERENT DIRECTIONS AT RAS EL-BAR

part near the existing groin on the estuary was protected to a length of 400.0 meters by a sea wall. The first of the new groins will start immediately after the sea wall. Three groins are planned for this year as an experimental stage, before covering the whole beach with groins. The distance between the groins is taken 350 m. The groins are extending 120 m in the sea and 30.0 m as a tie to the land. A representative cross-section of the groin is shown in Fig.(7). The seaward end of the groins are protected by heavy hollow squares. Artificial feeding of coarse sand will be supplied from a nearby quarry and dumped between the groins and to the west of westward groins. These groins may be sufficient to preserve the beach, however, some periodical artificial feeding might be needed after the storm season every year.

(b) Damietta Estuary

Before 1964, which is the year during which the High Dam started preventing the sediment being carried out by the Nile, the estuary used to be open to navigation. After that it is changed into a tidal inlet with a very small tidal prism.

The field studies carried out by the Suez Canal Research Centre for the Ministry of Scientific Research(6)

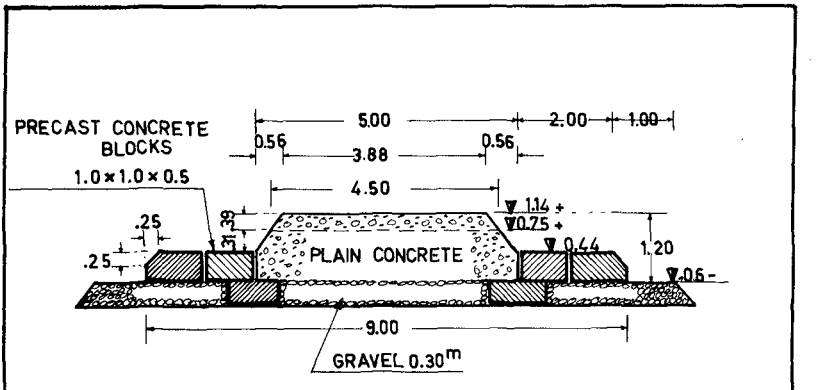

FIG (7) CROSS SECTION OF RAS EL-BAR GROIN

indicated the changes shown on Fig.(8). These cross-sections were sounded after completely dredging the inlet for navigation. Field indications and calculations of the stability of the inlet indicated that the stable area of the exit is about 100 m distributed over a wide section. Thus, no depth is left for safe navigation of fishing boats.

Model experiments by the Suez Canal indicated that the inlet can best be protected by a groin built on the eastern side. This groin starts just a little west of the nodal point, formed by the diffracted waves, and projects out in the direction of the tip of the existing groin as shown in Fig.(9). Pitching of the eastern side of the inlet might prove necessary, also some minor periodical dredging after some time.

2. Burullos Lake Exit

The situation in Burullos Lake Exit is quite different from that of Damietta estuary. Burullos Lake is a big lake receiving the drainage water from almost all the middle part of the Nile Delta. The people of El-Borg, just east of the exit, earn their living from fishing. When the exit closes up for navigation during storms, and it is not kept open by dredging, fish will not go in and out and the fishing boats cannot pass. At the same time the beach is eroding tremend-

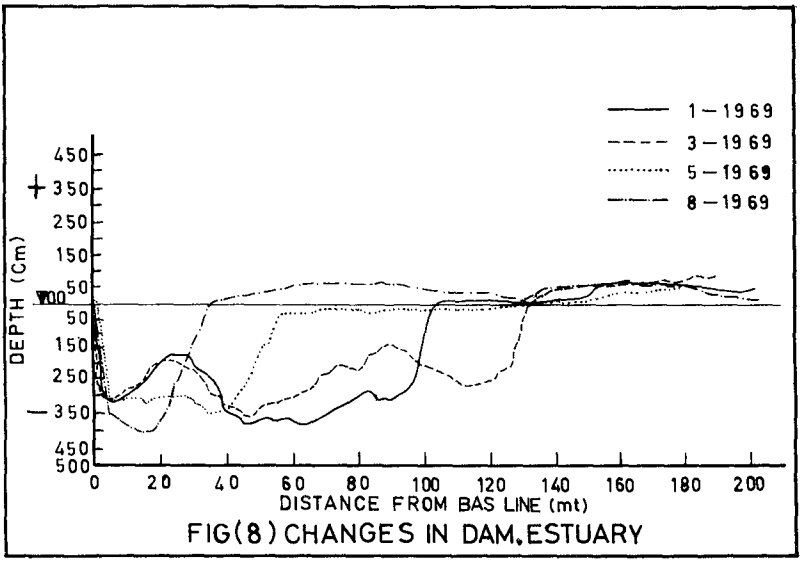

FIG(8) CHANGES IN DAM. ESTUARY

ously fast to such an extent that the village of El-Borg is said to be transferred about 2.0 km to the south during the last century. Now the sea forms the northern border of the village. Fig. (9) shows the situation at this area. During the fourties, it was found necessary to build a seawall north of ths village with some short groins to preserve the beach. However, the groins were too short to be effective but ths village was protected from the attack of the sea.

A short study was carried out by the Suez Canal Research Centre in 1969 for the Ministry of Scisntific Research[7], to determine the necessary information on which a fast temporary measure can be taken to keep the exit open.

This study showed that the littoral drift is going predominantly from the west to the east. It also showed that the current in the exit is not strong snough to give the required depth and width for navigation and safe fish migrations. Sediment samples were collected which showed distinctly that the sediment in this area is coarser than Ras-El-Bar.

Based on the above studies a groin was proposed and executed west of the exit, as shown in Fig.(9). The groin starts west of the exit and extends in a direction 15^{0} west of north. The total groin length is planned to be 200 m in the sea and

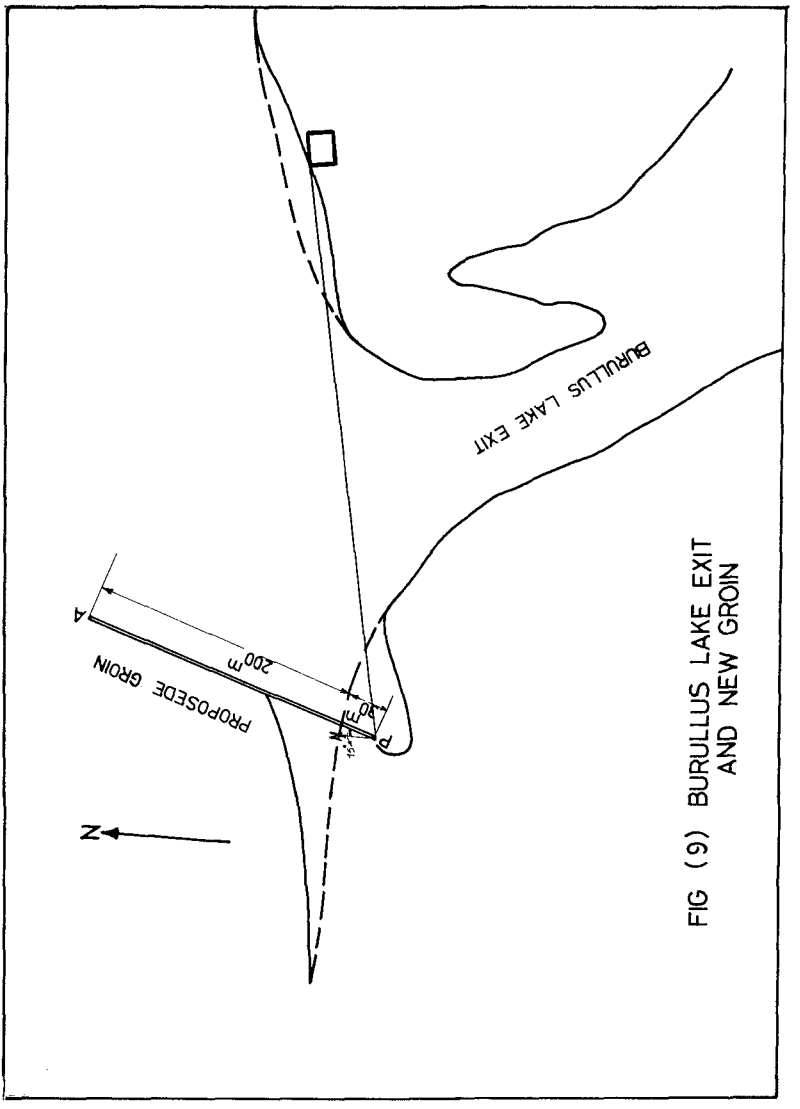

FIG (9) BURULLUS LAKE EXIT AND NEW GROIN

20 m as a tie to the land.

Execution started April 1971. By the end of 1971, 130 m were executed in the sea and it was found that it is necessary to extend the shore tie to about 40.0 m. The executed part of this groin proved to be a success. The beach west of the groin started building up. By the end of 1971, about 40 m of beach was gained. A navigable channel was opened by the flowing water, without any dredging, with its depth reaching about 2.5o m allowing a fair size of fishing boat to go in and out. The groin will be completed to its planned length this year. Fig.(10) shows a representative cross-section of the groin.

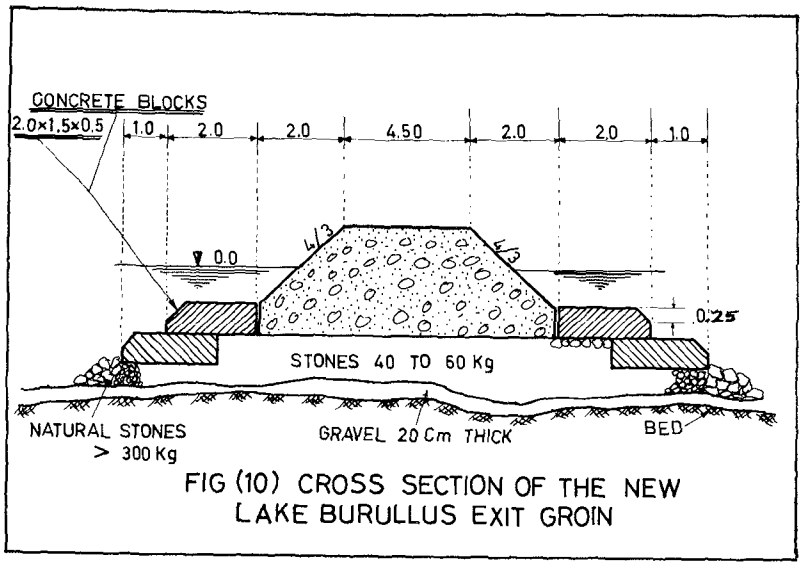

FIG (10) CROSS SECTION OF THE NEW LAKE BURULLUS EXIT GROIN

3. Idku Lake Exit

The village of El-Maadia is situated directly west of the exit. The problem there started as a fishing problem.

The exit used to be quite blocked for navigation. In the fourties the eastern groin was constructed. Sand accumulated east of it, but it did not solve the problem of clearing the exit. Then during the fifties the western groin was constructed and the eastern groin extended inwardly in the exit. The waves entering the exit obliquely are reflected on the eastern groin and hit the shore south of the western groin causing a big belly in the exit, and started attacking the village houses and destroy them. Moreover, the village level was quite low, therefore during the storms the village is almost completely flooded. Sand accumulated also directly west of the western groin. Idku lake is a medium size lake which receives the drainage water of the lands west of the Nile Delta. The outward flow is quite heavy. Thus with the two groins east and west of the exit, it can keep a good navigation channel for fishing boats. However, they might need a little extention. But the village have to be protected from the high water and the fast erosion that is taking place in front of it.

A short field study programme was carried out also by the Suez Canal Research Centre for the Ministry of Scientific Research[8], which revealed most of the facts discussed. It revealed also that the littoral drift in this area is sometimes to the west and sometimes to the east. Hydrographic and topographic surveys were carried out. Current measurements in the exit and on the beach were made. Water level variations were recorded and soil characteristics studied.

The above studies allowed the planning of the project to give immediate protection for the area. The general plan of the project is shown skematically on Fig.(11). Execution started in April 1971 and was completed early this year.

In all the above areas, records are going to be made continuously on the effect of such structures on the beach, at the same time testing the durability of the tried types of structures. This will help in the long period studies as field experiments for the overall protection project of the Delta.

The Long Term Plan

The establishment of satisfactory solutions for the various problems on the Delta coasts require full knowledge of the following three main groups of factors :

1. Historic development of the Delta shores
2. Present state of the Delta shores
3. Forces acting on the Delta shores

With regard to the historic development of the Delta shores, the present stats of knowledge indicates that it has been formed by the continuous discharge of large quantities of sediments into

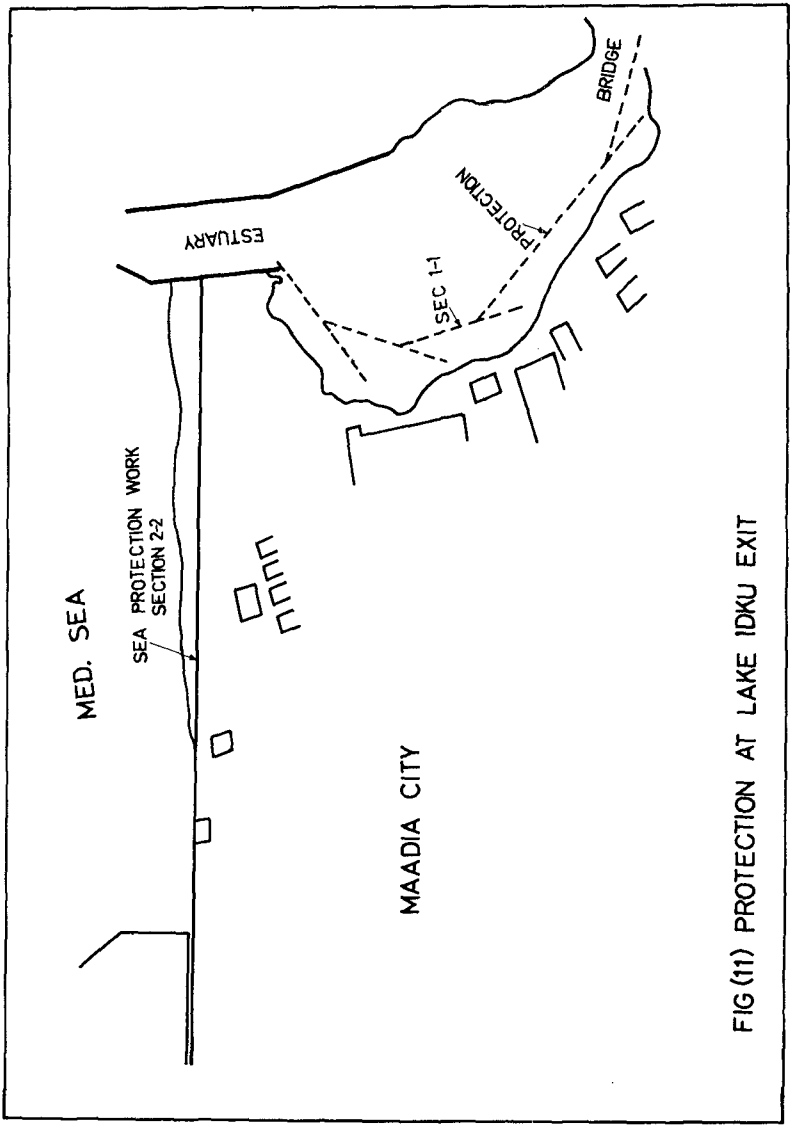

FIG (11) PROTECTION AT LAKE IDKU EXIT

the Mediterranean by the River Nile during thousands of years. The positive instability of these shores, causing accretion, seemed somehow to be reversed to negative instability causing erosion. What happened in the different phenomena involved in causing that change represents the first challenge to the shore protection experts in Egypt for the next few years. Whether it is regulating structures on the river Nile that caused decreased amount of sediments, or some cyclic changes of the meteorology of the Mediterranean Sea, or some changes in the climatology of the Nile origin in Abyssinia, that remains to be completely studied.

The construction of the Aswan High Dam might have changed the entire hydraulic regime of the Delta. This may cause difficulty in using the presently collected data in hindcasting what might had happened in the past and again what may occur in the future. This will need a careful and extremely thorough study of the existing situation and of any changes that take place. Therefore, a complete description of the Delta shores, from Alexandria to Port Said, should be completed and followed up as soon as possible.

This forms the base of planning for the long term study. The required description of the Delta shores consists of the following three groups of information :

i - Geographical, geological and geomorphological description

ii - Description of the meteorological conditions

iii - Description of the hydraulic conditions of the sea area, river mouths and the Lake outlets, including the characteristics and movements of sediments

The long term plan started in the middle of 1971 and the project personnel started collecting and analysing the following data :

A. Topographic work

1. Detailed topographic maps
2. Geological, lithological and geomorphological data
3. 83 profiles seaward to 6.0 m water depth and landward from the coast lines have been carried out. This will be repeated yearly to follow up the changes in the beach.

B. Hydraulic data

1. Water level variations along the coast and in the Lakes and the relation between them
2. Characteristics of the sea and lake water and their variations

3. Lake exits discharge measurements
4. Current measurements in the sea
5. Wave measurements, forecasting and hindcasting
6. Littoral drift measurements using radioactive or fluorescent tracers and other means
7. Model experiments for special areas

C. Meteorological Observations

D. Soil Samples

This includes surface soil samples, deep and shallow borings both on land and in the sea.

The United Nations Special Fund assisted the project by an amount of about £ 1.000.000 in the form of special equipment, some experts and some fellowships for training some of the project personnel abroad.

The first phase of this project is planned to be covered in about 3 years, ending in 1974. By that time the Institute of Coastal Studies and Protection is planned to be in full operation .

Conclusion

From the above discussions and presentation, it can be concluded that many studies are needed in order to protect the Nile Delta coast. The studies in progress might prove to be an opening to a diversity of some more studies both applied and academic. However, the short term plan is obviously needed to protect the dangerously attacked areas, until the final long term studies are ready to be applied. Also they are needed as full-scale field experiments from which data can be used in further protection structures along the coast.

References

1. Thabet,R.A., "Lake Menzala Exit Studies".Suez Canal Research Centre Report No. 26, 1964.
2. Mobarak,I.E., Kadib,A.A.,El-Ghamry M., "New Harbour at Damietta, Field Investigations". Suez Canal Research Centre Report No.34, 1966.
3. Diffrawy,H.A., and others,"Lake Burullos Exit",Experiment and Research Station, Barrages, Ministry of Irrigation, 1967 (In Arabic).
4. Wiegel,R.L., "Oceanographical Engineering", Prentice Hall Math.. series, 1965.

5. Kadib,A.A., "Litoral Drift at Ras-El-Bar Using Fluorescent Tracers".Suez Canal Research Centre Report No.38.

6. Kadib,A.A., "Damietta Estuary". Suez Canal Research Centre Report No.58.

7. Hilaly,N.A., "Burullos Lake Exit". Suez Canal Research Centre Report No.55.

8. Marzouk,N.A., "Lake Idku Exit". Suez Canal Research Centre Technical Report (in press).

CHAPTER 79

SYSTEMATIC STUDY OF COASTAL EROSION AND DEFENCE WORKS IN THE SOUTHWEST COAST OF INDIA

by

N.S. MONI **

ABSTRACT

The SouthWest coast of India is subjected to severe erosion due to attack by waves and tidal overflow. Through the years the problem has intensified as beach front areas have become more extensively developed and subject to greater damage from the force of the sea. More than 300 kms of the coast is subjected to severe erosion due to constant attack by waves and tidal overflow, resulting in continuous recession, loss of valuable property and affecting many aspects of its economy. The paper presents the problem at the proper perspective. It describes the various physical factors of the Southwest coast of India, namely the geomorphology, winds, waves, tides and currents, littoral drift, material characteristics, shore line and shore depth changes, effects of inlets and mudbanks. The study, evolution and development of different coastal defense works and their behaviour and effectiveness is also presented.

INTRODUCTION

The Southwest coast of India runs north - south along the Arabian Sea and extends 560 kms. This coast is characterised by a barrier strip of lowlying land between the Arabian Sea and a continuous chain of lagoons and backwaters. The coast line has helped in establishing a number of minor ports, in addition to maintaining a flourishing fishing industry. It is in this coastal strip, that the industrial, agricultural and other economic activities of this region are concentrated (Fig.1).

** Deputy Director, Coastal Engineering Division, Kerala Engineering Research Institute, Peechi, Kerala - INDIA.

It is estimated that out of the 560 km of coast line more than 300 km is subjected to erosion, due to the constant attack by waves and tidal overflow resulting in continuous recession, loss of property and affecting many aspect of the economy. Hence the problem is to stabilise the southwest coast of India in its present position by suitable protective measures after a detailed study.

PHYSICAL FACTORS

GEOMORPHOLOGY:

The Southwest coast of India is of recent age geologically, its formation dating back to the early tertiary period. Borings at Cochin show that there are deposits of alluvial material for 100 to 125m, overlying rock. It is also noticeable that the portion of the coast from Thottappalli to Quilandy (where the phenomenon ofmud banks is known to occur) is an alluvial belt backed by laterite deposits. Heavy mineral deposits ranked as world's largest and richest occur in the coastal area between Kayamkulam and Neendakara. There are forty four rivers, forty one of which flow westerly, from the mountains, to the low areas of backwaters and lagoons, near and at the coast. The average river length in 60 km. In the coastal region the rivers are generally interconnected and tidal (See Fig.1.).

TIDES AND STORM TIDES:

The mean tidal range varies from 0.9m at the south to 1.8m at the north. The tides are of the semidurinal type. The coast line is very low and coastal areas are flooded by storm tides in many sections, during the southwest monsoon. The storms raise the water level upto a meter or more at many sectors.

WAVES:

The sea is rough during the monsoon months (May to September) when the high waves with the storm surges attack the coast. The highest waves average 3.2m (highest ten percent) and the wave periods of 5 to 12 secs are observed. The direction of high waves is mostly from West during the monsoon period.

LITTORAL DRIFT:

Littoral drift is the beach material moved parallel to the coast in the near shore region of the sea caused

by waves approaching the beach at an angle. In the analysis of the coastal erosion problem, the direction, amount and character of littoral drift is of utmost importance for developing economical designs.

Direction and Quantum of Littoral Drift:

The following points are pertinent:

1) From the analysis of the developed data from charts, existing marine and coastal structures and position of headlands and embayments, it is found that the dominant direction of littoral drift in the Southwest coast of India is towards south.

2) The unimproved inlets in the region have the tendency to migrate to the southso also the sand spits at Periyar river outlet. These indicate southerly movement of drift. (Fig.7).

3) Mud banks are littoral barriers. The shore line of the most severely eroding sectors on the SouthWest coast are situated south of the general limits of migration of the two major mud banks - the Aleppey Mud-bank (now at Nirounnam) and the Narakkal mud bank. This indicates that the dominant direction of drift is towards south in these regions.

4) The curvature of the coast line of Kerala tending to form a line in the NNW - SSE direction is also conductive to form a southward drift, as the dominant waves are from due west during the monsoons.

5) So also the dominant direction of wind during the Southwest monsoon is from West and West North West, for most part of Kerala coast which aid in southerly drift.

6) The dominant direction of surface currents from April to September is from North to South on the West coast.

7) There is seasonal reversal of littoral drift all along the coast. The trend indicate southward movement during May to August (Southwest Monsoon period) and northward movement during the rest of the year.

8) Local reversal of drift due to topographical factors, inlet interferences, coastal works are also noted.

9) The quantum of gross littoral drift work out to (about) 1.25 million cubic meters per year.

CHARACTERISTICS OF BEACH MATERIAL:

Most of shores of Southwest coast of India are sandy. The average grain size of sand in these beaches ranges from fine to medium (0.15mm to 0.6mm). Adjacent to the coastal inlets it is fine sand (0.15mm)

EROSION

CAUSES OF EROSION:

A beach is in an eroding condition when more material is eroded away, than supplied. A permanent erosion is a result of a relative lack of supply of sand at the updrift end of the stretch in question. Usually there are two types of erosion namely (i) natural erosion from natural causes such as storms, tides, rise in sea level, due to tectonic upheavels etc and (ii) man made erosion. Man harnesses the rivers and bottles up their bed load. He builds breakwaters and jetties thereby, bar littoral drift, dredges huge quantities of sand and uses them for reclamation and thereby rob the coast. The building of fixed structures along the coast create excessive turbulence and increase the eroding action of waves. Both ~~cases~~ of natural erosion and man made erosion are existing in the Southwest coast of India.

The causes of severe coastal erosion in the Southwest coast of India is attributed to one or a combination of the following factors.

1) Early onslaught of the monsoon:

The southwest monsoon with its full fury enters the Indian peninsula at the Southwest Coast and this coast have to bear the brunt of the full blast of the monsoon storms with the incident high and steep waves, rise in water level, causing severe erosion and tidal overflow.

2) Geological Factors:

The Kerala shores is of subrecent to recent sediments. As a result, the coast is still in an unconsolidated stage and is yet to reach equilibrium conditions.

3) Level of Backshore and steepness of foreshore and inshore:

The back shore level is low (less than 1.5 meters above MSL) in many places causing severe tidal overflow during storms and during the monsoon season. The foreshore and inshore are comparatively very steep.

4) Mud Banks:

The mudbanks present along this coast are decisively influencing the shore processes and are effectively disturbing the equilibrium conditions of the coast adjacent to them, causing very severe erosion on its downdrift side. (eg. Purakkad, Chellanam).

HISTORICAL CHANGES:

Historical investigation of old and new maps and charts reveal specific locations of permanent erosion in the coast of Kerala. Comparison surveys prepared from authentic maps available from 1850 indicate, that there is consistent retrogression of shoreline. There is a net loss of land at the rate of 2m to 5.5m per year resulting in cumulative loss of precious land year after year. (Fig.2).

SEASONAL CHANGES:

Field observations at selected reaches for the past four years have indicated that there are seasonal changes also in the beaches of Kerala. Erosion is experienced from April to September (during Southwest monsoon). After this period the beach begins to accrete. The berm crest fluctuates to more than 50m in a season. Costly construction in this zone of seasonal fluctuations must be avoided. A typical example is given in Fig.3.

NATURAL EROSION:

Natural erosion is experienced in many parts of Kerala due to severe wave action, storm surges and also due to the numerous inlets present. These inlets act as littoral barriers causing leeside erosion at its south. (eg.) Muthalapuzhi, Kayamkulam, Azhikode, Chettua Velliyancode, Kallayi, Elathur, Murat, Azhikal etc.

MAN MADE EROSION:

Erosion is also caused as a result of man made marine

constructions for the development of ports and harbours. The construction of 5 km long approach channel for the development of Cochin port, the breakwaters at Neendakara and Mopla Bay had contributed to the disturbance of equilibrium conditions of the coast on either side of it. The reaction of the beach to the coastal constructions like groin system had caused downdrift erosion in many reaches.

OFFSHORE AND FORESHORE ZONES:

The continental shelf has a gradual slope upto 10 fathoms after which there is a steep fall. The distance of 100 fathom line from the shore varies, reducing from 82 km near Calicut to 45 km near Trivandrum. The offshore bottom profiles are gentle and uniform in gradient upto 45-50 fathoms line after which the slope of 1 on 5 to 1 on 12 above LW and 1 on 25 to 1 on 40 from LW to 3-4 m depth contour.

BEACH PROFILES:

The width of backshore and steepness of the beach profiles depend on the characteristics of the waves and the beach material. The beach material is generally of fine to medium sand with coarser fractions adjacent to bluff areas. Typical eroding profiles of the beach in the different sectors are given in Fig.4 Beach profiles are steeper in the eroding zones, with the foreshore having a slope of 1 on 5 to 1 on 12 above, with flatter under water slopes. Fig. 4 (a) shows the beach profile development at Thottappalli. The material eroded from the beach is deposited offshore and does not migrate to the south fast enough to balance the deposition. Fig.4 (b) shows the development of a profile at Chellanam where the beach is protected by a seawall, deep water erosion takes place and the profiles as a whole steepens. Fig.5 shows the difference in the beach slope within and adjacent to the mudbank at Aleppey.

MUD BANKS:

The formation and behaviour of 'mud banks' is a phenomenon peculiar to the Southwest coast of India. Similar phenomenon has not been reported in any other part of the world. The mud bank may be defined as an inshore area having a special property of dampening wave action and producing regions of calm water, even during the rough monsoon season, due to the dissipation of wave

energy in the large quantity of colloidal suspension in the region. The mud banks form part of the sediment activity along the coast. The mud bank region is considered to be a 'boon' by the local populace, as these areas, which are calm during the monsoon abound in Prawns, Sardines, Mackerals and Soles. Mud Banks are known to have existed in the Southwest Coast of India from ancient times and the earliest written account of the mud bank dates as far back as 1678 and 1723. There are four well known mudbanks - one near Alleppey and two near Kozhikode. (Ref. Fig.1).

Mud Banks affect the coastal processes in the following ways:

1) Traps the littoral material from the updrift side and there by prevent its down coast movement.

2) Causes accretion within the mudbank area. A typical profile showing the accretion of beach in the mud bank area is given in Fig.6.

3) Causes refraction and diffraction of waves on its sides.

It must be mentioned that the mud banks are decisively disturbing the equilibrium conditions of the coast adjacent to them. It is noteworthy to mention the fact that coastal erosion is historically severe in the coasts adjacent to the principal mudbanks, one south of Aleppey and the other south of Cochin. (Fig.2.).

COASTAL EROSION CONTROL

MEASURES AGAINST EROSION:

In selecting the shape, size and location of protection works, the objective should be to design the work which will accomplish the desired result most economically and with full consideration of its effects on adjacent shorelines. The analysis, of the data collected and field studies will permit the selection of structures that will attain the desired objective. The cost, maintenance as well as interest on amortization of first cost must always be evaluated. The types of coastal protective works adopted are the seawall, bulkhead, rivetments, jetties, groins, breakwaters (shore connected and offshore), artificially nourished and protective beaches and sand dikes, dune stabili-

sation by wind fencing and vegetation, uses of precast blocks (like tetrapods, tribars, hollow tetrahedron, stabit, Akmon, Svee, Dolos, Stapods etc.)

EARLY COASTAL PROTECTION WORKS:

Prior to 1953, the construction of shore protection works was only on a very limited scale. Groins of dumped granite rubble were constructed at a place called Chilakoor nearly eight years ago (1890) Bunds of laterite and granite rubble masonry with a sand core were raised north of Cochin outlet sixty years ago (1910-1914 before the construction of the approach navigation channel at Cochin).

DEVELOPMENT OF PRESENT COASTAL PROTECTION WORKS:

Although the problem of coastal erosion was existing for quite a long time, protection of coasts in a systematic way was initiated in the early fifties. The early pioneering structures were necessarily experimental.

Experimental Seawall at Cochin (1954-1957).

It was in 1953, when severe erosion caused serious damages particularly near Cochin, that recognition was given, for protection of this region. An experimental granite rubble wall for 1.6 km (one mile) was constructed during 1954-1957 at Mannassery, Cochin as a prototype study. The first 0.8 km (0.5 mile) of the seawall was of dumped granite rubble and the next 0.8 km (0.5 mile) was constructed with a sand core overlaid by rubble with cement grouting in the joints. Ten groins of different length and spacings were also constructed. Out of this, one groin was constructed with precast concrete blocks (0.61 m x 0.61 m x 0.3m) as armour stones and 20 to 40 dm^3 size stones as inner core. During the monsoon of 1956, the dry rubble portion of the seawall sank considerably. Noteworthy is the fact that the groyne constructed with cement concrete blocks has withstood the wave attack better than the other groins constructed with rubble.

Experimental Groins: (1959-1960).

Experimental groin with coconut piles was tried unsuccessfully in 1959 at Puthenthodu, Cochin.

of drainage facilities for overtopped water to flow back into the sea (v) The position of the seawall being close to the water line.

Sea walls constructed in the back shore with a beach infront gave better performance than those constructed in the forward portion (within the sweep zone). Hence seawalls may be located as far landward in the backshore beyond which further recession is not to be permitted. Considering the above factors the original section of the seawall was revised and a new design was evolved in 1970. This included a filter system, backfill and armour stones of increased weight and dimension. The fig. 10 gives details of the same. This design is now being tried in critical reaches.

ARTIFICIAL NOURISHMENT:

The problem that confronts the coastal engineer is 'what is the best and most economical method of protecting a beach that receives and inadequate supply of beach material' . The problem appears to be simple in that all that is required is to establish the supply material. Hence when studying an erosion problem it is always advisable to investigate the feasibility of mechanically placing beach material on the shore in such a manner than an adequate beach, will be maintained (in addition to the other remedial measures considered). An important advantage is, that this treatment remedies directly the basic cause of most erosion problems (ie; a deficiency in natural sand supply). Thereby it benefits, rather than damages the shore beyond the immediate problem area. Also it is the one system that maintain the balance of nature and is relatively free of the undesirable features of other systems. An obvious and important consideration is the availability of suitable sand for the purpose. The basic methods of nourishment are (i) stock pilemethod which is placing the fill at one point and allowing it to function as a feeder beach (ii) direct placement method which involves placing the material along the beach and creating an adequate beach width for immediate protection (iii) continuous supply method-where a fixed or semifixed plant interoepts and by passes the littoral drift to the down drift side and (iv) offshore dumping method.

Coastal protection by artificial nourishment was conducted at Purakkad (near Alleppey) during

Inclined groins, twenty in number were constructed in the Chellanam Coast, Cochin in 1959-1960. They were found to be not as effective as the groins normal to the shore.

Experimental Seawall with Bituminous Grouting:(1959)

As an experimental measure, a seawall with bitumastic grouting was constructed for 215 m at Soudhi, Cochin. A sand core, formed with a slope of 3:1 was covered with stones and the crevices filled with bitumastic grout. This seawall could not withstand the wave attack and failed within an year after construction.

Seawall and Groin System(1959-1963).

Dumped granite seawall and groins system as per design given Fig.8 was tried from 1959 at the critically eroding region at Chellanam. Between 1959 and 1963 nearly 40 kms of the worst affected reaches were protected by this method.

The seawall and groin system, helped to protect the coastal area behind it. However the groins trapped part of the littoral transport and therefore the downdrift region was depleted of its natural supply which caused severe erosion in the lee regions. Also, since there is time reversal of littoral drift all over the Coast, both the northern and southern extremities of the sewall and groin systems were affected and they posed new problems. As a consequence, continuous extension of seawall and groin system was found necessary in several regions (Thottappalli, Purakkad, Chellanam, Vypeen etc.)

Evolution of Seawall Design (1963):

In 1963 a design of seawall of a stabler section was evolved from the available data (Fig.9) Nearly forty kms of the coast was protected by the seawall (between 1963 and 1969). The speoial good features of this design are the flatter slopes and heavier armour stones. Prototype observations and studies conducted between 1964 and 1969 indicated the following: (i) A good filter at the bottom and on the land side is necessary (ii) Proper protection at toe with heavier stones and filter is necessary (iii) Low crest elevation cause overtopping by the waves, exposing the rivetment and the land behind to scour and consequent settlement (iv) Lack

during April - 1964. The reach selected was 1.6 km (1 mile) in length (north of the seawall and groyne system) which was severely eroding at the time of experiment. The direct placement method was adopted. The sand available at the outer channel of Thottappalli spillway was conveyed to the test by 5 tons trucks and placed in the reach directly. A total quantity of 47500 cum. of sand was dumped during the two months.

Even though the experiment was inconclusive, accretion was noted in this area in November-December 1964, subsequent to beach fill operations. Hence it can be inferred that if sufficient sand is available and if it can be placed at a rate fast enough to replenish the lost material, the shore line can be preserved in a satisfactory manner by this method. But a study of the collected boring charts of indicate that the availability of suitable sand that can be economically utilised is limited.

DUNE CONTROL:

Sand dunes act as barriers against action of the normal and storm tides and also reduce the action of onshore winds. Suitable stabilisation measures should be done by the use of fences, coats of crude oil or by dune vegetation to hold the sand that might otherwise migrate. The sand dunes not only act as protective barriers but also as stockpiles to feed littoral streams. The problems of dune control resolves itself to stabilisation and maintenance of dunes where they exist and inducement and stabilisation of protective dune where they do not exist naturally.

Wind Fencing:

The purpose of wind fencing is to arrest wind blown materials on the beaches and cause their accumulation at the fence, in locations where a sandy beach exist. Sand dunes will thus be created, which will raise the beach level and offer greater protection to the coast. Wind fences had been erected at two locations for trial length of 100m each at Munambam and West Hill as an experimental measure during the end of 1968. Two types of wind fencing are constructed. The one at West Hill is constructed using split bamboo where as the other at Munambam consists of prefabricated units using G.I.sheet strips.

Dune Vegetation:

A method of stabilisation of the dune is by vegetation. An experiment for a trial length of 100 m has been initiated in January 1969 at West Hill (Kozhikode) to study the use of beach grass (which is locally available) in stabilising the dune.

GABIONS:

In certain coasts, the placing of an impermeable object may cause boundary conditions of scour, and also cause uneven settlement due to poor subsoil condition. These difficulties can be mitigated by the use of a permeable and flexible structure. Gabions can be successfully used in such cases. They are metal cases (covered with protective plastic) or of high tensile steel mesh filled by natural stones of small size which are readily available. Crates of nylon are also used. Sand filled plastic or jute bags also used. Crates of 0.25 cum made of nylon nets and filled with small sized stones were tried with limited success at one groin location near Cochin.

USE OF PRECAST UNITS, AS ARMOUR LAYER OF SEAWALL, GROINS ETC.

Precast armour units have been developed in an effort to provide adequate armour units for seawalls, groins, jetties and breakwaters where stones of required size and durability could not be economically obtained. The first of these is the now famous tetrapod. Those which are subsequently developed and being used include tribars, hollow Tetrahedron, hollow square block, Tribars, Stabit, Quadriped, Akmon, Svee, Dolos, Stapod, Pentacon, Hexalegblock, Crossblock, Trilegs, Dugon, Hexapod etc. In the Southwest coast of India, the use of precast armour units is now confined to the armour units of breakwaters. The use of Precast interlocking concrete block rivetment is now suggested. Rectangular concrete blocks had been used with success in groin.

EVALUATION

The protection of the existing coast line of Southwest coast of India and their improvement is of importance. Through a great number of years, beaches have been lost and an all out effort is being made

to stabilise the coast line. It is too early to evaluate completely the coastal processes and the overall behaviour of the treatment effeced. It is hoped that the remedial measures evolved from the systematic study will help to stabilise the shores of SouthWest coast of India in the near future.

REFERENCES

1. Gole C.V., Hira Nandini M.G. 'Shore line advance ment by seawall and groynes at Cochin' , Proceedings of Seventh Conference on Coastal Engineering, Hague, 1960.
2. Moni,N.S., Nambiar.K.K.N., 'Study of artificial nourishment at Purakkad coastal area, Kerala' , Thirtyfifth Annual Research Session of C.B.I.P., India, 1965.
3. Moni, N.S., Nambiar,K.K.N., 'A study of littoral transport along the sandy coasts of Kerala' , Thirty Sixth Annual Research Session of C.B.I.P., India, 1966.
4. Moni.N.S., Nambiar K.K.N., 'Investigation of Seasonal variations in the beaches of the Kerala coast' , Journal of Irrigation and Power, April, 1967.
5. George M.Watts, 'Field Inspection of Erosion Problems in India' , Shore and Beach, October. 1968.
6. Moni.N.S., Nambiar.K.K.N., 'A study of Coastal erosion in Kerala' , Bhagirath, Irrigation and Power quarter yearly, January 1970.
7. Moni.N.S., 'Study of Mudbanks along the Southwest coast of India' , Proceedings of Twelfth Conference on Coastal Engineering, Washington D.C., 1970.
8. Moni.N.S., et al 'Shore history of specific reaches of Kerala' , Symposium on Coastal Erosion and Protection, Kerala Engineering Research Institute, India, 1971.
9. Moni.N.S., M.J.Fernandez., 'An evaluation of studies on coastal processes and coastal protection works of Kerala' , Forty first Annual Research Session of CBIP., India, 1971.
10. Moni.N.S., Fernandez.M.J., 'Seawall design for the coast of Kerala, India' , Forty-First Annual Research Session of CBIP, India, 1971.

...

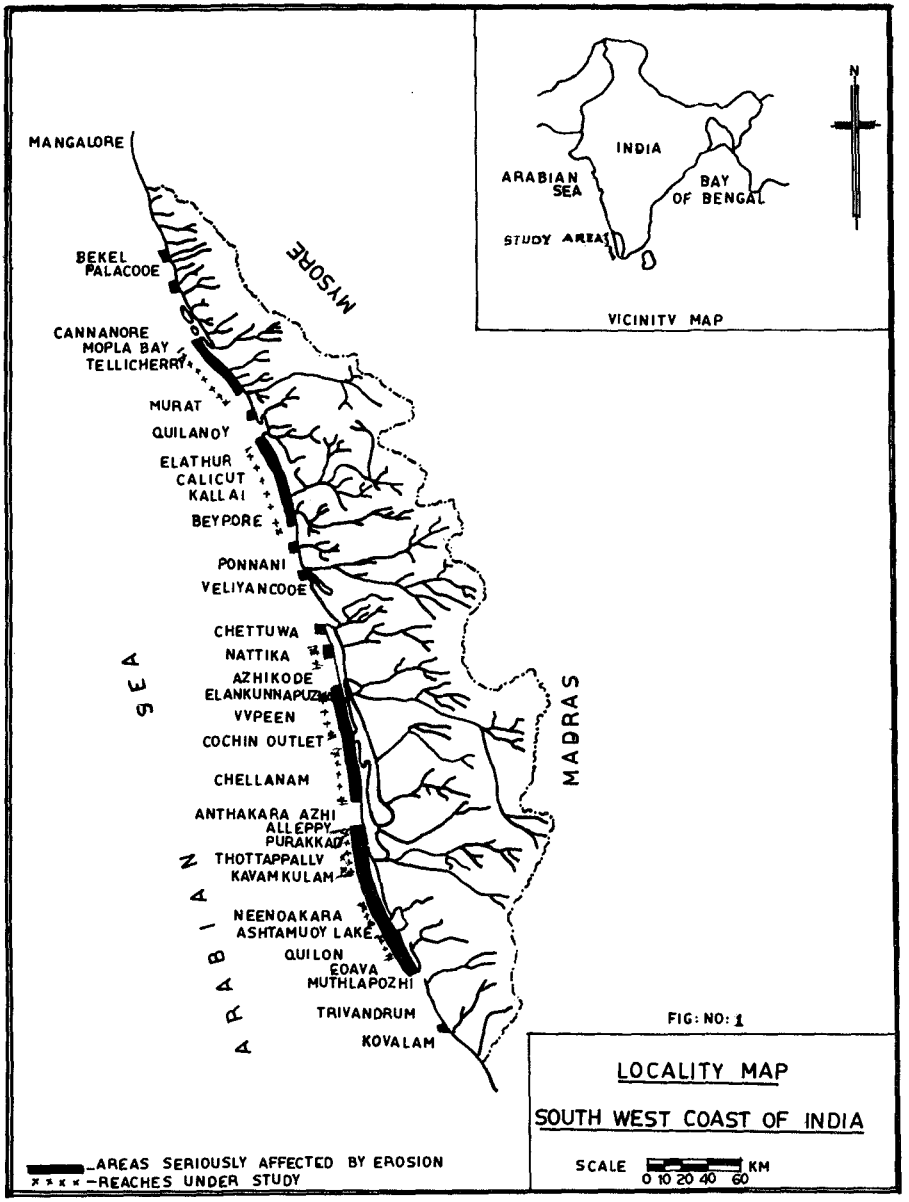
MANGALORE
BEKEL
PALACODE
CANNANORE
MOPLA BAY
TELLICHERRY
MURAT
QUILANDY
ELATHUR
CALICUT
KALLAI
BEYPORE
PONNANI
VELIYANCODE
CHETTUWA
NATTIKA
AZHIKODE
ELANKUNNAPUZ
VYPEEN
COCHIN OUTLET
CHELLANAM
ANTHAKARA AZHI
ALLEPPY
PURAKKAD
THOTTAPPALLY
KAVAMKULAM
NEENDAKARA
ASHTAMUDY LAKE
QUILON
EDAVA
MUTHLAPOZHI
TRIVANDRUM
KOVALAM
MYSORE
MADRAS
ARABIAN SEA
INDIA
BAY OF BENGAL
STUDY AREAS
N
VICINITY MAP
FIG: NO: 1
LOCALITY MAP
SOUTH WEST COAST OF INDIA
SCALE
0 10 20 40 60 KM
-AREAS SERIOUSLY AFFECTED BY EROSION
-REACHES UNDER STUDY

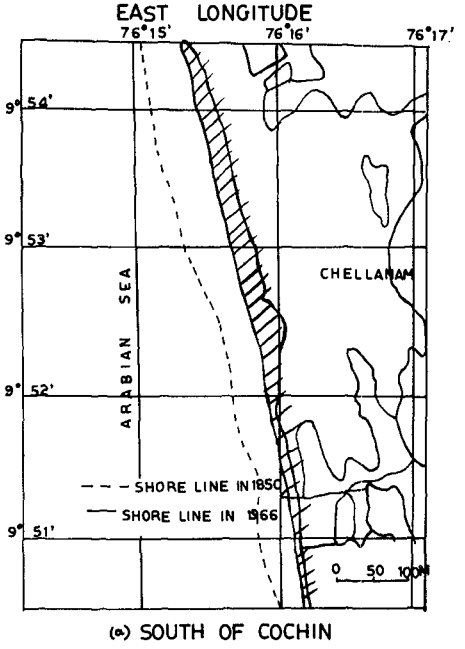

(a) SOUTH OF COCHIN

FIG:NO: 2(a)

SHORE LINE CHANGES IN SOUTH WEST COAST OF INDIA

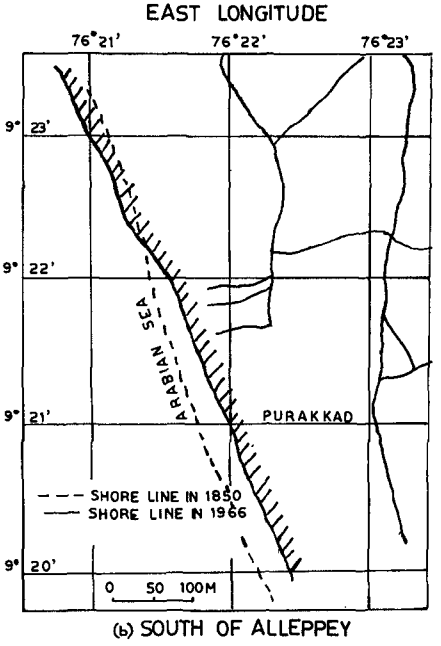

(b) SOUTH OF ALLEPPEY

FIG: NO: 2(b)

SHORE LINE CHANGES IN SOUTH WEST COAST OF INDIA

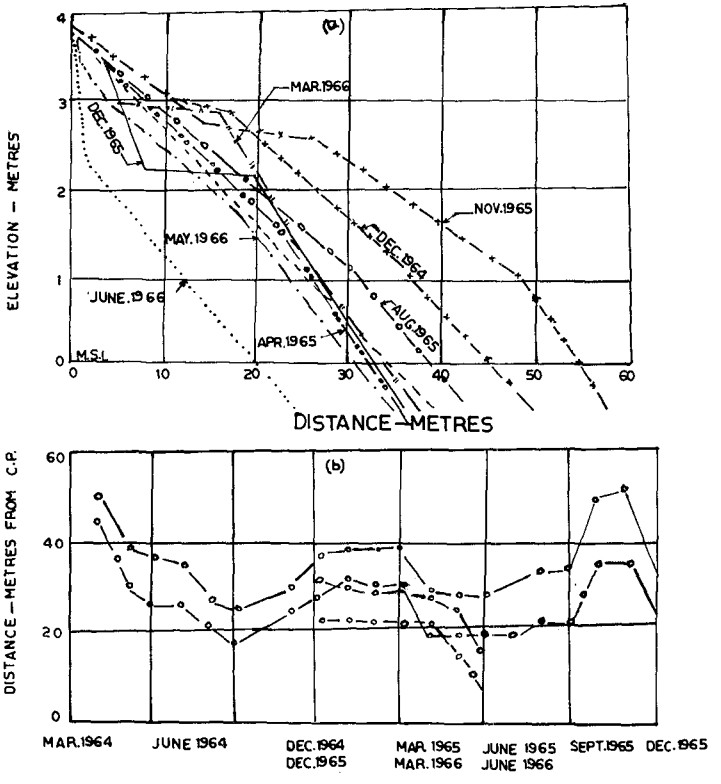

(a) PROFILE AT PURAKKAD

(b) CHANGES OF 1M AND 2M CONTOUR – PURAKKAD

FIG: NO: 3.

SEASONAL CHANGES OF BEACH PROFILE

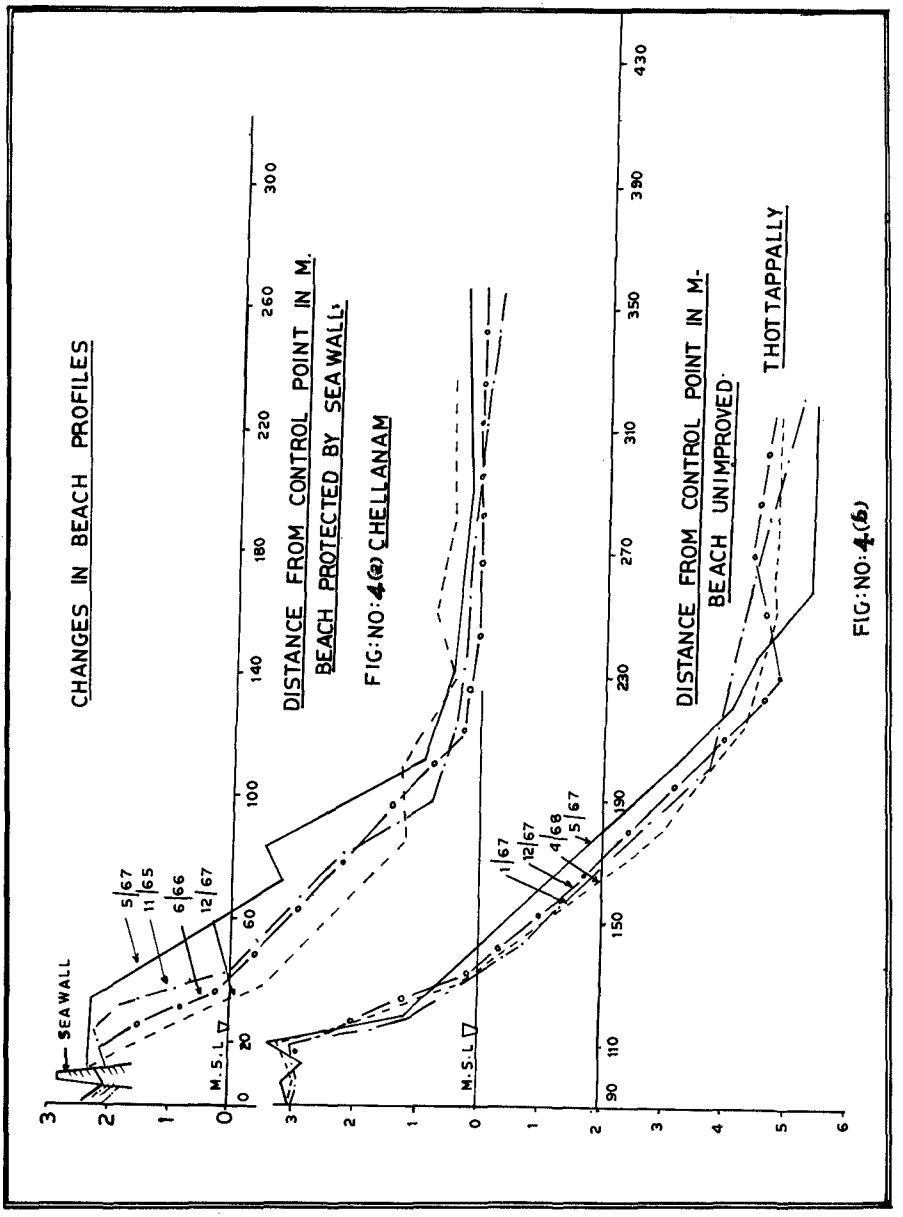
CHANGES IN BEACH PROFILES
SEAWALL
5/67
11/65
6/66
12/67
M.S.L
DISTANCE FROM CONTROL POINT IN M.
BEACH PROTECTED BY SEA WALL
FIG:NO:4(a) CHELLANAM
1/67
12/67
4/68
5/67
M.S.L
DISTANCE FROM CONTROL POINT IN M-
BEACH UNIMPROVED
THOTTAPPALLY
FIG:NO:4(b)

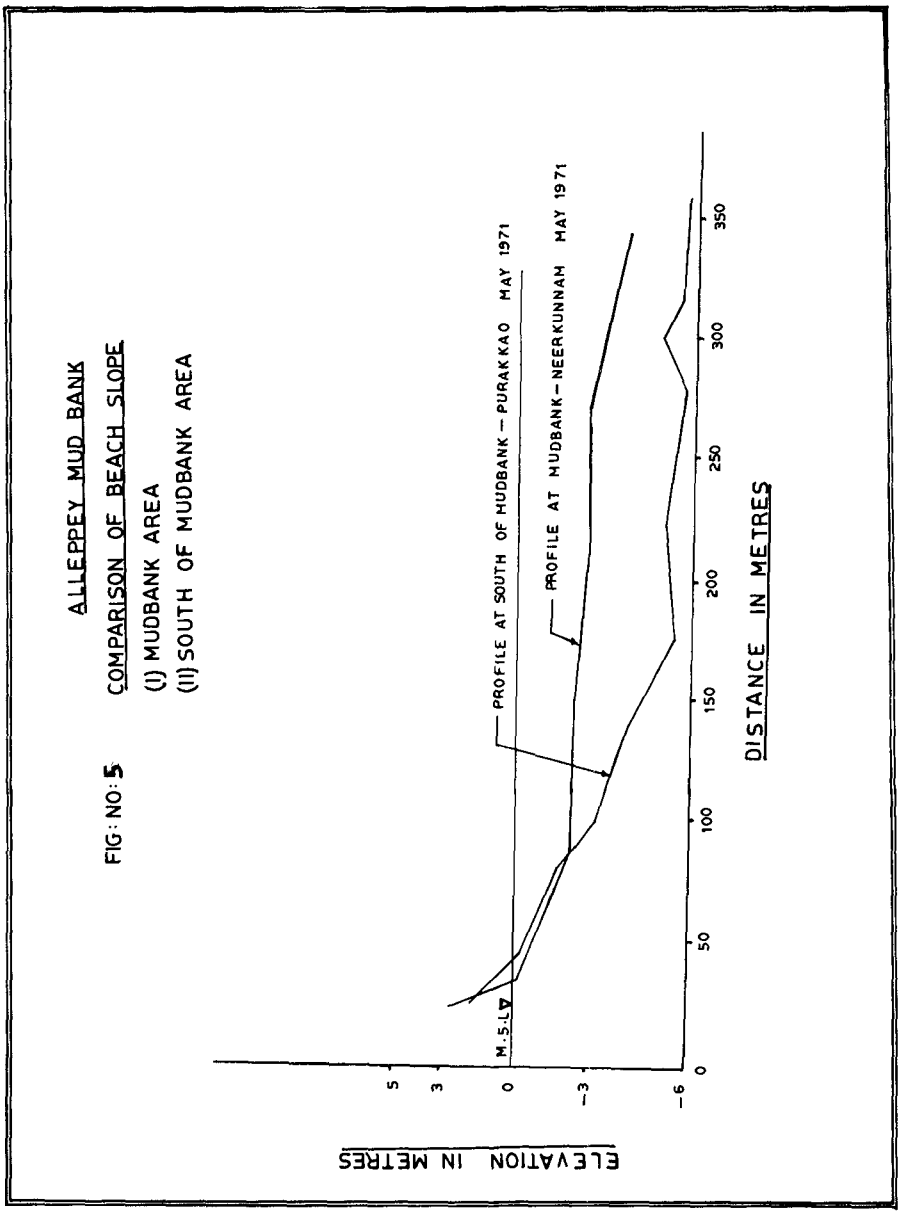
ALLEPPEY MUD BANK
COMPARISON OF BEACH SLOPE
(I) MUDBANK AREA
(II) SOUTH OF MUDBANK AREA
PROFILE AT SOUTH OF MUDBANK – PURAKKAO MAY 1971
PROFILE AT MUDBANK – NEERKUNNAM MAY 1971
M.S.L.
ELEVATION IN METRES
DISTANCE IN METRES
5
3
0
-3
-6
0
50
100
150
200
250
300
350

FIG: NO: 5

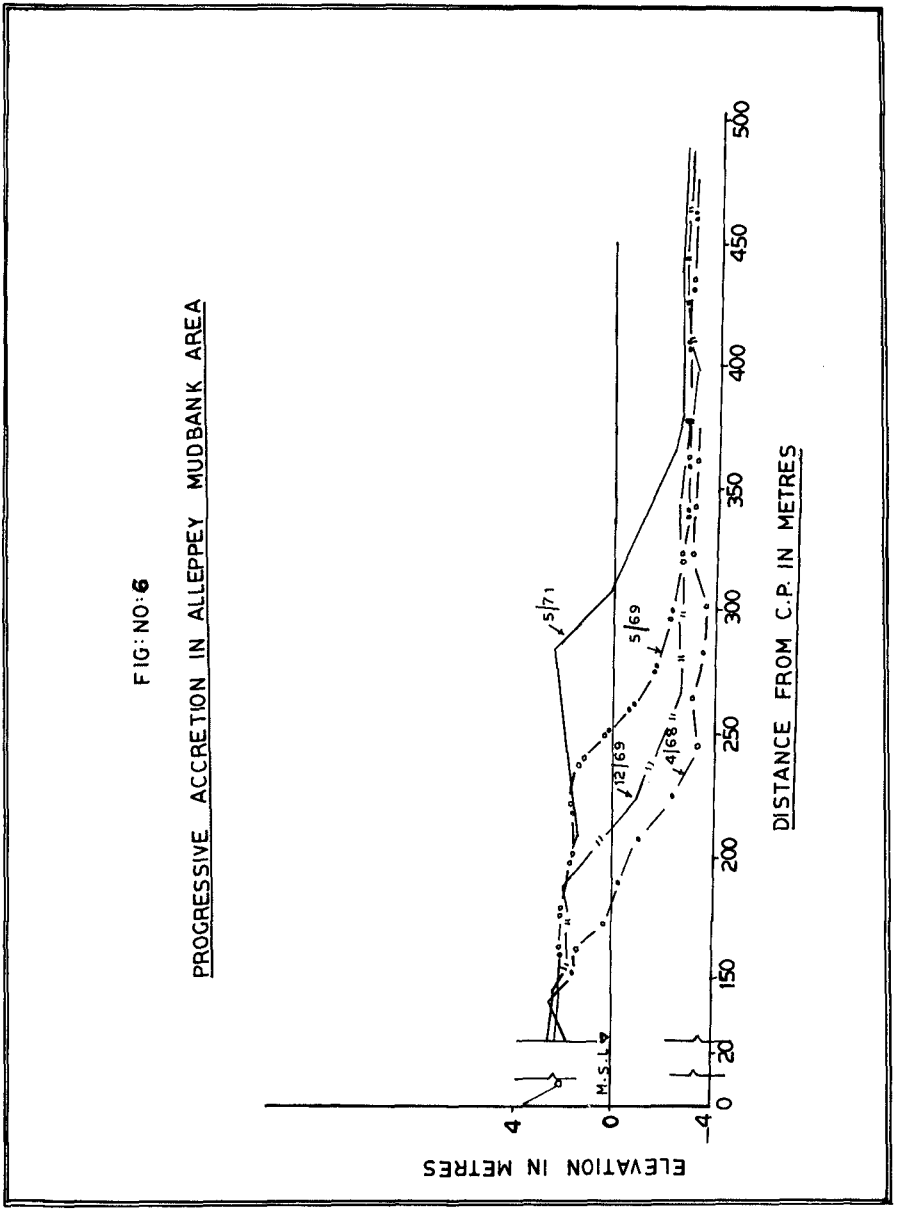
FIG: NO: 6
PROGRESSIVE ACCRETION IN ALLEPPEY MUDBANK AREA
ELEVATION IN METRES
DISTANCE FROM C.P. IN METRES
M.S.L.
5/71
5/69
12/69
4/68
4
0
-4
0
20
150
200
250
300
350
400
450
500

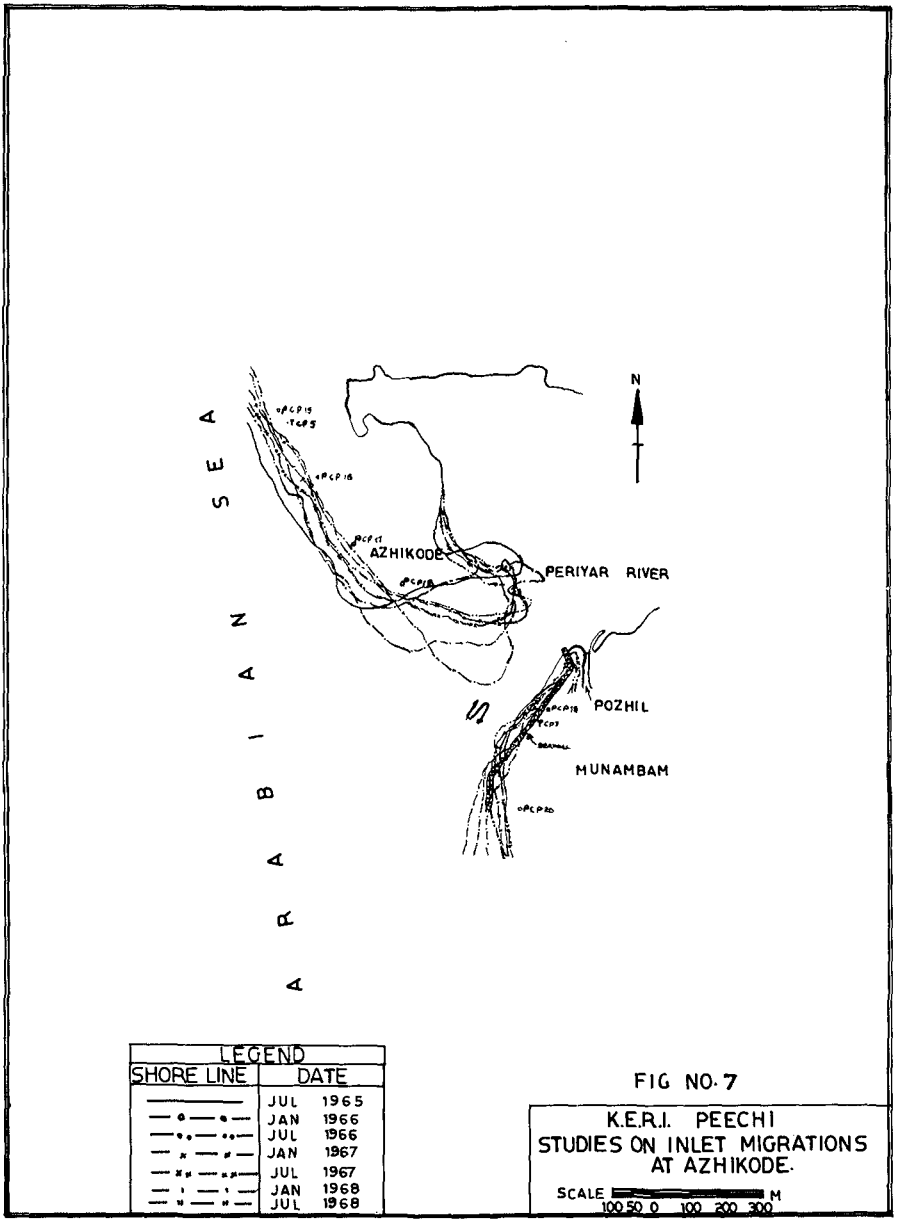
ARABIAN SEA
N
AZHIKODE
PERIYAR RIVER
POZHIL
MUNAMBAM
LEGEND
SHORE LINE
DATE
JUL 1965
JAN 1966
JUL 1966
JAN 1967
JUL 1967
JAN 1968
JUL 1968
FIG NO. 7
K.E.R.I. PEECHI
STUDIES ON INLET MIGRATIONS AT AZHIKODE.
SCALE
M
100 50 0 100 200 300

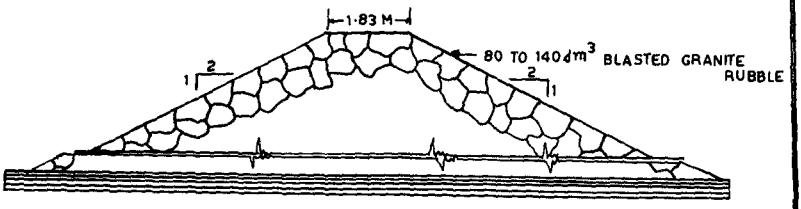

SECTION OF GROYNE

SCALE 1 0·5 0 1 2 3 4 M

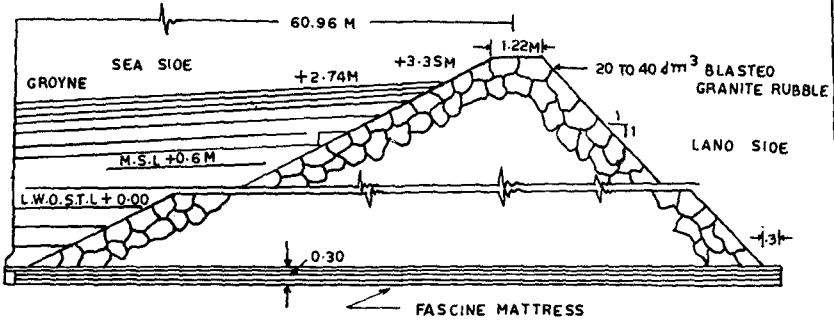

SECTION OF SEAWALL

SCALE 1 0·5 0 1 2 3 4 M

FIG:NO:8

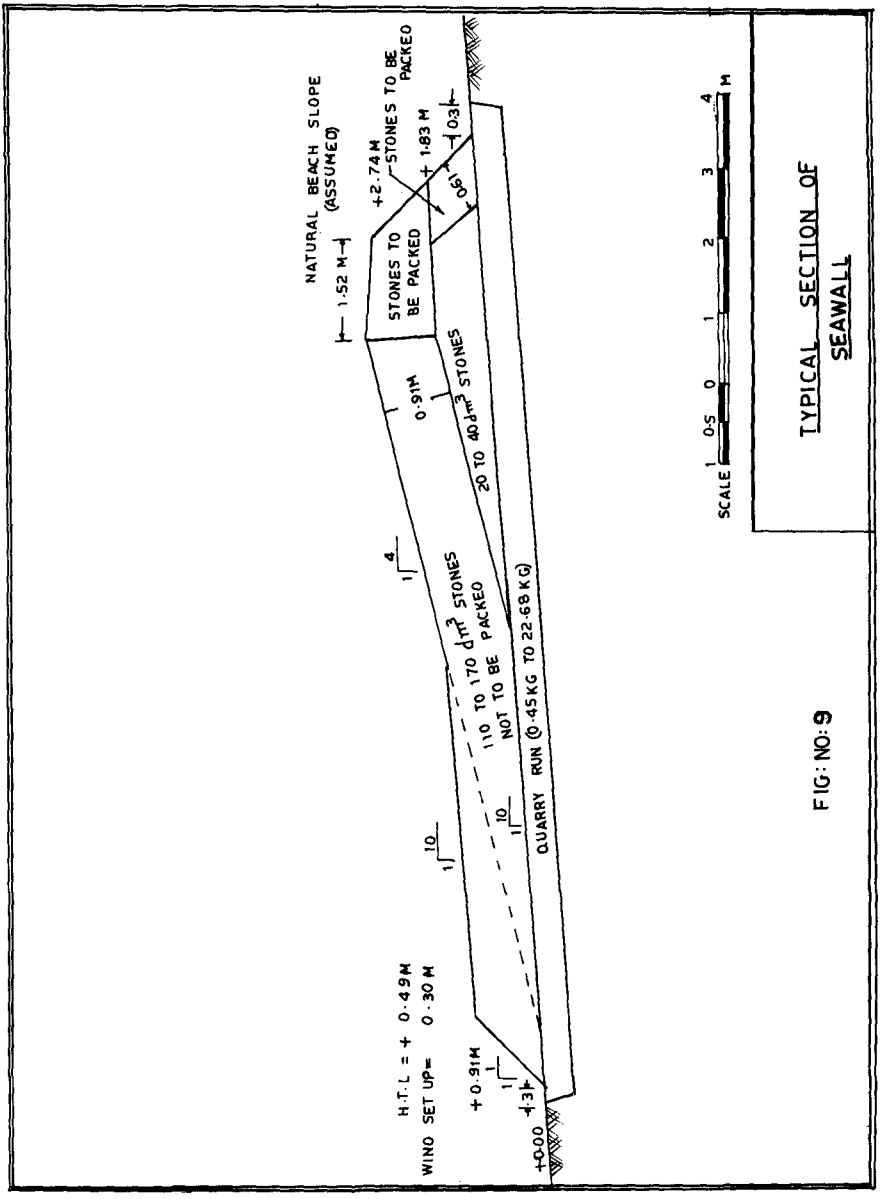
NATURAL BEACH SLOPE
(ASSUMED)
1:52 M
+2.74 M
STONES TO BE PACKED
+1.83 M
0.3
0.6
STONES TO BE PACKED
0.91M
20 TO 40 dm³ STONES
4
1
110 TO 170 dm³ STONES
NOT TO BE PACKED
10
1
10
1
QUARRY RUN (0.45 KG TO 22.68 KG)
H.T.L = + 0.49M
WIND SET UP = 0.30 M
+0.91M
1
1
+0.00
1.3
SCALE
1 0.5 0 1 2 3 4 M
TYPICAL SECTION OF SEAWALL
FIG: NO: 9

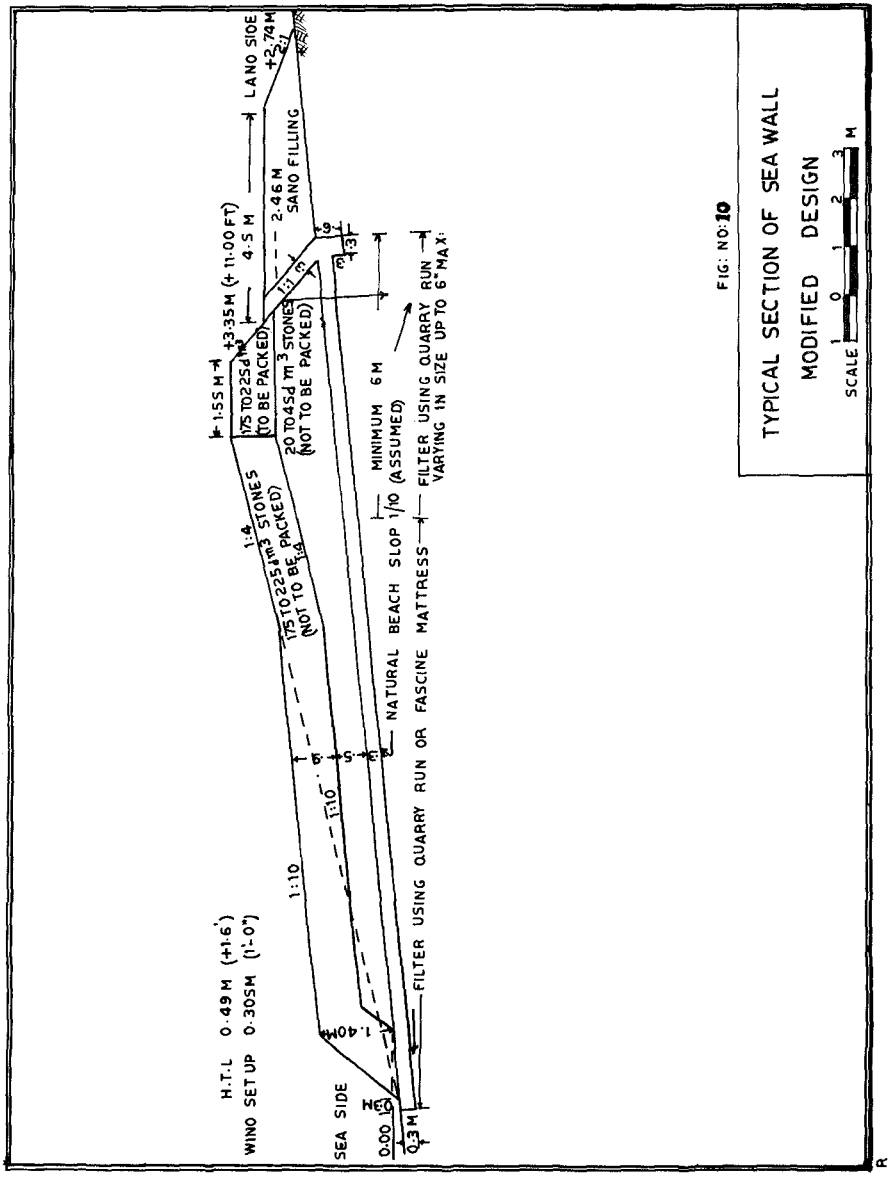
TYPICAL SECTION OF SEA WALL
MODIFIED DESIGN
SCALE 0 1 2 3 M
LAND SIDE
+2.74M
2.46 M SAND FILLING
+3.35 M (+11.00 FT)
4.5 M
1.55 M
1.75 TO 2.25 m³ STONES (TO BE PACKED)
20 TO 45 d m³ STONES (NOT TO BE PACKED)
1.75 TO 2.25 m³ STONES (NOT TO BE PACKED)
1:4
1:1
1:3
1:10
1:10
MINIMUM 6 M
NATURAL BEACH SLOP 1/10 (ASSUMED)
FILTER USING QUARRY RUN OR FASCINE MATTRESS
FILTER USING QUARRY RUN VARYING IN SIZE UP TO 6" MAX
SEA SIDE
0.00 M
0.3 M
H.T.L 0.49 M (+1.6')
WIND SET UP 0.305M (1'-0")
FIG: NO: 10

CHAPTER 80

ARTIFICIAL NOURISHMENT OF COPACABANA BEACH

By Daniel Vera-Cruz
Civil Engineer, Research Officer, Laboratório
Nacional de Engenharia Civil, Lisboa, Portugal

ABSTRACT

Results concerning the artificial nourishment of Copacabana Beach (Brazil) with sand are described. The beach, 4.2 km long, was formerly about 55 m wide. After an artificial nourishment with 3.5 million c.m. of sand, a mean width of about 140 m was reached. From that total of sand, 2.0 million c.m. were dumped offshore and the remaining amount stockpiled on the foreshore. Prototype and model results agree quite well. Comments are made on the efficacy of the offshore dumping method and recommendations concerning its use in future cases are presented.

INTRODUCTION

Different methods have been used in artificial nourishment of beaches, namely stockpiling, continuous supply and direct placement. Another method was tried in the past, the offshore dumping, which in many cases makes a large supply of beach material available at low cost, when hopper dredges are used. This is particularly true when feeding material comes from maintenance operations of harbors. Results of past experience of this method, however, were not encouraging. One can say, with J.V.HALL Jr. and George WATTS [1], that those results were negative.

The purpose of this paper is to present a practical case where the offshore dumping method was used with full success in the widening of Copacabana Beach (Brazil).

BRIEF HISTORY

Copacabana Beach is a sandy beach located in the west coast of Brazil, very near Rio de Janeiro, Fig. 1.

Its shape in plan is like a crescent, its length is around 4.2 km and its mean normal width formerly was about 55 m, Fig. 2.

For various reasons, SURSAN - Superintendência de Urbanização e Saneamento do Estado de Guanabara, Brazil, decided to widen the beach from the original mean width of 55 m to about 140 m.

The necessary studies to prove the feasibility of the project were ascribed to LNEC - Laboratório Nacional de Engenharia Civil, in Lisbon, Portugal. A field observation program was prepared and data collected along two years. The analysis of those data allowed to characterize the behavior of the beach and to explain its shape fluctuations. Based on the conclusions of that analysis, a small-scale model was designed, calibrated and run.

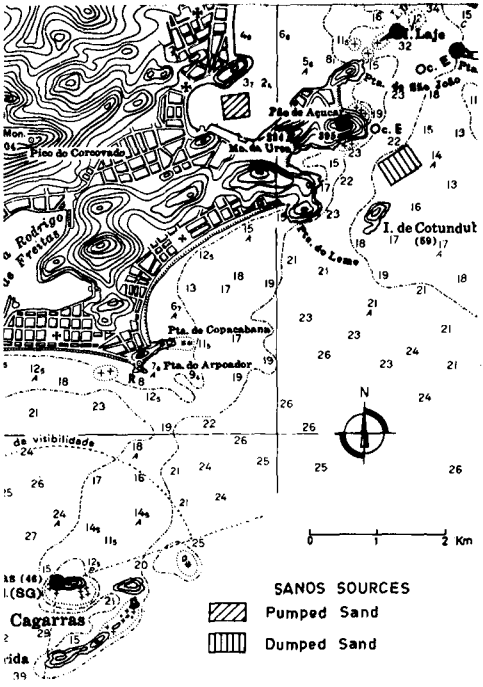

FIG. 1 - Location of Copacabana. Sources of Sand.

BEACH DATA

The field observation program included [2]:

a) Waves

Heights, periods and directions were observed twice a day. The observed values during two years allowed the definition of the local gravity wave regime as follows, summarily:

Heights: 90 % of the significant waves fall below 1.8 m and 50 % below 0.7 m; the highest significant observed height did not reach

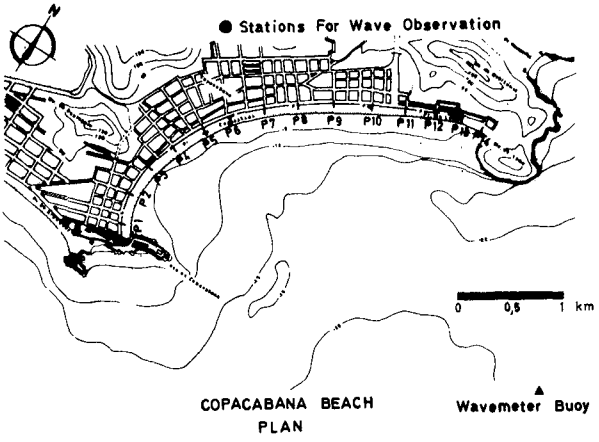

FIG. 2 Location of Surveyed Profiles

4.0 m; in 12 observations the significant height was above 3.0 m; the heights were measured at a depth around 20 m contour;

Periods: 70 % of the mean wave periods were between 9 s and 15 s and 50 % between 10 s and 14 s.

Directions: Wave directions before breaking were concentrated around S-SE. In 70 % of the observations, wave directions were between S-20°-E and S-25°-E.

b) Surveys

A general hydrographic survey in scale 1/2000 was done down to depths around 20 m. During two years 14 cross profiles (Fig. 2) of the shore were plotted every 15 days. When important changes occurred, the cross profiles were extended down to depths of about 10 m.

c) Tides

The tides are of the semi-diurnal type. The tidal ranges are of small amplitude: maximum of about 1.4 m and minimum of about 0.3 m.

d) Sand characteristics

Samples were collected once a month at the mean sea level at sites corresponding to the cross profiles alignments. A first general collecting was done at different levels from shore to offshore. Mineral analysis did not show significant variations. The sand, of which the unit weight was 2.6 gr/c.c., was fine to medium: median diameter from 180 μ to 420 μ. The prevailing median diameter at mean sea level was 300 μ to 400 μ .

FIG. 3 - Effects of Storm Waves

e) Wind

High velocity winds are not usual. Winds blowing at as much as 40 knots are very infrequent and of very short duration. Usually the maximum speed with significant frequency falls between 20 and 30 knots. Winds blow more frequently from WSW, W, WNW and ESE. This last direction is able to generate some local sea in Copacabana.

MAIN RESULTS OF DATA INTERPRETATION

The analysis of the fluctuations of the cross profiles led to the conclusion that cross movements of sand are very important and that there is not a predominant littoral drift direction. Considering the HWL the surveys revealed recession of about 30 m or more by storm waves. Relating profiles changes with wave condition, the general conclusion is that in Copacabana waves higher than 2 m tend to cause recession and that lower waves tend to rebuild the beach until the equilibrium shape is reestablished. Large recessions are recorded with one day storm duration, while it takes some weeks or even a few months to rebuild the beach.

Although recession is simultaneous all along the beach, some stretches are more vulnerable than others. In fact, the shore can in some points be completely washed out, causing the waves to bump a wall which

borders an avenue running along the beach. Fig 3 shows the beach during a storm, and one can see the waves arriving at the bordering wall along a certain stretch.

Storm waves originate sand movements at levels lower than (-10 m). At this level, depth fluctuations before and after storm sometimes reach 2 m.

THE CALIBRATION OF THE MODEL

The model was built with horizontal scale 1/300 and vertical scale 1/75. The sand was represented by crushed bakelite.

The model project was based on VALEMBOIS criterion [3]. The first stage of the calibration of the model consisted in reproducing an equilibrium shape of the beach similar to the prototype, for normal wave condition. During this stage, a few alterations were introduced in the model limits, to correct wave reflection and diffraction patterns. Such corrections derived mainly from the fact that, in order to respect wave refraction, the wave lengths were reproduced according to the vertical scale. The second stage consisted in trying to reproduce erosion in the model by storm waves. The model behavior at this stage was most satisfactory, the beach being more eroded in the model at points corresponding to the more vulnerable areas in the prototype.

The third stage consisted in, after a storm, reproducing again the normal conditions, which were expected to rebuild the beach. Again the model behavior was very satisfactory.

At this point the model was considered as calibrated and the next phase, artificial nourishment, started.

ASSUMPTIONS ON THE BEHAVIOR OF THE BEACH WHEN NOURISHED

As no predominant littoral drift existed, the cross movements of the beach being important and the general shape in plan being a crescent in any stage, this shape was considered as being the equilibrium shape for the natural agents prevailing on the beach.

According to such an assumption, if stockpiles of sand were distributed along the beach or, on the extreme case, if sand were stockpiled in a restricted area on the foreshore, the stockpiles should be acted on by the waves and the sand carried in such a way as to preserve the crescent shape of the beach. Moreover, while sand losses around the rocky arms delimiting the beach do not occur, a certain widening, depending on the sand volume stockpiled, must result.

The first runs of the model were based on such assumptions.

ARTIFICIAL NOURISHMENT IN THE MODEL

General description

Two main nourishment methods were tested: stockpiling on the foreshore, and offshore dumping. Both methods were tested either separately or jointly. When jointly applied, a mixed method results. Two different mixed methods were tested: the non-programmed method and the programmed one.

Stockpiling method

This method was used in two ways. First, in the distributed way, bakelite was stockpiled at regular time intervals at four different points more or less equidistant (3 m in the model). Simultaneously, 1 li

ter of bakelite was unloaded each 20 min in points P-3, P-6, P-9 and P-12 (Fig. 2). Second, in the concentrated way, 10 litres of bakelite were stockpiled each 20 min over the foreshore stretch between P-11 and P-12.

Offshore dumping

In this method 4 litres of bakelite were unloaded every 20 minutes along the model contour corresponding to -5 m in the prototype, taking into account that the loaded draught of the hopper to be used was ~ 6 metres.

Mixed methods

Non-programmed

In the non-programmed method both previous basic methods - stockpiling and offshore dumping - were used simultaneously, in a random way. In this way, the same beach stretch could be nourished at the same time by both methods.

Programmed

The programmed method avoided to nourish simulteaneously the same area of the beach by both methods. Stockpiles took place in points P-3, P-6, P-9 and P-12; however, those points were not fed at the same time. In fact, stockpiling took place only at two of those points each time, while offshore dumping occurred on areas far away from the areas receiving stockpiles. From time to time the method being used in a certain stretch was changed in such a way that the interference of the other method could be considered negligible.

Model study results

The model behavior confirmed the assumptions made. In fact, using the stockpiling method, either in 4 points or on a limited stretch of the foreshore, the material was carried by the waves in such a way that the final plan shape of the beach was similar to the original shape. It must be said also that the model beach cross sections agreed well with the natural beach cross sections.

The concentrated stockpiling [2] was tested with the main aim of confirming the general assumption on the beach material distribution by waves and it could be proved that, although slowly, the bakelite was carried all along the beach until final equilibrium shape was reached.

The model tests showed that the offshore dumping, although displaying more material losses and taking more time than the stockpiling, was efficient. In fact, referring to the mean widening of the beach at +1.1 m level (HWL), the necessary volume of sand to get an enlargement of 85 m would be, according to the model, as follows:

Stockpiles in four points: 2.5×10^6 c.m.
Offshore dumping : 4.0×10^6 c.m.

To reach that enlargement, it was enough to run the model for 30 hours, with the stockpiling method, and for 60 hours with offshore dumping. Later on, based on further model results and on practical considerations, a new approach was made concerning the total stockpiled volume, which was estimated at 3×10^6 c.m. With the mixed method it was expected that a volume between 3×10^6 c.m. and 4×10^6 c.m. would be enough. However, with the non-programmed mixed method a total volume of sand of 4.4×10^6 c.m. was necessary, with a model running time of 53 hours [4]. In that total volume, 2.4×10^6 c.m. were stockpiled and 2.0×10^6 c.m. were dumped. This fact was explained as resulting from an inconvenient interference of the two methods, the falling of the stockpiled sand to deep levels counteracting the climbing of the dumped

sand to high levels.

In trying to prove this explanation, the programmed mixed method was tested. The 85 m mean widening was reached stockpiling 1.5×10^6 c.m. and dumping 2.0×10^6 c.m., total of 3.5×10^6 c.m. of sand. This result is considered as a proof of the inconvenient interference of the two methods when used simultaneously in a non-programed way [5].

RECOMMENDATIONS BASED ON MODEL TESTS

Although, according to model tests results, offshore dumping proved to be efficient, those results should be accepted with caution, considering past experience. On the other hand, the fact that dumping sand was much cheaper than stockpiling was a temptation.

Weighing these and other aspects of the problem, a compromise solution was proposed by the Laboratório Nacional de Engenharia Civil: the beach nourishment should start with offshore dumping, not more than half the anticipated total volume of sand should be dumped and stockpiling should start after the dumping operation was over and maintained until the desired final width was reached.

The sand to be used should fulfill specifications particularly as regards mean diameter and percentage of very fine grains. The mean diameter should be not less than that on the natural beach sand and the maximum percentage of fine grains was established according to the size distribution of the natural beach sand.

On this basis, a total volume of sand was estimated around $3.5 \times \times 10^6$ c.m. to reach the final width.

FIELD OPERATIONS PROGRAM

General

The Laboratory recommendations could not be entirely accomplished in the field program, first of all owing to the short time in which the work had to be done and also because the hopper dredge started dumping a couple of months out of schedule.

The final program had to fit the new circumstances and, according to them, the field nourishment started with the stockpiling method at the end of Oct. 1969 and was completed at the beginning of May 70. During this time 1.5×10^6 c.m. of sand was stockpiled in 6 different points of the beach.

The hopper started dumping at the end of Dec. 69 and stopped by the middle of Apr. 70, delivering 2×10^6 c.m. It is to be noticed that stockpiled and dumped sand volumes are the same which were used in the programmed mixed method in the model. In the field works an effort was made to program the sand nourishment as much as possible according to the model program. This was not entirely possible, because the hopper operation started too late. On account of that and because the hopper output was greater than that of the stockpiling method, some areas of the beach were sometimes nourished by both methods simultaneously.

Some details on dredging operations

The stockpiled sand came from a protected bay, Fig. 1, pumped by two cutter suction dredges with 24" delivery pipes. The total length of pipes was around 5 km. The estimated monthly production of sand was 315000 c.m. and the average solid-liquid mixture was supposed to contain about 15 % of sand with mean diameter equal to 300 mic.. The water depth on the dredging area was around 13 m. The power calculation to attend those requirements recommended the installation of two floating booster stations of 24" and one 20" booster on shore [6]. To obtain greater flexibility in the dredging operations, the two parallel lines

FIG. 4 - The Dredge dumping Sand

of pipes were connected in X, so that any of the two dredges could pump to any of the discharge points. The actual percentage of solids in the solid-liquid mixture was about 12.5 %. During the operation the 500 m floating pipeline was occasionally damaged by wave action, resulting breaking of ball-joints and collars. Also the spud of one of the dredges was once broken by wave action.

The sand dumped on the offshore (between -4.0 m and -6.0 m contours) was carried by a hopper which dredged in the open sea at depths about 10 to 15 m, about 4.5 km away from the center of Copacabana Beach, Fig. 1. The hopper had the following characteristics:

Overall length : 95 m

Beam	:	16 m
Loaded draught	:	6 m
Hopper capacity	:	3,000 c.m.
Suction tubes	:	32"
Dredging pumps	:	2 number-driven by 2×800 h.p engines

The hopper peculiarity consisted of gates sliding on the flat bottom of the hopper. This allowed opening of the gates even when the stem touched the sea bottom. In fact, the hopper approached the beach until touching the bottom. At this moment the foregates were opened, the fore draught decreased and the ship could go a little more ahead. This operation continued until the stern gate was opened and the discharge finished. Fig. 4 shows the hopper in operation.

The normal output for the hopper varied between 15.000 and 25.000 c.m. a day. The rate of discharge was about one discharge each two and a half hours.

Sand samples taken during the works showed that the mean diameter of the stockpiled sand was around 300μ . The hopper sand had a mean diameter greater than 400 μ and frequently greater than 500μ . Only in a few samples was the percentage of fine sediment more than that allowed. On the whole, the new sand is coarser than the previous one.

BEACH BEHAVIOR DURING AND AFTER NOURISHMENT

The 14 profiles located as shown in Fig. 2 were surveyed to observe the beach behavior before, during and after the artificial nourishment.

The beach width referred to the +1.1 m level (HWL).

The initial mean width in each profile was computed as the average of 20 surveys made during the last 10 months which preceded the sand nourishment. The net widening in each profile, during and after the nourishment referred to the former mean width.

The mean widening of the beach is defined as the average of the measured widenings in the 14 profiles. The mean widening in a stretch of the beach is defined as the average of the measured widenings in the profiles included in that stretch. As a similar criterion was adopted during the model tests, the comparison between model and field behavior was very easy. During the works, a few surveys were run along each profile down to depths around the -10 m contour.

Sand samples were taken, either from the hopper dredge, or from pumping pipes, or from points at MWL along the beach, and size distribution plotted.

All the field control program was performed by the Technical Department of SURSAN.

Unfortunately, wave heigth measurement could not be done during the beach nourishment.

In Fig. 5, mean beach widenings according to model study and to field surveys are plotted. Graphs M-1, M-2 and M-3 refer to the model and graph P to the prototype. To plot graphs M-1 and M-2, the sand volumes discharged along the time by the dredge or stockpiled on the foreshore, respectively, were considered; graph M-3 results from adding M-1 and M-2. In plotting M-3, two weeks were assigned to the offshore dumping, concerning its contribution to the foreshore widening. This time lag cannot be proved, since it results from scare indications of field observations of very difficult interpretation.

One can see that the mean beach widening in the prototype exceeds, in the first months, what was expected from the model. This may be a consequence of the exceptionally low waves prevailing during the first 3 months following the beginning of stockpiling. In fact, during that

time, only from 10 to 12 Jan are high waves reported, buy it was estimated that they did not reach 2 m.

A decreasing of beach width starts at the middle of March, when the theoretical graph M-3 was very close to the actual one, P. Such decreasing of the beach width is closely associated with wave heights. In fact, after a long period of very low waves, high waves appeared in the first days of Mar., rough sea persisted practically throughout that month, with very high waves being reported from the 25th to the 28th, when the maximum wave height was estimated around 3.5 m. Although sand nourishment was maintained - except the hopper operation which underwent interruptions of a few days in the whole - the mean width of the beach decreased by 15 m during that month. Once the rough sea was over, beach re-formation started and at the end of April, when sand nourishment finished, the beach width had surpassed its previous maximum. By the end of May and, later on, during the last days of Jun and the first days of Jul., new recessions were caused by heavy sea, with subsequent re-formation in both cases. It is to be noticed that beach width at the end of each re-formation phase is always larger than it was at the end of similar phases that had occurred before. This is also true throughout the months following the end of offshore dumping (middle of Apr.) and the end of foreshore stockpiling (beginning of May.). In fact, in spite of alternating recession and re-formation, the evolution of the beach shows a clear trend for increasing widths from May to Oct. The mean net widening in that period was about 15 m. During Oct. and Nov. 1971 the beach seems to have reached its final stage of evolution, with mean widening varying between 85 m and 90 m. The trend showed by the beach for increasing width after the last nourishment operation is considered as a strong confirmation of the contribution of dumped sand for the foreshore widening. Two other factors reinforce this opinion. First, the practically exact prediction by the model concerning the total amount of sand to be used in order to reach the desired width; second, the fact that sand size distributions tend to show an increase of the median diameter compared with the sand existing before nourishment. This is only possible by an important contribution of the material dumped offshore, coarser than the original sand, since the sand stockpiled on the foreshore was slightly finer or at least not coarser than the sand formerly existing.

Fig. 5 still shows mean widening variations of different stretches of the beach. Except as regards the stretch between profiles P-1 and P-3, the fluctuations observed in the other ones closely agree with the fluctuations of the whole beach, which is considered as supporting the criterion adopted for observing the beach evolution.

The singular behavior of the stretch from P-1 to P-3, characterized by a much slower evolution, is firstly explained by the exceptional location of that stretch, where the wave pattern is influenced by diffraction around the rocky spit. This limitation was pointed out in the model study report, which says that, wave diffraction similitude not being reproduced in the model, the results of the tests concerning that corner should be considered with reserve. Besides, no important nourishment was made directly in that stretch, either in the offshore, or on the foreshore. The dredge could not aproach close enough, because the bottom is too flat there; the pipes could not be extended so far, for physical reasons. And, as that stretch of the beach is the one where wave action is the slightest, the sand artificially placed on other areas of the beach takes much longer to come into that corner, by a natural process.

The comparison of Fig. 6 which shows the original beach and Fig.7 which shows the new beach one year after starting artificial nourishment, gives an idea of the work done during that period of time.

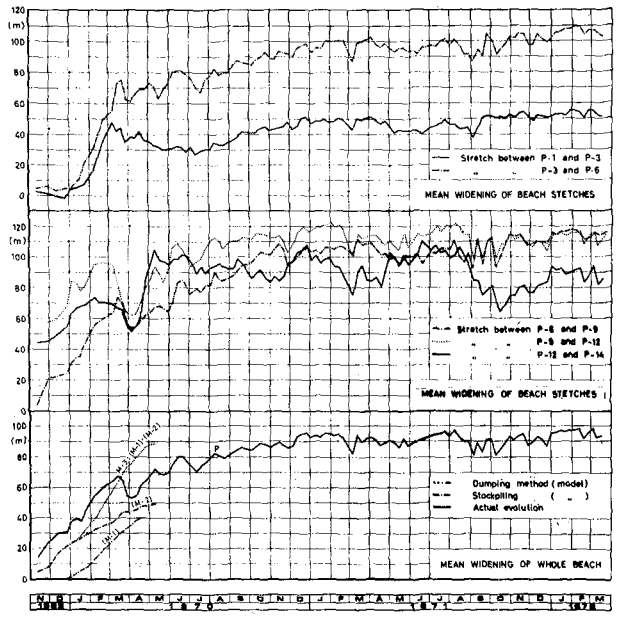

FIG. 5 - Beach Evolution during and after Nourishment

CONCLUSION

The good results obtained in the widening of Copacabana Beach (Brazil) by artificial nourishment of sand, stockpiled on the foreshore and dumped offshore, confirmed the predictions based on the results of a hydraulic model study, specifically run for that purpose. Such a practical success of the offshore dumping method will open new possibilities for its use in similar works in the future.

The use of offshore dumping, however, should result from the analysis of the specific conditions in each case. Knowledge of the coastal history and its correlation with natural agents is of prime importance.

FIG. 6 - View of the Beach before Nourishment

While more experience is not achieved on the offshore dumping method, it is advisable to use it in combination with other methods whose efficacy is already well controlled.

ACKNOWLEDGMENTS

The author is indebted to a number of people for advice and suggestions before and during the study of Copacabana Beach. He particularly wishes to acknowledge the advice and suggestions of Messrs. G. Watts (C.E.R.C., U.S.A. Army) and J. Valembois (E.D.F., Chatou, France).

The Memory of Mr.J.V.Hall Jr., whose contribution to the study of beach processes must be emphasided, is reminded by the author.

FIG. 7 - View of the beach one year after beginning of nourishment

REFERENCES

[1] HALL Jr., J.V.and WATTS, G. - "Beach Rehabilitation by Fill and Nourishment"; Transactions ASCE, Vol. 122, Paper No. 2853, 1957.

[2] "Praia de Copacabana - Estudo em modelo reduzido"; LNEC, Report May 1968.

[3] "Praia de Copacabana - Estudo em modelo - Alimentação submarina"; LNEC, Report Dec. 1968.

[4] "Praia de Copacabana - Estudo em modelo - Alimentação mista"; LNEC, Report July 1969.

[5] "Praia de Copacabana - Estudo em modelo - Alimentação mista programada"; LNEC, Report Nov. 1969.

[6] NICOLETTI, Marcos V. - "The Copacabana Beach - Reclamation Project"; Companhia Brasileira de Dragagem, Rio de Janeiro, 1970.

CHAPTER 81

ARTIFICIAL BEACH NOURISHMENT ON THE GERMAN NORTH SEA COAST

By Johann KRAMER*

A b s t r a c t

Several artificial beach nourishments were completed during the last twenty years on the German North Sea coast. Investigations made it possible to settle different problems connected with artificial beach nourishment and to gain additional information and experience. At present beach nourishments at Langeoog and Sylt will be realized in a way which is expected to bring the highest effectiveness. The hydrodynamic processes in connection with these beach nourishments and their change in shape will be subject to the paper.

Introduction

The East Friesian and North Friesian islands are spread along the German North Sea coast (Fig. 1). To the open sea, the islands have expansive sandy beaches, which are exposed to tidal currents and wave action. In order to maintain the beaches for the protection of the islands with their bathing resorts, people started to construct embankments and groynes more than 100 years ago. The coastal protection works, however, did not achieve the expected success on these stretches of sand, where more sand was eroded than supplied.

Thorough investigations in the years 1949/50 showed that the most economical way of carrying on the necessary island protection could be achieved by artificial beach nourishment (1). This was also a satisfactory solution for the bathing resorts in that they were provided with a beach. In this way, the "classical construction form" of island protection by means of embankments and groynes on the German North Sea coast was passed over for the first time in 1951/52 with the beach fill on Norderney.

A second beach fill followed in 1967. Beaches were also filled artificially with sand in various other islands, such as Föhr 1963, Baltrum 1968, Borkum 1969/70 and Langeoog in 1971. A further beach fill will take place on Sylt at Westerland in 1972.

---

* Leitender Baudirektor Diplomingenieur at the Wasserwirtschaftsamt, 296 Aurich, W. Germany

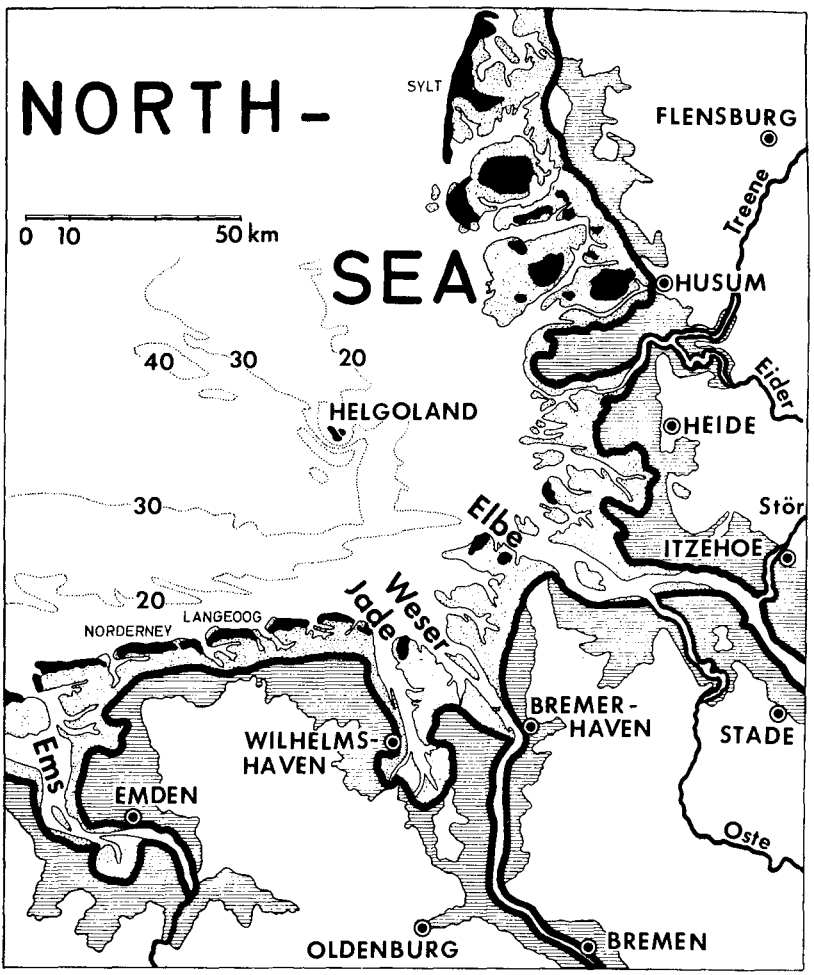

Fig. 1: The German North Sea coast

The technical development of artificial beach nourishment should be shown through the examples of Norderney 1951/52 and 1967, as well as Langeoog 1971 und Sylt 1972. The other mentioned examples of beach nourishment can go without comment as they do not differ basically from the artificial beach nourishment in Norderney. The experience gained in Norderney was taken into account when planning the beach nourishment programmes for Langeoog and Sylt.

The first Beach Nourishment in Norderney 1951/52

I have already described the planning, technical performance as well as the results of the beach fill in 1951/52 at the VIIth Conference on Coastal Engineering in Scheveningen in 1961 (2), so that it is possible to limit myself here to the basic problems.

The sand for the beach fill 1951/52 (Fig. 2) was dredged from the tidal flats south of the island and was transported by means of barges to the boster pump. From there, the sand-water mix was sucked from the barges and distributed over the beach areas through pipelines 60 - 70 cm in diameter.

Contrary to the original intention, the beach was filled with a continuous slope, as the originally planned fill dykes were destroyed very quickly by wave action. In this manner, at the end of the fill process, a high-water safe beach was created with a width of approx. 100 m, which, however, was lost in the following winter. The development of the beach fill was controlled by repeated beach surveys. In all, a total amount of 1,816,500 cubic meters (m^3) of sand was transferred in the years 1951/52. At the conclusion of the fill process, 1,245,500 m^3 of sand of the total amount still remained on the beach, giving a total fill loss of 31 % of the transferred amount of sand (2). Concerning the sand loss during and after the beach fill, it is important to note that the sand material used in the fill was finer than the sand originally present on the beach.

Behaviour of the first Beach Nourishment in Norderney after 1951/52

In the years following, a varying behaviour pattern set in in the beach areas. In the beach fill area of 1951, there was only approx. 3/4 % of the amount still left above the mean low water line by Spring 1959. In the beach fill area of 1952, a more

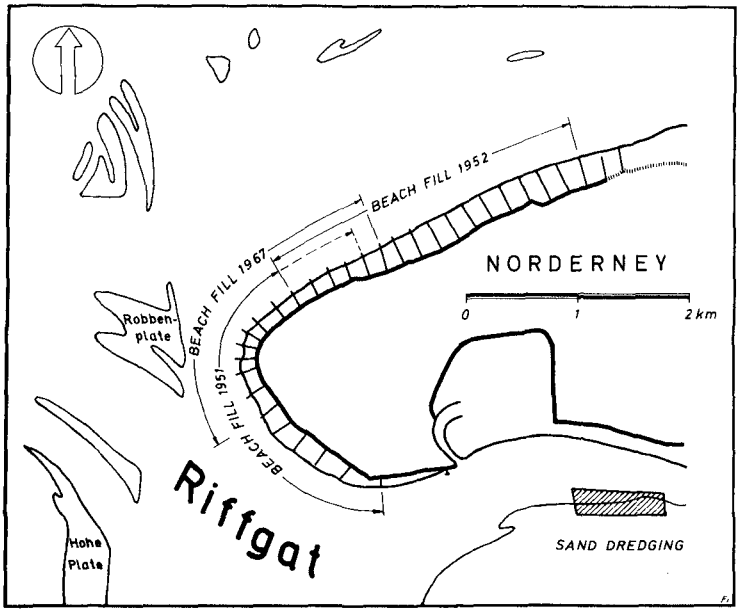

Fig. 2: Artificial beach nourishment on Norderney 1951/52 and 1967

favourable behaviour set in, which was not only attributable to the fill because further sand was added to the beach through the supply of sand deriving from sandbanks in front of the island.

It could be observed that in places where due to erosion the earlier beach height had been reached again, that the same inclination of the beach had been formed. It is therefore obvious that the beach height, incline, size of grain material, is dependent upon wave action conditions. No results were achieved in the efforts to correlate the erosion of sand to the natural parameters such as tide water levels, tidal currents and wave action. It is

merely the level of the established quantities of sand in the individual groyne fields that contribute to the judgement and assessment of the beach fills.

Second Beach Fill Norderney 1967

In 1967 a new beach fill was carried out in the immediate area of the West Beach (3). Here in parts, the beach had receded so far that the tops of the sheet pilings at the foot of the embankment and the groynes had been laid free to a very great extent and also the existence of the protection works endangered.

One of the experiences gained at the beach fill in 1951/52 was not to make a fill on a beach which was too high or had too strong an incline, as such a beach was particularly exposed to wave action, and consequently, the loss of sand particularly great. Therefore, in the fill area, the beach was only filled up to NN + 0,50 m up to the height of the sheet pilings, where a uniform beach incline of 1:50 could be expected, which corresponded to the natural incline of the beach. The amount of sand necessary for this was estimated to be approx. 200,000 m^3. Reference is made to the fact that in 1951/52 356,000 m^3 of sand was filled into the same area.

At the end of the beach fill in 1967, it was established that 240,500 m^3 of sand had been filled in. The storms of October 1967 brought forth a loss of 22 % of the total reserves above the mean low water line. Favourable weather conditions in the spring of 1968 until April 1969 and wind transport from the East of the island brought a small increase, so that after three years, in the spring of 1970, the total loss amounted to merely 16 %.

The total quantities of sand on the beach above the mean low water line as a result of the beach fills 1951/52 and 1967 were:

1951/52	854 500 m^3	-	100 %
1961	444 900 m^3	-	52 %
1962	365 800 m^3	-	43 %
1963	386 600 m^3	-	45 %
1964	377 900 m^3	-	44 %
1965	389 600 m^3	-	46 %
1966	344 300 m^3	-	40 %
1967	355 900 m^3	-	42 %
1968	346 600 m^3	-	41 %
1969	381 300 m^3	-	45 %

The total balance of the beach fills at Norderney can be estimated as good. However, the experiences already gained in 1951/52 repeated themselves in that a connection between loss of sand and wind/hydrological fringe conditions could not be deduced.

Experiences and Conclusions from the Beach Fills in Norderney

The experiences made with the beach fills 1951/52 and 1967 encourage the continuation of the described form of beach preservation in the western part of the Norderney island. However, further considerations over the optimal sand supply of future artificial beach nourishments will be necessary.

The amount of sand used in the beach fill of 1951/52 was too large. The amount of sand filled in above the mean high tide water line was already lost again in the following winter. On the other hand, the amount of sand added in 1967 was too small. Even though the sand balance developed positively on a whole and the loss ration of 16 % up to 1970 for the total amount above the mean low water line is relatively low, the aims were attained short-term only.

From the experiences gained in the beach fills in Norderney, it was realized that the fills should be done in a different manner. The regional distribution of the sand proved to be of different value to the whole reach of beach protection. As a result of the effect and direction of the current, the sand in the outer fields on the edges of the areas where sand is lacking, is lost more quickly than that which is transported with the current from the middle of the area lacking sand out to the edges. Preference should therefore be given to a punctated fill rather than a regional fill. The punctated supply of sand would slowly be carried by the currents to the neighbouring fields and finally to the edges of the deficient beach, so that on the whole, it would remain effective on the beach for a longer period of time. In that way, every cubic meter of the applied sand material would be used to the utmost. Therefore, the greatest efficiency in beach fill is achieved where every cubic meter of sand stays hydraulically effective over a longer period of time, although in a different place, which is not the case with regional sand supply.

Beach Nourishment Langeoog 1971/72

Until a few years ago, enough sand was transported to the beach on the island of Langeoog through arriving sandbanks so that a sufficient beach was present from which also the dunes could replenish themselves. However, in recent years, fairly large sand losses occurred on the northern side of the island, because the sand supply stopped when the sandbanks failed to appear. The result was that the dunes too were seriously affected.

A hydromechanical investigation (4) of the sand losses showed that the dune foot lay too low and that the beach was too steep. The result is that normal beach surf changes into a cliff surf with its disadvantageous effects, even at slightly raised water levels. On a beach of normal height and shallow incline, with uninterrupted beach surf, there is a greater area at the disposal of the transformation of wave energy. When the waves break, they end in a raised swell. On the contrary, with cliff surf, the cliff suddenly brakes the raised swell, causing a reflection where high pressures are set against the cliff wall and the cliff is exposed to considerably more wave energy than with beach surf. Higher turbulence and in addition a higher transport capacity of the cliff surf are the results. At raised water levels it can happen that the waves break directly at the foot of the cliff and transfer their whole energy directly on to the cliff with impact and foam. In this case, erosion and the longitudinal transport of the sand reaches a maximum. On the other hand, with even higher water levels, it can happen that the waves do not break at the cliff, but form a stationary wave. Then the wave energy is not transposed into another form of energy, but is reflected. Although serious damage occurs to the cliff as before, the damage is not as high as when the waves break on the cliff foot. That explains the fact that an extremely high tidal wave, with full reflection on the cliff wall, is not so damaging as a series of mediumly high waves, where the waves break directly on the cliff foot.

In order to preserve the dunes, the effect of the surf action had to be withheld from their base. Therefore, beginning in 1971, the beach in front of the dune foot is being raised and widened to such an extent (Fig. 3) that even with a storm surge, a natural surf takes place on the beach in front of the dune foot. In order to estimate the necessary amount of sand, a yearly erosion rate of 77 m^3/m of the beach in the erosion area had to be taken into consideration. With an increase, this requires an amount of 100 m^3/m and per year for the erosion area of approx. 2,000 meters in length on the northern side of Langeoog. This means that the beach can be raised by one meter for every 100 meters in width. However, as long as the present sand loss continues, one must

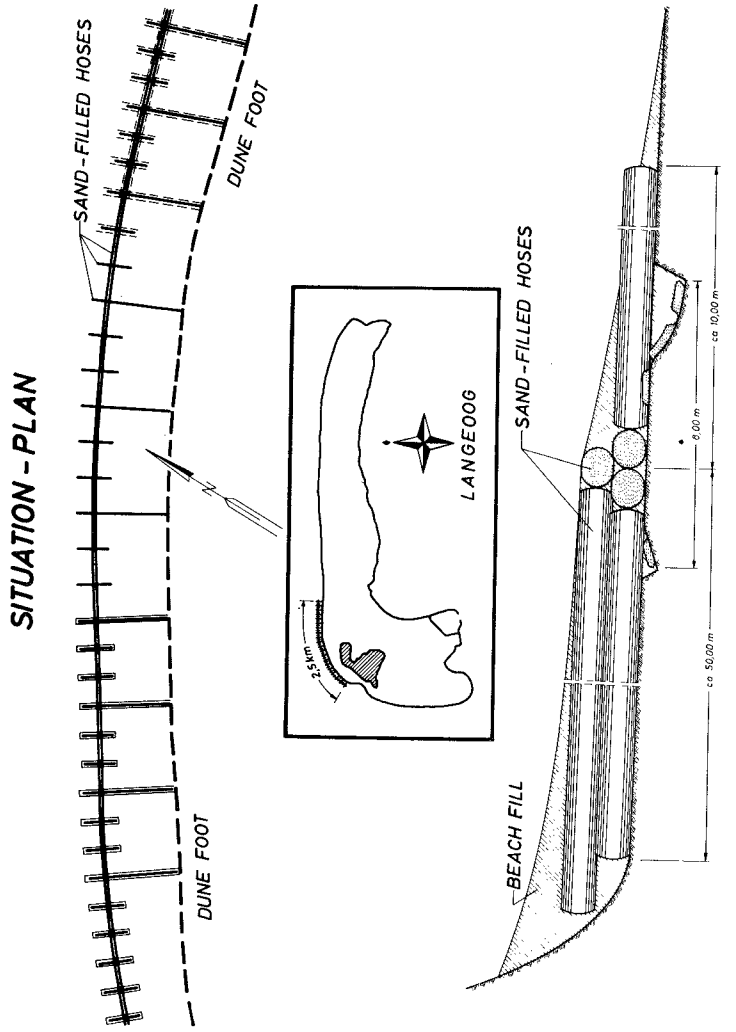

Fig. 3: Sand-filled hoses and beach nourishment at Langeoog 1971/72

reckon with a further yearly fill requirement of 200,000 cubic meters of sand. At a rough estimate, the costs for a continuous 5-yearly sand fill would be in the region of 2 Mio. DM. This is no comparison to the costs for groynes and embankments, which would be at least 50 Mio. DM, without the guarantee that they would eliminate the sand erosion.

The special purpose of this fill is to raise the dune foot and not a beach fill (4). In order to keep the filled-in sand material directly at the foot of the dunes, a longitudinal construction of sand-filled synthetik hoses has been set up (Fig. 3). This construction has been laid 50 m in front of the cliff base so that the filled area in front of it can develop into a natural beach even in raised tidal water levels. The top of the hose construction with a diameter of 1 m lies approx. NN + 2,0 m, i.e. the height of the previous cliff foot. The grain used for the fill was similar to that already on the beach (fine sand), so that by uninterrupted nourishment, the beach fill can also adjust itself to approximately 1:50.

The waves can break freely on this newly-made beach. The cliff foot, with its new high position, is only reached by incoming waves during very high storm surges, and this is only breaking surf.

As the berms are only reached by water during storm surges and for the rest of the time are in the dry, aolian sand transport can be expected with certain winds. Preliminary dunes can be won from the sand with the help of fence traps. Although these dunes are destroyed again by storm surges, they have a positive effect on sand economy.

With a difference in levels of 1,0 m in front of the longitudinal construction (Fig. 3), there is the possibility through reflection, that the beach in front of the hoses will be excavated and the construction itself in danger of being washed away. For this reason, the beach is built up so that it reaches the upper edge of the construction. This beach has to be maintained with a steady yearly refill, estimated at up to 200,000 m^3. The construction should only come into effect to protect the berms in storm surges when the beach in front of the construction is eroded.

The construction (Fig. 3) consists of two hoses laid down side -by-side and at intervals a further pipe laid on top. Washing away should be prevented by a woven mat which is 5 m long on the landward and seaward side and is buried to a depth of one meter on the seaward side.

Because longitudinal currents develop, due to the exposed construction and inclining wave action, causing erosion grooves in front of the construction as well as on the berms behind the construction, short rejectors - groynes made out of sand-filled hoses - have been installed (Fig. 3). These constructions are 10 m in length and are placed about 20 m apart and extend into the berm area. The whole berm area is intersected by sand-filled hoses with spacing of 60 m.

The work of building the hose construction and carrying out the beach fill was completed a month ago. The success of these measures will be seen in the coming years. This beach fill will still be economical in comparision to the construction of heavy embankments and groynes, even if 200,000 m^3 of sand have to be nourished yearly.

Experiences gained from the up to now Beach Nourishment Programmes

Experiences gained are as follows:

1. A minimum fill amount is necessary, otherwise no success can be expected.
2. Nourishment with sand of a coarser grain than that present on the original beach should be aimed at. Coarser grain has a higher layer stability and makes it possible to install a steeper beach where the base of the fill remains within the groyne fields.
3. The nourishment programme has to be adapted to the local currents, where the fill should take place either at lowtide or hightide, thus preventing any serious fill losses.
4. It is sufficient for a fill to be concentrated on a limited area of the beach (feeder beach) if the currents and wave action re-direct the sand material into the neighbouring areas, thus also achieving a sufficient rise in the beach level there.
5. Clay particles found in the fill material, which have to be endured in the first instance for reasons of reclamation, will soon be washed out, so that pollution of the sand beach does not occur.
6. There is no damage whatsoever to the flora and fauna in the vicinity of the beach fill.
7. Due to wave action, much higher sand losses occur on a beach built up high over the mean high water line than on a lower lying beach with a flatter profile.
8. A continual beach fill is appropriate, if it is necessary to replace the same amount of sand yearly.

Fundamentals of the artificial Beach Nourishment in Westerland/Sylt 1972

The island of Sylt, the most northerly of the North Friesian islands, extends for about 40 km north to south (Fig. 1). The island is strongly exposed to wave attack in westerly winds, which has caused, since time immemorial, erosion of the coastal area. As a result of this, the west coast of the island recedes, on an average, one meter per year. It has therefore been attempted for the past century to protect the island of Sylt from further damage by constructing groynes and embankments. It is particularly important to guard against damage to the town of Westerland, a significant bathing resort situated in the centre of the island, and to maintain a bathing beach there.

Since the 1950's, numerous hydrometrical, morphological, geological and sedimentological tests have been carried out to find the reason for this continuous recession (5). The cause lies in the negative balance of sand. A steady sand erosion is present in the middle of the island, but there is no sand supply to compensate for the loss.

The most varied methods were tried out in the construction of groynes and embankments, but although they delayed sand erosion, could not prevent it. On the basis of this knowledge and experience gained elsewhere in the meantime, the most economical solution for beach preservation at Westerland would seem to be artificial beach nourishment. The rudiments for this nourishment programme (5) were worked on by a group of experts of which the writer is a member.

The task of nourishing the beach at Westerland by the raising and widening of the beach, in order to safeguard the endangered coast protection works, will be even better accomplished, the more effectively the fill is combined in a positive sense with the natural processes. These can be characterised as follows:

On average, the beach and inshore zone extend to a width of 600 m to the seaward bar in front of the island (Fig. 4). Exposed to the power play of the currents and wave action, this stretch of the area shows the quickest changes. Re-direction of sand, diagonally and longitudinally, usually increases with the height of the waves. In this way, the sand transport on the beach is dependent upon the direction of the waves. Waves coming from the West bring little longitudinal transport. The waves, with their prevailing sloping attack, cause mass re-direction with a displacement parallel to the coast. The transport parallel to the beach is southerly with waves coming from the north-west and northerly with waves coming from the south-west. The longitudinal transport proceeds mainly in two sand flows, one in the surf region on the beach and the other in

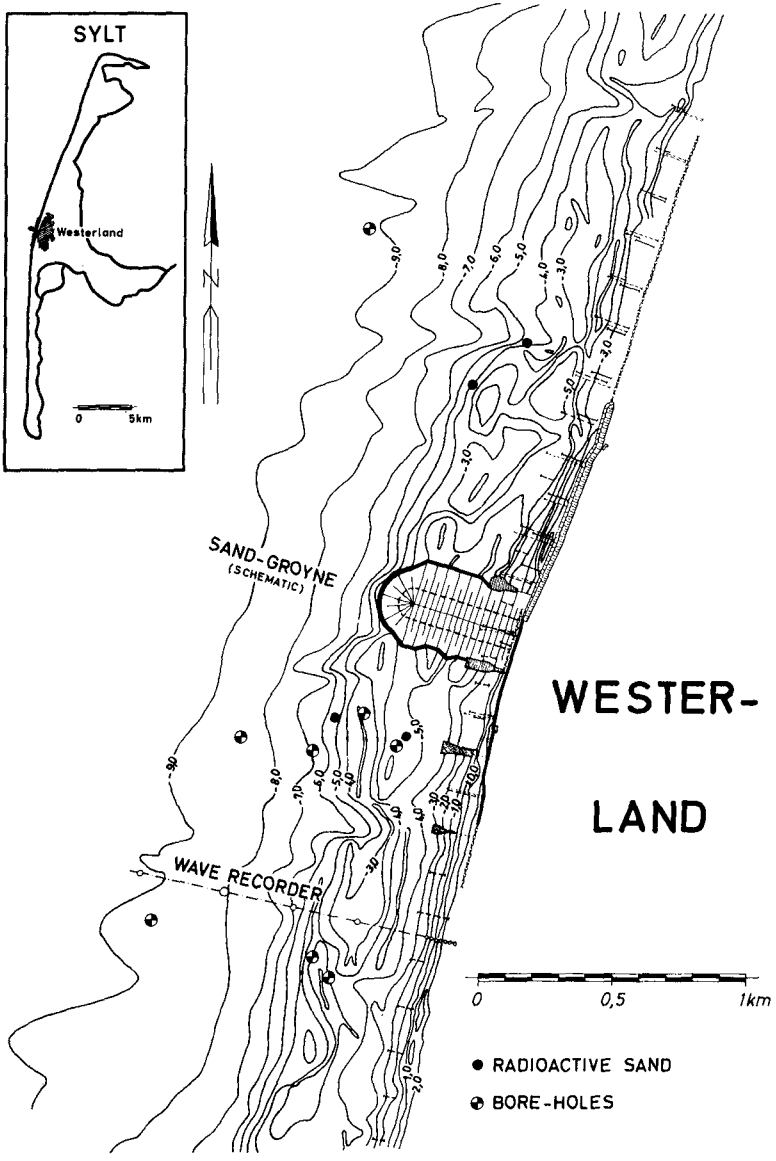

Fig. 4: The beach in front of Westerland/Sylt with the sand groyne (schematic) and investigation points

the surf region on the bar. According to the respective positions of the surf regions and their type of breakers, the sand transport also shifts its position and force. If no bar surf occurs, i. e., during high tides or with only moderately high waves, then, in the main, a sand transport only occurs on the beach, whose width extends approximately from the breaking point of the waves to their limit of uprush. On the other hand, in the case of bar surf, two sand flows are running in the same direction, one on the beach and one on the bar and the transport on the bar is the more powerful, the more wave energy is transformed into surf.

Large deviations in the height of the beach are possible, independent of weather conditions. These changes in a beach profile amounted to almost 5 m during a period of 10 months in 1954; the greatest change registered in the average beach height was 1.60 m from one day to the next. Data on the average yearly amount of sand loss on the beach of Sylt are uncertain. Specifications should be based on the many years of observation which showed a yearly average of 525,000 m^3 of sand.

Conclusions for a Beach Nourishment on Sylt with a Sand Groyne

There was a choice between four different methods of beach nourishment (5):

a) Indirect beach restoration through the build-up in layers of dredging on the offshore.

b) raising of the beach with a direct fill,

c) nourishment of locally restricted sand areas, and

d) continual fills.

Regional nourishment proves to be most suitable for the conditions on the coast of Sylt. In this way, direct protection is achieved for the beach protection works. The groyne system will probably offer no significant advantage in the nourishment programme. When the groynes are covered with sand they are ineffectual and uncovered, they give, as before, only little protection and merely lessen the effect of the surf currents.

In future planning, it should be borne in mind that there are still reliable methods for a quantative evaluation of wandering sands at present, but that qualitative theoretical models are available which can support such reflections. The fill in the form of beach widening and raising is possible. However, it is more advantageous to construct a type of sand groyne (Fig. 4). Changes and developments to this sand groyne are determined by natural occurrences, especially surf and sand transport. The aim is, therefore, to influence the present and unchangeable surf process in such a way that as little as possible of the newly added sand is lost after

the fill has taken place.

Additionally, contrary to the previous regional nourishment programmes on Norderney and Langeoog, an attempt is being made on Sylt to catch additional aand from the natural longitudinal transport by means of the sand groyne (Fig. 4). The basic idea is to fill in a sand structure vertical across the channel to the bar, which, in its initial form, would have the appearance and effect of a very flat groyne.

During construction, waves affect the sand structure. Contrary to groynes of normal shape, with such flat sand constructions, not only does wave diffraction occur, but also considerable wave refraction, because the dimensions of the aand groynes and their gradients amount to a multiplication of the lengths of the arriving waves. In this manner, the appearance of the surf is completely different from that at beach groynes of traditional construction. Figure 5 A shows a sketch of wave and surf conditions on the sand structure while under construction. The sand structure is indicated by two vertical contour lines. Wave attack on the beach is perpendicular; i.e. there is no longitudinal transport in the beach surf, which runs up both sides of the sand groyne unhindered. At the sand groyne itself, one must differentiate between the head and flank surf. Greater wave heights occur in the head surf than in the simultaneous beach surf, because on the cone of the groyne head, refraction causes concentration of wave energy. On the other hand, flank surf shows lesser wave heights. By normal wave attack on the beach, only refraction is present and no diffraction.

In any case, damage occurs on the top of the groyne through the head surf, which becomes greater as wave height increases. Surf currents directed landwards develop from the flank surf, which transport the material eroded from the head of the groyne landwards. As the waves do not decrease in height on the flanks, in the course of events, this material is accumulated on the flanks (Fig. 5 A). Due to the vertical wave attack, no material is extracted from the sand construction, but merely a shifting of the sand landwarda occurs. No additional sand, however, is retained from the natural sand transport under this type of wave attack.

It is known that additional sand, that does not originate from the construction, can be expected on the luff-side of the sand groyne by diagonal wave attack (Fig. 5 B), if the groyne projects far enough out of the beach surf. Apart from that, especially on the luff-side, sand from the top of the groyne is carried landwards by the flank surf, where two surf currents meet on the luff-aide of the groyne root. The point of the heaviest wave attack is moved from the top to the flank on the luff-side; on the other hand the

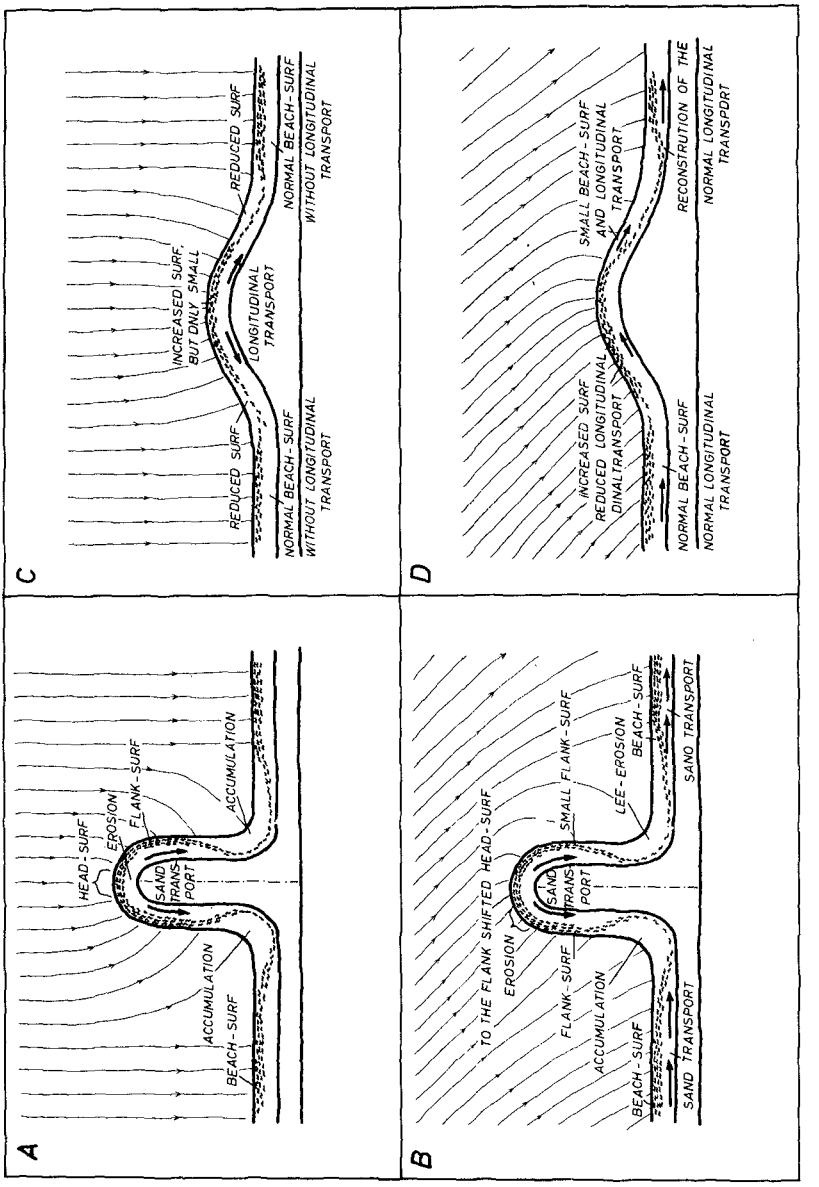

Fig. 5: Wave and surf conditions on the sand groyne

lee-side flank is exposed to much smaller wave force becsuse diffraction is added to refraction so thst here too a landwards transport dominates. On the lee-side of the beach a lee erosion is possible, but is not to be expected in the same intensity as with a solid groyne construction, because sand is supplied from the lee flank. Even diagonal wsve attack on the sand construction leads only to s landwards sand transport, although, by cutting off the surf current on the beach, additional ssnd can also be retained from the natural ssnd transport.

During the nourishment progrsmme, the sand groyne will be subject to the constsnt chsnging effects of the waves' forces. Waves from all directions have the uniform tendency of eroding the top of the sand groyne and shifting it landwards. At the same time, accumulation occurs at its root and the neighbouring flank sections, which are partly supplied from the ssnd construction and partly come from additionally retained ssnd volume.

Transformation of the Ssnd Groyne into a Sand Hoft

If the sand groyne is left to its own resources without further sand nourishment st its hesd, then s gradual transformation into a less projecting, flat ssnd construction, s "sand hoft", through the already described effect of the waves, takes place (Fig. 6 A) Later on, this ssnd hoft will extend even further along the beach while its projection snd height decrease. The speed of this trsns-formation depends upon the grsin of the sand, but mainly on the wave climate. In any case, the larger the sand mass st the begin-ning, the longer this process tskes. Simulsrly, the transformstion will take place more quickly at the beginning than later on, when the sand hoft has alresdy sdspted its shspe to the effect of the waves, and also when the waves have adapted themselves to the shape of the ssnd hoft.

During vertical wsve attack, the transportstion of sand landwards on the flanks of the sand hoft is light, for then the waves, due to refraction, meet the vertical contour lines practically vertically in compsrison to the ssnd groyne (Fig. 5 C). In a sloping wave sttack, the sand csn be transported around the sand hoft, as all surf currents, contrary to the sand groyne, run in the ssme direction (Fig. 5 D). The surf area on the beach extends round the whole ssnd hoft, during vertical as well as by sloping wave attack, and with its sand trsnsport, provides for an equable sand balance.

Continuous swell from only one direction over a longer period of time deforms the ssnd hoft assymetrically, whereby the luff-side flank becomes longer than that on the lee-side. A change in wsve direction then conveys a part of the ssnd transported around the

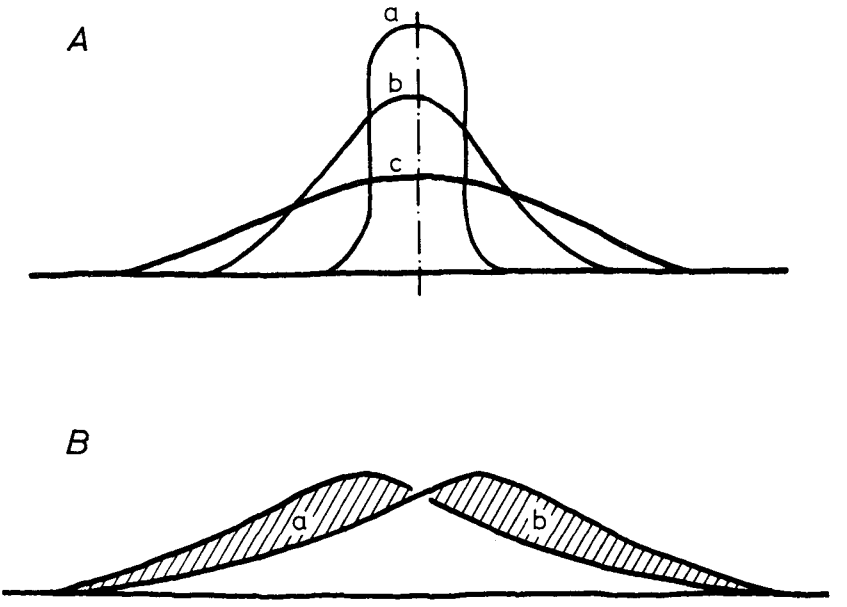

Fig. 6: A: Transformation of the sand groyne into a sand hoft (phase a-b-c)
B: Shuttled sand mass (phase a-b)

top of the sand hoft in the opposite direction, so that one can speak of a "shuttled sand mass" (Fig. 6 B). The stabilising effect that develops when part of the sand from the long-distance passes into the short-distance transport, is also very advantageous here.

The life of such a sand hoft, i.e. its stability, is longer, the more vertical the relation of the average landward current direction and energy is to the beach. It can be raised when the sand groyne is filled up to the bar, because there is already a saturated sand transport in the bar surf and therefore a decrease in the erosion at the head is conceivable. After the transformation of the sand groyne into a sand hoft, the bar surf at the top of the sand hoft changes over directly into beach surf. Because part of the wave energy reaches the lee-side flank through diffraction and refraction during a sloping wave attack on the lee-side, it is possible that the sand flow below the bar surf will be partially tapped.

Execution and Expectations of the artificial Beach Nourishment at Westerland

The construction of the sand groyne is undertaken with a daily amount of about 10,000 cubic meters of sand in order to advance the sand groyne in relation to the daily damage rate. In the favourable season, during summertime, it is possible to fill 900,000 m^3 within three months. On subtracting 1/3 of the sand volume as fill loss, 600,000 m^3 of sand remain for the sand groyne. Its length will amount to approx. 400 meters and its average width at the base approx. 300 meters with an average height of 7 meters from the bottom (Fig. 4).

The sand for the nourishment of the sand groyne is obtained from the eastern side of the island, where there is a range of Kaolin sand to a depth of 40 meters. The grain size practically corresponds with the existing sand material on the beach. The sand is conveyed from the withdrawal to the nourishment area by means of a pipeline approx. 8 km in length. Besides the suction dredge which obtains the sand, three intermediate pumping stations have been connected up in order to overcome the great distance involved in this transfer fill. The costs for the artificial beach nourishment are approx. 6,000,000- DM.

In addition, a sum of approx. DM 1,5 Mio. will be spent on investigations in order for a statement to be made under natural conditions on the success of this large effort. Numerous current and wave surveys will also be carried out in the area surrounding the sand groyne, which will be complemented by sedimentological tests (6). For that reason it is expected, that the execution of the present nourishment attempt at Sylt will lead to new and valuable knowledge of the suitability of artificial beach nourishment for island protection.

REFERENCES

1. KÜSTENAUSSCHUSS NORD- UND OSTSEE, ARBEITSGRUPPE NORDERNEY

Gutachtliche Stellungnahme zu den Untersuchungen über die Ursachen der Abbrucherscheinungen am West- und Nordweststrand der Insel Norderney sowie zu den zum Schutz der Insel vorgeschlagenen seebautechnischen Maßnahmen.

Die Küste, Jg. 1, H. 1, 1952

2. KRAMER, J.

Beach rehabilitation by use of beach fills and further plans for the protection of the island of Norderney

Proc. of VII Conference on Coastal Engineering, Vo. 2, 1961

3. LUCK, G.

Die zweite Strandaufspülung am Weststrand von Norderney

Jahresbericht der Forschungsstelle Norderney 1968, Bd. XX, 1970

4. KÜSTENAUSSCHUSS NORD- UND OSTSEE, GUTACHTERGRUPPE LANGEOOG

Gutachten über die Dünen- und Strandsicherung im Nordwesten der Insel Langeoog (1. Teil)

Hannover/Bad Tölz 1971 (Unpublished Report)

5. KÜSTENAUSSCHUSS NORD- UND OSTSEE, GUTACHTERGRUPPE SYLT

Gutachten zur Vorbereitung und Durchführung der vom Land Schleswig-Holstein für das Jahr 1971 geplanten Sandvorspülung am Weststrand der Insel Sylt - Vorschläge zur Einspültechnik - Teilgutachten B

Aurich 1971 (Unpublished Report)

6. KÜSTENAUSSCHUSS NORD- UND OSTSEE, GUTACHTERGRUPPE SYLT

Gutachten zur Vorbereitung und Durchführung der vom Land Schleswig-Holstein geplanten Sandvorspülung am Weststrand der Insel Sylt - Veranlassung und Aufgabenstellung - Teilgutachten A

Aurich 1970 (Unpublished Report)

CHAPTER 82

LA PROTECTION DES PLAGES DU LITTORAL DU LAC SAINT-JEAN

par

Richard Baivin [1]
Yvan Cousineau [2]

PREAMBULE

Avant l'apparition des premiers aménagements hydro-électriques de l'ALCAN, le niveau du lac Saint-Jean accusait des variations saisonnières considérables. Aux périodes de grandes crues et d'inondations du printemps succédaient les périodes de basses eaux de la mi-été qui donnaient lieu à de fréquentes tempêtes de sable et à la formation de dunes sur les berges. L'implantation du barrage d'Isle-Maligne et l'élargissement des gorges des Grande et Petite Décharges, en 1924, permirent de minimiser les dangers d'inondation au printemps et de maintenir en été un plan d'eau régularisé dont devaient tirer profit à la fois les exploitants des sites hydro-électriques et de nos jours les estivants et adeptes des sports aquatiques et nautiques. En contrepartie, le relèvement du niveau moyen du lac eut pour effet d'amorcer une érosion des berges en prévision de laquelle l'ALCAN avait d'ailleurs acquis les terrains en bordure du lac.

Le littoral ayant atteint, avec les années, un nouvel état d'équilibre, l'ALCAN a consenti à laisser s'établir, par voie locative, des chalets de plus en plus nombreux sur les terrains mêmes qu'elle avait acquis avant l'exhaussement du lac.

Vers 1960, à la suite de la mise en service de nouveaux aménagements hydrauliques, les consignes d'exploitation ont été modifiées (le niveau du lac étant gardé au voisinage de la cote maximale autorisée beaucoup plus tard en été et en automne) et les phénomènes d'érosion

---

(1) Ingénieur principal, Laboratoire d'Hydraulique LaSalle, Montréal
(2) Ingénieur-conseil, Division de la production électrique du Québec, ALCAN

qui s' étaient graduellement atténués après quelque quarante ans d' exploitation dans les conditions antérieures ont réapparu; l' ALCAN a alors confié au Laboratoire d' Hydraulique LaSalle l' étude des conditions hydrographiques (niveaux, vagues, vents, granulométrie des matériaux et profils-en-travers des plages) nécessaires à l' intelligence du régime du littoral et à la définition de mesures de protection appropriées.

La vocation touristique du rivage et le coût peu élevé de ce genre de solution ont incité à préférer, partout où cela semblait possible, le remblayage artificiel des plages (à l' aide d' apports prélevés au large) à une protection longitudinale du rivage.

La réalisation de ce vaste programme de remblayage, entreprise en 1966, a permis de protéger à ce jour une longueur de 95,000 pieds de plage, le volume total des apports nécessaires atteignant 1,500,000 verges cubes.

La note qui suit représente une tentative d' évaluation des résultats du programme, à l' aide des données disponibles (analyses granulométriques, levés bathymétriques, conditions d' attaque houle et niveaux).

IDENTIFICATION DU PROBLEME

Au cours des années 1962, 1963 et 1964, il est apparu nécessaire de combattre l' érosion des principales plages du lac, qui offraient depuis plusieurs années un équilibre satisfaisant. Ces plages, disséminées entre des zones de côte rocheuse et argileuse, ont une longueur totale d' une vingtaine de milles. Elles sont constituées de sables fins et moyens dont les pentes d' équilibre sont très douces et se prêtent bien à la baignade.

L' étude des conditions hydrographiques effectuée en 1965 a permis de conclure que l' érosion des plages s' opérait principalement par transport des matériaux vers le large [3], sous l' action conjugée des vagues (dont

---

(3) L' étude permit aussi de déceler quelques échanges longitudinaux, parallèles au rivage, résultant d' une attaque oblique des vagues, et des échanges fluvio-maritimes assez complexes, au débouché des rivières, mais ces phénomènes restaient secondaires dans la mesure où même les zones d' accumulation créées à la faveur des échanges restaient soumises au processus général d' érosion frontale.

l'attaque est généralement perpendiculaire au rivage dans la zone de mise en mouvement des matériaux), des courants de masse associés aux vagues (les "mers de vent" étant caractérisées par un courant de fond vers le large) et des niveaux (dont le régime a été modifié à partir de 1962, le niveau étant maintenu plus près de la cote maximale permise durant tout l'été et l'automne).

Les niveaux, en vertu des plans de régularisation en vigueur avant 1962 (voir figure 1), n'atteignaient la cote maximale +17.5' (4) qu'au cours des 5 à 7 semaines qui suivent la crue du printemps. A compter de 1962, le niveau fut maintenu plus près de la cote maximale durant tout l'été et l'automne. Les tempêtes se produisant avec un niveau aussi élevé ne tardèrent pas à endommager les berges. Les "mers de vent" auxquelles elles étaient soumises sont en effet très érosives, proportionnellement plus que ne l'est la houle océanique, car le vent qui souffle de l'eau vers la terre, au voisinage de la plage, accélère le mouvement des particules d'eau en surface vers la côte, tout en créant, en compensation, un courant de fond vers le large, opposé au courant de masse et pouvant provoquer le départ du matériau même s'il n'est pas mis en suspension (voir figure 2). Les plages saumises à ces conditions présentent des pentes très plates, ainsi qu'en témoignaient les profils-en-travers établis en 1965 (voir figure 3).

PRINCIPE DE LA METHODE DE PROTECTION ADOPTEE

Le principe de la méthode de protection adoptée découle directement du processus d'érosion lui-même; les plages sont reconstituées au moyen d'apports provenant de bancs au large (probablement les anciennes berges du lac, situées au-delà des remaniements récents contenus à l'intérieur des limites des profils-en-travers relevés en 1965). Ces apports sont mis en place au moyen d'une drague suceuse-refouleuse.

Dans la mesure où la granulométrie des apports reste comparable à celle des plages avant remblayage, il n'y a pas lieu de craindre une trop grande dispersion des éléments mis en place et l'on peut escompter que des profils d'équilibre comparables à ceux des plages d'origine pourront être réalisés avec des volumes d'apport assez limités.

---

(4) Ces niveaux sont lus à l'échelle de Roberval, dont le zéro est 316' au-dessus du niveau moyen de la mer.

REALISATION EFFECTIVE DU PROGRAMME

Dès 1966, l' ALCAN passait à la réalisation effective du programme. Elle entreprit, à titre expérimental, le remblayage d' un tronçon de plage de 3,460 pieds, situé à Saint-Henri de Taillon, au nord-est du lac (voir figure 4). Comme l' on n' avait pas encore fait l' acquisition d' une drague, les travaux durent être effectués avec des moyens terrestres (bulldozers, scrapers) concentrés sur la plage durant la courte période (environ une semaine) qui s' écoule entre la fonte des glaces sur les berges et la remontée du niveau consécutive à la crue du printemps (voir planches photographiques, vue "a"). Ces travaux permirent de déplacer un peu plus de 26,000 verges cubes de sable depuis une distance de 400 ou 500 pieds, au large, jusque sur les berges, pour constituer un remblai d' environ 7.5 verges cubes/pi. de plage.

En 1967, l' on faisait l' acquisition d' une drague suceuse-refouleuse (tuyau d' aspiration: 12"Φ, de refoulement: 10"Φ), d' une capacité de 250 verges cubes à l' heure, ayant un déplacement de 61 tonnes et un tirant d' eau de 26", ainsi qu' un remorqueur de 10 tonnes(tirant d' eau: 39") et 2,000' de conduite de refoulement en acier de 10"Φ), en longueurs de 40', montée sur flotteurs de 8' x 3' et pouvant être déplacée en marche à l' aide d' une débusqueuse (tracteur utilisé en forêt pour le transport des arbres); (voir planches photographiques, vues "b","c", et "d").

L' acquisition de cet équipement a permis de lancer les opérations de remblayage hydraulique qui se sont poursuivies chaque été depuis et sont devenues familières aux riverains du lac. Les opérations durent 5 mois l' an, 24 heures/jour, avec relâche le dimanche, et nécessitent 1 maître-dragueur, 3 chefs d' équipe (opérateurs de la drague), 3 opérateurs du remorqueur et six manoeuvres.

La figure 4, sur laquelle on a porté le bilan annuel des opérations (volume d' apport, longueur protégée, localisation) permet d' apprécier l' importance du programme mis en oeuvre. A la fin de 1971, le volume total des apports atteignait 1,500,000 verges cubes, la longueur de plage protégée 95,000 pieds, le tout représentant un volume moyen d' apport de 15.8 verges cubes/pi. de plage. Le prix de revient des apports est évalué à $ 0.55/vge cube.

EVALUATION DES RESULTATS A C E JOUR

Comment aborder le problème? Il convient d' abord de rappeler qu' il n' entrait pas dans la philosophie de la solution que le sable déversé sur les plages put être stable au sens où on l' entendrait pour une carapace de gros blocs. Le matériau d' apport doit forcément être dispersé afin de trouver sa pente d' équilibre. S' il s' agit d' un sable fin, la pente d' équilibre est assez douce, ce qui conduit à employer une grande quantité de matériau; au contraire, un gros sable, en raidissant la pente, permet d' éviter une trop grande dispersion.

L' analyse granulométrique du sable d' apport apparait donc comme l' un des éléments les plus importants du diagnostic que nous allons tenter.

Les levés bathymétriques disponibles (limités aux plages de Saint-Henri de Taillon et de Desbiens) fournissent un moyen de contrôle direct des résultats, mais couvrent des périodes assez courtes (3 et 2 ans, selon le cas).

Il est également intéressant de considérer les conditions d' attaque (vagues) auxquelles ont pu être exposés les apports et les variations de niveaux qui ont été enregistrées au cours de la même période.

A) Granulométrie des apports

Des échantillons du sable d' apport ont été prélevés à St-Jérôme (section 1), Desbiens (section 4), Pointe Bleue (section II), St-Méthode (section 5), Vauvert (section 7) et St-Henri de Taillon (section 9).

Nous avons établi les courbes granulométriques de ces échantillons afin de les comparer à celles du sable qui se trouvait déjà dans la partie haute des plages d' origine. Cette comparaison, dont les éléments essentiels sont regroupés dans le tableau 1, révèle que le matériau d' apport avait une granulométrie plus forte que celle du matériau d' origine à St-Jérôme, Desbiens, Pointe Bleue et Vauvert, et était plus fin que le matériau d' origine à St-Méthode et St-Henri de Taillon.

Or, le sable de la partie haute des plages primitives, auquel nous nous référons, était peu susceptible d' être dispersé, s' étant déjà appauvri des éléments fins qui avaient été rejetés au bas des plages sous l' effet de triage des vagues. Un sable plus gros devrait "à fortiori" être très peu dispersé et permettre une réduction intéressante des volumes d' apport, tout au moins là où le classement des matériaux réflète une action purement maritime (par opposition aux influences fluvio-maritimes). Par contre, il y a lieu de prévoir, là où le matériau d' apport était plus fin, qu' une plus grande dispersion des éléments interviendra, nécessitant des apports plus considérables.

B) Profils-en-travers de St-Henri de Taillon et Desbiens

Des levés de contrôle des fonds ont été exécutés annuellement par les services topographiques de l' ALCAN:

à Saint-Henri de Taillon d'abord, dès 1966 (année où l'on a effectué la première opération de remblayage) jusqu'en 1970, alors que l'on a procédé au rechargement de la plage. Les profils-en-travers ont une longueur approximative de 250 pieds, sont équi-distants de 100 pieds et couvrent une longueur de plage de 3,700 pieds;
à Desbiens, de 1969 (année du remblayage à cet endroit) jusqu'en 1971, compris. Ces profils-en-travers mesurent environ 250 pieds de longueur, sont équi-distants de 100 pieds et couvrent une longueur de plage de 3,000 pieds.

Ces levés bathymétriques démontrent que les matériaux déversés sur la plage de St-Henri de Taillan ont été davantage dispersés qu'à Desbiens. En effet, un calcul des quantités (voir tableau 2) indique que 95% des apports étaient restés en deçà des limites du levé bathymétrique après 2 ans, à Desbiens, contre 67% à St-Henri de Taillan. Ce pourcentage est du reste tombé à 42% à St-Henri de Taillan l'année suivante.

Ces chiffres semblent confirmer le rôle déterminant que tient la granulométrie dans le processus de dispersion des apports, sous réserve que d'autres facteurs ne soient intervenus tels la fréquence et la sévérité des tempêtes, au sujet desquelles nous n'avons que des indications générales (antérieures à la période 1965 - 1970), et les niveaux dont nous connaissons les variations de 1965 à 1970.

Rappelons à cet égard que les plages de St-Henri de Taillan et de Desbiens (ainsi, d'ailleurs, que celles de St-Jérôme et de St-Gédéan) sont très exposées, à la fois en ce qui a trait à l'amplitude et à la fréquence des tempêtes, les vents du sud-ouest, d'ouest et du nord-ouest soufflant avec force et représentant à eux seuls:

(a) 58% des vents de mai
(b) 61% des vents de juin
(c) 66% des vents de juillet
(d) 68% des vents d'août
(e) 67% des vents de septembre
(f) 66% des vents d'octobre, et
(g) 60% des vents de novembre

L'examen des enregistrements de niveaux de 1965 - 1970 révèle par ailleurs que des variations de cote assez marquées ont été observées, les niveaux en période d'eau libre ayant varié entre +12.5' et +17.5' . Des variations encore plus marquées auraient été enregistrées en 1971.

---

(5) La plage de Vauvert peut aussi être soumise à des conditions d'attaque assez dures (en raison de la longueur du "fetch" sud-est), mais la fréquence d'apparition de ces conditions est moins grande. Les plages de Pointe-Bleue et de St-Méthode sont les moins exposées du groupe.

Ces variations du niveau favorisent la dispersion des apports. En effet, le classement des matériaux dans une plage se fait suivant le niveau d'attaque. Pour chacun des niveaux, un tri des matériaux s'opère à la faveur duquel les éléments les plus gros sant abandonnés sur place, ou repaussés plus haut, tandis que les éléments plus fins sont rejetés plus au large; des variations de niveau marquées favarisent donc l'étalement des matériaux.

Considérans, par exemple, la plage de St-Henri de Taillan. Les apparts mis en place au printemps 1966 ant été attaqués sous des niveaux variant entre +16' et +17.5' durant le mois de juin, les 3 dernières semaines d'août, et les mois de septembre, actabre, navembre et décembre 1966 (le niveau variant entre +15' et +16' en juillet et durant la première semaine d'août). Ces conditions ont cammencé à adoucir la pente du remblai, qui s'est étalé sur une centaine de pieds de largeur (voir figure 5-a).

En 1967, le niveau s'est maintenu au voisinage de +14' de la mi-juin au début d'octabre, déplaçant le paint d'attaque au-dessus des matériaux remaniés l'année précédente, paur les repausser plus au large (vair encore la figure 5-a). Cette périade de bas niveau fut suivie, de la mi-actobre à la secande semaine de décembre, de niveaux campris entre +16' et +17.5', qui ant reparté l'attaque vers le haut de la plage.

L'année 1968 a donné lieu à des niveaux encore plus bas (la cate +12.5' ayant été atteinte à la mi-juillet), qui ont dû contribuer à repousser encore un peu plus loin les matériaux déjà déplacés sous la cote +14' l'année précédente.

Campte tenu de cette dispersion (dont les variatians de niveau et la granulométrie ont été les agents principaux), le volume d'apport initial de 7.5 v.c./pi. constituait un stock insuffisant pour permettre l'amorce véritable de nouveaux profils d'équilibre et il valait mieux entreprendre sans plus attendre le rechargement des profils comme on l'a fait en 1970.

Il est probable que la granulométrie des apparts frais ressemble à celle des apparts de 1966 et que les variations du niveau cantribueront encore à disperser les matériaux plus qu'on ne le voudrait, mais le volume d'apport supérieur que l'on a utilisé cette fois-ci (12.8 v.c./pi.), combiné au volume de 1966, devrait donner des résultats plus satisfaisants, qu'il faudrait continuer de contrôler chaque année.

Il est intéressant de souligner que bien que la plage de Desbiens ait été elle aussi soumise à des variations notables de niveau (6), l'an n'y a pas observé de dispersion notable (vair la figure 5-b), cette supériarité relative paraissant liée à la granulométrie des apports. La plage évalue tout de même lentement, comme en témoigne la figure 5-b, la partie haute du profil s'appauvrissant graduellement au prafit de la

---

(6) Le niveau est descendu à +15' en 1969, +14.5' en 1970 et plus bas encore en 1971 (valeurs non canfirmées à cette date...).

partie basse. Un rechargement pourrait donc là aussi devenir nécessaire, mais les résultats déjà acquis sont très encourageants.

C) Autres plages

Il est difficile de prédire le comportement des autres plages à partir des seuls renseignements actuellement disponibles, sauf pour St-Jérôme, où l'on est en droit de dire que les conditions (granulométrie des apports, quantités mises en place, mode d'attaque) ne sont pas moins favorables qu'à Desbiens, et St-Gédéon (plage comprise entre La Belle rivière et le ruisseau Grand Mont), où l'on peut aussi anticiper des résultats très satisfaisants, pour autant que la granulométrie des apports y soit aussi favorable qu'à St-Jérôme.

La solution est plus incertaine à Vauvert, Saint-Méthode et Pointe Bleue, où le régime des berges est marqué par des influences fluvio-maritimes qui viennent perturber le mécanisme d'érosion frontale due aux vagues en fonction duquel la méthode de protection a été conçue.

CONCLUSIONS

La méthode de protection a été conçue en fonction d'un processus d'érosion frontale due aux vagues. Ce processus caractérise le régime de l'ensemble des plages, mais il est brouillé par des influences fluvio-maritimes, au débouché des rivières, et par des échanges longitudinaux, en certaines portions du littoral (généralement des segments assez courts, que l'on identifiera "in situ") où l'attaque est nettement oblique.

La méthode a donc de meilleures chances de réussite là où le mécanisme d'érosion frontale peut être considéré comme prépondérant par rapport aux autres facteurs d'équilibre. Les plages de St-Henri de Taillon, St-Gédéon, St-Jérôme et Desbiens appartiennent en gros à cette catégorie. Elles sont malheureusement, par ailleurs, les plus exposées.

Le volume d'apport nécessaire pour y constituer de nouveaux profils d'équilibre parait fortement lié à la granulométrie des apports. Il est également influencé par les variations de niveau assez marquées qui caractérisent le régime du lac.

Les analyses granulométriques permettent d'anticiper que des volumes d'apports assez limités seront suffisants à Desbiens et St-Jérôme, mais qu'une dispersion plus considérable est à craindre à St-Henri de Taillon. Les levés bathymétriques exécutés à Desbiens et St-Henri de Taillon viennent d'ailleurs confirmer ces tendances. Les résultats de Desbiens et St-Jérôme seraient extrapolables à St-Gédéon (plage comprise

entre La Belle rivière et le ruisseau Grand mont) pour autant que la granulométrie des apports y doit aussi favorable, ce qui n' a pas été vérifié.

Les autres plages (Vauvert, St-Méthode, Pointe-Bleue...) ont un régime d' équilibre plus complexe et la solution y est plus incertaine, encore qu' elle puisse réussir en certains cas.

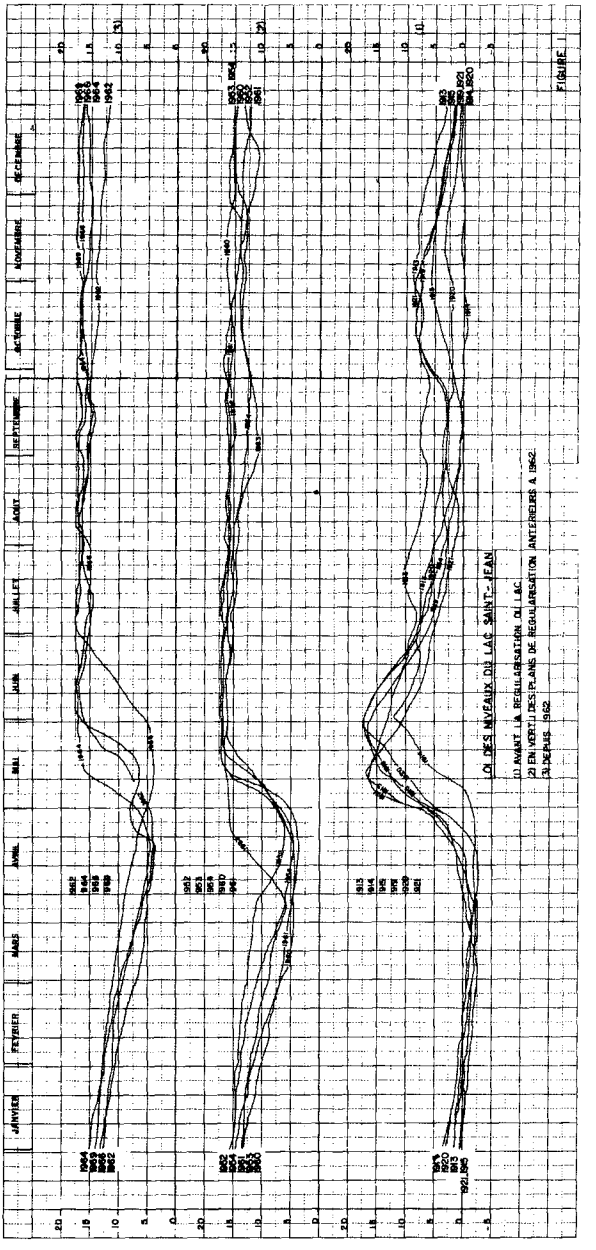
JANVIER
FEVRIER
MARS
AVRIL
MAI
JUIN
JUILLET
AOUT
SEPTEMBRE
OCTOBRE
NOVEMBRE
DECEMBRE
LOI DES NIVEAUX DU LAC SAINT-JEAN
1) AVANT LA REGULARISATION DU LAC
2) EN VERT) DES PLANS DE REGULARISATION ANTERIEURS A 1962
3) DEPUIS 1962
FIGURE 1

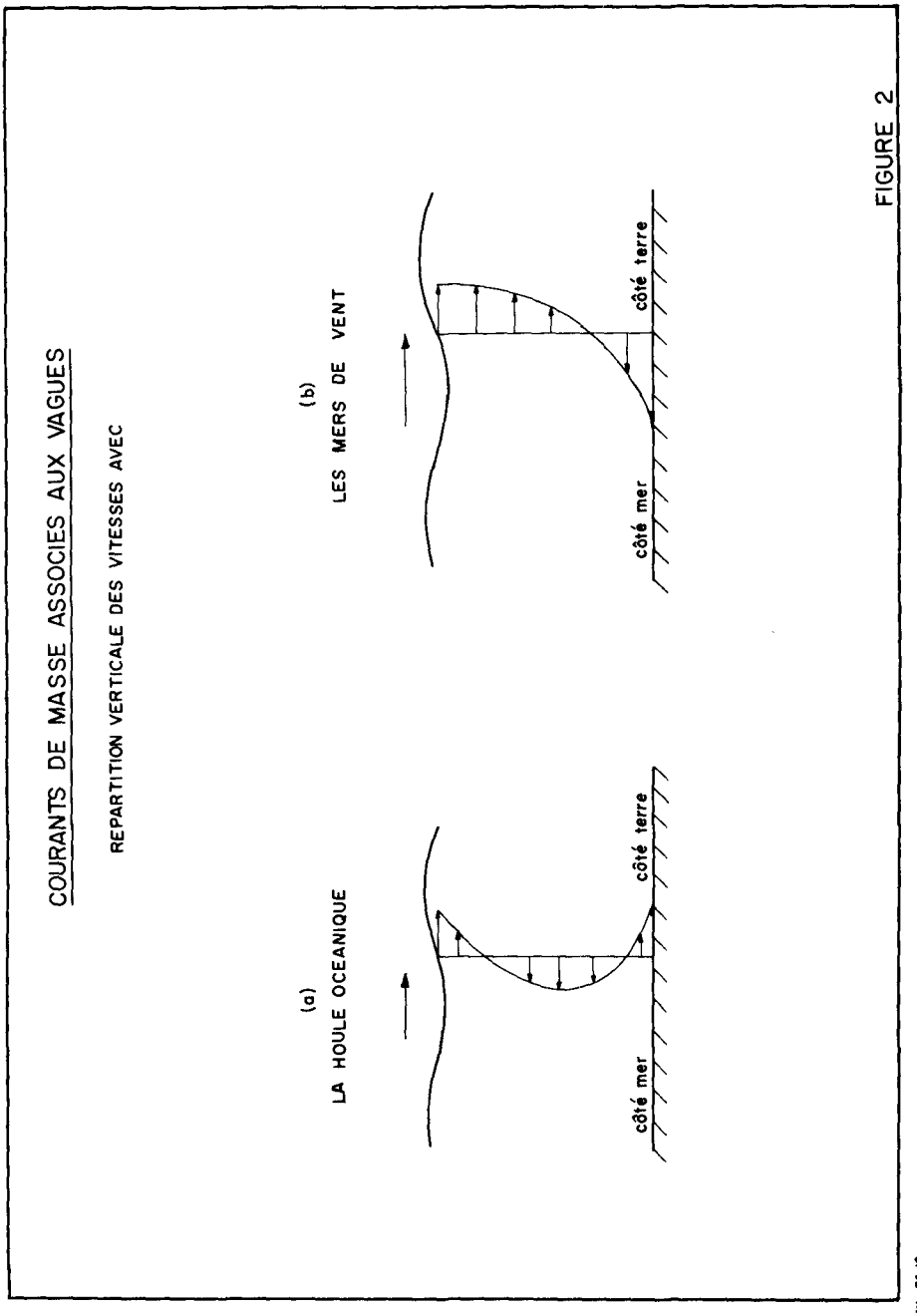

FIGURE 2

LHL. 3C.12

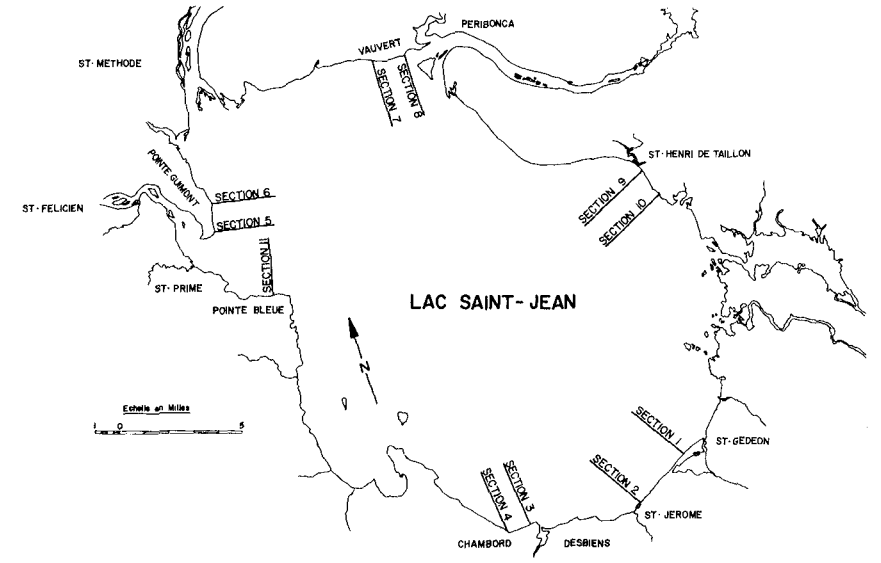

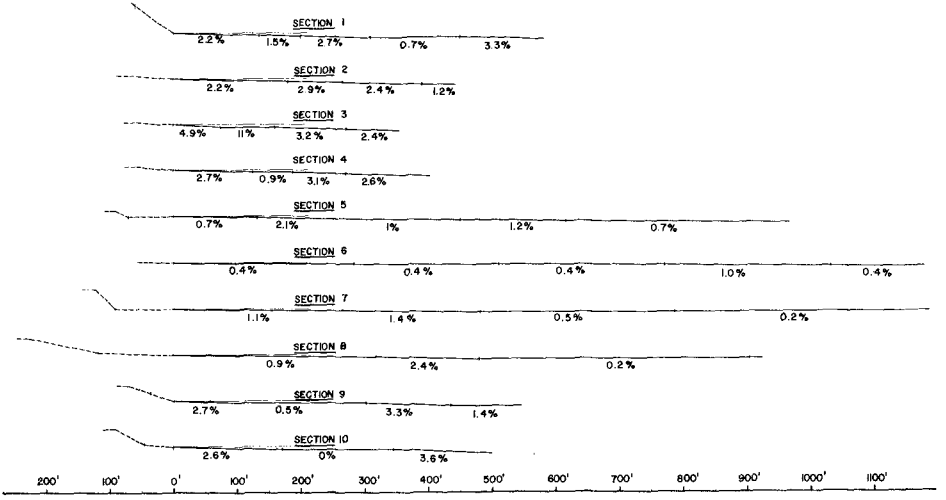

PROFILS EN TRAVERS DES PLAGES
(Etablis en 1965)
FIG : 3

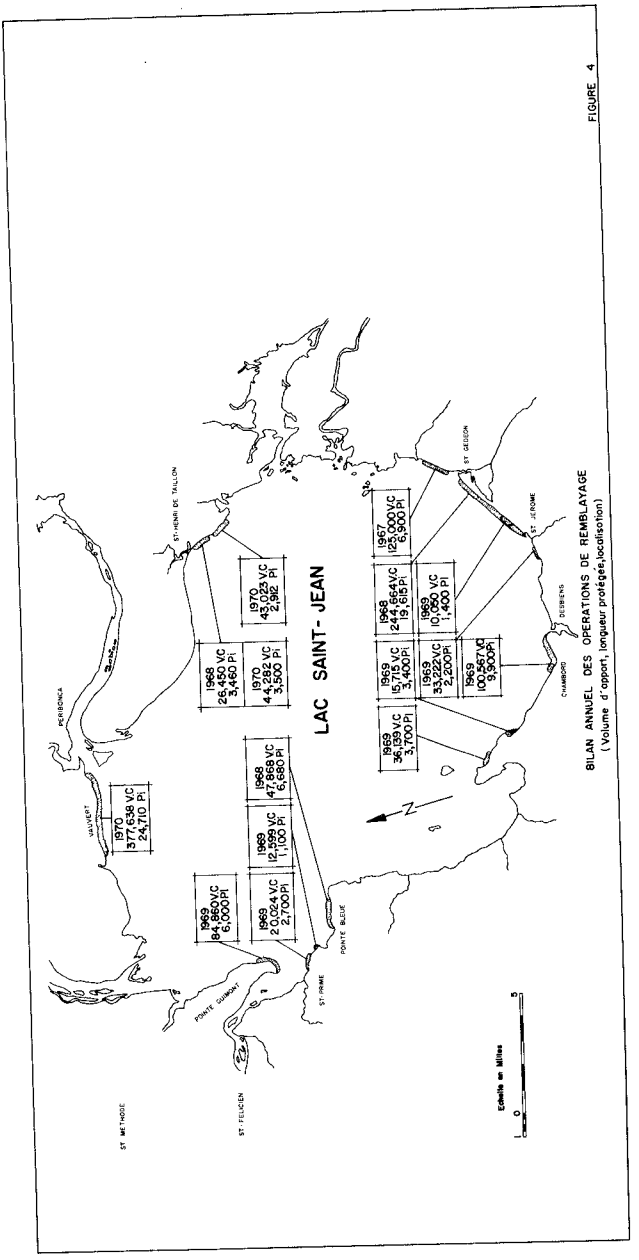
LAC SAINT- JEAN
ST-HENRI DE TAILLON
ST GEDEON
ST JEROME
DESBIENS
CHAMBORD
PERIBONCA
VALLEYFIELD
POINTE GIRARD
POINTE BLEUE
ST-PRIME
ST FELICIEN
ST METHODE
1970 377,638 VC 24,710 Pi
1969 84,860 VC 6,000 Pi
1969 20,024 VC 2,700 Pi
1969 12,599 VC 1,100 Pi
1968 47,868 VC 6,680 Pi
1968 26,450 VC 3,460 Pi
1970 44,282 VC 3,500 Pi
1970 43,023 VC 2,912 Pi
1969 36,139 VC 3,700 Pi
1969 15,715 VC 3,440 Pi
1969 33,222 VC 2,200 Pi
1969 100,567 VC 9,300 Pi
1968 244,644 VC 18,650 Pi
1969 10,000 VC 1,400 Pi
1967 185,000 VC 6,900 Pi
Echelle en Milles
0
5
N
BILAN ANNUEL DES OPERATIONS DE REMBLAYAGE
(Volume d'apport, longueur protégée, localisation)
FIGURE 4

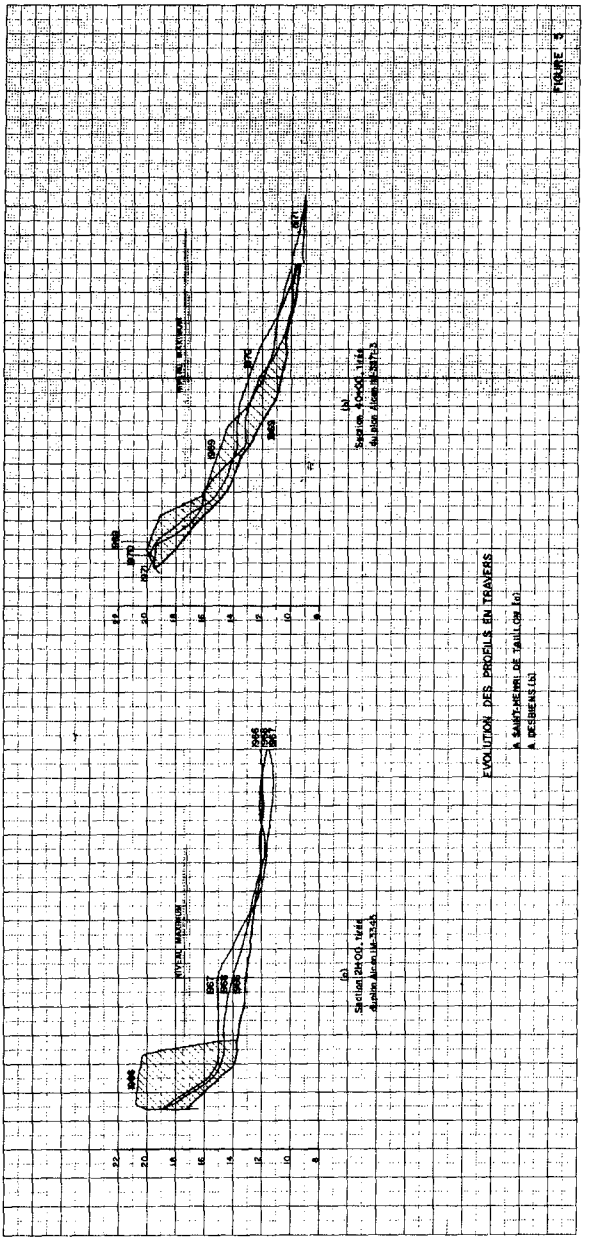
EVOLUTION DES PROFILS EN TRAVERS
A SABLE MOYEN DE TAILLE (Ø 50)
A DESSINER (1)
PLAGE 5

TABLEAU 1 : COMPARAISON ENTRE LA GRANULOMETRIE DES APPORTS ET CELLE DU SABLE QUI SE TROUVAIT DANS LA PARTIE HAUTE DES PLAGES D' ORIGINE

ENDROIT	Diamètre 50 %	Diamètre 90 %	Diamètre 10 %
Saint-Jérôme (section 1)			
Apports	0.7 mm	1.1 mm	0.5 mm
Matériau d' origine	0.40 mm	0.75 mm	0.25 mm
Desbiens (section 4)			
Apports	0.6 mm	0.95 mm	0.42 mm
Matériau d' origine	0.5 mm	0.75 mm	0.34 mm
Pointe-Bleue (section 11)			
Apports	0.60 mm	1.09 mm	0.37 mm
Matériau d' origine	0.5 mm	1.0 mm	0.22 mm
Vauvert (section 7)			
Apports	0.45 mm	1.1 mm	0.17 mm
Matériau d' origine	0.10 mm	0.29 mm	0.05 mm
St-Henri de Taillon (section 9)			
Apports	0.35 mm	0.45 mm	0.23 mm
Matériau d' origine	0.47 mm	0.72 mm	0.3 mm
Saint-Méthode (section 5)			
Apports	0.39 mm	0.5 mm	0.22 mm
Matériau d' origine	0.46 mm	0.60 mm	0.38 mm

TABLEAU 2 : CALCUL DU VOLUME D'APPORT DEMEURE EN DEÇA DES LIMITES DU LEVE BATHYMETRIQUE EN FONCTION DU TEMPS

PLAGE DE ST. HENRI DE TAILLON					PLAGE DE DESBIENS			
SECTION	1966	1967	1968	1969	SECTION	1969	1970	1971
0 + 00	100%	100%	222%	170%	25 + 00	100%	132%	106%
1 + 00	100%	100%	169%	203%	26 + 00	100%	115%	82%
4 + 00	100%	34%	51%	24%	27 + 00	100%	84%	108%
5 + 00	100%	60%	36%	66%	28 + 00	100%	80%	67%
6 + 00	100%	87%	75%	26%	29 + 00	100%	90%	103%
7 + 00	100%	55%	59%	50%	30 + 00	100%	103%	76%
8 + 00	100%	45%	58%	63%	31 + 00	100%	111%	99%
9 + 00	100%	44%	55%	39%	32 + 00	100%	97%	96%
10 + 00	100%	26%	64%	45%	33 + 00	100%	87%	112%
11 + 00	100%	39%	20%	10%	34 + 00	100%	100%	111%
12 + 00	100%	66%	54%	40%	35 + 00	100%	112%	116%
13 + 00	100%	89%	77%	63%	36 + 00	100%	110%	102%
14 + 00	100%	62%	67%	64%	37 + 00	100%	112%	94%
15 + 00	100%	97%	103%	66%	38 + 00	100%	113%	86%
16 + 00	100%	65%	79%	26%	39 + 00	100%	100%	107%
17 + 00	100%	72%	73%	17%	40 + 00	100%	112%	152%
18 + 00	100%	51%	70%	56%	41 + 00	100%	82%	161%
19 + 00	100%	65%	26%	4%	42 + 00	100%	77%	134%
20 + 00	100%	92%	73%	36%	43 + 00	100%	84%	108%
21 + 00	100%	79%	36%	16%	44 + 00	100%	111%	105%
22 + 00	100%	100%	52%	27%	45 + 00	100%	130%	97%
23 + 00	100%	65%	38%	9%	46 + 00	100%	168%	98%
24 + 00	100%	55%	46%	30%	47 + 00	100%	73%	96%
25 + 00	100%	82%	65%	34%	48 + 00	100%	84%	80%
26 + 00	100%	128%	101%	50%	49 + 00	100%	119%	78%
27 + 00	100%	111%	112%	19%	50 + 00	100%	69%	104%
28 + 00	100%	32%	31%	9%	51 + 00	100%	82%	139%
29 + 00	100%	124%	75%	39%	52 + 00	100%	107%	93%
30 + 00	100%	73%	33%	29%	53 + 00	100%	90%	111%
31 + 00	100%	119%	46%	6	54 + 00	100%	89%	102%
32 + 00	100%	69%	94%	49%				
33 + 00	100%	78%	65%	21%				
34 + 00	100%	57%	70%	34%				
35 + 00	100%	66%	55%	27%				
36 + 00	100%	117%	22%	12%				
37 + 00	100%	42%	69%	57%				
MOYENNE	100 %	73 %	67 %	42 %	MOYENNE	100 %	92 %	95 %

LABORATOIRE HYDRAULIQUE LASALLE LTÉE LASALLE HYDRAULIC LABORATORY LTD.

PHOTOS

(a)

du chantier 1966

(b)

de la drague à l'oeuvre

LABORATOIRE HYDRAULIQUE LASALLE LTÉE LASALLE HYDRAULIC LABORATORY LTD.

PHOTOS

(c)

du remorqueur

(d)

de la
"débusqueuse"

CHAPTER 83

COASTAL SAND MANAGEMENT SYSTEM

by

Birchard M. Brush

Scripps Institution of Oceanography, University of California

La Jolla, California 92037

ABSTRACT

Interruption of sand transport is the most persistent worldwide coastal problem. Wave action produces sand transport which is not a problem in some areas but in others results in coastal erosion, obstruction of harbor entrances, and permanent loss of sand. Conflict between saving sand and bypassing it is caused by a lack of methods to manage this valuable resource. Separate elements of control have been used with varying degrees of success; now it is proposed to incorporate subsystems into an integrated system for management of the littoral transport. A coastal sand management system is to be evaluated using three principal subsystems: (1) a mobile jet pump for use with a crater sink and fluidization accessories; (2) interlocking inertial modules which simulate structural materials because of high intergrain stresses; and, (3) the tactical deployment of phase dependent roughness elements to direct (or reverse) the net transport of sand.

A coherent sand management system promises to make a start toward true control of littoral sand transport. In addition, there is the prospect of eventually establishing the first self maintaining harbors.

It is attractive to consider systems which would be operative within reasonable cost, which may be entirely submerged, and which are capable of operating without regard to surface seakeeping problems.

Some aspects of the system indicate possible use of the mobile jet pump as a means for estimating longshore transport in the field, use in archaeology, and as a dredging and maintenance tool for small nations whose investment capital could not support massive dredging operations.

INTRODUCTION

Everything in the coastal zone, as with life in general, turns into a system. It can be a system at the outset, or through insufficient planning, become one at a less convenient time. An example is the construction of a coastal feature which may have been erected without regard to all of the factors bearing upon the problem, and which then possibly caused new problems by its presence.

Historically, there did exist unique and systematic means of coping with littoral drift around 1500 B. C. Two types of harbors are known to have existed during those times; continuous self-flushing harbors, which accomodated large numbers of ships even by today's standards, and; flushable harbors, which were periodically flushed in the manner of a modern tank toilet, for the removal of sand and silt. Exemplary were the harbors of Tyre (rhymes

with fire) and Sidon (rhymes with widen) on the coast of Phoenicia, locations that on modern maps are on the southern coast of Lebanon.

In 332 B. C., a year before his death, Alexander The Great laid seige to Tyre. To gain access to the walled city which was on a small offshore island, he built a causeway which interrupted the current flow through the harbor, and the divided portions of the harbor began to accrete; the causeway became a tombolo through continued accretion of sand. The method of cleaning the harbor was lost at the time of the Romans and the harbor remains sand covered today.

The harbor at Sidon was flushed by a system of two large sea water storage tanks filled by wind driven swell in the absence of large tidal range which when discharged into the harbor could cause enough current to entrain sediment and thus make it available to bypass along the coast. While wise enough not to resist Alexander, this knowledge of the harbor's manner of operation was lost in about the second century A. D.

In spite of the fact that the resourceful methods of maintaining these harbors were rediscovered in the 1930's by a remarkably astute French priest-archeologist, Pere A. Poidebard, a harbor built by modern engineers in 1958 at Tyre, to provide a Mediterranean terminus for the Saudi-Arabian petroleum pipeline during the Suez crisis, silted up in four months (McKee, 1969).

Modern techniques were not available to the ancients, and because of that fact, they were quite resourceful and innovative. It would appear that today we are 'hoist by our own technological petard' in that sand handling and dredging skills are available only in single expensive remedies, if at all.

At the Scripps Institution of Oceanography, a coastal sand management system is now under study. Its aim is to establish methods for remedial sand bypassing. The coastal sand management system consists of (but is not limited to) three principal subsystems: (1) the crater sink sand transfer system with optional fluidization; (2) ballasted interlocking inertial modules; and, (3) the tactical deployment of phase dependent roughness elements to direct the net transport of sand (Inman and Tunstall, 1972) (Figure 1).

The Crater Sink

The 'jet pump', a form of eductor using the kinetic energy of pumped clear water to entrain sediment laden water, has undergone design and performance improvements in recent years. Originally used in the 1840's for water wells, and more recently as an aid in maintaining suction lift for dredge mounted centrifugal pumps, it now promises to become a dredging means when used alone (it was first proposed for coastal sand handling in 1911) (Knowles and Rice, 1911). The jet pump may be used to form and maintain its own crater (Inman and Harris, 1971), thus maintaining an intentional and purposeful sink. A header of flow controlled valves may be used as an adjunct to the crater. It would use a portion of the driving water to fluidize the sand bottom; the increase in pore pressure reduces the coefficient of internal friction of the sand and permits it to flow freely under the influence of currents and gravity. The current which feeds secondary flow to the inlet of the jet pump would then carry additional sand to the crater where the inlet to the jet pump would be enriched.

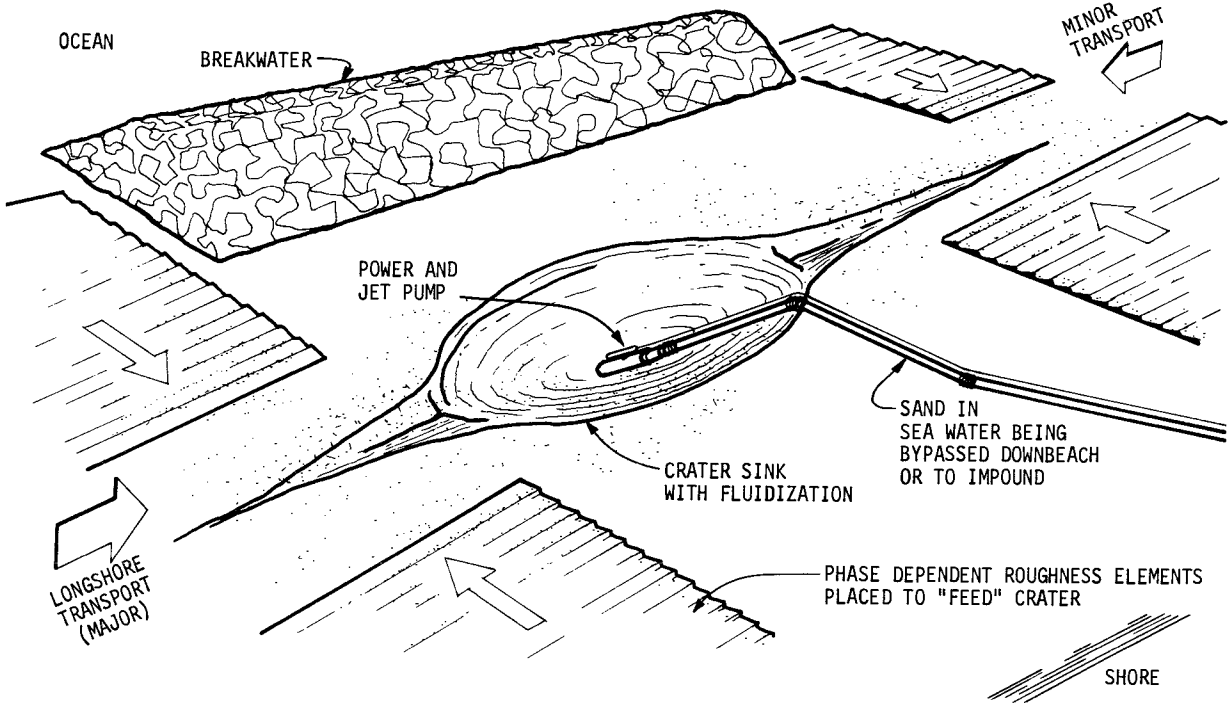

Figure 1. A coastal sand management system. Shown schematically are the crater-sink sand transfer systems, ballasted interlocking inertial modules assembled, for example, into a breakwater or other energy attrition means, and phase dependent roughness elements deployed to influence the direction of sand movement and enrich the crater. These elements are now under intensive study at the Scripps Institution of Oceanography.

A portable system is being assembled which consists of a trailer mounted power supply to drive a jet pump. This unit, fully instrumented, will be transportable. It will be tested in the Scripps Hydraulics Facility especially built slurry test loop. The closed loop test fixture will provide baseline data on carrying capacity, ability to maintain crater geometry by establishing quasi-equilibrium repose angle, ability to pump the crater free of induced cave-ins, ability to pump against slopes, and will continuously record the parameters of interest (Figure 2).

The desired information will include hydraulic head differentials, mass transport, flow velocities and establishment of Newtonian vs Bingham-plastic relationships. After completion of the laboratory phase, the design will have been refined in such a manner that it may be transported to a field location. The packaging will include a mobile power pack consisting of: engine, hydraulic pump, fuel, and instrumentation panel. Standard process electromagnetic flow meters, an important adjunct, will be used both in the test loop and hopefully, be modified for underwater use in the field. A submerged drive will power the pump from as near as possible to the water pump to avoid paying the hydraulic head penalty associated with surface pumping (Hammond, 1969). An air boost is an option which will be studied to determine its contribution as a velocity modulator, and as a means to augment hydraulic head differential.

It should be noted that this method holds promise for use in shallow water dredging, for which no satisfactory method now exists. In addition to a static application such as a crater sink, it has application to dynamic methods such as: 1) programmed 'sweeping' of a river channel or harbor entrance, or in response to wave climate information from sensors; 2) riding on the decks of ships using the harbor entrance (the hitch-hiking feature could be a portion of the harbor fees) for tide phased agitation dredging (Figure 3); 3) arrayed in fixed grids on the bottom. Units would be operable singly or in groups in response to storm impulses or wave climate changes either by operator choice, or as part of a feedback loop; and, 4) arrayed in series along a channel to resuspend sediment and eventually direct it to a crater sink.

In addition to the above direct applications for a mobile shallow water sediment bypassing system, the following uses should be studied: 1) the removal of sediment from dams and other river and stream obstructions; 2) use as a means of excavating a reference crater or channel along a sandy coast or harbor channel for the purpose of estimating littoral drift or channel accretion; 3) use for dredging sediment containing trapped gas (presently considered impossible to dredge because gas pockets break the suction on surface mounted centrifugal pump dredging equipment); 4) use for shallow water archaeology; and inland excavation by wetted crater if clear water may be pumped to the excavation (crater) site.
N. B: The only present options available to underwater archaeologists are the air lift, which requires large hydraulic head differences; and the water jet, which suspends as well as removes sediment thus limiting underwater visibility and not remotely relocating the sediment. 5) use in nations whose economic capability is limited, who cannot afford monster-dredge overkill. Many small harbors (for example; fishing harbors and marinas) could benefit by a small, efficient portable machine to control sediment. Further, the possibility of enhancing sediment movement by the use of two pipes, properly sized, with no machinery or external energy requirements should be studied

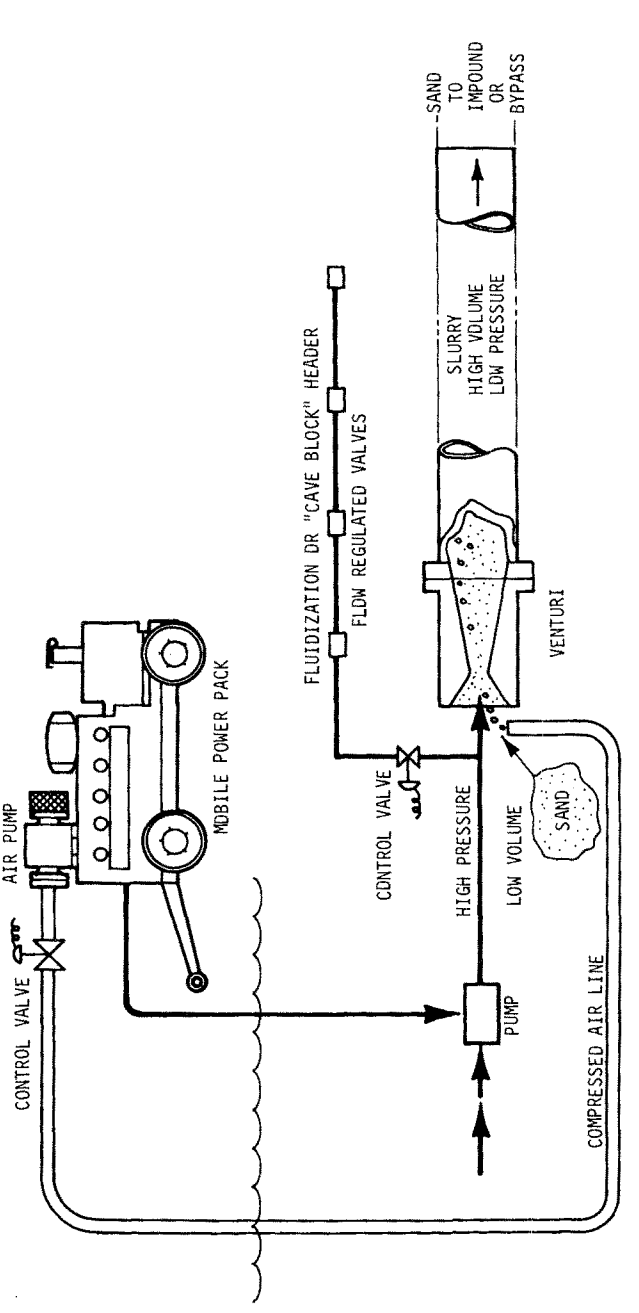

Figure 2. Schematic of the mobile power pack and pump which will be used to investigate sand transfer capabilities of a moderately sized unit. Single, two-phase, and three phase flows will be parametrically evaluated. The three-phase studies are a hybrid design, yet to be proven; but considered promising. "Cave block" refers to a possible technique for eroding the crater, thus enriching secondary flow to the jet pump.

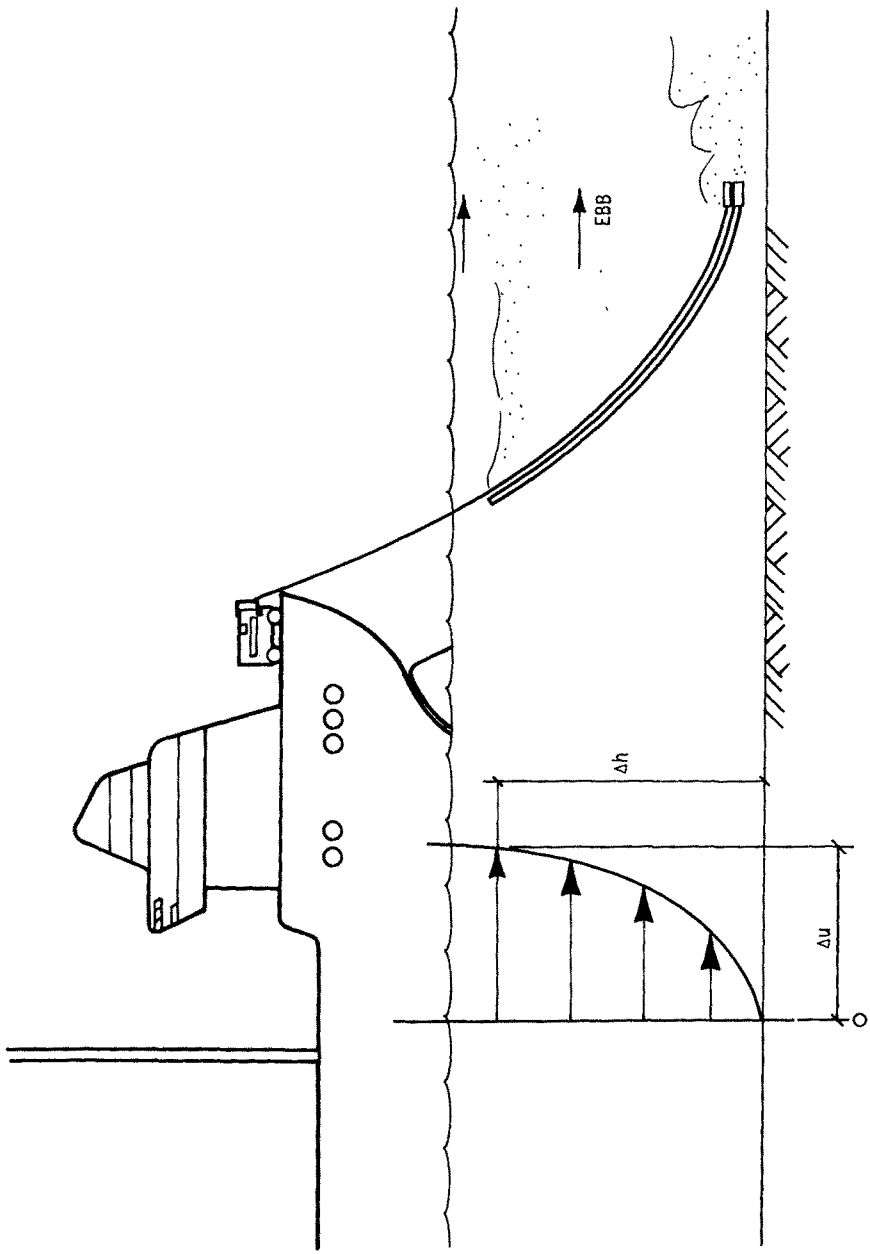

Figure 3. Current or tide-phased "agitation" dredging will be evaluated using the mobile power pack and jet pump. Δh and Δu interact to enhance the optimum relocation of sediment. For less affluent ports and harbors; the hitch-hiking mobile unit could offset, partially, the usual port fees.

(Figure 4). A series of pipes could be placed in a portion of a channel cross section offering the greatest velocity, and by means of a venturi tube, allow a smaller pipe to lift sediment from the bottom. Thus, periodically resuspended by these units at appropriate intervals, sediment could be relayed along, powered solely by the velocity due to the flowing water.

Ballasted Inertial Modules

Techniques to alter the angle of incidence, cause shoaling, or other encouragement of energy control for waves may be enhanced by manmade forms which ideally would utilize native materials, minimize labor, and be low in capital investment. Rocks, riprap, and other native forms have occasionally been augmented or replaced by manmade concrete forms whose inertia and dimensions tend to resist overturn, sliding or rolling by wave action. With the availability of manmade fibers which do not degrade rapidly in the marine environment or from ultraviolet degradation, a new generation of modules should be studied which would take advantage of the requirements listed above. For example, the tetrahedral shape (the botanical or medieval caltrop) may be placed in sites by pumping a dense sand and water mixture into a shape, manufactured of loosely woven polyvinyl alcohol fibers, or an equally durable material.

The water used to pack the sand into the shape would be forced out through the coarse weave, leaving a densely packed rigid form. The forms then could be arrayed in patterns which would endure for a reasonable economic period. Unlike the virtually permanent commitment of rock or concrete shapes, the fabric shapes could be slit and emptied, if necessary, by a diver with a knife. The prospect of searching for optimum shapes with rapid computer graphics is attractive, although regular polyhedra will pack to fill a space (Figure 5). This elegant and efficient technique forms the basis for much of R. Buckminster Fuller's structures (Fuller, 1969). By combining regular shapes to fill space, the critical shear stress for incipient movement becomes much larger, since it is nominally proportional to $(\text{volume})^{1/3}$. In addition, free body diagrams within the space indicate excellent resistance to internal shear because of the efficiently spaced ligaments which were the original shape boundaries. Tetrahedra may be formed when cut from continuous tubes, the method is well known in packaging technology; if a continuous tube with a circumference of four units is cut to a length equal to $\sqrt{3}$ units and the end seams are 90^{o} out of phase, the result will be a regular tetrahedron similar to the small diary product containers found in the U. S. Grain to grain stress may be increased, and specific gravity of sand filled shapes of over 2.0 may be achieved by two methods; 1) after filling, a girth ring (of standard industrial plastic banding) may be tightened around, say a sand bag, and for a slight reduction in volume, a high intergrain stress results. A limp sand bag when stiffened in this manner behaves like a structural unit even though the girth ring causes a reduction in the section modulus of the shape; and, 2) if the external shape is critical and must not be distorted, a small bladder may be introduced inside and expanded to gain higher intergrain pressure (Brush, in preparation).

Inert "shapes" were made with sea water only. Common porous canvas duck was filled with sea water and a polymeric gel (American Cyanamid AM-9 Grout) added which gelled the entire mass; the specific gravity is, of course, virtually that of sea water but a dramatic change in viscosity is achieved thirty seconds (or less) after the introduction of a small amount of the agent in power form.

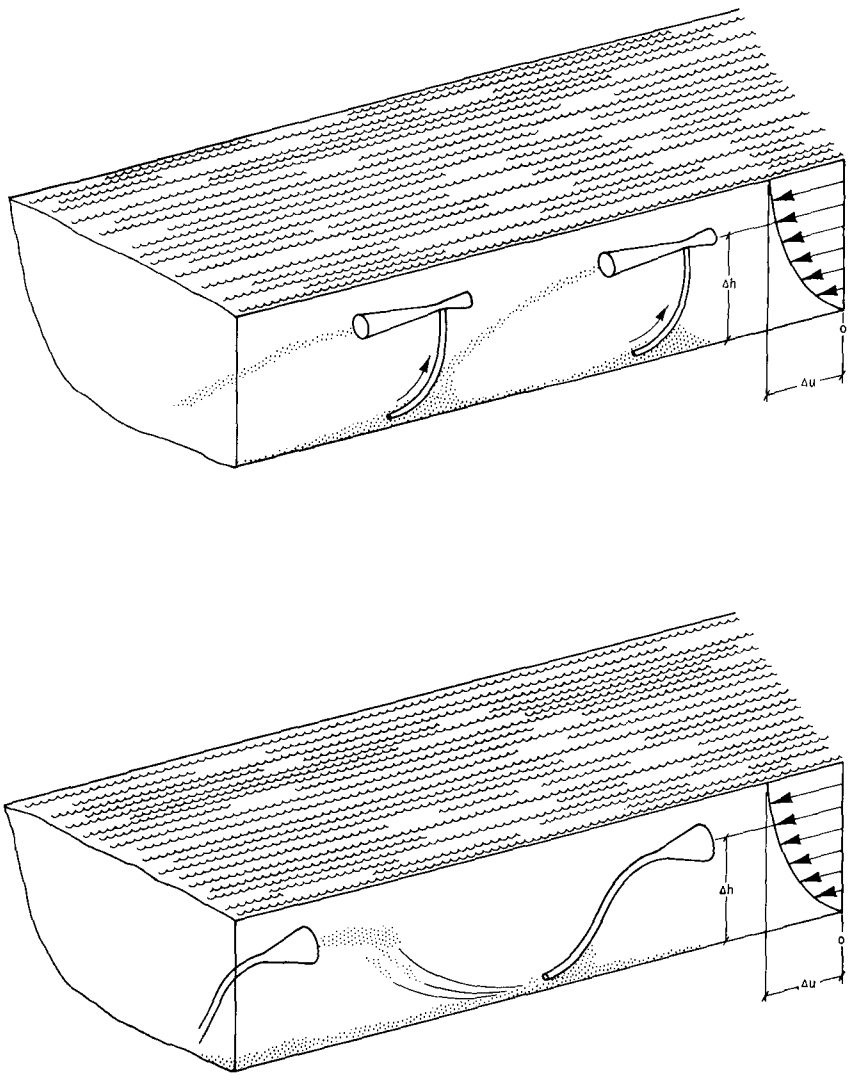

Figure 4. Cascade methods of enhancing sediment transportation need study to capitalize on difference in velocity potential in a fluvial system or in a harbor entrance. Tethered, buoyant units could capture the maximum velocity compatible with maximum ship depth and assist in channel maintenance without placing claims upon the earth's energy budget.

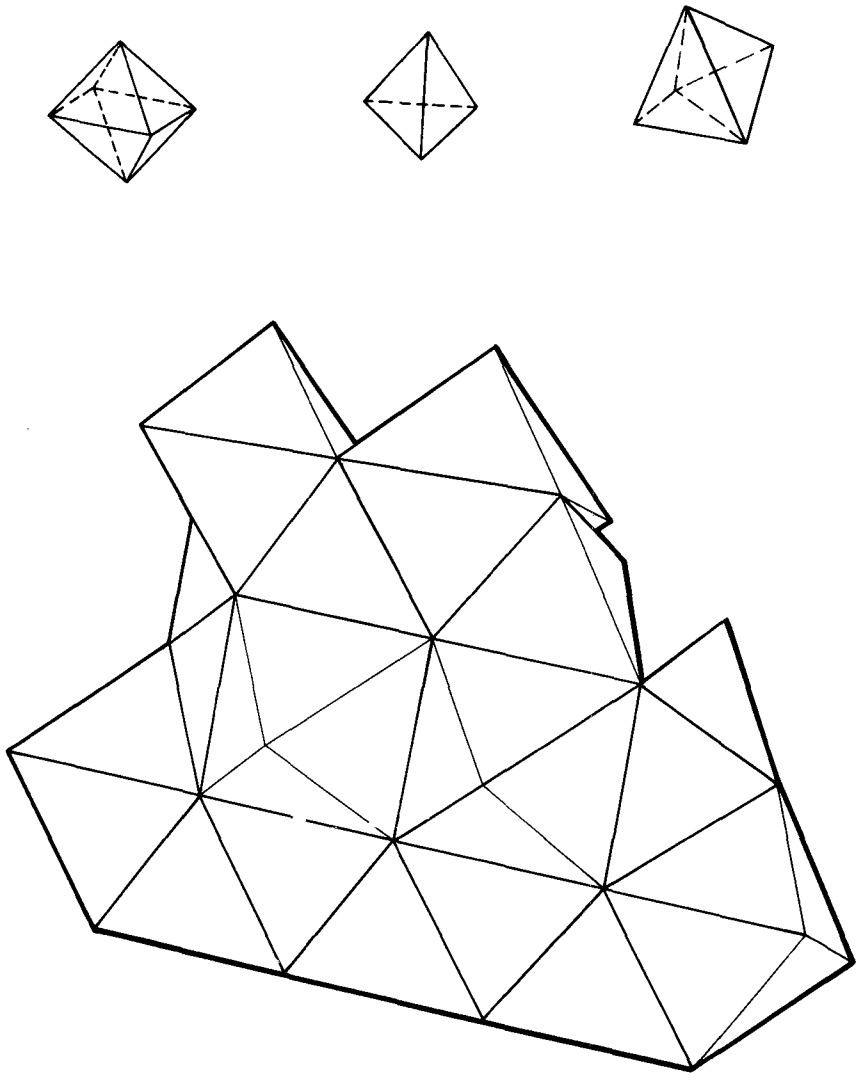

Figure 5. Regular polyhedra will pack to fill space in a complimentary manner. When space is filled in this manner, such as in the formation of a groin, the efficiently spaced ligaments (formed by the equilateral triangles that are the original boundaries of the shapes) have excellent resistance to internal shear.

Phase Dependent Roughness Elements

The importance of the shapes of ballasted modules becomes more evident when the phase dependent roughness elements which control, and even reverse sand transport are considered. Using shapes which, when filled, could be laid on the sea floor like a heavy carpet could enable sand to be directed by wave action to the jet pump from any desired direction.

The first models of elements were placed on the relatively smooth, sandy bottom of Scripps Beach in late 1971 and a larger array in the spring of 1972, all of these were rigid plaster or concrete forms and performed as laboratory studies had predicted. The first combined use of phase dependent elements with a flexible filled shape consisted of a frame of metal which dictated the height and wavelength of the elements. It was covered by a fabric "skin" whose panels had been partially rigidized with resin.

Recent laboratory tests and model experiments show that a remotely controllable array of elements may be made which will be movable, and respond to changes in wave climate, or to reversals in the direction of the principal sand transport. These modular shapes now are the precursors of elements whose slopes may be modified when control is achieved through a feedback loop in a given location. Changes in wave climate, fed into a computer, would cause modulation of the height-slope characteristics to cope with the changed conditions.

The System

When these subassemblies are integrated in order to act as a coherent system they promise to make a start toward true control of littoral sand transport (provided that the activities are preceeded by prudent and enlightened observation). In addition, there is the prospect of eventually establishing the first modern self-maintaining harbors. It is attractive to consider systems which would be operative within reasonable cost, which could be designed to be entirely submerged, and to operate without regard to surface seakeeping problems. The limitations of standard dredges have received comment (Wiegel, 1964), and additional incentives to the adoption of systems are the complicating factors of the 8 hour work day, and the forty hour week. These factors have forced costs higher because of the enormous cost attendant to the use of premium time, and multiple shift problems. One resort has been the use of larger and larger equipment to extract the maximum quantity from one 8 hour shift. The purpose of this contribution is to suggest that bigger is not necessarily better.

Conclusion

In a harbor which interrupts longshore drift, a system would provide an efficient and continuous means of bypassing or impounding sand for beach replenishment, commercial use, or simply to bypass downcoast. The prospect of maintaining deep channels for vessels drawing 70 feet or more is attractive because channels may be 'swept' using elements of this system. It would be possible to maintain a clear channel and manage the subaqueous profile of a sick harbor entrance. An economical method might make the competitive difference for a small harbor whose economic health was traffic dependent.

A form of jet pump has been in use for years in Colorado and in northern California for use in the extraction of heavy metals from crevices (Clark, 1972). It seems possible that the effort to continuously, or on a

sample basis, perform centrifugation of the effluent of the jet pump and sample the content of the crevices in the phase dependent elements, might result in enough income to partially defray routine maintenance expenses.

Some of the ideas advanced herein are admittedly conjectural but if successful and adequately promulgated, we may rest assured will be thoroughly dogmatized. The development of a coastal sand management system would provide a solution to an urgent and continuing problem.

Acknowledgements

I thank the U. S. Department of Commerce, NOAA, Sea Grant Program for providing an atmosphere which encourages innovation and dissemination without overpatronizing. The U. S. Army Corps of Engineers, Waterways Experiment Station, for supporting innovative research, and Professor Douglas Inman, Scripps Institution of Oceanography, for patient and helpful criticism.

REFERENCES

Brush, B. M., in preparation, "Ballasted interlocking inertial modules".

Clark, W. B., 1972, "Diving for Gold in California", California Geology, vol 25, no 6, p 122-143.

Fuller, R. B., 1969, Ideas and Integrities, MacMillan, New York, 318 pp.

Hammond, R., 1969, Modern Dredging Practice, Chapter 1, p 1-27, Fredrick Muller, London, 274 pp.

Inman, D. L. and R. W. Harris, 1971, "Crater-sink sand transfer system", Proc. Twelfth Coastal Engin. Conf., Amer. Soc. Civil Engin., New York, vol 2, p 919-933.

Inman, D. L. and E. B. Tunstall, 1972, "Phase dependent roughness elements", Thirteenth Int. Conf. Coastal Engin., Amer. Soc. Civil Engin., Abstracts Volume.

Knowles, M. and J. M. Rice, 1911, "Use of the water ejector for transporting sand", Jour. New England Waterworks Assoc., vol 25.

McKee, A., 1969, History Under the Sea, p 263, E. P. Dutton, New York, 342 pp.

ADDITIONAL REFERENCES OF INTEREST TO READERS

Diole, P., 1954, 4000 Years Under the Sea, Promenades d'archeologie sous-marine (trans. G. Hopkins) J. Messner, New York, 237 pp.

Frost, H., 1963, Under the Mediterranean: Marine Antiquities, Routledge and Kegan Paul, London, 278 pp.

CHAPTER 84

FAILURE OF SUBMARINE SLOPES UNDER WAVE ACTION

by

R. J. Mitchell [1]

K. K. Tsui [2]

D. A. Sangrey [3]

ABSTRACT

The results of model tests, carried out to evaluate the stability of submarine slopes under wave action are presented. A Bentonite clay was sedimented in a glass walled tank 6 feet long by 0.5 feet wide by 2.5 feet deep. The sedimentation and consolidation processes were studied and sediment densities were measured at various depths in the profile. Vane shear strength profiles were also measured at various average degrees of consolidation. Plastic markers were placed in the sediment adjacent to a glass wall so that the soil movements under both gravity and wave induced slides could be documented by photography. Dimensional similitude is discussed and the model test data are presented in a dimensionless form.

All instabilities were observed to be of the infinite slope type. Analysis of the data shows that wave action is instrumental in initiating downslope mass movements in gently to steeply sloping off-shore sediments. General lack of agreement between the model test results and published theoretical analyses was found but there was close similarity in the depths and form of failure under wave action and under gravity stresses alone. The loss of stability under wave action is analyzed on the concept that failure is gravity controlled and the soil strength is reduced to a value commensurate with gravity sliding by the cyclic shearing stresses imposed by progressive waves. A method of evaluating the stability of prototype slopes using a model test correlation and field vane strength measurements is proposed.

INTRODUCTION

Instabilities in submarine slopes have been observed or have been inferred over a wide range of slope angles from less than half a degree up to about 30°. These subaqueous landslides are believed to have caused rupture of submarine cables and to have generated many of the geomorphological features on the ocean bottom. There are numerous records describing these landslides but very few publications discuss the application of the principles of soil mechanics to the analysis of the stability of submarine slopes.

---

[1] Associate Professor of Civil Engineering, Queen's University at Kingston, Canada

[2] Soils Engineer, Geocon Ltd., Toronto, Canada

[3] Associate Professor of Civil Engineering, Cornell University, Ithaca, N.Y.

One of the particular features of many marine sediments is the time lag between the accumulation of sedimenting materials and the dissipation of excess pore water pressures which develop within the sediment. Such sediments are described as being underconsolidated. The excess pore water pressure at any level in the deposit will reduce the effective stresses and the undrained shear strength below values appropriate to the fully consolidated state. Underconsolidated sediments are, therefore, less stable than consolidated sediments.

In areas where oversteepening of slopes develops as a result of local erosion or crustal tilting gravitational forces may be sufficient to cause landslides (Terzaghi, 1956). Earthquakes and other seismic activity are widely accepted as causal agencies in submarine landsliding (Gutenberg 1939; Ambraseys 1960; Morgenstern 1967). Submarine landsliding has occurred in the absence of seismic activity however (Dill 1964; Chamberlain; 1964) and Henkel (1970) shows that the bottom pressure pulses due to ocean waves could be a major factor in initiating movements. This paper is concerned with the role of waves in initiating submarine landslides.

One of the effects of ocean waves is to produce pressure changes within the water below the surface and pressure pulses on the surface of the sediment. As a wave passes a pressure increases δp above the mean hydrostatic bottom pressure is felt below the crest while beneath the trough there is a pressure decrease $-\delta p$. The magnitude of the excess pressure δp, which is in phase with the wave, depends on the wave length L, wave period T, wave height H and the depth of water d, (Wiegel, 1964) and is given by:

$$\delta p = \frac{H}{z} \frac{\cosh k (z + d)}{\cosh kd} \cos (kx - \sigma t) \qquad (1)$$

where $k = \frac{2\pi}{L}$ and $\sigma = \frac{2\pi}{T}$

At the mudline ($Z = -d$) the excess bottom pressure is distributed as shown in Figure 1 and may be calculated as:

$$\delta p = K_p \eta \qquad (2)$$

where $K_p = \frac{1}{\cosh kd}$ is the pressure response factor on the top of sediment

$\eta = \frac{H}{2} \cos (kx - \sigma t)$ is the fluctuation of water level due to waves

Values of K_p are tabulated in standard oceanography texts. It may be noted that the excess pressure becomes negligable when the depth of water d is greater than half of the wave length L. Because of the difference in pressure under crest and trough, the passage of a wave induces shear stress in the soil. As the wave passes, soil at a particular point experiences cyclic fluctuation in magnitude and direction of these induced stresses.

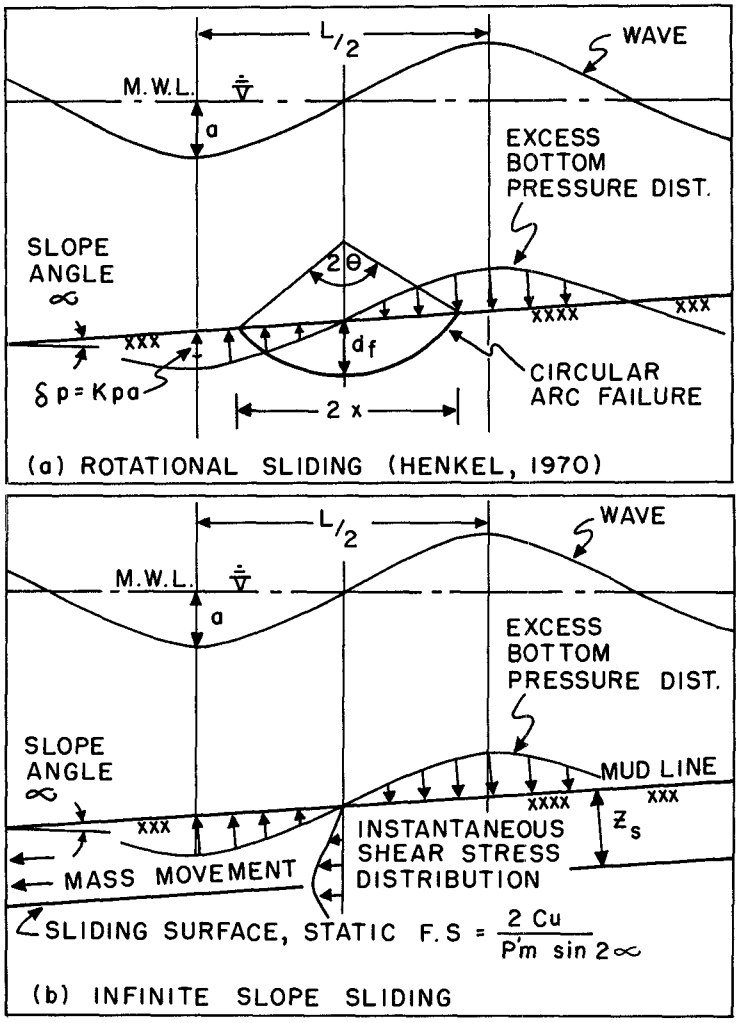

FIGURE 1 STATIC REPRESENTATION OF POSSIBLE FAILURE MODES

Considering static moment equilibrium on a circular arc sliding surface beneath a standing wave (Figure 1a) Henkel (1970) demonstrated that the excess bottom pressures at a given instant are sufficient to cause shear failure in underconsolidated soft sediments. Henkel substantiated his calculations using strength data from sediments in the Mississippi delta and he suggests that under a natural progressive train of waves, a sequence of circular arc slides would result in progressive down slope movement of the sediment. The critical depth of failure, d_f, in Figure 1a, is shown by Henkel to be a function of the wave length and excess bottom pressure. Henkel also calculates the subsurface pressure required to cause instabilities for a range of wave conditions.

Mass downslope movements of sediments could also develop in the form of infinite slope sliding as shown in Figure 1b. The distribution of shearing stresses in the sediment under a given excess pressure distribution may be estimated from the deformation characteristics of the soil (Wright and Dunham, 1972). At some depth in the sediment the shearing stresses may exceed the shearing strength and sliding would develop on a surface almost parallel to the mudline (for small slope angles). The depth of failure, Zs, in Figure 1b will be a function of the stress-strain strength properties of the sediment and the wave characteristics. Both failure mechanisms shown in Figure 1 are applied to the idealized situation of a uniform soil profile deposited and sedimented in a single layer. Layered materials and time dependent accumulation of sediments are not considered in this paper. Henkel's analysis is an upper bound solution while the analysis due to Wright and Dunham is a lower bound solution with soil movements being predicted using a non-linear stress-strain relationship.

Two dimensional model studies of slope failures initiated by wave action are described in this paper. The wave height (for a given d/L ratio) required to initiate failure, the depth of failure and the form of the soil movements were measured. The data are discussed with reference to the theoretical developments noted above.

MODEL STUDIES

Dimensional considerations

If the gravitational forces acting on an element of soil are to be correctly modelled it is generally necessary that the model and prototype be composed on the same material (Roscoe, 1969). A montmorillonite clay (commercial Bentonite) was chosen as the sediment and was mixed with distilled water which contained sodium chloride at a concentration of 35 p.p. thousand by weight. A 10 percent by weight suspension of clay was prepared for testing. Sea water was represented in the wave flume by a mixture of 35 parts sodium chloride per thousand parts of water. A model tank of dimensions 6 ft. long by 2 ft. deep by 0.5 ft. wide was chosen from the following considerations:

(i) the depth of sediment would be in excess of anticipated depths of failure.

(a) DRAINAGE CRACKS

(b) VANE SHEAR APPARATUS

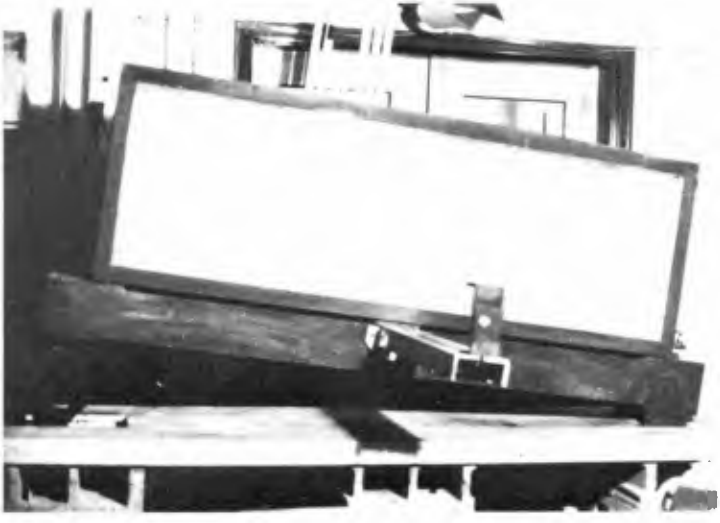

(c) SLOPE AFTER STATIC FAILURE

FIGURE 2 CONSOLIDATION AND STATIC TILTING EXPERIMENTS

(ii) the depth of water to wave length (d/L) ratio would be within the range where excess bottom pressure are considered significant in initiating sliding.

(iii) the tank length would be in excess of 1.5 wave lengths so that the form of the movements would not be unduly influenced by boundaries.

(iv) the width to length ratio of the tank would be representative of plane strain conditions.

(v) economic considerations.

In a sedimented underconsolidated or normally consolidated soil profile the undrained shear strength Cu of the soil is expected to increase linearly with depth and is generally expressed as a constant Cu/P_o' ratio where P_o' is the effective overburden pressure at a given depth ($P_o' = z\bar{\gamma}'$). This definition of p' does not account for any excess pore water pressure that will exist in underconsolidated soils. The consolidation process and average degree of pore water pressure dissipation may be characterized by two dimensionless parameters; the degree of consolidation $\bar{U}$ (often expressed as a percentage) and the time factor Tv which may be related to the soil compressibility, soil coefficient of permeability and length of the drainage path. For circular arc sliding in a soil exhibiting a linear increase in strength with depth, Gibson and Morgenstern (1961) have shown that the factor of Safety (F.S.) is independent of the slope height. The independence of failure on slope height is apparent for infinite slope sliding. Thus either of the failure mechanisms shown in Figure 1 could develop in the model tank. A slope studied in the model tank is considered to be identical to a prototype slope having the same slope angle α, and the same Cu/P_o' ratio. Measured depths of failure and wave heights (or excess bottom pressures) required to cause failure in the model slopes may be used to evaluate the theories advanced. The scale factor used for these parameters is in the order of 100 to 500.

Sediment preparation

The Sedimentation and consolidation processes were studied in the model tank shown in Figure 2c. Vane shear tests (Figure 2b) and excess pore water pressure measurements were carried out at various stages of consolidation. Variations in density through the soil profile were also measured. These studies were carried out to provide background data for interpretation of the stability studies and the details of apparatus and procedure are outlined by Tsui (1972). Only those data directly related to the stability problem are presented in this paper. A typical sedimentation-consolidation curve for the test sediment is plotted in Figure 3. During the latter stages of sedimentation drainage channels with associated surface boils were observed to form in the sediment (Figure 2a). The beginning of primary consolidation was marked by an abrupt change in the rate of settling of the mud line, closing of the drainage cracks and the commencement of excess pore water pressure dissipation. The average degree of consolidation defined by settlement of the mudline correlated well with the average degree of consolidation

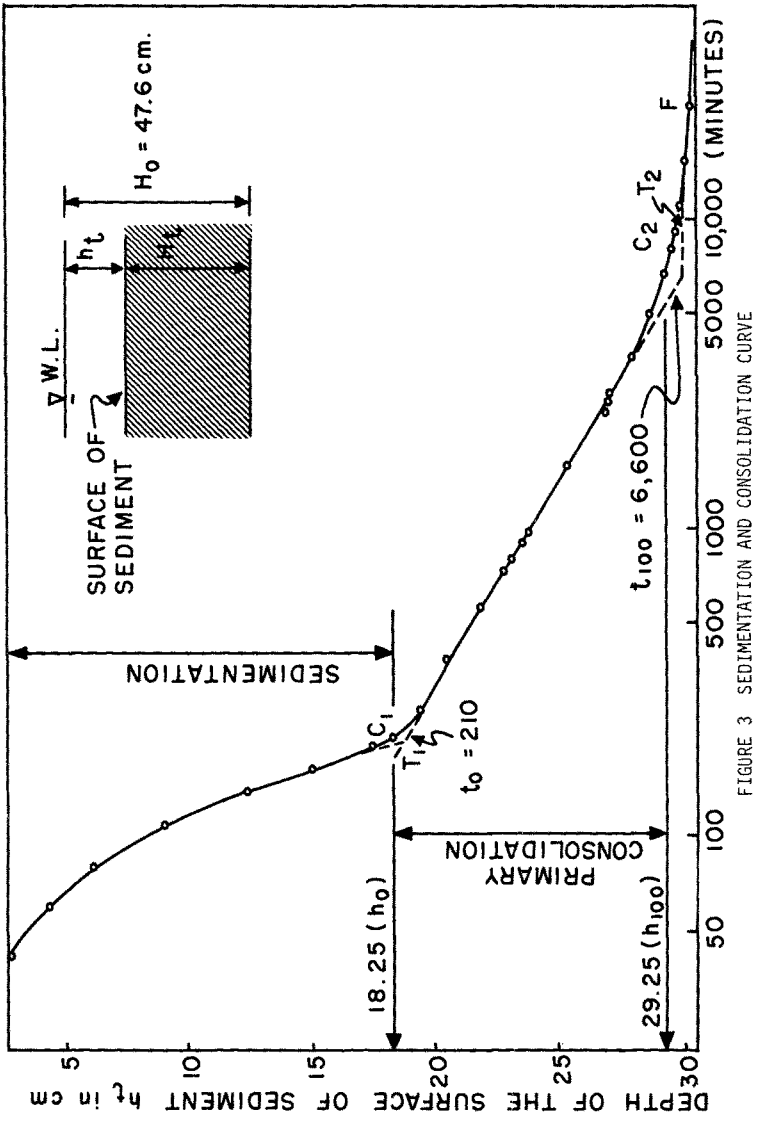

FIGURE 3 SEDIMENTATION AND CONSOLIDATION CURVE

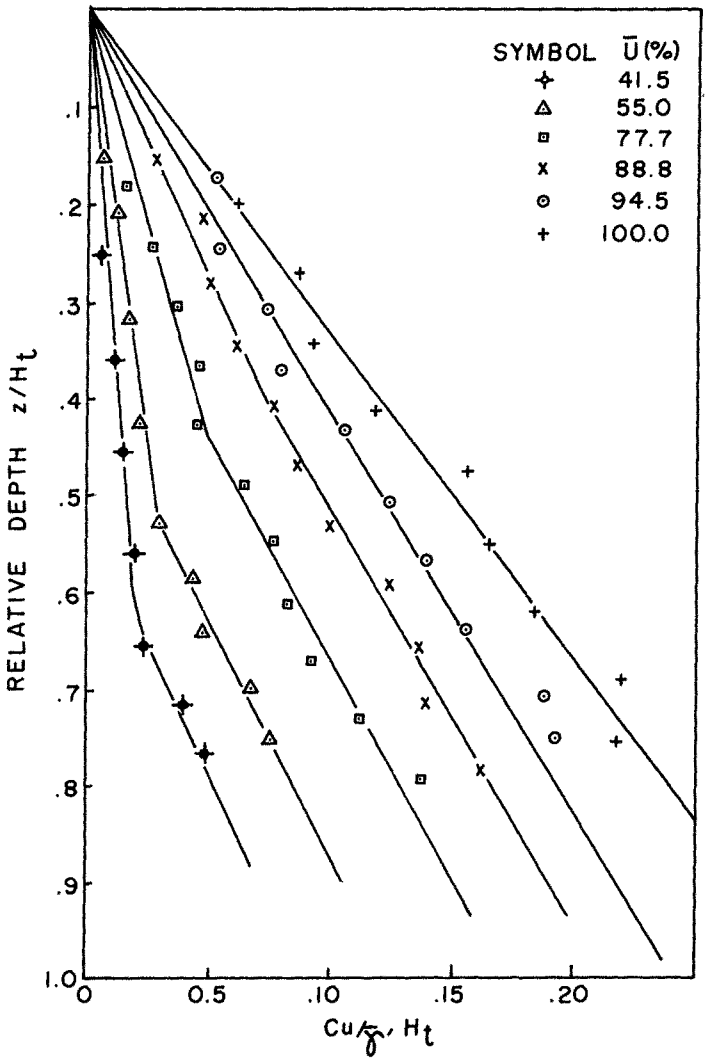

FIGURE 4 VANE SHEAR STRENGTH PROFILES

calculated from pore water pressure isochrones. After each experiment the soil was thoroughly mixed using an air injection stirring system and sedimented to the desired average degree of consolidation with reference to Figure 3.

Vane shear strengths, measured at various average degrees of consolidation, were found to vary non-linearly with depth as shown by Figure 4. This variation is thought to be related to density variations within the material or to thixotropic effects.

Static tilting tests

In order to arrive at suitable slope angles for the wave flume experiments a series of static tilting tests were carried out. Prior to these tests (at an average degree of consolidation of about 10%) plastic markers were inserted in the sediment adjacent to the glass wall. During latter stages of consolidation and subsequent slope deformations the movements of these markers were recorded by photography. Slope deformation and ultimate failure are produced by jacking one end of the tank such that the tilting rate was about 3 degrees per minute. Sequential photographs of the movements of plastic markers for a typical experiment are reproduced in Figure 5. Discontinuous curved shear surfaces were observed to form and produce a visible rupture zone when the displacements of the markers were quite small. Jacking was discontinued at this stage but the marker movements and rupture zone continued to develop with time. An enlarged view of the ultimate failure zone is shown in Figure 5. The displacements of markers at various times were measured from photographs with reference to a 2 cm. grid marked on the glass wall and are plotted for this typical test in Figure 6. The depth and thickness of the rupture zone and the depth of the ultimate failure plane were measured from visual observation and from the plotted marker displacements. These and other data from the series of static tilting experiments are summarized in Table 1. From the marker measurements the average shearing strain in the rupture zone at the time when this zone was first visible is estimated to be about 6%.

From equilibrium considerations it may be shown that, at failure

$$\frac{Cu}{\bar{\gamma}' z_s} = \frac{Cu}{\bar{P}'m} = \frac{1}{2} \sin 2\alpha f \qquad (3)$$

where z_s = depth to the sliding surface from the mud line.

$\bar{\gamma}'$ is the submerged density averaged over the depth z_s

αf is the angle at which rupture was initially observed (failure angle)

Cu is the undrained strength of the sediment at depth z_s

The values of undrained strength derived from static tilting experiments (equation 3) and those measured by vane tests are shown, on Figure 11, to be in good agreement. Up to about 50% of full primary consolidation the Cu/P_o' ratio

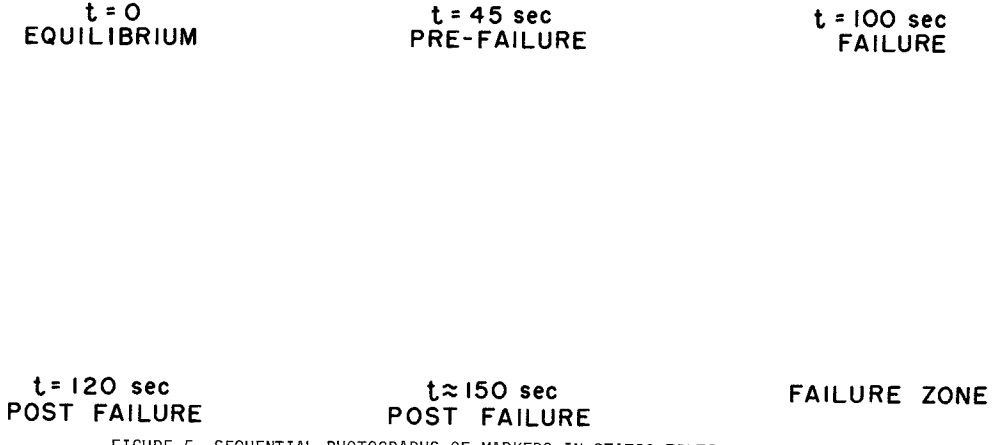

FIGURE 5 SEQUENTIAL PHOTOGRAPHS OF MARKERS IN STATIC TILTING EXPERIMENT

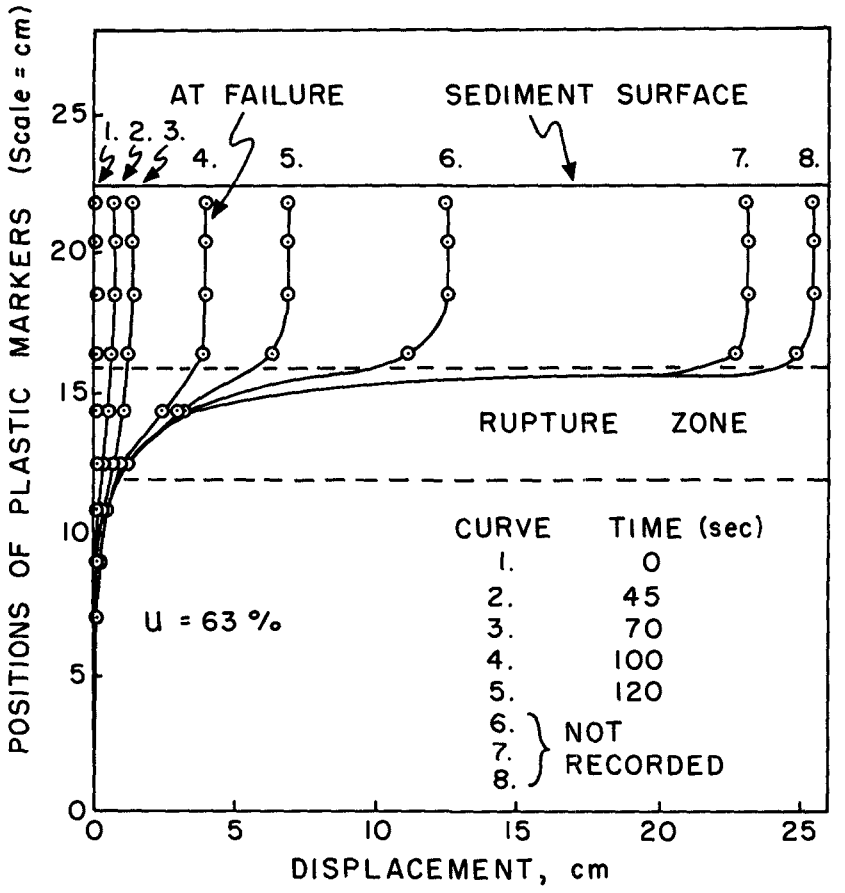

FIGURE 6 DISPLACEMENT OF MARKERS IN STATIC TILTING EXPERIMENT

TABLE 1 RESULTS OF STATIC TILTING EXPERIMENTS

NO. OF TEST	HEIGHT OF SEDIMENT H_t in cm	AVERAGE OEGREE OF CONSOLI-OATION $\bar{U}$ in %	FAILURE ANGLE OF SLOPE α_f IN OEGREES	C_u / p'_m RATIO	OEPTH OF SLIOING SUR-FACE z_s in cm	OEPTH OF RUPTURE ZONE z_f in cm	z_s / H_t	z_f / H_t
1	24.00	48.5	3.10	.0558	10.00	13.00	.417	.542
2	25.25	37.5	2.50	.0436	13.25	15.25	.525	.603
3	22.40	63.0	4.40	.0765	8.40	10.40	.375	.464
4	27.88	13.0	1.09	.0191	18.88	19.88	.676	.713
5	21.10	75.0	6.70	.1160	6.60	8.10	.313	.384
6	21.85	68.3	5.20	.0903	7.35	8.85	.336	.405
7	23.00	57.7	4.10	.0713	9.50	11.00	.413	.478
8	23.95	49.0	3.00	.0523	10.95	13.95	.457	.583
9	28.65	6.5	0.50	.0088	19.65	21.15	.690	.740
10	26.10	29.5	1.70	.0297	15.60	17.10	.598	.655
11	26.50	25.8	1.70	.0297	15.50	17.50	.585	.660
12	24.80	41.5	2.30	.0401	12.80	14.80	.516	.597
13	20.55	80.0	8.00	.1430	6.55	7.55	.319	.367
14	20.80	77.7	8.20	.1412	6.80	7.80	.325	.375
15	24.00	48.5	3.37	.0587	10.00	13.50	.417	.563
16	19.90	86.0	10.90	.1857	5.90	6.90	.297	.347

increases linearly with degree of consolidation (Figure 11) as predicted by Morgenstern (1967); for higher degrees of consolidation the rate of strength increase with consolidation is much higher. This behaviour may be a result of variations in submerged unit weight with depth, the large strains involved in consolidation under self weight, and possible thixotropic effects.

Tests under wave action

Figure 7 shows the model arrangement in the wave flume. The model tank used in the wave flume was equipped with sliding end sections that were lowered to the level of the mud line prior to each test. The artificial beach was adjusted to the elevation of the mudline to present a smooth continuous bottom transition from this beach to the mudline. The waves were generated by an adjustable wave paddle located in a deep section at the upstream end of the flume and the wave energy was dissipated on a horse hair beach at the downstream end of the flume. The flume is equipped with a wire mesh filter and partitioning board to prevent undesirable waves from reaching the test section. A smooth progressive sinusoidal wave train of constant characteristics was obtained over the test section.

Most of the tests were carried out using a wave length of 58 cm and a d/L ratio of about 0.35. The sediment was prepared in a manner identical to that used in the static tilting experiments and the tank was tilted to an angle such that the factor of safety against gravitational failure was at a known value between 1.25 and 2.80. Displacements of the plastic markers as a result of static tilting were quite small and an equilibrium condition was established immediately. The slope was then subjected to a progressive wave of small amplitude and the height of the wave was increased incrementally. Each increment of wave height was allowed to act on the sediments until the progressive downslope displacement of the plastic markers had terminated. Movements of markers in fixed elliptical orbits was considered to represent an equilibrium situation. The increment durations varied from about 2 minutes at the start of a test to about 10 minutes toward the end of a test. The incremental increases in wave height were chosen so that a failure condition, defined by continued and often accelerating downslope movements of the markers, was reached after five or six increments. Equilibrium positions of markers at the end of certain increments, as documented by photography, are shown for a typical test in Figure 8. A rupture zone with shear surfaces similar to these observed in static tilting and was found to develop with the larger slope movements associated with failure. The marker displacements measured from the photographs reproduced in Figure 8 are plotted in Figure 9 and a summary of data from a number of tests is presented in Table 2.

DISCUSSION OF MODEL TEST DATA

In all static tilting tests and all tests carried out under wave action the observed failure mode is best described as infinite slope sliding. The sketch in Figure 10 shows the approximate form of the rupture zone and the influence of the rigid ends of the model tank. The depth of this rupture

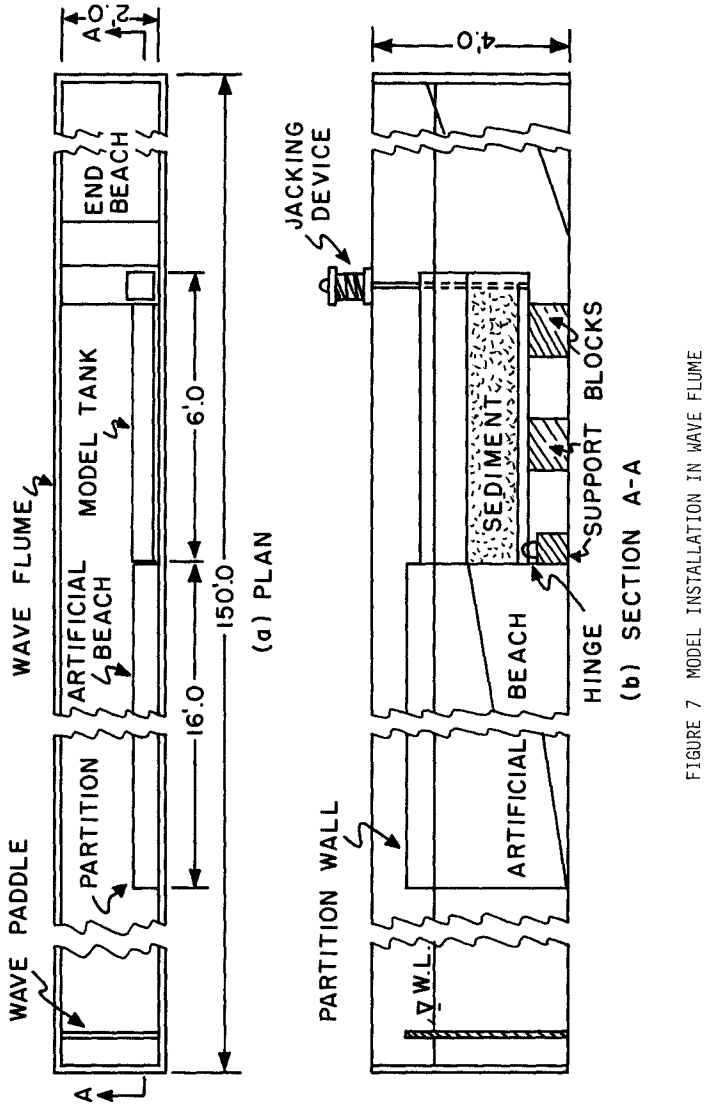

FIGURE 7 MODEL INSTALLATION IN WAVE FLUME

FIGURE 8 SEQUENTIAL PHOTOGRAPHS OF MARKERS UNDER WAVE ACTION

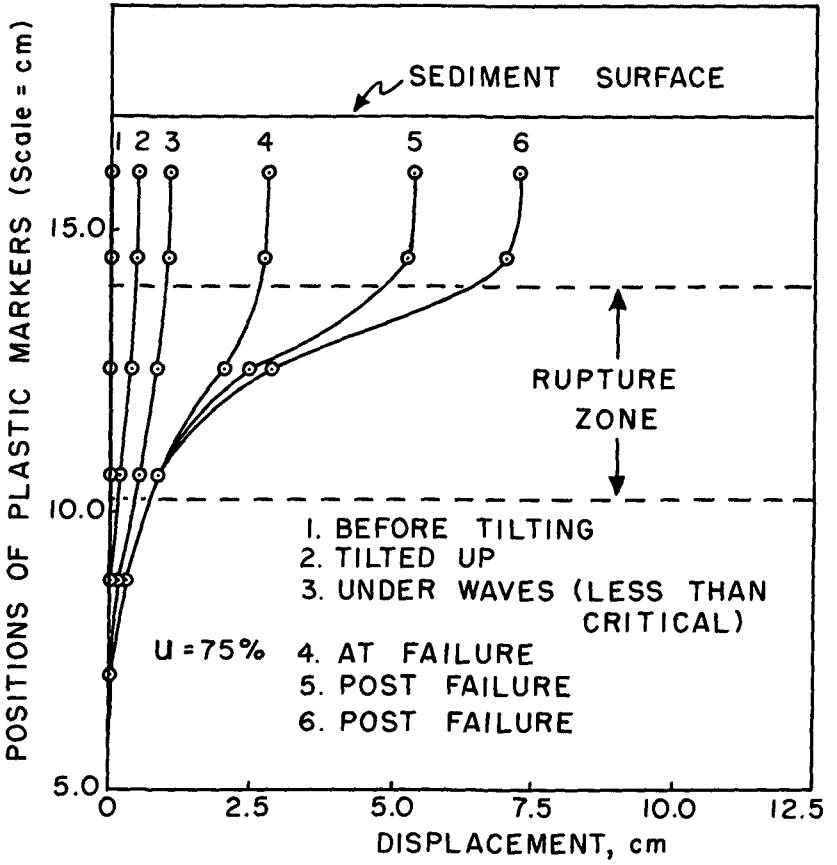

FIGURE 9 DISPLACEMENT OF MARKERS UNDER WAVE ACTION

TABLE 2 RESULTS OF STABILITY TESTS ON SLOPES SUBJECTED TO PROGRESSIVE WAVES

NO. OF TESTS	HEIGHT OF SEDIMENT H_t (in cm.)	AVERAGE DEGREE OF CONSOLIDATION $\bar{U}$ (in %)	FAILURE ANGLE OF SLOPE, α_f (in degrees)	ANGLE OF SLOPE α (in degrees)	FACTOR OF SAFETY F	DEPTH OF SLIDING SURFACE, z_s (in cm.)	DEPTH OF RUPTURE ZONE, z_f (in cm.)	z_s / H_t	z_f / H_t	DEEP WATER WAVE LENGTH L_o (in cm.)	WAVE HEIGHT H (in cm.)	DEPTH OF WATER d (in cm.)	d / L_o	PRESSURE RESPONSE FACTOR K_p	CRITICAL SUBSURFACE PRESSURE, δp_c (in gm/cm^2)	RESERVED STRENGTH, S_r (in gm/cm^2)
1	21.9	53.8	3.55	1.60	1.970	8.9	10.9	.406	.497	58	.75	22.4	.386	.1695	.0652	.0282
2	21.2	62.4	4.50	2.32	1.800	7.2	9.2	.340	.433	58	.73	21.7	.374	.1818	.0680	.0253
3	18.6	83.0	9.50	4.70	2.010	5.1	5.5	.270	.296	58	.75	17.3	.298	.2790	.1070	.0482
4	21.1	62.5	4.50	3.46	1.300	7.6	10.0	.360	.475	58	.45	18.6	.320	.2472	.0568	.0145
5	19.5	75.0	6.60	3.60	2.000	6.3	7.3	.325	.373	58	.80	19.7	.340	.2210	.0906	.0376
6	23.1	43.0	2.70	1.65	1.635	10.6	13.1	.458	.567	58	.50	21.1	.366	.1904	.0487	.0200
7	18.9	76.5	7.20	2.87	2.510	5.4	6.9	.286	.365	58	1.25	22.2	.382	.1735	.1110	.0407
8	20.6	62.5	4.55	1.60	2.840	6.6	8.6	.320	.417	58	1.20	24.2	.417	.1411	.0866	.0338
9	22.1	47.9	3.05	2.07	1.475	10.1	12.1	.457	.548	58	.53	21.4	.369	.1872	.0508	.0180
10	22.8	40.2	2.55	2.02	1.265	11.8	13.8	.517	.605	58	.30	20.7	.357	.2005	.0309	.0114
11	22.5	39.9	2.50	1.70	1.470	11.5	14.5	.511	.644	58	.45	22.1	.382	.1735	.0402	.0170
12	19.8	62.3	4.50	2.17	2.081	8.8	9.8	.419	.495	58	1.00	23.7	.409	.1480	.0758	.0353
13	20.4	52.3	3.30	1.50	2.200	9.4	11.4	.460	.560	58	1.05	25.6	.442	.1214	.0655	.0316
14	17.0	75.4	6.90	2.70	2.560	5.2	6.8	.306	.400	65	1.20	24.8	.381	.1745	.1075	.0388
15	18.0	60.8	4.33	2.15	2.020	7.6	9.6	.408	.516	58	.95	24.4	.421	.1378	.0671	.0311
16	20.3	46.0	2.90	1.50	1.930	10.3	12.3	.507	.606	65	.65	24.6	.378	.1776	.0593	.0271
17	21.7	33.9	2.15	1.10	1.940	11.7	13.7	.540	.631	74	.35	24.3	.328	.2506	.0450	.0225

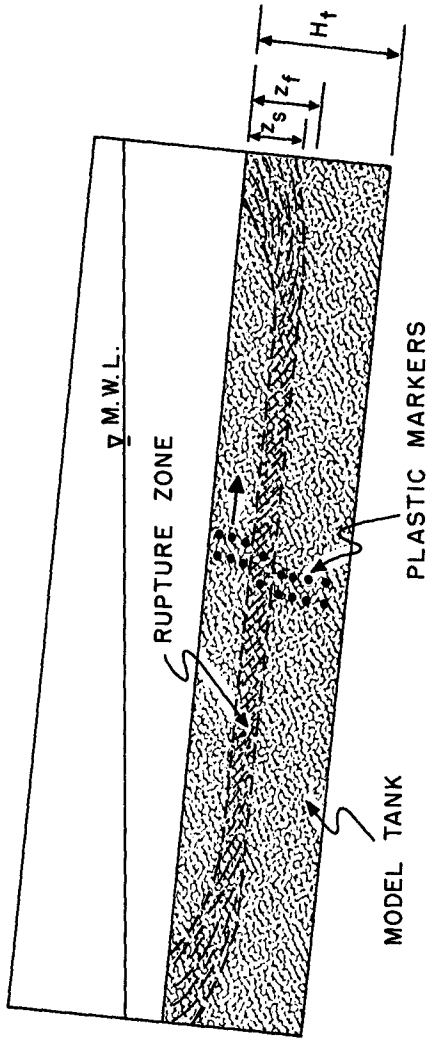

FIGURE 10 MODE OF FAILURE OF A SUBMERGED SLOPE IN STATIC AND WAVE EXPERIMENTS

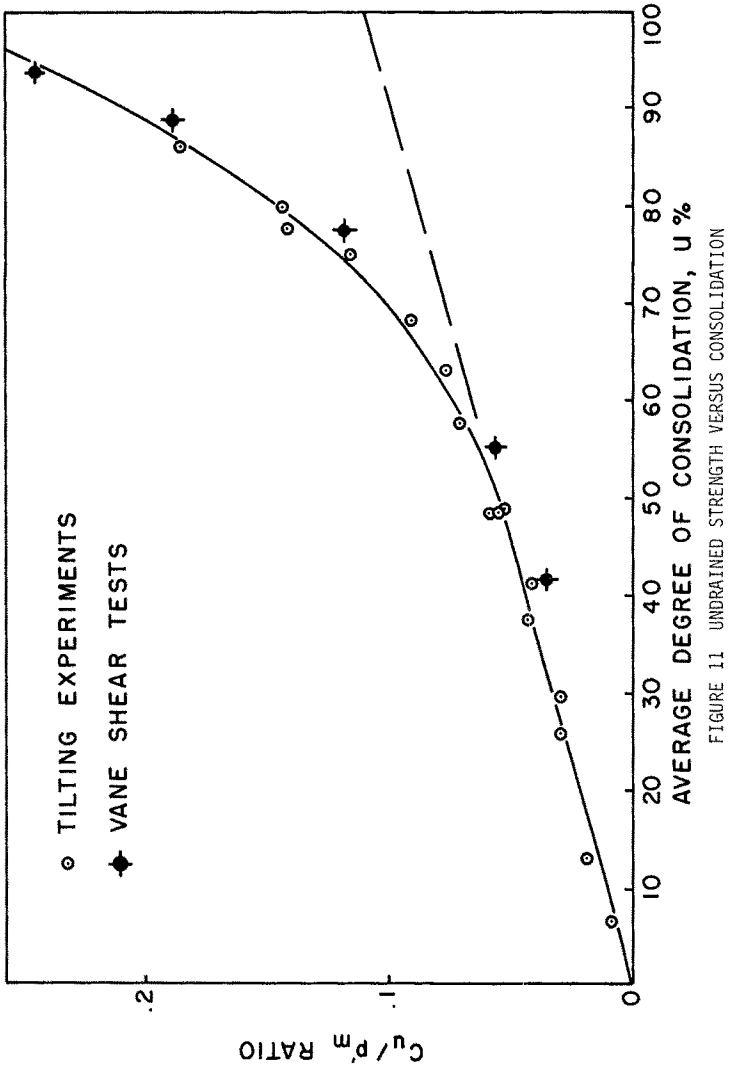

FIGURE 11 UNDRAINED STRENGTH VERSUS CONSOLIDATION

zone and the depth of the sliding surface was found to vary with the average degree of consolidation as shown on Figure 12. When the sediment was fully consolidated the downslope movement of sediment was confined to a thin surface layer. The few tests carried out using wave lengths different from 58 cm (hence a different d/L ratio for a given degree of consolidation) showed no influence of wave characteristics on the depth of failure. Since there is considerable variation in the strength-depth relationships in prototype situations (Bea, 1971; Sangrey, 1972) the relative influences of soil characteristics and wave characteristics on the depth of sliding appears to warrant further study. In an attempt to produce a circular arc slip a slope of about 10 cm in height was excavated in a fully consolidated sediment at an angle of approximately 25 degrees. When subjected to wave action this slope gradually flattered out by downslope transport of thin layers (2 cm thick) of sediment and no rupture or slip circle was observed.

The excess bottom pressure required to initiate mass movement of the sediment (critical bottom pressure, δp_c) increased with increased factor of safety (F.S.). In order to compare tests carried out at different F.S. a reserve strength (Sr) was defined as

$$Sr = \frac{\bar{\gamma}' z_s}{2} (\text{Sin } 2\alpha_f - 2\alpha) \qquad (4)$$

where α_f is the failure angle in static tests and α is the angle of the slope subjected to wave action.

From the plotted data in Figure 13 a linearly relation can be proposed between the critical bottom pressure and the reserve strength. Then the dimensionless parameter indicative of a failure situation is $\delta p_c/Sr$ and failure was observed to occur when

$$\delta p_c/Sr = 2.40 \qquad (5)$$

While it would be possible to use the model data presented in Figures 12 and 13 directly to analyze the stability of a prototype sediment having similar strength vs depth characteristics it is preferable to compare the model test observations to theoretical analysis in an attempt to evaluate a more general and rational approach to prototype stability calculations.

The fact that circular arc sliding was not observed should not be regarded as sufficient evidence to discard the upper bound stability analysis sketched in Figure 1a. The dynamic nature of the problem was recognized by Henkel (1970) and it is not difficult to picture that the cumulative effect of rotational movements under the action of progressive waves would be mass downslope movement. The circular arc is merely a convenient mechanism to obtain a numerical solution. The lower bound solution published recently by Wright and Dunham (1972), however, offers the advantage of making predictions of soil stresses and displacements prior to failure (or for bottom pressures less than the critical pressure) so that the effects of these movements on various types of foundations could be evaluated. The predictions of most general significance, however, are still the critical bottom pressures (or wave characteristics that will induce failure) and the maximum depths of the failures.

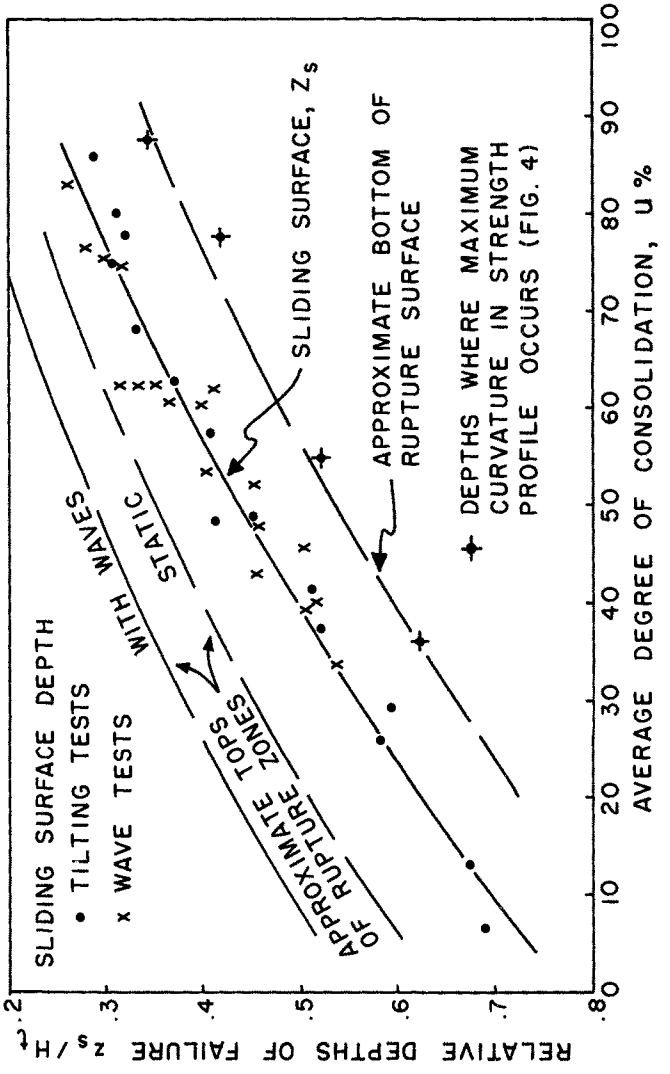

FIGURE 12 RELATIVE DEPTHS OF FAILURE VERSUS CONSOLIDATION

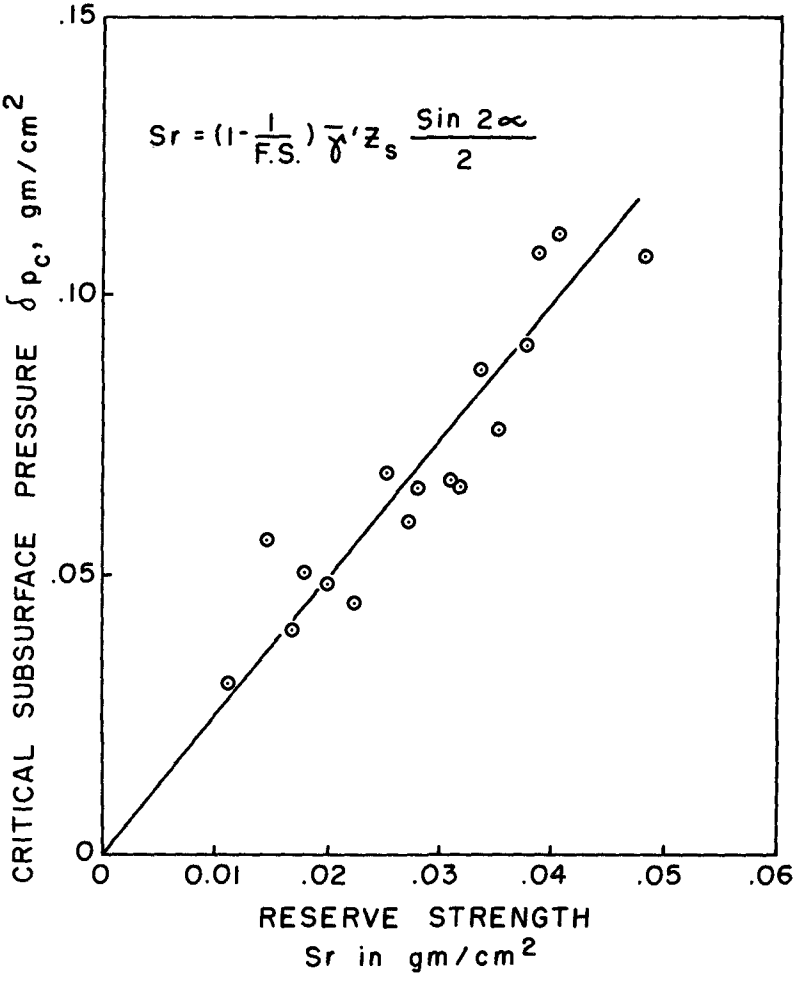

FIGURE 13 CRITICAL BOTTOM PRESSURES FOR SLOPES UNDER WAVE ACTION

For a simple soil profile having an undrained strength increasing linearly with depth both analyses indicate that failure begins at the mudline. Henkel's (1970) solution predicts a threshold value of excess bottom pressure, δp , when surficial soil failure begins. As δp increases this technique predicts an increasing depth below mudline for the failure. Model test failures did not begin as surficial or shallow displacements under small waves, instead the system was stable until an initial failure at significant depth. This is obviously inconsistent with Henkel's predictions; however, there was a reasonable relationship between the observed depth of failure and the prediction based on the waves acting at that time. Agreement between observed depth of failure and prediction was generally within 40%.

Wright and Dunham (1972) also predict that the maximum horizontal displacements and maximum ratio of applied stress to available strength will occur at the surface for a simple soil profile. Deeper stressed zones are associated with higher excess pressures. In general, this lower bound technique predicted maximum stress above the zone that actually failed in weaker soils and below the actual failure for stronger soils.

The discrepancies between the model test observations and the analytical predictions regarding the progress of failure from the mudline down may be due to the assumption that the soil has zero strength at the surface. It is more likely that the soil has a small finite strength at the surface derived from interpartical electro-chemical forces.

STRENGTH REDUCTION ANALYSIS

Previous analytical approaches are based on the concept that some additional downslope force must be provided to overcome a known shearing resistance. The discussion that follows is based on the concept that gravitational forces alone cause down-slope mass movement (failure) and the wave serves only to cause strength reduction in the soil. The undrained shearing strength at any depth in the soil profile may be effectively reduced due to excess pore water pressure build up or disturbances generated due to the cyclic shearing stresses (or strains) induced by a passing wave. To bring about failure the necessary percentage reduction in soil shearing resistance (or measured undrained strength) may be calculated as

$$R = \frac{S_r}{Cu} = \left(1 - \frac{\text{Sin } 2\alpha}{2Cu/p'm} \right) \times 100\% \qquad (6)$$

For a normally consolidated clay with a sensitivity of about 2, Sangrey, Henkel, and Esrig (1969) show that the strength can be reduced to the fully remoulded (not slickensided) critical state strength under cyclic loading. Following this general approach, and assuming that the minimum strength that can occur is the fully remoulded critical state strength, wave induced failure will occur only if the sensitivity of

the soil be greater than or equal to the factor of safety against gravitational failure. Thus, for waves to initiate failures

$$St = \frac{Cu \text{ undisturbed}}{Cu \text{ remoulded}} \geq F.S. \qquad (7)$$

In the model tests carried out in this study, values of factor of safety between 1.3 and 1.8 corresponding to strength reductions of 22% to 64% were used. It is expected that sedimented marine clays will have sensitivity ranging from about 0 to 10 (Sangrey, 1972). It may also be expected that the sensitivity will increase as the average degree of consolidation increases (see Figure 12).

For this series of model tests, equation 5 may be used directly with equation 6 to express the bottom pressure required to initiate failure (δp_c) in terms of the soil strength and the slope angle (or F.S. against gravitational failure) as:

$$\delta p_c = 2.4\ Cu \left(1 - \frac{\sin 2\alpha}{2\,Cu/p'_m}\right)$$

$$\delta p_c = 2.4\ Cu \left(1 - 1/F.S.\right) \qquad (8)$$

From these simple expressions the critical excess bottom pressure may be calculated at any depth for a given slope. As with former analytic approaches these expressions predict that surficial failure would develop initially for a simple soil profile (Cu/p'_0 constant). Since the failure is envisaged to be induced by wave action but gravity controlled, however, any increases in density with depth or any finite surface strength may lead to a more critical sliding surface at some depth in the profile. Using the measured vane shear strengths at the observed depths of failure, equation 8 was found to predict the value of δp_c to within ± 15% for the model tests.

Predicting the depth of failure appears to be a most formidable problem and should be done, in all cases, with respect to the strength profile. Weak layers or non-linear strength profiles may be considered directly using equation 8 although it is possible that extremely soft zones in some profiles (Bea, 1971) are wave induced (i.e. the soil has been softened or remoulded to some degree due to wave action). Equation 8 indicates that for a flat lying sediment (F.S. $\to \alpha$) an excess bottom pressure of 2.4 Cu would completely remould the soil to some depth. The depth of major remoulding may be expected to correspond with the depth of maximum cyclic shearing stress (or shearing strain). From the elastic predictions of Wright and Dunham (1972) the maximum shearing stress occurs at a depth of 0.19 Lo independent of variations in soil deformation modulus and is fairly uniform across the model. For the model value of Lo = 58 cm the depth of maximum cyclic shearing stress would then be 11 cm.

In discussing the general problems of submarine slope stability it

should be noted that the published theoretical solutions are essentially two dimensional. Henkel (1970) incorporates gravitational forces in his analysis but Wright and Dunham (1972) do not. Questions arise regarding the effect of a wave train progressing at some angle to the dip of the slope. The concept of wave action producing strength reduction and gravity producing slope instability is essentially independent of wave direction and mass movement would always occur down-dip. Model studies appear to be the most appropriate method of investigating this more general condition.

CONCLUSIONS

1. The usefulness of model studies in investigating submarine landsliding has been demonstrated. Model studies show that wave action can initiate an infinite slope type of failure in bottom sediments.

2. Contrary to analytical predictions the initial failure for a simple sedimented soil profile occurred at some finite depth in the profile. The depth of failure was observed to decrease almost linearly with increased average degree of consolidation.

3. The critical bottom pressure (calculated from the wave characteristics) required to initiate failure was found to increase linearly with the reserve strength (defined as the strength in excess of that required for stability of the slope in the absence of wave action).

4. For the observed depths of failure in sedimented soil profiles the upper bound solution due to Henkel (1970) appears to over-estimate the excess bottom pressure required to cause failure by a factor of 1.5 to 2.0.

It is suggested that the mechanism of failure may involve strength reduction due to cyclic shearing stresses (or strains) induced by wave action. An alternative method of calculating the critical excess bottom pressure is proposed. This method uses an empirical relationship derived from the model tests together with insitu vane strength data. The proposed failure mechanism is independent of wave train orientation and indicates that wave action cannot induce mass movement unless the soil has a sensitivity greater than or equal to the gravitational factor of safety.

ACKNOWLEDGEMENTS

The assistance of Mr. D.J. Davis, chief technician at the Coastal Engineering Laboratories, Queen's University at Kingston is gratefully acknowledged. The interest and contributions of Messrs. G.H. Sterling, R.G. Bea, P. Arnold, and E. Doyle of Shell Oil Company during the preparation of this paper are much appreciated. The model studies were carried out with financial support from the National Research Council of Canada.

REFERENCES

Ambraseys, N.N. (1960): "The Seismic Sea Wave of July 9, 1956, in the Greek Archipelago". Journal of Geophysical Research, Vol. 65.

Bea, R.G. (1971): "How Sea-floor Slides Affect Offshore Structures". The Oil and Gas Journal, Nov. 1971, pp. 88-92.

Chamberlain, T.K. (1964): "Mass Transport of Sediment in the Heads of Scripps Submarine Canyon, California". Papers in Marine Geology, Miller, R.L. ed. New York, The MacMillan Company.

Dill, R.F. (1964): "Sedimentation and Erosion in Scripps Submarine Canyon Heads". Papers in Marine Geology, Miller, R.L. ed. New York, The MacMillan Company.

Gutenberg, G. (1939): "Tsunamis and Earthquakes". Bulletin of the Seismological Society of America, Vol. 29.

Henkel, D.J. (1970): "The Role of Waves in Causing Submarine Landslides". Geotechnique, Vol. 20.

Morgenstern, N.R. (1967): "Submarine Slumping and Initiation of Turbidity Currents". "Marine Geotechnique", University of Illinois Press.

Roscoe, K.H. (1969): "Soils and Model Tests". Cambridge University Engineering Laboratory report.

Sangrey, D.A. (1972): "Obtaining Strength Profiles for Marine Soils Deposits". ASTM - STP 501, Page 106-120.

Sangrey, D.A., Henkel, J.D. and Esrig, M.J. (1969): "The Effective Stress Response of a Saturated Clay Soil to Repeated Loading". Can. Geot. J. Vol. 6, No. 2, pp. 241-252.

Terzaghi, K., (1956): "Varieties of Submarine Slope Failures". Proceedings of the Eighth Texas Conference on Soil Mechanics and Foundation Engineering, ASCE.

Tsui, K.K. (1972): "Stability of Submarine Slopes". Ph.D. Thesis, Queen's University at Kingston, Canada.

Wiegel, R.L. (1964): "Oceanographical Engineering". Prentice Hall, Inc. Englewood Cliffs, New Jersey.

Wright, S.G., and Dunham, R.S. (1972): "Bottom Stability Under Wave Induced Loading". Offshore Technology Conference, Dallas, Texas. Paper No. OTC 1603.

LIST OF SYMBOLS

α	Half of the wave height, H .
C_u	Undrained strength
d	Mean depth of waver above mud line
d_f	Depth of circular arc failure
F.S.	Factor of safety of a slope against gravitational sliding
H	Wave Height
H_t	Height of sediment at time t
k	$2\pi/L$
L	Wave length
L_o	Deep water wave length
p'_o	Vertical effective stress calculated from $Z\bar{\gamma}'$
p'_m	Vertical effective stress at depth of failure
R	Strength reduction factor
S_r	Reserve strength
T	Wave period
U	Average degree of consolidation
z_f	Depth of rupture zone
z_s	Depth of sliding surface
α	Angle of slope
α_f	Failure angle of slope
$\bar{\gamma}'$	Average submerged density
η	Fluctuation of water level due to wave
σ	$2\pi/T$
δp_c	Critical maximum wave pressure at slope failure
δp	Maximum wave pressure under crest of wave

CHAPTER 85

SEA-BED CONFIGURATION IN RELATION TO BREAKWATER STABILITY

J.H. van Oarschat and A. Wevers

Delft Hydraulics Labaratary, Delft, The Netherlands

ABSTRACT

Stability tests an the Eurapaart breakwaters, situated on a shallow foreshare, clearly demanstrated the effect af the foreshore canfiguration on the averall stability. The present article gives a descriptionaf the stability experiments and the interpretatian leading ta general canclusians regarding fareshare effects in combination with hydraulic canditions such as wave period, water depth and wave height. Bath regular and irregular waves have been used. The experiments, carried aut in commission of the Netherlands Government Department of Public Warks (Rijkswaterstaat) were af an applied nature and were not directed primarily ta the systematic study of foreshare effects.

1. INTRODUCTION

In designing and testing breakwater structures, generally main stress is laid upan the hydraulic conditions such as wave heights, currents and tides, with less attentian being paid to the relation between significant wave heights and average wave periods. The wave period is often considered to be a parameter of minor impartance in this respect. Moreover, the geametry of the sea-bed in frant of the breakwater and its indirect effects an the behaviaur of that structure are seldam taken inta consideration. The authors have come acrass anly a few examples where these fareshare effects have knowingly been taken inta account (Refs. 1 and 2).

Nevertheless, the geametry af the foreshare in cambination with bath the wave height and wave periad may in particular situatians be af major impartance in determining design conditians.

The profile af the foreshare will generally anly be variable to a limited extent, as it depends on the ariginal sea-bed configuration, the type af structure and the erasion and/or accretion ta be expected.

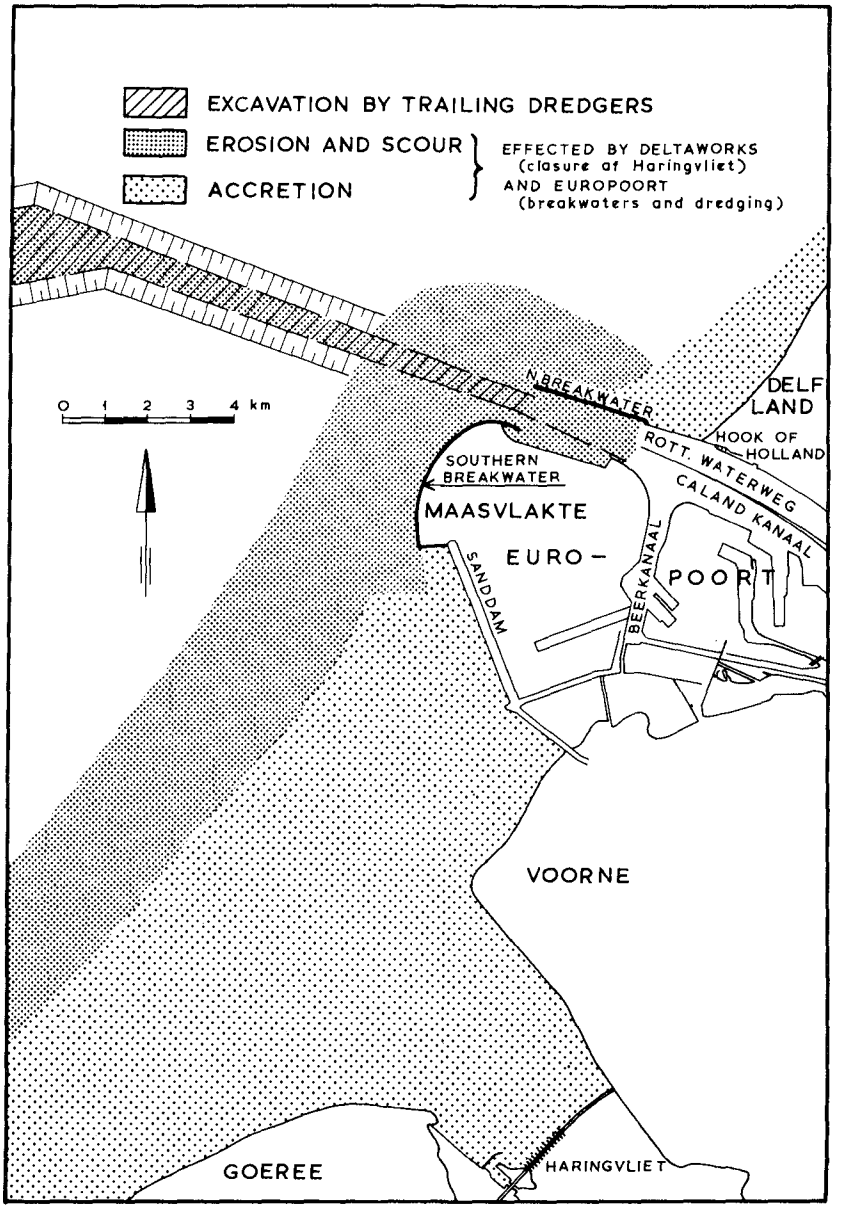

Fig. 1 Expected coastal erosion and accretion near Hook of Holland

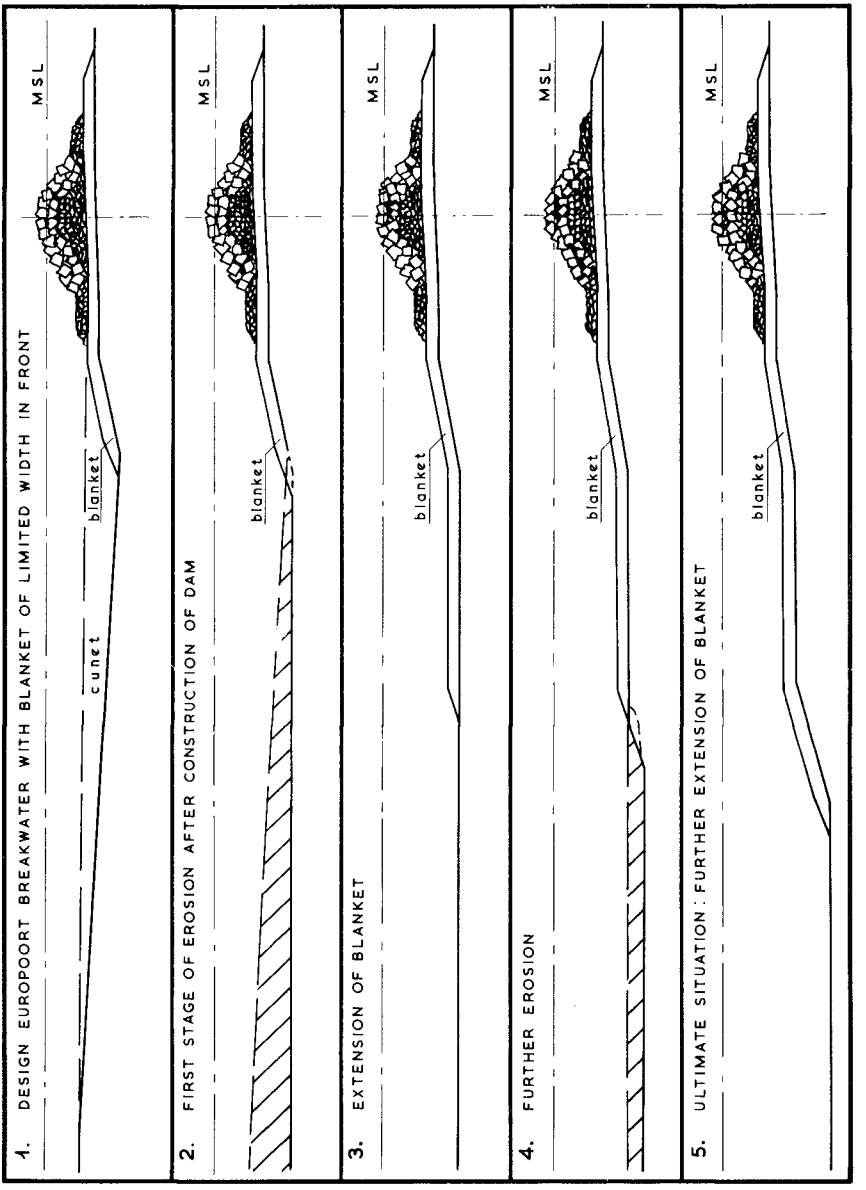

Fig. 2 Program for bottom protection in front of southern Europoort breakwater

The construction of a special foreshore substructure as part of the total structure may be considered for the design of deep-harbour protection works. Here the question may arise whether it will economically be more feasible to build the actual breakwater on a mound of relatively small-sized material and with such a configuration that the actual wave attack on the superstructure will be limited by the interaction of the incident wave motion with the substructure. This may lead to the use of smaller armour units in the superstructure. However, the amounts of material involved are huge, so that in most cases the sea-bed profile will be composed of the existing sea-bed configuration with possible erosion and/or accretion.

The effect of the foreshore configuration on the overall stability of the breakwater has been clearly demonstrated by model experiments carried out for the design of the Europoort breakwaters at the new harbour entrance to Rotterdam in commission of the Netherlands Government Department of Public Works (Rijkswaterstaat). These breakwaters will partly be constructed in relatively shallow water. After the new entrance has been completed, the depth in front of the bed protection can be expected to increase due to the contraction of the tidal currents and large-scale dredging, as is shown in Figure 1. In addition, design conditions are such that wave attack increases with depth. The final depth cannot be determined accurately at all places, partly because of the uncertainties in the development of ship sizes and partly because of the complexity of the coastal development. Therefore, when the deepening tends to exceed a certain value, a fixation of the sea-bed over a sufficiently large area is envisaged rather than a design based on the most unfavourable conditions that might occur. The different stages of construction are indicated in Figure 2.

2. GEOMETRY OF THE BREAKING WAVE

Maximum wave attack can be expected to occur when a structure is subjected to plunging breakers. After the waves have become initially unstable, they will progressively deform up to a point where part of the wave front becomes vertical, after which the crest will fall as a free-falling jet (i.e., the so-called plunging breaker). The place where the wave front becomes vertical is called here the breaking-point. Dependent on the location of the breaking-point and the path of the plunging wave, the falling jet moy hit the front face of the structure at about the still water level, or may fall into the water of the wave trough preceding the

breaking wave. In the latter case, a substantial amount of wave energy is converted into splash and turbulence, resulting in a largely reduced wave attack.

According to shallow water wave theory, the velocity of wave propagation is equal to:

$$v = \sqrt{g \cdot d}$$

where v = velocity of wave propagation
g = acceleration of gravity
d = water depth.

On the analogy of this equation, the horizontally-directed velocity of the breaking wave crest is equalized by:

$$v_B = \sqrt{g \cdot y_B}$$

where v_B = horizontally-directed velocity of the breaking wave crest at the breaking-point
g = acceleration of gravity
y_B = vertical distance from breaking wave crest up to the bottom at the breaking-point.

This latter equation has also been verified experimentally.

Assuming that the breaking wave crest at the breaking-point is exposed to gravity only, the path of the breaking wave tongue can be computed, starting from the horizontal initial velocity at the wave crest. In illustration: for the Europoort breakwater it may be assumed for the water depth at the breaking-point, d_B = 13.5 m, the breaking wave height, H_B = 10.0 m, and the vertical distance from the wave crest to the bottom, y_B = 21.0 m. Then the horizontal velocity of the wave front at the breaking-point equals v_B = 14.5 m/sec, whilst the plunging distance x_p, i.e., the horizontal distance from the breaking-point up to the point where the falling jet intersects the still water level, amounts to 19.5 m. From Figure 3 it follows that if the wave starts to break at the beginning of the horizontal bottom protection, the plunging jet will fall into the wave trough preceding the breaking wave, whereas if the wave breaks at the end of the horizontal bottom protection the falling jet will hit the front face of the breakwater.

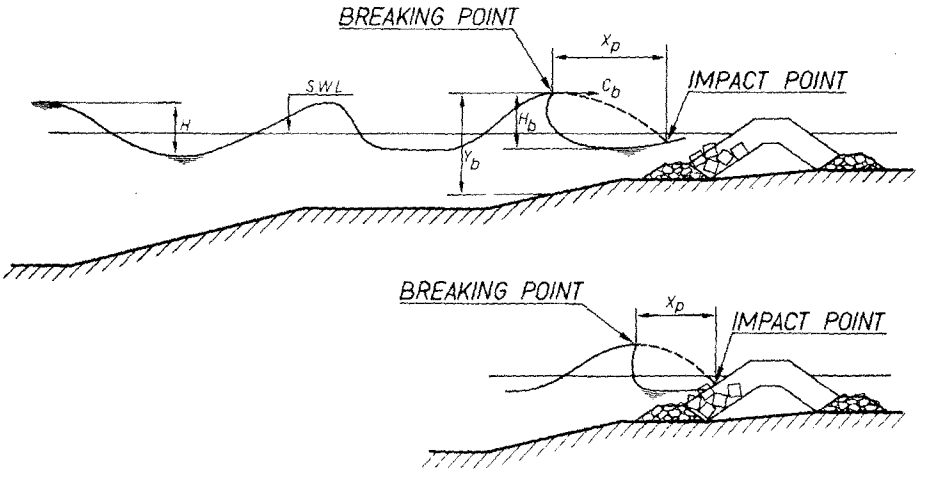

Fig. 3 Breaker geometry

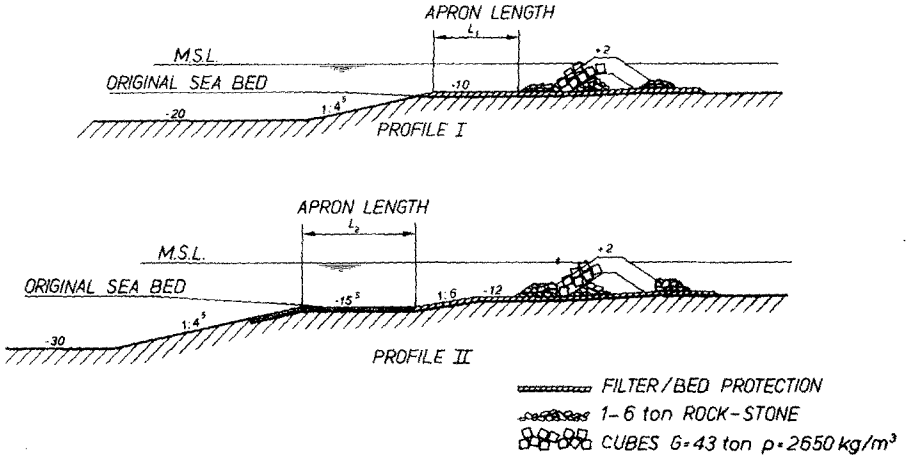

Fig. 4 Europoort breakwater profiles

From the foregoing it will be clear that the location of the breaking-point together with the wave dimensions at the breaking-point will strongly influence the amount of damage to be expected. Exact breaker dimensions as a function of foreshore configuration, water depth and wave periode cannot be predicted from theorerical considerations, nor are sufficient experimental results available, so only general tendencies can be derived from available theoretical and experimental investigations.

Assuming that the ratio between the breaking wave height above the still water level over the total breaking wave height will be nearly constant, the following general tendencies can be predicted with respect to the values of d_B, i.e., the water depth at the breaking-point, and H_B, i.e., the breaking wave height:

- An extension of the foreshore in a seaward direction, at constant wave period and water depth, can be regarded as a flattening of the slope, which will result in a decrease of the ratio H_B/d_B. This means that if d_B is kept constant, lower wave heights will form plunging breakers at corresponding depths in case of the longer foreshore.
- An increase of the wave period, at constant water depth and bottom configuration, has the same effect as the extension of the foreshore. Due to the increase of bottom friction, lower wave heights will start to break at corresponding depths when there are longer wave periods.
- At constant wave period and bottom configuration but increasing water depth, wave heights have to increase equally with water depth to form plunging breakers at corresponding depths.

3. STABILITY EXPERIMENTS

3.1. General

The effect of the foreshore geometry in relation to the wave characteristics will now be discussed on the basis of a selection of experiments carried out on two profiles (viz., Profiles I and II of Figure 4). Profile I is a "shallow" water profile which will be constructed in a previously-dredged trench (cunet). After completion of the breakwater, deepening in front of the breakwater will occur, but is not expected to exceed the level M.S.L. - 20.0 m. Tests with irregular waves were carried out to determine the effect of the apron length L_1 on the stability of the superstructure.

Profile II is a sa-called "deep" water prafile, which also will be canstructed in a previausly-dredged trench. Deepening which will occur in front af the breakwater is limited by a bed protection, as outlined in Figure 2, and is not expected to exceed the level of M.S.L. - 30.0 m. Experiments with both regular and irregular waves were carried out in order ta determine the optimum horizontal apron length L_2 of the bottom protectian, so that the same armour units (viz., concrete cubes af 43 tons with a specific density of 2,650 kg/m^3) can be used in all cases. The eroded sea-bed in front af bath aprons has been schematized by a fixed slape of 1 : 4.5.

3.2. Madels and Testing Facilities

Tests with regular waves have been carried aut in the wave basin af the Laboratory De Vaarst, in which waves are generated by a piston-type wave generator. The distonce between wave generator and model was abaut 19 m. During each test, wave period and water level were kept constant, whilst the wave height was increased in steps, each step lasting abaut 8 hours pratatype. At the end af each step the damage was recorded and classified accarding ta sa-called damage functians, as shown in Figure 5. During the tests visual abservatians af the breaker geometry, and especially the locatian of the impact paint, were made.

Tests with irregular waves have been carried out in the wind-wave flumes of the Delft Laboratory (Ref. 3), in which irregular waves with any arbitrary wave spectrum can be generated by a programmed wave generator. The testing procedure was similar to that for the regular waves.

3.3. Results

The experiments with regular waves an the "deep" water Prafile II were carried out with wave periods of 12, 14 and 15.5 secs, water levels of M.S.L. + 0.50 m and + 1.50 m, and apron lengths, L_2, of 30 m and 50 m.

Damage functians are given an Figures 5, 6 and 7. The wave period and the apran length as well as the water level appear to have a more or less significant effect on the stability of the structure.

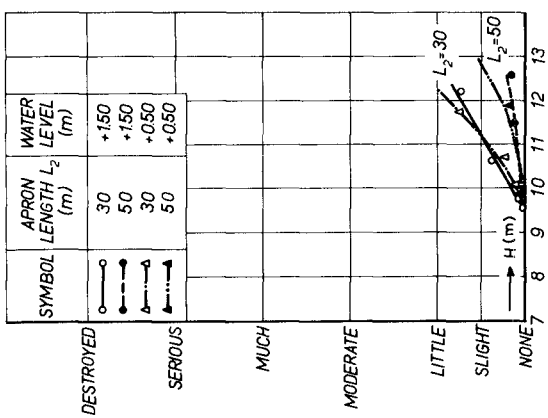

Fig. 5 Damage functions, profile II

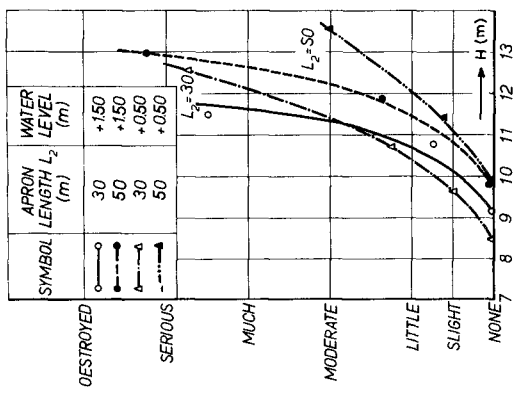

Fig. 6 Damage functions, profile

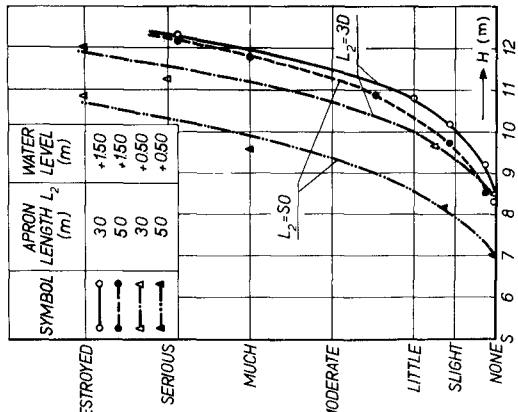

Fig. 7 Damage functions, profile II

The results on Figures 5, 6 ond 7 have been summarized on Figure 8 by characterizing each damoge curve by the wave height which couses a "little" damage to the breakwater.

On analysing these results it appeared that for the most dangerous combination, viz. T = 15.5 sec, L_2 = 50 m, and water level M.S.L. + 0.50 m, critical breaking conditions, as described in Chapter 2, occurred at a wave height of 8.5 - 9.5 m. At that time waves were just breaking at the toe of the structure, ond the front face of the breakwater was heavily attacked by the plunging jet, whilst the stability of the blocks wos olready reduced by the downrush and outflow of the water.

At a higher water level and/or shorter apron length the incident wave height hod to be increased beyond 10 m to have the impact point at a similar pasitian an the breakwater face. Lower wave heights were observed to merely surge over the crest of the breakwater.

With decreasing wave periods and constant wave heights the rate of deformation of the wave decreoses as a result of the diminishing effect of the bottom friction. For T = 14 secs and L_2 = 50 m plunging breakers which start to break at a critical distance in front of the breakwater only occur for incident wave heights which are considerably higher than those at T = 15.5 secs. The absolute difference in rate of deformation between the wove periods T = 15.5 secs and T = 14 secs is less for the apron length L_2 = 30 m than for L_2 = 50 m, which may explain the small difference in the wave heights, causing "little" damage, between T = 15.5 secs and T = 14 secs at this shorter apron length.

With a further decrease of the wave period to 12 secs, incident waves were observed either to surge over the breakwater crest or to fall into the water in front of it when the plunging jet did not reach the front face of the breakwater when breaking. On increasing the wave heights, the breaking-point moved more offshore, resulting in largely reduced wave attack. In two such situotions the damage described as "little" wos not even reached.

In general, it may be concluded that the foreshore acts as an obstacle on which the waves become unstable and subsequently may break at a certain distance from the breakwater. The initiation of damage, however, depends entirely on a very subtle combination of water depth, sea-bed configuration, wave period and wave height.

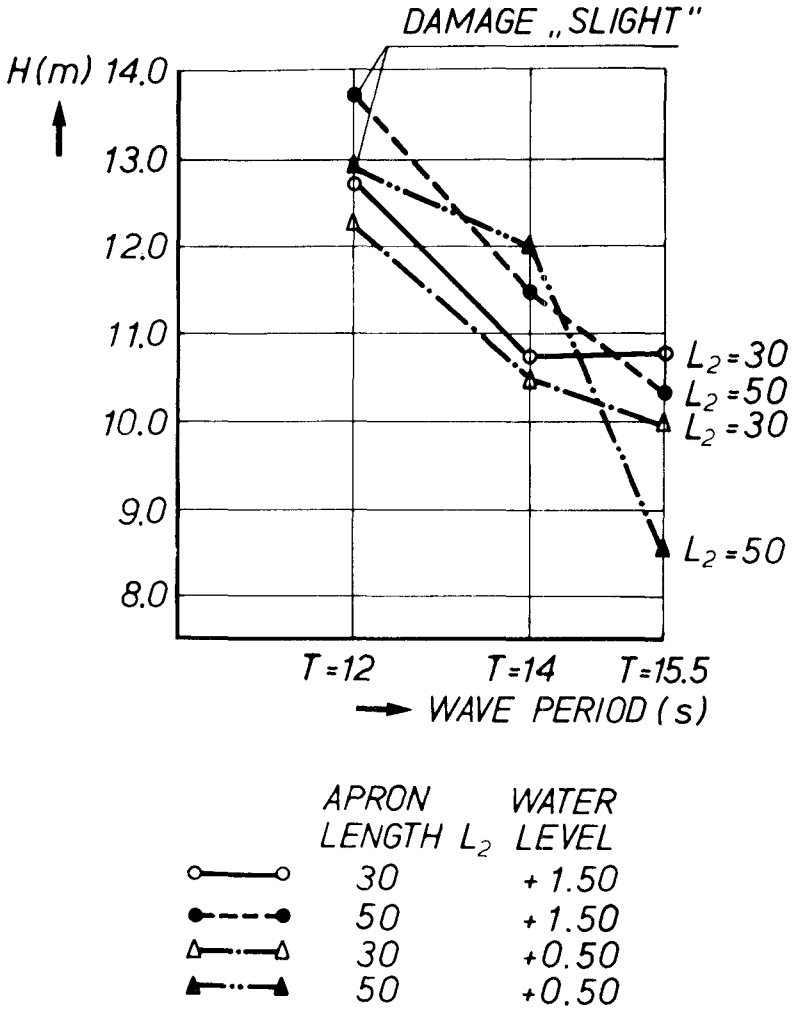

WAVE HEIGHT FOR DAMAGE „LITTLE" VERSUS WAVE PERIOD. PROFILE II

Fig. 8 Relatian wave height for damage "little" versus wave periad

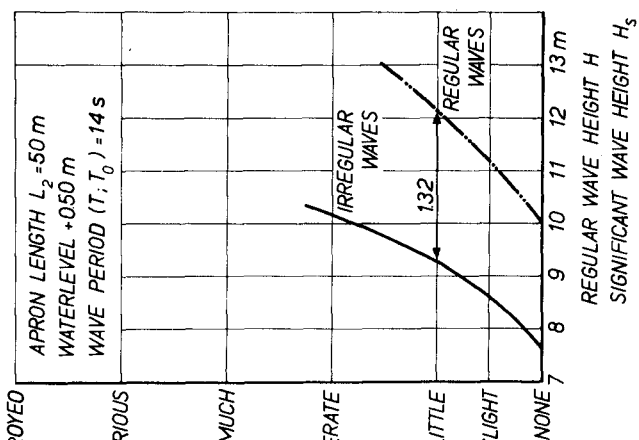

COMPARISON DAMAGE FUNCTIONS FOR REGULAR AND IRREGULAR WAVES (PROFILE II)

Fig. 9 Comparion damage functions

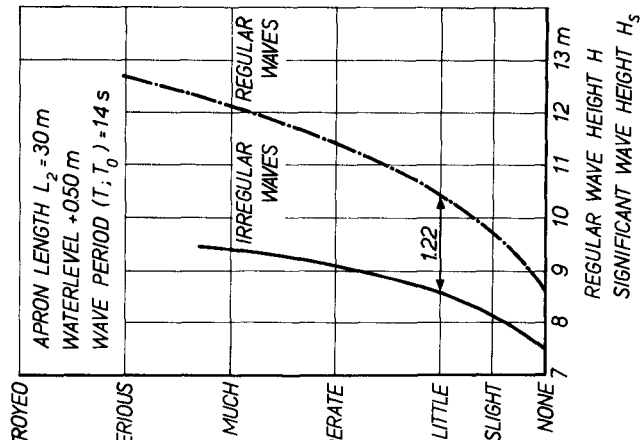

COMPARISON DAMAGE FUNCTIONS FOR REGULAR AND IRREGULAR WAVES (PROFILE II)

Fig. 10 Comparison damage functions

In addition to the experiments with regular waves, tests with irregular waves have been carried aut. In this case, the significant wave height was increased in steps, every step lasting about 8 hours prototype, whilst the top periad, i.e., the period in the wave energy spectrum with maximum energy density, was equal to T_o = 12 secs and T_o = 14 secs. Some of the results, summarized in damage functions, are shown in Figures 9 and 10. A total of six different combinatians of water level, apron length and wave period were tested.

Comparing the damage functions for irregular and regular wave action, both for a "little" damage, it was found that the ratio of the significant wave height H_s, and the regular wave height, H_r to cause similar damage was equal to:

$$\frac{H_r}{H_s} \simeq 1.15 \text{ to } 1.33.$$

So on the average equal damage will occur when

$H_r \cong 1.25 \times H_s$, or $H_r \cong H_{4\,\%}$, where $H_{4\,\%}$ is the wave height which is exceeded by 4 % of all waves, provided thot the regular wave period is equal to the top period of the wave spectrum and that the duration of the tests is also equal.

It is often ossumed, partly on the basis of experiments with porticular breakwater profiles, that H_r shauld be equal ta H_s in order to produce equal damoge (Ref. 4). Although this relation may be correct for particular breakwater crass-sections and a rather high extent of damage, it seems to be purely accidental and it is certainly not generally applicable, as already indicated. In fact, there is no physical basis whatsoever for this equality, as the significant wave height H_s is a more or less arbitrarily chosen characteristic height of an irregular train of waves. In this respect reference is also made to Ref. 5, where from experiments on rip-rap revetments of various slopes and compositions it was concluded that $H_r \cong H_{1\,\%}$.

A direct relationship between breaker distance and wave attack can be shown from the experiments with Profile I. These experiments were carried out with irregular waves only and with T_o = 14 secs and 4 different apron lengths.

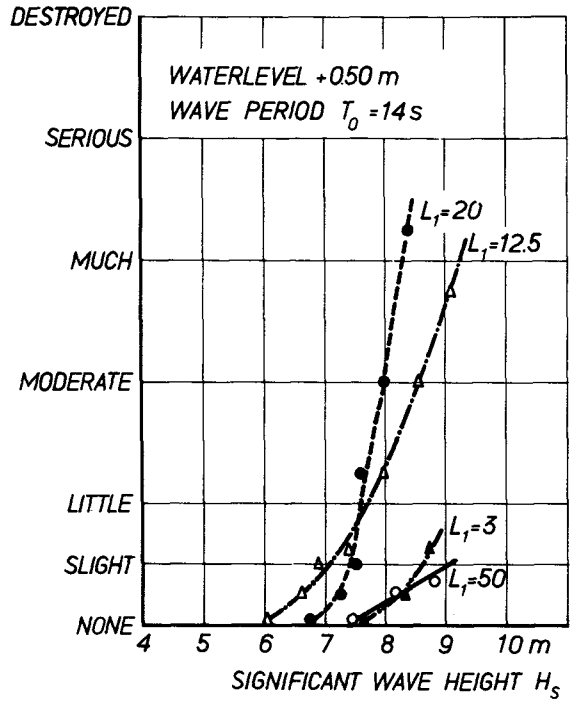

DAMAGE FUNCTIONS, PROFILE I

Fig. 11 Damage functions, profile I

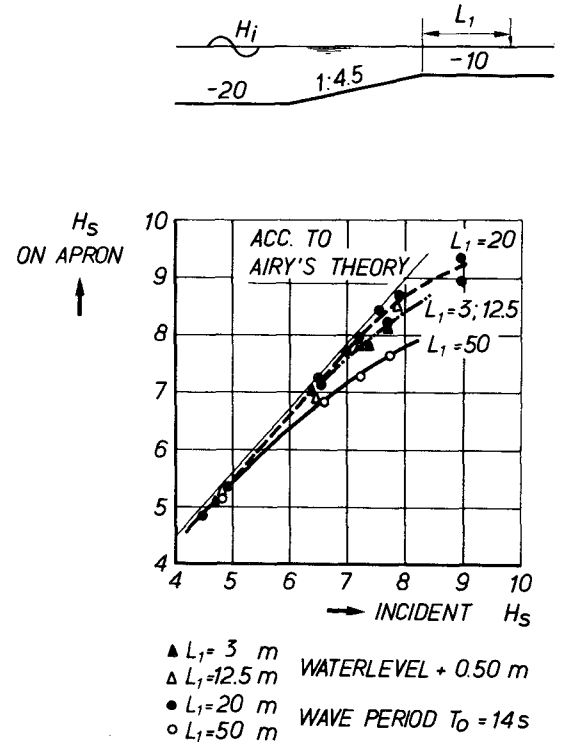

VARIATION OF WAVE HEIGHT ON APRON

Fig. 12 Voriation of wave height on opron

Damage functions are presented on Figure 11. Serious damage accurred under design conditions (i.e., H_s = 8.5 m) with the originally proposed apron length L_1 of 20 m. Moreover, the damage increased rapidly with a small increase of wave height. The damage was considerably less for apron length of L_1 = 3 m and L_1 = 50 m. For L_1 = 3 m waves were observed not to break in front of the breakwater, but on the breakwater itself, which causes the wave to surge over the crest, whereas for L_1 = 50 m the impact point of the higher waves is located so far seaward of the breakwater that the wave energy is reduced substantially.

In this respect reference is made to Figure 12, which indicates the relatian between the incident wave height and the wave height on the apron in the absence of a structure.

4. CONCLUSIONS

- The provision to extend the bottom protection seaward, entailing the construction of a relatively high foreshore in front of the Europoort breakwater if the depth in front tends to exceed a certain value, proved to be a helpful means of limiting wave farces which would otherwise become prohibitive. However, the design of this foreshore profile should be tested with a large variaty of preferably irregular wave conditions, as particular combinations of wave characteristics and foreshore profiles may give rise to extra large damage.

- The occurrence of maximum wave attack on the Europoort breakwater can be related to the distance between the front face of the structure and the breaking-point. The exact location of the breaking-point and the conditions on which this breaking will occur are very difficult to predict, as they depend on a rather subtle combination of water depth, foreshore configuration, wave period and wave height.

- Experiments with regular waves only give qualitative information, as it is not clear beforehand which wave height within the statistical variety of natural wave heights should be selected as the representative one. The frequently used assumption that $H_{regular}$ has to be equal to the significant wave height H_s may be correct in particular situations, but is in general purely accidental.

5. REFERENCES

1. Galvin Jr., C.J., Breaker travel and choice of design wave height; Proc. Am. Civ. Engrs., 95, no. WW2, May, 1969.

2. Führböter, A., Der Druckschlag durch Brecher auf Deichböschungen; Mitteilungen Franzius - Institut, Heft 28, 1966.

3. Von Oorschot, J.H. and d'Angremand, K., The effect af wave energy spectra on wave run-up; Proc. af the Eleventh Canf. an Caastal Eng., Landan. 1968.

4. Rogan, A.J., A camparisan of regular and wind-generated wave action on rubble-maund breakwaters; Proc. Sympasium Research on Wave Action, Delft, 1969.

5. Hydraulics Research Station Wallingford, Rip-rap protection for slopes subject to wave attack; Hydraulics Research, 1966.

6. Ferguson, H.A., The use of model tests for the design of maritime structures with regard ta wave action; Proc. Sympasium Research an Wave Action, Delft, 1969.

CHAPTER 86

ENGINEERING PROPERTIES OF SEA FLOOR SEDIMENTS FROM LA JOLLA CANYON

by: Iraj Noorany[1] and Robert A. Zinser[2]

Abstract

Near surface sea floor sediments were obtained by the tracked underwater vehicle RUM from four locations on the floor of the La Jolla Canyon. The sediments were clayey silts of high plasticity. The engineering properties of the sediments, including grain size, index properties, strength and compressibility, were determined.

Introduction

This paper covers the engineering properties of sediment samples from four locations on the floor of the La Jolla Canyon, north of San Diego on the Pacific coast, at waters ranging in depth from 1256 feet to 1334 feet. The samples were taken by a 2.875 in. in diameter, 22 in. long sampler attached to the RUM (Remote Underwater Manipulator), a research vehicle of the Marine Physical Laboratory of the Scripps Institution of Oceanography, University of California.

The RUM, (Fig. 1), is an unmanned tracked vehicle designed for sea floor explorations in water depths of more than 6000 feet (1,2,3). An umbilical cable connects RUM with a surface support platform. RUM has been equipped with a remotely controlled sediment corer, vane shear device, (Fig. 2), and cone penetrometer, (Fig. 3). A description of the sampling and in situ testing operations by RUM on the floor of the La Jolla Canyon was given by Anderson et al (3). Fig. 4 shows the sample locations. Water depths and the burial depths of the samples are given in Table 1.

Table 1 - Site Data

Sample	Location	Water Depth Feet	Burial Depth Inches
A-5	1	1256	8
B-6	2	1369	9
C-8	3	1275	13
D-9	4	1334	6

(1) Professor of Civil Engineering, California State University, San Diego, California.

(2) Graduate Research Assistant, California State University, San Diego, California.

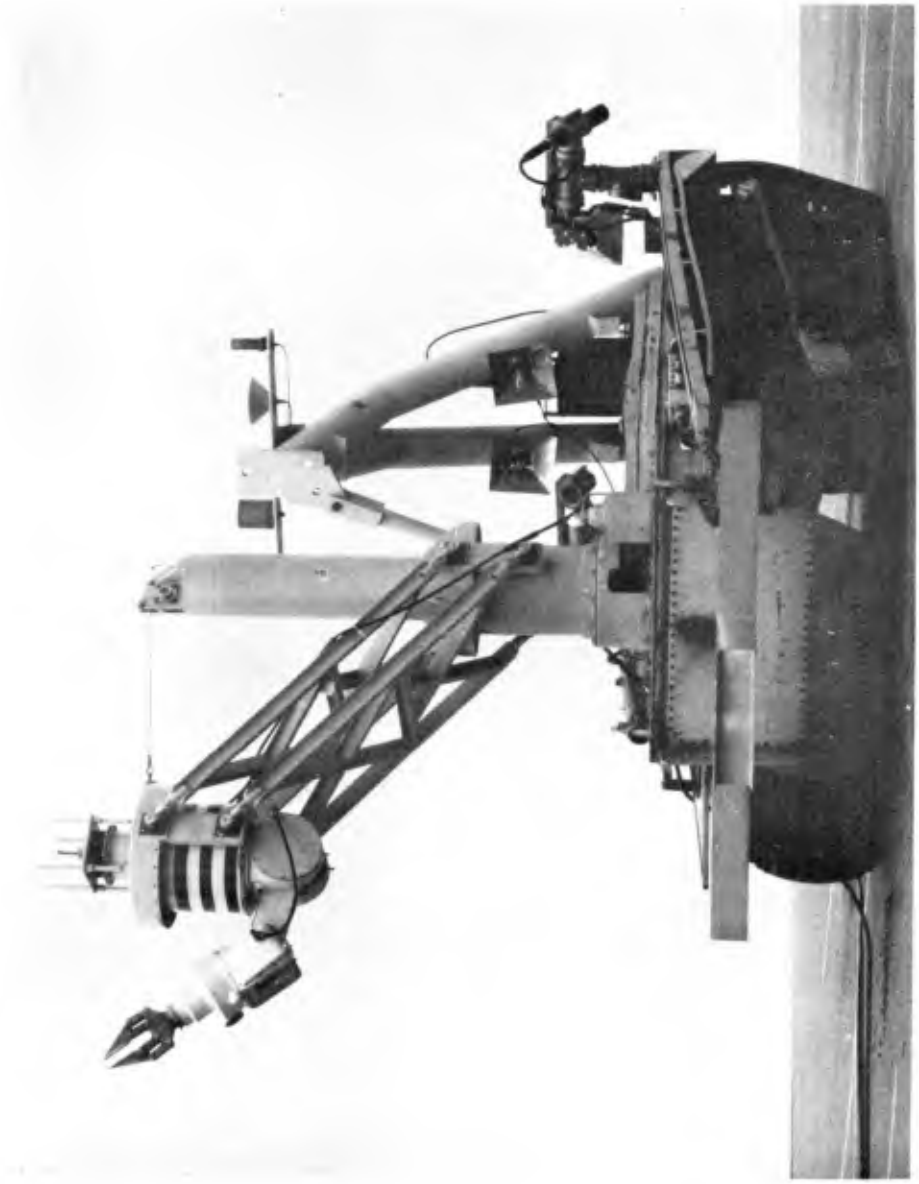

FIG. 1 THE RUM (COURTESY OF MARINE PHYSICAL LABORATORY, SCRIPPS INSTITUTION OF OCEANOGRAPHY, UNIVERSITY OF CALIFORNIA, SAN DIEGO)

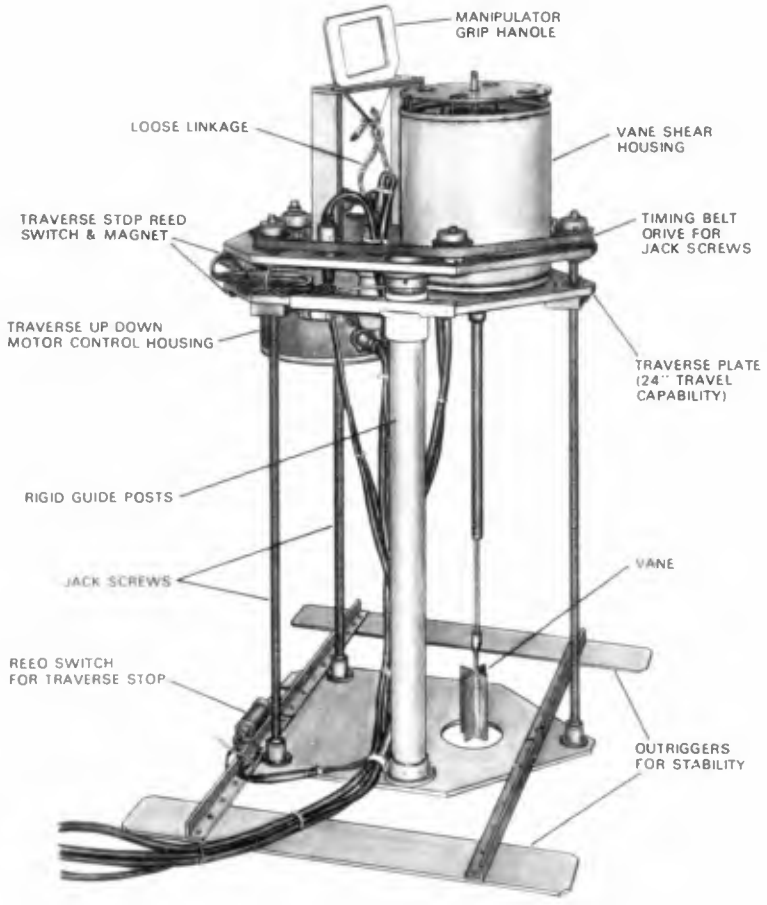

FIG. 2 THE RUM VANE SHEAR DEVICE

(COURTESY OF MARINE PHYSICAL LABORATORY, SCRIPPS INSTITUTION OF OCEANOGRAPHY, UNIVERSITY OF CALIFORNIA, SAN DIEGO)

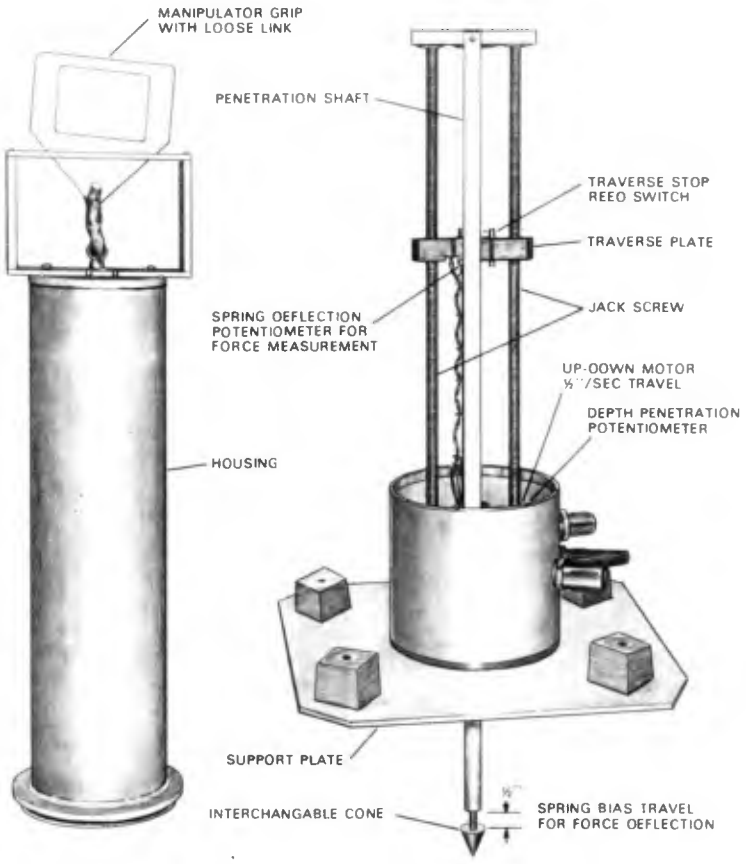

FIG. 3 THE RUM CONE PENETROMETER

(COURTESY OF MARINE PHYSICAL LABORATORY, SCRIPPS INSTITUTION OF OCEANOGRAPHY, UNIVERSITY OF CALIFORNIA, SAN DIEGO)

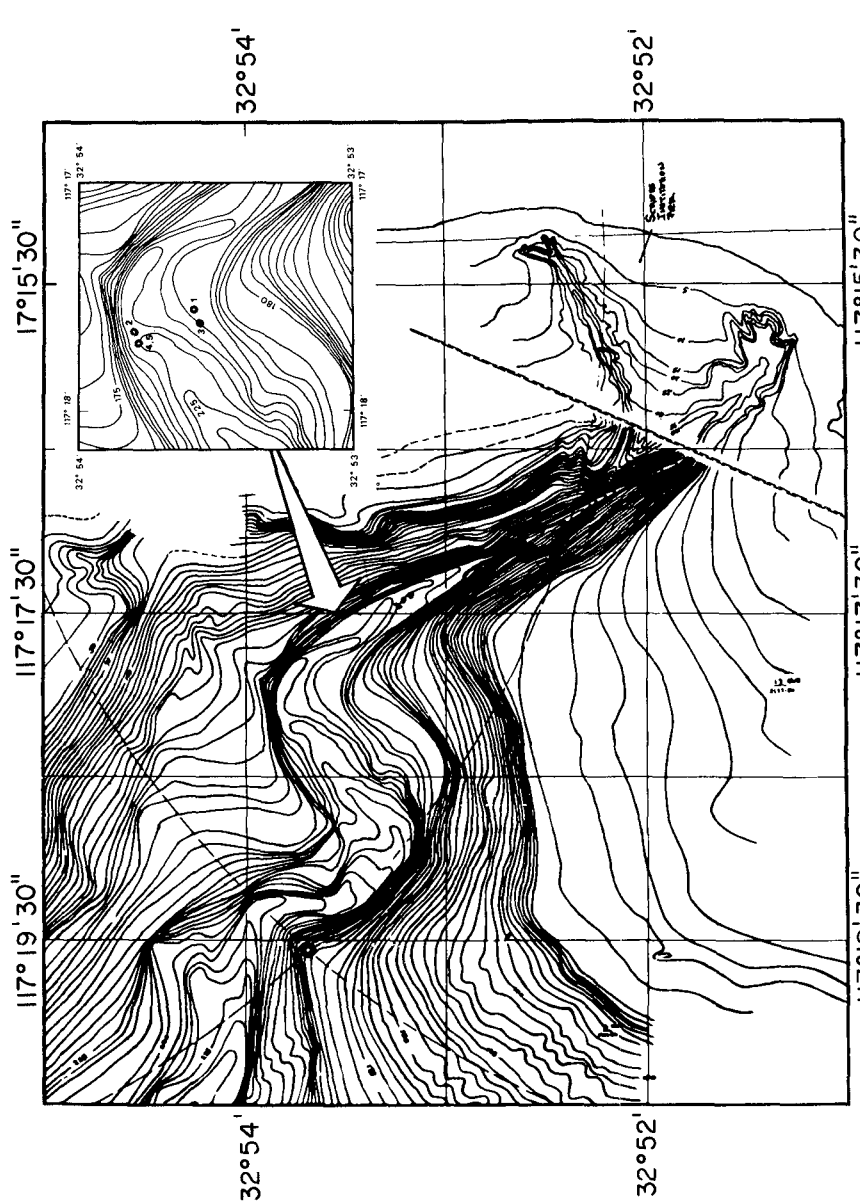

FIG. 4 SAMPLE LOCATIONS IN LA JOLLA CANYON (FROM REF. 3)

Index Properties

The samples recovered were gray-green organic clayey silts of high plasticity which classify as MH-OH according to the Unified Classification System. The gradation curves, (Fig. 5), for the samples indicated 86 to 94 percent material finer than 0.074 mm (U.S. Standard Sieve No. 200), and approximately 5 percent clay size material (finer than 2 microns). The index properties of the sediments are given in Table 2. The water contents listed might be slightly lower than the in situ values because the samples were very soft and tended to compress under their own weights in the sampling tube during the storage period prior to testing. This may be the main reason for the differences between the water contents reported in Tables 2 and 3.

Table 2 - Index Properties*

Sample	w %	G_s	S %	γ pcf	γ_d pcf	w_L	I_p	LI
A-5	106.6	2.75	99.9	90.0	43.7	84	44	1.5
B-6	108.1	2.70	100.0	90.3	43.3	81	39	1.4
C-8	96.9	2.70	100.0	92.5	46.8	71	33	1.9
D-9	97.5	2.73	99.3	91.5	46.4	77	33	1.6

* w is water content (ratio between weight of water and weight of solids); G_s is specific gravity of solids; S is degree of saturation; γ is unit weight; γ_d is dry density (ratio between the dry weight and total volume); w_L is liquid limit; I_p is plasticity index and LI is liquidity index.

Shear Strength

The undrained strength of each sample, determined by laboratory vane shear test, is given in Table 3. Fig. 6 shows a typical result of the laboratory vane shear test. The value of shear strength measured on sample D-9 appears high because of the reduction of water content caused by compression of the sample under its own weight in the sampling tube during the storage period. Sensitivity (the ratio between the undisturbed strength and fully remolded strength) values of 2 to 4 indicate "medium sensitivity." However, the actual sensitivities might be higher since disturbance and other changes caused by sampling and handling undoubtedly decreased the undrained strength of the samples. In situ vane shear tests by the RUM (3) in location No. 3 indicated a shear strength of approximately 0.5 psi at a depth corresponding to the burial depth of sample C-8 for which the laboratory vane shear was 0.3 psi.

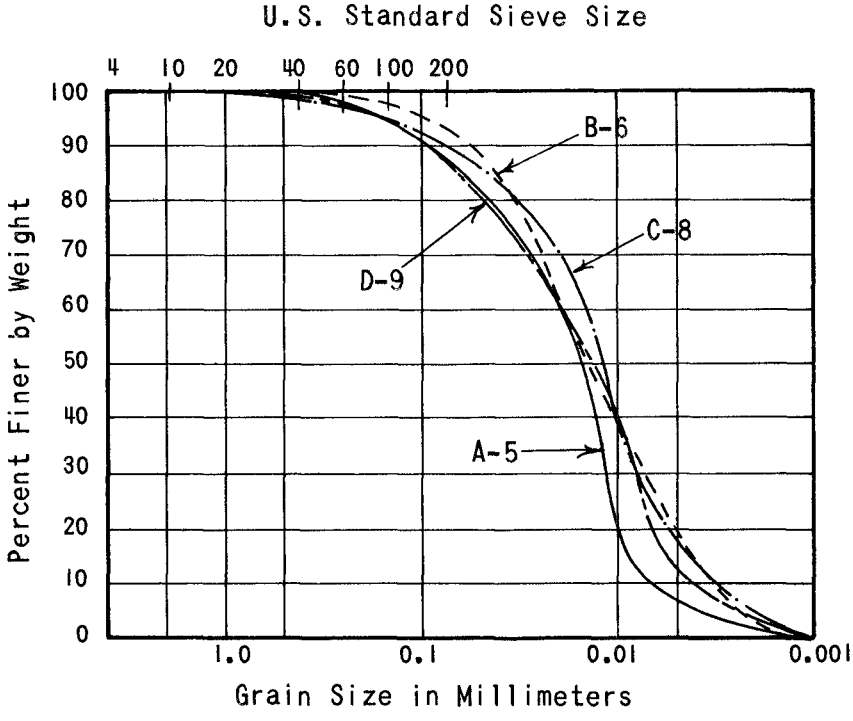

FIG. 5 GRADATION CURVES

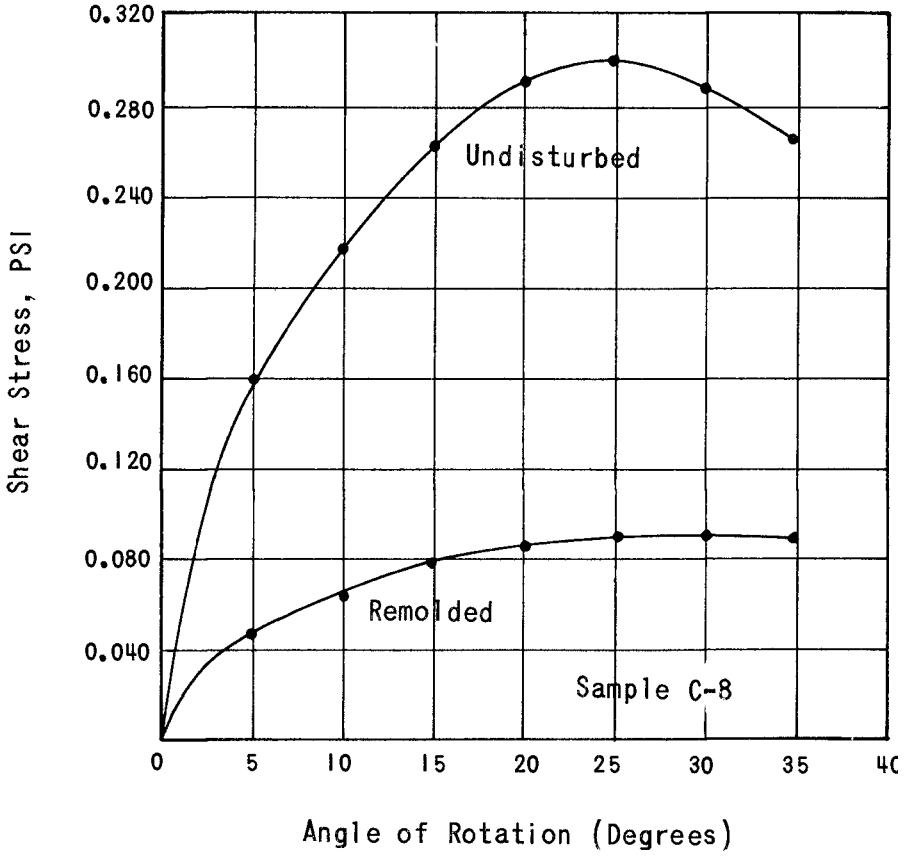

FIG. 6 RESULTS OF VANE SHEAR TEST

Compressibility

Consolidation tests were performed on 2.5 in. in diameter, 1 in. thick samples using a load increment ratio $\Delta p/p=1$, starting at a low stress of about 0.015 Kg/cm^2 (0.21 psi). Fig. 7 shows a typical result of consolidation test. Data from consolidation tests are summarized in Table 4. Fig. 8 shows a comparison between the compressibility characteristics of the clayey silt sea floor sediments tested and those of soft clays. The somewhat lower compressibility properties of these sediments are partly due to their high silt content. However, the values of the compression indices in situ might be higher than those determined from the samples because of the influence of sampling and disturbance on the compressibility characteristics of these sediments.

Table 3 - Undrained Shear Strength

Sample	Location	Water Content %	Vane Shear Strength, Su psi	Sensitivity
A-5	1	113	0.13	2.8
B-6	2	101	0.28	2.3
C-8	3	105	0.30	3.3
D-9	4	63	0.54	3.2

Table 4 - Compressibility Data

Sample	Water Content %	Initial Void Ratio e_o	Compression Index, C_c	$C_c/1+e_o$
A-5	106.6	2.93	0.72	0.18
B-6	108.1	2.91	0.78	0.20
C-8	96.9	2.61	0.66	0.18
D-9	97.5	2.66	0.63	0.17

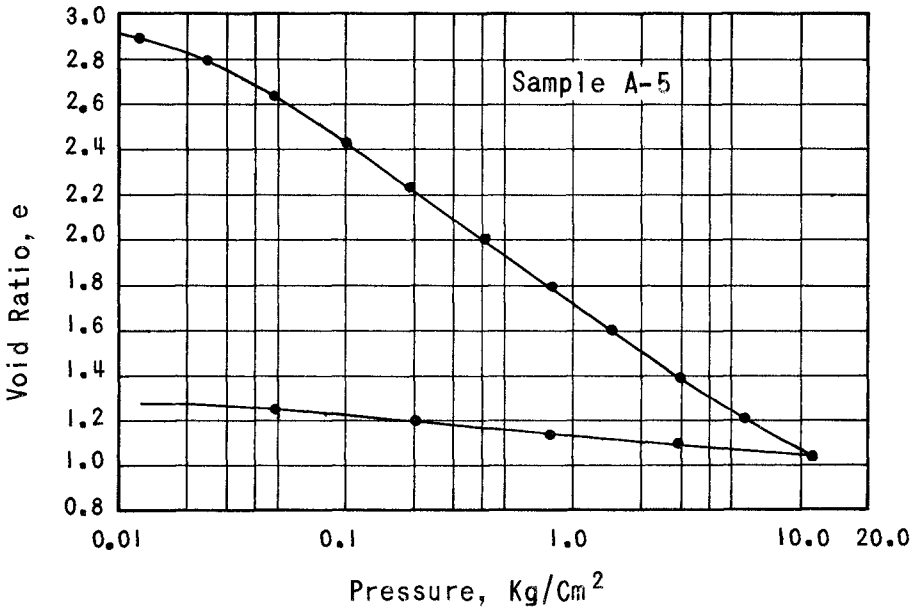

FIG. 7 RESULTS OF CONSOLIDATION TEST

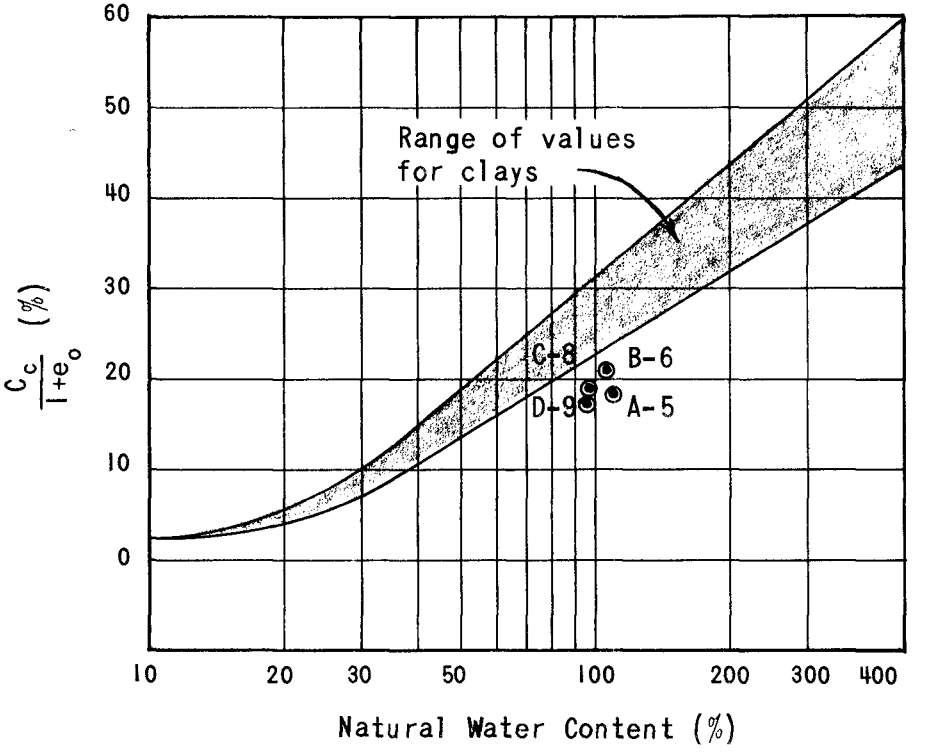

FIG. 8 WATER CONTENT vs. $C_c/1+e_o$

Summary

The engineering properties of near surface sediments obtained by the RUM from four locations on the floor of the La Jolla Canyon in waters ranging in depth from 1256 to 1334 feet were determined. The samples, which were clayey silts of high plasticity, had water contents higher than their liquid limits, had very low strengths (less than 0.5 psi) and medium sensitivities. The samples were highly compressible, but their virgin compression behavior, as evidenced by the $C_c/1+e_o$ values, were somewhat lower but not very different from those of other known marine cohesive soils (4,5).

Acknowledgment

The samples tested were provided by Dr. Victor C. Anderson of the Marine Physical Laboratory of the Scripps Institution of Oceanography. This work is a result of research sponsored by NOAA Office of Sea Grant, Department of Commerce, under Grant #USDC 2-35208 with the Institute of Marine Resources. The U.S. Government is authorized to produce and distribute reprints for governmental purposes notwithstanding any copyright notation that may appear hereon.

References

1. Anderson, V. C., Gibson, D. K. and Kirsten, O. H., "RUM II - Remote Underwater Manipulator (a Progress Report)," Marine Technology Society, 6th Annual Preprints, July, 1970.

2. Noorany, I., "Underwater Sampling and In Situ Testing: State-of-the-Art Review," American Society of Testing and Materials Special Technical Publication STP 501, March, 1972.

3. Anderson, V. C., Clinton, J. R., Gibson, D. K. and Kirsten, O., "Instrumenting RUM for In Situ Sub Sea Soil Surveys," American Society of Testing and Materials Special Technical Publication STP 501, March, 1972.

4. Noorany, I., and Gizienski, S. F., "Engineering Properties of Submarine Soils: State-of-the-Art Review," Proceedings, Journal of Soil Mechanics and Foundations Division, ASCE, September, 1970, pp 1735-1762.

5. Noorany, I., "Engineering Properties of Submarine Clays from the Pacific," Proceedings of the First International Conference on Port and Ocean Engineering, Technical University of Norway, August, 1971.

CHAPTER 87

COASTAL SAND MINING IN NORTHERN CALIFORNIA, U.S.A.

by

Orville T. Magoon[1], M. ASCE
John C. Haugen[2], A.M. ASCE
Robert L. Sloan[3]

ABSTRACT

The commercial mining of sand at coastal locations along California has been a continuing activity at some sites, sporadic at others and altogether discontinued at still other sites. This mining activity includes all methods of sand mining (dragline, self-propelled bottom-dump scrapers, diesel shovels, etc.) and may be classified by littoral zone location as (1) mining from a beach foreshore or backshore area wetted by the normal tidal range, (2) mining within a river mouth or other estuary upstream from the ocean but still within the tidal zone, and (3) mining from bluff or dune areas not wetted by the normal range of tides but still within the littoral system. Processing of the sand thus mined takes place when the material is transported from the mining site, usually by end dump trucks or belt conveyor to either a fixed or a portable plant.

Commercial uses of the sand thus mined fall into two general categories, (1) construction and (2) special purposes. Construction usage includes aggregate for concrete, asphalt, mortar, plaster and stucco, base material in road construction, and fill and structural backfill. Specialty uses include sand blasting and filtration material, foundry and engine sands, and raw material for manufacture of glass and ceramics.

Within the area studied (see Figure 1) the Monterey Bay area has the highest concentration of mining activity. To the north, the area around Fort Bragg yields significant quantities to the commercial miner. Most of the remaining coastal sand mining activity is concentrated in the San Francisco area.

[1]Special Assistant to the Director, U.S. Army Coastal Engineering Research Center, Washington, D. C., U.S.A.

[2]Civil Engineer, Navigation and Shoreline Planning Branch, Engineering Division, U.S. Army Engineer District, San Francisco, California, U.S.A.

[3]Civil Engineer, Chief, Navigation and Shoreline Planning Branch, Engineering Division, U.S. Army Engineer District, San Francisco, California, U.S.A.

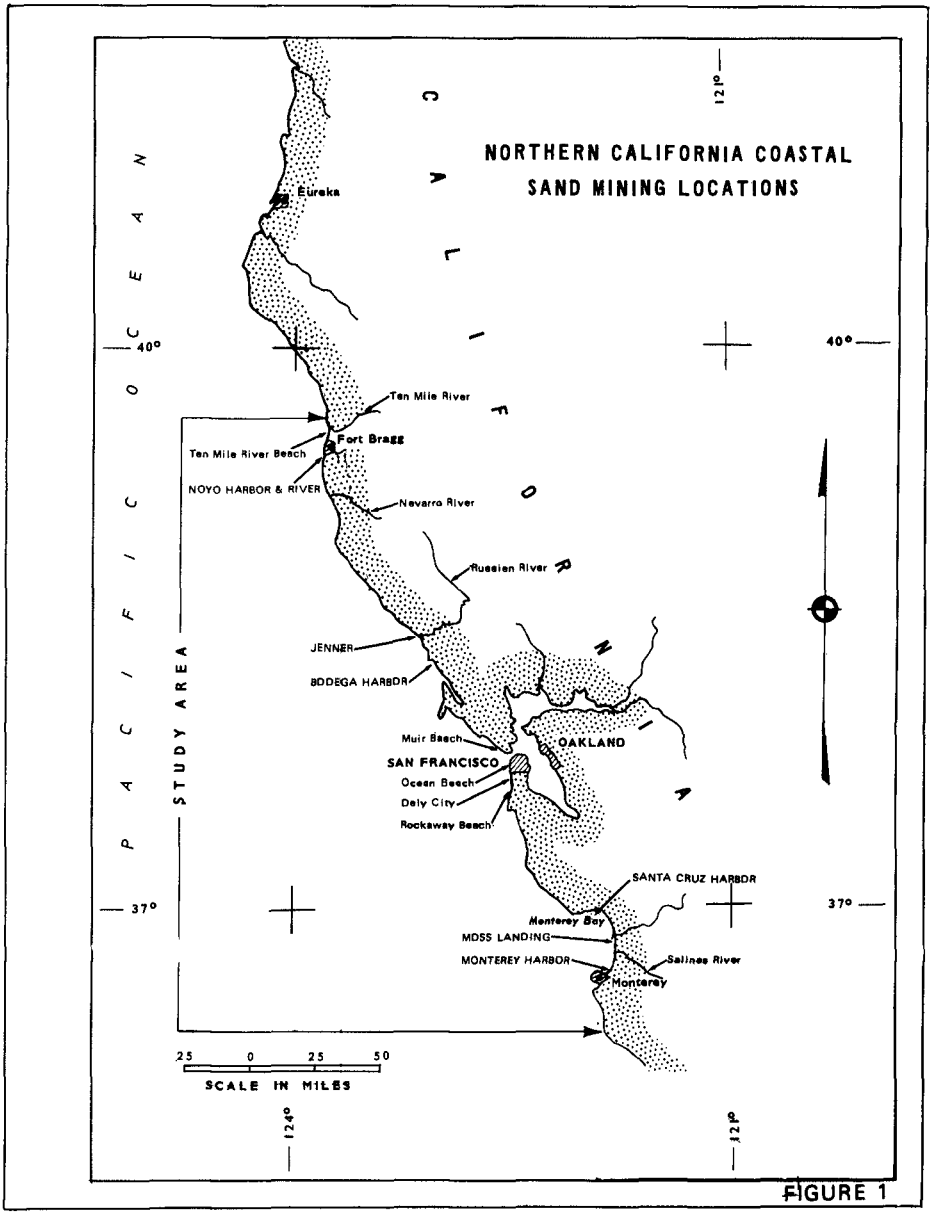
NORTHERN CALIFORNIA COASTAL
SAND MINING LOCATIONS
PACIFIC OCEAN
CALIFORNIA
STUDY AREA
Eureka
Ten Mile River
Fort Bragg
Ten Mile River Beach
NOYO HARBOR & RIVER
Navarro River
Russian River
JENNER
BODEGA HARBOR
Muir Beach
SAN FRANCISCO
OAKLAND
Ocean Beach
Daly City
Rockaway Beach
SANTA CRUZ HARBOR
Monterey Bay
MOSS LANDING
MONTEREY HARBOR
Salinas River
Monterey
40°
37°
124°
122°
25 0 25 50
SCALE IN MILES

FIGURE 1

Total sand (and gravel) production in California is increasing at a rate that is rapid even when compared with the production increases of other minerals in the state. Although that portion of total sand production occurring in the shore zone is extremely small compared to the vast quantity of sand comprising the present littoral system, the mining of sand does reach significant magnitudes in specific physiographic reaches along the coast. This is important inasmuch as sandy beaches represent a major recreational asset to certain coastal areas of the world.

INTRODUCTION

The study area for this paper extends from the Monterey Bay Area on the south to the vicinity of Fort Bragg on the north, or a total distance of about 230 nautical miles. San Francisco and San Francisco Bay are located about midway between Monterey and Fort Bragg (see Figure 1). Although the investigation of particular sites is limited to this portion of the California coastline, the paragraphs discussing the California sand and gravel industry in general apply statewide. Raised numbers in parentheses throughout the text refer the reader to the list of references at the conclusion of this paper for source material. Additional references of interest are listed following these under the heading "General References."

THE SAND AND GRAVEL INDUSTRY IN CALIFORNIA[1][2]

The economic and population growth of California has been paralleled by that of one of its leading non-metallic commodities - sand and gravel. This fact is clearly illustrated on Figure 2 which shows total sand and gravel production in the State of California for the years 1920 through 1964. California's total production in 1920 was almost 5 million tons and by 1964 this had risen to over 100 million tons. To further illustrate this growth, by 1969 total production had risen to 125 million tons, by 1970, 140 million tons and last year, 1971, 145 million tons. Since 1942 California has led the nation in the production of sand and gravel, with only petroleum products and cement outdistancing sand and gravel in total production within the state. About two percent of California's total output of sand and gravel is produced from beach and dune deposits.

USES OF SAND AND GRAVEL[1][3][4]

About nine-tenths of the state's output is used as aggregate in mixtures of either Portland Cement or asphaltic compounds for use in construction or road building. The remaining one-tenth is specialty sand, mostly used in glass making, sandblasting, filters and foundry processes. This breakdown of sand and gravel into use categories applies to sand alone as well. Commercial uses

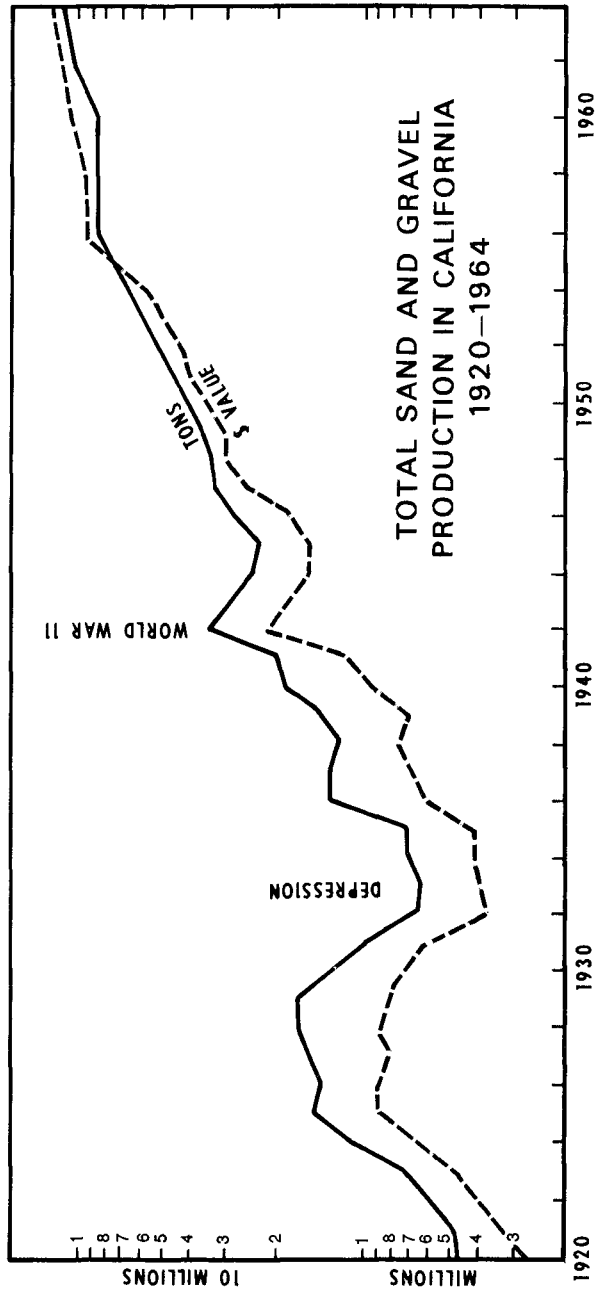
TOTAL SAND AND GRAVEL
PRODUCTION IN CALIFORNIA
1920—1964
TONS
$ VALUE
WORLD WAR II
DEPRESSION
MILLIONS
10 MILLIONS
1920
1930
1940
1950
1960

FIGURE 2

of sand fall into two general categories, (1) construction and (2) special purposes. A further breakdown as to specific uses under each general category may be helpful. The "construction" use category includes:

a. Aggregate for portland cement, concrete, asphalt concrete, mortar, plaster and stucco.

b. Base materials in road construction.

c. Fill and structural backfill.

Included under "specialty purposes" we find:

Glass Making	Specialty Aggregate
Foundry and Engine Sand	(granules for roofing,
Paint Filler	landscaping or aquariums)
Enamels	Sandblasting
Pottery and Ceramics	Filtration
Abrasives	

SOURCES OF SAND AND GRAVEL(1)(4)(5)(6)

Sand for commercial purposes is commonly found in three different types of source materials: Quaternary[1/] beach and dune deposits, Quaternary stream deposits in channels, floodplains, terraces and alluvial fans and older formations. Much of the sand and practically all of the gravel used in construction comes from Quaternary stream deposits. Specialty sands and granules, on the other hand, are obtained almost entirely from Quaternary beach and dune deposits. The latter deposits are also important sources of construction sand. A small amount of road construction material has been obtained from older formations of sand and gravel.

HISTORY OF SAND MINING

Sand mining activity along the coast can be traced backward in time to about 1865 when California's first State Geologist, J.S. Whitney,(7) reported that large quantities of white sand suitable for glass manufacture existed in the Monterey Bay-Carmel Bay area at Cypress Point and Pescadero Beach. The first reported use of sand from coastal sources such as these began in Monterey

1/ The last one million years, in terms of geologic time, are referred to as the Quaternary Period.

at least as early as 1867 when it was mined for use by the San Francisco glass industry to make lighthouse glass and wine bottles. J.R. Browne[8] reported that two of the glassworks employed 150 men and boys and annually produced $250,000 worth of glassware, using the deposits "near the harbor of Monterey" as the chief source of sand.

PRESENT ACTIVITY

Present sand mining activity on the reach of coast from Monterey to Fort Bragg is still concentrated in the Monterey Bay area with the remaining activity essentially limited to the Fort Bragg and San Francisco areas.

SPECIALTY SANDS[1]

Keeping in mind the specific uses for specialty sands, in 1964, California produced 1,482,000 tons of specialty sands, or about 1.5 percent of the state's total sand and gravel production for that year. The value of the 1964 production of specialty sand was over $6,000,000. The following tabulation presents the use breakdown for the 1964 production:

Glass Making	65%
Sandblasting	13
Grinding and Polishing	6
Engine Sand	4
Other Uses	12
	100%

As stated previously, the specialty sands used in California consist largely of material from Quaternary beach and dune deposits and early Tertiary sandstones. Most specialty sands are obtained from the purest available sand deposits that can be economically worked. A high content of quartz makes the sand physically durable and chemically inert, and also provides silica as an ingredient of glass and soluble silicates.

Recent beach and dune sands along the Pacific Ocean, in general, contain a lower percentage of quartz and a higher percentage of feldspar, dark mineral grains, and rock fragments than the Tertiary sandstones that are mined for high silica specialty sands. Beach sands, therefore, are used for minor applications that do not require high purity silica sand. Most beach sand deposits are measurable in millions of tons, have little or no overburden and can be mined inexpensively. Most of the beach and dune sand that is mined in California for specialty uses is obtained from two areas in Monterey County; one immediately southwest of Pacific Grove and the other along the shore of Monterey Bay. The deposits southwest of Pacific Grove are unlike any others in California because of their very

white color and general lack of clay, iron-bearing minerals and rock fragments (Figure 3). The east shore of Monterey Bay is formed almost entirely of sand dunes which have an appreciably higher content of iron than the Pacific Grove sand (Figure 4).

FIGURE 3. Remaining dune deposits Southwest of Pacific Grove

Most of the beach and dune sands in Northern California contain large proportions of dark mineral grains and dark rock fragments, and have been much less extensively used as specialty sands than those from Monterey Bay and southward. In 1963, for example, all of the specialty sand recovered from California beaches was obtained from 7 operations, 5 in the Monterey Bay area and 2 in Southern California.

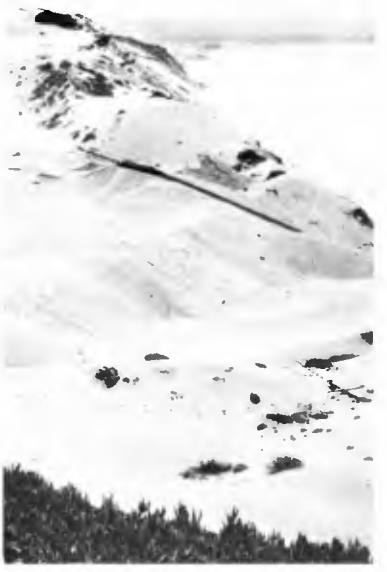

FIGURE 4. East shore of Monterey Bay

METHODS OF EXTRACTION[4][5][6]

How is the sand extracted in coastal mining operations? Most of the operators on Monterey Bay, for example, dredge the sand from the surf zone using a dragline bucket (Figure 5). Some dune sand is also mined in this manner. Other equipment used includes clamshells, diesel or electric shovels, frontend loaders (Figure 6) and bulldozers. Processing of the sand thus mined takes place when the material is transported from the mining site to either a fixed or portable plant. Modes of transportation used include end dump trucks, tractor scrapers, self propelled bottom dump scrapers and conveyor belts (Figure 7). This paper will not attempt a discussion of plant facilities, however, an excellent and detailed discussion of those in the Monterey Bay area is contained in Earl W. Harts 1966 report entitled, "Mines and Mineral Resources of Monterey County."[4]

FIGURE 5. Dragline bucket in surf zone.

FIGURE 6. Removal of sand using front-end loader and dump truck.

FIGURE 7. Transportation of sand from mining site to plant via conveyor belt.

DISCUSSION OF SPECIFIC SITES

The remainder of this paper will be devoted to a discussion of specific operating sites along the coast, beginning on the north near Fort Bragg and proceeding downcoast to the Monterey Bay area. Table 1 gives the distances between these sites in nautical miles. A listing of discontinued operations follows the "MONTEREY PENINSULA" discussion under the heading, "INACTIVE SITES."

TABLE 1

Distances Between Mining Operations Discussed

Site	Miles
Ten Mile River	
	0-5.0
Ten Mile River Beach	
	4.0-9.0
Fort Bragg	
	75.0
Mouth of Russian River	
	60.0
Golden Gate	
	5.0
Ocean Beach	
	6.0
Daly City	
	80.0
Mouth of Salinas River	
	12.0
Monterey	
	4.0-8.0
Monterey Peninsula	

In discussing quantities in the Monterey Bay area it has been necessary to do so in broad terms, i.e., no breakdown is available for each operator. This is, of course, due to the proprietary nature of this information. Another real problem in discussing total quantities for any given reach of coast is that of sand mining done extra-legally. (State and Federal permits are required for any mining activity seaward of the mean high tide line.) These operations go on undetected and the quantities, of course, are never reported. To further compound the problem of how to accurately estimate total quantities, much of the legal sand mining activity occurs above the mean high tide line and may or may not be reported since it's beyond the purview of the regulatory agencies.

FORT BRAGG AREA

Ten Mile River

A Fort Bragg gravel company mines the Ten Mile River streambed deposit which extends for about five miles upstream from a point one mile east of the Highway 1

Bridge. The material is excavated with a dragline to a depth of five feet and then hauled by trucks to the plant about one mile away. Reported capacity of the plant is 300-500 cubic yards per day. Products are essentially concrete sand and gravel and bituminous sand and gravel.

Ten Mile River Beach[9]

From the mouth of the Ten Mile River, approximately nine miles above Noyo Harbor, to Laguna Point, approximately 4.3 miles above Noyo Harbor, the coast is low and contains an extensive beach, locally known as Ten Mile River Beach. Portions of this beach have been intermittently mined for sand by the same Fort Bragg gravel company since about 1961.

At Mean Higher High Water, the beach is about 100 feet wide. The beach consists of a dark sand with a median-grain size at mean sea level of between 0.52 and 0.90 millimeters (mm). The backshore grain size varies considerably from 2.0 mm to 0.52 mm. Ten Mile River Beach is backed by prominent sand dunes. These dunes extend inland approximately 0.8 mile, and are traveling to the southeast under the influence of the predominent northwest wind at an average rate of about two feet per year and at a maximum rate of four feet per year (Figure 8).

FIGURE 8. Inland advance of Ten Mile River Beach dunes.

The State of California is in the process of acquiring Ten Mile River Beach for inclusion in the State Park system. Once included, commercial sand mining on the beach would be prohibited. However, until the transaction is finalized there is nothing to prevent the continuing removal of beach sand. During a period of about one month in the spring of this year, the company mined about 5,000-7,000 cubic yards from two separate beach sites (Figure 9).

FIGURE 9. Upper beach mining site - Ten Mile River Beach

Jenner (Mouth of the Russian River)

The area near the mouth of the Russian River is presently an untapped source of sggregate material (Figure 10). Reliable estimates place the sand and gravel deposit in this area at 60,000,000 tons. A San Francisco based construction and mining company negotiated a lease contract in 1966 with the California State Lands Commission. This gave the company the exclusive right to remove sand and gravel from the bed of the Russian River in an area within 4-1/2 miles of the river mouth. In payment for this privilege, the State could either accept cash royalties or parcels of real property for use as part of a State park. The mining company was unable to extract sand snd gravel subsequent to execution of

the contract due to their inability to maintain a channel opening at the river mouth. The company had planned to use ocean going barges to transport the material to their San Francisco Bay processing plant. Then in 1970, strong objections to the proposed operation were raised on environmental grounds and in September 1970 the county of Sonoma turned down the company's permit application.

FIGURE 10. Mouth of the Russian River.

SAN FRANCISCO AREA

San Francisco County - Ocean Beach[10][11]

In 1953, the city of San Francisco first took bids from private contractors for the mining of sand from Ocean Beach. Between June 1959 and June 1967 a total of 176,000 cubic yards of sand was removed from the section between Sloat Boulevard and the Cliff House. The city dictates how much sand will be removed, and from where. The contractor removes it, and gives the city whatever it needs, for asphalt mix, backfills and sandboxes. The contractor may sell whatever is left, paying the city a specified figure (forty-six cents per cubic yard in 1964, ninety-six cents in 1967).

Because of this operation, an argument has raged for years between local beach buffs who insist the city is ruining the beach for the sake of the "almighty dollar" and the city whose officials defend the sand removal as necessary to prevent closure of the Great Highway by blowing sand. Short periods of closure have been necessitated in the past due to blowing sand and sand on the roadway.

The last collection of money by the city of San Francisco for the selling of sand took place on 14 July 1967. At that time the contractor was instructed to cease his operation, however, he was still conducting unauthorized sand removal activities through October of that year. Shortly thereafter, however, the commercial operation was brought to a final halt.

Subsequent to cessation of the commercial operation in 1967, the city and county of San Francisco has continued periodically to remove sand from the dune and beach sreas, presumably to lessen the impact of blowing sand (Figure 11). However, no quantities are available from 1967 to the present.

FIGURE 11. Sand removal from Ocean Beach area - San Francisco

Daly City

According to newspaper accounts in late 1971,[12][13] the mining of sand from the ocean front near Mussel Rock (Daly City-Pacifica boundary) by a San Franciaco acavenger company had, at that time, been going on for about aix years (Figure 12). This sand removal was halted in 1971 when the company was notified that they were conducting the operation without the required Federal (Corps of Engineers) or State (State Lands Commission) permits.

FIGURE 12. Scavenger Company sand mining operation - Daly City

This sand removal beginning in 1965 was necessitated, according to the company, to permit the laying of a foundation for a seawall along a 1,900-foot stretch of beach from Mussel Rock north. The necessity for the seawall was, in turn, attributed to wave action which had, at that time, uncovered an abandoned dump. Refuse from this dump had begun to float to sea and adjacent beaches were being polluted resulting in a cease and desist order from the State Water Quality Control Board pertaining to the dumping site. Construction of the seawall was necessary to satisfy the Board.

According to a company spokesman, only about 2,500 cubic yards of sand were exported over a 10-month period. This material was sold for forty cents a cubic yard. Others estimate this quantity to be much higher and the mining activity to have extended over a longer (6-year) period of time.

MONTEREY BAY AREA[4]

Mouth of Salinas River[14]

It has been reported that the Monterey County Flood Control District has been removing sand from the river mouth periodically over a period of about ten years. This is done to provide better flow characteristics thereby reducing flood hazards in the lower reaches of the river. The sand removed by the county is placed alongside the mouth and some of this is probably removed by private interests for varied uses. Although much of the area is owned by a private concrete aggregate company, it is not believed that the company uses any of this material for commercial purposes.

Along Monterey Bay (General)

Sand is obtained from well established plants operating from about two miles south of the Salinas River mouth to the city of Monterey (Figure 13). The mouth of the Salinas River is shown near the lower right-hand corner of Figure 13. Due to the fact that these beaches are either advancing or retreating, sand producers here have some difficulty in locating draglines and equipment.

Total production along Monterey Bay since inception of this industry has been estimated at about 9,000,000 tons.

Lone Star Industries-Lapis Deposit

This site, two miles north of Marina and about two miles downcoast from the mouth of the Salinas River is the northernmost operation in the Monterey area and has been operating since 1906. Since 1929 it has been operated by Pacific Cement and Aggregates, now Lone Star Industries. Processing equipment is now used to produce sand for concrete aggregate and mortar and sand for sandblasting and other specialty uses.

The modern beach sand has not been used much since 1959. The operator is now using an older beach deposit about one-quarter mile inland from the shoreline. The coarser sand is excavated using a suction dredge floating in a circular pit about 400 feet in diameter. The material is pumped to the plant where it is sorted hydraulicly, classified and dried. Sand is shipped from the plant by truck and rail, dry or wet, bulk or sacked.

FIGURE 13. Monterey Peninsula and East shore of Monterey Bay.

Seaside Sand and Gravel Company

This plant is located about one mile northwest of Marina, just north of the Monterey Sand Company's Marina plant and about one mile downcoast from the Lone Star Industries-Lapis Deposit (Figure 14). Since 1957 coarse sand has been taken

FIGURE 14. Seaside Sand and Gravel Company.

from the breaker zone using a dragline scraper. The dunes are not high in this reach of shoreline. The sand is moved to a nearby surge pile and conveyed to washing and screening equipment. Principal products are blasting sand, plaster sand, concrete sand and roofing granules. Sand is shipped in bags or bulk.

Monterey Sand Company-Marina Deposit

This beach sand deposit was developed in approximately 1944 and is located about one mile north of Marina and less than one mile downcoast from the Seaside Sand and Gravel Company operation. The material taken from beach is coarse and well sorted. It is mined from surf zone using a typical dragline scraper. It is then taken from the surge pile, washed and classified. Blasting and plastering sands are the principal products, but the plant also produces engine and filter sand and roofing granules (Figure 15).

FIGURE 15. Monterey Sand Company - Marina Facility.

Lone Star Industries-Prattco Deposit

This deposit is located further downcoast in Sand City but still about five miles upcoast from Monterey. Beach sand mining has occurred at this site since 1921. The present operator, formerly Pacific Cement and Aggregates, produces sand for concrete, blasting and stucco. Dragline scrapers remove sand from both the surf zone and the extensive dune deposits (Figures 16 and 17). The sand is

stockpiled, psrtially sorted and blended. Medium grained sand is taken from the dunes and coarser sand from the beach. Dredging from the beach is often discontinued during the summer when the sand becomes too fine. On the whole, however, more beach sand than dune sand is excavated. The equipment is located on the dunes about thirty feet above sea level.

FIGURE 16. Lone Star Industries-Prsttco Deposit, surf zone mining.

FIGURE 17. Lone Star Industries-Prattco Deposit, dune mining.

Granite Construction Company Deposit

Located in Sand City, this plant has produced fine aggregate for concrete and asphalt since the late 1940's. Coarse beach sand is taken from the surf zone with a dragline scraper, and medium grained sand is taken by dragline scraper from the dunes. Material over 4-mesh size is removed and the dune and beach sands are blended, stored and trucked unwashed to the concrete and asphalt batch plants one-quarter mile to the east.

Monterey Sand Company-Sand City Deposit

Located in Sand City, this is the last operation before coming to the city of Monterey. This deposit has been worked since before 1931. The present company has been operating here since 1946. Coarse beach sand is taken from the surf zone using a dragline scraper (Figure 18). Dune sand is also taken. From the surge pile the sand is moved by conveyor to the washing-classifying section. It is hydraulicly sorted, blended and stored for bulk shipment by truck. The principal products are concrete fine aggregate, plaster sand and blasting sand. The company owns a drying-screening plant two-thirds of a mile to the south.

FIGURE 18. Monterey Sand Company - Sand City Facility.

MONTEREY PENINSULA[4]

General

Along the scenic Monterey Peninsula coastline (Figure 13) between Monterey and Carmel, beach deposits are scant, but extensive dunes once stretched up to one-half mile inland and over 200 feet above sea level in height in some areas. The white sand found in these dunes has been used for glass manufacture and specialty construction purposes. It is a medium-grained sand consisting almost entirely of equal parts of quartz and feldspar. These dunes have been mined extensively since about 1903 and the original sand resource is now largely depleted. Figure 19 shows an area that was once covered by extensive dunes. At present two companies have mining operations and/or processing plants on the peninsula coast.

FIGURE 19. Area formerly covered by extensive dunes.

Owens-Illinois Moss Beach Deposit

The first of these is Owens-Illinois whose Moss Beach deposit is located at the southern part of Moss Beach along the Seventeen Mile Drive. The property is owned by Del Monte Properties Company and leased to Owens-Illinois. Dunes up to forty feet in height formerly covered this area reaching about one-half mile inland. Dune sand has been bulldozed to a surge pile and moved on a half-mile long conveyor belt (Figure 20) to the processing plant. Since 1903 this operation has depleted nearly all of the dune resource at this site. The sand from this deposit is classified and extensively washed and cleaned at the processing plant. This process provides the company with the feldspathic raw material for the production of flint and colored glass. A small amount of the sand has been used for other specialty purposes.

FIGURE 20. Surge pile and conveyor belt - Owens-Illinois Moss Beach Deposit.

Del Monte Properties

The other peninsula operator, Del Monte Properties, is presently limited to the processing of sand trucked in from inland deposits. The company had been operating dune deposits at Moss Beach and Fan Shell Beach, but these resources are nearly depleted.

INACTIVE SITES

Based on a reconnaissance of the study area in 1961, the following coastal sand mining sites were reported as active at that time. In the case of Muir Beach, a field estimate of the total quantity mined was made:

Site	County	Total Quantity Mined (Cubic Yards)
Navarro River	Mendocino	Unknown
Muir Beach	Marin	5,000
Rockaway Beach	San Mateo	Unknown

SUMMARY

In conclusion then, what are the problems facing the sand miner, and conversely, what is mining's effect on the sand resource? One of the miner's problems has just been covered. In areas where mining activity has been going on since the beginning of this century, the sand resource has been noticeably depleted. This is especially true along the Monterey Peninsula where replenishment by wind and wave action is less than the excavation rate. Near population centers, another problem emerges, that of recreational and residential development, such as the golf course shown on Figure 21, further limiting utilization of the remaining beach and dune deposits.

Finally, then, and to repeat an earlier statement, although only about two percent of California's total output of sand and gravel is produced from beach and dune deposits and although this is quite small when compared to the vast quantities of sand comprising the present littoral system, the mining of sand does reach significant magnitudes in specific physiographic reaches along the coast. This is important inasmuch as sandy beaches represent a major recreational asset to certain coastal areas of the world.

FIGURE 21. Golf course, Monterey Peninsula.

ACKOWLEDGMENT

Acknowledgment is gratefully made to the Corps of Engineers, U. S. Army, for access and permission to use this study material. The views of the authors do not purport to reflect the position of the Corps of Engineers, Department of the Army, or Department of Defense.

REFERENCES

1. Mineral Resources of California, 1966, Bulletin 191, California Division of Mines and Geology.

2. California Ceology, February 1972, Volume 25, Number 2, pg. 41.

3. Mineral Commodities of California, 1950, Bulletin 156, Division of Mines.

4. Hart, Earl W., 1966, Mines and Mineral Resources of Monterey County, California, County Report 5, California Division of Mines and Ceology.

5. Goldman, Harold B., 1964, Sand and Cravel in California, an Inventory of Deposits, Part B - Central California, Bulletin 180-B, California Division of Mines and Ceology.

6. Goldman, Harold B., 1961, Sand and Cravel in California, an Inventory of Deposits, Part A - Northern California, Bulletin 180-A, California Division of Mines.

7. Whitney, J. D., 1865, Ceology 1. Report of Progress and Synopsis of the Field Work from 1860 to 1864: California Geology Survey, 498 pgs.

8. Brown, J. R., 1868, Mineral Resources of the States and Territories West of the Rocky Mountains: U. S. Covernment, pgs. 244, 251.

9. U. S. Army Engineer District, San Francisco, 1962, Review of Reports, Noyo River and Harbor, California.

10. Person, Wayne, 1972, City and County of San Francisco, Department of Public Works, personal communication.

11. Thurber, Scott, 1967, The Carrying Off of Ocean Beach, San Francisco Chronicle, November 13, 1967, pg. 4.

12. LaPierre, Frank, 1971, A Beach Sand Debate, The Milpitas Post, December 1, 1971, pg. 10.

13. Hollis, Robert, 1971, Daly City Sand Mining Is Stopped, San Francisco Examiner, November 22, 1971, pg. 1.

14. Welday, E., 1972, California Division of Mines and Geology, personal communication.

CENERAL REFERENCES

California Ceology, September 1971, Volume 24, No. 9, pgs. 170, 171.

Cherry, John, 1964, Sand Movement Along a Portion of the Northern California Coast, Hydraulic Engineering Laboratory, University of California, Technical Report No. HEL-4-3.

Directory of Mineral Producers in California for 1969, California Division of Mines and Ceology.

Johnson, J. W., 1963, Sand Movement on Coastal Dunes, Hydraulic Engineering Laboratory, University of California, Technical Report No. HEL-2-3.

Marine Technology Society Journal, July-August 1971, Vol. 5, No. 4, pgs. 35-43.

Minard, Claude R., Jr., 1964, The Erosional and Depositional History of the Coast of Northern California, Hydraulic Engineering Laboratory, University of California, Technical Report No. HEL-2-10.

Snow, David T., 1962, Beaches in Northwestern California, Hydraulic Engineering Laboratory, University of California, Technical Report Series 14, Issue 25.

Trask, Parker D., 1958, Beaches Near San Francisco, California, 1956-1957, Beach Erosion Board Technical Memorandum No. 110.

Zeller, R. P., 1961, A General Reconnaissance of Coastal Dunes of California, Hydraulic Engineering Laboratory University of California, Technical Report Series 72, Issue 6.

CHAPTER 88

ESTABLISHMENT OF A COASTAL SETBACK LINE IN FLORIDA

By

James A. Purpura
Associate Professor

Coastal and Oceanographic Engineering Laboratory
University of Florida, Gainesville, Florida, U. S. A.

ABSTRACT

The Florida Legislature passed a law in 1971 requiring the establishment of coastal construction setback lines on a county basis along the sand beaches of the State of Florida fronting on the Atlantic Ocean and the Gulf of Mexico.

Florida's beach areas (valued in $ billions) are being developed at an accelerated rate, however the coastline is in a general state of serious erosion. These factors combine to make implementation of the above law extremely urgent.

The Coastal and Oceanographic Department of the University of Florida has a contract with the Florida Department of Natural Resources to furnish a comprehensive engineering study of the various coastal counties of Florida in order to provide the technical information and make recommendations for the establishment of such setback lines.

A typical coastal county study is described. The study included historical data related to shoreline stability, field measurements, computations and evaluation of all pertinent factors. Some factors considered were dune elevations, foreshore-offshore slopes, erosion trends, storm surge, vegetation bluff line, wave setup, uprush, coastal structures and upland development.

Analysis of the pertinent factors resulted in formulation of criteria that were applied in recommendation of the setback line. The criteria-application is described along with adoption procedures as required by law.

I. INTRODUCTION

Chapter 161.053, Florida Statutes, enacted by the 1971 session of the State Legislature, provides that the Department of Natural Resources (Governor and Cabinet) shall set a Coastal Construction Setback Line along the Gulf and Atlantic shores of the State. This law prohibits any construction, excavation, damage to dunes or vegetation and driving of vehicles on dunes, seaward of the established setback line.

The purpose of this law is the protection of upland properties and the control of beach erosion by preservation of the natural beach-dune system.

This law states that the setting of this line shall be based on data resulting from comprehensive engineering and topographic-hydrographic surveys, erosion trends, predictable storm tides, wave runup, the vegetation bluff line, and other technical data.

Subsequently, the Department of Natural Resources, through the Bureau of Beaches and Shores, entered into a contract with the Coastal and Oceanographic Engineering Department of the University of Florida's College of Engineering for the required studies and surveys.

II. PROBLEM BACKGROUND

Florida's coastline has been considered one of the most beautiful recreational areas in the world. It has over 800 miles of sand beaches fronting the Atlantic Ocean and the Gulf of Mexico. It has beautiful dune formations, clean white sand and a sub-tropical climate which attracts over 25 million tourists per year.

Its sandy beaches backed by dunes constitute a natural defense against the sea. The beach area is highly dynamic, and seasonal fluctuations of the shoreline are a normal occurrence, However, Florida is subjected to winter northeast storm and tropical hurricanes, and abnormal assaults on the coastline may result in severe erosion or wild fluctuations. Sand dunes are nature's "insurance" in these instances. Although showing the scars of battle (scarps), nature usually provides a healing or rebuilding time before the next abnormal onslaught. In undeveloped beach areas bounded by natural dunes, the shoreline fluctuations are not readily apparent to the casual observer. Thus, parts of Florida's coastline have been considered relatively free of beach erosion and fluctuations. However, coastal development by man encroaching on the dynamic beach area provides "reference point" whereby natural shoreline fluctuations and beach erosion becomes readily apparent.

Recent history (geologically speaking) has shown that Florida's shorelines are in a general state of natural erosion (submergence), due mainly to a rise in sea level. But man's actions have and still are the biggest contributing factor to the State's shoreline problems.

Development of the coastline has progressed at an ever increasing pace. Unfortunately, with a complete lack of or poor zoning laws, man has encroached on the beaches and in the process has hampered or destroyed nature's defense against the sea. In fact, development has, in many instances, magnified erosive forces (vertical seawalls), inhibited natural rebuilding processes and placed older existing structures, once relatively safe, in jeopardy. Sections of the natural dune line have been removed and/or flattened and in many instances, structures have been erected in front of existing dunes. Large portions of the coastline and development worth billions of dollars are now subjected to flooding by storm tides as a result of these practices. The "improvement" and construction of several inlets around the coastline has further aggravated shoreline problems.

As a consequence of man's encroachment, destructive actions and magnification of erosive forces we now find that Florida has a serious beach erosion problem. A forewarning of this problem was pointed out in a 1962 publication[1] of the Coastal Engineering Laboratory of the University of Florida. The problem has been increasingly apparent as further development, above normal tides and wave conditions, have caused extensive damage to coastal structures and dune formations.

III. SETBACK LINE INVESTIGATION

The location of a setback line from a coastal engineering point of view depends upon certain physical conditions. Factors to be considered in a broad sense are shoreline stability (fluctuations, erosion trends) and topography as

related to storm/hurricane tides and wave action. To properly evaluate shoreline stability, there is a need for historical data of long duration.

The first step in a study is to survey the area in question to determine the need, if any, for a setback line. If the need is established, all available historical data should be collected, and a topographic and hydrographic survey of the area should be carried out.

1. Study Area

Based on existing shoreline conditions, and at the request of local officials, the Bureau of Beaches and Shores designated Martin County as the first county in which the required studies would be made. The study area consists of 22 miles of Atlantic Ocean beachfront dissected by St. Lucie Inlet, a major tidal inlet. The area consists of barrier islands, namely Hutchinson Island between the north Martin County line and St. Lucie Inlet and Jupiter Island from St. Lucie Inlet to the Palm Beach County Line. The locality is shown on USC & GS charts Nos. 846, 1247, 1248 and Figure 1 of this report.

Martin County has a long history of beach erosion and/or storm damage to its Atlantic Coastline. Jupiter Island has been noted for severe beach erosion problems and Hutchinson Island has suffered from erosion and damage especially during hurricanes and northeast storms.

Testimony and exhibits presented at a prestudy public hearing in Stuart on October 6, 1971 described some of the erosion and damage problems that have occurred in the past.

Of particular interest was the account of the August-September 1949 hurricane as reported in the Stuart News. It described how Martin County's "first ocean front tourist colony," at Jensen Beach was reduced to a pile of rubble. The colony was described as 5 deluxe, reinforced concrete cottages.

Also described at the hearing was the severe erosion south of the inlet, a breakthrough to the bay at Pecks Lake and a history of the development of St. Lucie Inlet.

A comprehensive report of the coastline problem in Martin County has been issued by the Department of the Army, Jacksonville District, Corps of Engineers dated September 16, 1968. The report entitled, Beach Erosion Control Study on Martin County, Florida, with its detailed descriptions and historical data was a valuable aid in the study. The above data and public hearing, confirmed the need of a setback line in Martin County.

2. Field Programs

The general case in Florida will show a lack of historical and good statistical data so, therefore, much reliance must be made on comprehensive topo-hydro field studies correlated with the measured physical parameters of the area.

A comprehensive field investigation of the study area was carried out as follows: As required in the law, monumented stations approximately 900 ft. apart were placed parallel to the shoreline (127 stations) from the northern county line along the coast to the southern county line, a distance of approximately twenty-two miles. (Figs. 2 and 3). Each station was carefully

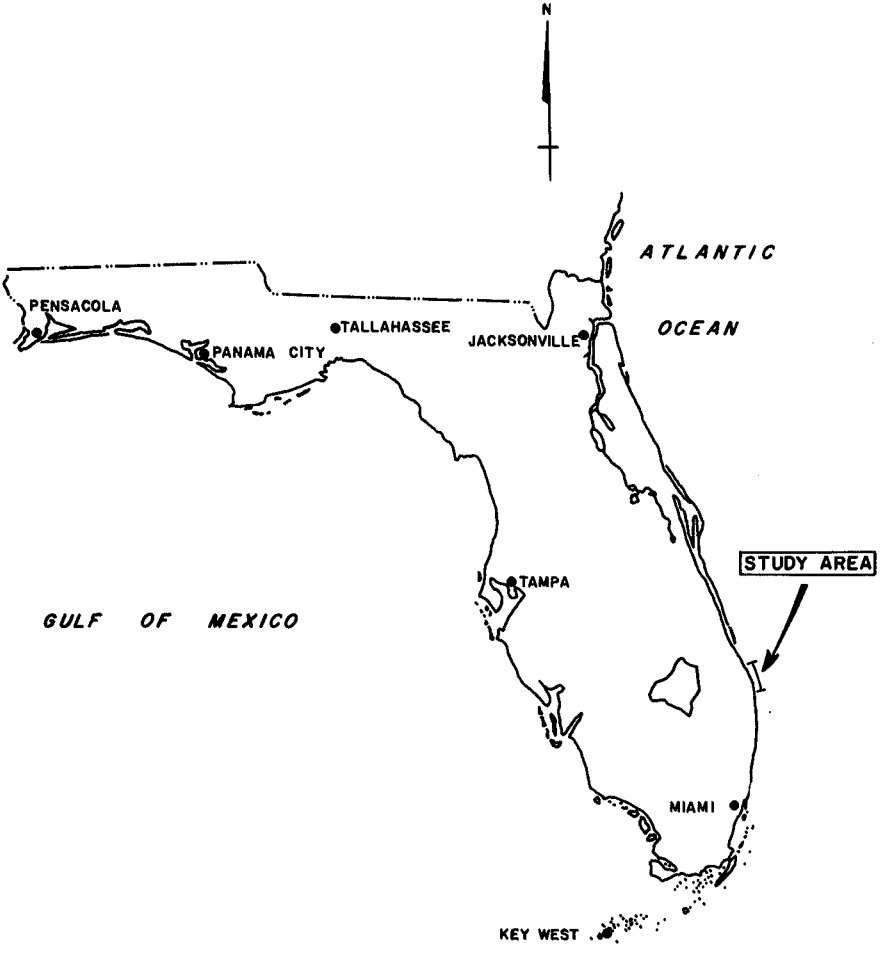

FIGURE 1 LOCATION MAP

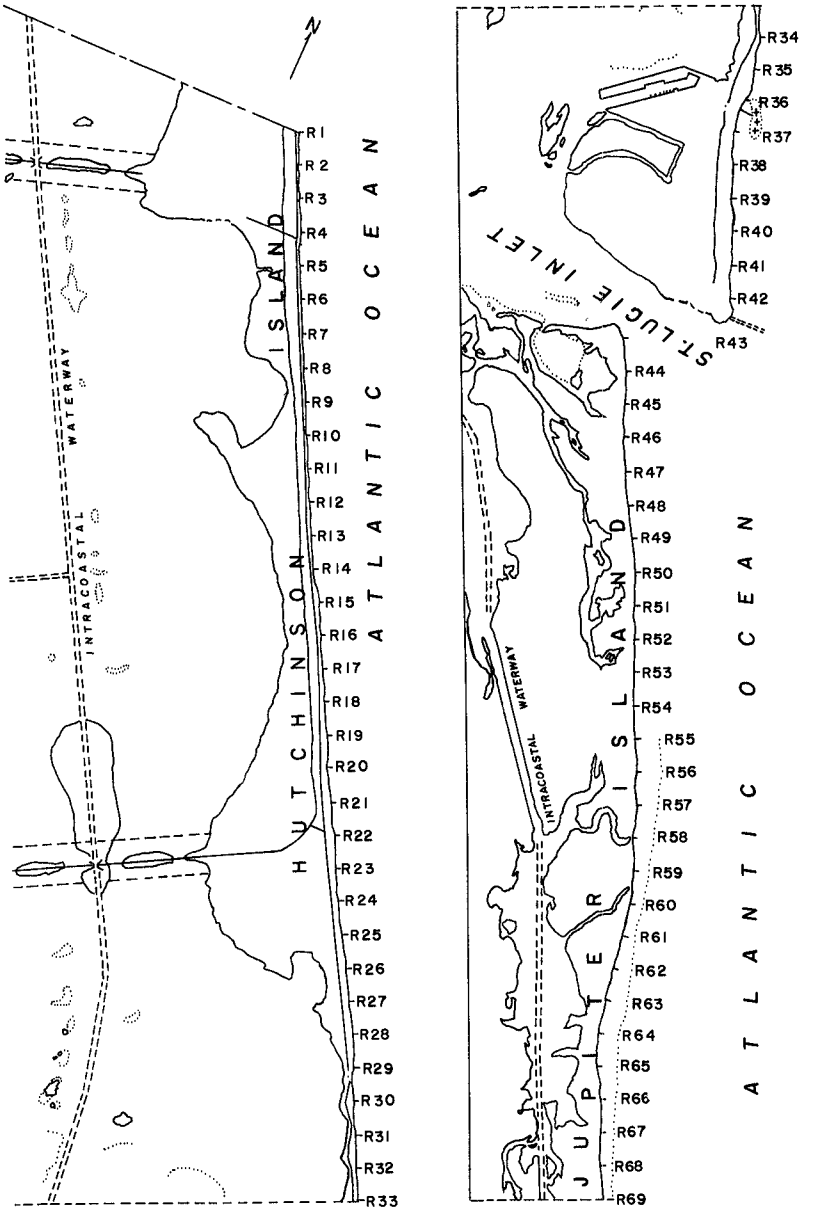

FIGURE 2 PROFILE STATIONS

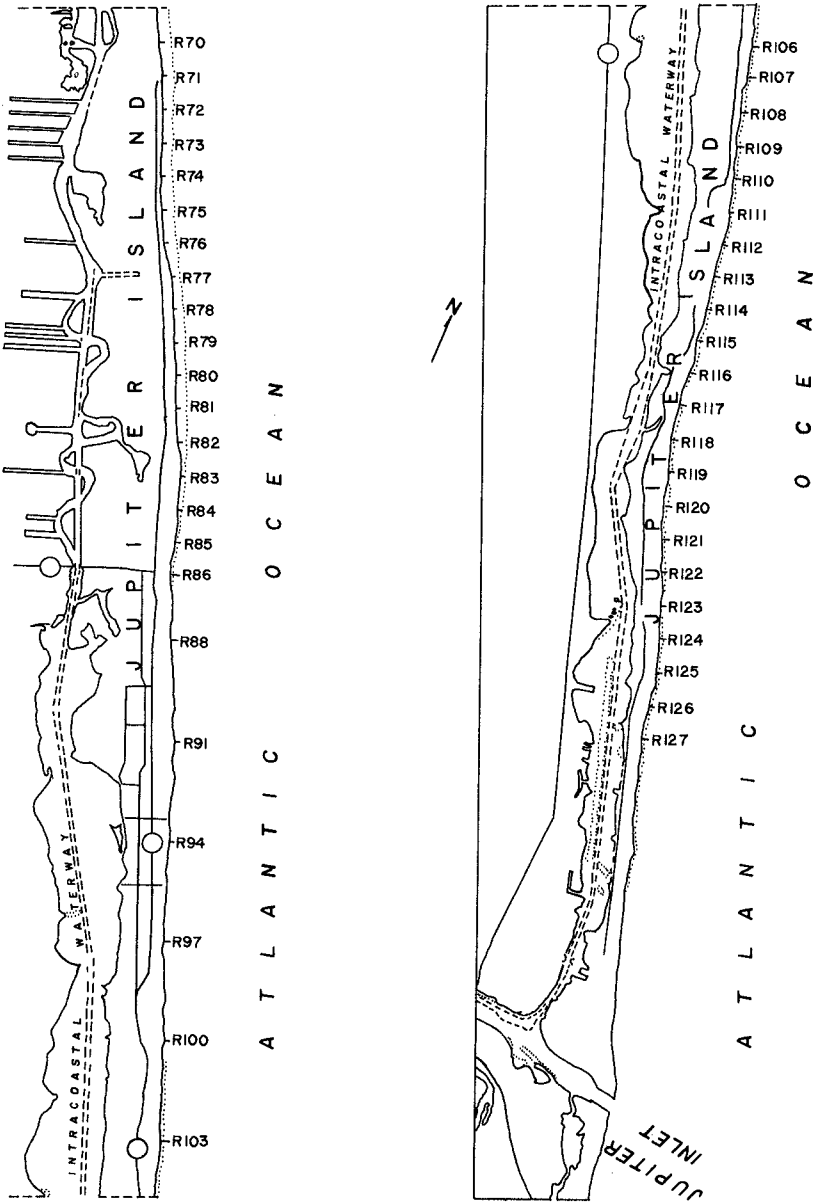

FIGURE 3 PROFILE STATIONS

surveyed in and tied to the State Plane Coordinate System.

Beach profiles from the back of the dune (where existing) to a wading depth were completed from each station. Profiles were repeated after two winter storms to determine profile fluctuations.

An automatic tide recorder was placed in operation on an ocean pier and recorded continuously during the study.

Using targeted stations as control, stereoscopic aerial coverage of the study area was flown and mylar reproductions at a scale of 1" = 100' were obtained.

Approximately 40 offshore soundings from the beach to a depth of about 30 ft. were completed.

Intensive ground coverage was carried out taking special note of beach material and composition, rock strata, vegetation-bluff-scarp lines, wave uprush, dune stability (blowout-gaps, etc.), existing coastal structures and their behavior, present construction and upland development. All of this data was carefully recorded and supplemented with photographs.

IV. PERTINENT FACTORS

1. Erosion Trends

Historical data are extremely valuable in determining the shoreline trend and erosion-accretion rates for use in determining a setback line location. Fortunately, there are sounding data of 1882, 1928-1930, 1946 and 1964 for Martin County. Much use was also made of historical aerial photographs, local news stories, local land surveys and public testimony. Long term trends, however, do not always indicate the short term fluctuations that occur on the beach. These fluctuations can be quite large in magnitude over a short term as a result of certain tide-wave conditions. During the recent surveys, areas of the county shoreline which have an apparent long term trend of stability were, noticed to suffer quite severe erosion with subsequent accretion-erosion cycles. These cycles are dependent on wave conditions, however, severe damage (i.e. loss of vegetation, structures, etc.) may result during these fluctuations.

2. Wind-Waves-Tide

It is important to obtain long term records of wind, waves and tides because of their direct bearing on the coastline stability. This is especially true for the short term trends or fluctuations of the beaches. Florida's coastline suffers from severe northeastern storms on an annual basis. These storms although "normal", can in many instances, if long enough in duration, cause considerably more beach erosion and coastline damage than many hurricanes. The following data was obtained for the Martin County area.

Tides - Tide records in this area, collected from previous studies and currently furnished by a tide recorder at Seminole Shores pier on Hutchinson Island, show that the tide is semi-diurnal with a rather large daily inequality. Tide tables of the U.S. Coast and Geodetic Survey list the average tidal range for the ocean tide off Martin County as 2.6 ft. and the average spring tidal range as 3.0 ft. The actual mean sea level (MSL) is 1.08 ft. above mean low

water (MLW) and 1.83 ft. below mean high water (MHW) (furnished by the Army Corps of Engineers, Jacksonville District).

Winds - The most comprehensive offshore wind speed and direction data in this area are compiled by the U. S. Naval Weather Service Command. According to this publication, 85.5% of the time the wind speed is between 4 and 21 knots. Wind direction frequencies are rather evenly distributed among the eastern semicircle with slightly higher frequency from east (21.7%) and northeast (16.7%).

Waves - In accordance with the wind direction, higher percentage of waves are from the east (22.4%) and northeast (17.2%). Waves with a height between 3 and 6 ft. are the most frequent (48.4%). Waves higher than 6 ft. have a frequency of 12.9%. The prevailing wave periods are between 3 and 4 sec. (30.7%), 1 and 2 sec. (26.0%) and 5 and 6 sec. (17.9%).

3. Longshore Current and Littoral Drift

The currents which affect the open coast are the longshore currents created by breaking waves at an angle to the shore. The magnitude of the longshore current depends on the breaking wave characteristics, breaking angle and local bottom and shore configurations.

The longshore currents are responsible for sand transport along the coast. For the study area, the littoral transport is generally southward during the period September through February, northward from June through August and directions uncertain during the rest of the months. The predominant or net littoral drift is from north to south and is estimated to be about 200,000 to 250,000 cu. yds. a year inside the 20 ft. contour.

4. Storm Surge and Wave Setup

In addition to the astronomic tide, storms, hurricanes and waves are capable of creating extreme high water levels, especially on shallow coastal areas.

Storm surge is the vertical rise in the still water level near the coast caused by wind stresses on the water surface. No reliable records are available of water levels on the open coast during major hurricanes which have occurred in the past few decades. In a study of storm tides in Florida[2], the Department of Coastal and Oceanographic Engineering, University of Florida has analyzed the normal yearly high tides and high water levels caused by hurricanes and expressed the results as frequency of occurrence for a certain water level to be equaled or exceeded. In that study, all available normal and storm tide data before 1959 along the coast of Florida were analyzed and correlated to provide the tidal level-frequency information for the open coast of Florida. Unfortunately there were a lack of data for the study area. Thus the interpolated storm surge frequencies given in that report may be less reliable than the new information furnished by National Oceanic and Atmospheric Administration (NOAA). For this reason, it is chosen to adopt the NOAA's information for use in this study. Figure 4 shows the storm surge elevation and frequency.

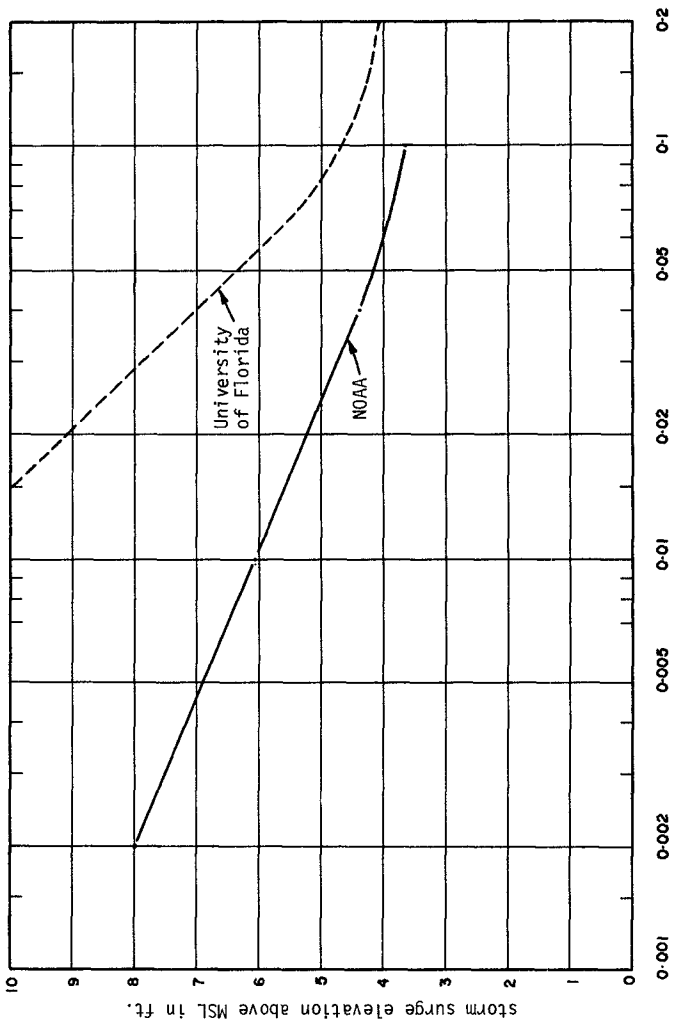

FIGURE 4 STORM SURGE FREQUENCIES

For comparison the interpolated surge elevation-frequency curve in the Univerversity of Florida's report is also shown in Figure 4 which indicates a much higher trend. In view of the documented[3] surge of 8.5 ft. (MSL) in St. Lucie River caused by the August 1949 hurricane, the curve with higher surge trend may prove to be valid, however, the newly compiled curve by NOAA was used for this study.

Wave setup is the superelevation of the water surface over normal surge elevation due to onshore mass transport of the water by wave action alone. There is no record of wave setup for this area. During a "Standard Hurricane" such as Hurricane Audrey (1960), the wave setup is estimated to be about 2.0 ft. in the study area.

Another factor which may cause an increase in water level is the effect of rainfall. Since hurricanes are often associated with excessive rainfall, an increase in storm tidal levels may occur in coastal areas in the neighborhood of creeks, rivers and inlets.

The water level rise due to reduced atmospheric pressure associated with a hurrican is considered to be included in the original storm tide data.

5. Wave Uprush

Wave uprush is the rush of water up onto the beach following the breaking of a wave. How high or how far the uprush will reach depends on the wave characteristics and the steepness and roughness of the beach surface. Due to the fact that each beach profile is highly irregular in shape and widely varying in elevation from place to place, the wave uprush is expected to vary accordingly. Since a setback line should not be exposed to direct wave attack of a certain frequency, the uprush would be a minimum elevation (or distance) beyond which the setback line should be located. While not much field data are available, laboratory test results have been utilized to assist in uprush computations. For a complicated beach surface with changing slopes, the composite slope method[4] has proven to be applicable. Laboratory tests[5] also showed rough surfaces could reduce uprush considerably.

A computer program was developed to perform the calculations of uprush on each of the profiles by employing the composite slope method.[4] Field data could be directly fed into the computer which would compute the wave uprush under any given wave height and period superimposed on any water level. Many different water levels (surge frequencies) and combinations of wave periods could be computed in an extremely fast, efficient manner.

6. Topographical Conditions and Existing Structures

As mentioned in Section III-2, Field Program, intensive ground surveys were carried out. Factors such as beach composition, coastal structures, upland development, vegetation (types-density), visible erosion and/or dune damage are all important considerations. Controlled, vertical aerial photographs of the coastline were flown and proved to be extremely valuable. These aerials were reproduced on mylar sheets at a scale of 1" = 100' and showed the position of each permanent monument (profile station) as well as the state plane coordinate lines.

V. SETBACK LINE ANALYSIS

In making the analysis for the setback line the objectives were two fold. To prevent beach encroachment that would endanger the natural beach-dune system and to prevent upland development from being unreasonably subjected to great or irreparable damage. The analysis considered these factors: topographic features, which included dune elevation, foreshore and offshore slopes, beach material and width, coastal structures, vegetation and bluff lines; the dynamic features, which included storm surge elevations, erosion rates, wave set up and uprush, tides and short term fluctuations of the beach profiles.

1. Criteria

For Martin County the guidelines and standards that were chosen for positioning the setback line are as follows:

A storm surge of 4.2 ft. MSL, 2.0 ft. wave setup and a 1.8 ft. MSL spring tide were combined in the determination of a still water level of 8.0 ft. MSL under storm conditions.

A wind wave of 6.5 ft. in height with a period of 8.0 sec. was chosen for computing the uprush by composite slope method[4] under the storm condition on each of the profiles. This will yield the information about how far landward the uprush may reach.

Long term erosion trends were compiled for each profile station and reduced to an annual average. Short term fluctuations were used to determine what order of magnitude may be expected on a 5 year frequency. Pertinent topographical features (materials, vegetation, etc.) were incorporated into these guidelines.

Existing coastal structures and upland development were studied for efficiency, durability, continuity and affect on adjacent properties.

2. Application

Using the above criteria, the uprush limits were plotted on the beach profile and aerial plans as a first approximation of the setback line.

A minimum distance of 40 ft. from the present dynamic beach face was used to provide for the extraordinary beach fluctuation. This distance was further adjusted to the annual erosion rate using a further setback of annual rate times 5 years.

A minimum distance of 25 ft. from the most seaward dune crest (if present) was used for protection of the dune system.

Adjustment of coastal structures - upland development was then applied where deemed necessary.

Further adjustment was made to avoid discontinuity, zig-zags or other irregularities which showed up on the plotted setback line.

Figures 5 to 8 show some typical profiles with the setback line (SBL), surge level (20 year frequency, see V.1.), and computed wave uprush.

VI. ADOPTION OF SETBACK LINE

As required by law, a public hearing in Martin County was held prior to recommendation to the Governor and Cabinet for adoption of the line.

Prior to the public hearing, notice was given to all county residents and interested parties. Plans showing the recommended setback line along with reports and other supporting data were placed on public display well in advance of the hearing.

At the public hearing all arguments and evidence for support or in opposition to the recommended line were recorded for study by the staff of the Department of Natural Resources. As a result of the hearing, one adjustment to the line was made by the hearing officer.

The line was recommended to the Governor and Cabinet for adoption. Further arguments and evidence were presented at the time. The setback line was adopted by a unanimous vote.

A legal description of the adopted setback line was then recorded at the Martin County Clerk Office.

The law provides for variances of the setback line to be granted by the Oepartment of Natural Resources if such variances are fully justified. The law further provides that the setback line be reviewed at five year intervals or sooner if proven necessary.

ACKNOWLEDGEMENTS

This study is supported by the Bureau of Beaches and Shores, Department of Natural REsources, Tallahassee, Florida. Bureau Chief, Mr. W. T. Carlton and Engineer, Mr. William Sensabaugh provided valuable assistance throughout the study. Special acknowledgement belongs to Mr. T. Y. Chiu of the Coastal and Oceanographic Research Laboratory who spearheaded the office work force and personally contributed so much to the project. Mr. Hal Bean, Field Supervisor and Mr. Stan Rising, also deserve special recognition for their untiring efforts in providing field data.

REFERENCES

1. Bruun, Morgan, Purpura, "Review of Beach Erosion and Storm Tide Conditions in Florida," Technical Progress Report #13, EIES, College of Engineering, University of Florida, 1961-1962.

2. "Storm Tides in Florida as Related to Coastal Topography," Bulletin Series No. 109, Florida Engineering and Industrial Experiment Station, University of Florida, 1962.

3. "Survey Report," by the Corps of Engineers, Jacksonville District, September 1961.

4. Saville, T., Jr., "Wave Run-up on Composite Slopes," Proc. of the 6th Conference on Coastal Engineering, Council of Wave Research, University

of California, 1958.

5. Savage, R. P., "Wave Run-up on Roughened and Permeable Slopes," Proc. of ASCE, Waterways and Harbors Division, WW3, Paper 1640, 1958.

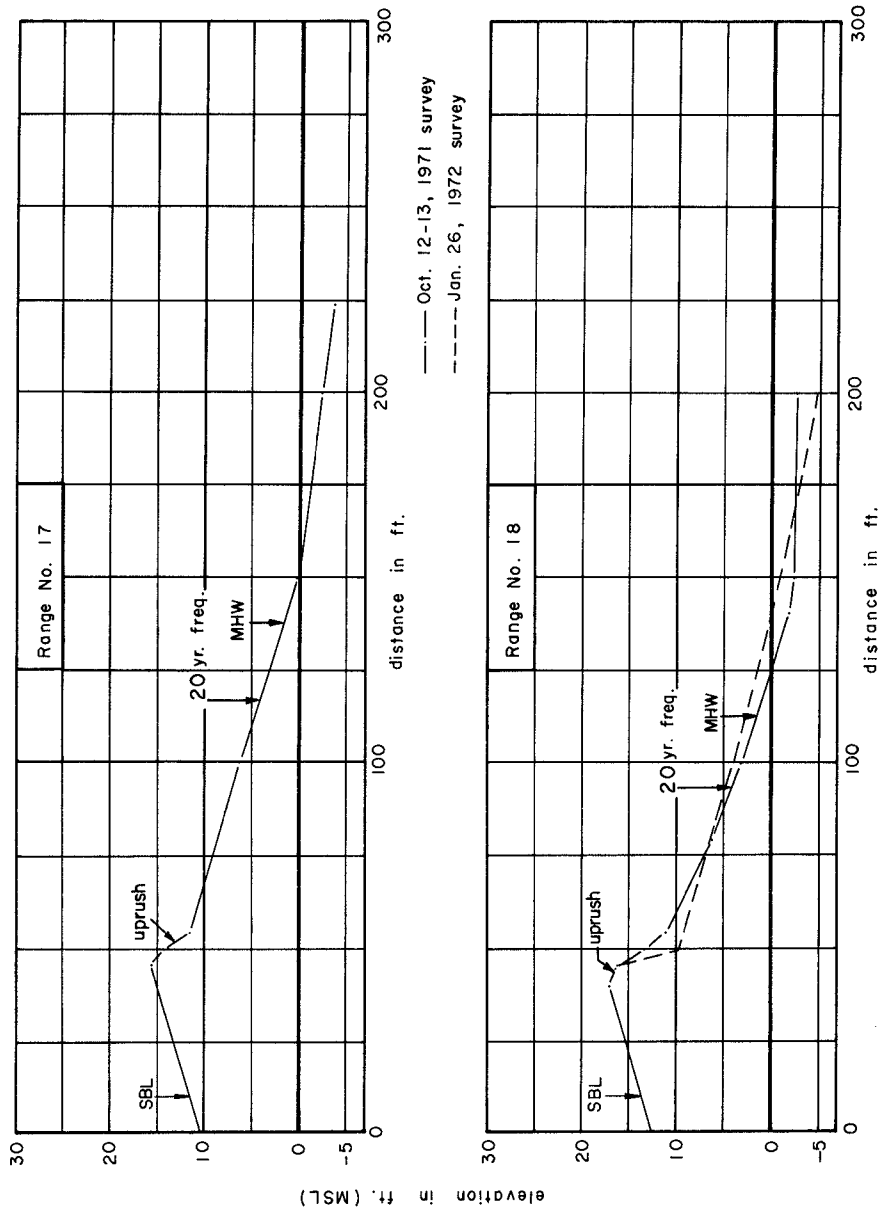

FIGURE 5 BEACH PROFILES

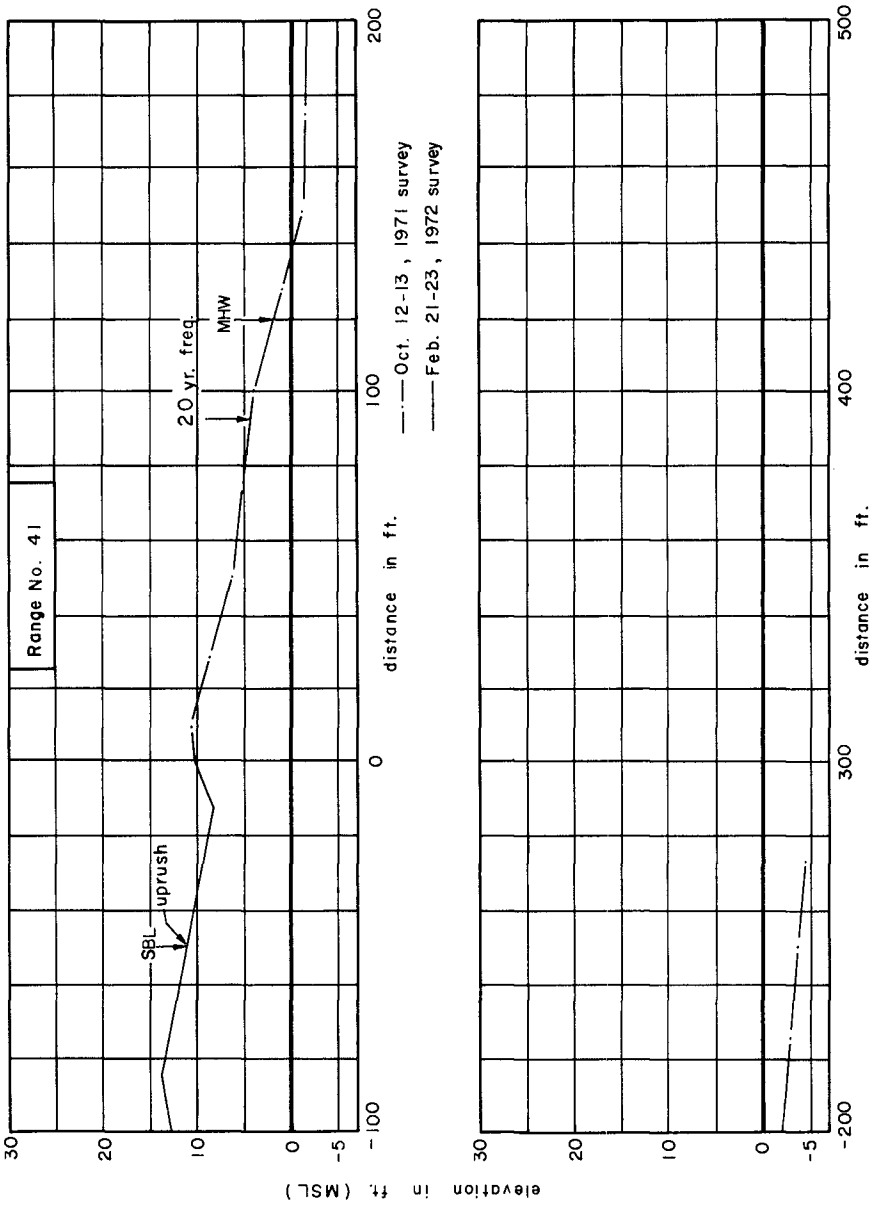

FIGURE 6 BEACH PROFILES

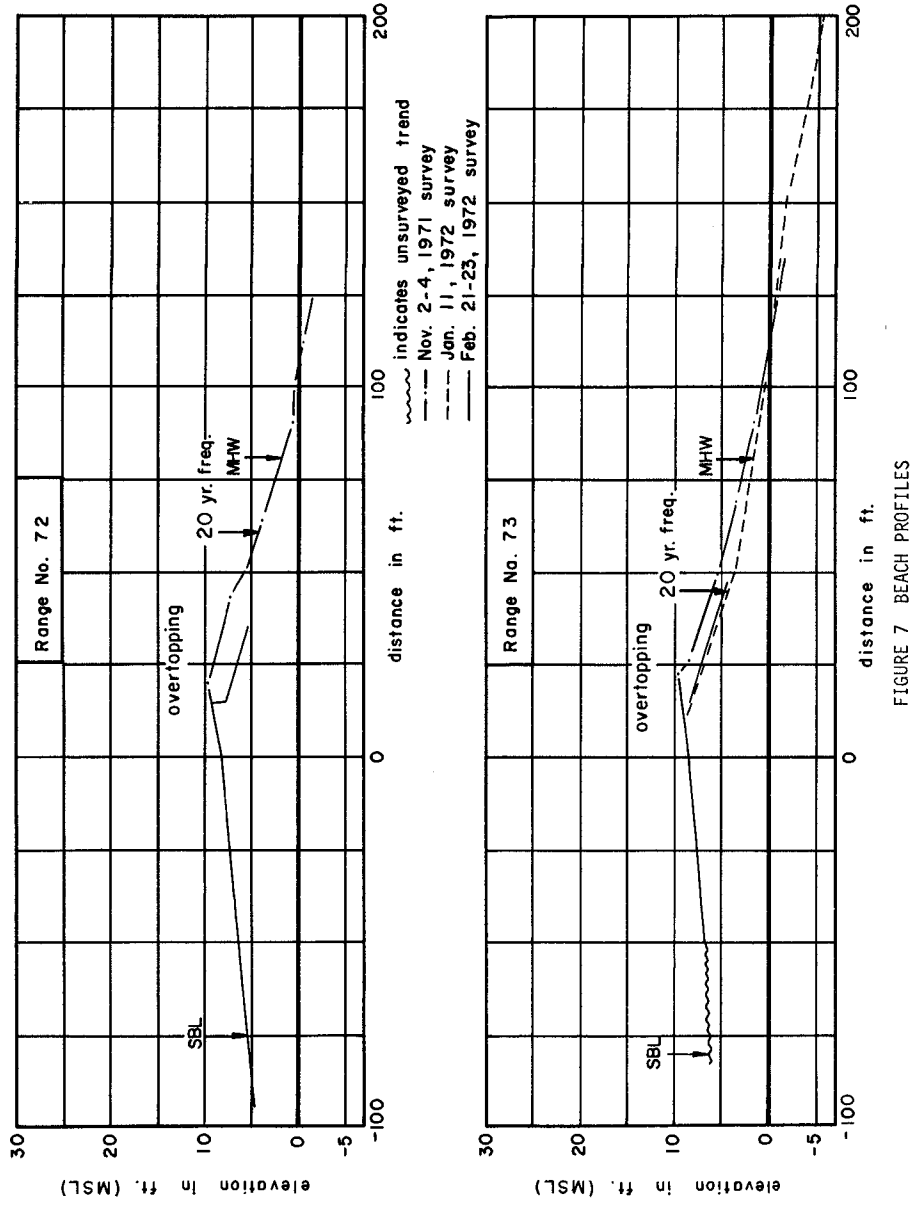

FIGURE 7 BEACH PROFILES

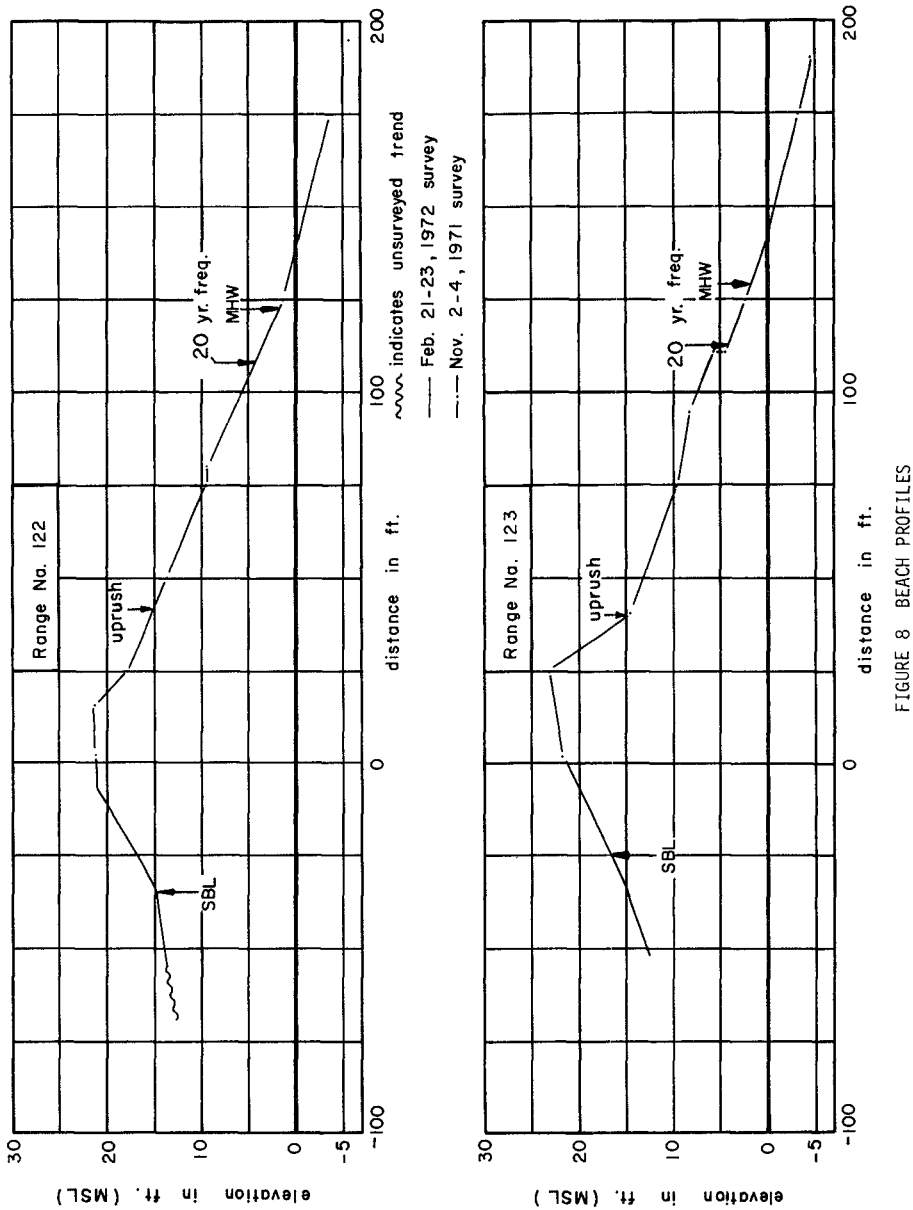

FIGURE 8 BEACH PROFILES

CHAPTER 89

CHARACTERISTICS OF SALTATION OF SAND GRAINS BY WIND

Yoshito Tsuchiya

Professor of Coastal Engineering
Disaster Prevention Research Institute
Kyoto University

and

Yoshiaki Kawata

Postgraduate, Department of Civil Engineering
Kyoto University, Kyoto, Japan

ABSTRACT

Although the phenomenon of saltation of sand grains in a sand storm is very complicated, there exists the successive saltation defined by the authors. The height and distance of saltation of sand grains in successive saltation by wind are compared with the theory of successive saltation proposed by the authors. The concentration of sand grains and velocity profile in a saltation layer are theoretically investigated with the aid of the results of experiment.

INTRODUCTION

In sand storms, the sand grains on the bed are moved by aerodynamic forces due to wind. After rolling and sliding for a distance less than a grain diameter, the sand grains which are so massive as to fail to begin suspension come into collision with other sand grains and then begin jumping motion. Such a motion is considered as saltation in this paper. The most important aspect in the motion of saltating sand grains is that the grains move intermittently in contact with the uneven, movable sand bed. In establishing the law of sediment transport by wind, the mechanics of such a motion of sand grains should be developed.

In 1941, Bagnold made a comprehensive study of the sand transport by wind. About twenty years ago Kawamura(1951) proposed an excellent theory of sand movement by wind based on the equation of motion of a sand grain. Recently Owen(1964) also investigated the interaction between a turbulent wind and the motion of uniform saltating sand grains to discover the velocity profile in a saltation layer and the law of sediment transport. There are fruitful suggestions for establishing the mechanics but the distributions of saltation height of sand grains should be taken into account in the development. More recently the present authors have investigated the mechanics of saltation of sand grains by wind and proposed a theory of successive saltation based on the equation of motion of a sand grain and the dynamic characteristics of collision between a saltating sand grain and bed sand grains.

In this paper, experimental considerations of the height and distance

of saltation of sand grains in the successive saltation are presented and a comparison between the theory of successive saltation and the experimental results is also described in comparison with the saltation of sand grains in water. Furthermore, the concentration of sand grains in a saltation layer is theoretically investigated based on the equations of sand movement and the stochastic approach to the distribution of saltation height of sand grains. An approach to discover the velocity profile in a saltation layer is presented with the aid of the momentum equation taking into consideration the bottom shear stress, the additional shear stress due to saltating sand grains and the Reynolds stress.

EXPERIMENTAL APPARATUS AND PROCEDURE

(1) Experimental Apparatus Experiments were carried out with a wind tunnel, 0.9 m wide, 11 m long and 0.39 m high. The tunnel was constructed of steel, but with both sides made of glass for observations. The velocity at the center of the section of tunnel is changed from 2 m/sec to 24 m/sec by a variator. The velocity measurements were made using a hot wire anemometer with a protecter of net. The characteristics of sand grains used in the experiment are shown in Table 1 with the experimental conditions carried out.

Table 1 Characteristics of sand grains used and experimental conditions carried out

(a) Fixed bed

No.	Dimeter of grains d cm	Kind of grains	Specific gravity σ/ρ_0	Density ratio σ/ρ	Shear velocity u_* cm/sec	Dimensionless tractive force (flow intensity) $u_*^2/(\sigma/\rho-1)gd$
1	0.225	sand grains	2.624	2235	97.9	0.0204
2	〃	〃	〃	〃	105.7	0.0227
3	〃	〃	〃	〃	119.0	0.0287
4	0.184	〃	2.523	2120	102.1	0.0273
5	〃	〃	〃	〃	114.8	0.0345
6	〃	〃	〃	〃	120.2	0.0378
7	〃	seeds	1.155	969	69.9	0.0280
8	〃	〃	〃	〃	83.3	0.0398
9	〃	〃	〃	981	67.8	0.0260
10	〃	〃	〃	〃	73.4	0.0305
11	〃	〃	〃	〃	82.4	0.0384
12	0.144	sand grains	2.474	2081	105.9	0.0382
13	〃	〃	〃	〃	122.0	0.0507
14	〃	seeds	1.155	981	76.9	0.0428
15	〃	〃	〃	〃	98.8	0.0706

(b) Movable bed

No.	d cm	σ/ρ_0	σ/ρ	u_*cm/sec	$u_*^2/(\sigma/\rho-1)gd$
1	0.225	2.528	2172	112.2	0.0262
2	〃	〃	〃	113.0	0.0267
3	〃	〃	〃	116.5	0.0286
4	0.184	2.550	〃	101.7	0.0266
5	〃	〃	〃	105.9	0.0287
6	〃	〃	〃	113.0	0.0326
7	0.144	2.528	2158	90.2	0.0267
8	〃	〃	〃	96.6	0.0307
9	〃	〃	〃	104.3	0.0358

(2) Experimental Procedure In the experiment in the case of fixed bed, the sand grains were uniformly coated on the tunnel bed. In the case of movable bed the sand grains were spread over the tunnel bed with a 2 cm thickness. After the sand bed was leveled, each run was started with the wind velocity shown in Table 1. The saltating sand grains in both the cases of fixed and movable beds were photographed with a Miliken high speed cine camera. The analysis of the trajectory of a saltating sand grain and the concentration of sand grains in a saltation layer were made with a film motion analyzer.

CHARACTERISTICS OF SALTATION

(1) Trajectory of Saltating Sand Grains Fig. 1 shows some examples of the trajectories of saltating sand grains in a saltation layer. It was concluded from the observation through the film motion analyzer that there

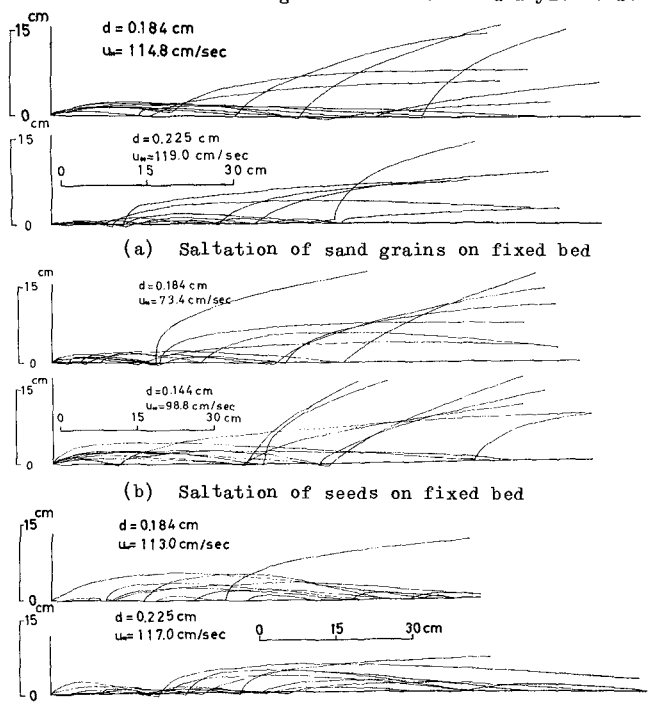

(a) Saltation of sand grains on fixed bed

(b) Saltation of seeds on fixed bed

(c) Saltation of sand grains on movable bed

Fig. 1 Trajectories of grains in saltation layer in cases of fixed and movable beds

exists similar seven elementary phenomena in the saltation as those in a water stream, such as the stationary state of a sand grain, the beginning of motion due to hydrodynamic forces, the beginning of motion due to collision,

the saltation, the collision among saltating sand grains, the rebound and the stop of saltation. Since the momentum of a successively saltating sand grain increases generally with order of saltation, the saltating sand grain often makes one more sand grains start to saltation. Because of the fact the mechanism of collision between saltating sand grains and bed sand grains is very important to consider the mechanics of sand transport by wind.

(2) Height and Distance of Saltation in Successive Saltation In the previous paper, the authors presented a theory of successive saltation of sand grains. The main formulations firstly can be summerized as follows. Based on the equation of motion of a sand grain, the vertical and horizontal velocities of saltation can be written approximately as

$$\left.\begin{aligned} &\bar{W} = \pm a_1\sqrt{\bar{H}-\bar{\eta}}\ ,\quad \bar{U} = \bar{U}_0 + a_1(\sqrt{\bar{H}} \mp \sqrt{\bar{H}-\bar{\eta}})\{(\bar{u}-\bar{U}_0)/K\}^2 \\ &\bar{W} = W/u^*,\ \bar{U} = U/u^*,\ \bar{\eta} = z/d\ ,\quad K^2 = (4/3)\{(\sigma/\rho-1)gd/u^{*2}\}(1/C_D) \\ &a_1^2 = K^2\{(3/2)C_D/(\sigma/\rho+1/2)\} \end{aligned}\right\} \quad (1)$$

in which u* is the shear velocity, W the vertical velocity of a sand grain, W_o the initial one, U the horizontal velocity, U_o the initial one, d the grain diameter, σ/ρ the specific gravity, g the acceleration of gravity, C_D the drag coefficient and z the coordinate.

The height and distance of saltation of a sand grain can approximately be given respectively as

$$\left.\begin{aligned} &\bar{H}\ (=H/d) = (\bar{W}_o/a_1)^2 \\ &\bar{L}\ (=L/d) = 4\bar{U}_o\bar{W}_o/a_1^2 \end{aligned}\right\} \quad (2)$$

And the relationships between the velocity components just before and after the collision of a saltating sand grain with bed ones can be expressed approximately as

$$\bar{U}_o = e\bar{U}_1\ ,\quad \bar{W}_o = e(t_1\bar{U}_1 + t_2\bar{W}_1)/\{t_3 + t_1(\bar{W}_1/\bar{U}_1)\} \quad (3)$$

in which $t_1 = (1+e)\tan\gamma$, $t_2 = 1-e\tan^2\gamma$, $t_3 = \tan^2\gamma - e$, e is the rebound coefficient of a sand grain and γ a parameter expressing the bed condition.

In the successive saltation in which the initial velocity of a sand grain holds constant, the height and distance of saltation can be given approximately as

$$\left.\begin{aligned} &\bar{H} = \left\{(1/2)\lambda\left[(1+e)-\sqrt{(1-e)^2+2(1-e)/\lambda(\bar{u}/K)^2}\right](\bar{u}/a_1)\right\}^2 \\ &\bar{L} = \lambda\left\{\left[(1+e)-\sqrt{(1-e)^2+2(1-e)/\lambda(\bar{u}/K)^2}\right](\bar{u}/a_1)\right\}^2,\quad \lambda = 4\bar{H}/\bar{L} \end{aligned}\right\} \quad (4)$$

respectively. The density functions for the distributions of height and distance of saltation can be formulated respectively as

$$\left.\begin{aligned} &f_1(\bar{H}) = (1/2\sqrt{2\pi})(1/\varepsilon\sqrt{\bar{H}\bar{H}_m})\exp\{-(\sqrt{\bar{H}}-\sqrt{\bar{H}_m})^2/2\varepsilon^2\bar{H}_m\} \\ &f_2(\bar{L}) = (1/2\sqrt{2\pi})(1/\varepsilon\sqrt{\bar{L}\bar{L}_m})\exp\{-(\sqrt{\bar{L}}-\sqrt{\bar{L}_m})^2/2\varepsilon^2\bar{L}_m\} \end{aligned}\right\} \quad (5)$$

in which H_m is the mean value of saltation height, L_m the mean value of saltation distance and ε the standard deviation. Using the above re-

lationships, the height and distance of saltation of a sand grain in the successive saltation can be calculated based on the results of experiment of the empirical constants in the theoretical formulations. Fig. 2 shows changes of the parameters characterizing the sand bed condition which are the empirical constants in the theory with order of saltation in the cases of fixed and movable beds. Although the data shown in the figure are fairly scattering, it is seen that the angle of departure of a sand grain at the moment of beginning of movement β and the ratio of the height to the distance of saltation have a tendency to somewhat increase with order of saltation. The trend of decrease in the rebound coefficient may suggest the possibility of loss of momentum of a saltating sand grain due to bottom friction and the movability of the bed sand grains at the moment of collision.

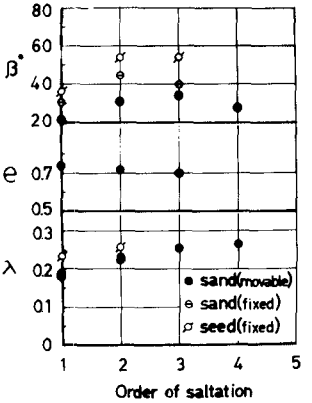

Fig. 2 Changes of parameters characterizing sand bed conditions with order of saltation

Fig. 3 shows an example of changes of the height and distance of saltation of a sand grain with order of saltation in comparison between the theoretical curves calculated by the above theory and the results of experiment in which the solid line indicates the result calculated by Eqs. (2) and (3) using the height and distance of saltation in the first saltation and the dimensionless representative velocity in the saltation layer $\bar{u} = 20$, and the broken line the similar one but the value of $\bar{u}$ is used as the velocity corresponding to the saltation height in each saltation. The height and distance of saltation of a saltating sand grain more radically increase with order of saltation than those in a water stream, since the rebound coefficient of a saltating sand grain in air is usually compared to be large with the one in water. It is concluded from the comparison that the theoretical curves for the height and distance of saltation in the successive saltation are in good agreement with the experimental values and that the height and distance of saltation become constant nearly at sixth order of saltation.

Fig. 4 describes a comparison between the theoretical curves for the stationary saltation in which the initial velocity of a saltating sand grain holds constant and the experimental values of height and distance of saltation obtained using sand grains and seeds on the fixed or movable bed, including the data in sediment transport in water obtained by the authors. A similar comparison has been presented in the previous paper but the figure is misdrawn. It is seen from the figure that the effect of the rebound coefficient of a saltating sand grain is very significant to estimate the height and distance of saltation. It is seemed that the height and distance of saltation approach to the theoretical curves for the stationary saltation if the successive saltation is continued.

CONCENTRATION OF SAND GRAINS IN A SALTATION LAYER

The saltation layer is formed when the shear velocity due to wind action much exceeds the initial value for sand movement. The concentration of sand grains is defined as the mass of saltating sand grains per unit volume in a saltation layer. In order to investigate the concentration of sand grains, Kawamura's approach can be applied on the basis of the characteristics of saltation of sand grains described already.

Consider the concentration of sand grains at any order of saltation. The concentration of sand grains having the saltation height between H and H + dH, $\psi_H dH$ can be written as

$$\psi_H dH = 2 G_0 f_1(H) dH / W \tag{6}$$

in which G_0 is the mass of sand grains emitting from unit area of the bed per unit time. Integration of Eq. (6) using Eqs. (1) and (5) gives an expression for the concentration of sand grains at the distance from the bed as

$$C(\eta) = (\bar{G}_0 / \sqrt{2\pi}\, a_1 \varepsilon / \bar{H}_m) \int_\eta^\infty (1/\sqrt{\bar{H}(\bar{H}-\eta)}) \exp\{-(\sqrt{\bar{H}}-\sqrt{\bar{H}_m})^2 / 2\varepsilon^2 \bar{H}_m\}\, d\bar{H} \tag{7}$$

in which

$$C(\eta) = \psi(\xi)/\sigma, \quad \psi(\xi) = \int_\xi^\infty \psi_H dH, \quad \bar{G}_0 = G_0/\sigma u^*$$

Therefore, if partition of number of saltating sand grains at any order of saltation is estimated, the concentration of sand grains in a saltation layer can be calculated by summing up the concentration function for every order of saltation. Fig. 5 shows an experimental result for the change of succession ratio of saltation. Using the result of Fig. 5, the concentration of sand grains can be calculated as shown in Fig. 6. It is concluded from the figure that the theoretical concentration curve is in good agreement with the results of experiment and that the concentration of sand grains does not decreases exponentially.

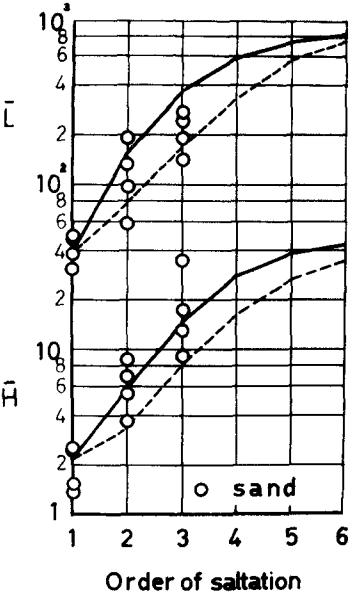

Fig. 3 Changes of height and distance of saltation of sand grain with order of saltation

VELOCITY PROFILE IN A SALTATION LAYER

Since the momentum transfer in a saltation layer occurs due to action of saltating sand grains, changes in the velocity profile in the layer take place. The shear stresses due to wind and saltating sand grains are considered to be composed with the Reynolds stress by wind and the additional shear stress due to saltating sand grains. From the point of view the shear stress can be expressed as

$$\tau = \tau_w + \tau_s \tag{8}$$

in which τ is the total shear stress, τ_w the Reynolds stress by wind and τ_s

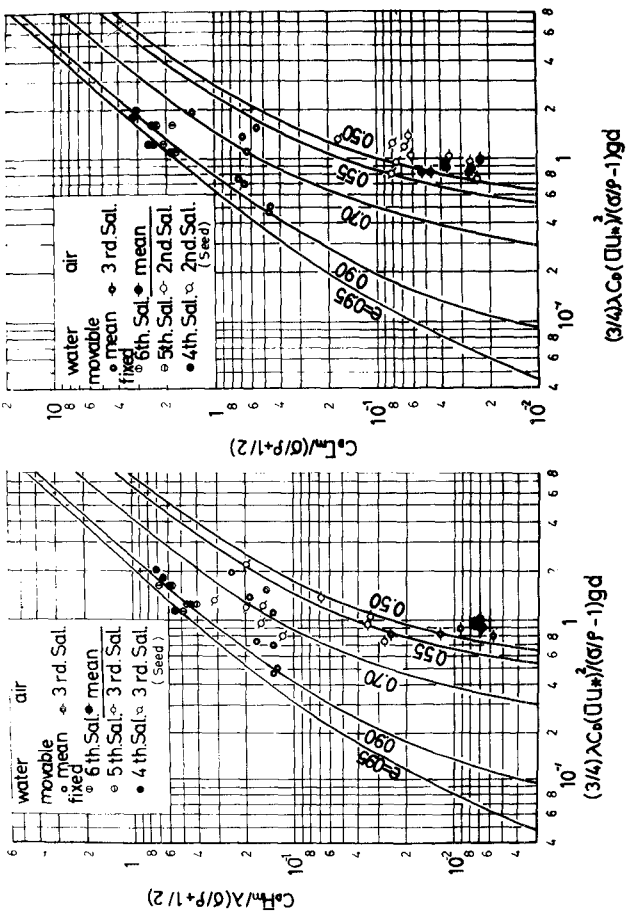

Fig. 4 Comparison between theoretical curves of height and distance of saltation of sand grain in stationary saltation and experimental values

the additional shear stress due to saltating sand grains. It is assumed that the additional shear stress is proportional to the mean value of the product of horizontal and vertical velocities of sand grains $\langle UW \rangle$ which is written as

$$\langle UW \rangle = \int_0^\infty UW f_1(H)\, dH \qquad (9)$$

based on the momentum transfer theory. Eq. (8) can finally be written as

$$\tau = \rho \{1 - \psi(z)/\sigma\} \ell^2 (du/dz)^2 - \psi(z) \langle UW \rangle \qquad (10)$$

in which ℓ is the mixing length assumed to be κz and u the wind velocity. Integration of Eq. (10) using Eqs. (1), (5) and (7) can approximately be made. It is concluded from some results of computation of

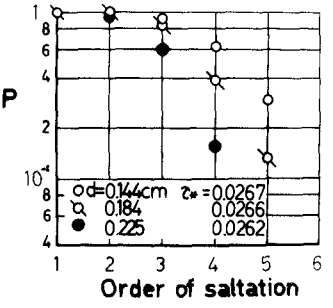

Fig. 5 Succession ratio of saltation of sand grains with order of saltation

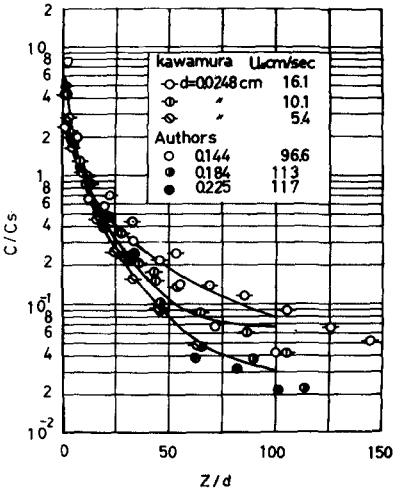

Fig. 6 Comparison between theoretical curves of concentration of sand grains in saltation layer and experimental values

Eq. (10) that the defect in velocity profiles in a saltation layer increases with the increase of the bottom shear stress due to wind action or the height of saltation of sand grains. Since a basic experiment of velocity profiles in a saltation layer has been carried out, comparison between the theoretical velocity profile and the result of experiment will be presented in the next paper.

CONCLUSIONS

Based on the detailed experiments on the successive saltation of sand grains by wind, an applicability of the theory of successive saltation is mainly considered in connection with the saltation by water. The main results obtained can be summerized as follows.

It was concluded that changes of the height and distance of saltation of sand grains with order of saltation are in good agreement with the theoretical curves and that the height and distance of saltation approach the stationary ones nearly at sixth order of saltation. The theoretical relationships of stationary saltation are applicable to express the characteristics of saltation of sand grains both in air and in water. The concentration of sand grains in a saltation layer can be theoretically formulated using the characteristics of saltation. In addition, an attempt to derive the velocity profile in a saltation layer is presented based on the momentum transfer theory taking into consideration the additional shear stress due to saltating sand grains.

REFERENCES

Bagnold, R. A. (1941). The physics of blown sand and desert dunes: Methuen & Co. Ltd., London.

Kawamura, R. (1951). Study of sand movement by wind: Report Tech. Res. Inst., Univ. of Tokyo, Vol. 5, pp. 95-112(in Japanese).

Owen, P. R. (1964). Saltation of uniform grains in air: Jour. Fluid Mech., Vol. 20, Part 2, pp. 225-242.

Tsuchiya, Y. (1969). Mechanics of the successive saltation of a sand particle on a granular bed in a turbulent stream: Bull. Dis. Pre. Res. Inst., Kyoto Univ., Vol. 19, Part 1, No. 152, pp. 31-44.

Tsuchiya, Y. (1970). Successive saltation of a sand grain by wind: Proc. Twelfth Conf. Coastal Engg., Vol. 1, pp. 1417-1427.

Stanley Park, Vancouver, B.C.

PART III

COASTAL STRUCTURES AND RELATED PROBLEMS

Ross Bay, Victoria, B.C.

CHAPTER 90

STANDING WAVES IN FRONT OF A SLOPING DIKE

by

Nobuo Shuto

Asian Institute of Technology, Bangkok, Thailand

Abstract

A solution of two-dimensional long waves on a beach of uniform slope is connected with that in water of constant depth, in order to yield an approximate solution for standing waves in front of a sloping dike. Wave motions are expressed in the Lagrangian description.

The highest possible standing waves as well as the reflection coefficient are calculated according to the Miche's conception. Theoretical results show a good agreement with the experimental results of Murota and Yamada.

It is also predicted that there is a relationship between the wave overtopping quantity and the quantity of water of standing waves above the crest height of the dike.

As for the wave pressure of standing waves, a simple formula in the Eulerian description is derived for relative-dike length $\ell/L < 0.16$ by allowing 6% error.

Introduction

Although a sloping face structure is more practical than a structure with vertical wall, no theoretical work except that of Keller & Keller[1] has been done to solve the standing waves in front of the former. At the point where the slope of the dike intersects the horizontal sea bottom, there is an abrupt change in slope. Difficulty in mathematical approach arises from this point. Since the direction of motion of water particles at the bottom is parallel to the bottom, the water particles should change their direction abruptly at the point. It is hard to satisfy this condition mathematically.

In the following analysis, an approximate theory is developed. The entire region is divided into two regions; [I] region of uniform water depth, and [II] region of a constant slope. Solutions of standing long waves in each regions are obtained at first independently and are connected so that the horizontal and vertical motions of water particles are continuous across the boundary between the two regions.

There are several theories for waves in water of uniform depth. Solution for long waves to the first order approximation is applied, assuming that the relative water depth in front of the structure is shallow enough and the motion is small, although the result is found applicable to such a higher waves as waves breaking on the slope.

Only a few wave theories are available for waves on a sloping beach. Miche[2] obtained a solution for waves over beaches sloping at special angles, by using the Lagrangian description. In his paper, surface waves were discussed. Since nodal line in case of standing surface waves are not straight lines in vertical direction, Miche's theory introduces another complexity if it is connected with a solution of waves in water of uniform depth. Lewy[3], or Isaacson[4] extended the Miche's theory for surface waves, but for slopes of more general angles or for all angles. Carrier & Greenspan[5] solved long wave motion on a sloping beach, using the shallow water theory in terms of the Eulerian description. As the horizontal coordinate in their result is a function of local wave height which varies with time, it is not convenient to use their solution in the case, because no such a theoretical result is available for case of long waves in water of uniform depth. Keller & Keller[1] applied the Isaacson's solution to the practical problems similar to the present problem. They obtained a result which corresponds to wave run-up height.

The author[6],[7] obtained a theory of long waves on a sloping beach in the Lagrangian description. Although his theory is of the first order of approximation, the result was comparable to that of Carrier & Greenspan. In addition, it is easy to obtain long wave motion in water of uniform depth. Therefore, this theoretical result is used in the present paper.

Theory

Let us consider the two-dimensional motion of an inviscid fluid. The position of the water particle, which is at the point (x_o, y_o) at t=0 is (x,y) at the time t=t. The pressure acting on this water particle is denoted by p. The still water surface is chosen as the horizontal axis and the y-axis is taken positive upwards.

Equations of continuity and motion are

$$\frac{\partial(x,y)}{\partial(x_o,y_o)} = 1 \tag{1}$$

$$\frac{\partial^2 x}{\partial t^2} = -\frac{1}{\rho}\frac{\partial(p,y)}{\partial(x_o,y_o)} \tag{2}$$

$$\frac{\partial^2 y}{\partial t^2} = -g - \frac{1}{\rho}\frac{\partial(x,p)}{\partial(x_o,y_o)} \tag{3}$$

where the symbol $\frac{\partial(u,v)}{\partial(x_o,y_o)}$ denotes the Jacobian

$$\frac{\partial(u,v)}{\partial(x_o,y_o)} = \begin{vmatrix} \frac{\partial u}{\partial x_o} & , & \frac{\partial u}{\partial y_o} \\ \frac{\partial v}{\partial x_o} & , & \frac{\partial v}{\partial y_o} \end{vmatrix} \tag{4}$$

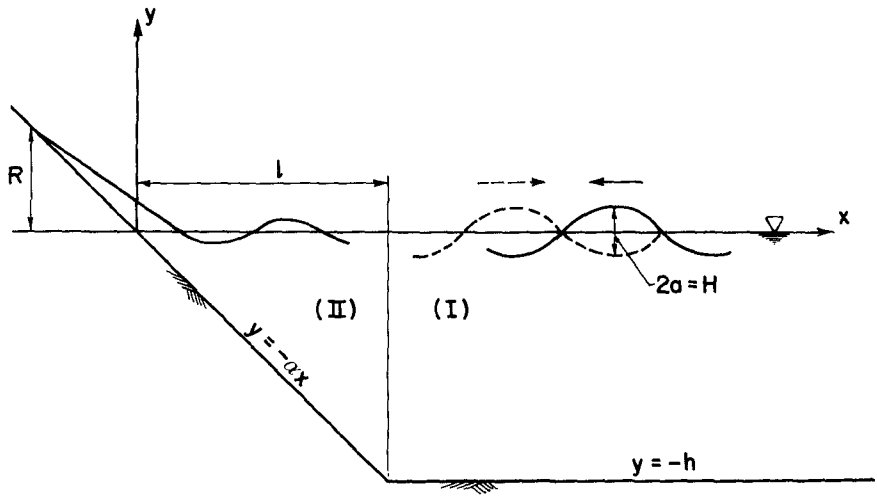

Fig.1. Definition Sketch

Let x_1, y_1 and p_1 be the small fluctuations around the zeroth order terms x_o, y_o and p_o, then

$$x = x_o + x_1 + \ldots\ , \quad y = y_o + y_1 + \ldots\ , \text{and} \quad p = p_o + p_1 + \ldots \tag{5}$$

We assume the long wave motion in which $\frac{\partial^2 y}{\partial t^2}$ is negligible compared with other terms up to the first order approximation.

The terms of the zeroth order approximation yield the equations,

$$l = l \tag{6}$$

$$\frac{\partial p_o}{\partial x_o} = 0 \tag{7}$$

$$\frac{\partial p_o}{\partial y_o} = -\rho g \tag{8}$$

and the first order terms yield the equations

$$\frac{\partial x_1}{\partial x_o} + \frac{\partial y_1}{\partial y_o} = 0 \tag{9}$$

$$\frac{\partial^2 x_1}{\partial t^2} + \frac{1}{\rho}\frac{\partial p_1}{\partial x_o} + g\frac{\partial y_1}{\partial x_o} = 0 \tag{10}$$

$$\frac{1}{\rho}\frac{\partial p_1}{\partial y_o} - g\frac{\partial x_1}{\partial x_o} = 0 \tag{11}$$

The water particles forming the free surface at the initial instant remain on the free surface throughout the succeeding motion. The water pressure acting on these particles is taken equal to the atmospheric pressure.

$$p = p_o + p_1 + \cdots = 0 \qquad \text{for particles satisfying } y_o = 0 \tag{12}$$

The water particles initially on the bottom cannot depart from the bottom. In the region [I], the vertical coordinates of these particles should satisfy the following equation

$$y = -h = y_o + y_1 + \cdots$$

which yields

$$y_o = -h,\ y_1 = 0 \qquad \text{for particles satisfying } y_o = -h \tag{13}$$

In the region [II], the slope of the dike is given by

$$y = -\alpha x$$

and bottom condition is written as

$$y_o = -\alpha x_o,\ y_1 = -\alpha x_1 \qquad \text{for particles satisfying } y_o = -\alpha x_o \tag{14}$$

Equations (1) through (3) yield the zeroth order solution

$$p_o = -\rho g y \tag{15}$$

which indicates the hydrostatic pressure distribution.

Equation (9) is integrated from the bottom to y_o

$$gy_1 = -g\int_{\text{bottom}}^{y_o} \frac{\partial x_1}{\partial x_o}\, dy_o - g\alpha x_1(x_o, -\alpha x_o; t)\,\delta_{i\,II} \tag{16}$$

where $\delta_{i\,II}$ is $\delta_{I\,II} = 0$ and $\delta_{II\,II} = 1$ for i=I, II. Equation (16) satisfies the bottom boundary condition.

Equation (11) is integrated from the free surface to y_o so as to satisfy the proposed boundary condition on the free surface, and is given by

$$\frac{p_1}{\rho} = g\int_o^{y_o} \frac{\partial x_1}{\partial x_o} dy_o \tag{17}$$

Substituting Eqs. (16) and (17) into Eq.(10), we have

$$\frac{\partial^2 x_1}{\partial t^2} + \frac{\partial}{\partial x_o}\left[g\int_o^{\text{bottom}} \frac{\partial x_1}{\partial x_o} dy_o - g\alpha x_1(x_o, -\alpha x_o; t)\, \delta_{i\,II}\right] = 0 \tag{18}$$

which determines the required solution.

In the region [I], Eq.(18) is written as

$$\frac{\partial^2 x_1}{\partial t^2} + g\frac{\partial}{\partial x_o}\int_o^{-h} \frac{\partial x_1}{\partial x_o} dy_o = 0 \tag{19}$$

Let $x_1 = X(x_o)\, Y(y_o)\, T(t)$. From Eq.(19), $Y(y_o)$ is concluded to be constant. Terms X and T should satisfy the equation

$$XT'' - gh\, X''T = 0$$

where each prime denotes the differentiation once with respect to the particular independent variable. A solution of standing waves is given by

$$\left.\begin{aligned} T &= \cos \sigma t \\ X &= \cos\left(\frac{\sigma}{\sqrt{gh}} x_o + \delta\right) \end{aligned}\right\} \tag{20}$$

where $\frac{\sigma}{\sqrt{gh}} = k$ is the wave number and δ the phase lag which is included because the point $x_o = 0$ does not always coincide with the antinode of the standing waves in the region [I].

Solution for y_1 and p_1 are obtained by Eqs.(16) and (17). With appropriate coefficients, a set of solutions is given for standing waves in the region [I] as follows:

$$\left.\begin{aligned} x_1 &= \frac{2a}{kh}\cos(kx_o + \delta)\cos\sigma t \\ y_1 &= \frac{2a}{h}(y_o + h)\sin(kx_o + \delta)\cos\sigma t \\ p_1 &= -\rho g\frac{2a}{h}y_o \sin(kx_o + \delta)\cos\sigma t \end{aligned}\right\} \qquad (21)$$

where a denotes the amplitude of the incident waves, $\sigma = 2\pi/T$ the frequency and $k = 2\pi/L$ the wave number.

Equation (18) is written, in the region [II], as

$$\frac{\partial^2 x_1}{\partial t^2} + g\frac{\partial}{\partial x_o}\int_o^{-\alpha x_o}\frac{\partial x_1}{\partial x_o}dy_o - g\alpha\frac{\partial}{\partial x_o}x_1(x_o, -\alpha x_o; t) = 0 \qquad (22)$$

Since the second and third terms in the above equation are functions independent of y_o, x_1 is a function of x_o and t only. Equation (22) is reduced to

$$\frac{\partial^2 x_1}{\partial t^2} - g\alpha\frac{\partial^2}{\partial x_o^2}(x_o x_1) = 0 \qquad (23)$$

Let $x_1 = X(x_o)\,T(t)$ and we have

$$\frac{T''}{T} = \frac{g\alpha[x_o X'' + 2X']}{X} = -\sigma^2 \qquad (24)$$

Functions X and T for standing waves are given by

$$\left.\begin{aligned} T &= \cos\sigma t \\ X &= \frac{1}{\sqrt{x_o}}J_1\left(\frac{2\sigma}{\sqrt{g\alpha}}\sqrt{x_o}\right) \end{aligned}\right\} \qquad (25)$$

First order terms are given as follows for standing waves on a sloping beach, with a coefficient A to be determined later.

$$\left.\begin{aligned} X_1 &= \frac{A}{\sqrt{x_o}}J_1\left(\frac{2\sigma}{\sqrt{g\alpha}}\sqrt{x_o}\right)\cos\sigma t \\ Y_1 &= A\left[(y_o + \alpha x_o)\frac{\sigma}{\sqrt{g\alpha}}\frac{1}{x_o}J_2\left(\frac{2\sigma}{\sqrt{g\alpha}}\sqrt{x_o}\right) - \frac{\alpha}{\sqrt{x_o}}J_2\left(\frac{2\sigma}{\sqrt{g\alpha}}\sqrt{x_o}\right)\right]\cos\sigma t \\ P_1 &= -\frac{\rho g\sigma}{\sqrt{g\alpha}}\frac{y_o}{x_o}A\,J_2\left(\frac{2\sigma}{\sqrt{g\alpha}}\sqrt{x_o}\right)\cos\sigma t \end{aligned}\right\} \qquad (26)$$

where y_1 and p_1 are determined by Eqs.(18) and (17), and J_n is the n-th Bessel Function of the first kind.

Two coefficients, A and δ, which are undetermined connect the two regions. Consider the particles which are, at the initial instant, at the point $x_o = \ell$ which is the boundary between two regions. Two expressions of the horizontal movements of these particles should be the same. As for the vertical movement, we cannot connect it for all water particles locating on $x = \ell$. However, the most important factor to be considered is the vertical displacement of the water particle on the free surface. As the first order pressure is the hydrostatic pressure, any discontinuity in water levels between the two regions might have a big influence. Therefore, this condition is adopted as one of the conditions. We have

$$\ell + \frac{2a}{kh}\cos(k\ell+\delta)\cos\sigma t = \ell + \frac{A}{\sqrt{\ell}}J_1\left(\frac{2\sigma}{\sqrt{g\alpha}}\sqrt{\ell}\right)\cos\sigma t \qquad (27)$$

and

$$\frac{2a}{kh}\sin(k\ell+\delta)\cos\sigma t = \frac{A}{kh}\left[\frac{\sqrt{\alpha}}{\sqrt{g}}\sigma J_2\left(\frac{2\sigma}{\sqrt{g\alpha}}\sqrt{\ell}\right) - \frac{\alpha}{\sqrt{\ell}}J_1\left(\frac{2\sigma}{\sqrt{g\alpha}}\sqrt{\ell}\right)\right]\cos\sigma t \qquad (28)$$

Eliminating δ, A is determined as

$$A = \frac{2a}{kh}\sqrt{\ell}\left[J_o^2\left(4\pi\frac{\ell}{L}\right) + J_1^2\left(4\pi\frac{\ell}{L}\right)\right]^{-1/2} \qquad (29)$$

in which the following relation is used.

$$\frac{2\sigma}{\sqrt{g\alpha}}\sqrt{\ell} = \frac{4\pi}{\sqrt{gh}\,T}\sqrt{\frac{h\ell}{\alpha}} = 4\pi\frac{\ell}{L} \qquad (30)$$

Run-up Height

Wave run-up on the dike is given by the vertical location of a particle corresponding to $x_o = 0$ and $y_o = 0$.

$$y\big|_{x_o=0,\ y_o=0} = A\left[\frac{\sigma}{\sqrt{g\alpha}}\frac{y_o}{x_o}J_2\left(\frac{2\sigma}{\sqrt{g\alpha}}\sqrt{x_o}\right) - \frac{\alpha\sigma}{\sqrt{g\alpha}}J_o\left(\frac{2\sigma}{\sqrt{g\alpha}}\sqrt{x_o}\right)\right]\cos\sigma t\Big|_{x_o=0,y_o=0}$$

$$= -A\sigma\sqrt{\frac{\alpha}{g}}\cos\sigma t \qquad (31)$$

Relative wave run-up height is given by

$$\frac{R}{2a} = \left[J_o^2 \left(4\pi \frac{\ell}{L}\right) + J_1^2 \left(4\pi \frac{\ell}{L}\right) \right]^{-\frac{1}{2}} \tag{32}$$

The result coincides with the amplification factor of Keller & Keller.

Figure 2 shows the relationship between $\frac{R}{2a}$ and $\frac{\ell}{L}$, and its asymptotic expressions:

$$\frac{R}{2a} = \sqrt{2}\,\pi \left(\frac{\ell}{L}\right)^{\frac{1}{2}} \qquad \text{for large value of } \frac{\ell}{L} \tag{33}$$

$$\frac{R}{2a} = 1 + 2\pi^2 \left(\frac{\ell}{L}\right)^2 \qquad \text{for small value of } \frac{\ell}{L} \tag{34}$$

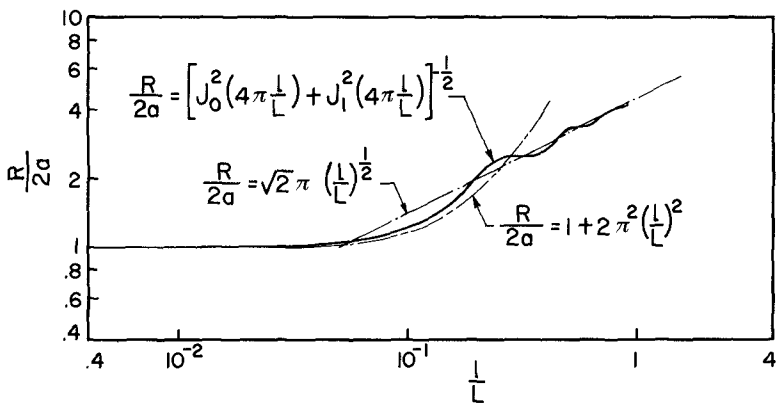

Fig.2. Relative Wave Run-up

Breaking Condition

Local wave steepness at the wave front cannot be steeper than the inclination of the slope. Therefore,

$$\left.\frac{dy}{dx}\right|_{x_o = 0,\ y_o = 0} = \left.\frac{\partial y/\partial x_o}{\partial x/\partial x_o}\right|_{x_o = 0,\ y_o = 0} = -\alpha \qquad (35)$$

gives the critical condition. This is the Miche's criterion for breaking. From Eqs.(5) and (26),

$$\left.\frac{\partial y}{\partial x_o}\right|_{x_o = 0,\ y_o = 0} = A\frac{\sigma^3}{g\sqrt{g\alpha}}\cos\sigma t$$

and

$$\left.\frac{\partial x}{\partial x_o}\right|_{x_o = 0,\ y_o = 0} = 1 - \frac{\sigma^3 A}{2g\alpha\sqrt{g\alpha}}\cos\sigma t$$

Equation (35) is written as

$$-\alpha + \frac{\sigma^3 A}{2g\sqrt{g\alpha}}\cos\sigma t = \frac{\sigma^3 A}{g\sqrt{g\alpha}}\cos\sigma t$$

Introducing the critical amplitude a_m of the incident wave which just breaks on the slope, the breaking condition is given by

$$\frac{2a_m}{L}\frac{1}{\alpha} = \frac{2}{\pi}\left(4\pi\frac{\ell}{L}\right)^{-1}\left[J_o^2\left(4\pi\frac{\ell}{L}\right) + J_1^2\left(4\pi\frac{\ell}{L}\right)\right]^{\frac{1}{2}} \qquad (36)$$

Figure 3 shows the relation above with the two approximate expressions;

$$\frac{2a_m}{L}\frac{1}{\alpha} = \left(\frac{1}{2\pi^2}\right)^{3/2}\left(\frac{\ell}{L}\right)^{-3/2} \quad \text{for large value of } \frac{\ell}{L} \qquad (37)$$

$$\frac{2a_m}{L}\frac{1}{\alpha} = \frac{1}{2\pi^2}\left(\frac{\ell}{L}\right)^{-1} - \frac{\ell}{L} \quad \text{for small value of } \frac{\ell}{L} \qquad (38)$$

Figure 4 provides a comparison of theoretical results with experimental results by Murota and Yamada.[8] For a relative depth $h/L = \alpha\ell/L$ and an incident wave steepness $2a/L$, an angle, α, of the slope on which waves just break is uniquely determined by Eq.(36), and is expressed in degree in the figure.

Reflection Coefficient

According to the Miche's definition, the reflection coefficient, r, of a slope is given by

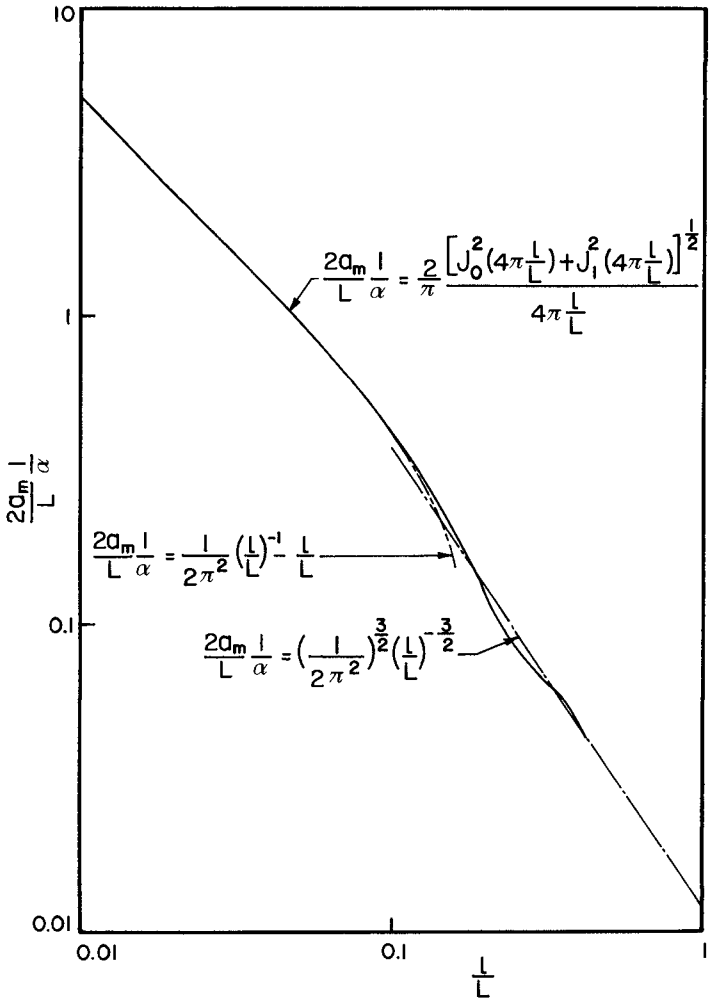

Fig.3. Breaking Condition

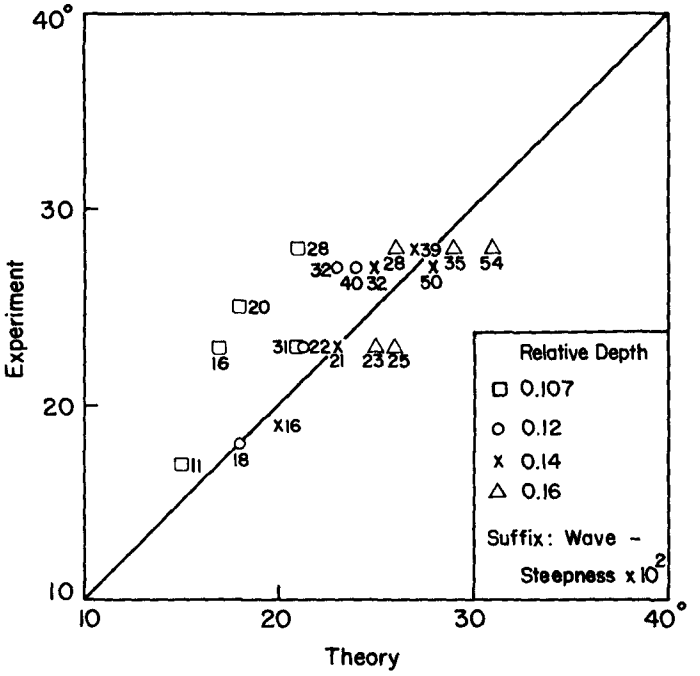

Fig.4. Theoretical Breaking Condition Compared With Murota & Yamada's Experiment.

$$\left.\begin{aligned} r &= 1 && \text{for } H_i \leq 2\,a_m \\ &= \frac{2\,a_m}{H_i} && \text{for } H_i \geq 2\,a_m \end{aligned}\right\} \qquad (39)$$

in which H_i is the incident wave height and $2a_m$ is the critical height of the incident wave which just breaks on the slope.

Wave smaller than $2a_m$ can be totally reflected by the slope, while a part of waves corresponding to $2a_m$ is considered to be reflected in case of bigger waves and the rest is considered to be lost due to the breaking.

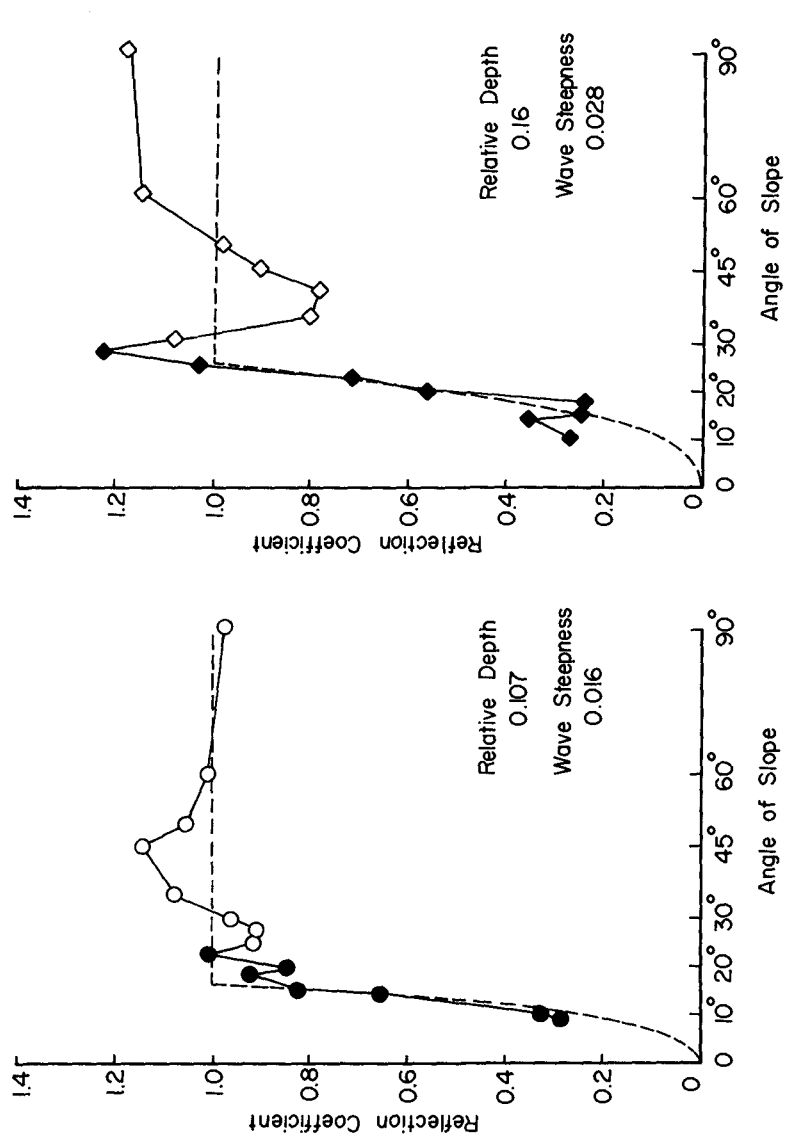

Fig.5 (a) Reflection Coefficient

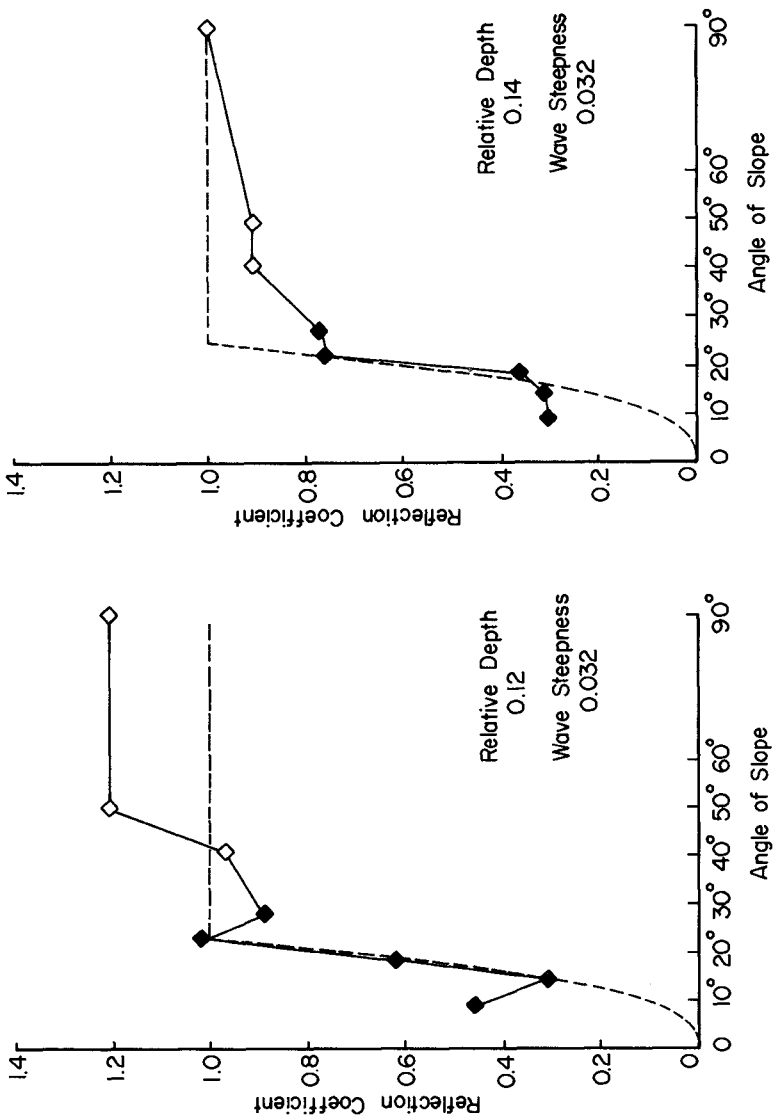

Fig.5 (b) Reflection Coefficient

Figures 5 - (a), (b) show examples of the comparison of theoretical result with the experimental results of Murota and Yamada. They carried out experiments in a wave flume which was divided into two parallel parts of the same width by a separator set along the centerline. At the end of the one part they placed a slope, while at the same end of another part a wave absorber was set to generate only the progressive waves in this part. Wave gauges were set in both parts at the same distance from the wave generator. Signals from wave gauges were electrically subtracted to separate the reflected waves from standing waves. For waves of bigger height, effect of nonlinear interaction may affect the magnitude of the reflected waves as was pointed by Goda and Abe[9], but in their experimental results no correction was made. This is considered a reason why they obtained the reflection coefficients bigger than unity under some conditions. In the figures, black marks correspond to waves which break on the slope, white marks correspond to non-breaking waves and the broken lines are theoretical results.

Wave Overtopping

In Figure 6, the rate of overtopping is compared with the volume of water above the crown height of the dike at the time when a crest of standing waves appears on the dike. Wave profile in front of the dike is drawn for water particles $y_o = 0$ at the time $\cos \sigma t = -1$ by using Eqs.(5) and (26), at first assuming the crown height of the dike is high enough to allow no overtopping. Then, the volume of water above the crest height is calculated. The experimental results are taken from one of the author's experiments. The figure suggests there is a close relationship between wave overtopping and the volume of water determined by the method above.

Wave Pressure

Pressure acting on the slope when maximum wave run-up occurs is given as follows by setting $\cos \sigma t = -1$, $y_o = -\alpha x_o$ and $y_1 = -\alpha x_1$ in Eqs.(5), (15) and (26).

$$\left.\begin{aligned} p &= \rho g \alpha x_o - \frac{\rho g \sigma}{\sqrt{g\alpha}} \alpha A \, J_2\left(\frac{2\sigma}{\sqrt{g\alpha}} \sqrt{x_o}\right) \\ x &= x_o - \frac{A}{\sqrt{g\alpha}} J_1\left(\frac{2\sigma}{\sqrt{g\alpha}} \sqrt{x_o}\right) \end{aligned}\right\} \qquad (40)$$

In order to calculate the pressure acting at x, the initial position, x_o, of the particle is determined by the second equation of Eq.(40), and is substituted into the first equation of Eq.(40).

As the procedure above is troublesome, an approximate expression is derived as follows. Introduction of non-dimensional variables defined as

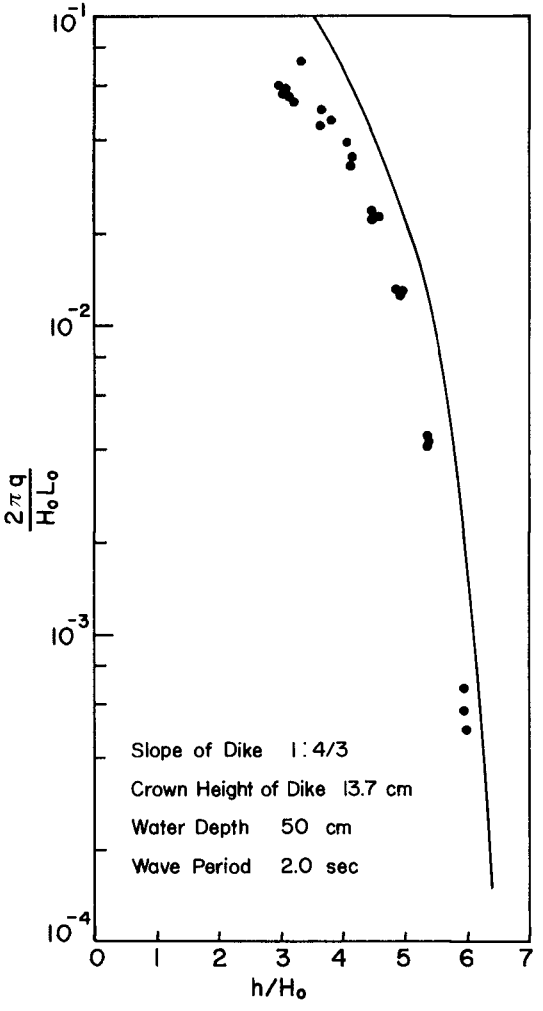

Fig.6. Wave Overtopping

$$\sqrt{X_o} = \frac{2\sigma}{\sqrt{g\alpha}}\sqrt{x_o}\ , \quad \sqrt{X} = \frac{2\sigma}{\sqrt{g\alpha}}\sqrt{x}\ , \quad P = \frac{4\sigma^2}{g\alpha}\frac{p}{\rho g\alpha}$$

and

$$D = \frac{4\sigma^2}{g\alpha}\ \frac{\sigma}{\sqrt{g\alpha}}\ A$$

reduces Eq.(40) to the followings

$$\left.\begin{aligned} P &= X_o - D\ J_2(\sqrt{X}_o) \\ X &= X_o - 2D\frac{1}{\sqrt{X}_o}\ J_1(\sqrt{X}_o) \end{aligned}\right\} \qquad (41)$$

For small X_o Eq.(41) is approximated by

$$\left.\begin{aligned} P &= X_o - D\frac{X_o}{4}\left[\frac{1}{2} - \frac{X_o}{24}\right] \\ X &= X_o - D\left[1 - \frac{X_o}{8}\right] \end{aligned}\right\} \qquad (42)$$

Error in the value of pressure given by Eq.(42) is less than 6% for $X_o \leq 4$, which is equivalent to $\ell/L \leq 0.16$

An Eulerian expression of the pressure is given by

$$P = \frac{8 - D}{8 + D}\ (X+D) + \frac{2}{3}D\ \frac{(X+D)^2}{(8+D)^2} \qquad (43)$$

Figure 7 shows the wave induced pressure for case of $D = 0.5$. First term of the above equation is a simple expression accurate enough in this case. Including the second term, Eq.(43) coincides with the theoretical result, Eq.(41).

The term D is also a function of ℓ/L, and it is approximated by, for small relative dike length, ℓ/L,

$$D = \frac{8\pi}{\alpha}\frac{H}{L}\ 4\pi\frac{\ell}{L}\left[1 + 2\pi^2\left(\frac{\ell}{L}\right)^2\right] \qquad (44)$$

where $H = 2a$.

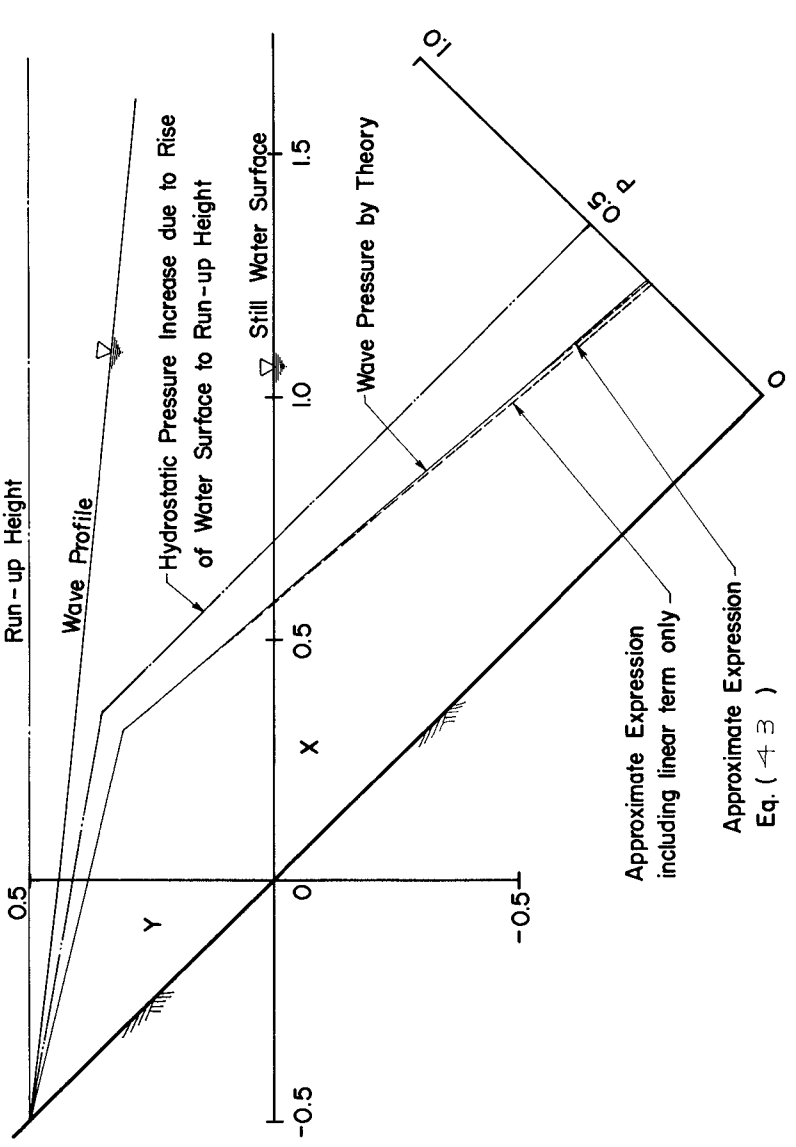

Fig.7. Wave Pressure Distribution At The Time When Wave Crest Appears At The Dike.

With dimensional variables, total pressure is written in the Eulerian description as follows.

$$\frac{p}{\rho g} = \frac{\alpha - 4\pi^2 \frac{H}{L}\frac{\ell}{L}\left\{1 + 2\pi^2\left(\frac{\ell}{L}\right)^2\right\}}{\alpha + 4\pi^2 \frac{H}{L}\frac{\ell}{L}\left\{1 + 2\pi^2\left(\frac{\ell}{L}\right)^2\right\}}\left[\alpha x + 2H\left\{1 + 2\pi^2\left(\frac{\ell}{L}\right)^2\right\}\right]$$

$$+ \frac{4}{3}H\left\{1 + 2\pi^2\left(\frac{\ell}{L}\right)^2\right\}\left[\frac{2\pi^2\frac{\ell}{L}\frac{\alpha x}{L} + 4\pi^2\frac{H}{L}\frac{\ell}{L}\left\{1 + 2\pi^2\left(\frac{\ell}{L}\right)^2\right\}}{\alpha + 4\pi^2\frac{H}{L}\frac{\ell}{L}\left\{1 + 2\pi^2\left(\frac{\ell}{L}\right)^2\right\}}\right]^2 \qquad (45)$$

Conclusion

A theory is developed to describe the standing long wave motion in front of a sloping dike. Relative run-up height, breaking condition, reflection coefficient and pressure distribution are given. The breaking condition and the reflection coefficient are compared with the experimental results, and good agreements between the theory and experiments are shown. A method is proposed to predict the wave overtopping. Comparison with experimental results shows utility of this method.

Although the theory has several approximations from mathematical and physical point of view, it provides a useful basis for practical design.

Acknowledgements

The author wishes to express his gratitude to Dr. K. Kajura, Professor of the Earthquake Research Institute, the University of Tokyo, for his helpful discussions and encouragements. Thanks are also due to Mr. H. Nishimura, Lecturer of the University of Tokyo, who pointed out mistakes in the first manuscript. This research was supported in part by the Matsunaga Science Foundation and in part by Science Research Fund of the Ministry of Education, Japan.

REFERENCES

1) Keller, J.B. and H.B. Keller: Water wave run-up on a beach, Research Report No.NONR-3828(00), Office of Naval Research, Dept. of the Navy, 1964.

2) Miche, A.: Mouvements ondulatoires de la mer en profondeur constante ou decroissante, Annales des ponts et chaussees, 1944.

3) Lewy, H.: Water waves on sloping beaches, Bulletin of the American Mathematical Society, Vol.52, 1946.

4) Isaacson, E.: Water waves over a sloping bottom, Communications on Pure and Applied Mathematics, Vol.3, 1950.

5) Carrier, G.F. and H.P. Greenspan: Water waves of finite amplitude on a sloping beach, Journal of Fluid Mechanics, Vol.4, 1958.

6) Shuto, N.: Run-up of long waves on a sloping beach, Coastal Engineering in Japan, Vol.10, 1967.

7) Shuto, N.: Three-dimensional behaviour of long waves on a sloping beach, Coastal Engineering in Japan, Vol.11, 1968.

8) Murota, A. and T. Yamada: Basic study on reflection, Proc. of the 13th Conference on Coastal Engineering in Japan, 1966.(in Japanese).

9) Goda, Y. and Y. Abe: Apparent coefficient of partial reflection of finite amplitude waves, Report of the Port and Harbour Research Institute, Vol.7, No.3, 1968.

CHAPTER 91

PRESSURE UPON VERTICAL WALL FROM STANDING WAVES

By Prof. Dr. Eng. Sci. V.K. SHTENCEL.*

When surge waves approach a vertical wall a standing wave is formed ahead of the latter. This is the only case when the interaction between waves and structure result in a stable mode of motion with distinct kinematic characteristics. Such motion can be described by equations of hydromechanics without the introduction of any hydraulic coefficients; a comparison of various theoretical solutions with experimental data can serve as an additional criterion for evaluating the accuracy of this or that solution.

The first theoretical solution for wave pressure acting upon a vertical wall under the effect of standing waves at a finite depth has been published by Sainflou in 1928 (1).

By correlating motion equations for surge waves derived by Gerstner as early as 1802 and Flamani's equations for standing waves on an infinite depth, Sainflou derived for the case of standing waves on a finite depth the following relations:

$$x = x_o - 2\, r \cos 6t \sin kx_o$$
$$y = y_o + 2\, r_1 \cos 6t \cos kx_o + 2\, krr_1 \cos^2 6t \qquad (1),$$

In Eq. (1) :

$$r = \frac{h}{2} \frac{\operatorname{ch} k(H + y_o)}{\operatorname{sh} kH}; \quad r_1 = \frac{h}{2} \frac{\operatorname{sh} k(H + y_o)}{\operatorname{sh} kH};$$

* Head of the Chair of Ports of Leningrad Water Transport Institute
Dvinskaja 5/7 Leningrad, 198035.

x_o and y_o - ordinates of a particle at rest;
h, λ and τ - respectively height, length and period of a wave;

H - depth; $k = \frac{2\pi}{\lambda}$; $\sigma = \frac{2\pi}{\tau}$;

abscissae axis coincides with still water level; ordinate axis coincides with wall surface and is directed upwards.

When deriving the pressure relation Sainflou utilized the hydrodynamic equilibrium equation in terms of Lagrange variables:

$$\frac{1}{\rho}\frac{\partial p}{\partial x_o} = -\frac{\partial^2 x}{\partial t^2}\frac{\partial x}{\partial x_o} - \left(g + \frac{\partial^2 y}{\partial t^2}\right)\frac{\partial y}{\partial x_o}, \qquad (2)$$

$$\frac{1}{\rho}\frac{\partial p}{\partial y_o} = -\frac{\partial^2 x}{\partial t^2}\frac{\partial x}{\partial y_o} - \left(g + \frac{\partial^2 y}{\partial t^2}\right)\frac{\partial y}{\partial y_o}.$$

After substituting all the partial derivatives - taking into account the second order terms in relation to wave height we have:

$$\frac{1}{\rho}\frac{\partial p}{\partial x_o} = 2(gkr_1 - \sigma^2 r)\cos\sigma t \sin kx_o + 2k\sigma^2(r^2 - r_1^2)\cos^2\sigma t \sin 2kx_o \qquad (3)$$

$$\frac{1}{\rho}\frac{\partial p}{\partial y_o} = -g - 2gkr\cos\sigma t\cos kx_o - 2gk^2(r^2 + r_1^2)\cos^2\sigma t + 2\sigma^2 r_1\cos\sigma t\cos kx_o + 4k\sigma^2 rr_1\cos^2\sigma t + 4k\sigma^2 rr_1\cos 2\sigma t \qquad (4)$$

The continuity equation is satisfied on condition

$$k(r^2 - r_1^2) \approx 0 \qquad (5)$$

By omitting in integrating (3) and (4) all terms with second and higher order factors in relation to wave

height, Sainflou arrives to the following relation for pressure upon a wall (with $x_o = 0$):

$$\frac{p}{\gamma} = - y_o - 2h \frac{\operatorname{sh} \frac{ky_o}{2kH}}{\operatorname{sh} 2kH} \cos \sigma t \qquad (6)$$

By substituting in (6) $\cos \sigma t = 1$ we derive pressures on approach of wave crest; substitutinn of $\cos \sigma t = -1$ gives respectively the pressure at trough approach.

For plotting pressure diagrams we preset n 5 or 7 values of ordinates of resting particles y_o, then calculate the pressure using Eq.(6), and apply it to points, the positions of which are derived from the equation:

$$y = y_o + 2r_1 \cos \sigma t + 2rr_1 \cos^2 \sigma t \qquad (7)$$

From the moment of its first publication relation (6) was generally used for practical calculations all over the world. Only in the fifties the works of Miche (2) demonstrated that in some cases the method implies considerable errors. According to Sainflou (6) maximum excess wave pressure upon a wall always tekes place on the approach of the crest ($\cos \sigma t = 1$), and pressure value is positive for all points acrosss the height (Fig.1a). But practically Miche was the first to demonstrate (1) that at considerable depth ahead of the wall maximum pressure can occur not on crest approach, but in some intermediate moment; during the approach of the crest even negative pressures can possibly occur near the bottom (Fig. 1b). Calculation methods were developed, which take into account the second order terms in relation to wave height. Rundgren's (3) and Kuznetsov's (4) methods are among the most widely known.

Rundgren's paper, published in 1958, completes the investigations that were started by Miche (2) and Biesel (5). The solution procedure is as follows: basic motion characteristics are found as polynomials and are expanded by the smaller parameter powers in relation to wave

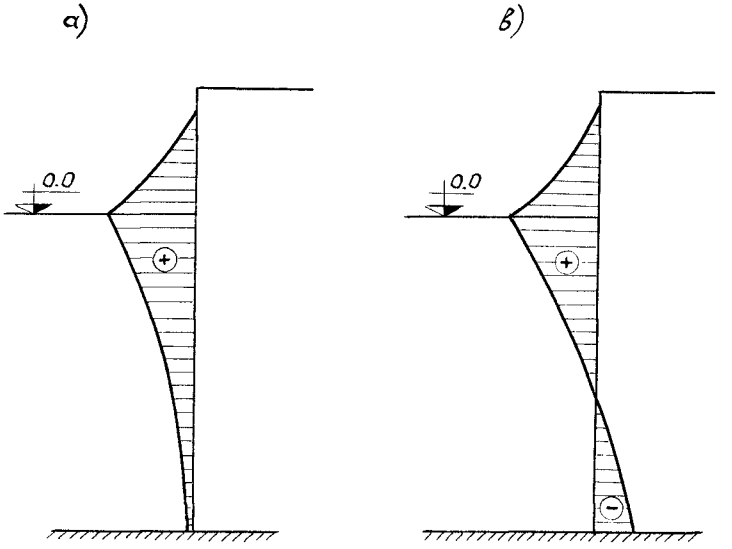

Fig.1. Character of Pressure upon Vertical Wall Diagrams.
a - Sainflou, b - second approximation formulae.

height (retaining second order terms). Final relationships give a good agreement with experimental results; at relatively low heights there however appear considerable errors. This is explained by the appearance of a surplus term in the Cauchy integral, this term becoming markedly increased as relative depth H/λ is decreased. Therefore a limit for utilization of calculation formular $H/\lambda = 0.132$ is set; if relative depth would be greater, then Miche-Biesel - Rundgren equation would give inevitably wrong results. Therefore even though this solution is rather widely used (see e.g. Kamel's paper (6) published in 1971) a search for a new and more accurate calculation method would be very desirable.

Kuznetsov's solution (4) has many important theoretical errors, which are analyzed in (7). Owing to a correction achieved by introducing empirical coefficients for small depths, this solution is in good agreement with experimental results, but for relatively large depths total pressure can be found to be two or more times the true value.

We feel that the cause of inadequacy of all the presently known methods lies in the fact that neither of them takes into account the specific character of wave motion. When studying fluid motion, hydrodynamics neglects particle deformations. It brings no errors into final equations for all types of motion except those for wave motion, since the deformations are of random character. But in wave motion particle deformations are periodical and undirected for significant areas (8). Therefore it is the deformations that undoubtedly affect the motion kinematic, and any accurate solution would be impossible if we do not take them into account. Author's attempts of taking into account particle deformations when deriving equations for surge waves and standing waves revealed great mathematical difficulties awaiting the investigator on this way.

Search for an approximate solution brought the author to the conclusion, that calculation formulae yielding practically acceptable results for all the range of rated depths can be derived from Eq.(1). And indeed, many of the investigators who carried out laboratory experiments on standing waves found that wave profile derived from Eq.(1) gives the best agreement with experimental data for all the depth range. This leads to a suggestion that the discrepancy between experimental pressure diagrams and those calculated from (6) is caused by the approximation in its derivation.

Turning now back to Eqs. (3) and (4) it should be noted that they can be integrated without omitting the second order terms. If we assume a limiting condition for surface $p = 0$ with $y_o = 0$, then - proceeding from assumption (5) - we derive from (3):

$$g = \frac{\sigma^2}{k} \operatorname{cth} kH \qquad (8)$$

Integrating (4) on substitution of (8) and dividing the result by "g" we get:

$$\frac{p}{\gamma} = - y_o - 2r_1 \cos \sigma t \cos kx_o - 2krr_1 \cos^2 \sigma t +$$

$$+ 2r \operatorname{th} kH \cos \sigma t \cos kx_o + k(r^2 + r_1^2) \operatorname{th} kH \cos^2 \sigma t +$$

$$+ k(r^2 + r_1^2) \operatorname{th} kH \cos 2\sigma t + F(t) \qquad (9)$$

To simplify the final expressions it would be reasonable to transform the fifth term having in view the relationship (5):

$$k(r^2 + r_1^2) \operatorname{th} KH \cos^2 \sigma t = 2kr^2 \operatorname{th} kH \cos^2 \sigma t \qquad (10)$$

(A chek proved that it gives an error in the final result which lies within 1 to 2%).Function F(t) will be found from limiting conditions on surface: $p = 0$ if $y_o = 0$.

Taking into account that on surface $r = r_1$ cth kH, and substituting (10) we have:

$$F(t) = -\frac{kh^2}{2} \operatorname{cth} 2kH \cos 2\sigma t \qquad (11)$$

Assumin $\cos kx_o = 1$ and substituting (10) into (9) we obtain the final expression for pressure in any point:

$$\frac{p}{\gamma} = -y_o - 2h\frac{\operatorname{sh} ky_o}{\operatorname{sh} 2kH}\cos\sigma t - kh^2\frac{\operatorname{sh} ky_o \operatorname{ch} k(H+y_o)}{\operatorname{sh} 2kH \operatorname{sh} kH}\cos^2\sigma t -$$

$$-\frac{kh^2}{2}\frac{\operatorname{ch} 2kH - \operatorname{ch} 2k(H+y_o)}{\operatorname{sh} 2kH}\cos 2\sigma t. \qquad (12)$$

Since Eq.(12) gives pressure value in Lagrange variables, for finding the loading point calculated for a particle with $y_o = a$ we have to find the current ordinate of the particle by substituting $y_o = a$ into Eq. (7)*.

With unlimited depth Eqs. (12) and (7) become considerably simplified:

$$\frac{p}{\gamma} = -y_o - \frac{kh^2}{2}(1 - e^{2ky_o})\cos 2\sigma t \qquad (12a)$$

$$y = y_o + he^{ky_o}\cos\sigma t + \frac{kh^2}{2}e^{2ky_o}\cos^2\sigma t \qquad (7a)$$

Practically when $H \geqslant 0.4\lambda$ calculations can be begun using Eqs. (12a) and (7a).

For plotting an excess wave pressure diagram we have to set 5 to 7 y_o- values, then to calculate p/γ pressure values; then diagram of full pressure is plotted and the hydrostatic pressure subtracted.

The value of full pressue resultant can be derived

---

*) In the publication of our relationship in Khaskhachik G.D. & O.M.Vanchagov's work (9) a misprint has slipped in: in the second term of Eq. (2) factor "cosσt" is erroneously omitted.

by integrating Eq. (12):

$$\frac{R}{\gamma} = \int_{0}^{-H} \frac{p}{\gamma} \frac{\partial y}{\partial y_o} dy_o \qquad (13)$$

Excess wave pressure resultant will obviously take the form:

$$\frac{\Delta R}{\gamma} = \frac{R}{\gamma} - \frac{H^2}{2\gamma} \qquad (14)$$

Omitting cumbersome calculations of this value we give here only the final equation:

$$\frac{\Delta R}{\gamma} = \frac{h^2}{2}\left(\frac{4}{kh} \text{ th } kH \cos\sigma t + 6kH \frac{\cos^2\sigma t}{\text{sh } 2kH} + \cos 2\sigma t + \right.$$

$$\left. + \cos^2\sigma t - 2kH \text{ cth } 2kH \cos 2\sigma t\right) \qquad (15)$$

As seen from (15) the maximum of excessive wave pressure resultant is time-dependent. The value of phase which corresponds to maximum pressure is derived by taking a derivative of (15) and equalizing it to zero.

As a result we derive two radicals:

$$\cos\sigma t = 1 \qquad (16)$$

$$\cos\sigma t = \frac{2 \text{ th } kH}{kh\left(4kH \text{ cth } 2kH - \frac{6kH}{\text{sh } 2kH} - 3\right)} \qquad (17)$$

It was found that if $\cos \sigma t$ calculated from (17) yields a value $0 < \cos \sigma t < 1$, then this very moment will correspond to the maximum value of excessive pressure resultant. If however this condition is not fulfilled, then the maximum of resultant will occur when the first radical (16) is used, i.e. at the moment of maximum wave crest rise at the wall.

For a case of $H \geqslant 0.4\lambda$ Eq.(17) takes a simpler form:

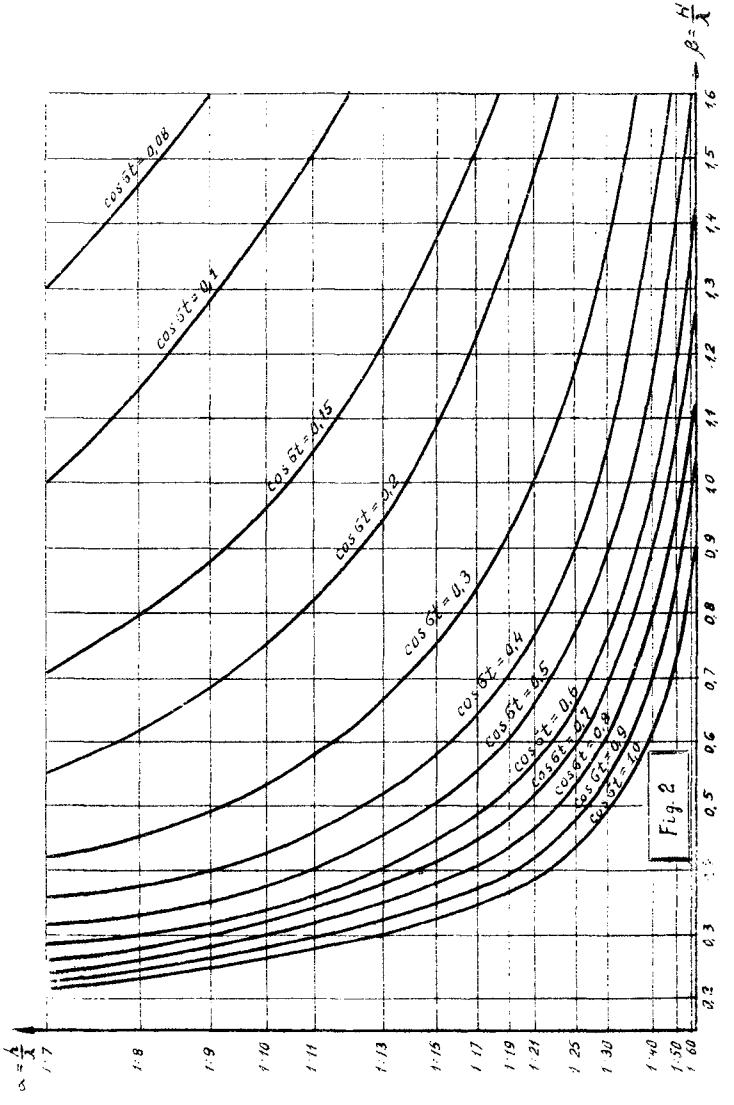
cos 5t = 0,08
cos 5t = 0,1
cos 5t = 0,15
cos 5t = 0,2
cos 5t = 0,3
cos 5t = 0,4
cos 5t = 0,5
cos 5t = 0,6
cos 5t = 0,7
cos 5t = 0,8
cos 5t = 0,9
cos 5t = 1,0
Fig. 2

$$\cos 6t = \frac{\lambda}{H(8\frac{H}{\lambda} - 3)} \qquad (17a)$$

To simplify the calculations we plotted a diagram of relationships between cos t and relative wave heights $\alpha = h/\lambda$ and depths $\beta = H/\lambda$ (Fig.2). As seen from the diagram the increase in relative depth as a rule leads to $\cos 6t < 1$ and the maximum of excessive wave pressure resultant does not coincide with the moment of maximum wave crest rise at the wall.

If we derive by similar integration the resultant moment in relation to wall bottom and then determine the phase which corresponds to moment maximum, then it will be seen, that this phase does not coincide with that of the resultant maximum. The recommended method of calculations reflects all the peculiarities of pressure variations that were found by other investigators. Excess pressure at the bottom at $y = \infty$ will then be:

$$\frac{p_b}{\gamma} = -\frac{kh^2}{2} \cos 2\sigma t \qquad (18)$$

N.N.Zagriadskaya has collected all published data on experimental laboratory investigations of the action of standing waves upon a vertical wall, and made a comparison with theoretical data. She found (10) thereby that the method recommended in the present paper should be considered as preferable when compared to Miche - Biesel - Rundgren method and to that of Kuznetsov, since it gives the best agreement with the results of laboratory experiments.

REFERENCES

1. Sainflou G. Essai sur les digues maritimes verticals. Ann. Ponts & Chaussées, 1928, v.4.
2. Miche M. Mouvements ondulatoires de la mer en profondeur constante et décroissante. Ann. Ponts & Chauss. v.114, n.n. 1-4, 1944.
3. Rundgren L. Water Wave Forces. Bull. Inst. Hydr., n.54, Stockholm, 1958.
4. Kusnetsov A.I. Interaction between Standing Waves and Vertical Walls. "Trudy MISI" (Proc. Mosc. Eng.Constr. Inst.) n.20, Moscow, 1957.
5. Biesel F. Equations générales du second de la houle irréguliére. La Houlle Blanche, n.3, 1952.
6. Kamel H. Wave Pressure on Seawalls and Breakwaters. Bull. PIANC, v.2, n.8, 1971.
7. Shtencel V.K. Determination of the Action of an Unbroken Standing Wave upon a Vertical Wall. "Trudy LIVT" (Proc. Leningr. Inst. Water Transp.) n. 88, Leningrad, 1967.
8. Shtencel V.K. Specific Character of Wave Motion of a Fluid and its Contributions in the Theory of Sea Waves. "Oceanology", v.6,n.5. Ac.Sci.USSR, Moscow.1966.
9. Khaskhachik G.D., Vanchagov O.M. Regular Wave Effects on Walls Made of Cylinders. J.Waterways, Harbours, & Coastal Engng. Div. Proc. A.S. of C.I. n.11, 1971.
10. Zagriadskaya N.N. In the Proc. of Coordination Conf. on Hydroengineering. n.50, 1969; n.61, 1970. Energy. Leningrad.

CHAPTER 92

PRESSURE UPON VERTICAL WALLS FROM OVERTOPPING WAVES

by

M.E.Plakida[x)]

A B S T R A C T

This paper is concerned with the study of wave pressures exerted upon breakwaters of the vertical type from overtopping waves.

The formulae for maximum wave pressure upon vertical walls and the wave crest elevation for overtopping waves are suggested by the author. The phase interval method for the maximum wave pressure is also given.

---

x) Chief of Wave Laboratory of Moscow Branch of Water Transport Engineering Institute; Bolschaya Ordynka Street 19, Moscow, J-35. U.S.S.R.

INTRODUCTION

The following symbols are used in this paper:

h – wave height;

λ – wave length;

τ – wave period;

H – depth of water measured from the still water level (SWL);

Z_{sw} – elevation of wave crest above SWL for a standing wave at 90° ($t = 0{,}25\tau$);

Z_{max} – maximum elevation of wave crest from overtopping wave;

P_{sw} – wave pressure intensity for a standing wave at SWL;

P^{o}_{max} – maximum wave pressure intensity from overtopping wave at SWL.

Experimental model study shows that elevation of wave crest and wave pressures upon a vertical wall from an overtopping waves decrease in comparison with conditions without overtopping. Wave pressures upon vertical walls decrease with the loss of the wall elevation above SWL.

The construction of a breakwater for overtopping waves requires less expenses than for a full profile of walls, but it is necessary to take into consideration increasing degree of agitation in harbours.

Overtopping of waves over sea-walls is a very complicated hydraulic phenomenon which consists of partial standing waves (clapotis partial - French) and of periodical flow with a variable water discharge.

The trajectories of the four indicators small balls of bitumen and paraffin with the liquid specific weight are shown on fig.1. On fig.1 the two of the indicators namely I and II are to the left from the knot; and two other indicators III and IV are between the knot and

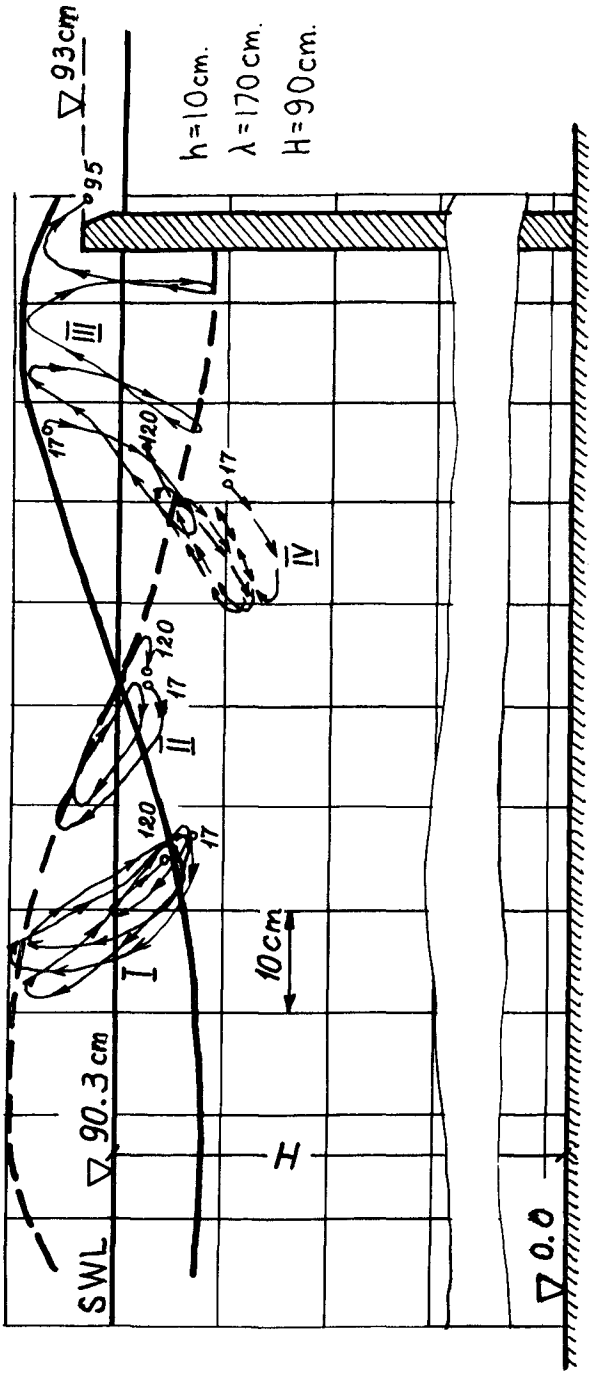

Fig. 1. Movement of particles. (Film 24 cd/sec.)

the wall. The surface indicators I and II move along trajectories, which are typical curves of partial standing waves. There is no water current influence due to overtopping waves here.

The indicators III and IV show a complicated simultaneous movement of particles is inherent in the partial standing wave and the flow with variable discharge. As a result the indicator III move along a loop-type trajectory.

The mathematical description of this phenomenon is very difficult. The author has decided to use a wave flume in order to clarify the questions with the help of hydraulic models within the given experimental parameters.

We use the standing wave theory and experimental data, giving the coefficients for computation of the maximum wave crest elevation and wave pressures upon a vertical wall from overtopping waves.

MODEL AND EQUIPMENT

This study has been carried out by the author in a wave flume of a rectangular cross-section 23 m in length and 0.50 m wide with a water depth of 0.90 m.

The wall model was represented by a concrete block with a wood screen. Seven wave pressure-gauges and one

level-gauge were sunk into the screen surface. The installation scheme and the placing all the gauges is given on fig.2.

The crest wall elevation above SWL is equal α =2.7cm The investigation has been carried out for the following parameters (see tabl. 1).

Table 1

h cm	λ cm	τ sec	$\frac{h}{\lambda}$	$\frac{H}{\lambda}$	$\frac{\alpha}{h}$
1	2	3	4	5	6
10	170	1,06	0,06	0,53	0,27
17	210	1,20	0,08	0,48	0,16

The wavegenerator of a flap type was used to generate regulars waves with different wave periods and wave heights.

The wave pressures were measured by tensemetric gauges having a frequency 140 cycles per second. The wave heights were measured by electrical gauges. A sample of an oscillograph record is given on fig. 2.

Phases of wave indulations and the movement of ball indicators were recorded on a 35 mm film at 24 frames per sec. A sample of a film record is shown on fig.1. The trajectories of indicators I, II and IV from 17 up to 120 frames and the trajectory of the indicator III up to 95 frames are seen on this figure.

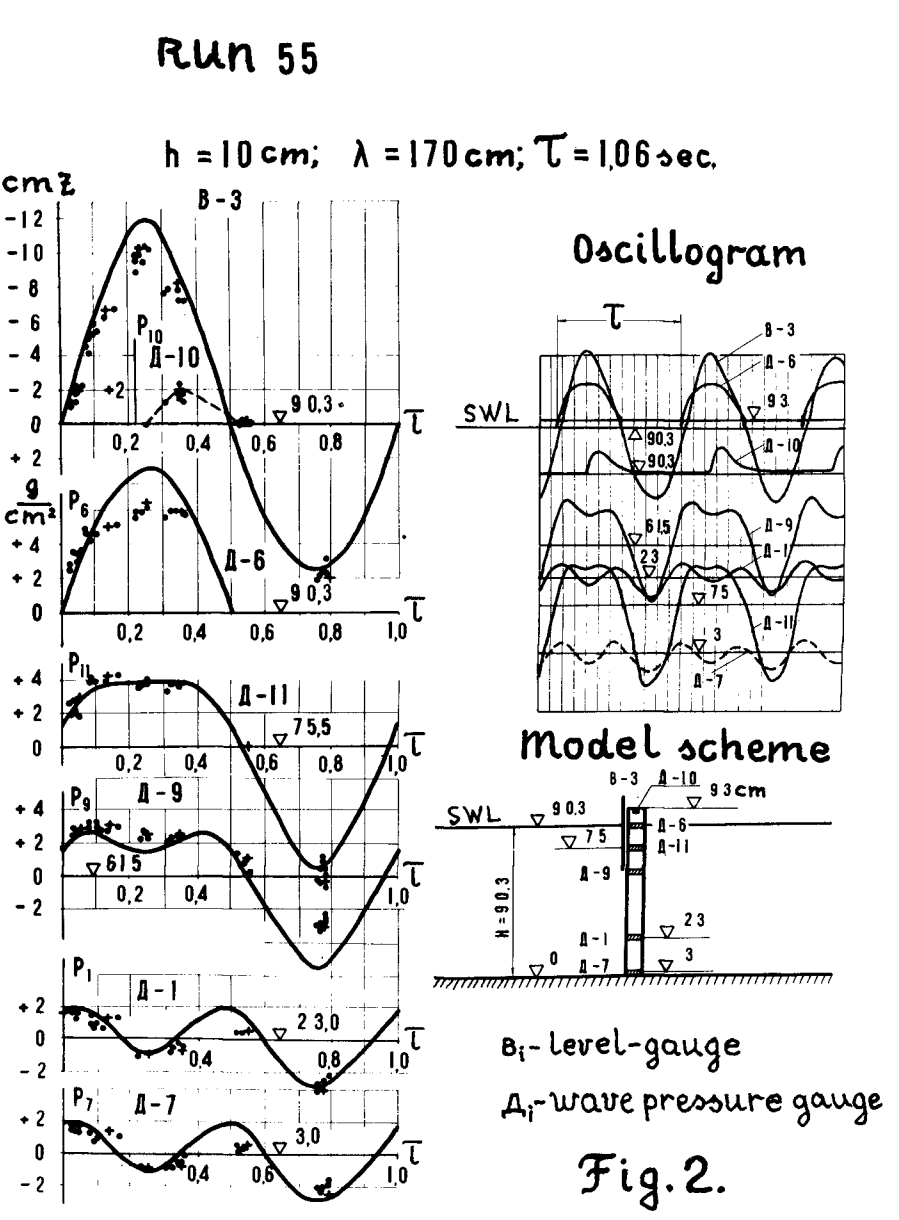
RUN 55
h = 10 cm; λ = 170 cm; τ = 1,06 sec.
cm z
B-3
P10
Д-10
P6
Д-6
P11
Д-11
P9
Д-9
P1
Д-1
P7
Д-7
g/cm²
τ
Oscillogram
SWL
B-3
Д-6
Д-10
Д-9
Д-1
Д-11
Д-7
Model scheme
93cm
H = 90.3
Bi - level-gauge
Дi - wave pressure gauge

Fig. 2.

RESULTS

On fig.2 graphs of water level oscillation and wave pressure are shown by a continuous line according the calculation by the standing wave theory (1, 2 and 3) at condition without overtopping. Experimental data are also shown by points.

The decreases of water level elevation (see B-3) and wave pressures in the vicinity of still water surface (see Д-6) are clear from these graphs for overtipping waves in comparison with waves without overtopping.

Within the scope of experimental parameters:

- maximum wave crest elevation Z_{max} from overtopping waves is given by formula

$$Z_{max} = 0,8\ Z_{sw}$$

- maximum wave pressure at still water level from overtopping waves will be

$$P^{o}_{max} = 0.8\ P_{sw}$$

Values of wave pressures equal and below the level of 75 cm (see fig.2) up to from the bottom are practically equal to values calculated by the standing wave theory. Thus the decrease of wave pressures up to 20% due to wave overtopping are only noted from the still water level down to a depth about (1.0 ÷ 1.5) h.

Maximum resultant of wave pressures occurs at phase intervals from 0.10τ to 0.15τ (zero phase corresp-

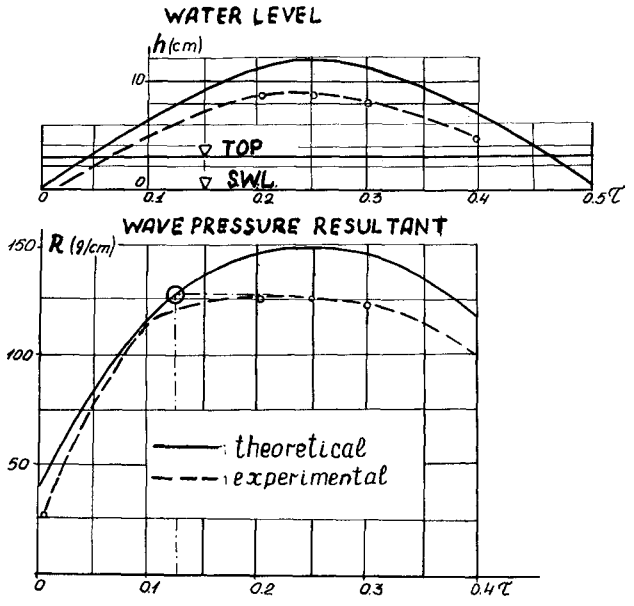
WATER LEVEL
h(cm)
10
0
TOP
SWL
0
0.1
0.2
0.3
0.4
0.5τ
WAVE PRESSURE RESULTANT
150
R (g/cm)
100
50
theoretical
experimental
0
0.1
0.2
0.3
0.4τ

Fig. 3.

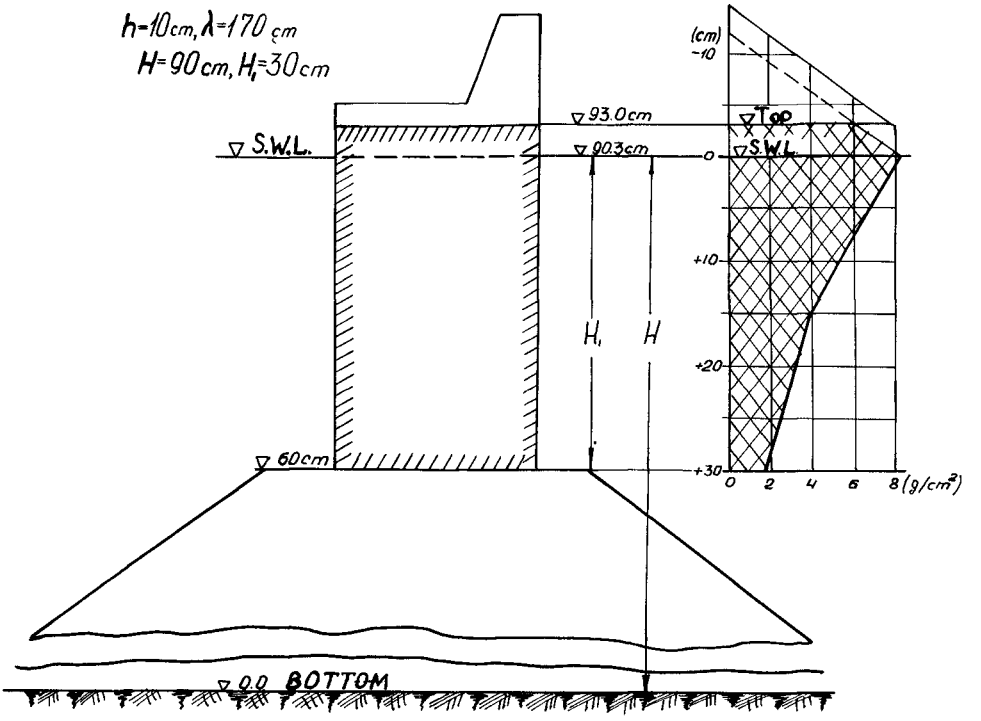
h=10cm, λ=170 cm
H=90cm, H1=30cm
S.W.L.
93.0cm
90.3cm
60cm
0.0 BOTTOM
H1
H
(cm)
-10
0
+10
+20
+30
T90
S.W.L.
0 2 4 6 8 (g/cm²)

onds to the coincidence of the upsurging wave surface with SWL).

Computation of the maximum resultant of wave pressure may be carried out by a graphical method based on the standing wave theory for 4-5 phases values of the resultant in a phase interval from 0.10τ up to 0.15τ

The graphs of change the water level and the wave pressure resultant for semiperiod of wave calculated by the standing wave theory and by experimental data are given on fig.3. These curves of the wave pressure resultant are in corresponding to the wave pressure scheme indicated above on fig.3.

C O N C L U S I O N

Wave crest elevationd and wave pressures upon vertical walls decrease from overtopping waves in comparison with a full wall.

Decrease of wave pressures occur only from SWL down to depth of about (1.0 ÷ 1.5) h.

Maximum resultant of wave pressures due to overtopping waves occurs at a phase interval from 0.10 τ up to 0.15 τ for the scope of our experiments.

REFERENCE

1. Biésel. Equation générales au second ordre de la houle irrégulière. La Houille Blanch N.3, 1952

2. Г.Г.Метелицына. Исследование стоячей волны на вертик. стенку.Тр.ЦНИИЭВТ, вып.XIX. Москва,1960.

G.G Metelithyna. Investigation of standing wave pressure upon vertical wall. Proc.CNIIWT Vol.XIX, Moscow, 1960.

3. М.Э.Плакида. Современный метод расчета волнового давления от стоячей волны на вертикальную стенку. Гидротехническое строительство №5, 1963

M.E.Plakida. Modern method of calculating of wave pressure on vertical wall from standing wave. Hydrotechnical Construction N.5, 1963

CHAPTER 93

NEW DESIGNS FOR BEACH PROTECTION STRUCTURES

by

G.D.Khaskhachikh, Candidate of Science
G.A.Tsaturiyan, Candidate of Science
Ya.S.Shulgin, Engineer.

All-Union Research Institute of Transport Construction
Igarskaya proezd, 2, Moscow I-329, USSR.

Along some length of the Black Sea coast line there are beach protection structeres largely represented by groins and traverses in conjunction with wave resisting embankment walls. The groins are built of 30 to 100 t concrete blocks and set on a rubble-mound foundation levelled by sea divers.

In the course of building and exploitation of these structures, a number of disadvantages have been revealed. These are:

- The groin structure is affected by the waves that scour the rubble-mound foundation at the bottom and thereby disturb it. Failures occur more frequently at the head (seaward) part of the groin;
- The rubble-mound is concerned with having to perform a great deal of heavy and harmful to health diving job, such as underwater excavation, filling and levelling the stone material, etc.;
- The rubble-mound cost and labour involved are estimated to be high.

An example of deformation of such a groins is shown in figure 1.

Investigations were carried out in order to develop more reliable and industrialized designs of groin and traverse for use in soils subjected to scouring by waves. This resulted in achieving some new concepts of groin design which were then realised in construction on the Adler site of the Black Sea coast. The site was situated on a huge accumulation promontory formed by sand-shingle deposits. Reaching the shore, there were the sea waves up to 5-6 m. Due to a deficiency of sediments in that area an erosion process had already started involving the shore slopes, beaches and the sea bottom near the shore. The stabilization required for this section of the shore was being achieved by building a system of beach-protection structures, such a groins, stepped-slope sea-walls, submerged breakwaters, and by making artificial beaches. This system of beach protection has proved to be highly efficient in stabilizing the shores. Beside the conventional structures set on the rubble-mound foundation, two groins of a new design set on reinforced concrete hollow cylindrical piles were used there.

The experimental construction was aimed at field examination of the erection procedure for these structures, as well as to define their reliability in the course of application.

The first of the two test groins, shown in figure 2, is comprised of to 4 x 5-6 m, 2-4.5 m high concrete blocks weighing up to 100 tons.

Each block has a central hole 1.7m in diameter for a prestressed concrete hollow cylindrical pile 1.6m in diameter to be driven through it by vibrodriver. There are also semicircular slots on the butts for 20-t concrete keys. 1.6m in diameter to be inserted in them. These slots can as well be used for driving the piles. The head portion of the groin consist of two blocks fixed in place by

Fig. 1. Deformation of the conventional groin.

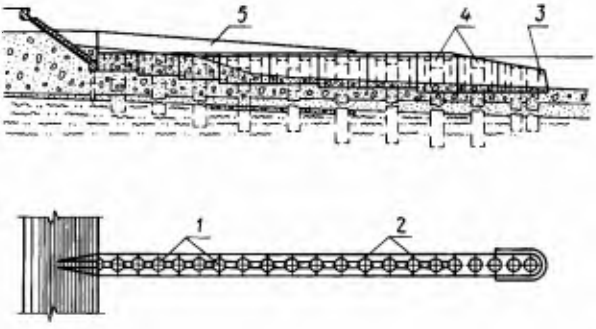

Fig. 2. Scheme of the concrete block groin set on cylindrical hollow pile foundation.

1- concrete blocks; 2- concrete keys; 3- head block; 4- cylindrical hollow piles; 5- cast-in-place concrete.

three hollow cylindrical piles. On the whole, the 60-m long groin is comprised of ten blocks, nine keys, and ten 8-10m length piles which are driven to the depth of 5 to 6 meters. The concrete blocks function as a reliable conductor in driving the piles, and as a means of protection for the latter from the sea-water abrasion.

Connection of the groin with the sloping wall was performed with cast-in-place concrete, also used in forming the levelling plate and profile crest.

The erection procedure for the groins consist of the following steps:

- pit excavation using a floating crane with a grab;
- installation of prismatic blocks;
- installation of the keys;
- installation and vibrodriving the hollow cylindrical piles;
- placing the cast-in-place concrete.

The groin under construction is shown in figure 3, and the same groin fully completed is shown in figure 4.

The second test groin is a reinforced concrete structure composed of slubs that fit into the slots of the concrete bearing blocks. These slabs are also supported by the hollow cylindrical piles driven through the holes in the blocks (see fig. 5).

The 60-m length groin structure consist of four intermidiate 60-t bearing blocks; a 65-t head portion; six hollow cylindrical piles; and ten 4-7m length, 0.6m thick concrete slabs weighing from 11 to 26 tons. The slabs are placed in two cources by height. The thin-walled groin structure is more acceptable from the economic point in view, though special means are needed to protect its slabs from abrasion by shingle deposits. For this purpose the high-strength concrete with a polimer-concrete covering is used, as well as the cast-in-place concreting for all of the other members of the structure. The erection procedure for this groin is principally the same as that for the former. A general view of the groin under construction is shown in Fig.6

Fig. 3. Groin made of concrete blocks under construction.

Fig. 4. Groin made of concrete blocks is fully completed.

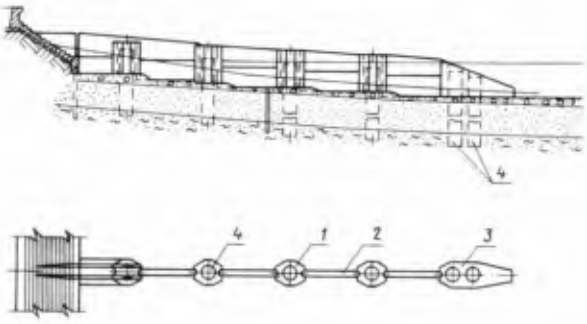

Fig. 5. Scheme of the groin made of reinforced concrete slabs.

1- bearing blocks; 2- renforced concrete slabs; 3- head block; 4- cylindrical hollow piles.

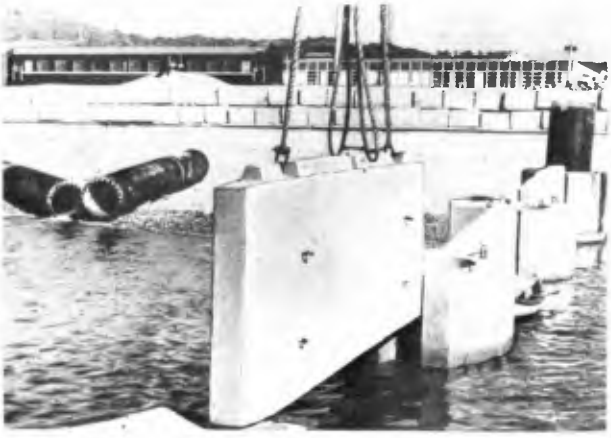

Fig. 6. Groin made of reinforced concrete slabs under construction.

For all of the blocks and screening slabs in these test structures, the footing was installed below the active layer of deposits. In order to improve the block-pile connection, the piles were driven 1.5m further down below the block surface.

During the construction period and successive two years of exploitation, the new groins were subjected to repeated attacks of heavy and long storms with the waves up to 5-6 meters, but according to detalied examinations of these structures no damage has been recorded.

The test groin investigations have enabled designing a combined groin structure for shores with shingle deposits prevailing. The on-shore portion of such a groin is composed of prismatic blocks while the head portion is of thin-walled slabs.

Such a design is more suitable for the groin operation under these conditions.

CHAPTER 94

A PROBABILISTIC APPROACH TO DETERMINE WAVE FORCES ON OCEAN PILE STRUCTURES

by

G. I. Schuëller* and H. C. Shah**

ABSTRACT

Multiple linear regression analysis is applied to predict horizontal velocities and acceleration of water particles subjected to waves. Furthermore it was used to predict the coefficient of drag for circular piles. The mean value functions of the parameters are calculated and the assumption of their lognormal distribution reasonably well verified. The method used here is free from theoretical assumptions about wave mechanisms and, hence, explains the behavior of experimental results.

Using Monte Carlo simulation these regression relations were then utilized to generate the distribution functions of wave forces. Using the Morison force equation, in this simulation, the distribution function for the drag and the inertial components of the force are determined separately. A linear superposition of those time varying processes was performed to obtain the distribution of the total maximum force. Finally a probabilistic wave height-wave force relationship was developed for the purpose of creating a force distribution function given a random sea state.

1. INTRODUCTION

Circular piles are often used to support various ocean structures. The wave forces to which they are subjected are of utmost importance for the design of such structures.

The actual situation in the ocean presents a confusing and often frustrating problem to the engineer. Our limited knowledge about the ocean waves has made engineering design extremely difficult, resulting in a number of failures in

---

* Assistant Professor, The George Washington University, Dept. of Civil Engineering, Washington, D. C.

** Associate Professor, Stanford University, Dept. of Civil Engineering, Stanford, California.

the past.

The following factors complicate the design considerably: first, wave characteristics change continuously as the wave travels. Secondly, even the forces exerted by identical waves vary greatly. This variation is caused by fluctuations in the fluid particle velocities and accelerations as well as eddies around piles caused by the rapidly reversing flow. These random phenomena can only be handled using a probabilistic approach.

A cumulative distribution function of wave forces created from field data would give the engineer sufficient information for his design. In reality most of the available data on ocean waves consist of records of wave height, period and length, three easily measured properties. However, useful wave force measurements have been conducted very seldom due to high cost and extraordinary experimental difficulties involved.

Therefore a method is proposed which transforms available data into useful form. In other words, records of wave heights, periods and lengths can be converted in cumulative distribution functions of wave forces. The method utilizes a multiple regression analysis to develop a relationship between those easy to measure wave properties and the parameters used in the Morison[1] force equation. These parameters include water particle velocities and accelerations as well as the coefficients of drag and inertia. Using Monte Carlo simulation these regression relationships are then the basis of the development of the cumulative distribution function of the wave forces. Given this distribution, the engineer can make reliability statements about his design. This information developed above can then be utilized to create a probabilistic wave force-wave height relationship. This relationship enables one to take the randomness of the sea into account. The most likely cumulative distribution function of the wave forces for a particular wave height distribution given a wave period can be determined. Integration over all possible periods for a fully developed sea leads to a cumulative distribution function of the force, which again can be used for reliability statements.

2. DEVELOPMENT OF THE MAXIMUM FORCE DISTRIBUTION FUNCTION

The generally accepted and most widely used formula for a force on a pile is the so-called Morison formula,[1]

$$F = \frac{1}{2} D\rho C_D |u|u + \rho \frac{\pi D^2}{4} C_M \frac{\partial u}{\partial t} \qquad (1)$$

The first part of this equation represents the form drag caused by surface shear. The second part of the equation is the acceleration force on the displaced volume of fluid including the virtual mass effect. Although the particle motion in waves is orbital, the method is based on rectilinear flow. Morison also assumed that the drag force and the inertia force can be treated separately, and that the total force can be obtained by adding the solutions linearly.

The fluid density ρ and the pile diameter D are assumed to be constant. However, based on experimental evidence[2,3,4,5,6] the water-particle velocity u, the acceleration $\partial u/\partial t$, the coefficient of drag, C_D, and the coefficient of mass, C_M, are considered random variables. Their mean value functions and distributions are developed by utilizing available experimental data [2,3,4] and applying the mathematical method of multiple linear regression analysis. The results obtained are the following:[7]

$$u^* = \exp(0.442 + 0.04L^* - 0.231d^* + 0.221S^*) \qquad (2)$$

where $u^* = \frac{uT}{H}$, $L^* = \frac{L}{H}$, $d^* = \frac{d}{H}$, $S^* = \frac{S}{H}$,

and

$$a^* = \exp(2.856 + 0.04L^* - 0.28d^* + 0.127S^*) \qquad (3)$$

where $a^* = \frac{aT^2}{H}$

and

$$C_D = e^{0.484}(Re)^{-0.694}(H^*)^{0.067}(T^*)^{0.115} \qquad (4)$$

where $H^* = \frac{H}{D}$, $T^* = \frac{uT}{D}$

Note that the equations (2), (3) and (4) represent mean value functions. The assumption of the lognormal distribution of the dependent parameters u^*, a^* and C_D was reasonably well verified by means of probability and error plots.[7] The coefficient of mass, C_M, was assumed to be lognormally distributed with a mean value of 2.5 and a standard deviation of 1.2. Equations (2) and (3) represent the maximum water particle velocities and accelerations within a wave.

These equations can be expressed as a function of time

as

$$u(t) = u \cdot \cos\omega t \tag{5}$$

$$a(t) = a \cdot \cos\omega t \tag{6}$$

where $\omega=2\pi/T$, the angular frequency. Substituting equations (5) and (6) in equation (1) the following expression is obtained:

$$F_T(t) = C_D\left(\frac{\rho D}{2}\right)\left(\frac{H}{T}\, u^*\right)^2 \cos\omega t|\cos\omega t| + C_M\left(\frac{\rho\pi D^2}{4}\right)\left(\frac{H}{T^2}\, a^*\right)\sin\omega t \tag{7}$$

Since the drag component is 90° out of phase with the inertia component, the maximum drag force occurs when the wave crest or trough passes the pile. The maximum inertia force occurs when the wave passes the still water level. The maximum total force exerted by a wave is derived by setting the first derivative of equation (7) to zero. This results in the following equation:

$$F_{T_{max}} = C_D\left(\frac{\rho D}{2}\right)\left(\frac{H}{T}\, u^*\right)^2 \left\{1 + \frac{1}{4}\left[\frac{C_M\left(\frac{\rho\pi D^2}{4}\right)\left(\frac{H}{T^2}\, a^*\right)}{C_D\left(\frac{\rho D}{2}\right)\left(\frac{H}{T}\, u^*\right)^2}\right]^2\right\} \tag{8}$$

The expression $F_{T_{max}}$ in equation (8) is a function of the previously determined random variables u, a, C_D, C_M and is therefore also a random variable. Equation (8) can be written:

$$f_{F_{T_{max}}}(f_{T_{max}}) = f_{C_D}(C_D)\left(\frac{\rho D}{2}\right)\left(\frac{H}{T}\, f_{u^*}(u^*)\right)^2 \cdot \left\{1 + \frac{1}{4}\left[\frac{f_{C_M}(C_M)\left(\frac{\rho\pi D^2}{4}\right)\left(\frac{H}{T^2}\, f_{a^*}(a^*)\right)}{f_{C_D}(C_D)\left(\frac{\rho D}{2}\right)\left(\frac{H}{T}\, f_{u^*}(u^*)\right)^2}\right]^2\right\} \tag{9}$$

The maximum total force probability density function $f_{F_{T_{max}}}(f_{T_{max}})$

can be obtained rigorously by derivation of the distribution as a function of the random variables u, a, C_D and C_M which are assumed to be lognormally distributed. Although the probabilistic portion of the derivation of the distribution is a rather direct problem, the calculus needed to evaluate the resulting integrals seems to be intractable. Fortunately, an approximate method for creating derived distributions, the Monte Carlo Method,[8] furnishes a distribution of sufficient accuracy.

3. DEVELOPMENT OF A PROBABILISTIC WAVE FORCE - WAVE HEIGHT RELATIONSHIP FOR AN OCEAN SURFACE

In the previous section it was shown how to obtain a maximum wave force probability density function for a single wave.

The actual situation in the ocean presents a complex and confusing problem. The local wind generated waves are superimposed on the large ocean waves whose origin may be thousands of miles away. A deterministic approach to ascertain the wave heights of ocean waves is impossible because of the present inadequate understanding of complicated wave systems. However, by observing the random nature of the ocean waves, it is plausible that some statistical regularity can be found.

3.1 Statistical Distribution of Wave Heights

Wiegel et al.[4] measured the forces exerted by ocean waves on vertical circular cylindrical piles near Davenport, California, in water ranging from 45 feet to 50 feet deep. The relation of H versus T of the measured data is plotted in Figure 1. The data show a considerable amount of scatter, indicating the presence of waves with various combinations of H and T in the ocean. To gain insight into this apparent randomness, the data are grouped into several ranges of the period T as follows:

Period Group		Average Period Representing the Range (sec.)
1	$6 \leq T < 10$	$T_1 = 8$
2	$10 \leq T < 12$	$T_2 = 11$
3	$12 \leq T < 14$	$T_3 = 13$
4	$14 \leq T < 16$	$T_4 = 15$
5	$16 \leq T < 20$	$T_5 = 18$

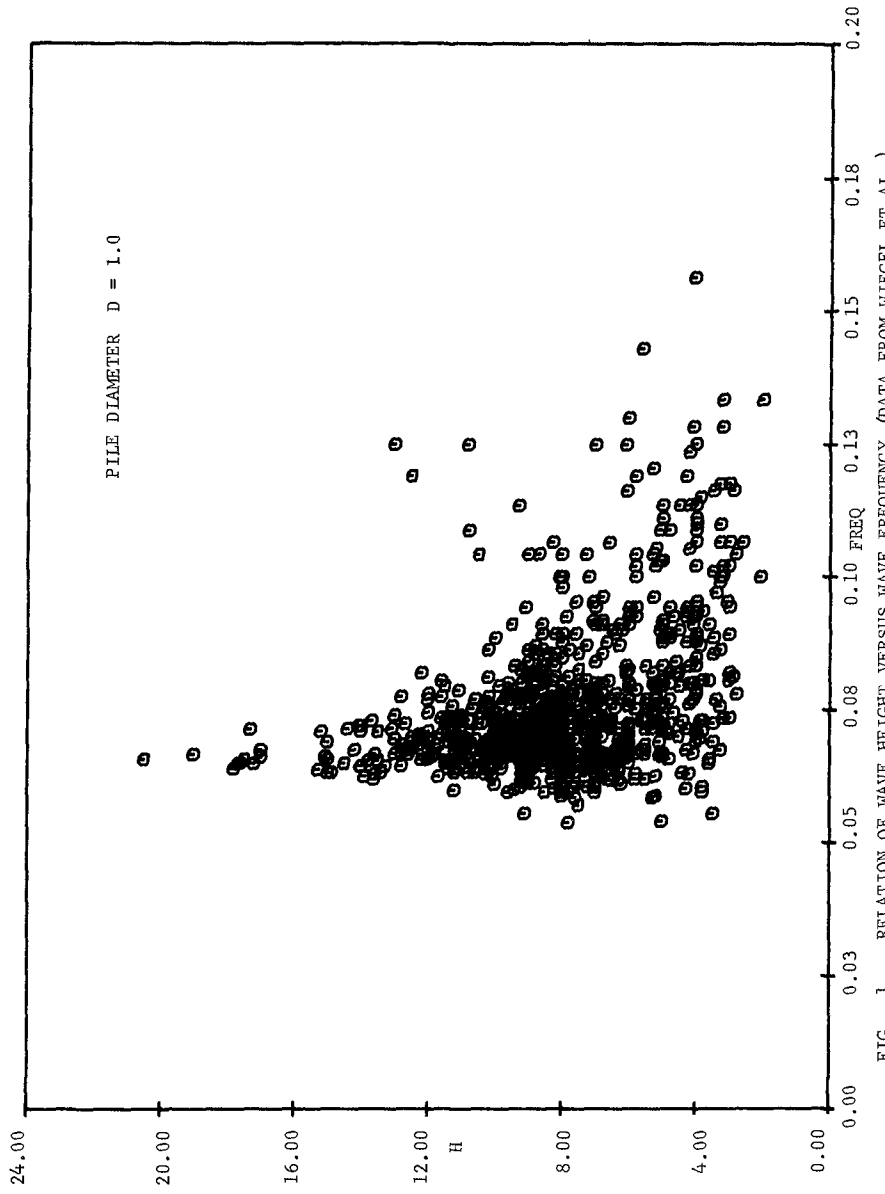

FIG. 1 RELATION OF WAVE HEIGHT VERSUS WAVE FREQUENCY (DATA FROM WIEGEL ET AL.)

Histograms are then constructed for each period. By normalizing the histogram and dividing the resulting probability mass function by the size of the H interval, the frequency function of H for each period group is obtained. These frequency functions are shown in Figure 2(a)-(e). It is interesting to see that the distribution of H resembles the Raleigh distribution whose PDF is given by

$$f_H(h) = \begin{cases} (2h/c^2)\exp(-h^2/c^2), & \text{for } h \geq 0 \\ 0, & \text{otherwise} \end{cases} \tag{10}$$

where h represents a particular realization of the random wave height, H, and c^2 is the mean square of H.

The idea that the wave heights follow the Raleigh distribution was introduced by Longuet-Higgins[9] in his theory for waves having narrow band spectra.

In the derivation of equation (10), Longuet-Higgins assumes that the ocean waves involved were nondirectional and infinitesimal so that simple linear wave theory would apply. Borgman[10] argued that although for large waves the data are not exactly distributed according to the Raleigh distribution, the Raleigh curve appears similar enough to the data to justify its use in most engineering approximations. However, for this problem it is only of importance that there is some statistical regularity in the distribution of H. Figures 2(a)-(e) indicate that such regularity exists.

3.2 Functional Relationship Between H and F

The analytical tools which are employed to find the functional dependence of F on H are the regression analysis and the Monte Carlo simulation. From Section 2, it can be seen that the functional relation between H and F is a probabilistic one. Equation (9) shows how to obtain the maximum total force probability density function. For this equation every parameter is given in Wiegel's data[4] except the wave length L. However, L can be approximated by utilizing the linear wave theory[5]

$$L = \frac{gT^2}{2\pi} \tanh\left(\frac{2\pi d}{L}\right) \tag{11}$$

Equation (11) is an implicit formula for L which may be solved

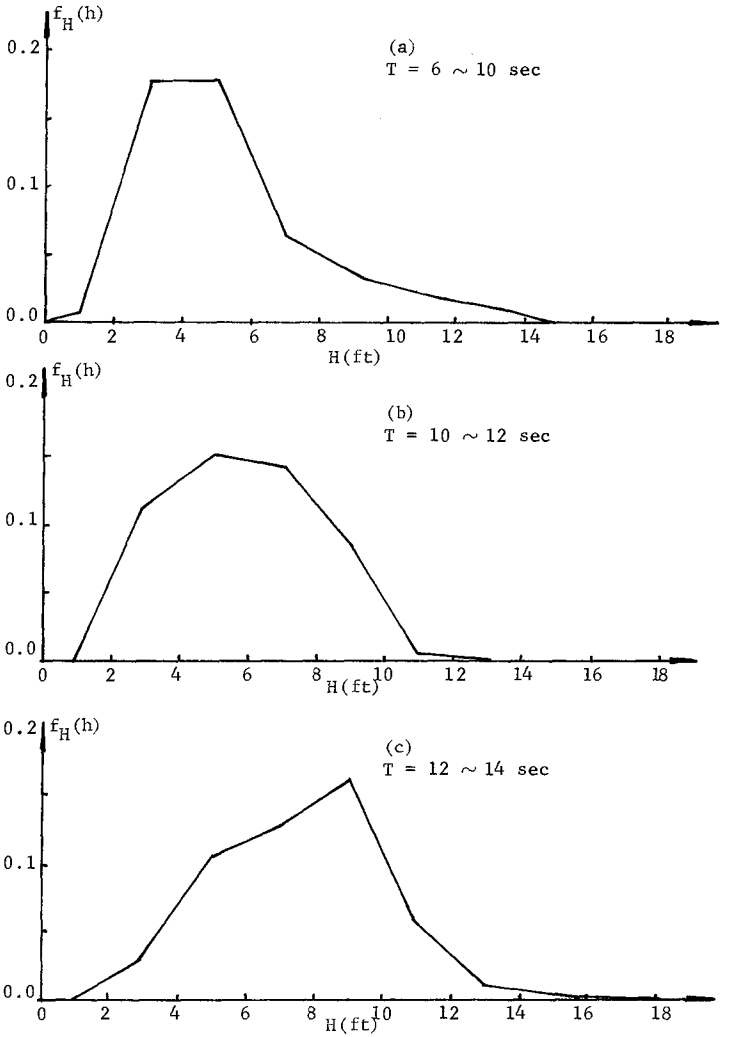

FIG. 2. WAVE HEIGHT FREQUENCY FUNCTIONS
(a) FOR T = 6 ~ 10, (b) T = 10 ~ 12,
(c) T = 12 ~ 14 sec. [continued]

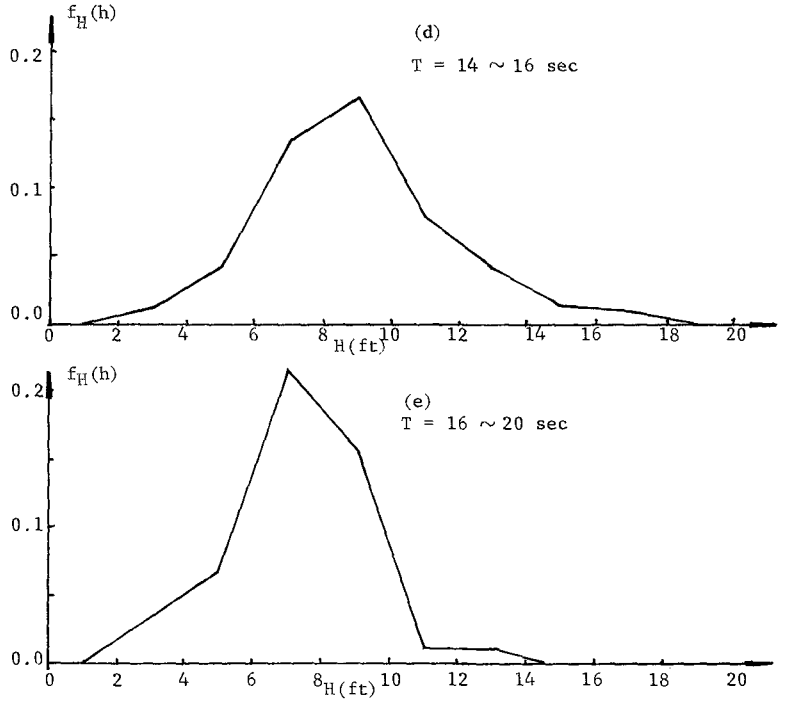

FIG. 2. WAVE HEIGHT FREQUENCY FUNCTIONS
(d) FOR T = 14 ~ 16, (e) T = 16 ~ 20 sec.

by using the Newton-Raphson method.

To develop the mean value functions of the wave forces, Monte Carlo simulations must then be performed for constant wave periods T and various wave heights H. This process results in a family of mean value functions, shown in Figure 3.

Figures (4)-(8) show the coaxial diagrams which demonstrate the relationships between H, T and $F_{T_{max}}$. Part A of the graphs contains the CDF for the wave height, determined from field data. Part B relates the wave height to wave force for a given value of T.

Since the relationship between H and T is probabilistic, each T curve is a mean value function. Part C is a CDF for the wave force which is derived from parts A and B of the graphs as illustrated in the diagram. This process can be easily performed since the relationship between $F_{T_{max}}$ and H is a monotonically increasing function. Because the height-force relationship is probabilistic, the CDF of the wave force is a graph of the most likely force to be expected. Thus the method of coaxial relationships shown here can be used to generate a CDF for wave forces for a particular period and a given wave height distribution.

3.3 Application of the Method Proposed in Design

In order to apply this method in design more extensive data are needed on wave height distributions. If a pile is to be designed to last several years then the statistical frequency of unusual high waves must be known. The data series used to determine the CDF of H would consist of wave data for large storms or a tabulation of those waves exceeding a certain wave height in a given record. For example, in the Gulf Coast, hurricane data would probably be used in design. It may also be necessary to consider the probability of hurricane or storm occurrence in the analysis.[11]

4. CONCLUSIONS

This analysis has demonstrated a method for determining the cumulative force distribution of piles caused by a given wave height distribution. To create a force distribution the Morison force equation was used to develop the relationship between wave force ans several wave properties using experimental data. In utilizing the Morison equation, the horizontal water particle velocity and acceleration as well as the coefficients of drag and mass were considered random variables. The mean value functions and variances of these random variables were developed using multiple linear regression analysis and

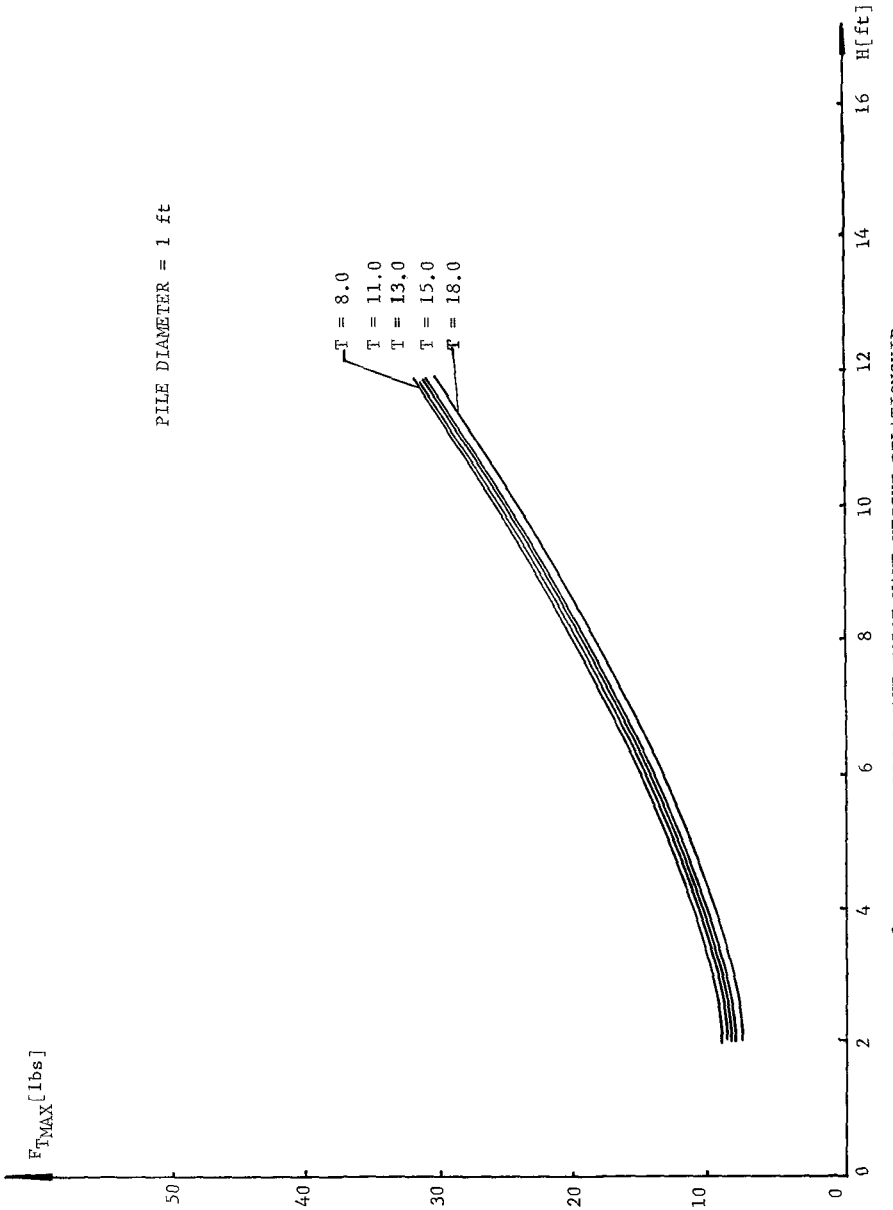

FIG. 3. PROBABILISTIC WAVE FORCE-WAVE HEIGHT RELATIONSHIP.

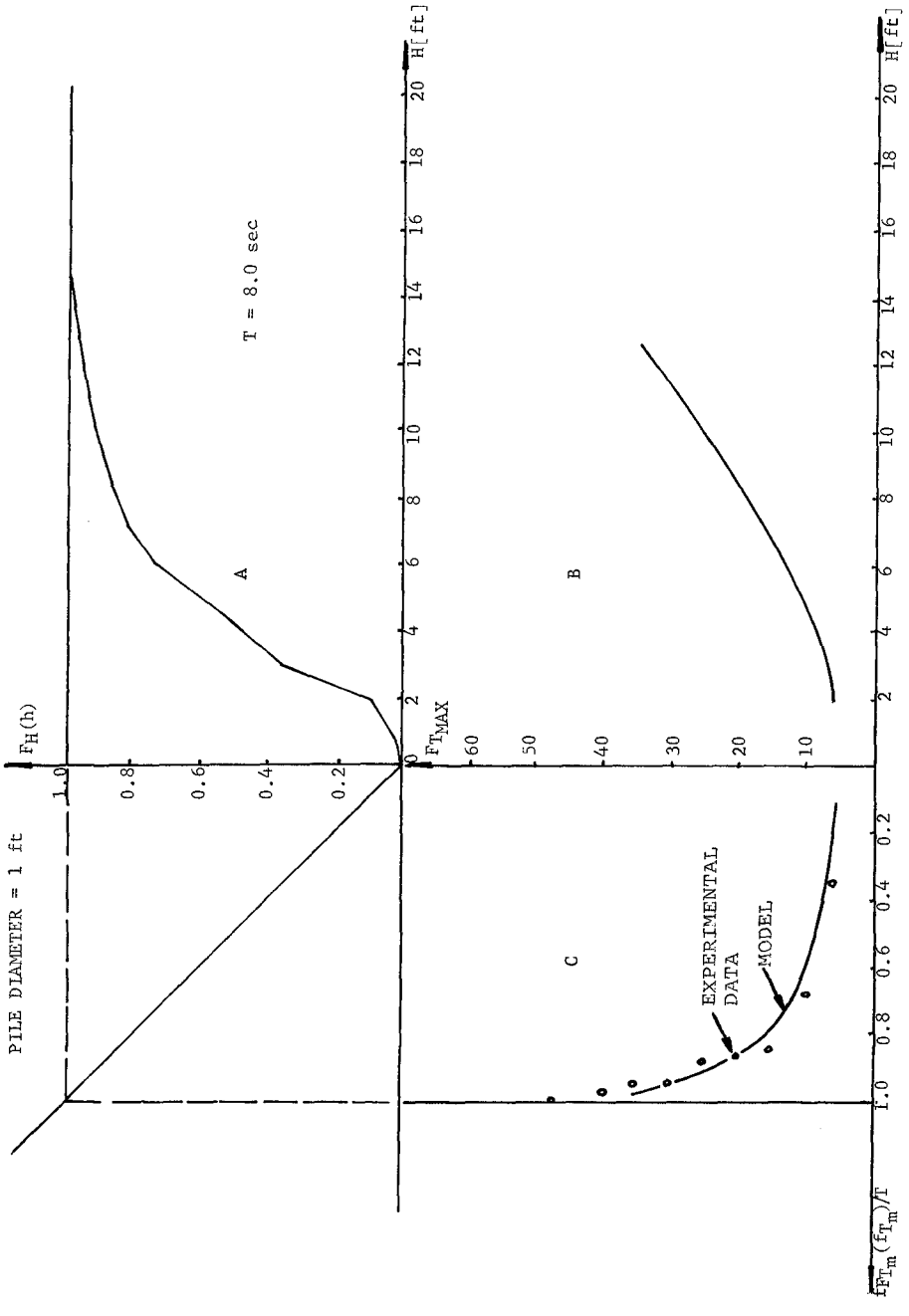

FIG. 4. CO-AXIAL DIAGRAM FOR RELATIONSHIP BETWEEN H, T, AND F_{MAX} FOR T = 8 SEC.

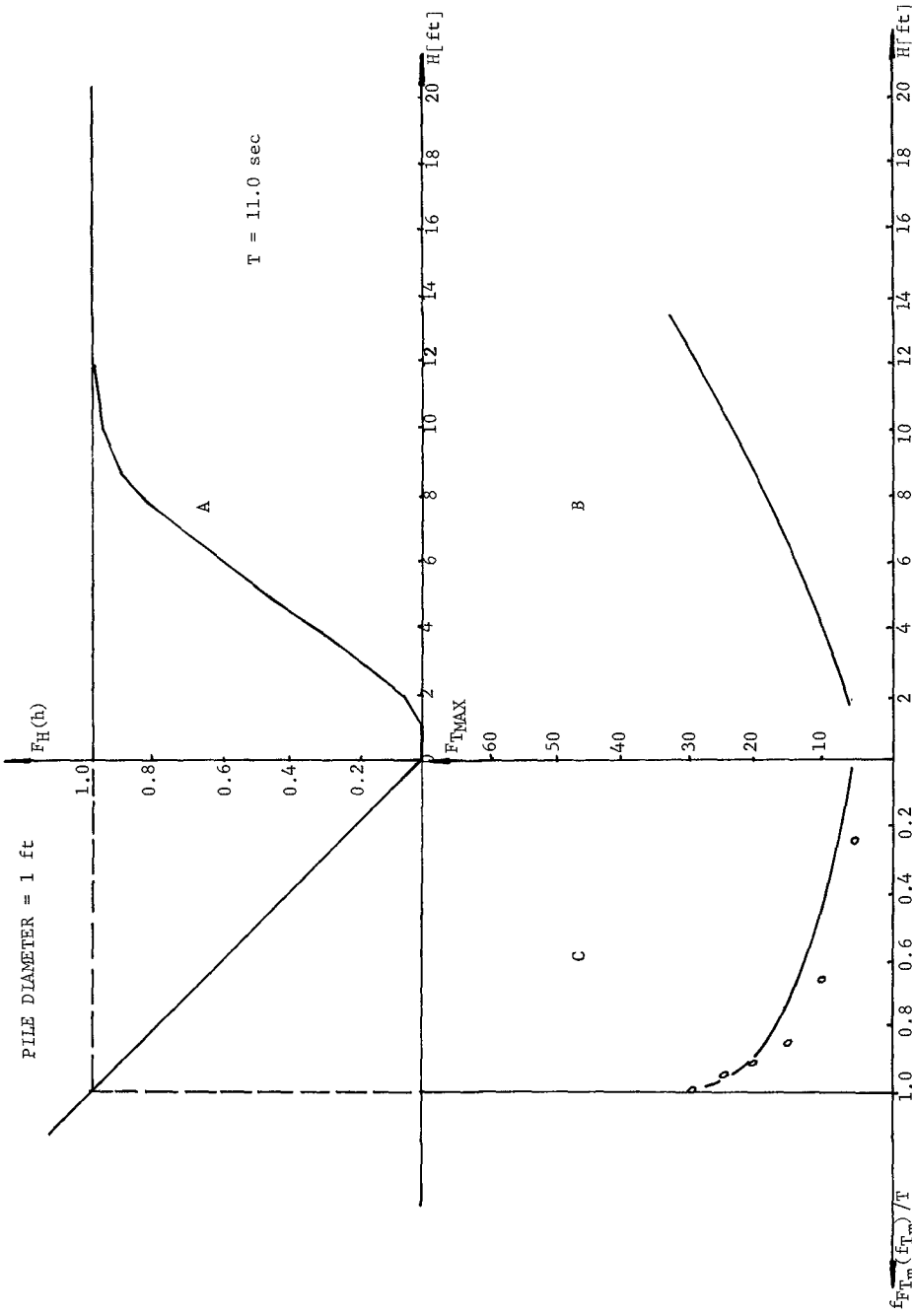

FIG. 5. CO-AXIAL DIAGRAM FOR RELATIONSHIP BETWEEN H, T, AND F_{MAX} FOR T = 11 SEC.

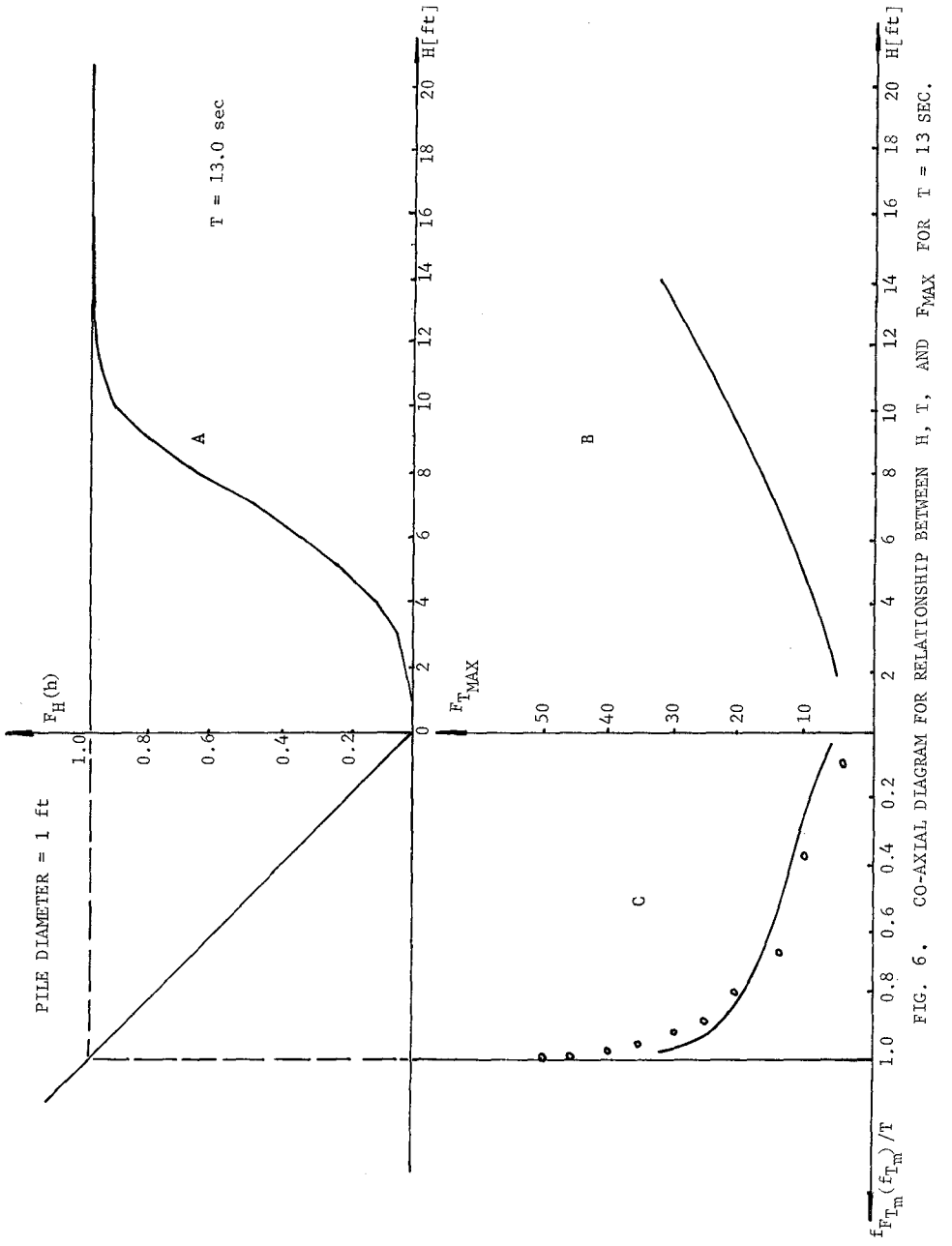

FIG. 6. CO-AXIAL DIAGRAM FOR RELATIONSHIP BETWEEN H, T, AND F_{MAX} FOR T = 13 SEC.

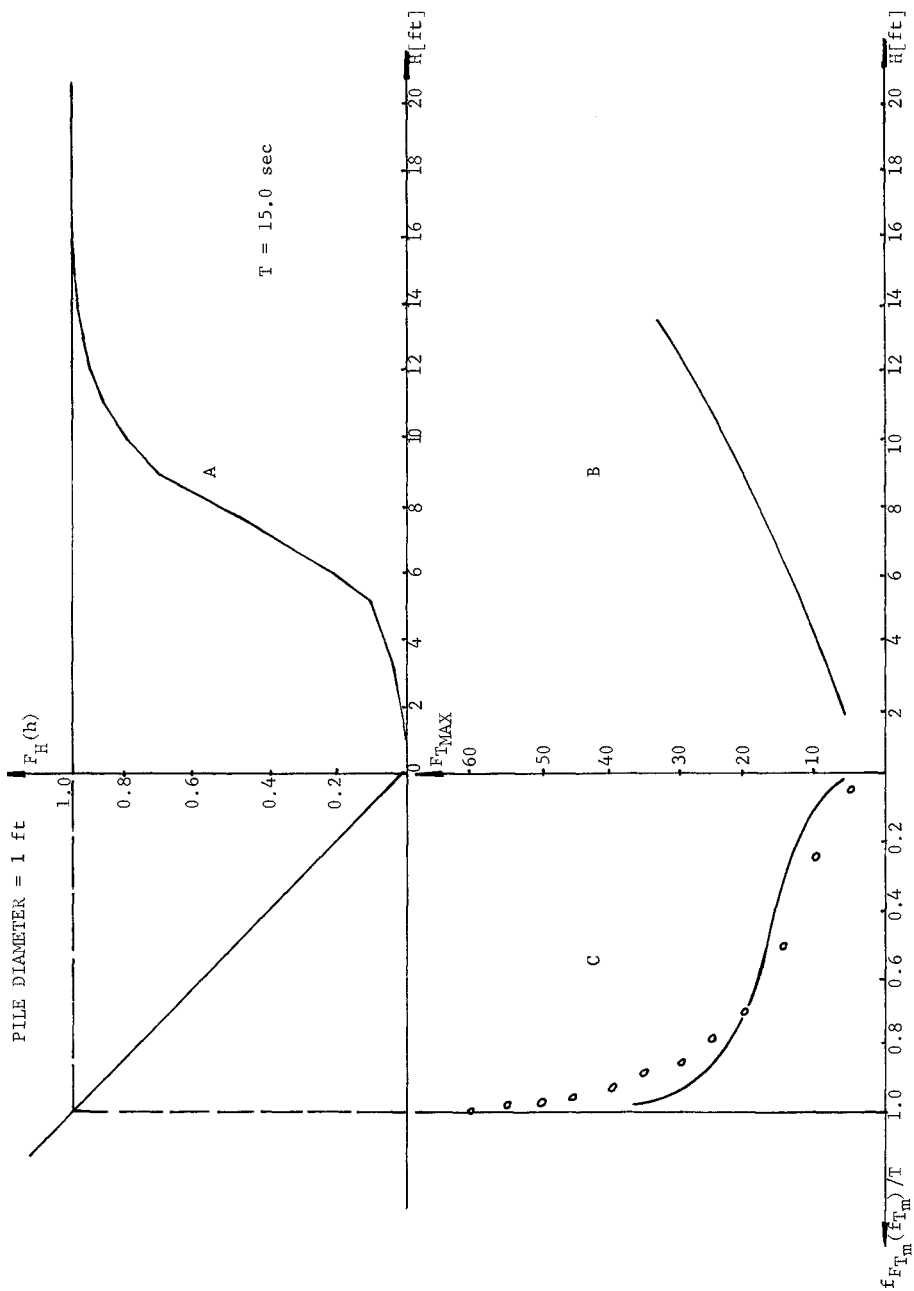

FIG. 7. CO-AXIAL DIAGRAM FOR RELATIONSHIP BETWEEN H, T, AND F_{MAX} FOR T = 15 SEC.

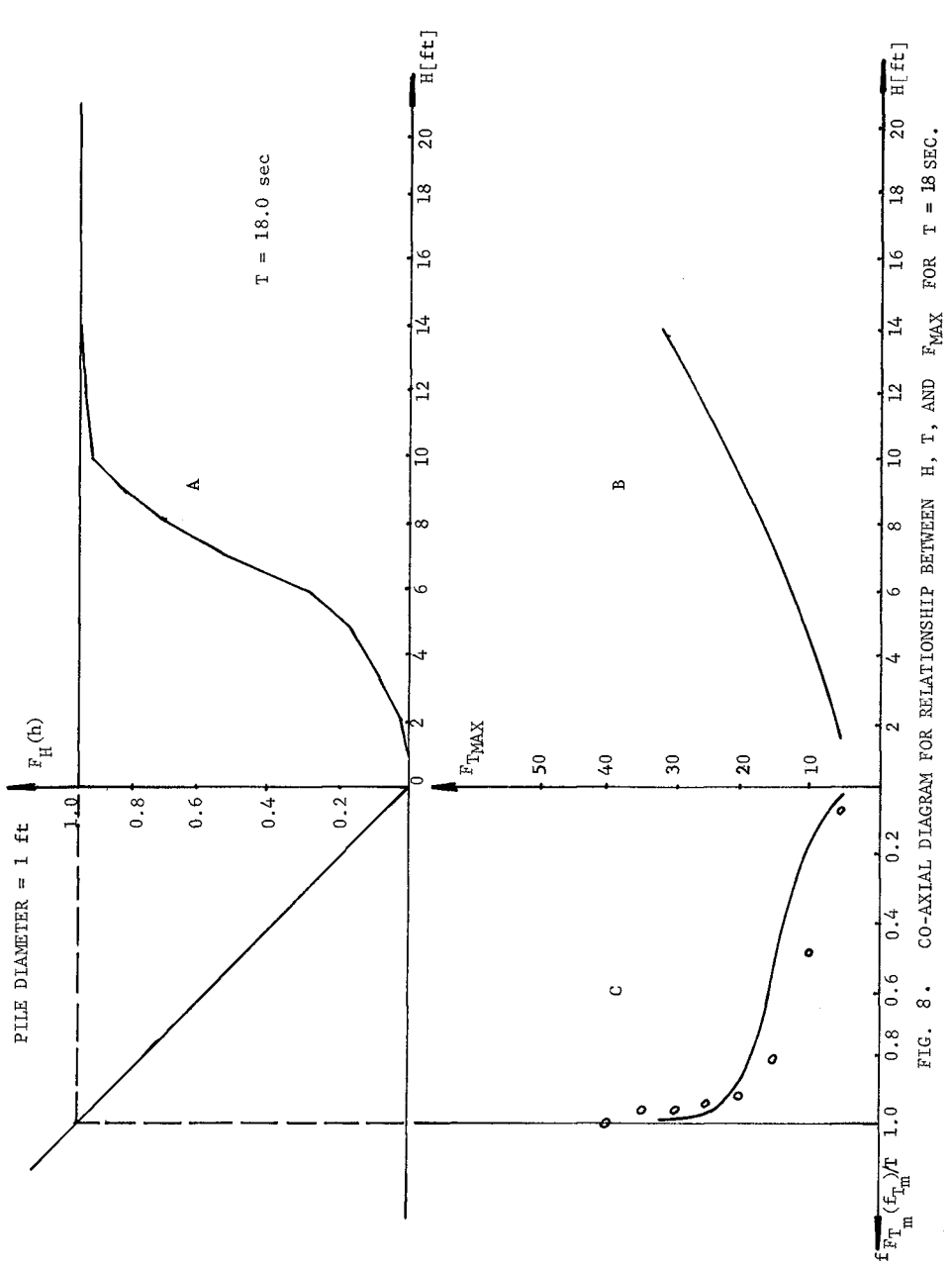

FIG. 8. CO-AXIAL DIAGRAM FOR RELATIONSHIP BETWEEN H, T, AND F_{MAX} FOR T = 18 SEC.

assumed to be lognormally distributed.

Unfortunately, the prediction equations developed are valid only for the range of the original data. The valid range of these prediction equations could be expanded considerably if data were available in other ranges. Currently, experimental data for water particle velocity, and acceleration are seriously lacking. Data are also needed for long-crested, low amplitude waves with large periods and for low amplitude waves with large water depths.

Although prior knowledge of the relationships between the wave particle velocity acceleration and other wave properties is known from linear and other wave theories, an extrapolation beyond the data cannot be justified.

In the development of the regression equation of the drag coefficient considerably more data were available. The big advantage of this equation is that it makes possible the development of a probability density function which is related to particular measured wave properties.

Experimental data used for the determination of the drag coefficient were taken at the still water level. If experimental data were available for different values of S (water particle depth) then a study of the variation of the drag coefficient for different mean water particle positions could be performed. This additional information would give much more insight into the problem.

The Monte Carlo simulation technique was employed to derive the maximum wave force probability density function using the regression equations previously developed.

Finally, a method was proposed which makes the creation of cumulative force distributions for given wave height distributions possible. For this purpose a probabilistic wave height-force relationship was developed. This method also takes the probability of occurrence of extreme waves into account. The agreement between the experimental data and the model is quite acceptable.

NOMENCLATURE

a ..... pile diameter

c^2 ..... mean square of H

C_D ..... coefficient of drag

C_M ..... coefficient of mass

d ..... water depth

D ..... pile diameter

$f_{F_{T_{max}}}(f_{T_{max}})$ ..... maximum wave force probability density function

F_T ..... total wave force

h ..... particular realization of H in Raleigh distribution

H ..... wave height

L ..... wave length

S ..... mean water particle depth

T ..... wave period

u ..... water particle velocity

ρ ..... fluid density

REFERENCES

1. Morison, J. R., O'Brien, M. P., Johnson, J. W. and Schaaf, S. A., 1950, "The Force Exerted by Surface Waves on Piles", Petroleum Transactions, Amer. Inst. Mining Engineers, Vol. 189, pp. 149-154.

2. Morison, J. R. and Crooke, R. C., 1953, "The Mechanics of Deep Water, Shallow Water, and Breaking Waves", Beach Erosion Board, Tech. Memo. No. 40, March 1953.

3. Elliot, J. H., 1953, "Interim Report", Calif. Inst. Tech., Hydro. Lab., Contract NOy-12561, July 1953. (Unpublished).

4. Wiegel, R. L., Beebe, K. E. and Barry, R. W., 1954, "Ocean Wave Forces on Piles", Technical Report Series 35, Issue 9, Inst. of Eng. Research, Univ. of Calif., Berkeley, September 1954.

5. Wiegel, R. L., 1964, "Oceanographical Engineering", Prentice-Hall, Inc., Englewood Cliffs, N. J.

6. Lé Mehauté, Divoky, D. and Lin, A., 1968, "Shallow Water Waves: A Comparison of Theories and Experiments", Tetra Tech, Inc., 630 North Rosemead Blvd., Pasadena, Calif., August 1968, 22 pp. (Unpublished report).

7. Schueller, G. I., 1972, "A Probabilistic Method for Predicting Velocities and Accelerations of Water Wave Particles", Offshore Technology Conference (1972), Paper No. OTC 1615.

8. Benjamin, J. R. and Cornell, C. A., 1970, "Probability Statistics and Decision for Civil Engineers", McGraw-Hill Book Company, New York.

9. Longuet-Higgins, M. S., 1952, "On the Statistical Distribution of the Heights of Sea Waves", Journal of Marine Research, Vol. 11, 1952, pp. 245-266.

10. Borgman, L. E., 1965 a, "Wave Forces on Piling for Narrow-Band Spectra", J. Waterways Harbors Div., Proc. ASCE, Vol. 91, No. WW3, Proc. Paper 4443, August 1965, pp. 65-91.

11. Russell, L. R. and Schueller, G. I., 1971, "Probabilistic Models for Texas Gulf Coast Hurricane Occurrences", Offshore Technology Conference (1971), Paper No. OTC 1344.

CHAPTER 95

WAVE FORCES ON SUBMERGED PIPE LINES

by

Ernest F. Brater[1] and Roger Wallace[2]

ABSTRACT

This is a presentation of the analyses of data obtained from a laboratory investigation of horizontal forces produced by oscillatory waves on submerged pipes. The research program was planned to help solve design problems for pipe lines located on or below the bottom in the oceans or the Great Lakes. The project was financed by the National Science Foundation.

A continuous record of wave height and horizontal force was obtained for pipes of four diameters, for three wave heights and three wave lengths. Forces were measured at four locations below the water surface, the lowest position being as near the bottom as possible. Other tests were conducted with the pipes located in various positions within trenches of several different shapes. The actual pipe diameters, wave heights and wave periods used in the laboratory tests were such that on the basis of a scale ratio of 1 to 75 the range of prototype parameters would include pipe diameters varying from 8 to 15 feet, wave heights varying from 8 to 23 feet and wave periods in the range from 6 seconds to 12 seconds. Results are presented in the form of coefficients of inertial resistance and drag which can be used with the Airy equations to compute forces.

INTRODUCTION

The increasing use of submerged pipelines for water intakes and sewer outfalls and for the transportation of oil, gas and other chemicals has created considerable interest and concern regarding the magnitudes of design forces. Not only are failures of such pipelines very costly but there is an increasing concern because of the almost irrepairable environmental damage that might occur. A review of various aspects of the problem has been presented by Ralston & Herbich (1969). In a summary of the various hazards to submerged pipelines, Ried (1954) has placed wave action at the top of the list. Grace (1971) has summarized previous research on this topic.

1 Professor of Hydraulic Engineering, Department of Civil Engineering, University of Michigan

2 Hydraulic Engineer, Michigan Water Resources Commission

The investigation of forces created by oscillatory waves on submerged structures was started at the University of Michigan Lake Hydraulics Laboratory with tests on a proposed off-shore drilling structure (Brater and Maugh, 1953). The first basic research effort dealt with forces on barge-like shapes (Brater, McNown & Stair, 1961). Interest in a second project dealing with forces on submerged pipelines arose because of the senior author's involvement in re-designing pipelines which had failed due to wave forces. Such failures occurred at depths of from 20 to 40 feet with the pipes exposed in trenches. Estimates of the necessary coefficients could be made from values determined for vertical piling (Morrison, Johnson & O Brien, 1954). However, because of the uncertainties involved the designs were probably somewhat conservative. The previous experience with research on wave forces indicated that a laboratory testing program would supply the necessary design information. Accordingly, application was made to the National Science Foundation for financial assistance. The grant was made and the research was carried out over a period of five years.

HYDRAULICS OF OSCILLATORY WAVES

The water motion associated with oscillatory waves is one of rotation in nearly closed circular or elliptical orbits. When wave motion is from left to right the orbital motion is clockwise. If one envisions a sinusoidal wave form* as sketched in Fig. 1, then phase angles (θ) can be used to designate points between successive crests. One can either visualize the motion at a point with respect to time (t) or instantaneous conditions at location (x) as indicated in Fig. 1. The time and horizontal space parameters can be combined into the following equations for θ and the water surface profile (y). In these equations L is the wave length and T is the wave period.

$$\theta = 2\pi \left(\frac{x}{L} - \frac{t}{T}\right) \tag{1}$$

$$y = \frac{H}{2} \cos \theta \tag{2}$$

The corresponding directions of water movement for any phase angle are as depicted by the solid arrows in Fig. 1. The orbital velocities create drag forces on submerged bodies of the form expressed by Eq. (3) in which A is the projected area

$$F_d = C_d \rho A \frac{u^2}{2} \tag{3}$$

on a plane perpendicular to u, C_d is the drag coefficient and ρ is fluid density. It will be seen that drag forces on a fixed body are in the direction of wave motions when a crest

---

* The water motion will be described and the force equations developed on the basis of the Airy theory. Thereafter some implications of the Stokes theory will be discussed.

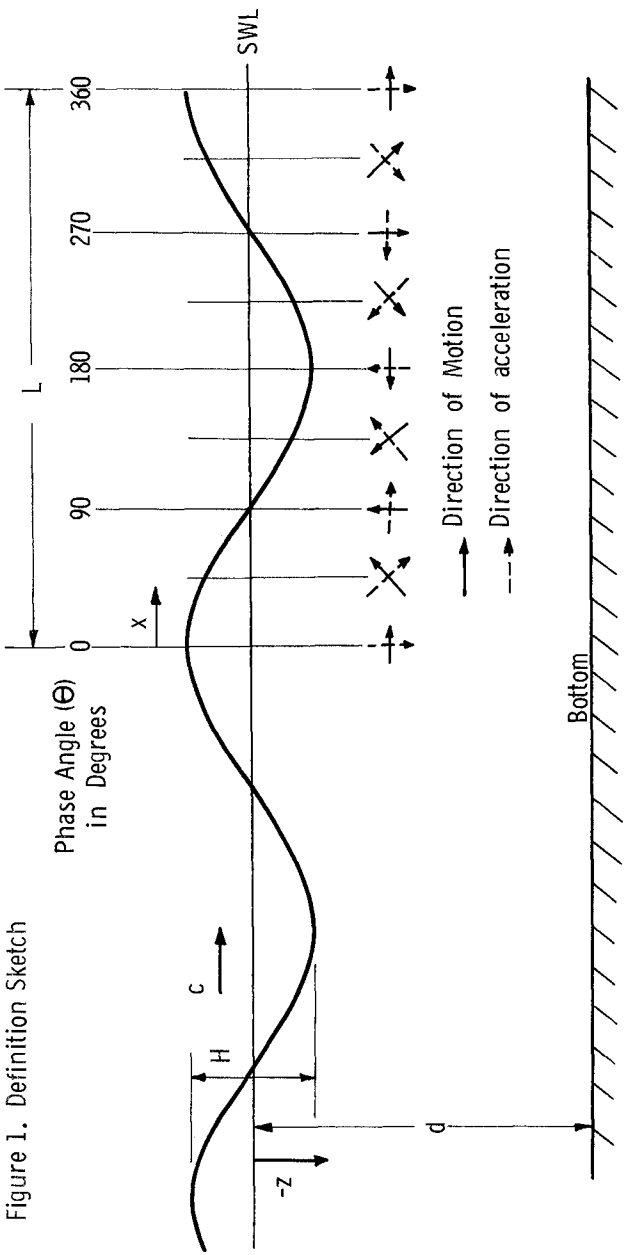

Figure 1. Definition Sketch

is above the body and that the drag force rotates in a clockwise direction thru 360 degrees with the passage of each wave. This variation in direction of the horizontal drag force is expressed analytically in terms of component in the x direction as shown by Equation (4).

$$F_{dx} = C_{dx} \rho A_x \frac{u_x^2}{2} \tag{4}$$

The value of u_x is given by Equation 5.

$$u_x = \frac{\pi H}{T} \frac{\cosh 2\pi (d+z)/L}{\sinh 2\pi d/L} \cos \theta \tag{5}$$

The other type of force produced by the orbital motion is caused by pressure differences and is called the inertial force (King and Brater, 1963). This is the force which would have been required to accelerate the fluid displaced by the solid body plus the additional force due to the flow disturbance caused by the presence of the solid body. This additional force is taken care of by including a coefficient of inertial resistance (C_m) in the expression for this force shown in Eq. (6), in which V is the volume of the submerged body. The

$$F_i = C_m \rho V \frac{\partial u}{\partial t} \tag{6}$$

amount that Cm exceeds unity may be thought of as related to the additional mass of fluid affected by the presence of the body and is sometimes called the coefficient of virtual mass, hence the use of the subscript m in on the coefficient. This force acts in the direction of wave motion for $\theta = 90^o$ and, as can be seen by the dotted arrows in Fig. 1, it is 90^o out of phase with the drag force. The horizontal component of the inertial force is shown by Eq. 7.

$$F_{ix} = C_{mx} \rho V \frac{\partial u}{\partial t} \tag{7}$$

The value of $\frac{\partial u_x}{\partial t}$ is given by Eq. (8).

$$\frac{\partial u_x}{\partial t} = \frac{2\pi^2 H}{T^2} \frac{\cosh 2\pi (d+z)/L}{\sinh 2\pi d/L} \sin \theta \tag{8}$$

Referring to Equations (4) and (7) and to Fig. 1 it may be seen that both forces have positive components in the x direction for $0 < \theta < 90$ and negative components in the x direction for $180 < \theta < 270$ thus creating the possibility that the maximum horizontal force (F_x) will be a combination

of F_m and F_d at intermediate phase angles. The expression for F_x is

$$F_x = F_{dx} + F_{ix} \tag{9}$$

Differention of F_x with respect to θ and setting the result equal to zero yields the following expression for the angle of maximum combined force.

$$\sin \theta_{max} = \frac{2C_m V}{C_d A_x H} \frac{\sinh 2\pi d/L}{\cosh 2\pi (d+z)/L} \tag{10}$$

One difficulty in dealing with Eqs. (4), (5), and (7) and (8) is that values of u and $\partial u/\partial t$ vary from point to point and therefore in estimating forces on submerged bodies a weighted average value of u and $\partial u/\partial t$ should be used. For the case of inertial forces on very large structures this problem has been solved conveniently by writing Eq. (7) in terms of pressure differences (Brater, McNown & Stair, 1962). For most pipelines the size of the structure is so small compared to stormwave lengths that the weighted average differs little from the value at the center of the body.

Perhaps the most troublesome decision that must be made in developing an analytical basis for computing wave forces is the choice of the theory to be used for computing u and $\partial u/\partial t$. The Airy equations which have been used in this discussion have the tremendous advantage of simplicity. Even though tables (Skjelbreia, 1958) have been developed which make it much easier to use the Stokes equations it would require a great improvement in accuracy to warrant the expenditure of the additional time. Actually the differences between computed values of orbital velocity and acceleration are small.

From the point of view of finding an adequate analytical approach for computing maximum wave forces the most important difference between the Airy and Stokes theories is the difference in the phase angles of the maximum acceleration. According to the Airy theory these phase angles (θ_m) are 90 and 270 degrees. Within the range of H, L and d for these tests, values of θ_m computed from the Stokes equations (Skjelbreia, 1958) are also 90° for downwave acceleration for L = 2.6 feet but for L = 4.1 feet θ_m varies from 86 to 88 degrees and for L = 6.7, θ_m varies from 72 to 83 degrees. This would mean that for large values of L a measured value of θ_m as small as 72 degrees might indicate that the maximum force is entirely of the inertial type and that F_d is negligible. This point becomes academic however, when one considers Eq.'s (4), (5), (7) and (8) for the case where θ is 72°. The value of $\sin 72^\circ$ is 0.95 and that of $\cos^2 72^\circ$ is 0.10. Therefore for

phase angles of 72^{o} the Airy theory would give practically the same answer whether the forces were computed from Eq. (9) including both types of forces or from Eq. (7) with $\sin \theta = 1$.

EXPERIMENTAL PROCEDURE

Waves were generated by a plunger type wave machine located near one end of a tank 93 feet long and 14 feet wide. The wave machine was capable of generating waves with heights as large as 0.35 feet and with periods as short as 0.7 seconds. A mat of plastic hair was placed behind the wave machine as well as at the opposite end of the tank to dampen reflections. Although this material is very efficient very small reflections were returned from the far end of the tank but in all cases the test run was completed before those reflections returned to the dynamometer.

The test specimen was suspended from a dynamometer located about 40 feet from the wave generator. The test specimens were 4.5 feet long. Additional pipe of the same diameter was mounted at either end of the test specimen so that the pipe extended for the full width of the wave tank except for the small gap between the test specimen and the dummy end sections. Horizontal forces exerted on the test specimens were transmitted to vertical cantilever beams upon which strain gages were mounted. The signals from the strain gages were amplified and recorded with a pen recorder. The dynamometer was calibrated for both up-wave and down-wave forces. The relation was nearly linear and varied little from one test to the next but was re-checked frequently during tests.

Wave heights were measured by a resistance gage located about six feet in front of the dynamometer and on the center line of the tank. The gage was calibrated by raising it and lowering it known amounts, within the tank at its permanent location. The calibration changed very little but was checked frequently. Its output was recorded by pen on an oscillograph chart. A hook gage mounted on the same truss as the wave gage was used to check the water surface elevation in the tank. The time relation of horizontal forces to wave form was determined by mounting a second wave gage above the center of the test specimen. The output from this gage was recorded on the same chart as the wave force trace.

The wave period was determined from the wave trace knowing the rate of movement of the chart paper. Wave lengths were then computed from the periods. It was also necessary to run force tests to determine the corrections for the forces on the portion of the dynamometer which extended below the water surface. Even though this portion of the dynamometer was slender the forces were sufficient to require a small correction particularly when the specimen was located near or below the bottom. Several experimental difficulties were

encountered in conducting these tests. Fully 80 per cent of the time was spent in eliminating problems which affected the quality of the results. The most difficult problem was that of extraneous input to the force recorder. This was solved only after the measurement of vertical forces was abandoned and an electronic filter was installed in the system.

EXPERIMENTAL PROGRAM

A continuous record of wave height and horizontal force was obtained for pipes of four diameters, for three wave heights and three wave lengths. For each set of test parameters forces were measured at four locations (-z) below the water surface, the lowest position being as near the bottom as possible. Other tests were made with pipes placed in various locations in trenches of several different shapes. The water depth was kept at one foot at all times. Numerical values of the parameters are shown in Table 1.

TABLE 1

TEST PARAMETERS

Pipe Diameters (D) in ft.	0.104	0.140	0.159	0.198	
Wave Heights[1] (H) in ft.	0.11	0.21	0.31		
Wave Lengths[1] (L) in ft.	6.1	4.1	2.6		
Distances Below Water Surface[1] (-z/d)	0.25	0.50	0.75	0.96[2]	1.2[3]

(1) These are typical values for each group. Individual values varied slightly.
(2) Pipe very near the bottom.
(3) Pipe in a trench.

The only conditions in this array that were not tested were the cases of the largest wave height (.31') combined with the shortest wave length (2.6') which resulted in waves which were very steep and unstable. The ranges of the ratios of wave height, depth and pipe diameter to the wave length were $.016 < H/L < .081$, $.149 < d/L < .385$ and $.016 < D/L < .076$ respectively.

The tests conditions for pipes located in trenches are illustrated in Fig. 2. The condition shown in Fig. 2a simulates a pipe half burried in the bottom. Figures 2b and 2c show conditions which are similar to those that might exist in an open trench. The various circles in Fig. 2(b)

Figure 2. Types of Trenches

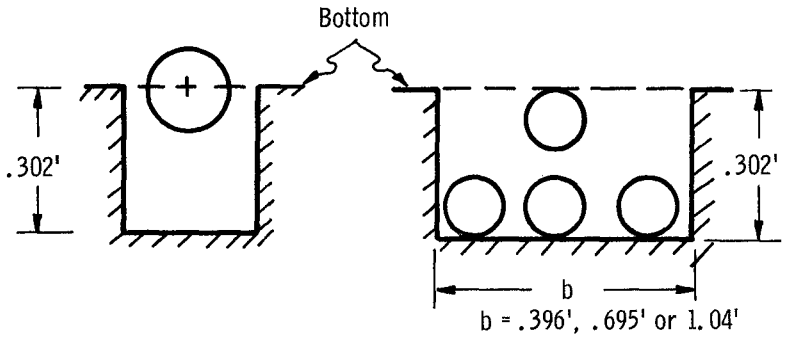

(a) (b)

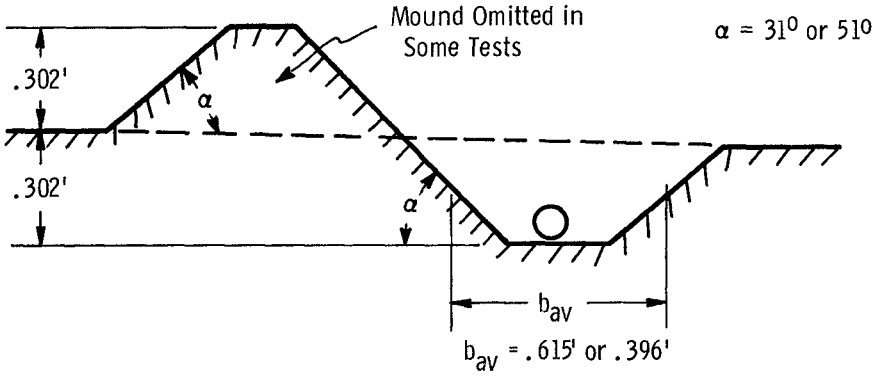

(c)

show the locations at which the pipe was placed. With the pipes in a trench, a full range of wave parameters was tested only for a pipe diameter of 0.159 feet but a limited number of parameters were studied for the other three diameters.

ANALYSIS OF RESULTS

Phase Angles of Maximum Forces. The phase angles (θ_p) at which the positive or the down-wave forces are a maximum would be expected to occur in the range from 0 to 90 degrees based on the Airy theory and phase angles at the maximum negative or up-wave forces (θ_n) in the range from 180 to 270 degrees. This is illustrated in Figure 3 which shows computed values of Fd and Fi as well as measured and computed values of (F_d+F_i) for conditions from Test 83. The measured value θ_p and θ_n were 63° and 250° respectively. In the interest of simplicity, only θ_p will be used in this discussion. Average measured values of θ_p for the various diameters varied from 65° for the smallest diameter to 77° for the largest.

It was found that the dimensionless number, D^2/HL, is a useful parameterin decidingwhether θ_p or θn would differ substantially from the phase angle of the maximum inertial force. Values of θ_p are plotted against D^2/HL in Fig. 4. This criterion is not the complete answer because as shown by the symbols one can detect slightly different trends for different pipe diameters. Yet, the relation is good enough to indicate for example that when $D^2/HL < .025$, θ_p may be less than 65° and the drag force should be included in the computations for the maximum force.

Coefficients of Inertial Resistance. Because the inertial force as given by Eq. (6) is usually the predominant force, values of the coefficient of inertial resistance (C_m) were considered as the most important contribution of the research program. Values computed from Eq. (7) from the average forces at $\theta = 90°$ and 270° were called CM. These values might be considered the true values of C_m except that it has been shown in the previous discussions that the maximum positive acceleration probably occurs at an angle somewhat smaller than 90° in many cases.

Another set of values of C_m was computed from Eq. (7) using the average of the maximum positive and negative forces. These were called CMM. The positive forces were sometimes greater and sometimes less than the maximum negative forces. The differences of the averages of the maximum positive or maximum negative forces from the average for both directions varied from 3.3 per cent for the smallest pipe diameter to 1.6 per cent for the largest diameter. In all cases the average of the

Figure 3. Measured and Computed Forces

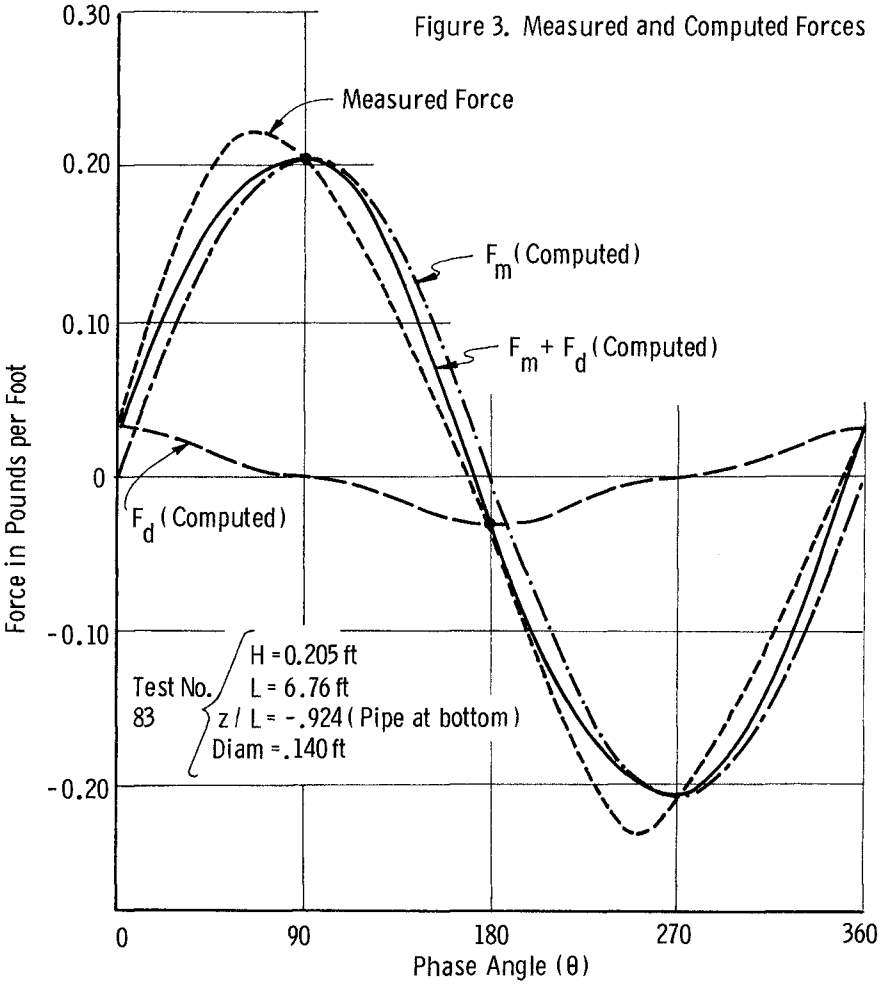

Figure 4. Phase Angles of Maximum Positive Forces

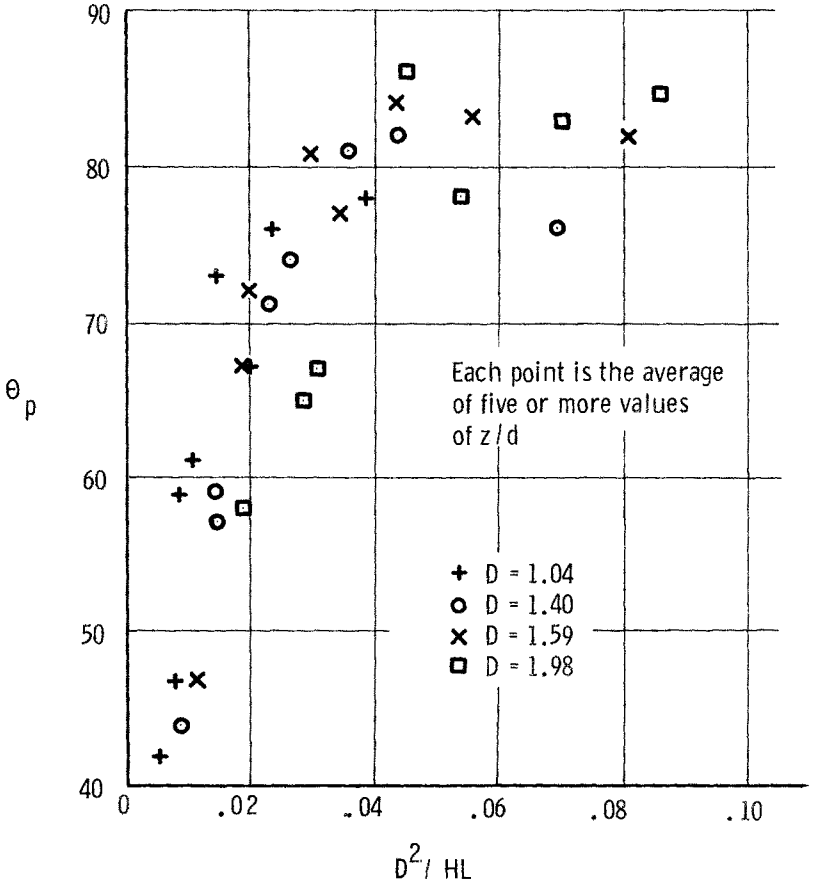

negative forces was greater than the average of the positive forces. The values of CMM could be used to estimate the average total force, assuming the drag force to be negligible.

Another set of values of C_m was derived from the maximum forces obtained from each test and irregardless of the direction of the force. These coefficients were designated as CMMM. They might be used for conservative estimates of the maximum forces assuming the drag forces to be negligible.

In considering various ways of presenting the derived values of C_m it was found that values were relatively independent of D and H but varied in a very orderly linear manner with z/L. Therefore this method of presenting the data was selected. A computer program was written to determine the optimized least square fit for the points in various categories. The values determined were the slope (m), the intercept (b), the linear correlation coefficient (r) and the standard deviation from the regression (S_r). The first six lines of Table 2 give the coefficients for three locations above the bottom. The four pipe diameters were analyzed separately, then all diameters together and finally all diameters except the smallest (D = 0.104). In all cases all three wave heights are included in each category. The next category includes all diameters and wave heights with the pipe very near the bottom (line 7, Table 2). Values of z/d differ somewhat for this category because of the differences in pipe diameters, z being the distance from the water surface to the center of the pipe. Therefore -0.9 is a nominal value of z/d. The final category, for which coefficients are given in line 8, represents a half buried pipe for all diameters and wave heights.

The linear correlation coefficients (r) are measures of the likelihood that the sets of points should be represented by the least squares linear equation. Values of r_1 shown in the table represent one per cent confidence limits which suggest the value of r for which the likelihood that it could be achieved accidentally is only 1 in 100. Since the values of r for these tests are all very much larger than values of r_1 one must conclude that it is no accident that the groups of values of C_m and - z/L are fitted by straight lines. The values of S_r shown in Table 2 are for the equations representing CMM. The values of S_r for CM and CMMM were very similar in magnitude.

In the categories for $0.25 < -z/d < 0.75$ for the four diameters there are 12 equations (lines 1 thru 4 in Table 2) representing four pipe diameters and three ways of computing C_m. If one were to plot all of these they would, with two exceptions fall very near together. The two exceptions are CMM and CMMM for the smallest pipe diameter (0.104).

Table 2

CORRELATIONS OF C_m WITH z/L

		CM					CMM					CMMM					
D (Ft)	z/d	b	m	Eq. No.	r	r_1	b	m	Eq. No.	r	r_1	b	m	Eq. No.	r	r_1	S_r
.198	-0.25 to -0.75	1.37	6.56	11	0.88	0.39	1.59	5.82	12	0.87	0.39	1.79	5.33	13	0.81	0.39	0.26
.159		1.41	6.36	14	0.83	0.46	1.69	5.41	15	0.79	0.46	1.91	4.96	16	0.72	0.46	0.33
.140		1.26	5.87	17	0.86	0.48	1.56	5.50	18	0.84	0.48	1.75	5.22	19	0.81	0.48	0.26
.104		1.49	6.65	20	0.90	0.49	2.04	5.32	21	0.82	0.49	2.38	4.84	22	0.72	0.49	0.26
All		1.38	6.36	23	0.85	0.23	1.73	5.37	24	0.79	0.23	1.97	4.87	25	0.69	0.23	0.32
All except .104		1.34	6.41	26	0.85	0.25	1.61	5.64	27	0.84	0.25	1.81	5.22	28	0.78	0.25	0.29
All	-0.9	2.59	4.83	29	0.63	0.37	3.07	4.13	30	0.57	0.37	3.20	4.16	31	0.57	0.37	0.52
All	-1.0	0.83	3.11	32	0.74	0.42	1.01	2.85	33	0.70	0.42	1.14	2.78	34	0.60	0.42	0.25

m and b are coefficients in the equation $C_m = b + m\ (-z/L)$

r is the linear correlation coefficient

r_1 is the value of r for a one per cent confidence limit

S_r is the standard deviation from the regression

CM, CMM and CMMM are values of C_m derived as described in the text.

This is to be expected because as shown in the previous section it is only for the smallest sizes that drag forces tend to make an important contribution to the maximum total forces. It might be concluded that the following equations (line 6 of Table 2) for all values of D except D = .104' may be used when $D^2/HL < .02$.

$$CM = 1.34 + 6.41\ (-z/L) \quad (26)$$

$$CMM = 1.61 + 5.64\ (-z/L) \quad (27)$$

$$CMMM = 1.81 + 5.22\ (-z/L) \quad (28)$$

For small sizes, where $D^2/HL < .02$, it would be better to use the Equations (20), (21) and (22) (line 4 of Table 2) derived for the smallest diameter, D = 0.104'. It may be questioned whether such refinements are desirable or necessary because the differences among the various equations are probably very small compared with uncertainties in the selection of a design wave. It would be quite appropriate for design purposes to use Equations (23), (24) and (25) (line 5 of Table 3) derived for all diameters irregardless of any size criterion.

The equations for the pipe on the bottom (z/d = -0.9) have excellent correlation coefficients. The standard deviations from the regressions are somewhat larger than for the other equations. These equations have much practical importance because they provide design values for the most vulnerable position in which a pipe can be placed. The equation numbers and coefficients are presented in line 7 of Table 2.

Equations (32), (33) and (34) (line 8, Table 2) give values of Cm for the case of a half buried pipe (z/d = -1.0). It should be noted that in computing values of C_m from the test data by means of Eq. (7) the volume was taken as the entire volume of the pipe. Forces computed in this same manner would include the assumption that pressure differences would penetrate the bed material at least to the bottom of the half buried pipe.

The equations for C_m which apply when the pipes are located in trenches of various shapes were not computed by means of a least squares procedure because most of the data were obtained for z/L of about -0.29 (32 tests). A smaller number of values were obtained for a z/L of approximately -.19 (six tests) and z/L = -.47 (four tests). It was assumed that the relationship would be similar to the ones obtained for the other eight categories. Therefore the large number of tests for a z/L of about -0.29, for which the average value of CMM was 1.42, was used to determine the location of the line. The less well defined values for z/L = -.19 and -.47 respectively were used to determine the slope. In this manner the following equation was derived for pipes in a trench.

$$CMM = 1.0 + 1.4\ (-z/L) \quad (35)$$

The values of CM and CMMM appears to be smaller and larger than CMM respectively in about the same proportions as for all of the other categories. It did not seem to be worthwhile to try and distinguish differences between coefficients for various shapes of trench or positions of the pipes within the trench. It appeared that when the width of the trench was about 7 times the pipe diameter that conditions were approaching those without a trench.

In order to provide a visual presentation of the relation of the relationships for various conditions all of the Equations for CMM are plotted in Figure 5.

Drag Coefficients. It has been shown in the previous sections that the drag forces play a much less important role in determining the total maximum horizontal forces than do the inertial forces. However, there are situations in which the quantity D^2/HL is very small (less than 0.02) in which it may be desirable or necessary to include the drag force. The drag coefficients were plotted against the Reynolds number (R) which was defined as shown by Eq. (36) in which D is the pipe diameter, u is the orbital

$$R = \frac{Du}{\upsilon} \tag{36}$$

velocity and υ the kinematic viscosity. The plotted points showed definite trends but were widely scattered. It should be recalled that the drag coefficients were determined from forces at phase angles of 0 to 180 degrees. Since the forces were relatively small at these phase angles and also changing rapidly it might be expected that measured forces might have errors that are larger than in the measured values of the maximum or near maximum forces. It was found that for the range of z/L from -0.25 to -0.75 the points needed to be plotted separately for different values of d/L, but that for each value of d/L the full range of wave heights and pipe diameters could be included. An example is shown in Fig. 6 in which the plotted points are for a nominal value of d/L of 0.24. The solid line was plotted thru these by judgement. On the same graph are also shown the lines but not the points obtained in the same manner for nominal values of d/L of 0.16 and 0.38.

For the case of the pipe on the bottom the values of C_d for all values of d/L were plotted together as shown in Fig. 7. Symbols were used which identify the values of D and d/L for each point. The line representing these points was drawn by judgement.

A similar plotting for the case where the pipe is half burried (z/d = -1) is shown in Figure 8. These groups of points included all values of d/L. In all cases the value of Ax in Eq. (6) was taken as the entire area of the pipe and values of R were always computed using the full diameter. This creates an anomaly for the half burried pipe. One can either use the total pipe area as was done here or use only the exposed area

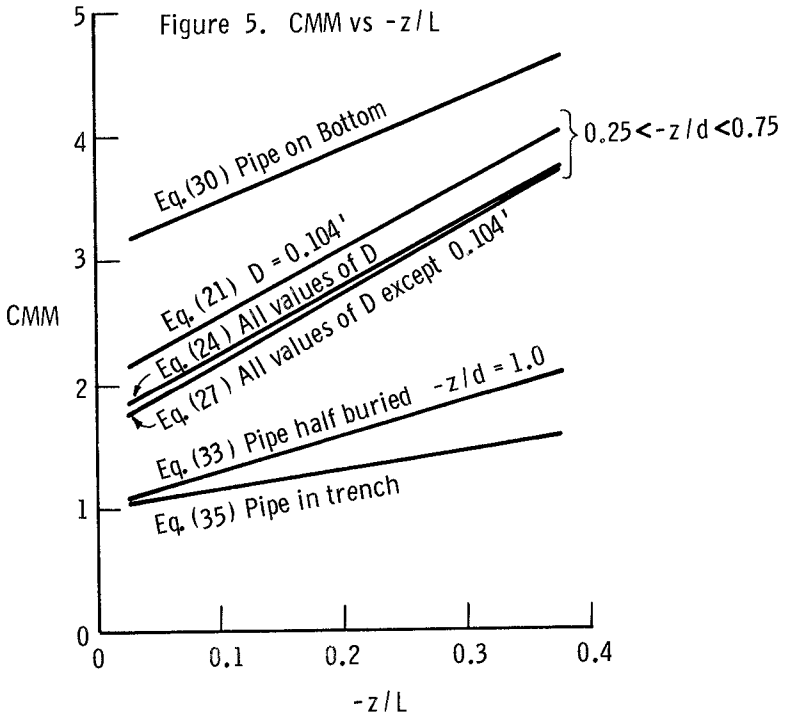
Figure 5. CMM vs -z/L
CMM
-z/L
Eq. (30) Pipe on Bottom
Eq. (21) D = 0.104'
Eq. (24) All values of D
Eq. (27) All values of D except 0.104'
Eq. (33) Pipe half buried -z/d = 1.0
Eq. (35) Pipe in trench
0.25<-z/d<0.75
0
1
2
3
4
5
0
0.1
0.2
0.3
0.4

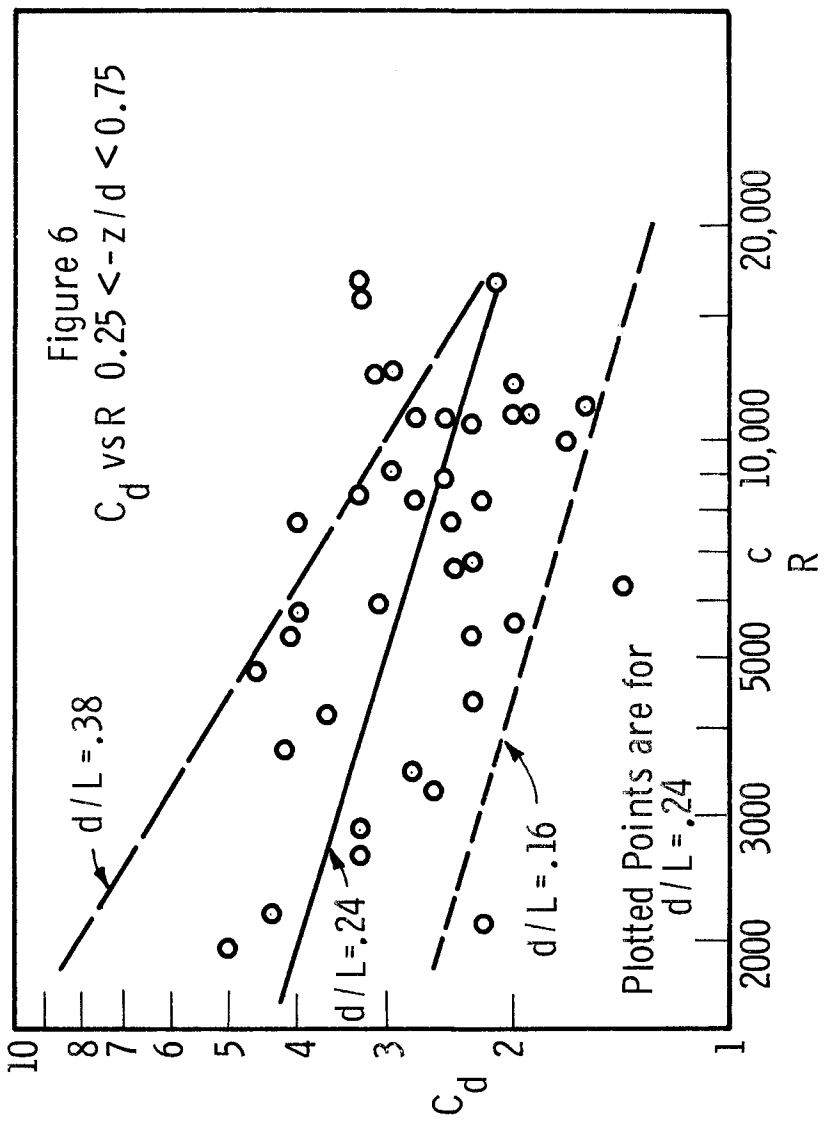
Figure 6
C_d vs R 0.25 < -z/d < 0.75
d/L = .38
d/L = .24
d/L = .16
Plotted Points are for
d/L = .24
C_d
R
10
8
7
6
5
4
3
2
1
2000
3000
5000
10,000
20,000

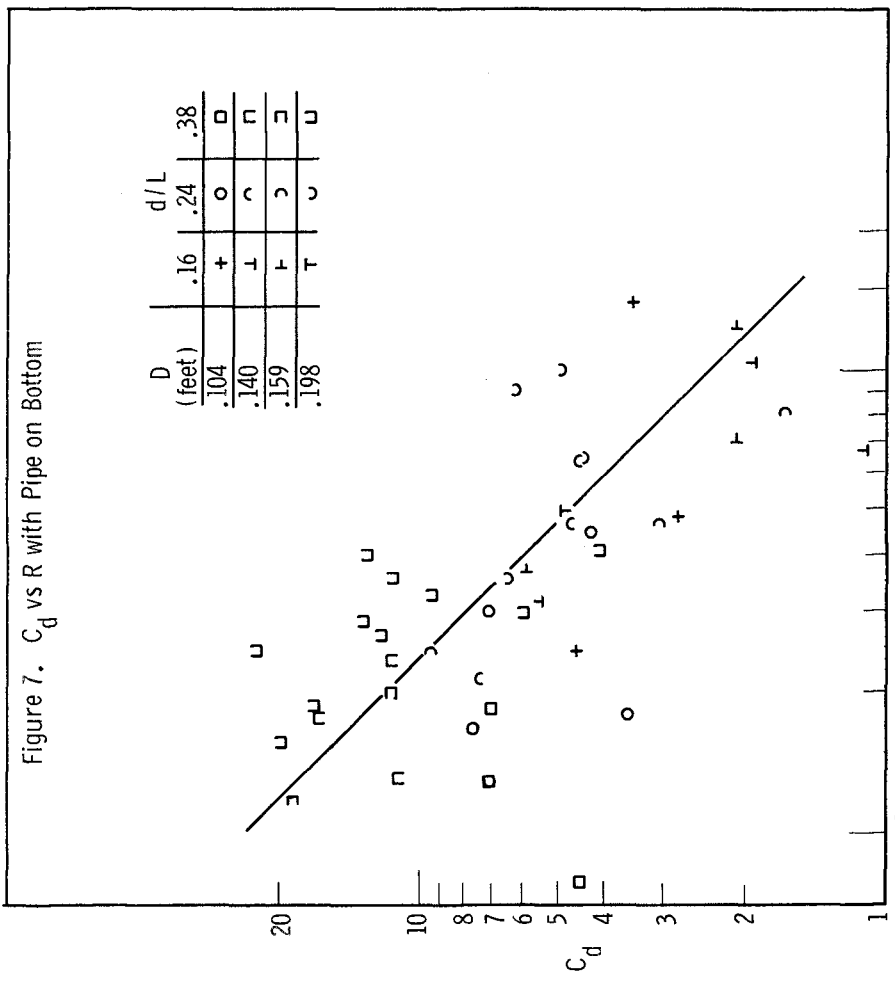

Figure 7. C_d vs R with Pipe on Bottom

and double the values of C_d. Similar lines, but not the points, representing values of C_d for the pipe located in a trench are also shown in Fig. 8.

SUMMARY AND APPLICATIONS

Coefficients of inertial resistance for use in Eqs. (7) or (9) and drag coefficients to be used in Eqs. (4) or (9) were derived for a wide range of pipe diameters, wave heights, wave lengths and pipe locations. Results were plotted against dimensionless parameters which make them suitable for use in practical design problems. The tests showed that the inertial force as given by Eq. (7) predominated but that in the smallest pipe size tested the drag forces were producing noticeable contributions. This could be recognized by the deviation of the phase angles of the maximum forces from those of the maximum inertial forces. The parameter D^2/HL was used to indicate the type of force which is active. When $D^2/HL < 0.02$ the drag forces became important. The coefficients of inertial resistance computed from the average of the maximum positive and negative forces (CMM) or those computed from the maximum force (CMMM) are the most usefull for practical applications. In the range covered by these tests either CMM or CMMM could be used with Eq. (7) to estimate design forces without including a component of the drag force.

REFERENCES

1. Brater, E. F. and L. C. Maugh, "Model Study of an Offshore Drilling Structure," Tech Rept. No. 6, Lake Hydraulics Lab, Dept. of Civil Eng., University of Michigan, 1953.

2. Brater, E. F., John S. McNown and L. D. Stair, "Wave Forces in Submerged Structures, " Trans. ASCE, Vol. 126, 1961.

3. Grace, R. L.,"Submarine Pipeline Design Against Wave Action," LookLab/Hawaii, Univ. of Hawaii, Vol. 2, No. 2, 1971.

4. King, H. W. and E. F. Brater, "Handbook of Hydraulics," McGraw-Hill Book Co., Inc. 1963, pp. 10-44 to 10-51.

5. Morrison, J. R., J. W. Johnson and M. P. O'Brien, "Experimental Study of Forces on Piles," Proc. 4th Conf. on Coastal Eng., Engineering Foundation, 1954.

6. Ralston, Derwood O., and John B. Herbich, "The Effects of Waves and Currents on Submerged Pipelines," Sea Grant Publ. No. 101, Texas A. & M. University, 1969.

7. Ried, R. O., "Oceanographic Consideration in Marine Pipeline Construction," Contributions in Oceanography and Meteorology, Texas A. & M. University, No. 3, 1950-54.

8. Skjelbreia, Lars, "Gravity Waves, Stokes Third Order Approximation, Table of Functions," Council on Wave Research, Engineering Foundation, 1958.

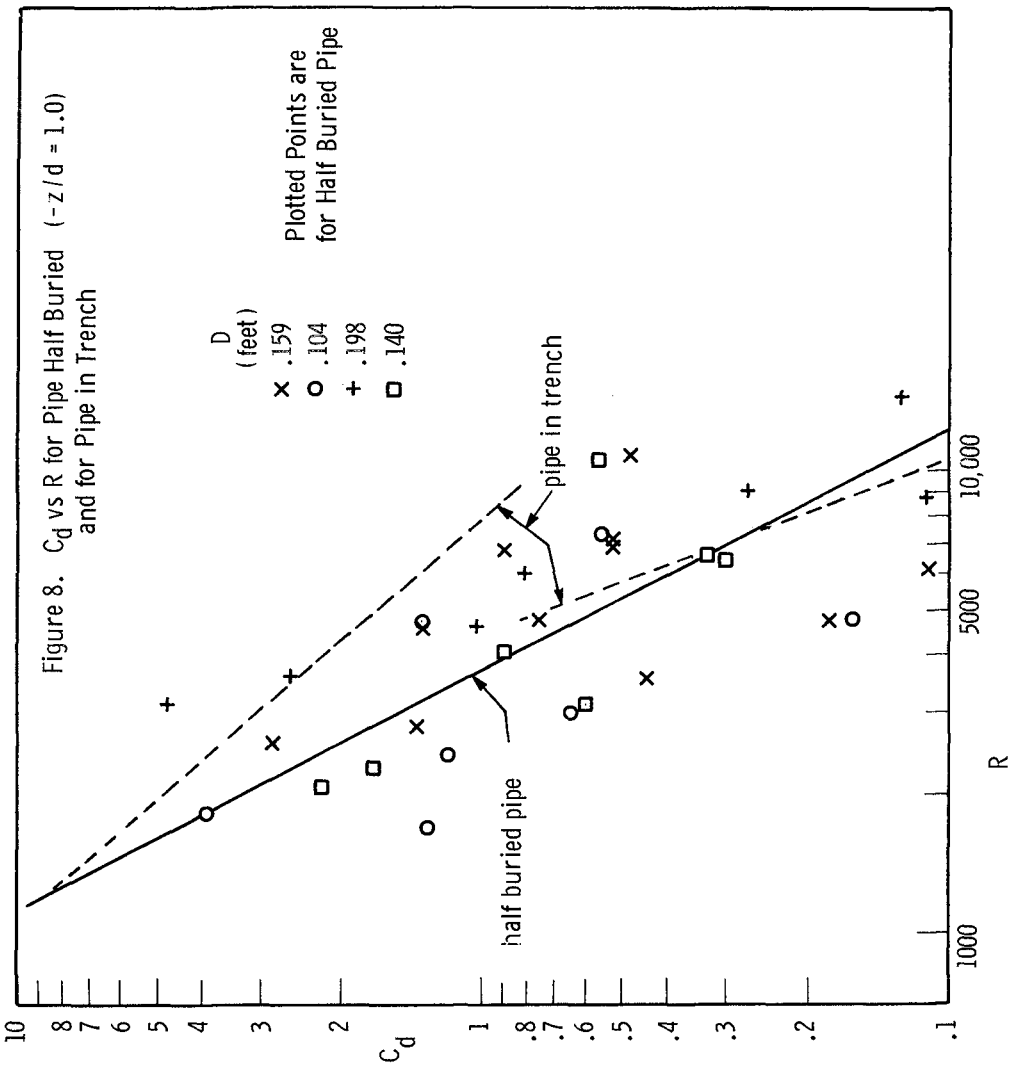
Figure 8. C_d vs R for Pipe Half Buried (-z/d = 1.0) and for Pipe in Trench
Plotted Points are for Half Buried Pipe
D (feet)
× .159
o .104
+ .198
□ .140
pipe in trench
half buried pipe
C_d
R
10
8
7
6
5
4
3
2
1
.8
.7
.6
.5
.4
.3
.2
.1
1000
5000
10,000

CHAPTER 96

WAVE FORCE ON A VESSEL TIED AT OFFSHORE DOLPHINS

Yoshimi Goda
and
Tomotsuka Yoshimura

Marine Hydrodynamics Division, Port and Harbour Research Institute, Ministry of Transport, Nagase, Japan

ABSTRACT

The solution of wave scattering by a vertical elliptical cylinder is applied to calculate the wave forces exerted upon it. The wave forces in the directions of long and short axes of ellipsis are shown in nondimensional forms as the functions of the angle of wave approach, the diameter-to-wavelength ratio, and the aspect ratio of ellipsis. The results of wave force computed are also shown in terms of the virtual mass coefficients associated with the reference volume of the circular cylinder the diameter of which is approximately equal to the apparent width of the elliptical cylinder observed from the direction of wave approach.

Theory is further applied for the wave forces acting upon a vessel moored tight at offshore dolphins and the forces transmitted to the dolphins through the vessel. The vessel is approximated with the fixed elliptical cylinder having the same width-to-length ratio. The computation with directional wave spectra shows that a tanker of 200,000 D.W.T. may exert the force of about 1,400 tons at the one-third maximum amplitude to each breasting dolphin when the tanker is exposed to the incident waves of $H_{1/3}$=1.0m and $T_{1/3}$=10 sec from the broadside.

INTRODUCTION

Modern tankers and ore carriers are in a steady increase in their size in order to lower the transportation cost of their cargo. A number of berthy facilities for them have recently been constructed in the offshore. The berthing facilities are called sea berths.

Engineers examine the conditions of winds, waves, tidal currents, tides, soils, and earthquakes in the design of a sea berth, but the major design load usually comes from the impact of ship's berthing or the earthquake force. The wave forces acting upon breasting dolphins through the vessel moored are not taken into design in spite of their apprehended importance, because their magnitude has yet been uncertain.

When a tanker with the length of 300 to 400 m is moored at a sea berth, it behaves like a kind of an insular breakwater and is expected to receive

large wave forces. The forces must be transmitted to the dolphins. Thus, the wave forces can be one of major design factors for offshore dolphins.

The authors have previously derived the solution of wave scattering by a vertical, elliptical cylinder, and have confirmed its validity for the case of insular breakwaters through several experiments.[1] The solution is extended in this paper to yield the wave forces exerted upon an elliptical cylinder. The solution is applied for wave forces upon a vessel, the geometry of which is approximated with the elliptical cylinder having the same aspect ratio. The vessel is also assumed to be tightly fixed at two breasting dolphins. Computation of wave forces are made for incident waves having directional spectrum. The computed irregular forces are shown with the one-third maximum value as the representative of the force spectra.

SOLUTION OF SCATTERED WAVES BY AN ELLIPTICAL CYLINDER

The potential theory is presumed in order to solve the scattering of small amplitude waves. From the presumption, the fluid motion and boundary conditions are expressed as

$$\frac{\partial^2 \Phi}{\partial x^2} + \frac{\partial^2 \Phi}{\partial y^2} + \frac{\partial^2 \Phi}{\partial z^2} = 0 \qquad \text{(in fluid)} \tag{1}$$

$$\left.\begin{aligned} \frac{\partial \zeta}{\partial t} &= \left(\frac{\partial \Phi}{\partial Z}\right)_{z=0} \\ \zeta &= -\frac{1}{g}\left(\frac{\partial \Phi}{\partial t}\right)_{z=0} \end{aligned}\right\} \qquad \text{(on water surface)} \tag{2, 3}$$

$$\frac{\partial \Phi}{\partial n} = 0 \qquad \text{(on the obstacle surface and the sea bottom)} \tag{4}$$

where x and y are the coordinates on the still water surface, z is the coordinate measured from water surface positive upward, ζ is the water surface displacement, g is the acciration of gravity, and n is the coordinate normal to the boundary surface.

The velocity potential Φ which satisfies the boundary condition at the sea bottom is expressed as

$$\Phi = \phi_0 \phi \cosh k(h+z) \exp(i\sigma t) \tag{5}$$

where ϕ_0 is a constant, ϕ is a function describing the profile of water surface, $k=2\pi/L$, $\sigma=2\pi/T$, L is the wavelength, T is the wave period, and h is the water depth.

The relation among wave period, wave length and water depth is derived from Eq. (2), (3) and (5) as

$$\sigma^2 = g\, k \tanh kh \tag{6}$$

By the substitution of Eq. (5) into Eq. (1)

$$\frac{\partial^2 \phi}{\partial x^2} + \frac{\partial^2 \phi}{\partial y^2} + k^2 \phi = 0 \tag{7}$$

In the case that the boundary is represented with a vertical elliptical cylinder the problem is better treated by transfering the coordinates (x, y) with the elliptical coordinates (ξ , η) shown by Fig. 1 as

$$\left.\begin{aligned} x &= \frac{B}{2} \cosh \xi \quad \cos \eta \\ y &= \frac{B}{2} \sinh \xi \quad \sin \eta \end{aligned}\right\} \tag{8}$$

where B is the distance between the focuses of the ellipsis. By using Eq. (8) Eq. (7) is transformed as

$$\frac{8}{B^2(\cosh 2\xi - \cos 2\eta)} \left(\frac{\partial^2 \phi}{\partial \xi^2} + \frac{\partial^2 \phi}{\partial \eta^2}\right) + k^2 \phi = 0 \tag{9}$$

The water surface function ϕ can be expressed with the addition of ϕ_{in} of the incoming waves and ϕ_{sc} of the scattered waves by the principle of linearity. Since $\lim_{\xi \to \infty} \phi_{sc} = 0$, both ϕ_{in} and ϕ_{sc} must be the solution of Eq. (9).

Presuming that ϕ is expressed as the product of the function $R(\xi)$ of only ξ and $Q(\eta)$ of only η , Eq. (9) is

$$\frac{d^2R}{R\, d\xi^2} + 2k_1^2 \cosh 2\xi = -\frac{d^2Q}{Q\, d\eta^2} + 2k_1^2 \cos 2\eta = A \tag{10}$$

In Eq. (10) A is the characteristic number which is determined with only k_1^2 , where $k_1 = B\, k/4 = \pi B / 2L$.

Equation (10) can be separated into two equations for $R(\xi)$ and $Q(\eta)$.

$$\frac{d^2Q}{d\eta^2} + (A - 2k_1^2 \cos 2\eta)\, Q = 0 \tag{11}$$

$$\frac{d^2R}{d\xi^2} - (A - 2k_1^2 \cosh 2\xi)\, R = 0 \tag{12}$$

When $\eta = \eta^* + n\pi$ is substituted into η in Eq. (11), the form of the equation does not change. Therefore, one of the solutions of Eq. (11) has a periodic function with the period of π or 2π . When $\eta = \xi / i$ is substituted into η in Eq. (11), Eq. (11) become the same equation with Eq. (12). Thus the solutions of either equations, (11) or (12), immediately yield the solutions of another. Equations (11) and (12) are the Mathieu differential equation and the moditied Mathieu differential equation.[2)]

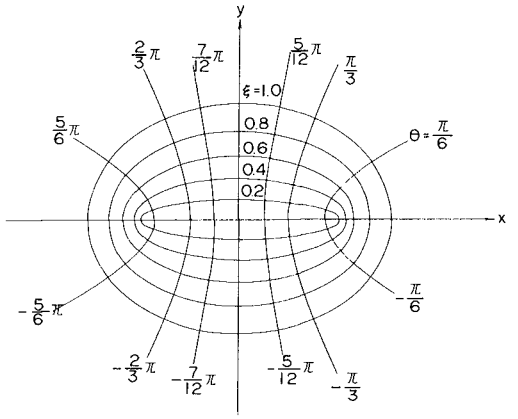

Fig. 1 Elliptical coordinates

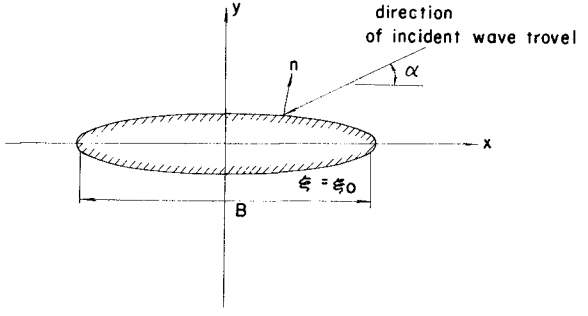

Fig. 2 Elliptical cylinder and direction of incident wave travel

When the incident waves approach the elliptical cylinder from the direction shown in Fig. 2, the waves are expressed as the series of the solutions of Eq. (11) and (12).

$$\phi_{in} = \sum_{n=0}^{\infty} \left[\frac{2}{p_{2n}} Ce_{2n}(\xi)\, ce_{2n}(\eta)\, ce_{2n}(\alpha) \right.$$

$$+ \frac{2}{s_{2n+2}} Se_{2n+2}(\xi)\, se_{2n+2}(\eta)\, se_{2n+2}(\alpha)$$

$$+ i \left\{ \frac{2}{p_{2n+1}} Ce_{2n+1}(\xi)\, ce_{2n+1}(\eta)\, ce_{2n+1}(\alpha) \right.$$

$$\left. \left. + \frac{2}{s_{2n+1}} Se_{2n+1}(\xi)\, se_{2n+1}(\eta)\, se_{2n+1}(\alpha) \right\} \right] \tag{13}$$

The functions $ce_n(\eta)$ and $se_n(\eta)$ are the solutions of Eq. (11); the former is the even function and the latter the odd. The functions $Ce_n(\xi)$ and $Se_n(\eta)$ are the solutions of Eq. (12) and correspond to $ce_n(\eta)$ and $se_n(\eta)$ respectively. The terms p_n and s_n are constants.

Considering that the scattered waves progress outward from the cylinder, ϕ_{sc} can be expressed as

$$\phi_{sc} = \sum_{n=0}^{\infty} C_{2n} Me^{(2)}_{2n}(\xi)\, ce_{2n}(\eta)\, ce_{2n}(\alpha)$$

$$+ S_{2n+2} Ne^{(2)}_{2n+2}(\xi)\, se_{2n+2}(\eta)\, se_{2n+2}(\alpha)$$

$$+ C_{2n+1} Me^{(2)}_{2n+1}(\xi)\, ce_{2n+1}(\eta)\, ce_{2n+1}(\alpha)$$

$$+ S_{2n+1} Ne^{(2)}_{2n+1}(\xi)\, se_{2n+1}(\eta)\, se_{2n+1}(\alpha) \tag{14}$$

The functions $Me^{(2)}_n(\xi)$ and $Ne^{(2)}_n(\xi)$ in Eq. (14) are the another solutions of Eq. (12) and correspond to the second kind of the Hankel function. The constants C_n and S_n are determined by the boundary condition on the elliptical cylinder of the following.

$$\left(\frac{\partial \phi_{in}}{\partial \xi}\right)_{\xi=\xi_0} + \left(\frac{\partial \phi_{sc}}{\partial \xi}\right)_{\xi=\xi_0} = 0 \tag{15}$$

The water surface function ϕ is thus obtained from Eq. (13), (14) and (15).

$$\begin{aligned}\phi &= \phi_{in} + \phi_{sc} \\ &= \sum_{n=0}^{\infty} \Bigg[\frac{2}{p_{2n}} \left(Ce_{2n}(\xi) - \frac{Ce'_{2n}(\xi_0)}{Me^{(2)\prime}_{2n}(\xi_0)} Me^{(2)}_{2n}(\xi) \right) ce_{2n}(\eta) ce_{2n}(\alpha) \\ &\quad + \frac{2}{s_{2n+2}} \left(Se_{2n+2}(\xi) - \frac{Se'_{2n+2}(\xi_0)}{Ne^{(2)\prime}_{2n+2}(\xi_0)} Ne^{(2)}_{2n+2}(\xi) \right) se_{2n+2}(\eta)\, se_{2n+2}(\alpha) \\ &\quad + i \Bigg\{ \frac{2}{p_{2n+1}} \left(Ce_{2n+1}(\xi) - \frac{Ce'_{2n+1}(\xi_0)}{Me^{(2)\prime}_{2n+1}(\xi_0)} Me^{(2)}_{2n+1}(\xi) \right) ce_{2n+1}(\eta) ce_{2n+1}(\alpha) \\ &\quad + \frac{2}{s_{2n+1}} \left(Se_{2n+1}(\xi) - \frac{Se'_{2n+1}(\xi_0)}{Ne^{(2)\prime}_{2n+1}(\xi_0)} Ne^{(2)}_{2n+1}(\xi) \right) se_{2n+1}(\eta) se_{2n+1}(\alpha) \Bigg\} \Bigg]\end{aligned} \tag{16}$$

When the incoming wave height is H_{in}, ϕ_0 can be obtained from Eq. (3) as

$$\phi_0 = \frac{g H_{in}}{2\sigma \cosh kh} \tag{17}$$

The velocity potential of Φ becomes

$$\Phi = \frac{g H_{in}}{2\sigma} \phi \frac{\cosh k(h+z)}{\cosh kh} \exp(i\sigma t) \tag{18}$$

Before the calculation of the wave form and forces by the velocity potential of Eq. (18), the characteristic number and other constants must be computed. The number of terms in the summations is determined from the convergency of the series of Eq. (16). The number generally becomes large as B/L increases. In the present paper the number is determined with sufficient accuracy as shown in Table 1.

Table 1. Number of Terms

B/L	≤ 1.2	≤ 2.4	≤ 3.2	≤ 4.5	≤ 5.5	≤ 6.5	≤ 7.5	≤ 8.0
Number of Terms	1～2	1～3	1～4	1～5	1～6	1～7	1～8	1～9

THE WAVE FORCES ACTING UPON THE ELLIPTICAL CYLINDER

The formula of the wave pressure at the point (ξ_0, η, z) on the cylinder surface is derived from the velocity potential of Eq. (18) by the use of the Bernoulli equation as

$$p = -i\frac{w_0 H_{in}}{2}\frac{\cosh k(h+z)}{\cosh kh}(\phi)_{\xi=\xi_0} \tag{19}$$

in which w_0 is the specific weight of water. The functions $ce_n(\eta)$ and $se_n(\eta)$ in $(\phi)_{\xi=\xi_0}$ are rewritten with the Fourier series of η for the sake of fast convergence as:

$$\begin{aligned}
ce_{2n}(\eta) &= \sum_{r=0}^{\infty} A_{2r}^{(2n)} \cos 2r\eta \\
ce_{2n+1}(\eta) &= \sum_{r=0}^{\infty} A_{2r+1}^{(2n+1)} \cos(2r+1)\eta \\
se_{2n+1}(\eta) &= \sum_{r=0}^{\infty} B_{2r+1}^{(2n+1)} \sin(2r+1)\eta \\
se_{2n+2}(\eta) &= \sum_{r=0}^{\infty} B_{2r+2}^{(2n+2)} \sin(2r+2)\eta
\end{aligned} \tag{20}$$

The terms $A_r^{(n)}$ and $B_r^{(n)}$ are functions of k_1^2.

The total wave forces exerted upon the cylinder are obtained by the double integrations of wave pressure from the bottom to the still water level and around the cylinder. The total forces are separated into the component forces Fx and Fy in the x- and y-directions. The results of calculations are:

$$\left.\begin{aligned}
Fx &= \frac{\pi w_0 bH_{in}}{4k}\tanh kh \exp(i\sigma t) \\
&\times \sum_{n=0}^{\infty}\frac{2A_1^{(2n+1)}}{P_{2n+1}}\left\{Ce_{2n+1}(\xi_0) - \frac{Ce'_{2n+1}(\xi_0)}{Me^{(2)\prime}_{2n+1}(\xi_0)} Me^{(2)}_{2n+1}(\xi_0)\right\} ce_{2n+1}(\alpha) \\
Fy &= -\frac{\pi w_0 aH_{in}}{4k}\tanh kh \exp(i\sigma t) \\
&\times \sum_{n=0}^{\infty}\frac{2B_1^{(2n+1)}}{S_{2n+1}}\left\{Se_{2n+1}(\xi_0) - \frac{Se'_{2n+1}(\xi_0)}{Ne^{(2)\prime}_{2n+1}(\xi_0)} Ne^{(2)}_{2n+1}(\xi_0)\right\} se_{2n+1}(\alpha)
\end{aligned}\right\} \tag{21}$$

where a and b are the long and short axes of ellipsis, respectively.

Figures 3 and 4 show the variation of the nondimensional forms of Fx and Fy with respect to the ratio a/L in the case of b/a = 0.15. The nondimensional forces are Fx/w_oH_{in} b h K_F and Fy/w_oH_{in} a h K_F, where K_F is the coefficient derived from the wave pressure of a small amplitude wave:

$$K_F = \frac{\tanh kh}{k\ h} \tag{22}$$

The nondimensional forces exhibit undulations, but the periods and amplitudes of undulations vary according to the angle α of the incident wave approach and the ratio of a/L. The nondimensional force in the y-direction has the maximum value at about a/L = 0.4 in every value of α, and decreases rapidly in the range of a/L>1.0 except for $\alpha = 90^o$. The undulation of Fx in nondimensional form is larger than that of Fy, but the maximum value of Fx is almost constant regardless of the incident angle α. The heavy lines in Figs. 3 and 4 indicate the nondimensional forces upon a circular cylinder.

VIRTUAL MASS COEFFICIENTS OF THE ELLIPTICAL CYLINDER

The amplitude of wave forces of Fx and Fy can be expressed in terms of the virtual mass coefficient associated with the accelation of water particles under progressive waves. Since the virtual mass coefficient depends on the parameters of a/L, α, and b/a, the variation of its value is much complicated. To simplify the computation the reference volume of a circular cylinder is applied. The diameter of the circular cylinder is taken approximately equal to the apparent width of the elliptical cylinder observed from the direction of the incident wave approach. The diameter of D is expressed as

$$D = (a - b)\sin\alpha + b \tag{23}$$

The diameter D in Eq. (23) satisfies the definition of apparent width at certain conditions of α, a, and b as follows

$$\left.\begin{array}{lll} D = b & \text{at } \alpha = 0 & \\ D = a & \text{at } \alpha = \pi/2 & \\ D = a = b & \text{at } a = b & \text{(circular cylinder)} \\ D = a\sin\alpha & \text{at } b = 0 & \text{(plate)} \end{array}\right\} \tag{24}$$

The virtual mass coefficients of Cmx and Cmy can be computed from Eq. (25)

$$\left.\begin{array}{l} Fx = \dfrac{w_o}{g}\, Cmx\, \dfrac{\pi}{4}D^2 \displaystyle\int_{-h}^{o} \frac{\partial u}{\partial t}\, dz \\ Fy = \dfrac{w_o}{g}\, Cmy\, \dfrac{\pi}{4}D^2 \displaystyle\int_{-h}^{o} \frac{\partial v}{\partial t}\, dz \end{array}\right\} \tag{25}$$

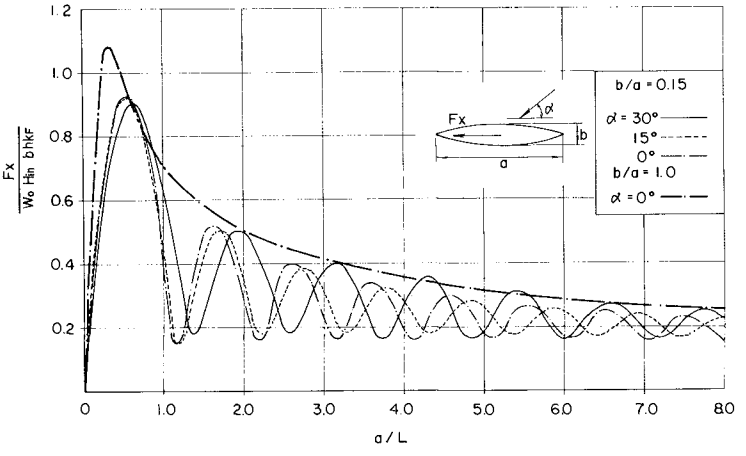

Fig. 3 Variation of nondimensionarized force of Fx

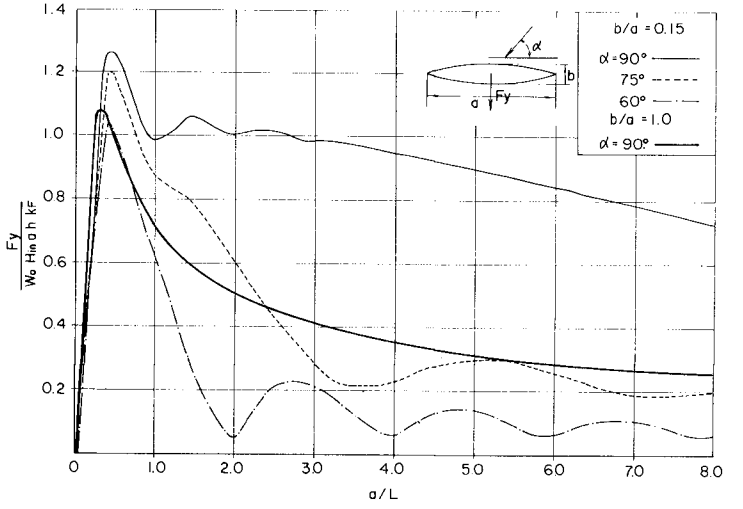

Fig. 4 Variation of nondimensionarized force of Fy

The symbols u and v in Eq.(25) denote the water particle velocity in x- and y-direction under progressive waves without the obstacle. Figures 5 and 6 show examples of the variations of Cmx and Cmy with respect to D/L for $\alpha = 90^{o}$ and 60^{o}, respectively. There is no line of Cmx in Fig. 5 for $\alpha = 90^{o}$ because of Fx = 0 at $\alpha = 90^{o}$.

The line of b/a = 0.0001 gives the asymptote to the virtual mass coefficient of a plate, and the line of b/a = 1.0 represents the virtual mass coefficient of a circular cylinder computed by the formula derived by MacCamy & Fuchs.[3] The coefficient Cmy for b/a = 0.0001 at D/L = 0 and $\alpha = 90^{o}$ has the value of 1.0, which is equal with the theoretical value of a plate.

Diagrams of Cmx and Cmy for other directions of wave approach can be found in reference (4).

IRREGULAR FORCES ACTINC ON A VESSEL AND OFFSHORE DOLPHINS

(1) Wave Spectrum

The relation between the frequency wave spectrum of $S_{\zeta\zeta}(f)$ and the directional wave spectrum $S_{\zeta\zeta}(f,\theta)$ is

$$S_{\zeta\zeta}(f) = \int_{-\pi}^{\pi} S_{\zeta\zeta}(f,\theta)\,d\theta \tag{26}$$

The directional wave spectrum $S_{\zeta\zeta}(f,\theta)$ is expressed as the product of frequency-wise function $S_{\zeta\zeta}(f)$ and directional function of $h(\theta)$ which satisfies the condition of

$$\int_{-\pi}^{\pi} h(\theta)\,d\theta = 1, \tag{27}$$

then $S_{\zeta\zeta}(f)$ coincides with the frequency wave spectrum. The functional forms of frequency wave spectra have been proposed by Neumann[5], Bretschneider[6], Pierson & Moskowitz[7], and etc. The forms of the angular distribution of $h(\theta)$ have been investigated in the wave measurements by Cote et. al.[8] and Ewing[9], but the functional form has not been settled on account of scanty measurements.

In this paper, the following Bretschneider's spectrum modified to satisfy the condition of $\overline{\zeta^2} = \int_0^{\infty} S_{\zeta\zeta}(f)\,df$ is used as the frequency wave spectrum.

$$S_{\zeta\zeta}(f) = 0.430\left(\frac{\bar{H}}{g\bar{T}}\right)^2 g^2 f^{-5} \exp\left\{-0.645\,(\bar{T}f)^{-4}\right\} \tag{28}$$

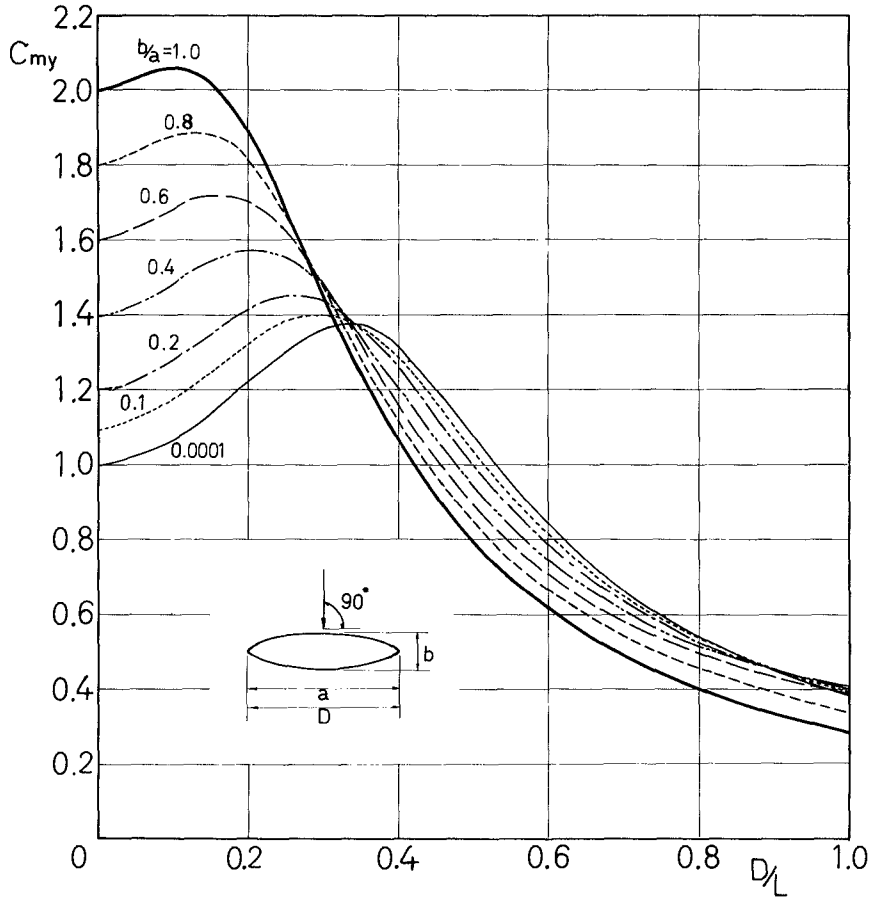

Fig. 5 Virtual mass coefficient Cmy

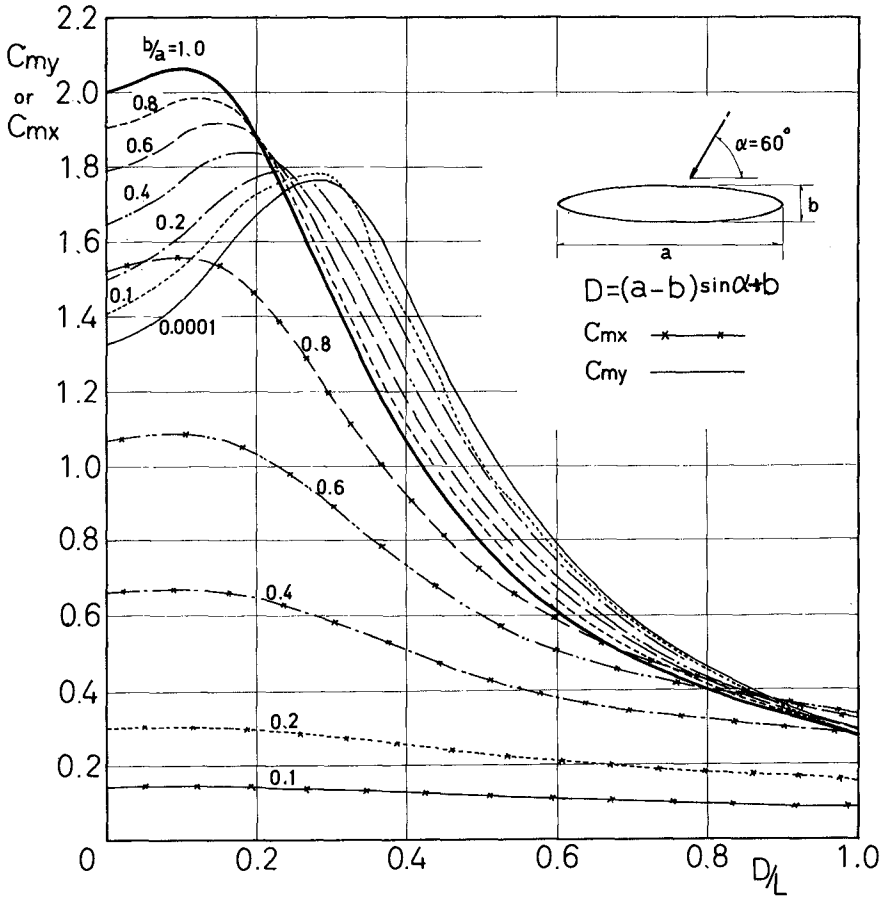

Fig. 6 Virtual mass coefficients Cmx and Cmy

As to the angular distribution satisfying Eq. (27), the following form is employed;

$$h(\theta)\begin{cases} = \dfrac{2^{2s}(s!)^2}{(2s)!\,\pi}\cos^{2s}\theta & (\theta = 1, 2, \cdots\cdots)\ (|\theta| < \dfrac{\pi}{2}) \\ = 0 & (|\theta| > \dfrac{\pi}{2}) \end{cases} \tag{29}$$

Computation of irregular wave forces is made with the relations of $\bar{H} = 0.625\ H_{1/3}$ and $\bar{T} = 0.9\ T_{1/3}$, where $\bar{H}$ and $\bar{T}$ are the mean wave height and period, and $H_{1/3}$ and $T_{1/3}$ are the wave height and period of the significant wave.

(2) Representative Value of the Irregular Forces

Because the wave forces are linear to the displacement of the water level as shown in Eq. (21) and the displacement almost has the Gaussian distribution, the irregular wave forces are expected to follow the same distribution. Longuet-Higgins has proved that the maxima of the wave configuration have the Rayleigh distribution in the case of the narrow-band spectra[10]. Although the spectral band of the sea waves is wide, the investigations of sea waves by field measurements[11] and by numerical simulation[12] have demonstrated that the wave heights closely follow the Rayleigh distribution as long as they are defined by the zero-up-crossing method. Therefore, if the maxima of irregular wave forces are defined as the maximum between two successive zero-up-crossing points of a wave force record, the newly defined maxima will follow the Rayleigh distribution.

The one-third maximum force of $F_{1/3}$ and one-tenth maximum force of $F_{1/10}$ can be calculated under the Rayleigh distribution as

$$\begin{aligned} F_{1/3} &= 1.416\sqrt{\overline{F^2}} \fallingdotseq 2.00\sqrt{\int_0^\infty S_{FF}(f)\,df} \\ F_{1/3} &= 1.800\sqrt{\overline{F^2}} \fallingdotseq 2.55\sqrt{\int_0^\infty S_{FF}(f)\,df} \end{aligned} \tag{30}$$

The selection of which statistical values of $\sqrt{\overline{F^2}}$, $F_{1/3}$, or $F_{1/10}$ for the design of offshore structures cannot be easily determined without due consideration of the dynamic response or allowable strength of the material of the structures.

In this paper, $F_{1/3}$ is employed as the representative value of the irregular wave forces, and the results of the computations are expressed with it. It must be made clear that $F_{1/3}$ should not be taken as the design load because the force larger than $F_{1/3}$ is expected to occur during the given wave condition. If the design load is to be taken as the maximum force with the occurrance probability less than μ during the continuation of N waves, the maximum force can be calculated as:

$$(Fmax)_{\mu} = 0.708 F_{1/3} \sqrt{\ln\left(\frac{\ln N}{\ln 1/(1-\mu)}\right)} \qquad (31)$$

With the occurrence probability selected at $\mu = 0.10$, $(Fmax)_{\mu}$ becomes 1.85 $F_{1/3}$ for 100 waves, and 2.14 $F_{1/3}$ for 1000 waves.

(3) Forces Acting upon the Vessel Tied at Offshore Dolphins

In the computation of wave forces acting upon a vessel moored tight at the offshore dolphins, the following four assumptions are introduced.

1) The geometry of the vessel is represented with a virtical, elliptical cylinder of Fig. 7 with the draft of h_1.
2) The vessel is considered to be rigidly tied at two breasting dolphins without movement though actual vessels in mooring have the freedom of limited motion. The wave forces computed under these assumptions will exceed those acting upon movable vessels and will provide the asymtotic values of thrusts and pulls.
3) The presence of the gap between the vessel's bilge and the sea bottom is assumed not to affect the pressure distribution along the vessel.
4) The wave force of Fx in the direction of the vessel length is taken by the tie ropes.

The two breasting dolphins are located at (x_R, y_R) and (x_L, y_L) shown in Fig. 7. In the formulation, the symbols in Fig. 7 is used.

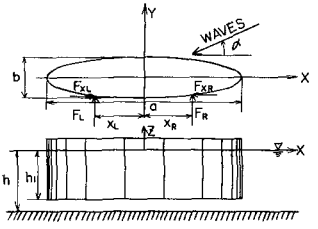

Fig. 7 Characteristics of computed tanker

Forces equilibrum equations are represented as

$$\left.\begin{aligned} &Fx_L - Fx_R = 0 \\ &F_L + F_R + Fy = 0 \\ &-F_L x_L - F_R x_R + M_O + Fx_L y_L - Fx_R y_R = 0 \end{aligned}\right\} \qquad (32)$$

The forces Fx and Fy are the x and y component of the wave force acting upon the vessel, and can be computed under the previous assumptions. The symbols M_o denotes the moment by the wave force arround the origin. Fx_R and Fx_L are the forces generated by Fy for the existence of the curvature of the elliptical cylinder at the fixed points.

It is considered that $|y_R - y_L|$ is much shorter than x_L and x_R, and Fx_R and Fx_L are much smaller than Fy. When the terms containing Fx_R and Fx_L are neglected, F_L and F_R can be obtained from Eq. (32) as follows

$$\left.\begin{aligned} F_L &= -\frac{M_o + Fy\ x_R}{x_R - x_L} \\ F_R &= \frac{M_o + Fy\ x_L}{x_R - x_L} \end{aligned}\right\} \tag{33}$$

The value of Fx will determine the necessary strength of tie ropes and is obtained as

$$\begin{aligned} Fx &= \int_0^{2\pi}\int_{-h_1}^{0} \left(-\frac{B}{2}\sinh\xi_0\cos\eta\right) p\ dz\ d\eta \\ &= \frac{H_{in}}{2}\exp(i\sigma t)\sum_{n=0}^{\infty}(\Psi_{Fx})_n \end{aligned} \tag{34}$$

where,

$$(\Psi_{Fx})_n = -\frac{\pi w_o b}{2k}\ \frac{\sinh kh - \sinh k(h-h_1)}{\cosh kh}$$

$$\times\left\{\frac{2A_1^{(2n+1)}}{p_{2n}}\left\{Ce_{2n+1}(\xi_0) - \frac{Ce'_{2n+1}(\xi_0)}{Me^{(2)\prime}_{2n+1}(\xi_0)}\ Me^{(2)}_{2n+1}(\xi_0)\right\}ce_{2n+1}(\alpha)\right\} \tag{35}$$

The force Fy can be easily obtained in the form similar with Eq. (35) in reference of Eq. (21). The moment M_o is

$$M_o = \int y\ dFx - \int x\ dFy \tag{36}$$

The forces of F_L and F_R is obtained by substituting Fx, Fy, and M_o into Eq. (33).

When $(\Psi_F)_n$ of each force is given in the same form with Eq. (35), the spectrum of each force of $S_{FF}(f)$ is calculated as:

$$S_{FF}(f) = \int_{-\pi}^{\pi} \left\{ \sum_{n,m=0}^{\infty} (\Psi_F)_n (\Psi_F)_m^* \right\} S_{\zeta\zeta}(f,\theta)\, d\theta$$
$$= S_{\zeta\zeta}(f) \int_{-\pi}^{\pi} \left\{ \sum_{n,m=0}^{\infty} (\Psi_F)_n (\Psi_F)_m^* \right\} h(\theta) d\theta \qquad (37)$$

where $(\Psi_F)_n^*$ is the conjugate complex number of $(\Psi_F)_n$.

When the main directional angle of the irregular wave approach is θ_o θ in Eq. (37) is given with $\theta = \alpha - \theta_o$.

The computations of the force spectra are made for a taker of 200,000 D.W.T. with the length of Ls = 352m, the width of Ws = 50.3m, and the draft of h_1 = 17.8m. The locations of the dolphins are assumed at x_R = 88m and x_L =-88m, which are a quarter of the length of the tanker.

Two types of the irregular incident waves are used in the computations. One is the swell of $H_{1/3}$ = 1.0m and $T_{1/3}$ = 10 sec. The other is the waves with a long period of $H_{1/3}$ = 0.2m and $T_{1/3}$ = 30 sec which are considered to exert a very strong force to the tanker. The water depth is constant as h = 20m.

Figure 8 shows the variation of the one-third maximum force of each irregular force to θ_o in the case of $H_{1/3}$ = 1.0m and $T_{1/3}$ = 10 sec and the parameter of s = 1 in Eq. (29).

Each one-third maximum force is maximum at θ_o = 90°. The one-third maximum forces of Fy, F_L and F_R decrease rapidly as θ_o decrease, but the decrease of $Fx_{1/3}$ is very small as $Fx_{1/3}$ = 300 tons at θ_o = 90° and 200 tons at θ_o = 0°. In spite of the small height of significant waves, $H_{1/3}$ = 1.0m, the one-third maximum force of Fy acting upon the tanker is 1,950 tons at θ_o = 90°, and both $F_{L1/3}$ and $F_{R1/3}$ acting upon the dolphins are 1,400 tons at the same angle.

Figures 9 and 10 show the variation of $Fy_{1/3}$ and $F_{R1/3}$ to the parameter of s in the case same with Fig. 8. The force $Fy_{1/3}$ is maximum at θ_o = 90° and its value depends on the parameter s. For example, $Fy_{1/3}$ is 4,200 tons with s = ∞ , 2,500 tons with s = 4 and 1,950 tons with s = 1 at θ_o = 90°. But $Fy_{1/3}$ with s = ∞ decreases most rapidly as θ_o decreases from 90°. The variation of $F_{R1/3}$ has almost same tendency with that of $Fy_{1/3}$ except that $F_{R1/3}$ is maximum at about θ_o = 80° with s = ∞ .

Figure 11 shows the variation of each one-third maximum force in the case of $H_{1/3}$ = 0.2m, $T_{1/3}$ = 30 sec and s = 1. Though the incident wave height is one-fifth of the previous cases, $Fy_{1/3}$ of 910 tons and $F_{L1/3}$ = $F_{R1/3}$ of 590 tons are about one halves of those in Fig. 8. These forces decrease rapidly with the decrease of θ_o, but $Fx_{1/3}$ is almost constant.

When it is considered that even incident waves of a small wave height can exert very large forces to the tanker and the offshore dolphins

as mentioned above, the wave forces will be realized as one of major factors in the planning and design of offshore dolphins. The direction of the sea berth should be determined with due consideration for the direction of the swell approach because the wave force decreases rapidly as θ_0 deviates from $\theta_0 = 90^\circ$. The long period waves should also be prevented from approaching the sea berth.

There remain several problems in the computation of wave forces. They are:

1) The equations on the wave forces have not been confirmed in the experiments though the equations on the reflection and the diffraction by insular breakwaters have been confirmed in the experiments[1].
2) The influence of the clearance between the vessel and the sea bottom on wave forces has not been clarified. The influence is expected to increase as the clearance becomes large.
3) The movement of vessels in mooring is not taken into account. Theory should be developed with experimental verification.
4) The form of the angular distribution or two dimensional wave spectral form should be made clear by the investigation of actual sea waves.

The first two problems are under study in the authors' laboratory and the results will be reported in near future.

CONCLUSION

(1) The theoretical solution of the wave action upon the elliptical cylinder is derived and computation is made for wave forces. The component wave forces in x- and y-direction for the aspect ratio of $b/a = 0.15$ differ depending upon the angle of the wave approach, but the non-dimensional force of Fy has the maximum at about $a/L = 0.4$ irrespective of the angle of wave approach.

(2) The virtual mass coefficients of the elliptical cylinder vary with parameters of b/a, D/L, and α ; they are shown in graphical forms.

(3) The irregular wave forces acting upon the vessel fixed in position have been computed with the approximation of the geometry of a vessel with the elliptical cylinder having the same width-to-length ratio.

(4) Wave forces in the direction of beam decrease rapidly as the angle of wave approach deviates form the beam, but the forces in the longitudinal direction vary a little with the angle of wave approach.

(5) The forces acting upon the offshore dolphins through the vessel are demonstrated to be one of major design factors; the one-third maximum value of thrusts and pulls to a dolphin is estimated as 1,400 tons even for the waves of $H_{1/3} = 1.0$m, $T_{1/3} = 10$ sec, approaching from the beam.

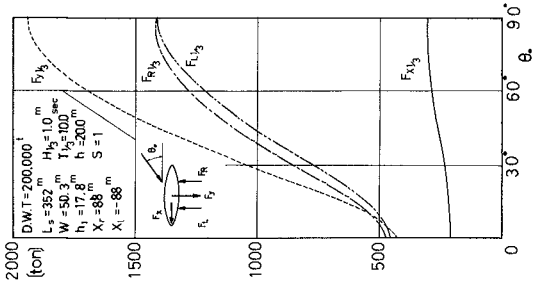

Fig. 8 Variation of one-third maximum forces ($H_{1/3}$ = 1.0m, $T_{1/3}$ = 10 sec)

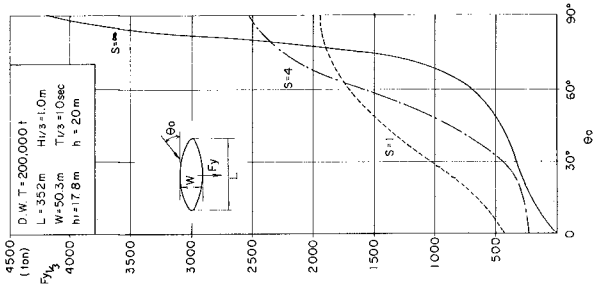

Fig. 9 Variation of $F_{y1/3}$ for s ($H_{1/3}$ = 1.0m, $T_{1/3}$ = 10 sec)

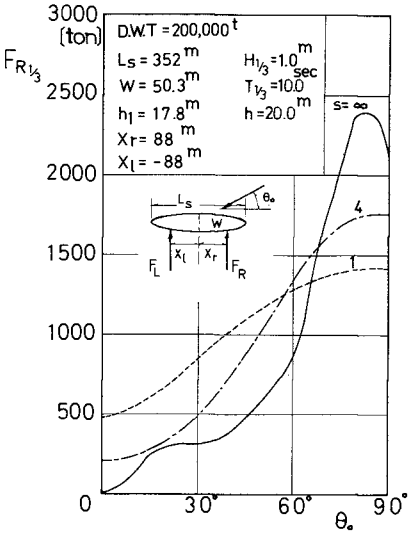

Fig. 10 Variation of $F_{R1/3}$ for s
($H_{1/3}$ = 1.0m, $T_{1/3}$ = 10 sec)

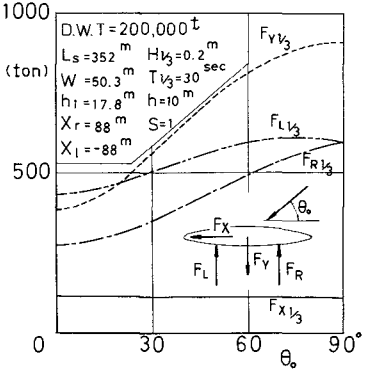

Fig. 11 Variation of one-third maximum
forces ($H_{1/3}$ = 0.2m, $T_{1/3}$ = 30 sec)

REFERENCES

1) Goda, Y., Yoshimura, T., and Ito, M. (1971) : Reflection and diffraction of water waves by an insular breakwater, Report of the Port and Harbour Research Institute, Vol. 10, No.2, pp.3 - 52 (in Japanese)

2) Mclachlan, N.W. (1964) : Theory and application of Mathieu functions, Dover Pub. Inc. New York.

3) MacCamy, R.C. and Fuchs, R.A. (1959) : Wave force on piles; diffraction theory, Tech. Mems, No.69, BEB

4) Goda, Y. and Yoshimura, T. (1971) : Wave force computation for structures of large diameter, isolated in the offshore, Report of the Port and Harbour Research Institute, Vol.10, No.4, pp.3 - 52(in Japanese)

5) Neumann, G. (1953) : On the ocean wave spectra and a new method of forecasting wind-generated sea, Tech. Memo., No.43, BEB

6) Bretschneider, C.L. (1959) : Wave variability and wave spectra for wind-generated gravity waves. Tech. Memo., No.118, BEB

7) Pierson, W.T. and Moskovitz, L.(1965) : A proposed spectra form for fully developed wind sea based on the similarity theory of S.A. Kitaigoloskii, Jour. Geophysical Res., Vol.69, No.24, pp.5181 - 5190

8) Refered from Ocean physics III (1971) by Nayata, U., Hikosaka, S. and Miyazaki, M., pp.53 - 87 (in Japanese)

9) Ewing, J.A. (1969) : Some measurement of the directional wave spectrum, Jour. Marine. Res., Vol.27, No.2, pp.163 - 171

10) Longuet-Higgins, M.S. (1952) : On the statistical distribution of the heights of sea waves, Jour. Marine. Res., Vol.XI, No.3, pp.245 - 266

11) Goda, Y., Nagai, K. and Ito, M. (1971) : Wave observation at the Port of Nagoya, third report. Diffraction and statistics of wind waves, Tech. Note of the Port and Harbour Research Institute, No. 120, P.24 (in Japanese)

12) Goda, Y. (1970) : Namerical experiment on wave statistics with spectral simulation, Report of the Port and Harbour Research Institute, Vol. 9, No. 3, pp.3 - 51

CHAPTER 97

Studies on the Navigation Buoy for Strong Tidal Currents and Large Waves

by

Shoshichiro Nagai*

Kazuki Oda**

Katsuhiko Kurata***

ABSTRACT

Up to the present time, some researches have been done about hydrodynamic forces and tensile forces on mooring cables and configuration of cables in uniform and ununiform currents.[1] Recently, the dynamic problems on the mooring system of buoy in waves are being studied by means of analytical and numerical methods. Authors have studied about a large navigation buoy exposed to strong tidal currents and large waves by means of model tests in an open channel and a wave tank.

INTRODUCTION

A big project of the construction of three long bridges linking between the Main Land of Japan and Shikoku Island is about to start almost simultaneously at the three routes. All of them will cross narrow straits with strong tidal currents which are dangerous paths in a point of view of safety navigation. One of them, the Akashi Straits of about 4 km width has a maximum tidal current velocity of 8 knots. And in addition, quite a many ships more than 2000 a day pass through the straits. About more than 90 % of them are small ships less than 1000 gross tonnage. These small ships have often caused many marine accidents in such narrow straits.

---

* Professor of Hydraulic Engineering, Faculty of Engineering Osaka City University, Osaka, Japan

** Assistant Professor of Hydraulic Engineering, Faculty of Engineering, Osaka City University, Osaka, Japan

*** Research Associate of Hydraulic Engineering, Faculty of Engineering, Osaka City University, Osaka, Japan

During the construction work of the piers, it is expected that ship collisions against the boring towers, the erection piers and other temporary structures may happen during bad weather, thick fog or night. After the completion of the piers ships would also collide against the piers.

For the purpose of preventing the ship collisions against these structures, several kinds of equipments for security of ships navigating through the straits are required not only at the upstream and downstream sides of the piers but also on the piers to show and control the navigation channels of the ships.

As one of the equipments, navigation buoys equipped with electric lights, electric horns, radar reflectors and transponders were required to anchor at the upstream and downstream sides of the structures.

As was mentioned, the straits over which the bridges will span have strong tidal currents. And the maximum height of waves estimated at the Akashi Straits is as large as 7 meters.

A committe was organized by the Honshu Shikoku Bridge Authority in order to investigate and design the special buoys to withstand the severe environmental conditions.

DESIGN CRITERIA FOR THE BUOY

The committe has decided the design criteria for the buoy as follows.

(1) A maximum tidal current velocity of 8 knots
(2) A ten-minutes mean wind velocity of 45 m/sec
(3) A maximum instantaneous wind velocity of 60 m/sec
(4) A maximum wave height of 7 m
(5) A water depth of 100 m
(6) A maximum movable radius of 85 m
(7) Steel chains were recommended to be used for the mooring line, because synthetic fiber ropes, for example, nylon ropes are much inferior to chains in the shear strength and the durability though the weight per unit length is much less than that of steel chains.

PRELIMINARY MODEL TESTS

At the beginning of the investigation, three shapes of buoys which were circular cylindrical, ship- and discus-type buoys and two kinds of

mooring systems which were single buoy system and two buoys system with a submerged mid-float were selected by the committe as the buoys to be studied.

The first step of the study is to evaluate the characteristics of three shapes and two mooring systems of the buoys in the tidal currents and waves. The outlines of the surface buoys and the submerged mid-float are shown in Figs. 1 (a),(b),(c) and Fig. 2.

The original three surface buoys were made nearly equally in the total weight which was about 4.2 tons to 4.5 tons, and in horizontal cross-sectional area which was 15.9 m^2 except the discus-type buoy which had a larger cross-sectional area of 50.3 m^2 because of a smaller draft.

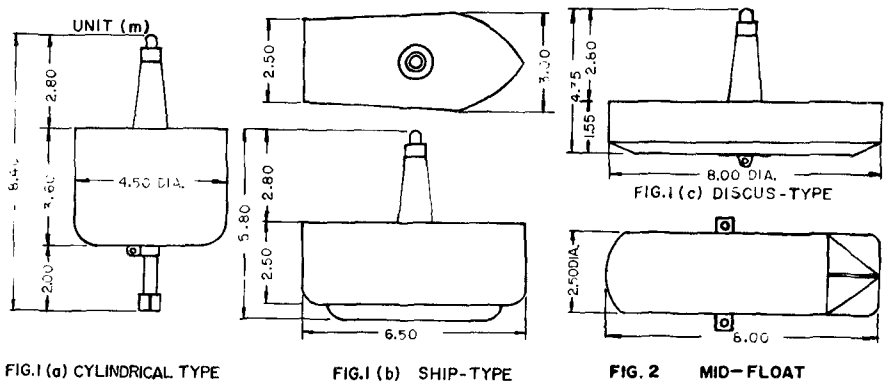

Fig. 1.Outlines of Surface Buoys

Fig. 2.Outline of Mid-Float

According to the results of the preliminary model tests for the original three buoys, the circular cylindrical type buoy was not suitable for the special buoy because of large drag force exerted on the hull and consequently, larger tension acted on the mooring chains under the co-existence of tidal currents and waves.

REFORMED BUOYS

From the results of the preliminary model tests, ship- and discus-type were selected for the buoy hull and they were reformed in shape and diminished in dimensions on the basis of the fundamental plan of the mooring system as shown in Fig. 3. Fig. 3 (a) shows the case of two

buoys system in deeper sea with a water depth of 100 m. Fig. 3 (b) shows the case of single buoy system in shallower sea with a water depth of 30 m. In such relatively shallow sea where the depth of water is shallower than about 100 m, single buoy system is better and more economical than two buoys system.

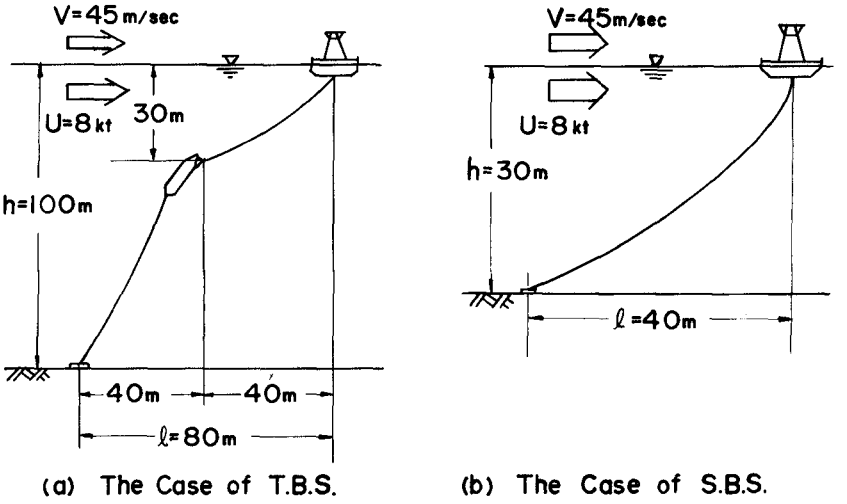

Fig. 3. Fundamental Plans of Mooring System

Fig. 4 (a) shows the outline of the reformed ship-type buoy. The total height from the top to the bottom of the reformed ship-type buoy is 5.99 m and the width is 2.0 m. The horizontal cross-sectional area is 9.5 m^2. The total weight is 5.5 tons. The total buoyancy is 13.7 tons. Fig. 4 (b) shows the outline of the reformed discus-type buoy. The total height is 5.55 m. The diameter is 4.5 m. The horizontal cross-sectional area is 15.9 m^2. The total weight and the total buoyancy are almost the same as ones of the ship-type buoy.

HYDRODYNAMIC FORCES EXERTED ON THE BUOYS

In the second step of the study, further model tests for the reformed buoys were carried out.

The hydrodynamic forces exerted on the reformed buoys by steady

flows were measured. The scale of model to prototype was 1/20. For the experiments, an open channel, 40 m long, 1.2 m wide, 0.8 m deep with the maximum flow discharge of 550 l/sec, in Osaka City University was used. The total drag forces, including the wave making drag, the pressure drag and the skin friction drag, were measured by using a flat steel bar with 4 strain gages.

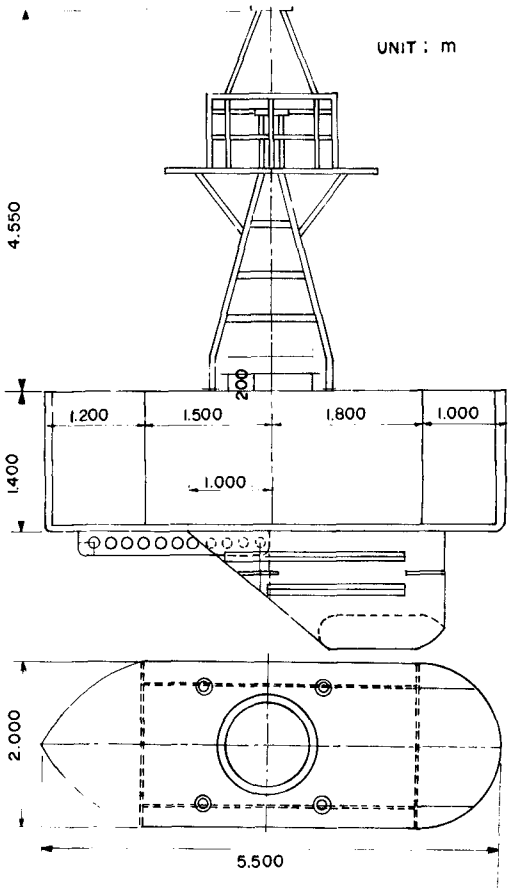

(a). Outline of reformed ship-type buoy

Fig. 4.Outline of Reformed Buoys

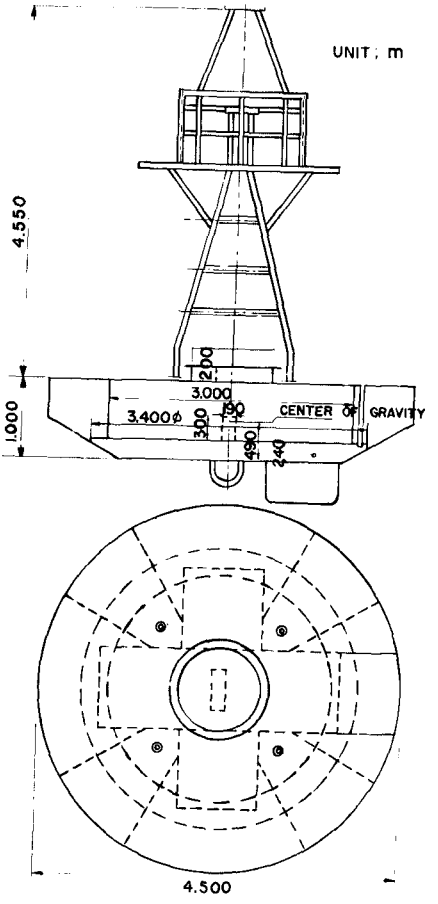

(b) Outline of reformed discus-type buoy

Fig. 4. Outline of Reformed Buoys

The hydrodynamic forces exerted on the buoys parallel to the current direction may generally be represented in the following expression.

$$F = \frac{1}{2} \rho C_R A U^2, \qquad (1)$$

in which F defines the total drag force exerted on a buoy, A is the projected area perpendicular to the current direction, U denotes the

current velocity, ρ is the mass density of water and C_R defines the total drag coefficient.

The total drag coefficients C_R of the reformed ship- and discus-type buoys are shown in Figs. 5 (a) and (b) .

Most of the total drag forces on the buoy may be the wave making drag for relatively large velocities. Consequently, C_R seems to depend on the shape, the draft of the buoy, h_d , and Froude Number $F_r = U/\sqrt{g\ h_d}$

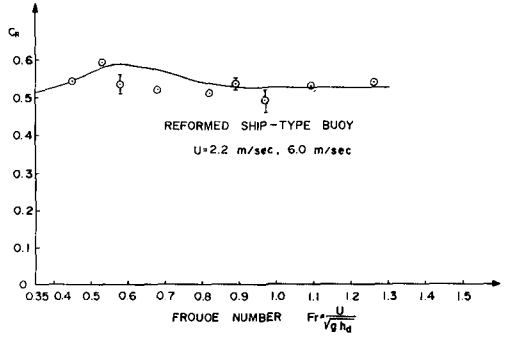

(a) Reformed Ship-Type Buoy

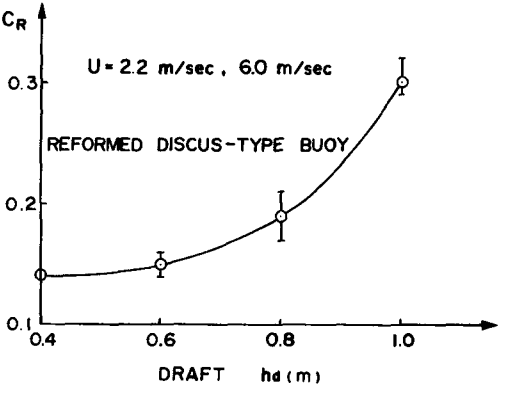

(b) Reformed Discus-Type Buoy

Fig. 5.Total Drag Coefficients of Reformed Buoys

A negative up-lift force acts downwards on the surface buoys perpendicular to the current direction.[2] In order to investigate negative up-lift forces, the upper tensions on the mooring line were measured by using a small ring gage with two strain gages, and the vertical components of the upper tensions T_V were compared with the increases in the buoyancy of the buoy ΔP corresponding to the increases in the draft of the buoy in the current from the draft in the still water. The difference between T_V and ΔP is equivalent to the negative up-lift force. According to the experimental results, the negative up-lift forces on the reformed ship-type buoy seem to be 2 % to 4 % of the total buoyancy P_V which is equal to the weight of the water volume equivalent to the volume of the submerged part of the buoy. And the negative up-lift forces on the reformed discus-type buoy seem to be 3 % to 9 % of P_V.

According to the results of the experiments concerning the negative up-lift forces on the another model buoy of the circular cylindrical shape with a hemispherical bottom as shown in Fig. 6, the negative up-lift forces seem to be 1 % to 3 % of the total buoyancy. Fig. 7 shows the one example of the pressure distribution on the bottom surface at $\theta = 0^\circ$, in which θ defines the horizontal angle measured from the upstream stagnation point.

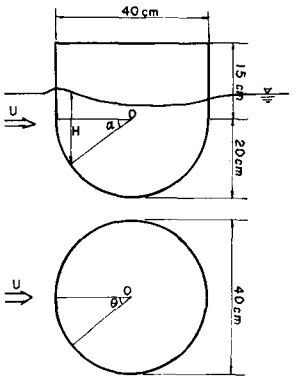

Fig. 6. Circular Cylindrical Type Buoy with Hemispherical Bottom

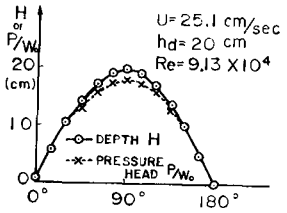

Fig. 7. Pressure Distribution on the Hemispherical Bottom

The solid line shows the depth H of the bottom surface from the water surface. The dotted line shows the pressure head distribution on the bottom surface. The difference between them contributes to the negative up-lift force.

For the buoys of such shapes as used in our experiments, it seems that the negative up-lift forces on the buoys do not have so important meaning from a practical point of view.

MODEL TESTS IN WAVES

1/15-scale model tests concerning the reformed buoys exposed to the tidal currents and waves were carried out in a large wave tank, 60 m long, 10 m wide and 2.5 m deep, in Osaka City University. For the purpose of simplification of model tests, it was assumed that the influences of the tidal currents and waves exerted on the moored buoy are independent. The effects of the hydrodynamic forces on the moored buoy by the tidal currents were simulated roughly by the use of a special coil spring with constant reaction, as shown in Fig. 8, in a wave tank. This special coil spring has such a characteristic that the reaction is almost constant regardless of the elongation. The reaction P is represented by following equation.

$$P = \frac{E\ I}{2\ R_0^2} \qquad (2)$$

in which, E is Young's modulus, I is geometrical moment of inertia of coil spring and R_0 is a radius of curvature of coil. (See Fig. 9) This spring is coiled around a pully with very small friction. The coil spring was set in a case as shown in Fig. 10.

At the beginning of the experiment, the horizontal force equivalent to the total drag force on the buoy, that is, the horizontal component of the upper tension on the mooring chains calculated by Wilson's tables and diagrams[1] was given on the bottom of the moored model buoy by pulling with the special coil spring. (See Fig. 11) The weight per unit length of the model chains was taken $(1/15)^2$ times as much as the prototype on the basis of Froude law of similarity. As shown in Fig. 12, the curve of the mooring chain in the wave tank does not agree with the curve of the chain in the uniform tidal current. The model chain forms

the catenary curve in the wave tank. Moreover, the upper end of the mooring chain in the model tests moves to more downstream side than the location estimated in the uniform currents. These caused the upper tension T_u on the mooring chain in the model tests to become smaller than that in the uniform tidal current, because the effect of the hydrodynamic force exerted on the mooring chain by tidal currents was not simulated in the model tests. In order to simulate the effect more correctly, the horizontal force given by the coil spring and the weight per unit length of the mooring chain were taken larger than those calculated, but leaving the length of the mooring chain just as it was.

Fig. 8.Special Coil Spring with Constant Reaction

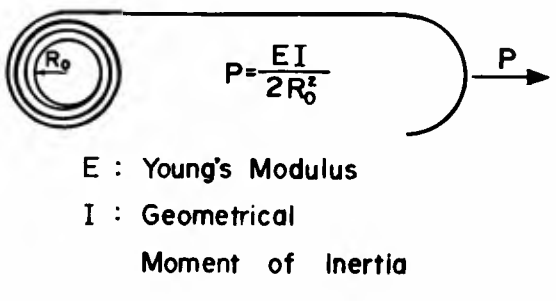

Fig. 9.Special Coil Spring with Constant Reaction

Fig. 10.Special Coil Spring Set in a Case

Fig. 11.Model Buoy Pulled with the Special Coil Spring

As the result of this adjustment, both the upper tension and the curve of the mooring chain in the model tests almost agreed with calculated ones in the tidal currents.

By the way as above mentioned, the initial equilibrium condition of the moored buoy in the tidal currents was formed in the wave tank as shown in Fig. 13. The upper tension on the mooring chain was measured by

the use of a small ring gage with two strain gages. Fig. 14 shows the relationships between the upper tensions and wave heights at a wave period of 8 sec for the single buoy system of the reformed ship- and discus-type buoys. The criteria of the mooring buoy used in Fig. 14 were a water depth : 30 m, a maximum movable radius of a buoy : 40 m, a tidal current velocity : 8 knots, a ratio of chain length to water depth : about 1.70 and a weight per unit length of the mooring chain in water : 33.5 kg/m.

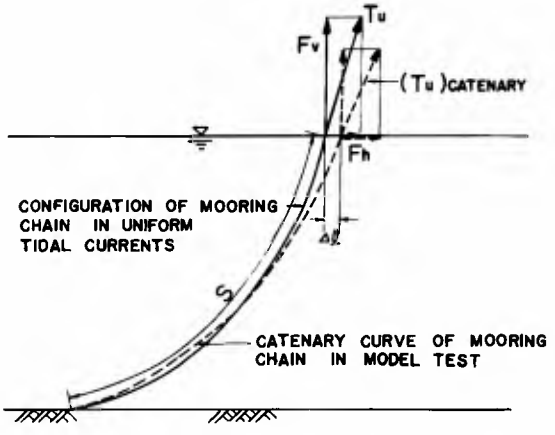

Fig. 12.Curves of Mooring Chains

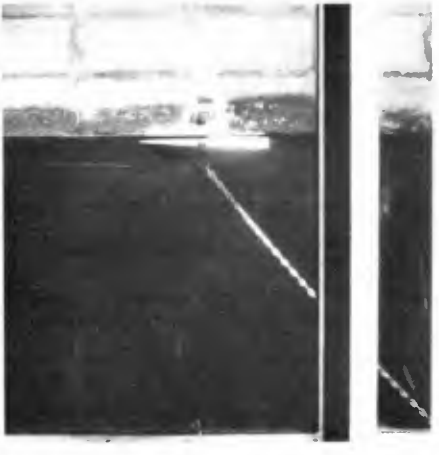

Fig. 13.Initial Equilibrium Condition of Moored Buoy

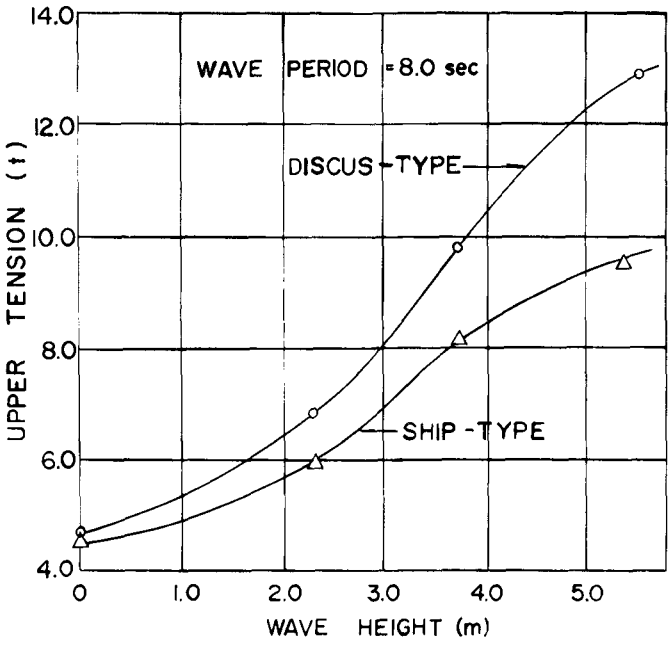

Fig. 14. Relationships between the Upper Tensions and Wave Heights

From Fig. 14, it may be concluded that the upper tensions for the discus-type buoy are larger than those for the ship-type buoy though their initial upper tensions are almost the same. The reason may be attributed the fact that since the discus-type buoy has larger bottom area than the ship-type buoy, the impact forces caused by the upward motion of the wave on the bottom of the discus-type buoy are larger than those on the ship-type buoy.

Further detailed experimental results for the reformed discus-type buoy under the same mooring criteria for wave periods of 6.0 sec, 8.0 sec and 10.0 sec are shown in Fig. 15. Fig. 15 shows that shorter period-waves may cause larger upper tensions on the mooring chains than longer period-waves.

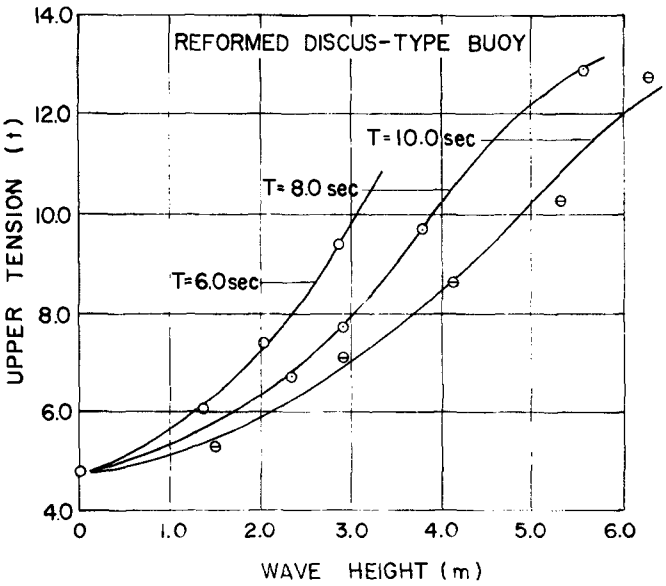

Fig. 15.Relationships between the Upper Tensions, Wave Heights and Wave Periods

OSCILIATORY MOTIONS OF BUOYS

The reformed ship-type buoy has two periods of the free oscillation of 4.4 sec for tolling and 2.4 sec for pitching, moreover their damping is very slow. On the other hand, the discus-type buoy has one period of the free oscillation of 2.1 sec regardless of the mode of oscillation except heaving, besides the damping is very fast. Therefore the ship-type buoy is apt to roll and pitch with large inclination caused by the resonance with waves with period of 2 sec to 4 sec, while the discus-type buoy does not oscillate so much as the ship-type buoy does because of its large damping effect, even in waves with a resonant period. Waves with periods of 2 sec to 4 sec have been often caused by winds with velocities of 10 m/sec to 15 m/sec in the Seto Inland Sea. In addition,

waves generated by ships which navigate through the straits also have such a shorter periods.

CONCLUSION ON SHAPE OF BUOY

From a practical point of view, it may be concluded that the ship-type buoy is not suitable for the special buoy. Finally, the discus-type buoy was selected for the special buoy, though the upper tension is larger than that in the ship-type buoy.

TWO BUOYS SYSTEM WITH SUBMERGED MID-FLOAT

According to the results of additional experiments for the two buoys system, it was found that the upper mooring chains tend to twist about the mid-float at slack tide. But if the length of the upper mooring chain is taken shorter, the large impact forces are caused on the mooring chains by the movement of the surface buoy due to the waves.

PROTOTYPE BUOY

On the basis of the results of these studies, the discus-type buoy was designed and several were manufactured in 1971 for the practical use.

Two discus-type buoys in the Akashi Straits and other discus-type buoys in the Bisan Straits have been moored for the navigation buoys in single buoy system to show and control the navigation channels to ships navigating around the boring towers erected in those straits. (Fig. 16 and Fig. 17)

ACKNOWLEDGEMENT

Part of this study was supported by a grant of the MATSUNAGA SCIENCE FOUNDATION. The writers wish to express their appreciation for its support.

REFERENCES

(1) B.W.Wilson : Characteristics of Anchor Cables in Uniform Ocean Currents, Bulletin of P.I.A.N.C., Vol.1 and Vol.2, 1964.

and others.

(2) S.Nagai : Hydrodynamic Forces on Light Buoy in Strong Tidal Currents, 11th Conf. of I.A.H.R., Sept., 1965.

Fig. 16

Fig. 17

Fig. 16 and Fig. 17. Discus-Type Buoy Moored in the Akashi Straits

CHAPTER 98

WAVE FORCES ON A PLATFORM WITH A RIBBED BOTTOM

Keith H. Denson
Professor of Civil Engineering
Mississippi State University
State College, Mississippi

Melville S. Priest
Director
Water Resources Research Institute
Mississippi

ABSTRACT

Observation of hurricane damage along the Mississippi Gulf Coast has stimulated studies of wave action on structures which permit the waves to pass beneath the floor or bottom surface. This paper reports a laboratory study which compares relative drag and lift forces on a structure with a plane, horizontal bottom surface to those on a structure with a ribbed bottom surface, for various conditions of relative wave height and relative clearance of the structure above the stillwater surface. Also, the effects of relative depth of ribs, relative spacing of ribs, and end webs or diaphragms are noted. The study was limited to the condition for which the bottom ribs were transverse to the general direction of wave motion. The results, which are presented in graphical form, clearly show the effects of the ribs.

INTRODUCTION

It is a rather common occurrence along portions of our coasts that structures supported on piles have encroached upon the sea to such an extent that, during the high stages of a storm surge, waves of considerable magnitude may actually pass beneath the structures. The authors[1] have reported on lift and drag forces exerted by waves on elevated platforms with plane, horizontal bottoms and plane, vertical sides, for the case of normal wave incidence. The waves were considered to be of the type which, in passing from deep water into shallow water, tend to behave more nearly as individuals than as parts of an oscillatory system. That is, wave period was not considered to be a significant quantity.

Observation of hurricane damage to elevated platforms with structural ribs, such as stringers, joists, girders, or T-beams, on the bottoms led to an extension of the earlier study by the authors[1] to determine the relative effects of the ribs on lift and drag forces, as compared to such forces on platforms with plane, horizontal bottoms. The results of this extension of the study are reported herein.

The lift and drag forces exerted by waves are time-dependent variables. However, the interests of this study were in the extreme values. Consequently, only maximum and minimum values of lift and drag are considered herein. The results are presented in graphical form, through dimensionless parameters which enable some degree of generalization.

DIMENSIONAL CONSIDERATIONS

For the previous, related study by the authors[1], in which the structure had a plane bottom surface, the physical quantities which were found to be useful in describing the lift force (F_l) or the drag force (F_d) were specific weight (γ) of the water, stillwater depth (D), wave height (H), clearance (Δ) between the horizontal bottom of the structure and the stillwater surface, width of structure (W), length of structure (L), and horizontal area (A) of the bottom surface.

For the study reported herein, some additional lengths are necessary for describing the geometry of the ribbed bottom. Specifically, the lengths are rib depth (δ), rib thickness (t), and rib spacing (S). Conditions with and without end diaphragms between ribs were studied, but no additional physical quantities are introduced to describe the diaphragms.

For purposes of generalization, the above mentioned physical quantities might be arranged into the dimensionless parameters shown in the implicit function

$$\Omega_1\left(\frac{F_l}{\gamma DA} \text{ or } \frac{F_d}{\gamma DA}, \frac{H}{D}, \frac{\Delta}{D}, \frac{W}{D}, \frac{L}{D}, \frac{\delta}{D}, \frac{t}{D}, \frac{S}{D}\right) = 0 \quad \ldots\ldots \quad (1)$$

in which it is evident that the quantity chosen as common to all parameters is the stillwater depth (D).

During the study reported herein, the width of structure (W), length of structure (L), and rib thickness (t) were held constant, as was the stillwater depth (D). Consequently, for purposes of analysis, Eq. 1 might be rewritten

$$\Omega_2\left(\frac{F_l}{\gamma DA} \text{ or } \frac{F_d}{\gamma DA}, \frac{H}{D}, \frac{\Delta}{D}, \frac{\delta}{D}, \frac{S}{D}\right) = 0 \quad \ldots\ldots\ldots\ldots\ldots \quad (2)$$

EQUIPMENT AND EXPERIMENTAL PROCEDURE

The study made use of a wave basin in a laboratory of the Water Resources Research Institute, Mississippi State University. Interior dimensions of the basin are 30 ft width, 40 ft length, and 2½ ft depth. The wave generator is of the vertical plunger type. Stroke and speed are adjustable. Waves move from the deeper water near the generator over a ramp to the study area, which has a horizontal bottom, and on to a sloping gravel bank which serves as a wave attenuator.

The basic test structure was a plastic box with a horizontal bottom of rectangular shape and vertical sides. Plastic ribs were attached to the bottom, with the exterior ribs flush with the front and rear walls of the basic box and the interior ribs located so as to obtain equal spacing throughout. This box was suspended from a metal frame by means of members upon which strain gages were mounted. The support system permitted adjustment of clearance between structure and stillwater surface. The electrical system of which the strain gages and an amplifier-recorder were parts was calibrated for measurement of lift and drag forces. Wave height and stillwater depth were measured by means of hook-point gages.

The common or reference values of physical quantities which appear in the independent parameters of the problem were H = 3.44 in, Δ = 0.25 in, W = 15.00 in, L = 12.00 in, δ = 0.38 in, t = 0.25 in, S = 3.92 in, and D = 8.00 in. All of the ribs and the end diaphragms were cut from one-quarter inch plastic sheets. When end diaphragms were used, they were the same depth as the ribs.

Data were collected to show the relation between maximum and minimum values of each of the dependent parameters $F_l/\gamma DA$ and $F_d/\gamma DA$ and the independent parameter H/D for various values of Δ/D, δ/D, and S/D, and to show the effects of end diaphragms. The results are presented in a graphical form which enables comparison with results from the earlier study by the authors[1], in which the bottom of the test structure was a plane surface.

RESULTS

Each of the Figures 1, 3, and 5 relates maximum and minimum values of $F_l/\gamma DA$ to H/D for a particular value of Δ/D, and each of the Figures 2, 4, and 6 relates maximum and minimum values of $F_d/\gamma DA$ to H/D for a particular value of Δ/D, for various bottom configurations of the structure.

Each of the figures provides a comparison of conditions with ribs versus those without ribs. In addition, Figures 1 and 2 are intended to show the effects of rib depth (δ/D), rib spacing (S/D), and the use of end diaphragms on maximum and minimum values of $F_l/\gamma DA$ and $F_d/\gamma DA$, respectively, for the common or reference value of Δ/D.[1] Figures 1-6 are intended to show the effects of clearance (Δ/D), with rib depth (δ/D) and rib spacing (S/D) at common or reference values, and no end diaphragms.

CONCLUSIONS

Within the limits of this study, it appears that the most significant effect of using ribs is some tendency to magnify the maximum and minimum values of $F_l/\gamma DA$ and $F_d/\gamma DA$, the degree of magnification increasing as H/D increases.[1] Both verification and limitations of the foregoing statement should become evident from inspection of the figures and the following comments.

As indicated in Figures 1 and 2, an increase in rib depth, which was an increase in δ/D, resulted in an apparent decrease in maximum values of $F_l/\gamma DA$ at moderate values of H/D and an increase at higher values of H/D. The effect of the increase in rib depth on the maximum values of $F_d/\gamma DA$ was to magnify them. The effect on minimum values of both $F_l/\gamma DA$ and $F_d/\gamma DA$ was, for the most part, to magnify them.

Again, as indicated in Figures 1 and 2, a decrease in rib spacing, which was a decrease in S/D, resulted in maximum values of both $F_l/\gamma DA$ and $F_d/\gamma DA$ that were lower at moderate values of H/D and higher at higher values of H/D. The effect of the decrease in rib spacing on minimum values of $F_l/\gamma DA$ was to magnify them. The effect, if any, on minimum values of $F_d/\gamma DA$ at moderate values of H/D was not clear, but there was a tendency to magnify at higher values of H/D.

As indicated in Figures 1 and 2, the use of end diaphragms resulted in some increase in maximum values of both $F_l/\gamma DA$ and $F_d/\gamma DA$ at moderate values of H/D. Otherwise, the effect on maximum values was slight. The effect of end diaphragms on the minimum values of $F_l/\gamma DA$ was a considerable magnification of them. The effect, if any, on minimum values of $F_d/\gamma DA$ was not clearly defined.

The maximum values of $F_l/\gamma DA$ were considerably different for conditions with and without ribs only for the intermediate clearance, for which $\Delta/D = 0.031$, and for initial submergence, for which $\Delta/D = -0.047$, at higher values of H/D. The minimum values of $F_l/\gamma DA$ were considerably different for conditions with and without ribs only for initial submergence, for which $\Delta/D = -0.047$, at higher values of H/D. The pattern of difference between maximum values of $F_d/\gamma DA$ for conditions with and without ribs appears to be more or less the same regardless of clearance, for values of Δ/D in this study. There was little difference between minimum values of $F_d/\gamma DA$ for conditions with and without ribs regardless of clearance.

ACKNOWLEDGEMENT

Funds for support of this study were derived from the State of Mississippi and administered by the Water Resources Research Institute, Mississippi State University.

REFERENCE

1. Denson, Keith H., and Priest, Melville S., "Lift and Drag Forces Due to Wave Action on Elevated Platforms," Paper No. 1559, Offshore Technology Conference, Houston, 1972.

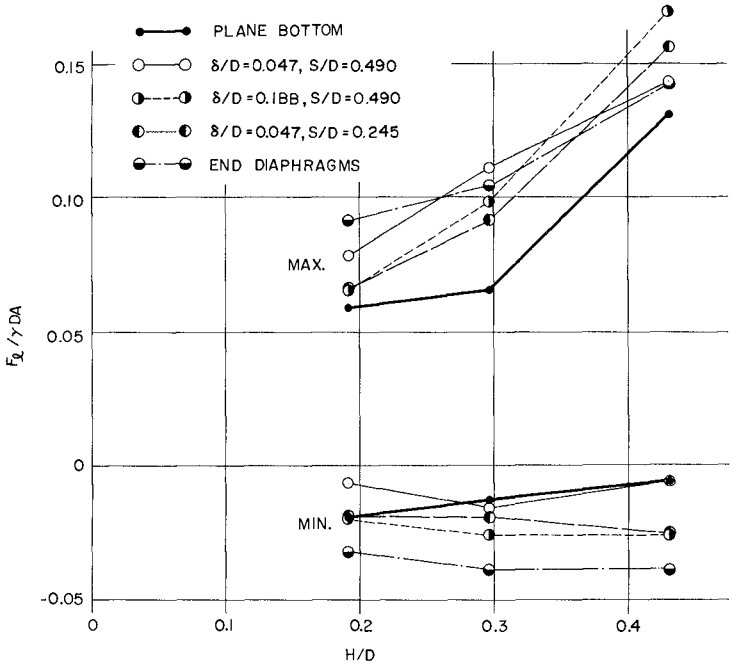

FIG. 1 - THE EFFECT OF BOTTOM RIBS ON LIFT FOR $\Delta/D=0.031$

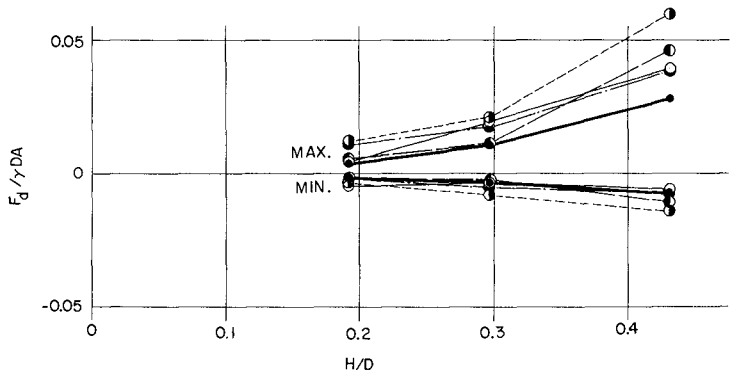

FIG. 2 - THE EFFECT OF BOTTOM RIBS ON DRAG FOR $\Delta/D = 0.031$

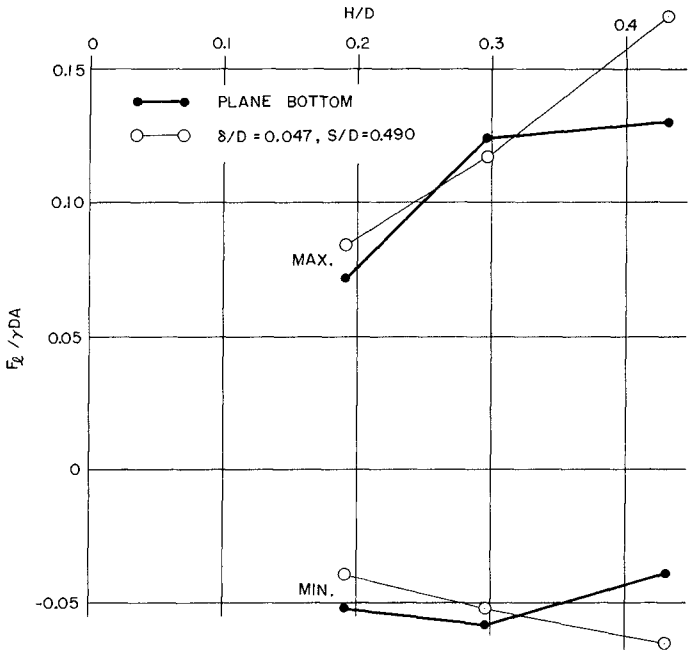

FIG. 3 - THE EFFECT OF BOTTOM RIBS ON LIFT FOR Δ/D = -0.047

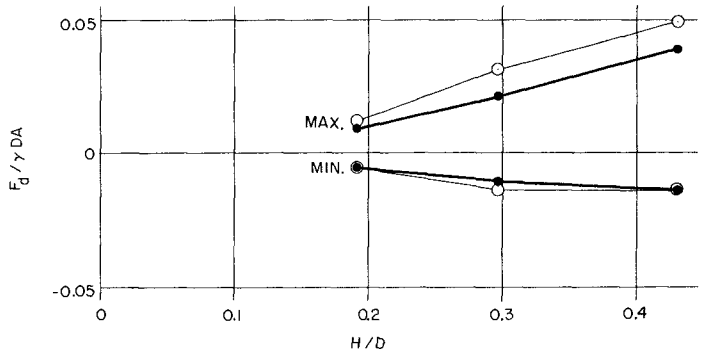

FIG. 4 - THE EFFECT OF BOTTOM RIBS ON DRAG FOR Δ/D = -0.047

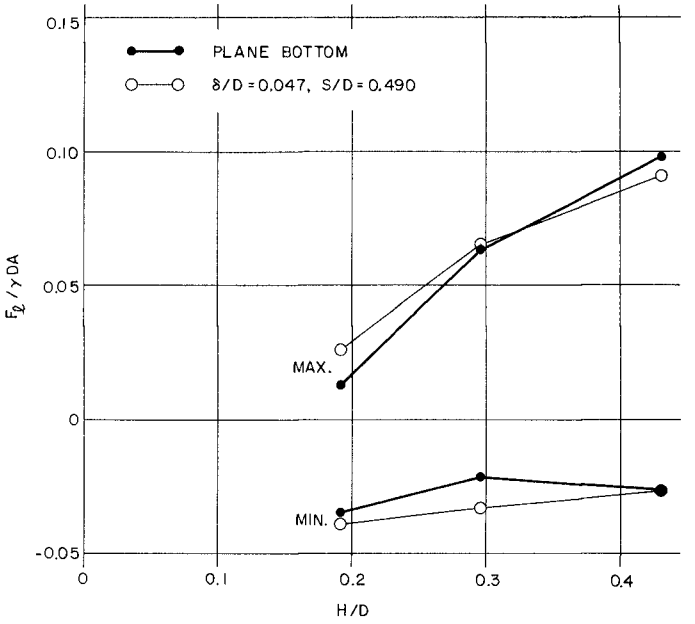

FIG. 5 - THE EFFECT OF BOTTOM RIBS ON LIFT FOR $\Delta/D = 0.109$

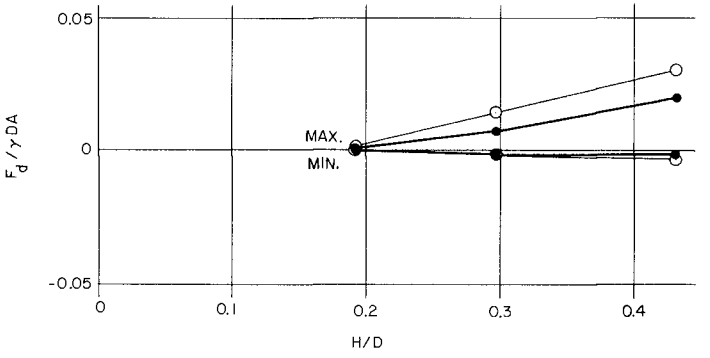

FIG. 6 - THE EFFECT OF BOTTOM RIBS ON DRAG FOR $\Delta/D = 0.109$

CHAPTER 99

FLUID FORCE ON ACCELERATING BODIES

Wallis S. Hamilton[1]

Abstract

The force exerted by a liquid on a moving body always depends on the preceding velocity and acceleration of the body.

The Basset-Lai equation, derived from the linearized equation of motion, gives the force on spheroids when convective acceleration of the water particles may be ignored. Examples prove that the history integral it contains accounts for a large portion (even all) of the force. Measured forces on a cylinder anchored in accelerating water show that history is equally important when convective accelerations are large. An important unanswered question is whether history terms that will fit a range of motions can be invented for simple non-linear problems.

For non-linear repetitive motion, such as the force exerted on piles by regular waves, no explicit history term is needed. The usual division of force into inertia and velocity portions is possibly less sound than a suggested alternative form from dimensional analysis.

One cannot expect to unravel the hydrodynamics of irregular wave forces, but he may use similarity principles to predict their probability distribution from measurements made elsewhere. Irregular waves will be statistically similar, altho mean heights may differ greatly, if the probability distributions of suggested characteristics of the gage records are alike. Given similar waves and structures scaled to the waves, the probability distributions of dimensionless wave forces also will be alike, and the forces at one place can be predicted from measured forces at another.

Introduction

Coastal engineering problems often involve the force exerted by water on a body when the water and/or the body are accelerating. Examples are wave forces on piles, the fluid force on a dam or underwater structure during an earthquake, and the traction on particles during bed-load movement.

If a body moves unsteadily thru a liquid, as when one stirs coffee with a spoon, the velocity pattern in the fluid at a given instant evidently depends upon the prior motion of the body. If, at the instant of interest, the velocity vector and its time rate of change were known at all points in the flow field, and if the shear and normal stress components at one point also were known, one could integrate the Navier-Stokes equations numerically to find the instantaneous stresses, and

[1] Professor of Civil Engineering, The Technological Institute, Northwestern University, Evanston, Illinois 60201.

consequently the force, exerted by the fluid on the body. Since the velocity pattern was generated by a sequence of body motions, the instantaneous force also will depend upon this sequence, i.e., upon the history of the acceleration of the body.

Similarly, if irregular waves move past a stationary pile, the velocity and acceleration of the water particles near the body at a chosen time will depend partly upon the eddies in the wakes generated by antecedent waves. Consequently the instantaneous force on the pile will depend somewhat on the recent local wave history. Thus the maximum force exerted on a pile by a wave of given height and length is not a fixed number but a variable that depends upon the sizes of the two or three waves immediately preceding it.

The above reasoning and example suggest that a comprehensive equation for the force on a body accelerating in a fluid should contain the usual instantaneous velocity and acceleration terms plus corrections based on the acceleration that took place before the instant of interest--history terms. A review of the literature, however, shows that most authors have avoided using history terms in the force equation, even tho they recognized a general need, by choosing types of motion that do not require them. For example, References [1] thru [10] show that there is no lack of analyses of pendulums that oscillate harmonically in a fluid or of forces exerted by uniform oscillatory waves on cylinders and other objects. In such uniform periodic motion, the fluid velocity pattern changes continually during a cycle, but the succession of patterns is repeated during the next cycle and the next. Hence the force becomes a periodic function of time, altho not necessarily sinusoidal, and may be expressed in terms of phase or instantaneous velocity and acceleration.

Another group of authors [11] thru [14] has tried to avoid using history terms by treating other special problems such as (a) suddenly started, (b) constantly accelerated, or (c) freely falling objects.

While the need to study different types of accelerated motion case by case is genuine, the analyst who always thinks about the influence of antecedent motion on the present force will have a better grasp of the physical problem than one who does not. In some instances, moreover, he will be able to present the results of both mathematical analysis and experiment in best form if he uses a history term in the force equation.

The purposes of this paper are: (1) to present examples that show how important history may be; (2) to divide unsteady force problems into three categories according to the motion history, namely, (a) simple non-repetitive motion, (b) simple repetitive motion, and (c) irregular and random motion; and (3) to suggest a suitable way of expressing the fluid force for each category.

Definition

Both linear and non-linear flow problems will be considered in the paragraphs that follow. If the convective acceleration term $(\vec{u}\cdot\vec{\nabla})\vec{u}$[2] in the Navier-Stokes equation is small enough, compared to the other terms,

[2] $\vec{u}$ is the fluid velocity vector, a function of space and time.

to be ignored, the problem is linear. Physically this means that separation and turbulence will be absent altho the maximum Reynolds number may be quite large. Conversely, of course, convective accelerations are not negligible in non-linear problems, and wakes behind blunt bodies are to be expected.

Solution to a Linear Problem

By neglecting convective accelerations, Lai and Mockros [15] were able to formulate a mathematical solution to the problem of the force on a spheroid moving along its axis of symmetry. The resulting equation can be used to calculate the fluid force for linear problems of motion--repetitive, non-repetitive, and irregular. Further, it contains an explicit history integral and thus can be used to illustrate the importance of accelerations that take place before the instant at which the force is calculated. The Lai equation becomes identical to the Basset [16] equation when major and minor axes of the spheroid are equal, i.e., when the body is a sphere. The general form is

$$-F(t) = C_A m \frac{dv}{dt} + C_V 3\pi\mu D v + C_H \sqrt{\pi\mu\rho}\,\frac{D^2}{4}\int_0^t \frac{dv}{d\tau}(t-\tau)^{-\frac{1}{2}}\,d\tau \quad \ldots\ldots\ldots (1)$$

in which F(t) is the fluid force at time t, C_A, C_V, and C_H are the added mass, velocity, and history coefficients, m is the mass of displaced fluid, v is the velocity of the spheroid, and D its diameter normal to the axis of symmetry, μ and ρ are the viscosity and density of the fluid, and t and τ are time measured from the beginning of motion. For a sphere: $C_A = \frac{1}{2}$; $C_V = 1$; $C_H = 6$.

It is worth noting that the first term on the right of Eq. (1) is the resistance due to the irrotational added mass, and the second is the steady-state viscous drag.

Simple Non-Repetitive Motion

We introduce as an example a body that has been moving thru an incompressible fluid for a long time at constant velocity. An external force then stops the object quite rapidly. During deceleration and when it is stationary the body obstructs the forward flow it previously generated. Thus the fluid will exert a forward force on the body, i.e., a force opposite in direction to the original drag force. The magnitude of the forward force cannot be expressed as a function of the instantaneous velocity and acceleration of the object after the object has stopped; history terms are required.

Other examples of simple non-repetitive motion are: constant acceleration or deceleration from one steady state velocity to another; acceleration from rest by a constant external force such as gravity or buoyancy; and the deceleration that a body falling thru air may experience as it enters water. In each of these examples the force at a given instant depends on the antecedent motion as well as on the instantaneous velocity and its derivatives. By definition then, motion may be classified

as simple and non-repetitive if the fluid force on the body at any instant can be expressed by a manageable equation in which history terms need to appear.

Suppose the body in the first example is a small sphere moving in oil. Then values of diameter, viscosity and velocity may be chosen to satisfy linear problem requirements and make Eq. (1) valid. The writer chose as a sample problem a sphere 0.01 ft. in diameter traveling with an initial velocity of 0.1 ft./sec. thru SAE30 oil. The ball was brought to rest in 1/90 sec. by a suddenly applied external force that produced $\frac{dv}{dt}\Big|_0 = -9$. The resulting fluid force calculated from Eq. (1) is shown in dimensionless form in Fig. 1. Note that the time scale is made logarithmic to expand the deceleration period and that the actual time in seconds is one-tenth of the dimensionless time. The deceleration began arbitrarily at 10^{-4} on the dimensionless time scale.

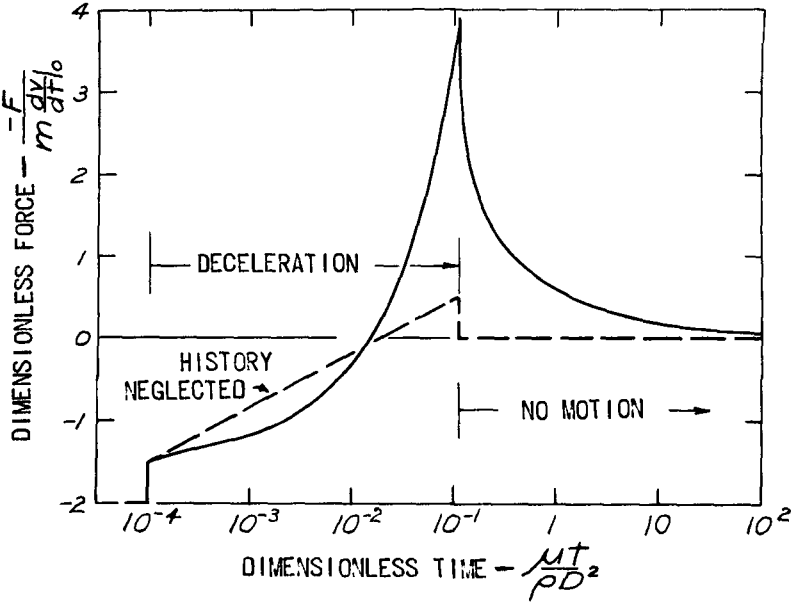

Fig. 1 Influence of history on fluid force acting on small sphere stopped in oil

The dimensionless force on the sphere changed from a steady state drag of -2 to -1.5 as soon as the deceleration began, rose to a maximum value of 3.88 (in the forward direction) just as the body stopped, and then decayed toward zero during a comparatively long period. The large effect of the history integral is apparent, since the maximum forward force is 0.5 if this term is omitted and no force occurs after the motion stops.

Other authors have used the fluid force given by Eq. (1) to study such matters as spheres falling thru a fluid and the response of a submerged sphere mounted on a vertical cantilever spring. Hjelmfelt and Mockros [17], for example, published the curves shown in Fig. 2, which show that a spherical sand grain falling from rest in water (density ratio 2.65) will take about three times as long to reach 0.6 of its terminal velocity as it would if there were no history force. Mockros and Lai [18] compared the same linearized falling-sphere theory with experiments. They found better agreement between the two when the history term was included than when it was not.

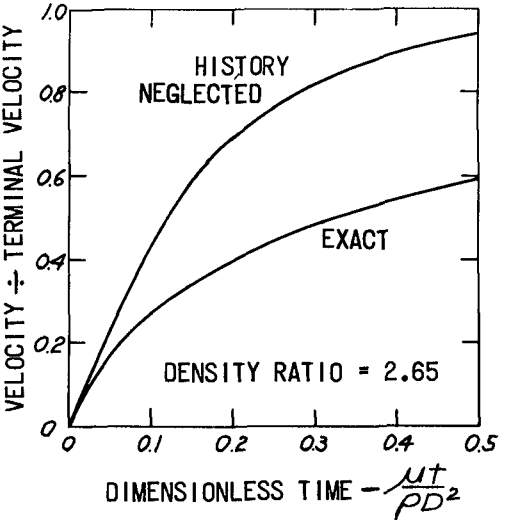

Fig. 2 Influence of history on velocity of sand grain falling from rest in water

For a submerged spherical mass on a spring Hjelmfelt et al., [19], discovered that the history term prevents critical damping if the mass is displaced from its equilibrium position and released. The moving fluid always pushes the mass past the equilibrium point.

We now turn to non-linear problems in the simple non-repetitive motion category. In the first place no general mathematical solution like Eq. (1) is available for any shape of body. Second, one must suppose that prior motion influences the present force altho the Basset history integral may have little resemblance to the kind of history terms required. Third, an empirical equation should give the proper force when the body has been moving with constant velocity for a long time and when it begins to accelerate from rest or from a long period of constant velocity.

Suppose we choose that the history terms, whatever their form, amount to zero after a long period of rest or constant velocity and hypothesize that the correct force is given by

$$-F(t) = C_A m\frac{dv}{dt} + C_V\frac{\rho A|v|v}{2} + \text{History terms} \quad \ldots\ldots\ldots\ldots\ldots\ldots\ldots\ldots(2)$$

in which A is the appropriate cross-sectional or wetted area. To satisfy the constant velocity condition, C_V must be the steady state drag coefficient, and to give the proper force at the instant acceleration from rest begins, C_A must be the irrotational[3] added mass coefficient. Consequently if the hypothesis is to be correct, the irrotational C_A must apply at the instant a body begins to accelerate from constant velocity. Hamilton and Lindell [20] have shown, using spheres towed in water, that it does apply for low velocities (Reynolds numbers less than 35,000). More evidence is desirable.

The history terms of Eq. (2) remain to be invented by studying experimental data. As an example of the job that these terms need to do, the writer has used Eq. (2) and data published by Sarpkaya [21] to prepare Fig. 3. Sarpkaya measured the fluid force on a 2.75-inch circular cylinder fixed in a water tunnel. Its axis was normal to the flow. The water, initially at rest, was given an essentially constant acceleration for about 0.12 sec., producing a velocity which thereafter remained essentially constant at 3.1 ft./sec.

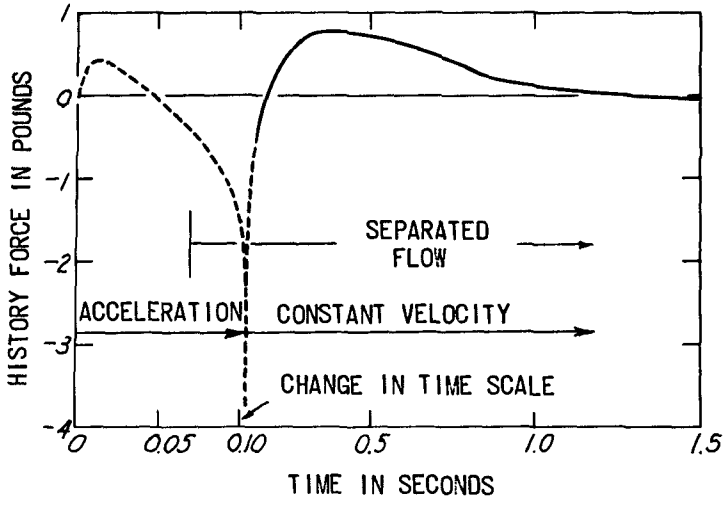

Fig. 3 History force on a cylinder fixed in rapidly accelerated water

[3]For supporting evidence see Mellsen et al. [14] and Hamilton and Lindell [20].

For Fig. 3 the history force was calculated by subtracting the calculated added mass force and the calculated steady state drag from the measured force. The irrotational coefficient C_A for fluid accelerating past a fixed cylinder is 2.00 and the steady state drag coefficient C_V was taken from a standard plot. The instantaneous velocity was used to compute the Reynolds number.

Referring now to Fig. 3, we see that for a short time after acceleration began the history force was positive, meaning that the added mass and drag terms were not quite large enough to make up the total force. This is compatible with linear theory, which may be expected to apply for a very short time after the beginning of motion. But after about 0.02 sec. the required history force begins to depart from what the linear history integral would indicate, and by the end of the acceleration period it reaches a poorly defined negative value. This simply means that, although separation has begun, the wake is much smaller than the steady state wake at the instantaneous velocity. Thus the drag term is much too large and a negative correction is needed. On the other hand, the wake overexpands by time = 0.2 sec. and the steady state drag is inadequate from then until about time = 1.3 sec. In this region a positive history correction is required.

This example shows that adopting Eq. (2) for non-linear force problems puts the burden of correcting the drag for transient wakes onto the history terms. They would also need to compensate for the existence of a laminar boundary layer when the steady state drag at the instantaneous Reynolds number presumes a turbulent one--and vice versa.

In the more general problem we have a change from one speed to another. The magnitude and duration of the corrections depend upon the initial and final velocity, the magnitude of the acceleration (or deceleration), the fluid properties, and the size and shape of the object. And the essence of the force problem is to discover whether or not there are similarities in flow behavior that permit unique history terms or any other explicit expression to apply to a range of problems rather than to one special case.

Simple Repetitive Motion

An example of this kind of motion is a steady state oscillation, not necessarily harmonic, but with an easily identified period. Uniform waves are repetitive; a damped oscillation is not. The basic reason for introducing the repetitive category is that no history terms or history integrals are needed in a fluid force expression. The force is a function of phase.

To illustrate the linear case let us consider a sphere oscillating in a liquid according to

$$v = b\sigma \sin \sigma t \qquad (3)$$

in which b and σ are the amplitude and frequency.

When Eq. (3) is differentiated and substituted into Eq. (1) and the integral evaluated from $\tau = -\infty$, when the motion began, to $\tau = t$, the present time, the result may be put into the alternative forms

$$-F(t) = m\left(\frac{1}{2} + \frac{9}{2}\alpha\right)\frac{dv}{dt} + 3\pi\mu D\left(1 + \frac{1}{2\alpha}\right)v \quad \ldots\ldots\ldots\ldots\ldots\ldots\ldots\ldots(4)$$

or

$$-F(t) = C(\alpha)mb\sigma^2 \sin\left[\sigma t + \varphi(\alpha)\right] \quad \ldots\ldots\ldots\ldots\ldots\ldots\ldots\ldots\ldots\ldots(5)$$

in which $C(\alpha)$ is a force coefficient, $\varphi(\alpha)$ is a phase shift, and

$$\alpha = \left(\frac{2\mu}{\rho\sigma D^2}\right)^{\frac{1}{2}}, \qquad \tan\varphi(\alpha) = \frac{1 + 9\alpha}{9\alpha + 18\alpha^2},$$

$$C(\alpha) = \frac{1}{2}\left[(1 + 9\alpha)^2 + (9\alpha + 18\alpha^2)^2\right]^{\frac{1}{2}} \quad \ldots\ldots\ldots\ldots\ldots\ldots\ldots\ldots\ldots\ldots(6)$$

Form (4) is due to Stokes [1]. Since the coefficient of dv/dt contains α and thus depends on viscosity, this form is sometimes used to support the argument that added mass coefficients depend on viscosity. But whether they do or not is entirely a matter of definition since there is no a priori rule that says all multipliers of the instantaneous acceleration must be included as part of the added mass. The writer prefers to regard m/2 as the added mass, which is the value for a sphere from irrotational theory, and recognize $m\left(\frac{9}{2}\alpha\right)\frac{dv}{dt}$ as part of the history integral.

In form (5) the force is a harmonic function with a known amplitude. It leads the velocity function by a known phase angle. By deriving a similar expression with the history integral omitted and comparing it with Eq. (5), one may show that the amplitude of the force always is increased by the history integral. This is consistent with the result of Hjelmfelt and Mockros [22] who determined how well sand particles would follow straight line oscillations of a liquid in which the particles were suspended. They found that including the history integral increased the ratio of the amplitude of the particle motion to the amplitude of the water motion. Their result applies to sand transport by waves.

Stokes' [1] form for expressing the fluid force on an oscillating sphere in the linear case, Eq. (4), has been carried over to non-linear oscillation problems by numerous authors[4] who like to use

$$-F(t) = C_M m\frac{dv}{dt} + C_D\frac{\rho A|v|v}{2} \quad \ldots\ldots\ldots\ldots\ldots\ldots\ldots\ldots\ldots\ldots(7)$$

in which C_M and C_D are experimental inertia and velocity coefficients which may or may not vary during a cycle.

---

[4] For example, see References [5] thru [10] and [23].

This form has become a standard one for expressing the wave force on piles. The horizontal components of acceleration and velocity of the approaching water particles are calculated from one of the oscillatory wave theories, and the coefficients, assumed constant thruout a cycle, usually are based on tests. Values often are chosen to produce the proper maximum and minimum forces.

It is instructive to compare Eq. (7) with Eq. (2) Eq. (2) has been recommended for non-repetitive motion, but is valid for periodic motion.[5] The equations are similar except that (2) contains explicit history terms and (7) does not. Since the wave force on a pile at any chosen value of the phase depends on the prior motion, C_M and C_D in Eq. (7) must absorb the influence of history. Hence, at best, their values can equal C_A and C_V in Eq. (2) only under particular circumstances. C_M and C_D depend on phase and wave height divided by pile diameter, whereas C_A and C_V are irrotational added mass and steady state drag coefficients respectively.

Eq. (7) cannot be put into the harmonic form of Eq. (5) because the drag force in (7) is proportional to the velocity squared. Nevertheless, the fluid force in any repetitive motion is a repeating function of the phase, which may be expressed non-dimensionally as t/T, where T is the period. The dimensionless displacement of the body (or of the fluid in the absence of the body if the fluid moves), say S/D, is presumed to be a known function of t/T. (Here D is a suitable body dimension, usually transverse.) It produces a measured fluid force pattern F(t/T) which may be written in dimensionless form as

$$\frac{F}{\rho D^2 b^2/T^2}\left(\frac{t}{T}\right) = \frac{F_{max}}{\rho D^2 b^2/T^2} \times f\left(\frac{t}{T}\right) \quad \ldots\ldots\ldots\ldots\ldots\ldots\ldots\ldots\ldots\ldots (8)$$

where $f\left(\frac{t}{T}\right)$ = the measured $F\left(\frac{t}{T}\right)$ divided by the measured F_{max}, and b is a pertinent amplitude such as the maximum displacement.

Further, for a particular repetitive motion $\frac{F_{max}}{\rho D^2 b^2/T^2}$ will depend on $\frac{b}{D}$ and $\frac{\rho D b}{\mu T}$. Consequently

$$\frac{F}{\rho D^2 b^2/T^2}\left(\frac{t}{T}\right) = \frac{F_{max}}{\rho D^2 b^2/T^2}\left(\frac{b}{D}, \frac{\rho D b}{\mu T}\right) \times f\left(\frac{t}{T}\right) \quad \ldots\ldots\ldots\ldots\ldots\ldots\ldots (9)$$

The form of Eq. (9) makes the maximum force an easily described function but provides the option of expressing the force detail thruout the cycle by plotting $f\left(\frac{t}{T}\right)$.

---

[5] Odar and Hamilton [24] used Eq. (2) for the force on a sphere oscillating in oil and invented a history term based on the Basset history integral.

For the force exerted on objects by regular waves the counterpart of Eq. (9) is

$$\frac{F}{\rho D^2 H^2/T^2}\left(\frac{t}{T}\right) = \frac{F_{max}}{\rho D^2 H^2/T^2}\left(\frac{h}{D}, \frac{H}{D}, \frac{H}{gT^2}, \frac{\rho DH}{\mu T}\right) \times f\left(\frac{t}{T}\right) \quad \text{.....(10)}$$

in which H is the wave height, h is the water depth, and g is the acceleration of gravity. Eq. (10) assumes that surface tension may be neglected and that the wavelength will be fixed by the choice of h, H, and T. The viscous parameter may be unimportant. Also for objects that are large compared to the water particle displacements, acceleration forces will dominate, and a more suitable dimensionless force is $\frac{F}{mH/T^2}$. Garrison and Perkinson [25] have used a set of dimensionless parameters somewhat like those suggested to express the maximum wave force on horizontal cylinders.

Obviously the writer prefers Eq. (10) to Eq. (7). Eq. (7) uses inertia and drag coefficients that are too easily confused with irrotational added mass and steady state drag coefficients.

Irregular and Random Motion

In this class belong vibrations generated by earthquakes, turbulence, and the particle motions caused by irregular waves. The dispersion or settling of particulate matter in turbulent flow is a linear force problem involving random motion. A non-linear problem, of course, is the force exerted by irregular waves on piles.

As in previous examples, the fluid force at a particular time is conditioned by eddies or velocity patterns set up by prior motion. Thus, since irregular motion is not repetitive, an attempt to express force details in terms of instantaneous velocity and acceleration is fundamentally unsound. But if the motion is truly irregular or random, the task of unraveling the contributions of innumerable possible histories, except in special linear problems to which Eq. (1) applies, is overwhelming. Therefore non-linear problems, at least, should be handled statistically. For an example, let us focus on forces exerted by irregular waves.

Grace [10] found that seemingly identical ocean swells produced quite different forces on a submerged sphere. He attributed the discrepancies to probable differences in water particle motions under waves of equal height and period. But suppose waves (a) and (b) have identical particle motions, yet wave (a) is preceded by a smaller wave and wave (b) by a larger one. Then the forces exerted by (a) and (b) would differ because the motion history is different.

The data published by Wiegel [7] for forces exerted by ocean waves on piles show practically no correlation between wave height and force. Nevertheless, according to Borgman [26] an analysis of some of these data showed that the spectral density of force was similar to the spectral density of height except in the high-frequency off-peak region. Borgman used constant coefficients in Eq. (7), first-order wave theory to get particle motions, and a Gaussian wave-height distribution to prove that this similarity should exist. He set up a procedure for transferring from one spectrum to the other.

Aware of Borgman's work Paape [27] measured the forces exerted on piles subjected to irregular waves in the laboratory. Spectral densities of force and wave height calculated from his data were not similar and he failed to find a satisfactory transfer function. Thus one must conclude that the spectra may or may not be similar and that Borgman's assumptions oversimplified matters.

It is unfortunate that the designer cannot rely upon similarity between force and wave height spectral densities. For resonance problems he needs to know the frequency at which the force "energy" peaks. Perhaps Paape's tests and others may be used to find how much the frequency at the peak of the force spectrum may differ from the frequency at the peak of the wave height spectrum.

Because wave forces and heights do not correlate, Bretschneider [28] recommends ranking the heights and maximum forces[6] in order of magnitude and working with cumulative probability plots of wave height and force. His idea makes sense because it avoids any inference that the present wave alone is responsible for the present force. Bretschneider developed the idea into a method for analyzing measurements and predicting magnitudes of design forces for statistically similar wave sequences. An alternative method follows.

Suppose we have force and wave height measurements for a particular body shape in a particular irregular sea. How can one arrive at the force that, say, would be equaled or exceeded five percent of the time if a similar sea of greater magnitude acted upon a similar structure? Note first of all that this is a model-prototype kind of problem and one must be able to identify a similar sea. Criteria will appear presently.

We attribute the force at a given instant to the unbalanced shear and normal stresses exerted by the fluid on the body. They are caused by the instantaneous velocities and accelerations of the fluid particles in a rather large region surrounding the object. The motion pattern in the region, of course, is caused by the waves and the presence of the object, but the only index of velocity available is H/T and of acceleration H/T^2. H may be defined as the height of a crest above the surface depressions before and after it and T as the time interval between the two depressions. Both are often a matter of judgment.

Altho these indices represent the particle motion quite inadequately, the dimensionless acceleration H/gT^2, where g is the acceleration of gravity, is certainly a variable on which the force depends. Using γ as specific weight, we may write for a particular wave

$$\frac{F_{max}}{\gamma D^3} = \frac{F_{max}}{\gamma D^3}\left(\frac{h}{D}, \frac{\gamma DH}{g\mu T}, \frac{H}{D}, \frac{H}{gT^2}, \text{History}\right) \quad \ldots\ldots\ldots\ldots\ldots\ldots\ldots\ldots\ldots\ldots (11)$$

The history term is a reminder that a range of values of $F_{max}/\gamma D^3$ may accompany each set of values of the other four variables.

---

[6] He separated drag and inertia forces by picking values at wave peaks and zero crossings respectively.

For a given sea state and a particular structure the variables

$$\frac{\gamma DH}{g\mu T}, \frac{H}{D}, \frac{H}{gT^2}, \text{ as well as } \frac{F_{max}}{\gamma D^3},$$

will have permanent probability distributions. That is, if the gage height record may be taken as a stationary time series, the statistical properties of the force record also will be permanent. Hence we may avoid history and hydrodynamics by writing

$$\left\{\frac{F_{max}}{\gamma D^3}\right\} = \left\{\frac{F_{max}}{\gamma D^3}\left(\frac{h}{D}, \left\{\frac{\gamma DH}{g\mu T}\right\}, \left\{\frac{H}{D}\right\}, \left\{\frac{H}{gT^2}\right\}\right)\right\} \quad \ldots\ldots(12)$$

in which the braces are used (unconventionally) to mean the probability distribution of the quantity enclosed.

Let us compare these variables for two cases, model m and prototype p. If the model is built to the proper length scale ratio and the model sea is similar to the prototype sea,

$$\frac{h}{D}\Big|_m = \frac{h}{D}\Big|_p \quad \ldots\ldots(13)$$

$$\left\{\frac{H}{D}\right\}_m = \left\{\frac{H}{D}\right\}_p \quad \ldots\ldots(14)$$

$$\left\{\frac{H}{gT^2}\right\}_m = \left\{\frac{H}{gT^2}\right\}_p \quad \ldots\ldots(15)$$

$$\left\{\frac{\gamma DH}{g\mu T}\right\}_m \neq \left\{\frac{\gamma DH}{g\mu T}\right\}_p \quad \ldots\ldots(16)$$

Because of Ineq. (16) $\left\{F_{max}/\gamma D^3\right\}_m$ will not be exactly equal to $\left\{F_{max}/\gamma D^3\right\}_p$. In what follows we shall assume that all the Reynolds numbers are large enough and the structure blunt enough to make the inequality unimportant. Then

$$\left\{\frac{F_{max}}{\gamma D^3}\right\}_p \simeq \left\{\frac{F_{max}}{\gamma D^3}\right\}_m \quad \ldots\ldots(17)$$

and if the right hand probability distribution is known, the probability distribution of $F_{max}|_p$ is obtained simply by multiplying the numbers on the abscissa scale by the constant $\gamma D^3|_p$ as indicated in Fig. 4. (In the figure the measurements have been grouped into eight class intervals.) Then the distribution of $F_{max}|_p$ may be summed to get the cumulative probability of the prototype force and answer the question of what force will be equaled or exceeded five percent of the time.

Similar seas have been assumed. Now we must face the question of how to identify statistically similar seas. The definition itself can vary, depending on why they are defined. We are interested in making Eq. (17) true when surface tension and viscosity are unimportant.

The first requirement is that Eq. (15) be satisfied, but it says nothing about the sequences of changes in wave height. From a history standpoint these sequences have an important influence on the force

distribution. Hence $\left\{\frac{H}{gT^2}\right\}$ is a necessary but insufficient index for similar seas and an equation involving differentials such as

$$\left\{\frac{(H_j-H_i)^2/\overline{H^2}}{(t_j-t_i)^2/\overline{T^2}}\right\}_m = \left\{\frac{(H_j-H_i)^2/\overline{H^2}}{(t_j-t_i)^2/\overline{T^2}}\right\}_p \quad \text{.....(18)}$$

is indicated. Wave j follows wave i.

Moreover, since Eq. (14) scales the structure to the waves it does not pertain to identifying wave similarity only. Hence for sea similarity an equation such as

$$\left\{H^2/\overline{H^2}\right\}_m = \left\{H^2/\overline{H^2}\right\}_p \quad \text{.....(19)}$$

is more appropriate. Thus for the present purpose, similar seas probably exist if Eqs. (15), (18), and (19) are satisfied. Experimental data are required to find if they are adequate or not. For example, altho the orientation of the structure with respect to the dominant wave direction presumably is part of the modeling, no account has been taken of the directions of component waves in the description of the sea.

In addition to dimensional analysis and hopefully some physical insight in the choice of dimensionless variables, the writer has used two rather self-evident requirements if force and wave height records from one situation are to be used to find forces in another:

(a) The wave records at the two locations must have certain similarities.

(b) The structure size must be scaled to the wave size, Eq. (14).

These conditions are no different from the ones required in the case of regular waves, Eq. (10), for which wave similarity is implied by a choice of h/D, H/D, and H/gT^2.

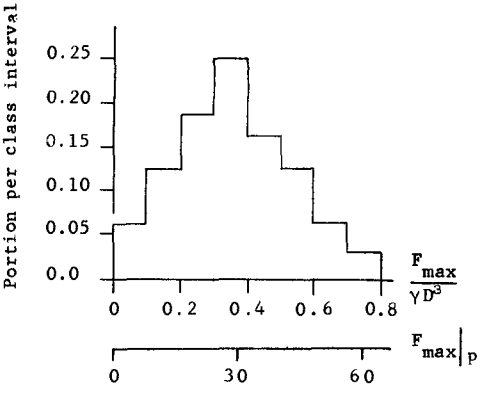

Fig. 4

For regular wave problems engineers use data from tests containing a range of dissimilarities, get a range of coefficients of some sort, and use average coefficient values to calculate approximate forces. Sometimes they calculate extremes to find how much error may be involved.

If similarity requirements are ignored, corresponding errors will occur when statistical quantities, such as probability distributions, are used for analyzing irregular wave and force measurements. To isolate variations due to scale differences, one might well test several sizes of pile, for example, as Wiegel [7] did, but test them simultaneously in the same wave environment.

Bibliography

1. Stokes, G., "On the Effect of the Internal Friction of Fluids on the Motion of Pendulums," Cambridge Trans., Vol. 9, No. 8, 1851 (also Mathematical and Physical Papers, Cambridge Univ. Press, Vol. 3).

2. Yu, Yee-tak, "Virtual Masses and Moments of Inertia of Disks and Cylinders in Various Liquids," Journal of Applied Physics, Vol. 13, Jan. 1942, p. 66.

3. Stelson, T. E., and Mavis, F. T., "Virtual Mass and Acceleration in Fluids," Proceedings, ASCE, Vol. 81, Separate No. 670, April 1955.

4. McNown, J. S., "Drag in Unsteady Flow," Proceedings 9th International Congress of Applied Mechanics, Brussels, 1957, p. 124.

5. Keulegan, G. H., and Carpenter, L. H., "Forces on Cylinders and Plates in an Oscillating Fluid," Journal of Research, National Bureau of Standards, Vol. 60, No. 5, May 1958, p. 423 (also Research Paper 2857).

6. Morison, J. R., et al., "The Forces Exerted by Surface Waves on Piles," Petroleum Transactions, American Institute of Mining, Metallurgical, and Petroleum Engineers, Vol. 189, 1950, TP 2846, p. 149.

7. Wiegel, R. L., et al., "Ocean Wave Forces on Circular Cylindrical Piles," Journal of the Hydraulics Division, ASCE, Vol. 83, No. HY2, April 1957, paper 1199.

8. Harleman, D. R. F., et al., "Experimental and Analytical Studies Of Wave Forces on Offshore Structures, Part I," MIT Hydrodynamics Lab. T. R. No. 19, May 1955.

9. Brater, E. F., et al., "Wave Forces on Submerged Structures," Journal of the Hydraulics Division, ASCE, Vol. 84, No. HY6, Nov. 1958, paper 1833.

10. Grace, R. A., and Casciano, F. M., "Ocean Wave Forces on a Submerged Sphere," Journal of the Waterways and Harbors Division, ASCE, Vol. 95, No. WW3, August 1969, p. 291.

11. Goldstein, S., and Rosenhead, L., "Boundary Layer Growth," Proceedings Cambridge Philosophical Society, Vol. 32, 1936, p. 392.

12. Keim, S. R., "Fluid Resistance to Cylinders in Accelerated Motion," Journal of the Hydraulics Division, ASCE, Vol. 82, No. HY6, Dec. 1956, paper 1113.

13. Laird, A. D. K., et al., "Water Forces on Accelerating Cylinders," Journal of the Waterways and Harbors Division, ASCE, Vol. 85, No. WW1, March 1959, p. 99.

14. Mellsen, S. B., et al., "Real Fluid Effects on an Accelerated Sphere before Boundary-Layer Separation," ASME Paper 66 WA/UNT-6, Annual Meeting Preprint, Nov. 1966.

15. Lai, R. Y. S., and Mockros, L. F., "The Stokes-flow Drag on ... Spheroids ...," Journal of Fluid Mechanics, Vol. 52, Pt. 1, 1972, p. 1

16. Basset, A. B., "On the Motion of a Sphere in a Viscous Liquid," Philosophical Transactions, Royal Society of London, Vol. 179, 1888, p. 43.

17. Hjelmfelt, A. T., and Mockros, L. F., "Stokes Flow Behavior of an Accelerating Sphere," Journal of the Engineering Mechanics Division, ASCE, Vol. 93, No. EM6, Dec. 1967, p. 87.

18. Mockros, L. F., and Lai, R. Y. S., "Validity of Stokes Theory for Accelerating Spheres," Journal of the Engineering Mechanics Division, ASCE, Vol. 95, No. EM3, June 1969, p. 629.

19. Hjelmfelt, A. T., et al., "Dynamic Response of a Restrained Sphere in a Fluid," Journal of the Engineering Mechanics Division, ASCE, Vol. 93, EM1, Feb. 1967, p. 41.

20. Hamilton, W. S., and Lindell, J. E., "Fluid Force Analysis and Accelerating Sphere Tests," Journal of the Hydraulics Division, ASCE, Vol. 97, No. HY6, June 1971, p. 805.

21. Sarpkaya, T., "Separated Flow about Lifting Bodies and Impulsive Flow about Cylinders," Journal of American Institute of Aeronautics and Astronautics, Vol. 4, No. 3, 1966, p. 414.

22. Hjelmfelt, A. T., and Mockros, L. F., "Motion of Discrete Particles in a Turbulent Fluid," Applied Scientific Research, Vol. 16, 1966, p. 149.

23. Lee, T. T., "Research Deficiencies--Wave Force on Piles," Look Lab Hawaii, University of Hawaii, Vol. 1, No. 3, July 1970, p. 38.

24. Odar, F., and Hamilton, W. S., "Forces on a Sphere Accelerating in a Viscous Fluid," Journal of Fluid Mechanics, Vol. 18, Pt. 2, Feb. 1964, p. 302.

25. Garrison, C. J., and Perkinson, B. T., "Wave Forces on a Horizontal Circular Cylinder," Conference Abstracts, Thirteenth International Conference on Coastal Engineering, Vancouver, July 1972, p. 459.

26. Borgman, L. E., "The Spectral Density for Ocean Wave Forces," Coastal Engineering, Santa Barbara Specialty Conference, October 1965, ASCE, 1966, p. 147.

27. Paape, A , "Wave Forces on Piles in Relation to Wave Energy Spectra," Proceedings Eleventh Conference on Coastal Engineering, London, ASCE, Sept. 1968, p. 940.

28. Bretschneider, C. L., "On the Probability Distribution of Wave Force ... Correlation Drag Coefficient ...," Coastal Engineering, Santa Barbara Specialty Conference, Oct. 1965, ASCE, 1966, p. 183.

Notation

A = cross-sectional or wetted area
b = amplitude of a harmonic or periodic motion
C = dimensionless force coefficient
C_A = added mass coefficient--irrotational motion
C_D = velocity coefficient--unsteady motion
C_H = history coefficient
C_M = inertia coefficient
C_V = steady state drag coefficient
D = diameter or other significant length
F = force exerted by fluid
F_{max} = maximum fluid force in repetitive motion or when a wave passes
f = force-variation coefficient
g = acceleration of gravity
H = wave height
h = water depth
i,j = subscripts to indicate one wave and the next
m = mass of fluid displaced by a body; also subscript indicating model
p = subscript indicating prototype
S = displacement during repetitive motion
T = period of a repetitive motion or time interval between waves
t = time at which force is calculated or measured
$\vec{u}$ = velocity of fluid particle
v = speed of body

$\alpha = (2\mu / \rho \sigma D^2)^{\frac{1}{2}}$
γ = specific weight of fluid
μ = viscosity of fluid
ρ = density of fluid
σ = frequency, radians/second
τ = time during history of motion--an integration variable
$\vec{\nabla}$ = space derivative operator

$\{\}$ indicate probability distribution of the quantity enclosed

CHAPTER 100

MATHEMATICAL MODELING OF LARGE OBJECTS IN SHALLOW WATER WAVES AND UNIFORM CURRENT

by

Hsiang Wang

University of Delaware, Newark, Delaware

Abstract

A mathematical model is presented which portrays the physical system of a large axially symmetric structure in a flow field of finite water depth, large amplitude wave and strong current. The flow field, which enters as the input, is derived from a velocity potential similar to that of the cnoidal wave of Keulegan and Patterson. The inclusion of a uniform velocity in the derivation of velocity potential results in a cross interference term in addition to the well known Doppler shift effect.

The numerical results are compared with experiments on a bridge pier (Ref. 6) which is partially cylindrical with base diameter equivalent to 100 feet in prototype; close to the surface, where the wave action is greatest it is conical. These results are also compared with theoretical calculations based on linear wave theory and fifth-order wave theory. It is concluded that the results based on the modified cnoidal wave theory come closest to the experimental value.

Introduction

A computer simulation is developed which portrays the physical system of an arbitrarily shaped large structure situated in a flow field where the water depth is finite, the wave is large and the current is not negligible. The structure is large in the sense that its charcteristic length is at least the same order of magnitude as wave length; the wave is large and the water is shallow in that the ratio of wave height to water depth is not infinitesimal. While the presence of a large structure causes wave reflection and diffraction, the existence of a uni-directional current results in the modification of the wave kinematics and, possibly, causes wake formation. As a consequence of large amplitude waves, the convective inertia cannot be neglected. The combination of a large amplitude wave and a large object makes it necessary to compute the wet line around the structure.

The present study is motivated by an earlier experimental work (Wang, 1970). Those laboratory measurements were performed to determine pressures, forces and moments exerted on a large bridge pier. This bridge pier had a cylindrical base and a conical top. When converted from a model into a prototype, such a bridge pier, with a base diameter of 100 feet, would be situated in water 100 feet deep with waves up to 25 feet and current up to 8 knots. The experimental results were later compared with theoretical calculations based on linear wave theory (MacCamy and Fuch, 1954) and on fifth-order wave theory (Clavier, 1967). The comparisons were unfavorable as both theories yielded much too small maximum horizontal forces and moments compared to the experimental values. Since physical situations similar to those described are quite common in engineering, a better predictive technique is, therefore, attempted.

The incoming wave field, in the absence of objects, is first derived from the cnoidal wave of Keulegan and Patterson (1940) incorporated with the effect of a uniform current. The incorporation of a current is not a trivial task as non-linear interaction occurs which results in dispersions of both wave amplitude and wave length.

Since the obstacle is not necessarily in cylindrical shape, the outflows created by the obstacle cannot be expressed in terms of known functions such as Bessel functions of the second kind used by MacCamy and Fuch. A near field wave is sought through Taylor's expansion of wave potential at the obstacle. The outflow potential at the obstacle is then expressed in terms of inflow wave potential and its derivatives normal to the object. The normal derivatives are introduced to fulfill the non-linear free surface condition. Physically, one can reason that the scattering of an incoming wave at a distance should be proportional to the variations of the incoming wave from the distance to the object.

Because of the complicated nature of the problem a computer program is developed using the Burroughs 5500 to facilitate numerical computations of pressure distributions, forces, and moments exerted on the structure.

Incoming Flow

In this section we shall seek a solution for surface waves of finite height superimposed on a uniform current in water of finite depth in the absence of the obstacle. Flow characteristics derived from the wave field will be used as the incoming flow conditions.

General Equations

It will be supposed that the velocity field is irrotational and the fluid is incompressible:

$$\vec{u}' = -\nabla\phi' \tag{1}$$

and

$$\nabla^2\phi' = 0 \tag{2}$$

where $\vec{u}'$ is the velocity vector and ϕ' is the corresponding velocity potential.

A solution of ϕ' will be sought that satisfies the appropriate boundary conditions. Referring to Fig. 1 where the uniform velocity U is oriented into the positive x-direction, we can separate the velocity potential ϕ' into two parts:

$$-\phi' = Ux - \phi \tag{3}$$

where ϕ is the unsteady part of the velocity potential. Then, we have

$$-\phi'_x = U - \phi_x = U + u \tag{4}$$

and

$$-\phi'_y = -\phi_y = v \tag{5}$$

where the subscripts refer to derivatives (as will be used throughout this paper) and where u and v are time-periodic velocities in the x and y directions, respectively.

The boundary conditions to be satisfied are at the surface, i.e., $y = \eta + h$

$$\frac{p}{\rho} = -g(y - h) + \phi_t + U\phi_x - \frac{1}{2}(\phi_x^2 + \phi_y^2) = 0 \tag{6}$$

and

$$\frac{d}{dt}[y - (\eta + d)] = 0 \tag{7}$$

where η is the free surface variation with respect to the calm water and

$$\frac{d}{dt} = \frac{\partial}{\partial t} + \nabla\phi\cdot\nabla \tag{8}$$

and at the bottom, $y = 0$

$$\phi_y = 0 \tag{9}$$

For shallow water waves, we adopt for the potential ϕ the power series (Keulegan and Patterson, 1955):

$$\phi = \sum_{n=0}^{\infty} \phi_n y^n, \quad \phi_1 = 0 \tag{10}$$

Substituting this expression for ϕ in Eq. (2), the following series is obtained

$$\phi = \phi_o - \frac{y^2}{2!}\frac{\partial^2\phi_o}{\partial x^2} + \frac{y^4}{4!}\frac{\partial^4\phi_o}{x^4} - \frac{y^6}{6!}\frac{\partial^6\phi_o}{\partial x^6} + \ldots \tag{11}$$

Differentiating with respect to y,

$$\frac{\partial\phi}{\partial y} = -y\frac{\partial^2\phi}{\partial x^2} + \frac{y^3}{3!}\frac{\partial^4\phi_o}{\partial x^4} - \frac{y^5}{5!}\frac{\partial^6\phi_o}{\partial x^6} + \ldots \tag{12}$$

The function ϕ_o is a function of x and t only.

First Order Solutions

If the velocity square terms in Eq. (6) are negligible in comparison with gh and the expansions in Eqs. (11) and (12) are cut short at the first term, wave equations of the first order can be derived. Since (in our case) we are not particularly interested in infinitesimal waves detailed presentations of first order appromimation are omitted. It is sufficient to point out that, to the first order, the effect of a uniform stream superimposed on a wave field is the well-known Doppler shift, i.e.,

$$C_1 = U + C_o = U \pm \sqrt{gh} \tag{13}$$

and

$$\omega_1 = \sigma + kU \tag{14}$$

where C is the apparent wave celerity with current
C_o is the wave celerity with no current and is equal to $\sqrt{gh}$ for the shallow water cause
ω_1 is the apparent wave frequency with current
σ is the wave frequency with no current
k is the wave number which remains unchanged with and without the current.

Second Order Solutions

When the ratio of wave height to water depth becomes appreciable, such as the present situation, first order approximation is no longer satisfactory. Second order approximation is sought, therefore. Retaining two terms in Eqs. (11) and (12) and substituting them into Eqs. (2), (6), and (7), the following set of equations are obtained:

$$(g + \frac{UC_o}{h})\eta - \frac{\partial\phi_o}{\partial t} + \frac{g}{2}\left[\frac{\eta^2}{h} + h^2(1 + \frac{U}{C_o})\frac{\partial^2\eta}{\partial t^2}\right] = 0 \tag{15}$$

and

$$\frac{\partial \eta}{\partial t} - h \frac{\partial^2 \phi_o}{\partial x^2} + U \frac{\partial \eta}{\partial x} + C_o \frac{\partial}{\partial x} \left(\frac{\eta^2}{h} - \frac{h^2}{6} \frac{\partial^2 \eta}{\partial x^2} \right) = 0 \tag{16}$$

Eliminating ϕ_o from the above equations results in the following expressions for the water surface variation (η):

$$\eta_{tt} = (C_o + U)^2 \eta_{xx} + gh\left[\left(\frac{3}{2} + \frac{U}{C_o} \right) \frac{\eta^2}{h} + \frac{h^2}{3} \left(1 + \frac{U}{C_o} \right) \frac{\partial^2 \eta}{\partial x^2} \right] \tag{17}$$

This equation is valid to the second order approximation. The corresponding wave celerity can be shown as equal to:

$$C_2 = U + C_o \left[1 + \frac{1}{4} \frac{(3 + 2U/C_o)}{1 + U/C_o} \frac{h}{\eta} + \frac{1}{6} \frac{h^2}{\eta} \eta_{xx} \right] \tag{18}$$

In the absence of a current the above expression reduces to

$$C_2' = C_o \left(1 + \frac{3}{4} \frac{\eta}{h} + \frac{1}{6} \frac{h^2}{\eta} \eta_{xx} \right) \tag{19}$$

which is the same as that obtained by Keulegan and Patterson (1940). Thus, to the second order, simple Doppler's shift is not applicable. An interference term:

$$\frac{1}{4} \frac{(3 + 2U/C_o)}{1 + U/C_o} \frac{\eta}{h} \tag{20}$$

exists. This term manifests the fact that the uniform current not only transports the waves but also does additional work on them. Longuet-Higgins and Stewart (1960) have found a similar term for deep water waves and have defined a radiation stress tensor to express the work done by a current of unit strength against the waves. This interference term can be rewritten as

$$\gamma(U/C_o) \cdot \frac{\eta}{h} \tag{21}$$

where (U/C_o) is a function of U/C_o alone. When this function is plotted against U/C_o as shown in Fig. 2, the effects of current on waves is clearly illustrated. For the condition of counter current, that is U/C_o is negative, energy is fed into the wave; the wave steepens and finally breaks. For the condition of concurrent, on the contrary, energy is extracted from the wave and the wave flattens. All of these phenomena are commonly observed but cannot be explained so far without an energy exchange mechanism.

The water surface variation can also be expressed explicitly by solving Eq. (15) with the assumption of a permanent wave form, i.e.,

$$\frac{d\eta}{dt} = \frac{\partial \eta}{\partial t} + C_2 \frac{\partial \eta}{\partial x} = 0 \tag{22}$$

or

$$\frac{\partial \eta}{\partial t} = - C_2 \frac{\partial \eta}{\partial x} \tag{23}$$

Following closely the derivations outlined by Keulegan and Patterson (1940) by substituting Eq. (20) into Eq. (15) and integrate twice one obtains

$$\eta = - \eta_2 + H\, Cn^2\left[\sqrt{\frac{3C + 2U}{4(C+U)h^3}}\ \frac{1}{k}\ \sqrt{H}\,(x - C_2 t), k\right] \tag{24}$$

where H is the wave height
Cn is one kind of the Jacobian functions of modulus k which is related to wave length (see Eq. (23)), and

$$\eta_2 = H\left[\frac{E_1(k) + k^2 - 1}{F_1(k)k^2}\right] \tag{25}$$

$F_1(k)$ and $E_1(k)$ are the elliptic integrals of the first and second kind respectively. The wave length is found to be

$$L = \sqrt{\frac{16(C_o + U)h^3}{(3C_o + 2U)H}}\ kF_1(k) \tag{26}$$

which is seen to be a function of the uniform velocity. Differentiating Eq. (21) twice and then substituting into Eq. (16), one obtains the speed of the wave crest as:

$$C_{c2} = U + C_o\left[1 + \frac{3 + 2U/C_o}{8\ (1 + U/C_o)}\frac{H}{h} + \frac{16}{3} F_1{}^2(k)\ \frac{h^2}{L^2}\right] \tag{27}$$

If we define T as the wave period, we have by definition

$$C_{c2} T = L \tag{28}$$

From Eqs. (23), (24) and (25), the effects of current on wave length as well as on wave height can be brought out. Referring to Fig. 3, it becomes obvious that for the case of counter current the wave length shortens, whereas the reverse is true for the case of concurrent flow. Figure 4 shows the effects of current on wave height. As expected, for counter current, the wave height increases whereas for concurrent flow the wave height diminishes.

The velocity potential of the incoming flow field can be obtained from Eq. (16). We first substitute η_t by $-\frac{\partial(\eta C_2)}{\partial x}$ into Eq. (16) and then integrate it with respect to x twice

$$\phi_o = \frac{1}{h}\int (U - C_2)\eta dx + \frac{g}{2h^2}\int \eta^2 dx - \frac{gh}{12}\eta_x \tag{29}$$

The task now reduces to an evaluation of $\int \eta dx$ and $\int \eta^2 dx$. The integrations are lengthy but straightforward. The resulting ϕ_o becomes:

$$\phi_o = a + b + c \tag{30}$$

where

$$a = \frac{U - C_2}{h} \left\{ \frac{HLE(\phi)\ (k)}{2F_1(k)k} + z_d x + \frac{HL(1 - k)}{k}\ \theta \right\}$$

$$b = \frac{g}{2h^2} \left\{ z_d^2 x + 2 z_d a + H^2 \left[\frac{1}{3}\ \mathrm{snX\ cnX\ dnX} + \frac{2 + k^2}{3k^4} F_1(\phi)\ (k) - \frac{2(1 + k^2)}{3k^4}\ E_1(\phi)\ (k) \right] \right\}$$

$$c = - \frac{gh}{12} \times 4\ \frac{H}{L} F_1(k)\ \mathrm{snX\ cnX\ dnX}$$

$$= - \frac{1}{3}\ gh\ \frac{H}{L} F_1(k)\ \mathrm{snX\ cnX\ dnX}$$

where

$$\phi = \sin^{-1} [\mathrm{snX}]$$

and

$$X = \left[2F(k)\ \left(\frac{x}{L} - \frac{t}{T} \right),\ k \right]$$

Outflow Generated by the Obstacle

Since the characteristic length of the obstacle is, in the present suudy, assumed to be comparable to that characteristic of the wave field, the disturbance to the flow field created by the obstacle must be taken into consideration. In other words the outflow generated by the obstacle must be determined. Because an exact irrotational solution for a pile of irregular shape in a gravity wave field has not been found, an approximate solution is proposed to yeild near field flow information from which pressure and force on the pile can be calculated.

As the surface of the obstacle is bounded by closed curves, it is natural to define its contour in appropriate cylindrical coordinates (R, θ, y) (Fig. 5):

$$R = R\ (\theta, y) \tag{31}$$

where R prescribes the contour of the obstacle. A local coordinate system (ℓ, m, n) is also defined such that ℓ is tangent to the contour curve, m is the bi-normal, and n is the normal at any station.

The near field potential is expressed in Taylor's series of velocity potential on the obstacle:

$$\phi = \sum_{k=0}^{\infty} \frac{n^k}{k!} \frac{\partial^k \phi(p)}{\partial n^k} \tag{32}$$

where $\phi(p)$ is the velocity potential at the obstacle and n is the local normal as defined earlier.

The task now reduces to finding the velocity potential on the object.

The velocity potential on the object can be separated into two parts:

$$\phi(p) = \phi_{in}(p) + \phi_{out}(p) \tag{33}$$

where $\phi_{in}(p)$ is the inflow velocity potential that exists if the object is removed and $\phi_{out}(p)$ is the velocity potential generated by the obstacle.

The inflow velocity potential on the object is determinable from the inflow potential described in the previous section. The outflow potential on the object needs to be developed. We assume that $\phi_{out}(p)$ can be expanded in terms of functions determinable from $\phi_{in}(p)$ and its derivatives in the normal direction, i.e.,

$$\phi_{out}(p) = \sum_{k=0}^{\infty} \alpha_k \frac{\partial^k \phi(p)}{\partial n^k} \tag{34}$$

This assumption is believed to be valid for several reasons. From the point of view of mechanics, the response must be determinable from the excitation. From the mathematical point of view, many exact solutions exist in which the outflow potential created by the obstacle is, on the surface of the obstacle, proportional to the incoming potential. Outstanding examples are a submerged cylinder and a sphere. For a submerged cylinder, for instance, the outflow potential at the surface of the cylinder is equal in magnitude, to the inflow potential at the surface. Furthermore, the non-linearity of the free surface is none other than the continuous scatterings of the incoming flow by the obstacle at a distance. Thus, it is plausible to include normal derivative terms of incoming flow potential in the representation of outflow potential.(i.e., ϕ_{out} depends on the variations of ϕ_{in} with distance to the obstacle).

After one has selected the functional representations of outflow potential, the coefficients, α, can be determined through appropriate boundary conditions. These boundary conditions are:

$$p \approx 0 \tag{35}$$

$$\frac{dp}{dt} = \frac{\partial p}{\partial t} + \nabla\phi \cdot \nabla p = 0 \tag{36}$$

at the free surface. And

$$\frac{\partial \phi}{\partial n} = 0 \tag{37}$$

at the surface of the obstacle and at the bottom. These equations, (35), (36) and (37), are applied to the total potential, of course.

Since we are interested in the velocity potential at the obstacle, simultaneous solution of Eqs. (35) and (36) defines a wet line on the obstacle. It should be noted that for a finite term of expansion of ϕ_{out}, the conditions p = 0 and dp/dt = 0 cannot be satisfied exactly. One usually has to settle for an approximation such as

$$|p|_{max} \leq \Gamma_1$$

or

$$\left|\frac{dp}{dt}\right|_{max} \leq \Gamma_2$$

where Γ_1 and Γ_2 are the pre-determined maximum tolerable errors.

Once we determine the velocity potential, the pressure distribution around the obstacle can be obtained through Bernolli Equation. The total force and moment exerted on the obstacle are then calculated through numerically integrating the following equations:

$$F = 2\int_o^{\Pi} \int_o^{\eta} p \cos\theta \, Rd \, yd\theta \tag{38}$$

and

$$M = 2\int_o^{\Pi} \int_o^{\eta} p \cos\theta \, Ry \, dyd\theta \tag{39}$$

Numerical Computations

Numerical computations are performed for an axial-symmetric pier of configurations shown in Fig. 6. The pier is 100 feet in diameter with a cylindrical base 80 feet high and a conical top of 45 degrees extruding out of the water level which is 100 feet above the mud line. The incident wave is 7.6 seconds long in period and 14 feet high. The current velocity is null. This combination is chosen so that the numerical results can be compared with experiments of an identical situation (Wang, 1970).

To facilitate numerical computation, the pier is divided into

grids; 19 azimuthal stations from o to π, 8 depth stations on the cylindrical sections and 25 depth stations on the conical section (Fig. 6). The oncoming potential is calculated first according to Eq. (30) using a method similar to that developed by Wang and Hwang (1970).

The outflow potential is calculated by cutting short Eq. (34) to retain only the first two terms, i.e.,

$$\phi_{out}(\text{pile}) = \alpha_o \, \phi_{in}(\text{pile}) + \alpha_1 \frac{\partial \phi_{in}(p)}{\partial n} \tag{40}$$

The coefficients α_o and α_1 are obtained through iterative processes so that both boundary conditions, Eqs. (35) and (36) are approximately satisfied. In essence, the iterative scheme consists of the following manipulations:

1. Select a value of α_o (1 is selected for the present calculation because it leads to the case of cylindrical diffraction) and maintain C_1 to be zero. From Eq. (32), cutting short at two terms,

$$\phi = \sum_{k=0}^{1} \frac{\eta^k}{k!} \left[\frac{\partial^k \phi_{in}(p)}{\partial n^k} + \frac{\partial^k \phi_{out}(p)}{\partial n^k} \right]$$

and Eq. (30), we obtain a tentative velocity potential.

2. From Eq. (35), letting Γ_1 be equal to zero (exact solution) i.e.,

$$\frac{p}{\rho} = - \, g\eta + \phi_t + U\phi x - \frac{1}{2}(\nabla\phi)^2 = 0$$

a value of η can be obtained. Numerically, it is achieved by computing p at consecutive depth stations from the sea floor until p changes sign. If, for instance, the change of sign occurs between y_L and y_{L+1}, one calculates

$$\alpha = \frac{p_L}{p_L + p_{L+1}}$$

where p_L is the value of p at y_L and p_{L+1} that at y_{L+1}. The value of η is then determined as

$$\eta = y_L + \alpha \Delta y_L$$

If no change of sign occurs within reasonable range, the value of C_o needs to be adjusted.

3. If the value of η falls within a reasonable range, Eq. (36),

$$\frac{dp}{dt} < \Gamma_2$$

is used to check the validity of the solution. For the case $\frac{dp}{dt} > \Gamma_2$, letting $\Gamma_2 = 0$, we solve for α_1.

4. The above procedures are repeated until suitable sets of values of α_o and α_1 are obtained for all the azimuthal stations for a designated time station.

We have to confess that up to date no systematic method has been developed for the proper selection of α's. In the computer program, we have made the assumption that α_o varies from 1 (reflection from cylindrical surface) to 0 (the object has no influence on the wave field), and , varies from -1 to +1. Indeed, the results to date fall into this range. It is also impossible, at present, to establish the uniqueness of these solutions. At this moment, like many engineering problems, we rely on the actual physical situation to test the validity of our solution.

After we have obtained the velocity potential, the numerical computation of pressure distribution, forces and moments are rather straightforward. Only horizontal force and horizontal moments are being calculated.

Comparision of Theoretical and Experimental Results

Numerical computations are performed for the following input conditions:

pier diameter: 100 feet
water depth: 100 feet
wave height: 14 feet
wave period: 7.6 second
current velocity: 0 knots

These conditions are chosen so that the results can be compared with that obtained from earlier wave tank measurements. The experiments are described by Wang (1970). The essential results are summerized in Table 1. In this table, theoretical results based on linear wave theory and fifth-order wave theory are also included.

	Experiment	Cnoidal Wave	Fifth-Order Wave	Linear Wave
Wave Force (kips)	6,300	5,050	2,900	4,000 (est.)
Force Center (ft.)	53 (ave.)	49.5	49	

Table 1. Comparison of Experimental and Theoretical Results

From these results, it is clear that the results based on the modified cnoidal wave theory come closest to the experimental value. All three theories, however, yield smaller values than the experiment.

The total maximum horizontal force exerted on the pier is predicted by the cnoidal analysis to be approximately 20 percent smaller than the experiment, whereas the discrepancies become 30 percent and 45 percent for the cases of linear and fifth order wave methods, respectively. To explain why theories predict lower values than the experiments, several possibilities are examined.

All the theories are based on the assumption that the fluid is inviscid. As a consequence, viscous force, or velocity related force, is completely ignored in the computation. This assumption may or may not be valid, particularly in a scaled down model. If the viscous force cannot be ignored, the theoretical results would naturally be expected to yield smaller values than the experiments. In the report of experimental results, this possibility has been examined and discounted; because in the experiment, the observed wake is very small and the maximum horizontal force occurs at the instant when the water particle acceleration is maximum and its velocity is null at the center of the pier. This conclusion is further confirmed through comparing the theoretical pressure distribution with that of the experiment (Fig. 7). It is obvious from Fig. 7 that the effects of wake (from 150° to 180°) to the horizontal force is very small. The discrepancy actually occurs at the middle section of the pier.

A second possibility why the theoretically predicted force is smaller than the experiment is that the tank test was performed in a channel of finite width with channel width to pier diameter ratio equal to 4 to 1 whereas the theories deal with an infinite flow field. Thus, the blocking effect which might be expected to occur in the tank test has not been taken into consideration in the theoretical formulation. This blocking effect is believed to be the major contributing factor to the discrepancy between theoretical and experimental results.

Yet there exists a third possibility; namely, the selected wave theory does not truly represent the actual wave motion in the tank. This difficulty is rather insurmountable at this time. One can only hope that the selected wave theory is one of the better fits to the physical situation to be described. LeMéhante and Divoky (1968) have shown that among various wave theories, the cnoidal wave of MacCamy and Fuch comes closest to describing the water particle motions (rather than water surface variations which sometimes can be forced to fit) in shallow water. The present study seems to confirm, at least that among linear, fifth order and cnoidal, the cnoidal wave is a better choice. It is worthwhile to observe that under the combinations of shallow water and large obstacles, fifth order wave theory yields the largest discrepancy between theory and experiment. One may speculate that when the diameter of the object is of the same order of magnitude as the wave length, effects due to higher harmonics may nullify each other or may even interfere with that created by the basic harmonics.

Finally, in Fig. 8 the wet line on the cone-shaped surface of the pier is shown in comparison with the undisturbed wave shape (the wet line which occurs under the condition that the obstacle has no effect on the wave field) and with a fully reflected line (linear wave fully

reflected by a cylindrical structure). From the Figure, it is obvious that a cone-cylinder shaped structure causes far less surface disturbance than that caused by a cylindrical structure. As a consequence, a cone shaped structure also offers significant advantages over cylindrical structures in reducing wave forces. These phenomena concur the experimental results cited previously.

In summary, the mathematical model and the computer program developed provide a means of calculating wave forces and moments on large structures of irregular shapes in a wave field where the current effect cannot be neglected. The mathematical model, however, yields smaller wave forces than those obtained through experiment. It is believed to be suitable for engineering purposes provided that the characteristic length of the object is at least the same order of magnitude as the wave length and that the object is situated in a shallow-water wave environment. It is further stressed that this model will not yield validate information when the object is small compared to water depth and wave dimensions such as pilings and drill strings.

It is worth mentioning that in the derivation of inflow wave field, certain resilient figures of non-linear interference between current and shallow water waves have been discovered; those include wave length and wave height dispersions. Explicit expressions have been provided for these dispersions. Further pursuit in this direction should yield enlightening information in wave mechanics.

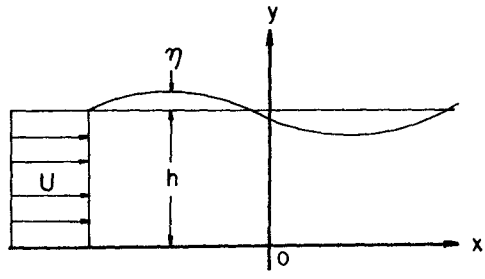

Figure 1. Definition sketch

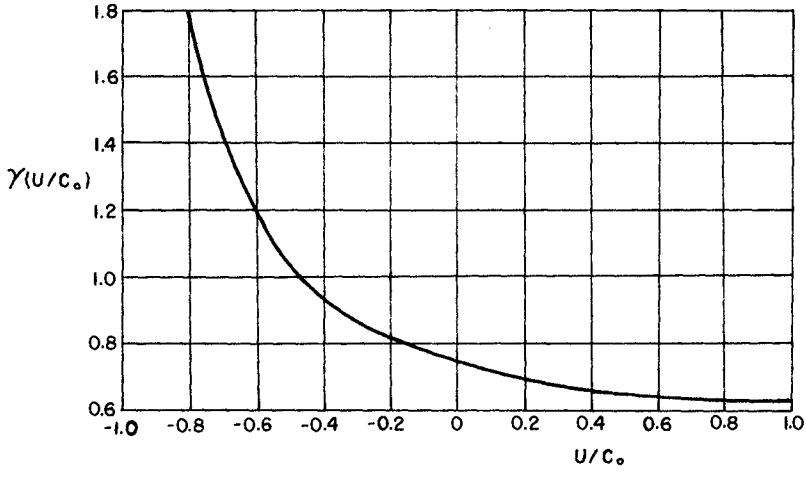

Figure 2. Variation of $\gamma(U/C_o)$ versus U/C_o

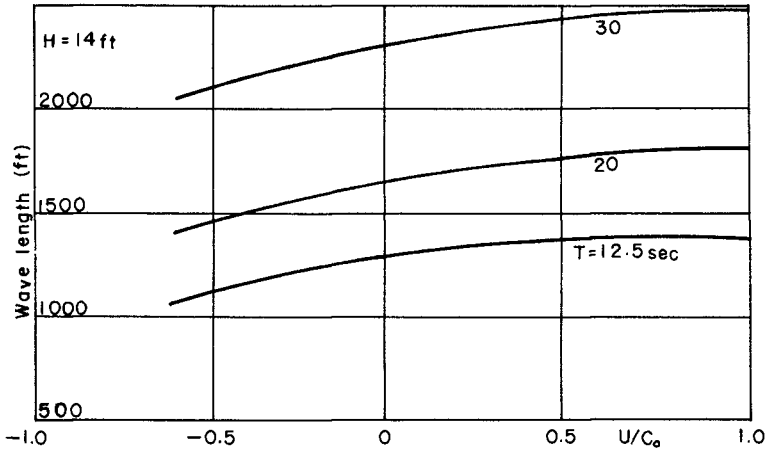

Figure 3. Current effect on wave length

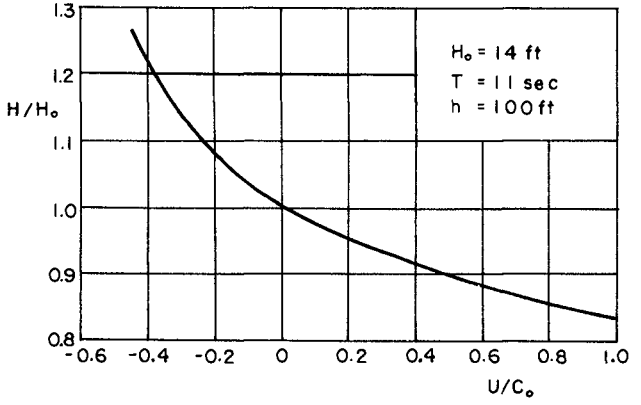

Figure 4. Current effect on wave height

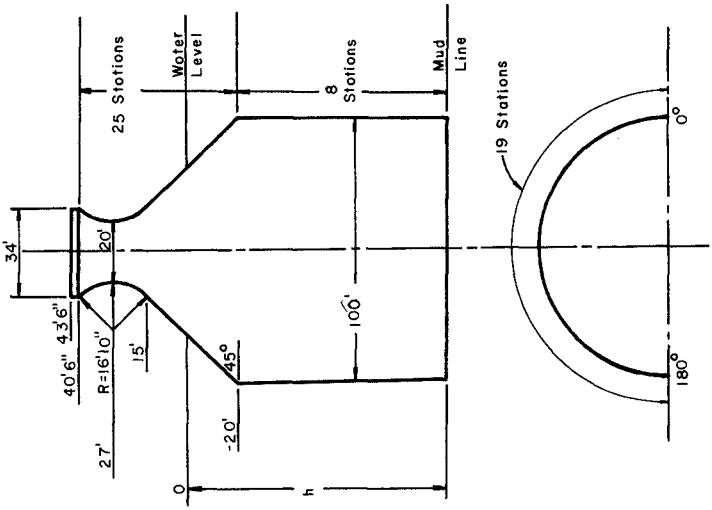

Figure 6. Grid system applied to obstacle for numerical computation

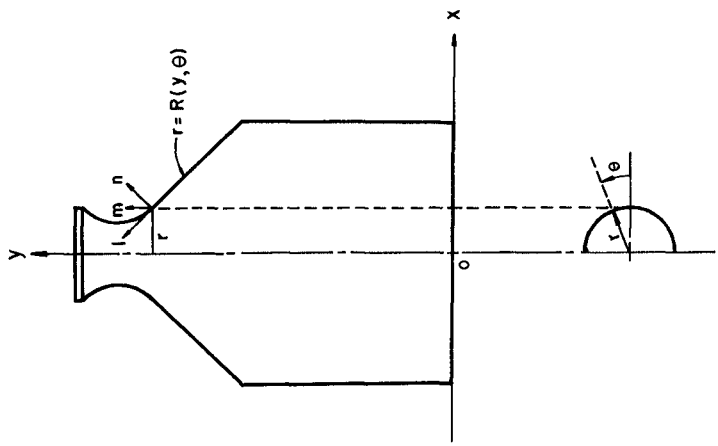

Figure 5. Definition and coordinate systems of obstacle

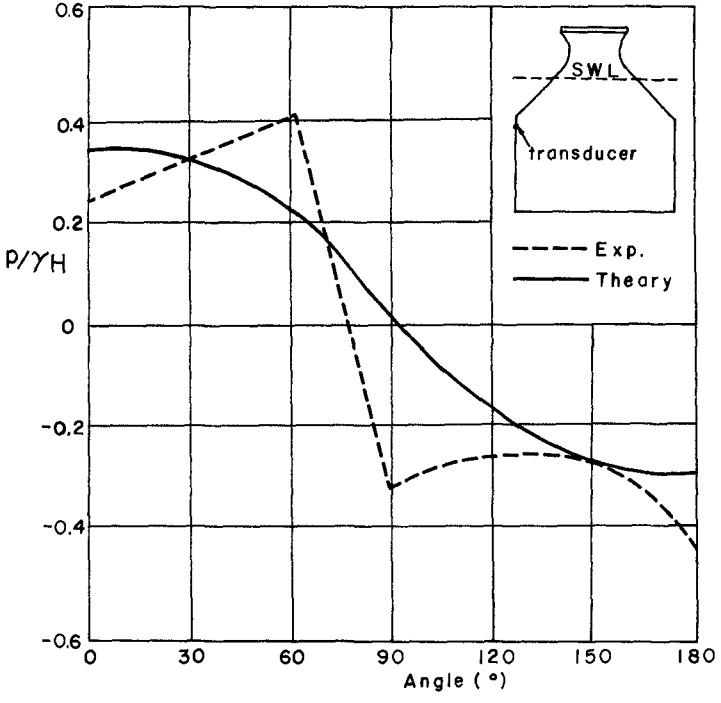

Figure 7. Pressure distributions about the obstacle at F_{max}

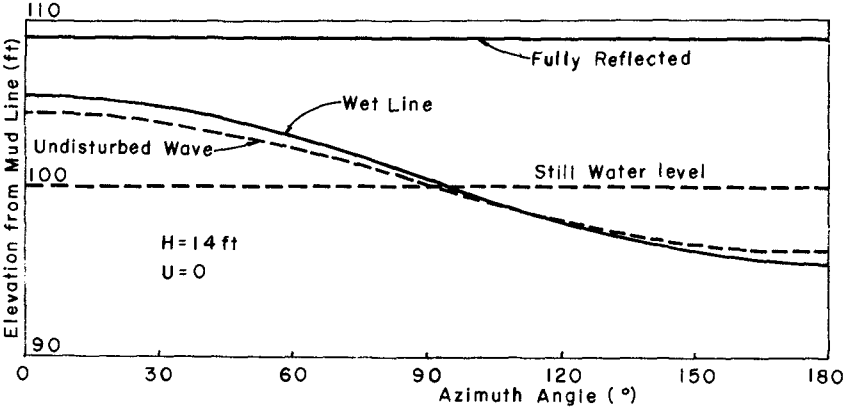

Figure 8. Wetline around the obstacle

References

1. Clavier, P. A., "Wave Effects on Piles of Any Symmetry in the Presence of Current," Supplement SN-425, National Engineering Science Co., 1967.

2. Le Méhauté, B., et.al., "Shallow Water Waves: A Comparison of Theory and Experiments," Proc. 11th International Conference on Coastal Engineering, 1968, pp. 86-107.

3. Longuet-Higgins, M. S. and Stewart, R. W., "Changes in the Force of Shut Gravity Waves on Long Waves and Tidal Current," Journal of Fluid Mechanics, 1960, pp. 565-583.

4. Keulegan, C. H. and G. W. Patterson, "Mathematical Theory of Irrotational Translation Waves," National Bureau of Standards, Paper RP1272, 1940.

5. MacCamy, R. C. and Fuch, R. A., "Wave Force on Piles; A Diffraction Theory," U. S. Army Corps of Engineers, Beach Erosion Board, T. M. No. 69, 1954.

6. Wang, H., "Loadings on Large Piers in Waves and Currents," Proc. 12th International Coastal Engineering Conference, pp. 1491-1511, 1970.

7. Wang, H. and Hwang, L. S., "Behavior of a Slender Body in Shallow-Water Waves," Proc. 12th International Coastal Engineering Conference, pp. 1723-1744, 1970.

CHAPTER 101

ICE EFFECTS ON COASTAL STRUCTURES

by

H.R. Kivisild

Director of Research and Development
FENCO, Toronto

and

G.D. Ransford

Chief Research Engineer
FENCO, Toronto

Introduction

Ice effects on coastal structures, and more particularly the maximum forces caused by ice action, depend on a number of factors, such as:-

(a) The physical properties of the ice encountered.
(b) The thickness of ice formations.
(c) The size of these formations, and their motion.
(d) The shape and size of the structures concerned.

Past history of ice accumulations is important too, not only in relation to ice properties (as when new ice and multi-year ice are found together at the one location), but also for instance when structures become frozen in, or when ice debris accumulates on sloping faces or when ice bustles form around piers. The very considerable difficulties in carrying out insitu experimental work, not only on the overall effects of interest to engineers such as ice thrust on fixed structures, but also on ice properties themselves, mean that there are still large gaps in our knowledge of the subject. Finally, the non-isotropic nature of the naturally occurring ice, and the broad spectrum of ice behaviour under loading (brittle,ductile or, when creep predominates, viscous), contribute still further to the complexity of the subject.

Physical Properties of the Ice Encountered

A sharp distinction should be made between freshwater ice, which exhibits brittle failure under commonly prevailing rates of load application, and sea ice, which is much more plastic. The added plasticity of the latter offsets the lower strength due to brine inclusions; sea ice in effect tends to mould itself around an obstacle producing higher crushing forces than when brittle behaviour prevals.

Ice masses which engineering structures must withstand differ in many respects from samples of ice studied in the laboratory. The use of carefully chosen small samples in evaluating the crushing resistance of ice overestimates the crushing strength of large masses of ice which naturally contain imperfections; the strength ratio, which is typically of the order of 2 : 1, cannot yet be estimated with high precision.

In the case of sea ice, brine pockets cause a reduction in strength. If the salinity is known, the brine volume may be found as a function of temperature. A reduction ratio may then be used to scale down the expected strength of the sea ice, as compared with that of freshwater ice at the same temperature; unfortunately, the reduction is not known with precision. It should be added that a rise in temperature leads to a reduction in strength of pure ice. This effect compounds the loss of strength suffered by sea ice on account of increasing brine volume at higher temperatures for a given salinity.

Much discussion has taken place in the past about the effect of rate of loading on the crushing resistance of ice. It has been inferred from past tests on sea ice specimens that a peak resistance occurs at a certain rate of loading, with strength reductions at either higher or lower rates. Our own re-evaluation of the earlier data referred to tallies with recent research (1) to the effect that while compressive strength drops off with a reduction in rate of strain, there is no peak value reached at a definite finite rate of loading. Highest strengths are found when impact is fastest, giving in effect brittle, rather than plastic failure.

Thickness of Ice Formations

The thickness of unbroken sheet ice forming on the sea or in bodies of freshwater can be estimated with adeuqate precision by a variety of formulae. One of the earliest of these formulae is Zubov's:

$$T^2 + 50T = -8\Sigma\Theta$$

where T is the ice thickness attained in cm after $\Sigma\Theta$ freezing ^0C - days, measured rather illogically for sea ice, from 0^oC down rather than from the actual freezing point of sea water. Later workers allow for snow cover, wind velocity, etc., but the results given do not vary much from Zubov's simple estimate based on average conditions for sea ice in the arctic.

Ice moving against an offshore structure may however have been subjected to prior crushing with the formation of rafted covers or of ridges. In the process, the original cover will have been fractured so that when recently formed, ridges or rafted formations may actually be weaker than the unbroken cover. For

design purposes, however, it is essential to consider the effect of subsequent annealing. In the extreme case of multiyear arctic ice in which the annealing is caused by snowmelt water giving nearly pure ice of high strength, the resulting formations may present a formidable obstacle to shipping. Coastal structures, other than drilling rigs in exposed locations, will fortunately not have to cope with such extreme types of ice hazard in general. Partly-annealed ridges may have to be considered, though; we are only now acquiring reliable data (2) concerning not only the expected sail and keel shapes of ridges (which are generally not in isostatic equilibrium)but also the shear strength built up within the keel by the snowmelt water filtering down. This paucity of information is of course not surprising, in view of the experimental difficulties involved.

Close into shore in many regions hummocked ice is found which is thicker than elsewhere, principally on account of repeated crushing of floating ice against the ice fixed to the shore. Coastal structures will not be established in such zones. More importantly, the existence of such areas of ice may effectively bar winter access by icebreaker to harbours established within sheltered areas of the coast, e.g. in the mouths of rivers. An added source of ice thickening arises in this case too; fresh water brought down by the rivers will lead to thicker ice, as fresh water freezes more readily than salt. Problems of this nature plague the Hudson Bay shipping route, for example.

Thickness and age of an ice formation are two parameters from which expected salinities, so important in assessing crushing strength, may be assessed. As sea water freezes, brine is trapped between the surrounding ice crystals; however, with the passage of time, or by virtue of a melting and refreezing process occurring in multiyear arctic floes, the brine inclusions tend to disappear leaving much stronger ice behind.

The rate of thickening of ice, and the general conditions under which growth occurs, will affect the grain structure too. Though past tests have shown that grain orientation plays a very important role in relation to crushing strength (ice crystals growing parallel to one another in a typical thick sheet behave in rather the same way as lubricated bundles of rods), not enough is known yet to introduce grain orientation as an independent factor in crushing strength formulae for real, composite ice sheets as opposed to laboratory specimens.

Icebergs constitute a separate problem, fortunately in rather restricted areas of the globe. It is difficult to see as yet what means are available to cope with the iceberg danger as it affects fixed offshore structures, e.g. fixed rigs off the Labrador coast. The problem is not only one of the enormous masses of ice involved, but also of instability; icebergs may so readily overturn.

Size of Ice Formations, and their Motion

From the standpoint of structural design, a broad distinction serving to illustrate the principles involved may be made between two categories of ice:

(i) "Infinite" ice masses (sheets or icebergs)

These may or may not develop the maximum crushing force which the ice can in theory deliver, depending on the rate of movement of the ice. Generally a large ice floe moving against a fixed structure will do so at a velocity such that the maximum crushing force (brittle failure of the ice) occurs. The only possible relief from these high forces will result from substituting floating (non-fixed) structures for fixed ones wherever possible, e.g. by using barges instead of fixed offshore platforms for drilling. The floating structure will however be rendered unserviceable each time the ice hits.

Under this heading, the forces exerted by ice sheets undergoing thermal expansion, subsequent on a rise in air temperature, between fixed structures or obstacles may also be considered. It should be noted that the latter problem, despite much excellent research work (3), still sets the designer a difficult task; not only must the flexibility of the structure be allowed for, but also the transmission of shear between successive layers of the ice sheet must be considered, as these undergo differential expansion. Thus extensive ice sheets will predictably arch and crack, giving lower thermal forces than smaller sheets subjected to the same thermal effects.

In practice, it has been shown that successful engineering designs using light structures can be evolved by making proper use of flexibility.

(ii) Finite ice masses (small floes or growlers)

The maximum crushing force may or may not be developed in this case, depending on the momentum of the ice mass as it hits the structure; the flexibility of the latter also plays a minor role.

In designing against such ice impacts, considerable thought must be given to the probable size of the floes likely to occur at the site, the velocity of approach of the floes (depending for example on wind and durrents and to some extent on the roughness of the floe itself) as well as to the physical properties of the ice. Thus free-moving floes may only arise in the spring, when ice masses break loose and disintegrate; a careful estimate of probable ice temperature, salinity and residual thickness is required in such cases.

The Shape and Size of the Structures

Depending on whether the impact is delivered by a mass of ice of effectively infinite size, or by a mass of ice of finite size, one may have to consider respectively

(i) The effect of the ice impact over the whole exposed surface of the structures; or

(ii) Local effects occurring while the impacting mass is being brought to a standstill.

Of course, in case (1), the structure must be designed in such a way that local stresses occurring are also properly absorbed. Hence the case of an "infinite" ice mass is the more general one.

Structures, looked at as a whole (i.e. without reference to local effects) may be categorized in a number of ways. The simplest shape is that of a plane face, which may be vertical or sloping. In theory, at least, an ice sheet exerts far less force against a sloping face to which it does not adhere than against a vertical one. For reasons given at the outset, it is not proven that real benefits accrue from sloping faces as opposed to vertical ones, at least in the arctic.

Whereas, in the case of a plane face of considerable width struck by an ice mass, the proper crushing strength is that derived by compression testing of similar ice with due allowance for scale effects, temperature and salinity variations throughout the sheet, etc. the problem of choosing the correct equivalent crushing strength for the case of a cylindrical structure is somewhat more complicated, even if one assumes that prior to impact the ice sheet was preformed to the exact cylindrical shape in question. Part of the ice will shatter upwards, part downwards and obviously, in the case of a relatively slender cylinder at least, part will shatter out laterally. Certain rupture patterns can be devised in an effort to describe the impact phenomena; even if these are not perfectly coherent, and there are difficulites in developing a shatter mechanism that satisfies all the rules of logic, they should at least err on the safe side. Unpublished work has achieved this goal to a large extent, except in relation to one factor which must serve to reduce overall forces in the case of large engineering structures. This is the fact that, in considering the impact of ice masses not previously adhering to a structure, contact of the ice and subsequent failure at maximum stress will not occur at all points simultaneously over the face of the structure. A ratchet motion will in effect prevail, and this has been observed. The problem of determining just what scale-down factors should be used, without committing oneself to unsafe design, is as yet unsolved. Field tests of a particularly costly and difficult type are called for; some headway has been made, but only on thin, fast moving floes not typical of many locations (4).

In designing multileg offshore structures, to which category piled quaywalls belong, arbitrary allowance is generally made when studying overturning or sliding of the structure as a whole for the non-simultaneity of the forces acting on different legs or piles. Once again, more rational design procedures are desirable, but the problem is to obtain site data for this.

Reference has been made to the combination of failure modes, upward, downward and lateral, in the impact of ice on cylindrical structures. In the case of small ice formations, rather than of the large ones discussed hitherto, the gradual spreading of the contact zone as the ice hits the structure has to be considered. Various phases can be identified, e.g. in the case of a plane ice surface hitting a rounded structure. The local resistance of the structural plating or members affected must be checked against the force delivered by the ice. Local stresses can exceed the unconfined compressive strength of ice cylinders very markedly, while the contact zone is first expanding outwards. Subsequent phases of impact introduce the problem noted earlier: at how many points will contact develop simultaneously?

Overall forces in the case of very small floes or growlers may be restricted by splitting of the entire floe. The contact force in this case is limited by the tensile strength of ice, rather than by the compressive strength. High velocities of impact are the only ones of concern to the designer.

In the case of a floe of limited size hitting a large cylindrical structure, the ice may be brought to rest. The retardation of the floe as it comes to rest should be analyzed (5) in relation however to the limited momentum in the impacting ice, and possibly the give in the structure itself.

The added forces, if any, caused by unconsolidated ice ridges may be analyzed along fairly straightforward lines, at least in the case of simple cylindrical structure. Unpublished studies have shown that, to the extent that the ice sheet within such ridges may be thinner than elsewhere (on the assumption that ridging cannot occur in rafted and annealed ice, which is the most dangerous type of sheet), ridges may not exert supplemental forces on structures as compared with the surrounding cover. As previously noted, consolidation in ridges will present an entirely different problem.

The adhesion of ice to structures partly depends on the nature of the surface. Thus ice bustles, or ice accretions around piles brought about by tidal movement, occur on steel surfaces but not on creosoted timber ones. Freezing-in of structures will lead to a considerable increase (approximately to the doubling) of ice forces once the surrounding sheet begins to move. Finally many of the theories will be in default should adfreezing occur.

REFERENCES

1. Ivor Hawkes and Malcolm Mellor
"Deformation and Fracture of Ice under Uniaxial Stress"
Journal of Glaciology, Vol II, No. 61, 1972 pp 103-131

2. W.F. Weeks, A.Kovaks and W.D. Hibler
"Pressure Ridge Characteristics in the Arctic Environment"
Proc. lst International Conference on Port and Ocean Engineering under Arctic Conditions, Trondheim, Norway, 1971, Vol I, pp 152-183

3. Marc Drouin
"Les poussées d'origine thermique exercées par les couverts de glace sur les ouvrages hydrauliques"
D.Sc. thesis, Universite Laval, Quebec, October 1971

4. K.A. Blenkarn
"Measurement and Analysis of Ice Forces on Cook Inlet Structures"
Paper OTC 1261, Offshore Technology Conference, April, 1970, Houston, Texas

5. R. Frederking and L.W. Gold
"Ice Forces on an Isolated Circular Pile"
Proc. lst International Conference on Port and Ocean Engineering under Arctic Conditions. Trondheim, Norway, 1971, Vol I, pp 73-92

CHAPTER 102

CONSIDERATIONS ON FACTORS IN BREAKWATER MODEL TESTS

by Yvon Ouellet, D.Sc.

Assistant Professor, Civil Engineering Department

Laval University, Quebec, Canada.

ABSTRACT

In the light of tests on breakwater armor units conducted at Laval University on behalf of the Department of Public Works of Canada, a discussion on various factors involved in model tests on breakwater armor units is presented in comparison with previous studies made on the subject. Tests have been carried out on natural stones, tetrapods and mainly dolosse.

Various factors whether they pertain to waves or to the structure are analysed in view of the factors resulting from the interaction of both of them, that is stability of the armor units, damage to the structure or run up of the facing. These factors are the ones for which model tests are conducted. The interpretation of results for the given test conditions should not be evaluated without considering possible scale effects.

From the analysis of test results presented by different investigators, a need for the standardization of test results became apparent. Recommendations are made concerning the presentation of results for their future use in engineering design. A standard weight of 100 grs with a standard length of 100 cms for model values are proposed to present the results on a diagram showing significant wave height versus damage, where damage should be expressed in terms of the number of units displaced in the area between $\pm$ the wave height giving 1% damage.

INTRODUCTION.

Scale model tests of rubble-mound breakwaters is concerned with factors resulting from the interaction of waves and the structure itself. As shown in fig. 1, these are commonly referred to as stability, damage and wave run up. On one side the factors pertaining to the structure could be divided into the structure itself, that is its slope, its orientation with respect to wave attack and whether its trunk or its head is attacked by waves, the units, their weight, density and shape and the layers that is their thickness, porosity and the way the units are placed in them. On the other side the waves which are caracterized by their height, period and duration, can act under different conditions such as whether they are shallow or deep water, breaking or non breaking, linear or non linear, regular or irregular, overtopping or non overtopping.

Because of the great difficulty in obtaining prototype results, a great amount of scale model tests of breakwaters have been carried out in different laboratories over the world. The tests were first conducted on natural stones then later on artificial concrete blocks in order to get a stability formula, that is the required weight of given units for no damage under certain wave conditions. Afterwards the notion of damage to the structure was introduced above this level, which in turn made other factors such as storm duration, wave period, types of waves, run up and overtopping, intervene in this kind of study. All these tests were done in view of making possible a better design of the structure. With the knowledge of damage suffered by a breakwater under different wave conditions of which the frequency of occurence is known, it was then possible to think of achieving an optimum design by comparing the construction cost versus the cost of damage risks including the malfunction of the structure. This is the ultimate goal to be obtained in a study of that sort after all the factors involved have been taken into account.

EFFECT OF WAVE HEIGHT.

The wave height is the primary factor belonging to waves for the study of rubble-mound breakwaters. Whether constant or significative wave height is used, it is always referred to the incident wave characteristics. It is the factor most involved concerning the stability, damage or run up incurred on the breakwater. Imprecision in measuring the wave height will result in the scattering of the results.

EFFECT OF WAVE PERIOD.

The wave period is of secondary importance on stability as long as we are near the value of maximum interest. For given conditions, a small change in wave period near value does not affect much stability.

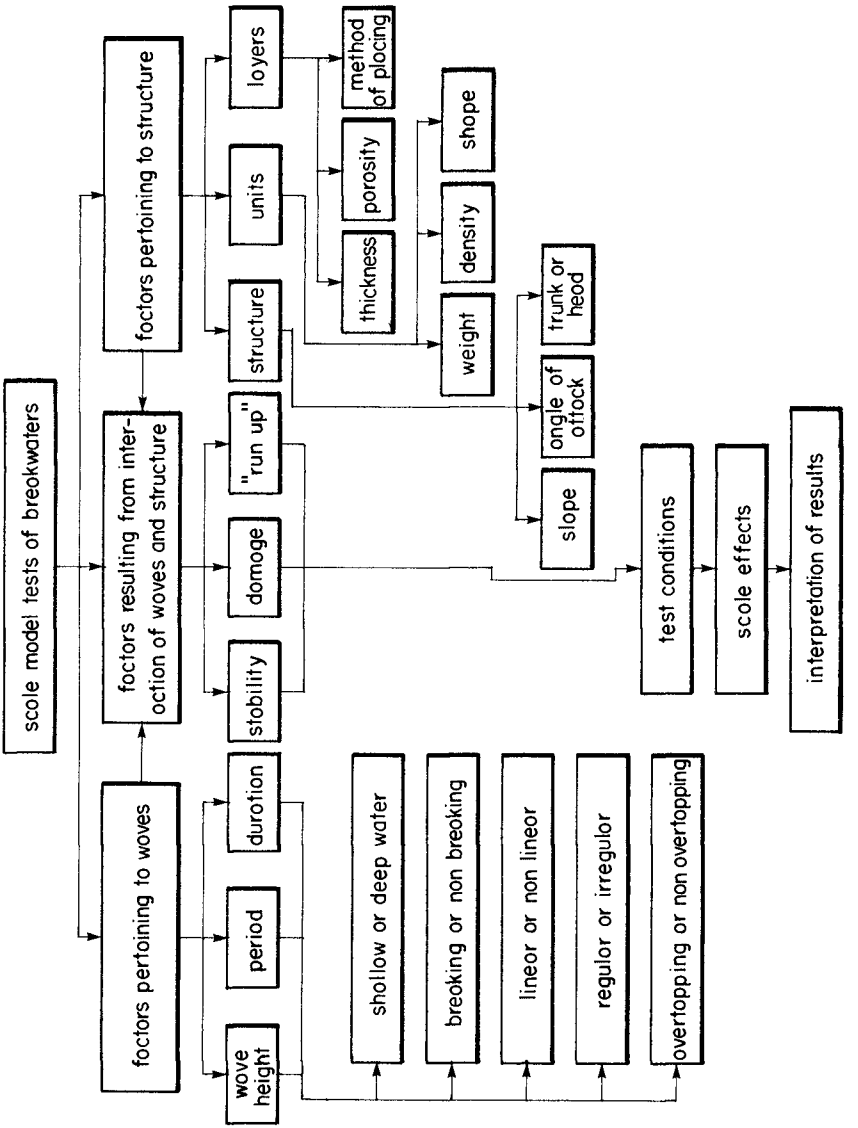

Fig. 1.—FACTORS CONCERNED WITH SCALE MODELS TESTS OF BREAKWATERS

The values of prototype wave periods reported in the literature should not be taken as such since they depend on the scale adopted by the author (see table 1) and accordingly on the size of the prototype units which results. In order to make possible a comparison, we have reported all values to a standard model weight of 100 grs by scaling down the true weight of the units used for model tests given in table 1 to this standard weight. By taking the cubic root of this scale we get the length scale which is given in table 2 with the other corresponding values scaled accordingly. It can be seen that the range of most damaging model wave periods is between 1.5 to 2.0 seconds. In fact a variation should take into account other factors such as the wave height which results in wave steepness and the water depth which results in relative depth for non breaking wave conditions. As reported by hydraulic Research Station, Wallingford, it appears that the effect of wave period is more important in the advanced stage of damage.

EFFECT OF STORM DURATION.

The storm duration is specified in terms of the number of waves attacking the structure. This factor, which is important in the scattering of test results is of considerable importance in the advanced stage of damage. Above a certain level of wave height, damage to the structure will increase if sufficient duration is allowed. Below this level the damage to the structure stops to a certain limit where a new equilibrium profile is obtained. The limit would then approximatively be when for the new equilibrium profile the protective layer is uncovered.

Which is of interest regarding storm duration is the time history of wave attack, that is whether the new built structure is first attacked by smaller or bigger waves. Most of the time for model tests wave heights are increased in steps until the maximum conditions are obtained. This sometimes permits to some units to get into a more stable position before the higher waves come. However some tests conducted directly with greater wave heights on a newly placed facing have shown a slight difference between these two test conditions.

EFFECT OF STRUCTURE.

Many tests have been conducted on breakwater with slope of facing in the range of 1 in 1.5 to 1 in 3, which is in the limit of most of the breakwaters built. Outside this range few tests are available because of their less practical interest. The variation of slope affects the wave form in the vicinity of the breakwater and in this way the conditions of attack of the protective layer. The most interesting point concerning the slope is its variation towards a new equilibrium composed of three different slopes when serious damage is suffered by the structure.

When waves arrive at an angle with the structure, the effect is less severe than perpendicular wave attack. However not much reduction is for angles smaller than 45°.

TABLE 1- CHARACTERISTICS OF MODEL UNITS USED BY DIFFERENT INVESTIGATORS.

AUTHOR YEAR PLACE	NAME OF UNITS	VOLUME OF UNITS	WEIGHT OF UNITS	SPECIFIC GRAVITY	SPECIFIC WEIGHT	WATER DEPTH	WAVE HEIGHT (UP TO)	WAVE PERIOD	SCALE
---	---	cc	grs	---	lbs/ft^3	feet	feet	sec.	---
HUDSON 1959 Vicksburg, U.S.A.	Quarry stones Tetrapods (concrete) Tetrapods (leadite)	14-48 35-48 43-48	41-140 82-100 95-105	2.66-3.08 2.16-2.46 2.14-2.28	166-192 135-154 134-142	1.26-2.0 1.26-2.0 1.26-2.0	0.70 0.70 0.70	0.88 to 2.65	No scale
SINGH 1961 Wallingford, England	Stabits	55	129	2.32	145	1.0	0.68	1.45 1.75	1:47
PAAPE & WALTER 1962 Delft, Netherlands	Akmons Quarry stones Cubes Tetrapods Tripods Bipods	38 38 38 38 38 38	84 84 84 84 84 84	2.2 2.2 2.2 2.2 2.2 2.2	137 137 137 137 137 137	1.4 1.4 1.4 1.4 1.4 1.4	0.6 0.6 0.6 0.6 0.6 0.6	1.4 1.4 1.4 1.4 1.4 1.4	No scale
MERRIFIELD & ZWAMBORN 1965 C.S.I.R. South Africa	Dolosse Dolosse Dolosse Tetrapods Rectangulars Rectangulars Tetrahedrons	479 218 94 385 536 394 304	993 427 185 834 1262 929 594	2.07 1.96 1.96 2.16 2.36 2.36 1.95	130 123 123 135 148 148 122	2.5 2.5 2.5 2.5 2.5 2.5 2.5	1.2 1.2 1.2 1.2 1.2 1.2 1.2	1.2 2.4 and 3.0 for each units	1:25
CARSTENS & ALS. 1966 University of Norway	Quarry stones	104	280	2.70	168	3.3	1.0	0.5 to 3.0	No scale
FONT 1968 Central University Venezuela	Rocks Rocks Rocks	94 70 38	255 190 102	2.71 2.71 2.71	169 169 169	1.75 1.75 1.75	0.5 0.5 0.5	1.58 1.58 1.58	No scale
KREEKE 1969 University of Florida U.S.A.	Granite stones	0.65	1.86	2.86	178	1.0	1.0	0.75	No scale
OUELLET 1969 University Laval Canada	Quarry stones Tetrapods Tetrapods Dolosse Dolosse Dolosse Dolosse	457 325 155 69 66 66 20	1475 780 340 165 156 143 43	2.65 2.40 2.16 2440 2.40 2.16 2.16	165 150 135 150 150 135 135	1.8 1.8 2.5 1.8 2.5 2.5 2.5	1.0 1.0 1.2 1.0 1.2 1.2 0.6	2.0 2.0 2.0 2.0 2.0 2.0 2.0	1:16
RAICHLEN 1969 Caltech, U.S.A.	Tribar	20.8	46.7	2.25	141	0.76	0.40	1.75	1:75
ROGAN 1969 Chatou, France	Quarry stones	24	63	2.6	162	1.15	0.4	1.0 to 2.0	No scale
FONT 1970 Central University Venezuela	Rocks Tetrapods	38 39	102 87	2.71 2.23	169 139	1.31 1.31	0.5 0.5	1.58 1.58	No scale
WHILLOCK 1970 Wallingford, England	Dolosse Dolosse	39.5 6.3	91.0 14.5	2.30 2.30	144 144	1.20 0.65	0.63 0.34	1.6 to 2.4 1.2 to 1.8	1:40 1:73.7
ERGIN & PORA 1971 Metu, Turkey	Stones	17.3	45	2.60	162	1.6	0.4	1.3	1:50
TETMOPOULOS 1972 Chatou, France	Stones	23.6	61.3	2.60	162	0.33 to 0.80	0.42	1.0 to 2.0	1:40

TABLE 2- MODEL UNITS SCALED DOWN TO A STANDARD WEIGHT OF 100 GRS

AUTHOR YEAR PLACE	NAME OF UNITS	VOLUME OF UNITS	WEIGHT OF UNITS	SPECIFIC GRAVITY	SPECIFIC WEIGHT	WATER DEPTH	WAVE HEIGHT (UP TO)	WAVE PERIOD	SCALE
---	---	cc	grs	---	lbs/ft^3	feet	feet	sec.	---
HUDSON 1959 Vicksburg, U.S.A.	Quarry stones Tetrapods (concrete) Tetrapods (leadite)	32-38 40-46 44-47	100 100 100	2.66-3.08 2.16-2.46 2.14-2.28	166-192 135-154 134-142	1.1 to 2.6	0.6 to 0.9	0.84 to 3.0	1:0.74 to 1:1.12
SINGH 1961 Wallingford, England	Stabits	42.7	100	2.32	145	0.92	0.63	1.40 to 1.70	1:1.09
PAAPE & WALTER 1962 Delft, Netherlands	Akmons Quarry stones Cubes Tetrapods Tripods Bipods	45.2 45.2 45.2 45.2 45.2 45.2	100 100 100 100 100 100	2.20 2.20 2.20 2.20 2.20 2.20	137 137 137 137 137 137	150 150 150 150 150 150	0.64 0.64 0.64 0.64 0.64 0.64	1.5 1.5 1.5 1.5 1.5 1.5	1:0.94 1:0.94 1:0.94 1:0.94 1:0.94 1:0.94
MERRIFIELD & ZWAMBORN 1965 C.S.I.R. South Africa	Dolosse Dolosse Dolosse Tetrapods Rectangulars Rectangulars Tetrahedrons	48.2 51.0 51.0 46.2 42.4 42.4 51.3	100 100 100 100 100 100 100	2.07 1.96 1.96 2.16 2.36 2.36 1.95	130 123 123 135 148 148 122	1.16 1.54 2.03 1.23 1.07 1.19 1.38	0.56 0.74 0.98 0.60 0.52 0.57 0.66	0.6 to 2.6 2.6 2.6 2.6 2.6 2.6	1:2.15 1:1.62 1:1.23 1:2.03 1:2.33 1:2.10 1:1.81
CARSTENS & ALS. 1966 University of Norway	Quarry	37.1	100	2.70	168	2.34	0.71	0.42 to 2.53	1:1.41
FONT 1968 Central University, Venezuela	Rocks Rocks Rocks	36.8 36.8 36.8	100 100 100	2.71 2.71 2.71	169 169 169	1.28 1.41 1.74	0.43 0.45 0.50	1.35 1.42 1.58	1:1.37 1:1.24 1:1.01
KREBEL 1969 University of Florida U.S.A.	Granite stones	34.9	100	2.86	178	3.77	3.77	1.46	1:0.265
OUELLET 1969 Laval University Canada	Quarry stones Tetrapods Tetrapods Dolosse Dolosse Dolosse Dolosse	37.8 41.7 46.2 41.7 41.7 46.2 46.2	100 100 100 100 100 100 100	2.65 2.40 2.16 2.40 2.40 2.16 2.16	165 150 135 150 150 135 135	0.73 0.91 0.66 1.52 2.15 2.22 3.31	0.41 0.51 0.80 0.85 1.03 1.06 0.80	1.30 1.42 1.64 1.84 1.72 1.88 2.30	1:2.45 1:1.98 1:1.50 1:1.18 1:1.16 1:1.12 1:0.75
RAICHLEN 1969 Caltech, U.S.A.	Tribar	44.5	100	2.25	141	0.98	0.52	2.0	1:0.78
ROGAN 1969 Chatou, France	Quarry stones	38.4	100	2.60	162	1.34	0.47	1.10 to 2.26	1:0.85
FONT 1970 Central University Venezuela	Rocks Tetrapods	36.8 36.8	100 100	2.71 2.23	169 139	1.30 1.38	0.50 0.53	1.58 1.62	1:1.01 1:0.95
WHILLOCK 1970 Wallingford, England	Dolosse Dolosse	43.4 43.4	100 100	2.30 2.30	144 144	1.24 1.24	0.65 0.65	1.6 to 2.4 1.6 to 2.4	1:0.97 1:0.53
ERGIN & PORA 1971 Metu, Turkey	Stones	38.4	100	2.60	162	2.10	0.52	1.5	1:0.77
TZIMOPOULOS 1972 Chatou, France	Stones	38.5	100	2.60	162	0.4 to 0.9	0.5	1.1 to 2.2	1:0.85

It is well accepted that the head of a breakwater is more vulnerable than the trunk and accordingly should be more protected. Model tests on trunk section are one-dimensionnal while tests on the head are two-dimensionnal.

EFFECT OF UNITS.

The weight of the units is quite important in breakwater model tests. They should be small enough so that they are within the capabilities of test conditions but not too small otherwise scale effects result.

The density of the units tested are mainly those resulting from using rocks or concrete in salt or fresh water that is from 2.2 to 2.7. This factor is taken into account in Hydson's stability formula.

The shape, which could be more or less sophisticated, is responsible for the fact that units are more or less stable with respect to one another. This factor is taken care of in stability formulas by a coefficient which includes the degree of interlocking.

Tests with dolosse of approximataly the same weight 143 and 156 grs but with different densities 2.16 and 2.40 have been carried out under similar test conditions. A plot of damage coefficient K_D versus pencentage damage (fig. 2) shows a great scatter of test results. However these same results when plotted on a graph of wave height versus damage are grouped together (fig. 3). This would mean that for these units Hudson's formula would not apply.

Such a remark has also been made by Hydraulic Research Station, Wallingford with respect to a change of slope from 1:1.5 to 1:3 with the same kind of units. One can find the explanation of this phenomena by returning to the derivation of Hudson's formula in which the inertia term in the induced forces has been neglected with respect to the drag force and the friction and interlocking terms neglected with respect to buoyant wieght in the resistive forces. In case of dolosse, interlocking effect is more important than buoyant weight for the stability of the units.

EFFECT OF LAYERS.

The most important factors with respect to layers are related to the method of placing the units and the effect of the underlayers.

Most of the time units are randomly placed in two layers with some exceptions of units such as tribars where a one layer of uniform placing is used. This is an important factor in the scattering of results. It is more relevant in the early stage of damage where poorly placed units are displaced for lower wave heights.

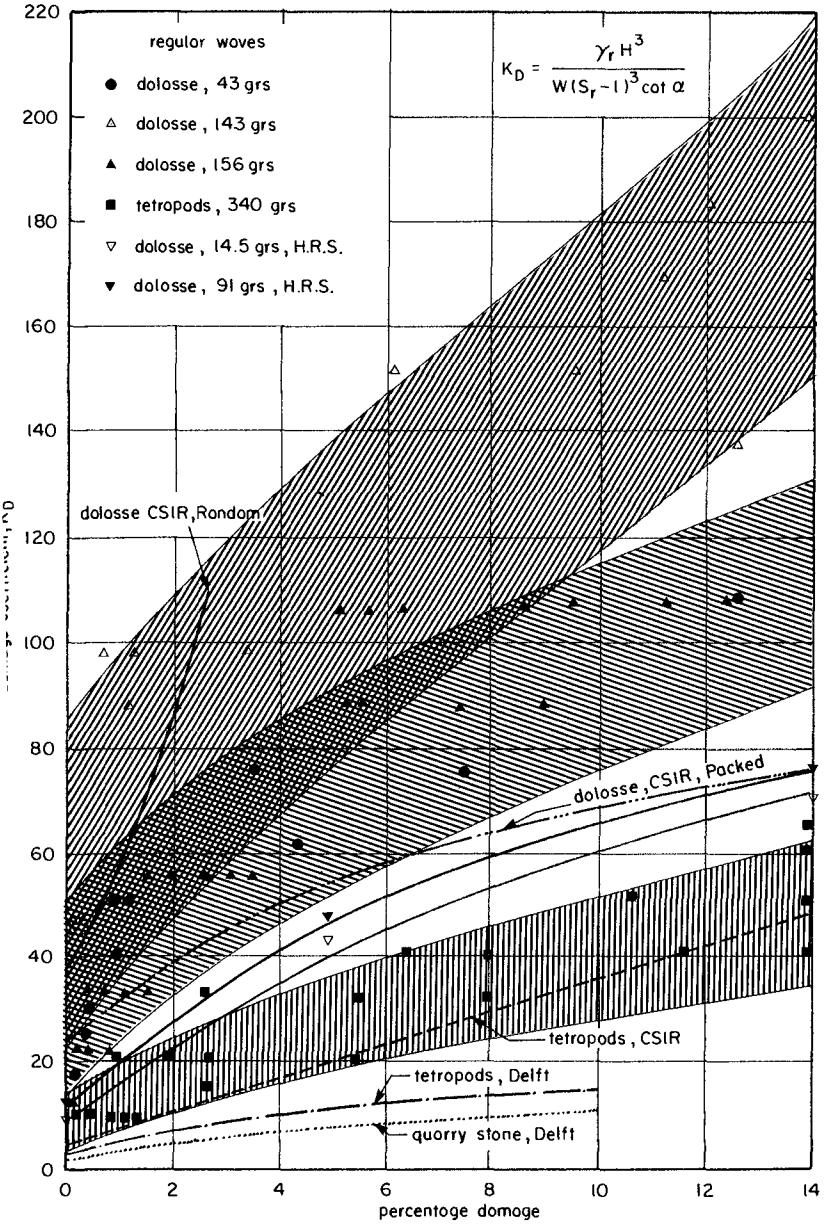

Fig.2—DAMAGE COEFFICIENT VERSUS PERCENTAGE DAMAGE.

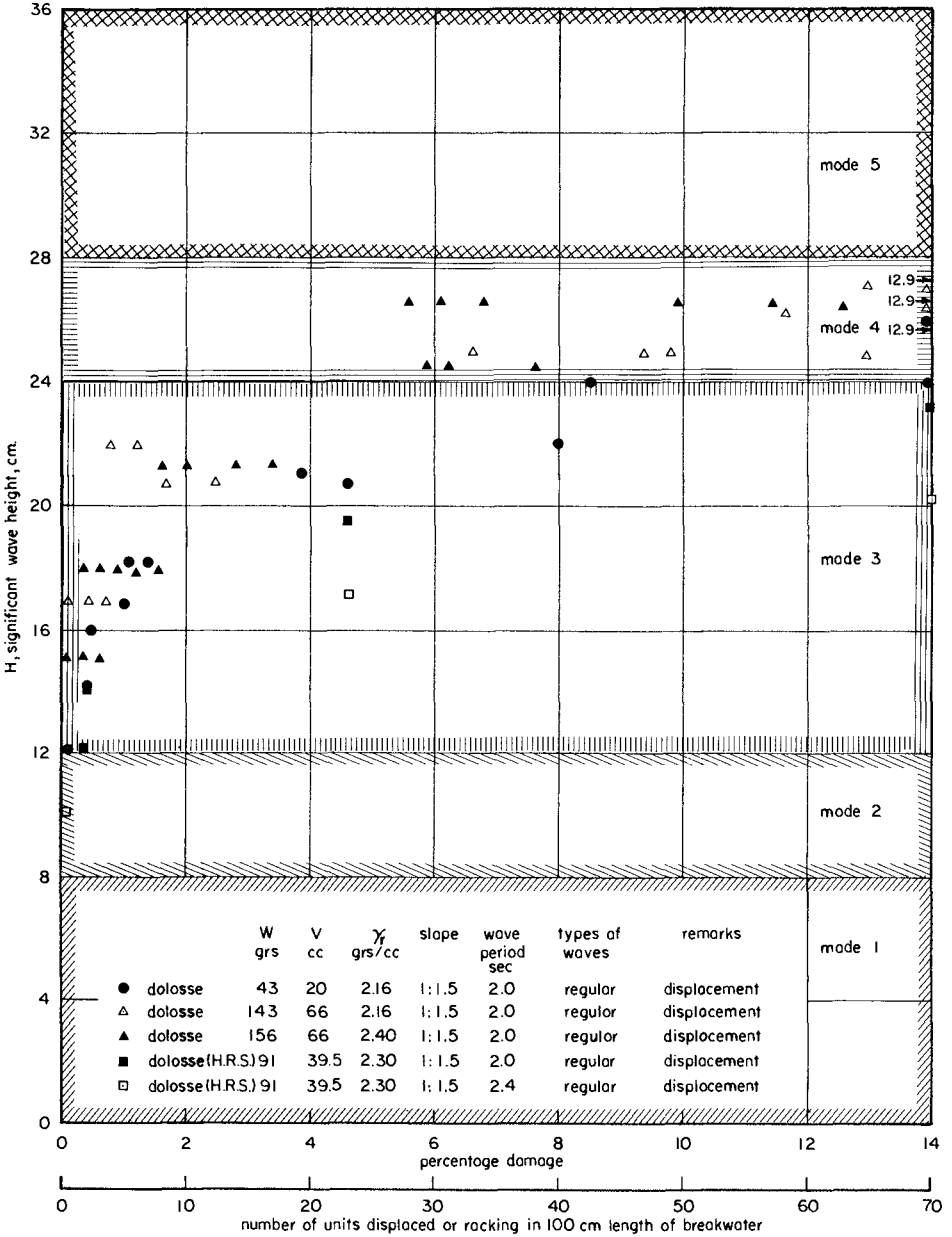

Fig. 3— SIGNIFICANT WAVE HEIGHT VERSUS DAMAGE FOR UNITS WITH AN EQUIVALENT WEIGHT OF 100 grs.

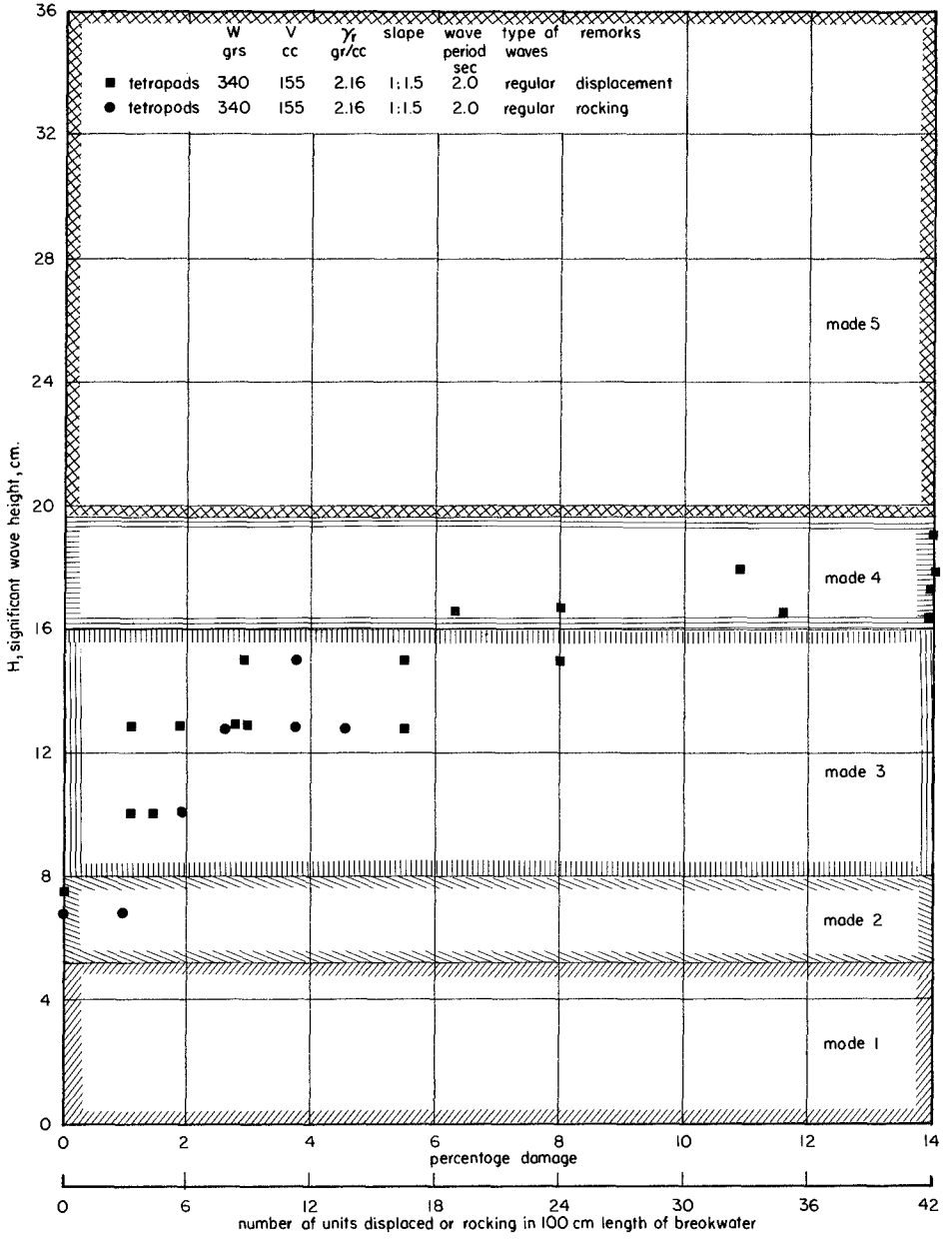

Fig. 4 — SIGNIFICANT WAVE HEIGHT VERSUS DAMAGE FOR UNITS WITH AN EQUIVALENT WEIGHT OF 100 grs.

The underlayers are built in order to present finer particles to escape through the cover layers and create enough friction between layers to prevent sliding of layers with respect to one another. Although literature reports the effect of underlayers is more or less of importance on stability, it is believed that its effect should not be overlooked when designing breakwaters, because these results come from model tests where scale effects could be important and limited amount of test results are available.

TEST CONDITIONS.

Scale model tests of breakwaters are conducted in order to evaluate the stability of the units, the damage to the structure for higher waves and the run up on its facing to determine its crest elevation. The interpretation of results should not be done without taking into account test conditions under which model testing have been conducted.

The depth of water and the bottom slope are responsible for the change of wave characteristics approaching the structure that is whether waves are shallow or deep water, breaking or non breaking, linear and non linear. In shallow water the wave height is limited by the water depth but in some cases the toe of the structure should be protected. These factors do not seem to have much influence on stability as long as the same wave height reach the structure.

The most important factors to take into account are those related to irregular waves and wave overtopping. From the few tests conducted with irregular waves, it is now accepted that the significant wave height of wave spectra having a Rayleigh type distribution is comparable to a corresponding regular wave height. Although wave run up, wave energy or the ratio of maximum wave height to the significant wave height are factors which have been proposed for consideration for describing irregular wave trains, it will necessitate more test results to specify the type of wave spectra.

When the crest elevation is not high enough, overtopping occurs and this happens when still water level is approximately equal to 60% of the breakwater height. In this case the leeside is in general more vulnerable than the seaside and maximum damage occurs when the still water level is slightly below the crest of the breakwater. The limited amount of tests have shown that the slope on leeside is less important than on the seaside, although overtopping height is difficult to estimate because of turbulence.

FACTORS RESULTING FROM INTERACTION OF WAVES AND STRUCTURE.

Scale model tests on breakwaters are usually conducted to determine the stability of the armor units, the damage to the structure or the run up on the facing. The most important factor is the damage in-

curred on the structure since it includes the stability of the units and that wave run up is an additionnal factors to be measured.

The wave run up which is of the order of the wave height delineates the breakwater height for non overtopping condition. It depends on many factors such as the slope of the facing, wave steepness, relative depth, permeability and roughness of the breakwater facing and angle of wave attack. Its measurement is made difficult because of the porosity of the layers.

Although the damage suffered by the structure is very important, it is one of the most confused term used by different investigators. Whether it refers to rocking, displacement or fracture of the units, its definition expressed in terms of percentage varies from one another. The unit displacement and unit rocking as proposed on reference 3 should be maintained in future tests. The difference comes from whether the distance of the movement of a unit is more or less than the overall length of the unit. Its description has mainly been used in terms of percentage with respect to a certain number of units placed in the test section.

But confusion introduced from the fact that the expression of percentage damage is referred to different numbers of units placed in the test section has led to define the damage by the number of units displaced in a given standard length. But since this number varies with the weight of the unit it is not as indicative as a percentage value to express the amount of damage produced. To remedy this, a new proposition is made further in this paper.

It is well known that the damage is located mainly in the area around still water level. This occurs mostly in sliding of isolated units which, although some of them are detached during the rush up, are deposited down the slope. A new equilibrium profile composed of three different slopes is attained if damage to the structure is not sufficiently high enough to produce failure of the structure which happens when the first underlayer becomes uncovered. The wider the test section, the more precise is the damage measured.

Comparison of damage is usely done in graphs showing damage coefficient versus percentage damage or wave height versus damage. A damage band rather than a damage curve is obtained and from these curves, a design wave exceedance versus damage (fig. 5) can be obtained for future use in a optimum design procedure. Comparing the curves shown in figure 5, it is expected that a single curve would apply for most of the units used as armor units on the recommended sections given in Technical Report no 4. This would be obtained by a small change in the value H_{S0} which is much influenced by the method of placing the units.

Consideration of these curves and observation of the armor layers under wave attack led to the conception of modes of failure, where the approximative limits are given in terms of the design wave height (no damage criteria):

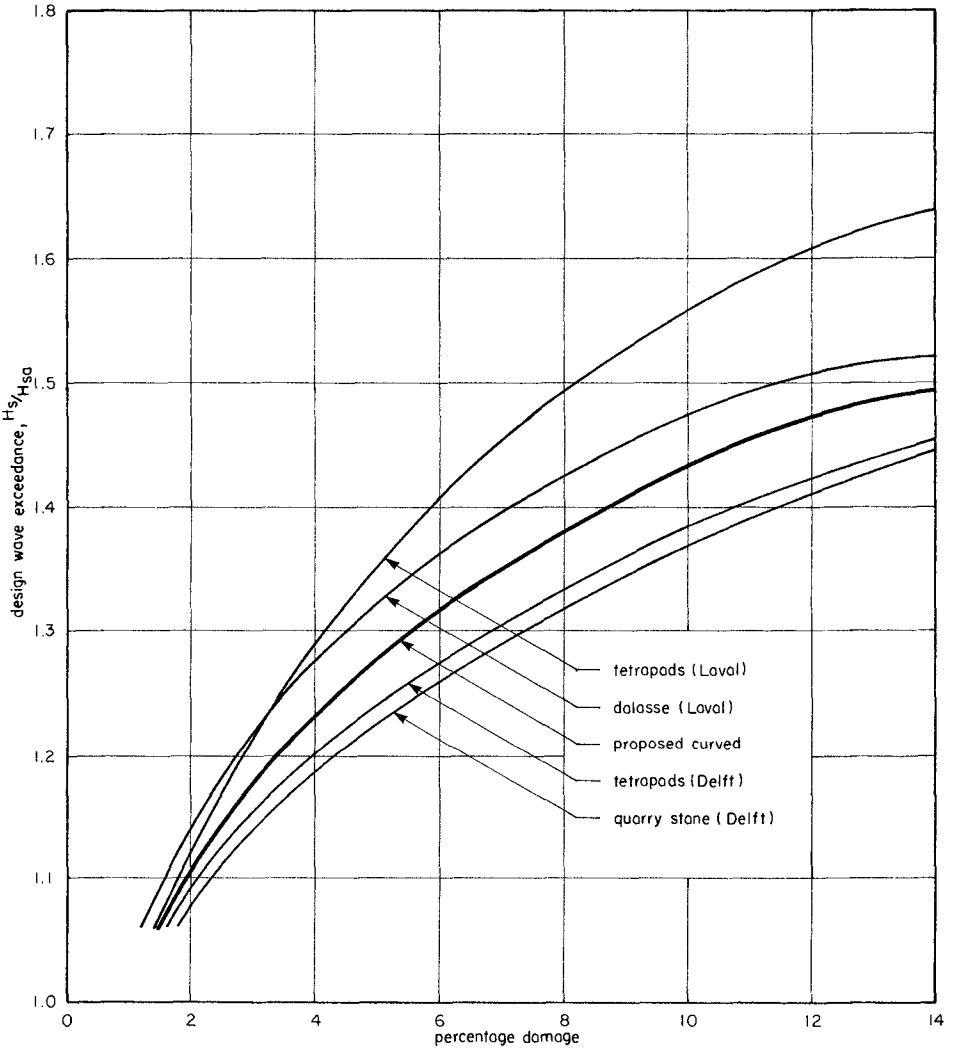

Fig. 5 — DESIGN WAVE EXCEEDANCE VERSUS PERCENTAGE DAMAGE.

Mode 1:	0 H - 0.5 H	No movement of the units.
Mode 2:	0.5 H - 0.9 H	Rocking of the units but no displacement.
Mode 3:	0.9 H - 1.5 H	Some units are displaced but the armor layer remains stable.
Mode 4:	1.5 H - 1.8 H	Units are displaced and the armor layer would fail if time is allowed.
Mode 5:	above 1.8 H	Immediate failure of the armor layer.

These modes of failures can be show as in figures 3 and 4 on a wave height versus damage diagram and could be useful to design engineers.

SCALE EFFECTS.

The interpretation of results or their transposition from model to prototype depends on scale effects for the given test conditions. For a model based on Froude's similarity, the inertial forces should be large compared to viscous forces or otherwise the Reynolds number should be high enough that the flow is turbulent for both model and prototype. For breakwater scale model tests, this intervenes in the drag forces expressed in terms of a drag coefficient which is affected by the Reynolds number and by the flow through a porous structure according to Darcy's law. Such effect occurs when the weight of the units is relatively small. From our tests, a weight of 100 grs seems to appear as a lower limit in order not to have scale effects.

But many other factors can produce scale effects. For example is the flow in the underlayers to scale? What is the effect of using a board which permits to vary the slope? What are the effects of the types of waves whether regular or irregular if they are produced either by wind or paddle movement? Are the test conditions, that is the history and the duration of wave attack to scale? These are as many questions concerning scale effects which would be difficult to answer. Moreover one can add other factors such as reflexion of waves in the flume, side wall effects, stopping and starting the machine, etc...

RECOMMENDATIONS FOR BREAKWATER MODEL TESTS.

Since Hudson's formula seems not to apply when interlocking effects are more important, like it is the case for dolosse compare to natural stone, a plot of significant wave height versus damage with the different modes of damage on it (Fig. 3 and 4) appears more valuable than a plot showing damage coefficient versus damage. In this case the other parameters such as the density of the units, the slope, the wave period, etc... should be indicated. It can be seen that the scatter of test results are less spread on the former graph than on the latter one.

The damage used as such should mean the unit displacement that is the act of a unit moving a distance greater than its overall length. If unit rocking is referred to, it should be indicated.

The idea of expressing the damage as percentage of a certain number of units should be maintained since it is indicative of the amount of damage suffered by the structure. In order to make any comparison possible, it is suggested in the light of past experiments that these are referred to the number of units placed in the area between ± the wave height giving 1% damage.

If one likes to express the damage in terms of the number of units displaced in a given length of breakwater, the same weight of units has to be used in order to make possible any comparison. A standard weight of 100 grs with a standard length of 100 cms are proposed for presenting the test results (fig. 3 and 4).

For the determination of the wave height giving 1% damage, it is proposed to estimate it from the limit between mode 3 and mode 4 which is less influenced by the way of placing the units. In this case some help can be received from a graph showing the design wave exceedance versus damage.

The presentation of results could be standardized on a plot of significant wave height versus damage by adopting a standard weight of 100 grs and a standard length of 100 cms. By scaling other test conditions to these standard values, comparison between results is made possible. It would also be easy from such a figure to obtain prototype values corresponding to a given design wave height from Froudian scales.

CONCLUSION.

An analysis of various factors concerned with breakwater scale model tests reveal the need for a standardization of the presentation of test results. A simple method which does not included any formulas is proposed for the presentation of these results.

Although it is not the intention of the author to exclude any further need of research on the knowledge of what is damage related to, wave energy, wave power, wave steepness, wave height, wave run up, ... the presentation as suggested does not take that into account. To the author's point of view, it appears that better chances of success appear in locking in a correlation between damage and wave run up.

The ultimate goal to be obtained from such model testing is towards a better design of rubble-mound breakwater. For use in optimum design breakwater, it is proposed that only unit displacement be considered for damage. Since damage in mode 3 is not cumulative, it should be considered only once and for practical reasons this damage is not repaired after a storm has passed. Finally storm duration in mode 4 should be considered such that it is smaller than an usual duration of a storm and for that reason breakwater will fail if wave height is in that mode.

The proposed standardization is not intended to be final, but the author's goal would be attained if only this paper would sensitize those concerned with breakwater design on the various factors involved in breakwater model tests and that the presentation of test results asks for a plea of uniformity.

ACKNOWLEDGEMENT.

This paper is the outcome of a series of breakwater model tests carried out for the Department of Public Works of Canada. Collaboration and assistance provided by people of the Marine Engineering Design Branch are greatly appreciated.

REFERENCES

1.- OUELLET, Y.: "Effects of Irregular Wave Trains on Rubble-Mound Breakwater". Journal of Waterways, Harbors and Coastal Engineering Division, Proc. A.S.C.E., February 1972.

2.- TZIMOPOULOS, C.: "Premiers résultats de recherches sur des profils d'ouvrages en enrochements, économiques, stables et non franchis par une houle de caractéristiques données". La Houille Blanche, No 1, 1972.

3.- PAUL, M.W. & BAIRD, W.F.: "The Design of Breakwater Armor Units". Conference on "Port and Ocean Engineering in Artic Conditions" Norway, August 1971.

4.- LORDING, P.T. & SCOTT, J.R.: "Armor Stability of Overtopped Breakwater". Journal of the Waterways, Harbors and Coastal Engineering Division, Proc. A.S.C.E., WW2, May 1971.

5.- ERGIN. A & PORA, S.: "Irregular Wave Action on Rubble-Mound Breakwater". Journal of the Waterways, Harbors and Coastal Engineering Division, WW2, May 1971.

6.- FONT, J.B.: "Damage Functions of Rubble-Mound Breakwater". Proceedings of the 12th Conference on Coastal Engineering, Washington, 1970.

7.- KAMEL, A.M.: "Laboratory Study for Design of Tsunami Barrier". Journal of the Waterways, Harbors and Coastal Engineering Division, WW4, November 1970.

8.- HYDRAULICS RESEARCH STATION WALLINGFORD: "High Island Water Scheme Hong-Kong: A Study on the Use of Dolos Armor Units for Wave Protection on the Seaward Face of the Easters Dam". Report No EX.532, October 1970.

9.- GAMOT, J.-P.: "Stabilité des carapaces en tétrapodes de brise-lames à talus". La Houille Blanche, No 2, 1969.

10.- VAN DE KREEKE, J.: "Damage Functions of Rubble-Mound Breakwaters". Journal of Waterways and Harbors Division, Proc. A.S.C.E., WW3, August 1969.

11.- FONT, J.B.: "Effect of Storm Duration on Rubble-Mound Stability". Proceedings of the 11th Conference on Coastal Engineering, London 1968.

12.- ROGAN, A.: "Destruction Criteria for Rubble-Mound Breakwater". Proceedings of the 11th Conference on Coastal Engineering, London 1968.

13.- SINGH, K.Y.: "Stabit; A New Armor Unit". Proceedings of the 11 th Conference on Coastal Engineering, London 1968.

14.- CARSTENS, T., TORUM, A. & PARK, A.G.: "The Stability of Rubble-Mound Breakwater against Irregular Waves". Proceedings of the 10th Conference on Coastal Engineering, Tokyo, 1966.

15.- MERRIFIELD, E.M. & ZWAMBORN, J.A.: "The Economic Value of a New Breakwater Armor Unit 'Dolos'". Proceedings of the 10th Conference on Coastal Engineering, Tokyo 1966.

16.- U.S. ARMY COASTAL ENGINEERING RESEARCH CENTER.: "Shore Protection Planning and Design". Technical Report No 4, 1966.

17.- PAAPE, A. & WALTER, A.W.: "Akmon Armor Unit for Cover Layers of Rubble-Mound Breakwaters". Proceedings of the 8th Conference on Coastal Engineering, Mexico 1962.

18.- PER ANDERS, H.: "Stability of Rock-Fill Breakwaters". Goteberg, Elanders Boktrykeri Aktiebolag, Sweden, 1960.

19.- DANEL, P., CHAPUS, E. & DHAILLE, R.: "Tetrapods and Other Precast Blocks for Breakwater". Journal of Waterways and Harbors Division, Proc. A.S.C.E., WW3, September 1960.

20.- HUDSON, R.Y.: "Laboratory Investigation of Rubble-Mound Breakwaters". Journal of the Waterways and Harbors Division, Proc. A.S.C.E., WW3, September 1959.

CHAPTER 103

WAVE TRANSMISSION THROUGH PERMEABLE BREAKWATERS

by

Charles K. Sollitt, Asst. Professor
Oregon State University
Ralph H. Cross, Coastal Engineer
Alpine Geophysical Assocs., Inc.

Abstract

A theory is derived to predict ocean wave reflection and transmission at a permeable breakwater of rectangular cross section. The theory solves for a damped wave component within the breakwater and matches boundary conditions at the windward and leeward breakwater faces to predict the reflected and transmitted wave components. An approximate solution to conventional rubble mound breakwater designs is formulated in terms of an equivalent rectangular breakwater with an additional consideration for wave breaking. Experimental and theoretical results are compared and evaluated.

Introduction

It is common practice in coastal engineering design to account for wave transmission past rubble mound breakwaters by considering two possible transfer mechanisms: 1) diffraction through navigation openings in the structure, and 2) overtopping across the crest of the structure. Standard optical techniques have been modified to account for the diffraction process. The overtopping process is less well defined, however, recent semi-empirical methods (Cross, Sollitt, 1971) have improved design capabilities.

Both procedures are based on the assumption that the structure itself is impervious. However, field and laboratory observations raise some doubts about the universal applicability of this assumption. Calhoun (1971) has recorded transmission coefficients up to 40% resulting from the transmission of low crested swell directly through the pores of the rubble mound breakwater at Monterey Harbor, California. Similar observations have been reported by the New England Division, Army Corps of Engineers for the Isle of Shoals breakwater off the Maine-New Hampshire coast. This behavior is aggravated by long wave excitation and may be an important consideration in harbor seiching.

Neglecting the effect of direct transmission can be a significant omission in breakwater and harbor design. The analysis described in this study provides a technique which may be used to evaluate this important characteristic of permeable breakwaters.

Problem Statement

Wave interaction with permeable breakwaters excites wave motion within the interstices of the structure as well as producing reflected and transmitted waves. As an incident wave encounters a breakwater face part of the wave is reflected back out to sea, some energy is lost to wave breaking and the remaining energy is transmitted to the breakwater interior. The wave inside the structure decays as it propagates through the pores. Upon reaching the leeward face, the wave is partially transmitted to the lee side of the breakwater and is partially reflected back to the interior of the structure. This process yields two wave trains propagating in opposite directions within the structure, a reflected wave train propagating back out to sea and a transmitted wave train propagating beyond the lee side of the breakwater. In order to predict the characteristics of the wave which is ultimately transmitted beyond the breakwater, it is necessary to develop an analysis which properly identifies the reflected and interior wave motion as well.

The analytical approach used in this study begins with the unsteady equations of motion for flow in the pores of a coarse granular medium. The equations are linearized using a technique which approximates the turbulent damping condition inside the medium. This yields a potential flow problem satisfied by an eigen series solution. Linear wave theory is applied outside the breakwater and the excitation is provided by a monochromatic incident wave. The solutions are matched at the sea-breakwater interfaces by requiring continuity of horizontal mass flux and pressure. The amplitude and phase of the unknown wave components are solved from the latter boundary condition.

The Equations of Motion

A complete derivation of the theory is presented in a separate report by the authors (Sollitt, Cross, 1972). The major features are outlined herein.

The fluid motion in the interstices of the structure is described in terms of the seepage velocity and pressure. These are conceptual quantities which are averaged over finite and continuously destributed pore volumes. The incompressible equations of motion reduce to the following form:

$$\frac{\partial q}{\partial t} = -\frac{1}{\rho}\nabla (p + \gamma z) + \text{resistance forces}$$

$$\nabla \cdot q = 0 \qquad (1)$$

where q is the instanteous Eulerian velocity vector at any point, p is the corresponding pressure, γ is the fluid weight density, ρ is the fluid mass density, z is the vertical coordinate, t is time and ∇ is the gradient operator.

The gross effect of local spatial and temporal perturbations in the velocity field are accounted for by the resistance forces. The convective acceleration term is ignored because finite amplitude waves are quickly dissipated within coarse granular media.

The resistance forces in Eq. (1) are evaluated by combining known steady and unsteady stress relationships. Ward (1964) has demonstrated that under steady flow conditions the pressure drop through large grain permeable media is specified by

$$-\frac{1}{\rho}\nabla\,(p+\gamma z) = \frac{\nu}{K_p}\,\varepsilon q + \frac{C_f}{\sqrt{K_p}}\,\varepsilon^2\, q\,|q| \qquad (2)$$

where ν is the kinematic viscosity, K_p is the intrinsic permeability, C_f is a dimensionless turbulent resistance coefficient and ε is the porosity of the medium. The linear term governs low Reynolds number flow and the square law term dominates high Reynolds number flow.

In the present application, it is hypothesized that unsteadiness may be accounted for by introducing an additional term which evaluates the added resistance caused by the virtual mass of discrete grains within the medium. The resistance force due to the virtual mass is equal to the product of the displaced fluid mass, the virtual mass coefficient, and the acceleration in the approach velocity. The resulting force is distributed over the fluid mass within the pore so that the force per unit mass of fluid is simply

$$\frac{1-\varepsilon}{\varepsilon}\,C_M\,\frac{\partial q}{\partial t}$$

where C_M is the virtual mass coefficient of medium grains. C_M is a known quantity for isolated simple shapes, but generally is unknown for random, densely packed materials.

Combining the steady state damping law proposed by Ward with the additional inertial damping law proposed by the authors yields the appropriate replacement for the resistance forces in Eq. (1).

$$\frac{\partial q}{\partial t} = -\frac{1}{\rho}\nabla\,(p+\gamma z) - \frac{\nu}{K_p}\,\varepsilon q - \frac{C_f}{\sqrt{K_p}}\,\varepsilon^2\, q\,|q| - \frac{1-\varepsilon}{\varepsilon}\,C_M\,\frac{\partial q}{\partial t}$$

$$\nabla \cdot q = 0 \qquad (3)$$

The non dissipative inertial resistance term may be transposed to the left hand side of the equation and an inertial coefficient, S, defined as

$$S = 1 + \frac{1-\varepsilon}{\varepsilon}\,C_M \qquad (4)$$

then the equation of motion becomes

$$S\frac{\partial q}{\partial t} = -\frac{1}{\rho}\nabla(p+\gamma z) - \frac{\nu}{K_p}\varepsilon q - \frac{C_f}{\sqrt{K_p}}\varepsilon^2 q|q| \qquad (5)$$

$$\nabla \cdot q = 0$$

Note that Eq. (5) reduces to Darcy's Law for low Reynolds number, steady flow.

Linearzation Technique

In order to find an analytical solution to Eq. (5) some linearizing is necessary. The specific technique employed is as follows. The dissipative stress term in Eq. (5) is replaced by an equivalent stress term linear in q, i.e.,

$$\frac{\nu\varepsilon q}{K_p} + \frac{C_f\varepsilon^2}{\sqrt{K_p}} q|q| \rightarrow f\sigma q \qquad (6)$$

where σ is the angular frequency of the periodic motion and f is a dimensionless friction or damping coefficient. The coefficient σ is introduced to make f dimensionless and for subsequent algebraic expediency. To evaluate f in terms of the known damping law it is required that both the linear and non-linear friction laws account for the same amount of energy dissipation during one wave cycle. This is commonly referred to as Lorentz's condition of equivalent work.

The resistance term in the equation of motion, expressed in either form of Eq. (6) represents a friction force per unit mass acting at a point in the flow field. If this term is multiplied times the mass flux per unit volume flowing in a direction opposed to the friction force, the resulting quantity is the power dissipated per unit volume. If the power dissipation per unit volume is integrated over the volume of the flow field, ₩, and the wave period, T, the resulting quantity is the total energy consumed by friction in the volume of interest during one wave period. According to Lorentz's hypothesis, this quantity must be the same for all legitimate damping laws describing the same process. In equation form, this constraint is written

$$\int_{₩}\varepsilon d₩\int_{t}^{t+T} f\sigma q\cdot\rho q\,dt = \int_{₩}\varepsilon d₩\int_{t}^{t+T}\left\{\frac{\nu\varepsilon q}{K_p} + \frac{C_f\varepsilon^2}{K_p} q|q|\right\}\cdot\rho q\,dt$$

Thus a unique relationship exists between the medium parameters (ε, K_p, C_f), the flow field parameters (ν,q) and the friction coefficient, f. With f evaluated as a constant throughout $\forall$, this relationship may be written

$$f = \frac{1}{\sigma} \frac{\int_{\forall} d\forall \int_{t}^{t+T} \varepsilon^2 \left\{ \frac{\nu q^2}{K_p} + \frac{C_f \varepsilon}{K_p} |q|^3 \right\} dt}{\int_{\forall} d\forall \int_{t}^{t+T} \varepsilon q^2 \, dt} \tag{7}$$

The medium parameters in Eq. (7) are determined from steady state tests on small samples of the breakwater material. The velocity field is determined from the theoretical solution. Therefore, an iterative procedure is to be anticipated in the solution to f and q.

Substituting the linearized damping term into Eq. (5) yields the linearized equation of motion

$$\begin{aligned} S \frac{\partial q}{\partial t} &= -\frac{1}{\rho} \nabla (p + \gamma z) - f\sigma q \\ \nabla \cdot q &= 0 \end{aligned} \tag{8}$$

Potential Flow Field

The equation of motion is linear in both q and p. As a result, a simple harmonic excitation will yield a simple harmonic solution to the equation. The excitation in this study is assumed to be a monochromatic sea surface. It is consistent with Eq. (8) to equate the frequency of oscillation within the medium to the frequency of the excitation, σ, so that

$$q(x,y,z,t),\ p(x,y,z,t) = \{q(x,y,z),\ p(x,y,z)\}\ e^{i\sigma t}$$

and

$$\frac{\partial}{\partial t} \{q,p\} = i\sigma \{q,p\}$$

Substituting into Eq. (8) yields

$$(i\sigma S + f\sigma)\ q = -\frac{1}{\rho} \nabla (p + \gamma z)$$

Performing the curl operation on this equation demonstrates the irrotationality of the seepage velocity field, that is

$$\sigma(iS + f)\ \nabla \times q = -\frac{1}{\rho} \nabla \times \nabla (p + \gamma z) = 0$$

Thus, $\nabla \times q = 0$, the flow field is irrotational and a velocity potential, Φ, may be defined wherein

$$q = \nabla\Phi \tag{9}$$

Combining Eq. (9) with the incompressible continuity equation yields Laplace's equation

$$\nabla \cdot q = \nabla \cdot \nabla\Phi = \nabla^2\Phi = 0$$

which must be satisfied throughout the flow field.

Substituting Eq. (9) into (8) and removing the gradient operator leads to

$$S \frac{\partial\Phi}{\partial t} + \frac{1}{\rho}(p + \gamma z) + f\sigma\Phi = 0 \tag{10}$$

This is the linearized unsteady Bernoulli equation for flow in large scale granular media with quasi-linear damping. Along with Laplace's equation, it describes the flow and pressure field within the interstices of the granular media. In order to completely specify the problem, it is necessary to resolve the boundary conditions.

Boundary Value Problem

A vertical section of the solution domain is specified by a horizontal bottom at depth $z = -h$ and a free surface $z = \eta$, referenced to the still water level.

Capillarity and surface tension are negligible phenomena due to the large scale of the pores in media of interest. Consequently, the fluid pressure at the free surface is atmospheric pressure. The dynamic free surface condition is obtained by evaluating the Bernoulli equation at the free surface with $p = 0$ at $z = \eta$, thus

$$\eta = -\frac{1}{g}\left(S \frac{\partial\Phi}{\partial t} + f\sigma\Phi\right)_{z = \eta = 0} \tag{11}$$

where $g = \frac{\gamma}{\rho}$, the acceleration due to gravity. In order to avoid the difficulties of a transcedental solution and in keeping with the small amplitude wave assumption, the surface boundary condition is evaluated at $z = 0$.

The rate at which the free surface rises and falls about the still water lever (SWL), $d\eta/dt$, is equal to the vertical velocity component in a pore at the free surface, $\partial\Phi/\partial z$. This specifies the kinematic free surface condition as

$$\frac{d\eta}{dt} = \frac{\partial\eta}{\partial t} + \frac{\partial\eta}{\partial x}\frac{dx}{dt} = \left.\frac{\partial\Phi}{\partial z}\right|_{z = 0} \tag{12}$$

The convective term is of second order and may be ignored. Substituting Eq. (12) into (11) and applying the simple harmonic time dependence to the velocity potential yields the homogeneous free surface boundary condition

$$\left[g \frac{\partial \Phi}{\partial z} + \sigma^2 \, (if - S)\Phi \right]_{z = 0} = 0 \tag{13}$$

Breakwaters are commonly constructed on natural bottoms of very low permeability (sand, shale or bedrock). It is consistent to regard such a foundation as being impervious. It follows that the vertical velocity component must vanish at z = -h, i.e.,

$$\left. \frac{\partial \Phi}{\partial z} \right|_{z = -h} = 0 \tag{14}$$

Laplace's equation, along with the homogeneous boundary conditions expressed in Eqs. (13) and (14) specify the general form of the boundary value problem.

Throughout the domain: $\nabla^2 \Phi = 0$

At z = 0 : $g \frac{\partial \Phi}{\partial z} + \sigma^2 \, (if - S)\Phi = 0$

At z = -h : $\frac{\partial \Phi}{\partial z} = 0$

General Solution

This study seeks a two dimensional solution to the equations of motion. The longitudinal coordinate is in the direction of incident wave propagation. The homogeneous boundary value problem may be solved using a separation of variables technique. In the absence of a superimposed current, the general solution is

$$\Phi_n = i(a_{1n} e^{-iK_n x} + a_{2n} e^{iK_n x}) \frac{g}{\sigma(S - if)} \frac{\text{ch } K_n(h + z)}{\text{ch } K_n h} e^{i\sigma t} \tag{15}$$

where

$$\sigma^2 (S - if) = gK_n \text{ th } K_n h \tag{16}$$

and ch, th represent the hyperbolic cosine and tangent functions, respectively.

Equation (16) is a characteristic equation which specifies an infinite number of acceptable values to the complex eigen value K_n. For each eigen value, K_n, there is one eigen function, Φ_n, with its own arbitrary constants, a_{1n} and a_{2n}. Each eigen function is a solution to the boundary value problem. The total solution is the sum of all eigen functions. In theory, an infinite number of eigen functions exist, but in practice it is found that only a finite number of eigen functions need be summed to specify a problem to a reasonable degree of accuracy. Thus, the total solution is

$$\Phi = \sum_{n=1}^{\infty} \Phi_n \tag{17}$$

Equation (16) is equivalent to the dispersion equation in linear wave theory. Separating K_n into real and imaginary parts

$$K_n = \Gamma_n (1 - i\alpha_n) \tag{18}$$

and substituting into Eq. (16) yields a pair of dispersion equations for the real quantities Γ_n and α_n.

$$\frac{S\sigma^2}{g} = \Gamma_n \operatorname{th} \Gamma_n h \; \frac{1 - \dfrac{\alpha_n \sin 2\alpha_n \Gamma_n h}{\operatorname{sh} 2\Gamma_n h}}{1 - \dfrac{\sin^2 \alpha_n \Gamma_n h}{\operatorname{ch}^2 \Gamma_n h}} \qquad \frac{f}{S} = \alpha_n \; \frac{1 + \dfrac{\sin 2\alpha_n \Gamma_n h}{\alpha_n \operatorname{sh} 2\Gamma_n h}}{1 - \dfrac{\alpha_n \sin 2\alpha_n \Gamma_n h}{\operatorname{sh} 2\Gamma_n h}}$$

Note that with no damping (f = 0) and no virtual mass effect (S = 1.0), the above reduce to the linear wave theory velocity potential and dispersion equations.

Substitution of Eqs. (15), (16) and (18) into the dynamic free surface condition yields

$$\eta_n = a_{1n} e^{-\alpha_n \Gamma_n x} e^{i(\sigma t - \Gamma_n x)} + a_{2n} e^{\alpha_n \Gamma_n x} e^{i(\sigma t + \Gamma_n x)}$$

Thus, the surface profile is composed of a series of exponentially damped sinusoids propagating in both the positive and negative x directions. The real part of the complex wave number, Γ_n, specifies the spatial periodicity while the imaginary part, α_n, specifies the decay rate.

Vertical Face Breakwaters

The two dimensional velocity potential described by Eq. (15) applies to a media of finite depth and arbitrary longitudinal extent. To specify the potential for a breakwater of finite width, b, consider a crib style breakwater, located in a monochromatic sea environment, as sketched in Fig. 1. As an incident wave encounters the breakwater face at x = 0, a reflected wave is formed and a wave propagates through the structure to x = b where it is partially reflected, partially transmitted.

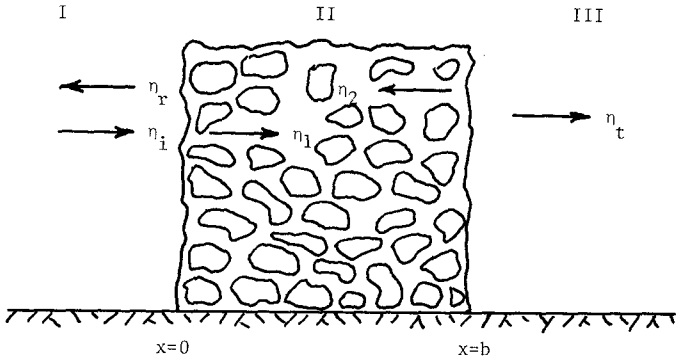

Figure 1. Crib Style Breakwater

A series of eigen modes is generated in each of the four resulting wave trains. Linear wave theory applies in regions I and III where f = 0 and S = 1.0. In these two regions, only the progressive modes propagate away from the breakwater. The local modes, characterized by imaginary wave numbers, are necessary to satisfy the interfacial boundary conditions but decay rapidly away from the breakwater.

The general solutions in each of the three regions are known. To apply the general solutions to this particular problem, the phase of the unknown amplitudes must be referenced appropriately. The incident, reflected and positively directed interior waves are referenced to the x = 0 face. The transmitted and negatively directed interior waves are referenced to the x = b face. A summary of the solutions, in terms of unknown amplitudes is given below.

Region I

$$\Phi_I = \Phi_i + \sum_{n=1}^{\infty} \Phi_{rn}$$

$$\Phi_i = i\, a_i e^{-ik_1 x} \frac{\sigma}{k_1} \frac{\operatorname{ch} k_1(h+z)}{\operatorname{sh} k_1 h} e^{i\sigma t}$$

$$\Phi_{rn} = i a_{rn} e^{ik_n x} \frac{\sigma}{k_n} \frac{\operatorname{ch} k_n(h+z)}{\operatorname{sh} k_n h} e^{i\sigma t}$$

$$\frac{p_I}{\rho} = -i\sigma\Phi_I - gz \quad , \qquad \sigma^2 = gk_n \operatorname{th} k_n h$$

Region II

$$\Phi_{II} = \sum_{n=1}^{\infty} \Phi_n$$

$$\Phi_n = i(a_{1n}e^{-iK_n x} + a_{2n}e^{iK_n(x-b)}) \frac{\sigma}{K_n} \frac{\text{ch } K_n(h+z)}{\text{sh } K_n h} e^{i\sigma t}$$

$$\frac{p_{II}}{\rho} = -(iS + f)\Phi_{II} - gz \quad , \quad \sigma^2 (S - if) = gK_n \text{th } K_n h$$

Region III

$$\Phi_{III} = \sum_{n=1}^{\infty} \Phi_{tn}$$

$$\Phi_{tn} = ia_{tn}e^{-ik_n(x-b)} \frac{\sigma}{k_n} \frac{\text{ch } k_n(h+z)}{\text{sh } k_n h} e^{i\sigma t}$$

$$\frac{p_{III}}{\rho} = -i\sigma\Phi_{III} - gz \quad , \quad \sigma^2 = gk_n \text{ th } k_n h$$

These equations contain 4n unknowns, i.e., n unknowns for each of the amplitude series a_{rn}, a_{1n}, a_{2n} and a_{tn}. In order to evaluate these unknowns, 4n additional boundary conditions are needed. Since the solutions in adjacent regions must be continuous at the interface between regions, it is apparent that the appropriate boundary conditions are continuity of pressure and horizontal mass flux at x = 0 and x = b. In equation form, the boundary conditions may be summarized as:

x = 0

$$u_I = \varepsilon u_{II} \quad \text{or} \quad \frac{\partial \Phi_I}{\partial x} = \varepsilon \frac{\partial \Phi_{II}}{\partial x}$$

$$p_I = p_{II} \quad \text{or} \quad \Phi_I = (S - if)\Phi_{II}$$

x = b

$$\varepsilon u_{II} = u_{III} \quad \text{or} \quad \varepsilon \frac{\partial \Phi_{II}}{\partial x} = \frac{\partial \Phi_{III}}{\partial x}$$

$$p_{II} = p_{III} \quad \text{or} \quad (S - if)\Phi_{II} = \Phi_{III}$$

Applying the above conditions directly yields a 4n x 4n complex matrix when evaluated at n different values of the depth, z. Considerable simplification may be gained by utilizing the orthogonal properties of the eigen functions. Orthogonality is the characteristic that the integral of the product of two eigen functions vanishes over the limits of the vertical domain if the eigen values are not equal, that is

$$\int_{-h}^{0} \Phi_m \Phi_n \, dz = 0, \; m \neq n$$

It is the z dependent terms that are orthogonal. To utilize this property, the interfacial boundary conditions are multiplied through by ch $K_m(h + z)$

and integrated over the full depth. The results, after much algebraic manipulation, are given below:

$$\sum_{n=1}^{\infty} C_{rn} \frac{K_m^2 - k_1^2}{K_m^2 - k_n^2} \left(\frac{k_n}{k_1} + \frac{\varepsilon}{S - if} \frac{K_m}{k_1} \right) +$$

$$e^{-iK_m b} \sum_{n=1}^{\infty} C_{tn} \frac{K_m^2 - k_1^2}{K_m^2 - k_n^2} \left(\frac{k_n}{k_1} - \frac{\varepsilon}{S-if} \frac{k_m}{k_1} \right) = 1.0 - \frac{\varepsilon}{S-if} \frac{K_m}{k_1}$$

$$\sum_{n=1}^{\infty} C_{rn} \frac{K_m^2 - k_1^2}{K_m^2 - k_n^2} \left(\frac{k_n}{k_1} - \frac{\varepsilon}{S-if} \frac{K_m}{k_1} \right) +$$

$$e^{-iK_m b} \sum_{n=1}^{\infty} C_{tn} \frac{K_m^2 - k_1^2}{K_m^2 - k_n^2} \left(\frac{k_n}{k_1} + \frac{\varepsilon}{S-if} \frac{K_m}{k_1} \right) = 1.0 + \frac{\varepsilon}{S-if} \frac{K_m}{k_1}$$

$$C_{1m} = \frac{S-if-1}{\varepsilon} \frac{k_1 K_m}{K_m^2 - k_1^2} \frac{sh\, K_m h\, ch\, K_m h}{sh\, K_m h\, ch\, K_m h + K_m h} \{1.0 +$$

$$\frac{\varepsilon}{S-if} \frac{K_m}{k_1} - \sum_{n=1}^{\infty} C_{rn} \frac{K_m^2 - k_1^2}{K_m^2 - k_n^2} \left(\frac{k_n}{k_1} - \frac{\varepsilon}{S-if} \frac{K_m}{k_1} \right) \}$$

$$C_{2m} = \frac{S-if-1}{\varepsilon} \frac{k_1 K_m}{K_m^2 - k_1^2} \frac{sh\, K_m h\, ch\, K_m h}{sh\, K_m h\, ch\, K_m h + K_m h} \{$$

$$- \sum_{n=1}^{\infty} C_{tn} \frac{K_m^2 - k_1^2}{K_m^2 - k_n^2} \left(\frac{k_n}{k_1} - \frac{\varepsilon}{S-if} \frac{K_m}{k_1} \right) \}$$

where $C_{rn}, C_{1n}, C_{2n}, C_{tn} = \frac{a_{rn}}{a_i}, \frac{a_{in}}{a_i}, \frac{a_{2n}}{a_i}, \frac{a_{tn}}{a_i}$

A brief inspection of the above equations reveals that the solution has been reduced to a 2n x 2n complex matrix for the dimensionless amplitudes of the reflected and transmitted waves and two linear vector equations for the dimensionless amplitudes inside the breakwater. It is apparent from the terms appearing in these last four equations that the solution ultimately depends on: the structural properties of the breakwater width and depth, b and h; the media properties of porosity and damping, ε and f; and the wave properties as described by the wave numbers inside and outside the breakwater, K_n and k_n.

Long Wave Solution

The complete solution is difficult to interpret qualitatively because of the series form of the complex matrix. Some insights into the general solution behavior may be gained, however, by considering the relatively simple case of long wave excitation. This condition is attained when the wave length exceeds the water depth by a factor of twenty so that the hyperbolic and trigonometric functions are equivalent to the values of their respective arguments. Then the dispersion equations become

$$\frac{\sigma^2 h}{g} = k_n h \, \text{th} \, k_n h \cong (kh)^2$$

$$\frac{\sigma^2 h}{g} (S - if) = K_n h \, \text{th} \, K_n h \cong (Kh)^2 \qquad (19)$$

Each equation reduces to a single positive root and the depth dependence drops from the equations of motion. Only a single eigen value exists for the solution in each of the three regions prescribed in Fig. 1. Thus, the total solution reduces to one component in each of the four unknown wave trains.

Substituting $Kh = \Gamma h(1-i\alpha)$ into Eq. (19) and separating real and imaginary parts yields

$$\Gamma^2 h^2 = \frac{1}{2} \frac{\sigma^2 h}{g} S \left(1 + \sqrt{1 + f^2/s^2}\right), \quad \alpha = \frac{\sqrt{1 + f^2/S^2} - 1}{f/S} \qquad (20)$$

Note that the effect of the damping coefficient, f, is to increase the long wave number inside the breakwater relative to its value outside. This causes the wave length to shorten, a result which one might anticipate. In general, friction inhibits wave propagation, therefore the celerity and wave length should be decreased, as indicated by Eq. (20).

The breakwater depth and width are of the same order of magnitude so that small Kh implies small Kb. Utilizing the small argument identities for the hyperbolic and trigonometric functions and evaluating the general series solution for a single eigen value yields the following for the dimensionless long wave complex amplitudes:

$$C_r = \frac{S - if - \varepsilon^2}{S - if + \varepsilon^2 - i2\varepsilon \frac{\sqrt{gh}}{\sigma b}} \qquad C_t = \frac{1}{1 + \frac{i}{2\varepsilon} \frac{\sigma b}{\sqrt{gh}} (S - if + \varepsilon^2)}$$

$$C_1 = \frac{\left(1 + \frac{\sqrt{S-if}}{\varepsilon}\right)\left(1 + \frac{i\sigma b}{\sqrt{gh}} \sqrt{S-if}\right)}{2 + \frac{i}{\varepsilon} \frac{\sigma b}{\sqrt{gh}} (S - if + \varepsilon^2)} \qquad C_2 = \frac{1 - \frac{\sqrt{S-if}}{\varepsilon}}{2 + \frac{i}{\varepsilon} \frac{\sigma b}{\sqrt{gh}} (S - if + \varepsilon^2)} \qquad (21)$$

These equations represent an exact solution to the permeable break-

water problem for the specific case of an incident wave which is very long with respect to water depth and breakwater width. The simple form of the equations allows one to easily interpret the effect of various independent parameters on the solution. Some pertinent limiting conditions are: As the medium takes on the properties of pure sea water, i.e., 100% porosity and no damping, transmission becomes complete and no reflection occurs ($f \to 0$, $\varepsilon \to 1$ with $S = 1$ yields $C_t \to 1$, $C_r \to 0$). As the porosity approaches zero, the breakwater assumes the characteristic of a solid vertical wall and no transmission occurs while reflection becomes perfect ($\varepsilon \to 0$ yields $C_t \to 0$, $C_r \to 1$). As the damping properties of the medium become severe (either inertial or dissipative) the transmission drops to zero and the reflection becomes perfect (f or $S \to \infty$ yields $C_t \to 0$, $C_r \to 1$). As the breakwater becomes very thin, the transmission becomes nearly complete while the reflection becomes negligible ($b \to 0$ yields $C_t \to 1$, $C_r \to 0$). Finally, as the wave period becomes very long, such as a tidal oscillation, the transmission becomes complete and no reflection occurs ($\sigma \to 0$ yields $C_t \to 1$, $C_r \to 0$. These same trends have been observed in the solution to the general problem for shorter waves.

Equation (21) verifies that increasing the friction coefficient, f, or the product of f with the wave frequency, σ, causes a relative decrease in the long wave transmission coefficient. This behavior also applies to the short wave solution. It will be useful, therefore, to be able to predict the dependence of $f\sigma$ on the wave and breakwater characteristics. Lorentz's condition of equivalent work, as given by Eq. (7) specifies this dependence. The friction coefficient characterizes the damping throughout the breakwater so the volume integral in Eq. (7) may be replaced by a double integral on x and z with the submerged portion of the breakwater as limits of integration.

$$f\sigma = \frac{\int_{h}^{0} dz \int_{0}^{b} dx \int_{t}^{t+T} \varepsilon^2 \left\{ \frac{\nu q_R^2}{K_p} + \frac{C_f \varepsilon}{\sqrt{K_p}} \left| q_R \right|^3 \right\} dt}{\int_{-h}^{0} dz \int_{0}^{b} dx \int_{t}^{t+T} \varepsilon q_R^2 \, dt} \qquad (22)$$

where q_R is the real part of the complex velocity, q. The numerator includes a term which is proportional to the cube of the velocity whereas the denominator is proportional to the square of the velocity. Consequently, relative increases in the velocity will cause relative increases in $f\sigma$. The velocity inside the breakwater is proportional to the product of the wave amplitude and wave frequency. The amplitude and frequency of the wave components inside the breakwater increase monotonically with increasing amplitude and frequency of the incident wave. Consequently, if the wave frequency is held constant then a relative increase in the incident amplitude will cause a relative increase in $f\sigma$. Likewise, if the amplitude is held constant, then a relative increase in the frequency, i.e., decrease in period and wave length, will cause an increase in $f\sigma$. Since increasing $f\sigma$ causes a decrease in the transmission coefficient it may be concluded that the transmission coefficient will decrease for increasing wave steepness or increasing wave number.

Solution Method

The solution method is a straight forward iterative technique. An outline of the procedure is given below.

1) Assume an initial value for f, e.g., f = 1.0.
2) Solve the dispersion equation, (16), for n eigen values. n ≈ 5 yields better than 95% convergence for kh ≤ π.
3) Solve the complex matrix for the amplitude and phase of n-modes in each unknown wave train.
4) From 3) determine q and solve the Lorentz equation, (22), for f.
5) Compare the calculated f with the assumed f and iterate if necessary (return to 2)).
6) The absolute values of C_r and C_t are the reflection and transmission coefficients for the structure.

The iteration scheme typically closes after two to eight cycles and is efficiently performed on a digital computer.

Conventional Breakwater Schemes

The preceding discussion has been limited to permeable structures of rectangular form. The inclusion of layered, trapezoidal shaped breakwaters greatly complicates the problem. A rigorous analytical solution is virtually impossible due to the non-homogeneous boundary conditions and wave breaking which occurs at the inclined breakwater slopes. To circumvent these difficulties this study introduces an approximate equivalent rectangular breakwater solution.

The simplified approach replaces the actual structure with an equivalent rectangular breakwater which has the same submerged volume as that of the trapezoidal breakwater. That is, a hypothetical breakwater is formed by bisecting the slopes between z = 0 and z = -h with vertical planes, as in Fig. 2. Within the confine of these planes, the rectangular breakwater has the same internal structure as the trapezoidal breakwater, and the crib style breakwater solution of the previous section is used to describe the flow field. Exterior to these planes, linear wave theory is applied to describe the incident, reflected and transmitted wave trains. The two solutions are matched at the hypothetical interfaces to satisfy continuity of pressure and horizontal mass flux and thereby solve for the unknown modal amplitudes.

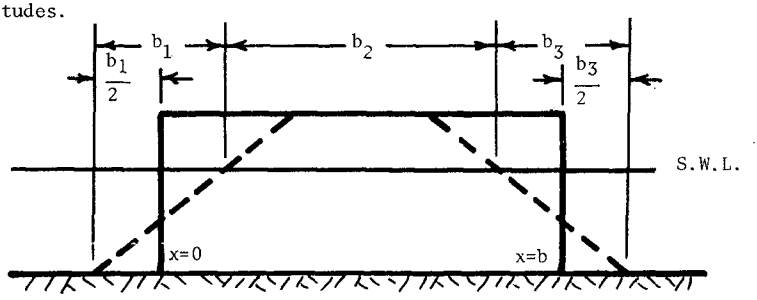

Figure 2. Equivalent Rectangular Breakwater

Lorentz's condition of equivalent work is used to evaluate a linearized damping coefficient, f, which applies throughout the hypothetical rectangular breakwater. However, unlike the condition derived for the crib style breakwater, the new equivalent work principle attempts to account for the effect of energy dissipation due to wave breaking on the windward slope. This is accomplished by modifying a theory attributed to Miche (1951) which estimates the wave energy losses on impermeable slopes. These losses are added to the frictional losses in the numerator of Eq. (22) to yield a revised estimate to the damping coefficient, f. Thus,

$$f\sigma = \frac{\int_{h}^{0} dz \int_{0}^{b} dx \int_{t}^{t+T} \varepsilon^2 \left\{ \frac{\nu q_R^2}{K_p} + \frac{C_f \varepsilon}{\sqrt{K_p}} |q_R|^3 \right\} dt + \frac{\dot{\bar{E}}_{loss}}{\rho}}{\int_{-h}^{0} dz \int_{0}^{b} dx \int_{t}^{t+T} \varepsilon q_R^2 \, dt} \qquad (23)$$

where $\dot{\bar{E}}_{loss}$ is the period averaged power lost to breaking. In this manner surface breaking losses are combined with internal friction losses. The effect is distributed among the various modal components in the reflected and transmitted wave trains through the dependence of the interfacial boundary conditions on f.

The details required to evaluate $\dot{\bar{E}}_{loss}$ are presented in the reference by Sollitt and Cross (1972). The calculation is empirical but facilitates enumeration of breaking losses in the absence of precise analytical methods. As improved methods become available, they may be incorporated into the calculation. The intent of the present discussion is to identify the concept and relegate the mechanical details to the parent reference.

Summarizing, the conventional sloping face breakwater problem is solved by adding breaking losses to the crib style breakwater solution. This effectively increases the friction coefficient f and reduces the transmission coefficient accordingly.

Experimental Results

Experimental results for two model breakwater configurations are presented. The first model is a homogenous, vertical walled breakwater composed of 3/4" gravel contained in a wire screen crib. The model is twelve inches wide and extends well above the height of maximum clapotis. The water depth is twelve inches.

The second model is a layered trapezoidal shaped structure dimensioned as in Fig. 3. The media properties are also tabulated in the figure. The properties of the second layer correspond to those of the crib style breakwater as well.

A complete documentation of the experimental program is presented in the reference by Sollitt and Cross (1972). Sample results are presented in the following figures. The crib style breakwater behavior is displayed in Figs. 4 and 5. The trapezoidal layered breakwater behavior is displayed in Figs. 6 and 7. The reflection and transmission coefficients are presented as functions of wave steepness and wave number. A dominant feature is the

decrease in the transmission coefficient with increasing wave steepness. This characteristic is due to non-linear damping as predicted by the theory. The reflection coefficient is relatively insensitive to wave steepness for the crib style breakwater case but decreases due to wave breaking on the sloping face breakwater. The reflection and transmission coefficients decrease with increasing wave number (decreasing wave length) for both configurations.

Comparison of Theory and Experiment

The theory is evaluated using the given breakwater properties and five terms in the eigen series solution. The virtual mass coefficient, C_M, is unknown and is taken equal to zero by default. Theoretical reflection and transmission coefficients are solved using the iteration procedure discussed previously. The results are presented as continuous and dashed lines on the experimental plots.

Figures 4 and 5 reveal that the theory tends to underestimate the reflection coefficient and slightly overestimate the transmission coefficient for the crib style breakwater. The correlation is improved by taking non-zero values for the virtual mass coefficient. One cannot predict the magnitude of this coefficient apriori because the virtual mass of densely packed fractured stone is not known. Evaluation of C_M, however, may serve as a calibrating link between theory and experiment in future studies.

Theory and experiment also tend to diverge for very small values of the incident wave amplitude in both models. This response is apparent at small H_i/L on the constant kh curves, and at large kh on the constant H_i/L curves. It can be shown that this occurs when the scale of the fluid motion becomes smaller than the aggregate scale on the breakwater surface. As the wave amplitude becomes very small, the wave field orbit diameters are exceeded by the individual rock diameters on the slope. Then the waves begin interacting with individual pieces of gravel rather than a continuous porous slope. The reflection process is modified as waves are partially reflected directly off particle surfaces and the theoretical assumption of a continuum no longer applies.

Correlation between the conventional trapezoidal shaped breakwater theory and experiment is quite favorable. The results, however, are contingent upon proper evaluation of the breaking losses, and further insights into the breaking process are needed.

Conclusions

Theory and experiment for both breakwater configurations generally concur that: 1) the transmission coefficient decreases with decreasing wave length, breakwater porosity and permeability, and increasing wave height and breakwater width. 2) The reflection coefficient decreases with decreasing breakwater width and wave length and increasing porosity and permeability.

Correlation between experiment and theory is best when the incident wave height exceeds the particle diameter of the medium. Although additional work is needed to improve the breaking wave calculation, the predicted reflection and transmission coefficients are very useful design estimates.

Acknowledgements

The study was conducted at the Massachusetts Institute of Technology and sponsored by the U.S. Army Coastal Engineering Research Center.

References

Calhoun, R. J., "Field Study of Wave Transmission Through a Rubble Mound Breakwater", M.S. Thesis, U.S. Navy Postgraduate School, March 1971

Cross, R. H., Sollitt, C. K., "Wave Transmission by Overtopping", Massachusetts Institute of Technology, Hydrodynamics Laboratory Technical Note No. 15, July 1971

Miche, M., "Pouvoir Réfléchissant des Ouvrages Maritimes Exposes a l'Action de Houle", Annales des Ponts et Chaussees, May-June 1951, pp. 285-319

Sollitt, C. K., Cross, R. H., "Wave Reflection and Transmission at Permeable Breakwaters", Massachusetts Institute of Technology, R. M. Parsons Laboratory Technical Report No. 147, March 1972

Ward, J. C., "Turbulent Flow in Porous Media", Proc. ASCE, J. Hyd. Div., Vol. 90, No. HY 5, Sept. 1964, pp. 1-12

Layer	ϵ	C_f	K_p	diam.
1	0.434	0.282	$0.482 \cdot 10^{-5}$	1.37"
2	0.439	0.295	$0.1138 \cdot 10^{-5}$	0.774"
3	0.430	0.4056	$0.375 \cdot 10^{-6}$	0.382"

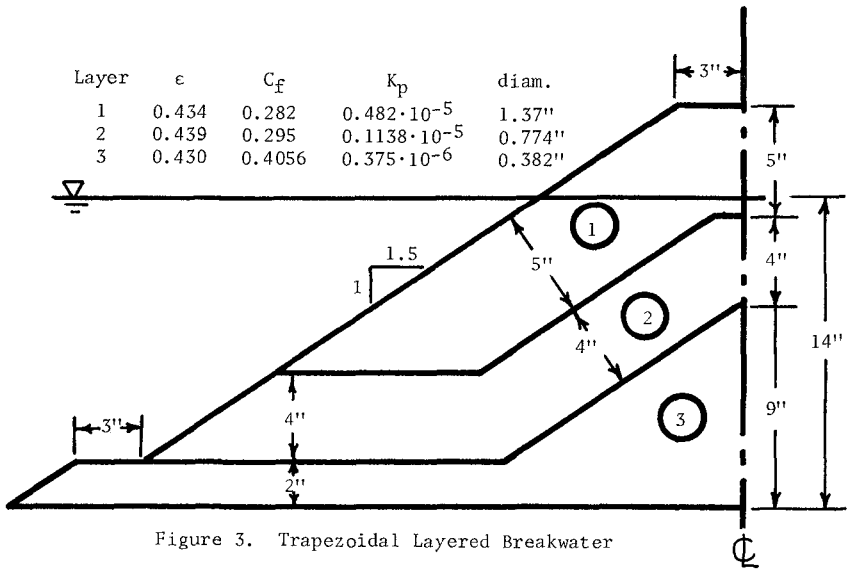

Figure 3. Trapezoidal Layered Breakwater

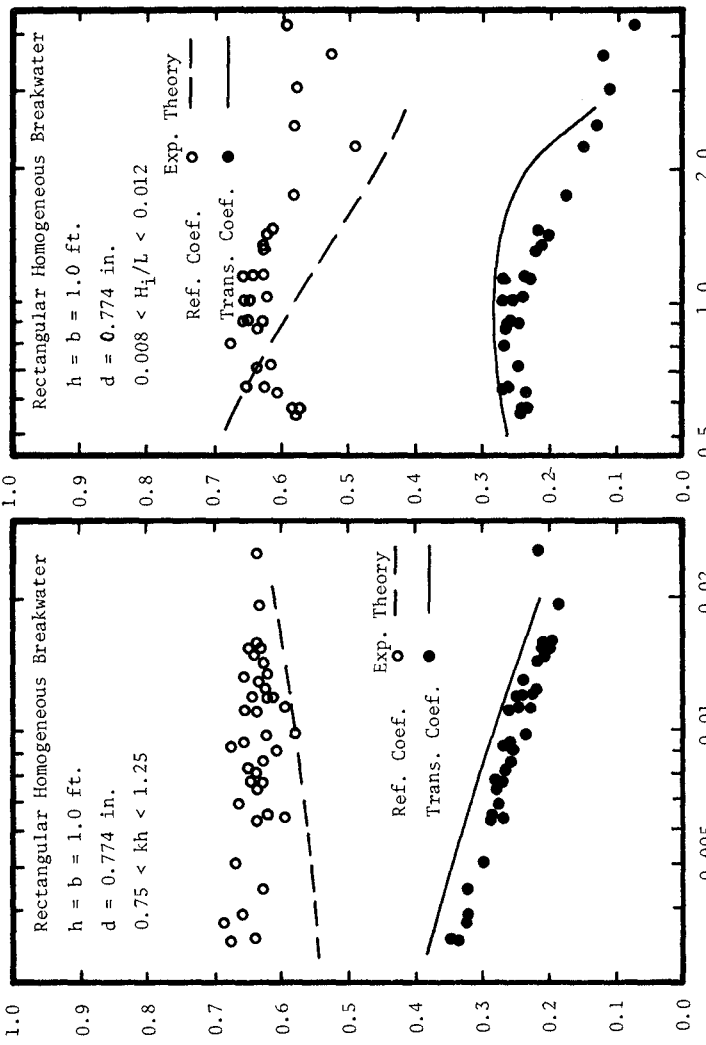

Figure 4. Reflection, Transmission Coefficient Dependence on Wave Steepness

Figure 5. Reflection, Transmission Coefficient Dependence on Wave Number

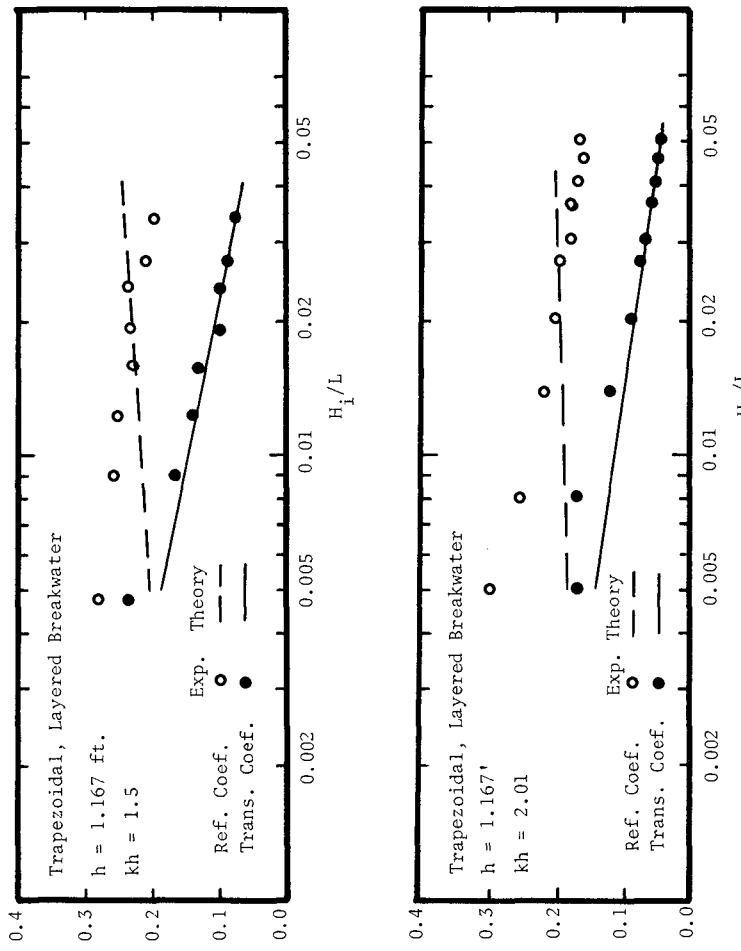

Figure 6. Reflection, Transmission Coefficient Dependence on Wave Steepness

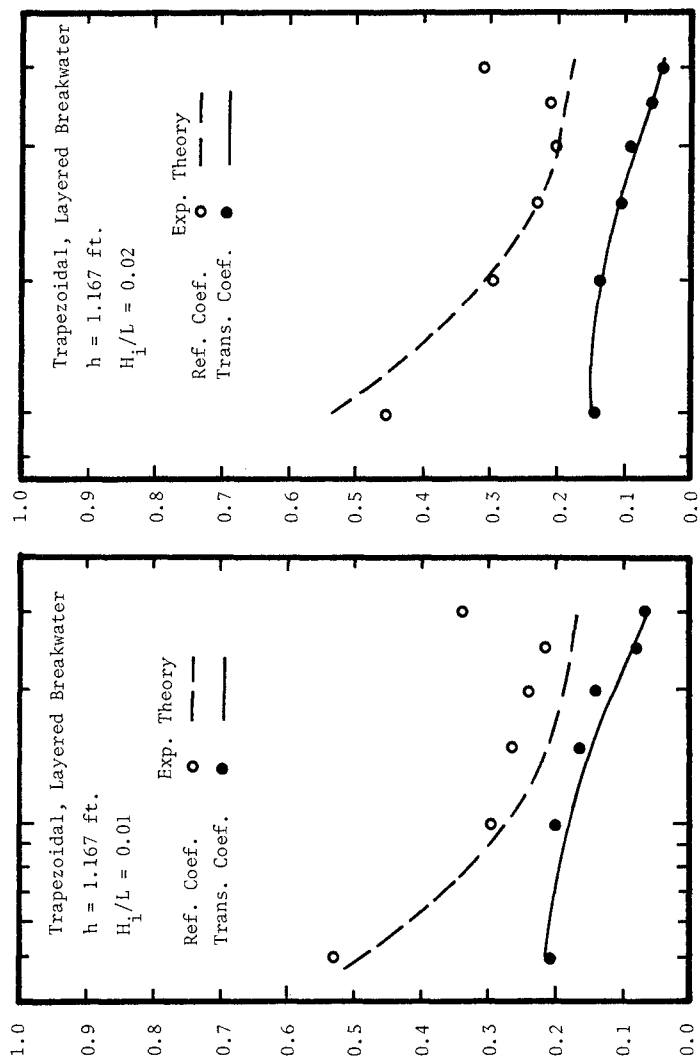

Figure 7. Reflection, Transmission Coefficient Dependence on Wave Number

CHAPTER 104

REFLECTION AND TRANSMISSION FOR A POROUS STRUCTURE

by

Hideo Kondo, Associate Professor
Satoshi Toma, Research Associate

Department of Civil Engineering
Muroran Institute of Technology
Muroran, Japan

ABSTRACT

Effects of characteristics of incident waves and of the thickenss of structure on wave reflection by and transmission through a porous structure were studied. Use of an idealized porous structure which is a lattice composed of circular cylinders was made. The relative thickness of structure B/L was found to have appreciable effects on reflected and transmitted wave energies.

The reflection coefficient Kr reaches to a maximum of it for B/L of about 0.2 to 0.25, then decreases as B/L increases, and remains approximately uniform for B/L larger than about 0.6. The transmission coefficient Kt, however, decreases nearly exponentially as B/L increases.

Measurement of wave height within structure revealed a pattern of standing waves having a loop at the front face and a node at the rear face of it. That relates to the trend of Kr.

Analytical approaches to predict the transmitted wave height, and wave heights before and within porous structures are found to be useful.

1. INTRODUCTION

Various porous structures including common rubble-mound breakwaters have been being constructed in harbor and coastal areas to dissipate strong ocean wave energy. A porous structure allows a part of the incident wave energy to penetrate through it into the protected water area at the same time to reflect a part of the energy. Reflection by and transmission through a porous structure of the incident wave energy are dominated by hydraulic characteristics of the structure and of the incident wave. Several studies on porous structures have been disclosed for transmitted waves through and reflected waves by specific types of porous structure, such as rubble-mound breakwaters.[1),2),3)] However, our knowledge about effects of hydraulic characteristics, such as thickness, porosity and loss coefficient of a porous structure on the reflection and the transmission is not enough to apply for design purpose. The present study aims to clarify effects of the thickness of porous structures on wave reflection by and transmission through them, as well as effects of incident wave characteristics.

2. A SIMPLIFIED POROUS STRUCTURE

Several difficulties lie in finding definite effects of a hydraulic characteristic experimentally for practical rubble structures. One of them is that it is difficult to vary it alone while keeping others constant. Another is that wave motion within them hardly measured.

In the present study use of an idealized porous structure was made in order to avoid the difficulties. It is a vertical-faced lattice type of porous structure made of circular polyvinyl chloride cylinders which were glued together vertically and horizontally in a pitch of the diameter to produce uniform pores within the structure (see Fig.1). The porosity of the structure in hydraulic sense is to be approximately the following value, that is derived according to Fig.2.

$$\lambda = \left\{1 - \frac{2(\pi D^2/4)\cdot 2D}{2D^3}\right\} = 1 - \frac{\pi}{8} = 0.6075 \qquad (1)$$

where D is diameter of cylinders.

Flow resistance of the structure for steady flow was measured for the structure of different sizes of diameter. Results of flow resistance to the direction of wave propagation (Fig.1), are shown in Fig.3, in which ordinate is a loss coefficient of porous structures determined following to the equation.[1)]

$$C_1 = \frac{2g\lambda^5 D}{V^2}\left(\frac{\Delta h}{\ell}\right) \qquad (2)$$

where g is a accerelation of gravity, $\frac{\Delta h}{\ell}$ is energy slope, and V is mean flow velocity. Abscissa is Reynolds number defined by

$$Re = \frac{VD}{\nu} \qquad (3)$$

where ν is kinematic viscosty of fluid. It can be seen in Fig.3 that in the range of Reynolds number tested, turbulent property is stronger than that of laminar. Flow resistance to vertical direction to the structure was found a little larger than the data in Fig.3.

In Fig.3 loss coefficients of rubbles and spheres obtained by several authors are depicted for the case of λ of 0.4. It may be said about rubble that not only porosity and size but also shape and roughness have considerable influence on the coefficient. The average of the coefficients for turbulent flow through rubble is about twice of that for the present porous structure.

The following analytical expression for C_1 is often applyed for practical purpose.

$$C_1 = \frac{C_2}{Re} + C_3 \qquad (4)$$

For example C_1 of rubble was tried to be expressed with $C_2 = 28$ and $C_1 = 0.2$ in Eq .4,[1)] which is shown in Fig.3 by ④

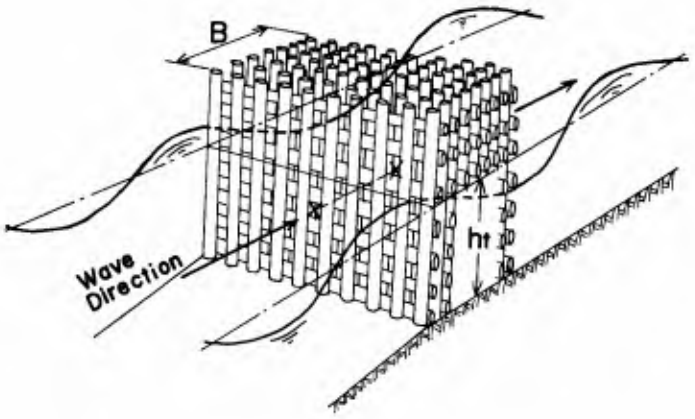

Fig.—1 Sketch of the porous structure

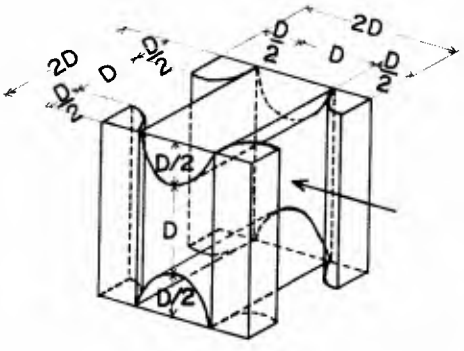

Fig.—2 Details of Void

Photo.—1 Horizontal Bottom

Photo.—2 Sloping Bottom

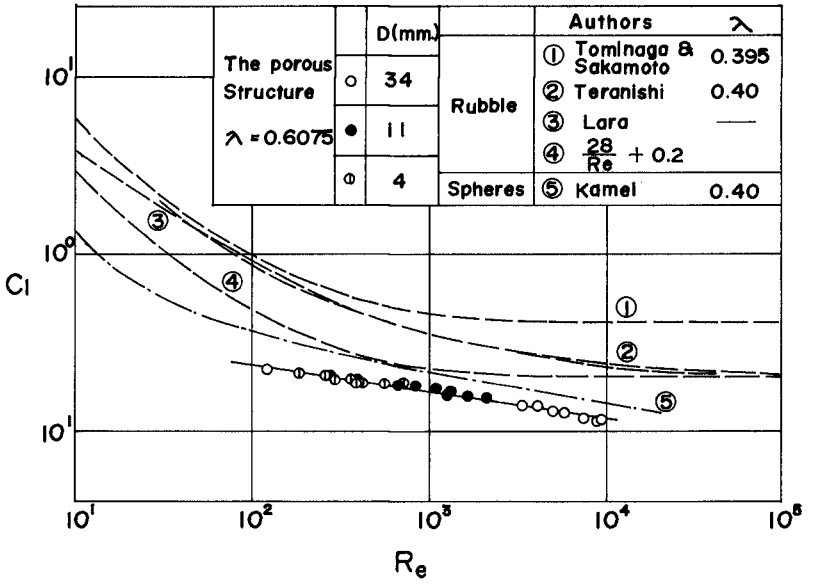

Fig.-3 Loss Coefficients

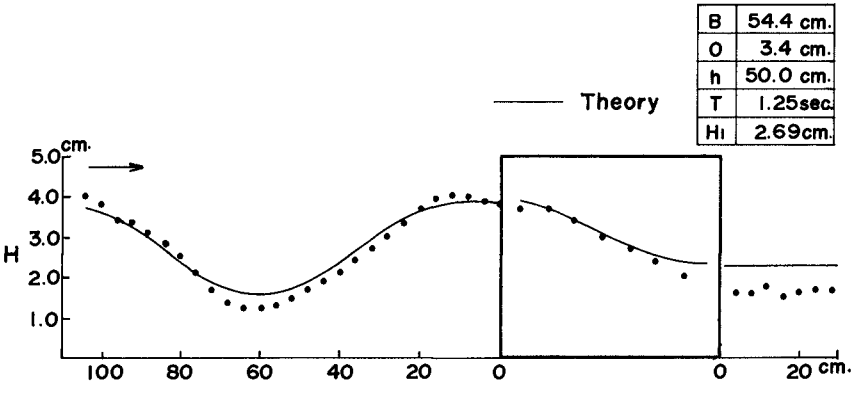

Fig.-4 Wave Heights around and within the structure

3. EXPERIMENTAL PROCEDURE

The experimental works were performed both over a horizontal bottom in a wave channel 1 meter deep, 0.4 meter wide and 18.5 meter long (Photo.1), and a sloping bottom 1/40 in another outdoor channel 0.5 meter deep, 1 meter wide and 35 meter long (Photo.2). Each channel was equipped with a flap-type wave generator. The maximum water depth tested for the former channel was 50 centimeters, while that for the latter was 13.5 centimeters at the toe of structure.

Parallel-wire wave gages were used to measure wave heights. In order to determine incident and reflected wave heights, two wave gages were installed at locations seaward where a loop and a node of partial clapotis were formed, respectively. They were about a half and a quarter of wave length seaward from the front face of structure. Also the method of a moving wave gage recording the water surface fluctuation while moving along the channel axis was used partly to determine the incident and the reflected wave heights. Leeward of the structure a wave gage was installed for transmitted waves. When wave height distribution before and after structure was investigated, wave gages were moved consecutively along the channel axis with a constant pitch between runs of a test. Wave heights within the structure were measured by inserting small wave gages vertically to pores between cylinders of the structure. The output was amplified and recorded on a multi-channel magnetic oscillograph.

4. RESULT AND DISCUSSION

The energy in incident wave which impinge on a porous structure is divided into reflected energy, transmitted energy and the energy dissipated on the surface of and within the structure. Owing to imperfect reflections of incident waves by both the front and the rear faces of a porous structure, standing waves are formed before and within it. Examples of wave height measured around the present porous structure are depicted in Fig.4, which confirm the above-stated. They tell us also that transmitted waves are considered to be progressive.

1) Reflection and Transmission Coefficients

The transmission coefficient is the ratio of transmitted wave height Ht, to incident one Hi, and is denoted Kt in this paper. The reflection coefficient Kr, is defined as that of reflected wave height Hr. The effects of incident wave characteristics, such as Hi, incident wave length L, and water depth at the toe of structure ht, on Kt are more or less similar to those known to rubble structures by several investigators.[1),2),3)] Kt decreases as Hi increases, as wave period T decreases, and ht decreases for both experiments over the horizontal bottom and those over 1/40 sloping bottom, as shown in Figs.5 and 6. There is no abrupt change in Kt between non-breaking waves and breaking waves, which can be seen in Fig.6. Kt for breakers may be well predicted by extending average of Kt for non-breaking waves along Hi/ht.

Data of Kr are more scattered compared with those of Kt. Reasons of the scattering of Kr may be sought in the effects of finite amplifude, the method to separate Hr, and the sensitiveness of interation between waves and porous structures. Effects of Hi and T on Kr are not clear as those on Kt are. Kr increases at ht increases. The statement above is limited to effects of incident wave characteristics themselves on Kt and Kr.

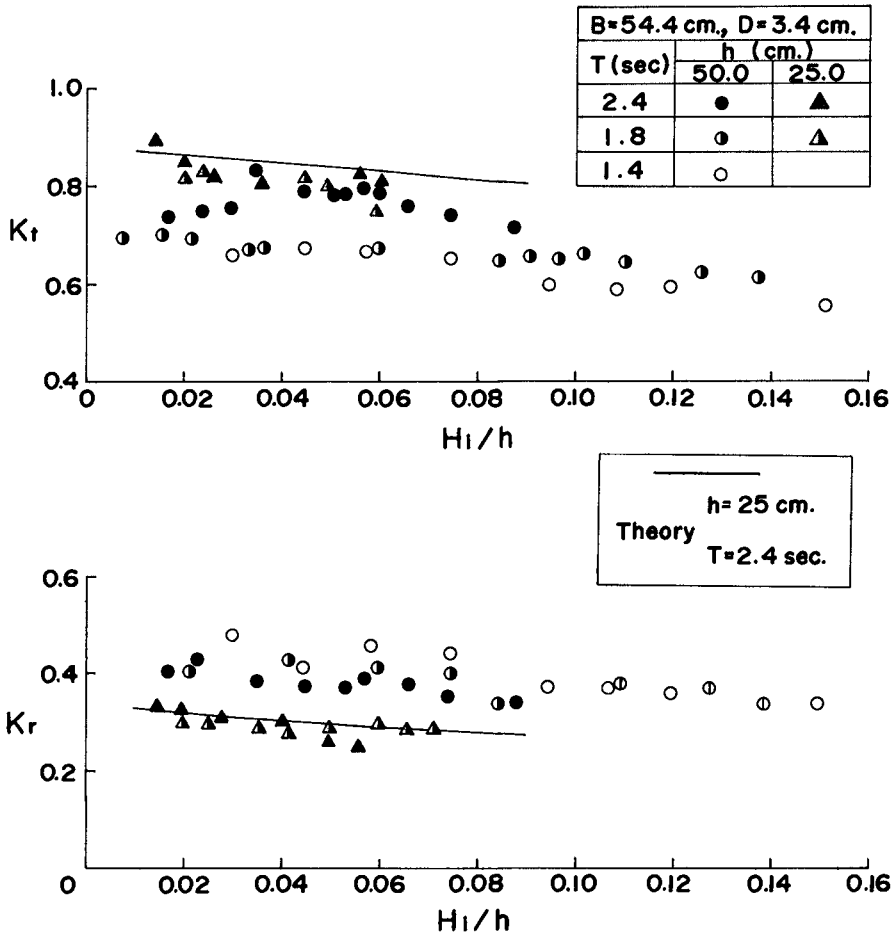

Fig.-5 K_t & K_r versus H_1/h (Horizontal Bottom)

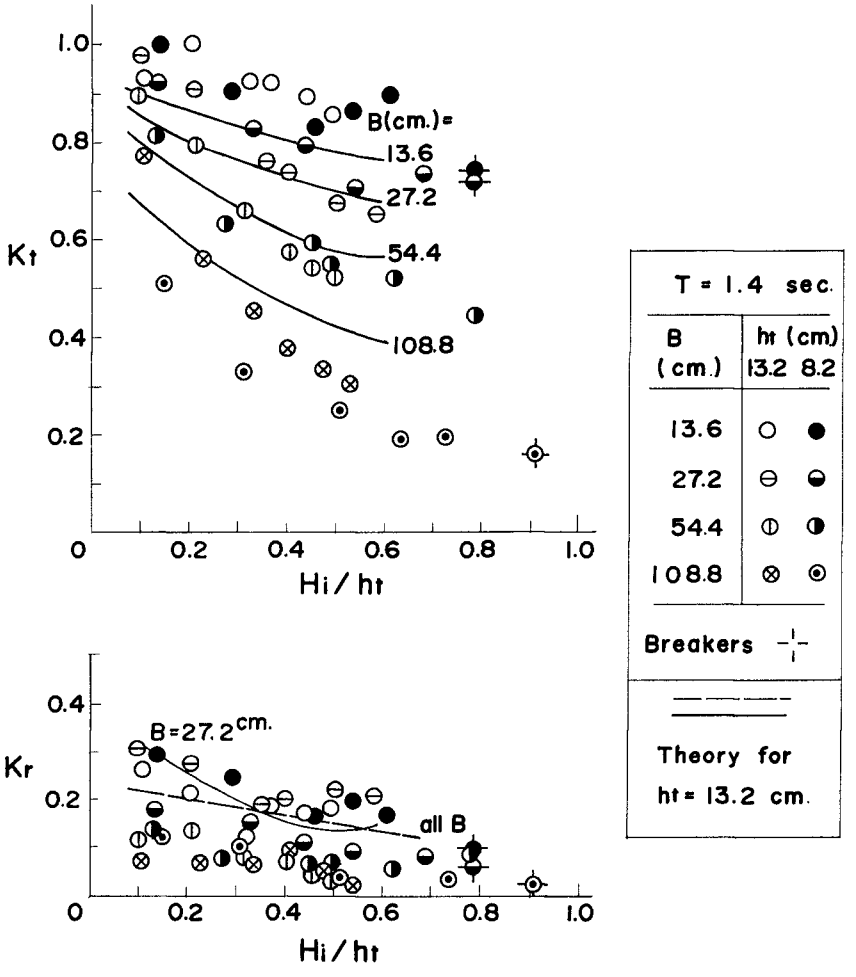

Fig.-6 Kt & Kr versus Hi/ht
(1/40 Sloping Bottom)

Among hydraulic characteristics of the structure the thickness was varied widely. A part of the results is shown in Figs.7 and 8 of which abscissas are relative thickness of structure B/L, where B is thickness of porous structures. Kt decreases approximately exponetially with increase B/L. Kr, however, increases with increase of B/L for very small B/L, reaches to the maximum for that of around 0.2 to 0.25, then becomes smaller, and remains nearly uniform for that greater than about 0.6. This trend about Kr is observed clearly for waves of relatively greater ht and of smaller Hi and perhaps for structures less resistance. In that case Kr fluctuates with a interval of about 0.5X(B/L) as shown in Fig.7. The effect of B/L on Kr is much interesting since it has not been reported for practical porous structures such as rubble breakwaters, though similar effects have been observed to several types of breakwater having a chamber with porous walls,[4)-6)] and to submerged breakwater.[7)] To examine whether structures made of rubble or other granular materials have the effects similar to that obtained here or not, experimental data for packed rubble by LeMehaute[1)] and packed spheres by Kamel[3)] were examined. Figs.9 and 10 are the results obtained respectively, which show clearly there are similar effects of B/L for these porous structures. Surveying Fig.3,7,9 and 10, it is concluded that the greater the flow resistance of a porous structure is, the greater Kr becomes, the smaller B/L for (Kr)max is, and the less Kr decreases after the maximum. Further study on effects of the relative thickness will require to measure the wave length within structure.

2) Wave Height Distribution

Because of existence of not only the transmitted waves but also the waves reflected by the rear face, wave height within a porous structure is not necessarily progressive and shows more or less a pattern of standing waves, which was already observed for pile arrays by Costello[8)]. It is expected naturally that values of B/L influence the distribution greatly. Fig.11 shows examples of the wave height in structure for several B/L values of constant B. Also Fig.12 shows those for constant T. From these figures it is observed for waves of B/L smaller than 0.25, wave height in the structure decreases from the front face to the rear face, but at least a maximal or a minimal of wave height is found within it for waves of B/L greater than 0.25. They show that waves within the structure tend to form a loop of standing waves at the front and a node at the rear face of the structure, respectively. When wave length coincides to this boundary condition, a resonance may occur. Owing to this, strong patterns of standing wave height distribution appears for the waves as shown Figs.11 and 12.

Thus waves of B/L about 0.25 bring larger reflected wave energy and so larger Kr. On the contrary waves of B/L about 0.5, may bring smaller Kr because of a cancelling effect of the two waves at the front face. The above statement is considered to be the reason of the effects of B/L which have been discussed in the preceding section.

3) Scale Effects

Scale effects on wave transmission and reflection for the present structure were tested by making use of the structures of different size. They are made of cylinders of 34, 18, 11 and 4 millimeters, respectively. Tests for the last three of them were operated to be models of those for the first one determined

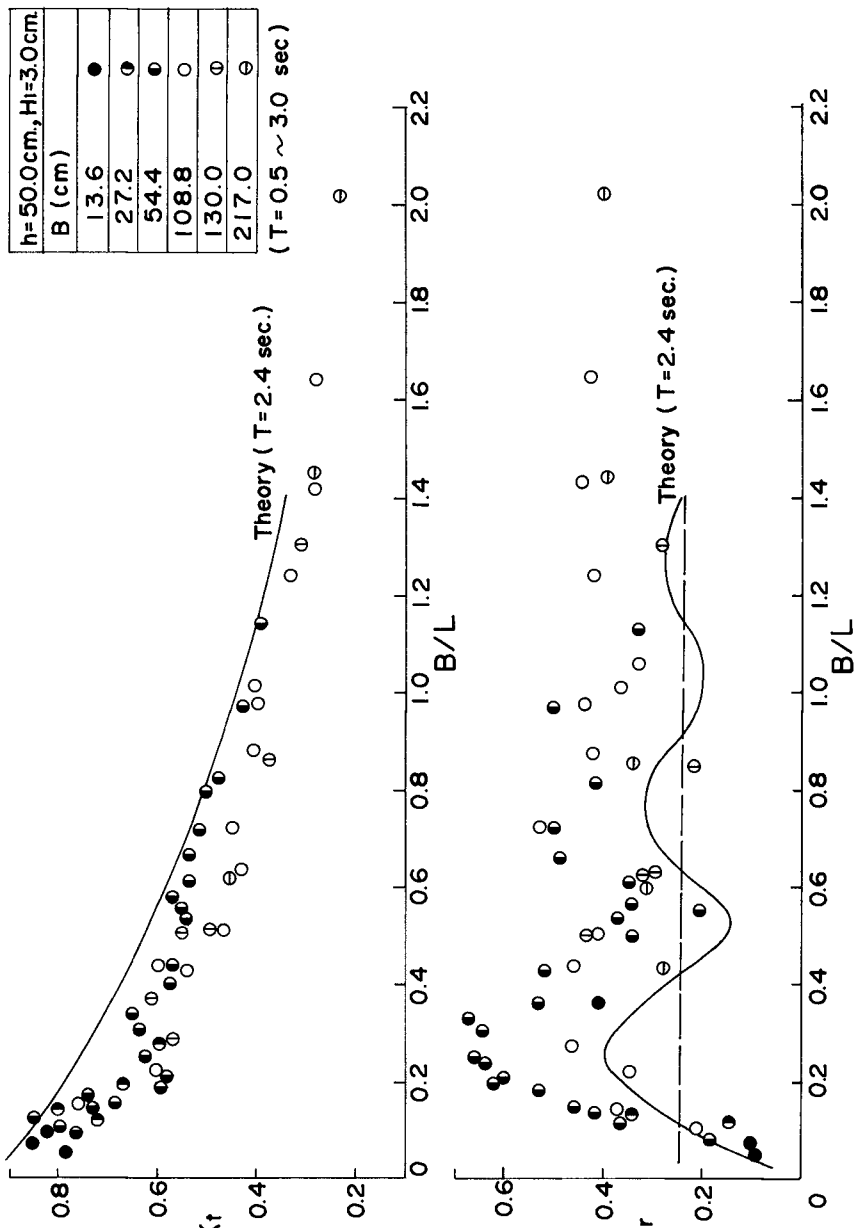

Fig.–7 Kt & Kr versus B/L (Horizontal Bottom)

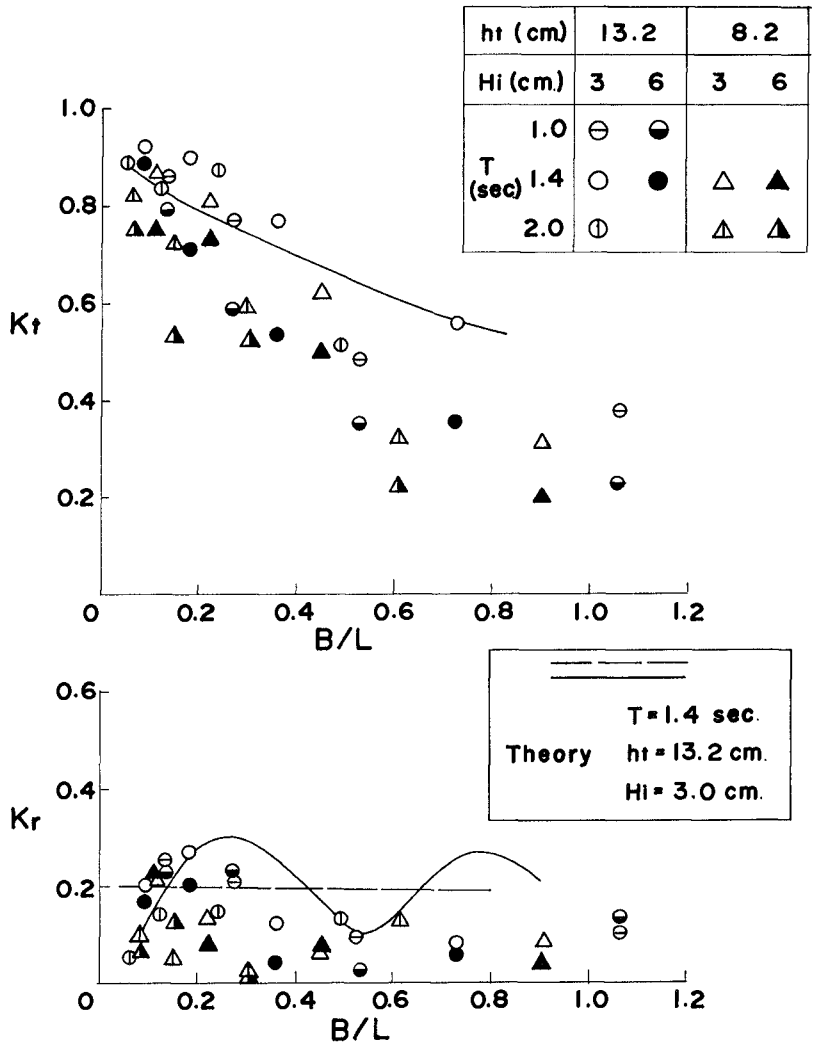

Fig.-8 Kt & Kr versus B/L
(1/40 Sloping Bottom)

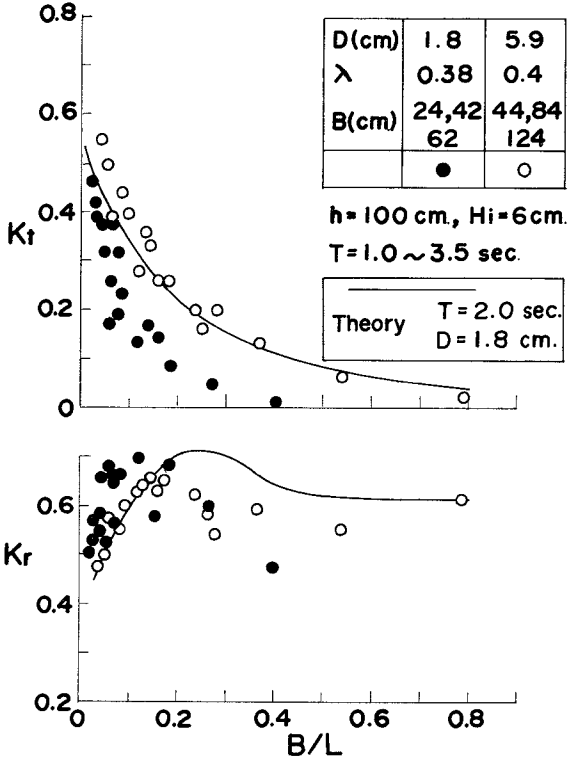

Fig.–9 Kt & Kr for Rubble Structure
(Produced from data by Le Mehaute, 1957)

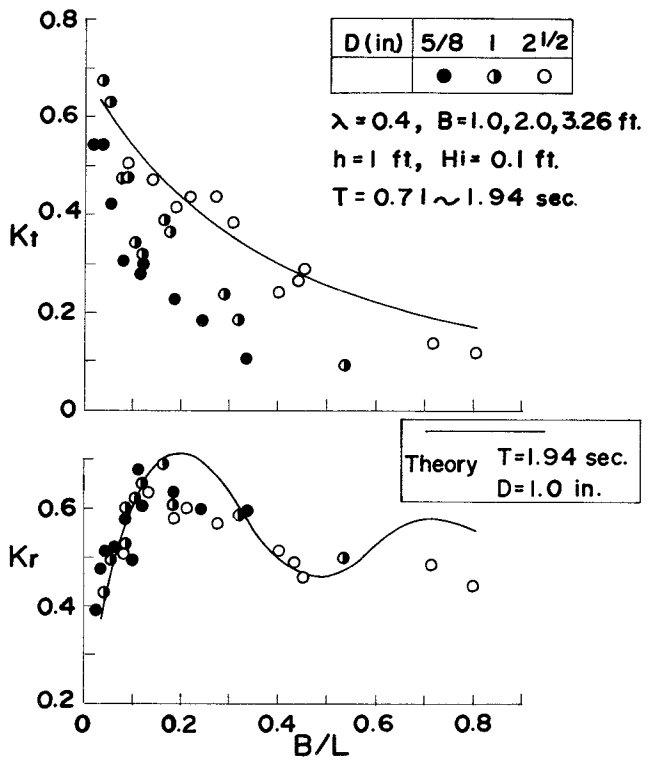

Fig.–10 Kt & Kr for Packed Spheres
(Produced from data by Kamel, 1969)

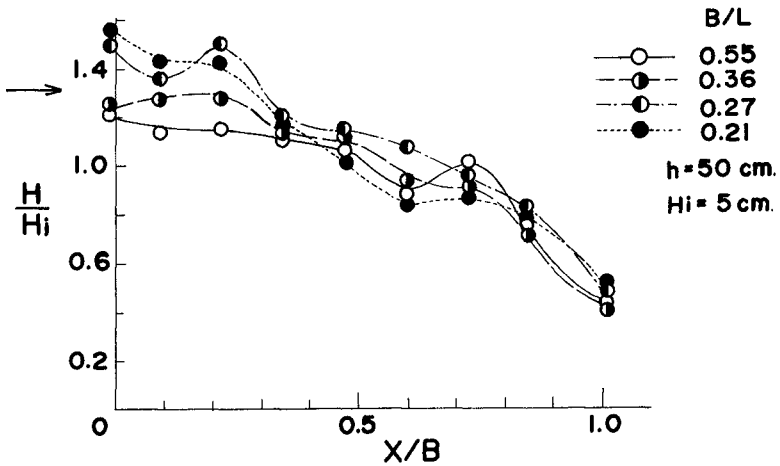

Fig.-11 Wave Height within Structure
(B=54.4 cm., Horizontal Bottom)

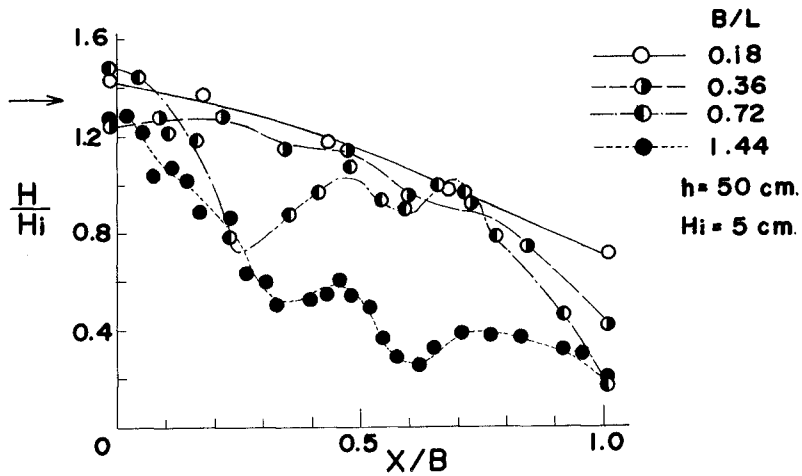

Fig.-12 Wave Height within Structures
(T = 1.0 sec., Horizontal Bottom)

by the Froude law with the length ratios being 18/34, 11/34 and 4/34, respectively. The result on Kt is shown in Fig.11, which indicates that the scale effects exist.

Scale effects on wave transmission for porous structures were studied for rubbles by LeMehaute[1] and Johnson, Kondo and Wallihan[9], for packed spheres by Delmonte[10]. Since loss coefficient of the structure is smaller and more turbulent, the effects on the structure is less than those on the others. As far as Kr concerned scale effects were not clearly observed in the present study.

5. THEORETICAL APPROACHES

1) Kt

Theoretical approaches to predict Kt and Kr for a vertical-faced porous structure from characteristics of incident wave and those of the structure have been proposed by LeMehaute[1], Tominaga and Sakamoto[11], and the first writer[12].

In the writer's approach, incident waves are assumed to be of shallow water but the energy loss at the faces as well as within the structure can be considered. Examples of the theoretical values by the writer's method for Kt are shown in the several figures appeared in the preceding chapters. Generally speaking, the theory well predict Kt for waves of larger period, and smaller depth and wave height, and for structures of thinner width. For other waves than those mentioned above it gives greater Kt than experiment does because of loss due to vertical motions being neglected in the theory. Comparison of theoretical and experimental Kt was performed for wide range of incident waves and of B. The results for waves of relatively shallower water depth are shown in Fig.14. From the figure it is concluded that the theoretical approach to predict Kt is useful for waves of h/L smaller than 0.1.

2) Wave Height before the Structure

The water surface displacement measured from the undisturbed surface before a porous structure can be expressed by superposition of the incident and the reflected waves as shown Fig.15.

$$\eta = \eta_i + \eta_r \tag{5}$$

where η_i and η_r are of the incident and the reflected waves, respectively. They are given by Eqs.6 and 7 by taking the origin of x at the front face of structure.

$$\eta_i = \frac{Hi}{2} \sin (\sigma t - m_o x) \tag{6}$$

$$\eta_r = \frac{Hr}{2} \sin (\sigma t + m_o x + \alpha_r) = Kr \frac{Hi}{2} \sin (\sigma t + m_o x + \alpha_r) \tag{7}$$

where $m_o = 2\pi / L$.
Substituting Eqs.6 and 7 into Eq.5, it can be rewritten as

$$\eta = \frac{Hf}{2} \cos (\sigma t - \theta_f) \tag{8}$$

where

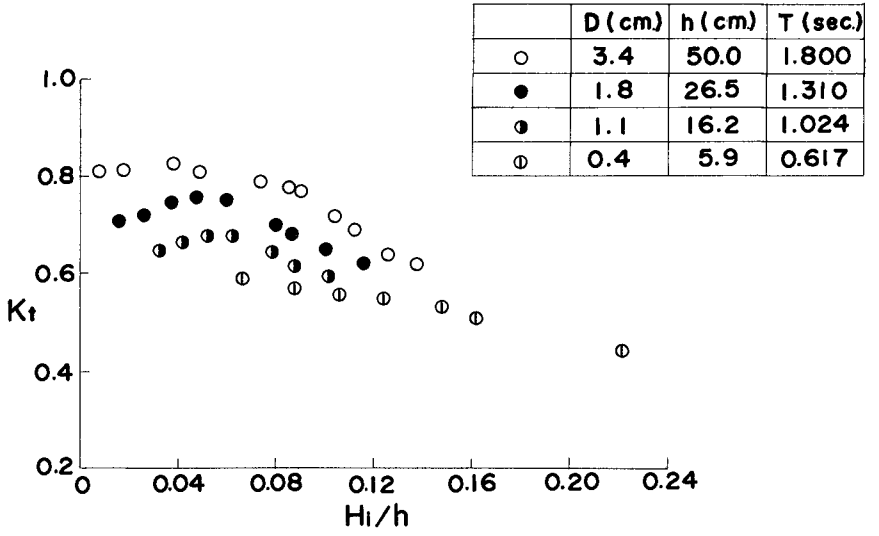

Fig.–13 Scale Effect on Kt

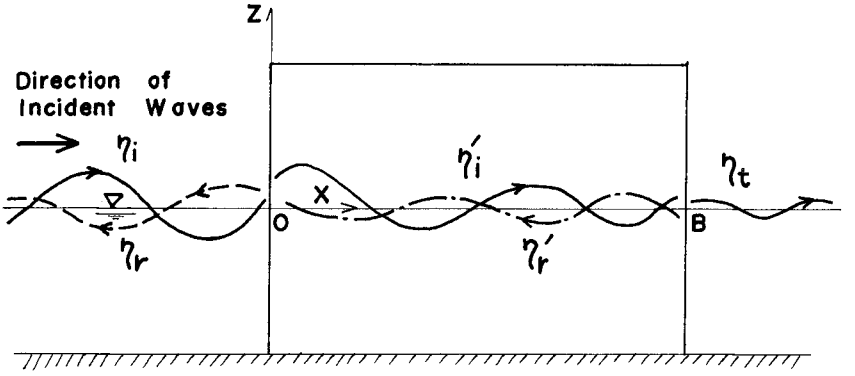

Fig.–15 Sketch of Waves around and within a porous structure

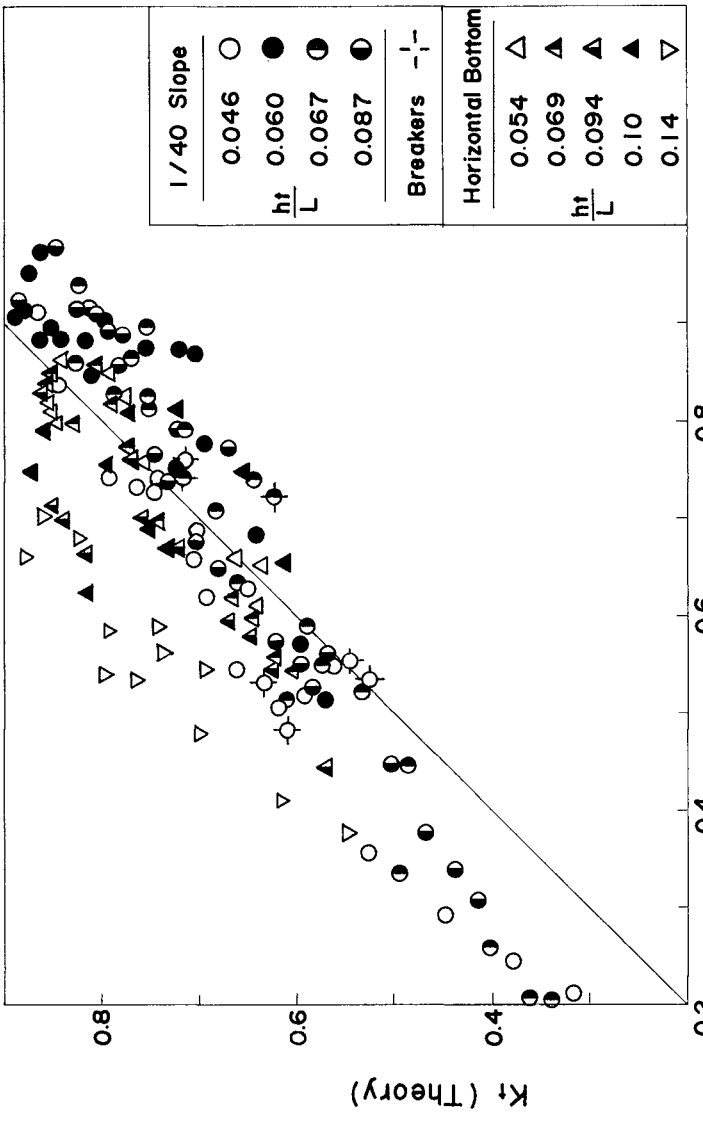

Fig.-14 Comparison of Theory with Experiment

$$Hf = Hi\sqrt{1 + Kr^2 + 2Kr \cos (2m_o x + \alpha r)} \tag{9}$$

$$\theta f = \tan^{-1}\left[\frac{\cos m_o x + Kr \cos (m_o x + \alpha r)}{-\sin m_o x + Kr \sin (m_o x + \alpha r)}\right] \tag{10}$$

3) Wave Height Distribution within Structure

The water surface displacement of progressive long waves in a porous medium is expressed[12]

$$\eta = \frac{Hor}{2} e^{-nx} \cdot \sin (\sigma t - mx) \tag{11}$$

in which Hor denotes wave height at the origin, i.e., x = 0, σ is $2\pi/T$, m and n are given by

$$m = \sqrt{\frac{\sigma^2 \tau}{2gh}\left[\sqrt{1 + (\frac{\lambda g}{\tau \sigma k^*})^2} + 1\right]} \tag{12}$$

$$n = \sqrt{\frac{\sigma^2 \tau}{2gh}\left[\sqrt{1 + (\frac{\lambda g}{\tau \sigma k^*})^2} - 1\right]} \tag{13}$$

in which τ is the square root of tortuosty of the medium. k* is given by

$$k^* = k / (1 + \frac{8\beta U^*}{3\pi}) \tag{14}$$

where k is the coefficient of permeability, U* is the muximum horizontal velocity at the location concerned. β is a coefficient which is given by Eq.15 when C_1 is expressed by Eq.4.

$$\beta = C_3 D / C_2 \nu \tag{15}$$

The water surface displacement within structure is expressed in a similar way to the preceding section as

$$\eta' = \eta_i' + \eta_r' \tag{16}$$

$$\eta_i' = \frac{Hi'}{2} e^{-n_i x} \cdot \sin (\sigma t - m_i x) \tag{17}$$

$$\eta_r' = \frac{Hr'}{2} e^{n_r (x-B)} \cdot \sin (\sigma t + m_r x - 2m_i B + \alpha_r) \tag{18}$$

where subscripts i and r refer to incident and to reflected waves from the rear face, respectively (Fig.15). Hi' and Hr' are given by[12]

$$Hi' = Ktf \cdot Hi \tag{19}$$

$$Hr' = Krb \cdot Hi' \cdot e^{-n_i B} = Ktf \cdot Krb \cdot e^{-n_i B} \cdot Hi \tag{20}$$

Ktf is the transmission coefficient at the front face. Krb is the reflection coefficient at the rear face. Let us express η' as

$$\eta' = \frac{Hs}{2} \cos (\sigma t - \theta s) \tag{21}$$

then,

$$Hs = Hi\, Ktf \sqrt{\frac{e^{-2n_i x} + Krb^2\, e^{-2[(n_i+n_r)B - n_r x]}}{+ 2Krb\, e^{-(n_i+n_r)B-(n_i-n_r)x} \cos [(m_i+m_r)x - 2m_i B + \alpha r]}} \tag{22}$$

$$\theta s = \tan^{-1}\left[\frac{e^{-n_i x} \cdot \cos m_i x + Krb \cdot e^{-(n_i+n_r)B+n_r x} \cdot \cos (m_r x - 2m_i B + \alpha r)}{-e^{-n_i x} \cdot \sin m_i x + Krb \cdot e^{-(n_i+n_r)B+n_r x} \cdot \sin (m_r x - 2m_i B + \alpha_r)}\right] \tag{23}$$

4) Kr

In the analytical approach to predict Kr which had been proposed by the first writer in 1970[12], the reflected wave energy by the front face of structure is only considered. So the computed Kr by the theory shown with broken lines in the several foregoing figures does not vary with B. Owing to the retrogressive wave energy through the front face after being reflected by the rear face of structure, they deviate appreciably from theexperimental ones especially for those of smaller B/L. An analytical approach for Kr which contains the two kinds of reflected wave is derived as following.

The water surface displacement of the combined reflected waves can be expressed

$$\eta_r = \eta_{rf} + \eta_{rb} \tag{24}$$

where η_{rf} and η_{rb} are the water surface displacement for the reflected waves by the front face and by the rear face, respectively. Subscripts f and b for Kt, Kr, αt and αr refer to the front face and the rear face of structure, respectively.

$$\eta_{rf} = \frac{Hi}{2} \cdot Krf \cdot \sin\left(\sigma t + m_o x + \alpha rf\right) \tag{25}$$

The water surface displacement of the incident waves for η_{rb} is obtained by making use of of Eq.4 as

$$\eta_r' = \frac{Hi}{2} \cdot Ktf \cdot Krb \cdot e^{-(n_i+n_r)B} \cdot \sin\left(\sigma t + m_r x - 2m_i B + \alpha rb + \alpha tf\right) \tag{26}$$

Since η_{rb} is that of the transmitted waves of η_r', it is obtained as

$$\eta_{rb} = \frac{Hi}{2} Ktf\ Krb\ \bar{K}tf\ e^{-(n_r+n_i)B} \sin\left(\sigma t + m_o x - 2m_i B + \bar{\alpha}tf + \alpha rb + \alpha tf\right) \tag{27}$$

where $\bar{}$ refer to the retrogressive waves from the structure to the front water area. When we write η_r as following,

$$\eta_r = \frac{Hi}{2} Kr \cdot \sin\left(\sigma t + m_o x + \alpha r\right) \tag{28}$$

then,

$$Kr = \frac{\sqrt{Krf^2 + Ktf^2 \cdot Krb^2 \cdot \bar{K}rf^2 \cdot e^{-2(n_i+n_r)B} + 2Krf \cdot Ktf \cdot Krb \cdot \bar{K}tf}}{\times e^{-(n_i+n_r)B} \cos\left(-2m_i B + \bar{\alpha}tf + \alpha rb + \alpha tf - \alpha rf\right)} \tag{29}$$

$$\alpha r = \tan^{-1}\left[\frac{Krf \sin \alpha rf + Ktf\ \bar{K}tf\ Krb\ e^{-(n_i+n_r)B} \sin\left(-2m_i B + \alpha rb + \bar{\alpha}tf + \alpha tf\right)}{Krf \cos \alpha rf + Ktf\ \bar{K}tf\ Krb\ e^{-(n_i+n_r)B} \cos\left(-2m_i B + \alpha rb + \bar{\alpha}tf + \alpha tf\right)}\right] \tag{30}$$

Since the K and α values in the right sides of the above two equations can be obtained[12], Kr and αr are calculated. The computed Kr values are shown with solid lines in Figs.6-10. They fit the experimental ones much better than those of the former approach shown with broken lines, though the degree of fitness is not good as those of Kt. Also computed wave heights before and within the structure with Eqs. 9 and 22 are shown in Fig.4 with solid lines, which confirm usefulness of these approaches. In the course of computing Hs by Eq.22 and Kr by Eq.30, m_i and m_r are assumed to be m_o because the incident waves are not necessarily of shallow water.

6. CONCLUSIONS

1) The transmission coefficient Kt is greater for waves of smaller height, longer period and smaller thickness. The effects of the above characteristics on the reflection coefficient Kr themselves are not clear as those on Kt are.

2) The relative thickness of structure B/L, has definite effects on Kt and Kr. Kt decreases nearly exponentially with increase of B/L. Kr increases with B/L for small values of that, reaches to the maximum for that abuot 0.2 to 0.25, then decreases, and remains nearly uniform for waves of that greater than 0.6. Similar effects of B/L are found for rubbles and for packed sphers.

3) Waves within structures show a pattern of standing waves because not only the progressive waves but also retrogressive waves reflected by the rear face of the structure exist. Since a loop of standing wave tends to form at the front face and a node at the rear face, the pattern is emphasized for waves B/L about 0.25, which is considered to be the reason of the maximum Kr.

4) Scale effects of the structure bring smaller Kt for structure of smaller size. No appreciable effects on Kr are observed for the structure.

5) Kt of waves of relative depth h/L less than 0.1 including breaking waves is well predicted by the theoretical method developed previously by the first writer. the approaches to predict Kr, wave heights before and within structures are presented, uefulness of which is confirmed by the comparison with experiment.

ACKNOWLEDGEMENTS

The writers would like to gratefully acknowledge the encouragement and valuable suggestions of Professor Akira Ozaki of Hokkaido University, who was the chairman of the research project, " Study on Coastal Disasters and their Countermessures ", conducted during the period of 1969-1971 with a research grant of the Ministry of Education, which supported the present study partly.

The writers wish to express their gratitudes to Professor Takao Sakai, Department of Civil Engineering, Muroran Institute of Technology, for his constant encouragement during the course of the study.

REFERENCES

1) LeMehaute, B.: Pèrmèabilitè des digues en enrochements aux ondes gravitè pèriodiques, La Houille Blanche, No.6, 1957 et No.2, No.3, 1958.

2) Kondo, H.: Wave transmission through rubble, M.S. Thesis in Civil Engineering, University of California, Berkeley, September 1965.

3) Kamel, A. M.: Water wave transmission through and reflection by pervious coastal structures, WES. Research Report H-69-1, October 1969.

4) Bovin, R.: Comments on vertical breakwaters with low coefficients of reflection, The Dock & Harbor Authority, 45, pp.56-61, June 1964.

5) Terret, F. L., J. D. C. Osorios, and G. H. Lean: Model Studies of a perforated breakwater, Proc. 11th Conf. on Coastal Engrg., vol.II, pp.1104-1120, 1968.

6) Richey, E. P. and C. K. Sollitt: Wave attenuation by porous walled breakwaters, Jr. of Waterway, Harbors and Coastal Engrg. Div., Proc. of ASCE, vol.96, WW3, pp.643-663, Aug. 1970.

7) Dick, T. M. and A. Brebner: Solid and permeable submerged breakwaters, Proc. of 11th Conf. on Coastal Engrg., vol.II, pp.1141-1158, 1968.

8) Costello, R. D.: Damping of water waves by vertical circular cylinders, Transaction of A. G. U., vol.33, No.4, pp.513-519, Aug. 1952.

9) Johnson, J. W., H. Kondo and R. Wallihan: Scale effects in wave action through porous structures, Proc. of 10th Conf. on Coastal Engrg., vol.II, pp.1022-1024, Sept. 1966.

10) Delmonte, R. C.: Breakwater constructed by closely packed spheres, University of California, Berkeley, 1972, (see chapter 105).

11) Tominaga, M. and T. Sakamoto: Study on the wave deformations due to the permeable coastal structures (1), Proc. of 16th Conf. on Coastal Engrg., JSCE, pp.309-319, Dec. 1969 (in Japanese)

12) Kondo, H.: An anlytical approach to wave transmission through permeable structures, Coastal Engineering in Japan, vol.13, pp.31-42, Dec. 1970.

NOTATIONS

B	thickness of porous structure
C_1, C_2, C_3	loss coefficient of porous structure
D	diameter of cylinder, or rubble, or sphere
g	accerelation of gravity
H	wave height
Hf	wave height before porous structure
Hi	incident wave height
Hor	progressive wave height at the origin in porous structures
Hr	reflected wave height
Hs	wave height within porous structures
Ht	transmitted wave height
h	water depth
ht	water depth at the toe of structure
$\Delta h/\ell$	energy slope
i	subscript about incident waves
Kr	the reflection coefficient (= Hr/Hi)
Kt	the transmission coefficient (= Ht/Hi)
k	a coefficient of permeability (cm/sec)
L	incident wave length
r	subscript about reflected waves
t	subscript about transmitted waves
T	wave period
U*	a representative horizontal water particle velocity within structures
V	mean steady flow velocity
α	a phase angle to incident wave
β	a coefficient
η	water surface displacement from still water
θ_f	a phase angle for waves before structure
θ_s	a phase angle for waves within structure
λ	porosity of porous structure
τ	square root of tortousty
ν	kinematic viscosify of fluid

CHAPTER 105

SCALE EFFECTS OF WAVE TRANSMISSION THROUGH PERMEABLE STRUCTURES

by

Richard C. Delmonte*
University of California
Berkeley, California

The energy in waves which impinge on a porous structure, such as a rubble mound breakwater, is divided into reflected energy, transmitted energy, and the energy dissipated by turbulence within the structure. Numerous studies on various aspects of this problem have been made in the past, the most recent of which are those by Kondo (1970) and Sollitt and Cross (1972). The reader is referred to these latter papers for a literature review and the presentation of the theory of wave transmission through a porous media (also see the previous chapters by these same authors). In the studies by Sollitt and Cross (Chap. 103), the porous media consisted of crushed stone; whereas, in the tests by Kondo (Chap. 104) the porous structure consisted of a lattice of circular cylinders. Experimental data which supplement the data obtained in the tests of Kondo, Sollitt and Cross where made at the University of California on a series of three structures constructed of closely packed uniform spheres. Each structure was installed in turn in a wave channel and subjected to wave action with the wave height being measured both seaward and leeward by resistance-type wave gages. The experimental procedure and results are summarized as follows.

EXPERIMENTAL PROCEDURE

The experimental work was performed over a horizontal bottom in a wave channel 3 ft deep, 1 ft wide and 106 ft long. Plastic-coated horsehair was placed in the ends of the wave tank to damp wave energy reflections (Fig. 1). The wave flap could be adjusted to the desired frequency by use of a vari-drive electric motor. Also the eccentrlcity could be adjusted to produce a wide range of wave heights.

Using the Froude law for scaling and considering the largest structure to be the control model with the smaller units as models, the following conditions were used in the tests of the three structures (see Table 1).

A structure was placed in the wave tank at the desired location. Side effects were minimized by extending the test section across the full width of the channel, thus simulating the condition of an infinitely wide structure.

---

* Formerly Graduate Student, Dept. of Civil Engineering

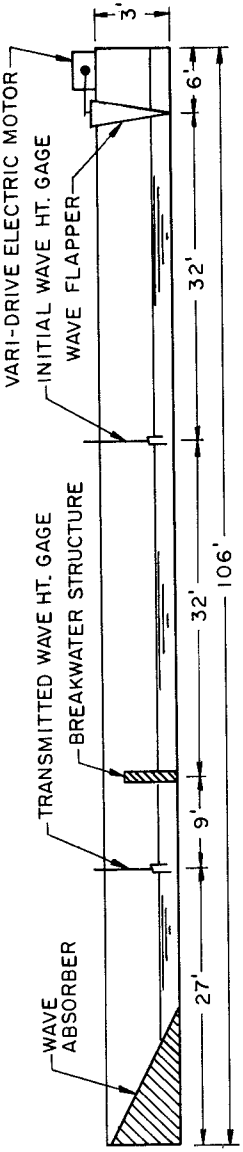

FIG. 1 SKETCH OF 3' x 1' x 106' WAVE CHANNEL

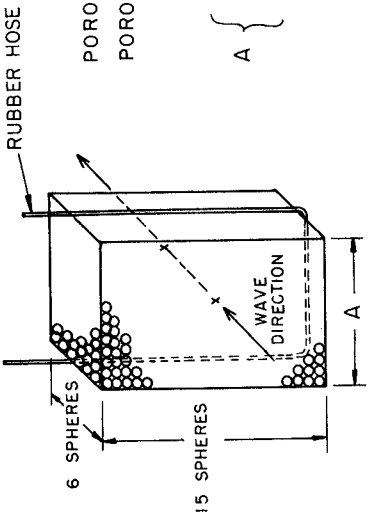

FIG. 2 SKETCH OF BREAKWATER STRUCTURE

To prevent leakage between the structure and the walls of the wave channel, a rubber hose was extended around the bottom and sides of the structure (Fig. 2). The water depth and wave period was selected from Table 1 for a particular structure.

TABLE 1.--TEST CONDITIONS

Structure	Structure Length (ft)	Water Depth (ft)	Sphere Diameter (in)	Porosity of Structure (%)	Wave Period* (sec)	Reynolds No. $d^2/T\nu$
Control Model	1.0	1.6	2.125	40	1.9	1360
1:2 Model	0.5	0.8	1.063	40	1.34	481
1:4 Model	0.25	0.4	0.532	40	0.95	170

*Time scale = square root of length scale.

A parallel-wire resistance type wave gage and strip-chart recorder were used to record the incident and transmitted wave height. With the water level in the wave tank motionless, the experiment was begun by starting the strip-chart recorder and the wave generator. Recorded data were the incident wave height (H_i) and the transmitted wave height (H_t). Measurements taken from the wave records were based on fully developed waves, uninfluenced by reflection distortions, beats, or standing waves.

The wave characteristics were obtained as follows: d/L was held constant by maintaining a constant wave length (constant wave period) while adjusting the height of the incident wave (see Table 2).

RESULTS AND DISCUSSION

Using the experimental data the transmission coefficient (H_t/H_i) was calculated and plotted against the wave steepness (H_i/T^2) for each structure as shown in Fig. 3 (For the plotted relationships, H_i/T^2 replaced H_i/L, where L is wave length).

Examination of Fig. 3 shows that the Froude law is not the only factor involved in this model study. This is evident particularly at small wave steepnesses, (H_i/T^2). Using the experimental data, when (H_i/T^2) = 0.02, H_t/H_i = 0.5, 0.4 and 0.3 for the control model, model 1:2, and model 1:4, respectively. The reflected energy is probably a function of the Froude number as well as the porosity of the structure; that is, the energy dissipated by turbulence within the structure is probably a function of a Reynolds number.

TABLE 2

TABULATION OF H_t/H_i vs. H_i/T^2

RUN NO.	H_t/H_i	H_i/T^2	
1	1.08	.0032	
2	.924	.0054	
3	.842	.00772	
4	.598	.0137	
5	.565	.0159	
6	.535	.0188	Control Model
7	.492	.0224	T = 1.9 sec.
8	.487	.0240	$1/T^2 = 2.77 \times 10^{-1}$ sec.$^{-2}$
9	.434	.0277	
10	.436	.0291	
11	.482	.0277	
12	.467	.0294	
13	.467	.0294	
14	.468	.0308	
1	.402	.0153	
2	.344	.0259	
3	.288	.0368	
4	.265	.0474	
5	.260	.0557	
6	.244	.0664	Model #1
7	.192	.0770	T = 1.34 sec.
8	.174	.0849	$1/T^2 = 5.57 \times 10^{-1}$ sec.$^{-2}$
9	.157	.102	
10	.149	.1085	
11	.144	.1210	
12	.141	.1235	
13	.136	.1290	
14	.129	.1360	
1	.219	.0304	
2	.194	.0487	
3	.174	.0703	
4	.164	.0914	
5	.160	.111	
6	.143	.132	Model #2
7	.126	.150	T = 0.95 sec
8	.114	.171	$1/T^2 = 1.11$ sec.$^{-2}$
9	.130	.153	
10	.135	.132	
11	.137	.137	
12	.114	.130	
13	.130	.123	
14	.108	.123	

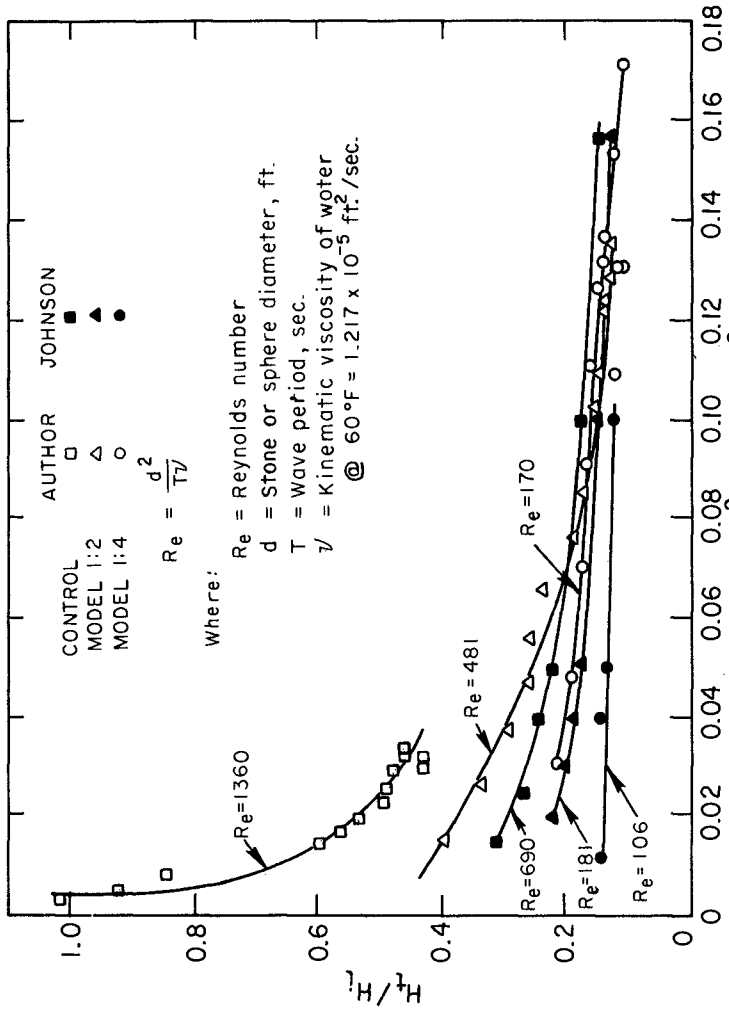

FIG. 3 PLOT OF TRANSMISSION COEFFICIENT (H_t / H_i) VERSES WAVE STEEPNESS (H_i / T^2)

Obviously, additional and more controlled experiments are required to completely define the limits in which scale models can be used to predict the transmission of wave energy through breakwater structures.

REFERENCES

Kondo, H. (1970). An analytical approach to wave transmission through permeable structures, Coastal Engineering in Japan, Vol. 13, 1970, pp. 31-42

Sollitt, C. K. and Ralph H. Cross, III (1972). Wave reflection and transmission at permeable breakwaters. Ralph M. Parsons Laboratory for Water Resources and Hydrodynamics, Report No. 147, March 1972.

CHAPTER 106

SCALE EFFECTS IN RUBBLE-MOUND BREAKWATERS

by

Kenneth W. Wilson[1] and Ralph H. Cross[2]

ABSTRACT

In conducting model tests of wave transmission through permeable rubble-mound breakwaters, it is impossible to satisfy simultaneously the Froude and Reynolds criteria for dynamic similarity. The common practice has been to scale the wave parameters and breakwater dimensions in accordance with the Froude Number, and to use large models.

This study represents an attempt to develop theoretical expressions for the coefficients of reflection and transmission as functions of the effective porosity of the breakwater structure, as influenced by the Reynolds-dependent boundary layer growth on the pores. These expressions use linear wave theory and boundary layer theory to estimate the effective decrease in pore diameter due to growth of the displacement boundary layer thickness in the pore.

The theoretical expressions were compared with experimental results from a series of three model tests with breakwaters having vertical faces and using gravel with diameters of 1.37 in., 0.762 in., and 0.324 in. respectively. The prototype to model ratios (using the largest model as the prototype) were 1/1.80 and 1/4.23 respectively.

The experimental results show clearly the existence of scale effects in both coefficients of reflection and transmission. The theoretical expressions were found to overestimate the scale effect in reflection and to underestimate it in transmission.

[1] Engineer, Department of Water Resources, Province of British Columbia

[2] Ocean Engineer, Alpine Geophysical Associates, Inc., Norwood, New Jersey

THEORETICAL DEVELOPMENT

This estimation of the scale effects for reflection and transmission proceeds in two steps: First, the establishment of a simple theory for the wave reflection and transmission coefficients depending only on the porosity of the structure (it being assumed, for the moment, that all other factors scale with the Froude Number, and may therefore be neglected); and second, the calculation of the Reynolds-dependent boundary layer growth inside the pores of the structure, and the resulting effects on the apparent porosity and thus the reflection and transmission coefficients.

Reflection-Transmission Theory

This theory describes wave reflection and transmission into the structure (H_r and H_{ti}, Fig. 1), it being assumed that $H_t \propto H_{ti}$ for the present purposes. The two basic assumptions are that energy is conserved; for a constant group velocity, this reduces to

$$E_i = E_r + E_{ti} \tag{1}$$

where E_i is the wave energy corresponding to the incident wave, H_i, given by linear wave theory as $\gamma H_i/8$, etc.; and that the water surface elevation is continuous across the face of the structure,

$$\eta_i + \eta_r = \eta_{ti} \tag{2}$$

where η_i is the total instantaneous water surface elevation associated with the incident wave, etc. Again, using linear wave theory,

$$\eta_i = a_i \cos (kx - \sigma t) \tag{3}$$

where the incident wave amplitude, $a_i = H_i/2$; x is the horizontal coordinate in the direction of wave advance; σ is the radian wave frequency, $2\pi/T$; T is the wave period; and t is time.

Assuming that the energy flux of the wave being transmitted through the structure is the same as that of the same wave in open water, but reduced by the fraction of the water volume occupied by rock;

$$C_g E_{ti} = C_g m \frac{\gamma A_{ti}^2}{2} \tag{4}$$

where m is the porosity and C_g the group velocity.

With the introduction of the appropriate additional expressions from linear wave theory, the above assumptions yield the following expressions for the wave reflection and "transmission" coefficients:

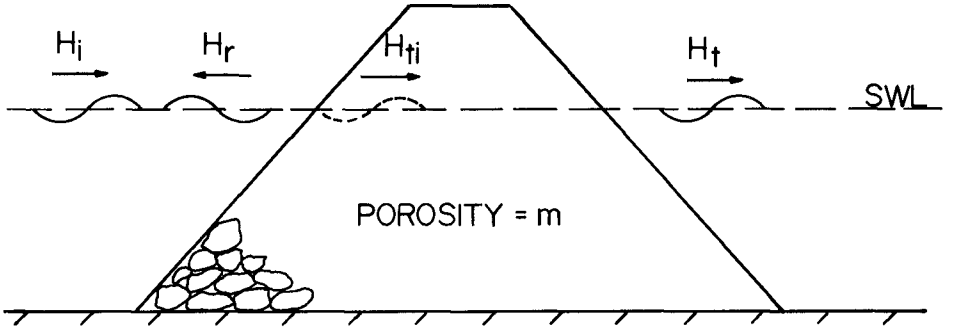

FIGURE I. WAVE REFLECTION AND TRANSMISSION

$$K_r = H_r/H_i = \frac{1-m}{1+m} \qquad (5)$$

$$K_{ti} = H_{ti}/H_i = \frac{2}{1+m} \qquad (6)$$

The above development is essentially identical to that for the reflection and transmission of waves encountering a contraction in width in a channel of constant depth.

Boundary Layer Effects

The growth of the boundary layer near the leading edge of a flat plate, or inside a short tube, represents the retardation of the flow velocity due to the presence of the solid boundary. In a short tube, this results in a reduction in the total flow discharge through the tube. One way of describing this discharge reduction is to calculate the displacement boundary layer thickness, δ^*, and to reduce the tube radius by this amount. From the definition of δ^*, then, the discharge obtained from the partly retarded flow velocity distribution in the original tube (Fig. 2). If we characterize the pores in the structure as tubes, this reduction in size of the tubes represents a reduction in porosity that can be applied to Eqs 5a & 5b to obtain the effect on K_r and K_{ti}.

First, the dimensions of the tube equivalent to the interstitial pores must be found. The tube length, ℓ, was arbitrarily chosen as 1/4 D, where D is the rock diameter. The tube diameter, D_p, was calculated from the hydraulic radius, R_h, as for a pipe: $D_p = 4\ R_h = 4\ A/P$. Here, A is the cross-section area of the pore, and P the wetted perimeter. Both these parameters are hard to measure; however, if both A and P are multiplied by a length (for example, D), they become proportional to the porosity, m, and the particle surface area per unit volume of structure, (1-M)S, where S is the specific surface, or surface area of the stones per unit volume of solids. For spheres, S=6/D; thus

$$D_p = \frac{4m}{1-m} \quad \frac{D}{6} \qquad (7)$$

To calculate the boundary layer growth, the flow velocity must be known. For the present purpose, the linear theory flow velocity at the water surface corresponding to H_{ti}, averaged over half a wave period, is taken as characteristic:

$$U = \frac{2H_i\ K_{ti}}{T \tanh kh} \qquad (8)$$

where h is the water depth.

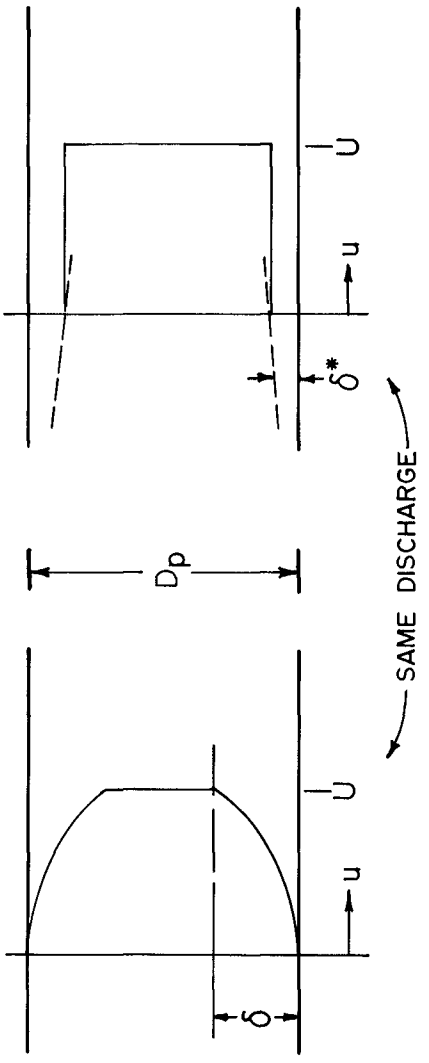

FIGURE 2. DISPLACED BOUNDARY LAYER EFFECT

For a laminar flow, the boundary layer thickness δ and the displacement thickness δ^* are given by

$$\delta = \frac{5x}{R_x^{1/2}} \tag{9}$$

and

$$\delta^* = \frac{1.73x}{R_x^{1/2}} \tag{10}$$

For the tube, x becomes ℓ, and the Reynold's number R_ℓ is given by $U\ell/\gamma$, where γ is the kinematic viscosity of the water. The maximum value of δ in the tube is limited to $D_p/2$, so that

$$\delta^* \text{ max} = 1.173\ D_p \tag{11}$$

The reduced porosity, m_r, is calculated as the reduction in cross-section area of the tube

$$m_r = m[1 - \frac{2\ \delta^*}{D_p}]^2 \tag{12}$$

To summarize, the following calculations are performed for both model and prototype:

1. The wave conditions, water depth and structure porosity are known for model and prototype.

2. K_{ti} is estimated from eq. 5b, and used to find U from Eq 7. D_p and ℓ are calculated using eq. 6 for D_p.

3. δ^* and m_r are calculated, using Eq 10 for m_r and Eqs 8b or 9 for δ^* (or empirical relations for turbulent boundary layers if R_ℓ exceeds 300,000).

4. K_r and K_{ti} are obtained from m_r using Eqs 5a and 5b. The estimate in step 2 is checked, and the calculations are revised as necessary.

5. The model-to-model prototype ratios for K_r and K_{ti} are obtained to find the scale effect.

Sample Calculations

Calculations of the scale effects were made for a hypothetical breakwater under the following prototype conditions:

Water Depth	$h = 40$ ft
Rock Diameter	$D = 3$ ft
Porosity	$m = 0.42$
Wave Period	$T = 8$ sec
Wave Heights	$H_i = 2$ and 10 ft

The results are presented as the reflection coefficient, $K_r = H_r/H_i$, and the transmission coefficient, equal to $K_{ti} = H_{ti}/H_i$, in the ratios of model to prototype (it being understood that the model values are first scaled up by the Froude laws).

TABLE I - Calculated Example

$H_i = 2.0$ Ft

Scale Ratio	Rock Dia., Inches	Reduced Porosity	Scale Ratios Trans.	Reflec.
1/1	36	.408	1.00	1.00
1/5	7.2	.385	0.99	1.05
1/10	3.6	.362	0.97	1.12
1/20	1.8	.325	0.95	1.21
1/50	0.72	.234	0.87	1.28
1/100	0.36	.177	0.79	1.44

$H_i = 10.0$ Ft

1/1	36	.411	1.00	1.00
1/5	7.2	.404	0.99	1.00
1/10	3.6	.393	0.98	1.02
1/20	1.8	.372	0.98	1.10
1/50	0.72	.331	0.95	1.19
1/100	0.36	.288	0.91	1.32

As expected, the transmission is reduced and the reflection increased in the smaller models. Assuming a 5% accuracy of laboratory wave measurements, the scale ratios where Reynold's scale effects become detectable are 1/5 for the 2-ft wave, and perhaps 1/15 for the 10-ft wave. A 1/5 model of a 40-ft high breakwater is still 8 ft high, and an expensive proposition.

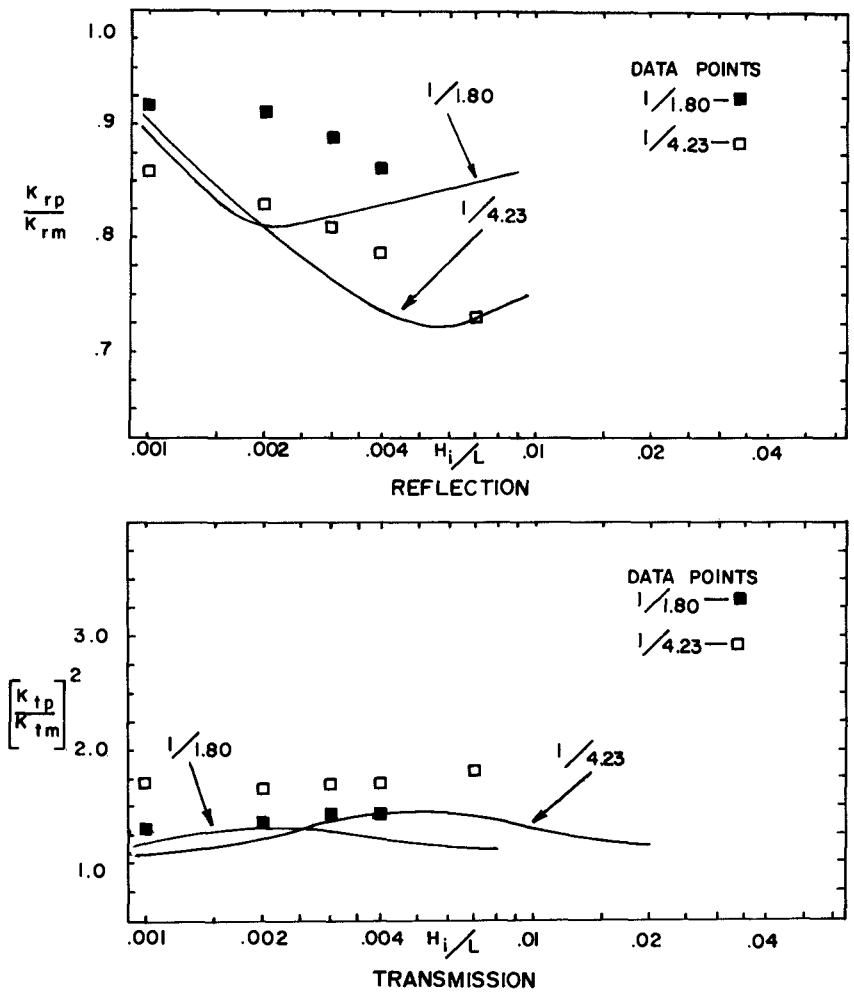

FIGURE 3. REFLECTION AND TRANSMISSION $kh = 0.5$

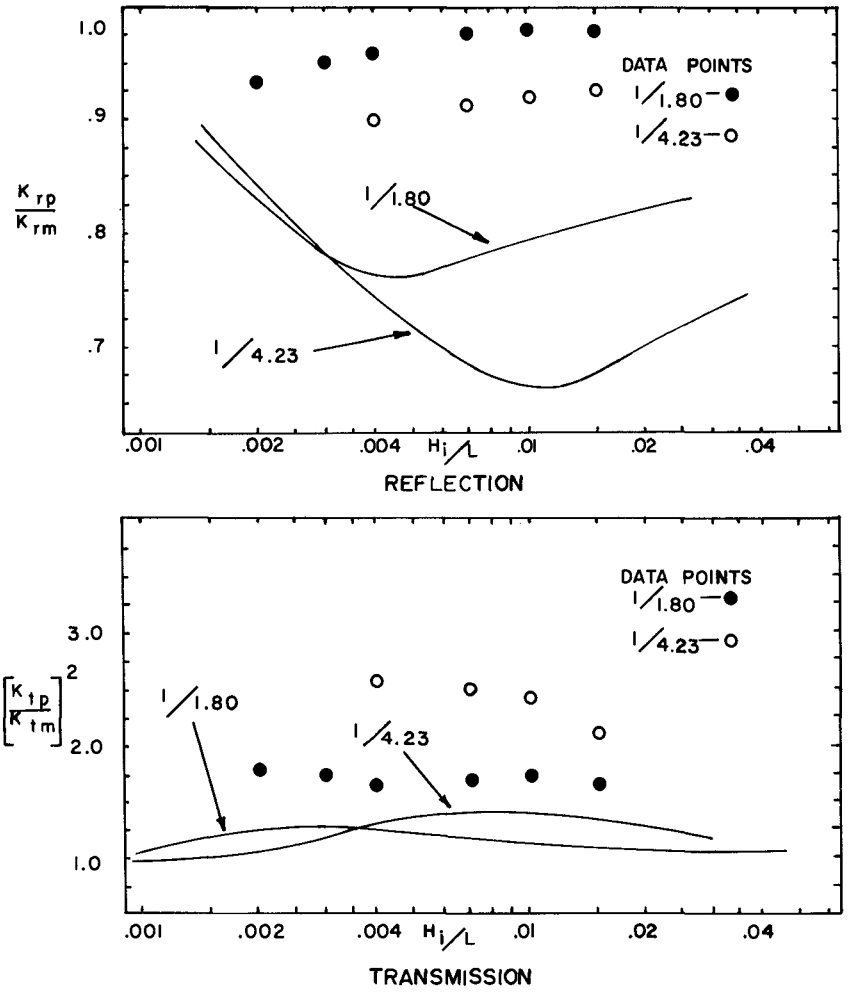

FIGURE 4. REFLECTION AND TRANSMISSION kh=1.0

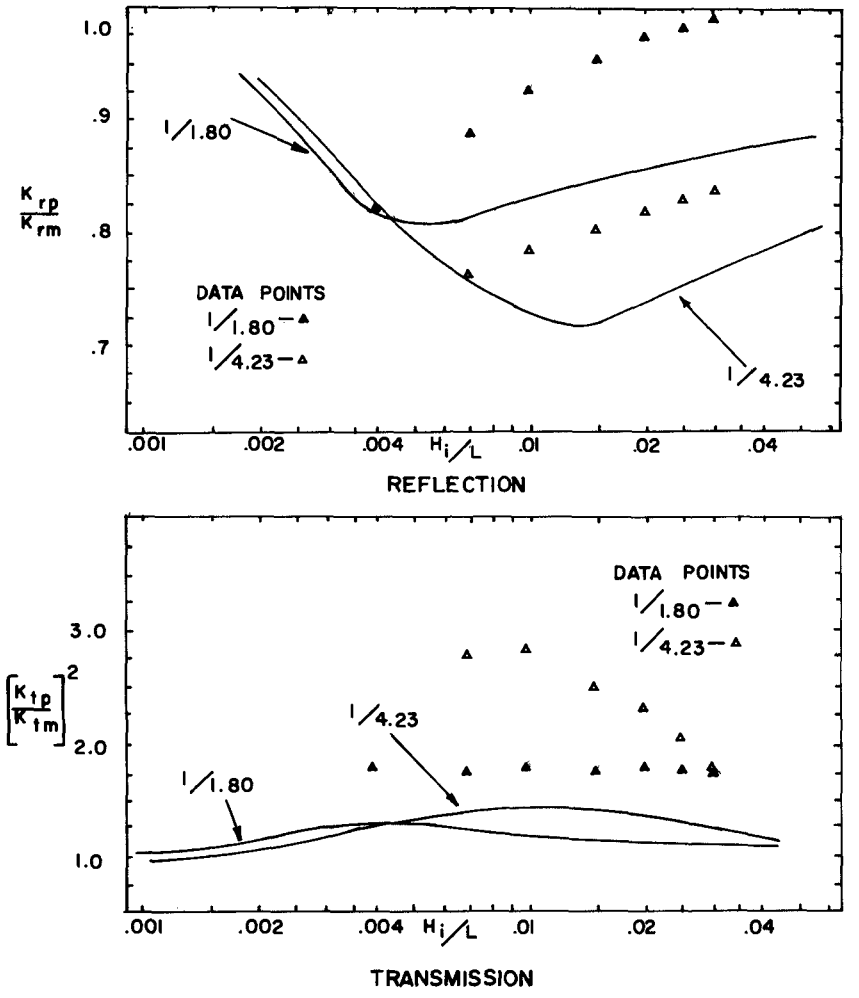

FIGURE 5. REFLECTION AND TRANSMISSION kh= 1.5

EXPERIMENTS

Several series of experiments were run in the large wave tank in the Hydrodynamics Laboratory at M.I.T. Crushed stone was graded, and placed in rectangular wire baskets to represent breakwaters of rectangular cross-section. The stone size (equivalent sphere diameter) was obtained from the number of particles, their weight and specific gravity, and the porosity in place from the basket size, stone weight and specific gravity. The three sizes used were as follows:

Stone	Diameter	Porosity	Scale Ratio
Large	1.37 inches	.437	1/1
Medium	.762	.411	1/1.80
Small	.324	.428	1/4.23

Wave heights (H_i, H_r, and H_t) were measured with parallel-wire resistance gages, with the gage on the "seaward" side mounted on a carriage to obtain the envelope of the partial reflection, and thus the height of the incident and reflected waves and the coefficient.

Results (as prototype/model ratios) for kh = 0.5, 1.0 and 1.5 are shown in Figs 3, 4 & 5. The agreement between the theoretical curves and the data is not particularly good. This may be due to several causes:

1. The assumption that H_t is proportional to H_{ti} (and thus $K_{ti} = K_t$) is particularly open to question; a better relationship, including scale effects, is needed.

2. Throughout the calculations, the "characteristic" dimensions and quantities used were chosen for convenience, with the implicit assumption that using a "characteristic" value instead of, say, a physically meaningful average value, was justified by similarity. Moreover, several phenomena such as energy losses at the seaward face were neglected, or assumed to scale by Froude laws. It is doubtful whether these are strictly correct, as these values and assumptions are used in computing Reynold's effects, which do not scale by Froude similarity.

3. The experiments are not really representative of a typical model=to-prototype relationship. Referring to the calculated example presented earlier, the experiments represent scales of 1/20 to 1/100, compared to a reasonable prototype. In this range, Reynold's effects are extensive, and, as the boundary layer nearly fills the assumed tube, the flat plate expressions used become doubtful.

CONCLUSIONS

The above calculations represent a very simplified "first approximation" at what is obviously a more complex phenomenon. Some large-scale data is needed to provide a proper evaluation of this level of analysis. The next level of sophistication in refining the analysis should be to incorporate a proper relationship between K_{ti} and K_t.

REFERENCES

Daily, J. W., and D. R. F. Harleman, Fluid Dynamics, Addison-Wesley Publishing Co., Inc., Reading, Mass., 1966.

Ippen, A. T. (Editor), Estuary and Coastline Hydrodynamics, McGraw-Hill Book Co., New York, 1966.

Wilson, K. W., Scale Effects in Rubble-Mound Breakwaters, S. M. Thesis submitted to the Department of Civil Engineering, M.I.T., Cambridge, Mass., June, 1971.

ACKNOWLEDGEMENTS

This investigation was sponsored by the Coastal Engineering Research Center, U. S. Army Corps of Engineers, under Contract No. DACW-72-68-C-0032, and performed in the Ralph M. Parsons Laboratory for Water Resources and Hydrodynamics at the Massachusetts Institute of Technology.

The preparation and presentation of this paper was supported by Alpine Geophysical Associates, Inc.

CHAPTER 107

WAVE ENERGY DISSIPATION IN ROCKFILL

by

John A. McCorquodale,* MEIC, A.M.ASCE.

ABSTRACT

Wave motion in a rockfill embankment is solved by a finite element approach. Lagrangian coordinates are used to trace the movement of fluid particles on the free surface.

INTRODUCTION

Very little literature exists on the subject of unsteady non-Darcy flow in coarse granular media. However, unsteady non-Darcy flow is encountered in a few important hydraulic problems, for example,

(a) Wave absorption and transmission in rubble-mound break-waters;
(b) Water level fluctuations in the rockfill and filter zones of a dam subjected to wave action;
(c) Transmission of floods or tides through rockfill dams and causeways.

A mathematical model, to simulate the internal Darcy and/or non-Darcy flow in an embankment subjected to wave action, would permit an improved analysis of: the stability of the embankment; the stability of the armour layer; and the absorption and dissipation of wave energy by the rockfill. Since the internal flow in the embankment and the external wave action are interdependent, a complete model requires the simulation of both of these flows. Such a model would permit the computation of wave run-up and reflection. The present report is limited to the simulation of the unsteady internal flow. Heitner and Housner (4), using a finite element method, have developed an external wave action simulation for Tsunamis. The author is presently attempting to couple the internal and external models.

BACKGROUND

Experimental studies of wave absorption and transmission through rockfill models, have been reported by Johnson et al (5). The flow in their models was probably non-Darcy.

Numerous (1, 3, 7, 10, 11, 12, 13) studies have been carried out to establish the governing equations for non-Darcy flow. Saturated flow in a porous medium may be characterized (12, 13) by one of the following regimes:

(a) Microseepage (non-Newtonian flow at extremely low velocities),
(b) Darcy flow (Laminar Newtonian flow with negligible inertial effects),
(c) Non-linear laminar flow (steady streamline flow in the pores but with significant inertial effects),
(d) Turbulent transitional flow (some of the streamlines in the pores become unstable or turbulent due to inertial effects although viscous forces are still important),
(e) Fully turbulent flow (inertial effects predominate over viscous effects).

Experimental and theoretical (1, 7) studies indicate that the governing equation, for the piezometric slope, i, in steady, one-dimensional, non-Darcy flow in regimes (c) and (d), has the form

---

*Associate Professor, Department of Civil Engineering, University of Windsor, Windsor, Ontario, Canada.

$$i = |\nabla\phi| = (a + bq)q \qquad \text{.....(1)}$$

where a and b are constants for a given medium, fluid and flow regime; q = magnitude of the macroscopic or bulk velocity. The piezometric slope, for the fully turbulent regime, is described by

$$i = |\nabla\phi| = bq^2 \qquad \text{.....(2)}$$

in which $|\nabla\phi|$ = the magnitude of the piezometric gradient $\nabla\phi$.

Polubarinova-Kochina (11) gives the unsteady non-Darcy flow equation

$$i = aq + bq^2 + c\frac{\partial q}{\partial t} \qquad \text{.....(3)}$$

in which c is a constant.

The author (7) has generalized equation 3 with the limitation that the effect of convergence, divergence or curvature of the macroscopic streamlines on the conductivity is negligible; the general equation for 2 or 3 dimensional non-Darcy flow is

$$\vec{q} = -\left(\frac{1}{a+bq}\right)\left(\nabla\phi + \frac{1}{gm}\frac{\partial \vec{q}}{\partial t}\right) \qquad \text{.....(4)}$$

in which $\vec{q}$ = macroscopic velocity; g = acceleration of gravity; m = porosity.

The internal flow is subject to the continuity equation

$$\nabla.\vec{q} = 0 \qquad \text{.....(5)}$$

Hence the internal governing equation is

$$\nabla.\left\{\frac{1}{(a+bq)}\left[\nabla\phi + \frac{1}{gm}\frac{\partial \vec{q}}{\partial t}\right]\right\} = 0 \qquad \text{.....(6)}$$

Equation 6 is to be solved for $\phi = \phi(x,y,t)$ within a time varying solution domain, subject to a set of initial conditions and certain time dependent (periodic) boundary conditions (see figure 1). An important aspect of the wave action problem is the determination of the phreatic surface (in the rockfill) as a function of time.

Lean (6) has solved the problem of wave action in a highly permeable wave absorber by invoking the Dupuit assumption to obtain the following equations for the wave motion:

$$\frac{\partial n}{\partial t} = -\frac{\partial (h_o u)}{\partial x} \qquad \text{.....(7)}$$

$$\frac{\partial u}{\partial t} = -g\frac{\partial n}{\partial x} - \frac{ku|u|}{h_o} \qquad \text{.....(8)}$$

where the variables are defined in figure 2.

Equations 7 and 8 were solved analytically by linearizing the friction term.

Another possible method of solution (2, 7) which has been developed by M. S. Nasser at the University of Windsor, is the method of characteristics; however in order to obtain a practical formulation of the problem, it is again necessary to

use the Dupuit assumption. The characteristic solution can be developed from

$$\begin{bmatrix} (h_o + \eta)/m & 0 & u/m & 1 \\ u/m & 1 & gm & 0 \\ dx & dt & 0 & 0 \\ 0 & 0 & dx & dt \end{bmatrix} \begin{Bmatrix} \frac{\partial u}{\partial x} \\ \frac{\partial u}{\partial t} \\ \frac{\partial \eta}{\partial x} \\ \frac{\partial \eta}{\partial t} \end{Bmatrix} = \begin{Bmatrix} 0 \\ -gm\,F(u)\,u \\ du \\ d\eta \end{Bmatrix} \qquad \text{.....(9)}$$

in which $F(u) = a + b|u|$.

Lean's method and the method of characteristics are useful for and applicable to the case in which the inertial effects are large compared with the friction effects. However, in the case of unsteady flow through sand and gravel embankments the friction effects predominate over the inertial effects and often the Dupuit assumption is not justified because of the two dimensional nature of the flow. The method described in this paper is applicable to the latter case.

MATHEMATICAL FORMULATION

Simplified Equations

If the inertial term, $(1/gm)\partial\vec{q}/\partial t$, in Eq. 6, is small compared to $|\nabla\phi|$ and has nearly the same line of action as $\nabla\phi$ and $\vec{q}$, then the transformation

$$\nabla\zeta = \nabla\phi + \frac{1}{gm}\frac{\partial\vec{q}}{\partial t} \qquad \text{.....(10)}$$

can be introduced in order to reduce Eq. 6 to

$$\nabla.\{K(|\nabla\zeta|)\nabla\zeta\} = 0 \qquad \text{.....(11)}$$

The macro-velocity is now approximated by

$$\vec{q} = -K(|\nabla\zeta|)\nabla\zeta \qquad \text{.....(12)}$$

in which $K(|\nabla\zeta|) = \frac{a}{2b}\left\{\frac{\sqrt{1 + c|\nabla\zeta|} - 1}{|\nabla\zeta|}\right\}$ .....(13)

and $c = 4b/a^2$.

The variational form of Eq. 11 is, (7,8,9),

$$\delta\chi = \int_{t_o}^{t}\int_{A(\tau)} \delta[K(|\nabla\zeta|)(|\nabla\zeta|)^2 + G(|\nabla\zeta|)]\,dA\,d\tau = 0 \qquad \text{.....(14)}$$

in which t_o = initial time;

$$G(|\nabla\zeta|) = \frac{a}{6bc}(2 - c|\nabla\zeta|)\sqrt{1 + c|\nabla\zeta|} \qquad \text{.....(15)}$$

$A(\tau)$ = solution domain.

The boundary conditions for the transformed variable ζ are (see figure 3):

(a) on $\underline{E}\,\underline{A}\,\underline{B}$:- $\frac{\partial \phi}{\partial n} = 0$ and $\frac{\partial \zeta}{\partial n} = 0$;

(b) on $\underline{E}\,\underline{D}$:- $\phi \simeq y_D$ and $\frac{\partial \phi}{\partial y} \simeq 0$ and

$\zeta \simeq \phi$ and $\frac{\partial \zeta}{\partial y} \simeq 0$;

(c) on $\underline{D}\,\underline{C}$:- $\phi \simeq y \simeq \zeta$;

(d) on $\underline{C}\,\underline{B}$:- $\phi = y$; ζ is found from Equation 10; a particle on the free surface remains on the free surface.

Within the approximation of the original transformation, the transformed boundary conditions satisfy the self-adjoint requirement for the variational format.

THE FINITE ELEMENT MODEL

The finite element method is useful for solving free surface problems because of the ease with which certain boundary conditions and variable geometry can be met. The solution domain, A(t), can be discretized by elements of the type shown in figure 4. Figure 3 shows a typical discretization at an instant in time.

The variation of ζ within each element is assumed to be

$$\zeta^e = (\beta_1 + \beta_2 x + \beta_3 y)t + \beta_4 + \beta_5 x + \beta_6 y \qquad \text{.....(16)}$$

where β_i are defined in terms of the six nodal conditions on ζ, x, y and t; thus for $0 \leq t \leq \Delta t$

$$\begin{Bmatrix} \beta_4 \\ \beta_5 \\ \beta_6 \end{Bmatrix} = \begin{bmatrix} 1 & x_\ell & y_\ell \\ 1 & x_m & y_m \\ 1 & x_n & y_n \end{bmatrix}^{-1} \begin{Bmatrix} \zeta_\ell \\ \zeta_m \\ \zeta_n \end{Bmatrix} \qquad \text{.....(17)}$$

and

$$\begin{Bmatrix} \beta_1 \\ \beta_2 \\ \beta_3 \end{Bmatrix} = [(\Delta t)^{-1}] \begin{bmatrix} 1 & x_i & y_i \\ 1 & x_m & y_m \\ 1 & x_k & y_k \end{bmatrix}^{-1} \begin{Bmatrix} \Delta\zeta_i \\ \Delta\zeta_j \\ \Delta\zeta_k \end{Bmatrix} \qquad \text{.....(18)}$$

in which

$$\Delta\zeta_i = \zeta_i - (\beta_4 + \beta_5 x_i + \beta_6 y_i) \qquad \text{.....(19)}$$

is the change in ζ_i during an interval Δt.

The finite element equivalent of Eq. 14 is

$$\frac{\partial \hat{\chi}}{\partial \zeta_i} = \Sigma \frac{\partial \hat{\chi}^e}{\partial \zeta_i} = 0 \qquad \text{.....(20)}$$

where

$$\frac{\partial \hat{\chi}^e}{\partial \zeta_i} = \int_0^{\Delta t} \int_{A(t)^e} \{\frac{\partial}{\partial \zeta_i} [K(|\nabla \zeta^e|)(|\nabla \zeta^e|)^2 + G(|\nabla \zeta^e|)]\} \, dA dt \qquad \text{.....(21)}$$

Substituting from Eq. 16 for ζ^e yields, after integration

$$\sum_{j=i}^{k} \sum_{e=1}^{N} \frac{\bar{K}^e \bar{A}^e}{A_1^e} [3(\beta_5 b_i + \beta_6 c_i)^e + S_{ij}^e \Delta \zeta_j] = 0 \qquad \text{.....(22)}$$

in which $\bar{K}^e = (K^e_{t=o} + K^e_{t=\Delta t})/2$;

$\bar{A}^e = (A_1^e + A_2^e)/2$;

A_1^e = area of triangle ijk;

A_2^e = area of triangle ℓmn;

$S_{ij} = (b_i b_j + c_i c_j)/A_1^e$;

$b_i = y_j - y_k$;

$c_i = x_k - x_j$;

N = number of elements.

CALCULATION OF THE FREE SURFACE MOVEMENT

The position of the free surface after a time increment Δt can be found from

$$\vec{s}(X,Y,\Delta t) = \vec{\bar{q}} \Delta t/m + \vec{s}(X,Y,O) \qquad \text{.....(23)}$$

where $\vec{s}(X,Y,t)$ = position of a free surface particle at time t (lagrangian form); $\vec{\bar{q}}$ = average 'bulk' velocity of the surface particle for the interval Δt (see figure 5). Since $\vec{\bar{q}}$ depends to some extent on the new free surface position, the computation of $\vec{\bar{q}}$ must be obtained by an iterative of trial and error process. Eq. 23 was also utilized to predict the motion or the outcrop point, C. The coordinates of the internal nodes of the elements must be adjusted as the free surface moves.

At each time step, Δt, a new free surface ϕ is computed from $\phi = y + C$; Eq. 10 is used to obtain the corresponding ζ. A transformation is obtained by integrating Eq. 10 along a streamtube to yield approximately

$$\zeta = \phi + \frac{1}{gm}\left(\overline{\frac{\partial q}{\partial t}}\right) S_p \qquad \text{.....(24)}$$

in which $\overline{(\partial q/\partial t)}$ is a representative average value of $\partial \vec{q}/\partial t$ along the streamtube, and S_p is the length of the streamtube. Since the inertia term is assumed to be small compared with friction, the values for S_p can be estimated on the basis of a solution in which $\zeta \equiv \phi$.

JUSTIFICATION OF ASSUMPTIONS

A one dimensional solution of Equation 6, for accelerating flow in a typical gravel, (8), indicates that the time required to reach 90% of the terminal (friction) velocity, corresponding to i = 1, is given by

$$t \simeq \frac{0.1}{gmb} \qquad \text{.....(25)}$$

or approximately .06 seconds for 4.4 cm crushed rock. With zero applied piezometric gradient, the maximum terminal velocity will decay to 10% of its value in

$$t \simeq \frac{.6}{gmb} \qquad \text{.....(26)}$$

or 0.4 seconds for 4.4 cm rock which corresponds to a particle displacement of about one grain diameter.

The case of rapid drawdown in a rockfill has been solved using Equation 6 without the inertia term (9), and with the inertia term (8). The results of these studies are summarized and compared with experimental results in figure 6. It is noted that the effect of the inertia term is small (as assumed in this paper) and that the numerical results are in agreement with the experimental results.

NUMERICAL ANALYSIS

Equations 22 and 23 were utilized to simulate wave motion in an embankment of 4.4 cm crushed rock (a = .005 sec/cm; b = .004 sec^2/cm^2; m = 0.40), as shown in figure 3. The right hand rockface is subjected to a periodic hydrostatic force produced by varying the external water depth according to

$$y_D = \bar{y}_o - A_o \sin\left(\frac{2\pi t}{T}\right)$$

in which $\bar{y}_o$ = mean tail water level (56 cm); T = wave period (2π seconds); A_o = wave amplitude outside rockfill (20 cm). The initial condition is $h_o = \bar{y}_o$ = 56 cm.

It is assumed that the internal free surface level at C will always be equal or higher than y_D.

The solution of Equation 22 and 23 is summarized in the flowchart, figure 7. Equation 22 was linearized and solved by successive over-relaxation (SOR factor = 1.65) at each time step ($0.05 < \Delta t < .2$ sec). In order to start the solution of Eq. 22 the free surface DB at the end of interval Δt is initially assumed to be the same as at the beginning of Δt; on this basis the necessary surface velocities for the application of Eq. 23 are obtained and hence a new free surface can be estimated.

As figure 7 indicates, this approximate solution is 're-cycled' to correct for non-linearities in the system and thus to improve the solution. The computation at a particular time step is complete when successive estimates of the free surface are within a specified tolerance.

The computations were carried out on an IBM 360/40 computer. A typical computer solution for the wave action on certain selected points is shown in figure 8. About 10 minutes of computer time was required for this solution.

EXPERIMENTAL VERIFICATION

Experimental studies, using a wave flume, are now under way to test the proposed numerical simulation. Figure 9 compares the predicted and preliminary experimental wave transmission curve, for a 4.4 cm rock embankment.

CONCLUSIONS

The proposed finite element model for unsteady non-Darcy flow is developed for the case when the influence of $(1/gm)\partial q/\partial t$ is small compared to the influence of turbulence. The available experimental studies appear to indicate that the proposed model is valid for unsteady flow in rockfill for rock sizes up to about 4 cm.

LIST OF REFERENCES

1. Ahmed, N., and Sunada, D. K., 'Nonlinear Flow in Porous Media', Journal of the Hydraulic Division, ASCE, Vol. 95, HY6, Nov. 1969.
2. Dracos, T., 'Calculation of the Movement of the Outcrop Point', Proc. XIII, Congress of the IAHR, Paper D-2, Kyoto, Japan, 1969.
3. Dudgeon, C. R., 'Flow of Water Through Coarse Granular Materials', Master of Engineering Thesis, University of New South Wales, 1964.
4. Heitner, K. L., and Housner, G. W., 'Numerical Model for Tsunamic Run-up', Journal of the Waterways and Harbour Division, ASCE, Vol. 96, WW3, August 1970.
5. Johnson, J. W., Kondo, H., and Wallihan, R., 'Scale Effects in Wave Action Through Porous Structures', Proc. 10th Conference on Coastal Engrg, Tokyo, 1966.
6. Lean, G. H., 'A Simplified Theory of Permeable Wave Absorbers', J. of Hydraulic Research, Vol. 5, No. 1, 1967.
7. McCorquodale, J. A., 'Finite Element Analysis of non-Darcy Flow', Ph.D. Thesis, Department of Civil Engineering, University of Windsor, Canada, 1970.
8. McCorquodale, J. A., 'The Finite Element Method Applied to Unsteady non-Darcy Flow', 18th Annual Special Conference, Hydraulics Division, ASCE, University of Minnesota, 1970.
9. McCorquodale, J. A., 'A Variational Approach to non-Darcy Flow', Journal of the Hydraulics Division, ASCE, Vol. 96, HY11, Nov. 1970.
10. Nasser, M. S. 'Radial non-Darcy Flow Through Porous Media', M.A.Sc. Thesis, Department of Civil Engineering, University of Windsor, 1970.
11. Scheidegger, A. E. ed., 'The Physics of Flow through Porous Media', 2nd ed., University of Toronto Press, Toronto, Canada, 1960.
12. Ward, J. C., 'Turbulent Flow in Porous Media', Journal of the Hydraulics Division, ASCE, Vol. 90, HY5, Sept. 1964.
13. Wright, D. E. 'Nonlinear Flow Through Granular Media', Journal of the Hydraulics Division, ASCE, Vol. 94, HY4, July 1968.

LIST OF SYMBOLS

a	=	a constant;
A	=	area;
A^e	=	area of an element;
A_o	=	wave amplitude;
b	=	a constant;
b_i	=	$y_j - y_k$;
c	=	a constant;
c_i	=	$x_k - x_j$;
e	-	superscript indicates element;
g	=	acceleration due to gravity;
h_o	=	depth measured from the initial mean water level;
i	=	slope of the piezometric grade line;
i,j,k l,m,n	-	indices;
k	=	constant;
$K(-)$	=	hydraulic conductivity;
m	=	porosity;
$\vec{q}$	=	macroscopic velocity;
$s(X,Y,t)$	-	Lagrangian coordinates;
S_{ij}	=	$(b_i b_j + c_i c_j)/A_1^e$;
S_p	=	streamtube length;
t	=	time;
T	=	period;
u	=	horizontal component of velocity;
(x,y,z)	-	Cartesian coordinates;
y_o	=	mean tailwater depth;
β_i	-	coefficients in the elemental representation of ζ^e ;
η	=	height of perturbation measured from initial mean W-L;
ϕ	=	piezometric head;
χ	=	functional;
ζ	=	transformed dependent variable.

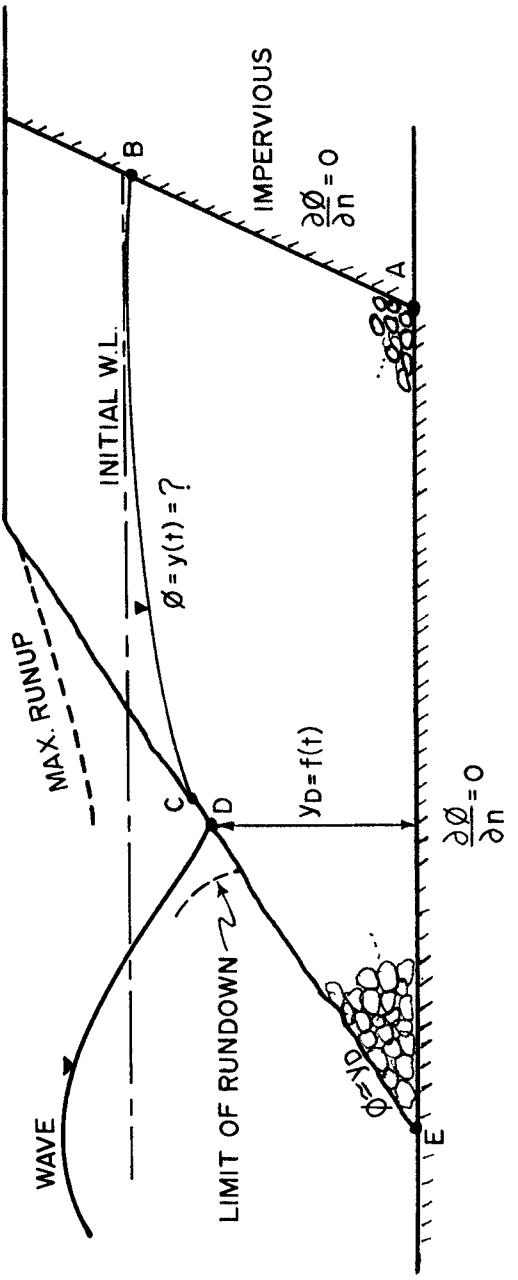

FIGURE 1 Typical Unsteady Non-Darcy Flow Problem.

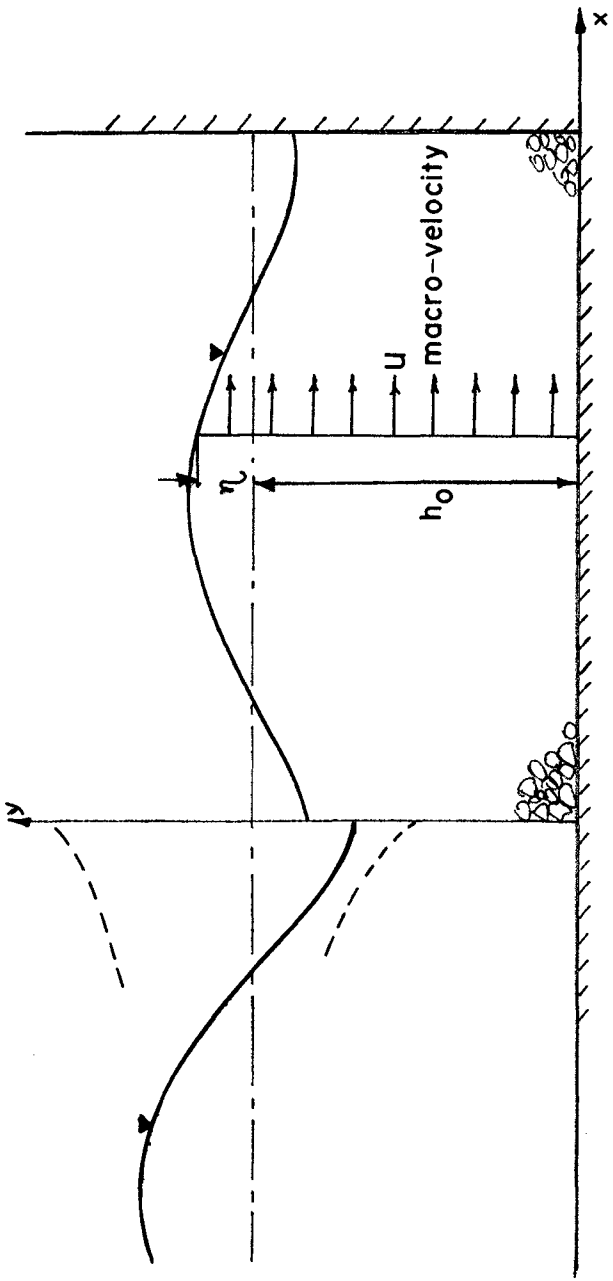

FIGURE 2 Defining Diagram.

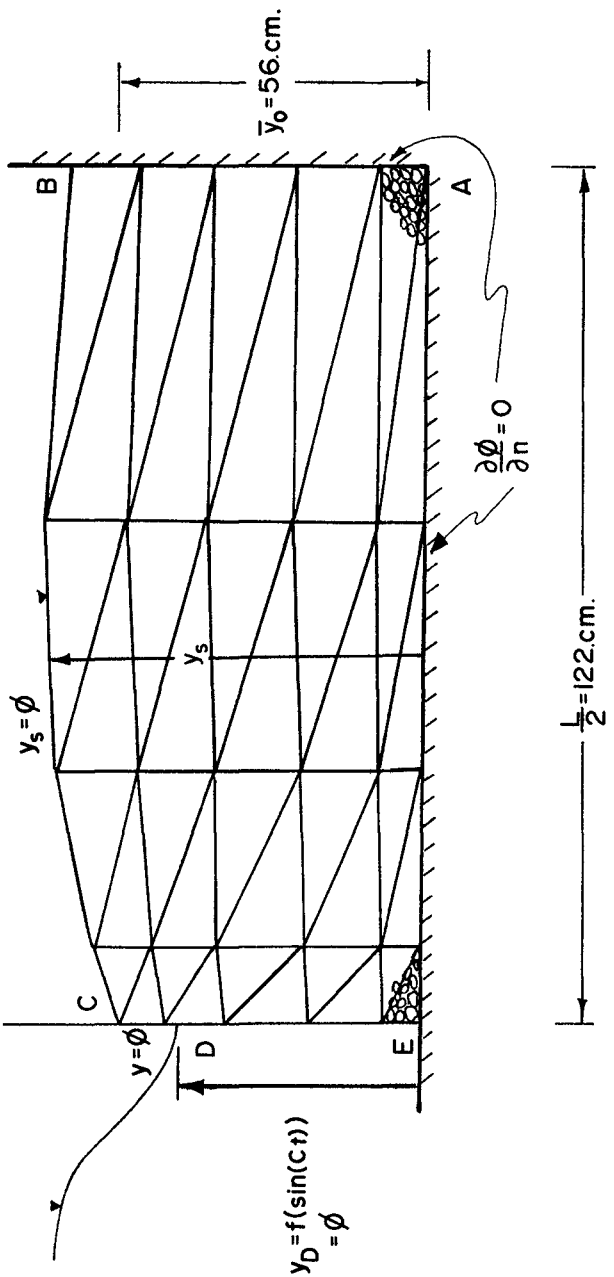

FIGURE 3 Boundary Conditions and Finite Element Discretization for the Illustrative Non-Darcy Flow Problem.

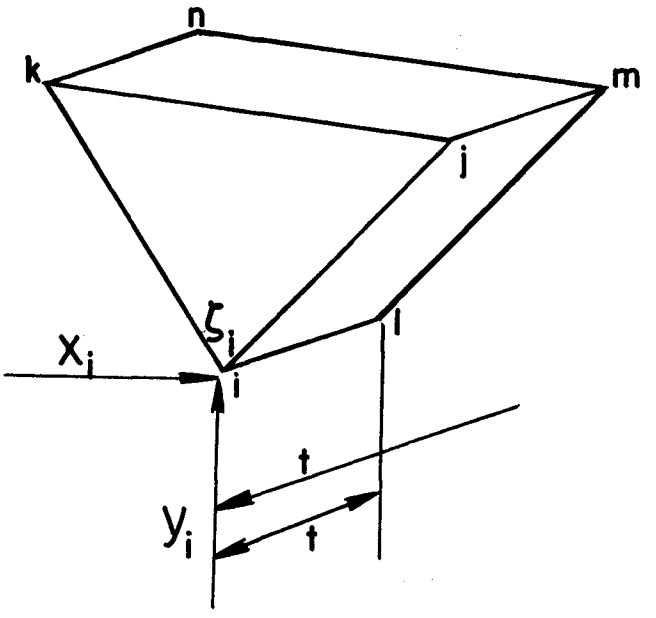

FIGURE 4 Typical Element in (x-y-t) Space.

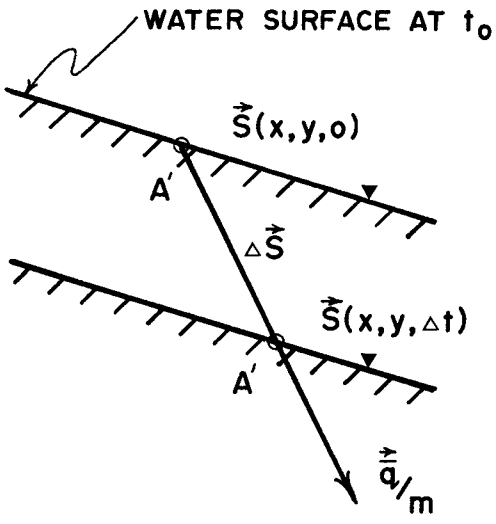

FIGURE 5 Lagrangian Approach to Tracing Particles on the Free Surface.

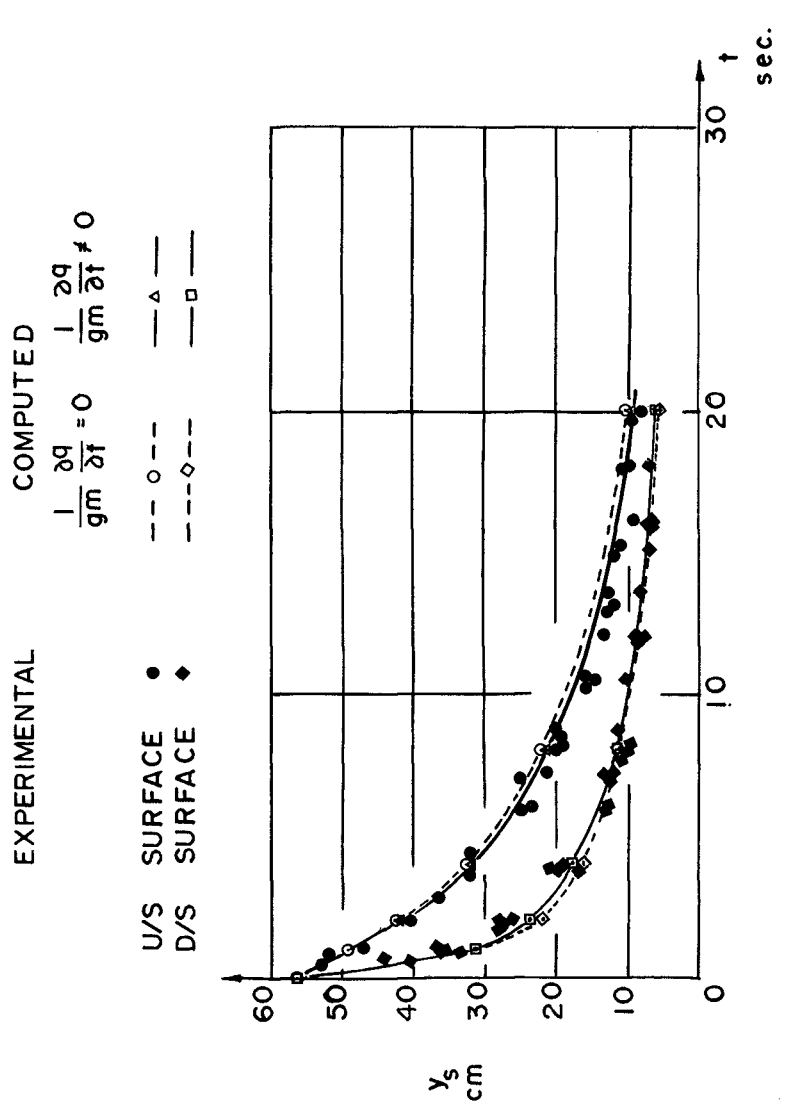

FIGURE 6 Experimental and Numerical Recession Curves for Rapid Drawdown in a Crushed Rock Embankment (4.4 cm. Rock).

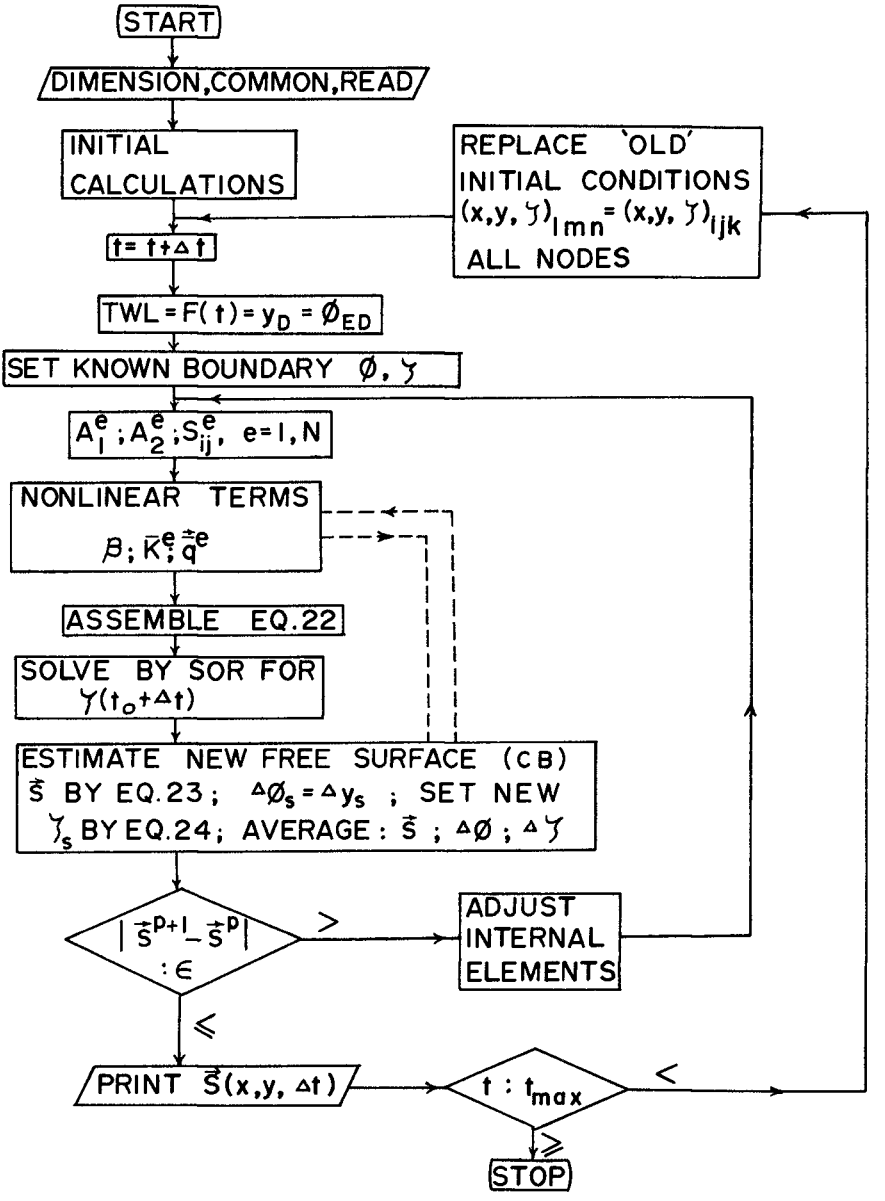

FIGURE 7 Computer Flow Chart.

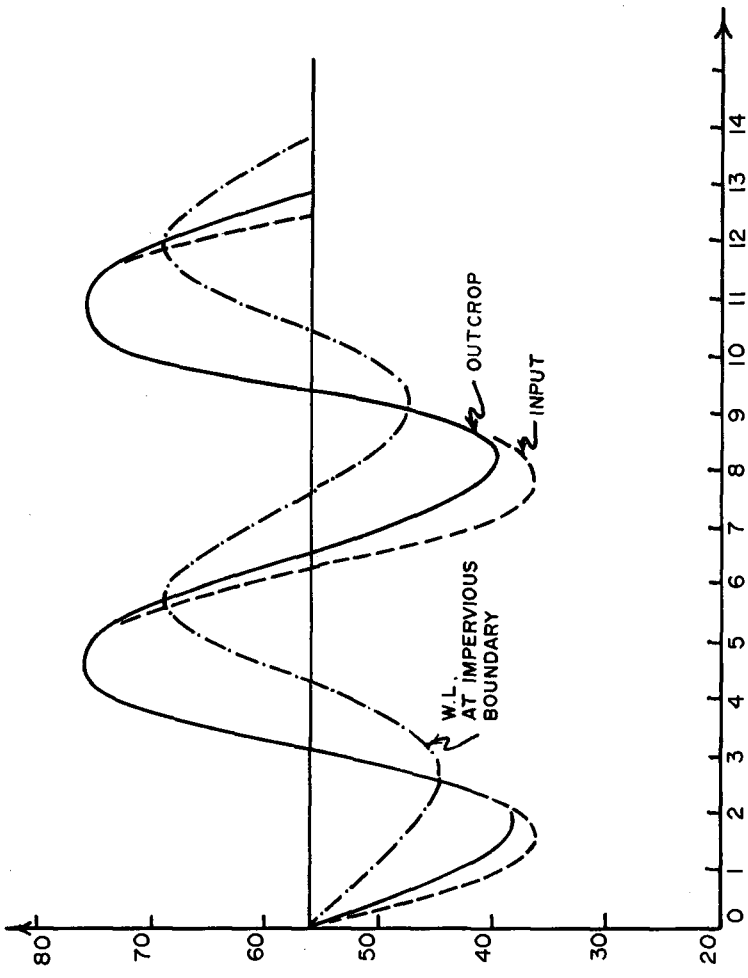

FIGURE 8 Computed Wave Motions at Selected Verticals.

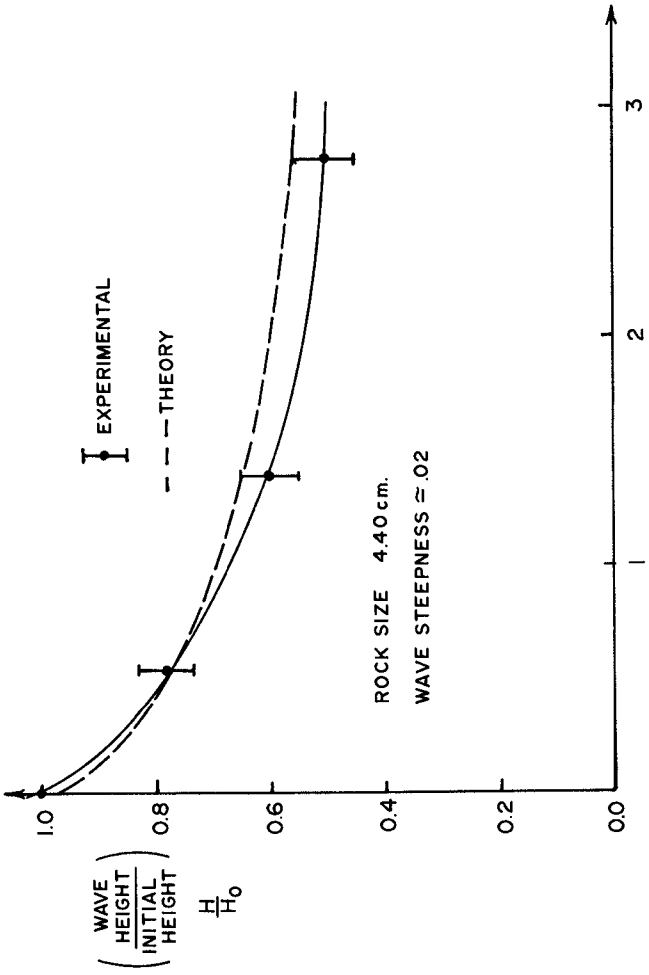

FIGURE 9 Computed and Preliminary Experimental Wave Transmission Curves for 4.4 cm. Crushed Rock.

CHAPTER 108

DISCONTINUOUS COMPOSITE WAVE ABSORBER STUDIES

Anthony R. Fallon
Research Engineer
Chevron Oil Field Research Company
La Habra, California

An experimental study was conducted to determine the energy dissipation characteristics of a discontinuous wave absorber consisting of an impervious lower slope and a stone-filled upper slope. The purpose was to determine the wave energy absorption as a function of the incident wave parameters and the wave absorber geometry. Parameters varied were wavelength, wave height, lower and upper absorber slopes, berm depth and width, and stone size. For virtually all test conditions, a minimum wave reflection was found when the discontinuity (berm) depth was at one-quarter to one-half the water depth below the water surface. The overall wave absorption increased under the following conditions: an increase in horizontal berm width of up to five layers of stone; a decrease in the angle of the upper (stone-filled) slope when the berm depth is below one-fifth the water depth; and a decrease in the angle of the lower (impervious) slope when the berm depth is above one-half the water depth. The results should be useful where water wave reflections must be minimal and space is limited, such as in harbor walls or for hydraulic models.

INTRODUCTION

The purpose of this study was to experimentally determine wave reflection as a function of wave absorber parameters. The absorber consisted of a stone-filled upper slope and an impervious lower slope. The series of over 400 wave absorber tests was run at the Look Laboratory of the Department of Ocean Engineering at the University of Hawaii. The author conducted the tests as a Master of Science thesis research project (Fallon, 1970). This paper presents the significant results.

TESTING PROCEDURE

The experimental configuration is shown schematically in Figure 1. Tests were conducted in a 48 ft-long x 9 in-wide x 13 in-high plexiglass flume. The wave generator was a paddle hinged at the top. Wave reflection was measured by moving the three wave gages (suspended from a trolley) slowly through a partial standing wave set up in front of the wave absorber test section. The resistance gages each measured a node and a loop (anti-node) as they moved through the standing wave. The oscillograph records (Figure 2) were used to determine a reflection coefficient based on linear wave theory. The reflection coefficient (R) is defined as:

$$R = \frac{HL-HN}{HL+HN}$$

where HL is the loop height and HN is the node height. The reflection coefficients for each gage were then averaged to obtain a representative reflection coefficient.

Computer simulations of the testing procedure were run to determine the error resulting in using the moving probe method for determining reflection coefficients. For R near unity, or a high probe velocity relative to the wave celerity, a large error resulted that was biased toward low values of R. However, when the reflection coefficient was less than 50%, as was the case in nearly all the test conditions run, this error was found to be less than 5%.

The wave absorber section is shown schematically in Figure 3. It consisted of an impervious lower slope (A) and a stone-filled upper slope (B), both of which were varied from 18° to 90°. Previous investigators have found that the reflection coefficient could vary with the stone placement. Therefore, to insure consistent absorber characteristics the stones were hand sorted, and flat or oblong stones were rejected. The stones were 1/2" and 3/4" in diameter and the void ratio for these stones was approximately 50%. The berm width (W) was varied from 0 (no stone) to 14 times the stone diameter. The berm depth (Z), found to be a very sensitive parameter, was varied in small increments; from 9 to 17 different values were used for each test condition. The relative berm depth (Z/D), where D is the water depth, was varied from 0 (all impervious slope) to 1.0 (all stone-filled slope). The water depth was 4 inches.

The nature of the apparatus limited the test wave characteristics. The ratio of wavelength to depth (L/D) was varied from 9 (in most tests) to 24. Relatively flat waves were used; their steepness (H/L) was varied from 0.004 to 0.012, 0.008 being used for most.

RESULTS

The primary result of these tests was the determination of the reflection coefficient variation as a function of the berm depth. This is illustrated in Figure 4 for an upper slope of 18° and a lower slope of 34°. The reflection coefficient decreases with increasing berm depth (that is, with extension of the rocks below the surface) reaching a minimum at about Z/D = 0.45. There the reflection coefficient levels off or even begins to rise for a further increase in the berm depth. This trend was observed in virtually all tests with a minimum reflection coefficient at Z/D values from 0.25 to 0.5. A point of minimum reflection was observed in the configuration

with no stones and only the geometric discontinuity present (Figure 5). It also occurred when the upper slope was rock-filled and at the same angle as the impervious lower slope. Figure 6 shows such results, for slopes of 18 degrees.

The effect of changing the berm width, which can be considered a measure of the number of layers of stones used, is illustrated in Figure 7. The reflection coefficient is plotted versus berm depth for various berm widths. The berm width is expressed in the dimensionless parameter W/d, which is the berm width divided by the average stone diameter (d). There is little wave absorption gained by increasing the berm width beyond five stone-diameters for the conditions tested.

The effect of changing the upper absorber slope is shown in Figure 8. When Z/D is less than 0.2, the angle of the upper slope has little effect on R. However, for Z/D greater than 0.2, R increases with an increase in the upper slope angle, as might be expected.

In Figure 9 is illustrated the effect of lower absorber slope on R. The angle has little effect when Z/D is greater than 0.5. However, when Z/D is less than 0.5, R decreases significantly with an increase in lower absorber slope.

No correlation was found between wave absorption and stone size, possibly because (1) the range of sizes tested was rather small, and (2) the void ratios were all approximately the same for these sorted stones.

The general results related to incident wave parameters were that wave absorption increased with wave steepness but did not correlate with wave length.

Because these tests were conducted in a relatively small wave flume, it was desirable to compare the results with those for similar larger scale tests. Look Laboratory had conducted two-dimensional wave absorber tests of about four times this scale in 1969 as part of a hydraulic model testing program (Look Laboratory, 1969). The results are shown with comparable ones from the present series in Figure 10. Correlation is good, indicating that the results of the present study may be applied to larger-scale situations.

Based on the results of this experimental investigation a general "best design" can be suggested that will minimize the use of both the horizontal space and the number of stones required. An effective design would have (1) an upper (stone-filled) slope with a berm width five times the average stone diameter and the face inclined at an angle of 18°, (2) a berm depth of 1/2 the water depth, and (3) a nearly vertical lower (impervious) slope. Sea walls and harbor walls are possible applications for such

a design. On a smaller scale, the walls of hydraulic models can be lined with this type of wave absorbers, as has been done at Look Laboratory.

REFERENCES

Fallon, Anthony R., Laboratory Studies of a Discontinuous Wave Absorber, M.S. Thesis; Ocean Engineering Department, University of Hawaii, December 1970.

Look Laboratory of Oceanographic Engineering, Study of Proposed Barbers Point Harbor, Hawaii, Technical Report No. 4, Center for Engineering Research, University of Hawaii, February 1969.

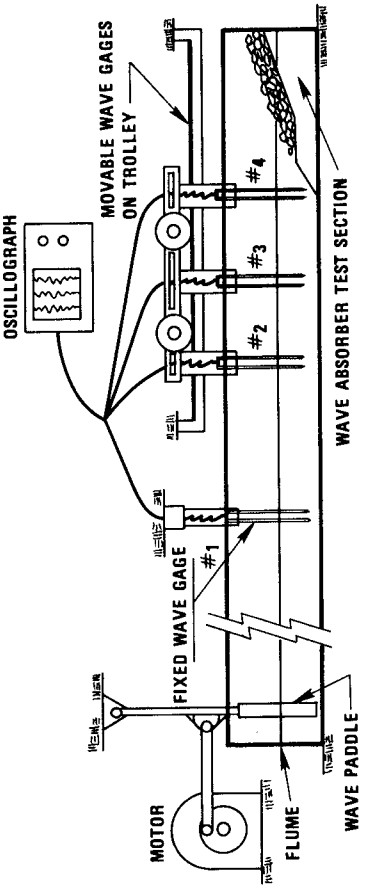

FIGURE 1
SCHEMATIC DIAGRAM OF WAVE ABSORBER TESTING APPARATUS.

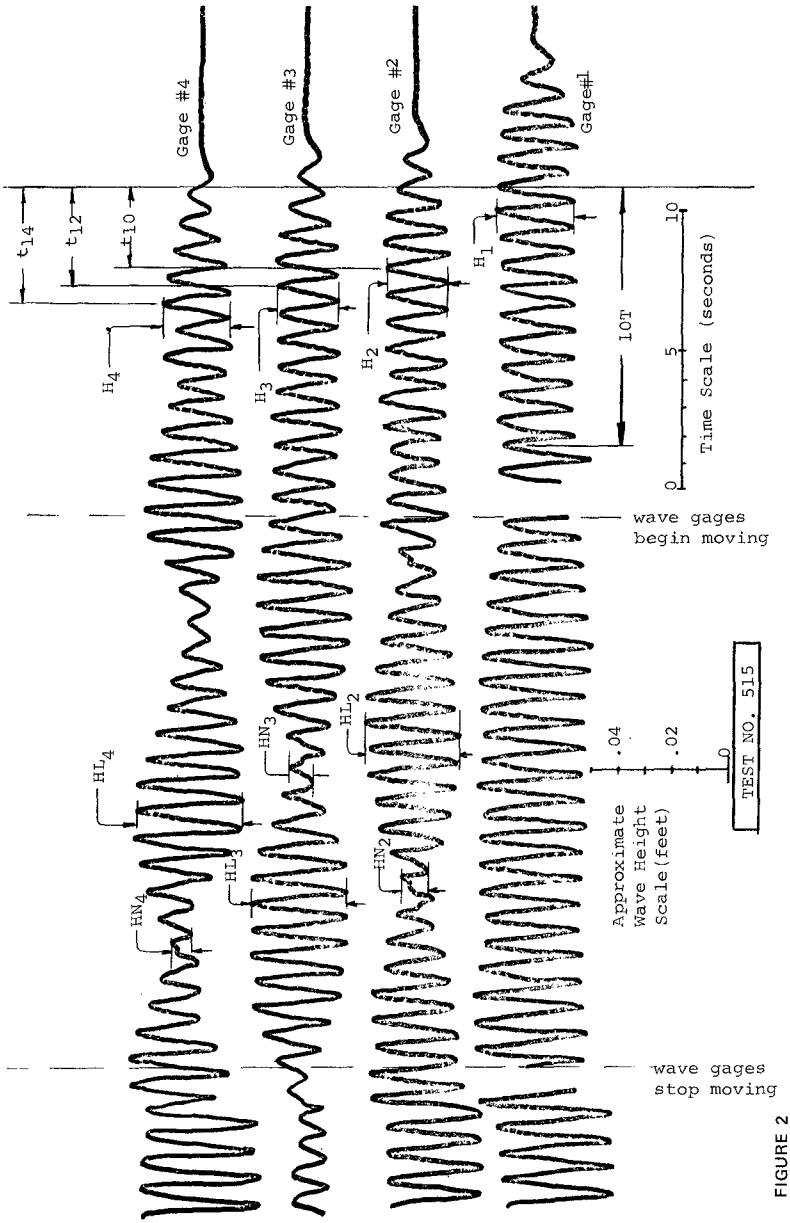

FIGURE 2
OSCILLOGRAPH RECORD FOR TEST No. 515

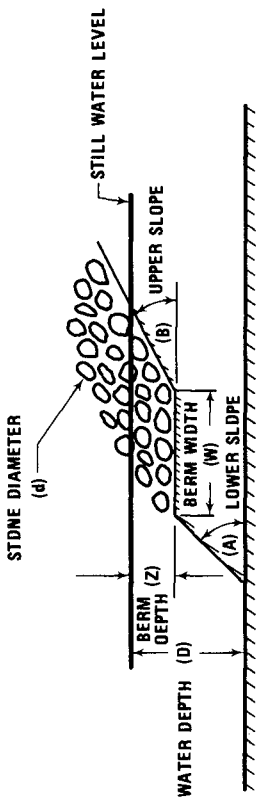

FIGURE 3
SCHEMATIC DIAGRAM OF WAVE ABSORBER
TEST SECTION

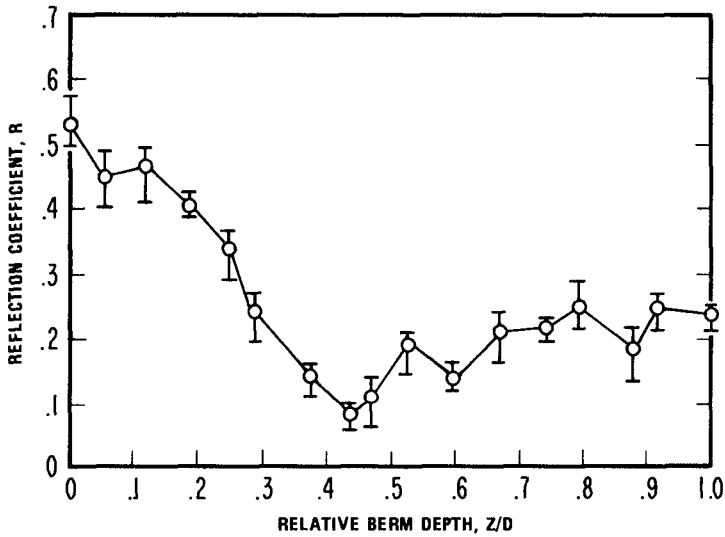

WAVELENGTH TO DEPTH RATID L/D = 9
WAVE STEEPNESS H/L = .008

WATER DEPTH D = 4.0"
LOWER SLOPE A = 34°
UPPER SLOPE B = 18°
BERM WIDTH W = 6.0"

STONE DIAMETER d = 0.64"

FIGURE 4
TEST RESULTS FOR TYPICAL CONDITIONS.

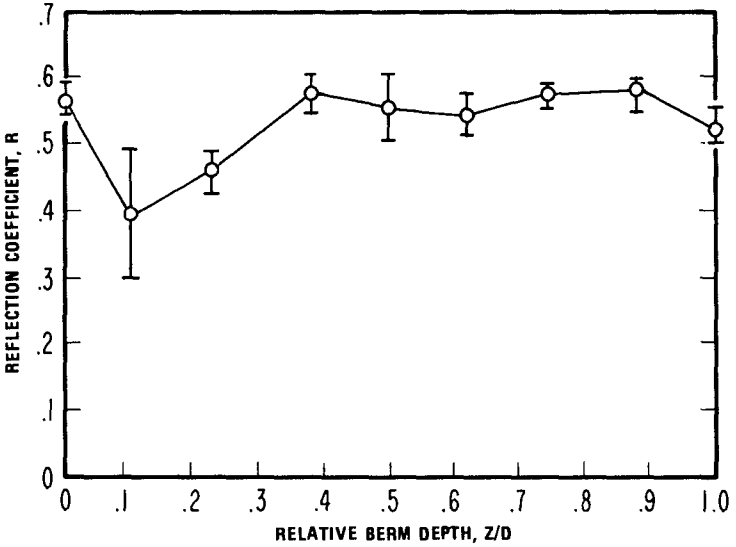

WAVELENGTH TO DEPTH RATIO L/O = 9
WAVE STEEPNESS H/L = .008

WATER DEPTH O = 4.0 INCHES
LOWER SLOPE A = 34°
UPPER SLOPE B = 18°

FIGURE 5
TEST RESULTS FOR NO STONES.

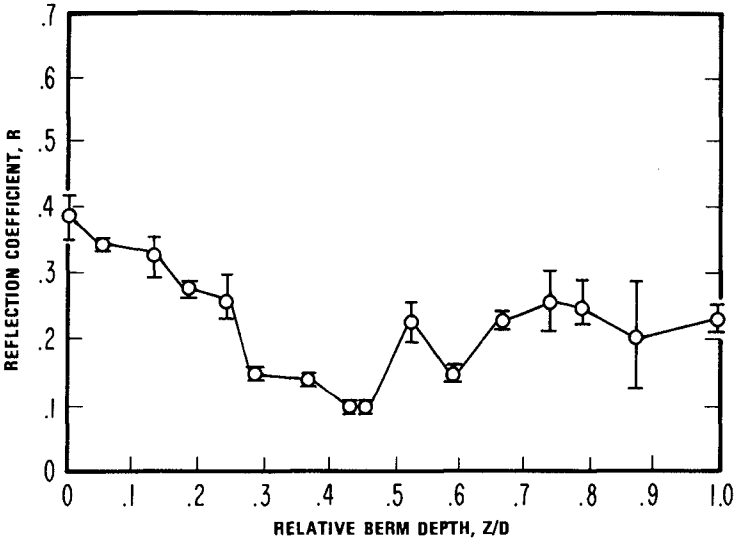

WAVELENGTH TO DEPTH RATIO L/D = 9
WAVE STEEPNESS H/L = .008

WATER DEPTH D = 4.0 INCHES
LOWER SLOPE A = 18°
UPPER SLOPE B = 18°
BERM WIDTH W = 6.0 INCHES

STONE DIAMETER d = 0.64 INCHES

FIGURE 6
TEST RESULTS FOR NO SLOPE DISCONTINUITY

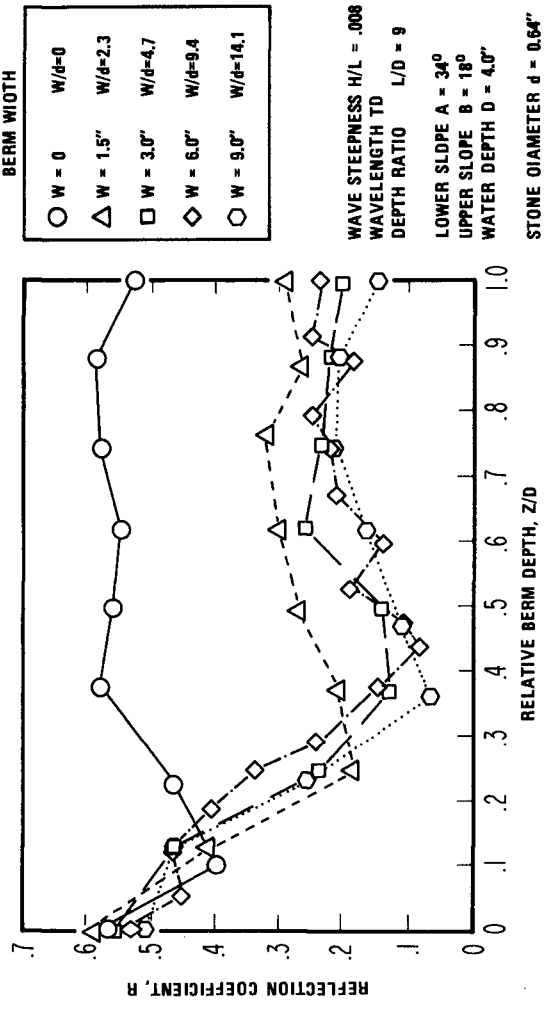

FIGURE 7
EFFECT ON REFLECTION COEFFICIENT
OF BERM WIDTH

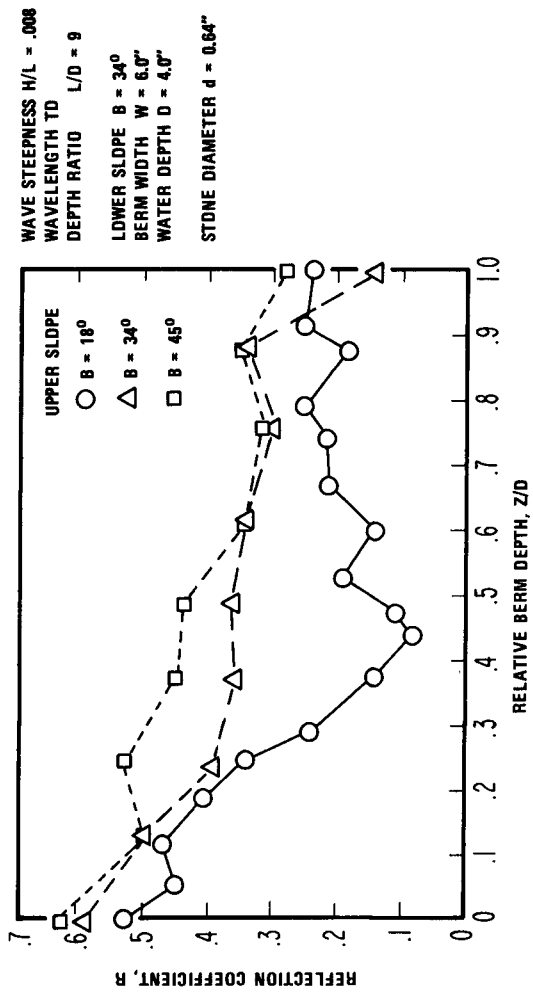

FIGURE 8
EFFECT ON REFLECTION COEFFICIENT
OF UPPER SLOPE

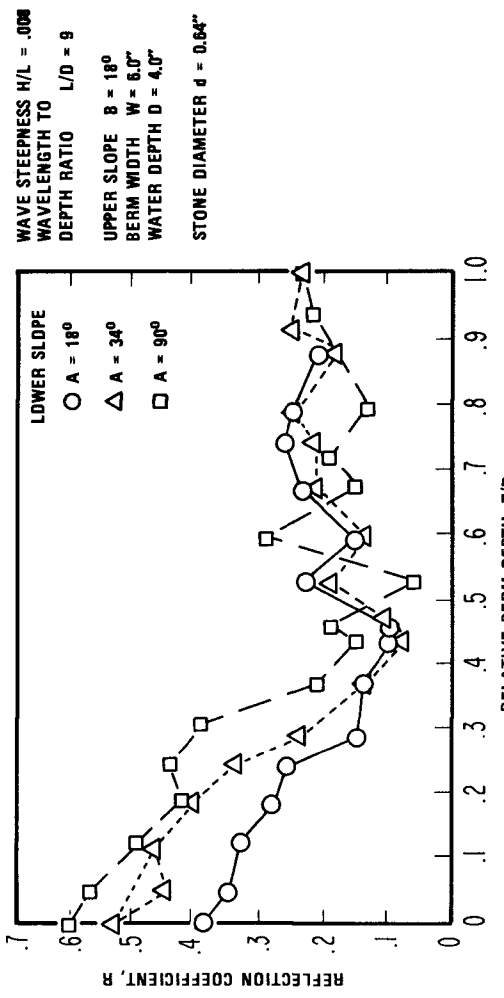

FIGURE 9
EFFECT ON REFLECTION COEFFICIENT
OF LOWER SLOPE

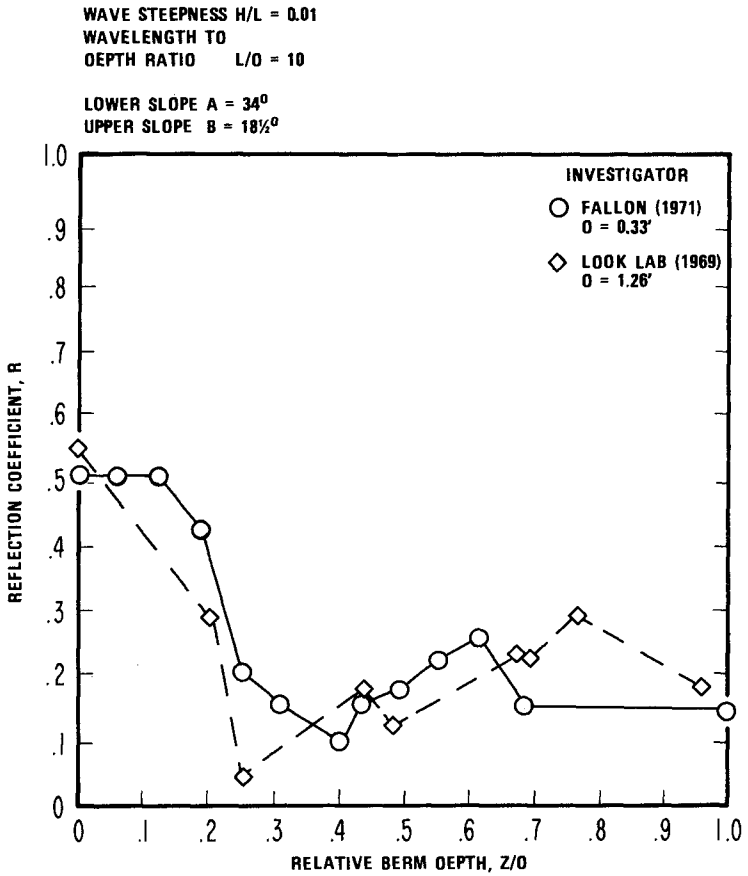

FIGURE 10

COMPARISON OF REFLECTION COEFFICIENTS FROM A DISCONTINUOUS, ROCK–FILLED WAVE ABSORBER FOR L/D = 10

CHAPTER 109

DESIGN OF FILTER SYSTEM FOR RUBBLE-MOUND STRUCTURES

Theodore T. Lee
Researcher

Look Laboratory of Oceanographic Engineering
Department of Ocean Engineering, University of Hawaii
Honolulu, Hawaii, U. S. A.

ABSTRACT

The rubble-mound seawalls, groins, breakwaters and ripraps around ocean-fall pipelines are still the most common type of shore-protection structures currently in use. Major reasons include: easiness to construct and repair, flexible with respect to settlement, favorable wave-energy dissipation, fitness for any water depth and any foundation, and because of its economical nature if rubble-stones are readily available. However, the importance of a filter system in the stability of such structures must be emphasized. More recently, the submerged rubble-mound structures have become very popular due to aesthetic reasons. A filter system is considered a must to protect such a structure against erosion as a result of wave overtopping.

Following a brief review of the problems, general discussions are made of the specific causes of failures including piping, overtopping, and nonstability. The physical factors that would affect the filter design are discussed in detail. Methods for design of filter system is presented including those applicable to the gradation of filter layers and to the plastic filters. The design procedure involves (a) making mechanical analysis of the backfill and base material, (b) estimating sizes of voids in the rubble-stones, (c) designing filter by Terzaghi criteria as revised by U.S. Army Waterways Experiment Station.

A sample design of graded filter system behind rubble-mound seawalls is given.

The procedure for the selection of plastic filters is also included.

A comparison of the merits and demerits of these two types of filter systems will be made. This comparison will take into account the model test results conducted in the Look Laboratory. However, the readers are cautioned about the scale effects of the scour characteristics particularly on those tests with light-weight model sediments.

This paper is intended as a general guideline for practicing engineers who will be responsible for design and construction of rubble-mound marine structures.

INTRODUCTION

The rubble-mound seawalls, groins, breakwaters, and ripraps around ocean outfall pipelines and oil production structures are the most common types of marine structures currently in use. Major reasons are: (1) have good wave-energy dissipation characteristics thereby reducing wave run-up and bottom erosion, (2) easy to construct and to repair damages, (3) flexible in response to settlement, (4) suitable for use in any water depth or with any type of foundation, and (5) economical since rubble-stones usually are readily available near site. Unfortunately, many rubble-mound structures have failed due to faulty design and construction. In some instances, the interaction between waves, storm surges, wind-driven currents and the structure is not well defined and failures occur due to instability of the structure. In the past, emphasis has been placed on the effect of size or weight of the rubble-stones and/or armour units on the desirable stability. The importance of the foundation characteristics has been overlooked. Undoubtedly, many failures were caused by inadequate foundation protection. For example, a lack of proper rubble-stone gradation and filter system behind the seawall at the Sangley Point, Philippines has resulted in the leaching of the backfill behind the seawall, and in foundation erosion. More recently, the submerged breakwaters have become very popular in the United States due to aesthetic and environmental reasons. A filter system is considered a must to protect such a structure against erosion as a result of wave overtopping.

Most experimental studies on the stability of breakwaters have been conducted in a fixed-bed model without due consideration of the effect of foundation erosion on the stability of the armour units.

This paper is aimed to improve the design of the filter and rubble gradation system of a rubble-mount structure subject to a given critical ocean environment. Both graded and plastic filters will be discussed. It is intended as a general guideline for practicing engineers who will be responsible for design and construction of rubble-mound marine structures. The paper is also intended to call the attention of researchers to consider foundation erosion and protection by filter system in their future experimental studies on stability of rubble-mound type structures.

STATEMENT OF THE PROBLEM

A complete failure of the rubble-mound structure can be expected if the stone gradation is improper or if the filters are not provided, or are improperly constructed to specification. Many failures have been attributed to internal erosion wherein beach materials are removed by percolating water, such as that due to water waves, surface runoff, and tidal flow. As a wave and/or tide rises on a pervious wall, water fills all the voids back to the impervious section or until the soil is saturated. When the wave recedes, this water must be permitted to escape immediately or the hydrostatic pressure will cause the facing to be dislocated by piping action in the soil foundation unless a filter is provided. Washing-out of the backfills, settlement of the main structure and overtopping of the subsequent waves will follow eventually. Overtopping could also occur due to tsunami or hurricane wave effects.

To reduce the danger of piping, either a drainage filter system or an impervious membrane should be considered.

A drainage filter system consists of a narrow vertical or sloped layer or layers of graded stone, gravel, and sand behind the rubble-mound structure underneath the foundation toe. The impervious membrane or cutoff wall is composed of such materials as steel sheet piling or plastic blankets (Barrett, 1966). These impervious layers are designed respectively to penetrate into or to cover beach areas so as to lengthen the path of seepage. This tends to prevent the water from reaching the backfill or beach soil. The filter system is preferable. However, it should be noted that filters cannot function effectively unless they are free of fines.

Generally, four types of rubble-mound seawalls may be designed with graded filters as shown in Fig. 1. The size of stones is of primary importance. It may vary from top to bottom of the wall depending on such parameters as wave height, slope of wall and specific weight of stones. Design principles are presented by the Bank Protection Committee, California (1960), and by the U.S. Army Coastal Engineering Research Center (1966). If the seawall includes a hand-laid steep section, heavy face stones are generally required. For a flatter slope, the size of stone can be materially reduced. A slope of 1.5 on 1 is used generally but 1.2 on 1 is not uncommon.

DESIGN CRITERIA FOR GRADED FILTER SYSTEM

The gradation of the filter material depends on the characteristics of the backfill or beach materials and on the voids of rubble stones or armour units. The filter material should be uniformly graded from fine sands, coarse sands, gravels such that it will not wash into it. The material could be in two or more protective layers.

The design procedure involves (a) making mechanical analysis of the backfill and/or base materials, (b) estimating sizes of voids in the cover rubble-stones, and (c) designing filter by Terzaghi criteria as revised by U.S. Army Engineer Waterways Experiment Station (Posey, 1961 and 1971). It stipulates that:

$$\frac{D_{15}\ \text{Filter}}{D_{85}\ \text{Base}} < 5$$

$$4 < \frac{D_{15}\ \text{Filter}}{D_{15}\ \text{Base}} < 20$$

$$\frac{D_{50}\ \text{Filter}}{D_{50}\ \text{Base}} < 25$$

$$\frac{D_{85}\ \text{Filter}}{D_{\text{voids, stones}}} > 2 \quad \text{(Seelye, 1965)}$$

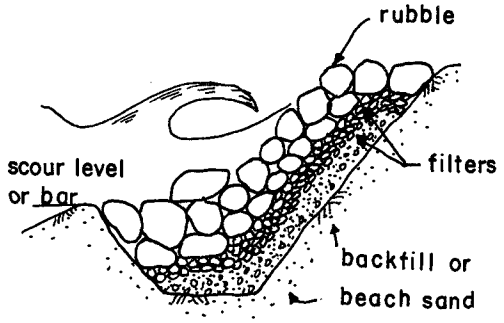

(a) Type I Revetment - Slope Protection

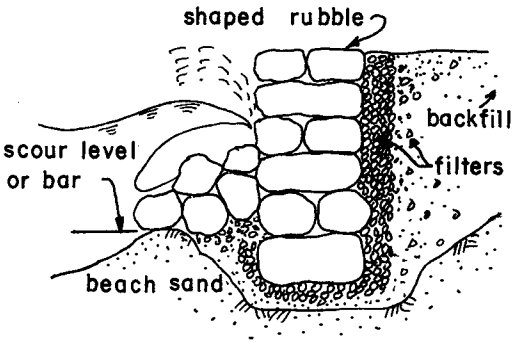

(b) Type II Hand-Laid Rubble Wall

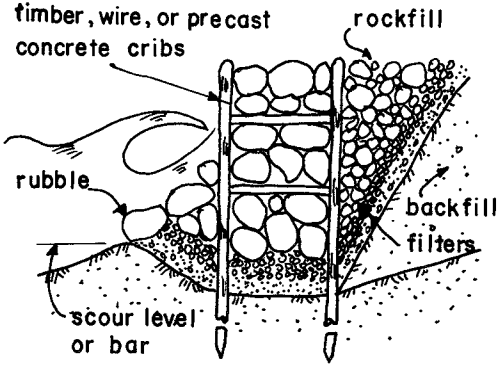

(c) Type III Crib Wall

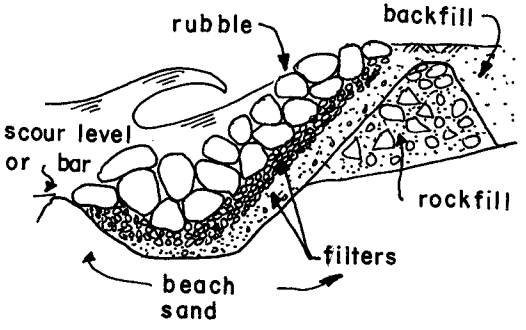

(d) Type IV Rubble Mound Wall

FIG. 1 TYPICAL RUBBLE-MOUND SEAWALLS WITH GRADED FILTERS

where D = nominal diameter of grain size usually in mm, and for example D_{50} means 50% grain size

The thickness of the filter material should be adequate for a complete coverage of subgrade and backfill materials. In prototype, a layer of 6 to 12 inches is considered adequate. For rubble-mound structures with large voids, it is necessary to design a multilayer filter system. The first layer filter material is protected by another layer with its size distribution governed by the same design criteria as indicated above. This process is continued until filter material size is large enough to resist washing away through the voids formed in contact with ocean waves on the outermost layer of the rubble stones.

A sample design of a graded filter system behind rubble-mound seawalls is given in Figure 2.

DESIGN OF PLASTIC FILTER SYSTEM

In the event of unavailability of aforementioned graded materials suitable for local ocean conditions, a new type plastic filter has been found effective in increasing the stability of shore protection structures such as rubble revetments, seawall toe protection, bulkheads, rock groins, breakwaters, legged drilling platforms, and drainage systems (Fig. 3). The use of plastic filters as a replacement for graded filter systems and filter blankets in coastal structures was discussed by Barrett (1966, 1972).

In general, the plastic filter is woven of synthetic fibers such as polyvinylindene chloride resin monofilament yarns and polypropylene monofilament yarns which have higher tensile strength and higher resistance to abrasion than the former. Its filtering ability (permeability and soil particle retention) can be designed to meet individual requirements. Depending upon local soil conditions, the water volume and type of flow expected the permeability and filtration requirements of the plastic filter may vary from one project to another in an identical structure. In cases where thickness is required, this element would have to be realized by adding a layer of gravel or crushed stone. If the soil to be protected has an excessively high silt content, it would be advisable to place a sand pad beneath the plastic filter. Important design considerations include: the type of structure, weight and type of armour units, method of construction, and forces the structure is designed to withstand (wave action, water volume and hydraulic gradient oscillations, velocities). These variables determine the necessary abrasion resistance, tensile strength, puncture, and burst strengths of the plastic filter cloth, as specified. In all, the plastic filter must be so designed to be effective to retain soil and remain permeable to water under both laminar and turbulent flow conditions. If a particular plastic filter is selected, it is advisable that laboratory tests be conducted to determine permeability and filtration properties in the base materials to be protected, so as to ensure the filtering effectiveness as expected.

A comparison of the merits and demerits of these two types of filter systems is given in Table 1. This comparison takes into account the model test results

GIVEN

1. Mechanical analysis of a subgrade backfill or base material to be protected (Curve I): D_{15}=0.21 mm, D_{50}=0.31 mm, and D_{85}=0.52 mm; maximum
2. Maximum voids of face stones 300 mm.

REQUIRED

1. Gradation limits of 1st filter material (II) for protection of base material (I).
2. Gradation limits of filter material (III) for protection of filter material (II).

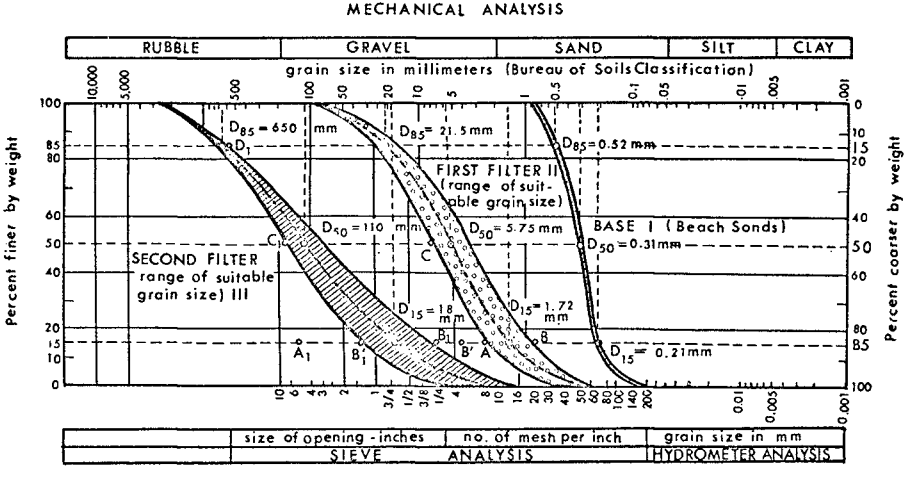

TYPICAL RUBBLE-MOUNTED SEAWALLS

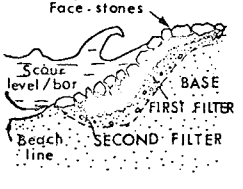

SOLUTION

1. First filter layer:
   - Maximum 15% filter (II) size = 5x0.52mm
     - Criteria (1) = 2.60mm (Point A)
   - Minimum 15% filter (II) size = 4x0.21
     - Criteria (2) = 0.84mm (Point B)
   - or Maximum 15%=20x0.21 = 4.2mm (Point B')
   - Maximum 50% filter size = 25x0.31mm
     - Criteria (3) = 7.8mm (Point C)

   Answer: Selected first filter layer (II): D_{15}=1.72mm; D_{50}=5.75mm; D_{85}=21.50mm

2. Second filter layer (III):
   - Maximum 15% filter (III) size = 5x21.5mm
     - Criteria (1) = 122.50mm (Point A_1)
   - Minimum 15% filter (III) size = 4x1.72mm
     - Criteria (2) = 6.88mm (Point B_1)
   - or Maximum 15%=20x1.72 = 34.40mm (Point B'_1)
   - Maximum 50% filter (III) size = 25x5.75mm
     - Criteria (3) = 143.75mm (Point C)
   - Minimum 85% filter (III) size = 2x300=600mm (Point D_1)

   Answer: Selected second filter layer (III): D_{15}=18mm; D_{50}=110mm; D_{85}=650mm

Fig. 2 A Sample Design of a Graded Filter System Behind Rubble-Mound Seawalls

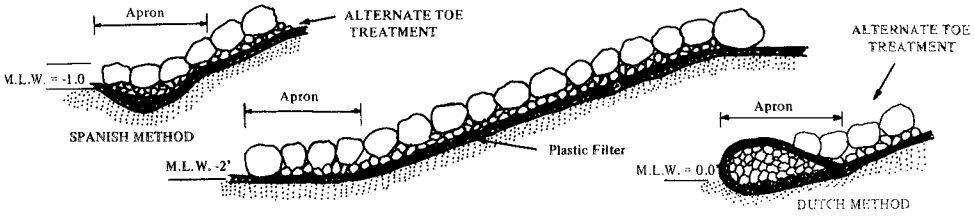

(a) Permeable rock revetment

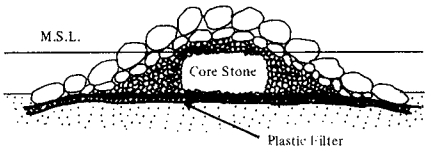

(b) Rock breakwater/jetty/groin

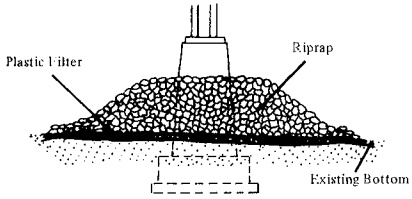

(c) Legged platform erosion protection

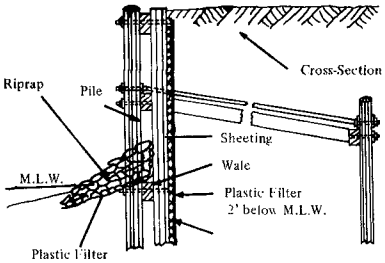

(d) Timber bulkhead

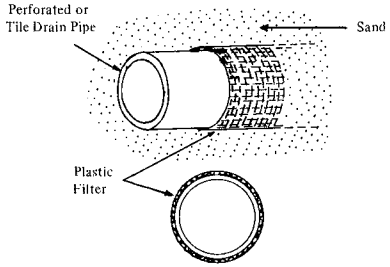

(e) Pipe wrapping drainage system

FIG. 3 TYPICAL APPLICATIONS OF PLASTIC FILTERS IN COASTAL STRUCTURES (Courtesy of R.J. Barrett of Carthage Mills, Inc.)

TABLE I A COMPARISON OF THE MERITS AND DEMERITS OF PRADED AND PLASTIC FILTER SYSTEMS

Filter Type	Merits	Demerits
Graded Filter System	1. most likely available 2. widely accepted practice 3. less effect of long-term operation on permeability and filtration may be expected. 4. the effectiveness will not be affected due to bio-deterioration	1. very difficult to construct to specification under water 2. difficult to determine the voids of the armour stones as required to design filter gradation 3. rock filter has not independent strength because it depends on soil condition for its stability
Plastic Filter System	1. filtering ability can remain the same during installation 2. have an independent tensile strength 3. eliminate screening process required for the graded filter 4. permit greater opportunity for consistency in filter design 5. plastic filter can be applied without too much concern on the geographic location and availability of graded materials	1. the plastic filter materials may not be readily available 2. initial cost may be higher than graded filter 3. more difficulty to maintain the permeability and filtration ability over long-term operations 4. the effectiveness may be reduced due to bio-deterioration

conducted in the Look Laboratory which will be described in the following paragraphs. However, the readers are cautioned about the scale effects of the scour characteristics particularly on those tests conducted with light-weight (walnut shells, ground) model sediments.

LABORATORY EXPERIMENTS IN DETERMINING THE STABILITY OF RUBBLE-MOUND BREAKWATER WITH FILTER SYSTEMS

An undistorted, two-dimensional hydraulic model study was conducted to test the stability and sensitivity of rubble-mound type jetty design with graded and/or plastic filter systems. Particular attention was given to the characteristics of the armour stone, secondary layers, core materials and characteristics of scour at the toe and under the foundation of the jetty. Model scales selected were: 1:24.5, 1:23.4, and 1:20 respectively.

A review of the considerable literature concerning hydraulic model studies on breakwater stability revealed that most study tends to neglect the effect of a movable bed on stability, including the characteristics of scour under the foundation, particularly under overtopping storm wave conditions. The scale similitude and significant findings were described previously by Lee (1970). The purpose of this section is to point out the importance of erosive type model and the phenomenon of permeability and filtration observed in the movable-bed model.

Two types of model sediments were used, i.e. fine sands and ground walnut shells. Their size distributions are shown in Fig. 4 respectively. The characteristics of jetty materials in model is shown in Table 2.

The general dimensions of final test sections of the jetty with and without plastic filters are shown in Fig. 5. The effectiveness of the graded or plastic filter are indicated in Fig. 6. Both are quite effective in reducing the scouring at the jetty toe, as compared with excessive scour depth when the jetty is designed with minimum or no toe protection.

It is interesting to note that the permeability and filtration characteristics are significantly different without toe protection and with protection by graded and/or plastic filters (Fig. 7). For the same duration of wave actions, the permeability and filtration is much greater for the jetty with no toe protection.

To demonstrate the effect of model sediment property on the scouring characteristics, tests were conducted for identical jetty design but two different sediments (sands and ground walnut shells) were used. The scouring at jetty toe are compared in Fig. 8. It should be noted that time scales for them must be taken into consideration in order to have a fair comparison. The permeability and filtration for the two different materials are similar as shown in Fig. 9.

It was found that: (1) To prevent scouring under the jetty, it is necessary: (a) to extend a layer of core materials beyond the armour-stone toe, and then place two layers of secondary stones over this core layer with proper gradation, or (b) as an alternative, a plastic filter may be placed under the jetty and

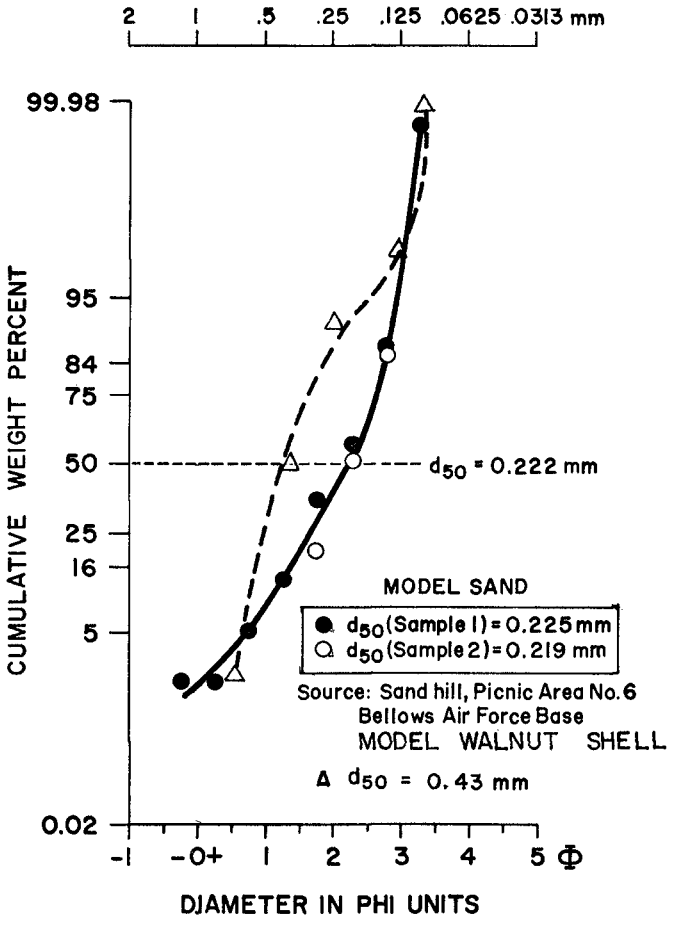

FIG. 4 SIZE DISTRIBUTION OF BEACH SANDS USED IN MODEL

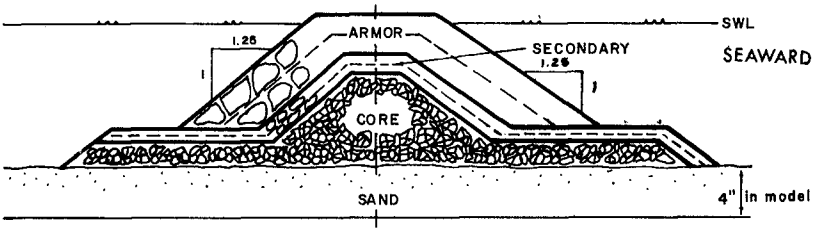

(a) without plastic filter, graded filter only
(Test Section 6)

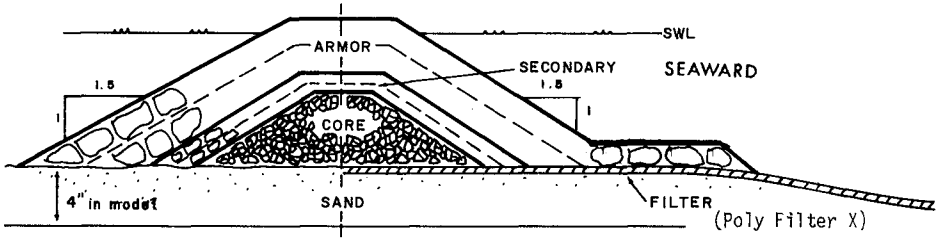

(b) with plastic filter
(Test Section 3)

FIG. 5 GENERAL DIMENSIONS OF FINAL TEST SECTIONS OF THE JETTY WITH AND WITHOUT PLASTIC FILTERS

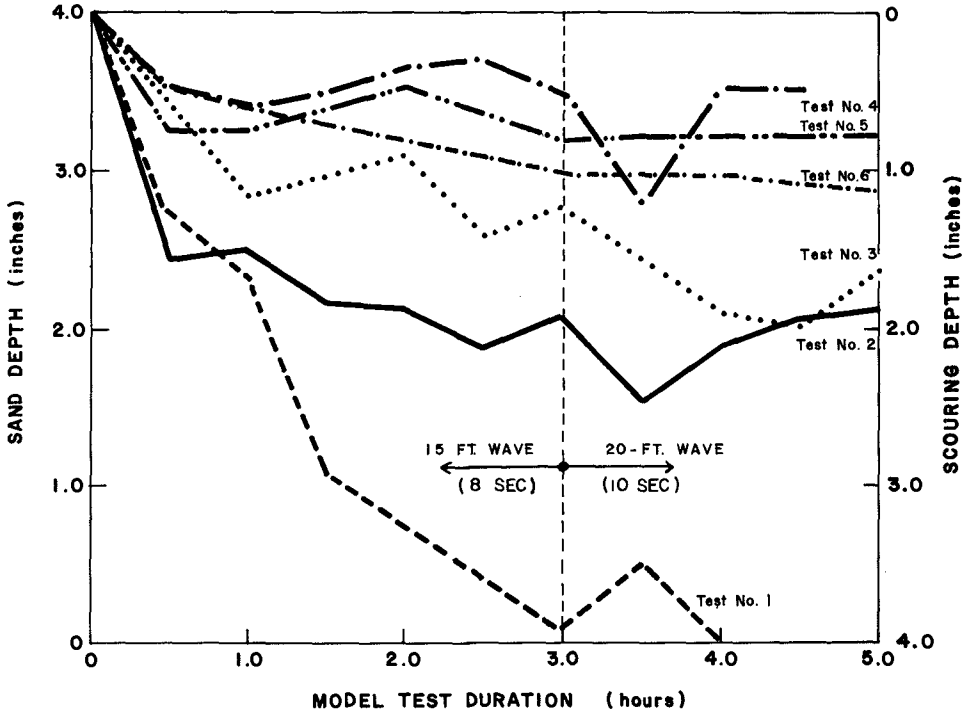

FIG. 6 SCOUR CHARACTERISTICS OF JETTY TOE AS A FUNCTION OF DEGREE OF PROTECTION

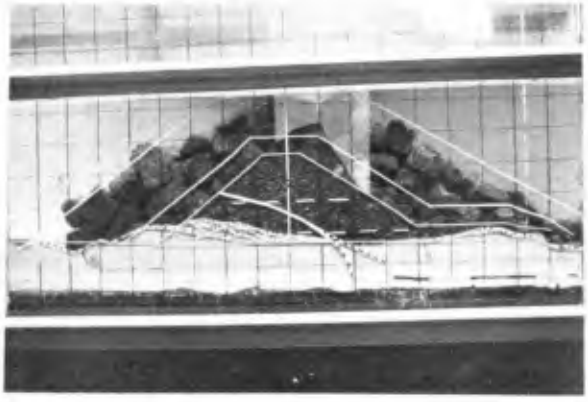

Without plastic filter
(15ft, 8 sec, 2 hr.)

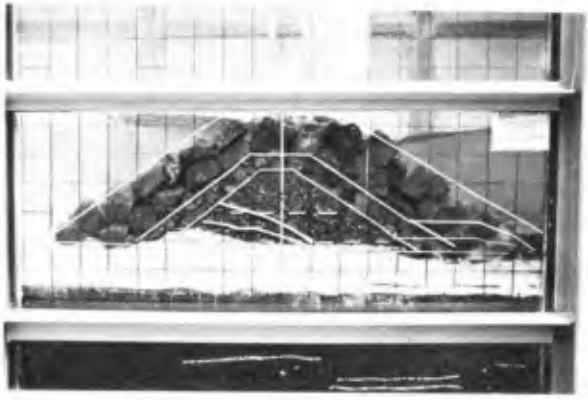

With plastic filter
(15 ft, 8 sec, 2 hr.)

FIG. 7

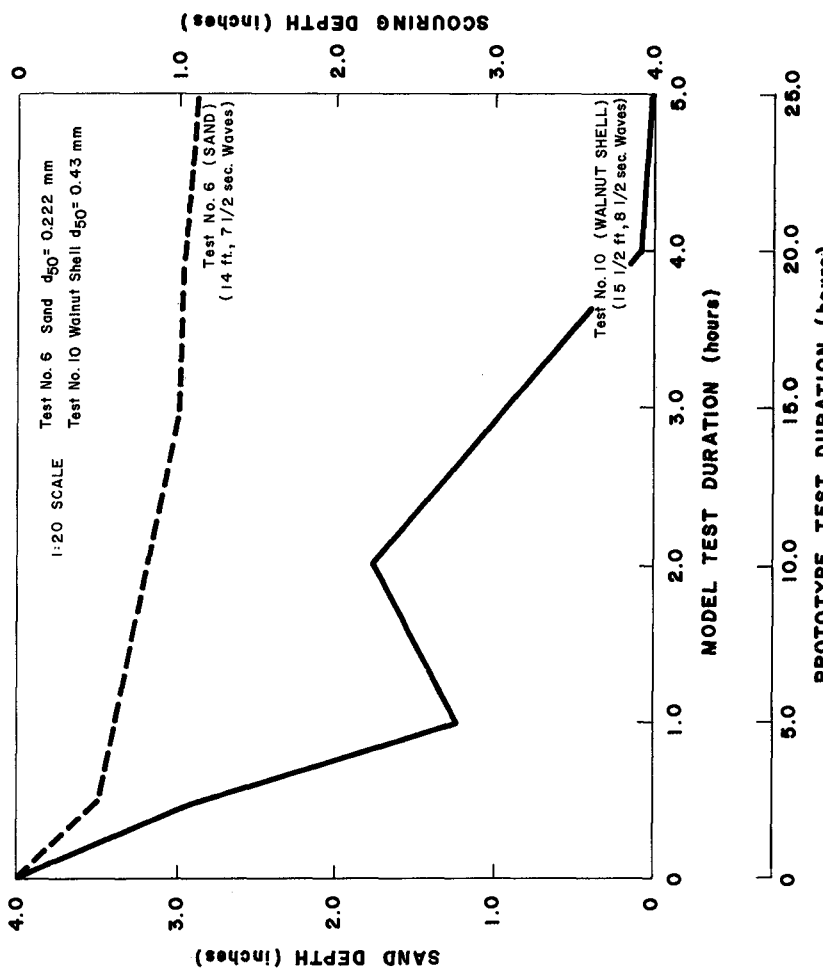

FIG. 8 SAND SCOURING AT JETTY TOE (TESTS 6 AND 10)

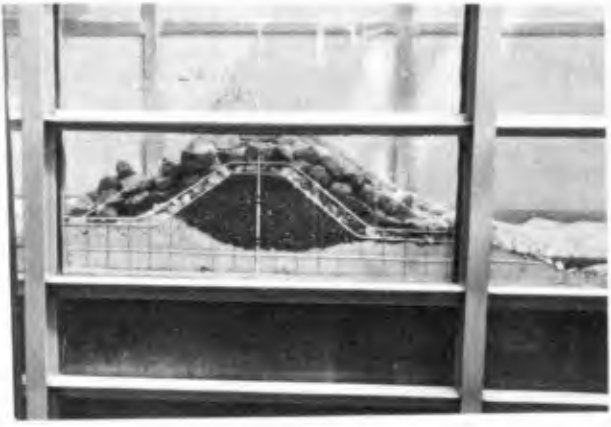

(a) Sands — 2 hrs of 20 ft, 10 sec waves & 3 hrs of 14 ft, 8 sec waves (TEST SECTION 5)

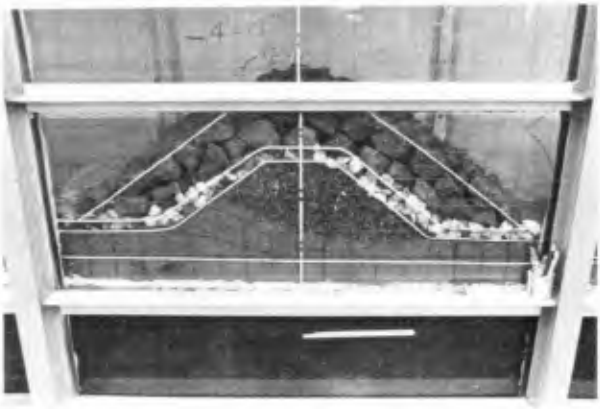

(b) Walnut shell — 5 hrs of 15 ft, 8 sec waves (TEST SECTION 10)

FIG. 9

extend beyond the toe with secondary stones over it; (2) a filter layer, preferably plastic, is necessary in the prototype construction between the core material and the sandy beach; and (3) quantitative experiments on the scouring depth at the jetty with different model sediments need to be studied further.

The stability of the rubble-mound structure should be studied in a movable bed model, particularly the structure is founded in a depth shallower than the critical depth for sand movement. Otherwise, the designer should specify that the jetty bottom should either extend below scour depth yet to be determined, or it should be rest on a plastic filter. Also, the filter system for a jetty should be designed with extreme care, particularly if translatory currents induced by tidal and river flow along the longitudinal axis of the jetty are significant.

SUMMARY

The need for a properly designed and constructed filter system is obvious in the stability of rubble-mound marine structures. The design criteria given in this paper would be helpful to practical engineers to select either graded or plastic filters to suit local environmental and resources conditions. The gradation of filter materials is dependent on the characteristics of base sands and cover-stones of armour units. The plastic filter must be selected to meet the requirements of permeability and soil-particle retention, preferably determined from laboratory tests under a variety of flow conditions anticipated at site.

A movable-bed type test should be conducted for future studies on the stability of rubble-mound structures to determine the scouring characteristics with due consideration of model scale effects.

ACKNOWLEDGMENTS

The author is indebted to Mr. R.J. Barrett of Carthage Mills, Inc. who furnished valuable information and fruitful discussions.

Mr. A.R. Fallon, then Graduate Assistant and now of Chevron Oil Field Research Co., California, conducted the laboratory investigation on the stability of breakwater using a movable-bed hydraulic model in two dimensions.

REFERENCES

1. Barrett, R.J. (1966), "Use of Plastic Filters in Coastal Structures," Proceedings of 10th International Conference on Coastal Engineering, (September 1966, Tokyo, Japan), Chapter 62, p. 1048, American Society of Civil Engineers, New York, N.Y., 1967.

2. Barrett, R.J. (1972), "Design and Application of Plastic Filters," letter communication with T.T. Lee furnishing most recent information including a Plastic Filter Handbook, giving methods of design and installation of plastic filters, laboratory tests of permeability and filtration, and listing of coastal installations during the period of 1961 to 1971, in U.S. and Canada, Bank Protection Committee, California (1960), "Bank and Shore Protection in California Highway Practice," Department of Public Works, Division of Highways, California, November 1960.

3. Lee, T.T. (1970), "Estuary Inlet Channel Stabilization Study Using a Hydraulic Model," Proceedings of 12th International Conference on Coastal Engineering, (September 1970, Washington, D.C.) Chapter 71, p. 1117, American Society of Civil Engineers, New York, N.Y., 1970.

4. Posey, C.J. and J.H. Sybert (1961), "Erosion Protection of Production Structures," Proceedings of Ninth Convention of International Association for Hydraulic Research, Dubrovnik, 1961.

5. Posey, C.J. (1971), "Protection of Offshore Structures Against Underscour," ASCE Journal of Hydraulics Division, Proceedings of American Society of Civil Engineers, Vol. 97, No. HY7, July 1971.

6. Seelye, E.E. (1956), "Foundations Design and Practice," John Wiley and Sons, Inc., New York, 1956, pp. 14-21.

7. U.S. Army Coastal Engineering Research Center (1966), "Shore Protection, Planning and Design," Technical Report 4, U.S. Army Corps of Engineers, Washington, D.C. (Originally published in 1953, as revised in 1957, 1961, and 1966).

CHAPTER 110

WAVE REFLECTION AND TRANSMISSION FOR PILE ARRAYS

by
Brian J. Van Weele, Head
Hydraulics and Hydrology Section
Parson, Brinckeroff, Quade & Douglas, Inc.
New York, New York
and
John B. Herbich, Ph.D., P.E.
Professor and Head
Coastal and Ocean Engineering Division
Texas A&M University
College Station, Texas
(Currently the U.N. Expert in Coastal Engineering)

ABSTRACT

A group of piles in a specific geometric pattern may represent a part of a foundation supported by multiple pilings or a porous sea wall or other type of porous coastal structure. "Wave characteristics" of such a structure will include not only the wave transmission but also wave reflection characteristics.

Most of the experiments in the past on pile groups were mainly concerned with wave transmission characteristics as a function of wave height and period. The main purpose of these previous studies was to evaluate the absorption characteristics of pile groups, and wave reflections were generally not measured, or evaluated.

Variables in this study included wave characteristics such as wave height and length and three types of symmetric pile arrays, two providing clear spacing in the direction of the wave between pile rows and one with a staggered arrangement.

The results presented in dimensionless form show the effect of pile geometry and wave steepness on the coefficient of reflection and transmissibility.

INTRODUCTION

Wave reflection from solid sea walls and other objects is an important phenomenon in ocean engineering. When the structure is permeable or porous, the *transmission of waves* through it as well as *wave reflection* from it must be considered in evaluating the "wave characteristics" of the structure.

A group of piles in a specific geometrical pattern might be generalized as a porous structure or porous sea wall. Many such types of porous structures were investigated before the invasion

of Normandy during World War II (1)*.

Most of the experiments in the past on pile groups were mainly concerned with the transmission character of the particular group, and with the effect of various types of waves upon the transmission characteristics, also called *transmissibility*. It can be said that in the previous studies the pile groups were considered mostly as breakwaters, and their wave absorption characteristics were of main concern.

A vast amount of research has also been focused in the past upon the wave forces acting on the piles (1,2,3,4).

Very little research has been performed on the wave reflection from cylindrical piles. It is true that in some reports mention is made of magnitudes of wave reflection from pile groups and the effect of spacings of the piles in the pile groups, but conclusions, if any, are quite general. This rather vague and small amount of information on the reflection from pile groups prompted the interest in this investigation. A further motivation was a report by Wiegel, which read: "*For a given number of piles, there does not appear to be any appreciable difference in the effect of the various array configurations upon the effectiveness of the structure as a breakwater.*" (1)

BRIEF REVIEW OF EARLIER STUDIES

Wiegel developed a formula for the transmissibility of a single row of piles (1). In assuming that the portion of power transmitted through the pile row is proportional to the portion of gaps between the piles, the following formulas,

$$\frac{H_T}{H_I} = \frac{P_T}{P_I} = \frac{b}{D+b} , \qquad (1)$$

can be derived, where

H_T = the transmitted wave height,

H_I = the incident wave height,

P_T = the transmitted power,

P_I = the incident power,

b = the distance between piles, and

D = the diameter of the piles.

However, Wiegel found that the measured transmitted wave height in a model was almost 25 percent greater than the trans-

* Numbers in parenthesis refer to references listed at the end of the paper.

mitted wave height predicted by Equation 1. The discrepancy was attributed to wave diffraction effects.

Wiegel also pointed out that if a group or configuration of piles is used which has more than one row, the problem of calculating the power transmitted, and consequently the transmitted wave height, becomes more complicated. This is due to a number of factors, namely, reflection of the energy, scatter of the energy, and the energy dissipated by skin drag and form drag.

Reid and Bretschneider (4) commented that the results of studies seem to indicate that the mutual interference of piles apparently does have an effect on the wave characteristics if the spacing is less than two pile diameters. However, it is mentioned further that for greater spacing the effect is slight and probably can be ignored in most piling structures.

An investigation of the effect of mutual interference of piles was reported by Morison, et al. (2) Although the interference concerns the ratio of the maximal moment on the center pile of a column or row to the maximal moment on a single pile, the results showed that at spacings of less than 1-1/2 times the pile diameter in the row arrangement (perpendicular to wave travel) interference effects are noticeable on the three-pile row used in the study. Also, this interference effect on the row of piles was concluded to be negligible for spacings of 1-1/2 times the pile diameter or greater.

Costello (5) studied the wave-height transmission capacity of dense pile structures, comparing the effects of spacing between piles transverse to the wave front to the effects of longitudinal spacing of piles. The results of his studies indicate that the relative depth, d/L, may be neglected in the comparison of various transmission capacities. Costello also noted that increasing the number of rows by 100 percent resulted in an average decrease in wave transmission of only 18 percent, irrespective of the configuration and density of the cylinders. Furthermore, from the data obtained within the pile group itself, Costello concluded that approximately 50 percent of the total decrease in wave transmission occurred within a distance of less than 1/4 of the wave length, measured from the incident face of the group of cylinders. In an abstract of the paper Costello states that: "*The overall results of the experiments show rather conclusively that a moderately dense piled structure is highly selective in its capacity to reduce wave action.*" (5)

Joshi (6) studied the relation of the coefficient of reflection to several wave characteristics, such as L/D, and steepness for a single row of piles.

EXPERIMENTAL STUDIES

1. *Test Facilities*

The experiments were conducted in a wave tank having an overall length of 67.5 feet, a depth of 2 feet, and a width of 2 feet. Waves were produced mechanically by an oscillating pendulum-type wave generator. The wave tank was equipped with efficient wave absorbers. Wave profiles, wave reflections and other wave characteristics were measured by capacitance-type probes and recorded electronically.

The pile configurations consisted of groupings of sixteen pipes, each having a diameter of 3/4 inch, in all cases except for one arranged in a rectangular array. The particular patterns of the piles were set up by using two pieces of 3/8 inch marine plywood with the pattern holes drilled through them. Pins were placed through the four corner pipes directly above the piece of plywood on the bottom of the tank and directly below the piece on the top of the tank. The pile group was then firmly held in place when clamped down as shown in Figure 1.

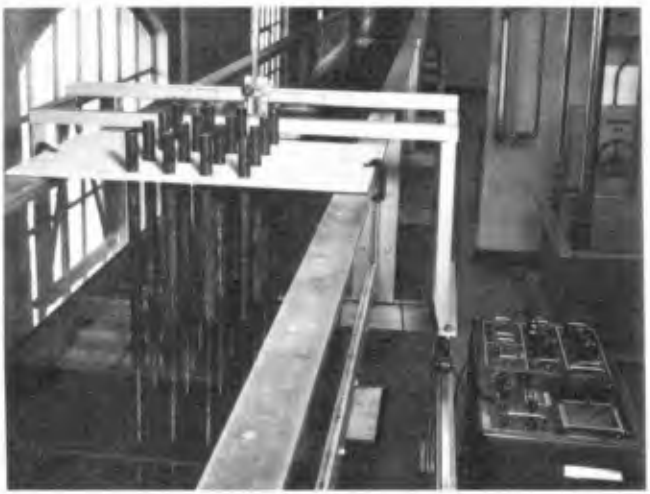

Figure 1 Pile Group Arrangement

2. *Experimental Procedure*

The depth of water used throughout the testing was held constant at 1 foot. Also held constant was the L/d ratio (length of wave/depth of water) equal to 3.70. The wave period, T, was computed using the Airy equation:

$$L = T\sqrt{\frac{gL}{2\pi}\tanh\frac{(2\pi d)}{L}} \qquad (2)$$

where g = acceleration of gravity. The wave period was then set on the wave generator and remained constant for all tests.

For measurement of wave reflection the probe was placed on the approaching wave side of the pile group.

After starting the wave generator, the stylus of the recorder was slowly moved back and forth in the longitudinal direction at the center line of the pile group for a distance slightly more than that of the wave length. This was repeated with the probe moved to be in line with the outer column of the pile group, in order to obtain an average reading. The data were collected for three wave steepnesses (H/L). The methods used in determining both the incident wave height and the reflection coefficient are described in References 7 and 8. Measurements of the transmitted wave height were taken on the opposite side of the pile group.

3. *Cases Tested*

Three cases were studied. Cases I and II were similar in that a basic pattern of four columns and four rows was used. Case I involved tests on groups of piles with the clear space transverse to the oncoming wave being the variable and keeping the clear space parallel to the oncoming wave constant at two pile diameters (2D). Case II involved tests on groups of piles with the clear spacing parallel to the oncoming wave being the variable and keeping the clear space transverse to the oncoming wave constant at 2D. For both Case I and II the clear spacing used were D, 1.5D, 2D, 3D, and 4D, making a total of 9 different cases.

Case III consisted of just one pattern of the piles in which they were staggered, the clear space between them being equal to 2D. Figure 2 shows all pile arrays, and Figure 3 shows the staggered array in Case III.

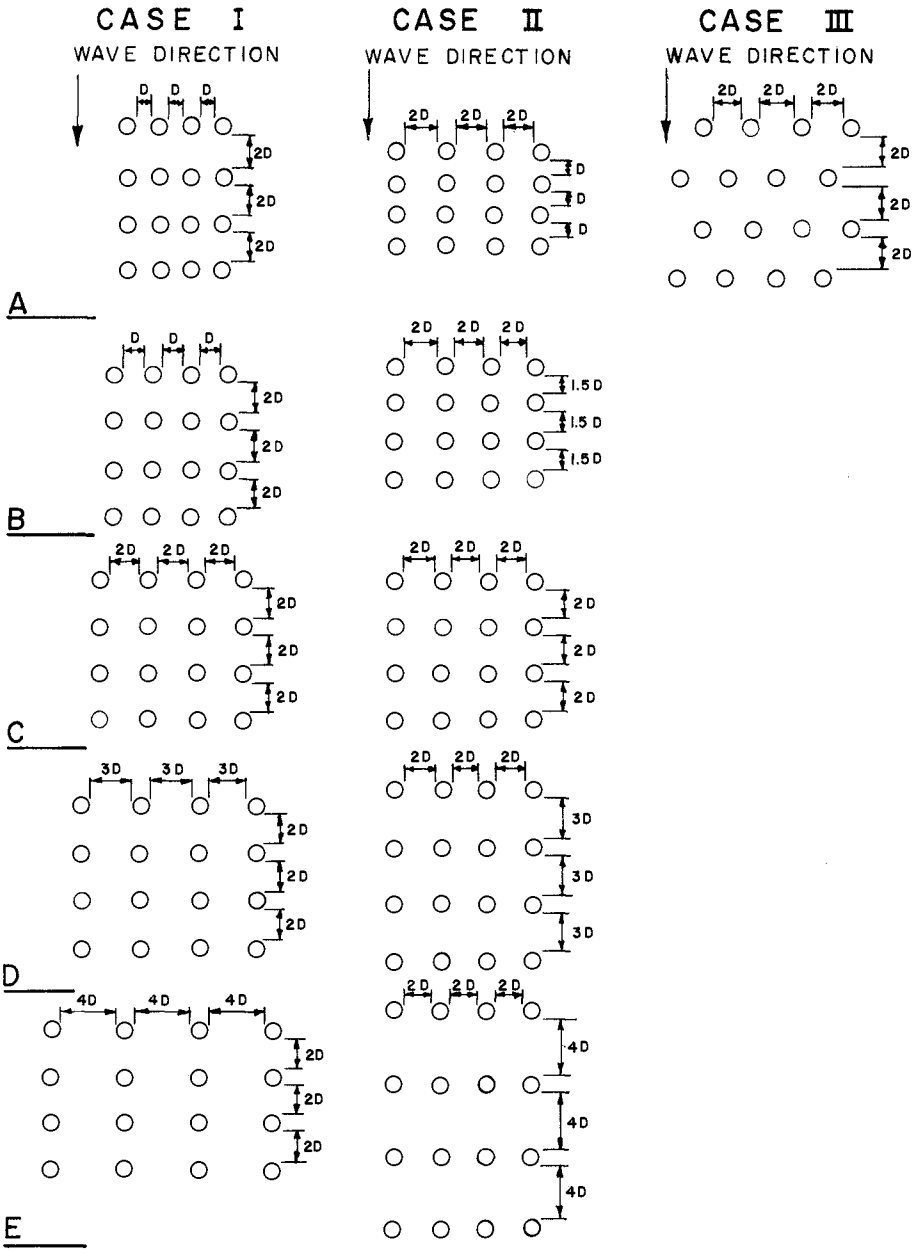

Figure 2 Pile Arrays

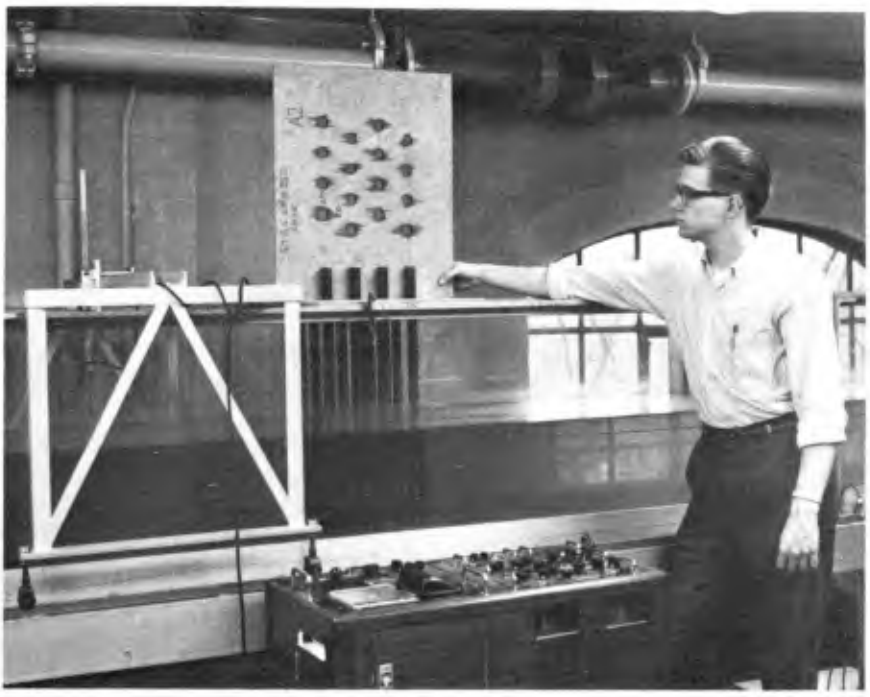

Figure 3 Staggered Pile Arrays. Case III.

RESULTS

The results of the study can best be expressed by examining the graphs developed from the experimental data. The following five variables were employed in the plots: *wave reflection coefficient, wave transmissibility, wave steepness, transverse pile spacing "a", and longitudinal pile spacing "b".*

Figures 4 and 5 show *transmissibility* as a function of *wave steepness*. These curves are similar to curves presented by both Wiegel and Costello and demonstrate the trend of slightly decreasing transmissibility with increasing steepness. In Figure 4 the cases investigated seem to indicate that as the spacing "a" increases the transmissibility decreases. This however seems contrary to expectations and will be investigated further in a subsequent plot. In Figure 5 the trend is as expected because here as the spacing "b" increases so does the transmissibility. This will also be discussed in more detail.

Figures 6 and 7 present the effect of *wave steepness* on *coefficient of reflection*. In both Case I and Case II the trend of the reflection coefficient decreasing with increasing steepness is apparent from the lowest steepness to approximately 0.065.

In general the decrease in reflection coefficient is at a faster rate at the low steepness portions of the curves for small spacings of piles, and at a faster rate of decrease on the high steepness portions of the curves for larger spacings. The reflection coefficient decreases with increasing spacing as was expected. It also is interesting to note that both the largest and smallest magnitudes of the reflection coefficient were obtained in Case II as shown in Figure 7.

The relationship between the *reflection coefficient* and both the *transverse* and *longitudinal spacings* is shown in Figures 8 and 9. It can be seen that the reflection coefficient steadily decreases with an increase in the spacing for both cases tested. It is also noticed that Case II produces both the highest and lowest magnitudes of reflection; but now it can be seen directly that in Case II the rate of reduction in reflection coefficient is definitely greater. Thus with regard to the patterns tested, it is beginning to appear as that the spacing "b", is of equal, if not more, importance than the spacing "a", as far as the reflection coefficient is concerned. However, it is possible that, had another spacing between piles been chosen to be held constant, the results might have been different.

Figure 10 is an interesting plot drawn for Case I showing how the transmissibility is affected by the transverse spacing, "a", of the pile arrays. As revealed by Figure 4, it is again shown that the lowest steepness gives the highest transmissibility with a particular spacing or pattern. However, the shape of the curves is particularly interesting. If some thought is given as to why

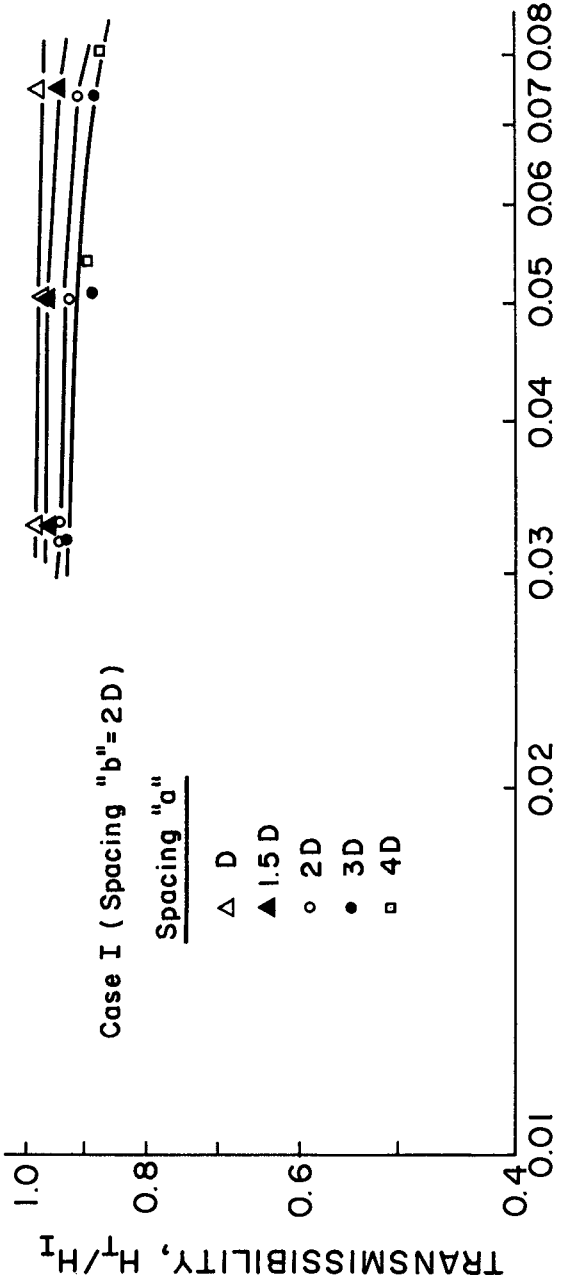

Figure 4 Case I, Transmissibility as a Function of Wave Steepness

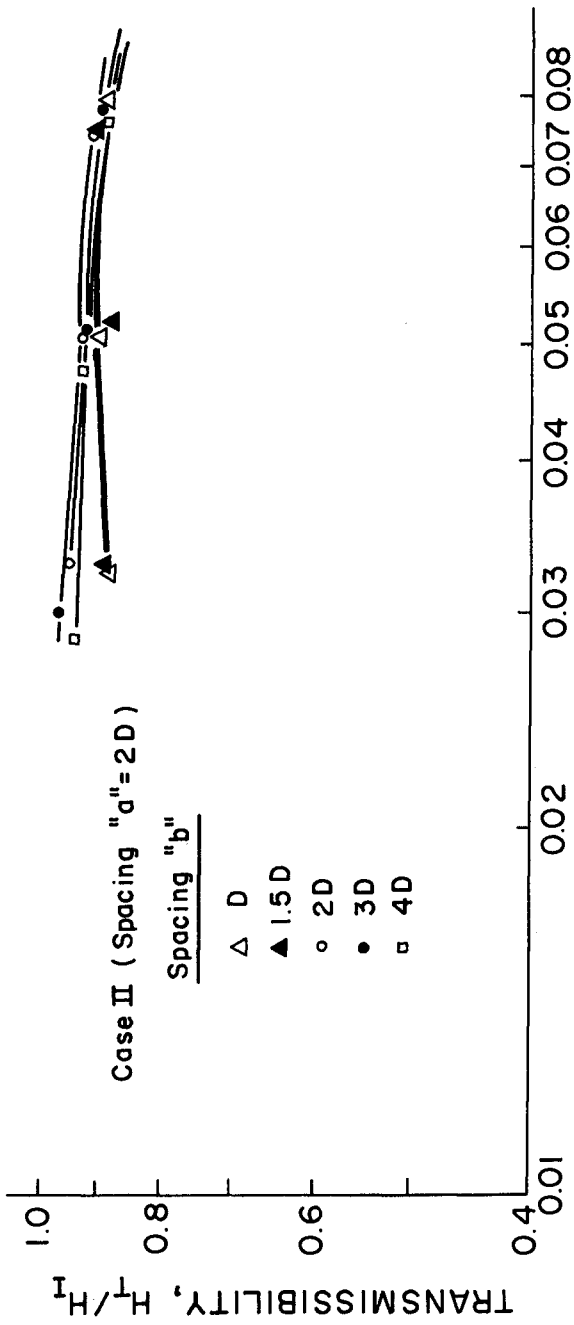

Figure 5 Case II, Transmissibility as a Function of Wave Steepness

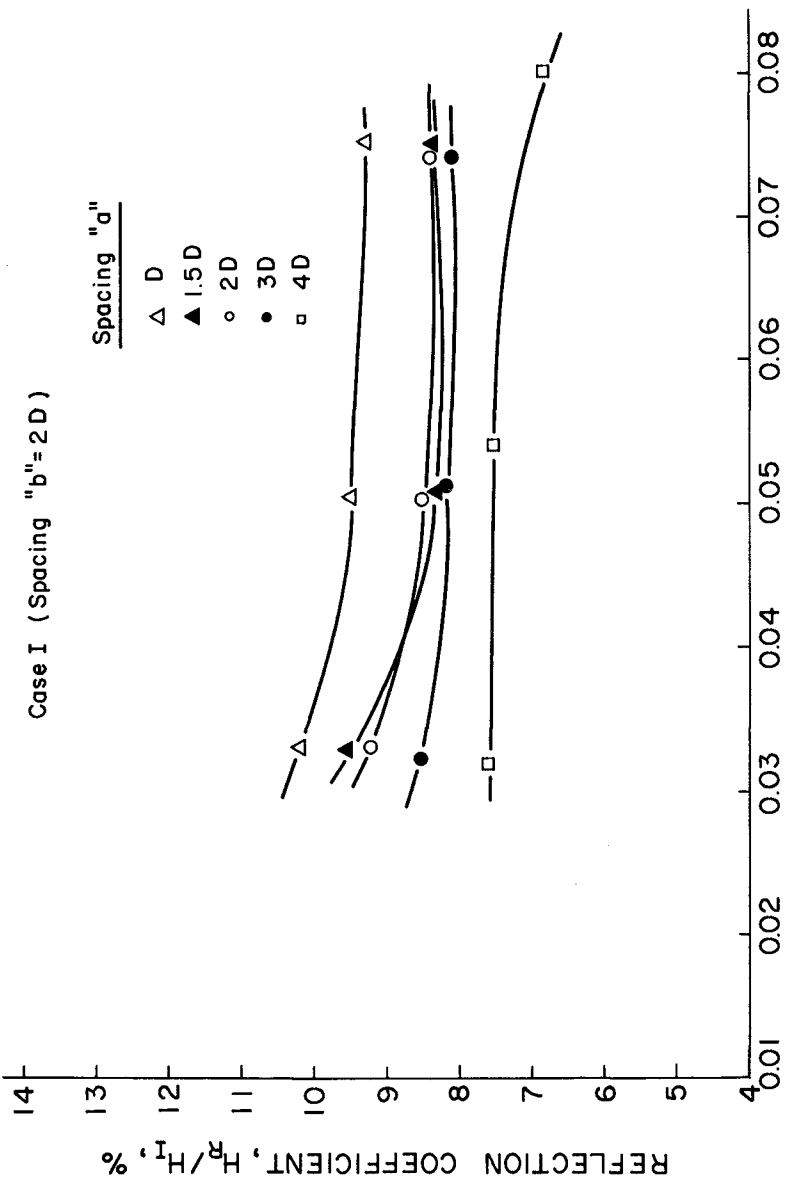

Figure 6 Case I, Reflection Coefficient as a Function of Wave Steepness

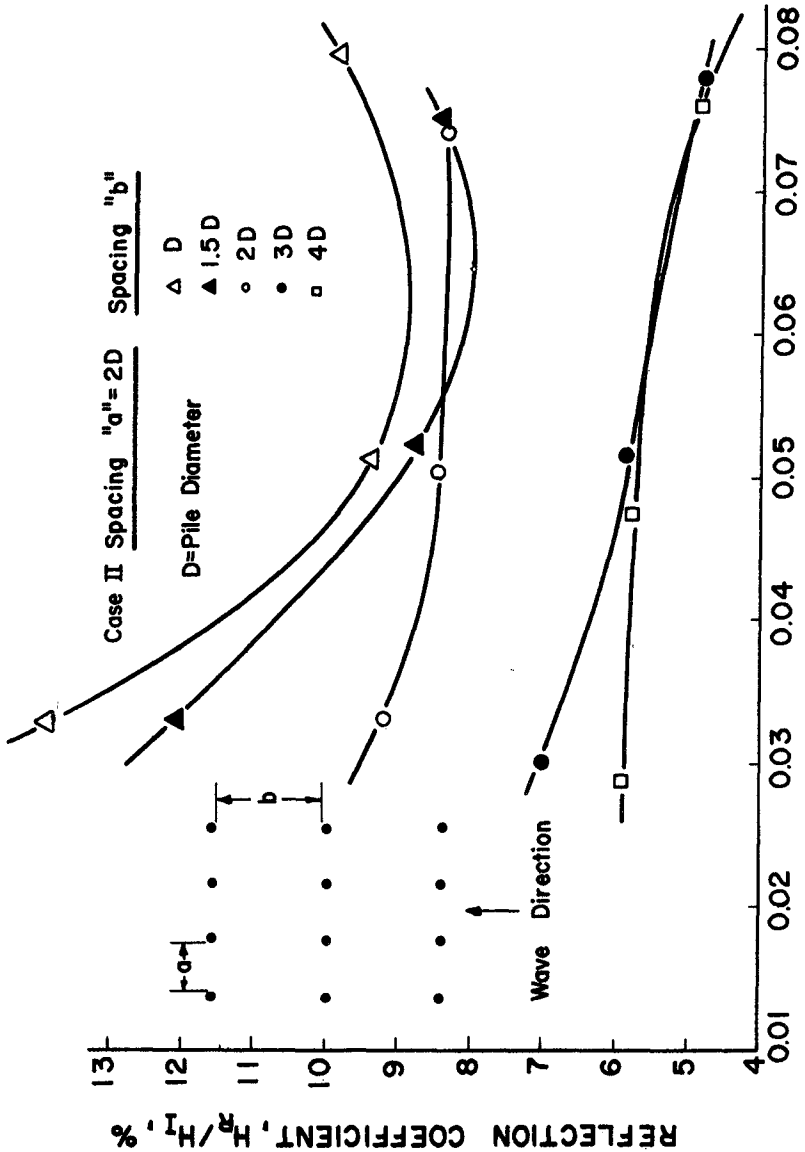

Figure 7 Reflection Coefficient as a Function of Wave Steepness

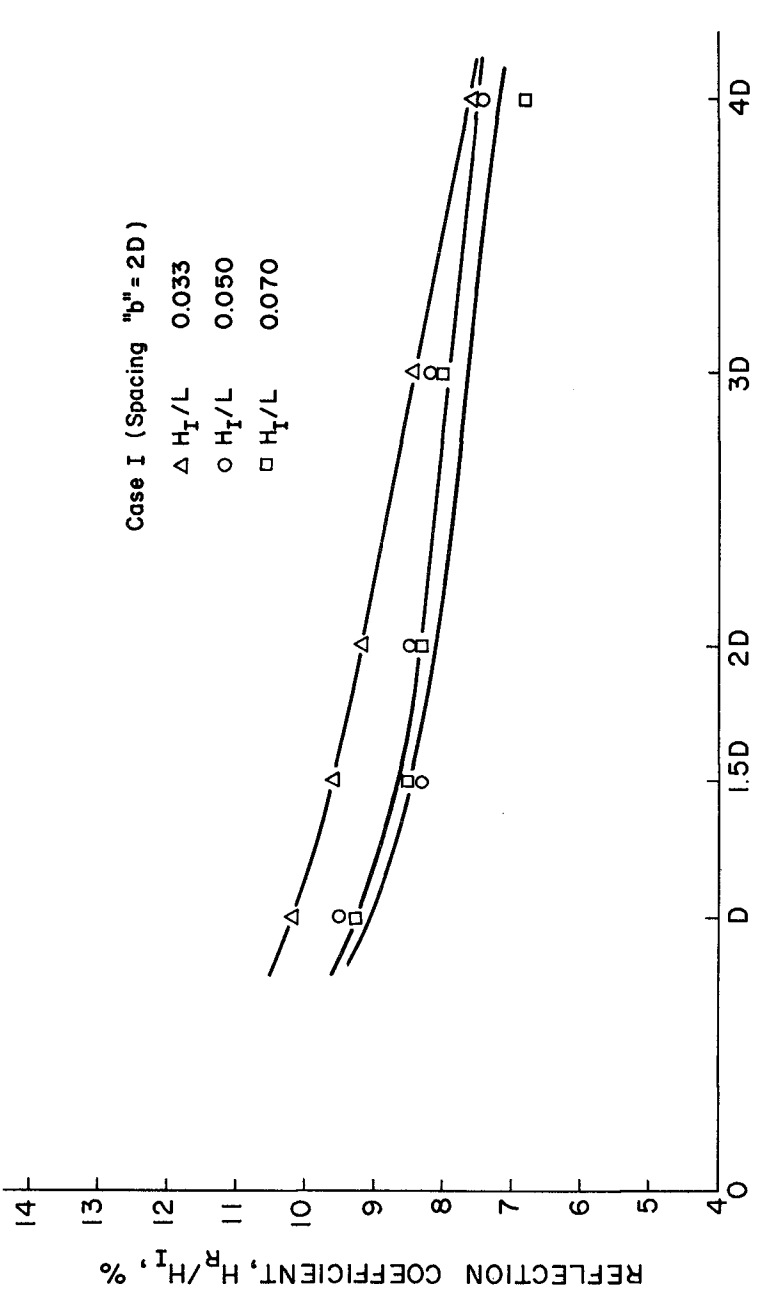

Figure 8 Case I, Reflection Coefficient as a Function of Spacing "a"

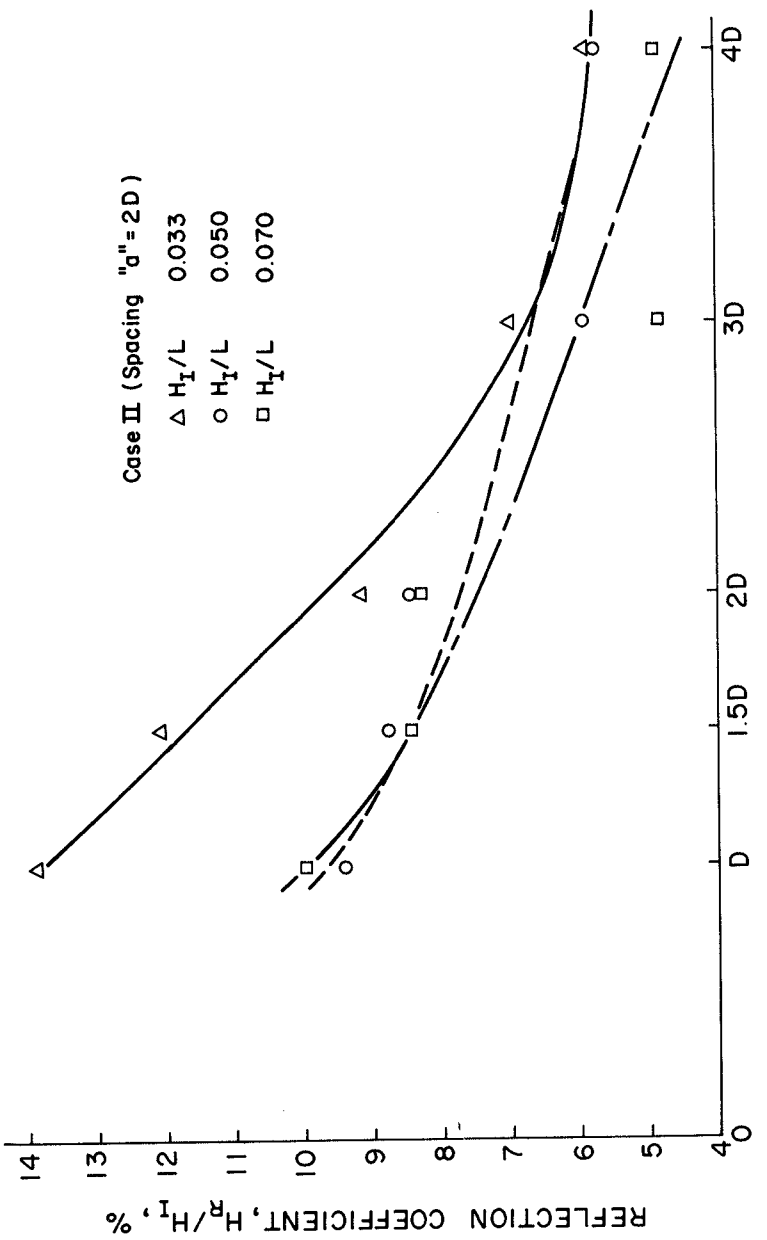

Figure 9 Case II, Reflection Coefficient as a Function of Spacing "b"

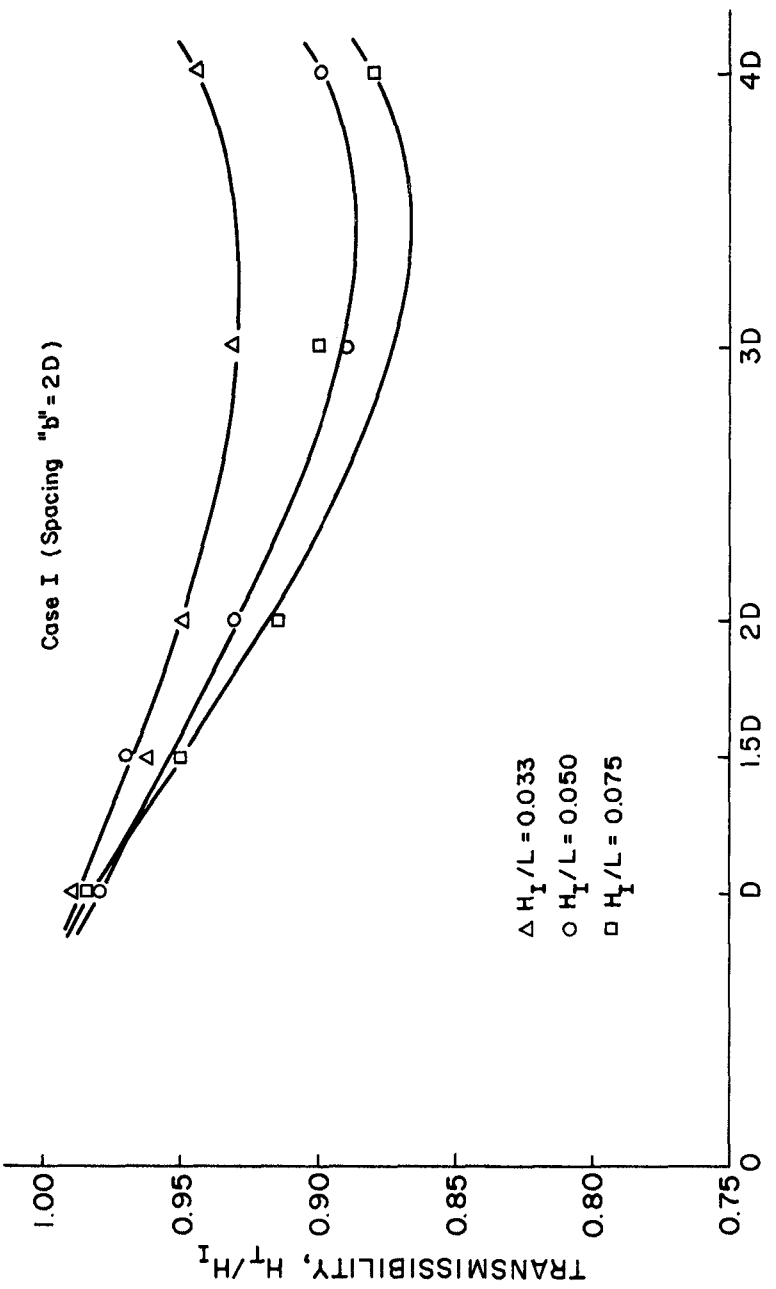

Figure 10 Case I, Transmissibility as a Function of Spacing "a"

the transmissibility increases, it appears logical that as the spacing increases less energy will be lost. Hence, the transmissibility will rise. Why does the transmissibility then at first decrease as the spacing increases? A possible explanation to this question is available if we examine the two major types of energy losses encountered when a wave passes through a pile group. The two losses are: reflection loss and energy loss as a result of eddy formation. Now, if energy loss due to eddy formation is considered to be significantly higher than that due to reflection for this particular case ("b" = 2D), it can be surmized then that as the spacing increases from a comparatively dense arrangement the transmissibility will decrease mainly due to larger eddy losses. As the spacing becomes very large however, the effectiveness of the pile group as an energy dissipator decreases. Thus, the shapes of the curves in Figure 10 can be explained. It should also be noted that the decrease in transmissibility in Figure 10 might not be as steep as it appears. The reason for this is that, when the small spacing groups of Case I were tested, there appeared a "peaking" of the waves behind the pile groups due to the higher ends of the wave along the tank walls moving transversely toward the lower or center part of the wave. This made it difficult to obtain an accurate measurement of the transmitted wave height.

For an idea of how transmissibility is affected by the parallel spacing, "b", of the piles (Case II), Figure 11 can be examined. Again it is shown that the lowest steepness yields the highest transmissibility with a particular spacing. The shape of the curves in this plot also merit special attention. If the pattern with "b" = D is used, it can be assumed that the energy loss is due mainly to reflection because the spacing parallel to the oncoming wave is not yet sufficient to yield great eddy losses. Hence, the transmissibility increases as the spacing becomes larger and the effect of reflections becomes less pronounced. But now as the spacing, "b", gets larger than 2D, the eddy loss becomes considerable, and the transmissibility will decrease slightly. Although Figure 11 seems to indicate this decreasing trend might continue, it is highly probable that the curves will again start to rise and continue rising asymptotically toward $H_T/H_I = 1$, beyond some spacing larger than 4D.

Case III consisted of a single test performed on a pile arrangement in which the piles were staggered and evenly spaced both transversely and longitudinally by 2D. This test can then be compared with the rectangular array, spaced 2D by 2D. It was found that the reflection coefficient for the staggered array was slightly less than that for the rectangular array. The reason for this is not clear, because it would seem that the reflection coefficient would be larger for the staggered array owing to the fact that more surface area would be directly in the way of the incident wave. However, the average difference of reflection coefficient between the two pile groups was less than 1%, which very well might be less than the experimental error. The staggered array produced a transmissibility which was less for each wave than that produced by the 2D by 2D rectangular array. This result agrees with the statement

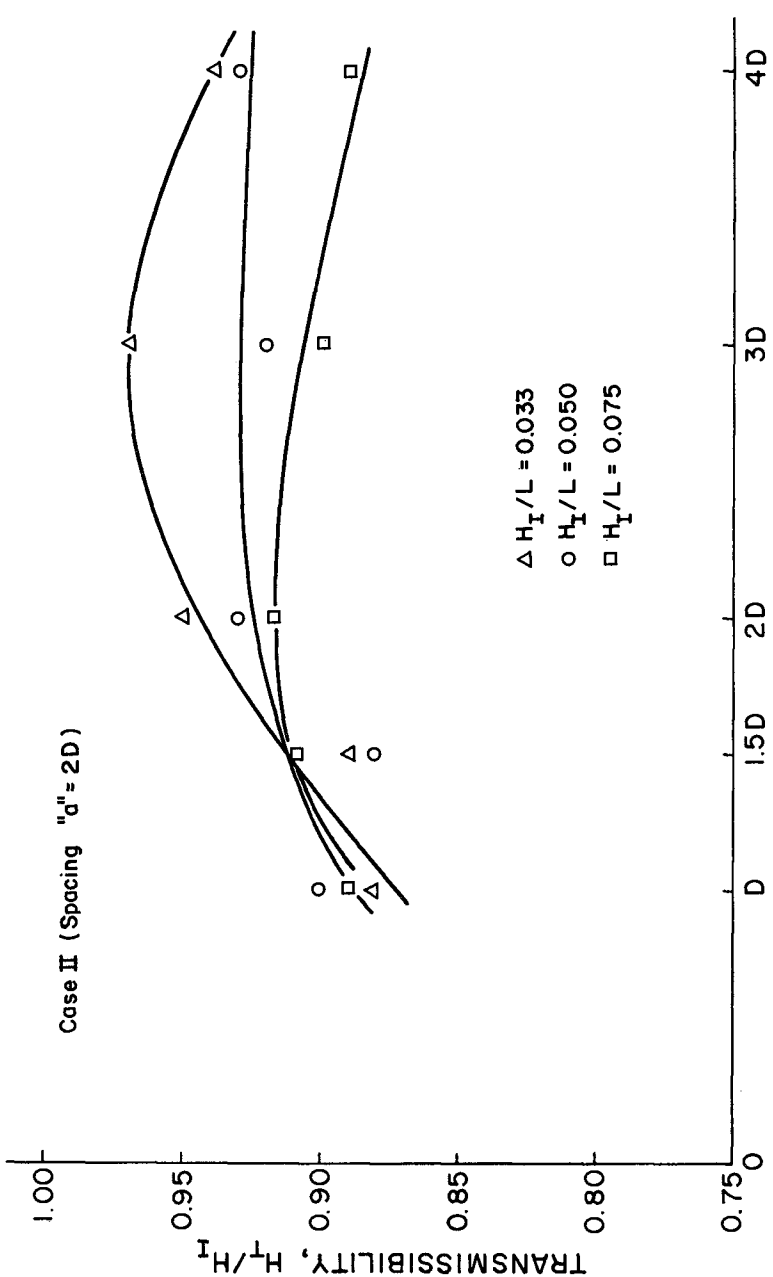

Figure 11 Case II, Transmissibility as a Function of Spacing "b"

found in Costello's report which reads: *"The head loss across uniformly spaced banks of tubing was greater for a staggered array than for rectangular spaced tubes."* (5)

The subject of reflections from staggered arrays warrants further experimentation.

CONCLUSIONS

(1) The transmissibility of a particular pile group decreases with a decrease in the steepness of the waves passing through the group.

(2) In general, the reflection coefficient of a particular pile group also decreases with a decrease in the steepness of the waves passing through the group.

(3) The reflection coefficient decreases with an increase in the longitudinal and transverse spacing between piles.

(4) It appears that the longitudinal spacing, "b", is of equal, if not more, importance than the transverse spacing, "a", in regard to the reflection coefficient of pile groups. This is based on the facts that the case of longitudinal spacing had the largest and smallest reflection coefficients and consequently a greater rate of reduction in reflection coefficient for an increase in spacing.

(5) The variation in transmissibility between different pile groups depends considerably on the spacings between the piles and the corresponding combinations of reflection loss and eddy loss.

(6) The reflection coefficient does not appear to be significantly changed by staggering the piles.

(7) Staggering the piles does decrease the transmissibility.

REFERENCES

1. Wiegel, R.L., OCEANOGRAPHICAL ENGINEERING, Prentice-Hall, Inc., 1964.

2. Morison, J.R., Johnson, J.W., and O'Brien, M.D., "Experimental Studies of Forces On Piles", Proceedings of Fourth Conference on Coastal Engineering, Chapter 25, 1953.

3. Morris, H.M., APPLIED HYDRAULICS IN ENGINEERING, Ronald Press, 1963.

4. Reid, R.O., and Bretschneider, C.L., SURFACE WAVES AND OFFSHORE STRUCTURES, The Agricultural and Mechanical College of Texas, Department of Oceanography, October, 1953.

5. Costello, R.D., "Damping of Water Waves by Vertical Circular Cylinders", Transactions, American Geophysical Union, Vol. 33, No. 4, p. 513-519, August, 1952.

6. Joshi, D.R., REPORT ON STUDY OF THE GRAVITY WAVE REFLECTIONS FROM CYLINDERS, Lehigh University, Fritz Engineering Laboratory, May, 1962.

7. Herbich, J.B., FLUID MECHANICS LABORATORY MANUAL, Lehigh University, Fritz Engineering Laboratory, 1960.

8. Herbich, J.B., EXPERIMENTAL STUDIES OF WAVE FILTERS AND ABSORBERS, University of Minnesota, St. Anthony Falls Hydraulic Laboratory, Project Report 44, 1956.

9. Van Weele, B.J., WAVE REFLECTION AND TRANSMISSION FOR CYLINDRICAL PILE ARRAYS, Lehigh University, Fritz Engineering Laboratory, May, 1965, Report No. 293.4.

CHAPTER 111

WAVE RUNUP ON VERTICAL CYLINDERS

by

C. J. Galvin[1] and R. J. Hallermeier[2]

ABSTRACT

Wave height at a point on vertical cylinders is measured as a function of the orientation angle, α, between the normal from the point on the cylinder and the direction of travel of a single periodic train of waves. The wave height distribution, $H(\alpha)$, has a broad maximum around $\alpha = 0^\circ$ (facing into the waves) and a more restricted maximum at $\alpha = 180^\circ$. The maximum at $\alpha = 0^\circ$ increases with wave height in all cases, and the superelevation has about the magnitude of the velocity head in the wave crest. In 21 different $H(\alpha)$ for which it is possible to determine the axis of symmetry by a simple objective test, 14 $H(\alpha)$ have axes of symmetry within $\pm 3^\circ$ of the direction of wave travel. Most of the variation in $H(\alpha)$ is due to variation in crest elevation; trough elevation remains relatively constant for the 360° range of α. The shape of $H(\alpha)$ depends more on height and cylinder cross section than on period, although the variation in $H(\alpha)$ as a function of cross section is significantly less than the extreme variations in tested cross sections. Applications of these results to wave direction measurement and to interpretation of wave records from surface-piercing wave gages are discussed.

INTRODUCTION

As a wave passes a vertical cylinder, its shape, including its height, is affected by the presence of the cylinder. The purpose of this paper is to present measurements of wave height very near the surface of cylinders of selected cross sections. These experiments are motivated by the possibility that the wave height distribution around a cylinder can be used to measure wave direction. The height data in this paper are for periodic laboratory water waves propagating in one direction.

When a wave passes a vertical cylinder, the principal effects of the resulting wave-cylinder interaction are scattering by the cylinder and viscous dissipation in the wake of the cylinder (Chen and Mei, 1971). The parameter, $\pi X/L$, where X is the nominal cylinder diameter and L is the wavelength, describes the wave scattering, and the parameter, H/X, where H is the incident wave height, describes the wake effects. There should be a critical value of each parameter above which respective effects are significant, but these critical values are not known. Bidde (1970) suggests that eddy shedding by waves around a cylinder depends on a Keulegan-Carpenter number, $K = UT/X$, where U is the maximum fluid velocity and T is the wave period. In Bidde's (1970) experiments, eddy shedding occurs when $K \geq 3$.

---

[1]Chief, Coastal Processes Branch, U. S. Army Coastal Engineering Research Center, Washington, D. C.

[2]Oceanographer, Coastal Processes Branch, U. S. Army Coastal Engineering Research Center, Washington, D. C.

The three dimensionless numbers, $\pi X/L$, H/X, and K, are collectively referred to in this paper as wave interaction parameters.

Only two previous experimental studies of wave height distribution around vertical cylinders are known to the authors (Hellström and Rundgren, 1954; Laird, 1955), and both of these studies are for a limited range of wave interaction parameters (Table 1). These early studies verify even casual observations that the wave height distribution around vertical cylinders is approximately symmetric about an axis given by the direction of wave travel.

TABLE 1. WAVE INTERACTION PARAMETERS* IN EXPERIMENTAL STUDIES OF WAVE HEIGHT AT CYLINDERS

		(1) $\pi X/L$	(2) H/X	(3) UT/X
This paper	Circular cylinders and H-beams	0.015 to 0.15	0.25 to 4.0	2 to 15
Hellström and Rundgren, 1954	Cylindrical model lighthouse	$\sim$1.0	$\sim$0.4	
Laird, 1955	Cylindrical model island	$\sim$1.0	$\sim$0.05	

*Column (1) is the scattering parameter; column (2) is the wake parameter; column (3) is the Keulegan-Carpenter number for eddy shedding (Bidde, 1970). X is diameter of cylinder, H is wave height, T is wave period. Both L (wavelength) and U (maximum particle velocity) are computed from linear theory.

TEST VARIABLES

Data were collected in CERC wave tanks 96 feet long by 1.5 feet wide, and 85 feet long by 14 feet wide. Each tank has a piston-type wave generator consisting of a vertical flat plate constrained to move horizontally in approximately simple harmonic motion, so that the generator motion is uniquely determined (in theory) by the period, T, and eccentric, E, of the driving arm (Galvin, 1964). In practice, the generator in the 85-foot tank vibrates badly, introducing higher frequency bumps in the wave record, especially for low waves.

The downstream end of the tanks have absorbing beaches designed to minimize reflection, and reflection was not considered a problem in these tests.

The wave height distribution around the cylinder depends on three sets of independent variables:

$$\text{Height Distribution} = f(H, \text{Cylinder, Gage}) \quad (1)$$

The first set, including 4 variables, determines the wave height, H, in the absence of the cylinder

$$H = H(T, E, d, x_g) \quad (2)$$

where d is the water depth and x_g is the distance from the generator to the cylinder. Distance, x_g, is required because the wave deforms nonlinearly as a function of distance traveled (Galvin, 1972).

The second set of independent variables describe the cylinder, including cylinder shape, size, and material. For the purpose of this paper, the term 'cylinder' includes any shape that can be formed by moving a vertical line around a closed curve. In this sense, the 7 shapes shown in Figure 1 are sections of cylinders. Cylinders A and B are circular cylinders; Cylinder C is the finned cylinder; Cylinders D, E, and F are the deep H-beam, the square H-beam, and the shallow H-beam, respectively; and Cylinder G is the flat plate. These cylinders vary in dimensions from a minimum of 0.5 inches for the thickness of the flat plate to a maximum of 12 inches for the diameter of the outer circumference of the finned cylinder. Cylinders A through F were made of Plexiglas: 1/8-inch thick for Cylinders A and E, and 1/4-inch thick for Cylinders B, C, D, and F. Cylinder G is varnished plywood. In addition to those shown on Figure 1, a number of other cylinders were tested for special purposes, including scale effects.

The third set of independent variables are the characteristics of the wave gage used to measure the height, including accuracy, distance between cylinder surface and gage, and position of the gage with respect to the cylinder cross-sectional shape. Accuracy and distance from the cylinder are discussed in the next section. The position of the gage on the cylinder for non-circular cylinders is always between flanges and as close as possible to the middle of the web surface (Figure 2).

The angle, α, to which the height distribution is referred, is the angle between the incoming wave direction and a line from the cylinder axis to the wave gage (Figure 2). The wave height distribution is then indicated by $H(\alpha)$, which was measured by rotating the cylinder-gage combination through 360° in 5 or 10-degree increments.

The range of conditions tested at each of the cylinders is shown on Table 2. The variables, H, T, and d were chosen to be Froude models of representative wave conditions at the CERC wave gage on the end of the Atlantic City, New Jersey, Steel Pier (1:15 for 96-ft tank; 1:6 for 85-ft tank). Because of test restrictions, including size of available wave gages, the cross sections of the laboratory cylinders are larger than required by the model scales, if existing piling and H-beams in the field are considered to be prototype (see Figure 1).

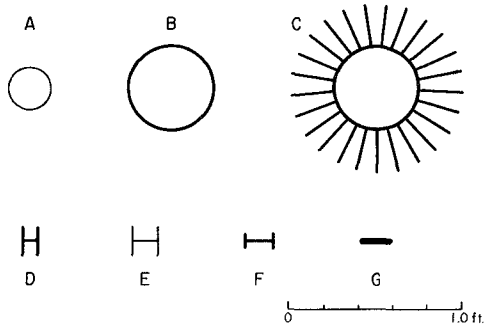

Figure 1. CROSS-SECTION OF TEST CYLINDERS

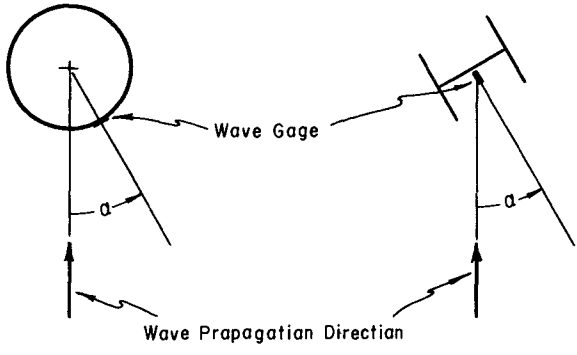

Figure 2. ORIENTATION ANGLE, α

TABLE 2. TEST CONDITIONS

Water Depth*, d, ft	Wave Period, T, sec	Wave Length**, L, ft	Wave Height, H, ft	Cylinders Tested
1.00	1.55	8.1	0.12-0.30	A,D,E,F,G
1.00	2.32	12.7	0.08-0.48	A,D,E,F,G
1.00	3.10	17.4	0.06-0.26	A,D,E,F,G
2.33	2.35	18.8	0.26-0.71	B,C,E
2.33	3.55	29.4	0.29-0.78	B,C,E
2.33	4.70	40.4	0.42-0.88	B,C

*x_g = 25.05 ft for 1.0 ft depth; 19.5 ft for 2.33 ft depth.

**Computed from linear theory for indicated depth and period.

WAVE HEIGHT ACCURACY

Three variations of the CERC parallel wire gage (Stafford, 1972) were used to measure H(α). Gages were checked for calibration and drift before and after each run, and in the case of the circular cylinders, some runs were checked independently by marking the height distribution with grease pencil (china marker) on the cylinder and by slipping a sheet of bond typing paper around the cylinder and letting the waves record their own crest height distribution in wetting the papers. These checks indicate that the data are internally consistent and usually repeatable to within a few percent. In one repeat test, a wetting agent (Edwal Kwik-Wet) was added to give the tank a 40 ppm solution of water with low surface tension. With this solution, the observed H(α) was not significantly different from H(α) without the solution, except over about 15% of the circle where the solution seemed to accentuate two minimums in H(α) by up to 20%. Changing the cylinder-to-gage distance by 3/4 to 1 inch changes wave height by 2 to 3% and crest height by 1 to 8%. These tests indicate that cylinder-to-gage distance does not significantly affect the conclusions of this study.

RESULTS

Experimental results presented here include information on wave shape (Figures 3, 4, 5, 6), symmetry of height distribution (Figure 7), effect of period on height distribution (Figure 8), and effects of height and cylinder cross section on the height distribution (Figures 9, 10, 11, 12, 13, 14).

Wave Shape. Experience shows that it is useful to define the height, H, as the sum of a crest height, P, and trough height, Q, as shown on Figure 3

$$H = P + Q \tag{3}$$

In terms of height distributions, the height at orientation angle α is

$$H(\alpha) = P(\alpha) + Q(\alpha) \tag{4}$$

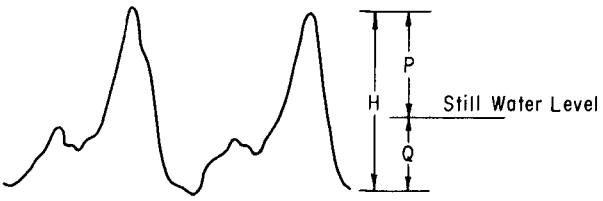

Figure 3. WAVE HEIGHT DEFINITIONS

Experiments show that most of the variation in $H(\alpha)$ is due to variation in $P(\alpha)$ (Figure 4), so that variations in $H(\alpha)$, which are the primary interest of this study, are also illustrated by variations in $P(\alpha)$. Since this crest height distribution, $P(\alpha)$, is easier to reduce from wave records than $H(\alpha)$, the remainder of the paper contains data in terms of $P(\alpha)$, unless otherwise stated. For easier comparison of results, the observed $P(\alpha)$ is divided by P, the crest height in the absence of the cylinder, in Figures 8 through 14.

The shape of the wave measured at the surface of the cylinder depends on the nonlinear deformation of the wave during its travel from the generator to the cylinder, and on the interaction between the cylinder and the wave. For d/L ratios less than about 0.1, individual water waves separate into 2 or more waves (solitons) of unequal height whose speeds are related to their respective heights (Galvin, 1972). Because their speeds differ, the separation between two solitons is a function of x_g, the distance from the generator. Thus, on Figure 5, the separation is greater between solitons than on Figure 6 because the dimensionless travel, x_g/L, is 1.97 for Figure 5, compared to 0.66 for Figure 6. Soliton separation does affect the shape, but not the basic symmetry of $H(\alpha)$. Only two values of x_g were used for data reported here (Table 2).

Figure 5 shows the effect of the wave-cylinder interaction due to: (1) wave steepness (compare low steepness shapes in left column with high

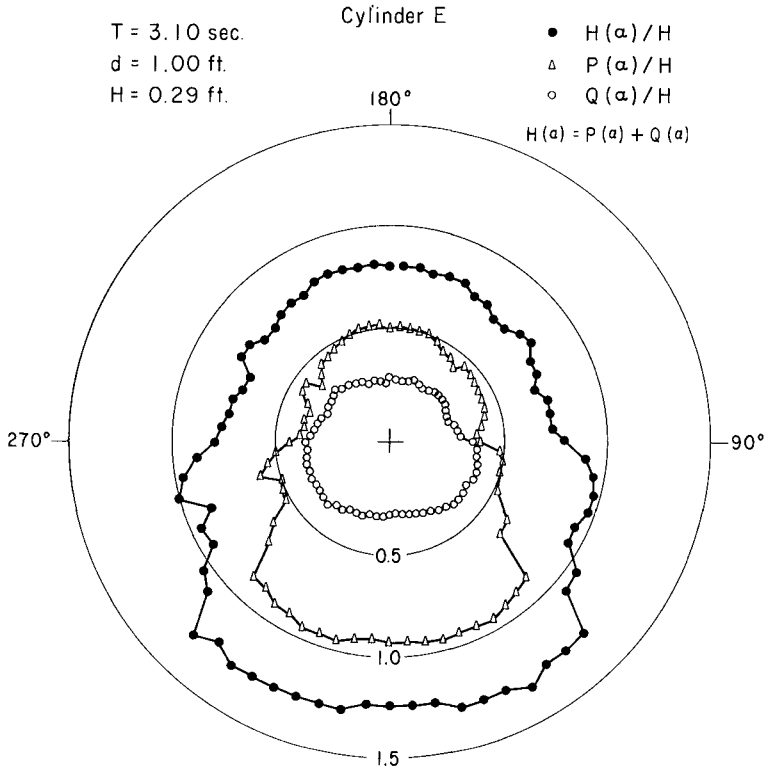

Figure 4. SIMILARITY BETWEEN H(α) AND P(α) IN SQUARE H-BEAM

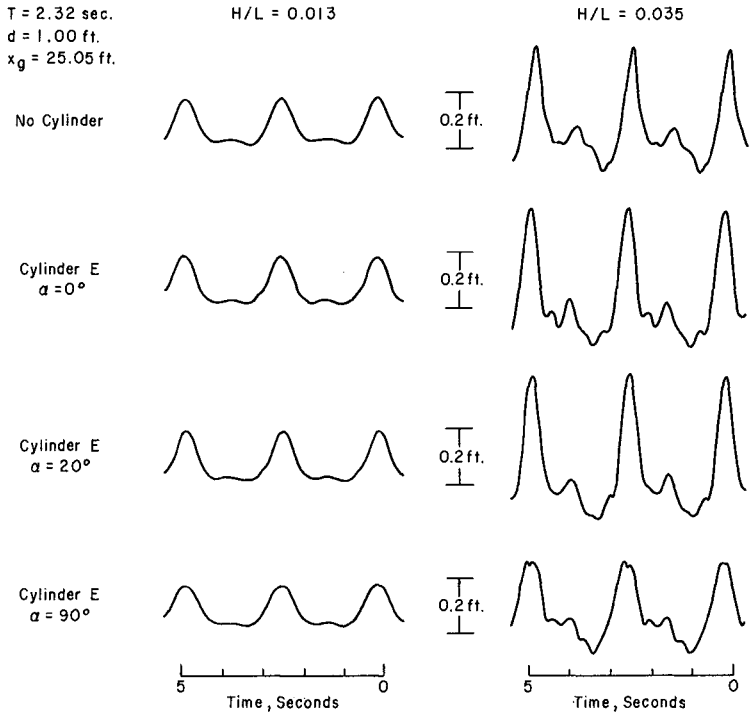

Figure 5. WAVE SHAPE IN SQUARE H-BEAM FOR TWO STEEPNESSES AND THREE ORIENTATIONS

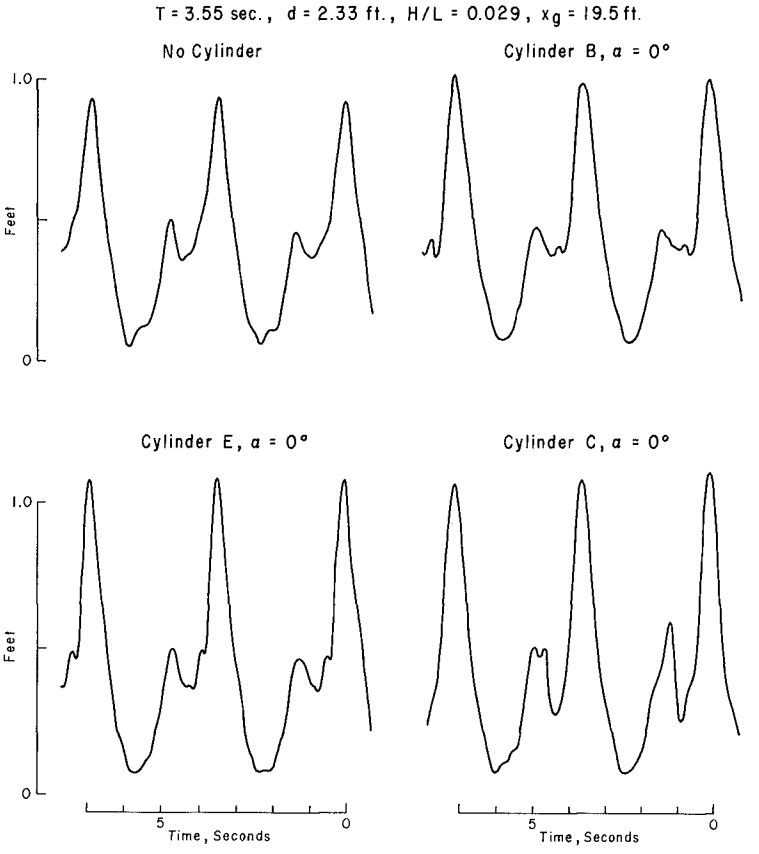

Figure 6. WAVE SHAPE AT THREE CYLINDERS FOR α = 0°

steepness shapes in right column); (2) presence of H-beam (compare top wave shapes without the H-beam to the remaining shapes with the H-beam); and (3) orientation angle ($\alpha = 0^{\circ}, 20^{\circ}, 90^{\circ}$). At low steepness, wave shape is not affected much either by the presence of the H-beam or by orientation. At high steepness, the cylinder and α alter both the crest elevation and the higher frequency oscillations in the trough. Among other phenomena, the steep wave at $\alpha = 20^{\circ}$ for these test conditions is repeatably smoother than the same wave with no H-beam (Figure 5).

Figure 6 shows wave shapes at three very different cylinders (circular cylinder, finned cylinder, square H-beam). Each of the cylinders amplifies the crest elevation compared to the elevation in the absence of the cylinder, but the shape of the wave does not differ much among cylinders. The amplification of the smaller soliton peak at the finned cylinder (lower right of Figure 6) appears to be due to a resonance excited by the subsiding crest of the larger soliton in the slot between fins.

Symmetry. On Figure 4, the $H(\alpha)$ and $P(\alpha)$ have obvious symmetry about the direction of wave travel. For simple symmetric distribution of $H(\alpha)$, the difference between $H(\alpha)$ and $H(\alpha + 180^{\circ})$ is necessarily zero at right angles to the axis of symmetry. (This result holds for symmetric distributions whose maxima occur on the axis of symmetry. It does not necessarily hold, even though the distribution is symmetric, if pronounced maxima or minima occur off the axis of symmetry, e.g., rectangular distributions on a polar plot.)

Figure 7 shows a typical plot of the 180° differences for both $H(\alpha)$ and $P(\alpha)$. The zero crossing is 2 or 3° from the 90° position required by symmetry. A total of 26 separate $P(\alpha)$ distributions are illustrated on the Figures of this paper. Of these, 21 have the simple distributions that require zero crossing at $\alpha = 90^{\circ}$ if symmetric. Of these 21, the zero crossings of 14 are within $\pm 3^{\circ}$, and 17 are within $\pm 5^{\circ}$, of $\alpha = 90^{\circ}$. The exceptions in the 26 cases are the deep H-beam, which gives a rectangular distribution, and very low waves, where the 180° difference becomes about equal to the expectable error in measured $P(\alpha)$.

Period Effect. Figure 8 shows the $P(\alpha)/P$ distribution for 3 test conditions in which period varied but depth and height were held constant. These data show that the shape is approximately independent of period, although the amplification of height around $\alpha = 0^{\circ}$ is 15% greater for the steepest wave. Because period has relatively little effect on the height distribution, the remainder of this paper concerns tests run at a single period, $T = 2.32$ seconds in 1.0 ft depth, or its Froude-related value of 3.55 seconds in 2.33 ft depth (Table 2). Since the Keulegan-Carpenter number is greater than 3 in most of these tests, variation in T only affects the scattering parameter (Table 1). Since there is little variation of shape of $P(\alpha)$ with T, it appears that the wave height distributions are relatively independent of scattering effects in these tests.

Crest Height Distribution. Figures 9 through 13 show the effect of varying wave height, at $T = 2.32$ seconds and $d = 1.0$ ft, on the 3-inch circular cylinder (Figure 9), deep H-beam (Figure 10), square H-beam (Figure 11),

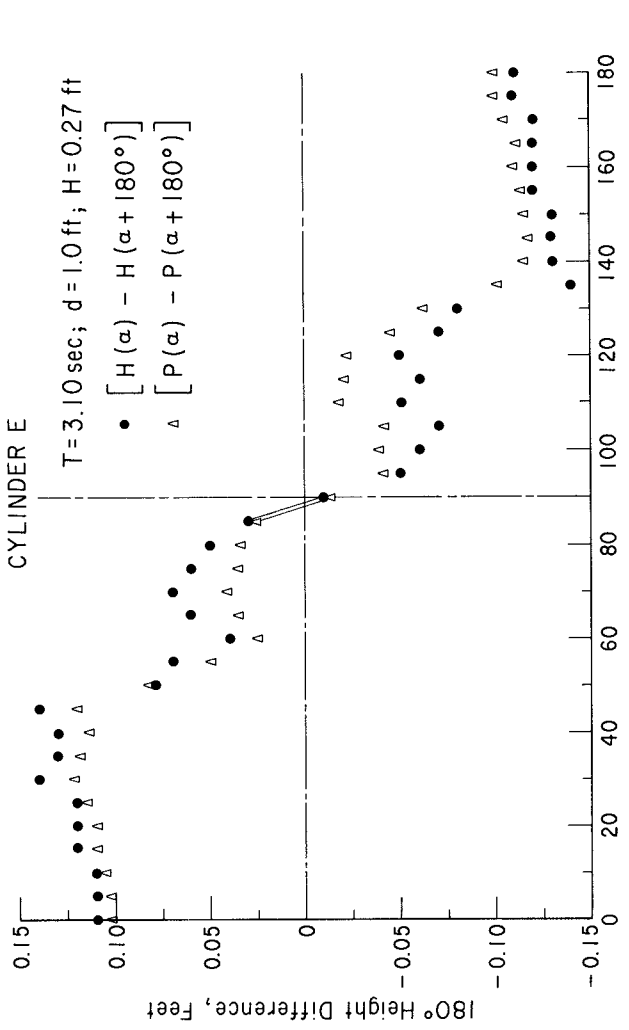

Figure 7. DEPENDENCE OF $[H(\alpha) - H(\alpha+180°)]$ AND $[P(\alpha) - P(\alpha+180°)]$ ON ORIENTATION ANGLE α (SQUARE H-BEAM)

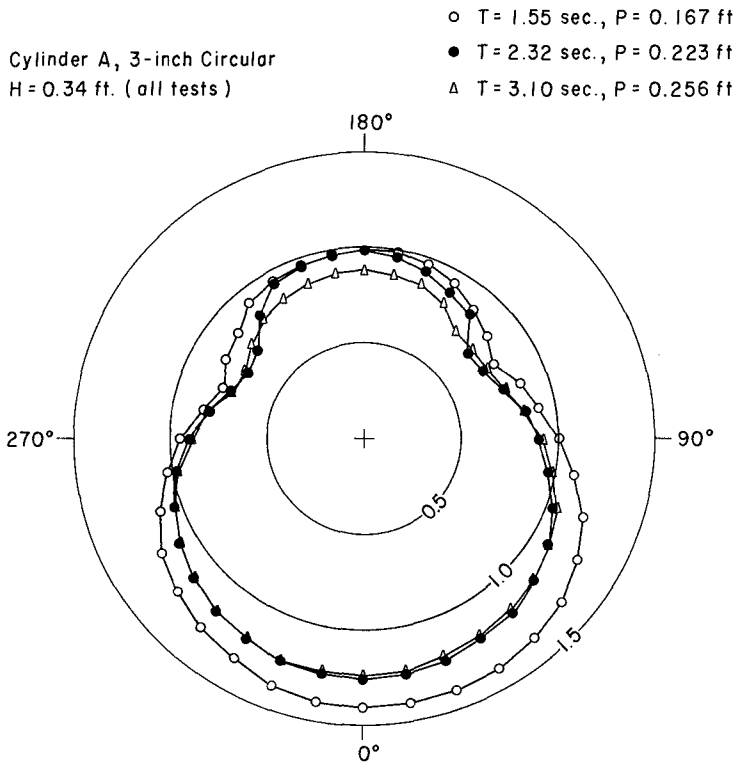

Figure 8. PERIOD EFFECT ON CREST HEIGHT DISTRIBUTION, P(α)/P, FOR 3 PERIODS AT CONSTANT HEIGHT

shallow H-beam (Figure 12), and flat plate (Figure 13). Figure 14 (the last figure) compares the $P(\alpha)/P$ for 6-inch circular and finned cylinders. Figures 9 through 13 all have the same format, displaying $P(\alpha)/P$ for four test heights on three polar plots. The distribution for the lowest test height is repeated on each of the three polar plots as a reference distribution from which relative changes may be more easily judged.

For all distributions on Figures 9 through 13, the maximum value of $P(\alpha)/P$ occurs near $\alpha = 0^{\circ}$, or symmetrically about $\alpha = 0^{\circ}$. This front maximum has a magnitude that increases from about 1.0 to about 1.4 as P increases. On Figure 8, the maximum increases as T decreases. These facts are consistent with the hypothesis that runup on the front of the gage is the velocity head of the water particle in the wave crest. Use of linear or solitary wave theory to predict this runup gives results that are within a factor of 2 of observed values.

For almost all height distributions shown, there is also a pronounced maximum at $\alpha = 180^{\circ}$ (see Figure 12), but the value of this 180° maximum is not simply related to the wave height. This maximum in the rear is mainly stagnation head of converging flow in the rear of the cylinder as the crest passes, and it typically has a value between 0.8 and 1.0.

The existence of maxima at $\alpha = 0^{\circ}$ and $\alpha = 180^{\circ}$ requires minima at intermediate angles. These minima are observed to be related to separation points on the circular cylinder. From the data available, it appears that the minima on the equidimensional cylinders (circular cylinders and square H-beam) shift toward 180° as P increases (see Figures 9 and 11).

As a general test result, the shape of $P(\alpha)/P$ does not vary as much as the shape of the cylinder cross section. It appears that stagnation in the front of the cylinder and separation in the rear reduce the effect of cylinder shape on the flow.

ENGINEERING APPLICATIONS

Wave Direction Measurement. The symmetry in the $P(\alpha)/P$ distributions about the direction of travel suggests that the wave runup around a cylinder might be used to measure wave direction. Proposed wave direction instruments reported in the literature include: wave gage arrays, airborne cameras (Stilwell, 1969), radar (Oodshorn, 1960), acoustic (Multer, 1970) and electromagnetic sensors; devices to measure forces on small objects (Banwell, 1965), and vanes to align with or against the flow (Hall, 1950). Of the instruments suggested, wave gage arrays appear to have attracted the most attention (Barber, 1954, p. 1048; Panicker and Borgman, 1970, p. 117; Ploeg, 1972, p. 331; Chakrabarti and Snider, 1972, p. 657; Wiegel, Al-kazily, and Raissi, 1972), but techniques of processing and interpreting the data are still under development. Except possibly for aerial photography, none of the proposed methods (including the method proposed here) have satisfactorily solved the problem of distinguishing directions when more than one wave train occurs at the same time. At present, no instrument is accepted as providing an economic, automatic field measurement of nearshore wave direction that is reliable to within 5 degrees. Due to refraction, at least 5 degree accuracy is needed for waves near the littoral zone. Considerable experience at the Coastal Engineering Research Center (Galvin and Seelig, 1971) and elsewhere (Zwamborn, et al, 1972) suggests that the best existing engineering solution to the problem of obtaining nearshore wave direction is visual observation.

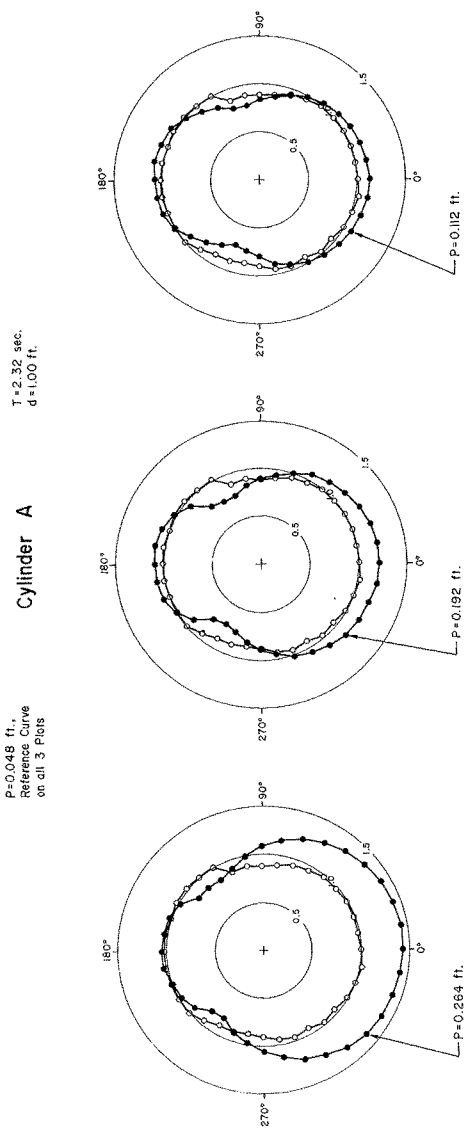

Figure 9. CREST HEIGHT DISTRIBUTION, P(α)/P, FOR 4 HEIGHTS, CIRCULAR CYLINDER

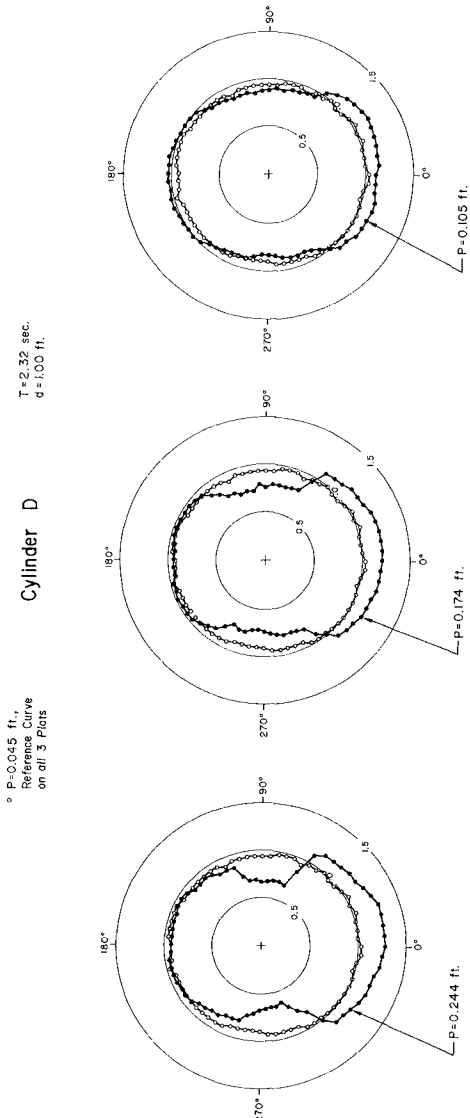

Figure 10. CREST HEIGHT DISTRIBUTIONS, P(α)/P, FOR 4 HEIGHTS, DEEP H-BEAM

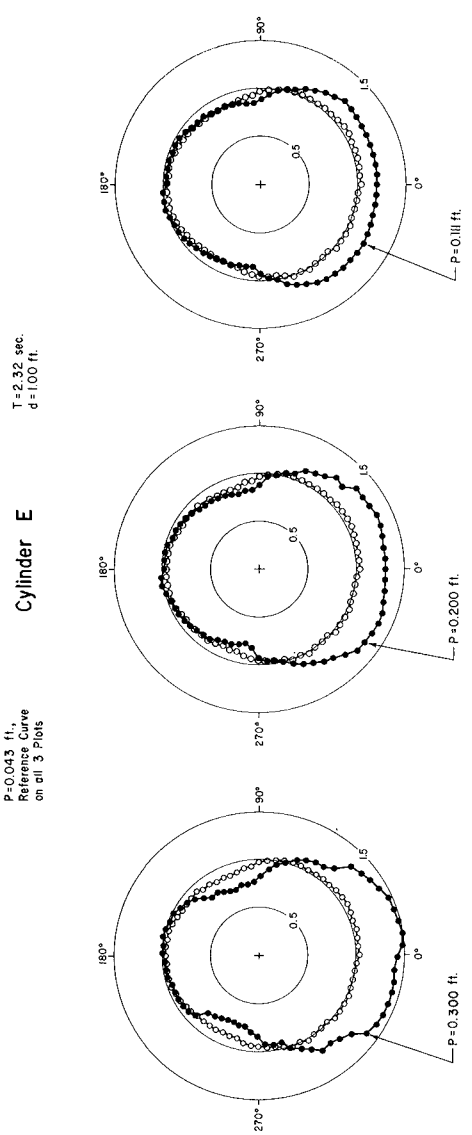

Figure 11. CREST HEIGHT DISTRIBUTIONS, P(α)/P, FOR 4 HEIGHTS, SQUARE H-BEAM

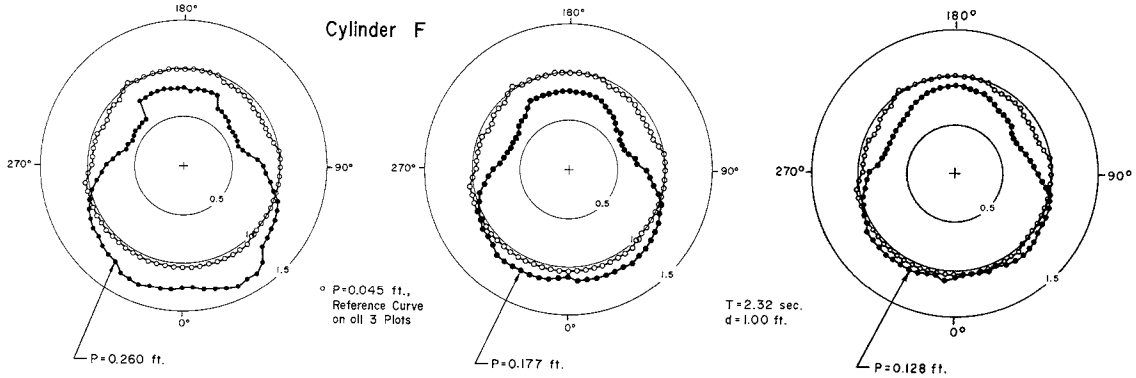

FIGURE 12. CREST HEIGHT DISTRIBUTIONS, P(α)/P, FOR 4 HEIGHTS, SHALLOW H-BEAM

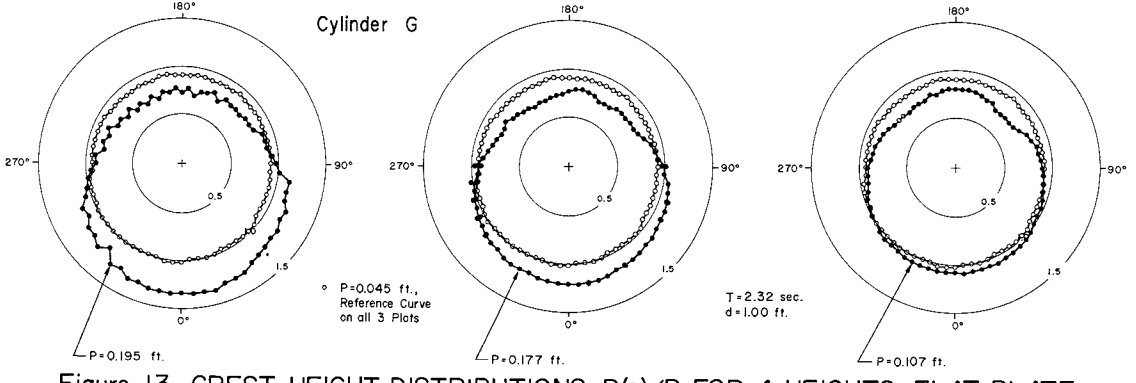

Figure 13. CREST HEIGHT DISTRIBUTIONS, P(α)/P, FOR 4 HEIGHTS, FLAT PLATE

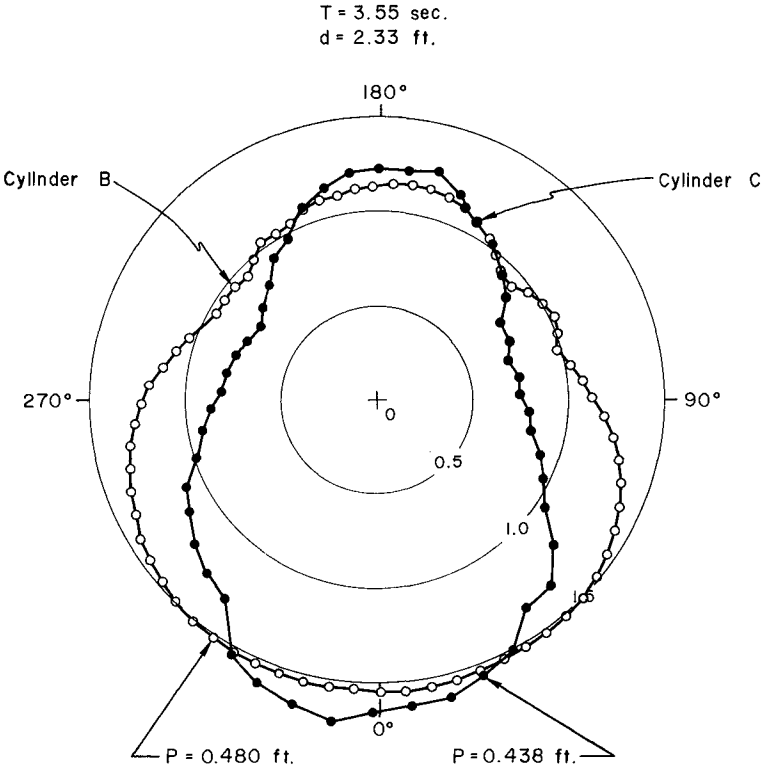

Figure 14. CREST HEIGHT DISTRIBUTIONS, $P(\alpha)/P$, FOR SIMILAR HEIGHTS, AT FINNED(•) AND 6-INCH (○) CYLINDERS

The experiments of this paper suggest the use of wave gages mounted around a vertical cylinder as an instrument to measure wave direction. Advantages of this proposed method, that are not simultaneously present in other proposed methods, include: (1) effectively point measurement; (2) use of existing, field-proven sensors (wave gages or pressure sensors); (3) no moving parts; (4) performance that improves rather than degrades due to eddy-shedding and other viscous effects. The authors are unaware of published work on such an application, but field pressure records from around instrumented towers are now being analyzed for direction at the University of Florida with promising initial results (R. G. Dean, 1972, personal communication). A number of difficulties are anticipated in applying the proposed method, including the previously mentioned multiple wave train problem, as well as reduced sensitivity to low or short-crested waves, and design problems in developing a reliable field instrument.

Wave Gage Interpretation. Data from this study might be used to interpret wave height statiatics obtained from surface-piercing wave gages mounted on structures. The step resistance wave gage that has been used for many years by the Coastal Engineering Research Center is typically mounted in an H-beam which is attached to a pier pile. These gages show heights that are higher than heights measured at the same point by wire surface-piercing gages or by submerged pressure gages (see Esteva and Harris, 1970, Figure 5). The difference increases with increasing height, which is consistent with wave runup on the gage as the cause, since velocity head in the wave crest is proportional to the square of the wave height. If real, these runup effects on wave gages overrepresent the high waves at a locality, and they could result in over conservative design. It was the field observation of runup effects on step resistance gages by one of the authors that led to the present study.

In addition to possible applications to wave direction measurement and to interpretation of some wave gage records, the data from this study have basic application to the problem of wave action on cylinders, a subject of continuing interest to coastal engineers.

ACKNOWLEDGEMENTS

The experiments and data reduction that form the basis of this paper were done between February 1970 and August 1972 by R. J. Karlitskie, C. R. Schweppe, R. E. L. Ray, and J. C. Jones at the U. S. Army Coastal Engineering Research Center. Data presented in this paper, unless otherwise noted, were obtained from research conducted by the United States Army Coastal Engineering Research Center under the Civil Works research and development program of the United States Army Corps of Engineers. Permission of the Chief of Engineers to publish this information is appreciated. The findings of this paper are not to be construed as official Department of the Army position unless so designated by other authorized documents. The contents of this paper are not to be used for advertising or promotional purposes. Citation of trade names does not constitute an official endorsement or approval of the use of such commercial products.

REFERENCES

Banwell, T.J., "The TCB Wave Cage: A New Instrument for the Measurement of Ocean Waves", Ocean Science and Engineering, Vol. 2, pp. 1069-1087 (1965).

Barber, N.F., "Finding the Direction of Travel of Sea Waves", Nature, Vol. 174, 1954, pp. 1048-1050.

Bidde, D.D., "Wave Forces on a Circular Pile Due to Eddy Shedding", U. of California (Berkeley), Hydraulic Engineering Lab Report No. HEL 9-16, June, 1970.

Chakrabati, S.K., and R.H. Snider, Laboratory simulation of multidirectional spectra of ocean waves, Offshore Technology Conference, Preprints, Volume II, paper OTC 1691, pp. 657-668, May 1972.

Chen, H.S. and C.C. Mei, "Scattering and Radiation of Gravity Waves by an Elliptical Cylinder", MIT Parsons Laboratory Report No. 140, Aug 1971, 149 pp.

Esteva, Dinorah, and D. Lee Harris, "Comparison of Pressure and Staff Cage Records", Proceedings of the 12th Conference on Coastal Engineering, ASCE, 1970, pp. 101-116.

Galvin, C.J., "Finite-amplitude, Shallow-water Waves of Periodically Recurring Form, Proceedings of Symposium on Long Waves, Newark, Delaware, (in press), 1972.

Calvin, C.J., "Wave-Height Prediction for Wave Generators in Shallow Water", CERC T.M. No. 4, 1964.

Calvin, C.J., Seelig, W.N., "Nearshore Wave Direction from Visual Observations", EOS Abstract, AGU, Volume 52, No. 4, April 1971.

Hall, Jay V., "The Rayleigh Disk as a Wave Direction Indicator", Beach Erosion Board, T.M. No. 18, July 1950.

Hellstrom, B., and L. Rundgren, "Model Tests on Olands Sodra Grund Lighthouse", R. Inst. Tech. Stockholm, Bull. No. 39 of Inst. of Hydr., 1954, 64 pp.

Laird, A.D.K., "A Model Study of Wave Action on a Cylindrical Island", Trans American Geophysical Union, 36, 1955, pp. 279-285.

Multer, R.H., "Measuring a Directional Velocity in Water Waves with an Acoustic Flowmeter", USAE Coastal Engineering Research Center T.M. No. 31, (1970).

Oudshoorn, H.M., "The Use of Radar in Hydrodynamic Surveying", Proceedings of the 7th Coastal Engineering Conference, The Hague, Netherlands, Vol. 1, pp. 59-76, (1960).

Panicker, N.N., and L.E. Borgman, "Directional Spectra From Wave-Cage Arrays", 12th Coastal Engineering Conference, Washington, D.C., Sept. 1970, pp. 117-137, (ASCE).

Ploeg, J., "Results of a Directional Wave Recording Station", Abstracts of 13th International Conference on Coastal Engineering, Vancouver, Canada, July 1972, pp. 331-337.

Stafford, R.P., "Investigation and Procedure for Calibration of CERC Laboratory Wave Cage, FWK Model-1", CERC Laboratory Report (MFR), 27 July 1972.

Stilwell, D., Jr., "Directional Energy Spectra of the Sea from Photographs", Journal of Geophysical Research, 74, pp. 1974-1986, (1969).

Wiegel, R.L., M.F. Al-kazily, and Hooshang Raissi, "Wind Generated Wave Diffraction by a Breakwater, University of California Technical Report HEL 1-19, 130 pp., December 1971.

Zwamborn, J.A., K.S. Russell and J. Nicholson, "Coastal Engineering Measurements", Thirteenth International Conference on Coastal Engineering Abstract

CHAPTER 112

RELATIONS BETWEEN THE RUN-UP AND OVERTOPPING OF WAVES

by

Shoshichiro Nagai*

Akira Takada**

ABSTRACT

The quantitative relationships among run-up, overtopping and reflection of waves are presented in this paper. In addition, the authors have proposed several empirical relationships to calculate the height of wave run-up and the quantity of wave overtopping in the region of standing waves.

INTRODUCTION

The run-up, overtopping and reflection of waves are mutually interrelated through the medium of wave energy, and these phenomena are remarkably affected by the slope of the sea-wall, the slope of the sea bottom, the wave steepness and the water depth at the toe of the sea-wall, showing complicated variation. Studies of this kind are few up to now, and several problems have been yet unsolved.

The slope of the sea-wall has much influence on the height and wave profile of run-up, the quantity of wave overtopping and the rate of reflection of waves. In this paper, the quantitative relationships among the phenomena of run-up, overtopping and reflection of waves are shown.

In addition, several empirical relationships have been proposed to calculate the height of wave run-up and the quantity of overtopping in the region of $h_1 \geq (h_b)_p$, in which h_1 is the water depth at the toe of a sea-wall and $(h_b)_p$ is the water depth of breaking of progressive waves, as shown in Fig. 1.

The definition diagram is shown in Fig. 2. In conducting the experiments, the impermeable and smooth slope was used.

---

* Professor of Hydraulic Engineering, Faculty of Engineering
Osaka City University, Osaka, Japan

** Associate Professor, Department of Civil Engineering
Chubu Institute of Technology, Nagoya, Japan

RATE OF WAVE REFLECTION, r

When the water depth at the toe of a sea-wall is larger than the depth of breaking of incident waves, the waves impinging against the slope of the sea-wall may be classified into the two kinds of surging waves and breaking waves, depending upon the slope of the sea-wall and the wave steepness. [3),(4)]

Miche (1951) found that if the slope of the sea-wall was gentler than the critical slope, the waves in front of the sea-wall broke on the slope. The angle of the critical slope of the sea-wall, θ_c, which is related to the wave steepness in the deep water, H_0' / L_0, was given by the following Eq. (1) by Miche. [4]

$$\frac{H_0'}{L_0} = \sqrt{2\theta_c / \pi} \cdot (\sin^2\theta_c / \pi) \qquad (1)$$

According to Miche, [4] the rate of wave reflection are given by

$$\frac{r}{\zeta} = 1 \quad \text{for} \quad \theta \geqq \theta_c \qquad (2)$$

$$\frac{r}{\zeta} = \sqrt{2\theta / \pi} \cdot (\sin^2\theta / \pi) \cdot (H_0' / L_0)^{-1} \qquad (3)$$

$$\text{for} \quad \theta < \theta_c$$

in which ζ is a correcting coefficient of reflection (approximately equal to unit).

Eq. (2) and Eq. (3) have been already confirmed experimentally as shown in Fig. 3.

HEIGHT OF WAVE RUN-UP, R

It is hard to say that quantitative investigations on this problem have sufficiently been made so far. The authors have investigated the relationships between deep-water-wave steepness, H_0' / L_0 , and the slope of the sea-wall giving the highest run-up as shown in Fig. 4.

(1) For Surging Waves ($H_0' / L_0 \leqq \sqrt{2\theta / \pi} \cdot \sin^2\theta/\pi$)

The height of wave run-up, R , may be obtained by making use of both Miche's linear solution for surging waves and non-linear effect for finite amplitude standing waves as follows.

$$\frac{R}{H_0'} = K_S \left(\sqrt{\pi / 2\theta} + \delta \right) \qquad (4)$$

in which H_0' : wave height in deep water, θ : angle of inclination of a sea-wall to the horizontal plane, K_S : shoaling factor ($= H_1 / H_0'$, H_1 : wave height at the toe of a sea-wall), δ : the term representing the non-linear effect

$$\delta = \left(\eta_{(t)_{max}} - H_1 \right) / H_1 .$$

δ_S of Sainflou's equation[7] for finite amplitude standing wave is given by

$$\delta_S = \frac{1}{2} k_1 H_1 \coth k_1 h_1 \qquad (5)$$

in which h_1 : water depth at the toe of a sea-wall, $k_1 = 2\pi / L_1$, and L_1 : wave length at h_1 .

δ_{II} of the second-order solution[1] for finite amplitude standing wave is given by

$$\delta_{II} = (1/8) k_1 H_1 (3 \coth^3 k_1 h_1 + \tanh k_1 h_1) \qquad (6)$$

δ_{III} of the third-order solution[8] for finite amplitude standing wave is given by

$$\delta_{III} = \varepsilon_A^2 \cdot \delta_{II} \qquad (7)$$

in which ε_A (≤ 1) is expressed by

$$\varepsilon_A = S^{1/3} \left\{ \left(\frac{1}{2} + \sqrt{\frac{1}{4} + \frac{S}{27}} \right)^{1/3} + \left(\frac{1}{2} - \sqrt{\frac{1}{4} + \frac{S}{27}} \right)^{1/3} \right\} \qquad (8)$$

in which S is expressed by

$$S = \frac{2}{H_1^2 k_1^2 (b_{11} + b_{13} + b_{31} + b_{33})} \qquad (9)$$

in which b_{11} , b_{13} , b_{31} and b_{33} are expressed as follows.

$$b_{11} = (1/32)(3\omega^{-2} + 6\omega^{-1} - 5 + 2\omega) \quad (10)$$

$$b_{13} = (3/128)(9\omega^{-2} + 27\omega^{-1} - 15 + \omega + 2\omega^{2}) \quad (11)$$

$$b_{31} = (1/128)(-3\omega^{-2} - 18\omega^{-1} + 5) \quad (12)$$

$$b_{33} = (3/128)(9\omega^{-3} - 3\omega^{-2} + 3\omega^{-1} - 1) \quad (13)$$

in which $\omega = (\tanh k_1 h_1)^2$ (14)

δ_{IV} of the fourth-order solution[9] for finite amplitude standing wave is given by

$$\delta_{IV} = \delta_{III} + (1/6.)(k_1 H_1)^3 \varepsilon_A^4 (b_{02} + b_{22} + b_{42} + b_{04} + b_{24} + b_{44}) \quad (15)$$

in which b_{02} , b_{22} , b_{42} , b_{04} , b_{24} and b_{44} are shown as follows.

$$b_{02} = (1/512\sqrt{\omega})(-27\bar{\omega}^{2} + 288\bar{\omega}^{1} + 168 - 210\omega - 45\omega^{2} + 18\omega^{3}) \quad (16)$$

$$b_{22} = (1/512\sqrt{\omega})(-81\bar{\omega}^{4} - 54\bar{\omega}^{3} + 423\bar{\omega}^{2} - 583\bar{\omega}^{1} + 108 - 195\omega - 18\omega^{2}) \quad (17)$$

$$b_{24} = \{ 1/512 (3+\omega)\sqrt{\omega} \} (324\bar{\omega}^{3} + 2484\bar{\omega}^{2} - 1152\bar{\omega}^{1} - 2072 + 1092\omega + 420\omega^{2} - 72\omega^{3}) \quad (18)$$

$$b_{04} = (1/512\sqrt{\omega})(54\bar{\omega}^{3} + 243\bar{\omega}^{2} + 198\bar{\omega}^{1} + 6 - 198\omega + 63\omega^{2} + 18\omega^{3}) \quad (19)$$

$$b_{42} = \{ 1/512 (3+4\omega)\sqrt{\omega} \} (-81\bar{\omega}^{3} - 1053\bar{\omega}^{2} + 63\bar{\omega}^{1} - 283 + 282\omega) \quad (20)$$

$$b_{44} = \{ 1/512 (5+\omega)\sqrt{\omega} \} (405\bar{\omega}^{4} + 81\bar{\omega}^{3} + 522\bar{\omega}^{2} - 262\bar{\omega}^{1} + 1 + 21\omega) \quad (21)$$

The calculated values of the term representing the non-linear effect, δ were compared with the experimental values, as shown in Fig. 5.

In Fig. 5, δ_{III} or δ_{IV} give generally quite appropriate values in the region of standing waves, but they give slightly smaller values in the region of breaking waves on $\tan\alpha = 1/30$ or $1/10$. The reason was considered that the small amplitude wave theory was used for the calculation of K_s and there were some sprays of waves on the slopes.

On the other hand, δ_{II} gives larger values in general but gives suitable values in the region of breaking waves on the slope of the sea-bottom bottom $\tan\alpha = 1/30$ or $1/10$.

Therefore, it was decided to use δ_{II} from a point of view of the practical use.

(2) For Breaking Waves ($H_0' / L_0 > \sqrt{2\theta/\pi}\cdot\sin^2\theta/\pi$)

Hunt (1959) proposed a formula to calculate the height of wave run-up in the breaking waves region.[3]

However, in Hunt's equation, the condition near the boundary between the surging waves region and the breaking waves region are not considered as shown in Fig. 6.

Therefore the Eq.(22) was proposed for the cases when the slope of a sea-wall $\tan\theta \geqq 1/8$,

$$\frac{R}{H_0'} = K_s \left(\sqrt{\pi/2\theta_c} + \delta \right) \left(\tan\theta / \tan\theta_c \right)^{2/3} \qquad (22)$$

in which, θ_c is the angle of the gentlest slope that produces surging waves which can be calculated in Eq.(1).

Fig. 7 shows the comparisons of the experimental values with the calculated values of the height of the wave run-up, R/H_0' , indicating a fairly good agreement of the experimental values with the calculated values. The values of δ_{II} shows a considerable aplicability as shown in Fig. 8.

QUANTITY OF WAVE OVERTOPPING, Q

The phenomena of wave overtopping occur when the crown height of the sea-wall is lower than the height of the wave run-up.

As to the maximum quantity of overtopping, the relationships between the slope angle of the sea-wall and the deep-water-wave steepness were studied by experiments. Fig. 9 shows the results. According to Fig. 9, the maximum overtopping of waves occurs at the critical region between surging waves and breaking waves.

There are two methods to relate the height of wave run-up to the quantity of overtopping. One is the method which uses the profile of wave run-up,[10] and the other uses the surface elevation of wave run-up on the front of the sea-wall.[11] [12]

This study is concerned with the former, but whichever method is used, it is thought to be of practical importance to find out a response function against the incident waves.

(1) For the Vertical Wall

It was assumed that the quantity of overtopping for a constant wave period, Q, is proportional to the water volume of the run-up wave above the crown height of the sea-wall, V. From Fig. 10,

$$Q = a\ B\ V \tag{23}$$

in which a : the coefficient for quantity of overtopping, B : the width of overtopping.

If the wave profile obtained from the second-order approximation is used of finite amplitude standing wave theory without overtopping, the water quantity of overtopping can be calculated.

$$\begin{aligned} Q &= a_{II}\ B \int_0^{x_c} \{\ \eta_{II}(x) - H_c\ \}\ dx \\ &= a_{II}\ B\ [\ (\ H_1 / k_1\ )\ \sin k_1 x_c \\ &\quad + (\ H_1^2 / 16\ )\ (\ 3 \coth^3 k_1 h_1 + \tanh k_1 h_1\ )\ \sin 2 k_1 x_c \\ &\quad - H_c\ x_c\ ] \end{aligned} \tag{24}$$

in which H_c : the crown height of a sea-wall from the still water level, $\eta_{II}(x)$: the profile of wave run-up of the second-order solution of finite amplitude standing wave theory, and x_c ($< L_1/4$) can be obtained by $\eta_{II}(x) = H_c$.

$$\cos k_1 x_c = (\ 1 / 4 d\ )(\ \sqrt{H_1^2 + 8 d\ (\ d + H_c\ )}\ - H_1\ ) \tag{25}$$

in which

$$d = (\ 1 / 8\ )\ k_1 H_1^2\ (\ 3 \coth^3 k_1 h_1 + \tanh k_1 h_1\ ) \tag{26}$$

when $h_1 \geq (\ h_b\ )_s$, in which $(\ h_b\ )_s$ defines the water depth of breaking of standing waves, a_{II} is given by the following equation, which was obtained by the experiments

$$a_{II} = 9.3\ (\ H_0' / L_0\ )\left(\frac{R_{II} - H_c}{H_1}\right)^{1/2} \tag{27}$$

in which R_{II} shows the height of wave run-up of the second-order approximation of finite amplitude standing wave theory.

The quantities of overtopping obtained by the experiments were compared with the calculated ones, as shown in Fig. 11.

Fig. 11 shows that Eq.(24) may be stated to be in a fairly good agreement with the experimental values. The mean value of Q_{exp} / Q_{cal}, ($\overline{Q_{exp} / Q_{cal}}$), and the standard deviation, σ , are given by

$$\overline{\left(Q_{exp} / Q_{cal} \right)} = 0.98$$

and

$$\sigma = \sqrt{\frac{1}{N} \sum_{i=1}^{N} \left\{ \frac{Q_{exp}}{Q_{cal}} - \left(\frac{Q_{exp}}{Q_{cal}} \right) \right\}^2} = 0.28 \tag{28}$$

When $h_1 = (h_b)_p \sim (h_b)_s$ and $\tan \alpha = 1/10$, in which $(h_b)_p$ denotes the water depth of breaking of progressive wave and $\tan \alpha$ is the slope, a_{II} is given by

$$a_{II} = 5.5 \left[h_1 / (h_b)_s \right]^{2/3} (H_0' / L_0) \left(\frac{R_{II} - H_c}{H_1} \right)^{1/2} \tag{29}$$

Values of $\overline{\left(Q_{exp} / Q_{cal} \right)}$ and σ for Eq.(29) are given by

$$\overline{\left(Q_{exp} / Q_{cal} \right)} = 1.10$$

and

$$\sigma = 0.40 \tag{30}$$

Further investigations are needed to get higher accuracy.

(2) For the Sloping Wall

If the wave profile running up on the slope of the sea-wall in the case of non-overtopping of waves can be approximated by a trapezoid, as shown in Fig. 12. The quantity of overtopping is obtained by the following equation.

$$\begin{aligned} Q &= a_\theta B V \\ &= (a_\theta)_{II} B \left[\frac{(1 + \cot^2 \theta)(R_{II} - H_c)^2}{2 (\cot \gamma - \cot \theta)} \right. \\ &\quad \left. + 0.15 H_1 (R_{II} - H_c) \right] \end{aligned} \tag{31}$$

in which $(a_\theta)_{II}$ denotes the coefficient for quantity of overtopping, γ is an angle at the edge of the profile of run-up wave. cot γ is given by the following equations, obtained by the experiments,

when $\cot \theta \geq 1$,

$$\cot \gamma = 67 (H_1 / L_1) (\cot \theta)^{1.6} \tag{32}$$

when $\cot \theta = 0 \sim 1$,

$$\cot \gamma = \left\{ n + \frac{n (n - 1)}{2} \cot^2 \theta \right\}^{1/2} \cot \theta \tag{33}$$

in which

$$n = -3.224 \log_{10} \left\{ \frac{1}{1 + (67 H_1 / L_1)^2} \right\} \tag{34}$$

Fig. 13 shows that the comparison between the experimental and calculated values may be stated to be in a fairly good agreement.

When $h_1 \geq (h_b)_s$, $(a_\theta)_{II}$ is given by the following equation obtained by the experiments.

$$(a_\theta)_{II} = 7.6 (\cot\theta)^{0.73} (H_0' / L_0)^{0.83} \tag{35}$$

Fig. 14 shows that the comparison between the experimental and calculated values may be stated to be in a fairly good agreement.

Values of $\overline{(Q_{exp} / Q_{cal})}$ and σ calculated by Eq.(35) are

$$\overline{(Q_{exp} / Q_{cal})} = 1.00$$

and (36)

$$\sigma = 0.35$$

When $h_1 = (h_b)_p \sim (h_b)_s$ and $\tan\alpha = 1/10$, $(a_\theta)_{II}$ is given by the following equation.

$$\log_{10}(a_\theta)_{II} = \log_{10} 6.6 + 1.8 \log_{10}\{h_1 / (h_b)_s\} + 2\left\{\frac{(h_b)_s - h_1}{(h_b)_s - (h_b)_p}\right\} \log_{10}\left(\frac{R_{II} - H_c}{H_1}\right) + 0.73 \log_{10}\cot\theta + 0.83 \log_{10} H_0' / L_0 \tag{37}$$

Values of $\overline{(Q_{exp} / Q_{cal})}$ and σ calculated by Eq.(37) are

$$\overline{(Q_{exp} / Q_{cal})} = 1.00$$

and (38)

$$\sigma = 0.51$$

Further experiments are needed to get higher accuracy.

CONCLUSIONS

In the previous studies, the run-up, overtopping and reflection of waves were studied as an independent phenomenon, and their interrelationships have never been discussed adequately.

In this paper, the calculation formulae were proposed for the height of wave run-up and the quantity of overtopping, and proved to give fairly good values to the experimental values.

Furthermore, relationships between the height of wave run-up, quantity of overtopping and the rate of reflection of waves were investigated by experiments. Their correlations were presented in details, and summarized in Fig. 15.

It is clear in Fig. 15 that the slope which produces the highest run-up of waves is nearly in agreement with not only the slope which produces the maximum overtopping, but also the gentlest slope that produces the total reflection. In other words, the highest run-up of waves and the maximum overtopping of waves arise generally in the critical region between surging waves and breaking waves. The equation for the critical condition is generally shown in Eq. (1) for the region of standing waves.

REFERENCES

(1) Miche, M. : Mouvements ondulatoires de la mer en profondeur constane ou décrissante. (I ∿ IV), Annales des Ponts et Chaussées, Vol.121, pp. 25 ∿ 78, 131 ∿ 164, 270 ∿ 292, 369 ∿ 406, 1944.

(2) Kishi, T. : Researches on sea-walls (2) - On the shallow clapotis of finite amplitude -, The Public Work Research Institute, Ministry of Construction, Vol. 90, pp. 27 ∿ 54, March, 1955, (in Japanese).

(3) Hunt, I. A. : Design of sea-walls and breakwaters, Proc., ASCE, Vol. 85, No. WW3, Sep., 1959.

(4) Miche, M. : Le pouvoir reflechissant des ouvrages maritimes, Annales des Ponts et Chaussées, May-June, 1951.

(5) Murota, A : Experimental researches on reflection of roughness slopes, Proc., 14th Conf. on Coastal Engineering in Japan, pp. 45 ∿ 48, Oct., 1967, (in Japanese).

(6) Le Méhauté, B., Koh, R. C. Y. and Hwang, Li-San : A synthesis on wave run-up, Proc., ASCE, Vol. 94, No. WW1, Feb., 1968.

(7) Sainflou, G. : Essai sur les disques maritimes verticales, Annales des Ponts et Chaussées, Vol. 98, No. 4, 1928.

(8) Tadjbakhsh, I. and Keller : Standing surface waves of finite amplitude, Journal of Fluid Mechanics, Vol. 8, pp. 442 ∿ 451, 1960.

(9) Goda, Y. : The Fourth order approximation to the pressure of standing waves, Coastal Engineering in Japan, Vol. 10, pp. 1 ∿ 11, Vol. 11, 1967, (Errata, Coastal Engineering in Japan, Vol. 11, pp. 197, 1968)

(10) Takada, A. : On relations among wave run-up, overtopping and reflection, Proc., The Japan Society of Civil Engineers, No. 182, pp. 18 ∿ 30, Oct., 1970.

(11) Shiigai, H. and Kono, T : Analytical approach on wave overtopping on levees, Proc., The 12th Coastal Engineering Conference, Vol. 1, pp. 563 ∿ 573, Sep., 1970.

(12) Takada, A. : Wave overtopping quantity correlated to the surface elevation of finite amplitude clapotis, Proc., The Japan Society of Civil Engineers, No. 201, pp 61 ∿ 76, May, 1972, (in Japanese).

(13) Hamada, T. : Secondary interaction of surface waves, Report of Port and Harbour Research Institute, Ministry of Transport, Japan, No. 10, 1965.

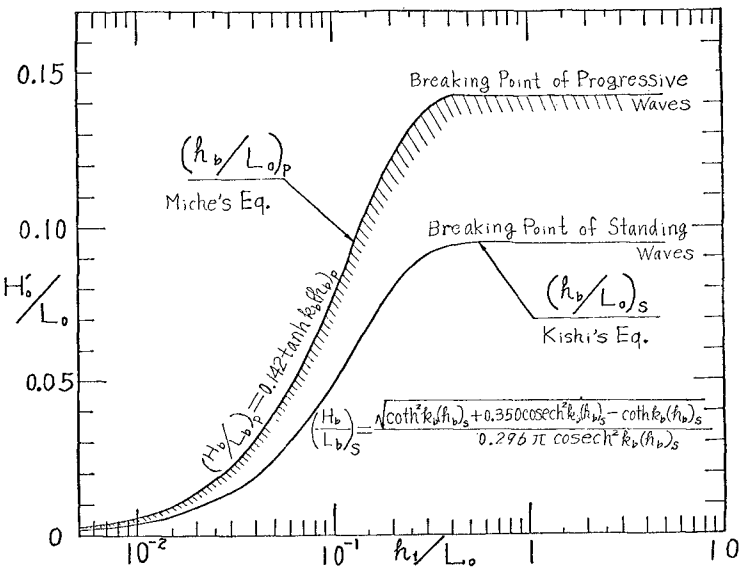

Fig. 1. Breaking point of progressive waves and standing waves (Applicable region in this paper)

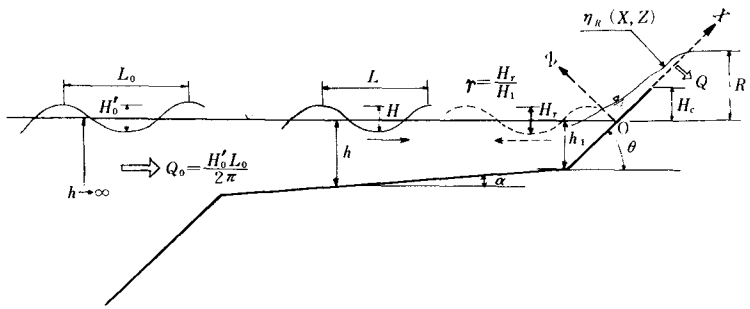

Fig. 2. The definition diagram in this paper

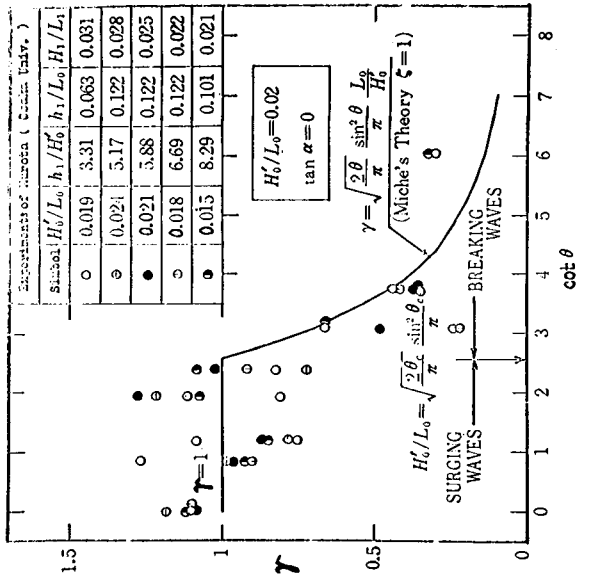

Fig. 3. Comparison between theoretical and experimental values of the rate of reflection

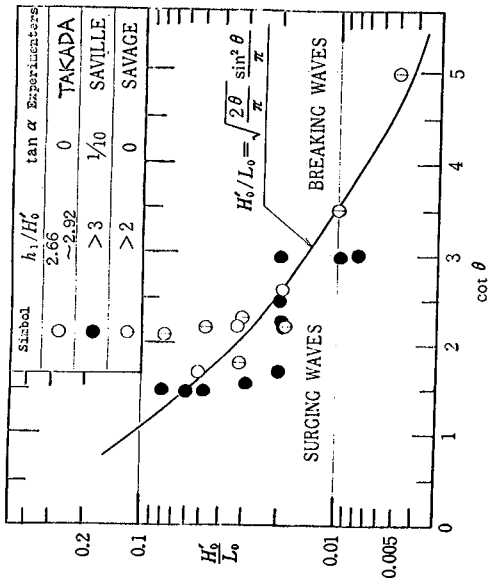

Fig. 4. Condition generating the maximum height of wave run-up, R_{max}
(Relations between cot θ and H_0'/L_0)

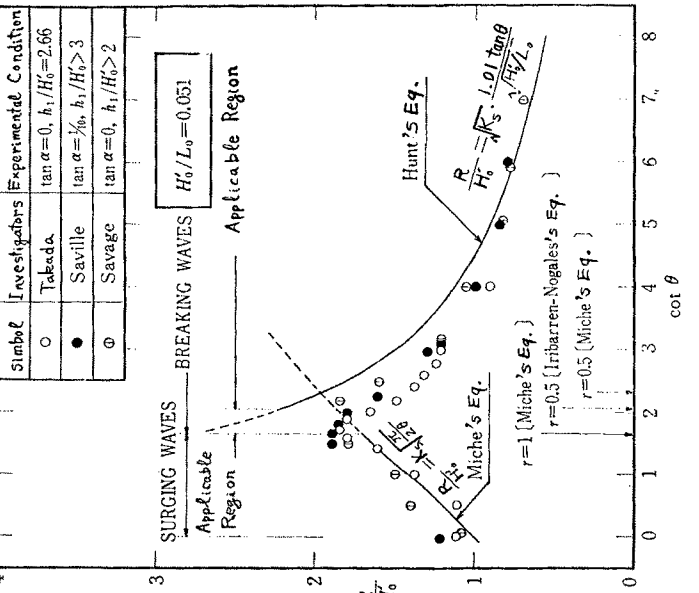

Fig. 6. Miche's equation and Hunt's equation of wave run-up R / H0' (Comparison between calculated and experimental values)

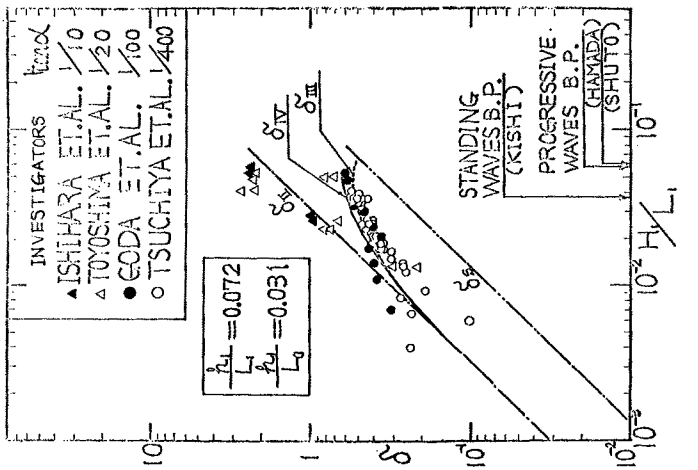

Fig. 5. Comparison between theoretical and experimental values of the term representing the non-linear effect, δ

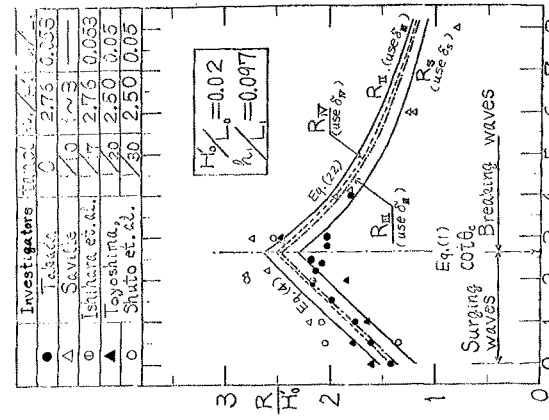

Fig. 7. Comparison between calculated and experimental values of the height of run-up, R / H_0'

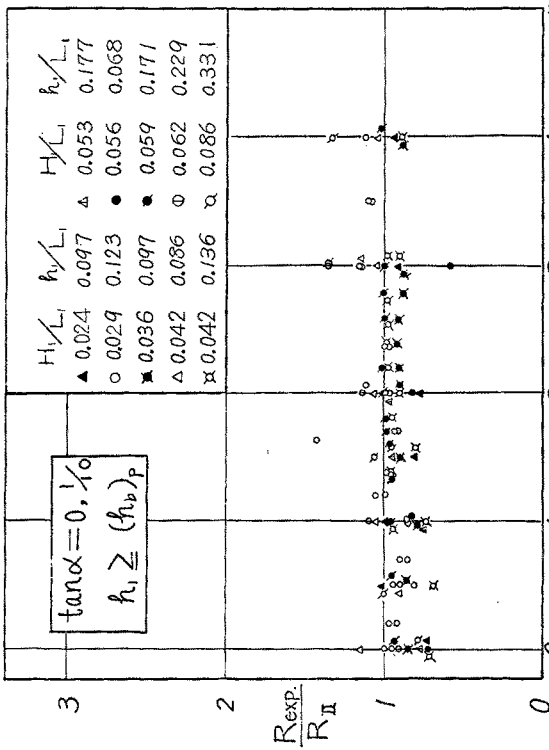

Fig. 8. Comparison between calculated values using δ_{II} and experimental values of the height of wave run-up, R

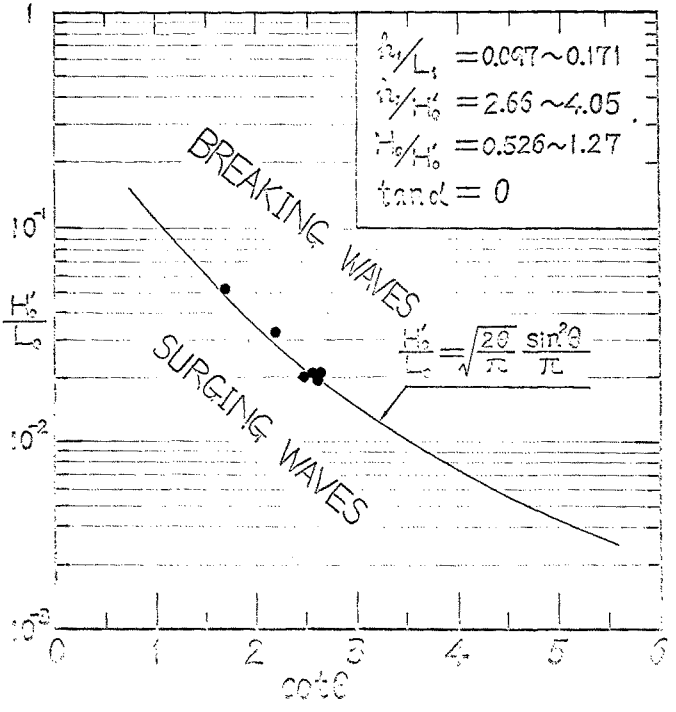

Fig. 9. Condition generating maximum quantity of wave overtopping, Q_{max}
(Relations between cot θ and H_0' / L_0)

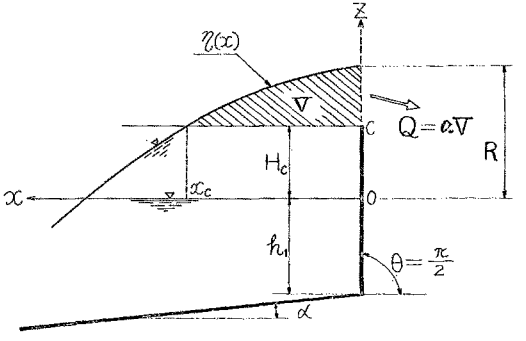

Fig. 10. Relations between a profile of run-up wave and the quantity of wave overtopping for vertical wall

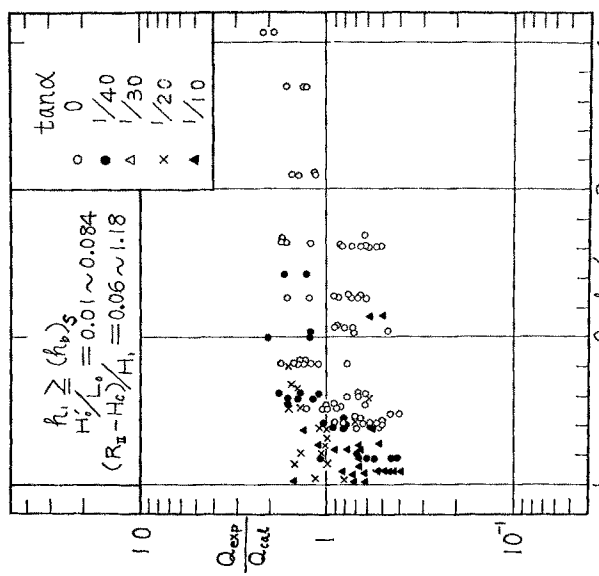

Fig. 11. Comparison between calculated and experimental values of quantity of wave overtopping for $h_1 \geqq (h_b)_s$

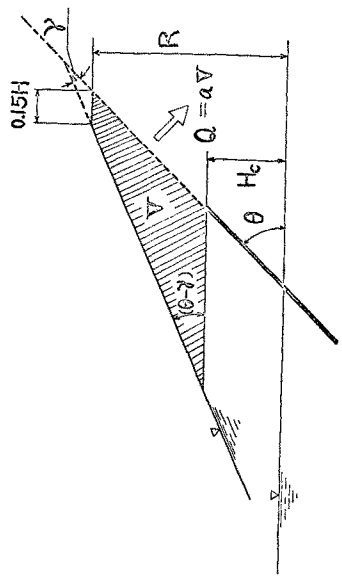

Fig. 12. Relations between wave profile of run-up and quantity of wave overtopping for sloping wall

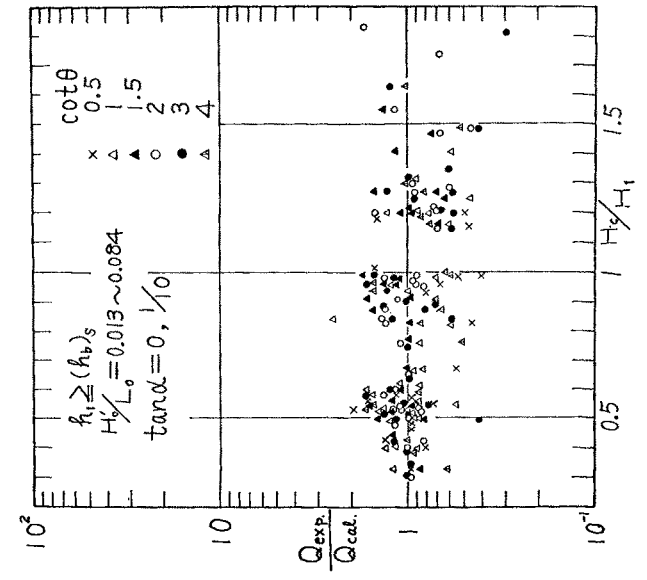

Fig. 14. Comparison between calculated and experimental values of quantity of wave overtopping for $h_1 \geqq (h_b)_s$

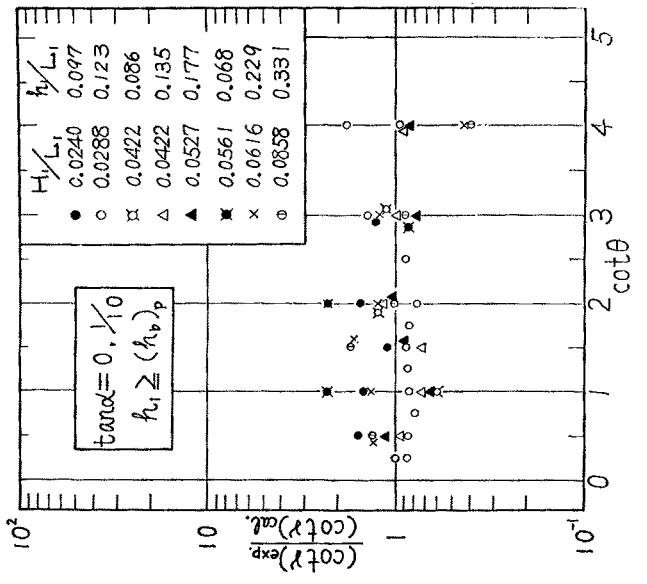

Fig. 13. Comparison between calculated and experimental values of an angle at the edge of the profile of wave run-up, cot γ

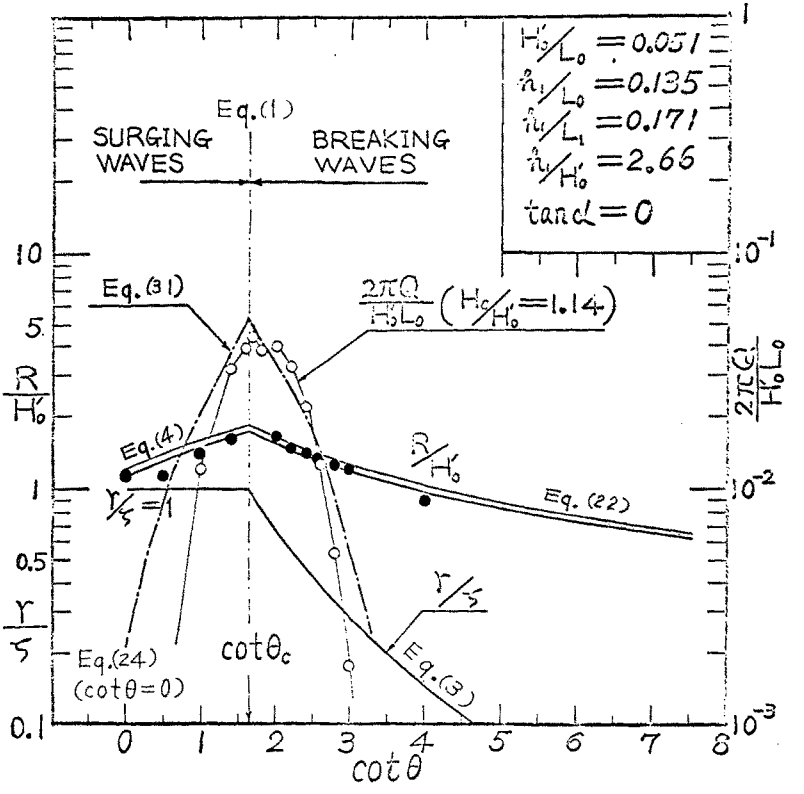

Fig. 15. Correlation characteristics among run-up, overtopping and reflection of waves

CHAPTER 113

SET-UP DUE TO IRREGULAR WAVES

J.A. Battjes
Dept. of Civil Engineering
Delft University of Technology
Delft, Netherlands

ABSTRACT

Energy losses in breaking irregular waves are estimated on the assumption that a wave, while breaking, loses only that portion of its height which would be in excess of the breaker height for the given wave period and the mean local depth. This leads to expressions for the magnitude of the radiation stresses as a function of the distance offshore. From this the variations in mean water level and the longshore current velocity are calculated with existing methods. Laboratory measurements of set-up in two-dimensional irregular waves are described. The data appear to some extent to be internally inconsistent; this may be due to enclosed air bubbles.

1 INTRODUCTION

The water motion in and near the surf zone is of prime importance in many coastal engineering problems. Theoretical studies of its dynamics have been made mainly since the last world war. However, it is only since the introduction of the concept of radiation stress that a satisfactory formulation has been obtained. This had led to quantitative predictions concerning the change in mean water level, and the generation of longshore currents, due to regular waves. For application to natural waves these results should be extended so as to include the wind-wave variability. A description of the wave field in terms of a linear spectral model is not suitable in the surf zone because of the strong nonlinearities. In the following a semi-theoretical approach is used which deals with average properties of individual waves in the space-time domain. Only quasi-two-dimensional situations are considered, i.e. straight, parallel depth contours and average flow parameters which do not vary in the longshore direction. The symbols are defined in Appendix 2.

2 REVIEW OF ESTABLISHED RESULTS

2.1. Radiation stress

Consider a situation in which it is possible to define a mean motion and a superimposed relatively rapidly fluctuating motion. The momentum balance for the mean motion then contains terms representing average momentum transfer caused by the fluctuations. These are equivalent to stresses. They are called Reynolds stresses in the case of turbulence.

When the fluctuating velocity field is due to waves they are called radiation stresses, following Longuet-Higgins and Stewart (1960), who formally introduced the concept. (It was developed independently by Dorrestein (1961) for the calculation of wave set-up, and by Lundgren (1963), who called it "wave thrust".) The term radiation stress actually refers to the contribution of the waves to the time average of the vertically integrated horizontal flux of horizontal momentum. In contrast to the Reynolds stresses in turbulence, the radiation stresses can be readily calculated in terms of external flow (wave) parameters. The principal radiation stresses in long-crested, progressive sinusoidal waves are proportional to the mean energy density E, with coefficients of proportionality which are functions of the depth-wavelength ratio only:

$$S_{11} = (2n - \tfrac{1}{2})\, E \qquad (1)$$

$$S_{22} = (n - \tfrac{1}{2})\, E \qquad (2)$$

in which

$$n = \tfrac{1}{2} + Kd/\sinh 2Kd \qquad (3)$$

The gradients of the radiation stresses appear as driving forces in the momentum equations for the mean motion. The complete equations can be found elsewhere (Bowen, 1969) and will not be reproduced here.

2.2. Set-up and longshore currents due to regular waves.

Several effects of the waves on the mean motion can be calculated by means of the concept of radiation stress, provided it is possible to estimate the wave parameters. This is most difficult for the wave energy. For regular waves useful results have been obtained on the supposition that energy losses can be neglected outside the surf zone, and by assuming that in the surf zone the wave height decays in a constant proportion to the local mean depth (Longuet-Higgins and Stewart, 1963; Bowen et al, 1968):

$$H(x) = \gamma \{h(x) + \bar{\zeta}(x)\} = \gamma d(x) \qquad (4)$$

Set-up. The differential equation for the set-up $\bar{\zeta}$ due to waves of perpendicular incidence reads

$$\frac{d\bar{\zeta}}{dx} = -\frac{1}{\rho g(h+\bar{\zeta})} \frac{dS_{11}}{dx} . \qquad (5)$$

Integration of this equation, with S_{11} calculated on the basis of the assumed wave height variation described above, leads to a predicted set-down of the mean water level outside the surf zone, and a set-up shoreward of the breakerline, as indicated schematically in Fig. 1. The theoretical predictions have been verified experimentally (Bowen et al, 1968). The coefficient γ is a function of the incident wave steepness and the beach slope.

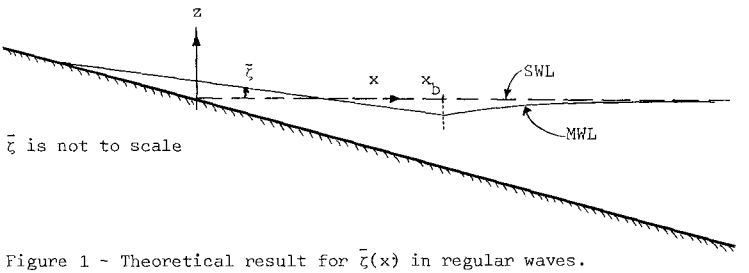

Figure 1 - Theoretical result for $\bar{\zeta}(x)$ in regular waves.

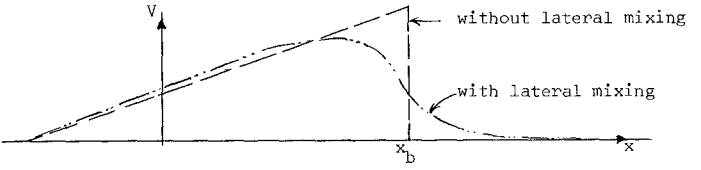

Figure 2 - Theoretical result for V(x) due to regular waves.

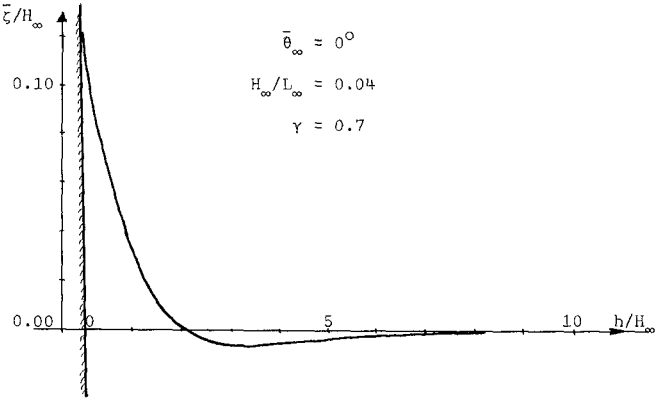

Figure 3 - Calculated set-up in irregular waves.

Longshore current velocities. (Bowen, 1969; Thornton, 1969; Longuet-Higgins, 1970). Obliquely incident waves exert a longshore thrust on the water mass in the surf zone, driving the longshore current. The net driving force per unit horizontal area has been shown to be proportional to the local rate of energy dissipation per unit area. It changes discontinuously from zero outside the breakerzone to a maximum immediately shoreward of the breakerline, due to the assumed wave height variation. In steady uniform flow this driving force is balanced by bottom friction and lateral friction due to molecular or turbulent viscosity. These should be expressed in terms of wave parameters and the longshore current velocity in order to calculate the distribution of the latter in the direction perpendicular to the shore. The computed velocity profile is discontinuous at the breakerline if lateral turbulent momentum exchange is neglected. Inclusion of some form of lateral mixing smoothes the velocity profile, but does not alter it drastically in the surf zone on gently sloping beaches, except of course near the breakerline (Fig. 2).

2.3. Discussion.

In the theories referred to in the preceding paragraph the variation of mean wave energy density with distance offshore plays a predominant role. For regular waves useful approximations were obtained by distinguishing two regions with different regimes, separated by a well-defined breakerline with fixed position. However, this method fails for irregular waves because no point can be defined inshore of which all the waves are breaking while offshore from it no waves would break. Instead, at each point only a certain percentage of the waves passing it are breaking or broken, while this percentage in general varies gradually with distance offshore. Associated herewith is a gradual variation of average values of other wave parameters, such as energy density, energy flux, momentum flux, etc. The problem is how these can be estimated in terms of the characteristics of the incident irregular waves. The attempt to find a solution to this problem includes the choice of a mathematical model for the description of irregular waves. Two such models are in general use: the linear spectral model on the one hand and the wave-by-wave description on the other. The former operates in the frequency domain, and is suitable for relatively low waves. The latter operates in the space-time domain and utilizes theoretical and empirical probability distributions characterizing individual waves. The applicability of this method is not restricted to low waves. For this reason it can be used with advantage in situations where nonlinearities are important. The procedure then is to use relationships for periodic nonlinear waves as a basis for the calculation of the corresponding probabilities in irregular waves. This approach has been applied to calculate distributions of wave forces on piles (Borgman, 1965; Pierson and Holmes, 1965), of run-up on slopes (Saville, 1962; Battjes, 1971) and of breakers on a beach (Collins, 1970). Although this method can make no claim to rigor, it is probably more rational for the present problem than the linear spectral model because of the essential role of wave breaking, which is a highly nonlinear phenomenon occurring to individual waves (crests) in physical space, and not to individual spectral components. For this reason it was decided to utilize the wave-by-wave description of the irregular waves. The adaptation of this method which was used is described in the following paragraph.

3 ENERGY LOSSES IN BREAKING IRREGULAR WAVES

An application of the wave-by-wave description to the problem of irregular breaking waves has been given by Collins (1970). Energy losses are incorporated in the model by assuming that the height of a wave after initial breaking decays in constant proportion to the mean local depth. Two different breaking criteria are used. They are taken from theoretical and experimental results for regular waves; their validity is restricted to shallow-water conditions.

The model used herein is based on a breaking criterion which should be approximately valid in shallow water as well as in deep water, while the decay of the wave height after breaking is assumed to be such that a height is maintained equal to the local breaker height. In other words, only the energy corresponding to the height in excess of the local breaker height is assumed to be dissipated. It is expected that this a more realistic model for the waves which break in not-very-shallow water than that used by Collins.

The breaking criterion for regular waves which has been adopted for use is based on Miche's formula for the limiting steepness of stable periodic waves in water of constant depth:

$$\left(\frac{H}{L}\right)_{max} = 0.14 \tanh \frac{2\pi d}{L} , \tag{6}$$

which in shallow water approximates to

$$\left(\frac{H}{d}\right)_{max} = 0.28\pi \approx 0.88 \tag{7}$$

Since we are here dealing with deforming waves in water of variable depth, Miche's formula cannot be expected to apply. It is known empirically that the H/d ratio for waves breaking on a beach in shallow water varies mildly with the initial wave steepness and the beach slope. (It ranges approximately between 0.6 and 1.2.) In view of this the following breaking criterion was chosen:

$$\frac{H_b}{L} = 0.14 \tanh \left(\frac{\gamma}{0.88} \frac{2\pi d}{L}\right) \tag{8}$$

which in shallow water approximates to

$$H_b = \gamma d \tag{9}$$

The value of γ varies with beach slope and, to a smaller extent, with the steepness of the incident waves. In applications to irregular waves it will be treated as a constant for given beachslope and mean wave steepness. The wavelength L in Eq. 8 is calculated from the wave period T and the mean water depth d by means of the classical formula for sinusoidal gravity waves in water of constant depth. Eq. 8 then defines a breaker height H_b for any given depth and wave period. The effects of period variability on H_b are not considered in the following; if necessary they can be taken into account numerically without changing the essence of the approach.

For calculating the mean energy density at some point it is assumed that those wave heights which in absence of wave breaking would exceed H_b are reduced by breaking to the value H_b. Let the (fictituous) wave heights $\tilde{H}$ in absence of breaking be Rayleigh-distributed with rms value H_o. For given incident waves, H_o can be calculated at any point with existing methods, taking shoaling, refraction and bottom friction into account. The fictituous wave height distribution would then be known, and given by

$$\begin{aligned} \tilde{F}(h) = Pr(\tilde{H} \leq h) &= 0 && \text{for } h < 0 \\ &= 1 - \exp(-h^2/H_o^2) && \text{for } h \geq 0 \end{aligned} \tag{10}$$

where

$$H_o^2 = E\{\tilde{H}^2\} \tag{11}$$

This distribution will be clipped at $h = H_b$ in order to obtain an approximation of the actual wave height distribution:

$$\begin{aligned} F(h) = Pr(H \leq h) &= 0 && \text{for } h < 0 \\ &= 1 - \exp(-h^2/H_o^2) && \text{for } 0 \leq h \leq H_b \\ &= 1 && \text{for } h > H_b \end{aligned} \tag{12}$$

The mean square value of H, which is approximately proportional to the mean wave energy density, can be calculated from this distribution function using the definition

$$H_{rms}^2 = E\{H^2\} = \int_{-\infty}^{\infty} h^2 \, dF(h) \tag{13}$$

which gives

$$H_{rms}^2 = \tilde{F}(H_b) \, H_o^2 \tag{14}$$

or

$$H_{rms}^2 = (1-\tilde{Q}_b) \, H_o^2 \, , \tag{15}$$

in which

$$\tilde{Q}_b = 1 - \tilde{F}(H_b) = Pr(\tilde{H} > H_b) = \exp(-H_b^2/H_o^2) \tag{16}$$

is the fraction of the waves that break at the point with breakerheight H_b. From a comparison of Eq. 11 and Eq. 15 it follows that clipping the upper fraction $\tilde{Q}_b$ of the fictituous wave height distribution gives a relative reduction of mean square value equal to $\tilde{Q}_b$. Only the Rayleigh distribution has this property.

It can happen that in very shallow water $H_b^2/H_o^2 << 1$. In that case Eq. 14, upon substitution of Eq. 10, reduces approximately to

$$H_{rms}^2 = H_b^2 \tag{17}$$

It may be seen that H_{rms} in this limiting case equals the value which it would have for regular waves with height H_b. This is to be expected because the approximation involved in effect consists of considering almost all the wave heights to be equal to H_b, while neglecting the contributions to $E\{H^2\}$ from wave heights less than H_b. Note that the condition $H_b^2/H_o^2 << 1$ may not be fulfilled anywhere if gradual energy dissipation by processes other than breaking is important, as can happen on very gentle slopes.

The condition $H_b^2/H_o^2 << 1$ usually implies $d/L << 1$, in which case Eq. 9 is a valid approximation of Eq. 8. With this substitution Eq. 17 becomes

$$H_{rms}^2 = \gamma^2 d^2 , \tag{18}$$

so that the energy variation in irregular breaking waves according to this model approaches that which is usually assumed for regular waves (Eq. 4) as the relative water depth decreases.

Regarding the validity of the approximations given above, it should be remembered that only the final result (H_{rms}) is used in the subsequent calculations of the radiation stresses and their effects on the mean motion. The actual wave height distribution in the surf zone is undoubtedly smoother than the clipped distribution given by Eq. 12, which at $h=H_b$ increases discontinuously from $1-\hat{Q}_b$ to 1. However, with a suitable choice of γ the actual cumulative probability of the wave heights may be overestimated for $h < H_b$ and underestimated for $h > H_b$, which should result in relatively smaller errors in the calculated mean square wave height than in the probability function.

4. CALCULATED SET-UP AND LONGSHORE CURRENT VELOCITIES

The expressions for H_{rms} obtained in the preceding paragraph have been used in calculations of set-down and set-up and of longshore current velocities. Some results will be geven here, with omission of computational details.

The radiation stresses were calculated from Eqs. 1, 2, and 3, where E was taken equal to $\rho g H_{rms}^2/8$, and n was determined from the mean wave period and the local depth. Energy dissipation by bottom friction was neglected. Thus, only shoaling and, where applicable, refraction have been taken into account in the determination of the fictituous rms wave height H_o. The waves were assumed to have a rather narrow distribution of energy with respect to frequency and direction.

Set-up. Eq. 5 for the set-up of waves with perpendicular incidence was integrated numerically for $\gamma = 0.7$ and an incident wave steepness $H_\infty/L_\infty = 0.04$, where H_∞ is the rms wave height in deep water, and L_∞ the deep water wavelength calculated from the mean wave period. The resulting set-down and set-up given in Fig. 3. The vertical scale is exaggerated.

Longshore current velocity. The formulation given by Thornton (1969) and Longuet-Higgins (1970) was used as a basis for the calculation of the longshore current velocity profile. The same linearization of the longshore bottom shear component was employed. However, no shallow-water approximations were used. Lateral momentum exchange due to turbulence was neglected. Some results are given in Fig. 4, in which the normalized local mean longshore current velocity is plotted against the relative depth, with the mean angle of incidence at deep water as a parameter. The normalizing factor is proportional to the ratio between the mean depth gradient and the bottom friction factor c_f ($= \tau_B/\rho u_B^2$), and to the rms orbital velocity in deep water. The calculated normalized velocity reaches its greatest value for an angle of incidende near 60°. The current is confined to a rather narrow zone for very oblique incidence, due to the pronounced effects of refraction which then occur.

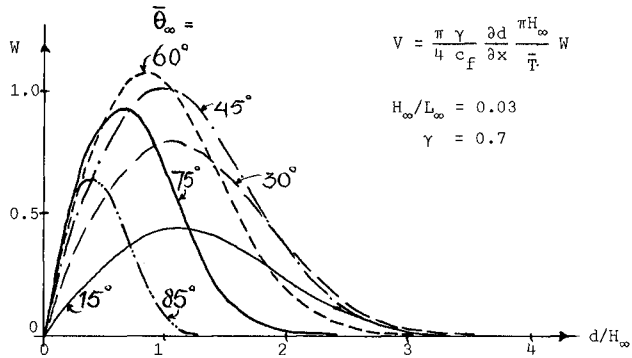

Figure 4 - Calculated longshore current velocities due to irregular waves.

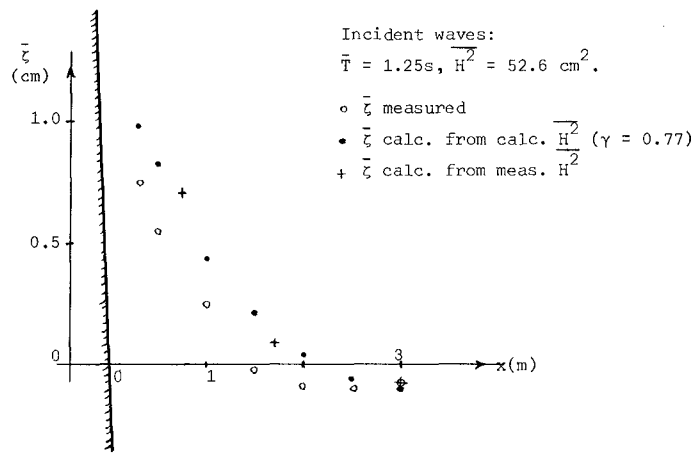

Figure 5 - Measured and calculated set-up.

It should be noted that in the figures 3 and 4 the independent wave parameters are characteristics of the incident waves in deep water. This is in contrast with known formulas for the longshore current velocity due to regular waves, most of which are expressed in terms of wave characteristics at breaking.

It has already been mentioned that the effects of variability of wave period and direction were not taken into account in the preceding calculations. It has been shown elsewhere (Battjes, 1972) that in particular the angular distribution, if not narrow, can strongly affect the radiation shear stress, which provides the driving force for the longshore current. Treating deep-water wind-driven waves (as opposed to swell) as if they were long-crested would result in overestimating the total longshore thrust by more than 100%. This effect should therefore be accounted for if longshore currents are to be calculated from deep-water waves with a rather broad angular spreading of the energy.

5. LABORATORY MEASUREMENTS

A few measurements were carried out in a wave flume of the Delft Hydraulics Laboratory in order to check the validity of the approach outlined in the paragraphs 3 and 4. The results are briefly described in this paragraph. They will be more fully reported in a forthcoming publication, after the completion of additional tests.

5.1. Experimental arrangement

The wave flume is 100 m long and 2 m wide; the water in the constant depth portion of the flume was about 0.55 m deep. A hydraulically driven wave board capable of generating irregular waves is located at one end of the flume. At the other end a 1:20 staight plywood slope was installed. For measurements of the change in mean water level, particularly the set-up, 7 pressure taps (I.D. 4 mm) were provided, flush with the slope. The taps were connected by plastic tubes to a 15 cm I.D. vertical cylindrical well, where a vibrating-point gauge sensed the water surface elevation to an accuracy of approximately 0.1 mm. The amplified signals were recorded on paper. The water level was adjusted in such a manner that the pressure taps, including the uppermost one, would be submerged all the time during a run, or very nearly so, so that a valid reading of the mean water level could be obtained.

Four resistance type wave gauges were installed. The gauges in a mean depth less than 20 cm were inserted through the plywood slope in order to maintain the minimum submergence necessary for a linear gauge response. As a consequence of this arrangement these gauges could not easily be moved. The signal from each gauge was fed into analog equipment for the on-line determination of wave height histograms (based on 1000 wave heights between zero-crossings) and power spectra. The signals could also be recorded.

A rms incident wave height of 7 cm to 8 cm was used in all runs. It was kept more or less constant so that the pressure taps and the shallow-water wave gauges would be in the zone of breaking without being moved between runs. The mean wave period was approximately 1.2s and 2.0s. The width of the energy spectrum of the waves was varied as much as possible with the available equipment.

5.2. Experimental results

It appeared from the measurements that the applied variation of the width of the energy spectrum hardly affected the wave energy decay and the set-up. Its influence will not be further discussed.

Wave height. A comparison of measured and calculated mean square wave heights is given in table 1. The values of γ on which the calculations were based are also given in the table; they were chosen so as to optimize the overall agreement between measured and computed values. It may be seen that γ for the longer (less steep) waves is greater than that for the shorter (steeper) waves.

wave gauge no.	mean depth d (cm)	$\bar{T}$=1.25s; γ = 0.77				$\bar{T}$=2.0s; γ = 0.88			
		$\overline{H^2}$ (cm^2)				$\overline{H^2}$ (cm^2)			
		meas	calc	meas	calc	meas	calc	meas	calc
1	55	52.6 →	52.6	56.1 →	56.1	52.7 →	52.7	63.7 →	63.7
2	36	-	51.0	46.5	55.0	-	58.2	58.8	69.4
3	16	47.4	50.2	47.8	51.9	70.8	71.3	77.9	80.7
4	8.8	32.6	29.5	36.3	31.2	42.6	45.0	48.8	45.4
5	5.1	12.5	11.5	-	11.6	20.3	18.7	-	19.0

Table 1

This is in agreement with what is known for regular waves. Inspection of table 1 shows that the variation of $\overline{H^2}$ with distance offshore is satisfatorily described by Eqs. 15 and 16.

Set-up. An example of measured and computed set-up is given in Fig. 5. (The set-up curves which are not shown are essentially the same as those in fig. 5, and will not be presented individually). The set-up was calculated on the basis of Eq. 5 and the assumptions outlined in the paragraphs 3 and 4. Its value was taken to be zero at the toe of the slope. The set-up (set-down) appears to be fairly well predicted by the theory at $x \approx 3$ m ($h \approx 15$ cm), which is the most seaward measuring point, where only a small fraction of the waves is breaking. However, shoreward of this point, from $x \approx 3$ m to $x \approx 1.5$ m, the computed and measured values diverge, the computed values showing a rise towards the shore which is almost absent in the measurements. The maximum difference is about 2.5 mm. Shoreward of $x \approx 1$ m ($h \approx 5$ cm) both sets of points follow very nearly the same trend.

The discussion of the results described above naturally centers on the area of strongest disagreement between theory and measurements. If the disagreement were used as an argument to reject the theory then the question arises: which parts of the theory? It was found to describe the rms wave height variation fairly well. In order to eliminate any uncertainties which nevertheless might be present in the theoretically calculated wave heights, the set-up between three wave gauges was computed using measured rather than calculated wave heights. The result is given in Fig. 5. As expected, the disagreement has hardly diminished. The conclusion is that the measurements are in error, and/or that the theory used in relating

wave characteristics and set-up is in error, particularly Eq. 5. The latter possibility is regarded as very unlikely because Eq. 5 has been confirmed in previous tests with regular waves (Bowen et al, 1968). The wave height measurements in the present tests are considered reliable, due to frequent calibrations, which moreover showed good linearity and no measurable drift. Another possibility might be that the set-up measurements are in error. The recording system of the water level variation inside the stilling wells was frequently calibrated and is not suspect. Air bubbles were sometimes present in the tubes connecting the wells to the pressure taps; this was concluded from the recorded signals which in those cases did not go back to the original still water value after a run. All such measurements were discarded and the air bubbles removed. Thus it is believed that the recordings of the vibrating-point gauges give a good measure of the change in the mean static head at the location of the pressure taps due to the waves. It has been shown by Dorrestein (1961) for water of constant density that this change is equal to the change in mean depth if the waves are statistically stationary in time and in the horizontal coordinates. The latter condition is not exactly met in the present tests but an analysis such as given by Dorrestein shows that errors arising from horizontal inhomogeneities cannot account for the observed discrepancy. Lacking further information, it is believed that the inconsistencies may have originated in the neglect of air entrapment during breaking. Air content with concentration C would cause a systematic underestimation of the true mean water level by an amount approximately given by

$$\Delta = \int_0^d \overline{C(z)}dz$$

The concentration $\overline{C}$ varies with the intensity and the frequency of breaking. The difference Δ should be almost zero in relatively deep water where breaking occurs very infrequently, and increase in the shoreward direction as more and more waves are breaking. In very shallow water it may diminish again with the decreasing depth d. The air concentration which would be necessary to account for the observed discrepancies is of the order of a few percent, averaged over the depth and the time. This does not appear to be impossible. However, without additional supporting data the explanation given above should be considered as purely conjectural. It is planned to carry out additional tests from which perhaps more definitive conclusions can be drawn.

APPENDIX 1 - REFERENCES

Battjes, J.A., "Run-up distributions of waves breaking on slopes", Journal of the Waterways, Harbors and Coastal Engineering Division, ASCE, 97, Feb. 1971, pp. 91-114.

Battjes, J.A., "Radiation stresses in short-crested waves", J. of Mar.Res. 30, 1, Jan. 1972, pp. 56-64.

Borgman, L.E., "The statistical distribution of ocean wave forces on vertical piling", Techn.Mem. No. 13, U.S. Army Coastal Eng. Res. Center, July 1965, 31 pp.

Bowen, A.J., Inman, D.L., and Simmons, V.P., "Wave 'set-down' and set-up", J. of Geoph. res., 73, 8, 1968, pp. 2569-2577.

Bowen, A.J., "The generation of longshore currents on a plane beach", J. of Marine Res., 27, 2, 1969, pp. 206-215.

Collins, J.I., "Probabilities of breaking wave characteristics", Proc. 12th Coastal Eng. Conf., Washington, D.C., 1970, I, pp.399-414.

Dorrestein, R., "On the deviation of the average pressure at a fixed point in a moving fluid from its 'hydrostatic' value", Appl. Sci. Res., A, 10, 1961, pp. 384-392.

Dorrestein, R., "Wave set-up on a beach", Proc. Second Techn. Conf. on Hurricanes, June 1961, Miami Beach, Washington, D.C., 1962, pp. 230-241.

Longuet-Higgins, M.S. and Stewart, R.W., "Changes in the form of short gravity waves on long waves and tidal currents", J. of Fluid Mech., 8, 1960, pp. 565-583.

Longuet-Higgins, M.S. and Stewart, R.W., "A note on wave set-up", J. of Mar. Res., 21, 1963, pp. 4-10.

Longuet-Higgins, M.S., "Longshore currents generated by obliquely incident sea waves", J. of Geoph. Res., 75, 33, 1970, pp. 6778-6801.

Lundgren, H., "Wave thrust and energy level", Proc. IAHR Congress, London, 1963, pp. 147-151.

Pierson, W.J., Jr. and Holmes, P., "Irregular wave forces on a pile", J. of the Waterways and Harbors Division, ASCE, 91, WW4, 1965, pp. 1-10.

Saville, T., Jr., "An approximation of the waverun-up distribution", Proc. 8th Coastal Eng. Conf., Mexico, 1962, pp. 48-59.

Thornton, E.B., "Longshore current and sediment transport", Tech. Rep. 5, Dept. of Coastal and Oceanographic Engineering, Univ. of Florida, Gainesville, Florida, 1969.

Thornton, E.B., "Variation of longshore current across the surf zone", Proc. 12th Conf. on Coastal Eng., Washington, D.C., 1970, I, pp. 291-308.

APPENDIX 2 - LIST OF SYMBOLS

c_f	bottom shear stress coefficient
C	volume concentration of air in water
d	mean depth (= h + $\overline{\zeta}$)
E	mean wave energy per unit area
E {.}	expectation of quantity in brackets
F	cumulative probability of H
$\tilde{F}$	cumulative probability of $\tilde{H}$
g	gravitational acceleration
h	still-water depth
h	realization of H or $\tilde{H}$ (in Eqs. 10 through 13 only)
H	wave height (total range in water surface elevation between two successive downcrossings of mean level)
$\tilde{H}$	fictituous wave height in absence of breaking
H_o	rms value of $\tilde{H}$
H_∞	rms value of incident wave height in deep water
k	$2\pi/L$
L	wavelength
L_∞	deep-water value of L calculated from $\overline{T}$ of incident waves
n	coefficient (eq. 3)
Q	probability of exceedance
S_{11}	largest principal radiation stress
S_{22}	smallest principal radiation stress
T	wave period (between successive downcrossings of mean level)
u_B	orbital velocity near the bottom acc. to potential theory
V	longshore current velocity, averaged over depth and time
W	normalized value of V (see fig. 4)
x	horizontal coordinate, positive seawards
z	vertical coordinate, positive upwards
γ	coefficient in breaker criterion
Δ	error in set-up measurements
ζ	elevation of water surface above still-water level
θ_∞	angle between direction of wave propagation in deep water and normal to the depth contours
τ_B	bottom shear stress

subscript "b" refers to "breaker"
an overbar denotes time average or arithmetic average

CHAPTER 114

EXCITATION OF WAVES INSIDE A BOTTOMLESS HARBOR

by

Noboru Sakuma[1], Johannes Bühler[2] and R. L. Wiegel[3]

1. INTRODUCTION

In planning enclosed areas in the ocean, such as offshore harbors for fishing or recreational boats, one has to consider very carefully the problem of forced seiches due to surface water waves. A number of papers have been written on this problem, but to the authors' knowledge, only one of them has treated the case of an artificial bottomless circular harbor in the open ocean, for which the walls extend only part way to the sea floor. A bottom to such a harbor, which would be expensive, can only be omitted if the effect of its absence on the sea surface inside the harbor is not overly detrimental.

C.J.R. Garrett (1970) made a theoretical study of the excitation of waves inside such a harbor for the 'no-entrance' case. The object of this paper is to evaluate experimentally the behavior of the sea surface inside such a harbor, to compare the results with the theoretical values obtained by Garrett, and to extend the observations to the case for which there is an entrance to the harbor.

2. THEORY

A theory of the excitation of waves inside a partially immersed bottomless vertical circular cylinder was developed by C.J.R. Garrett. In this theory, the free surface displacement may be described by real partof $\zeta e^{-i\sigma t}$, where the incident wave is given by

$$\zeta = \zeta_o e^{ikx} \tag{2.1}$$

$$= \zeta_o \sum_{m=o}^{\infty} \epsilon_m i^m J_m (kr) \cos m\theta \tag{2.2}$$

where $\epsilon_o = 1$, and $\epsilon_m = 2$ for $m \geq 1$; ζ_o is the amplitude of the incident wave. Disturbances within a circular cylinder can be expressed approximately by

---

1 Research Engineer, Public Works Research Institute, Ministry of Construction, Japan (formerly graduate student, Dept. of Civil Engrg., Univ. of California, Berkeley, California

2 Graduate student, Dept. of Civil Engrg., Univ. of California, Berkeley, California

3 Professor, Dept. of Civil Engrg., Univ. of California, Berkeley, California

$$\zeta\ (r,\theta) = \zeta_o \sum_{m=o}^{\infty} \varepsilon_m\ i^m\ \chi_m\ (r)\ \cos\ m\theta \tag{2.3}$$

The corresponding displacement potential (the product of $\frac{1}{-i\sigma}$ and the velocity potential) is

$$\zeta(r,\theta,z) = \zeta_o \sum_{m=o}^{\infty} \varepsilon_m\ i^m\ \psi_m(r,z)\ \cos\ m\theta \tag{2.4}$$

where

$$\chi_m(r) = \frac{\partial \psi_m}{\partial z}\ \Big|_{z=d} \tag{2.5}$$

In order to satisfy the kinematic free surface condition, φ must also satisfy

$$\nabla^2\ \varphi = 0 \tag{2.6}$$

$$\sigma^2\ \varphi - g\ \frac{\partial\ \varphi}{\partial\ z} = 0 \quad \text{on } z = d \tag{2.7}$$

$$\frac{\partial\ \varphi}{\partial\ z} = 0 \qquad \text{on } z = 0 \tag{2.8}$$

$$\frac{\partial\ \varphi}{\partial\ r} = 0 \quad \text{on } r = a \text{ for } h \le z \le d \tag{2.9}$$

Garrett found that the appropriate expansion of ψ_m could be expressed as follows. In $r \ge a$

$$\psi_m(r,z) = J_m(kr) - \frac{J_m'(ka)}{H_m'(ka)}\ H_m(kr)\ \frac{Z_k(z)}{Z_k'(z)} + \sum_{\alpha} F_{m\alpha}\ \frac{K_m(\alpha r)}{\alpha K_m'(\alpha a)}\ Z_\alpha(z) \tag{2.10}$$

where

J_m, Y_m; ordinary Bessel functions

I_m, K_m; modified Bessel functions

$H_m = J_m + iY_m$; the Hankel function of the first kind

$$Z_k(z) = N_k^{-\frac{1}{2}} \cosh kz \tag{2.11}$$

$$Z_\alpha(z) = N_\alpha^{-\frac{1}{2}} \cos \alpha z \tag{2.12}$$

$$N_k = \tfrac{1}{2}\,[1 + (\sinh 2kd/2kd)] \tag{2.13}$$

$$N_\alpha = \tfrac{1}{2}\,[1 + (\sin 2\alpha d/2\alpha d)] \tag{2.14}$$

$$F_{m\alpha} = \frac{1}{d}\int_0^h f_m(z)\, Z_\alpha(z)\, dz \tag{2.15}$$

In $r \leq a$

$$\psi_m(r,z) = \sum_\alpha F_{m\alpha}\frac{I_m(\alpha r)}{I_m'(\alpha a)}\, Z_\alpha(z) \tag{2.16}$$

Using Eqs. (2.5) and (2.16), the free surface elevation of Eq. (2.3) is, for $r \leq a$

$$\chi_m(r) = A_m J_m(kr) + {\sum_\alpha}' F_{m\alpha}\frac{I_m(\alpha r)}{\alpha I_m'(\alpha a)}\, Z_\alpha'(d) \tag{2.17}$$

where

$$A_m = F_{mk}\frac{Z_k'(d)}{kJ_m'(ka)} \tag{2.18}$$

The solution for $r \geq a$ may be written

$$\chi_m(r) = J_m(kr) + B_m H_m(kr) + {\sum_\alpha}' F_{m\alpha}\frac{K_m(\alpha r)}{\alpha K_m'(\alpha a)}\, Z_\alpha'(d) \tag{2.19}$$

where

$$B_m = (A_m - 1)\frac{J_m'(ka)}{H_m'(ka)} \tag{2.20}$$

The first term on the right hand side of Eq. (2.17) is the most important contribution to the wave motion inside the cylinder; the other terms describe waves which are generally confined near $r = a$.

Garrett made numerical calculations of A_m for several conditions. These have been reproduced in Figs. 1 and 2, in order that they can be compared with experimental results.

3. EXPERIMENTAL ARRANGEMENTS AND PROCEDURE

The experimental study reported herein was made in the hydraulic model basin (150 ft. by 63 ft. by 2½ ft.) at the Richmond Field Station of the University of California.

3.1 Conditions Tested

The conditions that were tested in the experiment are as follows (for definition of the symbols, see Fig. 3):

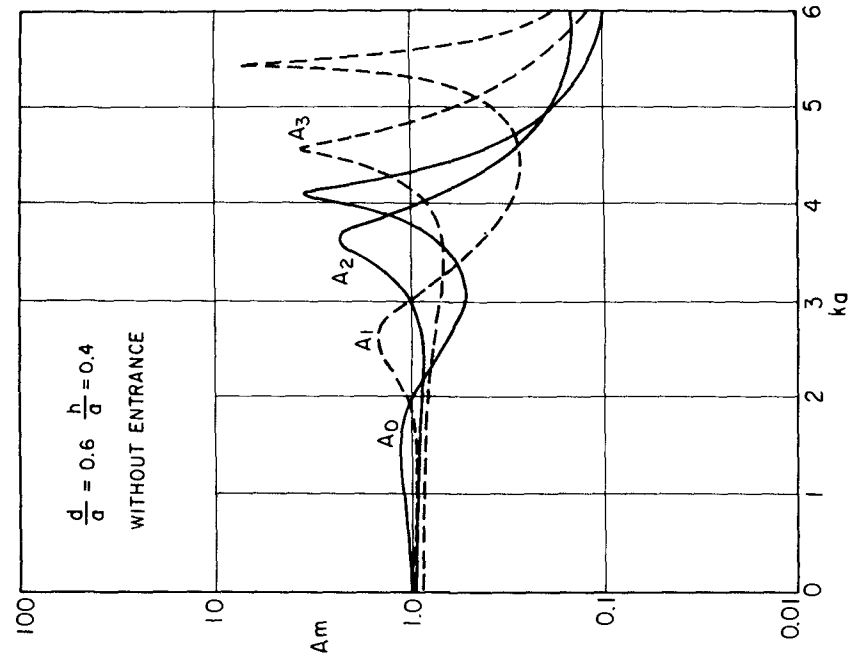

FIG. 2 THEORETICAL VALUES OF Am VS. ka
(from Garrett)

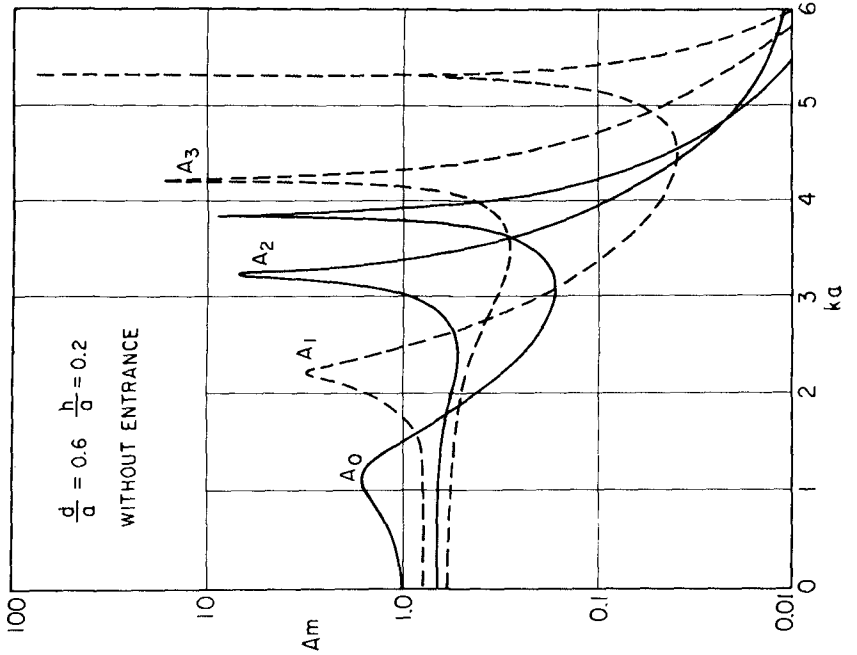

FIG. 1 THEORETICAL VALUES OF Am VS. ka
(from Garrett)

CASE NO.	$\frac{d}{a}$	$\frac{h}{a}$	NOTES
1	0.6	0.2	Without entrance.
2	0.6	0.4	
3	0.6	0.2	With an entrance in the rear.
4	0.6	0.4	
5	0.6	0.2	With an entrance on the side.
6	0.6	0.4	
7	0.6	0.2	With an entrance at the front.
8	0.6	0.4	

with d = 0.9 ft.; a = 1.5 ft.; h = 0.3 ft., and $ka = 2\pi a/L = 0.5 \sim 8.0$.

Two different experimental arrangements were used. The first series of experiments were conducted in a section of the model basin for cases 1 and 2. This arrangement is shown in Fig. 4 (small basin). The experiments were then repeated with an arrangement as shown in Fig. 5 (large basin) and the results compared. Because of the reduced reflection effects, the remaining cases were then studied in the large basin.

3.2 Experimental Arrangements and Procedures

Wave heights and wave periods inside and outside the cylinder were measured by means of parallel wire resistance type wave gages and a multichannel rectilinear writing oscillograph (Wiegel, 1953).

Four wave gages were used to measure the waves; one was used to measure the incident waves, and three were used to measure the waves inside the cylinder. The wave gage that was used for measuring incident waves was installed as far away from the cylinder as possible in the model basin in order to minimize the effect of wave reflection from the cylinder (see Figs. 4 and 5). The other three wave gages were installed inside the cylinder to enable measurement of the maximum wave height for each mode of harbor water surface oscillation.

In measuring the forced surface oscillations inside the cylinder and in interpreting the results, it is useful to consider the modes of oscillation to be the same as the modes of free oscillation inside a vertical circular harbor which extends to the bottom. This case has been studied theoretically and experimentally by J. S. McNown (1951; 1952) and by Goda (1963). The water surface elevations inside a vertical circular cylinder are expressed as

$$\zeta = C_m J_m(kr) \cos m\theta \qquad (3.1)$$

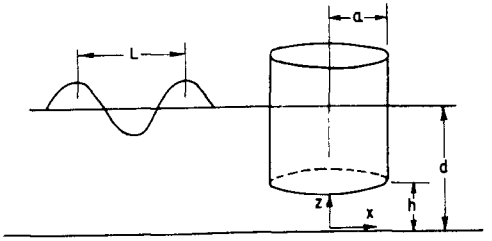

FIG. 3 DEFINITION SKETCH OF BOTTOMLESS VERTICAL CIRCULAR CYLINDER PARTIALLY IMMERSED

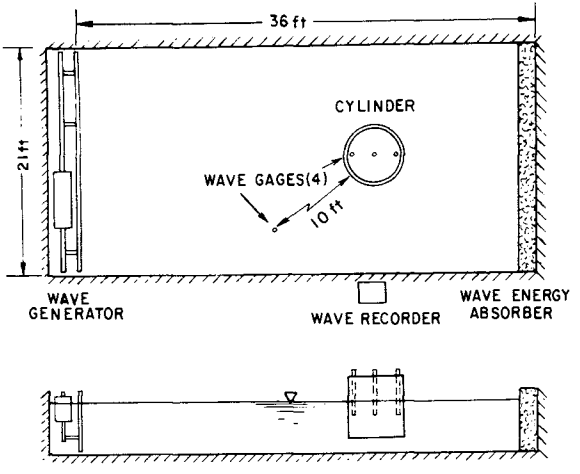

FIG. 4 EXPERIMENTAL ARRANGEMENT SMALL BASIN

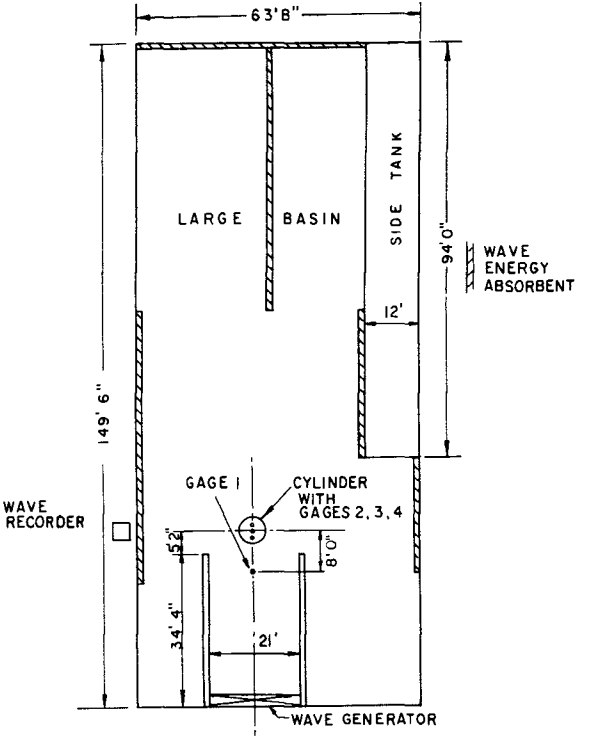

FIG. 5 EXPERIMENTAL ARRANGEMENT LARGE BASIN

where C_m is a coefficient related to the wave amplitude, k is the wave number $(2\pi/L)$, L is the incident wave length, r is the radial coordinate, θ is the angular coordinate, m is an integer and J_m is the Bessel's function of order m. Some of the possible modes expressed by the above expression are shown in Fig. 6.

In the experiment, however, it appeared that the mode or modes occurring within the cylinder were mostly of the lowest order of m; in other words, 0_1, 1_0, 2_0, 3_0 (Fig. 10) were observed, even though theoretically the number of modes possible for a given value of ka is infinite.

The places where the maximum wave elevation were observed in the cylinder were either at the center of the cylinder or near the wall of the cylinder. The orientation of the nodal lines of mode 1_0, for instance, would be normal to the direction of advance of incident waves. Therefore, for almost all of the experimental runs the three gages inside the cylinder were installed as shown in Fig. 7.

The cylinder which was used as a model of a circular harbor was made of steel and had three legs to hold it at the desired elevation above the bottom. After a number of measurements were made, an entrance to the harbor was made by cutting out a section of the cylinder, as shown in Fig. 8. For additional measurements without an entrance, the section was put back in place and the gaps closed with a plastic sealant.

An example of an incident wave record is shown in Fig. 9. It was difficult to define a "height of the incident wave," especially at higher wave numbers ka. When the generator was started, the waves gradually increased in height. The effects of reflection became evident before a uniform height was reached. The incident wave height was defined as the equilibrium wave height after a long time. This includes reflections from the walls of the basin and the cylinder itself. The final tests were made in the large basin in order to minimize the effect of these reflections. Reproductions of the records of representative samples of nearly all conditions have been reproduced in a laboratory report (Sakuma, Bühler and Wiegel, 1971).

From this incident wave height ζ_o, the corresponding values of A_m' can be calculated as follows. From Eq. 2.17, except near the wall, $X_m(r)$ can be approximated by

$$X_m(r) = A_m J_m(kr) \tag{4.1}$$

as the first term on the right hand side of Eq. 2.17, $A_m J_m(kr)$, is a much more important contribution to the wave motion inside the cylinder than is the second term. Substituting Eq. 4.1 into Eq. 2.3 results in

$$\zeta(r,\theta) \doteq \zeta_o \sum_{m=o}^{\infty} \varepsilon_m i^m A_m J_m(kr) \cdot \cos m\theta \tag{4.2}$$

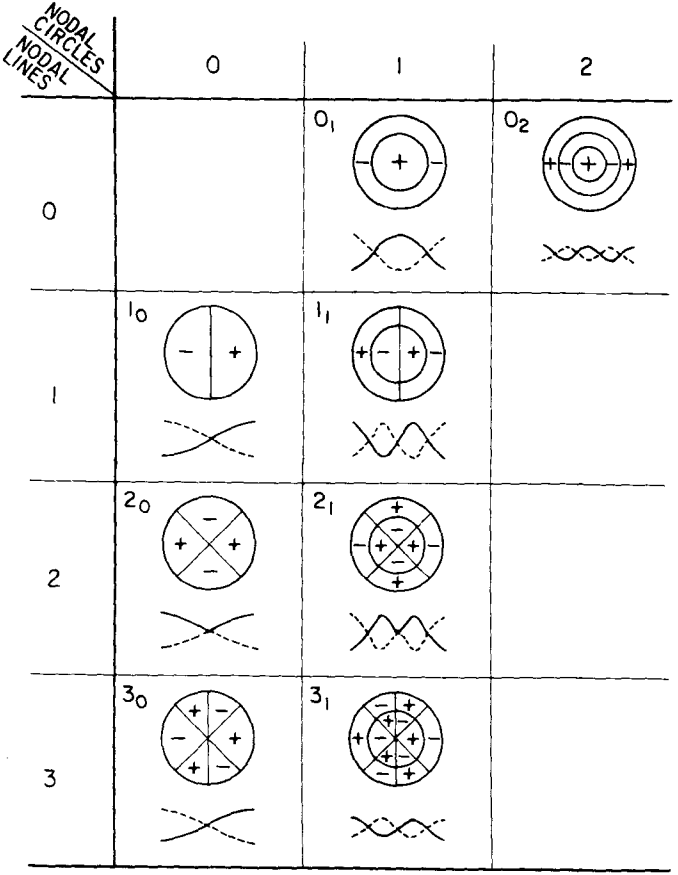

FIG. 6 SOME MODES OF FREE OSCILLATIONS IN A VERTICAL CYLINDER

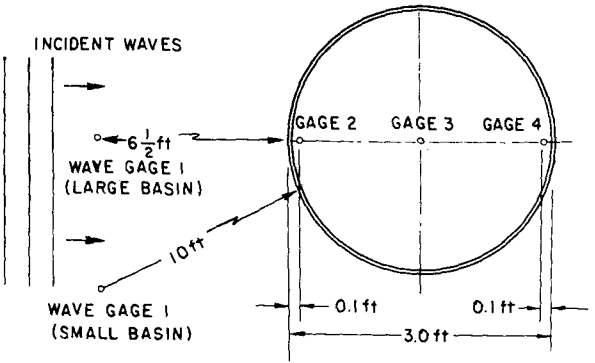

FIG. 7 WAVE GAGE LOCATIONS

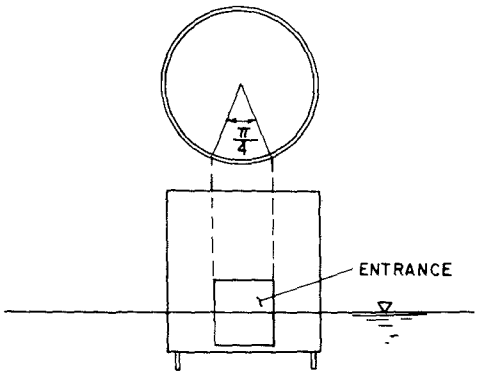

FIG. 8 CYLINDER WITH ENTRANCE

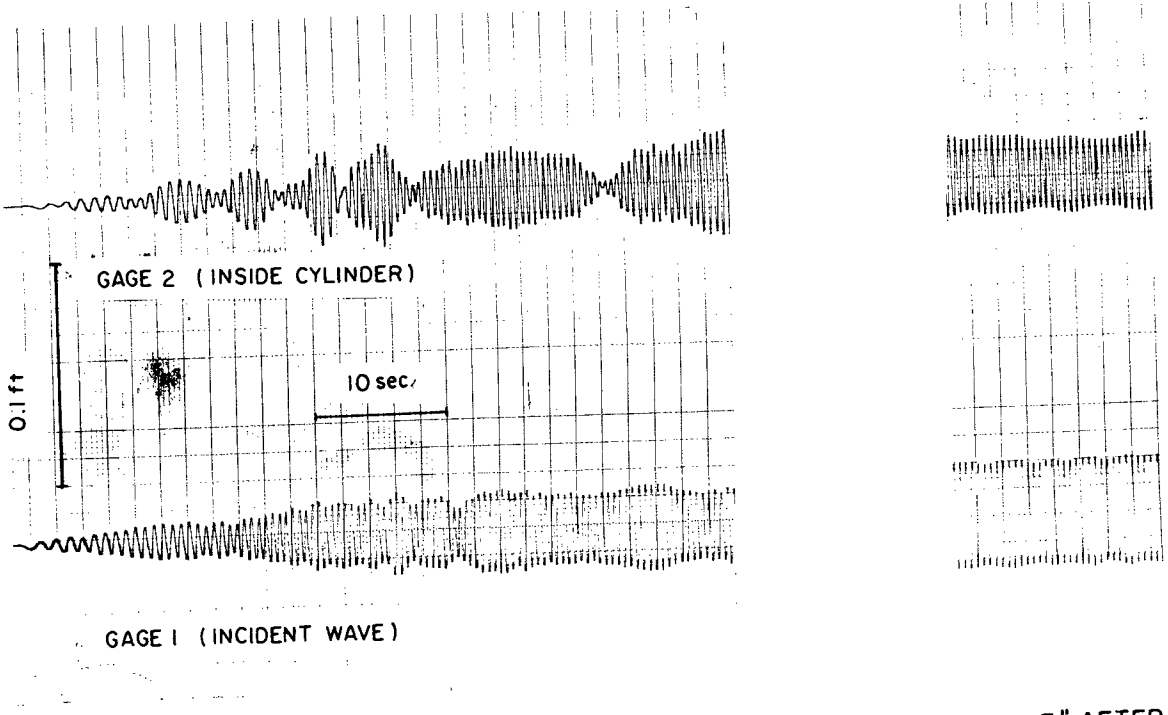

DEVELOPING WAVES
T = 0.625 sec.

"STABLE VALUE" AFTER 3 min.

FIG. 9 EXAMPLE OF WAVE RECORD

so

$$Am = \frac{\zeta(r,\theta)}{\zeta_o \sum_{m=o}^{\infty} \varepsilon_m i^m J_m(kr)\cdot\cos m\theta} \tag{4.3}$$

where $\varepsilon_o = 1$, and $\varepsilon_m = 2$ for $m \geq 1$. Defining A_m' as

$$A_m' = \frac{\zeta_{max}(r,\theta)}{\zeta_o \sum_{m=o}^{\infty} \varepsilon_m i^m [J_m(kr)]_{max}} \tag{4.4}$$

with $[\cos m\theta]_{max} = 1$, and $\zeta_{max}(r,\theta)$ is the maximum wave height in the cylinder.

When m = o, Eq. 4.4 will be

$$A_o' = \frac{\zeta_{max}(r,\theta)}{\zeta_o[J_o(kr)]_{max}} \tag{4.5}$$

$$= \frac{\zeta_{max}(r,\theta)}{\zeta_o} \tag{4.6}$$

since $[J_o(kr)\ max = 1$.

When m = 1:

$$A_1' = \frac{\zeta_{max}(r,\theta)}{2\ \zeta_o[J_1(kr)\ ]_{max}} \tag{4.7}$$

$$= \frac{\zeta_{max}(r,\theta)}{2(0.58)\ \zeta_o} \tag{4.8}$$

$$= 0.86\ \frac{\zeta_{max}(r,\theta)}{\zeta_o} \tag{4.9}$$

when m = 2:

$$A_2' = \frac{\zeta_{max}(r,\theta)}{2\ \zeta_o\ [J_2(kr)\ ]_{max}} \tag{4.10}$$

$$= \frac{\zeta_{max}(r,\theta)}{2\ \zeta_o[J_3(kr)}_{max} \tag{4.11}$$

$$= 1.04\ \frac{\zeta_{max}(r,\theta)}{\zeta_o} \tag{4.12}$$

when m = 3

$$A_3' = \frac{\zeta_{max}(r\theta)}{2\,\zeta_o [J_3(kr)]_{max}} \tag{4.13}$$

$$= \frac{\zeta_{max}(r,\theta)}{2(0.44)\,\zeta_o} \tag{4.14}$$

$$= 1.14\ \frac{\zeta_{max}(r,\theta)}{\zeta_o} \tag{4.15}$$

and so on.

As stated previously, the modes of oscillation which were observed in the cylinder were mostly of the J_0, J_1, J_2, J_3 types, or a combination of two or more of these modes. The fact that higher modes of oscillation were not observed, combined with the likely accuracy of the experimental measurements, A_m' can be approximated by:

$$A_m' \approx \frac{\zeta_{max}(r,\theta)}{\zeta_o} \tag{4.16}$$

for most practical purposes. This approximation was used to calculate A_m' as shown in Figs. 12 - 18.

4. RESULTS AND DISCUSSION

4.1 Small Basin

The results obtained for the small basin are shown in Figs. 12 and 13.

Each observed mode of oscillation is assigned a symbol. The symbols are defined in Fig. 10. The modes were recognized by a combination of visual observation and a study of the recordings of the outputs of the three wave gages within the cylinder. Generally, it was very difficult to tell which mode or modes of oscillation were occurring in the cylinder; sometimes two or more were observed at the same time, especially for the case of the cylinder with an entrance. As stated before, the modes recognized in the cylinder were either one of the lowest order possible or a combination of two or more such modes. Modes of higher orders might have existed in the cylinder in the experiment but they were not clear enough to be recognized. The orientation of the observed nodal lines were as shown in Fig. 10.

One has to be careful about ζ_{max}. For mode 1_0, for example, one would expect that the wave height at the location where wave gage #2 was installed would be the same as the wave height at wave gage #4 for the "no entrance" case. However, it was found that the wave height at wave gage #4 was larger than the height at wave gage #2 except for $ka > 4.5$ with $h/a = 0.2$ (Fig. 11, Small Basin). It is important to note in this regard that McNown (1951; 1952) found such a non-symmetry for the case of waves with a period close to two resonant conditions having nearly equal periods.

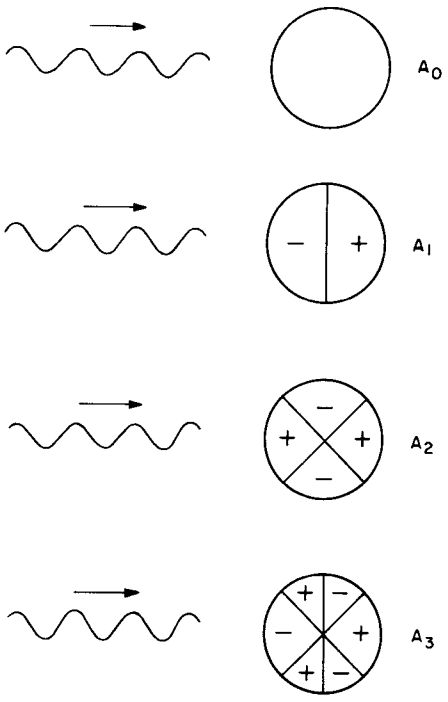

FIG. 10 OBSERVED ORIENTATIONS OF NODAL LINES

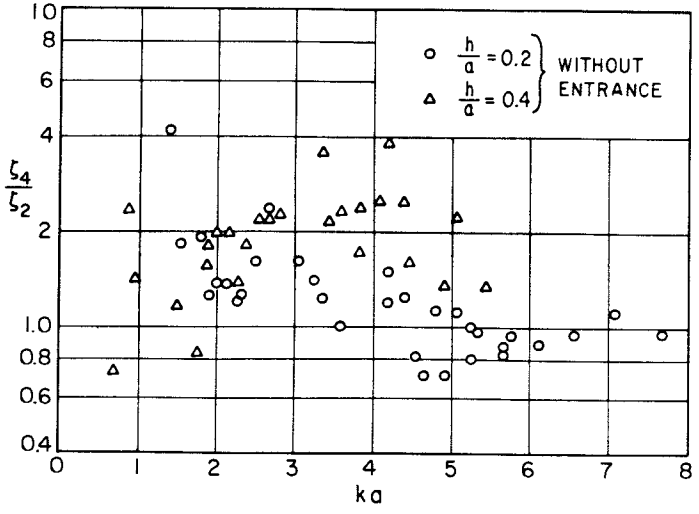

FIG. 11 RATIO OF WAVE HEIGHTS, WAVE GAGES 2 AND 4 SMALL BASIN

In calculating values of A_m' , the maximum value of ξ observed at any one of the 3 gages was used.

Consider the theoretical and experimental results for case 1 with h/a = 0.2 as shown in Figs. 1 and 12. The resonance patterns are alike; the values of ka for which peaks for different modes of oscillation appear in Fig. 12 are very similar to those in Fig. 1. The calculated response curves show very sharp peaks for the larger values of ka, while a substantial damping effect is apparent in the experiment data.

In regard to the results for case 2 with h/a = 0.4 (see Figs. 2 and 13), the damping effect is smaller than for the case of h/a = 0.2. In addition, the ratio of the wave height at wave gage #4 to the wave height at wave gage #2 is larger compared with the case of h/a = 0.2 (Fig. 11). The maximum value of A_m' is about the same for both cases. $A_m' = 2.5 \sim 2.8$.

4.2 Large Basin

The results for cases 1 and 2 are shown in Figures 12 and 13. The modes of oscillation agreed well with the ones observed in the small basin for corresponding wave numbers. The peak values of A_m' appear at the same values of ka as for the small basin.

The values of A_m' for ka $\geq$ 3 are smaller for the large basin. This is mainly due to reflections from the back wall of the small basin.

As third and fourth case, a bottomless, vertical circular cylinder with an entrance in the rear was studied (see McNown, 1951 and 1952, for a theoretical and laboratory study of a circular cylindrical harbor extending to the bottom). The authors are not aware of any theoretical studies of this case. Figs. 14 and 15 show the experimental results, with no designation for different modes of oscillation as the modes observed in the cylinder were not clear. The surface oscillations within the cylinder appeared to be a combination of two or more modes, and, in addition, were affected by the disturbances due to the flow through the entrance.

It is interesting to note that a nodal line did not form at the entrance; instead, quite a large amplitude of oscillation was observed. Wave diffraction was observed at the entrance. The wave heights are generally smaller than for the harbor without entrance except at high wave numbers for h/a = 0.2 (Fig. 14). The peak value at ha = 4 in Fig. 14 is not well defined, amplitude of the incident wave was fluctuating.

Figures 16 and 17 show the behavior of the harbor with the entrance in different locations. For the entrance in the rear, the oscillations inside the harbor decrease rapidly with increasing wave number. For the entrance at the front, the oscillations are larger at high wave numbers. The high peaks near ka = 4 and ka = 7 are not well defined. The maximum and minimum values of 5 runs are connected by vertical bars to give an estimate of the width of the fluctuations. The recordings of both incident

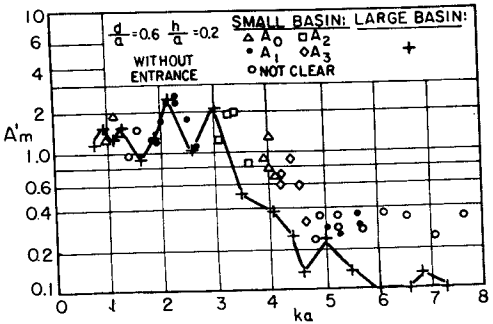

FIG12 EXPERIMENTAL VALUES OF A'm vs ka WITHOUT ENTRANCE, d/a=0.6 h/a=02

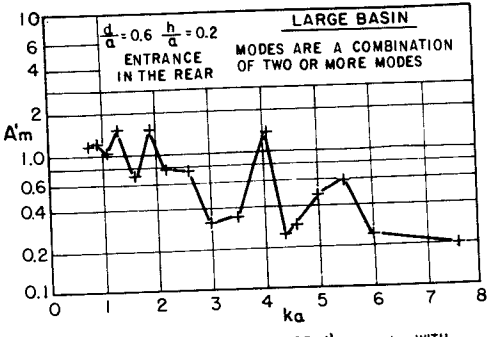

FIG14 EXPERIMENTAL VALUES OF A'm vs ka WITH ENTRANCE, d/a=0.6 h/a=0.2

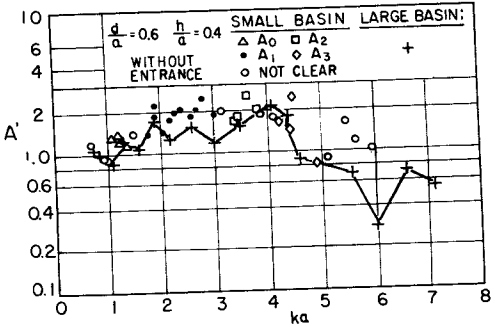

FIG13 EXPERIMENTAL VALUES OF A'm vs ka WITHOUT ENTRANCE, d/a=0.6 h/a=0.4

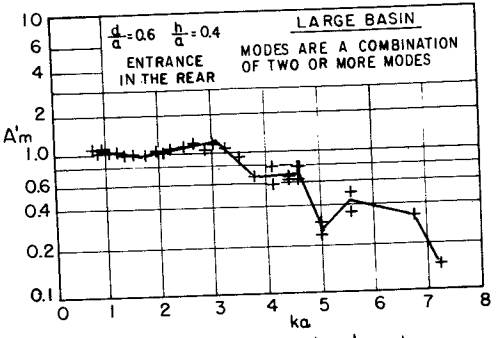

FIG15 EXPERIMENTAL VALUES OF A'm vs ka WITH ENTRANCE, d/a=0.6 h/a=0.4

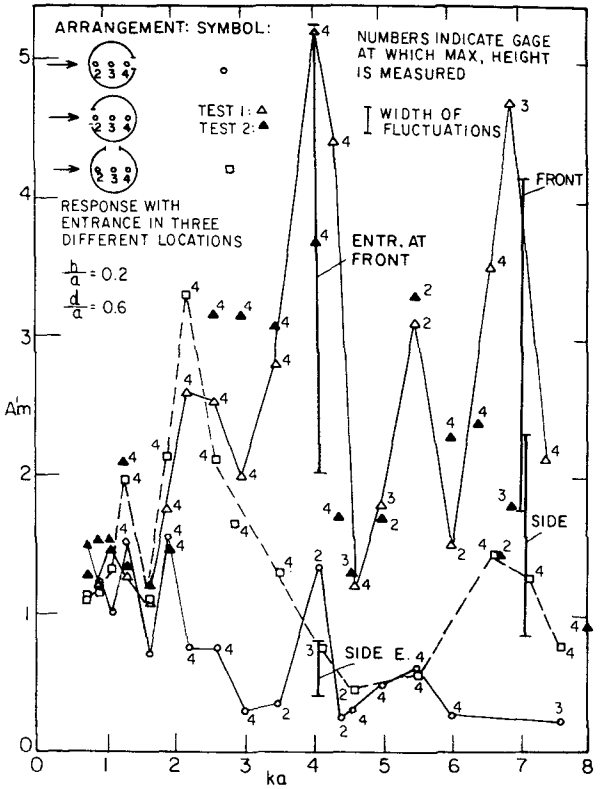

FIG.16 EXPERIMENTAL VALUES OF A'm vs ka

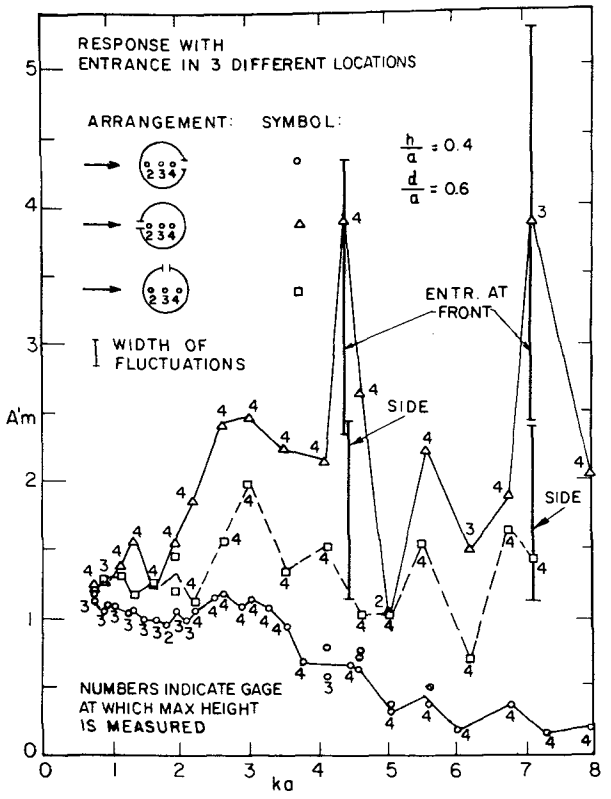

FIG.17 EXPERIMENTAL VALUES OF A'm vs ka

wave height and harbor oscillations showed large amplitude fluctuations at these values of ka. It was evident from observations made during the tests that reflections were the cause of this behavior.

Fig. 18 shows the maximum values of A_m for 3 different gage arrangements for the harbor with the entrance on the side. The largest oscillations of the water level occur in the center of the harbor for low wave numbers and at the remote end of the harbor for high ones. It is thus concluded that even for the case of an entrance on the side, the arrangement of the gages parallel to the direction of wave incident gives the maximum wave heights.

5. CONCLUSIONS

5.1 Harbor Without Entrance

1) Waves having the values of ka for which the resonance peaks of the J_0, J_1, J_2, and J_3 modes occurred, were generated in the laboratory, as well as waves of a series of other values of ka. Resonant peaks were observed in the laboratory study for the same values of ka at which the theoretical resonant peaks occur.

2) Damping of the wave amplitudes within the cylinder was found to be relatively large in the laboratory experiments for the larger values of ka.

3) The results of the experiments made with the cylinder without an entrance show the maximum values of A_m' to be from 2.0 to 2.5 (large basin). The maximum values occur at wave numbers ka smaller than 4.

5.2 Harbor With an Entrance

1) The modes of oscillation were usually complex and could not be classified according to Fig. 10.

2) The measurements showed that the oscillations were smaller for an entrance in the rear than for all entrance at the front, especially for wave numbers ka larger than 2.0.

3) With an entrance in the rear, the maximum values of A_m' were 1.1 for h/a = 0.4 and 1.6 for h/a = 0.2. The maximum values were observed at wave numbers ka smaller than 4.0.

4) With an entrance on the side, a maximum value of A_m' was observed at a wave number ka between 2.0 and 3.0. This maximum value of a'm was 2.0 for h/a = 0.4 and 3.2 for h/a = 0.2.

5) With an entrance at the front, large amplitude fluctuations were observed near ka = 4.0 and ka = 7.0. As an example, the values of a'm ranged from 2.4 to 5.3 at ka = 6.8 for h/a = 0.4. The fluctuations were due to the reflection of waves from the boundaries of the basin.

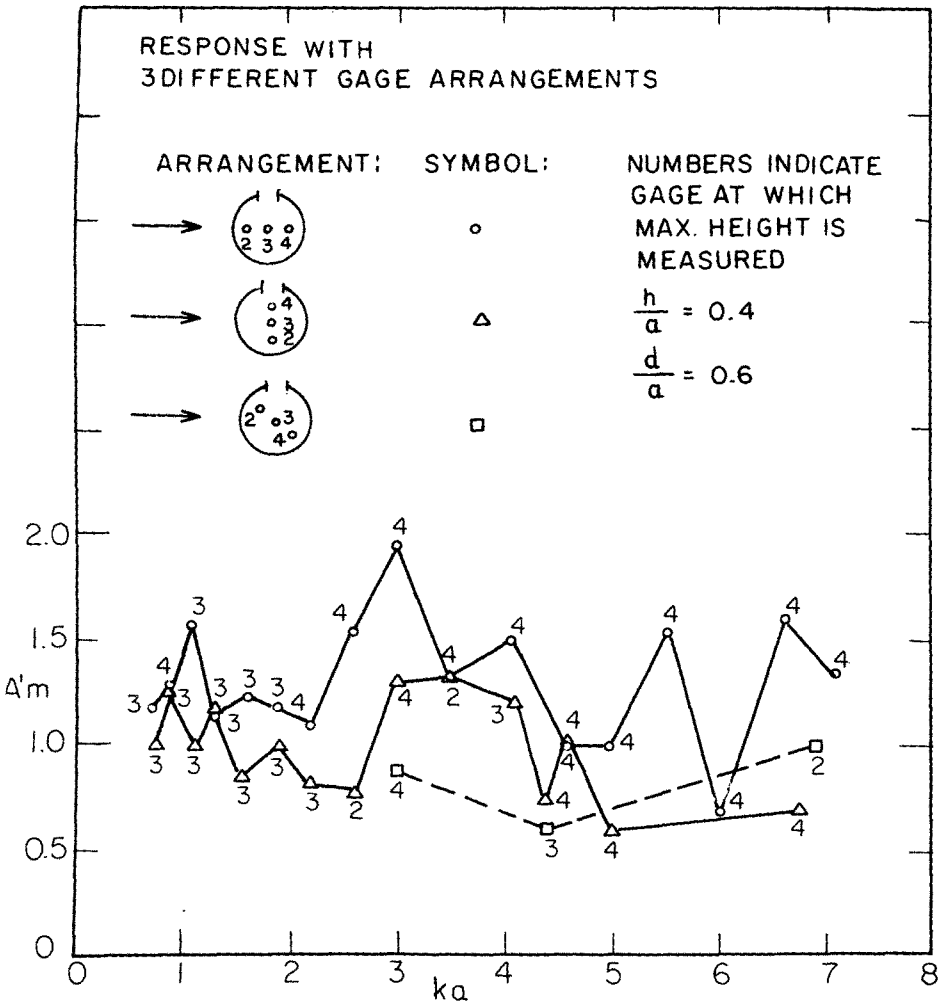

FIG.18 EXPERIMENTAL VALUES OF A'm vs ka

6. ACKNOWLEDGEMENTS

The senior author gratefully wishes to acknowledge the support of the Japan Public Works Research Institute, which made it possible for him to undertake graduate studies at the University of California.

The work reported herein was partially supported by the Coastal Engineering Research Center, Corps of Engineers, U.S. Army.

7. SYMBOLS

a = radius of circular cylinder

A_m = defined by Eq. (2.18)

B_m = defined by Eq. (2.20)

C_m = a coefficient related to the wave amplitude in Eq. (3.1)

d = water depth

g = acceleration of gravity

h = vertical distance from sea floor to bottom of cylinder

H_m = Hankel function of the first kind

I_m = modified Bessel function

J_m = ordinary Bessel function

k = wave number, $2\pi/L$

L = wave length

m = an integer, 0,1,2...

r = radial coordinate

T = wave period

x = horizontal coordinate in the direction of incident wave advance

z = vertical coordinate, $z = 0$ at undisturbed water surface

α = a real positive solution of $\alpha \tan \alpha d + \frac{\sigma^2}{g} = 0$

ϵ_m = a number; $\epsilon_o = 1$, and $\epsilon_m = 2$ for $m \geq 1$

ζ = water surface elevation

ζ_o = amplitude of incident waves

θ = angular coordinate

$\sum_{\alpha}$ = summation over α including α + -ik

$\sum_{\alpha}'$ = summation over only the real roots, i.e., α = -ik is excluded

σ = wave frequency, $2\pi/T$

$\varphi(r,\theta,z)$ = displacement potential

$\chi(r)$ = defined by Eqs. (2.17) and (2.19)

$\psi_m(r,z)$ = defined by Eq. (2.10)

8. REFERENCES

Garrett, C.J.R., "Bottomless Harbors," Journal of Fluid Mechanics, Vol. 43, Part 3, pp. 433-449, 1970.

Goda, Y., "On the Oscillations in a Rectangular Harbor and a Sector-Shaped One," The 10th Coastal Engineering Conference, Japan, 1963, in Japanese.

McNown, J.S., Sur l'entretien des Oscillations des Eaux Portuaires, sous l'Action de la Haute Mer., These, Faculte des Sciences, Univ. Grenoble, France, August 1951.

McNown, J.S., "Waves and Seiche in Idealized Ports," Gravity Waves, U.S. Dept. of Commerce, National Bureau of Standards, Circular No. 521, 1952, pp. 1953-164.

Sakuma, Noboru, Johannes Bühler and R. L. Wiegel, Experimental Study of the Excitation of Waves Inside a Bottomless Harbor, Technical Report HEL 1-17, Hydraulic Engineering Laboratory, University of California, Berkeley, California, May 1971, 36 pp.

Wiegel, Robert L., Parallel Wire Resistance Wave Meter, Coastal Engineering Instruments, Council on Wave Research, The Engineering Foundation, 1953, pp. 39-43.

Wiegel, Robert L., Oceanographical Engineering, Prentice-Hall, Inc., Englewood Cliffs, N.J., 1964.

Ucluelet, B.C.

PART IV

COASTAL, ESTUARINE, AND ENVIRONMENTAL PROBLEMS

Ocean Falls, B.C.

CHAPTER 115

REMOTE SENSING IN THE STUDY OF COASTAL PROCESSES

by
Orville T. Magoon[1], M. ASCE
Douglas M. Pirie[2]

ABSTRACT

The quantifiable determination of important coastal parameters remotely rather than by in situ measurements combined with automatic data reduction and analysis will result in a greatly increased understanding of the parameters being studied. This paper gives a progress report on joint Corps of Engineers-National Aeronautics and Space Administration (NASA) efforts to apply remote sensing in coastal studies. The devices used were multiband photography, the infrared scanner, the Side Looking Airborne Radar and various image enhancement and processing devices.

INTRODUCTION

The quantifiable determination of movement of sedimentary material along a coastline (or longshore transport) represents a major challenge facing coastal planners, coastal engineers and property owners.

Although littoral processes are conceptually understood, it is as yet not possible to adequately describe or quantify long or short term forecasts of the effects of improvements or modifications to the shoreline. In some instances, past shoreline changes have resulted in costly damage worth millions of dollars. Research in coastal processes at CERC is currently directed toward efforts to improve the state of the art on quantitative and qualitative approaches to this problem. These efforts are directed toward understanding of coastal phenomena based on extremely complex and relatively short lived in situ sediment transport measurements or experiments (such as radioisotope or fluorescent tagging of sand grains).

In addition to the examination of in situ sediment movement, it is also necessary to describe and quantify the major coastal processes which occur on a larger spatial basis.

The purpose of this study was to obtain imagery of a variety of coastal phenomena using available state-of-the-art devices, and to use appropriate enhancement and viewing equipment to evaluate the use of

[1]Special Assistant to the Director, U. S. Army Coastal Engineering Research Center, Washington, D.C., U.S.A.
[2]Ocean Engineer, Navigation and Shoreline Planning Branch, U. S. Army Engineer District, San Francisco, California, U.S.A.

this imagery and techniques in the study of various coastal processes. On 4 October 1971 the National Aeronautics and Space Administration (NASA), Manned Spacecraft Center, Houston, Texas furnished the NASA 927 NP3A Earth Observation Aircraft Program research aircraft for a flight of the central and southern California coast. Seven flight lines were flown along the California coast using an RS-14 infrared scanner and photographic data runs with altitudes from 500 to 10,000 feet. A similar number of flight lines using Side Looking Airborne Radar (SLAR) offset roughly two nautical miles from the coast match the photographic flight lines and are flown at an altitude of 5,000 feet. The NASA 927 aircraft is an experimental platform in which may be installed a number of optical electronic or other experimental sensing packages. Photographic equipment consisted of four KA-62 cameras and two RC-8 metric cameras. Various filter/film combinations were employed to optimize imagery.

The RS-14 scanner is a radiometer that optically/mechanically scans successive contiguous lines across the flight path and records simultaneously in two spectral intervals the energy reflected or emitted by earth features. This device includes internal calibration sources and a number of thermal infrared detectors which may be used as desired. For this particular flight, wave lengths from 8 to 14 μm were recorded on film and wave lengths from 3 to 5.5 μm were stored on analog tape.

The 16.5 GHz (SLAR) is a radar mapping device which transmits a series of pulses of 16.5 GHz radiation in a narrow fan shaped beam from an antenna mounted on the aircraft. The transmitted pulses alternate between horizontal and vertical polarization and back scatter energy is received in both polarizations. The device produces a photograph-like image and was operated to optimize and enhance water and wave action return. Of particular interest to coastal investigators is the onboard navigation system which automatically controls aircraft flight on selected latitude and longitude points.

The multiband and infrared imagery was processed on an I^2S multiband camera film viewer (MCFV) in Houston at the NASA Manned Spacecraft Center. This device is a high resolution 1,000 line system scanning three channels of multiband imagery. The MCFV provides a calibrated output from each of the three channels for viewing in composite true color analog, false color and digitized enhanced false color. By use of this device imagery from the three channels of coastal data were synergistically combined to produce the desired enhancements. Examples will be shown of various enhancement combinations.*

Ground/sea truth measurements were also taken. These measurements include observations at Project LEO sites and special measurements at selected points within the flight areas. Experiments are limited to the

*Color flight imagery shown in Vancouver Conference. Presentation could not be included in this presentation.

coastline of the State of California. Work was sponsored jointly by the NASA and the Corps of Engineers, Coastal Engineering Research Center.

NASA FLIGHT

On 4 October 1971 the National Aeronautics and Space Administration (NASA) Manned Spacecraft Center (MSC), Houston, Texas, furnished the NASA 927 NP3A aircraft for a flight over the central and southern California coast. Ten flight lines along the California coast had the RS-14 infrared scanner and photographic data runs with altitudes flown from 500 to 1,000 feet. Seven flight lines of SLAR data offset roughly two nautical miles from the coast matched the photographic flight line and were flown at an altitude of 5,000 feet.

FLIGHT OPERATIONS

In flying this mission, the NASA 927 aircraft was staged out of Moffett Field, California. The predawn flight containing 14 flight lines extended from approximately Ano Nuevo, San Mateo County, to just north of San Clemente, Orange County, California. The flights were generally flown with an equal balance of land and water or to be fairly biased, toward a larger percentage of water than land, but generally strict tangent flight lines. A summary map is shown in Figures 2A and 2B. A listing of the precise location of imagery was generated from the onboard data processing system (ADIAZ) obtained from the automatic inertial guidance system on NASA 927. This system simultaneously logged physical parameters relating to the flight for subsequent printing.

REMOTE SENSING SYSTEMS

Remote Sensing Devices

For this particular flight, and to be described in the next sections, the following devices were installed:

a. Camera System:

Camera	Position	Type	Film	Filter	Lens	Forward overlap, percent
RC-8	1	Color	SO-397	Haze	6 in.	60
RC-8	2	Color IR	2443	12	6 in.	60
KA-62	1a	Color	SO-397	12	3 in.	60
KA-62	2	B&W	2402	25A	3 in.	60
KA-62	3	B&W	2402	58	3 in.	60
KA-62	4	B&W IR	SO-246	89B	3 in.	60
SLAR boresight		Color	2448			

1/ KA-62 camera #1 with color film was overexposed one f-stop over a normal land return exposure in order to achieve water penetration.

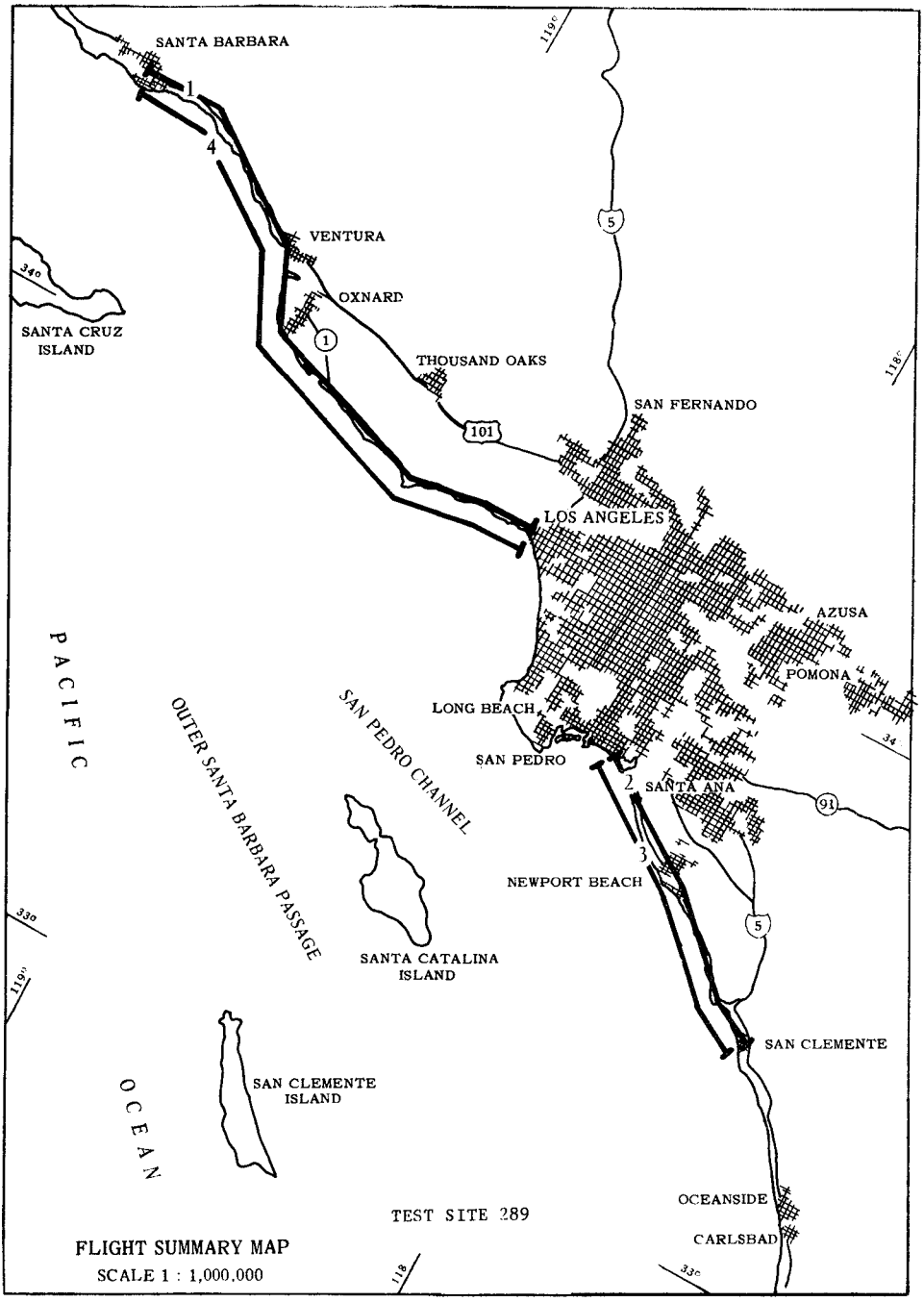
SANTA BARBARA
VENTURA
OXNARD
THOUSAND OAKS
SAN FERNANDO
LOS ANGELES
AZUSA
POMONA
LONG BEACH
SAN PEDRO
SANTA ANA
NEWPORT BEACH
SAN CLEMENTE
OCEANSIDE
CARLSBAD
SANTA CRUZ ISLAND
SANTA CATALINA ISLAND
SAN CLEMENTE ISLAND
PACIFIC
OCEAN
OUTER SANTA BARBARA PASSAGE
SAN PEDRO CHANNEL
TEST SITE 289
FLIGHT SUMMARY MAP
SCALE 1 : 1,000,000
1
2
3
4
5
101
91
119°
118°
34°
33°
340
330

FIGURE 2A

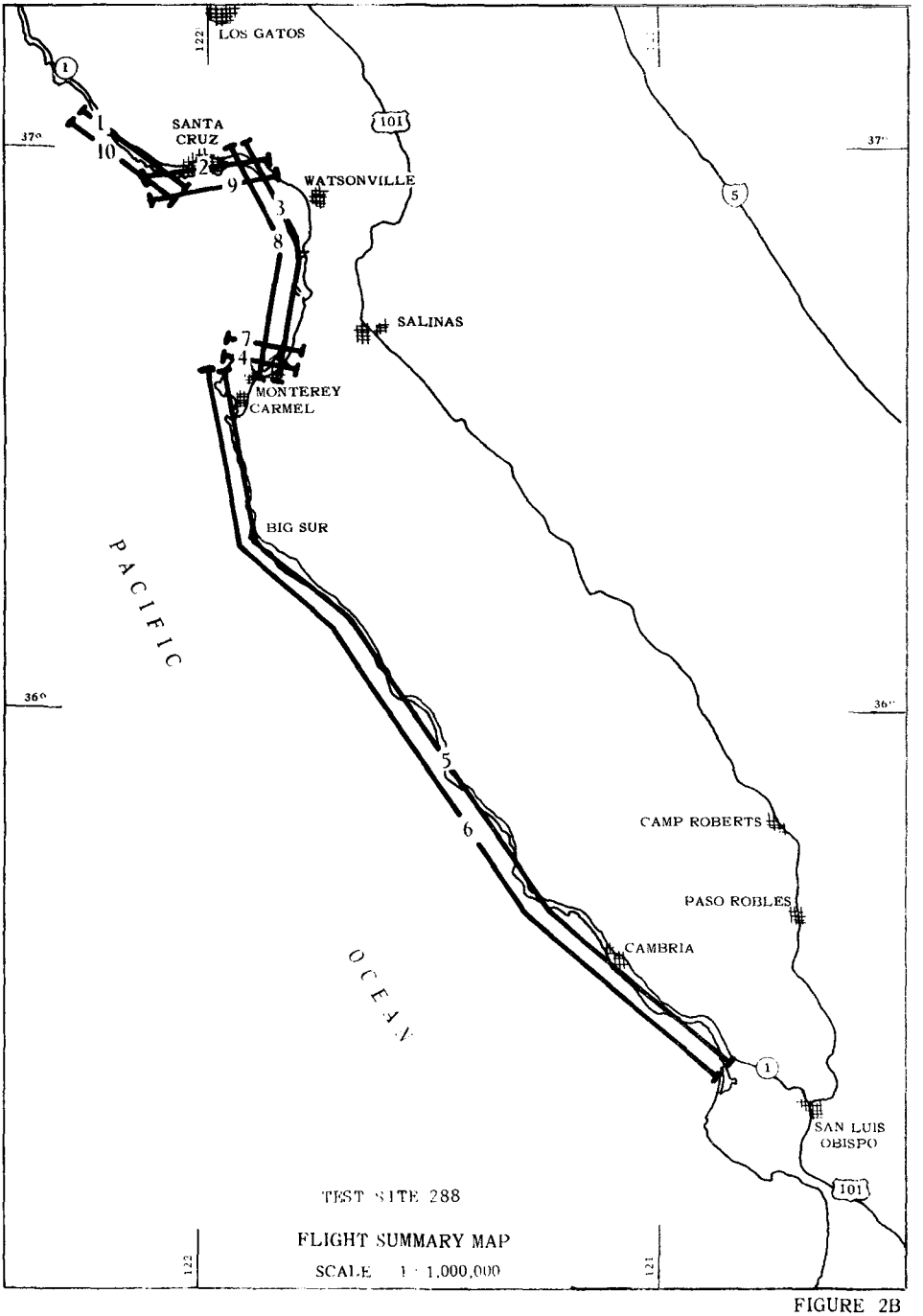
LOS GATOS
SANTA CRUZ
WATSONVILLE
SALINAS
MONTEREY
CARMEL
BIG SUR
PACIFIC
OCEAN
CAMP ROBERTS
PASO ROBLES
CAMBRIA
SAN LUIS OBISPO
101
5
1
122
121
37°
36°
TEST SITE 288
FLIGHT SUMMARY MAP
SCALE 1 : 1,000,000

FIGURE 2B

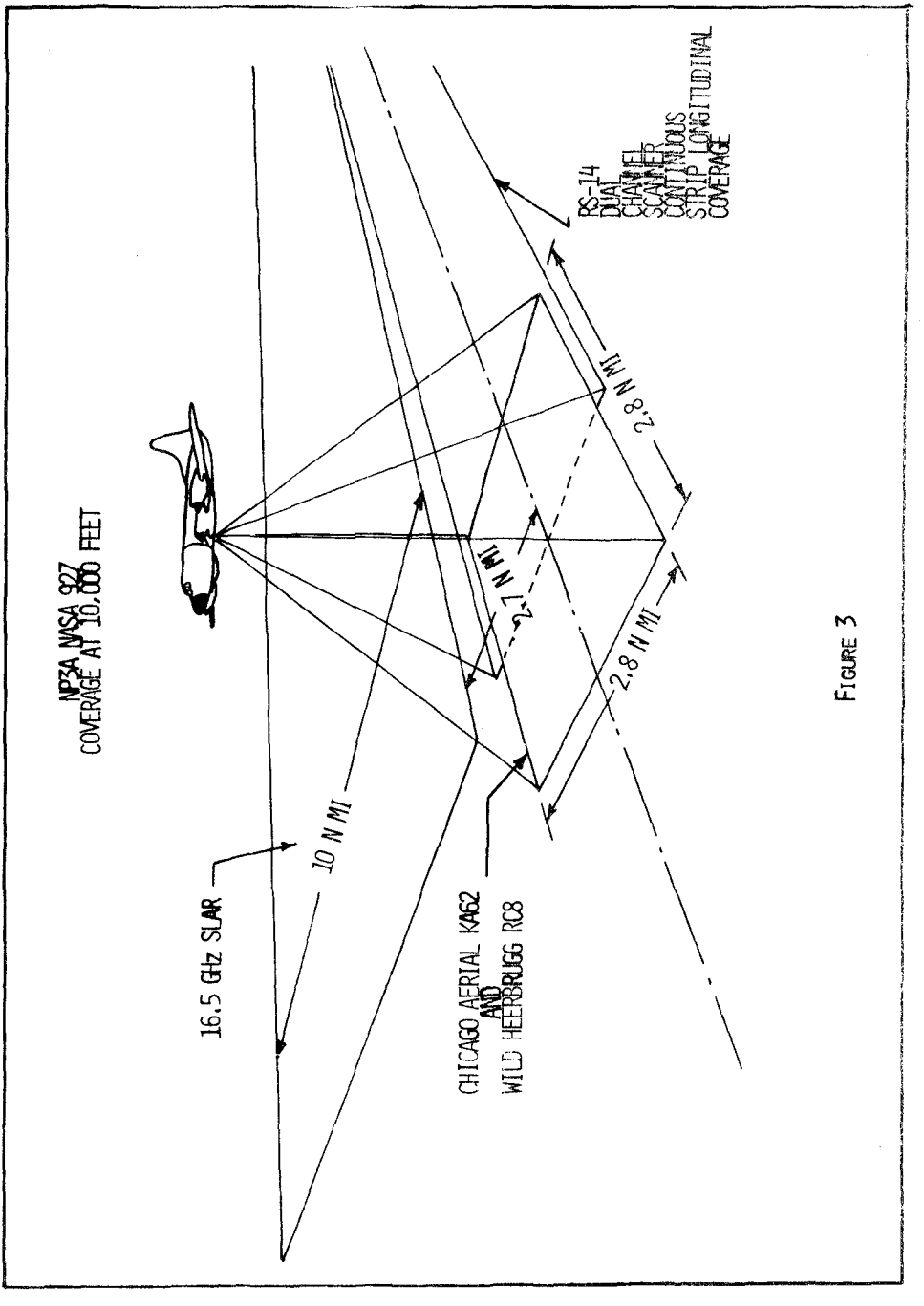
NP3A NASA 927
COVERAGE AT 10,000 FEET
16.5 GHz SLAR
10 N MI
CHICAGO AERIAL KA62
AND
WILD HEERBRUGG RC8
2.7 N MI
2.8 N MI
2.8 N MI
RS-14
DUAL
CHANNEL
SCANNER
CONTINUOUS
STRIP LONGITUDINAL
COVERAGE

FIGURE 3

b. RS-14 Scanner:

(1) Channel 1 - 3 to 5.5 μm
(2) Channel 2 - 8 to 14 μm

c. 16.5 GHz SLAR:

(1) Optimized settings to enhance water and wave action return.
(2) Full polarization matrix.

d. PRT-5: Recorded on onboard strip chart and magnetic tape.

e. Atmospheric sensors: Temperature, dew point, and liquid water content.

f. LTN-51

Cameras:

RC-8 Metric Camera. The Wild-Heerbrugg RC-8 metric, general mapping cameras employ a 6-inch focal-length, Universal Aviogon lens capable of color, color infrared, or conventional black and white on 9-inch format photo film. The camera is primarily employed as a high resolution terrain correlation and indexing device as described in the NASA MSC publication, "Earth Observation Aircraft Facility of the Manned Spacecraft Center, Vol. I."

The camera incorporates two separate data systems: an electromechanical events counter and a data recording cathode ray tube (CRT). The CRT displays encoded auxiliary data (ADAS) pertinent to camera operation and aircraft flight. The events counter registers the frame number and fixed data consisting of lens serial number and focal length. The events counter and fixed data is displayed on the edge of the film and CRT data is displayed on a corner of each frame.

The RC-8 cameras were mounted in T-28A-6 stabilized camera platform which increase camera steadiness and vertical accuracy under all conditions of flight within the range of the platform's freedom of movement. The platform is electronically controlled and gyroscopically stabilized to:

Provide a stabilized platform to support the RC-8 aerial camera in the aircraft

Maintain the optical axis of the camera fized with respect to vertical

Increase image resolution by reducing the effects of aircraft vibration and roll and pitch motion

Provide remote positioning of the camera azimuth to correct for the "crab" of the aircraft.

The maximum limits of correction for the T-28A-6 stabilized platform are as follows:

Azimuth	±15°
Roll	± 8°
Pitch	± 8°

KA-62 Camera System. The KA-62 is a serial frame camera employing spectral bandpass filters, a 3-inch focal length lens, and a 4.5-inch square image format. Depending on the filters installed, the camera may be used for broadband photography or for photographs sensitized to a selected portion of the spectrum.

A multiband camera system is formed by boresighting the cameras in the aircraft and using a different spectral bandpass filter with each camera. In the multiband application, the cameras are operated synchronously; photographs obtained show differences in tone density because of differential reflectance, thus accurately representing characteristics of the terrain.

The KA-62 camera incorporates two separate data systems: a 4-digit, cumulative, resettable, electromechanical events counter, and a data recording cathode ray tube (CRT) with their respective optical projection systems. The CRT displays encoded auxiliary data on camera operation and aircraft flight. The events counter registers the frame number and fixed data consisting of lens serial number and focal length. The events counter display is recorded on the edge of the film and the CRT data is recorded on a corner of each frame.

Image motion compensation (IMC) capability is provided to allow operation within a wide range of aircraft altitude and ground speeds. The KA-62 camera may be operated using either modified pulse mode or modified IMC pulse mode, controlled by remote switching in the Aircraft Camera Control System (ACCS).

An 89B filter is used with infrared aerographic film when operating only one camera with IR film; if two cameras are used with IR film, a 25A filter is used with the second camera.

Infrared

RS-14 Dual Channel Infrared Imaging Scanner. The Texas Instruments RS-14 Scanner detects infrared or ultraviolet radiation and processes the detected signals as video, displays the video as an intensity-modulated CRT trace, and projects the CRT trace on traveling photographic film. Infrared energy received is reflected through the scanner optical system and is focused upon a detector enclosed in the vacuum chamber of a closed-cycle refrigerator or cooler. Either two or four infrared detectors are available, depending upon preflight selection and

installation of detectors for the particular mission. A fifth sensor, a photomultiplier tube that may be installed before flight in place of two of the four IR detectors, detects ultraviolet and visual radiation.

While recording during flight, the selected detector converts received infrared or ultraviolet visual energy variations into electrical signals. The sensor output is processed into video and displayed as an intensity-modulated trace on a 5-inch CRT in the recorder unit. The CRT trace image is optically coupled to the film magazine unit, exposing the film to produce a rectilinear map.

Figure 4 is a simplified operating diagram of an IR scanner. In addition to the video calibration sources, a 10-step calibration scale and auxiliary data are displayed on the film. The system compensates for aircraft roll by use of inputs from a vertical gyro in the scanner.

Principles of Operation. The RS-14 IR Scanner is a passive, airborne, infrared and ultraviolet imaging system. The instrument scans the ground surface along the aircraft flight path and produces a rectilinear photographic image of the terrain. The system is passive in that it detects and records variations in the radiant energy emanating from earth terrain. Information received by the scanner is converted to video intelligence and processed through the scanner. The video intelligence is converted to visible energy via a CRT for recording on photographic film within a film magazine. A heat exchanger, part of the cryogenic cooling system, maintains the low temperature necessary to operate the infrared detectors located within the scanner. A power supply provides system operating voltages.

Precision Radiation Thermometer. In order to determine precise temperatures directly below the aircraft and to appropriately adjust the RS-14 radiometer, a Barnes Precision Radiation Thermometer (PRT-5) was operated during the times that the RS-14 was in operation.

The Barnes PRT-4 has a 2° field of view. The detector is an immersed thermistor bolometer. The absolute system accuracy of ±0.5°C (claimed) is achieved by controlling the temperature of a heated in-line reference cavity within the optical head of the PRT-5. Incoming target radiation (8 to 14 microns) is compared continuously with the known radiation of the internal reference. The difference is converted into a proportional electrical signal that is equivalent to the target radiation temperature. The output of the PRT-5 is proportional to the fourth power of the absolute radiation temperature; thus, a correction should be made to any linear interpolation between the high and low range marks.

SIDE LOOKING AIRBORNE RADAR (SLAR)

In an attempt to determine the applicability of side looking airborne radar (SLAR), a 16.5 GHz SLAR was operated on 14 flight lines of the 4 October 1971 NASA flight.

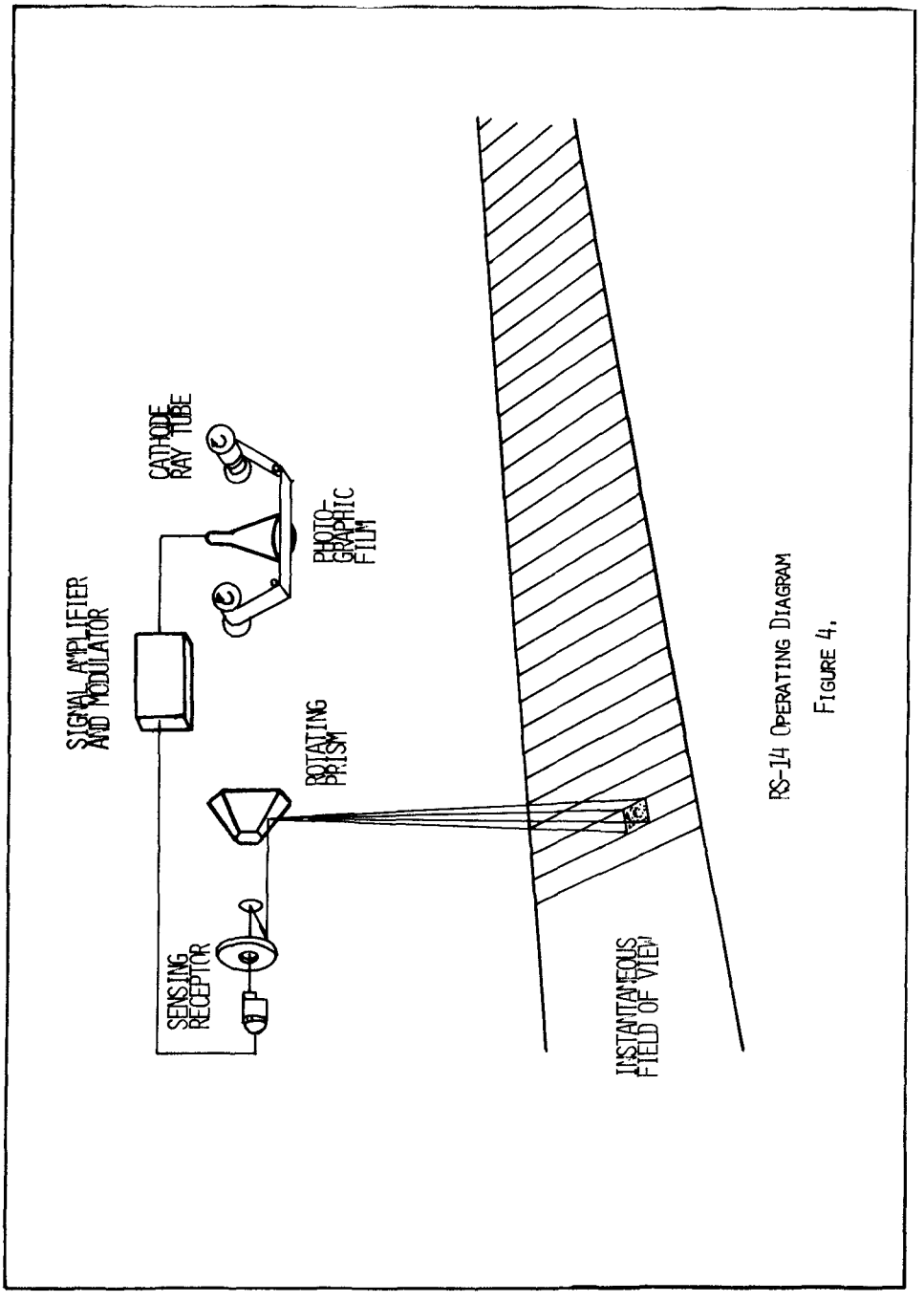

RS-14 Operating Diagram

Figure 4.

The SLAR is an unfocused, synthetic aperature, airborne, radar mapping device which scans the terrain on the starboard side of the aircraft's ground track. The AN/DPD-2 radar was modified by Philco-Ford to provide a dual polarization capability, with the radar data formatted into four separate polarization information channels for film recording.

The microwave energy scattering characteristics of physical objects provide a wide range of identifiable radar backscatter, or return. The differences between these returns enables use of radar to map a given area. The results may be interpreted through an understanding of the characteristic returns as more data is obtained on these characteristic returns. The 16.5 GHz SLAR provides high resolution ground mapping by utilizing a short pulse-width for range resolution (across-track) and a long, synthetically obtained antenna aperture for azimuth resolution (along-track).

The SLAR generates four 10-nautical mile-wide strip map images of the area on the right side of the aircraft. The strip map images (one parallel and one cross polarization for both horizontally and vertically polarized transmissions) are recorded on film during flight. All radar data processing needed to produce a map image is completed before recording on film.

The radar operator may select one of five slant-range swath positions (0 to 10 n.mi., 1.4 to 11.4 n.mi., 2.7 to 12.7 n.mi., 4.0 to 14.0 n.mi., or 5.4 to 15.4 n.mi.) to map the desired area.

As the aircraft flies over the selected terrain, a pulse generator circuit produces a continuous train of pulses. The pulses are used to drive the transmitter and to initiate the sweep on the CRTs which expose the film. The transmitter converts each pulse received into a burst of radio frequency (RF) energy. The duplexer, a switching device used to connect or disconnect the antenna to or from the transmitter or the receiver, connects the antenna to the transmitter during the brief pulse period when RF energy is generated. The antenna radiates the energy toward the terrain below in a narrow, shaped beam. Because of the depression angle (the angle below horizontal at which the energy is directed), the wave front contacts the ground at a point Q (see Figure 9 on the following page) and continues to sweep outward to point T. The antenna receives the backscatter, and because it is connected by the duplexer to the superheterodyne receiver, feeds the microwave energy into the electronic network. The backscattered energy is converted into voltage variations which in turn modulate the intensity of two CRTs. The recording film is transported across the face of the CRTs at a rate proportional to the aircraft's ground speed. The CRTs expose the film in "sweeps" or lines in synchronism with the RF energy wave front "sweep" over the terrain (see Figure 10). The transmitter utilizes a ferrite switch to control polarization of transmissions.

16.5 GHz SLAR Antenna Pattern Diagram

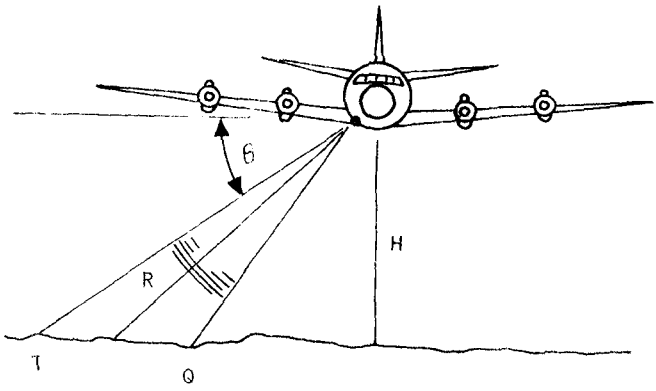

Figure 9

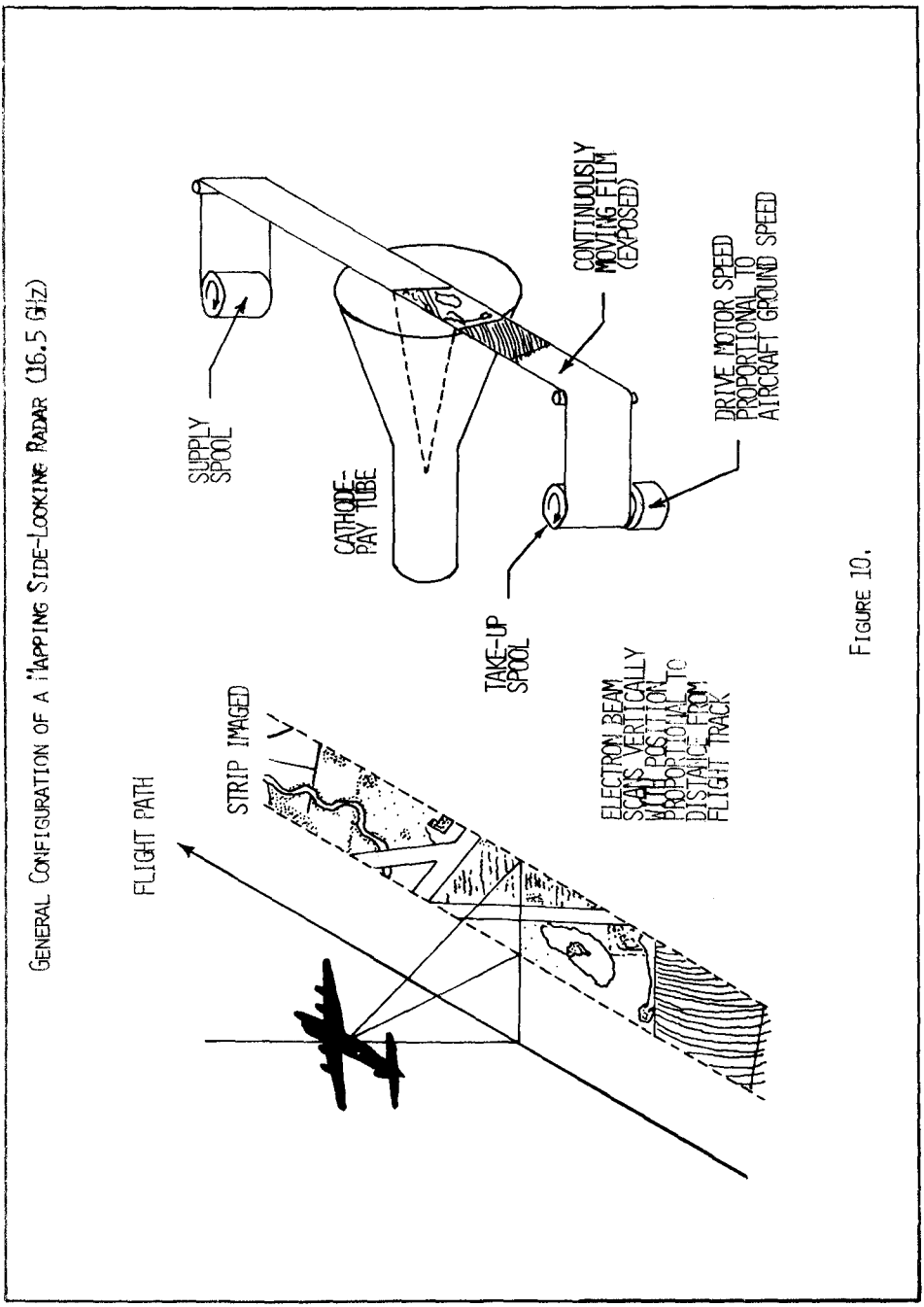
GENERAL CONFIGURATION OF A MAPPING SIDE-LOOKING RADAR (16.5 GHz)
FLIGHT PATH
STRIP IMAGED
SUPPLY SPOOL
CATHODE-RAY TUBE
CONTINUOUSLY MOVING FILM (EXPOSED)
DRIVE MOTOR SPEED PROPORTIONAL TO AIRCRAFT GROUND SPEED
TAKE-UP SPOOL
ELECTRON BEAM SCANS VERTICALLY WITH POSITION PROPORTIONAL TO DISTANCE FROM FLIGHT TRACK

FIGURE 10.

ENHANCEMENT AND IMAGE PROCESSORS

In the process of obtaining coastal information from imagery generated during this flight, a number of optical and electronic devices were used in an attempt to obtain maximum information from the available imagery. In cooperation with the NASA Manned Spacecraft Center, the Corps of Engineers personnel processed imagery on various devices at the MSC Earth Resources Systems in the Agena Building, Clear Lake City, Texas. The basic equipment used in this effort consisted of three systems, as follows:

The Multiband Camera Film Viewer (MCFV)
The Additive Color Viewer Printer
The Datacolor System

Multiband Camera Film Viewer (MCFV). The Multiband Camera Film Viewer, developed by I^2S, is a three-channel electronic system, capable of converting image data, stored on 70 mm or 5 x 5-inch format film, into electronic form, and digitally processing these data, in a high speed real time mode, into a special form for presentation on a high resolution 1,000-line color display. The three key elements of the MCFV system are the scanner, control, and display subsystems.

The scanner subsystem is housed in a console which provides an isolated, stabilized structure to support the various components. These components include a high resolution (1,000-line) CRT, beam splitters, lens, film transports, film holders, film gate drives, condenser lenses, the photomultiplier assembly and the associated drive electronics. The support provided for these components consists of a rigid optical bench assembly, supported and stabilized by three automatically leveled pneumatic struts.

The video signals generated by the scanner are processed by the components of the control subsystem housed in the display console. The two major components of the control subsystem are the Analog Signal Processor (ASP), and the Digital Image Processor (DIP).

The display subsystem consists of a triniscope, housed in the display console. The components of the system include three CRTs, one for each primary color, and an optical assembly. Associated with the CRTs are their electronic chassis, and adjustable CRT/Monitor mounts. The optical assembly is also supported by an adjustable mount. Inputs to the display subsystem are the analog outputs of the Digital Image Processor. These video signals are converted by the triniscope into monochrome or color displays for viewing or photo recording. This device is described in "An Electronic Viewer for Multiband Imagery" by Howard M. Roberts, American Society of Photogrammetry, Washington, D.C. meeting, March 12-17 1972.

SUMMARY OF RESULTS

Color views and enhancements presented during the Vancouver conference cannot be presented in this paper, however, summaries of the resulting image analysis are given below:

a. RC-8 position 1 (color) produced excellent presentation of land features, and limited information from sea and subsurface features.

b. RC-8 position 2 (color IR) produced presentation of the size and quality of marine kelp beds, but provided no way of determining whether the kelp is on the surface.

c. KA-62 position 1a (color). The yellow wratten 12 filter on overexposed color film was found to give the most useful information for the analysis of current and sediment patterns. Material from sewer outfalls is clearly seen on this imagery. It also provided good water penetration.

d. KA-62 position 2 (red). With normal exposure, this camera produces primarily water surface information and is thus useful in enhancement combinations. If this combination is overexposed 1 "f" stop, considerable additional sedimentary information is obtained.

e. KA-62 position 3 (green). Provides good information for the analysis of current and sediment patterns, but with normal exposure, does not produce as good results as KA-62 position 1a. Better results would probably be produced with overexposure.

f. KA-62 position 4 (B&W IR). The infrared (IR) energy can only penetrate a short distance into seawater and is highly reflected by vegetation including algae. Therefore, only the surface canopy of nearshore kelp is seen in this photograph. The near IR film is excellent for use in the analysis of waves breaking upon a beach. Since the IR film is not sensitive to a response by sediments and bottom colors, a good photograph can be obtained of coastal waves, beach cusps, and refraction patterns. It was unfortunate that at the time of this flight, there were only small waves in the central California area; however, other imagery seen by the authors has shown that the use of near IR black and white or false color IR techniques are invaluable in the analysis of ocean wave phenomena.

g. SLAR Boresight Camera. Of little value due to inability to depress at same coverage angle as SLAR on this mission.

h. RS-14 IR Scanner. This device provided detailed information from which current and/or sediment movement may be implied. Man-made discharges produced good sources for tracing current movements.

i. 16.5 GHz SLAR. Due to low wave heights and frequency, only limited information is obtained and that is in the zone of breaking waves. In order to obtain information on sea and swell waves lower frequencies would probably be required.

j. Enhancements. Image enhancements produced by the various devices tested yielded impressive results. Of the devices tested, the MCFV produces the best opportunity to synergistically combine various images to display a typical desired parameter (such as offshore kelp beds) with the ultimate view of producing automatic processing of imagery.

CONCLUSION

Based on the summary of the results of the coastal remote sensing flight described in this paper, it is concluded that remote sensing provides valuable tools in the study of coastal processes. It is further concluded that remote sensing combined with appropriate enhancement and automatic data processing will lead toward the development of remote sensing/analysis systems that will not only record the phenomena under study but will also produce the desired numerical values of the appropriate parameters describing the phenomena.

ACKNOWLEDGMENTS

This work was jointly sponsored by the U. S. Army Coastal Engineering Research Center, Washington, D.C., and Earth Observations Aircraft Program of the National Aeronautics and Space Administration (NASA). Acknowledgment is gratefully made to NASA for the aircraft mission support, and subsequent image processing and enhancement assistance. Financial support of the Coastal Engineering Research Center for data analysis and report preparation are also gratefully acknowledged. The views presented are those of the authors and do not purport to reflect the position of the National Aeronautics and Space Administration or the Corps of Engineers, Department of the Army, or Department of Defense.

In the work reported on in this paper, Mr. Orville T. Magoon was the Principal Investigator (PI) and Mr. Douglas M. Pirie was a Co-Principal Investigator (COPI) and Mr. Allan Williams of the Los Angeles District was responsible for the image analysis of the southern California coast. The authors also gratefully acknowledge the friendly cooperation of the NASA personnel both in NASA headquarters, Washington, D.C.; and in the Manned Spacecraft Center, Houston, Texas, and especially to Mr. Gordon Hrabal, the NASA Mission Manager.

The authors also gratefully acknowledge the extensive Sea/Ground Truth support provided by the Department of Parks & Recreation, State of California, Dr. Ed Thornton, USN Postgraduate School, Monterey, California, and supporting personnel at CERC.

CHAPTER 116

COASTAL ENGINEERING APPLICATIONS OF AERIAL REMOTE SENSING

Donald B. Stafford, A. M. ASCE[1]

ABSTRACT

This paper reviews the important coastal engineering applications of aerial remote sensing techniques and provides a current state of the art summary of the utilization of aerial remote sensors in coastal engineering studies. The sensors discussed include conventional black and white aerial photographs, black and white infrared aerial photographs, color and color infrared aerial photographs, multispectral aerial photographs, satellite photographs, infrared imagery, multispectral imagery, and radar imagery.

The field of coastal engineering is considered in a broad context to include all important applications of aerial remote sensing that relate to coastal engineering problems. The use of remote sensors to monitor coastal changes, study coastal landforms, examine storm effects, map coastal areas, determine nearshore hydrography, and monitor the environmental effects of coastal engineering projects, a topic of considerable current concern, is described.

The important characteristics of the various aerial remote sensors are described briefly. The advantages and limitations of the aerial remote sensing techniques for different coastal engineering studies are noted. The review and state of the art summary of the applications of the aerial remote sensors can be used by coastal engineers as guidelines in employing the sensors in future coastal engineering investigations.

INTRODUCTION

A considerable amount of literature exists which describes various applications of aerial remote sensing techniques in the field of coastal engineering. The increased interest in aerial remote sensors as a tool in coastal engineering investigations is indicated by the increasing number of papers describing the use of these techniques that have been presented at the Coastal Engineering Conferences in recent years. It is quite probable that the uses of aerial remote sensors in coastal engineering will continue to expand in the future as coastal engineers become more familiar with the techniques and improvements in aerial remote sensing techniques are developed.

---

[1]Associate Professor, Department of Civil Engineering, Clemson University, Clemson, South Carolina 29631

Aerial remote sensing techniques have several important advantages over other possible approaches to many coastal engineering studies. In many instances, a savings in the cost of data collection can be achieved. In other coastal engineering studies, the use of aerial remote sensing techniques makes it possible to collect data that could not be obtained by any other method or only at a cost that would be prohibitive. The use of aerial remote sensors also makes it possible and economically feasible to obtain more complete data on certain coastal conditions and processes than can be obtained by alternative data collection techniques. The continuous coverage of the terrain available with aerial remote sensors also permits very limited field observations to be used to characterize conditions over very large areas.

Certainly one of the most important advantages of aerial remote sensing techniques is a direct result of the aerial vantage point that is inherent in all of these techniques. The use of the aerial vantage point provides an overall view of terrain features that can be very useful in analyzing coastal landforms and processes. The aerial remote sensors provide synoptic coverage of the terrain that permits the coastal engineer to examine the relationship between various coastal features and processes. The continuous coverage and the aerial vantage point that are provided by the aerial remote sensors are particularly important in analyzing rhythmic coastal features such as sand waves that cannot be observed easily on the ground.

A variety of aerial remote sensors are available for use in coastal engineering applications. The most common sensors include black and white, black and white infrared, color, and color infrared aerial photographs, multispectral aerial photographs, satellite photographs, infrared imagery, multispectral imagery, and radar imagery. Each of these sensors has characteristics and capabilities that make it particularly suitable for certain types of coastal engineering investigations. It is imperative that coastal engineers be sufficiently familiar with the primary characteristics of the various sensors if the optimum sensor for a particular coastal engineering application is to be selected. Consequently, the following paragraphs describe the important characteristics and coastal engineering applications of the various sensors and summarize the advantages and limitations of the sensors.

APPLICATIONS OF AERIAL REMOTE SENSORS

Black and White Aerial Photographs

Conventional black and white or panchromatic aerial photographs have been used for many years in various coastal engineering applications. At the present time, black and white aerial photographs are the most widely used aerial remote sensor, primarily because these photographs are readily available for coastal areas. Black and white aerial photographs have been used both as graphic display tools or maps to illustrate coastal features and as a source to extract quantitative data concerning various coastal features and processes. Because of the aerial vantage

point, aerial photographs have a unique capability to depict many coastal features and processes. In many instances, the relationship between various coastal features and processes can be examined more thoroughly from aerial photographs than from ground observations.

One of the most useful coastal engineering applications of black and white aerial photographs is to detect and measure changes in dynamic coastal landforms by comparing photographs taken with some time lapse. Aerial photographs are made by various governmental agencies and private firms for many different purposes, and consequently several coverages of aerial photographs taken over the past 30-40 years exist for most coastal areas in the United States and many other areas of the world. Therefore, several increments of change in coastal features can be determined by making measurements on each set of available photographs. Aerial photographs can be used to determine changes that result from long-term coastal processes and from short-term effects such as storms and hurricanes. If an effort is made to minimize the detrimental effects of the inherent errors in aerial photographs caused by scale variation, tilt, and relief distortion, accurate measurements of coastal changes can be made. An important recent development in the use of aerial photographs for coastal engineering studies is that the Coastal Engineering Research Center has initiated a program to compile a list of all existing aerial photographs of coastal areas in the United States.

Athearn and Ronne (1963), Cameron (1965), El-Ashry (1963 and 1966), El-Ashry and Wanless (1965, 1967, and 1968), Moffitt (1969), and others have described the results of studies which used panchromatic aerial photographs to determine changes in coastal landforms. Stafford (1968 and 1971) presented a detailed description of a procedure for conducting beach erosion surveys by making measurements on comparative aerial photographs. The results obtained in conducting an erosion survey along the entire 330-mile length of the North Carolina Coast were presented by Langfelder, Stafford, and Amein (1968 and 1970).

Many other coastal engineering applications of panchromatic aerial photographs have been described by various investigators. Examples of these applications include studies of wave refraction patterns, rip currents, coastal mapping, land use mapping, storm effects on coastal landforms, water current direction and velocity, coastal landform and geomorphology research, and wave patterns. Sonu (1964) reviewed the use of black and white aerial photographs in studies of coastal processes.

Black and White Infrared Aerial Photographs

Black and white infrared aerial photographs have been used in certain coastal engineering applications for many years. For coastal applications, the primary characteristic of infrared photographs is that they produce a sharp contrast between water bodies and the beach. This feature is the result of the marked difference in reflectance characteristics of water and earth materials in the near infrared wavelengths. Water bodies photograph in a dark gray or black tone which contrasts distinctly with the white to light gray tone of the materials

composing the beach and other land features. Consequently, black and white infrared aerial photographs are very useful in shoreline delineation studies and particularly in locating the shoreline or waterline at different stages of the tide. By taking aerial photographs at specific levels of the tide, the location of the water line corresponding to any desired tidal stage can be determined. Black and white infrared aerial photographs have been used extensively by the National Ocean Survey and its predecessor, the U. S. Coast and Geodetic Survey, for various coastal mapping applications. Consequently, there are several coverages of black and white infrared aerial photographs available for many areas along the coast of the United States. It should be noted that black and white infrared aerial photographs can be used very effectively in conjunction with panchromatic aerial photographs in examining changes in coastal landforms.

Another characteristic of black and white infrared aerial photographs that can be useful for certain applications in the coastal environment is that these photographs have better haze penetration capability than panchromatic photographs. This capability results from the fact that the near infrared radiation used to expose black and white infrared film has a significantly longer wavelength than the visible spectrum radiation used to expose panchromatic film. The longer wavelength radiation is less susceptible to atmospheric scattering by thin clouds, fog, haze, dust, or air pollution than the shorter wavelength visible spectrum radiation in accordance with Rayleigh's Law. The increased haze penetration can be useful in a variety of coastal engineering applications in urbanized areas where air pollution is common or in areas where meteorological conditions frequently produce fog or haze.

Color and Color Infrared Aerial Photographs

Color and color infrared aerial photographs have been used in several coastal engineering applications. The addition of color to the aerial photograph provides a supplementary detection and discrimination capability that can be very useful in investigating many coastal features and processes. The additional cost of color or color infrared aerial photographs as compared to black and white photographs can be justified by the additional information content of color photographs in many coastal engineering applications. Several studies have shown that color photographs are most appropriate for some coastal engineering applications and color infrared photographs are the optimum type of aerial photograph for other coastal engineering applications. Thomas (1971) compared the coastal engineering applications of color and color infrared aerial photographs using the southern coast of Long Island, New York, as a study site. He found that color photographs were best for investigating underwater phenomena such as sediment patterns, water depths, and mapping shoal areas. Color infrared aerial photographs were found to be best for examining coastal features on land and for coastal vegetation studies. Consequently, obtaining both color and color infrared aerial photographs should be considered for comprehensive coastal engineering studies if the added expense can be justified.

Color aerial photographs have been used extensively by the National Ocean Survey in preparing and revising coastal charts because of their ability to provide water penetration and show submerged features. Color aerial photographs have been found to be useful in planning hydrographic surveys, in conducting storm damage surveys in coastal areas, and in revising nautical charts made obsolete by storm induced changes in coastal landforms.

Several studies of water penetration and water depth determination using color aerial photographs have been conducted in recent years. Much of the work in investigating the water penetration characteristics of color aerial photographs has been a preliminary step toward developing a technique for depth determination. Geary (1968) and others have described successful tests of water depth determination from color aerial photographs. Many studies have documented the superior water penetration capability of color aerial photographs as compared to color infrared photographs (Thomas, 1971). A special color film in which the blue sensitive emulsion layer was eliminated has also been used in depth penetration studies, apparently with considerable success. However, Ross (1969) and others have cast considerable doubt on the utility of a non-blue sensitive color aerial film for depth penetration applications. Several investigators have discussed important considerations in selecting the proper photographic techniques to achieve maximum depth penetration and to record subsurface details with color aerial photographs. Several studies have shown that a higher than ordinary exposure of the aerial film is necessary to produce maximum depth penetration, and this usually results in overexposure of the film for surface features. It is also important to have an understanding of the light transmission characteristics of water in planning depth determination projects using color aerial photographs. Continued development of techniques for determining water depths from aerial photographs can be expected.

Color aerial photographs have been used successfully in determining water current direction and velocity by photogrammetric techniques. Color aerial photographs have also been used in examining the flow patterns of water discolored by suspended sediment, pollutants, or dye. James and Burgess (1970) described a very sophisticated technique for investigating ocean outfall dispersion based on an analysis of color aerial photographs of a dye tracer. Waste concentrations, dispersion coefficients, and water current direction and velocity were determined by this technique.

Color infrared aerial photographs have some of the same characteristics commonly associated with black and white infrared aerial photographs. Color infrared photographs have better haze penetration than color photographs and they also give a sharper line of demarcation between water bodies and land features. These properties can be useful in several coastal engineering applications. The sensitivity of color infrared aerial film in the near infrared portion of the spectrum and the high reflectance of vegetation in the near infrared band cause vegetation to appear in a deep red or magenta color on color infrared aerial photographs. The variation in infrared reflectance characteristics of

different vegetation species is sufficient to permit the differentiation of vegetation species by examining the intensity of the reddish color of vegetation on color infrared aerial photographs. Color infrared aerial photographs have been used extensively for mapping marshland vegetation species in the coastal zone (Pestrong, 1969). Color infrared aerial photographs may also be useful in monitoring the environmental effects of various activities in marshlands, estuaries, and other coastal areas.

Multispectral Aerial Photographs

Multispectral or multiband aerial photographs have only recently begun to be utilized for coastal engineering applications. Multispectral aerial photographs consist of two or more photographs of the same area that have been exposed by using different portions of the electromagnetic spectrum. Multispectral aerial photographs produced by multiple lens cameras with different film and/or filter combinations have an increased capability for the detection and analysis of various coastal features and processes. This increased detection capability results from the fact that multispectral photographs provide additional information on the interaction of terrain features and the electromagnetic energy employed in making the photographs. The selection of the different film and filter combinations can be made in such a manner that the maximum amount of information for a particular coastal engineering application can be obtained from the multispectral aerial photographs. In coastal areas, one wavelength band could be chosen to give maximum water penetration, another wavelangth band chosen to provide the maximum capability to delineate the land-water boundary, another wavelength band could be chosen to provide the maximum capability to discriminate between coastal vegetation species, and the other wavelength band or bands selected to optimize the capability to detect some other coastal feature or process of interest to the investigator. Research has shown that four multispectral photographs consisting of the blue, green, red, and near infrared bands are adequate for many applications.

Pestrong (1969) examined the utility of multispectral aerial photographs in investigating several aspects of the coastal environment, including water depth penetration, land-water boundary delineation, drainage feature mapping, and vegetation mapping. He found that four photographs consisting of color, color infrared, black and white infrared, and a photograph in the 550-630 millimicron wavelength band would constitute an optimum multispectral system. Ross (1969), Wenderoth (1969), and Yost and Wenderoth (1968 and 1971) have used multispectral aerial photographs extensively to investigate the water depth penetration capability of aerial photographs. Several important aspects of the depth penetration problem such as photographic techniques for achieving maximum penetration, the effects of suspended particulate matter on penetration, and the attenuation characteristics of light in various wavelength bands in different types of coastal water have been examined and the results have been reported. It has been shown that the light transmission characteristics of water are an important factor that must be considered in planning multispectral aerial photography missions for coastal engineering applications that involve water penetration.

Recently considerable progress has been made in the analysis techniques for multispectral aerial photographs. The development of various image enhancement techniques and particularly the additive color viewing approach has greatly increased the capability to extract data on different features depicted in the multispectral aerial photographs. Available techniques and equipment can be used to combine the multispectral photographs in combinations that simulate regular color, color infrared, and other false color images. Therefore, the multispectral aerial photographs and the additive color viewing technique can be used to obtain the maximum amount of information about the coastal zone terrain and thus provide essential data for coastal engineering investigations. Multispectral aerial photographs and additive color viewing appear to have considerable potential in coastal zone vegetation studies and this approach may be useful in examining the environmental effects of some coastal engineering projects.

Satellite Photographs

Satellite photographs have been used in examining certain coastal and oceanographic phenomena that can be observed from satellite altitudes. Fortunately, a number of important coastal and oceanographic features are visible on satellite photographs. The primary advantage of satellite photographs is the large area of coverage provided by each photograph. The large area of coverage permits features and processes that occur on a large scale to be observed in their entirety rather than in small segments as is commonly the case with ground observations or even other aerial remote sensors. Therefore, the photographs are suited ideally to the analysis of large coastal phenomena such as littoral currents, suspended sediment patterns, river effluent dispersion, and regional coastal landform studies. Satellite photographs can provide synoptic coverage of large scale coastal features and processes that can be used to evaluate the relationship between various landforms and features observed in the photographs. Satellite photographs may be particularly useful for providing more complete information on small scale problems that are created by large scale processes whose role is not completely understood or which cannot be observed using low altitude aerial remote sensors or ground observations.

The combination of the high altitude and the small scale that is used in producing satellite photographs results in a relatively low resolution as compared to other photographic aerial remote sensors. Satellite photographs commonly have a resolution in which the smallest features that can be observed are in the 200-300 feet range. Although the low resolution limits the type of coastal features that can be examined on satellite photographs, the resolution is not a severe handicap when large scale features are being investigated.

The applications of satellite photographs to coastal engineering studies have been severely restricted by the fact that the photographs have been available for only limited areas. However, the Earth Resources Technology Satellite (ERTS) program to obtain repeat coverage with multispectral satellite photographs on an 18-day cycle for most coastal

areas promises to open a new era in the coastal engineering applications of satellite photographs. The repeat coverage will be particularly useful in investigating large time-varying coastal zone phenomena. The amount of satellite photography that will be available for study will increase dramatically as the ERTS and Skylab missions are conducted. Also, the combination of multispectral satellite photographs and analysis techniques such as additive color viewing offers considerable potential for coastal engineering applications.

One of the most important investigations of coastal processes by the use of satellite photographs was conducted by Mairs (1970). This study was based on an analysis of Apollo 9 photographs and it involved a detailed analysis of the origin, movement, and dissipation of turbid water plumes near Cape Hatteras, North Carolina. The observed plumes were concluded to be the ebb tide discharge of highly turbid water containing sediment derived from the bottom of Pamlico Sound. Mairs (1970) concluded that satellite photographs were a useful tool in studying coastal water circulation, flushing, and mixing patterns.

Nichols (1970) described several coastal processes that can be examined on satellite photographs, including turbid water plumes being transported by currents and circulation patterns. He noted the need for and the difficulties encountered in collecting adequate ground truth data to use in calibrating data extracted from satellite photographs.

Lepley (1968) investigated coastal water clarity by examining Gemini mission satellite photographs. The primary objectives of this study were to estimate the portion of the world's coastline that had sufficiently clear water to permit mapping of nearshore topography by using aerial remote sensing techniques and to investigate the feasibility of using satellite photographs to obtain data on water clarity. Lepley (1968) concluded that 35 percent of the world's coastal waters were sufficiently clear to allow mapping of sea floor topography to depths of 20 meters by aerial photographic techniques.

The satellite remote sensing data that will be generated in the near future appears to have considerable potential for coastal engineering applications. The availability of almost complete coverage of coastal areas at 18-day intervals will provide a capability for monitoring large scale coastal processes that has not previously existed. Hopefully, the apparent potential of this sensor will be realized in the near future so that this new tool can provide essential data needed in conducting comprehensive coastal engineering investigations.

Infrared Imagery

Infrared imagery is a non-photographic sensor that is produced by an optical-mechanical scanning device. The scanner is equipped with a detector which senses radiation in the infrared band. The infrared detector changes the incoming radiation into an electrical signal which can be recorded on magnetic tape or amplified and converted into an image on photographic film. The scanner is designed to scan a narrow band of

terrain perpendicular to the flight line of the aircraft. As the aircraft travels along the flight line, successive scan lines provide continuous coverage of a band of terrain beneath and on each side of the aircraft. The infrared detector can be selected to provide sensitivity in the portion of the infrared spectrum where the maximum amount of information on a particular application can be obtained. The size of the infrared detector can also be selected to provide the proper balance between spatial resolution and thermal sensitivity. Taylor and Stingelin (1969) have presented an excellent description of the operating characteristics of infrared scanners.

An important characteristic of infrared energy is that bodies emit radiation in proportion to their temperature. Therefore, the intensity of the infrared energy emitted by an object can be used as an indication of the temperature of the body. The gray tone or film density of the infrared imagery represents the intensity of the infrared emission and the temperature of terrain objects depicted in the imagery. On positive prints of infrared imagery, white or light gray tones represent high temperatures and dark tones represent low temperatures. Consequently, infrared imagery is often referred to as thermal imagery or thermal infrared imagery. The fact that infrared imagery can be used to obtain data on temperature makes this sensor an ideal tool for a variety of applications in which temperature is an important variable. Some infrared scanners have provisions for the scanner to observe the infrared emission of a body having a known temperature incorporated into the device. This provides a technique to calibrate the gray tone of infrared imagery. The ability to quantify the gray tones on infrared imagery greatly increases the utility of the imagery. Taylor and Stingelin (1969) have reported that temperature differences as small as one degree centigrade can be detected on infrared imagery.

An important characteristic of infrared imagery is that it has day and night capability. Infrared imagery does not require sunlight for illumination because the infrared energy emitted from the terrain is a function of the terrain temperature. Generally, infrared imagery is made at a time when the feature of primary interest has maximum temperature contrast with the surrounding terrain. By having day and night capability, infrared imagery is less restricted than aerial photography if coverage during a particular tidal stage or other specific time period is desired.

Infrared imagery has been used only to a limited degree for coastal engineering applications. Because of the relation between the gray tone of infrared imagery and temperature, infrared imagery is particularly applicable to studies in which temperature is an important variable. In the coastal environment an important terrain feature that is particularly temperature sensitive is water. Thus, most coastal applications of infrared imagery have involved investigations of various characteristics of water bodies that can be indicated by temperature differences. Studies of water pollution, thermal pollution, and tidal flushing of coastal water bodies are investigations in which infrared imagery can be used successfully.

Several studies of water currents in the coastal environment have utilized infrared imagery. Some of these studies have monitored the movement of cool groundwater being discharged by springs into warmer ocean water to evaluate current patterns. Other studies have examined current patterns by relying on the existence of natural water temperature differentials or heated industrial effluent and noting the movement of these water masses.

Taylor and Stingelin (1969) investigated current patterns in the Merrimack River estuary of Massachusetts by using infrared imagery taken at night. In particular, the effect of tidal stage on current patterns was of interest and infrared imagery taken at different tidal stages was examined. The movement of polluted water and the boundary between river water and sea water under the influence of tidal action was also evident on the infrared imagery.

Taylor and Stingelin (1969) and others have demonstrated the tremendous potential of infrared imagery for thermal pollution studies in the coastal environment. The dispersion patterns of thermal effluents can be easily traced on the infrared imagery. The influence of tidal currents on thermal effluent dispersion can be investigated by using infrared imagery taken at different tidal stages. As more nuclear and fossil-fueled power plants are constructed in coastal areas and possibly offshore, infrared imagery will provide a powerful tool to monitor the effects of the thermal discharges of these plants in the coastal environment. Infrared imagery can also be used effectively in a variety of environmental studies such as monitoring industrial effluents, determining oil pollution sources and dispersion patterns, and examining certain aspects of tidal marsh ecology.

Multispectral Imagery

Multispectral imagery is a relatively new remote sensing tool that has not been used to a significant degree in coastal engineering applications. The basic concepts and the equipment used in obtaining multispectral imagery are similar to those used in obtaining infrared imagery. However, multispectral imagery is a more comprehensive sensor because data is collected in several bands of the spectrum. The spectral range that can be covered in obtaining multispectral imagery ranges from the ultraviolet through the visible region to the infrared band. The multispectral scanner collects data in a number of spectral bands over this range.

The mode of operation of a multispectral scanner is quite similar to that of an infrared scanner. The optical-mechanical scanner scans an area beneath and on each side of the flight path. Each scan line covers a narrow band perpendicular to the flight line. As the aircraft moves forward successive scan lines combine to provide continuous coverage of the area. The incoming radiation is separated into several discrete wavelength bands and transmitted to detectors sensitive to the proper wavelength band. The intensity of the radiation in each band is translated into an electrical signal by the detector and the electrical signal for each spectral band is stored on magnetic tape. Multispectral

scanners having the capability to obtain data in as many as 24 discrete bands have been developed. Multispectral imagery in approximately five to seven bands is adequate for most applications.

When the multispectral data that is stored on tape is returned to the laboratory, the data in any of the spectral bands can be transformed into a photographic image. The gray tone or film density of the image corresponds to the intensity of the energy reflected or emitted in each particular band. It should be recognized that the energy emanating from the terrain represents primarily reflected energy in the ultraviolet, visible, and near infrared bands and emitted energy in the infrared spectral regions. Multispectral imagery commonly includes the infrared portion of the spectrum, and the infrared region is frequently separated into two or more bands corresponding to the infrared windows in the atmosphere.

The availability of data in several spectral bands provides a unique capability for discriminating between objects and for detecting the presence of specific features. The individual multispectral images reflect the spectral reflectance and emission characteristics of the terrain in each spectral band. Thus, the multispectral images can be used for detailed studies of terrain properties. Since many terrain features have unique spectral signatures or spectral signatures that are somewhat different from the signatures of the surrounding terrain, the multispectral images which reflect the spectral response of the terrain can be used to identify specific features.

One of the most advantageous aspects of multispectral imagery is the analysis techniques that are available. The multispectral data stored on tape can be processed and used as input to computer programs to analyze the data. By comparing the characteristics of the spectral response of the terrain with known spectral response data obtained from field measurements, the computer can identify certain terrain features. For instance, the ratio of the spectral response at different wavelengths may be used to identify certain features. Also, the computer output consisting of the predicted occurrence of selected features can be printed in a map showing the distribution of the features. This approach provides a degree of automation in the interpretation and analysis of aerial remote sensing data that is not available with other remote sensors. This technique is a powerful tool for analyzing multispectral imagery. However, it should be recognized that information on the spectral response of the features of interest must be known so that the computer analysis system can be calibrated.

One important and potentially very useful coastal engineering application of multispectral imagery that has been reported is water depth determination. Polcyn and Sattinger (1969) have described a technique for using multispectral imagery to map shallow water depths. The technique consists of the computer analysis of the energy reflected from the bottom at two different wavelengths. The depth determinations produced by the computer analysis are used to print a map of water depths. Thus, the computer performs the data analysis and also produces a

convenient presentation of the water depth data. Even though the water depth data may not be sufficiently accurate for some detailed coastal engineering investigations, the technique appears to have considerable potential for applications where data on water depths are required. It should be noted that this technique is in an early stage of development and considerable improvement in the method may be forthcoming in the near future. Combining a laser device for measuring water depths with the multispectral technique provides a method of calibrating the water depth data and improving the accuracy of the depth determinations.

Techniques for using multispectral imagery and computer processing to classify vegetation have been described by several investigators. The successful use of multispectral imagery and computer processing has been reported for a number of other applications. These techniques have been used to classify soils, investigate hydrologic features, and many other similar applications. It appears that these techniques may also be useful in investigating various aspects of the coastal environment other than water depths and vegetation. All that is required is that the features to be investigated have a sufficiently unique spectral signature that the presence of the feature can be predicted from an analysis of the multispectral imagery. Another requirement is that information on the spectral response of the feature of interest must be known and this information can be obtained from field measurements.

When the existing and potential uses of multispectral imagery and computer processing techniques are considered, this approach appears to have considerable potential for coastal engineering applications. Also, it is quite likely that the quality of multispectral imagery and available analysis techniques for multispectral imagery will realize significant improvement in future years. Consequently, multispectral imagery will probably be used more widely for coastal engineering applications in the future.

Radar Imagery

In contrast to all photographic sensors, infrared imagery, and multispectral imagery which are passive sensors, radar imaging systems are active sensors. This means that the radar sensor provides its own source of illumination rather than relying on reflected energy from the sun or emitted energy from the terrain. This property provides radar imaging systems with a day or night capability. The radar system transmits a pulse of energy in a narrow beam perpendicular to the flight path of the aircraft and monitors the returning or reflected signal. The returning signal is processed and used as input to a cathode ray tube device which produces a photographic image. Successive impulses of radar energy are transmitted from an antenna and the reflected signals are monitored to provide continuous coverage of a band of terrain on one side of the aircraft. Because the radar imaging system is an active sensor which illuminates the terrain with radio waves and monitors the reflected signal, it measures the reflective characteristics of the terrain.

The radar imaging system is a side-looking device which scans a band of terrain on one side of the aircraft. Radar imagery is frequently referred to as SLAR or SLR imagery which are acronyms for side-looking airborne radar or side-looking radar. Although the view of the terrain taken by the radar system is similar to the view in an oblique aerial photograph, the radar imagery is produced in a format that has a uniform scale. Mosaics of radar imagery can be compiled to provide continuous coverage of large areas.

Another important characteristic of radar sensors is that the long wavelengths that are commonly used are not significantly attenuated by the atmosphere even when clouds, fog, haze, or air pollution are present. This provides radar imaging systems with an all weather capability. Only heavy precipitation has the effect of degrading radar imagery. When the all weather and day and night capability are considered in combination, radar imaging systems have considerable versatility. The all weather capability can be a particularly advantageous characteristic in tropical areas where cloud cover is almost constant. The successful use of a radar imaging system in a tropical environment has been demonstrated in the Darien Province of Panama where good quality radar imagery was obtained in an area where it has never been possible to obtain complete aerial photographic coverage.

Some of the radar imaging systems have provisions to control the polarization of the signal that is transmitted and received by the sensor. For instance, a signal polarized in a horizontal plane can be transmitted, and a signal polarized in a horizontal plane can be received. Alternatively, a horizontally polarized signal can be transmitted and only vertically polarized signals received. The radar images produced by these two polarization combinations are defined as like and cross polarized images, respectively. It has been shown that having both a like and a cross polarized image can increase the ability to detect linear features associated with natural terrain and cultural development. One typical radar system provides adjacent like and cross polarized radar images for analysis and interpretation.

The synthetic aperture radar system operates in a slightly different manner and provides radar imagery with higher resolution than other radar systems. The primary characteristic of the synthetic aperture system is that the electronic equipment used for radar energy transmission and receiving is designed to produce a synthetic or fictitious antenna in space so that the flight path of the aircraft acts as an antenna in transmitting and receiving the radar pulses. The longer synthetic antenna improves the resolution of the imagery and provides for uniform resolution throughout the entire band of coverage. In the synthetic aperture radar system, the energy reflected from the terrain is received, changed into an electrical signal, and stored on film. The filmed data is processed optically in the laboratory to produce the radar imagery.

Radar imagery is usually produced at a relatively small scale. Also, the resolution of the best radar imagery available on the civilian market is approximately 50 feet. Thus, radar imagery is rather limited

when detailed analyses of terrain features are contemplated. On the other hand, the small scale radar imagery is particularly advantageous for conducting reconnaissance surveys of large areas. The side-looking radar imagery provides a wide band of coverage for each flight line which can be a useful feature.

Imagery produced by side-looking airborne radar systems has been employed by geoscientists for numerous applications related to geologic studies, geologic mapping, and terrain evaluation. However, the coastal engineering applications of radar imagery have been limited. However, it has been shown that many coastal landforms and features can be identified on radar imagery. Radar imagery can be used as as a map of coastal areas and the imagery can be interpreted to obtain data on the geology and other characteristics of coastal terrain.

One of the most extensive applications of radar imagery in coastal studies has been described by MacDonald, et al. (1971). This study involved an investigation of the use of radar imagery in coastal mapping and coastal geomorphology studies in Panama. The advantages and disadvantages of radar imagery in coastal studies were discussed and the types of coastal landforms visible on radar imagery were described. The importance of the all weather capability of radar sensors in obtaining satisfactory coverage of perennially cloud covered tropical areas was emphasized. The coastal landforms and features identified and examined on the radar imagery included tidal mud flats, estuarine features, surf, beach ridges, and a variety of other beach features. The low spatial resolution and lack of data on water depths, nearshore processes, and submerged features were noted as limitations of radar imagery in detailed coastal studies.

Lewis and MacDonald (1970) investigated the characteristics of estuarine drainage patterns by using radar imagery. The primary features examined were estuarine meanders consisting of oblong channels separated by depositional spurs. These landforms provide information on the balance between marine and fluvial processes and on other characteristics of the coastal environment. Other investigators have noted that radar imagery is very useful in delineating drainage patterns.

Orr and Quick (1971) investigated the use of radar imagery and other aerial remote sensors in coastal terrain studies. Radar imagery was found to be the optimum sensor for conducting a regional analysis of coastal terrain. A number of coastal landforms and features could be identified on the radar imagery. A ranking of the capability of radar imagery and several other aerial remote sensors in investigating various aspects of the coastal environment was presented.

Radar imagery with its day or night and all weather capability has the potential to be a useful sensor in selected coastal engineering investigations. Radar imagery can be particularly useful for coastal mapping in cloud prone tropical areas and in extreme northern or southern latitudes which have long periods of darkness. Radar imagery can also be advantageous in conducting reconnaissance surveys of long

sections of coastline. For certain types of coastal studies, radar imagery may be useful as a supplement to other aerial remote sensors. Improvements in radar imaging systems to increase the resolution may be available in the future.

Other Aerial Remote Sensors

Several other aerial remote sensors have been developed and used for certain coastal and oceanographic applications. Some of these sensors may prove to be useful for selected coastal engineering investigations. The sensors that appear to have the greatest potential for coastal engineering applications are described briefly in the paragraphs below.

Laser devices for determining water depths from aircraft have been developed recently. These devices are in a state of testing and development and information on the characteristics and accuracy of the devices is rather limited. The laser depth ranging devices may be particularly useful for calibrating water depth data obtained from other aerial remote sensors such as multispectral imagery or multispectral aerial photographs. Practical laser devices to differentiate between suspended sediment and true bottom may also be developed in the near future. Laser devices for measuring water depths appear to have considerable potential for coastal engineering applications, particularly if further development of the technique can improve the accuracy of the depth data obtained. It should be noted that laser devices for obtaining ground surface profiles or cross-sections of land features are available.

Meteorological satellites have had a tremendous impact in the field of meteorology and these satellites have also produced a considerable amount of data that is useful in oceanographic applications. Data on weather conditions obtained from meteorological satellites may be useful to coastal engineers in developing synoptic weather charts for use in wave propogation studies. Meteorological satellites can also be useful in examining severe storms such as hurricanes and relating the storm location to wave conditions and storm damage along coastlines.

Scientists at the U. S. Geological Survey have developed and tested a prototype model of an airborne fluorometer (Stoertz, et al., 1969). The device has the capability to measure fluorescence from dyes in aqueous solution in daylight from an airborne platform. The device can be very useful in monitoring dye tracers in water current and dispersion studies in bays and estuaries. The device can be used with clear or turbid water and very low concentrations of dye tracer can be detected. The airborne fluorometer appears to have considerable potential for coastal engineering applications such as hydrodynamic investigations and water pollution studies. Further improvements to overcome some of the problems with this new aerial remote sensor may be forthcoming.

Several other aerial remote sensors may have potential in certain coastal engineering studies. These include infrared radiometers, radar scatterometers, active microwave sensors, passive microwave sensors, and microwave scatterometers. Although not an aerial remote sensing

technique, terrestrial photogrammetry which is closely related to aerial photogrammetry also has potential in coastal engineering investigations both in the laboratory and the field.

CONCLUSIONS

Each of the aerial remote sensors has characteristics which make it particularly suitable for certain coastal engineering applications. Therefore, it is important to have an adequate knowledge of the capabilities of the aerial remote sensing techniques so that the optimum sensor can be selected for a particular application. By employing the type of aerial remote sensor that is most appropriate for a given task, coastal engineers can take maximum advantage of aerial remote sensing as an analysis tool, and considerable economic savings or improvements in data collection capability can frequently be realized in conducting coastal engineering investigations. Hopefully, the information presented herein can be used by coastal engineers as guidelines in employing aerial remote sensing techniques in future coastal engineering investigations.

Several of the aerial remote sensors appear to be particularly notable from the standpoint of future potential. Satellite remote sensing data that will be collected by the ERTS program in a multispectral format and with repeat coverage provided on an 18-day basis appears to be a particularly useful tool for monitoring large scale coastal processes of interest to coastal engineers. Image enhancement techniques such as additive color viewing should provide an improved capability to extract coastal engineering data from multispectral aerial and satellite photographs. The potential coastal engineering applications of multispectral imagery and computer processing techniques also appears to be substantial.

The field of aerial remote sensing has experienced rapid development in the past ten years, and this trend will probably continue in future years, although possibly at a slower pace. Consequently, significant improvements in the aerial remote sensors that currently exist can be expected to occur in the future. Also, new aerial remote sensors that are not available presently will probably be developed. The improvements that occur in the future may produce higher quality aerial remote sensing data, or they may consist of better techniques for analyzing aerial remote sensor data. The improved and new aerial remote sensors may improve the capability of these sensors for coastal engineering applications. The future developments in aerial remote sensors should be monitored closely to detect new techniques that are applicable to coastal engineering investigations.

One important factor that must be considered in coastal engineering investigations which employ aerial remote sensors is the provision for obtaining adequate ground truth data to calibrate the information obtained from the aerial remote sensors. For best results, ground truth data should be collected simultaneously with the aerial remote sensing mission, although this is not always possible. Obtaining current ground truth data is particularly important when coastal processes that are

heavily time dependent are under investigation. There is little doubt that many aerial remote sensing missions have been less than completely successful because of inadequate ground truth data. The expense of obtaining aerial remote sensing data has been essentially wasted on some projects because of the lack of satisfactory ground truth data that could have been obtained at minimal additional cost. It is important to make detailed plans for the ground truth data collection program so that unanticipated problems will not prevent satisfactory data from being collected. In some instances, the type of ground truth data that can be collected at reasonable cost may be a significant factor in selecting the type of aerial remote sensor that should be employed. It should be noted that one of the primary advantages of aerial remote sensing techniques is that they permit limited field observations to be extended throughout the area of coverage, and it is the ground truth data that form the basis for this process.

NOTE CONCERNING ILLUSTRATIONS

The oral presentation of this paper was accompanied by illustrations consisting of black and white and color 35mm slides. These slides illustrated several aerial remote sensor displays of coastal features. Because of the loss in quality that would result from the printing of the color illustrations in a black and white format, the decision was made to delete the illustrations in printing the paper. The interested reader is referred to the publications listed in the bibliography and other aerial remote sensing publications for illustrations of the aerial remote sensor displays of coastal zone landforms, features, and processes of interest to coastal engineers.

ACKNOWLEDGEMENT

This paper is based on research conducted by the writer under Contract DACW72-70-C-0034 with the Coastal Engineering Research Center, U. S. Army Corps of Engineers. A report entitled A State of the Art Survey of the Applications of Aerial Remote Sensing to Coastal Engineering which presents the results of this research program has recently been published and is listed in the references below (Stafford, 1972). The paper presented herein has been adapted from the contents of this report. The financial support of the Coastal Engineering Research Center in conducting the research program is gratefully acknowledged.

LIST OF REFERENCES

Athearn, W. D., and F. C. Ronne. 1963. Shoreline changes at Cape Hatteras: an aerial photographic study of a 17-year period. Naval Research Reviews, No. 6, June, pp. 17-24. Office of Naval Research, Washington, D. C.

Cameron, H. L. 1965. Sequential air photo interpretation in coastal change studies. Maritime Sediments, Vol. 1, No. 2, April, pp. 8-12.

El-Ashry, Mohamed T. 1963. Effects of Hurricanes on Parts of the United States Coastline as Illustrated by Aerial Photographs. Unpublished Master of Science Thesis, Department of Geology, University of Illinois, Urbana, Illinois, 73 pages.

El-Ashry, Mohamed T. 1966. Photointerpretation of Shoreline Changes in Selected Areas along the Atlantic and Gulf Coasts of the United States. Ph.D. Dissertation, Department of Geology, University of Illinois, Urbana, Illinois, 197 pages.

El-Ashry, Mohamed T., and Harold R. Wanless. 1965. Birth and early growth of a tidal delta. The Journal of Geology, Vol. 73, No. 2, March, pp. 404-406.

El-Ashry, Mohamed T., and Harold R. Wanless. 1967. Shoreline features and their changes. Photogrammetric Engineering, Vol. 33, No. 2, February, pp. 184-189.

El-Ashry, Mohamed T., and Harold R. Wanless. 1968. Photo interpretation of shoreline changes between Capes Hatteras and Fear (North Carolina). Marine Geology, Vol. 6, pp. 347-379.

Geary, Edmund L. 1968. Coastal hydrography. Photogrammetric Engineering, Vol. 34, No. 1, January, pp. 44-50.

James, Wesley P., and Fred J. Burgess, 1970. Ocean outfall dispersion. Photogrammetric Engineering, Vol. 36, No. 12, December, pp. 1241-1250.

Langfelder, L. Jay, Donald B. Stafford, and Michael Amein. 1970. Coastal erosion in North Carolina. Proceedings of the American Society of Civil Engineers, Journal of the Waterways and Harbors Division, Vol. 96, No. WW2, May, Paper No. 7306, pp. 531-545.

Lepley, L. K. 1968. Coastal water clarity from space photographs. Photogrammetric Engineering, Vol. 34, No. 7, July, pp. 667-674.

Lewis, Anthony J., and Harold C. MacDonald. 1970. Significance of estuarine meanders identified from radar imagery of Eastern Panama and Northwestern Columbia. Modern Geology, Vol. 1, No. 3, June, pp. 187-196.

MacDonald, Harold C., Anthony J. Lewis, and R. S. Wing. 1971. Mapping and landform analysis of coastal regions with radar. Geological Society of America Bulletin, Vol. 82, No. 2, February, pp. 345-357.

Mairs, Robert L. 1970. Oceanographic interpretation of Apollo photos. Photogrammetric Engineering, Vol. 36, No. 10, October, pp. 1045-1058.

Moffitt, Francis H. 1969. History of shore growth from aerial photographs. Shore and Beach, Vol. 37, No. 1, April, pp. 23-27.

Nichols, Maynard M. 1970. Coastal processes from space photography. Proceedings of the Twelfth Coastal Engineering Conference, September 13-18, 1970, Washington, O. C., Vol. 2, pp. 641-649. Published by the American Society of Civil Engineers.

Orr, Oonald G., and James R. Quick. 1971. Construction materials in delta areas. Photogrammetric Engineering, Vol. 37, No. 4, April, pp. 337-351.

Pestrong, Raymond. 1969. Multiband photos for a tidal marsh. Photogrammetric Engineering, Vol. 35, No. 5, May, pp. 453-470.

Polcyn, Fabian C., and I. J. Sattinger. 1969. Water depth determinations using remote sensing techniques. Proceedings of the Sixth International Symposium on Remote Sensing of the Environment, University of Michigan, Ann Arbor, October 13-16, pp. 1017-1028.

Ross, Oonald S. 1969. Enhanced oceanographic imagery. Proceedings of the Sixth International Symposium on Remote Sensing of Environment, University of Michigan, Ann Arbor, October 13-16, pp. 1029-1044.

Sonu, Choule J. 1964. Study of shore processes with aid of aerial photogrammetry. Photogrammetric Engineering, Vol. 30, No. 6, November, pp. 932-941.

Stafford, Donald B. 1968. Development and Evaluation of a Procedure for Using Aerial Photographs to Conduct a Survey of Coastal Erosion. A Report Prepared for the State of North Carolina. Oepartment of Civil Engineering, North Carolina State University, Raleigh, August, 219 pages.

Stafford, Oonald B. 1971. An Aerial Photographic Technique for Beach Erosion Surveys in North Carolina. Technical Memorandum No. 36, U. S. Army Corps of Engineers, Coastal Engineering Research Center, Washington, O. C., October, 115 pages.

Stafford, Oonald B. 1972. A State of the Art Survey of the Applications of Aerial Remote Sensing to Coastal Engineering. Department of Civil Engineering, Clemson University, Clemson, South Carolina, May, 192 pages.

Stoertz, George E., William R. Hemphill, and Oavid A. Markle. 1969. Airborne fluorometer applicable to marine and estuarine studies. Marine Technology Society Journal, Vol. 3, No. 6, November, pp. 11-26.

Taylor, James I., and Ronald W. Stingelin. 1969. Infrared imaging for water resources studies. Proceedings of the American Society of Civil Engineers, Journal of the Hydraulics Division, Vol. 95, No. HY1, January, Paper No. 6331, pp. 175-189.

Thomas, Reuben S. 1971. Comparison of the Coastal Engineering Applications of Color and Color Infrared Aerial Photographs. Unpublished Master of Science Project Report, Department of Civil Engineering, Clemson University, Clemson, South Carolina, August, 67 pages.

Wenderoth, Sondra. 1969. Hydrographic and oceanographic applications of multispectral color aerial photography. Seminar Proceedings - New Horizons in Color Aerial Photography, Sponsored by the American Society of Photogrammetry, Held in New York City, June 9-11, pp. 115-125.

Yost, Edward, and Sondra Wenderoth. 1968. Coastal water penetration using multispectral photographic techniques. Proceedings of the Fifth Symposium on Remote Sensing of Environment, University of Michigan, Ann Arbor, April 16-18, pp. 571-586.

Yost, Edward, and Sondra Wenderoth. 1971. Coastal and Estuarine applications of multispectral photography. Proceedings of the American Society of Photogrammetry Fall Convention, San Francisco, September 7-11, American Society of Photogrammetry, Falls Church, Virginia, pp. 515-530.

SUPPLEMENTAL BIBLIOGRAPHY

American Society of Photogrammetry. 1968. Manual of Color Aerial Photography. John T. Smith, Jr., Editor-in-chief, American Society of Photogrammetry, Falls Church, Virginia, 550 pages.

Berryhill, Henry L., Jr. 1969. Remote sensing techniques as applied to coastal sedimentation, South Texas. Second Annual Earth Resources Aircraft Program Status Review, Vol. 1, Geology and Geography, Section 6, pp. 1-15, National Aeronautics and Space Administration, Manned Spacecraft Center, Houston, Texas, September 16-18.

Duxbury, Alyn C. 1967. Currents at the Columbia River mouth. Photogrammetric Engineering, Vol. 33, No. 3, March, pp. 305-310.

Keller, Morton. 1963. Tidal current surveys by photogrammetric methods. Photogrammetric Engineering, Vol. 29, No. 5, September, pp. 824-832.

National Aeronautics and Space Administration. 1970. Ecological Surveys from Space. NASA Special Publication 230, Office of Space Science and Applications, National Aeronautics and Space Administration, Washington, D. C., 75 pages.

Tewinkel, G. C. 1963. Water depths from aerial photographs. Photogrammetric Engineering, Vol. 29, No. 6, November, pp. 1034-1042.

CHAPTER 117

COASTAL APPLICATIONS OF THE ERTS-A SATELLITE

by
Orville T. Magoon[1], M. ASCE
Douglas M. Pirie[2]
John W. Jarman[3]

ABSTRACT

This paper describes the Earth Resources Technology Satellite (ERTS) placed in orbit in July 1972 and the ERTS simulation high altitude aircraft flights which have been flown for approximately one year. The ERTS satellite and simulation programs conducted by the National Aeronautics and Space Administration (NASA) have been developed to demonstrate the techniques for efficient management of the earth's resources. To achieve this objective the ERTS-A satellite provides for the repetitive acquisition of high resolution multispectral data of the earth's surface on a global basis. Two sensor systems have been selected for this purpose: a four-channel multispectral scanner (MSS) subsystem for ERTS-A and a three-camera return beam vidicon (RBV) system. Systematic repeating earth coverage under nearly constant observation conditions is provided for maximum utility of the multispectral images collected by the ERTS satellite, which operates in a circular sun synchronous nearly polar orbit at an altitude of 494 nautical miles. It circles the earth every 103 minutes completing 14 orbits per day and views the entire earth in 18 days. The orbit has been selected so that the satellite ground trace repeats its earth coverage at the same local time every 18-day period within 20 nautical miles. A number of data output products are available from this satellite which include 70 mm products for precise location of topographic features, 9.5 inch positive or paper prints and also computer compatible tapes or punched cards.

Also described are the results of the ERTS-A simulation flights flown at an altitude of 65,000 feet as related to coastal studies. Simulations of both the RBV and MSS in coastal areas are presented.

OBSERVATORY

The ERTS Observatory (Figure 1) satellite weighs approximately 2,100 pounds (953 kg) with a height of about 10 feet (3 meters), a diameter of 5 feet (1.5 meters) and with solar paddle assemblies extending out to about 13 feet (4 meters). A detailed description of this satellite is available in Data Users Handbook, NASA Earth Resources Technology

[1]Special Assistant to the Director, U. S. Army Coastal Engineering Research Center, Washington, D.C., U.S.A.
[2]Ocean Engineer, Navigation and Shoreline Planning Branch, U. S. Army Engineer District, San Francisco, California, U.S.A.
[3]Civil Engineer, Office Chief of Engineers, Corps of Engineers, U. S. Army, Washington, D.C., U.S.A.

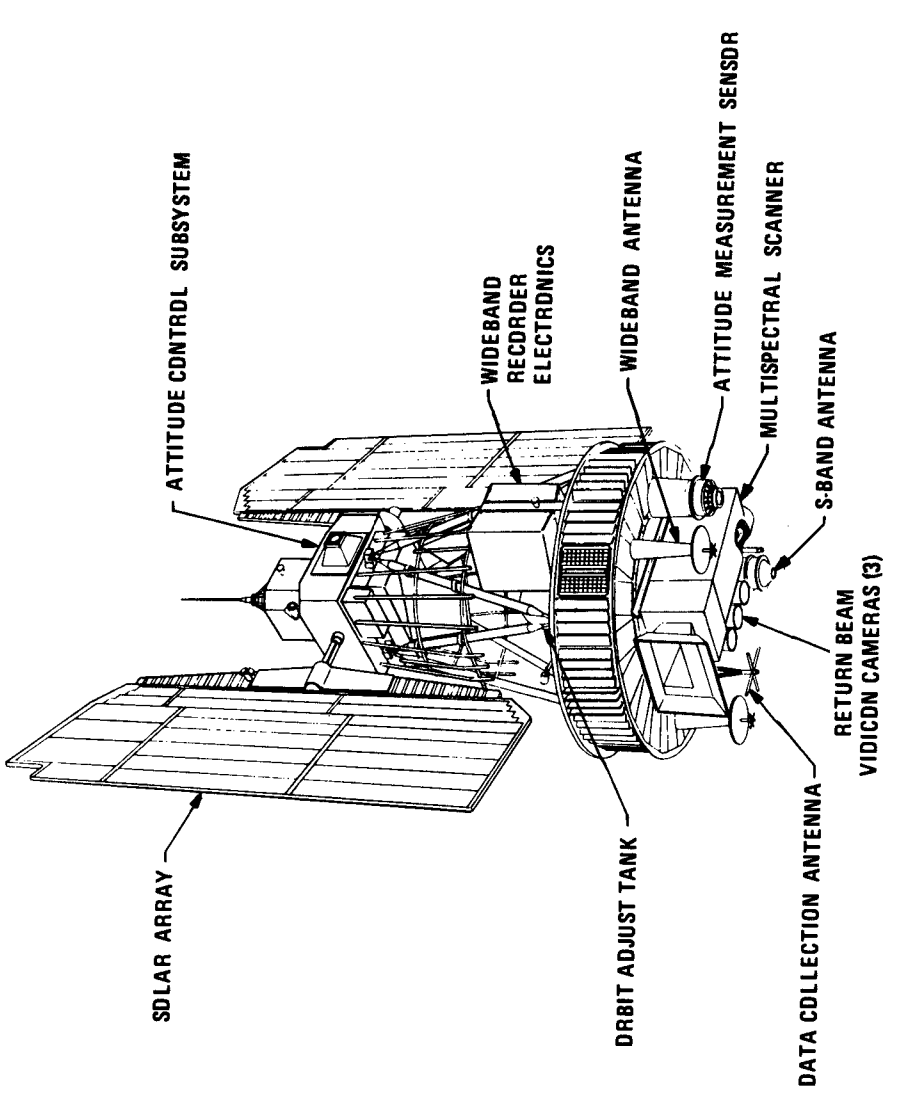
ATTITUDE CONTRDL SUBSYSTEM
WIDEBAND RECORDER ELECTRONICS
WIDEBAND ANTENNA
ATTITUDE MEASUREMENT SENSOR
MULTISPECTRAL SCANNER
S-BAND ANTENNA
RETURN BEAM VIDICON CAMERAS (3)
SOLAR ARRAY
ORBIT ADJUST TANK
DATA COLLECTION ANTENNA

Figure 1

Satellite, Goddard Space Flight Center, Greenbelt, Maryland 20771, U.S.A., Attention: Mr. Thomas M. Ragland, Code 430. The basic remote sensing subsystems of interest to the coastal engineer are the Return Beam Vidicon Camera and Multispectral Scanner to be described below. This was also described by Magoon, et al[1] 1971.

The Return Beam Vidicon (RBV) consists of three independent cameras sensing the following bands: RBV No. 1 0.48 - 0.575 (blue-green); RBV No. 2 0.58 - 0.68 (yellow-orange); RBV No. 3 0.69 - 0.83 (red) microns. As these bands are in the visible spectrum, this subsystem is operated only during daylight hours. The viewed ground scene which is roughly 100 (185 km) by 100 (185 km) nautical miles produces overlapping images every 25 seconds. The RBV camera orientation is shown on Figure 2.

The Multispectral Scanner (MSS) continuously scans a ground swath perpendicular to the spacecraft velocity as shown on Figure 3. Optical energy is sensed from four spectral bands as follows:

Band 1	0.5 to 0.6 micrometers
Band 2	0.6 to 0.7 micrometers
Band 3	0.7 to 0.8 micrometers
Band 4	0.8 to 1.1 micrometers

The ERTS provides repeating earth coverage under nearly constant observation conditions. The satellite's ground trace repeats its ground coverage every 18-day period within 20 nautical miles. A typical ERTS daily ground trace (daytime passages only) is shown in Figure 4.

SIMULATION FLIGHTS

In order to provide the ERTS user community with examples of imagery, NASA is operating two high altitude aircraft as a part of the airborne research program Earth Resources Aircraft Project (ERAP). These planes, Lockheed U-2's, are providing repetitive flights at 65,000 feet (20,014 meters) over 5 test sites. The time interval between flights, timed to simulate satellite coverage is approximately 18 days. The data collection system carried in the aircraft used for direct ERTS simulation consists of three cameras coupled to make three simultaneous images over 196 square nautical miles in the test site. The cameras have a focal length of 45 mm and use 70 mm roll film. A system of filters permits only selected portion of the spectrum which correspond to ERTS measurement to be recorded on the film. The spectral regions viewed by the cameras are in the 475-575 nanometer band width (green) the 580-680 nm band width (red), and the 690-760 nm band width (near IR or very red). The fourth camera identical to and coupled with the

---

(1) Magoon, et al, Use of Satellites in Coastal Engineering, Port and Ocean Engineering Under Arctic Conditions, Trondheim, Norway, 1971.

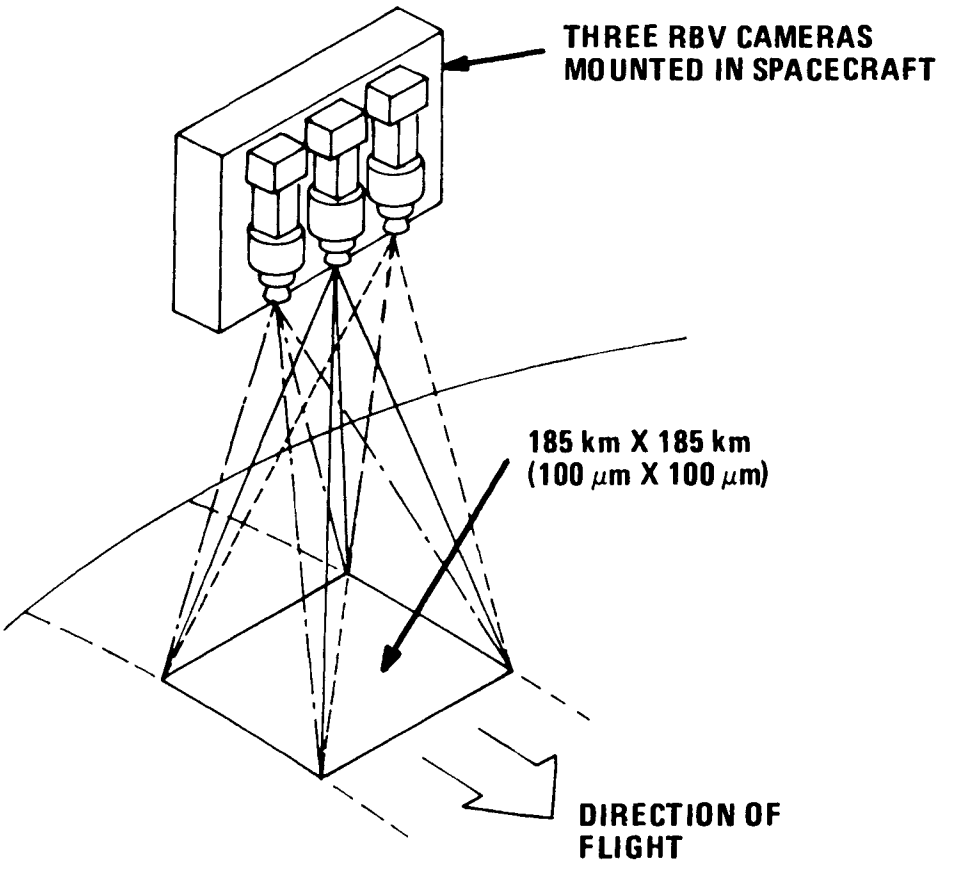
THREE RBV CAMERAS
MOUNTED IN SPACECRAFT
185 km X 185 km
(100 μm X 100 μm)
DIRECTION OF
FLIGHT

Figure 2

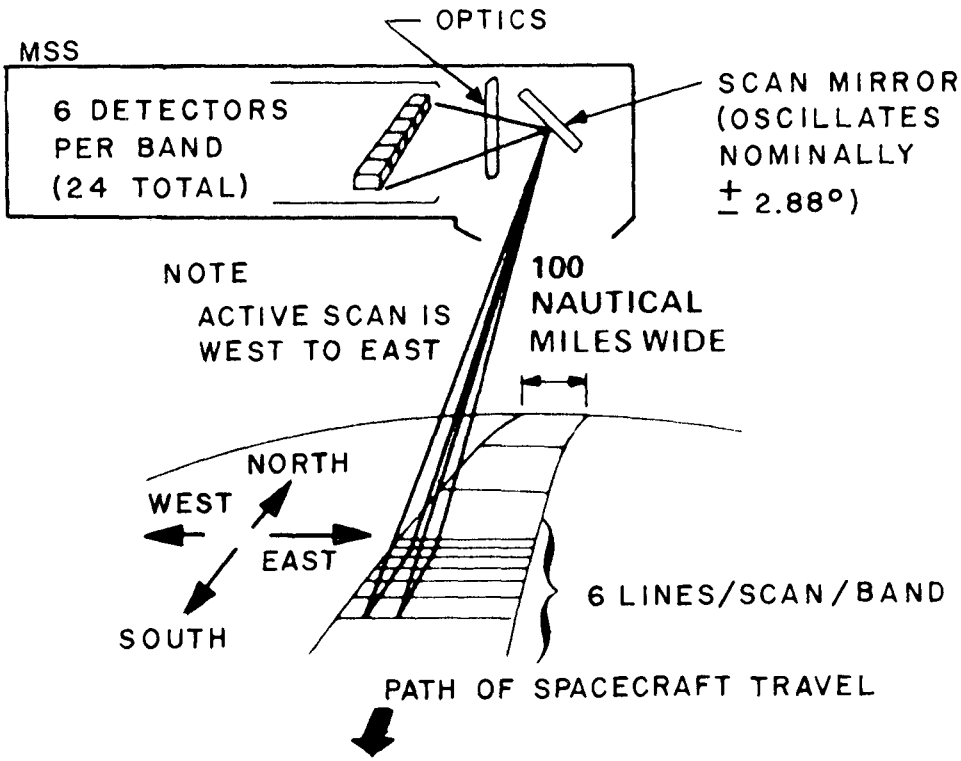
OPTICS
MSS
6 DETECTORS
PER BAND
(24 TOTAL)
SCAN MIRROR
(OSCILLATES
NOMINALLY
± 2.88°)
NOTE
ACTIVE SCAN IS
WEST TO EAST
100
NAUTICAL
MILES WIDE
NORTH
WEST
EAST
SOUTH
6 LINES/SCAN/BAND
PATH OF SPACECRAFT TRAVEL

Figure 3

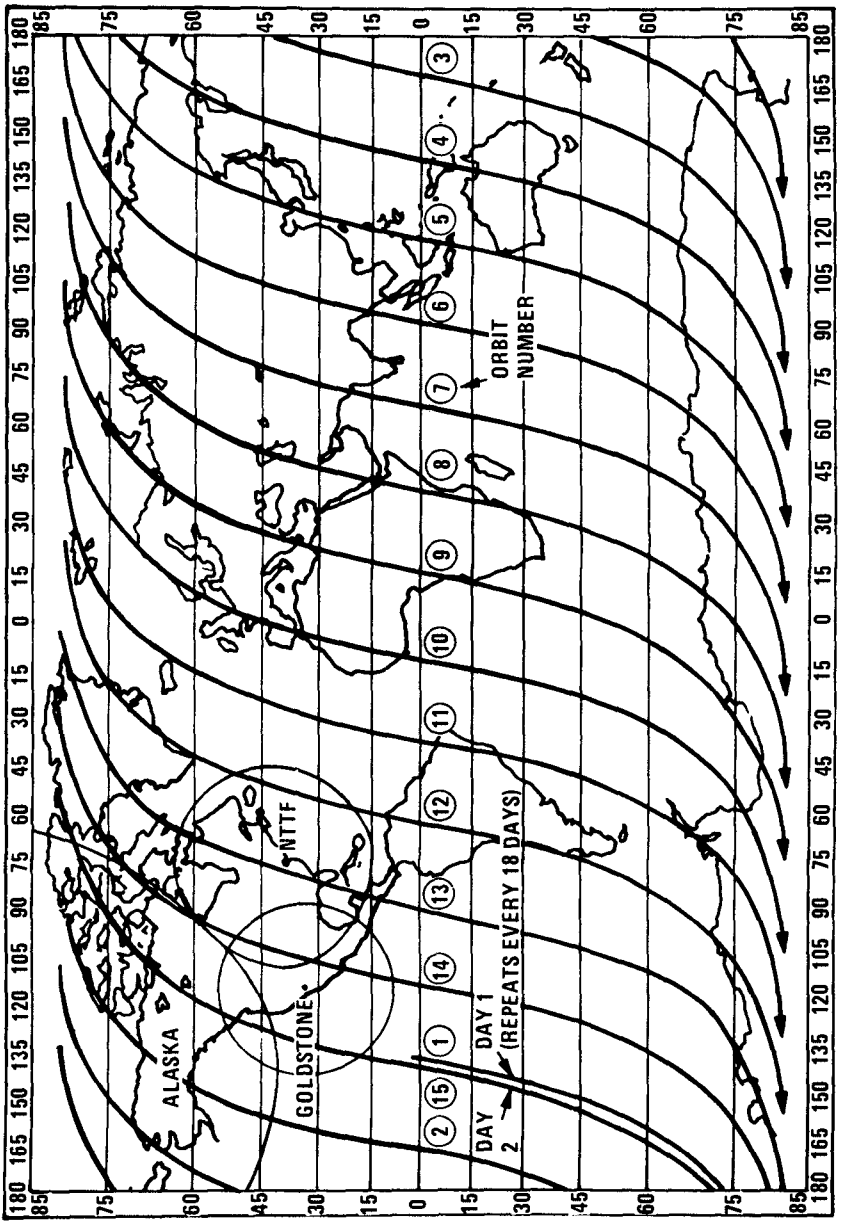
ALASKA
GOLDSTONE
NTTF
DAY 1
(REPEATS EVERY 18 DAYS)
DAY 2
ORBIT NUMBER

Figure 4

three primary cameras uses color infrared film to produce general purpose earth resources information in the 590-850 nm band width. The cameras automatically record images every 105 seconds over the test site. The number of frames exposed over the sites varies from 79 for the California Feather River and Lake Tahoe to 163 for the Chesapeake Bay. Data flights over all of the test sites are originated from NASA/Ames with exception of the Chesapeake Bay site which is staged from NASA's Wallops Island Station in Virginia.

Upon examination of the imagery supplied in conjunction with the NASA U-2 flights a number of coastal applications for this imagery and presumably the ERTS satellite imagery were noted for the purposes of this discussion, three general areas of interest are noted as follows:

a. Studies of the nearshore and coastal water movement by observing photographed sediment plumes or patterns,

b. Observing changes in inlet configurations and barrier beach or spit configurations, and

c. Studies relating to determination of wave direction

These general areas are discussed separately below.

NEARSHORE SEDIMENT MOVEMENT

A coastal area-inlet problem of considerable interest has been the area in the vicinity of the entrance to San Francisco Bay (Golden Gate). In this general area particular interest in the technical literature has been paid to Bolinas Bay and the entrance to Bolinas Lagoon. Recent literature describing Bolinas Bay are given by Johnson[2] and Wilde and Yancey[3]. Of particular interest are the hypothesized circulation in Bolinas Bay taken from Wilde and Yancey. Additional study of this site is currently underway by Ritter[4]. Wilde and Yancey and Ritter give somewhat conflicting views of sedimentation movement and inferred water circulation. Of particular interest in the Bolinas site is that the coast from the entrance to Bolinas Lagoon to Ducksbury Reef contains an eroding bluff which contains a sufficiently large amount

---

[2] Johnson, J. W., "Seasonal Bottom Changes - Bolinas Bay, California", 1970 12th International Coastal Engineering Conference, pp. 138-139.

[3] Wilde, P. and Yancey, T., "Sediment Distribution and Its Relation to Circulation Patterns in Bolinas Bay, California", 1970 12th International Conference on Coastal Engineering, pp. 1397-1415.

[4] Ritter, J., "Sedimentation and Hydrology of Bolinas Lagoon, Marin County, California, open file report", U. S. Dept. of Interior, Geol. Survey, Water Res. Div., Menlo Park, Calif.

of fine material to produce a natural pollution source which is readily visible to the unaided eye.

Inasmuch as the ERTS simulation photography of the San Francisco Bay test site overflies the Bolinas Bay/Bolinas Lagoon area ERTS simulation imagery was examined with an attempt to infer the water circulation at the time the photography was taken.

Repeated views taken by the ERTS simulation flights of the sediment plume from this source were seen extending out away from the bluff. False color enhancements of this imagery were made by use of the NASA/Houston Multiple Camera Film Viewer (MCFV) described in "Remote Sensing in the Study of Coastal Processes" by Magoon and Pirie printed elsewhere in these Proceedings. This device takes the three images and assigns colors to grey scales and then recombines the three separate color images to a single image.

Based on this imagery, it is concluded that the ERTS RBV will produce a viable product for coastal sediment studies.

In the analysis of the U-2 imagery major coastal sediment plumes were noted along many sections of the California coast. A particularly noticeable plume was seen off of Point Reys, California.

INLET CONFIGURATIONS

A second coastal inlet problem of major interest is the understanding and quantification of changes to inlets in barrier beaches and coastal bars and spits. These highly variable geomorphological features are extremely difficult and costly to study by conventional means, such as surveying, due to the extremely high cost associated with conventional ground surveys. Additionally, conventional low level photography, i.e., 10,000-foot range, normally results in the generation of large amounts of film and imagery and by and large results in greater detail than is necessary for general conformal studies. Of particular interest were ERTS simulation flights of the Delmarva Peninsula in Accomac County, Virginia, where major changes in coastal areas are readily detected from the ERAP images. In a sequence of views of these islands taken from the CARETS test site imagery, gross changes in inlet configuration can be readily detected. It is also important to note that the imagery for the entire 32,600 square mile area of the Chesapeake site can be contained in a very small space, i.e., a roll of film 70 mm wide and one inch in diameter. The Vinten cameras resolve scenes down to about 50 feet while the 24-inch cameras will resolve scenes down to about 3 feet.

WAVE DIRECTION

It is technically accepted that ocean waves produce one of the major forces that are associated with the configuration and establishment of coastal inlets. The technical literature contains vast numbers of references relating to correlation between coastal movements and ocean wave conditions. One of the important parameters that investigators have looked for is a viable system for measurement of wave direction. Unfortunately the theoretical analyses of the available wave direction models are subject to question due to the fact that there is little factual data on the configuration of deep water waves. This is in part due to the lack of a suitable platform to observe the major wave phenomena. Based on the work of Dr. D. Lee Harris at the Coastal Engineering Research Center it appears that the U-2 aircraft operating at an altitude of approximately 65,000 feet provides a unique platform for obtaining imagery related to wave direction.

CONCLUSIONS

Based on the imagery supplied by the NASA ERTS simulation efforts, it is concluded that ERTS imagery will be of use to coastal investigators in two principal areas: study of coastal sediment and related water mass movement through the repeated monitoring of coastal sediment plumes, and for the study of changes in highly variable sections of coasts such as offshore barrier islands and erodible shoals. Use of ERTS imagery in studies relating to deep water wave direction is problematical depending on the resolution of water surface waves in the final data products received from NASA.

ACKNOWLEDGMENTS

Acknowledgment is gratefully made to the National Aeronautics and Space Administration (NASA), the Corps of Engineers, U. S. Army, for access and permission to use this study material. The views of the authors do not purport to reflect the position of the National Aeronautics and Space Administration or the Corps of Engineers, Department of the Army, or Department of Defense.

Contents of this paper are not to be used for advertising or promotional purposes. Citation of trade names does not constitute an official endorsement or approval of the use of such commercial products.

CHAPTER 118

THERMAL POWER PLANT ENVIRONMENTAL STUDIES

by

M. J. Doyle, Jr.,[1] and R. F. Cayot[2]

ABSTRACT

Once-through cooling water systems for thermal power plants offer an economical means of dissipating the differential energy of modern-day turbines.

Before the decision to proceed with the design of a once-through cooling water system is made, a considerable study effort must be undertaken in order to determine that no harmful effects will accrue to the environment from the plant's operation.

These studies must include:

1. A comprehensive literature search
2. Field investigations of the air and water
3. Analytical evaluation of the field data

The Pacific Gas and Electric Company has been conducting environmental studies at its operating thermal power plants and at proposed sites since 1958.

This paper describes the approach used by the Company in conducting environmental studies. Meteorological data were obtained from on-site sensors, stored on magnetic tape, and subsequently computer-processed. Oceanographic data in the form of water temperatures, salinity, and dissolved oxygen profiles, as well as current speed and direction, were obtained from surface vessels. Remote sensing systems were used to obtain dispersion and dilution information, sea-surface temperature data, and aerial photographs of flora indigenous to the study area. All remote-sensed data, except for the aerial photographs, were stored on magnetic tape, in flight, and later processed in the computer with graphic off-line printout.

[1]Engineer, Department of Engineering Research, Pacific Gas and Electric Company, Emeryville, California

[2]Chief, Department of Engineering Research, Pacific Gas and Electric Company, Emeryville, California

Introduction

The National Environmental Policy Act, enacted in 1970, the State of California through its local Regional Water Quality Control Boards, the Atomic Energy Commission, and many other regulatory agencies require environmental studies at all operating and proposed power plant sites. Pacific Gas and Electric Company (P G and E) has conducted environmental studies at its operating plants and proposed sites in the marine environment since 1958 (1, 2, 3, 4, 5, 11). The basic philosophy of these studies has remained unchanged from 1958 to the present; however, the methods and techniques have undergone substantial development (6). The primary objective of each study has been to (1) develop an understanding of the physical and biological characteristics of the marine environment, and (2) determine the effects of the plant or potential plant on the marine environment.

Many disciplines are represented in a comprehensive environmental study. In coastal areas, these include oceanography, engineering, biology, meteorology, photogrammetry, and others. Proper interfacing of each is required in order to obtain meaningful results. Each is complementary to the other.

The normal process of most studies in on a "begin-end" basis. Environmental studies for new plant sites seemingly do not fit this pattern at this time. There is a start-point, but, because of the magnitude and variability of the factors involved, there is no end-point. They can be described as "preoperational" and postoperational."

In the preoperational period, the site environs are studied qualitatively and to some extent quantitatively, so that it can be evaluated with respect to physical and biological processes. It is important to study these processes during the different oceanographic seasons. Temperature and salinity distributions, for example, vary seasonally in coastal waters. The basic study program is designed to interface synoptic with on-going studies so that their seasonal changes can be documented for comparison of long-term data. Modeling studies are made, based in part, on field study data.

The postoperational study period differs in length from the preoperational period. Studies at many P G and E plants are continuing to date, even though in some cases the plants have been operational for more than 20 years.

Literature Search

A logical starting point for an environmental study is in the reference library. Marine investigations have been made and reported along the California coastline for over a hundred years. A large compendium of information can be found in the archives of the National Oceanographic Data Center (NODC), Washington, D.C. Information available includes climatology, sea-state conditions, surface and subsurface water temperature, salinity and dissolved oxygen data, and wave height, direction, and period information. Data can be retrieved from the archives in many formats.

The basic selection is made by isolating the smallest geographical area of interest available (Marsden sub-square) and recalling the data.

In addition to NODC, many other data sources are available to the investigator. These include publications of state and federal agencies, privately endowed research organizations, and universities and colleges. The literature search, up to this point, has been confined to descriptions of the environment in or near the power plant site.

The next area of search deals with methodology. The literature is constantly being expanded to include work done in many areas of the world. Although most environmental studies share a common goal, all studies are not conducted in exactly the same manner. For this reason, methodology is constantly being expanded; and one basis for this expansion is motivated by the literature search.

Field Investigations of the Air and Water

The second step in the environmental study is to develop a program which details the organization of the study. At a minimum, this program will include the following main points:

1. On-site recording systems
   - Water temperature
   - Tide stage
   - Meteorological
     - Wind speed and direction
     - Barometric pressure
     - Solar radiation
     - Relative humidity
     - Precipitation
2. Synoptic studies
   - Shipboard
     - Surface and subsurface
       - Salinity
       - Temperature
       - Dissolved oxygen
       - Turbidity
       - Current speed and direction
   - Airborne
     - Sea-surface temperature
     - Dispersion and dilution (dye) studies
     - Photography (i.e., kelp beds)

Figure 1 shows a flow diagram of data acquisition to analysis of an environmental study.

The methodology shown in Figure 1 is the result of many years of effort by the Pacific Gas and Electric Company to improve the quality of each environmental study. Noteworthy of these are the use of magnetic-tape recording systems (computer-compatible) for meteorological data and airborne

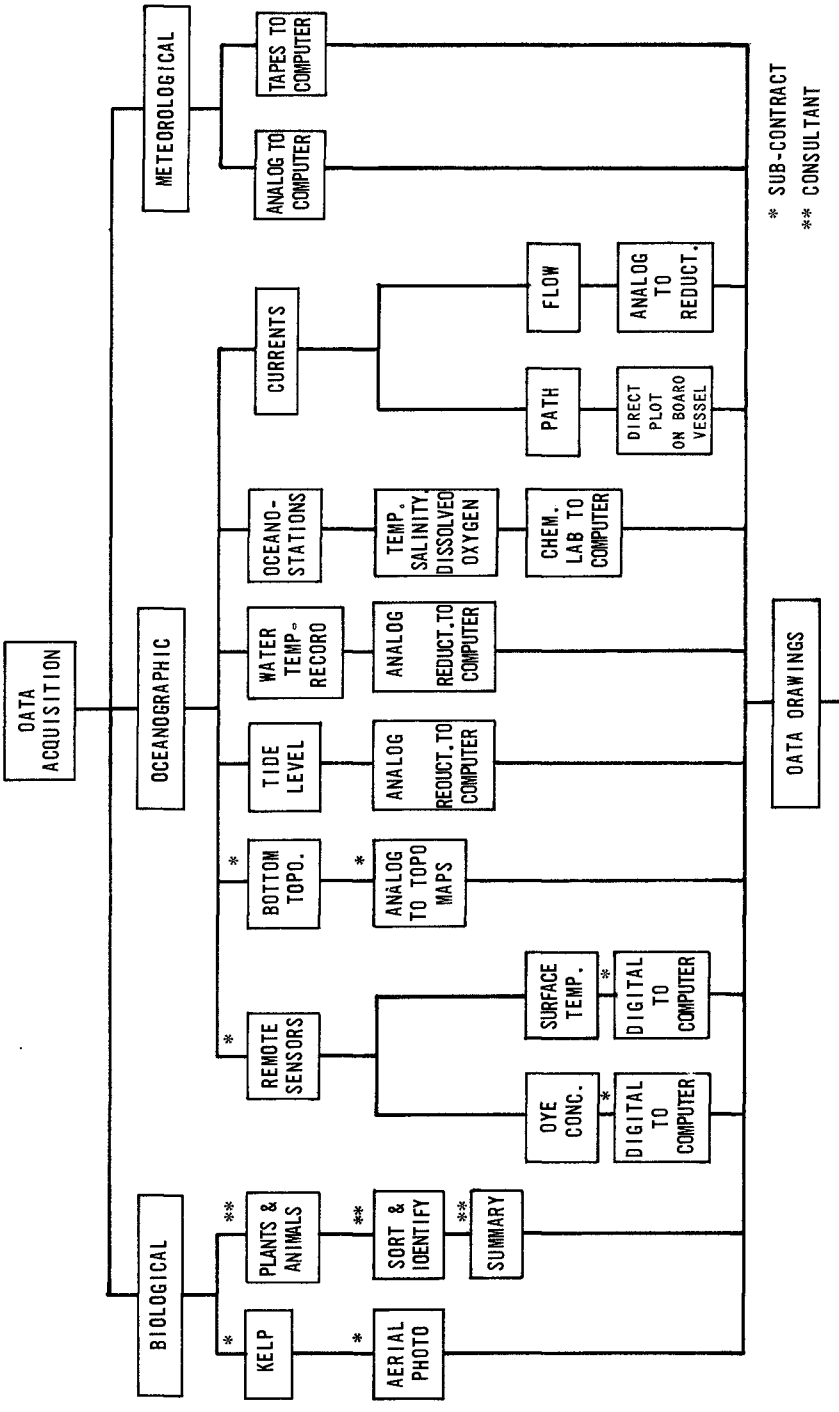

FIG. 1 - ENVIRONMENTAL STUDIES, FIELD STUDIES DATA FLOW

remote-sensing systems (see Figures 2 and 3). There are many advantages in the use of tape systems. Obvious among these are the amount of data that can be obtained, stored, and processed; and the low cost. In addition, with the information in a computer-compatible format, the routining possibilities are expanded.

Instrumentation. Instrumentation used by the company ranges from rather simple water temperature recorders to sophisticated infrared line scanners. Some of these instruments and related support equipment are shown in Figure 4. These items are utilized from a chartered 65-foot steel-hulled commercial fishing vessel, which serves not only as a platform but also provides the quarters for test personnel. Typical field synoptic study periods last from seven to ten days and are conducted on a 24-hour per day basis. Airborne systems, including an infrared scanner and a high altitude reconnaissance camera, are shown in Figures 5 and 6.

Methodology. The shore-based systems are operated for the duration of the study. The airborne systems are operated at selected intervals of current and tidal stage periods. One of the advantages of infrared line scanners is their ability to operate during any portion of the lunar day (for sea-surface temperature data-gathering). On board the primary research vessel, temperature, salinity, and dissolved oxygen data are obtained from surface to near bottom at each oceanographic station. These data are reduced on board and organized for subsequent onshore computer processing. Temperature and salinity data are processed for density and stability determinations.

Current speed and direction are determined by three methods:

1. Current meter (flow)
2. Radar-tracked drogue (path)
3. Dye-path drift

Remote-sensing systems, excluding aerial photography, combine the operation of the instruments in the aircraft with related or supporting systems aboard the research vessel. These surface vessel systems are commonly referred to as "ground truth systems." For sea-surface temperature, the airborne infrared scanner is determining the water temperature ($\pm$ 1°F) to a depth of approximately 20 microns (7). A precise inflight calibration of the scanner can only be made by comparing the scanner values (voltage/temperature) with surface temperature values obtained by a system operating in the same bandwidth (8-14 microns) as the scanner. This is accomplished by the use of an infrared radiometer on board the surface vessel. Ground-truth data are obtained for the scanner, when it is operating in the tracer dye mode, by the use of water sample data obtained through the use of a fluorometer operating on board the surface vessel. Dye concentrations can be determined by the scanner to 0.1 PPB (8).

Analysis

Most environmental studies are designed to cover annual cycles. In some coastal areas, such as California, the annual cycle consists of three

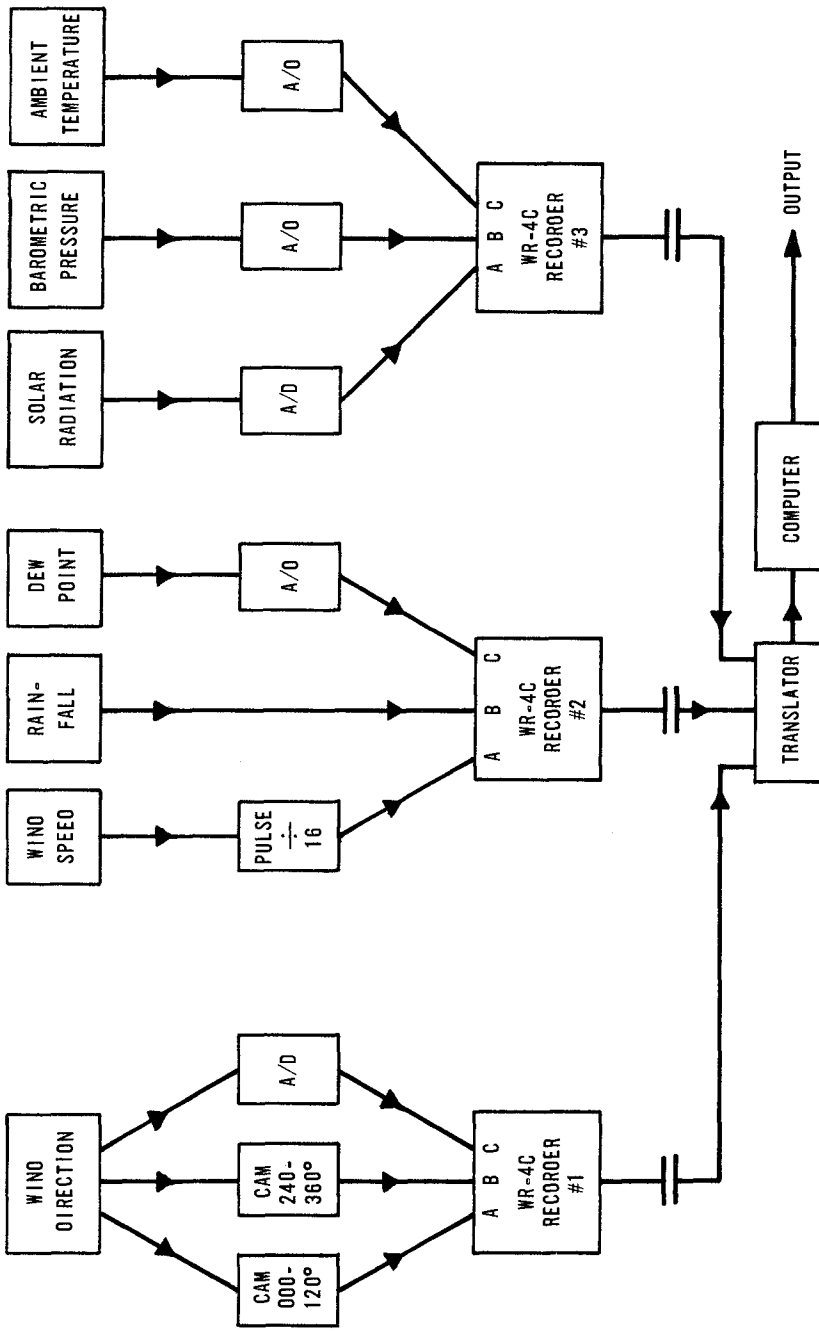

FIG. 2 ENVIRONMENTAL DATA ACQUISITION SYSTEM

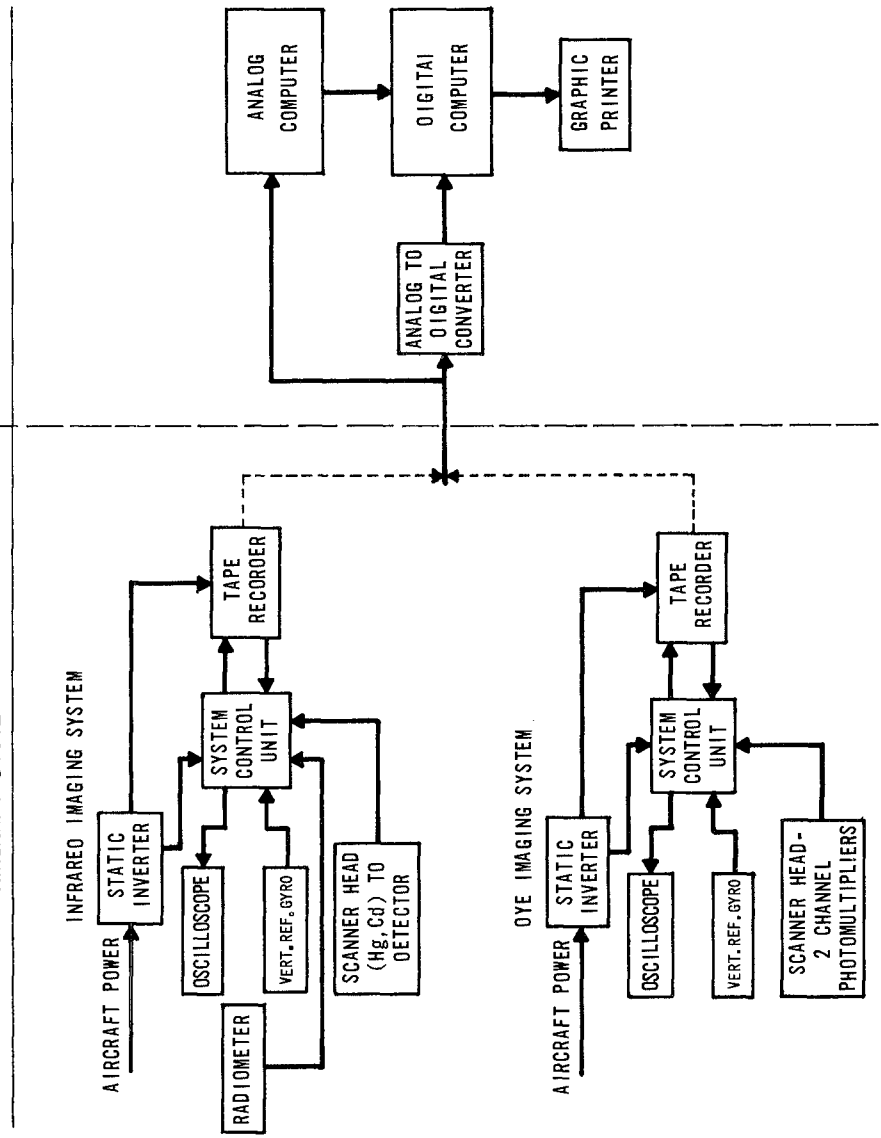

FIG. 3 - BLOCK DIAGRAM OF DATA FLOW FROM ACQUISITION TO GRAPHIC PRINTER

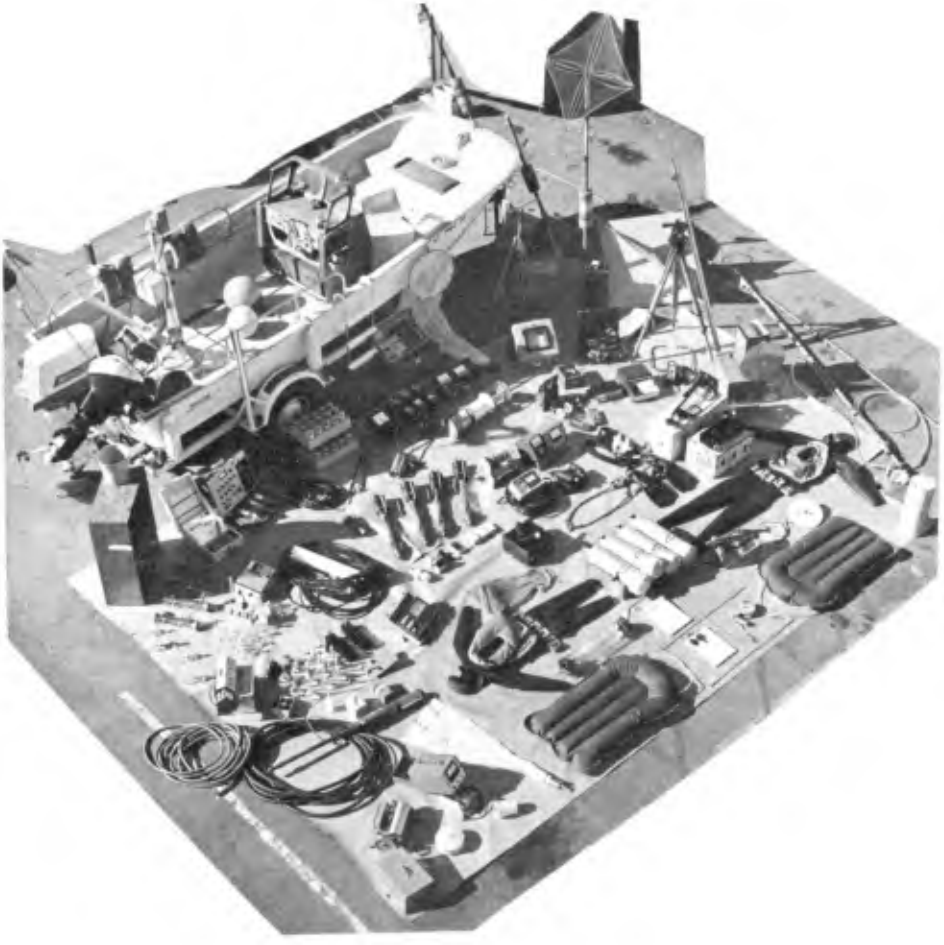

Figure 4 - Equipment Used in Environmental Field Studies

Figure 5 - Airborne Infrared Scanner-Control Systems, Reference Units and Magnetic Tape Recorder Located Inside Aircraft

Figure 6 - High Altitude Recon Camera - Infrared Type 2443 Aero Neg Film used for Kelp Mapping Flights

seasons, while in inland or estuarine areas there are four seasons. Summary data analysis is therefore made of the full year's cycle.

From the literature search, it has been determined what data exists for the area under study. An example of this is shown in Figure 7. Data from two shore stations and from NODC (Marsden Sub-square 83) are compared. In this case, sea-surface water temperature data (mean, maximum, and minimum - monthly), covering a time period 1847-1970, have been plotted. Data obtained during our studies are then compared against the long-term data to determine if significant variations existed during our study period.

Similar comparisons can also be made with meteorological, wave height, wave period, salinity, and temperature with depth data.

With these data in this format, it is then possible to analyze both the old and the new data with respect to the following:

1. Basic ranges - minimums and maximums
2. Short-term vs. long-term mean variations
3. Seasonal variations

Sea-surface temperature and dispersion and dilution data obtained by the airborne remote-sensing system are graphically displayed for analytical purposes.

Figure 8 shows examples of both black-and-white imagery and computer output (5). Both show a view of the thermal effluent from a power plant operating at a load of 1500 MWe, a flow of 1350 CFS, and a temperature difference (intake-discharge) of 22°F. The difference in the two figures is that the black-and-white imagery is qualitative, while the computer output shows the actual areas in square feet contained within each isotherm. The task of analyzing the plant thermal output has thus been quantified.

The data obtained during environmental studies, whether it be physical, biological, or related disciplines, are complementary. For example, physical data are directly related to model studies. The suitability of a physical or analytical model can be verified by studies at operating power plants (10). This paper has covered the physical studies needed as input to biological assessment which must be pursued in a parallel mode of investigation.

Summary

Thermal power plant environmental studies are designed to document the characteristics of the impact area of the plant. They should include a thorough literature search of previous studies in the area. A comprehensive study plan must be developed. It should be designed to include all seasons of the year. Whenever possible, acquired data should be stored in a computer-compatible format. The analysis should include the interfacing of all disciplines within the study.

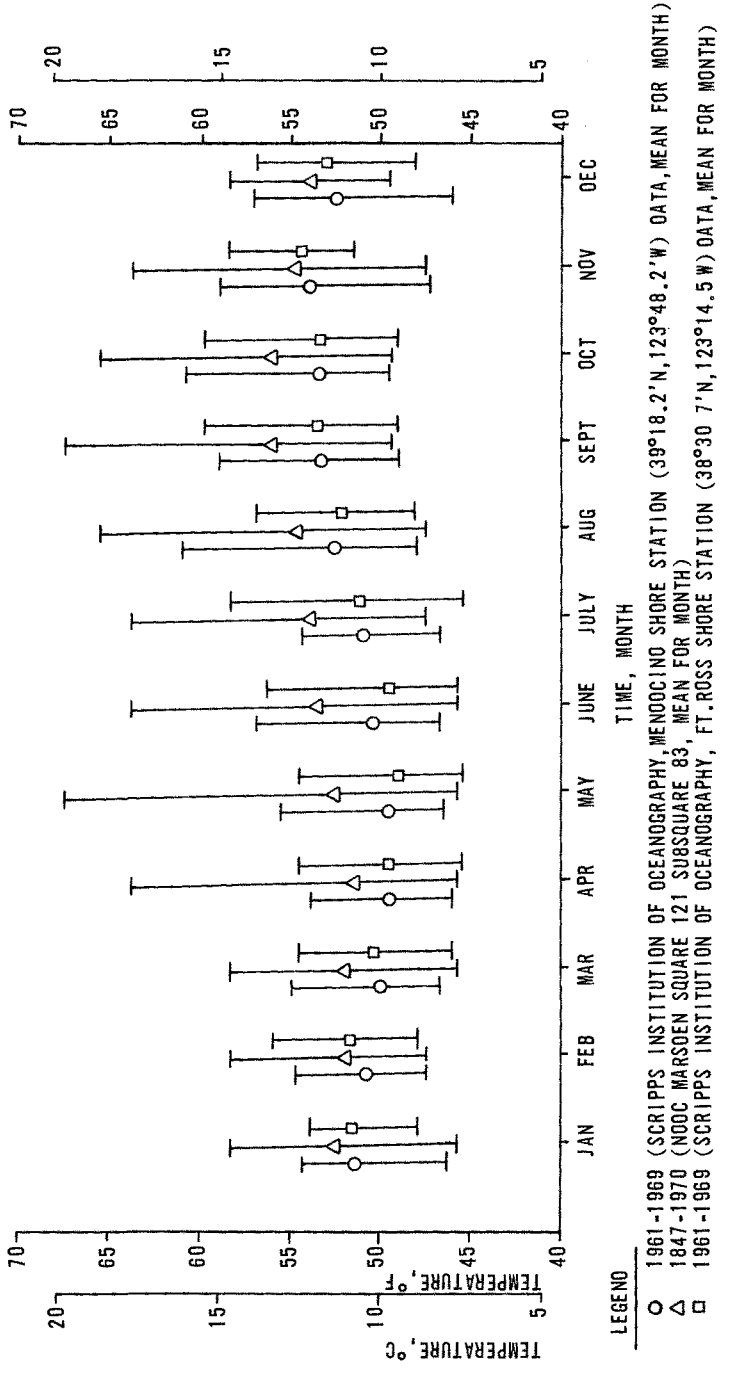

FIG. 7 - MEAN, MAXIMUM AND MINIMUM MONTHLY SEA SURFACE WATER TEMPERATURES RECORDED NEAR PT. ARENA, CALIFORNIA

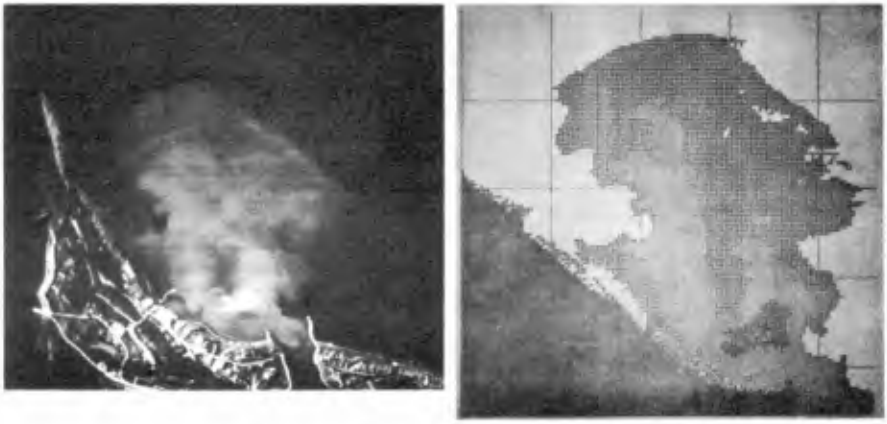

LEVELS 1 2 3 4 5 6 7 8 9 10 11 12 13

LEVEL	TEMP. (DEG. F)	NUMBER OF AREA ELEMENTS	AREA (SQ.FT.)
1	56.99 - 58.00	4917	6053900
2	58.00 - 60.00	2302	2834300
3	60.00 - 62.00	147	180991
4	62.00 - 64.00	43	52942
5	64.00 - 66.00	18	22161
6	66.00 - 68.01	11	13542
7	68.01 - 69.99	7	8617
8	69.99 - 72.00	1	1230
9	72.00 - 74.00	1	1230
10	74.00 - 76.00	1	1230
11	76.00 - 78.00	2	2461
12	78.00 - 80.00	0	0
13	80.00 - 82.00	0	0

AREA OF ONE ELEMENT (SQ. FT.) = 1231.74
TIME OF PASS = 1345
ALTITUDE (FEET) 7000
HEADING (DEG. FROM NORTH) 50
SPEED (MPH) 100
GRID SIZE IN FEET = 1000
MOSS LANDING IR TEST 12/6/70

FIGURE 8 - Thermal scan (left) and computer constructed surface isotherms (right) for the Moss Landing Power Plant Units 6 and 7 at a load of 1500 MWe, a cooling water flow of 1350 cfs, and a temperature difference of 22^{o}F, December 6, 1970.

REFERENCES

1. ADAMS, J. R.
1968 Ecological Investigations Around Some Thermal Power Stations in California Tidal Waters. Presented at 2nd IBP Workshop of the Effects of Thermal Additions in the Marine Environment. Chesapeake Biological Laboratory, Solomons, Maryland, November 1968.

2. ADAMS, J. R., H. J. GORMLY, AND M. J. DOYLE, JR.
1969 Ecological Investigations Related to Thermal Discharges. Presented at Pacific Coast Electrical Assoc. E. & O. Section. Annual Meeting, Los Angeles, California (March 13-14, 1969): 16p. mimeo.

3. ADAMS, J. R.
1970 Thermal Effects of Electric Power Plants. Hearings before the Joint Committee on Atomic Energy, Congress of the United States, Ninety-first Congress, on the Environmental Effects of Producing Electric Power, February 24-26, 1970. Washington, D.C.: U.S. Government Printing Office: Part 2 Vol. 1: 1781-1800.

4. ADAMS, J. R., H. J. GORMLY, AND M. J. DOYLE, JR.
1970 Thermal Investigations in California, Marine Pollution Bulletin, Volume 1 (NS) No. 9 (September 1970) pp 140-142.

5. ADAMS, J. R.
1971 Statement before the Committee on Public Works, Honorable John A. Blatnik, Chairman, Sept. 14, 1971. in Water Pollution Control Legislation - 1971. Hearings before the Committee on Public Works, House of Representatives, 92nd Congress, 1st. Session, Washington, D.C. US GPO: 1184-1214.

6. CHENEY, W. O. and G. V. RICHARDS
1966 Ocean Temperature Measurements for Power Plant Design. Proc. ASCE 1965 Coastal Engr. Conf. Santa Barbara, California: 955-989.

7. ELIASON, J. R. , H. P. FOOTE, and M. J. DOYLE, JR.
1970 Remote Sensing Techniques for Tracing the Movement of Industrial Wastes in Surface Waters. Proceedings Pacific Northwest Industrial Waste Conf. 1970: 22p.

8. ELIASON, J. R., H. P. FOOTE, and M. J. DOYLE, JR.
1971 Surface Water Movement Studies Utilizing a Tracer Dye Imaging System. Proceedings of the Seventh Annual International Symposium on Remote Sensing of the Environment, Ann Arbor, Michigan (May 1971): 20p.

9. GORMLY, J. J.
1972 Correlation Studies of Thermal Effects from Steam Electric Power Plants and Thermohydraulic Models. ASME Publication 72-Pwr-2 (February 1972): 7p.

10. MINER, R. M., P. D. HINDLEY, and R. F. CAYOT
1971 Thermal Discharge: A Model-Prototype Comparison. Presented at ASCE National Water Resources Engineering Meeting, Phoenix, Arizona. January 11-16, 1971. 40p.

11. NORTH, W. J. and J. R. ADAMS
1968 The Status of Thermal Discharges on the Pacific Coast. Proceedings of 2nd Workshop on Effects of Thermal Additions in the Marine Environment, Solomons, Md. (November 1968), Chesapeake Science 10 (3-4): 139-144.

CHAPTER 119

LAND USE AS A FACTOR IN COASTAL WATER QUALITY

by

P. H. McGauhey
Professor Emeritus
University of California
Berkeley

Public Concern for the Coastal Zone

Recognition of coastal and estuarine waters as a part of the overall water resources of a nation is a development that became evident only in quite recent years in the United States. To a significant degree it is associated with an aroused public concern for the quality of something currently described loosely as "the environemnt" — a concern which initially reached a critical mass in about the year 1969. To be sure, the oceans have always fascinated men of all sorts from adventurers to scientists, but the emergence of a broad public interest in the quality of ocean water, particularly in the coastal zone, is the result of several factors, not all of which are scientifically defensible. One such factor is the notion that the oceans are teeming with life which may well become man's final source of food when he has overwhelmed by sheer numbers the physical and biological carrying capacity of the land. Such an estimate of the potential of the sea seems to have been obtained by multiplying the volume of the oceans by the biomass concentration typical of the continental shelves. That it is a vast exaggeration in no way detracts from its potential to energize public reaction. However, the truth that aquatic life is most abundant in the coastal zones, and the prospect that man must manage this zone in a better manner if that life is to continue to contribute to his well being, only makes it the more important that the quality of coastal waters be a matter of concern and of purposeful management. To this end a considerable degree of public overestimation of the role of the sea in sustaining human life is a force that can be harnessed to productive programs of intelligent action. In fact, an appreciable amount of purely emotional concern for such catchwords as "ecosystems," "endangered species," "habitat," etc. can be tolerated and often used productively without any debating of its validity as long as it does not impose a serious constraint upon society without generating any corresponding benefit to either man or his fellow creatures.

But concern for coastal waters and the problems of their quality cannot be confined to food for man nor to habitat for marine biota. It is an inescapable spinoff of urbanization and an aspect of the need of urban man for recreational facilities. Nor is this situation likely to get any better, because the tendency for human beings to become urban dwellers is a worldwide phenomenon. In the U.S.A. the 1970 census revealed that 75 to 80 percent of its citizens were living on less than 10 percent of the land. Various estimates anticipate that by the year 2000, 90 percent of some 300 million people in the United States will live on 3 to 5 percent of the land. More significant, however, is the census finding that 73 percent of the U.S. population live within 50 miles of the sea coast or the Great Lakes. Thus it must be presumed that the coast is a factor in the life of more than

three-quarters of our people at some time during each year. Similar statistics for other nations are not at hand at this writing but one may readily presume that the percentage of Canadians, for instance, who are similarly influenced by the ocean is no less than that of the United States.

What does urban man demand of coastal waters? First he wants access to them, generally to a degree far in excess of that readily available in the vicinity of any large concentration of population. He wants beaches for his bathing and basking. He wants marinas for his boat; open water for water skiing; room to sail or to speed under power. He wants an aesthetically pleasing water. He wants fish and wildfowl; and he wants clean water free from health hazards, nuisance conditions, and whatever other aspects he may associate with another of his catchwords — "pollution."

The Coastal Zone as a Factor in Water Quality

The quality of coastal waters is inescapably a function of what happens on the land, especially within the coastal zone. Man not only wants the physical and psychological benefits of an unpolluted nearshore water, but also he wants to occupy on a continuous and permanent basis both the shoreline and the landward coastal zone; and he prefers for this purpose the estuaries and embayments that mark the terminus of coastal and inland valleys. Here he seeks both economic gain and the accommodation of large numbers of people, on which such gain depends, by erecting high-rise water-front apartments with a superior, and often a preemptive, view of the water. He wants to, and does, reserve to individuals the beach and marina areas, thus limiting public access to the shoreline or concentrating recreationists in a few inadequate beach parks. He wants and needs harbor facilities for commercial shipping. In fact, urban settlements to a large degree began along the seacoasts and other major waterways where transportation by boat and barge might serve the human needs and the search for wealth that goes with commerce. In terms of coastal water quality this phenomenon had several major effects.

One such effect is the result of the natural untidiness of man. It involves the desire of people to be rid of unwanted wastes in the least expensive and troublesome manner. Because essentially all coastal cities have been long in their development, waste discharge practices began when man's tolerance level for the unaesthetic was somewhat higher than it is today. Consequently, the method of dealing with domestic and industrial wastewaters was to pipe them in a raw state directly to an estuary or embayment by the shortest route from the area of origin. This compounded the number of points of discharge of sewage as the city grew. In many cities, both storm water and sewage flowed through the same conduit. Initially such a waste disposal practice may have had little effect on the life of coastal waters. Later, as the extent of the population concentration increased, the oxygen demanding potential of decomposing organic matter came to endanger the oxygen resources required by aquatic organisms. Moreover, the presence of bacteria of intestinal origin became a hazard to the health of people using beaches and coastal waters, or eating shellfish taken from them.

The development of industry, which made large cities possible, increased the range of "pollutants" in sewage to include toxic metals and exotic chemicals, leading to a new spectrum of dangers to the users of coastal waters — be they men or creatures less able to control their own destiny.

Concerning domestic and industrial sewage discharges it may be said that both man's aesthetic sense and his ability to increase the volume and variety of waterborne wastes have grown faster than his willingness to depart from ancient practices, faster than his knowledge of the effects of wastes on marine life, and faster than his economic and technological progress in collecting together the discharges from dozens of outfalls and upgrading them to levels which he is still trying to establish as appropriate. Therefore it may be said that sewerage of man's homes and factories in the coastal zone can contribute to coastal waters such things as unsightly floating debris and grease, toxic ions and chemicals, oxygen consuming organic matter, nutrients, and bacteria and viruses. The effects of these may include loss of clarity of water, aesthetic nuisance, health hazards to man, and observable direct, or little understood indirect, effects on aquatic biota. Not all effects of waste discharges, however, are necessarily detrimental. The amount and the state of nutrients in human wastes may be suited to the support of a thriving marine community. The point, in the context of the present discussion, is that wastewater discharge from urbanized land is a major factor in the quality of coastal waters bordering such land.

A second factor in land-water quality relationships in urban development derives from the physical use of the land itself. Coastal valleys in nature intercept some of the sediment brought down by natural floods. Typically such valleys also contain low lying marshy land which intercepts surface runoff and serves as habitat for plants and wildfowl, as well as for mosquitoes and other insects which man in his own interest dare not tolerate. As the city grows, these valley and marsh lands come under development. Swamps are drained of water and of stored organic nutrients. Natural stream beds are straightened and lined with concrete or replaced with conduits. These measures hasten both flood and less severe surface runoff to the sea. Roofs, streets, and paved parking lots, which characterize urban development, likewise hasten rain water to the sea. One effect on coastal water quality is to increase the drop in salinity resulting from fresh water inputs, and to discharge to the coastal water a variety of debris generated by men living in large concentrations, carrying on his industry, and wearing down countless automobile tires in the streets.

There are also other aspects of urbanization that affect the quality of waters moving from the land to the sea. Both the search for a view and the limited availability of valley land encourages urban development of hills and mountain sides. On steep land, as on flat land, the most economic use of costly equipment during land development is to prepare the entire site quickly. Thus, stripping of vegetation and reshaping of land surface generates a source of sediments which may in time of heavy rainfall be disastrous to aquatic biota or habitat. Conversely, protecting a city from floods by control reservoirs may so reduce the sediment budget of a coastal area that long existing beaches disappear.

Associated with the drainage of urbanized land may be water quality factors resulting from the commercial and household use of pesticides; and from fertilizing of gardens, lawns, and parks. Although the alarmist may fear that toxic materials from such sources may harm marine life, or that nutrients may stimulate excessive growth of aquatic plants, little is known of the effects in either a general or a specific case of human occupancy of land. The same holds true for surface runoff from agriculturally or industrially developed land. What is known then is the kind of water quality factors that urban land development generates and, more important, that if one does not like the presence of such factors in coastal waters he shall have to look to land use management practices to determine what he can do about it.

Controlling the Quality of Coastal Waters

The foregoing conclusion is deliberately drawn before it is thoroughly documented in order to facilitate an examination of our traditional control measures and an evaluation of our areas of ignorance of appropriate objectives for coastal water quality control.

Most anyone familiar with North America will agree that the freedom to own and to use and abuse land is a heritage of Americans much harder to invade than that of their freedom similarly to abuse water. Moreover, what is today considered an improper use of a land resource may at some earlier date have been its highest beneficial use. Specifically, in pioneer times when agriculture was the strongest base of local economy and land ownership the symbol of affluence, a man's livelihood depended upon subduing wilderness, not upon creating one by legislation. Furthermore, society is yet far from ready to consider its vast system of scientific agriculture as a pollution of the land which must summarily be ended. In fact, the continuance and the success of agriculture is perhaps the most institutionalized aspect of our civilization.

With water the story is different. Concern for the quality of water developed slowly. Knowledge of the role of water quality in health is scarcely a century old. Nevertheless in the case of drinking water it is a comparatively well resolved problem. The concept of other beneficial uses for which quality should be considered, however, has been institutionalized less than 25 years. To control water quality the abuser of water becomes known as a "polluter," the abuse itself as "pollution," and "pollution control" as the appropriate regulatory response. But most of this charade began with fresh water and with flowing water, which differs from land in a special way — it is a transport system rather than a sink; and its capacity to suffer pollution is one of concentration or degree. This led men naturally in the direction of "pollution control" aimed at the local discharge and at the control of its concentration at the source. Once such a concept was institutionalized it took a considerable period of years to come around to the viewpoint that water is a resource like air and land and so should be protected as a resource. The extension of this concept to that of protecting water quality for environmental reasons is little more than three years old.

Consequently, slowly developing water quality standards and objectives have been concerned with water per se and have had but limited secondary effects on restraining the use of land.

Coastal waters, with the exception of health and nuisance oriented factors, were not given particularly wide attention from a quality of resource viewpoint until "environmental quality" became a catchword. Prior to that time the ocean was considered as the earth's ultimate sink and all but hopeless in quality; quality, of course, being measured in terms of physical condition and chemical and microbiological constituents rather than in terms of its suitability for marine ecosystems.

Popular concern for "environemnt" and "ecology" aroused interest in protecting the quality of coastal waters for environmental objectives. Understandably, the effort is taking the "pollution control" route long applied to fresh waters. Thus, unwittingly the initial attempt is to overcome the results of poor or nonexistent land use planning and management by imposing increasingly severe restrictions on the quality of water discharged by land-based industries, cities, and agriculture. That this will have any important feedback effect in controlling land use in such a manner as to attain coastal water quality must be considered a forlorn hope.

Consideration is, of course, being given at many governmental levels of how land use management for protecting the air, water, and land environments as a single unit might be initiated. Generally proposals in this context take the form of greater governmental control by new agencies so broad in concept that simply organizing the agency and institutionalizing its power should allow the ocean to get a great deal saltier before its quality is related to the land in any specific way. Nevertheless, efforts to protect the quality of coastal waters are in evidence. In 1971 federal and state regulatory agencies began demanding that storm water runoff from coastal cities be collected and treated to some degree before permitting it to enter coastal waters. Just how this is to be accomplished in a city such as San Francisco with hills draining in three directions into the ocean and the Bay is less clear than is the evidence that authority will demand it. However, in evaluating such factors as those herein presented one thing does become quite clear. That is, that land as well as water will have to be managed simultaneously if national objectives related to coastal waters are to be realized.

The Search for Criteria

It is, of course, one thing to demonstrate rationally that the quality of coastal waters can be managed only by controlling how man husbands the land, but quite another to identify the appropriate land-water relationship, and to establish criteria suited to protecting both the quality of coastal waters and the quality of life within such water. It is at this point that we must recognize that our environmental goals are in danger of outrunning the limits of either understanding or good sense. Two boundary conditions can be set, neither of which makes sense of any kind. One is to do nothing to protect the quality of coastal waters; the other is to do nothing that

could conceivably pollute them. Few men can be found to advocate the first, whereas a loud and organized group of "true believers" have persuaded themselves that the latter must prevail — presumably without terminating mankind. Unfortunately, man simply does not have the knowledge necessary to establish realistic objectives, to evaluate the tradeoffs necessary to achieve such objectives, nor even to judge how much of the violence done an ecosystem in a given coastal area is attributable to nature and how much to man — or by what chain of circumstances it occurred. We may as well confess that despite our current zeal to save the oceans we really do not know what to save them from nor precisely for what purpose they are to be saved. But that does not mean that we should not try to find out.

Numerous studies to shed light upon the darkness I have indicated are in progress. To undertake a catalog of all ongoing work having land-water-ecosystems relationships in coastal zones is beyond the scope of this paper. Right here in Vancouver studies are aimed at evaluating the land-water relationships east of Vancouver Island and in the Frazier River. All I know of the early results of this study is that the chap who built Vancouver Island is going to have a hard time justifying it to the Sierra Club.

Work with which I am personally familiar is in progress in Hawaii under a Sea Grant to the University of Hawaii for studies which include the quality of coastal waters. There are several reasons why this particular study has a unique potential for developing criteria to relate coastal water quality to land management practices and for evaluating the resources of the coastal zone both landward and seaward of the shoreline.

To begin with, essentially all of inhabited Hawaii is shoreline or coastal zone, thus coastal waters are little influenced by what man does on inland rivers. Moreover, there are still situations in which the discharge from land to water, and consequently the coastal water environment is little affected by the presence of humans. This affords an opportunity to establish some baseline against which to evaluate human activity on land — a need which cannot be overemphasized. Next there are situations as at Kaneohe Bay where intense urbanization of a coastal valley has occurred and changes in water quality and biota have been observed in the presence of treated sewage. Moreover, plans to discharge sewage elsewhere are in progress and the opportunity is developing to observe changes in the environment and in the biota of Kaneohe Bay when only urban runoff afflicts its waters.

"Before" and "after" studies with raw sewage are in prospect and in progress in relation to Honolulu's sewage discharge at Sand Island. The sugar cane industry has likewise been isolated for evaluation of "before" and "after" effects of sugarcane culture and milling operations. Thus, Hawaii, by reason of its coastal zone and shoreline development and the relative ease of segregating the effects on water quality and biota of urban, agricultural, and industrial development of land, affords a particularly good place for land use versus coastal water quality evaluations which lead on to needed criteria. The state has certain other characteristics of significance. Water temperatures and weather permit almost uninterupted year round work in the ocean. Having no continental shelf, deep water exploration and resource studies are especially convenient. This same

phenomenon, however, accentuates Hawaii's need for information on dozens of the subjects which appear on the program of this Conference.

Of course a very great percentage of the coastline of the North American continent is influenced by what man does on inland rivers and tributary land. Here again we need some baseline data to differentiate between what man and what nature does to coastal water quality. Perhaps here in western Canada, where great upriver cities have not yet overwhelmed nature is the best place to seek such baseline criteria.

Conclusion

Nature has long used the ocean as a sink. If the quality of coastal waters which, as I noted earlier is the critical zone, is to be maintained as near as possible in some optimum condition, then it will never be enough merely to take up a sample of the water, frown over it in the laboratory, and lower the values in an increasing spectrum of "standards." We shall have to know more of how land use, land development, and land management practices, especially in the coastal zone, affects the quality of coastal waters, and what that quality means to life in that water. Then we shall have to know enough about natural shifts in ecosystems and what kind of ecosystems we want to maintain, or can possibly maintain, to make intelligent tradeoffs between land and water quality decisions. Finally, we shall have to reexamine the degree of freedom that goes with our land in order to adapt it to a population load which now brings these waters to a condition with which man must become concerned.

ABSTRACT

Coastal and estuarine waters are only now being fully recognized as a major sector of America's overall water resource. Protection of the quality of such waters for environmental objectives has understandably followed the same "pollution control" route long applied to fresh waters. This leads to attempts to overcome the results of poor or nonexistent land management regulations by imposing increasingly severe restrictions on the quality of water discharged by land-based cities and industries. Human occupancy of the coastal zone leads inevitably to the straightening and lining of drainage channels, the paving of streets and parking lots, the stripping of vegetation from land during subdividing, the overloading of land area with housing, the commercial and industrial use of pesticides and fertilizers, and various other phenomena which contribute to the degradation of the quality of coastal waters and water environments. Although freedom to own and abuse land is a heritage of Americans somewhat more difficult to invade than is their freedom similarly to abuse water, it is becoming clear that land as well as water will have to be managed if national objectives related to coastal waters are to be realized. Upriver activities lead to degradation of coastal waters in some situations. In others occupancy of the coastal zone is the major factor.

CHAPTER 120

EFFECTS OF WASTEWATERS ON MARINE BIOTA

Whseler J. North
W. M. Keck Engineering Laboratories
California Inetitute of Technology

ABSTRACT

The ocean provides enormous oapacity for dispersion and assimilation of human and natural wastes. Indsed marine ecosystsms dspend on such terrestrial sources for their nutrient supplies. It is incumbsnt on man to cause minimal disruption and, if possible, beneficial sffects from dispersing his wastss in the eea. The Southern California Bight receives the most intenss exposure to discharged sewage of any exposed region along the Pacific coast of North America. Evidenose of significantly altsred chemical and biological conditions in southsrn California have been demonstratsd. Elevated ooncentrations of csrtain metals occur in sediments nsar some large sewage outfalls. Pseticide rseidues wers extremely high in sand crabs from southern California. Beds of giant kelp decreased nsar eome, but not all,sewage outfalls. Correctional measurss ars disoussed. Ecological surveys ars currsntly used to provide early warning of potential biological problems near some southern California outfalls. A survsy nsar an outfall removed from service indicatsd moet ohanges in fish and macroinvsrtebrate populations occurred within a few months after the discharge oeased.

INTRODUCTION

Ecological consequences of discharging liquid wastes to the marine environment form a complex subjsct, involving an sxtensivs literature. To restrict this discussion to reasonable space limits, I shall consider only waste disposal to the open sea. I will rely primarily on data gathered in ths southsrn California region, the arsa with which I am most familiar.

From the outset I would like to eliminate certain emotions many of us oarry with reference to liquid waste. In the nursery we are all taught that human wastss are rspulsive and should be strongly avoidsd. What is valid in the nursery may not be true for the remainder of the world. Oceanic biota utilizs and depend on many wastes of terrestrial origin. Without nutrient input from streams and rivers, life in the ssa would be greatly reduced. Precise sources of these nutrients are of little ovsrall importancs. That is, it is immaterial to a marine plant whether phosphate ions come to it from rock erosion, decay procssses in soils, or releass as wastes from the bodies of man or other animals. Ws must, however, be careful to inject our nutrient subetances into the marins world in ways that do not disrupt ecosystems (i.e. avoid eutrophication problems). We must also be csrtain that the disposal operation does not significantly alter the physical and chemical environment.

The ocean is viswed as an attractive recsptacle by engineers charged with managing large volumes of liquid wastes generated by large metropolisss. The great expanse of the sea provides enormous oapacity for assimilation and dispersion. Soonsr or later most of our liquid wastes end up in the sea whether thsy are first discharged to rivers and streams or more directly placed in bays and sstuaries, or actually discharged in the ocean.

POPULATION DISTRIBUTION ALONG THE U.S. PACIFIC COAST

As a rough guide to intensity of waste generation, let us consider the distribution of human population along the Pacific United States. The combined populations of Washington, Oregon and California are about 25.5 million humans. (Statistical Abstract, 1970). About 11.3 million, or 44 percent of the three-state total, reside within "discharge distance" of the sea in the region between Ventura and San Diego (about 150 miles of coastline). More than a billion gallons of liquid wastes are discharged daily into the Southern California Bight . (1) No other region of our Pacific Coast is exposed to such an intensity of waste disposal. If marine waste disposal does affect marine biota, the Southern California Bight is a logical region for detecting and analyzing such effects.

The Southern California Bight is a major indentation in the coast just south of Point Conception (Figure 1). The seaward boundary exhibits a chain of islands lying some 25 to 50 miles offshore. The main current systems (California and Davidson Currents) usually do not affect coastal waters in southern California. Coastal currents in the regions receiving discharged wastes are sluggish and oscillatory, typically ranging up to 0.3 knots. Action from long period swell is reduced along those portions of the mainland that lie in the lee of offshore islands.

Four major outfalls account for approximately 90 percent of the sewage effluent discharged to the Southern California Bight. These facilities are operated by the City of San Diego (CSD, approximately 80 MGD), Orange County Sanitation Districts (OCSD, 135 MGD), Los Angeles County Sanitation Districts, (LACSD, 360 MGD) and the City of Los Angeles (CLA, 330 MGD) (Table 1). A number of minor municipal and industrial outfalls are scattered irregularly along the coast. Some of the minor outfalls have been studied intensively. Few, if any, ecological affects have been reported. About 90 percent of the discharged sewage effluent receives only primary treatment.

ENVIRONMENTAL IMPACT OF MARINE WASTE DISPOSAL

For sewage outfalls discharging in water of adequate depth and using diffusers, changes in oceanic temperature, salinity, pH and dissolved oxygen, are nearly always negligible. Although extensive plankton blooms occur in California's waters, all evidence indicates that these are natural phenomena and nutrients from discharged wastes are a negligible stimulus (3). Potential problem areas may exist with regard to toxicants, disease, sedimentation, and induced changes in species composition. These are fields where further research is clearly indicated.

Concentrations of toxic substances in receiving waters of well-designed outfalls are low, typically below threshold levels for overt distress symptoms during short term exposures for test organisms. In recent years, however, there have been indications that subtle mechanisms in the environment are able to concentrate toxicants to levels that may be biologically damaging. Consequently any evidence that such mechanisms may be operating near a sewage outfall, is cause for concern. Wastewaters are probably not the only sources of toxic inputs. Freshwater and airborne sources must also be considered and still require considerable investigation.

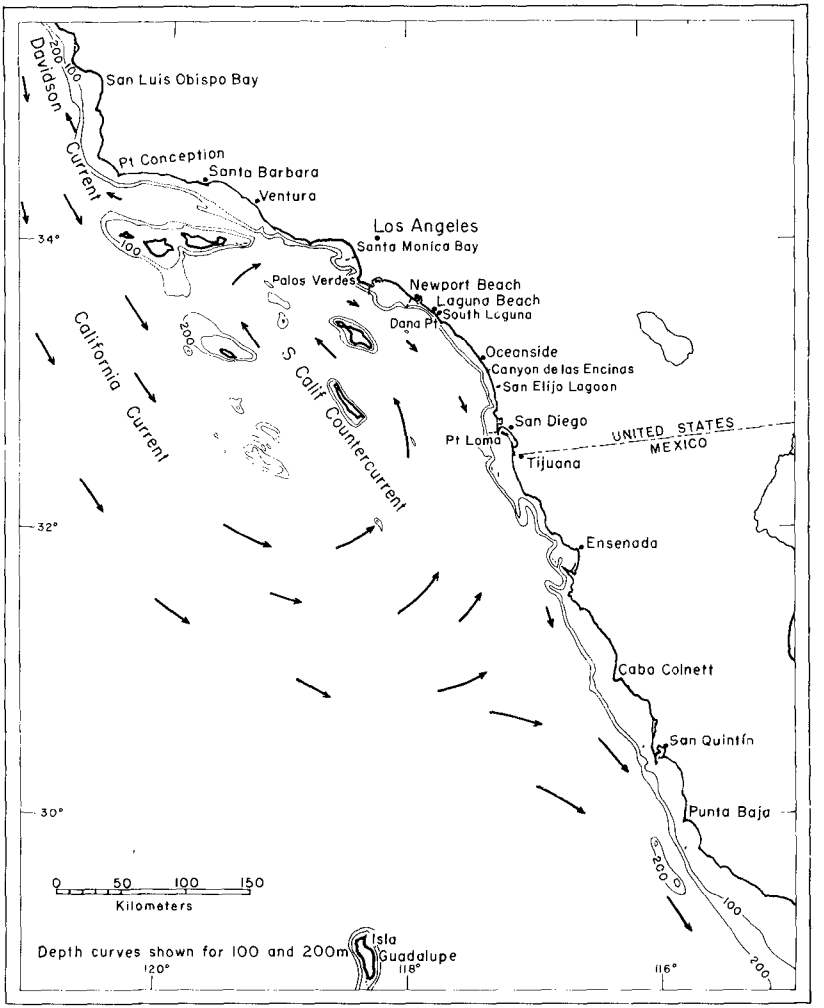

Figure 1. Chart of southern California and northern Baja California showing general current systems and their relations to the Southern California Bight, modified from Jones (2). The offshore California Current moves sluggishly most of the year but a reversal, the Davidson Current, can occur from August to November.

Table 1

Effluent volumes in millions of gallons per day versus time for four major southern California discharges. Data supplied by City of San Diego, Orange County Sanitation Districts, Los Angeles County Sanitation Districts, and City of Los Angeles.

Year	San Diego	Orange County	L. A. County	L. A. City
1972			360*	329*
1971	83	135	370	336
1970	81	130	371	330
1969	84	125	373	344
1968	80	120	348	323
1967	73	114	336	317
1966	71	107	318	316
1965	63	95	302	293
1964	61	89	293	287
1963	48	82	288	283
1962	49	75	280	278
1961	48	66	274	261
1960	48	54	264	259
1959	45	52	248	262
1958	44	44	220	267
1957	43	37	195	256
1956	40	31	183	249
1955	39	24	180	244
1954	39		176	239
1953	38		154	230
1952	37		147	219
1951	32		125	193
1950	28		114	194
1949	25		104	199
1948	23		82	184
1947	21		59	178
1946	23		53	161
1945	22		52	160
1944	9.7		52	162
1943	5.2		47	148
1942	↓		35	143
1941	↓		34	144
1940	↓		29	133
1939	↓		25	130
1938	↓		23	131
1937	↓		20	131
1936	↓		19	114
1935	↓		18	113
1934	↓		17	107
	1887			1894

*Estimate based on portion of year

Klein and Goldberg (4) have demonstrated increases in sedimentary Mercury in the vicinity of the LACSD discharge. Young (1) recently summarized all information concerning Mercury distribution in the Southern California Bight. Galloway (5) demonstrated increased levels of Zinc, Copper, Lead, Cadmium, and Chromium in sediments near the LACSD and CLA outfalls, vs. background values from distant samples. Burnett (6) examined DDT levels in sand crabs, Emerita analoga, as a function of distance from the Los Angeles region. Crabs from the Los Angeles area yielded DDT concentrations two orders of magnitude greater than collections from remote areas in central California.*

There is thus clear evidence that potential toxicants are being concentrated at certain locations in the Southern California Bight. Ecological consequences of these phenomena await analysis. If significant adverse effects exist, source control of toxicants may be necessary. It should be mentioned that Clendenning (7) found that short term exposures (up to 96 hours) of giant kelp tissues (Macrocystis) to 100:1 dilutions of sewage in seawater (composite sewage samples provided by LACSD and CSD), stimulated photosynthesis as much as 50 percent, presumably an effect from nutrients in the sewage.

Investigations of disease among organisms near sewer outfalls are presently only in preliminary phases. Collections have indicated some association of abnormal conditions among certain fish species captured near outfalls. Abnormalities may also be found, albeit with reduced frequencies, in the same species from areas well removed from outfalls. Thus Russell and Kotin (8) noted an 0.3 incidence of papillomas in white croaker (Genyonemus lineatus) from Santa Monica Bay vs. none among specimens from a control area. Halstead and Young (9) described a variety of afflictions in various fish species, which they believe were related to discharged wastes. The Southern California Coastal Water Research Project (10) is collecting and analyzing incidence vs. distribution data. Etiology of these diseases remains unknown. North (11) observed tumorlike growths on stipes and bladders of kelps near the San Diego outfall.

Grigg and Kiwala (12) believed that light sedimentation upon normally rocky surfaces was responsible for reduction in numbers of species that they recorded near the LACSD sewer outfall. These authors reasoned that even a thin film of sedimented material might prevent settling by microscopic planktonic larvae seeking solid rock substrate. The LACSD discharge in recent years has discharged about 500 tons daily of suspended solids (13). Although much of the suspended solids would not settle unless floculation occurred, the quantities liberated are very large and comparable to the natural coastal transport of sediments in some areas. There is not evidence that sedimentation poses problems on normally sedimentary bottoms, although Carlisle (14) has suggested that distributions of fishes may change in such areas.

There are indications that marine waste disposal may cause significant alterations in distributions of ecologically important species. One such species is giant kelp, Macrocystis pyrifera. Giant kelp develops a treelike structure underwater. Populations of plants form a forest habitat that comprises the base of diverse and productive communities. The kelp bed association provides commercial and recreational sources of fishes and shellfish. Kelp canopies are harvested and processed as food additives and for alginates. Kelp beds near Los Angeles and San Diego began declining in the early 1940's and were virtually nonexistent by 1960 (15). In general, the first indications

*DDT discharge by LACSD has been essentially eliminated.

of permansnt large-scale disappearance occurred in those portions of the beds closest to sewage outfalls (Figure 2). Deterioration spread from this local rsgion. During the period of decline, volumes of discharged effluent increased continually (Table 1).

Surveys in the deteriorating kelp beds typically revealed large-scale destruction of kelp holdfasts (the plant's anohoring mechanism) by swarms of grazing sea urchins. Deterioration of the Point Loma kelp bsd near San Diego was halted and reversed (16) after urchin populations were brought under control (Figure 3). Pearse et al. (17) showed that urchins oculd absorb organics from seawater through the dermis and utilize them. Analyses by Clark (18) indicatsd that dissolved organic substances near the LACSD sewer outfall were significantly elsvated vs. a control arsa. She oalculated that dissolved fres amino acids alone were present in sufficient concentration near the LACSD outfall to provide significant nourishment to urohins of the region. The restored kelp bed off Point Loma perhaps now benefits from nutrisnts discharged from the San Diego outfall. An indication is offsred by the high productivity of this kelp bed. The bed's present area is considerably less than 10 percent of all kelp beds in California, yet Point Loma yields about 25 percent of the annual harvest.

DETECTING ECOLOGICAL CHANGE

It is clear that effects of sewer outfalls on marine ecosystems can be subtle, complex, and at times unprediotable. To protect biota of the Southern California Bight, regulatory agencies have defined beneficial uses to be protscted that include preservation of fishes and other aquatic life. In addition, ths State of California sponsored an extsnsive survey of the southern California continental shelf by the Allan Hancock Foundation of the University of Southern California (USC). The study's purpose waa to establish background conditions to aid in evaluating future change. The investigation gathsred data on water temperature, salinity, dissolved oxygen, phosphate, silicats, nitrate, pH, transparency, transmissivity, sedimentary characteristics, microplankton, sedimentary fauna, foraminifera, and intertidal algae from 1956 to 1960, occupying 732 stations (19). For several reasons, usage of the data has only been modsrate. For sxample, different sampling and analytical techniquss now in oommon use may not yield comparable data. Likewise data may be needed for specific locations not sampled during the USC study.

The USC and subsequent investigations (20, 21) have demonstrated the great complexity of ths nearshore environment. Distributions of organisms are usually patchy, posing difficult sampling and analytical problems. Even restricted areas may support hundreds of plant and animal species, displaying great ranges of densities. Sorting and idsntifying organisms can be an snormous and tsdious burden. Specialists are usually needed to identify the difficult groups such as Polychetes, Amphipods, Isopods, and Mollusks. Initially, monitoring programs sought to dsfine the entire scosystem but costs and the hopelessness of such efforts have caussd a shift in emphasis. A recently designed study, conducted by OCSD, utilizes trawling to characterize fishes and macroinvertebrates. Fishes are components of a wide variety of food chains. If a significant ecological disruption developsd, changes in fish populations would probably occur at a fairly early stage and provide ths necessary warning of an impending problem. Southern California fishes have been studied thoroughly, so identification and sorting efforts in the OCSD monitoring program are relatively small.

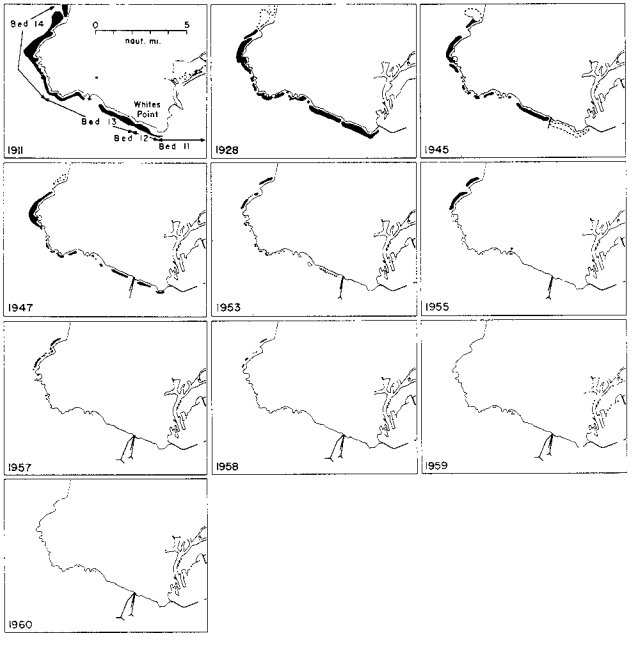

Figure 2. Historical series of charts of the Palos Verdes Peninsula showing status of kelp beds and construction of outfall system off Whites Point. Kelp beds shown as black. Data gathered from maps and aerial photos. Where a portion of the coast was missing in a series of aerial photos, the outline of kelp beds from the previous chart is shown as a dotted line. Abnormally high water temperatures from 1957 to 1959, seriously damaged existing kelp.

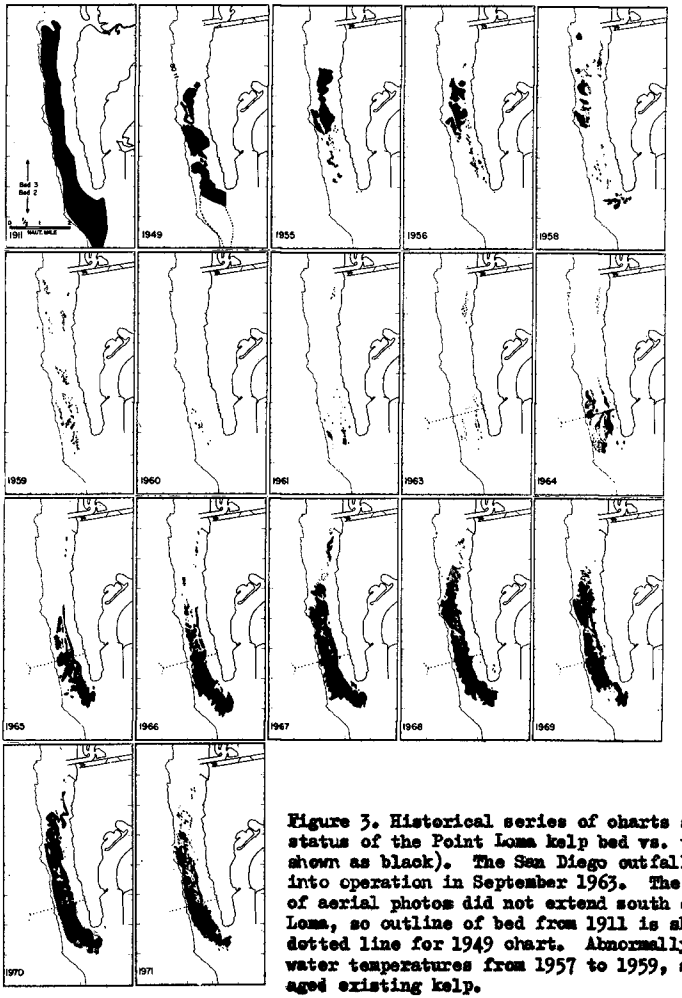

Figure 3. Historical series of charts showing status of the Point Loma kelp bed vs. time (kelp shown as black). The San Diego outfall was put into operation in September 1963. The 1949 series of aerial photos did not extend south of Point Loma, so outline of bed from 1911 is shown as dotted line for 1949 chart. Abnormally high water temperatures from 1957 to 1959, seriously damaged existing kelp.

Monitoring at the San Diego outfall presently places emphasis on sedimentary fauna. The voluminous data have been periodically analyzed by independent contractors (22,23,24). No significant adverse effects have appeared. Abundances of some groups increased substantially after discharge commenced in 1963.

Marine populations frequently undergo changes in response to natural environmental events as well as to other human activities such as fishing, accidents, construction, dredging, etc. To identify such effects it is important that control stations be included in monitoring programs.

OTHER BENTHIC STUDIES

A review paper by Gunnerson in 1961 (25) summarized most of the early literature. Relatively little biological work near Pacific coast outfalls had been published at that time. The large background survey of the Allan Hancock Foundation (19) and the first kelp studies (15) were still in progress. Since then, a number of studies (apart from routine monitoring) have sought to evaluate conditions near sewage outfalls.

Point Loma

Much additional survey and collection work off Point Loma was undertaken in 1965 by diving biologists from the Department of Fish and Game. Their study indicated a diverse and abundant fauna and flora existed on the rocky shelf inshore from the outfall and no adverse effects attributable to the discharge were observed (20). Grab samples of sediment close to the terminus did not yield sludge but species composition of the infauna suggested influence by the discharge.

San Elijo Lagoon

A 6 MGD ocean outfall near the mouth of the San Elijo Lagoon discharges domestic sewage through a diffuser at a depth of 60 feet. Biota was surveyed and described just before outfall construction in 1964 (26). The same region was resurveyed in 1969 after nearly five years of discharging had occurred (27). Of eleven species or groups observed along the sedimentary outfall transect in 1964, eight were recorded again in 1969. Missing organisms were a red alga, *Agardhiella*, a gastropod, *Acteon*, and a sea star, *Luidia*, none of which had been highly abundant. In 1969, however, the region near the outfall yielded an additional seven algal and 97 animal species not recorded from this transect in 1964. The presence of the nearby solid outfall structure was probably responsible for many but not all of the increased numbers of species. The outfall terminus yielded 105 species and varieties. Numbers of fishes were greater at the terminus than along the shallower section of the pipe that supported a lush growth of kelp (kelp is usually highly attractive to fishes).

Density of giant kelp in the area was determined by Strachan in 1969 for three established kelp beds previously studied by North in 1963-64 (28). Standing crops in 1969 had increased at all three stations by factors ranging from about double to nearly 18 times the 1964 values. Considerable marine life was noted remaining throughout the region. The richest transect was one-half mile north of the outfall and yielded nine algal, 144 invertebrate,

and five fish species vs. eight algal, 118 invertebrate, and fifteen fish species in 1964. It appeared, therefore, that the outfall had produced little, if any detrimental effect. The increased abundance of giant kelp might represent a nutritional stimulus such as reported by Clendenning (7).

Canyon de las Encinas

Department of Fish and Game divers conducted background (1962) and post-discharge surveys near the small (2.2 MGD) sewer outfall off Canyon de las Encinas to note any changes caused by the operation. Principal changes involved increased abundances of sea anemonies, hermit crabs, sand stars, and white urchins (29). Diversities and abundances of species colonizing the outfall structure were considered normal for the age of the "reef". Overall, no adverse influences of outfall operation were noted.

Pre- and post-discharge studies were conducted on kelp beds near Canyon de las Encinas (30, 31). Parameters measured were kelp abundance, plant size, growth rate, mortality, and reproduction as evidenced by abundance of juveniles. No adverse effects were found. The beds have remained luxuriant (as indicated by surface canopies) up to the present.

Central Orange County

Three small (6MGD) outfalls discharge in nearshore waters at depths from 30 to 80 feet at Laguna Beach, South Laguna, and Dana Point in central Orange County. Distances between adjacent outfalls varies from $2\frac{1}{2}$ to 5 miles. The region was surveyed by Andersen and North (32), comparing conditions near the outfalls to control areas two or more miles away from discharge sites. Quantitative sampling indicated concentrations of a worm, Pherusa, and a sea star, Astropecten, were reduced near the Laguna Beach outfall while another worm, Diopatra, was much more abundant (values highly significant) near the Laguna Beach and South Laguna outfalls. Diversity was greatly reduced near the Dana Point outfall and its control station compared to the other sites. Recent construction of a harbor in the Dana Point area may have affected biota at this outfall and its control station.

Orange County Outfall

Diving biologists from the Department of Fish and Game surveyed biota near the Orange County Sanitation Districts discharge off the Santa Ana River in early 1965. A nearby artificial reef was also inspected. Numbers and kinds of sedimentary fauna appeared normal as did communities encrusting most of the outfall structure (33). The last 100 feet of outfall pipe displayed reduced species diversity and there were indications of impoverishment on the artificial reef. The general biological impact of the discharge was nonetheless considered small. This outfall has been retained on a standby basis since March 1971 and the new 4 mile pipe carries effluent to a much deeper discharge site. A decrease in sedimentary sulfide levels was observed near the old outfall after discharge operations ceased (10).

PLANKTONIC STUDIES

Gunnerson (25) stated that "evidence for greater production of marine plankton in the vicinity of sewage-effluent discharges is strong", citing studies from Florida, Oslo Fjord, and the Mediterranean as support. This conclusion has since been verified for southern California waters by Tibby et al. (34;

see also 19). These workers found an initial depression of phytoplankton productivity as sewage and seawater became mixed near the Orange County outfall. After about eight hours a substantial increase in carbon-14 uptake was noted, lasting about two hours. No correlations were found between productivity and concentrations of phosphate, silicate and ammonia. Stevenson and Grady (35) usually found increases in planktonic concentrations near outfall "boils". Occasionally the effect could be traced to a 12,000 foot distance. These authors did not believe that effluent mixtures caused plankton "blooms" (marked concentration increases) but they surmised that discharged nutrients might enhance bloom intensities. Gunnerson (25) could find no convincing evidence that the subtle fertilization effects of sewage could lead to dense plankton bloom or eutrophication in open coastal waters although such effects may occur in semi-enclosed situations. Tibby et al. concurred (19). Comparing microplankton counts from 59 stations near outfalls, with counts from all 800 stations surveyed, the Allan Hancock Foundation was unable to find any differences among numbers of dinoflagellates recovered, but reported a significantly greater mean value for diatoms from the outfall stations (differences in means were 2.9 times the standard error). Influences on individual species were not determined.

Clendenning and Sweezey (36) believed that there may have been an association between sewage effluent and cryptomonads in San Diego Bay. The City of San Diego conducted surface to 20 foot depth plankton tows for five years near their Point Loma outfall (a discharge that rarely, if ever, extends to within 20 feet of the surface). A total of 80 groups that included 35 species were segregated during processing. Several species may have responded to the Point Loma discharge (Ceratium dens, Ceratium furca, and Noctiluca sp. may have increased temporarily, Skeletonema costatum and Oxytoxum sp. may have increased, particularly during a period of sludge discharge). Overall, however, it was ooncluded that influences on planktonic communities were negligible (22,23). This study was certainly the most detailed effort and the most carefully analyzed work of its kind ever conducted on the Pacific coast. As a result, the Regional Water Quality Control Board was convinced that the San Diego discharge was not influencing planktonic communities significantly and the City was allowed to discontinue this exceedingly costly program.

The problems associated with conducting meaningful plankton studies have plagued almost every survey that has examined this type of community near outfalls. Species identification requires highly specialized and painstaking efforts from collection to identification (37). Personnel with necessary skills are often unavailable. The City of San Diego studies were hampered by high turnover rates among technical personnel. Abundance variations even for a single species can be enormous, sometimes spanning five or six orders of magnitude during a single collection series. Vertioal migrations, tendencies to form stratified distributions under certain (usually unknown) conditions, horizontal transport by currents, and other factors introduce transients leading to profound abundance fluctuations within hours or even minutes.

In designing dispersal characteristics for a proposed ocean outfall for the City of San Francisco, bioassays were conducted on common marine animals to determine toxicity thresholds (38). The most sensitive species proved to be larvae of the bay shrimp (Crago nigrocauda) and of the market crab (Cancer magister).

STUDIES NEAR A DISCONTINUED DISCHARGE

An interesting study has been conducted by Marine Biological Consultants, funded by the County Sanitation Districts of Orange County (39). Trawling was used to define any macrofaunal changes following cessation of discharge from the District's Ocean Outfall No. 1. The outfall had been operating since 1954 and dispersed about 135 MGD of primarily treated effluent from a diffuser at a depth of approximately 55 feet. This system was removed from operation in March 1971 and thereafter effluent was dispersed from a newly-constructed outfall at a depth of 195 feet about three miles south from the former site of discharge.

The trawling studies involved quarterly collections using a 24 foot otter board trawl with a 1½ inch mesh body and a ½ inch mesh liner in the cod end. Each trawl occupied ten minutes of bottom fishing time. Collections were made at depths of about 50 feet, approximately 100 yards west of the outfall. Similar trawls were conducted at a control station of comparable depth and substrate, about four miles easterly. Studies ran continuously from August 1969 to the present (i.e. comprising twelve collection series).

The collections yielded a total of 75 invertebrate and 65 fish species. The outfall site produced 42 invertebrate and 52 fish species while the control yielded 61 invertebrates and 44 fishes. Most species appeared so sporadically that no relation to cessation of the discharge could be established. Among those species recovered fairly frequently and/or abundantly, 20 appeared to be relatively indifferent to the presence or absence of the discharge, nine showed tendencies to be less frequent near the outfall station before March 1971. Three species displayed reduced frequencies and/or abundances at the outfall station after March 1971 (i.e. there may have been some attraction by the discharge for these species: Table 2). Total species recovered per trawl fluctuated widely but after March 1971, values remained consistently high at both stations.

The data were thus fairly conclusive and revealing for certain species. When changes occurred, they usually appeared shortly after the discharge ceased. Obviously trawling is a highly selective operation, recovering primarily larger epibenthic invertebrates and intermediate-sized fishes. Even so, the data are useful in demonstrating character and rapidity of the changes involved.

CORRECTIONAL MEASURES

In-depth discussion of correctional measures is far beyond the scope of this paper. Needs for correction may become apparent from *in situ* observations gathered by monitoring programs or from external sources - generally research conducted elsewhere on problems aggravated by special circumstances. Correction, if needed, may take several forms including increased waste treatment effort, source control, or in certain cases, legislative action. Decisions are often costly and consequences far-reaching. Obviously both society and the environment benefit most if decisions are not made in a hysterical atmosphere.

Table 2

Summary of trawling studies comparing the Orange County Sanitation Districts Ocean Outfall No. 1 with a control area about 4 miles away. Sewage disposal at this outfall was terminated in March 1971. Numbers represent individuals recovered per ten minute trawl. Data from Marine Biological Consultants (39). Num = numerous; P = present.

Species	Station	Trawling Date											
		8/19/69	11/29/69	2/20/70	5/26/70	8/19/70	12/9/70	2/16/71	5/25/71	8/19/71	12/10/71	2/11/72	5/12/72
		INDIFFERENT SPECIES											
	Outfall		1							1		1	
Polinices draconis	Control												
	O			Num.				1			P		
Balanus concavus pacificus	C		10	1	36			4		P	3		
	O			5	.			2	1		1	1	
Cancer anthonyi	C				3					1			1
	O	4	3	39	8	3		9	15		2	8	2
Cancer gracilis	C				2		1		7	16			
	O	12	86	76	13	2		43	227	35	33	51	12
Crago nigromaculata	C		2	1	5			14	82	4	7	2	5
	O		7	2	4	1		73	24	75	2	4	
Lironeca vulgaris	C		13	3	28			118	46	29	P	3	54
	O	7	7	38	22	6		24	7	41	34	20	67
Astropecten verrilli	C		49	6	12			64	3	24	18	158	9
	O	2	3	5	2			8	1	9	2	5	9
Pisaster brevispinus	C						2		3		1		
	O			16	25			19	2				2
Citharichthys sordidus	C			135				1352	37		19	20	56
	O	38	69		18	45		543	449	300	287		99
Citharichthys stigmaeus	C		30			64			796	979	310	405	448
	O	2			1		14		15	9		11	2
Embiotoca jacksoni	C												
	O	1034	4	18		77		36				2	
Engraulis mordax	C												
	O	2	2				2		2	6		4	
Hyperprosopon argenteum	C												
	O				14			1	12				
Microstomus pacificus	C				9			1	1	28			10
	O	14	15	8	17		11	17	28	33	4	5	1
Phanerodon furcatus	C			7	2			1	7	8			3
	O	1				1	4		4	1	4	9	
Pleuronichthys verticalis	C		1	4	1		3	2	2	7	5	11	7
	O							156	4				
Sebastes semicinctus	C					2			8		1	1	
	O	577	36	75	34	8			1			248	
Seriphus politus	C								1				
	O	9	4	12	5	4	3	12	6	13	14	5	
Symphurus atricauda	C			5	3		7	10	10	27	26	16	16
	O				1			5	16			15	
Zalembius rosaceus	C							1	22			1	34

Table 2 (continued)

Species	Station	Trawling Date											
		8/19/69	11/29/69	2/20/70	5/26/70	8/19/70	12/9/70	2/16/71	5/25/71	8/19/71	12/10/71	2/11/72	5/12/72
SPECIES THAT INCREASED													
	Outfall								1			2	1
Flabellinopsis iodinea	Control			1				2	3			1	8
	0								6			1	3
Petalaster foliata	C		5	11							2	3	1
	0										2		2
Hippoglossina stomata	C		1		11		3	5	2	5	6	2	10
	0							2		6	1	1	1
Hypsopsetta guttulata	C										2		1
	0	1			1		2	2		5	3	15	1
Paralichthys californica	C						3			2	3	3	3
	0				1	4			8		1	4	7
Parophrys vetulus	C		1		3	1	3	1		9	6	12	32
	0								4	1		2	3
Pleuronichthys coenosus	C		4	2		2			3				4
	0						2		7	15		7	3
Pleuronichthys decurrens	C						3	5	157	29	17	1	7
	0						2	4	8		4		7
Scorpaena guttata	C			1				2	1	4	2		11
SPECIES THAT DECREASED													
	0	26	190	16	15	142		33	36	7		11	
Cymatogaster aggregata	C			38	7	4			9				3
	0	1024	160	293	455	578	254	103	6	11		32	
Genyonemus lineatus	C									2			2
	0	55		1		1	3						
Palometa simillima	C												
Species per trawl	0	22	18	24	21	14	17	29	35	28	23	35	25
	C	-	16	23	26	7	15	27	38	36	37	32	33

CONCLUSION

It is evident that marine waste disposal can and has produced significant changes among nearshore ecosystems in the Southern California Bight. This does not mean that deterioration has been complete or irreversible. The majority of the Southern California coastline still displays healthy, productive, and diverse marine communities. A major adverse effect, deterioration of the important kelp bed association, can be corrected, if given adequate effort. Clearly there is need for improvement and continued learning. I am optimistic that a time will come when we will know enough about ecological effects of marine sewage disposal to indeed be able reliably to fertilize and benefit the sea with our discarded nutrient materials.

REFERENCES

1. "Mercury in the Environment: a Summary of Information Pertinent to the Distribution in the Southern California Bight," by D. A. Young, Southern California Coastal Water Research Project, 1971.

2. "General Circulation and Water Characteristics in the Southern California Bight," by J. H. Jones, Southern California Coastal Water Research Project, 1971.

3. "Eutrophication in Coastal Waters: Nitrogen as a Controlling Factor," by University of California, Institute of Marine Resources, Wtr. Qual. Off. Env. Prot. Ag., Proj. 16010 EHC, 1971.

4. "Mercury in the Marine Environment," by D. H. Klein and E. D. Goldberg, Environ. Sci. Technol., Vol. 4, 1970, pp. 765-768.

5. "Man's Alteration of the Natural Geochemical Cycle of Selected Trace Metals," by J. N. Galloway, University of California San Diego, PhD Dissertation, 1972.

6. "DDT Residues: Distribution of Concentrations in Emerita analoga (Stimpson) along Coastal California," by R. Burnett, Sci.,Vol. 174, 1971, pp. 606-608.

7. "Laboratory Investigations," by K. A. Clendenning, University of California, Institute of Marine Resources, Effects of Discharged Wastes on Kelp, Quarterly Progress Reports: IMR Ref 58-11, pp. 27-29; IMR Ref 60-10, 1960, pp. 7-11.

8. "Sqamous Papilloma in the White Croaker," by F. E. Russell and P. Kotin, Jour. Natl. Cancer Inst., Vol. 18, 1957, pp. 857-861.

9. "Toxicity of Marine Organisms Caused by Pollutants," by B. W. Halstead, FAO Tech. Conf. Mar. Pol. Effects on Living Resources Fish., FAO Fish. Rpt. 99, FIRM/R99 (En), 1971, pp. 104-105 (abstract).

10. "Southern California Coastal Water Research Project Progress Report 9," ed. M. Sherwood, So. Calif. Coastal Wtr. Res. Proj., 1972.

11. "Kelp Bed Restoration Activities," by W. J. North, Ann. Rpt., Kelp Habitat Imp. Proj., Calif. Inst. Tech., 1966, p. 18.

12. "Some Ecological Effeots of Discharged Wastes on Marine Life," by R. W. Grigg and R. S. Kiwala, Calif. Fish & Game Quart., Vol. 56, 1970, pp. 145-155.

13. "Southern California Coastal Water Research Project, Waste Inventory and Pollutant Input," mimeo compilation presented at State Watsr Resources Control Board hearing, Dec. 1971.

14. "Results of a six-year trawl study in an area of heavy waste discharge," by J. G. Carlisls Jr., Calif. Fish & Game Quart., Vol. 55, 1969, pp. 26-46.

15. "An Investigation of the Effects of Discharged Wastee on Kelp," State Wtr. Qual. Cont. Bd. Pub. 26, 1964.

16. "Eoological Relationships Bstween Giant Kelp and Sea Urchins in Southsrn California," by D. L. Lsighton, L. G. Jones, and W. J. North, Proc. Vth Intl. Ssaweed Symp., Pergamon, 1967, pp. 141-153.

17. "Marine Waste Disposal and Sea Urchin Ecology," by J. S. Pearse, M. E. Clark, D. L. Leighton, C. T. Mitchell, and W. J. North, Appendix in Ann. Rpt. Kelp Habitat Improvement Proj., 1969-1970, Calif. Inst. Teoh.

18. "Dissolved Free Amino Acids in Sea Water and their Contribution to the Nutrition of Sea Urchins," by Mary E. Clark, Ann. Rpt., Kelp Habitat Improvement Proj. 1968-69, Calif. Inst. Tech., pp. 70-93.

19. "An Oceanographic and Biological Survey of the Southsrn California Mainland Shelf," State Wtr. Qual. Cont. Bd. Pub. 27, 1965.

20. "The Marine Environment offshore from Point Loma, San Diego County," by C. H. Turner, E. E. Ebert, and R. R. Givsn, Dept. Fish & Game Fish Bull. 140, 1968.

21. "Man-made Reef Ecology," by C. H. Turnsr, E. E. Ebert, and R. R. Given, Dept. Fieh & Game Fieh Bull. 146, 1969.

22. "Analyeis of Oceanographic and Ecological Monitoring Program at the City of San Diego Point Loma Outfall," by Marine Advisers, State Wtr. Qual. Con Bd., 1965.

23. "Effects of Ocan Disoharge of Waste Water on the Ocean Environment near the City of San Diego Outfall," by Water Resources Eng., State Wtr. Qual. Cont. Bd., 1967.

24. "Effects of San Disgo's Wastewatsr Discharge on the Ocean Environment," by C. W. Chen, Jour. Wtr. Pol. Cont. Fsd., pp. 1458-1467.

25. "Marine Disposal of Wastes," by C. G. Gunnerson, Jour. San. Eng. Div., Proc. Am. Soc. Civ. Eng., Vol. 87, 1961. pp. 23-56.

26. "Survey of ths Marine Environment offshore of San Elijo Lagoon, San Diego County," by C. H. Turner, E. E. Ebert, and R. R. Given, Calif. Fish & Game, Vol. 51, 1965, pp. 81-112.

27. "The Marine Environment Offshore of San Elijo Lagoon (a Post-Construction Submarine Outfall Area) and the San Dieguito River Mouth (a Pre-Construction Submarine Outfall Area)," by Alec R. Strachan, Calif. Dept. Fish & Game, MRR Ref. 71-1, 1971, 107 pp.

28. "An Ecological Study of the Kelp Bsds in the Vicinity of San Elijo Lagoon, San Diego County," by W. J. North, Final Rpt. on Std. Agreement 12-1, Stats Wtr. Qual. Cont. Bd., 1964, 26 pp.

29. "Survey of a Marine Environment Subsequent to Installation of a Submarine Outfall," by C. H. Turner, A. R. Strachan, and C. T. Mitchell, Calif. Dept. Fish & Game, MRO Rsf. No. 67-24, 1967, 65 pp.

30. "An Ecological Study of the Kelp Beds in ths Vicinity of Canyon de las Encinas, San Diego County," by W. J. North, Final Rpt. on Std. Agreement 12-12, State Wtr. Qual. Cont. Bd., 1963, 27 pp.

31. "An Ecological Study of the Kelp Beds in the Vicinity of Canyon de las Encinas, San Diego County," by W. J. North, Final Rpt. on Std. Agresment 12-7, State Wtr. Qual. Cont. Bd., 1968, 30 pp.

32. "A Marine Biological Survey of Central Orange County near Three Sewage Outfalls," by E. K. Anderson and W. J. North, Final Rpt. on Std. Agresment 0-2-63, State Wtr. Res. Cont. Bd., 1972, 73 pp.

33. "The Marine Environment in the Vicinity of the Orange County Sanitation District's Ocsan Outfall," by C. H. Turner, E. E. Ebert, and R. R. Given, Calif. Fish & Game, Vol. 52, 1966, pp. 28-48.

34. "The Diffusion of Wastes in Open Coastal Watsrs and thsir Effects on Primary Biological Productivity," by R. B. Tibby, J. E. Forworthy, M. Oguri, and R. C. Fay, Proc. Symp. Pol. Mar. Microorg. Prod. Petrol., Monaco, Com. Int. Explor. Sci. Mer Medit., 1964, pp. 95-113.

35. "Plankton and Associated Nutrients around Three Outfalls in Southsrn California," by R. E. Stevenson, and J. R. Grady, Allan Hancook Foundation, Univ. So. Calif., 1956.

36. "Phytoplankton in Coastal Waters," by K. A. Clendenning and B. Sweeney, Effects of Discharged Wastes on Kelp, Ann. Rpt., 1957-8, Univ. Calif. Inst. Mar. Rss., IMR ref 58-11, 1958, pp. 36-37.

37. "The Status of Plankton Detsrmination in Marine Pollution Analyses," by J. B. Lackey, Proc. 1st Intl. Conf. on Waste Disp. in the Mar. Env., 1960, pp. 404-412.

38. " Oceanographic and Ecological Base Data Acquisition and Evaluation of Alternative Locations. A Predssign Rsport on Marine Waste Disposal, City and County of San Francisoo," by Brown and Caldwell Eng., 1971.

39. "The Benthic Environment off Orange County Sanitation Districts Ocean Outfall No. 2," by Marine Biological Consultants, Mimeo Quart. Prog. Rpts, for 8/19/69, 11/29/69, 2/20/70, 5/26/70, 8/19/70, 12/9/70, 2/16/71, 5/25/71, 8/19/71, 12/10/71, 2/11/72, and 5/12/72.

ACKNOWLEDGEMENTS

It is a pleasure to acknowledge help and suggestions on the manuscript from personnel of the Bureau of Sanitation, City of Los Angeles; Sanitation Districts of Los Angeles County; Sanitation Districts of Orange County; Department of Watsr Utilities, City of San Diego; and Marine Biological Consultants, Inc. The manuscript was typed by Barbara H. Britten. Laurence G. Jones prepared the drawings.

CHAPTER 121

MARINE MONITORING OF THE VICTORIA SEWERAGE SYSTEM

by

Norval Balch, Derek V. Ellis and Jack L. Littlepage*

ABSTRACT

The Capital Regional District of British Columbia, Canada, is implementing for the Greater Victoria area, a major sewerage plan based mainly on marine discharge by submerged outfalls. To assess effects on the receiving ecosystem, a thirty month monitoring program has been carried out at the site of a newly constructed 6000 foot marine outfall. Of the standard water quality parameters, several were established during the pre-discharge period as "gross sewage field indicators" at beach outfalls: nitrite, phosphate, total and fecal coliform bacteria, Secchi depths, Forel colour and salinity. The remaining parameters were not sensitive to the presence of effluent: temperature, dissolved oxygen, nitrate, silicate and chlorophyll. In the water surrounding the diffuser of the extended outfall, only total coliform values showed the presence of effluent once discharge was diverted from the beach outfall. Profiling techniques were employed for measuring chlorophyll, turbidity and Rhodamine dye. A method was developed for mapping coliform bacteria in the sediment surrounding the diffuser, as an index of the ability of the receiving water to assimilate effluent loads being discharged into it. It is stressed that monitoring programs should be included in plans for any major coastal operation.

INTRODUCTION

Long marine outfalls for discharging sewage effluent have been in operation at many locations and for many years along the west coast of the United States, and have in several cases been accompanied by extensive monitoring programs (eg. State Water Pollution Control Board 1956, Garber 1960, Ludwig & Onodera 1964, Ludwig & Storrs 1970). However, the Canadian west coast has only recently begun to consider the use of long outfalls, as well as their environmental suitability and hence the need for adequate monitoring.

Specifically, the Greater Victoria area is in the early phases of implementing a major sewerage disposal plan based mainly on marine discharge by extended outfalls, to replace a number of outfalls which discharge untreated municipal sewage at the shoreline. The rationale behind considering long marine outfalls for untreated sewage, rather than the construction of sewage treatment plants at this time, is that the area being serviced (FIG. 1) is surrounded by marine waters with a great deal of tidal flushing.

---

* Department of Biology, University of Victoria, Victoria, B.C., Canada

Tidal currents of up to 2-3 knots (1.0-1.5 m/sec) result in continuous and large scale mixing off most of the coastline and should result in high dilution rates for discharged effluent.

When in April 1969 the provincial regulating authority issued a permit to the Capital Regional District for the construction and operation of a 6000 foot long outfall at Macaulay Point on the south coast of the area (FIGS. 1 & 2), it was stipulated that it should "carry out a sampling and surveillance program ... on the beaches and in the waters adjacent to the outfall and Macaulay Point". The reasons for requiring such a monitoring program were given in the letter of transmittal which read: "although there is a wealth of information throughout the world in support of the proposed method of disposal authorized, we have decided in the public interest to use the proposed outfall as a research project. It is the intention of the Pollution Control Branch to use the information gathered .... to verify the effectiveness of the proposed method of disposal and to document for future reference the suitability of long outfalls for the disposal of sewage in the coastal waters of British Columbia."

Accordingly, a group within the Department of Biology of the University of Victoria was requested to carry out an intensive two year monitoring program in order to collect data on the response to the discharged effluent of the receiving marine ecosystem. The program was designed to cover one year before and one year after operation of the outfall commenced in the summer of 1971. A program was established combining routine monitoring of a number of standard chemical, physical and biological parameters along with several more research-oriented projects aimed at studying the possible effects of the discharged effluent on certain components of the surrounding ecosystem. Members of the same group have also carried out a number of studies at several other outfall locations but the most extensive study has been carried out at the Macaulay Point outfall.

This outfall consists of a 36 inch (0.9 m) pipe, 6000 feet long (1829 m) with a multiport 500 foot (152 m) diffuser and discharging into approximately 200 feet (60 m) of water. Initial average daily discharge rates have been between 5 and 28 CFS (3 - 15 MGD, 14 - 68 X 10^6 l/day) with average flows of 45 CFS (24 MGD, 109 X 10^6 l/day) projected for the year 2015.* Prior to construction of this extended outfall, discharge was directly at the low water mark.

In order to obtain background data prior to initiation of discharge from the new outfall, sampling began in May of 1970. The University is scheduled to continue the initial program until the end of October 1972, thus giving 16 months of pre-discharge data and 14 months of post-discharge data.

In designing a monitoring program for a specific outfall, there are two basic aims: (1) to delimit the spatial extent of the effluent field, i.e. where is it? how concentrated is it? and (2) to estimate its impact on certain

* And if a recent engineering study is put into effect, another outfall will be built in the same area, with projected flows in 2015 of close to 90 CFS (48 MGD, 218 X 10^6 l/day).

critical chemical and biological parameters. The latter of these two questions is the more complex and difficult, for it is impossible to monitor every aspect of the ecosystem in order to see what perturbations may be occurring. Thus we must fall back on a few selected, accurately measurable, indices. But even the relatively simple problem of delimiting the effluent field poses many problems, especially in an area such as the one under consideration where relatively low discharge rates couple with very large dilution rates to make the actual field an extremely elusive target.

METHODS

A sampling grid was established (FIG. 2) which included 10 offshore stations (W) and 6 shoreline stations (S). Subsequently, in response to a request from public health authorities for additional coliform data near the shore, an additional 8 shoreline stations (K) were established, for coliforms only. Sampling was carried out from a 30 foot (9 m) oceanographic launch, which allowed the shoreline stations to be occupied within 15 to 50 feet (5 - 15 m) of the actual shore. The stations have been sampled at approximately 3 week intervals. In addition, two control stations were sampled 3 or 4 times a year. They were located in the middle of the Juan de Fuca Strait and were intended to provide data on open water conditions so that data will be available which can unequivocally be considered as being removed from localized influence of either terrestrial runoff or sewage effluent.

Two of the shore stations were located within a few feet of two separate outfalls (S3, S6), one of which (S3) ceased operation in August 1971 while the other is still in operation. This means that data were available for indicating immediate and gross effects of relatively undiluted effluent, for indicating the clean-up effect of cessation of flow at an outfall,as well as for indexing the effects of putting a new offshore outfall into operation. In essence, there were two types of control data: one from open marine waters and one from a still-discharging shoreline outfall.

The parameters routinely measured at the surface were the following: temperature, Secchi depth, salinity, nitrite, nitrate, phosphate, silicate, oxygen, chlorophyll, total and fecal coliforms, and Forel colour.

On alternate sampling dates depth profiles were taken of salinity, temperature (BT) and total coliforms at 0, 4, 25 and 50 m.

RESULTS

A. Pre-Discharge Data

The 16 months pre-discharge data supply the information necessary for the selection of those parameters which were reliable gross sewage field indicators. FIGS. 3, 4, 5 and 6 are time series plots of four such parameters (nitrite, phosphate, total coliforms and fecal coliforms) and show the high values for stations S3 and S6, with S3 values dropping to background values following diversion of discharge to the 6000 foot outfall.

Of the 12 parameters routinely measured, 7 indicated the presence of effluent at the two shore outfall stations: nitrites, phosphates, water coliforms (total and fecal), Secchi, Forel and salinity. These can be called "gross sewage field indicators" since the observed changes were from water samples normally collected only a few feet from the two shoreline, surface, non-diffuser outfalls. They cannot therefore all be thought of as necessarily useful indicators of a well-diffused effluent field. Indeed we have found that in the water around the new extended outfall, these indices cannot be distinguished from stations farther removed, even the offshore control stations. The one possible exception was coliform bacteria. The remaining standard water quality indices appear to have little value for effective monitoring since they did not show any marked effluent effect even in the plumes of the two active shoreline outfalls. These parameters were: dissolved oxygen, nitrate (FIG. 7), silicate, chlorophyll (FIG. B).

Though it might be expected that chlorophyll levels could be reduced in the extremely turbid effluent plume, this cannot be substantiated because of the problem of filtering such water and obtaining suitable chlorophyll extracts.

It might also be expected that dissolved oxygen would be severely reduced in the effluent plume, but this was not shown to be the case. Apparently, even with the relatively low dilution values in effect close to these outfalls, the dissolved oxygen in the receiving waters was sufficient to make up for any oxygen deficiency in the discharged effluent.

Silicates and nitrates also did not show elevated values at these outfall stations, apparently due to their natural high levels in the receiving waters.

B. Post-Discharge Data

After 59 years of discharge of untreated sewage from the old shoreline Macaulay Point outfall, effluent was diverted to the new 6000 foot outfall on August 24, 1971. On the immediate following sampling date (2 days later) at S3, water coliforms, nitrites, phosphates, salinity, Secchi and Forel had returned to normal shoreline background levels. (FIGS. 3, 4, 5 & 6). In the 11 months of data collected since then this pattern has not changed, while at the offshore (W) stations surrounding the diffuser there have been no detectable changes, with the possible exception of coliform bacteria.

Though only preliminary analysis of the data has been carried out to date, it suggests that from the time that discharge from the new outfall began, there has been a slight elevation of coliform values at some of the offshore stations surrounding the diffuser. The frequency of total coliform values greater than 1000 MPN/100 ml (the locally required water quality standard) was calculated and showed that stations W4 and W1 had the most frequent occurrence of such values. This was in contrast to the pre-discharge data in which stations W6 and W9 showed the highest frequency. Note that W6 is in fact a shoreline station and is expected to be high. Two other

methods of analyzing the data (so that all coliform values were used, not just values greater than 1000 MPN) suggested slightly different distribution patterns, though all methods examined showed W4 as being consistently high during the post-discharge months. This distribution agrees with the most frequent direction of tidal flow (between east and south-east) which should give a higher frequency of elevated coliforms at W4.

One of the most probable reasons that well-marked effects have not been observed in the receiving waters is that the outfall was designed to carry much higher flows than presently in effect. The present dilution rates should thus be much higher than for the flow rates eventually anticipated. Indeed, the intermittent pumping regime presently in effect (5 min. on, 20 min. off) makes it doubly difficult to locate the effluent field with any of the standard parameters since there is not a steady state plume issuing from the diffuser but pulses of effluent that are rapidly diluted.

Using published values (Associated Engineering Services Ltd. 1966) for two constituents of effluent, it was possible to make a preliminary estimate of the dilutions involved in the receiving waters at Macaulay Point. The maximum total coliform level measured in raw sewage was 33×10^6 MPN/100 ml. The maximum level measured at W stations since discharge was 24×10^2 MPN/ml. Thus the most conservative estimate of a dilution rate (ignoring bacterial die-off) is 1.5×10^4. A similar dilution rate would be necessary to reduce the measured levels of phosphate (42 mg/l) in sewage to those encountered at the W stations. Thus a preliminary estimate of the dilutions in effect by the time the field has surfaced would be in the order of 1.5×10^4.

Because of the high dilutions in effect, it has proved difficult to determine from water quality measurements whether the field has been surfacing. It has been commonly noted that an aggregation of seagulls on the surface near the diffuser appeared to be related to the presence of visible particulate sewage. In order to determine whether these gulls might be a reliable indicator of the surfacing field, on each sampling date that the gulls were present, water samples were taken at the centre of the aggregation, designated as station WO. However, there has been no evidence from the water quality data that effluent is present at that station. In particular, there appeared to be no trend of elevated coliforms. On two occations more intensive surveys have been carried out at WO, by taking a number of coliform samples in a line through the apparent centre of the aggregation of gulls. But even these intensive surveys have been inconclusive in showing a correlation between the presence of gulls and the presence of effluent, as indexed by coliform bacteria. TABLE 1 shows that on February 15, 1972, there were no elevated coliform values, while on March 13, 1972, high values did occur but were well to one edge of the gulls. Subsequently surface samples containing apparent gross floatables have been collected and tested for coliforms. Both total and fecal values so obtained had high values, proving their sewage origin. It is these particles that are probably being fed on by the gulls. The fact that standard water coliform samples are not elevated at WO results from high sub-surface dilution of the effluent. The buoyant phase however will concentrate at the air-water interface close to the diffuser.

Another method employed for field delimitation has been the use of the fluorescent dye, Rhodamine WT, injected into the pipe at the pumphouse and then traced in the water column by vertical and/or horizontal profiling using a subsurface pumping system flowing through a continuously recording fluorometer. In a dye study on April 13, 1972, the diffusing dye was located at depth very near the diffuser. It could then be traced to the surface and thereafter at the surface for a distance of some two miles over a time period of two hours. Even with a strong onshore wind, there was no apparent impinging by the effluent field on the shore, due to a strong tidal current parallel to the shore. However, the ability of a single boat to give an adequate three-dimensional picture of the movement of the dye was severely limited, so aerial photography is being included in the dye study program.

Ideally it would be advantageous to have a technique that allowed three-dimensional profiling of the effluent field, without introduction of expensive tracers such as dye or a radioactive material. One such method tested at the Macaulay Point outfall has involved the use of a transmissometer for measuring turbidity. However, with the high dilutions in effect at the Macaulay Point outfall, it was not found possible to detect the field with this instrument. At other outfall locations the instrument has proved to be more successful. Two sewage fields (one from a beach outfall, the other from a sub-tidal outfall at 50 foot depth) were detectable by means of a towed transmissometer (α meter) to distances of 2000 - 2500 feet from their sources. Comparison of analyses of discrete samples with turbidity (α values) indicated that effluent field profiles can be expressed in terms of coliform levels, though profile interpretation will be site-specific as well as season-specific, due to variations in turbidity caused by phytoplankton or by the particulate component of the sewage itself. This turbidity profiling technique also has been applied with positive results to outfalls for mining wastes discharges.

Recognizing the difficulties involved in tracing an effluent field in the water column itself, it would seem advantageous to use the underlying sediments in some manner so as to obtain a cumulative chart of the extent of horizontal movement of the effluent field. A sensitive index that can be obtained from the sediments is the presence of coliform bacteria. Since these bacteria sediment out, and are relatively specific to sewage. their presence in the sediments should be an indication of the persistent presence of effluent in the overlying waters. Using divers in the shallow waters around several shoreline outfalls, the extent of the sewage fields could be mapped. However, there was a large degree of variability resulting both from field sampling and laboratory analysis, so a more reproducible sampling technique was sought. This was particularly imperative since diver sampling was not feasible around the Macaulay Point outfall at depths of around 200 feet (60 m). A technique has been developed which employs VanVeen grab samples. Replicate subsamples can be obtained from the grab sample by coring into the sediment with a ½ inch diameter, sterile glass tube. Although there is still a large degree of sample variability, differences between stations close to and distant from the diffuser can readily be discerned (TABLE 2). The value of this technique lies in the fact that it is a cumulative index of the extent of the field, as well as an indicator of the ability of the receiving waters to assimilate the effluent loads being introduced into it. A field of fixed size and concentration would suggest that the interaction

between effluent and the receiving waters had reached a steady state. On the other hand, a steady growth of the size of the field as well as in the numbers of organisms encountered would suggest that the overlying water column is not capable of "treating" the wastes being discharged to it. It thus should be an extremely valuable long term monitoring index.

Discussion so far has been mainly with regard to effluent field delimitation. What about some of the critical biological components of the ecosystem? The enriching effect of injecting large quantities of nutrients into receiving waters is one that has become of paramount importance in many fresh water systems where the resulting eutrophication has severely downgraded the usefulness of many of our lakes and rivers. The same principles apply in marine ecosystems: if nutrients are added, they must go somewhere. They must be taken up by primary producers (phytoplankton), raise the reservoir of inorganic nutrients in the water, or sediment out. But the inescapable fact is that most of them must enter biological processes and in so doing change the balanced relationships that have evolved in the evolutionary time scales preceeding such a man-induced change. The real problem is, however, to quantify the impact that such enrichment has on the environment. With marine waters already being heavily laden with essential nutrients, it could well be that even massive injections of nutrients would have no measurable effect. On the other hand, localized effects might well be of significance; or a long term, low rate of eutrophication might be occurring, but virtually impossible to detect. We could well pose the question as to what is the long term, cumulative effect of all the nutrients being discharged into the Straits of Georgia and Juan de Fuca, a marine system that is in essence a large estuary and has on its boundary urban centres such as Vancouver, Seattle,and Victoria,as well as a number of large pulp mills discharging large amounts of wastes (FIG. 1). For instance, the relatively small urban area of Victoria will be discharging something like 2600 tons of nitrogen, 1700 tons of phosphate a year over the next forty years (Associated Engineering Services Ltd. 1966). Are we unwittingly working toward a Great Lakes situation even here?

Routine sampling of chlorophyll (an index of phytoplankton biomass) should be able to detect any long term rise in primary productivity in a marine area, if carried out over a long enough time scale so that normal yearly variations can be taken into account. But this sort of approach is an extremely long term one, for slow eutrophication may well take decades before it is detectable. A small scale localized monitoring program is not in a position to carry out the necessary work for such a project. The sampling required should be over large areas since spatial variability of phytoplankton growth is very important. The Macaulay Point monitoring program has investigated whether a point source of nutrients such as the Macaulay Point outfall may be contributing to small scale, localized phytoplankton growth. The method employed has been continuous chlorophyll profiling using a pumping system in line with a continuously recording fluorometer. With this system, fairly detailed maps of phytoplankton concentrations can be prepared (eg. FIGS. 9 & 10). The results show that distribution of planktonic plants in an inshore environment is very complex; that surface runoff of nutrients, local topography and weather plus inputs from various types of effluent, all contribute

to phytoplankton patchiness. To select out the possible enriching effect of a particular outfall will entail continued profiling over several years. However, these data are essential before it will be possible to say whether or not sewage disposal is effecting this critical component of the ecosystem.

One of the sampling problems involved with monitoring primary productivity is the large degree of temporal variability, making results dependent on the particular conditions of a specific sampling day. It would be advantageous to be able to measure some component of the ecosystem that is more fixed and which might show the cumulative effects of the presence of effluent. Fortunately such a component does exist, since the bottom communities of animals are much more stable than planktonic communities. Sampling of these bottom dwelling animals has been carried out around several of the outfalls under study. In particular, pre-discharge and post-discharge samples have been obtained around the Macaulay Point outfall. These collections are still being worked on but preliminary results show a marked increase of scavenger-type organisms such as large hermit crabs, Paguristes turgidus. The samples are to be checked for species associational and biomass changes, with interpretation in terms of changes in trophic structure and production.

Apart from planktonic plants and benthic animals, there are a large number of other crucial components of the ecosystem that can be influenced by the operation of marine outfalls, eg.planktonic animals, pelagic fish, bottom fish, seaweeds, marine mammals, protozoans and bacterial populations. Their numbers, species diversity and distribution can all be influenced, but to monitor them all would be extremely expensive as well as probably redundant. However, the other side of the problem is that "a priori" we can never be certain just which are the crucial parameters to measure, so judicious choices must be made when designing monitoring programs. The shotgun approach of many early monitoring programs can now begin to be replaced by much more carefully designed programs where the parameters measured, the number of stations and replications as well as sampling frequency can all be selected site-specifically on the basis of past experience with a view to optimizing useful results. It is no longer good enough to measure something just because we know how to or because everyone else is doing it.

Another crucial component of a well-designed monitoring program should be that such a program be initiated prior to the construction or operation of any structure that is liable to disrupt the environment. Even with well-documented control stations, it is not always possible to interpret data collected after the event, if there is no background, pre-event data against which to compare it. Thus, in the planning stages for any major coastal development, parallel with engineering discussions, consideration should be given to an appropriate monitoring program which should be implemented early enough so that background data can be obtained prior to construction.

It will increasingly become the responsibility of any developing agency to take environmental factors into consideration and at as early a stage as possible predict any major physical, chemical and biological effects that may occur. Environmental safety margins must become as important a criterion as engineering safety margins. However, for these to be realistic they must be based on predictions that arise from adequate oceanographic and marine ecological information obtained from well designed monitoring programs.

REFERENCES

Associated Engineering Services Ltd., 1966. Sanitary Sewerage Study of the Greater Victoria Area. A Report to the Joint Sewerage Committee.

Ludwig, F.L. and P.N. Storrs. 1970. Effects of waste disposal into marine waters. A survey of studies carried out in the last ten years. Water Research, vol. 4, pp. 709-720.

Ludwig, F.L. and B. Onodera. 1964. Scientific parameters of marine waste discharge. Advances in Water Pollution Research, vol. 3, pp. 37-56.

Garber, W.F. 1960. Receiving water analyses. Waste Disposal in the Marine Environment, Pergamon Press.

State Water Pollution Control Board. 1956. An investigation of the efficacy of submarine outfall disposal of sewage and sludge. Publication No. 14.

TABLE 1

Coliform transects (MPN/100 ml) across seagull aggregations near end of Macaulay Point Outfall.

A. February 15, 1972. Stations approximately 20 feet apart.

							Aggregation of Gulls									
Station	4	5	6	7	8	9	10	11	12	13	14	15	16	17	18	19	20
Total	70	40	<30	90	40	40	40	40	40	<30	<30	40	40	90	40	90	40
Fecal	<30	<30	<30	<30	<30	<30	40	<30	<30	<30	<30	<30	<30	<30	<30	40	40

B. March 13, 1972. Stations approximately 15 yards apart.

				Aggregation of Gulls								
Station	1	2	3	4	5	6	7	8	9	10	11	12
Total	70	90	<30	40	90	70	430	640	430	11,000	640	430
Fecal	<30	<30	<30	<30	40	<30	40	90	430	150	90	70

TABLE 2

Sediment coliform levels in the area of the Macaulay Point Outfall. Replicate samples were taken at W1 (at the diffuser) and W2 (½ mile offshore from diffuser).

Station	Subsample	Coliform Values (MPN/100ml) Total	Fecal	Station	Subsample	Coliform Values (MPN/100ml) Total	Fecal
W1	1	46,000	43,000	W2	1	930	430
W1	2	46,000	24,000	W2	2	4,300	90
W1	3	>110,000	43,000	W2	3	2,100	90
W1	4	110,000	7,500	W2	4	930	90
W1	5	>110,000	7,500	W2	5	2,100	230
W1	6	46,000	4,300	W2	6	1,500	40
W1	7	15,000	930	W2	7	750	40
W1	8	46,000	4,300	W2	8	93	>30
W1	9	46,000	2,100	W2	9	4,300	40
W1	10	110,000	2,400				
	Mean	68,500	13,903		Mean	1,889	120
	Standard Oeviation	36,942	16,671		Standard Deviation	1,509	131

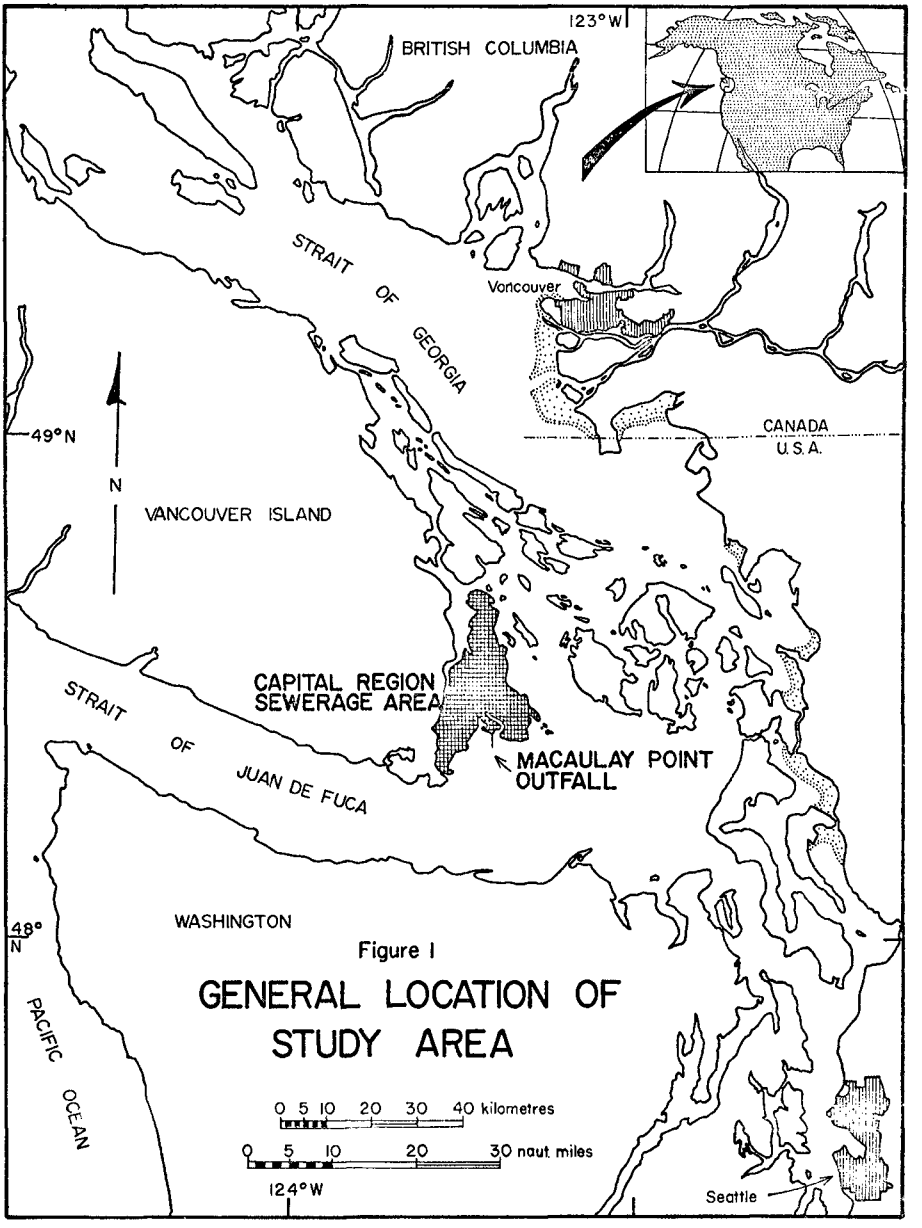

Figure 1

GENERAL LOCATION OF STUDY AREA

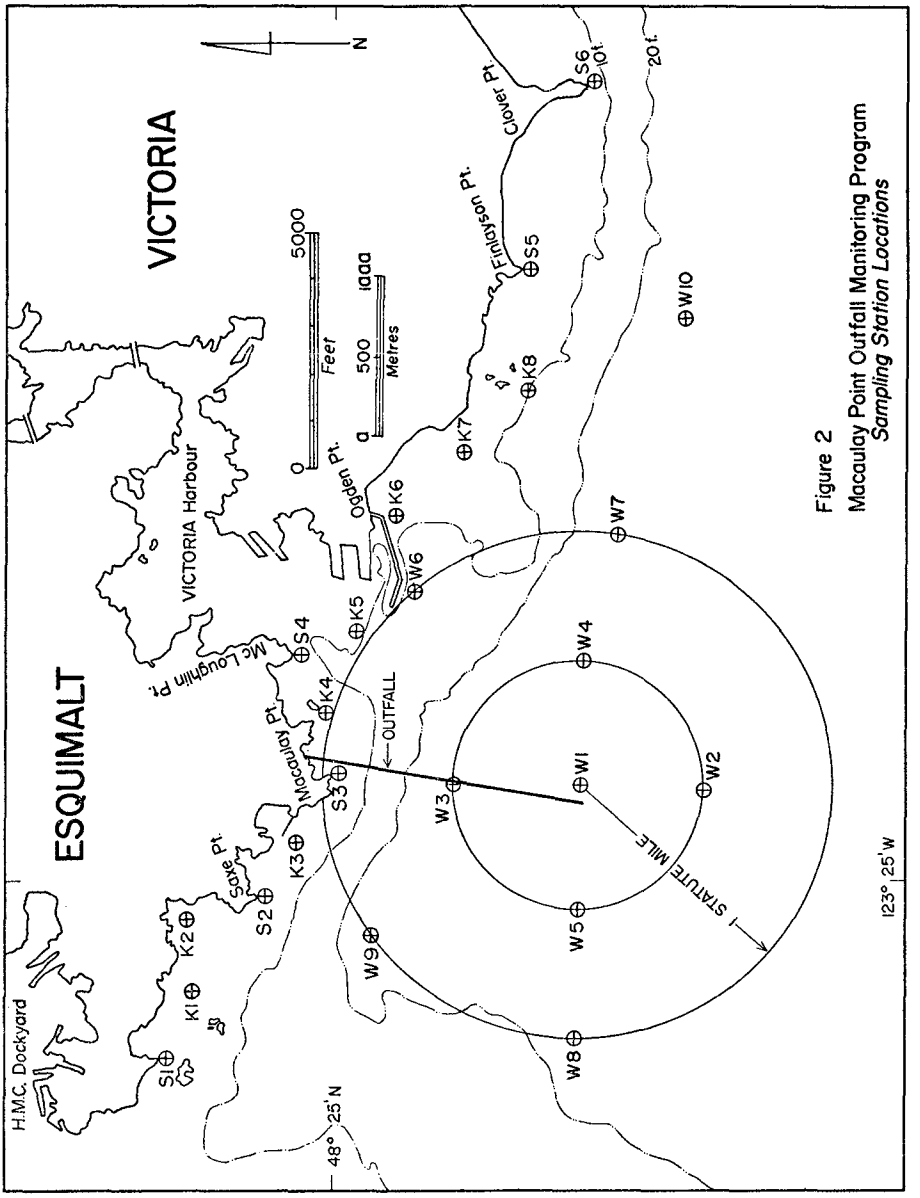

Figure 2
Macaulay Point Outfall Monitoring Program
Sampling Station Locations

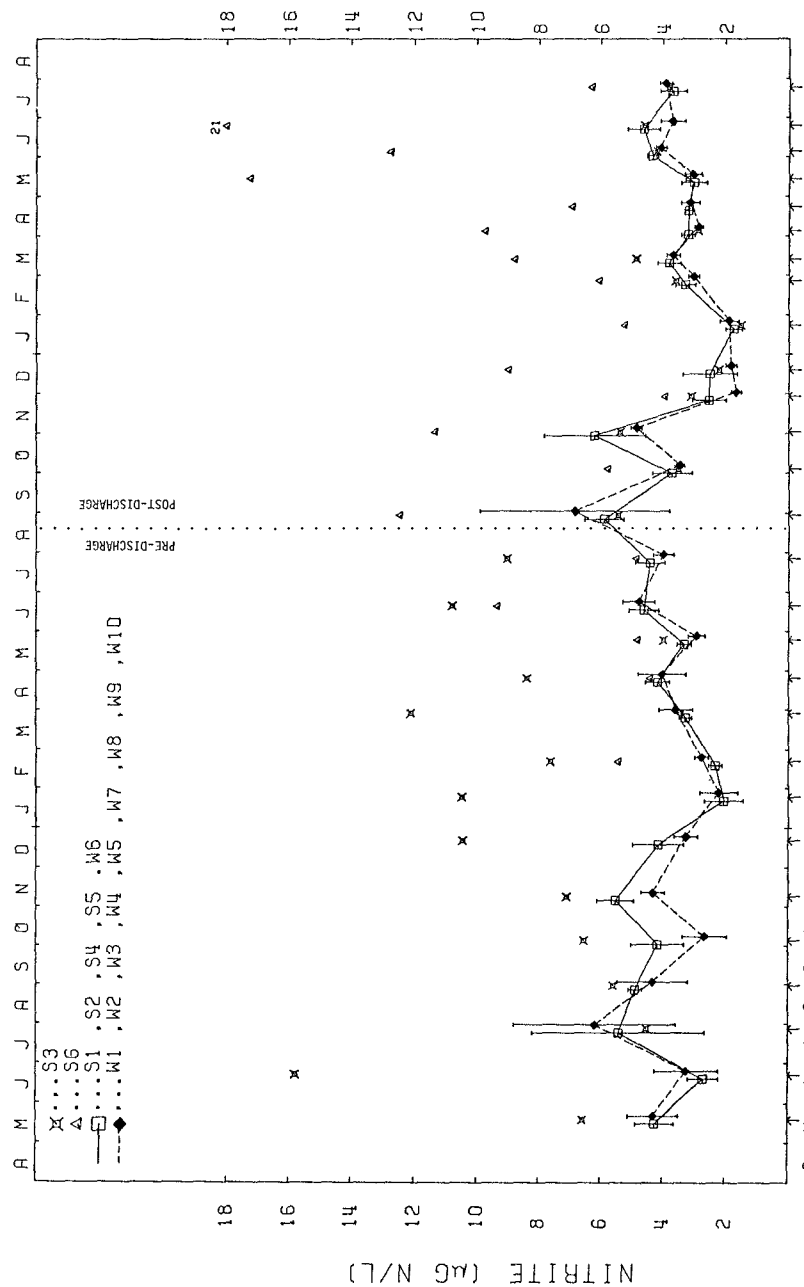

FIGURE 3. MEAN NITRITE VALUES (computer-drawn time series)
Vertical lines represent ± 1 standard deviation of the mean. Arrows on X axis denote sampling dates. Note symbol displacement to left and right of sampling date in order to reduce overlap.

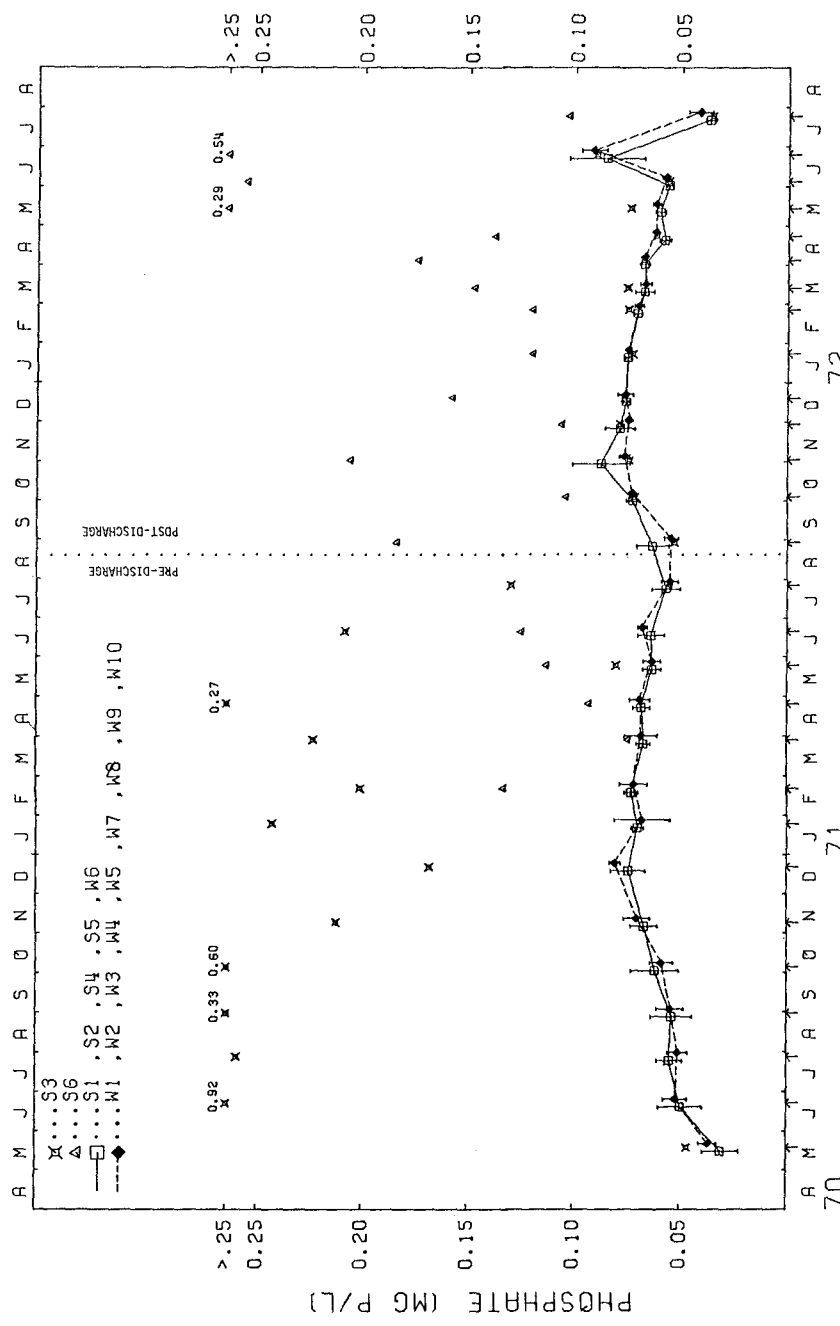

FIGURE 4. MEAN PHOSPHATE VALUES (computer-drawn time series)
Vertical lines represent ± 1 standard deviation of the mean. Arrows on X axis denote sampling dates. Note symbol displacement to left and right of sampling date in order to reduce overlap.

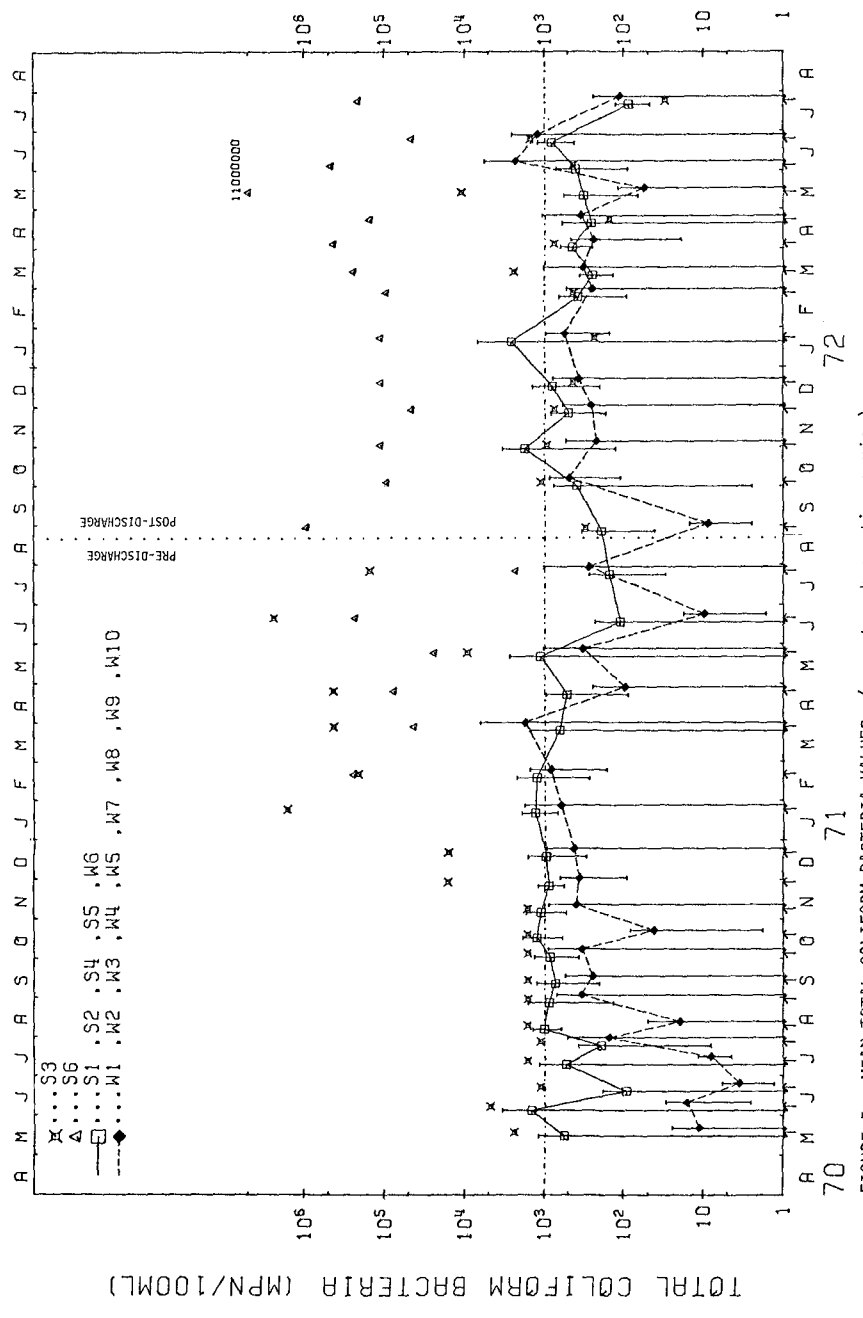

FIGURE 5. MEAN TOTAL COLIFORM BACTERIA VALUES (computer-drawn time series)
Vertical lines represent ± 1 standard deviation of the mean. Arrows on X axis denote sampling dates. Note symbol displacement to left and right of sampling date in order to reduce overlap.

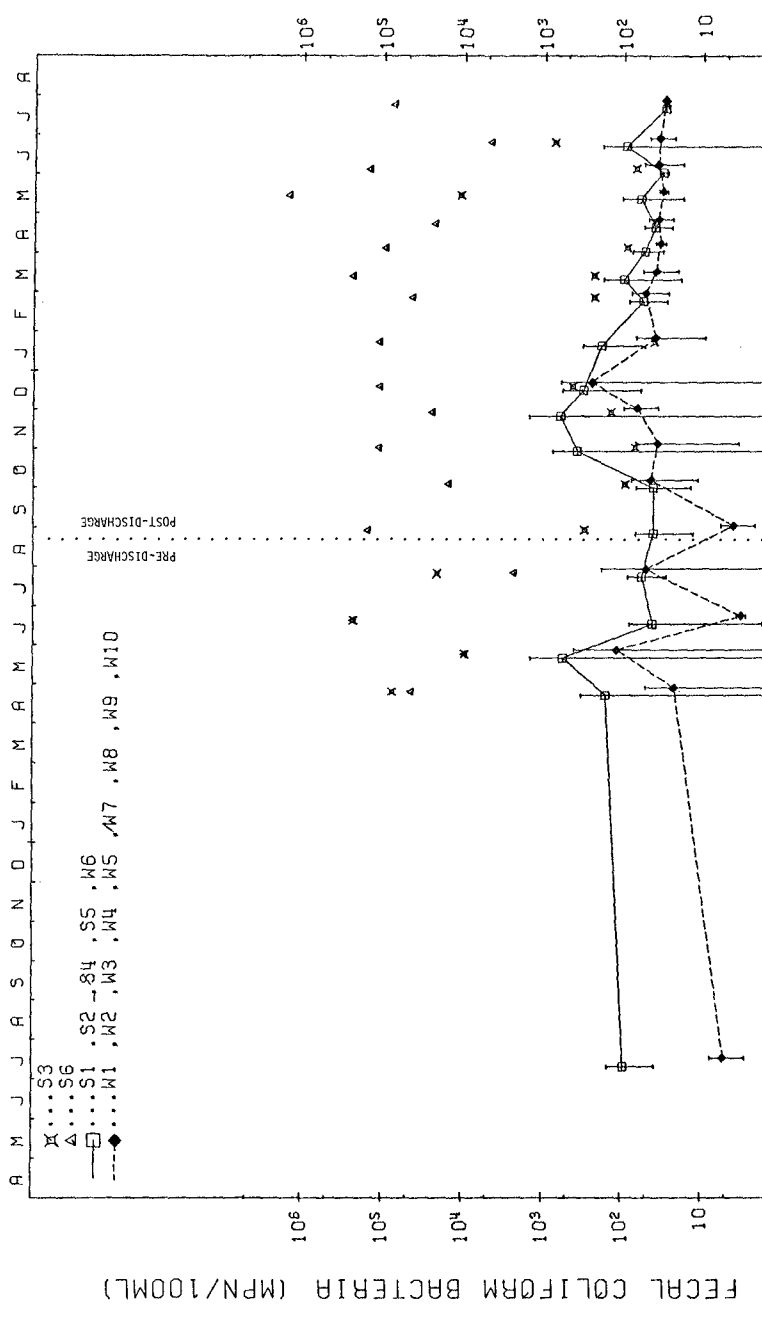

FIGURE 6. MEAN FECAL COLIFORM BACTERIA VALUES (computer-drawn time series) Vertical lines represent ± 1 standard deviation of the mean. Arrows on X axis denote sampling dates. Note symbol displacement to left and right of sampling date in order to reduce overlap.

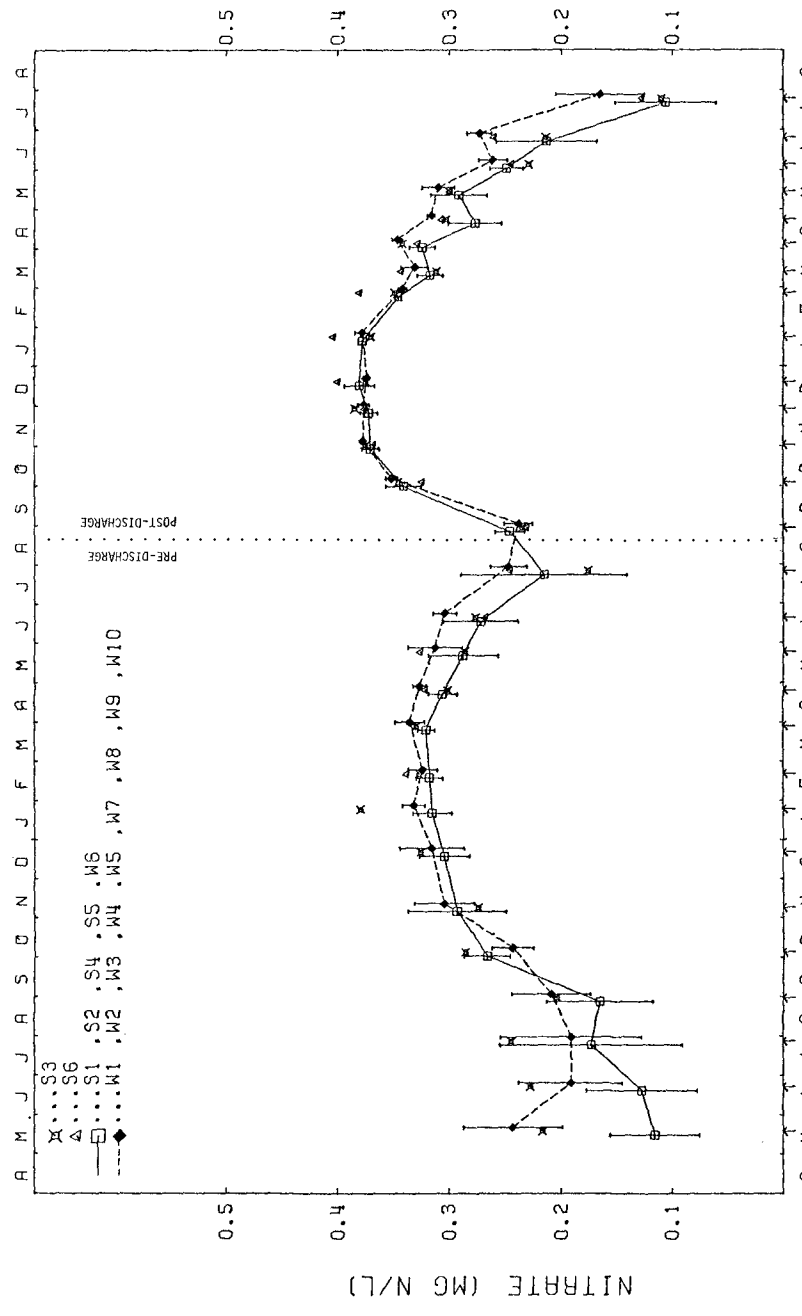

FIGURE 7. MEAN NITRATE VALUES (computer-drawn time series)
Vertical lines represent ± 1 standard deviation of the mean. Arrows on X axis denote sampling dates. Note symbol displacement to left and right of sampling date in order to reduce overlap.

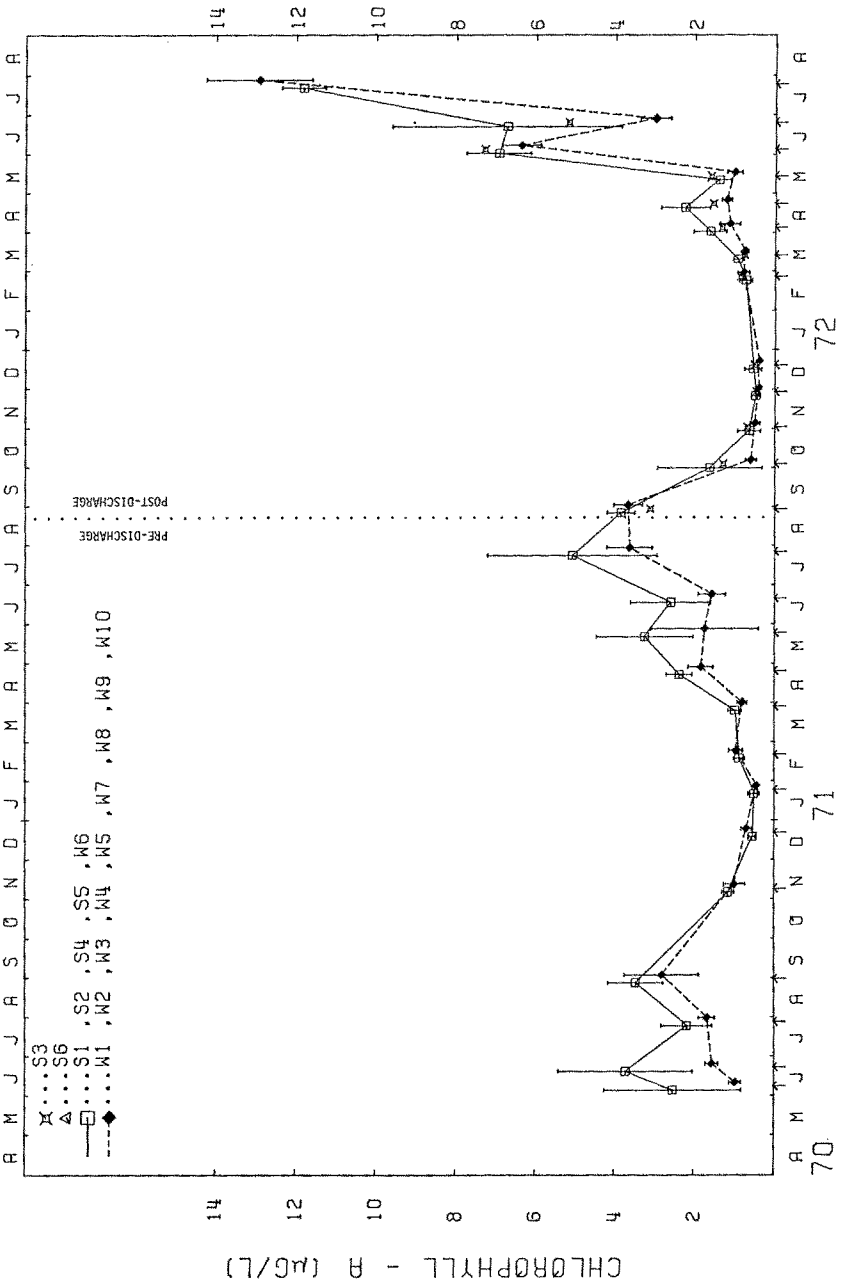

FIGURE 8. MEAN CHLOROPHYLL-A VALUES (computer-drawn time series)
Vertical lines represent ± 1 standard deviation of the mean. Arrows on X axis denote sampling dates. Note symbol displacement to left and right of sampling date in order to reduce overlap.

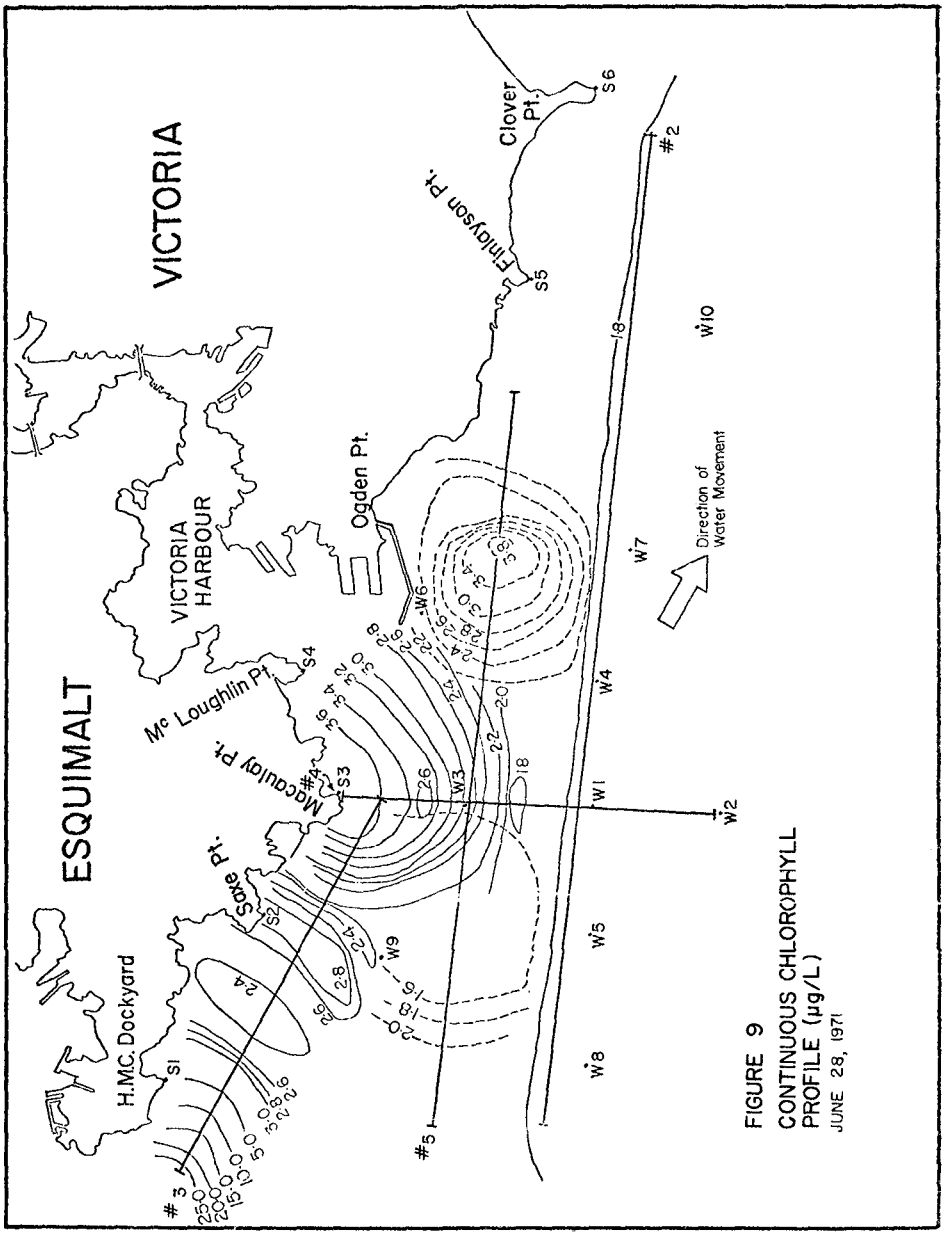

FIGURE 9
CONTINUOUS CHLOROPHYLL PROFILE (µg/L)
JUNE 28, 1971

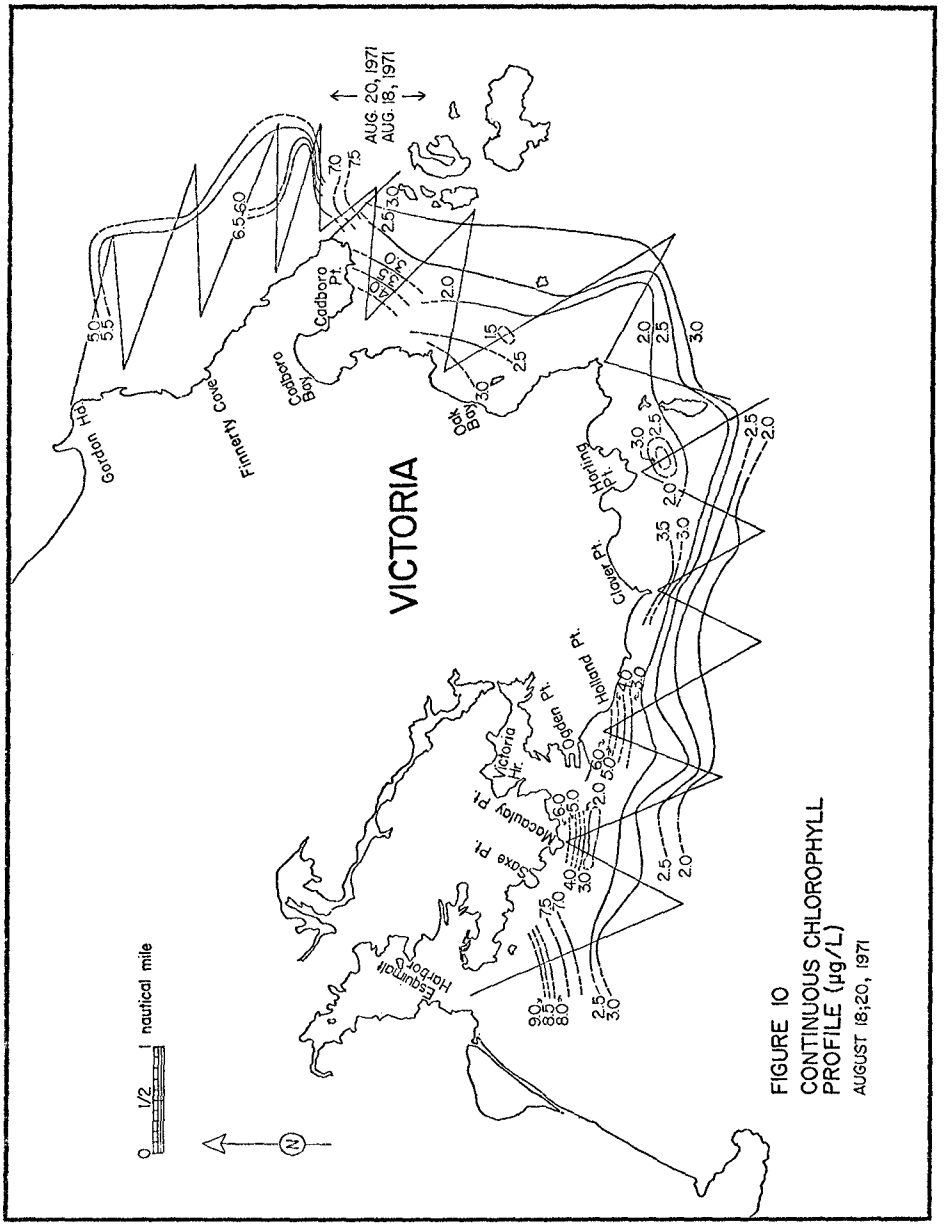

FIGURE 10
CONTINUOUS CHLOROPHYLL PROFILE (µg/L)
AUGUST 18;20, 1971

CHAPTER 122

INDUSTRIAL SEWAGE IN THE WESER ESTUARY

by GÜnter Luck

Director of the Researchstation for Island- and Coastprotection, Norderney, West-Germany.

ABSTRACT

The in former years nearly exclusively agriculturally structured coastal areas of Lower Saxony recently undergo an increasing industrialisation. This process was introduced by the settlement of a Titandioxyd factory at the Weser estuary, which releases acid sewage. The problems, connected with the discharge of this sewage are discussed, as well as the tests performed in order to prevent a possible overstrain of the Weser water. The hitherto gained results are described and preliminarily interpreted. The recent, partly surprising biological development cannot be traced back to a measurable ecological change in the Weser estuary and therefore is inducement to think over critically the applied procedure.

In recent years the German coastal area was almost exclusively agriculturally structured. (Figure next page). Accordingly the coastal waters and affluxes were charged preponderantly with agricultural and domestic waste, and for its decomposition the self-purification-power of the used water was sufficient. Compared with this the industrial and professional sewage was altogether insignificant and only in the worst cases caused local concerns. The higher amount of waste, increasing with


N O R D S E E
N o r d -
f r i e -
s i s c h e
J n s e l n
N o r d -
f r i e s -
l a n d
D e u t s c h e
B u c h t
O s t f r i e s i s c h e J n . s e l n
O s t f r i e s l a n d
Sylt
Rantum
Föhr
Dagebüll
Amrum
Oland
Langeneß
Gröde
Nebel
Hallig en
Hooge
Nordstrandmoor
Norderoog
Pellworm
Süderoog
Südlatt
Husum
Nordstrand
Tönning
Eider
Helgoland
Düne
Blauort
Büsum
Trischen
Scharhörn
Neuwerk
Cuxhaven
Elbe
Wangerooge
Spiekeroog
Langeoog
Minsener Oldoog
Norderney
Baltrum
Mellum
Juist
Hemmert
Borkum
Riffgat
Norden
Jever
WILHELMSHAVEN
Jade
Weser
BREMERHAVEN
Jade Busen
Ems
Aurich
Emden
Dollart
0 10 20 30 40km

improving sewerage, could mostly be neutralized by sewerage plants.

More imperiled were the estuaries of Elbe, Weser, Jade and Ems Rivers, which had to receive the not yet eliminated wastes of the big rivers and the harbours as well as of the port-towns. Though in these areas, too, expecially in the Elbe River, the strain of the water locally led to not unobjectionable situations, the disturbance of the biological equilibrium altogether remained in tolerable limits.

The desire of industries, producing a high amount of sewage, especially of chemic giants, for deep water, which commenced in Germany in about 1965, meanwhile resulted in the settlement of a number of bigger factories. Further settlements are in discussion or already projected. Herewith possibly a development is commenced, which in many estuaries of Europe and other continents already causes severe concerns (1).

The process of industrialization of the Lower Saxonian coastal area was introduced by the settlement of a Titandioxyd factory at the Weser estuary, on the Blexener Groden opposite of Bremerhaven, which started production in 1969. (Figures next page. Top: Sewage discharge area of the Titan factory in the Weser estuary. Bottom: View to Blexener Groden with Titan factory after commencement of production). In the permission-procedure for the discharge of preponderant acid sewage was stated, that the Titan factory intended to deposit the in the production process recoverable weak acid in the North Sea, northwestward of Helgoland Island, and to discharge the not recuperative rest-acids into the Weser River at km 65,8. In this paper it shall not be talked of the Helgoland release area, but only of the conditions in the Weser estuary. Due to the statement of the Titan management the rest-acids should contain the following pollutants:


BREMER
HAVEN
DIE WESER

$FeSO_4$	0,71	g/l	270 kg/h
H_2SO_4	0,68	g/l	1080 kg/h
$(NH_4)_2SO_4$	0,14	g/l	220 kg/h
$TiOSO_4$	0,10	g/l	160 kg/h
$MgSO_4$	0,013	g/l	16 kg/h
TiO_2	0,004	g/l	7 kg/h

Total amount of sewage: 38 200 m^3/d.

The planned release of thus big amounts of chemical sewage in an on the whole only little polluted estuary and the with view to the environment-protection world-wide raised demands for maintenance of the purity of our living space as well as the local very insufficient experiences, concerning the behaviour of liquid wastes in brackish water, made the treatment of the involved problems especially difficult.

The in the thereby commenced discussion repeatedly uttered thought, to prevent an industrialization of our coast at all in order to preserve the waters, is opposed by a number of economic-political aspects. The objective of Lower Saxony and its adjacent countries, concerning the industrial development of coastnear living spaces and economic domains, is influenced by the modern industrial society. In the coastal area Lower Saxony needs capable industries to establish safe working places, in order to retrench the gradient of prosperity, directed from north to south, and last not least to gain the growing taxable capacity, connected with any economical animation. These economic objectives however have to be confronted with very hard demands for the protection of our environment, especially of the coastal waters. Misconceptions, concerning these processes, could be irreparable for decades or even for ever.

In the German legislation and in the Lower Saxonian water law, which has to be applied for the case in question, the conditions are laid down, which have to be observed or found in case of release and transportation of waste. According to this law the minimum-requirements have to be quoted, to which the water

quality has to conform. The law further prescribes, that certain substances are not allowed to be released, which influences have to be warded off, by which the water consistence can be detrimentally influenced, and others. Further here the legal procedure is settled, which is authoritative at water usufruct. Accordingly for the water usufruct a "permission" or a "concession" can be imparted. The permission revocably authorizes to make use of a water in an appointed manner and can be timed. The concession however has a stronger legislative validity and is imparted for an appropriate time, which in special cases even may transgress 30 years. The permission allows in difficult cases and at unforeseen damages, to impose the water usufructuary subsequently and short-dated with additional conditions for the water usufruct. For this reason at industrial sewage discharge usually only a "permission" is imparted.

For the water legal procedure in question therefore above all a number of expert opinions was demanded, which should allow an estimation of the consequences to be expected at the planned sewage release and which should prove, under what conditions a permission can be imparted at all. Three complexes of questions seemed to be of special importance:

1. In what time and on which way the pollutants will be mixed with the water of the Weser estuary by tide and current?

   The studies proved, that at mean tides and upstream water conditions in the Weser water soon a dilution rate of 1 : 1500 is obtained. As expected the waste particles - oscillating saw-shaped in the tide rhythm in front of the point of release - transpose resultingly seaward. A sewage release only at certain tidal phases is of no effect (2).

2. Will the chemistry of the Weser water be in any way impaired by the release of the acid sewage respectively is even a change of pH from alkaline to acid value to be expected

and will there be an increase of sedimentation owing to the flocculation of ferro-hydroxide?

Orientated at the hydrographic results the chemical studies allowed the interpretation, that due to the expected dilution-rate a chemical change of the Weser water was not to be expected. The acid neutralization capacity respectively the rate of carbonate of the water would be sufficient for the neutralization of the appearing sulfuric acid and the iron and titan, bound to sulphates, and would be bound up only to 3,25% even under the most adverse circumstances. The expected ferro-hydroxide flocculation would be entirely insignificant compared with the normal suspended load of the Weser River (3).

3. Will there be any influences on the local biocoenosis at continued release of sewage?

The in this respect performed physiological experiments in a tank, supplied with additional acid, which was in keeping with the quality of the sewage of the Titan plant, had the preliminary result, that the lethal limit of most of the test animals is reached at a dilution rate of 1 : 3,3 to 1 : 4 and that concentrations up to 1 : 13 can be born. At the actual rate of dilution therefore a disturbance of the biological equilibrium would not have to be feared (4).

As physiological tests in tanks with simulated boundary conditions are contested in any case, and only adults were used for the tests, these results were accepted with great skepsis. Actually later experiments proved, that the limits of compatibility for herring eggs and larvae range at a much higher rate of dilution (5).

These experiments were fundamental to the lastly in 1966 confered permission for the release of sewage in the applied quality and quantity. A number of internal and external conditions were imposed to make sure, that the sewage release

doesn't slip out of control and possible damage can be avoided respectively recognized in time. Some of these conditions were: Inlet of the waste with overpressure square to the current direction in order to guarantee an instantaneous thorough mingling, fixation of the pH of the waste at the point of inlet to 1,8, restriction of the standard of solid matters to 0,5 mg/l, prohibition of additional inlet of oil and other floating substances, mechanic clarifying of additional domestic waste etc. In the Weser River in a distance of 500 m from point of inlet, horizontal as well as vertical, the pH of the polluted water is not allowed to range below 6,5. The rate of iron, solved in the water, must not exceed an increase of 0,5 mg/l and the rate of colloidal ferrous an increase of 0,5% - related to the solid matter substance.

The condition, prescribing, that in 500 m distance from the point of inlet the pH must not undercut 6,5, was violently contested. For one was due to the chemical examination to be expected, that the acid neutralization capacity of the Weser water was strong enough, that a pH reduction in such dimension is not thinkable. If on the other hand the acid neutralization capacity was not sufficient, a drop of pH in such dimension could not be tolerated, for herewith an acid bar across the Weser River would be built up, the influence of which to the biologic conditions would be immeasurable and possibly would commence a not predictable future development. But due to the fact, that the pH seemed most endangered by the release and in order not to neglect anything, this condition was finally maintained.

The Titan factory was obliged to equip their plant with the necessary constructions and measuring devices in order to control the conditions. Further biologic/ecologic first-investigations were demanded to estimate possible, later appearing damages in the Weser estuary, to fix the state being and to make possible comparative studies after the factory's setting to work. Herewith should be guaranteed,

that quality deteriorations of the Weser water can be intercepted in time by additional conditions.

With these biological studies to a certain extent unknown territory was entered. In Germany comparative studies in brackish water and under tidal conditions hitherto were not performed to that extent, therefore own experiences were not available. The foreign and especially the very abundant American technical literature substantially describes - as far as we were able to evaluate it in the short time - damages in their estuaries, caused by human influences. Furthermore results, gained otherwhere, hardly could be transferred to our situation without modification, due to different hydrographic boundary conditions. Further a complete seizing of the Weser biocoenosis - apart from interesting detail-results - did not exist.

For the first-investigations only one year was at our disposal, what made the whole problem still more difficult. Additional difficulties rose by the without that short-dated strong fluctuations of the pH of the Weser water from 7,1 to 7,9, caused by the release of potash-waste into the upland-Weser-river. The ecologic boundary conditions, changing with the tides - altering salt contents, shift of the boundaries of the brackish water in dependency on upland discharge etc. - had no simplifying effect, either. Furthermore, while still performing the tests, another factory - intending to release gypsum sewage - extended its production.

The studies were extended to an area of 15 km upstream to 20 km downstream from the point of release and to the tidal flats situated within this area. (Figure next page). This district comes up to approximately the mean brackish water area of the Weser estuary. The test material was gained in 10 sections during 10 excursions from December 1967 to November 1968. This guaranteed the full valuation of the seasonable fluctuations of the vegetation. Simultaneously to the collecting of the biological test portions chemical water analysis were performed

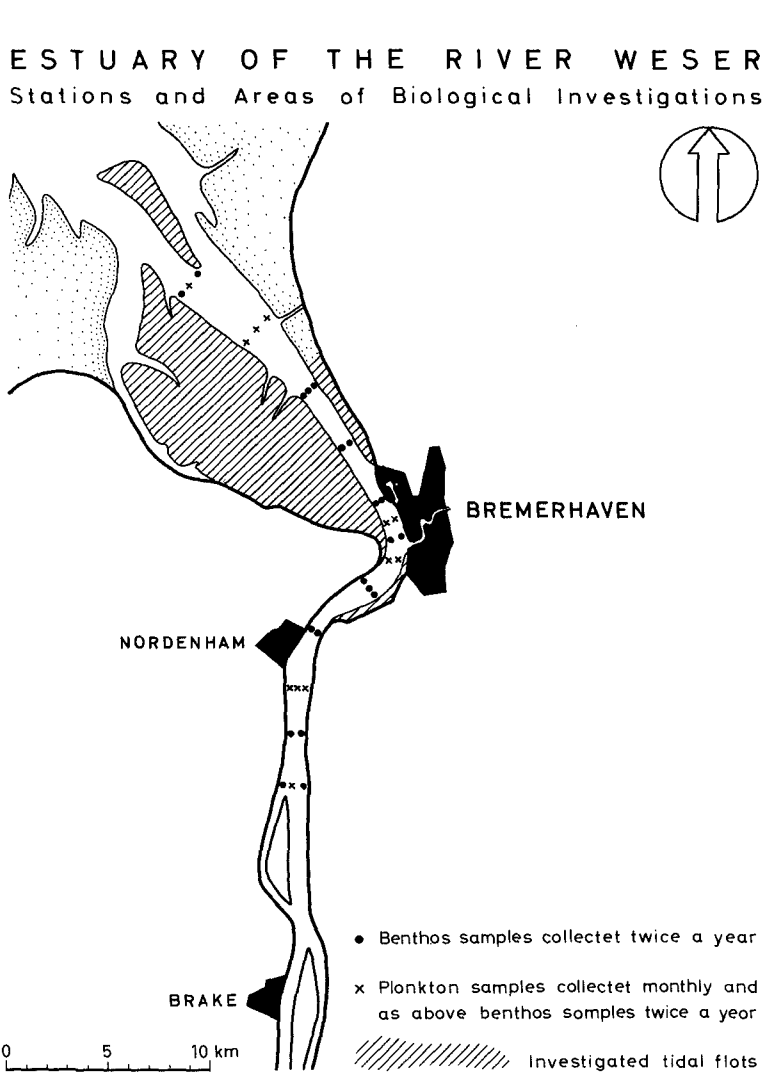
ESTUARY OF THE RIVER WESER
Stations and Areas of Biological Investigations
BREMERHAVEN
NORDENHAM
BRAKE
0 5 10 km
• Benthos samples collectet twice a year
x Plonkton samples collectet monthly and as above benthos samples twice a yeor
Investigated tidal flots

in order to safe the ecological parameter.

In detail on each excursion bottel plancton, net plancton and macrobenthos was tested. The samples in question were gained on the water surface and near the bottom. The evaluation was emphasised on the quantitative, spatial and temporal distribution. A taxanomically complete study was not planned and due to the short time, available for the investigations, not possible. The evaluation of the rich material took several years in any case. The tidal flats were only once macrobiologically mapped, as due to the short range of time multy mapping was not possible (6).

After having concluded the primary tests and having been able to develop clear conceptions regarding the biology of the test area, in the year 1971 - i.e. two years after the Titan factory's commencement of production - first comparative studies were performed.

These studies - the detailed description of which would be too prolix - had a surprising result, which is also inducement to think over again critically the whole method of the biological/ ecological analysis with regard to future similar problems.

The primary test had - at least with respect to the diatom flora - the unexpected result, that - in spite of an increase of eutrophication and an intensified strain of the oxygen-household of the Weser River - the conditions qualitatively hardly had changed since the turn of the century. The then performed diatomee-tests by the way represent the beginning of the studies of protisten-plancton in the Weser River. The macrobenthos was only very insignificantly developed and lacked completely in large areas. Possibly this has to be reduced to the exclusively mechanic influences of the dredging in the Weser River. But it is also thinkable, that by the repeated deepening of the bottom ground-materials were carved, which as substratum don't suit for brackish water benthos. Altogether

in the test-area the Weser River looked as though it was so far healthy, respectively the self-purifying power was still sufficient for the decomposition of the rest-deterioration of the upland discharge as well as of additional sewage release. After all the experience of the penury of species and individuals, typical for the brackish water, was affirmed.

In 1971 comparative studies at random were performed. They had - first of all qualitatively - completely different results. Above all the feared reduction of pH in the release area nearly failed entirely. Only at turn of low water the pH of the Weser water near the point of release dropped significantly below 7, and short-dated a weak acid sewage effluent developed, which reached over the control section. At more significant current and at high water only in the immediate neighbourhood of the point of release an influence of the sewage was perceptible. The internal conditions, which were controlled simultaneously, were observed. In the test area a perceptable increase of the rate of sedimentation could not be ascertained. Compared with the natural conditions it remained neglectably small.

The at the same time achieved biological drains in the test area revealed, compared with the primary studies, qualitatively entirely different results. Conditions were ascertained, which nearly reached up to a status of depopulation. A such severe deterioration of the Weser water in so short a period was surprising. It cannot, or at least not only, be reduced to the release of waste of the Titan factory.

For one the short-dated and locally very limited reduction of pH in the release area seemed not to be significant enough to be able to become ecologically decisively effective. Other ecological changes, reducible to the Titan sewage, were not perceptable. On the other hand it was striking, that the biological samples lacked marine as well as limnetic detritus, which was still found in larger quantities at the primary studies.

Consequently the initial events for the biological deterioration in the Weser estuary had to be searched byond the test area. A causal effect could not be imputed to the small rate of oxygen content, having a saturation of less than 50% when performing the controll-measurements, as similar rates were found already at the primary studies. The organisms, living in brackish water, develop due to the frequently altering living conditions a strong resistance against outer influences, as is known.

Therefore for the moment only hypothesis can be developed to explain the phenomenon of depopulation. An overstrain of the Weser upland discharge in so short a time can be set aside as reason for the depopulation, as there the development is kept under control. It is possible, however, that the upland discharge is efficient indirectly, because at the comparative measurements the Weser River already for a longer time only led very little water. This could explain, too, that the limnetic detritus was no more traceable. On the other hand this is no explanation for the absence of marine detritus. So far the suppositions, basing on the hydrographic boundary conditions, are little satisfactory. It is also thinkable, that population-dynamic developments took place, which already happened elsewhere, too, without an alteration in the ecological paramenters beeing traceable. (Figure next page: Population dynamic at a test station in the tidal flat near Norderney Island as example of possible fluctuations, which were not caused by human influence.) Probably here a number of influences, which are for the time being still unknown to us, are commonly efficient. Therefore the studies shall be continued and deepened.

Nevertheless the now present experiences are inducement to think over critically the studies, performed in the Weser estuary, and to draw conclusions for subsequent similar investigations.

Above all it has to be appointed, that the time, being available

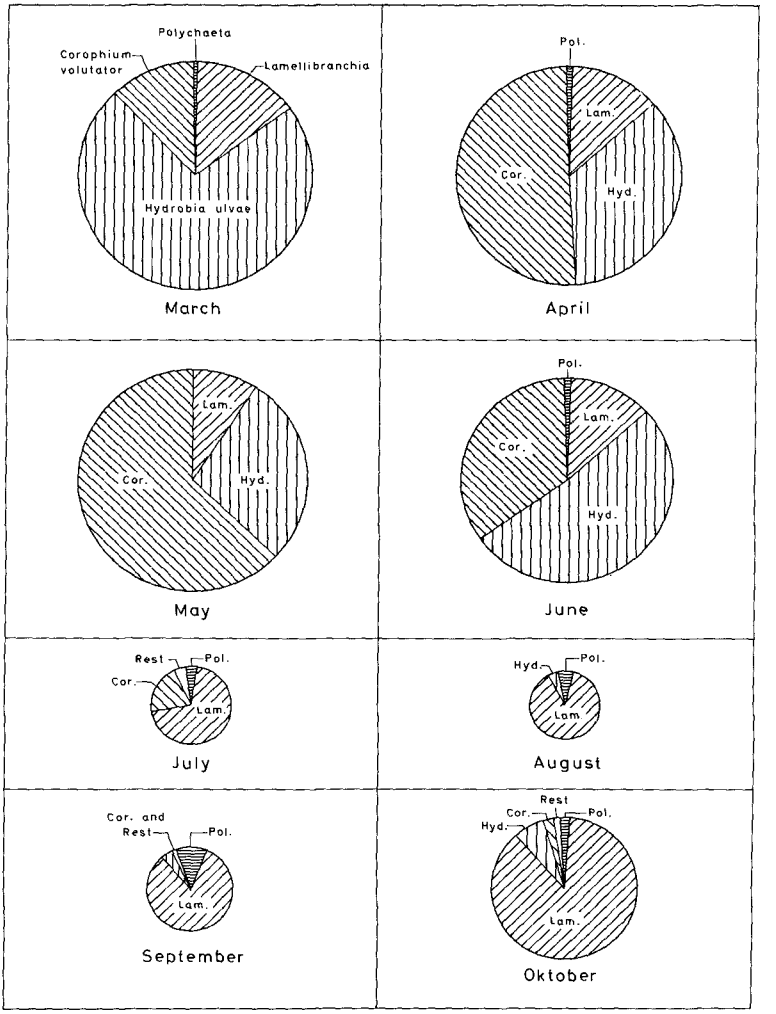

Changes in quantity and composition of the bottom fauna at a station in the eastfrisian waddensea. Sections representing number of individuals.

for contenting studies was far insufficient. Therefrom anew resulted spacial restrictions in the test area and a too coarse-meshed net of test-stations. Only by this the interpretation of the results is already extremely obstructed. Furthermore the tests and the interpretation of the results revealed exceedingly the deficiencies of our biological knowledge. In a speech a very ingenious German biologist once observed, the progress in the biological research would finally throw us back to our biological instinct. Exact scientific assertions would be an attempt of a gross illusion. This conclusion however should not be valued as oath of manifestation of the biology. It only reveals the extraordinary multiple states and ecological/biological causative relations in the lively nature. Nevertheless the instinct has to be sharpened by the augmentation of our knowledge and experiences.

Already for this reason the biological study of coast-near sea-areas and esturies should be commenced without urgent reason. We believe, that we have done our best in the Weser estuary and still are doing it. Many decisions however would have been easier and many a development would have been prognosticated better, if long-dated biological/ecological observations would have been available at the beginning of the studies, which in this case only would have been to be completed in detail.

In the meanwhile in the other German estuaries, too, similar studies have been commenced, induced by industry-settlements. Though, while studying the Weser River, we have become aware of the today's limits of these investigations, we nevertheless believe, that with increasing experiences we will become able improvingly to steer the strain of our water, which presently just is necessary in a closely colonized industrial country.

REFERENCES

1. Luck, G.: "Gefährdung der Küstengewässer durch Abwassereinleitungen", Neues Archiv für Niedersachsen, Bd 20, H 3, 1971.

2. Hensen, W.: "Gutachten zum Antrag der Titangesellschaft auf Einleitung von Abwasser in die Unterweser bei Blexen vom 12.2.1966", nicht veröffentlicht.

3. Viehl, K.: "Gutachten zum Antrag der Titangesellschaft auf Einleitung von Abwasser in die Unterweser bei Blexen, 22.4.1966", nicht veröffentlicht.

4. Meyer-Waarden: "Gutachten über die Einleitung der Abwässer der Titan-Gesellschaft m.b.H., Leverkusen, in die Weser bzw. die Nordsee, 7. Juni 1966", nicht veröffentlicht.

5. Kinne O. und H. Rosenthal: "Effects of sulfuric water pollutants on fertilization, embryonic development and larvae of the herring, Clupea harengus". Marine Biology, International Journal on Life in Oceans and Coastal Waters, Vol. 1, Nr. 1, June 1967.

6. Michaelis, H.: "Untersuchungen über das Schöpfplankton der Wesermündung", Jahresbericht 1970, Bd XXII, der Forschungsstelle für Indel- und Küstenschutz, Norderney.

CHAPTER 123

AN EVALUATION OF MIXING IN THE TAY ESTUARY

J. R. West * and D. J. A. Williams **

ABSTRACT

The authors consider the derivation of an sxprsssion for ealinity distribution in an sstuary, from an instantaneoue mass balance equation for a solute in a continuum. Ths exprsssion is compatible with existing field instrumentation and limited economic resources. Details are given of a prototype survsy which included continuous monitoring of the salinity distribution of the Firth of Tay, an estuary subject to a wide range of fluvial and marine influencee. The survey results enabled an apparent dispersion coefficient to be svaluated and an estimate to bs made of the net mixing.

INTRODUCTION

An important feature of estuarine management and research is a knowledge of the temporal and spatial distribution of salinity with respect to fluvial and marine influences.

At present there exists an incomplete understanding of the solute transport aesociated with turbulent flow in the prssence of density gradients, that is characteristic of many partially and apparently well mixed estuaries. Study of this phenomenon is hindered by the difficulty of directly monitoring turbulent fluctuations of fluid velocity and soluts concentration, and the wide range of the tsmporal and spatial variation of theee variables for given influences sxternal to the estuarine system. A further difficulty is that in many estuariee, the components of these marine and fluvial influences exhibit wids variations in both magnitude and time ecale.

A mathematical representation of solute distribution may be formulated from the fundamental principle of mass balance. Its practical application in the absence of a priori relationehips for the variables describing mass traneport, can only bs achieved by the application of statistical averaging, which leads to the assumption of empirical functions that requirs evaluation through the comparison of thsory with prototype data.

The results predicted with such a modsl must be treated with caution unless ths dependence of ths empirical functions is wsll understood for ths relevant input conditions to ths system. The expense and difficulty of collecting prototype data requires the use of the simplest form of model compatible with an adequate return of information.

* Eaet of Scotland Water Board, Invergowrie, Dundee, Scotland
** Department of Chemical Enginesring, University College, Swanssa, Wales

In thie papsr, a description ie given of the use of a ons dimsneional form of the solute mass balance squation in ordsr to obtain a mathematical repressntation of salinity dietribution in the Tay Estuary. Refersnce ie made to the proper reduction of dimensionality and time averaging of the inetantaneous three dimeneional soluts mass balance equation. The conditione of significant tidal variation of both channel cross eectional area and solute concentration are recognieed. An apparent coeffioient of diepereion and a net mixing term are defined, svaluatad and correlatad to fluvial discharge and distance along the estuary.

THE TAY ESTUARY

The estuary links a catchment having an area of approximately 7,500 km^2 through 50 km of tidal watere to the North Ssa. The River Tay and ite main tributary, the River Earn, have mean discharges of 160 cumecs and 20 cumecs (1) reepectively. The combined monthly mean dischargee ehows an annual variation ranging from 60 cumecs to 250 cumece (calculated from 15 yeare data).

The mean tidal ranges of epring and neap tides are 4.7 m and 2.3 m at the bar (2). Ths amplitude of the tidal wave ie similar at the mouth of the eetuary and at Dundee, and thence it undergoes a gradual reduction until the relevant tidal limit is reached.

The crose eectional area of flow at mean water level is fairly conetant as far as Dundee and then decreasee approximately linsarly with longitudinal dietance to Newburgh where the channel becomee of the more uniform nature characterietic of a fluvial regime. Betwsen Newburgh and Balmerino, a main channel, bordered by tidal flats, closely follows the southern shore. It then aesumee a more central poeition through the moving sand bank complex upstream of Broughty Ferry, whereafter it reachee the mouth of the setuary in a well defined channel bordered by ehoale and tidal flate. A maximum depth of 30 m occurs near Broughty Ferry, but generally depths range from 20 m to 2 m relative to low elack water levels. A datailed description of the bathymetry and eedimsntological featuree of the eetuary ie given slsewhere (3).

The ealinity intrueion extends to the Newburgh region during low river flowe. Generally the difference between ealinity near the free surface and near the bed rangee from leee than 0.1 ppt to the order of 2 - 3 ppt. For particular conditions of wind and tide, or near slack water, coneiderably greater differences may occur.

ONE DIMENSIONAL REPRESENTATION OF SOLUTE DISTRIBUTION

A eolute mase balance equation bassd on fundamental physical principles may be derived for turbulent flow in eetuariss. Aseuming the variation in fluid daneity to bs small compared with that of the other variablee, and that the effects of molecular diffusion may be neglected, then the equation for a/

conservative solute may be written as

$$\frac{\partial C}{\partial t} + \frac{\partial}{\partial x_i}(U_i C) = 0 \qquad (1)$$

where i = 1, 2 or 3, refers to a cartesian coordinate system

C = Solute concentration

U_i = Component of fluid velocity

t = Time

The reduction of dimensionality of equation (1) has been shown by Pritchard (4), with the "turbulent" terms introduced by a temporal average over a small time interval, to give

$$\frac{\partial}{\partial t}(C_A A) + \frac{\partial}{\partial x}(A U_A C_A) + \frac{\partial}{\partial x}(A \langle\langle u'C' \rangle_{\Delta t} + \langle u'_A C'_A \rangle_A) = 0 \qquad (2)$$

where x = Distance from mouth of estuary

A = Lateral cross sectional area of channel

Δt = A small time interval

$f_d = \langle f \rangle_d = \frac{1}{d}\int_d f\, dd$ & $f = f_d + f'_d$

f = A function dependent on d

Further temporal averaging over a tidal period has been considered by Okubo (5) and modified by Williams and West (6) for the case where there exists a significant tidal variation of cross sectional area and of the spatial mean value of solute concentration. Assuming steady state conditions gives

$$\frac{\partial}{\partial x}(C_{AT} Q_T) + \frac{\partial}{\partial x}(\langle A(u'_{AT} C'_{AT} + \langle\langle u'C' \rangle_{\Delta t} + \langle u'_A C'_A \rangle_A + A'_T C'_{AT} u_{AT} \rangle_T) = 0 \qquad (3)$$

where $f_{AT} = \frac{1}{T}\int_T f_A\, dt$

f_A = Function dependent on t

T = Tidal period

Q = Fluvial discharge

An inspection of the terms in equation (3) is useful at this stage. A value of the term Q_T may be obtained by standard river gauging techniques and a good estimate of C_{AT} for salinity at any section may usually be calculated from data acquired using a small fast craft and in situ salinity measurement procedures.

To the authors knowledge, the useful measurement of the turbulent perturbations U_i and C_i in estuarine flow is impractical at present. The measurement of turbulent mean velocity components ($\overline{U}_i$) is technically feasible, but gathering detailed data is generally economically prohibitive in most natural tidal channels having an irregular cross section.

Thus in practice it is convenient to rewrite equation (3) using a/

coefficient $D_{x_{AT}}$ to give

$$\frac{\partial}{\partial x}\left(C_{AT}Q_T\right) - \frac{\partial}{\partial x}\left(A_T D_{x_{AT}} \frac{\partial c_{AT}}{\partial x}\right) = 0 \qquad (4)$$

where $D_{x_{AT}}$ is dsfined as

$$D_{x_{AT}} = -\frac{1}{A_T \frac{\partial c_{AT}}{\partial x}}\left(\langle A\left(u'_{AT}c'_{AT} + \ll u'c' \gg_{\Delta t} + u'_A c'_A\rangle_A\right) + A'_T C'_{AT} u_{AT}\rangle_T\right) \qquad (5)$$

The precise physical meaning of $D_{x_{AT}}$ is not easily understood. Howsver, its use introducss uniformity and simplicity into the algebra and psrmits practical rssults to be achieved. The intuitive uss of a turbulent diffusion coefficient (D_{ij}) has besn discusssd by many authors (for example Okubo (7)) but further progress to a ussful end, analytically or numerically of necsssity requirss the condition.

$$D_{ij} = 0 \qquad i \neq j$$

where D refers to elements of the turbulent diffusion

and i, j = 1, 2 or 3

This assumption is difficult to justify in the light of the present understanding of estuarins flow, but is often accspted in the processs of model development. On this basis the tsrm $D_{x_{AT}}$ is proposed. It is a function of mean (A, T) concentration gradient, the spatial and temporal variation of fluid velocity and solute concentration, and the temporal variation of cross sectional area. Herein ths term $D_{x_{AT}}$ is loossly termsd an apparent dispersion cosfficisnt. It should be noted that it is necsssary to include a convective term with the non-convective terms.

DATA ACQUISITION AND ANALYSIS

Turbulent mean values of salinity at a point are likely to bs ths combined result of marine and fluvial inputs to the estuarinssystem over a psriod of time of the order of weeks. To establish the magnitude and tims scale of these effects the continuous monitoring of salinity, with respect to tidal range and fluvial discharge, was arranged at a point approximatsly equidistant bstwsen the mouth of the estuary and the upstream limit of salinity intrusion. Ths tidal exc ursion in the Tay is such that at a point so placed, the mean (T) salinity is a function of conditions ovsr 75% of the intrusion length.

Water sampling instrumentation and a water levsl recordsr wers installed at Newport Pier. The sits had the advantages of being accsssibls in all anticipated weather conditions and was for most of a tidal cycls subject to a strong tidal current. Hourly water samplss having a volume of 600 - 800 ml were

collectsd and analysed for salinity using a salinity/temperaturs bridge. The automatic sampler (North Hants. Eng. Co. MK IV) consists essentially of twenty four evacuated bottles with clockwork actuated valves. To be independent of mains electricity on an sxposed site was considersd to be important. The suotion head of 7 m at low tide made ths use of a battery powered sampler unattractive.

The water level recorder produced quarter hourly readings on water rssistance computer compatible punched tape. Economic and site conditions limited the stilling well size to 100 mm and float diameter to 80 mm. Calibration (8) indicated an accuracy of $\pm$ 13 mm though during quiet surface wave conditions the effect of interference betwesn float and countsrweight can be observed in figure (3).

River discharge data was supplied by the Dept. of Agriculture, Fisheries and Food for Scotland as mean daily discharges. Hydrographic data was taken from charts prepared by the Dundee Harbour Trust and by the Admiralty.

The salinity record was examined with respect to salinity in the main channel at that section and for ths sffects of tidal range and river flow.

Confirmation that the autosampler data reflected conditions elsswhere on the cross section was sought by comparing the autosampler data with spatial mean valuss of vertical profiles measured in the main channel, whsre the lateral salinity variation was known to be small. The results shown in fig (2) ars typical of the three periods monitorsd. The lag of the point values on the flood is more likely to be the effect of the main flood current tending to flow to the north of ths ebb current (10) rather than vertical salinity gradients.

The tidal dependence of the salinity time series was demonstrated through the use of the least squares criteria to approximate to the data a function of the form (9)

$$y = a_0 + a_1 \sin \omega t + a_2 \cos \omega t \qquad (6)$$

where

$$\omega = \frac{2\pi}{T}$$

a_0, a_1, a_2 = constants

$\sqrt{a_1^2 + a_2^2}$ = amplitude

The period was varied from 11.90 hr to 13.00 hr in steps of 0.01 hr. This revealed for both the water level and salinity data the existence of large values of amplitude for the semi-diurnal (12.42 hr) and 14 day (12.00 hr) components.

Insight into the salinity river flow relationship was achieved by filtering a major part of the tidal effects by approximating equation (6) to various intervals of data and taking a_0 as parametric representation of salinity in that interval. An interval of 24 hr was found to be a satisfactory compromise between loss of detail of the record and of the smoothing of the semi-diurnal tidal/

effects. During psriods of steady fluvial discharge when the tidal effects on mean (T) salinity might be expectsd to bs apparent, the changes in value of a_o suggest a steady trsnd towards an equilibruim value for that flow. However, the tidal range was found to be related to the salinity range, to a first approximation by a linear function.

The values of a_o wsre plotted against an arithmetic average of the msan daily fluvial flow for the precsding 7 days. Study of the records of several floods indicated that 7 days was approximately the average time between peak discharge at the Ballathie (R. Tay) gauging station and ths corresponding minimum value of mean (24 hr) salinity at Newport Pier.

A linear relationship could be approximated to the salinity river flow data. Such a rslationship must of necessity bs of an approximate nature bscause of the dynamic features of the system and of ths variability in the maximum flow, volume and duration of fluvial floods. Data for effectively steady state conditions is givsn in figure (4).

Having sstablished that salinity data might be detected and charactsrissd, salinity rsadings were taken at fivs stations in the main channel (approx 4 km apart) for several tidal rangss and river flows, and examined for a similar relationship. At each station vertical profiles of salinity distribution were measured at intervals of about 20 mins for complete flood and ebb tides (i.e. bstween slack water). Field msasurements showed that cross sectional area msan values of salinity could often be estimated to better than 1 ppt from channel station data. An sstimats of the spatial msan was obtainsd by assuming a linear variation between measured values and thsn taking a spatial avsrage. The spatial mean values of salinity were then approximated to a sixth order polynomial and the mean (A, T) salinity evaluated from this function by temporal avsraging.

At Pool, Broughty Ferry, Newport and Flisk, the rslationship betwesn mean (A, T) salinity and mean (7 day) fluvial discharge closely approximated to a linsar function. The regression linss are shown in figure (4). The lack of variation in river flow on the occasions that the station at Balmerino was monitored serves to indicate reproducibility of results for those conditions at that station. As the slopes of the mean salinity/fluvial discharge functions are similar at Newport and at Flisk, a like value of slope was assumed for the function at Balmerino.

Plotting of the mean (A, T) longitudinal salinity distribution for various flow conditions, figure (5), enabled the abstraction of the data necessary in order to obtain estimates of the value of the apparent dispersion cosfficient.

The variation of the apparent dispersion coefficient with mean (7 day) river flow and distance along the estuary is shown in figures (6) and (7). The coefficient is sensitive to the effects of the variation of river flow. At the

three upstream sampling stations, the observed data indicates that the coefficient passes through a maximum value as the river flow increaees. A marked epatial variation is exhibited near the mouth of the estuary, elsewhere there is a comparatively gradual linear variation.

It is difficult to gain physical information from the apparent dispersion coefficient. An indication of the magnitude of the net effecte of the physical proceeees over a tidal cycle may be obtained from the net advective salt flux during a tidal cycle, here defined as the net mixing. The net mixing is a function of turbulent effects as well as epatial and longer term temporal variations. A good estimate can be obtained from the term $Q_T\ C_{AT}$ if the term $A'_T\ C'_{AT}\ U_{AT}$ may be assumed to be comparatively small, as is generally the caee for the Tay Estuary.

The linear relationship between the mean (A, T)salinity and mean (7 day) river flow,

$$C_{AT} = b_o + b_1 Q_T \qquad (7)$$

where b_o, b_1 = Constante at a point x
leads to a second order relationship for the net mixing F,

$$F = Q_T\ C_{AT} = b_o\ Q_7 + b_1 Q^2_7 \quad (8)$$

Equation (8) indicatee that the net mixing is also sensitive to the effects of mean river flow variation and that a maximum value is passed through as mean river flow increaeee (Figure (9)). The existence of this maxima are not confirmed for all the etations as some occur outwith the limits of conditions observed in the field. The field data indicates a nearly linear increaee in mixing along the estuary (Figure (8)).

CONCLUSION

The one dimensional solute mass transport equation in a tidally averaged form is a useful preliminary approach to the study of mixing in an estuary. While unsatisfactory from a physical point of view, the introduction of an apparent dispersion coefficient provides, along with other functions, an algebraic representation of the effects of processes that lead to what is here called the net mixing. The yield of physical information is limited to an estimateof the net effects of the physical processes of solute transport over a tidal cycle. In the Tay Estuary the apparent dispersion coefficient and net mixing are highly dependent upon distance along the eetuary and mean river flow.

ACKNOWLEDGEMENTS

The work described in this paper was carried out while both authors were members of the Dept. of Civil Engineering of the University of Dundee. It forms a part of an interdisciplinary study of the Tay Estuary supported by the University of Dundee, Science Reeearch Council and Natural Environment Research Council.

REFERENCES

1. - The Surface Water Year Book of Grsat Britain 1965-66 H.M.S.O. (1971)

2. - Admiralty Tide Tables Vol. 1 1970

3. Buller, A.T. McManus, J and Williams, D.J.A. Ressarch Report No. 1, University of Dundee (Tay Estuary Research Centre) 1971, p 15

4. Pritchard, D.W. J. Mar. Res. 1958 17, p 412.

5. Okubo, A. in Studies in Oceansography, Hidaka Jubilee Committee, Geophys. Inst., University of Tokyo, 1964, p 216.

6. Williams, D.J.A. and West, J.R. Symposium on Mathematical and Hydraulic Modelling of Estuarine Pollution, W.P.R.L. Stevenage (in press)

7. Okubo, A. Chesapeake Bay Institute, Topical Report, Ref. 69-1

8. Lsnnon, G.W. et al Int. Rep. No. 9 Liverpool Tidal Institute 1966

9. West, J.R. and Williams, D.J.A. 5th I.A.W.P.R. Conference, Hawaii 1970 Pergamon Press 1971.

10. McManus, J West, J.R. Williams, D.J.A. Proc. Geol. Soc. London 1970 No. 1662 p 71

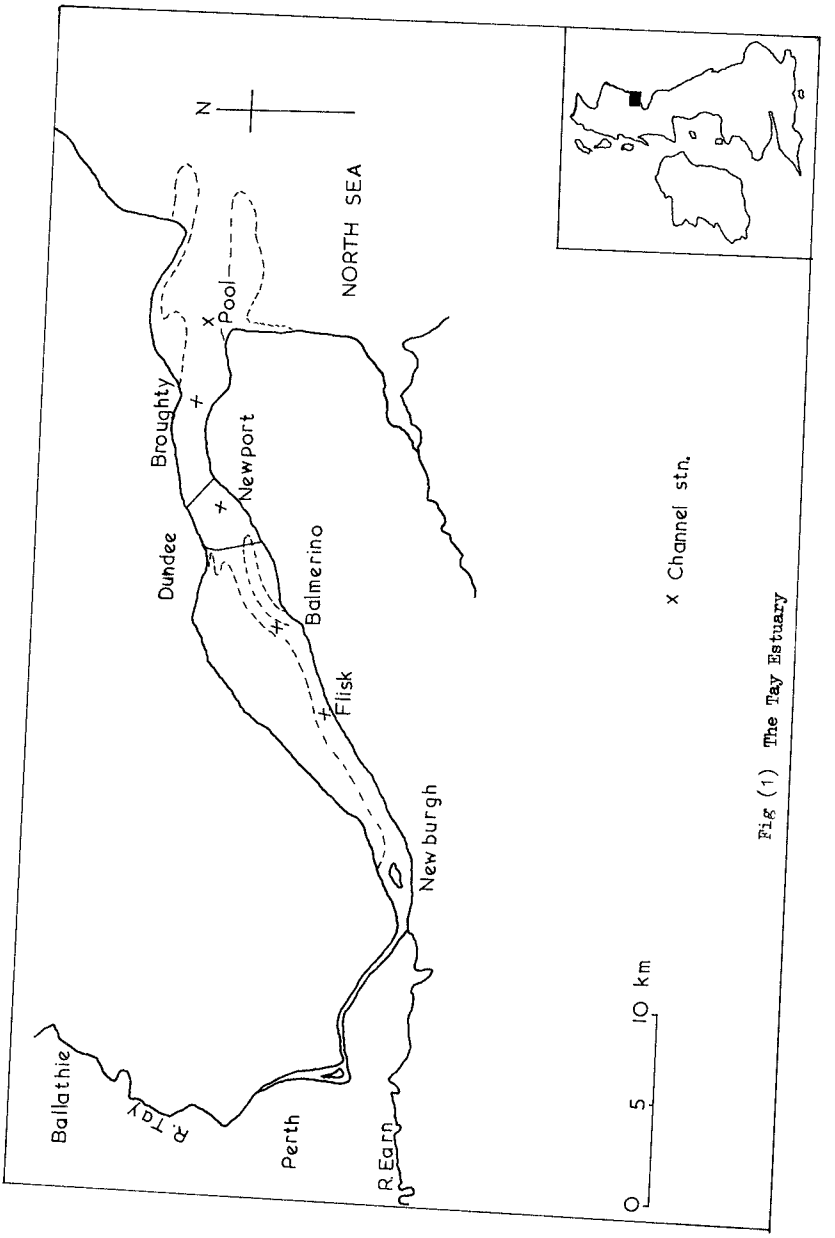

Fig (1) The Tay Estuary

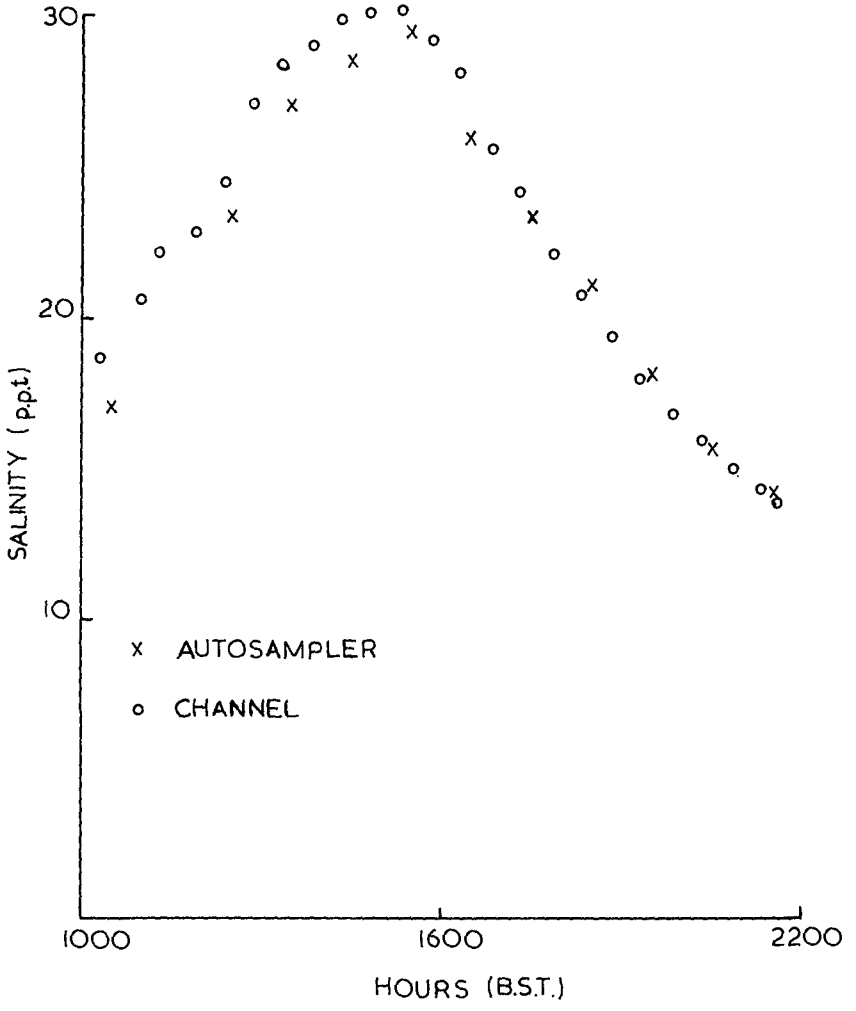

Fig. (2) Comparison of autosampler data with channel mean salinity data at Newport

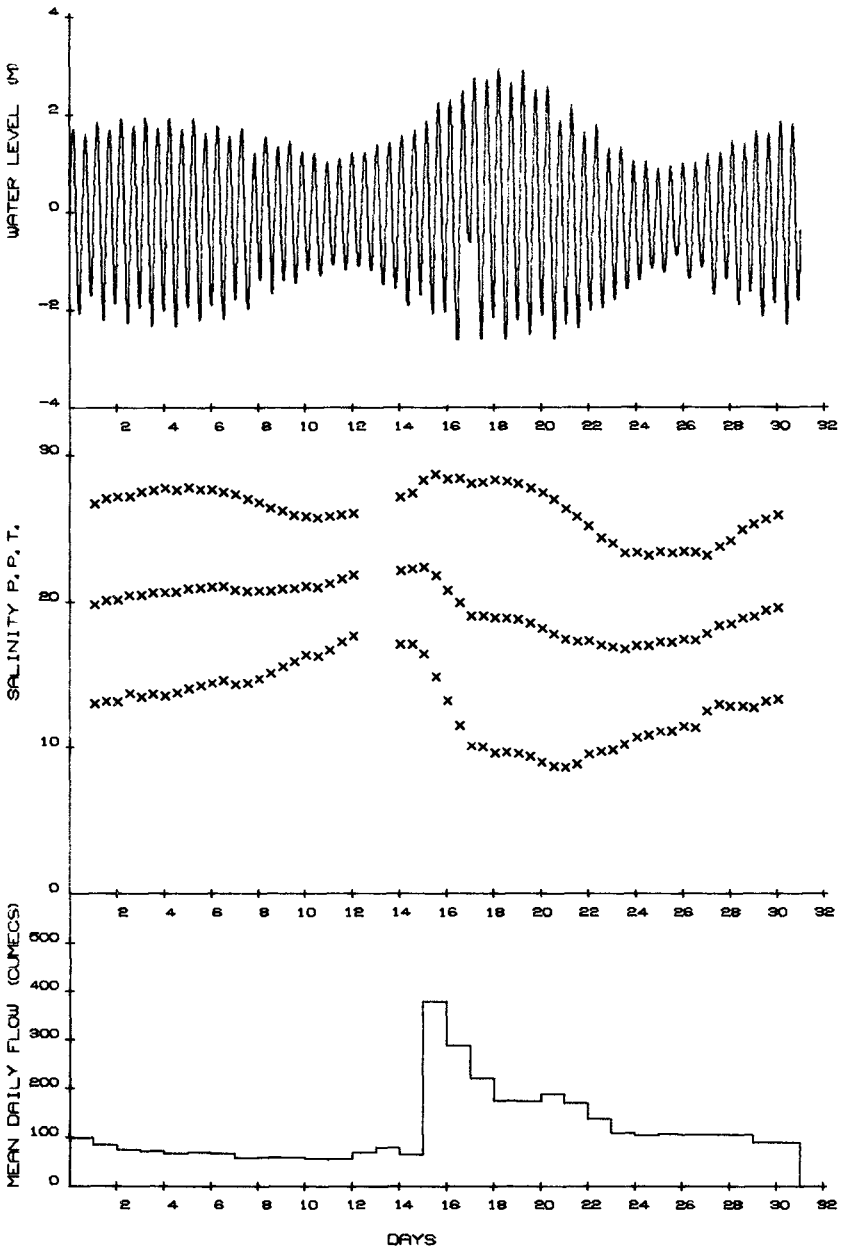

MONTH 8 YEAR 70

FIG 3 MAX, MEAN & MIN SALINITY (NEWPORT), WATER LEVEL (NEWPORT) & RIVER DISCHARGE (TAY & EARN) VARIATION WITH TIME.

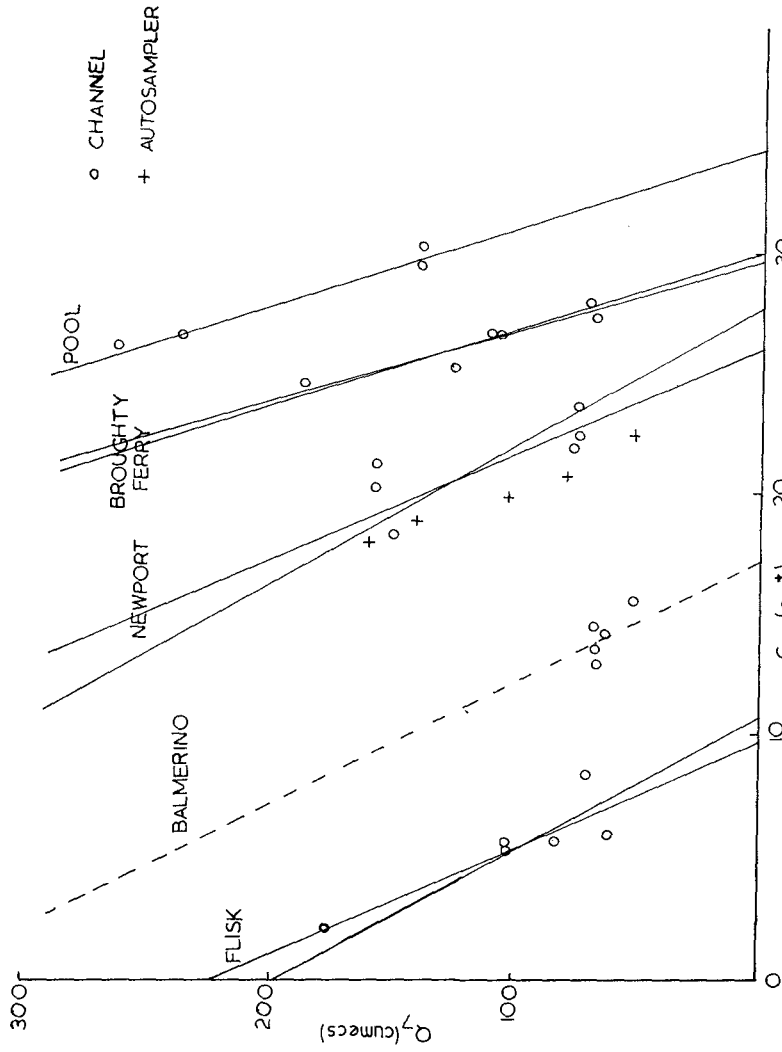

Fig. (4) Variation of mean (A,T) salinity with mean (7 day) fluvial discharge

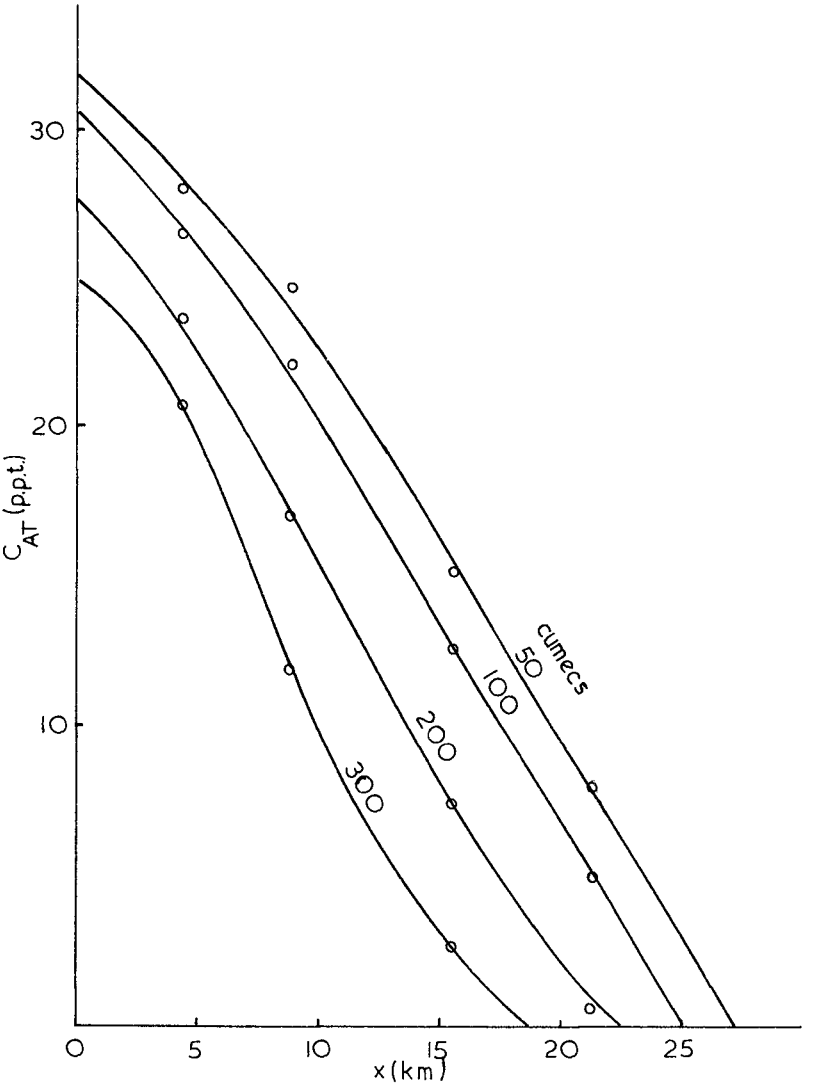

Fig. (5) Longitudinal mean (A,T) salinity distribution as a function of mean (7 day) river flow

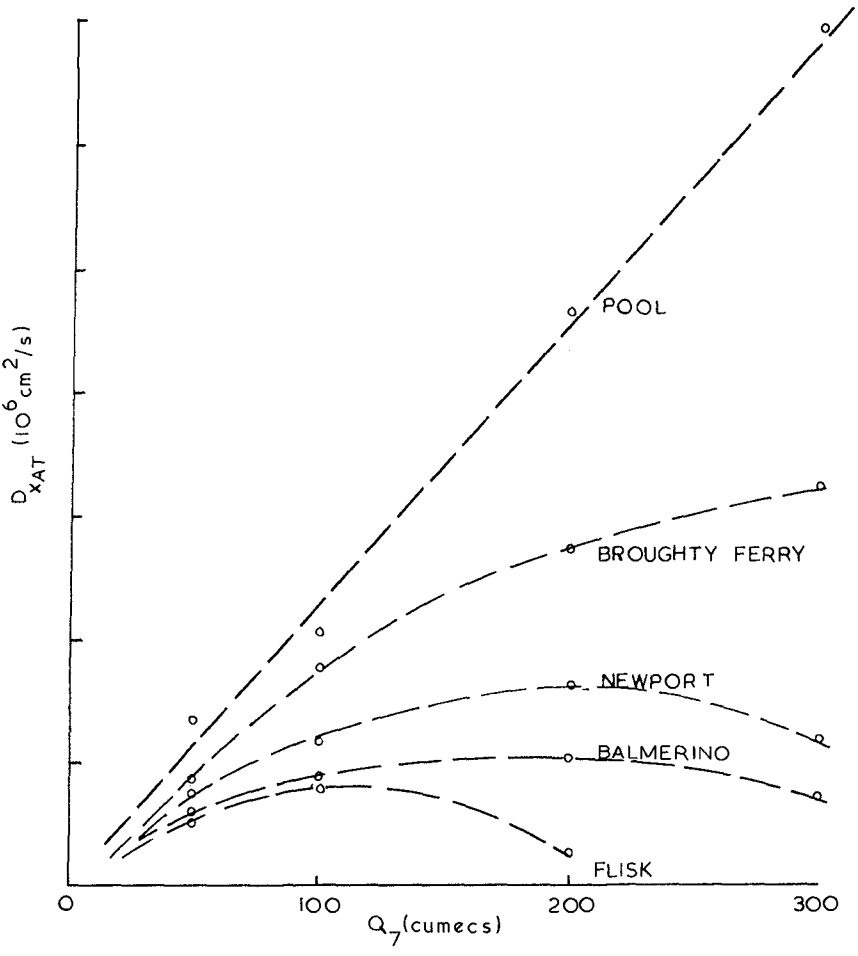

Fig. (6) Variation of apparent dispersion coefficient $D_{x_{AT}}$ with mean (7 day) river flow Q_7

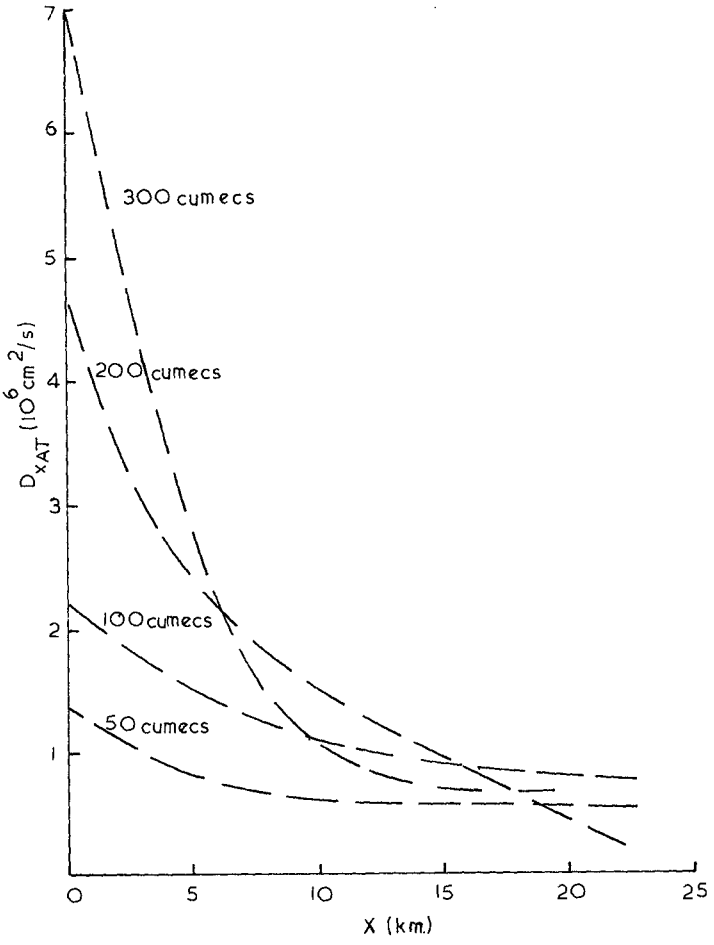

Fig. (7) Apparent dispersion coefficisnt $D_{x_{AT}}$ as a function of distance x from estuary mouth

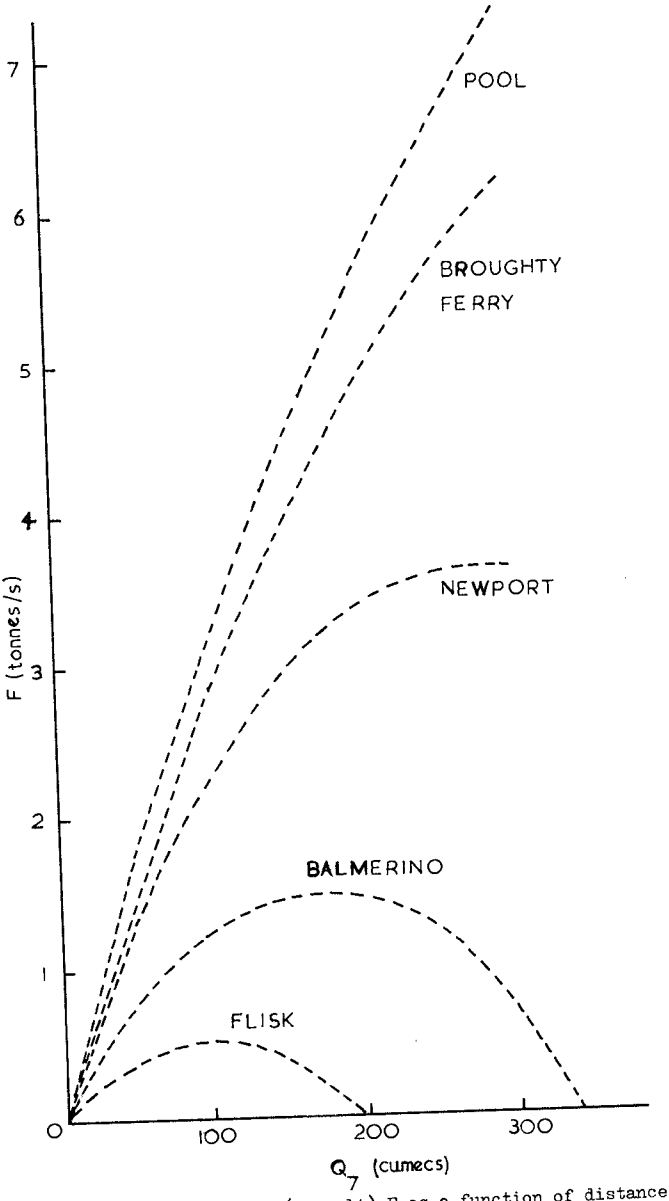

Fig. (8) Net mixing (of salt) F as a function of distance x from estuary mouth

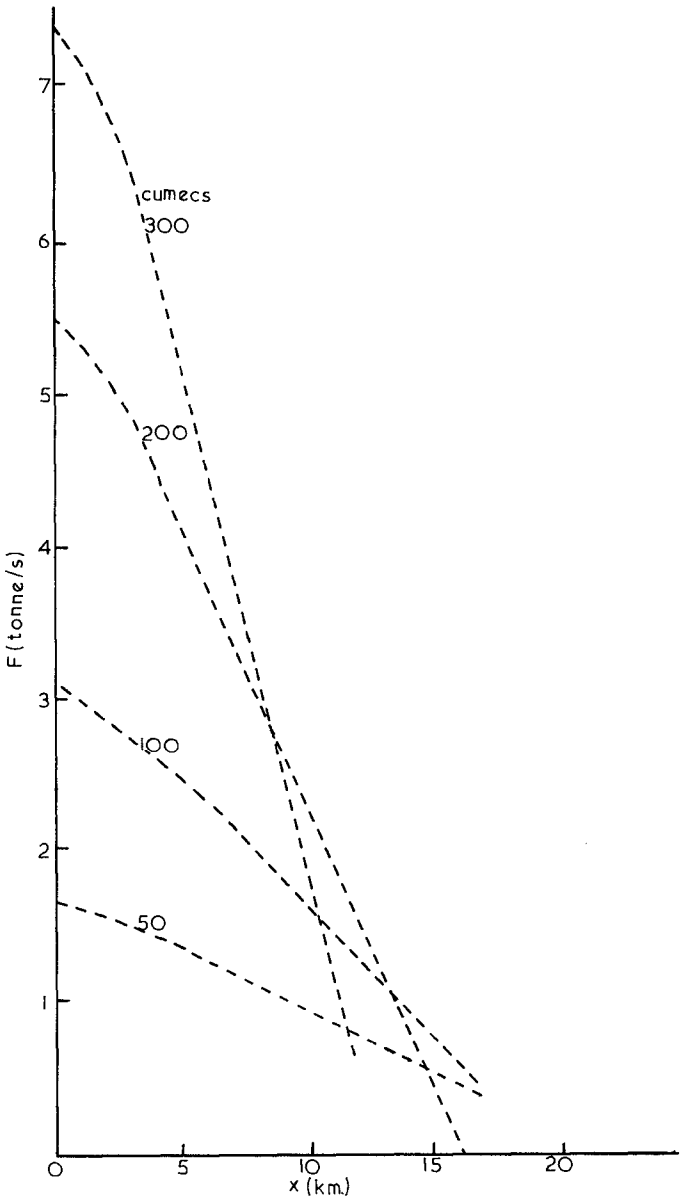

Fig. (9) Variation of net mixing (of salt) F with mean (7 day) river flow Q_7

CHAPTER 124

USE OF MIXING TUBES ON MARINE OUTFALLS

by

Richard Silvester
Department of Civil Engineering
University of Western Australia

and

Mana Patarapanich
Postgraduate Student
University of Strathclyde
Scotland

ABSTRACT

To optimise dispersion from marine outfalls multiport diffusers have been developed. The addition of mixing tubes to such outlets can create an ejector action and so cause pre-mixing before discharge to the receiving mass of water. The characteristics of such water jet-pumps in this submerged condition have been derived elsewhere, but are applied herein to the dilution of effluents. For a range of jet to mixing tube area ratios optimisation has been carried out on a computer, thus indicating the densimetric Froude numbers and depth ratios at which dilution exceeds that for the plain jet. Even for a stagnant ambient medium dilution in experiments exceeds that predicted, possibly because of macro-turbulence not accounted for in the theory available. Turbulons developed in a mixing tube are larger than any emerging from a plain smaller jet and may thus promote better mixing from its exit to the sea surface. Mixing tubes have obvious applications in shallow water and where an effluent is particularly obnoxious.

INTRODUCTION

With the increased concentration of industry and population on coasts and waterways, for the sake of cooling water and sea transport, greater demands are being made on the coastal waters for the disposal of liquid effluent. At the same time these beach areas are required for recreation of the populace, so that higher standards of purity are being demanded for river, estuarine and coastal waters. This situation has promoted the use of multiple ports in outfalls(1), so that warm water or effluent alike can be well mixed with the receiving liquid. Because such diffusion takes some time and distance to be effective the hydraulics of mixing tubes will be outlined.

Although the waters of coastal zones and estuaries are in continual motion, due to tidal currents, the diffusion analyses generally assume a stagnant ambient fluid. A design based upon this adverse condition is reasonable since at high- or low-water-slack the receiving liquid is stagnant for a period of 2 or 3 hours, in which time a sizable volume of effluent could accumulate.

An outfall may have ports which discharge horizontally or vertically or both. At the outlet the jet contains a certain kinetic energy in the form of momentum. Due to the normal density difference of the effluent and the medium a certain potential energy is exerted on the jet in the form of buoyant uplift. As the jet travels through the stagnant liquid it draws some of it in, so increasing the area through the jet and diluting its contents. The further from the port the greater is the proportion of buoyant force to vertical momentum, any horizontal momentum remaining steady, although the velocity associated with this approaches zero as the area of the jet increases.

Many workers have supplied analyses and experimental data on this topic, but those who have provided comprehensive reports suitable for ready application are Abraham(2) plus Fan and Brooks(3). Both of these are mathematical treatments which include constants derived from experimental work of their own or of other workers. Abraham treats vertical and horizontal jets in ambient fluid of constant or variable density. Fan and Brooks have generalised the analysis to cover discharge at any angle and to vary the constants over the depth, rather than a step change at mid-depth. Both reports contain graphs for circular orifices or continuous slots, only the former will be discussed here.

CIRCULAR JET IN UNIFORM DENSITY MEDIUM

A jet of diameter D is depicted in Fig. 1 issuing with a velocity U_o at an angle θ_o to the horizontal into an ambient liquid of uniform density ρ_s. At the nozzle the density and concentration of the effluent is ρ_o and C_o respectively. At the end of flow establishment (6.2 D from the nozzle) the centre-line concentration C is given by

$$C_o / C = 1.15 \qquad \ldots\ldots\ldots\ldots\ldots\ldots\ldots\ldots\ldots\ldots (1)$$

whilst at a height y above this point the centre-line concentration C_y

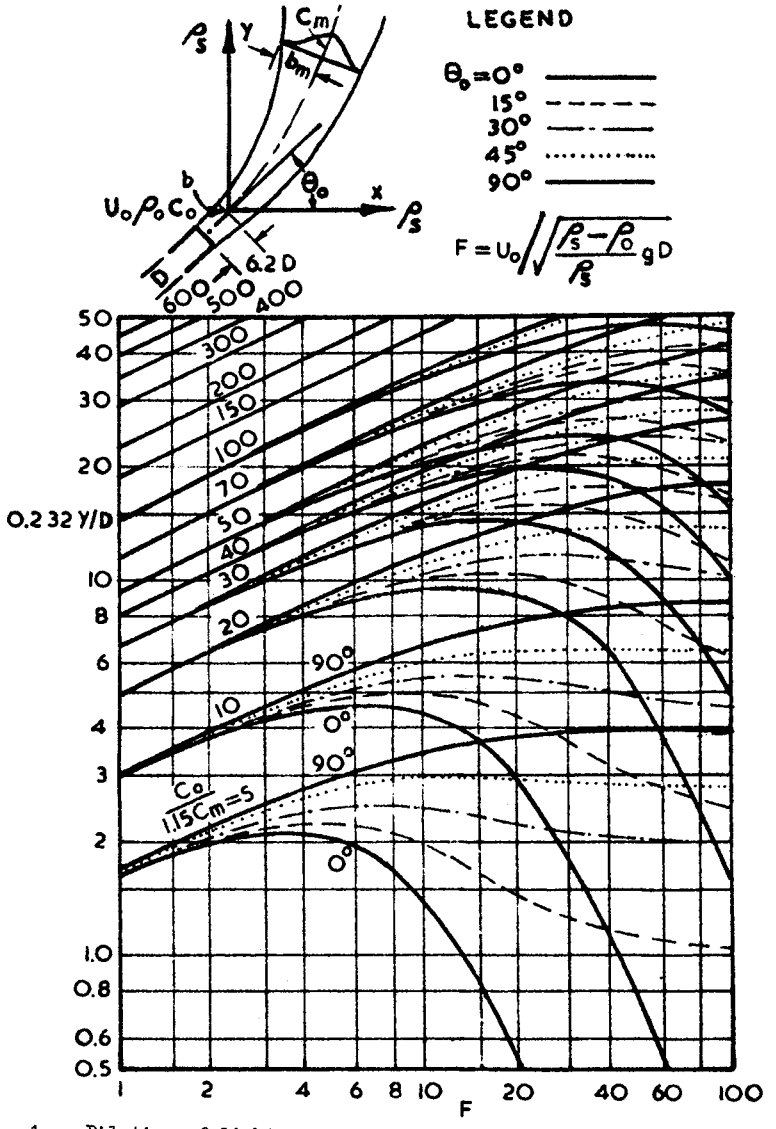

1. Dilution of lighter circular jet in ambient fluid of uniform density.

is given by the curves in Figure 1. These vary with y/D, θ_o and densimetric Froude number F defined by

$$F = U_o \Big/ \sqrt{\frac{\rho_s - \rho_o}{\rho_s} gD} \qquad \text{.....(2)}$$

The graphs of Fan and Brooks[3], from which Figure 1 has been prepared, were presented with an abscissa of dimensionless momentum flux which at the nozzle (M_o) is related to F by

$$F = \frac{\lambda}{2^{\frac{1}{4}} \alpha^{\frac{1}{2}}} M_o^{\frac{5}{4}} \qquad \text{.....(3)}$$

where α is the coefficient of entrainment, assumed from Rouse et al[4] to be 0.082. This is noted since Fan and Brooks[3] state that if new values of α and λ emerge from future tests then a new multiplying factor can be derived for use with the same graphs. For the sake of simplicity the values of $\alpha = 0.082$ and $\lambda = 1.16$ have been employed, resulting in the abscissa of F, also used by Fan and Brooks as an alternative scale. For $F = \infty$ a value of $\alpha = 0.057$ is suggested.

To obtain the vertical height from the nozzle to the trajectory point where the concentration is C_m the component of the distance for flow establishment must be added, that is

$$y_m/D = y/D + 6.2 \sin \theta_o \qquad \text{.....(4)}$$

The dilution curves ($C_o/C_m = S_m$) in Figure 1 for $\theta_o = 90^\circ$ rise consistently with F, whereas those for $\theta_o \leq 45^\circ$ reach a peak y/D and then fall, thus giving two locations at which the same dilution or concentration occurs. At small F the jet rises almost vertically from the nozzle and reaches a given dilution at a specific height (e.g. F = 1, $C_o/1.15\ C_m = 10$ at 2.32 y/D = 3). As the jet discharge is increased, and so F, so is the height of y/D for the same dilution until F is large enough for the trajectory length to permit enough mixing for the dilution to become similar at the same height (e.g. F = 20 gives the same conditions as before).

Sharp[5] has described the mechanism for small F as that of "starving" the jet. In this situation the buoyant force predominates and stretches the system, so causing gusts which expedite mixing. The condition for minimal dilution is therefore the Froude number at which the jet reaches the surface on the point of being starved. Operation at these maxima on the curves of Figure 1 should be avoided. Conditions should be chosen either side of these F values, preferably smaller ones as these demand less power. It is seen that for any given Froude number the greatest dilution is achieved by the horizontal jet, but other angles must be considered so as to prevent interaction of jets.

The co-ordinates of the trajectory with respect to the origin of established flow are given in Table I in terms of x/D and y/D. The width ratio b_m/b (see Figure 1), where b is the half jet width at the

end of flow establishment ($\approx D/\sqrt{2}$), and b_m is the half width where the central concentration is C_m is also listed. The concentration at any radius r from the centre-line is given by the Gaussion distribution

$$C_r/C_m = e^{-r^2/(\lambda b_m)^2} = e^{-0.74(r/b_m)^2} \quad \ldots\ldots\ldots\ldots\ldots\ldots (5)$$

MIXING TUBES

Several devices were used by Hansen and Schroeder[6] to break the jet into parts, in order to effect greater dilution. They concluded: "Dilution of a jet can be increased by use of a special nozzle design, but the possibilities in this direction are reduced considerably when complicated devices are avoided and little or no additional loss of energy is allowed." In multiport diffusers deflection of one jet into the path of another serves little purpose. Also, such appendages must be added to the outfall when it is in place, which can be a costly operation.

However, under certain conditions of insufficient depth, or improving the dilution of an existing outfall, the addition of a mixing tube may be found economical. This consists of a cylinder, larger in diameter than the port or 'nozzle' which is placed in line with the jet, with its flared entrance in close proximity to the outfall (see Figure 2). The jet then draws seawater into the tube and mixes with it before discharging at a lower velocity at the outlet. Design graphs have been presented[7] for this water-jet-pump action and its application to sewage outfalls presented by Silvester[8].

The initial dilution S_i effected in the mixing tube is in proportion to the water drawn in (Q_s) and the discharge of the driving jet (Q_n), so that

$$S_i = \frac{Q_n + Q_s}{Q_n} = \frac{Q_m}{Q_n} \quad \ldots\ldots\ldots\ldots\ldots\ldots\ldots (6)$$

The ratio Q_m/Q_n depends upon the ratio (R) of the area of the nozzle ($a = \pi D^2/4$) to the area of the mixing tube ($A = \pi D'^2/4$). For the specific condition of a plain cylindrical mixing tube with flared entrance a characteristic curve as in Figure 2 can be derived[7]. This is based upon the criterion that the mixing tube length is 7 times its diameter (i.e. = 7D'), which has been found to be that for maximum mixing with least friction loss [9].

The discharge velocity from the mixing tube is much lower than that from the nozzle and, in spite of the increased diameter, the densimetric Froude number is decreased, such that

$$F_m/F_n = (Q_m/Q_n)R^{\frac{5}{4}} \quad \ldots\ldots\ldots\ldots\ldots\ldots\ldots (7)$$

where $$F_m = U_m / \sqrt{\frac{\rho_s - \rho}{\rho_s} gD'} \quad \ldots\ldots\ldots\ldots\ldots\ldots\ldots (8)$$

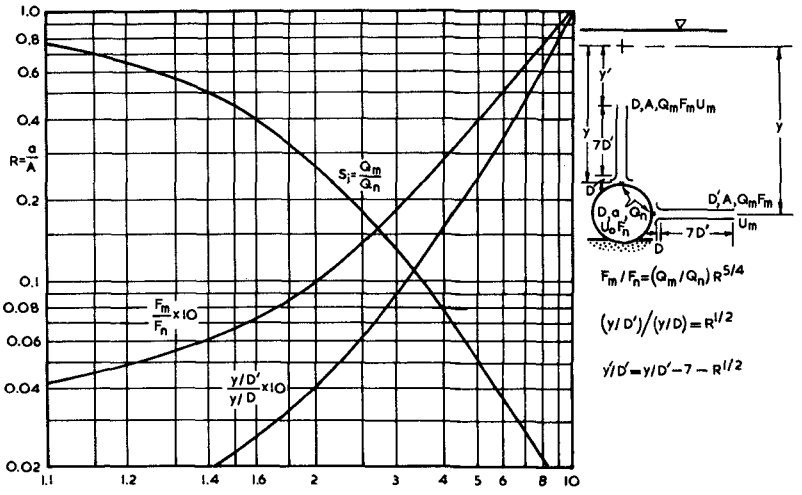

2. Initial dilution, change of densimetric Froude number, and change of dimensionless height by using a mixing tube on horizontal or vertical circular jets.

where U_m is the discharge velocity from the mixing tube ($= 4Q_m/\pi D'^2$)

ρ is the density of the diluted effluent leaving the mixing tube.

Equation (7) has been plotted against R in Figure 2.

The mixing tube now serves as the nozzle for the further dilution (S'_m) of the jet as it rises to the surface. The height ratio for the design chart of Figure 1 must now be based on the mixing tube diameter D', which can readily be determined from Figure 2, for any chosen R value. When the mixing tube is vertical the remaining height for dilution (y'/D') is the height from the nozzle (y/D') less the height from the end of the mixing tube to the nozzle ($7D' + D = 7D' + D'R^{\frac{1}{2}}$). The nozzle exit is placed one diameter (D) from the entry point of the cylindrical mixing tube for optimum efficiency(9).

A typical variation of initial dilution (S_i), dilution beyond the mixing tube (S'_m), and total dilution ($S_t = S_i \times S'_m$) is given in Figure 3. This is for a specific area ratio R and specific depth ratio y/D. It is seen that as R increases (i.e. mixing tube smaller) initial mixing decreases whilst dilution from the exit to the surface increases. The product of these two dilutions decreases as R increases, approaching ultimately the dilution from the original nozzle as R reaches 1.0. Thus for all values of $R < 1.0$ the total dilution is greater than that from the single nozzle, for the case of F = 15 and y/D = 60.

It should be noted that as greater dilution is effected so will the volume or depth of ambient liquid taken up by effluent. This necessarily

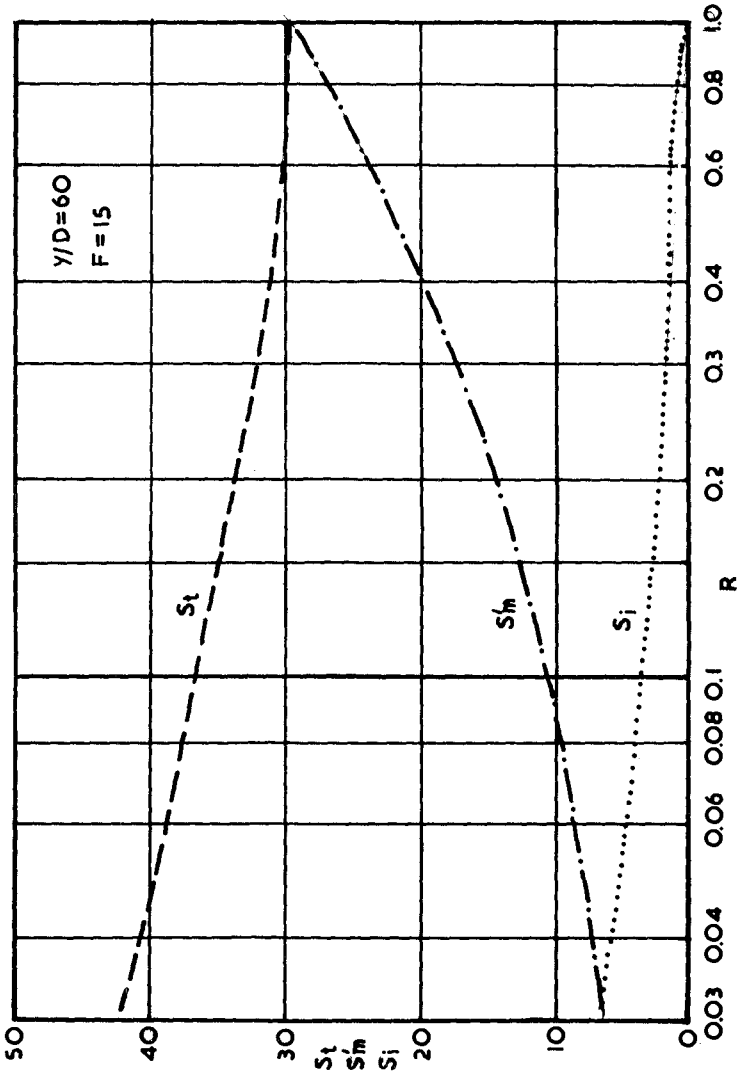

3. Variation of initial dilution (S_i), buoyant dilution (S'_m) and total dilution ($S_t = S_i \times S'_m$) with area ratio R for a specific F and y/D.

decreases the active height (y) available for diffusion. However, currents and waves influence this thickness of polluted water in ways yet to be determined, so that refinements in assessment of this decreased depth ratio is not warranted at present except qualitatively.

Similar curves to Figure 3 can be derived for other area and depth ratios, from which an improvement factor can be derived ($= S_t/S_m$). A multitude of area ratios (R) could be selected for such a comparison, making the choice of a mixing tube tedious unless other design criteria limit this choice. In order to optimise the total dilution (S_t) for a horizontal jet a computer study was carried out[10], the result of which is presented in Figure 4.

It may seem strange that placement of an apparent obstruction in the flow path of a jet will achieve greater dilution with the surrounding medium. However, it should be realised that a plain jet effects mixing by drawing in ambient fluid through shear stresses at its boundaries. This process is maximum near the nozzle where velocities are greatest. When this stress is exerted within the confines of a mixing tube the stagnant fluid is accelerated and mixed completely within a short distance of the nozzle. The ejector tends to pump ambient fluid into the jet rather than leave it to the peripheral shear stress to accelerate some boundary layer thickness to the speed of the plume.

Equation (2) may be re-written as

$$F = Q \Big/ \frac{\pi}{4} D^2 \sqrt{\frac{\rho_s - \rho_o}{\rho_s} gD} \qquad \text{.....(12)}$$

Thus for a specified dilution (C_o/C_s) in Figure 1 and an F value on the left of the maximum of the horizontal jet curve, any reduction of F to effect greater dilution (for a given discharge Q) implies a larger D and hence smaller y/D. This traverse to the left and downwards would probably mean arriving back on the same dilution curve, or below it, so that optimum design can be reached. When a mixing tube is used a similar change of D and F occurs, but an initial dilution is also produced. As seen above the product of S_i and S'_m can be greater than dilution (S_m) from the plain jet, when y/D, F and R are within certain limits. It is seen that greatest gain derives for large y/d, small F and small R. These are rather conflicting demands since smaller F and smaller R may result in a condition where the jet from the nozzle is insufficient to drive the "jet-pump". The smaller R also implies a relatively large D' and hence length 7D'. But Figure 4 could serve as a starting point for the design of an outfall, which should then be tested in the laboratory.

A similar optimization curve is presented in Figure 5 for a vertical jet, in which y/D has been separated from F, because no benefit accrues until y/D = 120. This is because the height for dilution S'_m is reduced as the mixing tube length increases vertically. The major benefit from this type of installation is that F is reduced to the stage where "Starvation" of the plume occurs and hence mixing promoted. If insufficient height is left for this to take place no increase in dilution over that from the plain jet results.

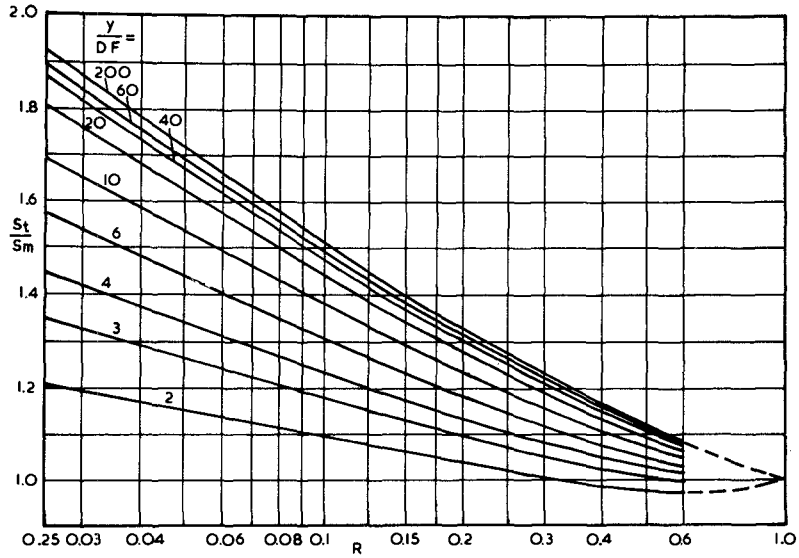

4. Design chart for selecting size of mixing tube for a horizontal jet.

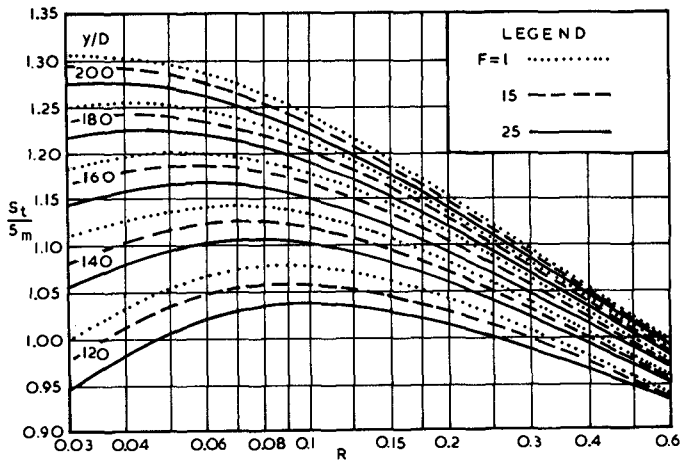

5. Design chart for selecting size of mixing tube for a vertical jet.

EXPERIMENTAL VERIFICATION

Tests on plain horizontal jets have been reported by Cederwall[11]. Using a semi-empirical relationship derived by Bousanquet et al[12], he has reported them as explicit analytical solutions

$$S_m = 0.54\ F(y/DF)^{7/16} \qquad \text{.....(9)}$$

for $y/D < 0.89F$, and

$$S_m = 0.54\ F(0.38\ y/DF + 0.68)^{5/3} \qquad \text{.....(10)}$$

for $y/D > 0.89F$

where $$S_m = C_o/C_m \qquad \text{.....(11)}$$

Equations (9) and (10) have been graphed in Figure 6A, together with a similar presentation of $y/D\ S_m$ verses y/DF for the solutions of Abraham[2] and Fan and Brooks[3]. The latter includes the dilution factor for flow establishment, which correction could be applied to the curves of Cederwall and Abraham, since their solutions apply to established flow only.

The parameters as outlined above are the best for comparing the experimental results from several workers[6][10][11][13][14]. This has been done in Figure 6B and indicates that better mixing is obtained even in the laboratory than that predicted by theory. In this respect the theoretical solution is conservative. With the aid of further macro-turbulence available in the prototype (through scale effects alone) it would be expected that greater dilution could ensue. Hansen and Schroeder[6] accepted the deviation from theory as a "factor of safety".

In respect to laboratory experiments it has been noted[10][13] that time is required in experiments for the dilutions to reach a steady state. For jets of $\frac{1}{8}$ to $\frac{1}{4}$ inch diameter about 10 to 20 minutes is required at $y/D \geq 50$. Closer to the outlet equilibrium is reached much sooner.

Laboratory tests for jets with mixing tubes[10] have shown that total dilution as indicated in Figures 4 and 5 is possible. In fact, dilution in excess of the theoretical prediction was obtained, as has been experienced with plain jets. It could be anticipated that this improvement, which probably emanates from the macro-turbulence not accounted for in the theory, might be greater due to the larger turbulons generated in the mixing tube. The tests referred to utilised nozzles of $\frac{1}{8}$ to $\frac{1}{5}$ inch diameter and mixing tubes of $\frac{1}{4}$ to $\frac{1}{2}$ inch diameter[10]. Further experiments are warranted, since economical improvements on existing outfalls may be possible, especially where discharge is from a plain end or a few large ports.

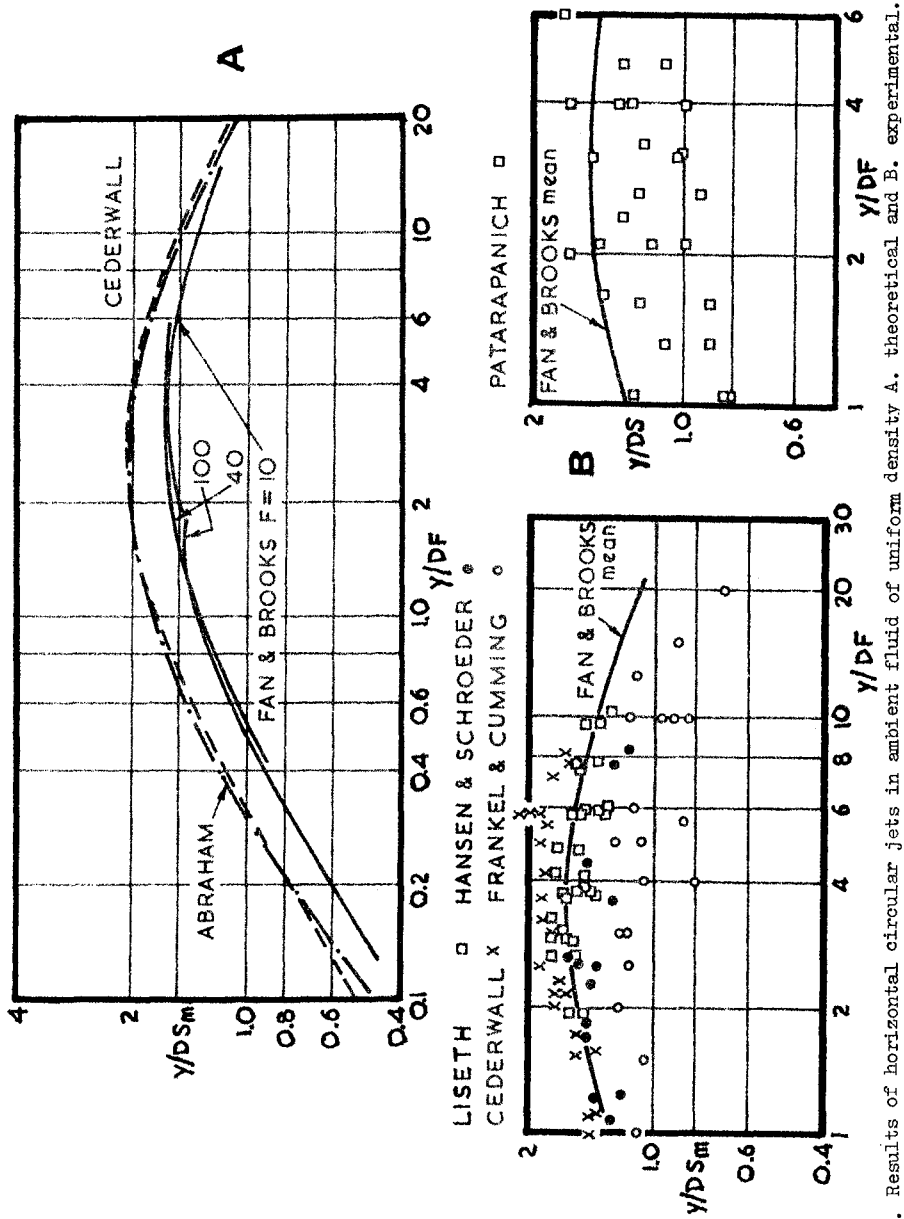

6. Results of horizontal circular jets in ambient fluid of uniform density A. theoretical and B. experimental.

APPLICATION OF MIXING TUBE CONCEPT

The addition of mixing tubes to the ports of an outfall does not impose any extra pressure head load on the system. The discharge from each outlet could, in fact, be increased due to the slight suction created at the entrance of the mixing tube.

One installation in a river has been reported[15], although the mixing tube in this case was not of correct proportions for optimum mixing[8]. The concept is particularly applicable when an effluent as supplied for discharge is very obnoxious to marine fauna and flora, making swift initial mixing desirable. It could also serve in density-stratified situations, to reduce the mixture density to a value where the effluent could be retained below the surface.

Pearson[16] made a comprehensive survey of sewage outfalls and provided details of 148 installations throughout the world. This report contains some 250 references on this topic. These outfalls were investigated by the authors to see what improvement in dilution could be effected by the addition of mixing tubes. Only 42 could be analysed due to lack of information or inappropriate nozzle shape (slots etc). Of these 26 could be so improved by percentages ranging from 25 to 245%. The largest percentage gains applied to discharges direct from the end of an outfall into shallow water, for which an R ratio of 0.1 was used, implying a mixing tube diameter of about three times the port outlet or a length of around 20 times this dimension. The addition of mixing tubes to a newly constructed outfall presents the same problem as modifying an outfall that has been in commission for some years. A little thought would soon devise a plastic or fibre glass appendage which could be readily clipped on to each port with the minimum of handling by divers. By such pre-mixing, existing outfalls could be made to carry larger loads, or new outfalls could be of shorter length.

CONCLUSIONS

1. Greater demands on coastal waters for recreation has raised their pollution standards and caused marine outfalls to be taken further seawards and multiple ports diffusers to be utilised.

2. A mixing tube with a flared entrance placed co-axially with a port or nozzle of an outfall will promote initial mixing and produce greater overall dilution in certain circumstances.

3. Graphs have been prepared which indicate the densimetric Froude numbers and depth ratios required for a mixing tube, of specific area ratio to the initial jet, to optimise dilution.

4. Experiments with small scale mixing tubes have shown that dilution is greater than that predicted by semi-empirical relationships, in a similar way to those for plain jets.

5. Larger scale tests may confirm the supposition that discharge from a mixing tube can produce better dispersion because of the larger

sized turbulons they could produce.

6. Pre-mixing might be useful for an obnoxious effluent, whether of chemical or temperature nature, so that its concentration is reduced sufficiently for it not to affect the marine biota.

7. Pre-mixing could produce sufficient immediate dilution to retain an effluent within the body of a fluid medium with a density gradient.

8. Application of mixing tubes to many existing outfalls could increase their capacity for diluting effluents, particularly in the case of single, or a few, large ports in shallow conditions.

REFERENCES

1. Rawn, A.M., F. Bowerman and N.H. Brooks "Diffusers for disposal of sewage in seawater" Proc.A.S.C.E. 86 (SA2), 1960, 65-106.

2. Abraham, G. "Jet diffusion in stagnant ambient fluid" Delft Hyd. Lab. Publ.No. 29, 1963.

3. Fan, L.N. and N.H. Brooks "Numerical solutions of turbulent buoyant jet problems" Cal.Inst.Tech.Rep. No. KH-R-18, 1969.

4. Rouse, H., C.S. Yih and H.W. Humphreys "Gravitational convection from a boundary source" Tellus 4, 1952, 201-210.

5. Sharp, J.J. "Physical interpretation of jet dilution parameters" Proc.A.S.C.E. 94 (SA1), 1968, 55-64.

6. Hansen, J. and H. Schroeder "Horizontal jet dilution studies by use of radioactive isotopes" Acta Polytechnica Scandinavica, Civil and Bldg.Const.Ser.No. 9, 1968.

7. Silvester, R. and N.H.G. Mueller "Design data for the liquid-liquid jet pump" J.Hyd.Res. 6, 1968, 129-162.

8. Silvester, R. "Jet mixers in sewage outfalls" J.Inst.Engrs. 39, 1967, 33-37, 95.

9. Mueller, N.H.G. "Water jet pump" Proc.A.S.C.E. 90 (HY3), 1964, 83-113.

10. Patarapanich, M. "Use of mixing tube in marine sewage disposal" Thesis presented to Asian Institute of Technology, Bangkok, in partial fulfilment of Master Eng. degree, 1971.

11. Cederwall, K. "Hydraulics of marine waste water disposal" Chalmers Inst. of Tech., Gotcborg. Rep.No. 42, Hyd.Div., 1968.

12. Bousanquet, C.H., G. Horn and N.W. Thring "The effect of density differences on the path of jets" Proc.Roy.Soc. A263, 1961, 340-352.

13. Liseth, P. "Mixing of merging buoyant jets from a manifold in stagnant receiving water of uniform density" Uni. of Cal., Rep.No. HEL 23-1, 1970.

14. Frankel, R.J. and J.D. Cumming "Turbulent mixing phenomena of ocean outfalls", Proc.A.S.C.E. 91 (SA2), 1965, 33-59.

15. Anon. "Jet mixer on effluent main for Surfers Paradise sewerage" J.Instn.Engrs.Aust. 38, 1966, 74-76.

16. Pearson, E.A. "Investigation of the efficacy of submarine outfall disposal of sewage and sludge" Californian Water Pollution Control Board, Publ.No. 14, 1956.

TABLE I

Coordinates of trajectory and jet width for circular jet in uniform density medium.

Values of 0.232x/D (upper) and b_m/b (lower)

θ_o	0.232 y/d	F = 1	2	4	8	16	32	64	128
0	5	0.5	1.5	2.5	4.5	7.5	12.5	20.5	33.5
		3.5	4.0	4.5	6.0	8.5	13.0	20.5	33.0
	10	0.7	1.6	3.0	5.5	9.7	16.2	26.5	42.0
		6.5	7.0	7.5	8.5	11.0	17.0	26.5	41.5
	20	1.0	2.0	3.5	6.5	11.9	20.0	33.5	53.7
		12.0	12.5	13.0	14.5	17.0	22.5	33.5	52.0
	30	1.0	2.0	3.5	7.5	13.0	22.5	37.6	61.2
		19.0	19.5	20.0	21.0	23.0	29.0	39.0	60.0
	40	1.0	2.0	3.5	7.6	14.0	24.5	41.0	67.0
		25.0	25.5	26.0	27.0	29.5	34.0	45.0	64.0
	50	1.0	2.0	3.5	7.9	14.5	26.4	44.0	72.0
		30.5	31.0	31.5	33.0	35.0	40.5	51.0	68.0
15	5	0.5	1.4	2.4	4.0	6.6	10.0	12.6	16.5
		3.5	4.0	4.5	5.5	8.0	11.0	14.0	18.0
	10	1.0	1.5	3.0	5.0	8.5	13.4	19.2	27.0
		6.5	7.0	7.5	8.5	11.0	15.0	20.0	29.0
	20	1.0	1.8	3.5	6.0	10.5	17.5	27.2	40.0
		12.0	13.0	13.5	14.5	17.0	21.0	29.5	41.5
	30	1.0	2.0	3.6	6.9	11.8	20.0	32.0	48.5
		18.0	18.5	19.0	20.5	22.0	27.0	36.0	50.0
	40	1.0	2.0	3.8	7.1	13.7	21.9	35.6	55.2
		25.0	25.5	26.0	27.0	29.0	33.0	41.5	58.0
	50	1.0	2.0	3.9	7.4	13.5	23.2	37.5	60.5
		30.5	31.0	31.5	33.0	34.0	38.0	46.0	63.0

(Continued)

TABLE I (continued)

ϕ_o	0.232 y/d	F = 1	2	4	8	16	32	64	128
30	5	0.5	1.0	1.9	3.1	4.5	6.2	7.5	8.5
		3.5	4.0	4.5	5.5	6.5	8.5	9.5	10.5
	10	0.6	1.1	2.3	4.1	6.6	10.0	13.4	16.0
		6.5	7.0	7.5	8.5	10.0	13.0	17.0	20.0
	20	0.6	1.2	2.7	5.3	8.9	14.0	20.8	27.2
		12.5	13.0	13.5	14.5	16.0	20.0	26.0	32.0
	30	0.7	1.3	3.0	5.7	10.1	16.5	25.5	35.7
		18.0	18.5	19.0	20.5	22.0	26.0	32.0	42.0
	40	0.8	1.4	3.1	6.0	11.0	18.4	29.0	42.2
		25.0	25.5	26.0	27.0	28.5	32.0	39.0	50.5
	50	0.9	1.5	3.2	6.4	11.5	19.5	31.5	47.0
		30.5	31.0	31.5	32.0	34.0	38.0	44.0	55.0
45	5	0.3	0.9	1.5	2.4	3.2	4.2	4.8	5.2
		3.5	4.0	4.5	5.0	6.0	7.0	8.0	8.5
	10	0.4	1.0	1.9	3.2	5.1	7.0	8.8	9.6
		6.5	7.0	7.5	8.0	9.5	12.0	14.0	15.0
	20	0.5	1.1	2.3	4.0	6.9	10.6	14.7	17.5
		12.5	13.0	13.5	14.0	15.5	18.0	22.0	26.0
	30	0.6	1.2	2.4	4.7	7.9	12.7	18.6	24.5
		18.0	18.5	19.0	20.0	21.5	25.0	30.0	35.0
	40	0.7	1.3	2.5	5.0	8.5	14.2	21.5	29.7
		25.0	25.5	26.0	26.5	27.5	30.5	36.0	43.0
	50	0.7	1.4	2.6	5.1	9.0	15.2	24.0	34.1
		30.5	31.0	31.5	32.0	33.0	36.0	42.0	51.0

CHAPTER 125

HYDRODYNAMIC ANALYSIS OF SLUDGE DUMPED IN COASTAL WATERS

Billy L. Edge, A.M. ASCE[1]

ABSTRACT

Due to increased environmental pressures, there is a rapidly growing tendency to shift from traditional land disposal of dredged material to offshore or ocean disposal. The quantities of such materials are quite large, resulting in a very serious disposal problem. For example, maintenance dredging alone produces approximately six million cubic yards of material annually in Charleston Harbor. Existing techniques are reasonably adequate to describe the transport and settling characteristics of coarse, sandy dredge materials discharged from barges or hopper dredges at sea. However, such approaches need to be modified to describe the transport of fine-grained clay and silt materials. This material constitutes a significant portion of the dredged material resulting from both new harbor and channel construction and maintenance dredging along the coast of the Carolinas and Georgia. These fine-grained materials are subject to many additional physical forces as well as chemical phenomena, e.g., flocculation, salinity and temperature variations, etc. A hydrodynamic model for fine-grained dredged material has been developed which considers many of these forces. It is also applicable for describing the transport mechanisms associated with barge disposal of wastewater sludges from municipal and industrial sources. The results of the model indicate what discharge strategies are necessary for placing the sludge at a desired location or depth with a predetermined concentration.

INTRODUCTION

Increased industrialization and urbanization has resulted in an increasing demand for siting activities in estuarine areas. As a result, there is little room left for creating fill areas on land or in the marshes to dispose of the great quantities of dredged material. In addition, many of the fill or disposal areas which have been used in the past are thought to be creating environmental problems and may never serve any beneficial purpose. Because of these ecological problems and as a consequence of demands for increased dredging depths, consideration is being given to disposing of most dredged materials in the future into the ocean environment. More than 112 sites are already being used for offshore disposal of waste and dredged material. A significant and growing portion of the public as well as some governmental agencies see this as a serious problem whereas other groups view this as the only economic solution for future dredging.

In the ocean environment, much of the dumped material is subject to complicated energy forces which vary from hour to hour. Wind forces appear to exert very strong influences in shallow waters; however, in deeper areas

[1]Associate Professor, Department of Civil Engineering, Clemson University, Clemson, South Carolina, 29631.

a different relationship exists among the governing forces. Because of this complex situation, much more information is needed on winds, tides, currents, and other hydrological phenomena before the fate of dumped materials can be predicted with any reasonable accuracy and an effective program of disposal wisely managed. Additional information would also provide a firmer basis for setting standards and providing guidelines for disposal.

One of the important quantifiable variables that affects the ultimate location of the dumped material is the disposal characteristics of the barge or dredge. The officer in charge may not be particularly concerned with dumping fine-grained sediment or "fluff" directly over the disposal areas since the material if dumped just outside of the dredging site or channel on the littoral downstream side may pass over the disposal area. Physically the material is then out of the channel, but the determination of its ultimate location for a true evaluation of the environmental impact will be impossible under these circumstances using currently-employed techniques.

A characteristic of a large percentage of the dredged material is that it is very fine-grained and therefore has a very low settling rate. An additional complicating factor in the disposal of fine-grained sediments is the effect of the thermocline on the settling and flocculation characteristics of the sediments. It has been shown that some of the fine-grained taconite tailings which are being dumped in Lake Superior are settling only to the thermocline (21). The tailings are then transported with the natural current along the surface of the thermocline as on a conveyor belt to some other location where they ultimately settle out of suspension. The same phenomena may very well be occurring with a significant proportion of the fine-grained material that is currently being dumped at sea as suggested by Amos et al. (2).

The disposal of dredged material quite often results in increased turbidities and changes the bottom configuration as well as alters the hydrodynamic characteristics of the local area. All of these factors can adversely or beneficially affect the aquatic environment. According to Horne, et al. (14), an accumulation of as little as 30 cm/yr may be great enough to exterminate certain benthic organisms. Conceivably, dredging may be offered as a tool for removing objectionable bottom deposits such as the sludge banks below municipal and industrial wastewater treatment plants in large coastal cities. The disposal of such material is of prime importance when it is recognized that the ultimate location will be yet another benthic community.

The Corps of Engineers has estimated that about 45 percent of the dredged material on the Atlantic Coast is polluted (8). The sources of this pollution are quite numerous and include industries, municipalities, and agriculture as well as natural benthic sources. Dredge spoils account for 80 percent, or 34 million tons annually, of all ocean dumping.

New and improved techniques for determining sedimentation rates have been recommended as a high-priority research area by a recent study (20). That study recommended "increased knowledge of the effects of offshore and nearshore dumping" and "increased knowledge of the sources and rates of sedimentation and the effects of sedimentation on the ecosystem."

The National Academy of Sciences and the National Academy of Engineering provided advice to the Federal government on management of waste in the coastal marine environment (18). An extensive study was carried out by a group of consultants to answer various questions concerning the effect of dumping waste in the ocean. Some of the conclusions of their study were:

1. For barge dumping of *sludges* in the ocean, research is needed on flows generated by suddenly released sinking sludge in a stratified environment.

2. There is need to develop *predictive models* for gross spreading of patches and plumes in the ocean from the combined effects of eddy diffusion (both horizontal and vertical) and shear in the mean velocity field.

3. A study should be made of the physical-chemical factors and the role of organisms in effecting the *flocculation rates* of sediments in estuaries and coastal waters. (Emphasis added.)

Pollution resulting from the dumping of waste material into the ocean is now recognized as a serious, complex, and rapidly-growing problem in the management and use of the Nation's ocean resources. The public has become very aware of the existing and potential adverse environmental effects from the discharge of waste material on the continental shelf. The lack of reliable means to determine the ultimate effects of the dumped materials has caused much concern and apprehension over the present, oftentimes seemingly arbitrary, approach to dumping at various sites throughout the Nation's coastal zone. The work outlined in this paper is aimed directly at this problem and should provide a useful tool for evaluating the ultimate location of waste material which is dumped on the continental shelf. The results of this study should be quite beneficial to those agencies responsible for establishing disposal criteria as well as for those who must prepare environmental impact statements for their dredging programs.

SIMULATION MODEL

Because of the many forces, both physical and chemical, which influence the dynamics of material which is dumped into the ocean, it is necessary to make several assumptions regarding the forces which have a significant influence in this problem. The developed simulation procedure, then, does not include all forces which enter into this problem. Instead a mathematical model has been built for those parameters and forces which are considered to be most significant. In this framework, the model can be used as a tool together with sound judgment to provide a description of the transport mechanisms which can be used in evaluating various dumping operations.

The mathematical model for simulating the disposal of wastes at sea is composed of a combination of jet theory and sedimentation theory. The model is essentially composed of two parts: first, a simulation of a negatively-buoyant jet discharged downward into a stratified environment; and, second,

sedimentation theory is used to provide a description of the transport of material from the end of the jet to the floor of the ocean. A similar approach is presented by Clark et al. (7) in which they present a technique for analyzing disposal from a hopper barge.

As shown in Figure 1, the transport of the discharged material to the bottom begins from an outlet which is located some distance below the water surface and through which is pumped the waste to be disposed. In the figure is shown the disposal system from a barge. The operating system considered here will be a barge which discharges through a set of large pipes. As the waste exits from the pipes, it follows a jet pattern and the waste will ultimately come to rest on the ocean floor since it is negatively buoyant. However, if the waste in the jet is sufficiently diluted with entrained fluid, then it may not necessarily reach the bottom before it becomes neutrally buoyant and stabilizes at some intermediate depth. As shown in the figure, when the jet reaches this equilibrium depth it still has a small amount of momentum and is carried somewhat below this depth but then rises up in the form of a buoyant plume. At this point, the inertia loses importance and the material is affected by local currents, flocculation, and gravitational attraction. The material then settles toward the bottom while being moved about by currents and turbulence. The ultimate location, spread, and density are the final results that must be obtained to completely and adequately describe the process of dumping wastes at sea.

There are several theories available for predicting the discharge of buoyant jets into still environments. All of these theories are based on the integral conservation equations. The general case of a buoyant jet inclined at an arbitrary angle has been studied by Fan and Brooks (10) for a linearly stratified, quiescent environment. Cederwall (6) has studied, experimentally, the flow of a buoyant slot jet into stagnant or flowing environments. Cederwall did not consider a stratified situation. A good summary of these studies is given by Baumgartner and Trent (4). The most general analytical treatments available are given by Ditmars (9) and Hirst (12). The formulation proposed by Hirst is for jets discharged to flowing, stratified environments. The development of the governing differential equations from their basic integral form can be found in Hirst (12).

Consider the pipe shown in Figure 2, from which is discharged a negatively buoyant jet. The assumptions made concerning the jet flow are:

1. steady flow
2. imcompressible flow
3. fully turbulent jet
4. similar, axisymmetric velocity profiles
5. hydrostatic pressure
6. small jet curvature
7. longitudinal turbulent transport is less than convective transport
8. constant fluid properties

The similarity profiles are Gaussian in form and are given as:

$$u^*(s,r) = \Delta u(s)e^{-r^2/b^2} + U\cos\theta \qquad (1)$$

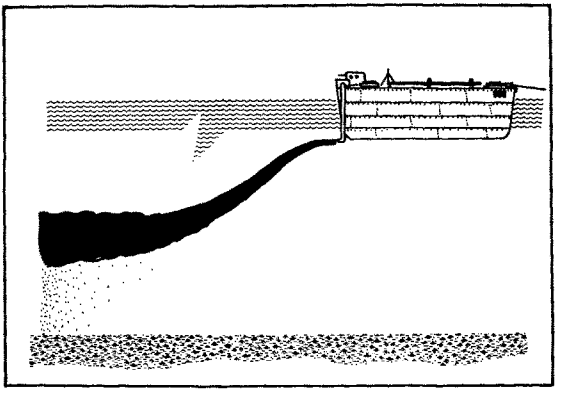

Figure 1. A towed barge discharging waste through a pumped system.

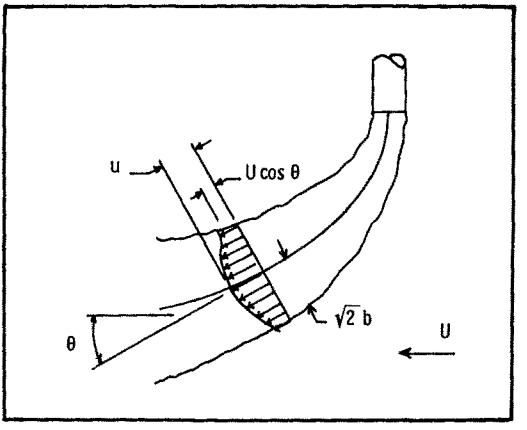

Figure 2. Geometry of a negatively-buoyant jet.

$$\rho^*(s,r) - \rho_\infty = \Delta\rho(s)e^{-r^2/(\lambda b)^2} \quad \ldots\ldots(2)$$

$$c^*(s,r) = c(s)e^{-r^2/(\lambda b)^2} \quad \ldots\ldots(3)$$

where

$$\Delta u = u - U\cos\theta$$

$$\Delta\rho = \rho - \rho_\infty$$

and where

$u(s)$ = centerline velocity
$\rho_\infty(s)$ = ambient density
$\rho(s)$ = centerline density
$c(s)$ = centerline tracer concentration
b = a measure of the jet radius
$1/\lambda^2$ = turbulent Schmidt number
$(\ )^*(s,r)$ = refers to parameters across the jet profile
U = speed of cross flow (speed of barge)

The parameter λ is considered the ratio between density and velocity profiles. The velocity $u(s)$ is an absolute velocity. To make the problem static, a uniform velocity has been added to the water column so that barge has zero velocity.

Use of the above assumptions and the similarity profiles with the integral equations yields the following differential equations:

$$\frac{d}{ds}\left[\frac{b^2}{2}\tilde{u}\right] = E \quad \ldots\ldots(4)$$

$$\frac{d}{ds}\left[\frac{b^2}{2}\left(\tilde{u} + (\lambda^2-1)U\cos\theta\right)\Delta\rho\right] = -\frac{1+\lambda^2}{\lambda^2}\frac{d\rho_\infty}{ds}\frac{b^2}{2}\tilde{u} \quad \ldots\ldots(5)$$

$$\frac{d}{ds}\left[\frac{b^2}{4}\tilde{u}^2\cos\theta\right] = EU + F_D\sin\theta \quad \ldots\ldots(6)$$

$$\frac{d}{ds}\left[\frac{b^2}{4}\tilde{u}^2\sin\theta\right] = -\frac{1}{2}g\lambda^2b^2\frac{\Delta\rho}{\rho_0} - F_D\cos\theta \quad \ldots\ldots(7)$$

where

$\tilde{u} = u + U\cos\theta$
$F_D = C_D\sqrt{2}bU^2\sin^2\theta$
C_D = coefficient of drag
ρ_0 = initial ambient density at outlet
E = entrainment function

These equations represent the conservation of mass, momentum in the x and y directions and the buoyancy, respectively.

The entrainment coefficient, or volume flux relationship, is derived in general terms by Hirst (13). However, a more convenient and proven form is given by Abraham (1).

$$E = b\left(\alpha_m(u - U\cos\theta) - \alpha_b U\sin\theta\cos\theta\right) \quad \ldots\ldots(8)$$

This equation is for a negatively-buoyant jet. The coefficient α_m is used to describe the entrainment due to the initial jet action and α_b is due to the negative buoyancy. Abraham gives a value of 0.5 for α_b.

Using Equation 8, Equations 4-7 can be rewritten, after some simplification, as:

$$\frac{d\bar{u}}{ds} = -\frac{4}{\bar{u}b^2}\left[\frac{1}{2}g\lambda^2 b^2\frac{\Delta\rho}{\rho_0}\sin\theta - E\left(U\cos\theta - \frac{\bar{u}}{2}\right)\right] \quad \ldots\ldots(9)$$

$$\frac{d\theta}{ds} = -\frac{4}{\bar{u}^2 b^2}\left[\frac{1}{2}g\lambda^2 b^2\frac{\Delta\rho}{\rho_0}\cos\theta + EU\sin\theta + F_D\right] \quad \ldots\ldots(10)$$

$$\frac{db}{ds} = -\frac{1}{\bar{u}b}\left[\frac{b^2}{2}\frac{d\bar{u}}{ds} - E\right] \quad \ldots\ldots(11)$$

$$\frac{d\Delta\rho}{ds} = -\frac{2}{b^2}\left(\bar{u} + (\lambda^2 - 1)U\cos\theta\right)^{-1}\left[\Delta\rho\left(E + (\lambda^2 - 1)bU\left(\cos\theta\frac{db}{ds} - \frac{b}{2}\sin\theta\frac{d\theta}{ds}\right)\right)\right.$$
$$\left. + \frac{1+\lambda^2}{\lambda^2}\sin\theta\frac{d\rho_\infty}{dy}\frac{b^2}{2}\bar{u}\right] \quad \ldots\ldots(12)$$

These equations are combined with:

$$\frac{dx}{ds} = \cos\theta \quad \ldots\ldots(13)$$

$$\frac{dy}{ds} = \sin\theta \quad \ldots\ldots(14)$$

and can be solved simultaneously. A digital computer solution has been used for this system employing a Runge-Kutta-Gill integration technique.

To solve the above equations, it is necessary to have appropriate values of α_m and λ in addition to the initial jet characteristics. Fan and Brooks (10) found $\alpha = 0.082$ and $\lambda = 1.16$ to be quite satisfactory for their work in linearly stratified environments for buoyant jets. There is not sufficient data yet available to validate these coefficients for negatively-buoyant jets, but these numbers will be used for illustrative purposes until better numbers are available.

Since the above solution is only valid for the zone of established flow, the initial values of the jet characteristics must be corrected for the changes which occur in the zone of flow establishment. This zone of flow establishment has been analytically studied by Hirst (7). A simple method for correcting the jet characteristics is to consider that: (1) the jet issues from the pipe and travels a straight-line distance of 6.2D, where D is the pipe diameter; (2) at the end of the zone of flow establishment, (6.2)D, the initial jet half-width $b = D/\sqrt{2}$; and (3) the initial value of $\Delta\rho$, $\rho - \rho_\infty$, is $(1+\lambda^2)/2\lambda^2$ times the difference at the source. At this point, the above equations can be solved with these initial conditions.

If a tracer is contained in the jet, and is not present in the ambient fluid, the following equation can be used to describe the dilution of the substance:

$$\frac{d}{ds}\, cb(u - U\cos\theta) = 0 \qquad (15)$$

or:

$$cb(u - U\cos\theta) = c_0 b_0 (u_0 - U_0 \cos\theta_0) \qquad (16)$$

in which c_0 is the initial concentration at the beginning of the zone of established flow or $(1+\lambda^2)/2\lambda^2$ times the effluent concentration.

The analysis which has been presented thus far is for describing the transport of the dumped material from the barge down to a level of neutral buoyancy. Since the jet overshoots this neutral level, it will rise up to this level of velocity reversal. This is illustrated in Figure 3 which is from the results of Ditmars (9). It has been implied that the ocean floor is sufficiently below the maximum descent to keep from invalidating the technique. From the level of neutral buoyancy, the entrained material in the remaining fluid from the jet will begin to settle to the bottom under gravitational influence. From this point onward, the influencing forces are much more complicated than have been considered thus far. The material is now influenced by even the smallest prevailing currents, including harmonic tidal currents and local turbulence, as well as the chemical factors. If colloidal material is in suspension, it will settle in the form of flocs much more rapidly than otherwise. This flocculation is rapidly advanced in the initial stages of the sedimentation process. Within the process of flocculation a large complex of problems is involved since the flocculation characteristics of various mineral components of clays are at present unknown under saline conditions.

The flocculation rate and magnitude depend upon the different types of clays which are present. The most common clay minerals are kaolinite, illite, and montmorillonite which are hydrous silicates of aluminum, iron, and magnesium. Chemical and particle-size properties combine to produce different flocculation rates for the same concentration of suspended sediment; and, of course, the rate is heavily dependent upon the concentration. Moreover, the amount of flocculation decreases exponentially with time.

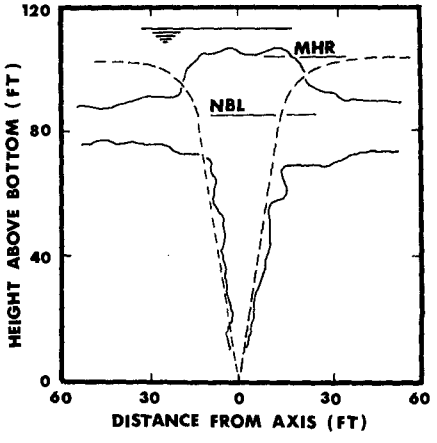

Figure 3. Comparison of a computed profile of a buoyant jet with an observed profile.

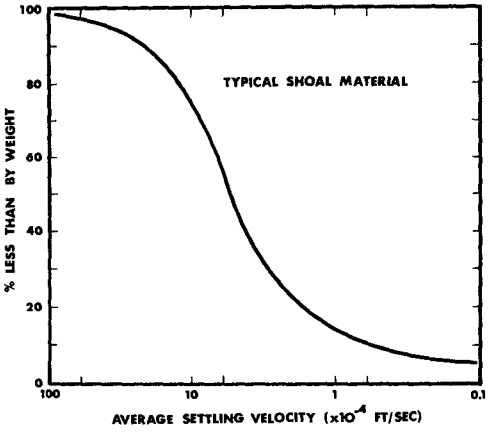

Figure 4. Distribution of settling velocity for shoal material in Charleston Harbor.

The flocs grow to a size and at a rate that is dependent upon the local turbulence. Brownian motion would be much too slow to provide the size flocs that actually exist. Rather, the presence of internal shear flows serve to bring particles into contact more rapidly than could Brownian motion alone. As the particles grow and begin to settle they make contact with other particles for additional growth. The local turbulence also acts to limit the maximum size of the flocs by breaking them apart if they grow too large.

To simplify this analysis, consider that a distribution of settling velocity is available for the material under consideration such as that shown in Figure 4. As the material settles from the cloud at the level of neutral buoyancy, it is affected by local turbulence and is dispersed in the horizontal direction. The scale of turbulent dispersion in the vertical direction is much smaller due to greater stability added by the stratification and will be neglected at this point. Consider also that there is a small cross-current, w, which is constant with depth. The 4/3 law of eddy dispersion:

$$D = CE_r^{1/3} L^{4/3} \quad \ldots\ldots\ldots\ldots\ldots\ldots\ldots\ldots\ldots\ldots\ldots\ldots\ldots\ldots\ldots\ldots\ldots\ldots\ldots\ldots\ldots\ldots (17)$$

where:

D = dispersion coefficient

C = coefficient

E_r = rate of energy dissipation per unit mass

L = Lagrangian eddy size

has been assumed applicable to ocean dispersion in many cases, and will be used in this analysis.

Orlob (9) obtained the relationship:

$$D = 0.00016L^{4/3} \left[ft^2/sec\right] \quad \ldots\ldots\ldots\ldots\ldots\ldots\ldots\ldots\ldots\ldots\ldots\ldots\ldots\ldots\ldots\ldots\ldots\ldots\ldots\ldots\ldots\ldots (18)$$

from field data taken by others. For a particular site, of course, a study should be undertaken to adequately evaluate the appropriate relationship. The eddy size is taken to be $L = 4\sigma$ where σ is the standard deviation of material in the moving, spreading patch. If the patch of material, with $\sigma = \sigma_b$, is at the level of neutral buoyancy, then Koh (17) has shown that the horizontal dispersion can be characterized by:

$$\sigma = \sigma_b \left(1 + 4^{2/3} \frac{2}{3} \frac{(0.00016)t}{\sigma^{2/3}}\right)^{2/3} \quad \ldots\ldots\ldots\ldots\ldots\ldots\ldots\ldots\ldots\ldots\ldots\ldots\ldots\ldots\ldots\ldots\ldots\ldots\ldots\ldots\ldots\ldots (19)$$

in which t is the time after the cloud has moved from the line of neutral buoyancy. Now, since the different size particles settle at different velocities, the cloud will not maintain its integrity. The above equation can be used however by applying it for each particle size. In other words, the cloud will be growing at all depths at the same rate.

From knowledge of the distribution of material with settling velocity, the total accumulation of material can be obtained by application of the above equation. A simple extension of this describes the distribution of the material that accumulates on the bottom in the presence of a small current. In fact, this is the result that will be of most benefit in the description of the ultimate fate of dredged materials which are dumped at sea. This result will tell which materials may not have settled in the dumping area as well as the rate of growth (height) of the bottom in the disposal area.

ILLUSTRATIVE EXAMPLE

To provide a meaningful example of the application of this technique, the spoil material is taken as that found in shoals in Charleston Harbor, South Carolina. The settling velocity distribution for this material is shown in Figure 4. The material is assumed to be transported to sea in a 3,000 ton barge. The barge is fitted with two discharge pipes which are both 0.707 feet in diameter. Since the pipes discharge adjacent to one another, they are considered as a single outflow with a diameter of 1.00 feet. The discharge outlet is 10 feet below the water surface. The barge carries a slurry which consists of 300 tons of fixed solids with a specific gravity of 2.5. Thus the total volume of solids discharged per load is 4,320 cu. ft. The barge discharges in water 200 feet deep.

Several situations are considered in this example. First the barge is assumed to be stationary and the jet velocity is varied from 5 fps to 10 fps. The density profile shown in Figure 5 indicates a high degree of stratification and is typical of summer conditions. Conversely, the winter situation shown in this figure was used to compare the effect of highly stratified and slightly stratified ocean environments on the characteristics of the jet model. The winter condition was run only for a velocity of 5.00 fps.

The results for a velocity of 5 fps and 1.00 ft. diameter are shown in Figure 6. It is emphasized that in the description of the plume width, Figure 6, the ultimate width at the neutral buoyancy line is given by the width at the maximum point of travel shown in the figure. The neutral buoyancy level is indicated on the figures by the line of squares. The maximum point of travel of the jet is the level indicated in this figure. The results for a velocity of 10 fps are given in Figure 7. It can be seen from these figures that, as the initial jet velocity increases, the time required for the material to settle to the continental shelf decreased markedly. In Figure 8, the centerline velocity distribution for an initial velocity of 10 fps is presented. The apparent discontinuities in the profile are a result of the sharp breaks in the given density profile. The case of an initial velocity of 12.5 fps was considered, but the jet reached the bottom before it stopped. The theory on which this analysis is based does not consider this effect therefore the results were discarded.

In Figure 9, the total depth of bottom sediment from the discharge of

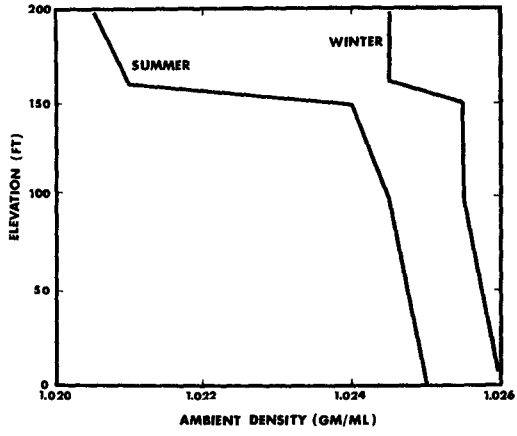

Figure 5. Density distribution during summer and winter conditions.

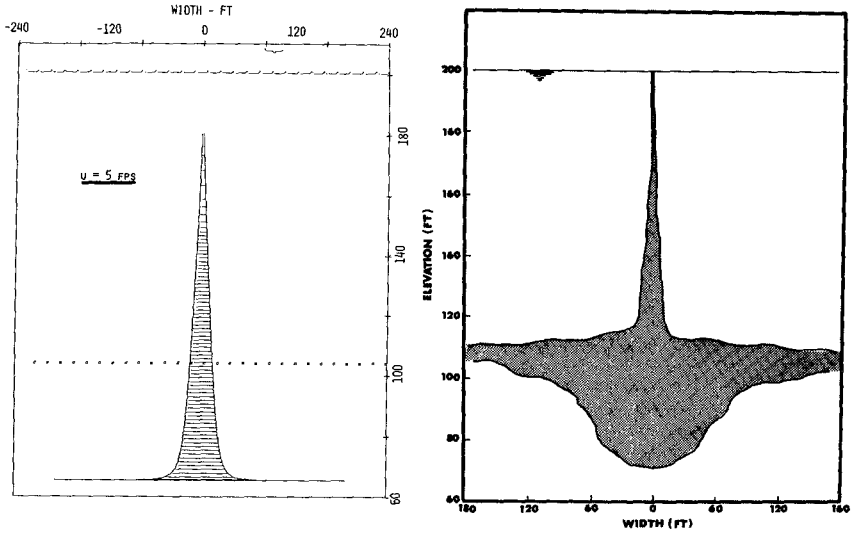

(a) Results of mathematical model (b) Physical interpretation of results

Figure 6. Variation of jet width with elevation (u_0 = 5 fps).

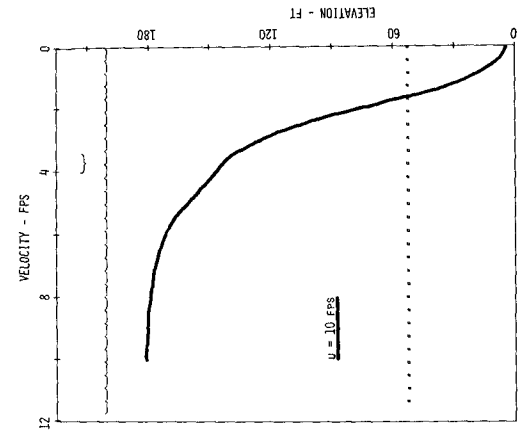

Figure 8. The centerline jet velocity variation with depth (u_0 = 10 fps).

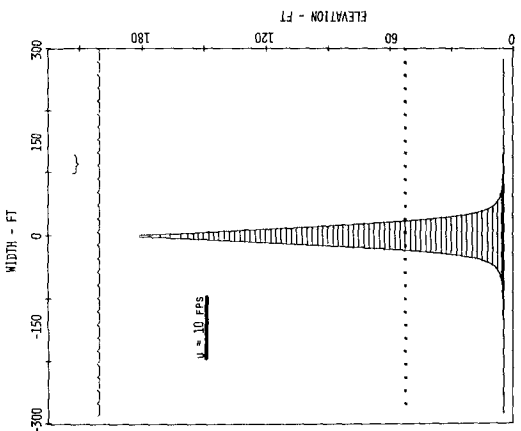

Figure 7. Variation of the jet width with elevation (u_0 = 10 fps).

one barge is given. This depth is across the center of the circular disposal pattern. It is emphasized that for this case there is no cross current. The top line gives the total depth while the bottom lines indicate the contribution from particles with different settling velocities. In Figure 10, the distribution of time for settlement is given for velocities of both 5 fps and 10 fps. It is obvious from the figure that very little material will settle out of the suspension within a day. If more than one load is dumped within a short interval of time, it is probable that the concentrations would increase to the extent that flocculation may occur and more rapid sedimentation could result. In this analysis it has been assumed that flocculation does not occur. This is a valid assumption since the volume percentage of sediment is less than 0.1% at the neutral buoyancy level.

The jet diameter was changed to 1.5 ft., and for an initial velocity of 5 fps the jet reached the bottom and established neutral buoyancy at an elevation of 40 ft. From this it would appear that the neutral buoyancy level and thus the ultimate sediment distribution on the bottom is more sensitive to changes in jet diameter than jet velocity. Also it may be desirable to keep the jet from reaching the bottom and resuspending the sediment there.

For the winter density profile, the jet plume reached the bottom while establishing neutral buoyancy at 30 ft. This case, with an initial velocity of 5 fps indicates a considerable difference in the ultimate location of the spoil material when compared with disposal under summer conditions. Although this result was anticipated, it nevertheless firmly establishes the large differences which can exist between the ultimate disposition of material dumped in the winter and the summer.

Lastly the settling material was exposed to an ambient current of 0.1 fps. This current was small enough to have no effect on the jet characteristics, yet it did have a significant effect on the material settling from the neutrally buoyant cloud. In Figure 11 is an illustration showing the ultimate location of the material. It is seen that much of the material has been carried a great distance from where it was originally dumped. The discontinuous nature of the results stems from the fact that the continuous settling distribution was divided into ten discrete segments. Thus it is very probable that if fine-grained material is dumped into an environment in which there is a small current the material could be carried a considerable distance before it settles. This partially explains the situation described by Baxter (3) in which he indicated that no traces of Philadelphia's digested sludge that was dumped into the Atlantic Ocean could be found. It is quite possible that the material was swept out of the 1-mile by 2-mile disposal area before it settled to the bottom.

Consider now the situation in which the barge is moving at a speed of 7 fps and discharging material at 10 fps. The movement of the material as shown in Figure 13 is from the barge with an initial angle of zero to the depth at which the jet stops. From this point the movement of the material is like a plume and not a jet. When the jet stops, however, the material contained in it is still heavier than the ambient water. Thus the material continues to travel downwards as a negatively-buoyant plume without momentum.

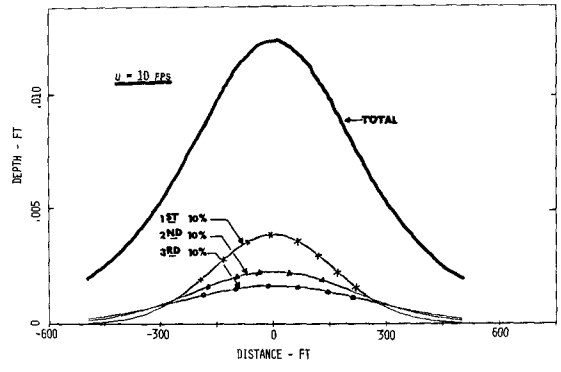

Figure 9. Total depth of bottom sediment discharged from one barge load and the contributions from each of the first three settling groups.

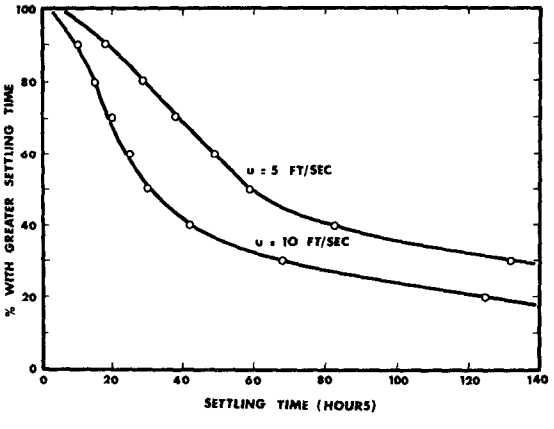

Figure 10. Distribution of time for settlement for initial jet velocities of 5 and 10 fps.

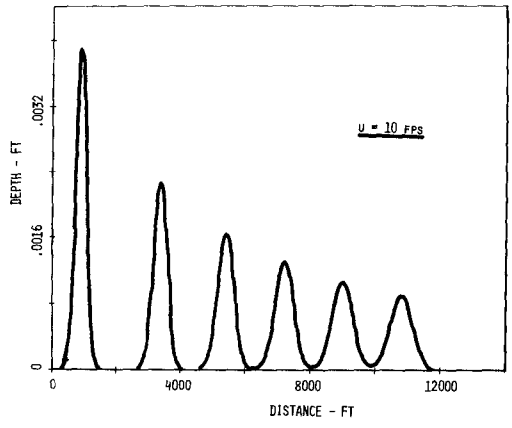

Figure 11. Total depth of bottom sediment discharged from one barge load in the presence of a current of 0.1 fps (u = 10 fps).

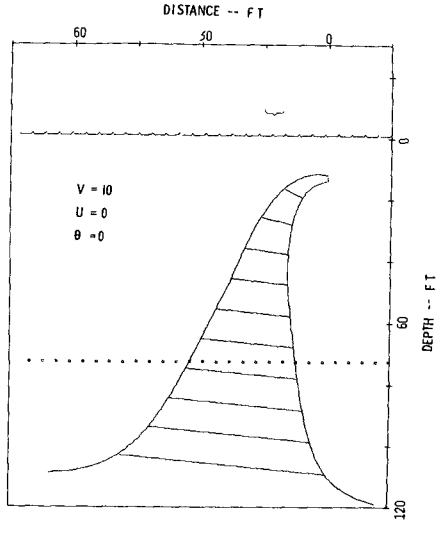

Figure 12. Trail of waste discharged from a stationary barge with an initial velocity of 10 fps and angle of zero. The width of the jet is at the same scale as the depth.

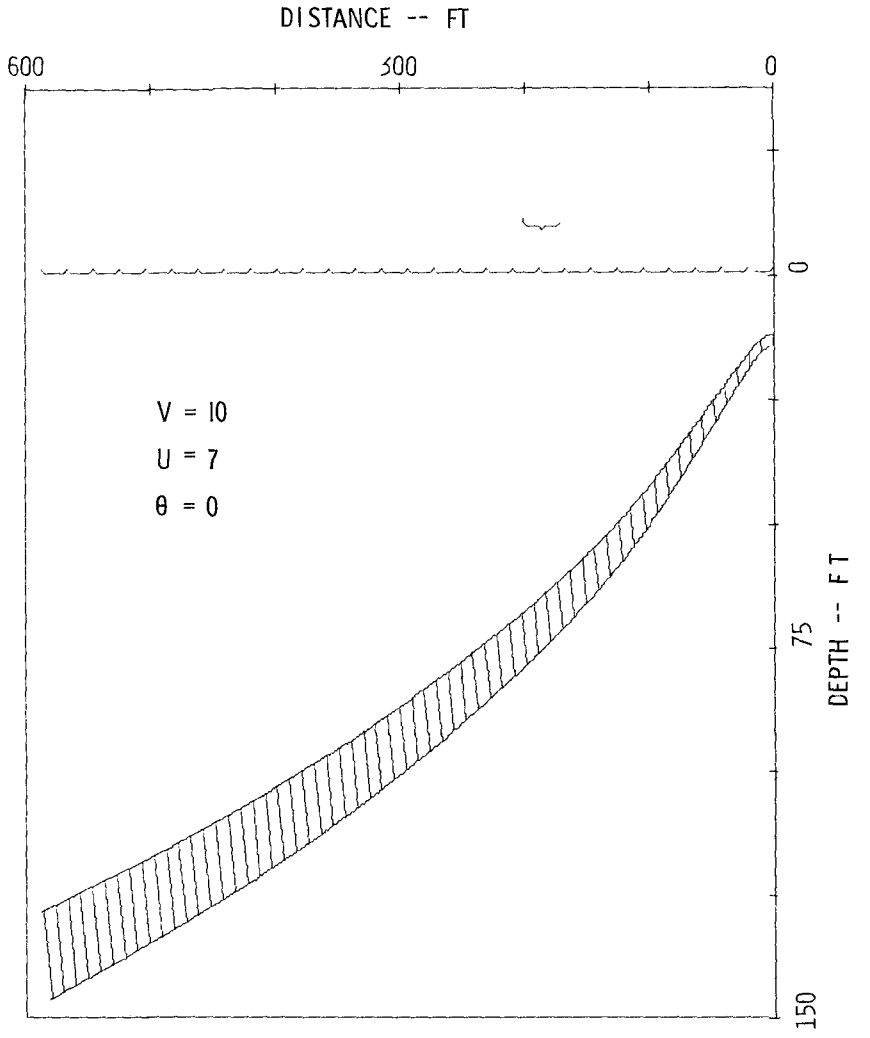

Figure 13. Trail of waste discharged from a barge moving at 7 fps, discharging at 10 fps, and at an initial angle of zero. The width of the jet is at the same scale as the depth.

On the other hand, if the barge is traveling slower, the material does reach a neutral-buoyancy level as shown in Figure 12 for the case of a stationary barge.

The effective dilution of the waste was not significantly different for the case of the barge moving, 76, than for the stationary case, 68. An interesting situation results for the discharge in the vertical direction; for no movement the dilution is 109, whereas for a barge velocity of 7 fps the dilution is only 33. The location where the jet breaks down into a plume or stops is significantly different for these situations.

It appears that through judicious discharge strategies the waste material can be placed at any desired depth at the necessary concentration according to the environmental conditions and requirements.

CONCLUSIONS

A mathematical model has been developed to simulate the transport of material that is discharged from a barge into the ocean. The objective of this simulation was to quantify the ultimate location of the material when it reaches the bottom. The first part of the mathematical model describes the action of the barge discharge as a negatively-buoyant jet which is moving into a stratified environment. This model describes the maximum depth of the jet travel and the level at which the fluid in the jet will come to rest and be neutrally buoyant. The second part of the model simulates the dispersion and transport characteristics of the sediment particles as they settle to the bottom.

The model was used to simulate the dumping of fine-grained sediment into a disposal area 200 ft. deep. In addition to showing the sensitivity of the model to the initial jet conditions, the model showed that the ultimate location of the material also depended largely on the initial jet characteristics. In the presence of a small cross-current much of the material was carried out of the designated disposal area before it could settle out of suspension. By varying the discharge conditions, however, the location of this material could be controlled to a greater extent. The disposal pattern is quite different for winter conditions than for the stratified, summer conditions. In the summer the material is much more likely to be carried out of the disposal area.

The model which was developed in this study has the capability to predict the ultimate location of waste that is discharged at sea. This capability is of course restricted by the assumptions made in the development of the model. The technique is restricted to a barge discharging to the open ocean through a pumping system while moving. With respect to these assumptions, this model offers much potential to assist in evaluating many ocean dumping operations.

From the results of this study, it appears quite obvious that discharge strategies can be developed that will allow the material to be placed on the ocean bottom with much more confidence than has been the case. In effect, the material can be discharged to any depth, at the end of the mixing region, with any desired concentration.

The discharge through a pumping system offers a clear advantage over disposal in the wake of the barge. Although the initial dilution may not be as great, the material is passed through the euphotic zone with the least possible damage. At the point where the material begins to spread and settle there may be considerably less marine life to be disturbed than on the ocean surface.

REFERENCES

1. Abraham, G., "The Flow of Round Buoyant Jets Issuing Vertically into Ambient Fluid Flowing in a Horizontal Direction," Preprint 111-15, Fifth International Conference on Water Pollution, San Francisco (1970).

2. Amos, A. F., C. Garside, K. C. Haines, and O. A. Roels, "Effects of Surface-Discharged Deep Sea Mining Effluent," Marine Technology Society Journal, Vol. 6, No. 4., pp. 40-46, July (1972).

3. Baxter, S. S., C. F. Guarino, R. A. Erb, and C. T. Davey, "Philadelphia's Ocean Sludge Disposal Experience and Studies," presented at 44th Annual Conference of the Water Pollution Control Federation, San Francisco, October (1971).

4. Baumgartner, D. J. and D. S. Trent, "Ocean Outfall Design. Part 1. Literature Review and Theoretical Development," Report from Pacific Northwest Water Laboratory, FWQA, 129 pp., April (1970).

5. Cable, Carl C., "Optimum Dredging and Disposal Practices in Estuaries," Journal of the Hydraulics Division, ASCE, Vol. 95, No. HY1, pp. 103-114, January (1969).

6. Cederwall, K., "Buoyant Slot Jets Into Stagnant or Flowing Environments," Report No. KH-R-25, W. M. Keck Laboratory of Hydraulics and Water Resources, California Institute of Technology, Pasadena, 86 pp., April (1971).

7. Clark, B. D., W. F. Rittall, D. J. Baumgartner, and K. V. Byram, "The Barged Ocean Disposal of Wastes: A Review of Current Practice and Methods of Evaluation," Report from Pacific Northwest Water Laboratory, EPA, 120 pp., July (1971).

8. Council on Environmental Quality, Ocean Dumping: A National Policy, 45 pp., October (1970).

9. Ditmars, J. D., "Mixing of Density-Stratified Impoundments with Buoyant Jets," Report No. KH-R-22, W. M. Keck Laboratory of Hydraulics and Water Resources, California Institute of Technology, Pasadena, 203 pp., September (1970).

10. Fan, L. N., and N. H. Brooks, "Numerical Solutions of Turbulent Buoyant Jet Problems," W. M. Keck Laboratory of Hydraulics and Water Resources, Report No. KH-R-18, California Institute of Technology, Pasadena, 94 pp., January (1969).

11. Hirst, E., "Analysis of Buoyant Jets Within the Zone of Flow Establishment,"ORNL-TM-3470, Oak Ridge National Laboratory, U. S. Atomic Energy Commission, Oak Ridge, Tennessee, 43 pp., August (1971).

12. Hirst, E., "Analysis of Round, Turbulent, Buoyant Jets Discharged to Flowing, Stratified Ambients," ORNL Rep. 4685, Oak Ridge National Laboratory, Oak Ridge, Tennessee, 37 pp. (1971).

13. Hirst, E., "Buoyant Jets Discharged to Quiescent Stratified Ambients," Journal of Geophysical Research, Vol. 76, No. 30, pp. 7375-7384, October (1971).

14. Horne, R. A., A. J. Mahler, and R. C. Rossello, "The Marine Disposal of Sewage Sludge and Dredge Spoil in the Waters of the New York Bight," Woods Hole Oceanographic Institution, Woods Hole, Massachusetts, January (1971).

15. Ippen, A. T., "Sedimentation in Estuaries," Chapter 15, Estuary and Coastline Hydrodynamics, edited by A. T. Ippen, McGraw-Hill, New York, 744 pp., (1966).

16. Ketchum, B. H., and W. L. Ford, "Rate of Dispersion in the Wake of a Barge at Sea," Transactions, American Geophysical Union, Vol. 33, No. 5, pp. 680-684, October (1952).

17. Koh, R. C. Y., "Ocean Sludge Disposal by Barges," Water Resources Research, Vol. 7, No. 6, pp. 1647-1651, December (1971).

18. National Academy of Science Committee on Oceanography and National Academy of Engineering Committee on Ocean Engineering, Wastes Management Concepts for the Coastal Zone: Requirements for Research and Investigation, 126 pp., (1970.

19. Orlob, G. T., "Eddy Diffusion in Homogeneous Turbulence," Transactions, ASCE, Vol. 126, Part 1, (1961).

20. U. S. Department of the Interior, The National Estuarine Pollution Study, Report of the Secretary of the Interior to the United States Congress, Senate Document No. 91-58, 633 pp., (1970).

21. Water Quality Laboratory, "Effects of Taconite on Lake Superior," Report of Environmental Protection Agency, Ouluth, Minnesota, (1970).

CHAPTER 126

REPRODUCTION OF PHYSICAL PROCESSES IN COASTAL AREAS

Hans-Gerhard Ramming x)

Summary

Physical processes in the ocean, adjacent and marginal seas are mainly of special interest for oceanography and related sciences, whilst the knowledge and the understanding of these processes in coastal areas, estuaries and tidal rivers is also of significant practical importance for coastal engineers. Just measurements and observations are not sufficient to obtain a comprehensive insight into these processes and to explain and to understand the spatial and temporal states and their variations. Hydrodynamical-numerical investigations are delivering a considerable assistance.

Within this paper my remarks will be restricted to some examples of the numerical reproduction of physical processes in shallow - water areas:

1) Dynamics depending on tides and wind;
2) Horizontal dispersion of suspended matter.

In concluding this paper I shall mention a special coastal model with a permanent refined grid-net, which is a part of the well - known North Sea model.

Using the vertically integrated hydrodynamic equations

$$u_t + \frac{ru\sqrt{u^2+v^2}}{h+\zeta} - fv + uu_x + vu_y + g\zeta_x = 0$$

$$v_t + \frac{rv\sqrt{u^2+v^2}}{h+\zeta} + fu + vv_y + uv_x + g\zeta_y = 0$$

$$\zeta_t + ((h+\zeta)u)_x + ((h+\zeta)v)_y = 0$$

x) Dr., Lecturer, Institut für Meereskunde, Universität Hamburg

where x,y space-coordinates
t time-coordinate
$h+\zeta$ actual waterdepth
f Coriolis parameter
g acceleration of gravity
r constant friction coeffdicient
u,v components of the mean velocity

transformed into difference equations, hydrodynamical models have been applied in previous years to describe physical processes in the ocean as well as in coastal regions. For the numerical treatment of hydrodynamical equations the natural conditions, such as depth distribution, boundary values and - as far as these are effective - meteorological data and density distribution have been considered. In many cases the quantitative reproduction of tides and storm-surges has been successful and good agreement between measured and computed values was obtained. Regarding the metbod I will not go into the details, see special publications by Hansen. The results of numerical investigations can suggest, in which areas or at whieh places measurements are necessary or of special interest. One must however verify the results of tbese numerical studies against observations, because there is no other possibility of testing them. Analytical solutions exist only in simple cases.

The motion in shallow areas, tidal estuaries and mud flats is very complicated. The tidal curves are particularly non-harmonic. The depth distribution and the nonlinear interaction at the bottom and at the surface are of great influence on motion processcs. Sands, flats and coastal areas fall dry for a limited time during a tidal period depending on its height.

When considering the actual water-depth in the equation of continuity and the quadratic friction term, which depends directly on the velocity and the water-depth, the differential equations become nonlinear. These nonlinear terms in the vertically integrated equation of continuity can be included in the numerical treatment. This seems to be very significant in order to reproduce motion processes in shallow-water areas, in which these terms are very essential, considering that tbe tidal range and the depth can be of the same order.

These nonlinearities are responsible for the non-harmonic behaviour of the tidal curves. A particular advantage of the numerieal approach is that a reasonable simulation of the bottom topography and coastal boundaries may be included in the model. It is only a question of grid-distance and expense of time on computers, if the bottom topography and the coast shall be approximated with high accuracy.

In order to prove the application of hydrodynamical-numerical models on extreme shallow-water areas, we have the problem that motion processes including the overflow of flats and drying banks should be reproduced. It is necessary to distinguish all possible cases. From time to time it may occur that there will be no water at some grid-points. One has to check the neighbourhood of each grid-point from time-step to time-step with regard to the actual water-depth, the depth-distribution and the physical possibility of transports and directions of transports. These and the former mentioned distinctions of several cases are formulated as a system of numerous questions for the computer. It is now necessary to prove the accuracy. Therefore, this numerical method was applied to some models, which permitted a comparison between analytical and numerical results. If the agreement of both of these results in the stationary state is sufficient, it may be assumed that the numerical treatment of the differential equations from the beginning of the computations until the stationary state approximates also the unknown nonstationary results.

A closed rectangular basin with a dimension of 36 km x 48 km was covered with a net-work of equal distances. In several models with constant depth of 0.5 m, 0.4 m and so on until 0.1 m a homogeneous constant wind-velocity of 5 m/sec, 10 m/sec and 20 m/sec in x-direction was applied. In the stationary state the transport disappears, and it follows that the vertically integrated velocities become zero.

Fig. 1 shows the slope of the sea-surface under the action of a homogeneous constant wind and a comparison between the analytical solution and the hydrodynamical-numerical treatment. The straight line L_o is the distance without water along the bottom. The agreement in this point of the comparison is remarkable and important for further investigations.

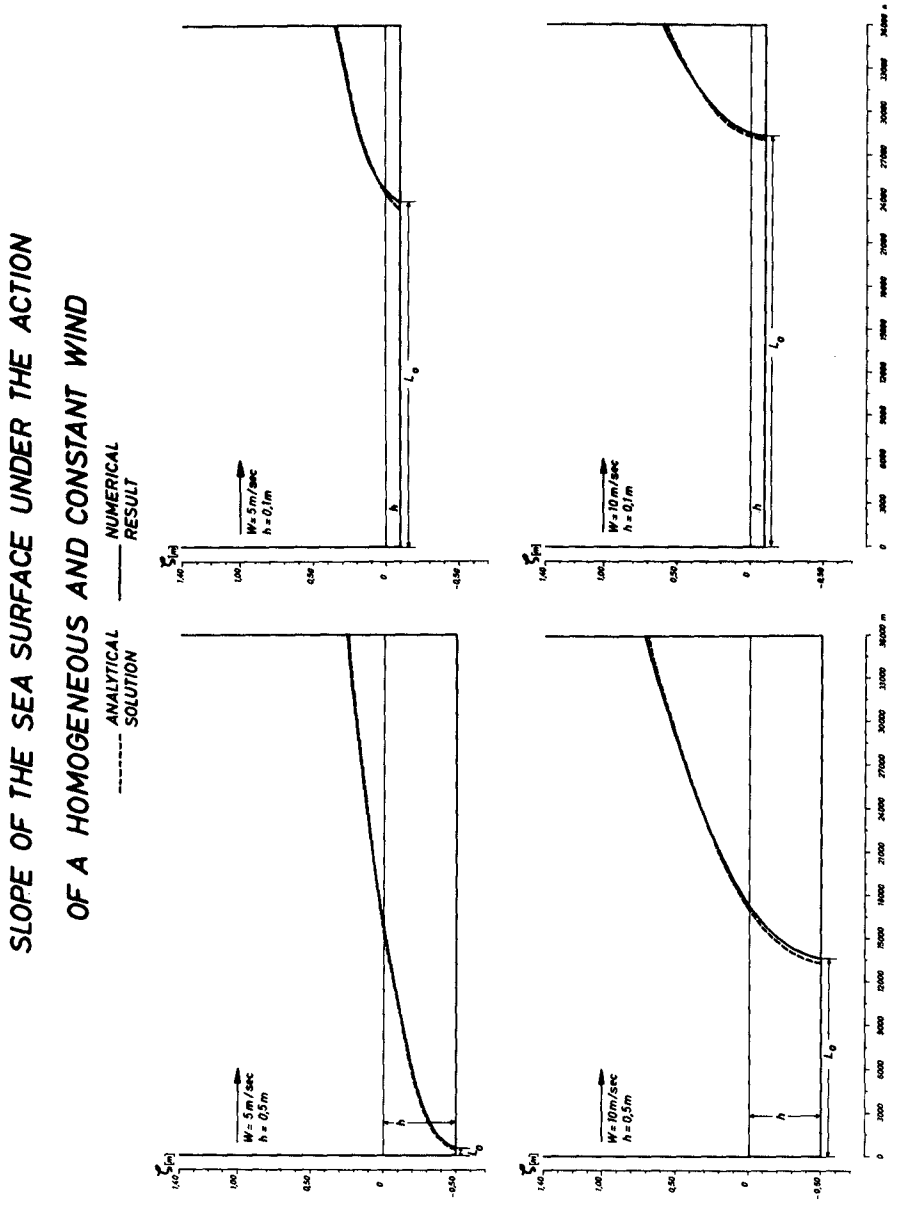
SLOPE OF THE SEA SURFACE UNDER THE ACTION
OF A HOMOGENEOUS AND CONSTANT WIND
NUMERICAL RESULT
ANALYTICAL SOLUTION
W = 5 m/sec
h = 0,1 m
W = 10 m/sec
h = 0,1 m
W = 5 m/sec
h = 0,5 m
W = 10 m/sec
h = 0,5 m
h
L_0

Fig. 1

After this theoretical example we can go to the next step and prove this method in a complicated natural model.

Fig. 2 shows a plan view of the outer Elbe with bottom topography and computational grid. A part of the "Neuwerker Watt" including the Isle of Scharhörn near the estuary of the Elbe River was covered with a rectangular net-work with a mesh-distance of 670 m. The water-levels determined by seven gauges around this area for the tidal periods from the 29th September until the 3rd October in 1967 were used as boundary condition. The figure also shows the water-level gauges and the boundary points. The depth-distribution of this region is very complicated and varies from NN - 16 m near the boundary to NN + 3.5 m in the inner part of this area. The observed water-level in the interior points A, B and C is known but not given in the computation.

In fig. 3 a comparison between computed and observed time variation of water-level in these three interior points is represented. The differences are less than $\pm$ 8 cm. The agreement during the period of extreme shallow-water is a remarkable result of this computation.

With respect to river tides hydraulic engineers applied the continuity equation to compute average velocities in cross-sections of the river from gauge records and measurements of fresh-water inflow from the upper river. The geometry of the river must be known. This method of cubature was applied to the Elbe River by Klein and others. This method represents the only possibility for the verification of numerically determined mean velocities. One example of the comparison for the interior points A, B, C and D is shown in fig. 4. The agreement seems to be sufficient, if you consider the rather complicated horizontal and vertical distribution of velocities.

It is necessary for further investigations to consider even this vertical distribution in connection with the problem of reproducing horizontal and vertical dispersion of suspended matter. In this connection I should like to mention a special publication by Sündermann (1971).

The reproduction of the water-levels and the vertically integrated velocities and the proof of the model's similitude with nature is an important supposition for hydrodynamical-numerical investigations

PLAN VIEW OF THE OUTER ELBE, SHOWING BOTTOM TOPOGRAPHY AND COMPUTATIONAL GRID.

COMPUTED AND OBSERVED TIME VARIATION OF WATER LEVEL AT THE THREE INTERIOR POINTS A, B AND C.

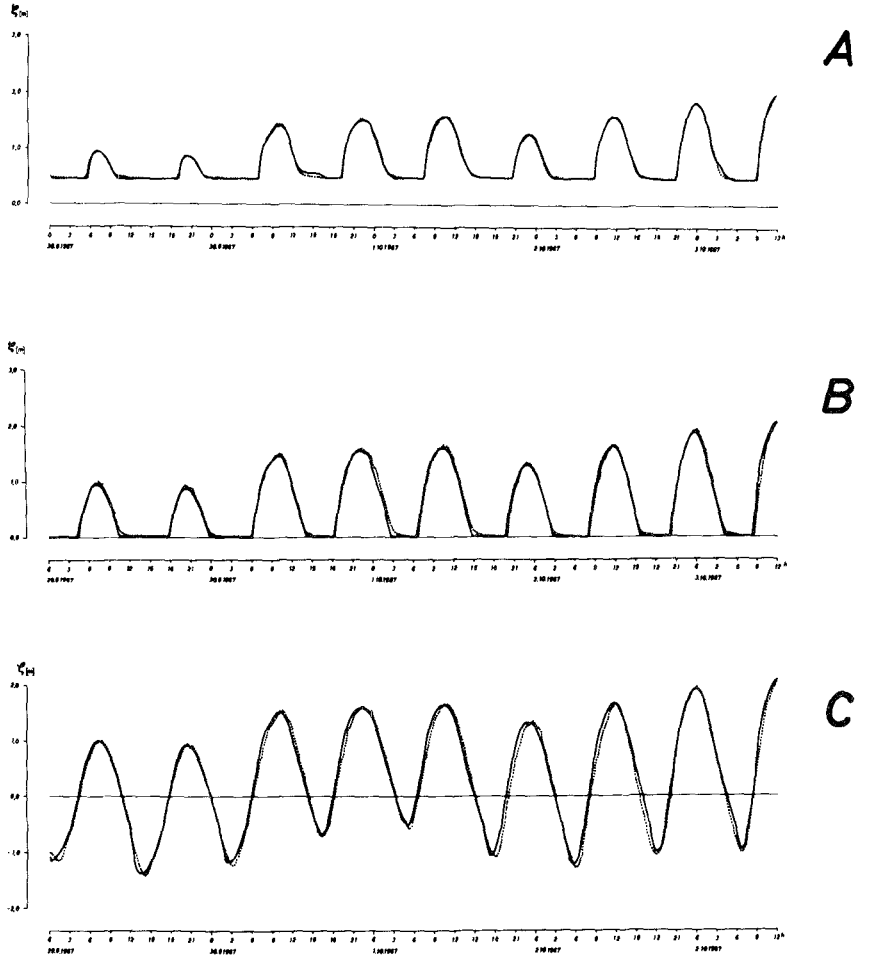

Fig. 3

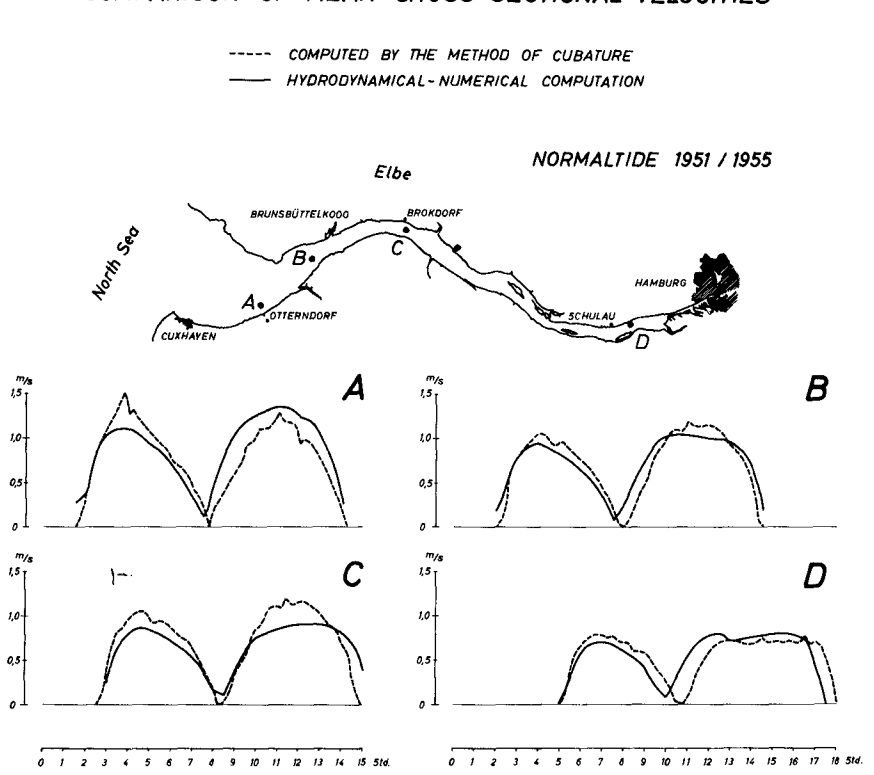
COMPARISON OF MEAN CROSS SECTIONAL VELOCITIES
----- COMPUTED BY THE METHOD OF CUBATURE
—— HYDRODYNAMICAL-NUMERICAL COMPUTATION
NORMALTIDE 1951 / 1955
Elbe
North Sea
BRUNSBÜTTELKOOG
BROKDORF
HAMBURG
SCHULAU
OTTERNDORF
CUXHAVEN
A
B
C
D
m/s
1,5
1,0
0,5
0
0 1 2 3 4 5 6 7 8 9 10 11 12 13 14 15 Std.
0 1 2 3 4 5 6 7 8 9 10 11 12 13 14 15 16 17 18 Std.

Fig. 4

of horizontal dispersion of suspended material. If this supposition is fulfilled, one can try to include the equation of mass-transport for example in the form

$$S + uS_x + vS_y = AS_{xx} + BS_{yy}$$

where S is the quantity of suspended material as a product of volume and concentration

A is the coefficient of horizontal eddy diffusivity in x-direction and

B the same in y-direction.

The physical process of horizontal dispersion is a turbulent process of transport depending on bottom topography and the motion of water in the vertical and horizontal direction. In the case of diffusing momentum the horizontal coefficient of diffusivity can be understood as an interior horizontal friction. If the density is equal to one, the dimension of these coefficients A and B is m^2/sec. Investigations by Elder and Bowden have shown that the following formula is applicable:

$$A = 5.9 \; r \; (h+\zeta) \; u$$
$$B = 5.9 \; r \; (h+\zeta) \; v$$

r is a non-dimensional constant friction parameter, equal to $3.0 \cdot 10^{-3}$ and $h+\zeta$ the actual waterdepth.

Before the equation of transport is applied to a hydrodynamical-numerical model, it is necessary to mention the substantial assumption used in the numerical treatment, in order to correctly interpret the results obtained. The material - in this connection marked - bas uniform quality and is an admixture of water in such a concentration as not to essentially change the density. The material remains in suspension during the dynamical process. Erosion and sedimentation have not been considered. It is assumed that the material is dispersed equally from the bottom to the surface. The investigated concentrations reproduce a mean distribution of the material at the grid - points, which are representative for a fixed area in tbe grid-net. A twodimensional model corresponding to tbe Elbe River in its given morphological structurs was used. In addition to the condition at the open boundary near Cuxhaven, observed waterlevel and - as a

function of time - the time-dependent concentration of suspended material is given according to measurements of Nöthlich. He specifies the average ouantity of seston during these measurements

with 28.6 mg/l dry weight at high-water-time

and 56.4 mg/l dry weight at low-water-time

at one point within the Elhe Estuary. It was assumed that this distrihution is valid for the whole cross-section at the mouth of the river.

The computation hegan at low-water-time, and the tide, averaged over the years 1951/55, was used. Because simultaneous measurements are unavailahle, it was only possible to compare the numerical results with measurements from tbe year 1967. It is well-known that the dispersion of suspended matter in a tidal river varies with the season and depends on meteorological circumstances and the salinity stratification of the estuary. As a first approximation it has been assumed that the main components of the transport of suspended matter during tbe time of measurements are the samc as over the averaged tidal cvcle. Tbe essential numerical results are presented in fig. 5. It shows the distrihution of seston conditioned by the dynamical processes in the Elbe River between Otterndorf and Stadersand. In the upper part the distrihution during the time of maximum, and in the lower part the distribution during the time of minimum, of seston concentration in Cuxhaven is shown. At high-water as well as at low-water-time in Cuxhaven a zone of higb seston concentration about 200 mg/l exists near Brunshüttel. During high-water-time this zone is broader than at low-water-time, whilst there is no difference in the length of the zone. This turbidity zone is a typical phenomenon in the Elbe River and is a result of an interaction between several components. Based on the qualitative reproduction of this turbidity zone hy means of hydrodynamical-numerical methods it can he concluded that the main reason for the situation of this zone is determined hy the hydrodynamics of the river. In this section the residual currents are very small.

A comparison between computed and measured mean concentration of seston in five sections of the Elbe River is shown in fig. 6. It must be noted that measurements were made at several places and at different tidal phases. The maximum and the minimum of seston at the

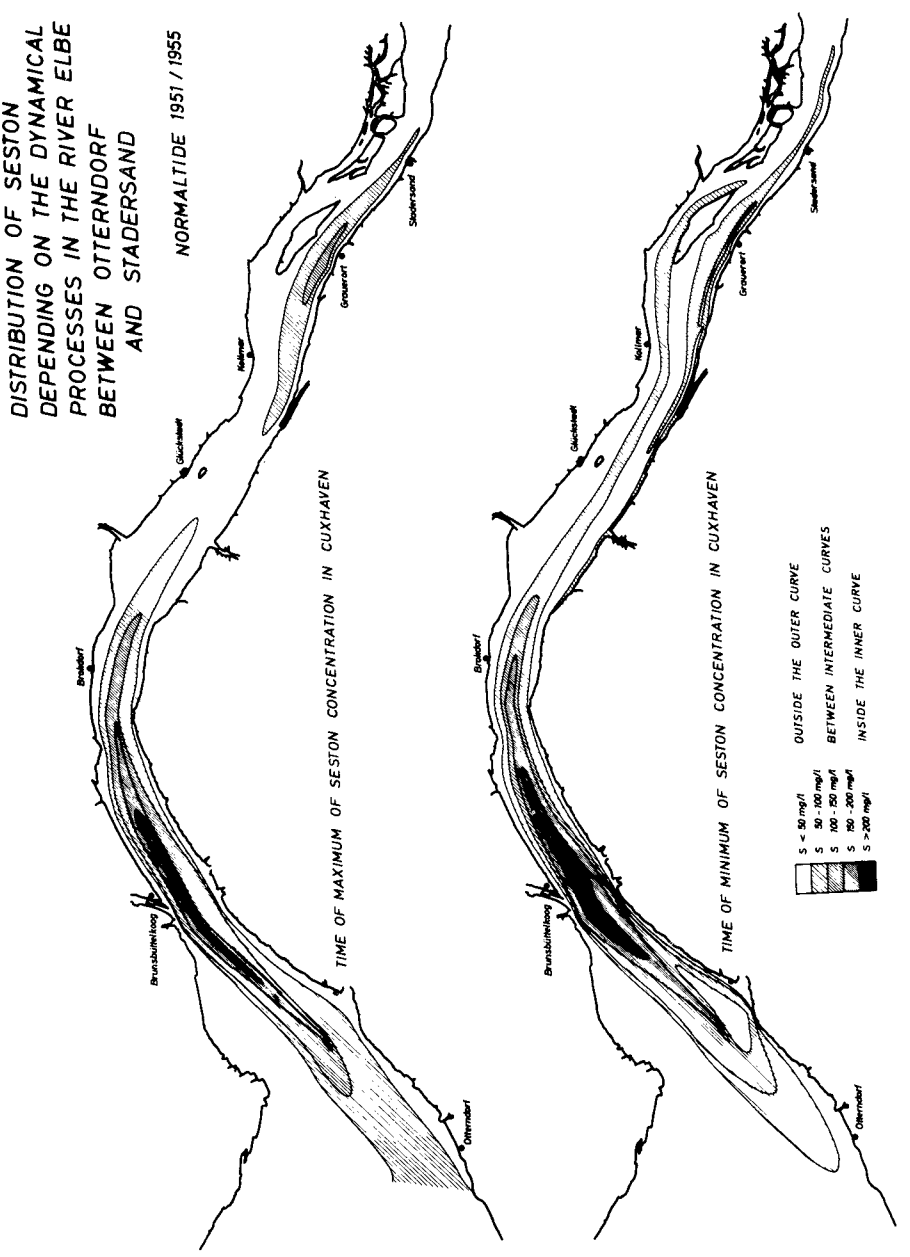
DISTRIBUTION OF SESTON
DEPENDING ON THE DYNAMICAL
PROCESSES IN THE RIVER ELBE
BETWEEN OTTERNDORF
AND STADERSAND
NORMALTIDE 1951 / 1955
TIME OF MAXIMUM OF SESTON CONCENTRATION IN CUXHAVEN
TIME OF MINIMUM OF SESTON CONCENTRATION IN CUXHAVEN
Brunsbüttelkoog
Brokdorf
Glückstadt
Kollmar
Grauerort
Stadersand
Otterndorf
S < 50 mg/l
S 50 - 100 mg/l
S 100 - 150 mg/l
S 150 - 200 mg/l
S > 200 mg/l
OUTSIDE THE OUTER CURVE
BETWEEN INTERMEDIATE CURVES
INSIDE THE INNER CURVE

Fig. 5

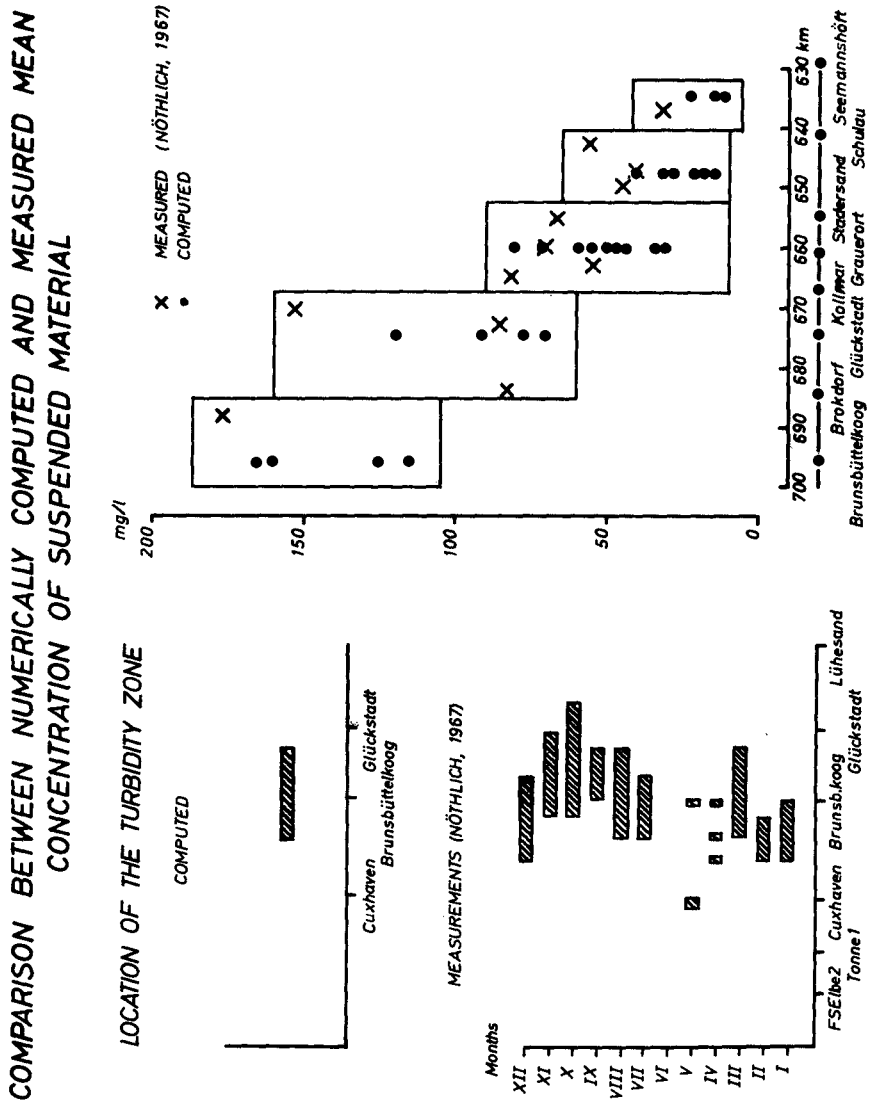
COMPARISON BETWEEN NUMERICALLY COMPUTED AND MEASURED MEAN CONCENTRATION OF SUSPENDED MATERIAL
LOCATION OF THE TURBIDITY ZONE
COMPUTED
Cuxhaven
Brunsbüttelkoog
Glückstadt
MEASUREMENTS (NÖTHLICH, 1967)
Months
XII
XI
X
IX
VIII
VII
VI
V
IV
III
II
I
FSElbe2
Tonne1
Cuxhaven
Brunsb.koog
Glückstadt
Lühesand
mg/l
200
150
100
50
0
MEASURED (NÖTHLICH, 1967)
COMPUTED
700
690
680
670
660
650
640
630 km
Brokdorf
Kollmar
Stadersand
Seemannshöft
Brunsbüttelkoog
Glückstadt
Grauerort
Schulau

Fig. 6

grid-points, which are situated near the points of observations, could be specified.

Taking into consideration the above-mentioned restrictions, one can see a general agreement between measured and computed values. On the left hand side of this figure the agreement between computed and measured location of the turbidity zone is shown.

These results suggest various possibilities of anplication with regard to the numerical methods, and they constribute to the development of a model, which is suitable for inclusion of other, for example hydrobiological, components. On the other hand it is possible to use models of this kind for prohlems of pollution. As a first approximation the location of the turbidity zone in the Elbe River can be explained as a consequence of the very small residual currents, which one can define as a mean velocity over one tidal period. It also means a very long hindrance of waste-water transport in this area. If the question arises of how to change this condition, then one has to consider many interacting components. It is thus important in certain coastal engineering projects not only to change the velocities and their directions, but also include into the consideration a variation of the residual currents.

The next figure 7 shows the distribution of residual currents during one M_2 tide in the North Sea. It may be mentioned that the M_2 tide introduced at the Dover Straits and on the northern entrance of the North Sea as a pure harmonic function of time, produced residual currents in the interior of the North Sea and accordingly, a circulation with an unperiodical watertransport. The largest transports in the eastern and the northern direction occur in the southern and eastern parts of the North Sea. This numerical result corresponds to observations. For the inner and deeper parts the above statement is sufficient. For coastal regions more information is required, hence, this figure should serve as an example only. In coastal areas one needs more detailed information about water-level and velocities, and other physical processes. The model shown before in figure 7 is thus not sufficient for considering the special physical processes, which occur in coastal regions and shallow water.

DISTRIBUTION OF RESIDUAL CURRENTS DURING ONE M_2 - TIDE IN THE NORTH SEA

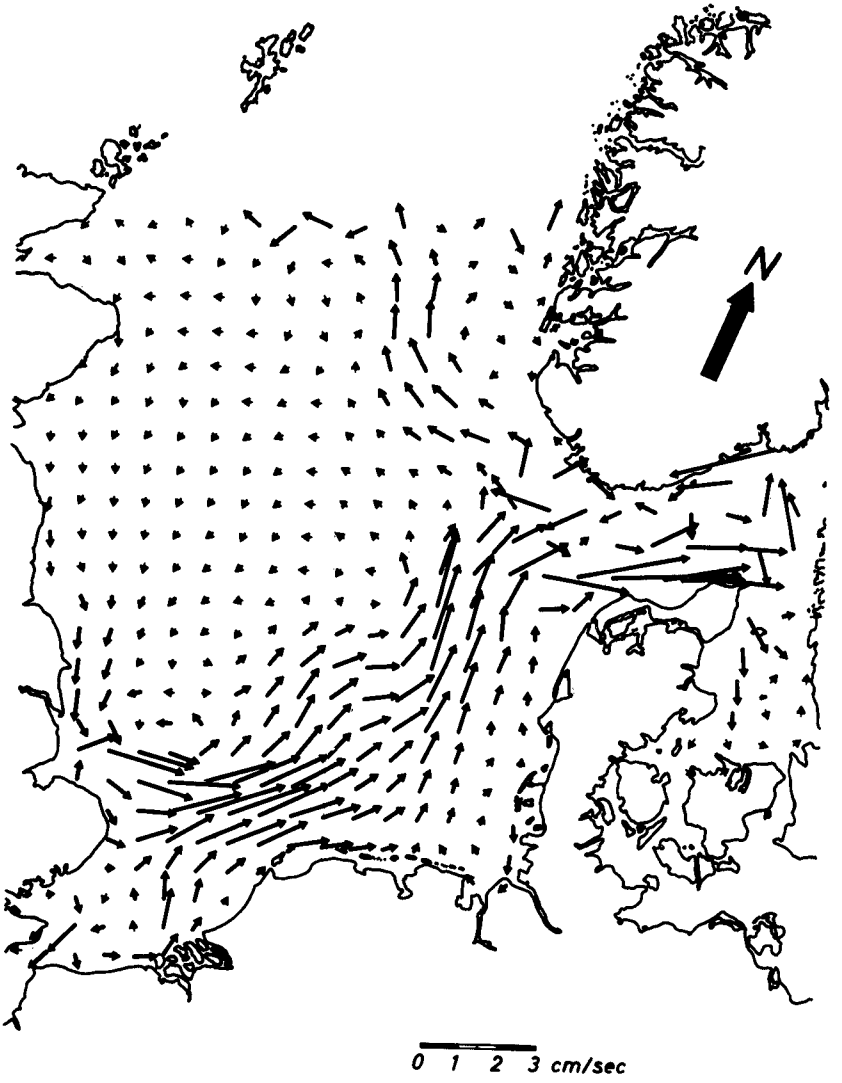

Fig. 7

In these areas it is necessary to refine the gridnet which is normally used in the open sea. A closer meshed network is advantageous for a good approximation of the bottom topography and coastal configuration. The numerical treatment is limited by the capacity of computers which are available, and the condition of numerical stability must he taken into account.

Figure 8 shows a model with a permanent refined network. A special technique makes it possible to refine the net in any choosen area. This figure gives an example of a section of a refined gridnet in the Elbe Estuary. This one third (1/3) refinement can be continued until the desired distance of the mesh-size is reached and the approximation of islands, sands, depth distribution and coastal configuration has the necessary accuracy. As a first result of these investigations figure 9 shows a refined representation of the distribution of residual currents over one tidal period in the Elbe Estuary.

This coastal area model of the German Bight and the Elbe Estuary shall be an example and a suggestion for coastal engineers. By using such models it is possible to study the influences of coastal buildings upon the variations of waterlevels, mean velocities and residual currents.

GRIDNET OF THE NORTH SEA AND REFINED GRIDNET IN THE GERMAN BIGHT

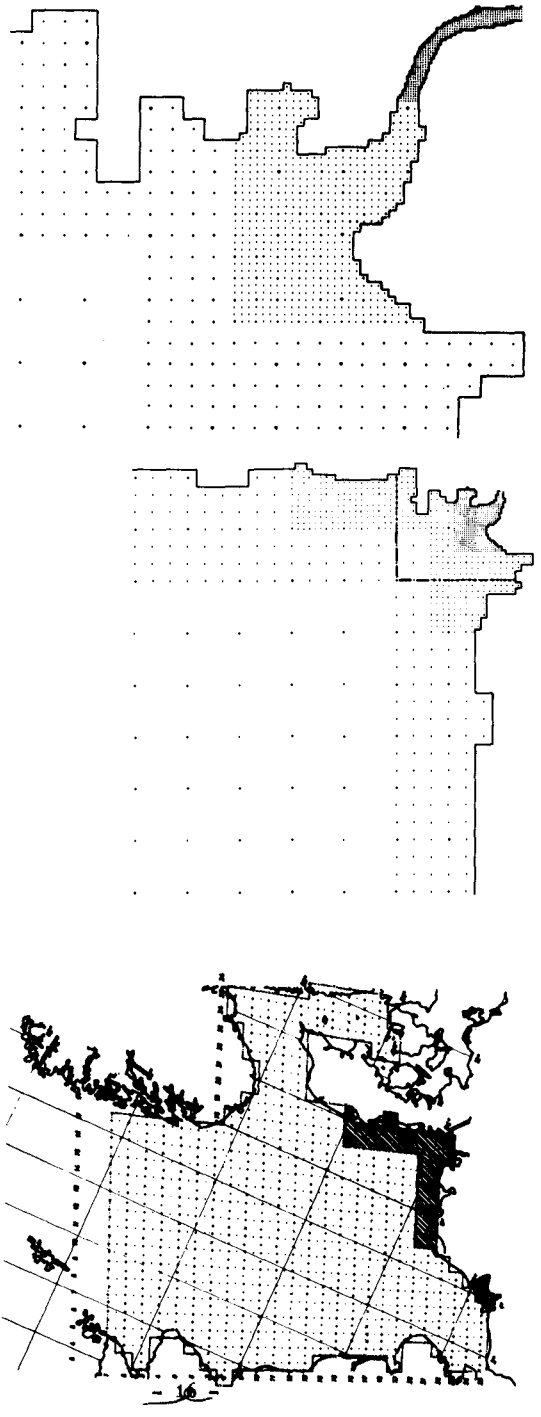

Fig. 8

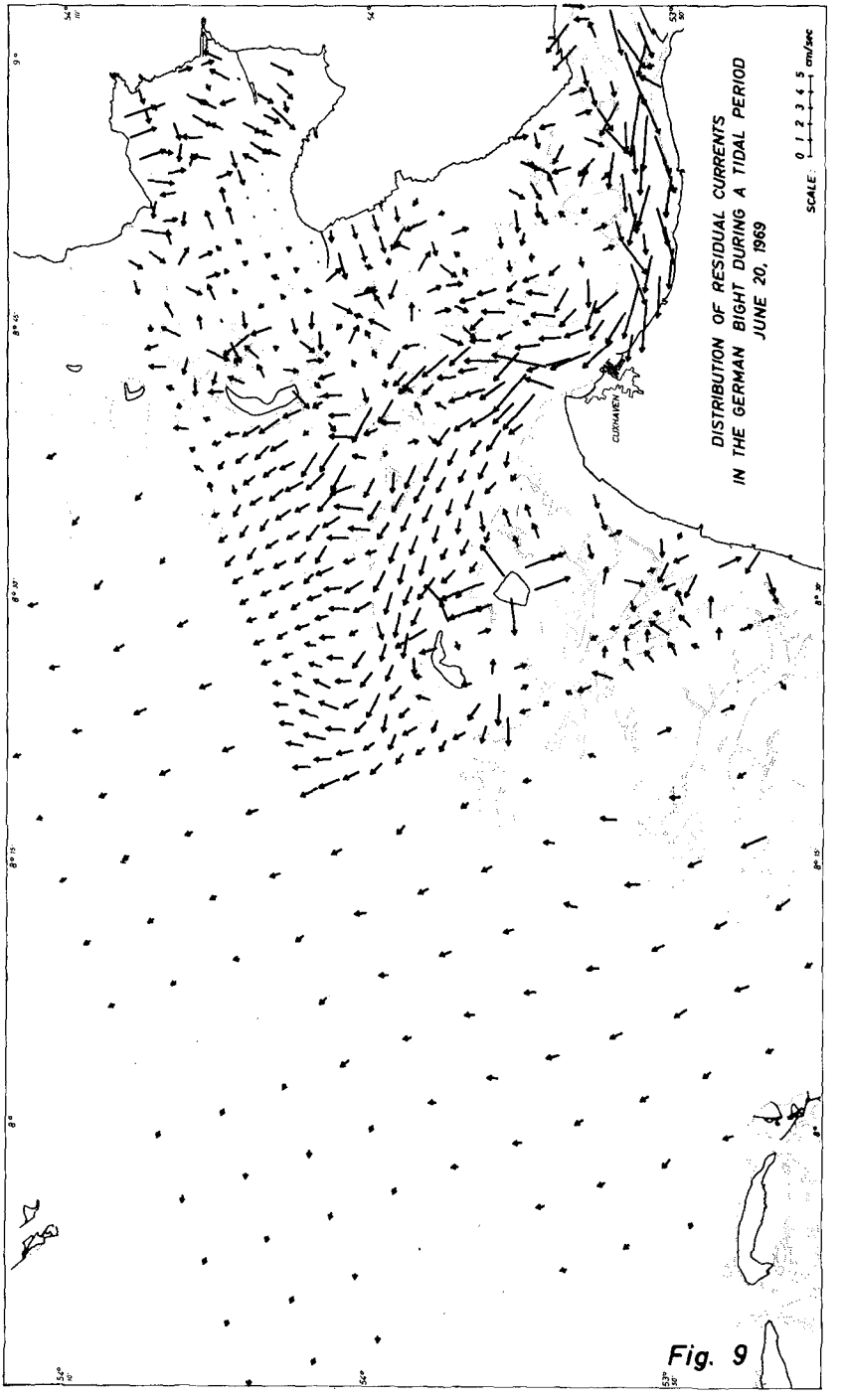
DISTRIBUTION OF RESIDUAL CURRENTS
IN THE GERMAN BIGHT DURING A TIDAL PERIOD
JUNE 20, 1969
SCALE 0 1 2 3 4 5 cm/sec
CUXHAVEN

Fig. 9

References:

HANSEN, W. — Einige Bemerkungen zur Ermittlung der Gezeiten auf großen Tiefen und in Flachwassergebieten
Archiv für Meteorologie, Geophysik und Bioklimatologie
Serie A, Meteorologie und Geophysik, Bd 7,1954

HANSEN, W. — Theorie zur Errechnung des Wasserstandes und der Strömungen in Randmeeren nebst Anwendungen
TELLUS No. 3, 1956

HANSEN, W. — Hydrodynamische Methoden in der Ozeanographie; Beiträge zur Physik der Bewegungsvorgänge im Meere
GEOFISICA PURA E APPLICATA - Milano Band 44 (1959/III)

HANSEN, W. — Hydrodynamical methods applied to oceanographic problems
Mitteilungen des Instituts für Meereskunde der Universität Hamburg, Heft I, 1962

HUBER, K. — Anwendung des hydrodynamisch-numerischen Verfahrens zur Interpretation und Reproduktion von Bewegungsvorgängen im flachen Wasser
Mitteilungen des Instituts für Meereskunde der Universität Hamburg, Heft XV, 1970

KLEIN, H.-A. — Strömungsverhältnisse und Wassermengen der Tide-Elbe
Mitteilungen der Wasser- und Schiffahrtsdirektion Hamburg, Heft 11, 1960

NÖTHLICH, I. — Untersuchungen über den Schlickhaushalt in der Unterelbe mit besonderer Berücksichtigung der biologischen Komponenten
Mitteilungen der Wasser- und Schiffahrtsdirektion Hamburg, Heft 17, 1967

NÖTHLICH, I. — Untersuchungen über Beziehungen zwischen Strömung und Schwebstoffgehalt in der Unterelbe
Unveröffentl. Bericht der Wasser- und Schiffahrtsdirektion Hamburg 1967

RAMMING, H. G. — Gezeiten und Gezeitenströme in der Eider
Mitteilungen des Instituts für Meereskunde der Universität Hamburg, Heft I, 1962

References (contd) :

RAMMING, H. G. Shallow Water Tides
Mitteilungen des Instituts für Meereskunde der Universität Hamburg, Heft X, 1966

RAMMING, H. G. Ermittlung von Bewegungsvorgängen im Meere und in Flußmündungen zur Untersuchung des Transportes von Verunreinigungen
Helgoländer wiss. Meeresuntersuchungen Heft 17, 1968

RAMMING, H. G. Investigation of motion processes in shallow-water areas and estuaries
Symposium on Coastal Geodesy, Munich, 1970

RAMMING, H. G. Hydrodynamisch-numerische Untersuchungen über strömungsabhängige Horizontalausbreitungen von Stoffen in Modellflüssen mit Anwendungen auf die Elbe
Mitteilungen des Instituts für Meereskunde der Universität Hamburg, Heft XVIII, 1971

ROSE, D. Über die quantitative Ermittlung der Gezeiten und Gezeitenströme in Flachwassergebieten mit dem Differenzenverfahren
Mitteilungen des Franzius-Instituts für Grund- und Wasserbau der Technischen Hochschule Hannover, Heft 18, 1960

SUNDERMANN, J. Die hydrodynamisch-numerische Berechnung der Vertikalstruktur von Bewegungsvorgängen in Kanälen und Becken
Mitteilungen des Instituts für Meereskunde der Universität Hamburg, Heft XIX, 1971

CHAPTER 127

NUMERICAL MODELING OF CONSTITUENT TRANSPORT IN BAY SYSTEMS

By R. G. Dean[1] and R. B. Taylor[2]

ABSTRACT

This paper describes the results of a numerical modeling study of the Lower Biscayne Bay system in southeast Florida. The purpose of the study is to predict the effects of cooling water intake and discharge associated with the Turkey Point Power Plant facility, which comprises two fossil-fueled units and two nuclear units. When completed the system will generate 2450 megawatts. One of the original (but since abandoned) operating plans considered would require intake by the plant ranging from 4250 to 10,600 cfs of Bay water for cooling and dilution purposes to be returned via a six-mile canal to the Bay system.

The Lower Biscayne Bay system comprises several bodies of water of 6 to 10 ft. depth which are connected over shallow limestone and mud sills. The numerical model incorporates an area of approximately 36 by 12 nautical miles divided into grid squares of 2 nautical miles on each side.

Available field data are used to calibrate the model. The results of the calibration and predictions of the effects of the plant withdrawal and discharge on the natural bay system flows are presented.

The primary features of interest of the study include: 1) the effect of the plant cooling water requirements on the Bay hydromechanics, including recirculation and flows through small inlets connecting the Bay to the Ocean; and 2) the concentration distributions of conservative constituents in the Bay system as affected by advective and dispersive processes. The numerical procedure consists of a non-dispersive and a dispersive model which are employed sequentially.

INTRODUCTION

This paper presents the background for and some results obtained from two numerical calculation procedures to simulate the tidal, wind-driven and other induced flows and mixing processes in the Biscayne Bay/ Card Sound System in Southeast Florida, see Figure 1. The two calculation procedures (or models) are employed sequentially to represent: (1) the non-dispersive hydromechanics of the bay system, and (2) the dispersive and advective transport of a constituent and the exchange with contiguous water systems.

[1]Professor, Coastal and Oceanographic Engineering Laboratory, University of Florida, Gainesville, Florida 32601.

[2]Research Assistant, Coastal and Oceanographic Engineering Laboratory, University of Florida, Gainesville, Florida 32601.

The numerical models described in this report are based on finite difference representations of the governing equations of motion and continuity and conservation of the constituent. Both dispersive and advective transport are included in the constituent transport considerations.

The non-dispersive numerical model utilizes and extends the techniques developed by Platzman[1], Miyazaki[2], Reid and Bodine[3], and represents an improvement of the numerical model developed by Verma and Dean[4] for the Biscayne Bay area.

For the appropriate geometry of the Bay system, the finite difference representations of the equations of motion and continuity are solved for time-varying forcing functions which can include:(1) ocean tide which could be composed of astronomical and barometric components, (2) wind shear on the surface of the bay system, (3) runoff along the boundaries of the bay, and (4) withdrawal and discharge of water by the Turkey Point Plant at any specified locations. The principal difficulty in applying the available methods to the Biscayne Bay/Card Sound area is that this area is perhaps unique due to the presence of a number of limestone sills, some of which are "laced" by numerous channels. When examined in detail, the variation of hydraulic "admittance" of these various features with tidal stage is quite important in representing the overall hydromechanic response of the bay system. The equations associated with the non-dispersive numerical model were programmed for solution on a digital computer; the results of these computations are Fourier coefficients which represent the time-varying water surface displacements and discharge components throughout the bay system. This output from the non-dispersive program serves as input to the companion dispersive model which predicts the concentrations and transport of a constituent introduced into the bay.

The dispersive model is based on a finite difference formulation of the two dimensional equations for conservation of a constituent. The present version of the model considers only conservative constituents; however, modifications are planned to represent the fate of non-conservative constituents by incorporating exchange mechanisms across the upper and/or lower surfaces to simulate transfer to the atmosphere and bottom sediments, respectively. Of particular interest is the representation of an anisotropic dispersion coefficient based on Elder's[5] study of dispersion in an open channel. This feature is of importance in areas where there is a strong predominance to the current direction.

The present paper does not present the underlying theory or numerical basis in complete detail; for a more complete treatment, the reader is referred to References (6) and (7).

DESCRIPTION OF PHYSICAL SYSTEM

The numerical model incorporates an area of approximately 36 by 12 nautical miles, and extends from the Rickenbacker Causeway (northern limit) to the southern limit of the model, which is located near the causeway between Barnes Sound and Blackwater Sound, see Figure 1. The model extends from the western boundary of the Biscayne Bay/Card Sound system to an

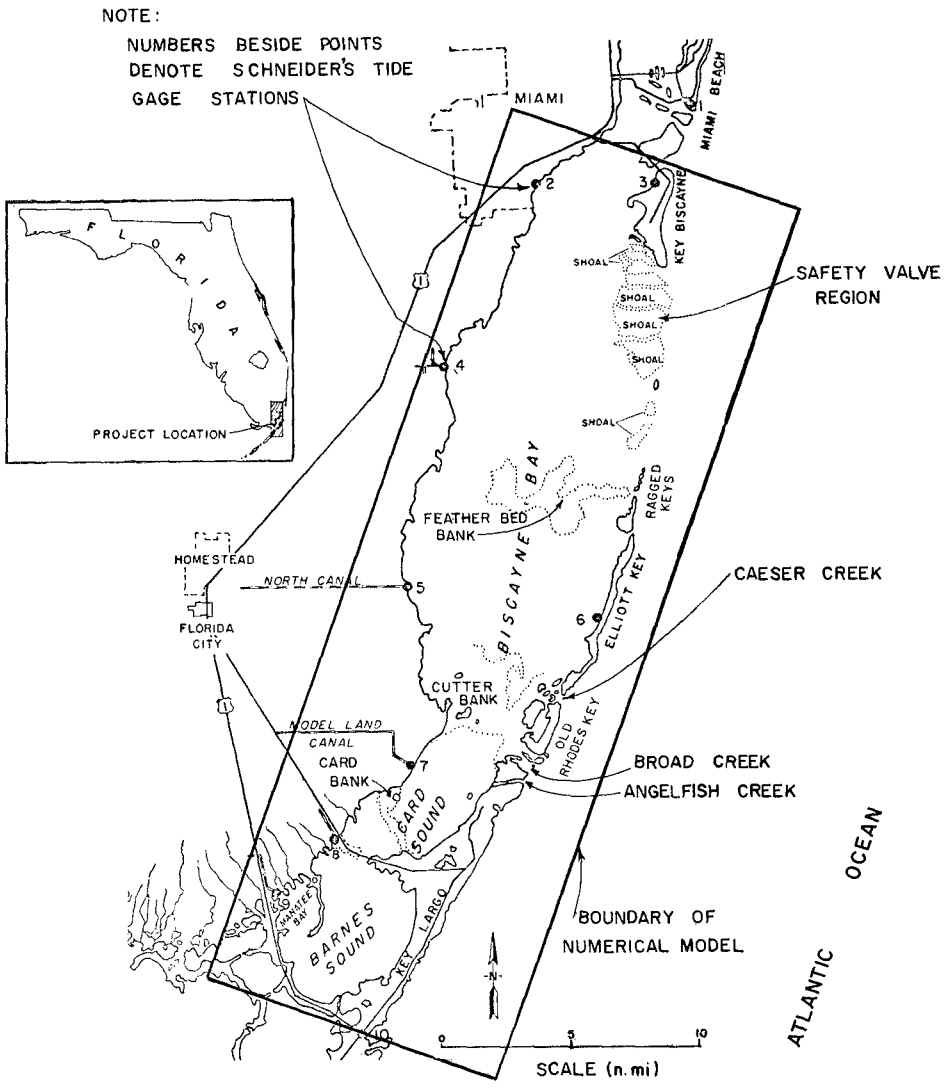

FIGURE 1. AREA INCLUDED IN NUMERICAL MODEL. THIS FIGURE ADAPTED FROM SCHNEIDER.[9]

eastern limit which is approximately 2 miles into the Atlantic Ocean.

The Biscayne Bay system comprises several water bodies which are connected via shallow sills. The primary flow into the Biscayne Bay/Card Sound System occurs through the "Safety Valve" region located at the northeastern limits of Lower Biscayne Bay. This entrance to the bay is approximately 9 nautical miles in length, and is characterized as a shallow limestone sill approximately 1/2 to 2 nautical miles in breadth, and at mean low water is 1 to 3 ft. in depth. The sill is interlaced by approximately 20 channels which, at mean low water, range up to 15 ft. in depth. The other inlets which are responsible for the major part of the remaining flow in and out of the bay system include Bear Cut which communicates with the Atlantic Ocean at the northeast corner of the bay system, the bridge in the Rickenbacker Causeway which communicates with lower Biscayne Bay to the north, and several inlet systems connecting Lower Biscayne Bay and Card Sound to the Atlantic Ocean. These inlets include Caesar Creek, which is located in lower Biscayne Bay between Elliott Key and Old Rhodes Key and transports water in and out of the Bay at this point. At the northern end of Card Sound, there is a series of channels which connect Card Sound to the Atlantic Ocean. These channels are fairly numerous, however, the major channels are Broad Creek and Angelfish Creek.

At the southern limit of Barnes Sound, Jewfish Creek connects Barnes Sound with Blackwater Sound, however, this is a relatively small channel and probably does not affect the region of interest significantly.

The bay system interior may be characterized as a number of shallow basins separated by much shallower limestone sills and mud banks, which affect the hydraulics considerably. Starting at the north end of the bay system, the average mean low water (MLW) depths are on the order of 7 ft. from the Rickenbacker Causeway for a distance of approximately 14 nautical miles to the south where a shallow sill "Feather-Bed Bank" is located. This sill varies considerably in depth, ranging from a mean low water depth of 6 ft. to areas where the sill is exposed; an average depth is on the order of 2 to 3 ft. mean low water. Continuing south from the Feather-Bed Bank a distance of approximately 9 nautical miles, a second limestone sill, "Cutter Bank" is located; this sill separates lower Biscayne Bay from Card Sound. There is also a lateral decrease in the width of the Bay; at this point the width is approximately 3 nautical miles. The depth at Cutter Bank ranges from about 1 to 3 ft. at mean low water. Card Sound is approximately 10 ft. in depth at mean low water and is partially isolated from Little Card Sound by "Card Bank" which is a mud sill of approximately 1 to 3 ft. mean low water depth. Little Card Sound is a small basin which is approximately 8 ft. in depth and is separated from Barnes Sound to the south by a lateral and vertical restriction. The Card Sound bridge and associated causeway result in a clear opening between Card Sound and Barnes Sound of about 2000 ft. The natural sill depth at this location is approximately 3 ft. Barnes Sound has a mean low water depth of 9 ft., and its connection with Blackwater Sound to the south is quite restricted, and occurs through Jewfish Creek. For the purpose of the numerical model described in this study, it is assumed that Barnes Sound and Blackwater Sound are completely isolated from each other.

The major physical characteristics of the Biscayne Bay/Card Sound system are shown in Figure 1.

THEORY AND FINITE-DIFFERENCE REPRESENTATIONS

Because of space limitations, the remaining portion of this paper will emphasize the results obtained from application of the numerical models. In this section, the basis for the theory and finite-difference representations is described briefly, however the reader interested in the details should refer to References (6) and (7).

Non-Dispersive Model - The governing equations for the non-dispersive model are the differential equations of motion and continuity. As in a number of previous studies, it is assumed that the water column is well-mixed, the vertical accelerations are negligible, and the convective accelerations are relatively small. This allows the equations of motion to be integrated over depth and to be expressed in terms of the transport components q_x and q_y and the total instantaneous depth. The bottom and surface stresses are retained in the equations of motion, however the lateral stresses on the water column are considered negligible. Anomalous features such as the shallow sills and inlets to the bay are represented in the form of stress terms, the characteristics of which were determined by calibration. The continuity equation is also integrated over depth to obtain the usual expression for the rate of change of water surface elevation in terms of the divergence of water transport.

The vertically-integrated equations of motion and continuity were cast in finite-difference forms, such that the time-marching solution was based on an explicit time- and space-staggered procedure, with quasi-linearization of the bottom and anomalous features stress terms.

Dispersive Model - The dispersive model is based on the differential equation for conservation of a constituent, c, including constituent transport due to advection and dispersion. The assumption is made that the water column is well-mixed, allowing the governing equation to be integrated over depth. Special features of the method employed in this model include the procedure of representing advective transport and the incorporation of anisotropic turbulent dispersion coefficients, in accordance with the results of Elder[5] and Bowden[8] and limited dye studies in the Bay system of interest.

RESULTS

The results obtained from the numerical calculation procedures are discussed separately under non-dispersive and dispersive sub-categories. However, it should be noted that the dispersive results include water level and transport results from the non-dispersive calculations.

Non-Dispersive Results

Three separate sets of computations were carried out using the non-dispersive model to demonstrate its present capabilities and to gain some

insight into future extensions of the model.

Run No. 1 - Two Nautical Mile Grid,Calibration with Schneider's Results, No Wind, No Plant Discharge

The first set of calculations was carried out to calibrate the model and to assess the confidence that could be placed in the use of the model. The grid employed was the 2-mile grid portrayed in Figure 2. The most complete data available for calibration were those collected by J. J. Schneider[9] in 1968, who monitored tidal elevations and set-up in the Biscayne Bay systems at nine locations (Figure 1). In order to calibrate and assess the model, a mean ocean tide of 2.44 ft. range was applied along the seaward grid of the schematized model. This corresponds to the grid line i = 6 as shown in Figure 2. The ocean tide input to the model was a sinusoid having the form

$$\eta = 1.22 \sin \left(\frac{2\pi}{12.4} \frac{t}{3600}\right)$$

in which t is the time in seconds.

In the calculations, which represent a "run" of the numerical model, a time step Δt = 220 sec. was employed. At each time step, the output of the numerical model includes tidal elevations at each of the centerpoints of the grids shown in Figure 2, and also the output includes the transport components (i.e. product of velocity component with total depth) normal to and located at the center of each of the grid lines shown in Figure 2. Figures 3, 4, 5 and 6 present a comparison of the calculations resulting from the numerical model.

Figure 3 presents a comparison of the measured and calculated tidal ranges at the locations of Schneider's tide gage stations. It was found that it was possible to calibrate the model by adjusting the hydraulic characteristics of the inlets and sills in the system so as to obtain agreement generally within 5%.

Figures 4 and 5 present comparisons between computed and measured time lags of the tide for high and low water respectively at Schneider's tide gage stations. Lags shown are with respect to the ocean tide measured at Government Cut. Agreement was generally obtained within $\pm$ 20 minutes except at Station 9.

One interesting phenomenon predicted by the model is the "tidal set-up" in the bay that results from the loss of tidal energy and reflection of tides within the bay. This tidal set-up is manifested as a mean tide elevation above the mean ocean level; this set-up increases toward the lower end of the Bay system. Figure 6 presents a comparison of the measured and computed half-tide planes which represent the set-up. Although the agreement may seem less than desirable, the following should be noted: (1) the magnitude of the quantities are small (maximum of approximately 3") and, (2) the leveling may be questionable. With regard to the latter point, Schneider has concluded the leveling of Tide Gage Location 8 to be in error and has arbitrarily adjusted this level by 0.2' which is almost as great as the maximum set-up.

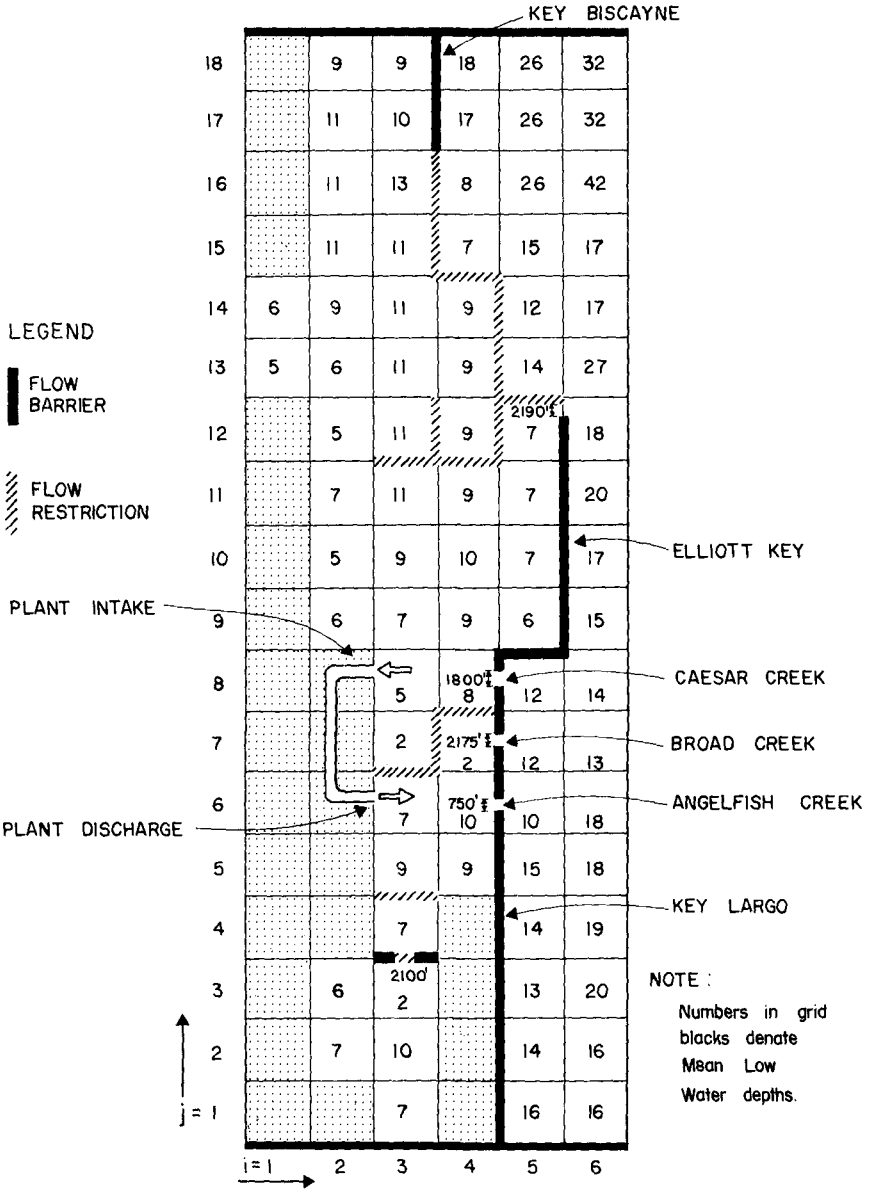

FIGURE 2 TWO MILE GRID SIMULATION OF THE BISCAYNE BAY / CARD SOUND SYSTEM

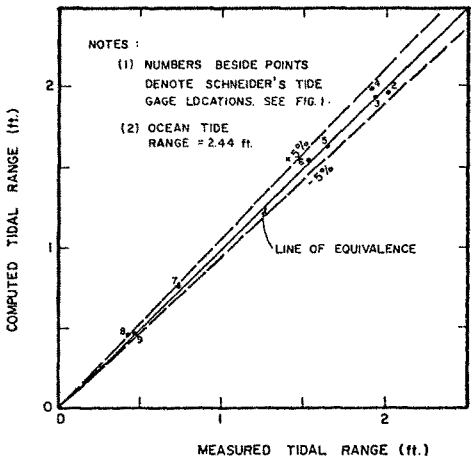

FIGURE 3 COMPARISON OF MEASURED AND COMPUTED TIDAL RANGES.

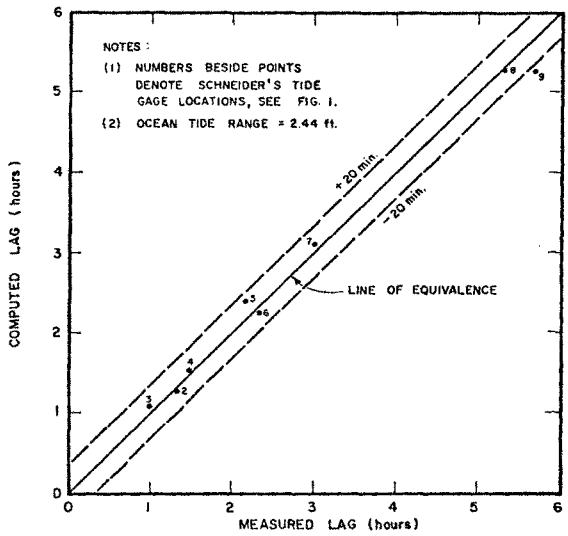

FIGURE 4 COMPARISON OF MEASURED AND COMPUTED TIDAL LAGS FOR HIGH WATER.

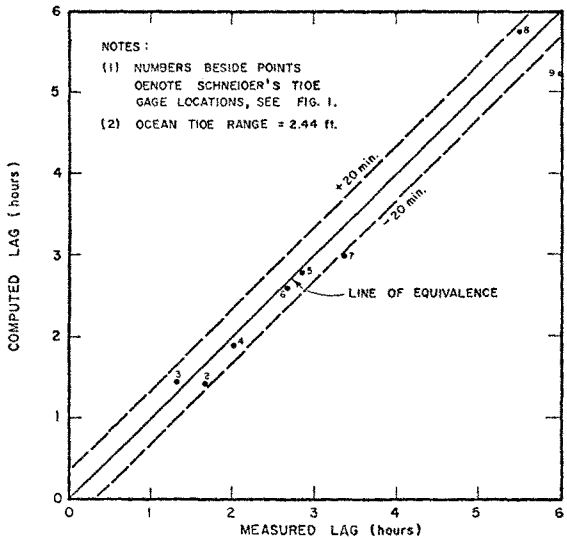

FIGURE 5 COMPARISON OF MEASURED AND COMPUTED TIDAL LAGS FOR LOW WATER.

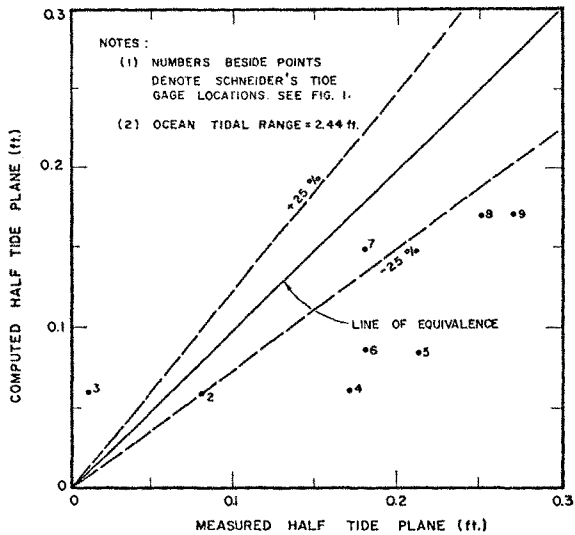

FIGURE 6 COMPARISON OF MEASURED AND COMPUTED HALF TIDE PLANES.

Figure 7 presents isolines of tidal range. The effect of the limestone sills in decreasing the tidal range is very evident from the steep tidal range gradient at these locations. The tidal ranges measured by Schneider at Stations 2-9 are also shown on this figure.

A comparison of mean tidal exchange volumes for Card Sound and the Ocean was made between the results of this model and those of earlier models by Verma and Oean[4], and Taylor[10]. The tidal exchange volume was selected as a representative measure of comparison between the various models because the exchange volume represents the total tidal flow through the inlet system over one-half of a tidal cycle and is therefore a better means of comparing the results of the models than is the peak flow rate which can vary considerably with the channel geometry for a given cross-sectional area.

Since the flow rate through an inlet and thus the exchange volume of the bay are roughly proportional to the square root of the amplitude of the ocean tide, the results of Verma and Oean, and Taylor models were adjusted so as to be representative of an ocean tidal range of 2.44 ft., the value used to calibrate the present model.

The comparable tidal exchange volumes of the three models for a tidal range of 2.44 ft. are as follows:

Present Model - 0.59×10^9 ft.^{3}

Verma and Oean - 0.79×10^9 ft.^{3}

Taylor - 0.93×10^9 ft.^{3}

It is believed that the actual value of the tidal exchange volume lies somewhere between 0.6×10^9 and 0.8×10^9 ft.^{3} which would indicate that the results from the previous models are high while the results of this model are slightly low. Support for this is given by O'Brien's relationship[11] between the cross-sectional area of the inlet at its most narrow section and the tidal prism of the bay. Using three inlets having mean water level cross-sectional areas of 2870, 9200, and 8180 ft.^{2} to represent Old Rhodes Channel, Broad Creek and Angelfish Creek, respectively, O'Brien's method yields a tidal exchange volume of 0.74×10^9 ft.^{3} for a tidal range of 2.44 ft.

Maximum discharge values computed at all grid lines in the Bay system indicate a reduction in magnitude of the peak transports in the southern portion of the system and a predominance of the longshore components in the Card Sound Basin.

Run No. 2 - Plant Discharge of 4250 cfs, No Wind, Mean Flow Distribution

Computations were carried out to demonstrate the capability of the model to predict:(1) the effect of a plant discharge of 4250 cfs, (2) the source of the water flowing into the plant, and (3) the disposition of the discharged water. Streamlines are calculated, based on the mean transport components; the streamlines represent the approximate mean flow paths of the water particles. The results are shown in Figure 8 and represent streamlines based on the discharge averaged over a full tidal cycle for zero wind and zero rainfall conditions.

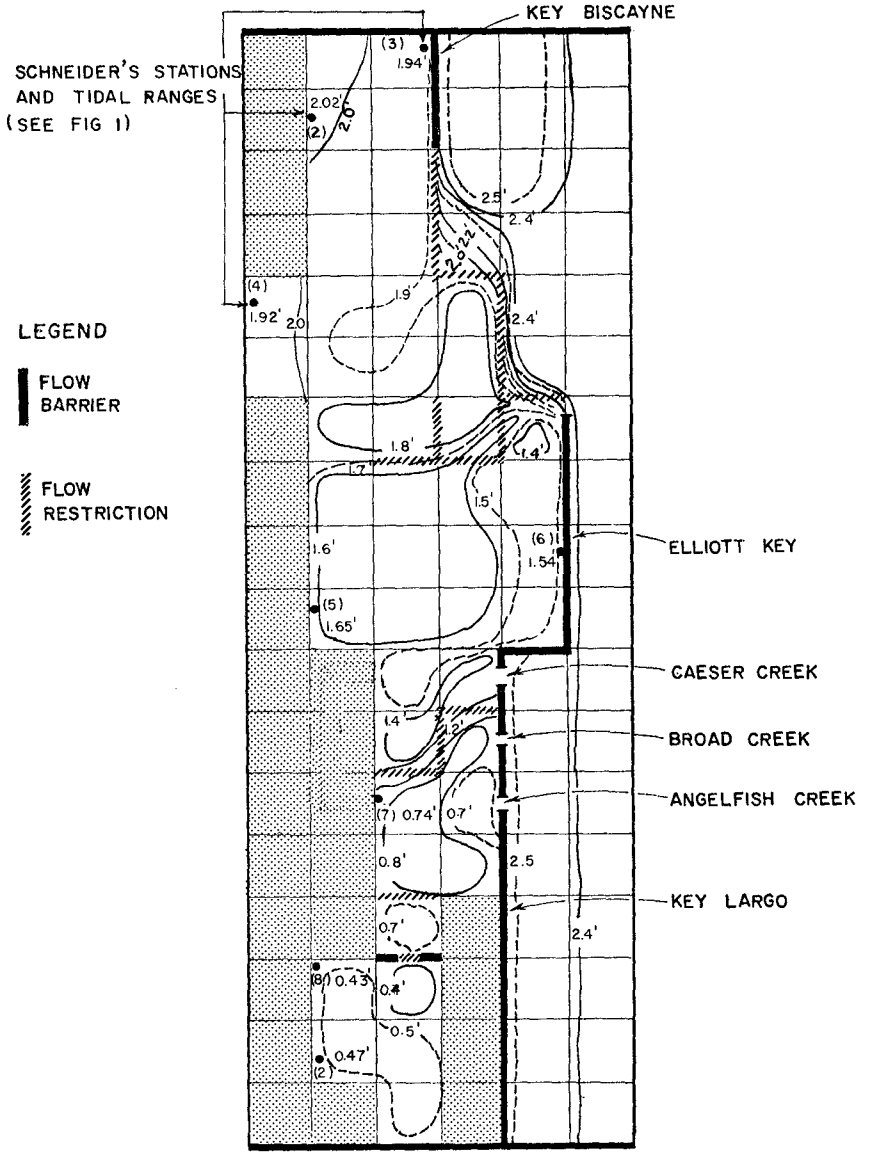

FIGURE 7 ISOLINES OF COMPUTED BAY TIDAL RANGE FOR AN OCEAN TIDAL RANGE OF 2.44 ft.; COMPARISON WITH SCHNEIDER'S DATA.

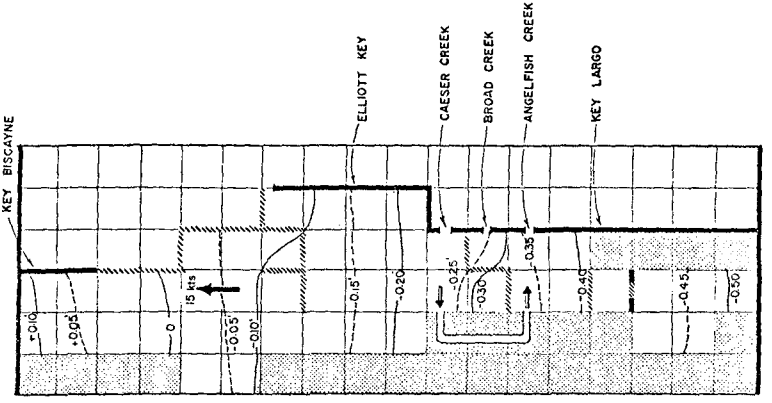

FIGURE 9 CHANGE IN MEAN WATER LEVEL DUE TO A 15 KNOT WIND BLOWING ALONG MAJOR AXIS OF BAY.

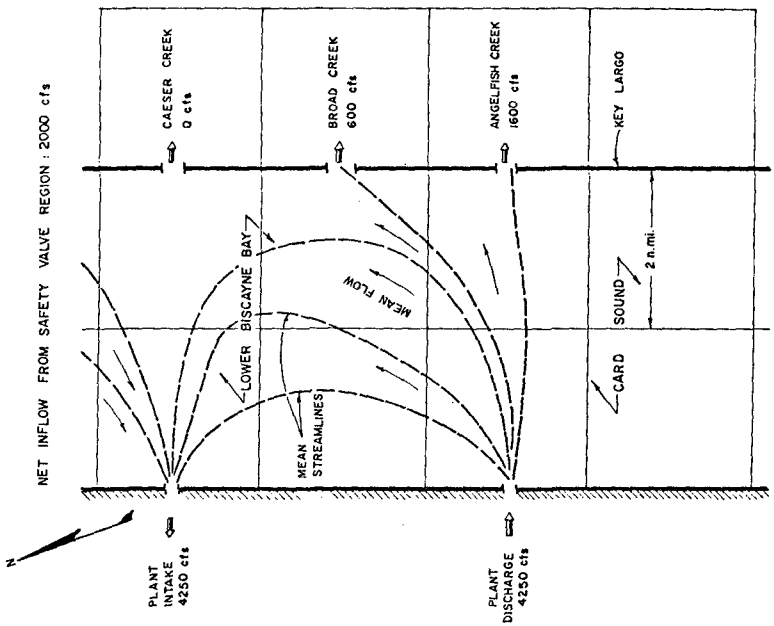

FIGURE 8 MEAN STREAMLINES AND DISCHARGES ASSOCIATED WITH PLANT FLOW OF 4250 c.f.s., WIND CONDITIONS : CALM.

From the mean discharge values, it is possible to determine a "dividing streamline" outside of which all water discharge from the Canal terminus at Card Sound is not redrawn into the Plant and inside of which all water is recirculated into the Plant. It is noted that approximately 50% of the water discharged into Card Sound flows from Card Sound to the Atlantic Ocean primarily via Broad and Angelfish Creeks. The remaining 50% is recirculated. To replace the 50% of the Plant flow out of the system, this same amount enters Biscayne Bay, primarily from the "Safety Valve Region", located at the north extremity of lower Biscayne Bay. These results do not reflect the effect of mixing of the Bay water which is treated by the dispersive model.

Run No. 3 - A Steady South-Southwest Wind of 15 Knots

In order to demonstrate the capability of the model in representing forcing functions in addition to the tides, Run No. 3 included the same tide and Plant discharges as Run No. 2, however, a steady wind of 15 knots along the axis of the Bay system was included. Resulting mean streamlines were then computed in a manner identical to that described above for Run No. 2. The associated wind stress applied to the Bay surface was 0.001 lb/ft.^{2}. The major effect of the wind stress resulting from the applied wind is to depress the mean water levels in the southern portions of the Bay and to cause "new ocean water" to be drawn in through Angelfish, Broad, and Caesar Creeks, and to circulate toward the north and for a net amount of water to be displaced out through the Safety Valve region. The change in mean water level due to the wind is shown in Figure 9 . It is noted that the maximum change of -0.5 ft. occurs in the Barnes Sound area.

Figure 10 shows the effect of the south-southwest wind on the mean discharges within Card Sound. Comparison of Figures 8 and 10 shows that without mixing, the plant mass recirculation has increased from 50 to 100% as a result of the wind.

Dispersive Results

Two runs will be presented which employ the companion non-dispersive and dispersive models.

Run No. 1 - Two Nautical Mile Grid,Calibration with Continuous Plant Discharge of 4250 cfs, No Wind

The first set of computations was carried out to: (1) calibrate the dispersive model for net exchange with the ocean, (2) illustrate the capabilities of the model for conditions in which the tides represent the only forces, and (3) to examine the required length of model run to achieve near-equilibrium conditions.

Computed water surface elevations and volumetric flow rates for each grid square as a function of time were obtained from the calibrated non-dispersive model using an ocean tidal amplitude of a = 1.22 ft., zero wind stress (no wind), and a plant discharge of 4250 cfs. These data were then introduced into the dispersive model which used the same grid scheme as the non-dispersive model (Figure 2). The power plant effluent or constituent was considered to have a volumetric concentration level of 1.0 as it entered Card Sound. In order to evaluate the time required to achieve near-equilibrium conditions in the Card Sound Basin, a prototype running time of 333 hours (approximately 14 days) was conducted.

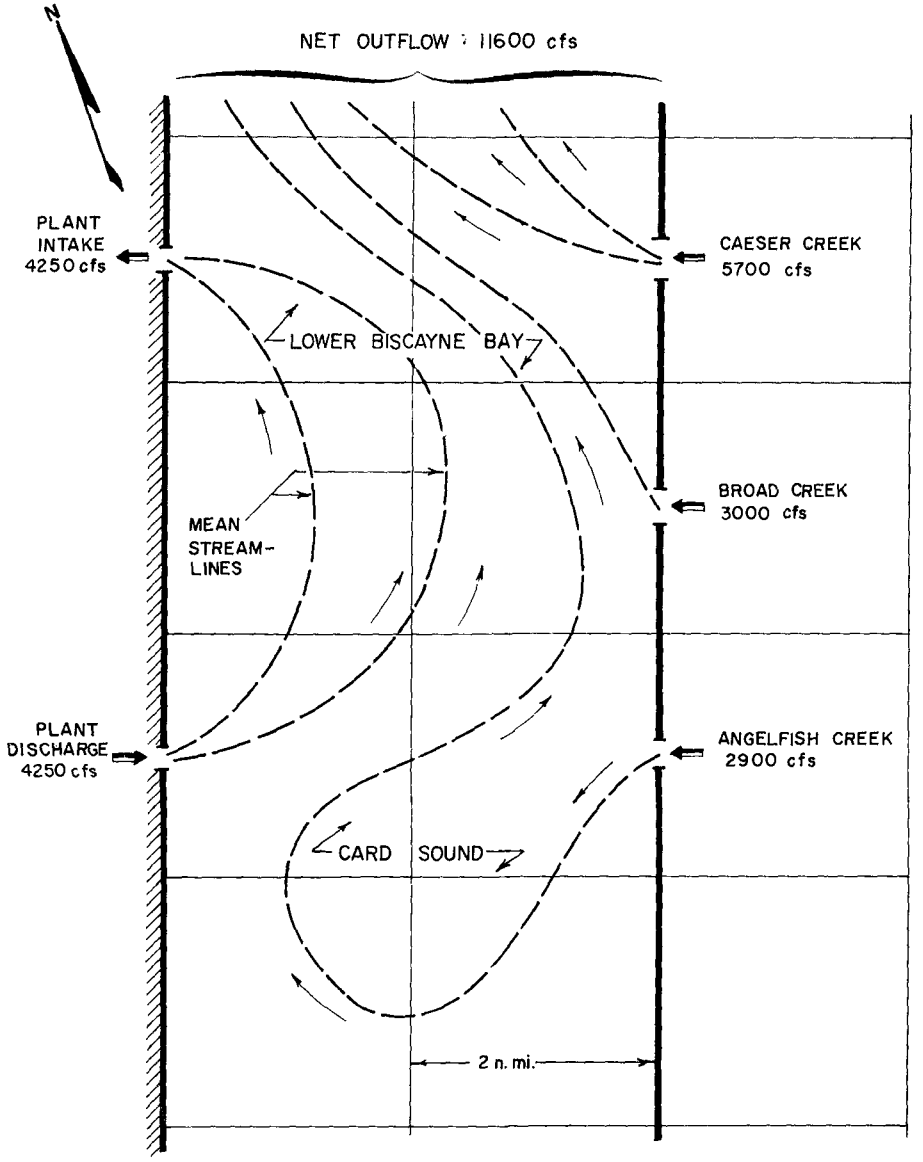

FIGURE 10 MEAN STREAMLINES AND DISCHARGES ASSOCIATED WITH A PLANT FLOW OF 4250 cfs AND A SUSTAINED SSW WIND OF 15 KTS.

For each "run", or set of calculations performed by the model, a time step of Δt = 5000 sec. was used. This is considerably larger than the value of Δt = 220 sec. utilized in the non-dispersive model, but is acceptable due to the more stable nature of the dispersive computation procedure. On the other hand, it will be seen that the dispersive mechanisms approach steady state much more slowly. At each time step, the output of the model includes tidal elevation and constituent concentration levels relative to the discharge point at each of the center points of the grid. Also calculated are velocities and total transport components of the constituent/bay water mixture normal to and located at the center of each of the grid lines shown in Figure 2.

To calibrate the model, values of constituent concentration levels in the ocean grid squares located in the extreme right column and adjacent to Caesar, Broad, and Angelfish Creeks, (6,6), (6,7) and (6,8) were adjusted to achieve the desired degree of mixing between the bay system and the ocean. Based upon limited field data obtained by the Coastal and Oceanographic Engineering Department of the University of Florida using rhodamine dye injection in Broad Creek, the ratio of the mean constituent concentration on the flood tide to the mean constituent concentration in the preceding ebb tide is approximately,

$$\frac{\overline{c}_F}{\overline{c}_E} \simeq 0.6$$

The resulting average obtained for use in the model was

$$\frac{\overline{c}_F}{\overline{c}_E} = 0.55$$

which states that during each tidal cycle, there is a 45% renewal of Card Sound water transported to sea on the ebb tide with ocean water. A more detailed description of the procedure is given in Reference (7). Field work is presently in progress to obtain additional data regarding the exchange coefficients associated with the inlets in the lower Biscayne Bay system.

The transport of power plant effluent to and from Card Sound and its contiguous bodies of water for time ranging from 312 to 330 hours for this example is illustrated by the solid curves in Figures 11, 12 and 13. The results obtained from these curves are summarized in Table I.

An inspection of Table I shows that with no wind, Biscayne Bay and the Atlantic Ocean receive nearly equal amounts of constituent, each being greater than the amount received by Barnes Sound. However, these data also show that at a time of 320 hours, there is still a net flow into Barnes Sound which implies that equilibrium has not been attained. This is to be expected since Barnes Sound is essentially a closed end basin, its equilibrium concentration levels should be the same as those at the lower end of Card Sound. Moreover, the weak tidal exchange between these two basins suggests that equilibrium values in Barnes Sound will be approached slowly.

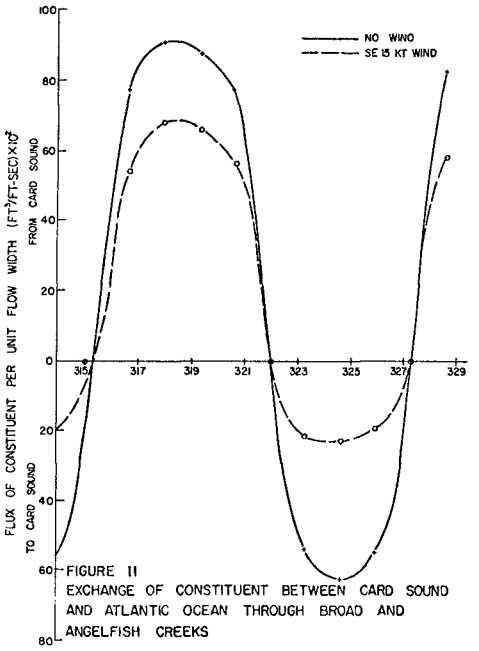

FIGURE 11
EXCHANGE OF CONSTITUENT BETWEEN CARD SOUND AND ATLANTIC OCEAN THROUGH BROAD AND ANGELFISH CREEKS

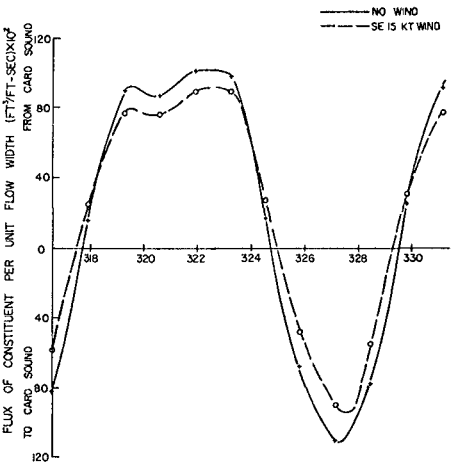

FIGURE 12 EXCHANGE OF CONSTITUENT BETWEEN CARD SOUND AND LOWER BISCAYNE BAY

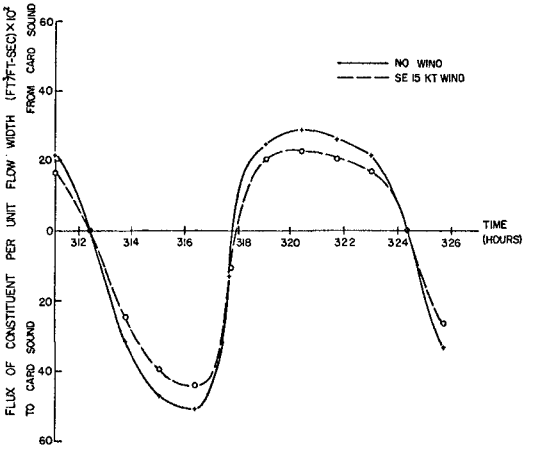

FIGURE 13 EXCHANGE OF CONSTITUENT BETWEEN CARD SOUND AND BARNES SOUND

TABLE I

NET EXCHANGE VOLUMES OF CONSTITUENT BETWEEN CARO SOUND ANO CONTIGUOUS BOOIES OF WATER FOR CONTINUOUS PLANT OISCHARGE = 4250 cfs ANO ZERO WINO CONOITIONS (T = 311 hrs. to T = 330 hrs.)

Contiguous Body of Water	Net Exchange Volume of Constituent (ft^3/ tidal cycle)	Per Cent Constituent Returned with Tide to Card Sound
Atlantic Ocean	9.48×10^7	55%
Lower Biscayne Bay	9.48×10^7	62%
Barnes Sound	2.29×10^7	74%

It should also be noted from Table I that the total net volume of constituent transported out of Card Sound to contiguous bodies of water during one tidal cycle exceeds by approximately 10% the volume of constituent discharges into Card Sound from the power plant during the same period. Realistically this cannot be true since the concentration levels in Card Sound during this period are still increasing. A more precise estimate of an 8% error was obtained using a Δt = 1000 sec. and running the model for the same wind, tide and plant operational conditions. The computed total constituent flux between Card Sound and all contiguous bodies of water is shown in Figure 14. Further investigations have indicated that the improper mass balance of constituent in Card Sound is the result of the technique employed to numerically represent the advective terms in the dispersion equation. The magnitude of this error is approximately 10 per cent.

The distribution of the power plant effluent as predicted by the calibrated dispersive model is illustrated in Figures 15 and 16 for times t = 322 hours. The curves in these figures represent approximate isolines of effluent concentration with values given in parts power plant effluent per 1000 parts bay water. The effects of tidal phase on the distribution of the plant effluent are evident by a comparison of these two figures.

Most of the results presented correspond to problem run times covering the twenty-sixth cycle (approximately 311 to 323 hours) after the initiation of the run, i.e. commencement of the plant discharge. To establish how near the constituent concentration values were to equilibrium and the time at which equilibrium conditions could be expected to be reached, computed maximum constituent concentration levels at two locations in Card Sound, as they occurred during each tidal cycle, were plotted versus time (Figure 17). As indicated by the curve shown in Figure 17 for grid location (3,7), the

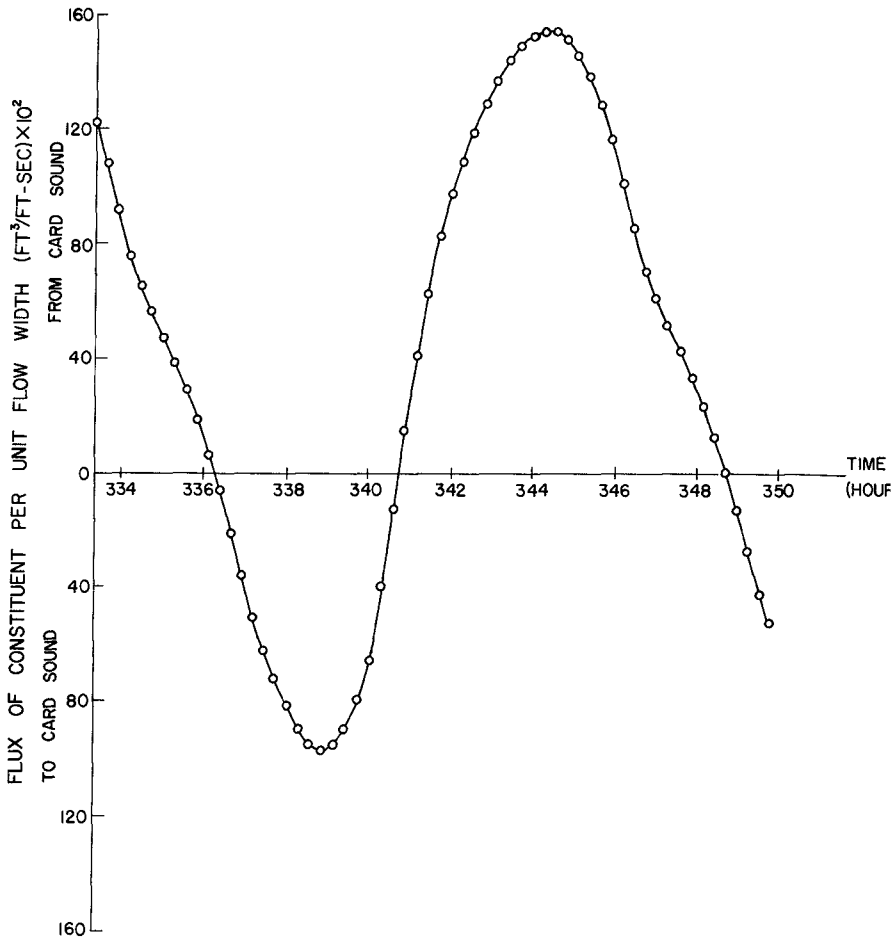

FIGURE 14 TOTAL EXCHANGE OF CONSTITUENT BETWEEN CARD SOUND AND ALL CONTIGUOUS BODIES OF WATER (USING MODEL $\Delta t = 1000$ SECONDS)

FIGURE 16 ISOLINES OF CONSTITUENT CONCENTRATION (PPT)
FOR HIGH TIDE AT MODEL LAND CANAL. PROTOTYPE
CONTINUOUS DISCHARGE TIME 329 HRS., NO WIND

FIGURE 15 ISOLINES OF CONSTITUENT CONCENTRATION (PPT)
FOR LOW TIDE AT MODEL LAND CANAL. PROTOTYPE
CONTINUOUS DISCHARGE TIME 322 HRS., NO WIND

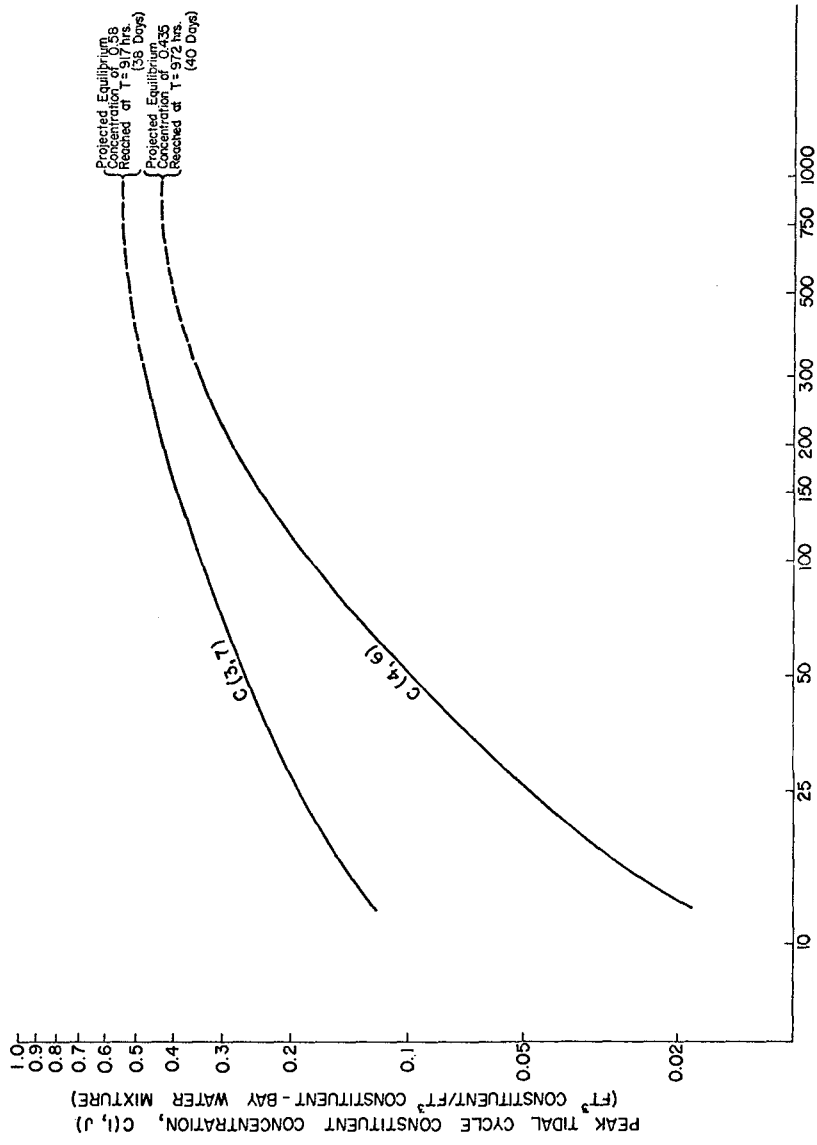

FIGURE 17 PLOT OF CONSTITUENT CONCENTRATION LEVELS AT GRID LOCATIONS (3,7) AND (4,6) VS. PROTOTYPE CONTINUOUS DISCHARGE TIME (NO WIND)

concentration at time T = 330 hours has reached approximately 88% of its extrapolated equilibrium value of 0.55 which is expected to occur 38 days after the commencement of discharge. Similarly, the concentration at grid location (4,6), which corresponds to the region in Card Sound directly east of the discharge canal, for time T = 330 hours has reached approximately 82% of its extrapolated equilibrium value of 0.435. The corresponding equilibrium time for this location is 40 days.

It is evident that the equilibrium time for a particular location in the absence of wind and other climatological variables is dependent upon: (1) the position of the location relative to the discharge point, (2) the presence of predominant currents, and (3) the amount of communication between a basin and adjoining bodies of water. Using these criteria it would be expected that the Card Sound 8asin would reach equilibrium concentration levels first along the western half followed closely by the seaward half. Biscayne 8ay and 8arnes Sound would of course lag Card Sound. Equilibrium conditions in 8arnes Sound, as noted earlier, would be approached very slowly due to the basin's closed nature and the small tides and therefore weak exchange with Card Sound.

Constituent concentration levels existing at the plant intake during the twenty-sixth tidal cycle varied between 28 and 35 per cent, depending on the phase of the tide. If it is assumed that these values are approximately 85 per cent of their equilibrium values (based on the previous discussion) then ultimately a range of 33 to 41 per cent mass recirculation could be expected.

Run No. 2 - Continuous Plant Discharge of 4250 cfs, Steady South-East Wind of 15 Knots

To demonstrate the capability of the dispersive model to describe the effects of varying forcing functions other than the tides, a steady south-east wind of 15 knots was introduced while the other parameters (ocean tide, plant discharge) remained the same. A wind stress of 0.001 lb/ft^2 was applied and surface elevations and volumetric flow rates per unit flow width were computed using the non-dispersive model for each grid element as before. These data were then used as input to the dispersive model which in turn computed the resulting constituent concentration levels, and total transport components of the constituent/bay water mixture as described for Run No. 1.

Due to space limitations, the results of Run No. 2 will be summarized briefly. By comparison of the results of Run Nos. 1 and 2, it was found that the effect of the wind: (1) causes significantly increased mixing of the water from Card Sound with that of the Atlantic Ocean and Lower Biscayne Bay, (2) increases the transport of constituent from Card Sound to Lower 8iscayne 8ay while inhibiting the movement of constituent eastward across Card Sound, and (3) increases slightly the recirculation of the discharged water to the plant intake (from 27-33% for no wind to 28-35% with wind).

SUMMARY

Two numerical models have been developed to represent the non-dispersive and dispersive hydromechanics of a bay system as influenced by tides, winds, runoff and any discharges into the bay system. These models have been applied

to the Biscayne Bay/Card Sound System and several examples presented illustrating the application of the model to calculating the behavior of the natural system and the influence of the discharge and withdrawal of water by the Turkey Point, Florida power plant. In particular, the mean flow field and the concentration distribution of a conservative constituent has been investigated. The numerical models provide satisfactory agreement with the limited available field data.

ACKNOWLEDGEMENT

The research described in this paper was supported by the Florida Power and Light Company as part of an extensive program on the hydrography of the Biscayne Bay/Card Sound system; the approval of Florida Power and Light Company to publish this paper is appreciated.

REFERENCES

1. Platzman, G. W., "A Numerical Computation of the Surge of 26 June 1954 on Lake Michigan", Geophysics, Vol. 6, 1958.

2. Miyazaki, M., "A Numerical Computation of the Storm Surge of Hurricane Carla 1961 in the Gulf of Mexico," Technical Report No. 1D, Department of Geophysical Sciences, University of Chicago, 1963.

3. Reid, R. D. and B. R. Bodine, "Numerical Model for Storm Surges in Galveston Bay," Journal of the Waterways and Harbors Division, ASCE, Vol. 94, No. WW1, pp. 33-57, February, 1968.

4. Verma, A. P. and Dean, R. G., "Numerical Modeling of Hydromechanics of Bay Systems," Proceedings, Civil Engineering in the Oceans, II, ASCE, pp. 1D69-1088, 1969.

5. Elder, J.W., "The Dispersion of Marked Fluid in Turbulent Shear Flow," Journal of Fluid Mechanics, Vol. 5, Part 5, pp. 544-56D, 1959.

6. Dean, R. G. and R. B. Taylor, "Numerical Modeling of Hydromechanics of Biscayne Bay/Card Sound System. Part I: Non-Dispersive Characteristics," Department of Coastal and Oceanographic Engineering, University of Florida, August, 1971.

7. Taylor, R. B. and R. G. Dean, "Numerical Modeling of Hydromechanics of Biscayne Bay/Card Sound System. Part II: Dispersive Characteristics," Department of Coastal and Oceanographic Engineering, University of Florida, July, 1972.

8. Bowden, K. F., "Horizontal Mixing in the Sea Due to a Shearing Current," Journal of Fluid Mechanics, Vol. 21, Part 2, pp. 83-95, 1965.

9. Schneider, J. J., "Tidal Relations in the South Biscayne Bay Area," U.S. Geological Survey, Water Resources Division Open File Report, January, 1969.

10. Taylor, R. B., "Numerical Modeling of Tidal Circulation of Inlet Systems as Applied to the Broad Creek, Angelfish Creek, and Old Rhodes Channel Complex in South Florida," Technical Report, Rosenstiel School of Marine and Atmospheric Sciences, University of Miami, June, 1971.

11. O'Brien, M. P., "Equilibrium Flow Areas of Inlets on Sandy Coasts," Journal of the Waterways and Harbors Division, ASCE.

CHAPTER 128

A NUMERICAL MODEL FOR THE HYDROMECHANICS OF LAGOONS

J. van de KREEKE[1]

ABSTRACT

A numerical model is presented to describe the hydromechanics of lagoons connected to the ocean by relatively narrow inlets. Because special attention is given to the flushing, all second order terms in the hydrodynamic equations are retained. The study is restricted to lagoons with a one-dimensional flow pattern and water of uniform density. In designing a numerical solution to the equations, the inlet equations are regarded as implicit boundary conditions to the equations describing the flow in the lagoon proper. The advantages of this approach are: (1) the size of the computational grid in the lagoon can be chosen independently of the relatively small dimensions of the inlets and (2) the flow at branching inlets (an inlet connecting a lagoon to the ocean such that branching of the inlet flow can occur) still can be described by a one-dimensional tidal model.

The predictive capability of the numerical model is confirmed by favorable comparison between measured and computed particle paths and net transport for a series of laboratory experiments. In the experiments a canal of uniform width and depth is freely connected to a tidal basin at one end and at the other end is connected to the same basin by a submerged weir.

INTRODUCTION

The computational model presented in this paper is designed to simulate the tidal motion in the inland coastal waters found along the Florida Atlantic coast and the Gulf of Mexico coast. Many of these waters, from now on designated as lagoons, are characterized by (1) an elongated shape, (2) narrow inlets connecting the actual lagoon to the ocean and (3) fairly large tidal amplitude to depth ratios. The elongated shape of the lagoons permits the use of the one-dimensional tidal equations. Because of (3), the non-linear terms in the equations are retained. Also, these terms must be accounted for to correctly reproduce the tide-induced flushing.

The numerical scheme for the lagoon proper is based on an explicit difference scheme described by Reid and Bodine [3]. The inlets are incorporated in the model using Dronkers [2] work on river junctions and the computational scheme presented by Balloffet [1]. The performance of the numerical model is evaluated by comparing computed and measured results for a series of laboratory experiments.

[1]Assistant Professor, Division of Ocean Engineering, Rosenstiel School of Marine and Atmospheric Science, University of Miami

NUMERICAL MODEL

Equations

The equations used to describe the flow in the lagoon are the equation of continuity

$$\frac{\partial \eta}{\partial t} + \frac{\partial q}{\partial x} = M \tag{1}$$

in which η = water surface elevation, q = discharge per unit width M = storage, t = time coordinate, x = space coordinate, and the equation of motion

$$\frac{\partial q}{\partial t} + \frac{1}{h}\frac{\partial q^2}{\partial x} + g(h + \eta)\frac{\partial \eta}{\partial x} = -\frac{Fq|q|}{(h + \eta)^2} \tag{2}$$

in which h = mean depth, g = gravitational acceleration, F = resistance coefficient. For the inlets, because of the complexity of the flow (contraction, lateral stresses), recourse is taken to a semi-empirical representation

$$Q = \pm \left(\frac{2g\bar{P}^2}{2FL + m\bar{R}} \right)^{\frac{1}{2}} \left[\bar{R} + \frac{B}{\bar{P}} \frac{(\eta_o + \eta_i)}{2} \right]^{\frac{3}{2}} \sqrt{|\eta_o - \eta_i|} \tag{3}$$

- sign for $\eta_i \leq \eta_o$

+ sign for $\eta_i \geq \eta_o$

in which Q = total discharge, $\bar{P}$ = wetted perimeter of inlet cross section measured at mean ocean level, $\bar{R}$ = hydraulic radius for the inlet cross section measured at mean ocean level, L = length of inlet, B = width of inlet, η_o = ocean tide η_i = lagoon tide, m = coefficient which accounts for entrance losses and the non-uniform velocity distribution.

Numerical Scheme

The numerical scheme for the lagoon is space and time staggered. Water levels are computed at $n\Delta t$ and discharges at $(n + 1/2)\Delta t$. The water levels apply at the center of the grid blocks and the discharges are computed at the gridlines; see Figure 1. The mean depth h and the lateral inflow or rainfall are given at the time level and location of η. The basic recurrence equations for the one-dimensional tidal equations are

$$q'(i) = \frac{1}{G(i-1)} \left[q(i) + \frac{g\Delta t}{2\Delta x} (D(i) + D(i-1))(\eta(i-1) - \eta(i)) \right] \tag{4}$$

$$\eta'(i) = \eta(i) + \frac{\Delta t}{\Delta x} (q'(i) - q'(i+1)) + M(i)\Delta t \tag{5}$$

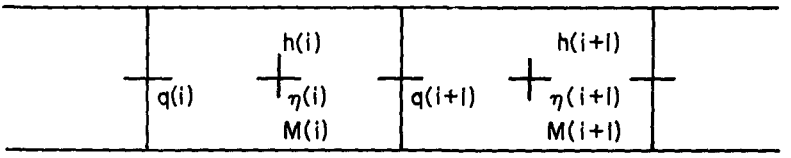

FIGURE 1. LOCATION OF VARIABLES IN THE NUMERICAL GRID

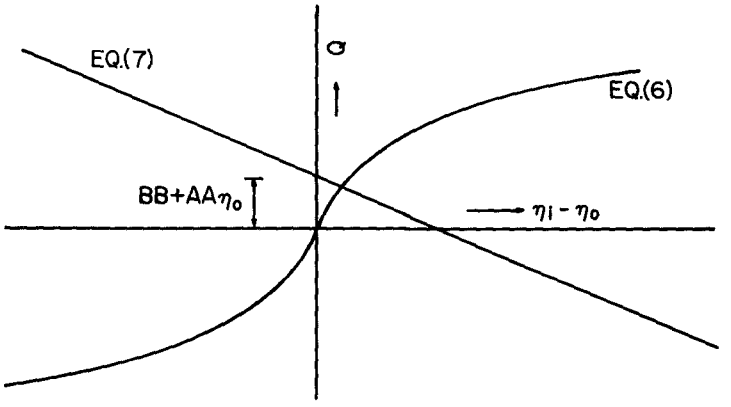

FIGURE 3. FUNCTIONS REPRESENTED BY EQUATIONS (6) AND (7)

in which

$$D(i) = \eta(i) + h(i)$$

$$G(i-1) = 1 + \frac{4F\,\Delta t\,|q(i)|}{(D(i) + D(i-1))^2} + 2\frac{\Delta t}{\Delta x}\frac{(q(i+1) - q(i-1))}{(h(i) + h(i-1)}$$

Primed symbols denote values of the variables at time step Δt later. Equations (4) and (5) are based respectively upon the differential Equations (2) and (1). The differential quotients in these equations are replaced by difference quotients using central differences. The difference quotients for Equation (1) are centered about $(n + 1/2)\Delta t$ and the location of η. The difference quotients for Equation (2) are centered about time level $n.\Delta t$ and are centered in space about the location of q. Starting from the initial conditions all the q's are computed for the next time level by means of Equation (4), then the η's are computed using Equation (5). It is noted that because of the convective acceleration, the recurrence formula (4) includes values as far apart as 2 space steps; see expression for G(i-1). This leads to difficulties when the boundary conditions at open boundaries are given as water levels. In that case, the convective acceleration is taken off center for the grids adjacent to those boundaries. After some algebraic manipulation, the following result is obtained.

$$Q = \pm\, DD\, \sqrt{|\eta_i - \eta_o|}$$
$$+ \text{ sign for } \eta_i \geq \eta_o \qquad (6)$$
$$- \text{ sign for } \eta_i \leq \eta_o$$

in which

$$Q = \frac{Q'(i+1) + Q(i+1)}{2}$$

$$DD = \sqrt{\frac{2g\bar{P}^2}{2FL + m\bar{R}}}\ (\bar{R} + \frac{\bar{B}}{\bar{P}}\ \frac{\eta_o + \eta_i}{2})^{3/2}$$

In the computational procedure the inlet equation, Equation (3), may be regarded as an implicit boundary condition for the flow in the lagoon.

The way in which this boundary condition is incorporated in the numerical scheme depends on the inlet configuration. The following two cases are considered:

- An inlet connecting a lagoon to the ocean such that no branching of the inlet flow occurs; see Figure 2A.

- An inlet connecting a lagoon to the ocean such that branching of the inlet flow can occur; see Figure 2B.

Consider the "nonbranching inlet"; see Figure 2A. The total discharge Q rather than the discharge per unit width, q, is used as a dependent variable. An auxiliary water level η_i is introduced which is computed at the same time level as the water levels in the lagoon. Starting from the initial conditions, all the discharges in the lagoon except Q(i + 1) can be computed using the procedure described before. The value of Q(i + 1) is then computed as follows. Q(i + 1) is related to the known ocean level η_o and the auxiliary level η_i by means of the inlet equation. A second equation relating Q(i + 1) and η_i is found by applying the dynamic equation, Equation (2), between the discharge stations Q(i + 1) and Q(i). Note that when computing the flow in the lagoon, the dynamic equation is applied between two water level stations. The difference form of the dynamic equation applied between Q(i + 1) and Q(i) yields

$$Q = AA(\eta_i - \eta_o) + BB + AA\,\eta_o \qquad (7)$$

in which

$$Q = \frac{Q'(i+1) + Q(i+1)}{2}$$

$$AA = \frac{-g\,D(i)\,B1\,\Delta t}{G\Delta x}$$

$$BB = \left\{Q(i+1) + Q(i) - Q'(i)\,.\,G + \frac{g\,B1\,D(i)\,\Delta t}{\Delta x}\,[\eta(i) + \eta(i-1)]\right\} \Big/ \left(2G + \frac{Q(i+1)}{2}\right)$$

$$G = 1 + \frac{F\Delta t\,|Q(i+1) + Q(i)|}{2D(i)^2 B1} + \frac{2\Delta t[Q(i+1) - Q(i)]}{\Delta x h(i) B1}$$

In determining the difference form, the terms in both the inlet and dynamic equation are centered about n . Δt.

The general shapes of the curves $Q = f(\eta_i - \eta_o)$ represented by the Equations (6) and (7) are indicated in Figure 3. Equation (7) represents

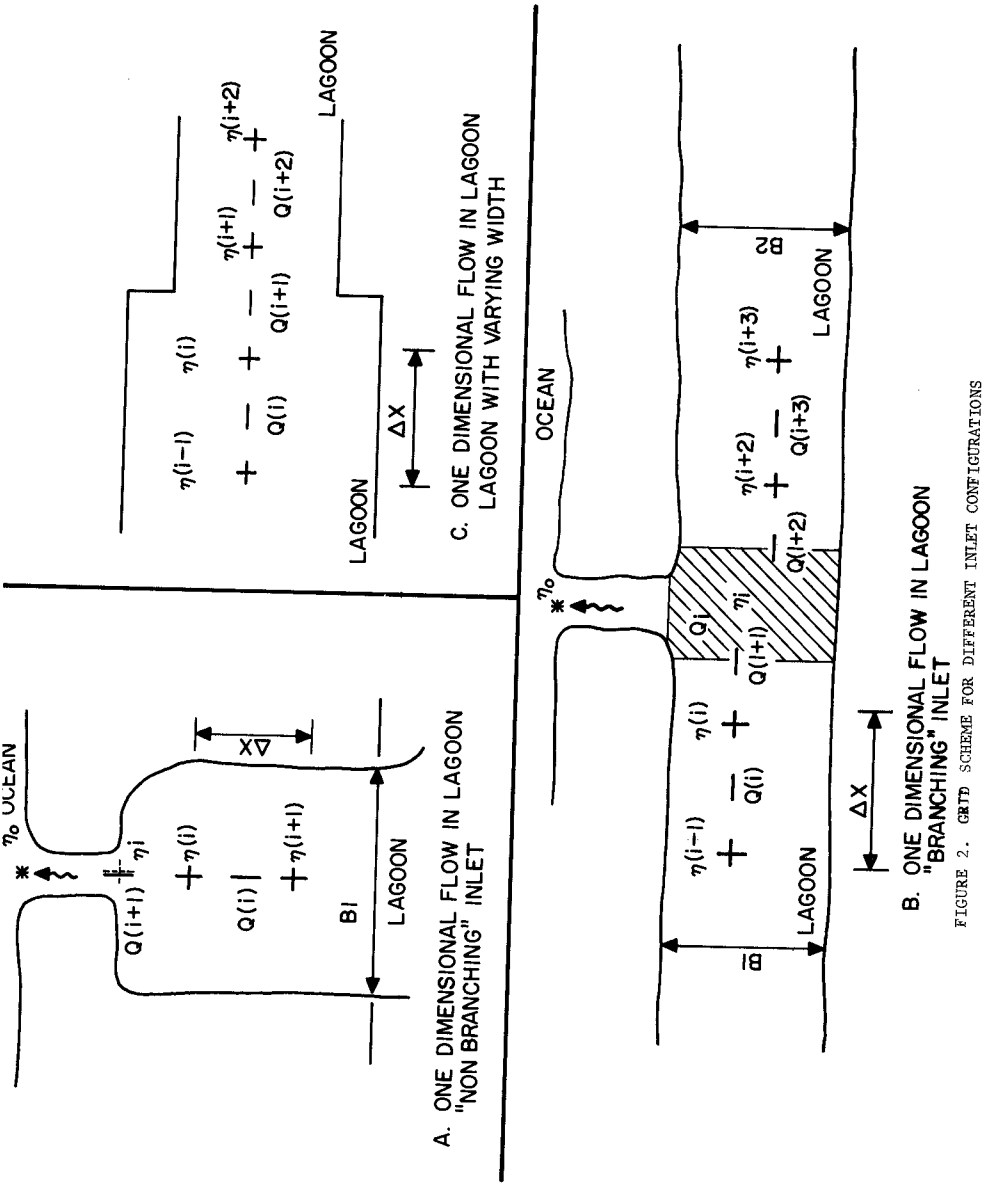

FIGURE 2. GRID SCHEME FOR DIFFERENT INLET CONFIGURATIONS

a straight line. The slope of this line, AA, is for most practical cases negative. Therefore, the sign of $(BB + AA\eta_o)$, which is a known quantity, determines the sign of $(\eta_i - \eta_o)$ which in turn determines the sign to be used in Equation (6). Eliminating $(\eta_i - \eta_o)$ between Equations (6) and (7) yields

$$Q = \frac{1 - \sqrt{1 - 4\frac{AA}{DD^2}(AA\eta_o + BB)}}{2\frac{AA}{DD^2}} \qquad (8)$$

for $(BB + AA\eta_o) \geq 0$

and

$$Q = \frac{1 - \sqrt{1 + 4\frac{AA}{DD^2}(AA\eta_o + BB)}}{-2\frac{AA}{DD^2}} \qquad (9)$$

for $(BB + AA\eta_o) \leq 0$.

Note that only the first order terms in $(\eta_i - \eta_o)$ are eliminated because second order terms are still present in the factor DD. Equations (8) and (9) therefore may be regarded as being quasi-linear, which suggests finding a solution by means of a perturbation method. First the value of $(\eta_i - \eta_o)$ in DD is taken equal to the value at the previous time step. The value of Q can then be found from Equation (8) or (9) depending on the sign of $(BB + AA\eta_o)$. Knowing Q, the value of $(\eta_i - \eta_o)$ is determined from either Equations(6)or (7). This value of $(\eta_i - \eta_o)$ is substituted in DD. The Procedure then is repeated until the difference between the computed and previously computed value of Q is within certain limits.

The numerical scheme for the "branching inlet" (see Figure 2B) involves four unknowns Q'(i+1), Q'(i+2), Q'(i+2), Q'_i and η_i as compared to only two, Q(i+1) and η_i, for the "nonbranching inlet". The four unknowns are related by the following four equations

- the inlet equation which takes the form of Equation (6) with $Q = \frac{Q'_i + Q_i}{2}$
- the dynamic equation applied between the locations of Q(i) and Q(i+1); this equation takes the form of Equation (7).
- the dynamic equation applied between the locations of Q(i+2) and Q(i+3); this equation takes the form of Equation (7) with

Q(i) replaced by Q(i+3), Q(i+1) replaced by Q(i+2), η(i) replaced by η(i+2), η(i-1) replaced by η(i+3), h(i) replaced by h(i+2), Δx replaced by $-\Delta x$, and B1 replaced by B2.

the continuity condition which, when assuming that the water level in the hatched area is the same everywhere, takes the form

$$Q(i+1) = Q_i + Q(i+2)$$

Elimination of Q(i+1) and Q(i+2) between the two dynamic equations and the continuity equation yields a relation between Q_i and η_i similar to Equation (7). This equation together with the inlet equation then can be solved following the procedure described before.

Finally, it is noted that in one-dimensional flow computations, it is often necessary to divide the lagoon into parts with different widths; see Figure 2C. The flow at the boundary of two such parts may be computed following a procedure similar to the one applied to the "nonbranching inlet", replacing the inlet equation by a second dynamic equation between the locations of Q(i+1) and Q(i+2).

COMPARISON WITH LABORATORY EXPERIMENTS

To evaluate the capability of the computational model to predict the water motion in lagoons, computed and measured float paths were compared for a series of laboratory experiments. A straight canal of uniform depth and width simulating a lagoon, was constructed in a tidal basin; see Figure 4. The canal was open at one end and at the other end provided with a submerged sharp crested weir. The average water depths used in the experiments were 5 cm and 6.5 cm, the wave amplitudes varied between 0.7 cm and 1.2 cm and the wave periods varied between 70 sec and 120 sec. Maximum velocities in the experiments varied between 3 cm/sec and 5 cm/sec, depending on water depth, amplitude and period. Reynolds' numbers ($Re = \frac{qD}{\nu}$) were larger than 800 (the limit for fully turbulent flow) 60% - 80% of the time (the exact percentage depending on depth, period and amplitude).

The floats used in the experiments were cylindrical and had a diameter of approximately 0.5 cm, the top was given a conical shape to minimize effects of surface tension. The length of the floats was chosen as large as possible to arrive at an average over depth particle path, but short enough that the float did not contact the bottom. Floats were released one at a time either in the middle of the lagoon or 5 cm from the side walls. Positions of the float were marked at each slack tide for a period of at least five tidal cycles.

Typical examples of measured and computed float paths are presented in Figure 5. In the computations the flow over the weir was described by

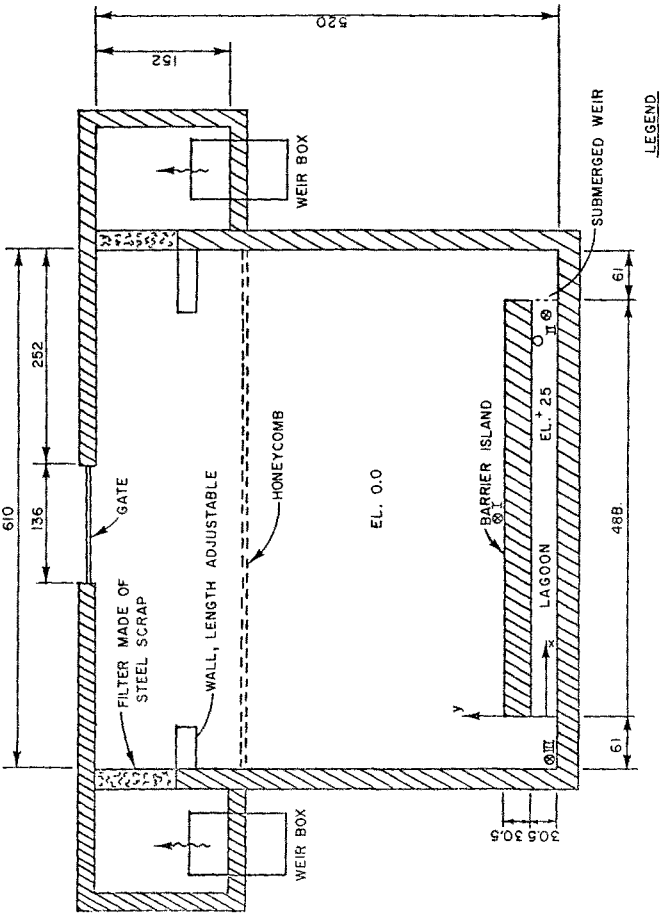

FIGURE 4 EXPERIMENTAL-SET UP

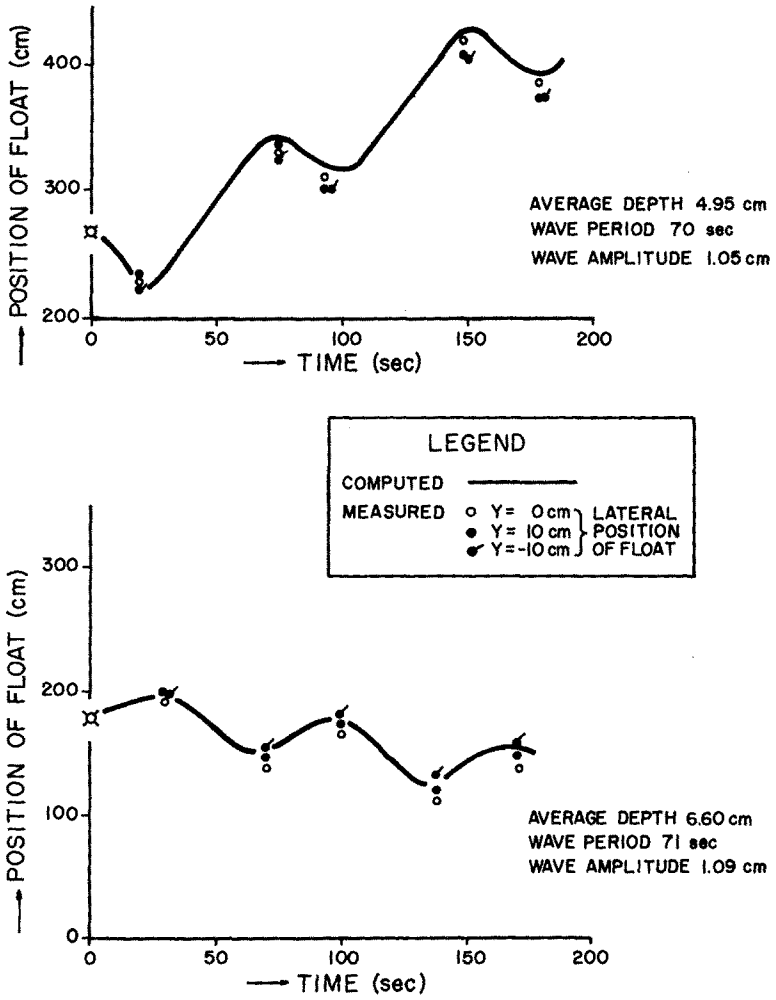

FIGURE 5. MEASURED AND COMPUTED FLOAT POSITIONS

an equation similar to Equation (3)

$$q_w = \pm \mu \pm h_w \sqrt{2g|\eta_o - \eta_i|} \qquad (10)$$

\+ sign for $\eta_i \geq \eta_o$

\- sign for $\eta_o \geq \eta_i$

In Equation (10)

q_w = discharge per unit width over the weir

$\mu_{\pm}$ = weir coefficient

h_w = total depth over weir

η_o = water level in tidal basin

η_i = water level in canal

For all the experiments the net discharge q was determined from the measured particle path using an empirical method described by van de Kreeke [4] and compared with the computed net discharge. The results are presented in Figure 6.

SUMMARY AND CONCLUSIONS

- The numerical model presented in this paper is especially designed for lagoons connected to the ocean by relatively narrow inlets and for which the flow field can be described by the one-dimensional tidal equations. The flow in the inlets is described by a semi-empirical relation. In the equations all non-linear terms are retained in order to correctly reproduce such phenomenon as tide-induced mass transport and variations in mean level along the longitudinal axis of the lagoon.

- The tidal equations are solved using an explicit difference scheme. In the computational model the inlet equations are regarded as implicit boundary conditions to the tidal equations. The advantages of this approach are: (1) the size of the computational grid in the lagoon can be chosen independently of the relatively small dimensions of the inlets and (2) the flow at branching inlets (an inlet connecting a lagoon to the ocean such that branching of the inlet flow can occur) still can be described by a one-dimensional model.

- The predictive capability of the model is confirmed by favorable comparison between measured and computed float paths and net dis-

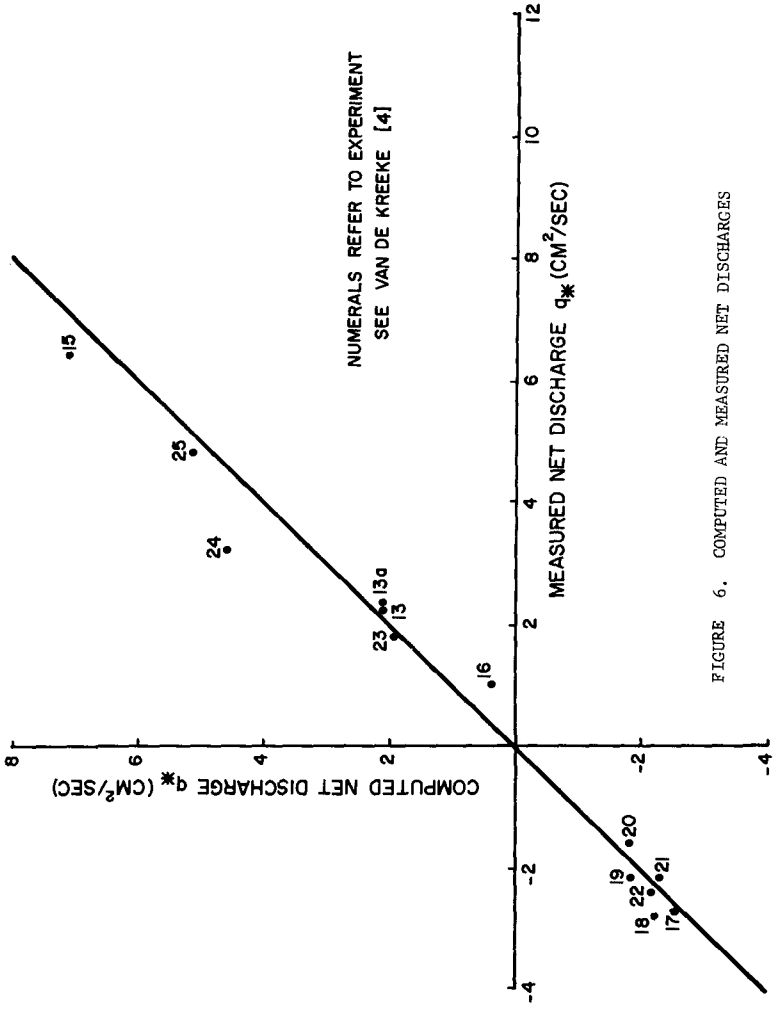

FIGURE 6. COMPUTED AND MEASURED NET DISCHARGES

charges for a series of laboratory experiments. For the experiments the relative magnitude of the different terms in the equations differs substantially from those found under prototype conditions. Therefore additional corroboration of the computational model at the prototype level is recommended.

ACKNOWLEDGEMENT

The author is indebted to R.G. Dean and B.A. Christensen for their suggestions and helpful criticism.

The study was in part supported by the Office of Water Resources Research, U.S. Department of the Interior.

REFERENCES

1. Balloffet, A., "One-Dimensional Analysis of Floods and Tides in Open Channels", Journal of the Hydraulics Division, ASCE. Vol 95, No. HY4, July 1969.

2. Dronkers, J.J. "Tidal Computations in Rivers and Coastal Waters", North-Holland Publishing Company, 1964.

3. Reid, R.O. and Bodine, B.R. "Numerical Model for Storm Surges in Galveston Bay", Journal of the Waterways and Harbors Division, ASCE, Vol. 94, No. WW1, February, 1969.

4. Van de Kreeke, "Tide-Induced Mass Transport in Shallow Lagoons", Department of Coastal and Oceanographic Engineering, University of Florida, Technical Report No. 8, October, 1971.

CHAPTER 129

A NUMERICAL MODEL OF ESTUARINE POLLUTANT TRANSPORT

by

Hugo B. Fischer
Associate Professor of Civil Engineering
University of California
Berkeley, California

I. INTRODUCTION

Pollutant transport studies in estuaries may be divided into two general types: firstly, those where a new pollutant will be discharged into an existing estuary; and secondly, those where the estuarine geomtry will be changed permanently. The first type of problem is analyzed more easily because distributions of existing natural or artificial tracers can be used to determine rates of transport and diffusion. For this type of problem one-dimensional or time-averaged two-dimensional models, employing apparent diffusivities evaluated from existing tracers, are often satisfactory. When permanent changes in the system are envisaged, however, it is likely that the bulk or apparent diffusivities of space and time-averaged models will be changed in unpredicatable ways. Hence to determine what will be the effect of dredging a new channel in an estuary, or permanently changing the distribution of fresh water inflow, more sophisticated models must include the underlying mechanisms of pollutant transport and diffusion. The purpose of this paper is to present a two-dimensional, non-time averaged model which is computationally fast, seems to be reasonably accurate, and can be used to predict the effect of permanent changes wherever a two-dimensional representation is satisfactory.

II. THE CONCEPT OF TWO-DIMENSIONAL MODELING

A computer program to solve the equations of motion and diffusion in three space dimensions and time for a real estuary is beyond the capacity of present day computers. Hence all computer models of estuaries are based on averaging, either over one or two space dimensions, or time, or both. The two-dimensional models discussed herein average only over the vertical dimension, so that the velocity and concentration are considered to be functions of the two horizontal dimensions x and y and time t, but not of the vertical dimension z. The equations to be solved are the vertically-integrated equation of motion,

$$\frac{\partial u}{\partial t} + u\frac{\partial u}{\partial x} + v\frac{\partial u}{\partial y} - fv + g\frac{\partial h}{\partial x} + g\frac{u\sqrt{u^2+v^2}}{C^2 h} = \frac{\tau_x}{\rho h} \qquad (1)$$

in the x direction, and a similar equation in the y direction, and the advective diffusion equation for a dissolved constituent,

$$\frac{\partial(ch)}{\partial t} + \frac{\partial}{\partial x}(uch) + \frac{\partial}{\partial y}(vch) = \frac{\partial}{\partial x}\left(D_x\, h\, \frac{\partial c}{\partial x}\right) + \frac{\partial}{\partial y}\left(D_y\, h\, \frac{\partial c}{\partial y}\right) \qquad (2)$$

In these equations u and v are velocities and D_x and D_y are diffusivities in the x and y directions, respectively, C is the Chezy coefficient, f is the Coriolis parameter, h is depth, τ_x is the x-component of the wind stress, and c is the concentration of a dissolved substance.

The restrictions on this concept are apparent. u and v are depth averaged velocities, so the velocity profile both in magnitude and direction is resolved into a single, depth averaged vector. The wind stress, which in the prototype exerts a stress on the water surface and produces a vertical, spiraling velocity profile, is resolved into an apparent body force inversely proportional to depth. The dispersive effect of the vertical velocity profile has to be expressed by the diffusivities D_x and D_y, which are therefore not turbulent diffusion coefficients at all, but rather dispersion coefficients depending on the direction, magnitude, and distribution of the velocity vector.

III. DESCRIPTION OF THE MODEL

The model to be described in this report is a two-dimensional model for use in large bays and estuaries with substantial open areas, where stratification is not important. The model is in two parts: first, a solution of the equations of motion, using the finite difference method given by Leendertse (1967); and second, a model for constituent transport developed by the writer and described in detail with a complete listing of the numerical program by Fischer (1970).

The hydrodynamic program is run first, and is operated until steady state is obtained (usually in the second tidal cycle). The x and y components of velocity at each grid point are stored on magnetic tape at hourly or half-hourly increments. This part of the procedure is similar to that used by Leendertse and Gritton (1971, a,b) in a modeling study of Jamaica Bay. Leendertse and Gritton have also developed and used a finite difference solution of the advective diffusion equation, using the same time step as for the hydrodynamic solution. In the present model, however, an alternate method is used, based on the method of superposition, which allows a substantially longer time step. The method of superposition, also called the convolution intergral, states that in steady uniform flow the solution to Equation 2, given a known concentration distribution at t = 0, is

$$c(x,y,t) = \iint_A \frac{c(\xi,\eta,0)}{4\pi t\sqrt{D_x D_y}}\, e^{\frac{1}{4t}\left(\frac{(x-ut-\xi)^2}{D_x} + \frac{(y-vt-\eta)^2}{D_y}\right)}\, d\xi\, d\eta \qquad (3)$$

This equation gives the concentration distribution resulting from any initial distribution after an arbitrarily long time, in the absence of boundaries. So long as the velocities remain constant there is no limit on the length of time step, and the accuracy of the solution depends only on the accuracy of the numerical integration.

In practice, of course, velocities in estuaries are neither steady nor uniform, and irregular boundary conditions must be satisfied. Furthermore, evaluation of the integral in Equation 3 is time consuming, even on modern numerical equipment, when many grid points are involved. The numerical scheme developed to satisfy these considerations, while still preserving the spirit of the method of superposition and taking advantage of its long time step, is illustrated in Figure 1. In place of the terms ut and vt, we use the approximations $\int_0^t u\,d\tau$ and $\int_0^t v\,d\tau$, where the time interval may be anything up to the time required for one tidal inflow or outflow. The integration is done in half-hourly steps, using the velocity field generated by the hydrodynamic program. The spatial integration in Equation 3 is replaced by a summation over a limited area, to increase computational speed. The scheme illustrated by Figure 1 uses a 5 point top hat distribution; to compute the concentration at the grid point I,J shown at the end of the path of arrows in Figure 1, we integrate the velocity field backwards in time to locate the closest grid point of origin, M,N, shown as the origin of the path or arrows. c(I,J) is computed by the relationship

$$c(I,J) = {}^1/_5 \left(c(M,N) + c(M+1,N) + c(M-1,N) + c(M,N+1) + c(M,N-1)\right) \qquad (4)$$

The boundary conditions of inflow from a river, or from the ocean, and the condition at the land boundary, are satisfied as follows. If the back calculation of the velocity field carries an indicator particle into the ocean, it is assigned the ocean concentration. Similarly, if a particle is carried into the river, it is assigned the river concentration, which may be a function of time given by another program. Obviously, no concentrations will be computed for points which are in fact on land; if, by chance, back integration of the velocity field carries the indicator particle out of the water field, its motion is stopped for the remainder of that time step, and it is assigned the nearest water concentration. Hence, all concentrations in the water field are computed by averaging concentrations around the grid point where the particle begins its motion. Diffusion, which is accomplished by the spatial integration of Equation 3, is carried out by the averaging procedure given in Equation 4. The magnitude of the apparent diffusivities, D_x and D_y, can be varied by varying the details of the averaging process, the time step, and the grid spacing. The 5 point averaging scheme shown in Equation 4 and Figure 1 is equivalent to selecting equal diffusivities D_x and D_y equal to $0.2\ (\Delta x)^2/\Delta t$, where, Δx is the distance between grid points and Δt is the duration of the advective time interval. The factor 0.2 is established by the probabilities of the diffusive motion, which in each direction during each time interval are 0.2 one step forward, 0.2 one step backward, and 0.6 no net motion. These probabilities could, of course, easily be changed by revising the averaging given in equation 4.

IV. AN EXAMPLE APPLICATION

The model has been applied to Botany Bay, New South Wales, Australia, as part of a major water quality study of the Georges River-Botany Bay system. The Georges River itself was modeled in one-dimensional segments, using the scheme described by Fischer (1972). Botany Bay is the downstream end of the river, and is a roughly circular embayment approximately three miles in diameter. The model was used to study the present geometry, and also a proposed geometry including a breakwater and port development. A one thousand foot grid was used, and an observed tide at the mouth of the bay was simulated. The model computed tidal elevations and velocities and the concentrations of six constituents throughout the bay and river system.

Figure 2 shows a typical example of currents computed in Botany Bay. These currents are used in the water quality model, and Figure 3 shows a typical result for a non-conservative constituent. Three constituent sources were modeled: the ocean, the Georges River, as a time-varying source computed by the river model, and a point source at the Cooks River. At the ocean mouth, a tidal exchange ratio of 75% was assumed. This was distributed over the tidal cycle by assuming that in the first hour of tidal inflow 50% of the inflowing water had just left on the previous tide, in the second hour 25%, and thereafter, zero. Wind stresses from winds coming from several directions were assumed, although in the simple geometry of Botany Bay wind driven circulations did not appear to be of major importance.

The model was first used to model salinity, because verification of a salinity distribution provides a good check on the physical description of the system. The salinity distribution in the Georges River was modeled with reasonable accuracy for a range of river discharges; unfortunately, this did not provide verification of the model in the bay, because the salinity within the bay is nearly constant. After the model was verified for salinity, concentrations were computed for biochemical oxygen demand, dissolved oxygen, coliforms, phosphorous, and nitrogen. To the extent that field data were available, reasonable verifications were obtained for all constituents.

V. DISCUSSION OF RESULTS

The water quality model presented herein represents a departure from the usual finite difference numerical method. The new method is always stable, by virtue of the method of averaging, and will always yield results which at least appear to be reasonable. When a very long time step is used the accuracy does, of course, suffer; in the present study, which used a six to eight hour time step, some of the details of the tidal flow were lost. On the other hand, the longer time step has the major advantage of permitting simulation of longer periods at reasonable cost. This is particularly important for water quality models, because while a hydrodynamic steady state may be achieved within two or three tidal cycles,

a steady state distribution of a constituent often requires as much as 30 to 60 tidal cycles, depending upon the size of the system. Ward and Fischer (1971) found, for example, that in the Delaware estuary a 30 day equilibrium time might be reasonable, and Hyer (1972) found that in some hydraulic model experiments 30 to 60 days were required to reach a salinity equilibrium. Thus, an important requirement for a water quality numerical model is an ability to run for 30 to 60 tidal cycles at reasonable cost.

In the present model, turbulent mixing both in the flow direction and transverse to the flow direction is simulated by mixing over a radius of 1000 feet at the end of every tidal inflow or outflow. This corresponds to assuming values of the turbulent mixing coefficients of approximately 10 $ft^2/sec.$ in each direction. These coefficients actually represent the effect of velocity shear in all directions, and their magnitudes in real estuaries are not well known. For dispersion in the flow direction, one can obtain the magnitude of the coefficient by using Elder's result $D_x = 6\ du^*$ where d is the depth of flow and u^* is the shear velocity. For Botany Bay, this would yield a value of the order of 10 $ft^2/sec.$ In the transverse direction, dispersion is probably caused by a rotation of the velocity vector with depth, as discussed by Ward (1972). Little can be said, however, about the magnitude of the transverse coefficient in real estuaries, as it is affected by a number of factors particular to each individual estuary. The assumption used for mixing in the present model, while very approximate, is probably as accurate a representation of what happens in real estuaries as can be devised from present knowledge. More field data on this aspect of dispersion are essential.

In summary, the model presented in this report represents an attempt to simulate the physical processes of transport and dispersion of constituents in estuaries. The time step used is long, permitting simulation of a long period of real time. Accuracy can probably be improved by shortening the time step and increasing the degree to which the details of convective transport are modeled. The model is presently being applied to several real estuaries and it is hoped that further development will provide a useful tool for water quality studies.

ACKNOWLEDGEMENTS

The study of Botany Bay described in this paper was sponsored by the Metropolitan Water Sewerage and Drainage Board, Sydney, Australia, and was carried out by Brown and Caldwell, Inc., consulting engineers. Funds for initial development of the numerical program were provided by the Water Resources Center of the University of California and by the National Science Foundation under Research Initiation Grant GK-3210.

REFERENCES

Fischer, H. B., 1970, "A Method for Predicting Pollutant Transport in Tidal Waters": Contribution 132, Water Resources Center, Univ. of Calif., 143 pp.

Fischer, Hugo B., 1972, "A Lagrangian Method for Predicting Pollutant Dispersion in Bolinas Lagoon, Marin County, California," U.S. Geological Survey Prof. Paper 582-B, 32 pp.

Hyer, Paul V., 1972, "Repeatability in Estuarine Hydraulic Model," J. Hyd. Div., Proc. ASCE, 98, 631-644.

Leendertse, J. J., 1967, "Aspects of a Computational Model for Long-Period Water-Wave Propagation", Memorandum RM-5294-PR, The Rand Corp., Santa Monica, Calif., 165 pp.

Leendertse, J. J., and E. C. Gritton, 1971a, "A Water-Quality Simulation Model for Well-Mixed Estuaries and Coastal Seas: Vol. II, Computational Procedures," The Rand Corp. R-708-NYC.

Leendertse, J. J., and E. C. Gritton, 1971b, "A Water-Quality Simulation Model for Well-Mixed Estuaries and Coastal Seas: Vol. III, Jamaica Bay Simulation," The Rand Corp. R-709-NYC.

Ward, Peter, R. B., 1972, "Transverse Dispersion of Pollutants in Oscillatory Open-Channel Flow," Report WHM-2, Hydraulic Engineering Lab., University of California, Berkeley, Calif.

Ward, P.R.B., and H. B. Fischer, 1971, "Some Limitations on Use of the One-Dimensional Dispersion Equation, with Comments on Two Papers by R. W. Paulson," Water Resources Research, 7, 215-220.

FIGURE CAPTIONS

Figure 1: Schematic drawing of particle motion in the transport model.

Figure 2: A typical computed velocity distribution in Botany Bay.

Figure 3: Predicted NO_2 and NO_3 levels (mg/l as N) in Botany Bay at low tide, July 1969.

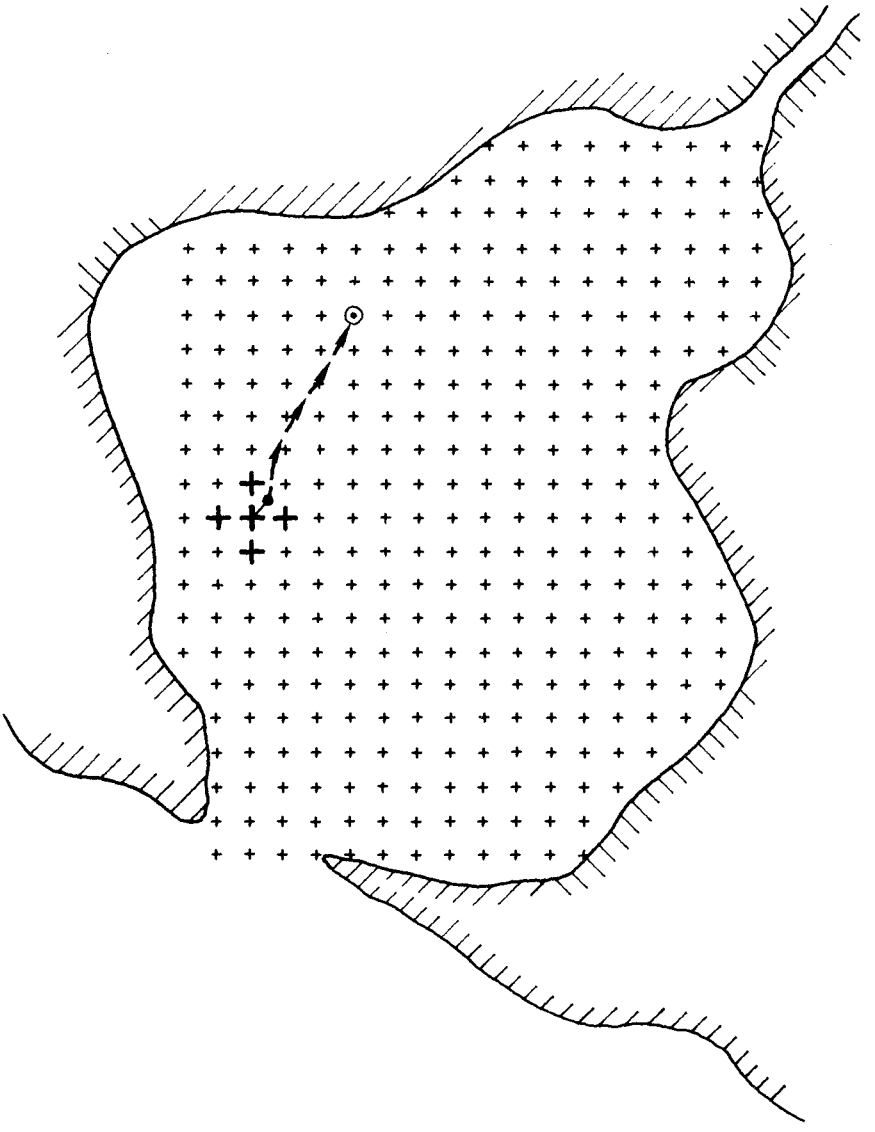

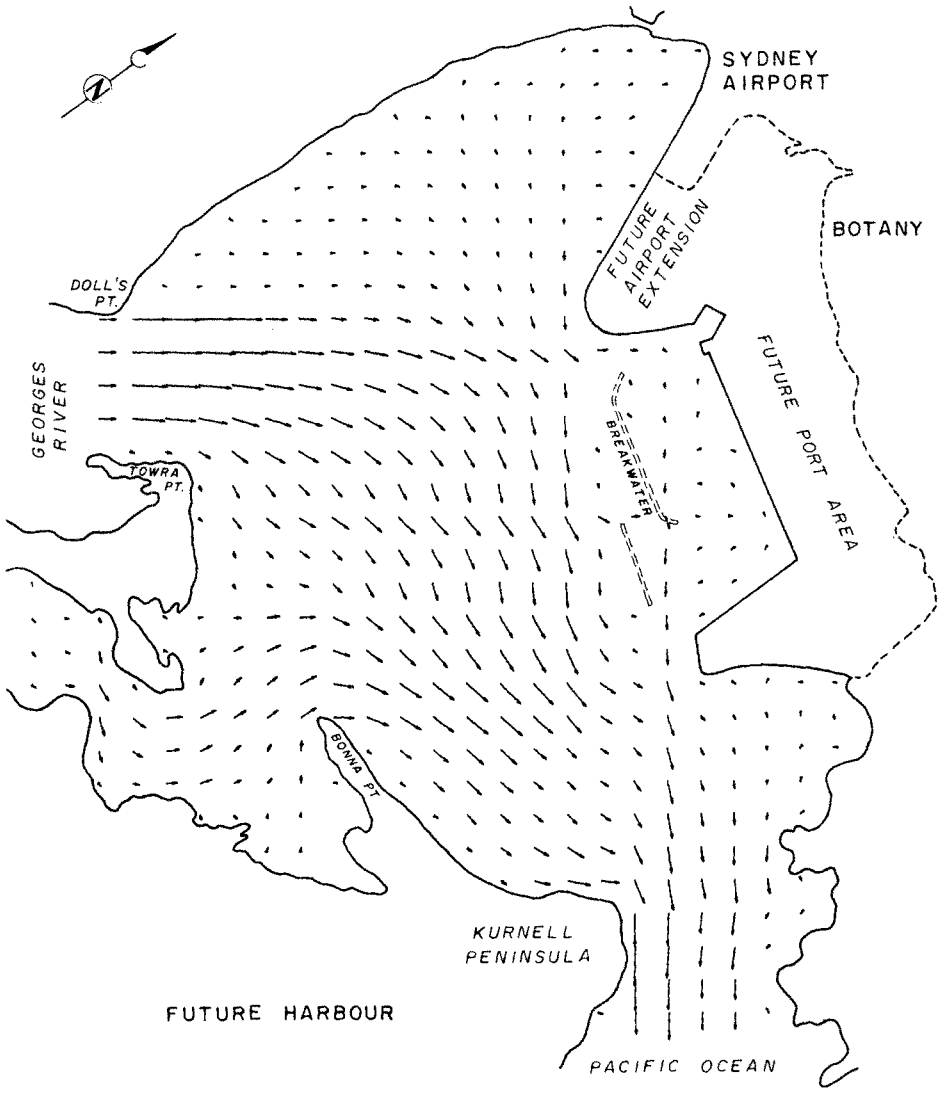
SYDNEY
AIRPORT
BOTANY
FUTURE
AIRPORT
EXTENSION
DOLL'S
PT.
GEORGES
RIVER
FUTURE PORT AREA
BREAKWATER
TOWRA
PT.
BONNA PT.
KURNELL
PENINSULA
FUTURE HARBOUR
PACIFIC OCEAN

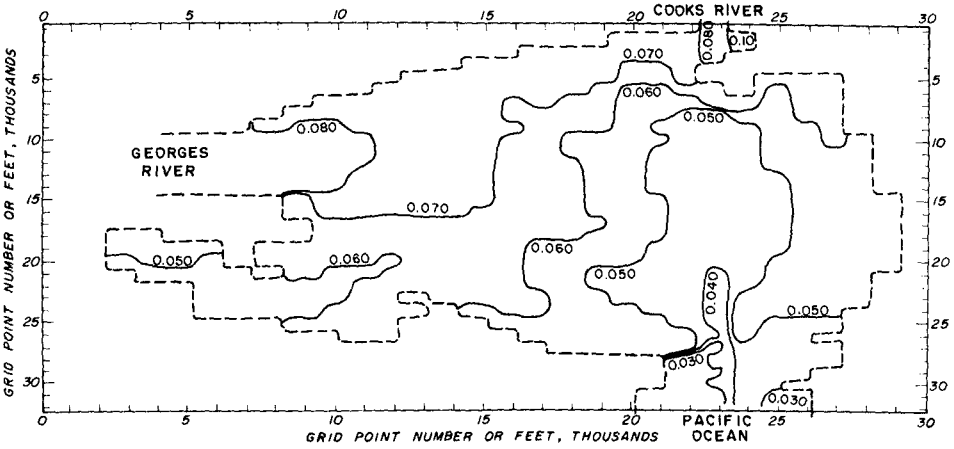
COOKS RIVER
GEORGES RIVER
PACIFIC OCEAN
0.080
0.070
0.060
0.050
0.040
0.030
0.10
GRID POINT NUMBER OR FEET, THOUSANDS
GRID POINT NUMBER OR FEET, THOUSANDS

CHAPTER 130

A MATHEMATICAL MODEL FOR SALINITY INTRUSION*

A. Y. Kuo and C. S. Fang
Department of Physical Oceanography and Hydraulics
Virginia Institute of Marine Science
Gloucester Point, Virginia 23062

ABSTRACT

A long term time-dependent mathematical model has been developed for predicting the salinity distributions in the upper York River System, including the tidal portions of the Mattaponi and Pamunkey Rivers.

The method of calculating the longitudinal dispersion coefficient is discussed in detail. The study area and field project are described. The downstream boundary condition was found from a scheme combining a semi-explicit technique and linear extrapolation. The mass-balance equation, averaged over a tidal cycle and solved numerically by the implicit finite difference scheme, provided a reasonable solution and afforded economy in computer time. Field data were compared with the corresponding model results, indicating the general accuracy of the methodology.

INTRODUCTION

The York River System of Virginia includes the Pamunkey and Mattaponi Rivers. The junction of the two rivers forms the York River which is an estuarine river with a 30 mile course from West Point to the Chesapeake Bay near Yorktown, Virginia. The tidal portion of the upper York River serves as a spawning and nursery ground for anadromous commercial and sport fish. The construction of a dam has just been completed on the North Anna River, a main tributary of the Pamunkey, and a second dam is proposed on the Pamunkey River. The effects of these dams will be the regulation and reduction of fresh water flow, thus altering the salinity regime and affecting the existing biota in the estuarine system.

This paper presents a mathematical model developed to study salinity intrusion in the upper York River System. It was used to assess the increased salinity intrusion due to various degrees of reduction of fresh water flow in the Pamunkey River. Predicted salinity distributions aid in regulating flows from the impoundments resulting from the dams.

*Virginia Institute of Marine Science Contribution No. 475.

MATHEMATICAL FORMULATION

The transport of salt in a roughly sectionally homogeneous estuarine river may be described by the one-dimensional mass balance equation

$$\frac{\partial}{\partial t}(AS) + \frac{\partial}{\partial x}(AUS) = \frac{\partial}{\partial x}\left(AE_s \frac{\partial S}{\partial x}\right) \tag{1}$$

where t is time, x is the distance along river, A is the cross-sectional area, E_s is the dispersion coefficient, U and S are the cross-sectional mean velocity and salinity, respectively. The lateral variation of axial velocity and the transport of salt due to lateral convection and diffusion are not explicitly represented in equation (1), but are lumped into a single dispersion term. The concept of dispersion in a shear flow was first illustrated by Taylor (1953, 1954), both theoretically and experimentally. Aris (1956) gave a rigorous mathematical proof of the dispersion representation of the transport due to interaction between lateral diffusion and velocity shear. Harleman (1971) has given a brief account of the subsequent extensions of the dispersion concept to natural bodies of water.

To describe the long term, such as seasonal, variation of salinity intrusion, a time increment of numerical computation larger than a tidal cycle is desirable. This large time increment can not be applied to equation (1) directly; it has to be applied to the equation averaged over a tidal cycle. Okubo (1964) performed the time average of equation (1) and arrived at

$$\frac{\partial}{\partial t}(\bar{A}\bar{S}) + \frac{\partial}{\partial x}(\bar{A}\bar{U}_f\bar{S}) = \frac{\partial}{\partial x}\left(E\bar{A}\frac{\partial \bar{S}}{\partial x}\right) \tag{2}$$

where the overbars represent the average over a tidal cycle, and U_f is the velocity due to fresh water discharge Q, given by

$$U_f = \frac{Q}{\bar{A}} \tag{3}$$

E is a dispersion coefficient including the time average of E_s and the effect of transport by oscillating tidal currents.

Since the York River model was to be used to predict the long term effect of fresh water reduction on salinity intrusion, the 'slack tide approximation' was chosen. In the model, only the maximum salinity in the tidal cycle, i.e., the salinity at high water slack, was predicted. No attempt

was made to predict the salinity variation within a tidal cycle. The variation of parameters within a tidal cycle may be written as

$$A = \bar{A} + A' \tag{4}$$

$$U = \bar{U} + U' \tag{5}$$

$$S = S_h + S' \tag{6}$$

$$E_s = \bar{E}_s + E' \tag{7}$$

where A', U' and E' are the deviation from the respective quantities averaged over tidal cycle, S_h is the salinity at high water slack and S' is the deviation from S_h. Substituting (4), (5), (6) and (7) into equation (1) and averaging over tidal cycle, the equation becomes

$$\frac{\partial}{\partial t}(\bar{A}S_h) + \frac{\partial}{\partial x}(\bar{A}U_f S_h) = \frac{\partial}{\partial x}\left(\bar{A}E\frac{\partial S_h}{\partial x}\right) \tag{8}$$

with

$$E = \bar{E}_s + E_t \tag{9}$$

where

$$E_t = -\frac{\overline{S'U'}}{\frac{\partial S_h}{\partial x}} \tag{10}$$

The one-dimensional continuity equation may be written as

$$\frac{\partial}{\partial t}A + \frac{\partial}{\partial x}(AU) = q \tag{11}$$

where q is the lateral fresh water inflow along a unit length of estuary. Averaging over a tidal cycle, equation (11) becomes

$$\frac{\partial}{\partial t}\bar{A} + \frac{\partial}{\partial x}(\bar{A}U_f) = \bar{q} \tag{12}$$

Substituting equation (12) into equation (8), the mass

balance equation becomes

$$\frac{\partial}{\partial t} S_h + U_f \frac{\partial}{\partial x} S_h = \frac{1}{\bar{A}} \frac{\partial}{\partial x} \left(\bar{A} E \frac{\partial S_h}{\partial x} \right) - \frac{\bar{q}}{\bar{A}} S_h \qquad (13)$$

FINITE DIFFERENCE APPROXIMATION

Equation (13) was applied to a part of the upper York River System, between transects upstream of the salt intrusion limits in the Pamunkey and Mattaponi Rivers and a transect four miles downstream of their junction in the York River. The inclusion of Mattaponi River in the model was necessary, even if the expected fresh water reduction was to occur only in the Pamunkey River. The Mattaponi River contributes about 35% of the fresh water discharge to the York River. The increased salt intrusion due to fresh water reduction in the Pamunkey will depend on the fresh water discharge in the Mattaponi while the salinity regime in the Mattaponi will be altered by the fresh water reduction in the Pamunkey. The two rivers are a coupled system and can not be separated.

The equation was solved numerically with an implicit finite difference scheme for each of the three rivers. Twenty, fifteen and four transects were chosen for the Pamunkey, Mattaponi, and York rivers respectively, with average distance between transects being about 3 miles. Except for the end transects of the three rivers, equation (13) was approximated by the following finite difference form for each of the transects.

$$\frac{S_{h,i}' - S_{h,i}}{\Delta t} + \frac{1}{2(\Delta x_{i-1} + \Delta x_i)} \left[U_{f,i}' (S_{h,i+1}' - S_{h,i-1}') + U_{f,i} (S_{h,i+1} - S_{h,i-1}) \right]$$

$$= \frac{1}{\Delta x_{i-1} + \Delta x_i} \left\{ \frac{1}{\bar{A}_i} \left[\left(\frac{\bar{A}_i E_i + \bar{A}_{i+1} E_{i+1}}{2} \right) \left(\frac{S_{h,i+1} - S_{h,i}}{\Delta x_i} \right) - \left(\frac{\bar{A}_{i-1} E_{i-1} + \bar{A}_i E_i}{2} \right) \right.\right.$$

$$\left. \left(\frac{S_{h,i} - S_{h,i-1}}{\Delta x_{i-1}} \right) \right] + \frac{1}{\bar{A}_i'} \left[\left(\frac{\bar{A}_i' E_i' + \bar{A}_{i+1}' E_{i+1}'}{2} \right) \left(\frac{S_{h,i+1}' - S_{h,i}'}{\Delta x_i} \right) \right.$$

$$\left. \left. - \left(\frac{\bar{A}_{i-1}' E_{i-1}' + \bar{A}_i' E_i'}{2} \right) \left(\frac{S_{h,i}' - S_{h,i-1}'}{\Delta x_{i-1}} \right) \right] \right\} - \frac{\bar{q}_i}{\bar{A}_i} S_{h,i} \qquad (14)$$

where the subscript i designates the quantities at the ith transect, subscripts i-1 and i+1 designate the upstream and downstream transects respectively, the prime quantities are

evaluated at the end of the time step Δt, unprimed quantities are evaluated at the beginning of the time step, Δx_i is the distance between the (i-1)th and the ith transects.

BOUNDARY CONDITIONS

The finite difference approximation of the mass balance equation transforms the differential equation into a system of algebraic equations. In this model, there are three systems of simultaneous equations, corresponding to the three branches of the estuarine river, the Pamunkey, the Mattaponi and the York. These three systems of equations are coupled with a mass balance equation for the element including the confluence. The three transects bounding the confluence are chosen to be so close together that the salinity may be assumed uniform within the circumscribed water body. This leaves two upper and one lower boundary condition to be established to close the whole system of equations. The two furthest upstream transects are located far beyond the salt intrusion limits in the Pamunkey and Mattaponi, hence their boundary conditions may safely be taken as zero salinity. The boundary condition at the downstream end in the York River imposes some difficulty. The technique used is a combination of a semi-explicit scheme and linear extrapolation. The salinity of the downstream boundary at the beginning of a time step is used as a boundary condition to estimate the salinity of other transects at the end of a time step. The boundary condition is refined by linear extrapolation from the estimated salinities at the two transects immediately upstream. The refined boundary condition is then used to calculate the salinity distribution at the new time step.

EVALUATION OF PARAMETERS

Convective Velocity. In this 'slack tide approximation' model, the convective velocity includes only the non-tidal component, which is given by

$$U_f(x,t) = \frac{Q(x,t)}{A(x,t)} \tag{15}$$

$Q(x,t)$ is the fresh water discharge from the drainage area upstream of the transect at distance x. This is estimated from the record of stream gauge stations located upstream from the tidal limits. At the ith transect, the fresh water discharge at the mth day is estimated by

$$Q_i(m) = Q_{i-1}(m-n) + I_{i-1,i}\ (m) \tag{16}$$

where $I_{i-1,i}$ is the total lateral fresh water inflow between the (i-1)th and ith transects, and assumed to be proportional to the drainage area increment between the two transects. A delay time of n days is allowed for the discharge Q_{i-1} to travel from (i-1)th transect to ith transect. This travel time is estimated from the average drifting velocity suggested by Pritchard (1958) as

$$U_d = \frac{Q}{\bar{A}} - \beta U_t A_t \tag{17}$$

where U_t and A_t are amplitudes of tidal current and cross-sectional area fluctuations, β is proportional to the correlation coefficient between the variations of tidal velocity and cross-sectional area.

The cross-sectional area averaged over a tidal cycle, $\bar{A}$, is the cross-sectional area corresponding to the fresh water discharge Q. Due to the large volume of average tidal discharge Q_t, $\bar{A}$ is a very weak function of Q except at the transects near tidal limits and at the time of flood. $\bar{A}$ is computed by the hypothetical formula

$$\bar{A} = A_r\left(1 + \frac{Q}{Q_t}\right)^b \tag{18}$$

where

$$Q_t = \frac{2}{\pi} U_t A_r \tag{19}$$

A_r is the cross-sectional area at zero fresh water discharge, and b is a constant less than unity. It may be inferred from calculations of Gallagher and Munk (1971) on the spectrum of tides in shallow water that A_r should be greater than the cross-sectional area below mean-sea level by less than 1% for the York River system.

Dispersion Coefficient. As shown in equation (9), the dispersion coefficient includes two components: one is $\bar{E}_s$, the time average of dispersion due to shear effect and the other is E_t, the dispersion due to the oscillating tidal current.

For a homogeneous estuarine river with a large width to depth ratio, Harleman (1971) suggested that

$$E_s = 77\, n\, h^{5/6} |U| \tag{20}$$

where n is the Manning friction coefficient, h is the hydraulic mean depth. If equation (20) is substituted into the dispersion term in equation (1) and averaged over a tidal cycle, it is determined that

$$\overline{E}_s = 77\, n\, \overline{h}^{5/6} \overline{|U|} \qquad (21)$$

to the first order approximation of two assumed small parameters. The parameters are the ratio of depth fluctuation to averaged depth $\overline{h}$ and the deviation of phase angle θ from $\pi/2$, where the angle θ is the phase between tidal current and tidal height. Equation (21) needs to be modified for use in case the estuarine river is not well mixed. No attempt was made to modify this expression for the present model for the following two reasons: first, the model was formulated primarily for predicting the effect of fresh water reduction on salinity intrusion (an estuary usually tends to be better mixed as the fresh water discharge decreases); second, since the empirical data for the dispersion coefficient in the 'slack tide approximation' model are much larger than E_s, it was expected that the modification would not change the total dispersion coefficient appreciably.

For this upper York River model, a simple dimensional argument was used to formulate the dispersion due to the oscillating tidal current. Dimensionally, the dispersion coefficient may be written as

$$E_t = \alpha u \ell$$

where u and ℓ are the velocity and length scale of the transport mechanism involved, α is a coefficient of order of unity. The apparent choice of the velocity scale would be the amplitude of oscillating tidal current U_t. There are several possible choices of length scale. The tidal excursion seems to be the obvious one. In most estuarine rivers of the Chesapeake Bay, including the York River System, the amplitude of the tidal current averages about 1.5 fps, which gives an excursion of 20,000 ft, and $u\ell$ roughly equal to 100 square miles per day, which is an order of magnitude larger than empirical values. Furthermore, if the tidal current is uniform throughout every cross-section of the river, the salt transported upstream during the flood tide will be carried downstream to the original longitudinal position in the ebb tide, even if some may have been diffused laterally or vertically. Thus, neglecting the fresh water flow and longitudinal turbulent diffusion, the same amount of salt will return to the original transect after a complete tidal cycle, resulting in no dispersion regardless of the tidal excursion. It is the non-uniformity of the tidal current within a cross-section which induces longitudinal dispersion.

Saline water is carried upstream faster in the mid-channel and part of it diffuses vertically or laterally. That diffused out of mid-channel will not be carried downstream to the original longitudinal position because of slower currents outside the mid-channel. Therefore, after a complete tidal cycle, salt originally in one transect will be spread out to other transects, resulting in longitudinal dispersion. For a straight estuarine river with large width-to-depth ratio, Holley et. al. (1970) showed that the time scale of lateral mixing due to turbulent diffusion is much larger than a tidal cycle while that of vertical mixing is much smaller. Therefore, the depth will be the choice of length scale. The depth averages 20 ft. for the upper York River and gives

$$u\ell \approx 0.1 \text{ mi}^2/\text{day}$$

an order of magnitude smaller than empirical data. In reality, in an estuarine river with large curvatures, secondary flows always exist; the time scale of lateral mixing may have the same order of magnitude as the vertical one. In this case, the choice of length scale would be the characteristic length of the cross-section such as the square root of the cross-sectional area. In this upper York River model, E_t was computed as:

$$E_t = \alpha U_t \sqrt{A}$$

where the coefficient α was adjusted until the model output agreed with 1970 field survey data, which gave $\alpha = 2.5$. The tidal velocity and cross-sectional area were calculated from field measurements.

FIELD MEASUREMENTS

Intensive hydrographic surveys were carried out in October, 1969. A total of 37 transects were occupied. Each transect had between one and four stations, depending on river width. Distance between transects averaged three miles. Transects located near sharp bends were positioned at least four river widths from the bend to insure representative measurements for the reach.

Salinity, temperature and velocity measurements were obtained at hourly intervals for twenty five consecutive hours at each station. Sampling depths were at six-foot increments from surface to bottom. Bathymetry of each transect was obtained with a recording sonic depth sounder.

Cross-sectional averages of the longitudinal component of velocity were calculated and plotted as function of time over 25 hours which gave the time variation of current for two

consecutive tidal cycles. The tidal amplitude was calculated as the average of the maximum flood and ebb currents. Cross-sectional areas were determined by planimetry of the bottom profile data collected from sounding.

For the purpose of model verification, a series of slack water surveys have been conducted since August, 1970. Salinity, as well as temperature, dissolved oxygen and biochemical oxygen demand, were measured at local slack water before ebb tide or slack water before flood tide. One station on each transect was sampled with measurements made three feet below the surface and three feet above the bottom.

RESULTS AND DISCUSSION

A mathematical model for salinity intrusion has been developed for the upper York River System. The model is based on the one-dimensional mass balance equation averaged over a tidal cycle. In the model, only the salinity at high water slack is predicted. No attempt is made to predict the salinity variation within a tidal cycle. The objective of this model is to simulate the long term variation of salinity intrusion and to assess the increased salinity intrusion due to various degrees of fresh water reduction in the Pamunkey River.

Figure 1 shows the comparison of the model output with field data of the York and Pamunkey Rivers. The slack water run data of August 14, 1970 was used as the initial condition of the model. Saline water intrudes further upstream in the dry season as indicated by the model output and the field data of late September and mid-November. Figure 2 shows the same comparison for the Mattaponi River. The agreement is not so good as that for the York and Pamunkey, particularly the comparison on November 15, which was four days after a large increase in fresh water discharge. It was observed that the model failed to yield satisfactory results with very high fresh water discharge, because the model responds too slowly to sudden large increases in fresh water discharge. Once it responds to flood conditions, all of the saline water is flushed out of the modeled portion of the estuary. Even after the flood recedes, the salt will not return because of the scheme for setting up the downstream boundary condition.

Figure 3 shows a sample of increased salinity intrusion due to fresh water reduction. With the dam on the North Anna River completed, one of the proposed fresh water flow regulations is a minimum of 40 cfs discharge from the reservoir during the dry season. Using the 1968-1969 fresh water discharge record as input, the solid curves show the salinity distributions with natural discharge and the dashed curves show the salinity distributions with the proposed regulation. In addition to the salinity increase at a particular location, it is also possible to follow the upstream movement of a

particular isohaline. The ecologist is usually more interested in this increased intrusion distance for given salinities, e.g. the 5‰ isohaline. Figure 4 shows the similar comparison for the Mattaponi River. Since only the discharge in the Pamunkey is regulated, the effect of the fresh water reduction decreases with distance upstream from the river's junction.

The model was developed to predict the effect of fresh water reduction on salt intrusion. The critical time of this effect is the dry season when the saline water intrudes furthest upstream. Therefore, the present model was verified with field data taken in the dry season and the constants in the model adjusted accordingly. It has been mentioned that the model failed to yield reasonable results for high fresh water discharge and caution should be taken in the application of the model.

ACKNOWLEDGEMENTS

Funding of the major portion of this research by the Division of Water Resources and State Water Control Board of Virginia is appreciated. We also thank Dr. P. Hyer and Mr. E. P. Ruzecki for their contributions in field data collection, Dr. B. Neilson and Mr. W. Athearn for their critical review of this paper.

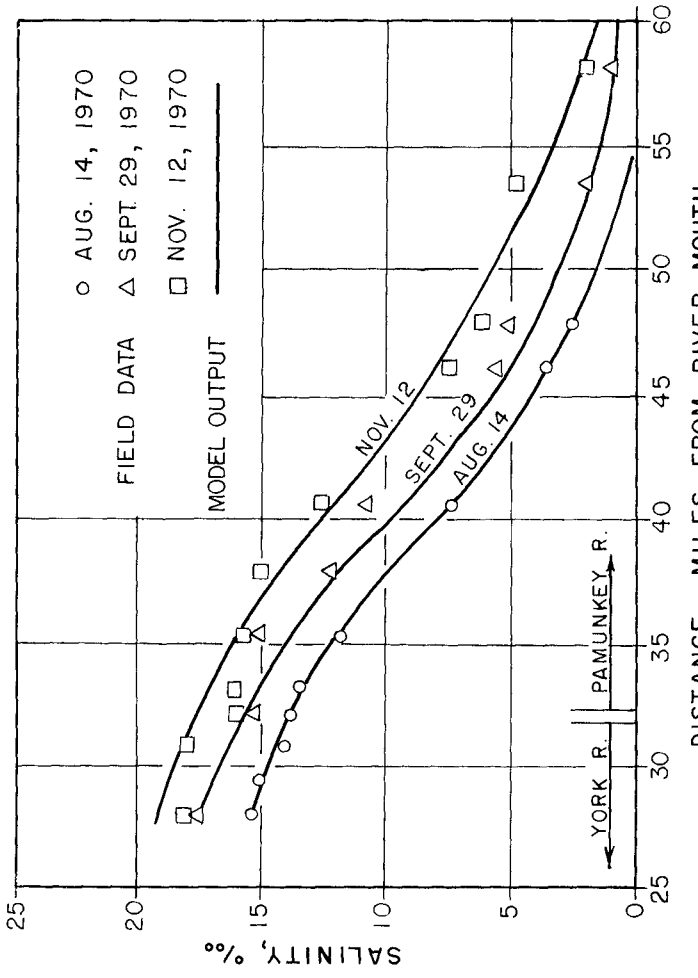

FIGURE 1. SALINITY DISTRIBUTION ALONG PAMUNKEY, 1970.

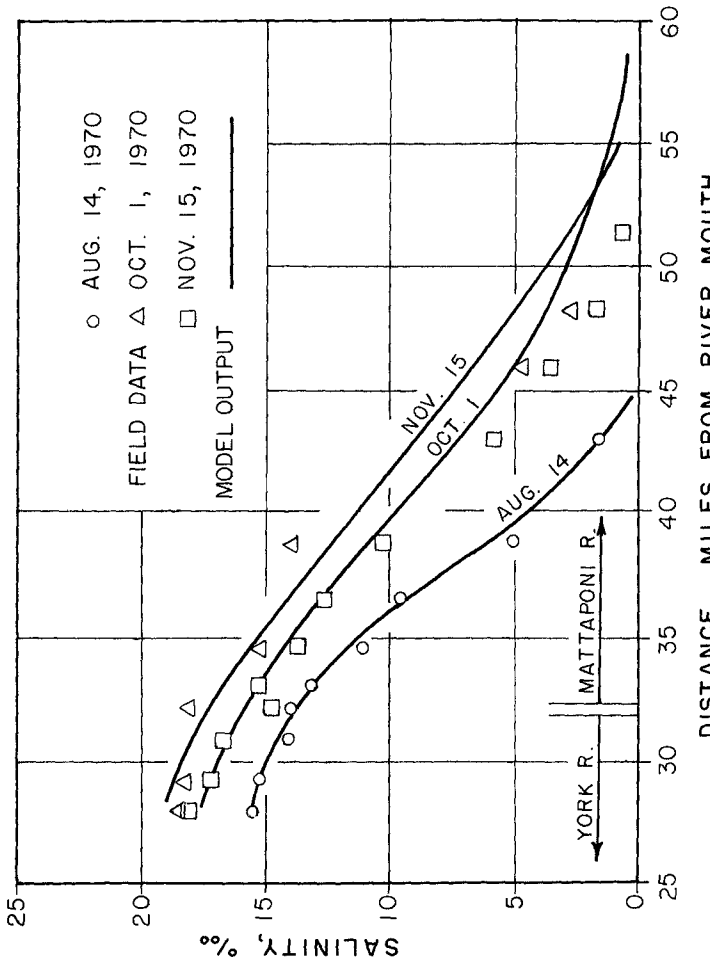

FIGURE 2. SALINITY DISTRIBUTION ALONG MATTAPONI, 1970.

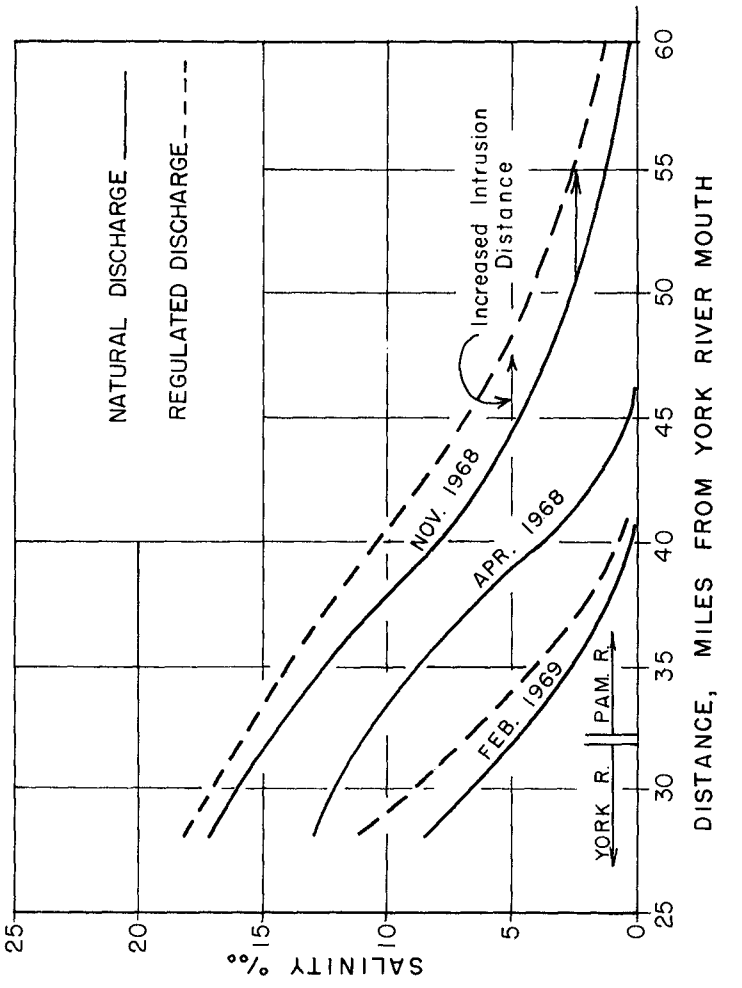

FIGURE 3. 1968-1969 SIMULATED RUN, PAMUNKEY.

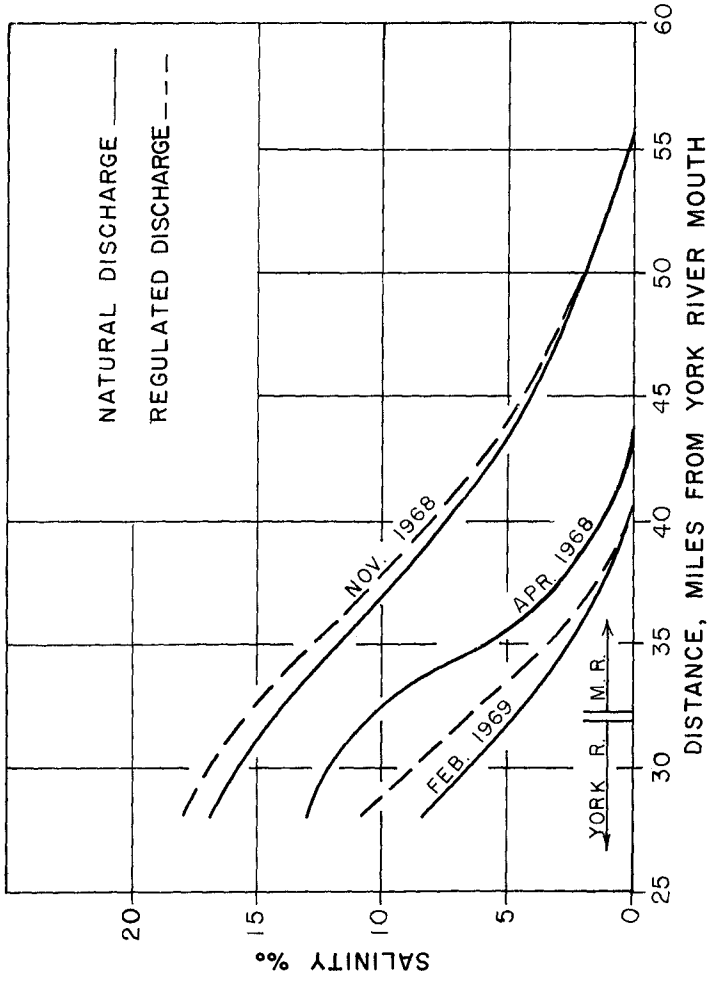

FIGURE 4. 1963-1969 SIMULATED RUN, MATTAPONI.

REFERENCES

Aris, R., "On the Dispersion of a Solute in Fluid Flowing through a Tube," Proc. Royal Society of London, Ser. A, Vol. 235, 1956, pp. 67-77.

Gallagher, B. S. and Munk, W. H., "Tides in Shallow Water: Spectroscopy," Tellus, Vol. 13(4-5), 1971, pp. 346-363.

Harleman, D. R. F., "One-Dimensional Models," Estuarine Modeling: An Assessment, Tractor, Inc., 1971, pp. 34-101.

Holley, E. R., Harleman, D. R. F. and Fischer, H. B., "Dispersion in Homogeneous Estuary," Proc. ASCE, Vol. 96(HY8), 1970, pp. 1691-1709.

Okubo, A., "Equations Describing the Diffusion of an Introduced Pollutant in a One-Dimensional Estuary," Studies on Oceanography, 1964, pp. 216-226.

Pritchard, D. W., "The Equations of Mass Continuity and Salt Continuity in Estuaries," J. of Marine Research, Vol. 17, Nov. 1958, pp. 412-423.

Taylor, G. I., "Dispersion of Soluble Matter in Solvent Flowing Slowly through a Tube," Proc. Royal Society of London, Ser. A, Vol. 219, 1953, pp. 186-203.

Taylor, G. I., "The Dispersion of Matter in Turbulent Flow through a Pipe," Proc. Royal Society of London, Ser. A, Vol. 223, 1954, pp. 446-468.

CHAPTER 131

A NUMERICAL MODEL OF THE ST. LAWRENCE RIVER

by

David Prandle*

ABSTRACT

A one-dimensional numerical model of a 340 mile section of the St. Lawrence River has been formulated to study tidal propagation. For a more detailed study of the flow distribution in a localised section of the river a two-dimensional model was used. A half mile square grid was used to schematise an area of approximately 20 miles long by 15 miles wide. This two-dimensional model was embodied within the one-dimensional model to permit a free interaction of flow across the boundaries.

For the one-dimensional case, a comparison of model and prototype results is included for both elevation and velocity. For the two-dimensional model a comparison of flow distribution was made by using field results obtained from photographing ice movement and from drogue movement.

To interpret the results of the two-dimensional model into a simple method of flow visualisation, use was made of animation techniques. A movie film was made that demonstrates both tidal rise and fall and the associated horizontal velocities. Elevation was reproduced by use of varying shades of coloured paper to simulate contours, velocities were represented by simulating drogue movement to produce smoke streaks.

INTRODUCTION

The St. Lawrence River extends from Lake Ontario to the Gulf of St. Lawrence connecting the International Great Lakes to the Atlantic Ocean. The region studied stretches from Father Point at the seaward end to the Port of Montreal, a distance of approximately 340 miles (Fig. 1).

Numerical simulation has been used extensively in studies of many areas of the river. The simulation techniques have included the methods of characteristics and finite differences. The latter method has been applied in both the implicit and explicit modes and for both one and two-dimensional applications. This paper describes a combined one and two-dimensional model employing an explicit finite difference solution.

*Assistant Research Officer, Hydraulics Laboratory, National Research Council, Ottawa, K1A 0R6, Canada.

Fig. 1. The St. Lawrence River

A detailed investigation was required of a section of the river approximately 20 miles long and varying in breadth from 2 to 15 miles (Fig. 2). The section included a number of channels interspersed by islands, the distribution of flow between these channels was of particular interest. A two-dimensional model with a half-mile square grid was used to represent this area. The boundaries of this model were extended to river sections where the lateral variations in flow were small. The flow conditions at these boundaries could not be specified from available field data, moreover they were subject to modification by engineering works within the area of interest.

This difficulty was resolved by extending the simulation of the river to sections where boundary conditions could be accurately specified and to where they would not be subject to modification. The river lengths between these external boundaries and those of the two-dimensional model were simulated by a one-dimensional numerical model.

The model was calibrated to reproduce tidal elevations throughout the river. For the two-dimensional model the friction coefficient was taken as constant throughout the area. The flow distribution obtained from the model was compared with prototype observations obtained from filming ice break-up and from drogue movements.

While the results of a model study of this nature are of fundamental importance for hydraulic engineering they may only constitute one of several factors which affect the decision making process in a comprehensive engineering scheme. In such instances a distinct limitation of numerical models has been the difficulty of presenting results in a form readily understood by the layman. Whereas for the alternative form of simulation by hydraulic scale models flow visualisation can be so gainfully exploited.

In an attempt to overcome this shortcoming of numerical models recourse was made to animation techniques. A description of the techniques developed in the compilation of the film is included.

MATHEMATICAL MODEL

(a) One-dimensional

The equations of motion may be written as follows:

Motion in the x-direction:

$$\frac{\partial U}{\partial t} + U \cdot \frac{\partial U}{\partial x} + g \cdot \frac{\partial H}{\partial x} + F = 0 \qquad (1)$$

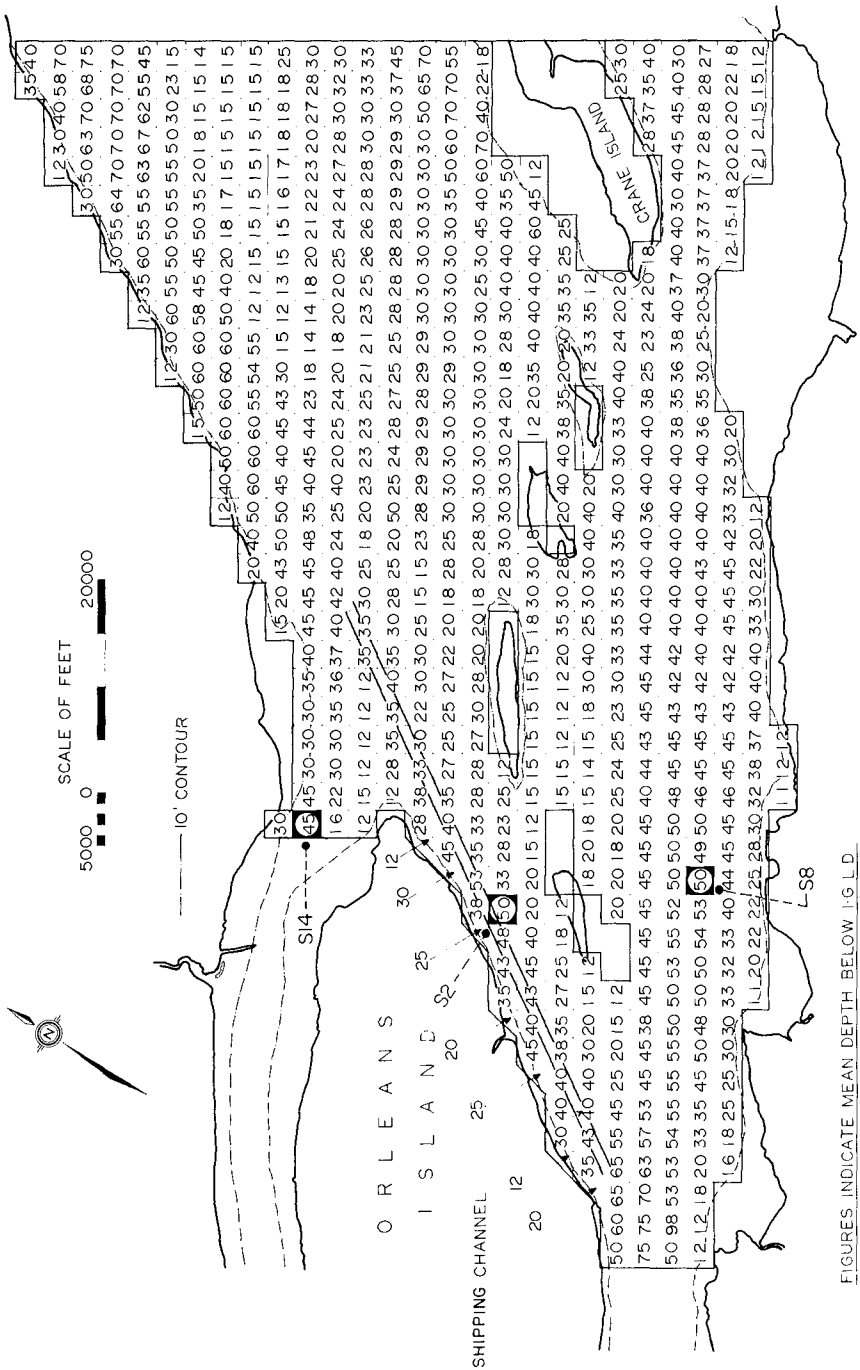

Fig. 2. Two-dimensional Schematisation

Continuity:

$$\frac{\partial Q}{\partial x} + B \frac{\partial H}{\partial t} - \partial \frac{Q_T}{\partial x} = 0 \qquad (2)$$

where x - a horizontal axis in the longitudinal direction of the river flow
t - time
U - velocity in the x-direction
g - acceleration of gravity
H - elevation of the water surface above a horizontal datum
Q - discharge = U · A, A area of cross-section
B - channel breadth
Q_T - tributary discharge.

The friction term F was represented in this case by the Chezy formula

$$F = \frac{g \cdot U \cdot |U|}{C^2 \cdot R}$$

C - the Chezy friction coefficient
R - the length parameter normally taken as the hydraulic radius but in this study the hydraulic mean depth is used.

An explicit finite difference solution was used to solve the above equations. The method of schematisation and the details of the numerical solution closely followed that described by Rossiter and Lennon*. The standard procedures for calibrating the model were adopted. The river was divided into ten sections within which the friction coefficient was considered constant. The optimisation of these ten coefficients was achieved after about five adjustments.

(b) Two-dimensional

The equations of motion may be written as follows:

In the x-direction:

$$\frac{\partial U}{\partial t} + U \cdot \frac{\partial U}{\partial x} + V \cdot \frac{\partial U}{\partial y} + g \cdot \frac{\partial H}{\partial x} + Fx - \Omega \cdot V = 0 \qquad (3)$$

In the y-direction:

$$\frac{\partial V}{\partial t} + U \cdot \frac{\partial V}{\partial x} + V \cdot \frac{\partial V}{\partial y} + g \cdot \frac{\partial H}{\partial y} + Fy + \Omega \cdot U = 0 \qquad (4)$$

*Rossiter, J.R.; Lennon, G.W.; "Computation of Tidal Conditions in the Thames Estuary by the Initial Value Method". Proc. Inst. Civil Eng., Vol. 31, May, 1965.

Continuity:

$$\frac{\partial H}{\partial t} + \frac{\partial}{\partial x}(U \cdot (H + D)) + \frac{\partial}{\partial y}(V \cdot (H + D)) = 0 \qquad (5)$$

where x,y - two orthogonal horizontal axes
U - velocity in the x-direction
V - velocity in the y-direction
H - elevation of the water surface above a fixed horizontal plane
D - depth of the bed below the same fixed plane.

Fx and Fy the friction terms in the x- and y-directions respectively were represented by the Chezy formula

$$Fx = \frac{g \cdot U \cdot |(U^2 + V^2)^{\frac{1}{2}}|}{C^2(H + D)}; \qquad Fy = \frac{g \cdot V \cdot |(U^2 + V^2)^{\frac{1}{2}}|}{C^2(H + D)}$$

$\Omega \cdot V$ and $\Omega \cdot U$ are the horizontal components of the Coriolis force. $\Omega = 2\Omega \sin \phi$, where ω is the angular velocity of the earth's rotation. ϕ is the latitude of the location.

The equations were solved using an explicite finite difference solution of the type described by Reid and Bodine*. The convective terms in Eqns. (3) and (4) were omitted to avoid instabilities and also to save computational effort. Their omission is unlikely to be of significance in a problem of this nature. There was not sufficient data to warrant a spatial variation in the value of the Chezy friction coefficient. It was taken as a constant equal to that used in the corresponding area in an earlier purely one-dimensional model of the river.

(c) Boundary of the One and Two-dimensional Model

At the junctions of the one and two-dimensional schemes the following techniques were used.

(i) The first water level position in the one-dimensional section is located at a distance $\Delta s/2$ from the limit of the two-dimensional scheme where Δs is the constant grid size used in the two-dimensional scheme.

(ii) For calculating the velocities at the boundary of the two-dimensional scheme it is assumed that the water level at the external grid point is equal to that given at the corresponding position in the one-dimensional model.

*Reid, R.O.; Bodine, B.R.; "Numerical Model for Storm Surges in Galvaston Bay". Proc. Am. Soc. Civ. Eng., Vol. 94, No. WW1, Feb., 1968.

(iii) For the calculation of this water level referred to in (i) and (ii) above, the following procedure is adopted.

The equation of continuity (2) is written as

$$b \cdot \frac{\partial h}{\partial t} + \frac{Q_1 - Q_2}{\partial x} = 0 \qquad (6)$$

where Q_2 refers to the discharge flowing from the two-dimensional model

and $$Q_2 = \sum_{i=1}^{i=N} U_i(H_i + D_i)*\Delta s$$

N is the number of lateral sections at the limit of the two-dimensional scheme. A complete description of the mathematical model is given by Prandle and Crookshank*.

MODEL RESULTS

A comparison of computed and recorded water levels over an eight day period is shown in Figs. 3 and 4 for four locations along the river. A velocity comparison at St. Francois is shown in Fig. 4.

To compare flow distribution in the two-dimensional model two techniques were used. The first, shown in Fig. 5, compares the predicted flow distribution with field measurements obtained from aerial photographs of ice movement. The field data applies to surface velocities and the ice movement is subject to the effect of wind, ice jams and inertial forces associated with its physical properties. However, the results show reasonable agreement and suggest that this technique for obtaining field results can be used to advantage. Further, the possibility of using the model to predict ice movement is an obvious corollary.

The second comparison of flow distribution was made by the use of drogues. Two drogues were released in the river simultaneously, one with a centre of drag at ten feet below the surface and the other at twenty feet below the surface. A comparison with the predicted path for such tests is shown in Fig. 6. Again, the drogues are subject to wind stress at the surface and do not represent depth-averaged velocities. However the comparison is reasonable and it is hoped to

*Prandle, D.; Crookshank, N.L.; "Numerical Model Studies of the St. Lawrence River". N.R.C. Report No. MH109, August, 1972, National Research Council, Ottawa, Canada.

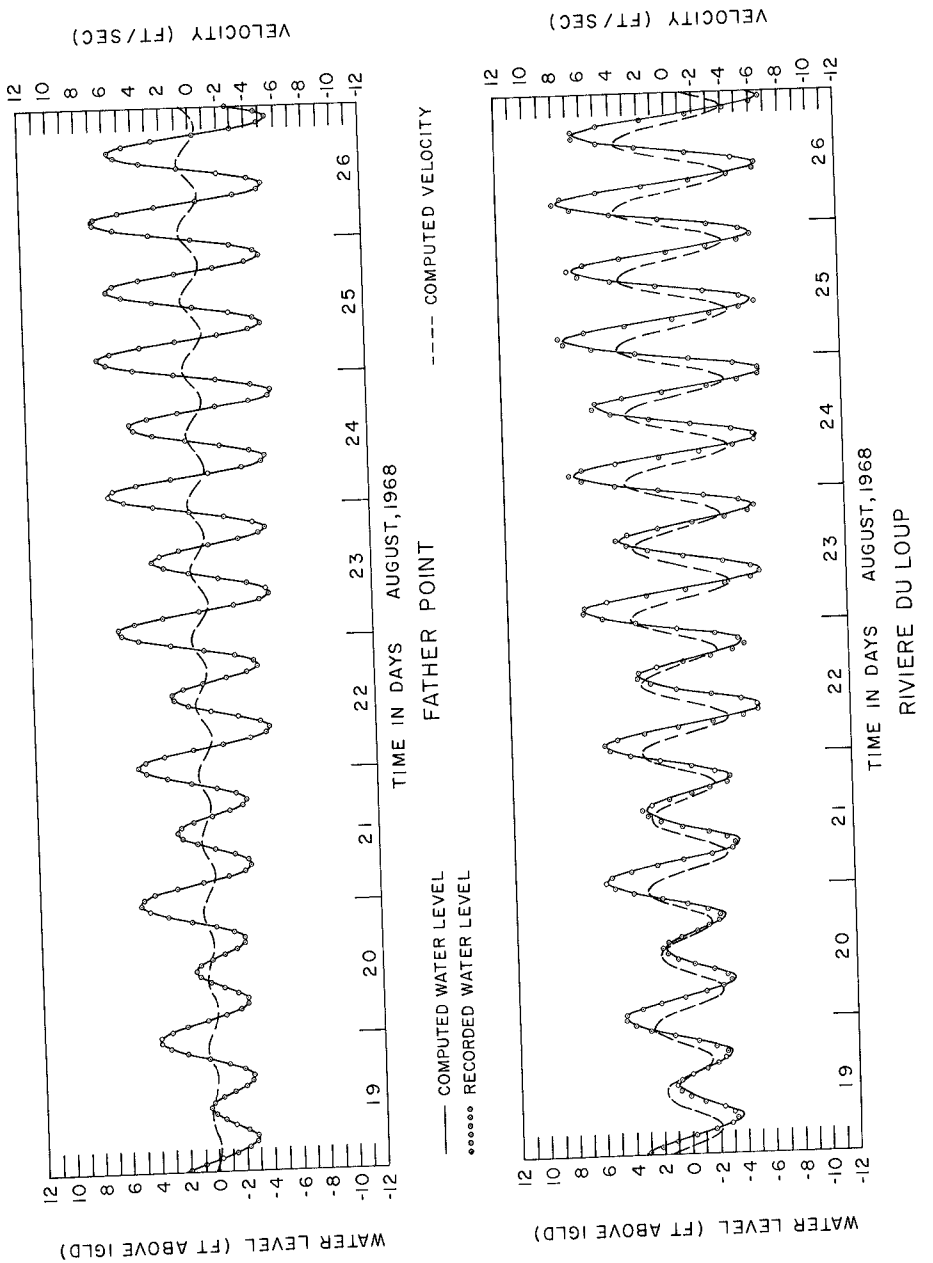

Fig. 3. Water Levels and Velocities; Computed and Recorded

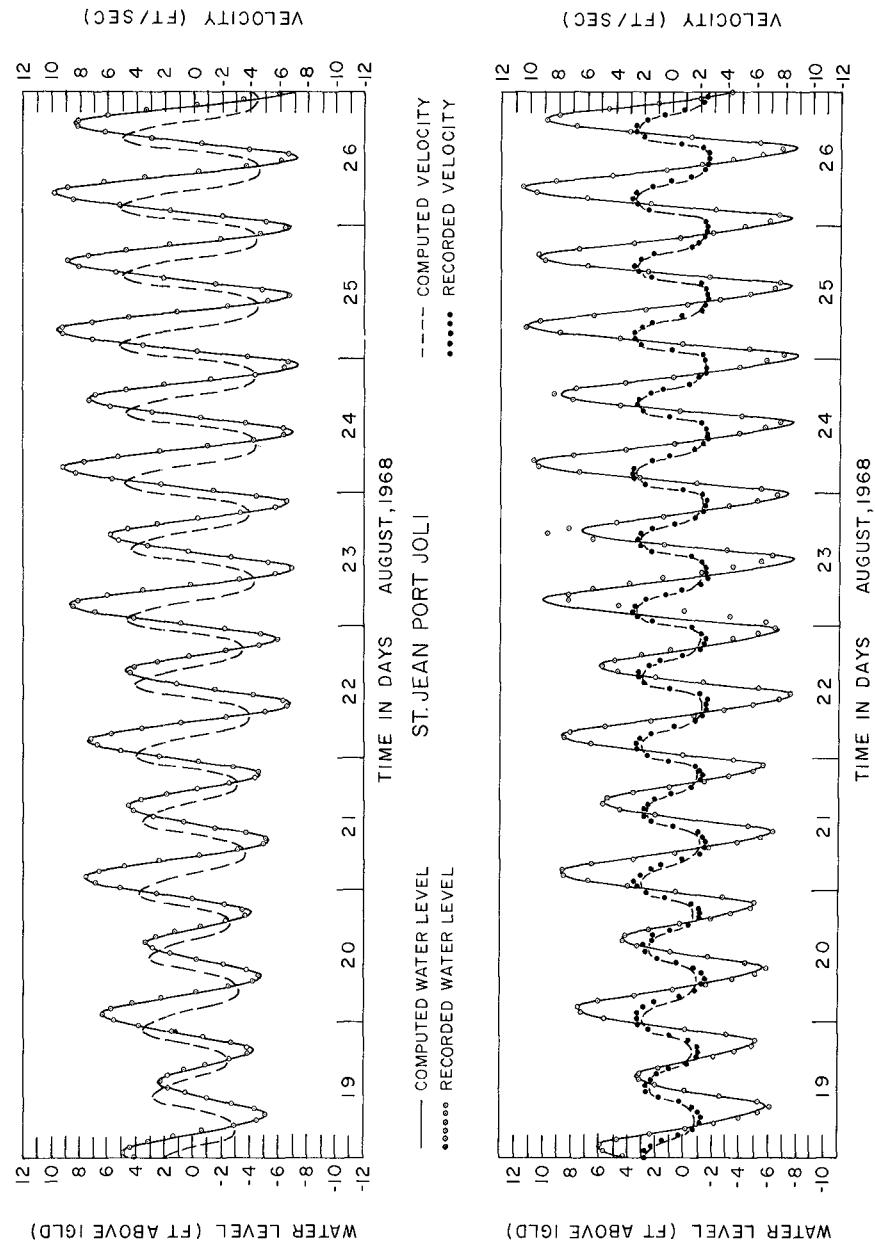

Fig. 4. Water Levels and Velocities; Computed and Recorded

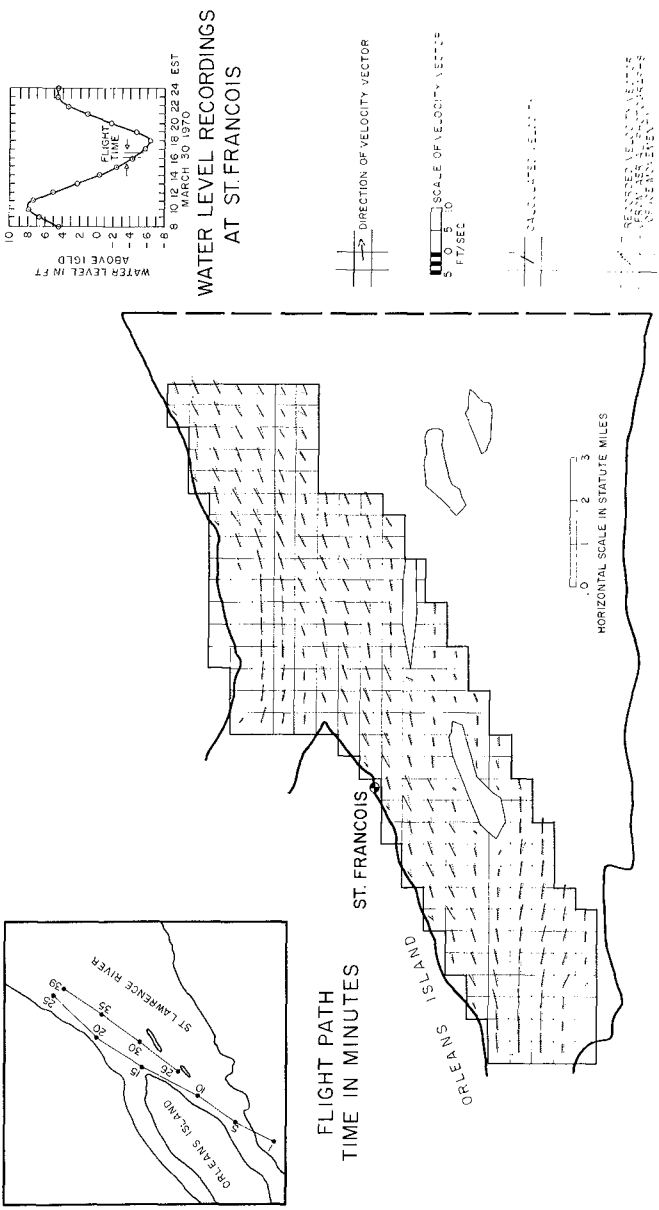

Fig. 5. Velocity Distribution From Ice Movement vs Computed Distribution

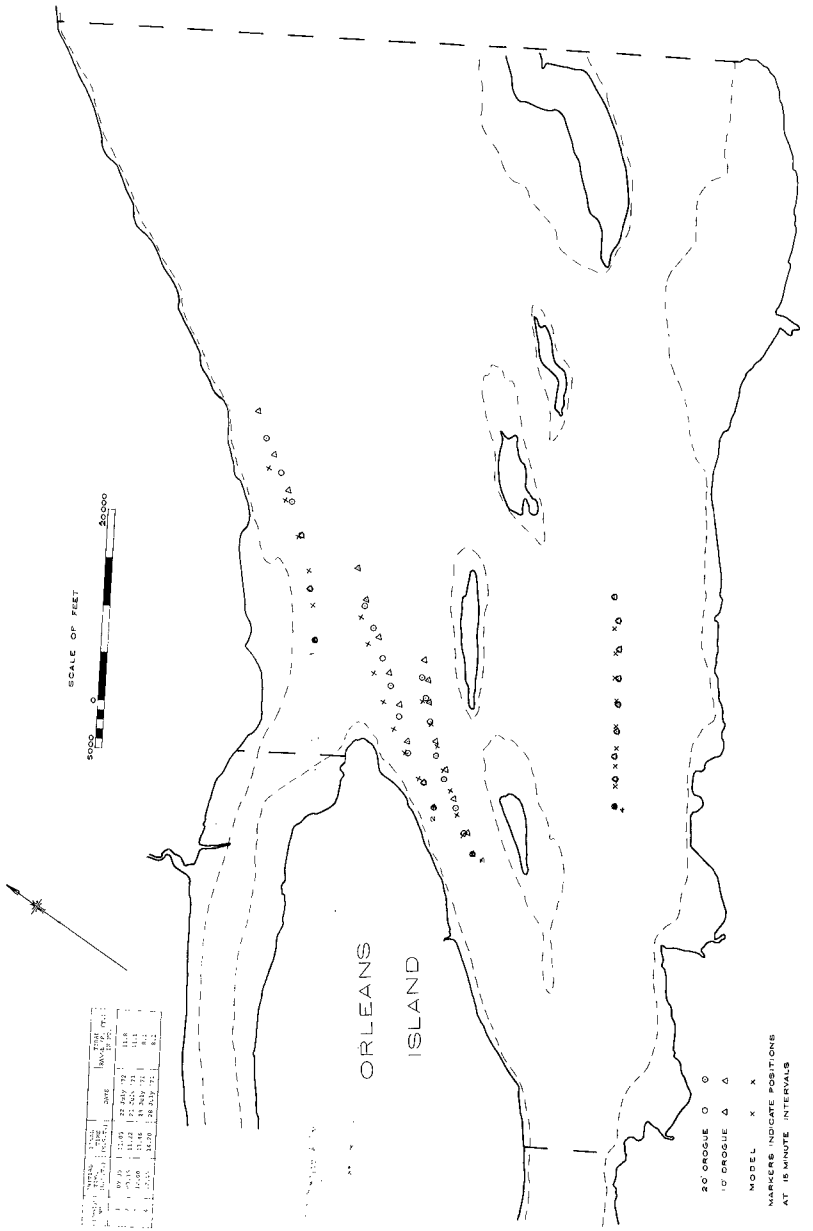

Fig. 6. Drogue Movements; Field and Model Results

extend the field tests to include measurements over a longer period of time. A comparable set of field measurements would be useful in calibrating the model and in studying dispersion or sediment movement.

To illustrate the instantaneous flow pattern computed by the model the form of presentation shown in Fig. 7 is used. By summing the vector velocities over a tidal cycle the net vector or drift velocity can be obtained. These values can be displayed in the same manner as Fig. 7; with due consideration for the limitations of the model this form of output can be extremely useful in many studies, particularly sediment transport.

The advantage in terms of flow visualisation of hydraulic scale models over numerical models is well recognised. This advantage of the scale model is fundamental. However, it is worthwhile to fully exploit the various methods of displaying the results of numerical models. An example of a particularly useful form of output is shown in Fig. 8 where the elevation of the water surface above chart datum at all points along the river is plotted for two complete days. This type of plot displays all the results (of level calculations) of the one-dimensional numerical model on a single figure and thus fully exploits the spatial resolution available from the model.

As an example of the use of this type of output the routing of a vessel entering the Port of Quebec is cited. The example considers the case of a vessel with a draught of 13 ft more than the minimum channel depth. The area where the available depth is limited is bounded by the two vertical lines. Assuming a vessel speed of 10 knots (relative to land for simplicity) the safest course is indicated in Fig. 8.

FLOW VISUALISATION BY ANIMATION*

The two parameters to be displayed are water level and velocity.

Water Level

Water level was simulated by the use of coloured contours. By examining the schemes used in topographical and hydrographical maps it was decided that the use of blue and grey colours would give the ten shades required and at the same time be consistent with standard colouring schemes used to represent water bodies.

---

*"Tidal Propagation in the St. Lawrence River". N.R.C. Film No. 31, 16 mm audio, 8 minutes.

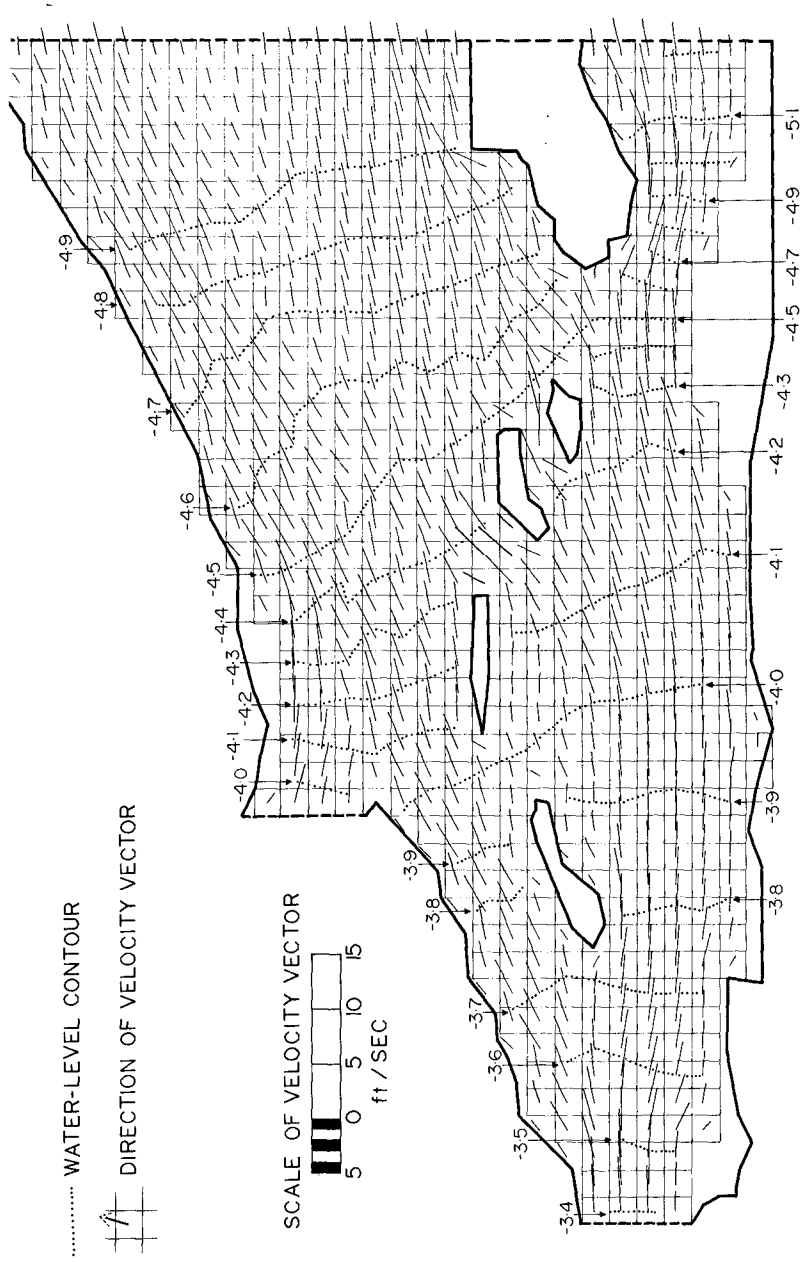

Fig. 7. Instantaneous Flow Pattern (Model Results)

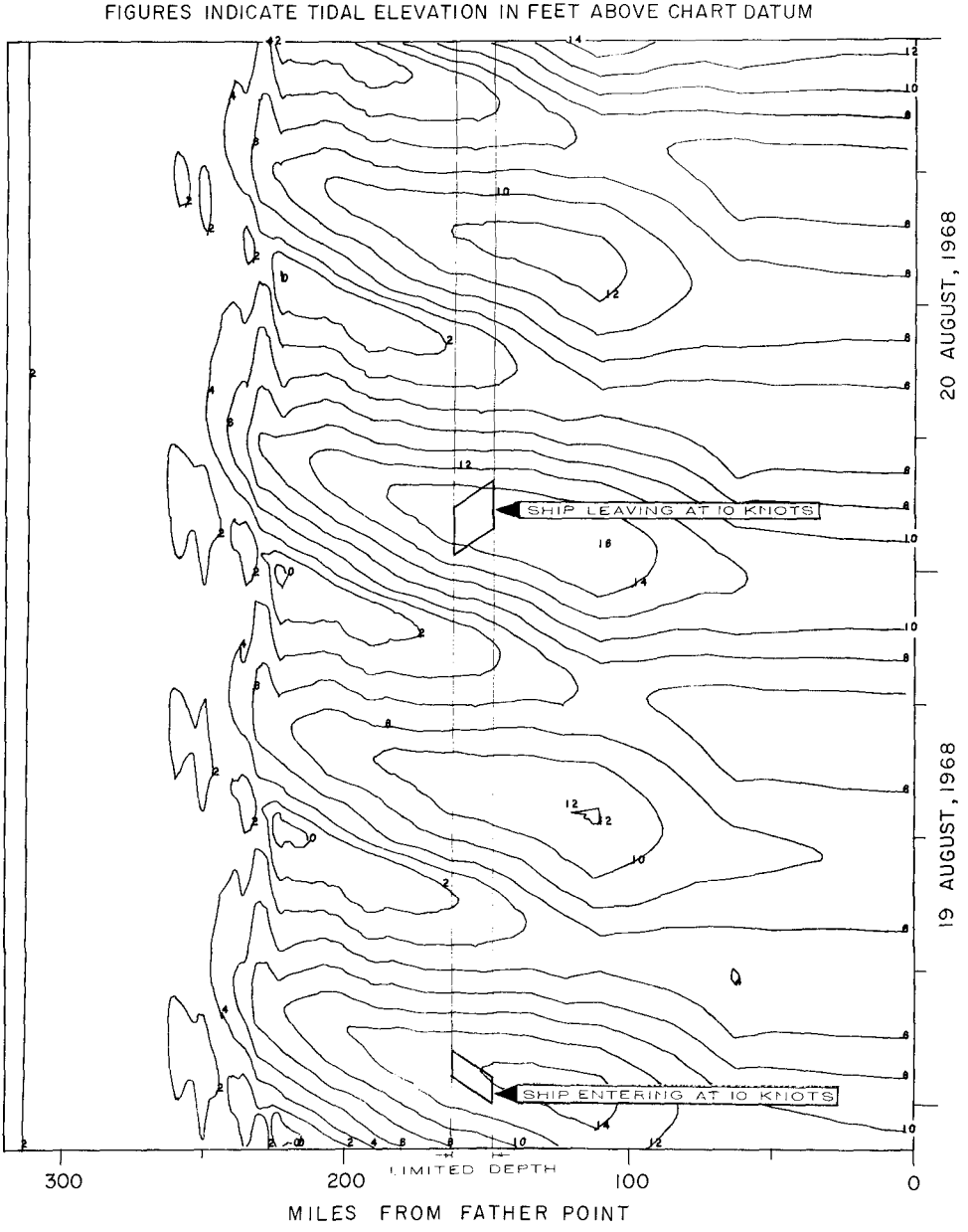
FIGURES INDICATE TIDAL ELEVATION IN FEET ABOVE CHART DATUM
SHIP LEAVING AT 10 KNOTS
SHIP ENTERING AT 10 KNOTS
20 AUGUST, 1968
19 AUGUST, 1968
LIMITED DEPTH
300
200
100
0
MILES FROM FATHER POINT

Having defined the interval of the water level contours, the datum should be set such that the level difference between high water and the highest contour is equal to that between the lowest level and the lowest contour. Failure to recognise this requirement unfortunately resulted, in this case, to an erroneous impression that "high water" persists for longer than "low water".

The physical procedure adopted in the compilation of each frame is shown in the film. The process is obviously tedious and has no particular merit. The objective of the programme was simply to investigate possible methods for flow visualisation. The ultimate aim is to display results using coloured television sets.

Velocity

Since the computational algorithm is based on a Eulerian scheme it is convenient to use an equivalent system for displaying velocities. This has been attempted by allowing the vectors shown in Fig. 7 to rotate and change in magnitude over a tidal cycle. However this did not present a satisfactory pictorial representation.

In hydraulic scale models useful methods for flow visualisation include dye injection and floats. An analogous technique was used for the numerical model by introducing marker particles at fixed intervals of time at the boundaries. These indicate instantaneous velocity and trajectories. The disadvantage of this Lagrangian form of representation is the loss of complete spatial resolution.

The techniques used in obtaining each frame are of interest and are included in the introduction to the film. The possibility of producing this sort of trace by using a cathode ray tube is immediately evident.

CONCLUSIONS

By combining a two-dimensional model with a one-dimensional model an accurate simulation of a particular short reach of a river was achieved. This technique has widespread applications subject to the limitations of the two-dimensional model.

The problem of flow visualisation associated with numerical models has been examined. For the one-dimensional model the use of contours to represent water elevation plotted against time and distance along the river has been found to be extremely useful. For the two-dimensional model animation techniques were used.

CHAPTER 132

Analytical Modeling of Estuarine Circulation

John S. Fisher[1]

John D. Ditmars[2]

Donald R. F. Harleman[3]

Abstract

A mathematical model is developed using analytical techniques to determine the longitudinal and vertical distributions of velocities and salinities, averaged over a tidal period, for mixed but partially stratified estuaries. The flow is assumed laterally homogeneous and the estuary width and depth are assumed to be functions of the longitudinal coordinate only. Required inputs to the model include the salt intrusion length, the ocean boundary salinity, the distribution of the depth-averaged salinity and the freshwater discharge.

The governing equations included in the model are the vertical and longitudinal equations of motion, continuity, salt conservation and an equation of state. The key assumption is made that the longitudinal salinity gradient is independent of depth. This decouples these equations and thus permits an analytical solution to be found.

Using data from laboratory flume tests and field surveys the model solutions are used to find correlations for the mean vertical transfer coefficients of mass and momentum with gross characteristics of the estuary. These correlations, plus the results from a one-dimensional numerical model, permit this analytical model to be used as a predictor of the velocity and salinity profiles in estuaries and to relate changes in freshwater discharge to possible changes in the location of shoaling zones.

[1]Assistant Professor, Department of Environmental Sciences, University of Virginia, Charlottesville, Virginia

[2]Assistant Professor, Department of Civil Engineering, and College of Marine Studies, University of Delaware, Newark, Delaware

[3]Professor of Civil Engineering, Head, Division of Water Resources and Hydrodynamics, Massachusetts Institute of Technology, Cambridge, Massachusetts

Introduction

Physical and mathematical models of estuaries are developed in order to represent the complex circulation of the prototype in a simplified form which can be tested and studied to determine the possible consequences of modifications of controlling factors on the natural circulation. Examples of such changes could include the dredging of a navigation channel, the diversion of freshwater inflow to other basins, or the placement of a diffuser for the heated condenser water of an electric power station. The former might seriously alter the salinity distribution while the latter could obviously influence normal biological cycles. Recourse to various types of models must be made to provide estimates of the impact of such changes.

At the present time, physical models of estuaries are the most important technique for determining the effects of changes in the prototype. Their great expense and slow building and operating times are drawbacks which sophisticated mathematical models may avoid. However, one can expect these physical models to continue to be important tools for estuarine analysis for a long time to come.

Mathematical models include both numerical and analytical models. At the present time, the numerical models available for engineering applications are of either the unsteady one- or two-dimensional type. A one-dimensional model averages all dependent variables over the cross-sectional area, and thus yields changes in mean values with time and along the longitudinal axis. These models can be used to predict water surface elevation, mean currents, and mean salinities. They can also be used with certain reservations to determine the cross-sectional mean concentration of a non-conservative water quality parameter, such as dissolved oxygen or biochemical oxygen demand.

Two-dimensional numerical models usually allow variations along the lateral as well as along the longitudinal axis. In this case, the only averaging is with depth. Again, these models can predict currents, water quality parameters, etc. These models are more complex than the one-dimensional case with regard to the computational techniques required.

This investigation develops a two-dimensional analytical model of estuarine circulation including vertical and longitudinal distributions of velocity and salinity. All equations are averaged over one or more tidal periods. This model can be coupled with a one-dimensional numerical model which is not time-averaged, but is averaged over a cross-section.

The ability to calculate vertical variations of the important flow parameters is often a useful tool for solving estuarine problems. Vertical salinity stratification is a key element in the circulation pattern of an estuary. Models which can predict the effects of changing geometry, freshwater inflows, etc. on this stratification are of great value. The modeling of vertical velocity profiles is another useful model capability. Many problems of shoaling in estuaries can only be properly studied with a knowledge of the vertical distribution of velocity.

If a model similar to the one described above is to have practical application as a predictive tool, all parameters included in the solution technique must be determinable in advance. Thus, an important part of the objectives of this study is to obtain relationships between the various time-averaged coefficients of turbulent diffusion and eddy viscosity included in the model and the gross parameters of estuarine circulation.

Previous Investigations

Pritchard (1952) describes the circulation in the Chesapeake Bay estuarine system, and in particular, in the James River estuary. Data from an extensive program of field surveys are discussed, in which salinities, temperatures and velocities were measured at several depths and stations and averaged over one or more tidal periods. The resulting net circulation and salinity distributions are typical for partially stratified conditions. A basic feature of this net circulation is a reversal in the vertical distribution of the time-averaged horizontal velocity. In the surface region, extending to about middepth, the net flow is towards the ocean, while the bottom region has flow in the opposite direction, towards the river end of the estuary. The depth integral of this velocity is equal to the net discharge of freshwater. Although two regions can be identified for the velocity, the vertical salinity distribution can not be separated into two distinct zones. In partially stratified estuaries, there is a continuous increase in salinity from the surface to the bottom, without a noticeable point of discontinuity.

Pritchard (1952, 1954) also identifies several interesting features of the longitudinal salinity gradient. For all depths, there is an increase in salinity from the freshwater region to the boundary salinity at the ocean end. In addition, over most of the estuary this longitudinal salinity gradient is nearly independent of depth, i.e., vertical position. This latter feature does not hold very near the ocean boundary or where the salinity goes to zero, upstream.

Hansen and Rattray (1965) present an analytical model of estuarine circulation averaged over one or more tidal periods. A simultaneous solution of the equations of mass and momentum conservation, assuming geometric similarity of velocity and salinity profiles and lateral homogeniety is developed. The estuary is divided into three regions inner, central and outer, for which different assumptions about salinity gradients and mixing coefficients are made.

McGregor (1972) develops an analytical model of the net, non-tidal bottom transport velocity for an estuary. This model is similar to other studies in that a longitudinal force balance includes only the pressure gradient and the vertical eddy stress gradient. For the pressure gradient, both a surface slope and density gradient are evaluated from recorded data for the Humber estuary. The solution technique introduces a number of empirical constants for fitting these distributions, as well as an empirical expression for the mean eddy viscosity. By proper fitting of the numerous constants, McGregor is able to match the net bottom velocity zero points with the shoaling zones for the Humber. The analysis is a good illustration of the roles of the surface slope, salinity gradient and river discharge in determining the zones of high rates of shoaling. However, due to the need to fit several constants to previous data, the model is of limited predictive capability.

Theoretical Considerations

The objective of the present study is to develop an analytical model of time-averaged estuarine circulation which will avoid the less tractable features of the previous models described above. The governing equations are similar to Hansen and Rattray's model, which was originally suggested by Pritchard's analysis of the James River estuary. A solution technique which is continuous over the entire length of an estuary is desired and which makes no assumptions about similarity of velocity or salinity profiles. Only the vertical eddy flux of salt and momentum are included, and thus only two eddy coefficients need to be specified.

In order to provide the analytical solution with a predictive capability, empirical correlations for these two parameters with gross characteristics of the flow field are sought, as a fundamental feature of the complete solution.

The model equations describing the circulation and distribution of salinity are the equations of motion, of continuity, of conservation of salt and an equation of state. The model is reduced to the longitudinal and vertical dimensions by assuming lateral homogeneity. The orientation of the coordinate system is with the x-axis positive towards the head of the estuary (upstream) and the y-axis positive downward. An additional simplification is made restricting the width $b(x)$ and the mean water level $h(x)$ to be functions of the longitudinal coordinate only. An inflow of freshwater Q_f occurs at the far upstream end.

For the conditions described, the conservation of momentum for the longitudinal direction can be written

$$\frac{\partial ub}{\partial t} + \frac{\partial u^2 b}{\partial x} + \frac{\partial uvb}{\partial y} = -\frac{1}{\rho}\frac{\partial p}{\partial x} b \tag{1}$$

where u is the velocity in longitudinal direction, v is the velocity in vertical direction, t is the time, ρ is the density, p is the pressure, x is the longitudinal direction, y is the vertical direction, and b is the width. This equation is a balance of forces for the estuary at any time in a tidal period, i.e., before time-averaging. The viscous frictional terms and Coriolis forces have been neglected. In addition, the approximation of Boussinesq has been applied to neglect density variations in all but the buoyancy terms. The pressure is for the fluid only, atmospheric pressure being assumed constant.

For the conservation of momentum in the vertical direction, hydrostatic conditions are assumed. Thus, inertial and convective accelerations are neglected. The vertical equation of motion can therefore be written

$$0 = -\frac{1}{\rho}\frac{\partial p}{\partial y} + g \tag{2}$$

where g is the acceleration of gravity.

The conservation of salt equation, before time-averaging, and neglecting molecular diffusion is

$$\frac{\partial sb}{\partial t} + \frac{\partial usb}{\partial x} + \frac{\partial vsb}{\partial y} = 0 \tag{3}$$

where s is the salinity and is a function of x, y, and t.

For incompressible flow, the two-dimensional equation of continuity is

$$\frac{\partial ub}{\partial x} + \frac{\partial vb}{\partial y} = 0 \tag{4}$$

There are three time scales of interest for the model being considered. Turbulent fluctuations of the dependent variables may be assumed to take place within a few minutes. These variables also have a diurnal or semi-diurnal component due to the tidal motion. Finally, slow variations over several tidal periods can result from the changing freshwater inflows and monthly changes in tidal amplitude. The details of the time-averaging of these equations is given by Fisher, et al. (1972).

From the analysis of the James River data, Pritchard (1954, 1956) argues that the dominant terms in the longitudinal equation of motion (1) are the pressure gradient and the vertical eddy flux of momentum, all other terms being of second order. This assumption is included in the present development. For the salt balance (3) the tidal cross-products and horizontal eddy flux are neglected by similar arguments. The reduced equations are further simplified by introducing mean eddy coefficients for the remaining turbulent terms

$$-\frac{\partial \overline{<u'v'>}}{\partial y} \equiv \frac{\partial}{\partial y}\left(D_y \frac{\partial U}{\partial y}\right) \tag{5}$$

$$-\frac{\partial \overline{<v's'>}}{\partial y} \equiv \frac{\partial}{\partial y}\left(K_y \frac{\partial S}{\partial y}\right) \tag{6}$$

where: $\overline{\quad}$ is average over turbulence, $< >$ is average over tidal period

where u', v', s' are turbulent components and U and S are averages over a tidal period of the horizontal velocity and salinity, respectively. D_y and K_y are mean eddy coefficients. These definitions for D_y and K_y are convenient with regard to reducing the mathematical complexity of the model. However, they are strictly artificial in that they do not preserve the mechanisms of turbulent mixing, i.e., tidal activity, in their formulation. In particular, Equation 5 relates the net turbulent momentum flux $\overline{<u'v'>}$ to the net, non-tidal velocity U. By purely physical arguments this flux should be related to the tidal velocity u_t. This apparent inconsistency is partially resolved since D_y is later correlated with the tidal velocity. The equations are now written

$$0 = -\frac{1}{\rho_m}\frac{\partial P}{\partial x} + \frac{1}{b}\frac{\partial}{\partial y}\left(bD_y \frac{\partial U}{\partial y}\right) \tag{7}$$

$$0 = -\frac{1}{\rho_m}\frac{\partial P}{\partial y} + g \tag{8}$$

$$\frac{\partial Ub}{\partial x} + \frac{\partial Vb}{\partial y} = 0 \tag{9}$$

$$\frac{\partial Sb}{\partial t} + \frac{\partial bUS}{\partial x} + \frac{\partial bVS}{\partial y} = \frac{\partial}{\partial y}\left(bK_y \frac{\partial S}{\partial y}\right) \tag{10}$$

The value and distributions of the mean eddy coefficients are unknown. If a solution to the above set of equations can be shown to match recorded data by proper fitting of D_y and K_y, one must assume that either all the neglected terms are zero, or more probably, that these neglected terms have been absorbed into these coefficients. A comparison of Equations 5 and 6 with the classical definitions of eddy viscosity and eddy diffusivity clearly shows the difference in the meaning of these terms

$$\frac{\partial}{\partial y}\left(\langle \varepsilon_y \frac{\partial \tilde{u}}{\partial y} \rangle\right) \neq \frac{\partial}{\partial y}\left(D_y \frac{\partial U}{\partial y}\right) \tag{11}$$

$$\frac{\partial}{\partial y}\left(\langle k_y \frac{\partial \tilde{s}}{\partial y} \rangle\right) \neq \frac{\partial}{\partial y}\left(K_y \frac{\partial S}{\partial y}\right) \tag{12}$$

More specifically, D_y and K_y are not simply ε_y and k_y averaged over a tidal period.

The effect of temperature on the relationship between density and salinity is not included in this model. A simple linear empirical expression is used

$$\rho = \rho_o(1 + \alpha s) \tag{13}$$

where ρ_o is a reference density and α is a conversion constant. The range of temperatures encountered in estuaries does not require a more complex expression, in light of other model assumptions.

Additional Assumptions

The governing equations developed in the preceeding sections can not be solved analytically in their present form. Previous investigators have introduced similarity assumptions for the velocity and salinity distributions as well as restrictions on the longitudinal salinity gradient. As stated in a preceeding section, the present investigation seeks to avoid the limitations of a similarity solution. However, as will be developed in the following sections, the longitudinal salinity gradient will be modified to allow an analytical solution to be found.

The Pritchard (1952, 1954) investigation of the James River revealed that for the stations and conditions of the survey, the longitudinal salinity gradient did not vary appreciably with vertical position. Harleman and Ippen (1967) showed a similar pattern for the analysis of data from a laboratory flume. Taken to the extreme, this observed feature suggests that the longitudinal salinity gradient may be assumed independent of its vertical position, i.e.,

$$\frac{\partial S}{\partial x} = \frac{\partial S}{\partial x}(x), \text{ although } S \approx S(x,y) \tag{14}$$

The longitudinal salinity gradient $\frac{\partial S}{\partial x}$ is replaced in Equations 7-10 with the longitudinal gradient of a depth averaged salinity S_d. Next, a steady-state condition is assumed. In addition, the two mean eddy coefficients D_y and K_y are assumed independent of vertical position. These coefficients have been shown to

represent the rather complex effects of time-averaging and of the neglecting of terms considered of smaller order. The vertical dependence of these coefficients is not known, although several investigators have attempted to analyse these terms from experimental and field observations. Thus, D_y and K_y are assumed to be independent of y, and are replaced with effective coefficients for the entire depth of flow, D and K, respectively.

As with most problems of fluid dynamics, it is convenient to develop analytical solutions in a non-dimensional form in order to permit generalized discussions of results. The choice of terms introduced to non-dimensionalize the various dependent and independent variables, although somewhat arbitrary, should recognize the possible difficulties in quantifying these new parameters. The following definitions will be shown to satisfy this condition:

$$\eta \equiv \frac{y}{h} \qquad \xi \equiv \frac{x}{L_i} \qquad \psi \equiv \frac{\Psi}{Q_f} \qquad \theta \equiv \frac{S}{S_o} \qquad \theta_d \equiv \frac{S_d}{S_o} \tag{15}$$

where L_i is the mean intrusion length, defined as the distance from the ocean boundary to a point where the time-averaged, depth averaged salinity is one percent of the ocean salinity. S_o is the ocean salinity, h is the depth of the mean water level and Q_f is the freshwater discharge, as previously noted.

Ψ is a stream function satisfying continuity. These quantities are introduced into the governing equations which have been reduced by assuming the Boussinesq approximation.

$$\left\{\frac{gS_o h^4 b}{L_i D Q_f}\right\} \frac{\partial \theta_d}{\partial \xi} = -\frac{\partial^4 \psi}{\partial \eta^4} \tag{16}$$

$$-\frac{\partial \Psi}{\partial \eta}\frac{\partial \theta_d}{\partial \xi} + \frac{\partial \theta}{\partial \eta}\frac{\partial \psi}{\partial \xi} = \frac{bKL_i}{Q_f h}\frac{\partial^2 \theta}{\partial \eta^2} \tag{17}$$

wherein ψ, θ, θ_d, ξ and η are all dimensionless variables. These equations can be further simplified by defining two coefficients,

$$C_1(\xi) = \frac{g\alpha S_o h^4 b}{L_i D Q_f} \tag{18}$$

$$C_2(\xi) = \frac{KL_i b}{Q_f h} \tag{19}$$

The boundary conditions included in this analysis are that the net velocity gradients at both the surface and the bottom are zero, that the depth-average of the velocity is equal to the freshwater velocity, that the vertical salinity gradient is zero at the surface, and that the depth-average of the salinity is equal to the specified mean value, S_d. In non-dimensional form these conditions are

$$\eta = 0; \quad -\frac{\partial^2\psi}{\partial\eta^2} = 0, \quad \frac{\partial\theta}{\partial\eta} = 0, \quad \psi = 1$$

$$\eta = 1; \quad -\frac{\partial^2\psi}{\partial\eta^2} = 0, \quad \psi = 0 \tag{20}$$

$$\int_0^1 \theta d\eta = Sd/S_o$$

The solution of Equation 16 is found by integration, and after substitution of the flow boundary conditions may be written

$$\psi = \frac{\partial\theta_d}{\partial\xi}\frac{C_1}{24}\{-\eta^4+2\eta^3-\eta\}-\eta+1 \tag{21}$$

This expression for the stream function is similar to the solution of Hansen and Rattray (1965) in form, differing only by the choice of boundary conditions and the restrictions on the longitudinal salinity gradient.

The solution of the salt balance Equation (17) is found by multiplying by an integration factor. The resultant equation for the salinity is

$$\theta(\xi,\eta) = \int f(\xi,\eta)d\eta+\theta_d-\int_0^1\int f(\xi,\eta)d\eta d\eta \tag{22}$$

where

$$f(\xi,\eta) = \exp(\int \frac{B}{C_2}\,d\eta)\int \frac{A}{C_2}\exp(\int -\frac{B}{C_2}\,d\eta)d\eta \tag{23}$$

$$+ b_1(\xi)\exp(\int \frac{B}{C_2}\,d\eta)$$

and

$$A(\xi,\eta) = -\frac{\partial\psi}{\partial\eta}\frac{\partial\theta_d}{\partial\xi} \qquad B(\xi,\eta) = \frac{\partial\psi}{\partial\xi}$$

The depth average of the salinity, averaged over a tidal period, S_d and its longitudinal gradient $\frac{\partial S_d}{\partial x}$ must both be specified in the solutions. For the purpose of evaluating the model from recorded data, these parameters can be simply backfigured from the measurements. However, in order for the analytical model to have a predictive capability, these terms must be predictable themselves. There have been numerous semi-empirical fits for this one-dimensional salinity distribution, Harleman and Ippen (1961), McGregor (1972) and others. However, a recently developed numerical model by Thatcher and Harleman (1972) permits one to compute a one-dimensional unsteady salinity distribution. This approach results in a general, non-empirical analysis for this input parameter. The intrusion length can also be evaluated by their technique.

The freshwater inflow and ocean boundary salinity are considered to be fundamental quantities, as are the depth and width distributions.

The remaining two quantities needed to evaluate the analytical solution are the eddy coefficients, K and D. Nothing can be said about these terms prior to their evaluation from recorded data. The procedure for their determination is to fit the analytical solutions for velocity and salinity with flume and field data and to pick the best fit values for K and D by trial and error. Since the stream function is dependent only on D, this procedure is not too cumbersome, even though the salinity is dependent on both D and K. This process of back-calculating D and K from recorded data has been repeated for several data sets. The resulting distributions of these coefficients was then correlated with parameters characteristic of the flow conditions.

Evaluation of Solution

The analytical solution for velocity and salinity distribution developed above was evaluated with laboratory data from the Vicksburg salinity flume, the Delft Hydraulic Laboratory salinity flume and the James River field study. This combined set of data covers a wide range of flow conditions and degrees of salinity stratification. For each case studied, a best-fit value for the two mean eddy coefficients was found at each longitudinal station.

The laboratory flume of the Corps of Engineers, U.S. Army, Vicksburg Waterways Experiment Station (WES), is described in detail in a WES report (1955). The flume is a lucite channel 327 ft. long, 0.75 ft. wide and 1.5 ft. in total depth. At the ocean end there is a tidal reservoir which can maintain a constant salinity and a periodic surface level. The opposite end has a freshwater reservoir. Roughness is achieved by 1/4 inch strips attached to the side walls on 2 inch centers. Different estuarine conditions are modeled by varying the freshwater inflow, the tidal amplitude and the basin salinity. Figures 1 and 2 compare the analytical solution with data from WES test 16. The solid lines are for the bottom boundary condition discussed above. The broken lines illustrate the analytical solution using a bottom condition of zero horizontal velocity. From these figures, and similar analysis for other flume tests, the condition of zero gradient was selected as the preferable condition for the model. Figure 1 shows how the analytical solution, using the longitudinal salinity gradient determined from the data, can follow the changes in the velocity distribution along the length of the flume. This characteristic of the solution enables the model to identify the limit of the upstream flow of saline water, the null point identified with shoaling zones in estuarine channels.

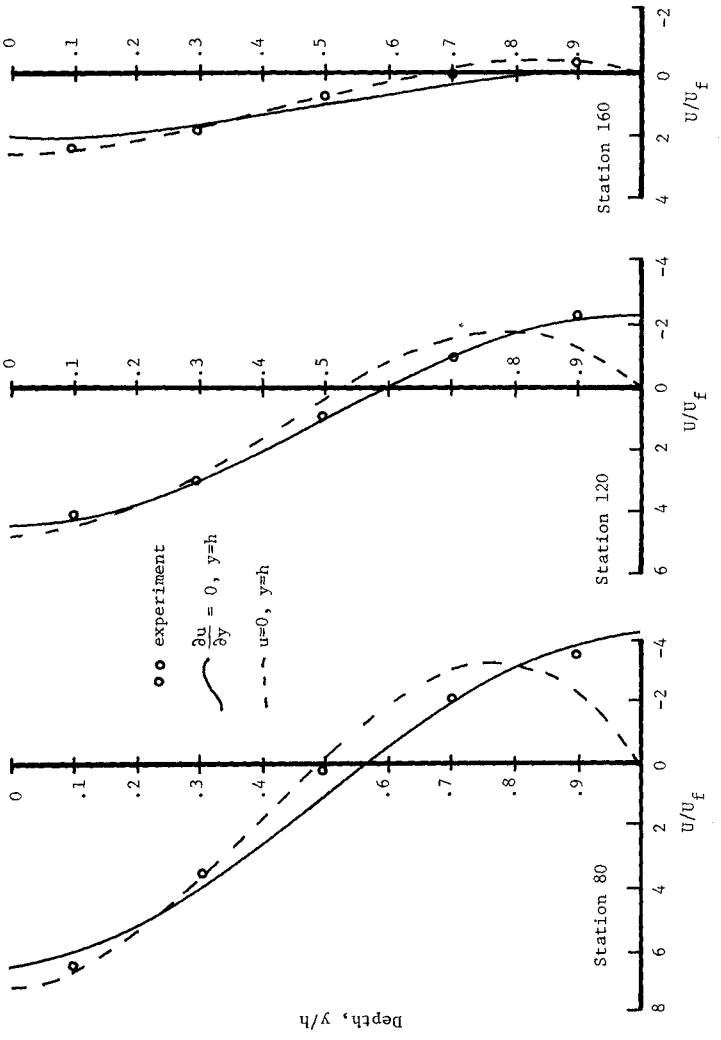

Figure 1 Horizontal velocity profiles, WES 16, stations 80, 120 and 160
U_f = 0.2 ft.sec., S_o = 29.2 ppt, tidal period = 600 sec., tidal amp. = .05 ft.

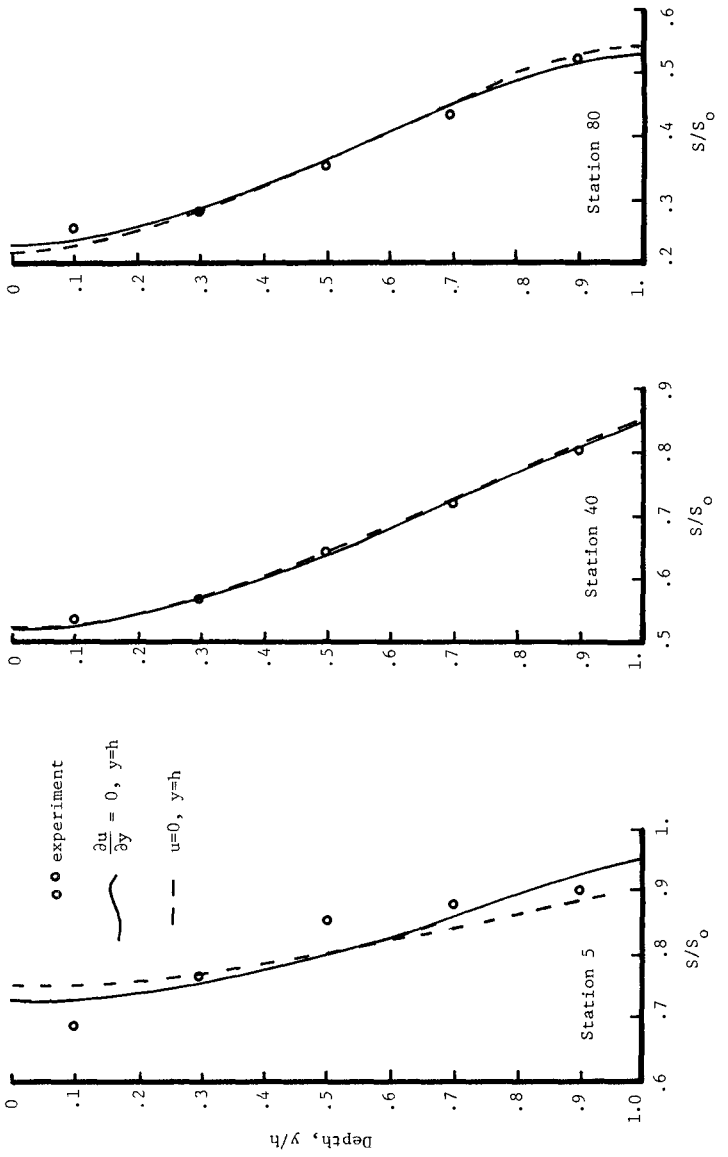

Figure 2 Salinity profiles, WES 16, stations 5, 40 and 80

At the Delft Hydraulics Laboratory an experimental investigation of salinity intrusion in estuaries similar to the Vicksburg studies has been carried out. The details of flume design and measurement technique are reported in Delft (1970). The flume is 546 ft. long, 2 ft. wide and 0.7 ft. deep (msl). For the Delft tests the bottom roughness was achieved by vertical bars .5 x .5 cm^2 in cross-section attached to the flume bottom. By changing the number of bars the roughness could be varied for different runs.

Four Delft tests were analysed with the analytical model. All the tests were for steady-state conditions and the longitudinal salinity distribution was back-figured from the recorded data as was done for the WES tests. Figure 3 illustrates the comparison between the analytical solution and flume data for test 116 at a central portion of the salinity regime.

A final example of the analytic solution is given in Figure 4 for the James River estuary. The difference between computed and actual velocities over most of the depth is probably due to several factors, including the uncertainty of time-averaged field measurements, and more importantly, the simplifying assumption of constant width with depth for the analytic solution. The salinity profiles for this same station show better agreement than the velocities. However, there appears to be a sharp vertical gradient near middepth for the field data which is not observed for the analytical solution. This difference may be a result of the same factors cited before for the velocity profile.

In general, the analytical model, although clearly capable of reproducing flume conditions more exactly, does not appear to break down for the prototype conditions and scales exemplified by the James River estuary.

Evaluation of Time-Averaged Coefficients

The evaluation of the mean eddy coefficients K and D was carried out for ten separate tests, including three field studies. These coefficients showed a varying degree of longitudinal dependence, as discussed by Fisher, et al. (1972). The longitudinal variations of the mean eddy coefficients suggested that although D and K are functions of x, this dependence is of secondary importance. By introducing the additional assumption that these mean eddy coefficients may be replaced with effective constant values for the entire longitudinal distance of the salinity regime, correlations of these coefficients are greatly simplified.

The significance of being able to use constant values for D and K, i.e., $\bar{D}$ and $\bar{K}$, is that only two unknown parameters need now be specified in order to apply the analytical model to a given set of estuarine conditions, i.e., freshwater discharge, ocean salinity, depth, etc. All other model parameters can be readily determined with the possible exception of the longitudinal salinity distribution. This latter input can be computed with the aid of a one-dimensional numerical model, as previously discussed. The determination of $\bar{K}$ and $\bar{D}$ for input to the model is made by using an empirical correlation of these constant coefficients with the gross characteristics of the estuarine system.

Following the arguments presented above for using constant values of $D(\xi) \simeq \bar{D}$ and $K(\xi) \simeq \bar{K}$, the dimensionless form of the governing equations suggests that a possible pair of useful parameters for correlating $\bar{K}$ and $\bar{D}$ is

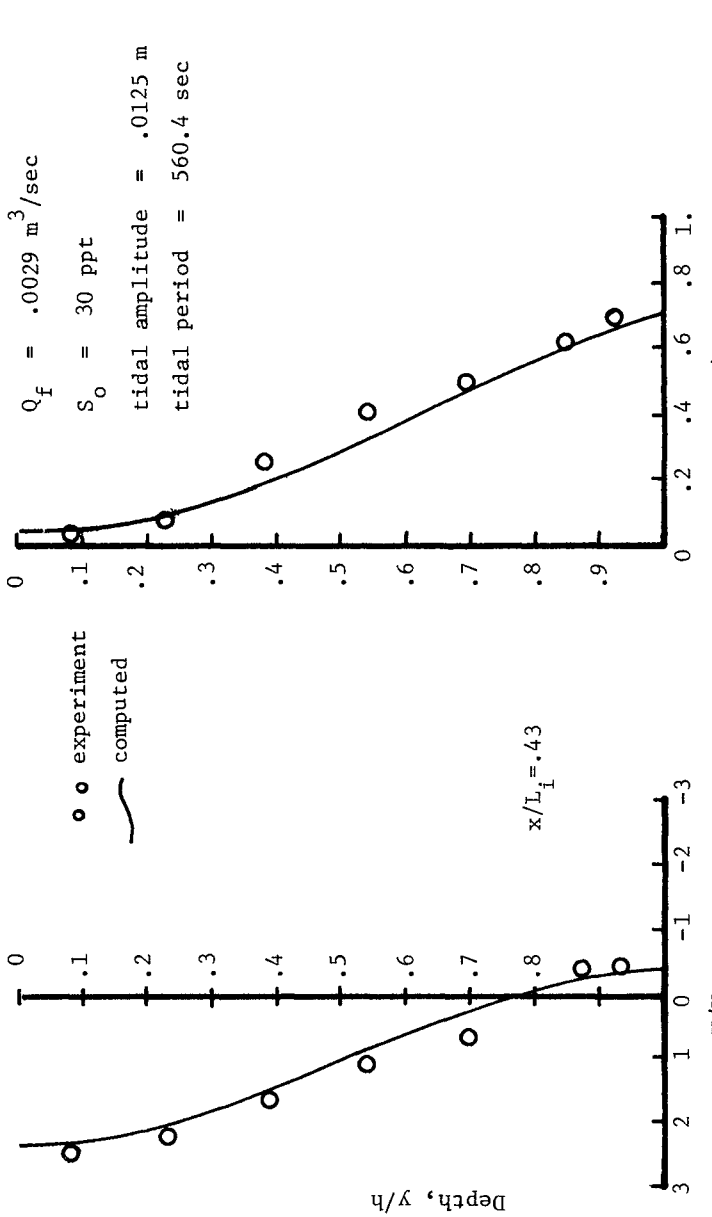

Figure 3 Horizontal velocity and salinity profiles, Delft 116

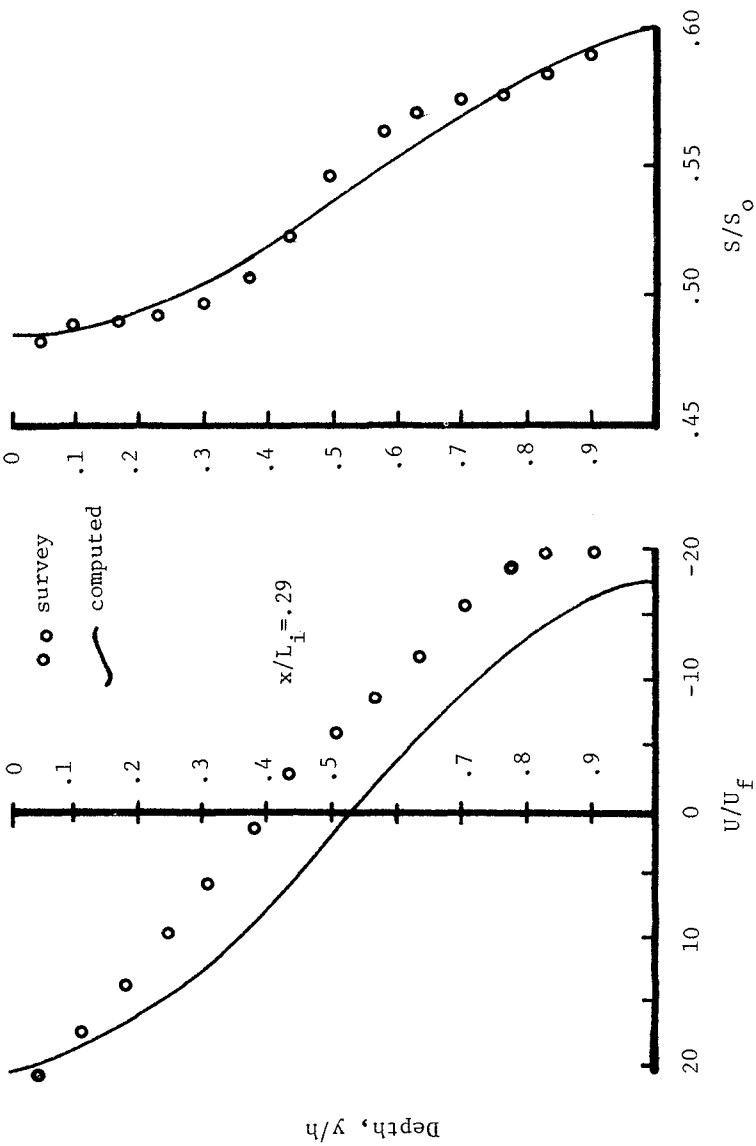

Figure 4 Horizontal velocity and salinity profiles, James River, 26 June - 7 July

$$\bar{C}_1 = \frac{g\alpha S_o h_o^4 b_o}{L_i Q_{fo} \bar{D}} \tag{24}$$

and

$$\bar{C}_2 = \frac{\bar{K} L_i b_o}{Q_{fo} h_o} \tag{25}$$

where the zero subscript, e.g., b_o, h_o, refers to the downstream limit or ocean boundary of the estuary. All terms in these new terms are assumed constant over the longitudinal and vertical dimensions, and the only unknown parameters are $\bar{K}$ and $\bar{D}$.

The values of $\bar{K}$ and $\bar{D}$ should be a function of the degree of mixing of the flow field which is in turn a function of the tidal activity. In recognition of this dynamic relationship of the physical system being modeled, $\bar{C}_1$ and $\bar{C}_2$ have been correlated with a characteristic non-time-averaged tidal velocity. To be consistent with the definitions above, this velocity is specified as the maximum entrance flood velocity u_o, non-dimensionalized by the freshwater velocity at this same boundary $\frac{Q_{fo}}{h_o b_o}$,

$$\bar{C}_3 = \frac{Q_{fo}/b_o h_o}{u_o} = \frac{U_{fo}}{u_o} \tag{26}$$

Figure 5 and 6 show the correlation of $\bar{C}_1$ with $\bar{C}_3$ and $\bar{C}_2$ with $\bar{C}_3$.

It is significant in these figures that both laboratory flume tests and prototype field surveys follow the same correlations. In addition, the range of degrees of stratification include the highly stratified Delft tests 121 and 122 as well as the nearly well mixed middle reaches of the James River estuary. Thus, this empirical approach to evaluating the effective coefficients of mean eddy flux, $\bar{D}$ and $\bar{K}$ is apparently applicable to naturally occuring estuarine conditions.

The Savannah Estuary - An Analytical Investigation of Estuarine Shoaling

The shoaling problems of the Savannah Estuary have been carefully reviewed by Simmons (1965) and Harleman and Ippen (1969). Both hydraulic models and field investigations have shown a relationship between the longitudinal location of maximum shoaling and a null point as indicated in Figure 6. From this figure it is seen that immediately downstream of Savannah Harbor, between stations 120 and 130, a zone of very high shoaling is located by comparison with the rest of the estuary. In addition, for the model data shown in Figure 6, with a freshwater flow equal to 7,000 cfs, the null point also occurs between these two stations.

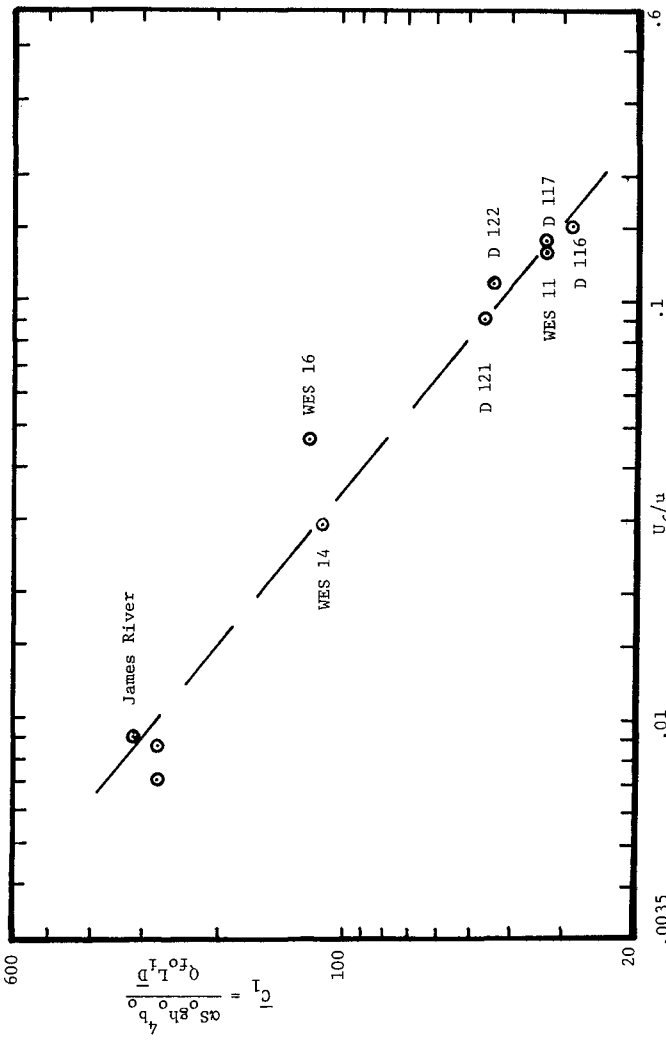

Figure 5 Correlation of $\bar{D}$

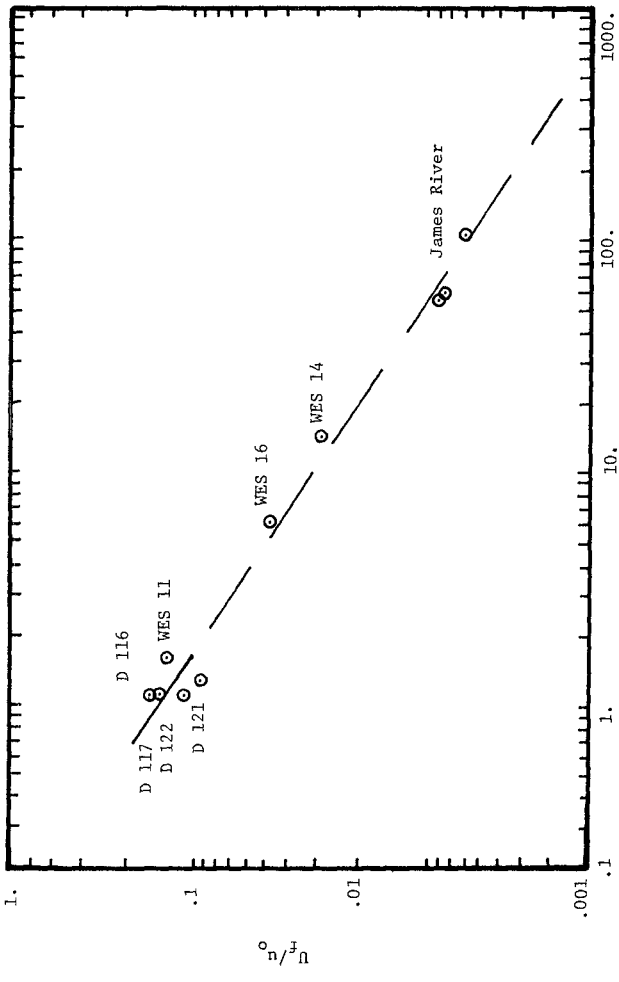

Figure 6 Correlation of $\bar{K}$

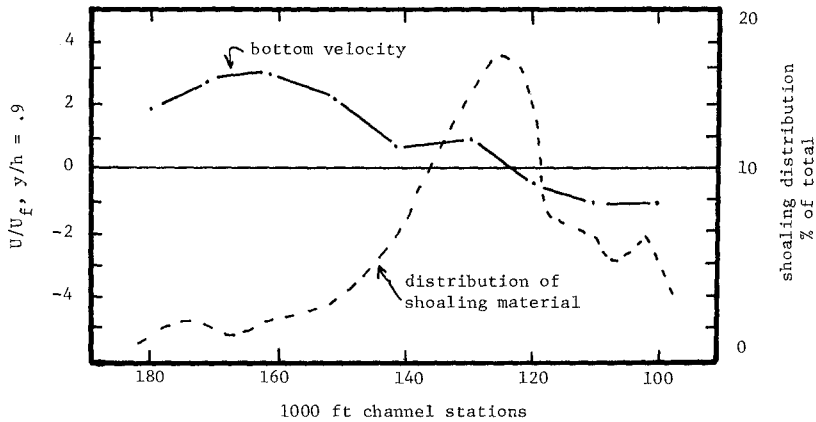

Figure 6 Longitudinal location of maximum shoaling in relation to null point for Savannah estuary, Q_f = 7000 cfs (from Harleman and Ippen 1969)

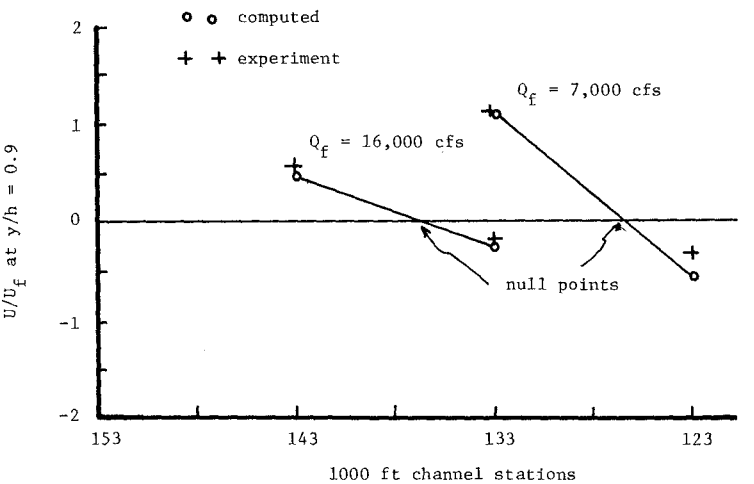

Figure 7 Null point location for Savannah estuary

In their report, Harleman and Ippen present the time- and depth-averaged longitudinal salinity distributions from the model for freshwater flows of 7,000 cfs and 16,000 cfs (their Figure 13). With these curves, and the correlation for eddy coefficients presented above, it is possible to apply the analytical model to this estuary and thus further investigate the null point dependence on freshwater flow rates.

Figure 7 illustrates the analytical results for the null point for the two freshwater flows. The connected circles are the computed values and the crosses are the hydraulic model data, as reported by Harleman and Ippen. The fairly close agreement between computed and experimental values indicates that the Savannah estuary prototype scales and conditions do not seriously violate the assumptions of the analytical model.

In Figure 7 it is seen that the null point shifts downstream about 1,000 feet when the freshwater discharge is increased to 16,000 cfs. Qualitative results of this nature illustrate the usefulness of the analytical model in the analysis of the many factors which determine the circulation patterns in estuaries. When used in conjunction with a numerical model, as discussed above, or a hydraulic model, as in the present illustration, this analytical model should prove to be a valuable aid to engineering analysis.

References

1. Delft Hydraulics Laboratory (1970) "Flume Study on Salinity Intrusion in Estuaries", M 896-X, 1970.

2. Fisher, J.S., Ditmars, J.D. and Ippen, A.T. (1972) "Mathematical Simulation of Tidal Time-Averages of Salinity and Velocity Profiles in Estuaries", Technical Report No. 151, Ralph M. Parsons Laboratory for Water Resources and Hydrodynamics, Department of Civil Engineering, Massachusetts Institute of Technology, 1972.

3. Hansen, D.V. and Rattray, M., Jr. (1965) "Gravitational Circulation in Straits and Estuaries", Journal of Marine Research, Vol. 23, No. 2, 1965.

4. Harleman, D.R.F. and Ippen, A.T. (1967) "Two-Dimensional Aspects of Salinity Intrusion in Estuaries: Analysis of Salinity and Velocity Distributions", T. B. No. 13, Committee on Tidal Hydraulics, U.S. Army Corps of Engineers, 1967.

5. Harleman, D.R.F. and Ippen, A.T. (1969) "Salinity Intrusion Effects in Estuary Shoaling", Journal of the Hydraulics Division, ASCE, Vol. 95, No. HY1, Proc. Paper 6340, 1969.

6. Ippen, A.T. and Harleman, D.R.F. (1961) "One-Dimensional Analysis of Salinity Intrusion in Estuaries", T. B. No. 5, Committee on Tidal Hydraulics, U.S. Army Corps of Engineers, 1961.

7. McGregor, R.D. (1971) "The Influence of Topography and Pressure Gradient on Shoaling in a Tidal Estuary", Geophysical Journal of Royal Astronomical Soc., 25, 1971.

8. Pritchard, D.W. (1952) "Salinity Distribution and Circulation in the Chesapeake Bay Estuarine System", Journal of Marine Research, Vol. 11, No. 2, 1952.

9. Pritchard, D.W. (1954) "A Study of the Salt Balance in a Coastal Plain Estuary", Journal of Marine Research, Vol. 13, No. 1, 1954.

10. Pritchard, D.W. (1956) "The Dynamic Structure of a Coastal Plain Estuary", Journal of Marine Research, Vol. 15, No. 1, 1956.

11. Simmons, H.B. (1965) "Channel Depth as a Factor in Estuarine Sedimentation", Tech. Bull. No. 8, Committee on Tidal Hydraulics, U.S. Army Corps of Engineers, Vicksburg, Mississippi, 1965.

12. Thatcher, M.L. and Harleman, D.R.F. (1972) "A Mathematical Model for the Prediction of Unsteady Salinity Intrusion in Estuaries", Technical Report No. 144, Ralph M. Parsons Laboratory for Water Resources and Hydrodynamics, Department of Civil Engineering, Massachusetts Institute of Technology, 1972.

13. U.S. Army Engineer Waterways Experiment Station (1955) Investigation of Salinity and Related Phenomena (Interim Report on Flume Control Tests), Vicksburg, Mississippi, 1955.

CHAPTER 133

COMPUTER STUDIES OF ESTUARY WATER QUALITY

by

Donald O. Hodgins[1]
Michael C. Quick[2]

A B S T R A C T

The convection and dispersion of pollutants in a deltaic estuary system are calculated using several interfaced computer programmes. The basic programme is a Dronkers type one dimensional hydrodynamic model, which is interfaced with a model of the salt water intrusion in the seaward reach.

The importance of Pitt Lake, a large fresh water but highly tidal lake, is discussed, inasmuch that it integrates water quality changes over long periods of time.

The salt wedge analysis reveals the nature of the interfacial stress which is not a function of velocity or velocity squared. It is shown that the interfacial stress is a function of entrainment, rather like a Reynolds stress, and plots are given of interfacial stress against local Richardson number multiplied by local upper layer velocity.

* * * * * *

The starting point of the study is to determine and trace the water movements resulting from tide and river flows in the Fraser River estuary. These water movements are calculated by determining numerical solutions of the hydrodynamic equations. These solutions are transferred to a convection and

---

1. Graduate Student, Department of Civil Engineering, UBC.

2. Assoc. Prof., Department of Civil Engineering, UBC.

diffusion computer sub-model as the basis for determining water quality conditions resulting from effluent discharges which enter the system at known points. The method is used to determine the convection and diffusion of conservative pollutants but later work will study non-conservative effects which may be time or flow dependent.

At the present time, the Fraser River is relatively undeveloped and flows are only slightly regulated. Also the river is one of the few remaining major salmon rivers and supports a major portion of both the Canadian and the United States salmon fishing industry. It is considered important to understand fully the behaviour of this estuary before too much development is begun. This study is one step in such a total study which is being actively pursued by a team of scientists and engineers.

The Fraser estuary has certain special features which must be considered and allowed for in the formulation of the computer modeling. The lower estuary divides into a delta with a South Arm which carries some 90% of the flow, a North Arm and a few lesser channels which are later subdivisions of the North and South Arms (Figure 1). There is a large fresh water lake, Pitt Lake, which connects to the estuary through a short channel at about the mid-point of tidal influence. The large flow reversals to and from this lake are frequently of the same order of magnitude as the mean annual fresh water Fraser River flows, and have resulted in a reverse delta extending into the lake. An important feature of the Fraser River is the large seasonal flow variation with winter flows of the order of 30,000 c.f.s. Summer flows have, historically, been as high as 600,000 c.f.s. (Figure 2). The tidal range at the mouth, with a maximum of about 15 feet, and the low winter river flows result in a fairly well stratified salinity intrusion in the seaward reaches. This salinity intrusion has almost certainly been increased by the dredging of the downstream channels. The influence of this flow variation on the tidal variation is indicated in Figure 3.

Pitt Lake is a particularly interesting feature of the estuary system. The large surface area of the lake allows it to accept large volumes of water on each tide so that it acts like a huge hydraulic damper on the tidal propagation. From the water quality viewpoint, Pitt Lake can be a valuable asset because it is continuously sampling the estuary water, so that the lake acts as a long-term integrator of water quality. This is particularly true during the summer months when the lake is stratified, because the cooler, inflowing estuary water plunges below the thermocline while the ebb tide flow is drawn from the surface layers. The lake's biological environment may prove to be a valuable long-term integrator of deteriorating water quality.

The basic hydrodynamic model follows work which is well documented in the literature (Dronkers (2)). This basic model

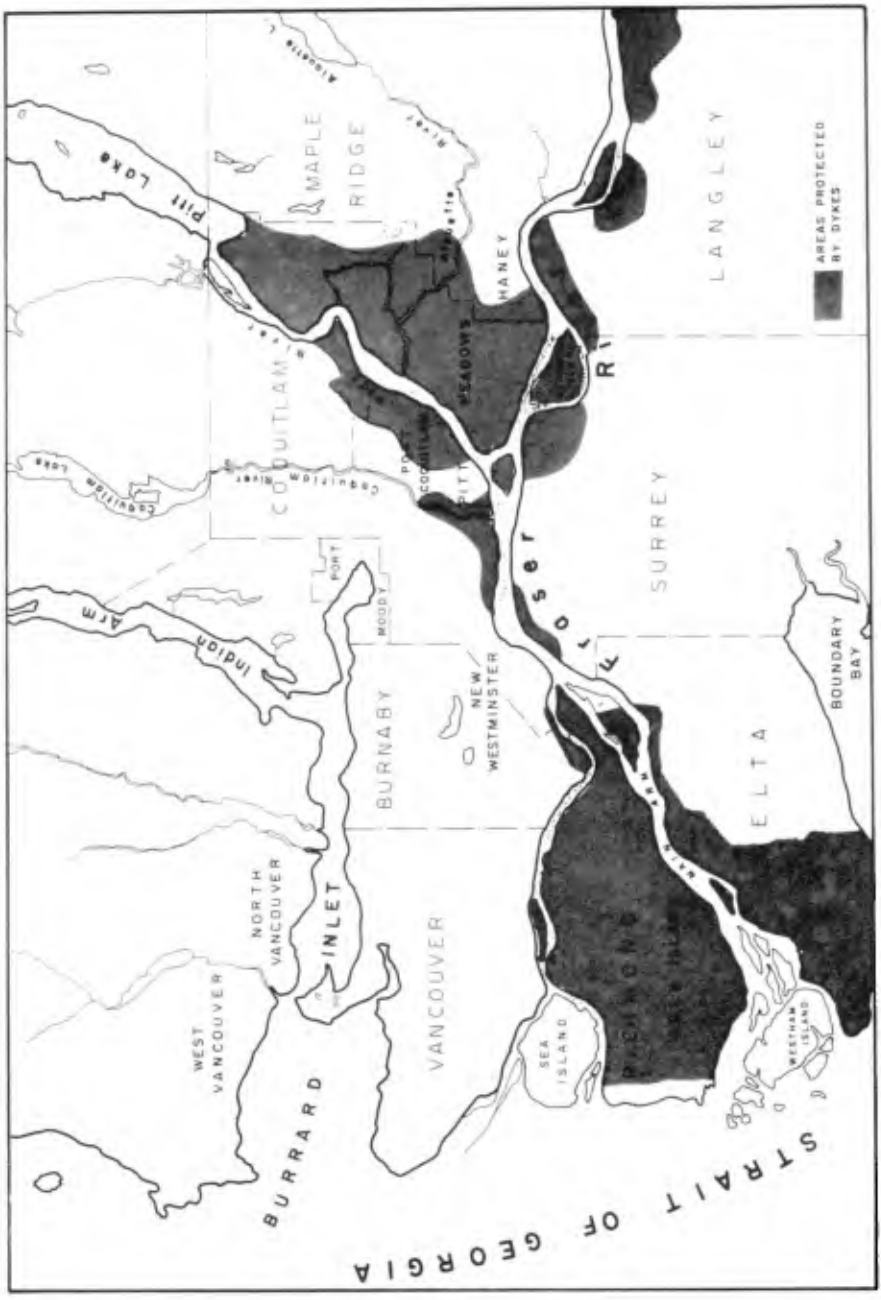

FIGURE 1. Lower Fraser Estuary

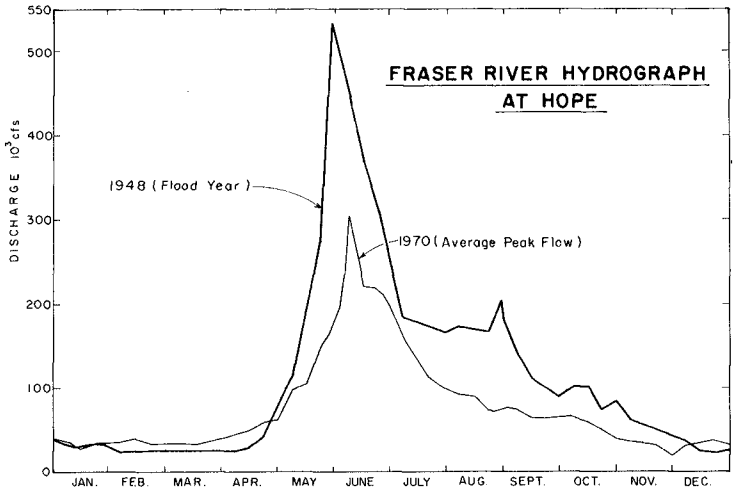

FIGURE 2. Typical Fraser River Discharges

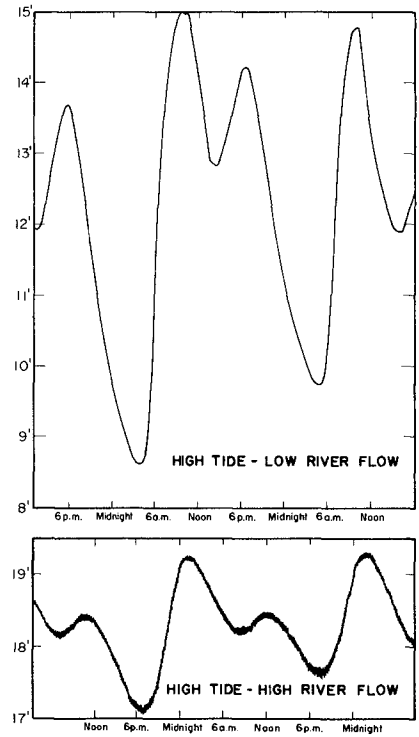

FIGURE 3. Tide Curves at Port Mann Showing Influence of High and Low Freshwater Discharge

is interfaced with more detailed local models which calculate such features as salinity intrusion and its modifications to the flow patterns, and local diffusion of effluents where concentration gradients are high. Finally, the convective model is abstracted from the output of the basic and local models. This convective model traces the movements of individual water masses and keeps account of concentrations.

The low freshwater discharge during winter months produces a density stratified estuary when saline water from the Strait of Georgia intrudes along the river bottom. Any numerical hydraulic modeling must therefore include the capacity to handle the stratified situation. A simple two-layer model for this purpose is presently under development, based on the following hydraulic equations. (Figure 4 shows the notation).

$z>-h_f$

$$\frac{\partial U}{\partial t} + U\frac{\partial U}{\partial x} + g\frac{\partial \eta}{\partial x} = -\tau_i/\rho(\eta+h_f) \tag{1}$$

$$\frac{\partial}{\partial t}(\eta+h_f) + \frac{\partial}{\partial x}[U(\eta+h_f)] = 0 \tag{2}$$

$-h_f>z>-h$

$$\frac{\partial U_s}{\partial t} + \frac{U_s \partial U_s}{\partial x} + \frac{\rho}{\rho_s} g\frac{\partial}{\partial x}(\eta+h_f) - g\frac{\partial h_f}{\partial x}$$

$$= (\tau_i-\tau_b)/\rho_s(h-h_f) \tag{3}$$

$$-\frac{\partial h_f}{\partial t} + \frac{\partial}{\partial x}[U_s(h-h_f)] = 0 \tag{4}$$

where τ_i and τ_b represent the interfacial and bottom shearing stresses respectively; ρ and ρ_s are the fresh and salt water densities. The velocities, U and U_s, represent mean values integrated over the depth of each layer. The boundary conditions corresponding to these equations are:

(i) the freshwater discharge at the upstream extremity of the salt water; and

(ii) the specifications of η_o and h_{f_o} at x=0 for all time.

Even the simple model involving equations (1) to (4) is computationally difficult and furthermore it contains more unknown quantities than equations. The usual approach is to replace the stress terms by functions of the other dependent variables; traditionally relations in terms of velocity shear. The solutions of these equations are sensitive to the assumption made for the interfacial stress. Therefore, a steady flow model has been extracted from this system of equations and solved to yield information on the interfacial stress term. The approach is similar

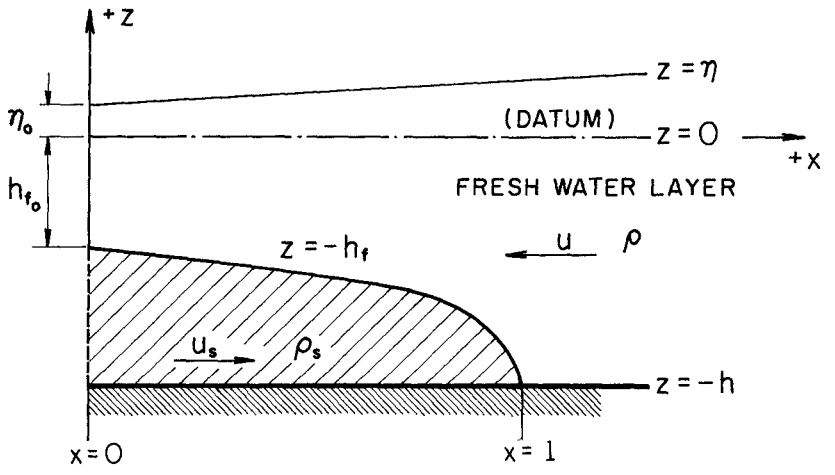

$$R^3 + (\eta'-2)R^2 = (2\eta' - \frac{(1+\eta')^2}{\varepsilon} + \frac{2C'}{\varepsilon})R - (\frac{2C'\eta'}{\varepsilon} - \frac{(1+\eta')^2\eta'}{\varepsilon} - \frac{2F^2}{\varepsilon}) = 0 \quad \ldots(9)$$

where

$$\varepsilon = (\rho_s-\rho)/\rho$$

$$\frac{2C'}{\varepsilon} = h'_{fo}(h'_{fo}-2) + \frac{(1+\eta'_o)^2}{\varepsilon} + \frac{2F^2}{\varepsilon(\eta_o + h_{fo})}$$

$$F = \frac{u_\ell(\eta_\ell+h)}{\sqrt{gh^3}} = \text{Froude Number}$$

$$R = h_f/h$$

$$\eta' = \eta/h,\ \eta'_o/h$$

$$h'_{fo} = h_{fo}/h$$

FIGURE 4. Stratified Flow Definition Sketch and Solution for Stationary Wedge

to Keulegan's (1) with respect to the starting equations.

The model which represents a simple balance of forces and continuity of mass in each layer, becomes:

$$z>-h_f \qquad U\frac{dU}{dx} + g\frac{d\eta}{dx} = -\tau_i/\rho(\eta+h_f) \tag{5}$$

$$\frac{d}{dx}[U(\eta+h_f)] = 0 \tag{6}$$

$$-h_f>z>-h \qquad \frac{\rho g}{\rho}\frac{d}{dx}(\eta+h_f) - g\frac{dh_f}{dx} = \tau_i/\rho_s(h-h_f) \tag{7}$$

$$U_s = 0 \tag{8}$$

A rectangular channel of constant width and depth, with no entrainment of salt water from the lower layer have been assumed. Equations (5) to (8) may be solved for the variable h_f, by eliminating the interfacial stress, τ_i, and using equation (6) to replace the velocity U by a discharge in the upper layer. This procedure results in an integrable differential equation whose final solution is a cubic in the interfacial depth h_f. This solution is an analytic function in terms of the surface elevation and freshwater discharge or Froude number and is shown in Figure 4.

In order to obtain information about τ_i, the surface profile for a given value of the freshwater discharge must be specified. The one-dimensional tidal equations (2) have been solved explicitly for tidal conditions and rectangular section geometries representative of the lower Fraser River. The results linking discharge and surface elevation have been used to estimate a range of values of these variables applicable to "balanced conditions" in the idealized estuary.

Salt wedge geometries (Figure 5) have been calculated for three discharges typical of velocities just after the turn to ebb tide. These solutions were obtained by imposing a *constant* surface slope in equation (9), (Figure 4), corresponding in an average sense to the discharge. In Figure 5 the penetration lengths have been normalized using the longest length obtained for the lowest discharge, $Q=-30$ ft^2/sec.

Once the salt wedge geometry has been obtained, equation (7) may be solved for the interfacial stress. These stresses are plotted in Figure 6 for the three discharges considered previously. In each case the stress increases to a maximum value near the upstream end and then decreases rapidly to a theoretical value of zero at the wedge toe.

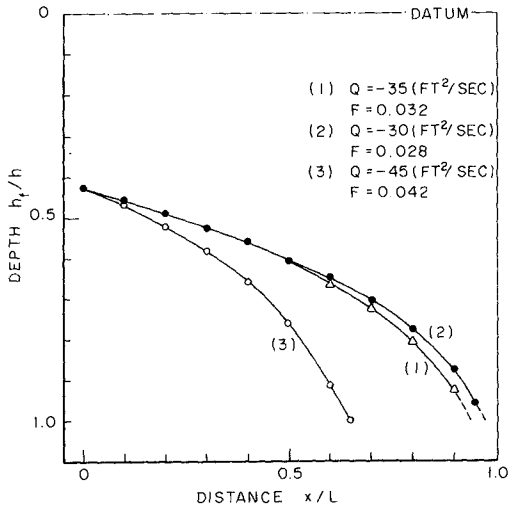

FIGURE 5. Calculated Salt Wedge for Three Different Fresh Water Discharges

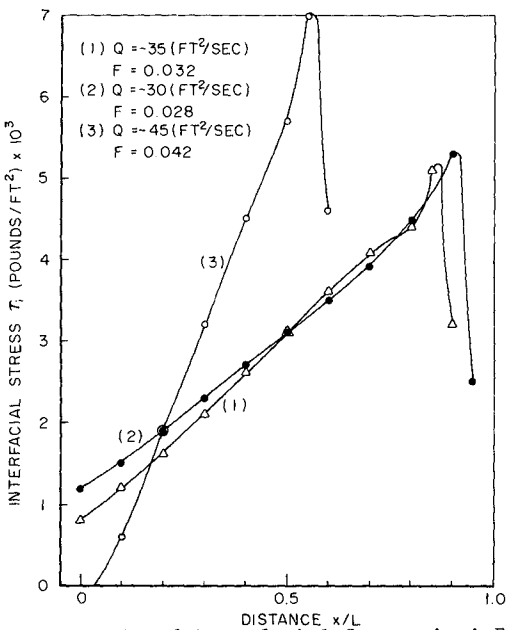

FIGURE 6. Calculated Interfacial Stress As A Function of Distance From Seaward End

We are now in a position to examine some assumptions about the variation of the interfacial stress term with respect to other flow variables. For example, if the stress is plotted against the freshwater velocity squared -- reflecting the mean velocity shear squared, since the salt water is assumed motionless -- the results shown in Figure 7 are obtained. The interfacial stress *decreases* in the direction of increasing velocity or velocity shear. If we think of velocity shear as the necessary mechanism for creating the stress, the results are contradictory.

The stress variations in Figure 6 were calculated from the pressure force in the lower layer and involve only the free surface and interfacial slopes. This can be seen if equation (7) is rearranged as:

$$\tau_i = \rho g(h-h_f)\left[\frac{d\eta}{dx} - \epsilon \frac{dh_f}{dx}\right] \qquad (10)$$

It is possible that the constant surface slope is an unreal boundary condition, resulting in a stress decrease in the seaward direction that is too rapid. However, equation (10) shows that, even if

$$\frac{d\eta}{dx} \to 0$$

as we move seaward,the interfacial stress will continue to decrease as

$$\epsilon \frac{dh_f}{dx}.$$

Evidence for a surface profile modification was obtained by applying the model for higher discharges and slope values. In such cases, the calculated stress reversed in direction when $\frac{d\eta}{dx}$ exceeded the value of $\epsilon \frac{dh_f}{dx}$. Clearly, such stress reversals are unphysical and suggest that $\frac{d\eta}{dx}$ approaches zero near the seaward end to maintain the correct force balances. The convective accelerations would account for such a modification as they create a retarding force on the flow acting like an adverse pressure force.

If the interfacial stress is principally a product of mixing; that is, a transfer of momentum across the interface like a Reynold's stress, then a seaward decrease in the force term may not be unreasonable. Indeed, preliminary field data indicate a higher degree of stratification near the seward end, and a better mixed region near the wedge toe. This suggests a greater interaction between the layers near the upstream end and the possibility of higher interfacial stresses in this region.

Assumptions made for the interfacial stress in the unsteady equations (1) and (3), will undoubtedly have a large influence on their solution. On the basis of the "steady-state" model, replacing this stress by functions of velocity or velocity

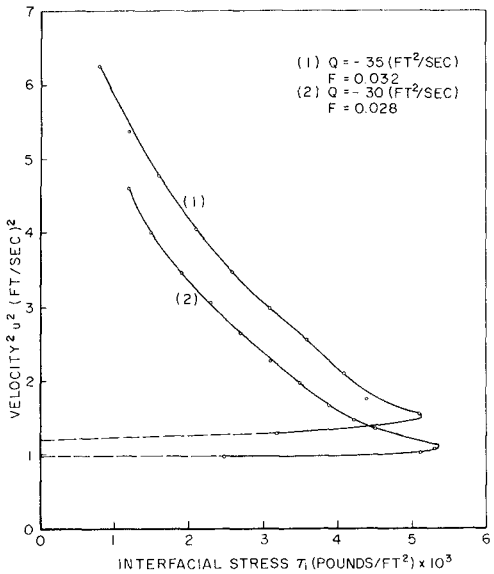

FIGURE 7. Interfacial Stress Plotted Against Velocity Squared, Showing Inverse Correlation

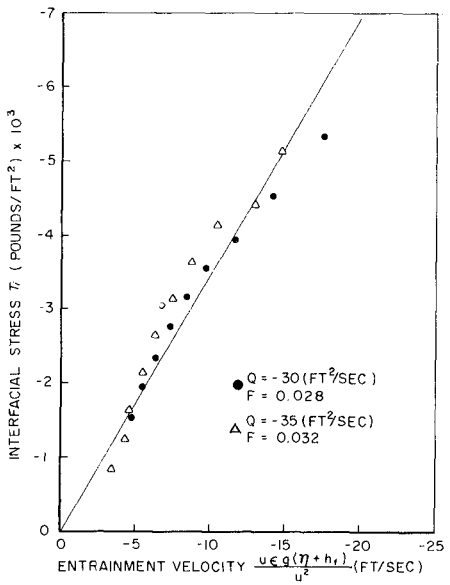

FIGURE 8. Interfacial Stress Plotted Against Velocity Multiplied by Richardson Number

squared will introduce incorrect stress variations with distance. Better representations may be found in terms of the surface slopes or parameters indicating the intensity of mixing. For example, if the interfacial stress, τ_i is plotted against an "entrainment velocity," the results in Figure 8 are obtained. This entrainment velocity is simply the average local velocity of the upper layer multiplied by the local Richardson number. This approach was suggested from a study of Ellison and Turner's work (3) although the results and formulation are not directly comparable or compatible. A similar, but slightly less good, fit is obtained by plotting stress against just Richardson number. As yet the actual mixing mechanism in the river regime is not well understood and presents perhaps the most challenging part of this problem.

The steady flow model has also shed light on the role of the convective acceleration term in equation (5). Equations (5) to (8) may easily be solved in the absence of the $u\frac{du}{dx}$ term; in which case the predicted salt wedge penetration averages approximately 40 per cent of the lengths shown in Figure 5. Thus the convective accelerations serve to reduce the transfer of momentum across the layer boundaries, thereby reducing the interfacial stress term. In the simple stationary model, this means the lower can now move further upstream and produce the longer penetration lengths. Thus it is necessary that any models of this nature retain the convective acceleration terms.

CONCLUSIONS

A digital computer model has been written which calculates the tidal flows in the Fraser River estuary. Information is extracted from this basic model to calculate convection and dispersion of conservative pollutants in the estuary system. In the seaward reaches of the estuary salt water intrudes during periods of moderate to low river stages and an additional model of this aspect has yielded some understanding of salt-fresh water interaction.

The solution of the salt water intrusion problem depends upon a correct representation of the interfacial stresses. A study of the arrested wedge reveals that this interfacial stress is not a function of velocity or velocity squared. In fact the interfacial stress is perhaps more nearly inversely proportional to velocity and is governed by entrainment, rather like a Reynolds stress. To confirm this result, a plot is given of local Richardson number multiplied by local upper layer velocity against computed stress. In this case the Richardson number is simply the inverse of the local densimetric Froude number.

A C K N O W L E D G E M E N T

Mr. Hodgins has been supported by a National Research Council of Canada Scholarship. The computational work has been financed both from a National Research Council grant and from additional funds received from the UBC Westwater Research Centre.

R E F E R E N C E S

(1) Ippen, A. T. *Estuary and Coastline Hydrodynamics*. McGraw-Hill Co. Inc., 1966, Chapter 11, pp. 546-74.

(2) Dronkers, J. J. "Tidal Computations for Rivers, Coastal Areas and Seas," *Journal of Hydraulics Division*, ASCE, No. HY1, Proc. Paper 6341, January, 1969.

(3) Ellison, T. H., and Turner, J. S. "Turbulent Entrainment in Stratified Flows," *Journal of Fluid Mechanics*, Vol. 6, 1959, pp. 423-448.

CHAPTER 134

DISTORTED MODELING OF DENSITY CURRENTS

J.J. Sharp, B.Sc., M.Sc., Ph.D., ARCST., C.Eng., P.Eng.*

ABSTRACT

The paper describes a method of choosing scales for the correct representation of convective spread in a hydraulic model involving densimetric phenomena. Although most prototype spreads are non-viscous in nature it is possible for small scale laboratory spreads to become affected by viscous influence when the spreading density front is remote from the outfall. This must be avoided if correct representation is to be achieved and the scales for the model must be chosen with this in view. It is often impossible to avoid viscous influence in a natural scale model of reasonable size and distortion of the vertical scale must then be employed.

INTRODUCTION

In attempting to design a physical model of phenomena involving densimetric spread, there are a number of aspects of the dispersion and diffusion process which must be considered. Ackers[1] has listed these as; jet diffusion, buoyant rise, convective spread, mass transport by ambient currents, ambient turbulent mixing and surface cooling (if applicable). Each of these has distinct scaling requirements and this paper concentrates on the requirements for convective spread with particular reference to outfalls located at the surface.

An existing procedure for convective spread is that due to Barr[2,3] and makes use of design diagrams obtained from lock exchange flow. Since the method to be described has been developed along lines suggested by Barr's approach, it is worthwhile to outline the basis of the lock exchange diagrams before proceeding to an evaluation of the new method.

* Associate Professor of Engineering, Memorial University of Newfoundland, St. John's, Newfoundland, Canada.

SCALING PROCEOURE BASEO ON LOCK EXCHANGE FLOW OATA

Figure 1 represents an illustration of basic exchange flow and it has been shown [2,3] that the distance travelled by the overflow, may be related to the time of travel by:

$$T/T_\Delta = \phi\left[L/H,\ \frac{(g')^{1/2}H^{3/2}}{\nu}\right] \quad \ldots\ldots\ldots (1)$$

where $T\Delta = (H/g')^{\frac{1}{2}}$; H = depth of flow; g' = 'reduced' nett gravitational acceleration at the outfall, $g\Delta\rho/\rho$; $\Delta\rho$ = density difference; ρ = base density; ν = kinematic viscosity; L = length of travel; T = time of travel.

Considerable experimental work resulted in a graphical representation of the relationship among these parameters, and this is shown in Figure 2, which forms the design diagram for choosing model scales.

A detailed explanation of Barr's method has been given elsewhere [1] but the method basically seeks to first establish details of an analogous, large scale, lock exchange mechanism which would give rise to the conditions expected to occur in the three dimensional prototype. Figure 2 can then be used to obtain scales which would allow of correct reproduction of rate of spread in a model lock exchange flow. It is surmised that if the scales are correct for the two dimensional phenomena they will also be correct for the three dimensional phenomena. Figure 2 indicates the effect of viscous influence on the rate of spread, the horizontal part of each curve of constant $T/T\Delta$ representing the region in which the spread is unaffected by viscous influence. Since most prototype spreads will be non-viscous, the objective is to ensure that the model relationship among the three parameters of Equation 1 is such that the model spread also lies outside the viscous zone.

Consider an analogous lock exchange flow in which

$(g')^{1/2}H^{3/2}/\nu = 1.06\times10^{6}$ and L/H = 267. (Longannet data:[2] $\Delta\rho$ = .0015 gm./ml., H = 15 ft., L = 4,000 ft., and ν = 1.2×10^{-5} ft.^{2}/sec.). From figure 2, $T/T\Delta$ = 500. In a natural scale model, the distance and time parameters must have the prototype values and, to avoid viscous influence, $(g')^{1/2}H^{3/2}/\nu$ must therefore be greater than approximately 2×10^{4}. (From Figure 2)

The limiting scale of the non-viscous, natural scale is thus given by

$$\frac{1}{x} = \frac{H_m}{H_p} = \left(\frac{2\times10^{4}}{1.06\times10^{6}}\right)^{2/3} = 1/14 \quad \ldots\ldots\ldots (2)$$

where 1/x = horizontal scale and suffixes m and p refer to model and

prototype respectively. A larger scale would allow the spread to travel further than the design extension with no viscous influence and a smaller scale would have the opposite effect.

If distortion is employed

$$(L/H)_m = (L/H)_p \cdot \frac{1}{e} \qquad \ldots\ldots\ldots (3)$$

$$(T/T_\Delta)_m = (T/T_\Delta)_p \cdot \frac{1}{e} \qquad \ldots\ldots\ldots (4)$$

$$\frac{(g')^{1/2} H^{3/2}}{\nu}_m = \frac{(g')^{1/2} H^{3/2}}{\nu}_p \cdot \left(\frac{x}{e}\right)^{3/2} \qquad \ldots\ldots\ldots (5)$$

The required horizontal scale is normally fixed by space considerations, and equations 3 - 5 and Figure 2 are sufficient to calculate the minimum distortion necessary to ensure viscous flow in the model. (3) Greater distortion has the same effect as increasing the scale of a non-distorted model.

For the Longannet model, the horizontal scale was set at 1/400 and on this basis the required distortion was found to be 6.7.

CRITICISM OF THE DESIGN METHOD

Various assumptions are implicit in the method, and these are worth comment.

1. The spread of a lock exchange flow is entirely convective compared with the normal circumstances of an outfall where there is almost certainly some jetting action. However, any element of forced flow in the model will inhibit viscous influence. Thus, if model scales are chosen to ensure that a convective flow is non-viscous, a forced flow in the model must also be non-viscous and would remain so at greater extensions than the design extension. Barr's design method is, therefore, conservative and errs on the safe side.

2. Figure 2 was prepared from experiments on two dimensional data and doubts have been raised (4) as to the applicability of that data to three dimensional spread. The validity of this criticism depends, to some extent, on site conditions which govern the shape of the spread, but the use of Figure 2 could be justified simply by the absence of more relevant information.

3. Before model scales can be chosen, it is necessary to assume a large scale lock exchange which is thought to be analogous to the prototype spread, i.e. one which will produce the same spread conditions as are expected to occur in the prototype. There can be

no doubt that this must be extremely difficult unless considerable first-hand experience of exchange flow is available and this severely limits application of the method.

DESIGN DIAGRAMS BASED ON THREE DIMENSIONAL SPREAD

A simple representation of three dimensional spread from a buoyant surface discharge is shown in Figure 3. It is assumed that an effluent discharge, Q, of density, ρ, flows through a circular pipe of diameter D into a quiescent homogeneous body of receiving fluid of density $\rho + \Delta\rho$. The effluent and the receiving fluid are miscible, and the kinematic viscosity of each, ν, is assumed to be the same.

By similitude reasoning it can be shown [5] that

$$\phi\left[\frac{L(g')^{1/5}}{Q^{2/5}}, \frac{T(g')^{3/5}}{Q^{1/5}}, \frac{Q(g')^{1/3}}{\nu^{5/3}}, \frac{D(g')^{1/5}}{Q^{2/5}}\right] = 0 \quad \ldots . (6)$$

where L = distance from source to tip of front
and T = time of travel.

The parameter $D(g')^{1/5}/Q^{2/5}$ is a form of outfall densimetric Froude number and, for constant values of $D(g')^{1/5}/Q^{2/5}$

$$\phi\left[\frac{L(g')^{1/5}}{Q^{2/5}}, \frac{T(g')^{3/5}}{Q^{1/5}}, \frac{Q(g')^{1/3}}{\nu^{5/3}}\right] = 0 \quad \ldots . (7)$$

Experiments conducted at two values of $D(g')^{1/5}/Q^{2/5}$ have indicated [5] that the relationship among the parameters of equation 7 is as given in Figures 4 and 5. These show similar features to Figure 2 and provide alternative design diagrams for scaling procedures.

Prior to experimental work, care was taken to ensure that the two values of $D(g')^{1/5}/Q^{2/5}$ chosen for study would be suitable for application to prototype outfalls.

Tamai [6] has suggested that most cooling water outfalls operate at densimetric Froude numbers of between 2.0 and 14.0 but, due to the size of apparatus available, it was not feasible to obtain the larger of these limits in the laboratory. Efforts were therefore concentrated on low values of the outfall Froude number and $D(g')^{1/5}/Q^{2/5}$ = 1.16 and 0.58 correspond to densimetric Froude numbers of 0.88 and 5.0 respectively.

SCALING PROCEDURE

The design method is basically similar to that described for lock exchange flow but is less dependent on assumed conditions.

For circular outfalls, values of the basic prototype parameters may be obtained directly from prototype data. Either diagram may be used depending on the proposed outfall conditions, and it may be necessary to estimate the final scales from calculations involving both diagrams. However, it will be shown later that the actual value of $D(g')^{1/5}/Q^{2/5}$ is not of great relevance during the scaling procedure.

Consider the Longannet outfall. Basic prototype data are; (2,7) Q = 3,200 ft.^{3}/sec., $\Delta\rho$ = .0015 gm/ml., L = 4,000 ft., and ν = 1.2 x 10 ^{5}ft^2/sec. (extension L = 4,000 ft. was chosen as the limit of spread for which correct representation was required in the model.)

Then $$\frac{L(g')^{1/5}}{Q^{2/5}} = 86.5 \qquad \ldots\ldots\ldots (8)$$

and $$\frac{Q(g')^{1/3}}{\nu^{5/3}} = 1.85 \times 10^{11} \qquad \ldots\ldots\ldots (9)$$

From Figure 4

$$\frac{T(g')^{3/5}}{Q^{1/3}} = 220 \qquad \ldots\ldots\ldots (10)$$

In a natural scale model, the time and distance parameters must have the same value as in the prototype. Thus the minimum model value of $Q(g')^{1/3}/\nu^{5/3}$ which would avoid viscous influence is

$$Q(g')^{1/3}/\nu^{5/3} = 0.6 \times 10^6$$

and for a natural scale model the scale is given by

$$\frac{1}{X} = \left(\frac{Q_m}{Q_p}\right)^{2/5} = \left(\frac{0.6\times10^6}{1.85\times10^{11}}\right)^{2/5} = 1/157 \qquad \ldots\ldots (11)$$

A similar process applied to Figure 5 leads to

$$\frac{1}{X} = \left(\frac{2.3\times10^6}{1.85\times10^{11}}\right)^{2/5} = 1/93 \qquad \ldots\ldots (12)$$

These scales show the beneficial effect of the outfall jetting action. Barr's data for convective flow leads to a natural

scale of 1/14. For an outfall with low jetting action (Figure 5) the limiting scale is 1/93, and with a greater forced element of flow (Figure 4) the scale is 1/157.

EFFECT OF DISTORTION

The effect of distortion is to reduce the required model value of $L(g')^{1/5}/Q^{2/5}$, thus allowing smaller $Q(g')^{1/3}/\nu^{5/3}$ without entering the viscous zone.

$$\text{ie} \quad \frac{L(g')^{1/5}}{Q^{2/5}}\,m = \frac{L(g')^{1/5}}{Q^{2/5}}\,p \cdot \frac{1}{e^{3/5}} \qquad \ldots\ldots (13)$$

$$\frac{T(g')^{3/5}}{Q^{1/5}}\,m = \frac{T(g')^{3/5}}{Q^{1/5}}\,p \cdot \frac{1}{e^{4/5}} \qquad \ldots\ldots (14)$$

$$\text{and} \quad \frac{Q(g')^{1/3}}{\nu^{5/3}}\,m = \frac{Q(g')^{1/3}}{\nu^{5/3}}\,p \cdot \frac{e^{3/2}}{x^{5/2}} \qquad \ldots\ldots (15)$$

For a horizontal scale of 1/400 and a distortion of 2, and taking the prototype values given in equations 8 - 10;

$$\frac{L(g')^{1/5}}{Q^{2/5}}\,m = 56.2 \qquad \ldots\ldots (16)$$

$$\frac{T(g')^{3/5}}{Q^{1/5}}\,m = 126 \qquad \ldots\ldots (17)$$

$$\frac{Q(g')^{1/3}}{\nu^{5/3}}\,m = 0.16\times10^{6} \qquad \ldots\ldots (18)$$

Figure 4 shows that these points lie just outside the viscous zone and thus, in a model, no viscous influence would be observed throughout a spread of 4,000 model feet.

Applying the same analysis to Figure 5 shows that, in the case of less jet action ($D(g')^{1/5}/Q^{1/5} = 1.16$) the model spread would become viscous in the latter part of the design extension. However, with a distortion of 4.0, both diagrams indicate freedom from viscous influence and thus, provided the outfall densimetric Froude number is greater than 0.88, a horizontal scale of 1/400 and a distortion of 4 would give a model spread, equivalent to 4,000 ft. prototype, free from viscous influence.

An additional constraint is that the correlation between the length and time parameters in the model must be identical to that obtained in the prototype. Figure 6 illustrates the experimentally determined correlation for non-viscous spread and shows that $D(g')^{1/5}/Q^{2/5}$ must have the same value in model and prototype. The outfall must thus be designed on a standard Froudian basis. Distortion effects are also given in Figure 6 which shows that any distortion alters the correlation in such a way as to reduce the required rate of spread in the model below that which will be achieved. The overall effect is, thus, twofold. Distortion can eliminate the gross errors of viscous influence, but at the same time reduces the possibility of achieving the correct rate of spread.

It is noticeable that the discrepancy increases as the distortion is increased, and it is therefore important, from the point of view of spread, to keep the design distortion to a minimum. Errors are greater at the higher value of $D(g')^{1/5}/Q^{2/5}$ than at the lower value, and this indicates that distortion causes greater misrepresentation of spread when the jetting action is low than would be the case for an outfall with a considerable element of forced flow. For $D(g')^{1/5}/Q^{2/5} = 0.58$ the errors are probably negligible.

These errors are not indicated by two dimensional data because in lock exchange flow there is little diminution of tip velocity as the spread moves away from the source. Thus a non-viscous spread diagram for lock exchange flow results in a straight line, and equations 3 and 4 show that exaggeration would simply move the prototype point (e = 1) along the line towards the origin.

RELEVANCE OF THE NON DIMENSIONAL GROUP $D(g')^{1/5}/Q^{2/5}$

As has been stated, the model outfall must be designed to have the same value of $D(g')^{1/5}/Q^{2/5}$ as the prototype. However, its actual value is not of great relevance for the purpose of choosing scales. The variation between the scales chosen on the basis of Figures 4 and 5 is not extreme. One diagram gives a natural scale of 1/93, the other 1/157. With a horizontal scale of 1/400, the calculated exaggerations are 2.0 and 4.0. Thus, it would not be difficult to estimate the required scales for an outfall having a value of $D(g')^{1/5}/Q^{2/5}$ between, or near, those chosen for the design diagrams. In any case, it is probable that most models involving outfall studies would require a greater exaggeration than 4.0 simply to obtain turbulent conditions, and this would ensure the formation of non-viscous spread for any densimetric Froude number greater than 0.88.

CONCLUSIONS

The new approach follows the lines laid down by Barr using two dimensional data [3] but has three distinct advantages.

1. There is no need to imagine an analogous lock exchange flow, and values of the relevant parameters can be calculated directly from prototype data.

2. The new approach makes use of three dimensional data instead of two dimensional data. Calculations have shown that exaggeration causes errors which are not indicated by Barr's congruency diagram but, for an outfall with $D(g')^{1/5}/Q^{2/5}$ less than 0.58, the magnitude of the discrepancy is relatively small.

3. The method includes consideration of the forced element of the flow and provides a more accurate result. There is less tendency towards over-design.

A comparison with Barr's method has shown that the Longannet model was probably distorted more than was necessary to obtain correct reproduction of the spread phenomenon. This resulted from scales being chosen from data pertaining to a purely convective flow. However, it is not suggested that the Longannet model was over-distorted. Other conditions, such as estuarine circulation and turbulence, are relevant, and what must be done is to ensure that the design distortion is not less than that required to provide conditions under which the model will correctly reproduce the prototype spread. Greater distortion than the minimum builds in a factor of safety against viscous influence but introduces errors, which may be important, and an effort should, therefore, be made to keep the design distortion to a minimum.

The scaling procedure may be criticised on the basis that it assumes dilution, velocity structure and depths of spread to be correctly simulated, provided rate of spread is accurately reproduced. Since the main aim of the design method is to ensure freedom from viscous effects, it is considered that this assumption is not unreasonable, but obviously there is a need for further data regarding the structure of three dimensional spread.

Application of the data to circular, closed conduit outfalls is straightforward, but it is more difficult to relate the data to channel outfalls. It may be that Figures 4 and 5 should be considered as interim design diagrams until information is available for open channel outfalls, but, until such time, they represent a more satisfactory design basis than is otherwise available.

In applying this scaling procedure it should be remembered that this applies to only one aspect of the spread phenomena. The other aspects which must be considered have different scaling requirements

and, to ensure a satisfactory model, it is necessary to choose a scale which will meet all requirements or, since this is often impossible, to determine the best possible compromise.

ACKNOWLEDGEMENTS

The Author wishes to acknowledge the usefulness of many discussions on this subject with his former colleague, Professor Barr. A brief, one paragraph synopsis of a similar paper [8] has been published in the Journal of the Institute of Civil Engineers, and their permission to reproduce the data contained therein is also acknowledged.

REFERENCES

1. Ackers, P., "Engineering Aspects of Thermal Pollution", Editors Frank L. Parker and Peter A. Krenkel, Chapter 6, Vanderbilt, May, 1969.

2. Frazer, W., Barr, D.I.H., and Smith, A.A., "A Hydraulic Model Study of Heat Dissipation at Longannet Power Station." Proc. Instn. Civ. Engrs., 1968, 39 (Jan.) 23 - 44.

3. Barr, D.I.H., "Densimetric Exchange Flow in Rectangular Channels - III - Large Scale Experiments." La Houille Blanche, 22, No. 6, 1967, 619-632.

4. Ackers, P., Price, W.A., Williams, J.M., Francis, J.R.D., Jaffrey, L.J., Allen, J., McDowell, D.M. and Engel, F.V.A., Discussion of reference (2) Proc. Inst. Civ. Engineers, Supplementary Volume, 1968, pp. 257-304.

5. Sharp, J.J., "Unsteady Spread of Buoyant Surface Discharge". Proc. ASCE., Vol. 97, No. HY9, September 1971.

6. Tamai, N., Wiegel, R.L. and Tornberg, G.F., "Horizontal Surface Discharge of Warm Water Jets." Proc. ASCE., 1969, 95, No. P02, (Jan.), 253-276.

7. Smith A.A. and Younger, J., "The Computer-Aided Analysis and Design of a Tidal Channel". Proc. Instn. Civ. Engrs., 1968, 40, (June), 135-153.

8. Sharp, J.J., "Scaling Procedures for Hydraulic Models Involving Densimetric Spread" (synopsis) Proc. I.C.E., Vol. 50, Nov. 1971, p. 355.

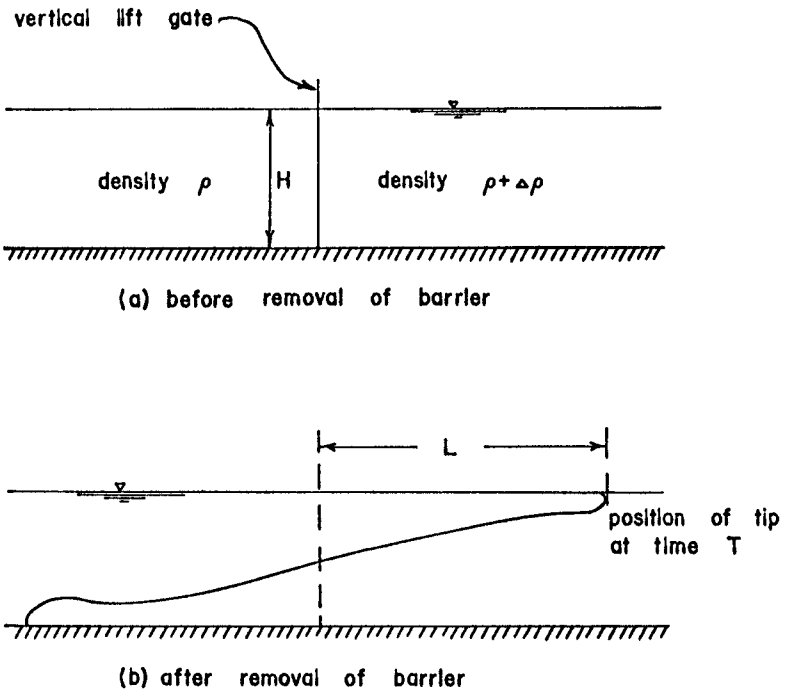

DIAGRAMMATIC ILLUSTRATION OF LOCK EXCHANGE FLOW

FIGURE 1

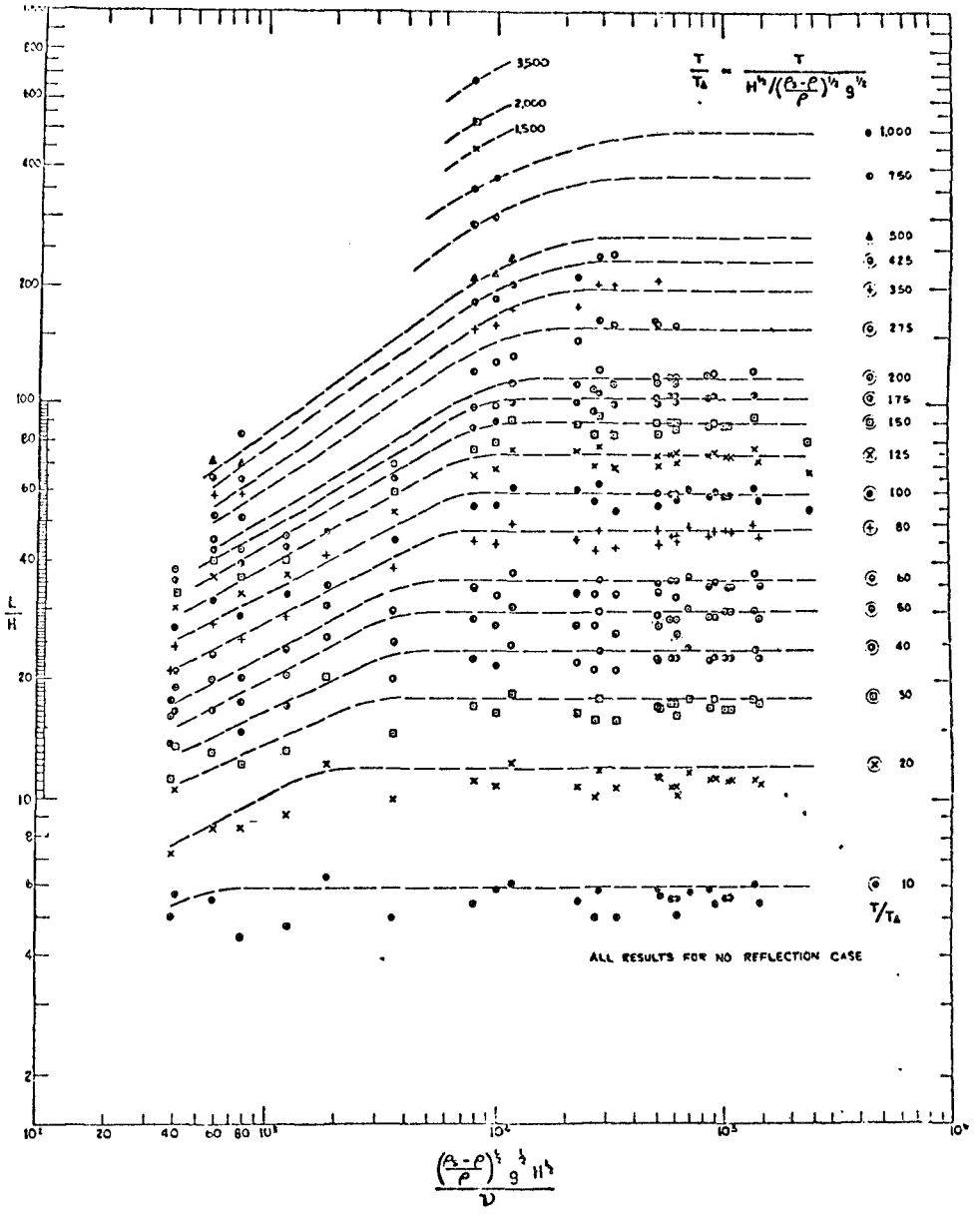

BARR'S CONGRUENCY DIAGRAM FOR OVERFLOW SPREAD

FIGURE 2

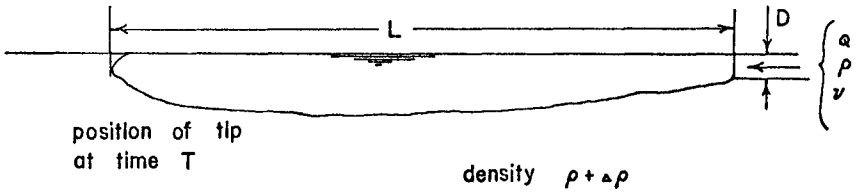

THREE DIMENSIONAL SPREAD

FIGURE 3

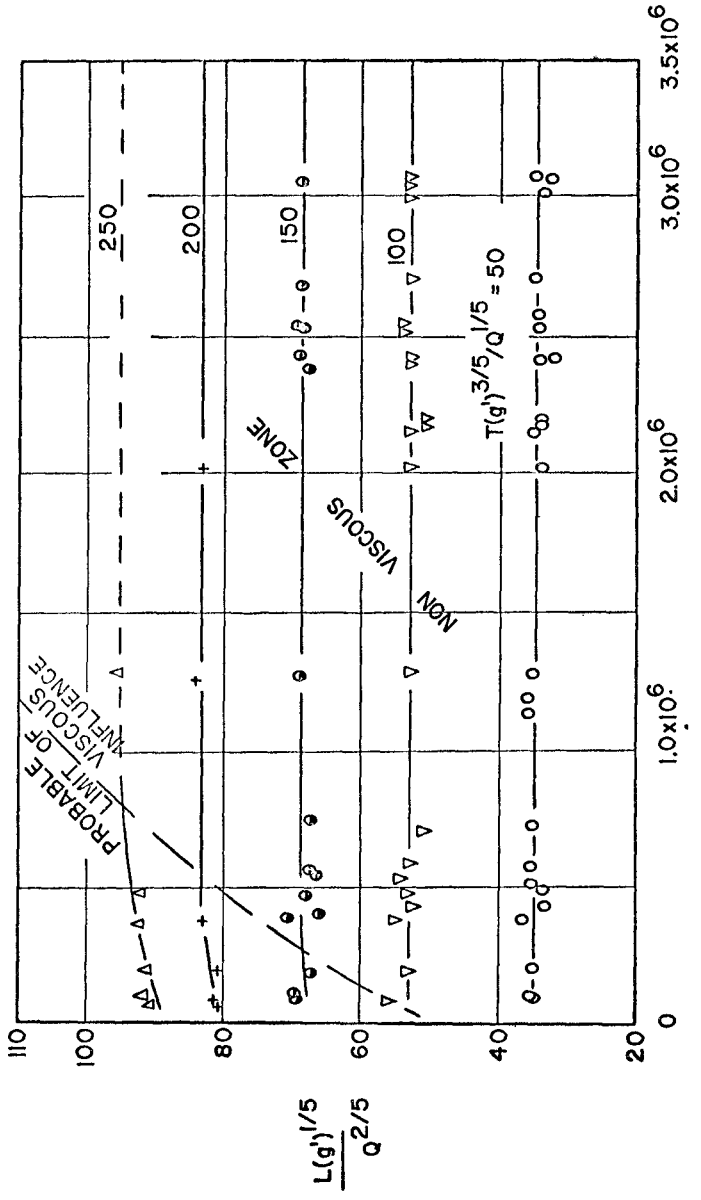
SPREAD DIAGRAM FOR $D(g')^{1/5}/Q^{2/5}=0.58$
$Q(g')^{1/3}/\nu^{5/3}$
$\frac{L(g')^{1/5}}{Q^{2/5}}$
$T(g')^{3/5}/Q^{1/5}=50$
NON VISCOUS ZONE
PROBABLE LIMIT OF VISCOUS INFLUENCE
250
200
150
100
110
100
80
60
40
20
0
1.0x10^6
2.0x10^6
3.0x10^6
3.5x10^6

FIGURE 4

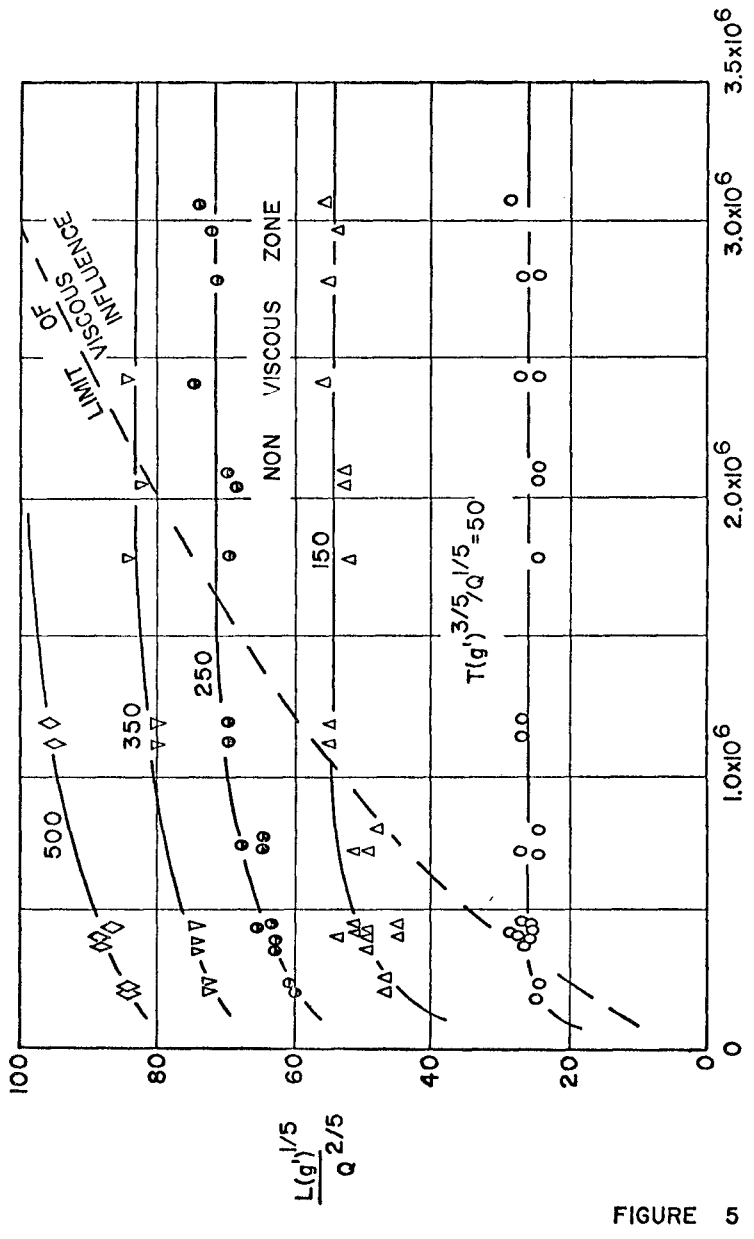

FIGURE 5

SPREAD DIAGRAM FOR $D(g')^{1/5}/Q^{2/5}=1.16$

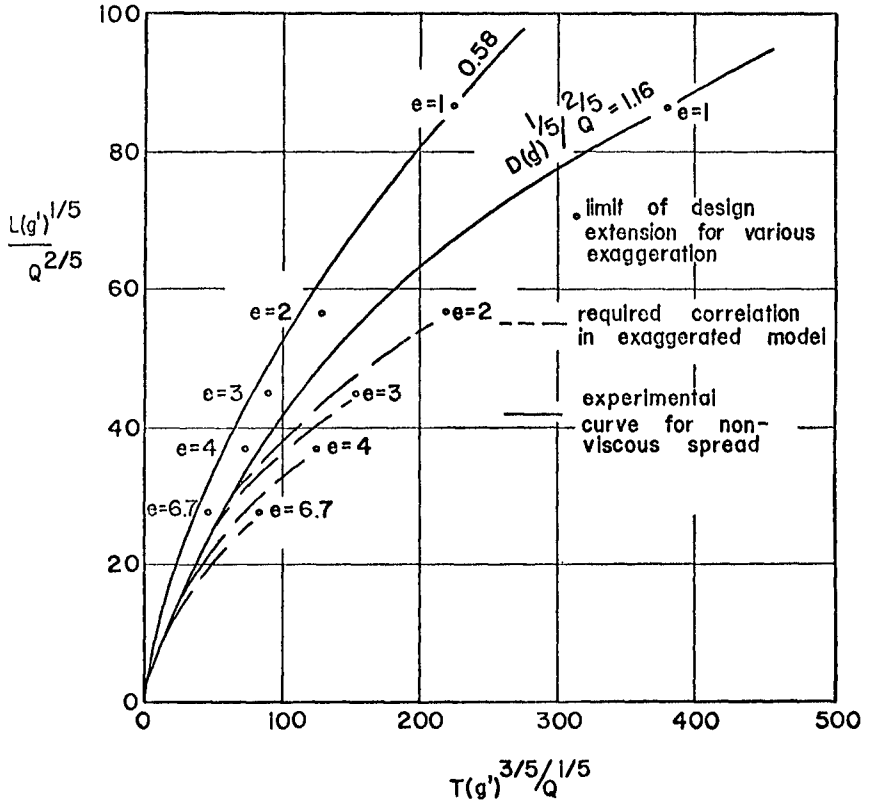

NON VISCOUS SPREAD

FIGURE 6

CHAPTER 135

EXPERIENCES WITH TIDAL SALINITY MODEL EUROPOORT

By: A.J. van Rees[*], P. van der Kuur[*] and H.J. Stroband[**]

SUMMARY

To guide the works for the new harbour entrance at Rotterdam-Europoort in 1965 a tidal salinity model (scales 1:640 hor., 1:64 vert.) was constructed. The model includes a part of the North Sea and the Rotterdam Waterway Estuary. For its regular adjustment, use could be made of extensive prototype measurements, two-dimensional tidal computations and tidal computations by msans of the DELTAR (analogue, one-dim.). The model has proved to be very valuable for predicting stream patterns for nautical purposes because the shipping (huge crude carriers) had to go on without danger while the works were being carried out. The model has also been used for the solution of harbour problems (design, siltation), for predicting cooling water recirculation, and for advice on salinity intrusion problsms.

1. Introduction

The seaward extension of the Europoort harbour system is being realised on the flats south of the mouth of the Rotterdam Waterway. Knowledge of the hydraulic conditions is of fundamental importance with the creation of complicated constructions in the field of coastal hydraulics. In the area at issue these are not only governed by the tidal movement but also to a considerable rate by density differences. To check the hydraulic aspects of the consequences of ths execution of the works, at the moment two methods are available: one- and two-dimensional mathematical models can be used without taking into account, however, density differences, and use can be made of hydraulic tidal ssa and estuary models reproducing three-dimensional flow and taking density differences into account. A combination of the two methods

[*] Delft Hydraulics Laboratory, Delft, the Netherlands

[**] Hydraulics Division, Delta Works, The Hague, the Netherlands

can also be applied, as shown later.

The prssent knowledgs on the physics of density currents is not so far advanced that computational methods can be successfully ussd for such a complicatsd pattern as the Europoort area with the inland tidal area of the Rotterdam Waterway Estuary. On ths other hand, there is sufficient knowledge about model laws for salinity models, so that a real chance of success may be expected. Consequently, at this moment the use of a hydraulic model is preferred in which ths tidal and density currents can be reproduced with a sufficient degree of accuracy. The construction of a hydraulic salinity model may thus be justified, and this has been affirmed by the results of the model tests carried out.

2. Preliminary Studies

In the years 1957-1962 the lay-out of the harbour entrance was investigated in a pilot model (tidal model scales 600/100, also tests not on Froude scals with wavss and mobile bed). Some aspscts wsre chscked in a detail modsl (harbour mouth with flood and ebb conditions, permanent flow, scales 375/125, also salinity aspects). The present model, which was commissioned in 1965 by the Rijkswaterstaat (Department of Traffic and Waterways) in ordsr to guids the works as an operational model, is a tidal salinity model with a fixed bsd.

In the years 1964-1967 an ad-hoc committee on tidal hydraulics (Rijkswaterstaat Services, Port Authority of Rottsrdam, Delft Hydraulics Laboratory) invsstigated future problems related with watsr, salt and sediment movement in the Rotterdam Waterway Estuary, which resulted in rscommendations for research. As a result, a tidal salinity flume was established to guide the above-mentioned Europoort model with respect to the fundamental aspects (a.o. selection of the scales).

To a certain extent data from field studies and computations were available. Since the beginning of this century many field data have been collected from ths Rotterdam Waterway Estuary. There was a substantial amount of know-how about the behaviour of the estuarine system (tide, currents and salinity aspects). For the Rotterdam Waterway Estuary as a part of the Delta system tidal computations had been executed and a great deal of experience was available in this field (including data from a tidal modsl, scales 2400/64 of the Delta area).

In 1965 no detailed information existed about the coastal region of the North Sea. There had been some float measurements for various purposes, amongst others to calibrate the pilot model of the mouth of the Rotterdam Waterway; but no detailed insight had been obtained of the flow distribution along the coast and the behaviour of the salinity distribution under the influence of the estuaries in the Delta region. The configuration of the sea bottom was well-known by soundings made by the hydrographic service of the Navy and the measuring services of the Rijkswaterstaat.

In 1965, moreover, no advanced computation methods existed for a detailed computation of the flow pattern in the coastal region. An idea of the effect of the new harbour mouth could be ascertained by simply applying the potential theory (obstacle in a parallel flow). This gave some insight into the flow pattern and the limits where the disturbance would be reduced to an acceptable degree. This information was required to estimate the position of the boundaries of the model. The tests in the pilot model also gave some information about this aspect. The stream atlasses available in 1965 showed that at an adequate distance from the coast, the velocities are directed almost parallel to a certain direction. For this reason (and for economic reasons) it was decided to have the western sea boundary parallel to the above direction and to have this limit as a closed model boundary.

3. Set-up of the Model (Fig. 1)

The conditions in the harbour mouth are governed by tidal and density currents. The tidal range is 1.60 m (mean tide), 1.35 m (neap tide) and 1.75 m (spring tide). The fresh water discharge from the Rotterdam Waterway is 1,000 m^3/s (mean value) and ranges roughly from 400 m^3/s to 4,000 m^3/s. The salinity of the North Sea is about 33 ppt. The current at sea runs almost parallel to the coast and during flood the flow is in a northerly direction. High water slack at sea is $3\frac{1}{2}$ hours after high water in the harbour mouth ($3\frac{1}{2}$ hours time lag). For the Europoort harbour there is no time lag and for the Rotterdam Waterway it is $2\frac{1}{2}$ hours.

Consequently the interaction of the currents is very complex, and is complicated even more by the action of strong density currents.

The boundaries of the eea section of the model were choeen on limite where disturbancee due to coastline modificatione are negligibly emall and where, except in eome caeee, the flow ie almoet homogeneous. The boundaries of the river system were choeen in the tidal region but beyond the region of salinity intrusion. There is one temporary non-homogeneous boundary (Haringvliet, before the closure of the eetuary).

The eelection of the scales of the model (1:640 horizontal dimeneion, 1:64 vertical dimeneion, 1:8 horizontal velocity, 1:80 time, 1:1 density) was based on eimilarity according to the Froude law and on coneideratione on diffusion. It ehould be mentioned that in 1965 no sound theoretical basis was available for the selection of the scalee; the tidal flume was not available in time to produce a physical backgrouud. Information from literature had to be the determining factor in the final decieion. It can now be said that the choice of the scales 640/64 hae been juetified by experimente with the model and by data from the tidal ealinity flume.

The eelection of the boundary conditions wae a major problem, being a determining factor for an efficient boundary control of the model. Apart from certain exceptione, the system has proved only well-defined if in the case of n boundary conditions in n-1 the flow and in one the water level ie prescribed. The boundary in which the water level ie prescribed was neceesary becauee of inaccuraciee and echematieations in the boundary conditions. This boundary had to be far enough from the problem area, sufficiently wide and without traneveree variation of flow and deneity. In the present model, the northern boundary fulfile these conditions best.

The bottom roughness of the model was brought to ecale by blocks (various sizes, for the greater part cubee with an edge of 0.05 m). In the river system it proved to be unneceseary to uee mixing devices (e.g., air bubble screens) in order to bring mixing to scale. It eeems that the compensating effect of the exaggerated wall roughnees in the highly dietorted channele is important. Though the sea part of the model ie quite large, it proved to be unneceeeary to have devicee for simulating Coriolis force. The effect of the Coriolis acceleration ie implicit in the boundary conditions as they were obtained from proto-

type data. For the internal area, two-dimensional tidal computations were executed with and without Coriolis acceleration, which have shown that there is no important difference in the tidal movement. It is obvious that the boundary conditions determine the phenomenon in the internal area to such an extent that no additional mechanism is necessary. A complicated problem could thus be avoided, for no experience existed about the effect of Coriolis devices (e.g., tops) in non-homogeneous flow, as in the internal area of the model.

A hall (3,000 m^2) was built for the model with its technical equipment and with facilities to make brine. The model was constructed on a concrete slab 1.25 m above the hall floor to provide space for reservoirs and other facilities. The sea part of the model consists of pre-stressed concrete plates following the bottom of the sea, while the other part of the model, including the problem area near the harbour mouth, was moulded in a sand bed. The water circulation system for the sea boundaries consists of a reservoir of 1,500 m^3 (below the model) and a closed canal to the boundaries, and in the system there are 3 pumps with a total capacity of 1.5 m^3/s. For the river boundaries there is a small reservoir with a pumping system to realise the tidal discharge and the fresh-water input; the most southern estuary branch (Haringvliet) has a reservoir (labyrinth) in which a two-phase system can be maintained so that a non-homogeneous boundary condition more or less can be realised. For the model the total use of salt is 1 ton (mean) and 4 tons (extreme) per hour.

The control of the model could not be realised as strictly as suggested earlier in this survey. The flow in the model is controlled (by means of a system with gates) at 12 points along the sea boundaries and at 3 points on the river boundaries. On the sea side gates are used with overflow, and on the river side with underflow. When calibrating the model, the gates are controlled in such a way that the currents on the boundaries are in accordance with prototype conditions. Once the movement of the gates is known, only the movement is reproduced (boundary control without feed back). Naturally the system in the final stage is very stable and the currents are very well reproduced, but it is very time-consuming to find the good calibration. This led to a switch-over to volumetric discharge control, a principle which is now being

adopted for the river boundaries. Density is controlled by injecting brine in the water circulation system of the sea boundaries, with samples being continuously extracted from the system and measured by means of a specific weight meter (gravitrol).

In the model the overall stream pattern is recorded by photographing floats (5 m, 10 m and 15 m lengths on prototype scale). To measure forces and moments (due to currents) along a certain shipping route (e.g., in the harbour entrance) a towed plate is used. The plate is towed into and out of the harbour, while the speed can be controlled and an angle with the route introduced. For tanker problems a plate of 300x15 m is used, and for coaster problems a plate of 100x5 m (prototype dimensions). For detailed measurements of the flow field, micro-propellers are used (in combination with a vane), and for measurements of the density distribution use is made of conductivity probes (in combination with a temperature meter). The tide is measured by water-level followers (vibrating needle principle). For the compilation and evaluation of the results a data-processing system (pencil follower, computer, plotter) has been available, but in 1972 a computer system is being introduced to take over the total data-processing, the checking of the model and in the near future also the boundary control of the model.

4. Boundary Conditions (Figs. 2 and 3)

To realise the tidal movement in the hydraulic model, the necesray tidal conditions must be given on the boundaries of the model: for instance, the vertical tide on the boundaries on the sea side together with the vertical tide on the inland boundaries. To obtain the salinity distribution, the river boundaries should be supplied with fresh water and the sea boundaries with salt water with a constant and homogeneously distributed salinity, except in some cases of non-homogeneous flow. These boundary conditions, together with the bottom configuration and data on flow resistance, provide sufficient information to realise the non-homogeneous tidal movement. The velocities could also be given, perpendicular to the sea boundaries of the model, provided at least one or more vertical tides were given at the same time for the involved tidal area, whereas on the inland boundaries the currents may be given, too. Generally, this boundary condition is more

strict than the vertical tide. The outline just given holds for a mathematical and a hydraulic model, although for the hydraulic model discussed in the preceding paragraph an extremely strict system of boundary conditions has to be used because of the reproduction of the salinity situation.

The next problem was to decide how the conditions on the sea boundaries and the inland boundaries could be obtained, together with sufficient information on the internal area. For this purpose, on June 15, 1966, extensive sea measurements were carried out by the measuring services of the Rijkswaterstaat, including detailed measurements of flow, density and silt distribution along rows corresponding with the boundaries of the model and in the internal area; water levels were measured at stations along the coast and at a few points in the sea and at regular distances along the Rotterdam Waterway Estuary. The sea measurements were so extensive,however, that it was impossible to carry out simultaneously flow and density measurements in the river system, so the river flow data had to be simulated by computation.

As the model could not be extended outside the tidal region, boundary conditions were required on boundaries inside. These data were computed starting from the data (at the river mouth) of the sea measurements of June, 1966, as boundary conditions. Computations were made by means of the DELTAR, which is an electrical analogon used by the Delta Division of the Rijkswaterstaat and simulating the tidal movement in the northern part of the Delta area (schematised to a system of tidal channels with a one-dimensional character) (Ref. 1). The DELTAR was essential during the operation of the model, particularly for the supply of data when conditions had changed, e.g., after the closure of the Haringvliet Estuary.

At the time of the sea measurements of June 15, 1966, the northern part of the Delta plan was not yet completed. As these works would already be finished at the time of completion of the Europoort Works, it was necessary to close the Haringvliet Estuary in the model for the realisation of the actual situation to be expected. By this, however, not only was the tidal movement in the adjacent sea area influenced, but at a more important rate the water movement in the inland tidal area. In consequence of this enclosure, a way had to be found to adapt

the boundary conditions to the new artificially-created circumstances. Due to the cutting-off of a volume of 550.10^6 m^3/tide (average value), it was to be expected that in particular the velocities at the southern tidal boundary would be changed.

By about 1968 the two-dimensional computations had developed so far that the measured 1966-situation could be modified. In connection with the developments along the Dutch coast as a result of the execution of the Delta plan, two-dimensional tidal computations were carried out for a rectangular sea area covering the coastal area of the North Sea, including the Delta region and ranging about 40 kms seaward (the Europoort area is within this rectangle). The dimensions of the computation molecules of the system were 1,600 m x 1,600 m (Ref. 2). In order to introduce the necessary vertical tidal boundary conditions to solve the tidal problem, measurements at sea were made on June 27, 1967, in which the vertical tides were measured along the above-mentioned rectangle. In the internal area of the rectangle, velocity measurements were also made for verification of the results of the two-dimensional computation.

The boundary conditions along the sides of the rectangle were assumed to be invariable. This means that the influence of the enclosure of the Haringvliet a priori was thought to be no longer noticeable on the vertical tides along the sea boundaries of the mathematical model. Consequently, by closing the Haringvliet and so putting the velocities there at zero, the changes of the velocities along the sea boundaries of the hydraulic model could be computed for the tide on the day of the sea measurements (June 27, 1967).

From the results of computation it appeared that water transportation through the southern part of the western sea boundary increased, while in the coastal region part of the southern sea boundary there was a considerable decrease. Along the northern sea boundary hardly any changes could be noticed. The vertical tide in the mouth of the Rotterdam Waterway, too, hardly changed after the enclosure of the Haringvliet.

The difficulty was now to translate the changes due to the enclosure of the Haringvliet, known from computation, into velocity changes on the model boundaries, corresponding with the tide on which the

model had been calibrated (June 15, 1966). This was done by expressing the changes of the normal velocities at the model boundaries in percentages, and by presuming that in similar phases these percentages would also apply to the changes of the velocities measured on June 15, 1966, thus adapting conditions along the sea boundaries to the new situation.

The realisation of the northern part of the Delta plan is changing considerably the inland boundary conditions which had originally existed. Of course, this was to be expected, as the tide used to penetrate into the northern part of the Delta area from three sides, viz., the mouth of the Rotterdam Waterway, the mouth of the Haringvliet and the inland connection with the southern part of the Delta area (Volkerak). If the entrances - Haringvliet and Volkerak - are left out, the tide in the northern part of the Delta area will be damped out considerably.

As already mentioned, the vertical tide in the mouth of the Rotterdam Waterway had hardly been changed by the enclosure of the Haringvliet. Consequently it could be introduced in the DELTAR as a tidal boundary condition and the tide of June 15, 1966, could thus be simulated for the completed northern part of the Delta area. The currents measured in the DELTAR at the already-mentioned inland boundaries of the hydraulic model were introduced in the model. Currents and water levels measured in the DELTAR along the Rotterdam Waterway Estuary could also be measured later in the hydraulic model. The current in the mouth of the Rotterdam Waterway as a function of time, proved to be in good agreement with the corresponding measuring results of the DELTAR.

5. Experimental Studies

5.1. Operational studies Europoort (Figs. 4, 5 and 6)

The main purposes of the model is research to support the works for the new harbour entrance at Rotterdam-Europoort (Ref. 3). The investigations were commissioned by the Rijkswaterstaat, Harbour Entrances Department.

The main aspects are:

(a) Operational research in connection with the making of a new entrance to the Europoort harbours and closing the temporary one.

(b) Additional rssearch for an optimum design of the combined harbour entrance to the Europoort basins and the Rotterdam Waterway.

(c) Operational research on the stages of exscution of the Northern and the Southern breakwaters.

(a) Operational research has been carried out for the rsalisation of a new sntrance to the Europoort harbours and for the closurs of ths tsmporary one. In four stages ranging from February 1970 up to April 1972 the planning for the exscution of ths works was tested and a number of alternative solutions wers examined. The opening of the new entrance was started by dredging from the inland side. A barrier, which was part of the old Southern breakwater was temporarily left, but in the final stages the breakwater was cut through. A gradual change occurred in the stream pattsrn in the harbour and in the temporary entrance. Howsver, as the least change could creats difficulties, because manoeuvring with big oil tankers in ths temporary sntrance was alrsady critical, the opening of the new entrancs had to be done vsry carefully. A jet stream into ths harbour would be dangerous for ths manoeuvring of the tankers in ths basin. It was known from DELTAR computations that above a critical size the connection between the new entrance and ths temporary one would operate as a shunt to the Rotterdam Watsrway. As a conssquence the stream pattern in the tsmporary entrance and in the harbour basin would change considerably, during ths flood period as well as the ebb period. This could bs dangerous for ths shipping, especially as manosuvrability is a big problem when ths speed is reduced considerably on sntering the harbour basin. The conclusions from DELTAR computations have been confirmed by the results from the modsl.

In the model stream patterns have been photographed for floats of various lsngths. For the junction of the temporary entrance with the Rottsrdam Waterway and for the main shipping routes in ths harbours, forces perpendicular to the routss have been computed bassd on velocity data from photographs.

(b) Additional ressarch is being done for an optimum design of the combined entrancs to the Europoort harbours and the Rotterdam Waterway. The works startsd from the south with a sand dam which joins up with the Southern breakwater through a transit structure. One problem

to be solved was the best length of this structure to guide the currents along the coast. To find an answer, stream patterns were photographed. The optimum length of the Northern breakwater had provisionnally been estimated from tests in the pilot model. This problem, which has important economic aspects, was also governed by other aspects apart from the hydraulic criteria (manoeuvring length, wind and waves, morphological problems, etc.). In the model the length was varied from 2,150 m to 2,950 m, measured from the old breakwater. This proved that the stream pattern was not very sensitive. Although a length of 2,550 m showed optimum with respect to the stream pattern, the design length of 2,750 m was maintained because of other aspects.
A big extension of the beach north of the Northern breakwater is in execution; the design was checked by photographing stream patterns in the model and found satisfactory.
The temporary entrance to the Europoort harbours will not be closed completely but an entrance for small shipping will be left and in this connection various alternatives have been tested by photographing stream patterns and by local velocity measurements.

(c) Operational research on the various stages of the execution of the Northern and the Southern breakwater has been carried out. Eight stages have been tested for the period April 1971 upto June 1974. For overall data stream patterns have been photographed. In the main shipping route, starting in the 66' approach gully and ending in the harbour, forces and moments have been measured by means of the towed plate and local velocity measurements were made at various locations where current concentrations were feared, for instance, at the end of dams. It proved that, starting from a very smooth stream pattern (April 1971), as the works proceed the stream pattern will gradually become less favourable (more concentrated between the dams), although in the final situation there will again be a slight improvement (smoother stream pattern). This is most important information for shipping.

Control measurements are regularly executed in prototype to check the results of the model. Though comparing the results is sometimes cumbersome because of different tidal conditions and fresh water flow, it has been shown that there is a good correspondence between

information from the model and that from nature. Extensive control measurements are those during closing the temporary entrance (an opening for small shipping was left) and regular measurements at sea in the approach route to the harbour mouth.

5.2. Other investigations

At the rsquest of the Electricity Board of Rotterdam research has been carried out on the dispersion of the cooling watsr of a huge electrical plant (in 1990 6,500 MW) to be situated in the new harbour area. The cooling water (250 m^3/s in 1990 and a temperature jump of 8^o C) can be taken from the harbour and released directly into the sea or in the opposite way. Four alternatives have been tested in the model.

The dispersion was photographed with fluorescine for a tracer and the concentration was measursd with rhodamine B. Density differences were simulated by adding fresh water to the salt water from the intake; a few tests were done with warm water, primarily to test thermovision techniques.

A major problem was the expected change in metsorological conditions (fog), which would be unfavourable for the quality of the harbour entrance. It turned out that this problsm was imaginary for about one kilometer from the outlet the warm water disappeared, and tests showed that a three-layer system had been established: from the bottom to the surface cold salt water, warm salt water, cold fresh water. The recirculation of cooling water to the intake proved to be unimportant, as even the most unfavourable alternative.

On assignment by the Port Authority of Rotterdam designs have been tested for a container harbour connected to the Rotterdam Waterway. The harbour lies in the estuarine region, and the flow conditions in the harbour mouth are governed by the tide and density differences. For overall data stream patterns have been photographed, and the nautical aspects have been analysed on the basis of forces computed along certain shipping routes. To analyse the morphological aspects the velocity distributions in various cross-sections have been measured and from velocity data in the harbour mouth the exchange flow (primarily due to density differences) has been computed, on the basis of

which and of the expected silt coneentration a prognosis of the siltation has been made. The effect of the harbour on the salinity intrusion has also been analysed.

At the request of the Rijkswaterstaat, Rotterdam Waterway Authority, the consequences of connecting a canal (depth 6 m, width 150 m, length 25 km) to the estuarine system havs been analysed. The canal is a part of the harbour system which leads from the inland side into the Europoort harbour area; it is connected by a sluice to the Old Meuse, a branch of the Rotterdam Waterway. Because of the ever-increasing shipping, particularly push tows, it is necessary either to build more sluices or to create an open connection. The latter solution has been investigated in the model. The criterion is the response at the salinity situation, although the steam pattern in the junction is also important for nautical reasons. By examining both situations (closed and open canal) in the same model experiment, maximum accuracy ($\pm$ 0.3 ppt in concentration difference and $\pm \frac{1}{2}$ km in intrusion length) could be achieved. Alternative configurations of the junction were analysed on the basis of photographs of stream patterns. Particularly interesting is the phenomenon in the mouth of the canal: because of the high tidal velocities and the small density differences, there is no dispersion due to critical flow conditions. The canal thus serves the function of a fresh water barrier.

6. Discussion of the Results

6.1. Analysis of the shipping problem (Fig. 7)

In the model the currents have been recorded as a function of place and time. But with these data alone the preparation of an advice on the navigability of a harbour entrance is a difficult task. The relation between navigability and currents (e.g., in a harbour entrance) is not well-known and the problem therefore involves the integration of the knowledge and experiencs of a number of disciplines Fortunately there exists a substantial know-how in various disciplines and information is available with respect to many aspects, a.o.:

1. Plots of tankers entering a harbour entrance, including the

recording of positions as function of time, drift angles and rudder angles; comments and interviews with pilots are simultaneously collected.

2. Experiences with sense perception-physiological research regarding the factor "man" in the system, e.g., from tests with ship simulators.
3. Response of model ships to certain types of currents in typical situations (e.g., influence of berths and bottom).
4. Measurements in prototype of the currents in the same situations as mentioned under 1 and/or simulations of the currents in a model.
5. Forces and moments on model ships towed along fixed routes with tests in a ship model basin, in addition to the information under 3. For purposes under 6, also tests with a towed plate have been done (Ref. 4).
6. Currents in a tidal salinity model. As this type of model is highly distorted, tests with model ships are not possible, therefore tests are made with a towed plate. In situations where this is not possible (e.g., in curved shipping routes), data are computed from stream patterns.

Much work is being done in this field, for a great deal by Rijkswaterstaat:

- Data are collected from existing situations to try and analyse the relation between current patterns and criticisms of the pilots. The effect of new situations is smoothed by instructing the pilots beforehand through stream atlasses about new situations, predicted from stream patterns measured in the tidal salinity model.
- On the initiative of Rijkswaterstaat a Nautical Committee has been formed on which the various disciplines and pilot organisations are represented. This committee co-ordinates the activities in the various fields and watches the nautical aspects with respect to the works in execution.

The lack of good criteria is obvious. Judgment of data for routes where there has been hardly any shipping or model data rising above limits known from the past, involves the danger that there are no criteria which indicate that the situation is inadmissible. Besides, the factor "man" is hard to judge; it has proved in some cases that

situations which initially were found difficult, did not create problems after some experience. In general, however, it is not necessary to judge the model data in an abeolute way as just described. A great part of the work consiets of comparison of mutual situations or comparison of situations with a reference situation. Nevertheless, not only forces and moments, but also gradients of these functions might have repercussions for shipping. There is an obvious lack of know-how to judge this; yet this problem can also be solved, in most cases by referring to known situations. The data on, for example, forces and gradients are tabulated as a function of place and time and are compared with similar data from a reference situation. Some well-eelected codes help to visualise the relative improvement or worsening, so that a final judgment can be made (in co-operation with the Nautical Committee).

6.2. Analysis of various problems (Fig. 8)

The analysis of dispersion due to density differences as with salinity intrusion problems, is based on intrusion lengths and longitudinal and vertical salinity distributions. When the model reproduces the tide (water level, flow) in an accurate way, the convective transports (in one-dimensional terms) are reproduced correctly. The reproduction of the dispersive transports can be checked by comparing these transports in model and prototype, and these data can be directly computed if the spatial distribution in a cross-section of horizontal velocity and concentration is known. The model has been scaled on a correct overall reproduction of horizontal dispersion; local diffusion aepects cannot be analysed in the model.

In the case of dispersion problems with no or very small density differences,a field in which the dispersion of cooling water from an electrical plant has been investigated, the success of the studies depends on whether the horizontal distribution of the effluent is the predominant phenomenon. As the model has been scaled on a correct reproduction of the horizontal dispersion (in longitudinal and in transverse directions), realistic results can be expected.

For siltation problems in a harbour a tidal salinity model is essential if the exchange due to density currents is predominant

(there is also an exchange in connection with the tidal prism and the effect of vortices in the mouth). The exchange flow can be computed from velocity data in the harbour mouth. When the silt concentration is known, the siltation can be predicted, if the longitudinal salinity distribution in the river is also known, by applying the formulas for the exchange flow in the sluice problem for this case (with the appropriate empirical coefficient).

For siltation problems in a river the model gives only little information. The predominance of the time mean value of the flow at the bottom is a criterion for siltation (no predominance means siltation), but for the Rotterdam Waterway it does not seem to be important. Sedimentation and erosion can hardly be predicted from the model. The velocity fields in a model with appropriate scales for a correct reproduction of salinity dispersion have some significance. For an overall impression a "bottom" velocity (1–2 m above the bottom) is generally used as a rough indication of changes in morphological conditions.

7. References

1. Schönfeld, J.C., and Stroband, H.J.: Tidal research by means of the hydraulic–electric analogy, Contribution in Final Report (English text) of the Delta Committee, Staatsdrukkerij, The Hague, 1960/61.

2. Dronkers, J.J.: Research for the coastal area of the Delta region of the Netherlands, Proc. 12th Coastal Engineering Conference, Vol. III, Washington, 1970.

3. Dixhoorn, J. van: Overall aspects of the design of the new harbour-entrance works at Hook of Holland, Contribution No. 5 (in Dutch) in a series of 13 articles on the construction of the new harbour mouth at Hook of Holland, "De Ingenieur" (Netherlands), 1969.

4. Measurement of forces and moments on a shipping model with various drift angles, Report No. 69–155–GBT (in Dutch), Netherlands Ship Model Basin, Wageningen, The Netherlands, 1969.

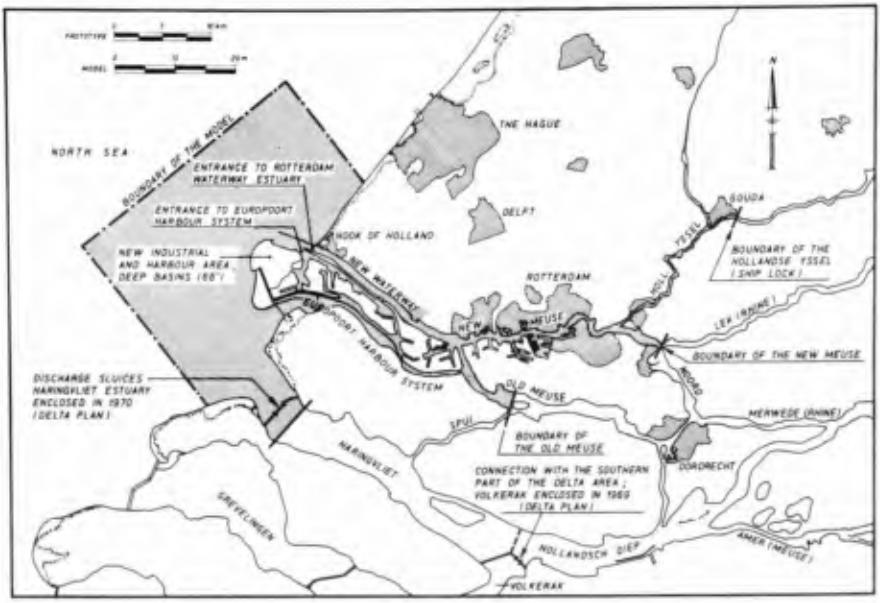

FIG. 1a PLAN OF THE MODEL AREA

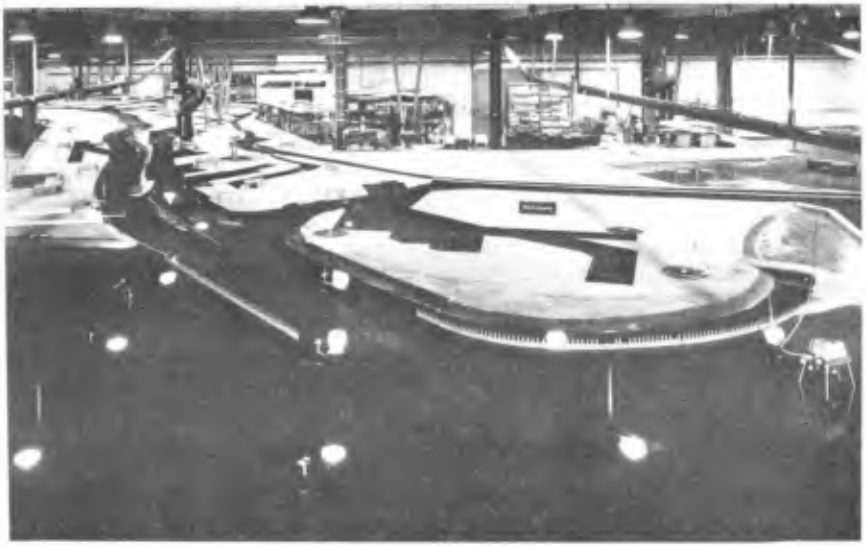

FIG. 1b VIEW OF THE MODEL

FIG. 1 GENERAL INFORMATION

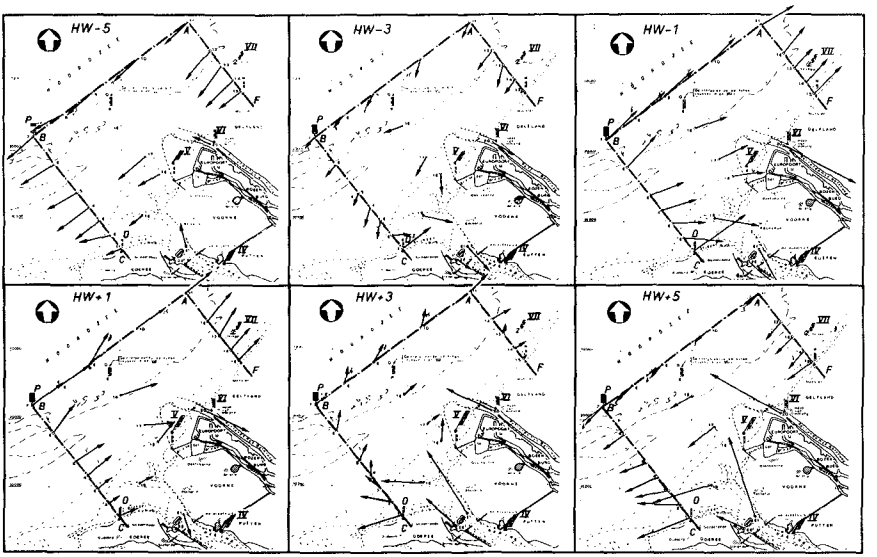

FIG. 2a VELOCITY DISTRIBUTION

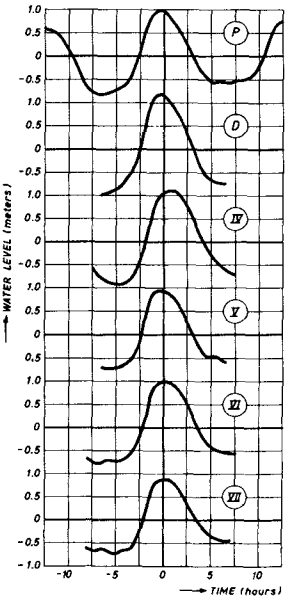

FIG. 2b DATA ON WATERLEVELS

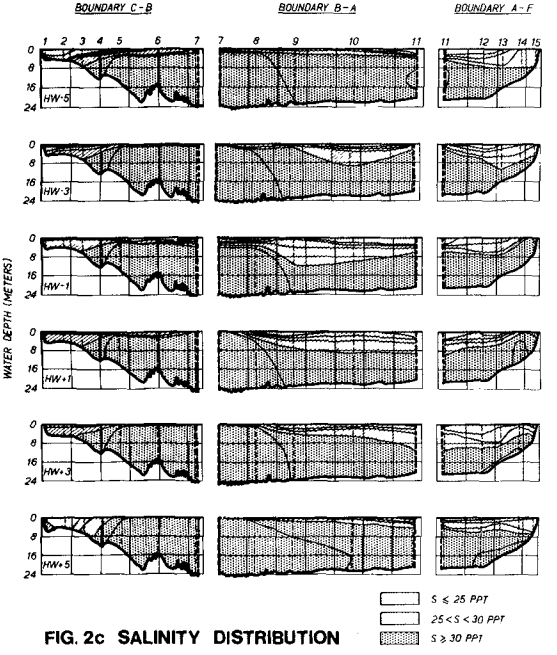

FIG. 2c SALINITY DISTRIBUTION

FIG. 2 PROTOTYPE SEA MEASUREMENT OF 15 JUNE 1966

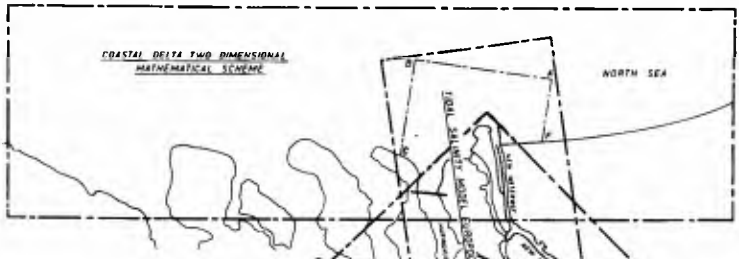

FIG. 3a COMPUTING SYSTEMS ANNEX HYDRAULIC MODEL

FIG. 3b VIEW OF THE "DELTAR"

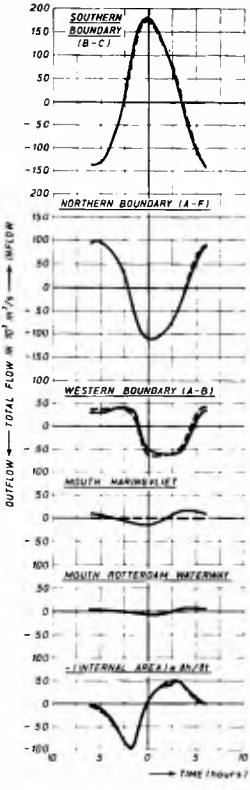

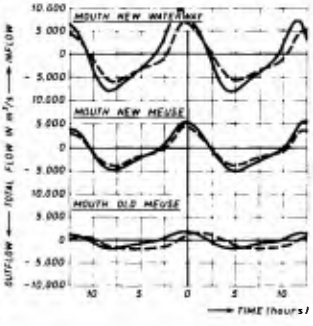

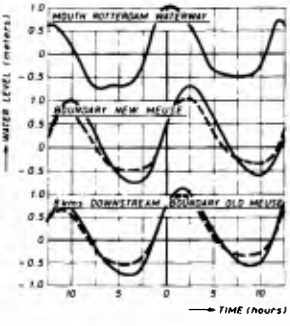

FIG. 3c DATA OF THE SEA AREA

FIG. 3d DATA OF THE RIVER SYSTEM

FIG. 3 COLLECTING DATA ON BOUNDARY CONDITIONS

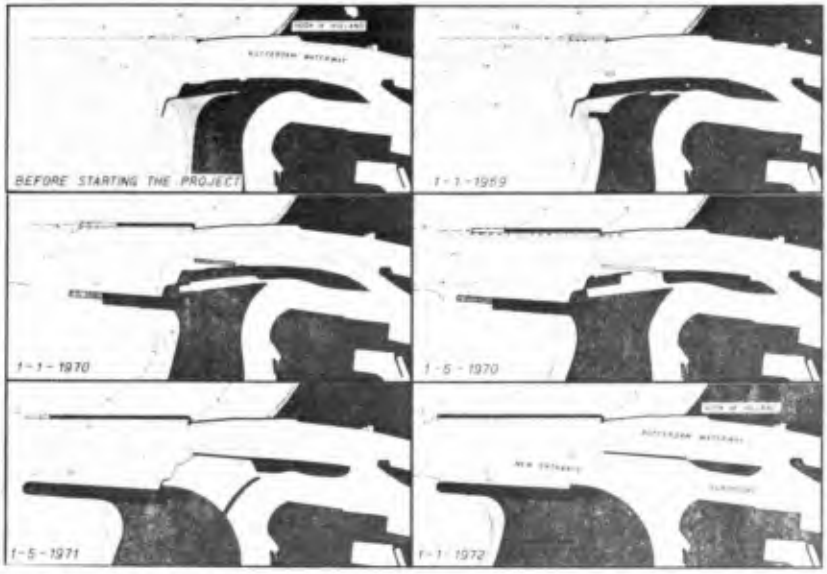

FIG. 4a STAGES OF EXECUTING THE NEW ENTRANCE EUROPOORT

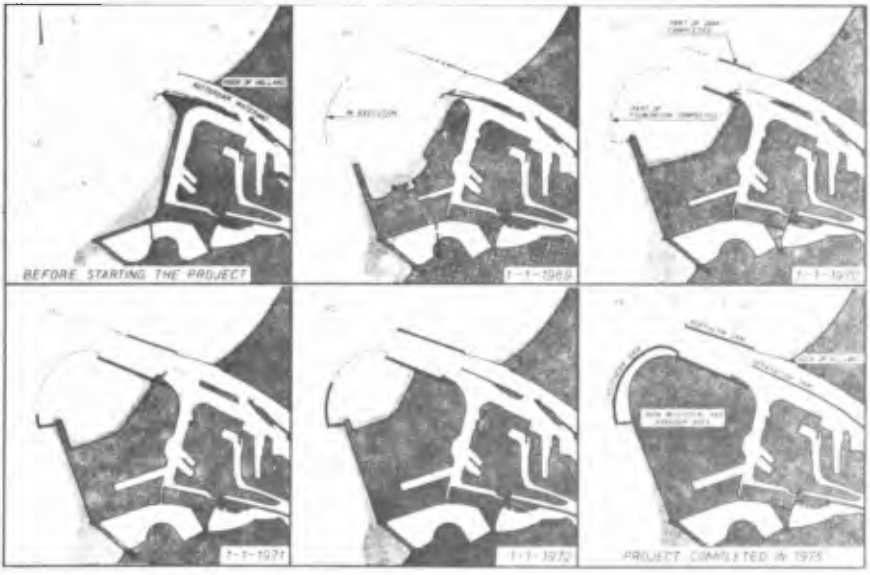

FIG. 4b STAGES OF EXECUTING THE TOTAL PLAN OF THE NEW HARBOUR MOUTH

FIG. 4 BUILDING STAGES NEW HARBDUR MOUTH ROTTERDAM-EUROPOORT

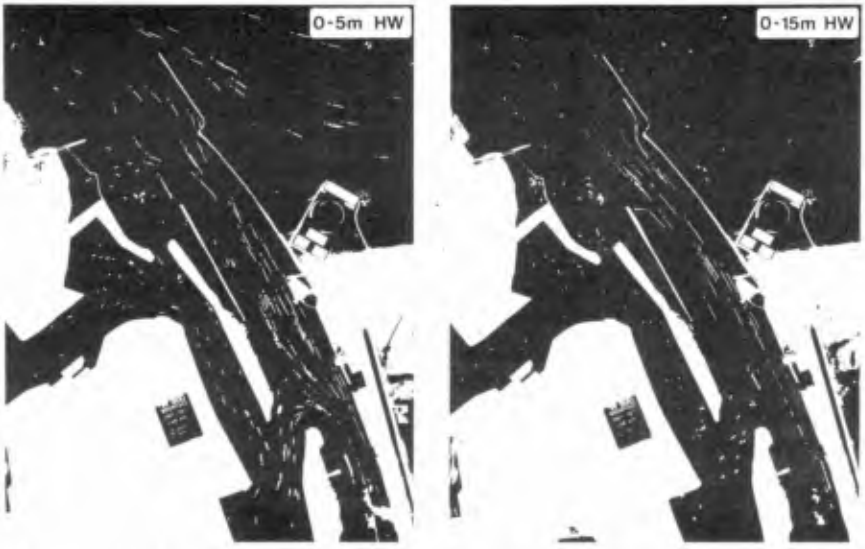

FIG. 5a FLOW PATTERN - BEFORE MAKING NEW ENTRANCE

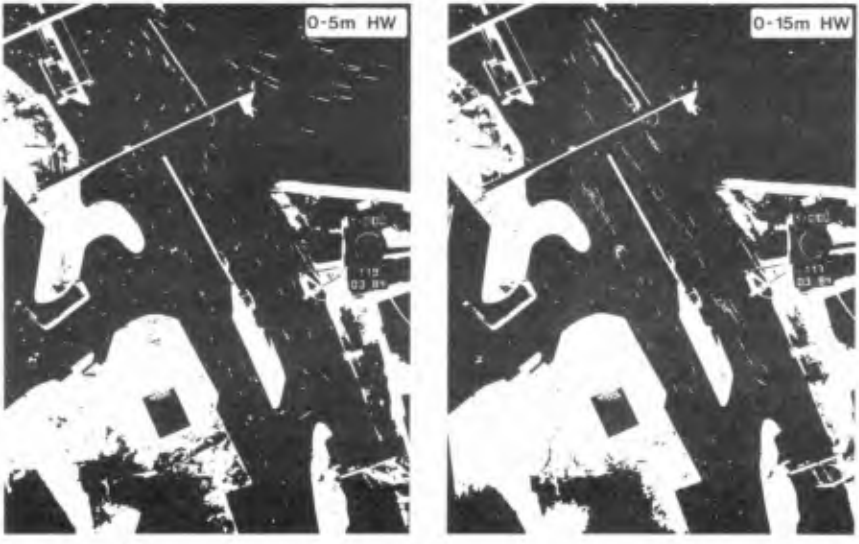

FIG. 5b FLOW PATTERN - AFTER REALISATION NEW ENTRANCE
(THE TIDAL VELOCITIES HAVE CHANGED TOO. BY THE ENCLOSURE OF THE HARINGVLIET)

FIG. 5 INVESTIGATIONS NEW ENTRANCE EUROPOORT

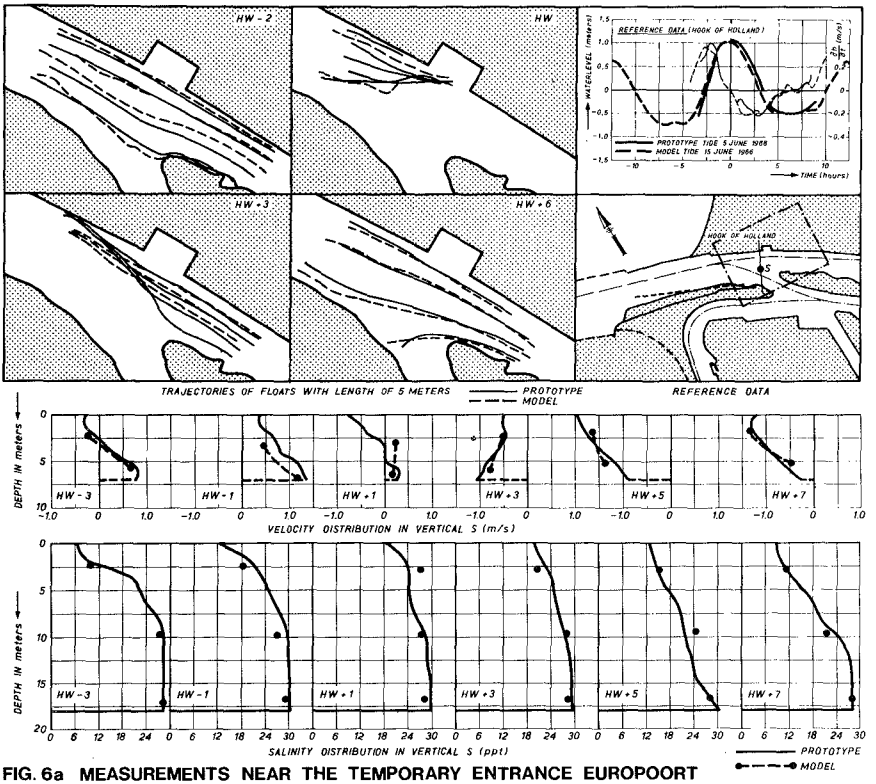

FIG. 6a MEASUREMENTS NEAR THE TEMPORARY ENTRANCE EUROPOORT

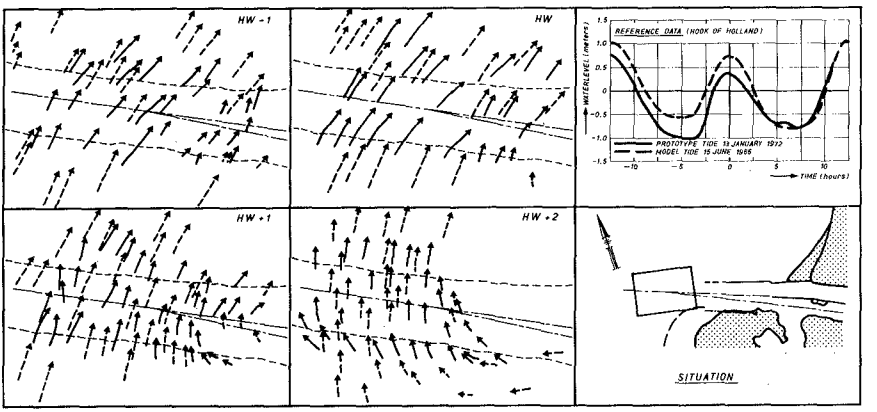

FIG. 6b MEASUREMENTS AT SEA IN THE APPROACH ROUTE

FIG. 6 VERIFICATION MODEL DATA BY MEASUREMENTS IN PROTOTYPE

FIG.7a SET-UP WITH TOWED PLATE

FIG.7b TYPICAL STREAMPATTERN

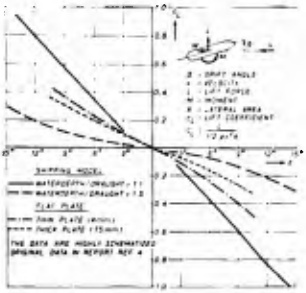

FIG.7c TESTS IN TOWING TANK

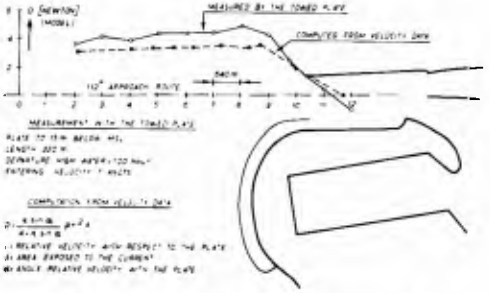

FIG.7d COMPARISON OF MEASURED AND COMPUTED FORCES

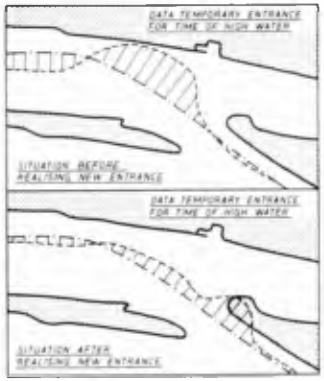

FIG. 7e FORCES IN TEMPORARY ENTRANCE (COMPUTED FROM VELOCITY DATA)

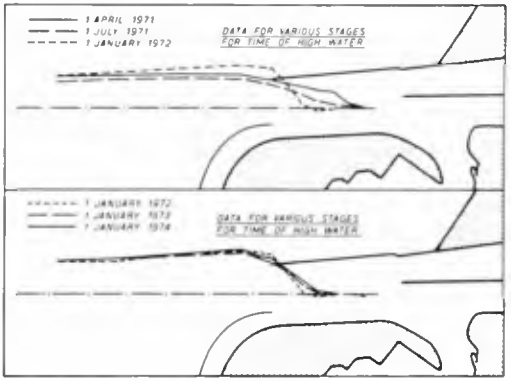

FIG.7f FORCES IN THE HARBOUR ENTRANCE (MEASURED WITH THE TOWED PLATE)

FIG.7 HANDLING THE SHIPPING PROBLEM (SAFE SHIPPING)

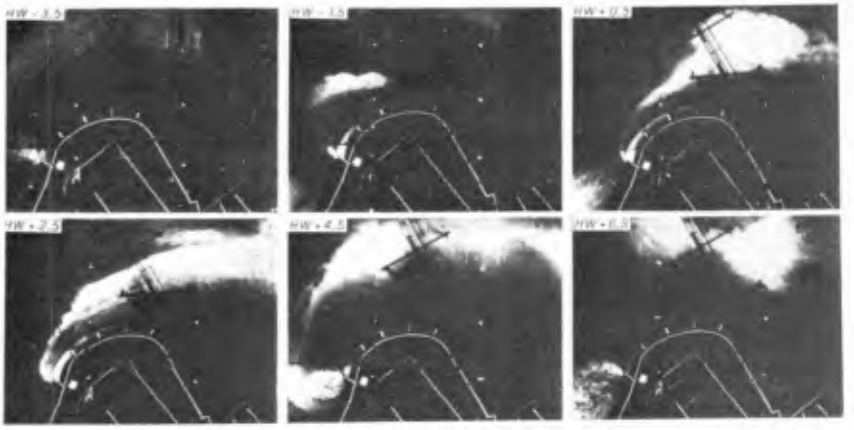

FIG. 8a RELEASE OF COOLING WATER

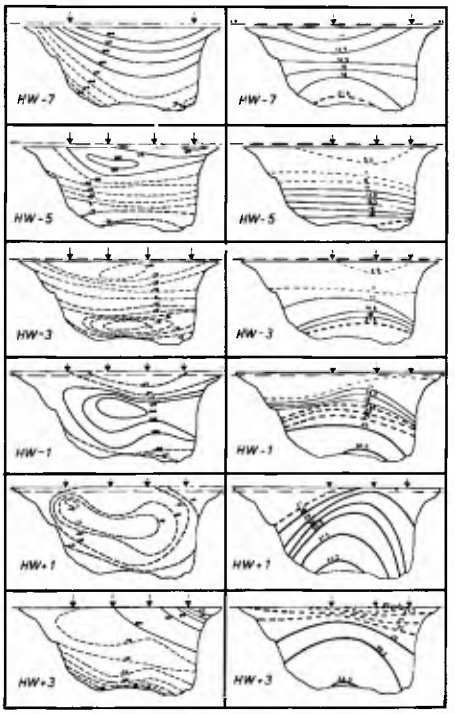

FIG. 8b VELOCITY AND SALINITY DISTRIBUTION
(DATA 21 JUNE 1956 MOUTH ROTTERDAM WATERWAY)

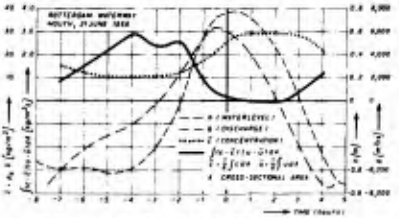

FIG. 8c DATA ON DISPERSION

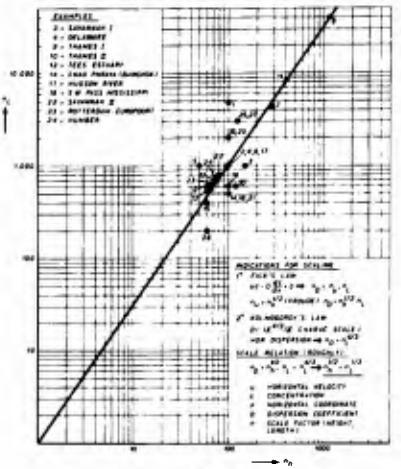

FIG. 8d MODELING OF DISPERSION

FIG. 8 HANDLING DISPERSION PROBLEMS

CHAPTER 136

The schematization for tidal computations in case of variable bottom shape.

by J.J. Dronkers [1])

Synopsis.

Mathematical and physical methods can be applied for tidal studies. After general considerations on these methods, some practical aspects of tidal computations are discussed, in particular the schematization for tidal computations in case of variable bottom shape in shallow coastal waters. The relation with the coefficient of friction is dealt with. A combined one- and two-dimensional tidal computation is considered. Also an example is given of the determination of the coefficient of friction in a very shallow region; the variations, which are found in this practical case are discussed.

1. General considerations on the application of mathematical and physical methods for tidal studies.

Tidal problems may be solved by means of mathematical or physical models. Both kinds of models are approximations of the reality; in some respects in a different way.

In the analytical methods the water motion is represented in a continuous way. They can explain general physical aspects, e.g. progressive standing and Kelvin waves. These methods can only be applied in case of schematical tidal regions, and simplified assumptions e.g. the equations must be linearized. The value of the analytical method may be doubtful when it is necessary to use a computer for evaluating the solution in a particular case. An example is the evaluation of the harmonic method on a computer. This method can be applied in case one or two harmonic components must

---

[1])Director, Hydraulics Division, Delta Works, The Hague, Netherlands.

be considered. In case of more components a computer evaluation of an analytical solution is not recommendable.

In a physical model the practical solution is obtained by measurements at certain locations. They can represent the tide in complicated tidal regions. They show more details, e.g. eddy streets, which occur at sharp bends, and in case piers are present. Such phenomenae cannot be represented in a sufficient way in the mathematical models considered till now. The shape of the bottom can also be represented better, although it is limited in case the distortion of the scale model is considerable. On the other hand it is difficult to represent the Coriolis forces in a sufficient way in case these forces have a considerable influence on the water motion.

The numerical tidal methods have qualities between the methods, mentioned above. They can describe the tidal motion in rather complicated tidal regions, and the Coriolis force can be included in a correct way. To which extent these methods can be used is still a point of discussion and experience. This depends on the phenomenae, which must be studied, on the required data, and on the accuracy, which is demanded.

The solution by means of a numerical method is a discrete solution of linear finite difference equations. In the finite difference solution the water levels and velocities are computed at certain grid points. Usually the grid points for the water levels are different from those for the velocities. The discretization of the equations causes however difficulties, which do not occur in analytical solutions, and in physical models. Moreover it is difficult to determine the accuracy of the finite difference solution by means of mathematical formulae. It must be obtained from experience.

Two numerical evalutation techniques exist: the explicit method and the implicit method. The non-linear terms in the finite difference equations are often represented in a different way by various authors. In the explicit method the water levels, and the velocities at a future time step are immediately computed from those at previous time-steps. In an implicit method they are obtained after the simultaneous solution of a set of linear equations. Therefore

the mathematical treatment of an implicit system of equations is more complicated than that of an explicit method. On the other hand in an explicit system the size of the grid net depends on a stability condition. This condition, which determines the time step, depends also on the friction, and the Coriolis coefficient. Such a condition is not necessary for an implicit system. The time step in case of the application of an implicit method, can be chosen several times greater than for an explicit scheme; it depends on the accuracy only. In particular this is of importance in coastal waters were deep gullies and shallows are found.

In the application of implicit and explicit methods instabilities of special kind, so called space-instabilities, may occur in the computation, in case the non-linear convective terms are included in the tidal equations. They may occur in particular in regions where large velocities, and variations in their directions occur, e.g. at sharp bends in an estuary. These instabilities do not occur when the convective terms are omitted. These problems are discussed in detail by Grammelveldt, 1969, and Kagan, 1970, for explicit schemes. It is shown that an explicit scheme e.g. that of Hansen's has a "computational viscosity", which depends on the grid size. In case of non-linear equations the "mathematical" wave interaction can induce a transfer of energy into the short wave range, in which it accumulates with time. Only a finite number of numerical waves can be resolved in a finite grid. This type of instability can be suppressed by introducing an artificial viscosity term, which causes a smoothing effect. However it is the question to which extent the accuracy is affected. Kagan shows that the minimum possible wave length, which is determined by the grid size, cannot be suppressed by an artificial viscosity term.

Obviously the introduction of the boundary conditions in mathematical models is much more simple than in physical models, where special apparatus must be applied.

From mathematical point of view the vertical tide, as well as the velocities should be introduced at the open boundaries, unless the convective terms in the equations of motion are small or may be neglected near the boundary. In this respect difficulties did

not occur in the two-dimensional tidal computations, applied in the coastal area of the coast of the Netherlands. At the open boundaries the water levels are introduced. The velocities obtained by measurements depend often on the local conditions determined by the bottom shape. Therefore they are not used as boundary conditions. The finite difference solution of the tidal equations is correct at some distance from the boundary. The inaccuracy of the results at the coast line may be a serious objection from practical point of view.

2. Schematization of tidal regions for two-dimensional tidal computation.

2a. General considerations on the size of grids.

A one dimensional case like a river is schematized into a number of sections of equal or unequal length. The length of a section is determined such that the variation in the bottom shape is limited as possible. Considerable variations can take place at the boundaries of the sections; if necessary a separate equation of Bernoulli must be considered at these transitions. Furthermore the length depends on the locations, where the water levels and the velocities must be computed, and on the required accuracy of the results. The length of the sections in the rivers of the Netherlands is about 5 to 10 km's.

In two dimensional regions a square net is applied for numerical computations. The size of such a grid depends on the bottom shape, and moreover on the importance of the convective terms in the equations of motion.

In the sea the convective terms cause rotating currents or circulation. Circulation is also caused by the Coriolis forces. The extent of these circulations to be considered in the computations cannot be smaller than double the grid size. If smaller circulations have to be considered the grid size must be taken smaller. Therefore a finer net is required when the convective terms are important. On the other hand the number of velocity and water level points, that can be considered in the computations on the computer, determines also the size of the grid net. E.g. in the Atlantic Ocean the size must be chosen many times greater than in the North Sea, where

30 km's or smaller is to be preferred. Large grid sizes can be applied whenever variations in the bottom shape are small with respect to the depth. Such variations are much greater in the coastal zones. Also the number of tidal data in the coastal zone to be required is much greater.
The size of the grid, considered in the coastal waters of the Netherlands, is 1.6 km. This zone extends from the coast line up to 30 km in the sea, and 150 km along the coast line. For more detailed and accurate information near the coast a smaller zone is considered. The size of this zone is about 10 km perpendicular to the coast line. The grid size is 0.4 km. In this region shallows and gullies occur, and moreover the irregular shape of the coast line must be represented. The boundary conditions at the sea side of the smaller zone are obtained from the results of tidal computations in the bigger zone, Dronkers 1970. The boundary of a smaller zone must be chosen such that the tidal data are not influenced noticeable by the tidal motion in the smaller zone.

Often a square grid cannot represent the bottom shape in the mouths of estuaries, where deep gullies and shallows occur, in a correct way. One square of the grid can cover the shallows as well as the gully. In this case it should be desired to determine separately an irregular net for the gullies and the shallows. Then the length and the width of the various rectangles of the grid may become unequal, and the accuracy of the finite differences in x-direction is different from that in y-direction.

In the immediate neighbourhood of the coast line beaches occur, which are dry during a part of the tide. The slope of the bottom may be of the order of 1 m per km or more. Because of the small depths it is necessary to consider very small grid sizes. Such detailed computations are not carried out till yet.

It is necessary to check the results of tidal computations by means of vertical tide and velocity measurements. In particular it is important in coastal waters, where small differences in the vertical tide may affect the directions of the velocities considerably.

2b. Improvement on the accuracy of tidal computations by introducing modified Chézy coefficients.

The most important forces, which determine the tidal motion in the sea are the inertia forces, the Coriolis force and the gravity force. Usually the friction is of less importance, Also the convection terms can often be omitted. Friction and convection become more important in coastal waters.

The results of the computations in the coastal region of the Netherlands' Delta show that the computed velocities in the gullies are often lower, and on the shallows higher than the velocities obtained from the measurements. Accordingly the schematization must be improved by taking smaller grid sizes, or by modifying the Chézy coefficient.

Fig. 1 shows the effect of modifications in the Chézy coefficients for a part of the mouth of the Haringvliet. The Chézy coefficient has been changed in the regions within the dotted lines from 60 to 90 $m^{\frac{1}{2}}/sec$.

From tidal computations in rivers a general knowledge exists ahout the values of the friction coefficient C (Chézy) or n (Manning), as a function of depth and bottom material. In all applications it is necessary to compare the resulting velocities and water levels with those obtained from measurements. In case considerable differences occur four factors must be considered: the size of the grid net; the influence of the location of the boundary conditions; the values of the Chézy coefficients, and the influence of the convective terms, due to the variations in the velocities. In the following it will be shown how the schematization can be improved by introducing modified Chézy coefficients, which take into account the variation of the bottom shape.

The modified Chézy-coefficient of a square ($\Delta x, \Delta y$) will be determined in case of the following assumptions. The values of C are known as a function of the depth. The velocity vectors in the square are parallel, and its magnitudes do not differ considerably from the mean value. These assumptions include that the convective terms in the equations of motion can be neglected in the square. Finally it is assumed that at a certain moment the difference in

head, due to the friction forces, is constant over the square.

The formula for the modified Chézy coefficient will be applied to the particular case that the velocities have directions parallel to the x-axis, and the variation in the bottom figuration only occurs in the y-direction. Let the square be subdivided in y-direction in n parts of equal depth. The total quantity of water in a cross-section of the square $\Delta x, \Delta y$ in the x-direction is,

$$a\, u \Delta y = a_1\, u_1\, \Delta y_1 + a_2\, u_2\, \Delta y_2 + \ldots + a_n\, u_n \Delta y_n \qquad (1)$$

in which a_i are depths and u_i are velocity components in x-direction. Because the values of the slope of the water surface $\frac{\Delta h}{\Delta x}$ are assumed to be constant in the square in x-direction, it holds according to the formula of Chézy,

$$\frac{\Delta h}{\Delta x} = \frac{u_1^2}{C_1^2\, a_1} = \frac{u_2^2}{C_2^2\, a_2} = \ldots\ldots = \frac{u_n^2}{C_n^2\, a_n} = \frac{u^2}{C^2 a}\,, \qquad (2)$$

in which the velocity u, the Chézy coefficient C, and the depth a are the mean values over the square.

It follows from (1) and (2) after replacing $u_m (m = 1,2 \ldots n)$ by $u \frac{C_m\, a_m^{\frac{1}{2}}}{C\, a^{\frac{1}{2}}}$, that

$$C\, a^{3/2} \Delta y = C_1\, a_1^{3/2} \Delta y_1 + C_2\, a_2^{3/2} \Delta y_2 + \ldots\ldots + C_n\, a_n^{3/2} \Delta y_n .$$

In case the depth changes continuously over the cross-section Δy, the following relation is obtained for the mean value of the Chézy coefficient, C, and the mean depth a,

$$\overline{C\, a^{3/2}}\, \Delta y = \int_0^y C(y)\, a(y)^{3/2}\, dy\,. \qquad (3)$$

In the general case the velocity has components in the x- and the y-direction. Then the variable y in (3) must be replaced by the variable y', which is determined by the rotation of the axes x and y over the angle α to the axes x' and y'; α is defined by the direction of the velocities in a square. Then the factor uV, respectively vV, in which $V = (u^2 + v^2)^{\frac{1}{2}}$ must be considered in the resistance terms. Because the velocity vectors are parallel,

V can be replaced by $\frac{u}{\cos\alpha}$, respectively $\frac{v}{\sin\alpha}$.
Let a square subgrid be formed over the square $(\Delta x, \Delta y)$ (fig.2). Then for each column in the y-direction formula (3) holds good. After addition of the results of the equation (3) for the subsequent columns, it is found,

$$\overline{C\, a^{3/2}}\, \Delta y\, \Delta x = \int_0^x \int_0^y C(x,y)\, a^{3/2}(x,y)\, dx\, dy, \qquad (4)$$

in which $\overline{C\, a^{3/2}}$ is the mean value of $C\, a^{3/2}$ over the square $(\Delta x, \Delta y)$. The formula (4) holds for the general case that the velocity vector is not parallel to the x-axis.

The modified value C_m of the square is obtained from $C_m\, a_m^{3/2} = \overline{C\, a^{3/2}}$, in which a_m is the mean depth in the square. Generally it holds $C_m > \bar{C}$. The analogous method can be applied to the river sections, Dronkers, 1964, Chapter XI.

3. The schematization for a combined two- and one dimensional tidal computation.

In this section the combined two-dimensional tidal computation for a part of the sea, and the one-dimensional computation for a river is demonstrated (fig.3). In case the grid size and the dimensions of the sections of the river are different, the schematization of the transition zone must be modified such, that the grid and the sections of the river fit together. In the transition section of the river this means that the width will become equal to the size of the grid: $\Delta x = \Delta y$, and that the mean velocity and the total quantity of water passing through the cross section, the discharge, does not change. This discharge is determined by the tidal conditions upriver of the transition section. Moreover the difference in head due to the resistance force must not change. Hence

$$b_1 a_1 = \Delta y\, a, \text{ and } C_1^2\, a_1 = C^2 a\ , \qquad (5)$$

in which a is the mean depth of the modified section, a_1 the depth of the original section; C and C_1 are the corresponding values of the Chézy coefficient.
These equations determine the modified depth a and coefficient C.

If the width of the mouth of the river, b_1, is more than twice

the value of Δy, more sections with equal width Δy, next to each other in the river mouth, must be considered.

The finite difference equations for the transition zone are mentioned below. The method for the solution of the tidal equations is dealt with in general terms.

In fig.4 the points are denoted, where the velocity components u and v, and the water levels h are computed in the transition zone from the sea to the river. An implicit scheme is applied, Leendertse, 1967. For the river the formulae of the third implicit scheme are applied, Dronkers, 1969. The water level and discharge, Q, or velocity, u, are taken at the same location, the beginning, or the end of each river section. The advantage of this method is that river sections with unequal length can be considered for the schematization of the river. An analogous method is applied in the schematization for the application of the harmonic method.

The convective terms are not considered in the formulae for the sea, however the Bernoulli term is included in the equations for the river.

Each time step consists of two parts. In the first half time step $t + \frac{1}{2}\tau$, the values of the velocity component in x-direction, u', and the water level with respect to the mean water level, h', are computed by means of implicit equations. The velocity component in y-direction in the sea, v', is determined by an explicit equation. In the second half time step $t + \frac{1}{2}\tau$, v'' and h'' are determined implicitly, and u'' is obtained from an explicit equation. No values of v have to be computed in the river, and therefore some modifications are to be made in the computational scheme.

In the following the finite difference equations are mentioned for the transition zone from the river to the sea. In fig.4 the locations of the variables with indices n and m are denoted. At the coast $m = M$, and for the river $n = N$. The most upriver section is denoted by $m = M_1$.

The squares of the grid in the sea which are on the same line as the river, have index m,N. For $M + 1 \leq m \leq M_1$, the equation of motion for the river is:

$$\frac{\delta h}{\delta x} = -\frac{1}{g}\frac{\delta u}{\delta t} - \frac{|u|u}{C^2(a+h)} - \frac{1}{g}u\frac{\delta u}{\delta x}, \qquad (6)$$

in which h is the water level, u the velocity, a the mean depth, and b_s the mean width of the river at time t and place x. This equation is replaced by

$$h'_{m+1} - h'_m = -\frac{(\Delta x)_m}{\tau g}\left[(u'_{m+1} - u_{m+1}) - (u'_m - u_m)\right] - \\ - \frac{(\Delta x)_m}{4}\,\frac{|u_{m+1}+u_m|\,(u'_{m+1}+u'_m)}{C_m^2\,(a_m + h_m)} - \frac{1}{2g}\,(u_{m+1}+u_m)(u'_{m+1}-u'_m)\,, \tag{7}$$

in which $(\Delta x)_m$ is the length of the m-th section and $\frac{1}{2}\tau$ is the half time step.

The equation of continuity,

$$b\,\frac{\delta h}{\delta t} = -\frac{\delta Au}{\delta x} \tag{8}$$

in which A is the area of a cross-section, and b the storage width, is replaced by

$$u'_{m+1} - u'_m = -\frac{(\Delta x)_m}{\tau}\,\frac{b_m}{A_m}\left[(h'_{m+1}-h_{m+1}) + (h'_m-h_m)\right] \tag{9}$$

These equations are written in the form:

$$h'_{m+1} - h'_m + \eta_m\,u'_{m+1} + \Theta_m\,u'_m = \mu_{m-1} \qquad (m = M+1,\ldots,M_1) \tag{10}$$
$$\nu_m(h'_{m+1} + h'_m) + u'_{m+1} - u'_m = \xi_m\,,$$

in which the coefficients depend on those of (7) and (8).

By means of the application of the sweep method in the upriver direction, the set of equations (10) can be rewritten in the form

$$u'_{m-1} = -q_{m-1}\,h'_m - t_m\,u'_m + s_{m-1} + b_{m-1}\,h'_{M+1}$$
$$h'_m = -p_m\,u'_m + r_m + a_m\,h'_{M+1}, \qquad M+2 \leqslant m \leqslant M_1 \tag{11}$$

Similar formulae are derived for the application of the sweep method in the downward river direction. Recurrent formulae for the computation of the coefficients q, t, etc. can he derived, Dronkers 1969.

After the successive elimination of h'_m and u'_m in the set of equations (11) in the upriver direction, and elimination in the

set of equations in the downriver direction, respectively, by means of the sweep methods, the following relations are obtained between $u'_{M+1,N}$, $h'_{M+1,N}$, $u'_{M_1,N}$ and $h'_{M_1,N}$ at the beginning and at the end of the river:

$$\begin{aligned} &h'_{M_1,N} + P_{M,N}\, u'_{M_1,N} + a_{M+1,N}\, h'_{M+1,N} + r_{M+1,N} = 0 \\ &P^*_{M+1,N}\, u'_{M+1,N} + h'_{M+1,N} + a^*_{M_1,N}\, h'_{M_1,N} + r^*_{M+1,N} = 0 \end{aligned} \tag{12}$$

The finite difference equations for the transition zone from sea to river follow next. First the equation of motion in x-direction is applied to square ABCD of fig.4 for the first half time step. This equation

$$\frac{\delta u}{\delta t} - \Omega v = -g\frac{\delta h}{\delta x} - \frac{gVu}{C^2 a},$$

in which Ω is the coefficient of Coriolis, is replaced by

$$\begin{aligned} u'_{m,n} = {} & u_{m,n} - \frac{g\tau}{2k}(h'_{m+1,n} - h'_{m,n}) + \frac{\tau\Omega}{8}(v_{m,n} + v_{m,n-1}) - \\ & - \frac{\tau g}{4}\left[\left\{(u_{m,N}+u_{m-1,N})^2 + (v_{m,N}+v_{m,N-1})^2\right\}^{\frac{1}{2}} + 2\,u_{m+1,N}\right] x \\ & x \frac{u'_{m,n}}{C^2_{m,n}(2a_{m,n}+h_m+h_{m+1,n})}, \end{aligned} \tag{13}$$

Then the equation of continuity is applied to the square EFGH,

$$\frac{\delta h}{\delta t} + \frac{\delta au}{\delta x} + \frac{\delta av}{\delta y} = 0.$$

The finite difference equation becomes,

$$\begin{aligned} h'_{m,n} = {} & h_{m,n} + \frac{\tau}{4k}(a_{m,n} + h_{m,n})\, u'_{m,n} - \\ & - (a_{m-1,n} + a_{m-1,n-1} + h_{m,n} + h_{m-1,n})\, u'_{m-1,n} + \\ & + (a_{m,n} + a_{m-1,n} + h_{m,n} + h_{m,n+1})\, v_{m,n} + \\ & + (a_{m,n-1} + a_{m-1,n-1} + h_{m,n} + h_{m,n-1})\, v_{m,n-1}. \end{aligned} \tag{14}$$

The explicit equation for $v'_{m,n}$ follows from the finite difference equation of the motion in y-direction (see square IJKL);

$$\frac{\delta v}{\delta t} + \Omega u = -g \frac{\delta h}{\delta y} - \frac{g\, Vv}{C_a^2} ,$$

$$v'_{m,n} = v_{m,n} - \frac{\tau\Omega}{8}\left(u'_{m,n}+u'_{m-1,n}+u'_{m,n+1}\right) - \frac{g\tau}{2k}\left(h_{m,n+1} - h_{m,n}\right) -$$

$$- \tau g \frac{\left[\frac{1}{9}\left(u'_{m,n} + u'_{m-1,n} + u'_{m,n+1}\right)^2 + v^2_{m,n}\right]^{\frac{1}{2}}}{C^2_{m,n}\left(a_{m,n} + a_{m-1,n} + h'_{m,n} + h'_{m,n+1}\right)} v'_{m,n} . \qquad (15)$$

The unknown values in equations (13) and (14) are $u'_{m,n}$, $h'_{m,n}$, $h'_{m+1,n}$, and $u'_{m-1,n}$ etc.; $v'_{m,n}$ is the unknown value in equation (15).

In the sea these equations are applied to the grid for $1 \leqslant m \leqslant M$; at the coast $m = M$. The index n varies between $n = 1$ and $n = N+1$ and from $n = N+1$ up to $n = N_1$. A solution by means of the sweep method, determines these values (Leendertse, 1967). Equation (15) determines v in the sea.

However for $n = N$ the equations (12) for the river must be added to the system of implicit equations mentioned in (13) and (14). Furthermore a relation between $u'_{m,N}$ and $h'_{M+1,N}$ (see fig.4) must be added to the equations (12). Applying the equation of continuity to the rectangle FBCG (fig.4), it follows,

$$a_{m,N}\left(u'_{M+1,N}-u'_{m,N}\right) = -\frac{k}{4\tau}\left[3\left(h'_{M+1,N}-h_{M+1,N}\right) + \left(h'_{m,N}-h_{m,N}\right)\right] \qquad (16)$$

The boundary condition at the coast is: $u_{m,n} = 0$ $(n \neq N)$. Also $h_{1,n}$ etc. are given at the boundary in the sea. The equations for the second time step can be set up in a similar way.

In this time step the unknown quantities are u'', h'' and v''. Then an implicit set of equations similar to (13) and (14) hold for h'' and v'', and an explicit equation for u''.

In equation (13), u' is replaced by v'', and the finite differences in x-direction are replaced by those in y direction. Furthermore the quantities which are defined for the time level t in equations (13-15) are replaced by the time level $t + \frac{1}{2}\tau$, in a way that they get the index ('). The equation of motion for the velocity component v is applied to square IJKL in fig.4, and the equation of continuity to the square EFGH.

Because in the equations for the river, v' and v'' do not occur, the solution of the complete set of equations of sea and river is different for the second time step. The values of v'' and h'' in the sea are determined by the set of implicit equations. The boundary value of $u_{M,N}$ at the mouth of the river is taken at time level $t + \frac{1}{2}\tau$, which is computed at the previous half time step. The equations for the river are not considered in this set of equations, because after the computation of v'' and h'', the values of u'' in the sea is determined by an explicit equation. Next values of u'' and h'' in the river are again found from a set of implicit equations for which $u''_{m,N}$ and $h''_{M_1,N}$ are the boundary condition. This set of implicit equations are solved in the same way as described above for h' and u'.

From the preceding computational scheme it appears that the dimensions of the section FB of which the length equals half of the size of the grid, must be modified such that the width is equal to the grid size k. The formulae for the modified dimensions are given in formula (5). The lengths, widths, storage widths and depths of the sections upriver of point follow from the schematization of the river.

4. The Chézy coefficient in very shallow regions.

The execution of tidal computations in very shallow regions of which the depth is small at low water or in which some parts are dry, encounter many difficulties. The convective terms can usually be neglected on the shallows because of the very small velocities. However the values and the directions of the velocities may change considerably in the transition zone from the channels to the shallow region. In this zone the values of the convective terms may be of the same order or larger in comparison with those of the other terms in the tidal equations. A very fine net must be considered for computations in such regions.

Friction forces are most important on the shallows. To get an impression about the Chézy coefficients in very shallow region, detailed tidal and velocity observations in a part of the Brouwershavense Gat of the Delta region in the Netherlands are carried out.

results are shown in relation to the depth.

It appears that considerable variations occur in the values of the Chézy coefficients for a certain depth, though in general the values decrease with decreasing depth in accordance with the expectation. Accurate computations cannot be carried out on shallows, because of the variable bottom-shape in the shallow region. This example appears too complex for schematization. Nevertheless the storage of the shallows must be taken into account in the tidal computations. Furthermore the friction term should be the only term to be considered in the equations of motion.

The determination of the Chézy coefficients in a river is dealt with by Dronkers, 1964. The measurements and computations mentioned in this section, are carried out by the Measuring Station at Zierikzee, Delta Works.

REFERENCES.

Dronkers, J.J., 1964, Tidal computations in rivers and coastal waters, North Holland. Publ. Comp. Amsterdam.

Dronkers, J.J., 1969, Tidal computations for rivers, coastal areas and seas, J. Hydr. Div. 6341, HY 1, Proc.Am.Soc. Civ.Eng., New York.

Dronkers, J.J., 1970, Research for the coastal area of the Delta region of the Netherlands, Coastal Engineering Congress, Washington, vol III, Chapter 108. Am.Soc.Civ.Eng., New York.

Grammeltvedt, A., 1969, A survey of finite-difference schemes for the primitive equations for a barotropic fluid, Monthly Weather Review, vol 97, no 5, New York.

Kagan, B.A., 1970, Properties of certain difference schemes used in the numerical solution of the equations for tidal motion, U.D.C. 551.466.71. lsw., Atmospheric and Oceanic Physics, Vol 6, no 7, pp. 704-714, translated by F. Goodspeed.

Leendertse, J., 1967, Aspects of a computational model for long period water wave propagation, Thesis, The Rand Corporation, Santa Monica, California.

The mean slope of the shallow in the direction of the coast is about 1:1500. The bottom material consists of fine sand (150 μ), mixed with silt.

Fig.5 shows the detailed contourlines of the depths of this region, and the locations where vertical tide and velocity measurements were taken.

The dimensions of this region are about: length 3 kms and width 2 kms. The region has been divided into 32 rectangles of which the dimensions are: length 750 m (x-direction), and width 250 m (y-direction, perpendicular to the coast). The mean depth in each rectangle has been determined with respect to the mean water level. The velocity vectors are resolved into the x-direction (u-component) and into y-direction (v-component). The tidal range was about 2.9 m. The maximum depth, where velocity measurements are taken was 3 m below mean sea level, and the minimum depth 1.4 m. The vertical velocity distribution are determined at intervals of 15 minutes. The minimum distance from the bottom was 0.2 m. The water levels are measured at intervals of 5 minutes at each gauge (see fig.5). A very accurate levelling of the gauges has been carried out for this purpose. The maximum differences in water level are of the order of 5 cm per km.

The mean velocities and their directions at any 15 minutes are represented graphically on the maps and decomposed in the x- and y-direction. The mean velocity components are determined on the sides of each rectangle (fig.5) by interpolation of the measured velocities.

After this preliminary work the equation of continuity, and the two-dimensional tidal equations of motion are applied to the water motion in each rectangle. The equation of continuity has been applied for the checking of the velocity measurements, because the quantity of water flowing to and from each rectangle at a certain instant must balance the quantity of water remaining within the rectangle at rising tide, or leaving the rectangle from high water to low water. The computations are carried out after each period of twenty minutes. The equations of motion are applied for the determination of the values of the Chézy coefficient. In fig.6 the

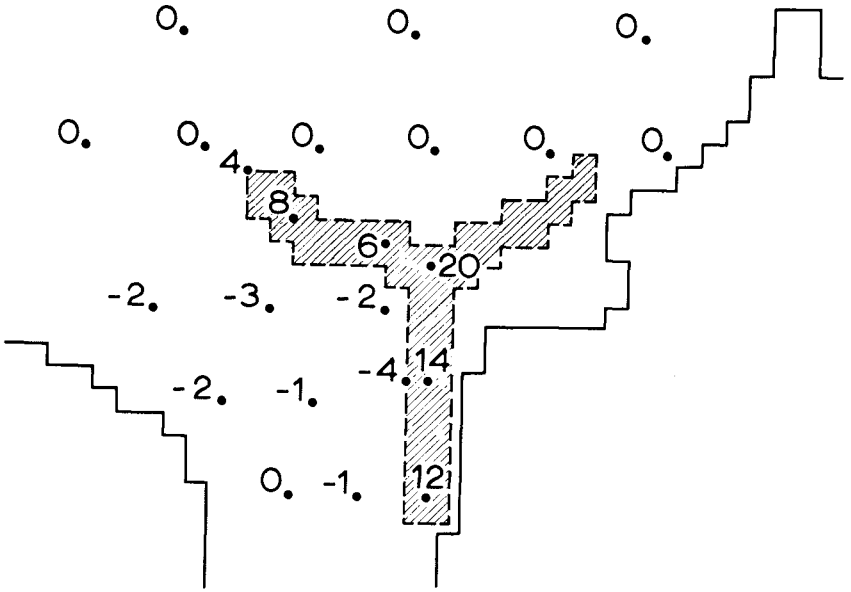

FIG. 1 INFLUENCE OF INCREASE OF CHEZY COEFFICIENT ON VELOCITIES (EXPRESSED IN %)

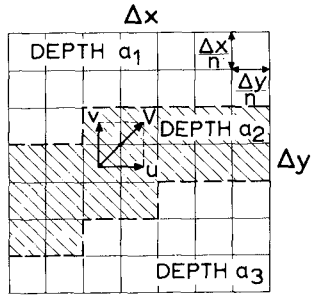

FIG.2 SCHEMATIZATION OF A SQUARE OF A GRID

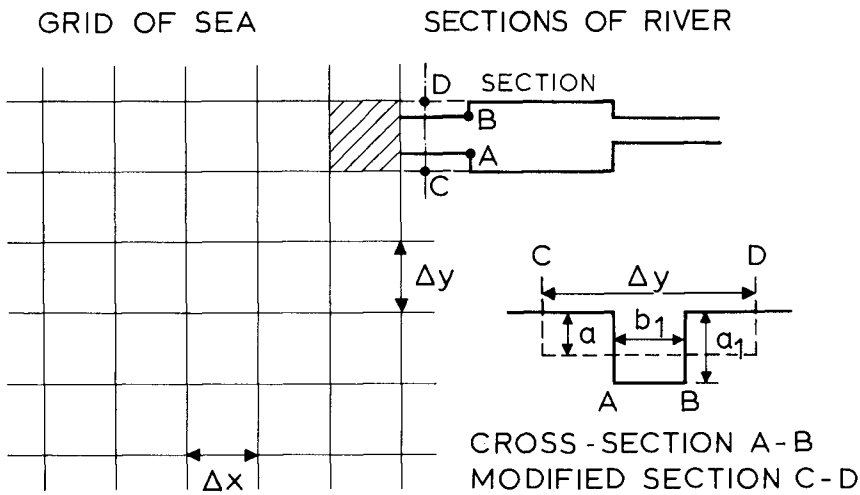

FIG. 3 COMBINED GRID OF SEA AND RIVER SECTIONS

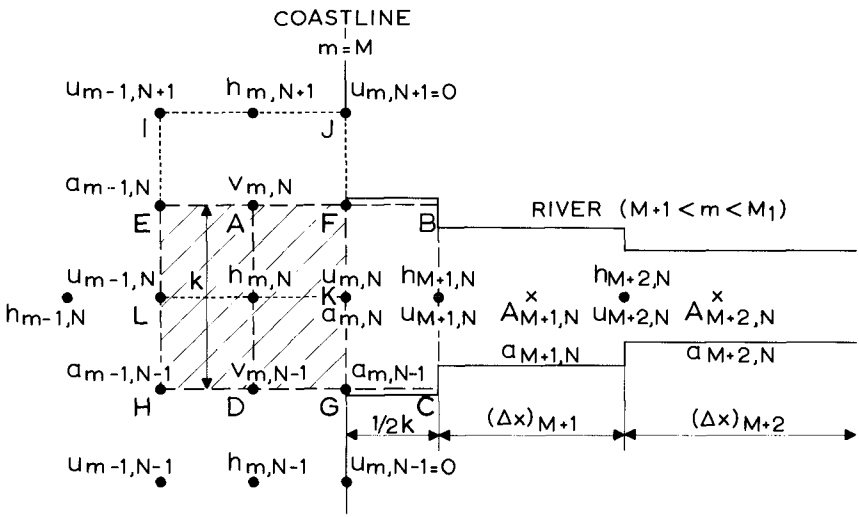

FIG.4 COMBINED GRID OF THE SEA AND RIVERSECTIONS

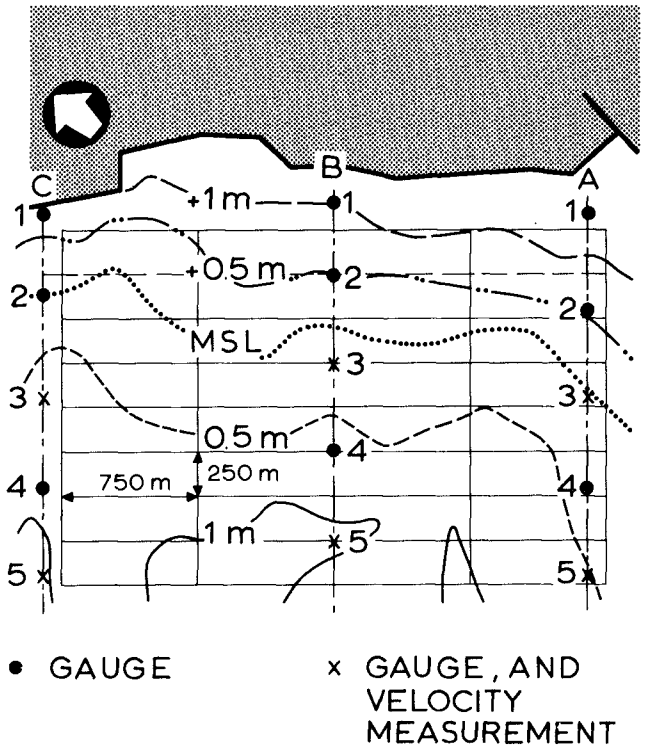

FIG. 5 CONTOUR LINES OF SHALLOW REGION, MEASURING POINTS AND GRID

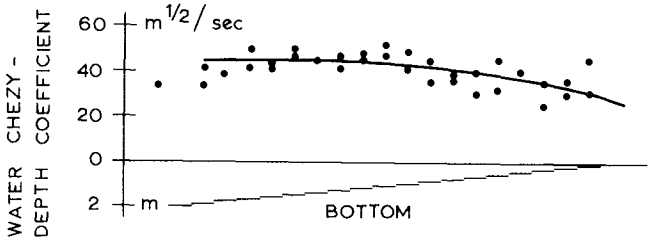

FIG.6 COEFFICIENT OF CHEZY AS FUNCTION OF DEPTH

CHAPTER 137

COMPUTER CONTROL AND DATA ACQUISITION OF A TIDAL MODEL

by

E.R. Funke*

ABSTRACT

A large tidal model of the St. Lawrence River covering the region from Montreal to Ile du Bic is connected directly to a mini computer for data acquisition and control of the tidal boundary. Some of the more important concepts for the design and operation of a computer based system for this application are described. Details of an adaptive feedback controller for diurnal tides are given.

A 16 mm film (N.R.C.-Division of Mechanical Engineering, film no. HYP 620, same title) describes the instrumentation and operation of the model. A report (N.R.C.-Division of Mechanical Engineering, Report No. MH-110, same title) provides further details of this system.

THE MODEL AND THE COMPUTER HARDWARE

The National Research Council under the sponsorship of the Ministry of Transport is operating a 750 ft tidal model of the St. Lawrence River covering a 325 mile section of the river from Montreal to Ile du Bic. The model has a horizontal scale of 1:2000 and a vertical scale of 1:120. Steady but adjustable tributary inflows are provided at various upstream locations. The model has one tidal boundary and a digital computer is used to control this boundary over one repeating diurnal cycle by means of a 35 cfs axial flow impeller pump. In addition one may use three 10 ft long weirs in this control which do not, however, significantly improve performance of the tidal control scheme.

The computer is an Electronics Associates Inc. EAI 640 with 16K words of 16 bit core, 1.65 microseconds cycle time, 2 disc drives, a teletype writer, a card reader, a drum plotter and a small magnetic tape recorder. In addition, there is an analog to digital interface with 96 single ended analog input and 8 analog output channels, 16 output control lines, 8 sense lines, 8 general-purpose interrupts and a digital timer.

---

*Associate Research Officer, National Research Council, Ottawa, Ontario, K1A 0R6.

THE ACTIVATORS

Pitch control of the tidal pump is primarily affected by a hydraulic feedback controller. The pilot valve of this controller is connected to a stepping motor through a precision screw drive. This stepping motor is driven directly by two output control lines from the digital computer. Similarly, stepping motors are attached to their weirs through screw drives and these motors are also driven through separate output control lines.

THE TRANSDUCERS

There are 48 floating bulb water level gauges (N.R.C. - Division of Mechanical Engineering, LTR-HY-30, "A Laboratory Type Water Level Gauge", J. Ploeg) and up to 20 velocity meters (N.R.C. - Division of Mechanical Engineering, LTR-HY-29, "A Drag Plate Velocity Meter for Use in Hydraulic Laboratories", B.D. Pratte, September 1972) are installed along the model. These are designed around Hewlett-Packard linear differential transformers. The level gauges are located in the model in the same geographic areas as tidal recording stations on the river. In addition to the measurement transducers there are several devices used for the monitoring of various operational and fault conditions. These include: -weir position, -pitch position, -weir or pitch limits, -power failure, -low hydraulic pressure, -butterfly or gate valve open or closed, -pump flow in or out, and others. Up to 6 multi-turn, manually operated potentiometers are provided which may be programmed to permit operator intervention in the functions of the control program.

OPERATIONAL FEATURES PROVIDED BY THE COMPUTER SOFTWARE

The computer software is almost entirely written in FORTRAN IV. It performs three distinct on-line functions; -the control of the tidal boundary, -the acquisition of measurement data and -the optional display of some data. These functions include the following features; -independent open loop control of three weirs, -control of one tidal pump by means of a feedback control function and a pump control table, -ability to evolve this pump control table, -monitoring and optional reporting of various fault conditions such as limits and jams, -data acquisition of 96 analog channels and 8 sense lines and their conversion to physical variables, e.g. levels to inches, currents to inch/sec and status to 'fault' or 'no fault', -storage on disc of converted data for the last 2 diurnal cycles,-calculation of tidal extremes over last diurnal cycle and mean discharges for up to 15 stations from current, elevation and cross-section area information, -the optional plotting of instantaneous water surface profiles and the optional typing of discharges or tidal extremes.

In the off-line mode the computer may be used to perform the following: -the optional smoothing of the pump control table by means of a Fourier transform algorithm,-the generation by means of a Fourier transform algorithm of a tidal profile over a diurnal cycle of 612 points using hourly readings as an input, -initialization of the control program including the calculation of head over weirs for any given overflow and the subsequent setting of the weirs to this elevation, -the facility to read and write various fixed parameters and control profiles via typewriter, card reader and magnetic tape, -the display by plotter of all experimental data. During run time the tidal elevations and velocities are stored on disc as blocks representing a scan of all gauges. The output program can select from one block, data from any number of level gauges and plot these as a function of distance from upper end of model or pick one gauge from all blocks and plot its output as a function of time. The tidal extremes may be plotted as a function of distance from upper end of model representing the envelope of tidal excursions for the entire river), -the plotting of a grid system as a function of distance from upper end of model, -the calibration of level gauges. (This feature provides for the automatic setting of weirs to a predetermined level and after excess water has run off and the model has settled, the program will take 50 consecutive readings over 40 seconds, and compute the average voltages and their standard deviations. This output represents one point on the calibration curve of all gauges. Repeated application of this procedure at different levels makes up a complete calibration run), -a quick check for all level gauges. (This is provided by computing the mean elevation of all gauges with the use of present calibration constants. Any gauge that is significantly out of calibration will reveal itself readily in comparison to all other gauges.)

DESIGN CONCEPTS FOR THE SOFTWARE SYSTEM

The Transducer Card

The transducer card is an IBM punched card associated with each transducer, potentiometer or switch and which contains all pertinent information such as station name, its analog channel number and its calibration constants. In addition there is a 'formula type number' which defines the particular conversion formula applicable to this transducer and, consequently, the manner in which the various constants are to be used. For example, a level gauge is converted according to $y = (v - B)/A + M$ and a velocity gauge is converted as $u = \text{sign}(A) \cdot \text{sign}(v) \cdot \sqrt{|v|/|A|}$, where v is the voltage reading, B is a bias voltage at mean water level, A is the sensitivity constant and M is the mean water level relative to datum. Both velocity and level gauges carry one constant D as a distance in miles from Montreal. This permits

the plotting of water surface profiles and the interpolations of elevations associated with discharge calculations. The conversion program currently in use handles up to 8 formulas, most of which are related to fault detection transducers.

Scale Factors and Data Types

Although conversion arithmetic is executed in floating point, for reason of economy all constants and variables are carried in storage in integer format. This leads to a choice of dimensions of variables suitable for this requirement, e.g. voltage readings are in millivolts, elevations are in inch/1000 and velocities are in (inch/1000) per second. The dimensions of some calibration constants are chosen to give at least 3 figure accuracy as, for instance, the constant A for level gauges which is in millivolts per inch. Dimensions of converted variables are usually carried in model units as this facilitates the evaluation of experimental data. However, at the time of final output of the measurement data, this is converted to prototype dimensions. This principle is, however, adaptable. The main objective is to reduce the amount of operator effort and if, for example, the run time calculations of discharges are more meaningful to the operator if carried in prototype units, then this will in fact be done.

Operator Control of Programs

The programs are packaged into 6 units. Each unit nearly fills the available core memory and includes a number of the described tasks. Each task is accessible to the operator through the typing of a one or two digit number which will cause the program to branch to the selected task. For the output program a control card is used to select a particular function and to specify pertinent parameters for this purpose. Consequently, the operator can prepare a deck of control cards that will cause the computer to carry out a pre-selected sequence of events. This control card is sufficiently simple to prepare so that the operator will not require any particular programming knowledge to modify it.

The Feedback Control Scheme for the Tidal Model

The feedback controller for this tidal model is basically a proportional plus derivative controller which is, however, augmented by an adaptive scheme. The fact that the tidal profile is repetitive is used to advantage, and the control scheme is programmed to learn from past mistakes and to take appropriate corrective action at an early enough time in the next tidal cycle.

The schematic of the control scheme is illustrated in

Fig. 1. In this diagram, the tidal profile, which exists in the computer as a table of numbers, is represented as a cam. As this hypothetical cam rotates, the corresponding movement in the computer is the stepwise incrementation of the table index every 0.8 seconds.

The reference input is taken from the 'cam' at a particular phase. This is compared to the water elevation at the control point, which is a gauge near the lower boundary of the model. This control transducer is substantially the same as the ones used for general data acquisition. The only difference is the choice of the linear differential transformer which has a ±3 inch range while most other transducers have a ±2 inch range. It is necessary to have an instrument with a large deflection range as there is a distinct danger that the water elevation might exceed these limits with a subsequent loss of signal. If this happens, the computer may compute an error of the wrong polarity and the system would then go completely out of control.

The transducers with a larger range have smaller resolution and accuracy in terms of absolute value. A typical figure quoted by Hewlett-Packard is .5%, which corresponds to an error due to non-linearity and resolution of .015 inch. Careful calibration will reduce this figure to .005 inch. So far the model control has proved adequate for the measurements that are being made. However, if it should become necessary to improve the accuracy of the feedback control, one may double up on the feedback transducer, one for fine control over the normal operating range and the other for coarse control in the fringe areas.

The areas in Fig. 1, which are surrounded by dashed/dotted lines, represent the jobs carried out by the various subroutines. In the normal feedback control situation the switch S_H is closed and S_G is open. The control function that is computed by the subprogram FDBCTR is based on present and previous errors and is given by

$$IEU_i = A_o*(E_i + E_{i-1})/2 + A_1*(E_i - E_{i-2})/2\Delta T.$$

The program remembers past values of error but discards those beyond $(i-2)\Delta T$.

Manual potentiometers are available to control the coefficients A_o and A_1. These 3-turn potentiometers are programmed through their transducer cards to give an output of one when turned fully clockwise and zero when turned fully counter clockwise. At the present time values of $A_o = .067$ and $A_1 = .05$ are used with the dimension of E being in inch/1000 and $\Delta T = 0.8$ seconds.

The feedback controller alone is not adequate for satisfactory operation. With the selected loop gains, control errors in the order of 0.1 inches are normal. Increased loop gains lead to instabilities. More sophisticated control functions which are designed around a lumped parameter approximation of the tidal basin proved critical. These lead to instabilities that are imperceptible at the control point but become undesirably amplified at several upstream locations with shallow water depth.

The method that is now being used with considerable success is based on the principle that a feedback controller should overcome primarily the unpredictable element in the control objective. Anything that is known a priori about the control task should not be achieved by the feedback error control. Rather, one should attempt to regulate the system as well as possible through an open loop control and whatever errors are made in this effort, due to random disturbances or misjudgement of system parameters, can then be corrected for by the feedback controller.

The open loop controller that is required here is a profile of control signals to the tidal pump that will regulate the impeller pitch to cause flow in and out of the tidal basin in such a way that the water elevation at the control point corresponds to the reference input. This profile is not easily determined by theoretical considerations or measurement. As a matter of fact, it was found that the simple placement of several roughness elements at certain places in the river model gave an almost imperceptible local change in water level, but could cause a major effect on the pump control profile. In addition, the pump has a nonlinearity in the vicinity of zero pitch which behaves more or less like a 'dead zone'. This nonlinearity is also a function of the head difference between the model and the sump which is variable. In the presence of these difficulties is was thought best to devise a scheme that would generate the required pump control profile through a learning procedure. This option is activated by closing S_G in Fig. 1.

When the controller recognizes an error and computed the corresponding control function IEU, then it is assumed that this corrective action, which is taken now, could yield better results if it had been taken a little sooner. For this reason, the quantity IEU_i is added to the pump control profile at a point just ahead of the current table index 'i'. If the pump control profile is $ITBL2C_i$ and the present value of the control function is IEU_i, then the learning function is expressed as

$$ITBL2C_{i-j}\Big|_{\text{next cycle}} = ITBL2C_{i-j}\Big|_{\text{this cycle}} + SO*IEU_i$$

where SO is an adjustable gain constant which is now always set to 1 and j is an adjustable phase control constant which is now set to 5 seconds/.8 seconds = 6 steps. Care is taken of course to recycle the index whenever table limits are exceeded.

When control conditions are changing or a new tidal profile is required, then it is necessary to place the computer system into this adaptation mode by closing the switch S_G. This is referred to as the 'updating' of the pump control profile. This procedure may take up to 8 diurnal cycles until the error has vanished to acceptable limits. After this it is customary to store all control parameters, including the tidal profile and the pump control profile, on digital magnetic tape. This allows the operator to recall from tape any particular tide which has been run previously and put the model into operation within minutes. Start-up transients at the control point for fully updated tides are shorter than one diurnal cycle.

CONCLUSIONS

The application of a computer based tidal control and data acquisition system has substantially improved convenience, accuracy and repeatability of experimental work on tidal models. These advantages are in addition to the obvious labour saving benefits. There are, however, two areas that require more development or study for further improvement. From a systems point of view it appears more desirable to restructure the software so that all model control and data acquisition programs are made fully compatible with a generalized data acquisition and data analysis system for a hydraulics laboratory. This would eliminate duplication in programming efforts. Secondly, the present feedback control scheme is considered unpractical for tidal profiles extending over more than two or three diurnal cycles. It is now felt the controller can be improved by the inclusion of a simple one-dimensional numerical approximation of the scaled model for the estimation of the dynamic storage at each time step. This study could lead to interesting extensions to two or three boundary models.

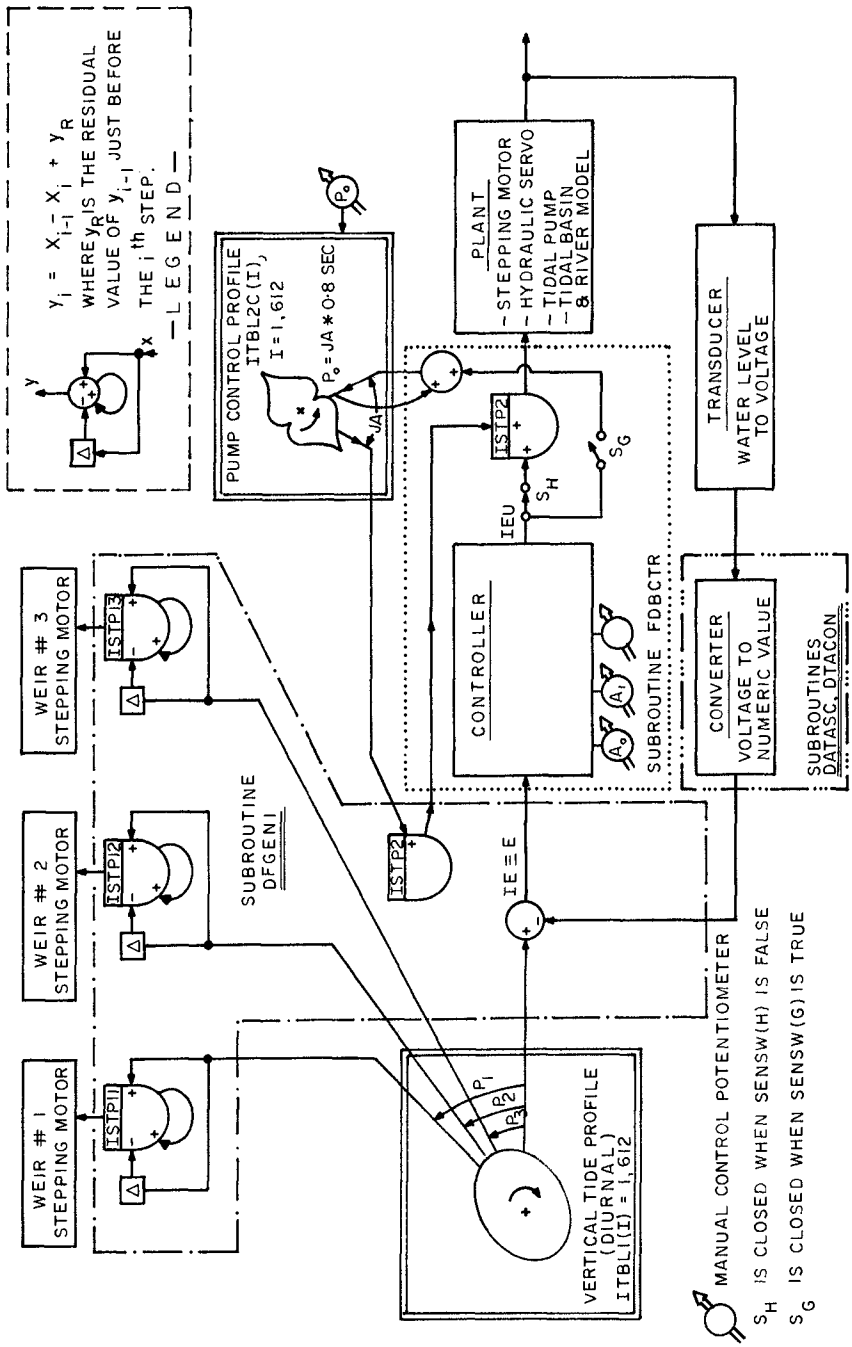

FIG.1 FEEDBACK CONTROL SCHEME FOR TIDAL MODEL

CHAPTER 138

DEFORMATION OF TIDAL WAVES IN SHALLOW ESTUARIES

by

CLAUDE MARCHE[1] and HANS-WERNER PARTENSCKY[2]

ABSTRACT

Several mathematical models have been lately presented which describe the tidal wave propagation within an estuary. The existing models derived from the method for damped co-oscillating tides are based on sinusoidal wave profile.

Meanwhile a tidal wave which moves upstream, generally exhibits a progressive deformation which tends to unbalance the length of time between flood and ebb tides. The actual profile is therefore no longer sinusoidal.

Our investigation uses the potential method, and takes into account the wave amplitude which is usually neglected compared with the water depth.

Finally, the velocity potential is obtained explicitely, using a double iterative method. Tidal elevation, particle velocities and trajectories are given by the same computer programmed algorithm.

Our study shows that 1) the phenomenon can be clearly visualized on the theoretical curves and 2) the magnitude of this deformation is inversely proportional to the water depth, becoming significant when the ratio η/h reaches the critical value of 1/10.

Damping and geometrical effects are also considered and the theory was applied to the St.Lawrence Estuary. A partial positive reflection of the incoming tidal wave is assumed at the narrow section near Quebec, whereas a complete negative reflection is assumed at the entrance to Lake St.Peter. The calculated and observed wave profiles, velocity distributions, and phase shifts are in good agreement.

I. INTRODUCTION

Several mathematical models have been developped, describing the tidal wave propagation in an estuary. The existing models, formulated by A.T. Ippen and D.R.F. Harleman, for the Delaware Estuary and the Bay of Fundy [1], as well as that of H.W. Partenscky for the St.Lawrence Estuary [2,3], made use of the method for damped co-oscillating tide, based on a sinusoidal wave profile.

---

1) Lecturer, Ecole Polytechnique, Montreal, Canada.
2) Director, Franzius Institute, Technical University of Hannover, Germany.

However, a tidal wave ascending an estuary, generally undergoes a progressive deformation which tends to unbalance the respective ebb and flood times of the water mass. The actual profile is therefore no longer sinusoidal. The theory, developped in this paper, allows us to explain and retrace this wave deformation, by taking the influence of the water depth into account.

II. DEFORMATION OF TIDAL WAVE IN A SHALLOW RECTANGULAR CHANNEL

1. Velocity potential and free surface elevation

The velocity potential of an oscillating wave of small amplitude propagating in the positive x direction is solution of the Laplace equation

$$\nabla^2 \phi_1 = 0$$

where index 1 indicates the incident wave.

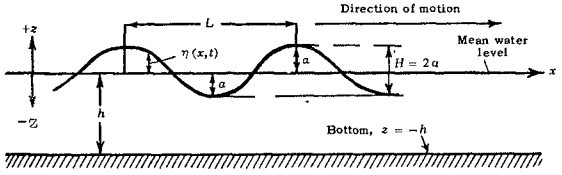

Fig. 1: Definition sketch

We consider the hypothesis of the small amplitude wave theory verified; however, we locate the free surface at elevation $z = \eta_1$, variable, and not at the mean elevation $z = 0$. The boundary conditions to be used to evaluate the resulting solution are:

at $z = \eta_1$:

$$-\frac{\partial \phi_1}{\partial t} + \frac{1}{2}\left(\frac{\partial \phi_1^2}{\partial x} + \frac{\partial \phi_1^2}{\partial y}\right) + g\,\eta_1 = 0$$

$$-\frac{\partial \eta_1}{\partial t} + \frac{\partial \phi_1}{\partial x} \cdot \frac{\partial \eta_1}{\partial x} - \frac{\partial \phi_1}{\partial z} = 0 \qquad (1)$$

at $z = -h$:

$$\frac{\partial \phi_1}{\partial z} = 0$$

By neglecting the higher order terms, the boundary conditions can be written in a simplified form:

$$\text{at } z = \eta_1 : \quad -\frac{\partial \phi_1}{\partial t} + g\,\eta_1 = 0 \qquad -\frac{\partial \eta_1}{\partial t} - \frac{\partial \phi_1}{\partial z} = 0 \tag{2}$$

$$\text{at } z = -h : \quad \frac{\partial \phi_1}{\partial z} = 0$$

We note that the boundary conditions (2) differ from the usual conditions for waves of small amplitude by an order of approximation. This leads us to assume as a first approximation an initial solution of the form:

$$\phi_1 = \frac{ag}{\sigma}\,\frac{\cosh G_1 (h+z)}{\cosh G_1 h}\cos(G_1 x - \sigma t) = \frac{A_1 g}{\sigma}\cos(G_1 x - \sigma t) \tag{3}$$

The boundary conditions (2) will now be applied to the velocity potential function ϕ_1. Solution (3) fulfills the boundary conditions if

$$\sigma^2 = g\,G_1 \tanh G_1 (h + \eta_1) \tag{4}$$

is verified. In the above equations, a is the amplitude of the tidal wave, η_1 is the instantaneous surface elevation given by

$$\eta_1 = \frac{1}{g}\,\frac{\partial \phi_1}{\partial t} \quad \text{and} \quad G_1 = \frac{2\pi}{L_1}$$

is the variable wave number.

It should be stressed the importance of equation (4) which shows that σ and G_1 are related by a variable expression depending on the elevation η_1, the latter being a function of time and space. Field measurements have shown the rigourous equality of the period of different tidal waves. This verification allows us to present the third equation needed:

$$\sigma = \frac{2\pi}{T} = \text{constant}$$

Equation (4) is an implicit equation in G_1, and an iterative computer programmed method will yield to a numerical solution in the system formed by equations (3) and (4). The uniqueness of the solution of this system is proved for all possible physical conditions. The deformation clearly appears when a comparison is made between the wave profile

obtained from this theory and the sinusoidal profile.

Figure 2 illustrates the type of deformation which a five feet amplitude wave undergoes, during propagation in a channel of fifteen feet depth. We note in particular a descending time of six tenth (6/10) period versus an ascending time of four tenth (4/10) of a period. Several similar curves, calculated for different water depths showed that the importance of the deformation becomes appreciable for a ratio of amplitude to depth of

$$\eta / h > 1/10$$

approximately.

The application of this theory to the potential of a wave reflected at x = B in the same rectangular channel leads to the following expression, with index 2 being used for the reflected wave:

$$\phi_2 = \frac{ag}{\sigma} \frac{\cosh G_2 (h+z)}{\cosh G_2 h} \cos(G_2 x - \sigma t + \delta) = \frac{A_2 g}{\sigma} \cos(G_2 x - \sigma t + \delta) \qquad (5)$$

with:

$$G_2 = \frac{2\pi}{L_2}$$

$$\sigma = g G_2 \tanh G_2 (h + \eta_2)$$

and

$$\delta = 2n\pi - 2 G_2 B$$

The velocity potential of the resulting wave is given by

$$\Phi = \phi_1 + \varkappa_r \phi_2 \qquad (6)$$

where $\varkappa_r$ is the reflection coefficient of the reflected wave at x = B.

2. Introduction of geometry and damping effects

The generalization of this theory to a practical application requires the introduction of two additional parameters: geometry and friction. In the most general case, the resulting wave profile is given by the expression

$$\eta = a\left(\frac{b_B}{b_x}\right)^{\frac{1}{2}} \left(\frac{h_B}{h_x}\right)^{\frac{1}{4}} \left[A_1 e^{-\mu(x-B)} \sin(G_1 x - \sigma t) - \varkappa_r A_2 e^{\mu(x-B)} \sin(G_2 x - \sigma t + \delta) \right] \qquad (7)$$

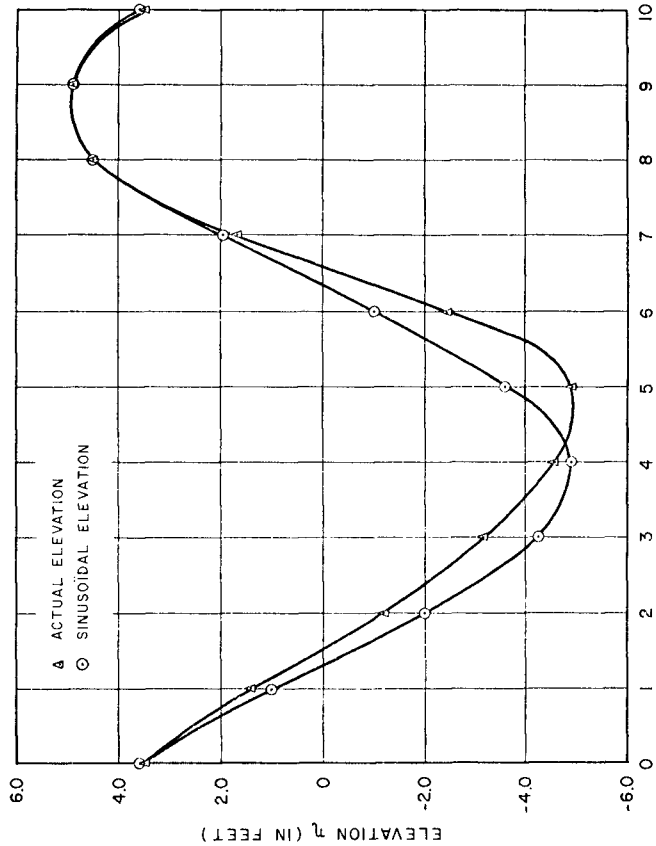

FIG. 2 DEFORMATION OF A TIDAL WAVE IN A RECTANGULAR CHANNEL

with the supplementary condition:

$$\sigma^2 = g\, G_1 \tanh G_1 (h + \eta_1) = g\, G_2 \tanh G_2 (h + \eta_2) \qquad (8)$$

where:

h is the mean water depth
b is the mean width
h is the overall damping coefficient
A_1 and A_2 are terms as defined in equations (3) and (5) respectively

Expression (7) is valid and may be used for any real estuary, with the condition that Green's Law be satisfied.

3. Water particle velocity

By virtue of the definition of the velocity potential, the horizontal and vertical components of a local fluid particle velocity due to the passage of the incident wave in a rectangular channel without friction are obtained by differentiation of the velocity potential in each direction:

$$U = -\frac{\partial \phi_1}{\partial x} = \frac{ag\, G_1}{\sigma} \frac{\cosh G_1 (h + \eta_1)}{\cosh G_1 h} \sin(G_1 x - \sigma t) \qquad (9)$$

$$V = -\frac{\partial \phi_1}{\partial z} = -\frac{ag\, G_1}{\sigma} \frac{\sinh G_1 (h + z)}{\cosh G_1 h} \cos(G_1 x - \sigma t) \qquad (10)$$

The implicit equation

$$\sigma^2 = g\, G_1 \tanh G_1 (h + \eta_1)$$

defining the term $G_1 = 2\pi/L_1$ used in the expressions (9) and (10). A numerical solution is utilized to determine the velocity components U and V as functions of x and z. Figure (3) shows a characteristic variation of the horizontal velocity during a wave period. We note from this curve a difference between the absolute values of minimum (5.20 feet/sec) and maximum (4.15 feet/sec) velocity of the particle considered: The velocity of reflux is of greater importance than the velocity of flux.

Therefore, for incompressible, two dimensional motion in the x, z plane the continuity equation requires that the corresponding period of time of rise and fall be unequal. This last observation corroborates

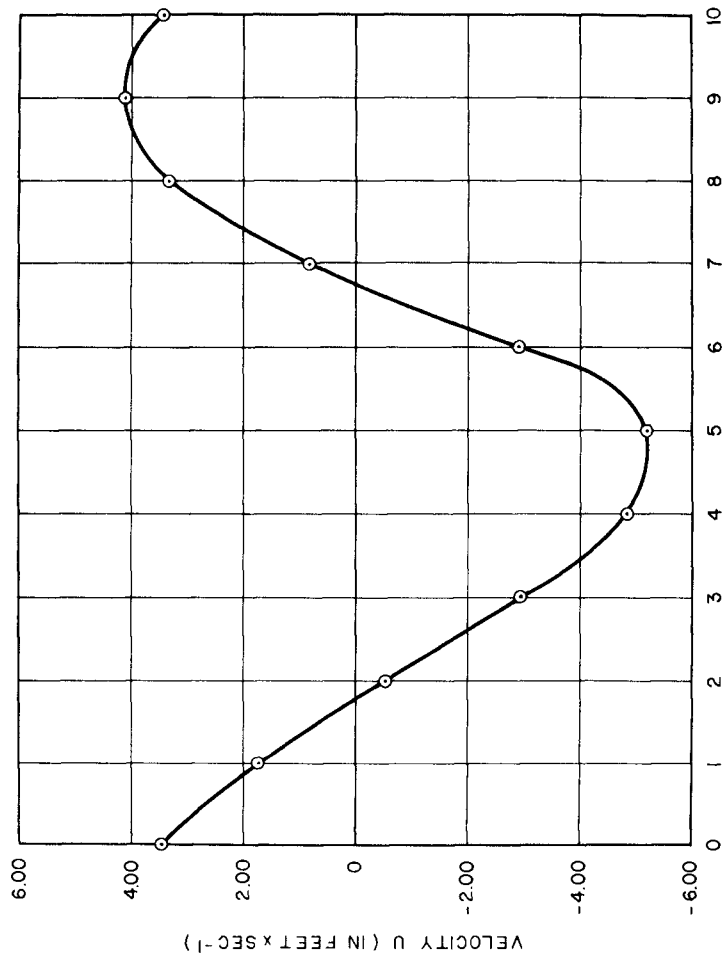

FIG. 3 HORIZONTAL VELOCITY CHANGE DURING A PERIOD

the mathematical and physical results concerning the tidal elevation, shown on figure (2).

4. Water particle trajectories

Another modification of importance given by this theory concerns the trajectories of particles. These are solution of the differential system

$$\frac{dx}{U} = \frac{dz}{V} = dt \tag{11}$$

In the integration of this system, we do not use the small particle movement hypothesis, thus allowing us to consider that particle velocity is only a time fonction. The complete integration of the system (11) may be made numerically, and without particular hypothesis, and leads to the following algorithm:

$$x_{t_n} = \sum_{n=1}^{n} \int_{(n-1)\frac{T}{m}}^{n\frac{T}{m}} U(x_{n-1}, t_{n-1})dt + x_o \tag{12}$$

$$z_{t_n} = \sum_{n=1}^{n} \int_{(n-1)\frac{T}{m}}^{n\frac{T}{m}} W(x_{n-1}, t_{n-1})dt + z_o \tag{13}$$

where:

x_{t_n} and z_{t_n} are the instantaneous horizontal and vertical displacements from 0 to t_n respectively and,

T/m is the increment of the numerical solution expressed as a fraction of the period.

Figure (4) illustrates the trajectory of a particle under the effect of a wave propagating in a very shallow region. We note that the initial ellipse obtained from the small amplitude wave theory is downward deformed.

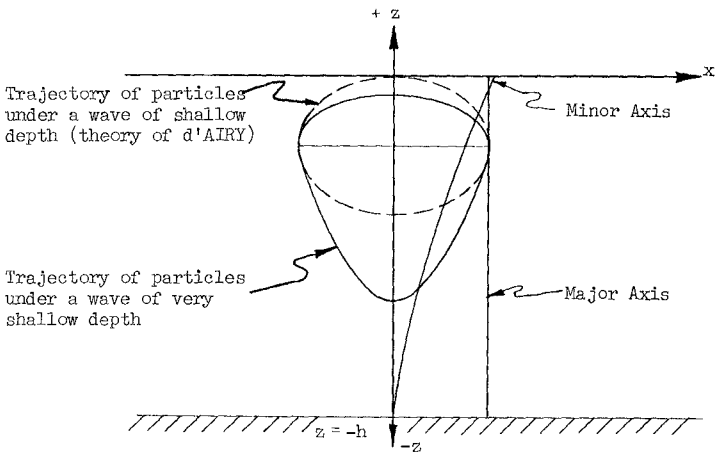

Figure 4

This deformation is easily explained by continuity by observing the velocity differences of flux and reflux. The calculated trajectories for different water depths show that there exists a variation in trajectory comparable to the well-known variation of ellipses in small amplitude wave theory. The major axis of the deformed ellipse remains constant at any depth, whereas the minor axis, in the vertical direction decreases with depth.

III. APPLICATION OF THE THEORY TO THE ST. LAWRENCE ESTUARY

1. Physical characteristics of the estuary

The St. Lawrence Estuary is composed of two parts of different geometry. The first concerning the estuary itself is a convergent form between its ocean entry and Quebec City. It is prolongated by a second part of more constant width and far shallower depths, bounded at the location of the enlargement known as Lake St. Peter.

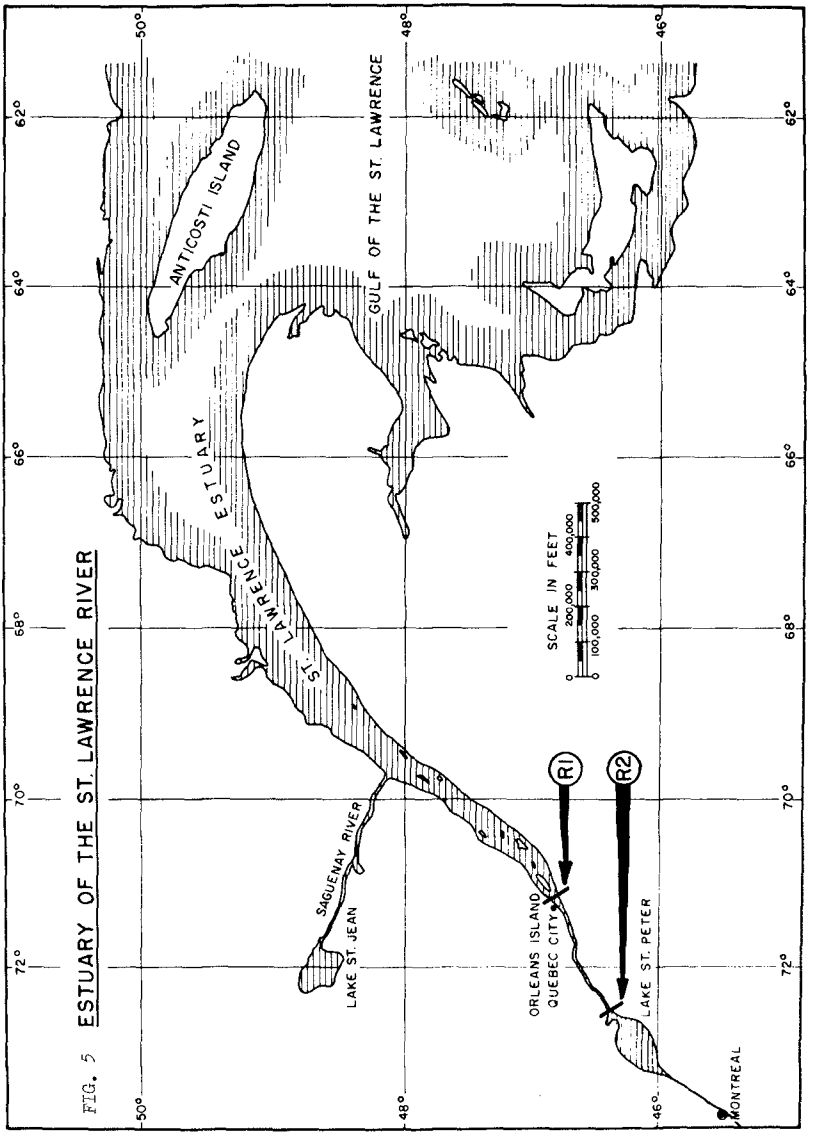
ESTUARY OF THE ST. LAWRENCE RIVER
ANTICOSTI ISLAND
GULF OF THE ST. LAWRENCE
ST. LAWRENCE ESTUARY
SAGUENAY RIVER
LAKE ST. JEAN
ORLEANS ISLAND
QUEBEC CITY
R1
R2
LAKE ST. PETER
MONTREAL
SCALE IN FEET
0
100,000
200,000
300,000
400,000
500,000
50°
48°
46°
62°
64°
66°
68°
70°
72°

These two distinct parts of the estuary, bring us to consider two successive reflexions of the ascending tidal wave: one partically positive at the straightening of Quebec (Section R_1), the other total and negative, at the sudden enlargement at Lake St. Peter (Section R_2).

2. Results

Some physical parameters are required for the solution of the actual conditions in the estuary. These are:

- The reflection and transmission coefficients particularly in the sections R_1 and R_2. These are furnished by a geometric study in that sector.

- The height of the tidal wave in the sections of reflection. These are found in the bibliography.

- The precise geometry of the estuary, the surface width and the average depth of each section under study.

Based on these informations, the application of the mathematical model allows us to predict the tidal elevation, the particle velocity and their trajectory at each section of the estuary, the instantaneous wave profile and the velocity distributions along the estuary at any time.

A comparison of the recorded and calculated elevations at the tidal stations of Neuville and Grondine (figure 5), which are located at the upper shallower part of the estuary, is shown on figure 6 and 7. These curves show the expected deviation from the pure sinusoidal motion due to the restricted water depth in this region. In the deeper part of the estuary, the graphs of $\eta(t)$ regain a more sinusoidal form.

Figure 8 presents the variation of the horizontal velocity of the particles at three sections of the upper part of the estuary: Neuville, Grondines, and Batiscan. We note from these three curves a difference between the absolute value of minimum and maximum velocities, which is proportional to the maximum velocity itself.

Figure 9 shows the trajectory of a particle initially located at Grondines and at a distance of seven feet above the bottom. We note that since the displacement is a periodic function of time in the expressions (12) and (13), the trajectories are closed curves. For comparison, the trajectory of a particle initially located at Batiscan above Grondines is shown on the same figure. We note that the conjugated effects of the damping and the geometry of the estuary tend to reduce the particle displacement in accordance with the wave propagation. In the deeper part of the estuary the trajectories appear elliptic.

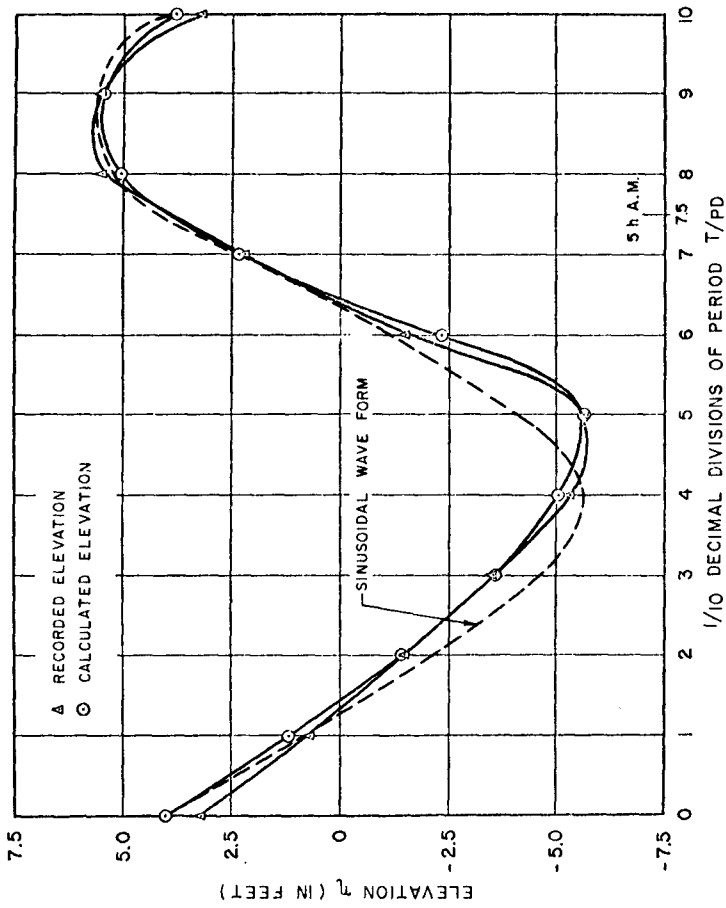

FIG. 6 COMPARISON OF TIDAL AMPLITUDES RECORDED AND CALCULATED AT NEUVILLE

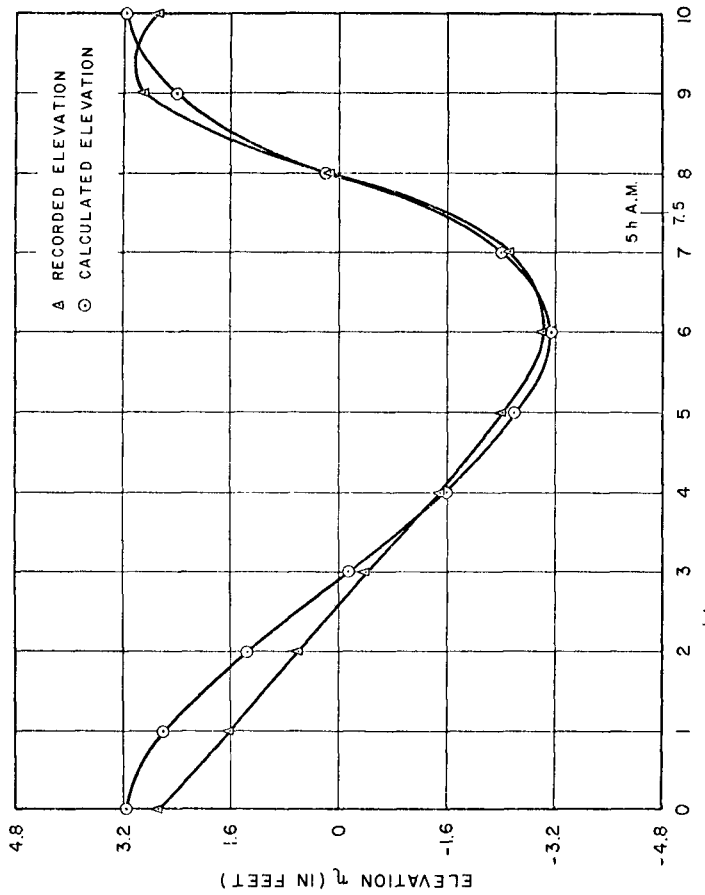

FIG. 7 COMPARISON OF TIDAL AMPLITUDES RECORDED AND CALCULATED AT GRONDINES

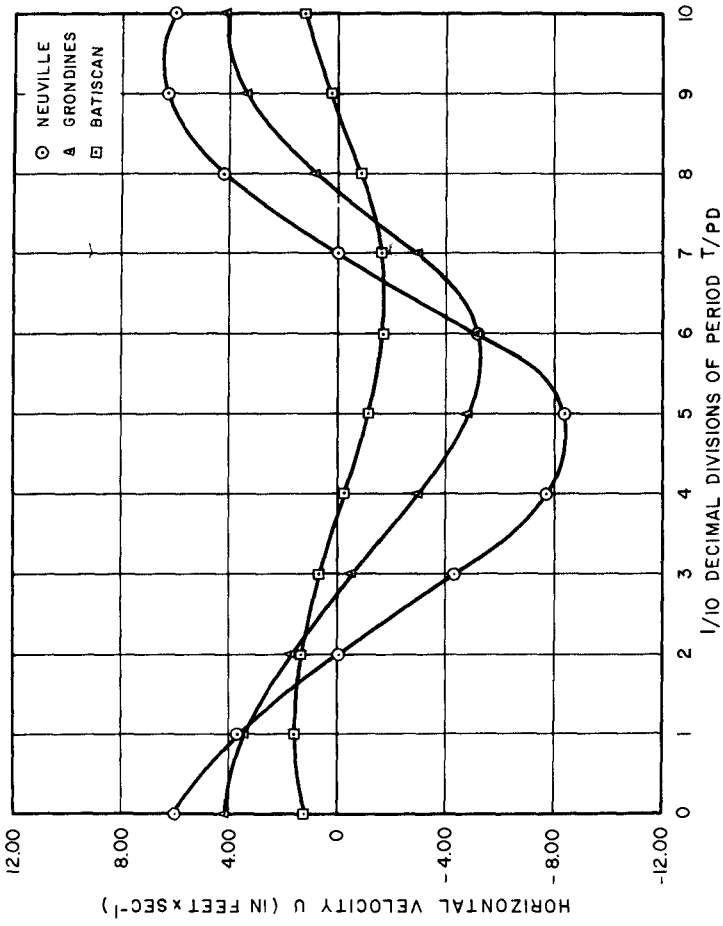

FIG. 8 HORIZONTAL VELOCITY CHANGE DURING A PERIOD AT NEUVILLE, GRONDINES AND BATISCAN

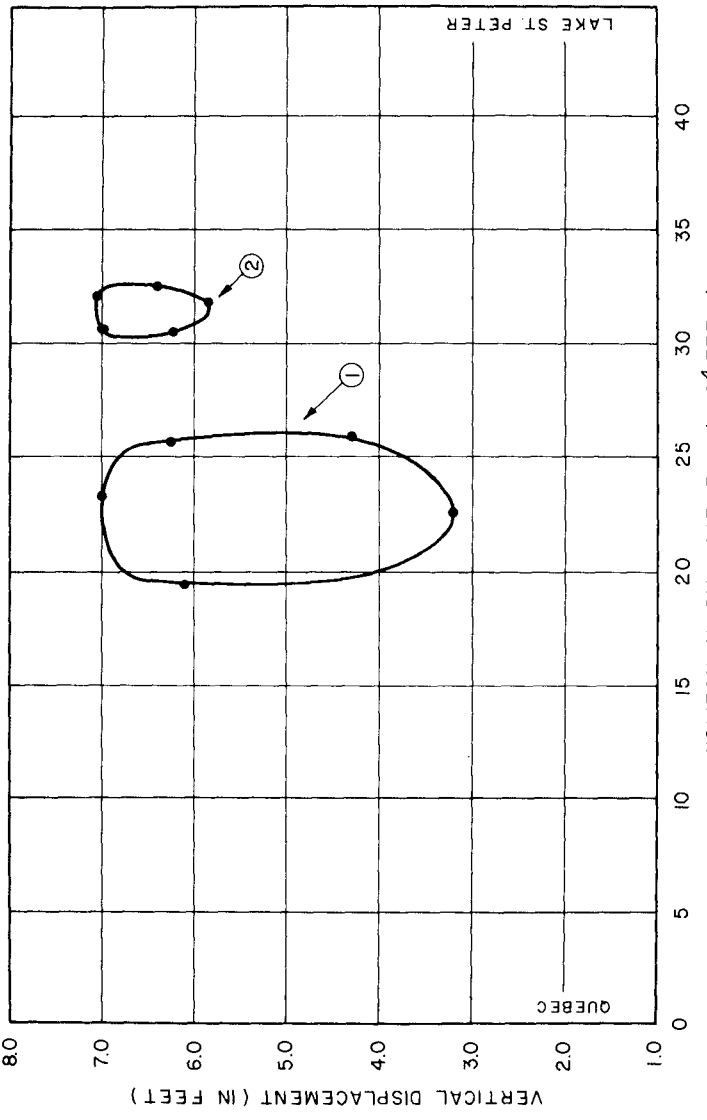

FIG. 9 COMPARATIVE PARTICULE TRAJECTORIES

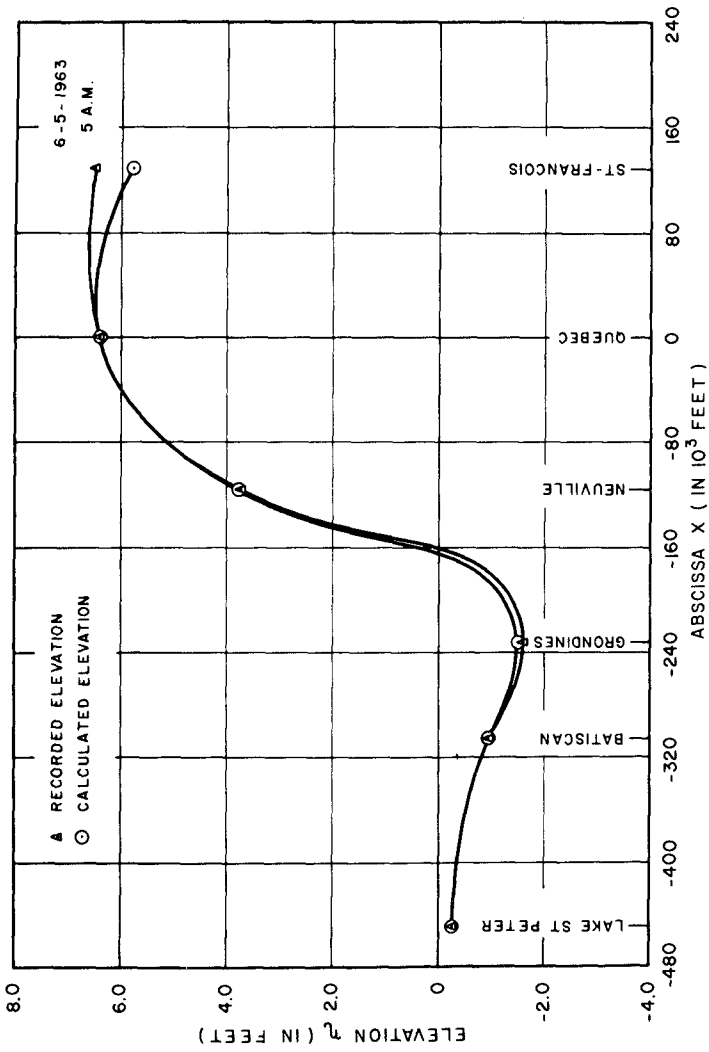

FIG. 10 INSTANTANEOUS PROFILE ALONG THE ESTUARY BETWEEN ST-FRANCOIS AND LAKE ST PETER

An instantaneous profile calculated for the upper part of the estuary is shown in figure 10. The calculation was made for 5 A.M. on May 5, 1963, a date for which a detailed recording was available. A comparison with the recorded data shows the accuracy of the theoretical values of the tidal elevations. On the other hand, these curves clearly show the effect of the total negative reflection of a tidal wave and its decline in the upper part of the estuary.

CONCLUSION

The mathematical model herein developped and applied to the St. Lawrence Estuary gives a good approximation of the tidal motion in both, the deeper and shallower part of the estuary. Especially in the shallower zone, the results show the well-known deformation of the wave profile which could not be predicted by preceeding mathematical models. The theoretical development used here, allows a computer oriented approach which could be modified to incorporate into the equations some of the more complex aspects of propagation of the tidal wave in an estuary, particularly the effect of the fresh water discharge, which was not yet included in the present study.

BIBLIOGRAPHY

(1) A.T. Ippen & D.R.F. Harleman : "Estuary and Coastline Hydrodynamics", McGraw-Hill, New York, 1965.

(2) H.W.Partenscky & R. Vincent : "Tidal Motion in the St. Lawrence Estuary", Xth Conference on Coastal Engineering, Tokyo, Sept. 1966.

(3) H.W. Partenscky & J.C. Warmoes : "A Study of the St. Lawrence River tides estuary using a linearized mathematical model", Ecole Polytechnique, Montréal.

(4) H.W. Partenscky & J.C. Warmoes : "Damped co-oscillating tides with negative reflection at the end of the estuary, IAHR, Kyoto, 1969.

CHAPTER 139

MATHEMATICAL AND HYDRAULIC MODELS OF TIDAL WAVES

by

Jürgen Sündermann[1] and Hans Vollmers[2]

ABSTRACT

A systematical comparison between experiments in hydraulic models and numerical computations for the case of the propagation of tidal waves in schematic estuaries is carried out. It is the aim of the investigations to present the advantages and disadvantages, the possibilities and limitations of the two models. The results show, generally, a fair agreement between measured and computed quantities even in the case of the occurence of horizontal eddies within the fluid.

INTRODUCTION

Whereas the hydraulic model has acted as an indispensable tool of coastal engineers in years past, purely mathematical methods gained in importance only in recent times. This development can be attributed primarily to the advances made in computer technology. In principle both methods the hydraulic model and the hydrodynamical-numerical (HN) method, are well suited in simulating the dynamics of natural water bodies. However, before one can ascertain how the two methods can be optimally combined so that the model simulates natural processes to a high degree of accuracy, it is first necessary to investigate the advantages and disadvantages of each, their possibilities and limitations. This paper presents further results of a systematic

1) Prof.Dr., Technische Universität Hannover
2) Dr.-Ing., Bundesanstalt für Wasserbau Hamburg
Germany

comparison of the two methods for tidal waves in schematic estuaries. Preliminary results were given by H. Vollmers at the 12th Coastal Engineering Conference [1].

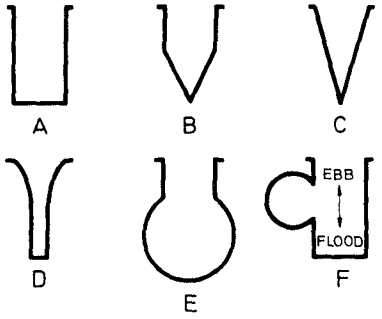

Fig. 1 Schematic estuaries

In order to gain experience and to determine some basic guiding principles, work commenced on simple, yet representative models. These are to be gradually adapted to natural configurations. Fig. 1 shows the forms of the schematic estuaries used. They are similar in shape to those found along the German North Sea coast. The special layout and dimension of the models was determined by the space available in the laboratory, to location and setup of the measuring apparatus and, also, the characteristics of the HN-models and the available computer capacity.

In each case, we assumed a constant depth of 15 m. The width at the entrance of the region was 4 km. Forms A to D, that's those more distinctly one-dimensional, had a length of 55 km. Forms E and F, more two-dimensional, had a length of 16 km. The diameter of the circular extensions was 10 km in case E (Jade) and 5 km in case F (Dollart). The coastal boundaries were approximated by vertical walls.

For the estuaries A to D, we studied the temporal and spatial behaviour of a M_2 tide of amplitude 1.5 m. For the cases E and F, the amplitude was increased to 3 m in order to obtain distinct measurable effects.

In the mathematical models used for comparison, the coriolis force was neglected as the hydraulic model could not simulate this effect. In order to obtain some first hand information on the effect of the coriolis force, in particular for case E and F, corresponding HN computations were carried out.

Due to core limitations, the mathematical model utilizes vertically meaned horizontal velocities. Comparison with measured velocities had therefore to be limited to mean values. A HN-model which includes the third dimension and thus permits a realization of the full 3-dimensional velocity structure, has now also been completed [2].

THE HYDRAULIC MODEL

As the current processes examined here are, to a large extent, influenced by inertial and gravity forces, we can assign to the transformation ratio nature/model the well-known Froude Number. In the hydraulic model the length and width scale was set at 1:1000, the depth scale was set at 1:100. With these scales a mean tidal period lasted 7.45 minutes. The model floor is composed of sand immobile under existing velocities. This floor, preformed by appropriate waves (approximately 1 cm amplitude) allowed us to simulate friction to a good degree. In Fig. 2 next to the just analyzed form E, we may also see the contours of form D, and the dimension of the 55 km long rectangular channel, form A.

The tidal waves were produced by a mechanical control system. During the experiments water levels and current speed were measured with vibrating points System Delft, self registering floating gauges and micro propellers. Directions were determined either with the help of small paper strips or photographically with a floating body free to rotate in the horizontal plane. As boundary conditions in the mathematical model we used the values at the entrance as measured in the hydraulic model. While

carrying out the speed measurements not only the time variations over a tidal cycle were determined but also the vertical distribution. Measuring locations in the hydraulic model were equivalent to corresponding grid points in the mathematical model.

Fig. 2 Model installation

THE MATHEMATICAL MODEL

The quasilinear, vertically integrated hydrodynamic equations were taken as the basis for the model. In order to solve the corresponding initial value problem numerically, an explicit method developed by Hansen, the HN method, was used [3]. The mathematical model based on this principle can be adapted to natural regions to a good degree. As empirical input data it is necessary to prescribe merely the tidal amplitude at the entrance and the geometry of the area in question.

The particular layout of the computational grid in the finite difference method is determined by the type of problem to be solved, the necessary accuracy one wishes to attain and the allowable computation expenditures. Model forms A to D were computed one-dimensionally, that is, not considering cross-streams but considering a variable cross-section. The estuary forms E and F were treated 2-dimension-

ally. The following differential equations are used

(1)

$$(1.1)\quad \frac{\partial u}{\partial t} + u\frac{\partial u}{\partial x} + v\frac{\partial u}{\partial y} + \frac{r}{h+\zeta}\sqrt{u^2+v^2}\,u - fv - A_H \Delta u + g\frac{\partial \zeta}{\partial x} = 0$$

$$(1.2)\quad \frac{\partial v}{\partial t} + u\frac{\partial v}{\partial x} + v\frac{\partial v}{\partial y} + \frac{r}{h+\zeta}\sqrt{u^2+v^2}\,v + fu - A_H \Delta v + g\frac{\partial \zeta}{\partial y} = 0$$

$$(1.3)\quad \frac{\partial \zeta}{\partial t} + \frac{\partial}{\partial x}\left((h+\zeta)u\right) + \frac{\partial}{\partial y}\left((h+\zeta)v\right) = 0$$

with u,v = components of the vertical meaned velocity vector in the x-, y-direction, respectively

ζ = deviation of the sea surface from the undisturbed level

h = mean water depth

t = time

A_H = horizontal eddy coefficient

f = coriolis parameter

g = acceleration of gravity

r = friction coefficient

This system of hyperbolic partial differential equations is nonlinear and hence particularly suited to shallow water dynamics which are known to be distinctly nonlinear.

In addition, boundary conditions must be added as follows

(2)

$$(2.1)\quad \underline{v}_n = 0 \qquad \text{along the coastline}$$

$$(2.2)\quad \zeta(t) = A\cos(\sigma t - \varkappa) \qquad \text{at the entrance of the estuary}$$

where A = amplitude

σ = frequency

$\varkappa$ = phase of the incoming tidal wave.

As initial conditions we assume a state of rest:

(3)

$$u = v = 0; \qquad \zeta = 0$$

In a one-dimensional calculation the equations are corresponding simplified.

Now a brief description of the HN models for the estuary forms A to F will be given. The appropriate grids and natural dimensions may be seen by Fig. 3. The layout of the grid points is well suited to the structure of the differential equations. The grid locations where tidal oscillation are generated are marked.

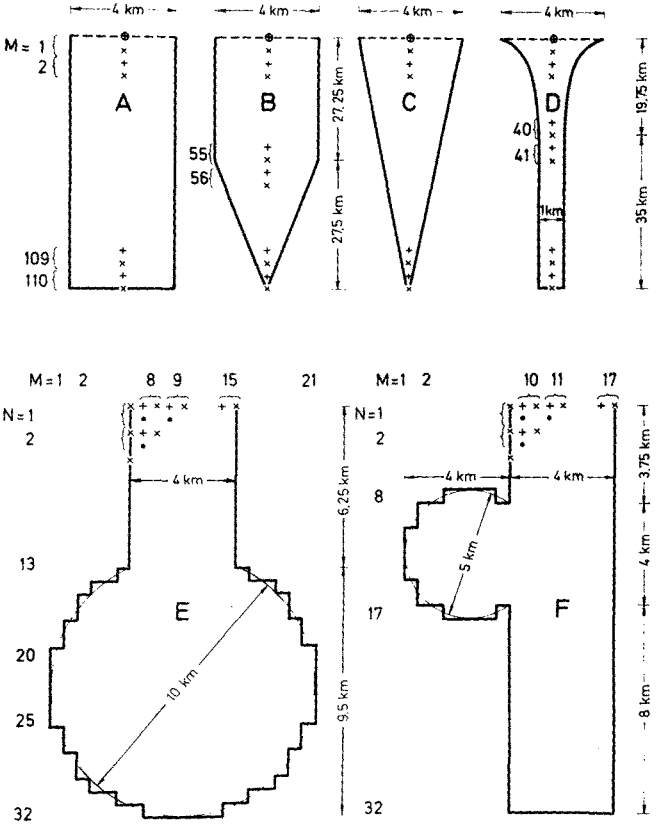

Fig. 3 Numerical grids for the estuaries

Sündermann

All models have the following scales:

$\Delta x = \Delta y = 500$ m	spatial grid distance between two similar computation points
$h = 15$ m	water depth
Models A to D: $\Delta t = 30$ sec Models E, F : $\Delta t = 25$ sec	time step

In each case, the computation were carried out until stationary conditions were achieved. The maximum time to reach this state was 5 tidal periods.

COMPARISON OF THE RESULTS

The numerous measurements and numerical results under consideration permit a very detailed comparison between the two methods. Within the limitations of this paper, only a representative selection can be given. Results will be given only to the extent where they extend those already reported at the Washington conference.

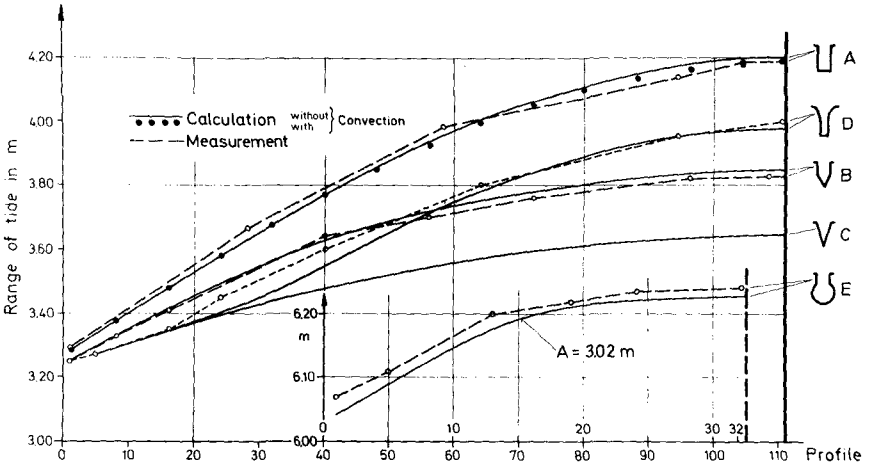

Fig. 4 Tidal ranges for different estuaries

Fig. 4 shows a comparison between the computed tidal amplitudes and the corresponding measured ones. The comparison is quite good. The maximum differences are of the order of a few centimeters; ever 50 % of the differences lie within measuring error. The convective terms were neglected in the equations of motion. Including these terms reduced the above differences. Fig. 5 shows a comparison between computed and measured tidal curves at cross-section 56 of estuary B (at the point of transition from rectangle to triangle) over several tidal periods. The agreement in both curves as regards form, amplitude and tidal duration is good.

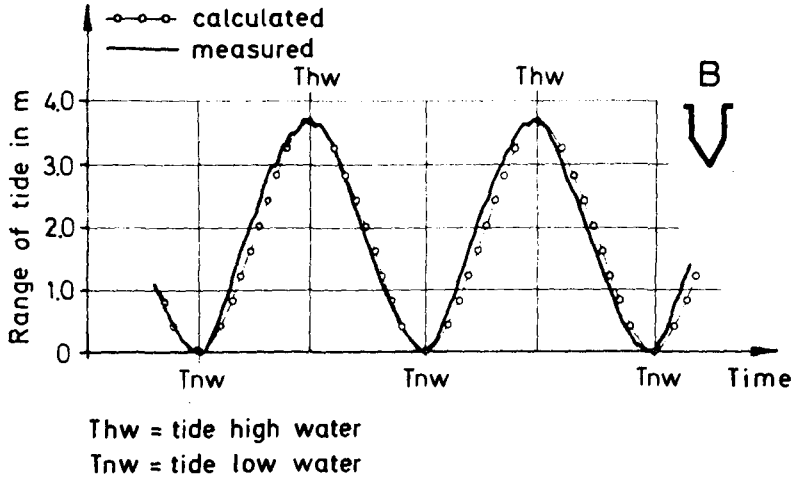

Fig. 5 Computed and measured tidal curve for the water elevation in cross-section 56 of estuary B

With estuary forms E and F we essentially wanted to compare the current structure in the whole model rather to make a detailed comparison of water level and current velocity. Fig. 6 shows a comparison between computed and measured current velocities over a tidal period. Flood and ebb curves are very similar; the agreement is adequate. Shown also are curves for profile 5 in model A. One can see that

the characteristic distribution of flood and ebb agree.

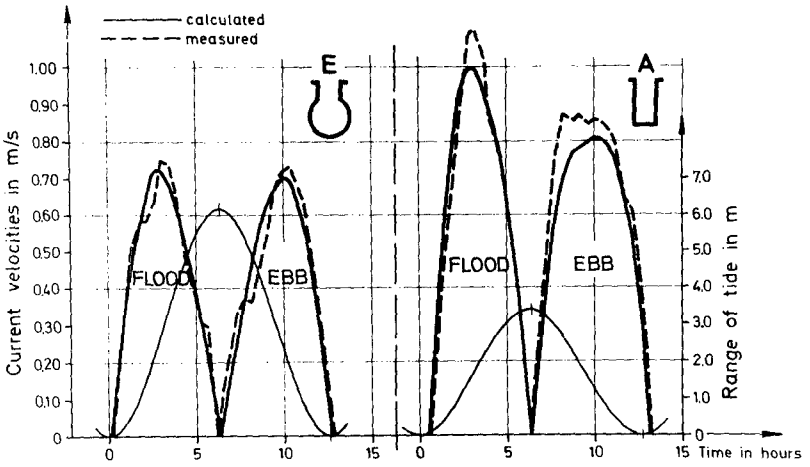

Fig. 6 Computed and measured current velocities during one tidal period in cross section 5 of estuaries A and E

Of particular interest is the comparison of the velocity structures for form E. One could expect that separation regions would form at the circular expansion areas especially at flood times. The development of these separation zones under nonstationary conditions is particularly instructive. Initial computations with the mathematical model however showed that, except during a short time interval at slack water, no separation occurred. It seems that sufficient conservation of vorticity was not achieved in this model. This failure could be eliminated by the inclusion of the convective terms. With help of synchronous output of the measured velocities, we were able to simulate and compare a classical vortex. The comparison was good.

Figures 7 (a) to (d) show the computed velocity fields (marked with arrows) with the corresponding fields in the hydraulic model for various sequential tidal phases. In Fig. 7 (a) the vortex has just started to be formed near

the expansion region. Fig. 7 (d) shows the vortex at its largest extension at the start of the ebb currents. It is just beginning to disintegrate. A boundary layer flow diminishes it in the central region of the estuary.

(a)

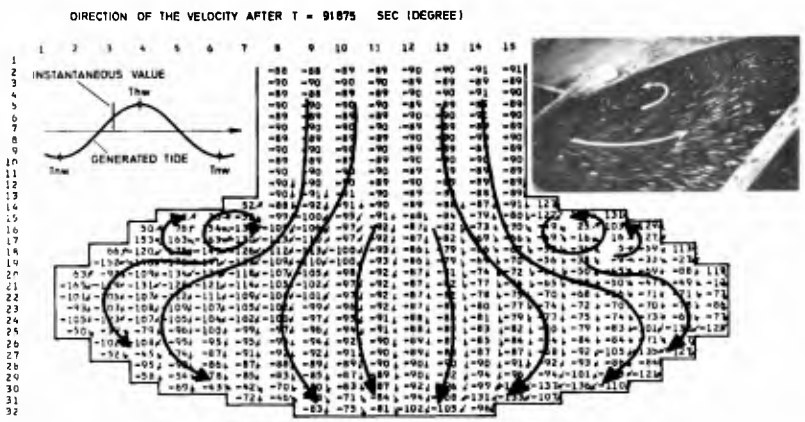

(b)

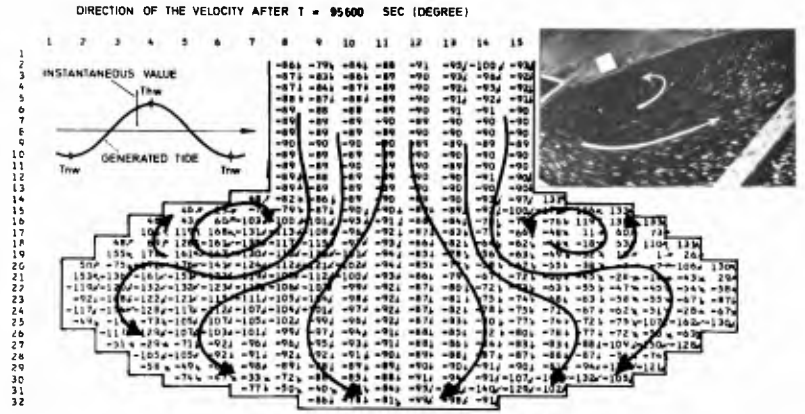

Fig. 7 a,b Computed and measured velocity fields in case of estuary E for two tidal phases separated by time interval of 1/12 tidal period

(c)

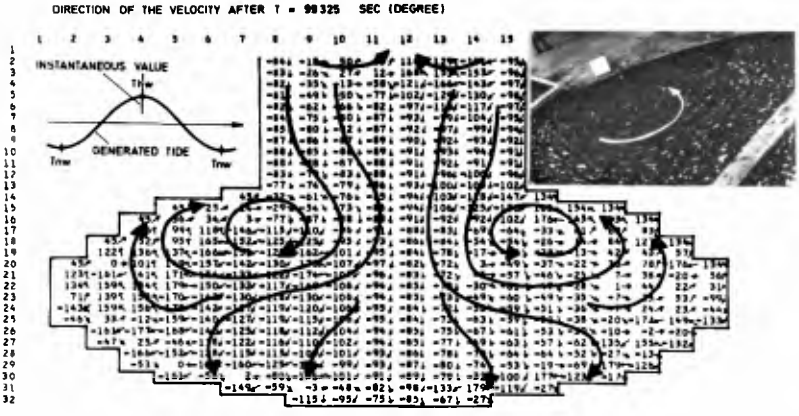

(d)

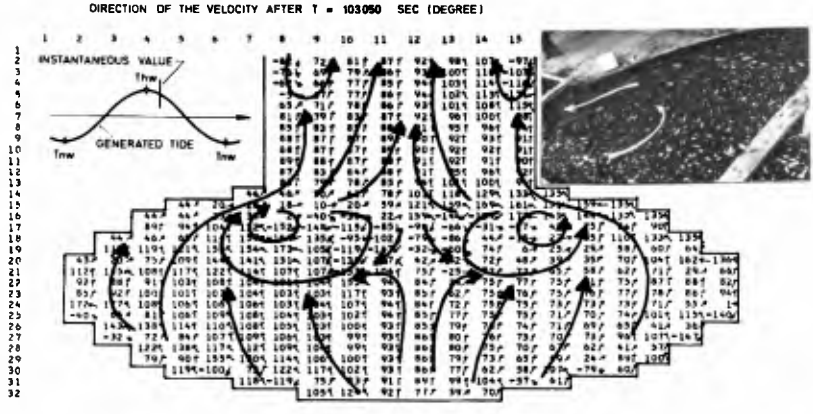

Fig. 7 c,d Computed and measured velocity fields in case of estuary E for two tidal phases seperated by time interval of 1/12 tidal period

The possible effect of the coriolis force in the more 2-dimensional formes E and F as also in nature is of particular interest. Computations showed that, although the water level distribution did not change significantly, the horizontal velocity structure at particular phases of the tide, were altered significantly. As an example, Fig. 8 shows the current distribution at the same time as in Fig. 7(d) but including the coriolis effect. One may see the large change - in particular the unsymmetric distribution of the direction field.

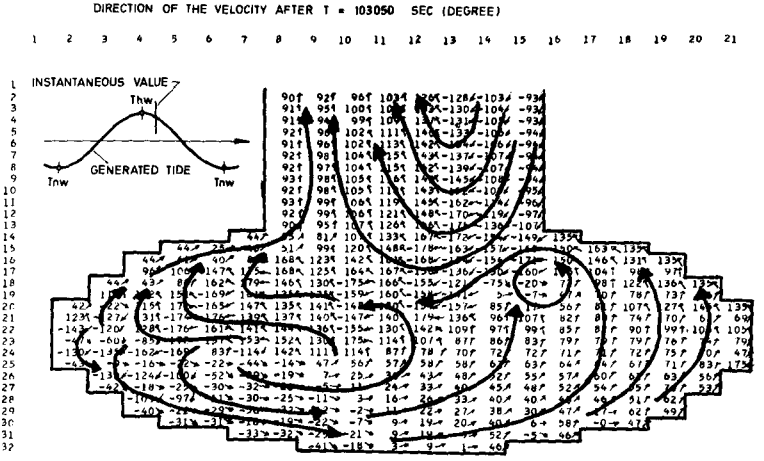

Fig. 8 Velocity fields as in Fig. 7 (d) including the coriolis force

Figures 9 (a) and (b) show two current situations for estuary F. Two eddies have formed in the expansion area. Just before slack water the whole circular basin consists one large vortex. To be noted is the good comparison as regards the area of deformation. Just at this time the eddy also extends somewhat into the rectangular canal and causes a deflection of the streamlines.

(a)

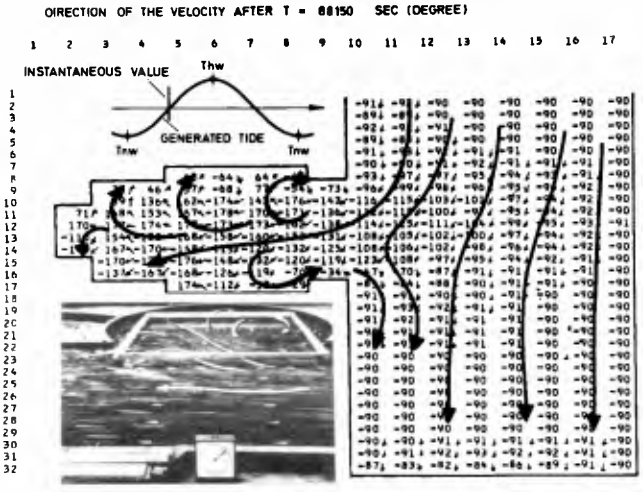

(b)

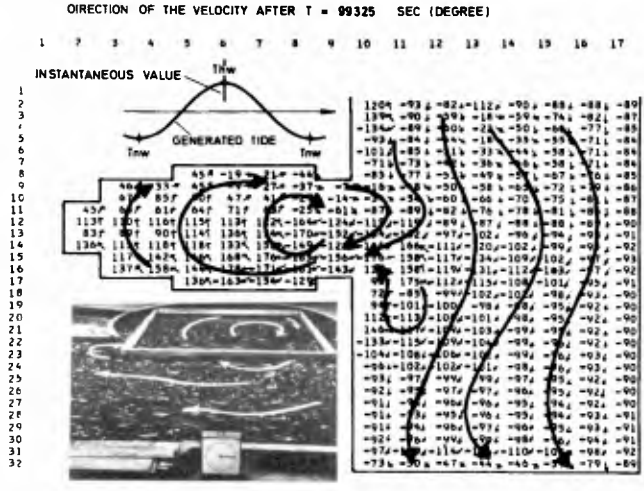

Fig. 9 a,b Computed and measured velocity fields in case of estuary F for two tidal phases separated by a time interval of 1/4 tidal period

CONCLUSIONS

Seen overall, the results of the hydraulic and mathematical model compare well for the tidal waves considered. The essential characteristics of the currents have been qualitatively reproduced. The quantitative comparison shows, nearly without exception, only small differences between measured and computed quantities. This is especially true for the simple forms A and B. For these forms the hydraulic model can be substituted by an equivalent mathematical one.

No detailed quantitative comparison have yet been made for the estuaries E and F. The development of the current system at particular tidal phases is however so similar in the two systems that, in general, the two methods can be considered equivalent.

On the basis of measurement we have some to the general important conclusion that for the HN models the convective terms could not be neglected when analyzing tidal phenomena. On the other hand, the insertion of a simple quadratic friction term with a constant friction parameter seemed adequate. A comparison of the computations, with and without the coriolis force, showed that for two-dimensional regions large differences can occur in the current patterns although the surface elevations are not appreciably changed.

The results presented here, indicate that it would be worthwhile to improve the mathematical model. Thus, we intend to include the vertical structure in future and, by using a variable spaced difference net, to be able to simulate the real geometry to a higher degree of accuracy. It would then seem possible to replace the hydraulic experiment, for cases similar to the ones examined by a HN model. The hydraulic model can, on the other hand, be utilized in those complex instances where satisfactory mathematical formulations do not as yet exist.

REFERENCES

[1] Vollmers, H.
Sündermann, J.
Tidal waves in schematic estuaries,
Proceedings of the 12th Coastal
Engineering Conference, Vol III,
Washington 1970

[2] Sündermann, J.
Die hydrodynamisch-numerische
Berechnung der Vertikalstruktur
von Bewegungsvorgängen in Kanälen
und Becken
Mitt. Inst. f. Meereskunde,
Universität Hamburg, Nr. 19, 1971

[3] Hansen, W.
Hydrodynamical methods applied to
oceanographic problems
Mitt. Inst. f. Meereskunde,
Universität Hamburg, Nr. 1, 1962

CHAPTER 140

TIDAL HYDRAULICS IN THE CAÑO MACAREO

Konstantin Zagustin, Ph.D.[1], Frank D. Masch, Ph.D., P.E.[2],
and Robert J. Brandes, Ph.D.[3]

ABSTRACT

Investigations have been undertaken to predict the tidal amplitudes and current patterns at the mouth of the Caño Macareo in Venezuela to the Atlantic Ocean. These studies were undertaken as part of a more comprehensive feasibility study sponsored by the Corporacion Venezolana de Guayana for location and orientation of a 60-foot deep navigation channel and for the design of related channel appurtenances. In the analysis, three simulation methods were employed conjunctively. These included one- and two-dimensional mathematical models and an electro analogical model. Model results have been supplemented with prototype data and other information based on field observations.

Analyses provided for determination of tidal hydraulics, first, to establish baseline conditions as they presently exist, and second, to evaluate the effects of various proposed channel alignments. The two-dimensional mathematical model and the electro analogical model both provided for inclusion of a pronounced longshore sea current which plays an important role in determining current patterns at the mouth of the Macareo. In addition, the use of a berm to modify the sea current in the vicinity of the channel entrance was investigated.

---

[1]Consulting Engineer, Associate Professor and Head, Hydraulic Laboratory, Central University of Venezuela.

[2]Principal, Water Resources Engineers, Inc., Austin, Texas.

[3]Senior Engineer, Water Resources Engineers, Inc., Austin, Texas.

INTRODUCTION

This paper describes a model study performed on the Caño Macareo estuary, a branch of the Orinoco River delta in Venezuela, Figure 1, to determine the best location for a navigation channel and the additional structures necessary to provide minimum maintenance dredging. The study is part of a total project being developed by the Corporacion Venezolana de Guayana to provide navigation for large vessels to the industrial area of Ciudad Guayana located on the Orinoco River. To minimize dredging of the 60-foot deep channel, the plan foresees the closure of the Caño Macareo 180 kilometers upstream of its mouth at "Boca de Serpientes", with provisions for inclusion of a lock system to cope with differences in water levels. This scheme will reduce sediment deposition along the channel while at the mouth of the river the tidally-generated currents should be sufficiently strong to keep sediments moving.

The model analyses, both mathematical and electro analogical, were undertaken to predict the flow behavior through the mouth of the Caño Macareo after the river is closed and a constant discharge is released to prevent salinity intrusion. Studies were also performed to determine circulation patterns produced by tidal influence in the vicinity of the river's mouth with the proposed channel and its appurtenances in place.

UNIDIMENSIONAL ANALYSIS

To determine the river discharge at ebb and flood conditions at the mouth, a one-dimensional numerical analysis of the tidal propagation along the river was made. Field work was undertaken to determine the cross-sections of the river at intervals of three kilometers, and equivalent rectangular cross-sections were computed for use in the numerical procedure. A typical tide was selected and computations were made for the natural conditions, first, to make a preliminary check on the available field data, and second, to adjust the friction factor and other parameters in the problem. When this initial step was completed a maximum typical

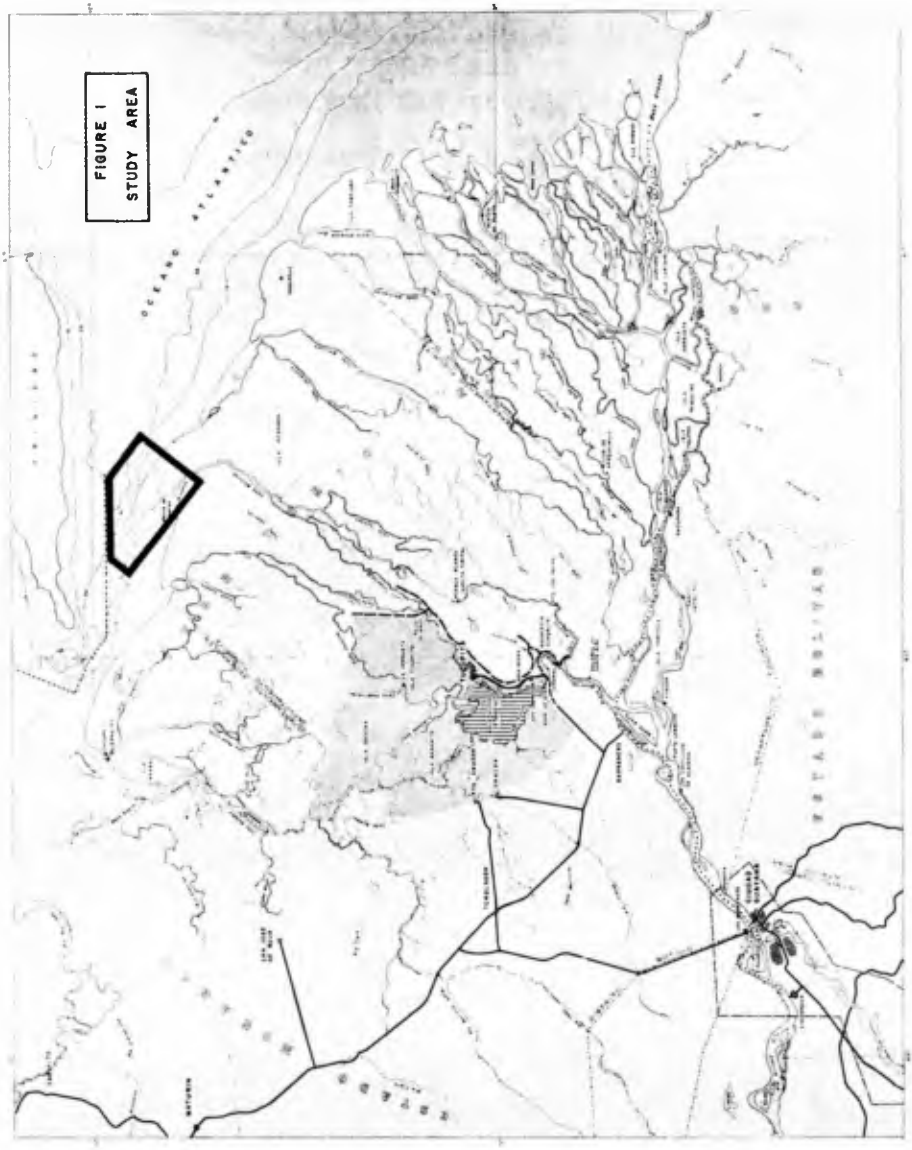
FIGURE 1
STUDY AREA
OCEANO ATLANTICO
ESTADO BOLIVAR

tide was used to run the one-dimensional numerical model for the case with the river closed 180 kilometers from its mouth. The results, as shown in Figures 2 and 3, provided boundary conditions in the form of the time-history of discharge and water surface elevation for use in the two-dimensional models of the river mouth area.

BIDIMENSIONAL ANALYSIS

Two-dimensional solutions of the flow field were obtained by two methods; a numerical scheme applied by Masch and Brandes and Zagustin's electro analogical model. The two-dimensional numerical solution used took into account all of the pertinent variables in the problem including the water level variation with time, spatial discharge variations with time, sea currents, depth variations, friction factors, and fresh water discharge. While the numerical procedure used provides a sufficiently accurate description of the physical processes involved, the spatial resolution of results, however, is somewhat limited by the grid size used because of computer time and storage requirements. The analogical solution, on the other hand, is restricted to ideal flow and cannot easily account for time variations, but can provide indications of the streamline patterns for ebb, and flood flows. These two conditions are important in the analysis of sediment motion, particularly since it was found from the one-dimensional results that there was a relatively long period when the flow characteristics remained nearly constant at each condition. The fact that depth variations could be reproduced accurately and that streamline configurations could be obtained as needed, provided additional complementary information for use with the numerical solution.

ELECTRO ANALOGICAL MODEL

The electrical analogy for determination of the streamline patterns is based on the similarity between eqs. (1) and (2). Equation (1) represents

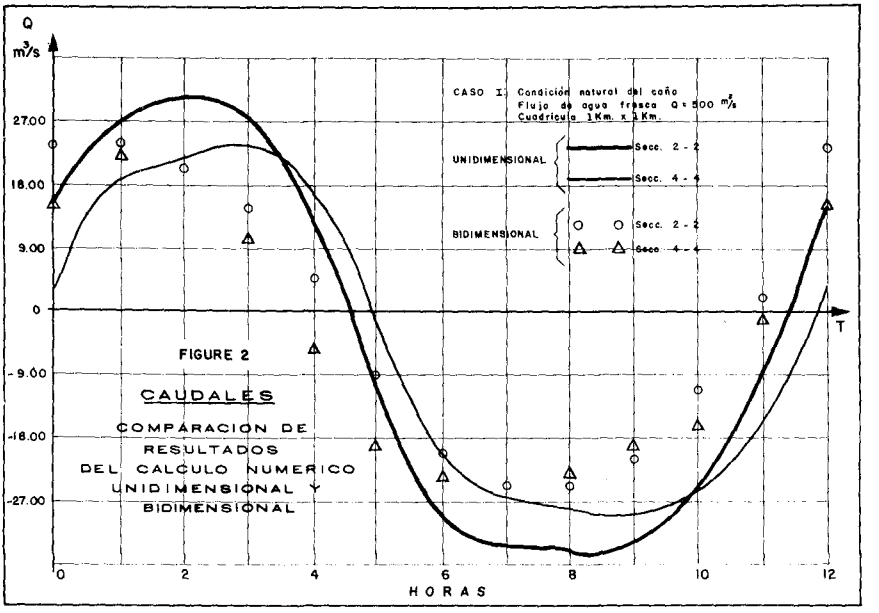

FIGURE 2

CAUDALES

COMPARACION DE RESULTADOS DEL CALCULO NUMERICO UNIDIMENSIONAL Y BIDIMENSIONAL

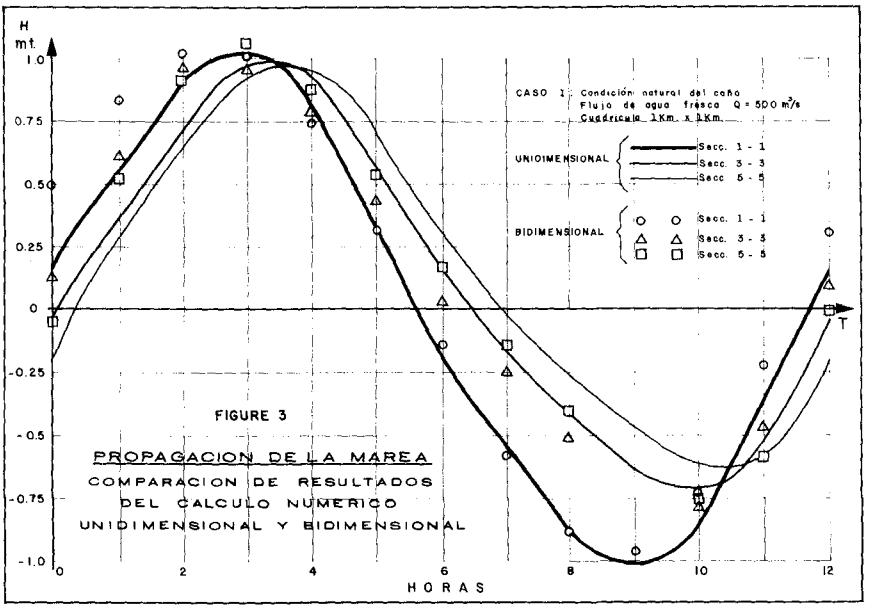

FIGURE 3

PROPAGACION DE LA MAREA

COMPARACION DE RESULTADOS DEL CALCULO NUMERICO UNIDIMENSIONAL Y BIDIMENSIONAL

the flow of an ideal irrotational fluid in a variable depth field and is given as

$$\frac{\partial}{\partial x}\left(\frac{1}{d_{xy}}\frac{\partial \Psi}{\partial x}\right) + \frac{\partial}{\partial y}\left(\frac{1}{d_{xy}}\frac{\partial \Psi}{\partial y}\right) = 0 \qquad (1)$$

where d_{xy} is the depth at a point (x, y) and Ψ is the stream function. The equation of electric potential in a uniformly conducting field with variable thickness, t_{xy}, is given as

$$\frac{\partial}{\partial x}\left(t_{xy}\frac{\partial e}{\partial x}\right) + \frac{\partial}{\partial y}\left(t_{xy}\frac{\partial e}{\partial y}\right) = 0 \qquad (2)$$

where e is the electric potential.

To have a correlation between streamline and equi-potential lines, the analogic model must be built with a thickness of conductor material inversely proportional to the depth. The analogic model built for this study utilized Teledeltos paper as a conducting medium, and hence the number of layers of the Teledeltos paper was maximum in the areas of low depth and minimum in areas of high depth. The applied voltage was proportional to the flow discharge in the river and the magnitude of the sea current established for each condition.

TWO-OIMENSIONAL HYDROOYNAMIC MOOEL

Mathematical characterization of the hydrodynamics of a two-dimensional estuarine system requires the simultaneous solution of the dynamic equations of motion and the unsteady continuity equation. The theoretical basis for these equations has been dealt with in detail in the literature and will not be repeated here.

Neglecting the convective acceleration terms but including wind stresses and the Coriolis acceleration, the equations of motion applicable

to tidal flow can be written as

$$\frac{\partial q_x}{\partial t} - \Omega q_y = - g d \frac{\partial h}{\partial x} - f q q_x + K V_w^2 \cos \Theta \qquad (3)$$

$$\frac{\partial q_y}{\partial t} + \Omega q_x = - g d \frac{\partial h}{\partial y} - f q q_y + K V_w^2 \sin \Theta \qquad (4)$$

The equation of continuity for unsteady flow can be expressed as

$$\frac{\partial q_x}{\partial x} + \frac{\partial q_y}{\partial y} + \frac{\partial h}{\partial t} = 0 \qquad (5)$$

In eqs. (3), (4) and (5), q_x and q_y are the vertically integrated flows per foot of width at time t in the x and y directions, respectively (x and y taken in the plane of the surface area); h is the water surface elevation with respect to mean sea level (msl) as datum; d is the depth of water at (x, y, t) and is equal to (h - z) where z is the bottom elevation with respect to msl; $q = (q_x^2 + q_y^2)^{1/2}$; V_w is the wind speed at a specified elevation above the water surface; Θ is the angle between the wind velocity vector and the x-axis; K is the non-dimensional wind stress coefficient; and Ω is the Coriolis parameter equal to $2 \omega \sin \Phi$ where ω is the angular velocity of the earth taken as 0.73×10^{-4} rad/sec and Φ is the latitude. The bed resistance coefficient, f, is computed from the Manning equation as $[gn^2/2.21\ d^{7/3}]$ where n is the Manning roughness coefficient. The Manning coefficient can be estimated either from the Stickler Formula knowing spatial and point distributions of sediments or it can be determined empirically from comparisons of measured and computed tide and velocity histories.

The numerical solution involved an explicit computational scheme in which the two-dimensional vertically integrated equations of motion and the unsteady continuity equation were solved over a rectangular grid of square cells used to represent the physiography of the system and to

specify boundary conditions. Two different grid networks were used to describe the study area at the mouth of the Caño Macareo. Resolutions of one and one-half kilometers were used in representing the area from deep water up to the point of river closure, Figures 4 and 5, respectively. The models were excited with representative tides in deep water, a longshore sea current over the continental shelf, and a constant release at the most upstream reach of the river.

The time histories of water surface elevation and component velocities for one tidal cycle were obtained for each water cell in each of the grid representations including the adjacent shallow areas subject to flooding at high tide. By scanning these results, velocities in each cell were resolved into vectors and then plotted at flood, ebb and slack conditions and compared with results of the electro analogical model.

DISCUSSION

The two-dimensional solutions of the tidal hydrodynamics with the numerical and the electro analogical procedures were carried out initially for natural conditions without channel improvements using boundary conditions determined from the one-dimensional analysis, Figures 2 and 3, and the available field data on the longshore sea current. The results obtained, also shown in Figures 2 and 3, compared satisfactorily with the field measurements of velocity magnitudes and directions at selected cross sections.

For the numerical solution with the one kilometer grid, a spiral type channel was included to take into account the storage effects of the river up to the point of closure. The depth and length of the spiral part of the channel was obtained by trial using the one-dimensional results as a reference. The magnitude of the sea current was divided into three parts and a variation of each magnitude with time was specified. In Figures 6 and 7, the comparison of Masch and Brandes' numerical computations and Zagustin's analogical results is presented for ebb and flood tide conditions.

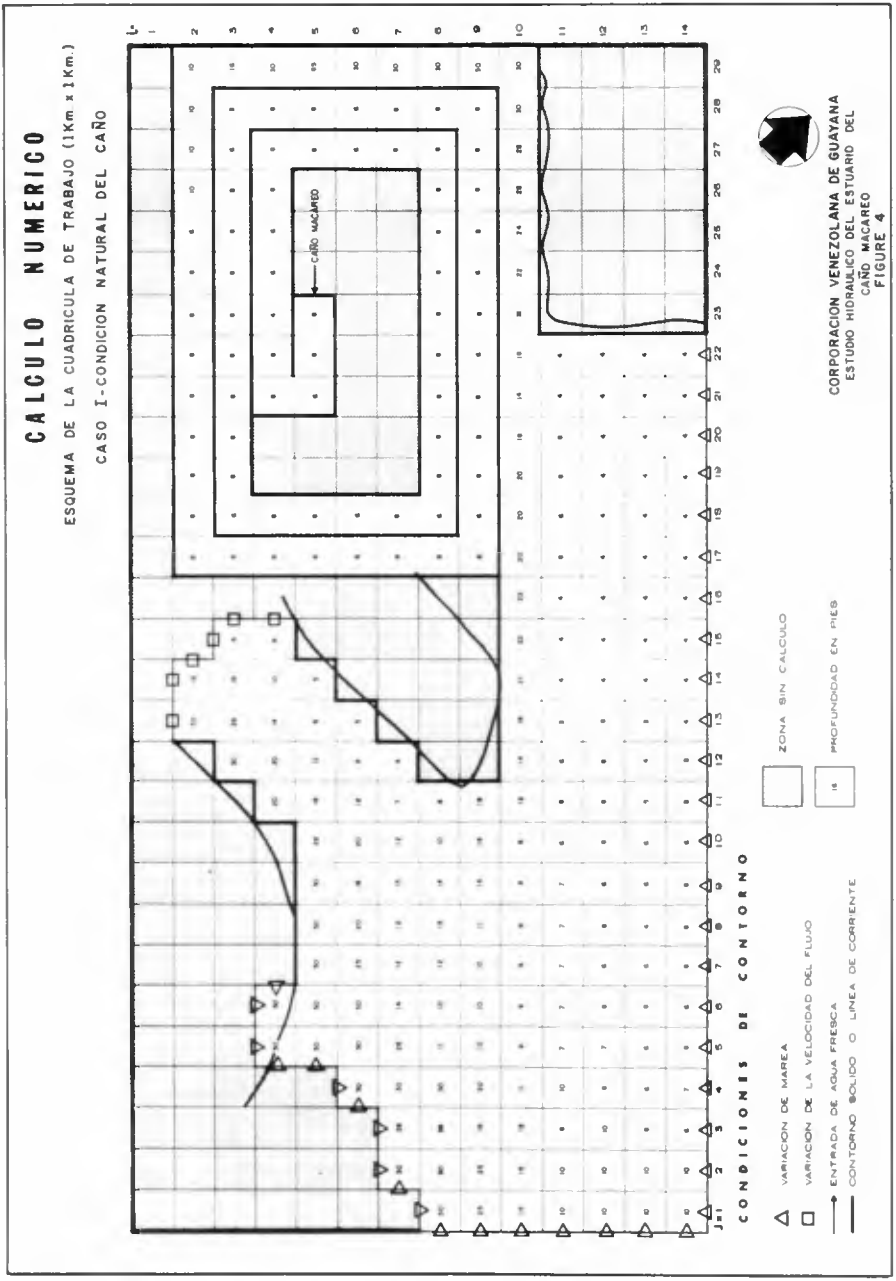
CALCULO NUMERICO
ESQUEMA DE LA CUADRICULA DE TRABAJO (1Km x 1Km.)
CASO I-CONDICION NATURAL DEL CAÑO
CAÑO MACAREO
CONDICIONES DE CONTORNO
VARIACION DE MAREA
VARIACION DE LA VELOCIDAD DEL FLUJO
ENTRADA DE AGUA FRESCA
CONTORNO SOLIDO O LINEA DE CORRIENTE
ZONA SIN CALCULO
PROFUNDIDAD EN PIES
CORPORACION VENEZOLANA DE GUAYANA
ESTUDIO HIDRAULICO DEL ESTUARIO DEL
CAÑO MACAREO
FIGURE 4

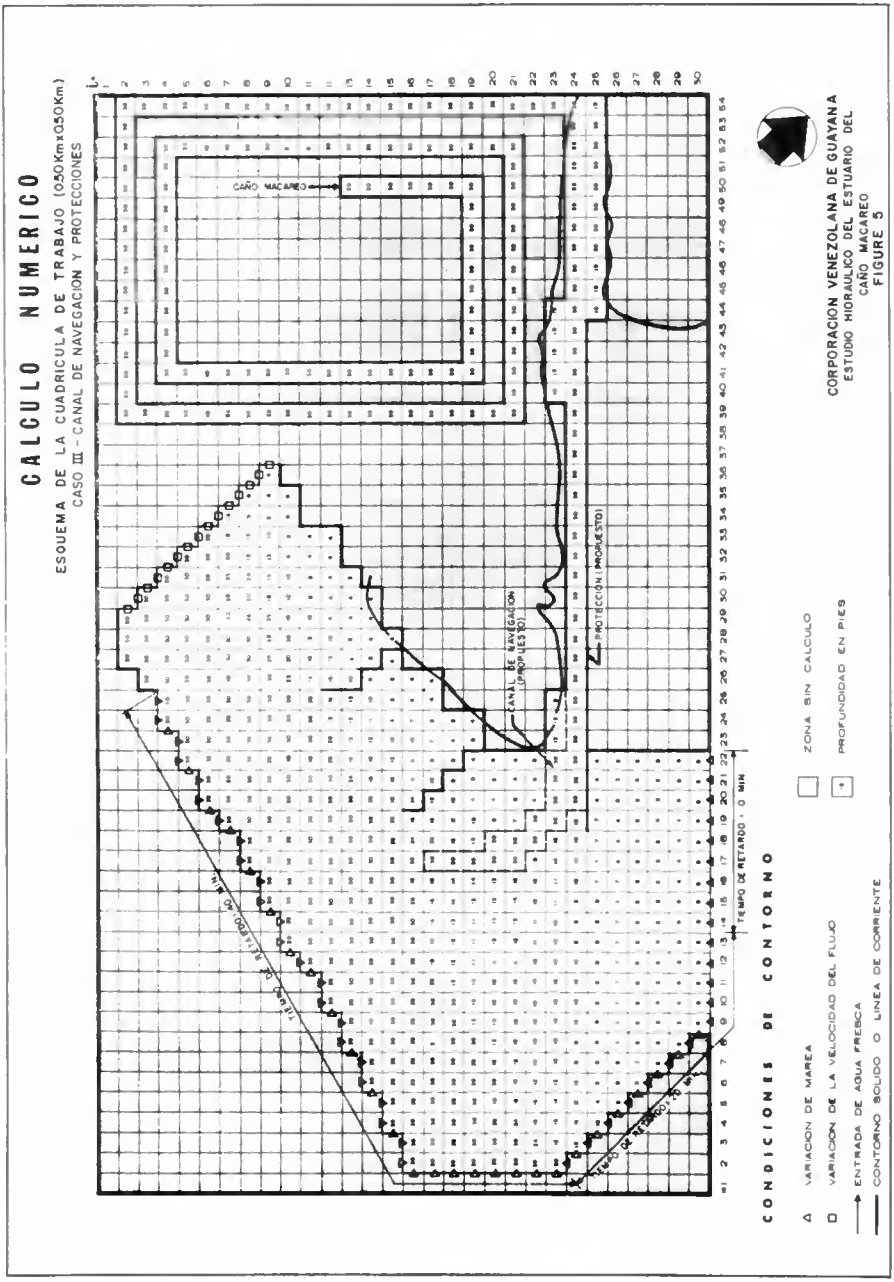
CALCULO NUMERICO
ESQUEMA DE LA CUADRICULA DE TRABAJO (0.50Km x 0.50Km.)
CASO III - CANAL DE NAVEGACION Y PROTECCIONES
CAÑO MACAREO
CANAL DE NAVEGACION (PROPUESTO)
PROTECCION (PROPUESTO)
TIEMPO DE RETARDO 1.0 MIN
CONDICIONES DE CONTORNO
VARIACION DE MAREA
VARIACION DE LA VELOCIDAD DEL FLUJO
ENTRADA DE AGUA FRESCA
CONTORNO SOLIDO O LINEA DE CORRIENTE
ZONA SIN CALCULO
PROFUNDIDAD EN PIES
CORPORACION VENEZOLANA DE GUAYANA
ESTUDIO HIDRAULICO DEL ESTUARIO DEL CAÑO MACAREO
FIGURE 5

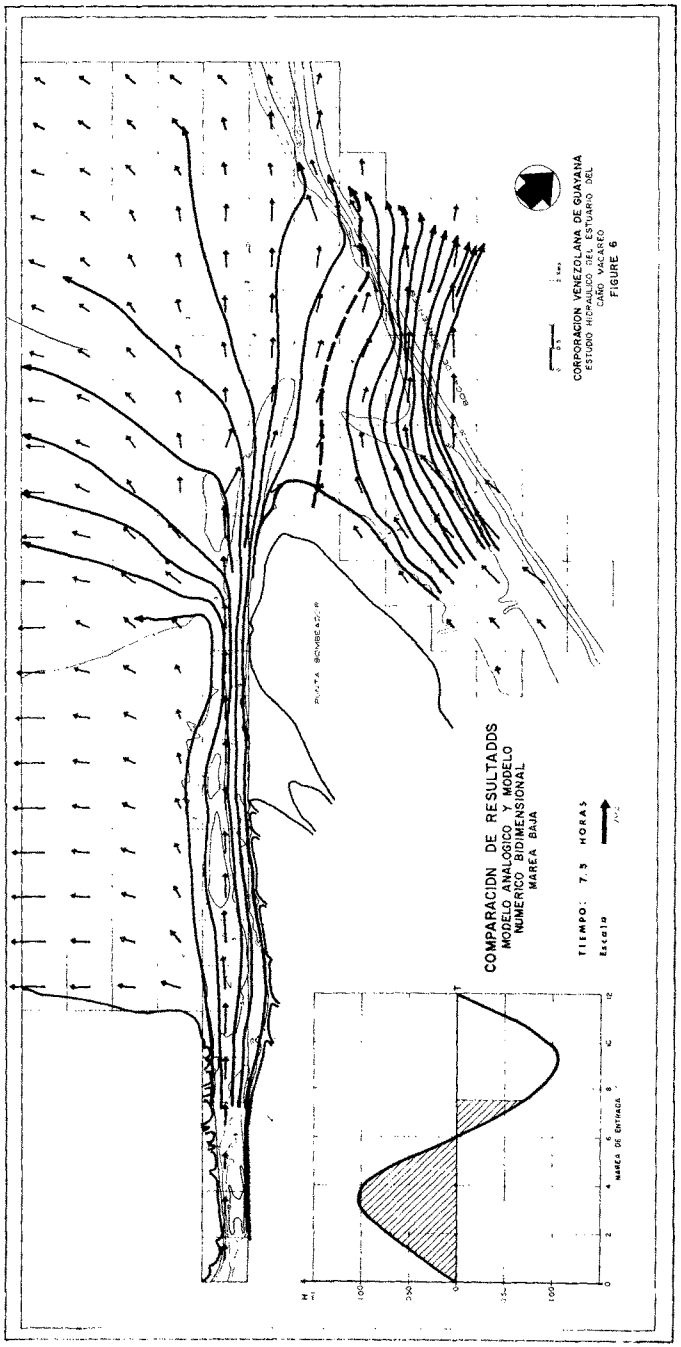
CORPORACION VENEZOLANA DE GUAYANA
ESTUDIO HIDRAULICO DEL ESTUARIO DEL
CAÑO MACAREO
FIGURE 6
COMPARACION DE RESULTADOS
MODELO ANALOGICO Y MODELO
NUMERICO BIDIMENSIONAL
MAREA BAJA
TIEMPO: 7.5 HORAS
Escala
MAREA DE ENTRADA
PLANTA BOMBEADORA

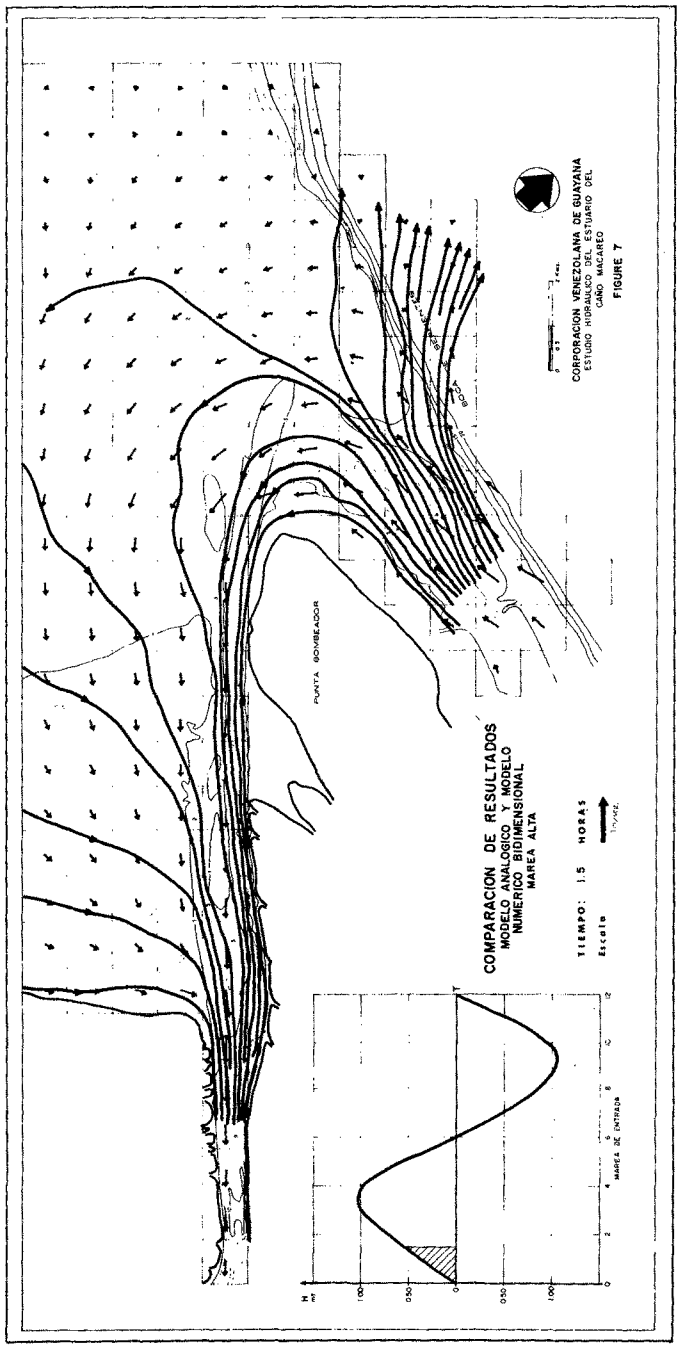
COMPARACION DE RESULTADOS
MODELO ANALOGICO Y MODELO
NUMERICO BIDIMENSIONAL
MAREA ALTA
TIEMPO: 1.5 HORAS
Escala
PUNTA BOMBEADOR
MAREA DE ENTRADA
CORPORACION VENEZOLANA DE GUAYANA
ESTUDIO HIDRAULICO DEL ESTUARIO DEL
CAÑO MACAREO
FIGURE 7

Partially as a result of the initial runs, it was decided that a lateral protection was required to maintain most of the channel length in the estuary free of sediment. Several combinations of barriers were tested to protect the channel at its exit to the sea. In these tests, the one-half kilometer grid was used with the numerical computations and a more detailed electro analogical model was also built. In both cases a more exact representation of the sea current was taken into account. Figures 8 through 11 show velocity patterns at flood, ebb and slack tide conditions as obtained from the models for a given geometrical configuration of the proposed barriers and channel alignment. After studying several combinations of berms, sea current barriers and channel alignment, a recommended layout, Figure 12, was selected based on minimizing sediment transport problems but still maintaining manageable velocities from the standpoint of navigation.

CONCLUSIONS

The numerical and analogical simulation models described in this paper have been shown to provide the capability for analyzing estuarial circulation patterns resulting from alternative channel configurations. The models which have been applied to the Caño Macareo, an estuary of the Rio Orinoco, were calibrated using data collected in the field and results obtained from a one-dimensional method of analysis. Several geometric configurations of channel alignment were investigated as well as different berm lengths and locations parallel to the channel and alongshore. For each configuration, velocity vectors were determined and then evaluated to select a recommended configuration to minimize sediment problems.

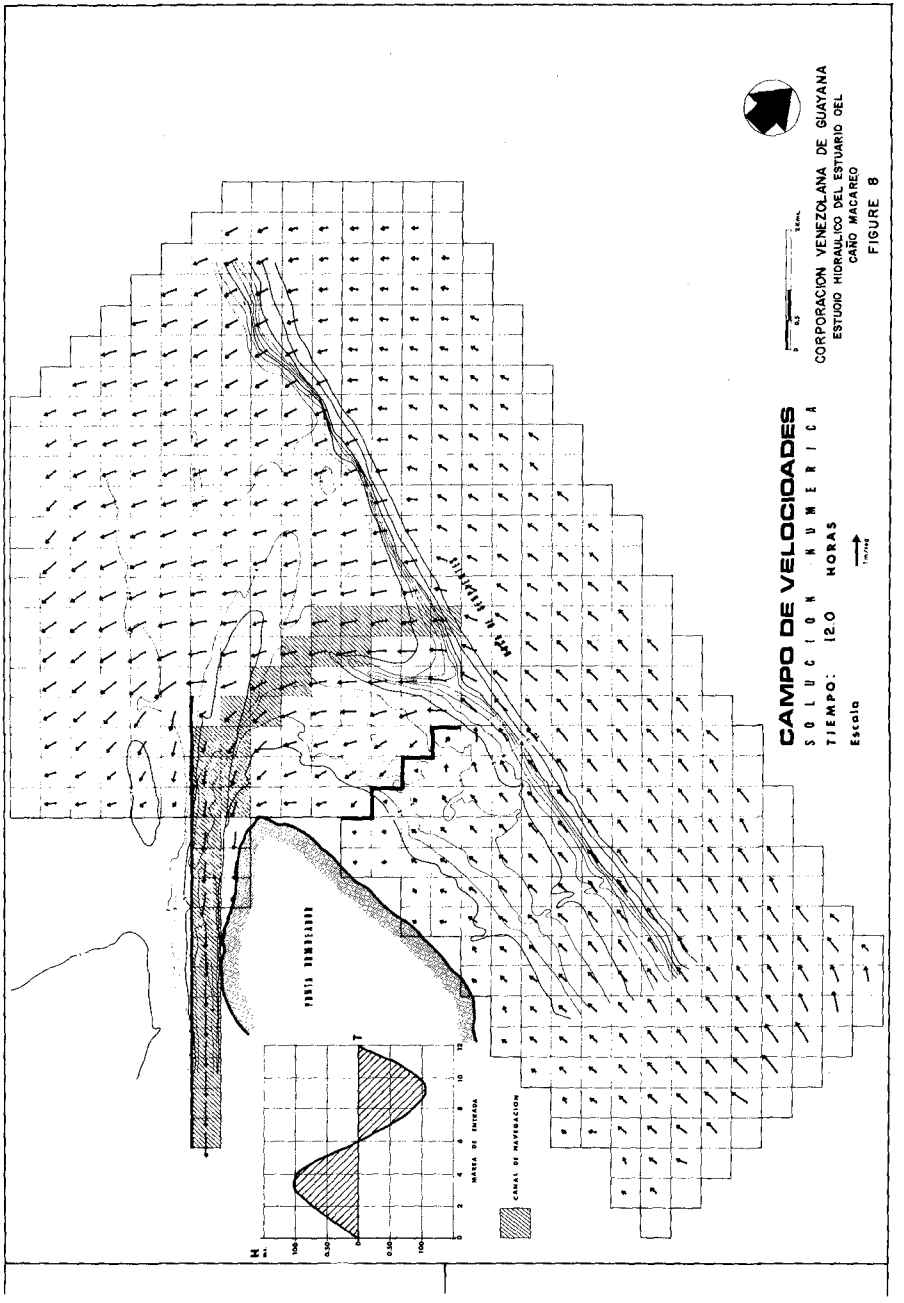
CAMPO DE VELOCIDADES
SOLUCION NUMERICA
TIEMPO: 12.0 HORAS
Escala
CORPORACION VENEZOLANA DE GUAYANA
ESTUDIO HIDRAULICO DEL ESTUARIO DEL
CAÑO MACAREO
FIGURE 8
CANAL DE NAVEGACION
MAREA DE ENTRADA

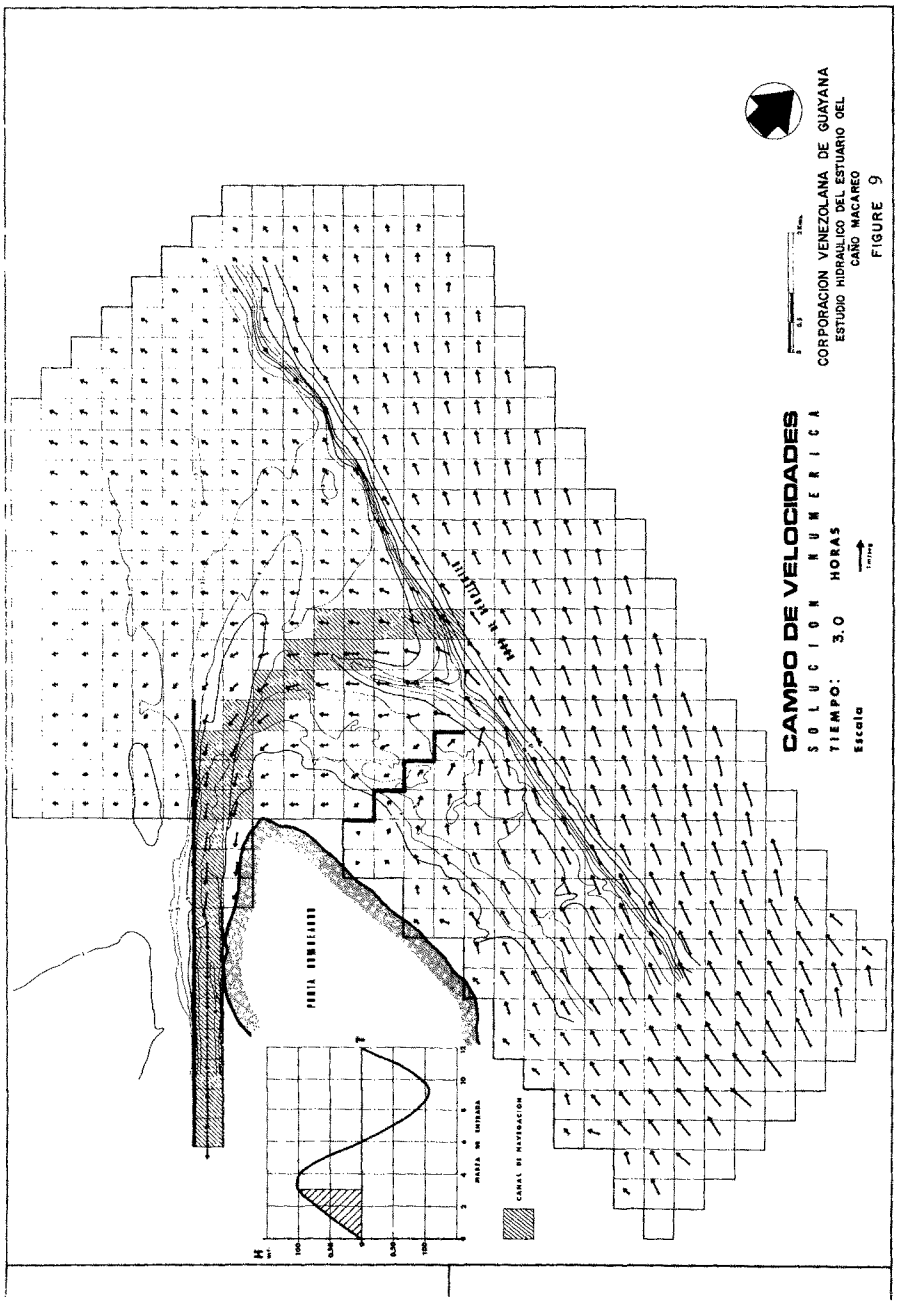
CAMPO DE VELOCIDADES
SOLUCION NUMERICA
TIEMPO: 3.0 HORAS
Escala
CORPORACION VENEZOLANA DE GUAYANA
ESTUDIO HIDRAULICO DEL ESTUARIO DEL
CAÑO MACAREO
FIGURE 9
PUNTA SOMBRERO
CANAL DE NAVEGACION

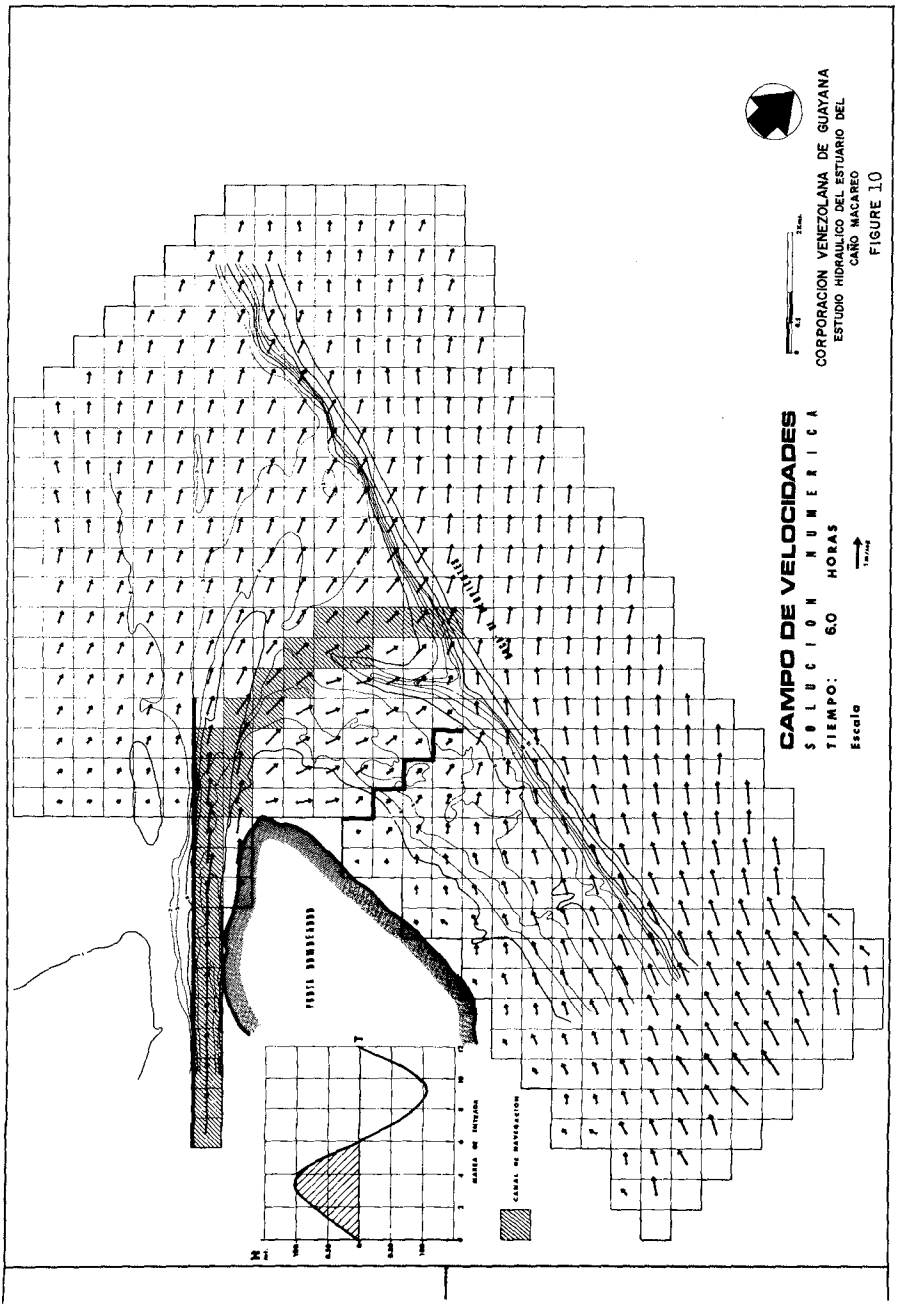
CAMPO DE VELOCIDADES
SOLUCION NUMERICA
TIEMPO: 6.0 HORAS
Escala
CORPORACION VENEZOLANA DE GUAYANA
ESTUDIO HIDRAULICO DEL ESTUARIO DEL
CAÑO MACAREO
FIGURE 10
CANAL DE NAVEGACION

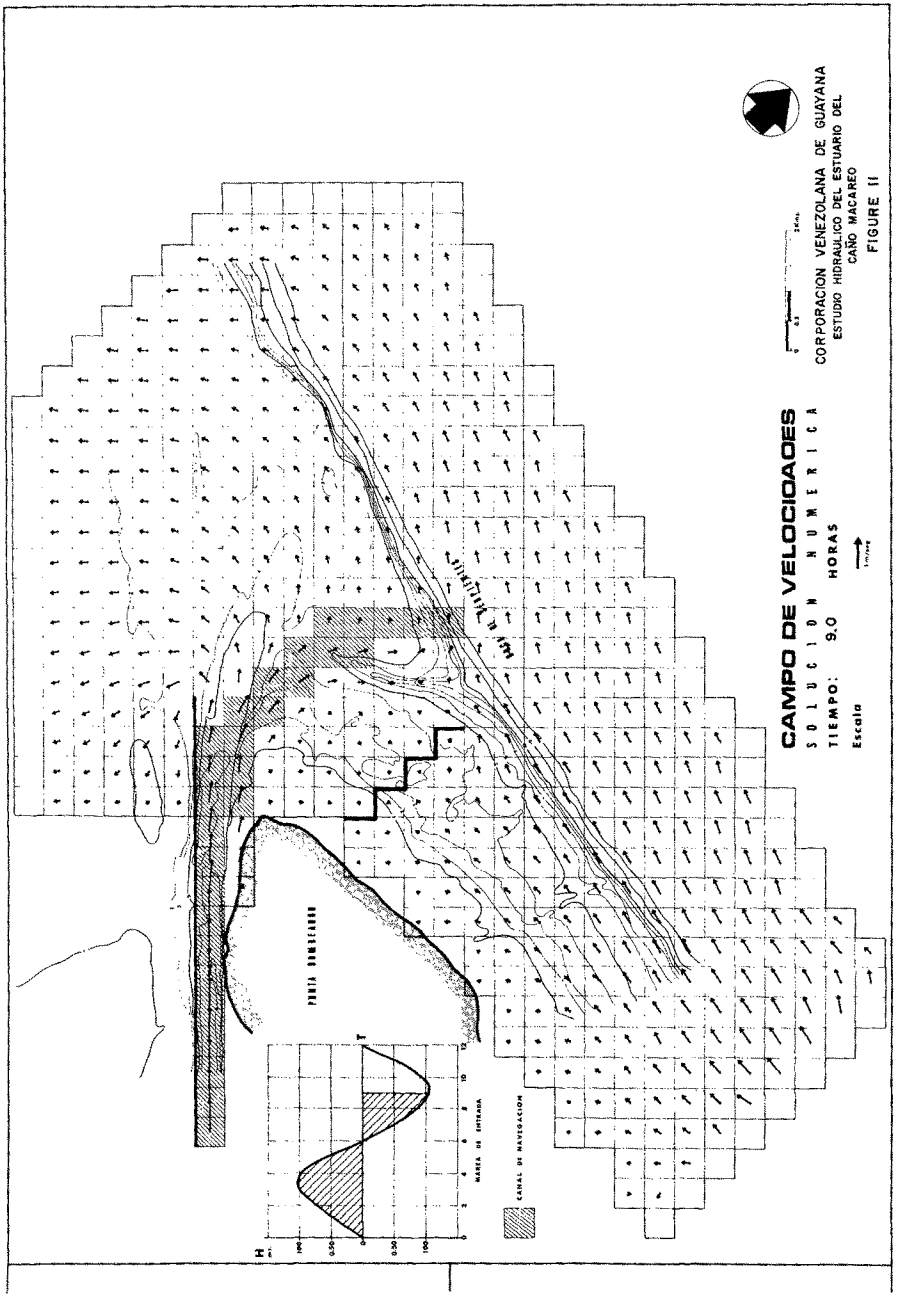
CAMPO DE VELOCIDADES
SOLUCION NUMERICA
TIEMPO: 9.0 HORAS
Escala
CORPORACION VENEZOLANA DE GUAYANA
ESTUDIO HIDRAULICO DEL ESTUARIO DEL
CAÑO MACAREO
FIGURE 11
PUNTA BARRIGUDA
CANAL DE NAVEGACION

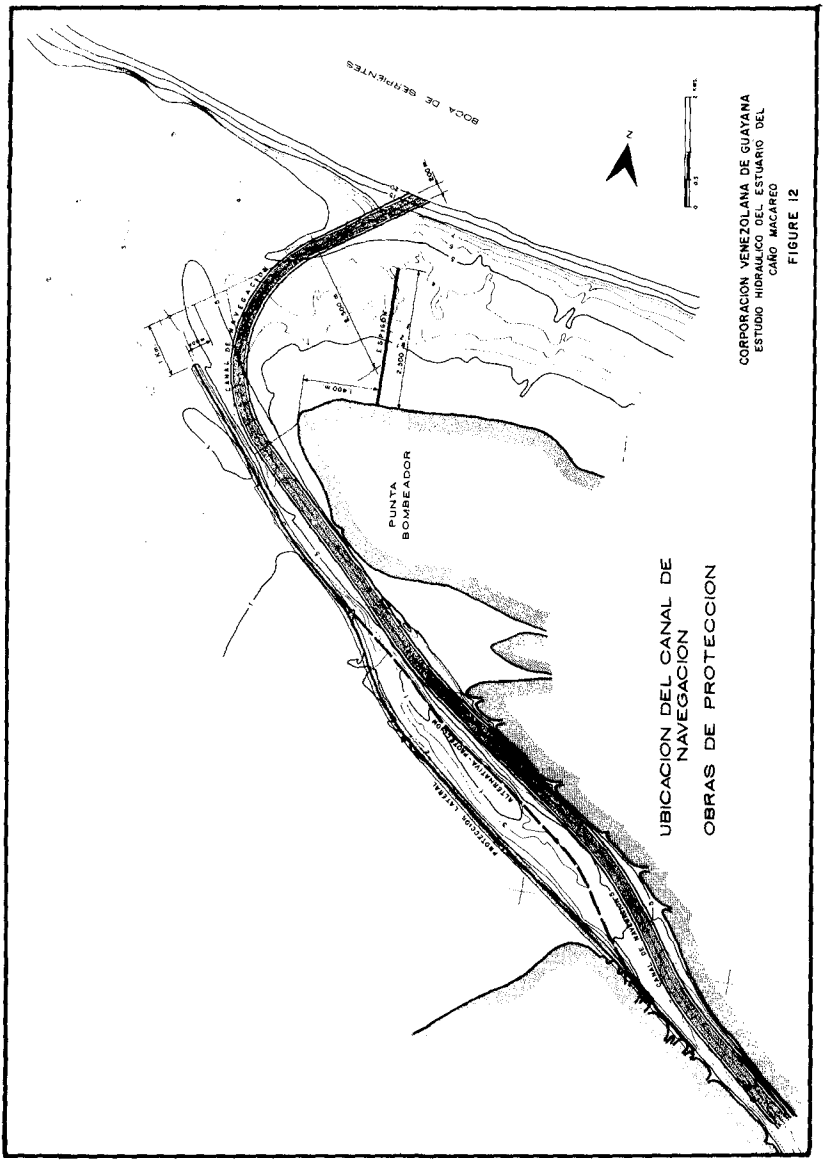
BOCA DE SEDIMENTES
PUNTA BOMBEADOR
UBICACION DEL CANAL DE NAVEGACION
OBRAS DE PROTECCION
CORPORACION VENEZOLANA DE GUAYANA
ESTUDIO HIDRAULICO DEL ESTUARIO DEL CAÑO MACAREO
FIGURE 12

CHAPTER 141

ELBE TIDAL MODEL WITH MOVABLE BED

by
Hans Vollmers[1] and Egon Giese[2]

ABSTRACT

The Bundesanstalt für Wasserbau (BAW) was charged to investigate an estuary tidal model of the Elbe-river (North Sea). The model, fitted with a movable bed, serves for special research with regard to suitable actions for the enlargement and maintenance of the main navigable channel in the sea area.

Because in tidal estuaries the interaction of fluid and solid material is extremely unknown, the investigation was undertaken to find out the arising morphological changes, only caused by tidal currents, considering structure or dredging works present or planned in prototype. The procedure seems advantageous and a better way as speculative interpretations of sediment movements, derived from flow velocities in a fixed bed model.

The horizontal scale of the model is 1:800, the vertical scale 1:100. After basic considerations as similarity, hydrology, morphology, respectively, specifications of the modelling technique are given and finally some test results are discussed.

SIMILARITY CONSIDERATIONS

In general the sediment transport in open channels cannot be described for models only by the Froude law, because

1 Dr.-Ing.
2 Ing(grad)
Bundesanstalt für Wasserbau, Hamburg, Germany

the perfect rough area of the resistance number is rarely available. Therefore it seems necessary to make compromises between the similarity laws of Froude and Reynolds.

The specific sediment transport can be expressed as

$$q_s' = f(\varrho, \varrho', g, \nu, D, w, u_*)$$

whereby $$u_* = \sqrt{g.h.I_e}$$

It denotes:

ϱ, ϱ_s	= specific density of the fluid and bed material	$[ML^{-3}]$
ϱ'	= relative specific density = $\frac{\varrho_s - \varrho}{\varrho}$	[1]
g	= gravitational acceleration	$[LT^{-2}]$
ν	= kinematic viscosity	$[L^2T^{-1}]$
w	= fall velocity of the grain in resting water	$[LT^{-1}]$
u_*	= shear velocity	$[LT^{-1}]$
h	= water depth	[L]
D	= characteristic grain diameter	[L]
I_e	= energy gradient	[1]
q_s'	= specific sediment transport	$[dynL^{-1}T^{-1}]$
κ	= Karman constant	[1]

Dimensionless parameters can be formed with these characteristic values:

Reynolds numbers:

$$R_* = \frac{u_* \cdot D}{\nu}; \quad R_w = \frac{w \cdot D}{\nu}$$

Transport numbers:

$$G_* = \frac{q_s'}{\varrho\, u_*^3}; \quad g_* = \frac{q_s'}{\varrho_s\, g\, D\, u_*}$$

Froude numbers:

$$F_* = \frac{u_*^2}{\varrho' g D}; \quad F_w = \frac{w^2}{\varrho' g D}$$

The term $Z = \frac{w}{\kappa u_*}$ shows advantageous the distribution of grains transported in suspension.

Sedimentological diameter:

$$D_* = \left(\frac{\varrho' g}{\nu^2}\right)^{1/3} D = \left(\frac{R_*^2}{F_*}\right)^{1/3} = \left(\frac{R_w^2}{F_w}\right)^{1/3}$$

It has been found out that the numbers F and R have their special significations for the outline of transport occurrences. Gehrig [1] has developed similarity relations by comparison of these numbers for model and prototype. These relations allow the estimation of horizontal and vertical model scales as well as details of material constants D and ϱ'. Conditions therefore are:
The model must be distorted and the resistance number is in the range of $R_* < 70$.

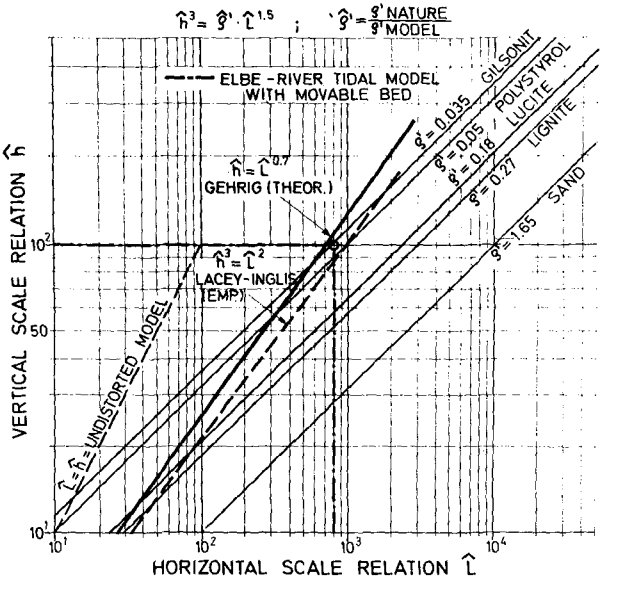

Fig. 1 Scale relations for movable bed models [1]

The starting equations are:

$$R_* = \frac{\sqrt{g\, h_N\, I_{eN}}\, D_N}{\nu_N} = \frac{\sqrt{g\, h_N\, K\, I_{eN}}\, D_N}{\sqrt{\hat{h}_N}\, \nu_N\, \hat{D}}$$

$$F_* = \frac{g\, h_N\, I_{eN}}{\varrho'_N\, g\, D} = \frac{g\, h_N\, I_{eN}\, K\, \hat{D}\, \hat{\varrho}'}{\varrho'_N\, g\, \hat{h}\, D}$$

The symbol $(\widehat{\ })$ denotes the reverse values of the similarity scale, $K = \frac{\hat{L}}{\hat{h}}$ is the similarity relationship of the distortion. Two terms can be derived from these definitions:

$$(\widehat{\ }) \quad h^3 = L^{1.5}\, s' \qquad (1)$$

$$(\widehat{\ }) \quad D^3 = s'^{-1} \qquad (2)$$

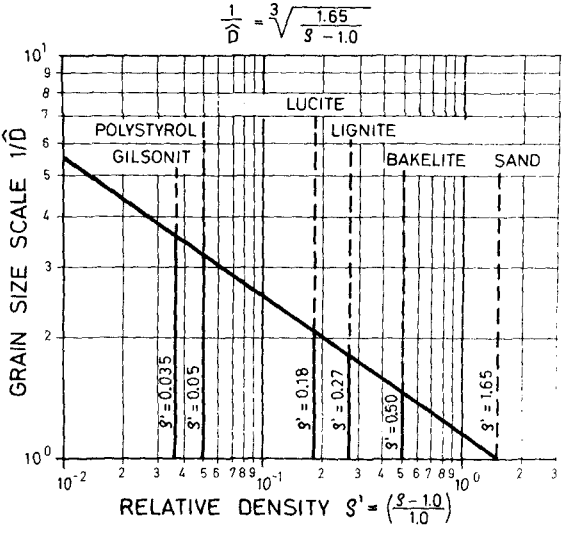

Fig. 2 Scale relations between density and grain diameter of the model bed material [1]

The Fig. 1 and 2 show the graphs of these equations. Suitable scale relations can be determined.

The following principles should be taken into consideration:

a) The horizontal relationship $\hat{L}$ of the model depends on the available area.

b) The vertical relationship $\hat{h}$ depends on the accuracy for the determination of the water levels.

c) Distortion and model discharge affect $\hat{L}$ and $\hat{h}$.

d) $\hat{D}$ and $\hat{S}$ will be determined adequate to available or buyable material.

e) In tidal models, the time scale for morphological changes can only be found empirically. (Historical tests).

HYDROLOGICAL AND MORPHOLOGICAL INFORMATIONS

The boundaries in the sea part of the tidal model (Fig. 3) were chosen with great accuracy after previous historical investigations [2]. The inlet contains special constructions for the adjustment of the tide wave generation. Flow velocities, flow directions and water-level slopes show good agreements between model and prototype for a great range of different tidal waves after adjustment.

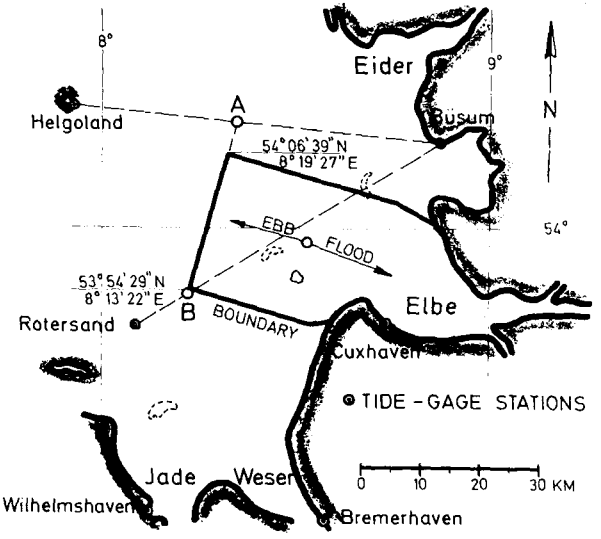

Fig. 3 Boundaries of the model in the sea area

Series of mean tides in the model did not satisfy natural occurrences. Therefore a month's cycle with 57 different tides was used with half monthly unequality between neap tide and spring tide (Fig. 4).

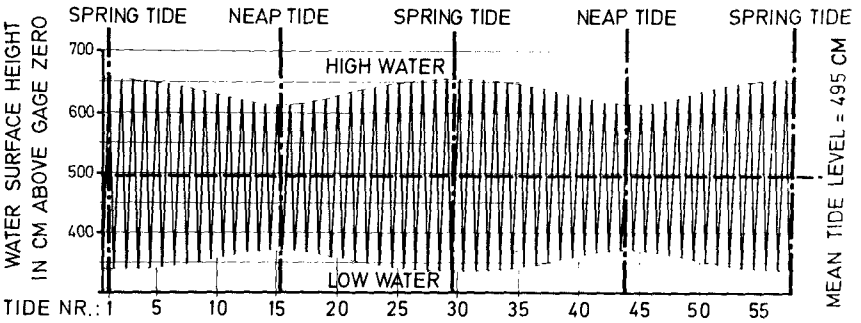

Fig. 4 Mean monthly tide curves (Cuxhaven)

The chosen scales for the model, required a very mobile bed material with a specific density of 1.05 g/ccm(gram per cubic centimeter). The material has a uniform grain diameter ($D \sim 2$ mm) and forms itself a good roughness under flow conditions. Because investigations will last several years, material should not change its characteristic. The plastic material POLYSTYROL satisfies requirements, but this material is very expensive. With a layer of about 10 cm, 120 000 kp (kilopond) were needed. The water-repellent property can be reduced by additives. In general, morphological changes observed in situ and model have been found in good agreement when the tide period in the model was modified.

Density currents and the coriolis acceleration are hardly to realize in distorted models with movable beds, here they were neglected, nevertheless the flow parameter are in good agreement.

MODEL CONSTRUCTION

The model was built from the mentioned boundary in the sea area up to the extreme point of the tidal influence at the weir Geesthacht. The length in axis is about 170 km. Hamburg, the main harbour of West Germany, has a distance of about 100 km from Cuxhaven at the river mouth (Fig. 5).

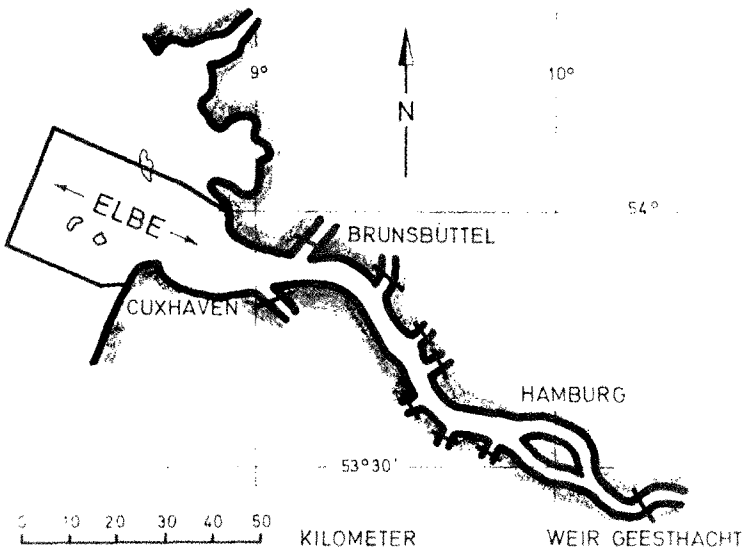

Fig. 5 The Elbe-River from the sea up to the extreme point of tidal influence (weir Geesthacht)

Besides special constructions for tide generation with a steerable sector gate, eleven adjustable pressure pipes, distributed over the width of the inlet (30 m), serves for exact quantitative water dispersion adequate to discharge cross-section. Before test runs the movable bed was moulded by placed tin profiles (later on removed), which are based on a step-like substructure of concrete (Fig. 6).

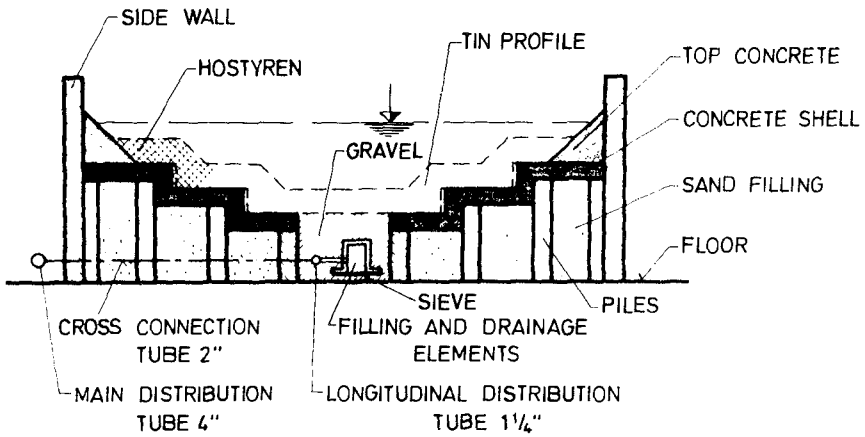

Fig. 6 Model cross-section for the movable bed part (schematical)

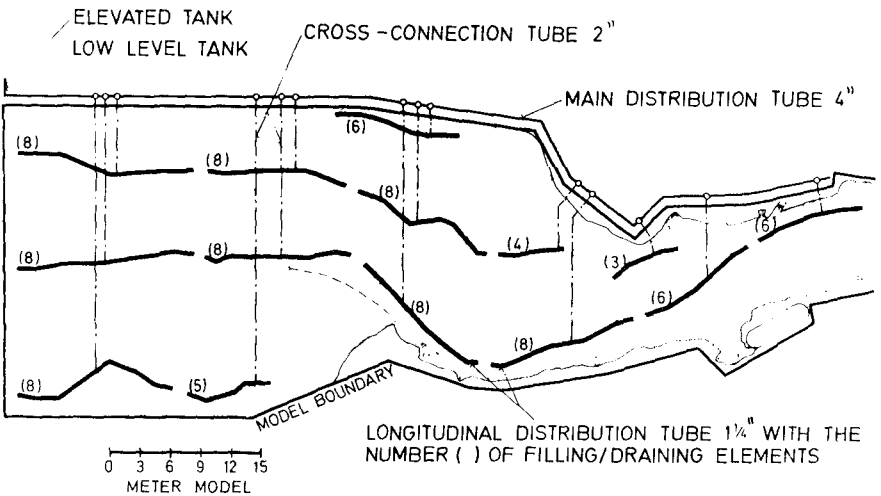

Fig. 7 Distribution system for irrigation and draining

The model has a square dimensional acting irrigation and drainage system, so that morphology cannot be destroyed during filling and draining (Fig. 7). Measurements and observations are possible from mobile bridges [3].

ELECTRONIC INSTRUMENTS

An electronic optical system reads tide curves, recorded on an endless tape as theoretical values. Vibrating points, system Delft, with remote control are installed as effective value for tide generation and as water-level gages. Steering and recording of data occurs in a central control station. Furthermore the following measurements are practicable (likewise by remote control): water-level slopes, velocities, measured with micro-propellers, flow directions, and the sounding of morphology with an optic-electrical system mounted on a float (Fig. 8). This instrument can be applied to a water-depth of 32 cm below a necessary cover height of 10 cm.

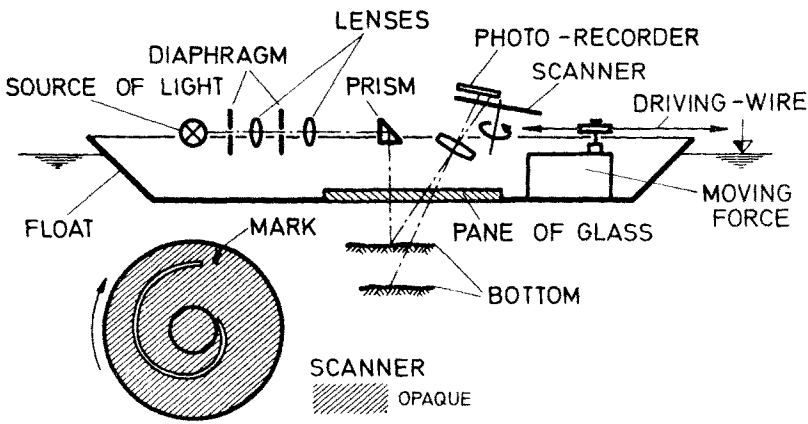

Fig. 8 Optic-electrical recording instrument for morphological sounding

This must be considered for the construction of the inlet. The profile sounding was realized after dark, because the influence of foreign light is extremely high.

SIMILARITY CONTROL

The verification of similarity occurs in two steps:

a) Dynamical similarity

b) Morphological similarity

To a. Test results of water-levels, flow velocities and flow directions as well as flood and ebb durations were compared between model and prototype. Therefore the Froude law was stated. The model area, later on fitted with a movable bed, was provided with a quasi fixed sand bed but with artificial formed surface roughness. All occurrences are in good agreement, as an example may serve the presentation of different measured tide curves (Fig. 9).

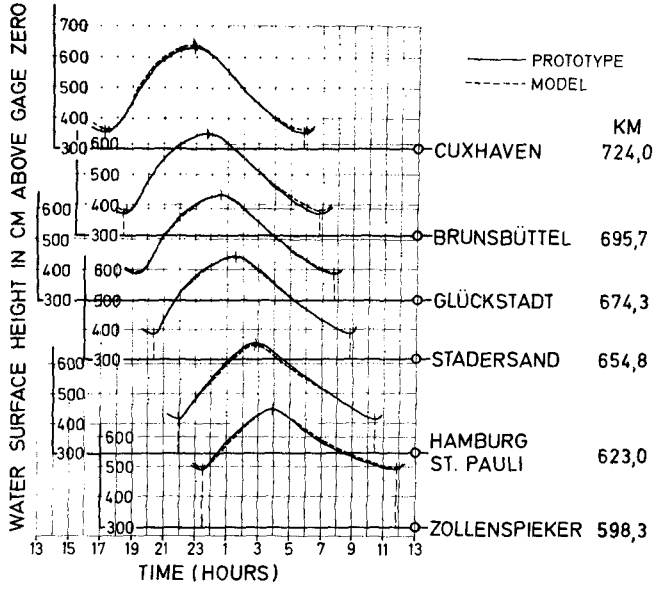

Fig. 9 Comparison of tide curves in model and prototype

To b. The morphological similarity can be expressed as a time relation, in which natural bed changes are reproducable in the model. Therefore historical tests were used in steps from 1910 to 1970. The tide period, derived from Froude, must be enlarged with a factor 1.4 to get favourable values for roughness and bed deformations. Finally the morphological time scale was found out with 1/705; (one day in nature is about two minutes in model).

FIRST PRACTICAL MODEL TESTS

The first tests have been carried out to prove the stabilization effect of a new main navigation channel, following natural canal development tendencies north-west of Cuxhaven.

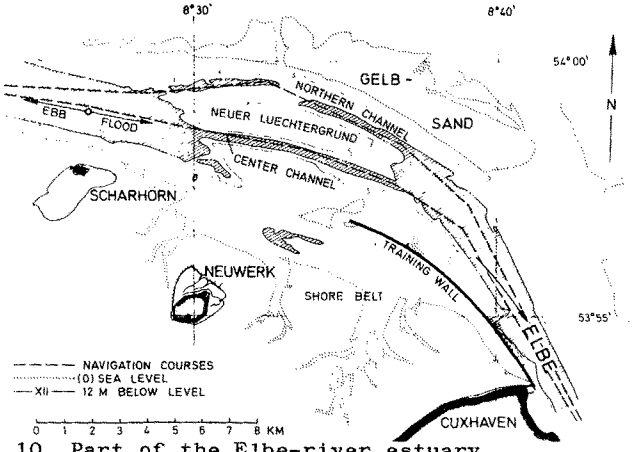

Fig. 10 Part of the Elbe-river estuary (north-west of Cuxhaven, 1969)

Till to-day sailing and arriving ships used two channels, the "Center Channel" and the "Northern Channel" (Fig.10). It is designed to widen and deepen the "Center Channel"for the whole traffic and especially for bigger ships. In the past decades the existing bipartition of the navigation channels leads to highly unstable conditions by different flood and ebb current directions and from this, likewise difficulties occur for navigation. With the completion of

a 9.25 km long training wall in the sea area 1968 (Fig.10), stabilization effects can be observed but the two navigation channels are still too flat. The new scheme for the widening of the "Center Channel" includes an additional extension of the training wall (about 3 km lengthening) and therefore two plans should be investigated in comparison with the existing wall length.

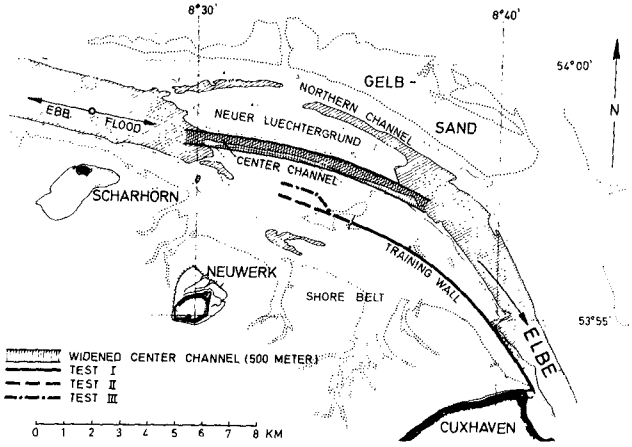

Fig. 11 Schemes of the training wall extension

In Fig. 11 denotes test I the existing length of the training wall, test II a tangential extension and test III an extension in a break off form, respectively. The existing longitudinal shape of the wall is given in Fig. 12. The wall is a riprap construction on fascine mattresses.

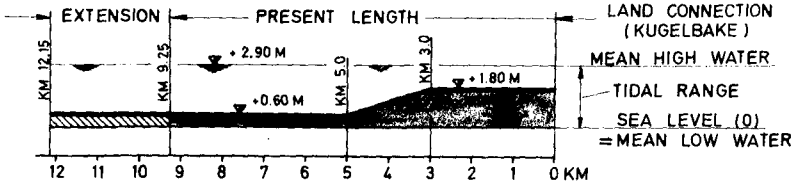

Fig. 12 Longitudinal section of the training wall with slope details

The new widened and deepened "Center Channel" (500 m width, 12 m depth below sea level), was considered as present in the model when the tests started. Each test lasted 186 hours in the model, what corresponds to a natural extrapolation time of 15 years in prototype. The measured silting rate at the end of this time, inside of the new dredged channel, was reduced to a year's rate and specified in per cent (Test I = 100 %).

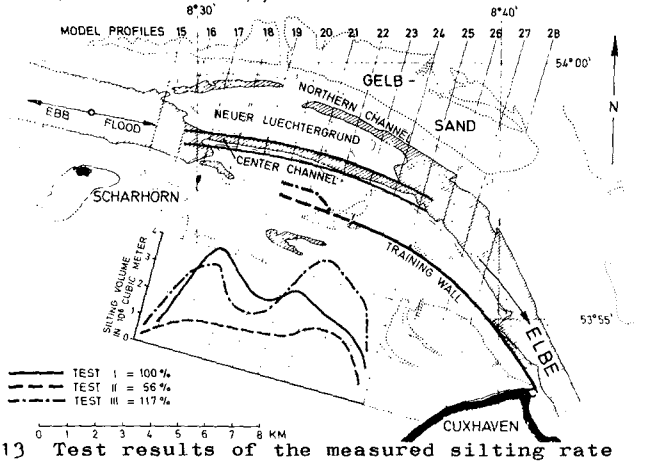

Fig. 13 Test results of the measured silting rate in the new "Center Channel" in relation to the training wall extension

The results given in Fig. 13 in per cent and with their local distribution, show a minimum rate for test II with the tangential extension. This is clearly more advantageous as the breaking form in test III with 117 %. In this case the break off form catches more material and compensates the training wall extension.

For test I with the existing training wall length the silting rate of the "Center Channel" was measured with 1.475 million cubic meter per year (model volume multiplied with model scales and devided through the number of test run years), for a channel width of 500 m. As a possible chance to compare dredging rates between model and prototype may serve Fig. 14.

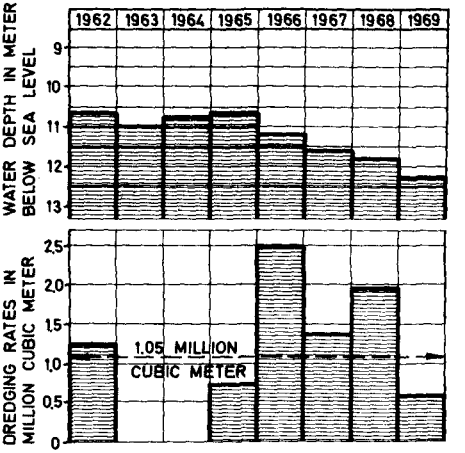

Fig. 14 Development of the mean water depth in relation to the dredging rates in prototype

The prototype informations show a mean dredging rate (1962-1969) of 1.05 million cubic meter per year for the mean channel width of 350 m. With the extension factor for the width of 500/350 = 1.43, this rate will be enlarged to 1.5 million cubic meter, similar as the rate, calculated from the model. This agreement is actual surprising but it is better to look not only at quantitative but more at qualitative results. However, the facts of these tests show obviously the possibility to minor the dredging rate in the "Center Channel" by extension of the training wall in form of test II.

The complex shoaling occurrences are outlined in Fig. 15. The different shoaling directions known in prototype and well simulated in the model too, are produced from diverging flood and ebb current directions. Resultant flow directions, noted for several measuring points, explain the relationship between sediment transport and flow directions and demonstrate the difficulties for the stabilization of the navigation channel.

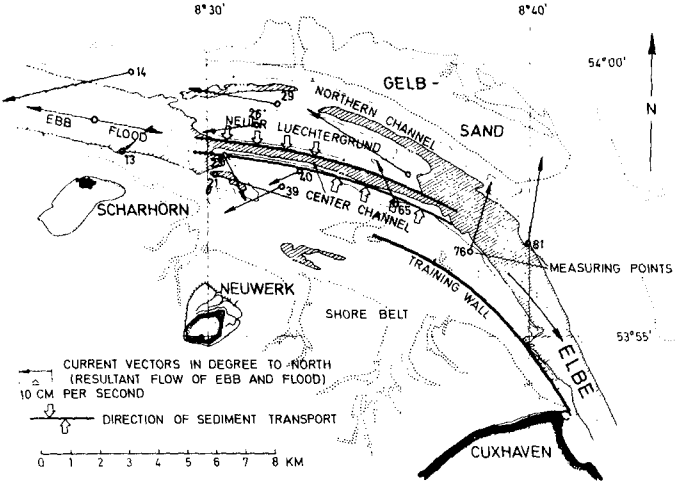

Fig. 15 Shoaling dynamic in the "Center Channel" area

Further testing sections considered changed position runs of the "Center Channel". Details are given in Fig. 16. The measured silting rates are also given in per cent with respect to test I. The training wall has here the extension of about 3 km with a total length now of 12.25 km for all variants (IV to VI).

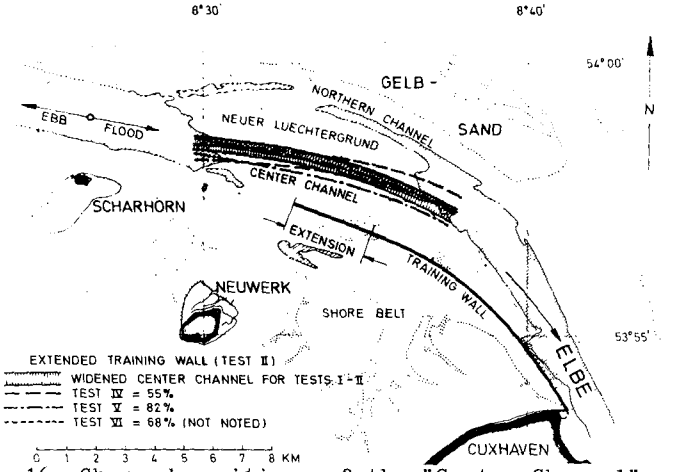

Fig. 16 Changed positions of the "Center Channel"

The results show, that a small turn of the "Center Channel" against clockwise direction (test IV), gives nearly the same per cent number as in test II (55 % to 56 %). However, in this case the navigation course is not advantageous.

Test V deals with a small approach of the "Center Channel" in direction to the training wall, but the shoaling rate increases (82 %). In Test VI a mixing of the "Center Channel" runs IV and V decreases again the shoaling rate (68 %). First of all, the tests to find out the optimum position showed the extreme sensibility of the movable bed and the influence on small constructional changes. On the other hand one can see that the natural developed channel, now stabilized by the training wall, is obviously the optimum channel course.

CONCLUSIONS

The presented study on a tidal model with a movable bed points out the successful reproduction of morphological occurrences in a tidal estuary. The valuation of the different construction plans of the training wall extension shows an optimum for the tangential lengthening (Test II), that means a minimum dredging rate for the "Center Channel", as the main navigation channel in the Elbe-river estuary. It is to mention that the measured quantitative shoaling rates were only used as a qualitative comparison basis. We know that it is impossible to reproduce all natural phenomena complex in a model, but in some instances, these models are a valuable help for the estimation of constructional or dredging works in coastal areas.

REFERENCES

[1] Gehrig — Über die Frage der naturähnlichen Nachbildung der Feststoffbewegung in Modellen
Mitteilungen des Franzius-Instituts für Grund-und Wasserbau der Technischen Hochschule Hannover, Heft 29, 1967

[2] Giese — Fahrwasserumbildungen in der Unter- und Außenelbe
Die Wasserwirtschaft, März 1971

[3] Giese, Teichert, Vollmers — Das Tideregime der Elbe, Hydraulisches Modell mit beweglicher Sohle
Mitteilungs-Blatt der Bundesanstalt für Wasserbau (BAW) Nr. 31, Karlsruhe 1972

CHAPTER 142

FIELD AND LABORATORY STUDIES; NAVIGATION CHANNELS OF THE COLUMBIA RIVER ESTUARY

M. P. O'BRIEN

Dean Emeritus, College of Engineering
University of California
Berkeley

INTRODUCTION

A model of the estuary of the Columbia River was built and tested at the University of California, Berkeley, during the years 1932 to 1936, to study the effects of proposed changes in the navigation channels on the currents and sediment movement. The project was sponsored by the North Pacific Division of the Corps of Engineers, and the engineering results were reported at that time in internal memoranda. The basis for the selection of the scale ratios and other factors affecting the design of the model were reported in some detail (O'Brien, 1935), but only a brief note was published regarding the operation and the accuracy of the model (Johnson, 1948). In some respects this model is still unique, and a description of it may be of interest to the coastal engineers.

This paper deals primarily with the model itself and not with the practical problems of channel maintenance and improvement, but some information regarding the regimen of the Columbia is necessary background for understanding the problems which were to be studied in the model. Figure 1 shows the configuration of the estuary, the jetties, and the ship channel. The river was then unregulated; the freshwater discharge exhibited an annual cycle with an average annual flow of 235,000 second-feet, an average summer freshet discharge of 660,000 second-feet, and an average low-water flow of 70,000 second-feet. The tide shows a diurnal inequality, with the long run-out following higher high water; the diurnal range of tide is 8.5 feet, and the average range is 6.5 feet. Freshet flows affect the range and lag of tide in the river section above the estuary to such a degree that the published USC and GS Tide Tables were valid only for the months September through May and not for the freshet season. The range of tide is approximately constant from the ends of the jetties to Harrington Point; the lag over this reach is approximately two hours. At low river stages the tide is evident as far as Bonneville, 140 miles from the mouth; the tide wave progresses with steadily decreasing amplitude and there are no nodal points. The tidal prism varies both with range of tide and river stage; at low river stages, the prism corresponding to an 8 foot range is between 600,000 and 700,000 acre feet.

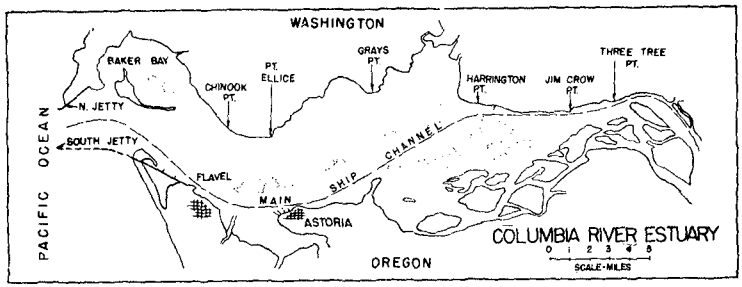

Fig. 1--Area covered in Columbia River Estuary model

The average annual suspended sediment load at the Dalles at that time, when the river was unregulated was 10,000 tons per year. The gradient of the river and the current velocity decrease, and the depth increases, below the Dalles; some of the suspended load at the Dalles probably moves as bed load in the lower river. At an average flow of 235,000 second-feet throughout the year, the average concentration of suspended material must be approximately 50 parts per million to transport 10,000,000 tons per year in suspension. However, the concentration in the estuary reached this level only at high freshet stages and was materially less throughout the remainder of the year. If the estimate of suspended load at the Dalles was correct, and if this load was transported through the estuary, high rates of net movement as bed load must occur there.

Two independent samplings of the bottom of the entire estuary showed the median diameter of a composite sample to be 0.0096 inches. The median diameter of samples from the beach and offshore was 0.0075 inches. The settling velocity of the estuary bottom material ranged from 0.10 to 0.15 ft. per sec.

OBJECTIVES OF THE MODEL STUDY

When model scale experiments were proposed, there were two unrelated problems in the area near the mouth of the Columbia; one concerned the channels in the estuary and the other the erosion of the ocean shore just south of the south jetty.

During the early stages of construction of the south jetty the shoreline of Clatsop Spit built seaward rapidly and the desired crest elevation of the jetty was attained with a lighter section than designed. Accretion continued for a few years but erosion followed; if erosion continued the light section at the base of the south jetty might be breached. It was thought that a scale model might provide the basis for correction of this problem. However, field studies of the movement of sand by wind on the

flat shore of Clatsop Spit and correlation of winds measured at the beach with those measured concurrently at North Head and at the Lightship showed that the observed erosion was caused by onshore winds transporting sand from the beach across the spit and into the lagoon (O'Brien and Rindlaub, 1934). Consequently, erosion of the outer beach was omitted from the program.

An interesting consequence of these studies of wind drift was a program of dune building and stabilization which was carried on for almost ten years. Its success was indicated by a recent paper (Kidby and Oliver, 1966) which reported that the dunes south of the south jetty are stabilized at about +25 ft. MLW and that the erosion of this shore appears to be approaching a terminal position asymptotically.

The other problem to be studied in the model was the location of the navigation channel between Harrington Point and the jetties. As it then existed, the ship channel made a sweeping curve, crossing the estuary to Tongue Point and following the south shore to the entrance (Fig. 1). A straight channel from Harrington Point to the entrance would be both shorter and easier to navigate, but this alignment would require dredging through the shoal area west of Harrington Point. Other less drastic changes were also under consideration.

At the time there was little experience with models involving both waves and tides, and the first question to be resolved was whether or not a scale model would furnish information regarding the currents and sediment movement in the estuary with the necessary accuracy, and in sufficient detail, to evaluate the proposed changes. The first phase of the study (O'Brien, 1935) was planned as a test of the validity of the model technique. It was anticipated that at least two horizontal scale ratios and several vertical scale ratios would be modeled and tested in the course of the program. The first model, built to a horizontal scale ratio of 3600, was thought to be the smallest in physical size which might yield reliable results.

FIELD INVESTIGATION

Elimination of the beach erosion problem from the scope of the model study considerably simplified the boundary conditions to be represented because it became unnecessary to reproduce ocean waves and this fact, in turn, permitted much greater flexibility in the choice of the horizontal and vertical scale ratios.

Reproduction of the currents required modeling of the entire estuary and river to the end of tide water. Surveys had been made frequently in the navigation channels, but the shoal areas, a major fraction of the area of the estuary, had been surveyed only infrequently. There was available a fairly complete survey made in 1935 and this survey was supplemented by

local surveys made at other times; these surveys formed the basis for the fixed-bed model (Univ. of Calif., 1936). Depths over the shoals probably show some seasonal variation, especially after the freshet season, and this fact should be kept in mind in appraising the reliability of this model.

Current measurements had been made by means of both current meters and surface floats. Current meter measurements were made at several boat stations across sections near Clatsop Spit in 1932 and near Clatsop Spit and Flavel in 1933; recordings were continuous at five points in the depth and over several days at each boat station. Float runs had been made at many points in the estuary over the years. In short, field data on the currents were sufficiently detailed and extensive that it was possible to construct a reasonably complete pattern of the currents at different ranges and phases of the tide. However, the current measurements were not made at the same time as the base survey.

The fresh water flow of the Columbia is relatively large, especially in the freshet season, and salinity gradients might possibly affect the currents in the estuary. No quantitative information was available on the salinity in the estuary and its spatial and temporal variations. Several salinity traverses were made along the ship channel at different river flows to establish the approximate magnitude and position of the maximum horizontal and vertical salinity gradients within the estuary proper. Since the heavier saline water tends to move inward along the bottom and the freshwater to move outward on the surface, the effects of a strong salinity gradient might have been appreciable on the currents and a major factor in the bottom sediment movement. Later, after the currents had been measured in the model, it was possible to correct the position of the isohalines to a constant phase of the tide and to determine the approximate horizontal motion of the salt wedge during a tidal cycle (Univ. of Calif., 1936); O'Brien, 1952). A study of the vertical variations in velocity at the current meter stations gave unmistakable evidence of net salinity currents, inward at the bottom and outward at the surface. Calculations from the field measurements showed that the inward salinity flow was approximately 100,000 sec. ft.

Earlier, extensive studies had been made at Berkeley of the movement of salt water through fresh water (O'Brien and Cherno, 1934), and this experience led to the conclusion that although salinity currents undoubtedly existed in the Columbia River estuary, representation of this phenomenon in this model would introduce severe complications, both in operation and in the interpretation of the results. There was no field evidence then available that flocculation occurred in the zone of increasing salinity or that the bottom salinity currents caused shoaling at particular points. Salinity effects were not represented in the model.

The internal summary report of these model studies (Univ. of Calif., 1936) contained this statement:

> "As regards the reliability of the model, it appears certain that failure to reproduce the salinity effects results in an error which is greatest in the region of the greatest rate of change of salinity... If the model were to be used to study the currents between the jetties, the effect of the salinity gradient would require more

careful study. However, the salinity survey showed that the salinity gradient is probably of negligible importance in the areas under study. Furthermore, comparison of model and prototype currents showed good agreement."

In recent years the currents near the Columbia River jetties have been studied in a model in which the salinity gradient was reproduced (Herrmann and Simmons, 1968).

Tongue Point in Astoria, Oregon is the primary reference tide station for this portion of the Pacific Coast, and a long period of tidal measurements was available. The tide generator in the model permitted continuous variation of range and duration and specific sections of the tide record could have been reproduced but at a considerable cost and delay of operations. An analysis was made of the frequency of different tidal ranges and of the duration of phase and it was found that the duration did not change appreciably with range and that range was the dominant variable. The energy transmitted by the tidal wave is proportional to the square of the range and this transmitted energy measures the capacity of the tide to generate currents and move bed material. Accordingly, the standard range reproduced in the model was the root-mean-square of the ranges, which was 8 ft., approximately the diurnal range. A standard tide curve was prepared for the model by averaging a number of consecutive tide cycles at Astoria measured concurrently with the 1932-33 Current Survey to obtain a curve representing percentage of range versus percentage of duration.

The tidal prism varies both with range and river flow. Adequate field data on river stage and tide range at points along the river to the limit of tidal effects were available for adjustment of the friction in the model to conform to the prototype.

In brief, the hydrographic and dynamic boundary conditions to be represented in the model were adequately defined and a valid appraisal of the accuracy or inaccuracy of the model was assured.

DESIGN AND CONSTRUCTION OF THE MODELS

Osborne Reynolds (1887) has pioneered the use of movable-bed tidal models with apparently valid results. In Table I (O'Brien, 1935), the characteristics of a number of earlier tidal models are compared with the first model of the Columbia River. By this comparison, the model seemed conservative but it represented a substantial extrapolation beyond the scale ratios and distortion of the few river models built in this country. For this reason, the first Columbia River model incorporating a movable bed was regarded more as an experiment on models than as a working model of the estuary. The extensive studies made as a basis for designing the movable-bed model were reported at the time (O'Brien and Rindlaub, 1934; O'Brien, 1935) and will only be summarized here.

The primary problems of designing a movable-bed tidal model are to select a material which will be moved by the tidal currents and to select vertical and horizontal scale ratios which will produce natural patterns of currents throughout the tidal cycle in those portions of the estuary under investigation, at velocities which will move this material, and at

Table I

CHARACTERISTICS OF IMPORTANT ESTUARY MODELS BUILT UP TO 1935

(From O'Brien, 1935)

Prototype	Mersey	Mersey	Seine	Rangoon	Severn	Columbia[a]
Experimenter	Reynolds, 1885	Vernon-Harcourt, 1886	Vernon-Harcourt, 1886	Alexander Gibbs and partners, 1932	A. H. Gibson, 1932	U. S. Engineers, 1934
Purpose	Effect of regulating works	Effect of regulating works	Channel-improvement	Channel through outer bar	Effect of barrage on silting and currents	Estuary- and bar-channels
Range of tide (ft)	.....	.....	24	16-21	21-41	8
Diameter of sand in prototype (in)	0.008	.....	.....	.....	0.009	0.008
Diameter of sand in model (in)	0.006	0.0065	.....	Same as Rangoon River	0.007	0.0076
Horizontal scale	31800 10600	30000	40000	8068 7050	8500	3800
Vertical scale	960 396	600	400	192	200	64
Period of tide in model (sec)	40 80	.....	25	76	74	99
Reproduction of tides	Hinged trough	Hinged trough	Hinged trough	Plunger	Plunger	Pumping and gravity
Waves	Used in part	.....	No	By fans	No	Yes

[a] Scales and sizes of model refer to first series of experiments.

a single scale ratio of volumetric transport. These are severe specifications and, clearly, cannot be fully realized. The practical question is whether bed material and scale ratios can be found which will yield acceptably close agreement with the prototype. The test of the validity of the model is to subject the model to proper boundary conditions of tide range and river flow and compare the model hydrography with past surveys in nature. If the model is thus verified, the assumption is made that changes in the configuraiton of the model will produce changes in its bed which will be predictive of corresponding conditions in the prototype.

Granular material is moved by water at rates which depend upon the tractive force of friction, which is in turn related to the average velocity and the depth. Experiments indicated that there is a critical velocity at the bed below which a material is not moved and that critical velocity reaches a minimum value below which it increases with decreasing

diameter of material, probably because the grains are so small as to be submerged in the laminar layer. In order to attain velocities in the model as large as possible, and necessarily above the critical velocity, over all areas of the estuary under invesitgation, the depths and range of tide in the model should be as large as possible, that is, the vertical scale reduction should be small. However, if this requirement is met and the same scale factor is applied to the horizontal dimension, the area of the model generally becomes too large and costly to be feasible. The usual solution of this dilemma is to distort the model by applying different scale ratios to all horizontal and vertical dimensions, both hydraulic and hydrographic.

Distortion of a model introduces many sources of discrepancy between model and prototype in addition to those inherent in small, undistorted models.

- The skin friction drag or hydraulic gradient will be less than that corresponding to the scale ratios. In the first Columbia River model, the friction slope in the model was approximately four times that in nature, whereas it should have been in the ratio of 3600/64. The tractive force on the bottom is correspondingly distorted.
- All of the bottom slopes will be greater in the model than in nature, and the form drag in the model will be relatively greater than in nature - by an unpredictable amount.
- Eddies with vertical axes may occur in the model behind projecting point at which the slope of the bottom has been greatly distorted but not in nature.
- The natural angle of repose of the model material and the bottom slopes in nature set a limit on the permissible distortion, if similarity is to exist.
- Ripple spacing and height appeared to depend on material size and current velocity, and hence would probably be related to the vertical scale ratio; ripple lengths would probably be relatively too large in the model.

These possible complications and the problem of selecting a suitable bed material led to much study and speculation before the design was completed.

If the velocities in the model are sufficient to move the material selected, turbulent flow will probably occur and the head losses will be approximately proportional to the square of the velocities, thus following the vertical scale ratio as requried. However, the magnitude of the energy loss in the estuary and the balance between skin friction and form drag on the bottom would affect the model response. The energy transmitted into the estuary by the tidal wave is proportional to WLH^2, where W is the width of the channel, H is the tide range, and L is the length of the tide wave in water of constant depth. Comparing the energy at the jetties and that at the entrance to the river at Harrington Point showed that the loss of energy in the estuary was approximately 75 percent of the 4×10^{12} ft lbs/tide which entered. Calculation of the loss by bottom friction gave 3×10^{12} ft lbs/tide, which is in agreement with the first calculation.

There was no evidence of appreciable reflection. Thus, it was established with reasonable accuracy that friction within the estuary plays a major role in determining the magnitude and distribution of the current velocities.

A possible type of hydraulic distortion which would increase the model velocities was to shorten the duration of the model tidal cycle. The velocity of advance of the tide is fixed by the depth, and the distortion would alter the phase relationship between elevation and velocity at different points along the channel but, since the vertical curvature of the surface is small, the cycle of current direction and phase might remain unaltered at each point with only an increase in velocity. Experiments on the model, with the tidal cycle shortened from 100 to 60 seconds, indicated that this technique is feasible technically, but this model tide duration proved to be too short for accurate control and measurement.

The time scale for the movement of corresponding volumes of sediment may be distorted by increasing the number of tidal cycles in a model year if the pattern of velocities in the model corresponds to the prototype and if the material in the model is kept in motion over the same fraction of the tidal cycle. This scale ratio can be determined empirically by operating the model until there is movement of volumes corresponding to measured changes in nature.

Consideration of the general model laws, the special factors mentioned, the space available, and the cost, the decision was made to model, with vertical boundaries, the high-water line of the estuary, river, and ocean shore to a scale of 3600. This arrangement would permit modeling different vertical scales without altering the plan form. The material used had approximately the same mean diameter as the weighted average of the material in the estuary*. The river section above Three Tree Point was represented by a labyrinth in which the bottom elevation and the width corresponded approximately to those of the river. The friction loss in the river section was adjusted by metal strips until the range and lag of the tide at each range of tide and river flow agreed with the prototype.

---

*Private communication from Prof. A. H. Gibson (dated Jan. 5, 1934) who had assisted Prof. Reynolds in the Mersey experiments:

> "As regards the question of sands for the bed materials, all models on which we have been working for the last 7 years or so have been those of tidal estuaries in which the flow has taken place alternately in both directions. We have, in these cases, determined the best bed material experimentally; that is, by choosing two surveys at a sufficiently long period apart, moulding the bed to the first survey, and running the appropriate number of tides and then re-surveying. We have then chosen the material which gave closest agreement with the second survey. In the case of our Severn model, we tried 12 materials of different grain sizes and densities, and finally adopted a sand whose mean diameter was about 25% less than that of the actual sand in the estuary.
>
> As it happens, the sands in the other estuaries which we have had to investigate were not very different in fineness from those in the Severn, and as a result we used the same type of bed material for these also."

MOVABLE BED MODEL

The movable bed model was built and operated to a vertical scale ratio of 64. The initial bed was leveled at an elevation corresponding to the average depth over the whole estuary. The average annual river flow of 235,000 sec-ft and the weighted tide range of 8 feet were applied. No measurement of the bed transport into the estuary had been made; the rate fed into the model at the river end was adjusted to maintain a constant bed level there. This rate, converted to prototype quantities at the model scale ratio, was 29×10^6 tons per year, which seemed high but possible, when compared to a suspended load of 10^7 tons per year at the Dalles.

The movable bed model was operated until the bed reached equilibrium. A good channel had developed along a straight line from Harrington Point to the jetties and there was no channel in the model corresponding to the navigation channel in the prototype. This negative result was discouraging at the time and it was concluded that a reliable movable-bed model would require a much larger horizontal scale. The decision was made to rebuild the model with a fixed bed to a vertical scale of 128.

Subsequent studies of the movement of powdered coal (specific gravity = 1.33; median diameter = 0.0041 inches) in the fixed-bed model showed that the sediment load brought down in the freshet season is deposited on the shoal area between Harrington Point and Point Ellice and that it is gradually moved out between the jetties during the remainder of the water year. The channel indicated by the model probably was in a good location under average conditions but it would have been closed completely after the freshet each year. Under regulated river flow, this straight channel might be feasible.

FIXED-BED MODEL

The 3600-scale model was molded in roughened concrete to a vertical scale of 128; the remainder of the program was carried out in this model. The bed conformed to the hydrographic survey made in 1935 which included most of the area of the estuary. Gaps in this survey were filled in from surveys made at other times. Depths in the estuary change both seasonally and from year to year, especially in the shoal areas where freshet flows deposited large quantities of sediment, and these deviations from the 1935 survey would affect current velocities and directions measured at other times.

The fixed-bed model program assumed that if the model currents conformed to measurements in the estuary the changes in currents due to dredging and training works could be predicted and that the trend of changes in bed configuration could be estimated from the currents.

Over the years, many current measurements had been made in the estuary using both current meters and floats. The hydrography at the time of these measurements was not known precisely and it was necessary to assume in making comparisons of the model with nature that the bottom was the same as shown in the 1935 surveys. Differences in depth between the dates of the current measurement and the bottom survey modeled probably caused

discrepancies in the comparison of velocities, particularly over the shoal areas. Other causes of disagreement between velocities in the model and in nature were:

1. Winds over the estuary are relatively strong and predominantly from the west. Some surface currents in the estuary probably were affected by winds at the time of measurement, particularly over shoal areas.

2. The model was out-of-doors. Much of the current data were obtained by timed photographs of confetti on the surface. Imperceptible air currents moved the confetti. Runs made while there were noticeable air currents were eliminated, but some remaining photographs undoubtedly were affected. These measurements in the model gave the surface current only.

3. The velocity and direction of the currents at each point varies with the phase of the tide. Comparisons must be made at the same phase of tide at each point. The celerity of the tide wave depends on the existing depth; it was difficult in some cases to determine the exact phase of the tide in nature during a specific float run.

4. A miniature propeller current meter was used in some of the model tests. The tidal cycle lasted only 100 seconds. An integral number of revolutions required a finite time; the measured peak velocities were lower than the true value.

5. The ocean tide varies continually in range, and to some extent in duration; the model was operated at the tide range and duration and the river flow existing at the time of field measurements, but the preceding sequence of tides was not followed.

6. There are unavoidable errors - and some blunders - in all field or laboratory measurements.

To minimize the effect of these possible causes of discrepancies, the field measurements were segregated in time into ten phases of the tide; comparisons of model and nature were made as precisely as possible in the same phase at the same location under the same range and duration of the tide and at the same river flow. Fortunately, the number of field measurements was sufficiently large to permit meaningful averages within these concurrent brackets of conditions to minimize the errors due to wind, changes in depth, and possibly salinity variations.

The model was controlled to match the prototype tide curve at Tongue Point, the reference station of the Tide Tables, and adjusted to yield the desired backwater curve at one discharge and the range of tide in the river to the limits of tidal effects. When so adjusted and controlled, the degree of agreement in tide range and backwater elevation was shown in Figure 2. The lag of the tide, which could not be adjusted independently was as shown in Figure 3. The range at the jetties in the model was 18

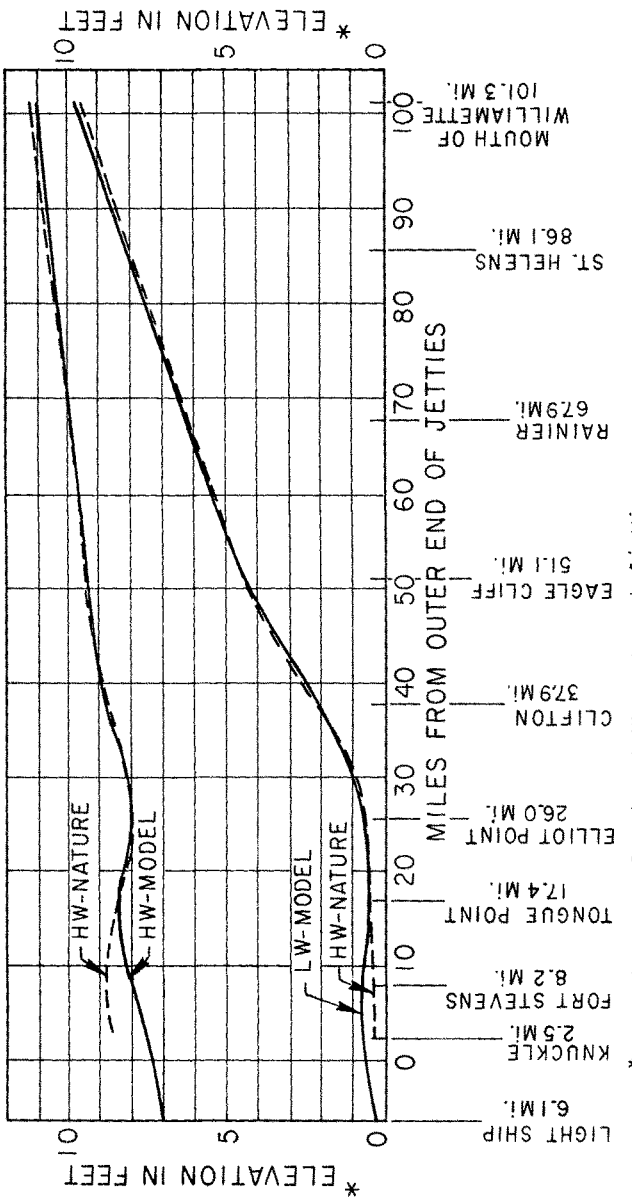

* Elevations are referred to MLLW at outer end of jetties

Model data taken from results of run Nos. 8-T-1 and 8-T-1d

Nature data from 1932 tide tables and U.S.T.M.L. dwg. Nos. D-8-1 and D-8-2

Average Normal Yearly Conditions for the Columbia and Williamette Rivers Excluding the Months of May, June and July

FIG. 2 COMPARISON OF MODEL AND NATURE, RANGE AND HEIGHT OF TIDE

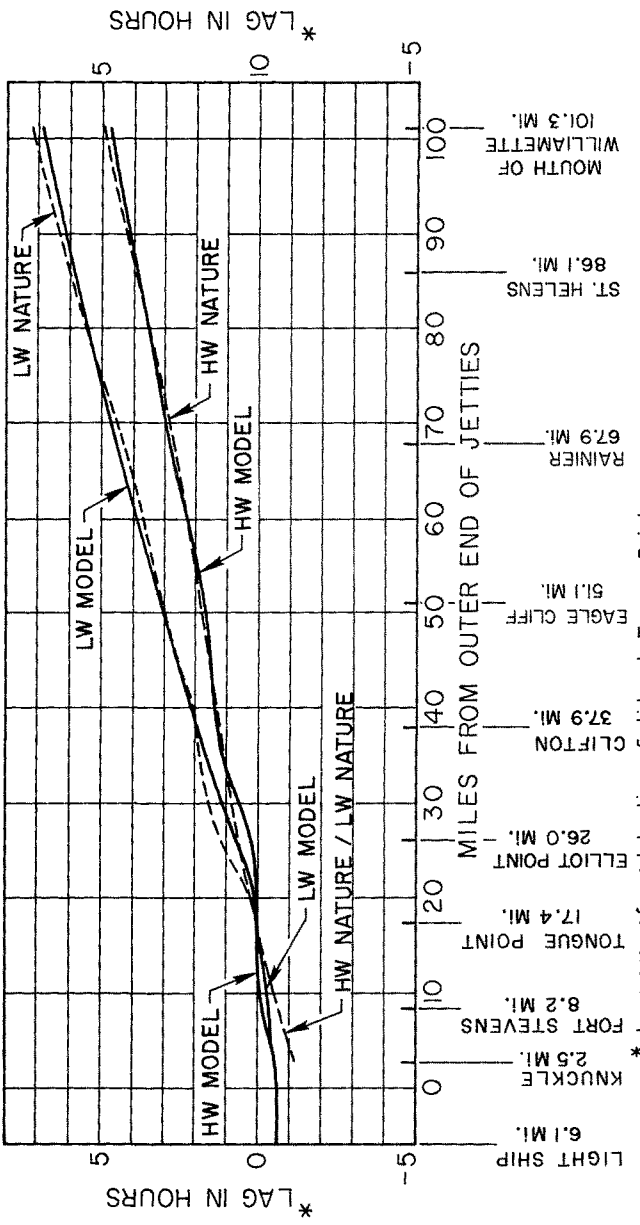

FIG. 3 COMPARISON OF MODEL AND NATURE, LAG OF TIDE

percent less, and the celerity of the tide through the estuary was greater than in the estuary. Similar comparisons were made at other river flows and tide ranges with similarly favorable results. The discrepancies were attributed to the relatively lower friction losses in the model which may have, among other effects, permitted some reflection of the tide seaward from the estuary, whereas no appreciable reflection was found in nature.

Many comparisons of model and prototype current velocities and directions were made and only a sampling of these results will be presented here to indicate the character of the results. Comparisons were made at corresponding tide ranges but exact duplication of tide was not always possible; the field velocities were corrected to the model range of tide by the relationship $V = V_{(observed)} \times \frac{8}{Range}$.

Table II shows one such comparison of float measurements at a fixed river discharge made during the central 40 minutes and 5 minutes of the tide phase. The phase divisions are referred to the tide at Tongue Point and Phase Division One follows high water. The exposure time for the photographs of the model was 0.63 seconds, corresponding to 3.5 minutes in nature. The agreement was improved in almost each case by considering the shorter time interval.

Table III shows a comparison of velocities measured by current meter in both model and prototype at a section across the estuary at Clatsop Spit. Figure 4 compares the variation in velocity over a tidal cycle. The field measurements were made in 1932; the bed of the model corresponded to the survey of 1935.

Most of the current measurements were made by photographing confetti strewn on the water surface. The exposure time was accurately controlled (see Figure 5).

The current directions scaled from drawings of field float observation and photographs of the model agreed within the precision of the measurements. The disagreement showed no regular variation with either location or phase. The average differences in direction during the division of the tidal cycle are shown in Table IV. The probable error in the model was ±5 degrees and in nature at least ±2 degrees.

The comparisons of model and prototype cited were made when the reliability of the model was still in question. The results indicated that a larger model would not be required and that the measurements in this model would provide a sound basis for engineering plans. The next step was to make more precise and detailed comparisions in the areas of particular interest.

Float measurements had been made in nature in considerable detail in the area near Harrington Point. These measurements were segregated by phase division in areas judged to have common hydraulic characteristics, and the average velocity and direction were computed for each group of measurements. The center of gravity of the field float runs was determined and the velocity and direction at this point in the model were measured by current meter and direction indicator. An excerpt from the report on this comparison appears in Table V.

TABLE II

Ratio of Field and Model Velocities for Tide Ranges between 7 and 9 feet. (Surface Floats)

	Phase Division										Average
	1	2	3	4	5	6	7	8	9	10	
Mouth to Fort Stevens	--	1.09	0.85	1.71	--	--	--	0.81 (0.76)	1.25 (1.15)	0.81 (0.85)	1.09 (0.94)
Channel to Astoria	--	--	--	--	--	--	0.80 (0.79)	0.89 (0.95)	1.51 (1.19)	--	0.95 (0.93)
Channel Astoria Tongue Pt.	2.06 (1.29)	1.25 (1.25)	--	--	--	--	--	--	--	--	1.43 (1.25)
Tongue Pt. Harrington Pt.	--	--	--	--	--	--	--	1.62 (1.77)	--	--	1.62 (1.77)
Harrington Pt.	1.41 (0.94)	1.24 (0.84)	--	1.76 (0.76)	--	--	--	--	1.05 (0.97)	--	1.09 (0.86)
Miller Sands Cut-off	--	--	0.68	1.03 (1.03)	0.99 (0.99)	--	--	--	--	--	0.82 (1.01)
Shoals at Miller Sands	--	0.78	1.03 (1.00)	1.25 (1.04)	--	--	--	--	--	--	1.15 (1.03)
Snag Island Jetty	3.08 (2.25)	1.34 (1.32)	0.82 (1.00)	0.70 (0.82)	1.05	--	--	--	--	--	0.90 (0.99)
Elliott Pt.	--	--	--	--	--	--	--	--	--	1.06 (1.06)	1.06 (1.06)
Average*	1.79	1.18	0.79	1.07	1.02	--	0.80	1.03	1.22	0.88	1.04 (0.99)

* The averages are computed from the summations of all float runs and not as straight numerical averages of the figures in the body of the table.

() Figures in parenthesis show the velocity ratio taken over the central 5 minutes of the phase division. Total of comparisons, 183.

TABLE III

Ratio of Currents at Five Clatsop Spit Stations in 1932-33 to the Model.
Field Velocities are the Average of Five Depths.
Range 7 to 9 feet in Nature. (Current Meters)

Date	Phase											Average
	Discharge	1	2	3	4	5	6	7	8	9	10	
9/13 to 9/15 1932	125,000	0.57	1.22	1.18	1.06	0.86	-	1.01	0.84	0.80	1.16	1.02
		Ebb phases, 1.06				Flood phases, 0.98						
4/6 to 4/8	320,000	2.16	1.32	1.19	0.99	0.77	-	0.86	0.82	0.80	0.98	1.00
		Ebb phases, 1.15				Flood phases, 0.85						

Average of all comparisons, 1.005

TABLE IV

Average Difference in Current Direction During
the Divisions of the Tidal Cycle

Phase	1	2	3	4	5	6	7	8	9	10	Average
Average difference in angle (degrees)	+3.3 (3)	-1.4 (17)	-7.0 (10)	-5.1 (19)	-0.6 (5)	-	-8.4 (5)	-2.4 (15)	+1.9 (19)	-2.6 (7)	-2.3

( ) Figures in parenthesis show number of float directions compared.

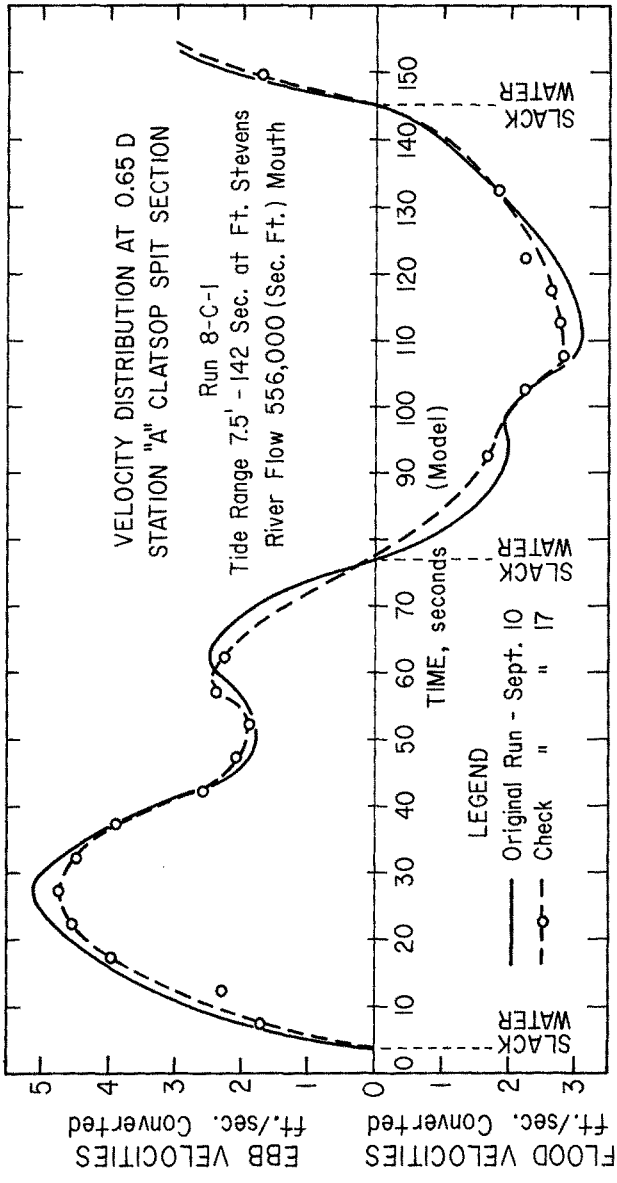

FIG. 4 MODEL MEASUREMENTS ON THE VARIATION IN VELOCITY OVER A TIDAL CYCLE

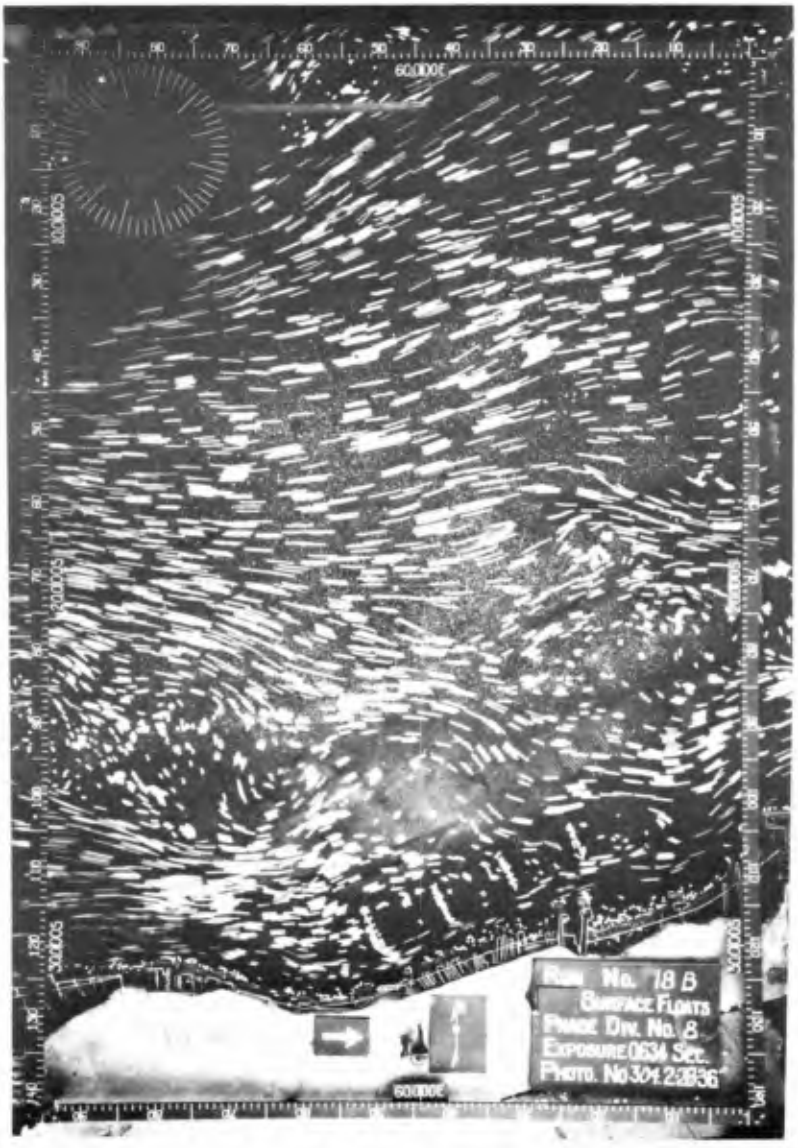

Fig. 5. Typical photograph for measurement of surface currents in the model.

TABLE V

Current Measurements at Harrington Point

Comparison of currents in model vectorially by phase divisions with those for nature given in Tech. Memo. No. 8, Low River Stage before Cutoff.

a) Run No. 9-C-D Per General Program, Run No. 9

Conditions: Corresponding to average in nature from HW at Tongue Point at 9.8 o'clock, Nov. 13 to LW at 18.7 o'clock, Nov. 16, 1933, the period during which float runs were made.

Range: 6.7 ft. at Tongue Point.
Elev. LW: 1.0 ft. at Tongue Point.
Period: 140 1/2 sec. (model)
River Flow: 152,000 sec. ft. (mouth)

Table of Comparison, Azimuths of Current Directions by Phase Divisions in Model with Directions of Velocity Vectors for Nature given in Tech. Memo. No. 8.

Area No.	Phase Divis.	Azimuth from True North: Model: Start of Phase Divis.	Model: End of Phase Divis.	Model: Middle of Phase Divis.	Nature
		degrees	degrees	degrees	degrees
XXI e	9			124	125
k	1			56	46
	2			*SW	*SW
	5			231	226
	10			57	53
XXIII e	2	95	*SW	*SW	86
	3			281	277
	4			285	290
	8	280	102	109	94
	9			99	99
XXV c	3			270	269
	4			272	275
	9			91	91
	10			91	93

*SW - Slack Water

b) Table of Comparison, Converted Model Phase Division Velocity Magnitudes with Nature as given in Tech. Memo. No. 8.

Area No.	Phase Divisions	Magnitude of Velocity: Model	Nature
		ft/sec.	ft/sec.
XXI k	5	2.8	3.6
XXIII e	3	3.2	1.6
	4	4.0	4.7
XXV c	3	2.4	3.0
	4	3.1	3.4
AV.		3.2	3.3

The agreement between model and prototype was good in the channels and deeper areas at strength of flood and ebb currents. The discrepancies between model and prototype were greatest over the shoal areas and near slack water.

MOVEMENT OF BED MATERIALS

Bed-movement was simulated in the fixed-bed model by using powdered coal having a specific gravity of 1.33 and a median diameter of 0.0041 inches. Theory and the observed behavior in the model indicated that this material was relatively more difficult to move as bed-load than the sand in the estuary; it was the most suitable material available for these qualitative experiments. Another technique used was to place permanganate crystals on the model surface at key locations. The important features of the pattern of bed movement were as follows:

- Under average conditions of river flow and tide, coal placed in the ship channel off Three Tree Point was moved rapidly, spreading both upstream and downstream along the ship channel and southward over the shoals as far as Snag Island Jetty. At the end of these runs, coal was found along the Ship Channel as far as Tongue Point and only a small amount had been carried onto the shoals west of Harrington Point.

- At freshet stage, coal placed in the main channel off Elliott Point passed through both the old channel and the Miller Sands Cut-Off. Part of the coal then followed the channel towards Tongue Point, but the major portion of it was carried onto the shoals west of Harrington Point. A very large accumulation of coal occurred west of Harrington Point along the line of the proposed channel "D". With channel "D" open, a greater percentage of the material reaching Harrington Point passed along this path than with it closed. West of Tongue Point the main bed-movement is outward across the estuary along the north side.

It was these experiments with coal in the fixed-bed model which answered the major question regarding channel location. The best channel indicated by the movable bed model from Harrington Point along the north side of the estuary to the jetties would be closed by sediment after each year's freshet.

In an effort to account for sand movement through the estuary, laboratory experiments were carried out on a number of sands, including one from the Columbia River estuary (O'Brien and Rindlaub, 1934; O'Brien, 1936). The work showed that the rate of transport was a function of $(V/D^{\frac{1}{4}})$ for a particular sand. Samples from the estuary showed a median diameter of 0.0096 inches. Local variations in sand size could not be considered in computing the bed-movement because of insufficient bottom samples, and the computations were made assuming a uniform sand size equal to that of the estuary sample tested in the laboratory.

Table VI shows the rate of movement at several points in the estuary during representative phase division. Table VII shows the rate of movement in pounds per hour at four sections in each of the ten tide phases, the net

TABLE VI

Bed-Movement Across Different Sections in Estuary

(in thousands of pounds of dry sand per hour)

Section		Average Norman Yearly Conditions				Freshet Conditions
		Ebb (Seaward) : Flood (Inward)				Ebb (Seaward)
		Phase Division				Phase Division
No.	Location	4	5	8	9	5
I	Ends of Jetties	46	16	64	69	72
II	Clatsop Spit	230	81	292	441	580
III	Chinook Dike	100	25	218	661	1,580
IV	Flavel	185	345	141	115	1,130
V	Astoria-Knappton	246	700	455	128	1,810
VI	Tongue Pt.-Grays Pt.	670	710	100	232	2,690
VII	Tongue Pt.-Harrington. N. bank of Channel	* 820	*1,630	108	3	* 3,860
VIII	Tongue Pt.-Harrington. S. bank of Channel	80	185	1	42	* 1,378
IX	Jim Crow Point	167	205	0	0	430

* Movement occurs in both directions across section.
Figure given is not movement in seaward or ebb direction.

TABLE VII

Bed Transportation
(pounds per hour)

ase	Section I (Jetties)		Section II (Clatsop Spit)		Section III (Chinook)		Section IX (Jim Crow Point)	
	Average	Freshet	Average	Freshet	Average	Freshet	Average	Freshet
1	* 1,000	* 96,000	* 1,000	* 225,000	*2,000	*28,000	0	0
2	*27,000	*390,000	*215,000	*1,270,000	*11,000	*360,000	0	*85,000
3	*90,000	*570,000	*197,000	*1,730,000	*95,000	*1,150,000	*19,000	*295,000
4	*46,000	*760,000	*230,000	*1,170,000	*200,000	*1,300,000	*167,000	*426,000
5	*16,000	*72,000	*81,000	*580,000	*25,000	*1,580,000	*205,000	*430,000
6	0	0	0	0	0	*36,000	*41,000	*1,300,000
7	-5,000	-64,000	-78,000	-246,000	0	-38,000	*27,000	*370,000
8	-64,000	-208,000	-292,000	-840,000	-218,000	-730,000	0	*82,000
9	-69,000	-150,000	-441,000	-890,000	-666,000	-1,300,000	0	0
10	0	0	0	-41,000	-3,000	-77,000	0	0
Net Movement per tide (pounds)	*52,000	*1,830,000	-194,000	*3,700,000	-810,000	*2,900,000	*570,000	*3,720,000
Net Movement per year+ (tons)	*17,000	*625,000	-37,000	*1,260,000	-277,000	*980,000	*195,000	*1,270,000

Notes:

* Indicates movement Seaward

\- Indicates movement Inward

\+ Taken as 680 tides

movement in pounds per tide, and the annual movement in tons in a year of 680 tides under average annual and freshet river flows. Figure 6 shows the computed rates of bed transport during Phase Division 4.

At an average flow of 225,000 second-feet throughout the year, the average concentration of suspended material must be approximately 50 parts per million to transport 10,000,000 tons in suspension - the amount indicated by measurements at the Dalles. Even at points of greatest agitation, such as over the hole off Tongue Point and around the old dikes at Harrington Point, the concentration of suspended material in the estuary reaches this value only at freshet stages. The average concentration throughout the year is believed to be materially less than 50 ppm and much of the material must move as bed-load if this annual load in the upper river is to be transported through the estuary.

The suspended load in the upper river amounted to 10,000,000 tons per year or 2,350,000 pounds per hour. At strength of ebb current under freshet conditions, with an extreme range of tides, bed movement exceeds this figure only at two sections within the estuary and is small at Jim Crow Point and Clatsop Spit.

This study of sediment movement in the estuary was not pursued farther because the other experiments described had provided answers to the engineering problems under study.

The analysis of bed-load movement indicated that regulation of the river in such manner as to reduce peak flows may have a disproportionately great influence on the channels of the river and the estuary. It has been estimated that at Wesport and Eureka bars, bed-movement is unimportant at fresh-water flows below 350,000 second-feet. Above this discharge, the transportation of material increases very rapidly and regulating the flow will reduce the total volume of material transported by the same total volume of water. The effect of such a change will vary with location in the river. Near tributaries which supply material, the average capacity to remove material will be reduced and shoaling will occur, whereas at points distant from sources of sand, depths should increase.

CONCLUSIONS

1. The movable bed model may have been more reliable than it was believed to be at the time, and this approach may have been abandoned prematurely.

2. The fixed-bed model to a vertical scale of 128 and a horizontal scale of 3600 reproduced with acceptable accuracy the range and lag of tide and the direction and velocity of the currents. The agreement was good in the channels and deepwater areas near strength of ebb and flood currents. Over shoals and around the time of slack water, the discrepancy between model and prototype was larger.

3. The movement of powdered coal in the model under average and freshet river flows appeared to agree qualitatively with the movement in the estuary.

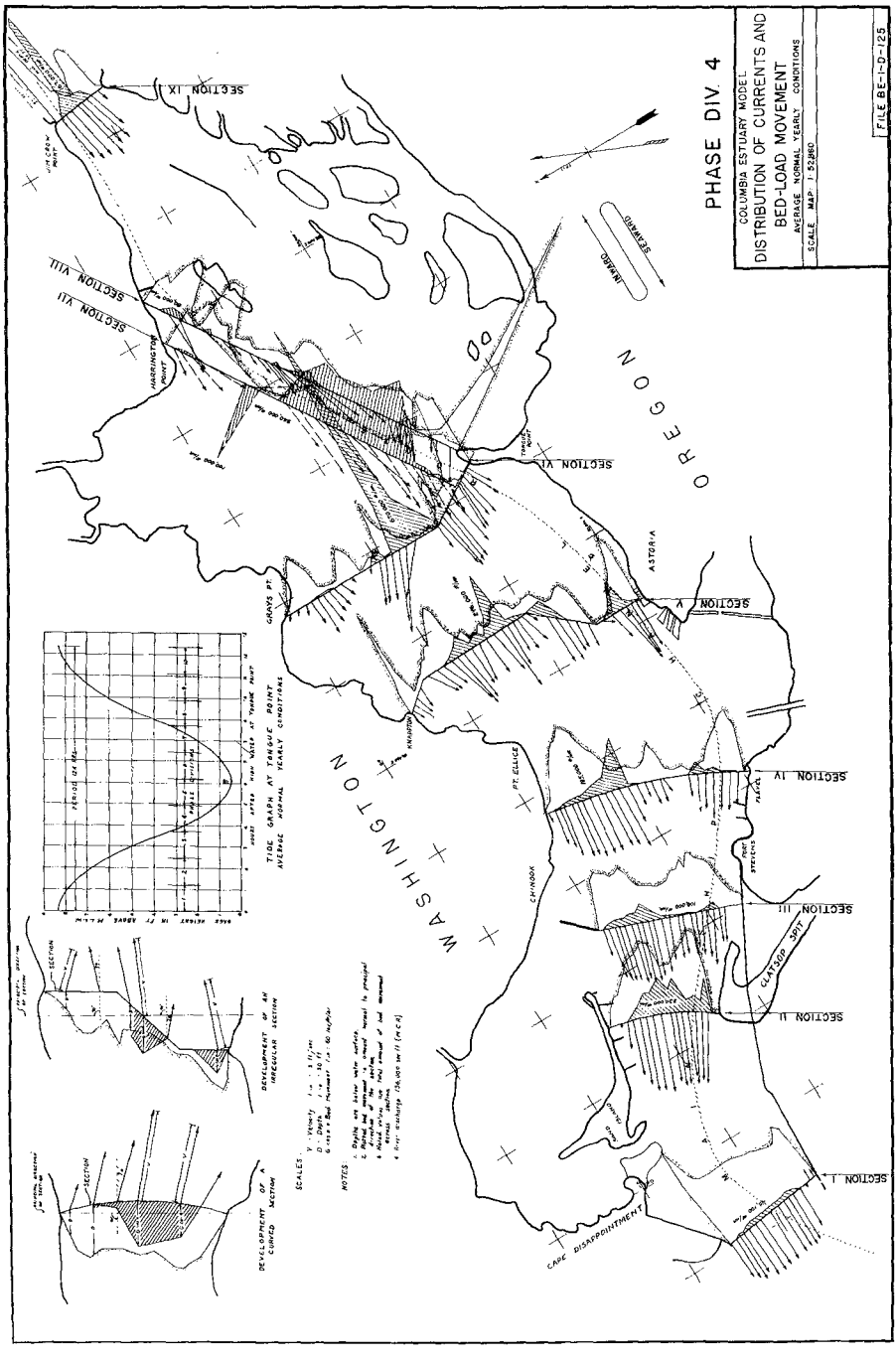

Fig. 6. Distribution of currents and bed-load movement.

4. Tidal models, which do not involve either wind waves or salinity gradients, may be modelled to small scales and large distortions with reliable results.

REFERENCES

Herrmann, F. A., Jr., and Simmons, H. B. (1968). Model studies of nagivatio improvements, Columbia River Estuary, Waterways Experiment Station, Tech. Report No. 2-735, Rept. 1, Hydraulic and Salinity Verification (Dec. 1968).

Johnson, J. W. (1948). Model studies made at the University of California River and Harbor Laboratory, Trans. Amer. Geophysical Union, Vol. 29, No. 1, Feb. 1948.

Kidby, H. A. and Oliver, J. E. (1966). Erosion and accretion along Clatsop Spit, Coastal Engineering, Santa Barbara Specialty Conference, Oct. 1965, Amer. Soc. of Civil Engineers, New York, pp. 647-672.

O'Brien, M. P. and Rindlaub (1934). The transportation of bed-load by streams, Trans. Amer. Geophysical Union, Part II, June 1934, pp. 593-603

O'Brien, M. P. and Cherno, J. (1934). Model law for the motion of salt water through fresh, Trans. Amer. Soc. Civil Engineers, Vol. 99, pp. 576-609.

O'Brien, M. P. (1935). Models of estuaries, Trans. Amer. Geophysical Union, Part II, Aug. 1935, pp. 485-492.

O'Brien, M. P. (1936). Notes on the transportation of silt by streams, Trans. Amer. Geophysical Union, Part II, pp. 431-436.

O'Brien, M. P. (1952). Salinity currents in estuaries, Trans. Amer. Geophysical Union, Vol. 33, No. 4, Aug. 1952, pp. 520-522.

Reynolds, Osborne (1887). On certain laws relating to the regime of rivers and estuaries, and on the possibility of experiments on a small scale, Report of the British Association for the Advancement of Science, 1887, pp. 555-562. Also see Reports of 1889, pp. 327-343; 1890, pp. 512-534; and 1891, pp. 386-404.

University of California (1936). Final report on field and laboratory studies of the navigation channels in the estuary of the Columbia River, U. S. Tidal Model Laboratory, Tech. Memo: No. 21, Berkeley, Dec. 28, 1936 (unpublished)

CHAPTER 143

FLUSHING CHARACTERISTICS OF SMALL-BOAT MARINAS

by

Ronald E. Nece[1] and E. P. Richey[2]

ABSTRACT

Results are presented for a laboratory study investigating the effectiveness of using a small-scale laboratory model to predict tidal flushing patterns in small-boat marinas. Laboratory results are compared with field measurements taken in an existing small-boat harbor.

Model limitations are indicated, but it is concluded that simple, small-scale models can constitute an effective, economical tool in the evaluation of designs of small, enclosed basins where water quality problems associated with circulation patterns in the basin are important. Some implications are made concerning the effect of basin planform upon circulation patterns.

INTRODUCTION

Most coastal engineering projects reported in the current literature are of such magnitude that design studies usually incorporate one or both of the following: a large-scale laboratory model study, in conjunction with a comprehensive program of field data acquisition needed for both model input and verification; or, a computer numerical model study of the harbor or estuary area concerned, again making use of field data to provide boundary conditions leading to solutions for currents, tidal elevations, and sometimes pollutant motions. As questions of water quality assume ever greater importance in coastal engineering works the continued use of the above methods, and especially the growth of numerical modeling, is both anticipated and logical. On the other hand, there will continue to be projects of a much smaller order of magnitude which do not justify the expense of a large-scale model study, for which two-dimensional numerical models with their required detailed field data input might represent a very uneconomical exercise in mathematics, and for which one-dimensional mathematical models would not be detailed enough and would mask significant local effects. For such lesser projects the use of small-scale laboratory models may be worthwhile and justified in project evaluation.

This paper reports on a preliminary study in which small-scale models are considered as a tool in the design and evaluation of small-boat harbors with respect to their flushing characteristics. In order to determine the

1. Professor of Civil Engineering, University of Washington, Seattle, Washington.
2. Professor of Civil Engineering, University of Washington, Seattle, Washington.

effectiveness of small laboratory models in describing water motions associated with harbor flushing, a model of an existing installation was constructed. Prototype vs. model performance could be obtained fairly simply by taking advantage of the conveniently located, small, well defined and relatively manageable tidal water body of the field installation.

Previous emphasis on small-boat basins, or marinas, has been on protection from wave action, but more marina installations will be examined in the future with special attention to their environmental impact. Concerns include how marinas respond to pollution sources and if marinas themselves constitute pollution sources, knowledge of current patterns for use in oil spill protection and/or cleanup, and how well marinas are self flushing.

The study reported here was influenced by regional needs in the Puget Sound area of the State of Washington, U.S.A. A 1968 study projected an increase in the number of permanent winter rental moorages in Puget Sound and adjacent waters from an existing 11,600 in 1966 to 74,300 in the year 2000 (1)[1]. While more recent demographic estimates may be more conservative, the magnitude of the problem still is large. It also has been estimated (1) that an average of 3 feet of shoreline is utilized at present for each moorage, and that approximately 200 miles of shoreline in Puget Sound are considered suitable for potential marina developments. Optimum siting and design of future marinas therefore will be of considerable environmental importance in the Puget Sound area, which can be considered representative of other coastal regions in terms of small-boat use.

Another factor bearing upon future installations is that many existing marinas no longer could be built in their present configurations under regulations enacted recently. In the State of Washington, marina bulkhead and/or breakwater configurations can have significant effect upon the mortality rate of migrating juvenile salmon because the migrating fry may be forced away from their desired shallow water routes into deeper water where they become subject to predator fish. Fisheries agencies have adopted revisions in breakwater and bulkhead standards (2); the effects of these revisions, which may require multiple harbor entrances, detached breakwaters, or navigation breaches in some cases, need investigation.

Many small-boat harbors allow a number of simplifications in model studies. Stratification is often negligible; breakwater-enclosed marinas typically are built where there is little or no fresh water inflow to the basin, and up to half of the tidal prism may be exchanged on a typical high tide. Wave effects are minimal, by design and by the small absolute size of the installation. Wind effects, while obvious on surface floatables and surface currents, are negligible on major currents. Tides are the dominant mechanism for producing water motions. Bottom frictional effects are not significant in the gross current patterns of the relatively short and deep water bodies. Consequently, model construction and operation can be simplified. Limitations on interpretation of model results then must be kept in mind; these will be discussed later.

---

1. Numbers in parentheses refer to entries listed in the References.

PHYSICAL CHARACTERISTICS OF MODEL AND PROTOTYPE

Prototype

The installation selected for the study was the City of Des Moines Small Boat Harbor, located on the east shore of Puget Sound about 15 miles south of the city of Seattle. The marina, built in 1970, was constructed on a tide flat area which was dredged to sufficient depth to allow movement of shallow draft pleasure motor and sail boats. Design dredging depths range from -8 feet MLLW at the south (closed) end of the marina to -13 feet MLLW at the entrance. Enclosing the marina is a rubble mound breakwater extending 500 feet seaward from the shoreline and then northward for 1,950 feet. The space between a timber pile breakwater and the northern end of the rubble mound breakwater provides a 175-foot entrance width at MWL. Fourteen floating piers within the marina provide 682 boat berths. Figure 1 is an aerial view of the installation.

Tides in Puget Sound are of the mixed type, with unequal lows. Mean sea level at Seattle is 6.8 feet above MLLW; the mean tide is 8.0 feet, and the average diurnal tide is 11.7 feet (3). At Des Moines there is zero height correction for low water, a 0.4-foot additive correction for high water, and an average lag of 6 minutes on Seattle for times of high and low water. The only direct fresh water inflow to the basin is sporadic and comes from storm sewer drains servicing streets immediately adjacent to the marina complex.

Model

The distorted laboratory model had a horizontal scale $L_r = 1{:}500$ and a vertical scale $Z_r = 1{:}50$. The corresponding velocity and time ratios were: $V_r = Z_r^{1/2} = 1{:}7.07$, and $t_r = L_r/V_r = 1{:}70.7$. The model, constructed primarily of plywood, was located in a tank having overall dimensions of 8 feet by 12 feet. For purposes of economy and simplicity of both construction and operation the enclosing breakwater was made impervious, the basin bottom was constructed to design dredging depths, and no attempt was made to simulate the floating piers or boats. Because currents in Puget Sound offshore from Des Moines are weak, there was no effort to model exterior currents. The model is shown in Figure 2.

Constant amplitude, constant period tides only, were produced in the model. The tidal generator was a variable-elevation waste weir, driven by a small motor through appropriate gear reducers and a Scotch yoke mechanism to obtain harmonic motion, and fed by a constant-rate water supply. Economy dictated this choice of a simple tide generator. The model tides were verified to be very nearly sinusoidal.

The model scale so selected was known to violate equality between prototype and model of some similarity parameters important in the modeling of pollutant motions in tidal basins, as summarized by Carstens (4). Despite the presence of jets and wakes formed by the tidal flows past the vertical breakwater at the entrance and past other sharp corners in the boundary planform, much of the model basin flow was in the laminar regime and had Reynolds numbers $\mathbb{R} = Vd/\nu$ (V = local depth-averaged velocity, d = corresponding water depth) considerably below the 1,000 value commonly associated

with the lower limit of turbulent free surface flow. In addition, there was no attempt to scale overall diffusion coefficients; hence, there was no reproduction of diffusion processes in the model.

Consequently, the small-scale model could not be utilized to reproduce either pollutant diffusion or the detailed velocity fields of the prototype; the model utility then had to be judged on how well it reproduced the gross tidal current structure of the prototype.

EXPERIMENTAL PROCEDURES

Tide Selection and Correlation

Tide curves showing typical spring tides occurring in one period during which field data were obtained are shown in Figure 3. The repetitive tide selected for use in the model had a nominal 10-foot (prototype) amplitude and a 12.4-hour (prototype) lunar tidal period; corresponding model values were 0.2 foot and 10.52 minutes, respectively.

Field current data were reduced to a common denominator for comparison with model measurements by the following process:

$$\frac{V_{ref}}{V_f} = \frac{\frac{h}{T_0}}{\frac{H}{T}} = \frac{h}{H}\,\frac{T}{T_0} \qquad (1)$$

where: V_{ref} = reference velocity, expressed in prototype units of feet/minute

V_f = current velocity measured in the prototype

h = equivalent prototype height of the model tide

$H = \frac{E + F}{2}$, the average of the prototype large ebb amplitude E and large flood amplitude F

T = time between high water levels enclosing the low water ebb slack tide

T_0 = equivalent prototype time of the model tidal period.

All current magnitudes shown on Figure 8 are given as values of V_{ref}, in feet/minute, prototype; times at which the velocities obtain are expressed in terms of the dimensionless time t/T, as defined on Figure 3. All field data were taken on the large ebb, E, or the large flood, F, in order to obtain more readily measurable current magnitudes.

Current Measurements

All current measurements in both model and prototype were taken with the use of drogues, or floats, which were tracked over time and space.

Most field measurements were made with the miniature drogues shown in Figure 4. The 4-inch by 3-inch cross-form plexiglass drogues could be positioned at any desired depth below the water surface; the color-coded fishing floats, which provided the necessary buoyancy as well as drogue identification, provided minimal exposure to wind drag above the water surface. Drogues were tracked by observers in small boats or standing on the piers; the piers provided ample reference points for distance and angle measurements. Except for the entrance region, velocities shown on the data figures are taken from drogues operating at a 6-foot depth, below the region of reduced velocities caused by the draft of the floating piers and moored boats.

Pathlines and velocities were measured on ebb flows near the outlet. For this purpose, the larger drogue shown in Figure 4 was used. A plane table and alidade, set up on the shore and used in conjunction with the thin stadia rod projecting above the water surface, allowed single-instrument determination of location vs. time of the drogue, from which local velocities at the 4-foot depth could be determined. The path followed by the drogue when it was released at the tip of the vertical timber breakwater provided the shape of the free streamline of the discharge jet at the marina mouth.

A simple visual method was used in the model in lieu of the more common streak photographs of confetti placed on the water surface to measure currents. Length of small, 0.10-inch diameter plastic-coated drinking straws, sealed and weighted at the bottom but open at the top, and with an equivalent prototype depth penetration of 10 feet, acted as drogues responding to an effective average velocity over the water column. Drogue locations were plotted at discrete time intervals by marking pen on a horizontal plexiglass sheet mounted above the model; the requirement that an observer sight down the open vertical bore of the straw cylinder was an effective method of reducing parallax errors. Individual drogues could be inserted at any location and at any time of the tidal cycle; drogue insertions at the same time and place, but on different tidal cycles, yielded pathlines in very close agreement and indicated model consistency.

MODEL-PROTOTYPE COMPARISONS

Ebb Flow at Entrance

Flow conditions in the harbor entrance area are such as might lend themselves to a first analysis utilizing ideal fluid, two-dimensional, free streamline methods if frictional resistance and effects of changing depth are neglected. Such an approach was used by French in considering the velocity distribution in the entrance region of a tidal flow through a relatively short channel into a lagoon (5).

In the present work, limited attention was given to the ebb flow only, in the vicinity of the timber breakwater. One set of drogue tracking data gave field observations of velocities and pathlines at the 4-foot depth. The observed separation streamline of the exit jet was compared with an estimated free streamline location determined by an (interpolated) adaptation of von Mises' two-dimensional contraction coefficients (6). No exact solution was attempted. An effective approach width of b = 175 feet between MWL on the

rubble mound breakwater and the tip of the timber breakwater was selected, as shown on Figure 5. The interpolated contraction coefficient $C_c = 0.58$ gave a predicted jet width of 100 feet. A flow net construction then gave the shape of other streamlines in the predicted jet.

Comparison between predicted and observed separation streamlines on Figure 5 shows that the predicted contraction was overestimated. The laboratory observation was closer to agreement with the predicted location. It is also very clear, however, that the separation streamline past the breakwater is indeed independent of the shape of the dredged channel.

Figure 5 indicates how predicted velocities, all based in part on the predicted free streamline location, compared reasonably well with field measurements. The predicted velocities were calculated by the one-dimensional continuity equation,

$$V = \frac{A_{basin}\left(\frac{dz}{dt}\right)}{a_{exit}} \qquad (2)$$

where: A_{basin} = total surface area of the marina behind the plane of a_{exit} ($A_{basin} = 1.05 \times 10^6$ sq. ft)

(dz/dt) = fall rate of water surface, from tide curves

a_{exit} = cross-sectional area of plane normal to the assumed uniform, one-dimensional velocity distribution in the jet where the jet surface width has become equal to $C_c b$.

Exit velocities measured in the model, while not shown on Figure 5, agreed well with field values.

Circulation Patterns within Marina Basin

The well defined basin geometry presented the temptation to treat ebb flows by potential flow methods -- i.e., by constructing a flow net for the basin configuration and extending Eq. 2 to yield local velocities at all points and at all times on the ebb flow. This procedure, a one-step refinement of rather common one-dimensional methods, could then yield water particle detention times. Both field and model observations confirmed the fallacy of such an approach.

The dominant feature of current patterns within the basin was the establishment of circulation cells initiated by flow separation around the timber breakwater on flood flows. Currents reversed direction almost everywhere in the channel at or very close to low water slack ($t/T = 0.5$). On the following inflow, separation flow past the timber breakwater created a counter-clockwise cell in the area behind the breakwater; this cell grew until it occupied about 40 percent of the basin area, and a second (clockwise) cell was formed and which filled most of the southern part of the basin. (A third, small counter-clockwise cell which formed at the extreme southern end of the enclosure contributed very little to general circulation patterns, but could lead to very long detention times for pollutants introduced in this part

of the basin). When the two primary cells were well established, by t/T ≈ 0.75, the primary inflow current near the middle of the basin was directed inshore and almost normal to the major axis of the marina.

This cellular flow structure is indicated by the float pathlines on Figure 6. Model and field pathlines at comparable t/T times show good agreement. Pathlines in the prototype are limited in length because the floats could not travel beneath piers. For repetive model tides, t/T values of 0.08 and 1.08 have the same meaning.

Angular momentum established during flood tide flows persisted into ebb flows. Outward flows were established in the main channel by the southerly of the two primary circulation cells prior to the time of high water slack. This effect is illustrated in Figure 7, where limited field tests were used to check the flow patterns observed in the model.

Slight errors were introduced in the model by making the exterior breakwater impermeable. Flows through the porous rubble breakwater were confirmed by dye observations in the field, and small head differences were measured by manometers between the interior and exterior faces of the breakwater during tidal flows. Pending the general lack of information in the literature on head loss relationships for flow through porous media of large 'grain' size, no attempt was made to calculate discharges through the breakwater. It is considered that any resulting discrepancies would be confined to regions adjacent to the breakwater and would have little if any effect upon general circulation patterns.

Existence of the two primary circulation cells is shown clearly in Figure 8, which indicates current patterns at t/T = 0.75. Although no direct comparison was reached between field and laboratory velocities at exactly the same time and place, agreement between model and prototype is adequate. Model-determined velocities shown at nearby points in Figure 8 are an indicator of the degree of consistency and reproducibility between repetitive tidal cycles as obtained by the simple visual observation procedures used in the laboratory.

CONCLUSIONS

The small single-entrance tidal water body studied has well defined boundaries; wind and stratification effects are negigible, so that tidal action is the dominant flow-producing mechanism. Despite the well defined boundary conditions, water motions within the basin are not easily predictable and cannot be treated by simplified calculation methods. Computation procedures such as those outlined by Leendertse (7), modified to incorporate the important separation effects, might be used to predict water motions; however, in terms of project sizes and costs as typified by the marina reported upon here, such methods might not be justified in terms of cost vs. useful output.

Planform geometry is seen to have a significant effect upon circulation patterns within the marina. Sharp corners, with resultant flow separation, promote circulation and mixing which may be helpful in the elimination of pollutants from the basin; effects of this additional mixing upon detention times of pollutants inserted at different locations in a basin likewise would

depend upon basin geometry. Asymmetry of single entrances appears to be advantageous in terms of promoting circulation within the marina. The number of circulation cells within a tidal basin would seem to be dependent largely upon entrance asymmetry and the length: width ratio of the planform. Investigation of the effects of such geometry parameters would be fruitful in considering designs of future, largely enclosed, marinas.

The laboratory model tested was found to give satisfactory reproduction of the gross velocity patterns within the existing marina. It is concluded that such small-scale models are a useful and economical tool to be used in the design and evaluation of proposed small-boat harbors.

ACKNOWLEDGMENT

Partial financial support for the laboratory activities was obtained from the Water Quality Training Program of the U.S. Department of the Interior. M. Maher, L. Lewis, T. Kearns, and C. Tweedt, graduate students at the University of Washington, contributed to various phases of the program.

REFERENCES

1. "Pleasure Boating Study, Puget Sound and Adjacent Waters, State of Washington", Report prepared for Puget Sound Task Force of Pacific Northwest River Basins Commission by Seattle District, U.S. Army Corps of Engineers and Pacific Northwest Region, Bureau of Outdoor Recreation, November 1968.

2. "Criteria Governing the Design of Bulkheads, Land Fills, and Marinas in Puget Sound, Hood Canal, and Strait of Juan de Fuca for Protection of Fish and Shellfish Resources", Washington State Department of Fisheries, Olympia, Washington, February 1971.

3. United States Coast and Geodetic Survey, "Tide Tables, West Coast North and South America", 1971.

4. Carstens, T., "Physical Modeling of Residence Times in Ocean Basins", Proc. 1972 Technical Conference on Estuaries of the Pacific Northwest, Oregon State University, Corvallis, Oregon, March 1972 (in press).

5. French, J.L., "Tidal Flow in Entrances", Committee on Tidal Hydraulics, U. S. Army Corps of Engineers, Technical Bulletin No. 3, January 1960.

6. Rouse, H., "Elementary Mechanics of Fluids", J. Wiley & Sons, New York, 1946 (p.57).

7. Leendertse, J. L., "Use of a Computational Model for Two-Dimensional Tidal Flow", Proc. Eleventh Conference on Coastal Engineering, London, 1968, pp. 1403-1420.

Fig. 1. Des Moines Small-Boat Harbor

Fig. 2. Laboratory Model

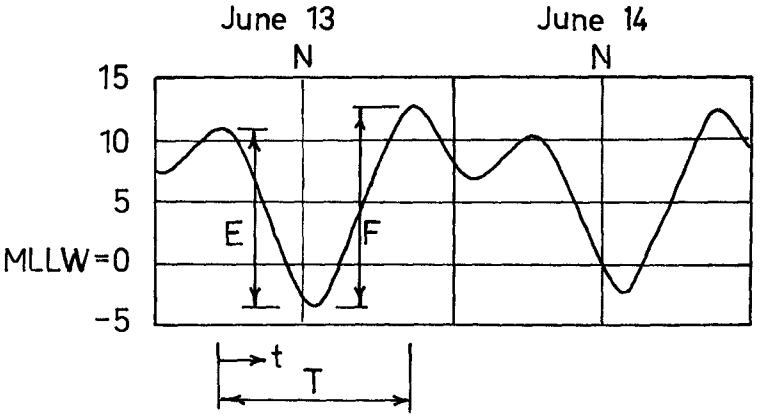

Fig. 3. Typical Tide Curves for Puget Sound, and Notation Definition

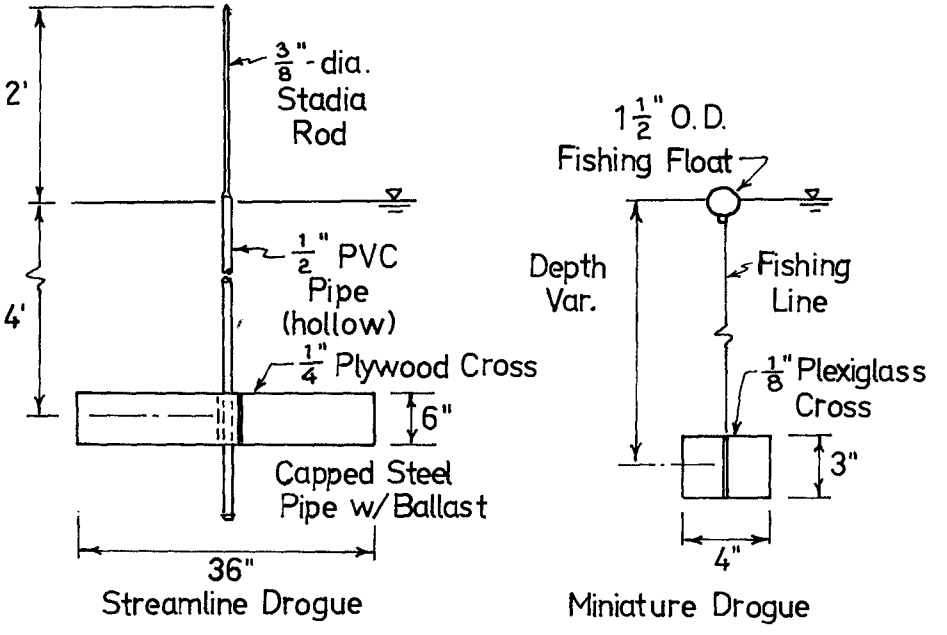

Fig. 4. Drogues Used in Field Studies

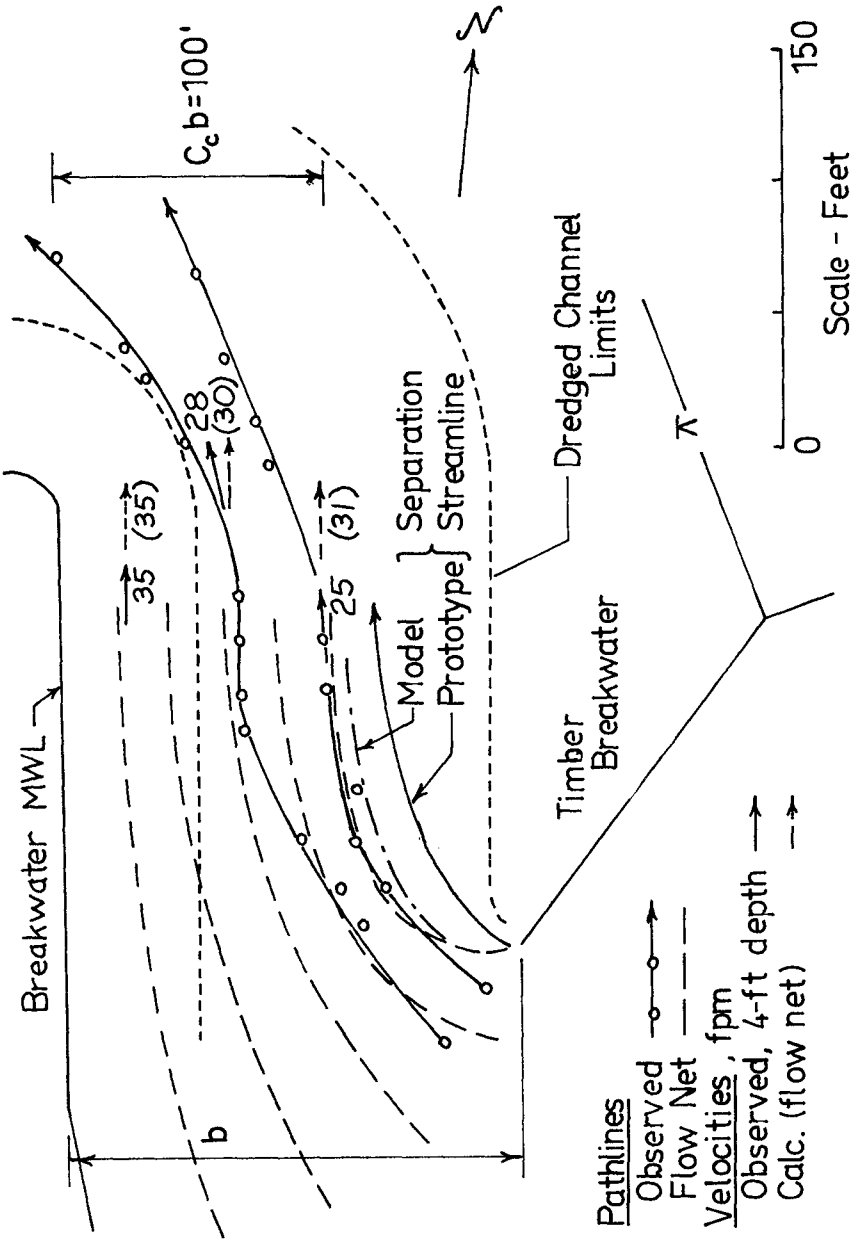

Fig. 5. Ebb Flow at Harbor Entrance

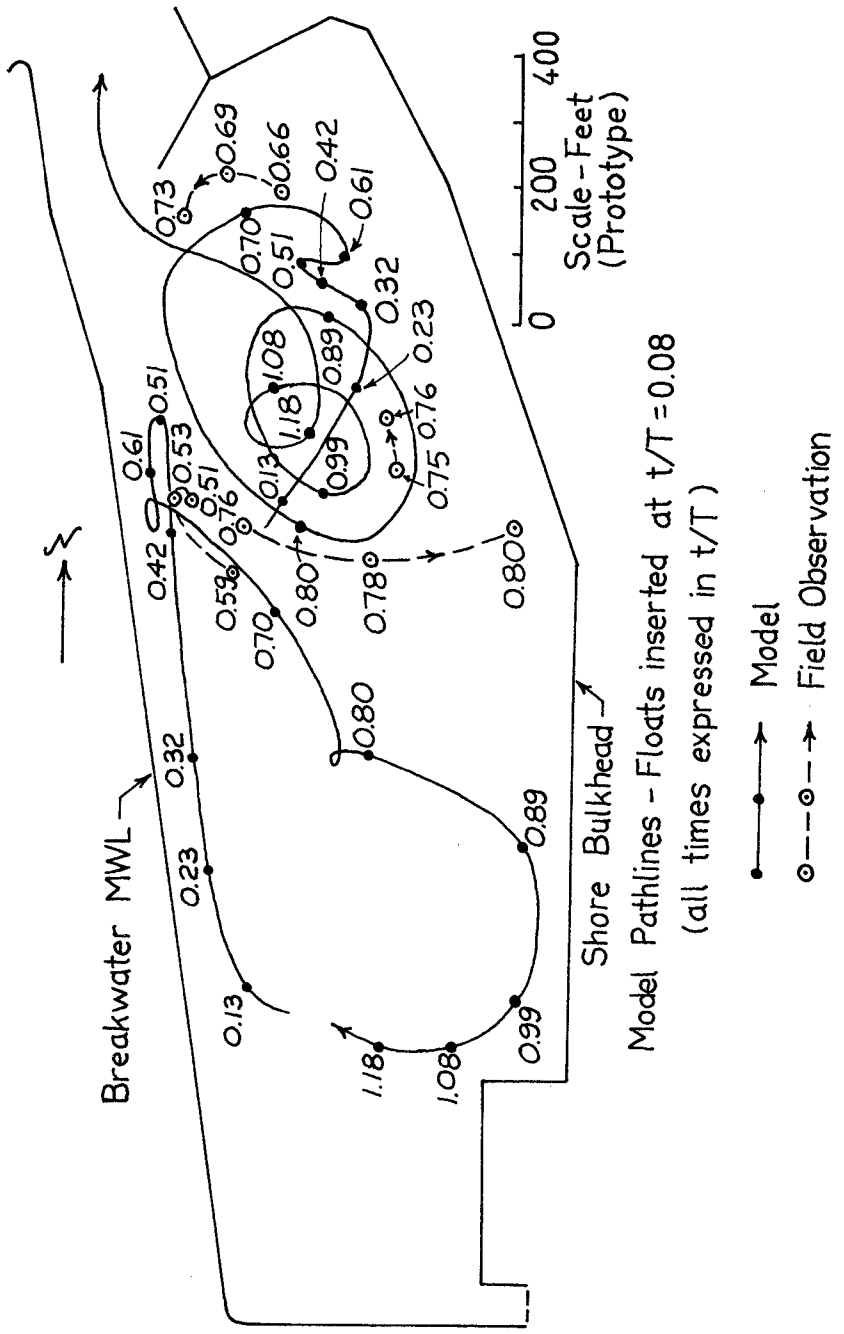

Fig. 6. Drogue Pathlines, Model-Prototype Comparison

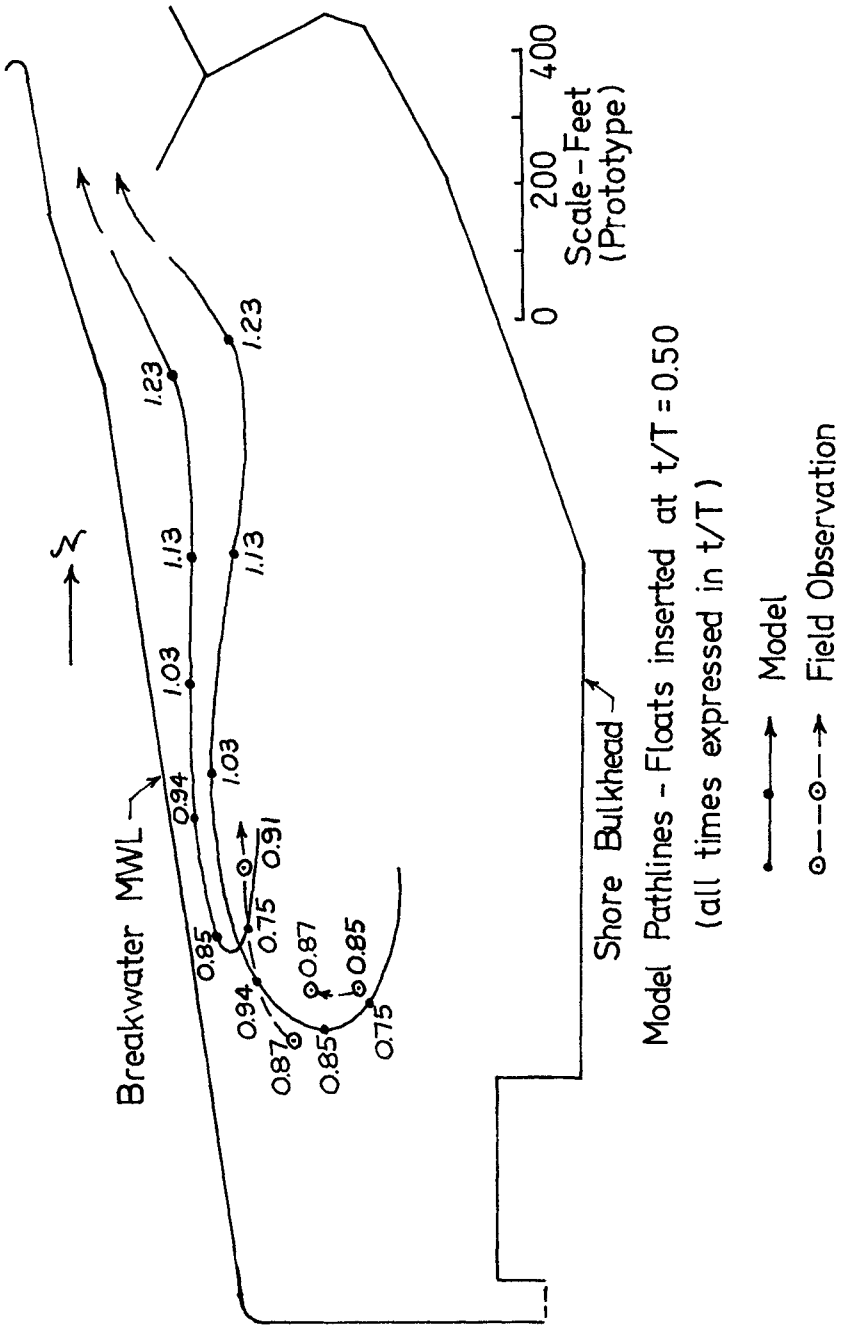

Fig. 7. Drogue Pathlines, Model-Prototype Comparison

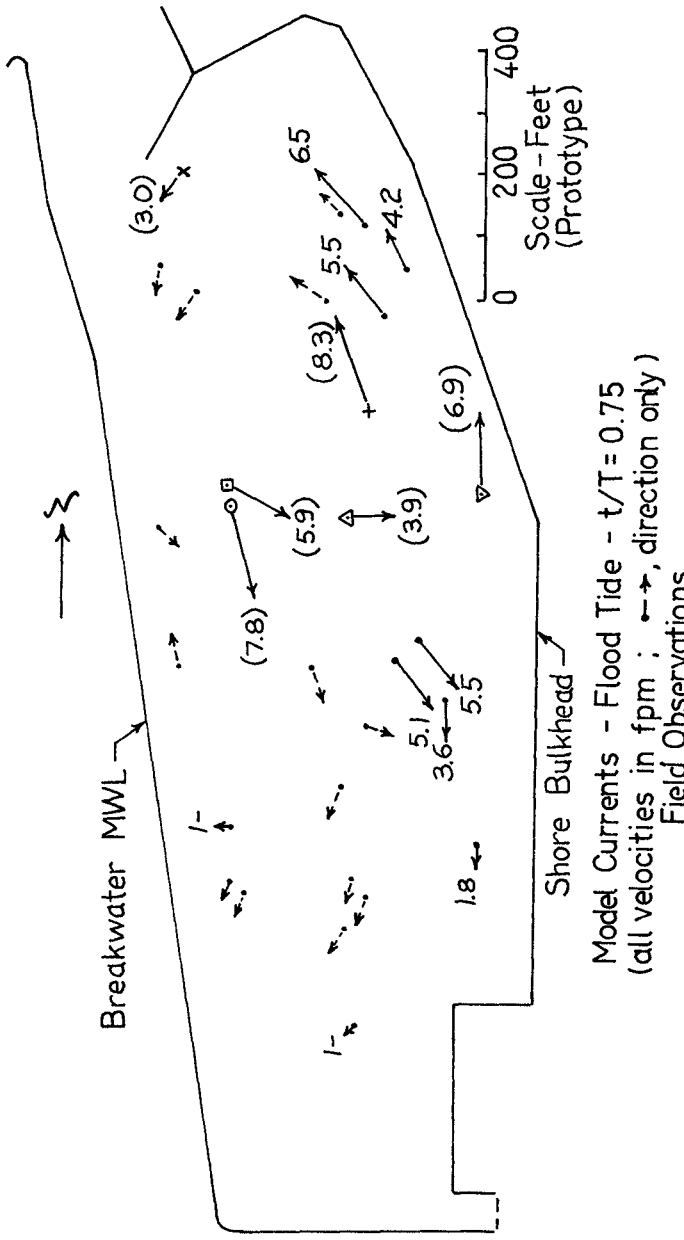

Fig. 8. Currents at t/T = 0.75, Model-Prototype Comparison

CHAPTER 144

NEARSHORE CURRENTS SOUTHEASTERN STRAIT OF GEORGIA

M. L. Schwartz, R. C. Fackler, E. A. Hoerauf, C. E. Larsen,
K. L. Lingbloom, M. A. Short
Coastal Studies Group, Department of Geology, Western Washington State College, Bellingham, Washington, 98225, U.S.A.

ABSTRACT

Nearshore water transport in the vicinity of Birch Bay and Cherry Point, Washington was investigated during the spring of 1971. The techniques used were: surface floats with variable depth drags, dye patches, streams of paper sheets, wind direction and velocity data, infrared and color aerial photography, and salinity and temperature readings from water samples. Birch Bay flood tide transports water into the bay, and ebb tide carries it out. The latter water either eddies off Point Whitehorn or moves out into the Strait of Georgia. Flood tide at Cherry Point transports water to the Point Whitehorn eddy or into Birch Bay, while on the ebb tide water moves from Cherry Point toward the vicinity of Neptune Beach and Sandy Point.

INTRODUCTION

Recent concerns regarding possible water pollution in the Strait of Georgia have led to an increased amount of scientific inquiry into the environmental factors affecting the nearshore oceanography of water transport. The authors have attempted to look into these factors over one ten-mile portion of Washington coastal water along the southeastern shore of the Strait of Georgia. More specifically, we have concerned outselves with Birch Bay and the coast south including an industrial area in the vicinity of Cherry Point (Fig.1). A sanitary sewer outfall located in Birch Bay has been proposed, and an oil refinery presently under construction will discharge its effluent at Cherry Point. Both projects have the potential of greatly affecting the ecology within nearby waters.

Environmental Overview:

A. Fraser River: Perhaps the single most dynamic factor affecting the Strait of Georgia is the Fraser River which drains much of interior British Columbia. Snow melt in the summer months adds great quantities of turbid fresh water to the Strait. Due to its lower density the river water creates a strongly stratified water column. Maximum flood water from the Fraser River may be observed to extend from its mouth near Vancouver, B.C. to Galiano Island on the opposite side of the Strait. Low density water also moves southward along the shore of the delta to the vicinity of Point Roberts off Birch Bay and Cherry Point (Kincaid et al, 1954; Sylvester et al, 1966; Waldichuk, 1968; Wennekens et al, 1955). Seasonal density stratification of coastal waters may be seen in figure 2 which utilizes data from a study done by the University of Washington (Sylvester et al, 1966) for the Intalco Corporation.

B. Surface Winds: Each past water pollution report on the subject area has presented early in its text the dichotomy between overall wind and tidal actions. The waves are the direct result of surface winds blowing across the water. Wave motion consists of nearly orbital movement of the water and transport in the direction of wave travel, both of which diminish rapidly with depth. Low density water and materials at or near the surface are thus transported in the wave direction.

Wind records for January at Bellingham show a high percentage of winds from the south, southeast, east and northeast. For July, west, southwest and south winds predominate (Phillips, 1966).

C. Coastal Geomorphology: The coastal landforms in the study area (Fig.1) are good indicators of the shoreward transport of sediment. Spits are common and provide tangible evidence. They show the resultant direction of transport of sediment along the shore by the wave generated processes--longshore drift and beach drift.

Sandy Point is a large spit actively building to the south from a bluff south of the Mobil Corporation refinery. The Birch' Bay Village spit within Birch Bay makes up part of the shore of the bay.

Yasso (1965) expressed a headland bay beach by its plan geometry. This type of beach is developed adjacent to a headland and is the result of the predominant direction of wave approach. The shoreline of the headland bay beach can be best described in plan view as having the curve of a logarithmic spiral, with its center near the headland. Studies made on Birch Bay by C. E. Larsen (paper in progress) have identified Birch Bay as such a beach. The maximum distance for wind wave development for Birch Bay is to the west and northwest. Waves entering Birch Bay from these directions are refracted around the headland and cause waves to approach the beach obliquely on the south shore. Longshore and beach drifting are directed along the beach in a counter-clockwise gyre. Wave energy decreases from south to north so that coarse sediments make up the southern beaches while there is a decrease in grain size to the north.

D. Tides: The area under study is subject to diurnal tides, with approximately a 2.5-foot range at neap and a 12-foot range at spring. There is a marked diurnal inequality within these cycles. Tidal currents are the prime cause of lateral water transport in the region. It is these currents with which this study is largely concerned.

METHODS

Several techniques were employed to study the effect of tidal currents on the transport of water from proposed sewage and effluent outfall sites at Birch Bay and Cherry Point respectively. The 32-foot research vessel, Mijada, was anchored at each of the proposed sites at the beginning of a spring ebb

or spring flood tide. Various markers were released in the water and, at given intervals, observers charted their position to gain an idea of the maximum transport effect of the tidal currents.

The Defence Research Establishment Pacific laboratory in Victoria, B.C. supplied fluorescene marker dyes. One container of dye was mixed with surface water in a one-gallon bucket and immediately poured into the water off of the stern of the anchored ship. This was repeated at regular intervals, and the progress of each dye patch was charted by the various observers. The first day dyes were released at one-hour intervals and observations from land were taken hourly. The dye disperses to the point where it is not visible from land in about 45 minutes, so on subsequent days the releasing and observation of the dye was done at half-hour intervals or less.

The second marking system employed was simply the releasing of sheets of paper from the stern of the anchored vessel. This was done at about 5-second intervals throughout the observation period. The paper was not visible from land, but it showed up well in aerial photographs and is an excellent indicator of the movement of surface water. Several types of paper were tried. Newspapers and computer print-out sheets were found to be too absorbant and sank readily from sight. A heavier grade of paper (water-stained scraps from the W.W.S.C. print shop) floated well and was the best paper for charting the currents.

The markers which were most easily sighted by the land-based observers consisted of wooden floats with weighted drags suspended at set depths below the surface, patterned after Scrimger (1960). The floats were 4-foot square sheets of 3/8" plywood. A 2-foot mast on each float was made of 3/4" dowelling. Each float was painted with different colors and designs and had various flags on the mast for easy identification. Suspended at set depths from the floats, by nylon cord, were drags made of two 4'x1' boards of 3/8" plywood joined so that there were four mutually perpendicular vanes, each 1'x2'. Each drag was held down by two four-pound lead weights tied to its base.

Three floats were used on each occasion. One had the drag nailed to the bottom of the float and was designated as the surface float. The two other floats had the drags suspended at various depths, depending on the depth of the water. At the Cherry Point site the vessel was in 50 feet of water, so the drags were set at 16 feet and 25 feet. At Birch Bay, in 25 feet of water, the drags were suspended at 8 feet and 16 feet below the surface.

Several methods were employed to chart the progress of the various markers in the tidal currents. The primary method involved two observers stationed on land, each with a clear view of the anchored ship and the floats. As the floats moved, however, it was sometimes necessary for one of the observers to move down-current to another position in order to stay within sight of them. The observers each had a plane-table on which was

mounted a map of the area being studied. Overlying the map was a sheet of Mylar drawing plastic on which the sighted positions of the markers at various times were noted and labeled. Alidades were used to locate the markers and to plot the lines of sight to the markers on the Mylar. Each observer also had a 2-way citizen's band radio with which they were in contact with the R/V Mijada. At given intervals, on signal from aboard the Mijada, each observer plotted and labeled the line of signt from his position to each float. Subsequent calculations utilizing the data from both observers aided in plotting the location of each float at each sighting. In this way the direction and rate of movement of each of the floats was charted.

As was stated earlier, the paper markers were never visible from land and the dye markers were only visible for about 45 minutes, so the floats were the only markers whose positions could be consistently charted from land. Another problem was the glare of the sun in the afternoons. It often made the locating of the floats difficult for the land observers. This problem was solved by having the R/V Mijada run down to the floats. The position of the boat could then be plotted by the land observers. This necessitated less regular observations, as the Mijada moved from float to float.

An airplane was available for use on two of the four days on which observations were made. On each of those days the plane made two flights at 2,000 and 4,500 feet over the area being studied. One flight was made one hour after slack tide and one flight at mid-tide. Aerial pictures were taken on each flight utilizing both infrared and color photography. The floats were plainly visible, and the dye was more easily visible from the air than from land. The paper markers were seen as a very fine line, charting the path of the surface water from the boat down-current. The ebb tide also exhibited bands where tidal currents of the warmer, shallow, bay water flowed out over the colder water of the Georgia Strait.

Float positions were also determined through the use of a sextant and a three-armed protractor. In this case the ship had to locate each marker. Upon pulling up to a float, someone on the ship would hold the sextant horizontally and read the angles between three prominant landmarks; first the angle between one of the outside landmarks and the center one of the three, then the angle between the center one and the landmark to the other side. By setting each of these angles between the arms of the three-armed protractor, the exact position of the ship and therefore the float could be determined. This method was tested and found to be as accurate as using the two land-based observers, so on the final day the group relied entirely on this method and the former land-based observers were aboard the ship to help take water samples.

Wind observations were taken using the ship's anemometer periodically during three days on which currents were being observed. Wind observations from the Blaine Air Force Radar Station, located in Birch Bay, for the years of 1968 and 1969 were also made available. They are thrice daily (0730, 1430, 2330) readings of wind velocity and directions. A computer program was developed to give average wind directions and velocities by the month and time of day, month only, and season only.

Water samples were collected in Birch Bay and at Cherry Point using Van Dorn bottles. The bottles were attached to a cable operated by a winch off the stern of the boat. The cable was clearly marked at ten-foot intervals, so the depth of the bottle could accurately be determined. Salinity and temperature values were obtained from each water sample. A salinity titration kit (LaMotte Chemical Products Co. model POL-H) was employed in the salinity determinations made aboard the R/V Mijada. Sampling stations are shown in figure 3.

OBSERVATIONS

Observations were made during the spring (maximum range) flood and ebb tides at the proposed outfall locations for Birch Bay's prospective sewage treatment plant and ARCO's industrial waste disposal to learn the maximum effect of tidal currents on the transportation of water at each of these sites.

On Sunday, March 21, 1971 high tide occurred at 8:38 a.m. and was +8.2 in Birch Bay. The R/V Mijada was anchored over the proposed sewage outfall location and the floats were released at 10:00 a.m. Dye was dropped at 11:00 and 12:00. The airplane flew over at 12:00 noon and 2:00 p.m.

Figure 4 is an aerial photo taken from 2,000 ft. at 12:00 noon. The dyes are not visible, but a faint line of paper can be seen in the photo, tracing the path of the surface water with the ebb tide current. The eight and sixteen foot floats can also be seen in the photo. These two floats moved at about the same rate of speed throughout the day. The surface float moved much faster. Figure 5 is an infrared photograph taken at 12:10 p.m. This time the plane was at 4,500 feet above sea level. The surface float can be seen in this photo. After only two hours, the surface float has traveled 2½ times as far as the floats with deeper drags. An outline of the warmer water from the bay as it flowed out into the Strait of Georgia is obvious in the photo. The land observers also noted that there were bands of calmer water along the paths of the floats, the currents manifesting themselves on the surface. Their "path" of calm water divided as it came out of the bay. Part of it continued south into the Strait while the other part turned in a large eddy south of Point Whitehorn. The surface float followed the current south into the Strait. The eight-foot float followed the eddying current. The sixteen-foot float dragged on the bottom coming around Point Whitehorn and had to be retrieved. The surface float was retrieved too, since it was travelling rapidly into the Strait. The R/V Mijada was able to follow the trail of paper markers to locate the surface float. There was also much debris concentrated along the path of the current.

Both the surface float and the sixteen-foot float were retrieved at 1:00 p.m. and were placed close to the position of the eight-foot float. From that time until 4:30 p.m. all three floats eddied off the southern side of Point Whitehorn, as can be seen in figure 7.

On April 4, 1971, a high tide of +6.8 feet occurred at 11:26 a.m. The R/V Mijada was anchored near the ARCO pier, close to the proposed effluent disposal site, and had markers in the water by 11:56 a.m. The airplane was scheduled to fly over at 1:30 p.m. Since the dye markers had dispersed too much to show up on the previous photos, they were released this time at fifteen minute intervals. The first dye was released at 12:45 p.m. and the fourth and last at 1:30 p.m., just before the plane flew over. Figure 6 is an aerial photo taken 2,000 feet above sea level at 1:30 p.m. The dyes can be seen to be spreading downwind as well as being carried south by the ebbing tidal current. As in Birch Bay the surface float moved the most rapidly.

The direction of the currents is southerly, parallel to the coastline. At 3:00 p.m. the surface float ran into the Intalco pier and had to be retrieved by the R/V Mijada. It was placed in the water farther from shore, so it would clear the pier.

At 10:32 a.m. on Saturday, April 24, 1971, there was a -1.9 foot low tide. An extra surface drag float was dropped just south of Point Whitehorn, in order to determine what would be the path of any water which had been in the eddy at ebb tide. The tidal current on the flood tide ran from south to north and carried the float into Birch Bay (Fig. 8). Later in the day the currents carried the float back out of the bay. The surface, sixteen and twenty-five-foot floats were dropped at 11:30 a.m. No dye or paper markers were used. The paths of the surface, sixteen and twenty-five-foot floats reversed, and with the ebb, the floats headed south. The aforementioned reversal of direction of the surface float out of the bay occurred in the middle of the flood tide. This is evidence of more complex tidal currents within the bay.

On Sunday, April 25, 1971, there was a low tide of -0.9 feet at 12:24 p.m. daylight saving time. At 12:40 p.m. the R/V Mijada was anchored over the proposed sewage outfall location at Birch Bay and the surface, eight and sixteen-foot floats were released. There were strong (10-20 knot) westerly winds on that day. By 2:00 p.m. all three floats had blown aground. The eight and sixteen-foot floats were retrieved and the eight-foot float was taken farther from shore and reset. Within an hour and a half it had blown aground again.

The surface and eight-foot floats were retrieved from the beach and placed in the water farther into the bay. They were retrieved before running aground. The effect of the strong westerly wind was more influential on the floats than were the tidal currents on this day.

CONCLUSIONS

Although the factors affecting the movement of surface waters are numerous, the most effective are tidal movements and effective wind direction. Only tidal movement and effective wind direction are reported on in detail in this paper. The conclusions of this paper are based on their combined effects as shown by actual measurement and observation of coastal processes.

It should be borne in mind that most effluents discharged into these waters will be warmer and less saline, therefore less dense, than the colder and more saline (denser) marine waters (Waldichuk, 1968). The effluents (and buoyant particulate matter) will rise and remain near the surface until effective mixing occurs. As noted in figure 2 and verified by our water samples, there is little stratification of the waters in the Strait of Georgia during the winter, but layering does occur there in the summer months (Sylvester, et al, 1966). Due consideration of these conditions should be included in any environmental planning that involves the Birch Bay-Cherry Point region.

Ebb Tide Transport

A. Birch Bay sewage outfall: Water leaving Birch Bay on an ebb tide (Fig. 7) can be thought of as a banded flow. The extensive intertidal zone creates an easily discernible band of water which has becomes less dense by the inflow of fresh water from numerous small streams and drainage ditches around the bay. The rapid warming of water in the shallow zone also enhances the decrease in water density.

This band of water generally conforms to the curve of the Birch Bay shoreline. It constitutes the surface water from the shore to approximately 3000 feet offshore and leaves the bay in a clock-wise gyre. At Point Whitehorn, the low density water enters the Strait of Georgia at an angle of about S45°W where it is deflected by the main force of a southward tidal current. It moves with the higher density, colder and more saline, waters of the Strait in the form of a large eddy. This eddy movement is visible both from the bluffs of Point Whitehorn and in aerial photographs (Fig. 5). Of special interest in this study was the debris in the center of the eddy. This material did not disperse during the ebb tide and was easily positioned to enter Birch Bay again on the next flood tide. Surface water, as shown by the movement of paper released from the research vessel, was carried deeply into the Strait only when the winds were directed offshore.

Effluent discharged into Birch Bay at the outfall location proposed by the consultants retained by the Birch Bay Water District is located at a greater depth than the low density water band leaving the bay. Should a high degree of mixing not be attained by the diffuser at this depth, material carried by the less dense fresh water from the sewer system will tend to collect in the water band leaving the bay. Although mixing may occur in the Strait of Georgia it is doubtful at this point that a complete exchange of water is attained. Further, evidence of surface materials concentrating in the center of offshore eddys suggests the possibility of this material re-entering the bay on the next flood tide.

B. Atlantic Richfield effluent outfall: Water movement on the ebb tide as recorded from the Atlantic Richfield outfall location (Fig. 8) is rather simple. All floats maintained a nearly uniform distance from shore. This

condition brought the floats to the vicinity of the Intalco pier and waste outfall to the southeast. This fact, combined with similar results measured from the Mobil Oil Co. pier (Kincaid et al, 1954) leads to the conclusion that water movement near Cherry Point is generally parallel to the shore. With this condition a case can exist where, with increased industrialization, one outfall may merge with the outfall of the neighboring industry.

Flood Tide Transport

A. Birch Bay Sewer outfall: Strong wind conditions on the day of float observations were not ideal for the actual measurement of tidal currents. However, information may be gleaned from the flood tide data from Cherry Point to Birch Bay (Fig 7 and 8). Surface water enters the bay from the south near Point Whitehorn and continues into the bay for some distance.

During our float studies, winds were of sufficient velocity from the effective wind direction to carry all floats ashore at Birch Bay State Park. This was also the case with floats dropped off near the mouth of the bay. Such an occurrence offers an example of the effects of wind wave action on materials carried into the bay during the flood tide.

Contrary to recommendations made during an earlier short-term float study (Berschauer and Olson, 1970) wastes discharged at the outfall site will be directed into the bay during flood tide.

B. Atlantic Richfield outfall: Flood tide transport of water, as shown in figure 8, follows the same basic pattern as does the ebb transport, i.e., movement tends to parallel the shoreline. In this case, however, transport is to the north towards Birch Bay rather than to the south. During the optimum tidal range of spring tides, water from Cherry Point can be expected to reach the mouth of Birch Bay. Float positions in this study indicated that this same water, and material carried by it, enter into the initial eddy formation off Point Whitehorn. Once more this offers the opportunity for wind wave activity to have an effect by either directing surface waste upon the beaches at Point Whitehorn, or by allowing it to enter Birch Bay. The flood tide movement of water intermediate between Cherry Point and Birch Bay enters the bay near Point Whitehorn and continues to near the proposed Birch Bay sewer outfall. Water initially near Point Whitehorn at the onset of flood tide may reasonable be expected to be carried along the southern shore of the bay for a yet greater distance. This condition would make contamination of these waters hazardous to the resort community of Birch Bay.

SUMMARY

The conclusions presented in this study show: (1) the proposed sanitary sewer outfall for the community of Birch Bay is located in such a position as to allow the reentry by tidal action of discharged wastes into the bay.

Materials released on a flood tide would be carried deep within the bay. Onshore winds may then drive material ashore on resort beaches. Ebb tide conditions at the bay are such that total exchange of water may not be complete. The mixing of water leaving the bay is only partially achieved. A substantial amount of surficial water is held in the center of an eddy movement south of Point Whitehorn where it may re-enter the bay on the following flood tide. (2) Wastes discharged by industrial sites in the vicinity of Cherry Point can be expected to parallel the shore under the effects of tidal currents. Water passing one industrial outfall can reach the adjacent outfall. Water receiving effluent at Cherry Point on a flood tide is easily carried to the mouth of Birch Bay where it can be driven ashore by effective winds. Water moving to the south on the ebb tide reaches the vicinity of Neptune Beach and Sandy Point.

ACKNOWLEDGEMENTS

This project has been funded in part by the Bureau for Faculty Research, Western Washington State College. We are also indebted to Mr. and Mrs. G. Garlick, Dr. F. Raney, and the W.W.S.C. Outdoor Program for further support; to Birch Bay Village for moorage facilities; and to the Defence Research Establishment Pacific for supplying fluorescene dye.

REFERENCES

Berschauer, W.L., and Olson, J.P., 1970, Engineering report on comprehensive water and sewerage plans for Whatcom County Water District No. 8: Hill Ingman, Chase, & Co., Seattle, 84 p.

Kincaid, T., Wennekens, M.P. and Sylvester, R.O., 1954, A study of the oceanographical and biological characteristics of southeast Georgia Strait prior to operation of the General Petroleum Corp. Refinery at Ferndale, WN.: U. of W., Seattle, 142 p.

Phillips, E.L., 1966, Washington climate for these counties: Clallam, Jefferson, Island, San Juan, Skagit, Snohomish, and Whatcom: W.S.U. Pullman, 64 p.

Scrimger, J.A., 1960, Temperature variations in Esquimalt Lagoon--a small landlocked body of water subject to tidal flushing: Limnology & Oceanography, 5:414-424.

Sylvester, R.O., Carlson, D.A., Christman, R.F., and Oglesby, R.T., 1966, A study of wastewater disposal for Intalco Aluminum Corp.: U. of W., Seattle, 82 p, with appendices.

Waldichuk, M., 1968, Waste disposal in relation to the physical environment oceanographic aspects: SYESIS, 1:4-27.

Wennekens, M.P., Kincaid, T., and Sylvester, R.O., 1955, A supplemental study of the oceanographic and biological characteristics of southeast Georgia Strait: U. of W., Seattle, 89 p.

Yasso, W.E., 1965, Plan geometry of headland bay beaches: Jour. of Geol., 73:702-714.

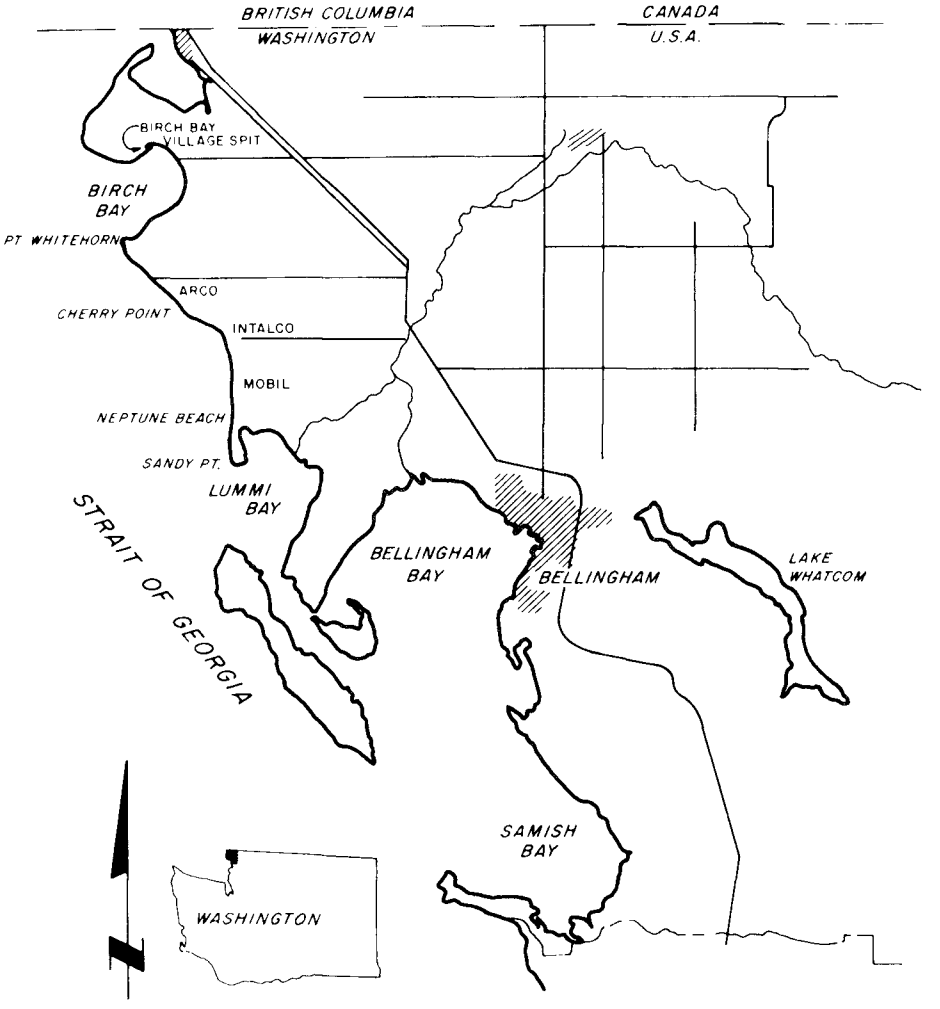

Figure 1 Location map of Birch Bay and Cherry Point, Washington.

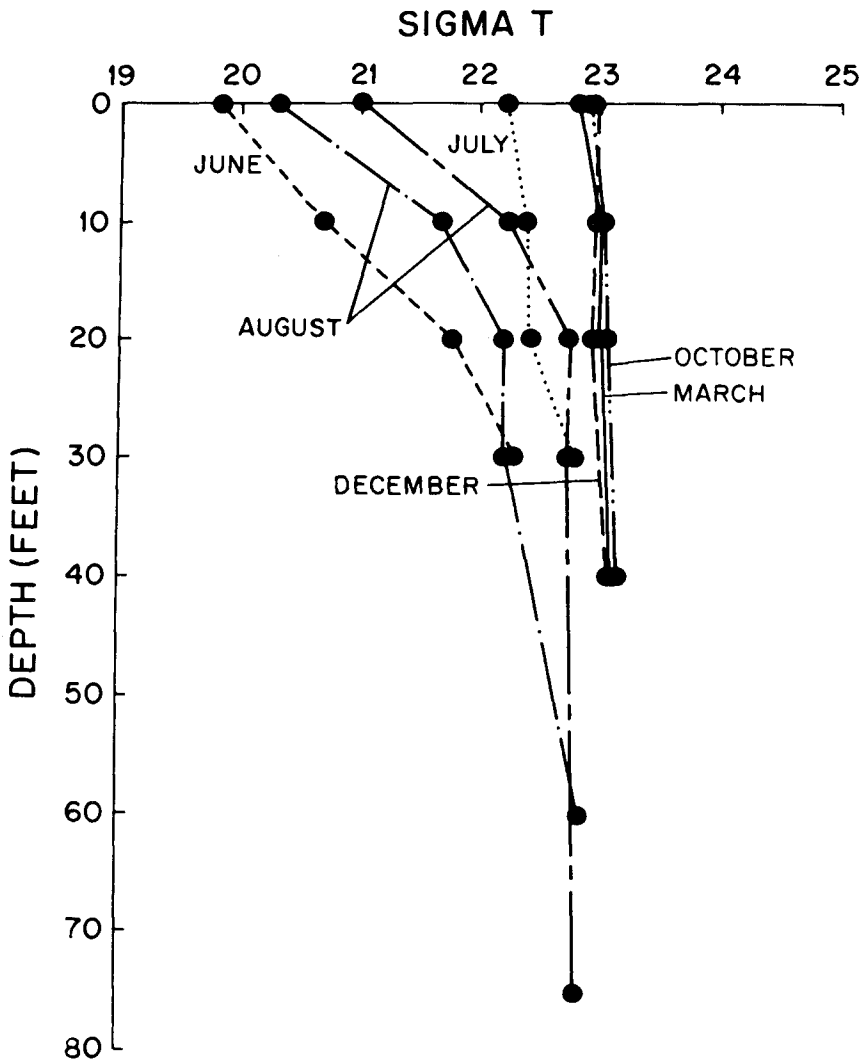

Figure 2 Density (sigma t) stratification in Georgia Strait (after Sylvester et al, 1966).

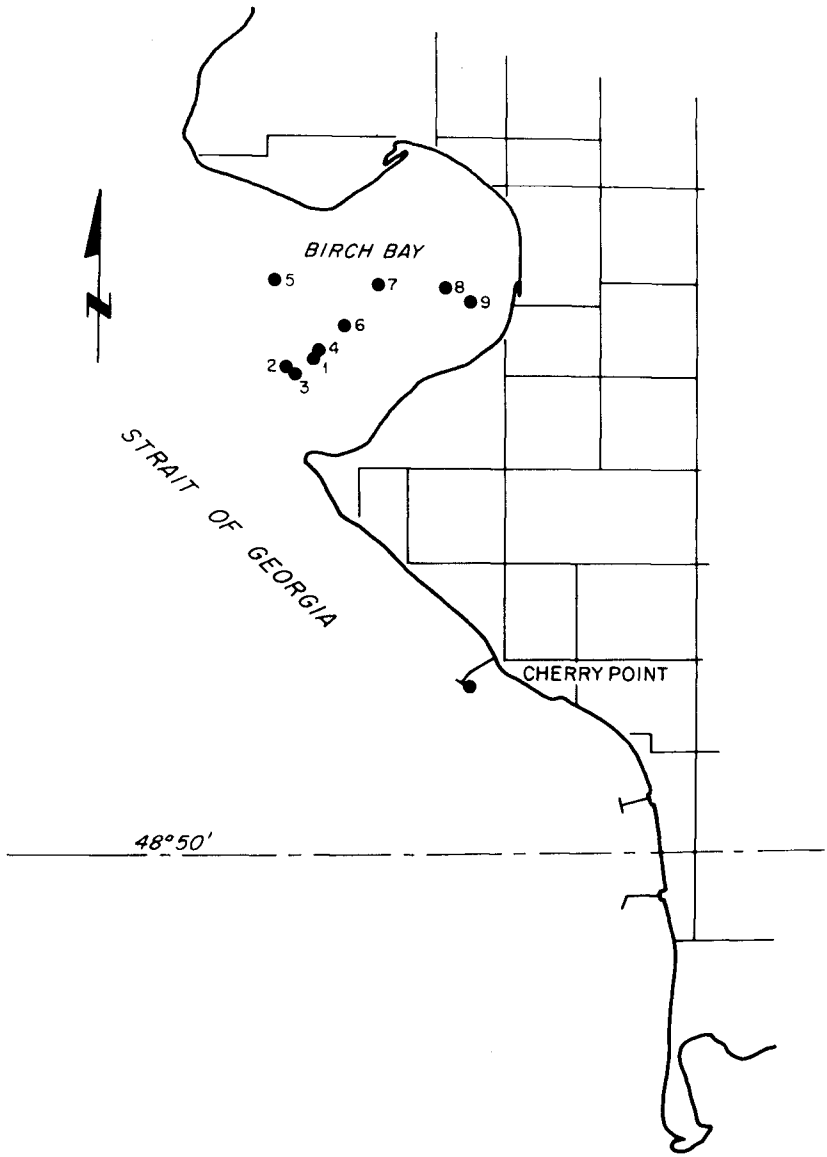

Figure 3 Water sampling stations.

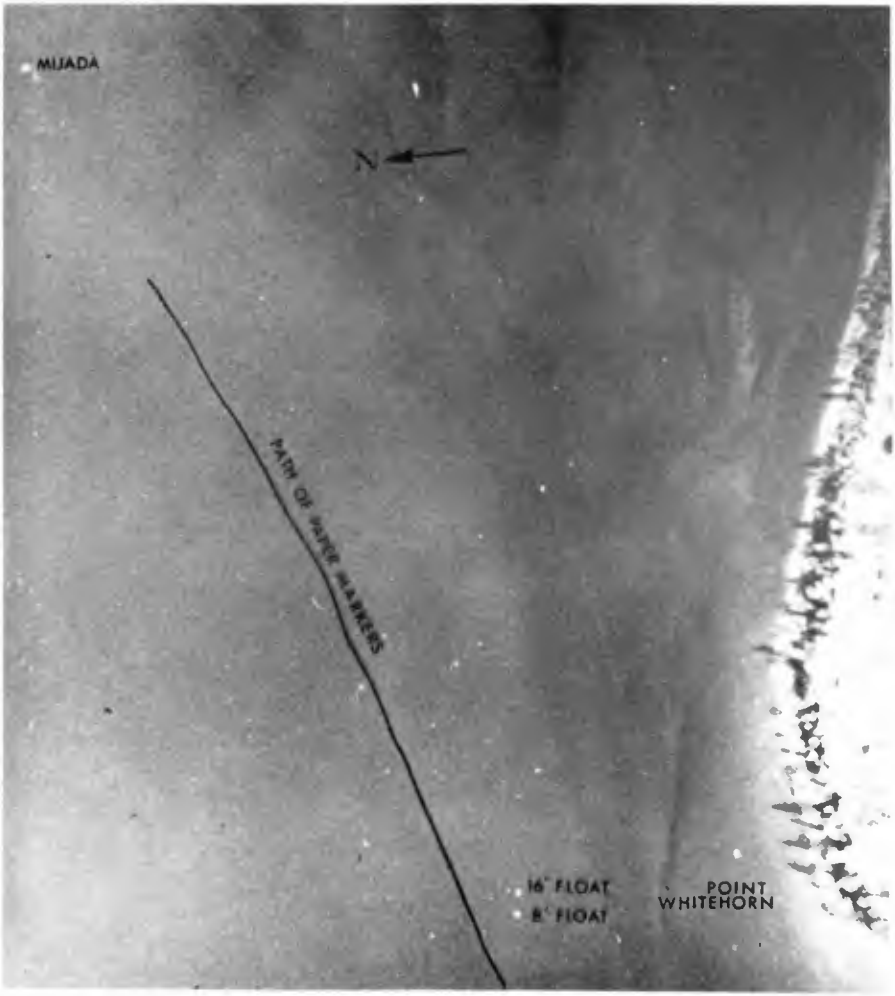

Figure 4 Aerial photo of path of ebb tide floating paper, taken from 2,000 feet over Point Whitehorn.

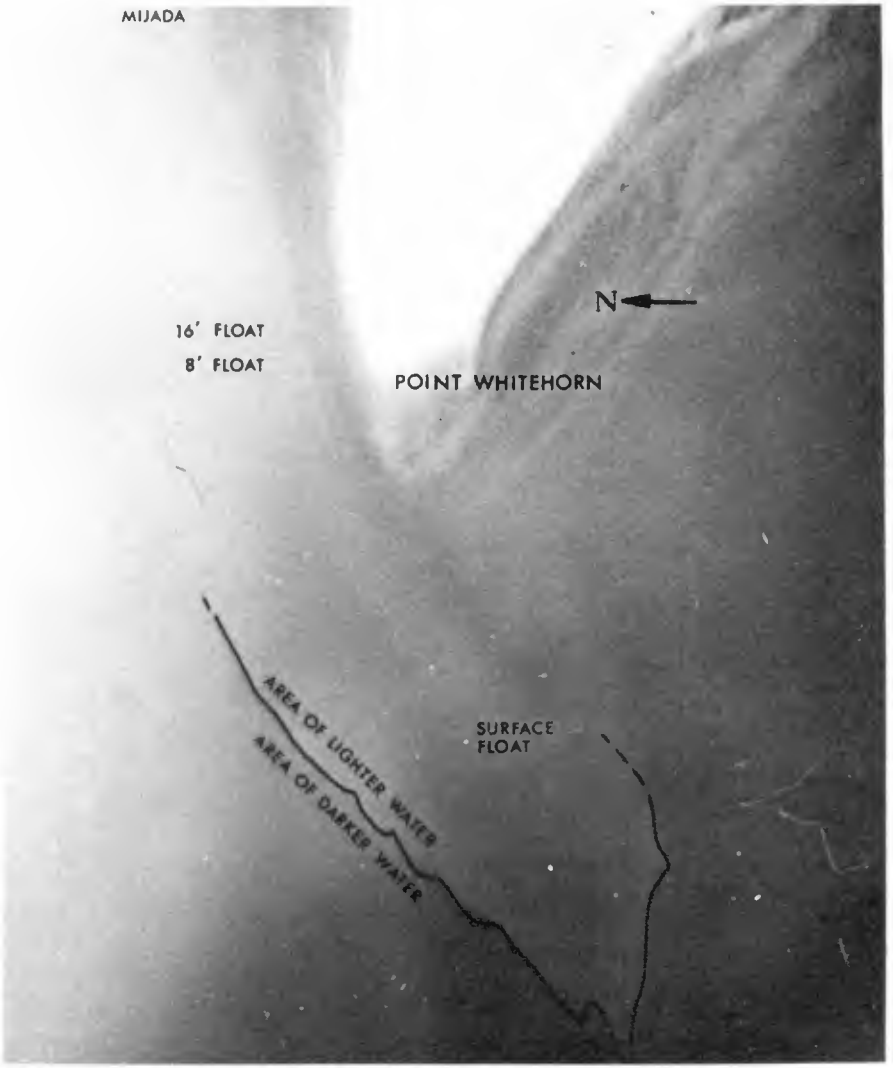

Figure 5 Infrared aerial photo, taken from 4,500 feet, of surface float location during ebb tide at Point Whitehorn.

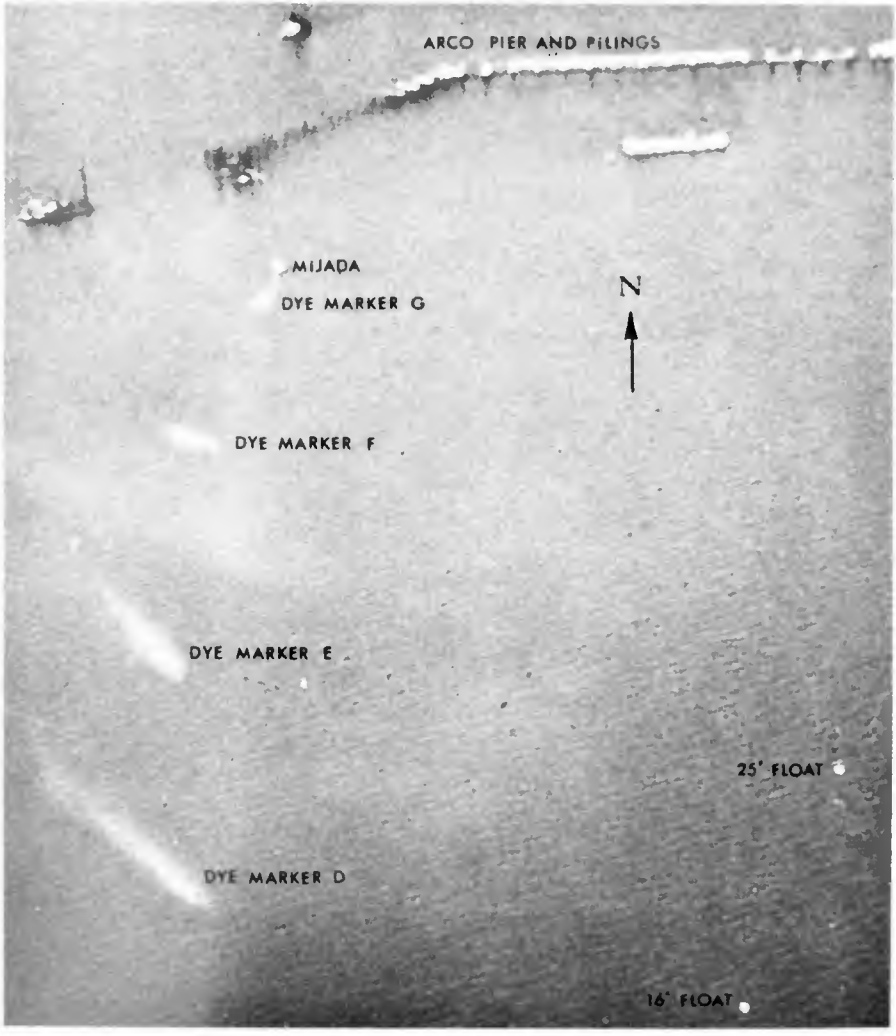

Figure 6 Aerial photo, taken at 2,000 feet, showing four dye patches released at 15 minute intervals from near the ARCO outfall site during ebb tide.

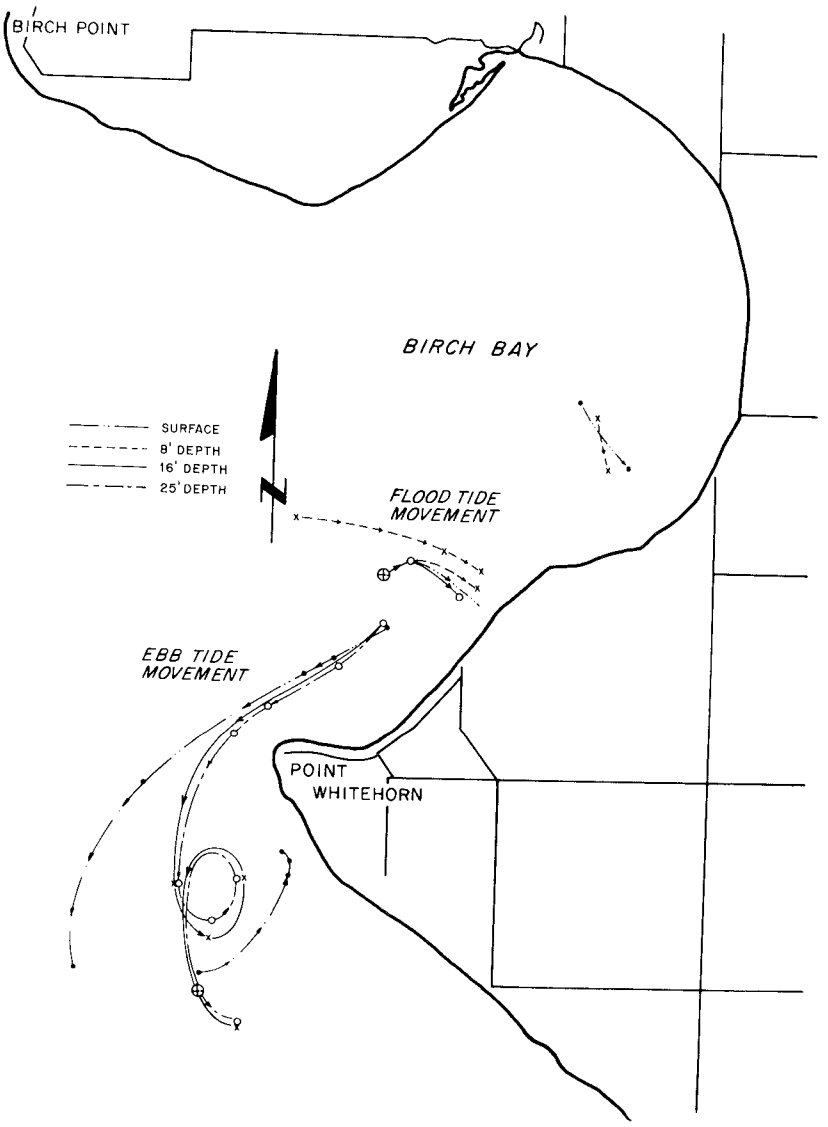

Figure 7 Float movements on flood and ebb tides at Birch Bay.

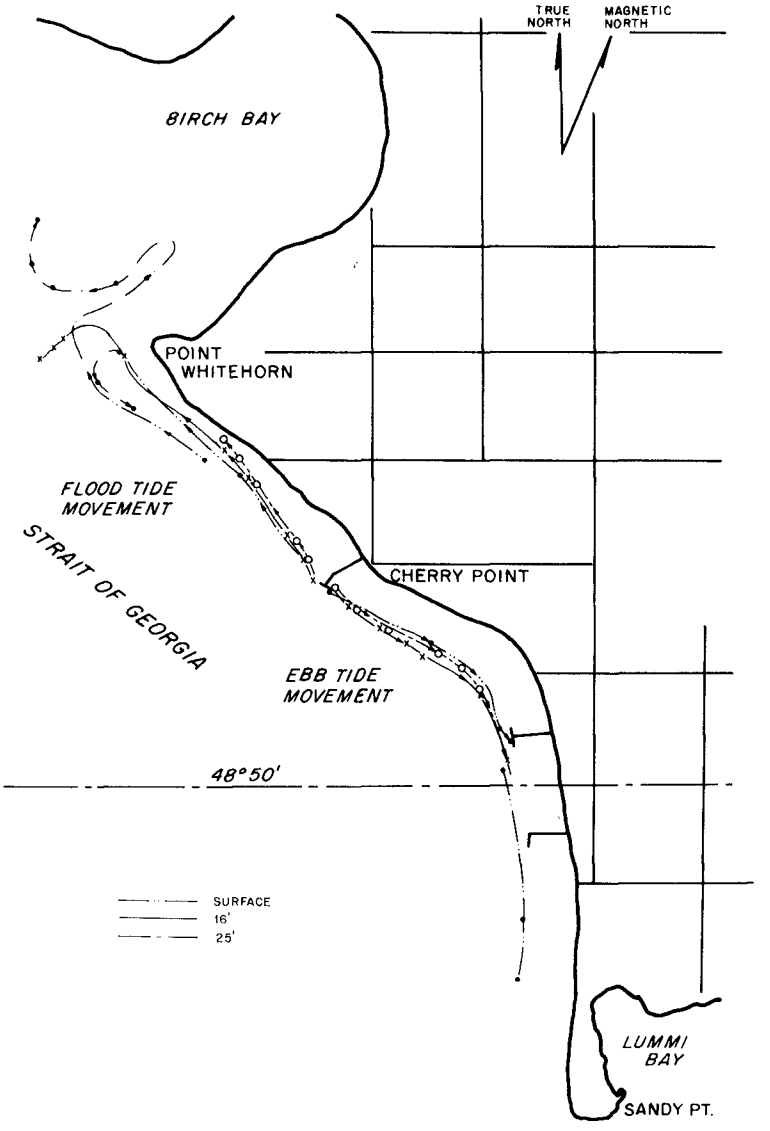

Figure 8 Float movement on flood and ebb tides at Cherry Point.

CHAPTER 145

WIND STRESS ON A COASTAL WATER SURFACE

S. A. Hsu
Coastal Studies Institute
Louisiana State University
Baton Rouge, Louisiana 70803

ABSTRACT

Simultaneous measurements of horizontal wind velocity above the water surface, air and water temperature difference, and water level were made during the summer of 1971 at an exposed field site off the northwest coast of Florida. Three identical vertical arrays of six-cup anemometers were used; they were located in the surf zone, in the area between the inner and the outer bars, and on the outer slope of the outer bar. The distances of these three stations from the mean shoreline were approximately 30, 130, and 230 m. Mean water depths were 1.5, 4.3, and 5.0 m.

Analysis of the profile data under adiabatic and onshore wind conditions indicates that better than 90 percent of the valid wind profile measurements are logarithmic. It was found from the nearly fifteen hundred 15-minute logarithmic wind profiles that the shear velocity U_* was not a linear function of wind speed, as is usually assumed in coastal applications, but had a functional relationship with velocity at 10 m or U_{10m} (from 0.5 to 8.5 m/sec), such that $U_* = 0.37\ U_{10m}^{2/3}$.

Comparison with similar investigations in deeper water and oceanic regions was also made.

INTRODUCTION

In the lowest turbulent layer of the atmosphere over water under adiabatic conditions, logarithmic wind-velocity distribution with height has been observed over the sea (see, e.g., Roll, 1965, and Ruggles, 1970) and in laboratory channels (Wu, 1968, and Lai and Shemdin, 1971). The logarithmic law states that

$$\overline{U_z} = \frac{U_*}{\kappa} \ln \frac{Z}{Z_o} \qquad (1)$$

where $\overline{U_z}$ is the mean horizontal wind velocity at a certain height z,

Fig. 1. Five identical cup anemometer arrays, located in the berm scarp, swash zone, surf zone, area between the inner and the outer bars, and on the outer slope of the outer bar on the coast of the Gulf of Mexico near Fort Walton Beach, Florida (see text for station identification). Three resistance-wire wave gages are shown on the left (cf. Fig. 2).

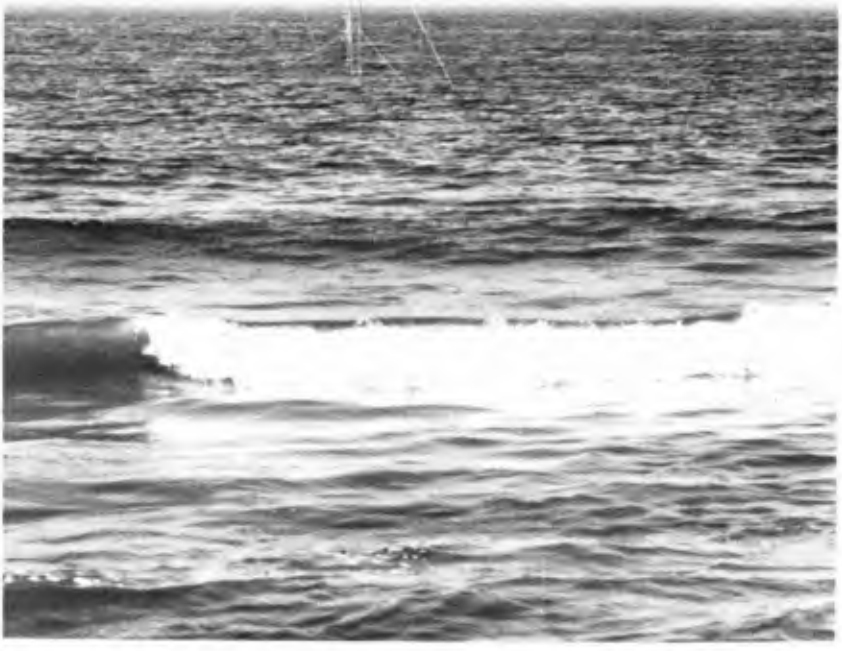

Fig. 2. One of the three identical cup anemometer arrays located on a fixed offshore mast in the area between the outer and the inner bars on the coast of the Gulf of Mexico near Fort Walton Beach, Florida. Two resistance-wire wave gages are shown in the background.

U_* is the shear (or friction) velocity [$= (\tau/\rho)^{1/2}$, where τ is the vertical transport of horizontal momentum and ρ is the air density], κ is the von Kármán constant ($\simeq 0.4$), and Z_o is the aerodynamic roughness parameter or the dynamic roughness obtained under the boundary condition that $\overline{U_z} = 0$ at $Z = Z_o$, where Z_o depends upon the boundary roughness as well as the characteristics of the boundary layer.

The wind stress τ ($= \rho U_*^2$) is of considerable importance because it plays an essential part in all processes of momentum transfer across the air-sea boundary, including generation of ocean surface waves and drift currents by wind action, wind set-up, and storm tides (Roll, 1965). The relationship between U_* and U_z or C_z [$= (U_*/U_z)^2$], the drag or resistance coefficient at a certain height z over the water surface, has been investigated for more than 30 years (see information compiled and summarized by Roll, 1965; Wu, 1969; and Kraus, 1972). However, there are no systematic and simultaneous measurements in the nearshore areas, ranging from swash zone, surf zone, area between the inner and the outer bars, and the outer slope of the outer bar. Therefore, in order to study the nearshore waves, currents, and other meteorologically related coastal engineering processes, drag coefficients obtained from deeper water or oceanic regions generally are assumed. The purposes of this paper are to provide wind-profile and stress measurements in these nearshore regions and to compare with similar investigations in deeper water and oceanic regions.

FIELD EXPERIMENT

This study is an integral part of an investigation undertaken by several related disciplines of the Coastal Studies Institute, Louisiana State University, of the dynamical processes operating near an open coast as a function of the sea-air-land interaction system (SALIS Project). The field program was carried out in June-July 1971 on Santa Rosa Island (Eglin AFB), Florida, where the mean tidal fluctuation was about 30 cm.

Instruments used for this study included three identical portable Thornthwaite Wind Profile Register Systems (C. W. Thornthwaite Associates, Model 106) with six-unit, three-cup, fast-response anemometers mounted at 145, 165, 205, 285, 365, and 445 cm above the mean water surface (Fig. 1). These three anemometer arrays were located in the surf zone, in the area between the inner and the outer bars, and on the outer slope of the outer bar. The distances of these three stations from the mean shoreline were approximately 30, 130, and 230 m. Their mean water depths were 1.5, 4.3, and 5.0 m. Some of the instruments are shown in Figure 2. The wind profile instrumentation and the data-reduction and analysis procedures have been described elsewhere (Hsu, 1971).

In addition, several other parameters were measured in the study area for reference purposes. They were air and water temperature differences at a distance of approximately 2.8 m (Weathermeasure Corporation, Model T-601), tidal fluctuation (a capacitance water level gage developed by N. H. Rector and R. G. Fredericks, of the Coastal Studies Institute),

and wind speed and direction at 10 m above the ground level (Science Associates, Inc., Model 162). Temperature and humidity gradients were also measured at 1.7, 3.6, and 5.5 m above a grass-free berm surface by three identical recording hygrometry systems (Taylor Instrument Company, Series 76J, having readings within $\pm$ 1 percent of any given chart range). The sensors were mounted on a 10-m meteorological tower. Furthermore, four resistance-wire wave gages were also installed in the study area (Fig. 2).

RESULTS

From June 15 through July 2, 1971, approximately fifteen hundred 15-minute wind profiles having statistically significant logarithmic wind distribution with height were obtained. When plotted on semi-logarithmic paper, straight lines with a correlation coefficient $\geq$0.98 were obtained. Some examples are shown in Figures 3 through 5. It should be noted that in this analysis only those onshore winds under adiabatic conditions were used (Roll, 1965, and Hsu, 1969). Note also that, for brevity, only those profiles which do not overlap are plotted in these figures. Figure 6 shows the wind stress under adiabatic onshore wind conditions as a function of wind velocity at 10 m above the mean sea surface for water depth $\leq$5 m. The vertical bars in this figure represent the variations of the mean U_* values obtained at three offshore stations, namely, in the surf zone, in the area between the inner and the outer bars, and on the outer slope of the outer bar.

It can be seen immediately that the difference of the mean U_* values at a given wind speed for these three stations is relatively small. It was also found from the present data that the shear velocity was not a linear function of wind speed, as is usually assumed in coastal applications, but has a functional relationship with wind velocity (from 0.5 to 8.5 m/sec), such that

$$U_* = 0.37\, U_{10m}^{2/3} \tag{2}$$

or

$$\tau = \rho U_*^2 = 1.64 \times 10^{-4}\, U_{10m}^{4/3} \tag{3}$$

in which U_{10m} is the wind speed in centimeters per second at the conventional reference level of 10 m above the mean sea surface. In Figure 6, comparison with similar investigations in deeper water ($\simeq$20 m) (Ruggles, 1970) and oceanic regions (Wu, 1969) is presented. The reason for the systematic discrepancy is not known because the three curves delineated in Figure 6 were not measured at the same period and in the same general region. It is suggested that such simultaneous measurements be executed in order to further our understanding of the interaction of the air-sea interface.

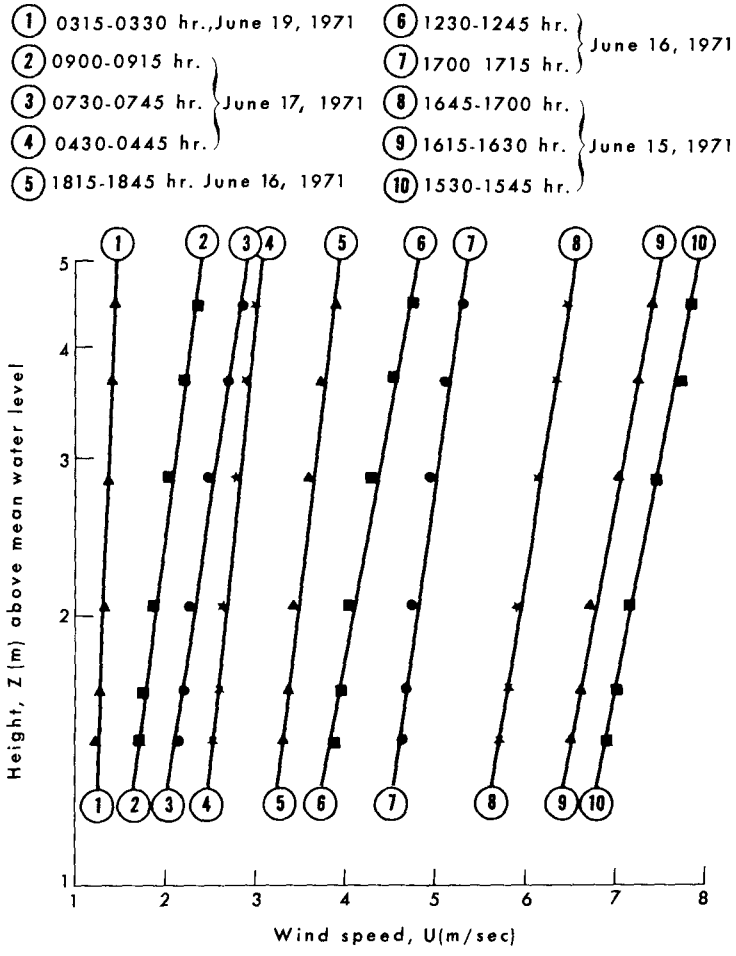

Fig. 3. Some examples of the 15-minute measurements of mean wind speed as a function of height (on a logarithmic scale) in the surf zone. Symbols represent measuring points.

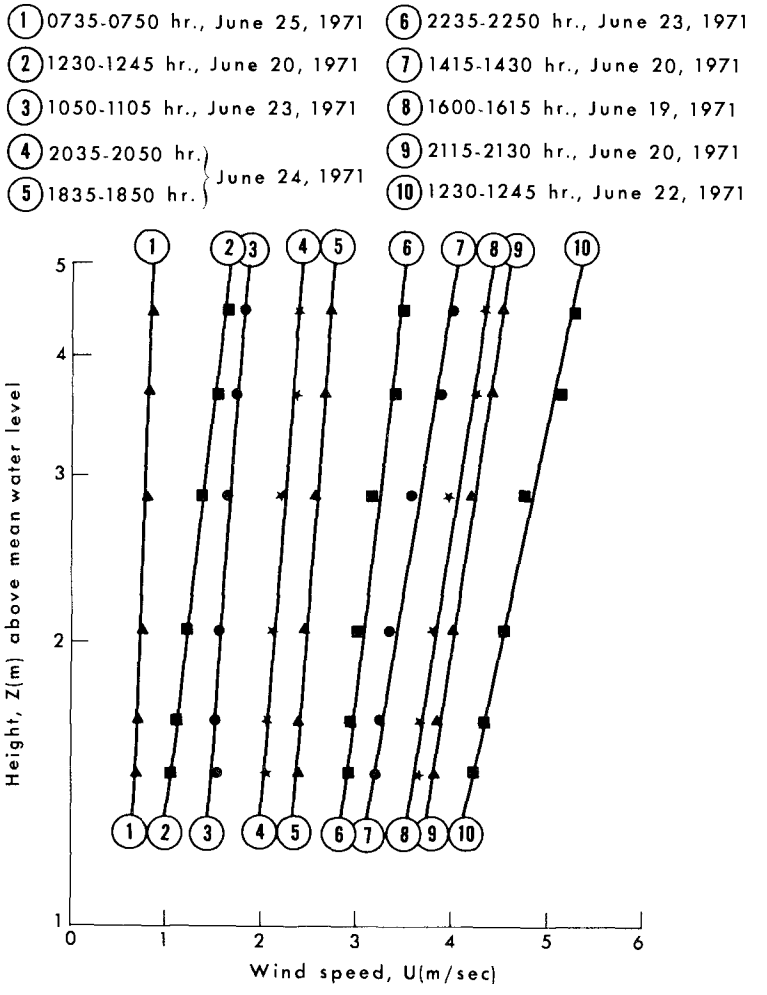

Fig. 4. Some examples of the 15-minute measurements of mean wind speed as a function of height (on a logarithmic scale) in the area between the inner and the outer bars.

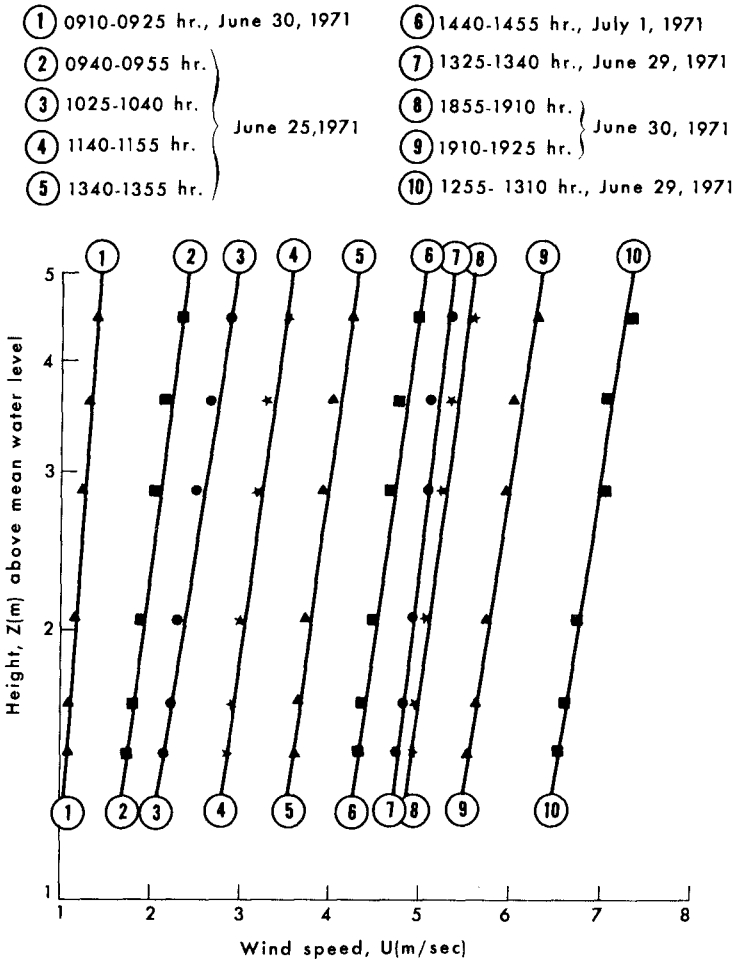

Fig. 5. Some examples of the 15-minute measurements of mean wind speed as a function of height (on a logarithmic scale) in the area on the outer slope of the outer bar.

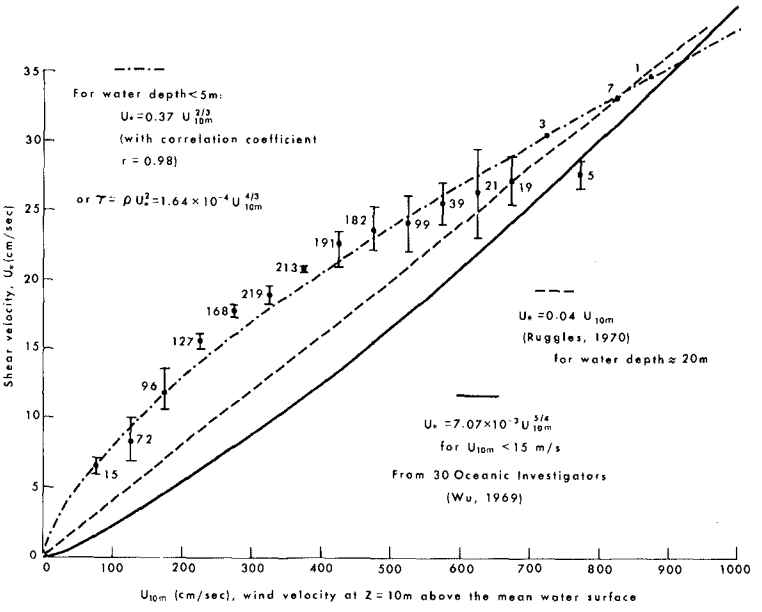

Fig. 6. Shear stress under adiabatic onshore wind conditions as a function of wind velocity at 10 m above the mean sea surface for water depth $\leq$5 m. The vertical bars represent the variations of the mean U_* values obtained at three offshore stations. Comparison with similar investigations under adiabatic conditions in deeper water and oceanic regions is also made.

CONCLUDING REMARKS

On the basis of nearly fifteen hundred 15-minute wind-profile measurements over a coastal water surface, it has been demonstrated that the atmospheric shear velocity and the wind speed are interrelated; these functional relationships are given in Figure 6. Since the logarithmic wind law can be valid only under the adiabatic condition (but not very close to the air-sea interface), the results presented in this study may not be applicable to synoptic and subsynoptic systems which have different atmospheric stability [e.g., sea breezes, when the synoptic effect is minimal in the Gulf of Mexico coastal regions (Hsu, 1970 a and b), some weather systems in the Atlantic Ocean (DeLeonibus, 1971), and air flows over the Beaufort Sea in the Arctic region, where, in addition, the possible effect of a humidity gradient on stability exists (Banke and Smith, 1971)].

Also, caution should be used in applying the present study to other phenomena, such as wave-induced perturbations and their importance in transferring momentum to waves; in this regard, DeLeonibus' (1971) field study and Lai and Shemdin's (1971) laboratory investigations may be consulted.

ACKNOWLEDGMENTS

This study was supported by the Geography Programs, Office of Naval Research, through the Coastal Studies Institute, Louisiana State University, under Contract N00014-69-A-0211-0003, Project NR 388 002. Appreciation is expressed to personnel of Eglin Air Force Base, particularly to Marshal Cartledge, for permission to occupy the site and use necessary facilities during the experiment. Thanks also go to Norwood Rector, Rodney Fredericks, and Bobby Montgomery, who helped to perform the experiment.

REFERENCES

Banke, E. G., and S. D. Smith, 1971, Wind stress over ice and over water in the Beaufort Sea. J. Geophys. Res., 76, 7368.

DeLeonibus, P. S., 1971, Momentum flux and wave spectra observations from an ocean tower. J. Geophys. Res., 76, 6506.

Hsu, S. A., 1969, Comments on a paper by J. Wu, 'Wind stress and surface roughness at air-sea interface.' J. Geophys. Res., 74, 5562.

_____, 1970a, Coastal air-circulation system: observation and empirical model. Monthly Weather Rev., 98, 487.

_____, 1970b, The shear stress of sea breeze on a swash zone. Proc. 12th Conf. Coastal Engr., Washington, D.C., Am. Soc. Civil Engrs., 1, 243.

_____, 1971, Measurement of shear stress and roughness length on a beach. J. Geophys. Res., 76, 2880.

Kraus, E. B., 1972, Atmosphere-ocean interaction. London (Oxford Univ. Press), 275 pp.

Lai, R. J., and O. H. Shemdin, 1971, Laboratory investigation of air turbulence above simple water waves. J. Geophys. Res., 76, 7334.

Roll, H. U., 1965, Physics of the marine atmosphere. Intern. Geophys. Ser., vol, 7, 426 pp., New York (Academic Press).

Ruggles, K. W., 1970, The vertical mean wind profile over the ocean for light to moderate winds. J. Appl. Meteorol., 9, 389.

Wu, J., 1968, Laboratory studies of wind-wave interactions. J. Fluid Mech., 34, 91.

_____, 1969, Wind stress and surface roughness at air-sea interface. J. Geophys. Res., 74, 444.

CHAPTER 146

PROBLEMS OF OIL POLLUTION ON COASTAL WATERS AND BEACHES

Uwe Carow

Landesamt für Wasserhaushalt und Küsten
Scholeswig-Holstein, Germany

In the coastal regions of the North- and Baltic-Seas of Germany more collisions with oil tankers have occured since 1955. These collisions have been followed by extreme pollution of the sea and coastal areas. In the following report the possibility of computing in advance the time and place of the landing of sludge, the advantages and disadvantages of chemical and mechanical treatment for the removal of the oil, the natural influences on the decomposition of the oil and the differences between oil-pollution on coasts with tides and on coasts without tides are explained and critizised.

Coastal areas and beaches are in danger of being polluted by oil. One part is the uncontrolled disposal of waste oil causing permanent pollution, the other part is the result of collisions with vessels. This danger is most threatening on much frequented shipping routes and in limited and relatively small sea-areas and bays of low depth, as it is the case with the North-and Baltic-Seas in the North of Europe.

6 oil tanker collisions since 1955 have caused considerable pollution in these areas. In the last three years 60 % of all oil-accidents have happened in coastal waters. You all remember the collision of the "Torrey-Cannyon" at the coast of Cornwall/ England causing a catastrophic oil-pollution. 90.000 to of oil ran out and the expenses for removing amounted to 1,6 Million Dollars.

The scope and the success of the technical measures taken against the oil are depending on different factors:

For instance cause, place and time of the accident, loaded and runout quantity of oil, kind - to say boiling point - of the oil as well as meteorological conditions.

Most important with the regard to a successfull fighting against the oil is to come in action quickly and expertly.

Generally an oil-pollution is governed by the following successive events: Outflow and spreading of the oil, drift of the contaminants,

landing of the contaminants.

The outflow of oil is depending on the kind of damage done to the tanker, a damage that may assume many forms. Resonable measures applied to the ship herself are apt to prevent the outflow of considerable amounts of oil. These measures consist primaryly in rendering the ship floatable again to enable her to be towed into a safe port. In many cases it will not be an advantage to burn out the wreck because by that the pollution is loaded into the atmosphere.

The kind of oil plays an important part in its expansion on the water. Precise measurements relative to speed of expansion and layer thickness of oil fields are not available. Following observations, a 1 mm to 4 mm thick layer will be buildt up very quickly. An oil-film of a thickness of one micron to 0,1 mm passing finally will be a little bit slower in forming.

We made an experiment spilling 11 to Arabian Light oil into the calm sea. 25 minutes later the oil had spread out on an 200 m wide and 400 m long expanse, the layer was 14-hundredth mm. After 6 hours the layer was 1,4 thousandth mm and extended to an expanse diameter of 1,7 n.m. (nautical miles).

Direction and speed of further expansion and drifting of oil fields are influenced by wind, state of sea, tidal currents and the so-called residual currents (that are streams without periodical proportions). In the German Bay just the flood-tide current has a speed of approximately 1.9 to - 2.8 n.m./h, the ebb-tide current a rate of round about 1,9 - 5,0 n.m./h. The drift of layers on the water surface can, thanks to tests with "drift cards" in plastic envelopes, be supposed to be 4,2 % of wind velocity in wind direction (German Bay). This value has been confirmed by observing drifting oil fields. In the case of prolonged drifting, there may arise an incertainty factor of $\pm$ 1 day. Therefore such drift computations should be verified by interim observations from airplanes and ships. But also without these crafts it will be possible (during fog and gale) to deliver relatively precise and timely forecasts as to the

coastal areas, where the oil will land, thus facilitating an efficient control of the oil. In one case it was possible to recalculate - on the basis of the landed oil - the way back to the place of the accident, with the conjectured place of accident thus being confirmed and the responsible tanker being found.

The control and calculation of the drift-way has three significant advantages:

1. You can follow the way also when it is not possible to observe from ships or airplanes.
2. If you know wind-velocity and wind-direktion you can forecast, which coastal region will be in danger to be polluted and you can warn the neighbour-land.
3. If there are larger oil-fields being sighted on the sea or being landed on the beach it is possible to pursue back the way of drifting in order to find the ship occasioning the pollution.

When it comes to "depositing" there exist - apart from the already mentioned influence factors - sea levels, vertical and horizontal coastal configurations, surf and "off-shore" factors which matter. The latter factors constitute a computational value composed of ebb-currents, surf streams and off-shore residual and drift currents. In the German part of the North Sea coastal area this parameter is assumed to be 0,5 n.m./h in direction NW. The medium residual current in the open sea amounts to 0.2 n.m./h, direction NE.

We differ between and mechanical methods of oil-removal at sea and on the beaches:

In eliminating oil pollution at sea, the following experiences have been gathered:

Although it is known that detergents together with oil are more toxic than chemical substances alone, emulsifying agents have been employed at sea. At some distance from the coast and with the sea being rough, immediate success was not noted. The mixture ratio of 1 : 1-necessary for a stable emulsion-has certainly

never been reached. It may, however, have facilitated the dispersion of the oil-surfaces. On the Baltic Sea, however, we had succeded in dispersing a thin-layer oil field, drifting immediately in front of a crowded bathing beach, by sprayed-on emulsifying agents and turbulence caused by screw propellers.

The application of emulsifying agents shouldn't be declined at any rate, you see, but it must be said, that emulsifiers - needed in mixture 1 : 1 - are very expensive.

In many cases it will be better to use binding-agents of solid substances. This is a kind of mineral-absorbent with a high surface area. It is hydrophobic and not toxic. The particle diameter is varying from 0,1 to 2 mm. Brought up to the oil, the floating mix will drift to shore in a very readily collectable form and it can be removed together with the bound oil. But there is one disadvantage: as a consequence of the little weight of the binding agents a strong wind will blow it away, so that you can use it only in times with low wind-velocities.

Swimming oil barriers - as a mechanical way - only may be used in calm waters as in rivers, river-mouths, creeks and harbours. In the rough sea or in the surf the oil will flow over or under the barrier under the influence of waves and currents.

In Germany just have been made successfull tests by dropping binding agents with helicopters. In contrast to wing-airplanes they have a slow dropping-speed, low flying-depth and a high loading-capacity.

On the beaches, the oil was primarily removed in a mechanical way. On the tidal beaches the oil is often spread by ebb and rising tide over a large expanse as far as to the foot of the dunes. To use bulldozers peeling off the oil-polluted sand layer, proved to be most efficient. Individually distributed oil areas or oil clods could be removed with shovels. The removal of oil on grassgrown dikes is very difficult. Damage done to the sod endangers the security of the dike. Here you have to proceed with caution and to remove carefully and manually the oil with the aid of shovels.

From the stone covers the oil only could be removed to a certain extent by means of emulsifying agents.

On the beaches not subject to varying tides - as on the shores of the Baltic-Sea - oil fighting is easier. Due to the limited fluctuations of the sea level, the landed oil will remain in only a small shore area. With the surf being strong, it has proved a success to heap up a sand mound at a distance of some meters from the water line to keep the remaining beach free from oil.

Nature, too, is very helpful in eliminating oil pollution on beaches. A quick disintegration of oil also was observed in deeper sand layers (up to 20 cm). Particularly efficient are high tides or storm tides returning the partially disintegrated oil into the sea, where it continues to be further decomposed.

The differences of the oil as to quantity and composition, in the place of the accident and on the beach, reveal a considerable influence of the natural disintegrating forces. These primarily are consisting in the evaporation of the volatile constituents of the oil, the photo-oxidation by sunrays and the decomposition by bacteria.

Model tests with four different types of crude oil have shown four manners of decomposition processes:

1. The evaporation of low-boiling compounds up to a loss of approximately 20 % of weight is a short-time process.
2. Further the formation of a water-oil-emulsion under influence of precipitation and water turbulence is a quickly developing reaction, causing a fundamental change in the properties of the oil.

3./4. Ageing and biochemical degradation are long-term processes. The first one especially changes the viscous properties and the second one effects the chemical composition.

During the Torrey-Cannyon accident there have been made tests with decomposition by bacteria. There were found in 1 ml at "oil in water" 1,5 millions of microorganisms and in "oil saturated sand" 24

millions of bacteria. It was also observed, that the bacteria are relatively resistant against chemical agents as for instance emulsifiers. Many model-tests are necessary to find more about the influence and effect of bacterial-decomposition on oil.

Last not least something about the identification of the responsible ship causing the oil pollution: In many cases we were succesfull to identify the run out oil on the beach and the oil loaded from the tanker. We are using chemical-analysis in a manner of infra-red-spectrum or atomic-absorption-spectral analysis. But it must be provided that the time between accident and landing - respectively moment of sampling - is short enough, so that above named decomposition processes won't have changed the characteristic properties of the oil.

Every tanker accident and the pollution resulting from that occur under different conditions. For that reason, each case requires special measures. Experience has shown, that to fight oil at seas is in many cases more expensive than on the beach. In view of the natural-disintegrating-forces any reasonable use of control mediums should also consider the time relative to the bathing season on the beaches. In the last analyses all the measures should be taken under careful consideration of all the above named influence factors, duly estimating the danger of oil pollution to the existence of man, animal and plant life.

This is not a hopeless task, but the problem of oil pollution will only be solved by international teamwork and by exchanging practical experiences on technical and organisational lines. The protection against the "black tide", however, is as difficult as the protection of our shores and beaches against the forces of sea-waves and - currents.

CHAPTER 147

THE CLEANING OF GRAVEL BEACHES POLLUTED BY OIL

E. H. Owens*

Abstract

An attempt to clean beaches without the use of dispersants was undertaken in Chedabucto Bay, Nova Scotia, following a spill of Bunker C oil from the tanker "Arrow" in the spring of 1970. Sand beaches account for less than 2% of the coast of Chedabucto Bay and those which were polluted were cleaned manually using peat moss, rakes, and shovels. Most sand beaches can be cleaned with relative ease, as oil does not permeate the sediments, and the angle of sand beaches is generally low so that mechanical methods can be applied without large-scale removal of beach sediments. Oil deposited on gravel beaches permeates below the surface layer and cleaning by mechanical methods involves excavation of beach sediments to depths of one metre or more. This method endangers the stability of a beach, particularly if the sediment supply is limited. Also this method was found to be ineffective in removing all contaminated sediments.

* Atlantic Geoscience Centre, Bedford Institute of Oceanography, Dartmouth, Nova Scotia, Canada;
and Coastal Research Division, Department of Geology, University of South Carolina, Columbia, South Carolina 29208

INTRODUCTION

The tanker "Arrow" ran aground on Cerberus Rock on February 4, 1970, and the resulting spill of Bunker C oil polluted more than 350 km of shoreline in Chedabucto Bay, Nova Scotia. The coast of Chedabucto Bay is made up of a variety of shoreline types ranging from rock or till cliffs to sandy beaches and sheltered lagoons. Attempts to clean sections of the polluted shoreline without the use of dispersants met with many difficulties. The effect of oil on the various shoreline types differs greatly so that no one cleaning technique could be applied to large sections of shoreline.

During the spring of 1970 a task force, established by the Canadian federal government to deal with the pollution problem, initiated a series of clean-up projects to restore contaminated beaches. Approximately 80 km of coast were selected for cleaning, based on their recreational value to the local residents and to tourists. Available dispersants were considered too toxic to marine life and the task force decided to clean the beaches by removing the contaminated sediments. The majority of beaches in Chedabucto Bay are made up of mixed sand-gravel sediments and in many locations oil had permeated up to 0.5 m or had been buried as much as 2 m below the surface, thus requiring the excavation of large volumes of beach sediment.

CLEAN-UP METHODS

Prior to the Chedabucto Bay spill, a great variety of techniques had been investigated for the containment and removal of oil from the surface of the sea, but relatively few studies had been concerned with shoreline clean-up technology. Even within the field of beach restoration, work had been concentrated on sand beaches with little attention to gravel and cobble beaches, tidal flats, or marshes. The problem of establishing criteria for the cleaning of shorelines is complicated by the different types of oil, each of which has different physical properties, and by the variety of coastal types in terms of different process environments and different erosional or depositional forms. The results of studies on oil contaminated sand beaches (e.g., F.W.P.C.A., 1970) could not be applied to gravel beaches, and adequate contingency plans for future spills must therefore take into account the nature of this particular coastal environment.

Various techniques have been discussed for the cleaning of oil-contaminated gravel beaches (Wardley Smith, 1968; 1969); these include burning, absorption, removal and dispersion of the oil with solvents. (i) Burning may be efficient but is costly and most types of oil are difficult to ignite and require constant application of heat. The warming of oil increases its mobility so that it permeates into the sediments. (ii) The use of absorbant materials is not always effective and requires mechanical or manual effort to apply and remove the absorbing material. (iii) Cleaning by the mechanical

removal of sediments poses many problems related to the natural beach equilibrium which may be disturbed and may result in more damage than that originally caused by pollution. (iv) The application of solvent-emulsifiers under controlled conditions appears to be the most effective way of removing oil without damage to the beach, but the dangers of toxicity to marine life have so far prohibited the large-scale use of this method. Eventually the best hope for efficient and practical removal of oil pollutants on coasts lies in the development of non-toxic chemical dispersants.

SEDIMENT REMOVAL

Sand beaches account for less than 2% of the coast of Chedabucto Bay (Owens, 1972) and those which were polluted were cleaned manually using peat moss, rakes, and shovels. On sand beaches oil rarely permeates below the surface and can be removed with relative ease. The only important geological concern in this part of the program was to minimize damage to backshore vegetation by vehicles gaining access to the beach.

On gravel beaches, oil was observed to have permeated up to 45 cm immediately following deposition in February and March, despite low air temperatures (Drapeau, 1970). Also, the normal processes of accretion on the beach led to burial of the oil-contaminated sediments in many localities. Subsequent periods of erosion frequently exposed layers of oiled sediments on the beach face slope. Attempts to clean these beaches involved excavation to depths in excess of one metre (Owens, 1971; Owens and Drapeau, 1972). This removal of sediment can lead to a serious disturbance of the existing beach equilibrium.

Mechanical equipment was used in Chedabucto Bay to clean 50 km of mixed sand-gravel beaches by removal of contaminated material. Data is available for some locations (Mackay, 1970) and it indicates that approximately 3 to 6 cubic metres were removed for each linear metre of beach. Most of this material was removed from the beach in the zone near or above high water level. Removal of sediment from this zone is particularly undesirable because natural replacement of material is slow, as areas above normal high water are only affected by littoral processes during periods of storm wave activity (Fig. 1a). At Indian Cove on the south shore of Chedabucto Bay the removal of sediments enabled waves to wash over the crest of the beach and this resulted in a retreat of the beach crest by 20 metres over a one year period (Fig. 1b).

The beach sediments in Chedabucto Bay are largely derived from the erosion and reworking of till deposits over the last 10,000 years during a period of rising sea level. Present-day processes do not provide sufficient

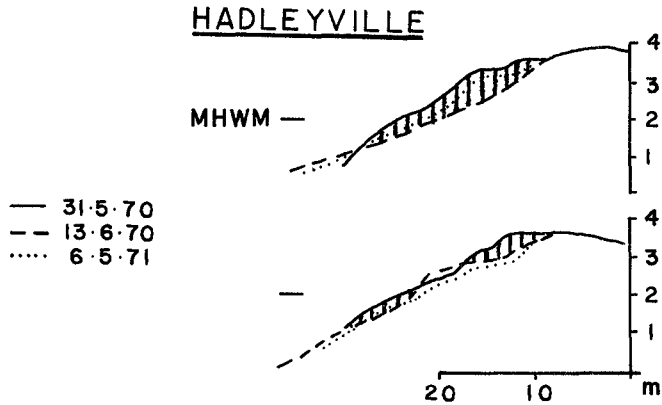

Figure 1a. Beach profiles at Hadleyville. Shaded area indicates sediment removed by beach cleaning. Most of the contaminated sediments on this beach on the west shore of Chedabucto Bay were removed from the zone above Mean High Water Mark.

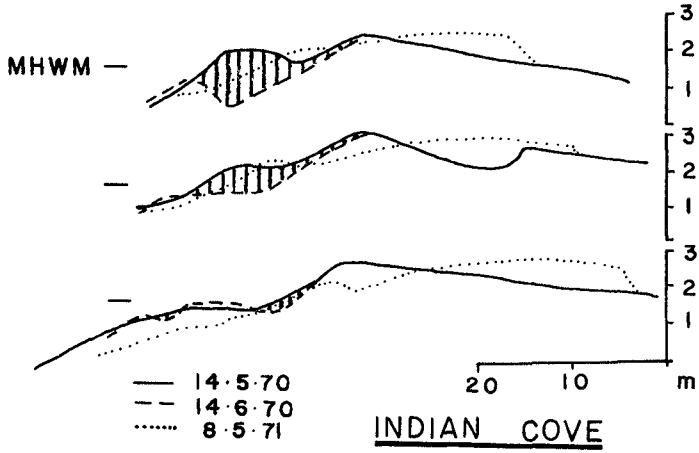

Figure 1b. Beach profiles at Indian Cove, a pocket beach on the south shore of Chedabucto Bay. Shaded area indicates sediment removed by beach cleaning. In certain sections sediments were removed to depths in excess of one metre. Within twelve months the beach crest retreated more than 20 metres.

sediment to the beach zone to replace large-scale losses. A similar situation is reported by Robinson (1961) who traces rates of shoreline retreat following sediment removal at Hallsands on the south coast of England. In both cases present-day sediment supply is limited and is unable to replace material lost by natural or human activity. Gravel is transported more slowly than sand and even if material is available for redistribution, serious damage to the beach equilibrium may be incurred before natural healing can take place.

NATURAL CLEANING

Many of the heavily polluted sand and gravel beaches in Chedabucto Bay were cleaned by normal wave action within a period of several months following contamination. This natural physical breakdown and removal of the oil was particularly evident on the beaches exposed to the full effect of waves from the Atlantic. Much of the oil had been deposited during a period of storm waves, and therefore contaminated material concentrated in the zone beyond the limit of normal wave action. This oil would only be removed by biodegradation or during subsequent periods of storms. However, the effectiveness of natural processes to clean beaches is important provided there is no urgent requirement for restoration of the beach.

Thomas monitored several intertidal locations of differing exposure over a one year period following the spill and reports (1971) that all locations showed significant reductions in oil coverage except for one site, a sheltered heavily-oiled lagoon. "Reductions in oil coverage were most noticeable at exposed locations. For instance at the Crichton Island study location the maximum percentage oiling of the intertidal zone (in April, 1970) was 10% in the upper portion while none of the remainder showed over 5% oiling. At maximum oil coverage, in June 1970, coverage ranged from 100% in the upper portion to 90-20% on the lower portion of the shore" (Thomas, 1971).

The northern coast of Chedabucto Bay is a lowland area which has been drowned to produce a complex series of islands, inlets, and bays. Most of this shoreline is not exposed to wave action from the open sea and in the sheltered low-energy environments oil was removed only very slowly by littoral processes. In such environments beach cleaning is valuable as physical processes are operating on a greatly reduced level. Contamination in sheltered localities is often more extensive and may be sufficient to prevent the normal movement of beach sediments. The immobilized beaches can be partly restored by the use of heavy equipment to break the surface layers which have been bound by the oil. In some cases this may be sufficient to permit wave processes to clean the sediments but in many areas further action may be necessary.

The beaches of low-energy wave environments are similar to many polar beaches and some measure of the probable effects of a spill in the Canadian arctic archipelago can be gained from the Chedabucto Bay area. In areas where

wave action is limited biodegradation is the only process that will break down the oil naturally and rates of biodegradation are greatly reduced in higher latitudes. The rate of natural cleaning in a low-energy wave environment in the arctic would be extremely slow.

CLEAN-UP OPERATIONS

Except in those areas where natural processes cannot clean beaches, due to low wave energy conditions or to excessive accumulations of oil, it is recommended that beach cleaning should only be undertaken at locations where contamination presents serious social or economic difficulties. Clearly, pollution of beaches frequently visited by tourists requires action but even in this case a spill occurring during the off-season could be left. Eventual cleaning before the tourist season would probably be necessary but this would be on a greatly reduced scale due to the effects of natural cleaning.

Whenever it is necessary to clean gravel or mixed sand-gravel beaches for social or economic reasons this should be accomplished without sediment removal. However, no techniques are available at present which can clean gravel beaches for recreational use without the application of dispersants, but two possibilities are suggested. One method which may be effective involves the use of a bulldozer to push contaminated material into the surf zone at low tide to allow normal wave processes to clean and redistribute the material. A second possibility involves the adaption of a technique developed in Bermuda for the cleaning of sand beaches repeatedly contaminated by oil (I.W. Hughes, pers. comm.). This process involves cleaning the sediment by washing with a dissolvant and then returning the material to the beach. Equipment could be designed to handle large volumes of gravel so that contaminated sediments could be excavated, fed into a tumbler system to dissolve or remove the oil, and then discharged for return to the beach. In this way oil could be removed rapidly without loss of beach sediment.

CRITERIA FOR CLEAN-UP OPERATIONS

Reaction to an oil spill which leads to pollution of the shoreline should be based on consideration of the socio-economic, geological, and wild-life factors within the area.

(1) The immediate response should be to protect those areas which would be most seriously affected by contamination, such as marshes and estuaries.
(2) Recreational or economic use will determine if any of the beach areas require cleaning. It may not be necessary to restore areas of shoreline which are little used and will, in time, clean themselves.

(3) If restoration is necessary then operations should only commence when there is no danger of recontamination.
(4) If natural cleaning would not be a feasible approach the available techniques must be evaluated to determine whether they can achieve the desired objective. There is little point in attempting to clean gravel or mixed sand-gravel recreational beaches with existing manual or mechanical methods as it is not yet possible to remove all contaminated material without the use of dispersants.
(5) A decision to adopt clean-up techniques which involve sediment removal must take into consideration the possible effects of lowering beach storm ridges, or of the destruction of backshore vegetation as this may lead to permanent damage, more serious than that caused by the original pollution.

CONCLUSIONS

The cleaning of shorelines contaminated by oil presents many problems, particularly on gravel beaches or in sheltered areas. As yet, there is no simple, efficient clean-up method and in some cases it may be necessary to suffer the inconvenience of a polluted coast rather than disturb the natural stability of a beach by large-scale sediment removal, resulting in more damage than that caused by the original pollution.

REFERENCES

Drapeau, G., 1970, Reconnaissance Survey of Oil Pollution on the South Shore of Chedabucto Bay, March 24 to 25, 1970. Unpub. Rept., Atlantic Oceanographic Laboratory, Bedford Institute, Dartmouth, Nova Scotia.

Drapeau, G., 1972, Natural Cleaning of Oil Polluted Beaches in Chedabucto Bay. 13th International Conf. Coastal Engineering, Abstract No. B 2.

F.W.P.C.A. (Federal Water Pollution Control Administration), 1970, Preliminary Operations Planning Manual for the Restoration of Oil Contaminated Beaches. URS Research Company Rept. to the F.W.P.C.A., Water Pollution Control Series Contract 14-12-811, 58 p.

MacKay, J.W., 1970, Beach Restoration Report. Unpub. MS., Dept. of Public Works, Halifax, Nova Scotia, 91 p.

Owens, E.H., 1971, The Restoration of Beaches Contaminated by Oil in Chedabucto Bay, Nova Scotia. Marine Sciences Branch, Ottawa, MS. Rept., Series No. 19, 75 p.

Owens, E.H., 1972, A Reconnaissance of the Coastline of Chedabucto Bay, Nova Scotia. Marine Sciences Paper No. 4, Information Canada, Ottawa, p. 24.

Owens, E.H., and Drapeau, G., 1972, Changes in Beach Profiles at Chedabucto Bay, Nova Scotia, Following Large-Scale Removal of Sediments (in preparation).

Robinson, A.H.W., 1961, The Hydrography of Start Bay and its Relationship to Beach Changes at Hallsands. Geog. Journ., v. 127, no. 1, p. 63-77.

Thomas, M.L.H., 1971, Spring 1971 Survey of Intertidal and Lagoonal Areas in Chedabucto Bay. Unpub. Rept. to the Project Oil Task Force, 3 p.

Wardley Smith, J., 1968, Recommended Methods for Dealing with Oil Pollution. Unpub. Rept., Min. of Technology, Warren Springs Laboratory, Stevenage, Herts, U.K., Rept. LR 79 (EIS), 22 p.

Wardley Smith, J., 1969, U.K. Ministry of Technology Work on Oil Pollution. Proc. API/FWPCA Joint Conf. on the Prevention and Control of Oil Spills, New York, p. 27-40.

CHAPTER 148

NATURAL CLEANING OF OIL POLLUTED SEASHORES

by

Georges Drapeau*

ABSTRACT

Field observations were carried out for a period of 20 months on the seashores of Chedabucto Bay, following the spillage of 108,000 barrels of bunker C oil in the bay by the tanker Arrow in February 1970. The main factors that control the natural cleaning of seashores are as follows:

1) Physico-chemical characteristics of oil: The bunker C-type fuel oil carried by the tanker Arrow forms, when spilled at sea, a very stable emulsion containing some 40 percent sea water. The emulsion formed is 40 times as viscous as pure bunker C (30,000 poises at 32°F).

2) Nature of polluted seashore: The natural cleaning of seashores is essentially mechanical. Abrasion of oil is most rapid on sand beaches because sand-size sediments are moved more vigourously by wave action. Such beaches clean within six months. Cobble and boulder beaches take one year to clean in Chedabucto Bay. Bedrock outcrops are still covered with a veneer of "dried" oil after 20 months of exposure to the surf.

3) Hydrodynamics of the environment: Wave action is the dominant source of energy that reaches the seashores of Chedabucto Bay and the cleaning of beaches is directly related to the amount of wave energy reaching different areas of the seashore.

*Atlantic Geoscience Centre
Bedford Institute of Oceanography, Dartmouth, N.S. Canada

Present address: Université du Québec (I.N.R.S.)
300 des Ursulines, Rimouski, Qué. Canada

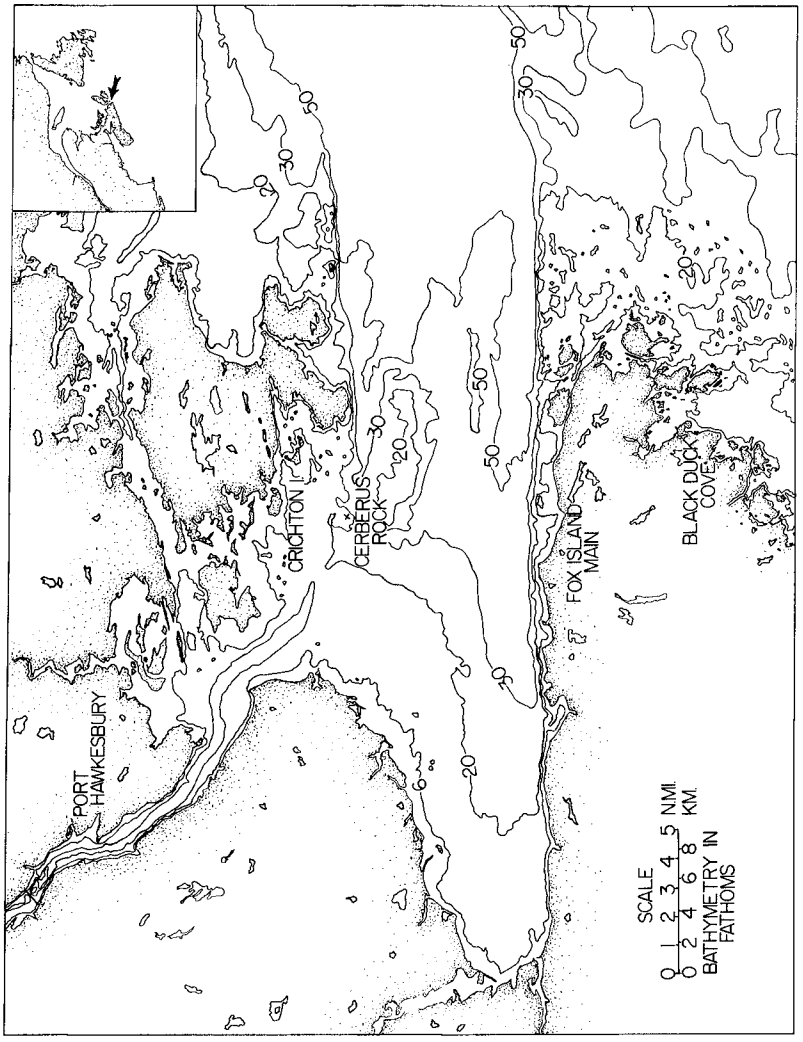

FIG. 1 Bathymetric map of Chedabucto Bay. Location of the map-area is shown in the upper right corner.

4) Climatic conditions prevailing when oil reached the seashore: The spillage of oil from the tanker Arrow took place during a period of wintry weather. High waves and high tides prevailed at that time. Much oil was then pushed very high on the beaches and remained unreached during the following summer season. Had the oil spill occured during the summer in calm weather, the pollution of seashores would have been much less extensive.

INTRODUCTION

The Liberian tanker Arrow grounded on Cerberus Rock in Chedabucto Bay, Nova Scotia (fig. 1). Chedabucto Bay, located on the Atlantic Coast of Canada between mainland Nova Scotia and Cape Breton Island, is a triangular bay 20 miles deep and some 10 miles wide. The south coast of the bay is developed along a fault zone and is consequently rectilinear and steep. By contrast, the north coast is characterized by a submerging, low-lying topography. The coast of Chedabucto Bay comprises a variety of rock outcrops, eroding till cliffs, gravel and mixed sand-gravel beaches (Owens, 1972 a). The Arrow lost 108,000 barrels of bunker C oil and approximately one third of that cargo reached the shore and polluted 190 of the 375 miles of seashore surrounding the bay. A task force was formed by the Canadian Government to contend with that accident and also to gain as much understanding as possible of oil spills in a wintry environment. A program of field observations of oil pollution on seashores was initiated as part of the Canadian Government Task Force (Drapeau, 1970). It is possible, after 20 months of field observations, to outline the main factors that control the natural cleaning of oil polluted seashores. These factors are: 1) Physico-chemical characteristics of oil, 2) nature of polluted seashore, 3) hydrodynamics of the environment, and 4) climatic conditions during the oil spill.

1) Physico-chemical characteristics of oil:

The oil spilled by the tanker Arrow is a bunker C-type fuel oil which is much heavier than the Kuwait crude spilled by the Torrey Canyon in the English Channel, or the crude oil released by the offshore well blowout and natural seepages in the Santa Barbara Channel.

The most significant characteristic of bunker C oil, as far as oil pollution of seashores is concerned, is that it forms a stable emulsion of sea-water-in-oil. A similar phenomenon has been observed for crude oils (Great Britain Cabinet Office, 1967; Benyon, 1969; Batelle Memorial Institute, 1969). Experiments carried out by the Canadian Government Task Force indicate that the exposure time in the sea necessary to increase the water content in bunker C by 30 percent is in the order of three days (Task Force - Operation Oil, 1970). Samples of

FIG. 2 Bunker C emulsion deposited on sand. The emulsion is so viscous that it does not permeate deeply into the sand. The "asphalt pavement" formed is approximately four inches thick (April 9, 1970).

FIG. 3 Indian Cove, south shore of Chedabucto Bay. Photograph taken one month after the oil spill, on March 25, 1970. The sandy portion of the beach is already clean, while the boulders are still heavily polluted.

FIG. 4 Same area as above photographed 14 months after the oil spill, in May 1971. The boulders are clean and oil has disappeared completely from that beach.

FIG. 5 Sand beach in a protected inlet (Black Duck Cove, see location in figure 1). That beach is "frozen" under a heavy coat of oil. Shallow channels developed in response to action of tides on the beach (March 25, 1970).

oil emulsion collected in different areas at different times contained between 33 and 53 percent water. The physico-chemical properties of the bunker C-sea water emulsion are substantially different from those of pure bunker C. As compared with pure bunker C, the viscosity of the emulsion is increased from 700 to 30,000 poises at 32°F (McKay, 1970; Richards, 1970). Time-lapse photography has shown that bunker C creeps slowly on bedrock surfaces, the rate of flow depending on the thickness of the slick, the ambient temperature, and the intensity of sunshine. Field observations indicate that the bunker C-sea water emulsion is very stable. Eighteen months after the spill, particularly on warm days (70°F, 21°C), heavy accumulations of bunker C emulsion appeared as fresh as at the time of the oil spill.

2) Nature of polluted seashore:

As the bunker C-sea water emulsion is chemically inert, the natural cleaning of seashores results from the mechanical abrasion of oil. Surfing waves are the main source of mechanical energy on the seashore, but wave energy is effective in cleaning the seashore in as much as it induces the movement of sediments on the beach. Sand beaches are easily stirred up by wave action and, as the bunker C emulsion is so viscous that it does not permeate deeply into the sand (fig. 2) sand beaches clean rapidly. Oil slicks one half inch thick that strand on moderately exposed sand beaches take only one to two months to disappear (fig. 3). The situation is different however if the oil cover is too thick; the beach is then completely "frozen" under the oil slick and the waves run on and off without cleaning the oil (fig. 5). Gravel beaches take longer than sand beaches to clean because gravel is not moved as easily by waves and also because the bunker C emulsion penetrates more deeply into a gravel bed (Owens, 1972 b). Boulder and bedrock seashores are not easily cleaned because they are immobile. The exposed boulder beaches in Chedabucto Bay cleaned within one year (fig. 4). Heavily polluted bedrock outcrops exposed to wave attack were still covered with a veneer of "dried" oil 20 months after the spill.

3) Hydrodynamics of the environment:

Wavc energy is the main source of mechanical energy prevailing on the seashores of Chedabucto Bay. The wave climate in the bay is moderate as compared with that of the open ocean. The fetch in Chedabucto Bay does not allow for the formation of waves exceeding a period of eight seconds, according to Bretschneider's (1952) diagram of maximum wave period versus fetch length. However, the bay is open to the Atlantic Ocean and long period waves coming from the east and southeast can penetrate deeply into the bay, which is 300 feet deep and eight miles across at the entrance. Because of its orientation, Cheda-

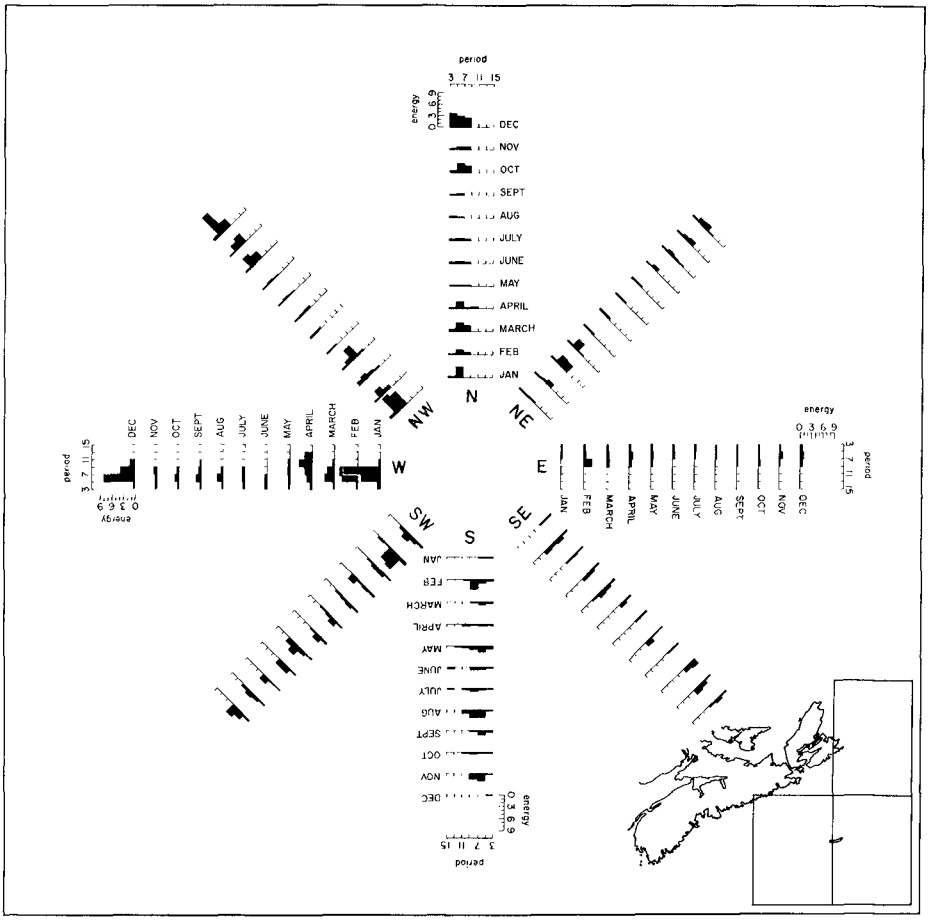

FIG. 6 Wave climate compiled from Wave Climate of the Canadian Atlantic Coast and Continental Shelf - 1970 (Neu, 1971). The areas used for compilation are outlined in the lower right corner.

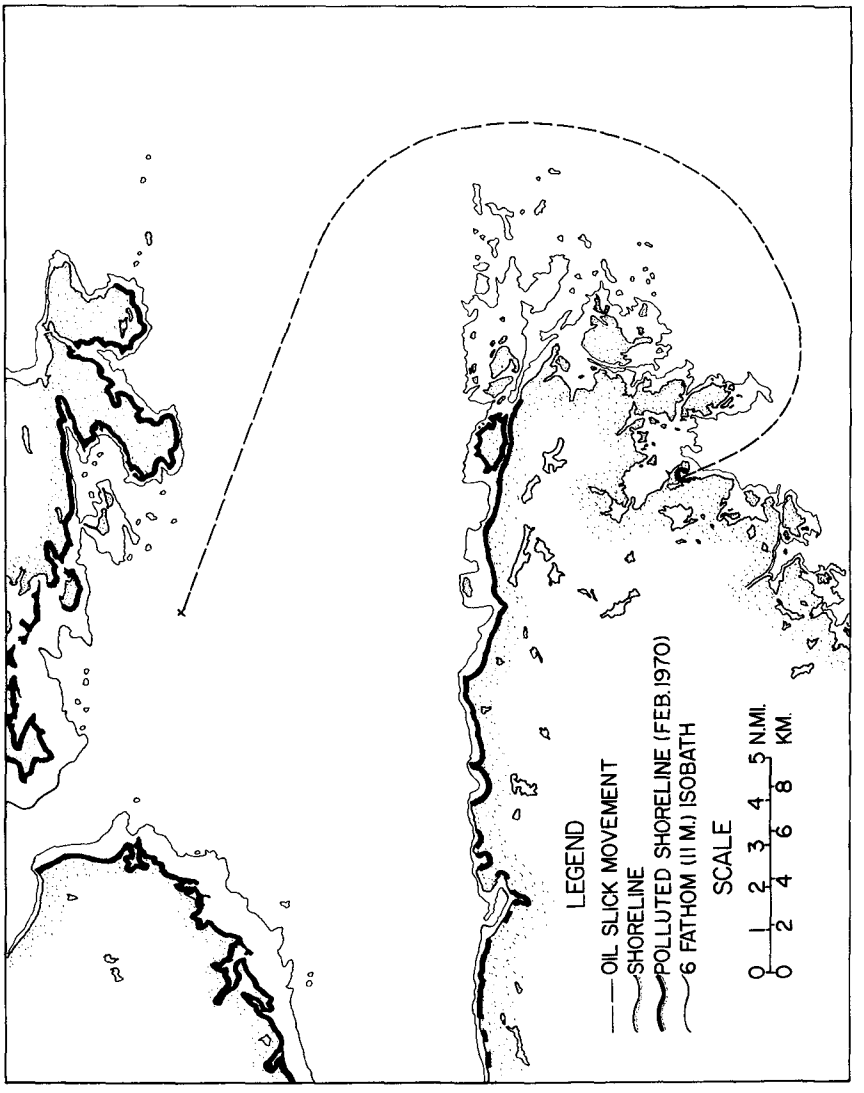

FIG. 7 Assumed track of a large oil slick that reached Black Duck Cove. Oil slicks can be brought into presumably protected areas by the combined action of winds and tides.

bucto Bay is protected from the strongest waves developing in that area of the Atlantic Ocean. The strongest ocean waves come from the north-west as outlined by the rose diagram (Neu, 1971) shown in figure 6. Direct wave measurements were taken near Cerberus Rock by Neu (1970) during the salvage operations. A maximum of 11 seconds was recorded for wave period and a maximum of 9.5 feet for wave height.

Tides in Chedabucto Bay are semi-diurnal and range between 4.4 and 6.9 feet (Canadian Hydrographic Service, 1971). Longshore currents in Chedabucto Bay result from the combined action of tides and winds and are in the order of 0.4 to 0.6 ft/sec. (Neu, 1970).

4) Climatic conditions during the oil spill:

Oil slicks are moved by the combined action of winds and tides. The wind was blowing from the south at the time of the grounding of the Arrow so that the first oil slicks were pushed on the shores of Isle Madame. The wind eventually turned and the oil escaping from the wreck was pushed onto the south shore of Chedabucto Bay and into the open ocean. The trajectory of oil slicks can be very intricate. A particularly striking case in Chedabucto Bay is the heavy pollution of Black Duck Cove, which can only be described as a "caprice de la nature" (fig. 7).

The stranding of oil on seashores bears many similarities with that of other floating debris. On seashores exposed to surf action, oil accumulates at the high-water level with driftwood and plastic containers (fig. 8). In areas protected from the surf, oil slicks are pushed slowly by the wind, and blanket large portions of the intertidal zone instead of accumulating at the high-tide level (fig. 5).

The heavy polluted south shore of Crichton Island (fig. 1) located 2.5 miles north of the ship wreck, was monitored in greater detail in order to understand more precisely the mechanisms of deposition and removal of oil from beaches. The section of beach studied is particularly interesting because it is in a delicate state of equilibrium with the environment (fig. 9). Part of the shore is protected by a sublittoral rock platform which modifies the wave approach (fig. 10) thus inducing the formation of a convex barrier as seen in figure 9. The height and the slope of the beach, as well as the texture of its sediments, are controlled by the hydrodynamics of the environment (fig. 11). Where the beach is not directly protected by the subtidal rock platform, the crest is higher, the slope is steeper, and the texture of sediments coarser, as compared with the crescentic portion of the beach

FIG. 8 Helicopter view of Crichton Island beach showing that oil accumulated at high-tide level, and above, in areas exposed to wave action (April 9, 1970).

FIG. 9 Crescentic beach on Crichton Island. Concentrations of oil are apparent at high-tide level and on bedrock (April 9, 1970).

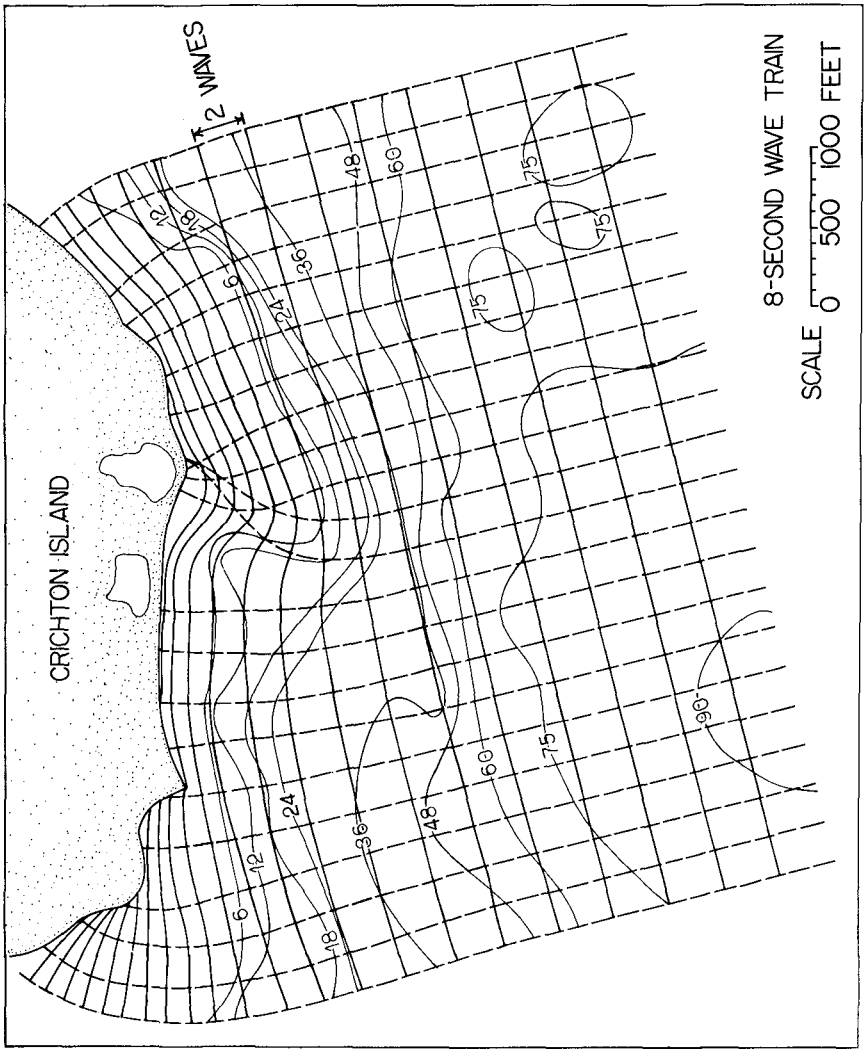

FIG. 10 Computer plotted (Vandall, 1972) wave refraction diagram for the beach shown in figure 9. The two ponds appearing behind the beach on the photograph are outlined under the words "Crichton Island" on the diagram.

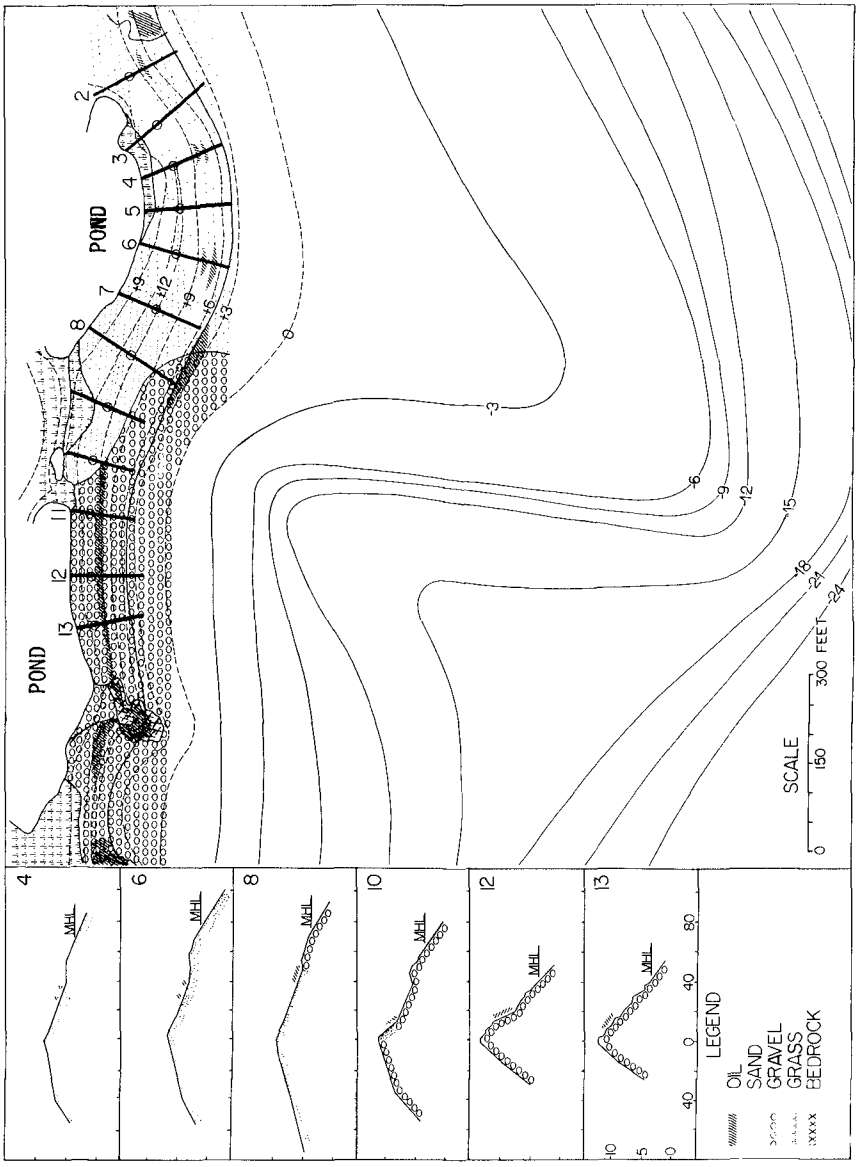

FIG. 11 Geological map and profiles of the beach shown in figures 9 and 10. The two ponds seen in figures 9 and 10 are identified on the map. The topography is contoured in feet with reference to the Canadian Hydrographic Service datum.

FIG. 12 Photograph taken in April 1970 facing profile 12 outlined in figure 11. Oil was pushed above higher high tide level which normally reaches the lower post seen on the photograph.

FIG. 13 Same area as figure 12 photographed in March 1971. This gravel beach is essentially clean. The profile of the beach has changed as indicated by the reference poles, but the gravel is clean underneath.

FIG. 14 Crichton Island beach. The lower edge of the photograph is parallel to profile 8 outlined in figure 11, and the portion of beach between profiles 8 and 13 appears on the photograph. Oil stranded at a lower level on the protected portion of the beach in the foreground, and was pushed higher along the more exposed section of the beach in the background.

directly protected by the offshore platform, where the profile is lower and the sediments are composed of sand instead of gravel. The deposition of oil on that beach follows a similar pattern. The oil was pushed higher on the gravelly, more exposed portion of the beach than on the less exposed sandy crescentic section, as shown in figure 11.

The grounding of the Arrow occured in a period of wintry weather during which waves in Chedabucto Bay presumably reached a height of 15 feet and the tides departed by more than 1.5 foot from predicted levels (Neu, 1970). Oil was then pushed very high on exposed seashores (Owens and Drapeau, 1972). On the most exposed portion of the beach monitored on Crichton Island, (profiles 12 and 13, fig. 11, and fig. 12 and 13) the oil was pushed sufficiently high to remain out of reach throughout the following summer season, so that portions of the beach were only cleaned during the storms of the following winter. Naturally oil was not pushed as high on the portion of the beach partly protected by the sublittoral platform (profiles 4, 6 and 8 in figure 11 and figure 14); therefore that oil was reached by summer waves and cleaned within six months.

The detailed monitoring carried out on Crichton Island shows then that the climatic conditions prevailing during an oil spill determine the extent of pollution on the seashore. Had the oil spill in Chedabucto Bay occured during a period of calm weather, the oil pollution on the shore would have been confined to the high water-level and would have been easily reached by the waves afterward.

CONCLUSIONS

In the eventuality of a major oil spill threatening a seashore, three points should be taken into consideration. Firstly, all efforts should be concentrated to prevent oil from entering inlets even if such areas do not seem as important as the exposed beaches used for recreation. Natural cleaning of exposed sand beaches is relatively rapid, but inlets remain polluted for a very long time and become a continuous source of contamination for the clean beaches. The experience of Chedabucto Bay has shown that sand beaches in the vicinity of polluted areas can be recontaminated to a greater or a lesser extent many times during one season. It takes very little oil to make a beach unsuitable for recreational purposes. Secondly, attention should be given to the fact that no detergents were used in Chedabucto Bay. The bedrock on exposed seashores that had been heavily polluted, was as clean eighteen months after the spill as if large quantities of detergents had been used immediately after the pollution occured. A slower but nonetheless efficient natural cleaning of bedrock surfaces is a better compromise than using large quantities of detergents that would jeopardize

the biological equilibrium of the environment. Thirdly, salvage operations or any type of operation involving a risk of oil spillage should be attempted only in calm weather and during periods of neap tides. Should then an oil spill occur, oil slicks would strand lower on the seashore. Detailed monitoring on Crichton Island has shown that the natural cleaning of exposed beaches is relatively rapid when oil does not extend above normal high tide level. By contrast, oil pushed by storm waves beyond the high-water mark stagnates on the berm until the next period of prolonged wintry weather. Furthermore, it takes considerably more wave energy to clean a beach than to pollute it. It is an important point to consider when assessments are made of the rate of natural cleaning.

ACKNOWLEDGEMENTS

The writer wishes to acknowledge the excellent support received from the Task Force-Operation Oil and from the Bedford Institute of Oceanography. The writer is particularly thankful to Dr. B. R. Pelletier for critically reading the manuscript, to Mr. P. Vandall for providing computer programs for the construction of wave refraction diagrams, and to Mr. R. Belanger for handling the photography and experimenting with new techniques.

REFERENCES

BATELLE MEMORIAL INSTITUTE, 1969, Review of Santa Barbara Channel Oil Pollution Incident: Federal Water Pollution Control Administration, Department of the Interior, Washington, D. C.

BENYON, L. R., 1969, Dealing with Oil Pollution at Sea and on Shore: Draft of paper presented at Oil Pollution Conference in Geneva, October 1969.

BRETSCHNEIDER, C. L., 1952, Revised Wave Forecasting Relationships: Proc. 2nd Conference Coastal Engineering, Council on Wave Res., Engineering Foundation.

CANADIAN HYDROGRAPHIC SERVICE, 1971, Canadian Tide and Current Tables, Vol. 1, Atlantic Coast and Bay of Fundy: Department of E.M. and R., Ottawa.

DRAPEAU, G., 1970, Reconnaissance survey of oil pollution on south shore of Chedabucto Bay, March 24-25, 1970; unpub. rep. Atlantic Oceanographic Laboratory, Dartmouth, N.S.

GREAT BRITAIN CABINET OFFICE, 1967, Committee of scientists on the scientific and technological aspects of the Torrey Canyon disaster: Her Majesty's Stationery Office, London.

MC KAY, G. D.M., 1970, Viscosity of emulsion of bunker C and sea water. Unpublished report: Department of Chemical Engineering, Nova Scotia Technical College, Halifax, N.S.

NEU, H.A., 1970, The hydrodynamics of Chedabucto Bay and its influence on the Arrow oil disaster: Bedford Institute, Nova Scotia, AOL report 1970-6.

NEU, H.A., 1971, Wave climate of the Canadian Atlantic Coast and Continental Shelf - 1970: Bedford Institute, Nova Scotia AOL Report 1971-10.

OWENS, E.H. 1972a, A reconnaissance of the coastline of Chedabucto Bay, Nova Scotia, Marine Sciences Paper No 4, Department of the Environment, Ottawa.

OWENS, E.H. 1972 b, The cleaning of gravel beaches polluted by oil: 13th International Congress on Coastal Engineering, in press.

OWENS, E.H. and DRAPEAU, G., 1972, Changes in beach profiles at Chedabucto Bay, Nova Scotia, following large-scale removal of sediments: Canadian Journal, Earth Sciences, in press.

RICHARDS, P., 1970, Effect of water concentration on viscosity of bunker C: unpub. rep., Department of Chemical Engineering, Nova Scotia Technical College, Halifax, N.S.

TASK FORCE - OPERATION OIL, 1970, Report of the Scientific Coordination Team to the Head of the Task Force. Operation Oil, Vol. II (Clean-up of the Arrow oil spill in Chedabucto Bay): Atlantic Oceanographic Laboratory, Dartmouth, N.S.

VANDALL, P.E., 1972, The construction of wave refraction diagrams by computer: Computer note BI-C-72 - Atlantic Oceanographic Laboratory, Bedford Institute of Oceanography, Dartmouth, N.S.

CHAPTER 149

CONTAINING OIL SLICKS IN FLOWS OF FINITE DEPTH

by

D.L. Wilkinson*

ABSTRACT

The hydrodynamics of oil slick containment are examined. It is shown that containment is only possible when a densimetric Froude number based on flow velocity and depth and the oil density is less than a critical value. Experiments confirmed that an oil slick was unable to maintain a stationary front when the Froude number exceeded the critical value.

It is also shown that viscous effects ultimately limit the thickness and therefore the length and volume of any real slick. Expressions are derived which enable these limits to be determined.

*Consultant, Hydraulics Laboratory, National Research Council of Canada, Ottawa, Ontario, K1A 0R6.

CONTAINING OIL SLICKS IN FLOWS OF FINITE DEPTH

INTRODUCTION

It is well known that when oil spills onto a water surface it spreads rapidly to form a thin film, eventually only thousandths of an inch thick. At present there is no known means of removing an oil film as such from a water surface other than by the natural processes of evaporation and biological degradation. The efficiency of man devised removal techniques increases rapidly as the thickness of the slick itself increases so that confinement of the slick is usually the first step in the clean-up procedure.

Oil booms, which restrict the movement of oil on the water surface, are commonly used as the confining apparatus. Wind and currents will cause oil to accumulate on the upstream side of any partially submerged barrier which impedes the flow of oil on the the water surface. Figure 1 shows an oil slick contained in a flowing stream.

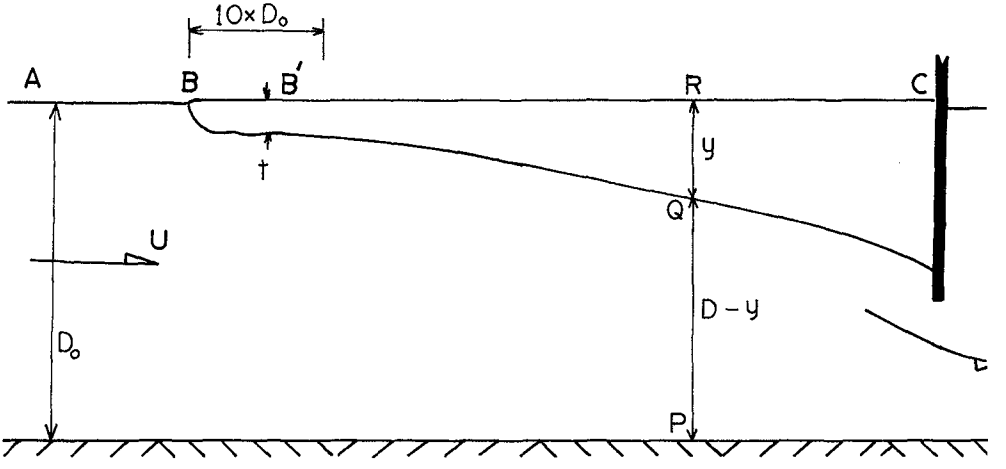

Fig. 1. Profile of a Contained Oil Slick

Unfortunately containment of oil slicks is not always possible as winds, waves and currents can cause oil to escape past a boom or even cause structural failure of the boom itself. This paper examines the effects of current on oil contained in a horizontal two dimensional channel. It is shown that viscous shear forces at the oil-water interface ultimately limit the length of any contained oil slick. Furthermore, dynamic considerations make containment of a slick impossible if the current flow exceeds a critical Froude number. Suggestions are madc as to how slicks might be contained under supercritical conditions by judicious alignment of an oil boom.

THE PHYSICS OF A CONTAINED OIL SLICK

Figure 1 shows the profile of a typical laboratory oil slick and it should be noted that the horizontal scale has been compressed by a factor of 50 compared with the vertical scale. Starting at the upstream end B, the slick can be divided into two distinct areas of influence. Firstly, an abrupt thickening occurs near the very front of the slick (B-B' in Fig. 1). This is a dynamic effect brought about by the presence of a current passing beneath the slick, and in a given channel the greater the current speed, the deeper will be the slick front. Viscous effects are relatively unimportant in this frontal zone so that its thickness can be predicted with reasonable accuracy using inviscid flow assumptions.

The analysis enables the frontal thickness ratio $\phi = t/D_o$, (where t is the frontal thickness of the slick and D_o the current depth upstream of the slick) to be expressed as a function of a densimetric Froude number F. The densimetric Froude number, hereafter simply termed the Froude number, is defined as

$$F = U/(\Delta g D_o)^{\frac{1}{2}}$$

where U = current speed upstream of the slick
$\Delta = \rho_{water} - \rho_{oil} / \rho_{water}$
and g = gravitational acceleration.

Unfortunately, solutions for ϕ are available only for a limited range of Froude numbers less than approximately 0.5. At Froude numbers in excess of this value a stable front is unable to form and oil will pass beneath any boom, no matter how deeply it is placed. The Froude number of the flow in Fig. 1 was 0.30 and the slick was therefore stable.

The downstream region of the slick is denoted by B'C and in this zone viscous forces are responsible for the further thickening of the slick. It can be seen in Fig. 1

that the interfacial slope increases with distance from the slick front. Obviously in flows of finite depth this process cannot continue indefinitely and ultimately the slick attains a critical thickness where additional oil cannot be contained and if oil is added to a slick at this stage an equal volume of oil will be displaced beneath the boom, irrespective of its depth.

Two practical points concerning boom immersion depths may be made at this stage. Firstly the skirt depth must at least exceed the dynamically induced thickness t otherwise virtually no oil will be contained at all. Secondly even when the Froude number is less than 0.5 there is a limit to the volume of oil which can be contained behind a single boom. This volume is dependent upon the Froude number of the flow and the interfacial stress. An increase in magnitude of either of these factors will reduce the volume of oil which can be contained. In order to retain the maximum amount of oil, that is achieve a slick of critical length, the skirt depth must exceed the critical slick thickness at C in Fig. 1. The ratio of this thickness to the upstream flow depth D_o can be expressed as a function of the Froude number F and is quite independent of the magnitude of the viscous forces even though it is these forces which cause the slick thickness to reach its limiting value. If the skirt depth of the boom is intermediate between the dynamically induced thickness t, and the maximum slick thickness, oil will be contained but less than if the skirt extended past the critical thickness of the slick.

THEORY

Benjamin (1968) examined the problem of an air cavity advancing into a horizontal box as fluid drained from its single open end. The fluid flow around the air cavity is similar in many respects to the passage of water beneath an oil slick contained in a horizontal channel. The main point of difference between the two phenomena is the existence of the stagnation point at the very front of the slick (B in Fig. 1) results in a superelevation (ε) of the level of the water surface. The superelevation is small compared with the slick thickness t but is important in determining the pressure distribution beneath the slick. However ε may be neglected when summed with t in the convective terms of the force balance equations. Benjamin's solution can be readily adapted to describe a contained slick (see Appendix 1) and the frontal thickness ratio (ϕ) is related to the Froude number of the flow by the equation

$$F^2 = \phi\left[\frac{2\phi}{1-\phi} + \frac{1}{1-\Delta}\right]^{-1}(2-\phi) \qquad (1)$$

Since the slick thickness ratio ϕ is derived from a momentum

pressure force balance relationship, Eq. 1 yields a ϕ value which in an inviscid fluid would be approached asymptotically. In real flows the thickness predicted by Eq. 1 is achieved 15 to 30 slick thicknesses from the front.

It will be apparent later that physical solutions are limited to thickness ratios between zero and approximately one third, depending upon the specific gravity of the oil. This range of solutions for Eq. 1 is plotted as the curve AB in Fig. 2. Frontal thickness of a number of laboratory oil slicks are in close agreement with Eq. 1.

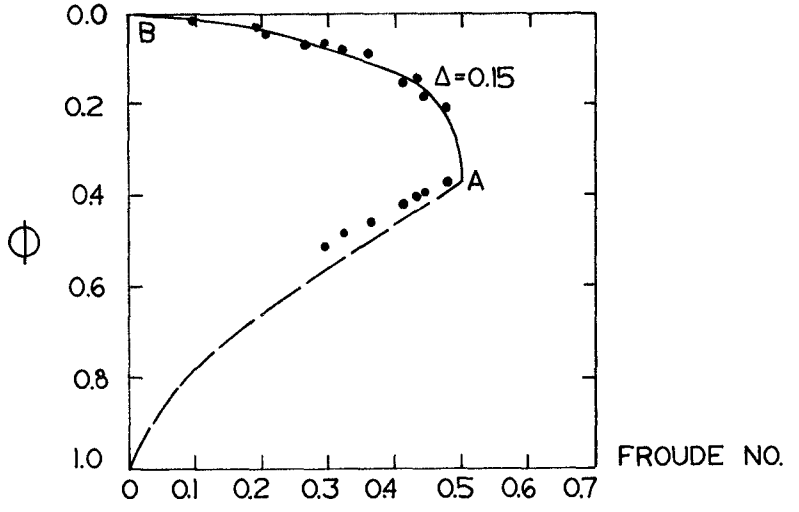

Fig. 2. Frontal Thickness Ratio as a Function of Froude Number

The significant point to note is that no solutions exist to the force balance equation for Froude numbers greater than approximately one half, and in the experiments it was found that slick containment became impossible at Froude numbers in excess of this value.

The relationships describing the equilibrium of the viscous zone of an oil slick, where flow conditions are slowly varying, are derived in Appendix 2. Briefly, an equation describing the flow force balance at a section is combined with the continuity equation to yield a relationship between the upstream Froude number F, the free surface slope $\frac{\partial D}{\partial x}$, the interfacial slope $\frac{\partial y}{\partial x}$, the slick thickness ratio at

the section of interest and the boundary shear stress τ_b acting on the flow at the channel bottom and sides. A second relationship is derived giving conditions for equilibrium of the slick itself and this equation involves all the previous variables except that the boundary stress is replaced by an interfacial stress τ_i which acts at the oil-water interface. The slope of the free oil surface, which is of no practical interest, can be eliminated between the above two equations leaving a single relationship for the interfacial slope given by:

$$\Delta\rho g y \frac{\partial y}{\partial x} \{1 - (\phi + \left[\frac{F}{1-\phi}\right]^2)\} = \frac{\tau_i}{1-\Delta} \{1 - \Delta(\phi + \left[\frac{F}{1-\phi}\right]^2)\} + \tau_b \phi \quad (2)$$

where ρ is the density of the water and
y is the slick thickness.

The two stress terms can be expressed in terms of a friction coefficient, the upstream Froude number and the local slick thickness ratio as below.

$$\frac{\tau_i}{\Delta\rho g D_o} = \frac{f_i}{8} \left(\frac{F}{1-\phi}\right)^2 \quad (3a)$$

and

$$\frac{\tau_b}{\Delta\rho g D_o} = \frac{f_b}{8} \left(\frac{F}{1-\phi}\right)^2 \quad (3b)$$

Values of the interfacial friction coefficient f_i must be determined from experiments while the boundary friction coefficient f_b is well documented elsewhere (Streeter, 1961).

It will be noted that Eq. 2 is singular when

$$\{1 - (\phi + \left[\frac{F}{1-\phi}\right]^2)\} = 0 \quad (4)$$

and at this point the interfacial slope becomes vertical. The gradually varied flow assumption upon which Eq. 2 is based is no longer valid and infact the slick thickness reaches its maximum value just before this critical point is reached. Experiments have shown that if oil is added to a slick which has reached critical length, oil will commence to flow beneath the barrier and escape, irrespective of how deeply the barrier is immersed in the flow. Oil will continue to be lost until the slick is again of critical size.

It can be seen in Eq. 4 that the critical thickness ratio is independent of the magnitude of the viscous stresses and depends only upon the upstream Froude number. The curve AO in Fig. 2 shows the critical thickness ratio plotted as a function of Froude number. The range of thickness of a slick possible at any given Froude number, can be determined

from the ordinate distance between the frontal thickness curve AB and the critical thickness curve AO. It could be anticipated from the decreasing ordinate distance that as the Froude number increases in value the volume of oil which may be contained in any given channel will also decrease. Experimental values of the critical slick thickness are in good agreement with Eq. 4.

Profiles of oil slicks can be calculated by numerical integration of Eq. 2 using Eq. 1 to predict the initial frontal thickness. Figure 3 shows the results of such a calculation for the laboratory oil slick shown in Fig. 1.

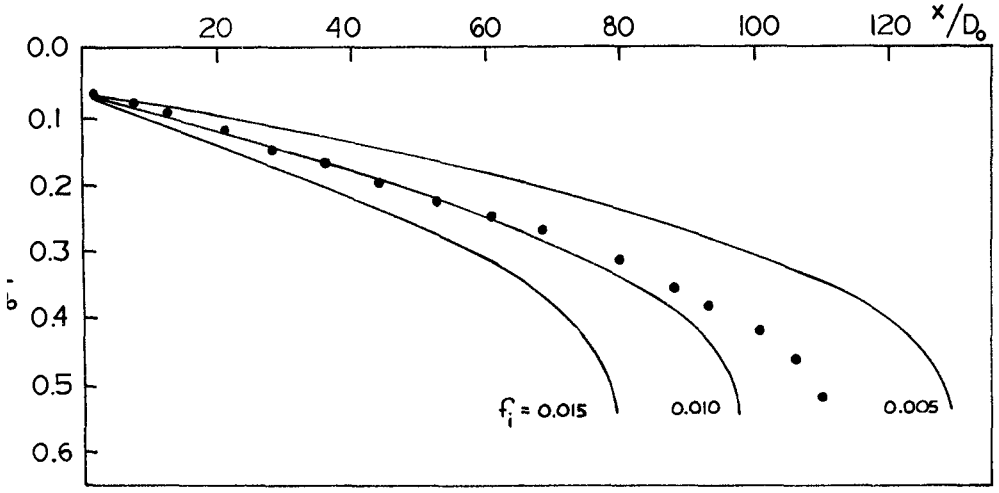

Fig. 3. Comparison of Calculated and Experimental Slick Profiles

The Froude number in this experiment was 0.30 and the mean Reynolds number in the flow passing beneath the slick was 5,400 yielding a friction coefficient of 0.038. Calculations were made for the profiles of slicks having the above Froude number and boundary friction coefficient and were repeated for four values of the interfacial friction coefficient. Each profile is shown in Fig. 3 together with the experimental profile. It appears that the interfacial friction coefficient decreases slightly in value along the length of an oil slick. Similar behaviour was noted in other oil slick experiments and is not unexpected as thickening of a slick results in a convective velocity increase along the length of a slick and hence a similar increase in the Reynolds number of the flow passing beneath the slick. Reynolds numbers of the flows in the experiments were in the range

5,000 to 15,000 where an increase in Reynolds number leads to a decrease in the boundary, and probably the interfacial friction coefficients. Similar effects would probably not be observed in large scale slicks. Interfacial friction coefficients measured in laboratory experiments are generally of the order 0.01, however it is expected that the development of interfacial waves in prototype slicks could result in an appreciable increase in this coefficient.

OPTIMISING BOOM LAYOUTS IN RIVERS AND ESTUARIES

Very few rivers or estuaries will conform to the highly idealised geometry considered so far in this paper. Generally velocities will vary considerably in the horizontal so that in a single river cross-section there might be areas where conditions are critical for containment, and areas where containment is feasible. The problem then becomes that of directing oil out of the critical areas into the quieter regions where it can be removed using skimmers or oleophilic belts. Figure 4 shows a typical Froude number distribution across a river channel and two possible boom layouts.

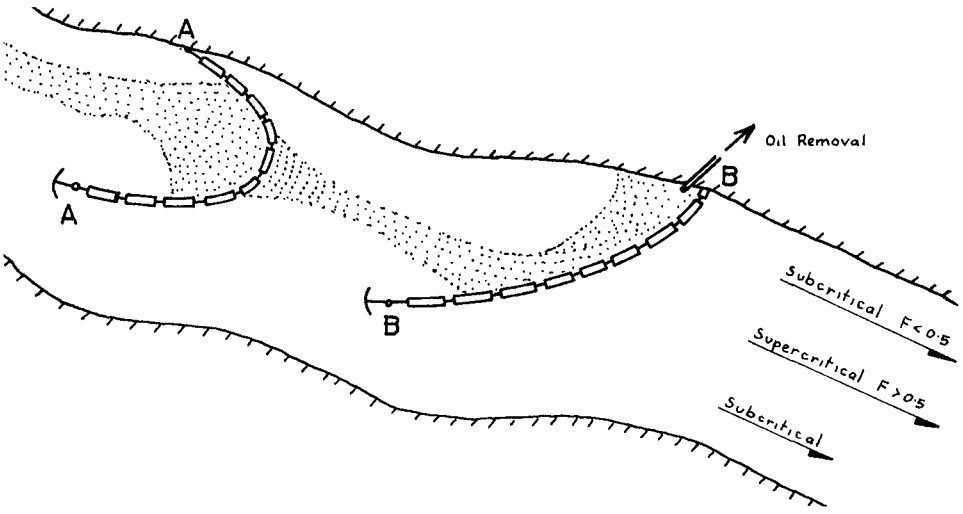

Fig. 4. Typical Boom Configurations

If a boom is set across the channel as in AA, oil would tend to accumulate in the area where the current speed was greatest, and as in this particular case the Froude number in this area

exceeds the critical value, the oil will pass beneath the boom and will be lost. The second layout BB is far preferable since by angling the boom across the maximum velocity region, the velocity component normal to the boom is substantially reduced and the oil will be diverted to quieter regions of the river where containment is possible.

CONCLUSIONS

1) Oil slicks cannot generally be contained in areas where the densimetric Froude number of the current exceeds approximately 0.5.

2) In any channel there is a limit to the volume of oil which can be contained as a single slick.

3) Judicious alignment of oil booms will often enable oil to be diverted from supercritical areas of a channel to quieter regions where containment and removal is possible.

APPENDIX 1
Analysis of the Frontal Region of a Contained Oil Slick

An expression is derived which relates flow conditions in a two-dimensional channel of finite depth, to the equilibrium thickness of an oil slick which can be contained on the water surface in the channel. The flow beneath the oil slick is assumed to be inviscid.

Consider the contained oil slick shown in Fig. 1. If one assumes steady uniform flow conditions exist at A and B' then the sums of horizontal momentum and pressure force per unit width will be equal at both sections and are given by:

$$\rho U^2 D_o + \frac{\rho g D_o^2}{2} = \frac{\rho U^2 D_o^2}{D_o+\varepsilon-t} + \frac{\rho(1-\Delta)g(D_o+\varepsilon)^2}{2} + \frac{\Delta\rho g(D_o+\varepsilon-t)^2}{2}$$

where U = velocity of flow upstream of the slick
ρ = density of the water
D_o = depth upstream of the slick (section 0)
g = gravitational acceleration
$\rho(1-\Delta)$ = density of the oil
t = frontal thickness of the slick
and ε = difference in elevations of the free surface at points A and B'.

In any real problem $\Delta\rho$ is small compared with ρ, and ε is very small compared with D_o. Consequently pressure force terms involving $\Delta\rho\varepsilon$ and ε^2 and momentum terms having ε as a numerator will be neglected in the expansion of the flow force equation above. The flow force equation then reduces to the simpler form:

$$\rho U^2 D_o + \frac{\rho g D_o^2}{2} = \frac{\rho U^2 D_o^2}{D_o - t} + \frac{\rho g D_o^2}{2} + \rho g D_o \varepsilon - \Delta \rho g D_o t + \frac{\Delta \rho g t^2}{2}$$

The difference in levels of the free surface at sections 0 and 1 can be obtained by considering the pressure at the stagnation point B on the streamline AB. As there is no energy dissipation between points A and B, the pressure (p) at B is given by the Bernoulli relationship

$$p = \frac{\rho U^2}{2}$$

This pressure is balanced by an elevation in the surface level of the oil slick,

$$p = \rho (1 - \Delta) g \varepsilon$$

and therefore

$$\varepsilon = \frac{1}{1 - \Delta} \frac{U^2}{2g}$$

The above equation can now be combined with the earlier flow force expression and non-dimensionalized to give

$$F^2 = \frac{F^2}{1 - \phi} + \frac{1}{1 - \Delta} \frac{F^2}{2} - \phi + \frac{\phi^2}{2}$$

and re-arranging we get

$$F^2 = \phi (2 - \phi) \left[\frac{2\phi}{1 - \phi} + \frac{1}{1 - \Delta} \right]^{-1}$$

where

$$F = \frac{U}{(\Delta g D_o)^{\frac{1}{2}}}$$

and

$$\phi = \frac{t}{D_o}$$

The flow force equation above relates the equilibrium thickness of a contained oil slick from conditions upstream of the slick.

APPENDIX 2
Analysis of the Viscous Zone of a Contained Oil Slick

The viscous zone of a contained oil slick may be analyzed by considering the equilibrium of the streamwise gradient of pressure and intertial forces and the boundary shear stress. Consider the slick shown in Fig. 1. The equilibrium of section PR is given by

$$\frac{\partial}{\partial x}\left[\frac{\rho g(1-\Delta)D^2}{2}+\frac{\Delta\rho g(D-y)^2}{2}+\frac{pq^2}{D-y}\right]=-\tau_b$$

where τ_b is the boundary shear stress and q is the flow per unit width beneath the slick. A similar expression can be derived for equilibrium of the slick itself (QR) yielding

$$(1-\Delta)gy\frac{\partial D}{\partial x}=\tau_i$$

where τ_i is the interfacial shear stress.

$\frac{\partial D}{\partial x}$ can be eliminated between the above two equations and non-dimensionalising gives

$$\Delta\rho gy\frac{\partial y}{\partial x}\left\{1-\left[\phi+\left(\frac{F}{1-\phi}\right)^2\right]\right\}=\frac{\tau_i}{1-\Delta}\left\{1-\Delta\left[\phi+\left(\frac{F}{1-\phi}\right)^2\right]\right\}+\tau_b\phi$$

REFERENCES

1. Benjamin, T.B. Gravity Currents and Related Phenomena. J. Fluid Mech., 1968, Vol. 31, pt. 2, pp.209-249.

2. Streeter, V.L. Handbook of Fluid Dynamics, Monograph, McGraw Hill, 1961.

CHAPTER 150

TSUNAMI GENERATION AND PROPAGATION

by

Joseph L. Hammack, Jr.[1] and Fredric Raichlen[2]

ABSTRACT

A linear theory is presented for waves generated by an arbitrary bed deformation (in space and time) for a two-dimensional and a three-dimensional fluid domain of uniform depth. The resulting wave profile near the source is computed for both the two and three-dimensional models for a specific class of bed deformations; experimental results are presented for the two-dimensional model.

The growth of nonlinear effects during wave propagation in an ocean of uniform depth and the corresponding limitations of the linear theory are investigated. A strategy is presented for determining wave behavior at large distances from the source where linear and nonlinear effects are of equal magnitude. The strategy is based on a matching technique which employs the linear theory in its region of applicability and an equation similar to that of Korteweg and deVries (KdV) in the region where nonlinearities are equal in magnitude to frequency dispersion. Comparison of the theoretical computations with the experimental results indicates that an equation of the KdV type is the proper model of wave behavior at large distances from the source region.

INTRODUCTION

The main body of tsunami research has originated in Japan as a natural consequence of the devastating effects of tsunamis on this nation. In early investigations of tsunami generation, e.g., Takahasi (1942, 1945, 1947), Ichiye (1950), Honda and Nakamura (1951), Nakamura (1953) integral expressions (based on a linear theory) were developed to describe the waves resulting from various bed deformations in both two and three-dimensional fluid domains. The difficulty in evaluating these complex expressions for the generated waves precluded a detailed understanding of their character. Webb (1962) and Momoi (1964) developed the wave profiles near the disturbance using high-speed computational facilities. (It should be noted that the bed deformation adopted by Webb is of special interest since it is also one of the models investigated in this study; it appears that an error was made in the earlier solution by Webb.) The waves at large distance from the source region (and at large times after generation) have been investigated by several authors including Keller (1963) and Kajuira (1963) using asymptotic methods such as the method of stationary phase. More recently Hwang and Divoky (1970) have developed a numerical model of tsunami generation based on the shallow-water-wave equations; this model has been applied to the Alaskan earthquake of 1964. The only experimental investigations of tsunami generation (using bed deformations to generate the waves) appears to be those of Takahasi (1963) and Takahasi and Hatori (1962).

[1] Research Fellow in Civil Engineering, W. M. Keck Laboratory of Hydraulics and Water Resources, California Institute of Technology, Pasadena, California, U.S.A.

[2] Professor of Civil Engineering, W. M. Keck Laboratory of Hydraulics and Water Resources, California Institute of Technology, Pasadena, California, U.S.A.

Although numerous authors have investigated the tsunami problem, none appear to have thoroughly studied the wave profiles generated over a full range of characteristic size and time scales for a specific bed deformation. In addition, no authors appear to have determined the restrictions on the applicability of the linearized description of wave behavior for generating and propagating a wave. In this investigation a linear theory has been adopted to describe the waves; however, the effects of nonlinearities during generation and propagation will be examined (for the two-dimensional model). A three-dimensional model of tsunami generation will be discussed, based on a linear theory, and differences between the results for the two and three-dimensional models near the region of generation will be examined. Experiments have been conducted in a wave tank equipped with a section of the bottom which can be moved in a programmed fashion by an hydraulic-servo-system, and these results are compared to the two-dimensional theory.

THEORETICAL ANALYSIS

Consider a fluid domain D as shown in Fig. 1 bounded above by the free surface, S_f, below by the solid boundary, S_b, and unbounded in the direction of wave propagation, i.e., $-\infty < x < \infty$. Initially the fluid is at rest, with the free

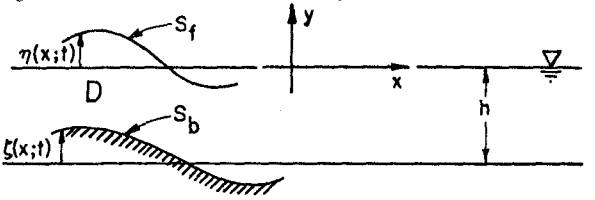

Fig. 1. Definition sketch of coordinate system.

surface and the solid boundary defined by y = 0 and y = -h, respectively. For t > 0 the bed (or solid boundary) is permitted to move in a prescribed manner given by $y = -h + \zeta(x;t)$ such that $\lim_{|x|\to\infty} \zeta(x;t) = 0$. The resulting deformation of the free surface, which is to be determined, is given by $y = \eta(x;t)$. Assuming the fluid to be incompressible and the flow irrotational, a velocity potential $\varphi(x, y;t)$ is known to exist such that $\vec{q} = \nabla\varphi$ where $\vec{q}$ is the velocity vector, i.e., $\vec{q} = (u, v)$. From the continuity equation $\nabla \cdot \vec{q} = 0$, it is found that:

$$\nabla^2\varphi = 0 \text{ in D.} \tag{1}$$

The kinematic conditions to be satisfied on the free surface and on the solid boundary are:

$$\varphi_y = \eta_t + \varphi_x\eta_x \qquad \text{on } y = \eta(x;t), \tag{2}$$

$$\varphi_y = \zeta_t + \varphi_x\zeta_x \qquad \text{on } y = -h + \zeta(x;t) \tag{3}$$

By further assuming the flow to be inviscid and surface energy effects to be negligible the dynamic condition to be satisfied by the fluid particles on the free surface becomes:

$$\varphi_t + \tfrac{1}{2}(\nabla\varphi)^2 + g\eta = 0 , \tag{4}$$

where the pressure on the free surface has been taken as zero.

Solution of Eqs. (1), (2), (3), and (4) is inherently difficult due to the nonlinear terms in the boundary conditions and the unknown location of the free surface on which the boundary conditions are to be applied. These difficulties can be circumvented by assuming the effects of the nonlinear terms to be small relative to the linear effects and applying the linearized boundary conditions at the original positions of the fluid boundaries. The linearized boundary conditions are given by:

$$\varphi_{tt}(x, 0;t) + g\varphi_y(x, 0;t) = 0 , \tag{5}$$

$$\varphi_y(x, -h;t) = \zeta_t(x;t) , \tag{6}$$

where the kinematic and dynamic conditions on the free surface have been combined into a single condition given by Eq. (5). The requirements necessary for this linearized approximation to provide an accurate description of the fluid behavior will be discussed in more detail shortly.

The solution of Eqs. (1), (5), and (6) for the previously stated initial conditions and an arbitrary bed displacement has been presented in detail by Hammack (1972). Using the Fourier transform with respect to the x-coordinate and the Laplace transform with respect to time, t, the water surface displacement was found to be:

$$\eta(x;t) = \frac{1}{2\pi}\int_{-\infty}^{\infty} e^{-ikx}\left\{\lim_{\Gamma\to\infty}\frac{1}{2\pi i}\int_{\mu-i\Gamma}^{\mu+i\Gamma}\frac{s^2 e^{st}\overline{\zeta}(k;s)}{(s^2+\omega^2)\cosh kh}\,ds\right\}dk , \tag{7}$$

where:
$$\omega^2 \equiv gk \tanh kh , \tag{8}$$

$$\overline{\zeta}(k;s) = \int_{-\infty}^{\infty} dx \int_0^{\infty} e^{ikx} e^{-st}\zeta(x;t)\,dt . \tag{9}$$

The bracketed quantity in Eq. (7) is the complex inversion integral for the Laplace transform; the remaining integration represents the inversion integral for the Fourier transform.

A specific bed deformation, $\zeta(x;t)$, must be prescribed before Eq. (7) can be simplified further. Of special interest in the present study is a bed deformation described mathematically by:

$$\zeta_e(x,t) = \zeta_o(1-e^{-\alpha t})\,H(b^2-x^2) \qquad \text{for } t > 0 , \tag{10}$$

where H( ) is the Heavyside step function. Eq. (10) indicates that a block section of the bed, symmetric about x = 0 with a length of 2b, moves in an asymptotic manner to an elevation of ζ_o which may be either above or below the initial bed location. This bed deformation can be characterized by three parameters: an amplitude, ζ_o, a size, b, and a characteristic time, t_c. For convenience the characteristic time which has been chosen is the time required for two-thirds of the movement to be completed, i.e., $t = t_c$ when $\zeta/\zeta_o = 2/3$ or $t_c = 1.11/\alpha$. This bed deformation will hereafter be referred to as the exponential bed motion.

Before Eq. (7) can be simplified, the bed motion, $\zeta_e(x;t)$, must be transformed by Eq. (9); performing these integrations yield:

$$\overline{\zeta}_e(k;s) = 2\zeta_o\frac{\sin kb}{k}\left[\frac{\alpha}{s(s+\alpha)}\right] . \tag{11}$$

Substituting Eq. (11) into Eq. (7), performing the integration around the Bromwich contour in the complex s-plane, taking only the real part of the results, and noting that the integrand is an even function of k yields:

$$\eta(x;t) = -\frac{2\zeta_o}{\pi}\int_0^\infty \frac{\cos kx \sin kb}{k \cosh kh}\left(\frac{\alpha^2}{\alpha^2+\omega^2}\right)\left[e^{-\alpha t} - \cos \omega t - \frac{\omega}{\alpha}\sin \omega t\right] dk \ . \qquad (12)$$

Eq. (12) represents the water surface movement resulting from the exponential bed displacement in a two-dimensional fluid domain; the remaining integration over k cannot be performed in closed form and numerical computations must be used.

Now consider a three-dimensional fluid domain, D, with cylindrical coordinates r, z, and θ, bounded above by a free surface, S_f, below by a solid boundary, S_b, and unbounded in the radial direction, i.e., $0 \le r < \infty$. Initially the fluid field is at rest with the free surface and bed located at $z = 0$ and $z = -h$, respectively. For $t > 0$ the bed is permitted to deform in a prescribed manner given by $z = -h + \zeta(r;t)$; hence, only axially symmetric deformations of the bed are considered in this model. The water surface displacement resulting from an axisymmetric bed deformation will also be independent of θ and is given by $z = \eta(r;t)$. Under the same assumptions stated previously for the two-dimensional fluid domain, the linearized description of fluid behavior is given by:

$$\varphi_{rr} + \varphi_r + \varphi_{zz} = 0 \qquad \text{in D,} \qquad (13)$$

$$\varphi_{tt}(r,0;t) + g\varphi_z(r,0;t) = 0 \ , \qquad (14)$$

$$\varphi_z(r,-h;t) = \zeta_t(r;t) \ . \qquad (15)$$

Eqs. (13), (14), and (15) are most easily solved by first using the Hankel transform of zeroth order with respect to the radial coordinate r and the Laplace transform with respect to t. (See Hammack (1972) for the details of this solution.) The resulting water surface displacement is found to be:

$$\eta(r;t) = \int_0^\infty k J_o(kr)\left\{\lim_{\Gamma\to\infty}\frac{1}{2\pi i}\int_{\mu-i\Gamma}^{\mu+i\Gamma}\frac{s^2 e^{st}\tilde{\zeta}(k;s)\, ds}{(s^2+\omega^2)\cosh kh}\right\} dk \ , \qquad (16)$$

where ω^2 is defined by Eq. (8) and the use of the tilda superscript with the bed displacement indicates:

$$\tilde{\zeta}(k;s) = \int_0^\infty dr \int_0^\infty r J_o(kr)\, e^{-st}\zeta(r;t)\, dt \ . \qquad (17)$$

The bracketed quantity in Eq. (16) again represents the complex inversion integral for the Laplace transform of a function while the remaining integration is the inversion integral for the Hankel transform of zeroth order. (The Bessel function of first kind and zero order in Eqs. (16) and (17) is denoted by $J_o(\ )$.)

In order to compare the wave structures resulting from similar bed deformations in the two-dimensional (2-D) and the three-dimensional (3-D) models of tsunami generation, consider a bed deformation for the 3-D model given by:

$$\zeta_e(r;t) = \zeta_o(1-e^{-\alpha t})\, H(r_o - r) \ , \qquad \text{for } t \ge 0 \ , \qquad (18)$$

where H( ) is the Heavyside step function. Eq. (18) represents a bed deformation in which a block section of the bed, circular in planform with a radius r_o, moves with the same time-displacement history as the block section of the bed in the 2-D model; hence, Eqs. (10) and (18) represent analogous bed deformations in the 2-D and 3-D models of tsunami generation, respectively. Three parameters again are required to characterize the bed motion given by Eq. (18): an amplitude, ζ_o, a size, r_o, and a characteristic time, t_c. The characteristic time will again be chosen as the time required for two-thirds of the bed displacement to be completed. Substituting $\zeta_e(r,t)$ as given by Eq. (18) into Eq. (17) yields:

$$\tilde{\zeta}_e(k;s) = \zeta_o \frac{r_o J_1(kr_o)}{k} \left[\frac{\alpha}{s(s+\alpha)}\right] , \qquad (19)$$

where $J_1( )$ is the Bessel function of first kind and order one. Substituting Eq. (19) into Eq. (16), performing the integration around the Bromwich contour, taking only the real part of the results, and noting that the integrand is an even function of k yields:

$$\eta(r;t) = -\zeta_o r_o \int_0^\infty \frac{J_1(kr_o) J_o(kr)}{\cosh kh} \left[\frac{\alpha^2}{\alpha^2+\omega^2}\right]\left[e^{-\alpha t} - \cos \omega t - \frac{\omega}{2} \sin \omega t\right] dk . \qquad (20)$$

The remaining integration over k cannot be performed in closed form and, as with the two-dimensional example, numerical computations must be used to approximate the results.

Eqs. (12) and (20) describe the water surface displacements resulting from similar bed deformations in a two and three-dimensional model of tsunami generation. It should be emphasized that these solutions are based on a linearized description of fluid behavior; hence, their applicability is restricted to bed motions in which the neglected nonlinear effects are small relative to the linear effects which have been retained.

PRESENTATION AND DISCUSSION OF RESULTS

The results presented in this study for the two and three-dimensional models of tsunami generation will be concerned primarily with the wave structure near the source region of the bed deformation. This area of the fluid domain will be referred to as the generation region and is given by $|x| \leq b$ for the 2-D model and $r \leq r_o$ for the 3-D model. Some comments on the propagation of waves outside of the generation region will be presented for the two-dimensional model.

The Generation Region – There are two positions in the generation region of the 2-D model which have been investigated both experimentally and theoretically; these positions are $x/h = 0$ and $x/b = b/h$. (For a discussion of the experimental equipment used to model the bed deformation for the two-dimensional model, see Raichlen (1970) or Hammack (1972).) Analogous positions in the 3-D model (which have been investigated only theoretically) are $r/h = 0$ and $r/h = r_o/h$. The results presented for the positions at the edge of the bed deformation, i.e., $x/h = b/h$ and $r/h = r_o/h$, are of special interest since the wave structure at these locations represents the type of wave which propagates from the source region.

It has been shown by Hammack (1972) that three dimensionless parameters are important in determining the characteristics of the waves in the generation region. These parameters are: ζ_o/h which represents a disturbance-amplitude scale, b/h or r_o/h which represents a disturbance-size scale, and $t_c\sqrt{gh}/b$ or $t_c\sqrt{gh}/r_o$ (hereafter referred to as the time-size ratio) which is the ratio of a disturbance-time scale, $t_c\sqrt{g/h}$, and the disturbance-size scale. The time-size

ratio may also be interpreted as the ratio of a characteristic distance a long wave will propagate during the bed motion to the characteristic length of the bed deformation. When the bed displacement is very rapid such that $t_c\sqrt{gh}/b$ (or $t_c\sqrt{gh}/r_o$) is much less than unity during the displacement interval, the effect of the bed deformation is confined to the neighborhood of the generation region. Bed motions of this type will be referred to as impulsive. When the bed displacement is very slow such that the time-size ratio is much greater than unity, the water surface elevations (depressions) which occur have sufficient time to propagate from the generation region during the displacement interval; hence, the displaced water volume is spread over a larger region of the fluid domain at the end of the bed displacement. Bed motions of this type will be referred to as creeping.

One of the more important characteristics of waves in the generation region is the maximum displacement of the water surface, η_o, which occurs at a particular location. Fig. 2 shows the experimental and theoretical variation at x/h = b/h of the ratio of the maximum wave amplitude, η_o, to the total bed displacement, ζ_o, as a function of the time-size ratio, $t_c\sqrt{gh}/b$. The results are presented separately for each of the five disturbance-size scales (b/h) investigated. Hollow symbols are used to indicate data for which a bed upthrust ($\zeta_o > 0$) occurred; shaded symbols indicate data for bed downthrows ($\zeta_o < 0$). The magnitude of the disturbance-amplitude scale for each experiment is shown in the legend of Fig. 2.

The general behavior of the theoretical variation of the relative wave amplitude, η_o/ζ_o, with the time-size ratio shown in Fig. 2 is similar for each size scale. For impulsive bed motions, i.e., $t_c\sqrt{gh}/b << 1$, the relative wave amplitude reaches a maximum and remains constant with decreasing time-size ratios. The results for impulsive bed motions of the larger size scales indicate that the maximum amplitude of the wave propagating from the generation region is equal to one-half of the total bed displacement; for the smaller size scales the maximum wave amplitude appears to be less than $0.5\,\zeta_o$. As the time-size ratio becomes very large, i.e., for creeping bed motions, the linear theory indicates that the relative wave amplitude becomes inversely proportional to the time-size ratio. (The range of time-size ratios between the impulsive and creeping range will be referred to as transitional.)

The linear theory presented in Fig. 2 for the three smaller size scales agrees well with the variation found from the experiments; however, it should be noted that no disturbance-amplitudes scales, ζ_o/h, greater than 0.2 (in absolute value) were used for these experiments. The experimental results presented for the two larger size scales in Fig. 2 indicate that nonlinear effects become important as the disturbance-amplitude scale exceeds 0.2 when the bed motion is either impulsive or transitional. In the creeping range the linear theory agrees well with the data regardless of the magnitude of ζ_o/h. (This suggested nonlinear behavior in the generation region due to large amplitude scales has been demonstrated analytically by Hammack (1972) for impulsive and creeping bed motions.)

In order to compare the behavior of the relative wave amplitude, η_o/ζ_o, between the two and three-dimensional models of tsunami generation, the theoretical variation of the relative wave amplitude for corresponding time-size ratios has been computed at the center of the disturbance (x/h = 0 and r/h = 0) and at the leading edge (x/h = b/h and r/h = r_o/h) for a size scale of b/h = r_o/h = 12.2. The results presented in Fig. 3 show that at x/h = b/h or r/h = r_o/h the computed variations are similar in shape; an impulsive, transitional, and creeping range of time-size ratios can be defined also for the 3-D model. The relative wave amplitude for the 3-D model is smaller than that

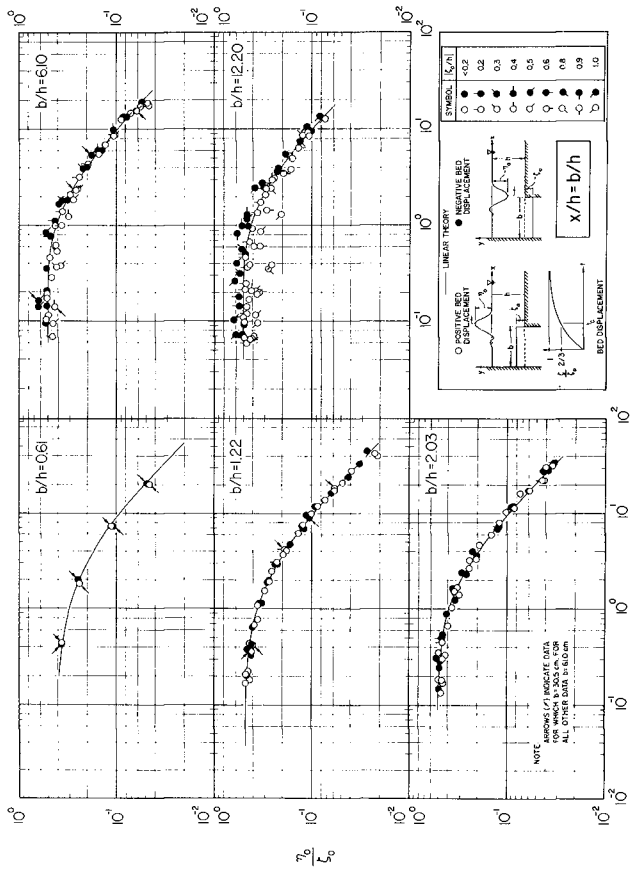

Fig. 2 Variation of the relative maximum wave amplitude, η_o/ζ_o, with the time-size ratio, $t\sqrt{gh}/b$, at $x/h = b/h$ for exponential bed displacements.

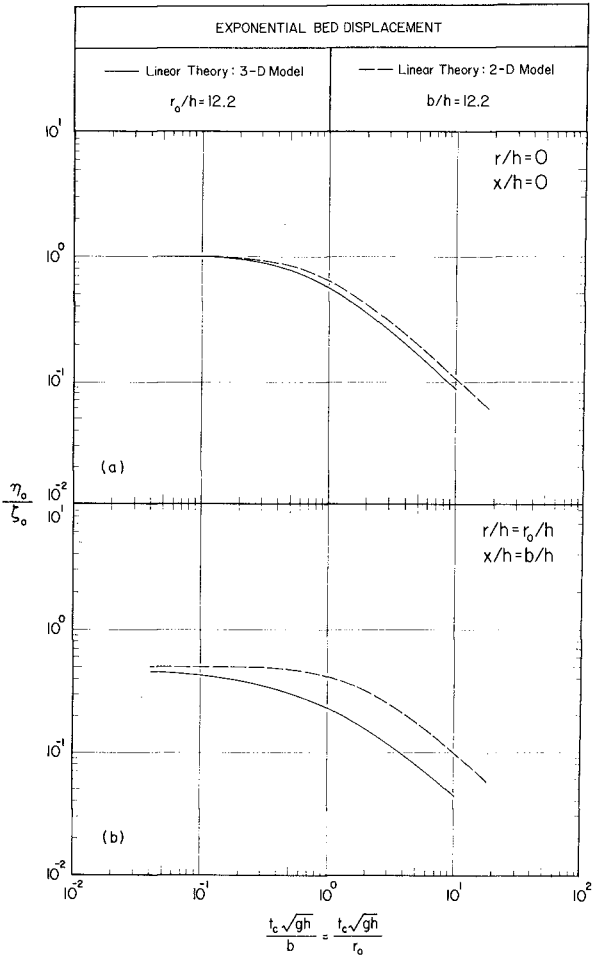

Fig. 3 Theoretical variation of relative maximum wave amplitude, η_o/ζ_o, with the time-size ratio, $t_c\sqrt{gh}/r_o$; a) at $r/h = 0$, b) at $r/h = r_o h$.

computed for the 2-D model over the full range of time-size ratios. At the center of the moving bed, i.e., $x/h = r/h = 0$, the relative wave amplitudes become equal to unity for impulsive bed motions; hence the water surface moves with the bed. In the transitional and creeping range of time-size ratios, the relative wave amplitude is slightly larger for the 2-D model; however, in both cases η_o/ζ_o becomes inversely proportional to the time-size ratio for creeping bed motions.

It was shown in Fig. 2 that the maximum value of the relative wave amplitude in the impulsive range of time-size ratios began to decrease below 0.5 as the disturbance-size scale became very small. This behavior is a result of the elliptic nature ($\nabla^2\varphi = 0$) of the response of the fluid field to an impulsive boundary condition. In order to investigate this behavior more thoroughly for both the two and three-dimensional models, computations of η_o/ζ_o as a function of the disturbance size scales (b/h or r_o/h) for impulsive bed motions have been performed. The results of these computations at the center ($x/h = r/h = 0$) and at the leading edge ($x/h = b/h$ and $r/h = r_o/h$) of the disturbance are shown in Fig. 4; the time-size ratios used for these computations were less than 10^{-2} and 10^{-3} for the two and three-dimensional models, respectively.

The results for the 2-D model indicate that η_o/ζ_o becomes equal to unity and to one-half at $x/h = 0$ and $x/h = b/h$, respectively, for size scales greater than approximately four. For smaller size scales the relative wave amplitude at each position begins to decrease and for $b/h < 10^{-1}$ at each position the relative wave amplitude become equal and directly proportional to the size scale.

For the 3-D model, Fig. 4 shows that η_o/ζ_o becomes equal to unity at $r/h = 0$ for size scales greater than approximately four (similar to the 2-D model); however, at $r/h = r_o/h$ the relative wave amplitude approaches a value of one-half in an asymptotic manner and doesn't become identical to the results of the 2-D model until approximately $r_o/h = 10^2$. For size scales such that $r_o/h < 10^{-1}$ the computations indicate that η_o/ζ_o is equal at both positions in the generation region; η_o/ζ_o also becomes proportional to $(r_o/h)^2$ in this range. Hence, the two and three-dimensional models of tsunami generation behave quite differently for small disturbance-size scales.

In addition to the maximum wave amplitudes, it is also of interest to examine the temporal variation of the water surface movement at a given location in the generation region. Since the temporal behavior of the water surface is similar in each of the three regions: impulsive, transitional, or creeping, it is sufficient to examine typical wave structures for each region. Examples of the theoretical and experimental wave profiles at the center and the leading edge of the bed deformation are presented in Fig. 5 for the 2-D model where the water surface elevation, η, has been normalized by the total bed displacement, ζ_o, and is shown as a function of the nondimensional time $t\sqrt{g/h}$. (The disturbance-size scale, b/h, is equal to 12.2 for each record; a disturbance-amplitude scale, ζ_o/h, has been chosen in each case for which the linear theory is expected to be applicable.)

For the impulsive bed motion shown in Fig. 5, the water level rises rapidly to a maximum elevation of ζ_o and $\zeta_o/2$ at $x/h = 0$ and $x/h = b/h$, respectively, remains at this elevation for an interval of time, and then rapidly returns to the still water level (SWL) about which it oscillates in a damped manner. Most of the wave energy is confined in a single lead wave which resembles the actual bed deformation. The linear theory agrees reasonably

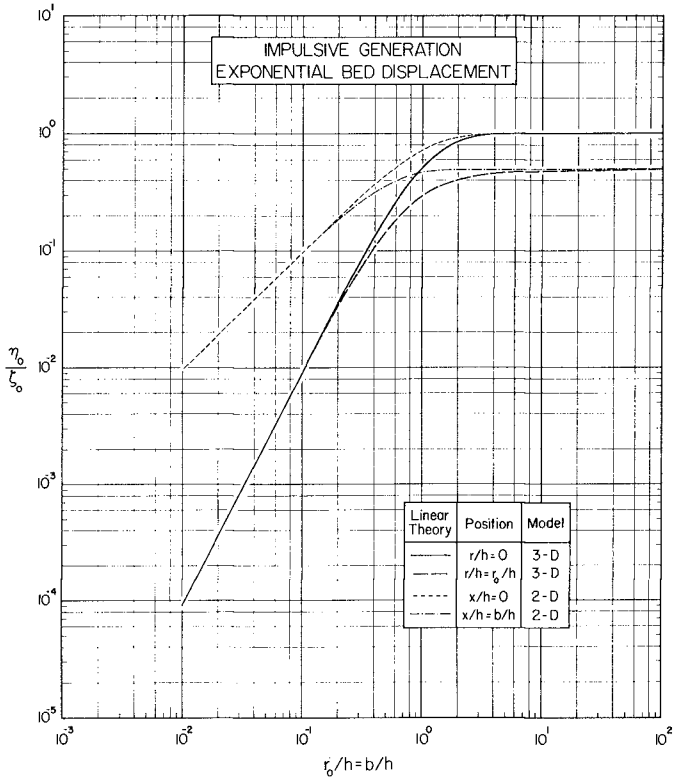

Fig. 4 Theoretical variation of relative maximum wave amplitude, η_o/ζ_o, with the disturbance-size scale, $r_o/h = b/h$, for impulsive bed displacements.

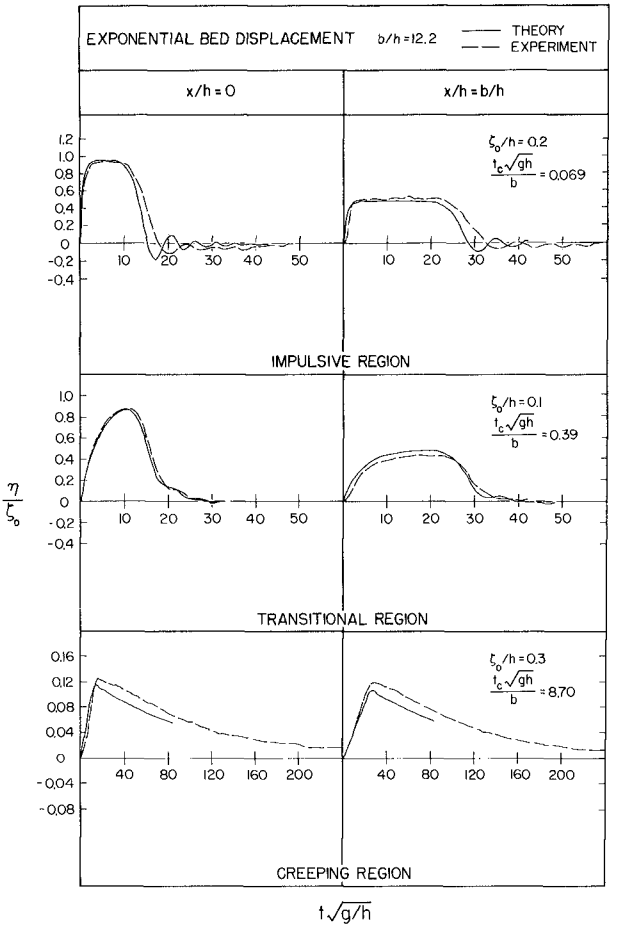

Fig. 5 Typical wave profiles in each region of generation at x/h = 0 and x/h = b/h generated by exponential bed displacements.

well with the measured profile; however, small differences do occur near the trailing portion of the lead wave. The wave profile at $x/h = b/h$ is typical of waves which propagate from the source region of an impulsive upthrust of a block section of the sea bed.

In the transitional and creeping ranges, the water level rises more slowly to a maximum elevation and immediately begins to return to the still water level. The rate of fall of the water level to the SWL for a creeping bed motion is so slow that the wave propagating from the generation region resembles a bore at $x/h = b/h$.

Typical wave profiles generated at the center ($r/h = 0$) and leading edge ($r/h = r_o/h$) of similar bed deformations for the 3-D model are shown in Fig. 6. The wave amplitude, η, again has been normalized by the total bed displacement, ζ_o, and is shown as a function of the nondimensional time, $t\sqrt{g/h}$. A disturbance-size of $r_o/h = 12.2$ has been chosen for each record; hence, a direct comparison is possible with the results presented in Fig. 5 for the 2-D model.

The lead wave at $r/h = 0$ resulting from an impulsive upthrust of the bed resembles that observed for the 2-D model at $x/h = 0$; however, after the water level returns to the SWL it now continues to decrease to a negative elevation of $-1.6\ \zeta_o$. Large amplitude oscillations then occur about a mean level which appears to be approaching the SWL. The positive lead wave that results at $r/h = r_o/h$ is now observed to be followed by a negative wave of comparable amplitude and period; no significant negative waves were observed to result in Fig. 5 from a bed upthrust in the 2-D model.

The positive lead wave resulting from a bed modtion in the transitional region in Fig. 6 is followed by a single negative wave with a larger period and a smaller maximum amplitude than that observed for an impulsive bed motion. When the time-size ratio indicates that the bed motion is creeping, a single positive wave is observed to propagate from the generation region; a similar wave also resulted for a creeping bed motion in the 2-D model.

Tsunami Propagation in a Two-Dimensional Fluid Domain of Uniform Depth. Once a wave propagates from the generation region of the two-dimensional model described in the previous sections, it enters a fluid domain of uniform depth. The linear theory derived in the previous section provides an adequate description of the propagating wave as long as the nonlinear terms which were neglected by this theory remain small compared to the linear terms which have been retained. It is well known that the magnitude of the nonlinear effects (or amplitude dispersion) in a long wave is characterized by the parameter, η_o/h, where η_o is the maximum wave amplitude and h is the water depth. The linear effects (or frequency dispersion) are characterized by $(h/\ell)^2$ where ℓ is a characteristic length of the wave. Hence, the relative importance of nonlinear effects is indicated by the ratio:

$$\underline{U} = \frac{\eta_o/h}{(h/\ell)^2} = \frac{\eta_o \ell^2}{h^3} \quad , \tag{21}$$

which will hereafter be referred to as the Ursell Number although Korteweg and de Vries (1875) as well as Ursell (1954) discussed the significance of this parameter in characterizing long wave propagation. When the Ursell Number is much less than unity for a wave, the linear theory provides an adequate description of wave behavior. When the Ursell Number is much greater than unity, the linear effect of frequency dispersion may be neglected and only the nonlinear effect of amplitude dispersion need be considered in approximating

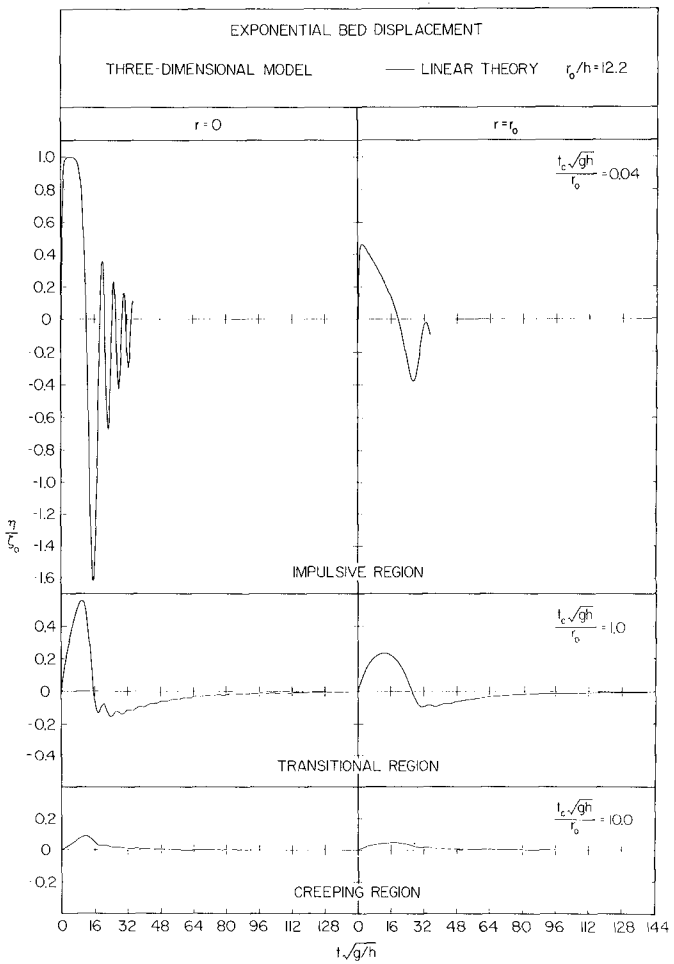

Fig. 6 Typical wave profiles in each region of generation at $r/h = 0$ and $r/h = r_o/h$ generated by exponential bed displacements.

the wave behavior. For the special case of small-but-finite non-linear effects such that η_o/h is of the order of $[(h/\ell)^2]$, a theory which describes the wave behavior must retain both amplitude and frequency dispersion effects; approximate theories such as those developed by Boussinesq (1872) or Korteweg and deVries (1895) provide an adequate description of wave behavior for this special case. It is well known that waves of permanent form (the solitary or cnoidal waves) exist for this special case, i.e., when the Ursell Number is about unity. These permanent form waves result as a balance between the competing effects of amplitude and frequency dispersion is achieved.

Ursell (1954) showed that nonlinear effects grow like $t^{\frac{1}{3}}$ for a long wave propagating in a two-dimensional fluid domain which is initially described by a linear theory (see Hammack (1972) for a more detailed discussion of this). Hence, the linear theory presented in the previous section will eventually become inadequate as a description of wave behavior and a theory such as that of Korteweg and deVries (KdV), which considers both amplitude and frequency dispersion (in an approximate manner), would appear to be required to describe the wave behavior.

The equation of Korteweg and deVries has been the subject of extensive research recently due to the discovery by Gardner et al (1967) of an exact solution algorithim for this equation with arbitrary initial conditions. The exact solution indicates that a finite number of solitary waves (or solitons) will emerge from an initial wave form; these solitons are ordered by decreasing amplitude toward the rear of the train and are followed by a dispersive train of oscillatory waves. Zabusky (1968) and Segur (1972) have shown that this pattern of wave behavior evolves when the initial wave contains a net positive volume. The Ursell Number for this train of solitary waves remains constant during further propagation, since these waves are permanent in form and the competing effects of amplitude and frequency dispersion are balanced.

These properties of the solution of the KdV equation for an initial wave $\int_{-\infty}^{\infty} \eta(x;\sigma)dx > 0$, i.e., the net wave volume is positive, suggest the following procedure for developing a uniformly valid solution of the wave behavior resulting from a bed upthrust for which a linear theory initially provides an adequate description of wave behavior, i.e., $U << 1$ near the generation region. The linear theory may be used to determine the wave behavior until the Ursell Number, computed in an appropriate manner, indicates that nonlinearities are becoming important; the wave profile computed using the linear theory can then be used as an initial condition for the KdV equation which may be solved to determine further wave behavior for all time. An example of this strategy will be presented shortly .

In order to apply the suggested strategy the Ursell Number must be evaluated for a variety of complex (non-sinusoidal) wave profiles in a reasonable way to indicate when frequency and amplitude dispersion are about equal. No single length may exist which adequately describes a complex wave; hence, the Ursell Number becomes a variable parameter in different regions of the wave. An appropriate definition of the length, ℓ, in a region of a complex wave is $\ell = 0\,(\eta/\eta_x)$ where η_x represents the slope of the wave. In order to determine a numerical value for ℓ, the following operational definition may be used:

$$\ell = |\eta_o| / |(\eta_x)_{max}| \,, \tag{22}$$

where $|\eta_o|$ is the absolute value of the total change in wave elevation within the region and $|(\eta_x)_{max}|$ is the absolute value of the maximum slope of the water surface in the region. Hence, the Ursell Number becomes:

$$\underline{U} = \frac{\eta_o |\eta_o|^2}{h^3 |(\eta_x)_{max}|^2} \quad . \tag{23}$$

An appropriate region of a complex wave can then be defined as the region between two successive positions of zero wave slope ($\eta_x = 0$). When Eq. (23) is applied to each region of a solitary wave, the Ursell Number is found to be approximately two; hence, an Ursell Number of about two when computed by Eq. (23) should indicate that frequency and amplitude dispersion are about equal. (It should be noted that the Ursell Number in the leading region of a complex wave will normally be the largest for the wave since the longest wave components travel the fastest.)

Due to the complexity of the method for the exact solution of the KdV equation, a numerical solution algorithim has been adopted. The numerical solution is similar to that introduced by Peregrine (1966) and is based on an equation of the KdV type in the form:

$$u_t + (1 + \frac{3}{2}u)\, u_x - \frac{1}{6} u_{xxt} = 0 \quad , \tag{24}$$

where us is a nondimensional velocity ($u = u^*/\sqrt{gh}$), x is a nondimensional space coordinate ($x = x^*/h$) and t is a nondimensional time ($t = t^*\sqrt{g/h}$). The velocity u, is related to the wave amplitude, η, to the same order of approximation, by:

$$\eta = u + \frac{1}{4}u^2 - \frac{1}{6} u_{xx} \quad . \tag{25}$$

A simple finite-difference approximation of Eq. (24) was found to be stable by Peregrine. The accuracy of this finite-difference approximation for a specific grid size is easily determined by propagating a solitary wave numerically; changes of the shape of this wave during propagation are due to the approximation. The accuracy of the finite difference model can be improved by decreasing the grid size.

In order to illustrate the suggested strategy for a bed upthrust, an experiment with the following generation parameters has been investigated:

$$\zeta_o/h = 0.1, \quad b/h = 12.2, \quad t_c\sqrt{gh/b} = 0.148 \quad . \tag{26}$$

From the previous discussion, a linear theory would be expected to accurately describe the waves near the generation region for the parameters of Eq. (26). Fig. 7a shows the measured wave profiles at the leading edge of the bed section, $(x-b)/h = 0$, and at three more positions downstream: $(x-b)/h = 20$, 180, and 400. The wave amplitude, η, has been normalized by the water depth and plotted as a function of the nondimensional time: $t\sqrt{g/h} - (x-b)/h$.

The measured wave observed to be leaving the generation region at $(x-b)/h = 0$ resembles the actual bed deformation. During propagation the single lead wave appears to separate into three individual waves (or solitons) and a dispersive wave train develops behind these leading solitons. The Ursell Number as calculated by Eq. (23) is indicated in Fig. 7a for the frontal region of the lead wave. At only twenty depths the Ursell Number is equal to 0.7; hence, frequency dispersion is only slightly larger than amplitude dispersion. At $(x-b)/h = 180$ and 400 the Ursell Number is two and three, respectively; thus, frequency and amplitude dispersion effects are about equal. (Only one significant digit for the Ursell Number is indicated in Fig. 7.)

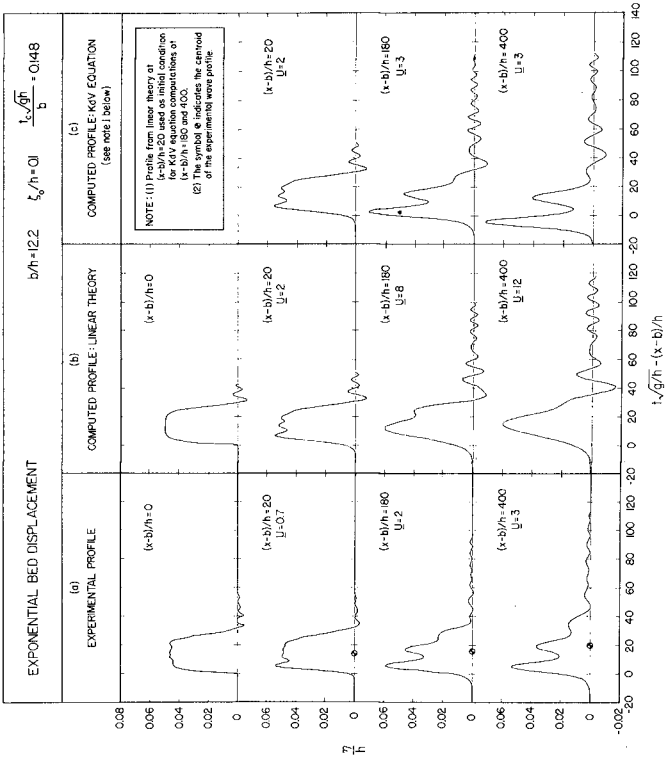

Fig. 7 Downstream wave profiles generated by an impulsive exponential bed upthrust; a) measured, b) computed by linear theory, c) computed by KdV equation.

Fig. 7b shows the wave profiles at each downstream position as computed by the linear theory, i.e., Eq. (12). The computed profiles at $(x-b)/h = 0$ and $(x-b)/h = 20$ agree well with the measured profiles in Fig. 7a; however, at the downstream positions of $(x-b)/h = 180$ and 400 the linear theory no longer predicts the measured wave structure well. Frequency dispersion, unhindered by amplitude dispersion in the linear theory, continues to disperse the wave into its spectral components. The continual growth of the Ursell Number in the front region of the lead wave from $\underline{U} = 2$ at $(x-b)/h = 20$ to $\underline{U} = 12$ at $(x-b)/h = 400$ is a result of this frequency separation.

Following the suggested strategy for determining wave behavior after nonlinear effects have become important, the linear theory at $(x-b)/h = 20$ (where $\underline{U} = 2$) has been used as the initial condition for Eq. (24). The profiles computed by this equation at $(x-b)/h = 180$ and 400 are shown in Fig. 7c. The temporal variation of these profiles agree well with the measured results in Fig. 7a. The Ursell Number for the front region of the lead wave in Fig. 7c remains constant at a value of three; hence, frequency and amplitude dispersion are of the same order during wave propagation and solitons are emerging.

The difference between measured and computed wave amplitudes in Fig. 7a and Fig. 7c are the result of viscous effects in the experimental model. Corrections applied to the experiments for these viscous effects (see Hammack, (1972)) indicate that Eq. (24) does predict these amplitudes well for a non-dissipative fluid medium.

Oscillating Bed Motions With a Mean Displacement - In the preceding sections only a simple time-displacement history of the bed motion was considered. In order to observe experimentally the effect of a more general time-displacement history on the resulting waves, experiments were conducted where an oscillating motion (or dither) was superposed on the mean displacement; the frequency and amplitude of this dither was varied. Fig. 8 abc shows the measured waves in the generation and downstream region resulting from three bed displacements with the same mean motion; the wave amplitude, η, has again been normalized by the water depth, h, and shown as a function of the nondimensional time $t\sqrt{g/h} - (x-b)/h$. The actual time-displacement history of the bed section is also shown in Fig. 8.

Waves resulting from the mean motion alone are shown in Fig. 8a. Note that this mean motion (termed the half-sine bed displacement) occurs in a finite time, t_c; the generation parameters for this motion are:

$$\zeta_o/h = 0.2, \quad b/h = 12.2, \quad t_c\sqrt{gh}/b = 1.10 \ . \tag{27}$$

The time-size ratio in Eq. (27) indicates that this bed displacement is near the boundary between the impulsive and transitional ranges of time-size ratios (see Hammack, 1972 for more details of this mean motion). The wave measurements in Fig. 8a for the mean motion again demonstrate the evolution of solitons from the positive lead wave which propages from the generation region. In Fig. 8b a dither is superposed on the mean motion with a period, τ, of one-half the characteristic time, t_c, of the mean motion and an amplitude, ζ_1, of one-half the total bed displacement. The lead region of the wave profiles in the generation region $(x-b)/h = -b/h$ and 0 resemble the actual bed displacement; the wave leaving the generation region at $(x-b)/h = 0$ contains several small oscillatory waves superposed on the larger wave which are apparently created by the mean motion alone. These oscillatory waves are left behind by the mean wave during propagation until, at $(x-b)/h = 400$, the measured wave resulting from this bed motion is almost identical to the results for the mean bed displacement alone in Fig. 8a.

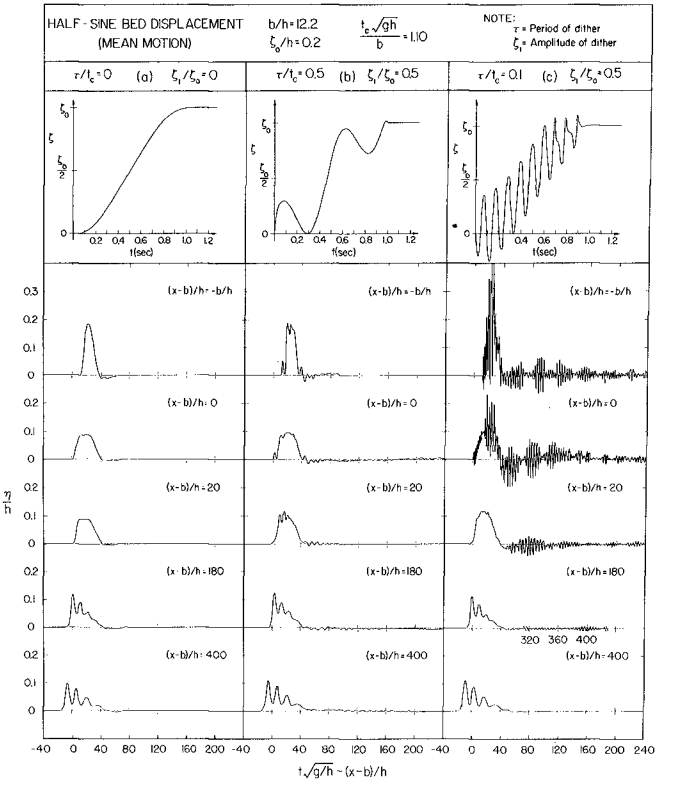

Fig. 8 Measured wave profiles; a) an impulsive half-sine mean motion, b), c) half-sine mean motion with a superposed oscillation.

Fig. 8c shows the waves generated when the period, τ, of the superposed dither is reduced to $0.1\ t_c$ while the amplitude, ζ_1, is maint ined at $0.5\ \zeta_o$. Large amplitude cross waves, i.e., waves propagating laterally across the wave tank, were created in the generation region by this bed motion. These cross waves also created high frequency oscillatory waves that propagated downstream as evidenced by the measurements at $(x-b)/h = 20$ and 180. These oscillatory waves appear to decay very rapidly (due to the combined effect of frequency separation and viscosity) and are again left behind by a large wave which is apparently created by the mean motion of the bed only. The measured wave at $(x-b)/h = 400$ is almost identical to the results found in Fig. 8a; hence, it appears that the detailed time-displacement history for an impulsive bed motion may not be of critical importance in determining the wave behavior downstream of the generation region. (It should be noted that the opposite was found to be true by Hammack (1972) for creeping mean motions with a superposed dither. A knowledge of the exact time-displacement history of the bed section is of major importance in determining the downstream wave behavior when the mean motion is creeping.)

CONCLUSIONS

The following conclusions regarding tsunami generation and propagation can be drawn from the theoretical and experimental models investigated in this study:

1) The maximum amplitude of the wave propagating from the generation region is approximately one-half of the total bed displacement for both the two and three-dimensional models of tsunami generation which were studied.

2) The linear theory appears to accurately predict the wave structure in the generation region whenever the disturbance-amplitude scale, ζ_o/h, is less than 0.2 in absolute value.

3) Major differences exist between the structure of the wave propagating from the generation region of the 2-D and 3-D models investigated; large negative waves can result from an impulsive bed uplift in the 3-D model while no large negative waves result from a bed uplift in the 2-D model.

4) Nonlinear effects grow during wave propagation in the 2-D model so that the linear theory eventually becomes an inadequate description of wave behavior; an equation similar to that of Korteweg and deVries was shown to be the proper model of wave behavior once linear and nonlinear effects become about equal.

5) A detailed knowledge of the time-displacement history of an impulsive bed motion may be unimportant in determining the wave behavior outside of the generation region.

ACKNOWLEDGMENT

This study was supported by the National Science Foundation under Grants GK-2370 and GK-24716 and was conducted at the W. M. Keck Laboratory of Hydraulics and Water Resources, California Institute of Technology.

LIST OF REFERENCES

Boussinesq, J. 1872 "Theorie des ondes et des remous qui se propagent le long d'un canal rectangulaire horizontal, en communiquant au liquide contenu dans ce canal des vitesses sensibilement pareilles de la surface au fond", J. de Mathematiques Pures et Appliquees, 2nd Serie, 17, 55-108.

Gardner, C.S., Greene, J.M., Kruskal, M.D., and Miura, R.M. 1967 "Method for Solving the Korteweg-deVries Equation", Phys. Rev. Ltrs, 19, 1095-1097.

Hammack, J. L., Jr., 1972 "Tsunamis - A Model of Their Generation and Propagation", Rep. No. KH-R-28, W.M. Keck Lab. of Hydraulics & Water Resources, California Institute of Technology.

Honda, H., and Nakamura, K., 1951, "The Waves Caused by One-Dimensional Deformation of the Bottom of Shallow Sea of Uniform Depth", Science Report Tohoku University, Sendai, Japan, 3, 133-137.

Hwang, L.S., and Divoky, D., 1970, "Tsunami Generation", JGR, 75, 6802-6817.

Ichiye, T., 1950, "On the Theory of Tsunami", Ocenographical Magazine, 2, 83-100.

Kajiura, K., 1963, "The Leading Wave of a Tsunami", Bull., Earthquake Research Institute, Tokyo University, 41, 535-571.

Keller, J.B., 1963, "Tsunamis - Water Waves Produced by Earthquakes", Intern. Union of Geodesy & Geophysics, Monograph No. 24, 154-166.

Korteweg, D. J., and deVries, G., 1895, "On the Change of Form of Long Waves Advancing in a Rectangular Canal, and on a New Type of Long Stationary Waves", London, Edinburgh, and Dublin Philosophical Mag., Ser. 5, 39, 422-443.

Momoi, T., 1964, "Tsunami in the Vicinity of a Wave Origin", Bull. Earthquake Research Institute, Tokyo University, 42, 133-146.

Nakamura, K., 1953, "On the Waves Caused by the Deformation of the Bottom of the Sea, I", Science Report, Tohoku University, Sendai, Japan, 5th Series, 5, 167-176.

Peregrine, D.H., 1966, "Calculations of the Development of an Undular Bore", J. Fluid Mech., 25, 321-330.

Raichlen, F., 1970, "Tsunamis: Some Laboratory and Field Observations", Proc. 12th Coastal Engineering Conf., Washington, D.C., 2103-2122.

Segur, H., 1972, "The Korteweg-deVries Equation and Water Waves. I. Solution of the Equation", submitted to the J. Fluid Mechanics.

Takahashi,R. 1942, "On Seismic Sea Waves Caused by Deformations of the Sea Bottom", Bull. Earthquake Research Institute, Tokyo University, 20, 275-400.

Takahashi, R., 1945, "On Seismic Sea Waves Caused by Deformations of the Sea Bottom, 2nd Report", Bull. Earthquake Research Inst., Tokyo Univ., 23, 23-35, (in Japanese).

Takahashi, R., 1947, "On the Seismic Sea Waves Caused by Deformations of the Sea Bottom, 3rd Report", Bull. Earthquake Res. Inst., Tokyo Univ., 25, 5-8.

Takahasi, R., 1963, "On Some Model Experiments on Tsunami Generation", Intern. Union of Geodesy & Geophysics, Monograph No. 24, 235-248.

Takahasi, R., and Hatori, T., 1962, "A Model Experiment on the Tsunami Generation from a Bottom Deformation Area of Elliptic Shape", Bull. Earthquake Research Institute, Tokyo University, 40, 873-883.

Ursell, F., 1953, "The Long-Wave Paradox in the Theory of Gravity Waves", Proc., Cambridge Philosophical Soc., 49, 685-694.

Webb, L. M., 1962, "Theory of Waves Generated by Surface and Sea-Bed Disturbances", Appendix 1, "The Nature of Tsunamis, Their Generation and Dispersion in Water of Finite Depth," Tech. Rep. SN 57-2, Natl, Engrg. Sci. Co.

Zabusky, N. J., 1968, "Solitons and Bound States of the Time-Independent Schrodinger Equation", Phys. Rev., 168, 124-128.

CHAPTER 151

RECREATIONAL SURFING ON HAWAIIAN REEFS

by

James R. Walker[1]

Robert Q. Palmer[2]

Joseph K. Kukea[3]

ABSTRACT

Recreational surfing has been studied in Hawaii to develop criteria for the preservation, enhancement and design of surf sites. The criteria will aid in planning compatible uses of the coastal zone. Surfing characteristics and wave transformations were studied in the field and related to ocean bottom features at prime surf sites. A small scale, three-dimensional, hydraulic model study was conducted to determine the effect that a given bottom feature had upon the surfing wave. A concept of a multiple-purpose surfing shoal to be compatible with several varied interests in the coastal zone was hypothesized from field, analytic, and model studies.

INTRODUCTION

Hawaii is the surfing mecca of the world. The ancient Hawaiians originated surfing, which has become a popular international sport. More than ten percent of the local population on Oahu surf (Anderson and Co, 1971). There are about 1,600 surf sites in Hawaii; however, many of these surf sites have good surfing conditions only under certain combinations of wind and wave conditions. Consequently, relatively few of these sites have good surfing conditions at a given time, and those sites with conditions conducive to surfing are generally overcrowded. The rapidly increasing popularity of surfing and the loss of surf sites due to construction projects contribute to the overcrowding of surf sites.

Overcrowding increases the frequency of injury and decreases enjoyment of the sport. Unlike skiing and golf, for which new recreational facilities may be built to meet the increased demand, surfing is confined

[1]Jr. Researcher, Dept. of Ocean Engineering, University of Hawaii

[2]Assoc. Researcher, Dept. of Ocean Engineering, University of Hawaii

[3]Grad. Student, Dept. of Ocean Engineering, University of Hawaii

to a limited number of natural surf sites, for given wind and wave conditions. Hence, an effort should be made to preserve and enhance these valuable natural surf sites and to develop design criteria for creation of multiple-purpose reefs.

ENVIRONMENT

There are eight major islands in the Hawaiian archipelago. All of the Islands have surf sites, however, Oahu, the island with the major population center, has the greatest number. This study was primarily conducted on the island of Oahu. Much of the bathymetry off Oahu is composed of fringing coral reef having ridges and sand-filled channels running seaward from shore. Surfing areas are generally found over the ridges, while the channels separate adjacent surf areas.

The stable coral and basalt reef formations, in contrast to sandy shoals, do not shift under wave attack. Stable shoals are conducive to the study of the surfing area because they induce relatively consistent wave transformations.

The location of some of the prime surf sites studied on Oahu are shown in Figure 1. The sites on the south shore, along the Ala Moana reef and at Queen's in Waikiki, have a fringing reef with steep seaward slopes to deep water. The north shore sites of Sunset, Pipeline, and Waimea are located in deeper water and generally have a flat, narrow shelf extending over a mile seaward from the 30-foot to the 60-foot depth contour. The bottom slopes on the leeward side, such as at Makaha, generally drop sharply to deep water. The shallow reefs on the windward side extend far seaward, then slope steeply to deep water.

In Hawaii, the northeasterly trade winds blow at ten to fifteen knots about 80 percent of the year. Local waves generated by the trade winds arrive at the windward coast with periods ranging from five to ten seconds and with breaker heights up to ten feet. Waves with similar characteristics occasionally occur on the southwestern shores during the winter months.

The big surf for which Hawaii is famous is due to waves generated by distant storms in the North Pacific, during the winter months, and in the Southern Hemisphere, during the summer months. These swell s break on island reefs far removed from their generating winds. Large, low pressure systems 1,000 to 2,000 miles northwest of the Islands generate surf on the northwestern shores with ten to fifteen second periods and with breaker

heights up to 30 feet. The southern swell may be generated more than 5,000 miles from the Islands. These waves generally have periods of 14 to 20 seconds and breaker heights of three to 15 feet. The waves from the southern swell generally arrive in groups of three to five waves with very regular periods, characterized by ten to twenty minute intervals between groups.

Hawaii has a semi-diurnal tide with a mean daily range of two feet. Even this small tide range significantly influences the breaking wave characteristics at certain sites.

SURFING

Surfing is the sport of riding a breaking wave. Surfing is practiced using various forms of equipment, such as a board, a canoe, a sailboat, or even using no equipment, except perhaps fins, for body surfing. The most popular surfing form is board surfing and is the form referred to in this paper, although the basic techniques pertain to all surfing forms in general.

Surfing is generally performed at a specific location called a "surf site." A "surf site" is an area in which waves break in a consistent and desirable form under given conditions. The popularity of a surf site depends upon several variables, including the frequency of occurrence of breaker characteristics, wind, water surface conditions, proximity of the site to population centers, suitability for surfing under a wide range of wave conditions, access, and hazards.

The mechanics of surfing are first for the surfer to attain a position just seaward of the breaker zone. When a desirable wave approaches, the surfer paddles with the direction of wave advance, utilizing the force of gravity relative to the slope of the wave face to attain a velocity equal to the velocity of the wave. This is termed "catching a wave" and is shown schematically by the sequence in Figure 2. Once the wave is caught, the surfer assumes a standing or crouching position. The surfer then slides, or "drops," forward down the face of the wave from near the crest toward the trough, traveling at a velocity greater than that of the wave. During the drop, which takes from two seconds at Queen's in Waikiki on a three-foot wave to five seconds at Waimea Bay on a 15-foot breaker, the wave begins to break. The breaking then proceeds shoreward and laterally along the crest. After the acceleration experienced during the drop, the surfer initiates a turn to the right or to the left,

escaping from the turbulent breaking region. The surfer maneuvers on the wave face in the vicinity of the junction of the unbroken wave and the breaking region, called the "peel," or "curl," by shifting his feet and weight to control the response of the surfboard. The surfer ends his ride when he "kicks out" back over the wave crest, or when he loses control of his board. If the surfer loses his board, it is transported by wind, wave, or current forces into the surfboard-recovery area. The surfer then must retrieve his board and return to the take-off area through the return zone. A schematic of these areas is shown in Figure 3.

WAVE TRANSFORMATIONS

Wave properties such as length, height, and asymmetry are modified as waves enter shallow water. The primary modifications influencing surfing are described by refraction, amplitude amplification, diffraction, and breaking. In addition, the incident wave system may induce secondary wave systems which influence the behavior of multiple breaking. Also, other non-linear effects such as breaking-wave-induced setup and currents influence the characteristics of surf sites and adjacent reefs and beaches.

Refraction plays two important roles in influencing the characteristics of a surf site. First, convergence of energy over a ridge, and divergence over a trough, result in wave height variations along the crest line. Secondly, refraction changes the direction of wave advance, tending to align the wave crest lines parallel with the bottom contours. The more closely aligned the crest lines and breaking depth contours become, the greater becomes the velocity that the surfer must attain to successfully ride the wave.

Wave height amplification due to shoaling water depths accounts for one of the most important wave transformations involved in forming the surfing wave. Over ridges, wave height is increased relative to wave height over the side channels. This amplitude differential induces waves to break along the channel edge, providing the peel where the wave is ridden. The amplification factor basically is dependent upon the water depth to wave length ratio, with the greater amplification factors found for the smaller ratios. Hence, the longer period waves are more sensitive to smaller depth variations and they break at a greater height relative to their deep water wave height. The longer period waves also tend to break in a more consistent pattern than do the shorter period waves.

Lateral transmission of wave energy induced by wave height variations along the crest line is not well understood. This effect, called diffraction, violates basic assumptions normally invoked in refraction analysis. Analytical description of wave benavior over shoals near the breaking region is therefore not reliable by conventional methods. Whalin (1970) has shown the degree of discrepency between refraction analysis and observed wave behavior in a convergence zone. Diffraction of water waves over a submerged shoal has been treated by Rao and Garrison (1970), but under non-breaking conditions. The primary influence of diffraction on surfing is to transmit wave energy laterally along the wave crest, thereby smoothing the response of the wave to the shoal. This suggests that the size and shape of the shoal are important factors in formation of a surfing wave.

In general, the most desirable surfing waves are those which break, although breaking is not a necessary condition for surfing. A condition for wave breaking occurs when the particle velocities of the wave crest equal the velocity of wave propagation (Stokes, 1847). Different wave theories predict this condition for breaking at different limits. The most commonly employed condition for breaking, due to McCowan (1894), is $H_b = 0.78d_b$, where H_b is the breaker height, and d_b is the breaking depth. Other investigators have employed various theories and have obtained different criteria for breaking, ranging from $H_b = 0.73d_b$ (Laitone, 1963) to $H_b = 1.0d_b$ (Dean, 1968).

Since wave theories are not generally valid near the breaker zone and the above criteria were developed for limiting waves traveling over a horizontal bottom, the reliability of the limits is questionable. Galvin (1969) reviewed data from several wave flume investigations and developed the following empirical relationships, which include the effect of beach slope, S: $d_b/H_b = 0.92$ when S is steeper than 14.3, and $d_b/H_b = 1.4 - 6.86/S$ when S is flatter than 14.3.

Breaker-type is also an important factor in surfing. Breaker-type is a classification of wave profile during breaking. Galvin (1968) studied movies of flume waves and derived the following expression for the breaker-type index, K: $K = H_b S/gT^2$, where g is the acceleration due to gravity, and T is the wave period. The suggested limits for breaker-type are: Surge when $K < 0.003$; Plunge when $0.003 \leq K \leq 0.068$; and Spill when $K > 0.068$. The most desirable surfing waves are those with breaker-

types in the plunge-spill region.

The descriptions of wave behavior given above were developed for waves propagating over straight, laboratory slopes. These methods are difficult to apply to the composite slopes found over the complex coral reefs found in nature. Camfield and Street (1968) observed that wave transformations over composite slopes responded to the slopes some distance seaward of the breaker point. This finding was also observed during the course of the present study. Therefore, the slope one-half wave length seaward of the breaking point was employed in describing the characteristics of the surfing waves of this study.

As the wave enters shallow water, the velocity of propagation decelerates. For wave lengths that are long compared to the water depth, the velocity of wave propagation, C, may be given by $C = \sqrt{gd}$ to the first approximation, and by $C = \sqrt{g(d + \eta)}$ to the second approximation, where is wave amplitude, and d is the still water depth. The second approximation appears to be more accurate; however it requires an a priori knowledge of η, which renders it more difficult to apply. The first approsimation may be used to predict the wave velocity in terms of breaker height by substituting $d_b = 1.28H_b$: $C = \sqrt{g(1.28)H_b}$. The expression indicates that the surfer must attain a greater velocity to catch larger waves and that the rides on larger waves tend to be faster than on smaller ones.

Non-linear effects, such as wave setup, induced currents, and energy decay, have important effects upon the surfing wave, as well as upon beach stability. A discussion of the relationship of these phenomena to surfing is given by Walker and Palmer (1971).

METHODS

Research methods involved primarily field observations of natural surf sites. Detailed bathymetric surveys of prime surf sites having desirable surfing characteristics were made. Water depths were measured using a recording echo sounder in water deeper than five feet and a sounding rod in depths of less than five feet. The bathymetric surveys were conducted during the season of calm seas. Wave transformations and surfing characteristics were observed and related to the bathymetry during the surfing season. Time-sequenced aerial photographs were taken, and their transparencies were projected over the bathymetric charts to study the wave transformations in relation to the bottom configuration. Land-

based triangulation techniques were used to track surfer riding paths to supplement the aerial studies.

Field observations were supplemented with a 1:75 scale, three-dimensional, hydraulic model study. The model study was conducted to determine the influence of various shaol features on the surfing wave. The model basin, described by Fallon, et al (1971), had been built for a boat harbor entrance channel improvement study. This study was initiated by the surfing community, which was concerned over the possible loss of a surfing site. After the harbor study, shoal features, including size, depth, and seaward slope, were tested to determine their influence on breaking wave patterns. The shoals were constructed with model stones which represented 500-pound prototype basalt. Due to time limitations for use of the model, tests were restricted to a single wave condition having a 13.5-second period and six-foot breaker height. This condition is typical of summer surf at the test location. Model observations were primarily confined to observing changes in breaking wave patterns which were influenced by the various shoal configurations.

OBSERVATIONS

The characteristics of a dozen surf sites were studied in detail; however, Queen's in Waikiki was the subject to the most thorough study. Queen's was selected as a typical surf site and one from which an artificial surf site might be modeled. The bathymetry of Queen's, located in Waikiki Bay, is shown in Figure 4. The coral reef shoal is 300 feet wide and 600 feet long. It has a 150-foot wide, seven-foot deep sand-filled channel on the left side and a 16-foot deep hole on the right side. The shoal starts to form a ridge at 12-foot depth. A seven-foot deep trench on the shoreward side separates the surf shoal from the beach and seawall. Queen's is surfed by 20 to 50 people at a time on waves from two to eight feet high.

Figure 5 is the third of a sequence of aerial photographs taken at five-second intervals over Queen's. The breaking wave height was six feet and the period was 20 seconds. The crest lines showing the wave propagating over the shoal are superimposed over the bathymetry in Figure 6. The take-off, riding, end-of-ride, and board-recovery areas are labeled. The approximate path of the surfer is plotted, and the breaking region is crosshatched.

At position t = 0, the incident wave is slightly divergent due to

the configuration of the bay in Waikiki. Upon traversing the shoal, the wave refracts and becomes convergent over the ridge comprising the Queen's shoal. Refraction and shoaling amplification increase the height rapidly over the 1:40 seaward slope, and the wave initially breaks in seven feet of water. The wave may be ridden to the left or the right. It should be noted that the breaking on the left generally follows the edge of the sand channel, and that the breaking on the right generally follows the 5.5-foot depth contour. The surfer maneuvers in the vicinity of the breaking region of the wave. This region, called the peel or curl, is outlined in the aerial photograph, Figure 5, by the white water patterns. Figure 7 illustrates a surfer riding in the peel. The rate of peel propagation along the wave crest line is termed the "peel-rate." The vector diagram in Figure 8 gives the relationship among the wave velocity, V_w, the velocity of the surfer, V_s, and the peel velocity, V_p. The included angle between the unbroken wave crest, along V_p, and the velocity of the surfer is termed the "peel-angle, α." At Queen's, in the above sequence, the peel-angle is 80 degrees to the left and 60 degrees to the right. The ride to the right is generally faster.

Peel-angle, breaker height, and breaker-type are important parameters defining the surfing wave. These characteristics are listed in Table 1 along with other observations made at study sites. Table 1 includes data taken from some of the most famous surf sites in the world. Pipeline is noted for its fast ride and hard, plunging breaker-type. Waimea Bay is noted for its large waves which are ridden by expert surfers. Queen's has small spilling waves ridden by average-skilled surfers. Figure 9 is a plot of peel-angle as a function of wave breaker height for observations listed in Table 1.

Based upon the observations of the skill level required to surf at the study sites, suggested conditions for surfable peel-angle are given in Figure 9. The peel-angle limit is also based upon the assumption that the velocity of a surfer is limited to about 40 feet per second or less over an extended length of ride. It is assumed that the surfer cannot successfully match the peel velocity for greater peel-angles for the given wave height. Also shown in Figure 9 are subjectively developed categorizations of surfer skill level to indicate the peel-angles and breaker heights preferred by surfers of different experience. It is emphasized that categories are not clearly differentiated from one another

and there is considerable overlap. Figure 9 could be of benefit in selecting design criteria for an artificial surf site.

To the first approximation, the peel-angle may be related to the breaker height, and velocity of the surfer by the expression $\sin \alpha = \sqrt{gH_b B}/V_s$, where B is a breaker height coefficient, d_b/H_b. Using the McCowan breaking criteria, B = 1.28 in the preceding equations, isolines of surfer velocity, V_s, are plotted in Figure 9. The peel-angle is related to the included angle between incident wave crest line and the breaking depth contour. Hence, surfing velocities are related to the incident wave and bottom characteristics.

The preceding discussion pertains primarily to fluid-bottom interactions. The breaking properties of height and form of waves and the water surface conditions are significantly influenced by the wind. A surf site has the most desirable conditions with a component of wind of less than 15 knots opposing the direction of wave advance. Stronger opposing winds tend to interfere with the surfing by lifting the surfboard nose out of the water and roughening the water surface. A component of wind following the direction of wave advance tends to prematurely topple the wave crest and spoil the water surface conditions by generating local chop. It should be noted, however, that many popular surf sites exist with strong following winds. These sites generally exist only under the adverse wind condition which generates the surfing wave.

Several observations of wave behavior at surf sites have been made. One of these is the effect of finite height waves and wave breaking on the refraction of waves propagating over a surf shoal. Figure 10 traces the history of a wave crest propagating over the Queen's surf shoal. Observed wave orthogonals are drawn and compared with orthogonals computed by linear wave theory ray tracing techniques. It whould be noted that the calculated orthogonals indicate the presence of a caustic. The observed orthogonals start to converge, but, during the breaking process, the wave crest approaches the trough and a divergence is observed. This divergence may be attributed to several phenomena, including the finite wave height effect on wave velocity of propagation, the wave-induced current over the shoal, and the increase in wave crest velocity as the crest slides down the face of the wave toward the trough. This latter effect has been observed causing large breaking waves to diverge from a shoal into navigation channels rather than refract into the adjacent reef.

These phenomena render standard wave ray tracing techniques invalid in the breaking zone. This is normally implied, but often ignored in practice.

Several important observations were made in the model study which supplemented the field observations. Since some of the prototype surf sites were modeled, it was readily verified that the model reasonably duplicated the breaking wave patterns under the conditions tested. Given below are pertinent results of the testing of shoal features required to induce favorable surf.

The first test series involved moving the 15-foot depth contour 100 feet seaward to make a 15-foot deep shoal. Shoal widths of 100-, 200- and 400-foot widths were tested. No noticeable changes in the wave breaking patterns due to the presence of the shoal were observed. The next test series involved moving the ten-foot depth contour seaward 100 feet to make shoals of the same widths noted above. The effect of these shoals was to move the breaking depth seaward 50 feet. The next test series involved moving the eight-foot contour seaward by similar shoal increments. The primary influence of the eight-foot deep shoal was to move the breaking position seaward 70 feet. The width of these shoals did not have a noticeable effect except to create a wider breaking area.

The abrupt depth transitions used in formation of the shoals are not usually found in the prototype; therefore, a 1:30 slope was extended from the eight-foot deep shoal to the existing bottom. The primary effect of the slope was to move the breaker position seaward another 30 feet to the eight-foot contour. The seaward slope has an important function in the formation of the surfing wave. The slope reduces reflection, influences breaker-type, and if shaped properly, causes a convergent zone.

Excellent surfing conditions are commonly found on both sides of natural and man-made channels. Channels are important features of surf sites since they separate adjacent sites, induce smaller amplitude amplification factors relative to those over the shoal, and help refract the wave over the surf shoal. A series of four tests involving channels with widths of 50, 100, 200 and 300 feet was conducted. The shoal depth was eight feet, the channel depth was 15 feet, and the shoal was 200 feet long and 700 feet wide. The 50- and 100-foot wide channels did not induce the expected refraction or the desired amplitude amplification differential relative to that over the shoal required to produce a desirable

surfing wave. In these cases, the wave broke completely across the channel. The 200- and 300-foot wide channels did induce a desirable surfing wave form.

MULTIPLE PURPOSE REEF CONCEPT

A general concept of a surf site has been hypothesized from field, analytic, and model observations. The bottom features required to produce the surf site features shown in Figure 3 are summarized in the following discussion and shown in Figure 11.

A seaward slope, in a ridge configuration, induces a convergence, influences the breaker type and height, and causes the wave to gradually increase in amplitude until it becomes a breaking wave. A flat seaward slope also causes the initial breaking to spread over a wide area, thereby allowing more people to surf the area. A steep transition from deep water to the breaker depth may produce a very hard, plunging wave whose amplitude and steepness increases so rapidly that the surfer cannot "catch" the wave. Such a condition occurs at the Makaha Bowl, where the depth shoals from 37 feet to 16 feet in less than 50 feet of wave travel distance. It is very difficult to catch a wave a this site at the peak.

Side channels separate a surf site from adjacent sites, create differential amplitude amplification factors relative to the shoal, and enhance refraction. The channels provide an area for the surfers to gain access to the site without interfering with others surfing. Breaking wave-induced rip currents moving seaward are generally found in the side channels. The alignment of the side channel relative to the direction of wave advance helps to control the peel rate.

The shoal provides an area for the wave to break and dissipate energy. The shoal should be of variable depth to allow for incident waves with a wide range of characteristics to break in a form desirable for surfing. The shoal should be long enough to provide a ten- to 30-second ride. Longer riding areas increase surf site capacity.

The trench is perhaps the most ideal type of board-recovery area because it isolates the surf site from the beach, swimming area, and structures. The trench should be wide enough and deep enough to stop the wave from breaking and to reduce the velocity of the wave-induced current.

There are many variations of this surf site concept which are typical of many natural sites. For example, the basic concept shown in Figure 11 has surfing to both the left and right. However, many surf sites are

located next to promontories where it appears that the shoal is a submerged projection of land. Makaha and Waimea have this configuration. The general concept is easily modified to describe this configuration by considering only half of the shoal. The other half of the shoal continues to rise above the water to the promontory.

In addition to surfing, other interests such as swimming, fishing, diving, boating, beach usage, land reclamation, and construction projects compete for usage of the coastal zone. Proper planning in the coastal zone could minimize conflicts and allow for several uses of the area. One such plan, which occurs naturally in some areas, is the "multiple-purpose reef." The plan incorporates an artificial reef designed according to the general surf shoal concept shown in Figure 11. The shoal would act as a submerged breakwater, dissipating wave energy by inducing the wave to break. The dissipation of energy would serve as an erosion control device, noted by Zwamborn, et al (1970), or to reduce the design wave at a structure. Natural shoals on the island of Maui have been observed to protect beaches from erosive wave action. The board-recovery trench would isolate the surf site from swimming areas, beaches, and structures. The side channels could be boat harbor entrance channels with return zones near the channel edge. If the shoal were made of coral, or were an artificial shoal made of rock or artificial concrete units, the voids would provide fish habitat. The shoal could be used as a diving area when the surf is down.

Surfing is an important recreation in many coastal zone communities. An effort should be made to preserve and enhance surf sites and to create new surf sites which would be compatible with other uses of the coastal zone. This investigation is only a first step in describing surfing characteristics. More intensive research is required to better define breaking wave behavior over complex bathymetry and on surfboard hydrodynamics.

ACKNOWLEDGEMENTS

The Surf Parameters study was funded by the Fifth and Sixth Legislatures of the State of Hawaii. This work was performed by the University of Hawaii, Department of Ocean Engineering at the J.K.K. Look Laboratory. The authors wish to thank the many members of the surfing community, especially Mr. John Kelly of Save Our Surf, for their assistance in conducting this study.

REFERENCES

Anderson, R. N. and H. Co, "Characteristics of Surfers in Hawaii," Dept. of Agricultural and Resource Economics, U. of Hawaii, July 1971.

Camfield, F. E. and R. L. Street, "The Effects of Bottom Configuration on the Deformation, Breaking, and Run-Up of Solitary Waves," Proc. 10th Conf. on Coastal Engineering, ASCE, London, 1968.

Dean, R. G., "Breaking Wave Criteria: A Study Employing a Numerical Wave Theory," Proc. 11th Conf. on Coastal Engineering, ASCE, London, 1968.

Fallon, A. R., F. Gerritsen, and R. Q. Palmer, "Model Investigation of Inprovements to Kewalo Basin, Honolulu, Hawaii," Look Lab TR-17, 1971.

Galvin, C. J., "Breaker-Type Classification on Three Laboratory Beaches," Journal of Geophysical Research, Vol. 73, No. 12, June 1968.

Galvin, C. J., "Breaker Travel and Choice of Design Wave Height," ASCE, Journal of Waterways and Harbors Division, WW2, May 1969.

Laitone, E. Ve., "Higher Approximations to Non-Linear Water Waves and the Limiting Heights of Cnoidal, Solitary, and Stokes' Waves," BEB, TM No. 133, February, 1963.

McCowan, J., "On the Highest Wave of Permanent Type," London, Edinburgh, and Dublin, Phil. Mag., V. 38, 1894.

Rao, V. S. and C. J. Garrison, "Interaction of a Train of Regular Waves with a Rigid Submerged Ellipsoid," Sea Grant Publication No. TAMU-SG-71-209, Texas A. and M. University, May 1971.

Stokes, G. G., "On Thoery of Oscillatory Waves," Trans. Cambridge Phil. Soc., V. 8, p. 441, 1847.

Walker, J. R. and R. Q. Palmer, "A General Surf Site Concept," Look Lab TR-18, U. of Hawaii, September 1971.

Whalin, R. W., "The Limit of Applicability of Linear Wave Refraction Theory in a Convergent Zone," U. S. Army Waterways Experiment Station, Vicksburg, Miss., December 1971.

Zwamborn, J. S., G. A. Fromme, and J. B. Fitzpatrick, "Underwater Mound for Protection of Durban's Beaches," Proc. 12th Conf. on Coastal Engineering, ASCE, Washington, D. C., 1970.

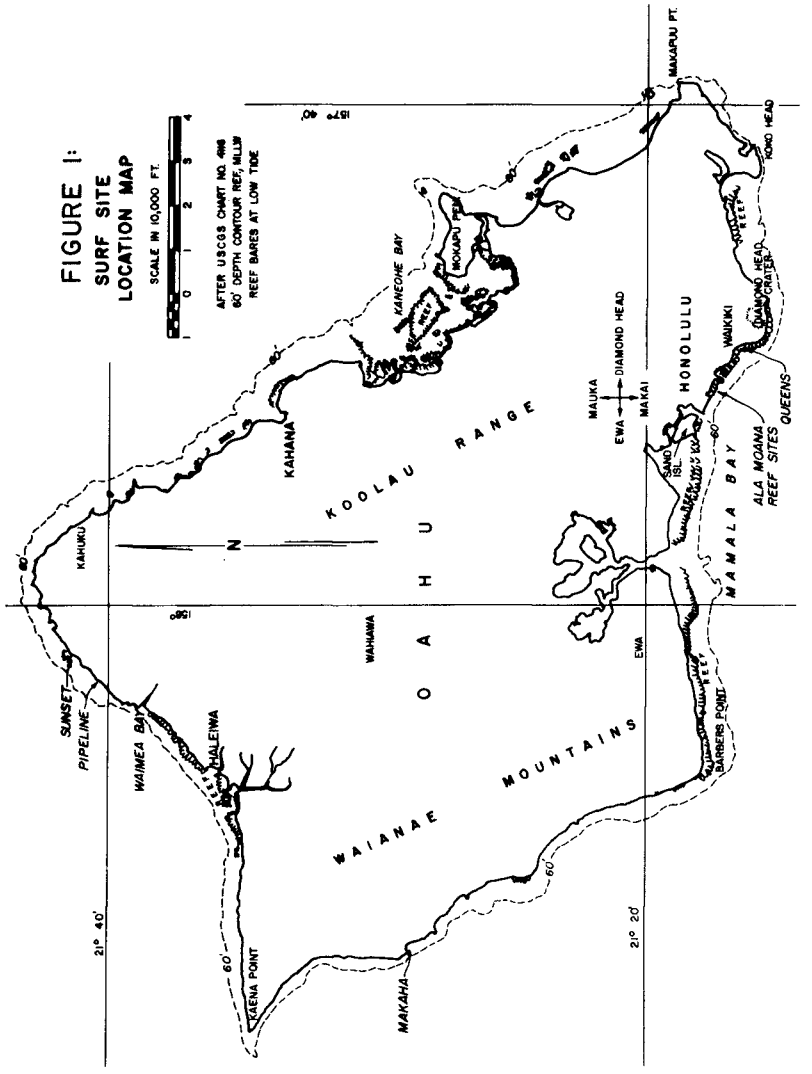
FIGURE 1:
SURF SITE
LOCATION MAP
SCALE IN 10,000 FT.
0 1 2 3 4
AFTER USCGS CHART NO. 4116
60' DEPTH CONTOUR REF, MLLW
REEF BARES AT LOW TIDE
157° 40'
MAKAPUU PT.
KAHANA
KANEOHE BAY
MOKAPU PEN.
KOOLAU RANGE
MAUKA
EWA
DIAMOND HEAD
MAKAI
HONOLULU
WAIKIKI
DIAMOND HEAD
ROAD
QUEENS
ALA MOANA
REEF SITES
MAMALA BAY
SAND ISL.
KUMUKAHI REEF
KAHUKU
N
OAHU
WAHIAWA
EWA
SUNSET
PIPELINE
WAIMEA BAY
HALEIWA
WAIANAE MOUNTAINS
BARBERS POINT
KAENA POINT
MAKAHA
21° 40'
21° 20'

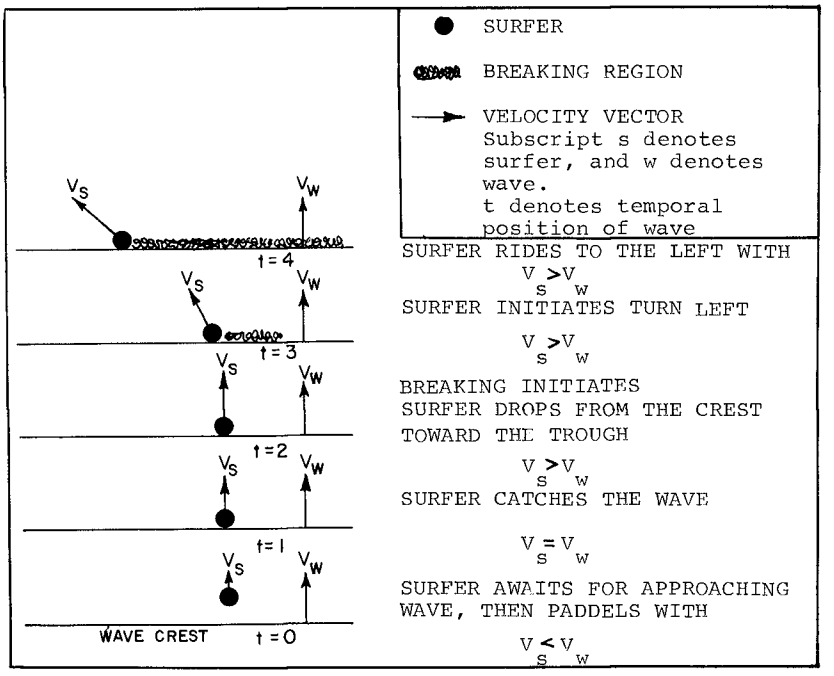

FIGURE 2: SURFING SEQUENCE SCHEMATIC

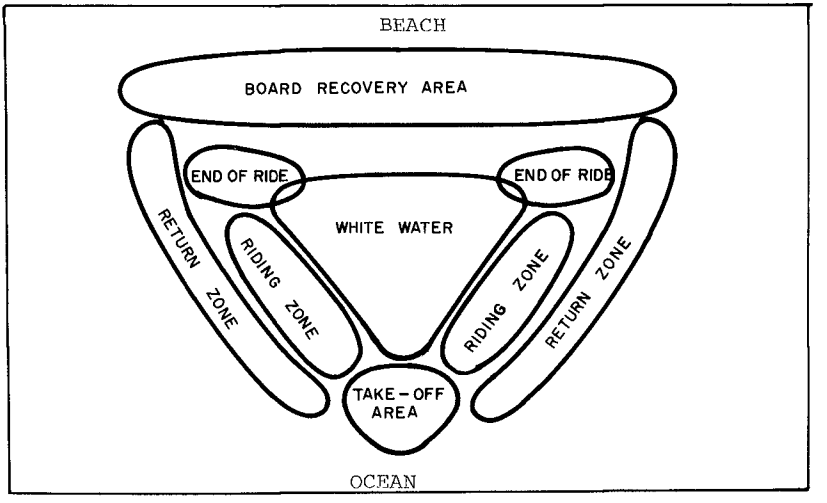

FIGURE 3: SCHEMATIC OF SURFING AREA

FIGURE 5: AERIAL PHOTOGRAPH THREE OF A SEQUENCE OF A SIX-FOOT HIGH BREAKER WITH A TWENTY SECOND PERIOD AT QUEEN'S IN WAIKIKI, APRIL 26,1972. THE TIDE ELEVATION WAS +1.0 FEET.

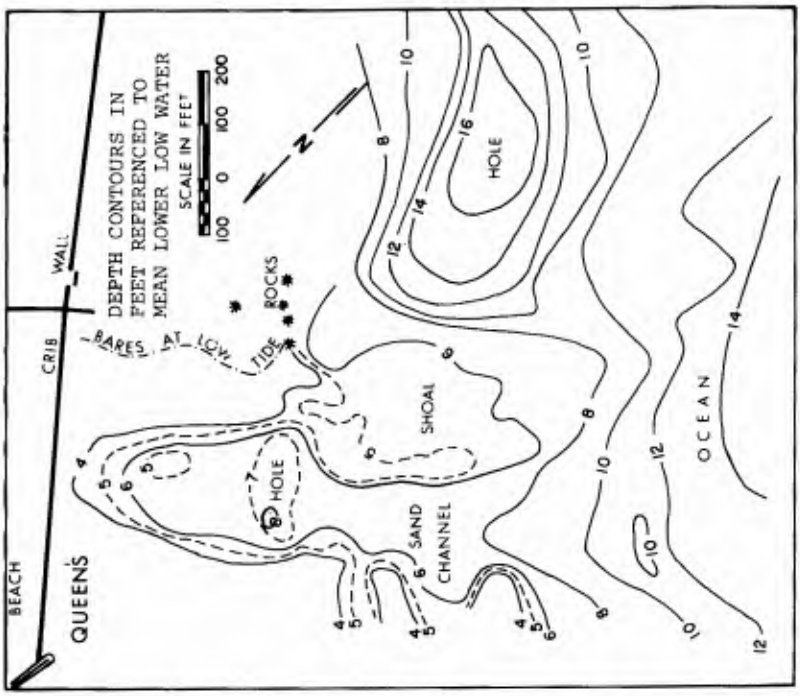

FIGURE 4: BATHYMETRY OF QUEEN'S SURF SITE

FIGURE 7: SURFER RIDING IN THE "PEEL" ON AN EIGHT FOOT BREAKER AT ALA MOANA, JUNE 5, 1972.

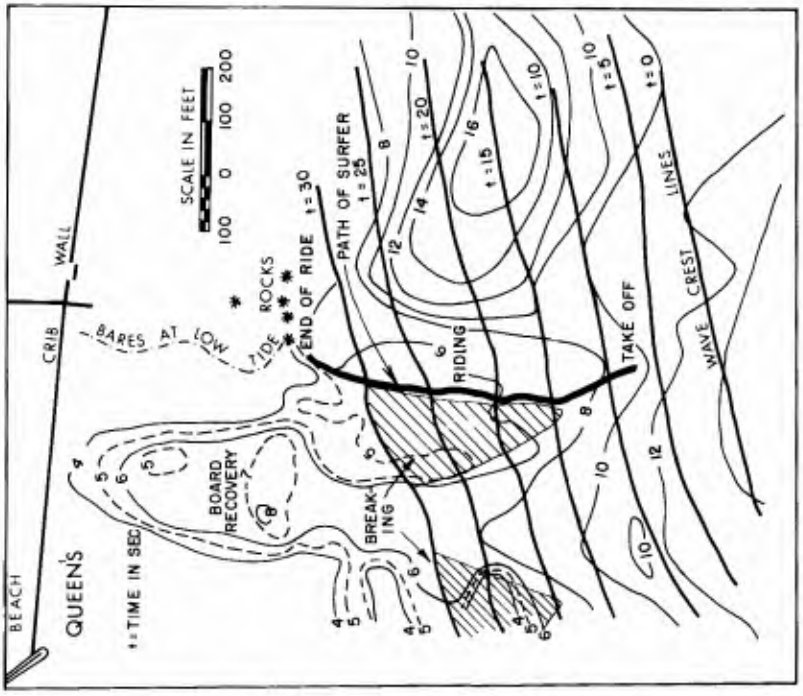

FIGURE 6: WAVE PROPAGATONG OVER QUEEN'S

TABLE 1: SURF SITE OBSERVATIONS

Data Pt	Site	Bottom Slope S	Breaker Height H_b (ft)	Wave Period T(sec)	Breaker Type Index	Surfer Velocity V_s (ft/sec)	Peel Angle α (degrees)	Breaker Type
1a	Queen's	40	4	12	0.035	18	60R	Spill
b	Queen's	40	7	20	0.022	22	65R	Spill-Plunge
c	Queen's	40	6	20	0.019	21	55R	Spill-Plunge
d	Queen's	40	6	20	0.019	18	80L	Spill-Plunge
2a	Ala Moana	33	6	17	0.021	30	35	Plunge
b	Ala Moana	20	10	20	0.015	30	38	Plunge
d	Ala Moana	25	9	20	0.017	30	32	Plunge
3a	Lefts	30	6	20	0.014	30	45	Plunge
4a	Kewalo	37	6	17	0.024	18	65	Plunge-Spill
5a	Makaha	60	6	14	0.057	28	65	Spill
b	Makaha	60	8	16	0.058	20	68	Spill
6a	Waimea	20	17	16	0.041	38	80	Plunge-Spill
7a	Pipeline	65	18	16	0.14	45*	35	Plunge
b	Pipeline	22	12	16	0.032	32	40	Hard Plunge
8a	Sunset	100	18	16	0.22	43*	40	Plunge-Spill
b	Sunset	100	15	16	0.18	33	65	Plunge-Spill

* Wave not ridden, R= ride to the right, L= ride to the left

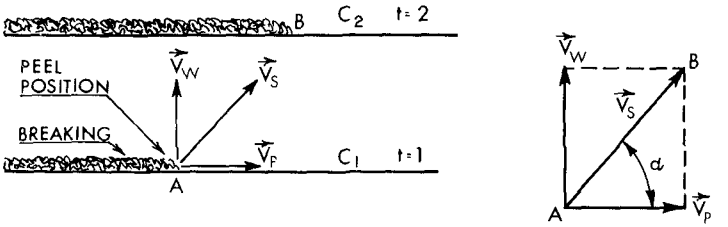

FIGURE 8: DIAGRAM SHOWING RELATION AMONG PEEL PARAMETERS

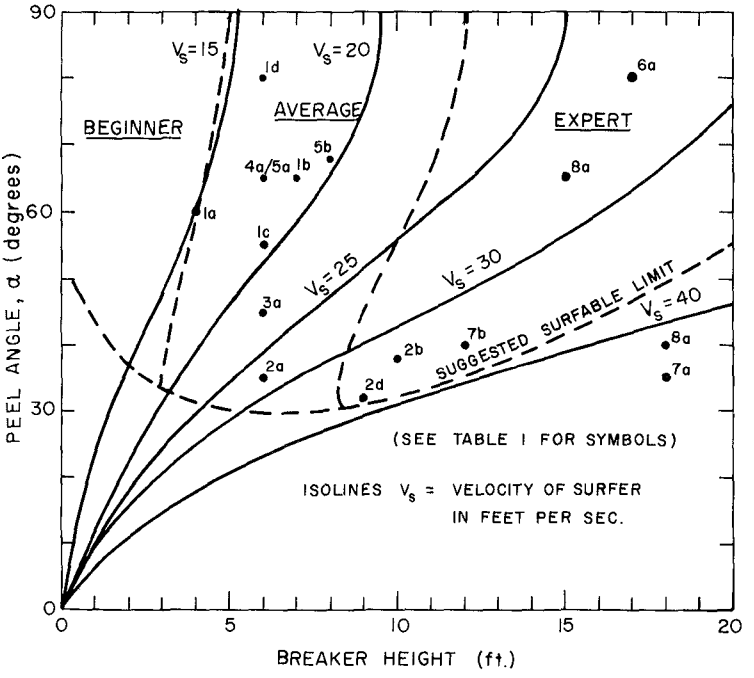

FIGURE 9: PEEL-ANGLE vs. BREAKER HEIGHT

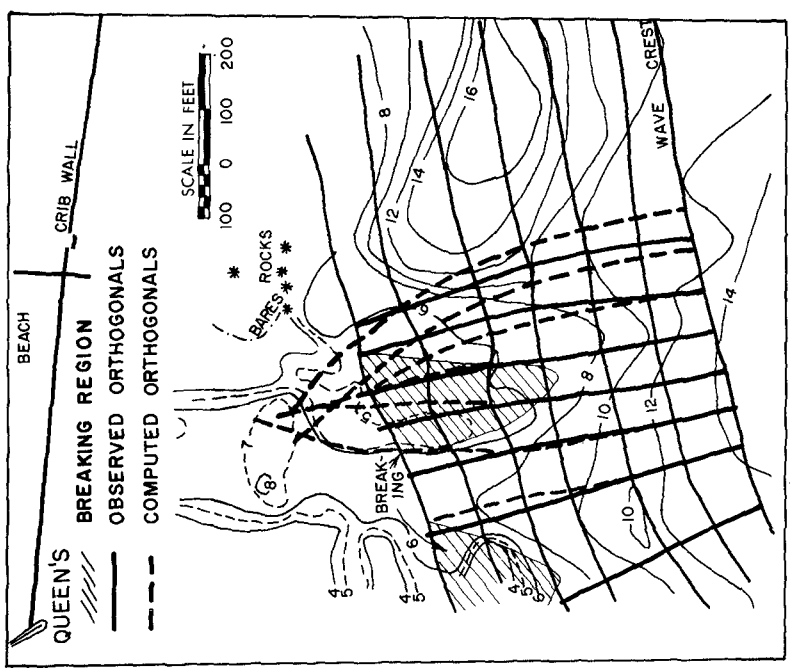

FIGURE 10: COMPARISION OF OBSERVED AND CALCULATED WAVE ORTHOGONALS

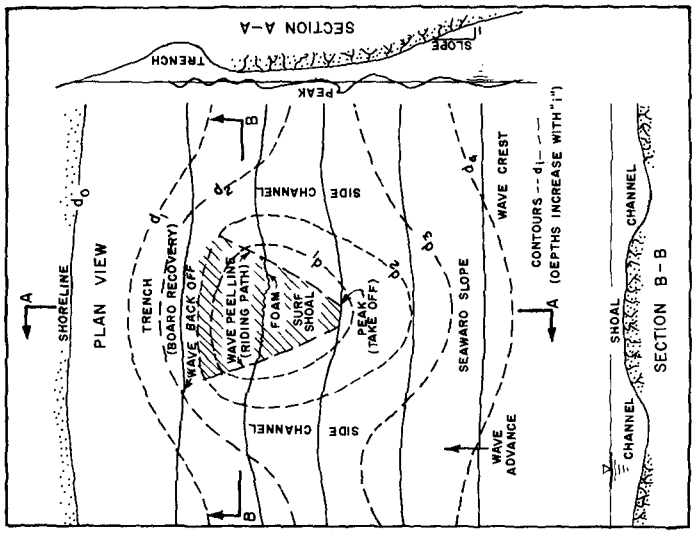

FIGURE 11: MULTIPLE-PURPOSE REEF CONCEPT

CHAPTER 152

SURGE IN THE SOUTHEAST BASIN, LONG BEACH HARBOR, CALIF.

By Basil W. Wilson[1], F. ASCE
James A. Hendrickson[2] and Juan Jen[3], A.M. ASCE

INTRODUCTION

Recent studies of the hydrodynamic responses of Los Angeles-Long Beach Harbors to the effects of long period waves [conducted in 1967-68 for the U.S. Army Corps of Engineers, Los Angeles District (35)], showed that the basins had characteristic modal periods of oscillation, which could be excited, apparently, on rather rare and largely unpredictable occasions. Available field data for confirmation of the mathematical results were largely non-existent at the time and satisfactory correlations were greatly hampered. In the interim the development of the Southeast Basin, Long Beach Harbor, for the reception of fast container ships has led to more detailed study and measurement of the responses of this particular basin to long period waves. The purpose of this paper is to present some of the original theoretical results of the 1968 study and examine their correlation with data of recent acquisition. Their bearing upon the motions in surge and sway of ships moored within the Southeast Basin will also be examined briefly in the light of some simple measurements of ship motions.

FREE UNDAMPED OSCILLATIONS OF HARBOR BASINS

Many approaches have been taken to the solution of the problem of the free oscillations of a basin of irregular planform and variable (or uniform) depth (4 , 5, 11 - 14, 20, 25, 34, 35). Some general review of these has been given elsewhere (32,33) and accordingly it will not be repeated here. Interest at the moment,

[1] Consulting Oceanographic Engineer, Pasadena, California

[2,3] Senior Engineers, Science Engineering Associates, Newport Beach, California, (Division of Dames and Moore)

specifically, is in results of the method followed by Wilson, et al (35).

The procedure follows from the equations of motion and continuity of a water particle in long waves of low amplitude, free from forced excitation and damping. These equations, referred to an x-y co-ordinate system in the horizontal plane, can be combined to yield (cf. 9, §193) a single equation governing water surface elevation η, namely

$$\frac{\partial^2 \eta}{\partial t^2} = g\left[\frac{\partial}{\partial x}\left(h \frac{\partial \eta}{\partial x}\right) + \frac{\partial}{\partial y}\left(h \frac{\partial \eta}{\partial y}\right)\right] \tag{1}$$

in which $h(x,y)$ is variable water depth according to location (x,y) and g the acceleration from gravity.

If the solution to Eq. (1) is taken of the form:

$$\eta = \zeta (x,y) \cos \omega t \tag{2}$$

where ζ is an amplitude function in (x,y) independent of time t and ω is an eigenfrequency (angular) of a mode of free motion, then substitution of Eq. (2) in Eq. (1) transforms the latter to

$$\frac{\partial}{\partial x}\left(h \frac{\partial \zeta}{\partial x}\right) + \frac{\partial}{\partial y}\left(h \frac{\partial \zeta}{\partial x}\right) + (\omega^2/g)\,\zeta = 0 \tag{3}$$

On expansion Eq. (3) becomes

$$h\left(\frac{\partial^2 \zeta}{\partial x^2} + \frac{\partial^2 \zeta}{\partial y^2}\right) + \frac{\partial h}{\partial x}\frac{\partial \zeta}{\partial x} + \frac{\partial h}{\partial y}\frac{\partial \zeta}{\partial y} + (\omega^2/g)\,\zeta = 0 \tag{4}$$

This equation can be integrated in closed form for only a limited number of relatively simple geometrical shapes of basins. However it may be solved numerically by a finite difference technique, which follows essentially the principles discussed by Stoker (24, §10.13).

In order to develop a proper degree of flexibility in the analysis, the equation is considered in relation to a rectangular co-ordinate grid system (Fig. 1 a) whose elemental distances δ in the directions of x and y are not necessarily equal. Thus the regime at any single point 0 can be specified in relation to that at each

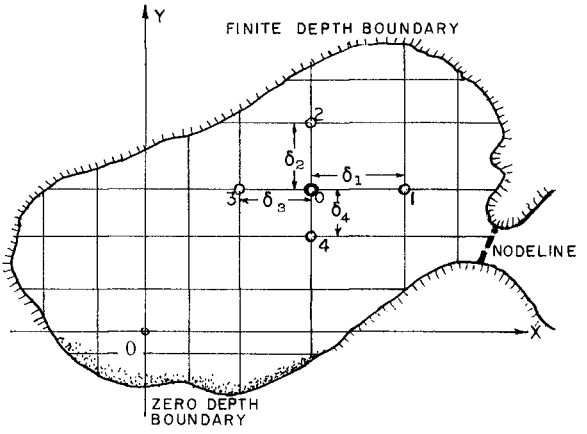

FIG. 1(a) - SCHEMATIC DIAGRAM OF RECTILINEAR COORDINATE GRID SYSTEM OVERLAID ON PLAN OF BAY OR HARBOR

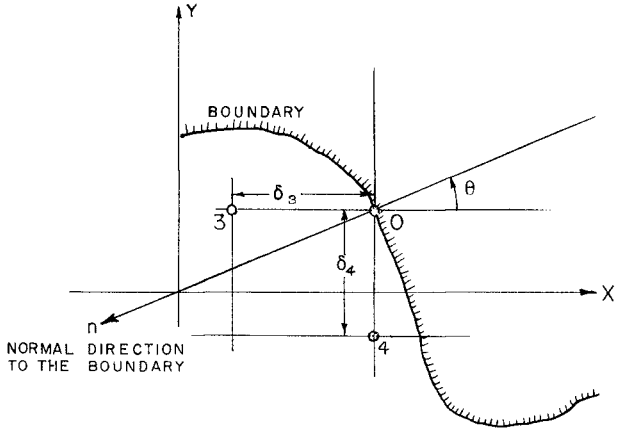

FIG. 1(b) - SCHEMATIC DETAIL OF GRID POINT DEFINING A BOUNDARY

of the four adjacent grid points, 1 to 4, in terms of the incremental distances δ_1, δ_2, δ_3, and δ separating the points. Thus the differential terms of Eq. (4) can be expressed as:

(i) $$\frac{\partial \zeta}{\partial x} = \frac{\zeta_1 \delta_3^2 + \zeta_0(\delta_1^2 - \delta_3^2) - \zeta_3 \delta_1^2}{\delta_1 \delta_3 (\delta_1 + \delta_3)} \qquad 5(a)$$

(ii) $$\frac{\partial^2 \zeta}{\partial x^2} = 2 \left\{ \frac{\zeta_1 \delta_3 - \zeta_0(\delta_1 + \delta_3) + \zeta_3 \delta_1}{\delta_1 \delta_3 (\delta_1 + \delta_3)} \right\} \qquad 5(b)$$

and

(i) $$\frac{\partial \zeta}{\partial y} = \frac{\zeta_2 \delta_4^2 + \zeta_0(\delta_2^2 - \delta_4^2) - \zeta_4 \delta_2^2}{\delta_2 \delta_4 (\delta_2 + \delta_4)} \qquad 6(a)$$

(ii) $$\frac{\partial^2 \zeta}{\partial y^2} = 2 \left\{ \frac{\zeta_2 \delta 4 - \zeta_0(\delta_2 + \delta_4) + \zeta_4 \delta_2}{\delta_2 \delta_4 (\delta_2 \delta_4)} \right\} \qquad 6(b)$$

with

(i) $$\frac{\partial h}{\partial x} = \frac{h_1 \delta_3^2 + h_0(\delta_1^2 - \delta_3^2) - h_3 \delta_1^2}{\delta_1 \delta_3 (\delta_1 + \delta_3)} \qquad 7(a)$$

(ii) $$\frac{\partial h}{\partial y} = \frac{h_2 \delta_4^2 + h_0(\delta_2^2 - \delta_4^2) - h_4 \delta_2^2}{\delta_2 \delta_4 (\delta_2 + \delta_4)} \qquad 7(b)$$

In Eqs (5) through (7), subscripts 0 to 4 identify the values of the function ζ at the points 0 to 4.

By substitution of Eqs (5) through (7) in Eq. (4) and by suitable algebraic manipulation, Eq. (4) can be converted to the form:

$$(\nu_k - a_0)\zeta_0 + a_1\zeta_1 + a_2\zeta_2 + a_3\zeta_3 + a_4\zeta_4 = 0 \qquad (8)$$

in which the eigenvalue ν_k (an unknown) is related to any kth eigenfrequency ω_k (k = 1, 2, 3,.....N) by

$$\nu_k = \omega_k^2/g \qquad (9)$$

and the coefficients a_i (i = 0, 1, 2, 3, 4) are constants calculable in terms of

the depths h_i and the distance increments δ_i (35).

If there are N reticulation points of the type 0 in the network, N equations of the type of Eq. (8) can be formed for the N unknowns of the function ζ_n (n = 1, 2, 3, ...N) in association with N possible eigenvalues ν_k = 1, 2, 3, ...N). Consequently an N x N matrix can be formed for determination of the eigenfrequencies ω_k and the surface elevations ζ_n from the corresponding eigenvectors.

Where the grid network intersects the boundaries of the basin, special conditions apply and some of the N equations of type Eq. (8) must express these conditions. In general the boundary can be of three forms; a zero-depth boundary such as a beach or sloping wall; a finite-depth boundary such as a vertical wall or cliff; and an open-mouth boundary such as a harbor entrance or bay-mouth. As shown in Fig. 1(b), through the versatility of a variable grid spacing, it is possible to ensure that a typical boundary condition can be expressed in terms of a grid point 0 located exactly on the boundary, at suitably small distances from adjacent grid-points 3 and 4 (for the configuration shown).

Zero-Depth Boundary:

The condition of zero depth (h_o = 0) causes the first terms of Eq. (4) to vanish. Eqs (5a) and (6a) correspondingly reduce to

$$\frac{\partial \zeta}{\partial x} = (\zeta_0 - \zeta_3)\,\delta_3 \tag{10a}$$

$$\frac{\partial \zeta}{\partial y} = (\zeta_0 - \zeta_4)/\delta_4 \tag{10b}$$

while Eqs (7a) and (7b) become:

$$\frac{\partial h}{\partial x} = -\,h_3/\delta_3 \tag{11a}$$

$$\frac{\partial h}{\partial y} = -\,h_4/\delta_4 \tag{11b}$$

Applications of Eqs (10) and (11) to Eq. (4), then yield the special zero-depth boundary condition:

$$\{(h_3/\delta_3^2) + (h_4/\delta_4^2) - \nu_k\}\,\zeta_0 - (h_3/\delta_3^2)\,\zeta_3 - (h_4/\delta_4^2)\zeta_4 = 0 \qquad (12)$$

Finite-Depth Boundary:

If the boundary at point 0 in Fig. 1(b) is one of finite depth, then there can be no horizontal flow of water normal to the boundary at that point. This requires that $\frac{\partial \zeta}{\partial n} = 0$ where n expresses the direction normal to the boundary. If θ be the angle which the normal direction makes with the x-axis, then

$$\frac{\partial \zeta}{\partial n} = \frac{\partial \zeta}{\partial x}\cos\theta + \frac{\partial \zeta}{\partial y}\sin\theta = 0 \qquad (13)$$

By use of Eqs (10), Eq. (13) then becomes the special finite depth boundary condition.

$$(\delta_3 \tan\theta + \delta_4)\,\zeta_0 - \delta_4\zeta_3 - (\delta_3 \tan\theta)\,\zeta_4 = 0 \qquad (14)$$

Open-Mouth Boundary:

At an open-mouth "boundary" (fictitious, of course), by which a basin or bay is considered connected to another body of water, there will be, in general, both horizontal flow and vertical surface elevation of the water. The condition of existence of an eigenfrequency oscillation in the basin, however, usually requires that a nodal condition ($\zeta = 0$) shall prevail along some nodal line across the mouth. If the basin entrance is a comparatively narrow one, without much neck or channel, it is usually safe to assume that the direct line of shortest distance connecting the promontories of the mouth will mark the position of a node, across which the flow is normal. If the mouth is a broad entrance to a bay the position of a node line will be less accurately definable, though its position may always be assumed, and, in this, sound judgement and experience can be helpful. Strictly the condition across the mouth needs to be defined by matching it with the motion behavior of the external body of water, but in this study this refinement and complication was considered unnecessary.

The boundary equation for a grid-point on the node line, is then simply

$$\zeta_0 = 0 \qquad (15)$$

VELOCITIES AND DIRECTIONS OF OSCILLATORY FLOW

The horizontal flow velocity, V, of the water at any point (x, y) in the free mode of oscillation (Fig. 2a) may be defined as to direction s by the angle ψ which the s-direction makes with the axis of x. For the long waves and small amplitudes which basin oscillations normally invoke, V may be considered uniform with depth. In terms of the velocity potential φ prevailing at the point (x, y) and the component velocities u and v, its value is

$$V = (u^2 + v^2)^{\frac{1}{2}} \approx \frac{\partial \varphi}{\partial s} \tag{16}$$

while the value of the potential φ itself is given by the generalized Bernoulli equation for the free surface, namely

$$\frac{\partial \varphi}{\partial t} = g\eta \tag{17}$$

From Eqs (2), (16) and (17), then, the velocity becomes

$$V = (g/\omega) \frac{\partial \zeta}{\partial s} \sin \omega t \tag{18}$$

Usually, because the velocity fluctuation is sinusoidal, the major interest is in knowing its maximum value, V_{max}, (at $\sin \omega t = 1$) and its direction of flow, s. In relation to values ζ_i ($i = 0, 1, 2, 3, 4$) for grid points surrounding a central point $i = 0$ (Fig. 2b), the vector magnitude and direction of velocity can be determined from:

$$V_{max} = (g/2\delta_1 \delta_2 \delta_3 \delta_4 \omega)[(\delta_2 \delta_4)^2 \{\delta_3(\zeta_1 - \zeta_0) + \delta_2(\zeta_0 - \zeta_3)\}^2 + (\delta_1 \delta_3)^2 \{\delta_4(\zeta_2 - \zeta_0) + \delta_2(\zeta_0 - \zeta_4)\}]^{\frac{1}{2}} \tag{19}$$

and

$$\tan \psi = \frac{\delta_1 \delta_3}{\delta_2 \delta_4} \cdot \frac{\delta_4(\zeta_2 - \zeta_0) + \delta_2(\zeta_0 - \zeta_4)}{\delta_3(\zeta_1 - \zeta_0) + \delta_1(\zeta_0 - \zeta_3)} \tag{20}$$

Thus velocities and directions of oscillatory flow are readily determined once the matrix solution of ζ has been achieved.

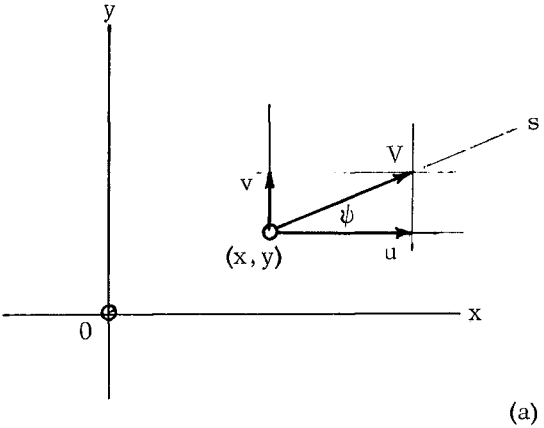

(a)

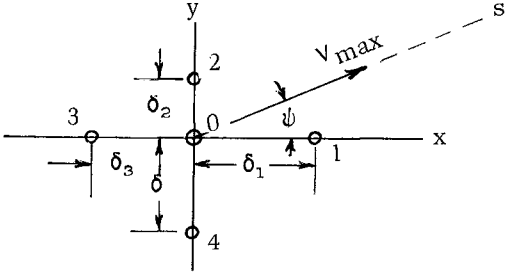

(b)

FIG. 2 - SCHEMATIC REPRESENTATION OF VELOCITY AT A POINT; (a) IN PLAN VIEW; (b) IN THE NUMERICAL GRID

NUMERICAL SOLUTION FOR SOUTHEAST BASIN SHAPE OF 1968

The Southeast Basin of Long Beach Harbor as it existed in 1967-1968 is shown in Fig. 3. Depths within the basin varied from about 35 ft to 55 ft in the deepest spot within Basin Six. The modelling of this basin for the numerical computation is shown by the grid of 88 points in Fig. 4 which cover the area and define the boundary. The sequence of points from 1 to 38 all lie upon the boundaries while the remainder from 39 to 88 encompass the interior area.

Results of the numerical calculations are given most readily in the form of contoured diagrams of normalized surface elevations expressing the generalization of Eq. (2), namely:

$$(\eta_k)_n = (\zeta_k)_n \cos \omega_k t \qquad (21)$$

where k(= 1, 2, 3, . . .) expresses the mode number and n the grid number (n = 1 to 88), for the condition that amplitudes are a maximum (cos $\omega_k t$ = 1). Thus Figs 5(a) and (b) give the mode shapes for the two lowest modes(k = 1 and k = 2), with contour lines in increments of 5, normalized to maximum positive surface elevation of 100. Arrows and small figures alongside grid points define directions and velocities in units per sec, normalized to maximum surface height variation (double amplitude) of one unit. Because values of velocity are of secondary interest in the present paper no attempt has been made to preserve the legibility of the velocity figures, as computer-plotted in these diagrams.

The fundamental mode oscillation (k = 1), with period T_1 = 14.2 mins, has just one node at the mouth of the basin (Fig. 5a); this is the so-called "pumping" mode for the Southeast Basin. In the second mode oscillation (T_2 = 7.0 mins), there are two nodes (Fig. 5b) and the entire basin oscillates in what is effectively a uninodal seiche between Basin Six and the Southeast Basin. Basin Six, however, at the same time displays its pumping mode response to the node at the entrance of the coupled basins.

In Fig. 6(a) the third mode oscillation (T_3 = 3.7 mins) turns out to be predominantly a diagonal (cross) seiche between extremities of the Southeast Basin.

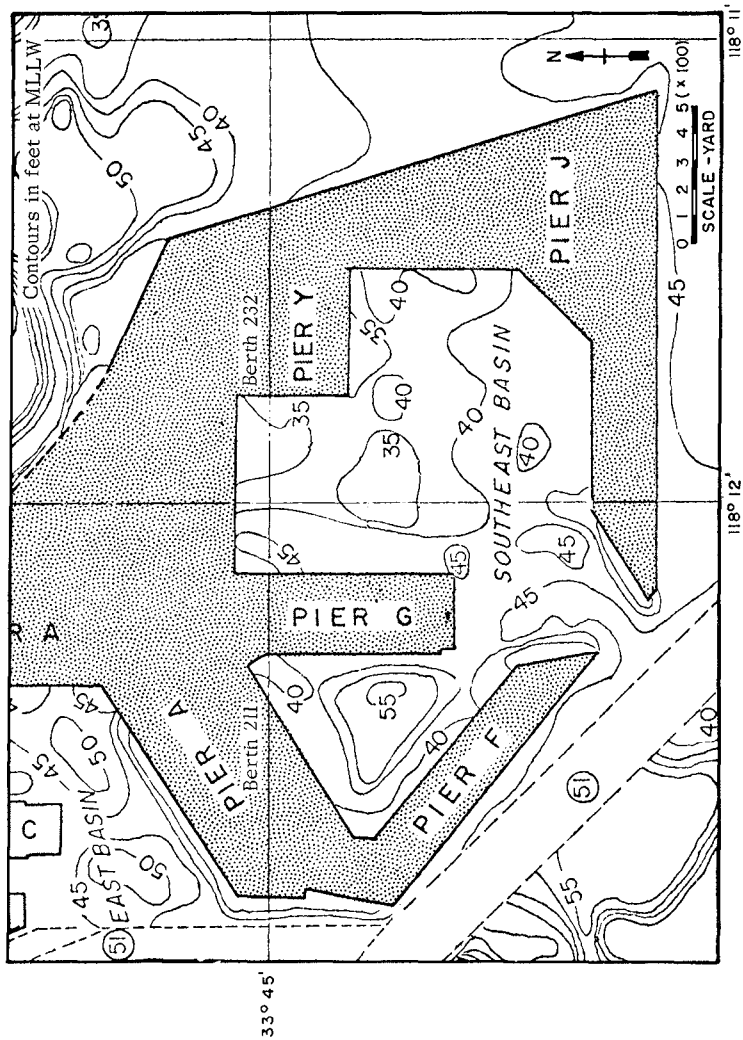

FIG. 3 - BATHYMETRY OF SOUTHEAST BASIN, LONG BEACH HARBOR (1967)

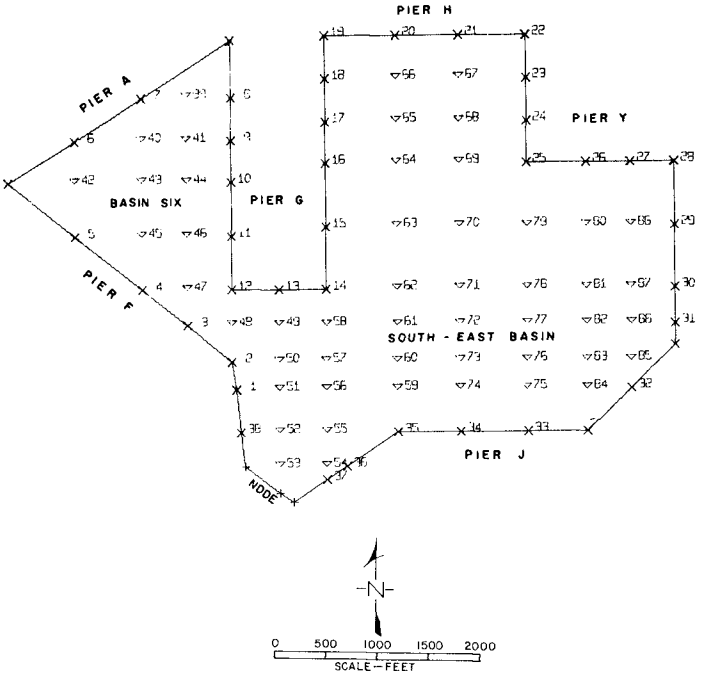

FIG. 4 - NUMERICAL GRID FOR MODELLING SOUTHEAST BASIN SHAPE OF 1967 - 1968

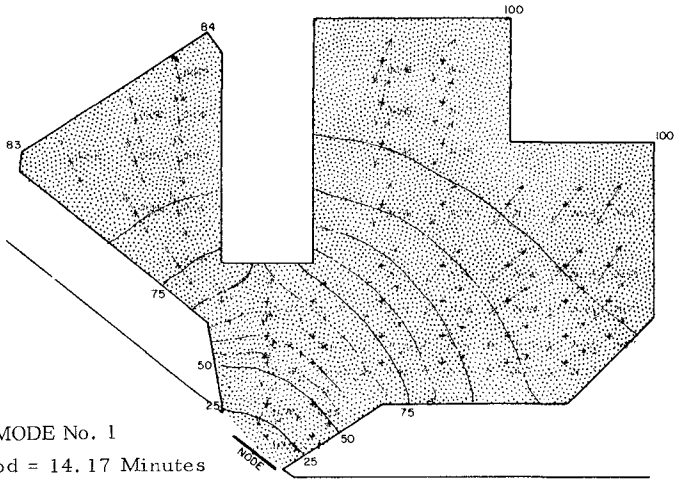

(a) MODE No. 1
Period = 14.17 Minutes

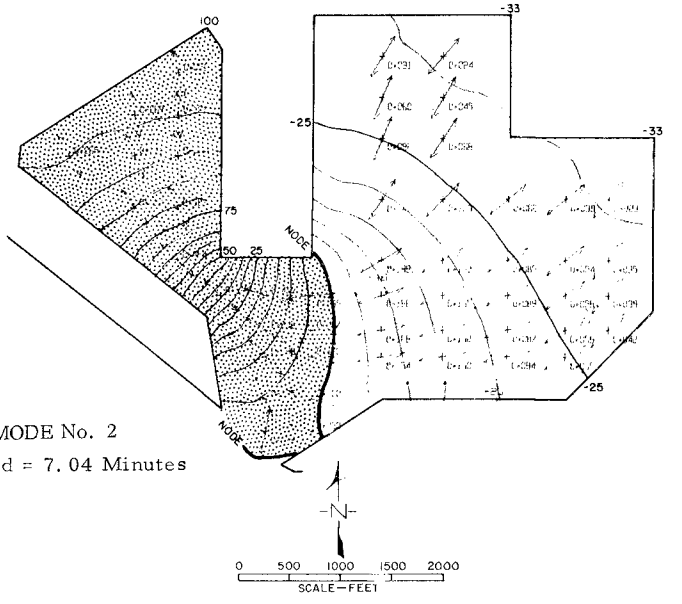

(b) MODE No. 2
Period = 7.04 Minutes

FIG. 5 - MODES OF FREE OSCILLATION OF SOUTHEAST BASIN (1968)
(a) 1st MODE; (b) 2nd MODE

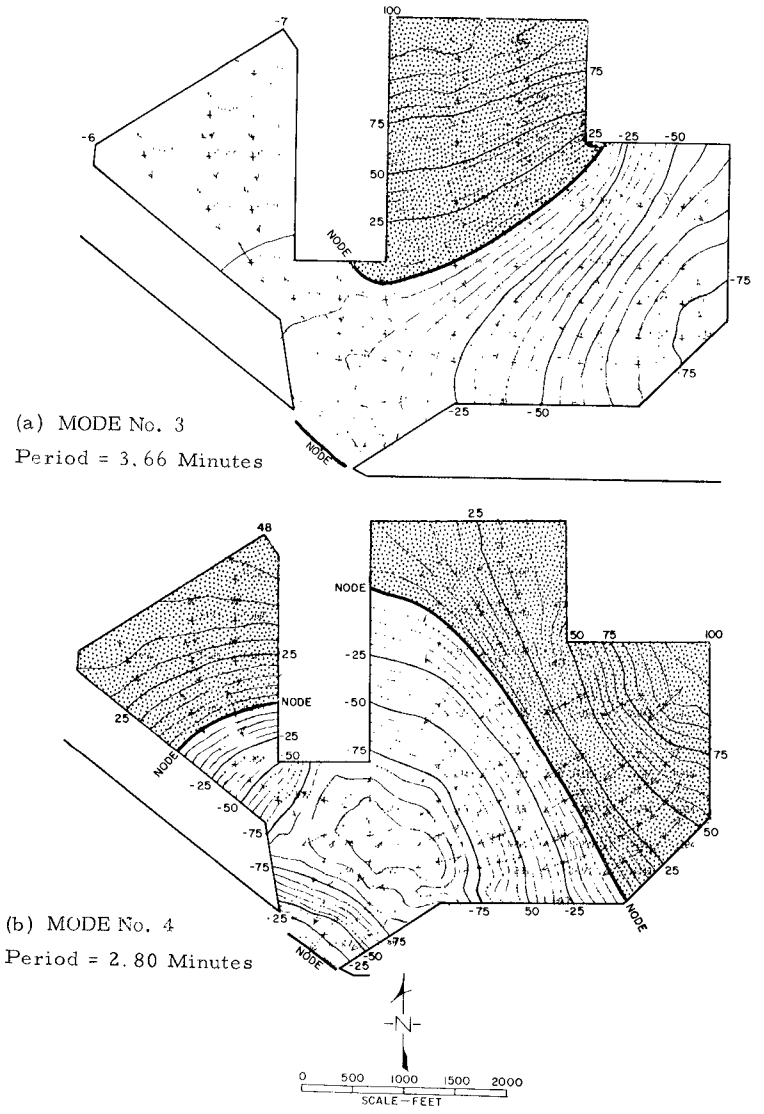

FIG. 6 - MODES OF FREE OSCILLATION OF SOUTHEAST BASIN (1968)
(a) 3rd MODE; (b) 4th MODE

Basin Six hardly responds at all.

The fourth mode oscillation (T_4 = 2.8 mins, Fig. 6b) is essentially the pure bi-nodal oscillation of the open-mouth connected basins. The Southeast Basin, with a normalized amplitude of 100 at the northeast corner, as compared with 48 in the north corner of Basin Six, obviously dominates the oscillation.

Configurations of higher modal oscillations are not given here for the basin shape of 1967-68, though they were recorded to the 10th mode (35). Numerical calculations were not pursued beyond the 10th mode because of the inherent decline in accuracy of the numerical method for large values of k.

CONFIRMATION OF THE NUMERICAL MATRIX SOLUTIONS FOR FREE OSCILLATIONS

By way of verifying the approach taken and the results thus far given, two different methods were used to evolve corroborative information. The first of these employed the time-marching technique of Leendertse (14) in propagating a long wave of given period into the Southeast Basin to establish its own oscillation. The second procedure used the impedance principle first developed by Rayleigh in 1877 (21) in acoustical problems and adapted by Neumann in 1944 to the study of seiches in connected bodies of water (17,18).

Numerical Time-Marching Technique

This method uses the integrated equations of motion and continuity, governing the propagation of long period waves, in two sets of difference equations for a step-by-step solution in increments of time of the water surface elevation and water particle velocities (14). The program of computation can be applied to a much finer grid than that used in the matrix solution and can thus define the shape and depths of a basin relatively more accurately. However, the method cannot establish an eigen period (free oscillation) except by trial and error solutions of effects from a large number of input periods, taken very close together.

As a check on the matrix solution results given in Fig. 6(b) a 2.8 mins period long wave was impressed on the entrance to the Southeast Basin with an arbitrary 15 cms amplitude at the star-positions just outside the basin mouth (Fig.7). The propagation of the wave was followed at time-steps of 6 secs over a 260-point spatial grid covering the Southeast Basin areas. The program, developed (and applied) by Leendertse (14), included the effects of bed friction and Coriolis force (though the latter effects would be almost negligible in so small a basin). After 85 time-steps the motion inside the basin reached the stable oscillation represented in Fig. 7. The oscillation established a node in a straight line across the entrance and a second node within the basins, characterizing it as the binodal resonant oscillation with respect the entrance, typical of an open-mouth basin. Fig. 7 is seen to be in good general agreement with Fig. 6(b), both as regards nodal and antinodal positions and also relative amplitudes. The mode shape contours of Fig. 7, however, may be expected to be more accurate than those of Fig. 6(b), because of the much larger number of grid points (260), [as compared with 88 for Fig. 6(b)], used in definition of spatial area and depth within the basins.

Neumann's Impedance Method of Seiche Analysis

The second method used in general confirmation of the matrix solutions required that the variable shape and depth of the Southeast Basin and Basin Six be approximated as a series of connected basins of uniform depth, width and length which are open-ended at connecting points and closed at terminal points and, of course, open-ended at the mouth. The adopted manner of dividing up the Southeast Basin into such a system is illustrated in Fig. 8(a) which gives also the "individual basin" dimensions of length, width and depth. The accompanying schematic circuit diagram for this array is shown in Fig. 8(b), in which the individual basins, in series or parallel, are designated from I to IX.

The details of the method for solving the eigen-frequencies of oscillation of the combined basin system will not be given here. The reader is referred to Defant (4), O'Brien (19) or Wilson (33) for particulars. The eigen-frequencies

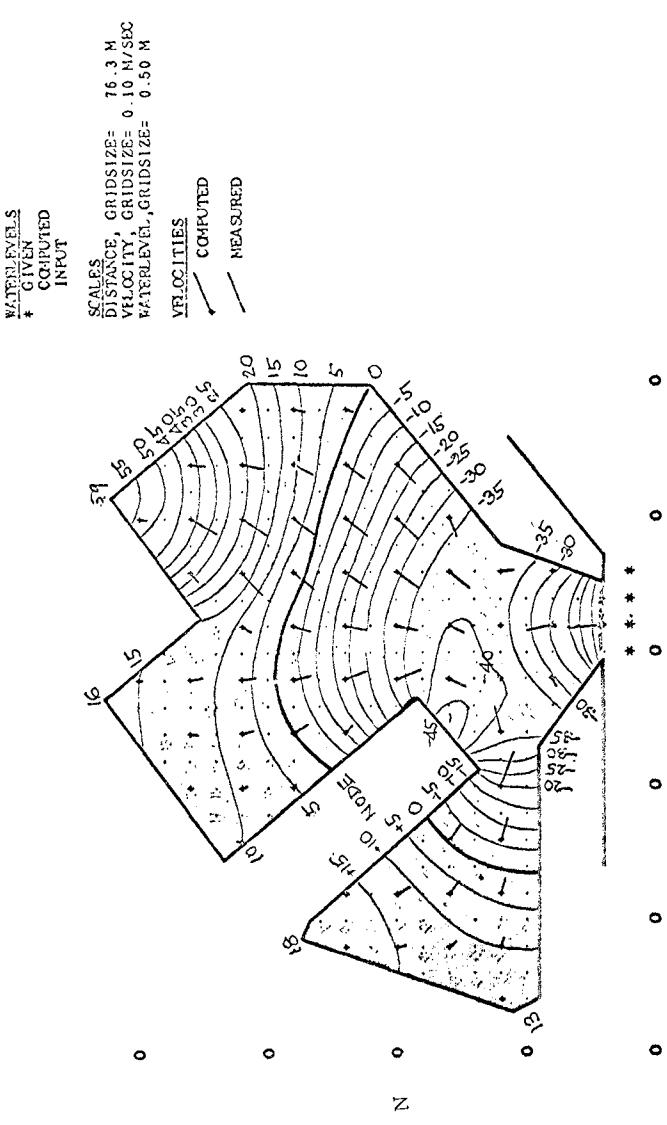

FIG. 7 - MODE OF OSCILLATION FOR SOUTHEAST BASIN, LONG BEACH HARBOR, DEVELOPING FROM 2.80 MIN PROGRESSIVE WAVE TRAIN ENTERING BASIN VIA MOUTH; NUMERICAL MARCHING TIME CALCULATION OF LEENDERTSE

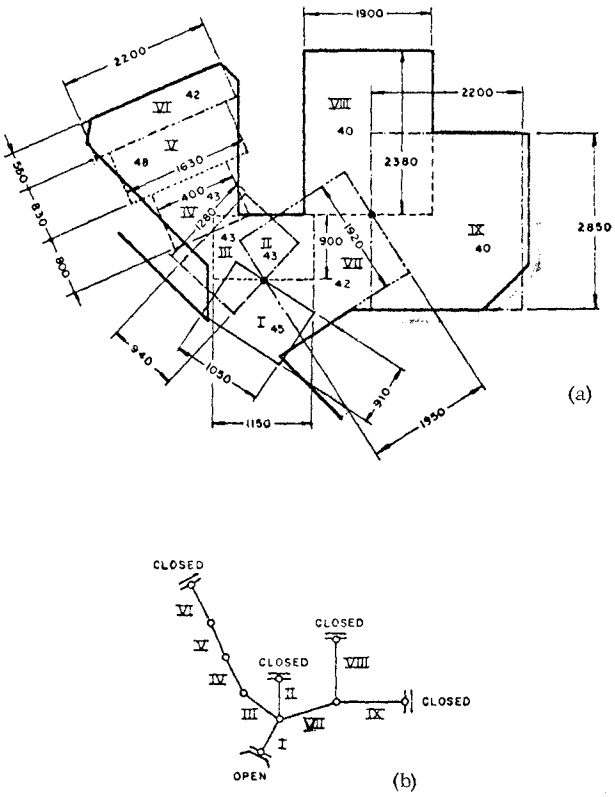

FIG. 8 - "IMPEDANCE" MODEL FOR SOUTHEAST BASIN, LONG BEACH HARBOR AS A CONNECTED SYSTEM OF RECTANGULAR BASINS (a) BASIN DIMENSIONS (b) EQUIVALENT CIRCUIT DIAGRAM

ω_k are obtained as the roots of two parametric equations, one of the variables of which is ω_k. Details of these equations may be found in Wilson (33) or Wilson, et al (35).

The sequence of modal periods evolving from the solutions to these equations are given in Table 1 in comparison with the modal periods derived from the matrix solutions.

TABLE 1 - COMPARISON BETWEEN MODAL PERIODS OF FREE OSCILLATION OF SOUTHEAST BASIN, LONG BEACH HARBOR, CALCULATED BY TWO METHODS

Method	Modal Period, T_m - (mins)									
	m=1	2	3	4	5	6	7	8	9	10
Matrix	14.2	7.0	3.7	2.80	2.02	1.80	1.76	1.58	1.54	1.44
Impedance	12.7	5.2	4.3	2.83	2.20	1.60	1.48	1.42	1.41	1.07

The comparison, although not too good as to accuracy, is quite acceptable as to order of magnitude. The test is a particularly severe one for the impedance method; its accuracy is only as good as the approximations made in simulating the Southeast Basin and Basin Six as an array of interconnected rectangular basins. It serves nevertheless to confirm the validity of the matrix solutions, whose accuracy also is necessarily limited by the matrix number (88 x 88) or the memory capacity of the computer.

NUMERICAL SOLUTION FOR SOUTHEAST BASIN SHAPE OF 1972

Developments in the Southeast Basin in the last few years have been towards reclaiming more warehouse and loading space and reducing the amount of water space in the basin. The new shape of the basin as of 1972 is shown in Fig. 9 which gives also the numerical grid adopted, in this case, with 83 points to identify the boundary and bathymetry. Identified also in Fig. 9 are two corner positions,

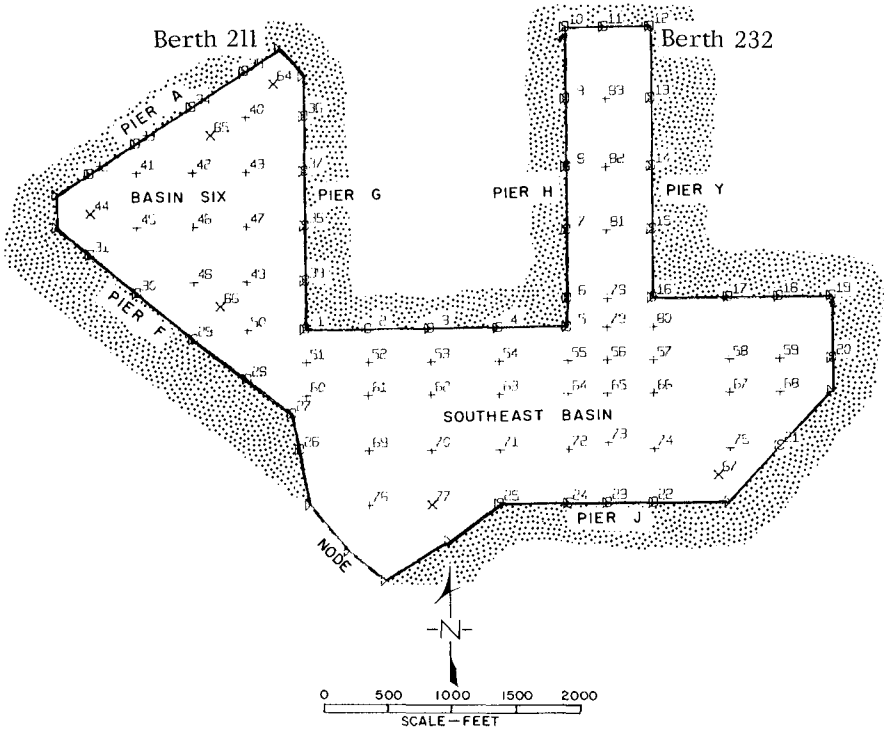

FIG. 9 - NUMERICAL MODEL OF SOUTHEAST BASIN (1971)

Berth 211 in Basin Six and Berth 232 in the Southeast Basin slip, at which special tide gages were established for recording long wave activity in the basins. These will be referred to later.

For the matrix solution of the new basin shape the whole basin system was assumed to have a uniform depth of 45 ft. In practice this depth has been increased to 55 ft throughout most of the Southeast Basin, but as the calculations were performed in 1967-68 for the lesser depth of 45 ft this must be borne in mind when comparisons are made (later) between calculated results and measurements.

The sequence of Figs 10 to 14 give the matrix solutions of the lowest modes of oscillation of the new basin shape, determined again on the assumption that a node develops across the mouth of the basin.

The lowest four modes, as might be expected, are quite similar in character to the corresponding modes of free oscillation for the 1968 basin. This is readily seen by comparison of Figs 5 and 10 and Figs 6 and 11. For modes higher than the fourth, the similarity ends and the behavior of the coupled basins becomes one of mutual interaction. It is noteworthy in Fig. 11(a) that in the third mode (k=3), the slip in the Southeast Basin is responding strongly to an oscillation which, though binodal for the entire basin system, is uninodal for the slip itself, as judged by the fact that the internal node is approximately at the mouth of the slip.

Fig. 12(a) can be recognized as a mode (T = 1.80 mins) which develops a tri-nodal seiche between the northern extremity of Basin Six and the eastern extremity of the Southeast Basin. The slip has a rather weak response.

At T = 1.65 mins, (Fig. 12b), Basin Six develops a strong uninodal oscillation between the north and west corners, while the Southeast Basin and slip oscillate rather moderately in what may be described as a clover-leaf pattern, the stem of which is the core of the white area enveloping the mouth of the slip and the petals the three shaded areas outside.

At k=7, T = 1.58 mins, the next mode (Fig. 13a), Basin Six continues to oscillate strongly between the north and west corners, while a moderately strong

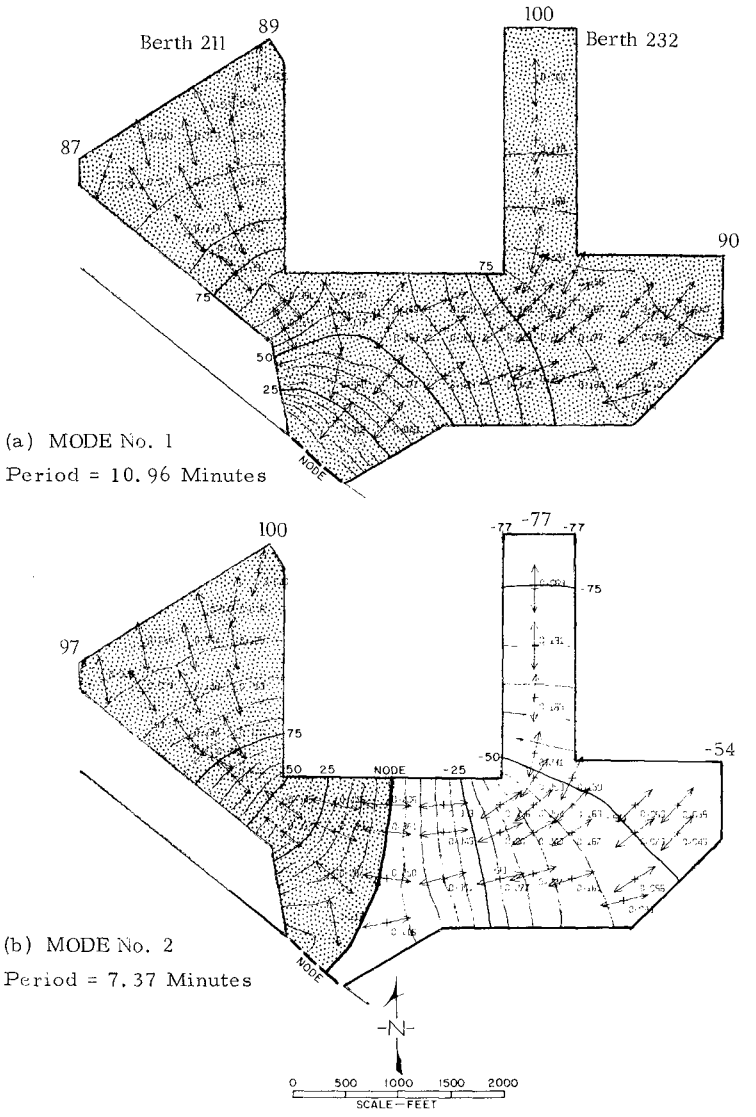

FIG. 10 - MODES OF FREE OSCILLATION OF SOUTHEAST BASIN (1971)
(a) 1st MODE; (b) 2nd MODE

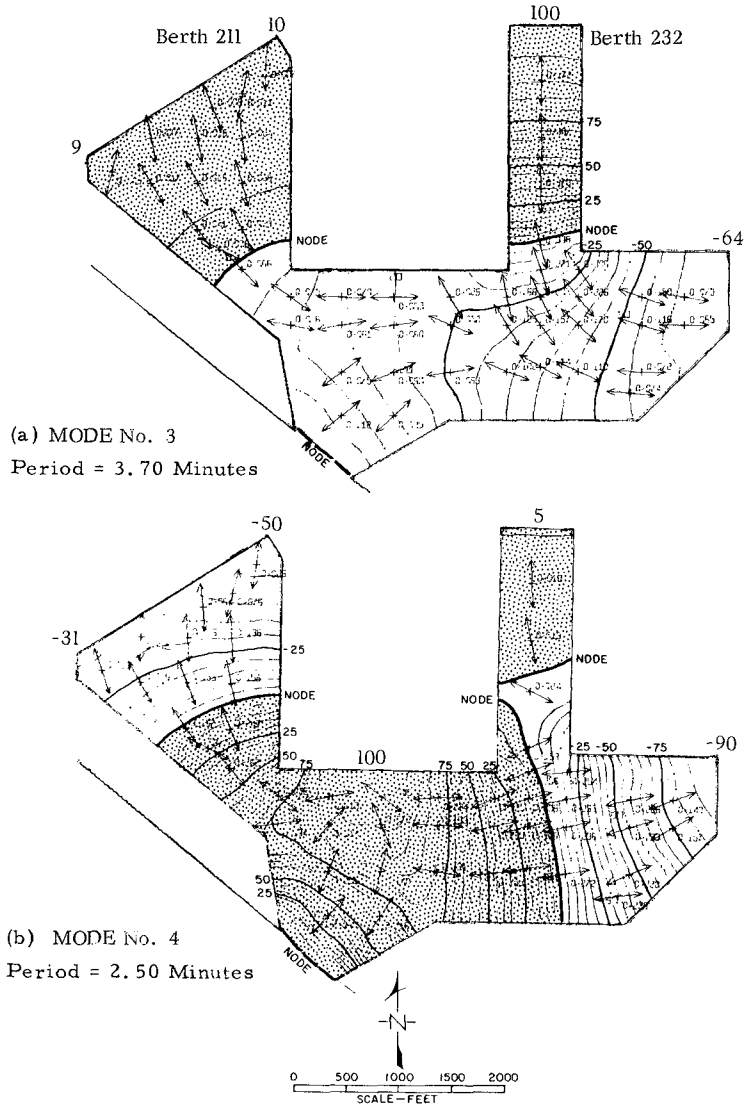

FIG. 11 - MODES OF FREE OSCILLATION OF SOUTHEAST BASIN (1971)
(a) 3rd MODE; (b) 4th MODE

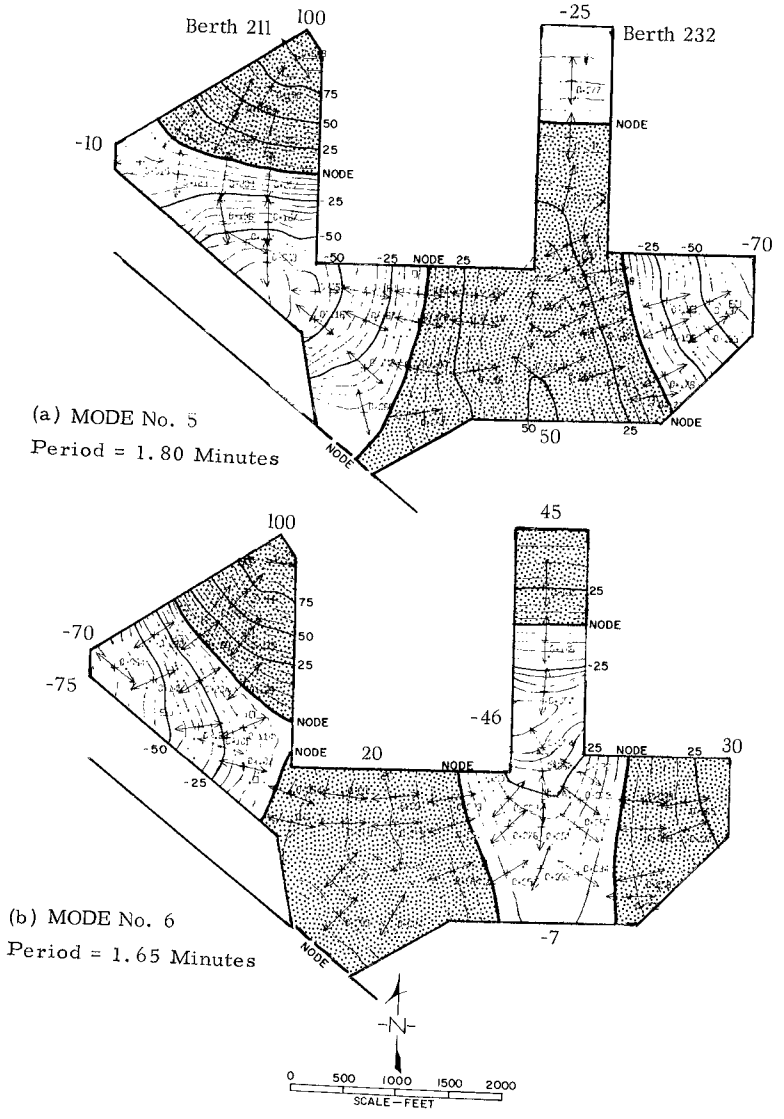

FIG. 12 - MODES OF FREE OSCILLATION OF SOUTHEAST BASIN (1971)
(a) 5th MODE; (b) 6th MODE

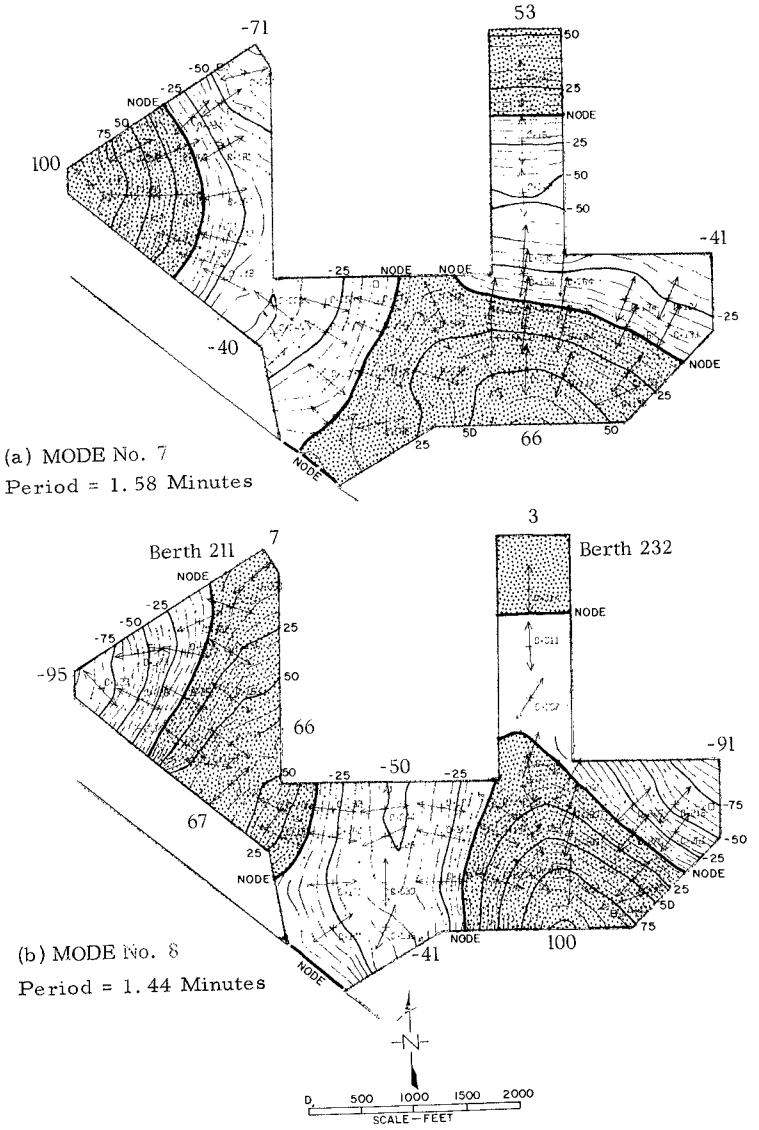

FIG. 13 - MODES OF FREE OSCILLATION OF SOUTHEAST BASIN (1971)
(a) 7th MODE; (b) 8th MODE

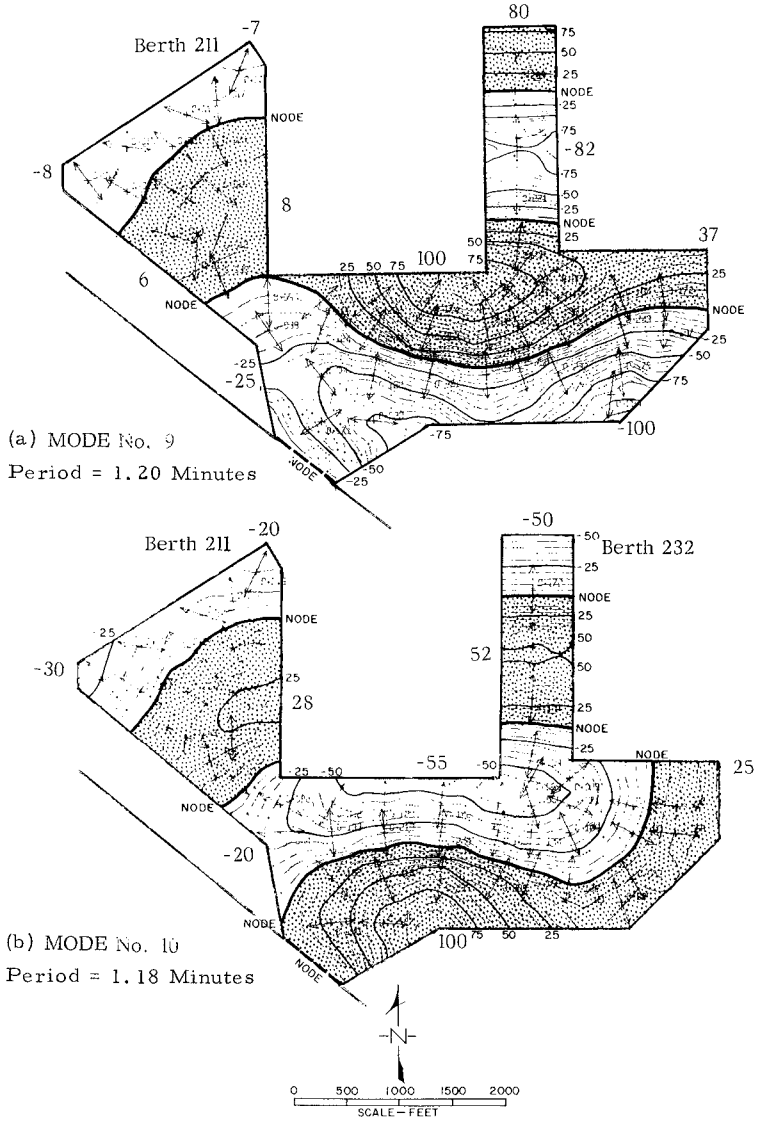

FIG. 14 - MODES OF FREE OSCILLATION OF SOUTHEAST BASIN (1971)
(a) 9th MODE; (b) 10th MODE

binodal oscillation develops between the head of the slip and south arm of the Southeast Basin (Pier J).

In the eighth mode (k = 8; T = 1.44 mins, Fig. 13 b), the oscillation is predominantly a quadrinodal seiche between the western and eastern extremities of the Southeast Basin, inclusive of Basin Six. In the slip at Berth 232 there is almost no response.

Fig. 14 (a) for the next higher mode (k = 9; T = 1.20 mins) suggests that the Southeast Basin develops a strong tri-nodal seiche between the northern extremity of the slip and the southern boundary at Pier J. The oscillation in the slip itself virtually conforms to a binodal seiche as if the slip was a closed-end basin. At the same time the oscillation in the area between Pier G and Pier J is virtually a uninodal transverse seiche with a node approximately axial to this part of the basin in an east-west direction.

Finally in the tenth mode (as far as calculations were pursued for k = 10; T = 1.18 mins) Fig. 14 (b) shows that the oscillation is a slight variation of the ninth mode, but has larger participation in Basin Six and weaker response in the remaining Southeast Basin.

In summary, the modal periods of free oscillation for the Southeast Basin in its 1971 configuration form the sequence

$$T \approx 11.0;\ 7.4;\ 3.7;\ 2.5;\ 1.80;\ 1.65;\ 1.58;\ 1.44;\ 1.20;\ 1.18;\ldots\text{mins} \qquad (22)$$

It is perhaps unfortunate that the numerical calculations could not have been pursued to higher modes than the tenth (k = 10), to reveal periods of response down to values as low as T = 30 secs. However it was judged that the close proximity of modal periods for $k > 8$ (as for example, T_8 and T_9 in Figs 14) and general declining accuracy would preclude reliability of results. It would have required a very much larger computer memory than was available in 1967-68 for coping with an enlarged N x N matrix to have increased the accuracy of results for $k > 10$, via a finer network of points covering the basin area and boundaries. In this connection it should be noted that pre-existing studies have concluded that

the critical periods for surge motion of ships in harbors cover mainly the period range from about 20 secs to 2 mins with periods in the neighborhood of 1 min predominantly important (2, 6, 7, 8, 22, 26, 30, 35). At least part of this period range is covered by the calculations of this paper.

It is rather easy to infer from Figs 14(a) and (b), that, had the calculations been pursued to the next few higher modes, the node near the mouth of Basin Six would advance farther into the basin, while that deeper in the basin would separate into two parts, each enclosing an approximately circular sector of unshaded area at the north and west corners of the basin. Such an oscillation in Basin Six, at expected periods of about 1 min, would then assume a 'cloverleaf' pattern with the three corners (petals) of Basin Six responding with in-phase elevation in opposition to the motion of the central part (stem) of the basin. The significance of this will be discussed later in relation to observational data.

OBSERVATIONAL EVIDENCE OF LONG WAVE ACTIVITY IN THE SOUTHEAST BASIN

Incidence of Surge in the Southeast Basin

It is no secret that Los Angeles-Long Beach harbors have been afflicted by troublesome surge problems on rather infrequent occasions over 60 years, ever since the construction of these ports. Long before the development of the Long Beach outer harbor, comprising the East and West Basins and the Southeast Basin, ship surging disturbances were being experienced on occasion in the outer harbor of Los Angeles, particularly in the East Channel (35). Fig. 15, which is adapted from Leypold (15), gives measurements of 1935 of typical effects in the East Channel. These disturbances would penetrate part way up the Main Channel (Fig. 15, inset) but die out within about a mile of its entrance. At the Berth 174 tide gage deep in the inner harbor, on the other hand, it was a common, almost daily, occurrence to find fairly prominent 60 min oscillations superimposed on the high tide. The latter phenomenon is believed to be a resonant response of the inner Los Angeles harbor and Cerritos Channel (Fig. 15, inset) to a continental shelf

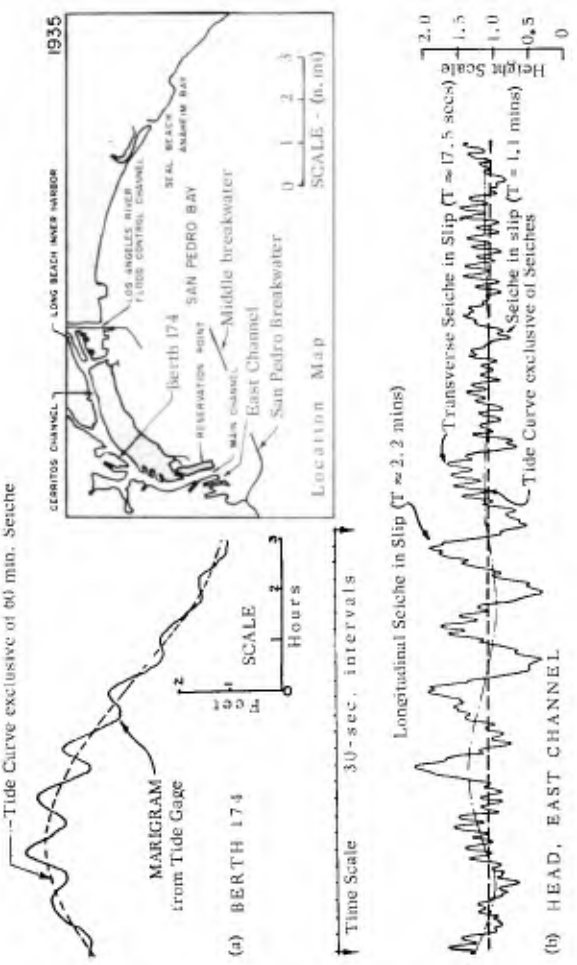

FIG. 15 - DATA INDICATIVE OF LONG PERIOD WAVE ACTIVITY IN LOS ANGELES HARBOR IN 1935-36: (a) TYPICAL TIDE CURVE, BERTH 174, L.A. INNER HARBOR (circa 1935-36); (b) MARIGRAM FOR HEAD OF EAST CHANNEL, L.A. OUTER HARBOR, DECEMBER 19, 1935 (adapted from Leypold, 1937)

oscillation off San Pedro Bay (31,35) and, so far from being troublesome, is beneficial in flushing the inner harbor with mild currents.

The incidence of surge action is believed to be secular in its frequency and severity, waxing and waning in apparent out of phase relationship with the sunspot cycle (29,35). Fig. 16, which shows the height of long period wave oscillations (solid black graph) as a function of time in relation to local sea level and weather parameters, for a tide gage station at Pierpoint (end of Pier A, East Basin, Fig. 3), suggests that from 1964 to 1967 activity was on the increase. The measure of "height of surge" in Fig. 16 was taken as the band width of the trace on the tide gage, which at a chart speed of 1 inch per hour, tended to fuse oscillations of less than 3 mins period. As expected from previous studies of surge action in harbors (27,29), there is no correlation between local weather effects and magnitude of surge, the latter being related rather to large cyclonic storms in the adjacent or distant oceans.

Fig. 17 presents in greater detail a portion of Fig. 16 covering the period between August 26 and September 14, 1967. Here, in the interval September 1 to 6, the surge index (solid black diagram) reached a highest peak, and various moored ships were reported in trouble at their berths. It may be noted, in this case, that peaks of the silhouette diagram correlate well with times of high tide. a peculiarity of surge action that had been noted in 1913 by Muñoz, a consultant to Los Angeles Harbor (16), and has been noted also in Table Bay Harbor, Cape Town, South Africa (29). It is probable that normal tidal influx into the harbor induces a degree of free oscillation at high tides which accounts for the peaks at these times and that it increases the magnitude of any long wave activity present from other sources.

In 1967-68 there existed no factual information on the surge responses of the Southeast Basin other than the calculations reported in this paper. However, some statistical information of wharfinger's estimates of surge conditions, made on occasions of berth occupancies, was used to develop criteria of relative susceptibilities of berths in Basin Six to "medium" surge conditions (35). These criteria

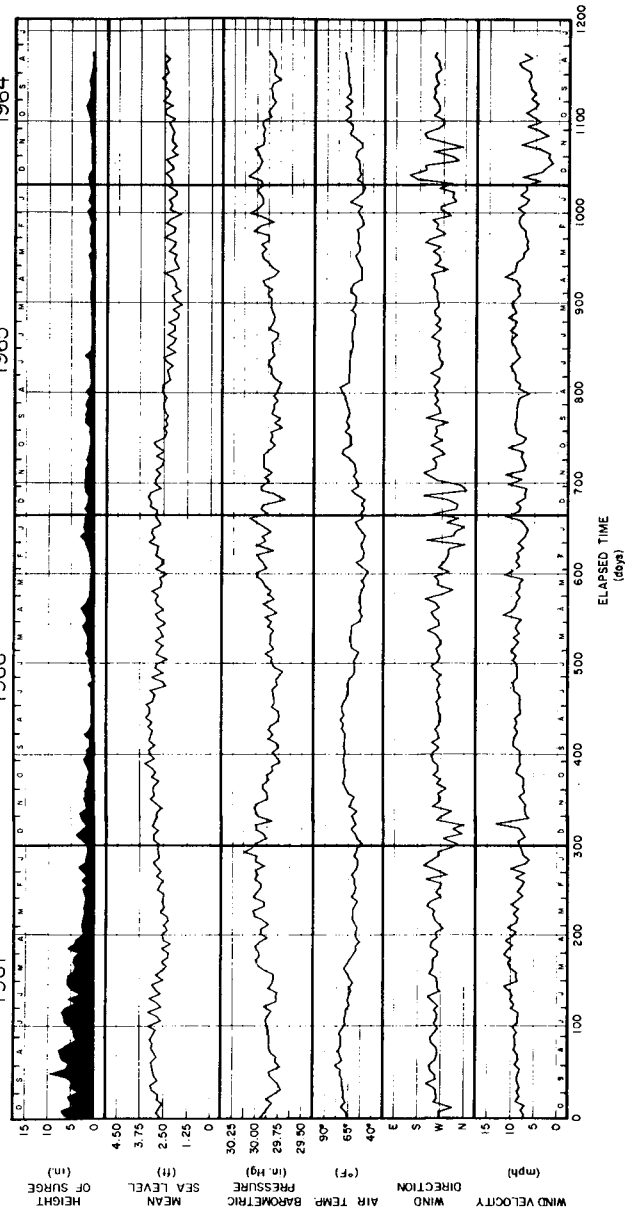

FIG. 16 - CONDENSED HISTORIES OF COMPARATIVE SURGE, TIDE AND LOCAL WEATHER CONDITIONS AT LONG BEACH HARBOR, 1964-67

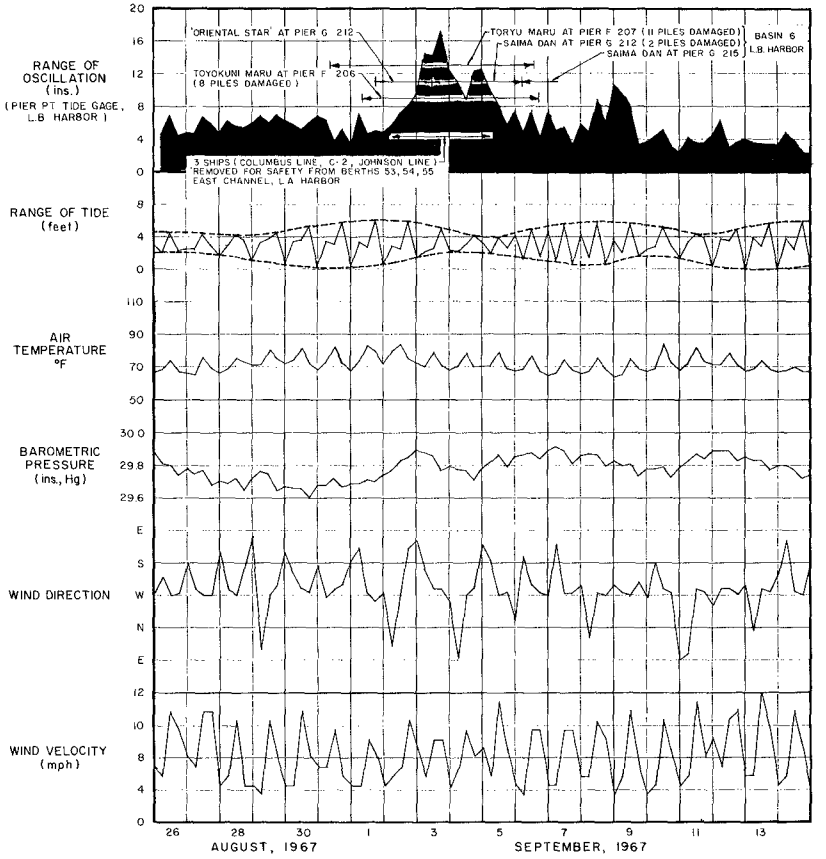

FIG. 17 - DETAILED HISTORIES OF COMPARATIVE SURGE, TIDE AND LOCAL WEATHER CONDITIONS AT LONG BEACH HARBOR, AUGUST 26 - SEPTEMBER 14, 1967

are shown in Fig. 18 as percentage figures flanking the berth numbers. The percentages express the mean annual probability (as of 1965-66) that medium surge would prevail during occupancy of a berth by a ship. The definition of "medium surge" was quite nebulous, but expressed a wharfinger's opinion that the surge was not "serious", but also not "light", and therefore presumably was able to cause motion in a moored ship, though not to the extent of being really troublesome.

Fig. 18 shows that Berth 210 on Pier A in Basin Six had the highest relative susceptibility to surge (21%) of any of the berths occupied in the period August 1965 to June 1966. Berths 207 and 208 at the southwest corner of the basin showed the highest susceptibility of 17 percent. Berth 213, was apparently not occupied, as also berths 204, 205, and 215, near the entrance of Basin Six. From the susceptibility distribution covering berths 206 to 212, it may be inferred that the surge oscillation most likely to give such a distribution would be one having the nodal lines shown in Fig. 18 and would probably be in the nature of a "cloverleaf" seiche, which by inference from the matrix calculations of the last section would be expected to have a period approximating 1 min.

It is possible to infer what the period of such an oscillation would be by another approach. Thus by regarding the access to one of the corners of the triangular Basin Six as a triangular canal of uniform depth, it is known from Lamb (9. §186) that the surface oscillation along the axis of such a canal would take the form

$$\eta \propto J_0(kx) \tag{23}$$

in which J_0 is a Bessel function of zero order, x the distance from the vertex of the canal along the axis or bisector of the angle and k a wave number defined by

$$k^2 = \sigma^2/gh \tag{24}$$

σ being the angular frequency of the oscillation and h the water depth. The Bessel function $J_0(kx)$ has unit value at $x=0$ (the vertex), zero value at $kx=2.41$ and maximum negative value (-0.428) at $kx=3.83$.

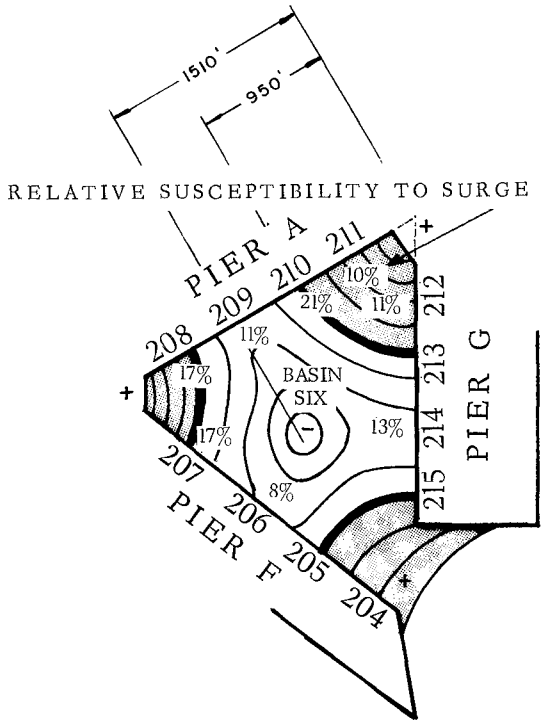

FIG. 18 - EXPECTED "CLOVER-LEAF" MODE OF OSCILLATION IN BASIN SIX, SOUTHEAST BASIN, LONG BEACH HARBOR, IN RELATION TO BERTH SUSCEPTIBILITY TO SURGE

Taking the cloverleaf oscillation to be most intense along the northeast bisector in accord with Fig. 18, the distance from the vertex to the node is 950 ft., yielding a value for k of $950k = 2.41$ or $k = 2.54 \times 10^{-3}$. Adopting h = 45 ft., Eq. (24) then yields the period of oscillation

$$T = 2\pi/\sigma = 1.08 \text{ mins} \tag{25}$$

The negative antinode of -42, relative to a normalized value of 100 at the northeast corner of Basin Six, would occur at $kx = 3.83$ or x = 1510 ft. This distance agrees satisfactorily with the anticipated stem of the cloverleaf oscillation (Fig. 18).

This quantitative conclusion thus supports the inference of the last section, and its deduction, from statistical information of berth susceptibility to medium surge action suggests that the 1.08 oscillation is a potent factor in the surging of ships, supporting conclusions arrived at by several investigators in other parts of the world (1, 6, 7, 22, 26-30, 35).

Spectrum Analyses of Tide Gage Records in the Southeast Basin

What might be called the first good factual data on long period disturbances experienced in the Southeast Basin were obtained as marigrams from two special tide gages located at Berth 211 in Basin Six and at Berth 232 in the slip of the Southeast Basin (Fig. 9). These marigrams, for the occasion of May 8, 1971, shown as curves a and A in Fig. 19, had sufficiently open time scales (1 inch = 15 mins) to permit of digitization of the records for numerical spectrum analysis.

In the first instance the digitized data were high-pass filtered for the elimination of frequencies below 0.025 cycles per hour (periods greater than 40 mins) leaving the residual traces b and B in Fig. 19. These residuals, covering a record length of $91\frac{1}{2}$ hours, or 2000 data points at time increments of 0.285 min, were then analyzed numerically for their wave energy spectra at 400 lags, or a frequency resolution of 0.0044 cycles/min. The resulting general spectra are shown in Figs 20(a) and 21(a), which show, typically, dominant peaks of energy suggestive of prominant oscillations at particular frequencies.

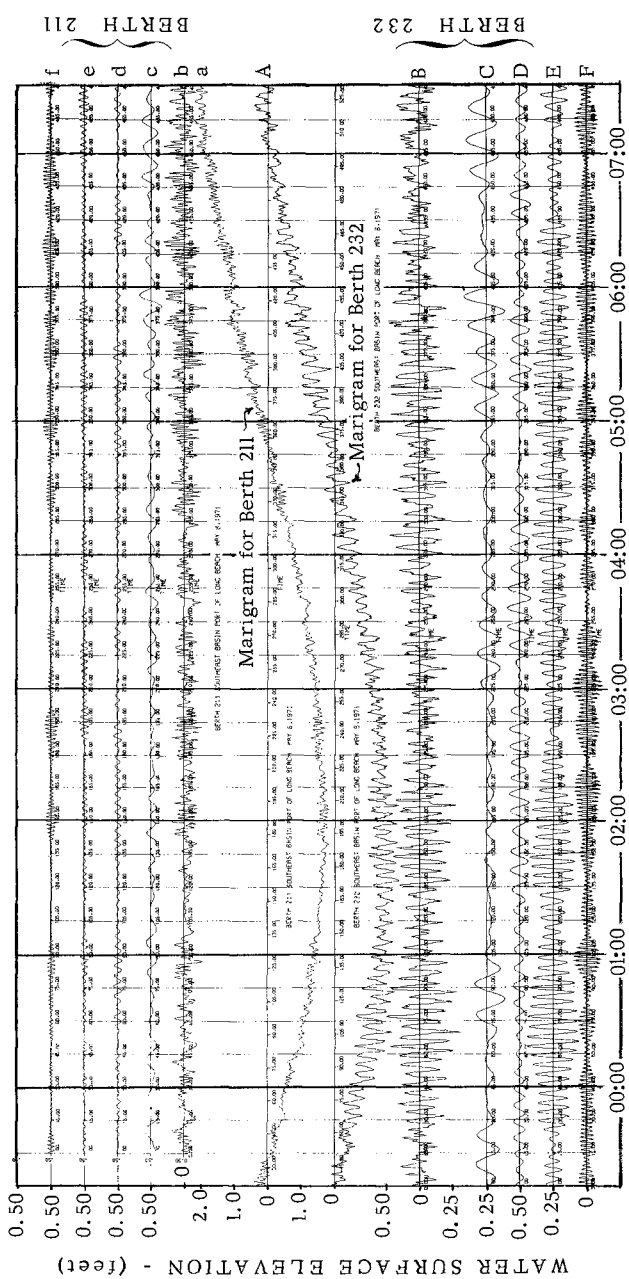

FIG. 19 - WAVE FORMS OF PRINCIPAL COMPONENTS IN MARIGRAMS OF MAY 8, 1971, FOR BERTHS 211 AND 232, SOUTHEAST BASIN, PORT OF LONG BEACH: (a) Marigram for Berth 211; (b) Residual of (a), filtered of tide; (c), (d), (e), (f), Components at periods $T \approx 13.3$, 4.3, 2.9, 1.7 mins, respectively; (A) Marigram for Berth 232; (B) Residual of (A), filtered of tide; (C), (D), (E), (F), Components at periods, $T \approx 13.3$, 8.9, 4.4, 1.9 mins, respectively

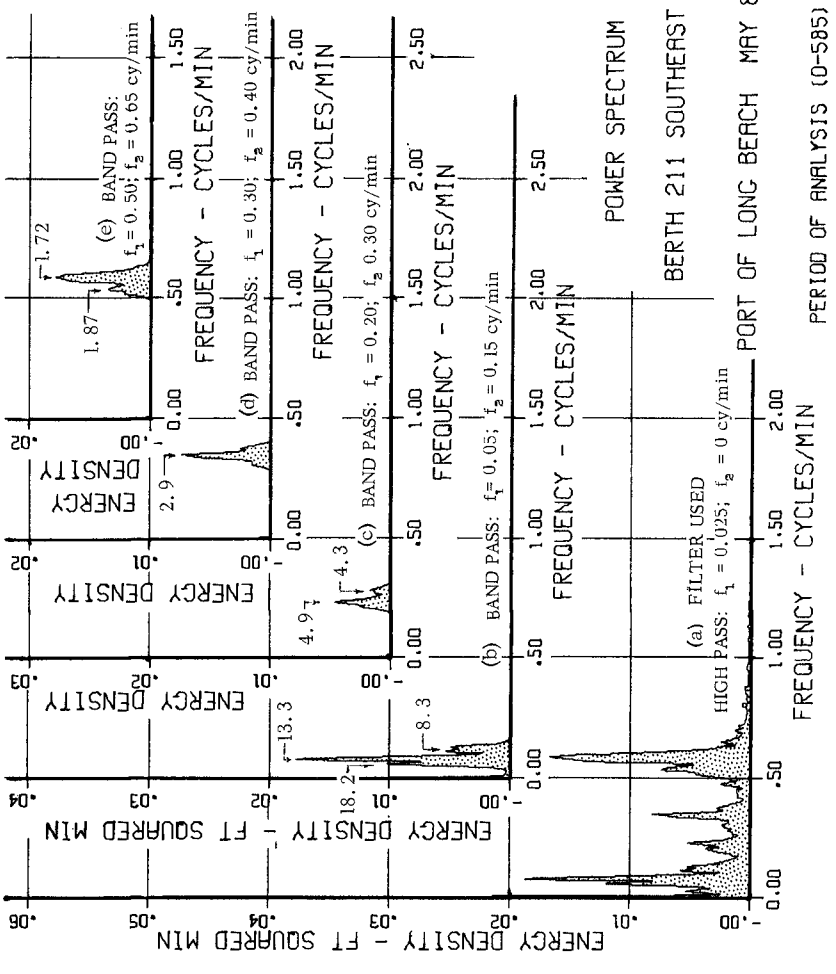

FIG. 20 - POWER SPECTRA FOR BERTH 211 MARIGRAM, MAY 8, 1971; (a) General Spectrum, prefiltered of tide; (b) to (e), band pass filtered spectra for isolation of principal components. (Figures at peaks are periods in mins)

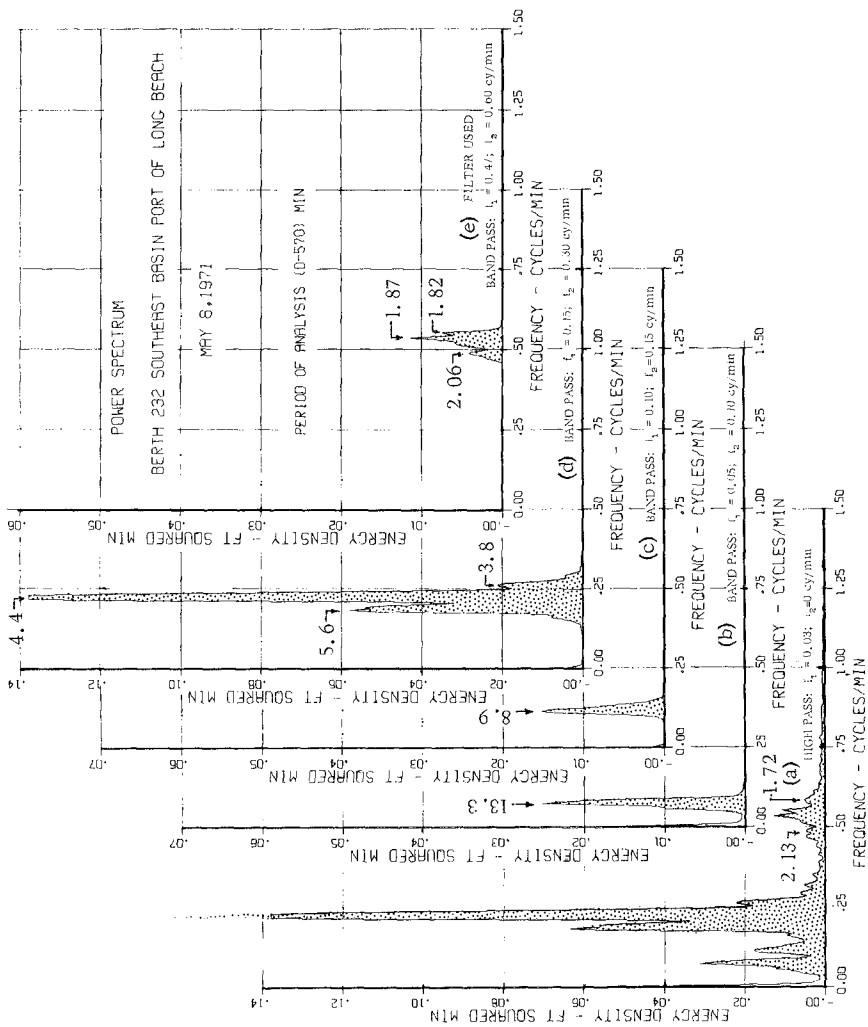

FIG. 21 - POWER SPECTRA FOR BERTH 232 MARIGRAM, MAY 8, 1971; (a) General Spectrum, prefiltered of tide; (b) to (e), band pass filtered spectra for isolation of principal components. (Figures at peaks are periods in mins)

The remaining wave energy spectra, given as Figs 20(b) to (e) and Figs 21(b) to (e), are the result of isolating parts of the spectra by selective band-pass filtering of the residual traces b and B in Fig. 19. As examples, by filtering the data of Fig. 19(b) through the numerical band-pass having frequency limits of 0.05 and 0.15 cycles/min, the isolated wave form (c) in Fig. 19 is found corresponding to the spectral energy of Fig. 20(b): similarly by filtering the data of Fig. 19(B) through a band-pass with frequency limits of 0.05 and 0.10 cycles/min, the resulting wave form (C) in Fig. 19 corresponds to the limited spectrum (b) in Fig. 21.

Although the trace (c) in Fig. 19 is composite of at least three frequencies (of periods 18.2, 13.3 and 8.3 mins), whereas trace (C) is essentially a pure wave form of 13.3 mins period, there are many in-phase similarities between (c) and (C), suggesting that an oscillation of 13.3 mins period was common to Basin Six (Berth 211) and the Southeast Basin slip (Berth 232).

The information of Figs 19, 20 and 21 is most readily compared with the results of calculations, given in the first part of this paper, by assembly in Table 2. Here, in the first four columns are set out the computed modal periods of the Southeast Basin, as given previously in Table 1 and Eq. (22). In the next five columns are observational results derived from the marigrams (a) and (A) of Fig. 19. Periods corresponding to spectrum peaks are tabulated in columns (5) and (7) and maximum wave heights, identified from the wave forms in Fig. 19, are recorded in columns (6) and (8). Column (9) contains periods identified in Fig. 19(A) by use of Chrystal's method of residuation (3). The choice of rows for listing the observational data in columns (5) to (9), has been made in accord with the approximate agreement of periods with calculated modal periods; there is, of course, no positive way of identifying mode numbers with observed periods. Figures underlined denote oscillations of greatest strength. Because the tide gages were damped against registration of short period perturbations, no perceptible wave energy was recorded at periods below those given in columns (5) to (8), or, if it was, it was eliminated by hand-smoothing to permit digitization of the data. Column (9) shows that in the marigram for Berth 232, a periodicity of the order of 0.9 min was in fact present in the original tide gage trace.

TABLE 2 - SURGE OSCILLATIONS IN THE SOUTHEAST BASIN, LONG BEACH HARBOR: COMPARISON (VIA DIFFERENT TECHNIQUES) BETWEEN THEORY AND OBSERVATION (May 8, 1971)

THEORY				OBSERVATION (Analysis of Marigrams for May 8, 1971)				
Numerical Matrix Solution			Neumann's Impedance Method (approx. only)	Numerical Spectrum Analysis				Chrystal's Method of Residuation (approx. only) Berth 232
				Berth 211		Berth 232		
Mode No.	Basin as of 1968	Basin as of 1971						
N (1)	Period T (mins) (2)	Period T (mins) (3)	Period T (mins) (4)	Period T (mins) (5)	Max. Height H (ft.) (6)	Period T (mins) (7)	Max. Height H (ft.) (8)	Period T (mins) (9)
1	14.2	11.0	12.7	18.2 13.3*	0.24 0.33	13.3	0.30	12.0
2	7.0	7.4	5.2	8.3	0.12	8.9	0.21	7.5
3	3.7	3.7	4.3	4.9 4.3	0.10 0.13	5.6 4.4 3.8	0.42 0.68 0.25	4.5 3.9
4	2.8	2.5	2.8	2.9	0.15	2.13 2.06	0.12 0.12	
5	2.0	1.80	2.2	1.87	0.14	1.87	0.23	
6	1.80	1.65	1.60	1.72	0.20	1.82	0.22	
7	1.76	1.58	1.48			1.72	0.13	
8	1.58	1.44	1.42					1.5
9	1.54	1.20	1.41					
10	1.44	1.18	1.07					0.9

* Figures underlined define strongest oscillations

Comparison of the theoretical and observational results in Table 2 suggests that the oscillations recorded on May 8, 1971, were probably indicative of several of the natural modes of response of the Southeast Basin. The 18.2 min period in column (5), however, is largely unexplained. Its presence in the Berth 211 record and absence at Berth 232 suggests that it may be fictitious and some sort of digitization error; any true oscillation of that period would have to pervade the basins as a whole. The periods at 13.3 and 8.3 - 8.9 mins in columns (5) and (7) or 12.0 and 7.5 mins in column (9) are probably evidence of the first and second modes of oscillation of the Southeast Basin system. Exact agreement of values is hardly to be expected because of real differences between the actual harbor and the mathematical modelling of it, as for example in water depths and in non-vertical basin side and end walls.

In the third mode row of Table 2, we find two periods listed in column (5), three in column (7) and two in column (9) against just one period for the comparable calculation in column (3). Any explanation for this has to be conjectural, but it may be assumed that some of the additional periods found in the May 8, 1971, data reflect the independent first modes of oscillation of Basin Six (for the Berth 211 record) and of the slip (for the Berth 232 record), as if these basins were entities in their own right. Reference to Fig. 11(a) suggests that at a slightly longer period than 3.70 mins the node for Basin Six as also for the slip would lie exactly at the mouths of these basins and would correspond to the uninodal oscillations for these open-mouth basins. In the case of the slip and the eastern portion of the Southeast Basin, it is also possible to suppose that this part of the total basin could also function as an independent open-mouth basin for which the fundamental mode oscillation would be one having a node at the approximate position of the -25 contour in Fig. 10(b). The period for such a mode would lie between the periods of Figs 10(b) and 11(a), that is, between 7.4 and 3.7 mins and might well account for the 5.6 min peak of energy recorded in column (7) of Table 2.

It becomes increasingly more difficult to identify positive association between observed and calculated periods at the higher modes. Nevertheless numerous near coincidences suggest modal correlations such as shown in Table 2.

PRELIMINARY OBSERVATIONS OF SHIP BEHAVIOR IN THE SOUTHEAST BASIN

The occurrence of surge activity in the Southeast Basin on May 8, 1971, found the harbor empty of ships because of the prolonged west coast shipping strike, so that observation of ship behavior at that time was not possible. In fact because of this and other factors,occasions for obtaining significant information on ship response to surge activity have been extremely few. In this section nevertheless are given the first measurements that were made of ship movements in correlation with sea disturbances on September 11, 1970, soon after the tide gage at Berth 211 had been placed in Basin Six, but before the tide gage at Berth 232 in the slip had become operative.

Figs 22 and 23 record the components of motion in surge and sway of the centers of gravity (midships) of two ships, respectively one of 10,000 DWT at Berth 206 in Basin Six, the other of 11,000 DWT at Berth 245 along Pier J of the Southeast Basin (see insets). The simultaneous trace from the marigram of the tide gage is also recorded in each figure and shows that 18 sec swells with a height in excess of 6 ins were penetrating into Basin Six along with longer period oscillations whose presence in the trace is seemingly not very apparent until identified by the median dash-dot curve.

Some degree of influence of the 18 sec swells is seen to pervade the surge and sway motions of the ships in the two locations, but the dominant motions in surge and sway are obviously being dictated by much longer period effects. In the case of the "Eastern Cherry" at Berth 206 in Basin Six (Fig. 22), surge motion is conforming to an approximate period of 1.5 mins. Reference to Fig. 13(b) suggests that the nodal current for this oscillation could be influencing the ship. In sway motion the "Eastern Cherry" was responding dominantly to a 1.7 min oscillation and Fig. 12(b) suggests that this could be the influence of the sixth mode oscillation for the Southeast Basin which is transverse for Basin Six and would induce current on the beam to a ship occupying Berth 206. There is also a detectable small influence of a period of about 1 minute on the ship motions in Fig. 22 and this could have relation to an oscillation in Basin Six of the type of Fig. 18.

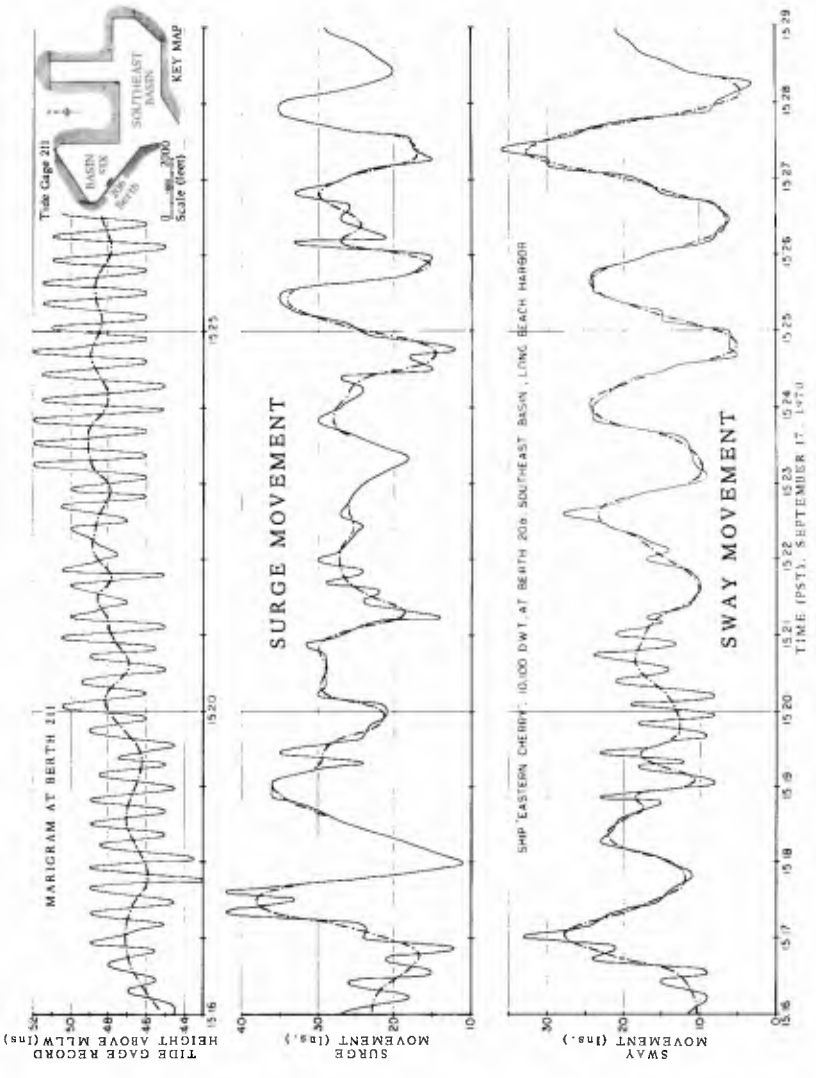

FIG. 22 - SURGE AND SWAY MOVEMENTS OF SS, "EASTERN CHERRY", 10,100 DWT, MOORED AT BERTH 206, BASIN SIX, SOUTHEAST BASIN, LONG BEACH HARBOR, IN RELATION TO SEA DISTURBANCE AT BERTH 211 ON SEPTEMBER 11, 1970

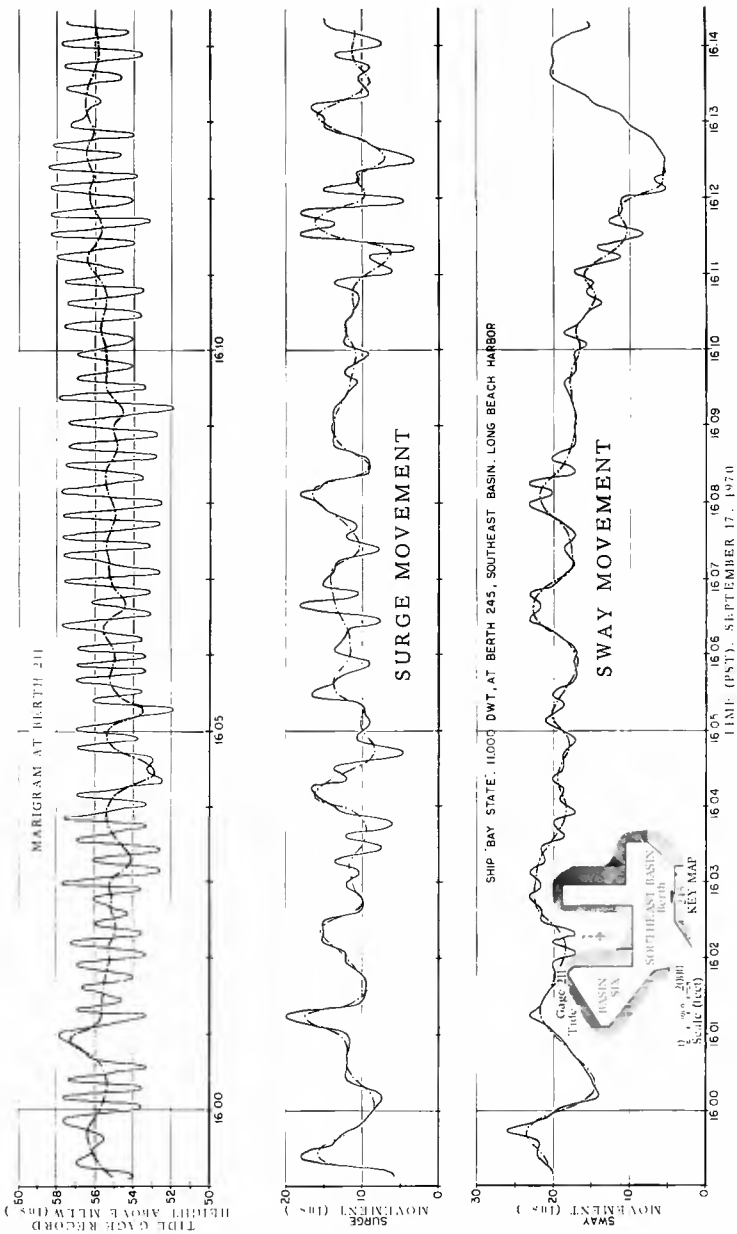

FIG. 23 - SURGE AND SWAY MOVEMENTS OF SS. "BAY STATE", 11,000 DWT, MOORED AT BERTH 245, SOUTHEAST BASIN, LONG BEACH HARBOR, IN RELATION TO SEA DISTURBANCE AT BERTH 211, BASIN SIX, ON SEPTEMBER 11, 1970

The motions of the "Bay State" at Berth 245, Southeast Basin are much less pronounced. Here again 18 sec swells are exerting strong influence at times on ship surging, but the underlying surge behavior appears to be composite of 1.5 and 1.0 minute oscillations. Here too Fig. 13(b), for the eighth mode of response of the Southeast Basin,could explain this effect because oscillatory current direction at $T \approx 1.4$ mins would favor ship motion along the quay. In sway motion, according to Fig. 23, movements appear to accord with periods of 1.2 to 1.5 mins. Fig. 14(a) then suggests that the ship was under the influence of the transverse mode of oscillation (k=9), producing oscillatory currents normal to the ship at Berth 245.

SUMMARY AND CONCLUSIONS

The numerical "matrix" method of solving the hydrodynamic long wave equations for the modes of free oscillation of a basin appears to be one of the few that can successfully cater to a completely arbitrary shape and bathymetry of the basin. Its accuracy is limited only by the memory capacity of the computer needed to handle the N x N matrix deriving from use of an N-point mesh to define the boundaries and intermediate depths of the basin. The method described uses a variable grid mesh which has the advantage that grid points can be made to fall precisely on the boundaries. Boundaries can be vertical walled, sloping, or opening upon larger bodies of water. In most cases of harbors and narrow mouth bays the nodal boundary condition at the mouth can be satisfactorily specified by the assumption of the nodal position. In bays having very wide mouths the assumption of a nodal position would call for a high degree of experience and judgement on the part of the operator, but,more accurately,such cases would need the extension of the mesh outside the bay as far as the continental shelf edge, where, along the sharp depth discontinuity, a nodal condition could reasonably be assumed again.

In application to the Southeast Basin of Long Beach Harbor the matrix method yields the modal periods, water surface elevation and oscillatory current patterns for the basin shape and depth in its condition of 1967-68 and for its present shape of 1971-72. To a reasonable degree of accuracy the eigen-periods for the

1967-68 shape have been checked by use of the "impedance" method of Neumann, and by the marching time-step method of Leendertse. They have also been confirmed in this paper to an acceptable extent with actual measurement of sea disturbances in the Southeast Basin, by correlation of the dominant frequencies uncovered by spectrum analysis of the records with the calculated modal periods. In another sense the rationality of the computed results has been demonstrated by the fact that the modal shapes of the basin oscillations accord with the expected manner in which the compartments of the Southeast Basin would naturally tend to oscillate. Intrinsically the Hamiltonian principle is satisfied by the results which show that particular modes of oscillation are frequently modal in character for a part of the total basin at the same time they are modal for the entire basin.

As against other systems of numeral calculation of the responses of basins of arbitrary shape to long period wave excitation, the method of this paper suffers from the disadvantage that it predicts only normalized eigen-responses (elevations and currents) and not the dynamic amplifications in relation to an external stimulation. However, it gives more readily the relative responses over the entire area of a basin and it treats more accurately variability of depth which is usually taken constant in other procedures. Dynamic amplifications over a basin area as a function of the frequency of an external excitation can always be obtained by use of an adjunct numerical procedure, such as Leendertse's (14), which introduces friction effects and allows for non-uniform depths.

Observations of the motions of two cargo ships moored in the Southeast Basin during an occurrence of long wave activity indicate that motions of surge and sway are plainly affected to a certain extent by 18 sec swell agitation in the harbor. However, major movements occur also at periods which appear to be combinations of 1.0, 1.2, 1.5 and 1.7 min periodicities. These periods accord with calculated and observed periods of oscillation of the Southeast Basin and the modal current directions are consistent with the surge and sway motions of the ships. It should be pointed out, nevertheless, that recent (unpublished) numerical calculations of the general motions of a moored ship in regular waves, by one

of the writers (Wilson),has shown that subharmonic effects are induced in which long period motions occur at periods several times that of the incident wave. The same effect in sway motion,in particular,has been observed and reported by Lean (10). The possibilities for grave resonance between these subharmonic motions and the stimulation of the longer period harbor oscillations is at once apparent.

ACKNOWLEDGEMENT

The main elements of the theoretical part of this paper are based upon work done for the U. S. Army Los Angeles District, Corps of Engineers under contract No. DACW 09-67-C-0065. The Port of Long Beach has provided the opportunity and assistance for acquisition of observational data on sea disturbances and ship motions in the Southeast Basin reported in this paper. The Chicago Bridge and Iron Co., Plainfield, Illinois, kindly provided assistance for the digitization of records and the numerical spectrum analyses. To all these authorities the writers express their sincere appreciation for permission to collect, correlate and publish the results. Finally credit is due to H. Soot for programming and processing the computer calculations and plot-outs.

APPENDIX - REFERENCES

1. Am. Soc. C. E., "Proceedings of the NATO Advanced Study Institute on Analytical Treatment of Problems of Berthing and Mooring Ships", ASCE, New York, N.Y., 1971, 344 pp.

2. Carr, J. H., "Long Period Waves or Surges in Harbors", Proc. Amer. Soc. Civil Eng., v. 78, Separate No. 123, 1952; also, Trans. Amer. Society Civil Eng, v. 118, 1953, pp. 588-603

3. Chrystal, G., "Investigation of the Seiches of Loch Earn by the Scottish Loch Survey. Parts I and II", Trans. Roy. Soc. Edinburgh, v. 45(2), 1906, pp. 361-396

4. Defant, A., "Physical Oceanography", Pergamon, Oxford, v. II, 1960

5. Hwang, L-S and Tuck, E. O., "On the Oscillation of Harbors of Arbitrary Shape", J. Fluid Mech., v. 42(3), 1970, pp. 447-464

6. Joosting, W. C. Q., "Investigation into Long Period Waves in Ports", Proc. XIX th International Navigation Congress, Sect. II, Communication 1, London, 1957, pp. 205-227

7. Kilner, F. A., "Model Tests on the Motion of Moored Ships Placed on Long Waves", Proc. 7th Conf. on Coastal Eng'g, (The Hague, Netherlands, Aug. 1960), Council on Wave Research, Univ. California, Berkeley, 1961, pp. 723-745

8. Knapp, R. T. and Vanoni, V. A., "Wave and Surge Study for the Naval Operating Base, Terminal Island, California", Tech. Rep. Hydraul. Struct. Lab., California Institute of Technology, Pasadena, Ca., 1945

9. Lamb, H., "Hydrodynamics", Dover, New York, 1945, (1932 ed.)

10. Lean, G. H., "Sub Harmonic Motions of Moored Ships Subjected to Wave Action", Proc. Royal Institution of Naval Architects, Paper WI, 1971, 12 pp.

11. Lee, J. J., "Wave-induced Oscillations in Harbors of Arbitrary Shape", Tech. Rep. No. KH-R-20, 1969, W. M. Keck Lab. Hydraul. Water Resour., California Institute of Technology, Pasadena, Ca.

12. Lee, J. J., and Raichlen, F., "Wave Induced Oscillations in Harbors with Connected Basins", Tech. Rep. No. KH-R-26, 1971, California Institute of Technology, Pasadena, California

13. Lee, J. J., and Raichlen, F., "Oscillations in Harbors with Connected Basins", Proc. ASCE, v. 98(WW3), Aug. 1972, pp. 311-332

14. Leendertse, J. J., "Aspects of a Computational Model for Long-period Water Wave Propagation", Memo RM-5294-PR, 1971, Rand Corp., Santa Monica, California

15. Leypold, H., "California Seiches and Philippine Typhoons", U.S. Nav. Inst. Proc., v. 63(6), 1937, pp. 775-788

16. Muñoz, A. C., "Surge Action in the Outer Harbor, Los Angeles, 1910-13", Letter of C. G. Muñoz, Report of Lt. Col. C. H. McKinstrey, Corps of Engineers, Document No. 896, House of Representatives, 63rd Congress, 2nd Session, Washington, D.C., Apr. 14, 1914

17. Neumann, G., "Die Impedanz Mechanischer Schwingungs-systeme und Ihre Anwendung auf die Theorie der Seiches", Ann. Hydraul. Mar. Met. 72, 1944, pp. 65-76

18. Neumann, G., "On Resonance Oscillations of Bights and the Mouth Correction for Seiches", Deut. Hydrogr. Z. 1, 1948, pp. 79-101

19. O'Brien, J. T., "Seiches and Other Causes of Motion of Ships Already Moored", in "Analytical Treatment of Problems of Berthing and Mooring Ships", ASCE, New York, N.Y., 1971, pp. 20-26

20. Raichlen, F., "Long Period Oscillations in Basins of Arbitrary Shapes", Proc. Amer. Soc. Civil Eng., Spec. Conf. Coastal Eng., 1965, Chap. 7, pp. 115-145

21. Rayleigh,Lord, "The Theory of Sound", Dover, New York, 1945, (1877 Edn.)

22. Russell, R. C. H., "A Study of the Movement of Ships Subjected to Wave Action", Proc. Inst. Civ. Engrs (London), v. 12, 1959, pp. 379

23. Sommet, J., "The Motion of a Ship under the Action of Seiche", Proc. Symp. "Behavior of Ships in a Seaway", Wageningen, Netherlands, 1957, v. 1, pp. 354-373

24. Stoker, J. J., "Water Waves", Wiley (Interscience), New York, 1957

25. Taylor, C., Patil, B. S. and Zienkiewicz, O. C., "Harbor Oscillation: A Numerical Treatment for undamped Natural Modes", Proc. Inst. Civil Eng., v. 43, 1969, pp. 141-155

26. Wilson, B. W., "Ship Response to Range Action in Harbor Basins", Proc. Amer. Soc. Civil Eng., v. 76, 1950, Separate No. 41; also, Trans. Amer. Soc. Civil Eng., v. 116, 1951, pp. 1129-1157

27. Wilson, B. W., "Origin and Effects of Long Period Waves in Ports", Proc. 19th Int. Navigation Congr., Sect. II, Commun. 1, London, 1957, pp. 13-61

28. Wilson, B. W., "The Energy Problem in the Mooring of Ships Exposed to Waves", Proc. Princeton Univ. Conf. Berthing Cargo Handling Exposed Locations, 1958, pp. 1-67; also, Bull. Int. Navigation Congr., (PIANC), 50 (1959)

29. Wilson, B. W., "Research and Model Studies on Range Action in Table Bay Harbour, Cape Town", Trans. S. African Inst. Civil Eng., v. 1(6), 1959, pp. 131-148; (7), pp. 153-177

30. Wilson, B. W., "Threshold of Surge Damage for Moored Ships", Proc. Inst. Civil Eng., v. 38, 1967, pp. 107-134; v. 40, 1968, pp. 363-382

31. Wilson, B. W., "Tsunami Responses of San Pedro Bay and Shelf, Ca.", Proc. Amer. Soc. Civil Eng. Conf. Civil Eng. Oceans, 1969, pp. 1099-1133; also, J. Waterways, Harbors Coastal Eng. Div., Proc. Amer. Soc. Civil Eng., v. 97(WW2), 1970, pp. 239-258

32. Wilson, B. W., "Harbor Oscillation: A Numerical Treatment for Undamped Natural Modes", [Discussion on (25)], Proc. Inst. Civ. Engrs (London), v. 44, 1970, pp. 203-210

33. Wilson, B. W., "Seiches", in "Advances in Hydroscience" (V. T. Chow, editor), Academic Press, New York, v. 8, 1972, pp. 1-94

34. Wilson, B. W., Hendrickson, J. A. and Kilmer, R. E., "Feasibility Study for a Surge-action Model of Monterey Harbor, California", Contract Rep. No. 2-136, 1965, Waterways Exp. Sta., U.S. Army Corps of Engineers, Vicksburg, Mississippi

35. Wilson, B. W., Jen, Y., Hendrickson, J. A. and Soot, H., "Wave and Surge Action Study for Los Angeles-Long Beach Harbors", Tech. Report to Los Angeles District Corps of Engineers, U.S. Army, Science Engineering Associates, San Marino, California, July 1968, (unpublished)

Subject Index

Author Index